MALAYSIAN JOURNAL OF ANALYTICAL SCIENCES

Published by The Malaysian Analytical Sciences Society

ISSN
1394 - 2506

Vol 20 No 1 (2016)

Vol 20 No 2 (2016)

Vol 20 No 3 (2016)

Vol 20 No 4 (2016)

Vol 20 No 5 (2016)

Vol 20 No 6 (2016)

2016

Malaysian Journal of Analytical Sciences Vol 20 No 1 2016

Page

1. ANTIBACTERIAL AND ANTIOXIDANT ACTIVITY OF LICHENS *Usnea rubrotincta, Ramalina dumeticola, Cladonia verticillata* AND THEIR CHEMICAL CONSTITUENTS 1
(Kajian Aktiviti Antibakteria dan Antioksidan Liken *Usnea rubrotincta, Ramalina dumeticola, Cladonia verticillata* dan Sebatian Kimianya)
Saranyapiriya Gunasekaran, Vinoshene Pillai Rajan, Surash Ramanathan, Vikneswaran Murugaiyah, Mohd. Wahid Samsudin, Laily B Din

2. MODIFIED DISPERSIVE LIQUID-LIQUID MICROEXTRACTION USING GREEN SOLVENT FOR DETERMINATION OF POLYCYCLIC AROMATIC HYDROCARBONS (PAHS) IN VEGETABLE SAMPLES 14
(Pengekstrakan Mikro Cecair-cecair Serakan yang Terubahsuai dengan Pelarut Hijau untuk Penentuan Polisiklik Aromatik Hidrokarbon (PAHs) dalam Sampel Sayur – Sayuran)
Chai Mee Kin, Premla Devi Chander, Wong Ling Shing

3. ENZYMATIC SACCHARIFICATION ON AMMONIA PRETREATED OIL PALM TRUNK BIOMASS FOR GLUCOSE PRODUCTION: AN OPTIMIZATION USING RESPONSE SURFACE METHODOLOGY 21
(Sakarifikasi Enzim pada Prarawatan Ammonia Biomas Batang Kelapa Sawit bagi Penghasilan Glukosa: Pengoptimuman dengan Kaedah Gerak Balas Permukaan)
Long Wee Lai, Siti Sarenah Mohd Yahya, Norakma Mohd Nor, Moohamad Ropaning Sulong

4. SPECTROSCOPIC ANALYSIS OF RHAMNOLIPID PRODUCED BY PRODUCED BY *Pseudomonas aeruginosa* UKMP14T 31
(Analisis Spektroskopik Ramnolipid yang Dihasilkan oleh *P. aeruginosa* UKMP14T)
Noramiza Sabturani, Jalifah Latif, Shahidan Radiman, Ainon Hamzah

5. PRODUCTION OF RARE EARTH ELEMENTS FROM MALAYSIAN MONAZITE BY SELECTIVE PRECIPITATION 44
(Penghasilan Unsur Nadir Bumi daripada Mineral Monazit Menggunakan Pemendakan Terpilih)
Che Nor Aniza Che Zainul Bahri, Wadeeah M. Al- Areqi, Amran Ab. Majid, Mohd Izzat Fahmi Mohd Ruf

6. NEW METHYLTRIMETHOXYSILANE-(3-MERCAPTOPROPYL)-TRIMETHOXYSILANE COATED HOLLOW FIBER-SOLID PHASE MICROEXTRACTION FOR HEXANAL AND HEPTANAL ANALYSIS 51
(Pengekstrakan Mikro Fasa Pepejal-Gentian Berongga Tersalut Metiltrimetoksisilana-(3-merkaptopropil)trimetoksisilana Baharu bagi Analisis Heksanal dan Heptanal)
Siti Munirah Abd Wahib, Wan Aini Wan Ibrahim, Mohd Marsin Sanagi

7. EFFECT OF SILVER NANOPARTICLE ADDITION ON THE STRUCTURE AND CHARACTERISTICS OF RADIO-PHOTOLUMINESCENCE GLASS DOSIMETER 64
(Kesan Penambahan Nanozarah Argentum Terhadap Struktur dan Sifat – Sifat Dosimeter Kaca Radio – Pendarcahaya)
Irman Abdul Rahman, Muhammad Taqiyuddin Mawardi Ayob, Hur Munawar Kabir Mohd, Ainee Fatimah Ahmad, Shamellia Sharin, Faizal Mohamed, Sidek Ab Aziz, Shahidan Radiman

8. THEORETICAL AND EXPERIMENTAL INVESTIGATION OF PYRIDYL-THIOUREA DERIVATIVES AS IONOPHORES FOR Cu(II) ION DETECTION 73
(Kajian Teori dan Eksperimen bagi Terbitan –Terbitan Piridil-Tiourea Sebagai Ionofor untuk

Pengesanan Ion Cu(II))
Wan Mohd Khairul Wan Mohamed Zin, Mohd Faizuddin Abu Hasan, Adibah Izzati Daud, Hafiza Mohamed Zuki, Ku Halim Ku bulat, Maisara Abdul Kadir

9. CHARACTERIZATION AND ANTIMICROBIAL STUDIES OF FIVE SUBSTITUTED BIS-THIOUREAS 85
(Pencirian dan Kajian Antimikrobial Terhadap Lima Sebatian Bis-Tiourea)
Nurulain Kamalulazmy, Sahilah Abd Mutalib, Fatin Ilyani Nasir, Nurul Izzaty Hassan

10. POLY(DIMETHYLSILOXANE)-POLY(VINYL ALCOHOL) COATED SOLID PHASE MICROEXTRACTION FIBER FOR CHLORPYRIFOS ANALYSIS 91
(Gentian Pengekstrakan Mikro Fasa Pepejal Tersalut Poli(Dimetilsiloksana)-Poli(Vinil Alkohol) untuk Analisis Klorpirifos)
Wan Aini Wan Ibrahim, Nor Fairul Zukry Ahmad Rasdy, Norfazilah Muhamad, Mohd Marsin Sanagi

11. ENHANCED ACTIVITY OF C3N4 WITH ADDITION OF ZnO FOR PHOTOCATALYTIC REMOVAL OF PHENOL UNDER VISIBLE LIGHT 102
(Peningkatan Aktiviti C3N4 dengan Penambahan ZnO untuk Fotomangkin Penyingkiran Phenol di bawah Sinaran Tampak)
Faisal Hussin, Hendrik O. Lintang, Leny Yuliati

12. SYNTHESIS AND CHARACTERIZATION OF 6,6'-BIS(2-HYDROXYPHENYL)-2,2'-BIPYRIDYL LIGAND AND ITS PLATINUM COMPLEX FOR THE INTERACTION WITH CT-DNA 111
(Sintesis dan Pencirian Ligan 6,6'-Bis(2-Hidroksifenil)-2,2'-Bipiridil dan Kompleks Platinum untuk Kajian Interaksi dengan CT-DNA)
Norhidayah Selamat, Lee Yook Heng, Nurul Izzaty Hassan, Nurul Huda Abd Karim

13. INVESTIGATION ON OPTICAL AND PHOTOELECTROCHEMICAL PROPERTIES OF SELF-ASSEMBLED TITANIA NANOTUBE ARRAYS PREPARED BY ANODIZATION 121
(Penyiasatan Sifat Optik dan Fotoelektrokimia Swahimpunan Nanotiub Titania Bertatasusunan yang Disediakan Melalui Penganodan)
Lim Ying Chin, Zulkarnain Zainal, Mohd Zobir Hussein, Tan Wee Tee

14. EPOXIDATION SYNTHESIS OF LINOLEIC ACID FOR RENEWABLE ENERGY APPLICATIONS 131
(Penghasilan Asid Linoleik Berepoksidasi untuk Penggunaan Tenaga yang Diperbaharui)
Bashar Mudhaffar Abdullah, Rahimi M. Yusop, Jumat Salimon, Darfizzi Derawi, Waled Abdo Ahmed

15. NUTRIENT REMOVAL OF GREY WATER FROM WET MARKET USING SEQUENCING BATCH REACTOR 142
(Penyingkiran Nutrien Air Basuhan dari Pasar Basah Mengguna Reaktor Kelompok Urutan)
Omar Danial, Mohd Razman Salim, Salmiati

16. PREPARATION AND CHARACTERIZATION OF GRAPHENE-BASED MAGNETIC HYBRID NANOCOMPOSITE 149
(Penyediaan dan Pencirian Nano Komposit Hibrid Magnetik Berasaskan Graphene)
Jashiela Wani Jusin, Madzlan Aziz, Goh Pei Sean, Juhana Jaafar

17. PENYEDIAAN DAN PENCIRIAN HIDROGEL BERASASKAN KANJI/AKRILAMIDA DARIPADA UBI *Stemona curtisii* 157
(Preparation and Characterization of Starch/Acrylamide-Based Hydrogel from Stemona curtissi Tuber)
Lim Wun Pin, Airul Ashri, Muntaz Abu Bakar, Wan Yaacob Wan Ahmad, Mohd Azwani Shah Mat Lazim

18. MODIFICATION OF TITANIUM DIOXIDE NANOPARTICLES WITH COPPER OXIDE CO-CATALYST FOR PHOTOCATALYTIC DEGRADATION OF 2,4-DICHLOROPHENOXYACETIC ACID 171
(Nanozarah Titanium Dioksida Terubahsuai Ko–Mangkin Kobalt Oksida untuk Degradasi Asid 2,4-diklorofenoksiasetik)
Leny Yuliati, Wai Ruu Siah, Nur Azmina Roslan, Mustaffa Shamsuddin, Hendrik O. Lintang

19. RESIDUE DETERMINATION AND MONITORING OF THE LEVELS OF METSULFURON METHYL IN SELECTED RIVERS AT TASIK CHINI, PAHANG, MALAYSIA 179
(Penentuan Residu dan Pemantauan Metsulfuron Metil di Sungai Terpilih di Tasik Chini, Pahang, Malaysia)
Khairiatul Mardiana Jansar and Ismail Bin Sahid

20. ADSORPTION OF Cu, As, Pb AND Zn BY BANANA TRUNK 187
(Penjerapan Cu, As, Pb dan Zn oleh Batang Pisang)
Nurzulaifa Shaheera Erne Mohd Yasim, Zitty Sarah Ismail, Suhanom Mohd Zaki, Mohd Fahmi Abd Azis

21. DITHIZONE MODIFIED SILVER ELECTRODE FOR THE DETERMINATION OF METAL IONS IN AQUEOUS SOLUTION 197
(Elektrod Perak Diubahsuai Ditizon bagi Penentuan Ion Logam dalam Larutan Akues)
Mohamad Aiman Firdaus Othman, Azrilawani Ahmad @ Othman, Hafiza Mohamed Zuki

MALAYSIAN JOURNAL OF ANALYTICAL SCIENCES
Published by The Malaysian Analytical Sciences Society
ISSN 1394 - 2506

ANTIBACTERIAL AND ANTIOXIDANT ACTIVITY OF LICHENS *Usnea rubrotincta*, *Ramalina dumeticola*, *Cladonia verticillata* AND THEIR CHEMICAL CONSTITUENTS

(Kajian Aktiviti Antibakteria dan Antioksidan Liken *Usnea rubrotincta*, *Ramalina dumeticola*, *Cladonia verticillata* dan Sebatian Kimianya)

Saranyapiriya Gunasekaran[1]*, Vinoshene Pillai Rajan[1], Surash Ramanathan[2], Vikneswaran Murugaiyah[3], Mohd. Wahid Samsudin[1], Laily B Din[1]

[1]School of Chemical Science and Food Technology, Faculty of Science and Technology
Universiti Kebangsaan Malaysia, 43600 UKM Bangi, Selangor, Malaysia
[2]Centre for Drug Research
[3]School of Pharmaceutical Sciences
Universiti Sains Malaysia, 11800 Gelugur, Penang, Malaysia

**Corresponding author: saranyapiriya89@gmail.com*

Received: 24 August 2015; Accepted: 4 November 2015

Abstract

The present study was carried out to evaluate the antibacterial and antioxidant activity of extract and chemical constituents of *Usnea rubrotincta*, *Ramalina dumeticola* and *Cladonia verticillata.* Acetone extract of *U. rubrotincta* showed promising antibacterial activity against Gram positive bacteria *Bacillus subtilis* with the lowest Minimal Inhibitory Concentration (MIC) value of (15.63 µg/mL). Six secondary metabolites were isolated using Preparative High Performance Liquid Chromatography (PHPLC) method from the two bioactive lichens *U. rubrotincta* and *R. dumeticola* (compound 1 – 6). Among all six compounds, compound (1) exhibited strongest activity against both the tested Gram positive bacteria at 7.81 µg/mL. Compound (6) had 69.57% scavenging activity against DPPH free radical while the rest only showed below 50% scavenging activity. This is the first evaluation of antibacterial activity of lichens found in Malaysia and to our knowledge, this is the first report of antibacterial and antioxidant activity of compound (3) and (5).

Keywords: antibacterial, antioxidant, *Usnea rubrotincta*, *Ramalina dumeticola*, *Cladonia verticillata*, usnic acid

Abstrak

Kajian ini dijalankan bagi menilai aktiviti antibakteria dan antioksidan sebatian kimia liken yang diekstrak iaitu *Usnea rubrotincta*, *Ramalina dumeticola* dan *Cladonia verticillata*. Ekstrak aseton terhadap *U. rubrotincta* telah menunjukkan aktiviti antibakteria yang memberangsangkan terhadap bakteria Gram positif *Bacillus subtilis* dengan nilai Kepekatan Perencatan Minimum (KPM) sebanyak (15.63 µg/mL). Enam metabolit sekunder telah dipencilkan daripada 2 liken bioaktif iaitu *U. rubrotincta* dan *R. dumeticola* menggunakan kaedah Kromatografi Cecair Prestasi Tinggi Preparatif (KCPTP) (sebatian 1 – 6). Daripada 6 sebatian, sebatian (1) telah memaparkan aktiviti yang paling kuat terhadap kedua-dua bakteria Gram positif yang dikaji pada kepekatan 7.81 µg/mL. Sebatian (6) mempunyai peratus pemerangkapan radikal bebas DPPH pada 69.57% manakala sebatian lain hanya menunjukkan aktiviti pemerangkapan kurang daripada 50%. Ini adalah penilaian pertama terhadap aktiviti antibakteria bagi liken yang dijumpai di Malaysia dan kepada pengetahuan kita, ini adalah laporan pertama bagi aktiviti antibakteria dan antioksidan sebatian (3) dan (5).

Kata kunci: antibakteria, antioksidan, *Usnea rubrotincta*, *Ramalina dumeticola*, *Cladonia verticillata*, asid usnik

Introduction

Lichens are self-supporting symbiotic association between a mycobiont and a photobiont. The mycobiont which is the fungus is unique and dominates the association while the photobiont is the algae or cyanobacteria. Many lichens are able to endure extreme environmental conditions hostile to the survival of the individual partners [1]. They are able to grow as scattered patches on stones, outcrops, on tree trunks or shrubs. Lichens mostly expose their vegetative parts to sunlight to enable the photobiont which harvest energy from solar radiation. These vegetative bodies are called thalli or lichenized stroma which contains characteristic secondary compounds [2].

To date approximately 1050 secondary metabolites have been identified [3] and most of them are considered to be very unique. The secondary metabolites found in lichens were reported to have multiple functions. They are light filters that protect the photobionts from excessive radiation [4], prevent damage from grazing by herbivores and have antibiotic properties to protect against microbial degradation [5]. Compounds like atranorin, fumarprotocetraric acid, gyrophoric acid, lecanoric acid, physodic acid, protocetraric acid, stictic acid and usnic acid have showed comparatively strong antimicrobial properties against bacteria and fungi, amongst which were human, animal and plant pathogens, mycotoxin-producers and food-spoilage organisms [6]. Several depsides (sekikaic acid, lecanoric acid and lobaric acid) are known exhibited radical scavenging activity comparable to rutin [7].

There are compelling reasons for the search of new antimicrobial agents, including from natural product drugs mainly because of the emergence of multi drug-resistant pathogens and the reduced effectiveness of currently used drugs. Besides, the rise of various diseases related to oxidative stress implicates the dire need of discovery of new antioxidant agents. Lichens can be a good source for the search due to the ability to survive in extreme conditions. Malaysia is abundant of highland and lowland lichens. Din et al. [8] profiled several types of chemical compounds derived from lichens collected from Bukit Larut, Peninsular Malaysia some of which have been reported previously to possess strong antibacterial and antioxidant activity. Four lichen species namely *Ramalina peruviana, Parmotrema tinctorum, Bulbothrix isidiza* and *Cladia aggregata* from Penang Hill, Malaysia were found to have significant antioxidant activity [9]. Hitherto there is no report on the antimicrobial activity of the lichens found in Malaysia. This study investigated antibacterial and antioxidant potential of various extracts of three different lichens from the species, *Usnea rubrotincta, Ramalina dumeticola and Cladonia vercillata* collected from the Malaysian highland area. Further to this, work was undertaken to isolate the chemical constituents from the active lichen extracts.

Materials and Methods

Lichen samples

Lichen *Ramalina dumeticola* was collected from Fraser Hill, Pahang, 3° 46 N' 111° 43 E', 1300m above sea level, voucher specimen number (F.H 1). Lichen *Usnea rubrotincta* and *Cladonia vercilata* were collected from Bukit Larut, Perak, 4° 50N', 100° 48 E', 1035m above sea level, voucher specimen number (B.L 1, B.L 2). Voucher specimens of these lichens have been deposited at the School of Chemical Sciences and Food Technology, Universiti Kebangsaan Malaysia.

Microorganisms and media

The bacteria used as test organisms are as follows: *Staphylococcus aureus* (ATCC 29213), *Bacillus subtilis* (ATCC 19659) and *Escherichia coli* (ATCC 25922) obtained from American Type Culture Collection/USA). Bacterial cultures were maintained on Muller Hinton agar substrates (Oxoid Ltd., Hampshire, England) and were stored at 4 ^{o}C.

Preparation of lichen extracts

The lichen samples were air dried at room temperature. Powdered lichen samples of 250 g were subjected to sequential soxhlet extraction with two types of solvent, acetone and methanol. All the extractions were repeated twice. The extracts were then filtered, concentrated *in vacuo* and air-dried under fume hood to obtain dry powdered extracts which were stored at 4°C.

Antibacterial studies

The minimal inhibitory concentrations (MIC) of methanol and acetone extract of the lichens were determined using the 96 well plate methods as described by Eloff [10] with some modification. Bacterial inoculums were obtained from bacterial cultures incubated for 24 hours at 37 °C on Müller-Hinton agar and diluted to 0.5 McFarland standard of approximately 10^8 CFU/mL. The extracts were screened for antibacterial potentials at 500 µg/mL. Extracts showing bacterial growth inhibition were further tested to evaluate its MIC. A two fold serial dilution of acetone extracts (500 – 7.81 µg/mL) in DMSO and methanol extracts in methanol were prepared in a sterile 96-well plate respectively. The percentage of solvent was kept below 1% throughout the experiment.

Bacterial suspensions (100 mL) were added to each well and the plates were incubated for 24 hours at 37 °C. After the incubation time, 50 mL of *p*-iodonitrotetrazolium *(p*-INT) (0.2 mg/mL) was added into all the wells, including the blank wells (containing methanol or DMSO), and further incubated for 1 hour. These plates were then observed for color changes. Wells with yellow color were interpreted as no growth, whilst purple color was interpreted as presence growth. The minimum inhibitory concentration (MIC) was determined as the lowest concentration of samples which inhibit any visible growth of bacteria. Chloramphenicol and vancomycin were used as positive controls (500 – 7.81 µg/mL). All experiments were performed in triplicate.

Antioxidant assay: Total phenolic content

Total phenolic content (TPC) were estimated by using the Folin – Ciocalteu method [11] with some modification. Stock solutions of 1 mg/mL extracts and gallic acid were prepared in DMSO and distilled water respectively. A series of gallic acid concentrations were prepared by diluting the stock solution with distilled water. Gallic acid of 250 µL was added into individual test tubes followed by addition of 1 mL of distilled water and 250 µL of Folin – Ciocalteu reagent. After thoroughly shaken, the test tubes are allowed to sit in room temperature for 6 minutes. Later, an amount of 2.5 mL of Na_2CO_3 was added and allowed to sit for another 2 hours in a dark room at room temperature. A 200 µL of solution from each test tube is transferred into 96-well plate and the absorbance were measured at 760 nm using a microplate reader. The experiments were performed in triplicates. Gallic acid (0–500 µg/mL) was used for calibration of a standard curve. The result was expressed as gallic acid equivalents (GAE)/g dry weight of lichen material.

Total flavonoids

The total flavonoid content (TFC) was determined using colorimetric method as described by Sakanaka et al. [12]. An amount 125 µL of 1 mg/mL extract or standard solution (quercetin) were mixed with 625 µL of distilled water in a test tube. Sodium nitrite (5%) solution of 37.5 µL is then added and incubated for 6 minutes. Aluminium chloride (10%) solution of 75 µL was later added and the mixture was allowed to stand for another 5 minutes. Thereafter, 250 µL of 1M sodium hydroxide was added. The mixture was brought up to 1.25 mL with distilled water and mixed well. The absorbance at 510 nm was measured immediately. Quercetin (0.5–0.02 mg/mL) was used to construct a standard curve. The results were expressed as quercetin equivalent (QE) per gram dry weight of lichen extract. The experiments were performed in triplicates.

1, 1-diphenyl-2-picryl-hydrazyl (DPPH) free radical analysis

A quantitative determination of free radical scavenging activity was measured by using DPPH assay as described by Shimada et al. [13]. The antioxidant activity was expressed as percentage scavenging of DPPH by extract compared to standard, Trolox. An amount of 20 µL extract (1 mg/mL) was added into 180 µL of 0.2 mM of DPPH solution in 96-well plate. The plate was incubated for 20 minutes and kept in the dark. The same steps were repeated for standard Trolox. The percentage of scavenging was calculated from the absorbance of decolorization which obtained spectrophotometrically at 550 nm. Scavenging of the DPPH radical by the sample was calculated according to the following Equation (1).

$$\text{DPPH scavenging activity (\%)} = [A0 - A1 / A1] \times 100 \quad (1)$$

where $A0$ is the absorbance of the control and $A1$ is the absorbance of the sample. Free radical scavenging activity is expressed as the percentage of DPPH scavenging activity. The experiments were performed in triplicates.

Isolation of chemical constituents from the bioactive extracts: Liquid-liquid extraction
2 g of bioactive extracts were subjected to liquid-liquid extraction using hexane and methanol at 1:1 ratio. The process was performed in a triplicate. The resulting fractions were pooled and dried. It was noticed that there were crystals formed, which was filtered and purified further by recrystallization.

Thin layer chromatography (TLC)
The fractions were dissolved in appropriate solvent before being spotted onto the TLC plate. Solvent systems used in this thin-layer chromatography were according to Culberson [14] and Culberson et al. [15] namely (a) benzene-dioxane-acetic acid (180:45:5, 230 mL), (b) hexane-diethyl ether-formic acid (130:80:20, 230 mL), (c) toluene-acetic acid (200:30, 230 mL) and (d) toluene-ethyl acetate-formic acid (139:83:8, 230 mL). The spots were viewed under long and short ultraviolet light before sprayed with 10% sulphuric acid and heated at 110 °C.

Column chromatography
Fractions that showed good separation on the TLC plate was subjected to column chromatography. The solvent system used was similar to the one used for TLC. An approximately 0.5 g of the fraction was dissolved in a small amount of solvent system to avoid solubility problems inside the column. Small amounts of solvent were filled into the column every 15 minutes. The sub-fractions were collected according to the bands formed in the column and air-dried before subjected to TLC.

Preparative high performance liquid chromatography
The column used for separation was a Phenomenex Hypersil 5µ C18 column (150 x 21.2 mm) with the gradient mobile phases of methanol (A) and 1% orthophosphoric acid (B) with a flow rate of 4 mL/min. The run started with 100% B and was lowered to 50% B within 5 minutes then to 40% B within a further 10 minutes, followed by 20% B within the next 30 minutes. Then 500 µg/ml of sample with the injection volume of 100 µl was injected. A photodiode array detector was used to detect the compound peaks and recorded at three different wavelengths of 222 nm, 230 nm and 280 nm. The fractions were collected according to the retention time.

Identification of chemical constituents
An analytical HPLC method adapted from Din et al. [8] was used to evaluate the purity of the compounds obtained. A Phenomenex Hypersil 3µ C18 column (250 by 4.6 mm) with a flow rate of 1mL/min was used. The mobile phases were 1% aqueous orthophosphoric acid (A) and methanol (B). The gradient system started with 100% A and was raised to 58% B within 15 minutes, then to 100% B within next 16 minutes, followed by isocratic elution in 100% B for a further 10 minutes. The compounds were further subjected for mass (LC-MS ToF), 1D NMR FT-NMR 600MHz Cryo (Fourier Transform Nuclear Magnetic Resonance 600MHz Cryoprobe) and 1D NMR FT-NMR 500MHz (Fourier Transform Nuclear Magnetic Resonance 500MHz) spectrometry.

Bioassay for isolated chemical constituents
The isolated chemical constituents were evaluated for antibacterial and antioxidant activity at 500 µg/mL using the methods described in section Antibacterial studies and Antioxidant assay. The active chemical constituents were further tested for their (MIC).

Results and Discussion

Chemical Constituents
Usnic acid, (1) was obtained as yellow needles from acetone extract of *U. rubrotincta*, (1190 mg, 6.62% yield); HPLC retention time: 28.76 minutes; Mass spectrometry data showed 345 m/z; ^{1}H NMR data and ^{13}C NMR data, see Table 1; Structure, see Figure 1.

Barbatic acid, (2) was obtained as colorless needles from methanol extract of *U. rubrotincta*, (0.13 mg, 0.31% yield); HPLC retention time: 29.02 minutes; Mass spectrometry data showed 360m/z; ^{1}H NMR data and ^{13}C NMR data, see Table 2; Structure, see Figure 1.

Table 1. ^{1}H and ^{13}C NMR spectral data (CDCl3) for compound (1)

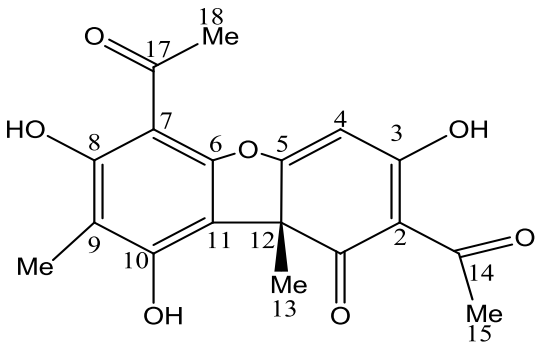
Analysis		**δH**		**δC**
NMR	C-1			198.06
	C-2			179.39
	C-3	-	s, 1H, OH-3	155.22
	C-4	5.986	s, 1H, H-4	191.73
	C-5			101.53
	C-6			98.35
	C-7			109.33
	C-8	13.320	s, 1H, OH-8	157.51
	C-9			103.97
	C-10	11.039	s, 1H, OH-10	163.88
	C-11			105.24
	C-12			59.08
	C-13	1.766	s, 3H, Me-13	27.93
	C-14			200.37
	C-15	2.669	s, 3H, Me-15	32.14
	C-16	2.111	s, 3H, Me-16	7.56
	C-17			201.80
	C-18	2.684	s, 3H, Me-18	31.31

Notes: Chemical shift values δ in ppm.

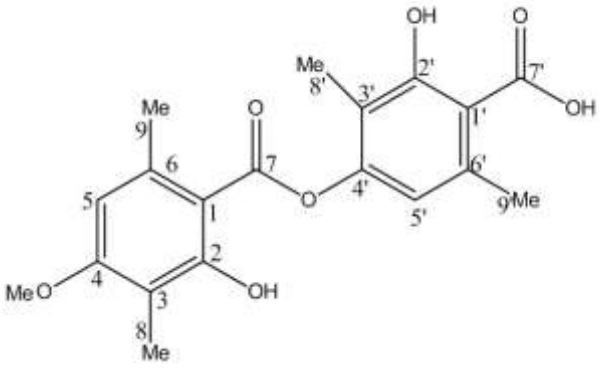
Table 2. ^{1}H and ^{13}C NMR spectral data (CDCl3) for compound (2)

Analysis	**δH**		**δC**
	C-1		110.17
	C-2		152.23
	C-3		104.25
	C-4	3.930 *s*, 3H, MeO-4	162.32
	C-5	6.559 *s*, 1H, H-5	106.19
	C-6		140.16
	C-7		170.01
	C-8	2.069 *s*, 3H, Me-8	6.53
	C-9	2.706 *s*, 3H, Me-9	23.59
	C-4-OMe		54.78
	C-1’		162.27
	C-2'		110.50
	C-3’		115.98
	C-4’		162.77
	C-5’	6.575 *s*, 1H, H-5’	140.75
	C-6'		115.70
	C-7'		173.77
	C-8’	2.054 s, 3H, Me -8'	7.99
	C-9'	2.595 *s*, 3H, Me-9'	24.30
		- *s*, 1H, 2-OH	

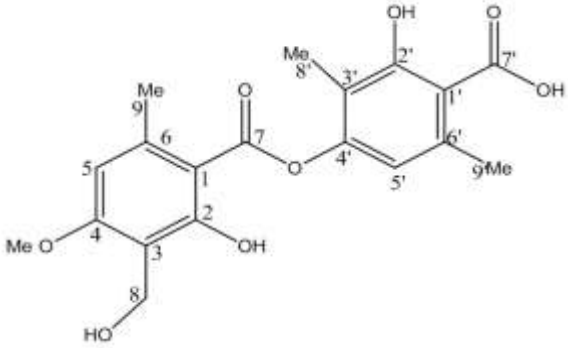
Notes: Chemical shift values δ in ppm.



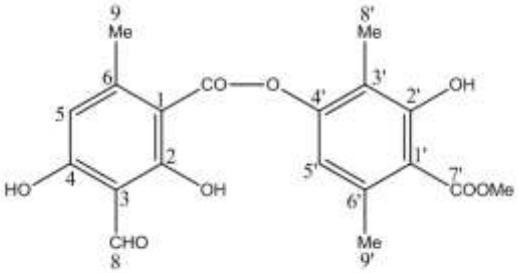
(1)



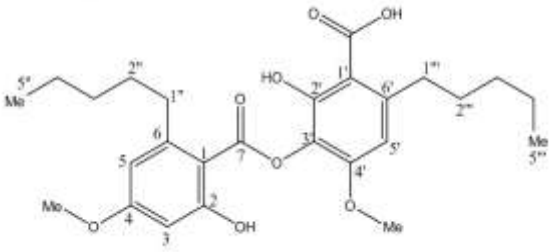
(2)



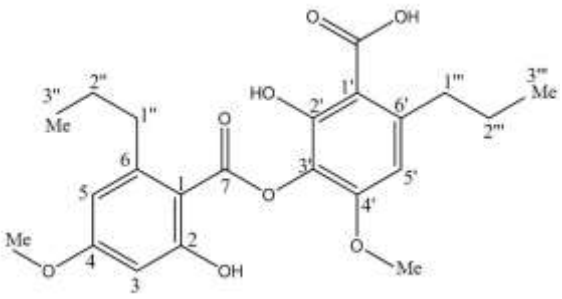
(3)



(4)



(5)



(6)

Figure 1. Chemical structure of (1) Usnic acid, (2) Barbatic acid, (3) 8-Hydroxybarbatic acid, (4) Atranorin, (5) Hyperhomosekikaic acid and (6) Sekikaic acid

8-Hydroxybarbatic acid, (3) was obtained as colorless crystals from methanol extract of *U. rurbotincta*, (5.18 mg, 0.01% yield); HPLC retention time: 28.94 minutes; Mass spectrometry data showed 391.29 m/z; ^{1}H NMR data see Table 3; Structure, see Figure 1.

Atranorin, (4) were obtained as colorless prisms from acetone extracts of *R. dumeticola*, (51.28 mg, 0.29% yield); HPLC retention time: 29.05 minutes; Mass spectrometry data showed 373.11 m/z; ^{1}H NMR data and ^{13}C NMR data, see Table 4; Structure, see Figure 1.

Table 3. ^{1}H NMR spectral data (CDCl3) for compound (3)

Analysis	**δH**	
	1.185	s, 3H, Me
	2.023, 2.031	s, 3H, Me
	2.104	s, 3H, Me
	2.522	
	2.556	
	2.618	
	3.424	s, 3H, OMe-4
	3.836	s, 2H, -CH2OH-8
	6.312	s, 1H, H-5
	6.478	s, 1H, H-5’
	11.424	s, 1H, 1-OH
	11.872	s, 1H, 1-OH

Notes: Chemical shift values δ in ppm.

Table 4. ^{1}H and ^{13}C NMR spectral data (CDCl3) for compound (4)

Analysis	δH		δC
C-1			102.901
C-2	12.503	s, 1H, OH-2	169.165
C-3	2.678	s, 3H, Me-9	108.606
C-4	12.551	s, 1H, OH-4	167.552
C-5	6.392	s, 3H, Me-5	112.926
C-6			152.527
C-7			169.776
C-8	10.349	s, 1H, CHO-8	193.932
C-9			24.130
C-1’			116.849
C-2’	11.962	s, 1H, OH-2’	162.949
C-3’			110.318
C-4’			152.037
C-5’	6.507	s, 1H, C-5’	116.091
C-6’			139.956
C-7’			172.285
C-8’	2.080	s, 3H, Me-8’	25.681
C-9’	2.536	s, 3H, Me-9’	9.456
COOMe-7’	3.969, 3.979	s, 3H, COOMe-7’	52.444
-			29.787

Notes: Chemical shift values δ in ppm.

Hyperhomosekikaic acid, (5) were obtained as colorless plates from acetone extract of *R. dumeticola*, (4.92 mg, 0.20% yield); HPLC retention time: 27.87 minutes; Mass spectrometry data showed 480 m/z; ^{1}H NMR data see Table 5; Structure, see Figure 1.

Sekikaic acid, (6) were obtained as colorless prisms from acetone extracts of R. dumeticola, (4.73 mg, 0.20% yield); HPLC retention time: 29.45 minutes; Mass spectrometry data showed 406 m/z; 1H NMR data see Table 6; Structure, see Figure 1.

Table 5. ^{1}H NMR spectral data (CDCl3) for compound (5)

Analysis	**δH**	
NMR	0.913, 0.926, 0.938	t, 3H, Me-5''
	0.985, 0.997, 1.009	t, 3H, Me-5'''
	1.128, 1.138	m, 6H, 3x -CH2
	1.290, 1.302, 1.314	
	2.158	
	2.93, 2.94, 2.96	t, 2H, -CH2- 1"
	2.98, 2.99, 3.009	t, 2H, -CH2- 1"'
	3.82	s, 3H, MeO- 4
	3.876	s, 3H, MeO- 4'
	6.365, 6.369	d, 1H, H-3'
	6.393, 6.397	d, 1H, H-5'
	6.548	s, 1H, H- 5

Notes: Chemical shift values δ in ppm.

Table 6. ^{1}H NMR spectral data (CDCl3) for compound (6)

Analysis	**δH**	
NMR	0.823, 0.838, 0.852	t, 3H, Me
	1.195, 1.212, 1.227	t, 3H, Me
	1.288, 1.295, 1.302, 1.316	-
	1.547, 1.561	q, 2H, -CH2
	1.608, 1.623, 1.639, 1.654	q, 2H, -CH2
	2.843, 2.859, 2.874	t, 2H, -CH2-1"
	2.909, 2.925, 2.941	t, 2H, -CH2-1"'
	3.343, 3.347, 3.350	
	3.730	s, 3H, -OMe
	3.784	s, 3H, -OMe
	6.274, 6.279	d, 2H, H-3
	6.302, 6.308	d, 2H, H-5
	6.448	s, 1H, H-5'

Notes: Chemical shift values δ in ppm.

Bioassay of extracts

The antibacterial activity and the (MIC) of extracts are summarized in Tables 7 and 8 respectively. Acetone extracts of *Usnea rubrotincta* and *Ramalina dumeticola* and methanol extracts of *Usnea rubrotincta* exhibited inhibitory activity against gram positive bacteria *S. aureus* and *B. subtilis*. However no activity against *E. coli*, gram negative bacterium was observed. The remaining lichen extracts were not active against the three test bacteria. The acetone extract of *R. dumeticola* exhibited highest activity against *S. aureus* followed by acetone and methanol extracts of *U. rubrotincta*. For negative control, DMSO did not exhibit any inhibition against all test organisms.

Table 7. Antibacterial activity of acetone and methanol extracts of various lichens at 500 µg/mL concentration

Test Organisms	***Usnea rubrotincta***		***Ramalina dumeticola***		***Cladonia verticillata***		**Chloramphenicol**	**Vancomycin**
	A	**M**	**A**	**M**	**A**	**M**		
S. aureus	+	+	+	-	-	-	+	+
B. subtilis	+	+	+	-	-	-	+	+
E. coli	-	-	-	-	-	-	+	+

Notes: A, acetone extract; M, methanol extract; +, had inhibitory activity against tested bacteria; -, had no inhibitory activity of extract against tested bacteria

Table 8. Minimal Inhibitory Concentration of bioactive extracts against selected gram positive bacteria

Test Organisms	***Usnea rubrotincta***		***Ramalina dumeticola***	**Chloramphenicol**	**Vancomycin**
	A	**M**	**A**		
	Minimal Inhibitory Concentration (µg/mL)				
S. aureus	125	500	31.25	31.25	7.81
B. subtilis	15.63	250	31.25	15.63	7.81

Notes: A, acetone extract; M, methanol extract

Both acetone and methanol extracts of *U. rubrotincta* showed activity against gram positive bacteria. The lowest MIC (15.63 µg/mL) was observed for acetone extract of *U. rubrotincta* against *B. subtilis* comparable to chloramphenicol. A similar activity against *B. subtilis* and *S. aureus* was reported for *Usnea barbata* acetone extract with MIC value of 0.1 mg/mL [16]. *R. dumeticola* acetone extract showed good antimicrobial activity against both gram positive bacteria with MIC values though it was approximately four times less potent than vancomycin (Table 8). Lichen from the same genus, *Ramalina farinacea* was also reported active against some gram positive bacteria including *B. subtilis* and *S. aureus* at MIC value of 264 µg/mL and 132 µg/mL respectively [17]. All the lichen extracts in this study showed no activity against gram negative bacteria. These findings are closely in agreement with report by Burkholder et al. [18] whom reported no activity of 42 tested lichens against gram negative bacteria *E.coli.*

The phenol and flavonoid contents of all three lichens were in the range of 43.12 – 101.62 mg of GAE/g extract and 24.92 – 165.03 mg of QE/g extract respectively. The DPPH assay showed scavenging activity lower than 50% of for all the studied lichens at 500 µg/mL. Results are summarized in (Table 9).

Table 9. Total phenolic content (TPC), Total flavonoid content (TPC) and DPPH radical scavenging activity of the lichen extracts

	Sample	**TPC (mg) of (GAE)/g dry weight of extract**	**TFC mg of (QE)/g dry weight of extract**	**% Scavenging** of **DPPH at 500µg/mL**
Acetone	RD	101.62 ± 3.51	24.92 ±1.06	27.21 ± 1.61
	U.R	63.05 ± 3.27	165.03 ±0.62	19.31 ± 0.25
	C.V	101.37 ± 3.31	108.09 ±3.95	33.09 ± 0.84
Methanol	R.D	48.74 ± 0.84	42.77 ± 1.13	16.4 ± 2.99
	U.R	43.12 ± 1.14	98.48 ± 2.13	11.42 ± 1.96
	C.V	48.61 ± 0.87	79.20 ± 1.65	17.25 ± 2.98
Trolox				98.19 ± 0.66

Another study [19] recorded (TPC: 115mg of (GAE)/g dry weight of extract) and (TFC: 1.625mg of rutin equivalent/g dry weight of extract) values of a different species of *Usnea* lichen which is *Usnea longissima.* The same study also reported high antioxidant activity (IC50 = 0.10 mg dry material). Phenolic compounds are a type of antioxidant agents which can adsorb and neutralize the free radicals [20], in which the phenol content in present study is lower than reported study [19]. This explains the low antioxidant activity of *U. rubrotincta* compared to *U. longissima. Cladonia foliacea* was investigated for its TPC and DPPH scavenging activity [21], which also reported low phenolic content (TPC: 78.12mg of (GAE)/g dry weight of extract) and weak scavenging activity at (IC50: 1000 µg/mL) which is in accordance with the present study. Lichen from the genus *Ramalina, Ramalina peruviana* was investigated for its phenolic content, as well as its free radical scavenging activity [9]. They also reported lowest total phenolic content in *R. peruviana* (27.1 mg GAE/g extract) compared to a few other lichen species studied, however the free radical scavenging activity was found to be relatively strong at (IC50 = 60.66 mg dry material). *R. dumeticola* was found to contain higher phenolic content but the free radical scavenging activity was only 27.21%. This can be due to different types and concentrations of phenolic compounds present in *R. peruviana* and *R. dumeticola*.

Since the antioxidant activity of the extracts was moderate compared to the antibacterial activity, the extracts selected for subsequent purification and isolation was based on the antibacterial assay results. A total of six secondary metabolites were isolated from acetone and methanol extract of *R. dumeticola* and *U. rubrotincta.* Compound (1) and (4) were found in both the lichen acetone extracts which were identified as usnic acid and atranorin respectively. Compounds (5) and (6) were isolated from acetone extract of *R. dumeticola* which was determined to be hyperhomosekikaic acid and sekikaic acid. With regards to the methanol extract of *U. rubrotincta,* two more compounds were isolated which were (3), 8-hydroxybarbatic acid and (2), barbatic acid.

Among all isolated chemical constituents, (1) exhibited highest inhibitory activity against both gram positive bacteria at (MIC: 7.81 µg/mL) which is comparable to standard vancomycin. Atranorin and (2) also showed active inhibitory potential at (MIC: 31.25 µg/mL) and (MIC: 15.63 µg/mL) against *B. subtilis.* The high antimicrobial activity of (1) has been reported previously by Tay et al. [17] in which the lowest inhibitory concentration against *S. aureus* was at (MIC: 3.1 µg/62.5 µl) and *B. subtilis* at (MIC: 0.78 µg/62.5 µl). Compound (1) has been observed to be present in high levels in both the active lichens which could partly explain the potency of the extracts comparable to the standard.

Lauterwein et al. [22] reported a MIC value range from 2 to 16 µg/mL for (1) against gram positive bacteria *S. aureus.* In this study, compound (4) has exhibited stronger activity than the report by Yilmaz et al. [23], where the inhibition potential was only at (MIC: 500 µg) against *S. aureus* and (MIC: 15.63 µg) against *B. subtilis*. Thadani et al. [24] reported similar activity of (4) and (6) against *B. subtilis* with inhibition at 100 µg/mL in a disk diffusion assay.

However, they also reported inhibition activity of (4) and (6) against gram negative bacteria *E. coli* and no inhibition of (4) and (6) against *S. aureus*. Both reports by Yilmaz et al. [23] and Thadhani et al. [24] have significant difference with this study due to method difference where the reported studies used disk diffusion assay compared to this study which uses the MIC method. Besides that, the bacteria strains are also different between this investigation and Yilmaz et al. [23]. Martins et al. [25] reported MIC values of 50-100 µg/mL for (2) against various strains of *S. aureus* which is similar to this study where we obtained MIC value of 62.50 µg/mL concentration. Disk diffusion method has its own disadvantages where zone sizes are affected by the media used and by the different growth rates of organisms being tested therefore MIC tests are more accurate with anaerobic bacteria [26].

All compounds exhibited below 50% scavenging activity against DPPH free radicals except compound (6). Sisodia et al. [27] reported close activity between the standard and compound (6) against DPPH free radical but in this study only 69.57% scavenging activity was recorded compared to standard Trolox. They also reported minimum scavenging activity of (4) in which is in agreement with this study. Compound (1) which is a phenolic compound, poorly scavenged the DPPH free radical which is in accordance with the findings of Devehat et al. [28] and Thadhani et al. [7]. The radical-scavenging effect of antioxidants on DPPH is a method to quantify the hydrogen donating potency of chemicals and compound (1) does not seem to have the labile hydrogen atoms to bind with the DPPH ions. Devehat et al. [28] studied the antioxidant capacity of compound (2) alongside other lichen compounds but did not report any scavenging activity which is in agreement with our findings where the activity was also very low in contrast to standard. Results are summarized in Table 10.

Table 10. Antibacterial and radical scavenging activity of the isolated compounds

Test Compounds	**MIC (µg/mL)**		**% DPPH radical scavenging at 100µg/ml**
	S. aureus	***B. subtilis***	
(1)	7.81	7.81	44.62 ± 0.22
(2)	62.50	31.25	29.29 ± 0.003
(3)	-	125	36.60 ± 0.001
(4)	62.50	15.63	27.79 ± 0.11
(5)	-	125	13.25 ± 0.002
(6)	-	125	69.57 ± 0.52
Chloramphenicol	31.25	15.63	
Vancomycin	7.81	7.81	
Trolox			98.41 ± 0.01

Notes: - mean no activity detected against tested bacteria

Conclusion

This is the first report on biological study in of lichens *Usnea rubrotincta*, *Ramalina dumeticola*, and *Cladonia verticillata* from Malaysia. Among the chemical constituents isolated in this study, 8-hydroxybarbatic acid from *U. rubrotincta* and hyperhomosekikaic acid from *R. dumeticola* has been investigated for its antibacterial and antioxidant capacity for the first time and were found to be considerably active against tested bacteria. Usnic acid and atranorin have been identified as active antibacterial agents while sekikaic acid as a considerable antioxidant agent. Further work should be done to enhance the knowledge on these chemical constituents.

Acknowledgement

This research was supported by Exploratory Research Grant Scheme (ERGS/1/2012/STG01/UKM/01/3), Ministry of Higher Education, Malaysia, Universiti Kebangsaan Malaysia, Malaysia, and Universiti Sains Malaysia, Malaysia.

References

1. Denton, G. H. and Karlen, W. (1973). Lichenometry: Its application to Holocene moraine studies in Southern Alaska and Swedish Lapland. *Arctic Alpine Research* 5:347 – 372.
2. Ahmadjian, V. and Reynolds, J. T. (1961). Production of biologically active compounds by isolated lichenized fungi. *Science* 133:700 – 701.
3. Stocker-Worgotter, E. (2008). Metabolic diversity of lichen-forming ascomycetous fungi: culturing, polyketide and shikimate metabolite production, and PKS genes. *Natural Product Reports* 25: 188 – 200.
4. Gauslaa, Y. and Solhaug, K. A. (2001). Fungal melanins as a sun screen for symbiotic green algaein the lichen *Lobaria pulmonaria*. *Oecologia* 126: 462 – 471.
5. Emmerich, R., Giez, I., Lange, O. L. and Proksch, P. (1993). Toxicity and antifeedant activity of lichen compounds against the polyphagous herbivorous insect *Spodopter alittoralis*. *Phytochemisty* 33:1389 –1394.
6. Rankovic, B. and Misic, M. (2008). The Antimicrobial Activity of the Lichen Substances of the Lichens *Cladonia furcata, Ochrolechia androgyna, Parmelia caperata* and *Parmelia conspresa*. *Biotechnology Biotechnological Equipment* 22: 1013 – 1016.
7. Thadhani, V. M., Choudhary, M. I., Ali, S., Omar, I., Siddique, H. and Karunaratne, V. (2010). Antioxidant activity of some lichen metabolites. *Natural Product Reports* 25: 1827–1837.
8. Din, L. B., Zuriati, Z., Samsudin, M.W., and Helix, J.A. (2010). Chemical Profile of Compound from Lichens of Bukit Larut, Peninsular Malaysia. *Sains Malaysiana* 39(6): 901 – 908.
9. Stanly, C., Hag Ali, D. M., Keng, C. L, Boey, P.L., and Bhatt, A. (2011). Comparative Evaluation of Antioxidant Activity and Total Phenolic Content of Selected Lichen Species from Malaysia. *Journal of Pharmacy Research* 4: 2824 – 2827.
10. Eloff, J. N., (1998). A Sensitive And Quick Microplate Method To Determine The Minimum Inhibitory Concentration Of Plant Extracts For Bacteria. *Planta Medica* 64: 711-713.
11. Singleton. V. L. and Rossi, J. A. Jr. (1965). Colorimetry of total phenolics with phosphomolybdic phosphotungstic acid reagents. *American Journal of Enology and Viticulture* 16:144 – 158.
12. Sakanaka S., Tachibana Y. and Okada Y. (2005). Preparation and antioxidant properties of extracts of Japanese persimmon leaf tea (kakinohacha). *Food Chemistry* 89:569 –575.
13. Shimada, K., Fujikawa, K., Yahara, K. and Nakamura T. (1992). Antioxidative properties of xanthone on the auto oxidation of soybean in cylcodextrin emulsion. *Journal of Agriculture Food Chemistry*. 40: 945–948.
14. Culberson, C. F. (1972). Improved conditions and new data for the identification of lichen products by a standardized thin layer chromatographic method. *Journal of Chromatography* 72: 113 – 125.
15. Culberson, C. F., Culberson, W. L. and Johnson, A. (1981). A Standardized TLC analysis of β-Orcinol Depsidones. *The Bryologist* 84 (1):16 – 29.
16. Madamombe, I. T. and Afolayan, A. J. (2003). Evaluation of Antimicrobial Activity of Extracts from South African *Usnea barbata*. *Pharmaceutical Biology*: 199 – 202.
17. Tay, T., Ozdemir, T. A., Yilmaz, M., Turk, H. and Kivanc, M. (2004). Evolution of the Antimicrobial Activity of the Acetone Extract of the Lichen *Ramalina farinacea* and its (+)-Usnic acid, Norstictic acid, and Protocetraric acid Constituents. *Zeitschrift fur Naturforschung*. C. 59: 384 –388.
18. Burkholder, P, R., Evans, A. W., McVeigh, I. and Thornton, H, K. (1944). Antibiotic Activity of Lichens. *Botany* 30: 250 – 255.
19. Sinha, S, N. (2013). Screening Of Phytochemicals and Assessment of Antioxidant Activity of *Usnea Longissima. International Journal of Universal Pharmacy and Life Sciences* 3: 2249 – 6793.
20. Florence, O, J, A. and Adedapo, A. (2011). Comparison of the nutritive value, antioxidant and antibacterial activities of *Sonchus asper* and *Sonchus oleraceus*. *Records of Natural Prod*ucts 5: 9 – 42.
21. Mitrovic, T., Stamenkovic, S., Cvetkovic, V., Tosic, S., Stankovic, M., Radojevic, I., Stefanovic, O., Comic, L., Dacic, D., Curcic, M. and Markovic, S. (2011). Antioxidant, Antimicrobial and Antiproliferative Activities of Five Lichen Species. *International Journal Molecular Sci*ences 12: 5428 – 5448.

22. Lauterwein, M., Oethinger, M., Belsner, K., Peters, T. and Marre, R. (1995). In vitro activities of the lichen secondary metabolites vulpinic acid, (+)-usnic acid and (-)-usnic acid against aerobic and anaerobic microorganisms. *Antimicrob. Agents Chemother* 39: 2541 – 2543.
23. Yilmaz Y., Turk A. O., Tay T. and Kivanc M. (2004). The antimicrobial activity of extracts of the lichen *Cladonia foliacea* and its (-)-usnic acid, atranorin and fumarprotocetraric consitituents. *Zeitschrift fur Naturforschung* C. 59: 249 – 254.
24. Thadhani, V. M., Choudhary, M. I., Khan, S. and Karunaratne, V. (2012). Antimicrobial and toxicological activities of depsides and depsidones. *Journal of National Science Foundation Sri Lanka* 40(1): 43 – 48.
25. Martins, M. C. B., Goncalves de Lima, M. J., Silva, F. P., Azevedo-Ximenes, E., Henrique da Silva, N., and Pereira, E. C. (2010). *Cladia aggregata* (lichen) from Brazilian Northeast: Chemical Characterization and Antimicrobial Activity. *Brazilian Achieve of Biology and Technology* 53(1): 115 – 122.
26. James H. J. and Mary, J, F. (1998). Antimicrobial Susceptibility Testing: General Principles and Contemporary Practices. *Clinical Infectious Diseases* 26: 973 – 980.
27. Sisodiaa, R., Geola, M., Vermaa, S., Ranib, A., & Durejaa, P. (2013). Antibacterial and antioxidant activity of lichen species *Ramalina roesleri*. *Natural Product Research* 27(23): 2235 – 2239.
28. Devehat, F., Tomasi, S., Elix, J.A., Bernard, A., Rouaud, I., Uriac, P. and Boustie, J. (2007). Stictic Acid Derivatives from the Lichen *Usnea articulata* and Their Antioxidant Activities. *Journal Natural Products* 70: 1218 – 1220.

MALAYSIAN JOURNAL OF ANALYTICAL SCIENCES
Published by The Malaysian Analytical Sciences Society
ISSN 1394 - 2506

MODIFIED DISPERSIVE LIQUID-LIQUID MICROEXTRACTION USING GREEN SOLVENT FOR DETERMINATION OF POLYCYCLIC AROMATIC HYDROCARBONS (PAHS) IN VEGETABLE SAMPLES

(Pengekstrakan Mikro Cecair-cecair Serakan yang Terubahsuai dengan Pelarut Hijau untuk Penentuan Polisiklik Aromatik Hidrokarbon (PAHs) dalam Sampel Sayur – Sayuran)

Chai Mee Kin[1]*, Premla Devi Chander[2], Wong Ling Shing[3]

[1]*Department of Civil Engineering, College of Engineering*
[2]*College of Graduate School*
Universiti Tenaga Nasional, 43000 Kajang, Selangor, Malaysia
[3]*Faculty of Science, Technology, Engineering & Mathematics,*
INTI International University, 71800 Nilai, Negeri Sembilan, Malaysia

**Corresponding author: mkchai@uniten.edu.my*

Received: 9 August 2015; Accepted: 11 December 2015

Abstract

According to International Agency for Research on Cancer (IARC), most of Polycyclic Aromatic Hydrocarbons (PAHs) known as genotoxic human carcinogen and mutagenic. PAHs represent as poorly degradable pollutants that exist in soils, sediments, surface water and atmosphere. A simple, rapid and sensitive extraction method termed modified Dispersive Liquid-Liquid Microextraction (DLLME) using green solvent was developed to determine PAHs in vegetable samples namely radish, cabbage and cucumber prior to Gas Chromatography Flame Ionization Detection (GC–FID). The extraction method is based on replacing chlorinated organic extraction solvent in the conventional DLLME with low toxic solvent, 1-bromo-3-methylbutane without using dispersive solvent. Several experimental factors such as type and volume of extraction solvents, extraction time, confirmation of 12 PAHs by GC-MS, recovery percentages on vegetable samples and the comparative analysis with conventional DLLME were carried out. Both DLLME were successfully extracted 12 types of PAHs. In modified DLLME, the recoveries of the analytes obtained were in a range of 72.72 – 88.07 % with RSD value below 7.5 % which is comparable to the conventional DLLME. The use of microliter of low toxic extraction solvent without addition of dispersive solvent caused the method is economic and environmental friendly which is fulfill the current requirement, green chemistry based analytical method.

Keywords: polycyclic aromatic hydrocarbons, modified dispersive liquid-liquid microextraction, gas chromatography flame ionization detection

Abstrak

Menurut agensi antarabangsa bagi penyelidikan kanser (IARC), kebanyakan Polisiklik Aromatik Hidrokarbon (PAHs) dikenali sebagai karsinogen genotoksik terhadap manusia dan mutagen. PAHs mewakili sebagai pencemar degradasi rendah yang wujud dalam tanah, enapan, air permukaan dan atmosfera. Satu kaedah pengekstrakan yang mudah, pantas dan sensitif yang digelar sebagai pengekstrakan mikro cecair – cecair serakan (DLLME) yang terubahsuai dengan pelarut hijau telah dibangunkan bagi penentuan PAHs dalam sampel sayur – sayuran iaitu lobak, kubis dan timun sebelum diukur menggunakan gas kromatografi – pengesan nyala pengionan (GC–FID). Kaedah pengekstrakan ini adalah berdasarkan penggantian pelarut pengekstrakan organik berklorin di dalam DLLME konvensional dengan pelarut rendah toksik, 1-bromo-3-metilbutana tanpa menggunakan pelarut penyebar. Beberapa factor eksperimen seperti jenis dan isipadu pelarut pengekstrakan, masa pengekstrakan, pengesahan 12

PAHs dengan GC-MS, peratusan perolehan semula sampel sayur – sayuran dan perbandingan analisis dengan DLLME konvensional telah dijalankan. Kedua – dua teknik DLLME telah berjaya mengekstrak 12 jenis PAHs. Bagi DLLME terubahsuai, perolehan semula analit berada dalam julat 72.72 – 88.07 % dengan nilai RSD adalah kurang daripada 7.5 % iaitu setanding dengan teknik DLLME konvensional. Penggunaan mikroliter pelarut pengekstrakan yang rendah toksik tanpa penambahan pelarut penyebar menyebabkan kaedah ini ekonomik dan mesra alam yang memenuhi keperluan semasa iaitu kaedah analisis berasaskan kimia hijau.

Kata kunci: polisiklik aromatik hidrokarbon, pengekstrakan mikro cecair-cecair serakan yang terubahsuai, gas kromatografi-pengesan nyala pengionan

Introduction

Polycyclic aromatic hydrocarbon (PAH) is a complex mixture of an end product, resulted from incomplete combustion of organic materials. It represents as poorly degradable pollutants that exist in soil, sediments, surface water and atmosphere [1]. Sixteen PAHs have been classified as genotoxic human carcinogen and mutagenic by the International Agency for Research on Cancer (IARC) and selected by US Environmental Protection Agency (EPA) as Constant Degree priority pollutants for regulatory process [2]. They are anthracene, fluoranthene, pyrene, benzo(b)fluoranthene, benzo(k)fluoranthene, acenaphthylene, acenaphthene, benzo(a)anthracene, benzo(a)pyrene, benzo(g,h,i)perylene, chrysene, cyclopenta(c,d)pyrene, dibenz(a,h)anthracene, dibenzo(a,l)pyrene, indeno(1,2,3-c,d)pyrene and 5-methylchrysene.

To assess the penetration of PAHs or their metabolites in the plant, it is important to develop a sensitive, rapid, simple, economic and environmental friendly extraction method. Various conventional extraction methods such as Liquid-liquid extraction (LLE) and Solid-phase extraction (SPE) have been implemented [3]. However, the presences of various plant pigments and the limitations of conventional extraction method lead to the failure of developing a compatible, efficient, economical and miniaturize extraction method. The discovery of Dispersive Liquid-Liquid Microextraction (DLLME) method by Assadi and teammates solved the drawbacks of conventional method and it is known to be rapid and low cost method [4]. In this procedure, the mixture of extraction solvent and dispersive solvent is rapidly injected into aqueous sample results the formation of fine droplets. These droplets increase the surface area between extraction solvent and sample solution and speed up the extraction [2, 4]. However, there are few drawbacks on this method as it acquired toxic halogenated solvents used as extraction solvent and dispersive solvent. DLLME also restricts implication on vegetable matrices due to interferences [5].

In this study, modified DLLME was developed to determine the PAHs from the vegetable samples followed by gas chromatography-flame ionization detector (GC–FID). In this procedure, only minimal amount (100µl) of low toxic extraction solvent is added into the vegetable sample compared to that two types of solvent (e.g. water immisicble and water miscible solvent) are needed in original DLLME to form the emulsion consist of fine droplets.

Materials and Methods

Reagents and Materials

Twelve types of PAHs (acenaphthylene, acenaphthene, fluorene, anthracene, phenanthrene, fluoranthene, pyrene, benzo(a)anthracene, chrysene, benzo(b)fluoranthene, benzo(k)fluoranthene and benzo(a)pyrene) were purchased from Supelco. 1-bromo-3-methylbutane, hexanol, heptanol, octanol, nonanol were purchased from Sigma-Aldrich. Acetone and Acetonitrile (HPLC Grade) were obtained from Merck. Deionised water (D.I.) was purified on a Milli-Q water system. Stock solution of PAH standards were prepared by dissolving PAHs standard at 10 ppm in acetonitrile. Working standard solutions of 12 types of PAHs were prepared in acetonitrile at concentration of 5 ppm to 0.1 ppm. The solutions were stored at 4 °C in a refrigerator. Vegetables namely radish (*Raphanus sativus),* cucumber *(Cucumis sativus) a*nd cabbage (*Brassica oleracea*) were purchased from the local organic market. The vortex agitator model no. VELP Scientifica ZX^3 (Usmate, Italy) and the centrifuger with a model no. Hettich ROTOFIX 32 Benchtop centrifuge (Tuttlingen, Germany) were used in this experiment.

Instrumentation

The chromatographic analysis was performed by using Gas Chromatography model Agilent 7890A equipped with a split/splitless injection inlet, flame ionization detector (FID) and a 7683 automatic liquid sampler. The optimization

of gas chromatography (GC-FID) condition was carried out and set up in which runtime of a sample requires 25 minutes. The 12 PAH compounds were separated by using HP-5 (5% phenyl-methylpolysiloxane) capillary column (30m x 320µm x 0.25µm). The optimum condition of the GC-FID for separation of 12 PAHs was oven temperature commenced at 100°C for 1 min and was raised by 15 ^{o}C min^{-1} to 280 ^{o}C for 10 mins. Helium as carrier gas in a constant flow of 1 mL min^{-1}, injector temperature of 290 ^{o}C and in splitless mode.

Gas Chromatography–Mass spectrometry (GC-MS Shidmazu QP2010) was used to perform the confirmation of 12 types of PAH. The applied column comprises of 30m x 0.25mm i.d. x 0.25µm firm thickness known as DB-5MS. The injection for analyte separation was made in splitless mode, injector temperature was maintained at 290°C and the injection volume was 1µL. Ultra-pure helium gas (99.9995%) was used as carrier gas with flow rate of 1.2 mL min^{-1}. The oven temperature programmed, where the initial temperature was 100°C and held for 1 min and ramp to 290 °C at 15°C min^{-1} and held for 20 minutes. Total run time was 33.67 min.

Sample Preparation

The vegetable sample was weighed, homogenized, centrifuged, filtered and spiked at 50 µL of 10 ppm of mixture of individual standard. The homogenized sample (5 ml) was transferred into conical centrifuge tube.

An appropriate amount of extraction solvent (e.g. 100 µL) was added into the sample and gently shaken. A cloudy solution formed due to tiny droplets of extraction solvent dispersing in the sample solution. After homogenization (vortex) and centrifugation process at rate of 3000 rpm for 10 minutes, the sedimented layer formed at bottom of the conical tube. The sediment layer further transferred into the glass insert in a 2 ml of vial using of microsyringe. 1 µL of the sediment solution was injected into GC–FID using autosampler for the analysis at optimized GC-FID condition. Three replicates were done for each trial.

The Selection of Extraction Solvent

The selection of an extraction solvent is crucial for the determination of extraction efficiency of the modified method. Five types of low toxic solvents namely hexanol, heptanol, octanol, nonanol and 1-bromo-3-methylbutane have been tested to obtain an optimal extraction solvent. The selection of low toxic extraction solvent was made based on few criteria's. The extraction solvent must be (a) high density than water, (b) low solubility in water, (c) achieves high percentage recovery of target analyte and (d) achieve good chromatographic behaviour. Besides, the toxicity level of the selected extraction solvent must be less hazardous compared with conventional DLLME extraction solvent (e.g. tetrachloroethylene, chloroform, chlorobenzene) and also an environmental friendly solvent in order to achieve the aim of green chemistry. The behaviour of toxicity and solubility in water of two conventional DLLME extraction solvents (tetrachloroethylene and chlorobenzene) and five selected extraction solvents (hexanol, heptanol, octanol, nonanol and 1-bromo-3-methylbutane) are tabulated in Table 1. Among all the tested solvents, 1-bromo-3-methylbutane has lowest toxicity and lowest solubility in water.

Table 1. Lethal Dose (LD_{50}) Toxicity of 7 types of Extraction Solvents

No	Extraction Solvent	$LD_{50\ (mg/kg,oral)}$ on rat	Solubility in water	Ref.
1	Tetrachloroethylene	2600/2629	206 mg/L at 25°C	[6]
2	Chlorobenzene	1437-3400	400 mg/L at 20 °C	
3	Hexanol	720	5000 mg/L at 20°C	
4	Heptanol	500	2850 mg/L at 100°C	
5	Octanol	5000	1000 mg/L at 20°C	
6	Nonanol	3.56	1000 mg/L at 20°C	
7	1-Bromo-3-methylbutane	6150	196 mg/L at 16.5°C	

The percentage of recovery (%) calculated based on the ratio of the concentration of peak area after extraction to the initial spiked concentrations of analyte in the sample solution.

Results and Discussion

Experimental parameters for the modified DLLME, including the types of low toxic solvent and its volume as well as the extraction time were optimized. From the Figure 1, 1-bromo-3-methylbutane yield the highest average recovery percentage (75.53 %) compare to other extraction solvents. Meanwhile, other extraction solvents failed to obtain the acceptable recovery range (70 – 120 %) set up by the International Conference on Harmonisation (ICH) on the validation of analytical procedures [7]. 1-bromo-3-methylbutane solvent was able to extract all the desired analytes well in the acceptable recovery range from the liquid matrices. Therefore it was ideal to select 1-bromo-3-methylbutane solvents as an extraction solvent in modified DLLME on the extraction of 12 PAHs in vegetable samples. Other four extraction solvents (hexanol, heptanol, octanol and nonanol) have the low recovery percentages. This may due to they are high solubility in water which exposed to the interferences that presence in water and caused the solvents loss interaction with analytes as 12 PAHs are immisible in water. Besides, these four extraction solvents are less dense (0.8 g/mL) than water leaded the failure of the formation of sedimented extraction phase. The droplets formation of extraction solvent floats on the surface of the sample solution causes the difficulties to extract the analytes from the sample solution. These are prove that the density of the solvent and its solubility in water are the important criteria's when selecting the extraction solvent as mentioned above.

Results showed that the sedimented extraction phase obtained is depending on the amount of extraction solvent used. The higher volume of extraction solvent used the larger amount of sedimented phase was obtained. However, the aim of the study is to find out the minimal usage of extraction solvent to extract all 12 PAHs. In fact, 50 µL of the extraction solvent produced minimal amount of sediment layer and caused the difficulties to transfer the sediment layer into the vial as the sediment layer was mixed up with the sample precipitate even though after long period of centrifugation process. In order to reduce the solid matrix interference problem, 100 µL was selected as an ideal volume as the study focuses on the minimal usage of solvent upon extracting 12 PAHs from solid matrices.

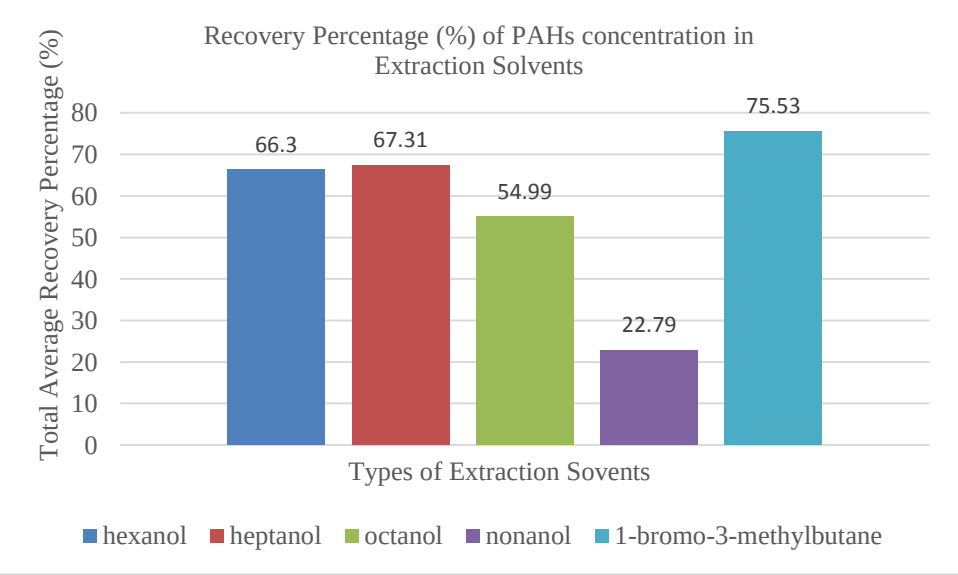


Figure 1. Recovery Percentage (%) of PAHs concentration in extraction solvents

Extraction time

In conventional DLLME, fine droplets of organic solvent are formed in the sample solution with the mixture of extraction solvent and dispersive solvent [8]. This may due to the quick mass transfer of analytes from the aqueous phase to the extraction solvent. Meanwhile in modified DLLME, homogenous fine droplets were formed reproducibly with aid of gentle shaken without addition of dispersive solvent. The extraction time is defined as shaking time. The results showed that there was no significant difference in the extraction recoveries for all the PAHs during the shaking time range (1, 2, 4, 6, 8 and 10 minutes). Since the extraction recovery with extraction time of 2 min lies within the acceptable range (70 to 120 %) with the low relative standard deviation (< 5%), 2 min shaking time was considered as optimal time for modified DLLME. Short extraction time required in modified DLLME is one of the most remarkable advantages of modified DLLME.

Confirmation of 12 PAHs by GC-MS

The mass spectrometry detector can be used for detection and identification purpose as well as for quantitation of analytes. In this study, gas chromatography couple with mass spectrometry detector was implemented only for analyte identification and confirmation. The sediment extraction phase was withdrawn and injected into GC-MS for full scan analysis. The total ion chromatogram of the target analytes under optimized GC-MS conditions was obtained and shown in Figure 2.

In MS full scan mode, all ions produced from each analyte peak in the MS was employed in confirmation of the targeted analytes. High reliability of identification was achieved by making comparison of the MS of the targeted analyte at the top of its chromatographic peak with the best matching compound in the standard mass-spectral libraries. From the results, it was known that all the 12 types of PAHs were successfully extracted using modified DLLME. The 12 types of PAHs were successfully identified and confirmed to be present in the sedimented extraction phase. The initial ion fragments for the first peak were formed at 7.27 minutes and ends at 18.604 minutes. The range of the ion fragments forms between 152.10 m/z to 276.15 m/z. The existing of molecular ions with highest m/z ratio similar to their respective molecular weight was shown to present in individual PAHs mass spectrum.

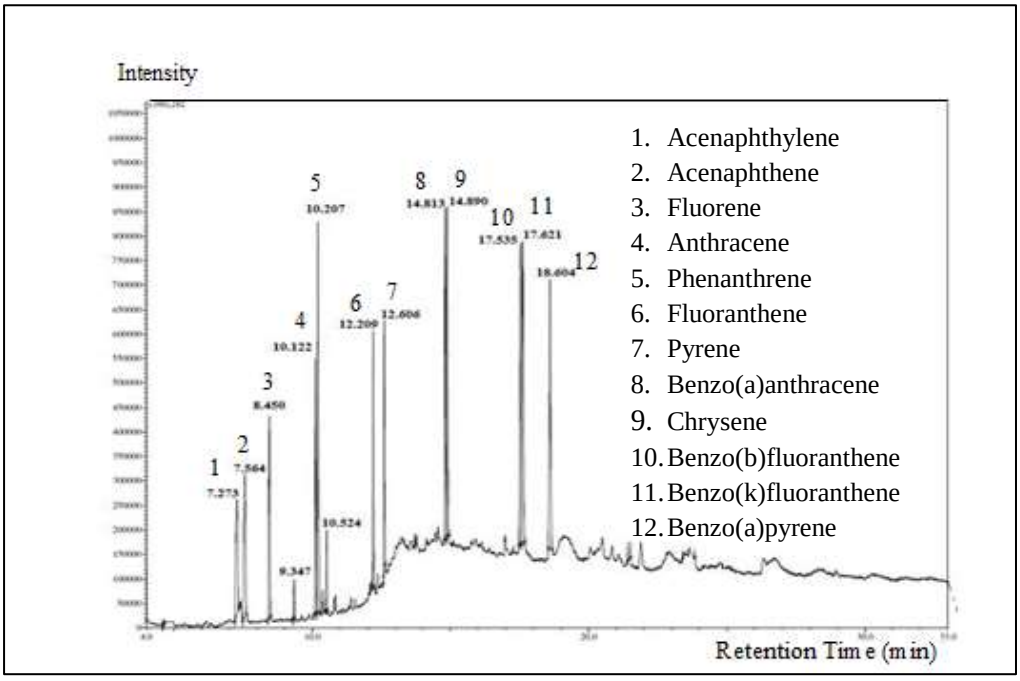


Figure 2. Chromatogram of 12PAHs obtained from modified DLLME in GC-MS Full Scan Mode

Comparison between Modified DLLME and Conventional DLLME

The modified DLLME was compared with conventional DLLME using the same three types of vegetable (e.g. radish, cabbage and cucumber). The purpose of this comparison is to determine the efficiency of the modified DLLME towards the vegetable matrix compared to the conventional DLLME. In conventional DLLME, the common implemented extraction solvent was tetrachloroethylene at 50 µL and the dispersive solvent was acetone at 100 µL. In modified DLLME, 1-bromo-3-methylbutane was used as extraction solvent at 100 µL and there is no addition of dispersive solvent. Each sample was injected three times and the recovery percentage and RSD value of both methods on three vegetable samples were calculated and tabulated in Table 2.

Table 2. Comparison of Recovery Percentage (%) of Modified DLLME with Conventional DLLME in the vegetable samples

PAH	Radish		Cucumber		Cabbage	
	Modified DLLME (%) (RSD%)	**Conven. DLLME (%) (RSD%)**	**Modified DLLME (%) (RSD%)**	**Conven. DLLME (%) (RSD%)**	**Modified DLLME (%) (RSD%)**	**Conven. DLLME (%) (RSD%)**
Acenaphthylene	83.05 (0.1)	76.83 (0.3)	85.29 (1.1)	82.35 (3.2)	80.47 (3.5)	75.64 (4.5)
Acenaphthene	87.88 (0.2)	86.48 (0.2)	81.94 (4.0)	78.32 (6.7)	78.18 (2.7)	76.26 (3.1)
Fluorene	88.07 (0.5)	80.39 (1.8)	80.26 (3.0)	79.92 (4.2)	76.67 (3.5)	74.35 (3.9)
Anthracene	82.14 (0.6)	77.27 (1.7)	76.40 (3.7)	73.43 (3.8)	77.96 (2.7)	72.50 (2.8)
Phenanthrene	81.81 (0.4)	76.36 (1.8)	75.64 (3.4)	71.89 (5.0)	76.29 (3.2)	71.64 (3.8)
Fluoranthene	78.02 (0.3)	74.24 (2.3)	78.53 (2.1)	74.35 (4.1)	77.86 (1.9)	74.11 (2.7)
Pyrene	78.68 (3.3)	72.65 (2.5)	77.29 (7.5)	75.90 (7.7)	75.08 (0.6)	72.60 (0.7)
Benzo(a)anthracene	77.18 (0.5)	75.41 (4.0)	74.37 (7.1)	71.13 (7.4)	74.23 (4.4)	73.08 (4.6)
Chrysene	75.79 (0.2)	73.85 (3.9)	78.52 (5.1)	75.76 (6.0)	74.61 (1.5)	70.44 (1.8)
Benzo(b)fluoranthene	80.94 (1.9)	75.64 (4.7)	74.68 (3.3)	72.50 (3.4)	75.56 (3.6)	73.81 (4.6)
Benzo(k)fluoranthene	75.38 (3.1)	71.34 (4.7)	73.05 (3.0)	71.28 (5.3)	74.25 (2.6)	70.36 (3.9)
Benzo(a)pyrene	72.72 (0.9)	71.93 (5.0)	72.45 (6.2)	70.59 (6.5)	75.62 (2.8)	71.08 (3.4)

From the results obtained, both methods successfully extracted all the 12 PAHs from the respective vegetables. However, modified DLLME yielded higher recovery percentages ranged from 72.72 % to 88.07 % in radish, 72.45 % to 85.29 % in cabbage and 74.23 % to 80.47 % in cucumber with minimal of RSD values from 0.1 % to 7.5 % compared to the conventional DLLME that yielded the recovery percentages ranged from 71.34% to 86.48% in radish, 70.59% to 82.35% in cabbage and 70.36% to 76.26% in cucumber with RSD values (%) from 0.2 % to 7.7 %.

1-bromo-3-methylbutane has higher density than water and low solubility in water leads to high extraction efficiency compared to tetrachloroethylene which used as extraction solvent in conventional DLLME. Without the addition of dispersive solvent, 1-bromo-3-methylbutane capable of forming the fine droplets and enhances the contact surface area between analyte and extraction solvent whereas chlorosolvents acquired dispersive solvent to extract the analyte (12 PAHs) from the vegetable sample. Low recovery of tetrachloroethylene in conventional DLLME may due to the low solubility of tetrachloroethylene towards the analyte [9].

Conclusion

A novel sample preparation method designated as Modified DLLME has been developed for the determination of PAHs in vegetable samples with only using minimal amount of low toxic solvent as extraction solvent without addition of dispersive solvent. Compared to conventional DLLME, modified DLLME yields higher efficiency recovery range from 72.72 – 88.07 % at minimal RSD value range from 0.1 – 7.5 %. Thus modified DLLME is a reliable alternative technique for sample pre-concentration in terms of performance and speed. Major advantages of this modified method are present at low cost and only usage of minimal amount of low toxic extraction solvent to form fine droplets. This method was applied on solid matrices as conventional DLLME majorly focused on the liquid matrices due to the inteference problems.

Acknowledgement

The authors express special thanks to the Ministry of Higher Education of Malaysia – Fundamental Research Grand No. FRGS/1/2013/ST01/UNITEN/02/1 for the financial supports, UNITEN Renewable Energy Centre and Faculty Science of University Malaya for the laboratory analysis.

References

1. Mohammadi, V. K., Mohammadi, A., Hashemi, M., Khaskar, R. and Haratian, P. (2012). Microwave-assisted extraction and dispersive liquid-liquid microextraction followed by gas chromatography-mass spectrometry for isolation and determination of polycylic aromatic hydrocarbons in smoked fish. *Journal of Chromatography A*, 1237: 30 – 36.
2. Hosseini, M. H., Mohamad, R., Akbarian, S., Mizani, F., Pourjavid, R. M. and Arabieh, M. (2013). Homogeneous liquid-liquid microextraction via floatation assistance for rapid and efficient determination of polycyclic aromatic hydrocarbons in water samples. *Analytica Chimica Acta*, 762: 54 – 60.
3. Tseng, W. C., Chen, S. P. and Huang, S. D. (2014). Optimization of two different dispersive liquid-liquid microextraction methods followed by gas chromatography-mass spectrometry determination for polycyclic aromatic hydrocarbons (PAHs) analysis. *Talanta*, 120: 425 – 432.
4. Leong, M. I., Chang, C. C., Fuh, M. R. and Huang, S. D. (2010). Low toxic dispersive liquid liquid microextraction using halosolvents for extraction of polycyclic aromatic hydrocarbons in water samples. *Journal of Chromatography A*, 1217: 5455 – 5461.
5. Guo, L. and Lee, H. K. (2011). Low density solvent-based solvent demulsification dispersive liquid-liquid microextraction for the fast determination of trace levels of sixteen priority polycyclic aromatic hydrocarbons in enviromental water samples. *Journal of Chromatography, A*, 1218: 5040 –5046.
6. Chemical Properties of Product. (2008). Access online from Chemical e-Book: http://www.chemicalbook.com/ProductChemicalPropertiesCB1394458_EN.html. Retrieved 15/8/2014.
7. Chai, M. K. and Tan, G. H. (2009). Validation of a headspace solid-phase microextraction with an internal standard method for the determination of pesticide residues in fruits and vegetables. *Food Chemistry* 117: 561 – 567.
8. Zang, X. H., WU, Q. H., Zhang, M. Y., XI, G. H. and Wang, Z. (2009). Developments of Dispersive Liquid-Liquid Microextraction Technique. *Chinese Journal of Analytical Chemistry*, 37(2): 161 – 168.
9. Zgola-Grzekowiak, A. and Grzeskowiak, T. (2011). Dispersive Liqiud-Liqiud Microextraction. Trends In Analytical Chemistry, 30(9): 1382 – 1397.

MALAYSIAN JOURNAL OF ANALYTICAL SCIENCES
Published by The Malaysian Analytical Sciences Society
ISSN 1394 - 2506

ENZYMATIC SACCHARIFICATION ON AMMONIA PRE-TREATED OIL PALM TRUNK BIOMASS FOR GLUCOSE PRODUCTION: AN OPTIMIZATION USING RESPONSE SURFACE METHODOLOGY

(Sakarifikasi Enzim pada Prarawatan Ammonia Biomas Batang Kelapa Sawit bagi Penghasilan Glukosa: Pengoptimuman dengan Kaedah Gerak Balas Permukaan)

Long Wee Lai*, Siti Sarenah Mohd Yahya, Norakma Mohd Nor, Moohamad Ropaning Sulong

Faculty of Science and Biotechnology,
Universiti Selangor,
Jalan Timur Tambahan, 45600 Bestari Jaya, Selangor, Malaysia

**Corresponding author: zki@unisel.edu.my*

Received: 14 August 2015; Accepted: 31 December 2015

Abstract

This paper reported the optimization of glucose production from ammonia pre-treated oil palm trunk biomass via enzymatic saccharification process using response surface methodology (RSM). A set of experiment was computed by face centered central composite design (FCCCD) using Design Expert software to statistically evaluate the findings. Three independent variables namely: temperature (35 – 55 °C), pH (4.5 – 6.5) and enzyme ratio (cellullase: *β*-glucosidase; 3:1 – 7:1) were investigated under the given conditions designed by RSM. The experimental result (4.964 ± 0.006 $g.L^{-1}$) was in good agreement with RSM model prediction (4.958 $g.L^{-1}$) with an error less than 0.2 %. The RSM design has been proven to successfully predict the glucose response in this study.

Keywords: oil palm trunk biomass, enzymatic saccharification, lignocellulosic substrate, ammonia pre-treament, response surface methodology

Abstrak

Kertas kerja ini melaporkan pengoptimuman hasilan glukosa daripada prarawatan ammonia biomas batang kelapa sawit melalui proses sakarifikasi enzim dengan menggunakan kaedah gerak balas permukaan (RSM). Satu set eksperimen telah dibentuk iaitu kaedah muka berpusat reka bentuk komposit dengan menggunakan perisian Design Expert bagi menilai penemuan kajian secara statistik. Tiga pembolehubah bebas iaitu: suhu (35 – 55 ° C), pH (4.5 – 6.5) dan nisbah enzim (selulase: β-glukosidase; 3:1 – 7:1) telah disiasat di bawah situasi yang direka oleh RSM. Hasil eksperimen (4.964 ± 0.006 $g.L^{-1}$) yang diperoleh berada dalam persetujuan yang baik dengan ramalan model RSM (4.958 $g.L^{-1}$) iaitu pada ralat kurang daripada 0.2 %. Reka bentuk RSM telah terbukti berjaya meramalkan respon glukosa dalam kajian ini.

Kata kunci: biomas batang kelapa sawit, sakarifikasi enzim, substrat lignoselulosa, pra-rawatan ammonia, kaedah gerak balas permukaan

Introduction

Oil palm (*Elaeis guineensis*) is broadly established in tropical countries such as Malaysia, Indonesia, and Thailand for its comestible oil [1]. In general, the oil palm starts bearing its oil in 2.5 years after being planted, and become

lower in productivity after 20-25 years [2, 3]. Therefore, it is necessary to cut the old oil palm tree and to replant new seedlings for sustainable palm oil.

This practise would generate abundance of felled oil palm trunk (OPT). As reported in 2013, Malaysia possesses an oil palm plantation area up to 5.038 million hectares and the oil palm industries have generated 59 million ton of solid biomass annually [4]. These oil palm residues (dry weight, %) include oil palm empty fruit bunch (30 %); oil palm frond (44 %) and oil palm trunk (26 %) respectively. The oil palm trunk like others part oil palm, consists of lignocellulosic biomass which rich in cellulose, hemicellulose and lignin. Consequently, the felled oil palm trunks can be used as one of vital biomass resource to generate beneficial products such as animal feed, biofertilizer, biodiesel, bioplastic and etc. [5].

Generally, the conversion of lignocellulosic biomass into fermentable monosaccharide (sugars) is inevitably through two major steps i.e. pre-treatment of raw materials and enzymatic hydrolysis of pre-treated material [4]. The pre-treatment step is aimed to breaking up the complex structure of lignocellulosic matrix so as to disrupt the crystalline structure of cellulose and thus enhance the enzyme digestibility during the hydrolysis reaction [6]. Up to date, pre-treatment processes such as chemical, physiochemical and biological have been employed to pre-treat the raw lignocellulosic biomass. However, none of the pre-treatment protocol is universal and economically viable to pre-treat different cellulosic biomass. Hence, the proper pre-treatment is essential for the efficiency of biomass conversion [7]. The pre-treatment objective is to eliminate lignin, detached cellulose and hemicellulose, increase the surface area accessibility and subsequently improving the accessibility of hydrolytic enzymes for the maximum emanation of fermentable monosaccharide.

To take full advantage of plentiful OPT residues, the present study has used OPT as a substrate candidate for glucose emanation. This study has utilized the hot dilute aqueous ammonia (7 %) to pre-treat the OPT biomass. The ammonia treated OPT was then subjected to enzymatic hydrolysis for glucose production. The main objective of this investigation is to determine the best hydrolysis conditions for the maximum glucose production. Hence, the RSM based on face centered central composite design (FCCCD) was employed as to identify the optimal enzymatic saccharification conditions in present study.

The response surface methodology (RSM) was used in the present study to analyse the effects of different independent variables (temperature, pH and enzyme ratio) and to optimise the response (glucose production). Generally, the RSM could be used to simplify the optimization by study the multi-parameters simultaneously [8]. By setting up the three dimensional plots, the overall behaviour reaction of experimental data could be easily understood as well as the interaction effects. The software also provides the statistical ANOVA analysis to identify the significant or insignificant factor in the experiment.

Materials and Methods

Raw material

The oil palm trunk (OPT) biomass was used as a substrate in present study. It was collected from Concept Renewable Energy Sdn. Bhd., Macap, Johor. The fresh pulverized OPT was dried at 45 ºC for 3 consecutive days and then it was sieved to get the particle size with less than 1.0 mm [4].

Ammonia pre-treatment method

The 5.0 g of sieved OPT biomass was soaked in 7 % ammonia solution at 80 °C for 8 hours [7]. Once completed, the slurry was recovered by passed thru the filter cloth and then followed by washing with plenty of distilled water until the pH of wash liquid has reached at neutral value. The treated OPT was dried at 45 ºC to constant weight. The chemical compositions of treated OPT contained 38.7 %, 14.7 %, 9.1 % 6.4 %, 2.3 % 19.4 % and 5.4 % (w/w) of glucan, xylan, arabinan, mannan, galactan, acid-insoluble lignin and ash, respectively on a dry weight basis [7].

Enzymes

Two commercial enzymes were used in this study namely: cellulase (Celluclast 1.5) from *Trichoderma reesei* ATCC 26921 and *β*-glucosidase (Novozym 188) from *Aspergillus niger*. The activity of both enzymes was

measured at 80.41 FPU.mL^{-1} and 134.68 CBU.mL^{-1}, respectively [9, 10]. The 40 FPU.g^{-1} and 100 CBU.g^{-1} of substrate were used throughout the study.

Buffer preparation

The sodium citrate buffer was made by mixing of citric acid monohydrate and trisodium citrate dihydrate. The 0.1 M concentrations for both solutions were prepared by dissolving 21.01 g.L^{-1} of citric acid and 29.41 g.L^{-1} of trisodium citrate dehydrate, respectively. The desired pH value could be attained by mixing both solutions to a total of 100 ml [11]. The 0.1 M sodium citrate buffer was then further diluted to desire 50 mM concentration for the whole investigation.

Experimental design

The response surface methodology (RSM) was employed to design the experiment. Three independent variables, namely: temperature, pH and enzyme ratio (cellulase: β-glucosidase) were examined to determine the effect of each factor on glucose production response. The total of 20-run was computed using face centered central composite design (FCCCD) with six center points of replicates and the alpha value of 1.0. The ranges and the designed levels of process variables are given in Table 1.

Table 1. Actual values of independent variables

Factors	Low level, (–1)	Center level, (0)	High level, (+1)
A: Temperature, °C	35	45	55
B: pH	4.5	5.5	6.5
C: Enzyme ratio (cellulase: β-glucosidase)	3:1	5:1	7:1

The quadratic model equation for predicting the optimal point is expressed by Eq. (1) as followed:

$$Y = \beta_0 + \Sigma \beta_i X_i + \Sigma \beta_{ii} X_i^2 + \Sigma \beta_{ii} X_i X_j + \mathcal{E} \quad (1)$$

where Y is the predicted response (glucose amount, g.L^{-1}), β_0 is constant coefficient, β_i, β_{ii} and β_{ij} are coefficient for the linear, quadratic and interaction effects, X_i and X_j are factors (independent variables) while $\mathcal{E}$ is the error.

The Design Expert 6.0.4 software was used for regression and graphical analyses of the attained data. Generally, a full second-order model with linear, quadratic and interaction term was fitted in order to conclude the optimum combinations of factors level [2]. Meanwhile, the main and interaction effects of model term were also statistically analysed using analysis of variance (ANOVA).

Enzymatic hydrolysis of treated OPT

The treated OPT substrate, 1 % (w/v) was added into a glass jar which contained 100 ml of 0.05 M buffer solution (pH 4.5 – 6.5) and 100 µl 0.2 % (w/v) of sodium azide. The glass jar was then transferred into water bath and heat-up to 35 - 55 °C for 15 min according to RSM design. Lastly, both enzymes with certain ratio (3:1 to 7:1) were discharged into glass jar to initiate the enzymatic hydrolysis reaction. All enzymatic hydrolysis reaction was performed in triplicate and the errors were within ± 5 %.

Glucose analysis

The withdrawal hydrolysate was mixed with 3, 5-dinitrosalicylic (DNS) reagent in ratio of 1:1 and brought to heating at 100 °C for 15 min to cease the enzyme activity. The mixture was cool-down to room temperature prior to read spectrophotometrically at wavelength of 540 nm [12]. The reducing sugars formed during the enzymatic hydrolysis were represented with glucose equivalent [10]. All hydrolysis experiment was conducted in triplicate and the obtained glucose data was presented in an average value.

Validation of RSM prediction points

The optimization predicted points, i.e. temperature, 44.23 ^{o}C; pH, 5.22 and cellulase: β-glucosidase 3:1 were recommended by the RSM software. These suggested parameters were tested in subsequent confirmation run in order to validate the RSM prediction points.

Results and Discussion

Optimization of glucose production

A total of 20-set run which divided into 3 blocks was computed based on face centered central composite design (FCCCD) protocol as shown in Table 2. The enzymatic hydrolysis reaction on ammonia pre-treated OPT biomass was conducted as per each set point as described. Table 2 also tabulates the glucose response for both experimental and predicted values.

The run-11 shows the highest glucose concentration up to 5.73 g.L^{-1} when the experimental conditions were set to temperature, 45 °C; pH, 5.5 and enzyme ratio 5:1, respectively. It was noticed that when the experiment was conducted in conditions at temperature, 55 °C; pH, 6.5, and enzyme ratio 3:1, the lowest glucose concentration was attained i.e. 0.20 g.L^{-1}.

Table 2. RSM design of experiment: experimental and predicted value

Run	Block	Factor A: Temperature	Factor B: pH	Factor C: Enzyme ratio	Response, Glucose (g.L^{-1})	
					Experimental	Predicted
1	Block 1	45.00	5.50	5:1	4.28	4.65
2	Block 1	55.00	4.50	7:1	1.24	1.27
3	Block 1	35.00	4.50	3:1	2.11	2.10
4	Block 1	55.00	6.50	3:1	0.20	-0.28
5	Block 1	45.00	5.50	5:1	3.96	4.65
6	Block 1	35.00	6.50	7:1	0.56	-0.06
7	Block 2	55.00	4.50	3:1	0.72	1.22
8	Block 2	35.00	4.50	7:1	2.04	2.40
9	Block 2	55.00	6.50	7:1	0.22	0.11
10	Block 2	35.00	6.50	3:1	0.42	0.27
11	Block 2	45.00	5.50	5:1	5.73	4.89
12	Block 2	45.00	5.50	5:1	4.66	4.89
13	Block 3	45.00	5.50	5:1	4.50	4.05
14	Block 3	45.00	5.50	3:1	4.22	4.35
15	Block 3	45.00	4.50	5:1	4.31	3.42
16	Block 3	45.00	5.50	7:1	4.11	4.45
17	Block 3	45.00	5.50	5:1	4.99	4.05
18	Block 3	55.00	5.50	5:1	0.95	1.01
19	Block 3	35.00	5.50	5:1	1.21	1.61
20	Block 3	45.00	6.50	5:1	0.34	1.69

A full quadratic regression model based on actual values was as shown in Eq. (2). The Eq. (2) has a high coefficient of determination, R^2 and adjusted coefficient of determination, R^2_{Adj} at 0.9057 and 0.7997, respectively. This

indicates the quadratic model could be well explained. There is merely 9.43 – 20.03 % of the variation occur might due to noise that cannot be explained by the model it self [14].

$$\text{Glucose} = -82.94287 + 2.31023*\text{Temp} + 14.78740*\text{pH} - 0.87010*\text{Enzyme} - 0.027414*\text{Temp}^2 - 1.49843*\text{pH}^{2+} 0.086392*\text{Enzyme}^2 + 0.020438*\text{Temp}*\text{pH} + 2.93125\text{x}10^{-3}*\text{Temp}*\text{Enzyme} - 0.018187*\text{pH}*\text{Enzyme} \quad (2)$$

The analysis of variance (ANOVA) for glucose content after enzyme hydrolysis was used to estimate the glucose response as a function of temperature, pH and enzyme ratio is shown in Table 3. Mathematically, when the Prob > F values greater than 0.05, those factors are considered statistically insignificant. Meanwhile when Prob > F values less than 0.05, it could be defined as a significant factor [14]. In present study, the quadratic model with 0.003 was significant. The "lack-of-fit" F-value of 4.52 implies that the "lack-of-fit" was insignificant relative to the pure error. There is a 12.2 % chance for the model that a "lack-of-fit" F-value of this large could occur due to noise. In general, the non-significant lack-of fit was good and implied that all data in this experiment were adequated as well as good predicatibility of the model [2].

Table 3. Analysis of Variance (ANOVA)

Source	**Sum of Square**	**DF**	**Mean Square**	**F value**	**Prob >F**	
Block	4.06	2	2.03			
Model	61.40	9	6.83	8.54	0.0030	Significant
A	0.90	1	0.90	1.13	0.3196	
B	7.51	1	7.51	9.40	0.0155	
C	0.03	1	0.03	0.03	0.8602	
A^2	20.2	1	20.2	25.2	0.0010	
B^2	6.03	1	6.03	7.54	0.0252	
C^2	0.32	1	0.32	0.40	0.5442	
AB	0.33	1	0.33	0.42	0.5360	
AC	0.03	1	0.03	0.03	0.8575	
BC	0.01	1	0.01	0.01	0.9112	
Residual	6.39	8	0.80			
Lack of Fit	5.64	5	1.13	4.52	0.1220	Not Significant
Pure Error	0.75	3	0.25			
Cor Total	71.88	19				

Note: A: Temperature; B: pH; and C: Enzyme ratio; $R^2 = 0.9057$, $R_{Ajd}^2 = 0.7977$

In present study, only the main effect, pH was significant where the value of Prob>F equal to 0.015. Others significant terms were of square effect of temperature (Prob>F = 0.001) and square effect of pH (Prob>F = 0.025). On the other hand, those insignificant factors were the main effect: temperature (Prob>F = 0.320) and enzyme ratio (Prob>F = 0.860); square effect of enzyme ratio (Prob>F = 0.5442); and all three interactive effects: temp*pH (Prob>F = 0.53), temp*enzyme ratio (Prob>F = 0.856) and pH* enzyme ratio (Prob>F = 0.911), respectively. Based on the ANOVA analysis, those insignificant factors whether main, square or interaction effect can be eliminated and therefore the new reduced quadratic model could be expressed in Eq. (3) as followed:

$$\text{Glucose} = -82.94287 + 14.78740*\text{pH} - 0.027414*\text{Temp}^2 - 1.49843*\text{pH}^2 + 0.020438*\text{Temp}*\text{pH} + 0.018187*\text{pH}*\text{Enzyme} \quad (3)$$

Although interaction effects such as temp*pH and pH*enzyme were insignificant, but they were still maintained in new model (Eq. 3) to retain the model hierarchy [13].

Normality test and predicted versus actual analysis

A graphical technique uses to regulate the relevance of assumption on normality is by plotting the data points on a normal probability paper. If a straight line can be draw through the plotted points, the assumption of normality is reflected to be rational. Figure 1 showed the obtained data were fall on the straight line.

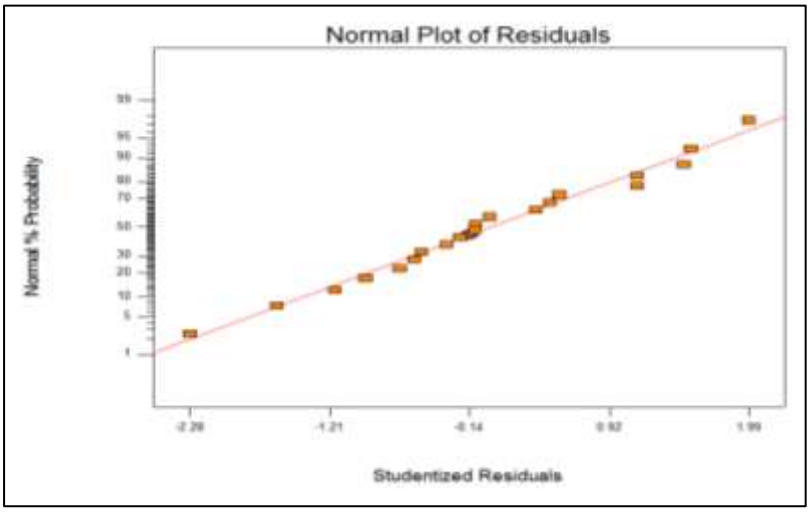


Figure 1. Normality plot of residuals

On the other hand, the data in Table 2 shows that the predicted values were in good agreement with the experimental values for glucose response. The results could be further corroborated as illustrated in Figure 2 which graphically depicts the correlation between the actual and predicted responses. All data point was closed to the straight line, demonstrating that no significant violations of the model were found. Moreover, the model should adequate to predict the glucose amount during enzymatic hydrolysis within the range in present study as it was highly significant, where the Prob > F value is 0.003. In fact, the coefficient of determination, R^2 = 0.9057, considered sufficient to identify the correlation between the actual and the predicted values [15].

Three-dimensional (3D) response surface plots

As shown in Table 3, the main factor: pH was statistically significant. Therefore, the interaction effects which involve Temp*pH and pH*Enzyme ratio should be remained. Further analysis on these interaction effects were carried out. The three-dimensional (3D) response surface plots of both interaction effects were illustrated in Figure 3 and Figure 4, respectively.

Interaction effects of temperature versus pH (temp*pH)

Figure 3 demonstrates the 3D response surface plot for the interaction effects of temperature versus pH. Both of the interaction effects were temperature and pH (varying from 35 – 55 ºC and 4.5 – 6.5, respectively) on the glucose production, while holding the enzyme ratio at its center point, *viz.* 5:1.

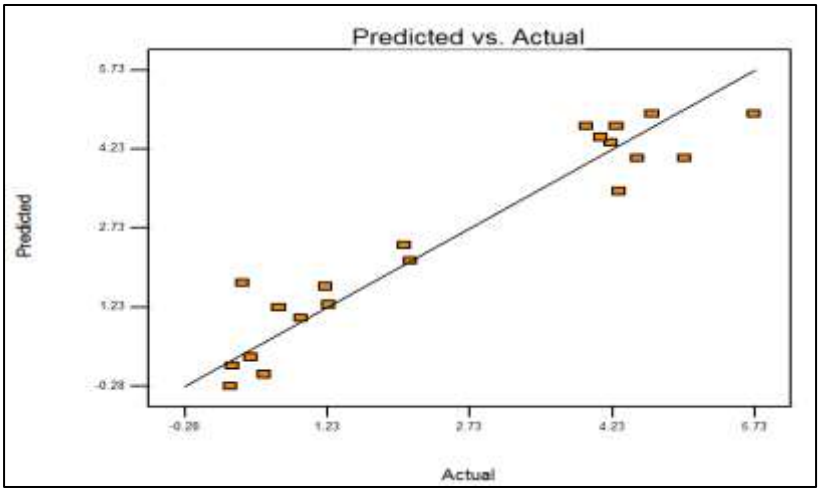


Figure 2. Actual and predicted plot of glucose response

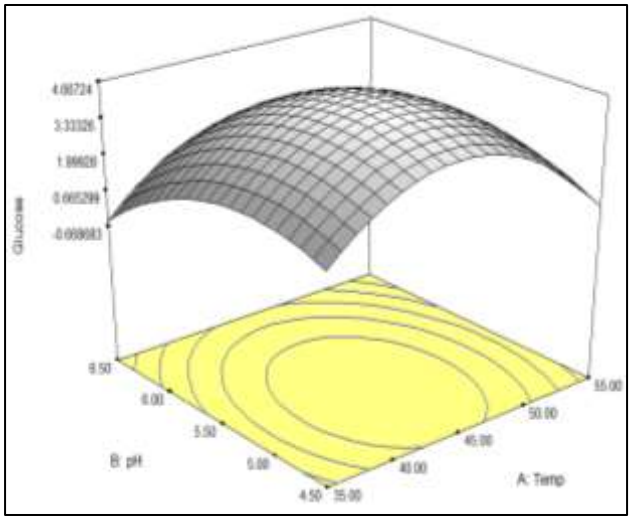


Figure 3**.** 3D response surface plot for interaction effects of temperature versus pH

It was noticed that the highest glucose concentration > 4.39 $g.L^{-1}$ could be attained when temperature at 45 ºC and pH in the range of 5.0 – 5.5, respectively. The pH range of 4.5 – 6.0 is favour the glucose production in all tested temperature ranging from 35 – 50 ºC. The glucose concentration was increased when the temperature was raised from 35 to 45 ºC. This could be explained as the enzyme-catalyzed reaction behaves like most chemical reaction, proceed at a faster velocity as the temperature is raised. An increase in temperatures, it would impart more kinetic energy to the reactant molecules resulting in more productive collision per unit time [16]. As a result, more glucose released when the temperature was raised from low to mid-point in present study. However, further increased of temperature (> 45 ºC), the glucose concentration was decreased. Figure 3 has obviously showed the raising of glucose amount from 35 – 45 ºC and sharply declined when the tested temperature was in range of 45 – 55 ºC. In general, an enzyme molecule is a very delicate and fragile structure. If the molecule absorbs too much energy, the

tertiary structure will be disrupted and the enzyme will lose its catalytic activity and eventually denatured. This is the main reason why low glucose concentration was detected when at higher temperature. In short, both cellulase and β-glucosidase enzymes were performed well and reach their optimum temperature point at 45 °C.

Interaction effects of pH versus enzyme ratio (pH*enzyme ratio)

Figure 4 reveals the interaction between pH and enzyme ratio on glucose production. When temperature was fixed at 45 °C, enzyme ratio and pH were set to 5:1 and 4.8 – 5.6; 4.65 $g.L^{-1}$ of glucose concentration is obtainable. Meanwhile, when the pH value greater than 5.6 the glucose amount was decreased.

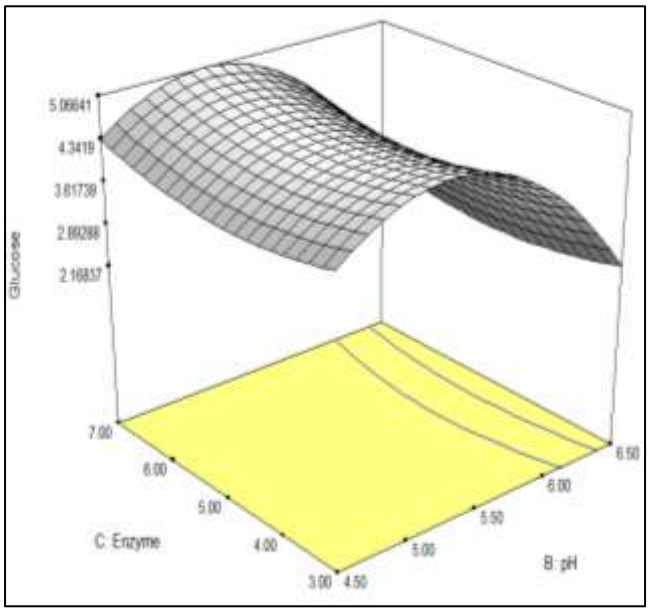


Figure 4. 3D response surface plot for interaction effects of pH versus enzyme ratio

Generally, enzymes have ionic groups on their active sites and must be in suitable environment either acid or base to function. A change of pH in the medium would lead to modification of enzyme in the ionic form of active site and its three-dimensional shape [17]. For these reasons, enzymes are only active over a certain pH range. Hence, the enzyme activity would be retarded once it is beyond the suitable pH range and thus impede the reaction rate. It was noticed that both cellulase and β-glucosidase was active at low acidic pH condition ranging from 4.5 – 5.5. The higher pH value (pH > 5.6) did not favour the enzyme hydrolysis in this study. This is a reason why the glucose content was lower at high pH condition compared to low pH circumstance. Figure 4 shows the 3D response surface plot where the glucose amount was increased from 4.5 to its optimum point 5.5 and declined with increment of pH values.

Prediction and verification of optimization conditions

Response optimizer function has provided a set of solutions that were used to predict the optimum conditions of glucose production from enzymatic saccharification of ammonia treated OPT substrate. The criteria of the variables were set accordingly as to maximize the response, i.e. glucose production. By following RSM prediction, ones could obtain the glucose at 4.958 $g.L^{-1}$ when the parameters were set to temperature, 44.23; pH 5.22 and enzyme ratio, 3:1, respectively. Moreover, the desirability value of this response is 1.00. It means when running the pre-set conditions, the experimental value should be the same as prediction. In order to ascertain the prediction, three replication runs were performed as to verify the RSM prediction. Table 4 tabulates both of the RSM prediction and experimental values for glucose production.

Table 4. Optimum conditions suggested by the RSM for glucose production

A Temperature	B pH	C Enzyme ratio	Glucose production, $g.L^{-1}$		Error, %
			RSM prediction	Experimental	
44.23	5.22	3:1	4.958	4.964 ± 0.006	0.12

In present study, the glucose concentration of 4.964 ± 0.006 $g.L^{-1}$ was obtained. Both predicted and experimental values were in closed agreement to each other with the error less than 0.2 %. Last but not least, the RSM model has successfully modelled the glucose production on ammonia pre-treated OPT substrate in present study.

Conclusion

This investigation studied three independent variables on glucose emanation from enzymatic saccharification of ammonia pre-treated OPT substrate using response surface methodology (RSM). Statistical optimization of enzyme hydrolysis for glucose production has been successfully carried out. The attained data could fit the second order equation well with an R^2 up to 90.57 %. The RSM optimization of glucose response, 4.958 $g.L^{-1}$ was achieved when the experiment was performed according to the software optimizing settings. The model suggested the best conditions when temperature, pH and enzyme ratio were set at 44.23 °C, 5.22 and 3:1, respectively.

Acknowledgement

The authors would like to thank the Faculty of Science and Biotechnology, Universiti Selangor for funding the project. Special thanks to Mr KV Lai, Concept Renewable Energy Resources Sdn. Bhd. who have provided the oil palm trunk sample for this investigation.

References

1. Chooklin, S, Kaewsichan, L. and Kaewsrichan, J. (2013). Potential Use of Oil Palm Sap on Lactic Acid Production and Product Adsorption on Dowex™ 66 Resin as Adsorbent. *Asia Pacific Journal Chemical Eng*ineering, 8(1): 23 – 31.
2. Amouzgar, P, Khalil, H. P. S. A, Salamatinia, B, Abdullah, A. Z. and Issam, A. M. (2010). Optimization of Bioresource Materials from Oil Palm Trunk Core Drying Using Microwave Radiation: A Response Surface Methodology Application. *Bioresource Technology*, 101: 8396 – 8401.
3. Yuanisa, A, Kafidul Ulum, K. and Wardani, A. K. (2015). Pretreatment of Oil Palm Trunk Lignocellulose as First Step to Produce Second Generation of Bioethanol: A Review. *Jurnal Pangan Agroindustri*, 3(4): 1620 – 1626.
4. Lai, L. W. and Idris, A. (2013). Disruption of Oil Palm Trunks and Fronds by Microwave-Alkali Pretreatment. *Bioresources*, 8(2): 2792 – 2804.
5. Sukri, S. S. M., Rahman, R. A., Illias, R. M. D. and Yaakob, H. (2014). Optimization of Alkaline Pretreatment Conditions of Oil Palm Fronds in Improving the Lignocelluloses Contents for Reducing Sugars Production. *Romanian Biotechnology Lett*er, 19(1): 9006 – 9018.
6. Binod, P, Satyanagalakshmi, K, Sindhu , R, Janu, K. U, Sukumaran, R. K. and Pandey, A. (2012). Short Duration Microwave Assisted Pretreatment Enhances the Enzymatic Saccharification and Fermentable Sugar Yield from Sugarcane Bagasse. *Renewable Energy*, 37: 109 –116.
7. Jung, Y. H, Lee, H. J, Seo, J. H, Kim, S, Seung, D, Choi, I. G, Yang, T. H, Park, Y. C. and Kim, K. H. (2012). Aqueous Ammonia Pretreatment, Saccharification, and Fermentation Evaluation of Oil Palm Fronds for Ethanol Production, *Bioprocess and Biosystems Eng*ineering, 35:1497 – 1503.
8. Wong, Y. C, Tan, Y. P, Taufiq, Y. Y. H. and Ramli, I. (2015). An Optimization Study for Transesterification of Palm Oil Using Response Surface Methodology. *Sains Malaysiana*, 44(2): 281 – 290.
9. Zhang, P. Y. H, Hong, J. and Ye, X. (2009). Cellulase Assay, In: Jonathan, R.M. (ed) Biofuels: Methods and Protocols, Methods in Molecular Biology. New York: Humana Press.

10. Bommarius, A. S, Katona, A, Cheben, S. E, Patel, A. S, Ragauskas, A. J, Knudson, K. and Pu, Y. (2008). Cellulase Kinetics as A Function of Cellulose Pretreatment. *Metabolic Engineering*, 10: 370 – 381.
11. Dawson, R. M. C, Elliot, D. C, Elliot, W. H. & Jones, K. M. (1986). Data for Biochemical Research (3rd ed.). U. K.: Oxford Science Publication.
12. Ghose, T. K. (1987). Measurement of Cellulase Activities. *Pure Applied Chem*istry, 59: 257 – 268.
13. Lai, L.W, Idris, A. and Yusof, N. M. (2014). Lignin extraction from oil palm trunk by Microwave-Alkali technique. *Malaysian Journal Fundamental Applied Science*, 10: 59 – 63.
14. Wee, L. L, Annuar, M. S. M, Ibrahim, S. and Chisti, Y. (2011). Enzyme-Mediated Production of Sugars from Sago Starch: Statistical Process Optimization. *Chemical Engineering Communications*, 198(11): 1339 – 1353.
15. Alshaibani, M, Yaakob, Alsobaai, Z. A. M. and Sahri, M. (2014). Optimization of Pd-B/γ-Al_2O_3 Catalyst Preparation for Palm Oil Hydrogenation by Response Surface Methodology (RSM). *Brazilian Journal of Chemical Engineering*, 31(1): 69 – 78.
16. Segel, I. H. (1976). Biochemical Calculations: How to Solve Mathematic Problem in General Biochemistry. USA: John Wiley and Sons.
17. Shuler, M. L. and Kargi, F. (1992). Bioprocess Engineering: Basic Concepts. New Jersey: Prentice Hall.

MALAYSIAN JOURNAL OF ANALYTICAL SCIENCES
Published by The Malaysian Analytical Sciences Society
ISSN 1394 - 2506

SPECTROSCOPIC ANALYSIS OF RHAMNOLIPID PRODUCED BY PRODUCED BY *Pseudomonas aeruginosa* UKMP14T

(Analisis Spektroskopik Ramnolipid yang Dihasilkan oleh *P. aeruginosa* UKMP14T)

Noramiza Sabturani[1], Jalifah Latif[2], Shahidan Radiman[3], Ainon Hamzah[1]*

[1]*School of Biosciences and Biotechnology*
[2]*School of Chemical Sciences and Food Technology*
[3]*School of Applied Physics*
Faculty of Science and Technology,
Universiti Kebangsaan Malaysia, 43600 UKM Bangi, Selangor, Malaysia

**Corresponding author: ainonh@gmail.com*

Received: 21 September 2015; Accepted: 20 November 2015

Abstract

Biosurfactant produced by *Pseudomonas aeruginosa* UKMP14T was optimized by growing the isolate in mineral salt medium (MSM) supplemented with 1% (v/v) glycerol and 1.3 g/L ammonium sulphate with C/N ratio of 14:1. The culture medium was incubated at 37°C, with an agitation speed of 150 rpm for 7 days. *P. aeruginosa* UKMP14T produced biosurfactant at 0.8 g/L after 7 days incubation. Anthrone assay proved biosurfactant was glycolipid. The biosurfactant was characterized by scanning electron microscope-energy dispersive X-ray spectroscopy (SEM-EDX) in addition to Fourier transform infra-red (FT-IR), nuclear magnetic resonance (NMR) and electrospray ionization-mass spectrometry (ESI-MS). The SEM-EDX analysis indicated the presence of carbon and oxygen elements by 78% and 22% (atomic %), respectively. FT-IR absorption spectra indicated the functional groups of rhamnolipid were located at 3308.46, 2922.91, 2857.09 and 1730.96 cm^{-1}. ESI-MS/MS analyses identified *P. aeruginosa* UKMP14T produced rhamnolipid with two fatty acids-nine congeners, L-rhamnosyl-L-rhamnosyl-β-hydroxydecanoyl-β-hydroxydecanoate (Rha-Rha-C_{10}-C_{10}) (*m/z* 649) which formed the main compound. The critical micelle concentration (CMC) of this rhamnolipid was established at 30 mg/L (32 dynes/cm). The characteristics of biosurfactant produced by *P. aeruginosa* UKMP14T indicated it has a high potential in industrial dan bioremediation application.

Keywords: biosurfactant, *Pseudomonas aeruginosa*, rhamnolipid, spectroscopic analysis, CMC value

Abstrak

Biosurfaktan dihasilkan oleh *Pseudomonas aeruginosa* UKMP14T dioptimumkan dalam medium garam mineral (MSM) yang ditambahkan dengan 1% (i/i) gliserol dan 1.3 g/L ammonium sulfat dengan nisbah C/N iaitu 14:1. Medium kultur ini dieram pada 37°C, dengan kelajuan goncangan pada 150 psm selama 7 hari. *P. aeruginosa* UKMP14T menghasilkan biosurfaktan sebanyak 0.8 g/L selepas 7 hari pengeraman. Asai antron membuktikan biosurfaktan terhasil adalah glikolipid. Biosurfaktan tersebut dicirikan oleh mikroskop pengimbasan elektron-spektroskopi tenaga serakan sinaran-X (SEM-EDX), dengan penambahan Infra-merah transformasi Fourier (FT-IR), resonan magnetik nuklear (NMR) daknn spektrometri jisim-pengionan elektrosemburan (ESI-MS). Analisis SEM-EDX menunjukkan kehadiran unsur karbon dan oksigen masing-masing sebanyak 78% dan 22% (% atomik). Spektrum penyerapan FT-IR menunjukkan kumpulan berfungsi ramnolipid pada 3308.46, 2922.91, 2857.09 dan 1730.96 cm^{-1}. Analisis ESI-MS/MS mengenalpasti *P. aeruginosa* UKMP14T menghasilkan ramnolipid dengan sembilan kongener-dua asid lemak, L-ramnosil-L-ramnosil-β-hidroksidekanoil-β-hidroksidekanoat (Rha-Rha-C_{10}-C_{10}) (*m/z* 649) sebagai sebatian utama. Kepekatan misel kritikal (CMC) ramnolipid ini dikesan pada 30 mg/L (32 dynes/cm). Ciri-ciri biosurfaktan yang dihasilkan oleh *P. aeruginosa* UKMP14T menunjukkan ia mempunyai potensi tinggi untuk di aplikasi dalam industri dan bioremediasi.

Kata kunci: biosurfaktan, *Pseudomonas aeruginosa*, ramnolipid, analisis spektroskopik, nilai CMC

Introduction

For decades, efforts have been made to find alternative surfactants to those chemically synthesized and as a result biosurfactants are more harmony with current trends towards global environmental awareness. There are several features that make biosurfactants commercially promising for industrial applications; their lower toxicity, higher biodegradability and effectiveness at extreme temperature, salinity and pH conditions. Their most important advantages are their ecological applicability, biodegradable and biosynthesized by a variety of microorganisms [1].

Among the different classes of biosurfactant such as glycolipids, lipopeptides, phospholipids, fatty acids, neutral lipids and polymeric compounds [2], ramnolipids members of glycolipid group, are the most extensively studied and characterized. The typical structure of rhamnolipid is determined by the number of rhamnose, fatty acids and the combination of fatty acids components. Two known major types of rhamnolipid species are L-rhamnosyl-3-hydroxyldecanoyl-3-hydroxydecanoate or mono-rhamnolipid (Rha-C_{10}-C_{10}) and L-rhamnosyl-L-rhamnosyl-3-hydroxyldecanoyl-3-hydroxydecanoate or di-rhamnolipid (Rha-Rha-C_{10}-C_{10}) [3]. Now, over 40 different ramnolipid congeners have been described and bacteria from genus *Pseudomonas* were found to be the most common producers of this compound [4].

Biosurfactant production including rhamnolipid is generally associated with the utilization of hydrocarbons by microbial community. The function of biosurfactants is often related to hydrocarbon uptake. Therefore, they are predominantly synthesized by hydrocarbon-degrading microorganisms. At low concentration, surfactant are soluble in water and with increasing concentrations, they form micelle in solution. The concentration at which micelle begins to form is called the critical micelle concentration (CMC); above the CMC, biosurfactants can solubilize hydrocarbons in soil-water system. Therefore, the biosurfactants may be useful in degradation of oil-contaminated area [5].

This study attempted to define the structures of these compounds by using a number of analytical methods such as Fourier transform infrared spectroscopy (FTIR) and mass spectrometry [6] and by utilizing SEM-EDX for the purposes of analysis. It is of interest to note SEM-EDX for the purposes of analysis had not been used in previous studies that were carried out. Therefore, the main objective of this study is to identify the rhamnolipid congeners produced by *P. aeruginosa* UKMP14T by using spectroscopic analyses including SEM-EDX and determination of CMC value of this surface active compound.

Materials and Methods

Biosurfactant-producing bacterium

P. aeruginosa UKMP14T used in this study were selected from 20 hydrocarbon-degrading bacteria for its potential in producing biosurfactant. These hydrocarbon-degrading bacteria were isolated from oil-contamined soil and water from oil refinery petroleum plants [7].

Media

The nutrient parameters such as carbon and nitrogen sources as well as the physical parameters (pH and temperature) have been optimized in a previous study [7]. The growth medium used in this study was mineral salt medium (MSM) [8] containing 0.1% (v/v) trace elements [9] and added with ammonium sulphate ($(NH_4)_2SO_4$) as a nitrogen source at 1.3 g/L with a C/N ratio of 14:1. The medium was adjusted to pH 9.0 and then autoclaved at 121°C, 15 psi for 15 minutes, cooled to room temperature (± 25°C) before added with 1% (v/v) of glycerol as a carbon source.

Production of biosurfactant

An amount of 10% (v/v) of standardized bacterial suspension of *P. aeruginosa* UKMP14T was prepared [10] and inoculated into a 250 mL conical flask containing 50 mL of MSM and added with 1% (v/v) glycerol. The culture was incubated at 37°C in an orbital shaker (Multitron, Infors HT, Switzerland) with an agitation speed of 150 rpm for 9 days. The culture medium was then centrifuged at 8022 g (RC5C Sorvall Centrifuge Instrument, USA) at 4°C

for 30 minutes. The supernatant was assayed with anthrone [11] and Bradford [12] methods for detection of sugar and protein, respectively. L-rhamnose solutions with a range of concentrations, 0.02-0.10 g/L for anthrone assay and bovine serum albumin (10-50 µg/mL) for Bradford assay were used for the standard curves. The bacterial growth was determined by spread plate method and pH was monitored using pH meter (Delta 320, Mettler-Toledo, China). Specific growth rate of this bacterial isolate was determined [13].

Scanning electron microscope – energy dispersive X-ray spectroscopy (SEM-EDX)
Samples of the culture medium for the production of biosurfactant by *P. aeruginosa* UKMP14T were taken after 4 and 7 days of incubation and centrifuged at 760 g for 10 minutes (IEC MicroCL 17 Centrifuge, Thermo Electron Corporation, Germany). The samples was then prepared [14] and viewed under SEM (LEO-SEM1450VP, UK) with integrated EDX spectroscopy (Incax-Sight, Oxford Instrument, UK).

Extraction of biosurfactant
To recover biosurfactant, cell free supernatant was subjected to an acid precipitation [15]. The supernatant was treated by acidification to pH 2.0 using 1.0 M HCl and left for four weeks at 4°C to complete the precipitation of the biosurfactant. After centrifugation at 8022 g at 4°C for 30 minutes, the precipitate was dissolved in 0.1 M $NaHCO_3$, pH 8.0, and then reacidified and recentrifuged. Later, the precipitate was extracted using chloroform-methanol (2:1, v/v). The organic phase was evaporated to remove the solvent, yielding a viscous dark-brown biosurfactant product.

Thin layer chromatography (TLC)
About 30 µL of the biosurfactant extract dissolved in chloroform was spotted onto TLC plates (silica gel 60 G Merck, USA) and developed in chloroform:hexane:methanol (5:4:1, v/v/v) as solvent system. For detection of glycolipid and protein, the plates were air dried, sprayed with anthrone and ninhydrin reagent, and heated at 100°C for 2 minutes. The appearance of yellow spots was regarded as positive for the glycolipid biosurfactant. On the other hand, red spots would be detected when protein was present in the sample.

High performance liquid chromatography (HPLC)
The extract was further partially purified by HPLC (Waters Alliance e2695 Separation Module, USA) equipped with C18-RP Waters Symmetry column and Waters 2998 Photodiode Array Detector. The mobile phase consists of aqueous solution of (A) water with 0.1% (v/v) formic acid and (B) 100% (v/v) methanol. The gradient system was used, starting with 10% to 90% B in 20 minutes and reversed from 90% to 10% in 10 minutes. The flow rate of the mobile phase was set at 1 mL/min and the sample injection volume was 50 µL. The fractions were collected with a fraction collector and then concentrated to dryness using centrifugal concentrator. After this process, spectroscopic analyses were done for the characterization of rhamnolipid congeners.

Fourier transform infra red (FT-IR) spectroscopy
The chemical bonds and functional groups present in the fractions collected from HPLC were elucidated using FT-IR spectrometry (Perkin Elmer Spectrum 400 FT-IR and spotlight 400 imaging system, USA). The spectrum was recorded at the range of 4000-650 cm^{-1}, resolution of 4 cm^{-1} with 4 times scans.

Nuclear magnetic resonance (NMR)
The extracted biosurfactant was redissolved in deuterated methanol (MeOD) and analyzed using 1D ^{1}H and ^{13}C NMR and 2D NMR experiments (Bruker/AVANCE III 600MHz cryoprobe, USA). Correlation spectroscopy (COSY), heteronuclear single quantum coherence (HSQC) and heteronuclear multiple-bond correlation spectroscopy (HMBC) were determined.

Electrospray ionization-mass spectrometry (ESI-MS and ESI-MS/MS)
The analyses were performed in Bruker MicroToF Q, USA in the negative-ion mode. The extracted biosurfactant was dissolved in methanol and introduced using direct infusion technique with a syringe pump at flow rate of 0.3 µL/min. ESI tandem mass spectra (ESI-MS/MS) were acquired by mass-selecting the target ion using a quadruple mass analyzer. The conditions of the analysis were capillary 3.0 kV and set collision cell RF 250.0 Vpp. Collision energy induced dissociation (CID) for the detection of biosurfactant was determined within the range of 10-17 eV.

CMC determination

A series concentration of extracted biosurfactant was prepared by dissolving biosurfactant in distilled water within a range of 5 to 100 mg/L. For a positive control, sodium dodecyl sulphate (SDS) (500-10 000 mg/L) was prepared. Distilled water was used as a negative control. The surface tension was measured using a tensiometer (Surface Tensiomat Model 21, Fisher Scientific, USA) [16].

Results and Discussion

Production of biosurfactant

The growth of *P. aeruginosa* UKMP14T began after 2 hours incubation and achieved exponential phase after 12-hours incubation with a specific growth rate (μ) of 0.27 h^{-1}. The stationary phase occurred after 18 hours incubation (~10^9 CFU/mL) and the number of bacteria remained constant until 9 days (Figure 1a). The surface tension (ST) of the culture medium was reduced to 52.8 dynes/cm (after 12 hours) compared to 61.8 dynes/cm at 0 hour incubation. The maximum decrease in the ST of the culture medium was 30 dynes/cm which occurred at 48 hours and it was constant until 9 days (Figure 1a). The presence of glycolipid biosurfactant of 0.017 g/L was detected within 12 hours incubation using anthrone assay. The maximum biosurfactant production was at day-7 with 0.802 g/L and reduced to 0.516 g/L after 9 days (Figure 1b). The pH of the medium decreased from pH 9.0 slowly to pH 5.0 at day-6 of incubation (Figure 1b). Protein was not detected in this biosurfactant.

The SEM-EDX analysis indicated the presence of carbon and oxygen elements in the structure of the biosurfactant based on the electron images taken from SEM after 96 and 168 hours of incubation. According to the EDX spectrum, the amount of carbon was estimated at 78% (atomic %) which is 5 times higher than the oxygen content, 22% (atomic %) (Figure 2b & c).

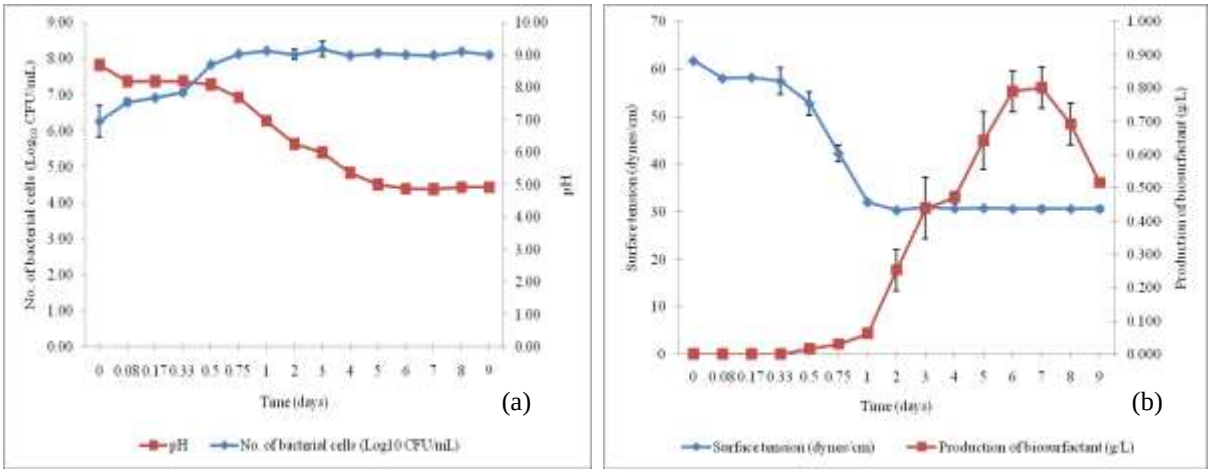


Figure 1. Production of glycolipid biosurfactant produced by *P. aeruginosa* UKMP14T when grown in MSM pH 9.0 with 1% (v/v) glycerol, 1.3 g/L of $(NH_4)_2SO_4$ with C/N ratio 14:1, temperature at 37°C, agitation speed of 150 rpm for a 9-days incubation time: (a) no. of bacteria (log_{10} CFU/mL) and pH; (b) surface tension (dynes/cm) and production of biosurfactant (g/L).

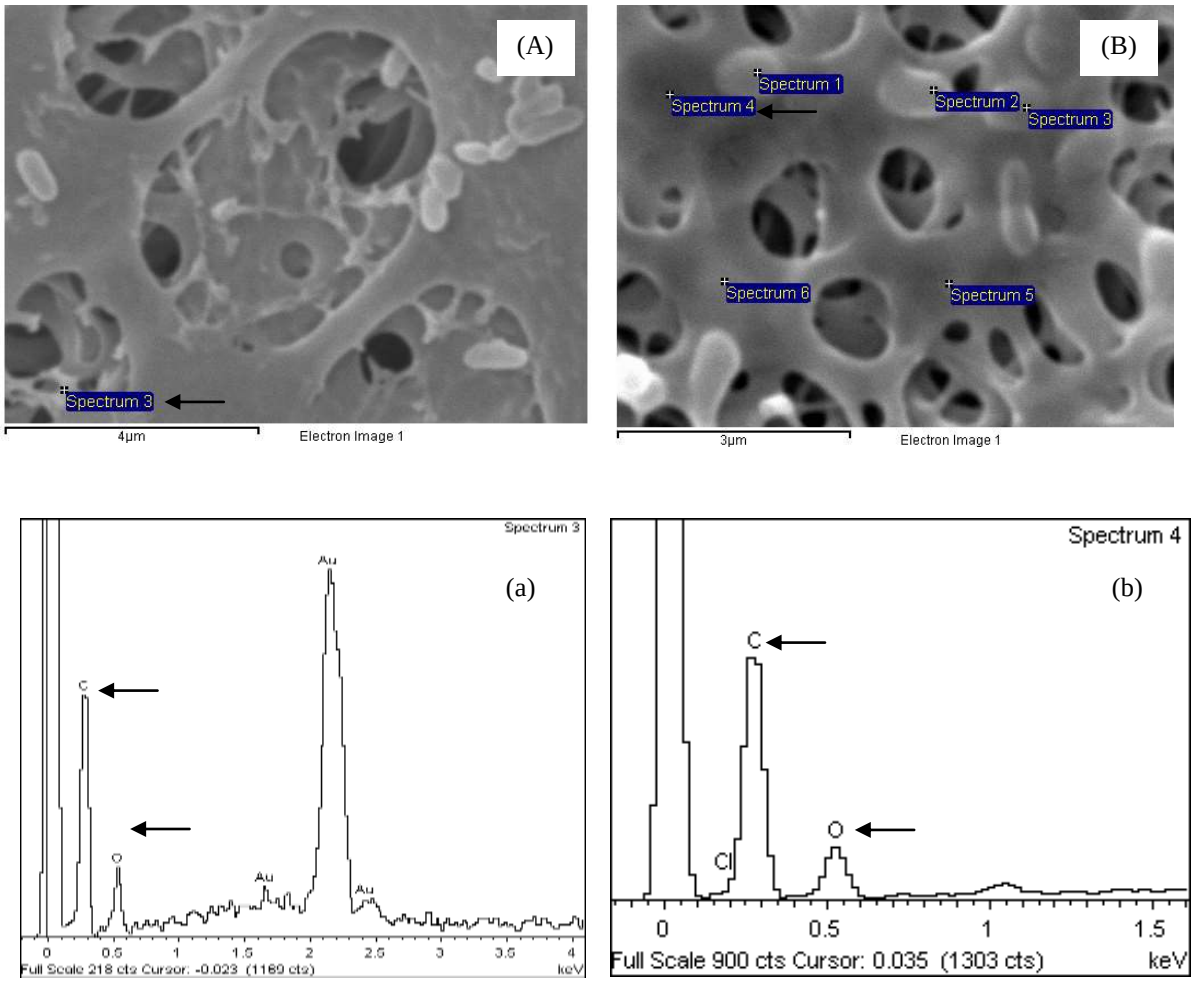


Figure 2. SEM-EDX analysis of biosurfactant produced by *P. aeruginosa* UKMP14T. Production of biosurfactant at different incubation time in optimum culture medium: A) 96 hours and B) 168 hours; EDX spectrum analysis: a) 96 hours and b) 168 hours.

The biosurfactant produced by *P. aeruginosa* UKMP14T was classified as glycolipid because of the presence of hexose sugar in the supernatant from the culture medium. In this study, anthrone assay was used for a purpose of detection. This glycolipid biosurfactant was categorized as secondary metabolite since it was produced during the stationary phase in acidic environment. The highest accumulated glycolipid biosurfactant occurred after 7 days incubation in culture medium. In this study, SEM can be utilized for high magnification imaging of the bacteria cells including the biosurfactant produced in the hydrated formed. SEM in combination with EDX, using electron images had successfully determined elements that were present in the real physical structure of biosurfactant. Moreover, through this analysis the group of biosurfactant can be distinguished by determining the atomic number of elements and their distribution. This study showed that only carbon and oxygen were present without the element of nitrogen in the biosurfactant produced. Therefore, this biosurfactant can be categorized in glycolipid group but not in lipopeptides or polymeric surfactants. The combination of these instruments (SEM-EDX) play a very important role in confirming the major elements and makes identification work easier as this will help in narrowing

the next step in the structural characterization study by providing solid preliminary data as reference. In addition, no previous work using SEM-EDX had been done before and this study was a pioneer in using these instruments for analysis.

The production of the biosurfactant by *P. aeruginosa* EM1 isolated from an oil-contaminated site was 4.9 g/L, when grown in MSM, pH 6.8 which contains 40 g/L of glycerol and 50 mM sodium nitrate ($NaNO_3$), grown at 37°C with an agitation speed of 200 rpm for 168 hours [18]. On the other hand, *P. aeruginosa* MR01 produced 2.1 g/L of biosurfactant, when grown in MSM, pH 8.0 with 1.2% (w/v) glucose and 0.1% (w/v) ($(NH_4)_2SO_4$), at 37°C with an agitation speed of 180 rpm for 48 hours [19]. Both studies showed a maximum decreased in the surface tension of the biosurfactant, about 30 mN/m, which is of the same value produced in this research. pH, agitation speed as well as C and N concentrations are major factors that effecting the microbial growth and inducing development component of protein for biosurfactant production. In addition, limitation of N nutrient (C:N ratio) is related to microbe lypogenesis. Limiting of certain nutrient in medium will accumulating intrasel lipid produced by microbe in medium. In rhamnolipid biosynthesis, the limiting step for this process is lipid formation, not carbohydrate [20, 21].

Chemical characterization of biosurfactant: TLC

Crude biosurfactant on TLC plate showing only yellow spots were detected and separated with different R_f values which 0.53, 0.36 and 0.26, respectively. Yellow spots with specific Rf values on TLC after sprayed with anthrone reagent showed the separation of the glycolipid biosurfactant from crude extract. The preliminary characterization method of TLC supported that biosurfactant produced by *P. aeruginosa* UKMP14T was a glycolipid.

HPLC

Five fractions of partially purified biosurfactant (F1, F2, F3, F4 and F5) were eluted and collected using HPLC at different elution times of 2.01, 2.27, 17.32, 21.56 and 23.01 minutes, respectively (Figure 3). The HPLC fractions were not mixed for further analysis and each fraction was analyzed individually. However, these fractions are partially purified using HPLC. Purposely to remove impurities and only mixtures of rhamnolipid congeners were collected. Each of these fractions were further analyzed individually with spectroscopic analyses such as FTIR, NMR and mass spectrometry for identification of the glycolipid biosurfactant.

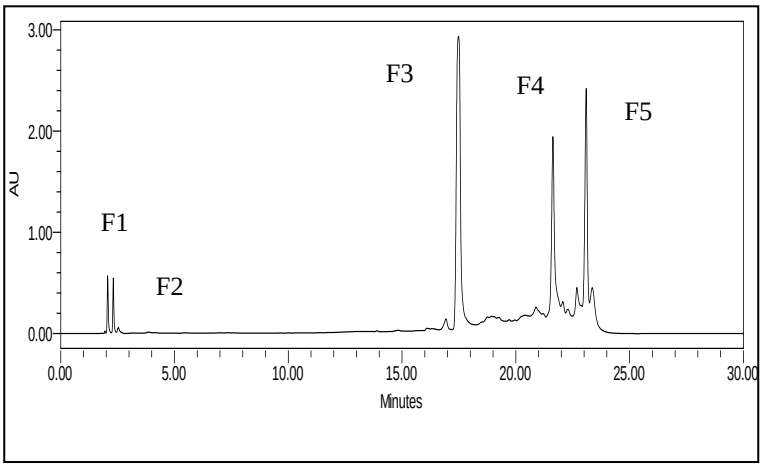


Figure 3. HPLC chromatogram of glycolipid biosurfactant produced by *P. aeruginosa* UKMP14T.

FT-IR spectrometry

Figure 4 represent FT-IR spectra from all HPLC fractions (F1, F2, F3, F4 and F5). The significance of these fractions is contained only mixtures of rhamnolipid congeners, since all the impurities were removed during separation using HPLC. FT-IR spectra of each HPLC fractions (F1-F5) indicated the functional groups of the glycolipid biosurfactant including rhamnolipid, where the important absorption spectra were located at 3308.46, 2922.91, 2857.09 and 1730.96 cm^{-1} (Figure 4). The spectra appearing at 3308.46 cm^{-1}, confirming for –OH stretching of hydroxyl group, 2922.91 and 2857.09 cm^{-1} showed the presence of –CH aliphatic stretching and $–CH_2$ methylene stretching and –C=O stretching vibrations of ester carbonyl group at 1730.96 cm^{-1}.

The FT-IR spectra revealed –OH stretching vibration for hydroxyl group, –CH aliphatic stretching, $–CH_2$ methylene stretching and ester carbonyl group (–C=O) elucidated the lipid moiety in glycolipid biosurfactant such as rhamnolipid.

This finding supported by FT-IR spectra from biosurfactant produced by *P. aeruginosa* DS10-129 (EBI accession no. AM419153) [22]. The broad spectrum appearing at 3368 cm^{-1} should be assigned to the –OH stretching vibration of hydroxyl group in the chemical structure. The strong absorption spectrum present at 2926 and 2856 cm^{-1} are expected to be the –CH stretching vibration of the hydrocarbon chain positions. Finally, the characteristic spectrum displayed at 1737 cm^{-1} confirmed the –C=O stretching vibrations of the carbonyl groups.

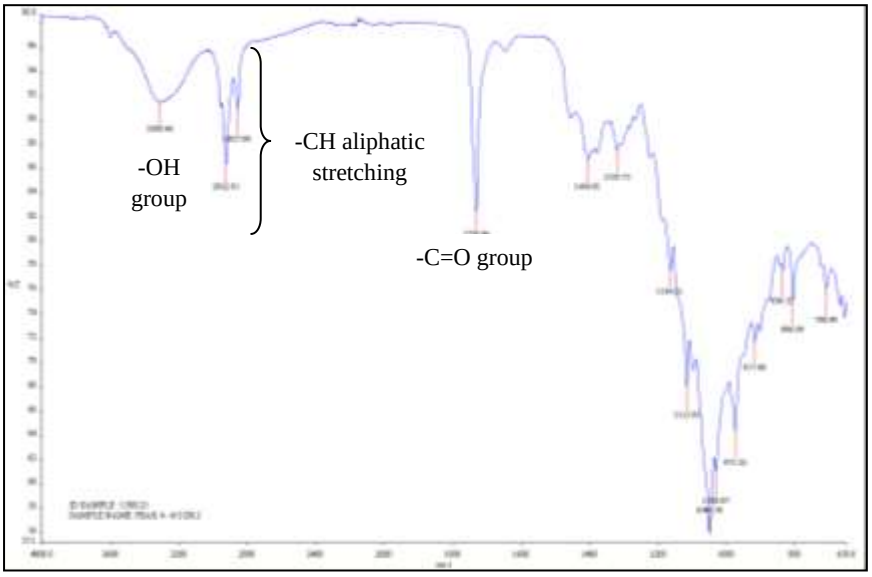


Figure 4. FT-IR spectra of HPLC fractions (F1-F5) from glycolipid biosurfactant produced by *P. aeruginosa* UKMP14T.

NMR spectrometry

The presence of di-rhamnolipid in fractions was detected by 1D ^{1}H and ^{13}C NMR analysis. The characteristics of rhamnose rings and lipid group were indicated by the appearance of the chemical shifts (δ) in the region of 0.90-4.93 ppm (Table 1) while the 2D NMR experiment, especially HMBC spectra, determined the satellites at chemical shift, δ 4.93/97.7 and 4.89/102.7 (Figure 5). Moreover, 1D and 2D NMR analyses exhibited the anomeric moiety at C1' and C1" as two rhamnose structures of di-rhamnolipid in fractions F1-F5, which is consistent with β-L-

rhamnopiranose(1'↔1)-hydroxyfatty acid and β-L-rhamnopiranose(1"→2')-β-L-rhamnopiranose linkages, respectively [23]. But in the lipid structure of rhamnolipid, long aliphatic hydrocarbon chain, as well as ester and carbonyl group, forming β-hydroxyfatty acid chain was confirmed. Since all of these fractions were partially purified, same results were obtained which is di-rhamnolipid after analysis and summarized in one table. Fraction F_2 is a set of data from other previous study as a comparison to this study.

Table 1. The ^{1}H and ^{13}C NMR data of fractions (F1-F5) and comparison with di-rhamnolipid, F_2

Moiety	Carbon	F1-F5 (δ_H, ppm[a])	F_2 (δ_H, ppm[b])	F1-F5 (δ_C, ppm[a])	F_2 (δ_C, ppm[b])
Sugar	C1'	4.93	4.746	97.7	94.9
	C2'	3.74	3.57	79.0	74.9
	C3'	3.69	3.562	68.8	68.5
	C4'	3.64	3.26	71.0	72.5
	C5'	3.70	3.59	70.9	70.5
	C6'	1.26	1.10	16.6	16.4
	C1"	4.89	4.730	102.7	102.5
	C2"	3.97	3.86	70.5	70.4
	C3"	3.63	3.4	68.7	68.1
	C4"	3.65	3.13	71.0	73.3
	C5"	3.67	3.56	70.9	70.9
	C6"	1.24	1.11	16.5	17.2
Lipid	C1	4.06	4.058	73.9	71.6
	C2	2.56	2.28	38.8	39.4
	C3	-	-	171.0	171.6
	COOH	-	-	173.4	173.8
	CH_3	0.90	-	12.9	14.0
	C4	5.26	5.24	70.9	70.8
	C5	2.57	2.38	38.8	38.9
	CH_2	1.34/1.55	1.37/1.404	22.17/31.4	22.1/34.2

[a]600 & 150 MHz (^{1}H & ^{13}C respectively), in MeOD
[b]400 & 100 MHz (^{1}H & ^{13}C respectively), in $CDCl_3$: MeOD: D_2O (1:1:1) [23]

Mass spectrometry

The characteristic of the lipid moiety in rhamnolipid congeners was identified using ESI-MS data from the HPLC fractions (F1-F5) (Table 2). The major rhamnolipid identified was L-rhamnosyl-L-ramnosyl-β-hydroxydecanoyl-β-hydroxydecanoate (Rha-Rha-C_{10}-C_{10}) (Figure 6) based on the pseudo-molecular ion peaks at *m/z* 649. In addition, eight other congeners based on the ESI-MS/MS analyses were detected. The congeners were Rha-C_{10}-C_{10} (*m/z* 503), Rha-C_8-C_{10} (*m/z* 475), Rha-C_{10}-C_8 (*m/z* 475), Rha-Rha-C_8-C_{10} (*m/z* 621), Rha-Rha-C_{10}-C_8 (*m/z* 621), Rha-Rha-C_{10}-$C_{12:1}$ (*m/z* 675), Rha-Rha-C_{10}-C_{12} (*m/z* 677) and Rha-Rha-C_{12}-C_{10} (*m/z* 677). This study revealed three mono-rhamnolipid and six di-rhamnolipid with two β-hydroxyfatty acid chains but no rhamnolipid with single β-hydroxyfatty acid chain was found. The length β-hydroxyfatty acid chain varied among minor homologues, C_8, C_{10} and C_{12} with one unsaturated $C_{12:1}$. It was noted that di-rhamnolipid congeners were the predominant congener as compared with mono-rhamnolipid congeners. Moreover, three isomeric pairs of congeners could be distinguished in this study, namely Rha-C_8-C_{10}/Rha-C_{10}-C_8, Rha-Rha-C_8-C_{10}/Rha-Rha-C_{10}-C_8 and Rha-Rha-C_{10}-C_{12}/Rha-Rha-C_{12}-C_{10}. These isomeric congeners showed that the shorter chains of β-hydroxyfatty adjacent to the sugar were found to be dominant as compared with the congeners with longer chains.

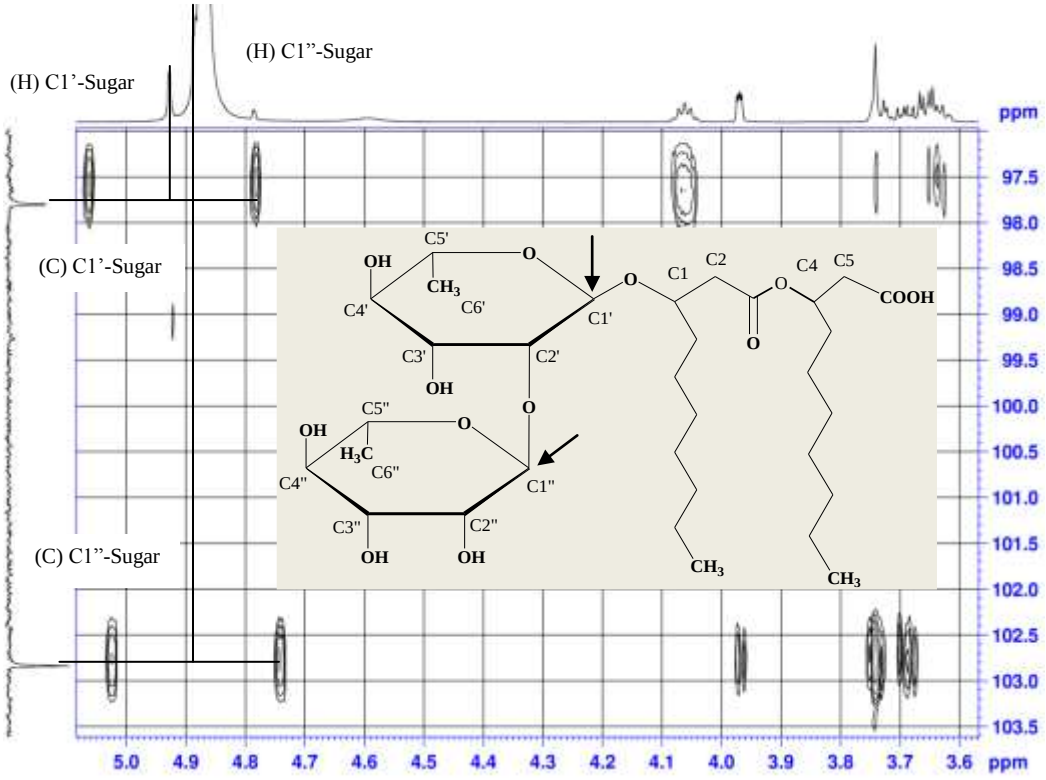


Figure 5. HMBC spectra of fractions F1-F5 (di-rhamnolipid), the glycolipid biosurfactant produced by *P. aeruginosa* UKMP14T showing the anomeric signals at δ 4.93/97.7 and 4.89/102.7 consistent with β-L-rhamnopiranose(1'↔1)-hydroxyfatty acid and β-L-rhamnopiranose(1"→2')-β-L-rhamnopiranose linkages, respectively.

Table 2. Chemical compositions with varies of fatty acids in rhamnolipid congeners produced by *P. aeruginosa* UKMP14T

Rhamnolipid congeners	**Fragmentations *m/z* (50-1000)**	**$[M-H]^-$ (*m/z*)**	**Difference between isomeric pairs $[M-H]^-$ (*m/z*)**
Rha-C_8-C_{10}	142, 163, 169, **305**, 311	475	**305** : Rha-C_8
Rha-C_{10}-C_8	141, 163, 170, **333**	475	**333** : Rha-C_{10}
Rha-C_{10}-C_{10}	163, 169, 170, 333, 339	503	
Rha-Rha- C_8-C_{10}	142, 169, 205, 311, **451**	621	**451** : Rha-Rha-C_8
Rha-Rha-C_{10}-C_8	141, 205, **479**	621	**479** : Rha-Rha-C_{10}
Rha-Rha-C_{10}-C_{10}	169, 205, 339, 479	649	
Rha-Rha-C_{10}-$C_{12:1}$	195, 205, 479, 365	675	
Rha-Rha-C_{10}-C_{12}	197, 205, **479**	677	**479** : Rha-Rha-C_{10}

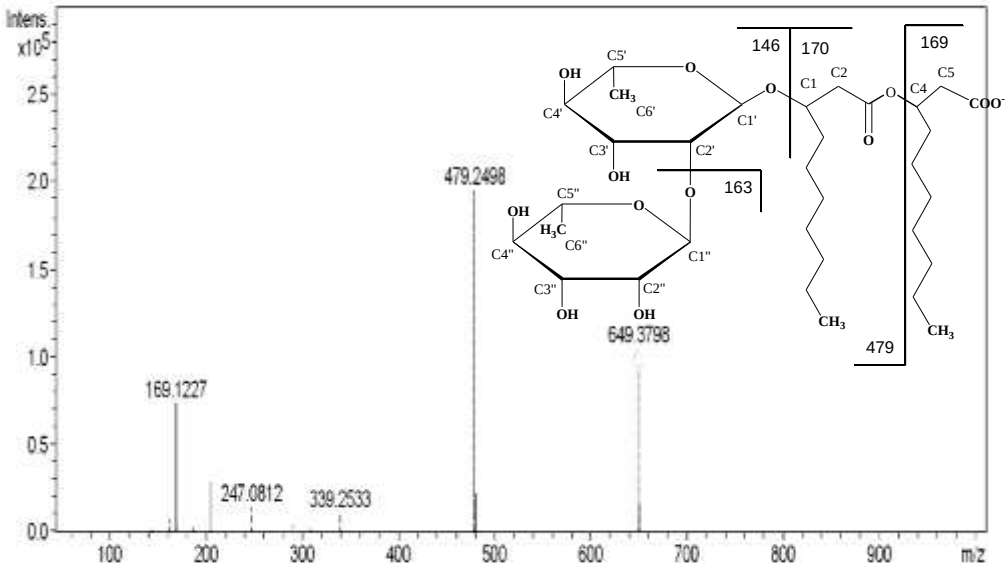


Figure 6. ESI-MS/MS spectra in negative ion mode of di-rhamnolipid (Rha-Rha-C_{10}-C_{10}) (*m/z* 649) produced by *P. aeruginosa* UKMP14T.

The length of the constituent fatty acids had been found to vary from C_8 to C_{14} and several single fatty acid-containing rhamnolipid compounds were also identified. Over 40 different rhamnolipid components had been described, all having molecular masses below 800 Da [4]. Five congeners where Rha-Rha-C_{10} act as main congener were produced by *P. aeruginosa* LBI when cultured with 3.2% (v/v) sunflower-oil refining waste as the main carbon source [24]. Whereas, *P. aeruginosa* strain MA01 produced 6 congeners, mixture of mono- dan di-rhamnolipid with ratio 1:1 when cultured with 10% (v/v) soybean oil [25].

In another study, it was reported that *P. putida* BD2, which was isolated from the Arctic soil, when grown in a medium containing 20 g/L glucose, produced only Rha-Rha-C_{10}-C_{10} [26]. The composition of the congeners is related to many parameters, the culture media composition, the culture condition as well as the age of the culture. The resulting mixture of the congeners determined the properties of the biosurfactant and even slight differences of the mixture can have great consequences on its physical-chemical properties. The presence of unsaturated bonds, the length of alkyl chain and the size of hydrophilic head group were correlated with surface-active properties of the biosurfactant. Furthermore, the presence of larger fatty acids chains plays a role in decreasing the CMC of rhamnolipid. For instance, mono-rhamnolipids are less soluble, adsorb onto surfaces more strongly and have a higher CMC value for hydrocarbon solubilization [27]. In this study, the two fatty acids-nine rhamnolipid congeners produced by *P. aeruginosa* UKMP14T were expected to have high surface active activity, thus increasing the efficacy of biosurfactant.

CMC determination

Rhamnolipid produced by *P. aeruginosa* UKMP14T was able to reduce surface tension of distilled water from 72 to 32 dynes/cm with the CMC value at 30 mg/L (Figure 7) as compared with the positive control SDS (40 dynes/cm) but at a much higher CMC value of 2000 mg/L (Figure 8).

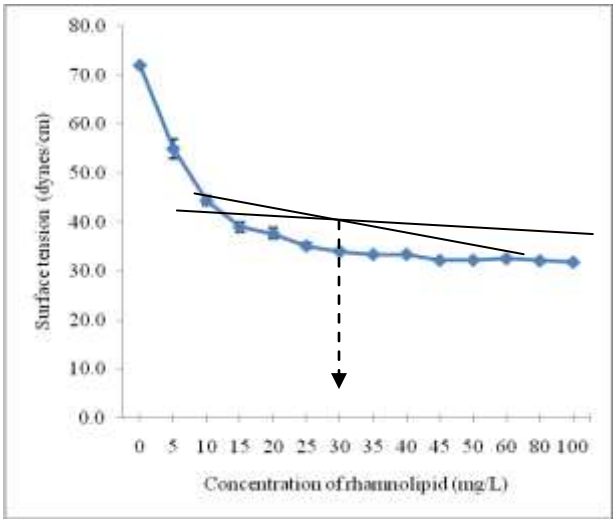


Figure 7. CMC value of rhamnolipid produced by *P. aeruginosa* UKMPT

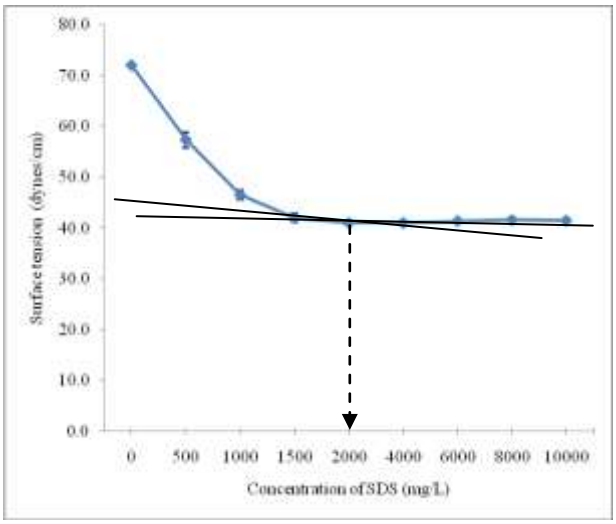


Figure 8. CMC value of sodium dodecyl sulphate (SDS)

Previous studies reported the CMC values of rhamnolipid varied based on *P. aeruginosa* strain and its culture conditions. Rhamnolipid with 13 congeners (main congener Rha-Rha-C_{10}-$C1_{2:1}$) produced by *P. aeruginosa* S6, was able to reduce ST of distilled water from 72 to 33.9 dynes/cm with CMC value 50 mg/L [28]. *P. aeruginosa* L2-1 also produced rhamnolipid with 16 congeners (Rha-Rha-C_{10}-C_{10}) with CMC value of 30 mg/L [29]. Interestingly, *P. aeruginosa* UKMP14T which produced ramnolipid with two fatty acids-nine congeners also has the same CMC value as *P. aeruginosa* L2-1, where all the congeners composed with two fatty acids. Therefore, this study put forth a suggestion that a higher amount of congeners in rhamnolipid does not necessarily lower the CMC value and that each congener present has important roles in determining the compounds surface active activities. Rhamnolipid with two fatty acids-nine congeners in this study acted as hydrophobic rhamnolipid. As a result, very low CMC value

was obtained that correlated to the higher surface activities. Moreover, determination of the CMC value is very important in the application of biosurfactant where aggregation structure of this compound will change based on this specific concentration. If it below the CMC value, the biosurfactant will exist in the form of monomers, but if it is above the CMC value, the concentration of monomers is constant and is balanced to form micelle. Micelle is a structure containing an arrangement of monomers molecule of biosurfactant by providing hydrophobic pseudo-phase inside the micelle and the hydrophilic phase outside the outer structure [30, 31]. Due to the unique characteristic of biosurfactant, it can replace the usage of synthetic surfactant in various industries including food, cosmetic, agricultural and pharmaceutical as emulsifier, stabilizer, thickener, lubricant agent, cleaner, biocontrol and anti microbial agent [32]. This study suggested the physicochemical characteristics of this rhamnolipid need to be further investigated with specific tests to determine its potential.

Conclusion

The new combination of rhamnolipid congeners produced by *P. aeruginosa* UKMP14T consist di-rhamnolipid (Rha-Rha-C_{10}-C_{10}) as main congener together with other two fatty acids-eight congeners. Spectroscopic analyses are very useful methods to elucidate structure, types of functional groups, weight and atomic percentage of different elements in the rhamnolipid. The low CMC value of this rhamnolipid indicated high surface active properties and for further study, the characteristics of physicochemical need to be determined for specification of its potential application.

Acknowledgement

Financial supports from Universiti Kebangsaan Malaysia (Grant No.: OUP-157-2012) and the National Science Fellowship (NSF) were highly acknowledged.

References

1. Benincasa, M., Marqués, A., Pinazo, A. and Manresa, A. (2010). Rhamnolipids surfactants: alternatives substrates, new strategies. In. Sen,. R. (Ed.). *Biosurfactants*, pages. 170 - 184. New York: Landes Bioscience and Springer Science+Business Media.
2. Shoeb, E., Akhlaq, F., Badar, U., Akhter, J. and Imtiaz, S. (2013). Classification and industrial applications of biosurfactants. *Part-I: Natural and Applied Sciences*, 4 (3): 243 - 252.
3. Sanket, K. G. & Yagnik, B. N. (2013). Current trend and potential for microbial biosurfactants. *Asian Journal Explore Biology Science*, 4 (1): 1-8.
4. Nie, M., Yin, X., Ren, C., Wang, Y., Xu, F. and Shen, Q. (2010). Novel rhamnolipid biosurfactants produced by polycyclic aromatic hydrocarbon-degrading bacterium *Pseudomonas aeruginosa* strain NY3. *Biotechnology Advances*, 28: 635 - 643.
5. Bordoloi, N. K. and Konwar, B. K. (2009). Bacterial biosurfactant in enhancing solubility and metabolism of petroleum hydrocarbons. *Journal of Hazardous Materials*, 170: 495 - 505.
6. Rakde, A. K., Kumbhar, A. B. and Chaudhari, P. D. (2013). Marine surfactants: A review. *Journal of Biochemical and Pharmaceutical Research*, 2 (2): 1 - 5.
7. Ainon, H., Noramiza, S. and Shahidan, R. (2013). Screening of biosurfactants produced by the hydrocarbon-degrading bacteria. *Sains Malaysiana*, 42 (5): 615 - 623.
8. Zajic, E. and Supplison, B. (1972). Emulsification and degradation of "Bunker C" fuel oil by microorganisms. *Biotechnology and Bioengineering*, 14: 331 - 343.
9. Bouchez, M., Blanchet, D. and Vandacasteele, J. P. (1995). Degradation of polycyclic aromatic hydrocarbons by pure strains and defined strain associations: inhibition phenomena and cometabolism. *Applied Microbiology Biotechnology*, 43: 156 - 164.
10. Hamzah, A., Rabu, A., Azmy, R. F. H. R. and Yussoff, N. A. (2010). Isolation and characterization of bacteria degrading Sumandak and South Angsi oils. *Sains Malaysiana*, 39 (2): 161 - 168.
11. Bailey, R.W. (1958). The reaction of pentoses with anthrone. *Biochemical Journal*, 68: 669 - 672.
12. Bradford, M. M. (1976). A rapid and sensitive method for the quantitation of microgram quantities of protein utilizing the principle of protein-dye binding. *Analytic Biochemistry*, 72: 248 - 254.
13. Chen, C.I. and Taylor, R.T. (1995). Thermophilic biodegradation of BTEX by two *Thermus* species. *Biotechnology & Bioengineering*, 48: 614 - 624.

14. Dykstra, M. J. and Reuss, L. E. (2003). *Biological Electron Microscopy, Theory, Techniques, and Troubleshooting*. Second Edition. US: Springer.
15. Zhang, Y. and Miller, R. M. (1992). Enhancement of octadecane dispersion and biodegradation by a *Pseudomonas* rhamnolipid biosurfactant. *Applied and Environmental Microbiology*, 58: 3276 - 3282.
16. Xia, W-J., Dong, H-P., Yu, L. and Yu, D-F. (2011). Comparative study of biosurfactant produced by microorganisms isolated from formation water of petroleum reservoir. *Colloids and Surfaces A: Physicochemical and Engineering Aspects*, 392: 124 - 130.
17. Lin, S-C., Sharma, M. M. and Georgiou, G. (1993). Production and deactivation of biosurfactant by *Bacillus licheniformis* JF-2. *Biotechnology Process*, 9: 138 - 145.
18. Wu, J-Y., Yeh, K-L., Lu, W-B., Lin, C-L. and Chang, J-S. (2008). Rhamnolipid production with indigenous *Pseudomonas aeruginosa* EM1 isolated from oil-contaminated site. *Bioresource Technology*, 99: 1157 - 1164.
19. Lotfabad, T. B., Shourian, M., Roostaazad, R., Najafabadi, A. R., Adelzadeh, M. R. And Noghabi, K. A. (2009). An efficient biosurfactant-producing bacterium *P. aeruginosa* MR01 isolated from oil excavation areas in South of Iran. *Colloids & Surfaces B: Biointerfaces*, 69: 183 - 193.
20. Saharan, B. S., Sahu, R. K. and Sharma, D. (2011). A review on biosurfactants: fermentation, current developments and perspectives. *Genetic Engineering and Biotechnology*, 29: 1 - 14.
21. de Sousa, J. R., Correia, J. A. d. C., de Almeida, J. G. L., Rodrigues, S., Pessoa, O. D. L., Melo, V. M. M. and Goncalves, L. R. B. (2011). Evaluation of a co-product of biodiesel production as carbon source in the production of biosurfactant by *P. aeruginosa* MSIC02. *Process Biochemistry*, 46: 1831 - 1839.
22. Mehdi, S., Dondepati, J. S. and Rahman, P. K. S. M. (2011). Influence of nitrogen and phosphorus on rhamnolipid biosurfactant production by *P. aeruginosa* DS10-129 using glycerol as carbon source. *Biotechnology*, 10 (2): 183 - 189.
23. Monteiro, S. A., Sassaki, G. L., De Souza, L. M., Meira, J. A., De Araujo, J. M., Mitchell, D. A., Ramos, L. P. And Krieger, N. (2007). Molecular and structural characterization of the biosurfactant produced by *Pseudomonas aeruginosa* DAUPE 614. *Chemistry and Physics of Lipids*, 147: 1 - 13.
24. Benincasa, M. and Accorsini, F. R. (2008). *P. aeruginosa* LBI production as a integrated process using the wastes from sunflower-oil refining as a substrate. *Bioresource Technology*, 99: 3843 - 3849.
25. Abbasi, H., Hamedi, M. M., Lotfabad, T. B., Zahiri, H. S., Sharafi, H., Masoomi, F., Moosavi-Movahedi, A. A., Ortiz, A., Amanlou, M. and Noghabi, K. A. (2012). Biosurfactant-producing bacterium, *P. aeruginosa* MA01 isolated from spoiled apples: Physicochemical & structural characteristics of isolated biosurfactant. *Journal of Biosciences & Bioengineering*, 113 (2): 211 - 219.
26. Janek, T., Lukaszewicz, M. and Krasowska, A. (2013). Identification and characterization of biosurfactants produced by the Arctic bacterium *Pseudomonas putida* BD2. *Colloids & Surfaces B: Biointerfaces*, 110: 379 - 386.
27. Pornsunthorntawee, O., Chavadej, S. and Rujiravanit. R. (2009). Solution properties and vesicle formation of rhamnolipid biosurfactants produced by *Pseudomonas aeruginosa* SP4. *Colloid and Surfaces B*, 72: 6 - 15.
28. Yin, H., Qjang, J., Jia, Y., Ye, J., Peng, H., Qin, H., Zhang, N. and He, B. (2009). Characteristics of biosurfactant produced by *Pseudomonas aeruginosa* S6 isolated from oil-containing wastewater. *Process Biochemistry*, 44: 302 - 308.
29. Costa, S.G. V. A. O, Nitschke, M., Lépine, F, Déziel, E. and Contiero, J. (2010). Structure, properties, and applications of rhamnolipids produced by *Pseudomonas aeruginosa* L2-1 from cassava wastewater. *Process Biochemistry*, 45: 1511 - 1516.
30. Mata-Sandoval, J. C., Karns, J. and Torrents, A. (2000). The influence of surfactants and biosurfactants on the bioavailability of hydrophobic organic pollutants in subsurface environments. *Review International Contamination Ambient*, 16 (4): 193 - 203.
31. Urum, K. and Pekdemir, T. (2004). Evaluation of biosurfactants for crude oil contaminated soil washing. *Chemoshere*, 57: 1139 - 1150.
32. Singh, A., Van Hamme, J.D. and Ward, O.P. (2007). Surfactants in microbiology and biotechnology: Part 2. Application aspects. *Biotechnology Advances*, 25: 99 - 121.

MALAYSIAN JOURNAL OF ANALYTICAL SCIENCES
Published by The Malaysian Analytical Sciences Society
ISSN 1394 - 2506

PRODUCTION OF RARE EARTH ELEMENTS FROM MALAYSIAN MONAZITE BY SELECTIVE PRECIPITATION

(Penghasilan Unsur Nadir Bumi daripada Mineral Monazit Menggunakan Pemendakan Terpilih)

Che Nor Aniza Che Zainul Bahri*, Wadeeah M. Al- Areqi, Amran Ab. Majid, Mohd Izzat Fahmi Mohd Ruf

Nuclear Science Program, School of Applied Physics,
Faculty of Science and Technology,
Universiti Kebangsaan Malaysia, 43600 UKM Bangi, Selangor, Malaysia

**Corresponding author: anizazainul@gmail.com*

Received: 2 November 2015; Accepted: 31 December 2015

Abstract

Rare earth elements (REEs) are very valuable and have high demands for advanced technology nowadays. REEs can be classified to light rare earth elements (LREEs) and heavy rare earth elements (HREEs). Malaysian rare earth ore especially monazite, is rich with LREEs compared to HREEs. Therefore a study was carried out to extract the REE from Malaysian monazite. The objectives of this study are to determine the content of REEs in Malaysian monazite leach solution, as well as to produce high grade of REEs. Concentrated sulphuric acid was used in digestion process and the filtrate containing the REEs was determined using Inductively Coupled Plasma- Mass Spectrometry (ICP-MS). Ammonia solution was used for REEs precipitation from monazite leach solution. The result indicated that REEs was successfully separated from monazite leach solution through selective precipitation using ammonia at pH 2.34 and the percentage of REEs that successfully separated was 70.03 – 81.85%. The percentage of REEs which successfully separated from final solution was 96.05 – 99.10%. Therefore, to have high purification of individual REEs, solvent extraction process should be carried out.

Keywords: monazite, rare earth elements (REEs), separation, selective precipitation

Abstrak

Unsur nadir bumi sangat berharga dan mempunyai permintaan yang tinggi dalam teknologi termaju masa kini. Unsur nadir bumi dapat dikelaskan kepada unsur nadir bumi ringan (LREEs) dan unsur nadir bumi berat (HREEs). Bijih nadir bumi Malaysia terutamanya monazit kaya dengan unsur nadir bumi ringan berbanding unsur nadir bumi berat. Dengan itu, satu kajian telah dilakukan untuk mengekstrak unsur nadir bumi dari monazit Malaysia. Objektif kajian ini adalah untuk menentukan kandungan unsur nadir bumi dalam larutan larut lesap monazit Malaysia serta menghasilkan unsur nadir bumi bergred tinggi. Asid sulfurik pekat telah digunakan untuk menghadamkan monazit dan hasil turasan yang mengandungi unsur nadir bumi ditentukan menggunakan ICP-MS. Larutan ammonia telah digunakan untuk memendakan torium daripada unsur nadir bumi dari larutan larut lesap monazit. Keputusan kajian mendapati unsur nadir bumi berjaya diasingkan dari larutan larut lesap monazit melalui mendakan terpilih menggunakan ammonia pada pH 2.34 dan peratus unsur nadir bumi yang berjaya diasingkan adalah antara 70.03 – 81.85%. Peratus unsur nadir bumi yang berjaya diasingkan daripada larutan akhir pula adalah 96.05 – 99.10%. Oleh itu, bagi menghasilkan unsur nadir bumi yang berketulenan tinggi maka proses pengekstrakan pelarut perlu dilakukan.

Kata kunci: monazit, unsur nadir bumi, pengasingan, pemendakan terpilih

Introduction

Rare earths elements (REEs) are series of chemical elements found in the rare earth's crust that are vital to many modern technologies including consumer electronics, computers and networks, clean energy, communication, advanced transportation, health care and many others. There are 17 elements that are considered to be rare earth elements which are 15 elements in the lanthanide series and 2 additional elements that share similar chemical properties. 15 elements in lanthanide series are Lanthanum (La), Cerium (Ce), Praseodymium (Pd), Neodymium (Nd) and Samarium (Sm) that are classified as light rare earth elements (LREEs) meanwhile Europium (Eu), Gadolinium (Gd), Terbium (Tb), Dysprosium (Dy), Holmium (Ho), Erbiumthulium (Er) and Ytterbium (Yb) are classified as heavy rare earth elements (HREEs). Another two additional elements are Scandium (Sc) and Yttrium (Y) [1].

REEs are often found together in nature at low concentrations in various minerals. About 95% of the rare earths occur in only three minerals: bastnasite, monazite, and xenotime [2]. In Malaysian, monazite and xenotime are minerals phosphates that are present as by-product of tin mining processing. Many reports cite that Malaysia has reasonably substantial amounts of REEs. In facts, Malaysia has about 30,000 tonnes of rare earths based on the finding in the residual tin deposits [3]. Monazite contains more LREEs compared to HREEs that are associated together with NORM (Thorium and Uranium) in significant concentration. Monazite concentrate commonly contains 24.0 – 29.0% of phosphate (P_2O_5), 55.0 – 60.0% rare earth metal oxides, 5.0 – 10.0% thorium oxide (ThO_2) and 0.2 - 0.4% uranium oxide (U_3O_8) [4].

Various processing routes have been developed to recover rare earths elements from minerals. After mining, ore is beneficiated by flotation, magnetic or gravity methods to produce rare earth concentrates, which then undergo hydrometallurgical processing to recover rare earth metals or compounds [5]. The chemical treatment of monazite can be carried out via the alkaline through sodium hydroxide or via the acid by means of sulphuric acid digestion. Sulphuric acid digestion is the classical method which has been used for many years by the processing industry. The monazite leach solution produced through digestion with sulphuric acid contains REEs and others elements such as Th, U as well as phosphoric acid and excess sulphuric acid. The reaction of monazite and concentrated sulphuric acid is shown by equation 1 – 3 below [4]:

$$2RE(PO_4) + 3H_2SO_4 \longrightarrow RE_2(SO_4)_3 + 2H_2PO_4 \quad (1)$$

$$ThSiO_4 + 2H_2SO_4 \longrightarrow Th(SO_4)_2 + SiO_2 + 2H_2O \quad (2)$$

$$Th_3(PO_4)_4 + 6H_2SO_4 \longrightarrow 3Th(SO_4)_2 + 4H_2PO_4 \quad (3)$$

The high commercial value of the REEs depends on their purity and the quality of the compounds. In order to separate REEs from monazite leach solution, first selective precipitate was used to remove the thorium. The most common and promising precipitation methods are acidity control using precipitating agent. Selection of precipitating agent will depend on the specific composition of monazite leach solution. Traditionally, precipitation has been viewed from a chemical equilibrium and an inorganic cation or anion removal perspective [2]. Reducing the acidity of monazite leach solution at a pH of 1, 3, and 6 can precipitate Th, REEs and U respectively [6 7]. Meanwhile study by Gupta & Krisnamurty (2005) was showed the monazite leach solution is subsequently diluted with precipitating agent for neutralization to yield precipitates containing mainly thorium at pH 1.05, rare-earth at pH 2.3 and uranium at pH 6 [5]. Davis used sodium carbonate or sodium hydroxide to partially neutralize the monazite leach solution [8]. Meanwhile ammonia hydroxide [9] or magnesia [10] could be used to partially neutralize the monazite leach solution.

Monazite concentrate can contain up to 70% of REEs [11]. An ability to separate the REEs more than 70% can produce high grade REEs. Therefore, the objectives of this study are to determine the content of REEs in monazite leach solution as well as to produce high grade of REEs.

Materials and Methods

Preparation of monazite leach solution

Monazite sample used in this study were originally from *'amang'* factory in Perak. The monazite leach solution were prepared by digesting approximately 25 g of monazite in 50 ml of 98% sulphuric acid for 3- 4 hours at 200 –

230°C on the stirring hot plate, the mixture then was cooled to room temperature. Distilled water was added to dissolve the metal sulphates, and filtered to produce a clear solution. This clear solution was called as monazite leach solution. The monazite leach solution was diluted with distilled water to 250 mL. The content of REEs in monazite leach solution was determined using ICP-MS. The ICP-MS instrument used was an ELAN 9000 (PerkinElmer SCIEX). Prior to ICP-MS analyses, standard solution was prepared using PerkinElmer Pure Plus (multi-element calibration standard 2). It is noted that 100 mL of the 250 mL monazite leach solution was taken for the REEs and thorium analysis.

Selective precipitation of REE with ammonia solution

The acidity of monazite leach solution which contains REEs, thorium and uranium was reduced at differences pH by using ammonia solution. The measurements of pH were done using EUTECH instruments pH700. 100 mL of monazite leach solution was adjusted pH around 1.08 – 1.84 with ammonia (13.4 M) and was filtered to separate thorium. The content of REEs in filtrate solution was determined via ICP-MS. The filtrate solution again was adjusted the pH 2.34 – 3.43 with ammonia (13.4 M) to precipitate the REEs. After filtration, total REEs concentrations in the REEs precipitate was determined by dissolving it in hydrochloric acid and analysed via ICP-MS and final solution was also determined for total content of elements. Separation percentage of REEs from monazite leach solution was calculated. The flowchart REEs separation from monazite was summarized as shown in Figure 1.

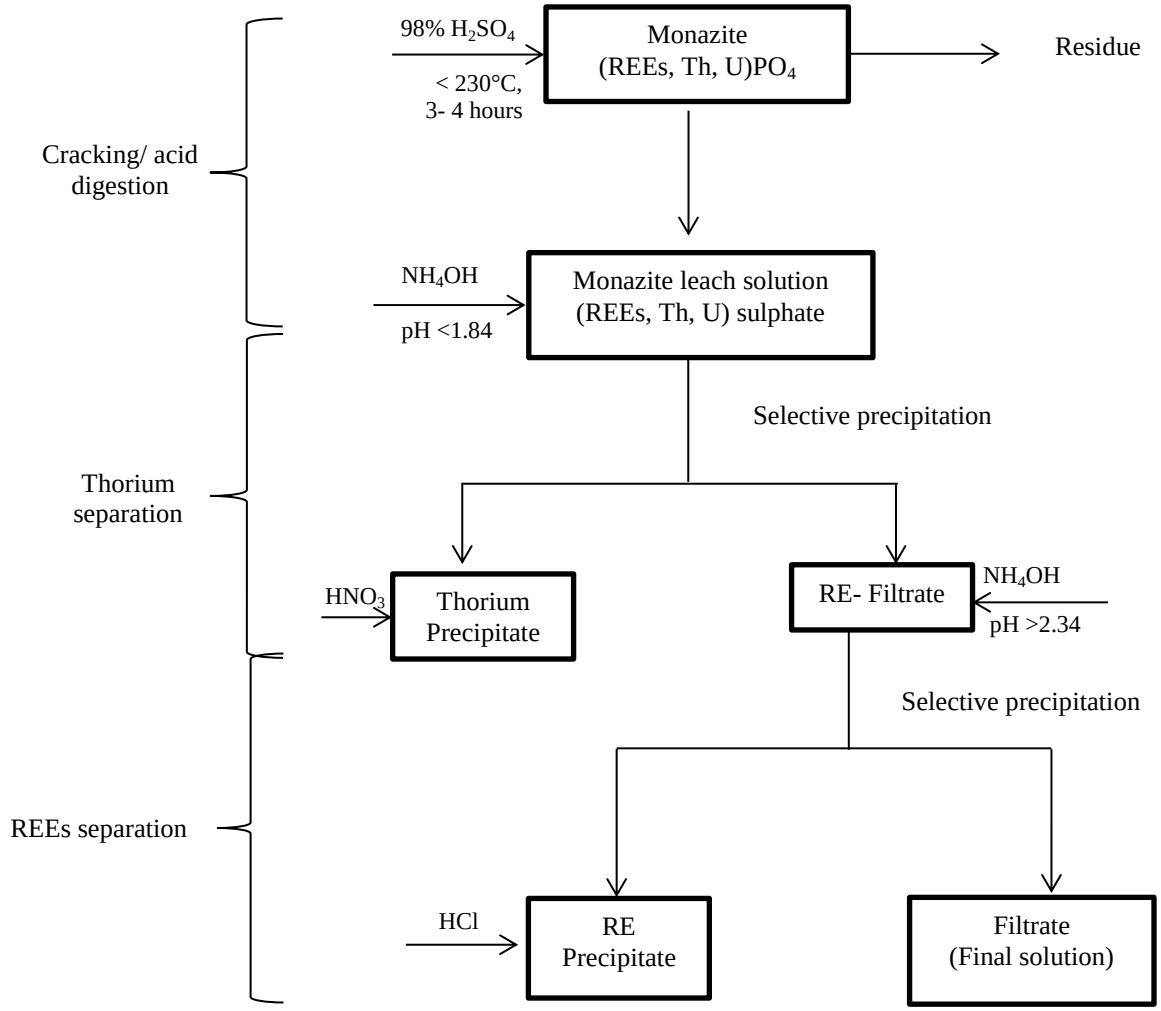


Figure 1. Simplified flowchart of REEs separation from monazite leach solution

Results and Discussion

The content of REEs in monazite leach solution

The result of REEs contained in 100 mL monazite leach solution was presented in Table 1. There are six LREEs and seven HREEs were determined by ICP-MS. The total concentration LREEs in 100 mL of monazite leach solution were Ce, La, Nd, Pr, Gd and Sm which contain 131.25, 75.87, 53.33, 14.77, 12.29 and 11.11 mg respectively. Meanwhile the HREEs determined were in range of 1.93–15.41 mg. The total content of LREEs were 298.62 mg and their amounts represent 69.17% of the total element in monazite leach solution. Monazite contains up to 70% REEs, primarily Ce and La as well as significant amount of Nd, Pr and Sm, from LREEs group [11]. The result shown clearly the content of LREEs was more abundant compared to HREEs in Malaysian monazite. Meanwhile, the monazite leach solution was prepared also contains significant amount of thorium. The presence of thorium in monazite leach solution was quite high, which is a concern in REEs separation processing. This study shown the percentage of thorium was contained in monazite leach solution more than HREEs. The percentage of thorium in 100 mL monazite leach solution determined was 19.40% compared to HREEs was 11.43%. This way was normal because the monazite mineral was considered as a source of world supply for both LREEs and thorium [12], whereas the higher content of HREEs could be found in xenotime and bastenite.

Table 1. The mean content of light rare earth elements, heavy rare earth elements and Thorium in 100mL monazite leach solution

LREEs	Total content of elements in 100 ml of leach solution (mg)	HREEs	Total content of elements in 100 ml of leach solution (mg)	NORM	Total content of elements in 100 ml of leach solution (mg)
La	75.87± 1.19	Tb	1.93 ± 0.02	Th	83.76± 1.17
Ce	131.25 ± 0.91	Dy	13.31 ± 0.10		
Pr	14.77 ± 0.26	Ho	3.07± 0.41		
Nd	53.33 ± 0.24	Er	11.14 ± 0.14		
Sm	11.11 ± 0.08	Tm	2.01 ± 0.36		
Gd	12.29 ± 0.21	Yb	15.41 ± 0.55		
		Lu	2.49 ± 0.09		
ΣLREEs	**298.62**	**ΣHREEs**	**49.36**	**ΣNORM**	**83.76**
%	**69.17**		**11.43**		**19.40**

Separation of REEs from monazite leaches solution

As mentioned above, monazite leach solution contains high concentration of thorium that should be removed first. Thorium is a radioactive element but it is valuable to use in nuclear reactor as nuclear fuel. Therefore, thorium was removed from monazite leach solution by gradually reducing the acidity until the insoluble thorium phosphate precipitated. The REEs phosphates were more soluble and remained in solution. Precipitation of thorium by ammonia solution at pH < 1.84 was done and the result was indicated in Table 2.

The result shown that an only small amount of REEs was precipitated and more than 96% of REEs left in the filtration. Kernal (1953) reported that at pH 1.6, 99% of thorium had precipitated together with only a few percent of REEs [13]. However, this study showed at pH 1.08 – 1.84 about 97.68% of thorium was precipitated with presence only 1.61- 3.08% of REEs. The total percentages of LREEs and HREEs in the filtrates are 97.33 and 97.93% respectively. It clearly showed that total percentage in rare earth filtrate for both LREEs and HREEs have no significant difference. The content of REEs in rare earth filtrate was in range 1.89 ± 0.06 - 127.58 ± 3.77 mg.

The higher content of REEs in rare earth filtrate was continued with second precipitation using ammonia solution at pH more than 2.34 and the result was shown in Table 3. The total content of LREEs and HREEs in rare earth precipitated were 230.95 and 36.21 mg respectively. From the result, the content of REEs determined in final solution very low was in range 0.04 – 2.59 mg. In comparison the total percentage of separation for LREEs and HREEs, the LREEs has shown the high total percentage separation was 98.18% whereas HREEs was 95.36%. The highest percentage separation was 99.10% of Sm while the separation of Ce which represents the major constituent of the LREEs was about 98.61%. On the other hand, for HREEs the Tb has shown high percentage of separation about 97.93%. Meanwhile, the content of thorium in final solution was 0.01 ± 0.00 mg and in percent of separation was 99.99%. Based on this result, it means almost all the thorium was successfully separated from the REEs.

Table 2. The mean content of REEs and Thorium in rich rare earth filtrate

Atomic number	**Elements**	**Total content of elements in 100 ml of leach solution (mg)**	**Total content of REEs in RE- filtrate (mg)**	**Percentage of separation (%)**
LREEs				
57	La	75.87± 1.19	74.28 ± 1.80	97.90
58	Ce	131.25 ± 0.91	127.58 ± 3.77	97.20
59	Pr	14.77 ± 0.26	14.32 ± 0.56	96.95
60	Nd	53.33 ± 0.24	51.69 ±1.41	96.92
62	Sm	11.11 ± 0.08	10.78 ± 0.37	97.03
64	Gd	12.29± 0.21	11.99 ± 0.43	97.56
	ΣLREEs	**298.62**	**290.64**	**97.33**
HREEs				
65	Tb	1.93 ± 0.02	1.89 ± 0.06	97.93
66	Dy	13.31 ± 0.10	13.02 ± 0.44	97.82
67	Ho	3.07± 0.41	3.01 ± 0.08	98.05
68	Er	11.14 ± 0.14	10.91 ± 0.28	97.94
69	Tm	2.01± 0.36	1.97 ± 0.04	98.01
70	Yb	15.41 ± 0.55	15.09 ± 0.28	97.92
71	Lu	2.49± 0.09	2.45 ± 0.06	98.39
	ΣHREEs	**49.36**	**48.34**	**97.93**
NORM				
90	Th	83.76± 1.17	1.94 ± 1.17	2.32

The percentage of individual precipitate at pH < 1.84 and pH > 2.34 was illustrated in Figure 2. It is clear that recovery of REEs at pH > 2.34 was above 70%. Meanwhile, less than 5% of REEs was precipitated at pH < 1.84. It can figure out that most of REEs was separated during ammonia precipitation and the optimum pH for REEs removal was in pH > 2.34. In addition to the effect of different pH, concentration of ammonia as a precipitant affect was affected of the separation percentage results. This study shown the percentage of REEs was successfully separated was in range 96.05 – 99.10%. Monazite can contain up to 70% REEs [11] and in this experiment was shown more than 70% of REEs was separated. It implies the high grade REEs was successfully produced via selective precipitation at selected pH value.

Table 3. The separation percentage of REEs and Thorium from monazite leach solution

Atomic number (Z)	Elements	Total content of elements in 100 ml of leach solution (mg)	Total content of Elements in RE precipitate (mg)	Total content of REEs in final solution (mg)	Percentage of Separation (%)
LREEs					
57	La	75.87± 1.19	62.10 ± 16.62	2.59 ± 0.92	96.59
58	Ce	131.25 ± 0.91	101.71 ± 18.86	1.82 ± 0.75	98.61
59	Pr	14.77 ± 0.26	10.94 ± 1.75	0.16 ± 0.06	98.92
60	Nd	53.33 ± 0.24	39.19 ± 6.50	0.54 ± 0.25	98.99
62	Sm	11.11 ± 0.08	7.78 ± 1.18	0.10 ± 0.05	99.10
64	Gd	12.29± 0.21	9.23 ± 2.33	0.22 ± 0.09	98.21
		298.62	**230.95**	**5.43**	**98.18**
HREEs					
65	Tb	1.93 ± 0.02	1.44 ± 0.37	0.04 ± 0.01	97.93
66	Dy	13.31 ± 0.10	9.68 ± 2.18	0.31 ± 0.11	97.67
67	Ho	3.07± 0.41	2.26 ± 0.55	0.09 ± 0.03	97.07
68	Er	11.14 ± 0.14	8.24 ± 2.05	0.44 ± 0.01	96.05
69	Tm	2.01± 0.36	1.50 ± 0.42	0.07 ± 0.02	96.52
70	Yb	15.41 ± 0.55	11.26 ± 2.68	0.44 ± 0.11	97.14
71	Lu	2.49± 0.09	1.83 ± 0.45	0.09 ± 0.02	96.39
		49.36	**36.21**	**2.29**	**95.36**
NORM					
90	Th	83.76± 1.17	2.49 ± 2.31	0.01 ± 0.00	99.99

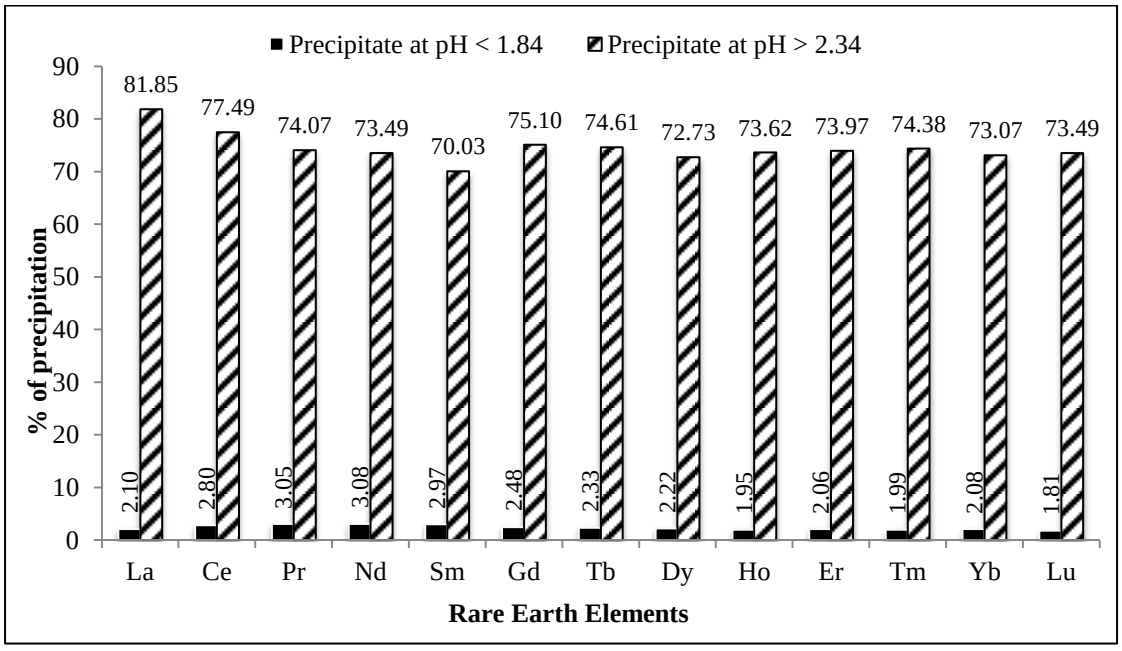


Figure 2. Percentage of individual REEs precipitated with ammonia solution at pH < 1.84 and pH > 2.34

This experiment will be continued by purification process to produce high-purity REEs. The resulting solution then will undergo further purification by solvent extraction with organic extractants in kerosene. Commercially, there are three organic extractant are chosen i.e di(2ethylhexyl)phosphoric acid (D_2EHPA), Tributylphosphate (TBP) and aliquat-336. The solvent extraction is usually used to separate individual REEs or produce mixed rare earth compounds.

Conclusion

Monazite leach solution was prepared by digesting the monazite with concentrated sulphuric acid. The content of REEs in the monazite leach solution is rich with LREEs with percentage 69.17% compared to HREEs only 11.43%. The presence of thorium in monazite leach solution was quit high. The REEs was separated from monazite leach solution through selective precipitation using ammonia at pH > 2.34 and the recovery percentage of REEs was 70.03 – 81.85%. The percentage of REEs was successfully separated from final solution was 96.05 – 99.10%. Therefore, high grade REEs can be obtained by selective precipitation from monazite leach solution. In order to have high purification of individual REEs, multistage solvent extraction should be carried out.

Acknowledgement

The authors would like to acknowledge the Ministry of High Education and Ministry of Science Technology and Innovation for the funding this work through FRGS/ 1/ 2013/ ST01/UKM/01/2 and FP0214D052-01-2.4 DSTIN respectively. Many thanks to Universiti Kebangsaan Malaysia for the support and encouragement.

References

1. Environment Protection Agency. (2012). Rare Earth Elements: A Review of production, processing, recycling and associated environmental issues.
2. Gupta C. K. and N. Krishnamurthy. (1992). Extractive metallurgy of rare earths. *International Materials Reviews* 1992, 37 (5): 197
3. Academy of Science Malaysia & The National Professors' Council. (2011). Rare Earth Industries: Moving Malaysia's Green Economy Forward. *Perpustakaan Negara Malaysia*. ISBN 978-983-9445-69-5.
4. Gupta C. K, and Mukherjee T. K. (1990). Hydrometallurgy in extraction process. *Library of Congress*, 1: 90-1561, ISBN 0-8493-6804. Printed by United States.
5. Gupta, C.K, and N. Krishnamurthy. (2005). Extraction Metallurgy of Rare Earths. *Taylor & Francis e-Library, Boca Raton, New York, Washington, DC*. ISBN 0-20367180-5.
6. Hughes, K. C. and Singh, R. (1980). The isolation of thorium from monazite by solvent extraction. *Hydrometallurgy*, 6 (1-2): 25 – 33.
7. Wickleder, M. S., Fourest, B. and Dorhout,P. K. (2010). Thorium. *The Chemistry of the Actinide and Transactinide Elements*, 1- 6 (4): 52 –160.
8. Davis, C. W. (1921). Thorium compounds from monazite sands. *U. S. Patent* 1,368,243.
9. Rollefson, A. K. and Hogeman, P. (1947). Chemistry of thorium. *Preliminary Draft PPR*. Vol. 17A. Ch. VII. *U. S. Atomic Energy Commission*, CB-3717. April 17, 1947.
10. Spencer, J. P. (1919). The metals of the rare earths. *London; Longmans, Green, and Co.*
11. Peelman, S. Sun, Z. H. I., Sietsma, J. and Yang, Y. (2014). Leaching of rare earth elements: past and present. *1st European Rare Earth Resources Conference* Milos|04-07/09/2014
12. Ahmed, S.H., Helaly, O. S., Abd El-Ghany, M. S. (2015). Evaluation of Rare Earth Double Sulphate Precipitation from Monazite Leach Solutions. *International Journal of Inorganic and Bioinorganic Chemistry*, 5(1): 1 – 8.
13. Kernal Glenn Shaw. (1953). A process for separating thorium compounds from monazite sands. *Iowa State University*. *Retrospective Theses and Dissertation.*

MALAYSIAN JOURNAL OF ANALYTICAL SCIENCES

Published by The Malaysian Analytical Sciences Society

ISSN 1394 - 2506

NEW METHYLTRIMETHOXYSILANE-(3-MERCAPTOPROPYL)-TRIMETHOXYSILANE COATED HOLLOW FIBER-SOLID PHASE MICROEXTRACTION FOR HEXANAL AND HEPTANAL ANALYSIS

(Pengekstrakan Mikro Fasa Pepejal-Gentian Berongga Tersalut Metiltrimetoksisilana-(3-merkaptopropil)trimetoksisilana Baharu bagi Analisis Heksanal dan Heptanal)

Siti Munirah Abd Wahib[1], Wan Aini Wan Ibrahim[1,2]*, Mohd Marsin Sanagi[3]

[1]Separation Science and Technology Group (SepSTec), Department of Chemistry, Faculty of Science
[2]Frontier Materials Research Alliance
[3]Ibnu Sina Institute for Scientific and Industrial Research
Universiti Teknologi Malaysia, 81310 UTM Johor Bahru, Johor, Malaysia

**Corresponding author: wanaini@kimia.fs.utm.my; waini@utm.my*

Received: 9 December 2014; Accepted: 16 October 2015

Abstract

Determination of volatile organic compounds (VOCs) in various matrices is often accomplished using solid phase microextraction (SPME) as a superior mode of extraction. Alternatively, another configuration of solid phase microextraction (SPME) namely hollow fiber-solid phase microextraction (HF-SPME) is a great approach to redress some limitations of the ordinary SPME fibers including fiber breakage, coating stripping and sample carry over. The HF-SPME technique highlights the use of hollow polypropylene (PP) membrane to hold and protect the adsorbent inside its lumen. Unlike the conventional SPME, the inexpensive HF device can be disposed after single use. Introducing extracting phase via sol-gel technology has gained great interest owing to its simple preparation method and promising way to obtain materials with good characteristics. In the present work, a new hybrid silica material based on methyltrimethoxysilane-(3-mercaptopropyl)trimethoxysilane (MTMOS-MPTMOS) was introduced as a new extractant of HF-SPME and the effectiveness of the proposed method was tested for analysis of hexanal and heptanal as the target VOC analytes. Preparation of the HF-SPME MTMOS-MPTMOS was simple in which the hybrid material was synthesized via sol-gel method and was self-polymerized in small segments of HF. Parameters affecting the efficiency of the HF-SPME MTMOS-MPTMOS in extracting both aldehydes were thoroughly investigated and analyzed by gas chromatography-flame ionization detection (GC-FID). It was found that the highest efficiency was achieved as the extraction was conducted in 30 min at a stirring rate of 1000 rpm in a 10 mL of sample solution whereby the back-extraction was performed via vortex for 3 min using 100 µL methanol as desorption solvent. Under the optimal conditions, linearity was observed over a range of 0.020-10.00 µg mL^{-1} with detection limits of 0.015 µg mL^{-1} and 0.010 µg mL^{-1} for hexanal and heptanal, respectively. The applicability of the HF-SPME MTMOS-MPTMOS for analysis of hexanal and heptanal in human urine sample was proven from the quantitative recoveries (> 90%) achieved. The HF-SPME MTMOS-MPTMOS offers an attractive alternative for rapid and convenient extraction tool and showed good potential for analysis of hexanal and heptanal from aqueous samples.

Keywords: hollow fiber-solid phase microextraction, sol-gel hybrid, methyltrimethoxysilane, (3-mercaptopropyl)tri-methoxysilane, hexanal, heptanal

Abstrak

Penentuan sebatian organik meruap (VOC) dalam pelbagai matriks sering dicapai dengan pengekstrakan mikro fasa pepejal (SPME) sebagai mod unggul pengekstrakan. Sebagai alternatif, pengekstrakan mikro fasa pepejal-gentian berongga (HF-SPME) adalah pendekatan yang baik untuk mengatasi kekangan gentian SPME biasa termasuk kerapuhan gentian, salutan tertanggal dan

baki sampel suntikan tertinggal. Teknik HF-SPME mengetengahkan penggunaan membran polipropilena (PP) berongga untuk memegang dan melindungi fasa pengekstrak dalam lumen HF. Tidak seperti konvensional SPME, alat HF yang murah boleh dibuang selepas sekali penggunaan. Menghasilkan fasa pengekstrak melalui teknologi sol-gel telah mendapat perhatian luas kerana kaedah penyediaan yang mudah dan cara yang memberangsangkan untuk menghasilkan bahan dengan ciri-ciri yang baik. Dalam kajian semasa, bahan silika hibrid baharu berdasarkan metiltrimetoksisilana-(3-merkaptopropil)trimetoksisilana (MTMOS-MPTMOS) telah diperkenalkan sebagai bahan penjerap baharu HF-SPME dan keberkesanan kaedah yang dicadangkan telah diuji terhadap analisis heksanal dan heptanal sebagai analit VOC sasaran. Penyediaan HF-SPME MTMOS-MPTMOS adalah mudah yang mana bahan hibrid ini telah disintesis menggunakan kaedah sol-gel dan telah diswapolimer di dalam segmen kecil HF. Parameter yang mempengaruhi kecekapan HF-SPME MTMOS-MPTMOS dalam mengekstrak kedua-dua aldehid telah dikaji dengan teliti dan dianalisis menggunakan kromatografi gas-pengesan pengionan nyala (GC-FID). Kecekapan tertinggi telah dicapai apabila pengekstrakan dijalankan selama 30 min pada kadar kacauan 1000 rpm di dalam 10 mL larutan sampel yang mana pengekstrakan-kembali dilakukan melalui vorteks selama 3 min menggunakan 100 µL metanol sebagai pelarut penyahjerapan. Pada keadaan optimum, julat linear ialah 0.020-10.00 µg mL^{-1} dengan had pengesanan bagi heksanal dan heptanal masing-masing ialah 0.015 µg mL^{-1} and 0.010 µg mL^{-1}. Kesesuaian HF-SPME MTMOS-MPTMOS untuk analisis heksanal dan heptanal dalam sampel air kencing manusia terbukti dengan perolehan kuantitatif yang dicapai (> 90%). HF-SPME MTMOS-MPTMOS menawarkan alternatif menarik sebagai alat pengekstrakan yang cepat dan mudah serta menunjukkan potensi yang baik untuk analisis heksanal dan heptanal daripada sampel akueus.

Kata kunci: pengekstrakan mikro fasa pepejal-gentian berongga, hibrid sol-gel, metiltrimetoksisilana, (3-merkaptopropil)-trimetoksisilana, heksanal, heptanal

Introduction

Aldehydes are common carbonyl compounds that take part in the pathology of certain diseases and their presence have been suggested as degradation products of lipid peroxidation [1, 2]. Besides, aldehydes were predominately VOCs biomarker found at elevated concentrations level in lung cancer subjects. In particular, hexanal and heptanal have been extensively studied as potential lung cancer biomarkers that can be measured in different biological samples [3 – 6]. The accurate determination of volatile compounds in biological samples is a major constraint due to the presence of overwhelming matrix effects and the analyte concentration might be too low to be analysed directly. Thus, searching for a reliable extraction technique is of vital importance. The prevalent extraction method employed to analyze aldehydes is solid phase microextraction (SPME) [2 – 6]. Specifically, carboxen/ polydimethylsiloxane (CAR/PDMS) [3] and polydimethylsiloxane/divinylbenzene (PDMS/DVB) [4 – 6] are two well-known SPME fibers that were used for the determination of aldehydes. SPME is a rapid and simple technique. Extraction, preconcentration and sampling can be carried out as a single step. However, SPME has certain limitations such as commercially available fibers are not chemically stable due to mere physical deposition or partial cross linking of the polymer coating. In addition, the ordinary SPME fibers suffer from low recommended operating temperature, fragile, limited lifetime and is expensive [7, 8]. Other than ordinary SPME fiber, several methods were developed for analysis of hexanal and heptanal in biofluids [9 – 11]. However, the proposed techniques involved complicated preparation material or extraction procedure. This is time consuming as it adds extra step in the sample preparation steps.

Sol-gel technology offers the simplest way to obtain adsorbent with good characteristic for extraction purpose. Various adsorbents were synthesized by sol-gel method including the combination of sol-gel precursors with other different coating materials to enhance the properties of extracting phase [12 – 16]. Some inherent advantages of sol-gel process that can redress the limitations of commercial SPME are; porous structure material with high surface areas for better analytes adsorption, coating is stable towards high temperature, good adhesion towards fiber as support owing to chemical bonding [17 – 19]. However, there are still several factors impeding the use of SPME fiber including troublesome in pre- and post-gelation treatment, long conditioning time needed before first use, and sample carryover during analysis. Emerging of different configurations of solid-based extraction is a promising solution and alternative to the above-mentioned problem.

Recently, Es'haghi et al. [20, 21] has come out with a new SPME approach namely hollow fiber-solid phase microextraction (HF-SPME). Instead of using a fiber, small segments of polypropylene HF were used for coating purpose. The possible memory effect can be avoided by discarding the HF tool after single use. Besides, the use of porous polypropylene enables to eliminate matrix interferences by prohibiting the larger molecules enter/adsorb

onto the coated material, thus, promotes clean extraction. HF-SPME technique was successfully applied for the determination of different types of compounds including phenobarbital [21] organophosphorus pesticides [22, 23] selected aflatoxins [20], diclofenac and piroxicam [24], diethylstilbestrol [25], metronidazole [26] and heavy metals [27]. Introducing HF-SPME extracting phase via sol-gel method is a good approach since the HF can act as a medium to hold the sol-gel material and in the same time, simple preparation of sol-gel material can be accomplished by in-situ gelation process of sol solution in the lumen of HF. To the best of our knowledge, no development of sol-gel hybrid materials for use as adsorbent material has been reported for the determination of hexanal and heptanal, particularly for HF-SPME. Therefore, in the present work, the sol-gel material based on methyltrimethoxysilane-(3-mercaptopropyl)trimethoxysilane (MTMOS-MPTMOS) is proposed to be employed as the main extractant of HF-SPME for the determination of hexanal and heptanal in aqueous samples.

Materials and Methods

Standards and Chemicals

Methyltrimethoxysilane (MTMOS), (3-mercaptopropyl)trimethoxysilane (MPTMOS), trifluoroacetic acid (95%) and polymethylhydroxysiloxane (PMHS) were obtained from Aldrich (St. Louis, MO, USA). HPLC grade methanol was purchased from Fisher Scientific (Leicestershire, UK) and deionized water was produced from a Millipore water purification system (Molsheim, France). Accurel Q3/2 polypropylene tubular membranes from Membrana (Wuppertal, Germany) with a wall thickness of 200 µm, pore size of 0.2 µm, and an ID of 600 µm were used for the HF-SPME device. Hexanal and heptanal were purchased from Merck Schuchardt (Hohenbrunn, Germany). Individual stock solution (1000 µg/mL) of hexanal and heptanal was prepared by dissolving the calculated amounts in HPLC grade methanol and fresh working solutions were prepared in methanol daily by further dilution of the stock solution.

Instrumentation

A 7820A Agilent GC from Agilent Technologies (Waldbronn, Germany) equipped with a HP-5 (5% phenyl methyl siloxane) column (30 m × 0.32 mm ID and 0.23 µm film thickness), a split/splitless injector and flame ionization detector (FID) was used for analysis of extracted hexanal and heptanal. Helium was used as the carrier gas at a flow rate of 1 mL/min. The flow rate of air as oxidant was set at 400 mL/min while the flow rate of hydrogen was set at 30 mL/min. All gaseous sources were supplied from Linde Malaysia (Kuala Lumpur, Malaysia). The oven temperature program was as follows: initial temperature of 50 °C, ramp to 80 °C at a rate of 10 °C/min, then to 180 °C at a rate of 40 °C/min to obtain a run time of 5.5 min. The inlet temperature used was 250 °C and the FID temperature was set at 280 °C.

The sol-gel MTMOS-MPTMOS was characterized using a Perkin Elmer FT-IR Spectrometer (Shelton, USA) in the region 650-4000 cm^{-1} via attenuated total reflectance (ATR) method. The images of the HF-SPME MTMOS-MPTMOS was captured with a Hitachi S3400N scanning electron microscopy (SEM) (Tokyo, Japan) using back-scattered electrons (BSE) mode at an accelerating voltage of 15 kV and low vacuum of 30 Pa.

HF membrane preparation

The polypropylene (PP) HF membrane was cut into ~ 2.5 cm segments and cleaned with acetone. It was then air dried before being injected with 6 µL of the prepared sol solution [22]. Both sides of the HF devices were heat-sealed before used. The sol solution was prepared by mixing appropriate volumes (µL) of precursors (MTMOS and MPTMOS), water, TFA (95%) as acid-catalyst, methanol (MeOH) as solvent and polymethylhydroxysiloxane (PMHS) in a 2 mL centrifuge tube to produce the desired mol ratios. The mixtures were vortexed for 2 min followed by centrifugation at 15 965 × *g* for 5 min. Then the homogenous solutions were directly injected into the lumen of the HF to allow for in-situ gelation. To ensure that the sol solidified in the HF, it was left at ambient temperature for overnight. The HF-SPME devices were then kept in an oven at 100°C for further drying before use.

HF-SPME Procedure

Typical HF-SPME extraction was performed using direct immersion mode in a sample vial containing 10 mL of deionised water spiked with an appropriate volume of a working standard hexanal and heptanal solution to obtain a final concentration of 10.0 µg/mL. To achieve the highest extraction efficiency, systematic studies were performed in triplicate for the optimization of several parameters including extraction time (15 - 70 min), sample volume (3 -

20 mL), sample stirring rate (450 – 1000 rpm) and salt addition (0 – 2.0%, w/v). After extraction, the PP HF membrane tool was transferred into a 2 mL vial containing an appropriate volume of suitable organic solvent (methanol, MeOH) prior to desorption process. For back-extraction, vortex-assisted method was selected to desorb the extracted analytes for 3 min. Parameters affecting desorption process including desorption solvent volume (80 – 500 µL) and vortex speed (15.8 – 86.4 × *g*) were also studied.

Preparation of real samples

The urine samples were obtained from healthy volunteers and stored at -2°C. An aliquot of the human urine samples was spiked with an appropriate amount of hexanal and heptanal. The urine samples were then diluted two times with deionised water and filtration through a 0.20 µm membrane filter prior to extraction. The same extraction procedure was applied for the spiked human urine and blank human urine sample (without spiking), similar to above-mentioned HF-SPME procedure.

Method Validation

The analytical performance of HF-SPME MTMOS-MPTMOS was validated in terms of repeatability, linearity, limit of detection (LOD) and limit of quantification (LOQ) using the optimized extraction conditions. The within batch and inter-batch precision were evaluated based on relative standard deviation in which the repeatability of extraction was calculated using 4 replicates. Linearity was obtained from the construction of calibration curve from 0.020 - 10.0 µg mL^{-1}. The LOD was determined at signal-to-noise ratio (S/N = 3) whilst the LOQ was determined at signal-to-noise ratio (S/N = 10). Accuracy (recovery) of the proposed HF-SPME MTMOS-MPTMOS method was assessed by spiking 1.0 and 0.25 µg mL^{-1} of hexanal and heptanal in human urine sample.

Results and Discussion

Preliminary Study

In order to assess the potential and effectiveness of the proposed sol-gel silica-based hybrid material in extracting hexanal and heptanal, effect of sol-gel process such as precursor, water, solvent and acid catalyst were optimized. Selection of optimal sol-gel synthesis was based on extraction efficiencies (measured by peak area response) obtained from GC-FID.

Effect of precursor

Precursors are the backbones of sol-gel polymer and synthesis of extracting phase using only precursors is much easier, faster, cheaper and more controllable as compared to addition of coating polymer [28]. In this study, the extracting phase was synthesized based on two precursors; MTMOS and MPTMOS. MTMOS is a good selection of precursor as the sol-gel network originating from an alkyl derivative of a tetraalkoxysilane precursor possesses a more open structure which can minimize cracking and shrinkage problems during drying step [29]. Meanwhile, the addition of MPTMOS that possess thiol (-SH) moiety can alter the polarity of the sol-gel hybrid formed thus enhance the possibility to extract the two mid-polar hexanal and heptanal more effectively.

Initially, the MTMOS amount was kept constant at 1 mmol whereas the addition of MPTMOS was evaluated at different mol ratios (1 – 7 mmol). Trifluoroacetic acid (TFA) as acid catalyst and methanol (MeOH) as solvent were fixed at a 2.5 and 6.0 mmol, respectively. PMHS as a deactivation agent (25 µL) was added to each sol solutions. As the mol ratios of MTMOS: MPTMOS was increased gradually from 1:1 to 1:4, better peak area response of hexanal and heptanal was obtained. However, further increase of MPTMOS from 5 mmol to 7 mmol resulted in a decrease of extraction performance for the two aldehydes. At higher mol of MPTMOS, the increase number of thiol moieties possibly led to covalent formation of disulphide (-S-S) [30]. This behavior decreased the number density of the bridging oxygen -Si-O-Si- as the network backbone thus alter the features of the sol-gel material in which the coated HF-SPME was easily ruptured. Therefore, the mol ratio 1:4 MTMOS: MPTMOS was selected as the optimum sol-gel composition and was used for further study.

Effect of water

Water is needed in sol-gel process to hydrolyze the precursors to form the reactive species for condensation reaction that leading to the formation of 3-D network [31]. In the present work, the sol-gel based on 1:4 mol ratio MTMOS: MPTMOS materials were prepared using different mol ratios of water from 3 mmol to 9 mmol, keeping the other

amount constant (6 mmol MeOH, 2.5 mmol TFA). Addition of 3 mmol water in sol solution resulted in the lowest extraction efficiency of hexanal and heptanal. It is possible that in the presence of small amount of water content in sol system, both precursors (MTMOS and MPTMOS) compete with each other to be hydrolyzed and only partial of the precursors enable to form reactive species for further reaction process. As the water content was increased from 3 mmol to 6 mmol, increasing in peak areas response were observed for hexanal and heptanal. Based on stoichiometric calculation, both MTMOS and MPTMOS have three methoxy groups each that can be hydrolyzed. This is parallel with the results obtained as the addition of 6 mmol of water in the sol system gave the highest peak area response. Further increase of water content from 7 to 9 mmol resulted in a reduction of extraction performance of the sol-gel hybrid material. It seems that the addition of higher volume of water content may not be necessary as water is also eliminated during the condensation process to produce the 3-D networks. In short, 6 mmol was selected as the optimum amount of water and was used for further investigation on sol-gel synthesis optimization.

Effect of acid catalyst

Catalyst plays a role in hydrolysis part of sol-gel process in which under acidic condition, the sol solution will undergo polymerization to form long, linear and poorly cross-linking material which is suitable for coating purpose or thin film end-product [32]. TFA, commonly used as acid catalyst, was adopted in this study. TFA is favourable since the organic acid could disperse in the organic matrix more evenly as compared to inorganic acid and enable to minimize crack formation as reported by Chen and co-workers [33]. The different mol of TFA varied from 1 mmol to 3.5 mmol were mixed in the sol solution consisting of 1 mmol MTMOS, 4 mmol MPTMOS, 6 mmol water and 6 mmol MeOH. According to the peak areas obtained (data not shown), using 2.5 mmol TFA (95%) gave the highest extraction efficiency, hence, was selected as the optimum acid mol in sol-gel MTMOS-MPTMOS.

Effect of solvent

Solvent is added in sol system to facilitate mixing of sol-gel precursors, water and deactivating reagents into a homogenous system [34]. In the current work, MeOH was used as the sol-gel solvent system and the effect of the solvent was investigated from 4-9 mmol. Higher peak areas of hexanal and heptanal were observed as MeOH was increased from 4 mmol to 7 mmol in sol solution. The apparent increase in signals is due to the increase amount of solvent which will favor more precursors to be solvated, hence increase the reaction rates of polymerization. However, addition of higher volumes of solvent (8 mmol and 9 mmol) caused a reduction in peak area performance for both hexanal and heptanal. This behavior is probably due to the excess amount of solvent which will dilute the sol solution and thus reduce the precursor concentration [31]. Thus, 7 mmol MeOH was selected as the optimum solvent to be added in the sol solution.

In brief, the optimum sol-gel MTMOS-MPTMOS in extracting the two aldehydes was 1 mmol MTMOS, 4 mmol MPTMOS, 6 mmol H_2O, 7 mmol MeOH, 2.5 mmol TFA (95%) and PMHS was added at a constant volume (25 µL) in the sol solutions. The optimization of sol-gel synthesis become more convenient and faster as the preparation of sol solution involved merely one-pot reaction at mild condition including vortex and centrifugation procedure before directly injected into the lumen of HF (the whole process takes ~10 min). Likewise, sol-gel hybrid is simply self-polymerized after left overnight and no troublesome post-gelation procedure is needed. SEM image of HF-SPME MTMOS-MPTMOS device is shown in Figure 1. It can be seen a thin layer coating surrounded the inner wall of hollow fiber with estimated thickness of 30 µm. Meanwhile, the small insert image indicates the sol-gel coating possesses a porous surface in which the pores are evenly distributed with average pore size of ~0.7 µm.

FTIR Characterization

To prove the existence of inorganic-organic networks in the synthesized material, the material was characterized using FTIR. The absorption bands of sol-gel hybrid MTMOS-MPTMOS spectrum are nearly identical to both spectra of MTMOS and MPTMOS precursors (Figure 2). The broad absorption band at wave number 3397.14 cm^{-1} corresponds to -OH stretching mode. This is possibly due to the presence of water or methanol in the sol-gel material. CH-stretching mode can be observed at wave number 2930.41 cm^{-1} but at lower intensity as compared to precursor's spectra. A very weak absorption band at 2556.02 cm^{-1} is due to the existence of thiol (-SH) functional group in the sol-gel hybrid. Even though the intensity is very low, it is similar to the absorption of pure MPTMOS precursor. Two wave numbers at 1000.15 cm^{-1} and 1091.13 cm^{-1} correspond to Si-O-Si absorption. The presence of the two bands with broader absorption at 1000.15 cm^{-1} and 1091.13 cm^{-1} as compared to spectra of MTMOS and

MPTMOS precursor indicates that siloxane chains become longer or branched, hence proved the successful polymerization of alkoxides to form Si-O-Si network.

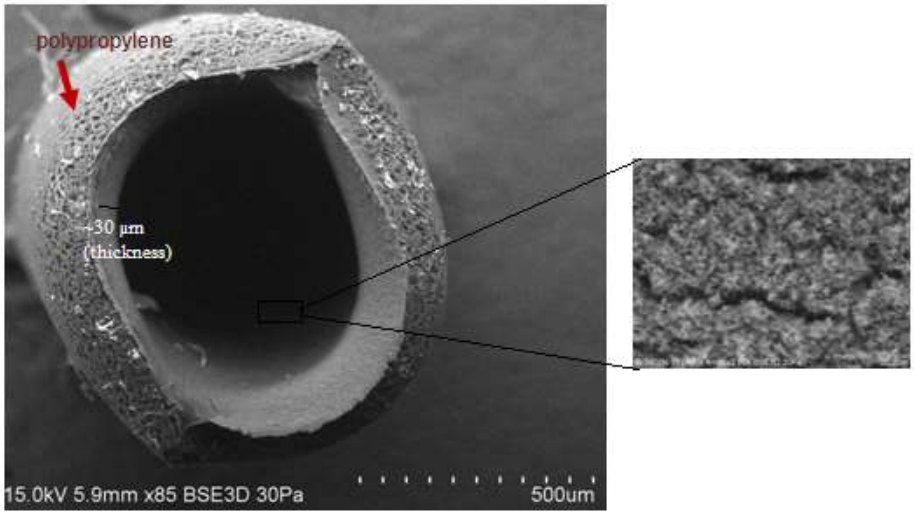


Figure 1. SEM images of sol-gel hybrid MTMOS-MPTMOS HF-SPME at × 85 magnification

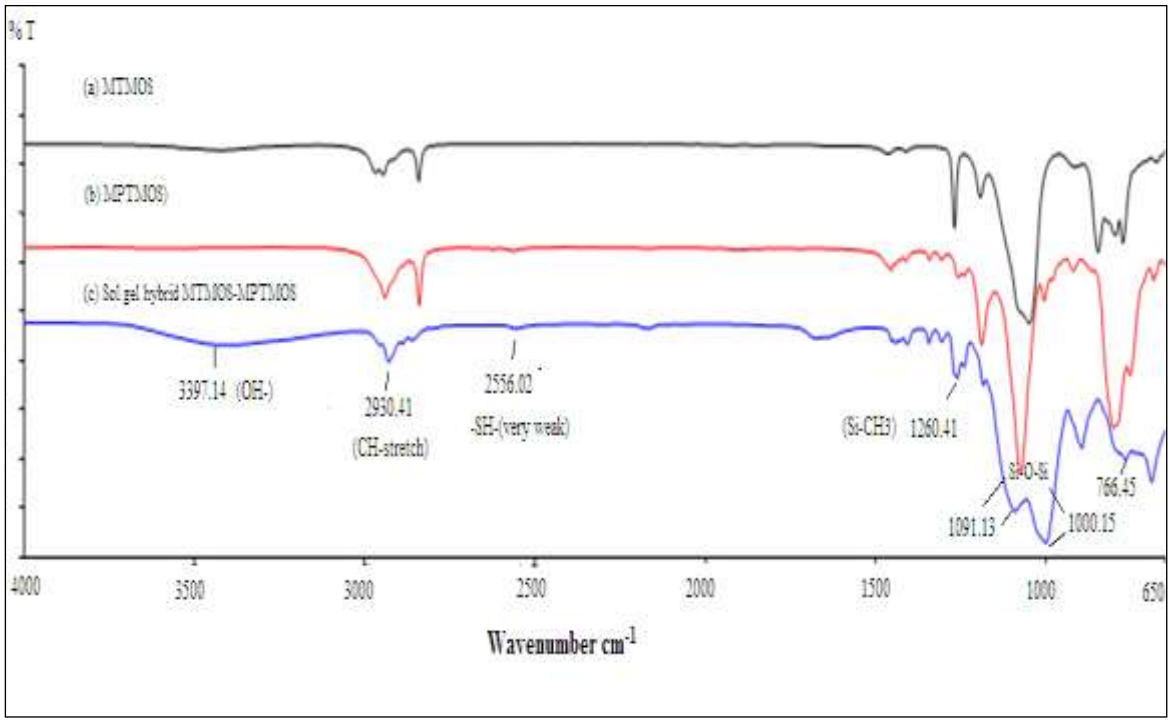


Figure 2. FTIR spectra of (a) MTMOS, (b) MPTMOS and (c) sol-gel hybrid of MTMOS-MPTMOS

Optimization of HF-SPME Performance

To obtain the highest extraction efficiency in extracting the two target aldehydes in aqueous samples, several parameters affecting the HF-SPME MTMOS-MPTMOS extraction performance were evaluated and optimized.

Selection of desorption method

Two desorption methods namely ultrasonication and vortex were used to back-extract the two analytes of interest. It was found that 20 min was the optimum desorption time using ultrasonication technique. In contrast, comparable peak efficiency for both aldehydes was obtained when desorption was performed via vortex for 3 min. As shorter analysis time is more practical, desorption via vortex for 3 min was selected for subsequent study.

Effect of extraction time

HF-SPME technique is based on an equilibrium process in which mass transfer is time-dependent. Thus, extraction time is a crucial factor to be optimized as the solute molecules need sufficient time to transfer from sample solution to HF interface and adsorbed onto the sol-gel material [21, 22]. In this work, different extraction times ranging from 15 min to 70 min were evaluated at ambient temperature and other extraction parameters were kept constant at a stirring rate of 600 rpm and sample volume of 10 mL while back-extraction was performed via vortex-assisted for 3 min using 100 µL MeOH (Figure 3). The selectivity of the fibre was found to be significantly higher for heptanal compared to hexanal. The extraction efficiency of hexanal and heptanal increased up to 30 min and no apparent signal differences was observed when extraction was increased from 40-70 min. Thus, 30 min was chosen as the optimum extraction time and was used for further study.

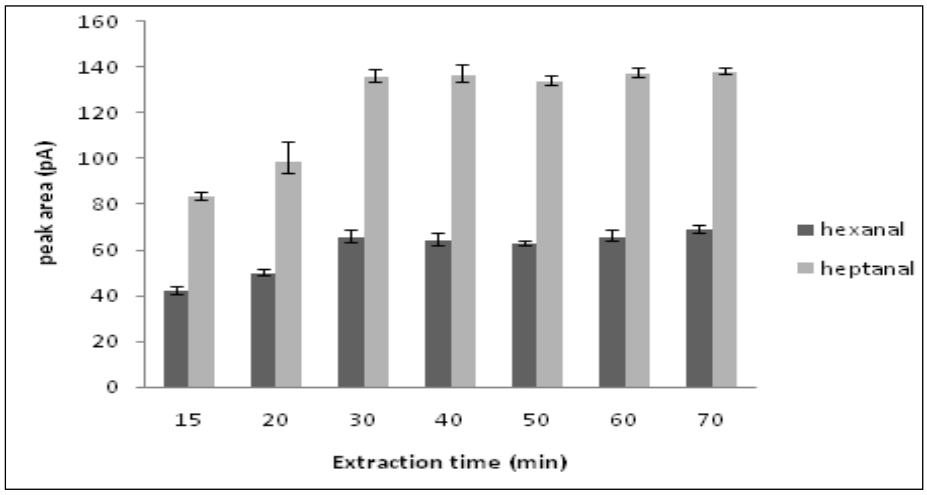


Figure 3. Effect of extraction time on the HF-SPME extraction efficiency (based on peak area). Extraction conditions: sample volume, 10 mL; stirring rate, 600 rpm. Desorption conditions: desorption solvent, MeOH; vortex assistance desorption for 3 min; vortex speed, 44.1 × *g*; desorption volume, 100 µL.

Effect of sample stirring rate and sample volume

Agitation of sample solution is favourable in extraction as it will shorten the required time needed for the analyte/s to reach equilibrium thus reduce the extraction time [21]. Effect of different stirring rate (450-1000 rpm) was tested for the HF-SPME MTMOS-MPTMOS extraction (Figure 4a). Higher stirring rate (beyond 1000 rpm) was avoided as it led to formation of excessive bubble during extraction and in the same time vigorous collision occurred between the HF and the vial wall. It was observed that higher stirring rate resulted in higher extraction efficiency as it can enhance the mass transfer of the analyte/s towards the extractant. Agitation at 1000 rpm showed the best extraction efficiency for hexanal and heptanal, thus, it was chosen as the optimum sample stirring rate.

During the HF-SPME process, the interaction between the analytes in the sample solution and the extractant is based on equilibrium, hence the ideal sample volume is also play a role to achieve the optimum extraction efficiency. Sample volume as a donor phase was varied from 3 – 20 mL (Figure 4b) for 30 min extraction time with an agitation rate of 1000 rpm while back-extraction was performed via vortex-assisted method for 3 min in 100 µL MeOH. Increasing the sample volume stepwise from 3 mL to 10 mL enhanced the peak areas of hexanal and heptanal. On the contrary, further volume increase to 15 mL and 20 mL gave poorer extraction efficiency for both aldehydes. This is probably due to poorer mass transfer kinetics in larger sample volume that resulted in the poor extraction efficiency observed. Therefore, 10 mL was chosen as the best sample volume for HF-SPME MTMOS-MPTMOS extraction.

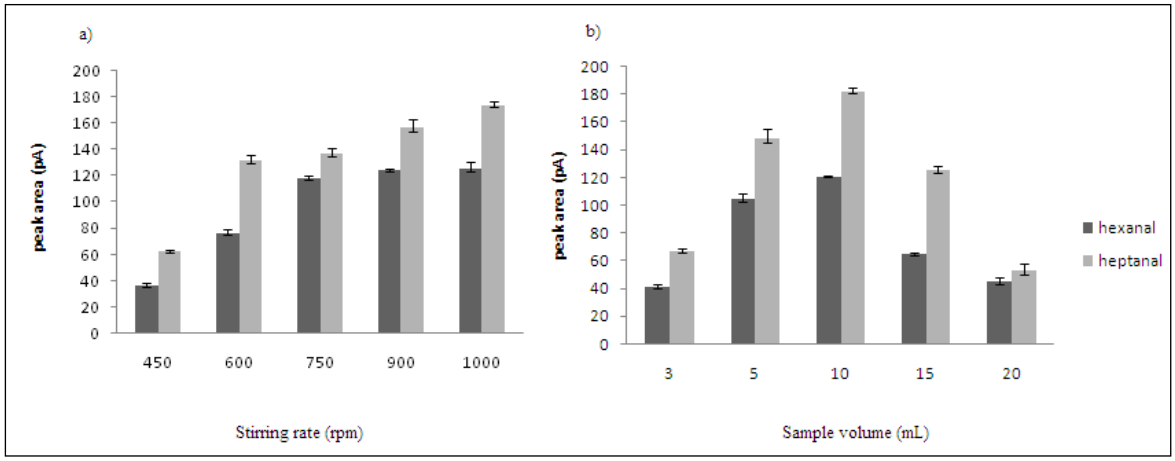


Figure 4. Effect of (a) sample stirring rate and (b) sample volume on the HF-SPME extraction efficiency (based on peak area). Other conditions are as in Figure 3.

Effect of salt addition

In most cases, salt is added to increase the ionic strength and to decrease the solubility of analyte/s in sample solution. In the present work, addition of sodium chloride was investigated at different concentrations from 0.5 - 2.0%, *w/v* (Figure 5) and the results were compared with the sample solution without the addition of sodium chloride. It was found that the higher the addition of salt concentration in sample solution, lower extraction efficiency of hexanal and heptanal was obtained. This is probably due to the presence of salt that can alter the properties of material coated in the tube of HF, change the diffusion rates hence, less analyte/s transfer to the extractant. Similar behavior was reported by Ebrahimi et al. [22]. Therefore, salt addition was not significant to be utilized for HF-SPME MTMOS-MPTMOS extraction of hexanal and heptanal.

Effect of desorption volume

Selection of appropriate volume of solvent is essential for the desorption capacity and to strip the analytes of interests from the sorbent phase. In this study, methanol was used as desorption solvent and the solvent volume was varied from 80 µL to 500 µL (Figure 6). Increase in extraction efficiency was observed for hexanal and heptanal when amount of the desorption volume was reduced. This is expected as the lower the desorption volume, the higher the preconcentration factor obtained. However, using a 80 µL desorption solvent resulted in peak decrease. The reason is, the volume level did not completely immerse the HF segments thus resulted in improper back-extraction of analyte/s. As the highest extraction efficiency was achieved using 100 µL of methanol, this volume was selected as the best desorption volume.

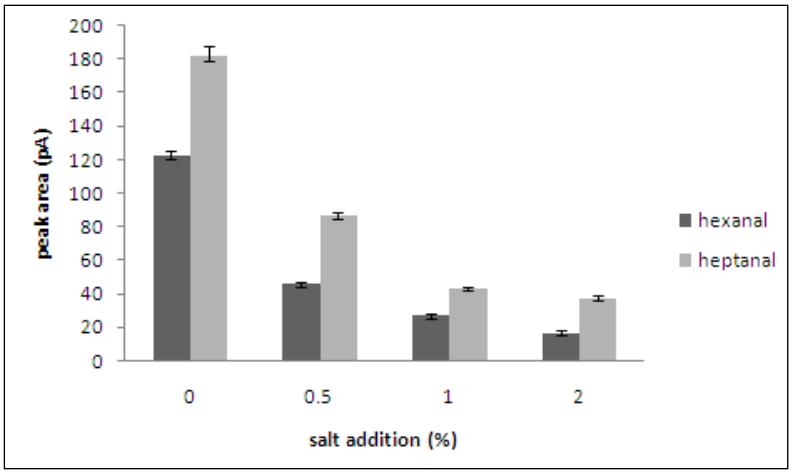


Figure 5. Effect of salt addition on the HF-SPME extraction efficiency (based on peak area). Other conditions are as in Figure 3.

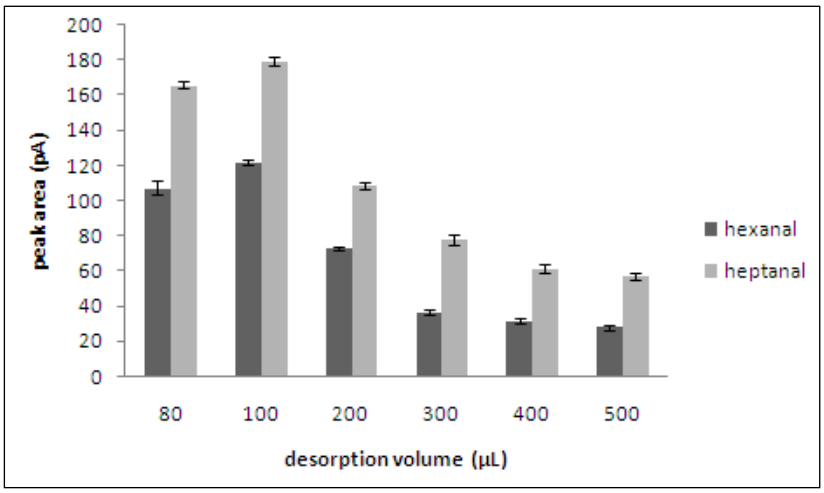


Figure 6**.** Effect of desorption volume on the HF-SPME extraction efficiency (based on peak area). Other conditions are as in Figure 3.

Effect of vortex speed

In this study, desorption was performed by vortex-assisted method. To select the ideal vortex speed, different vortex speed was explored within the range of 15.8 - 86.4 × *g* (Figure 7). As expected, increasing the speed of vortex provided higher extraction efficiency and the highest peak areas response of both aldehydes were obtained when the applied speed rate was 63.5 × *g*. Increasing the vortex speed to 86.4× *g* led to massive bubble formation and this is a fast speed to use to back-extract the analyte/s in 100 µL of desorption solvent, resulting in the reduction of extraction efficiency for both hexanal and heptanal. As vortex assistance desorption at 63.5 × *g* gave the highest extraction efficiency in determining hexanal and heptanal, it was chosen as the best vortex speed.

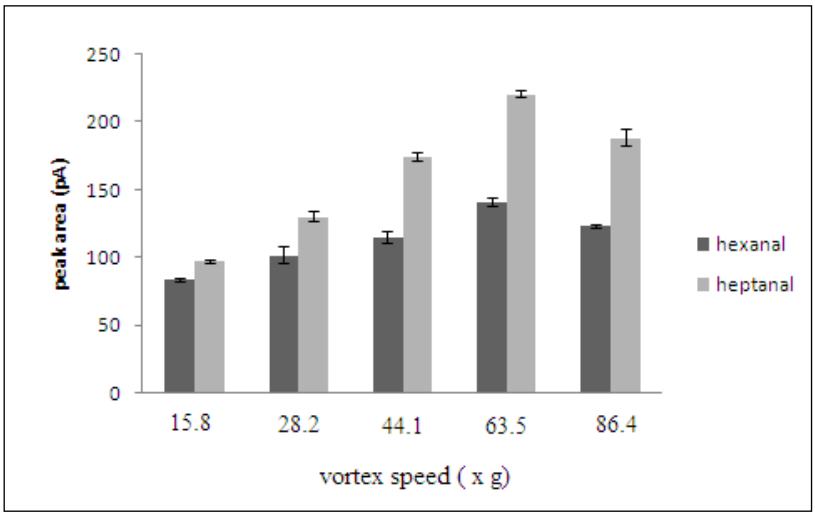


Figure 7. Effect of vortex speed on the HF-SPME extraction efficiency (based on peak area). Other conditions as in Figure 3.

Method Validation

Optimum extraction performance of hexanal and heptanal based on peak area response measured by GC-FID was achieved using 30 min extraction time, 1000 rpm agitation rate using 10 mL of aqueous sample, back-extraction of extracted analytes performed via vortex for 3 min at a speed of 63.5 × *g* using 100 µL methanol as the desorption solvent. Table 1 summarizes the calibration curve equation, limit of detection (LOD = 3 S/N), limit of quantification (LOQ = 10 S/N)) together with their coefficient of determination (R^2) and precision (intra batch and inter-batch) of HF-SPME MTMOS MPTMOS under the optimum extraction conditions. Linearity order observed was 500 with good coefficient of determination (> 0.996).

Table 1. Calibration curve equation, coefficient of determination, LOD, LOQ and precision values (within batch and inter-batch) HF-SPME at optimum conditions

Compound	Calibration curve Equation	Coefficient of determination (R^2)	LOD (µg/mL)	LOQ (µg/mL)	Within batch RSD (%, *n* = 4)	Inter batch RSD (%, *n* = 4)
Hexanal	y = 0.013x + 4.568	0.9985	0.015	0.040	3.82	7.86
Heptanal	y = 0.021x + 6.378	0.9969	0.010	0.030	3.25	9.36

Linear range: 0.020 –10.0 µg mL^{-1}

The applicability of the proposed HF-SPME MTMOS-MPTMOS method was tested on human urine from a healthy volunteer. Urine samples were spiked with hexanal and heptanal standard at certain concentrations after confirming the non-presence of the two aldehydes. Two levels of spiking were used in order to compare the recovery and precision values. Quantitative percentage recoveries were obtained for hexanal and heptanal (91.21 – 97.51 %, RSD < 5.5%, *n* = 3) (Table 2). Figure 8 shows the chromatograms of extract of blank and spiked urine samples (at 0.25 µg/mL of hexanal and heptanal) using HF-SPME MTMOS-MPTMOS. Based on the chromatograms, it is noticed that there was no significant interference from the sample matrix thus proved that HF-SPME method provided clean extraction.

Table 2. Average recovery of hexanal and heptanal in spiked urine sample

Analyte	Spiked concentration (µg/mL)	Average recovery (%)	RSD (%, *n* = 3)
Hexanal	1.0	97.51	3.28
	0.25	95.34	5.58
Heptanal	1.0	93.16	4.00
	0.25	91.21	2.78

**All extractions were carried out at optimum conditions*
**n = 3 (three different extractions)*

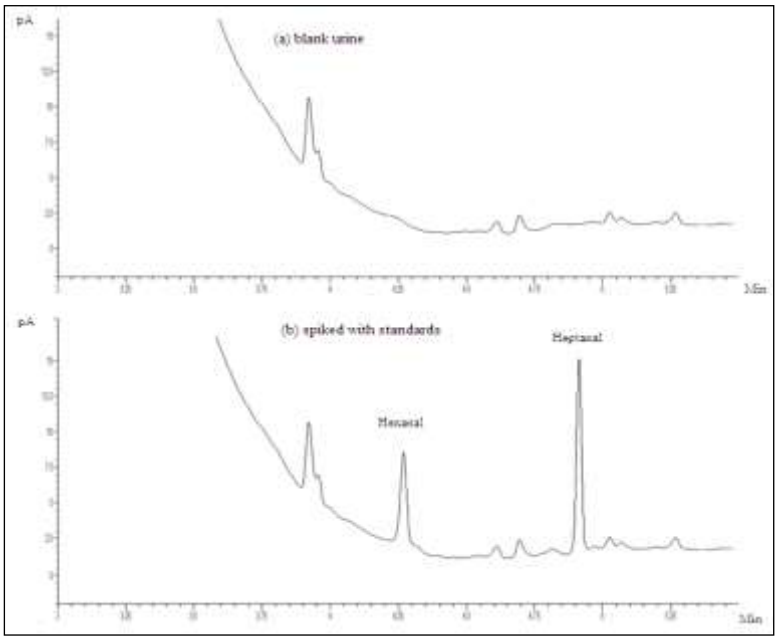


Figure 8. Chromatograms of a) blank urine sample b) extract of urine sample spiked with 0.25 µg/mL mixture of hexanal and heptanal using the proposed HF-SPME MTMOS-MPTMOS. Unknown peaks are most likely small molecular weight interferences from urine sample.

Conclusion

The sol-gel hybrid material, MTMOS-MPTMOS was successfully synthesized using mild conditions and used as a new adsorbent of HF-SPME for quantitative analysis of hexanal and heptanal from human urine samples with minimum sample preparation process. Several parameters affecting the extraction performance were successfully optimized and used in method validation. The proposed HF-SPME MTMOS-MPTMOS method is an easy and convenient microextraction technique that provides easy material preparation step and can be potentially applied for determination of hexanal and heptanal in human urine sample analysis.

Acknowledgement

The authors would like to thank Ministry of Higher Education Malaysia (MOHE) for the University Research Grant vote number 04H22 for the financial assistance. Ministry of Science, Technology and Innovation Malaysia (MOSTI) is also acknowledged for the MyBrain15 award to S. M. Abd Wahib.

References

1. Fathy Bakr Ali, M., Kishikawa, N., Ohyama, K., Mohamed, H. A-M., Abdel-Wadood, H. M., Mohamed, A. M. and Kuroda, N. (2013). Chromatographic determination of aliphatic aldehydes in human serum after pre-column derivatization using 2,2'-furil, a novel fluorogenic reagent. *Journal of Chromatography A*, 1300: 199 – 203.
2. Li, N., Denga, C., Yao, N., Xizhong Shen, X. and Zhang, X. (2005). Determination of Acetone, Hexanal and Heptanal in Blood Samples by Derivatization with Pentafluorobenzyl Hydroxylamine Followed by Headspace Single-drop Microextraction and Gas Chromatography Mass Spectrometry. *Analytica Chimica Acta*, 540: 317 – 323.
3. Deng, C, Zhang, X. and Li, N. (2004). Investigation of Volatile Biomarkers in Lung Cancer Blood using Solid-Phase Microextraction and Capillary Gas Chromatography-Mass Spectrometry *Journal of Chromatography B*, 808: 269 – 277.
4. Deng, C., Li, N. and Zhang, X. (2004). Development of Headspace Solid-Phase Microextraction with On-Fiber Derivatization for Determination of Hexanal and Heptanal in Human Blood. *Journal of Chromatography B*, 81 3: 47 – 52.
5. Poli D, Goldoni M, Corradi M. Acampa, O., Carbognani, P., Internullo, E., Casalini, A. and Mutti, A. (2010). Determination of Aldehydes in Exhaled Breath of Patients with Lung Cancer By Means of On-Fiber Derivatization SPME-GC/MS. *Journal of Chromatography B*, 878: 2643 – 2651.
6. Guadagni, R., Miraglia, N., Simonelli, A., Silvestre, A., Lamberti, M., Feola, D., Acampora, A. and Sannolo, N. (2011). Solid-phase Microextraction-Gas Chromatography-Mass Spectrometry Method Validation for the Determination of Endogenous Substances: Urinary Hexanal and Heptanal as Lung Tumor Biomarkers. *Analytica Chimica Acta*, 701: 29 –36.
7. Sarafraz-Yazdi, A. Dizavandi, Z. R. and Amiri, A. (2012). Determination of phenolic compounds in water and urine samples using solid-phase microextraction based on sol-gel technique prior to GC-FID. *Analytical Methods*, 4: 4316 – 4325.
8. Sarafraz-Yazdi, A., Ghaemi, F., and Amiri, A. (2012). Comparative Study of the Sol-Gel Based Solid Phase Microextraction Fibers in Extraction of Naphthalene, Fluorene, Anthracene and Phenanthrene from Saffron Samples Extractants. *Microchimica Acta*, 176: 317 – 325.
9. Xu, H., Wang, S., Zhang, G., Huang, S., Song, D., Zhou, Y. and Long, G. (2011). A Novel Solid-Phase Microextraction Method Based on Polymer Monolith Frit Combining with High-Performance Liquid Chromatography for Determination of Aldehydes in Biological Samples. *Analytica Chimica Acta*, 690: 86 – 93.
10. Song, D., Gu, Y., Liang, L., Ai, Z., Zhang, L., and Xu, H. (2011). Magnetic Solid-Phase Extraction Followed by High Performance Liquid Chromatography for Determination of Hexanal and Heptanal in Human Urine. *Analytical Methods*, 3: 1418 –1423.
11. Mieth, M., Kischkel, S., Schubert, J. K., Hein, D. and Miekisch, W. (2009). Multibed Needle Trap Devices for On Site Sampling and Preconcentration of Volatile Breath Biomarkers. *Analytical Chemistry*, 81: 5851 – 5857.
12. Wan Ibrahim, W. A., Farhani, H., Sanagi, M. M., and Aboul-Enein, H. Y. (2010). Solid Phase Microextraction using New Sol-Gel Hybrid Polydimethylsiloxane-2 Hydroxymethyl-18-Crown-6-Coated Fiber for Determination of Organophosphorous Pesticides. *Journal of Chromatography A*, 1217: 4890 – 4897.
13. Wan Ibrahim, W. A., Wan Ismail, W. N., Abdul Keyon, A. S. and Sanagi, M. M. (2011). Preparation and Characterization of a New Sol-Gel Hybrid Based Tetraethoxysilane Polydimethylsiloxane as a Stir Bar Extraction Sorbent Materials. *Journal of Sol-Gel Science and Technology*, 58: 602 – 611.
14. Zheng, Y., Wang, D. and Tian, J. (2012). Preparation and Application of Multiwalled Carbon Nanotubes Microspheres/Poly(ethylene glycol) Coated Fiber for SPME. *Advanced Materials Res*earch, 512-513: 2084 - 2087.
15. Wan Ibrahim W. A, Veloo, K. V. and Sanagi, M. M. (2012). Novel Sol-Gel Hybrid Methyltrimethoxysilane-Tetramethoxysilane as Solid Phase Extraction Sorbent of Organophosphorus Pesticides, *Journal of Chromatography A*, 1229: 55 – 62.

16. Gao, Z., Deng, Y., Hu, X., Yang, S., Sun, C. and He, H. (2013). Determination of Organophosphate Esters in Water Samples Using An Ionic Liquid-Based Sol-Gel Fiber for Headspace Solid-Phase Microextraction Couple d to Gas Chromatography-Flame Photometric Detector. *Journal of Chromatography A*, 1300: 141 –150.
17. Mu, Li., Hu, X., Weng, J. and Zhou, Q. (2013). Robust Aptamer Sol-Gel Solid Phase Microextraction of Very Polar Adenosine from Human Plasma. *Journal of Chromatography A*, 1279: 7 –12.
18. Zhou, Z. P., Wang, Z. Y., Wu, C. Y., Zhan, W. and Xu, Y. (1999). Sol-Gel Method for the Preparation of Solid -Phase Microextraction Fibers. *Analytical Letter*, 32: 1675 –1681.
19. Spietelun, A., Marcinkowski, Ł., de la Guardia, M. and Namieśnik, J. (2013). Recent Developments and Future Trends in Solid Phase Microextraction Techniques Towards Green Analytical Chemistry. *Journal of Chromatography A*, 1321:1 – 13.
20. Es'haghi, Z., Orayaei, H., Samadi, F., Masrournia, M. and Bakherad, Z. (2011). Fabrication of A Novel Nanocomposite Based on Sol-Gel Process for Hollow Fiber-Solid Phase Microextraction of Aflatoxins: B1 and B2, in Cereals Combined with High Performance Liquid Chromatography-Diode Array Detection. *Journal of Chromatography B*, 879: 3034 – 3040.
21. Es'haghi, Z., Rezaeifar, Z., Rounaghi, G-H., Nezhadi, Z. A., and Golsefidi, M. A. (2011). Synthesis and Application of A Novel Solid-Phase Microextraction Adsorbent: Hollow Fiber Supported Carbon Nanotube Reinforced Sol-Gel for Determination of Phenobarbital. *Analytica Chimica Acta*, 689: 122 –128.
22. Ebrahimi, M., Es'haghi, Z., Samadi, F. and Hosseini, M-S. (2011). Ionic Liquid Mediated Sol-Gel Sorbents for Hollow Fiber Solid-Phase Microextraction of Pesticide Residues in Water and Hair Samples. *Journal of Chromatography A*, 1218: 8313 – 8321.
23. Ebrahimi, M., Es'haghi, Z., Samadi, F. and Hosseini, M-S. (2012). Rational Design of Heteropolyacid-Based Nanosorbent for Hollow Fiber Solid Phase Microextraction of Organophosphorus Residues in Hair Samples. *Journal of Chromatography A*, 1225: 37 – 44.
24. Song, X-Y, Shi, Y-P and Chen, J (2012). A Novel Extraction Technique Based on Carbon Nanotubes Reinforced Hollow Fiber Solid/Liquid Microextraction for the Measurement of Piroxicam and Diclofenac Combined with High Performance Liquid Chromatography. *Talanta*, 100: 153 – 161.
25. Yang, Y., Chen, J. and Shi, Y-P. (2012). Determination of Diethylstilbestrol in Milk Using Carbon Nanotube-Reinforced Hollow Fiber Solid-Phase Microextraction Combined with High-Performance Liquid Chromatography. *Talanta*, 97: 222 – 228.
26. Li, J., Wang, Y-B., Wu, L., Li, K-Y. and Feng, W. (2014). Fabrication of Multi-Walled Carbon Nanotubes/ Oxide Reinforced Hollow Fibers by Sol-Gel Technique for Rapid Determination of Metronidazole in Milk. *Analytical Methods*, 6: 1404 –1411.
27. Su, S., Chen, B., He, M. and Hu, B. (2014). Graphene Oxide-Silica Composite Coating Hollow Fiber Solid Phase Microextraction Online Coupled with Inductively Coupled Plasma Mass Spectrometry for the Determination of Trace Heavy Metals in Environmental Water Samples. *Talanta*, 123: 1 – 9.
28. Bagheri, H., Piri-Moghadam, H. and Ahdi, T. (2012). Role of Precursors and Coating Polymers in Sol-Gel Chemistry toward Enhanced Selectivity and Efficiency in Solid Phase Microextraction. *Analytica Chimica Acta*, 742: 45 – 53.
29. Azenha, M., Malheiro, C. and Silva, A. F. (2005). Ultrathin Phenyl-Functionalized Solid Phase Microextraction Fiber Coating Developed by Sol-Gel Deposition. *Journal of Chromatography A*, 1069: 163 –172.
30. Mandal, B and Basu, B. (2014). Recent advances in S–S bond formation. *RSC Advances*, 4: 13854 – 13881.
31. Kabir, A., Furton, K.G. and Malik, A. (2013). Innovations in Sol-Gel Microextraction Phases for Solvent-Free Sample Preparation in Analytical Chemistry. *Trends in Analytical Chemistry*, 45: 197 –218.
32. Kumar, A., Gaurav, Malik, A. K., Tewary, D. K. and Singh, B. (2008). A Review on Development of Solid Phase Microextraction Fibers by Sol-Gel Methods and Their Applications. *Analytica Chimica Acta*. 610: 1 –14.
33. Chen, G., Li, W., Zhang, C., Zhou, C. and Feng, S. (2012). Preparation of a Novel Hyperbranched Carbosilane -Silica Hybrid Coating for Trace Amount Detection by Solid Phase Microextraction/Gas Chromatography. *Journal of Chromatography A*, 1256 : 213 – 221.
34. McDonagh, C., Bowe, P., Mongey, K. and MacCraith, B.D. (2002). Characterisation of Porosity and Sensor Response Times of Sol-Gel-Derived Thin Films for Oxygen Sensor Applications. *Journal of Non-Crystalline Solids*, 306: 138 –148.

MALAYSIAN JOURNAL OF ANALYTICAL SCIENCES
Published by The Malaysian Analytical Sciences Society
ISSN 1394 - 2506

EFFECT OF SILVER NANOPARTICLE ADDITION ON THE STRUCTURE AND CHARACTERISTICS OF RADIO-PHOTOLUMINESCENCE GLASS DOSIMETER

(Kesan Penambahan Nanozarah Argentum Terhadap Struktur dan Sifat – Sifat Dosimeter Kaca Radio – Pendarcahaya)

Irman Abdul Rahman[1,2]*, Muhammad Taqiyuddin Mawardi Ayob[1,3], Hur Munawar Kabir Mohd[1], Ainee Fatimah Ahmad[1], Shamellia Sharin[1], Faizal Mohamed[1,2], Sidek Ab Aziz[3], Shahidan Radiman[1,2]

[1]*School of Applied Physics, Faculty of Science and Technology*
[2]*Nuclear Technology Research Center, Faculty of Science and Technology,*
Universiti Kebangsaan Malaysia, 43600 UKM Bangi, Selangor Darul Ehsan, Malaysia
[2]*Department of Physics, Faculty of Science,*
Universiti Putra Malaysia, 43400 Serdang, Selangor Darul Ehsan, Malaysia

**Corresponding author: irman@ukm.edu.my*

Received: 9 December 2014; Accepted: 16 October 2015

Abstract

A series of silver-activated phosphate glass was prepared by melt quenching method. The effect of silver nanoparticle addition on the phosphate glass microstructure, composition and chemical characteristics was investigated using x-ray diffraction, fourier transform infrared and photoluminescence spectroscopy. Other physical property such as density was also evaluated. The density increased when the amount of silver ions were increased, due to the enhanced formation of non-bridging oxygen. In this study, we discuss the emission mechanism of two radio-photoluminescence peaks at 460 nm and 620 nm, where the electrons and holes produced by γ-irradiation a re-trapped by Ag^{+} ions to produce Ag^{0} and Ag^{2+} ions respectively, when the Ag^{+}-doped phosphate glass is exposed to γ-ray. We proposed that an emission mechanism of 460 and 620 nm radio-photoluminescence peaks with these Ag^{2+} and Ag^{0} ions. Furthermore, a correlation between the investigated properties and glass composition is discussed.

Keywords: silver nanoparticle, optical and physical properties, radio-photoluminescence glass dosimeter

Abstrak

Satu siri gelas argentum-aktif fosfat telah dihasilkan menerusi kaedah peleburan. Kesan penambahan nanobahan argentum ke dalam mikrostruktur gelas fosfat, komposisi dan sifat-sifat kimia dikaji dengan menggunakan pembelauan sinar-X, penjelmaan inframerah Fourier dan spektroskopi pendarcahaya. Sifat fizikal yang lain seperti ketumpatan kacaturut dikaji. Ketumpatan kaca bertambah apabila jumlah ion-ion argentum ditingkatkan, disebabkan oleh peningkatan pembentukan oksigen tanpa-hubung. Dalam kajian ini, kami membincangkan mekanisme pemancaran oleh dua puncak radio-pendarcahaya pada jalur 460 nm dan 620 nm, di mana elektron dan lohong yang terhasil daripada sinar-γ diperangkap oleh ion – ion Ag^{+} seterusnya menghasilkan ion – ion Ag^{0} dan Ag^{2+}, apabila kaca Ag^{+}-aktif fosfat didedahkan kepada sinar-γ. Kami turut membincangkan mekanisme pemancaran bagi setiap puncak radio-pendarcahaya pada jalur 460 dan 620 nm berdasarkan ion – ion Ag^{2+} dan Ag^{0} berkenaan. Tambahan lagi, hubung kait antara komposisi kaca dan sifat-sifat kaca yang terhasil turut dibincangkan.

Kata kunci: nanobahan argentum, sifat fizikal and optik, dosimeter kaca radio-pendarcahaya

Introduction

Recent technological applications have generated more interest in the study of glasses especially oxide glasses [1 – 6]. Among oxide glasses, phosphate based glasses are particularly attractive due to their ability to accommodate large concentrations of active ions without losing their useful properties of the material [1]. Phosphate glasses are relatively easy to prepare and offers a large range of compositional possibilities, which facilitates in tailoring the physical, chemical and optical properties of interest for specific technological applications [7]. In particular, embedding materials such as metal nanoparticles in glasses are expected to produce promising materials for functional optical devices due to a large third-order nonlinear susceptibility and an ultra-fast non-linear response [8]. The doping process plays an important role in the development of many optoelectronic devices especially dosimeters. Some dopants such as noble metal ions capture negatively charged electrons or positively charged holes, creating defects in the form of a change in their valence state through photo chemical reaction during exposure to successive gamma irradiation [6]. Radio-photoluminescence (RPL) in various glasses containing silver impurities has long been examined [9 – 11] for applications in personal solid-state dosimetry and radiation measurements. Yokota et al. [11] reported how to produce a glass element having low energy dependence, high sensitivity and good chemical stability. Moreover, the centers of luminescence will never disappear unless the glasses are annealed with high temperatures of about 400 $^{\circ}$C. This produces some excellent features such as repeatable measurement and small dispersions among samples [12].

In this study, phosphate glass dosimeters were prepared from reagent powders of P_2O_5, Li_2CO_3, $Al(OH)_3$, $NaNO_3$, $H_3BO_3$and silver nanoparticles. The optical and physical properties were determined with different silver ion contents within the phosphate base glass. The photoluminescence properties of silver-phosphate glass were studied. In addition, the density of the phosphate glass system was determined. The excitation and emission properties of radio-photoluminescence glass dosimeter in the form of Ag^+-doped phosphate glass and discussed the mechanism of RPL which is based on the excitation and emission properties also were evaluated.

Materials and Methods

Before synthesizing the Ag-doped phosphate glass, silver nanoparticles was firstly prepared. To obtain the Ag nanoparticles, 0.2 M of $AgNO_3$ (Aldrich; ≥ 99%) and 0.2 M of NaOH (Fluka; ≥ 97%) were dissolved in 100 ml of deionised water (resistivity = 18.2MΩ, TOC ≤ 5 ppb) under magnetic stirring at room temperature for 10 minutes. Triethanolamine (TEA) was poured into each solution at a molar ratio of 1:3 with excess TEA and continued stirring for 20 minutes. NaOH solution was added to the $AgNO_3$ solution during the ultrasound irradiation process (misonix-400, 60 Hz, 70 amplitude) for 60 minutes under nitrogen gas flow. The sample was then centrifuged and washed with excess deionised water to remove impurities and the excessive TEA used to cap the surface of the Agproducts, then dried overnight at 60 °C in the oven. The crystallinity and morphology of the products were later characterized by XRD (Bruker X-ray diffractometer) and TEM (Hitachi H-7100) instruments.

Secondly, phosphate glass for the solid state dosimetry was prepared from reagent grade powders of anhydrous P_2O_5, Li_2CO_3, $Al(OH)_3$, $NaNO_3$ and H_3BO_3. Silver nanoparticles were used as the main component for the radio-photoluminescence glass dosimeter. Silver-doped phosphate glasses were prepared by the melt-quenching method. The weight composition of the glass dosimeters were 9.26% $Al(OH)_3$, 7.34% Li_2CO_3, 2.0% $NaNO_3$, 2.72% H_3BO_3 and P_2O_5:Ag (73.58:5.1, 74.38:4.3& 75.18:3.5 respectively) in mol %, weighted using a digital weighing machine with an accuracy of ± 0.01 g, then mixed together using a mortar and pestle. Appropriate amount of each powder was melted in an alumina crucible which was placed in an electrical heated furnace in atmosphere. At a heating rate of about 10^0C/min, the temperature was gradually increased up to 600 $^{\circ}$C and kept at this temperature for 5 hours. Once the mixture was liquidised, the temperature was then increased again to 1250 $^{\circ}$C and left for one hour to obtain the appropriate viscosity. After the stirring and refining process, the glass liquid was then poured into a preheated stainless steel plate. At this point it then takes 24 hours to complete the annealing process at 350 $^{\circ}$C. The density of the glass samples were measured using the Archimedes principle, and distilled water was used as the immersion liquid. All samples were irradiated withγ-radiation, performed using a Co-60 source delivered at 1.8 kGy/h. In this work, the samples were irradiated such that the absorbed dose was 1 kGy. Excitation and emission measurements were performed at room temperature and RPL intensity was measured using FLS-920 spectrophotometer (excitation wavelength: 265 and 320 nm). The RPL emitted from the crystal was observed in a direction perpendicular to that

of the excitation beam and analysed using suitable filters with central wavelengths of 460and 620nm, respectively. The structure of the silver-phosphate glass was investigated using X-ray diffraction (Bruker X-ray diffractometer) and Fourier transform infrared spectroscopy (Perkin Elmer/Lamda 950).

Results and Discussion

The glass density values are lightly shifted in the range 2.48 to 2.67 g/cm^3, increasing with the silver content. With a high amount of Ag in the vitreous network the density increases up to 2.67 g/cm^3, possessing higher density values.

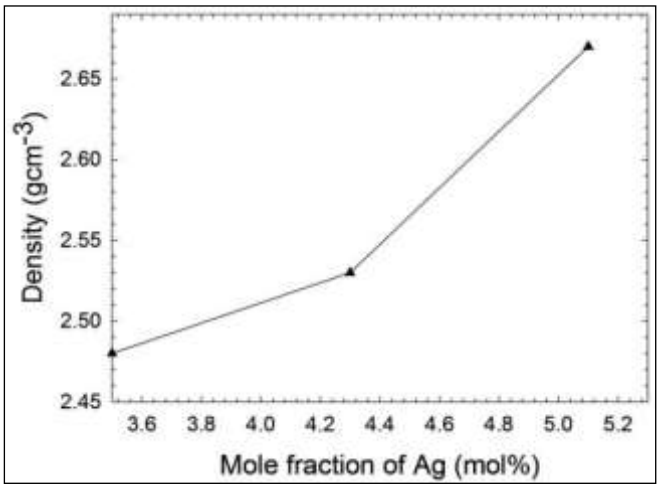


Figure 1. Density with different mole fraction (mol %) of silver-activated phosphate glass system

The micrograph of the Ag nanoparticles was obtained via TEM analysis is shown in Fig. 2(a). It shows structures consisting of irregular spherical metallic Ag with the average particle size estimated to be in range of 5 to 17 nm, determined by using the Sigma scan method as shown in Fig. 2(b).

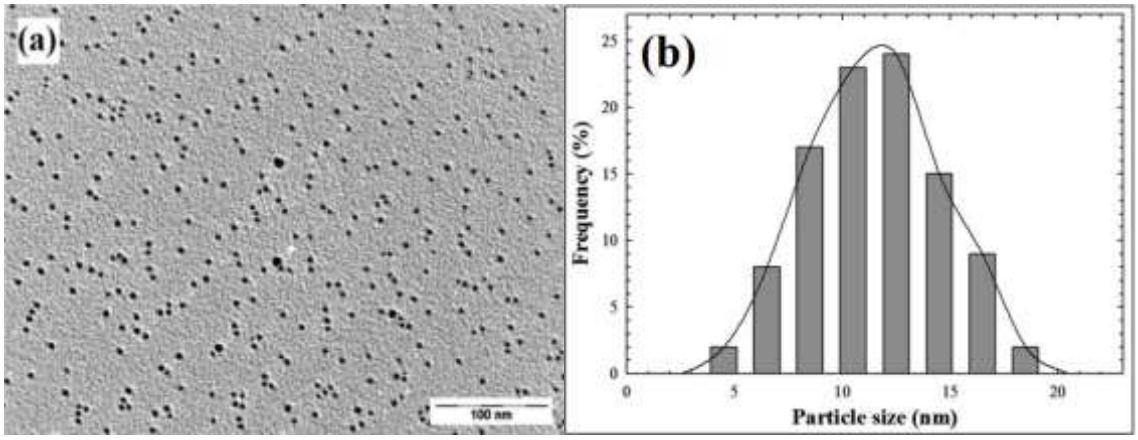


Figure 2. TEM micrograph of Ag nanoparticles prepared by sonication method

Aggregations occur due to large specific surface area and high surface energy, occurring during the process of sonication [13]. Due to the advantageous properties of silver nanoparticles, addition of these nanoparticles to phosphate glass increases the luminescence properties of the glass. Thus, it is interesting to study the effects of the addition of silver nanoparticles to phosphate glassesand the influence of its ions on the glass forming network.

The XRD pattern of Ag nanoparticles is shown in Fig. 3(a). The series of characteristic peaks have been indexed to metallic Ag indicating a face-centered cubic structure, according to JCPDS Card No. 1-87-717, with the lattice parameters; a = 4.0857 nm and space group fm-3m. No diffraction peaks of impurities have been observed, implying that all the $AgNO_3$was fully decomposed into Ag nanoparticles.

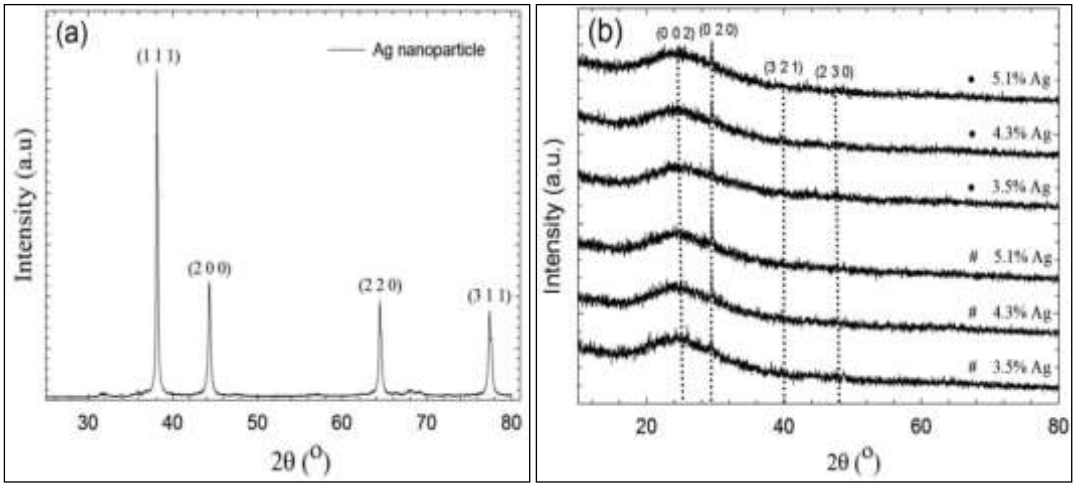


Figure 3. X-ray diffraction patterns of the (a) silver nanoparticles and (b) 3.5, 4.3 and 5.1mol % of Ag nanoparticles doped phosphate glasses before (#) and after (•) 1.0 kGy of γ-irradiation.

Figure 3(b) shows the pattern of the silver-activated phosphate glasses. The silver content was increase, no remarkablechange was exhibited in the XRD profiles of the six samples with differing silver contents (3.5, 4.3 and 5.1 mol %) before and after γ-irradiation. The overall features of these XRD curves confirm the amorphous nature of the glasses doped with silver nanoparticles. The pattern displays no sharp peaks, indicating the absence of any crystalline nature observed broad humps in the glass samples, characteristic of the phase at diffraction angles (2θ) to be fully amorphous, indicates that these glass samples are composed of a glassy phase. The series of characteristic peaks were indexed to monoclinic structure of silver phosphate with the lattice parameters; a = 11.86 nm, b = 6.06 nm, c = 7.31 nm and space group P21/n. From the XRD patterns, two strong peaks are present in the region at 24.38^o (0 02) and 29.51^o (0 2 0), which indicates that the material was silver doped in phosphate glass related in JCPDS Card No. 1-72-122. Therefore silver diffraction peaks were not well identified, since they were only present in the after mentioned bands. A great deal of interest has been shown in glasseswith implanted metallic clusters. As expected, the signal intensity of silver increased in the 5.1% sample, due to a higher amount of Ag nanoparticle.

In order to obtain more information about the prepared glasses, FTIR measurements were performed. Figure 4 shows the FTIR spectrum of each sample before and after gamma irradiation (1 kGy) for the silver doped phosphate glasses. The positions of the bands for the Ag-doped phosphate glass system are summarized in Table 1. A comparison of spectra in Figure 4 shows that the samples before and after γ-irradiation shows nearly similar IR transmission (absorption) spectra, which may be due to similar composition of the glass matrix, except for a change in the intensities of some peaks in same region for different amount of Ag, which seems to be having less or negligible effect on IR absorption spectra. Main observation after 1 kGy γ-irradiation is the generation of some new

peaks in the 800 – 1017 cm^{-1} range dominated by P-O-P linkages. This clearly indicates the breaking of these P-O-P linkages, which produces more non-bridging oxygen. This is associated with an increase in the intensity of band due to P=O bond at 1187 cm^{-1} (non-bridging oxygen), which confirms the idea of breaking P-O-P linkages in the glass. The bands in the region of 1400-500 cm^{-1} show a number of strong characteristic bands of phosphate glass. There is no significant difference in the line shapes of the spectra, because all of the samples contain > 50 mol% P_2O_5, which is as expected. These spectra consist of two main sets of IR absorption bands in the low and high frequency regions due to phosphate group and O-H molecule (bending mode), respectively. The three bands located in the range of 2346 – 2926 cm^{-1}were relatively weak and can be assigned to the stretching vibrations of P-O-H group in different structural sites, which was consistent in all samples. The shoulder observed at 1425 cm^{-1} is due to the characteristic stretching mode of the P=O bond.

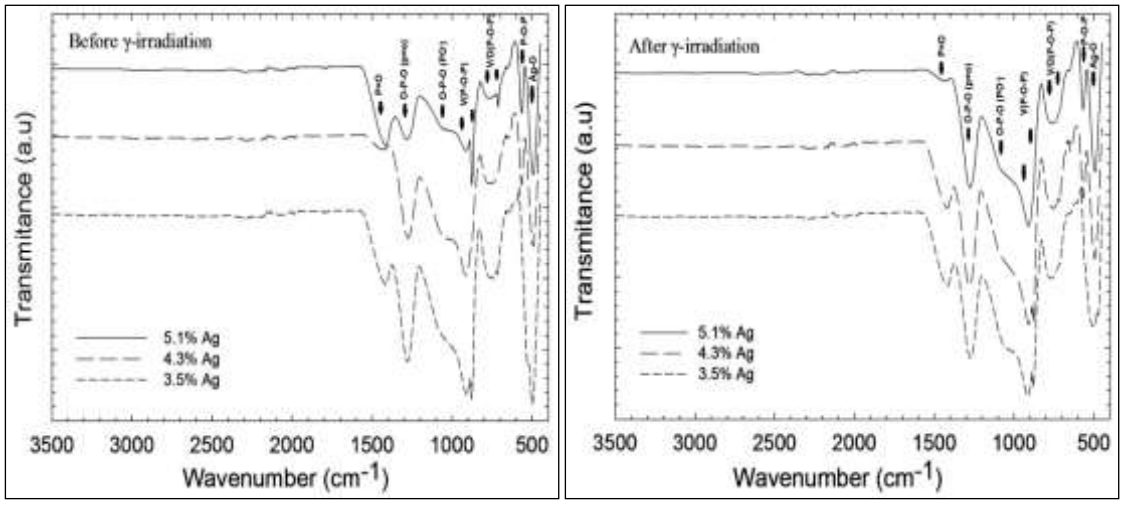


Figure 4. FTIR spectra for the phosphate glasses doped with 3.5, 4.3 and 5.1 mol % of silver nanoparticles.

Several authors have reported that the band corresponding to the stretching vibration of doubly bonded oxygen could be found in the frequency range of 1230 – 1390 cm^{-1}. The band at about 1281 cm^{-1} is assigned to the asymmetrical stretching vibration of O-P-O and P=O groups, ν_{as}(O-P-O)/ ν_{as} (P=O), while the medium broad band at 1100 cm^{-1} is related to the symmetric stretching vibration of that group, ν_s(O-P-O). The 1100 cm^{-1} band is the dominant feature of the spectra and has been assigned to P-O- groups. Moreover, increasing the quantity of the silver component, results in alteration of each band in the region of 1200 –1500 cm^{-1}, confirming the modifying behaviour of silver. The phosphorous non-bridging oxygen portion of PO_4 tetrahedra in a chain structure has been referred to as a $P\text{-}O^-$ unit. The asymmetric stretching vibration of the metaphosphate group, $\nu_{as}(PO_3)$ was observed in the range of 1012 –1153 cm^{-1}. This indicates that the bands due to $\nu_{as}(PO_3)$ can interfere with the band at 1100 cm^{-1}. The broadening observed in the region of 900 – 1105 may be due to the interference of $\nu_s(PO_3)$ with the spectral range 1000 – 1060 cm^{-1}. The shoulder around 878 cm^{-1} is assigned to the asymmetric stretching vibration of P-O-P linkages, ν_{as}(P-O-P), while the relatively weak band around 764 cm^{-1} is due to the symmetric stretching vibration of that linkage, ν_s(P-O-P). The region below 600 cm^{-1} is usually assigned to the vibration of metals [14]. The broad band at about 525 – 539 cm-1 may be assigned to the harmonics of P-O-P bending vibration as well as to the deformation mode of PO^- group. The wavenumbers of 480 and 510 cm^{-1} corresponds to the stretching and Ag-O symmetrical vibrations in PO_4. Piao et. al [15] describes that production of electron hole pairs during irradiation provides another path for bond rearrangement, reducing the constraints on structural relaxation. The relaxation process releases some of the excess energy stored in the structure, resulting in change in the bond angle.

Table 1. Vibrational assignment of the FTIR spectra of Ag-doped phosphate glass samples

No.	Vibrational mode	Wavenumber (cm^{-1})
1.	V_s(P-O-H)	2346-2926
2.	Stretching mode of P=O	1425
3.	Asymmetric stretching O-P-O V_{as}(O-P-O)/(P=O)	1281
7.	Symmetric stretching V_s(O-P-O)/PO^-	1100
8.	$V_{as}(PO_3)$	1012-1153
9.	$V_s(PO_3)$	1000-1060
10.	Asymmetric stretching P-O-P V_{as}(P-O-P)	878
11.	V_s(P-O-P)	764
12.	Harmonics of P-O-P bending vibration/deformation mode of PO^-	525-539
13.	V_s(Ag-O)	480 & 510

Figure 5 shows the radio-photoluminescence spectra of the silver-activated phosphate glass excited at 265 and 320 nm after gamma irradiation with an absorbed dose of 1 kGy.

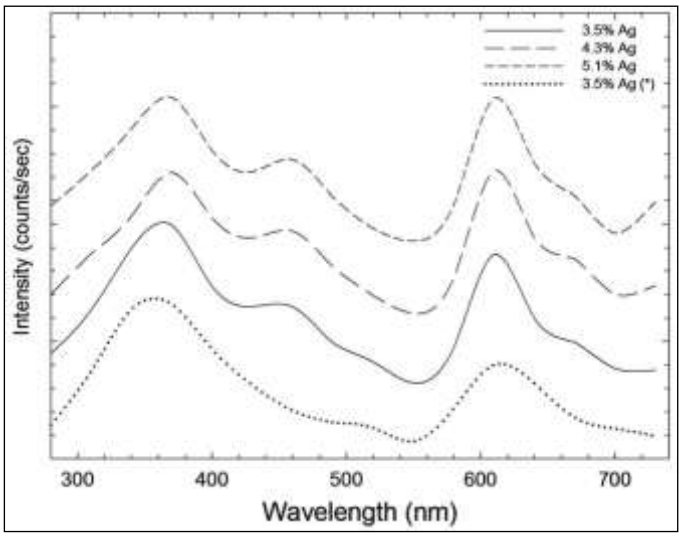


Figure 5. Radio-photoluminescence spectra of the silver-activated phosphate glass excited at 265 and 320 nm before (*) and after gamma irradiation with an absorbed dose of 1 kGy.

The PL spectra were measured to investigate the emission of silver ions corresponding to the dipolar electric transition $4d^{10} \rightarrow 4d^9 5s^1$. The main feature is composed of an excitation band at 265 nm, which consequently released an emission at 380 nm. Another excitation band can be seen at around 320 nm leading to emission between

450 up to 700 nm, with a band located around 460 nm and second band around 620 nm. This last intrinsic fluorescence is due to Ag^{+}–Ag^{+} pairs. One has to mention that for the lowest amount of Ag nanoparticles doped (3.5 %), the relative intensity of the band at 500 nm appears, to indicate that different nature of luminescent centers are most likely occurring. The existence of this emission band can be related to the formation of significant amount of Ag^{0} centers within the glass network. Even if the formation mechanisms of hole and electron traps are different, in all the irradiated cases, the 460 and 620 nm peak observed in the emission spectrum is believed to be due to aggregation of Ag^{0} and Ag^{+} ions which have possibly generated additional chemically stable clusters Ag_m^{x+} such as Ag_2^{+}, Ag_3^{2+} [9]. All these observations are consistent with a decrease of the emission of isolated silver ions showing that silver is definitely acting as the electron trap [16]. There is no emission peak observed for 3.5% of Ag-doped phosphate glass sample before γ-irradiation at 460 nm, which means there is no mechanism of hole and electron traps occurs and no Ag^{0} centreswere producedwithin the glass network.

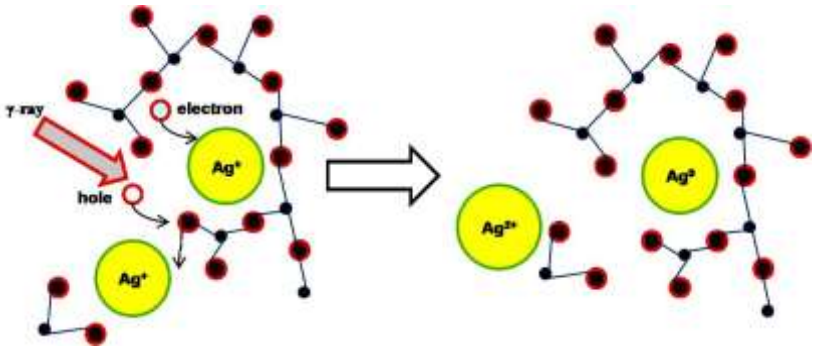


Figure 6. The colour centers formation mechanism of Ag-activated phosphate glass dosimeter

Radio-photoluminescence glass dosimeteris a mixture of inorganic amorphous solid and does not have lattice structure and lattice luminescence centers (molecular-level structures). Therefore, we can only establish the RPL model based on the energy of the excitation source and the energy of the released visible light. The networks of phosphate glass can be classified by the oxygen-to-phosphorus ratio, as set by the glass composition.The colour or luminescence centers are structured at the silver activated phosphate glass, as shown in Figure 6. The number of ionic silver is proportional to the numbers of electron traps. However, excessive numbers of ionic silver decreases the penetration efficiency of the pulse ultra-violet laser and increases energy dependence [17]. Therefore, a proper ratio of ionic silver is required for the best luminescence and excitation efficiency [18].

After γ-irradiation, the $AgPO_4$ in silver activated phosphate glass can be viewed as Ag^{+}/PO_4^{-}-related colour centres, produced inside the samples of Ag-doped phosphate glass (Equation 1). The glass changed colours from colourless to slightly yellow after γ-irradiation. When the tetrahedron of PO_4^{-} is exposed to radiation, it loses one electron and forms a positron hole, hPO_4 as shown in Equation 2. Equation 3 shows that the electron released from the PO_4^{-} will combine with Ag^{+} to form an Ag^{0}. In gamma irradiated silver-doped phosphate glasses, all electrons are trapped by Ag^{+} ions immediately after irradiation because Ag^{+} has a strong ability to trap electron. Similarly, hPO_4 will combine with Ag^{+} to become an Ag^{2+}as shown in Equation 4. The process where Ag^{+} ions trap holes is the main reason of the stabilization phenomenon of RPL centers. Both Ag^{0} and Ag^{2+} form the colour centers. The colour centers formation mechanisms are shown below.

$$AgPO_4 \rightarrow Ag^{+} + PO_4^{-} \quad (1)$$

$$PO_4^{-} \rightarrow hPO_4 + e^{-} \quad (2)$$

$$Ag^{+} + e^{-} \rightarrow Ag^{o} \text{ (electron trap)} \quad (3)$$

$$Ag^{+} + hPO_4 \rightarrow PO_4 + Ag^{2+} \text{ (hole trap)} \quad (4)$$

When these colour centers were excited with ~335 nm pulse ultra-violet lamp, the electrons in Ag^0 and $Ag^{2+}$are excited to higher energy levels and emit 600 – 700 nm visible orange light, then return to the original colour centers. These electrons will not return to the valence band of the glass material directly because the energy gained by electrons from the pulse ultra-violet laser is not high enough to let electron escape from colour centers. For electrons to gain enough energy to return to the valence band, the glass needed to be annealed at ~400 ^{0}C for one hour. The colour centers won't disappear after readout; hence, this glass can be read repeatedly.

Conclusion

In summary, optical, physical and chemical measurements on radio-photoluminescent silver-activated phosphate glass to clarify the origin and characteristics of the γ-induced colour centres was performed in this sudy. It was established that the phosphate glasses suitable for dosimeter control possess density values ranging from 2.48 to 2.67 g/cm^3. The glass density values are composition dependent, which the density increases with increasing Ag nanoparticles content in the vitreous network. FT-IR spectra of Ag-doped phosphate glasses have been studied before and after γ-irradiation. The FT-IR absorption spectra of Ag-doped phosphate glasses provide information about the main characteristics frequencies for phosphate bonds present in the glass network such as P=O, P-O-P, O-P-O and P-O-H. The presence of P-O-H bond indicates the hygroscopic nature of these phosphate glasses. The decrease in oxygen content of glass sample after γ-irradiation was indicating by bond breaking in the glass sample. This creates oxygen vacancy in the glass sample, which has been noticed as generation of defects in the optical observations. The optical properties such as RPL emission and excitation spectra of the Ag^+-doped phosphate glass were also investigated in this study. RPL emission spectrum consists of two emission bands peaked at about 460 nm and 620 nm. Blue RPL at 460 nm was closely connected to the 265 nm bands of the excitation spectrum. These bands were attributed to the Ag_2^+ and Ag^0 centres, respectively. On the other hand, orange RPL at 620 nm was associated with the 320 nm band in the excitation spectrum and this optical activity was due to the Ag^{2+} centres. Finally, the effect of gamma irradiation was observed in the form of change in the structural units of phosphate glass due to breaking and rearrangement of bonds in the glass network. All these changes were found to be dependent on the composition of the glasses system.

Acknowledgement

The authors wish to acknowledge the support from centre for research and instrumentation management (CRIM) for sample analysis and funding for this study from Universiti Kebangsaan Malaysia from grant DLP-2013-037, GUP-2014-17, UKM-DIP-2014-22 and FRGS/1/2014/5G06/UKM/02/3.

References

1. Andreeva, N. Z., Vil'chinskaya, N. N., Dmitryuk, A.V., Perminov, A. S., Petrovskii, G. T. and Savvina, O. C. (1985). Influence of activator concentration on the dosimetric properties of radio photoluminescent glasses. *Atom. Énergiya*. 58(2): 132 – 135.
2. Beekenkamp, P. (1965). Colorcenters in borate, phosphate and borophosphate glasses. Thesis, Technical University, Eindhoven, Philips Res., Suppl. 4.
3. Bishay, A. (1961). Gamma-ray induced coloring of some phosphate glasses. *J. Am. Ceram. Soc*. 44(11): 545-552.
4. Bishay, A. (1970). Radiation induced colorcenters in multicomponent glasses. *J. Non-Cryst. Solids*. 3: 54 –114.
5. Bocharova, T. V., Karapetan, G. O., Mironov, A. M., Khalilev, V. D. and Tagil'tseva, N. O. (2006). Gamma-induced absorption spectra as a new method for RE-ion environment study in a fluorophosphates glasses. *Opt. Mater*. 28: 1296 –1300.
6. Dmitryuk, A. V., Paramzina, S. E., Savvina, O. C. and Yashchurzhinskaya, O. A. (1989). Nature of radiophotoluminescent centers in silver-activated phosphate glasses. *Opt. Spectrosc*. 66: 1070 – 1075.
7. Hsu, S. M., Yang, H. W., Huang, D. Y. C., Hsu, W. L., Lu, C. C. and Chen, W. L. (2008). Development and physical characteristics of a novel compound radiophotoluminescent glass dosimeter. *Radiat. Meas*. 43: 538 – 541.
8. Takeda, Y., Plaksin, O. A. and Kishimoto, N. (2007). Dispersion of nonlinear dielectric function of Au nanoparticles in silica glass. *Opt. Express*. 15: 6010 – 6018.

9. Dmitryuk, A. V., Paramzina, S. E., Solov'eva, N. D. and Timofeev, N.T. (1996). The influence of glass composition on the properties of silver-doped radiophotoluminescent phosphate glasses. *J. Non-Cryst. Solids*. 202: 173 – 177.
10. Kurobori, T., Zheng, W., Miyamoto, Y., Nanto, H. and Yamamoto, T. (2010). The role of silver in the radio-photoluminescent properties in silver-activated phosphate glass and sodium chloride crystal. *Opt. Mater*. 32: 1231 –1236.
11. Yokota, R. and Imagawa, H. (1965). ESR studies of radiophotoluminescent centers in silver-activated phosphate glass. *J. Phys. Soc. Jpn*. 20: 1537 –1538.
12. Ahmed, I., Abou Neel, Valappil, S. P., Nazhat, S. N., Pickup, D. M., Carta, D., Carroll, D. L., Smith, M. E. and Knowles, J. C. (2007). The structure and properties of silver-doped phosphate-based glasses. *J. Mater. Sci. Mater. Med*. 42:9827 – 9835.
13. Birkin, P. R., Offin, D. G., Joseph, P. F. and Leighton, T.G. (2005). Cavitation, shock waves and the invasive nature of sonoelectrochemistry. *J. Phys. Chem. B*.109: 16997 –17005.
14. ElBatal, F. H., Ouis, M. A., Morsi, R. M. M. and Marzouk, S. Y. (2010).Interaction of gamma rays with some sodium phosphate glasses containing cobalt.*J. Non.-Cryst. Solids*. 356(1): 46-55.
15. Piao, F., Oldham, W. G. and Haller, E. E. (2000). The mechanism of radiation-induced compaction in vitreous silica. *J. Non-Cryst. Solids*. 276: 61 –71.
16. Maurel, C., Cardinal, T., Bellec, M., Canioni, L., Bousquet, B., Treguer, M., Videau, J. J. and Richardson, M. (2009). Luminescence properties of silver zinc phosphate glasses following different irradiations. *J. Lumin*. 129(12): 1514 –1518.
17. Zhao, Quan, Z., Qiu, J. R., Jiang, X. W., Zhao, C. J. and Zhu, C. S. (2004). Controllable precipitation and dissolution of silver nanoparticles in ultrafast laser pulses irradiated Ag^{+}-doped phosphate glass. *Opt. Exp*. 12(17): 4035 – 4040.
18. Yokota R. and Muto Y. (1971). Silver-activated phosphate dosimeter glasses with low energy dependence and higher sensitivity. *Health Phys*. 20: 662 – 663.

MALAYSIAN JOURNAL OF ANALYTICAL SCIENCES
Published by The Malaysian Analytical Sciences Society
ISSN 1394 - 2506

THEORETICAL AND EXPERIMENTAL INVESTIGATION OF PYRIDYL-THIOUREA DERIVATIVES AS IONOPHORES FOR Cu(II) ION DETECTION

(Kajian Teori dan Eksperimen bagi Terbitan –Terbitan Piridil-Tiourea Sebagai Ionofor untuk Pengesanan Ion Cu(II))

Wan M. Khairul[1]*, Mohd Faizuddin Abu Hasan[1], Adibah Izzati Daud[1,3], Hafiza Mohamed Zuki[2], Ku Halim Ku bulat[1], Maisara Abdul Kadir[1]

[1]*School of Fundamental Science*
[2]*School of Marine Science and Environment*
Universiti Malaysia Terengganu, 21030 Kuala Terengganu, Terengganu, Malaysia
[3]*Faculty of Engineering Technology,*
Universiti Malaysia Perlis (UniMAP),
Aras 1, Blok S2, Kampus UniCITI Alam, Sungai Chuchuh, 02100 Padang Besar, Perlis, Malaysia

**Corresponding author: wmkhairul@umt.edu.my*

Received: 5 November 2015; Accepted: 27 December 2015

Abstract

Copper (II) ion chemical sensors based on pyridine-thiourea derivatives; *N*-pyridyl-*N'*-(biphenyl-4-carbonyl)thiourea (**L1**), and *N*-pyridyl-*N'*-(3,5-dimethyoxybenzoyl)thiourea (**L2**) were synthesised, characterised, and studied as ionophores in the form of thin-films PVC membranes. The ionophores exhibited good responses towards copper (II) ion over the concentration range of 2 x 10^{-4} to 10 x 10^{-4} M with a limit of detection 1.34 x 10^{-5} to 1.48 x 10^{-5} M. The proposed sensors **L1** and **L2** revealed good performance in term of reproducibility and regeneration of the ionophores with low relative standard deviation (RSD) values 4.17 % and 2.74 % respectively. Besides, quantum chemical calculation performed using Gaussian 09 program indicated the oxygen (O) atom from carbonyl moiety (C=O) was the most favourite reactive site and mainly responsible for ionophore– Cu(II) interaction. The obtained data revealed pyridine-thiourea derivatives offered great potential as ionophore for the detection of Cu (II) ion.

Keywords: pyridine, thiourea, metal sensor, density functional theory, spectroscopic

Abstrak

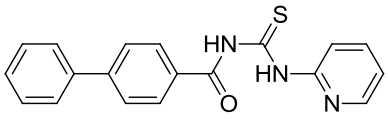
Pengesan kimia bagi ion kuprum (II) berasaskan terbitan piridil-tiourea; *N*-piridil-*N'*-(bifenil-4-karbonil)tiourea (**L1**), and *N*-piridil-*N'*-(3,5-dimetoksibenzoil)tiourea (**L2**) telah disintesis, dicirikan, dan dikaji sebagai ionofor dalam bentuk membran-membran PVC filem nipis. Ionofor – ionofor tersebut menunjukkan tindak balas yang baik terhadap ion kuprum (II) dalam julat kepekatan 2 x 10^{-4} to 10 x 10^{-4} M dengan had pengesanan 1.34 x 10^{-5} sehingga 1.48 x 10^{-5} M. Pengesan **L1** dan **L2** yang dicadangkan ini menunjukkan prestasi yang baik dari segi kebolehkeluaran semula dan penjanaan semula bagi ionofor – ionofor tersebut dengan nilai sisihan relatif piawaian yang rendah iaitu masing – masing 4.17% dan 2.74%. Selain itu, pengiraan kuantum kimia dilakukan dengan menggunakan program Gaussian 09 yang menyatakan bahawa atom oksigen (O) daripada moiti karbonil (C=O) adalah kawasan paling reaktif dan selalunya terlibat dalam interaksi ionofor-Cu (II). Data yang diperolehi menyatakan terbitan piridil-tiourea menawarkan potensi yang bagus sebagai ionofor bagi pengesanan ion Cu (II).

Kata kunci: piridina, tiourea, pengesan logam, teori fungsi ketumpatan, spektroskopi

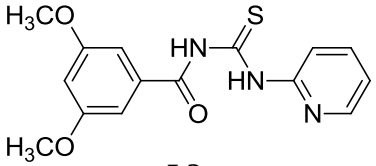
Introduction

In this developing era, industrial sector has rapidly become one of the most important sectors throughout the world. Production and manufacturing sectors gradually increase the rate of pollution as a result of the industrialisation process. Undoubtedly, metal as pollutant is known to be one of the common water pollution and has emerged as a harmful pollutant due to its toxicity at low concentration. Excessive amount of heavy metals will produce various toxicological effects and danger to most living organisms including to human [1, 2]. Among these, copper (Cu) which is classified as one of the metal pollutants which known to be toxic substance at certain concentration [3, 4]. Furthermore, Aziz et al. [5] reported the maximum limit under Standard B of Malaysian-Environmental Quality Act 1974 (Sewage and Industrial Effluents) 1979 is 1.0 mg/L which eventually make the detection process of this species to be such a challenge. Generally, metal detection in water samples depends on the utilization of expensive instrumentation techniques which at certain extend, can be rather complicated and time consuming [6 – 8]. Nowadays, there is a growing interest on research directed to the precaution of environmental control and industrial processes. Therefore, chemical sensor has arisen as an ideal option due to its rapid and simple approach towards detection. Thus, we proposed to synthesise and characterise a new class of ionophores featuring multi-chelating agent of pyridyl-thiourea derivatives which were fabricated into thin-film as molecular sensor towards copper (II) ion as an analyte of choice. A series of pyridine substituted thiourea compounds with different aromatic substituents namely biphenyl and 3,5-dimethoxybenzene were synthesised as proposed metal dication sensors prior treated as chemosensor for the detection of Cu (II) ion in the form of thin films. Figure 1 depicts all molecular structures of ionophores synthesised in this study.

Due to electronic conjugation system, multiple donor atoms (S, O and N) for complexation and ease of synthesis, thiourea moiety was chosen as material for development of potential chemical sensor. In order to enhance electronic conjugation of this system, several electron donor groups (R) were selected which expected to generate ideal flow of electrons via the progress of fair electronic conjugation in thiourea molecular framework. Besides, pyridine was introduced as substituent in this system to increase number of possible binding sites for interaction of metal ion. In order to specifically find the accurate interacting site of this molecule towards copper (II), density functional theory (DFT) calculation using Gaussian 09 was also carried out. The study on limit of detection, reproducibility and efficiency of these molecules in the form of thin films were carried out via UV-visible analysis. Result revealed that the efficiency and suitability of this system can be applied as chemical sensor for Cu^{2+} ion detection.



L1



L2

Figure 1. The molecular structures of pyridine-thiourea derivatives

Materials and Methods

Reagents

The chemicals used, namely ammonium thiocyanate, 2-benzylaminopyridine, biphenyl-4-carbonyl chloride, and 3,5-dimethoxy benzoyl chloride, were purchased from Sigma-Aldrich, Merck, Acrós Organics, and R & M Chemical. All solvents used in this study such as acetone, chloroform, dichloromethane, diethyl ether, ethyl acetate, hexane, methanol, and acetonitrile were purchased from Merck, Fisher Scientific, and R & M Chemical. For film membrane preparation, high molecular weight poly(vinyl chloride)(PVC), sodium tetraphenyl borate, tributyl phosphate, and tetrahydrofuran (THF) were used as received from Merck.

Characterisation

Infrared (IR) spectra were recorded using FT-IR Perkin-Elmer 100 spectrophotometer within spectral range 4000-400 cm^{-1}. CHNS microanalysis was carried out using a FLASHEA 1112 CHNS analyser for determination of

percentage of CHNS elements presence in the synthesised compounds. NMR spectra were recorded on Bruker Avance III 400 (^{1}H 400.11 MHz, ^{13}C 100.61 MHz) using deuterated chloroform ($CDCl_3$) at room temperature. The interaction between ionophores and Cu^{2+} were investigated using UV-visible spectrophotometer Shidmazu 1601 series in 1 cm path length quartz cell. Thin films membranes were fabricated via SCS 6808 spin-coater at angular speed of spinning at 2500 rpm. Theoretical evaluation was carried out to predict and investigate potential interaction between the synthesised compounds and Cu^{2+} ion via Gaussian 09 program package. The basic set used in the theoretical simulation was based on density functional theory (DFT) calculation at B3LYP/LANL2DZ to obtain several significant structural parameters.

Theoretical Evaluation on Interaction of the Pyridyl-Thiourea Compounds Towards Cu(II)

The theoretical analysis was carried out to observe several important parameters such as interaction behaviour, binding strength and binding mode of the pyridyl-thiourea derivatives (**L1** and **L2**) towards the tested analyte which undoubtedly contributed in sensing capability of each compound towards the studied metal ion using Gaussian 09 software. This theoretical analysis was based on DFT calculation at B3LYP/ 6-31G (d,p) for the thiourea compound and B3LYP/LANL2DZ for interaction of the synthesised compounds towards Cu (II) ion.

Synthesis of ionophores: Synthesis of *N*-pyridyl-*N'*-(biphenyl-4-carbonyl)thiourea (L1)

Ammonium thiocyanate (0.46 g, 6.00 mmol) in acetone was charged into a solution of biphenyl-4-carbonyl chloride (1.30 g, 6.00 mmol) to yield a suspension of pale yellow solution and white precipitate after *ca*. 4 hours of refluxed condition with constant stirring. The white precipitate was filtered. Then, a solution of 2-aminopyridine (0.56 g, 6.00 mmol) in acetone was added dropwise into the pale yellow filtrate. The reaction mixture was stirred at refluxed condition for *ca.* 6 hours. After adjudged completion by TLC (ethyl acetate: hexane; 1:4), the reaction was cooled to room temperature. Subsequent to addition of three ice cubes into the yellow filtrate, pale yellow precipitate was formed and filtered. The precipitate was recrystallized from methanol to produce yellow solid of **L1** (1.45 g, 73%).^{1}H NMR (400.11 MHz, $CDCl_3$): δ_H 7.13 (t, J_{HH} = 6 Hz, 1H, Ar-CH); 7.35 (d, J_{HH} = 7 Hz, 1H, Ar-CH); 7.39 (pseudo-d, J_{HH} = 6 Hz, 2H, Ar-CH); 7.55 (pseudo-d, J_{HH} = 6 Hz, 2H, Ar-CH); 7.66 (d, J_{HH} = 8 Hz, 2H, Ar-CH); 7.75 (t, J_{HH} = 8 Hz, 2H, Ar-CH); 7.92(d, J_{HH} = 8 Hz, 1H, Ar-CH); 8.36 (d, JHH = 8 Hz, 1H, Ar-CH); 8.72 (d, J_{HH} = 8 Hz, 1H, Ar-CH); 9.24, 13.24 (2 x s, 1H, NH); ^{13}C NMR (100.61 MHz, $CDCl_3$): δ_C 116.5, 121.4, 127.3, 127.8, 128.3, 128.6, 129.1, 130.1, 138.4, 139.3, 146.6, 147.5, 151.1 (13 x s, Ar); 166.1 (s, C=O); 177.3 (s, C=S); Elemental analysis for $C_{19}H_{15}N_3OS$: [Found (Calculated.)]: C = 69.12 (68.45); H = 4.73 (4.53); N = 12.55 (12.60); S = 9.96 (9.62).

Synthesis of *N*-pyridyl-*N'*-(3,5-dimethyoxybenzoyl)thiourea (L2)

Yielding pale yellow crystalline solid (64% yield), **L2** was prepared from 3,5-dimethoxybenzoyl chloride (1.51 g, 7.51 mmol), ammonium thiocyanate (0.57 g, 7.51 mmol), and 2-aminopyridine (0.71 g, 7.51 mmol) in the same manner as described in **L1**. ^{1}H NMR (400.11 MHz, $CDCl_3$): δ_H 3.80 (s, 6H, OCH_3); 6.62 (t, J_{HH} = 4 Hz, 1H, Ar-CH); 6.10 (d, J_{HH} = 2 Hz, 1H, Ar-CH); 7.84 (t, J_{HH} = 8 Hz, 1H, Ar-CH); 8.34 (d, J_{HH} = 6 Hz, 1H, Ar-CH); 8.67 (d, J_{HH} = 8 Hz, 1H, Ar-CH); 9.48, 13.47 (2 x s, 1H, NH); ^{13}C NMR (100.61 MHz, $CDCl_3$): δ_C 55.8 (s, OCH_3); 105.6, 106.0, 116.9, 121.4, 139.7, 150.6, 161.3 (8 x s, Ar-CH); 166.1 (s, C=O); 177.5 (s, C=S); Elemental analysis for $C_{15}H_{15}N_3OS$: [Found (Calculated.)]: C = 56.98 (56.77); H = 4.94 (4.76); N = 13.21 (13.24); S = 10.68 (10.10).

Preparation of film membranes

A solution of polyvinyl chloride (PVC) powder (120 mg), sodium tetraphenylborate (1.5 mg), tributylphosphate (240 mg), and of the compound (**L1** and **L2**) (80 mg) were dissolved in tetrahydrofuran (THF) with vigorous stirring for *ca.* 6 hours until the solution became a homogenous viscous solution [9]. The resulting solution was then transferred onto a glass slide of 5 cm x 0.5 cm which was placed in a SCS 6808 Spin Coater. The substrate was spun at high speed (2500 rpm) to obtain smooth and homogenous thin film.

Preparation for pH studies

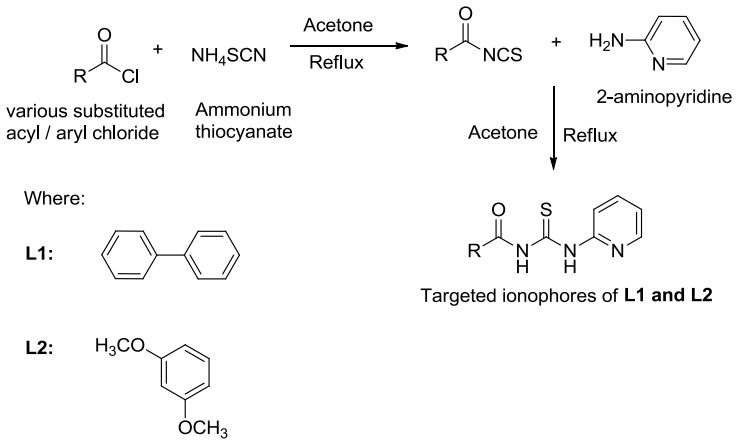
The study was carried out in pH buffered solution to minimise any change in pH due to the effects of temperature, light and the presence of carbon dioxide gas in air which can produce errors in the results. In this study, 1 mL of 5 x 10^{-4} M of Cu(II) ion solution was added to 5 ml of 5 x 10^{-5} M solutions of **L1** and **L2** prepared in different pH buffers (pH range from 3 to 10). A sample of the mixture was transferred into 1 cm^3 cuvette and the spectral

properties of these samples were recorded via UV-vis spectroscopy. Collected data was plotted to study effect of pH on response of **L1** and **L2** to sense the presence of Cu (II) ion.

Results and Discussion

Synthesis and characterisation of pyridine-thiourea

The pyridine-thiourea derivatives are proposed as ionophores (Figure 1) have their own advantages such as exhibit quick and ease of synthesis and purification. Scheme 1 shows the general synthetic work-up of the pyridine-thiourea derivatives synthesis. The molecular system featuring electron donating molecular framework has ability to increase their electron density throughout the molecular system, a desired feature to promote the binding ability of the ionophores with Cu (II) ion. Besides, **L1** and **L2** theoretically have known as multidentate ligand due to the existence of different coordination sites (N, O, and S) in particular geometry. Good yield of synthesised compounds were obtained of 73 %, and 89 % for **L1** and **L2** respectively.



Scheme 1. The general synthetic work-up of ionophores synthesis

The main IR bands of interest for **L1** and **L2** have been identified to show five absorption bands, namely, ν(N-H), ν(C-H), ν(C=O), ν(C-N), and ν(C=S). The first absorption band was assigned as the secondary amine N-H which could be observed at 3259 to 3267 cm^{-1} as medium intensity absorption band which was in a good agreement with previous works carried out by [10, 11] who reported the N-H stretching band was located in similar region. In most thiourea derivatives, N-H stretching band appeared at above 3200 cm^{-1} due to the influence of strong intramolecular hydrogen bond between N-H…O=C [12, 13] which led to the formation of broad and weak absorption band of N-H stretching [14,15]. Meanwhile, C-H alkane stretching bands could be observed in the region of 2974 to 3064 cm^{-1} as aromatic and alkyl type of CH groups were present in their molecular structures. In addition, in a range of 1524 to 1536 cm^{-1}, high intensity of ν(C-N) absorption band clearly been observed. Strong absorption band observed at 1670 cm^{-1} in both spectra were assigned as C=O absorption band. The appearance of the strong band was in a good agreement with previous studies carried out by [16 – 18]. The C=O stretch in all synthesised compounds were found at lower wavenumber compared with expected carbonyl stretching at around 1700 cm^{-1} as most carbonyl thiourea derivatives were stabilised by formation intramolecular hydrogen bond of C=O…H-N which led to emergence of pseudo-six-membered ring [19]. Consequently, formation of the intramolecular hydrogen bond interaction led to an increase in its polarity making the double bond character to be weaker and shifting the band to a lower wavenumber region [20]. The absorption band of C=S stretch for all synthesised compounds appeared as medium bands within range of 739 to 741 cm^{-1}. The presence of intramolecular hydrogen bonding between C=O with N-H moiety led to stronger electronegativity property of the N-H group which simultaneously enhanced double bond character of the C=S group [21] in which was found by several researchers [12, 22, 23].

In the ^{1}H NMR spectrum of **L2** a singlet resonance at δ_H 3.80 ppm was attributed to methoxy moiety in the compound. The O-CH_3 resonance was located at higher chemical as it was bonded to electronegative oxygen atom which pulled the electrons from proton methyl and deshielded the resonance to higher chemical shift region [24, 25]. High intensity singlet resonance with 6H integration shows that this resonance represents two symmetrical methoxy groups as reported by [26, 27]. The aromatic protons of both **L1** and **L2** can be observed at δ_H 7.13 – 8.74 ppm appeared as distinctive multiplet resonances due to the presence of unresolved aromatic protons [28]. The most common observation in ^{1}H NMR analysis of typical acyl thiourea molecular system is the presence of two singlet N-H resonances at the most downfield position [10, 11]. Both of these resonances were observed as distinctive broad singlets at the most deshielded region in the spectra. This is due to the presence of several electron-withdrawing moieties namely carbonyl and thiocarbonyl in the molecule which decreased electron density around the resonances and shifted the protons of N-H to downfield position [17, 29]. However, carbonyl-substituted N-H proton (NHCO) was found to be at lower chemical shift (δ_H 9.24 - 9.48 ppm) in comparison to thione-substituted N-H proton (NHCS) which is located at δ_H 13.24 - 13.47 ppm as the formation of intramolecular hydrogen bond between carbonyl moiety and thione-substituted N-H resonance produced stronger deshielding effect [12,15]. Carbon resonances in ^{13}C NMR spectra of **L2** could be observed at upfield position (δ_C 55.8 ppm) due to the presence of methyl moiety in molecular structure. However, CH_3 resonance of **L2** is observed at higher chemical shift (δ_C 55.8 ppm) as it was bonded to electronegative atom, oxygen, shifted the resonance to a higher chemical shift [30]. Resonances of aromatic carbon were observed at δ_C 105.5-161.2 ppm. Two distinctive resonances at the most downfield region (δ_C 166.0 and 177.3 ppm) can be observed which corresponded to carbonyl (C=O) and thione (C=S) respectively in both spectra of **L1** and **L2** [16, 31, 32]. This is due to formation of intramolecular hydrogen bonding and electronegativity effect of oxygen and sulphur atoms which pulled certain amount of electrons from both moieties and deshielded the resonances to higher chemical shift [13, 33]. The existence of several important resonances at expected regions in ^{1}H and ^{13}C NMR spectra of all synthesised compounds proved that pyridine-thiourea derivatives of both **L1** and **L2** were successfully synthesised.

Evaluation of sensing performances towards Cu (II) ion: Reaction responses

The reaction of the films towards different concentration of Cu (II) ion was investigated. Figure 2 and Figure 3 show the reaction response of **L1** and **L2** in the presence of Cu (II) ion within concentration range of Cu (II) ion was 2 x 10^{-4} M to 10 x 10^{-4} M. Upon exposure of Cu (II) ion to the film, the formation of absorption band of **L1** towards Cu (II) ion observed at wavelength of 385 nm. The higher the concentration of Cu (II) ion, higher the intensity of the absorption bands was observed. Similar observation was discovered in **L2** film with formation of medium absorption shoulder bands when Cu (II) ion was introduced to the film.

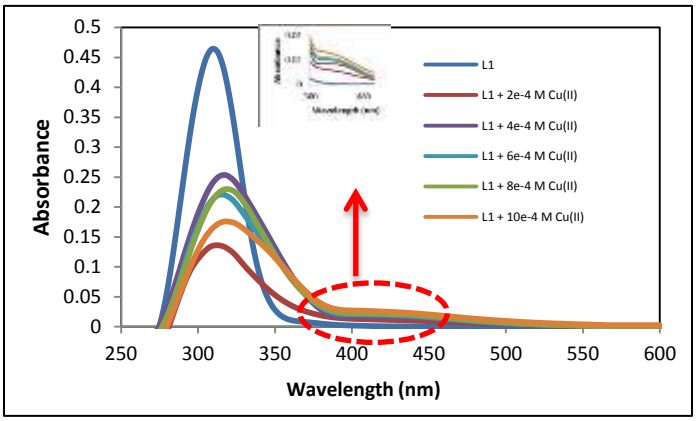


Figure 2. Reaction response of **L1** towards Cu (II) ion

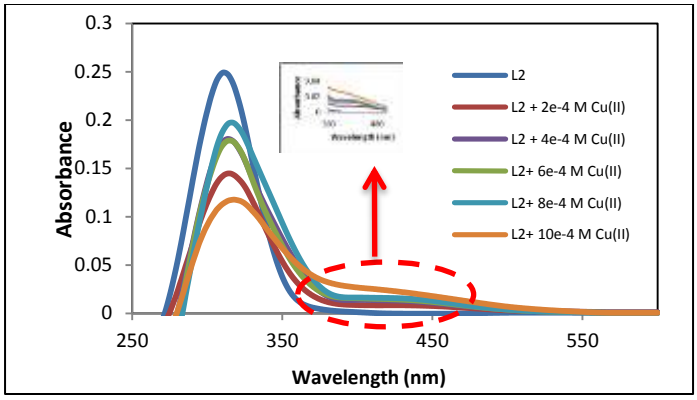


Figure 3. Reaction response of **L2** towards Cu (II) ion

Reproducibility of L1 and L2

A reproducible film will produce a stable and consistent data which is very crucial aspect in the sensing application. A number of 8 strips of samples were fabricated and used to complete the reproducibility test. Figure 4 shows reproducibility data behaviour of **L1** and **L2**.

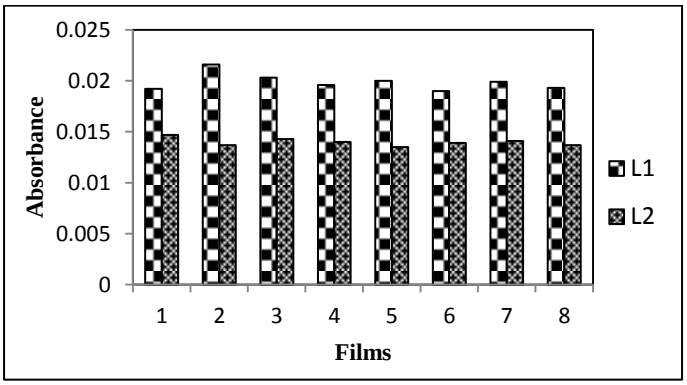


Figure 4. Graph of reproducibility studies for **L1** and **L2**

Figure 4 indicates stable and consistent reading for all films. Thus, the consistency in reading of the film showed that all films exhibited high reproducibility ability. Relative standard deviation (RSD) was calculated to prove and compare which film system possessed the best reproducibility. Table 1 shows the RSD value of **L1** and **L2** for their reproducibility property.

Table 1. RSD value of reproducibility for **L1** and **L2**

Film	Average, x	Standard Deviation	Relative Standard Deviation (%)
L1	0.019863	0.000828	4.17
L2	0.013988	0.000383	2.74

Table 1 revealed both **L1** and **L2** exhibited low value of RSD which were 4.17% and 2.74% respectively in which indicates higher ability of reproducibility [34, 35]. Therefore, it can be concluded that both L1 and L2 films exhibited reproducible results for detection of Cu(II) ion which is critical in order to produce uniform and accurate reading in its sensing performance. L2 exhibits the most effective reproducibility compared to L1. Higher RSD value might be caused by several technical errors during preparation of thin film such as uncontrollable thickness as well as uniformity of the films and amount of compound trapped in the films.

Regeneration of L1 and L2

Regeneration of chemosensor represents the ability of the sensors to be used repeatedly. An ideal sensor is a sensor with high regeneration property in which it can be used repeatedly and effectively for several measurements. Figure 5 shows regeneration data of all designated chemosensor (**L1** and **L2**).

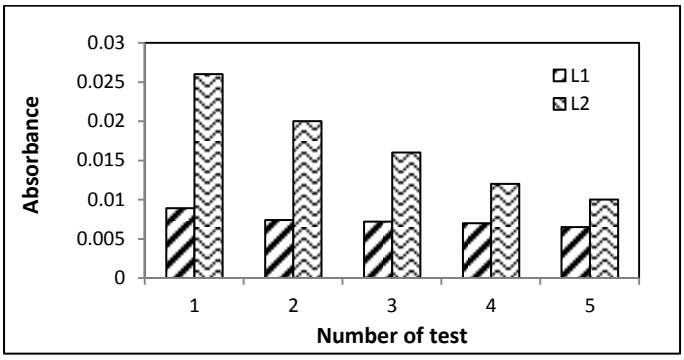


Figure 5. Graph of regeneration for **L1** and **L2**

L1 found to have ideal regeneration pattern up to 5 cycles which indicated multi-testing films. However, the sensing performance of **L2** decreased dramatically from the first to the fifth cycles compared to **L1** which showed gradual decreasing of its sensing performance. Based on Figure 5, **L1** offered ideal regeneration ability compared to **L2**. Table 2 shows the value of RSD in term of regeneration property of **L1** and **L2**.

Table 2. RSD value of regeneration for **L1** and **L2**

Film Cycle	**L1**		**L2**	
	Absorbance	**Percentage of regeneration (%)**	**Absorbance**	**Percentage of regeneration (%)**
1	0.0089	100	0.026	100
2	0.0074	83.15	0.020	76.92
3	0.0072	80.90	0.016	61.54
4	0.0070	78.65	0.012	46.15
5	0.0065	73.03	0.010	38.46
Mean, x	0.007400		0.016800	
Standard deviation (σ)	0.000903		0.006419	
RSD (%)	12.20		38.21	

The huge decrease of absorbance for both **L1** and **L2** films was contributed by the second cycle. This is due to the film which was used directly after fabrication process without any cleaning process to remove untrapped residue of the compound which led to involvement of the untrapped residue in the sensing mechanism. **L1** exhibits the lowest RSD value with 12.20% compared to **L2** with 38.21%. Large value of RSD for **L2** contributed from the leaching of compound from the film during the metal ion leaching process in EDTA solution which reduced the amount of compound to detect Cu (II) ion leading to lower sensing response in the following cycles. This is due to the strength of EDTA to bind to Cu (II) ion and unsurprisingly, it is also able to attract the compound-Cu(II) complex from the film. Besides, due to the unbounded compounds in the film on the glass substrate, the compounds were easily detached and leached off when the film became swollen during the sensing studies.

Limit of Detection (LOD)

In this respect, LOD of **L1** and **L2** films towards Cu (II) ion was carried out to investigate the efficiency and sensitivity of the sensors for Cu (II) detection which was calculated using Equation 1. Figure 6 shows the LOD graph of **L1** and **L2**.

$$LOD = \frac{3s}{\sigma} \quad (1)$$

where *s* is the standard deviation for the blank and σ is the slope of the LOD graph.

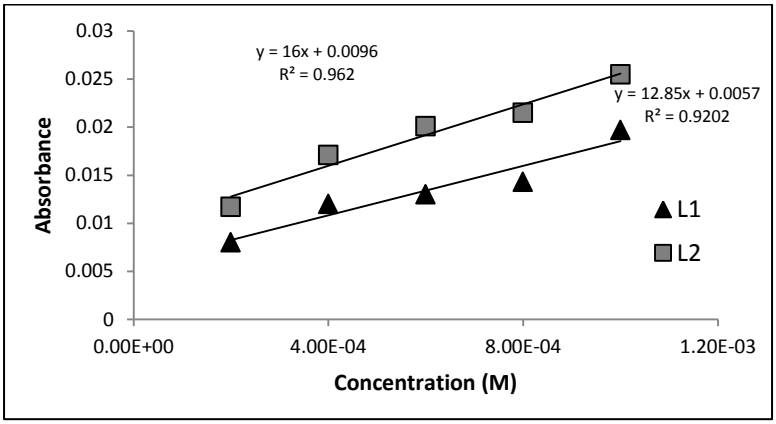


Figure 6. Calibration curves for LOD of **L1** and **L2**

LOD results revealed that, **L1** shows higher sensitivity towards detection of Cu (II) ion compared to **L2**. These experimental results were in good agreement with the theoretical investigation which **L1** exhibits higher response towards Cu (II) ion. In contrast, **L2** shows lowest sensitivity towards Cu (II) ion which was initially proven in the theoretical study on its binding mechanism and low interaction energy of **L2** towards Cu (II). Table 3 shows the data of LOD analysis of **L1** and **L2**.

Table 3. The data of LOD for **L1** and **L2**

Film	**L1**	**L2**
σ	12.85	16.00
s	5.76×10^{-5}	7.87×10^{-5}
LOD (M)	1.34×10^{-5}	1.48×10^{-5}

σ = slope of LOD graph; s = standard deviation

pH Effect

The reaction of metals with ligands is pH dependence. Therefore, pH study was carried out to find optimum pH condition for the reaction of Cu (II) ion with the selected compounds (**L1** and **L2**) which was carried out in the range pH 2 to pH 9. Figure 7 illustrates the effect of pH in the metal-ligand sensing performance.

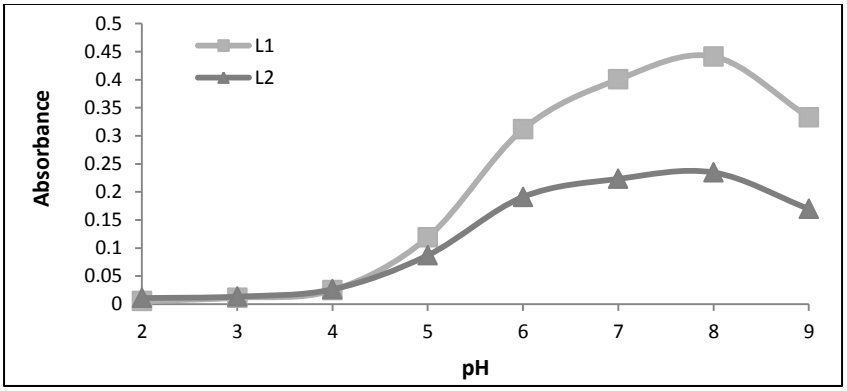


Figure 7. pH effect for metal-ligand sensing performance of **L1** and **L2**

Result obtained revealed that **L1** and **L2** showed quite similar patterns in the pH dependent graph which the curve started to increase at pH 4 then declined at pH 9. The most optimum pH for **L1** and **L2** compounds to sense Cu (II) ion was found at pH 8. This is due to the existence of intensive competition between H^+ and Cu (II) which decreased the ability of the compounds to form interaction with the metal ion resulting in lower response of absorbance at highly acidic condition [36]. Consequently, the absorbance of the compound-Cu (II) complex increased with increasing pH value.

Density functional theory (DFT) analysis

The ability of **L1** and **L2** to interact with Cu (II) was proven via density functional theory (DFT) analysis. Based on the analysis, **L1** and **L2** possessed ability to interact with the metal ion via C=O and C=S which acting as chelating ligand [37, 38]. Chelating behaviour of a ligand is known to have better and stronger interaction to enhance sensing performance of chemosensor. Similar binding behaviour observed in both **L1** and **L2** due to the presence of thiourea moiety in their molecular frameworks which is much dominant than other possible binding sites in the molecules. Based on the theoretical study, nitrogen atom of pyridine found to be twisted away from the interaction area which proved the pyridine portion was not involved in the interaction. There were several parameters which were taken into consideration in this analysis to compare capability of the compounds to interact towards Cu (II) such as interaction distance and binding energy. In term of interaction distance, **L1** indicated the lowest distance compared to **L2**. The interaction distance of **L1** via C=O and C=S towards Cu (II) are 2.027 Å and 2.520 Å respectively. The obtained distances were in the same region as reported by [31, 39]. This showed that **L1** has the highest strength to bind with Cu^{2+} followed by **L2**. Furthermore, in term of binding energy, the most negative value indicates optimum stability and strength of the interaction [40]. **L1** exhibits the most negative value of interaction energy (-230.34 kJ/mol) compared to **L2** -227.34 kJ/mol. The stronger binding energy and the shorter interaction distance of **L1** was caused by the stronger electron donating effect of biphenyl than 3,5-dimethoxybenzene groups in **L2**. Table 4 shows details on the theoretical evaluation data of these compounds via Gaussian 09 analysis.

Table 4. Theoretical interaction study between **L1** and **L2** towards Cu^{2+}

Compound	C=O···Cu (Å)	C=S···Cu (Å)	Binding Energy (kJ/mol)
L1	2.027	2.520	-230.34
L2	2.030	2.523	-227.34

Conclusion

On the basis of the results discussed in this paper, two new pyridine-thiourea derivatives **L1** and **L2** have been successfully synthesised and characterised prior to form active ionophores film entrapped in a PVC matrix for detection of Cu (II) ion. The reaction response of the ionophores towards different Cu (II) ion concentration was observed via difference in spectral features upon interaction with Cu(II). Apparently, **L1** exhibited good response with high sensitivity towards Cu(II) ion with limit of detection $1.34x10^{-5}$ M which was in good agreement with theoretical calculations. In fact, the theoretical analysis proved the oxygen (O) atom mainly defines its reactive site compared to sulphur (S) atom. Whilst, nitrogen (N) atom on pyridine moiety found to be twisted away from the interaction area; therefore, pyridine portion does not involved in the interaction mechanism with Cu (II). In addition, **L1** offered ideal interaction and binding energy for Cu (II) sensing (2.027 and -230.34 kJ/mol). In conclusion, a novel approach involving single molecular system of pyridine-thiourea (**L1** and **L2**) exhibited promising ability and potential for Cu (II) detection.

Acknowledgement

The authors would like to acknowledge the Ministry of Education (MOE) for the postgraduate student's scholarship (MyBrain15), and the School of Fundamental Science, Universiti Malaysia Terengganu for the research support and facilities.

References

1. Kaya, E. D., Söyüt, H. and Sükrü, B. (2013). Carbonic anhydrase activity from the gilthead sea bream (Sparus aurata) liver: The toxicological effects of heavy metals. *Environmental Toxicology and Pharmacology*, 36: 514 – 521.
2. Olawoyin, R., Oyewole, S. A. and Grayson, R. L. (2012). Potential risk effect from elevated levels of soil heavy metals on human health in the Niger delta. *Ecotoxicology and Environmental Safety*, 85: 120 – 130.
3. Viswanathan, K. (2012). Utilizing a tripeptide conjugated fluorescent hybrid nanoparticles as a fluorescence sensor for the determination of copper ions. *Sensors and Actuators A*, 175: 15 –18.
4. Lin, Q., Chen, P., Liu, J., Fu, Y-P., Zhang, Y-M. and Wei, T-B. (2013). Colorimetric chemosensor and test kit for detection copper (II) cations in aqueous solution with specific selectivity and high sensitivity. *Dyes and Pigments*, 98: 100 –105.
5. Aziz, H. A., Adlan, M. N. and Ariffin, K. S. (2008). Heavy metals (Cd, Pb, Zn, Ni, Cu, Cr (III)) removal from water in Malaysia: Post treatment by high quality limestone. *Bioresource Technology*, 99: 1578 –1583.
6. Bridgeman, J., Baker, A., Brown, D. and Boxall, J. B. (2015). Portable LED fluorescence instrumentation for the rapid assessment of potable water quality. *Science of the Total Environment*, 524: 338 –346.
7. Firooz, A. L., Ensafi, A. A., Karimi, K. and Khalifeh, R. (2013). Specific sensing of mercury (II) ions by an optical sensor based on a recently synthesized ionophore. *Sensors and Actuator B*, 185: 84 – 90.
8. Pradeep, T. (2009). Noble metal nanoparticles for water purification: a critical review. *Thin Solid Films*. 517(24): 6441 – 6478.
9. Bakker E, Simon W. (1992). Selectivity of ion-sensitive bulk optodes. *Analytical Chemistry*, 64(17):1805 – 1812.
10. Saeed, A., Shaheen, U., Hameed, A. and Naqvi, S. Z. H. (2009). Synthesis, characterization and antimicrobial activity of some new 1-(fluorobenzoyl)-3-(fluorophenyl)thioureas. *Journal of Fluorine Chemistry*, 130: 1028 – 1034.
11. Duan, X. –E., Wei, X. –H., Tong, H. –B., Bai, S. –D., Zhang, Y. –B. and Liu, D. –S. (2011). Ferrocene-modified pyrimidinyl acyl-thiourea derivatives: Synthesis, structures and electrochemistry. *Journal of Molecular Structure*, 1005: 91 – 99.
12. Karipcin, F., Atis, M., Sariboga, B., Celik, H. and Tas, M. (2013). Structural, spectral, optical and antimicrobial properties of synthesized 1-benzoyl-3-furan-2-ylmethyl-thiourea. *Journal of Molecular Structure*, 1048: 69 – 77.
13. Arslan, N. B., Kazak, C. and Aydın, F. (2012). N-(4-nitrobenzoyl)-N'-(1,5-dimethyl-3-oxo-2-phenyl-1H-3(2H)-pyrazolyl)-thiourea hydrate: synthesis, spectroscopic characterization, X-ray structure and DFT studies. *Spectrochimica Acta Part A-Molecular and Biomolecular Spectroscopy*, 89: 30–38.

14. Rahamathullah, R., Khairul, W. M., Salleh, H., Adli, H. K., Isa, M. I. N. and Tay, M. G. (2013). Synthesis. Characterization and Electrochemical Analysis of V-Shaped Disubstituted Thiourea-Chlorophyll Thin Film as Active Layer in Organic Solar Cells. *International Journal of Electrochemical Science*, 8: 3333 – 3348.
15. Zhang, L. –Y., Yuan, Y. –F., Hu, A. –G., Wang, J. –T. and Sun, J. (2001). Synthesis and molecular structure of a novel ferrocene-containing macrocyclic acyl thiourea derivative. *Journal of Organometallic Chemistry*, 637 – 639: 204 – 208.
16. Saeed, A., Erben, M. F., Abbas, N. and Flörke, U. (2010). Synthesis, crystal X-ray diffraction structure, vibrational properties and quantum chemical calculations on 1-(4-(4-Fluorobenzamido)phenyl)-3-(4-fluorobenzoyl)thiourea. *Journal of Molecular Structure*, 984: 240 – 245.
17. Tan, S. S., Al-abbasi, A. A., Mohamed Tahir, M. I. and Kassim, M. B. (2014). Synthesis, structure and spectroscopic properties of cobalt(III) complexes with 1-benzoyl-(3,3-disubstituted)thiourea. *Polyhedron*, 68: 287–294.
18. Atiş, M., Karicin, F., Sariboga, B., Tas, M. and Celik, H. (2012). Structural, antimicrobial and computational characterization of 1-benzoyl-3-(5-chloro-2-hydroxyphenyl)thiourea. *Spectrochimica Acta Part A-Molecular and Biomolecular Spectroscopy*, 98: 290 – 301.
19. Saeed, A., Erben, M. F. and Bolte, M. (2013). Synthesis, structural and vibrational properties of 1-(adamantine-1-carbonyl)-3-halophenyl thioureas. *Spectrochimica Acta Part A-Molecular and Biomolecular Spectroscopy*, 102: 408 – 413.
20. Koca, İ., Özgür, A., Coşkun, K. A. and Tutar, Y. (2013). Synthesis and anticancer activity of acyl thioureas bearing pyrazole moiety. *Bioorganic & Medicinal Chemistry*, 21(13), 3859 – 3865.
21. Estévez-Hernández, O., Otazo-Sánchez, E., Hidalgo-Hidalgo de Cisneros, J. L., Naranjo-Rodríguez, I., and Reguera, E. (2005). A Raman and infrared study of 1-furoyl-3-monosubstituted and 3,3-disubstituted thioureas. *Spectrochimica Acta Part A-Molecular and Biomolecular Spectroscopy*, 62(4-5): 964 –971.
22. Vinithra, G., Suganya, S. and Velmathi, S. (2013). Naked eye sensing of anions using thiourea based chemosensors with real time application. *Tetrahedron Letter*, 54(41): 5612 –5615.
23. Khairul, W. M., Yusof, M. F., Rahamathullah, R., Daud, A. I., Jasman, S. M., Hasan, M. F. A., Salleh, H., Adli, H. K. and Tay, M. G. (2013). Single Molecule Thin Film Featuring Disubstituted Thiourea (TU) Doped with Chlorophyll as Potential Active Layer in Photovoltaic Cell. *International Journal of Electrochemical Science*, 8: 8175 – 8190.
24. Farhan, H. M. (2014). Preparation and investigation of complexes (bisazo)-imidazole with Co (II) and Cu (II). *World Science Research Journals*, 2(2): 26 – 34.
25. Hasali, N. H. M., Omar, M. N., Zuberdi, A. M. and AlFarra, H. Y. (2013). Biotransformation of ethyl p-methoxycinnamate from Kaempferia galanga L. using Aspergillus niger. *International Journal of Bioscience*, 3(7): 148 –155.
26. Koleva, B. B., Kolev, T., Lamshöft, M., Mayer-Figge, H., Sheldrick, W. S. and Spiteller, M. (2009). Synthesis, spectroscopic and structural elucidation of 1-butyl-4-[2-(3,5-dimethoxy-4-hydroxyphenyl)ethenyl)]pyridinium chloride tetrahydrate. *Spectrochimica Acta Part A-Molecular and Biomolecular Spectroscopy*, 74(5): 1120 – 1126.
27. Sinha, S., Mandal, B. and Chandrasekaran, S. (2000). Selective para metalation of unprotected 3-methoxy and 3 , 5-dimethoxy benzoic acids with n- butyl lithium – potassium tert -butoxide (LIC – KOR): Synthesis of 3 , 5-dimethoxy-4-methyl benzoic acid. *Tetrahedron Letter*, 41: 3157–3160.
28. Yusof, M. S. M., Jusoh, R. H., Khairul, W. M. and Yamin, B. M. (2010). Synthesis and characterisation a series of N-(3,4-dichlorophenyl)-N′-(2,3 and 4-methylbenzoyl) thiourea derivatives. *Journal of Molecular Structure*, 975(1-3): 280 – 284.
29. Aydın, M., Ünal, B., Esat, B., Baykal, a., Karaoğlu, E., Toprak, M. S. and Sözeri, H. (2012). Synthesis, magnetic and electrical characteristics of poly(2-thiophen-3-yl-malonic acid)/Fe3O4 nanocomposite. *Journal of Alloys and Compounds*, 514: 45 – 53.
30. Zhang, X. H., Wang, L. Y., Zhan, Y. H., Fu, Y. I., Zhai, G. H. and Wen, Z. Y. (2011). Synthesis and structural studies of 4-[(5-methoxy-1H-indole-3-yl)-methylene]-3-methyl-isoxazole-5-one by X-ray crystallography, NMR spectroscopy, and DFT calculations. *Journal of Molecular Structure*, 994: 371 –378.

31. Koch, K. R., Hallale, O., Bourne, S. A., Miller, J. and Basca, J. (2001). Self-assembly of 2:2 metallomacrocyclic complexes of Ni(II) and Pd(II) with 3,3,3',3'-tetraalkyl-1,1'-isophthaloylbis(thioureas). Crystal and molecular structures of cis-$[Pd(L_2\text{-}S,O)]_2$ and the adducts of the corresponding Ni(II) complexes: $[Ni(L^1\text{-}S,O)(pyridine)_2]_2$ and $[Ni(L^1\text{-}S,O)(4\text{-dimethylaminopyridine})_2]_2$. *Journal of Molecular Structure*, 561: 185 –196.
32. Marquez, H., Loupy, A., Calderon, O. and Pérez, E. R. (2006). An eco-friendly protocol for synthesis of thiourea derivatives: 1-benzoyl-3-benzylguanidine and 1-benzoyl-3-benzyl-O-ethylisourea. A possible non-purely thermal microwave assisted reaction. *Tetrahedron*, 62(11): 2616 – 2621.
33. Khairul, W. M., Isa, M. I. N., Samsudin, A. S., Adli, H. K. and Ghazali, S. R. (2014). Conductive biodegradable film of N-octyloxyphenyl-N'-(4-methylbenzoyl)thiourea. *Bulletin of Material Science*, 37(2): 357 – 369.
34. Jain, P. S., Khatal, R. N. and Surana, S. J. (2011). Spectrophotometric Determination of Amodiquine in Bulk and in Pharmaceutical Formulation. *Research Journal of Pharmaceutical, Biological and Chemical Sciences*, 2: 120 –127.
35. Rohini, P., Madhusudhanareddy, I., Gupta, A., Lokeswara, B. V. and Sundharani, G. (2011). Method development and validation for estimation of nevirapine from tablets by RP-HPLC. *International Journal of Pharmaceutics*, 1(1): 29 –33.
36. Wilson, D., Arada, M. d. l. A., Alegret, S. and del Valle, M. (2010). Lead (II) ion selective electrodes with PVC membranes based on two bis-thioureas as ionophore: 1,3-bis(N'-benzoylthioureido)benzene and 1,3-bis(N'-furoylthioureido)benzene. *Journal of Hazardous Material*, 181: 140 –146.
37. Zhang, Y. –M., Pang, H. –X., Cao, C. and Wei, T.-B. (2007). Synthesis, crystal structure and biological activity of a new complex, + bis (1,1-diethyl-3-(3-fluorobenzoyl)-thiourea)nickel(II). *Indian Journal of Chemistry Section A-Inorganic Bio-Inorganic Physical Theoretical & Analytical Chemistry*, 46A: 1787 – 1791.
38. Jadhao, S. Z. and Rathod, M. S. (2012). Synthesis and Structural Investigation of Zinc Metal-Ligand (Thiourea Derivative) Complexes. *Journal of Chemical and Pharmaceutical Research*, 4(3): 1562 –1565.
39. Schwade, V. D., Kirsten, L., Hagenbach, A., Lang E. S. and Abram, U. (2013). Indium (III), lead (II), gold (I) and copper (II) complexes with isophthaloylbis(thiourea) ligands. *Polyhedron*, 55: 155 –161.
40. Kumar, A., Kumar, V., Diwan, U. and Upadhyay, K. K. (2013). Highly sensitive and selective naked-eye detection of Cu2+ in aqueous medium by a ninhydrin-quinoxaline derivative. *Sensors and Actuator B*, 176: 420 – 427.

MALAYSIAN JOURNAL OF ANALYTICAL SCIENCES

Published by The Malaysian Analytical Sciences Society

ISSN 1394 - 2506

CHARACTERIZATION AND ANTIMICROBIAL STUDIES OF FIVE SUBSTITUTED BIS-THIOUREAS

(Pencirian dan Kajian Antimikrobial Terhadap Lima Sebatian Bis-Tiourea)

Nurulain Kamalulazmy, Sahilah Abd Mutalib, Fatin Ilyani Nasir, Nurul Izzaty Hassan*

School of Chemical Sciences and Food Technology,
Faculty of Science and Technology,
Universiti Kebangsaan Malaysia, 43600 UKM Bangi, Selangor, Malaysia

**Corresponding author: drizz@ukm.edu.my*

Received: 4 November 2015; Accepted: 4 January 2016

Abstract

Thioureas play an important role in medicinal chemistry and agricultures due to their biological activity such as antibacterial, antifungal, antiviral, herbicides, rodenticides, phenoloxidase enzymatic inhibitors, anti-HIV and anti-tumor agents. In this study, five substituted bis-thioureas have been synthesized. The isophataloyl chloride and 2,6- pyridinedicarbonyl dichloride were easily converted to bis-isothiocyanate compound *via* the reaction with ammonium thiocyanate by solid–liquid phase transfer catalysis of polyethylene glycol-400 (PEG-400). Bis-isothiocyanate compound was reacted with aniline derivatives to produce substituted bis-thioureas in good yield at room temperature. All the novel compounds were obtained as yellow solid after recrystallization using DMF/EtOH/H_2O. Their chemical structures were confirmed by Infrared spectrosopy (IR), Nuclear Magnetic Resonance (NMR) ^{1}H and ^{13}C and mass spectrometry. The five synthesized compounds were screened for antimicrobial activities using disc diffusion method for antimicrobial activity against Gram-positive bacteria (*Bacillus Subtilis* and *Staphylococcus Aureus*), Gram-negative bacteria (*Escherichia Coli* and *Salmonella Typhi*) and a mold (*Aspergillus Niger*). All tested compounds showed low antimicrobial activity since the diameter of inhibition zone (IZ) measure was less than positive control inhibition zone.

Keywords: bis-thiourea, antimicrobial activities, PEG-400

Abstrak

Sebatian tiourea memainkan peranan penting dalam kimia perubatan dan pertanian kerana sebatian ini mempunyai aktiviti biologi seperti antibakteria, antivirus, herbisid, rodentisid, perencat enzim fenoloksidase, anti-HIV dan agen anti-tumor. Lima sebatian bis-tiourea telah disintesis dalam kajian ini. Sebatian bis-isotiosianat disintesis dengan mudah melalui tindak balas di antara sebatian isofataloil klorida atau 2,6-piridinadikarbonil diklorida dengan ammonium tiosianat melalui pemindahan mangkin fasa pepejal-cecair polietilena glikol-400 (PEG-400). Seterusnya, sebatian bis-isotiosianat ditindak balas dengan sebatian amina bagi menghasilkan sebatian bis-tiourea dengan hasil yang baik pada suhu bilik. Semua sebatian diperolehi dalam bentuk pepejal bewarna kuning selepas penghabluran semula menggunakan pelarut DMF/EtOH/H_2O. Pencirian struktur sebatian dibuat melalui kaedah spektroskopi Infra Merah (IR), Resonans Magnet Nukleus (NMR) ^{1}H dan ^{13}C dan spektrometer jisim (MS). Kajian aktiviti antimikrob bagi lima sebatian yang telah disintesis dibuat melalui kaedah resapan cakera melawan bakteria Gram positif (*Bacillus Subtilis* and *Staphylococcus Aureus*),bakteria Gram negatif (*Escherichia Coli* and *Salmonella Typhi*) dan kulat (*Aspergillus Niger*). Semua sebatian menunjukkan aktiviti antimikrob yang diperolehi rendah kerana diameter zon perencatannya (IZ) lebih kecil daripada zon perencatan kawalan positif.

Kata kunci: bis-tiourea, aktiviti antimikrob, PEG-400

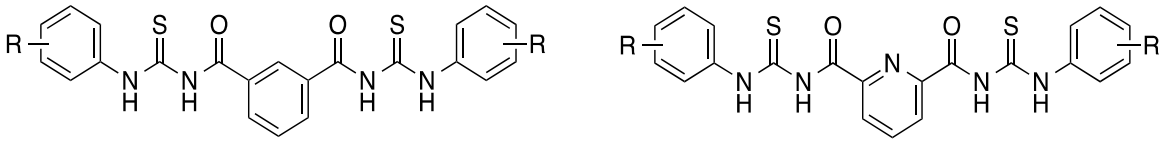
Introduction

Antimicrobial agents has received much attention in recent years due to the dramatically increased of bacterial and fungi infectious diseases. Since penicillin was introduced as antibiotics in 1940's and were among the first medications to be effective against many bacterial infections, antibiotics have been used widely in fight against infectious diseases caused by bacteria and fungi. However, the usage and misuse of antibiotics has led to the emergence of antibiotic-resistant pathogens including multidrug-resistant strains [1 – 3]. As consequence, it has caused failure in the treatment of infectious diseases. In that respect, there is growing interest in the discovery of new antibacterial agents.

Thioureas were first synthesized by Neuki in 1873 [4]. Thiourea derivatives exhibit various biological activities such as antiviral [5, 6], antibacterial [7], fungicidal [8, 9], herbicidal [10] and anti-HIV [11]. In 2011, Peng et al. have reported some 1,3-benzenedicarbonyl bisthiourea showed inhibition activities against cancer cells, such as human nasopharyngeal cancer cell line, CNE_2 and human oral cavity cancer cell line, KB with IC_{50} value 10.72 and 9.91 µm respectively [12].

Some example of bis-thiourea derivatives are N^3, $N^{3'}$-bis (disubstituted)isophatalyl-bis(thiourea), bis(thiourea)hydrazide [13], 2,2'-diaminobinapthalene-bis(thiourea) [14] and (bis)thiourea polyamine [15]. The derivatives of bis(disubstituted)isophtalayly-bis(thiourea) were also reported by Wang et al., Peng et al. and Jamil et al. research groups in 2005, 2011 and 2013, respectively [16, 17, 18]. In 2011, 1,2-Bis(*N*'-benzoylthioureidothioureido)-4-cholorobenzene was reported by Yamin research group [19]. The former compound is similar to 1,2-bis(*N*'-benzoylthioureido)benzene reported by Thiam and co-workers [20] during 2008 except for the presence of 4-chlorobenzene bridge at 1,2 position that connected the two benzoyl thioureido group.

In view of these observations, we have designed 1,3-benzenedicarbonyl and 2,6-pyridinedicarbonyl bisthiourea derivatives in order to investigate their antimicrobial activities. Herein, we report the syntheses of five bisthioureas compound **NA1-5** as shown in Figure 1 with the aid of solid-liquid phase transfer catalyst, PEG-400 [12]. Their structures of all the compounds were confirmed by IR spectroscopy and ^1H and ^{13}C Nuclear Magnetic Resonance (NMR). All compounds were screened for antimicrobial activities against Gram-positive bacteria, Gram- negative bacteria and a mold.



NA1: R = 4 - CH_3

NA2: R = 3,5 - $(CF_3)_2$

NA3: R = 4 - F

NA4: R = 4- CH_3

NA5: R = 3,5-$(CF_3)_2$

Figure 1. Chemical structures of substituted bis(thioureas)

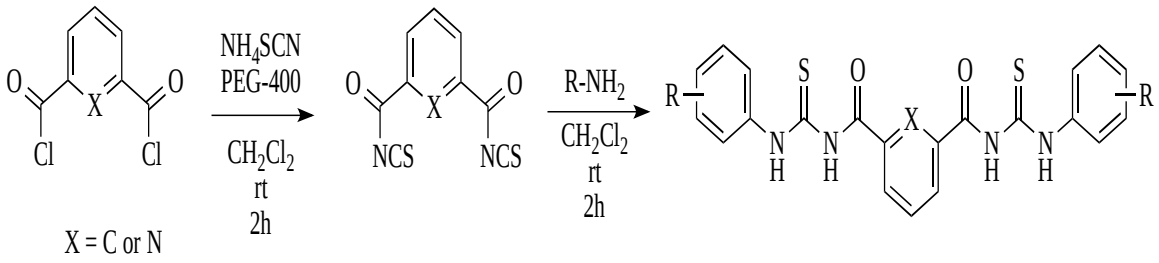
Materials and Methods

Chemicals (isophataloyl chloride, 2,6-pyridinedicarbonyl dichloride, aniline, 4-fluoroaniline, 3,5-bis(trifluoromethyl)aniline, ammonium thiocyanate, and PEG-400) and solvents (dichloromethane, dimethylformamide and ethanol) were purchased from Sigma Aldrich and MERCK and used directly without further purification. Melting points were determined by using BÜCHI Melting Point Model B-545. Infrared spectra were obtained using FTIR Perkin Elmer-1310 Spectrum GX Spectrophotometer in the spectral range of 4000

– 400 cm^{-1}. ^{1}H and ^{13}C were analysed by using Bruker Avance III 600 MHz and Jeol JNM-ECP 400MHz NMR spectrometer.

Synthesis of compounds

The general procedure for synthesizing compounds **NA1-5** (Scheme 1) was as follows. Isophataloyl chloride (2.46 mmol) or 2,6-pyridinedicarbonyl dichloride (2.45 mmol) was dissolved in 30 mL dichloromethane.
Subsequently, ammonium thiocyanate (7.38 mmol) and PEG-400 (0.22 mmol) were added to the solution and was stirred at room temperature for 2 hours. The resulting mixture was filtered to give isothiocyanate compound which was directly used without further purification. Aniline derivatives (5.15 mmol) was added and stirred for another hour. The yellow precipitate formed was filtered and washed with distilled water and purified by recrystallization using Dimethylformamide/Ethanol/Water.



Scheme 1. Synthesis of bis(thiourea) derivatives

Antibacterial screening

All synthesized compounds were screened for their antimicrobial activity by using disc diffusion method against five microbs (*Bacillus Subtilis, Staphylococcus Aureus, Escherichia Coli, Salmonella Typhi, and Aspergillus Niger*). Streptomycin (10µg) and Kinamycin (30µg) were used as positive control and Dimethyl sulfoxide as negative control. All bacteria were cultured in nutrient broth and incubated at 37 °C for 24 hours. After that, the agar media was prepared by pouring the nutrient agar solution into the sterilized petri dishes. Then, the cultures were spread on the surface of Nutrient Agar (NA). The discs (6 mm diameter) were impregnated with (10µL/disc) and (30µL/disc) test samples and then placed on the surface of the agar media. Experimental plates were incubated at 37 °C for 24 hours. Antimicrobial activity was determined by measuring the diameter of inhibition zone (IZ) and compared with positive control.

Results and Discussion

In this study, bis-isothiocyanate compound was not isolated and directly treated with respective aniline derivatives to give the corresponding bis-thiourea (**NA1-5**) in moderate to good yield *via* nucleophilic substitution mechanism. IR studies showed that, strong absorption in region 3250 – 3383 cm^{-1}, which corresponds to υ (N-H) stretching. The υ (C=O) absorption bands were observed in region 1650-1687 cm^{-1}. The medium intensity bands around 1152 – 1127 cm^{-1} attribute to the stretching of υ (C=S). All absorptions band value was in agreement with standard absorption value for thiourea compounds.

In the ^{1}H NMR spectra, the CONH protons appear as singlet in the range of δ 12.3 – 12.4 ppm whereas CONH protons appeared at δ 11.1 – 11.5 ppm. The appearance of N-H signals at higher frequency was due to the presence of carbonyl and thiocarbonyl groups which exert strong deshielding effect. The aromatic protons of parent 1,3-benzenedicarboxamide appeared around δ 8.5 –7.8 ppm. The aromatic protons of amine in compound NA1 and NA2 showed peaks in the range of δ 7.5 – 7.2 ppm and δ 8.8 – 7.9 ppm respectively. The protons signals of amine in NA2 were observed at higher frequency because the protons were deshielded by CF_3 groups. Compounds with parent 2,6-pyridinedicarboxamide protons signals were found at δ 8.0 –7.5 ppm while aromatic protons of amine in compound NA3, NA4 and NA5 appeared at δ 8.5 – 6.8 ppm. The aromatic protons signals of amine in compound NA3, NA4 and NA5 were slightly different from each other may be influenced by the nature of substituent group attached to the compound. Electronegative

atom reduced the electron density around those protons and hence the protons were deshielded. The ^{13}C NMR assignments showed that, the carbon signals for (C=S) and (C=O) appeared at δ 180.0 – 178.0 ppm and 167.2 – 162.0 ppm respectively. While aromatic carbon signals were observed at δ 154.1 – 116.9 ppm. All compounds were obtained as yellow solid after recrystallization using DMF/EtOH/H_2O. Their chemical structures were validated by FTIR, ^1H and ^{13}C NMR. The physical and spectroscopic data of the new compounds are shown below.

1,3-Benzenedicarboxamide, N^1,N^3-bis[[(4-methylphenyl)amino]thioxomethyl] **NA1:** Yield 78%, Yellow solid, m.p 222.0 °C, IR (KBr pellet, cm^{-1}) : υ (N-H) 3250.1, υ (C=O) 1655.9, υ (C-N) 1253.1, υ (C=S) 1151.0, ^1H (DMSO-d_6) $^{\delta}H$ (ppm): 12.4 (s, 2H, CSNH), 11.5 (s, 2H, CONH), 8.5 (s, 1H, Ar-H), 8.18 (d, J = 5.6 Hz, 2H, Ar-H), 7.8 (t, J = 8 Hz, 1H, Ar-H), 7.56 (d, J = 8.4 Hz, 4H, Ar-H), 7.24 (d, J = 8.0 Hz, 4H, Ar-H), 2.3 (s, 6H, CH_3), ^{13}C (DMSO-d_6) $^{\delta}C$ (ppm): 179.3 (C=S), 167.7 (C=O), 136.3 (Ar-C), 135.8 (Ar-C), 133.7 (Ar-C), 132.4 (Ar-C), 129.7 (Ar-C), 129.3 (Ar-C), 124.8 (Ar-C), 21.1 (CH_3).

1,3-Benzenedicarboxamide, N^1,N^3-bis[[(3,5-bis(trifluoromethyl(phenyl))amino]thioxomethyl] **NA2:** Yield 72%, Yellow solid, m.p 195.6 °C, IR (KBr pellet, cm^{-1}) : υ (N-H) 3232.8, υ (C=O) 1656.1, υ (C-N) 1245.8, υ (Ar-CF_3) 1280.0, υ (C=S) 1127.0, ^1H (DMSO-d_6) $^{\delta}H$ (ppm): 8.8 (s, 1H, Ar-H), 8.5 (s, 4H, Ar-H), 8.4 (d, J = 6.6 Hz, 2H, Ar-H), 7.9 (s, 2H, Ar-H), 7.8 (t, J = 7.2 Hz, 7.8Hz, 1H, Ar-H), ^{13}C (DMSO-d_6) $^{\delta}C$ (ppm): 180.0 (C=S), 167.1 (C=O), 140.1 (Ar-C), 133.4 (Ar-C), 132.5 (Ar-C), 131.7-131.0 (q, $^3J_{CE}$ = 33.9 Hz, C-CF_3), 129.6 (Ar-C), 127.9 (Ar-C), 126.0-120.6 (q, $^1J_{CF}$ = 270.1 Hz, CF_3), 119.5 (Ar-C).

2,6-pyridinedicarboxamide, N^1,N^3-bis[[(4-fluorophenyl)amino]thioxomethyl] **NA3:** Yield 53%, Yellow solid, m.p 210.4 °C, IR (KBr pellet, cm^{-1}) : υ (N-H) 3383.6, υ (C=O) 1679.7, υ (C-N) 1227.8, υ (C-F) 1352.8 υ (C=S) 1151.0, ^1H (DMSO-d_6) $^{\delta}H$ (ppm): 8.0 (d, J = 7.8 Hz, 2H, Ar-H), 7.94 (t, J = 8.4 Hz, 7.2Hz, 1H, Ar-H), 7.27-7.25 (m, 4H, Ar-H), 6.88-6.83 (m, 4H, Ar-H), ^{13}C (DMSO-d_6) $^{\delta}C$ (ppm): 178.9 (C=S), 163.7 (C=O), 160.9–159.3 (d, $^1J_{EC}$ = 242.8 Hz, C-F), 149.3 (Ar-C), 140.4 (Ar-C), 134.4 (Ar-C), 127.1-127.0 (d, $^3J_{EC}$ = 8.8 Hz, Ar-C), 126.9 (Ar-C), 115.4-115.5 (d, $^2J_{EC}$ = 21.9 Hz, Ar-C).

2,6-pyridinedicarboxamide, N^1,N^3-bis[[(4-methylphenyl)amino]thioxomethyl] **NA4**: Yield 65%, Yellow solid, m.p 177.0 °C, IR (KBr pellet, cm^{-1}) : υ (N-H) 3280.7, υ (C=O) 1656.0, υ (C-N) 1241.8, υ (C=S) 1144.2, ^1H (DMSO-d^6) $^{\delta}H$ (ppm): 12.3 (s, 1H, CSNH), 11.7 (s, 1H, CSNH), 11.1 (s, 1H, CONH), 10.9 (s, 1H, CONH), 8.2 (t, J = 8.4 Hz, 7.2 Hz, 1H, Ar-H), 7.7 (d, J = 8.0 Hz, 4H), 7.6 (d, J = 8.4 Hz, 1H, Ar-H), 7.5 (d, J = 1, 8.4 Hz, 1H, Ar-H), 7.2 (d, J = 8.0 Hz, 4H, Ar-H), 2.3 (s, 6H, CH_3), ^{13}C (DMSO-d_6) $^{\delta}C$ (ppm): 179.0 (C=S), 166.9 (C=O), 154.1 (Ar-C), 140.6 (Ar-C), 138.8 (Ar-C), 134.4 (Ar-C), 130.4 (Ar-C), 129.4 (Ar-C), 126.4 (Ar-C), 25.7 (CH_3).

2,6-pyridinedicarboxamide, N^1,N^3-bis[[(3,5-bis(trifluoromethyl(phenyl))amino]thioxomethyl] **NA5:** Yield 62%, Yellow solid, m.p 345.5 °C, IR (KBr pellet, cm^{-1}) : υ (N-H) 3296.0, υ (C=O) 1687.1, υ (Ar-CF_3) 1283.1, υ (C-N) 1246.6, υ (C=S) 1151.8, ^1H (Acetone-d_6) $^{\delta}H$ (ppm): 11.1 (s, 2H, CONH), 8.7 (s, 4H, Ar-H), 8.5 (d, J = 7.8 Hz, 2H, Ar-H), 8.4 (t, J = 7.2 Hz, 7.8 Hz, 1H, Ar-H), 7.8 (s, 2H, Ar-H), ^{13}C (Acetone-d_6) $^{\delta}C$ (ppm): 178.8 (C=S), 162.0 (C=O), 148.4 (Ar-C), 140.4 (Ar-C), 140.2 (Ar-C), 140.1 (Ar-C), 132.0-131.4 (q , $^3J_{EC}$ = 33.0 Hz, C-CF_3), 126.0 (Ar-C), 126.2-122.6 (q, $^1J_{EC}$ = 270.0 Hz, CF_3), 120.1 (Ar-C), 116.9 (Ar-C).

Antimicrobial activities

The antibacterial and antifungal activities of five new bisthioureas were tested against two Gram-positive bacterias (*Staphylococcus Aureus, Bacillus Subtilis),* two Gram-negative bacterias *(Escherichia Coli and Salmonella Typhi)* and single fungal strain - *Aspergillus Niger* using disc diffusion method. Streptomycin and Kinamycin were used as positive controls (Table 1).

Table 1. Antimicrobial result for five bis-thiourea compounds

Compound	Bacteria Inhibition Zone (mm)									
	Concentration (µg/disc)									
	A.Niger		***B.Subtilis***		***S.Aureus***		***E.Coli***		***S.Typhi***	
	10µg	**30µg**	**10µg**	**30µg**	**10µg**	**30µg**	**10µg**	**30µg**	**10µg**	**30µg**
NA1	-	-	6.5	6.5	7.0	7.0	6.5	6.5	-	-
NA2	-	-	6.5	6.5	7.0	7.0	6.5	6.5	-	-
NA3	-	-	7.5	7.5	7.0	7.0	6.5	6.5	-	-
NA4	-	-	6.5	6.5	6.5	6.5	6.5	6.5	6.5	6.5
NA5	-	-	7.0	7.0	6.5	6.5	6.5	6.5	8.0	9.0
Streptomycin 10µg	12.0		18.0		16.0		18.0		18.0	
Kinamycin 30µg	22.0		20.0		20.0		24.0		24.0	

Unfortunately, tested compounds did not display a remarkable activity against both type of bacteria and fungi. Nevertheless, compound NA5 showed valuable inhibitory activity. The activity of these compounds might be attributed to the presence of high electronegative substituent which enhanced the lipophilicity of the compounds. The lipophilicity of the compounds plays an important role in the penetration of solutes into the bacterial cell tissue [13]. The antibacterial activity of compound NA5 was higher than NA3 because NA5 contained multi fluoro group substituents which increase the lipophilicity of this compound. In contrary, all tested compounds had no activity against gram-negative bacteria. This observations showed that, the compounds were generally had better permeability towards gram-negative bacteria cell tissue.

Based on the test results, tested compounds had very low inhibition zone (IZ) values. It is known that thiourea compounds were generally exhibit good antimicrobial activities. However in this study, the results were contrary. This might be due to the solubility of the target compounds on the surface of the agar medium. Thus, the compounds were suspended on the agar surface and cannot reacted against those bacterias

Conclusion

In conclusion, five derivatives of 1,3-benzenedicarboxamide and 2,6-pyridinedicarboxamide bis-thiourea have been synthesized via solid-liquid phase transfer catalysis of PEG-400 and characterized by FTIR, ^{1}H and ^{13}C NMR. The preliminary studies on the antimicrobial activity via disc diffusion method showed that NA5 exhibit potential activity against *Staphylococcus Aureus*. For further research, we are planning to investigate the effect of transition metal complexation with these compounds toward their antimicrobial activity as some reports demonstrated that bis-thioureas antimicrobial activity were enhanced when complexed with transition metal. In addition, more sensitive antibacterial screening method such as dilution method should be used to evaluate the potential of synthesized compounds.

Acknowledgement

The authors would like to thank Universiti Kebangsaan Malaysia and the Ministry of Higher Education, Malaysia, for research grants FRGS/2/2013/ST01/UKM/02/1 and GUP-2014-015 respectively. Research facilities provided by PPSKTM and the Centre of Research and Instrumentation (CRIM) are very much appreciated.

References

1. Neucki, M. (1873). Zur kenntniss des sulfoharnstoffs. *Berichte der Deuschen Chemischen Gesellschaft,* 6 (1): 598 – 600.

2. Neu, H. C. (1992). The crisis in antibiotic resistance. *Science*, 257: 1064 – 1073.
3. Michel, M. and Gutmann, L. (1997). Methicillin-resistant Staphyllococus aureus and vancomycin-resistant enterococci: therapeut realities and possibilities. *Lancet*, 349: 1901–1906.
4. Normark, B. H. and Normark, S. (2002). Evolution and spread of antibiotic resistance. *Journal of Internal Medicine*, 252: 91 – 106.
5. Sun, J., Cai, H. and Mei et al. (2010). Molecular docking and QSAR studies on substituted acyl(thio)urea and thiadiazolo [2,3-α] pyrimidine derivatives as potent inhibitors of influenza virus neuraminidase. *Chemical Biology and Drug Design*, 76 (3): 245 – 254.
6. Sun, C., Zhang, X., Huang, H. and Zhou, P. (2006). Synthesis and evaluation of a new series of substituted acyl(thio)urea and thiadiazolo [2,3-α] pyrimidine derivatives as potent inhibitors of influenza virus neuraminidase. *Bioorganic and Medicinal Chemistry*, 14 (24): 8574 – 8581.
7. Zhong, Z., Xing, R., Liu, S., Wang, L., Cai, S. and Li, P. (2008). Synthesis of acyl thiourea derivatives of chitosan and their antimicrobial activities in vitro. *Carbohydrate Research*, 343 (3): 566 – 570.
8. Wang, F. H., Qin, Z. L. and Huang, Q. (2006). Synthesis and fungicidal activity of 1,3,4-oxadiazole substituted acylthioureas. *Frontiers of Chemistry in China*, 1: 112.
9. Ke, S. Y. and Xue, S. J. (2006). Synthesis and herbicidal activity of N(O)thioureas derivatives and related fused heterocyclic compounds. *Arkivoc*, 10: 63 – 68.
10. Xiao, L., Liu, C. J. & Li, Y. P. (2009). Ultrasound Promoted Synthesis of Bis(substituted pyrazol-4-ylcarbonyl)-Substituted Thioureas. *Molecules*, 14(4): 1423 –1428.
11. Vig, R., Mao, C., Venkatachalam, T. K., Tuel-Ahlgren, L., Sudbeck, E. A. and Uckun, A. (1998). Rational design and synthesis of phenethyl-5-bromopyridyl thiourea derivatives as potent non-nucleoside inhibitors of HIV reverse transcriptase. *Bioorganic and Medicinal Chemistry*, 6 (10): 1789 – 1797.
12. Peng, H., Liang, Y., Chen, L., Fu, L., Wang, H. and He, H. (2011). Efficient Synthesis and Biological Evaluation of 1,3-benzenedicarbonyl dithioureas. *Bioorganic & Medicinal Chemistry Letters*, 21: 1102 – 1104.
13. Klein, J. J. and Hecht, S. (2012). Synthesis of a new class of bis(thiourea)hydrazide pseudopeptides as potential inhibitors of β-sheet aggregation. *Organic Letters* 14 (11): 330 – 333.
14. Rampalakos, C. and Wulff, D. D. (2008). A Novel Bis-Thiourea Organocatalyst for the Asymmetric Aza-Henry Reaction. *Advanced Synthesis & Catalysis*, 350 (11-12): 1785 – 1790.
15. Verlinden, B. K., Beer de, M., Pachaiyappan, B., Besaans, E., Andayi, W. A., Reader, J., Niemand, J., Biljon van, R., Guy, K., Egan, T., Woster, P. M. & Birkholtz, L-M. (2015). Interrogating alkyl and arylalkylpolyamino (bis)urea and (bis)thiourea isosteres as potent antimalarial chemotypes against multiple lifecycle forms of ***Plasmodium falciparum*** parasites. *Bioorganic & Medicinal Chemistry*, 23 (16): 5131 – 5143.
16. Takacs-Novak, K., Noszal, B., Hermecz, I., Kereszturi, G., Podanyi, B. and Szasz, G. (1990). Protonation Equilibria of Quinolone. Antibacterials. *Journal of Pharmaceutical Sciences*, 79 (11): 1023 – 1028.
17. Xicun, W., Juan, L. and Zheng, L. (2005). An expenditious and solvent-free approach to substituted bis-thioureas and bis-thiosemicarbazides. *Journal of Chemical Research*, 791 –792.
18. Jamil, M., Zubair, M., Farid, M. A., Rashid, U., Rasool, N. and Islam, S. (2013). Antibacterial, cytotoxicity studies and characterization of some newly synthesized symmetrical N^3,$N^{3'}$-Bis (disubstitued)isophathalyl-bis(thioureas) and their Cu(II) and Ni (II) complexes. *Journal of Chemistry*, Hindawi.
19. Yamin, B. M. and Osman, U. M. (2011). *Acta Cryst.* E67, o1286.
20. Thiam, E. I., Diop, M., Gaye, M., Sall, A. S. and Barry, A. H. (2008). *Acta Cryst.* E64, o776.

MALAYSIAN JOURNAL OF ANALYTICAL SCIENCES
Published by The Malaysian Analytical Sciences Society
ISSN 1394 - 2506

POLY(DIMETHYLSILOXANE)-POLY(VINYL ALCOHOL) COATED SOLID PHASE MICROEXTRACTION FIBER FOR CHLORPYRIFOS ANALYSIS

(Gentian Pengekstrakan Mikro Fasa Pepejal Tersalut Poli(Dimetilsiloksana)-Poli(Vinil Alkohol) untuk Analisis Klorpirifos)

Wan Aini Wan Ibrahim[1, 2]*, Nor Fairul Zukry Ahmad Rasdy[1], Norfazilah Muhamad[1], Mohd Marsin Sanagi[3]

[1]*Separation Science and Technology Group, Department of Chemistry, Faculty of Science*
[2]*Frontier Materials Research Alliance*
[3]*Ibnu Sina Institute for Scientific and Industrial Research (ISI-SIR)*
Universiti Teknologi Malaysia, 81310 UTM Johor Bahru, Johor, Malaysia

**Corresponding author: wanaini@kimia.fs.utm.my; waini@utm.my*

Received: 9 December 2014; Accepted: 16 October 2015

Abstract

Traditional liquid – liquid extraction of pesticides consumes large volumes of organic solvent which are hazardous to the operator and is not environment friendly. Solid phase microextraction (SPME) is a solvent less extraction method which is safer to the operator and is environmental friendly. A sol-gel hybrid fibre coating material, poly(dimethylsiloxane)-poly(vinyl alcohol) (PDMS-PVA) was synthesized and used in head space solid phase microextraction (HS-SPME) of chlorpyrifos. The thickness of the synthesised PDMS-PVA fiber coating was 13.5 µm and it is thermally stable up to 400 °C. The PDMS-PVA sol-gel hybrid fiber was also stable to two organic solvents tested; acetonitrile and dichloromethane (1 hour dipping) and showed no significant changes in extraction performance for chlorpyrifos. Extracted chlorpyrifos was analysed using gas chromatography electron capture detector (GC-ECD). Optimum SPME parameters affecting the PDMS-PVA HS-SPME performance namely extraction time (15 min), extraction temperature (50 °C), desorption time (5 min), desorption temperature (260 °C) and stirring rate (120 rpm) were used for extraction. It was found that HSSPME using PDMS-PVA sol-gel fiber gave significantly better extraction performance of chlorpyrifos compared to commercial 100 µm PDMS fiber. The PDMS-PVA fiber showed excellent operational performances such as temperature stability (up to 380 °C), coating lifetime (up to 170 times use) and organic solvent stability. The PDMS-PVA-HS-SPME method showed excellent recovery for chlorpyrifos from tomatoes (98.0 %, 5.9% RSD) at 0.01 µg/g spiked level (5 times lower than maximum residue limit set by European Union).

Keywords: sol-gel hybrid, solid phase microextraction, chlorpyrifos, gas chromatography-electron capture detector

Abstrak

Pengekstrakan cecair – cecair tradisional bagi pestisid menggunakan isipadu pelarut organik yang banyak yang merbahaya kepada operator dan tidak mesra alam. Pengekstrakan mikro fasa pepejal (SPME) adalah teknik pengekstrakan tanpa pelarut yang lebih selamat kepada operator dan mesra alam. Bahan gentian tersalut hibrid sol-gel poli(dimetilsiloksana)-poli(vinil alkohol) (PDMS-PVA) telah disintesis dan digunakan untuk pengekstrakan mikro fasa pepejal ruang kepala (HS-SPME) klorpirifos. Ketebalan PDMS-PVA gentian tersalut yang telah disintesis ialah 13.5 µm dan stabil terma sehingga 400 °C. Gentian hibrid sol-gel PDMS-PVA juga stabil terhadap dua pelarut organik yang diuji, asetonitril dan diklorometana (1 jam celupan) dan tidak menunjukkan perbezaan ketara dalam prestasi pengekstrakan klorpirifos. Klopirifos yang telah diekstrak dianalisis menggunakan kromatografi gas-pengesan penangkapan elektron (GC-ECD). Parameter optimum SPME yang mempengaruhi prestasi PDMS-PVA-HS-SPME iaitu masa pengekstrakan (15 min), suhu pengekstrakan (50 °C), masa penyaherapan (5 min). suhu penyaherapan (260 °C) dan kadar putaran (120 rpm) telah digunakan untuk pengekstrakan. HS-SPME menggunakan gentian sol-gel PDMS-PVA menunjukkan prestasi pengekstrakan yang jauh lebih signifikan untuk klorpirifos berbanding dengan gentian komersial 100 µm PDMS. Gentian PDMS-PVA telah menunjukkan prestasi operasi yang cemerlang seperti kestabilan

suhu (sehingga 380 °C), jangka hayat salutan (sehingga 170 kali penggunaan) dan kestabilan terhadap pelarut organik. Kaedah PDMS-PVA HS-SMPE menunjukkan perolehan semula yang cemerlang untuk klorpirifos daripada sampel tomato (98.0 %, 5.9% RSD) pada aras pakuan 0.01 µg/g (5 kali lebih rendah daripada had maksimum residu yang ditetapkan oleh Kesatuan Eropah).

Kata kunci: hibrid sol-gel, pengekstrakan mikro fasa pepejal, klorpirifos, kromatografi gas pengesan penangkapan elektron

Introduction

The social concern about the levels of pesticides in the environment and the constant trend observed in current legislations to reduce their maximum residue levels allowed in a variety of matrices is increasing the number of samples to be analyzed well as the need for their accurate determination at very low levels. The help from the advance and improving technology especially in extraction and detection makes the study on pesticides more significant.

In recent years, separation and extraction sciences faced important developments. Starting with solid-phase extraction (SPE) in the 1980s, other modern methods, such as supercritical fluid extraction (SFE), supercritical fluid chromatography (SFC), solid-phase microextraction (SPME) and capillary electro-chromatography (CEC) have been introduced. Among the extraction methods available, SPME is more favorable due to its simplicity, solvent free application, rapid and versatility. Therefore to expand the potential of SPME as an extraction method is a very interesting challenge in improving separation science.

Commercial SPME fibers have generally good extraction properties compared to other conventional extraction method. However there are some drawbacks and certain aspects of their performance that can be improved. For instance, incomplete desorption that causes carry-over problems and a reduction of the lifetime of the fibers due to direct extraction of higher salt content samples and complex matrices, have been reported in the literature [1]. Furthermore, the low thermal stability, generally bleeding at high temperature (> 250 °C) and solvent stability can lower the extraction and desorption process. Recently, some new types of fibers, such as non polar silica particles bonded with C_8, C_{18} [2], pencil lead [3], graphite [4], nafion perfluorinated resin [5], polypyrrole [6], anodized aluminum wire [7], and molecularly imprinted polymer-coated fiber [8] have been prepared. However, almost all of these fibers coated with polymer are generally prepared by mere physical deposition, high temperature epoxy immobilization or partial crosslink of the polymer coating on the surface of the fused-silica fibers. The lack of proper chemical bonding between the polymer coating and fused-silica fiber surface may be responsible for the low thermal and chemical stability. The fiber coating lifetime is also limited, usually from 40 to 100 extractions [1]. In addition, the price of commercially available fibers is high due to their preparation process requiring expensive equipment.

Apparently the introduction of sol-gel technology has a promising alternative to overcome those problems. Sol-gel coating technology offers important advantages compared with conventional coating technique; strong adhesion between the coating and the bare fused-silica surface, the porous silica surface structure of sol-gel coating which can provide high surface areas and allow for high extraction efficiency and relative ease to change the composition of the coating which therefore will have different selectivity. This technology has been widely used to prepare SPME fiber because it can effectively create chemically bonded, porous and highly crossed coating on the fused silica fiber surface [9 – 12]. The simplicity of the sol-gel coating procedure provides excellent batch-to-batch reproducibility of the home-made fibers. A work done by Cajlakovic et al. [13] using poly(vinyl alcohol) (PVA) copolymer as optical pH sensing material offers a promising option for PVA to become as coating material in SPME fiber. This work successfully demonstrated that PVA with cross-linked produced a homogenous and crack-free membrane, making it more suitable for SPME fiber coating by sol-gel technology process.

In the current study, a simple and economical methodology for the determination of chlorpyrifos using headspace solid phase microextraction (HS-SPME) with an in-house silica-based sol-gel hybrid, polydimethylsiloxane-poly(vinyl alcohol) (PDMS-PVA) fiber coupled to gas chromatography equipped with an electron capture detector is presented and its use assessed in terms of thermal stability, solvent stability, reusability and application to real sample analysis of chlorpyrifos from water and tomato samples.

Materials and Methods

Reagents

Methyltrimethoxysilane (MTMOS), hydroxyl-terminated polydimethylsiloxane (OH-TPDMS), poly(vinyl alcohol) (PVA), trimethylmethoxysilane (TMMS), poly(methylhydroxysilane) (PMHS), and trifluoroacetic acid (TFA) were purchased from Sigma-Aldrich (USA). Sulfuric acid was obtained from Merck (Darmstadt, Germany). Hydrochloric acid and sodium hydroxide were purchased from Fluka Chemika (Switzerland). Chlorpyrifos was purchased from Dr. Ehrenstorfer (Augsburg, Germany). HPLC grade methanol was obtained from Merck (Schuchardt, Germany). Double-distilled deionized water of at least 18 MΩ was purified by Nano ultra pure water system (Barnstead, USA). Stock solution of 1000 ppm of chlorpyrifos was prepared in methanol. Working standard solutions was prepared by diluting the stock solutions with HPLC grade methanol. The stock solution and working standard was stored at 4 °C when not in use.

Preparation of fused silica fiber and PDMS-PVA sol-gel hybrid coating

Pieces of fused silica fiber were soaked in concentrated sulfuric acid for 3 h to remove original polyimide layer and to expose the fused silica core for sol-gel coating process. The fused silica fibers were then rinsed with distilled water and dipped into 1 M NaOH solution. The basic solution was removed and the fibers were exposed to 0.1 M HCl solution for 30 min to neutralize the excess NaOH. The activated fused silica fibres were then rinsed with distilled water, dried at 120 °C and stored for 12 h in a desiccator before use.

The PDMS-PVA sol phase was prepared by mixing 600 µL MTMOS, 300 mg OH-TPDMS, 80 mg PVA, 50 µL PMHS, and 400 µL of 95 % aqueous TFA in a glass tube. The mixture was vortexed for 2 min before being centrifuged at 12 000 rpm for 5 min. The top sol solution was used for fiber coating (1 cm length). After the treated fiber was dipped vertically into the sol solution for 20 min, a sol-gel coating was formed on the bare outer surface of the fiber end. For each fiber, this coating process was repeated three times with a freshly prepared PDMS-PVA sol phase. The coated fibers were then end-capped in a 20 % (v/v) methanolic solution of TMMS for 1 min. The in-house coated fibers were then mounted on used, discarded commercial SPME assemblies, after careful removal of the original fiber. Prior to use, the new PDMS-PVA fibers were conditioned in the GC injection port at 100°C for 2 h and then for 6 h at 280°C under 1 mL min^{-1} of Helium flow. The remaining sol from the fiber coating process was allowed to gel at room temperature for 2 h, ground, washed with distilled water and methanol, and conditioned under the same conditions as the fibers. It was used to run field emission-scanning electron microscopy (FE-SEM).and Fourier transform infrared spectroscopy (FTIR).

Characterization of sol-gel hybrid PDMS-PVA

The sol-gel PDMS-PVA composite was characterized using a 1600 series PE spectrophotometer (MA, USA) FTIR using KBR method in the range of 400 – 400 cm^{-1}. Thermal gravimetric analysis (TGA) was conducted using a Mettler Toledo TG-50 thermal analyser (Greifensee, Switzerland) within a temperature range 50 –800 °C. The thickness and surface morphology of the sol-gel hybrid PDMS-PVA was determined using a JEOL JSM-6710F FE-SEM (Tokyo, Japan).

Head space-solid phase microextraction

The fiber was conditioned by inserting it into the GC injection port at 250°C for a period of 30 min to 1 h. Then the fiber was repeatedly injected into the GC-ECD system until interfering peaks disappeared from the chromatogram monitored and satisfying baseline was obtained. Injection was performed under the same temperature programming for analysis. For HS-SPME mode, 2 mL of sample solution was placed in a 5 mL sample vial containing a magnetic stir bar and the vial was sealed with a PTFE septum. The vial was placed on a magnetic hot plate. Then the fiber was carefully introduced directly into the head space above the aqueous phase and stirred at a rate of 120 rpm for 15 min (temperature set to 20 °C). After the preset extraction time, the fiber was retrieved and introduced for a period of 5 min into the GC injection port for chlorpyrifos analysis.

Gas chromatography-electron capture detector conditions

The OPPs extracted by the SPME fiber was analyzed using an XL Perkin Elmer gas chromatography-electron capture detection (GC-ECD) system (CA, USA). For desorption of the analytes inside the GC injection port was set

at 280 °C. The column was kept at 180 °C for 2 min, then ramped at 4 °C min^{-1} to 200 °C, hold for 1 min and finally ramped at 10°C min^{-1} to 290°C, and hold for 1 min. The detector temperature was set at 300 °C. Helium was used as the carrier gas at a flow rate of 1.0 mL min^{-1} and nitrogen as a make-up gas was used at a flow rate of 32.4 mL min^{-1}. The pressure of the carrier gas was 10.0 psi. Peak areas of the ECD chromatogram signals were used to demonstrate the effect of parameters on the extraction efficiency of chlorpyrifos.

Real sample analysis

For real sample analysis, tomato (*Solanum lycopersicum*) was chosen as the sample as the matrix contains high colorant pigment due to the presence of carotenoid to assess matrix effect in PDMS-PVA-HS-SPME. The tomato was purchased from one of the local markets in Skudai, and stored in refrigerator to keep them fresh before analysis. The tomato was cut into small pieces and finely homogenized by using a chopper. Analytical portions of the tomato samples (10.0 g) were weighed in a 50 mL centrifuge tube and 20 mL deionized water was added. Then the sample was left to be extracted for 30 min on an ultrasonic bath. After the ultrasonication process, it was filtered through a filter paper. For analysis purpose, an aliquot of the sample (2 mL) was taken by micro-pipette to a SPME vial and followed by PDMS-PVA-HS-SPME procedure. For the accuracy test (recovery), the samples were fortified with chlorpyrifos at three different concentrations (0.005, 0.008 and 0.01 µg/g) and stored in refrigerator for one night to allow interactions between the chlorpyrifos and sample matrix. The chlorpyrifos concentration used is well below the MRL (5 – 100 times lower than the MRL) set by European Union for chlorpyrifos in tomato (0.5 mg/kg).

Results and Discussion

Preparation of sol-gel hybrid PDMS-PVA coating

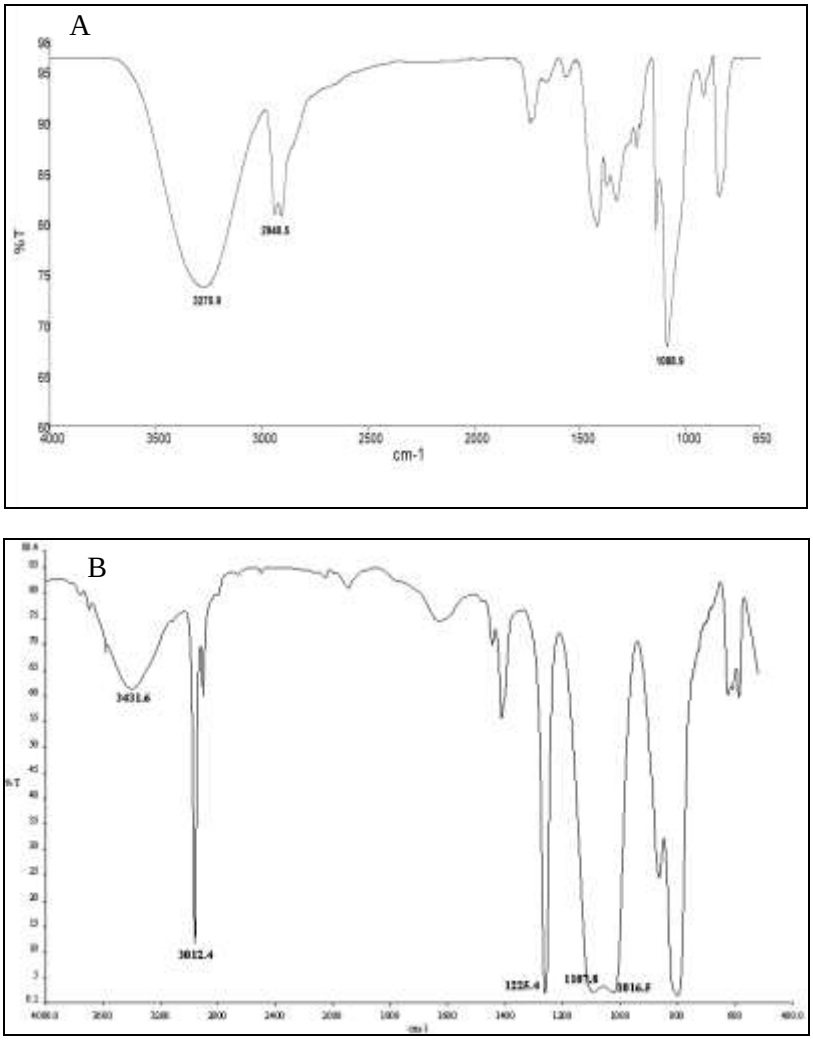
In this study, the sol-gel process was carried out using four principal ingredients which are, precursor, coating materials, deactivation reagent and acid catalyst. MTMOS was selected as precursor as it can avoid cracking and shrinkage of the coating during the gel-drying process. The sol-gel network originating from an alkyl derivative of precursor possesses a more open structure and can more effectively relieve stresses during drying, minimizing the cracking tendency [14]. PDMS is well known as a good non-polar stationary phase [15], but the addition of PVA is likely to improve the selectivity of fiber towards relatively polar or lower molecular weight compounds. As studied by Li et al. [16] who used terminated silicone oil as one of his coating material, it was not only to lengthen the silica network, leading to increase surface area of the fiber but also to spread the stationary phase of the fiber uniformly. In addition Cajlakovic et al. [13] proved PVA can be incorporated in sol-gel networks by the usual polycondensation processes and acts as a strong cross-linking agent. Another important ingredient used in the sol-gel coating process is PMHS, a well-known surface deactivation reagent in gas chromatography [10, 17]. Molecules of PMHS contain reactive hydrogen atoms capable of derivatizing silanol groups at elevated temperatures. Molecules of this ingredient get physically incorporated in the coating during the coating process. Post-coating thermal conditioning step leads to the deactivation of the fiber surface. The chemical structure of PMHS is very similar to that of PDMS, so it would not be a problem with PMHS as a deactivation reagent since its incorporation into the coating structure should have little effect on the sol-gel SPME fiber characteristic. Trifluoroacetic acid (TFA) was chosen as an acid catalyst to be added in the sol solution mixture. The reason for this is because during the sol-gel reaction, if the hydrolysis and polycondensation reaction rate is too fast, the coating stationary phase can hardly bond because of the space resistance of the three-dimensional network existed. Therefore, TFA is used to decrease the water reaction content in the sol, resulting in a slower hydrolysis reaction.

Characterization of sol-gel hybrid PDMS-PVA

Characterizations of the sol-gel hybrid PDMS-PVA were carried out on the in-house sol-gel PDMS-PVA fiber in order to verify whether the fiber was successfully synthesized. The physical characterizations included Fourier transform infrared (FTIR) spectroscopy, thermogravimetric analysis (TGA) and field emission-scanning electron microscopy (FE-SEM).

The FTIR spectra obtained from the sol-gel OH-TPDMS and PDMS-PVA composite were evaluated and subsequently compared. The spectrum of PDMS-PVA with the corresponding spectrum of the conventional PDMS from pure OH-TPDMS and PVA is also shown for comparison purposes (Figure 1). The position and characteristic of OH-TPDMS bands observed were in good agreement with those reported in the previous studies [18, 19]. The broad absorption band at 3436.7 cm^{-1} for sol-gel PDMS-PVA matches to the axial stretching of O-H bonds, and is

attributed to residual hydroxyl groups not eliminated after the end-capping treatment. However the intensity absorption present is small as the percentage transmittance is only 2 %. The decrease in hydroxy group peak in PDMS-PVA shows that it has been chemically bonded with other components. This band is also present in the OH-TPDMS with major intensity at 3431.6 cm^{-1}. Other absorption peaks match both those of sol gel PDMS-PVA and OH-TPDMS: 2965.0 cm^{-1} corresponds to the stretching of C-H bonds on methyl groups and 1022.3, 1096.1 and 1262.2 cm^{-1} corresponds to the stretching of Si-O bonds. However peaks at 2168.1 and 900.8 cm^{-1} present in sol-gel PDMS-PVA but not found in OH-TPDMS spectrum are attributed to Si-H bounds from PMHS, used as a surface deactivation reagent. The broad absorption peak around 1622.4 cm^{-1} found on PDMS-PVA can be attributed to the stretching of alkenic and vinylic C=C bonds, possibly formed by loss of water from poly(vinyl alcohol) (PVA) chains incorporated in the polymer framework. However, the presence of the hydroxyl absorption band suggests that the dehydration of the PVA chains have not been completed under the conditions used. This did not happen in PDMS-PVA fiber because the conditioning temperature for the fiber was up to 300°C compared to that the composite in example around 120°C for the maximum temperature.



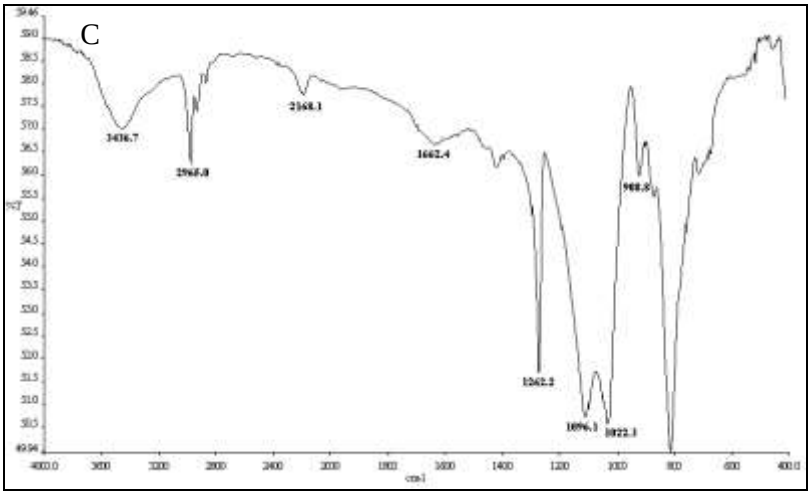


Figure 1. Infrared absorption spectra of: (A) PVA, (B) OH-TPDMS and (C) sol-gel PDMS-PVA

Thermal stability of the sol-gel PDMS-PVA fiber was studied using TGA in order to determine the limit of the operating temperature for the fiber and also helpful to enhance its coating lifetime. The TGA was performed under nitrogen gas and over the range temperature of 50-800°C at heating rate of 10°C min^{-1}. TGA curves (Figure 2) shows that the thermal degradation of the sol-gel PDMS-PVA composite occurs in three main stages. The first mass loss corresponds to slight degradation of PDMS-PVA which occurs at 240 °C. Between 240 °C and 330 °C, only 2 % of the total mass is lost for the sol-gel PDMS-PVA. The main mass loss step happens between 400 °C and 630 °C, corresponding to a loss 50 % of the initial mass with no other thermal series visible after this temperature. The last event was considered as characteristic of the thermal degradation of the sol-gel PDMS-PVA and can be assigned as its maximum practicable temperature. For the commercial PDMS SPME fiber, the maximum recommended operating temperature is only 280 °C; otherwise the fiber will deteriorate and affect analysis result negatively.

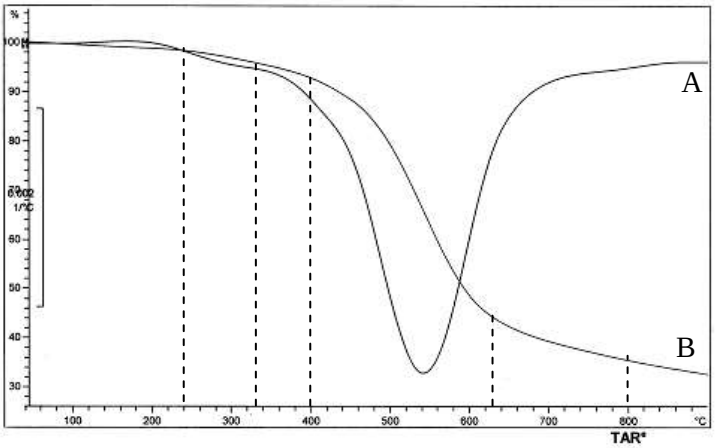


Figure 2. (A) TGA curve and (B) its first derivative of TGA curve for the sol-gel hybrid PDMS-PVA composite

The morphology of the sol-gel PDMS-PVA fiber surface was analyzed using FE-SEM. The average thickness of the sol-gel PDMS-PVA layer was estimated as being ~13 µm. This thickness is 6.5-8 times considerably thinner than most conventional coating thickness on commercial SPME fibers (100 µm for PDMS and 85 µm for polyacrylate). From this point of view, sol-gel coatings might seem inconvenient for SPME. However, the surface of the PDMS-PVA coating seems to be compact and smooth and also shows a high density of small particles with apparent rugged surface. Therefore increased in the availability of the surface area on the fiber thus enhanced the extraction performance.

Optimization of HS-SPME process

In order to optimize the HS-SPME technique, factors affecting the extraction efficiency such as extraction time, extraction temperature, stirring rate, desorption time, and desorption temperature were studied. Extraction time is determined by the length of time required for the analyte to reach equilibrium between the concentrations of analyte in the sample and the fiber stationary phase. Six different extraction times ranging from 5 to 40 min of HS-SPME with stirring rate fixed at 120 rpm have been studied. According to the literature [20 – 22], the extraction time can be shortened by working in the non-equilibrium area. Indeed, full equilibrium is not necessary as long as other parameters such as stirring rate and sampling time are kept constant and the result allowed a good and reproducible extraction response for chlorpyrifos. The optimum extraction time selected for the sol-gel PDMS-PVA fiber is 15 min (Figure 3). The rugged structure believed to be possessed by the PDMS-PVA fiber provided high surface area, allowing fast and effective extraction.

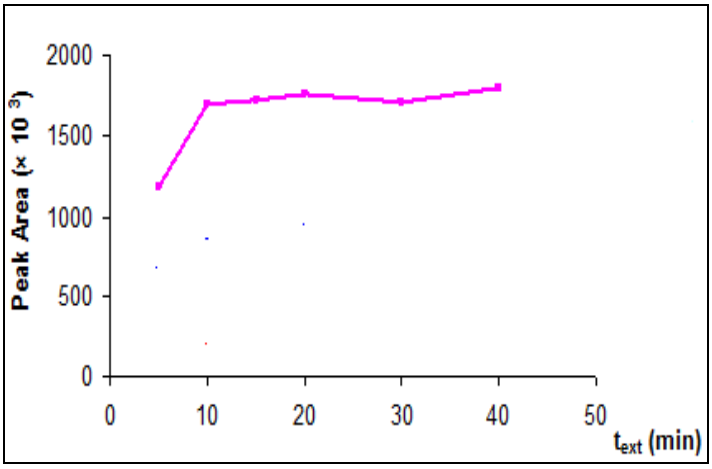


Figure 3. Extraction time profile for chlorpyrifos using PDMS-PVA fiber. HS-SPME conditions: t_{ext} 50 °C, t_{des} 5 min, T_{des} 250 °C, and stirring rate 120 rpm

The effects of extraction temperature ranging from 25 to 80 °C have been studied. In general with increasing temperature, the extraction ability of the fiber increased, this is because increasing temperature can significantly increase analyte evaporation rates (distribution constant) and mass transfer at the solution-gas interface (distribution velocity), which enhances the analytes to enter the gas phase and fiber coating. The extraction temperature profile for chlorpyrifos is shown in Figure 4. The figure shows that the equilibrium was established at extraction temperature of 50 °C. Consequently, 50 °C was selected as the optimum extraction temperature for PDMS-PVA fiber. The rate of diffusion of analytes through the static layer at the fiber solution interface increase with increasing temperature, so that more analytes are extracted at high temperature if equilibrium has not been reached [23].

Desorption time of the analyte from the fiber was studied to ensure complete desorption of the chlorpyrifos into the GC column. Six different desorption time varying from 1 to 10 min were studied. It was observed that desorption efficiency increase with an increase in desorption time from 1 to 5 min. After 5 min, there was no significant

increase in the peak area observed. Therefore 5 min of desorption time was selected as the optimum desorption time as it gave the highest amount of the analyte extracted (based on peak area).

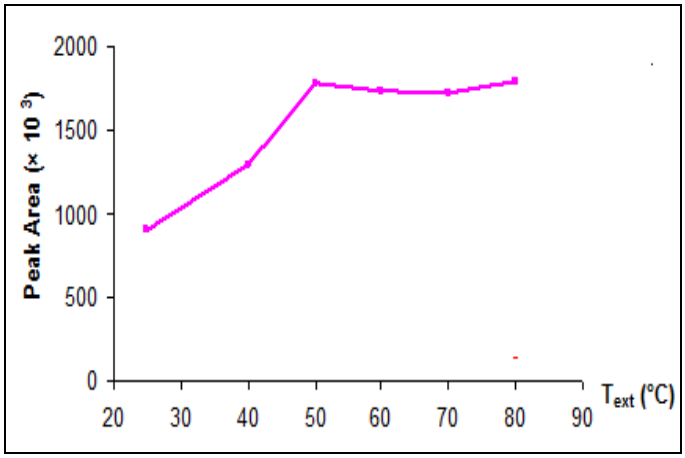


Figure 4. Extraction temperature profile for chlorpyrifos using PDMS-PVA fiber. HS- SPME conditions: t_{ext} 20 min, t_{des} 5 min, T_{des} 250 °C, and stirring rate 120 rpm

Desorption temperature of HS-SPME is measured from the GC injection port temperature indicator. In the current study, the effects of desorption temperatures ranging from 230 °C to 280 °C have been studied. Desorption temperature is important to guarantee complete desorption of the analyte studied to avoid carryover at the fiber. The result shows that there are no significant differences in peak area obtained at different temperature. Even though high temperature enhanced the desorption process but it can also degrade the analytes, worst it can damage the fiber and shorten its lifetime. Therefore, 260 °C was selected as the optimum desorption temperature since complete desorption the analyte studied were obtained from the coating. Furthermore, the PDMS-PVA fiber reveals that it can maintain the OPP peak area value obtained at different desorption temperature, which was almost the same.

Sample agitation or stirring was applied to enhance extraction and reduce extraction time, especially for higher molecular weight analytes with high diffusion coefficients. For practical purposes magnetic stirring bar was used in this study. It allows the control of the stirring rate and cyclic change in stirring direction. The effects of stirring rate ranging from 0 rpm to 600 rpm have been studied in the current work. The result obtained shows that the extraction efficiency increases as the stirring rate increased up to 120 rpm and decreases when the stirring rate further increased to 600 rpm. This agrees with the fact that SPME is a method based on equilibrium and that good diffusion through the phases is essential to reach equilibrium faster. Therefore a constant 120 rpm stirring rate was selected as the optimum stirring rate for HS-SPME of the chlorpyrifos.

Method validation

The optimized conditions for the HS-SPME extraction of chlorpyrifos using PDMS-PVA fiber are as follows; 15 min extraction time, 50 °C extraction temperature, 5 min desorption time, 260 °C desorption temperature and 120 rpm stirring rate. Under the optimum conditions, the PDMS-PVA-HS-SPME method was developed and validated for the extraction of spiked chlorpyrifos from water samples in terms of linearity, precision, limits of detection (LOD) and limits of quantification (LOQ). Good coefficient of determination was obtained (r^2 = 0.9972) within linearity range 0.001-0.1 ppm. The LOD at S/N = 3 obtained was 0.0076 ppm which is 5 –10 times lower than the maximum residue limit (MRL) set by the European Union (EU) [24].

Real sample analysis

The method developed for HS-SPME-PDMS-PVA for water samples was extended to tomato samples. Since no chlorpyrifos was detected in the tomato samples analysed, it was spiked with three different concentrations of

chlorpyrifos in order to determine the accuracy and precision of the PDMS-PVA HS-SPME method developed. It was found that at 0.01 and 0.008 µg/g spiking level, the accuracy of the PDMS-PVA-HS-SPME method developed was comparable with the commercial 100 µm PDMS-SPME. Sample matrix from the tomato samples was found not to significantly affect the accuracy of the PDMS-PVA-HS-SPME method. The precision of the PDMS-PVA-HS-SPME was better than the commercial 100 µm PDMS SPME. However, the accuracy of the commercial 100 µm PDMS SPME was better for samples spiked at the lowest level, 0.005 µg/g. The lower recovery obtained using the PDMS-PVA HS-SPME is probably due to the sample matrix effect which is more pronounced in the in-house SPME fibre. Comparable precision was obtained for samples spiked at 0.005 µg/g for both the SPME fibres (Table 1). Figure 5 shows the chromatogram of a spiked tomato sample analysis using the HS-SPME-PDMS-PVA.

Table 1. Percentage recovery and RSD of different concentrations of spiked chlorpyrifos from tomato sample using optimum HS-SPME conditions

Spiked concentration (µg/g)	**% Recovery (% RSD, *n* = 3)**	
	13 µm PDMS-PVA	**Commercial 100 µm PDMS**
0.005	62.64 (5.35)	76.86 (5.68)
0.008	85.65 (8.24)	85.62 (6.81)
0.01	98.01 (5.91)	91.70 (7.02)

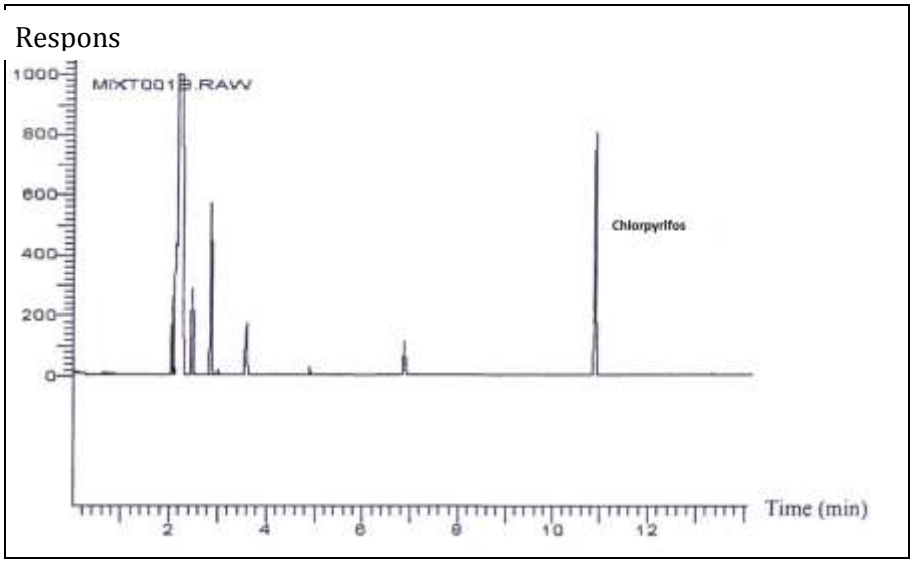


Figure 5. Chromatogram of spiked chlorpyrifos from tomato samples using the in house PDMS-PVA fibre. GC conditions:HP-5 column (30 m × 0.32 mm ID and 0.25 µm film thickness). Carrier gas: He at 1.0 mL min^{-1}. Detector: ECD. Injection port temperature: 280°C, Detector temperature: 300°C. Temperature programming: 180 – 290 ^{o}C at 4°C min^{-1} to 200°C (hold 1 min) and 10°C min^{-1} to 290°C (hold 2 min).

Conclusion

Sol-gel hybrid PDMS-PVA coating was successfully synthesized and applied as a SPME fiber coating for analysis of chlorpyrifos. The new sol-gel hybrid PDMS-PVA coating has high temperature stability up to 380 ^{o}C and showed comparable extraction performances to commercial 100 µm PDMS fiber in the extraction of chlorpyrifos

from tomato samples spiked at 0.01 and 0.008 µg/g. Matrix effect from the tomato samples did not significantly affect the extraction of chlorpyrifos spiked at these two levels (0.008 – 0.1 µg/g which is 5 – 60 times lower) below the MRL set by EU. The lower recovery of chlorpyrifos from tomato at a spiking level of 0.005 ppm (100 times lower than MRL) using the PDMS-PVA-HS-SPME could be due to matrix effect from the tomato samples. The sol-gel hybrid PDMS-PVA offers an alternative SPME coating of chlorpyrifos from water and vegetable samples such as tomato.

Acknowledgement

The authors would like to thanks the Ministry of Science, Technology and Innovation, Malaysia (MOSTI) for financial supports through IRPA Program Vote No. 74255 and 79085 and Department of Chemistry, Faculty of Science, UTM for facilitations**.**

References

1. Bartak, P. and Cap, L. (1997). Determination of Phenols by Solid-Phase Microextraction. *Journal of Chromatography A*, 767: 171 – 175.
2. Liu, Y., Lee, M. L., Hageman, K. J., Yang, Y. and Hawthorne, S. B. (1997). Solid-Phase Microextraction of PAHs from Aqueous Samples Using Fibers Coated with HPLC Chemically Bonded Silica Stationary Phases. *Analytical Chemistry*, 69: 5001.
3. Wan, H. B., Chi, H., Wong, M. K. and Mok, C. Y. (1994). Solid-Phase Microextraction Using Pencil Lead as Sorbent for Analysis of Organic Pollutants in Water. *Analytica Chimica. Acta*, 298: 219 – 223.
4. Kuo, C. P. and Shiea, J. (1999). Application of Direct Electrospray Probe to Analyze Biological Compounds and to Couple to Solid-Phase Microextraction to Detect Trace Surfactants in Aqueous Solution. *Analytical Chemistry*, 71: 4413 – 4417.
5. Gorecki, T., Martos, P. and Pawliszyn, J. (1998). Strategies for the Analysis of Polar Solvents in Liquid Matrixes. *Analytical Chemistry*, 70: 19 – 27.
6. Wu, J. C. and Pawliszyn, J. (2001). Polypyrrole-Coated Capillary Coupled to HPLC for In-Tube Solid-Phase Microextraction and Analysis of Aromatic Compounds in Aqueous Samples. *Analytical Chemistry*, 73: 55 – 63.
7. Djozan, D., Assadi, Y. and Haddadi, S. H. (2001). Anodized Aluminium Wire as a Solid-Phase Microextraction. *Analytical Chemistry*, 73: 4054 – 4058.
8. Koster, E. H. M., Crescenzi, C., Hoedt, W., Ensing, K. and Jong, G. J. (2001). Fibers Coated with Molecularly Imprinted Polyemers for Solid-Phase Microextraction. *Analytical Chemistry*, 73: 3140 – 3145.
9. Yu, J., Wu, C. and Xing, J. (2004). Development of New Solid-Phase Microextraction Fibers by Sol-Gel Technology for the Determination of Organophosphorus Pesticide Multiresidues in Food. *Journal of Chromatography A*, 1036: 101 – 111.
10. Malik, A., Chong, S. L., Wang, D. X., Hayers, J. D. and Wilhite, B. W. (1997). Sol-Gel Coating Technology for the Preparation of Solid-Phase Microextraction Fibers of Enhanced Thermal Stability. *Analytical Chemistry*, 69: 3889 – 3898.
11. Bigham, S., Medlar, J., Kabir, A., Shende, C., Alli, A. and Malik, A. (2002). Sol-Gel Capillary Microextraction. *Analytical Chemistry*, 74: 752 – 761.
12. da Costa, R. G. and Augusto, F. (2005). Highly Porous Solid-Phase Microextraction Fiber Coating Based on Poly(ethylene glygol)-Modified Ormosil Synthesized by Sol-Gel Technology. *Journal of Chromatography A*, 1072; 7 –12.
13. Cajlakovic, M., Lobnik. A. and Werner. T. (2002). Stability of New Optical pH Sensing Material Based on Cross-Linked Poly(Vinyl Alcohol) copolymer. *Analytical Chimica Acta*, 455: 207 – 213.
14. Dislich, H. I. (1998). *Sol-Gel Technology for Thin Films, Fibers, Performs, Electrons and Specialty Shapes*. Klein L. C edition, Noyes Publications, Park Riders, New Jersey.
15. Su, P. G. and Huang, S.D.(1999). Determination of Organophosphorus Pesticides in Water by Solid-Phase Microextraction. *Talanta*, 49: 393 – 402.
16. Li, X., Zheng. Z. R., Gao, S. Z. and Li, H. B. (2004). Preparation of Sol-Gel Coated Calix[4]arene Fiber for Solid-Phase Microextraction. *Journal of Chromatography A*, 1023: 15 – 25.
17. Hu, H. L., Yang, Y. Y., Huang, J. X. and Li, G. (2005). Preparation and Application of Poly(dimethylsiloxane)/β-cyclodextrin Solid-Phase Microextraction Membrane. *Journal of Chromatography A*, 543: 17 – 24.

18. Liu, M. M., Zeng, Z. R. and Fang, H. F. (2005). Preparation and Application of the Sol-gel derived acrylate/silicone co-polymer Coatings for Headspace Solid-Phase Microextraction of 2-Chloroethyl Ethyl Sulfide in Soil. *J. Chromatogr. A*, 1076: 16 – 26.
19. Liu, M. M., Liu, Y., Zeng, Z. R. & Peng, T. Y. (2006). Preparation and Characteristics of High pH Resistant Sol-gel Alumina-based Hybrid Organic-Inorganic Coating for Solid-Phase Microextraction of Polar Compounds. *Journal of Chromatography A,* 1108: 149 –157.
20. Kataoka, H., Lord, H. L. and Pawliszyn, J. (2000). Applications of Solid-Phase Microextraction in Food Analysis. *Journal of Chromatography A*, 880: 389 – 404.
21. Navalon, A., Prieto, A., Araujo, L. and Vilchez, J. L. (2002). Determination of Oxadiazon Residues by Headspace Solid-Phase Microextraction and Gas Chromatography-Mass Spectrometry. *Journal of Chromatography A*, 946: 239 –245.
22. Zambonin, C. G., Cilenti, A. and Palmisano, F. (2002). Solid-Phase Microextraction and Gas Chromatography-Mass Spectrometry for the Rapid Screening of Triazole Residues in Wine and Strawberries. *Journal of Chromatography. A*, 967: 255 –260.
23. Pawliszyn, J. (1997). *Solid-Phase Microextraction-Theory and Practice*. New York: Wiley-VCH.
24. European Database Pesticide Database. (2000). Retrieved from ec.europa.eu/sanco_pesticides/public [Access online on 8th August 2014].

MALAYSIAN JOURNAL OF ANALYTICAL SCIENCES
Published by The Malaysian Analytical Sciences Society
ISSN 1394 - 2506

ENHANCED ACTIVITY OF C_3N_4 WITH ADDITION OF ZnO FOR PHOTOCATALYTIC REMOVAL OF PHENOL UNDER VISIBLE LIGHT

(Peningkatan Aktiviti C_3N_4 dengan Penambahan ZnO untuk Fotomangkin Penyingkiran Phenol di bawah Sinaran Tampak)

Faisal Hussin[1], Hendrik O. Lintang[2], Leny Yuliati[2]*

[1]*Department of Chemistry, Faculty of Science,*
[2]*Centre for Sustainable Nanomaterials, Ibnu Sina Institute for Scientific and Industrial Research*
Universiti Teknologi Malaysia, 81310 UTM Johor Bahru, Johor, Malaysia.

**Corresponding author: leny@ibnusina.utm.my*

Received: 9 December 2014; Accepted: 3 January 2016

Abstract

Phenol is a stable and hazardous compound that is commonly found as an industrial effluent. Phenol can be treated by photocatalysis using zinc oxide (ZnO) as a photocatalyst. Unfortunately, the use of ZnO in photocatalysis is limited due to the poor response to the visible light. On the other hand, carbon nitride (C_3N_4) is able to absorb visible light. In the present study, a series of ZnO-C_3N_4 was prepared by impregnation method. The effect of zinc to carbon mol ratio (Zn/C) on the properties and photocatalytic activity was examined. X-ray Diffraction (XRD) patterns of the samples revealed that as the Zn mol ratio increased, the intensity of diffraction peaks for ZnO also increased but the intensity for C_3N_4 decreased. All prepared composite materials have an extended absorption band in the visible light region due to the presence of C_3N_4, as supported by DR UV-Vis spectra. The prepared ZnO-C_3N_4 composites were further investigated in the photocatalytic removal of phenol under visible light for 5 hours. All ZnO-C_3N_4 samples showed higher activity than the bare ZnO with Zn/C mol ratio of 1% showed the highest photocatalytic activity for removal of phenol among all the samples. The high activity observed on the ZnO-C_3N_4 would be due to role of ZnO to suppress electron-hole recombination and C_3N_4 to extend the absorption of ZnO in the visible light region.

Keywords: zinc oxide, carbon nitride, ZnO-C_3N_4 composites, impregnation method, phenol

Abstrak

Fenol adalah sebatian stabil dan berbahaya yang sering dijumpai sebagai efluen industri. Fenol boleh dirawat dengan cara fotopemangkinan menggunakan zink oksida (ZnO) sebagai fotomangkin. Malangnya, penggunaan ZnO di dalam fotopemangkinan adalah terhad disebabkan sedikit respons terhadap sinaran tampak. Sebaliknya, karbon nitrida (C_3N_4) mampu menyerap sinaran tampak. Dalam kajian ini, siri ZnO-C_3N_4 telah disediakan melalui kaedah pengisitepuan. Kesan nisbah mol zink kepada karbon (Zn/C) kepada ciri dan aktiviti fotomangkin telah diperiksa. Corak pembelauan sinar-x (XRD) daripada sampel – sampel membuktikan bahawa kesan nisbah mol Zn meningkat, keamatan puncak pembelauan untuk ZnO semakin naik tetapi keamatan untuk C_3N_4 semakin kurang. Semua bahan komposit yang disediakan mampu memperluaskan jalur penyerapan di dalam kawasan sinaran tampak disebabkan kehadiran C_3N_4 dan disokong oleh spectrum DR UV-Vis. Komposit ZnO-C_3N_4 yang disediakan selanjutnya dikaji di dalam fotomangkin penyingkiran fenol di bawah sinaran tampak selama 5 jam. Kesemua sampel ZnO-C_3N_4 mempunyai aktiviti yang tinggi berbanding hanya ZnO dengan 1% nisbah mol Zn/C menunjukkan aktiviti fotomangkin tertinggi dalam penyingkiran fenol. Aktiviti tinggi yang dilihat terhadap ZnO-C_3N_4 berkemungkinan disebabkan peranan ZnO untuk membantutkan penggabungan semula lubang elektron dan C_3N_4 untuk memperluaskan penyerapan ZnO di dalam kawasan sinaran tampak.

Kata kunci: zink oksida, karbon nitrida, komposit ZnO-C_3N_4, kaedah pengisitepuan, fenol

Introduction

Zinc oxide (ZnO) is one of the crucial multifunctional oxide materials for various applications, such as in sensors, solar cells and photocatalysis [1 – 9]. The ZnO has been investigated due to its unique property of wide band gap (3.37 eV), excitation binding energy (60 meV) at room temperature and good activity for photocatalytic decomposition reactions. Unfortunately, since ZnO has wide band gap and absorption only in the UV region [10], it requires large amount of energy in order to be active as a photocatalyst.

There are various ways to extend the absorption of ZnO to the visible light, such as by incorporating the ZnO with transition metal doping [11 –13], dye sensitizer [14 –15], and CdS [16]. Another feasible modifier is metal free graphitic carbon nitride (C_3N_4). The C_3N_4 has relatively lower band gap energy (2.70 eV) compared to the ZnO (3.37 eV), thus it is also able to absorb visible light region. Furthermore, the C_3N_4 has a strong covalent bond between carbon and nitrogen in the structure that makes it exhibit high stability under visible light irradiation, which can prevent photocorrosion effect that lead to the decreasing of activity. Due to these unique features, C_3N_4 is used as a visible light driven photocatalyst and it can be combined with other photocatalysts for better photocatalytic activity in the complete spectral region [17]. However, only few reports emphasizing on the incorporation of ZnO with the C_3N_4. It was reported that the modification of ZnO with C_3N_4 gave a promising result in the photocatalytic removal of methylene blue under visible light irradiation [18].

In this study, phenol was used as the model for organic pollutant. Phenol is considered as a toxic compound released from the industrial as an effluent. Moreover, phenol is very stable and it will remain in the waste water for a long term [19, 20]. Photocatalytic process is one of the available methods that offer both sustainable energy source and environmental friendly process. Since photocatalytic process involves minimum requirement of energy for decomposition of organic pollutant, it is believed that photocatalytic reaction is a green method for phenol decomposition. Moreover, it provides the possibility to utilize the solar light. Therefore, in this study, photocatalytic removal of phenol was investigated by applying visible light over the ZnO-C_3N_4 photocatalysts.

Materials and Methods

Preparation of carbon nitride (C_3N_4)

Urea ($CO(NH_2)_2$, Merck, 99.5%) was used as a source of carbon and nitrogen for preparation of the C_3N_4. The urea (300 g) was calcined under air atmosphere at a rate of 2.2 °C min^{-1} for 4 h in order to reach a temperature of 550 ^oC and tempered for 4 h at this temperature. The resulting yellow solid was ground before using it as the photocatalyst.

Preparation of ZnO

Zinc acetate dihydrate ($Zn(CH_3COO)_2.2H_2O$, QRëC, 99.5%) was used as the precursor to synthesize the ZnO. The $Zn(CH_3COO)_2.2H_2O$ (15 g) was calcined at 550 °C with a rate of 2.2 °C/min and tempered for another 4 h. The resulted solid was white in colour and was ground before it was used.

Preparation of ZnO-C_3N_4

Various ZnO-C_3N_4 samples were prepared by impregnation method with Zn/C ratios were 1, 5, 10, 20, and 50 mol percentage (mol%). The samples were labelled as ZnO-C_3N_4 (*x*) with *x* shows the ratio of zinc present in the sample. For a typical synthesis of ZnO-C_3N_4 (*1*), $Zn(CH_3COO)_2.2H_2O$ (0.0716 g) was dissolved in methanol (20 mL). The C_3N_4 (1 g) was then added slowly into the solution, stirred and dried at 80 °C on a hot plate until drying. The powder was then calcined at 550 °C for 4 h.

Characterizations

X-ray Diffraction (XRD, Bruker AXS Diffrac plus release 2000) was used to identify the structure of the prepared photocatalysts. The X-ray diffractogram of the catalyst was analyzed at 2θ range of 5-75° with scan rate of 0.05° s^{-1}. Diffuse reflectance Ultraviolet-Visible (DR UV-Vis, Shimadzu UV-2600) spectroscopy was used for measurement of absorption spectra of the prepared photocatalysts. Barium sulphate ($BaSO_4$) was used as the background reference with the scan range of 200-800 nm. Nicolet iS50 Thermo Scientific Fourier Transform Infrared Spectroscopy (FTIR) was used to detect the presence of functional groups in the composites. The measured wavenumber was in the range of 4000-400 cm^{-1} with the scan number of 32. Fluorescence spectroscopy (JASCO

Spectrofluorometer FP-8500) was used to obtain emission spectra of samples. The monitored wavelength was in the range of 200-600 nm. Potentiostat/Galvanostat/ZRA (Gamry Instruments Interface 100) was used for the photoelectrochemical studies. Typically, 0.01 g of C_3N_4, ZnO or ZnO-C_3N_4 composite was added to the solution containing of water (10 mL) and nafion (10 µL). Then, the solution was sonicated for 10 min. Afterward, the prepared sample (20 µL) was deposited onto the screen printed electrode (SPE) and then dried using a dryer for 10 min. Na_2SO_4 (0.01 M) and $K_3[Fe(CN)_6]$ (2.5 mM) aqueous solution was employed as an electrolyte. Before measurement, the prepared SPE was immersed in the electrolyte solution (6 mL) and the electrochemical impedance studies were conducted.

Photocatalytic activity test

The photocatalytic removal of phenol was conducted at room temperature. The photocatalyst (0.05 g) was dispersed in 100 mL of jacketed-beaker containing of phenol (50 ppm, 50 mL). Then, the beaker was placed on a stirring plate with cooling water system in a closed box for 30 minutes to let the adsorption reach the equilibrium. The reaction was carried out for 5 hours under visible light irradiation (150 W, $\lambda > 400$ nm, intensity of 100,000 lux). After reaction, the solution was taken and separated from the photocatalyst. The remaining phenol was measured by Gas Chromatography equipped with Flame Ionization Detector (GC-FID, Agilent 7820A).

Results and Discussion

Properties of C_3N_4, ZnO and ZnO-C_3N_4

In order to reveal the structure of the prepared samples, the diffraction patterns of the samples were recorded. As can be seen from Figure 1(a), the prepared C_3N_4 showed one intense peak at 2θ of 27.65°, which can be assigned as interlayer distances (d) of 0.32 nm, corresponding to the graphite-like C_3N_4 layer. An additional broad diffraction peak at 2θ of 12.95° with a d value of 0.683 nm showed a hole-to-hole distance of nitride pores, reflecting the geometric effect in pore walls of the prepared C_3N_4 sample [21]. The d values were obtained from the Bragg's law as shown in Equation 1.

$$n\lambda = 2d \sin \theta \quad (1)$$

where n is a positive integer, λ is the wavelength of the incident wave, d is the interplanar distance, and θ is the scattering angle. The presence of these diffraction peaks suggested that the C_3N_4 was prepared successfully. As can been observed from Figure 1(g), the diffraction peaks of the prepared ZnO can be indexed as a wurtzite structure, according to JCPDS file (JCPDS 89-1397).

For the ZnO-C_3N_4 composite samples, there were different trends of the diffraction peaks. For samples with low amount of ZnO (1 – 10 mol %), the samples showed the similar pattern as C_3N_4 with dominant peak at 2θ of 27.75°, suggesting the presence of C_3N_4 in these samples (Figure 1(b)-(d)). On the other hand, the samples with high amount of ZnO (20-50 mol %) showed similar diffraction patterns to the ZnO sample. This was reasonable as the amount of ZnO was larger than the C_3N_4. With the increase of the ZnO, the peak intensity of the C_3N_4 decreased. The XRD patterns clearly showed that the C_3N_4 and ZnO can be detected on the ZnO-C_3N_4 composite samples, depending on the amount of C_3N_4 and ZnO.

Figure 2 shows DR UV-Vis spectra for the ZnO and ZnO-C_3N_4 samples. For the C_3N_4 sample, it showed three strong absorption peaks at 277, 330 and 370 nm, corresponding to the N=C groups of aromatic 1,3,5-triazine, uncondensed C=O group and the terminal N-C group of C_3N_4, respectively (Fig. 2(a)). It was obvious that the C_3N_4 sample absorbed visible light up to *ca.* 450 nm. On the other hand, ZnO sample showed one absorption band centered at 320 nm due to the electron charge transfer in the Zn-O linkage, as shown in Fig. 2(g). For the ZnO-C_3N_4 samples, all samples showed the absorption peaks of both C_3N_4 and ZnO (Fig. 2(b)-(f)). As the mol ratio of Zn/C increased, the absorption edge of the samples showed blue-shifting from *ca.* 450 to *ca.* 380 nm. This was reasonable since when the amount of ZnO increased, the samples would behave like the ZnO, thus giving absorption spectra that were similar to that of the ZnO. From the DR UV-Vis measurements, it can be concluded that ZnO-C_3N_4 samples were successfully synthesized.

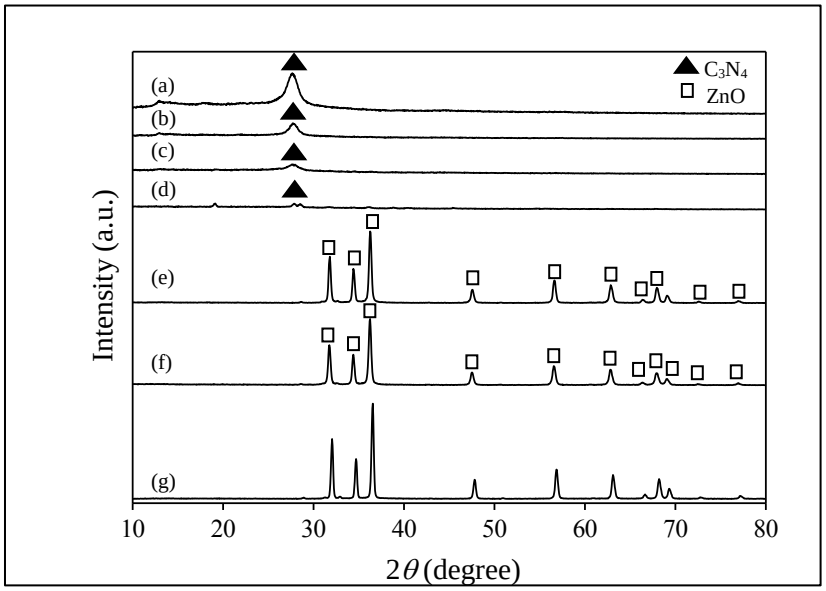


Figure 1. XRD patterns of (a) C_3N_4, (b) ZnO-C_3N_4 (*1*), (c) ZnO-C_3N_4 (*5*), (d) ZnO-C_3N_4 (*10*), (e) ZnO-C_3N_4 (*20*), (f) ZnO-C_3N_4 (*50*), and (g) ZnO.

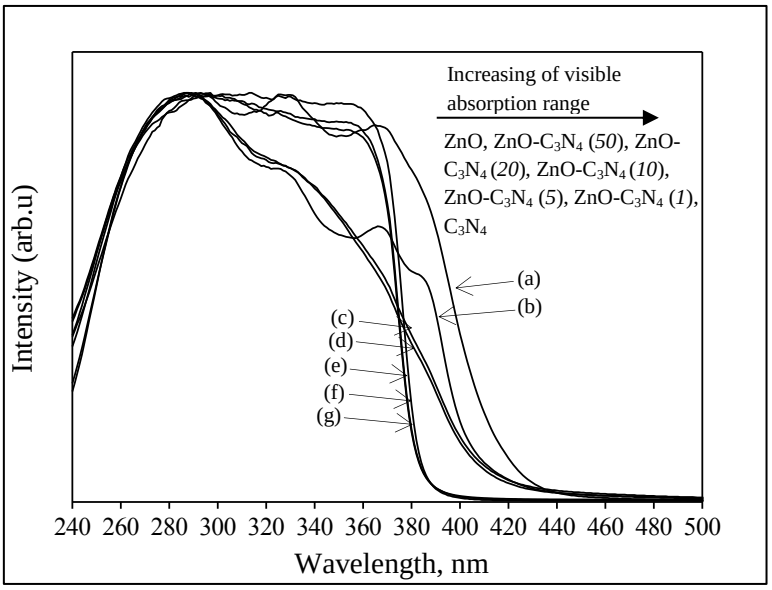


Figure 2. DR-UV Vis spectra of (a) C_3N_4, (b) ZnO-C_3N_4 (*1*), (c) ZnO-C_3N_4 (*5*), (d) ZnO-C_3N_4 (*10*), (e) ZnO-C_3N_4 (*20*), (f) ZnO-C_3N_4 (*50*), and (g) ZnO.

Figure 3 shows the FTIR spectra of C_3N_4, ZnO, and ZnO-C_3N_4 samples. As shown in Figure 3(a), the C_3N_4 showed several peaks due to the vibrations of some bondings occurred between carbon and nitrogen. The absorption peak at 810 cm^{-1} corresponded to the triazine unit of C_3N_4, while peaks at 1200 - 1600 cm^{-1} region corresponded to stretching modes of C-N heterocyclics. The absorption peaks at 1340 and 1640 cm^{-1} were related to the C-N and

C=N stretching modes. The broad absorption band at 3100 – 3300 cm^{-1} can be assigned as primary and secondary amines with their intermolecular hydrogen bonding interactions. All the observed peaks in the FTIR spectrum of C_3N_4 were similar to the absorption peaks reported previously [22 – 24], supporting the successful transformation of the urea precursor to the C_3N_4. The prepared ZnO showed an intense peak in the range of 400 – 500 cm^{-1} (Figure 3(g)), which was belonged to the Zn-O stretching. The FTIR spectra of the prepared ZnO-C_3N_4 samples are shown in Figure 3 (b)-(f). Similar to the results of XRD patterns and DR UV-Vis spectra, samples with low loading of ZnO showed the absorption peaks of C_3N_4 as the dominant species. The peaks assigned to the C_3N_4 decreased with the increase of Zn/C ratio. When the Zn/C ratio reached 50 mol%, the peaks related to the C_3N_4 were completely disappeared and only ZnO peak could be observed on the ZnO-C_3N_4 (50) sample, as shown in Figure 3(f).

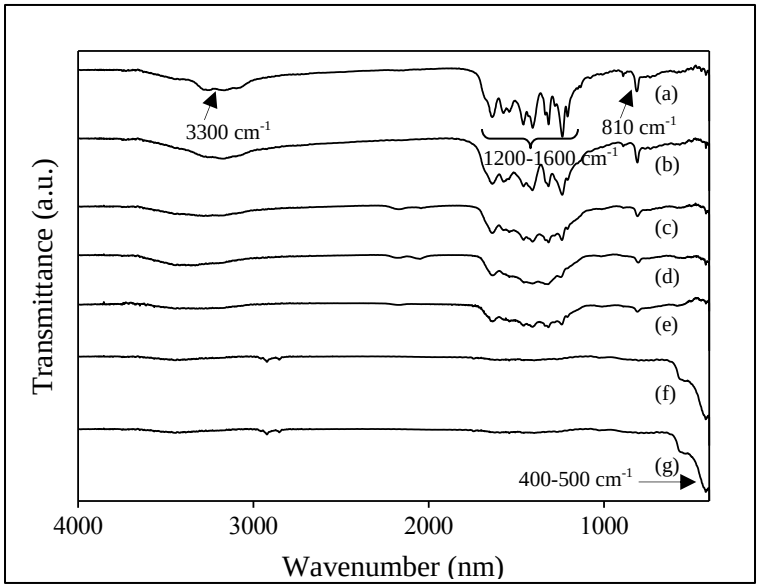


Figure 3. FTIR spectra of (a) C_3N_4, (b) ZnO-C_3N_4 (*1*), (c) ZnO-C_3N_4 (*5*), (d) ZnO-C_3N_4 (*10*), (e) ZnO-C_3N_4 (*20*), (f) ZnO-C_3N_4 (*50*), and (g) ZnO

Since the activity of the ZnO-C_3N_4 samples were evaluated under visible light irradiation, the charge transfer mechanism was investigated from the C_3N_4 site. The C_3N_4 exhibited two excitation peaks around 277 and 370 nm The excitation peaks at 277 nm would be related to the N=C groups of aromatic 1,3,5-triazine, while the peak of 370 nm would be due to the terminal N-C group of C_3N_4 [14, 22]. In order to investigate the effect of addition of ZnO on the emission of the C_3N_4, the emission spectra of the C_3N_4 and the ZnO-C_3N_4 samples were measured at the excitation wavelength of 277 and 370 nm, as shown in Figure 4. For both excitation wavelengths, the C_3N_4 showed two emission sites at 445 and 460 nm (Figure 4(a)). The emission intensity was found to decrease with the addition of ZnO (Figure 4(b)-(f)). The higher the amount of Zn/C ratio, the lower the emission intensity of the ZnO-C_3N_4 samples obtained. This result clearly suggested that there were interactions between the emission sites of C_3N_4 and the added ZnO particles. Since the emission is the result of electron-hole recombination, the low emission intensity would suggest the suppression of the electron-hole recombination. It can be proposed here that the addition of ZnO was able to suppress the electron-hole recombination of the C_3N_4. Therefore, under visible light irradiation, it can be suggested that the electrons from the conduction band of the C_3N_4 would be trapped by the ZnO, which would cause the less electron-hole recombination process. The mechanism of the electron charge transfer can be illustrated as in Figure 5.

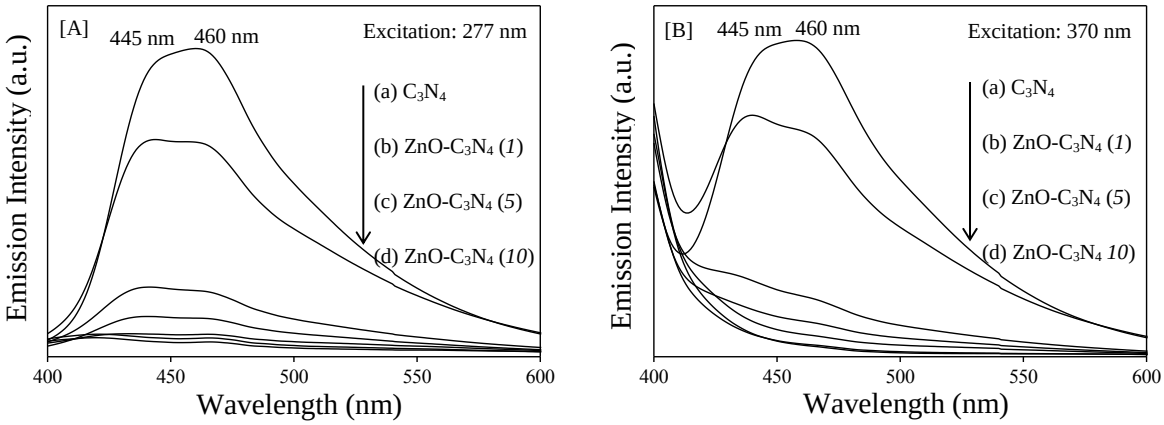


Figure 4. Emission spectra of (a) C_3N_4, (b) ZnO-C_3N_4 (*1*), (c) ZnO-C_3N_4 (5), (d) ZnO-C_3N_4 (*10*), (e) ZnO-C_3N_4 (*20*), (f) ZnO-C_3N_4 (*50*) and (g) ZnO monitored at the excitation wavelength of [A] 277 and [B] 370 nm.

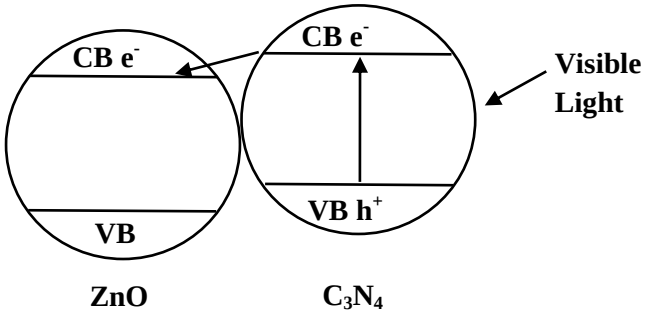


Figure 5. Schematic illustration of the electron charge transfer in the ZnO-C_3N_4 composite. CB and VB are conduction and valence bands, respectively.

In addition to the reduced electron-hole recombination, the lower emission intensity especially for samples with high loading of ZnO would be also caused by the smaller amount of the C_3N_4. This factor would also affect the photocatalytic activity of the ZnO-C_3N_4 composites under visible light irradiation.

Photocatalytic activity test

The C_3N_4, ZnO, and the ZnO-C_3N_4 samples were evaluated for the photocatalytic removal of phenol. Table 1 shows the percentage removals of phenol on the samples. The C_3N_4 showed 32% removal of phenol (Entry 1), while the ZnO showed 15% (Entry 7). The ZnO-C_3N_4 (*1*) showed 43% removal of phenol, which was three times higher than the activity of ZnO alone (Entries 2 and 7). It is worthy noted that the ZnO-C_3N_4 (*1*) showed higher activity than either C_3N_4 or ZnO. This result showed that there was a synergetic effect between the small amount of ZnO and the C_3N_4. As discussed previously, the small amount of ZnO would act to trap electron, thus inhibiting the electron-hole recombination process in the C_3N_4 sample. The less electron-hole recombination would be the key factor to get the improved photocatalytic activity.

Unfortunately, when the Zn ratio was more than 1 mol%, the activity was found to be gradually decreased with the increase of the Zn ratio (Entries 3 – 6). Therefore, the ZnO-C_3N_4 (*1*) showed the highest activity among the composite samples. As shown in the DR UV-Visible spectra, the ZnO-C_3N_4 (*1*) showed the most intense absorption

in the visible light. This property would be also one of the parameters that made it superior among the other composites. Moreover, as discussed in the characterization parts, samples with low loading of ZnO would behave like C_3N_4, while samples with high loading among would behave like ZnO. The ZnO-C_3N_4 (*50*) showed activity closer to the activity of the ZnO (Entries 6 and 7). Even though the activity decreased with the increase of the ZnO loading, it is clear that all ZnO-C_3N_4 composites showed better activities than the unmodified ZnO. This result also strongly suggested that the activity of C_3N_4 can be increased by the addition of ZnO.

Table 1. The percentages of phenol removal on ZnO and ZnO-C_3N_4 samples after 5 hours reaction under visible light irradiation[a]

Entry	**Samples**	**Percentage of phenol removal (%)[b]**
1	C_3N_4	32
2	ZnO-C_3N_4 (*1*)	43
3	ZnO-C_3N_4 (*5*)	34
4	ZnO-C_3N_4 (*10*)	33
5	ZnO-C_3N_4 (*20*)	26
6	ZnO-C_3N_4 (*50*)	21
7	ZnO	15

[a]Photocatalyst used was 0.05 g in the 50 mL solution of phenol (50 ppm)
[b]Percentage removal of phenol was calculated from the percentage ratio of reacted phenol to the initial concentration of phenol

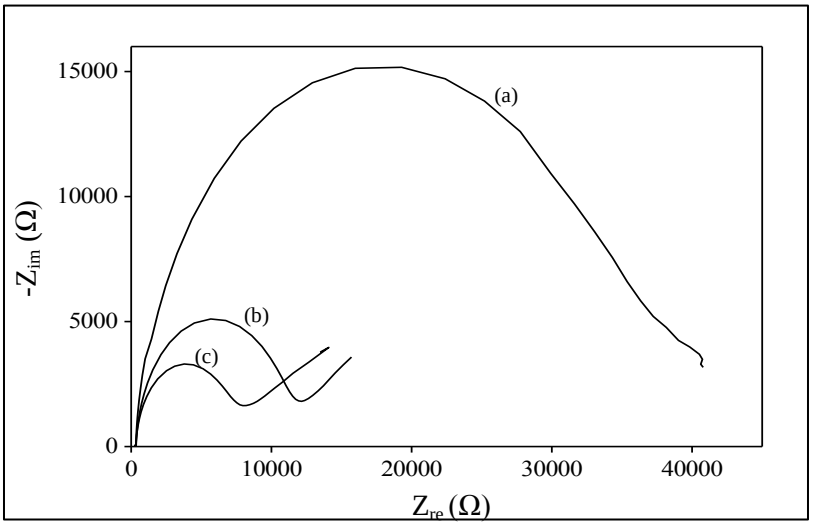


Figure 6. Nyquist plots of (a) ZnO, (b) C_3N_4, and (c) ZnO-C_3N_4 (*1*).

In order to obtain more detail information on the charge transfer and further support the synergetic effect between the ZnO and the C_3N_4, the electrochemical impedance measurement was carried out. Nyquist plots of the C_3N_4, the ZnO and the ZnO-C_3N_4 (*1*) composite were plotted with an open circuit between 1 MHz and 0.1 Hz as shown in

Figure 6. The ZnO-C_3N_4 (*1*) composite showed smaller semicircles compare to the bare ZnO and the C_3N_4, indicating the lower charge-transfer resistance on the surface of the composite [25]. With the suitable amount of ZnO, the charge transfer increased since C_3N_4 can transfer the electron to the ZnO thus, preventing the rapid electron-hole recombination. This synergetic effect resulted in the higher activity in the photocatalytic reaction.

Conclusion

The ZnO-C_3N_4 samples were prepared successfully by impregnation method. All the ZnO-C_3N_4 samples showed higher activity than the bare ZnO. The optimum amount of 1 mol% of Zn ratio gave *ca.* 3 times higher activity than unmodified ZnO. The ZnO-C_3N_4 (*1*) also showed higher activity than the C_3N_4. The synergic effect between the C_3N_4 and the ZnO was proposed, where the addition of C_3N_4 was able to extend the absorption of ZnO to visible light region and the small amount of ZnO would act to trap electron and suppress the electron-hole recombination.

Acknowledgement

This work was financially supported by the Ministry of Higher Education (MOHE, Malaysia) and the Universiti Teknologi Malaysia (UTM, Malaysia) through a Tier-1 Research University Grant (cost center code: Q.J130000.2509.06H66). F. H acknowledges the support of UTM through Zamalah Scholarships.

References

1. Wang, L., Kang, Y., Lui, X., Zhang, S., Huang, W. and Wang, S. (2012). ZnO Nanorod Gas Sensor for Ethanol Detection. *Sensors Actuators B: Chemical*, 162 (1): 237 – 243.
2. Wang, W., Huang, H., Li, Z., Zhang, H., Wang, Y., Zheng, W. and Wang, C. (2008). Zinc Oxide Nanofibers Gas Sensor via Electrospinning. *Journal of the American Ceramic Society*, 91 (11): 3817 – 3819.
3. Jean, J., Chang, S., Brown, P. R., Cheng, J. J., Rekemeyer, P. H., Bawendi, M. G., Gradečak, S. and Bulović, V. (2013). ZnO Nanowire Arrays for Enhanced Photocurrent in PbS Quantum Dot Solar Cells. *Advanced Materials*, 25 (20): 2790 – 2796.
4. Zhang, M.-L., Jin, F., Zheng, M.-L., Liu, J., Zhao, Z.-S. and Duan, X.-M. (2014). High Efficiency Solar Cell Based on ZnO Nanowire Array Prepared by Different Growth Methods. *RSC Advances*, 4 (21): 10462 – 10466.
5. Kaur, J., Bansal, S. and Singhal, S. (2013). Photocatalytic Degradation of Methyl Orange Using ZnO Nanopowders Synthesized via Thermal Decomposition of Oxalate Precursor Method. *Physica B: Condensed Matter.* 416: 33 – 38.
6. Kayaci, F., Vempati, S., Donmez, I., Biyikli, N. and Uyar, T. (2014). Role of Zinc Interstitial and Oxygen Vacancies of ZnO in Photocatalysis: A Bottom-up Approach to Control Defect Density. *Nanoscale*, 6 (17): 10224 –10234.
7. Tian, C., Zhang, Q., Wu, A., Jiang, M., Liang, Z., Jiang, B. and Fu, H. (2012). Cost-Effective Large-Scale Synthesis of ZnO Photocatalysts with Excellent Performance for Dye Photodegradation. *Chemical Communication*, 48 (23): 2858 – 2860.
8. Kumar, R., Kumar, G. and Umar, A. (2013). ZnO Nano-Mushrooms for Photocatalytic Degradation of Methyl Orange. *Materials Letters*, 97: 100 – 103.
9. Ameen, S., Akhtar, M.S., Nazim, M. and Shin, H.-S. (2013). Rapid Photocatalytic Degradation of Crystal Violet Dye over ZnO Flower Nanomaterials. *Materials Letters*, 96: 228 – 232.
10. Suchanek, W. L. (2009). Systematic Study of Hydrothermal Crystallization of Zinc Oxide (ZnO) Nano-Sized Powders with Superior UV Attenuation. *Journal of Crystal Growth*, 312 (1): 100 – 108.
11. Lu, Y.-H., Lin, W.-H., Yang, C.-Y., Chiu, Y.-H., Pu, Y.-C, Lee, M.-H., Tseng, Y.-C. and Hsu. Y.-J. (2014). A Facile Green Antisolvent Approach to Cu^{2+}-Doped ZnO Nanocrystals with Visible-Light Responsive Photoactivities. *Nanoscale*, 6 (15): 8796 – 8803.
12. Li, P., Wei, Z., Wu, T., Peng, Q. and Li, Y. (2011). Au-ZnO Hybrid Nanopyramids and Their Photocatalytic Properties. *Journal of the American Chemical Society*, 133 (15): 5660 – 5663.
13. Chauhan, R., Kumar, A. and Chaudhary, R.P. (2012). Photocatalytic Studies of Silver Doped ZnO Nanoparticles Synthesized by Chemical Precipitation Method. *Journal of Sol-Gel Science Technology*, 63 (3): 546 – 553.
14. Sarkar, S., Makhal, A., Bora, T., Lakhsman, K., Singha, A., Dutta, J. and Pal., S.K. (2012). Hematoporphyrin-ZnO Nanohybrids: Twin Applications in Efficient Visible-Light Photocatalysis and Dye-Sensitized Solar Cells. *ACS Applied Materials & Interfaces*, 4 (12): 7027 – 7035.

15. Yang, G. C. C. and Chan, S.-W. (2009). Photocatalytic Reduction of Chromium (VI) in Aqueous Solution using Dye-Sensitized Nanoscale ZnO under Visible Light Irradiation. *Journal of Nanoparticle Research*, 11 (1): 221 – 230.
16. Zou, X., Wang, P.-P., Li, C., Zhao, J., Wang, D., Asefa, T. and Li, G.-D. (2014). One-Pot Cation Exchange Synthesis of 1D Porous CdS/ZnO Heterostructures for Visible-Light-Driven H_2 Evolution. *Journal of Materials Chemistry A*, 2 (13): 4682 – 4689.
17. Yan, H., Chen, Y. and Xu. S. (2012). Synthesis of Graphitic Carbon-Nitride by Directly Heating Sulfuric Acid Treatment Melamine for Enhanced Photocatalytic H_2 Production from Water Under Visible Light. *International Journal of Hydrogen Energy*, 37 (1): 125 – 133.
18. Wang, Y., Shi, R., Lin, J. and Zhu, Y. (2011). Enhancement of Photocurrent and Photocatalytic Activity of ZnO Hybridized with Graphite-Like C_3N_4. *Energy & Environmental Science*, 4 (8): 2922 – 2929.
19. Pardeshi, S.K. and Patil, A.B. (2008). A Simple Route for Photocatalytic Degradation of Phenol in Aqueous Zinc Oxide Suspension Using Solar Energy. *Solar Energy*, 82 (8): 700 – 705.
20. Ahmed, S., Rasul, M. G, Martens, W. N., Brown, R. and Hashib, M. A. (2010). Heterogeneous Photocatalytic Degradation of Phenols in Wastewater: A Review on Current Status and Developments. *Desalination*, 261(1-2): 3 –18.
21. Pang, L.-L., Bi, J.-Q., Bai, Y.-J., Qi, Y.-X., Zhu, H.-L., Wang, C.-G., Wu, J.-W. and Lu, C.-W. (2008). Rapid Synthesis of Graphitic Carbon Nitride Powders by Metathesis Reaction between $CaCN_2$ and C_2Cl_6. *Materials Chemistry Physics*, 112 (3): 1124 –1128.
22. Sam, M. S., Lintang, H. O., Sanagi, M. M., Lee, S.L. and Yuliati, L. (2014). Mesoporous Carbon Nitride for Adsorption and Fluorescence Sensor of N-Nitrosopyrrolidine. *Spectrochimica Acta Part A: Molecular and Bimolecular Spectroscopy*, 124: 357 – 364.
23. Li, X., Zhang, J, Shen, L., Ma, Y., Lei, W., Cui, Q. and Zou, G. (2009). Preparation and Characterization of Graphitic Carbon Nitride through Pyrolysis of Melamine. *Applied Physics A*, 94 (2): 387 – 392.
24. Martha, S., Nashim, A. and Parida, K.M. (2013) Facile Synthesis of Highly Active g-C_3N_4 for Efficient Hydrothermal Production under Visible Light. *Journal of Materials Chemistry A*, 1: 7816 –7824.
25. Luo, Q.-P., Yu, X.-Y., Lei, B.-X., Chen, H.-Y., Kuang, D.-B. and Su, C.-Y. (2012). Reduced Graphene-Oxide-Hierarchical ZnO Hollow Sphere Composites with Enhanced Photocurrent and Photocatalytic Activity. *Journal of Physical Chemistry C*, 116: 8111 – 8117.

MALAYSIAN JOURNAL OF ANALYTICAL SCIENCES

Published by The Malaysian Analytical Sciences Society

ISSN 1394 - 2506

SYNTHESIS AND CHARACTERIZATION OF 6,6'-BIS (2-HYDROXYPHENYL)-2,2'-BIPYRIDYL LIGAND AND ITS PLATINUM COMPLEX FOR THE INTERACTION WITH CT-DNA

(Sintesis dan Pencirian Ligan 6,6'-Bis(2-Hidroksifenil)-2,2'-Bipiridil dan Kompleks Platinum untuk Kajian Interaksi dengan CT-DNA)

Norhidayah Selamat, Lee Yook Heng, Nurul Izzaty Hassan, Nurul Huda Abd Karim*

School of Chemical Sciences and Food Technology,
Faculty of Sciences and Technology,
Universiti Kebangsaan Malaysia, 43600 UKM Bangi, Selangor, Malaysia

**Corresponding author: nurulhuda@ukm.edu.my*

Abstract

A tetradentate ligand with four donor atoms OONN and its platinum metal complex were synthesized. Bis(phenoxy)bipyridine ligand was prepared by Suzuki coupling reaction between 6,6'-dibromo-2,2'-bipyridyl and 2-hydroxyphenylboronic acid with the presence of palladium (II) acetate. The formation of platinum complex was done by introducing the ligand with platinum (II) chloride in benzonitrile. Both ligand and complex structures were confirmed by ^{1}H, 2D cosy and ^{13}C NMR spectroscopy, ESI-MS spectrometry and FTIR spectroscopy. Binding studies of small molecules with DNA are useful to understand the reaction mechanism and to provide guidance for the application and design of new and more efficient drugs or sensors targeted on DNA. In this study, the binding interaction between the synthesized ligand and complex with calf thymus DNA (CT-DNA) has been investigated using UV-Visible and emission DNA titration. From the UV-Visible DNA study, it showed that platinum (II) bipyridine complex had higher affinity towards CT-DNA with binding constant K_b=(3.1 ± 0.02 x 10^5) ± 0.02 M^{-1} compared to that of bis(phenoxy) bipyridine ligand with binding constant (K_b) = (1.19 ± 0.08) × 10^3 M^{-1}. These findings will be valuable for the potential use of platinum (II) bipyridine complex as a phosphorescent probe in optical sensor DNA.

Keyword: bis(phenoxy)bipyridine, intercalating ligand, calf thymus-DNA, DNA interaction

Abstrak

Ligan tetradentat dengan empat atom penderma OONN dan kompleks platinumnya telah disintesis. Ligan bis(fenoksi)bipiridin disediakan melalui tindak balas pengkupelan Suzuki antara 6,6'-dibromo-2,2'-bipiridil dan asid 2-hidroksifenilboronik dengan kehadiran palladium(II) asetat. Pembentukan kompleks platinum dilakukan dengan menambahkan platinum(II) klorida terhadap ligan di dalam benzonitril. Kedua-dua struktur ligan dan kompleks dibuktikan dengan spekroskopi ^{1}H, 2D dan ^{13}C RMN, spektrometri ESI-MS dan spektroskopi FTIR. Kajian pengikatan terhadap molekul kecil dengan DNA sangat berguna untuk memahami mekanisme tindak balas dan untuk panduan bagi aplikasi dan reka bentuk dadah yang baharu dan berkesan atau sensor target kepada DNA. Dalam kajian ini, interaksi ikatan antara ligan dan kompleks terhadap DNA timus anak lembu (CT-DNA) dilakukan dengan kajian titratan ultra lembayung boleh Nampak dan titratan pendaflour. Kaedah tersebut membuktikan bahawa kompleks platinum (II) bipiridin mempunyai ikatan yang lebih kuat terhadap CT-DNA berbanding dengan ligan iaitu sebanyak K_b=(3.1 ± 0.02 x 10^5) ± 0.02 M^{-1} berbanding K_b=(1.19 ± 0.08) x 10^3 M^{-1}. Penemuan ini sangat bernilai dan berpotensi dalam menjadikan kompleks platinum (II) bipiridin sebagai prob fosforesen dalam sensor DNA optik.

Kata kunci: bis(fenoksi)bipiridin, ligan berinterkalasi, DNA timus, interaksi DNA

Introduction

The mix of pyridine–phenol ligand 6,6'-(2-hydroxyphenyl)-2,2-bipyridine has attracted the author's attention due to its bridging behaviour by phenolate residues attached to the end of a string of pyridyl donors which result in the formation of phenolate-bridged polynuclear complexes with interesting magnetic and spectroscopic properties [1 – 3]. Interestingly, the NNOO tetradentate conjugated aromatic ligands can coordinate with metal centre results in molecular planar and increase the structural flexibility. Since deoxyribonucleic acids (DNA) offers many potential binding sites due to its size and complexity, the coordination compound are able to bind to the DNA by non-covalent bonding through three binding modes which are groove binding, intercalation and external static electronic effects [4].

Metal complex DNA intercalators have been given more attention in the research field because they are widely used in pharmaceuticals as antibiotics, antibacterial and antitumor agents [5]. Some examples of DNA interactions using transition metal complexes include Ru [6] Co, Ni, Cu, Zn [7] and rare-earths compounds [8]. Platinum metal is chosen for the bipyridine complex in this study because it has been widely used in optical devices and has shown to have diverse applications in electroluminescence, photovoltaics, optical limiting, photocatalysis, and molecular probes [4]. Moreover, d^8 square-planar platinum (II) complexes with NNOO tetradentate conjugated aromatic ligands have shown to be highly phosphorescent at room temperature and thus have the potential to be developed as DNA optical sensor for the detection of DNA hybridization [9].

To date, no attempts have been made to explore the potential of platinum (II) bipyridine complex as a new phosphorescent DNA probe. In this present work, the ligand and its platinum metal complex are synthesized and it is the interest of this study to investigate the interaction between both compound and calf thymus DNA (CT-DNA). The overall aim is to investigate their optical properties towards DNA binding. It is predicted that platinum (II) bipyridine will bind stronger to CT-DNA due to the presence of platinum metal that enables the complex to become planar, thus allows them to π-π stack on the DNA bases and bind to DNA via intercalation [10]. It is expected that the bind to DNA will change the optical properties [11]. An enhancement of phosphorescence emission intensity upon the interaction with CT-DNA suggests that the platinum complex has the potential to be developed as a phosphorescence DNA sensor since there is still no report on this ligand and its complex for DNA probes sensor application [12]. Furthermore, there is a great market potential for simple, cheap, rapid, and quantitative detection of specific genes in the area of clinical, veterinary, medico-legal, environmental, and food industry.

Materials and Methods

Chemicals

The chemicals used in this work such as 6,6-dibromo-2,2'-bipyridyl, 2-methoxyphenylboronic acid, palladium (II) acetate, triphenylphospine, dimethoxyethane, pyridine hydrochloride, platinum (II) chloride and benzonitrile were purchased from Sigma-Aldrich and were used without further purification in the synthesis of ligand and complex. Calf thymus-DNA (CT-DNA) was obtained from Sigma (USA), agarose (molecular biology grade).

Physical measurement

^{1}H and ^{13}C NMR spectra of ligand were recorded using Bruker /AVANCE III 600 MHz Fourier transform nuclear magnetic resonance 600 MHz cryoprobe. The mass spectrometry was carried out using Bruker MicroTof Q Mass Spectrometer. IR spectra were recorded on KBr discs using FTIR Perkin-Elmer GX Model in the spectral range of 4000-400 cm^{-1}. The UV-Visible spectra were measured using Shimadzu UV-2450. Melting point was measured by using Barnsted electrothermal melting point IA9100 series.

Synthesis of 6,6'-bis(2-hydroxyphenyl)-2,2'-bipyridine ligand

Bis(phenoxy)bipyridine ligand was synthesized using the method patented by Nii et al. [12] with a slight modification. 6,6'-dibromo-2,2'-bipyridine (0.568 g, 1.81 mmol) and 2-hydroxyphenylboronic acid (0.499 g, 3.62 mmol) were refluxed for 4 hours in a mixture of dimethoxyethane (10 mL) and water (10 mL) with the presence of palladium (II) acetate (0.04 g, 0.18 mmol) under inert condition. After cooling the reaction solution to room temperature, chloroform (20 mL) and water (20 mL) were added to the reaction solution. The organic layer was concentrated and collected. Purification of the organic layer was carried out by column chromatography using dicloromethane:hexane (1:2) to obtain yellow crystal of 6,6'-bis(2-hydroxyphenyl)-2,2'-bipyridyl ligand. All

spectroscopic data for the ligand are in accordance to literature [13]. Yield : 0.3191 g (51%). ^{1}H NMR (600 MHz, $CDCl_3$) δ : 6.99 (t, 1H, , $^{3}J_{HH}$ = 8.4 Hz, arom), 7.09 (td, 1H, , $^{3}J_{HH}$ = 8.4 Hz, arom), 7.38 (td, 1H, , $^{3}J_{HH}$ = 7.2 Hz, arom), 7.89 (t, 1H, , $^{3}J_{HH}$ = 8.4 Hz, arom), 8.04 (m, 2H, bipyridine), 8.14 (dd, 1H, , $^{3}J_{HH}$ = 8.4 Hz H^{2}), 14.29 (s, 1H, -OH). ^{13}C NMR (600 MHz, $CDCl_3$) δ: 118.54, 118.80, 119.17, 119.22, 119.92, 126.64, 131.93, 139.27, 152.05, 157.90, 159.68. IR (cm^{-1}): 3434 (OH alcohol / phenol), 3083 (C-H aromatic), 1355 (C-N), 1563 (C=C aromatic), 1131 (C-O). ESI (+)- MS calculated for $C_{22}H_{16}N_2O_2$ [M+H] : 341.12 a.m.u. Melting point : 238.5 ± 1 ^{0}C.

Synthesis of 6,6'-bis(2-hydroxyphenyl)-2,2'-bipyridyl platinum complex

Platinum (II) chloride (0.133 g, 0.5 mmol) was added to the 6,6'-bis(2-hydroxyphenyl)-2,2'-bipyridine ligand (0.17 g, 0.5 mmol) and heated under reflux in 10 mL benzonitrile for 5 hours under inert atmosphere. After cooling the reaction solution to room temperature, methanol was added to the reaction solution to yield precipitation. The reddish colour precipitate was filtered and wash using methanol and diethyl ether to obtain 6,6'-bis(2-hydroxyphenyl)-2,2'-bipyridyl platinum complex. All spectroscopic data for the complex are in accordance to literature [13]. Yield : 0.0641 g (24%). ^{1}H NMR (600 MHz, $CDCl_3$) δ : 6.78 (m, 1H, , $^{4}J_{HH}$ = 1.8 Hz, arom), 7.15 (m, 1H, , $^{4}J_{HH}$ = 1.8 Hz, arom), 7.38 (m, 1H, , $^{4}J_{HH}$ = 2.4 Hz, arom), 8.24 (t, 1H, , $^{3}J_{HH}$ = 6.3 Hz, arom), 8.41 (t, 1H, , $^{3}J_{HH}$ = 12 Hz, arom), 8.54 (d, 1H, $^{3}J_{HH}$ = 12 Hz, arom) and 8.64 (t, 1H, , $^{3}J_{HH}$ = 12.6 Hz, arom). ^{13}C NMR (600 MHz, $CDCl_3$) δ: 116.65, 120.64, 121.15, 122.64, 124.55, 129.54, 131.84, 137, 149.28, 155.54, 162.16. IR (cm-1): 3089 (C-H aromatic), 1603 (C-N), 1346 (C=C aromatic), 1130 (C-O). ESI(+)- MS calculated for $C_{22}H_{16}N_2O_2$ [M+H] : 533.34 a.m.u.

DNA binding experiments: UV-Vis titration study

A calf-thymus (CT) DNA was dissolved in a 10 mM Tris-HCl /100 mM KCl (pH7.4) buffered overnight. The test compound was dissolved in a mixture of DMSO to give 5 mM stock solution. For working solution, the stock solution was diluted to 1 mM using DMSO and further diluted using the buffer to give appropriate concentrations [11]. A 1 cm pathlength quartz cuvette was used to conduct the measurements. The concentration of DNA used for the binding experiments was determined by measuring the absorption intensity at 260 nm with a molar extinction coefficient value of 6600 M^{-1} cm^{-1} [14]. The absorption titration experiments were performed by keeping the concentration of the ligand constant (20 μM) while varying the DNA concentrations (4.68×10^{-5} M to 1.26×10^{-3} M). Absorbance values were recorded after each successive addition of DNA solution and equilibration (Figure 5). The percentage of hypochromicity was calculated according to Equation (1):

$$\% \text{ hypochromicity} = [(\varepsilon \text{ free} - \varepsilon \text{ bound})/ \varepsilon \text{ free}] \times 100 \quad = \quad 16.04 \% \tag{1}$$

The intrinsic binding constant (K_b) of ligand - DNA was determined according to Equation (2):

$$\frac{DNA}{\Delta\varepsilon ap} = \frac{DNA}{\Delta\varepsilon} + \frac{1}{\Delta\varepsilon \times K} \tag{2}$$

where the apparent molar extinction coefficient, Δεap = |εA- εF|, εA= A observed /[ligand], Δε = |εB- εF|. The εF and εB represent the molar extinction coefficients for free ligand and DNA bound platinum ligand respectively. From the plotted graph of [DNA]/ (Δεap) versus [DNA], the y-intercept is equal to 1/ (Δεap × K), whereas the slope is equal to 1/ Δεap. K is obtained by dividing the slope value by the y-intercept [15]. Excitation wavelengths of 328 nm and 485 nm were used for DNA emission studies.

Emission study

Platinum (II) complex was dissolved in DMSO to yield 5 mM stock solutions. Prior to use, the compounds were diluted to 1 mM using DMSO. This was then further diluted using 10 mM Tris-HCl (pH 7.4) to appropriate concentrations. Aliquots of millimolar stock solution of DNA in Tris-HCl buffer (49 μM) were added to the solutions of the test complex (49 μM). The emission spectra were recorded at λ= 400–700 nm after 1 min equilibration and the luminescence enhancement at λ_{max} = 328 nm and 485 nm were determined.

Results and Discussion

Synthesis of 6,6'-bis(2-hydroxyphenyl)-2,2'-bipyridine ligand and its platinum complex

The 6,6'-bis(2-hydroxyphenyl)-2,2'-bipyridine ligand was successfully prepared via Suzuki coupling reaction using the starting material 2-hydroxyphenylboronic acid. The formation of the ligand was confirmed by spectroscopic and analytical methods. Platinum (II) chloride was introduced to the 6,6'-bis(2-hydroxyphenyl)-2,2'-bipyridine ligand and heated under reflux in 10 mL benzonitrile for 5 hours under inert atmosphere. The reaction scheme is shown in Figure 1. The formation of the platinum (II) complex was also confirmed by spectroscopic and analytical methods.

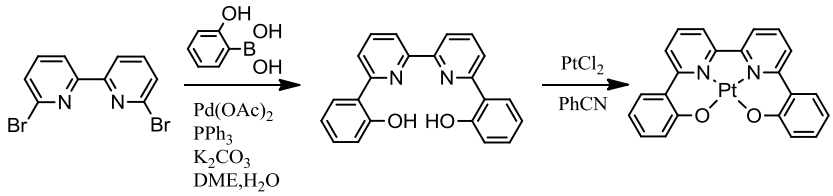


Figure 1. Synthesis of 6,6'-bis(2-hydroxyphenyl)-2,2'-bipyridine ligand via Suzuki coupling reaction and its coordination with metal

Figure 2 shows the NMR spectrum of 6,6'-bis(2-hydroxyphenyl)-2,2'-bipyridine ligand while Figure 3 shows the NMR spectrum of its platinum complex. The resonance at area 14.28 ppm from the spectrum of the ligand is assigned to the OH proton which is highly deshielded due to the large anisotropic field that is generated by the circulation of π electron in the aromatic ring. The disappearance of the resonance in the complex spectrum confirms that the deprotonation of OH groups occurred due to the coordination of oxygen atoms to the platinum (II) metal ion centre. The peaks at area 6.97 to 8.15 ppm in the ligand spectrum are assigned to the aromatic ring proton which is slightly shifted upfield compared to the corresponding peaks in the complex spectrum due to the presence of more electrons withdrawing OH group, and thus increases the shielding of the hydrogen, causing them to move upfield.

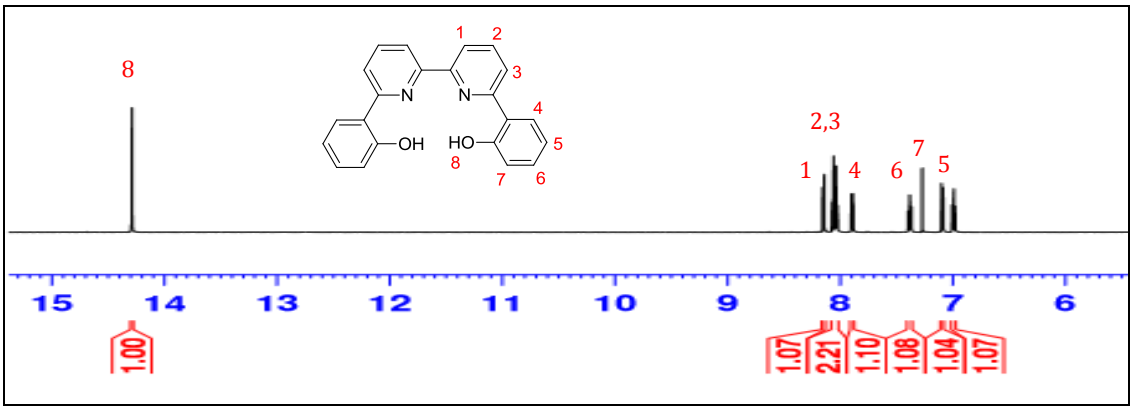


Figure 2. NMR spectrum of 6,6'-bis(2-hydroxyphenyl)-2,2'-bipyridine ligand

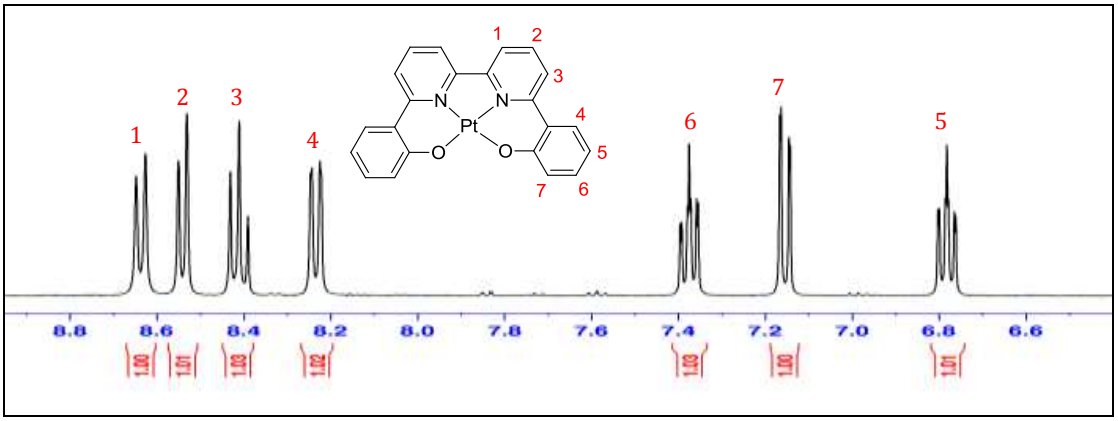


Figure 3. NMR spectrum of platinum (II) bipyridine complex

The assignment of both ^{1}H NMR spectra in $CHCl_3$ was also performed with the help of 2D-^{1}H-^{1}H NMR spectroscopy. The peaks around 7.04 – 8.5 ppm are assigned accordingly to the 2D-COSY NMR as shown in Figure 4(a) and Figure 4(b). The structure obtained was also confirmed by the ^{13}C NMR that shown on Figure 5(a) and Figure 5(b). From the spectrum, it is clearly shown that there was 11 signal peak that represented the presence of 11 carbon in the both structure, ligand and complex.

The infrared spectrum of the complex in Figure 6 represented the absorption band of azomethine –CH=N-, C-O, C=C aromatic and C-H aromatic at 1603 cm^{-1}, 1346 cm^{-1} and 3089 cm^{-1} respectively. The disappearance of hydrogen bonded OH absorption band at 3400 cm^{-1} in the complex spectrum supports the coordination of four donor atom N_2O_2 from ligand to platinum (II) metal ion centre, indicating a square planar geometry and aromatic rings structure. The formation of the ligand and complex was also supported by the mass spectrometry results in which the mass to charge ratio was [M+H] 341.12 a.m.u for the ligand and [M+H] 534.4 a.m.u for the complex. The melting point recorded for this ligand was 238.5 ± 1 ^{o}C.

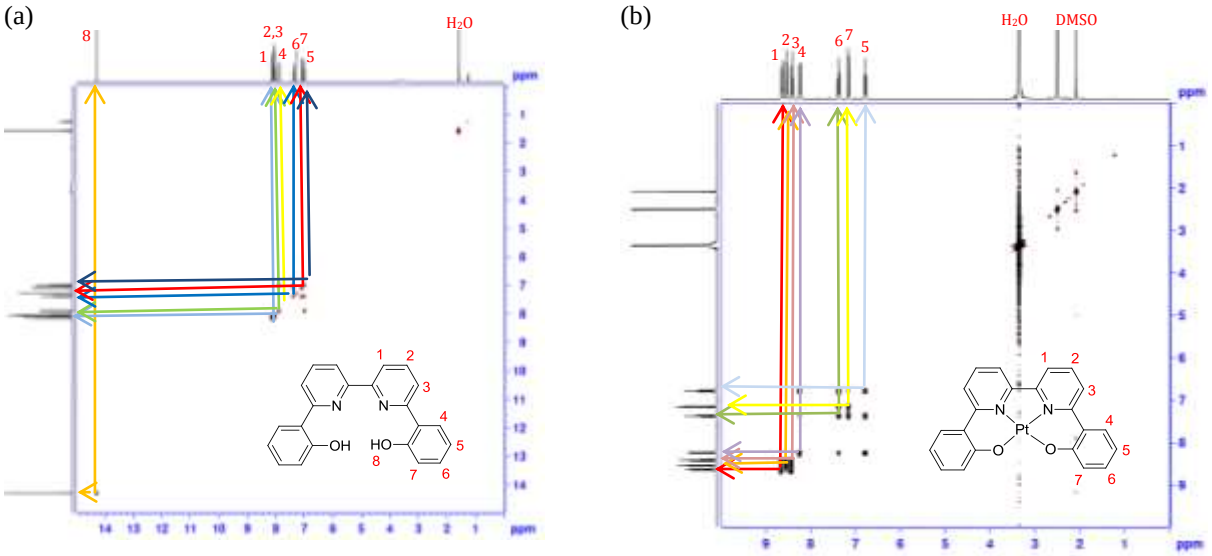


Figure 4. (a) 2D-COSY NMR of the ligand (b) 2D-COSY NMR of the complex

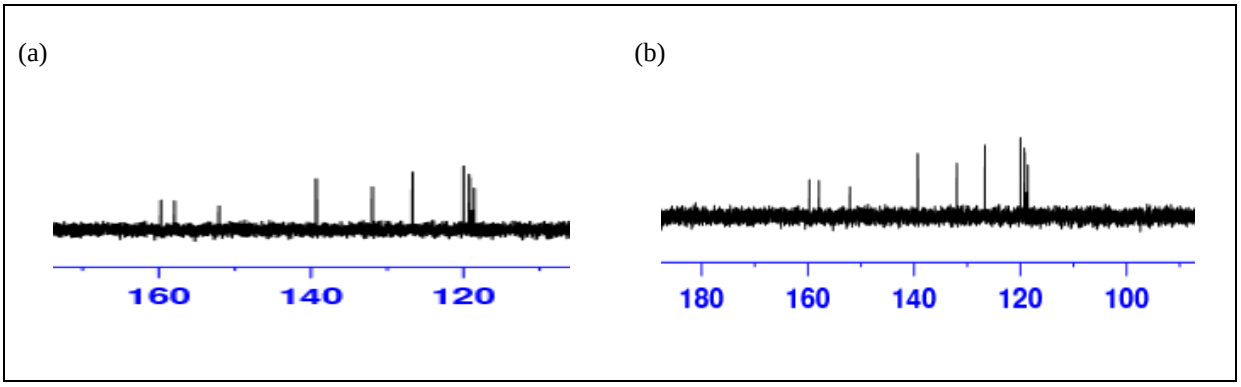


Figure 5. (a) ^{13}C NMR of the ligand (b) ^{13}CNMR of the complex

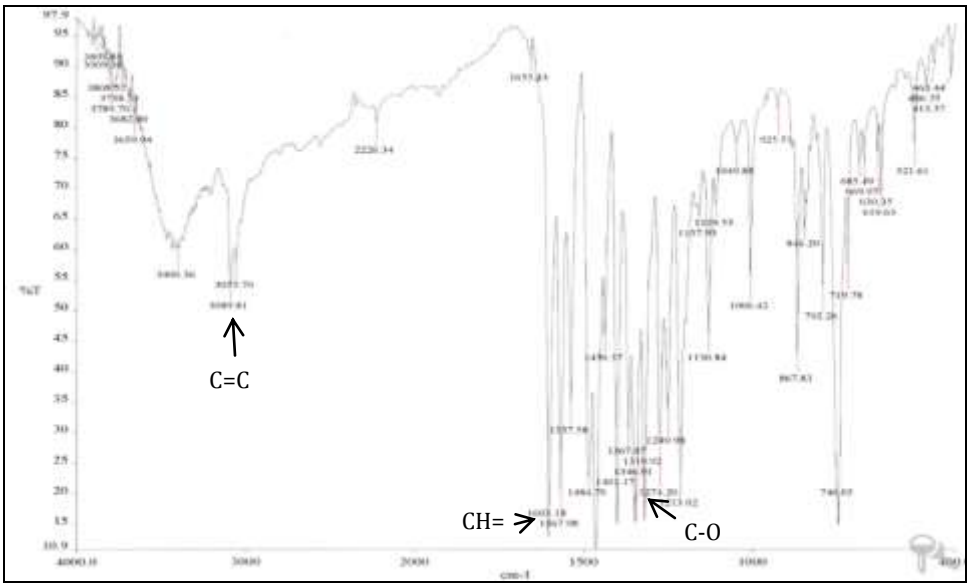


Figure 6. Infrared spectrum of the complex

UV-Vis DNA titration

The application of electronic absorption spectroscopy is one of the most useful techniques in DNA-binding studies. Since no DNA-binding studies have been reported yet on this ligand and its complex, the UV-Vis study was conducted to examine any susceptible interaction between both compound and CT-DNA, and also to study the comparison of the binding affinity between free ligand and with the presence of platinum metal centre ion. Generally, ligands that are coordinated to a metal centre result in a molecule planar and could increase its ability to intercalate between the DNA bases of double helix [15]. Therefore, the presence of metal ion will proposed the square planar geometry and thus will strongly bind to CT-DNA, presumably via intercalation mechanism compared to free ligand. The binding of intercalative compounds to DNA can be characterized by absorption spectral titrations, where lowering in absorbance (hypochromism) and shift to longer wavelengths (red shift) were observed [11]. Hypochromic effect is the spectral features of DNA concerning its interaction between the

electronic states of the compound and DNA base while red shift occurs due to the decrease in energy gap between HOMO and LUMO molecular orbitals after binding the complex to DNA [16].

The UV-Vis absorption spectra of the platinum complex showed three intense bands at 328 nm, 485 nm and 528 nm (Figure 7(a)). UV-Vis absorption spectra of the complex in Figure 7(a) demonstrated that the addition of increasing amounts of CT-DNA resulted in 16 % hypochromism at 528 nm and a slight red shift (3 nm). The hypochromism value was less compared to the absorption spectra of the ligand (Figure 8) which gave 46% hypochromicity upon the addition of increasing amounts of CT-DNA at 341 nm with the same red shift (3 nm). These results showed that there was an interaction between the electronic states of the chromophores in the both ligand and complex conjugates with DNA [5]. However, the intrinsic binding constant value (K_b) of the ligand was found to be $(1.19 \pm 0.08) \times 10^3$ M^{-1} which was 260-folds less the metal complex whose binding constant is $(3.1 \pm 0.02) \times 10^5$ M^{-1}. This means that the complex binds better than the ligand due to its planar aromatic rings structure. Square planar geometry can make the molecule planar, hence increases its intercalation properties [14].

The observed spectroscopic characteristics suggest that the complex interacts with CT-DNA through a mode that involves π-π stacking interaction between the aromatic rings of ligand and the base pairs of CT-DNA while the ligand bind to CT-DNA via outside binding mode interaction such as electrostatic [17] . Our results support the theory by Liu and Sadler [10], which stated that the square-planar platinum(II) complexes containing heterocyclic aromatic ligands bind to DNA duplexes non-covalently by intercalating between the base pairs. Besides, it is in good agreement with the data for other well-known intercalator metal complexes: hypochromicity values (15-30 %), red shift (3-5 nm) and binding constants 5.20×10^4 M^{-1} and 8.60×10^4 M^{-1} for 3-ethylpiperidineoxy-2-[(2-(piperidin-1-yl)ethoxy)phenyl]-pyridine)-2(N,O)-(5-nitro-8-quinolinolato) platinum (II) and *N,N'*-bis[4-[[1-(2-ethyl)piperidine]oxy]salicylidene]-4-(2-(piperidin-1-yl)ethoxy)-1,2-phenylenediamine-platinum(II), respectively [11].

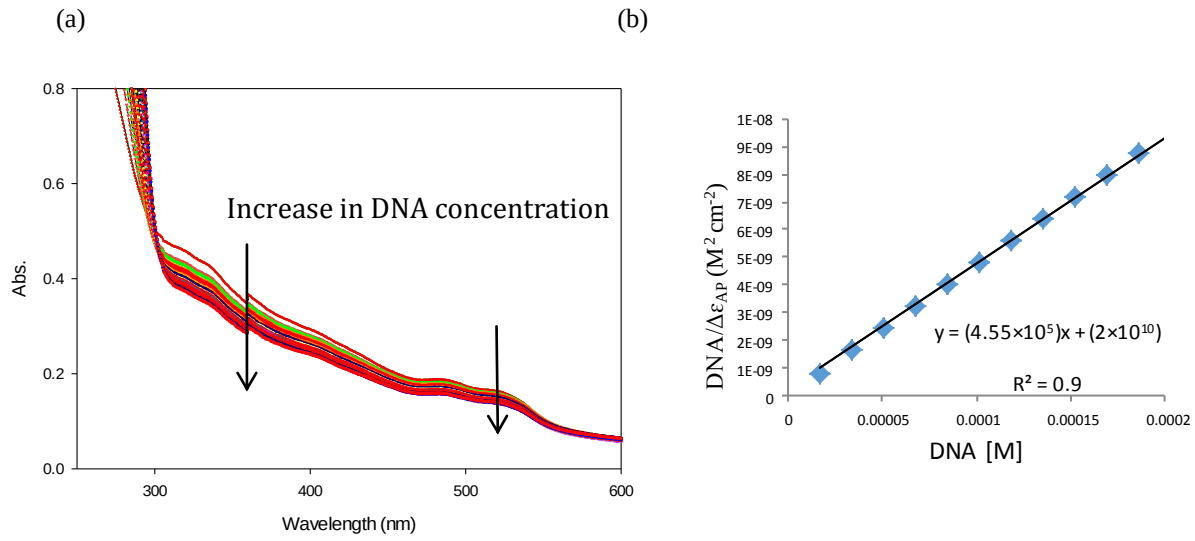


Figure 7. (a) Absorption spectral changes of complex (30 μM) in TRIS.HCl buffer (pH = 7.4) in absence and presence of increasing concentration of CT-DNA (4.68×10^{-5} M to 1.26×10^{-3} M) (b) the reciprocal plot that fits the absorbance data to obtain the binding constant.

(a) (b)

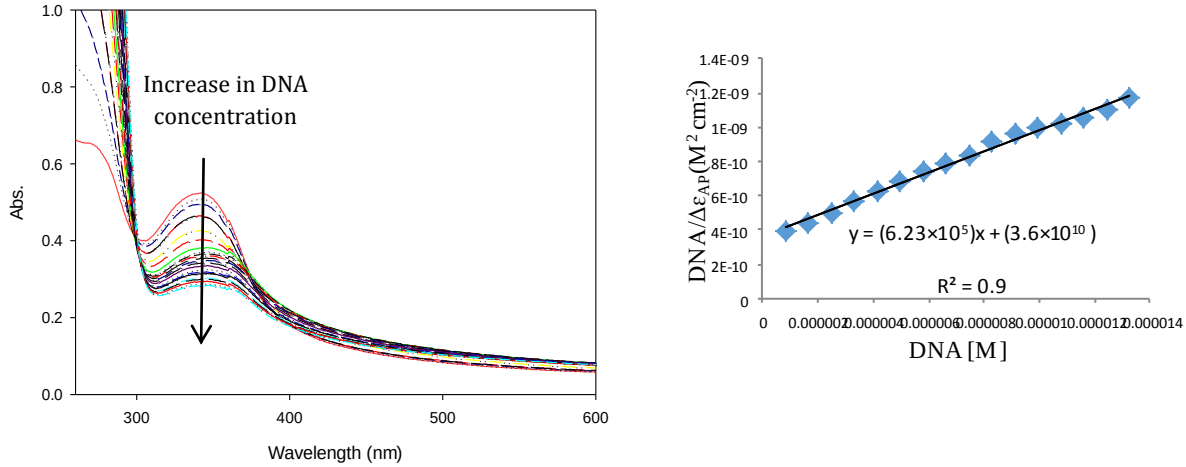


Figure 8. (a) Absorption spectral changes of ligand (30 μM) in TRIS.HCl buffer (pH = 7.4) in absence and presence of increasing concentration of CT-DNA ($4.68x10^{-5}$ M to $1.26x10^{-3}$ M). (b) The reciprocal plot that fits the absorbance data to obtain the binding constant.

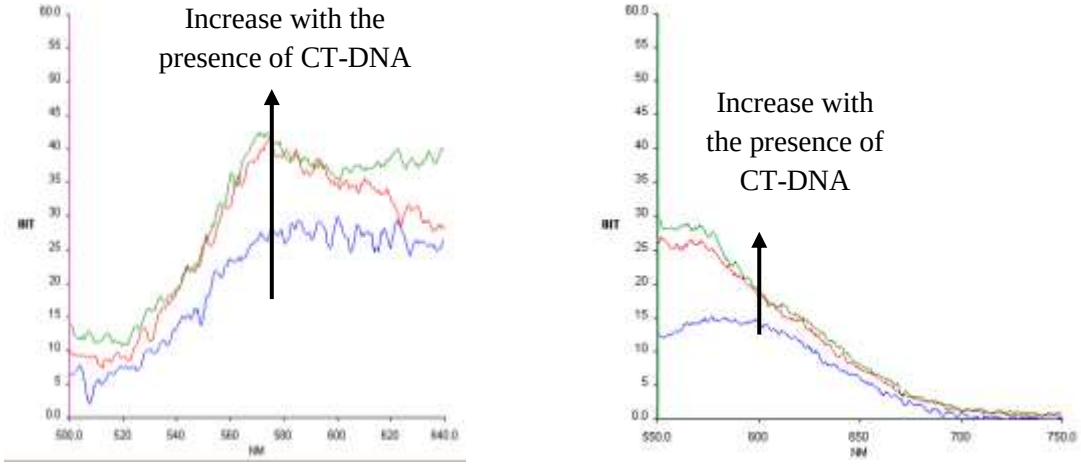


Figure 9. (a) Fluorescence emission spectra of platinum bipyridine complex (49μM) in TRIS.HCl buffer (pH = 7.4) in absence and presence of CT-DNA (λ excitation = 328 nm. λ emission = 570 nm). (b) Fluorescence emission spectra of platinum bipyridine complex (49μM) in TRIS.HCl buffer (pH = 7.4) in absence and presence of CT-DNA (λ excitation = 485 nm. λ emission = 570 nm)

Emission study

Platinum (II) complexes with a wide range of aromatic ligand are known to possess luminescent properties. Thus, it was the interest of this study to investigate whether the platinum bipyridine complex in this study is emissive and thus investigate their optical properties changes upon interaction with DNA. Emission titration experiments with 1:1 ratio were performed using constant concentration of complex and CT-DNA (49 µM) at different excitation wavelengths. Figure 9 shows the phosphorescence emission spectra in both the absence and presence of DNA in the Tris-HCl buffer. The platinum complex was found to be slightly emissive at λ_{max} = 328 and 485 nm respectively. Interestingly, the addition of CT-DNA resulted in an enhancement of phosphorescence emission intensity in both spectra. The emission spectra of the complex showed an increase in the intensity of emission by a factor of 1 indicating the interaction of the complex with DNA. These results confirmed that there was an interaction between phosphorescence platinum(II) bipyridine complex and DNA. These findings will be valuable for the potential use of platinum(II) bipyridine complex as a phosphorescence probe in optical sensor DNA.

Conclusion

The bis(phenoxy)bipyridine ligand and its platinum complex has been successfully synthesized and characterised. The ^{1}H, ^{13}C NMR, IR and mass spectrometry observations were used to elucidate the structure. UV-Vis DNA study showed that platinum complex might be a promising candidate compared to ligand for further applications as a DNA binder and anticancer drugs due to the interaction with CT-DNA via intercalation rather than outside binding. The coordination of ligand with metal centre increases the structural flexibility and thus increases the ability of the complexes to stack and intercalate between the DNA bases. An enhancement of phosphorescence emission intensity upon the interaction with porcine DNA suggests that the platinum complex has the potential as a phosphorescence DNA sensor. These findings will be valuable for the potential use of platinum (II) bipyridine complex as a phosphorescence probe for the detection of porcine DNA in food products.

Acknowledgement

The authors would like to acknowledge National University of Malaysia for providing the research facilities. This work has been carried out with the support of Malaysian Government through Ministry of Higher Education grant FRGS/1/2013/ST01/UKM/03/2, DIP-2014-016 and 06-01-02-SF0898.

References

1. Jeffery, J. C., Thornton, P. and Ward, M. D. (1994). An Unusual Chain-like Tetranuclear Manganese (II) Complex Displaying Ferromagnetic Exchange. *Journal of Inorganic Chemistry*, 33(16): 3612 –3615.
2. Bardwell, D. A., Jeffery, J. C. and Ward, M. D. (1995). Coordination Chemistry of Mixed Pyridine-phenol Ligands – Polynuclear Complexes of 6-(2-hydroxyphenyl)-2,2'-bipyridine with Ni(II), Cd(II), Mn(III) and Mn(II)/Mn(II), *Journal of the Chemical Society, Dalton Transactions*, 3071 – 3080.
3. Maher, J. P., Rieger, P. H., Thornton, P. and Ward, M. D. (1992). Coordination Chemistry of Mixed Pyridine Phenol and Phenanthroline Phenol Ligands, A Variable-Temperature Electron-Paramagnetic Resonance and Magnetic Susceptibility Study on 2 Binuclear Copper(II) Complexes. *Journal of the Chemical Society, Dalton Transactions*. 3353 – 3356.
4. Ramos, J. C. G., Morillo, R. G., Guzman, F. C. and Azuara, L. R. (2013). Metal Based Drug-DNA Interaction, *Journal of the Mexican Chemical Society*, 57(3): 245 –259.
5. Maryam, H., Mohammadjavad, P., Soheil, Z. M., Pouya, H., Nura, S. G., Maryam, Z., Elham, R., Hamed, K., Chung, Y. L., Hapipah, M. A., Nazia, A. M. and Mahmood., A. A. (2014). A Schiff Base-Derived Copper (II) Complex Is a Potent Inducer of Apoptosis in Colon Cancer Cells by Activating the Intrinsic Pathway. *Journal of Scientific World*, 2014: 1 – 12.
6. Barton, J. K., Kaiser, J. T. and Song, H. (2012). Crystal Structure of Δ-[Ru(Bpy)2dppz]2+ Bound to Mismatched DNA Reveals Side-By-Side Metalloinsertion and Intercalation, *Nature Chemistry*, 4: 615 – 620.
7. Zhou, C., Du, X. and Li, H. (2007). Studies of Interactions Among Cobalt(III) Polypyridyl Complexes, 6-Mercaptopurine and DNA. *Journal of Bioelectrochemistry*, 70(2): 446 – 451.
8. Wang, B., Yang, Z. and Li, T. (2006). Synthesis, Characterization, and DNA-Binding Properties of The Ln(III) Complexes With 6-Hydroxy Chromone3-Carbaldehyde-(2'-Hydroxy) Benzoyl Hydrazone. *Journal of Bioorganic and Medicinal Chemistry.* 14(17): 6012 – 6021.

9. Zhou, L., Feng, Y., Cheng, J., Sun, N., Zhou, X. and Xiang, H. (2012), Simple, Selective, and Sensitive Colorimetric and Ratiometric Fluorescence/Phosphorescence Probes for Platinum (II) Based on Salen-Type Schiff Bases, *Journal of RSC Advances*, 2(28): 10529 – 10536.
10. Liu, H. K. and Sadler, P. J. (2011) Metals Complex As DNA Intercalators, *Accounts of Chemical Research*, 44(5): 349 – 359.
11. Kashanian, S., Gholivand, M. B., Ahmadi, F., Taravati, A. and Colagar, A. H. (2007). DNA Interaction With Al–N, N′-Bis(Salicylidene)2,2′-Phenylendiamine Complex, *Spectrochimica Acta Part A: Molecular and Biomolecular Spectroscopy*, 67(2): 472 – 478.
12. Nii, K., Minami, A., Kousuke, W., Igarashi, I. T., Seiji, I. and Toshlhlro, I. (2012), Organic Electroluminescent Devices And Metal Complex Compound, *United States Patent* US8211553B2.
13. Orejon, A., Castellanos, A., Salagre, P., Castillon, S. and Claver, C. (2005), Oxidative Carbonylation Of Aniline With New Cobalt Catalytic Systems, *Canadian Journal Chem*istry 83: 764 – 768.
14. Chetana, P. R., Rao, R., Roy, M. and Patra, A. K. (2009), New Ternary Copper (II) Complexes of L-Alanine and Heterocyclic Bases: DNA Binding And Oxidative DNA Cleavage Activity, *Inorganica Chimica Acta*, 362(13): 4692 – 4698.
15. Vilar, R., Arnal, A. A., Buchholz, J. B. and Neidle, S. (2008), Effects of Metal Coordination Geometry on Stabilization of Human Telomeric Quadruplex DNA by Square-Planar and Square-Pyramidal Metal Complexes, *Inorganic Chemistry*, 47: 11910 – 11919.
16. Huda, N. (2012), Studies Towards Elucidating the Binding Modes between Metal-Salphen Complexes and G-Quadruplex DNA, Ph.D. Thesis, Imperial College London.
17. Shahabadi, N., Mohammadi, S. and Alizadeh, R. (2011). DNA Interaction Studies of A New Platinum (II) Complex Containing Different Aromatic Dinitrogen Ligands. *Bioinorganic Chemistry and Application*, 2011: 1 – 8.

MALAYSIAN JOURNAL OF ANALYTICAL SCIENCES
Published by The Malaysian Analytical Sciences Society
ISSN 1394 - 2506

INVESTIGATION ON OPTICAL AND PHOTOELECTROCHEMICAL PROPERTIES OF SELF-ASSEMBLED TITANIA NANOTUBE ARRAYS PREPARED BY ANODIZATION

(Penyiasatan Sifat Optik dan Fotoelektrokimia Swahimpunan Nanotiub Titania Bertatasusunan yang Disediakan Melalui Penganodan)

Lim Ying Chin[1]*, Zulkarnain Zainal[2], Mohd Zobir Hussein[3], Tan Wee Tee[2]

[1]School of Chemistry and Environment, Faculty of Applied Sciences,
Universiti Teknologi MARA (UiTM), 40450 Shah Alam, Selangor, Malaysia
[2]Department of Chemistry, Faculty of Science
[3]Advanced Materials and Nanotechnology Laboratory, Institute of Advanced Technology (ITMA)
Universiti Putra Malaysia, 43400 UPM Serdang, Selangor, Malaysia

**Corresponding author: limyi613@salam.uitm.edu.my*

Received: 9 December 2014; Accepted: 16 November 2015

Abstract

Well ordered and vertically oriented titania nanotubes (TNT) are of great scientific interest due to their high surface area, fewer interfacial grain boundaries and excellent charge transfer between interfaces; all are critical properties in photoelectrochemical and photocatalysis application. In this study, self-assembled TNT electrodes were synthesized by anodization of pure Ti in 0.5 wt.% NH_4F solution (NH_4F/H_2O), in mixture of aqueous-organic solution (NH_4F/H_2O/EG) and in an organic solution (NH_4F/EG). Choice of electrolytic medium has an influence on the crystalline structure, regularity, elemental composition and band gap of TNT. All the samples showed a red shift and stronger absorption in the wavelength between 500-700 nm ascribed to the surface colour and increase crystallinity upon calcination. TNT formed in NH_4F/H_2O solution has the highest direct band gap of 3.34 eV due to quantization effect. From Liner Sweep Photovoltammetry analysis, the lowest photocurrent was recorded for TNT anodized in NH_4F/H_2O and a twofold and fivefold increase on the magnitude of photocurrent was obtained for those formed in NH_4F/H_2O/EG and NH_4F/EG solution, respectively. Hence, highest photoefficiency of 2.79 % was recorded for TNT formed in NH_4F/EG probably due to the formation of longer length tube.

Keywords: titania, nanotube, anodization, photoefficiency, band gap energy

Abstrak

Nanotiub titanium dioksida yang bertertib rapi dan berorientasi mencancang (TNT) telah menarik perhatian disebabkan luas permukaan yang tinggi, sempadan butiran antara muka yang rendah dan pemindahan cas yang cemerlang di antara muka, yang mana semua ini merupakan ciri – ciri kritikal dalam aplikasi fotoelektrokimia and fotopemangkinan. Dalam kajian ini, swahimpunan TNT telah disintesis melalui penganodan plat titanium tulen dalam larutan 0.5 wt.% NH_4F (NH_4F/H_2O), campuran larutan akua-organik (NH_4F/EG/H_2O) dan larutan organik (NH_4F/EG). Pilihan media elektrolisis memberi kesan ke atas struktur hablur, keteraturan, komposisi unsur dan julang jalur TNT. Semua sampel mempamerkan anjakan merah dan penyerapan yang lebih kuat dalam julat gelombang 500 – 700 nm disebabkan warna permukaan sampel dan peningkatan kehabluran selepas pemanasan. Dari analisis fotovoltammetri pengimbasan linear, TNT yang teranod dalam larutan NH_4F/H_2O mencatatkan fotoarus yang terendah manakala peningkatan lipat ganda dua dan ganda lima dalam magnitud fotoarus boleh didapati untuk TNT yang teranod dalam larutan NH_4F/H_2O/EG dan NH_4F/EG. Oleh yang demikian, TNT yang dibentuk dalam latutan NH_4F/EG mencatatkan kecekapan foto yang tertinggi sebanyak 2.79 % mungkin disebabkan oleh pembentukan tiub yang lebih panjang.

Kata kunci: titania, nanotiub, penganodan, kecekapan foto, jalur jurang tenaga

Introduction

Titania (TiO_2) appears to be the most promising material to be used in photoelectrochemical applications due to its high efficiency, low cost, chemical inertness and photostability [1 – 4]. However, bulk TiO_2 materials have low surface area and therefore exhibit low adsorption property. Moreover, fast recombination rate of the photogenerated charge carriers deteriorate the performance of such materials especially in photoelectrochemical applications. In order to overcome such problems, much effort has been focused on fabrication of highly efficient materials with suitable architecture to minimize the recombination of electron-hole pairs. In this context, formation of highly ordered and oriented nanotubular or porous geometry is advantageous due to high surface-to-volume ratio and short diffusion path within enclosed nanoscale compartment [5]. Self-organized growth of TiO_2 nanotube arrays are of great interest due to its unique physical properties including larger surface area in a small geometrical area, fewer interfacial grain boundaries and superior charge transport, of which all are important properties governing its performance as photoanode in a photoelectrochemical cell. Therefore, the study aimed at synthesizing titania nanotubes in various electrolytic compositions in order to investigating the effects of electrolyte nature on the microstructure, optical and photoelectrochemical performance of the synthesized TNT.

Materials and Methods

Fabrication of titania nanotube arrays

A Ti foil (99.7%, Sigma Aldrich) was used for producing vertically oriented nanotubes. Prior to anodization, the Ti foils were cleaned by sonication in acetone, isopropanol, and deionized (DI) water respectively, followed by subsequent etching in 6 M HNO_3. They were then rinsed with DI water and dried in air. An electrochemical cell with a two-electrode configuration was used. The Ti foil served as the working electrode and high density graphite was used as the counter electrode and they were separated by approximately 2 cm. All the experiments were driven by a DC power source (Consort Mini, Cleaver Scientific Ltd) and were carried out at room temperature in three different types of electrolytes for 2 hours to form TNT. The composition of the three electrolyte solutions and voltage used for anodization were summarized in Table 1. After the anodization process, the samples were rinsed with DI water and dried in air. Subsequently, they were calcined at 500 ^oC in air for 2 hours with a heating rate of 2 ^oC/minutes. The resultant calcined TNT are hereinafter designated as C5TNT/H_2O, for the 0.5 wt% NH_4F solution adjusted to pH 4, C5TNT/EGH_2O, for the mixture of ethylene glycol containing 50 vol.% H_2O and 0.5 wt.% NH_4F and C5TNT/EG, for ethylene glycol containing 0.5 wt.% NH_4F. For comparison, the as-anodized samples without heat treatment were produced and were designated as AOTNT/H_2O, AOTNT/EGH_2O and AOTNT/EG, respectively.

Table 1. Summary of electrolyte compositions and voltage used producing TNT during anodization

Samples	Electrolyte composition	Voltage / V
TNT/H_2O	0.5 wt.% NH_4F adjusted to pH 4	20
TNT/EGH_2O	0.5 wt.% NH_4F + ethylene glycol + 50 vol.% H_2O	20
TNT/EG	0.5 wt.% NH_4F + ethylene glycol	65

Characterization of titania nanotube arrays

Phase identification was carried out using an X-ray diffractometer (XRD, Shimadzu D6000) with Cu K_α radiation (λ= 1.5406 Å). The morphology of the samples was characterized on TEM Hitachi H-1700 operating at an accelerating voltage of 200 kV. Quantitative measurements were done using image analysis software (Image J). Energy dispersive analysis of x-rays (EDX) was performed on JOEL FESEM JSM-7600F JOEL, Japan attached with Oxford INCA Energy 200 EDX to determine the purity and elemental composition in the as-anodized and

calcined samples. The optical absorbance behavior of TNT was characterized using a diffuse reflectance UV-VIS-NIR spectrophotometer (Model: UV-3600, Shimadzu Corporation, Kyoto, Japan) equipped with an integration sphere. $BaSO_4$ was used as a reflectance standard. The band gap energy (E_g) can be calculated using the absorbance data obtained following the Tauc Plot relation (Equation 1):

$$\alpha h\nu = A(h\nu - E_g)^n \quad (1)$$

where α is the absorption coefficient, h is the Planck's constant, ν is the wavenumber and A is a constant. The "n" depends on the types of band-to-band transition (for titania, n=2 for a direct band gap and n= ½ for a indirect transition between bands). The band gap energy could be obtained by extrapolating the straight line in the plot of $\alpha^{1/2}$ or $\alpha h\nu^2$ against $h\nu$ to the base line where $\alpha^{1/2}$ or $\alpha h\nu^2 = 0$. Thus, the E_g is equivalent to $h\nu$.

Photoelectrochemical test

Photoelectrochemical response of TNT was demonstrated using a three-electrode system with the synthesized TNT as the working electrode, a platinum wire as the counter electrode, and Ag/AgCl as the reference electrode. The photocurrent was measured with a scanning potentiostat (μAutolab type III) during a voltage sweep from +2.0 to –0.2 V with the sweep rate of 20 mV/s in 10 ppm methyl orange with 0.1 M KCl as the supporting electrolyte. All the potentials were quoted against Ag/AgCl reference electrode. A tungsten halogen lamp (300 W, 120 V) was used for illuminating the TNT samples and the light was intermittently chopped at a constant frequency to evaluate both the photocurrent and dark current. A UV lamp (B-100AP) with the incident power of 11 mW/cm^2 was used to evaluate the efficiency of photocurrent generated by TNT prepared in different electrolytic medium and the radiation source was placed 15 cm away from the cell. The solution used was 0.1 M KOH

Results and Discussion

Electrolyte composition is an important parameter influencing the structure, morphology and geometry (and thus the specific surface area) of the resulted nanotubes. The crystallinity and the isomorphs of TNT are critical in influencing their properties and potential applications. Figure 1 illustrates the XRD patterns of TNT as a function of electrolytic medium. No peak shift was observed as a function of electrolytic medium. For TNT/H_2O, a mixture of anatase at $2\theta = 25.4^o$ (JCPDS No. 21-1272) and rutile at $2\theta = 27.6^o$ (JCPDS No. 21-1276) was observed after calcination at 500 ^oC. As opposed to TNT/H_2O, only pure anatase phase at $2\theta = 25.4^o$, 38.0^o, 48.2^o, 54.0^o and 55.2^o corresponding to (101), (004), (200), (105) and (211) plane, respectively was obtained for TNT/EG and TNT/EGH_2O upon calcination at 500 ^oC as shown in Figure 1 (b-c). Our finding is in contradiction with the work reported by other researchers that the crystalline structures remained unaffected with different electrolytic media [6, 7]. It is also discernible that the (101) reflection exhibited greatest intensity as compared to the other anatase peaks for all samples, demonstrating the preferred growth orientation for nanotubes at this plane. For TNT/EG sample, almost tenfold increase on the intensity magnitude of (101) reflection compared to TNT/H_2O and a threefold increase for TNT/EGH_2O sample, probably ascribed to increase in length for samples prepared in different electrolytic medium.

TEM analysis was performed to gain information on the microstructure of the sample. Figure 2 shows the TEM image of all samples. Apparently, a single nanotube consisted of a closed bottom with a barrier layer thickness of 37 nm and ripples on sidewall were obtained in NH_4F/H_2O solution. Same observation on the formation of ripples was obtained for TNT/EGH_2O. These ripples could be formed due to current fluctuations occurred during anodization process. In contrast, well-dispersed and straight nanotubes with uniform wall thickness and smooth tube wall throughout the length of the nanotubes can be observed for TNT formed in NH_4F/EG. Therefore, the electrolyte composition is a crucial factor determining the morphology of the outer wall where ripples are observed in nanotubes grown in aqueous electrolytes, whereas nanotubes prepared in ethylene glycol can be either smooth or are having ripples depending on the water content (50 vol. % in this study).

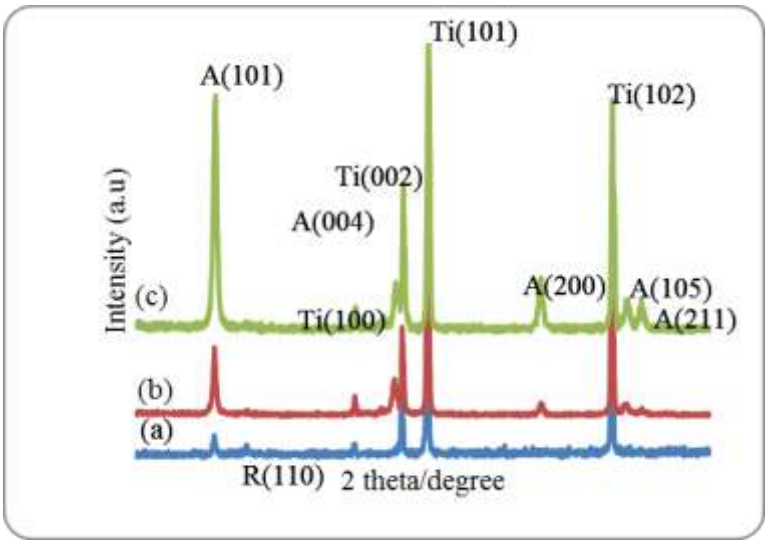


Figure 1. XRD patterns of calcined TNT synthesized at 20 V in different electrolytic medium with (a) NH_4F/H_2O (b) NH_4F/EG and (c) $NH_4F/EG/H_2O$ solution. A, R and Ti represent anatase, rutile and titanium, respectively

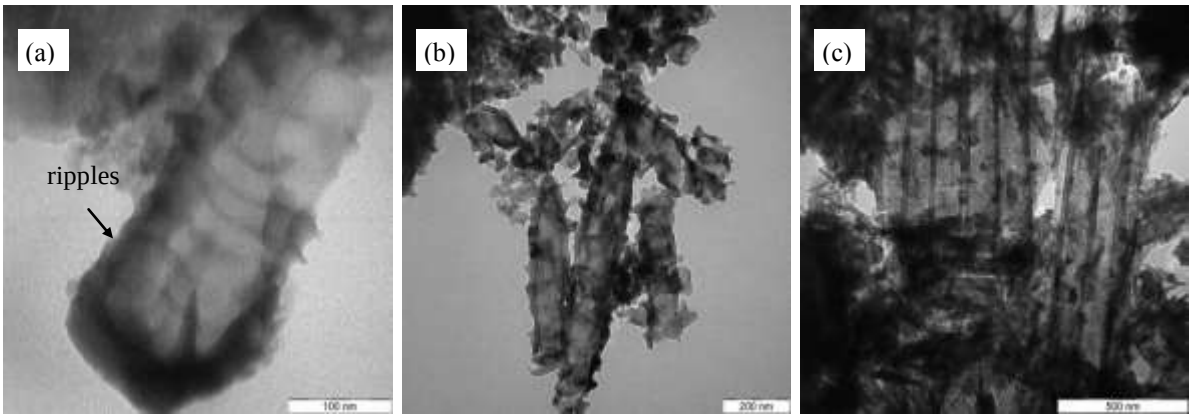


Figure 2. TEM images for (a) TNT/H_2O (b) TNT/EGH_2O and (c) TNT/EG

EDX analysis was done on blank Ti plate, as-anodized TNT and their calcined counterparts. The detailed compositions of the samples before and after calcination are shown in Table 2. For blank Ti, only Ti element was detected and C peak observed is due to carbon tape holding the sample. Evidently, Ti, O and F are found in the spectrum for $AOTNT/H_2O$, $AOTNT/EGH_2O$ and AOTNT/EG, with trace of carbon from the ethylene glycol observed for AOTNT/EG sample. The fluorine observed is due to the NH_4F added in the solution, which acts as a pore initiating agent. Calcination at 500 ^oC leads to a complete loss of the fluorine for C5TNT/EG and thus it is free from fluoride content and this result is similar with the work reported by Sreekantan et al. [8]. However, traces of F still can be detected for $C5TNT/H_2O$ and $C5TNT/EGH_2O$ but with almost negligible amount, indicating that the F is precipitated on the surface of sample during anodization and not incorporated into the TiO_2 lattice. In addition, all samples showed an increase in Ti and O content upon calcination. The molar ratio of Ti to O for calcined samples was close to the stoichiometric proportion, suggesting the samples were TiO_2.

For TNT/EG sample, a carbon rich layer could be probably obtained due to the voltage induced decomposition of the ethylene glycol as high voltage (65 V) is used during anodization of Ti. Therefore, higher C content (2.33 wt.%) was observed for AOTNT/EG sample. However, no C uptake from the solution occurs for C5TNT/EG given the C weight percent present is comparable to the blank Ti plate upon calcination at 500 ^{o}C. This result indicates that C from the ethylene glycol in AOTNT/EG could be easily removed via thermal treatment.

Table 2. Elemental analysis for Ti, as-anodised TNT and calcined TNT/H_2O, TNT/EGH_2O and TNT/EG

Sample	Weight percent (%)			
	Ti	O	C	F
Ti	99.44	-	0.45	-
AOTNT/H_2O	58.22	31.27	-	10.51
AOTNT/EGH_2O	51.20	38.53	-	10.27
AOTNT/EG	46.71	35.90	2.33	15.06
C5TNT/H_2O	61.83	36.11	-	2.06
C5TNT/EGH_2O	53.30	44.22	-	2.48
C5TNT/EG	63.11	36.60	0.29	-

Figure 3 shows the diffuse reflectance UV-Vis absorbance of both the as-anodized and calcined TNT prepared in different electrolytic medium. The absorbance response for AOTNT/H_2O, AOTNT/EGH_2O and AOTNT/EG exhibited lower absorption in the visible region, whereas the calcined counterparts showed a red shift and stronger absorption in the wavelength between 500−750 nm, with exception for C5TNT/EGH_2O. This can be attributed to the surface color and changes in crystalline structure of TNT. Generally, the color of C5TNT/H_2O was yellowish, dark green for C5TNT/EGH_2O and dark grey green for C5TNT/EG, respectively. In contrast, the as-anodized films were bright green, bright purple and bright grey for AOTNT/H_2O, AOTNT/EGH_2O and AOTNT/EG, respectively and this causes more adsorption in ultraviolet region and more reflection in the visible region. As shown in Figure 2, the absorption onset for C5TNT/H_2O, C5TNT/EGH_2O and C5TNT/EG was around 370, 380 and 390, respectively which was probably caused by increasing anatase content after thermal treatment. This is consistent with the changes in crystalline structure observed in XRD scan (Figure 1).

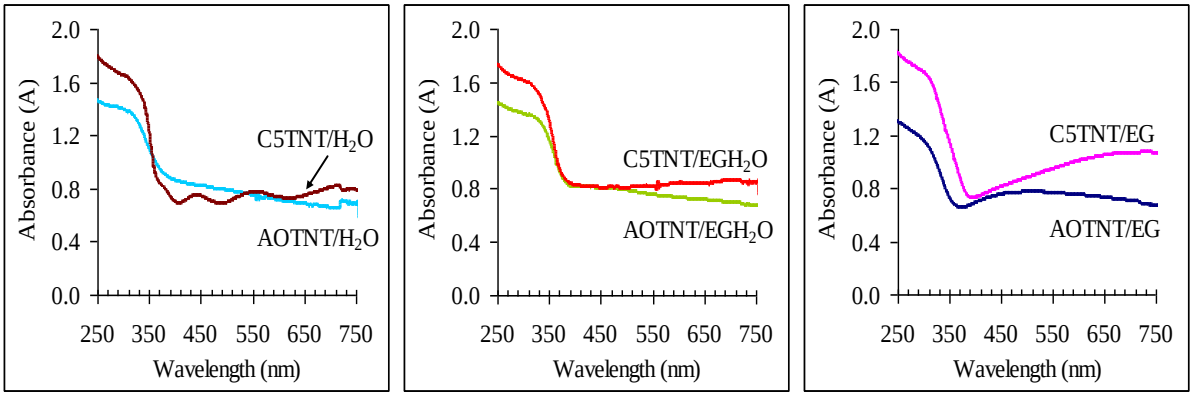


Figure 3. UV-Visible absorbance spectra of TNT/H_2O, TNT/EGH_2O and TNT/EG sample

In addition, the absorbency of visible light (< 550 nm) is higher for C5TNT/EG sample, which could mean that it possesses a higher efficiency of sunlight utilization compared to C5TNT/H_2O and C5TNT/EGH_2O sample. It is thus

expected that C5TNT/EG sample will result in an improvement in solar cell fabrication and in photocatalytic activity. Red shift in absorption wavelength in the visible region for C5TNT/EG might due to oxidation of ethylene glycol to carbonate type species which get adsorbed on the nanotube walls as an outer layer. Sohn et al. [9] also observed the introduction of carbon into TNT, which facilitates the improvement in visible light absorbance when employing ethylene glycol as electrolyte.

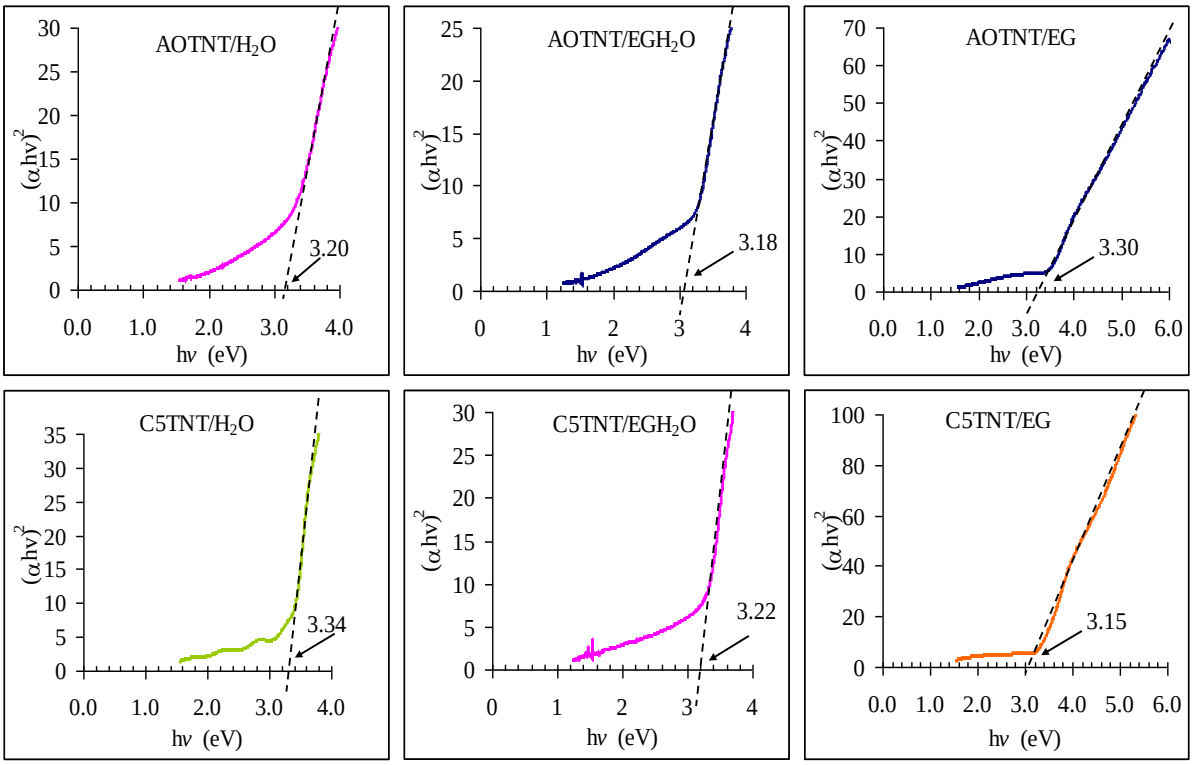


Figure 4. Plot of $(\alpha h\nu)^2$ versus $h\nu$ for AOTNT/H_2O, AOTNT/EGH_2O and AOTNT/EG and their calcined counterparts

Figure 4 shows the plot of $(\alpha h\nu)^2$ versus $h\nu$ for TNT prepared in different electrolytic medium. All the three as-anodised samples, AOTNT/H_2O, AOTNT/EGH_2O and AOTNT/EG have band gap energy of 3.18 – 3.30 eV with a direct transition and this result is similar with the work reported by Song et al. [10]. For the calcined samples, C5TNT/H_2O has the highest direct band gap of 3.34, which was higher than 3.2 eV for bulk anatase due to quantization effect of the nanosized titania. However, C5TNT/EGH_2O and C5TNT/EG exhibited a direct bandgap of 3.22 and 3.15 eV respectively, which was comparable to that of bulk anatase. The calcined samples demonstrated higher band gap than their as-anodised counterpart except for C5TNT/EG sample. From the EDX analysis (Table 2), no carbon was found for both the AOTNT/H_2O and AOTNT/EGH_2O samples whereas a 2.33 wt.% carbon content was found for AOTNT/EG sample.

The photocurrent generated by unmodified Ti and all as-anodized samples (AOTNT/H_2O, AOTNT/EGH_2O and AOTNT/EG) was almost negligible (~2 $\mu A/cm^2$) as they are amorphous without heat treatment. Therefore, the efficiency of generating photocurrent under halogen and UV lamp illumination in methyl orange was compared for all C5TNT/H_2O, C5TNT/EGH_2O and C5TNT/EG samples as shown in Figure 5. Apparently, the photocurrent generated for all samples illuminated with UV lamp was much higher than that observed with halogen lamp, demonstrating that the light from UV lamp (365 nm, 11 mW/m^2) is more efficient in generating and promoting the

electron-hole pairs activity than a halogen lamp (150 mW/m^2). Though halogen lamp exhibits higher photointensity, however, most of the light is given out as heat instead of promoting electron-hole activity. From the DR UV-Vis analysis as shown in Figure 4, the band gap energy for C5TNT/H_2O, C5TNT/EGH_2O and C5TNT/EG is 3.34, 3.22 and 3.15 eV, respectively. Therefore, the light from the UV lamp contains more number of photons with energy exceeding the band gap of TNT, and thus it can excite the TNT samples better compared to halogen lamp. Even though UV rays have higher energies than the light from halogen lamp, the hazardous effects possess by UV radiation is the draw back for the usage of such lamp in activating TNT.

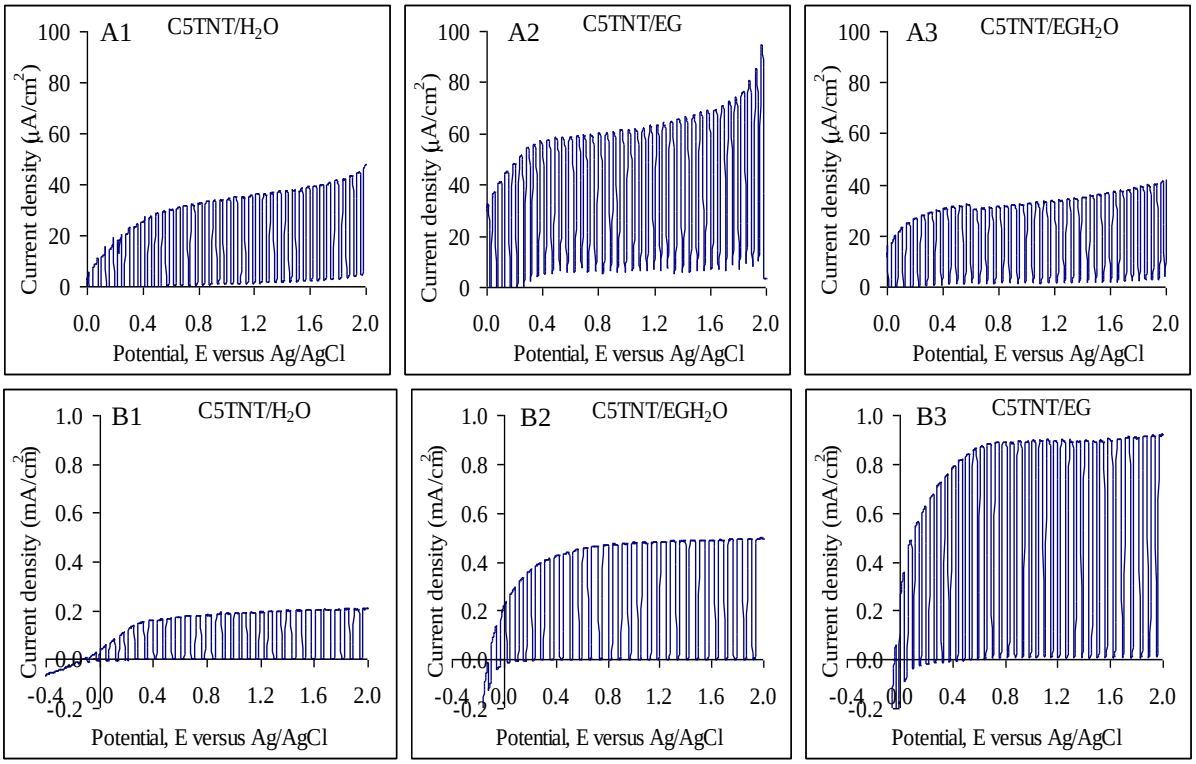


Figure 5. Comparison of the photocurrent potential curve for C5TNT/H_2O, C5TNT/EGH_2O and C5TNT/EG under illumination of halogen lamp (A) and UV lamp (B) in 50 mL 10 ppm methyl orange with 0.1 M KCl as supporting electrolyte

Table 3 shows the dimensional data and photocurrent current for TNT synthesized in different electrolytic medium when illuminated with UV lamp. The magnitude of photocurrent correlates to the efficiency of holes transfer at the oxide-electrolyte interface and electrons transport through nanotubes to the Ti substrate. The lowest photocurrent generated was found for C5TNT/H_2O and a twofold increase on the magnitude of photocurrent was observed for C5TNT/EGH_2O and the highest photocurrent was recorded for C5TNT/EG. Higher photocurrent response obtained for C5TNT/EG sample clearly indicates improved charge separation and greater electrons transport for sample with longer length and larger diameter tubes. In addition, longer length tubes also demonstrated greater surface areas that enhance the absorption of the incident photon, which in return increase the photocurrent response. However, the magnitude of photocurrent did not increase linearly with increasing length as the light intensity usually attenuates as it penetrates into the nanotubes. If the nanotubes have longer length than the effective depth of light penetration, the amount of incident photon absorb by the lower part of nanotubes will be lesser than that by the upper part. Therefore, light absorption by the TNT film will not increase further when the tube length exceeds a certain range.

Table 3. Dimensional data and photocurrent of TNT prepared in different electrolytic medium

Sample	Diameter (nm)	Length (μm)	Photocurrent[a] (mA/cm^2)
C5TNT/H_2O	75 ± 9	0.4 ± 0.01	0.16
C5TNT/EGH_2O	99 ± 10	2.6 ± 0.1	0.47
C5TNT/EG	141 ± 13	11.2 ± 0.3	0.79

[a] *Photocurrent is measured at 0.5 V versus Ag/AgCl in 10 ppm methyl orange solution*

Photoconversion efficiency, η% of light energy to chemical energy in the presence of an external applied potential for different nanotubes was calculated using Equation (2).

$$\eta\% = j_{ph} \left(\frac{[E^{o}_{rev} - |E_{app}|]}{I_o} \right) \times 100 \quad (2)$$

where I_o is the power density of the incident light (mW/cm^2), j_{ph} is the photocurrent density (mA/cm^2), E^{o}_{rev} is the standard reversible potential for water splitting reaction which is 1.23 V versus NHE and the applied potential, $E_{app} = E_{meas} - E_{aoc}$, where E_{meas} is the electrode potential (versus Ag/AgCl) of the working electrode at which photocurrent was measured under illumination and was taken as 0.5 V versus Ag/AgCl in this study. E_{aoc} is the electrode potential (versus Ag/AgCl) of the same working electrode under open circuit conditions, under the same illumination, and in the same electrolyte as shown in Table 4.

Table 4. Photoelectrochemical data and photoconversion efficiency of TNT prepared in different electrolytic medium

Sample	Photocurrent[a] (mA/cm^2)	E_{aoc} (mV)	Photoconversion efficiency (%)
C5TNT/H_2O	0.13	–435	0.49
C5TNT/EGH_2O	0.52	–550	1.23
C5TNT/EG	1.04	–539	2.79

[a]*Photocurrent was done in 0.1 M KOH at 0.5 V versus Ag/AgCl*

As the solar cell parameters such as open circuit potential and short circuit current are best obtained from a non-potentiostated cell configuration, therefore the assessing of the photoefficiency and the use of Equation 2 are only meant to afford figure-of-merit estimates. As shown in Table 4, the highest photoconversion efficiency was obtained for C5TNT/EG in agreement with the highest photocurrent density. Long nanotubes with ordered and well-defined morphology are necessary for good photoelectrochemical performance. The nanotube length obtained for C5TNT/EG is 11.2 μm, which is much longer than that for C5TNT/EGH_2O and C5TNT/H_2O and therefore showed a higher photoefficiency. Other researchers have reported higher photoefficiency with nanotubes length reaching up to 220 μm. For example, Mor et al. [11] had demonstrated that a photoconversion efficiency of 6.8 % was obtained for nanotubes formed in mixture of HF and acetic acid under UV illumination (337 nm). Later, TNT of 6 μm length, under a similar illumination shows a photoconversion efficiency of about 12.25 % [12]. 14.4 μm long TNT fabricated using a formamide-based electrolyte had achieved a photoconversion efficiency of 14.42 % and increased to 16.26 % for 24 μm long TNT fabricated in an ethylene glycol based electrolyte [13]. Nevertheless, it has been reported that the photoefficiency increased with increasing nanotube length up to 5 μm and thereafter tending toward a plateau [14]. Gratzel-type solar cells were fabricated after dye sensitizing the nanotubes layers. The

greatest overall light to electricity conversion efficiency reported for dye-sensitized solar cells based on the nanoparticles TiO_2 have achieved 11% [15]. For pure nanotubes layer, the record efficiency stands at 5.2 % [16] and 7 % for nanotube/nanoparticles mixtures [17].

Conclusion

In summary, titania nanotube arrays were successfully synthesized via electrochemical anodization of Ti in various electrolytic compositions. Choice of electrolytic composition has an effect on the microstructure, element composition, band gap and crystal structure of TNT. In addition, photocurrent response is enhanced using the calcined nanotubes and is affected by the morphology, dimensional changes; with higher photocurrent and photoefficiency conversion is associated with smooth and longer length tube. Highest efficiency was obtained for TNT/EG than those prepared in aqueous solution.

Acknowledgement

This material is based upon work supported by the Malaysia Toray Science Foundation through S&T research grant no. 100-RMI/PRI 16/6/2 (7/2014) and the Ministry of Education through FRGS grant no. 600-RMI/FRGS 5/3 (1/2014). The authors would also like to acknowledge Faculty of Applied Sciences, Universiti Teknologi MARA (UiTM) for the facilities provided.

References

1. Jen, H. P., Lin, M. H., Li, L. L., Wu, H. P., Huang, W. K., Cheng, P. J. and Diau, E. W. G. (2013). High-performance large-scale flexible dye-sensitized solar cells based on anodic TiO_2 nanotube arrays. *ACS Materials & Interfaces*, *5*(20), 10098 – 10104.
2. Yu, M., Long, Y. Z., Sun, B. and Fan, Z. (2012). Recent advances in solar cells based on one-dimensional nanostructure arrays. *Nanoscale*, *4*(9), 2783 – 2796.
3. Smith, Y. R., Sarma, B., Mohanty, S. K. and Misra, M. (2013). Single-step anodization for synthesis of hierarchical TiO_2 nanotube arrays on foil and wire substrate for enhanced photoelectrochemical water splitting. *International Journal of Hydrogen Energy*, *38*(5), 2062 – 2069.
4. Liu, Y., Cheng, Y., Chen, K., Yang, G., Peng, Z., Bao, Q. and Chen, W. (2014). Enhanced light-harvesting of the conical TiO_2 nanotube arrays used as the photoanodes in flexible dye-sensitized solar cells. *Electrochimica Acta*. 146: 838 – 844.
5. Masuda, H. and Fukuda, K. (1995). Ordered metal nanohole arrays made by a two-step replication of honeycomb structures of anodic alumina. *Science* 268(5216):1466 – 1468.
6. Ruan, C., Paulose, M., Varghese, O. K., Mor, G. K. and Grimes, C. A. (2005). Fabrication of highly ordered TiO_2 nanotube arrays using an organic electrolyte. *Journal Physical Chemistry B* 109(33):15754 – 15759.
7. Anitha, V. C., Menon, D., Nair, S. V. and Prasanth, R. (2010). Electrochemical tuning of titania nanotube morphology in inhibitor electrolytes. *Electrochimica Acta* 55(11):3703 – 3713.
8. Sreekantan, S., Saharudin, K., Lockman, Z. and Tzu, T. (2010). Fast-rate formation of TiO_2 nanotube arrays in an organic bath and their applications in photocatalysis. *Nanotechnology* 21:365603.
9. Sohn, Y. S., Smith, Y. R., Misra, M. and Subramanian, V. (2008). Electrochemically assisted photocatalytic degradation of methyl orange using anodized titanium dioxide nanotubes. *Applied Catalysis B: Environmental* 84(3-4):372 – 378.
10. Song, X. M., Wu, J. M. and Yan, M. (2009). Photocatalytic degradation of selected dyes by titania thin films with various nanostructures. *Thin Solid Films* 517(15):4341 – 4347.
11. Mor, G. K., Shankar, K., Paulose, M., Varghese, O. K. and Grimes, C. A. (2005). Enhanced photocleavage of water using titania nanotube arrays. *Nano Letters* 5(1):191 – 195.
12. Shankar, K., Mor, G. K., Prakasam, H. E., Yoriya, S., Paulose, M., Varghese, O. K. and Grimes, C. A. (2007). Highly ordered TiO_2 nanotube arrays up to 220 μm in length: Use in water photoelectrolysis and dye-sensitized solar cells. *Nanotechnology* 18(6):065707.
13. Paulose, M., Prakasam, H. E., Varghese, O. K., Peng, L., Popat, K. C., Mor, G. K., Desai, T. A. and Grimes, C. A. (2007). TiO_2 nanotube arrays of 1000 μm length by anodization of titanium foil: Phenol red diffusion. *Journal Physical Chemistry C* 111(41):14992 – 14997.

14. Watcharenwong, A., Chanmanee, W., de Tacconi, N. R., Chenthamarakshan, C. R., Kajitvichyanukuk, P. and Rajeshwar, K. (2007). Self-organized TiO_2 nanotube arrays by anodization of Ti substrate: Effect of anodization time, voltage and medium composition on oxide morphology and photoelectrochemical response. *Journal Material Research* 22(11):3186 – 3195.
15. Nazeeruddin, M. K., De Angelis, F., Fantacci, S., Selloni, A., Viscardi, G., Liska, P., Ito, S., Takeru, B. and Grätzel, M. (2005). Combined Experimental and DFT-TDDFT Computational Study of Photoelectrochemical Cell Ruthenium Sensitizers. *Journal American Chemical Society,* 127(48):16835 – 16847.
16. Roy, P., Albu, S. P. and Schmuki, P. (2010). TiO_2 nanotubes in dye-sensitized solar cells: Higher efficiencies by well-defined tube tops. *Electrochemistry Communications,* 12(7):949 – 951.
17. HyeokáPark, J. and GuáKang, M. (2008). Growth, detachment and transfer of highly-ordered TiO_2 nanotube arrays: use in dye-sensitized solar cells. *Chemical Communications,* (25):2867 – 2869.

MALAYSIAN JOURNAL OF ANALYTICAL SCIENCES
Published by The Malaysian Analytical Sciences Society
ISSN 1394 - 2506

EPOXIDATION SYNTHESIS OF LINOLEIC ACID FOR RENEWABLE ENERGY APPLICATIONS

(Penghasilan Asid Linoleik Berepoksidasi untuk Penggunaan Tenaga yang Diperbaharui)

Bashar Mudhaffar Abdullah[1], Rahimi M. Yusop[2]*, Jumat Salimon[2], Darfizzi Derawi[2], Waled Abdo Ahmed[2]

[1]*Clinical Investigation Centre,*
University Malaya Medical Centre, 13th Floor Main Tower, Lembah Pantai, 59100 Kuala Lumpur, Malaysia
[2]*Oleochemistry Programme, School of Chemical Sciences & Food Technology, Faculty of Science and Technology,*
Universiti Kebangsaan Malaysia, 43600 UKM Bangi, Selangor, Malaysia

**Corresponding author: rahimi@ukm.edu.my*

Received: 3 August 2015; Accepted: 4 November 2015

Abstract

Monoepoxidation linoleic acid (MEOA) has advantages for industrial applications. MEOA was synthesized using immobilized *Candida antarctica* lipase (Novozym 435®). At optimum conditions, higher yield (82.14 %) and medium oxirane oxygen content, OOC (4.91 %) of MEOA were predicted at 15 µL of H_2O_2, 120 mg of Novozym 435® and 7 hours of reaction time. Fourier Transform Infrared Spectroscopy (FTIR) spectra of the MEOA showed monoepoxide group at 820 cm^{-1}. ^{1}H NMR analysis confirmed the monoepoxide group at 2.92 – 3.12 ppm while the monoepoxide signals of ^{13}C NMR appear at 54.59 – 57.29 ppm. LC-MS analysis shows that of MEOA gives m/z at 296.22 as final product. MEOA exhibited good pour point (PP) of -41 ºC. Flash point (FP) of MEOA increased to 128 ºC comparing with 115 ºC of linoleic acid (LA). In a similar fashion, viscosity index (VI) for LA was 224 generally several hundred centistokes (cSt) more viscous than MEOA 130.8. MEOA was screened to measure their oxidative stability (OT) which was observed at 168 ºC. It is evident that increasing the hydrogen peroxide amount has a strong effect on the reaction kinetics; however, a large excess of hydrogen peroxide results in accumulation of peracid in the final product.

Keywords: linoleic acid, Novozym 435®, self-epoxidation, renewable energy

Abstrak

Mono-pengepoksidaan asid linoleik (MEOA) mempunyai kelebihan untuk aplikasi industri. MEOA telah disintesis menggunakan *Candida Antartika* lipase (Novozym 435 ®) pegun. Pada keadaan yang optimum, peratus hasil MEOA sebanyak 82.1 % dengan kandungan oksigen oksirana (OOC) sebanyak 4.91 % diperolehi dengan menggunakan 15 µL H_2O_2, 120 mg Novozym 435 ® dan 7 jam tindak balas. Analisis ^{1}H NMR mengesahkan kumpulan terepoksida pada 2.92 –3.12 ppm manakala isyarat ^{13}C NMR menunjukkan bacaan pada 54.59 – 57.29 ppm. Analisis LC-MS menunjukkan bahawa MEOA memberikan m/z 296.22 sebagai produk akhir. MEOA menunjukkan takat tuang yang baik pada suhu -41 ºC. Takat kilat MEOA meningkat pada suhu 128 ºC berbanding pada suhu 115ºC oleh asid linoleik (LA). Dalam keadaan yang sama, kebiasaanya VI untuk LA pada 224 beberapa ratus sentistok (cSt) lebih likat daripada MEOA 130.8. MEOA mempunyai kestabilan oksidatif pada suhu 168 ºC. MEOA berpotensi untuk dijadikan sebagai produk pertengahan dalam aplikasi tenaga keterbaharuan.

Kata kunci: asid linoleik, Novozym 435®, pengepoksidaan, tenaga diperbaharui

Introduction

Bio-renewable materials, such as plant oils and unsaturated fatty acid derivatives, have recently received increasing attention as a means of addressing environmental and economic concerns. Epoxidized oils are currently produced by the epoxidation of plant oils such as soybean, linseed oil [1] and *Jatropha curcas* seed oil [2].

Although the monoepoxidation of linoleic acid or its methyl ester has been carried out repeatedly in the past, it was only recently that a study of positional selectivity in the monoepoxidation of methyl linoleate was reported [3]. There are several methods to epoxidize the double bonds of unsaturated fatty acids, such as Prileshajev monoepoxidation reaction. In this reaction, a peracid from a short or long chain fatty acid and hydrogen peroxide (H_2O_2) under strong acidic conditions is used as the oxidizing agent. The peracid can either be added to the reaction mixture or is formed in situ, the latter being preferred due to safety reasons. The presence of the strong acid in the reaction mixture, however, causes the formation of side products, such as vicinal diols, estolides and other dimers. Although the careful choice of the peracid and the reaction conditions can help to minimize the epoxide loss, the selectivity of industrial monoepoxidation of unsaturated fatty acids rarely exceeds 80% [4].

The effect of reaction parameters on lipase-mediated chemo-enzymatic monoepoxidation of linoleic acid (LA) has been investigated [4]. H_2O_2 was found to have the most significant effect on the reaction rate and degree of epoxidation. An excess of H_2O_2 with respect to the amount of double bonds was necessary in order to yield total conversion within a short time period, as well as at temperatures above 50 °C to compensate for H_2O_2 decomposition. The reaction rate also increased by increasing the hydrogen peroxide concentration (between 10 and 50 wt-%), albeit at the expense of enzyme inactivation. LA was completely epoxidized when used at a concentration of 0.5-2 M in toluene at 30 °C, while in a solvent-free medium, the reaction was not complete due to the formation of a solid or a highly viscous oily phase, creating mass transfer limitations. Increasing the temperature up to 60 °C also improved the rate of epoxide formation. The monoepoxidation of methyl linoleate was examined using transition metal complexes as catalysts [5]. With a catalytic amount of MTO (4 mol%) and pyridine, methyl linoleate was completely epoxidized by aqueous H_2O_2 within 4 h. Longer reaction times (6 h) were needed with 1 mol% catalyst loading. Manganese tetraphenylporphyrin chloride was found to catalyze the partial epoxidation of methyl linoleate. A monoepoxidized species was obtained as the major product (63%) after 20 hours.

Objective of this study was attempted to improve the efficiency of monoepoxidation under milder conditions that minimize the formation of byproducts. Chemo-enzymatic monoepoxidation uses the immobilized lipase from *Candida Antarctica* (Novozym 435®) to catalyze conversion of fatty acids to peracids with 60% hydrogen peroxide. The fatty acid is then self-epoxidized in an intermolecular reaction. The lipase is remarkably stable under the reaction conditions and can be recovered and reused 15 times without loss of activity. Different lipase catalysts have been studied, of which Novozym 435®, a commercial preparation of *Candida Antarctica* lipase B, has been shown to be the most effective so far. Most of the investigations have involved dilution of the substrate in organic solvent. Recently, lipase mediated monoepoxidation in a solvent-free medium has also been reported [4]. LA, bearing two C=C double bonds, is one of the major components in *Jatropha curcas* seed oil. This study focuses on the impact of various reaction parameters on the monoepoxidation process, with the aim to determine optimal reaction conditions with regard to reaction efficiency and enzyme stability using D-optimal design. LA was used as the model substrate.

Materials and Methods

Experimental procedure

The enzymatic monoepoxidation was carried out using Novozym 435®, a commercial catalyst made up of lipase, from Candida Antarctica, immobilized on a polyacrylate resin [4]. Table 1 shows the different ratios of hydrogen peroxide (H_2O_2), different amounts of enzyme and different reaction times using D-optimal design. Three factors (variables) including hydrogen peroxide (µL, X_1), enzyme (mg, X_2) and reaction time (h, X_3) were performed for 18 experiments at the same experimental conditions.

In a typical chemo-enzymatic monoepoxidation of linoleic acid, 9(12)-10(13)-monoepoxy 12(9)-octadecanoic acid (MEOA), the LA (1.4 g) was dissolved in 10 mL toluene and the lipase was added. After stirring for 15 min, 15-20 µL of 30 % H_2O_2 was added and every 15 min the addition was repeated for 6 – 8 hours. Afterwards the lipase was removed by filtration, the mixture was washed with water to remove excess H_2O_2 and the organic phase was then

dried over anhydrous sodium sulphate; the solvent was evaporated in a vacuum rotary evaporator. The oxirane ring content (OOC %) [6], yield% and iodine value (IV) [7] were measured. The FTIR, ^{1}H, ^{13}C NMR and LC-MS were analyzed and the physicochemical properties of the product were studied [7].

Table 1. Independent variables and their levels for D-optimal design of the monoepoxidation reaction

Independent variables		**Coded Levels**		
		-1	**0**	**+1**
H_2O_2 (µL)	X_1	15	17.5	20
Enzyme (mg)	X_2	80	100	120
Time (h)	X_3	6	7	8

Experimental design and statistical analysis

To explore the effect of the operation variables on the response in the region of investigation, a D-optimal design at three levels was performed. H_2O_2 (µL, X_1), amount of enzyme (mg, X_2) and reaction time (h, X_3) were selected as independent variables. The range of values and coded levels of the variables are given in Table 1. A quadratic polynomial regression model was assumed for predicting Y variables. The model proposed for each response of Y was:

$$Y = ß_0 + \sum ß_i x_i + \sum ß_{ii} x_i^2 + \sum \sum ß_{ij} x_i x_j \quad (1)$$

Where $ß_0$; $ß_i$; $ß_{ii}$ and $ß_{ij}$ are constant, linear, square and interaction regression coefficient terms, respectively, and x_i and x_j are independent variables. The Minitab software version 14 (Minitab Inc., USA) was used for multiple regression analysis, analysis of variance (ANOVA), and analysis of ridge maximum of data in the response surface regression (RSREG) procedure. The goodness of fit of the model was evaluated by the coefficient of determination R^2 and the analysis of variance (ANOVA). Response surfaces and contour plots were developed using the fitted quadratic polynomial equations obtained from RSREG analysis and holding the independent variables with the least effect on the response at two constant values and changing the levels of the other two variables [8].

Results and Discussion

Reaction and mechanism of the monoepoxidation linoleic acid

Figure 1 demonstrates the scheme for the monoepoxidation reaction of LA (MEOA). MEOA results in a mixture of two monoepoxides (cis-9, 10-epoxy 12c- 18:1 and cis-12, 13 epoxy 9c- 18:1) with yield% of 75.82. H_2O_2 is an important reactant for the formation of peracids from fatty acids; hence, the influence of its amount on the monoepoxidation reaction was studied.

The addition of H_2O_2 solution to the reaction medium (toluene with LA) leads to the formation of two distinct phases, an organic phase and an aqueous phase show in Figure 2. The Novozym 435®, being adsorbed on a hydrophobic carrier, is mainly present in the organic phase. H_2O_2 will be partitioned in both the aqueous and the organic phases, with the concentration being higher in the aqueous phase (Figure 2) due to consumption of H_2O_2 for peracid formation in the organic phase.

The ratio of H_2O_2 to H_2O tends to decrease slightly in organic phase. Hence, for the reaction to proceed optimally, it is essential that the transport of the H_2O_2 from the aqueous phase to the organic phase is faster than its utilization in the enzymatic reaction [4].

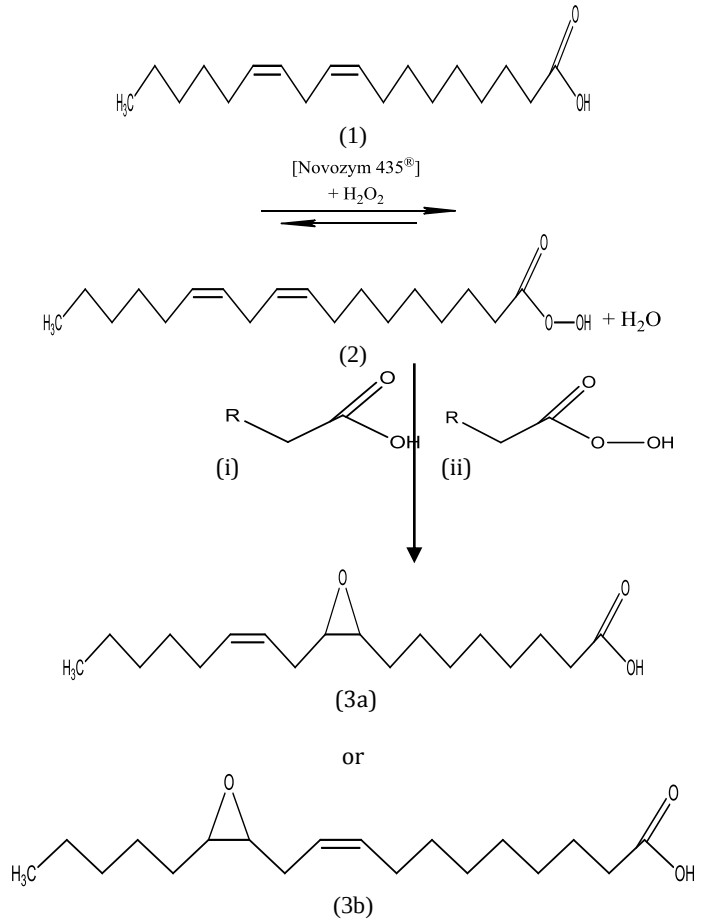


Figure 1. Chemo-enzymatic monoepoxidation of LA

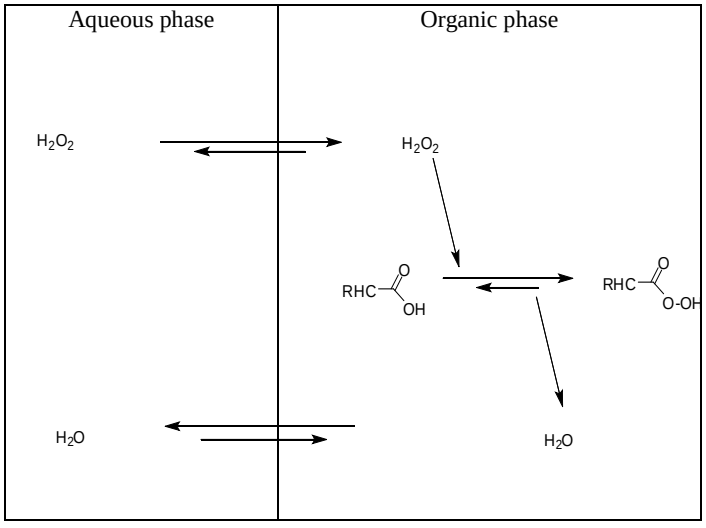


Figure 2. Transport of H_2O_2 and water in an organic-water biphasic system

The reaction synthesis was determined by varying amounts of H_2O_2 (15, 17.5 and 20 µL), which was added every 15 min, the addition was repeated 24 times. The different amounts of Novozym 435® (80, 100 and 120 mg) and different times (6, 7 and 8 hours) also have been used. A stoichiometric excess of the required amount of the H_2O_2 was used to compensate for its possible decomposition by light and temperature. Epoxide contains oxygen as one of the ring atoms. The mechanism of converting the peracid to epoxide involves one-step and the relative stereochemistry of the alkene is maintained in the epoxide [7]. The mechanism is shown schematically in Figure 3.

The double bond acts as the nucleophile with the π-electrons attacking the peracid oxygen. In one-step, the oxygen-oxygen bond breaks and the electrons shift over to form a new π-bond between oxygen and carbon. This causes the π-bond of the existing carbonyl to break and those electrons attack the terminal hydrogen. Finally, the electrons from the O-H bond, which is breaking, add to the alkene carbon to form the three-member ring epoxide [9].

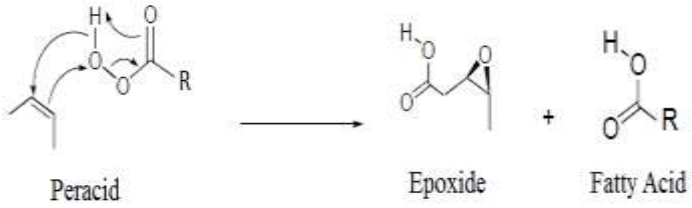


Figure 3. Mechanism of converting peracid to epoxide

Effect of process parameters and statistical analysis

This study demonstrates the application of the proposed response surface methodology (RSM) framework for the optimization of MEOA by using Novozym 435® catalytic monoepoxidation process. Hence, the knowledge about the process is relatively limited, and the design is used to obtain 18 design points within the whole range of three factors for experiments.

The designs and the responses yield percentage of MEOA (Y_1), oxirane oxygen content percentage (OOC, Y_2) and iodine value (IV mg/g, Y_3) are given in Table 2. Following the reaction experiments, the response surface is estimated by D-optimal design. Table 2 shows that the yield% of MEOA of Y_1 increased to (82.14 %) while OOC% of Y_2 (4.91) and IV of Y_3 (77.65) which is considerable compared to the theoretical OOC*t* (9.02) and initial iodine value IV◦ (157.35 mg/g). The conversion percentage of the MEOA is 81.35%. Subsequent experiments were performed using different amounts of H_2O_2 15, 17.5 and 20 µL for every 1.4 gm of LA in one single step. As seen in Table 2, there is a clear increase in the reaction rate (OOC percentage) and decrease iodine value (IV mg/g) with increasing H_2O_2 amount. With 15 µL, monoepoxidation was achieved at 7 h using 120 mg Novozym 435®.

The quadratic regression coefficients obtained by employing the least squares method technique to predict quadratic polynomial models for the yield percentage of MEOA (Y_1), OOC percentage (Y_2) and IV mg/g (Y_3) have been explained. For the yield percentage of MEOA (Y_1), the linear term of Novozym 435® catalyst amount (X_2), quadratic terms of H_2O_2 (X_{11}) and Novozym 435® catalyst amount (X_{22}) were significant ($p< 0.05$). The interaction between H_2O_2 (X_{11}) and Novozym 435® catalyst amount (X_{12}), and the interaction between H_2O_2 (X_{11}) and reaction time (X_{13}) were significant ($p< 0.05$), while its quadratic term of reaction time (X_{33}) was highly significant ($p<0.01$). Highly significant terms ($p< 0.01$) of OOC% (Y_2) and IV mg/g (Y_3) for the H_2O_2 (X_1) were linear. The linear term of IV mg/g for the reaction time h (X_3) was significant ($p< 0.05$).

The lack of fit *F*-value for all the responses shows that the lack of fit was not significant ($p> 0.05$) relative to the pure error. This indicates that all the models predicted for the responses were adequate. Regression models for data on responses Y_1, Y_2, and Y_3, were highly significant ($p<0.01$) with satisfactory R^2 (0.90, 0.69 and 0.79, respectively). However, the R^2 for Y_2 (0.69) was lower although the model was significant. Table 3 summarizes the analysis of variance (ANOVA) of all the responses of this study.

Table 2. D-optimal design arrangement and responses for MEOA

Run No.	Coded Independent			Responses					
	H_2O_2 (X_1)	Catalyst[a] (X_2)	Time (X_3)	Yield (Y_1, %)	OOC (Y_2, %)	RCO (%)	IV (Y_3, mg/g)	X (%)	SE
1	20	80	8	76.57	6.17	68.40	37.81	76.37	0.89
2	17.5	80	7	88.57	5.48	60.75	58.95	62.53	0.97
3	17.5	100	8	72.14	7.54	83.59	32.22	79.52	1.05
4	20	80	6	72.28	6.4	70.95	40.98	73.95	0.95
5	20	120	7	54.71	5.94	65.85	64.32	59.12	1.11
6	20	120	6	60.28	7.88	87.36	30.87	80.38	1.08
7	15	120	8	73.57	5.48	60.75	53.24	66.16	0.91
8	20	80	7	81.42	5.37	59.53	56.32	64.20	0.92
9	15	100	7	75.68	5.02	55.65	74.64	52.56	1.05
10	18.7	100	7	85.28	5.71	63.30	49.17	68.75	0.92
11	20	100	7	81.14	6.05	67.06	42.72	72.85	0.92
12	15	120	6	70.78	4.57	50.66	76.48	51.39	0.98
13	15	100	6	65.93	3.65	40.46	96.43	38.71	1.00
14	15	120	7	82.14	4.91	54.43	77.65	57.64	0.94
15	17.5	120	8	59.28	6.74	74.72	36.37	76.63	0.97
16	20	100	6	72.85	6.51	72.17	39.76	74.73	0.90
17	15	80	8	77.14	4.34	48.11	83.85	46.71	1.03
18	17.5	100	6	80.85	3.77	41.79	87.09	44.65	0.93

Notes: OOC, oxirane oxygen content; RCO, relative percentage conversion to oxirane; IV, iodine value; X, conversion to double bond; SE, oxirane oxygen selectivity; [a] catalyst Novozym 435® (mg)

Table 3. Analysis of variance (ANOVA) for all the responses of MEOA

	Source	*Df*	Sum of squares	Mean square	*F* value	*Prob>F*	
Y_1	Model	9	1298.00	144.22	8.22	0.0034	Significant
	Residual	8	140.36	17.55			
	Lack-of-fit	3	144.05	48.02	0.69	0.5763	Not significant
	Pure error	5	3.69	0.738			
Y_2	Model	3	13.62	4.54	6.74	0.0048	Significant
	Residual	14	9.43	0.67			
	Lack-of-fit	3	1.43	0.48	0.66	0.5956	Not significant
	Pure error	11	8.00	0.727			
Y_3	Model	3	4423.70	598.002	8.18	0.002	Significant
	Residual	14	2522.67	180.19			
	Lack-of-fit	3	734.74	244.91	1.51	0.2672	Not significant
	Pure error	11	1787.93	162.539			

These results suggest that linear effect of H_2O_2 is the primary determining factor for MEOA. The H_2O_2 had a very large effect on the results of their monoepoxidation study. The final equations in terms of actual factors are:

$$Y_1 = +87.53 -2.82X_1-4.50X_2 -0.14X_3 -9.06X_1^2 -5.43X_2^2 -9.81X_3^2 -9.74X_1X_2 -7.14X_1X_3 -7.80X_2X_3 \quad (2)$$

$$Y_2 = +5.59 +1.00X_1+ 0.58X_2 +0.51X_3 -0.37X_1^2 -0.099X_2^2 +0.31X_3^2 -0.22X_1X_2 -0.55X_1X_3 -0.27X_2X_3 \quad (3)$$

$$Y_3 = +56.24-18.82X_1-8.91X_2-10.57X_3 +8.06X_1^2+4.15X_2^2 4.41X_3^2+11.59X_1X_2+10.81X_1X_3 +5.42X_2X_3 \quad (4)$$

The significant interaction variables in the fitted models were chosen as the axes (amount of H_2O_2; X_1, amount of Novozym 435®; X_2 and reaction time; X_3) for the response surface plots. The relationships between independent and dependent variables are shown in the three-dimensional representation as response surfaces. Figures 4 to 6 are the Design plots for all the responses. In the MEOA, performing the technique using a low amount of H_2O_2 would give the desired OOC% of MEOA, as shown in Figure 5, while IV (Figure 6) was higher at this condition. As shown in Figures 5 and 6, increasing the amount of H_2O_2 led to an increase in the OOC percentage and a reduction of IV. The relationships between the parameters and MEOA were linear or almost linear. High OOC percentage could be obtained by using a high amount of H_2O_2 at high reaction time. Experimental variables should be carefully controlled in order to recover a medium percentage of MEOA of interest with reasonable yield [4].

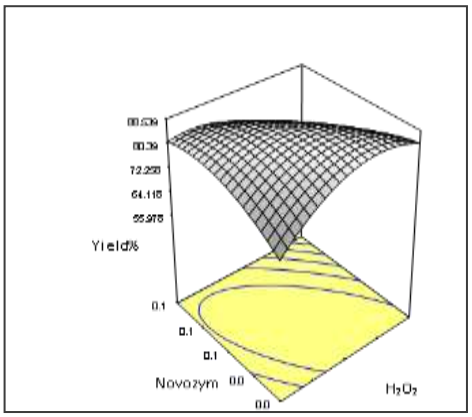


Figure 4. Response surface for the effect of the H_2O_2 (X_1, µL) and catalysts Novozym 435® (X_2, mg) on the yield% of MEOA

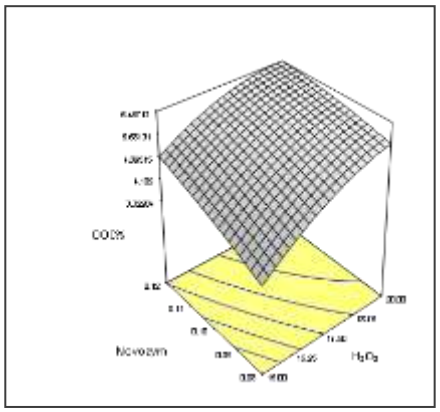


Figure 5. Response surface for the effect of the H_2O_2 (X_1, µL) and catalysts Novozym 435® (X_2, mg) on the OOC% of MEOA

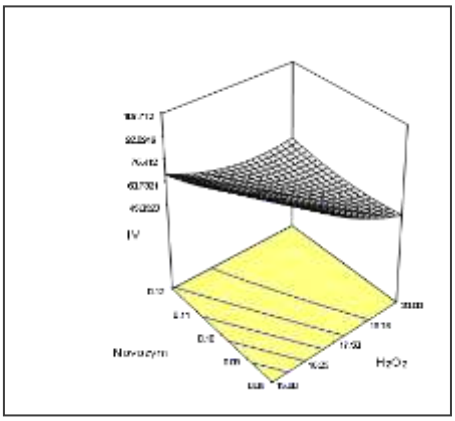


Figure 6. Response surface for the effect of the H_2O_2 (X_1, µL) and catalysts Novozym 435® (X_2, mg) on the IV mg/g of MEOA

The optimum conditions of the experiment to obtain a higher yield percentage of MEOA and medium OOC percentage were predicted at amount of H_2O_2 of 15 µL, catalyst Novozym 435® of 120 mg and 7 h reaction time. At this condition, the yield percentage of MEOA was 82.14%, 4.91% of OOC and 77.65 mg/g of IV. Reconfirmation of the optimal condition experiment was carried out at three replicate. While full epoxidation was observed within 10 h using 30 µL of H_2O_2, increasing the H_2O_2 amount used for the reaction results in the increasing formation of peracid. In the state of MEOA, the amount of peracids accumulated is not significant [10], due to the chemical reaction in which they are consumed is very fast. The reaction could indicate that with a high amount of catalyst, the utilization of H_2O_2 is so fast that the epoxidation of the double bonds does not keep pace with the formation of peracids. However, once all the double bonds are epoxidized, the remaining peracid is not consumed [4]. The observed value was reasonably close to the predicted value, as shown in Figures 7 – 9 respectively.

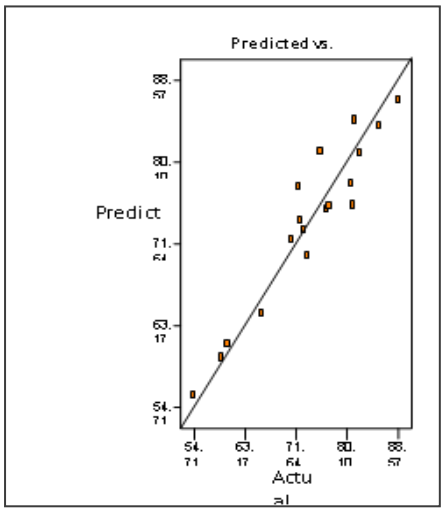


Figure 7. Predicated vs. actual plot of Y_1

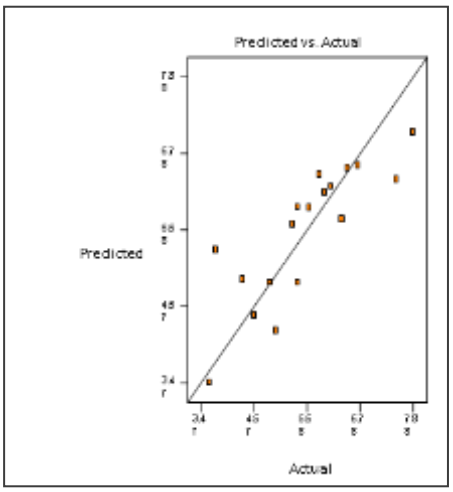


Figure 8. Predicated vs. actual plot of Y_2

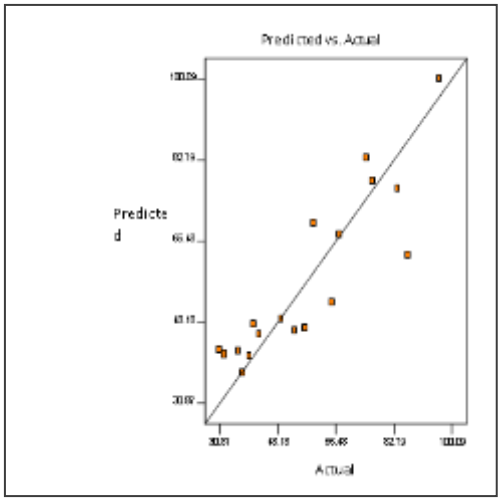


Figure 9. Predicated vs. actual plot of Y_3

FTIR analysis of MEOA

In order to prove the presence of the oxirane ring of MEOA, the final product was tested by FTIR. The oxirane ring of MEOA can be detected at 820 cm^{-1} [9]. For the carboxylic acid carbonyl functional groups (C=O), FTIR spectrum showed absorption bands of LA and MEOA at 1719 and 1711 cm^{-1}, respectively, while stretching vibration peak of C=C can be detected at wavenumber 3009 cm^{-1} [11]. Peaks at 2927 – 2856 cm^{-1} indicate the CH_2 and CH_3 scissoring of LA and MEOA. FTIR spectrum also shows absorption bands at 722, 723 cm^{-1} for (C-H) group vibration.

^{1}H and ^{13}C NMR Analysis of MEOA

The ^{1}H NMR spectroscopy shows the main signal assignments in LA, MEOA and di-epoxide LA. The ^{1}H NMR spectra for the products show some of the key features for a typical (-CH-O-CH-) at about 2.92 – 3.12 ppm of MEOA and about 2.99 – 3.13 ppm of di-epoxide LA. The distinguishable groups are the protons of the terminal methyl of the fatty acid chain. The signals at 0.88 – 0.86 ppm indicate the methylene group ($-CH_3$) of LA, which also appear in MEOA 0.86 – 0.88 ppm and di-epoxide LA 0.88 – 0.92 ppm next to the terminal methyl ($-CH_2$) at 1.30 – 2.06 ppm of LA, 1.29 – 2.03 of MEOA and 1.34 – 1.75 ppm of di-epoxide LA. However, the methane proton signals (-CH=CH-) were shifted upfield at about 5.35 – 5.36 ppm of LA and 5.38 – 5.49 ppm of MEOA while they disappeared in di-epoxide LA [12]. The signal at 7.27 ppm referred to the solvent D_2O for LA, MEOA and di-epoxide LA [7].

The ^{13}C spectroscopy shows the main signals assignment of the LA. The signals at 180.49 ppm refer to the carbon atom of the carbonyl group (carboxylic acid). The signals at 128.27 – 130.38 ppm refers to the unsaturated carbon atoms (olefinic carbons); 24.86 – 29.79 ppm due to methylene carbon atoms in fatty acid moieties of LA [13]. The results confirm the oxirane ring of MEOA 54.59 – 57.29 ppm and di-epoxide LA at about 54.61 – 57.32 ppm. Indeed, it appears that the signals were present in the MEOA, as four peaks of roughly equal intensity (132.89, 132.72, 130.15, and 124.02 ppm) were observed in the alkenic carbon region in the ^{13}C-NMR spectrum, [5], while they had disappeared in the di-epoxide LA.

The ^{13}C-NMR spectra indicate the existence of the carbonyl group (carboxylic acid) in their structure MEOA 179.32 ppm and di-epoxide LA at about 178.79 ppm. The other distinctive signals were aliphatic carbons MEOA at about 22.69 – 29.38 ppm and di-epoxide LA at about 22.77 – 29.44 ppm, which are common for these types of compounds [14]. The signals at 76.91 – 77.23 ppm refer to the solvent D_2O for LA, MEOA and di-epoxide LA [6].

Physicochemical Characteristics

This approach is used to study the low temperature flow behavior of fatty acids by monoepoxide ring. MEOA increased the pour point (PP) to 15 °C significantly comparing with LA at -2 °C. It can be assumed that the presence of the oxirane ring has a tendency to form crystalline structures that make it semi solid at low temperature through uniform stacking of the 'bend' epoxy ring [9]. Flash point (FP) is another important factor in determining how well oil will behave as a potential biolubricant. FP is often used as a descriptive characteristic of oil fuel, and it is also used to describe oils that are not normally used as fuels. FP refers to both flammable oils and combustible oils. Although there are various international standards for defining each, most agree that oils with a flash point of less than 43°C are flammable, while those having a FP above this temperature are combustible [7]. The FP of MEOA, which increased to 128 °C compared with 115 °C of LA, which means the result agrees with the various international standards. The efficiency of the biolubricant in reducing friction and wear is greatly influenced by its viscosity. Generally, the least viscous biolubricant that still forces the two moving surfaces apart is desired. If the biolubricant is too viscous, it will require a large amount of energy to move; if it is too thin, the surfaces will rub and friction will increase. The viscosity index highlights how the viscosity of a biolubricant changes with variations in temperature. The best oils (with the highest VI) will not vary much in viscosity over such a temperature range, and, therefore, will perform well throughout. In MEOA, the decreased viscosity index (VI) of 130.8 of MEOA is the result of less double bonds [7].

The ability of a substance to resist oxidative degradation is another important characteristic of biolubricants. Therefore, MEOA was screened to measure their oxidation stability using PDSC through the determination of OT.

PDSC is an effective method for measuring oxidation stability of oleochemicals in an accelerated mode [15]. The OT is the temperature at which a rapid increase in the rate of oxidation is observed at a constant, high pressure (200 psi). A high OT would suggest high oxidation stability of the material. OT was calculated from a plot of heat flow (W/g) versus temperature that was generated by the sample upon degradation and by definition. In this study, the OT of MEOA at 168°C was higher compared to LA at 159°C, indicating that the epoxy function either reduces the abstractibility of α-hydrogens or quenches the oxidation process [16].

Liquid Chromatography Mass Spectroscopy for the MEOA

Formed upon partial LA and MEOA were confirmed the liquid chromatography mass spectroscopy detection (LC-MS). The ion source was operated in the negative mode to produce $[M - H]^-$ precursor ions, which are prone to charge-remote fragmentation [4]. LC-MS analysis shows that of LA and MEOA gives m/z as 280.2335 and 296.2278 (Figure 10). LC-MS spectra obtained upon charge-remote fragmentation are usually straightforward to interpret and have been widely used for structural determination of fatty acids and related ester compounds [17].

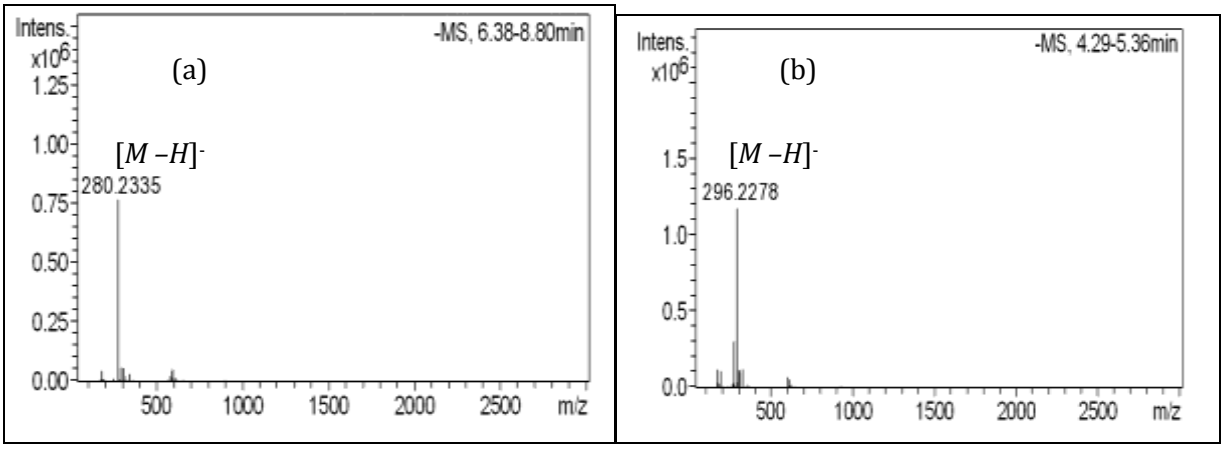


Figure 10. LC-MS analysis of LA (a) and MEOA (b)

Conclusion

It is evident that H_2O_2 is the most critical parameter influencing the chemo-enzymatic monoepoxidation reaction. Increasing the H_2O_2 amount has a strong effect on the reaction kinetics; however, a large excess of H_2O_2 results in the accumulation of peracid in the final product. At optimum conditions, a higher yield percentage of 82.14 and medium oxirane oxygen content OOC percentage of 4.91 and IV of 77.65 mg/g were predicted at 15 μL of H_2O_2, 120 mg of Novozym 435, and 7 h of reaction time. The conversion percentage of the MEOA is 81.35%. The MEOA exhibited high PP of 15°C. In a similar fashion, VI for LA was 224 generally several hundred centistokes more viscous than that MEOA (130.8).

Acknowledgement

We thank UKM and the Ministry of Science and Technology for research grant UKM-OUP-MI-2011, GGPM-2014-033 and DPP-2014-058.

References

1. Ruesch, M. and Warwel, S. (1999). Complete and partial epoxidation of plant oils by lipase-catalyzed perhydrolysis. *Industrial Crops and Products*, 9: 125 – 132.
2. Meyer, P-P., Techaphattana, N., Manundawee, S., Sangkeaw, S., Junlakan, W. and Tongurai, C. (2008). Epoxidation of soybean oil and *Jatropha* oil. *Thammasat International Journal of Science Technology*, 13: 1 – 5.

3. Ferrari, M., Ghisalberti, E. L., Pagnoni, U. M. and Pelizzoni, F. (1968). Monoepoxidation of methyl linoleate: (±)-methyl vernolate and (±)-methyl coronarate. *Journal of the American Oil Chemists' Society*, *45:* 649 – 651.
4. Orellana-Coca, C., Camocho, S., Adlercreutz, D., Mattiasson B. and Hatti-Kaul, R. (2005). Chemo-enzymatic epoxidation of linoleic acid: parameters influencing the reaction. *European Journal of Lipid Science Technology*, 107: 864 – 870.
5. Du, G., Tekin, A., Hammond, E. G. and Woo, L. K. (2004). Catalytic epoxidation of methyl linoleate. *Journal of the American Oil Chemists' Society*, 81: 477 – 480.
6. Siew, W. L., Tang, T. S. and Tan, Y. A. (1995). *PORIM test methods*. Volume 1. Palm Oil Research Institution of Malaysia.
7. Salimon, J., Salih, N. and Abdullah, B. M. (2011). Improvement of physicochemical characteristics of monoepoxide linoleic acid ring opening for biolubricant base oil. *Journal of Biomedicine and Biotechnology*, 2011: 1 – 8.
8. Salimon, J., Abdullah, B. M. and Salih, N. (2012). Selectively increasing of polyunsaturated (18:2) and monounsaturated (18:1) fatty acids in *Jatropha curcas* seed oil by crystallization using D-optimal design. *Chemistry Central Journal*, 2012: 6: 65 – 80.
9. Zubrick, J.W. (2000). *The Organic chem lab survival manual, 5th edition*, Wiley & Sons, Inc., New York.
10. Warwel, S. and Klaas, M.R.G. (1995). Chemo-enzymatic epoxidation of unsaturated carboxylic acids. *Journal of Molecular Catalysis B: Enzymatic*, 1: 29 – 35.
11. Socrates, G. (2001). *Infrared and Raman characteristic group frequencies: Tables and charts.* 3rd ed. John Wily & Sons Ltd. Chichester, England.
12. Hwang, H-S. & Erhan, S.Z. (2006). Synthetic lubricant basestocks from epoxidezed soybean oil and Guerbet alcohols. *Industrial Crops and Products*, 23: 311 – 317.
13. Abdullah, B. M. and Salimon, J. (2009). Physicochemical characteristics of Malaysian rubber (*Hevea brasiliensis*) seed oil. *European Journal of Scientific Research*, 31: 437 – 445.
14. Doll, K. M., Sharma, B. K. and Erhan, S. Z. (2007). Synthesis of branched methyl hdroxy stearates including an ester from bio-based levulinic acid. *Industrial and Engineering Chemistry Research*, 46: 3513 – 3519.
15. Zhang, Y.Y., Ren, T. H., Wang, H. D. and Yi, M. R. (2004). A comparative study of phenol-type antioxidants in methyl oleate with quantum calculations and experiments. *Lubrication Science*, 16: 385 – 392.
16. Samuelsson, J. and Johansson M. (2001). A Study of fatty acid methyl esters with epoxy or alkyne functionalities. *Journal of the American Oil Chemists' Society*, 78: 1191 – 1196.
17. Hsu, F-F. and Turk, J. (2004). Studies on sulfatides by quadrupole ion-trap mass spectrometry with electrospray ionization: structural characterization and the fragmentation processes that include an unusual internal galactose residue loss and the classical charge-remote fragmentation. *Journal of the American Society for Mass Spectrometry*, 15: 536 – 546.

MALAYSIAN JOURNAL OF ANALYTICAL SCIENCES
Published by The Malaysian Analytical Sciences Society
ISSN 1394 - 2506

NUTRIENT REMOVAL OF GREY WATER FROM WET MARKET USING SEQUENCING BATCH REACTOR

(Penyingkiran Nutrien Air Basuhan dari Pasar Basah Mengguna Reaktor Kelompok Urutan)

Omar Danial[1], Mohd Razman Salim[1,2], Salmiati[1,2]*

[1]*Department of Environmental Engineering, Faculty of Civil Engineering*
[2] *Center of Environmental Sustainabiliy and Water Security (IPASA), Research Institute for Sustainable Environment (RISE)*
Universiti Teknologi Malaysia, 81310 UTM Johor Bahru, Johor, Malaysia

**Corresponding author: salmiati@utm.my*

Received: 9 December 2014; Accepted: 16 October 2015

Abstract

Fresh water scarcity has become an important issue in this world today. Water reuse is known as one of the strategies to overcome this problem. Grey water is one of the sources of reused water. Several researches were carried out on water reuse, but limited attention was focused on reusing grey water from wet market, which contains high nutrient and organic matters. This study was carried out on nutrient removal from grey water using sequencing batch reactor (SBR). The grey water sample was taken from a wet market (Pasar Peladang, Skudai). About 1L of grey water was fed into the reactor with a total volume of 4L. Anoxic-aerobic phase were divided with a ratio of 30%-70% of total time respectively. Mixing was maintained at 30 rpm during the start of each cycle until settling phase to achieve uniform condition. Influent and effluent were set for 30 minutes. The SBR was operated with 3 cycles/day, temperature 30°C, cycle time 8 hours and hydraulic retention time (HRT) 1.2 days. Aeration at 35 L/min was induced for ammonia conversion and assisting nitrification.. The results show that the bacteria growing in alternating anoxic/aerobic systems could remove organic substrates and nutrient. The COD, Total Nitrogen and Total Phosphorus removal efficiencies were maximum at the levels of 94%, 88% and 70% respectively. Anaerobic-Aerobic-Anoxic phase was proposed to increase the removal percentage.

Keywords: SBR system, nutrient removal, grey water, hydraulic retention time, chemical oxygen demand

Abstrak

Kekurangan bekalan air bersih menjadi isu penting di dunia pada masa kini. Penggunaan semula air sisa yang telah diolah dikenali sebagai salah satu langkah strategik untuk mengatasi masalah ini. Penggunaan semula air basuhan telah menjadi salah satu sumber yang penting sebagai air sisa kitar semula. Beberapa kajian tentang perkara ini telah dijalankan, tetapi fokus yang berkaitan penggunaan semula air basuhan dari pasar basah, yang mengandungi nutrien dan permintaan oksigen kimia (COD) yang tinggi, agak terbatas. Kajian ini mengenai penyingkiran nutrien di dalam air basuhan dari pasar basah menggunakan reaktor kelompok urutan (SBR). Sampel air basuhan diambil dari pasar basah (Pasar Peladang, Skudai).Sebanyak 1L air basuhan telah dimasukkan ke dalam reaktor dengan jumlah isipadu total 4L. Nisbah tahap anoksik-aerobik ditentukan 30% -70% daripada jumlah masa total. 30 rpm pengaduk pencampuran dikekalkan pada awal setiap kitaran untuk mencapai tahap keadaan seragam. Influen dan efluen ditetapkan selama 30 minit. SBR telah dikendalikan dengan 3 kitaran / hari, suhu 30 ° C, masa kitaran 8 jam dan masa tahanan hidraulik (HRT) 1.2 hari. Pengudaraan pada 35 L/min telah dipasang untuk penukaran ammonia dan membantu nitrifikasi. Hasil kajian menunjukkan bahawa bakteria yang membiak dalam sistem anoksik / aerobik boleh menyingkir substrat organik dan nutrien. Tahap kecekapan maksimum penyingkiran COD, Nitrogen Jumlah dan Fosforus masing-masing adalah pada kadar 94%, 88% dan 70%. Fasa anaerobik-aerobik-Anoxic dicadangkan untuk meningkatkan peratusan penyingkiran.

Kata kunci: Sistem SBR, penyingkiran nutrien, air basuhan, masa tahanan hidraulik, permintaan oksigen kimia

Introduction

Scarcity of fresh water has become a global issues nowadays, which is already faced by almost one-fifth of the world's population (1.2 billion) [1]. Malaysia is not exempted from this problem. Although Malaysia received heavy rains all year around, approximately 2600 mm a year, it still cannot accommodate the increasing demand of fresh water. Fresh water problem in Malaysia needs to be viewed from economical consideration. While water rates keep increasing, the burden suffered by consumers especially high load consumer will help them when reuse water will lower the total costs of operation [2]. The need of water reuse is acceptable to cover such big activities as agriculture. Among all potential new sources of reused water is grey water that contribute 60 –75 % to domestic wastewater [3]. According to Lamine et. al. [4], grey water is wastewater produced from bath, showers, hand basin, washing machines, dishwashers, kitchen sink. This type of wastewater can be generated from household, office building and schools. Grey water is differentiated from black water, where sewage is excluded from grey water.

Grey water reuse has been applied in many countries, especially in the Middle East countries such as Lebanon and Palestine [5, 6]. These countries face a shortage of clean water hence grey water reuse has come into special focus to meet their basic needs. On the other hand, western countries such as Germany also applied grey water reuse even though the scarcity of fresh water did not come as special focus [7]. Grey water reuse can be applied to many hygienic activities. It can be used for toilet flushing, lawn, athletic field, cemeteries, park and golf courses, domestic garden, washing vehicle activities, fire protection, boiler feed water and concrete production [8 – 12]. However, different reuse purposes require different quality standards and thus different type of treatment [13].

Wet markets are fresh food markets that possess advantages in terms of costs, freshness and food preparation, which make them more attractive to consumers. According to Gorton [14], it is an important location to acquire the daily needs especially raw food at reasonable prices. Places that are easily approachable, affordable prices and a broad choice of goods and items make it more attractive to consumers. As wastewater generated from wet market is separated from toilet trench, it can be considered as grey water.

The purpose of this study was to investigate the application of sequencing batch reactor (SBR) technology for treating grey water collected at wet market effluent chamber. This study aimed to establish an approach in removing nutrients from grey water in an SBR. Wet market in Pasar Peladang, Skudai area was chosen for investigation to determine the process treatment of each type of wastewater and its possible re-use.

Materials and Methods

Wastewater characteristic

The grey water was collected from wet market effluent chamber. The sample was characterized to determine the properties of the water as it varies from source to source.

System configuration

Sequencing batch reactor (SBR) system was used in this study. It was fabricated from a transparent glass cylinder with a total volume of 5L and a working volume of 4L as shown on Figure 1.

Air (35 L/min) was provided by set of air pumps, model Atman HP-4000, equipped with two peristaltic pumps in charge of influent feeding and effluent discharging, respectively. A mechanical agitation (30 rpm) was operated whereby the wastewater is stirred or agitated so that well mixed wastewater achieved. The operation program of the SBR system consisted of five steps: fill, react (aeration), settle (sedimentation/clarification), draw (decant) and idle [15].

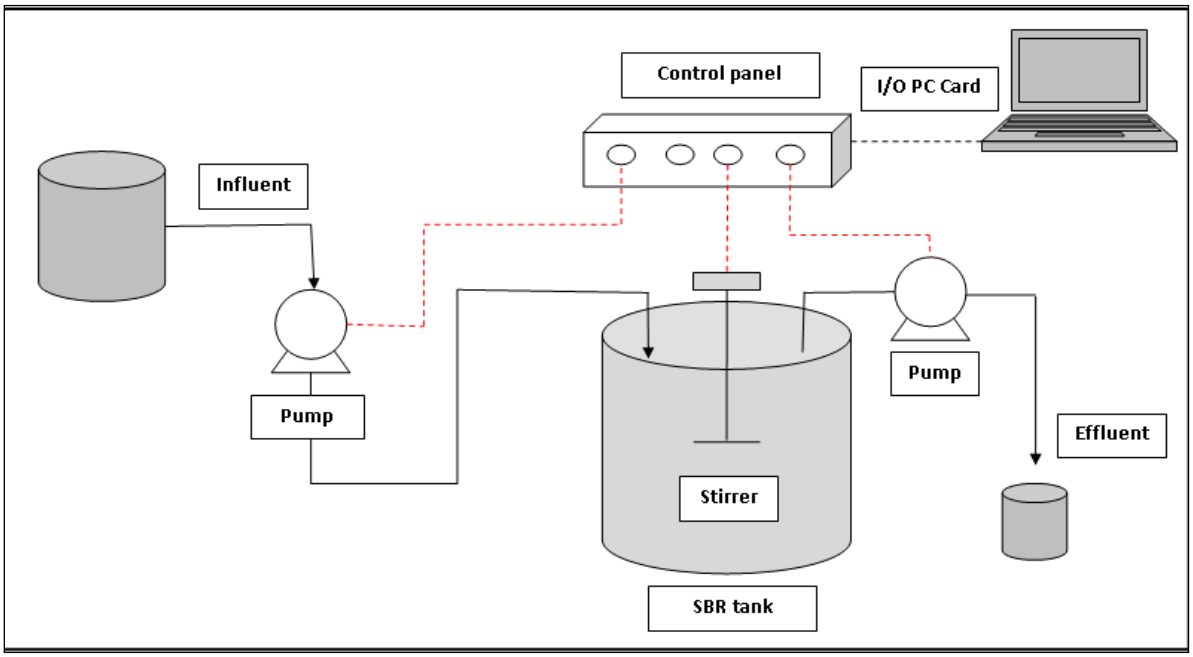


Figure 1. Schematic diagram of SBR system

Start-up of SBR

Bio-sludge to be used as inoculum during the start-up of the SBR was obtained from the sludge storage tank of a local municipal wastewater treatment plant (Taman Harmoni Wastewater Treatment Plant). The SBR was operated under alternating anoxic–aerobic conditions over 28 days. Activated sludge contained in the aeration basin in the activated sludge process (MLSS) was maintained at 3000 – 5000 mg/L. Within the process, pH was set at range 7.0 to 7.5 to ensure successful nitrification process. The reactor was operated at room temperature without control.

The process operates on batch basis. The SBR system worked at three cycles per day with 1.2 days hydraulic retention time (HRT). Each operating cycle consisted of four phases. They are FILL, REACT, SETTLE, and DRAW phases. During the filling process (0.5h), air pump was shut down to promote anoxic condition. The anoxic phase was then continued for 2 hours after feeding. Aeration phase was started for 4 hours when air pump was automatically switch on while mechanical agitation continuously operated. Aeration was then shut down for 1 hour. After 1 hour settling phase was occurred when aerobic phase finished. At the end of each cycle, supernatant of 1000 mL was removed from the SBR (0.5h).

Analytical procedure

Chemical oxygen demand (COD), Total Nitrogen (TN), Total Phosphorus (TP), Ammonia were analyzed using Spechtrophotometer DR5000. The pH value was measured using pH meter (HACH-Germany). Total suspended solids (TSS), MLSS and sludge volume index (SVI) concentrations were determined using standard method. [16].

Results and Discussion

The SBR performance was initially evaluated by measuring COD, TSS, TP, TN and Ammonia compounds in the effluent. The determined characteristics during the full operations are presented in Table 1.

The percentage COD removal in the grey water is shown in Figure 2. At the beginning of the run during start-up, the percentage COD removal was slow with the removal percentage of approximately 40 %. It was observed that

the removal percentage gradually increased, where after a month an increased in the measurement of oxygen equivalent of the organic material in wastewater that can be oxidized chemically was achieved. During the total operational period, high COD removal was achieved in the reactor and the effluent COD was nearly 90 %. This indicates that carbon removing bacteria were able to utilize carbon at pH level 7.0 to 7.5. The performance of grey water treatment in the SBR stabilized with low sludge production. The low production of sludge with good settling properties were also reported by Hernandez et. al. [17] for grey water treatment using SBR at an HRT of 12 hours and 1 day.

Table 1. Characteristics of effluent grey water

Parameters	**HRT = 1.2 days, Cycle time: 8 hours**		
	Average Influent	**Max Effluent**	**Average Removal**
COD (mg/l)	1708	97	94%
TSS (mg/l)	140	40	71%
TN (mg/l)	288	13	88%
TP (mg/l)	66	22	67%
NH_4-N (mg/l)	98	7	93%
NO_2-N (mg/l)	0.040	0.058	-
NO_3-N (mg/l)	0.01	38	-

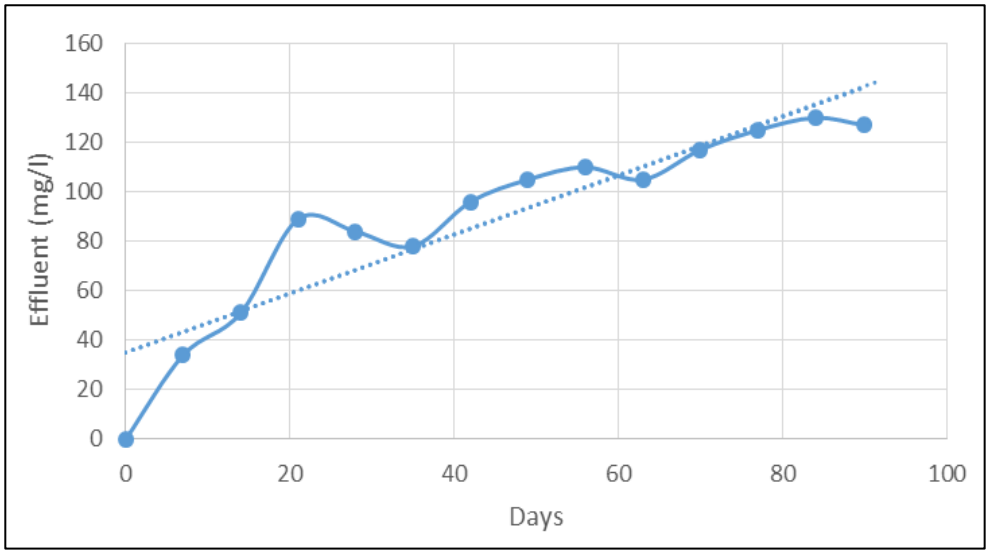


Figure 2. Percentage COD removal of grey water

The 8 hours cycle time with 4 hours aeration period was found to be enough in converting organic materials to CO_2, ammonia and water as expressed in Equation 1.

$$C_nH_aO_bN_c + dCr_2O_7^{2-} + (8d + c)\,H^+ \longrightarrow nCO_2 + \frac{a+8d-3c}{2}H_2O + cNH_4^+ + 2dCr^{3+} \quad (1)$$

The percentage removals of Total Nitrogen and Ammonia-Nitrogen are shown on Figure 3. This type of removal involved two step biological processes in which ammonia (NH_4-N) is oxidized to nitrite (NO_2-N) and nitrite is

oxidized to nitrate (NO_3-N) during the nitrification process. Akunna and Shepherd [18] using SBR to treat a mixture of black and grey water achieved ammonia-nitrogen content from 20 – 59 mg/L NH_3-N to 5 – 25 mg/L NH_3-N. This was then continued with denitrifcation process, where nitrate was reduced to small amount of nitric oxide and nitrous oxide, and mostly in the form of nitrogen gas, which escapes into the atmosphere. From the observation made, the slowly and persistence growth of bacteria occurred within two month. It was assumed that biological uptake of nitrogen for the growth of biomass, *Nitrosomonas* and *Nitrobacter* (nitrification bacteria) and *Nitrococcus*, *Nitrispira* and *Nitroeystis* in wet market wastewater was achieved.

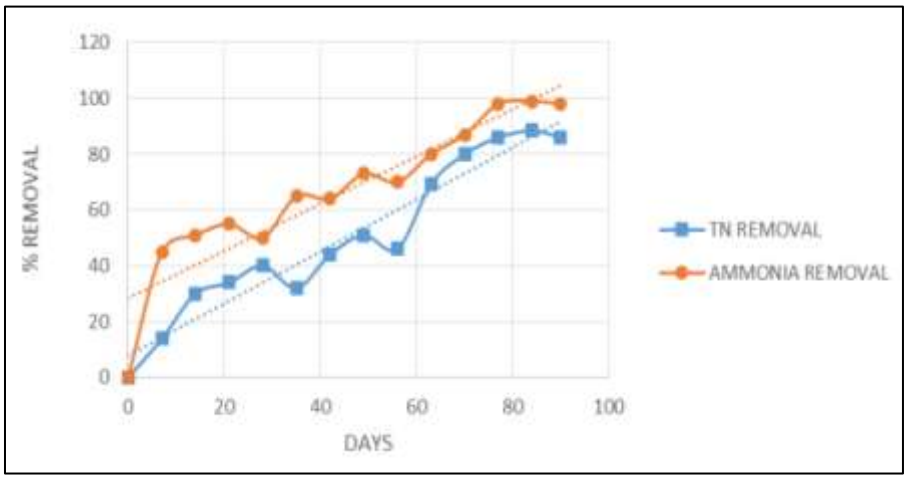


Figure 3. Percentage of Ammonia vs Total Nitrogen removal of grey water

The two lines of different removal (Ammonia-nitrogen and Total Nitrogen) showed that both parameters interlinked with each other. Successful total nitrogen removal must be started with great indicator of ammonification process which ammonia-nitrogen (NH_3-N) is converted to inorganic ammonium or ammonia with assistance of the catalysing by heterotrophic biomass concentration. Figure 4 illustrates the percentage removal of ammonia to nitrite and nitrate to nitrate in the grey water.

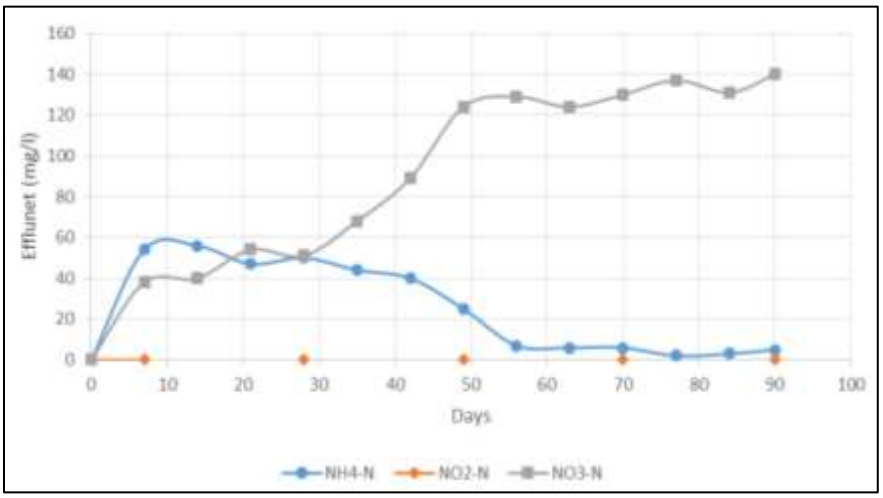


Figure 4. Percentage of Ammonia vs Nitrite vs Nitrate removal of grey water

The data was obtained by taking the effluent samples and tested for the removal performance. It was found that conversion of ammonia to nitrite and nitrate occurred successfully within four hours of aeration and two hours of anoxic stage. This indicated that the nitrification occurred during the first aerobic phase, where ammonia decreased to around 7 mg/L while nitrate increased until it peaked at 140 mg/L. This agrees with the result obtained by Puig et. al. [19], where the ammonia reduced from 9.6 to 0.7 mg/L with nitrate concentration peaking at 6.2 mg/L. The whole process of nitrification requires oxygen. Aerobic autotrophic bacteria are responsible for nitrification in activated sludge. In the first stage, ammonia (NH_4-N) is oxidized to nitrite (NO_2-N) by one group of autotrophic bacteria. In the second stage, nitrite (NO_2-N) is oxidized nitrate (NO_3-N) by another group of autotrophic bacteria.

It should be noted that at 0 – 20 days, the exchange of ammonia to nitrate is very low. This can be observed when the nitrate is in the range of 40 – 60 mg/L. This may cause the bacteria responsible for nitrification to grow much more slowly than heterotrophic bacteria. However, it is good to see uptrend movement despite of slow growth. On day 60 – 80 days, obvious conversion can be seen when the low ammonia and high nitrate effluent results were obtained. Nitrate is converted to nitrogen gas during the settling stage and the rest will be converted at anoxic stage in the next cycle. Also observed lower total nitrite stimulated seem invisible. This may be due to nitrite produced was directly converted to nitrate in the same cycle. If the number of high nitrite (NO_3-N) was seen in the effluent sample, this may be probably due by to the inadequate amount of oxygen or inappropriate pH level found in the system.

The total phosphorus removal average within 60 –70% as seen in Figure 5. The average result of removal may be caused by the initial phosphorus uptake becoming stunted by the long aeration time as observed by Hauschild et. al. [20] in their study. Phosphate accumulating organisms (PAOs), organisms that are capable of storing orthophosphate in excess of their biological growth requirements, are slow growing and normally surpassed by faster growing organisms (non-PAOs). It is suggested that an anaerobic zone is placed ahead of the aerobic zone [21]. This concurred with the finding by Puig et. al. [19], where the polyphosphate was found to be released during the anaerobic phase, while in the aerobic phase the PAOs in the reactor will quickly take up the phosphate.

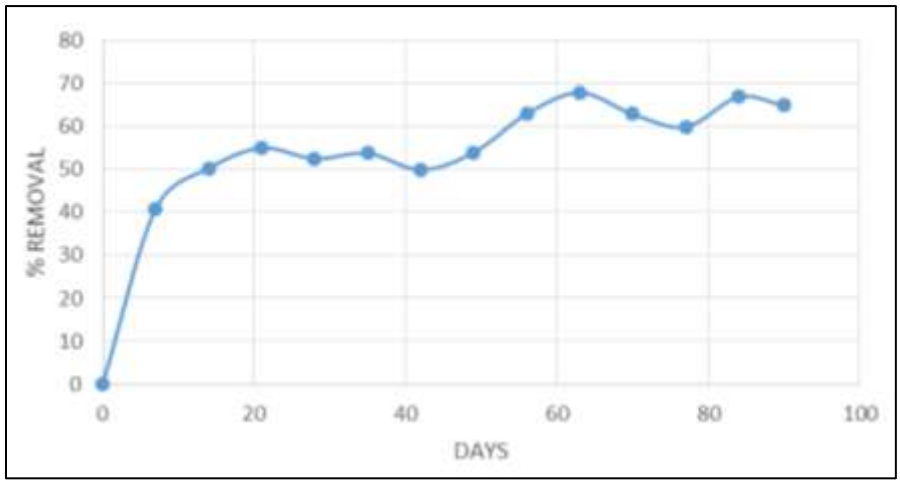


Figure 5. Percentage of Total Phosphorus removal of grey water

Conclusion

The SBR system can effectively remove nutrients and promote biodegradation of organic matter for wet market grey water when the reactor was operated with 1.2 day HRT (8 hours cycle time). The nitrification rate increased while the SBR reactor achieved above 90 % COD removal. The pH should be kept in the range 7.0 –

7.5 in order to prevent inhibition of the nitrifiers. Total phosphorus removal achieved was not above 80 %. It is suggested that aeration time should be increased to enhance poly P uptake.

Acknowledgement

The authors are pleased to acknowledge the Ministry of Higher Education, MOHE (Vot No.01H17) and Universiti Teknologi Malaysia (UTM) for funding this research.

References

1. Watkins, K. (2006). Human Development Report 2006 - Beyond scarcity: Power, poverty and the global water crisis. UNDP Human Development Reports (2006).
2. Eriksson, E., Auffarth, K., Henze, M. and Ledin, A. (2002). Characteristics of grey wastewater. *Urban Water*, 4(1): 85 – 104.
3. Ghunmi, L. A., Zeeman, G., Fayyad, M. and van Lier, J. B. (2011). Grey water treatment systems: A review. *Critical Reviews in Environmental Science and Technology*, 41(7), 657 – 698.
4. Lamine, M., Bousselmi, L. and Ghrabi, A. (2007). Biological treatment of grey water using sequencing batch reactor. *Desalination*, 215(1): 127 – 132.
5. Keough, N., Smira, S. and Benjamin, S. (2010). Lessons from a participatory approach to household greywater use in Jordan. In: Greywater Use in the Middle East, McIlwaine and Redwood (eds). IDRC.
6. Burnat, J. and Eshtayah, I. (2010). On-site grey water treatment in Qebi a Village, Palestine: Grey Water Use in the Middle East. 17.
7. Allen, L., Christian-Smith, J. and Palaniappan, M. (2010). Overview of greywater reuse: The potential of greywater systems to aid sustainable water management. Pacific Insfitute, November 2010, www. pacinst. org.
8. Karpiscak, M.M., Kennith, E. F. and Nancy, S. (1990) "Residential Water Conservation: Casa Del Aguai, 939 – 948.
9. Surendran, S. and Wheatley, A. D. (1998). Grey-water reclamation for non-potable re-use. *Water and Environment Journal*, 12(6): 406 – 413.
10. Okun, D. A. (1997). Distributing reclaimed water through dual systems. *Journal-American Water Works Association*, 89(11): 52 – 64.
11. Santala, E., Uotila, J., Zaitsev, G., Alasiurua, R., Tikka, R. and Tengvall, J. (1998). Microbiological greywater treatment and recycling in an apartment building. AWT98-Advanced Wastewater Treatment, Recycling and Reuse: Milan, 14 – 16.
12. Otterpohl, R., Albold, A. and Oldenburg, M. (1999). Source control in urban sanitation and waste management: Ten systems with reuse of resources. *Water Science and Technology*, 39(5): 153 – 160.
13. Gulyas, H. (2007). Greywater reuse–Concepts, benefits, risks and treatment technologies. In International Conference on Sustainable Sanitation–Food and Water Security for Latin America, Fortaleza, Ceará, Brazil.
14. Gorton, M., Sauer, J. and Supatpongkul, P. (2011). Wet markets, supermarkets and the "big middle" for food retailing in developing countries: evidence from Thailand. *World Development*, 39(9): 1624 – 1637.
15. Metcalf and Eddy. (1991). Wastewater Engineering: Treatment, Disposal, and Reuse. G. Tchobanoglous and F. L. Burton (Eds.). McGraw-Hill.
16. U.S.EPA (1999). Wastewater, Technology Fact Sheet: Sequencing Batch Reactors, U.S Environmental Protection Agency, Office of Water, Washington, D.C., EPA 932-F-99-037.
17. Hernandez, L., Zeeman, G., Temmink, H., and Buisman, C. (2007). Characterization and biological treatment of grey water. *Water Science and Technology*, 56: 193 – 200.
18. Akunna, J. and Shepherd, W. (2001) Comparison of RBC and SBR systems for the treatment of sewage from small communities. *Water and Environment Journal*, 15: 147 – 151.
19. Puig, S., Coraminas, Ll., Balaguer, M.D. and Colprim, J. (2007) Biological nutrient removal by applying SBR technology in small wastewater treatment plants: carbon source and C/N/P ratios effect. *Water Science and Technology*, 55(7), 135 – 141.
20. Hauschild, K., Leverenz, H. L. and Darby, J. L (2010) Development of Design Criteria for Denitrifying Treatment Wetlands. Water Environment Research Foundation (WERF) 3 – 11.
21. Nutrient Removal: WEF Manual of Practice (2005) No. 34. McGraw Hill Professional.

MALAYSIAN JOURNAL OF ANALYTICAL SCIENCES
Published by The Malaysian Analytical Sciences Society
ISSN 1394 - 2506

PREPARATION AND CHARACTERIZATION OF GRAPHENE-BASED MAGNETIC HYBRID NANOCOMPOSITE

(Penyediaan dan Pencirian Nano Komposit Hibrid Magnetik Berasaskan Grafin)

Jashiela Wani Jusin[1], Madzlan Aziz[1,2]*, Goh Pei Sean[2], Juhana Jaafar[2]

[1]*Department of Chemistry, Faculty of Science*
[2]*Advanced Membrane Technology Centre*
Universiti Teknologi Malaysia, 81310 UTM Johor Bharu, Johor, Malaysia

**Corresponding author: madzlan@utm.my*

Received: 9 December 2014; Accepted: 16 November 2015

Abstract

Graphene-based magnetic hybrid nanocomposite has the advantage of exhibiting better performance as platform or supporting materials to develop novel properties of composite by increasing selectivity of the targeted adsorbate. The hybrid nanomaterial was prepared by mixing and hydrolyzing iron (II) and iron (III) salt precursors in the presence of GO dispersion through co-precipitation method followed by in situ chemical reduction of GO. The effect of weight loading ratio of Fe to GO (4:1, 2.5:1, 1:1 and 1:4) on structural properties of the hybrid nanomaterials was investigated. The presence of characteristic peaks in FTIR spectra indicated that GO has been successfully oxidized from graphite while the decrease in oxygenated functional groups and peaks intensity evidenced the formation of hybrid nanomaterials through the subsequent reduction process. The presence of characteristic peaks in XRD pattern denoted that magnetite nanoparticles disappeared at higher loading of GO. TEM micrograph showed that the best distribution of iron oxide particles on the surface of hybrid nanomaterial occurred when the loading ratio of Fe to GO was fixed at 2:5 to 1. The reduced graphene oxide (RGO) sheets in the hybrid materials showed less wrinkled sheet-like structure compared to GO due to exfoliation and reduction process during the synthesis. The layered morphology of GO degrades at higher concentrations of iron oxide.

Keywords: graphene, graphene oxide, surface modification, chemical co precipitation, magnetic nanoparticles

Abstrak

Nano komposit hibrid magnetik berasaskan grafin mempunyai kelebihan dengan mempamerkan prestasi yang lebih baik sebagai platform atau bahan sokongan untuk mengembangkan sifat-sifat baharu komposit dengan meningkatkan pemilihan bahan terjerap yang disasarkan. Bahan nano hibrid telah disediakan dengan mencampurkan dan menhidrolisasikan pemula garam ferum (II) dan ferum (III) ke dalam sebaran GO melalui kaedah mendakan kimia diikuti oleh pengurangan kimia GO secara in situ. Kesan nisbah muatan berat Fe ke GO (4: 1, 2.5: 1, 1: 1 dan 1: 4) terhadap sifat struktur bahan nano hibrid telah dikaji. Kehadiran puncak berciri dalam spektrum FTIR menunjukkan bahawa GO telah berjaya teroksida daripada grafit manakala penurunan dalam kumpulan berfungsi oksigen dan keamatan puncak membuktikan bahawa terdapat pembentukan bahan nano hibrid berikutan melalui proses pengurangan. Kehadiran puncak berciri dalam corak XRD menandakan bahawa nano zarah magnetit hilang apabila muatan GO lebih tinggi. Mikrograf TEM menunjukkan bahawa pengagihan zarah ferum oksida yang terbaik di atas permukaan bahan nano hibrid berlaku apabila nisbah muatan berat Fe ke GO ditetapkan pada 2: 5 ke 1. Kepingan grafin oksida yang melalui proses pengurangan (RGO) dalam bahan hibrid menunjukkan struktur kedutan yang berkurang berbanding GO disebabkan oleh proses pengelupasan dan pengurangan semasa sintesis. Lapisan morfologi GO berkurang pada kepekatan ferum oksida yang lebih tinggi.

Kata kunci: grafin, grafin oksida, pengubahsuaian permukaan, mendakan kimia, nano zarah magnet

Introduction

Exposure to polluted water containing heavy metals and industrial waste can lead to major drawbacks to environment and pose risk to human health. In order to tackle these issues, various alternatives including membrane filtration [1], adsorption [2, 3], and ion exchange [4, 5] have been established. Recently, practical approaches have been made to develop a rapid nanocomposite adsorbent by incorporating magnetic nanoparticles (NPs) or nanocrystals into graphene or derivatives of graphene.

Graphene, a one-atom layer thick packed into a two-dimensional honeycomb sp^2 carbon lattice is currently an emerging new material in the world of science and technology because of their unique and outstanding properties [6, 7]. The production of graphene or reduced graphene oxide is preferably by using chemical route prior to its economical bulk synthesis. Meanwhile, high surface area and specific affinity for heavy metal adsorption from aqueous systems or wastewater samples can be provided by development of nanostructure metal oxides.

Among a wide range of magnetic materials, Fe_3O_4 NPs are becoming the topic of interest due to their unique magnetic separation performances by simply applying an external magnetic field. Besides that, magnetite nanoparticles are very well known for their established application in water treatment. In addition, magnetic particles-based composite adsorbents allowed rapid isolation from aqueous solutions for recycling or regeneration. The great advantage that arises from these two outstanding materials is essential to reduce the cost and time required for water or wastewater treatment.

Wu et al. reported the preparation of a graphene-based magnetic nanocomposite for the extraction of carbamate pesticides from environmental water samples [8]. Sheng et al. developed a versatile magnetic graphene oxide which has performed an efficient removal of arsenate [9]. Fan et al. also fabricated magnetic β-cyclodextrin-chitosan/graphene oxide as nanoadsorbent and applied into the application of removal and dye adsorption [10]. Despite having a lot of advantages, the formation of magnetic nanoparticles with graphene or its derivatives may involve particles aggregation thus the process remains challenging.

In this study, a graphene-based magnetic hybrid nanocomposite consisting magnetic nanoparticles that were incorporated on the surface of reduced graphene oxide through chemical co-precipitation of iron chloride salts solution and subsequent reduction of graphene oxide was developed. The properties of this hybrid material prepared with different loading ratios of graphene oxide and iron salt precursors were investigated. The synthesized nanomaterials were characterized by X-ray diffraction (XRD) and transmission electron microscopy (TEM) to study the nanoparticles crystallinity and morphology, respectively. The chemical compositions of the hybrid materials were investigated by Attenuated Total Reflectance Infrared spectroscopy (ATR-IR). It was expected that the further optimization of these hybrid materials based on various parameters such as type of reducing agent, reaction time, stirring rate and synthesis temperature can be implemented to produce a promising adsorbent for water treatment.

Materials and Methods

The materials used in the experiments were included of commercial graphite powder (60 – 85%) supplied by Superior Graphite Co. while hydrochloric acid (HCl, 37 %), sodium hydroxide (NaOH), hydrazine hydrate ($N_2H_4.H_2O$), and sulfuric acid (H_2SO_4, 95 – 97 %) were from Merck. Potassium permanganate ($KMnO_4$, 99 %) was purchased from Bendosen. Hydrogen peroxide (H_2O_2, 35 %), ferric chloride hexahydrate ($FeCl_3.6H_2O$) and ethanol (C_2H_6O) were supplied from QReC. Sodium nitrate ($NaNO_3$) and ferrous chloride tetrahydrate ($FeCl_2.4H_2O$) were obtained from Systerm. All materials were used as received. Distilled water was used throughout this study.

Preparation of Graphene Oxide (GO) films

Graphite oxide was first prepared from graphite powder in the presence of strong oxidizing agents according to modified Hummers method [11]. The proportion was scaled down during the synthesis process. Graphite powder (2 g) and $NaNO_3$ (1 g) were gradually added to a cold concentrated H_2SO_4 (98 %, 46 ml) followed by 30 minutes stirring in an ice bath. Subsequently, $KMnO_4$ (6 g) was slowly added to the mixture while maintaining the temperature below 20 ºC. After 2 hours stirring, the ice bath was removed and the mixture was stirred at 35 ºC for 30 minutes until it became pasty brownish. The reaction was continued with the addition of distilled water (92 mL)

resulting in sudden increase of the reaction temperature to 90 – 98 ºC which was maintained for 15 minutes. The mixture was diluted with distilled water and subsequently, H_2O_2 (30 %, 10 mL) was added to stop the oxidation process resulting the mixture turned to bright yellow with few bubbles existed. The mixture was left overnight with continuous stirring to make sure its homogeneity. The mixture then was centrifuged, rinsed with 5 % HCl solution to remove the residual metal ions followed by distilled water for several times to obtain neutral pH. Graphite oxide solution was subjected to ultrasonication to produce graphene oxide (GO). The resulting slurry was dried at 70 ºC for 24 hours to obtain GO films.

Preparation of Fe_3O_4-RGO Hybrid Nanomaterials

The procedure was modified from the previous literature where the molar ratio of Fe^{3+}:Fe^{2+} was fixed as 2:1 to synthesize the Fe_3O_4 nanoparticles [12]. GO (200 mg) was dispersed in distilled water (200 mL) by ultrasonication for 30 minutes to transform the carboxylic acid groups to carboxylate anions. Then $FeCl_3 \cdot 6H_2O$ (0.04 mol) and $FeCl_2 \cdot 4H_2O$ (0.02 mol) were dissolved in distilled water (100 mL), which then was added drop wise to GO dispersion at room temperature with vigorous stirring followed by sonication process for 30 minutes. Subsequently, 50 wt% NaOH solutions was added drop wise. The pH was constantly monitored to make solution of pH 11 – 12. The temperature of the solution was raised to 80 ºC and hydrazine hydrate (1.5 mL) was added with constant stirring for reduction of GO, resulting in a black solution. After being rapidly stirred for 5 hours the solution was continuously stirred for 12 hours at room temperature. The resulting precipitate was thoroughly washed with distilled water (3 times) and then followed by ethanol (3 times) to remove any impurities. The products were centrifuged for 15 minutes at 3000 rpm to discard excess water. The precipitate then was dried at 60 ºC for 8 hours. The dry product was then grinded into a fine powder. The same procedures were repeated to prepare different Fe to GO weight loading ratios of 1:1, 2.5:1. 4:1 and 1:4 (labeled as Fe/RGO 1:1, Fe/RGO 2.5:1, Fe/RGO 4:1, Fe/RGO 1:4 respectively).

Characterization of GO films and hybrid nanomaterials

FTIR was used to determine the chemical compositions of the prepared GO and hybrid nanomaterials. The prepared samples were characterized by using Attenuated Total Reflectance-Fourier Transform Infrared spectrometer (ATR-FTIR) with a resolution of 4 cm^{-1}. The crystallinity of GO and hybrid nanomaterials were examined based on XRD patterns obtained from PANalytical X'Pert Pro MPD HR-X-ray diffractometer, powered by Philips PW3040/60 with Cu-K_α radiation (λ = 1.5418 Å) generated from a Cu anode supplied with 40 kV and a current of 30 mA. The scan range for 2θ was from 5 to 90º. The surface morphology of the prepared samples was studied based on the TEM images captured with FEI/Philips CM12 transmission electron microscope operated at 120 kV.

Results and Discussion

Fourier Transform Infrared spectrometer (FTIR)

Figure 1 shows the FTIR spectra of graphite and graphene oxide (GO). The presence of few significant characteristic peaks in GO can be associated to the presence of oxygenated functional groups which were resulted from successful oxidation of graphite. The broad adsorption band at 3230.2 cm^{-1} is assigned to the O-H stretching vibrations while two adsorption bands appear at 1716.7 cm^{-1} and 1625.6 cm^{-1} are corresponding to the C=O stretching (from carbonyl and carboxyl groups) and aromatic C=C vibration (resulted from skeletal vibration from unoxidized graphitic domains) respectively. The peak observed at 1386.1 cm^{-1} can be assigned to the combination of C-O (carboxy) stretching vibration and deformation vibration of hydroxyl groups. Another peak presents at 1048.8 cm^{-1} can be attributed to the C-O (alkoxy) stretching vibration.

Figure 2 illustrated the FTIR spectra of GO and the hybrid nanocomposite with different loading ratio. The appearance of peak at 500-600 cm^{-1} differs GO from the hybrid nanocomposite in which it denoted the presence of Fe-O. The peak intensity of the hybrids was found to be very similar to each other except for Fe/RGO 1:4 which probably due to the higher loading ratio of GO presented in the hybrid. In general, the FTIR absorption bands of the hybrid nanocomposite showed much lower intensity compared to that of GO. The observation suggested that the oxygenated functional groups were partially removed from GO during the reduction process using hydrazine hydrate where GO has transformed into reduced graphene oxide (RGO) during the synthesis [13].

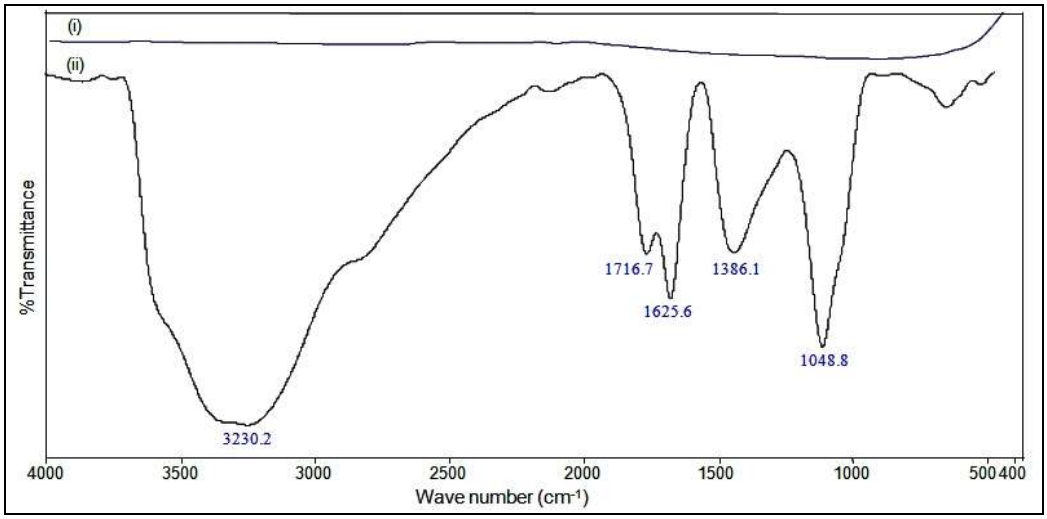


Figure 1. FTIR spectra comparison of (i) graphite and (ii) GO

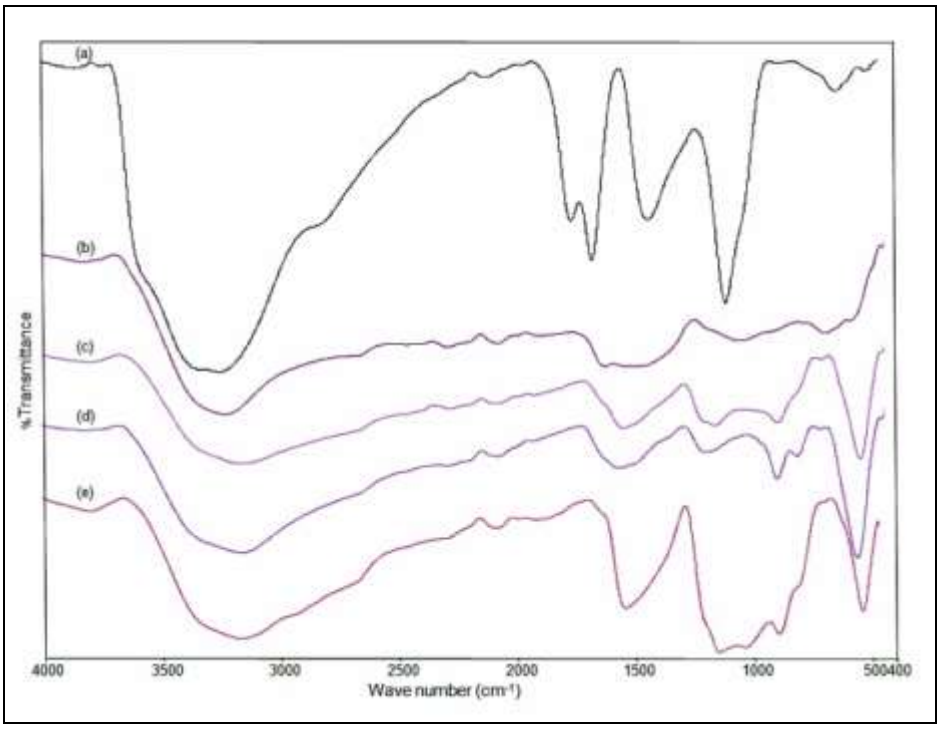


Figure 2. FTIR spectra comparison of (a) GO and hybrid nanomaterials with different weight loading ratios (b) Fe/RGO 1:4, (c) Fe/RGO 2.5:1, (d) Fe/RGO 4:1, and (e) Fe/RGO 1:1 respectively

X-Ray Diffraction (XRD)

XRD analysis was used to further confirm and compare the crystalline structure and composition of the obtained hybrid nanomaterials. XRD patterns of graphite, graphene oxide (GO) and hybrid materials synthesized at different weight loading ratios are shown in Figure 3. Graphite shows a very sharp diffraction peak at 2θ = 26.5° which corresponds to *d*-spacing of 0.34 nm with an index (002). Meanwhile, GO exhibits typical diffraction peaks centered at 2θ = 11.5° (001) corresponding to interlayer distance of ~ 0.77 nm and 2θ = 22.3° (100) which is consistent with the previous report [14]. The diffraction peak appears from GO is originated from (002) layer plane from graphite. The interlayer *d*-spacing of graphene oxide (0.77 nm) tends to be much larger than graphite (0.34 nm) due to the presence of many oxygen functionalities that attached to the surfaces of GO with some potential defects related to the strong oxidation process. A broad diffraction peak appears at $2\theta \approx 22.3^{o}$ due to the short range order of stacked graphene sheets.

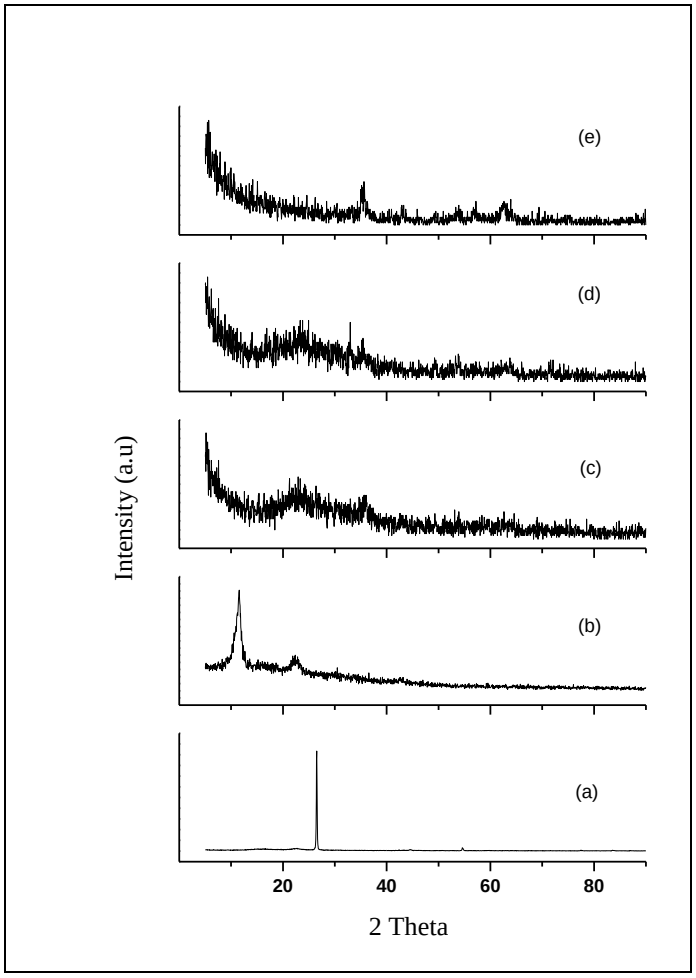


Figure 3. XRD patterns of (a) graphite, (b) GO, (c) Fe/RGO 1:1, (d) Fe/RGO 1:4, and (e) Fe/RGO 2.5:1

The XRD patterns of Fe/RGO nanocomposite with ratio of 1:1 and 1:4 are very similar. Both Fe/RGO 1:1 and Fe/RGO 1:4 showed the most intense diffraction peaks at $2\theta \approx 24^{o}$ and 23° respectively corresponding to the peak resulted from GO. However, both Fe/RGO 1:1 and Fe/RGO 1:4 do not show any peak that is corresponding to the magnetite compound. The Fe/RGO 1:1 is less likely to show magnetic properties due to the presence of minute amount of Fe_2O_3 particles in their composite. There are some diffraction peaks that are indexed to Fe_3O_4 particles in

Fe/RGO 2.5:1 with low intensity as compared to pure magnetic particles. The peaks of Fe/RGO 2.5:1 appear at $2\theta \approx 19.3^{o}$ (111), 35.4^{o} (311), 43.1^{o} (400), 53.7^{o} (422) and 62.5^{o} (440) indicated the characteristic of Fe_3O_4 nanoparticles while $2\theta \approx 24.5^{o}$ corresponds to the peak resulted from GO. However, formation of magnetite particles was not pure and might contain Fe_2O_3 particles and it was shown by at least two peaks of (220) and (511) indexes were missing. The synthesis reaction that was not carried out under nitrogen flow might be the reason for the unsuccessful magnetite formation since the ratio between Fe^{2+} and Fe^{3+} was probably disturbed during the fabrication process [15]. By using Scherer formula, average particle size of Fe/RGO 2.5:1 is estimated as 11.8 nm.

Transmission Electron Microscope (TEM)

The surface morphology of GO and the hybrid nanocomposites were studied by TEM whereby only GO and Fe/RGO nanocomposite with weight loading ratio of 2.5:1 and 1:4 were chosen as the representative samples (Figure 4). TEM analysis was performed on these two hybrids because Fe/RGO 2.5:1 presented the most significant characteristic peaks of XRD pattern while the analysis on Fe/RGO 1:4 was carried out to confirm that the higher loading ratio of GO might contribute to the disappearance of Fe-O absorption peak in the respective FTIR spectra. From the obtained TEM micrographs, there is significant difference between the as-prepared GO and RGO sheets in Fe/RGO 2.5:1 and Fe/RGO 1:4 hybrid. The RGO sheets present in the Fe/RGO 2.5:1 hybrid show less wrinkled sheet-like structure compared to GO and Fe/RGO 1:4 hybrid probably due to the exfoliation and reduction process during the synthesis. It has also been reported that, the layered morphology of GO tends to degrade at higher concentrations of iron oxide [16].

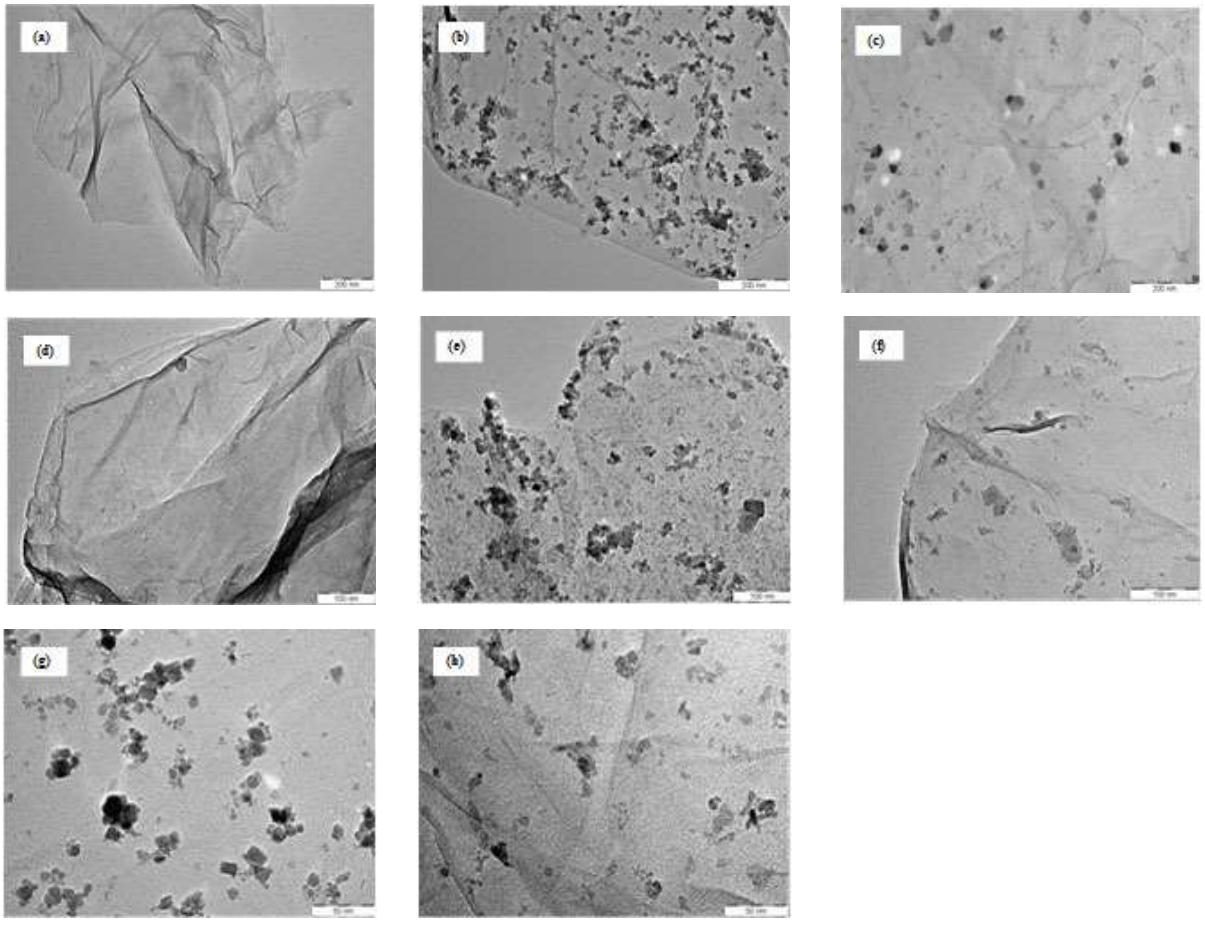


Figure 4. TEM micrographs of GO, Fe/RGO 2.5:1 and Fe/RGO 1:4 at magnification of 200 nm: (a, b, c), 100 nm: (d, e, f) and 50 nm: (g, h) respectively

Conclusion

The study on fabrication of hybrid nanomaterials was conducted by incorporating graphene oxide (GO) and magnetic nanoparticles altogether to achieve enhanced properties of conventional nanocomposite. The oxygen-rich functional groups allow GO to carry out secondary functionalization for the preparation of hybrid nanomaterials. In this study, magnetic hybrid materials were developed through chemical co precipitation from the mixture of iron (II) and iron (III) salt precursors, followed by in situ chemical reduction process of GO. From the FTIR spectra, it was shown that GO exhibited significant difference from graphite in terms of the amount of oxygenated functional groups. On the other hand, the hybrid nanomaterials exhibited absorption bands with much lower intensity compared to that of GO due to the partial removal of oxygenated functional groups during the reduction process. As higher loading of GO may have restricted the formation of iron particles onto the GO surface, the characteristic peaks that corresponding to magnetite nanoparticles were absent in the XRD patterns. The layered morphology of RGO sheets in hybrid nanocomposites showed less wrinkled sheet-like structure as compared to GO due to the exfoliation during the reduction process and probably because of the increasing iron oxide content. This study has shown that weight loading ratio of Fe to GO has significant effect in term of morphological and structural properties of the hybrid nanocomposites.

Acknowledgement

The authors acknowledge Ministry of Education Malaysia (MOE), Research Grant No. 4F257 and Universiti Teknologi Malaysia for the provided facilities and financial support throughout this study.

References

1. Blöcher, C., Dorda, J., Mavrov, V., Chmiel, H., Lazaridis, N. K. and Matis, K. A. (2003). Hybrid flotation—membrane filtration process for the removal of heavy metal ions from wastewater. *Water Research*, 37(16): 4018 – 4026.
2. Kadirvelu, K., Thamaraiselvi, K. and Namasivayam, C. (2001). Removal of heavy metals from industrial wastewaters by adsorption onto activated carbon prepared from an agricultural solid waste. *Bioresource Technology*, 76(1): 63 – 65.
3. Katsou, E., Malamis, S. and Haralambous, K. J. (2011). Industrial wastewater pre-treatment for heavy metal reduction by employing a sorbent-assisted ultrafiltration system. *Chemosphere*, 82(4): 557 – 564.
4. Dabrowski, A., Hubicki, Z., Podkościelny, P. and Robens, E. (2004). Selective removal of the heavy metal ions from waters and industrial wastewaters by ion-exchange method. *Chemosphere*, 56(2): 91 –106.
5. Qdais, H. A. and Moussa, H. Removal of heavy metals from wastewater by membrane processes: a comparative study. *Desalination*, 164(2): 105 – 110.
6. Geim, A. K. and Novoselov, K. S. (2007) The rise of graphene. *Nature Materials*, 6(3): 183 – 191.
7. Novoselov, K. S., Geim, A. K., Morozov, S.V., Jiang, D., Katsnelson, M. I., Grigorieva, I. V., Dubonos, S. V. and Firsov, A. A. (2005) Two-dimensional gas of massless Dirac fermions in graphene. *Nature*, 2005. 438(7065): 197 – 200.
8. Wu, Q., Zhao, G., Feng, C., Wang, C. and Wang, Z. (2011). Preparation of a graphene-based magnetic nanocomposite for the extraction of carbamate pesticides from environmental water samples. *Journal of Chromatography A*, 1218(44): 7936 – 7942.
9. Sheng, G., Li, Y., Yang, X., Ren, X., Yang, S., Hu, J. and Wang, X. (2012). Efficient removal of arsenate by versatile magnetic graphene oxide composites. *RSC Advances*, 2(32): 12400 – 12407.
10. Fan, L., Luo, C., Sun, M., Qiu, H. and Li, X. (2013). Synthesis of magnetic β-cyclodextrin–chitosan/graphene oxide as nanoadsorbent and its application in dye adsorption and removal. *Colloids and Surfaces B: Biointerfaces*, 2013. 103: 601 – 607.
11. Hummers, W.S. and Offeman, R.E. (1958). Preparation of Graphitic Oxide. *Journal of the American Chemical Society*, 80(6): 1339 –1339.
12. Yao, Y., Miao, S., Liu, S., Ma, L.P., Sun, H. and Wang, S. (2012). Synthesis, characterization, and adsorption properties of magnetic Fe3O4@graphene nanocomposite. *Chemical Engineering Journal*, 184(0): 326 – 332.
13. Ji, Z., Shen, X., Song, Y. and Zhu, G. (2011). In situ synthesis of graphene/cobalt nanocomposites and their magnetic properties. *Materials Science and Engineering: B*, 176(9): 711 – 715.

14. Zhu, S., Guo, J., Dong, J., Cui, Z., Lu, T., Zhu, C., Zhang, D. and Ma, J. (2013). Sonochemical fabrication of Fe3O4 nanoparticles on reduced graphene oxide for biosensors. *Ultrasonics Sonochemistry*, 20(3): 872 – 880.
15. Chia, C. H., Zakaria, S., Farahiyan, R., Liew, T. K., Khien L. N., Abdullah, M. and Ahmad, S. (2008). Size-controlled Synthesis and Characterization of Fe3O4 Nanoparticles by Chemical Coprecipitation Method. *Sains Malaysiana*, 37(4): 389 – 394.
16. Singh, V. K., Patra, M. K., Manoth, M., Gowd, G. S., Vadera, S. R. and Kumar, N. (2009). In situ synthesis of graphene oxide and its composites with iron oxide. *New Carbon Materials*, 24(2): 147 – 152.
17. Guo, J., Wang, R., Tjiu, W., Pan, J. and Liu, T. (2012). Synthesis of Fe nanoparticles@graphene composites for environmental applications. *Journal of Hazardous Materials*, 225–226: 63 –73.

MALAYSIAN JOURNAL OF ANALYTICAL SCIENCES
Published by The Malaysian Analytical Sciences Society
ISSN 1394 - 2506

PENYEDIAAN DAN PENCIRIAN HIDROGEL BERASASKAN KANJI/AKRILAMIDA DARIPADA UBI *Stemona curtisii*

(Preparation and Characterization of Starch/Acrylamide-Based Hydrogel from *Stemona curtissi* Tuber)

Lim Wun Pin, Airul Ashri, Muntaz Abu Bakar, Wan Yaacob Wan Ahmad, Mohd Azwani Shah Mat Lazim*

Pusat Pengajian Sains Kimia & Teknologi Makanan,
Fakulti Sains dan Teknologi
Universiti Kebangsaan Malaysia, 43600 UKM Bangi, Selangor, Malaysia

**Corresponding author: azwanlazim@ukm.edu.my*

Received: 13 July 2015; Accepted: 11 January 2016

Abstrak

Dalam kajian ini, hidrogel berasaskan kanji daripada ubi *Stemona curtisii* disintesis melalui kaedah pempolimeran radikal bebas menggunakan penyinaran gelombang mikro. Dalam kajian ini terdapat 3 jenis hidrogel dengan nisbah kanji kepada akrilamida yang berbeza dianalisis iaitu 1:3, 1:4 dan 5:3. Berdasarkan kepada ujian pembengkakan, hidrogel 1:3 mempunyai peratus pembengkakan paling tinggi dan ini dibuktikan dengan keputusan yang diperolehi daripada Mikroskop Pengimbas Elektron (SEM) di mana mikrograf SEM mempamerkan saiz liang pada hidrogel 1:3 adalah yang paling besar. Analisis menggunakan Spektroskopi Inframerah Transformasi Fourier-Jumlah Pantulan Teratenuat (ATR-FTIR) menunjukkan kehadiran puncak pada 1112 cm^{-1}, 1152 cm^{-1} dan 1150 cm^{-1} pada hidrogel 1:4, 1:3 dan 5:3 masing-masing yang menandakan pembentukan ikatan C-O-C hasil daripada proses pempolimeran taut silang. Analisis menggunakan Difraktometer Sinar-X (XRD) pula menunjukkan bahawa ketiga – tiga jenis hidrogel adalah amorfus. Kalorimeter Pengimbas Kebedaan (DSC) pula memberikan maklumat bahawa semua bahan yang digunakan untuk sintesis hidrogel adalah pada tahap kebolehcampuran yang baik dan hidrogel 1:4 menunjukkan suhu peralihan kaca (T_g) yang paling tinggi. Daripada termogram TGA/DTG pula, hidrogel 5:3 didapati lebih stabil terhadap haba berbanding hidrogel yang lain. Keputusan ujian Tegangan menggunakan Mesin Ujian Universal (UTM) telah mendapati bahawa hidrogel berasaskan kanji Ubi *Stemona curtisii* yang disintesis mempunyai potensi untuk diaplikasikan sebagai pembalut luka. Dalam ujian ini, hidrogel 1:4 yang mempunyai kandungan kanji yang paling rendah telah menunjukkan nilai modulus elastik Young yang paling tinggi.

Kata kunci: *Stemona curtisii*, hidrogel, pempolimeran radikal bebas, gelombang mikro

Abstract

In this study, hydrogel based on starch of *Stemona curtisii* was synthesized via free radical polymerization method by using microwave irradiation. In this study, there were three type of hydrogels formulated with different type of starch to acryamide been anaylyzed which were 1:3, 1:4 and 5:3. Based on swelling test, hydrogel with 1:3 was reported to have the highest swelling percentage where this is prove by Scanning Electron Microscope result. The SEM micrograph shows that hydrogel 1:3 have the largest pores size compare to the other two types of hydrogels. The polymerization reaction has been proven to occur successfully based on the analysis using Attenuated Total Reflection-Fourier Transform Infrared Spectroscopy (ATR-FTIR). Cross-linking polymerization process was determine by the present of peak at 1112 cm^{-1}, 1152 cm^{-1} and 1150 cm^{-1} in hydrogels 1:4, 1:3 and 5:3 respectively which indicate the formation of C-O-C bond.X-Ray Diffractometer (XRD) results showed that all starch-based hydrogels were amorphous. Differential Scanning Calorimeter (DSC) gave information that all the blending materials for hydrogel synthesis were of good miscibility and the hydrogel 1:4 was found to have the highest glass transition temperature. From the TGA/DTG thermogram, hydrogel 5:3 was reported to be more stable to heat as compared to other hydrogels. The results from Tensile test using Universal Testing Machine (UTM) have discovered that hydrogels based on the

starch of *Stemona curtisii* possess a potential to be applied as wound dressing. In this test, hydrogel with the lowest starch content, 1:4 showed the highest Young's elastic modulus value.

Keywords: *Stemona curtisii*, hydrogel, free radical polymerization, microwave

Pengenalan

Kajian tentang hidrogel telah mendapat perhatian semenjak 50 tahun yang lalu kerana sifatnya yang unik yang membolehkan ia digunakan di dalam pelbagai aplikasi. Selain itu, hidrogel juga mempunyai tahap fleksibiliti yang hampir sama dengan tisu tabii kerana kandungan airnya yang tinggi. Keupayaan hidrogel untuk menyerap air bergantung kepada kumpulan berfungsi hidrofilik yang terdapat pada tulang belakang polimer manakala ketahanannya terhadap pemelarutan berpunca daripada kewujudan taut-silang antara rantai rangkaian [1].

Pada awalnya, hidrogel disintesis secara kimia sama ada melibatkan proses satu langkah atau proses pelbagai langkah. Proses satu langkah yang sering digunakan seperti pempolimeran dan taut-silang selari yang dihubungkan oleh beberapa monomer. Proses pelbagai langkah pula melibatkan sintesis molekul polimer yang mempunyai kumpulan reaktif. Hidrogel boleh direka bentuk dan disintesis dengan kawalan berskala terhadap struktur hidrogel seperti ketumpatan pertautan-silang, ciri biodegradasi, kekuatan mekanikal, tindak balas kimia dan biologi hidrogel terhadap rangsangan [2]. Hidrogel kanji-akrilamida merupakan sejenis hidrogel yang peka terhadap suhu dan pH. Kepekaan hidrogel ini akan menentukan nisbah pengembangannya berdasarkan nilai pH apabila direndam dalam larutan penimbal. Secara tabiinya, hidrogel yang peka pH membengkak di dalam air pada pH tertentu. Hidrogel kanji-akrilamida boleh digunakan sebagai penyerap untuk kegunaan sisa buangan seperti pewarna metilena biru [3].

Para saintis telah mengkaji pempolimeran hidrogel berasaskan kanji dengan menggunakan gelombang mikro. Hasil kajian mereka menunjukkan terdapat tiga keadaan tindak balas akan berlaku dengan penggunaan gelombang mikro: pertama, semua kandungan tindak balas dalam larutan yang homogen adalah larut tanpa ada pemisahan fasa; kedua, bahan tindak balas sama ada polisakarida atau monomer yang tidak larut akan berada dalam larutan tindak balas sebagai ampaian; ketiga, apabila polisakarida dan pemula meresap pada penyokong pepejal tabii, mereka akan wujud sebagai fasa pepejal. Kajian awal turut menunjukkan penggunaan gelombang mikro dapat meningkatkan pembentukan kopolimer dan memberikan produk yang tinggi dalam masa yang singkat berbanding cara pemanasan langsung [4]. Secara umumnya, sinaran gelombang mikro merupakan satu cara pemanasan yang amat menarik. Gelombang ini boleh memanaskan bahan tindak balas terpilih secara langsung dan mempunyai pertukaran haba yang sederhana. Selain itu, kelebihan cara gelombang mikro yang paling ketara sekali adalah tindak balas pempolimeran menggunakan cara ini boleh dilakukan tanpa pemula atau kepekatan pemula yang sangat rendah. Tambahan pula, hidrogel yang dihasilkan melalui cara ini adalah bersifat lebih poros berbanding hidrogel daripada cara konvensional [5].

Ubi Kemili atau nama saintifiknya, *Stemona curtisii* (*Stemonaceae*) adalah sejenis ubi yang menjadi makanan ruji bagi penduduk di kawasan pantai timur Semenanjung Malaysia. Ubi ini juga dikenali sebagai sejenis herba saka berumpun yang ditanam sebagai tanaman semusim dengan pokoknya hanya boleh mencapai 60 – 90 cm sahaja. Oleh itu, kebanyakan hasil ubinya hanya bersaiz lebih kurang 2 – 4 cm panjang dan 0.5 – 2.0 cm lebar. Sejak dahulu, Ubi Kemili telah dikenali sebagai Galak Tua, Pokok Seratus atau Pecah Kelambu di kalangan masyarakat Melayu dan 'Bai-bu' dalam masyarakat Cina [6]. Kajian awal telah menunjukkan bahawa ubi spesies *Stemona curtisii* telah digunakan secara meluas dalam perubatan tradisional di China, Jepun dan Thailand untuk merawat penyakit pernafasan, batuk dan anti-kanser.Selain itu, kajian farmakologi telah menunjukkan bahawa ekstrak daripada spesies ini dapat menghalang pertumbuhan pelbagai jenis bakteria dan kulat di mana mereka telah digunakan sebagai racun serangga [7].

Bahan dan Kaedah

Pengekstrakan kanji daripada Ubi *Stemona curtisii*

Rajah 1 menunjukkan ubi *Stemona curtisii* yang digunakan dalam penyelidikan ini diperolehi dari Terengganu dan Kelantan, Proses pengekstrakan kanji dimulakan dengan proses basuhan ubi bagi menyingkirkan sebarang kotoran. Ubi dicuci dengan air yang mengalir dan kulitnya dibuang secara menggosok dengan tangan di bawah aliran air.

Langkah ini perlu diberi perhatian kerana ubi ini mudah teroksida. Oleh itu, ubi harus direndam dalam air suling sebaik sahaja dibuang kulitnya. Ubi dipotong kecil dan dikisar dengan menggunakan pengisar elektronik. Hampas ubi ditapis dengan menggunakan penapis kopi yang diperbuat daripada kain. Proses ini diulang beberapa kali bagi mendapatkan kandungan kanji yang tertinggi. Hasil tapisan dibiarkan selama lima jam untuk membenarkan kanji mendak ke dasar bikar. Kanji yang diperolehi dibasuh dengan menggunakan metanol dan dicuci sebanyak tiga kali lagi dengan air suling bagi menyingkirkan baki metanol yang terdapat pada kanji. Seterusnya kanji dikeringkan secara pengeringan sejuk beku dan dikisar menjadi serbuk.



Rajah 1. (a) ubi kemili (*Stemona curtisii*) dan (b) isi ubi kemili yang bewarna putih susu [7]

Sintesis hidrogel berasaskan kanji daripada Ubi *Stemona curtisii*

Untuk menghasilkan hidrogel mengikut kaedah yang dilaporkan oleh Pandey [8], sebanyak 2 g kanji ubi *Stemona curtisii* dilarutkan dengan menggunakan 15 mL larutan natrium hidroksida berkepekatan 1 M. Campuran ini dikacau berterusan sehingga kedua-dua fasa menjadi homogen dan larutan jernih berwarna kuning-keperangan terhasil. Kemudiaan, 4 g akrilamida dan 0.05 g kalium persulfat serta 0.2 g *N,N'*-metilenabisakrilamida (5 % daripada berat akrilamida) ditimbang dan dimasukkan ke dalam larutan kanji. Akrilamida dilarutkan terlebih dahulu dengan menggunakan 5 mL air suling manakala kalium persulfat dan *N,N'*-metilenabisakrilamida masing-masing dilarutkan dengan 2 mL air suling. Kesemua campuran dikacau dengan menggunakan pengacau bermagnet pada kelajuan 500 rpm selama 3 minit. Apabila larutan menjadi sedikit likat, ia dituang ke dalam piring petri kaca dan didedahkan kepada gelombang mikro berkuasa tetap 100 W selama 5 minit. Hidrogel yang dihasilkan dibiarkan kering semalaman di dalam kebuk wasap. Proses basuhan dilakukan bagi menyingkirkan bahan – bahan kimia yang tidak bertindak balas. Hidrogel kering direndam selama 2 jam di dalam air suling dan kemudiannya dikeringkan di dalam ketuhar pada suhu 40 °C selama 24 jam. Jadual 1 menunjukkan komposis berbeza bahan – bahan yang digunakan untuk mensintesis hidrogel.

Jadual 1. Komposisi kanji, AAm, KPS dan MBA yang berbeza di dalam penghasilan hidrogel

Nisbah kanji : akrilamida (AAm) (g/g)	**Pemula (Kalium Persulfat, KPS) /g**	**Agen taut silang (*N,N'*-metilenabisakrilamida,MBA)/g**
0:3	0.05	0.15
1:4	0.05	0.20
1:3	0.05	0.15
5:3	0.05	0.15

Ujian Pembengkakan Hidrogel
Dalam kajian ini, ujian pembengkakan hidrogel dilakukan dengan merendam hidrogel ke dalam air suling pada suhu bilik dan beratnya ditimbang setiap 10 minit selama 2 jam. Peratus pembengkakan dikira dengan menggunakan persamaan yang telah dilaporkan oleh Gulrez seperti persamaan berikut [9];

$$\text{Pembengkakan } (\%) = \frac{W_s - W_d}{W_d} \times 100$$

di mana, W_s adalah jisim hidrogel yang membengkak pada masa t (minit) dan W_d adalah jisim asal hidrogel.

Mikroskop Pengimbas Elektron (SEM)
Mikroskop Pengimbas Elektron (SEM) digunakan untuk menganalisis sifat morfologi permukaan hidrogel, keporosan hidrogel dan saiz keporosannya. Sebelum analisis dijalankan, sampel hidrogel dikeringkan terlebih dahulu dengan menggunakan pengering sejuk-beku. Sampel hidrogel kering diletakkan di atas stub aluminium dan disalut dengan emas menggunakan mesin penyalut (SC500, BioRad, UK). Imej morfologi hidrogel dicerap dengan menggunakan mikroskop pengimbas elektron (LEO 1450 VP, Germany)

Spektrometer Inframerah Transformasi *Fourier*-Jumlah Pantulan Teratenuat (ATR-FTIR)
Analisis menggunakan Spektroskopi Infra Merah adalah bertujuan untuk menentukan proses cangkukan telah berlaku di antara kanji dengan akrilamida. Spektrum Infra Merah direkodkan dengan menggunakan teknik spektroskopi Infra Merah (FTIR/NIR) model: *spectrum 400 FT-NIR and spotlight 400 imaging system*, Perkin Elmer USA. Sampel hidrogel dikeringkan terlebih dahulu dan spektrum dirakam pada nombor gelombang 400 – 4000 cm^{-1}. Jenis kristal yang digunakan dalam ATR adalah berlian.

Difraktometer Pembelauan Sinar-X (XRD)
Difraktometer Pembelauan Sinar-X (XRD) telah digunakan secara meluas dalam penentuan penghabluran pada granul kanji daripada ubi dan hidrogel [11,12]. Hidrogel yang disintesis dalam kajian ini dijadikan serbuk dan diuji dengan menggunakan instrumen XRD berjenama Bruker (Siemen) D-5000 pada sudut 2θ (5˚ - 80˚).

Kalorimeter Pengimbas Kebedaan (DSC)
DSC merupakan suatu teknik untuk merakam tenaga yang diperlukan untuk mendapatkan perbezaan suhu sifar di antara sampel dan bahan rujukan terhadap masa atau suhu apabila kedua-duanya didedahkan kepada persekitaran yang dipanaskan atau disejukkan pada kadar terkawal. Dengan memerhatikan perbezaan dalam aliran haba antara sampel dan bahan rujukan, jumlah haba yang diserap atau dibebaskan semasa peralihan itu dapat ditentukan (perubahan entalpi). Alat ini hanya boleh mengesan perbezaan suhu sampel di antara julat suhu (−70 ˚C hingga 700 ˚C) dengan bantuan gas nitrogen atau oksigen sebagai gas pembawa. Dalam kajian ini, DSC berjenama Mettler Toledo/822 e digunakan untuk menentukan suhu peralihan kaca (T_g) dan kebolehcampuran setiap komponen dalam sampel.

Analisis Termagravimetri (TGA)
TGA adalah satu kaedah yang digunakan untuk menentukan perubahan sifat-sifat fizikal dan kimia bahan polimer terhadap suhu. Biasanya, pemanasan yang berterusan dikenakan ke atas sampel untuk mengetahui kehilangan berat bahan polimer. Dalam kajian ini, TGA yang berjenama TA−60WS, Shidmazu Corporation (Kyoto, Japan) digunakan untuk mengetahui kestabilan hidrogel terhadap haba. Sampel hidrogel dikisar menjadi halus lalu pemanasan dilakukan pada julat suhu 0-600 ˚C dengan kadar pemanasan 20 ˚C/minit. Pada nilai suhu yang tertentu, hidrogel yang stabil akan menunjukkan perubahan jisim yang ketara di mana pengurangan jisim dapat dilihat pada cerun termogram pada nilai suhu itu [13].

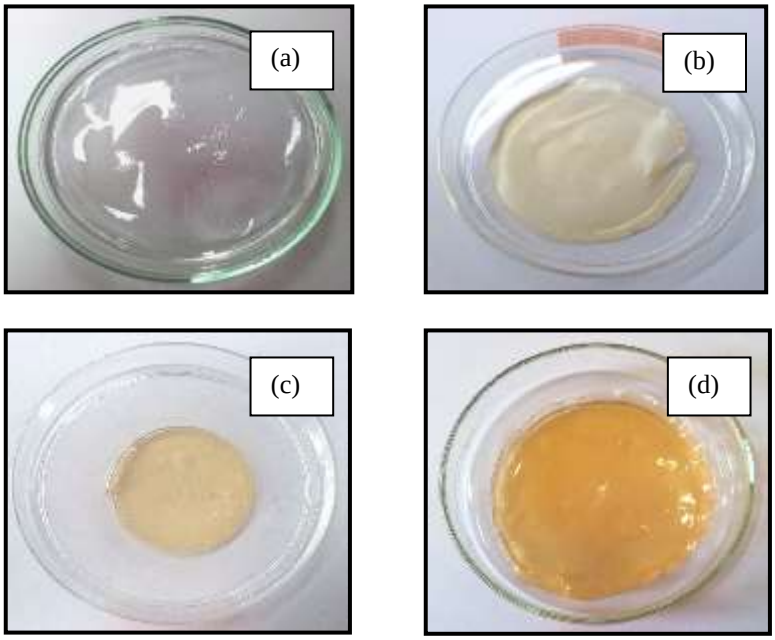
Ujian regangan hidrogel
Ujian regangan hidrogel ini dilakukan dengan menggunakan Mesin Ujian Universal (*Universal Testing Machine, UTM*) berjenama Instron/5566. Mesin ujian regangan universal adalah alat yang digunakan untuk mengukur kekuatan regangan, mampatan dan kekuatan ricih pada bahan. Sebelum ujian regangan dilakukan, sampel dipotong mengikut bentuk *'dumbell'* berdasarkan piawai ASTM (D 638−02a). Ketebalan sampel diukur terlebih dahulu

dengan menggunakan kaliper. Kemudian, sampel diapit pada Mesin Ujian Universal lalu duji pada kelajuan 3 mili meter/minit.

Keputusan dan Perbincangan

Penghasilan hidrogel

Rajah 2 menunjukkan hidrogel yang berjaya disintesis. Dalam penyelidikan ini, hidrogel berasaskan kanji daripada Ubi *Stemona curtisii* dihasilkan melalui aruhan gelombang mikro dengan menggunakan kalium persulfat, $K_2S_2O_8$ sebagai pemula radikal, akrilamida (AAm) sebagai monomer dan *N,N'*-metilenabisakrilamida (MBA) sebagai agen taut-silang telah berjaya dihasilkan.



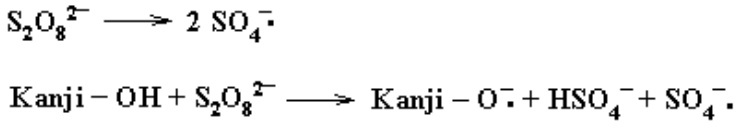
Rajah 2. (a) Hidrogel akrilamida (b) hidrogel dengan nisbah 1:4 (c) hidrogel dengan nisbah 1:3 dan (d) hidrogel dengan nisbah 5:3

Pemerhatian yang teliti terhadap hidrogel yang dihasilkan dari aspek fizikal seperti tahap kekenyalan, tekstur, permukaan dan warna seperti disenaraikan dalam Jadual 2. Cadangan tindak balas adalah seperti yang ditunjukkan dalam Rajah 3.

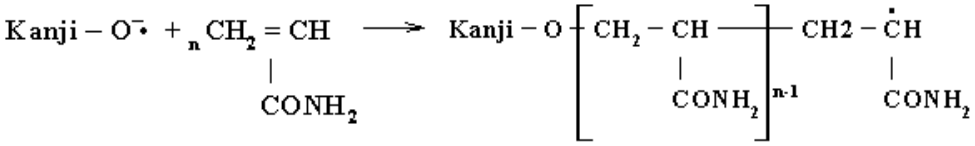
Jadual 2. Pemerhatian yang teliti terhadap hidrogel yang dihasilkan dari aspek fizikal seperti tahap kekenyalan, tekstur, permukaan dan warna.

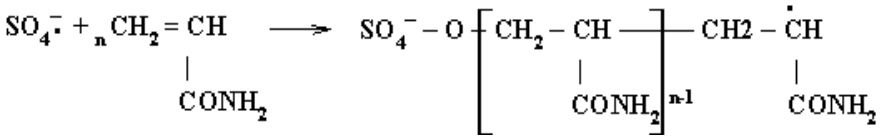
Hidrogel	Pemerhatian
Akrilamida	Berwarna putih lutsinar dengan permukaan yang sangat licin, mempunyai tekstur yang kurang lembut dan tidak kenyal.
Nisbah 1:4	Berwarna kekuningan dengan permukaan yang licin, mempunyai tekstur yang lembut dan sangat kenyal.
Nisbah 1:3	Berwarna kuning pudar dengan permukaan yang licin, mempunyai tekstur yang lembut dan kenyal.
Nisbah 5:3	Berwarna kuning gelap dengan permukaan yang kurang licin, mempunyai tekstur yang lembut dan kurang kenyal.

Permulaan rantai

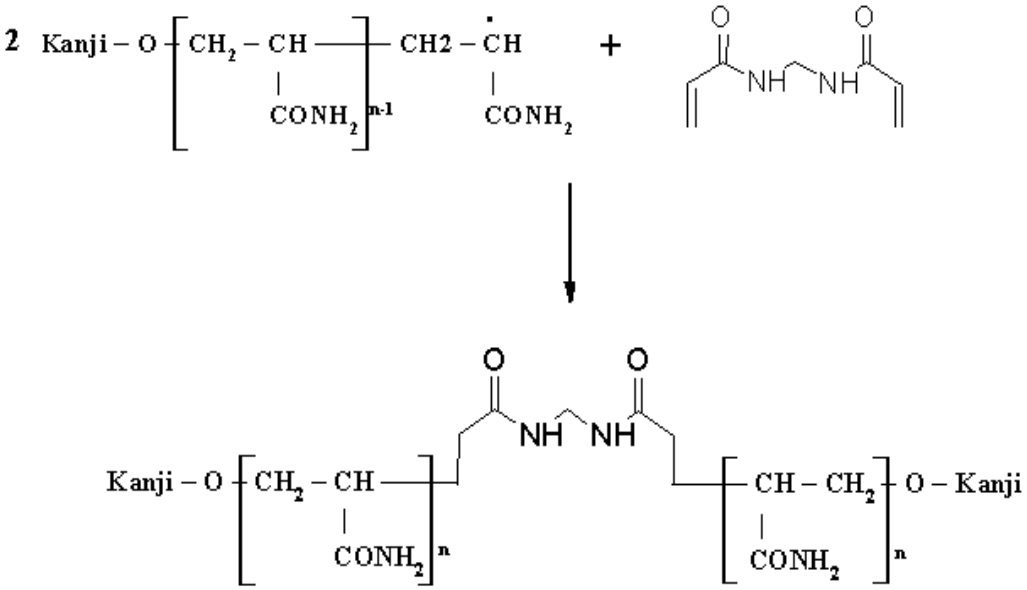


Perambatan rantai





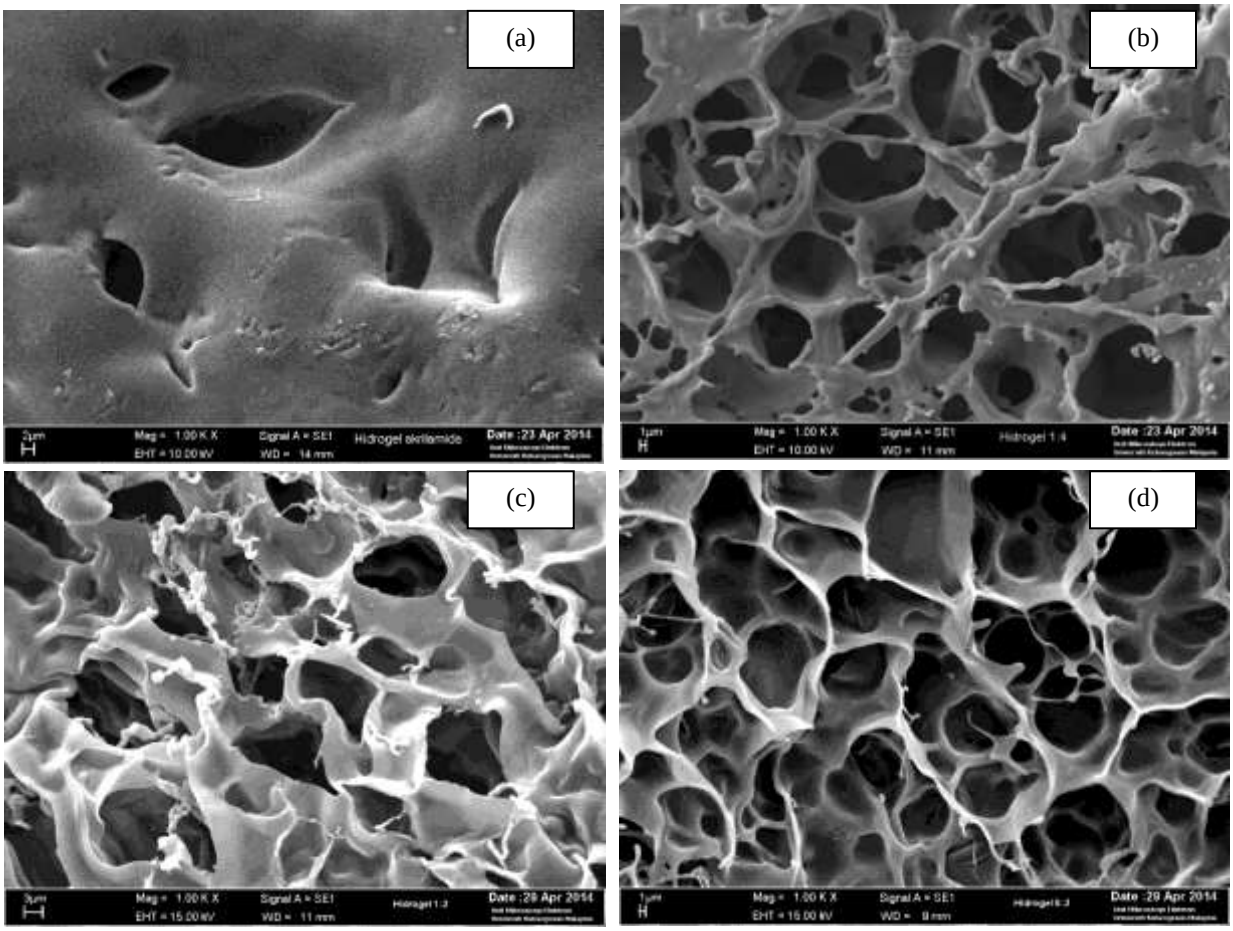
Penamatan rantai



Rajah 3. Cadangan tindak balas penghasilan hidrogel

Mikroskopi Pengimbas Elektron (SEM)

Dalam kajian ini, 4 jenis sampel hidrogel dengan nisbah yang berbeza yang telah dikeringkan secara pengeringan sejuk-beku telah dianalisis menggunakan SEM. Pengimbasan semua sampel telah ditetapkan pada 1,000 kali gandaan pembesaran dan mikrograf yang diambil seperti ditunjukkan dalam Rajah 4.



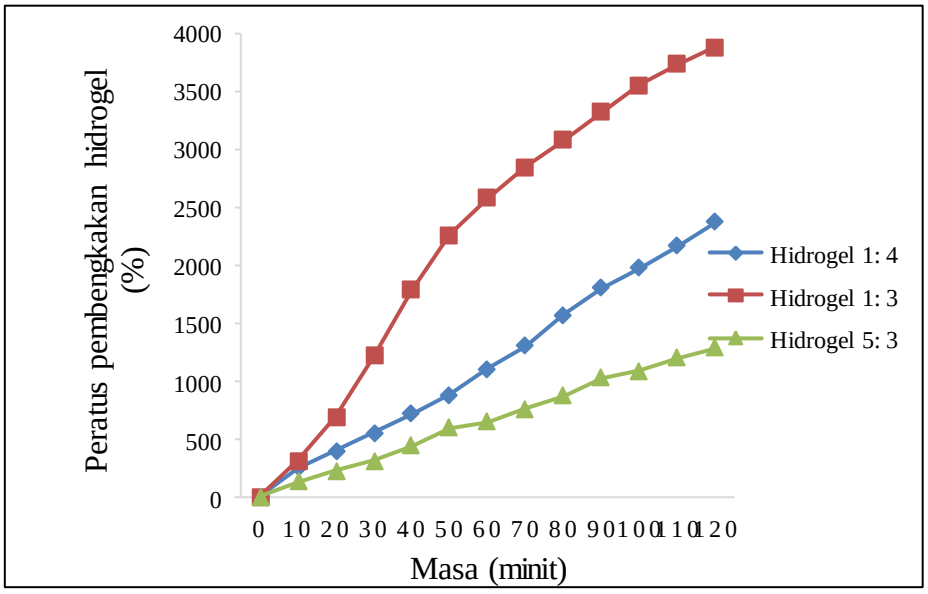
Rajah 4. Mikrograf bagi hidrogel dengan nisbah (a) 0:3, (b) 1:4, (c) 1:3 dan (d) 5:3 pada kuasa pembesaran 1000x

Perbandingan di antara mikrograf bagi sampel hidrogel (a), (b), (d) dan (d) jelas menunjukkan bahawa hidrogel 0:3 (a) mempunyai permukaan yang licin dan tidak poros. Ini membuktikan bahawa penambahan kanji ke dalam formulasi hidrogel dapat meningkatkan keporosan jaringan pada hidrogel [12].

Hidrogel 5: 3 (d) dengan kandungan kanji yang paling tinggi mempunyai banyak liang yang bersaiz kecil (13 –19 μm). Fenomena ini berlaku kerana penambahan kanji mengisi ruang antara rangkaian dan memadatkan lagi rangkaian taut-silang dalam hidrogel [13]. Dalam kata lain, darjah taut-silang yang tinggi dan rangkaian hidrogel yang tumpat akan mempunyai saiz poros yang kecil dan menghadkan ruang di dalam jaringan hidrogel. Berdasarkan mikrograf (c) hidrogel 1:3 mempunyai saiz liang yang lebih besar berbanding liang (d) hidrogel 1:4. Julat saiz bagi hidrogel 1:4 dan hidrogel 1: 3 adalah masing-masing di antara 11 – 22μm dan 10 – 26 μm.

Ujian pengembangan hidrogel

Berdasarkan kepada keputusan ujian pembengkakan yang ditunjukkan pada Rajah 5, hidrogel 1:3 mempunyai peratus pembengkakan paling tinggi iaitu 3881 % diikuti dengan hidrogel 1:4 sebanyak 2373 % dan seterusnya hidrogel 5:3 yang mencatatkan peratus pembengkakan paling rendah iaitu 1285 %.



Rajah 5. Graf peratus nisbah pengembangan hidrogel (%) bagi hidrogel 1:4, 1:3 dan 5:3 selama 2 jam

Hidrogel dengan kandungan kanji yang banyak akan meningkatkan sifat kebolehbasahan, sifat hidrofilik dan darjah pembengkakan [14]. Namun, darjah pembengkakan hidrogel bukan sahaja bergantung pada keadaan hidrogel dan media pembengkakan tetapi ia juga amat bergantung pada ketumpatan taut-silang hidrogel dan kepekatan bahan campur adun seperti kepekatan agen taut-silang dan kepekatan monomer [15].

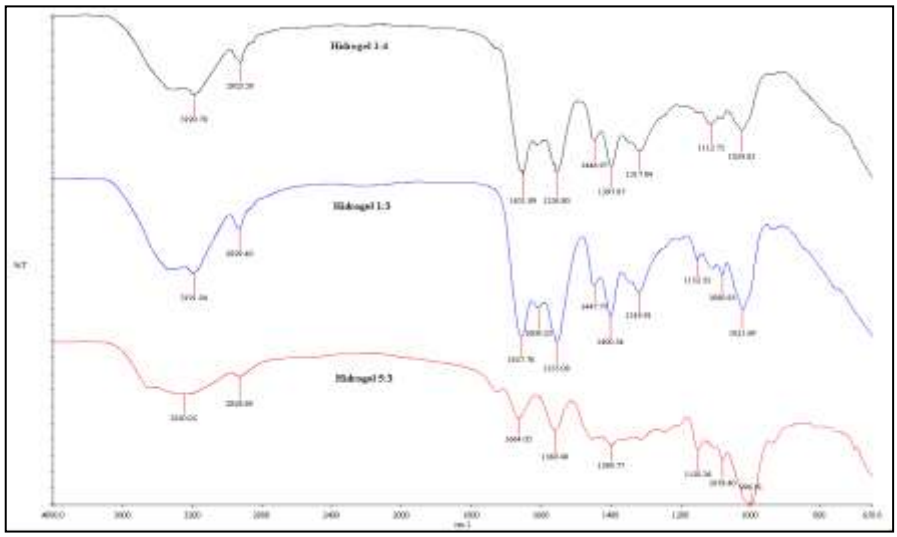
Dapat diperhatikan pada Rajah 5, hidrogel dengan kandungan kanji yang paling tinggi, 5: 3 mempunyai peratus pembengkakan yang paling rendah. Kandungan kanji yang tinggi dalam hidrogel mengakibatkan rangkaian hidrogel menjadi semakin tumpat. Ini menghadkan ruang di dalam jaringan hidrogel untuk mengembang [13]. Ruang yang terhadap ini secara langsung telah menghalang monomer AAm ataupun kanji untuk mengikat molekul air melalui ikatan hidrogen [15].

Hidrogel 1:4 pula mempunyai nisbah pembengkakan yang lebih rendah berbanding hidrogel 1:3. Hal ini berkaitan rapat dengan jumlah kepekatan komposisi campur-adun. Membandingkan hidrogel 1:3 dan 1:4, hidrogel 1:4 mempunyai kepekatan bahan campur-adun (kepekatanagen taut-silang, MBA dan monomer, AAm) yang lebih tinggi. Secara umumnya, agen taut-silang akan berada di antara rantai monomer untuk mentaut-silangkan rantai – rantai monomer tersebut. Maka, bilangan kumpulan hidrofilik yang tersedia untuk membentuk ikatan hidrogen dengan molekul air telah berkurang dan ini menyebabkan pembengkakan hidrogel 1:4 menjadi lebih rendah [16]. Selain itu, kepekatan monomer (AAm) yang lebih tinggi dalam hidrogel 1:4 memadatkan rangkaian polimer hidrogel dan air menjadi lebih sukar untuk meresap ke dalamnya [16]. Oleh itu, hidrogel 1:3 dengan jumlah kepekatan komposisi campur-adunyang lebih rendah mempunyai rangkaian yang tidak begitu padat. Rangkaian dengan ruang antaranya yang besar memudahkan pengikatan dengan molekul air berlaku dan peresapan air ke dalam rangkaian polimernya juga lebih mudah lalu nisbah pengembangan meningkat.

Analisis Spektrometer Inframerah Transformasi *Fourier*-Jumlah Pantulan Teratenuat (ATR-FTIR)

Rajah 6 menunjukkan spektrum ATR-FTIR bagi hidrogel yang disintesis dengan menggunakan nisbah kanji terhadap akrilamida yang berbeza. Puncak di antara 3400 – 3200 cm^{-1} terdapat pada ketiga – tiga spektrum yang mewakili kumpulan hidroksi pada kanji. Pempolimeran taut silang dikenal pasti telah berlaku berdasarkan kepada pembentukan ikatan C-O-C yang ditunjukkan pada frekuensi 1150 – 1100 cm^{-1}[17]. Puncak pada julat frekuensi

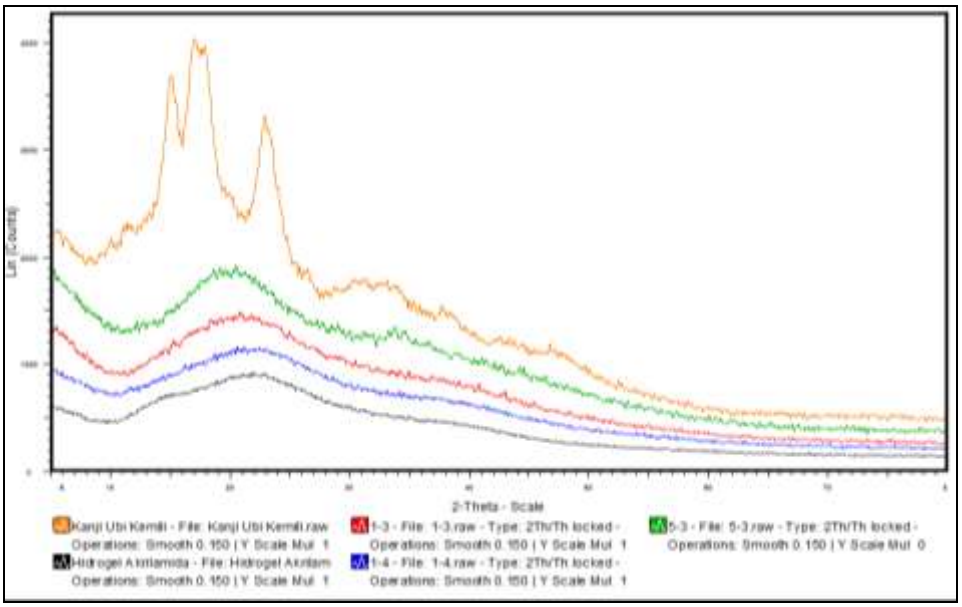
1000 – 800cm^{-1} juga telah hilang. Ini menandakan bahawa tindak balas pempolimeran antara kumpulan vinil pada monomer telah berlaku. [18].



Rajah 6. Perbandingan spektrum inframerah bagi hidrogel 1:4, hidrogel 1:3 dan hidrogel 5:3

Difraktometri Sinar-X (XRD)

Rajah 7 di bawah menunjukkan difraktogram pembelauan sinar-X bagi sampel kanji Ubi *Stemona curtisii*, hidrogel akrilamida dan hidrogel berkanji yang dihasil.



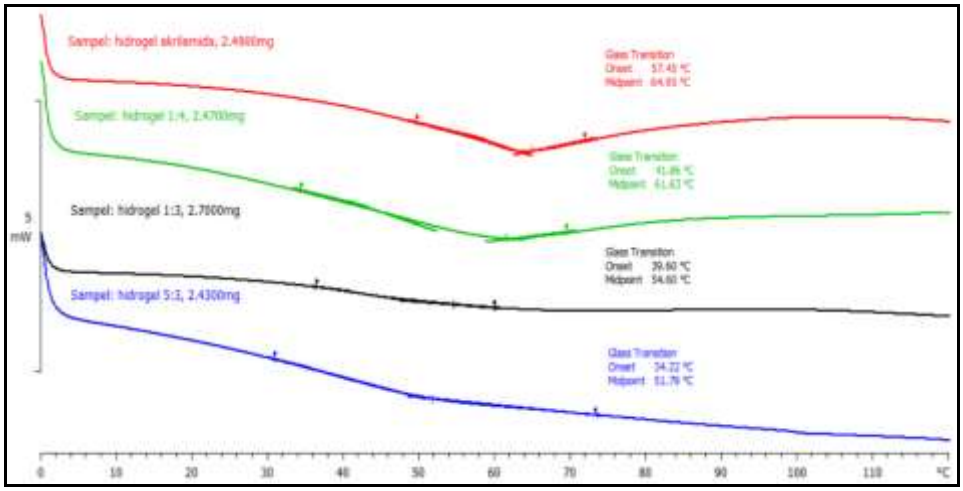
Rajah 7. Difraktogram pembelauan sinar-X sampel kanji, hidrogel akrilamida dan hidrogel berkanji yang dihasil

Berdasarkan Rajah 7, kanji Ubi *Stemona curtisi* menunjukkan sifat penghabluran dengan beberapa puncak keamatan yang tinggi pada belauan dengan skala 2θ 15˚, 17˚, 18˚ dan 23˚. Hal ini berlaku kerana disebabkan oleh kehadiran molekul berganda amilopektin di dalam struktur kanji yang boleh menghasilkan satu kawasan kristal jika molekul-molekul tersebut berada pada susunan selari antara satu sama lain manakala molekul amilosa hanya akan membentuk kelompok dan mewujudkan satu rantau tak berhablur yang membawa kepada sifat keamorfusan kanji [19, 20].

Berdasarkan kepada difraktogram pada Rajah 7, keempat-empat hidrogel menunjukkan sifat amorfus. Ini menunjukkan morfologi kanji telah berubah setelah proses pempolimeran/taut-silang untuk menghasilkan hidrogel berkanji. Puncak kanji yang tinggi pada belauan berskala 2θ 15˚, 17˚, 18˚ dan 23˚ tidak lagi wujud dalam difraktogram hidrogel. Menurut Bhattachary [21], hidrogel bersifat amorfus kerana taut silang dalam polimer hidrogel menghalang rangkaian daripada bersusun padat dalam orientasi berkala, rangkaian tidak dapat menggelongsor antara satu sama lain lalu tidak mempunyai sifat hablur tetapi menjana kekenyalan dalam hidrogel amorfus.

Kalorimeter Pengimbas Kebedaan (DSC)

Berdasarkan kepada Rajah 8 didapati bahawa setiap termogram sampel hanya terdapat nilai tunggal suhu peralihan kaca. Ini telah jelas menunjukkan bahawa semua bahan campur-adun yang digunakan untuk sintesis hidrogel adalah pada tahap kebolehcampuran yang baik. Menurut Diab [22] sistem polimer hidrogel yang terlarut campur dengan baik menunjukkan suhu peralihan kaca yang tunggal manakala jika suatu sistem itu tidak serasi akan mempunyai beberapa suhu peralihan kaca secara terasing yang mewakili setiap komponen dalam polimer hidrogel.



Rajah 8. Gabungan termogram DSC bagi hidrogel 0:3, hidrogel 1:4, hidrogel 1:3 dan hidrogel 5:3.

Jadual 3 menunjukkan suhu peralihan kaca bagi keempat-empat jenis hidrogel yang telah disintesis. Keputusan menunjukkan hidrogel kosong (0:3) mempunyai nilai T_g yang paling tinggi dan diikuti oleh hidrogel 1:4 (mempunyai kandungan kanji yang paling rendah), 1:3 (mempunyai kandungan kanji yang sederhana) dan 5:3 (mempunyai kandungan kanji yang paling tinggi). Ini telah menunjukkan bahawa kepekatan kandungan kanji mempengaruhi nilai T_g hidrogel yang dihasil. Semakin banyak kanji yang ditambahkan ke dalam sintesis hidrogel, semakin rendah nilai T_g hidrogel itu. Penurunan nilai T_g hidrogel ini berlaku disebabkan molekul air cenderung untuk mengikat pada molekul kanji dan menyebabkannya berfungsi sebagai pemplastik, maka hidrogel dengan kandungan kanji yang lebih tinggi akan mengalami penurunan nilai T_g akibat peningkatan sifat pemplastikan [17]. Hidrogel kosong pula mempunyai nilai T_g yang paling tinggi kerana ia tidak mempunyai kanji. Ketidakhadiran kanji menyebabkannya kurang sifat plastik dan mempamerkan nilai T_g yang lebih tinggi.

Kajian turut mencatatkan peningkatan penambahan monomer akrilamida dalam sintesis hidrogel meningkatkan nilai T_g hidrogel. Ini jelas dilihat daripada nilai T_g hidrogel 1:4 yang dihasil daripada paling banyak monomer adalah paling tinggi iaitu pada 65.0 ˚C. Peningkatan penambahan monomer (akrilamida) dapat meningkatkan nilai suhu T_g polimer hidrogel kerana ia menguatkan ikatan hidrogen antara rangkaian polimer lalu dapat menstabilkan polimer hidrogel [23]. Keputusan yang sama telah diperolehi oleh Painter [24] di mana mereka turut mencadangkan sifat ini sering dijumpai dalam adunan hidrogel kerana interaksi ikatan hidrogen.

Jadual 3. Suhu peralihan kaca bagi hidrogel yang berbeza komposisi bahan mula

Warna Termogram DSC	**Sampel**	**Suhu peralihan kaca hidrogel (˚C)**
Merah	Hidrogel 0 : 3	65.0
Hijau	Hidrogel 1 : 4	61.6
Hitam	Hidrogel 1 : 3	54.6
Biru	Hidrogel 5 : 3	51.8

Analisis Termogravimetrik (TGA)

Dalam kajian ini, analisis TGA dijalankan untuk mengetahui kestabilan/ketahanan hidrogel berasaskan kanji daripada Ubi *Stemona curtisii* terhadap haba. Data berkaitan dengan nilai peratus kehilangan jisim pada setiap peringkat, jumlah peratus kehilangan jisim dan peratus jisim yang masih ada pada suhu 600 ˚C dalam kanji Ubi *Stemona curtisii* dan setiap hidrogel yang disintesis telah disenaraikan dalam Jadual 4.

Jadual 4. Nilai peratus kehilangan jisim pada setiap peringkat, peratus kehilangan jisim maksima dan peratus jisim baki dalam kanji Ubi *Stemona curtisii* dan setiap hidrogel yang disintesis.

Sampel	**Peratus Kehilangan Jisim (%)**			**Peratus Kehilangan Jisim Maksima (%)**	**Peratus Jisim Baki (%)**
	Peringkat pertama (0 - 250 ˚C)	**Peringkat kedua (280 - 450 ˚C)**	**Peringkat ketiga (450 - 600 ˚C)**		
Kanji	10	76	-	-	-
Hidrogel 0: 3	9	59	11	79	21
Hidrogel 1: 4	7	44	23	74	26
Hidrogel 1: 3	7	47	18	72	28
Hidrogel 5: 3	12	38	19	69	31

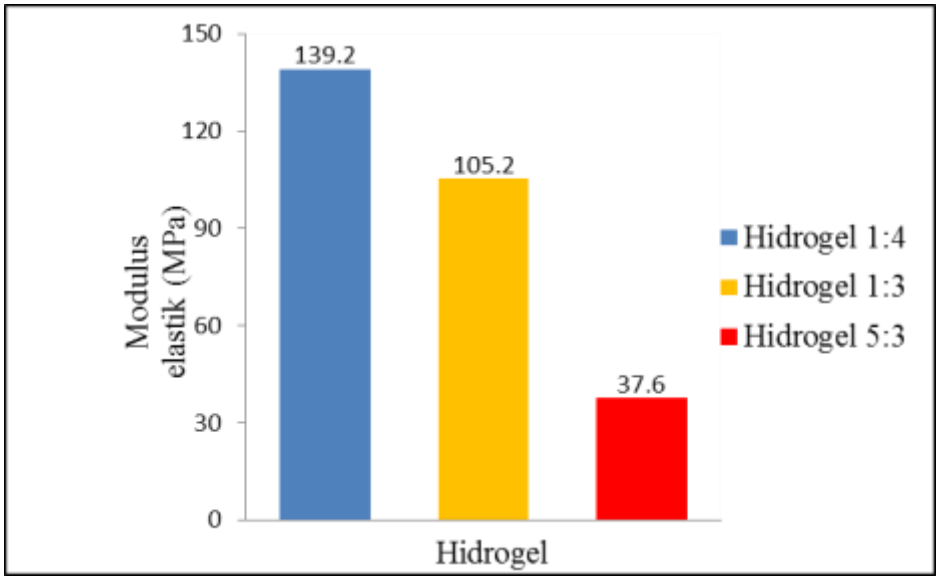
Peringkat pertama kehilangan jisim yang berlaku pada sekitar 0 – 250 ˚C boleh dikaitkan dengan penyejatan air yang terjerap secara fizikal atau kimia dalam semua sampel manakala peringkat penguraian yang lain adalah disebabkan oleh penguraian terma sampel [13, 25]. Secara keseluruhannya, semua hidrogel dengan kehadiran kanji mengalami peratus kehilangan jisim yang lebih rendah berbanding dengan hidrogel kosong. Hal ini kerana dalam hidrogel berkanji,atom hidrogen daripada kumpulan hidroksi primer dalam molekul kanji telah digantikan oleh monomer semasa perpautan-silang.Taut-silang antara monomer dan molekul kanji Ubi *Stemona curtisii* menghasilkan ikatan baru dan ikatan inilah yang menyebabkan hidrogel berkanji lebih stabil terhadap haba [17, 26].

Daripada keputusan kajian juga boleh dilihat hidrogel yang mempunyai lebih banyak kanji adalah lebih tahan haba dan mengalami peratus kehilangan jisim maksima yang lebih rendah. Hidrogel 5:3 (kandungan kanji paling tinggi) mempunyai jisim sampel yang paling tinggi pada suhu 600 ˚C diikuti oleh hidrogel 1:3 (kandungan kanji yang sederhana) dan hidrogel 1:4 (kandungan kanji paling rendah).Peratus jisim baki sampel-sampel tersebut pada suhu 600 ˚C adalah masing-masing 31, 28 dan 26 %. Kandungan kanji yang tinggi dalam hidrogel 5:3 menyebabkan rangkaiannya menjadi sangat padat dan mempunyai lebih banyak amilopektin (struktur rantai bercabang). Kandungan amilopektin mendorong kepada ketahanan sampel hidrogel terhadap haba kerana penguraiannya memerlukan suhu yang lebih tinggi berbanding rantai linear (amilosa) [17, 27].

Selain itu, tahap kestabilan/ketahanan sesuatu sampel terhadap haba juga berkait rapat dengan tahap penghabluran sampel itu. Peningkatan kandungan kanji dalam suatu sampel meningkatkan tahap penghabluran sampel dan meningkatkan tahap ketahanan sampel tersebut terhadap haba [28]. Oleh itu,semua hidrogel yang mempunyai kanji akan menunjukkan tahap ketahanan terhadap haba yang lebih tinggi berbanding hidrogel kosong [26].

Ujian tegangan hidrogel

Rajah 9 di bawah menunjukkan graf bar modulus elastik bagi setiap nisbah hydrogel yang telah disintesis. Berdasarkan Rajah 4.9, hidrogel 1:4 yang mempunyai kandungan kanji paling rendah telah menunjukkan nilai modulus elastik yang paling tinggi dan dikuti oleh hidrogel 1:3. Hidrogel 5:3 yang mengandungi berat kanji paling tinggi pula menunjukkan nilai modulus elastik dan tegasan tegangan yang paling rendah. Keputusan kajian menunjukkan tahap kekenyalan hidrogel menurun akibat peningkatan kandungan kanji (bahan asas) yang ditambah dalam sintesis hidrogel. Hal ini kerana penambahan kanji dalam hidrogel akrilamida menyebabkan sampel hidrogel itu menjadi lebih tegar. Hidrogel yang tegar menjejaskan kestabilan proses pemanjangannya kerana hidrogel yang tegar ini tidak akan terus memanjang untuk satu tempoh yang lama tetapi ia mudah putus. Maka, hidrogel yang mudah putus ini tidak bersifat elastik dan akan mempunyai nilai *Young's* modulus yang rendah [12]. Keputusan yang sama telah dilaporkan oleh [27]



Rajah 9. Graf bar modulus elastik bagi hidrogel dengan nisbah kanji : akrilamida 1 : 4, 1 : 3, 5 : 3.

Walau bagaimanapun, hidrogel berasaskan kanji daripada Ubi *Stemona curtisii* ini mempunyai potensi untuk diaplikasikan sebagai pembalut luka. Menurut laporan Gallagherdan [30] nilai kegagalan tegangan kulit adalah 34 MPa. Semua nilai modulus elastik hidrogel yang dihasilkan dalam kajian ini adalah lebih tinggi daripada nilai

kegagalan tegangan kulit. Oleh itu, hidrogel yang dihasilkan ini boleh digunakan untuk meliputi luka kerana tahap kekenyalannya yang tinggi boleh menahan tegasan geseran yang dan dapat menyerap tenaga tanpa pecah dan memberi kesan perlindungan terhadap luka [31].

Kesimpulan

Kajian yang dilakukan ini telah berjaya menghasilkan hidrogel berasaskan-kanji Ubi *Stemona curtisii* dengan menggunakan gelombang mikro. Penggunaan gelombang mikro membolehkan tindak balas berlaku pada kehadiran kepekatan bahan pemula yang lebih rendah dan lebih menjimatkan masa sintesis. Justeru, penghasilan hidrogel menggunakan kaedah gelombang mikro ini dilihat dapat dikomersilkan terutamanya di dalama bidang biobahan.

Penghargaan

Penulis ingin mengucapkan setinggi – tinggi penghargaan dan terima kasih kepada kakitangan makmal di Jabatan Kimia, Fakulti Sains dan Teknologi serta Universiti Kebangsaan Malaysia (FRGS/1/2014/ST01/UKM/03/1 dan PRGS/1/2014/TK04/UKM/03/1) di atas sokongan, bantuan dan bimbingan sepanjang tempoh kerja makmal dijalankan.

Rujukan

1. Hartmann, J. (1990). *Absorbent Polymer Technology*. The Netherlands: Elsevier Science Publishers B.V.
2. Burkert, S., Schmidt, T., Gohs, U., Dorschner, H. and Arndt, K. F. (2007). Cross-linking of poly(N-vinyl pyrrolidone) films by electron beam irradiation. *Radiation Physics and Chemistry* 76(8-9): 1324 – 1328.
3. Paulino, A. T., Guilherme, M. R., Reis, A.V., Campese, G. M., Muniz, E. C. and Nozaki, J. (2006). Removal of methylene blue dye from an aqueous media using superabsorbent hydrogel supported on modified polysaccharide. *Journal of Colloid and Interface Science* 301(1): 55 – 62.
4. Singh, V., Tiwari, A., Pandey, S. and Singh, S. K. (2006). Microwave-accelerated synthesis and characterization of potato starch-g-poly(acrylamide). *Starch - Stärke* 58(10): 536 – 543.
5. Yang, X. M., Liu, Q., Chen, X. L., Yu, F. and Zhu, Z. Y. (2008). Investigation of PVA/WS-chitosan hydrogels prepared by combined γ-irradiation and freeze-thawing. *Carbohydrate Polymers* 73(3): 401 – 408.
6. Zainura (2010). Galak tua (*Stemona*) – *Stemona tuberosa*. http://wannura.wordpress.com/2010/01/22 /galak-tua-stemona-stemona-tuberosa-lour/ [9 November 2013].
7. Zhao, W. M., Qin, G. W., Ye, Y., Xu, R. S. and Le, X. F. (1995). Bibenzyls from *Stemona tuberosa*. *Phytochemistry* 38(3): 711 – 713.
8. Pandey, M. and Amin, M. C. I. M. (2012). Accelerated preparation of novel bacterial cellulose/acrylamide-based hydrogel by microwave irradiation. *International Journal of Polymeric Materials and Polymeric Biomaterials* 62(7): 402 – 405.
9. Gulrez, S. K. H. and Al-Assaf, S. (2011). Hydrogels: Methods of preparation, characterisation and applications. Dlm. Carpi, P.A. (Ed.). *Progress in molecular and environmental bioengineering - from analysis and modeling to technology applications*, United Kingdom: InTech Europe: pp 646.
10. Dai, T., Qing, X., Wang, J., Shen, C. and Lu, Y. (2010). Interfacial polymerization to high-quality polyacrylamide/polyaniline composite hydrogels. *Composites Science and Technology* 70(3): 498 –503.
11. Zobel, H. F., Young, S. N. and Rocca, L.A. (1988). Starch gelatination: An X-ray diffraction study. *Cereal Chemistry* 65(6): 443 – 446.
12. Kenawy, E.-R., Kamoun, E. A., Mohy Eldin, M. S. and El-Meligy, M. A. (2013). Physically crosslinked poly(vinyl alcohol)-hydroxyethyl starch blend hydrogel membranes: Synthesis and characterization for biomedical applications. *Arabian Journal of Chemistry* 6(2): 1 – 9.
13. Abd El-Mohdy, H. L., Hegazy, E. A., El-Nesr, E. M. and El-Wahab, M. A. (2012). Synthesis, characterization and properties of radiation-induced starch/(EG-co-MAA) hydrogels. *Arabian Journal of Chemistry* 5: 1 – 9.
14. Li, A., Liu, R. and Wang, A. (2005). Preparation of starch-graft-poly(acrylamide)/attapulgite superabsorbent composite. *Journal of Applied Polymer Science* 98(3): 1351 – 1357.
15. Seddiki, N. and Aliouche, D. (2013). Synthesis, rheological behavior and swelling properties of copolymer hydrogels based on poly(N-isopropylacrylamide) with hydrophilic monomers. *Chemical Society of Ethiopia* 27(3): 447 – 457.
16. Isik, B. (1998). Swelling behavior of acrylamide-2-hydroxyethyl methacrylate hydrogels. *Turkey Journal of Chemistry* 24(2): 147 – 156.

17. Amin, M. C. I. M., Ahmad, N., Halib, N. and Ahmad, I. (2012). Synthesis and characterization of thermo- and pH-responsive bacterial cellulose/acrylic acid hydrogels for drug delivery. *Carbohydrate Polymers* 88(2): 465 – 473.
18. Zhao, Z., Li, Z., Xia, Q., Xi, H. and Lin, Y. (2008). Fast synthesis of temperature-sensitive PNIPAAm hydrogels by microwave irradiation. *European Polymer Journal* 44(4): 1217 –1224.
19. Blanche, S. and Sun, X. (2004). Physical characterization of starch extrudates as a function of melting transitions and extrusion conditions. *Advances in Polymer Technology* 23(4): 277 – 290.
20. Cheetham, N. W. H. and Tao, L. (1998). Solid state NMR studies on the structural and conformational properties of natural maize starches. *Carbohydrate Polymers* 36(4): 285 – 292.
21. Bhattachary, A., Rawlins, J. W. and Ray, P. (2009). *Polymer Grafting and Crosslinking*. United States of America: John Wiley & Sons Inc.
22. Diab, T., Biliaderis, C. G., Gerasopoulos, D. and Sfakiotakis, E. (2001). Physicochemical properties and application of pullulan edible films and coatings in fruit preservation. *Journal of the Science of Food and Agriculture* 2(81): 988 – 1000.
23. Xia, Y. Q., Guo, T. Y., Song, M. D., Zhang, B. H. and Zhang, B. L. (2005). Hemoglobin recognition by imprinting in semi-interpenetrating polymer network hydrogel based on polyacrylamide and chitosan. *Biomacromolecules* 6(5): 2601 – 2606.
24. Painter, P. C., Graf, J. F. and Coleman, M. M. (1991). Effect of hydrogen bonding on the enthalpy of mixing and the composition dependence of the glass transition temperature in polymer blends. *Macromolecules* 24(20): 5630 – 5638.
25. Bursali, E. A., Coskun, S., Kizil, M. and Yurdakoc, M. (2011). Synthesis, characterization and in vitro antimicrobial activities of boron/starch/polyvinyl alcohol hydrogels. *Carbohydrate Polymers* 83(3): 1377 – 1383.
26. Vakili, M. R. and Rahneshin, N. (2013). Synthesis and characterization of novel stimuli-responsive hydrogels based in starch and l-aspartis acid. *Carbohydrate Polymers* 9(8): 1624 – 1630.
27. Liu, X., Wang, Y., Yu, L., Tong, Z., Chen, L., Liu, H. and Li, X. (2013). Thermal degradation and stability of starch under different processing conditions. *Starch - Stärke* 65(1-2): 48 – 60.
28. French, D. (1972). Fine structure of starch and its relationship to the organization or starch granules. *Journal of Japanese Society for Starch Science* 19(1): 8 – 25.
29. Razzak, M. T., Darwis, D. and Zainuddin, S. (2001). Irradiation of polyvinyl alcohol and polyvinyl pyrrolidone blended hydrogel for wound dressing. *Radiation Physics and Chemistry* 62(1): 107 – 113.
30. Gallagher, A. J., Anniadh, A. N., Bruyere, K., Otténio, M., Xie, H. and Gilchrist, M. D. (2012). Dynamic tensile properties ofhuman skin. *International IRCOBI Conference on the Biomechanics of Injury*, pp 494 – 502.
31. Kunal, P., Banthia, A. K. and Majumdar, D. K. (2006). Preparation of transparent starch based hydrogel membrane with potential application as wound dressing. *Trends in Biomaterials and Artificial Organs* 20(1): 59 – 67.

MALAYSIAN JOURNAL OF ANALYTICAL SCIENCES
Published by The Malaysian Analytical Sciences Society
ISSN 1394 - 2506

MODIFICATION OF TITANIUM DIOXIDE NANOPARTICLES WITH COPPER OXIDE CO-CATALYST FOR PHOTOCATALYTIC DEGRADATION OF 2,4-DICHLOROPHENOXYACETIC ACID

(Nanozarah Titanium Dioksida Terubahsuai Ko–Mangkin Kobalt Oksida untuk Degradasi Asid 2,4-diklorofenoksiasetik)

Leny Yuliati[1]*, Wai Ruu Siah[1], Nur Azmina Roslan[2], Mustaffa Shamsuddin[2], Hendrik O. Lintang[1]

[1]*Centre for Sustainable Nanomaterials, Ibnu Sina Institute for Scientific and Industrial Research*
[2]*Department of Chemistry, Faculty of Science*
Universiti Teknologi Malaysia, 81310 UTM Johor Bahru, Johor, Malaysia

**Corresponding author: leny@ibnusina.utm.my*

Received: 9 December 2014; Accepted: 3 January 2016

Abstract

2,4-dichlorophenoxyacetic acid (2,4-D) is a common herbicide that has been used widely. Due to its excessive usage, the 2,4-D herbicides can cause contamination over agricultural land and water bodies. In the present work, a simple impregnation method was used to modify the commercial titanium dioxide (P25 TiO_2) nanoparticles with the copper oxide. The prepared samples were characterized by X-ray Diffraction (XRD), reflectance UV-visible and fluorescence spectroscopies. It was observed that the incorporation of copper oxide did not significantly affect the crystal structure of P25 TiO_2. On the other hand, the presence of copper oxide was confirmed by reflectance UV-visible and fluorescence spectroscopies. The activity of the prepared sample was evaluated for photocatalytic removal of the 2,4-D. The photocatalytic activity of the TiO_2 increased with the increase of copper oxide loading up to 0.5 mol%. Unfortunately, the higher loading amount of copper oxide resulted in the lower photocatalytic activity. This study suggested that the higher photocatalytic activities obtained on the low loading samples were due to the lower electron-hole recombination.

Keywords: P25 TiO_2, copper oxide, impregnation, photocatalyst, 2,4-D herbicide

Abstrak

Asid 2,4-diklorofenoksiasetik (2,4-D) adalah herbisid biasa yang telah digunakan secara meluas. Oleh kerana penggunaan yang berlebihan, herbisid 2,4-D boleh menyebabkan pencemaran di kawasan pertanian dan sistem air. Dalam kajian ini, satu kaedah pengisitepuan yang mudah telah digunakan untuk mengubahsuai nanozarah titanium dioksida komersial (P25 TiO_2) dengan kuprum oksida. Sampel yang disediakan telah dicirikan dengan XRD, spektroskopi pantulan serakan ultra lembayung-cahaya nampak, dan spektroskopi pendarfluor. Didapati pengubahsuaian P25 TiO_2 dengan kuprum oksida tidak memberi kesan yang signifikan kepada struktur kristal P25 TiO_2. Sebaliknya, kehadiran kuprum oksida telah disahkan oleh spektroskopi pantulan serakan ultra lembayung-cahaya nampak. Aktiviti sampel telah diuji untuk penyingkiran 2,4-D. Aktiviti fotomangkin TiO_2 meningkat dengan peningkatan jumlah kuprum oksida kepada 0.5 mol%. Malangnya, jumlah kuprum oksida yang lebih tinggi menghasilkan aktiviti fotomangkin yang lebih rendah. Kajian ini mencadangkan bahawa aktiviti fotomangkin yang tinggi diperolehi pada sampel loading rendah adalah disebabkan oleh penggabungan elektron-lubang yang lebih rendah

Kata kunci: P25 TiO_2, kuprum oksida, pengisitepuan, fotomangkin, 2,4-D herbisid

Introduction

The 2,4-dichlorophenoxyacetic acid (2,4-D) is one of the most used herbicides in the world and has been used since the 1940s. The 2,4-D is used widely to control broadleaf weeds in a variety of settings from crops, rights-of-way, lawns, forests to aquatic settings. In 1986, the International Agency for Cancer Research (IARC) classified the chlorophenoxy herbicides as a Group 2B (possible) carcinogen. Since then, various studies have been done on the toxicity and carcinogenicity of the 2,4-D. Recently, the 2,4-D epidemiology literature has been qualitatively reviewed [1]. Even though no convincing evidence for any chronic adverse effect of 2,4-D in human, studies in the removals of the 2,4-D in order to prevent the negative effects of the 2,4-D towards human and environment are still in progress.

One of the simple methods to remove the 2,4-D from water is by adsorption process. Some adsorbents have been reported to give good performance to adsorb the 2,4-D, such as the layered double hydroxides (LDH) [2 –5] and mesoporous materials [6] due to the large surface area, high anion capacity, and good thermal stability. However, rather than removing the 2,4-D by an adsorption process, degradation of the 2,4-D would be a great advantage to solve the environment problems. Degradation of the 2,4-D could be achieved by introducing the electrochemical assistance to a micobiological reduction system [7], and photooxidation via Fenton reaction and in the presence of strong oxidant such as hydrogen peroxide [8]. However, from the point of view of sustainability and environmentally safe process, photocatalytic reaction would be the promising method to degrade the 2,4-D herbicide [9 – 13]. Some studies also reported the combined method to degrade 2,4-D by the photocatalytic reactions with the use of strong oxidants and microwave [9, 10].

In general, photocatalytic removal of environmental pollutants has been a topic of great interest over the years [14]. One of the most widely used materials for photocatalytic degradation of environmental pollutants is titanium dioxide (TiO_2). As a photocatalyst, TiO_2 has a range of useful features, including high photocatalytic activity, stability, low toxicity, ready availability and low cost [15]. While TiO_2 is one of the most active catalysts for the degradation of a wide range of organic compounds, its catalytic activity should be further improved. Hence, there have been a great number of studies to modify the TiO_2 based photocatalysts. It has been reported that the TiO_2 bound with TiO_2 sol with the help of polymeric bonds showed better photocatalytic activity for degradation of 2,4-D than the unmodified TiO_2, owing to the better distributions of photons [11]. Another study reported that the addition of reduced graphene oxide and $CuInS_2$ on the TiO_2 improved its activity for degradation of the 2,4-D [12]. The addition of Ag/reduced graphene oxide was also reported increasing the activity of TiO_2 for the 2,4-D degradation [13]. The improved activity was closely related to the effective carriers separation and large adsorption capacity for the 2,4-D [12, 13].

While several studies have been reported to modify TiO_2 with noble metals, transition metal oxides and non-metal ions [15-18], in particular, it has been shown that transition metal oxides such as copper oxide have the potential of enhancing the photocatalytic activity of TiO_2 [19 – 21]. When applied to TiO_2 on the optimal composition, phase and size, these transition metal oxide nanoparticles can act as effective co-catalysts that improve the efficiency of TiO_2 photocatalysis. In the present work, a simple impregnation method was used to grow copper oxide nanoparticles on the surface of commercial P25 TiO_2 particles. The amount of copper incorporated on the surface of the P25 TiO_2 particles was varied in the range of 0.1 to 5 mol%. The effect of Cu loading on the photocatalytic activity of TiO_2 to degrade the 2,4-D was investigated.

Materials and Methods

Preparation of photocatalysts

P25 TiO_2 (Evonik) and copper(II) nitrate trihydrate (Aldrich, 99 – 104%) were used as received without any treatments. The required amount of copper(II) nitrate trihydrate was dissolved into 20 ml of distilled water. Then, the P25 TiO_2 (1 g) was dispersed in the copper nitrate solution by sonicating the mixture for 10 minutes. Under vigorous stirring, the resultant mixture was heated at 80 °C until the solvent was removed. The dried mixture was ground to a fine powder and calcined at 500 °C for 4 hours. The resultant powder was ground and stored under ambient conditions. The samples were labeled as *x* mol% Cu/P25 TiO_2, with *x* showed the ratio of Cu to Ti (mol%) and varied in the range of 0.1 – 5 mol%. For comparison, the P25 TiO_2 was also treated in the same manner to the samples, except for the addition of the copper(II) nitrate trihydrate.

Characterizations

X-ray Diffraction (XRD, Bruker AXS Diffrac plus release 2000) was used to identify the structure of the prepared photocatalysts. The optical properties of the samples were analyzed by an Avantes spectrophotometer AvaSpec-ULS2048 using a reflection probe holder with angle of 45° and PTFE-coated white material as the reference sample. The emission spectra were measured at room temperature on a Fluorescence Spectroscopy JASCO FP-8500. The spectra were monitored at excitation wavelength of 218 nm. The morphology and particle size of the samples were investigated by a transmission electron microscopy (TEM, JEM-2100) at an accelerating voltage of 200 kV. The sample was dispersed well in ethanol and then, put on a carbon-coated copper grid.

Photocatalytic activity test

The prepared samples were evaluated for removal of 2,4-D at room temperature under UV light irradiation. Prior to the irradiation, the sample (50 mg) was dispersed in 2,4-D solution (50 mL, 0.5 mM) and stirred in the dark condition for 1 hour to achieve the adsorption-desorption equilibrium. The reaction was carried out for 1 hour under irradiation by a 200 W Xe-Hg lamp, which light intensity was 15 mW cm^{-2} and it was equipped with an IR cut off filter. The remaining amount of 2,4-D after each reaction was determined by UV-Visible spectrophotometer using a Thermo Scientific Genesys 10S. The monitored wavelength was 283 nm. The percentage of 2,4-D removal was then calculated from the ratio of concentrations between the reacted and the initial 2,4-D.

Results and Discussion

Properties of Cu/P25 TiO_2 samples

Figure 1 shows the XRD patterns of P25 TiO_2 and the prepared Cu/P25 TiO_2 samples. All samples showed the diffraction peaks at 2θ of 25.30 and 27.43°, corresponding to the (101) plane of anatase TiO_2 and (110) plane of rutile TiO_2, respectively. These XRD patterns clearly suggested the presence of both anatase and rutile phases in the samples. However, no appreciable diffraction peak of copper oxide phase was observed on all of the Cu/P25 TiO_2 samples. This was mostly likely due to the small amount of copper oxide present in the sample. In addition, a high degree of dispersion of copper oxide on the TiO_2 support would result in the small particle size of the metal oxide, which would be beyond the detection limit of XRD.

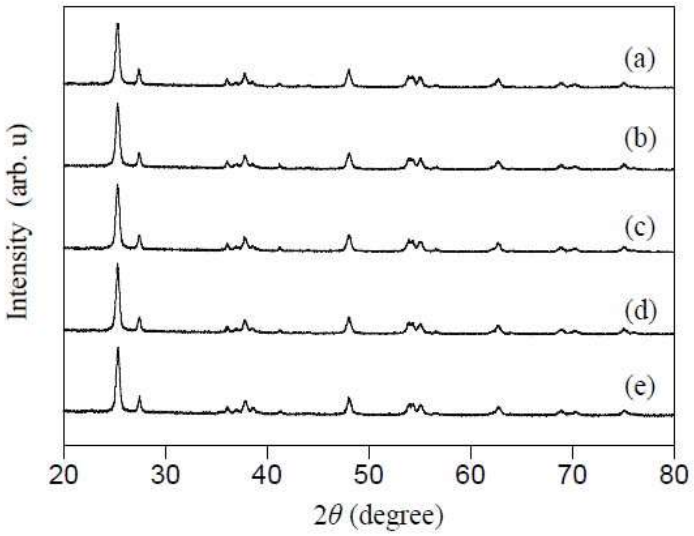


Figure 1. XRD patterns of (a) P25 TiO_2, (b) *0.1* mol% Cu/P25 TiO_2, (c) *0.5* mol% Cu/P25 TiO_2, (d) *1* mol% Cu/P25 TiO_2, and (e) *5* mol% Cu/P25 TiO_2 samples.

As shown in Figure 1, the XRD patterns of the Cu/P25 TiO_2 samples were very similar to that of the P25 TiO_2 sample. This result showed that the incorporation of copper oxide did not affect significantly the crystal structure of P25 TiO_2. Table 1 shows the crystallite size of anatase and the anatase to rutile ratio of the P25 TiO_2 and the prepared Cu/P25 TiO_2 samples. The crystallite size for anatase and rutile phase was determined by a Scherrer equation as shown in Equation 1, using the most intense peak of anatase (101) around 2θ of 25.3° and rutile (110) around 2θ of 27.4°, respectively.

$$t = \frac{K\lambda}{\beta\cos\theta} \tag{1}$$

where t is the average crystallite size in nm, while K is dimensionless shapes factor generally taken as 0.89, λ is the wavelength of the X-ray equals to 1.542 Å, β is full width at half maximum (FWHM) at 2θ of 25.3 or 27.4° and θ is Bragg's angle. The anatase to rutile ratio was also calculated based on the intensity of the most intense peaks at around 2θ of 25.3 and 27.4° for anatase (101) and rutile (110), respectively, as shown in Equation 2.

$$A(\%) = \frac{100 \times I_A}{I_A + 1.265 \times I_R} \tag{2}$$

where *A(%)* is the percentage of anatase, I_A and I_R correspond to the intensity of the anatase (101) and rutile (110) reflections, respectively.

As listed in Table 1, the crystallite size of P25 TiO_2 for both anatase and rutile phase was only slightly increased upon the addition of copper oxide. The average crystallite size for anatase phase was in the range of 17-21 nm, while for rutile phase was in the range of 60-72 nm. In addition, the anatase to rutile phase ratio of P25 TiO_2 likewise was not much affected by the incorporation of copper oxide. In order to support the crystallite size data, TEM images for the P25 TiO_2 and 0.5 mol% Cu/P25 TiO_2 are shown in Figure 2. The P25 TiO_2 showed irregular polyhedral shape nanoparticles (Fig. 2(a)). Most of the particles have size in the range of 15-25 nm due to the presence of anatase phase, while larger particles in the range of 50-70 nm were due to the presence of rutile phase. On the other hand, Figure 2(b) showed that no remarkable change in morphology and particle size could be observed on the 0.5 mol% Cu/P25 TiO_2. These results are in good agreement with the calculated average crystallite size from the XRD patterns shown in Table 1.

Table 1. Crystallite size and anatase to rutile ratio for P25 TiO_2 and Cu/P25 TiO_2 samples

Entry	Sample	Crystallite size (nm)[a]		Anatase to rutile ratio (%)[b]
		Anatase	Rutile	
1	P25 TiO_2	17.1	60.2	72:28
2	*0.1* mol% Cu/P25 TiO_2	18.1	67.8	74:26
3	0.5 mol% Cu/P25 TiO_2	18.5	71.9	74:26
4	*1* mol% Cu/P25 TiO_2	18.7	59.9	76:24
5	*5* mol% Cu/P25 TiO_2	20.3	62.0	74:26

[a]Estimated by the Scherrer equation shown in the Eq. 1.
[b]Estimated by the formula shown in the Eq. 2.

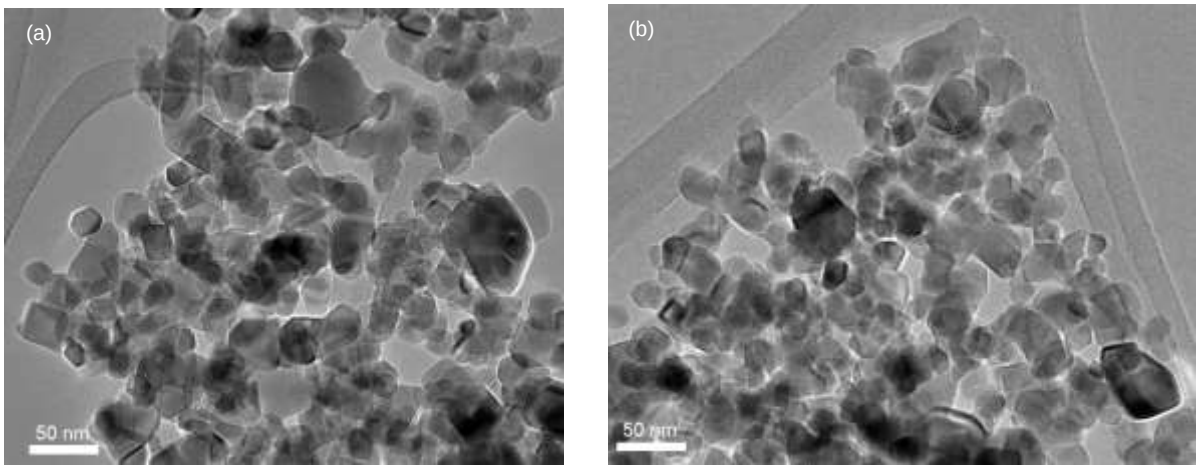


Figure 2. TEM images of (a) P25 TiO_2 and (b) *0.5* mol% Cu/P25 TiO_2 samples.

Figure 3 shows the reflectance UV-Vis absorption spectra of the P25 TiO_2 and Cu/P25 TiO_2 samples. The unmodified P25 TiO_2 sample has white colour as can be reflected in its UV-Vis absorption spectrum that displayed very low absorption intensity in the visible region of the spectrum (Fig. 3(a)). The addition of copper oxide resulted in the colour change from white to green. The colour became darker with the increase of the copper oxide loading. These changes could be observed in Figure 2, in which the Cu/P25 TiO_2 samples gave additional absorption in the visible light region and the absorbance increased with the increase of the copper oxide loading amount. The absorbance in the visible light region would be originated from the d-d transitions of the Cu^{2+} system [19], which were present on the surface of copper oxide modified TiO_2. While the Cu/P25 TiO_2 samples with low loadings of copper oxide did not much influence the band gap of the TiO_2, sample with high loading 5 mol% Cu/P25 TiO_2 slightly shifted the band edge absorption of P25 TiO_2 to longer wavelength. The shift indicated that some copper metal ions might alter the band gap of TiO_2 [16, 17].

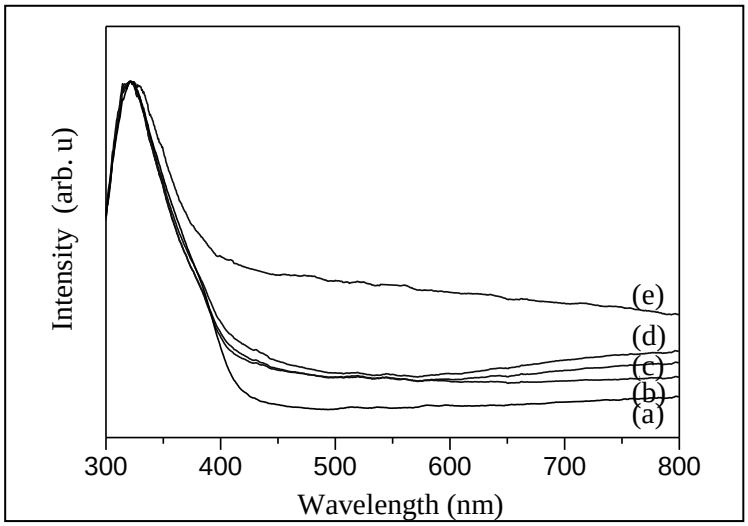


Figure 3. Normalized reflectance UV-Visible spectra of (a) P25 TiO_2, (b) *0.1* mol% Cu/P25 TiO_2, (c) *0.5* mol% Cu/P25 TiO_2, (d) *1* mol% Cu/P25 TiO_2, and (e) 5 mol% Cu/P25 TiO_2 samples

In order to study the interaction between the P25 TiO_2 and the copper oxide, the emission spectra of the samples were measured at the excitation of P25 TiO_2, which was at 218 nm. Figure 4 shows the emission spectra of P25 TiO_2 and the Cu/P25 TiO_2 samples. It was obvious that the emission intensity of P25 TiO_2 was reduced with the addition of copper oxide. The emission intensity was further reduced with the further increase of the copper oxide loading. This result clearly showed that there were interactions between P25 TiO_2 and the added copper oxide. Since emission intensity can be corresponded to the electron-hole recombination, the decreased emission intensity can be assigned to the suppression of electron-hole recombination.

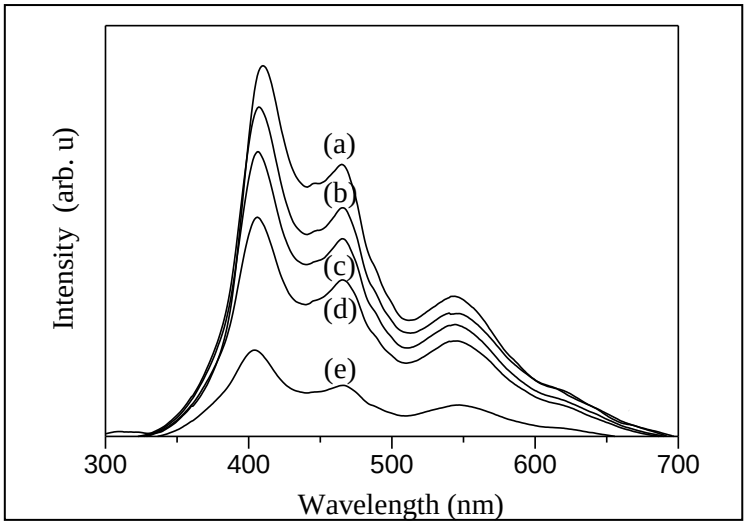


Figure 4. Emission spectra of (a) P25 TiO_2, (b) *0.1* mol% Cu/P25 TiO_2, (c) *0.5* mol% Cu/P25 TiO_2, (d) *1* mol% Cu/P25 TiO_2, and (e) *5* mol% Cu/P25 TiO_2 samples, monitored at excitation wavelength of 218 nm

As discussed previously, copper ions might alter the band gap energy of P25 TiO_2. Therefore, copper oxide might act as the co-catalyst to trap electron, thus enhancing the charge separation in the P25 TiO_2 that would lead to the enhanced activity. However, if the amount of copper oxide was too high, it would reduce the electrons in the conduction band of the P25 TiO_2 that might reduce the efficiency. Moreover, the large amount of copper oxide might also block the active sites of the P25 TiO_2 and reduce the photocatalytic activity. In other words, there would be an optimum amount of copper oxide that would give the optimum activity, which would be explained in the following part.

Photocatalytic activities of Cu/P25 TiO_2 samples

Figure 5 shows the photocatalytic removal of 2,4-D on the P25 TiO_2 and Cu/P25 TiO_2. It can be clearly shown that after 1 hour reaction, the photocatalytic activity of TiO_2 increased from 48.3 to 59.4 % with the increase of copper oxide loading up to 0.5 mol%. Unfortunately, the higher loading amount of copper oxide resulted in the lower photocatalytic activity. When the loading amount was 5 mol%, the activity decreased to 25.8 %. This result clearly suggested that the small amount of copper oxide, which was 0.5 mol%, was the optimum amount in this study to give the highest activity for the Cu/P25 TiO_2. The higher photocatalytic activity would be originated from the lower electron-hole recombination. On the other hand, the high loading amount of copper oxide might reduce the electrons in the conduction band of P25 TiO_2 or might block the active surface of P25 TiO_2, thus reduced the photocatalytic activity. Therefore, the optimum amount of copper oxide that would result in the optimum activity would be related to the optimum electron-hole separation, without reducing electrons in the conduction band of P25 TiO_2 and/or blocking active sites of the TiO_2. Similar results have been reported elsewhere [19 – 21]. The high amount of copper oxide may give masking effect on the P25 TiO_2, which prevented the UV light source to reach the active sites of TiO_2.

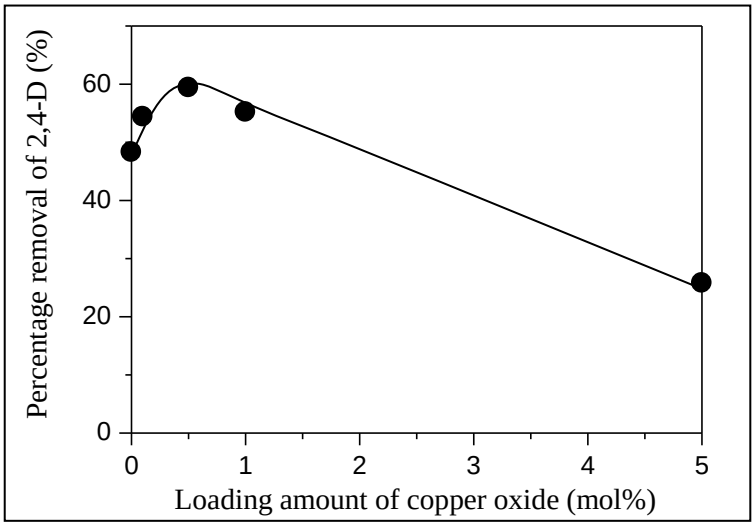


Figure 5. Photocatalytic removal of 2,4-D herbicide on the P25 TiO_2 and Cu/P25 TiO_2 samples.

Conclusion

The Cu/P25 TiO_2 samples were prepared successfully by an impregnation method. The addition of copper oxide did not much affect the crystallite size and the crystal phase of the P25 TiO_2. On the other hand, the addition of copper oxide increased the visible light absorption and slightly altered the band edge absorption of P25 TiO_2. Copper oxide also reduced the emission intensity, suggesting that optimum amount of copper oxide might act as good co-catalyst to trap electros, thus suppress the electron-hole recombination. The 0.5 mol% was found to be the optimum amount of copper oxide that enhance the activity of P25 TiO_2 for the photocatalytic removal of 2,4-D herbicide.

Acknowledgement

The research leading to these results has received funding from the European Union Seventh Framework Program (EU-FP7) under 4G-PHOTOCAT grant (agreement no.: 309636). This work has been also financially supported by the Ministry of Higher Education (MOHE) and Universiti Teknologi Malaysia (UTM, Malaysia) through the international contract matching grant (cost center code: R.J130000.7626.4C035).

References

1. Burns, C. J., and Swaen, G. M. H. (2012). Review of 2,4-Dichlorophenoxyacetic Acid (2,4-D) Biomonitoring and Epidemiology. *Critical Reviews in Toxicology*, 42 (9): 768 - 786.
2. Legrouri, A., Lakraimi, M., Barroug, A., De Roy, A. and Besse, J. (2005). Removal of the Herbicide 2,4-Dichlo-rophenoxyacetate from Water to Zinc–Aluminium–Chloride Layered Double Hydroxides, *Water Research*, 39 (15): 3441 - 3448.
3. Chao, Y.-F., Chen, P.-C. and Wang, S.-L. (2008). Adsorption of 2,4-D on Mg/Al-NO_3 Layered Double Hydroxides with Varying Layer Charge Density, *Applied Clay Science*, 40 (1-4): 193 - 200.
4. Chao, Y. F., Lee, J. J. and Wang, S. L. (2009). Preferential Adsorption of 2,4-Dichlorophenoxyacetate from Associated Binary-Solute Aqueous Systems by Mg/Al-NO_3 Layered Double Hydroxides with Different Nitrate Orientations, *Journal of Hazardous Materials*, 165 (1-3): 846 - 852.
5. Nejati, K., Davary, S. and Saati, M. (2013). Study of 2,4-Dichlorophenoxyacetic Acid (2,4-D) Removal by Cu-Fe-Layered Double Hydroxide from Aqueous Solution. *Applied Surface Science*, 280: 67-73.
6. Momcilovic, M. Z., Randelovic, M. S., Zarubica, A. R., Onjia, A. E., Kokunešoski, M., and Matovic, B. Z. (2013). SBA-15 Templated Mesoporous Carbons for 2,4-Dichlorophenoxyacetic Acid Removal. *Chemical Engineering Journal, 220: 276 - 283.*

7. Zhang, J. L., Cao, Z.P., Zhang, H.W., Zhao, L. M., Sun, X. D. and Mei, F. (2013). Degradation Characteristics of 2,4-Dichlorophenoxyacetic Acid in Electro-Biological System. *Journal of Hazardous Materials*, 262: 137 - 142.
8. Kwan, C. Y. and Chu, W. (2004). A Study of the Reaction Mechanisms of the Degradation of 2,4-Dichlorophenoxyacetic Acid by Oxalate-Mediated Photooxidation. *Water Research*, 38 (19): 4213 –4221.
9. Pei, C. C. and Chu, W. (2013). The Photocatalyic Degradation and Modeling of 2,4-Dichlorophenoxyacetic Acid by Bismuth Tungstate/Peroxide. *Chemical Engineering Journal*, 223: 665 - 669.
10. Lee, H., Park, S.H., Park,Y.-K., Kim, S.-J., Seo, S.-G., Ki, S.J. and Jung, S.-C. (2014). Photocatalytic Reactions of 2,4-Dichlorophenoxyacetic Acid using a Microwave-Assisted Photocatalysis System. *Chemical Engineering Journal*. 278: 259 - 264.
11. Vega, A. A., Imoberdorf, G. E. and Mohseni, M. (2011). Photocatalytic Degradation of 2,4-Dichlorophenoxy acetic Acid in a Fluidized Bed Photoreactor with Composite Template-Free TiO_2 Photocatalyst. *Applied Catalysis A: General*, 405 (1-2): 120 -128.
12. Liu, X., Tang, Y., Luo, S., Wang, Y., Zhang, X., Chen, Y. and Liu, C. (2013). Reduced Graphene Oxide and $CuInS_2$ Co-Decorated TiO_2 Nanotube Arrays for Efficient Removal of Herbicide 2,4-Dichlorophenoxyacetic Acid from Water. *Journal of Photochemistry and Photobiology A: Chemistry*, 262: 22 - 27.
13. Tang, Y., Luo, S., Teng, Y., Liu, C., Xu, X., Zhang, X. and Chen, L. (2012). Efficient Removal of Herbicide 2,4-Dichlorophenoxyacetic Acid from Water using Ag/Reduced Graphene Oxide Co-Decorated TiO_2 Nanotube Arrays. *Journal of Hazardous Materials*, 241-242: 323 - 330.
14. Malato, S., Fernández-Ibáñez, P., Maldonado, M. I., Blanco, J. and Gernjak, W. (2009). Decontamination and Disinfection of Water by Solar Photocatalysis: Recent Overview and Trends. *Catalysis Today*, 147 (1): 1-59.
15. Teh, C. M. and Mohamed, A. R. (2011). Roles of Titanium Dioxide and Ion-doped Titanium Dioxide on Photocatalytic Degradation of Organic Pollutants (Phenolic Compounds and Dyes) in Aqueous Solutions: A Review. *Journal of Alloys and Compounds*, 509 (5): 1648 - 1660.
16. Choi, W., Termin, A. and Hoffmann, M. R. (1994). The Role of Metal Ion Dopants in Quantum-Sized TiO_2: Correlation etween Photoreactivity and Charge Carrier Recombination Dynamics. *The Journal of Physical Chemistry*, 98 (51): 13669 - 13679.
17. Di Paola, A., Marcì, G., Palmisano, L., Schiavello, M., Uosaki, K., Ikeda, S. and Ohtani, B. (2001). Preparation of Polycrystalline TiO_2 Photocatalysts Impregnated with Various Transition Metal Ions: Characterization and Photocatalytic Activity for the Degradation of 4-Nitrophenol. *The Journal of Physical Chemistry B*, 106 (3): 637 - 645.
18. Dvoranová, D., Brezová, V., Mazúr, M. and Malati, M. A. (2002). Investigations of Metal-Doped Titanium Dioxide Photocatalysts. *Applied Catalysis B: Environmental*, 37 (2): 91-105.
19. Chiang, K., Amal, R. and Tran, T. (2002). Photocatalytic Degradation of Cyanide using Titanium Dioxide Modified with Copper Oxide. *Advances in Environmental Research*, 6 (4): 471 - 485.
20. Tseng, I.-H., Chang, W.-C. and Wu, J. C. S. (2002). Photoreduction of CO_2 Using Sol–Gel Derived Titania and Titania-Supported Copper Catalysts. *Applied Catalysis B: Environmental*, 37 (1): 37 - 48.
21. Slamet, Nasution, H.W., Purnama, E., Kosela, S. and Gunlazuardi, J. (2005). Photocatalytic Reduction of CO_2 on Copper-Doped Titania Catalysts Prepared by Improved-Impregnation Method. *Catalysis Communication*, 6 (5): 313 – 319.

MALAYSIAN JOURNAL OF ANALYTICAL SCIENCES
Published by The Malaysian Analytical Sciences Society
ISSN 1394 - 2506

RESIDUE DETERMINATION AND MONITORING OF THE LEVELS OF METSULFURON METHYL IN SELECTED RIVERS AT TASIK CHINI, PAHANG, MALAYSIA

(Penentuan Residu dan Pemantauan Metsulfuron Metil di Sungai Terpilih di Tasik Chini, Pahang, Malaysia)

Khairiatul Mardiana Jansar* and Ismail Bin Sahid

School of Environment and Natural Resource Sciences,
Faculty of Science and Technology,
Universiti Kebangsaan Malaysia, 43600 UKM Bangi, Selangor, Malaysia

**Corresponding author: mardiana@ukm.edu.my*

Received: 9 December 2014; Accepted: 16 October 2015

Abstract

The levels of metsulfuron methyl (methyl 2-(4-methoxy-6-methyl-1,3,5-trazine-2-ylcarbamoylsulfamoyl) benzoate (IUPAC) (MSM) and its metabolite IN-A4098 (4-methoxy-6-methyl-1,3,5-triazin-2-amine (AMMT) were determined from surface water samples of six rivers located at Tasik Chini, Pahang, Malaysia. The optimization analytical method was developed for the determination of the MSM herbicide and its metabolite, AMMT in surface water up to 0.05 ng/ml with good linearity in the calibration range 0.1 – 10 ng/ml. The procedure involves a clean-up process using the IST ISOLUTE ENV$^+$ solid phase extraction (SPE) method and the pesticide level are determined using the HPLC with variable wavelength detector (VWD) and 81 – 105 % recovery. The MSM compound represents one of main herbicides used in the Tasik Chini oil palm plantation. The method enables study to be made of the herbicide and its transformation products through simultaneous detection and quantification. In the field study levels of MSM in the surface water ranged from undetectable to 0.1378 ng/ml from the first season to forth season, while levels of the metabolite, AMMT ranged from undetectable to 1.473 ng/ml. The variation of the MSM and AMMT levels depended directly on the time of the pesticide application and the season.

Keywords: metsulfuron methyl, metabolite, solid phase extraction, Tasik Chini

Abstrak

Tahap pencemaran metsulfuron metil (metil 2-(4-metoksi-6-metil-1,3,5-triazin-2-ilkarbamoilsulfamoil) benzoat (IUPAC) (MSM) dan metabolit IN-A4098 (4-metoksi-6-metil-1,3,5-triazin-2-amina (AMMT) telah ditentukan daripada sampel air permukaan daripada enam batang sungai yang terletak di Tasik Chini, Pahang, Malaysia. Pengoptimuman kaedah analisis telah dibuat untuk menentukan kandungan herbisid MSM dan metabolitnya, AMMT dalam air permukaan dengan kepekatan minimum adalah 0.05 ng/ml dan julat kalibrasi adalah 0.1 – 10 ng/ml. Prosedur ini melibatkan satu proses pengekstrakkan menggunakan IST ISOLUTE ENV$^+$ kaedah pengekstrakan fasa pepejal (SPE) dan tahap herbisid ditentukan menggunakan HPLC dengan pengesan gelombang pelbagai (VWD) pada tahap perolehan semula adalah 81 – 105 %. Sebatian MSM merupakan salah satu daripada herbisid utama yang digunakan dalam ladang kelapa sawit Tasik Chini. Kaedah ini membolehkan herbisid dan metabolitnya dikesan dan dianalisis serentak. Di peringkat kajian lapangan, julat bacaan MSM dalam air permukaan adalah dari tidak dapat dikesan sehingga 0.1378 ng/ml dari musim pertama hingga musim keempat, manakala tahap pencemaran AMMT, yakni metabolitnya adalah dalam julat yang tidak dapat dikesan hingga 1.473 ng/ml. Tahap pencemaran MSM dan AMMT bergantung secara langsung kepada masa penyemburan herbisid dan musim kawasan tersebut.

Kata kunci: metsulfuron metil, metabolit, pengekstrakkan fasa pepejal, Tasik Chini

Introduction

Sulfonylurea herbicides are widely used in agriculture by reason of their low application rates, good crop selectivity and very low animal toxicity [1]. One of the common sulfonylurea herbicides used in oil palm plantations is metsulfuron methyl (MSM) which is often sprayed with glyphosate. MSM is particularly effective on some annual and perennial broad-leaved species and can be degraded by microbes into 4-methoxy-6-methyl-1,3,5-triazin-2-amine (AMMT). It is a selective, translocated herbicide that is mainly absorbed through leaves. Its main uses are for broad-leaved weed control in oil palm plantations in Malaysia, as a tank mix with glyphosate for pre-plant weed control and for the control of perennial weeds. Metsulfuron methyl acts on the plants, ALS enzyme (not present in animals) and this is the main reason for its low toxicity to mammals, birds and fish [2].

Pollution of surface water with metsulfuron methyl can occur when the pesticide is sprayed during the rainy season, at hilly areas, consisting of impermeable soil such as clay soil, or soil with low organic content and high pH [3, 4]. The indigenous tribes in Tasik Chini are still consuming the surface water of the lake for bathing and fishing, and some of the populations are using groundwater for their daily needs. Thus, it is important to monitor the level of pesticide in the lake (Tasik Chini) before it endangers human and aquatic lives. Contamination of groundwater can occur if the soil is sandy loam type because MSM is highly soluble in water, with log K_{ow} at 1.8 and 0.018 for pH5 and pH7 respectively (water solubility of MSM pesticide is pH dependent) [5]. It is not hazardous to the environment as its usage rate is low, it has low toxicity and degradation in the field is rapid. However, there are studies that contradict its low toxicity effects, whereby concerns arise with regard to the possibility of environmental contamination, mainly regarding the leaching potential into the ground water system [6, 7]. Besides, due to its high solubility in water there is a need to monitor and compare the level of metsulfuron methyl sprayed in the oil palm plantation area at different seasons (rainy and dry). No specific maximum residue limit (MRL) has been established; therefore a default MRL of 0.1mg/L applies to food [3]. Conversion of the sulphonylurea herbicide group has been studied [8] and initial cleavage of the sulphonylurea bridge has been identified as the main transformation reaction. The primary degradation occurs with DT_{50} in 81-148 days [8], whereby, the products subsequent from the cleavage (of metsulfuron-methyl) is include, 4-methoxy-6-methyl-1,3,5-triazin-2-amine (AMMT).

Recent years, many alternative techniques have been explored and established, these include using capillary electrophoresis, gas chromatography and liquid chromatography [10, 11, 12, 13] to extract metsulfuron methyl and its metabolite. Solid phase extraction (SPE) is the preferred method for environmental samples instead of liquid-liquid extraction due to its simple operation. A few studies on SPE type comparison have been conducted to select the SPE type that is suitable for sulfonylurea herbicide extraction. For the present study IST ISOLUTE ENV$^+$ cartridge was used. The quantification of extracted MSM and AMMT was detected by a high performance liquid chromatograph (HPLC) equipped with a variable wavelength detector. Liquid chromatography procedure used as the routine method in the laboratory was adapted from previous research [15].

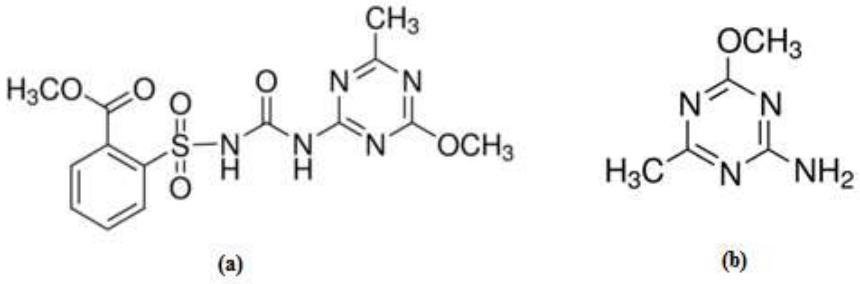


Figure 1. Molecular structure of (a) Metsulfuron methyl (MSM) and (b) 4-methoxy-6-methyl-1,3,5-triazin-2-amine (AMMT)

Materials and Methods

Study Area

Tasik Chini is located at the south eastern region of the state of Pahang, Malaysia and approximately 100 km from Kuantan, the capital of Pahang. The Tasik Chini lake system lies between 3°22´30" to 3°28´00" N and 102°52´40" to 102°58´10" E and comprises 12 open water bodies that are referred to as "laut" by the local people. There are a few groups of the indigenous Jakun tribe that live around the lake. Tasik Chini is the second largest natural fresh-water lake in Malaysia (after Tasik Bera). It covers 202 hectares of open water and 700 hectares of riparian, peat, hill and lowland Dipterocarp forests. There are three hilly areas surrounding the lake, namely Bukit Ketaya (209 m) in the southeast, Bukit Tebakang (210 m) at the north and Bukit Chini (641 m) located southwest. The study area has a humid tropical climate with two monsoon seasons, characterized by the following bimodal pattern: southwest and northeast monsoons bringing rainfall which varies from 1488 to 3071 mm annually. The mean annual rainfall is 2500 mm and the temperature range is from 21 to 32 °C. The lake drains northeasterly into the Pahang River through the Chini River, which flows for 4.8 km before it reaches the Pahang River. Sampling sites were selected according to land use and are shown in Figure 2.

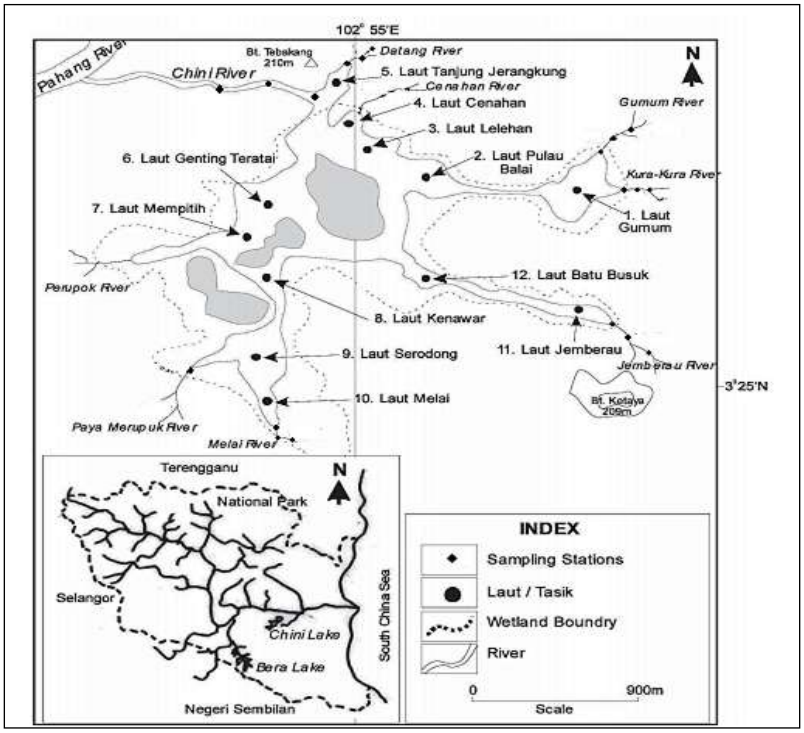


Figure 2. Map of the region: studied area and sampling sites

Sampling

Application of 150 gram/hectare MSM was applied on 15/12/2011, 14/03/2012, 13/06/2012 and 12/09/2012 to an individual oil palm plantation area near (20 meters) Sungai Jemberau (with the permission of the oil palm plantation owner and other pesticide applications were controlled). Herbicide application dates were decided by the researcher. The method of application involved spraying of the formulation using a backpack sprayer. Samples were taken one day after the MSM spraying and sampling details are as shown in Table 1 and Table 2 respectively. Water samples were taken from each sampling sites in accordance to standard methodology [12]. Samples were stored at glass containers in pH 5 – 6 (adjusted) for not more than one week at -4°C prior to analyses.

Reagents

All reagents and solvents used in the study were of HPLC grade. The MSM was purchased from Sigma Aldrich and the AMMT was purchased from Dr. Ehrenstorfer GmbH. The ultra-pure water was produced using of a sartorius water purification system (Sartorius, Germany). All calibration stock solutions of MSM and AMMT (500 mg/L) were prepared in methanol and stored at 4 ^{o}C for not more than six months. Working standards were prepared in methanol and used by the addition of the standard to samples for the recovery test and stored at 4 ^{o}C for less than one week. Each sample was analysed three times. Good linearity was obtained for the every signal for MSM and AMMT if no interfering pollutant was present.

Table 1. Identification of sampling time

Sampling Season	Sampling date	Description
M1	16/12/2011	Rainy season
M2	15/03/2012	Rainy season
M3	14/06/2012	Regular raining
M4	13/09/2012	Dry season

Table 2. Identification of samples taken from study area

Sampling	Location	Description
D1	Sungai Datang downstream	Forest area, fishing area
D2	Sungai Datang middle	Forest area, fishing area
D3	Sungai Datang up stream	Forest area, fishing area, oil palm plantation area
C1	Sungai Chini downstream	Recreation area, boating
C2	Sungai Chini middle	Recreation area, boating
C3	Sungai Chini up stream	Recreation area, boating
G1	Sungai Gumum downstream	Indigenous tribe settlement
G2	Sungai Gumum middle	Indigenous tribe settlement
G3	Sungai Gumum up stream	Indigenous tribe settlement
K1	Sungai Kura-kura downstream	Indigenous tribe settlement
K2	Sungai Kura-kura middle	Indigenous tribe settlement
K3	Sungai Kura-kura up stream	Indigenous tribe settlement
J1	Sungai Jemberau downstream	Oil palm plantation area
J2	Sungai Jemberau middle	Oil palm plantation area
J3	Sungai Jemberau up stream	Oil palm plantation area
L1	Sungai Melai downstream	Mining and logging activities area, Indigenous people settlement
L2	Sungai Melai middle	Mining and logging activities area
L3	Sungai Melai up stream	Mining and logging activities area

Instrumentation and chromatographic conditions

Liquid chromatographic analysis was performed with an Agilent 1220 Infinity LC System (Agilent, US) equipped with a dual plunger in series pump with proprietary servo-controlled variable stroke drive, an automatic injector,

and a variable wavelength detector (VWD). The Agilent 1220 instrument was controlled by computer (OpenLab Chemstation Edition software); data from the VWD was collected and evaluated by use of the same station after transfer via an analog-to-digital converter.

Separations were performed on a 150 mm, 4.6 x 150, 3.5 µm, Zorbax Eclipse XDB-C18 column (Agilent, USA), 3.5 µm internal diameter packed with high purity silica; The mobile phase was (A) methanol: acetonitrile: acetic acid = 50:50:0.01% and (B) 0.005 M phosphate buffers: acetic acid = 100:0.01% with adjusted pH to 2.5. Separation compound was achieved in a gradient condition, 15% B linear for 1.5minutes, increased to 60% B in 5.5 minutes, linear 60% B for 8 minutes, then returned to 15% B in 3 minutes. The column temperature was controlled at 40°C (sharpness of the compound peaks are better compared to uncontrolled temperature) and the volume of the sample injected was 20 µL. Variable wavelength detection, 200 nm, was used to monitor the products. A post-run period of 5 minutes was used for stabilisation. A total of 25 minutes of analysis was needed.

Sample Preparation and Clean-up Process

Water samples (1 liter) were collected in amber glass bottles and stored at -4ºC for a short term storage. After thawing, samples were filtered through a 0.45-µm nylon membrane filter and the filtrate was adjusted to pH 5 – 6 by addition of dilute hydrochloric acid (0.136 M). Samples were placed in ultrasonic bath for 15 minutes before the clean-up process. The targeted herbicide and its metabolite (MSM AND AMMT) were extracted by pulling the sample through a reverse-phase solid phase extraction (SPE) cartridge (ENV^{+} cartridge). Before pulling the sample through the cartridge, the cartridge was rinsed with 3ml of acetonitrile and 3 ml of water to reduce residual acidity within the cartridge, and then dried to remove any residual water. The analytes were eluted off the SPE cartridge using 8 ml of methanol. The resulting elute was evaporated near to dryness exactly at 1 ml. This final extract was filtered through a 0.20 µm membrane filter, and submitted for analysis.

Results and Discussion

The method optimised for detection of MSM and AMMT in water samples showed the following parameters: level of detection for water sample was 5µg/L for MSM and 1µg/L for AMMT with a good linearity in the standard addition calibration range 1 – 50 µg/L (r^2 = 0.998 – 0.999). Retention time for MSM was 3.176 minutes and for AMMT 10.721 minutes (Figure 3). Recovery rates of 83-110% were obtained for MSM and AMMT in water of pH 5.26. Figure 6 shows the recovery of 3 mg/L obtained for the pH range of 2.38 – 10.27. Using the gradient method, it was possible to perform simultaneous analysis for the herbicide (MSM) and its metabolites (AMMT). Thus, using the methods presented, it was possible to screen both MSM and AMMT simultaneously.

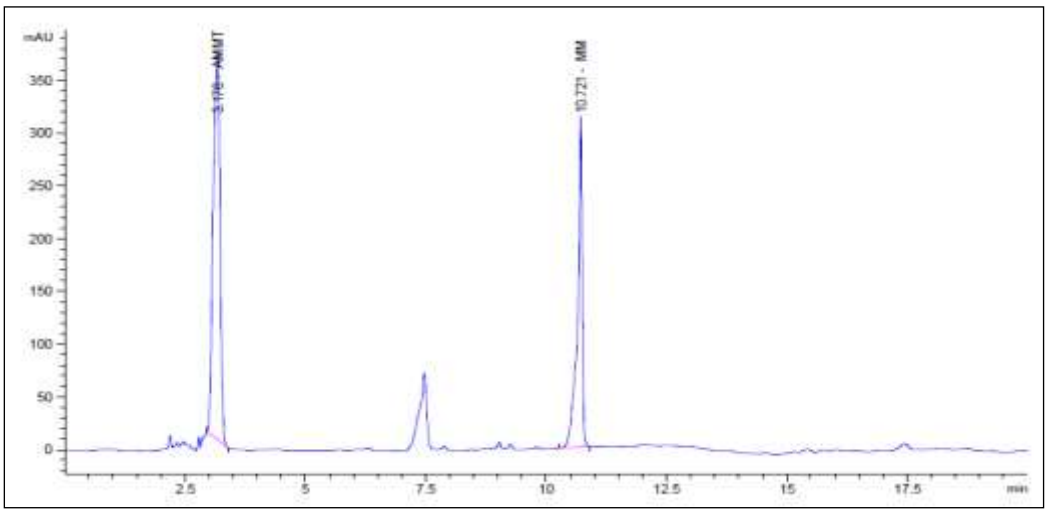


Figure 3. Gradient method: HPLC profile of spiked MSM and AMMT. Chromatogram has been corrected for baseline drift (overlay sample chromatogram on blank chromatogram)

In the present study, samples were collected four times from each of the 18 stations at six selected rivers during the wet and dry seasons. M1 and M2 represented the rainy season, with monthly average rainfall of 300 mm to 400 mm, meanwhile M4 represented the dry season, with a monthly average rainfall of 50 mm to 150 mm, and M3 the regular season, with a monthly average rainfall of 150 mm to 300 mm. The result obtained from water monitoring for MSM and AMMT from the sampling is provided in Figure 4 and Table 3. MSM concentration in the water ranged from undetectable to 604.4 µg/L (Figure 5). The amount of AMMT prevent in several stations and seasons shown in Table 3. A significant increase of the MSM concentration in the water was observed in the vary season (M1 and M2) in most of the rivers. The release of MSM can be associated with surface runoff from the oil palm plantation area and with soil exposure to MSM. These results showed the drift of MSM due to precipitation and related leaching in relation to its high solubility in water and its binding ability to the soil particles which drifted by the runoff [9]. In the present study, rain events played an important role transporting the MSM present in the soil towards the water stream through the mechanisms of dilution or drift of surface material by runoff. For Sungai Jemberau (J1, J2 and J3) the concentration increased from downstream to upstream possibly due to the location of the oil palm plantation area. A different patent occurred for Sungai Gumum (G1, G2 and G3) where the concentration decreased from downstream to upstream, perhaps due to the reduction of oil palm plantation area at the upstream area. Referring to the amount of AMMT in the water, there was no trend observed in the water bodies during the monitoring period and AMMT was found mainly during the dry season at low concentrations < 0.15mg/L.

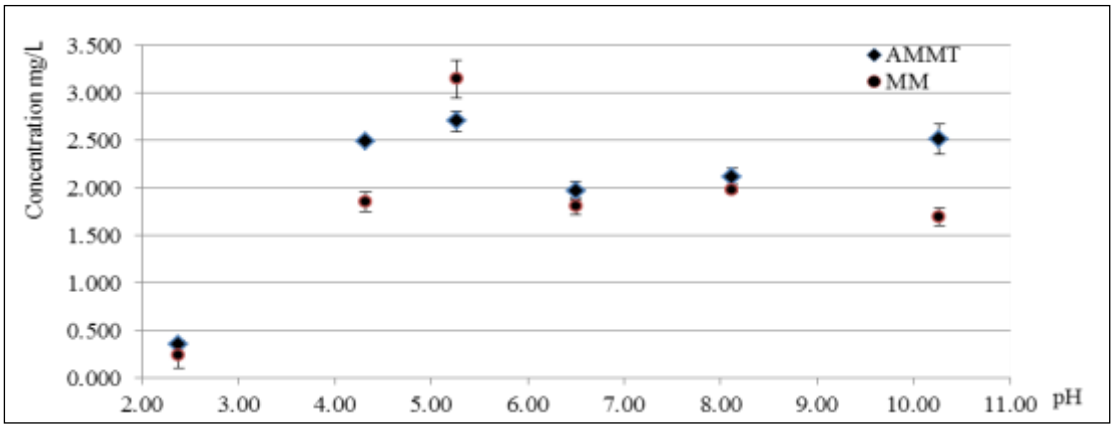


Figure 4. Recovery result of 3 mg/L for the pH range of 2.38 – 10.27

Table 3. AMMT concentration

Sampling	Sampling place	Concentration (mg/L)
Season 1	K3	0.0191
Season 2	D1	0.0510
Season 3	Every sampling point is not detected	
Season 4	CH2	0.0220
	D1	0.1390
	D2	0.0575
	K1	0.0472
	K2	0.1238
	K3	0.0381

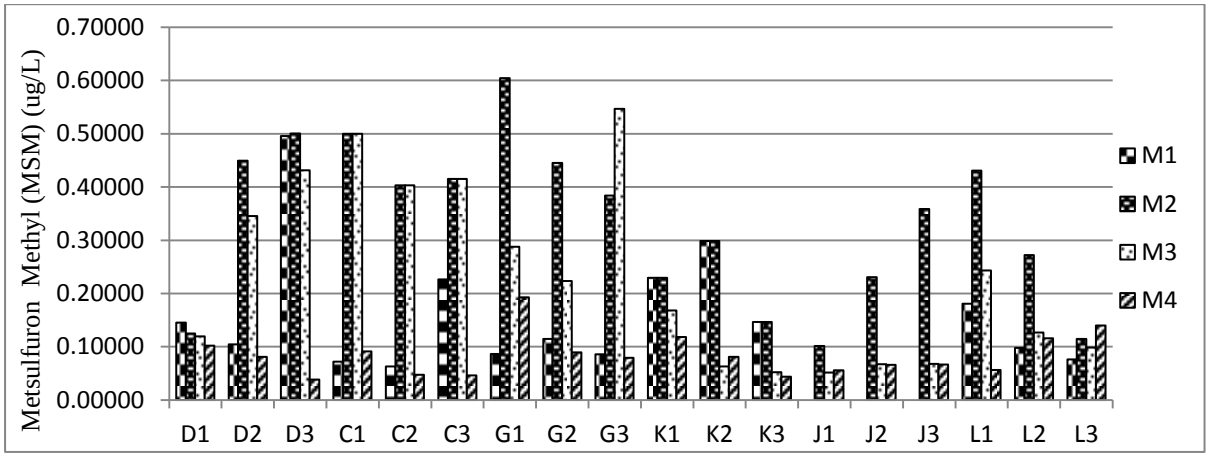


Figure 5. MSM concentration in water

Conclusion

The inclusion of the study of metabolites in monitoring programs and in experimental studies is mandatory. The optimized method used showed an adequate sensitivity for the detection of MSM and AMMT in water samples by a simple procedure. Concerning the levels of MSM detected in the water samples, there was no direct relationship observed between MSM application time and its detection in water. However, the rain events cause a rise in MSM concentration in the water. Finally, the contribution of this preliminary study is disclosed because there is little unpublished information in this region regarding pesticides application. Further studies for pesticide modeling on a monthly basis will be a useful tool for estimation of application rates.

Acknowledgement

The authors wish to thank the Ministry of Science, Technology and Innovation (MOSTI) for the grant (06-01-02-SF0827) to fund this project; Pusat Penyelidikan Tasik Chini and Faculty of Science and Technology, UKM for the research facilities.

References

1. Beyer, E .M., Duffy, M. J., Hay, J. V. and Schlueter, D. D. (1988). Sulfonylureas. In: Kearney, P.C., and Kaufman, D.D. (Eds.), Herbicides. Chemistry, Degradation and Mode of Action, Dekker, New York.
2. Ray, T. B. (1984). Site of action of chlorsulfuron: inhibition of valine and isoleucine biosynthesis in plants. *Plant Physiology, 75*, 827 – 831.
3. Health Canada Pest Management Regulatory Agency (2008). Re-evaluation Decision. Metsulfuron Methyl. Ontario: Minister of Public Works and Government Services Canada.
4. Abdullah, A. R, Saraswathy, S. and Norhayati, M. T. (2001). Adsorption-desorption and mobility of metsulfuron methyl in selected Malaysian agricultural soils. *Bulletin of Environmental Contamination and Toxicology* 66: 762 – 769.
5. Brown, H. M., Gaddamidi, V. and Lee, P. W. (1998). Sulfonylureas. In: Hutsons, D. H., and Roberts, T. (Eds.), Metabolic Pathways of Agrochemicals: Herbicides and plant growth regulators. The Royal Science of Chemistry, Cambridge.
6. Kjaer, C. M. Strandberg, and Erlandsen, M. (2006). Effects on hawthorn the year after simulated spray drift. *Chemosphere*. 63(5): 853 – 859.
7. Li, Z. J., Xu, J. M., Muhammad, A. and Ma, G. R. (2005). Effect of bound residues of Metsulfuron-methyl in soil on rice growth. *Chemosphere*. 58: 1177 – 1183.

8. Berger, B. M. and Wolfe, N. L. (1996). Hydrolysis and biodegradation of sulfonylurea herbicides in aqueous buffers and anaerobic water-sediment systems: assessing fate pathways using molecular descriptors. *Environmental Toxicology Chemistry*, 15:1500 – 1507.
9. Wang, H., Yang, F., Liu, G., Lei, Y. and Ye, Q. (2011). Monitoring of metsulfuron-methyl and its residues in an artificial pond. *Environmental Monitoring Assessment*, 174(1-4):597 – 604.
10. Singh S. B. and Paul, R. (2011). Gas chromatographic method for residue analysis of metsulfuron methyl from soil. *Bulletin of Environmental Contamination and Toxicology*, 86(2):149 – 151.
11. Bossi, R., Seiden, P., Andersen, S. M., Jacobsen, C. S. and Streibig, J. C. (1999). Analysis of metsulfuron-methyl in soil by liquid chromatography/Tandem Mass Spectrometry. Application to a field dissipation study. *Agricultural Food Chemistry*, 47(10):4462 – 4468.
12. National Council for Air and Stream Improvement, Inc. (NCASI) (2007). Hexazinone, Imazapyr, Metsulfuron Methyl, and Sulfometuron Methyl in Water by Solid Phase Extraction and HPLC/UV. NCASI Methods Manual. Research Triangle Park, NC: National Council for Air and Stream Improvement, Inc.
13. Shobha S. (2008). Persistence of metsulfuron-methyl in wheat crop and soil. *Environmental Monitoring and Assessment*, 147:463 – 469.
14. Halimah, M. Tan, Y. A. and Ismail, B. S. (2007). New and rapid method of analysis of metsufuron methyl in water sample. Proceedings of Product Development and Nutrition Conference: PIPOC 2007 International Palm Oil Congress: Palm Oil: Empowering Change. Kuala Lumpur (Malaysia), 26 – 30 Aug, 2007: pp 176.
15. Juhler, R., Sørensen, S. and Larsen, L. (2001). Analysing transformation products of herbicide residues in environmental samples. *Water Research*, 35(6), 1371–1378.

MALAYSIAN JOURNAL OF ANALYTICAL SCIENCES
Published by The Malaysian Analytical Sciences Society
ISSN 1394 - 2506

ADSORPTION OF Cu, As, Pb AND Zn BY BANANA TRUNK

(Penjerapan Cu, As, Pb dan Zn oleh Batang Pisang)

Nurzulaifa Shaheera Erne Mohd Yasim[1]*, Zitty Sarah Ismail[1], Suhanom Mohd Zaki[2], Mohd Fahmi Abd Azis[1]

[1]*Faculty of Applied Sciences,*
Universiti Teknologi MARA, 40450 Shah Alam, Selangor, Malaysia
[2]*Faculty of Business Management,*
Universiti Teknologi MARA, 26400 Bandar Tun Razak Jengka, Pahang, Malaysia

**Corresponding author: nurzulaifa@salam.uitm.edu.my*

Received: 9 December 2014; Accepted: 16 October 2015

Abstract

The purpose of this study is to investigate the effectiveness of banana trunk as an adsorbent in removal of heavy metals in aqueous solution. Functional groups of adsorbent were determined using Fourier Transform Infrared spectroscopy (FTIR). Batch experiments were conducted to determine the adsorption percentage of heavy metals (Cu, As, Pb and Zn). The optimum adsorption using banana trunk was based on pH difference, contact time and dosage. Adsorption percentage was found to be proportional to pH, contact time and dosage. Maximum adsorption percentage of Cu, As, Pb and Zn at pH 6, 100 minutes and 8 gram of dosage are 95.80 %, 75.40 %, 99.36 % and 97.24 %, respectively. Langmuir and Freundlich isotherms were used to determine the equilibrium state for heavy metals ion adsorption experiments. All equilibrium heavy metals were well explained by the Freundlich isotherm model with R^2 = 0.9441, R^2 = 0.8671, R^2 = 0.9489 and R^2 = 0.9375 for Cu, As, Pb and Zn respectively. It is concluded that banana trunk has considerable potential for the removal of heavy metals from aqueous solution.

Keywords: adsorption, heavy metals, banana trunk, pH, contact time

Abstrak

Kajian ini bertujuan untuk menyiasat keberkesanan batang pisang sebagai penjerap dalam penyingkiran logam berat di dalam larutan akueus. Kumpulan berfungsi penjerap ditentukan menggunakan Spektrospkopi Infra Merah Transformasi Fourier (FTIR). Eksperimen kelompok dilakukan untuk menentukan peratusan penjerapan logam berat (Cu, As, Pb dan Zn). Penjerapan optimum menggunakan batang pisang berdasarkan pH yang berbeza, masa sentuhan dan dos penjerap dianalisis dalam eksperimen kelompok. Peratus penjerapan didapati berkadar terus dengan pH, masa sentuhan dan dos penjerap. Peratus penjerapan maksimum Cu, As, Pb dan Zn pada pH 6, 10 minit masa sentuhan dan 8 gram dos penjerap masing-masing ialah 95.80 %, 75.40 %, 99.36 % dan 97.24 %. Isoterma Langmuir dan Freundlich telah digunakan untuk menentukan keadaan keseimbangan bagi eksperimen penjerapan logam berat. Semua keseimbangan logam berat dijelaskan dengan baik oleh model isoterma Freundlich dengan R^2 = 0.9441 , R^2 = 0.8671 , R^2 = 0.9489 dan R^2 = 0.9375 masing – masing untuk logam Cu, As, Pb dan Zn. Dapat disimpulkan bahawa batang pisang mempunyai potensi besar untuk penyingkiran logam berat daripada larutan akues.

Kata kunci: penjerapan, logam berat, batang pisang, pH, masa sentuhan

Introduction

The presence of heavy metals in the water bodies has caused severe health effects to people. Too much ingestion of copper (Cu) may bring about serious toxicological concerns, such as convulsions, vomiting, cramps or even death [1] while its deficiency may cause excessive accumulation of zinc (Zn) in human and animals which can reduce the immune system function. Among other effects include anemia, death of fetuses, liver, pancreas and kidney damage

[2]. Arsenic (As) is known as a poisonous element and very toxic to human. It can cause cancer and skin disorder besides non-cancerous diseases such as cardiovascular, pulmonary and neurological problems. Meanwhile, exposure to lead (Pb) resulted in a wide range of biological effects depending on the level and duration of the exposure.

Heavy metal sources can be natural or anthropogenic in origin. They existed naturally in a small amount on the Earth's crust and could not be degraded or eliminated. Higher concentration of heavy metals in the environment usually comes from anthropogenic activities such as copper (Cu) from electricity conductor, building materials and various alloys constituents. Zinc (Zn) is one of the transition elements possibly from refining and extraction industry while arsenic is contributed by human activities such as sewage and toxic chemicals disposals, industrial activities, vehicular emissions and erosion [3]. Finally, lead (Pb) is possibly coming from several other sources such as petrol, industrial processing, painting and soldering industries, water pathways and piping [4].

There are several conventional methods in removing heavy metals from water, which include precipitation, ion exchange, reverse osmosis, electrocoagulation and nanofiltration [5 – 7]. However, these methods are limited for the use of large industries since the operational cost is high [8]. Thus, using waste materials as an absorbent over activated carbon in removing heavy metals is wisely suggested since they are cheaper and effective.

The major aim of this study is to determine the potential of banana trunk as an adsorbent in removal of heavy metals in aqueous solution. Banana trunk is an agricultural waste generated from agricultural activities. It is chosen due to the waste generated is rising dramatically which can risk both human and ecosystem [9]. This waste can be converted into useful products through recycle which subsequently minimize the level of pollution caused by agricultural burning activities. From previous studies, agricultural wastes are potentially low cost adsorbent as they are unexploited resources, widely available, environmental friendly and also natural materials that exist in large quantities [10]. Many research had been conducted such as the study of the removal of Pb (II) by citrus pectin [11] and adsorption of Fe (II) using tamarind bark (*Tamarindus indica*) and potato peel waste (*Solanum tuberosum*) [12]. The optimum adsorption process was identified as a function of pH, contact time and dosage.

Materials and Methods

Chemical and stock preparation

5 ppm of each heavy metal solution was prepared from 100 ppm stock solution through dilution. The metal solutions were adjusted to pH 5 using 0.1 M of hydrochloric acid (HCl) [13]. It is recommended to shake the stock solution thoroughly prior to use and must not pipette directly from the bottle.

Sample preparation and analysis

The samples of banana trunk were obtained from banana plantation in Kuang, Selangor. The trunks were sliced into small pieces and washed thoroughly using distilled water. The trunks were air-dried for 4 – 5 hours before keeping them in the oven for 24 hours at 50 ºC. Then, the dried trunks were grounded and sieved and ready for FTIR-analysis [14]. This analysis is to determine the functional groups in banana trunk by scanning the sample from 4000 to 400 cm^{-1} at a 400 cm^{-1} resolution [15].

Batch analysis

50 mL of 5 ppm metal solution was mixed with 2 g of adsorbent in 250 mL flasks and agitated at 100 rpm for 60 min using an orbital shaker. The experiment was continued to identify the adsorption equilibrium dosage through mixing the solution with 4 – 10 g of dosage. The suspension was then separated by decantation. Determination of the rate of adsorption and adsorption equilibrium time was performed by determining the residual metal solution in the supernatant by allowing metal support-banana trunk fibers sorbent to equilibrate at different pH values of 2-10 for 60 min. Then, at the optimum pH and dosage, metal support-banana trunks were allowed to contact at different period between 5 – 150 min. The residual metal ion concentration was analyzed using Inductively Coupled Plasma-Optical Emission Spectrometer (ICP-OES). The percentage removal of heavy metal was calculated as equation 1 below:

$$\text{Adsorption (\%)} = \frac{(C_i - C_f)}{C_i} \times 100 \quad (1)$$

where, C_i and C_f are the initial and final concentrations of heavy metals present in the adsorption studies.

Adsorption isotherm

Analysis of adsorption under constant temperature was studied by using Langmuir and Freundlich equations. Langmuir isotherm assumes that there is an infinite number of binding sites having the same affinity for adsorption of mono layer and there is no interaction between the adsorbed molecules [16]. Based on the assumption, Langmuir isotherm represents the following equation 2:

$$q_e = \frac{q_m K_L C_e}{1 + K_L C_e} \quad (2)$$

The Langmuir equation is transformed into linear form to determine Langmuir adsorption parameters as expressed in Equation 3 below;

$$1/q_e = (1/q_m) + (1/q_m K_L)(1/C_e) \quad (3)$$

where q_e (mg/g) and q_m (mg/g) are the amount of adsorbed metal ions per unit mass of adsorbent and adsorption capacity, respectively. K_L is a constant related to the affinity of the binding sites (L/mg) and C_e is a un-adsorbed metal ion concentration in solution at equilibrium (mg/L).

The assumption of Freundlich isotherm is the adsorption energy of a metal binding to a site on an adsorbent depends on the vacancies of the adjacent sites and it is expressed by the following equation 4 [17]:

$$q_e = K_F C_e^{1/n} \quad (4)$$

In linear form, the Freundlich equation is expressed as follows:

$$\log q_e = \log K_F + 1/n \log C_e \quad (5)$$

where q_e the amount of metals adsorbed per unit mass of adsorbent (mg/g); C_e is the equilibrium concentration of metal ions (mg/L) while K_F (mg/g (L/mg)$^{1/n}$) and *n* (dimensionless) signify the adsorption capacity and adsorption intensity respectively. It can be defined as the adsorption or distribution coefficient and represents the quantity of dye adsorbed onto adsorbent for unit equilibrium concentration. 1/n is the heterogeneity factor and n is a measurement of the deviation from linearity of adsorption. The values indicate the degree of non-linearity between solution concentration and adsorption. The interpretations are as follow: If the value of *n* is equal to unity, the adsorption is linear; if the value is below unity, this implies that adsorption process is chemical, if the value is above unity adsorption is a favorable physical process.

Results and Discussion

Characterization of adsorbent

Based on the FTIR spectrum of banana trunk biomass shown in Figure 1, three different absorption peaks were detected. The peak at 3400.84 cm^{-1} represents the O-H functional group. The absorption band at 1624.01 cm^{-1} occurred for primary amine N-H functional group while the carboxylic acid (-COOH) group were detected at 1054.52 cm^{-1} wavelength. Previous study had stated that hydroxyl and carboxylic acid groups played a major role in the adsorption process [18]. According to [19], the hydroxyl group is highly effective towards adsorption rate and efficient through the exchange with metal ions. Meanwhile, the carboxylic acid group is relatively high adsorption rate due to the presence of more negatively charged groups on its surface [20].

Effect of adsorbent dosage

The effect of adsorbent dosage on the removal of selected heavy metals was investigated and shown in Figure 2. At the initial stage of batch experiment, the adsorption percentage of heavy metals increased with increasing of adsorbent dosage. This is probably due to the fact that by increasing the adsorbent dosage there will be numbers of active sites available for the adsorption of metal ions. However, further expansion of adsorbent dosage (> 8 g) did not significantly affect the percentage removal of heavy metals due to overcrowding of adsorbent particles [21].

Hence, the optimum dosage of banana trunk biomass for removing metal ions from liquid phase was 8 gram.

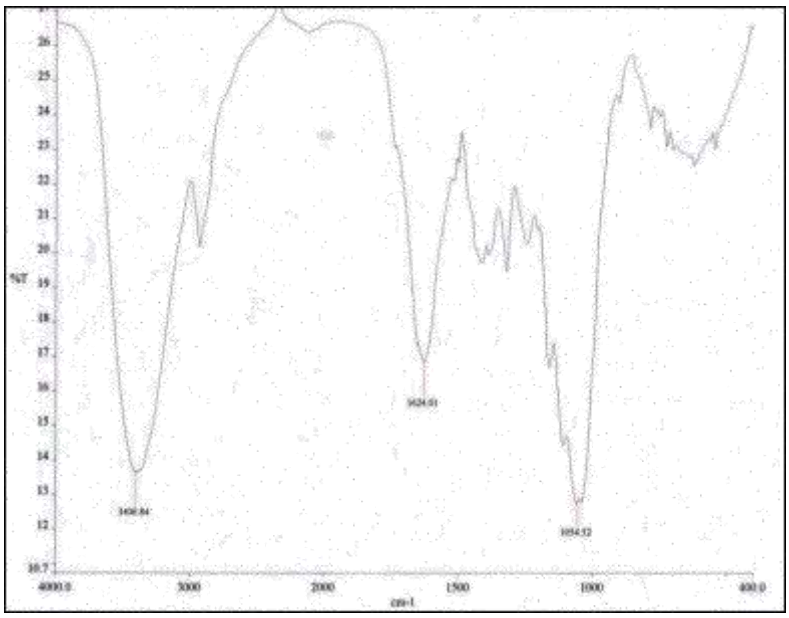


Figure 1. FTIR spectrum of banana trunk biomass (4000 cm^{-1} – 400 cm^{-1})

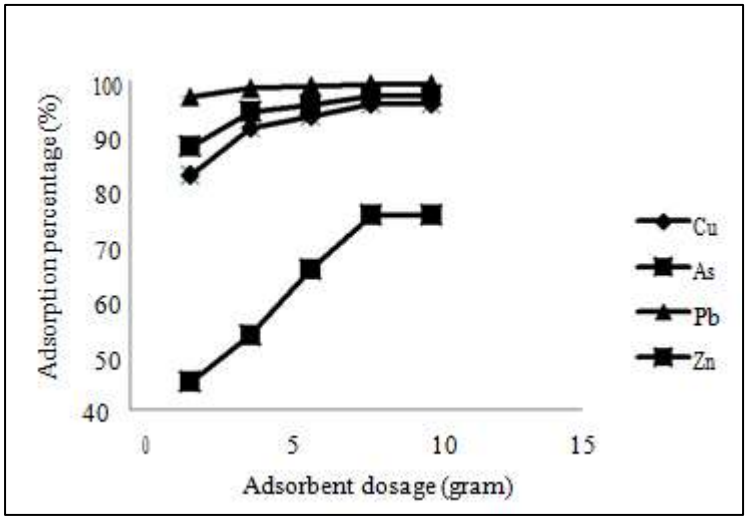


Figure 2. Graph of adsorbent dosage versus adsorption percentage

Effect of pH

Figure 3 shows the relationship between the adsorption percentages with pH for all the four heavy metals. The results obtained showing that there was a rapid removal of metal ions followed by slower adsorption process until the optimum pH was reached pH 6. It was noticed that the adsorption percentages for all four metals remained

constant as the pH increased beyond the optimum level. The tremendous metals removal as the pH increased is due to the reduction of competition between protons and metal cations for the same functional groups and by decreasing in the positive surface charge resulting in a lower electrostatic repulsion between the surface and metal ions [13]. It was recorded that the adsorption was at the least at the initial pH 2. The low adsorption percentage at the pH 3 and below is because of the H^+ ion competing with the metal cations for the adsorption site available whereas at the higher pH, the adsorption site is not active.

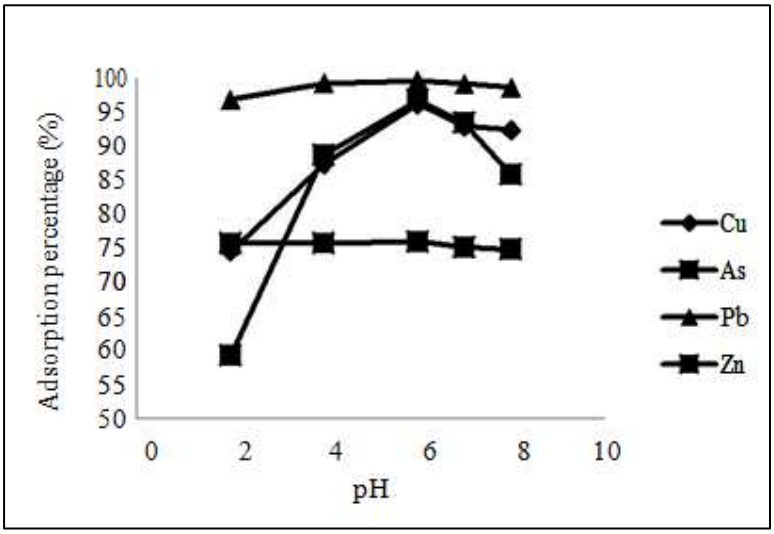


Figure 3. Graph of pH versus adsorption percentage

Effect of contact time

Optimum pH solutions were used for the determination of adsorption equilibrium time. Investigation of the effect of contact time in removal of heavy metals using banana trunk is explained in Figure 4. The removal of all four types heavy metal is increased with contact time until the optimum state is reached which was at 100 min. By extending the contact time beyond the optimum state, the process of removal of heavy metals was not significantly effective. On the other hand, the adsorption percentage was decreased due to the accumulation of metal ion species [22].

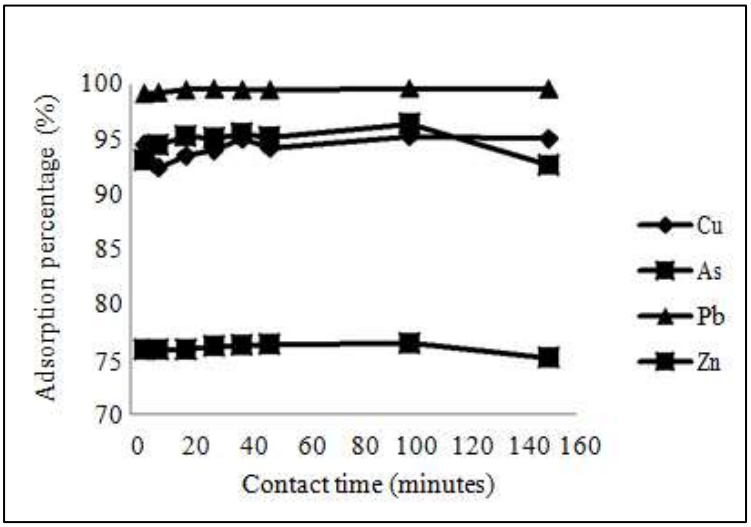


Figure 4. Graph of contact time versus adsorption percentage

Equilibrium studies

Langmuir and Freundlich isotherms were used to describe the equilibrium state of metal ions adsorption. The uptakes occur on a homogenous surface by monolayer sorption without any interaction between adsorbent molecules is described by Langmuir isotherm. This isotherm assumes there are no transmigration of metal ions in the plane of the surface and uniform energies of adsorption onto the surface. Langmuir isotherm constants were obtained from the plot of $1/q_e$ against $1/C_e$. Heavy metals (Cu, As, Pb and Zn) adsorptions that follow the Langmuir isotherm model are shown in Figure 5 whereas $1/q_e$ was plotted against $1/C_e$ and straight line was obtained for all studied heavy metals. The Langmuir parameters, q_m and K_L were calculated from the slope and interception of the isotherm as recorded in Table 1. From the Langmuir parameter, the adsorption capacities, (q_m), were identified in the sequence of Cu > Pb > As > Zn.

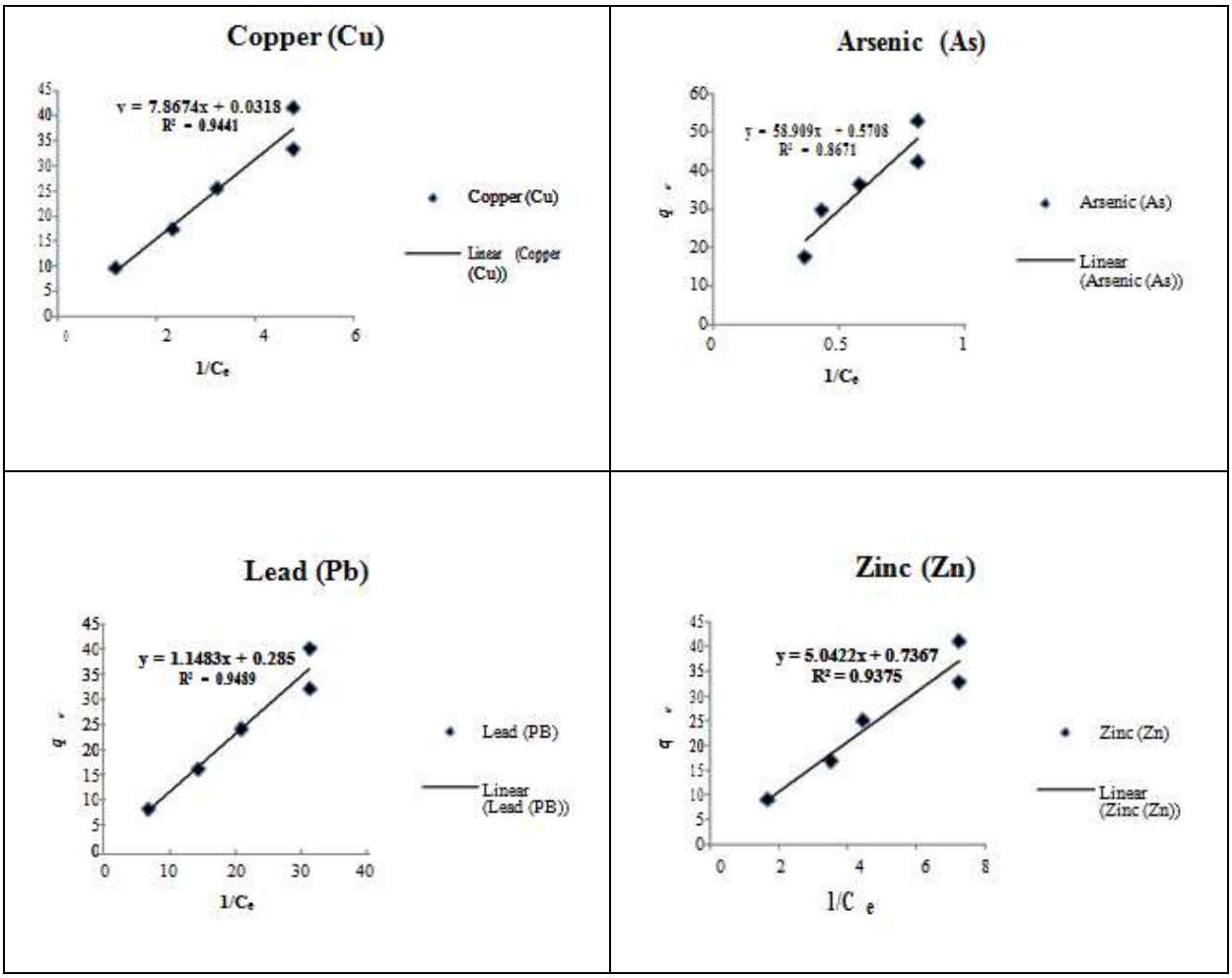


Figure 5. Plots of Langmiur isotherm for all heavy metals examined

The Freundlich isotherm describes the adsorption onto a heterogeneous surface. In Figure 6, when log C_e was plotted against log q_e, straight line was obtained representing that metal ions adsorption has followed the Freundlich isotherm model. Freundlich parameters which include *n* values and K_F values were computed from the slope and interception of the isotherm.

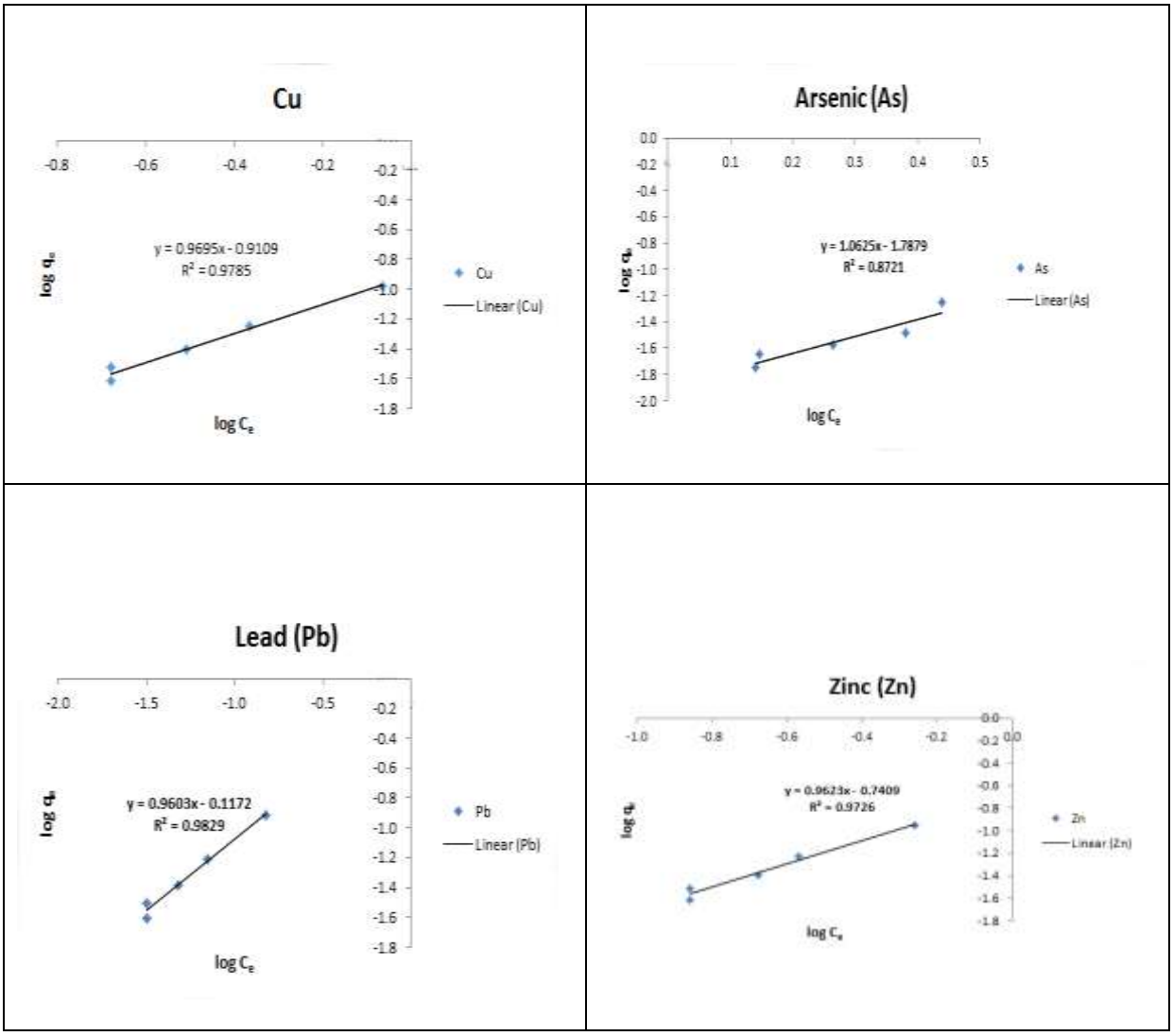


Figure 6. Plots of Freundlich isotherm for all heavy metals examined

Metal ions of Cu, Pb and Zn were favorably adsorbed by adsorbent since the n values are greater than 1. *N* values less than one indicate that the metal ions were not favorably adsorbed by adsorbent as shown in As adsorption. Table 2 shows the comparative evaluation of heterogeneous adsorption capacities onto various adsorbents.

The linear coefficient (R^2) was calculated to examine the fitness of the two isotherm models in the linear form. It is noted that Freundlich model describes the adsorption more successfully than Langmuir model where R^2 values of Langmuir model for all investigated heavy metals is higher and closer to unity compared to Freundlich model. According to Nady and Iman [23], if R^2 and $K_L < 1$, it is shown that metal ions are highly favorable adsorbed by prepared adsorbent. Thus, in this study, it is confirmed that banana trunk is effective in removal of heavy metals from aqueous solution.

Table 1. Langmuir and Freundlich parameters and correlation coefficient for the metals examined

Heavy Metals	Langmuir Isotherm			Freundlich Isotherm		
	q_m	K_L	R^2	n	K_L	R^2
Cu	31.45	4.04×10^{-3}	0.9441	1.03	0.12	0.9785
As	1.75	9.70×10^{-3}	0.8671	0.94	1.63×10^{-2}	0.8721
Pb	3.51	0.25	0.9489	1.04	0.76	0.9829
Zn	1.36	0.15	0.9375	1.04	0.18	0.9726

Table 2. Comparative evaluation of heterogeneous adsorption capacities onto various adsorbents

Metal	Adsorbent	Heterogeneous adsorption capacity (mg/g)	References
Cu	Banana trunk	1.03	Present study
	Banana peel	1.31	[24]
	Rock melon activated carbon	0.59	[25]
	Potato peel	1.86	[26]
Pb	Banana trunk	0.94	Present study
	Banana peel	1.40	[24]
	Orange peel	3.88	[27]
	Poly (vinyl alcohol)/chitosan	1.69	[28]
As	Banana trunk	1.04	Present study
	Orange peel	4.27	[29]
	Banana peel	1.35	[30]
Zn	Banana trunk	1.04	Present study
	Banana peel	1.58	[24]
	Potato peel	1.74	[26]
	Canola	1.85	[26]

Conclusion

In the present study it is proven that banana trunk has potential to be an effective and economically feasible adsorbent in removal of heavy metals. Three (Cu, Pb and Zn) out of four heavy metals achieved more than 90 % removals whereas As removal was only 75.40 %. In the batch experiment, it has been shown that the percentage removal is highly dependent on pH, contact time and dosage. The highest percentage removal for all investigated heavy metals was found at optimum pH 6, 100 min of contact time and 8 g dosage. The effectiveness of banana trunk as adsorbent in removal of heavy metals is confirmed by FTIR result that has detected three functional groups

including hydroxyl groups, carboxylic group and amine groups which played a major role in adsorption. The equilibrium adsorption data is best represented by Freundlich isotherm model compared to the Langmuir isotherm.

Acknowledgement

The authors would like to thank the University Teknologi MARA (UiTM) especially to Faculty of Applied Sciences, for giving the opportunity and providing the facilities to successfully perform this study.

References

1. Chen, T. C., Priambodo, R., Huang, R. L. and Huang, Y. H. (2013). The Effective Electrolytic Recovery of Dilute Copper from Industrial Wastewater. *Journal of Waste Management*. 2013: 1 – 6.
2. Perk, M. V. D. (2007). Soil and water contamination; from molecular to catchment scale. Utrecht, Netherland: Taylor & Francis. 128.
3. Garba, Z. N. and Hamza, S. A. (2010). Arsenic level speciation in fresh water from Karaye, local government area, Kano state, Nigeria. *International Journal Chemistry* 20 (2): 113 – 117.
4. Tong, S., Schirnding, Y. E. V. and Prapamontol, T. (2000). Environmental lead exposure: a public health problem of global dimensions. *Bulletin of the World Health Organization* 78(9): 1068 – 1077.
5. Kumari, P., Sharma, P., Srivastava, S. and Srivastava, M. M. (2006). Biosorption studies on sheeled Moringa oleifera Lamarck seed powder: Removal and recovery of arsenic from aqueous system. *International Journal of Mineral Processing* 78(3): 131 – 139.
6. Mondal, P., Majumder, C. B. and Mohanty, B. (2008). Treatment of arsenic water in a batch reactor by using ralstonia eutropha MTCC 2847 and granular activated carbon. *Journal of Hazardous Materials* 153(1-2): 588 – 599.
7. Rahman, M. S., Basu, A. and Islam, M. R. (2008). The removal of As (III) and As (V) from aqueous solutions by waste materials. *Bioresource Technology*. 99(8): 2815 – 2823.
8. Murugesan, G. S., Sathiskumar, M. and Swaminathan, K. (2006). Arsenic removal from groundwater by pretreated waste tea fungal biomass. *Bioresource Technology*. 97(3): 483 – 487.
9. Oladeji, Taiwo, J., Oyetunji and Ropo, O. (2013). Investigations into Physical and Fuel Characteristics of Briquettes Produced from Cassava and Yam Peels. *Journal of Energy Technologies and Policy* 3 (7): 40 – 46.
10. Deans, J. R. and Dixon, B. G. (1992). Uptake of Pb^{2+} and Cu^{2+} by novel biopolymers. *Water Resource* 26(4): 469 – 472.
11. Ankit, B. and Silke, S. (2008). Assessment of biosorption mechanism for Pb binding by citrus pectin. *Separation and Purification Technology* 63(3): 577 – 581.
12. Prasad, D. and Abdulsalam (2009). Biosorption on Fe (II) from aqueous solution using Tamarind Bark and potato peel waste; equilibrium and kinectic studies. *Journal Application Science in Environmental Sanitation* 4(3): 273 – 282.
13. Saeed, A., Akther, M. W. and Iqbal, M. (2005). Removal and recovery heavy metal from aqueous solution using papaya wood as a new biosorbent. *Separation and Purification Technology* 45 (1): 25 –31.
14. Kamsonlian, S., Balomajumder, C. and Chand, S. (2012). A potential of biosorbent derived from banana peel for removal of As (III) from contaminated water. *Journal of Chemical Sciences and Applications* 3(2): 268 – 275.
15. Sim, S. F., Murtedza, M., Lu, N. A. L. M. I., Sarman, N. S. P. and Samsudin, S. N. S. (2012). Computer-assisted analysis of Fourier Transform Infrared (FTIR) spectra for characterization of various treated and untreated agriculture biomass. *BioResources* 7(4): 5367 – 5380.
16. Ahmet, S. and Mustafa, T. (2008). Biosorption of total chromium from aqueous solution by red algae (*ceramium virgatum*): equilibrium, kinetic and thermodynamics studies. *Journal of Hazardous Materials* 160: 349 – 355.
17. Shugi, K., Singh, T. S. and Pant, K. K. (2003). Equilibrium and kinetics studies on removal arsenite by iron oxide coated activated alumina. *Indian Journal Environmental Health* 45: 151 – 154.
18. Hossain, M. A., Ngo, H. H., Guo, W. S. and Nguyen, T. V. (2012). Biosorption of Cu (II) from water by banana peel based biosorbent: experiments and models of adsorption and desorption. *Journal of Water Sustainability* 2(1): 87 – 104.
19. Wu, H. X., Wang, T. J., Chen, L. and Jin, Y. (2009). The roles of the surface charge and hydroxyl group on a Fe-Al-Ce adsorbent in fluoride adsorption. *Industrial Engineering Chemistry Research* 48: 4530 – 4534.

20. Chang, W. C., Deka, J. R., Wu, H. Y., Shieh, F. K., Huang, S. Y. and Kao, H. K. (2013). Synthesis and characterization of large pore cubic mesoporous silicas functionalized with high contents of carboxylic acid groups and their use as adsorbents. *Applied Catalysis B: Environmental* 142 – 143: 817 – 827.
21. Arunakumara, K. K. I. U., Buddhi, C. W. and Min-Ho, Y. (2013). Banana Peel: A Green Solution for Metal Removal from Contaminated Water. *Korean Journal of Environmental Agriculuture* 32 (2): 108 – 116.
22. Kamsonlian, S., Suresh, S., Majumder, C. B., Chand, S. (2011). Biosorption of As (V) from contaminated water onto tea waste biomass: sorption parameters optimization, equilibrium and thermodynamic studies. *Journal of Future Engineering and Technology* 7: 34 – 41.
23. Nady, A. F. and Iman, Y. E. S. (2011). Equilibrium Removal of Pb (II) Ions from Aqueous Solution onto Oxidized-KOH-Activated Carbons. *Carbon Letters* 12 (1): 1 – 7.
24. Muhammad, A. A., Abdul, W., Karamat, M., Mohd, J. M. and Ismail, Y. (2011). Low cos biosorbent banana peel (Musa sapientum) for the removal of heavy metals. *Scientific Research and Essays* 6 (19): 4055 – 4064.
25. Said, N., Amalina, R., Mazza, S. A. A., Syafiqah, A. K. and Hajar, A. M. S. (2015). Rock Melon Activated Carbon (RMAC) for Removal of Cd (II), Ni (II) and Cu (II) from Wastewater: Kinetics and Adsorption Equilibrium. *International Journal of Chemical Engineering and Applications* 6 (2): 105 – 110.
26. Morteza, F. and Mohsen, J. (2015). Removal of heavy metals from aqueous solution using sunflower, potato, canola and nut shell residues. *Journal of the Taiwan Institute of Chemical Engineers* 54: 125 – 136.
27. Ningchuan, F., Xueyi, G., Sha, L., Yanshu, Z. and Jianping, L. (2011). Biosorption of heavy metals from aqueous solutions by chemically modified orange peel. *Journal of Hazardous Materials* 185: 49 – 54.
28. Xiaoli, L., Yanfeng, L. and Zhengfang, Y. (2011). Preparation of macroporous bead adsorbents based on poly (vinyl alcohol)/chitosan and their adsorption properties for heavy metals from aqueous solution. *Chemical Engineering Journal* 178: 60 – 68
29. Suantak, K., Balomajumder, C. and Chand, S. (2012). Studies on surface characterization and isotherm modelling: Biosorption of Arsenic (III) onto low cost biosorbent derived from orange peel. *Journal of Scientific and Industrial Research* 71: 810 – 816.
30. Suantak, K., Balomajumder, C. and Chand, S. (2012). A potential of biosorbent derived from banana peel for removal of As (III) from contaminated water. *International Journal of Chemical Sciences and Applications* 3 (2): 269 – 275.

MALAYSIAN JOURNAL OF ANALYTICAL SCIENCES
Published by The Malaysian Analytical Sciences Society
ISSN 1394 - 2506

DITHIZONE MODIFIED SILVER ELECTRODE FOR THE DETERMINATION OF METAL IONS IN AQUEOUS SOLUTION

(Elektrod Perak Diubahsuai Ditizon bagi Penentuan Ion Logam dalam Larutan Akues)

Mohamad Aiman Firdaus Othman, Azrilawani Ahmad @ Othman, Hafiza Mohamed Zuki*

School of Marine Science and Environment,
Universiti Malaysia Terengganu, 21030, Kuala Terengganu, Malaysia

**Corresponding author: hafiza@umt.edu.my*

Received: 9 December 2014; Accepted: 16 October 2015

Abstract

Dithizone-PVC membrane was constructed and utilized as an ionophore reagent material for chemically modified silver (Ag) electrode. The modified electrode was characterized using cyclic voltammetry where the electrochemical behaviour of dithizone modified Ag electrode surface was investigated in the range of -0.6 to +0.6 V with 0.1 M KCl as supporting electrolyte. Comparative studies towards metal ions Cu^{2+}, Fe^{2+} and Pb^{2+} exhibited good responses for redox reactions with linear relationship between peak currents and concentrations. The correlation coefficients obtained were 0.9800, 0.9944 and 0.9949 while the evaluated limits of detection were 8.3 x 10^{-7} M, 4.7 x 10^{-7} M and 7.6 x 10^{-7} M respectively.

Keywords: PVC membrane, dithizone (1,5-diphenylthiocarbazone), cyclic voltammetry, redox reactions

Abstrak

Membran PVC-Ditizon telah dibina dan digunakan sebagai bahan reagen ionofora bagi elektrod perak (Ag) yang diubahsuai secara kimia. Elektrod yang diubahsuai telah dicirikan menggunakan voltametri berkitar di mana sifat elektrokimia bagi ditizon yang diubahsuai pada permukaan elektrod Ag telah dikaji di dalam julat -0.6 ke +0.6 V dengan 0.1 M KCl sebagai elektrolit sokongan. Kajian perbandingan terhadap ion-ion logam Cu^{2+}, Fe^{2+} dan Pb^{2+} mempamerkan respon yang baik bagi tindak balas redoks dengan hubungan linear antara arus-arus puncak dan kepekatan. Pekali korelasi yang diperolehi adalah 0.9800, 0.9944 dan 0.9949 manakala had pengesanan yang diukur adalah 8.3 x 10^{-7} M, 4.7 x 10^{-7} M dan 7.6 x 10^{-7} M masing-masing.

Kata kunci: membran PVC, ditizon (1,5-difeniltiokarbazon), voltametri berkitar, tindakbalas redoks

Introduction

Heavy metals pollution in environment is a global issue that has been discussed over the years. Heavy metals can enter the environment by both natural and anthropogenic sources including mining, agrochemicals, sewage and sludge applications and also industrial activity. Copper (Cu^{2+}), iron (Fe^{2+}) and lead (Pb^{2+}) are the most common existence of toxic metal ions in aqueous environmental solution. Although metal ions such as Cu^{2+} and Fe^{2+} are categorized as micronutrients at low concentrations, however, in excess contamination, these metals can be highly toxic [1].

Since the last few decades, the need to determine these heavy metal ions in aqueous environments has been highly focused especially in the field of environmental, pharmaceutical and biomedical studies [2, 3]. Electrochemical techniques in particular, chemically modified electrodes have received a great deal of attentions for determination of heavy metal ions [4]. These modified electrodes were prepared in varieties of specific modification processes in

order to improve the sensitivity and specification of the sensing purposes. Different modification processes such as physisorption [5], chemisorption [6], covalent attachment [7], modified polymers [8] and bulk modification of carbon composite materials [9] have been reported. In this study, surface modification of the electrode via polymerized chemisorption coating was applied using the specific and selective dithizone reagent. This method provides a particular function on the electrode surface such as a medium for metal ion bonding and unique properties of metal complexes [10].

Dithizone or 1,5-diphenylthiocarbazone (H_2D_Z) is an organic chelating reagent that was initially used for calorimetric determination of trace metal ions [11]. It was discovered by Helmuth Fischer, and the vast potential of dithizone has been reveiled in 1925 [12]. Through the years, applications of dithizone become widely used and continue to be expended in many analytical researches. Due to its capability in exhibit ions interesting redox chemistry, the electrochemical behaviour of dithizone has been studied [13]. With the presence of azo and sulfhydryl groups, the oxidation and reduction of dithizone can be characterized. Previous studies shown that dithizone has been exploited in chemically modified electrode as a modifier for determination of metal ions [14-15].

In this study, the immobilization of dithizone as a polymerized polyvinyl chloride (PVC) membrane was carried out in order to improve the stability and sensitivity of the reagent. PVC act as a polymer matrix that can be easily incorporated with an ionophore, and was commonly used in many electrochemical studies [16 – 17]. It was first investigated by Heineman and coworkers in 1980, which demonstrated the application of polymer film in chemically modified electrode [18]. A platinum (Pt) disk composed of PVC film impregnated with valinomycin can offer high selectivity and electrochemical activity on the PPy/PPS layer [19]. The modified electrode showed a stable standard potential of potassium ion. Recently, studies of PVC film coated in Pt electrode for the determination of chromium showed good detection limit of 6.8×10^{-8} M with linear concentration range of 8.4×10^{-8} M - 1.0×10^{-2} M. The sensor was successfully developed with the fast response time in 10 s [20]. Therefor, a new modified Ag electrode coated with polymerized chemisorption dithizone-PVC membrane as an electroactive reagent has been investigated. The electrochemical behaviour of the modified Ag electrode was described using cyclic voltammetric technique with several parameters studied.

Materials and Methods

Chemicals and reagent

All chemicals and reagent were of analytical grade and were used without further purification. Dithizone was obtained from Merck, Darmstadt, Germany. All metal salts, Copper (II) Sulphate, Iron (II) Chloride and Lead (II) Sulphate were of analytical grade from R & M Marketing, Essex, U.K. Other chemicals were polyvinyl chloride (PVC) from Sigma-Aldrich, tributyl phosphate (TBP), tetrahydrofuran (THF), sodium tetraphenylborate $NaB(C_6H_5)_4$ and hydrochloric acid (HCl) from Merck Darmstadt, Germany. Deionized water was used throughout the preparation of the samples.

Instrumentation

Electrochemical measurements were performed using Autolab model PGSTAT30 from Metrohm Ltd, Herisau, Switzerland.

Preparation of modified Ag electrode

Initially, dithizone-PVC membrane was prepared by mixing 120 mg of PVC powder, 10 mg of dithizone as ionophore and 1.5 mg of $NaB(C_6H_5)_4$ as a lipophilic additive with 240 mg of TBP. The mixture was dissolved in 6 ml of THF and was stirred for 3 hours. At the mean time, Ag electrode was polished repeatedly with sandpaper and was then thoroughly rinsed with acetone and followed by distilled water. Then, the Ag electrode was dipped into the dithizone-PVC membrane cocktail prepared, for 10 s. Finally, the modified Ag electrode was dried at room temperature for 1 hour before use.

Characterization of modified Ag electrode using cyclic voltammetry

All measurements were done using a conventional three electrode system. A Ag electrode modified with a dithizone-PVC membrane coating was used as a working electrode with a surface area of 0.60 cm^2. The Pt electrode and Ag/AgCl electrode were used as auxiliarly and reference electrodes, respectively. All electrochemical

experiments were carried out at room temperature and the potential was scanned in the range of -0.6 to +0.6 V at 0.1 Vs^{-1}.

Results and Discussion

Electrochemical characterization

The modified Ag electrode with dithizone-PVC membrane was characterized using cyclic voltammetry (CV) with and without the presence of metal ions containing 0.1 M KCl as supporting electrolyte. The CV was performed using a potential range between -0.6 to +0.6 V (vs. Ag/AgCl) with the scan rate of 0.1V s^{-1}. The voltammogram is represented in Figure 1. Line (a) shows the response of dithizone modified Ag electrode without metal ion, line (b), (c) and (d) show the responses of dithizone modified Ag electrode with $1x10^{-3}$ M Cu^{2+}, Pb^{2+} and Fe^{2+}, respectively. For modification of Ag electrode with Cu^{2+}, two reduction peaks can be observed from -0.1 to -0.3 V, corresponds to the two-electron reduction of Cu(II) to Cu(I) and Cu(0) (eq. 1 and Eq. 2). However, only one oxidation peak was observed at +0.2 V corresponding to the deposition of Cu(0) to Cu(I)/Cu(II) [21]. The proposed mechanism is illustrated as below:

$$Cu^{2+} + e^- \longrightarrow Cu^+ \quad (1)$$

$$Cu^+ + e^- \longrightarrow Cu^0 \quad (2)$$

The same reduction peaks also can be seen in modified Ag electrode with Pb^{2+} and Fe^{2+} from the range of -0.14 to -0.35 V and -0.15 to -0.36 V respectively. The reduction process for each metal ion showed that the dithizone-PVC membrane incorporates well with metal ions on the electrode surface, thus improved the electrode's performance. Meanwhile, the oxidation peak for modified Ag electrode with Pb^{2+} and Fe^{2+} was observed at +0.30 V and +0.20 V, respectively.

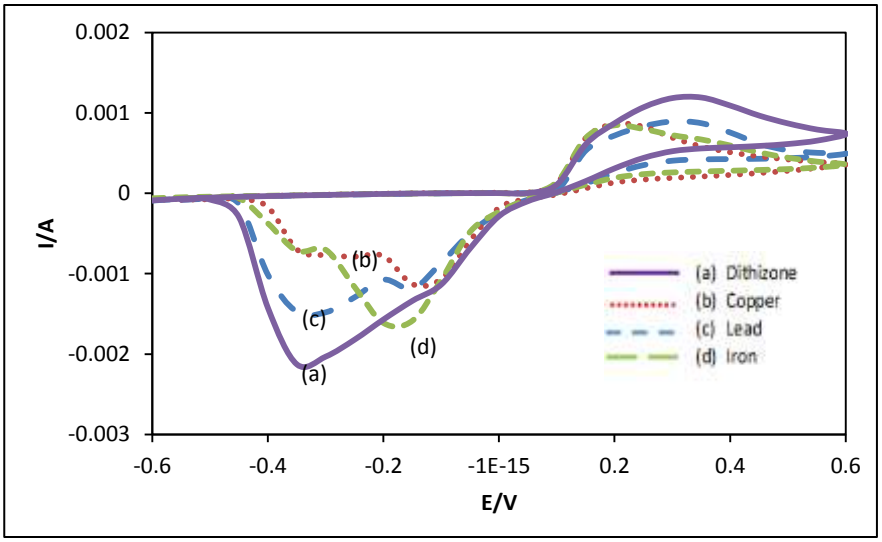


Figure 1. Cyclic voltammograms of (a) dithizone modified Ag electrode without metal (b) dithizone modified Ag electrode in Cu^{2+}, (c) dithizone modified Ag electrode in Pb^{2+}, and (d) dithizone modified Ag electrode in Fe^{2+}.

Effect of scan rates

In cyclic voltammetry, scan rate was used to determine the electrochemical behavior of a species generated at the modified electrode [22]. In this research, scan rate were optimized in order to characterized the redox reaction. Figure 2 (a), (b) and (c) show the effect of scan rates on the voltammogram of modified Ag electrode in the

potential range of 0.1 to 0.3 Vs^{-1} for Cu^{2+}, Pb^{2+} and Fe^{2+}. Increasing the potential scan rate influenced the change of peak current in both redox reactions. As it can be seen, the change of peak current in cathodic reaction shifted to more negative value with the increasing of scan rates for all metal ions.

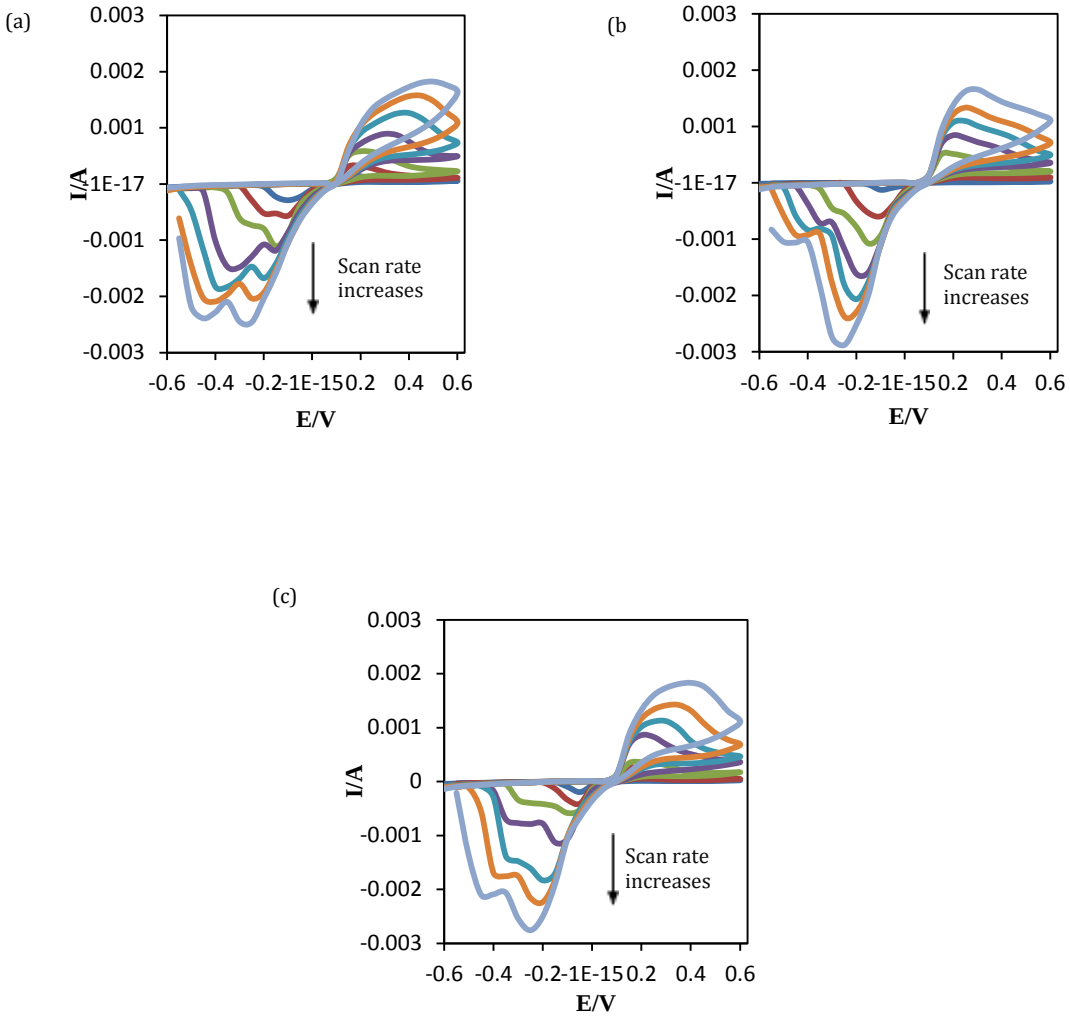


Figure 2. Optimization of scan rates on cyclic voltammograms of dithizone modified Ag electrode in $1x10^{-3}$ M of (a) Pb^{2+}, (b) Fe^{2+} and (c) Cu^{2+} with 0.1 M KCl as supporting electrolyte. (0.01 V, 0.025 V, 0.05 V, 0.1 V, 0.15 V, 0.2 V and 0.3 V).

The relationship between peak current densities, i_p, and peak on the square root of scan rate ($v^{1/2}$), can be determined using the Randles-Sevcik equation (Eq. 3) [23].

$$i_p = (2.69 \times 10^5) n^{3/2} A D^{1/2} v^{1/2} C \quad (3)$$

where n is the number of electrons passed per molecule, A is the electrode area (in cm^2), D is the diffusion coefficient of analytes (in $cm^2\ s^{-1}$) and C represents the concentration of analytes (in mol cm^{-3}). A graph on peak current densities (i_p) vs. square root of scan rate ($v^{1/2}$) was illustrated in Figure 3. The results show that the linear

relationships were obtained with the i_p is proportional to $v^{1/2}$ which indicates that the mechanism of mass transfer occurs from the bulk of the metal ion solution to the electrode surface by diffusion process. This behavior indicates that the electrochemical process was diffusion controlled [24-25].

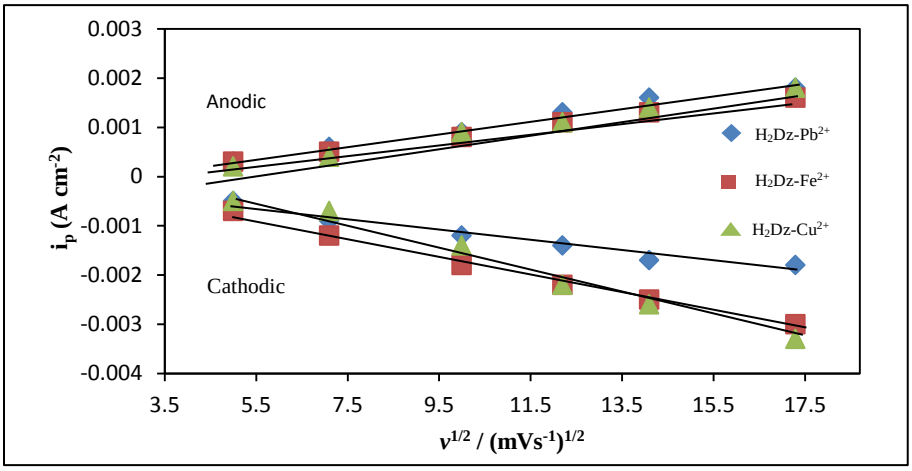
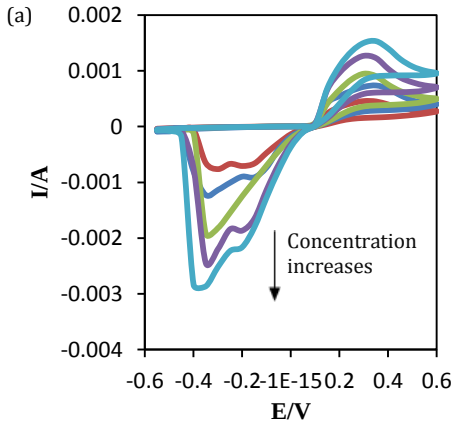
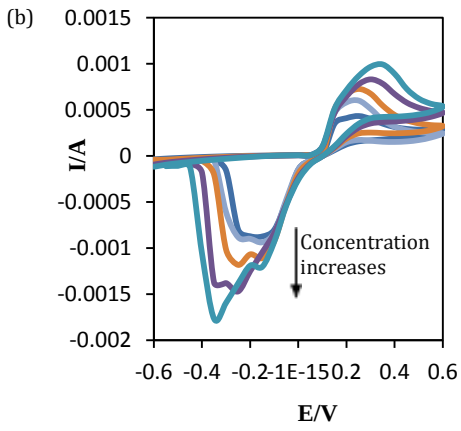


Figure 3. The relationship between peak current densities (i_p) on the $v^{1/2}$ for the H_2Dz modified Ag electrode in $1x10^{-3}$ M of Pb^{2+}, Fe^{2+} and Cu^{2+}.

Effect of different concentration

In order to investigate the influence of metal ions concentration on the cyclic voltammogram, study on different concentrations of metal ions Pb^{2+}, Fe^{2+} and Cu^{2+} were carried out. Figure 4 (a), (b) and (c) show the cyclic voltammogram for concentration of metal ions from 2 x 10^{-5} M to 10 x 10^{-5} M in 0.1 KCl at the scan rate of 0.1 Vs^{-1}. As can be seen from the figure, the anodic and cathodic peak current increase with the increasing of concentration. This indicates the concentration of metal ion Pb^{2+}, Fe^{2+} and Cu^{2+} are proportional to the electrochemical peak current.





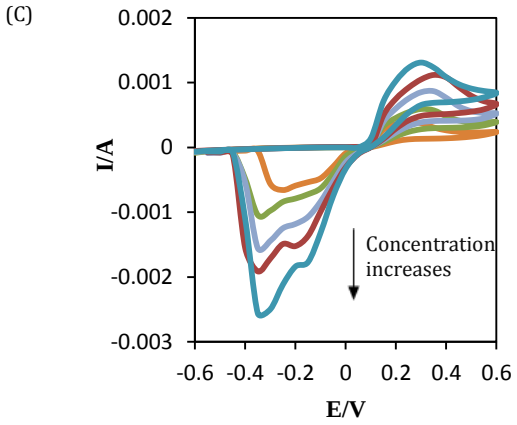


Figure 4. Cyclic voltammograms of different concentration of metal ions (a) Pb^{2+}, (b) Fe^{2+} and (c) Cu^{2+} deposited on the dithizone modified Ag electrode. (2 x 10^{-5} M, 4 x 10^{-5} M, 6 x 10^{-5} M, 8 x 10^{-5} M and 10 x 10^{-5} M).

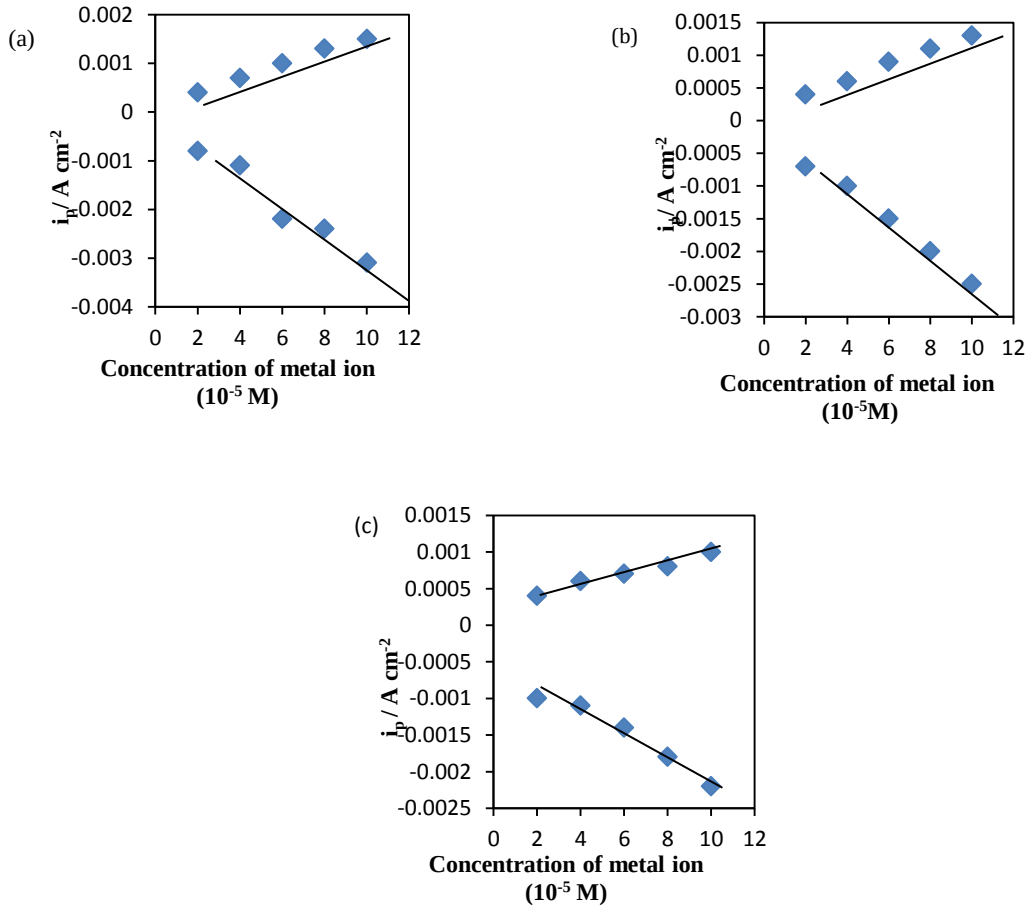


Figure 5. The relationship between peak current densities (i_p) on concentration of metal ions (a) Pb^{2+}, (b) Fe^{2+} and (c) Cu^{2+} at dithizone modified Ag electrode.

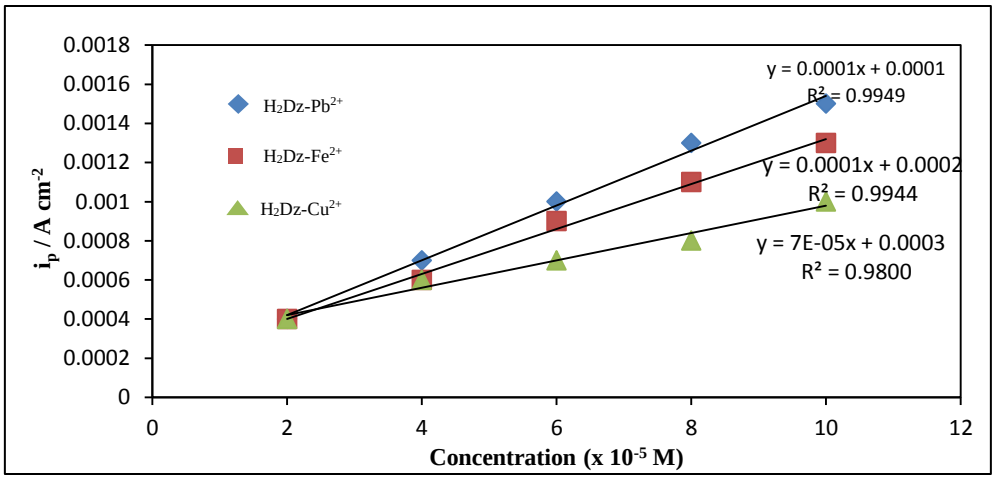


Figure 6. Calibration graph of peak current, i_p versus the concentration of metal ions using H_2Dz modified Ag electrode in 0.1 M KCl as supporting electrolyte.

Limit of Detection (LOD)

A calibration graph for the response of dithizone modified Ag electrode towards the metal ion Cu^{2+}, Fe^{2+} and Pb^{2+} has been plotted in Figure 6 to determine the sensitivity of the system. Within the potential range of -0.6 to +0.6 V, the correlation coefficient observed for Cu^{2+}, Fe^{2+} and Pb^{2+} were 0.9800, 0.9944 and 0.9949. From the results obtained, the evaluated values for LOD were 8.3 x 10^{-7} M, 4.7 x 10^{-7} M and 7.6 x 10^{-7} M, respectively.

Conclusion

The modification of Ag electrode based on dithizone as an ionophore reagent has been successfully developed to determine the concentration of Pb^{2+}, Fe^{2+} and Cu^{2+} in aqueous solutions. The modification using immobilized dithizone in PVC membrane via chemisorptions on the surface of Ag electrode exhibited irreversible process in a wide potential range from -0.6 to +0.6 V. The system showed excellent electrochemical characteristics with a good limit of detection in the range of 4.7 x 10^{-7} M to 8.3 x 10^{-7} M for those three metal ions studied. Hence, a new chemically modified electrode for detection of Pb^{2+}, Fe^{2+} and Cu^{2+} based on dithizone modified Ag electrode has been developed.

Acknowledgement

The authors would like to acknowledge Universiti Malaysia Terengganu and Ministry of Higher Education (MOHE) for the funding of this study (RAGS).

References

1. Schwartz, M. S., Benci, J. L., Selote, D. S., Sharma, A. K., Chen, A. G. Y., Dang, H., Fares, H., Vatamaniuk, O. K. (2010). Detoxification of multiple heavy metals by a half-molecule ABC transporter, HMT-1, and coelomocytes of Caenorhabditis elegans. *PLoS ONE* 5 (3): e9564.
2. Reeve, R. N. (2002). Introduction to Environmental analysis. (1st ed.) John Wiley & Sons Ltd.
3. Zejli, H., Sharrock, P., Hidalgo-Hidalgo de Cisneros, J. L., Naranjo-Rodriguez, I. and Temsamani, K. R. (2005). Voltammetric determination of trace mercury at a sonogel-carbon electrode modified with poly-3-methylthiophene. *Talanta* 68: 79 – 85.
4. Pournaghi-Azar, M. H. and Dastangoo, H. (2003). Electrochemical behavior of a novel palladium pentacyanonitrosylferrate modified aluminum electrode. *Electrochimica Acta* 48: 1797 – 1806.
5. Prieto-Simon, B. and Fabregas, E. (2004). Comparative study of electron mediators used in the electrochemical oxidation of NADH. *Biosensor Bioelectron* 19: 1131 – 1138.

6. Faucheux, N., Schweiss, R., Lutzow, K., Werner, C. and Groth, T. (2004). Self-assembled monolayers with different terminating groups as model substrates for cell adhesion studies. *Biomaterials* 25: 2721 –2730.
7. Wang, H., Xu, G. and Dong, S. (2001). Electrochemistry and electrochemiluminescence of stable (2,2'bipyridyl)ruthenium(II) monolayer assembled on benzene sulfonic acid modified glassy carbon electrode. *Talanta* 55: 61 – 67.
8. Kan, J., Pan, X. and Chen, C. (2004). Polyaniline-uricase biosensor prepared with template process. *Biosensor Bioelectron* 19: 1635 – 1640.
9. Calvo-Marzal, P., Torres, K., Hoehr, N., Neto, G. and Kubota, L. (2004). Determination of reduced gluthathione using an amperometric carbon paste electrode chemically modified with TTF-TCNQ. *Sensor Actuat* B 100: 337 – 344.
10. Toma, H. E., Zamarion, V. M., Toma, S. H. and Araki, K. (2010). The coordination chemistry at gold nanoparticles. *Journal Brazilian Chemical Soc*iety 21 (7): 1158 – 1176.
11. Tomcsányim, L. (1974). Investigations on the redox character of dithizone by voltammetric methods. Part I. The reduction of dithizone in aqueous solutions. *Analytical Chimica Acta* 70: 411 – 416.
12. Karel, G. V. E. and Jannie, C. S. (2010). Chemical and electrochemical oxidation and reduction of dithizone. *Polyhedron* 29: 1727 – 1733.
13. Jeanne, E. P., and Richard, P. B. (1981). Dithizone adsorption at metal electrodes. Electrochemical characterization of dithizone anion at silver electrode. *Journal of Electroanalytical Chem*istry 132: 291 – 309.
14. Kalcher, K. and Fresenius, Z. (1986). Voltammetrisches Verhalten von Gold an einer Dithizon-modifizierten Kohlenpasteelectrode. *Anaytical Chem*istry 325: 181 – 185.
15. Labuda, J. and Plaskon, V. (1990). Determination of mercury ions on a diphenylcarbazone bulk modified graphite electrode. *Analytica Chimica Acta* 228: 259 – 263.
16. Abbaspour, A., and Izadyar, A. (2001). Highly selective electrode for Nickel (II) ion based on 1,5-diphenylthiocarbazone (dithizone). *Microchemical Journal* 69: 7 – 11.
17. Singh, A. K., and Saxena, P. (2007). A PVC-based membrane electrode for nickel (II) ions incorporating a tetraazamacrocycle as an ionophore. *Sensors and Actuators B* 121: 349 – 355.
18. Heineman, W. R., Wieck, H. J. and Yacynych, A. M. (1980). Polymer Film Chemically Modified Electrode as a Potentiometric Sensor. Analytical Chemistry. *Analytical Chem*istry 52: 345 – 346.
19. Momma, T., Komaba, S., Yamamoto, M., Osaka, S. and Yamauchi, S. (1995). All-solid potassium-selective electrode using double-layer film of polypyrrole/polyanion composite and plasticized poly(vinyl chloride) containing valinomycin. *Sensors and Actuators* B24-B25: 724 – 728.
20. Abbaspour, A., Refahi, M., Khalafi-Nezhad, A., Rad, N. S. and Behrouz, S. (2010). Carbon composite-PVC based membrane coated platinum electrode for chromium determination. *Journal of Hazardous Materials* 184: 20 – 25.
21. Eliane, R. D. S., Edmar, P. M., Elizabeth, N. F., Jiujun, Z. and Aldalea, L. B. M. (2006). Graphite electrodes modified by 8-hydroxyquinolines and its application for the determination of copper in trace levels. *Journal Brazilian Chemical Soc*iety 17: 177 – 183.
22. Alice, D. L. (2011). Electrochemical analysis supported by macro and microelectrode array. Durham University, Durham, United kingdom.
23. Somerset, V., Leaner, J., Mason, R., Iwuoha, E. and Morrin, A. (2010). Development and application of poly(2,2-dithiodianiline) (PDTDA) coated screen-printed carbon electrode in inorganic mercury determination. *Electrochemical Acta* 55: 4240 – 4246.
24. Daud, N., Yusof, N. A., Nor, S. M. M. (2013). Electrochemical characteristic of biotinyl somatostation-14/Nafion modified gold electrode in development of sensor for determination of Hg(II). *International Journal Electrochemical Science* 8: 10086 – 10099.
25. Afkhami, A., Felehgari, F. S. and Madrakian, T. (2013). Gold nanoparticles modified carbon paste electrode as an efficient electrochemical sensor for rapid and sensitive determination of cefixime in urine and pharmaceutical samples. *Electrochemical Acta* 103: 125 – 133.
26. Zaky, A. M., Abd El-Rehim, S. S. and Mohamed, B. M. (2006). Effect of addition of sulphide ions on the electrochemical behavior and corrosion of Cu-Ag Alloys in alkaline solutions. *International Journal Electrochemical Science* 1: 17 – 31.
27. Riyanto., Othman, M, R. and Salimon, J. (2007). Analysis of ethanol using copper and nickel sheet electrodes by cyclic voltammetry. *Malaysian Journal of Analytical Sciences* 11 (2): 379 – 387.

Malaysian Journal of Analytical Sciences Vol 20 No 2 2016

Articles 11-24 are selected papers from the " International Conference on Applied Sciences and Industrial Technology (ICASIT 2015) for Chemistry and Environment Symposium, 24-26 February 2015, Grand Lexis, Port Dickson, Negeri Sembilan, Malaysia; organised by Faculty of Applied Science, Universiti Teknologi MARA, Shah Alam, Selangor, Malaysia."

Guest Editors: Rohaya Ahmad, Sabiha Hanim Saleh, Nesamalar V Kantasamy, Rozita Osman

Articles 25-30 are selected papers from the " UniSZA Research Conference 2015 (URC 2015), 14-16 April 2015, Universiti Sultan Zainal Abidin, Gong Badak Campus, Kuala Terengganu, Terengganu; organised by Centre For Research and Innovation Management (CRIM) UniSZA."

Guest Editors: Mohd Ekhwan Toriman, Mohd Khairul Amri Kamarudin, Hafizan Juahir, Roslan Umar, Azman Azid, Saiful Iskandar Khalit, Azizah Endut, Zarina Mohamad, Saiful Bahri Mohamed.

Page

1. CHROMATOGRAPHIC DETERMINATION OF TOLUENE AND ITS METABOLITES IN URINE FOR TOLUENE EXPOSURE – A REVIEW (Penentuan Kromatografi Toluena dan Metaboliknya di dalam Urin bagi Pendedahan Toluena – Satu Ulasan) 205
Mohamad Raizul Zinalibdin, Abdul Rahim Yacob, Mohd Marsin Sanagi

2. FAST AND SIMPLE FORENSIC RED PEN INK ANALYSIS USING ULTRA-PERFORMANCE LIQUID CHROMATOGRAPHY (UPLC) 224
(Analisis Forensik Cepat dan Mudah bagi Dakwat Pen Merah menggunakan Kromatografi Cecair Berprestasi Ultra)
Loong Chuen Lee, Seow Lay Ying, Wan Nur Syazwani Wan Mohamad Fuad, Ab Aziz Ishak, Khairul Osman

3. PENGGUNAAN KAEDAH PENYINARAN MIKROGELOMBANG DALAM SINTESIS TERBITAN TIOUREA 231
(An application of Microwave Irradiation Technique in Preparation of Thiourea Derivatives)
Hafizi Ahyak, Atisya Rohadi, Fatimatul Akma Awang Ngah, Bohari Yamin, Siti Aishah Hasbullah

4. TWO ISOLATED CRYSTALLINE SOLIDS FROM THE STEM OF *Entada spiralis* Ridl. (AKAR SINTOK) 238
(Pemencilan Dua Jenis Pepejal Kristal dari Batang Pokok *Entada spiralis* (Akar Sintok))
Aiza Harun, Siti Zaiton Mat So'ad, Norazian Mohd Hassan

5. STABILITY INDICATING RP-HPLC METHOD FOR SIMULTANEOUS DETERMINATION OF ASPIRIN AND CLOPIDOGREL IN DOSAGE FORM 247
(Kestabilan Kaedah KCPT-Indikator bagi Penentuan Serentak Asprin dan Clopidogrel Dalam Bentuk Dos)
Md. Gousuddin, Pinaki Sengupta, Vijaya Datt Tripathi, Arindam Das

6. REMOVAL OF MALACHITE GREEN DYE FROM AQUEOUS SOLUTION USING MULTI-WALLED CARBON NANOTUBES: AN APPLICATION OF EXPERIMENTAL DESIGN 258
(Penyingkiran Malakit Hijau daripada Larutan Akues Menggunakan Karbon Tiub Nano: Aplikasi Reka Bentuk Eksperimen)
Siti Aminah Zulkepli, Md Pauzi Abdullah, Wan Mohd Afiq Wan Mohd Khalik

7. UTILIZATION OF ENCAPSULATED $CaCO_3$ IN LIQUID CORE CAPSULES FOR IMPROVING LACTIC ACID FERMENTATION 272
(Penggunaan Kapsul Berteras Cecair yang Mengandungi $CaCO_3$ untuk Menambah Baik Penapaian Bakteria Asid Laktik)
Boon-Beng Lee and Nurul Ainina Zulkifli

8. CHEMOMETRIC ANALYSIS OF SELECTED ORGANIC CONTAMINANTS IN SURFACE WATER OF LANGAT RIVER BASIN 278
(Analisis Kemometrik Bahan Cemar Organik Terpilih dalam Air Permukaan Lembangan Sungai Langat)
Mohamad Rafaie Mohamed Zubir , Rozita Osman, Norashikin Saim

9. POLYVINYLPYRROLIDONE AS A NEW FLUORESCENT SENSOR FOR NITRATE ION 288
(Polivinilpirolidon Sebagai Sensor Pendafluor Baru Bagi Ion Nitrat)
Ing Hua Tang, Rita Sundari, Hendrik O. Lintang, Leny Yuliati

10. OXIDATION OF COMMERCIAL PETRONAS DIESEL WITH TERT-BUTYL HYDROPEROXIDE OVER POLYMOLYBDATE ALUMINA SUPPORTED CATALYST MODIFIED WITH ALKALINE EARTH METALS 296
(Pengoksidaan Diesel Komersial Petronas dengan Tert-Butil Hidroperoksida bersama Pemangkin Polimolibdenum Diubahsuai dengan Logam Alkali)
Wan Nazwanie Wan Abdullah, Rusmidah Ali, Wan Azlee Wan Abu Bakar

11. HYDROGEN PRODUCTION FROM GASIFICATION OF PALM KERNEL SHELL IN THE PRESENCE OF Fe/CeO_2 CATALYSTS 303
(Penghasilan Hidrogen daripada Pengegasan Isirung Kelapa Sawit dengan Kehadiran Mangkin Fe/CeO_2)
Anita Ramli, Mas Fatiha Mohamad, Suzana Yusup, Taufiq Yap Yun Hin

12. DEVELOPMENT OF CELLULOSE NANOFIBRE (CNF) DERIVED FROM KENAF BAST FIBRE AND IT'S POTENTIAL IN ENZYME IMMOBILIZATION SUPPORT 309
(Penghasilan Gentian-Nano Selulosa (CNF) diperolehi daripada Gentian Kulit Kenaf dan Potensinya sebagai Penyokong Pemegunan Enzim)
Safwan Sulaiman, Mohd Noriznan Mokhtar, Mohd Nazli Naim, Azhari Samsu Baharuddin, Mohamad Amran Mohd Salleh, Alawi Sulaiman

13. CHEMICAL PROFILING AND IDENTIFICATION OF ALKALOIDS AND FLAVONOIDS IN *Uncaria lanosa* var. *ferrea* VIA UHPLC-ORBITRAP MS 318
(Profil Kimia dan Pengenalan Alkaloid dan Flavonoid dalam *Uncaria lanosa* var. *ferrea* melalui UHPLC - Orbitrap MS)
Nursyaza Husna Shaharuddin, Nor Hadiani Ismail, Nurhuda Manshoor, Fatimah Salim, Rohaya Ahmad

14. EFFECT OF PALM OIL FIBER-TiO_2 RATIO IN THE COMPOSITE ON THE REDUCTION OF BTX AND FORMALDEHYDE IN THE AIR 324
(Kesan Nisbah Serat Kelapa Sawit-TiO_2 dalam Komposit bagi Pengurangan Kandungan BTX dan Formaldehid di Udara)
Nor Rahafza Abdul Manap, Roslinda Shamsudin, Mohd Norhafsam Maghpor, Muhammad Azmi Abdul Hamid, Azman Jalar

15. FRACTIONATION OF HEMICELLULOSE FROM RICE STRAW BY ALKALINE EXTRACTION AND ETHANOL PRECIPITATION 329
(Pemisahan Hemiselulosa daripada Hampas Batang Padi melalui Pengekstrakan Beralkali dan

Pemendakan Etanol)
Nur Hazlilla Zulyadi, Sabiha Hanim Saleh, Siti Halimah Sarijo

16. PREPARATION, CHARACTERIZATION AND PERFORMANCE STUDIES OF ACTIVE PVDF ULTRAFILTRATION-SURFACTANTS MEMBRANES CONTAINING PVP AS ADDITIVE 335
(Penyediaan, Pencirian dan Kajian Prestasi PVDF Aktif Ultraturasan-Surfaktan Membran mengandungi PVP sebagai Bahan Tambahan)
Nur Izzah Md Fadilah and Abdul Rahman Hassan

17. AN EXPERIMENTAL DESIGN METHOD FOR THE EXTRACTION OF EURYCOMANONE FROM TONGKAT ALI (*Eurycoma longifolia*) ROOTS USING PRESSURISED LIQUID EXTRACTION (PLE) 342
(Kaedah Reka bentuk Eksperimen bagi Pengekstrakan Eurikomanon daripada Akar Tongkat Ali (*Eurycoma longifolia*) Menggunakan Pengekstrakan Cecair Tekanan Tinggi)
Rozita Osman, Norashikin Saim, Mardiana Saaid, Nor Nasriah Zaini

18. MESOPOROUS SILICA ELECTROCHEMICAL SENSORS FOR THE DETECTION OF ASCORBIC ACID AND URIC ACID 351
(Sensor Elektrokimia Silika Berliang Meso untuk Pengesanan Asid Askorbik dan Asid Urik)
Hashazirah Mohamad Hassan, Nurul Barakah Ab Rahman, Mohammad Noor Jalil

19. EQUILIBRIUM AND THEMODYNAMIC STUDIES OF ANIONIC DYES REMOVAL BY AN ANIONIC CLAY-LAYERED DOUBLE HYDROXIDE 358
(Kajian Keseimbangan dan Termodinamik dalam Penyingkiran Pewarna Anionik daripadaTanah Liat Anionik-Dwi Hidroksida Berlapis)
Nesamalar Kantasamy and Siti Mariam Sumari

20. IDENTIFICATION OF HAZARDOUS EVENTS FOR DRINKING WATER PRODUCTION PROCESS USING MANAGED AQUIFER RECHARGE IN THE NAKDONG RIVER DELTA, KOREA 365
(Pengenalpastian Kejadian Berbahaya bagi Proses Pengeluaran Air Minuman Menggunakan Akuifer Terkawal Cas Semula dalam Delta Sungai Nakdong, Korea)
Sang-Il Lee and Hyon Wook Ji

21. ELECTROCHEMICAL SYNTHESIS OF ORDERED TITANIA NANOTUBES IN MIXTURE OF ETHYLENE GLYCOL AND GLYCEROL ELECTROLYTE 373
(Sintesis Nanotiub Titania Bertertib Secara Elektrokimia dalam Campuran Elektrolit Etilena Glikol dan Gliserol)
Lim Ying Chin, Zulkarnain Zainal, Zuraida Khusaimi, Siti Sarah Ismail

22. TEMPERATURE PROGRAMMED REDUCTION AND X-RAY DIFFRACTOMETRY STUDIES OF MoO_3 REDUCTION BY DIFFERENT CONCENTRATIONS OF CARBON MONOXIDE 382
(Kajian Penurunan Suhu Berprogram dan Pembelauan Sinar-X Terhadap Penurunan MoO_3 Menggunakan Kepekatan Karbon Monoksida Berbeza)
Alinda Samsuri, Tengku Shafazila Tengku Saharuddin, Fairous Salleh, Rizafizah Othaman, Mohamed Wahab Mohamed Hisham, Mohd. Ambar Yarmo

23. CHEMICAL CONSTITUENTS FROM THE LIANAS OF *Gnetum cuspidatum* Blume 388
(Sebatian Kimia dari Lianas *Gnetum cuspidatum* Blume)
Nik Fatini Nik Azmin, Norizan Ahmat, Nik Khairunissa Nik Abdullah Zawawi

24. EFFECT OF SUPPORT MATERIALS ON CATALYTIC ACTIVITY OF NANO RUTHENIUM CATALYST IN HYDROGENOLYSIS OF GLYCEROL 393
(Kesan Bahan Penyokong Terhadap Aktiviti Pemangkin Nano Ruthenium dalam Hidrogenolisis Gliserol)

Noraini Hamzah and Mohd Ambar Yarmo

25. *Moringa oleifera* SEED DERIVATIVES AS POTENTIAL BIO-COAGULANT FOR MICROALGAE *Chlorella* sp. HARVESTING 401
(Potensi Derivatif Biji *Moringa oleifera* sebagai Bio-Pengental untuk Penuaian Mikroalga *Chlorella* sp.)
Azizah Endut, Siti Hajar Abdul Hamid, Fathurrahman Lananan, Helena Khatoon

26. CHEMICAL AND BIOLOGICAL ANALYSES OF MALAYSIAN STINGLESS BEE PROPOLIS EXTRACTS 413
(Analysis Kimia dan Biologi Ekstrak Propolis Lebah Kelulut Malaysia)
Nurhamizah Ibrahim, Nurul Farah Shakila Mohd Niza, Muhammad Muslim Mohd Rodi, Abdul Jamil Zakaria, Zhari Ismail, Khamsah Suryati Mohd

27. CHARACTERIZATION OF $CaCO_3$ MICROSPHERES FABRICATED USING DISTILLED WATER 423
(Pencirian $CaCO_3$ Mikrosfera Difabrikasi Menggunakan Air Suling)
Intan Nabila Sabri, Nadiawati Alias, Abdul Manaf Ali, Javeed Shaikh Mohammed

28. EMULSION LIQUID MEMBRANE TECHNOLOGY IN ORGANIC ACID PURIFICATION 436
(Teknologi Emulsi Membran Cecair dalam Penulenan Asid Organik)
Norela Jusoh, Norasikin Othman, Nur Alina Nasruddin

29. THE POTENTIAL OF COCONUT SHELL POWDER (CSP) AND COCONUT SHELL ACTIVATED CARBON (CSAC) COMPOSITES AS ELECTROMAGNETIC INTERFERENCE (EMI) ABSORBING MATERIAL 444
(Potensi Serbuk Tempurung Kelapa (CSP) dan Karbon Teraktif Tempurung Kelapa (CSAC) Sebagai Bahan Penyerap Gangguan Elektromagnatik)
Siti Nurbazilah Ab. Jabal, Yew Been Seok, Wee Fwen Hoon

30. ANALYSIS OF SEASONAL SOIL ORGANIC CARBON CONTENT AT BUKIT JERIAU FOREST, FRASER HILL, PAHANG 452
(Analisis Kandungan Karbon Organik Tanah Secara Bermusim Di Hutan Bukit Jeriau, Fraser Hill, Pahang)
Ahmad Adnan Mohamed, Sahibin Abd. Rahim, David Allan Aitman, Mohd Khairul Amri Kamarudin

MALAYSIAN JOURNAL OF ANALYTICAL SCIENCES
Published by The Malaysian Analytical Sciences Society
ISSN 1394 - 2506

CHROMATOGRAPHIC DETERMINATION OF TOLUENE AND ITS METABOLITES IN URINE FOR TOLUENE EXPOSURE – A REVIEW

(Penentuan Kromatografi Toluena dan Metaboliknya di dalam Urin bagi Pendedahan Toluena – Satu Ulasan)

Mohamad Raizul Zinalibdin[1, 2], Abdul Rahim Yacob[1], Mohd Marsin Sanagi[1, 3]*

[1]*Department of Chemistry, Faculty of Science,*
Universiti Teknologi Malaysia, 81310 UTM Johor Bahru, Johor, Malaysia
[2]*Department of Chemistry,*
Johor Branch, Jalan Abdul Samad, 80100 Johor Bahru, Johor, Malaysia
[3]*Centre for Sustainable Nanomaterials,*
Ibnu Sina Institute for Scientific and Industrial Research,
Universiti Teknologi Malaysia, 81310 UTM Johor Bahru, Johor, Malaysia

**Corresponding author: marsin@kimia.fs.utm.my*

Received: 1 November 2015; Accepted: 10 March 2016

Abstract

The determinations of toluene and their metabolites in biological samples such as urine and blood allow the estimation of the degree of exposure to this chemical. Chromatographic methods and preliminary methods are now universally employed for this purpose. Preliminary color test methods are well established for qualitative determination of toluene and its metabolites. Mobile test kits using color test methods are a vast tool for screening urine samples but chromatographic methods are still needed for confirmation and quantitative analysis. Gas chromatography (GC) methods are well-adapted for the determination of toluene metabolite in urine, but these methods often require several pretreatment steps. Meanwhile, high performance liquid chromatography (HPLC) is becoming a powerful tool for the accurate and easy determination of toluene metabolites considering its decisive advantages for routine monitoring. Furthermore, recent development in HPLC could widen the usefulness of this method to solve the most complex analytical problems that could be encountered during the measurement.

Keywords: toluene, toluene metabolites, preliminary test, gas chromatography, high performance liquid chromatography

Abstrak

Penentuan toluena dan metabolitnya dalam sampel biologi seperti urin dan darah membolehkan anggaran tahap pendedahan terhadap bahan kimia ini. Kaedah kromatografi dan kaedah awalan merupakan kaedah yang sering digunakan untuk tujuan ini pada masa kini. Kaedah awalan menggunakan ujian warna telah dibangunkan untuk penentuan kualitatif toluena dan metabolit. Kit ujian mudah alih menggunakan ujian warna meluas digunakan bagi pemeriksaan sampel urin tetapi kaedah kromatografi masih diperlukan untuk pengesahan analisis kuantitatif. Kaedah kromatografi gas adalah kaedah yang kerap digunakan bagi menentukan metabolit toluena dalam urin namun kaedah ini sering memerlukan beberapa langkah rawatan awal. Sementara itu, kromatografi cecair berprestasi tinggi (HPLC) menjadi alat yang berkuasa untuk penentuan tepat dan mudah metabolit toluena memandangkan kelebihannya yang jelas untuk pemantauan rutin. Tambahan pula, perkembangan terkini dalam HPLC boleh memperluaskan kegunaan kaedah ini bagi menyelesaikan masalah analisis rumit yang boleh dihadapi semasa pengukuran.

Kata kunci: toluena, metabolit toluena, ujian awalan, kromatografi gas, kromatografi cecair berprestasi tinggi

Introduction

Volatile organic compounds (VOCs) are used as a component in a variety of domestic or industrial consumer products. This statement illustrates that humans always use and are frequently in contact with VOCs. Consumer products such as cleaning products, paints or thinner, glues, lighter, aerosols, cosmetics, fuels and others contain VOCs. Despite these, prolonged exposure to VOCs may lead to poisoning and sudden death [1, 2].

One of the major current issues among adolescents is misuse of the consumer products. In most of the cases, organic compounds contained in the consumer products are inhaled by them using different methods such as huffing, bagging and sniffing. Such conducts will deliver the desired effect such as feeling of pleasure, disinhibition, euphoria and hallucination [3, 4]. Unfortunately, the most difficult facet of the inhalant problem to confront is the fact that inhalants are everywhere.

Even though, there are many VOCs in consumer products, the concern is largely on toluene. This is because toluene has been the most widely used organic solvent in the industries since the second half of the last century [5-7].Such exposure to high concentrations of toluene has been reported by Watson [8]. Toluene biotransformation consists of several steps [9] involving side-chain oxidation where toluene is metabolized into benzoic acid and further conjugated with glycine to form hippuric acid [10]. Meanwhile, small amounts of absorbed toluene are oxidized at the aromatic ring and excreted in urine as *o*- and *p*-cresol.

This review aims to present a summary of the toluene exposure pertaining to toluene metabolites and its potential biomarker, preliminary tests for toluene metabolites, sample pretreatment and determination of toluene metabolites using various instrumentations. From this review, researchers in this area are expected to gain a good idea of analytical procedures, analytical techniques and analytical instrumentations involved. It is our hope that this review will facilitate researchers to plan their own research on toluene exposure and to develop fast method and new separation technique using green technology, electrochemical sensors with mobile instrumentation and other related techniques. The discussion begins with a general topic about toluene exposure and its effects on humans. The metabolism of toluene in human body from its inhalation until excretion in urine is then described. The selection of potential biomarkers and indicators of exposure to toluene are also described in a considerable detail.

Toluene exposure effects and analysis

The preliminary test has become a vast tool for on-site screening of urine sample as many drugs and other poisons give characteristic colors with appropriate reagents if present in sufficient amounts and in the absence of interfering compounds. A few of these tests are only for practical purposes but usually compounds containing similar functional groups will also react and thus interferences from other poisons, metabolites or contaminants are to be expected. Color tests for toluene metabolites have been described including for hippuric acid [11] and *o*-cresol [12].

Methods for toluene analysis and the identification of a reliable indicator in toluene exposure have been described by many researchers. High Performance Liquid Chromatography (HPLC) represents a valuable tool for the routine monitoring of workers exposed to toluene. The determination of urinary metabolites of toluene using HPLC has been extensively studied including those focusing on hippuric acid [13-17], cresol [18] and S-benzyl mercapturic acid [19-20]. For the urinary determination of solvent metabolites, especially for monitoring purposes, HPLC is becoming a method of choice. This method offers decisive advantages in this area as it permits the simultaneous determination of several metabolites whether it is run in isocratic mode or by gradient analysis. This method provides a complete metabolic profile, detection of isomer compound, it is easily automated, and does not require extraction, derivatization steps or pre-treatment of samples.

Determination of toluene metabolites in complex mixtures such as biological fluids is well-known and established. The separation of toluene metabolites from biological fluid can easily be achieved by gas chromatography (GC) with headspace method [21, 22]. However, gas chromatography-mass spectrometry (GC-MS) appears very suitable for the identification of toluene and their metabolites [23-27]. Unfortunately, not all target compounds are amenable to GC due to their poor thermal stability or volatility. Polar compounds are an example of analytes that need the pretreatment of sample using derivatization processes and these together rendered GC less widely-employed compared to HPLC in the analysis of toluene and its metabolites.

Metabolism and potential biomarker of toluene: Historical background

Hippuric acid has been a historical biomarker for toluene exposure but the validity of hippuric acid as an exposure marker is questionable as non-exposed subjects (background levels) were found to contain higher levels of hippuric acid compared to exposed subjects [28-31]. The value of the hippuric acid as a biomarker of occupational toluene exposure was further challenged by the presence of benzoate in some preservatives [32, 33] as benzoate is metabolized and excreted as a hippuric acid in urine [32, 34, 35].

Several researchers have considered a few other possible biomarkers for toluene exposure namely *o*-cresol [27, 36, 37], benzylmercapturic acid [19, 20, 38] and toluylmercapturic acid [39]. Although hippuric acid has attracted considerable attention as an indicator of exposure to toluene, the fact that it can deliver false results of toluene exposure has prompted a number of researchers to suggest *o*-cresol be used as a biomarker, especially for the determination of low-level exposures to toluene. However, it was found that urinary *o*-cresol demonstrated false results too when it involved smoking and drinking counterpart [40] where it can reduce the amount of this chemical particularly at low levels of toluene exposure.

More recently, researchers found a new specific biological marker for toluene metabolites namely S-benzylmercapturic acid (SBMA) [19, 20, 41]. SBMA was found to be a more specific biomarker compared to hippuric acid and *o*-cresol. It was found that SBMA was dependent only on airborne toluene and not effected by food preservative, smoking and drinking habit even at low level of exposure to toluene [42].

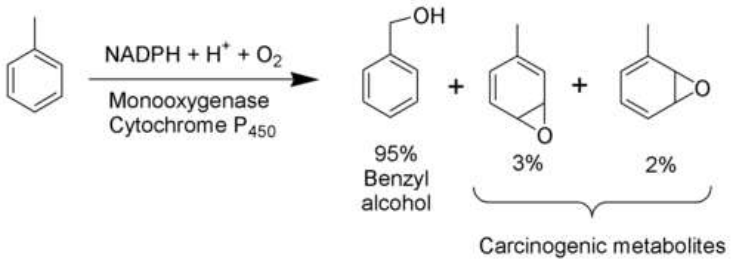
Toluene metabolism

According to Park et al. [43], toluene is the major solvent with the most documentation of abuse, possibly because of its relative low risk of sudden death and the ease of detection in blood. When many aromatic compounds such as toluene and benzoic acid are taken internally, they are converted to hippuric acid by reaction with the amino acid glycine [43]. In another paper, Anderson et al. [44] explained in detail that the principal metabolite of toluene is benzoic acid (approximately 80% of dose) which is conjugated with the glycine to form hippuric acid and directly excreted in urine (half-life of 2-3 hours).

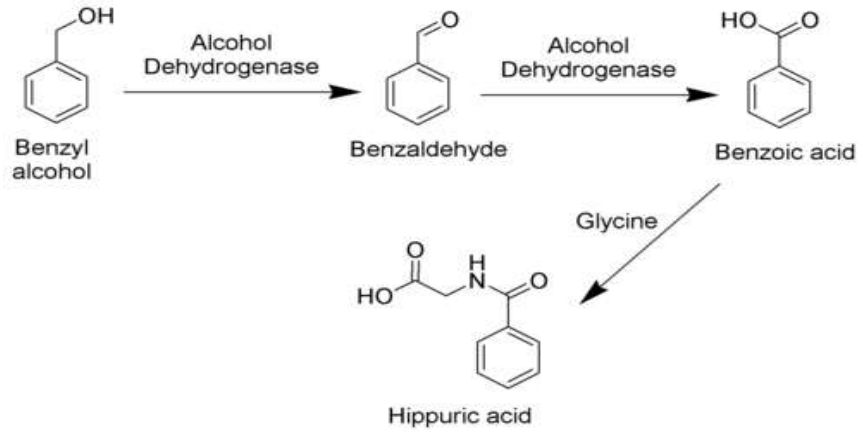
Toluene can be absorbed into the blood stream from the lung and the gastrointestinal tract and through the skin and mucosa. In late 1980s, Ameno et al. described that the brain and liver serve as reservoir for toluene [45]. A few years later, Yamazaki et al., in their work explained that more than 80% of absorbed toluene is metabolized by mix-oxidase enzyme system to benzoic acid and hippuric acid in the liver and kidney before excretion into the urine. Meanwhile, some absorbed toluene (0.4 – 1.1 %) is hydroxylated and excreted as a mixture of *ortho*-, *para*-, and *meta*-cresol. A schematic diagram for toluene metabolism in humans is shown in Scheme 1 [46].

Later on, Zuppi et al. [47] stated that the hippuric acid is biosynthesized from glycine, benzoic acid and CoA by enzymes located in the mitochondrial matrix of liver and kidney cells. This metabolic pathway provides an alternative flux of nitrogen from the usual urea precursors (ammonia, alanine and glutamate) to glycine and it is utilized for the detoxification of aromatic compounds such as toluene. Toluene is very hazardous to our health, with the potential of inflicting considerable pain and suffering until death to the sniffer.

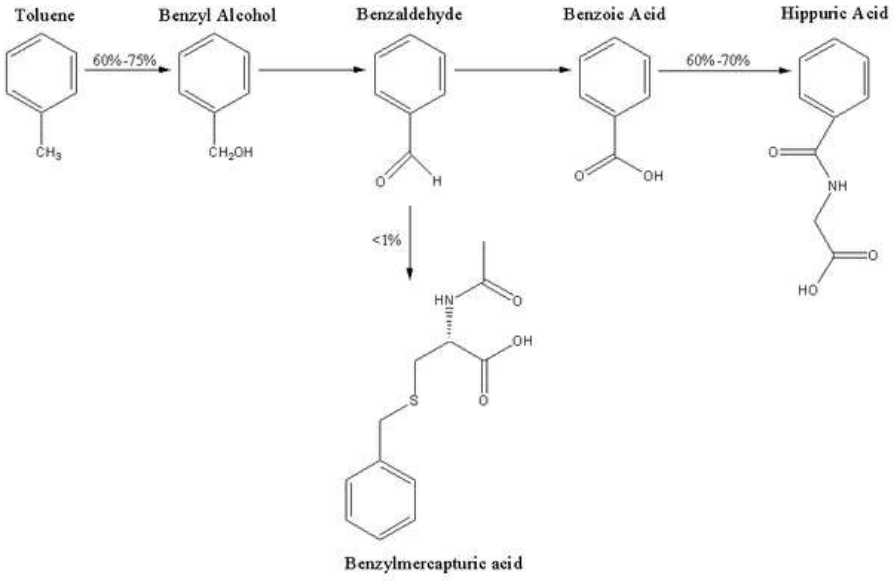
Following inhalation or oral exposure to toluene, approximately 60 – 75 % of absorbed toluene is metabolized to benzoic acid. The initial step involves side chain oxidation to benzyl alcohol by cytochrome P450 enzymes (Scheme 2). Benzyl alcohol is further oxidized to benzoic acid by alcohol dehydrogenase and aldehyde dehydrogenase. Benzoic acid is subsequently conjugated with glycine to form hippuric acid. Benzoic acid may also be conjugated with glucuronic acid to form benzoyl glucuronide in the urine. Less than 1% of absorbed toluene undergoes ring hydroxylation to form *o*-, and *p*-cresol, which are excreted in the urine as glucuronide or sulphate conjugates as reported by Amorim et al. [48].



Scheme 1. First step of toluene metabolism [46]



Scheme 2. Second step of toluene metabolism [46]



Scheme 3. Complete toluene metabolism in urine [47]

According to the World Health Organization (WHO), following inhalation, toluene is predominantly excreted in the urine as the metabolite, hippuric acid. Approximately 7 – 20 % of absorbed toluene is eliminated in air unchanged. Following a single acute exposure, toluene and its metabolites are almost completely eliminated within 24 hours [49].

Scheme 3 illustrates a full steps of toluene metabolism in urine. Approximately 60 to 75 % toluene is converted to benzyl alcohol before further oxidized to benzaldehyde. Less than 1 % benzaldehyde is converted to benzyl mercapturic acid while the rest is converted to benzoic acid. About 60 to 70 % hippuric acid is produced from conjugating benzoic acid with glycine.

Analytical methods: Sample collection and storage

It is a good practice that biological specimens should be stored at 4 ºC before transported to the laboratory. Exceptions to this include hair and nail, which are stable at room temperature and filter paper with adsorbed dried blood, which is a convenient way of storing and transporting blood samples for specified analyses whenever refrigerated transport and storage is not feasible [50].

Each specimen bottle should be securely sealed to prevent leakage and individually packaged in a separate plastic bag. Particular attention should be given to the packaging of the samples to be transported by post or courier in order to comply with current health and safety regulations. Sample volumes or amounts smaller than those indicated in Table 1 are often sufficient to complete the analyses required. However submission of very small sample may result in reduced sensitivity and scope of the analyses undertaken but nevertheless such samples should always be forwarded to the laboratory. Any residual specimen should be kept at -20 ºC or below until investigation of the incident has been concluded.

Table 1. Sample requirements for general analytical toxicology

Sample	Notes
Whole Blood	10 mL (lithium heparin or EDTA tube - use fluoride/oxalate/citrate if ethanol is suspected; plastic tube if paraquat is suspected; glass or plastic tube with minimal headspace if carbon monoxide or other volatile is suspected)
Plasma/Serum	5 mL (send whole blood if volatiles, metals and some other compounds are suspected)
Urine	20 - 50 mL (plain bottle, sodium fluoride)
Gastric contents	25 - 50 mL (plain bottle, no preservative)
Other samples	Vitreous humor (maximum available collect separately from both eyes), bile (2 mL) or liver (about 5g) can be a substitute for urine postmortem work. Other tissues (brain, liver, kidney, lung, and subcutaneous fat – 5g) may also be valuable, especially if organic solvents or other volatile poison is suspected.

Preliminary Test

Color tests are useful in minimizing the use of equipment and expertise required. However, the reagent has to be easily available and stable. Sensitivity is limited and the tests are usually applicable only to urine. It is possible to extract the metabolite and apply the color test to the residue, though this is rarely done for biological fluids. False negatives are a risk even when a test is used for its intended purposes in appropriate samples. Positive results with poison, metabolite or others serve to indicate the need for quantitative measurement. Urine samples are commonly used for preliminary test. This is because of urine is easy to collect and it can be useful to provide qualitative information about exposure to a particular substance (Table 2).

Researches in toluene exposure are extensive whether they involve quantitative or qualitative analyses. One of the most varied tools for qualitative analysis is a color test method. Many years ago, only a few of researchers

employed color test method to determine toluene metabolites [51]. Among the metabolites of toluene, hippuric acid is a traditional biomarker for the biological monitoring of toluene exposure but both *o*-cresol and hippuric acid are used by the endogenous and dietary sources [52].

Table 2. Color test methods for determination of toluene metabolites in urine

Sample Pre-treatment	Procedure[a]	Analysis Method	Color Changes	Detection Limit	Ref.
Extracted three times with methanol	Detection of hippuric acid based upon azlactone formation resulting from the reaction of an aldehyde with hippuric acid.Hippuric acid was converted to a deep orange-colored azlactone, 2-phenyl 4- (p-dimethylamino)benzal 5-oxazolone, by treatment of hippuric acid with acetic anhydride and p-dimethylamino-benzaldehyde.	Colorimetry method. λ_{max} = 410 nm	Yellow to deep orange color.	N.R	[52]
Acid extraction of urine sample	0.5 mL hippuric acid of pyridine (Pyr) solution mixed to 0.2 mL of benzenesulphonyl chloride (BSC). The solution was allowed to stand >20 min. It is then diluted to 5 mL with chloroform and recorded at 380 nm.	Colorimetry method. λ_{max} = 420 (red color) and 360 nm (orange color).	Yellow to orange red color within 40 min.	0.135 mg/mL	[53]
No extraction	0.5 mL of urine and 0.5 mL of Pyr were mixed and added with 0.2 mL of BSC and mixed for 5 s with a vibration mixer. The colored solution was allowed to stand for 30 min at room temperature, diluted to 5 mL with ethanol and mixed. The solution was centrifuged for 5 min to remove a little turbidity. The absorbance was determined at 410 nm in ethanol.	Colorimetry method. λ_{max} = 410 nm	Yellow to deep red color within 20 min.	0.20 mg/mL	[54]
No extraction	Urine sample (0.1 or 0.2 mL) was mixed with 0.25 mL Pyr, and subsequently with 0.1 mL BSC. Then, 0.125, 0.25, 0.5. 1.0 or 1.5 mL ultra-pure water was added.	Colorimetry method. λ_{max} = 410 nm	Yellow to deep red	0.125 mg/ml	[55]
No extraction	0.1 mL of urine added with 0.25 mL Pyr and 0.1 mL BSC and 1.0 mL distilled water.	Spectrophotomety UV at λ_{max} = 417 nm	Yellow to deep red within 1 min.	0.125 mg/ml	[11]

[a] Pyr, Pyridine; BSC, Benzenesulphonyl Chloride. N.R; Not reported.

Color test methods for hippuric acid have been developed since 1950s and further investigated by researchers in early 1980s. The founders of color reaction for hippuric acid, Gaffney et al. employed the formation of azlactone resulting from the reaction of an aldehyde with hippuric acid [51]. In this reaction, hippuric acid was converted to a deep orange colored azlactone, 2-phenyl-4-(p-dimethylamino) benzal-5-oxazolone by treatment of hippuric acid with acetic anhydride and p-dimethylaminobenzaldehyde. Urine sample was extracted three times with methanol for sample pre-treatment. The absorption was recorded with colorimetry method at λ_{max} = 410 nm.

A few years later, Umberger and Fiorese found a new method using pyridine and benzenesulfonyl chloride to develop deep red color in the presence of hippuric acid. Urine sample was extracted using ethyl acetate before recording using colorimetric method at λ_{max} = 420 nm (red) and 360 nm (orange) with detection limit of 0.135 mg/mL [53]. An investigation using colorimetric method was also reported by Tomokuni and Ogata [54]. The procedure employed 0.5 mL of urine, 0.5 mL of pyridine and 0.2 mL of BSC that were mixed for about 5 s with a vibration mixer and the colored solution was allowed to stand for 30 min at room temperature and then diluted with 5 mL of ethanol. Then the solution was centrifuged for 5 min to remove a little turbidity and the absorbance was determined at 410 nm in ethanol. This spectrophotometer method was simple but the yellow coloration obtained was indistinguishable from the yellowish color of urine because of the ethanol dilution.

In 2005, Yoshida et al. [55] modified the color test method that was established by Umberger and Fiorese, [53]. It involves a new color test method where the addition of pyridine and benzenesulfonyl chloride with existing distilled water develops a deep red color in the presence of hippuric acid. The colorimetric method for urine hippuric acid investigated in this study is based on the color reaction (reddening) of the specimen, which can be judged more clearly than the method of Tomokuni and Ogata [54] which involves a change to yellowish color. This method required only several minutes and used only commercially-available reagents without any pre-treatment. This work demonstrated the color changed but they it did not illustrate the color changes with different concentrations of hippuric acid. Besides that, the work was only focused on samples of people exposed to toluene and did not provide the equation and reaction of the color test method [55].

More recently, Yacob and Zinalibdin, developed a simple mobile test kit for screening and detecting glue sniffers based on the color test method [11]. The results obtained using the kit is are similar to those using UV–Vis result but it technique is faster with the results obtained within only 5 min and is also comparable to the dip strip urine drug testing kits. Thus, this kit can be a fast and in situ tool to help the National Anti-Drug agency for in the screening and detecting glue abusers among school students and teenagers [11].

Sample pre-treatment: Hippuric acid sample pre-treatment prior to HPLC

Liquid-liquid extraction (LLE) has been used for sample pretreatment of toluene metabolites. Poggi et al. illustrated the extraction procedure was performed on acidified urine, after addition of 4-hydroxybenzoic acid as internal standard using a butylchloride/isopropanol mixture and 0.5 mL of the organic layer was dried under nitrogen flow. The residue obtained was dissolved in 0.1 mL water/acetonitrile and 5 µL was injected into a HPLC [15]. Matsui et al. in his research used ethyl acetate for partial clean-up of biological samples [56]. Bevine et al. conducted a sample pretreatment which is made alkaline and extracted stepwise with methylene chloride and ethyl acetate and the addition of internal standard (3-methoxysalicylic acid) in plasma samples [57]. Meanwhile, several works have demonstrated sample pretreatments that do not require extraction step but effected only by dilution with distilled water followed by centrifugation [14, 58, 59].

Liquid-liquid-liquid microextraction (LLLME) method was developed for the determination of hippuric acid in urine and serum sample [60]. The analyte was extracted from an acidic aqueous sample solution (pH 3) through a thin layer of organic solvent membrane and back-extracted to a basic acceptor drop (pH 11) suspended on the tip of a 10-µL HPLC syringe in organic layer. Green technology was adapted in this method that offers the advantages of being simple, sensitive and inexpensive.

A simple molecularly imprinted polymer coated with modifed polysulfone membrane was introduced by Moein et al. [61]. The membrane was utilized for online extraction of hippuric acid in biological matrices. This method provided fast, sensitive, selective and robust sample preparation method for hippuric acid in biological fluids.

Hippuric acid sample pre-treatment and derivatization procedure prior to gas chromatography

Methods for the determination of hippuric acid based on GC usually require a derivatization procedure in the sample pretreatment step. A number of researchers have established the derivatization procedure for the analysis of toluene metabolites. Some researchers used diazomethane but it is an explosive, carcinogenic and highly toxic reagent [62-64].Other researchers used expensive substances as reagents to obtain methylsilyl derivatives which

require frequent cleaning of the GC detector [65, 66] and these derivatives are moisture-sensitive. In 1991, De Carvalho et al. [23] proposed the derivatization of hippuric acid using methanol in acid medium (HCl), a low-cost and low toxicity reagent. About ten years later, Kongtip et al. modified the method using a GC equipped with a DB-1 capillary column and a flame ionization detector [25]. The method successfully separated and eluted methyl esters of hippuric acid, *o*-, *m*- and *p*-methylhippuric acid within 11 min.

Extraction step is often the first step for the detection of toluene metabolites using GC. Before this century, many researcher used LLE as extraction step where the sample was acidified with acid and then the analyte was extracted using ethyl acetate [23, 25, 62-64]. The organic layer was collected for the derivatization step.

A novel approach of the extraction of hippuric acid using solid phase extraction [67] has been introduced. In the approach, an online automatic method for extraction of hippuric acid from urine sample using µ-solid phase extraction with polypyrrole adsorbent system was established [68]. However, post derivatization of hippuric acid by conversion to its methyl ester with methanol in hydrochloric acid was still needed for monitoring the toluene metabolites using GC.

Cresol pre-treatment prior to gas chromatography

The urinary cresol is present in urine sample usually as sulphate or glucuronic acid conjugates. For this reason, hydrolysis and neutralization steps are required to determine the urinary cresol. Truchon et al. in 1996 described a sensitive and reproducible gas chromatographic procedure for the determination of urinary *o*-cresol as follows. Acid hydrolysis was the first step encountered to produce unconjugated *o*-cresol. After extraction with methylene chloride at pH 2, the organic layer was concentrated by evaporation and the sample was analyzed by GC-flame ionization detection [27].

Solid phase microextraction (SPME) was established for determination of urinary *o*-cresol. Acid-hydrolyzed step is still required for the sample and a CW/DVB fiber was directly immersed in the sample solution for 20 min under magnetic stirring for the extraction. This SPME device was then introduced into chromatography injector port where the analyte is thermally desorbed from the fiber [26].

Analysis by High Performance Liquid Chromatography

Numerous sample pretreatment and HPLC methods have been proposed for the separation of toluene metabolites in biological samples, some of which are listed in Table 3. Several researchers have worked on the determination of hippuric acid in urine and blood samples. A few of them studied on the determination of hippuric acid in urine and blood for exposure of toluene, xylene and other chemicals for occupational and safety health. Ogata and his co-workers [59] determined hippuric acid as indicator of toluene exposure by HPLC. They used mixed solution of methanol-water-acetic acid (20: 80: 0.2) as the mobile phase and UV detection at 254 nm and without solvent extraction and pretreatment. Their results showed a low detection limit of 0.2 µg and analysis time of < 30 min.

HPLC method for simultaneous quantitative determination of the urinary metabolites of toluene, m-xylene and styrene (hippuric acid, *m*- methyl hippuric acid, phenylglyoxylic acid, mandelic acid) was described by Poggi et al. [15]. In the method, the residue obtained was dissolved in 0.1 mL of water/acetonitrile and 5 µL of the solution was injected into a HPLC system for analysis. Absorbance measurement was performed at 225 nm using UV detector. All metabolites were clearly separated within 12 min [15].

The direct determination of hippuric acid (HA) and *o*-, *m*- and *p*-methylhippuric acids (MHA) in the urine, metabolites of toluene and *o*-, *m*- and *p*-xylenes by HPLC have been described and established. A mixed solution of methanol-water-acetic acid (80: 20: 0.2) containing tetra-*n*-butylammonium bromide (0.2 % w/v) as mobile phase was used. Concentrations of HA and MHAs were estimated from their peak height at a wave length of 225 nm. Urine can be analyzed directly without solvent extraction or pretreatment to obtain complete separation of HA and *o*-, *m*- and *p*-MHAs. Authentic samples of glycine conjugates, HA and *o*-, *m*- and *p*-MHAs, in water and urine were well separated from each other and eluted within 25 min [69].

An automated HPLC method for the direct determination of urinary concentrations of hippuric acid (HA), and *o*-, *m*- and *p*-methyl hippuric acids (MH As), metabolites of toluene and *o*-, *m*- and *p*-xylenes, and of urinary phenyl glyoxylic acid (PGA) and mandelic acid (MA), metabolites of styrene or ethylbenzene have been described. Methanol was added to urine, the mixture was centrifuged and the supernatant was injected into HPLC A stainless-steel column packed with octadecyl silanized silicate was used and the mobile phase was a mixture solution of 5 mM potassium phosphate monobasic-acetonitrile (90:10) The method is simple and specific. Urine can be analyzed without solvent extraction. Analysis can be performed satisfactorily within 45 min for samples containing HA, MHAs, PGA and MA, and within 15 min for those containing HA, PGA and MA [70].

Matsui et al. [56] used HPLC for the determination of hippuric acid in urine sample. The separation was carried out on a reversed-phase column using 20 % methanol in 0.01 M potassium phosphate containing 0.5 % acetic acid as the mobile phase. The column effluent was monitored using UV detection at 254 nm. Hipuric acid was separated from other normal urine constituents in less than 10 min.

Kubota et al. [58] described the monitoring of hippuric acid and benzoic acid simultaneously in human biological fluids and considered it to be clinically important. They developed a simple and accurate HPLC method for the simultaneously determination of hippuric acid and benzoic acid in human urine and plasma. This research required no extraction step. Aliquots of urine and plasma were added to a solution of internal standard (*o*-chlorobenzoic acid) in acetonitrile and directly injected into a HPLC system using an acidic (pH 2.7) eluent and UV detection at 235 nm.

A method has been developed for the isocratic HPLC analysis of hippuric acid in human blood plasma. After the addition of internal standard (3-methoxysalicylic acid), plasma samples were made alkaline and extracted stepwise using methylene chloride and ethyl acetate. The detection limit was 50 pmol of hippuric acid per mL plasma. This work was conducted on samples from human occupationally exposed to organic solvent as described by Bevine et al. [57].

A simple HPLC procedure was described as a method for simultaneous determination of the six metabolites in urine namely hippuric acid , *o*-, *m*- and *p*-methylhippuric acid, phenylglyoxylic acid and mandelic acid. Urine analysis was selected in the study because of its non-invasive nature in sampling with minimal burden on exposed workers. A mobile phase of methanol-acetic acid-water (200: 8: 792) by volume was allowed to flow at a rate of 0.85 mL/min and monitored at a wavelength of 257 nm [13].

Yang [14] described a simple method for the simultaneous determination of creatine, uric acid, creatinine and hippuric acid in urine using HPLC. Chromatography was performed with a 0.02 M KH_2PO_4 as a mobile phase and UV detection at 220 nm without any extraction method. This method was applied for biomedical application to analyze urine samples from normal subjects and some patients. A HPLC method for determination of hippuric acid in urine was described by Yoshida et al. [55]. The mobile phase was 30% methanol containing 0.1% acetic acid and UV detection at 225 nm. No extraction method was used in this work. Urine samples were centrifuged (12 000 rpm, 10 min) and 5 µL supernatant was injected for analysis. This method was applied to the analysis of glue sniffer's urine [55].

A simple method for the simultaneous determination of hippuric acid and benzoic acid in urine using reversed-phase HPLC was described by Yacob and Zinalibdin [71]. Chromatography was performed with a mobile phase of mixed solution methanol-water-acetic acid (20: 80: 0.2) and UV detection at 254 nm in < 10 min. The detection limit of this method was 0.01 mg/L for hippuric acid and 0.06 mg/L for benzoic acid. This method was applied to the analysis of urine samples from the suspected of toluene abuser or glue sniffer among secondary school students. Meanwhile, Lee et al. [18] developed a simple and rapid HPLC-UV method for the simultaneous determination of eight urinary metabolites which is hippuric acid, mandelic acid, *o*-, *m*- and *p*-methylhippuric acid and *o*-, *m*- and *p*-cresols. All eight metabolites were successfully resolved within 5 min in 10 % aqueous ethanol containing 0.3 % acetic acid and 1.6 % β-cyclodextrin, using a gradient flow rate 1.0 - 5.0 mL/min [18].

Table 3. Conditions for sample pretreatment and HPLC separation of toluene metabolites in biological samples

Sample Pre-treatment[a]	**HPLC Column**	**Detection Limit**[b]	**Mobile Phase**[c]	**Detection wavelength**	**Target Analyte**[d]	**Ref.**
Acidified urine sample and extracted with ethyl acetate by shaking. Centrifuge for 5 min at 1000 rpm.	Bondapak C18 (30 cm × 4 mm) Flow rate : 0.70 mL/min Time : 11 min	N.R	20 % MeOH in 0.01M K_2PO_4 containing 0.5 % v/v HOAC.	254 nm	HA	[56]
Acidified urine, add 4-hydroxybenzoic acid using butylchloride/IPA and dried with N_2. Residue dissolve in 0.1 mL water /acetonitrile.	HC ODS Sil-X Flow rate: 1.0 mL/min Time: 12 min	MA: 25µg/mL HA: 7.5µg/mL m-mHA: 10µg/mL PHGA: 1µg/mL	Water: ACN: HOAC 95: 5: 0.02	225 nm	MA, HA, m-mHA, PHGA.	[15]
1ml MeOH mix with 1 mL urine and centrifuge at 2000 rpm for 5 min.	Silica gel Flow rate: 1.2 mL/min. Time: 25 min	N.R	MeOH-water-HOAC 80: 20: 0.2 With tetra-*n*-butyl ammonium bromide 0.2 % w/v	225 nm	HA, o-mHA, m-mHA	[69]
Urine dilute with mobile phase and centrifuge at 2000 rpm for 5 min.	Octadecyl-silanized silica gel (0.4 mm × 150 mm) Flow rate: 0.7 mL/min Time: 20 min	MA: 5ng/mL HA: 2ng/mL o-mHA: 4 ng/mL m-mHA : 4ng/mL PHGA: 1 ng/mL	0 mM KH_2PO_4 (pH3.3) containing 3 mM 1-decane-sulfonate/CH_3CN (85:15)	225 nm	HA, o-mHA, MA, Creatinine	[70]
100µl sample mix with 200µl contain ISTD	Yanapak ODSA (250 mm × 4.6 mm) Flow rate: 1.0 mL/min Time: 10 min	BA & HA: 1µg/mL	CAN-water-HOAC 35:63: 2	235 nm	HA & BA	58]

Table 3 (cont'd). Conditions for sample pretreatment and HPLC separation of toluene metabolites in biological samples

Sample Pre-treatment[a]	**HPLC Column**	**Detection Limit[b]**	**Mobile Phase[c]**	**Detection wavelength**	**Target Analyte[d]**	**Ref.**
Urine mix with MeOH and centrifuge 1600 rpm at 60 min	Intersil ODS-2 (4.6 mm × 250 mm) Flow rate: 0.85 mL/min Time: 20 min	HA: 0.5 mg/L o-mHA: 2.0mg/L m-mHA: 0.8 mg/L p-mHA: 0.2 mg/L PHGA: 0.1 mg/L MA: 3 mg/L	MeOH-HOAC-water 200: 8: 792	257 nm	MA, HA, o-mHA, p-mHA, m-mHA, PHGA.	[13]
N.R	Novapak- C18 (3.9 mm × 150 mm) Flow rate: 0.5 mL/min Time: 10 min		0.02 mol/L KH2PO4	220 nm	Creatine, Uric acid, Creatinine, HA	[14]
2 mL of urine centrifuge at 12000 rpm for 10 min.	Devolosil C18 (15 cm × 4.6 mm) Flow rate: 0.70 mL/min	HA: 0.1 ng/mL	MeOH-water-HOAC 20: 80: 0.2	254 nm	HA	[55]
Acidified urine and extracted with diethyl eter/methanol (9:1)	Novapak-C18 (3.9 mm × 150 mm) Flow rate: 1.0 mL/min Time: 8 min	HA: 0.01 mg/L BA: 0.06 mg/L	MeOH-water-HOAC 20: 80: 0.2	254 nm	HA & BA	[71]

Table 3 (cont'd). Conditions for sample pretreatment and HPLC separation of toluene metabolites in biological samples

Sample Pre-treatment[a]	HPLC Column	Detection Limit[b]	Mobile Phase[c]	Detection wavelength	Target Analyte[d]	Ref.
Vortex sample and ISTD. Dillute with 20 fold deionized water and centrifuge for 5 min.	Onyx Monolith RP-18 (4.6 mm × 100 mm) Flow rate gradient: 1.0-5.0 mL/min Time: 6 min	HA: 2µg/mL MA: 0.8 µg/mL o,m,p-mHA: 0.4 µg/mL o, m, p-cresol: 0.8 µg/mL	EtOH-HOAC-1.6% β-cyclodextrin 10 : 0.3 :90	225 nm	HA, MA, o,m,p-mHA, o, m, p-cresol	[18]

[a] IPA, Isopropanol; N_2, Nitrogen; MeOH, Methanol; ISTD, Internal Standard.
[b] NR, not recorded; MA, mandalic acid; HA, Hippuric acid; BA, Benzoic acid; o-mHA, o-methylhippuric acid; p-mHA, p-methylhippuric acid; m-mHA, m-methylhippuric acid, PHGA, phenylglyoxylic acid; o, ortho; p, para; m, meta.
[c] MeOH, methanol; K_2PO_4, Potassium phosphate; HOAC, acetic acid; ACN, acetonitrile; KH_2PO_4, Potassium dihydrogen phosphate; EtOH, ethanol.
[d] MA, mandalic acid; HA, Hippuric acid; BA, Benzoic acid; o-mHA, o-methylhippuric acid; p-mHA, p-methylhippuric acid; m-mHA, m-methylhippuric acid, PHGA, phenylglyoxylic acid; o, ortho; p, para; m, meta.

Analysis of VOCs by gas chromatography

Gas chromatography (GC) offers some advantages for determination of volatile substances such as toluene due to its easy procedure. Selected examples of conditions for sample pretreatment and GC separation of toluene metabolite in biological sample are listed in Table 4. Head space method can achieve good separation of volatile solvents from the biological matrix [22]. In addition, the determination of toluene and its metabolites was not a problem as the GC peaks were well separated [21].

De Carvalho in his work [23] described the determination of hippuric acid by GC-flame ionization detection. This research proposed the derivatization of hippuric acid using methanol in acid medium which is a low cost reagent with a low level of toxicity. After the extraction procedure, hippuric acid and internal standard were converted to the methyl esters using methanol in acid medium. All methyl ester were detected in < 45 min [23]. Besides that, a sensitive and reproducible GC procedure for the quantitative determination of urinary o-cresol was also described [27]. The first step involves acid hydrolysis (2 N HCl, 100 ºC, 10 min) which yields unconjugated *o*-cresol. After extraction (methylene chloride, pH 2), the organic layer is concentrated by evaporation and samples are analyzed by GC-flame ionization detection with a DB-5 column. The detection limit of the method is 0.36 µmol/L [27].

Determination of hippuric acid and *o*-, *m*- and *p*-methylhippuric acid in urine was described by Kongtip et al. [25]. These metabolites were extracted using ethyl acetate and then derivatized it to methyl ester derivatives and quantitated using a gas chromatography flame ionization detector and DB-1 capillary column. The derivative of hippuric acid and *o*-, *m*- and *p*-methylhippuric acid were well separated within 11 min [25].

Simultaneous determination of hippuric acid, *o*-, *m*- and *p*-methylhippuric acids, mandelic acid and phenyl glyoxylic acid was developed and described by Ohashi et al. and it proved to be a fast and sensitive technique [72]. These metabolites were converted to methyl esters derivatives using methanol in hydrochloric acid and then quantitated by gas chromatography-mass spectrometry (GC-MS) with selected ion monitoring using a DB-1 capillary column. The target analytes were quantitatively analyzed and resolved within 19 min with low detection limit.

Table 4. Conditions for sample pretreatment and GC separation of toluene metabolites in biological sample

Sample Pre-treatment[a]	**GC Procedure**[b]	**Target Analyte**[c]	**Derivatization Reagent**[d]	**GC Temperature**[e]	**Detection Limit**[f]	**Ref.**
Urine was acidified with 0.5 N HCl and extracted with ethyl acetate 20 min in horizontal shaker. Sample was centrifuged at 4000 rpm for 4 min and organic phase was collected.	SE-30 in Chromosorb W-Silanized glass column using GC-FID	PGHA, OA, *o*-mHA, *p*-mHA, BA, SA, MA, *m*-cresol	MeOH in HCl medium.	Carrier N_2 : 40 mL/min- TPGC Oven : 200 ºC Injector: 240 ºC Detector: 240 ºC	N.R	[23]
Hydrolyzed (2N HCl, 100ºC, 10 min) and extracted with methylene chloride, pH 2. Organic layer evaporated and collected	DB 5-column using GC-FID	o-cresol	Hydrolyzed using HCl and incubated in oven at 100 ºC for 10 min.	Carrier N_2 : 40 mL/min TPGC 30 ºC for 12 min and then increased 2ºC/min to 93 ºC	o-cresol: 0.36 µmol/L	[27]
1 mL of urine mix with 1 mL distilled water and acidified with 0.5M HCl then extracted with 3 mL ethyl acetate. Sample was evaporated to dryness and the residue reconstituted with derivatizing reagent and left in oven at 60ºC for 45 min. Solution was extracted with 1 mL chloroform and add 2 mL distilled water.	DB 1-column using GC-FID	HA, *o,m,p*-mHA	MeOH in HCl medium.	Carrier He: 10 mL/min Isothermal programmed Oven : 200 ºC Injector: 250 ºC Detector:250 ºC	HA: 0.05 mg/mL o,m,p-HA: 0.015 mg/mL	[25]
Acidified and extracted with diethyl ether. Sample was centrifuged at 2500 rpm for 10 min and dry incubated at 70ºC for 15 min. Next derivatize step was take part.	DB1-column using GC-MS. MA-mz:107 PHGA-mz: 105 HA-mz: 105 *o,p,m*-mHA-mz: 119	HA, o,m,p-mHA, MA, PHGA .	MeOH in HCl medium.	Carrier He: 1.8 mL/min TPGC 150 ºC for 3 min at 10 ºC/min and then increased 250 ºC for 7 min at 10º C/min Injector: 260 ºC Detector:260 ºC	HA, o,m,p-mHA, MA, PHGA : 8-27 pg/L	[72]

Table 4 (cont'd). Conditions for sample pretreatment and GC separation of toluene metabolites in biological sample

Sample Pre-treatment[a]	GC Procedure[b]	Target Analyte[c]	Derivatization Reagent[d]	GC Temperature[e]	Detection Limit[f]	Ref.
Acidified using HCl and kept in oven at 100ºC for 1 h. Hydrolyzed and adjusted pH 7 with NaOH & Na_2SO_4. Immersed with CW/DVB for 20 min under magnetic stirrer.	ZB-35 column using GC-FID	o-cresol	Hydrolyzed using HCl and kept in oven at 100ºC for 1 hour.	Carrier N_2: 8.0 mL/min Isothermal GC Oven: 190 ºC Injector: 210 ºC Detector:220 ºC	o-cresol: 0.1 mg/L	[26]
DI-SPME directly immersed in 10 mL vial for 20 min at 60ºC and under agitation for 20 min.	SLB-5 MS using GC-MS	FA, HA, m-mHA, MA, PGHA, SA trans muconic acid	Terimethyl-oxonium tetrafluoro-borate	Carrier He:1.2 mL/min TPGC 50 ºC (1min); increased at 10 ºC/min to 300 ºC (3 min).	FA: 0.9µg/mL, SA: 8.1 µg/mL, t,t-MA: 0.9 µg/mL.	[24]
Centrifuge urine at 4500 rpm for 10 min. µ-SPE system condition with 2.0 mL MeOH and 3.0 mL of Britton-Robinson buffer (3.0×10^{-3}mol/L, pH2). 0.1 mL aliquot sample dilute with Britton Robinson buffer at 10 mL volumetric flask. Preconditioned catridge 20 mg polypyrrole and washed with Britton Robinson buffer.	CP Sil 8 CB using GC-FID	HA in urine and water	MeOH in HCl medium.	Carrier He:10 psi. TPGC. 80 ºC (1 min) at 20 ºC/min to 140 ºC hold for 1 min at 20ºC/min then increased 280ºC (10 min). Injector: 280ºC Detector:280ºC	HA: Urine: 16.5 ng/mL Water: 12.1 ng/mL	[68]

[a]HCl, Hydrochloric acid; NaOH, Sodium hydroxide; Na_2SO_4, Sodium sulfate, CW/DVB, Carbowax-divinylbenzene; Direct immersion-solid phase microextraction, DI-SPME; MeOH, Methanol.
[b]GC-FID, Gas chromatography-flame ionization detector; GC-MS, Gas chromatograph-mass spectrometry; MA, Mandelic acid; PHGA, Phenyglyoxylic acid; HA, Hippuric acid; o-, ortho; m-, meta; p-, para; mHA, methylhippuric acid.
[c]HA, Hippuric acid; o-, ortho; m-, meta; p-, para; mHA, methylhippuric acid; MA, Mandelic acid; PHGA, Phenyglyoxylic acid; OA, Oxalic acid; SA, Stearic acid; FA, Furoic acid.
[d]MeOH, Methanol; HCl, Hydrochloric acid.
[e]N_2, Nitrogen; He, Helium; TPGC, temperature programmed GC.
[f]N.R, Not reported; HA, Hippuric acid; o-, ortho; m-, meta; p-, para; mHA, methylhippuric acid; MA, Mandelic acid; PHGA, Phenyglyoxylic acid; FA, Furoic acid; SA, Stearic acid; t-tMA, trans-trans muconic acid.

De Paiva et al. [26] developed a method for the determination of urinary *ortho*-cresol using solid-phase microextraction (SPME), followed by capillary GC-flame ionization detection (GC/FID). After optimization of the SPME variables and validation of the method, it was applied to analysis of *o*-cresol in urine collected from 27 workers exposed to solvents in automotive repair shops. The maximum extraction efficiency was obtained using a carbowax-divinylbenzene (CW/DVB) fiber (70 µm), immersed 20 min in acid hydrolyzed urine added with 3 g

Na_2SO_4 at pH 7.0 and under magnetic stirring. The SPME-GC/FID method –proved to be fast, simple and can be applied to the occupational toluene biomonitoring.

A method for the determination of the organic acids directly in the urine employing derivatization with trimethyloxonium tetrafluoroborate as a methylating agent and sequential extraction by head space and direct immersion-solid phase microextraction is reported. Furoic acid, hippuric acid, methylhippuric acid, mandelic acid, phenylglyoxylic acid and *trans*-muconic acid contained in urine and determined by GC-ion trap-mass spectrometry/tandem mass spectrometry analysis within 20 min [24].

Meanwhile, Ahmadi et al. [68] described a rapid, simple and high sensitive method for extraction of hippuric acid from human urine samples by using an automated micro solid phase extraction system (µ-SPE). However in order to increase sensitivity of gas chromatography with flame ionization detector, a post derivatization procedure was developed. In this work, a polypyrrole was synthesized by chemical oxidation of the pyrrole monomer in non-aqueous solution and applied as an excellent and efficient sorbent for µ-SPE. This method was successfully used to analyze trace amounts of HA in human urine samples without any interference from coexisting.

Conclusion

Biological monitoring of toluene exposure is a growing field of interest in toxicological and occupational laboratories. Chemical and biomedical analysts should be aware and have a broad knowledge to choose the most appropriate analytical method because it can remain a major problem. They are no ideal method *per se* but the best method selected should be able to deliver good results and compromise between several conflicting requirements.

Preliminary test is one of the indicators for screening purposes. It could be used on site for qualitative analysis with fast results using the mobile kit. The color test has proved a powerful method for preliminary test since early this decade. However, this method is not sensitive for low concentrations of toluene exposure and it can give a false results. Thus, quantitative instrumental analysis is still required for enforcement and research purposes such as using GC-MS and HPLC. Indeed, in these situations, cost, length, complexity and workload problems generated by the analytical method are not necessarily major concerns. In contrast, for the routine monitoring of toluene exposure and forensic cases in industrial environment and enforcement agency, the cost per determination, simplicity and automation will be important considerations.

HPLC appears to be the primary choice for the determination of toluene metabolites. The apparatus is relatively economical, automatable and sufficiently versatile to be used for other determination in related areas such as drug monitoring or clinical toxicology that are currently of interest in the same laboratory. As previously indicated, the analyst now has a choice between several methods, well adapted to routine and simultaneous determination of urinary metabolites of some common volatile solvents that require biological monitoring. Moreover, HPLC is also becoming an attractive tool in the growing field of more elaborate approaches with new urinary markers such as specific conjugates or isomers.

Acknowledgement

The authors would like to acknowledge Universiti Teknologi Malaysia for facilitations and the Department of Chemistry Malaysia and the Public Relations Department of Malaysia for studentship and financial support to Mohamad Raizul Zinalibdin.

References

1. Basselt, R. C. (2002). Disposition of toxic drugs and chemical in man, 6th Edition, .*Biomedical Publication*, Foster City pp. 5 – 1200.
2. Coopmana, V. A., Cordonniera, J. A. and de Meyere, C. A. (2005). Fatal workplace accident involving ethyl acetate: a distribution study. *Forensic Science International,* 154: 92 – 95.
3. Wille, S. M. R. and Lambert, W. E. E. (2004). Volatile substance abuse-post mortem diagnosis. *Forensic Science International,* 142: 135 –156.
4. Esmail, A., Pottier, L. and Wright, S. (1993). Deaths from volatile substances abuse in those under 18 years: results from a national epidemiological study. *Archives Disorder Children,* 69: 256 – 360.

5. Ukai, H., Inui, S., Takada, S., Dendo, J., Ogawa, J., Isobe, K., Ashida, T., Tamura, M., Tabuki, K. and Ikeda, M. (1997). Types of organic solvents used in small to medium scale industries in Japan: A nationwide field survey. *International Archives Occupational Environmental Health*, 70: 385 – 592.
6. Yasugi, T., Kawai, T., Endo, G., Monna, T., Odachi, T., Yamaoka, K., Hariguchi, S. and Ikeda, M. (1998). Types of organic solvents used in workplaces and work environment conditions with special references to reproducibility of work environment classification. *Industrial Health*, 36: 223 – 233.
7. Moon, C-S., Lee, J-T., Chun, J-H. and Ikeda, M. (2001). Use of solvents in industries in Korea; experience in Sinpyeong-Jangrim indusrial complex. *International Archives Occupational Environmental Health*, 74: 148 – 152.
8. Watson, J. M. (1982). Solvent abuse: presentation and clinical diagnosis. *Human Toxicology*, 1: 249 – 256.
9. Lof, A., Hansen, S. H., Naslund P., Steiner, E., Wallen, M. and Hjelm, E.W. (1990). Relationship between uptake and elimination of toluene and debrisquine hydroxylation polymorphism. *Clinical Pharmacology and Therapeutics*, 47: 412 – 417.
10. Ogata, M., Sugiyama, K. and Moriyasu, H. (1962). Studies on poisoning IV. Toluene concentration in air and urinary hippuric acid measured by paper chromatography and mass screening examination method. *Acta Medica Okayama*, 16: 283 – 292.
11. Yacob, A. R. and Zinalibdin, M. R. (2013). Detection of hippuric acid: A glue solvent metabolite using a mobile test kit. *Arabian Journal of Chemistry*, 6: 115 – 120.
12. Yacob, A. R. and Said, N. (2014). Ortho-Cresol as Indicator for Toluene Exposure among Workers. 2014 4th *International Conference on Environment Science and Engineering*, IACSIT Press, Singapore, 68: 14 –18.
13. Inoue, O., Seiji, K., Suzuki, T., Watanabe, T., Natkasuka, H., Satao, H. and Ikeda, M. (1991). Simultaneous determination of hippuric acid,o-, m -, and p -methylhippuric acid, phenylglyoxylic acid, and mandelic acid by HPLC . *Bulletin Environmental Contamination. Toxicology*, 47: 204 – 210.
14. Yang, Y. D. (1998). Simultaneous determination of creatine, uric acid, creatinine and hippuric acid in urine by high performance liquid chromatography. *Biomedical Chromatography*, 12 (2): 47 – 49.
15. Poggi, G., Giusiani, M., Palagi, U., Paggiaro, P. L., Loi, A. M., Dazzi, F. and Baschieri, L. (1982). High-performance liquid chromatography for the quantitative determination of the urinary metabolites of toluene, xylene, and styrene. *International Archives of Occupational and Environmental Health*, 50(1): 25 – 31.
16. Ogii K. (1988). Determination of Hippuric Acid in Cadaveric Urine and Urinary Stain by High Performance Liquid Chromatography. *Journal Tokyo Woman Medicine Collection*, 58: 627 – 636.
17. Fujii T., Kawabe S., Horike T., Taguchi T. amd Ogata M. (1999). Simultaneous Determination of the Urinary Metabolites of Toluene, Xylene and Styrene using High Performance Capillary Electrophoresis: Comparison with High Performance Liquid Chromatography. *Journal Chromatography B*. 41: 730 –740.
18. Lee, C. E., Lee, J., Lee, J., Eom, H.Y., Kim, M. K., Suh, J. H., Yeom, H., Kim, U., Youm, J. R. and Han, S. B. (2009). Rapid HPLC Method for the Simultaneous Determination of Eight Urinary metabolites of toluene, xylene and styrene. *Bulletin Korean Chemical Society*, 30(9): 2021 – 2026.
19. Inoue, O., Kanno, E., Yusa, T., Kakizaki, M., Ukai, H., Okamoto, S., Higashikawa, K. and Ikeda, M. (2002). Urinary benzylmercapturic acid as a marker of occupational exposure to toluene. *International Archives Occupational Environmental Health*, 75: 341 – 347.
20. Inoue, O., Kanno, E., Kasia, K., Ukai, H., Okamoto, S. and Ikeda, M. (2004). Benzylmercapturic acid is superior to hippuric acid and o-cresol as a urinary marker of occupational exposure to toluene. *Toxicology Letter*, 147: 177 –186.
21. Serap, A. A., Pembe, O., Yusuf, K.., Huseyin. K. and Suheyla, E. (2001). Medicolegal Aspects of Blood-Urine Toluene and Urinary Ortho-Cresol concentration in Toluene Exposure. *Turkish Journal Medical Science*, 31: 415 – 419.
22. Monteiro, C., Franco, J. M., Proença, P., Castañera, A., Claro, A., Vieira, D. N. and Corte-Real, F. (2014). Qualitative and quantitative analysis of a group of volatile organic compounds in biological samples by HS-GC/FID: application in practical cases. *Forensic Science International*, 243: 137 –143.
23. De Carvalho, D., Lanchote, V. L., Bonato, P. S., Queiroz, R. H. C., Santos, A. C. and Dreossi S. A. C. (1991). A new derivatization procedure for the analysis of hippuric acid and m-methyl-hippuric acid by gas chromatography. *International Archive Environmental Health*, 63: 33 – 37.

24. Pacenti, M., Dugheri, S., Villanelli, F., Bartolucci, G., Calamai, L., Boccalon, P., Arcangeli, G., Vecchione, F., Alessi, P., Kikic, I. and Cupelli, V. (2008). Determination of organic acids in urine by solid-phase microextraction and gas chromatography-ion trap tandem mass spectrometry previous 'in sample' derivatization with trimethyloxonium tetrafluoroborate. *Biomedical Chromatography*, 22: 1155 – 1163.
25. Kongtip, P., Vararussami, J. and Pruktharathikul, V. (2001). Modified method for determination of hippuric acid and methylhippuric acid in urine by gas chromatography. *Journal of Chromatography B: Biomedical Sciences and Applications*, 751(1): 199 – 203.
26. De Paiva, M. J. N., Martins, I. and de Siqueira, M. E. P. B. (2007). Analysis of o-cresol in urine by solid phase microextraction capillary gas chromatography. *Journal Brazillian Chemical Society*, 18 (5): 1034 –1039.
27. Truchon, G., Tardif, R. and Brodeur, J. (1996). Gas chromatographic Determination of urinary o-cresol for the monitoring of toluene exposure. *Journal of Analytical Toxicology*, 20: 309 – 312.
28. Ikeda, M. (1996). Selected solvents.4.6 Toluene. In: Mikheev MI (ed) Biological monitoring of chemical exposure in workplace. *World Health Organization, Geneva*, (1) 4: 205 – 217.
29. Ikeda, M. and Ohtsuji, M. (1969). Significance of urinary hippuric acid determination as an index of toluene exposure. *British Journal Industrial Medicine*, 26: 244 – 246.
30. Lauwerys, R. (1983). Toluene In: Alessio L, Berlin A, Roi R, Boni M (eds) Human biological monitoring of industrial chemicals, *Joint Research Centre Ispra Establishment* CEC 1: 159 – 175.
31. Siqueira, M. E. and Paiva, M. J. (2002). Hippuric acid in urine: references values. *Revision Saude Publica*, 36: 723 – 727.
32. Sugita, M., Aikawa, H., Suzuki, K., Yamasaki, T., Minowa, H., Etoh, R. and Kasuga, H. (1988). Urinary hippuric acid excretion in everyday life. *Tokai Journal Exposure Clinical Medical*, 13: 185 – 190.
33. Villanueva, M. B., Jonai, H., Kanno, S. and Takeuchi, Y. (1994). Dietary sources and background levels of hippuric acid in urine; comparison of Philiphine and Japanese levels. *Industrial Health*, 32: 339 – 346.
34. Michitsuji, H., Ohara, A., Yamaguchi, K. and Fujiki, Y. (1987). Effect of intake of refreshments in excretion of hippuric acid in urine. *Matsushita Medical Journal*, 26: 105 – 116.
35. Kawai, T., Yamauchi, T., Miyama, Y., Sakurai, H., Ukai, H., Takada, S., Ohashi, F. and Ikeda, M. (2007). Benzyl alcohol as a marker of occupational exposure to toluene. *Industrial Health*, 95: 143 – 150.
36. Hasegawa, K., Shiojima, S., Koizumi, A. and Ikeda M. (1983). Hippuric acid and o-cresol in the urine of workers exposed to toluene. *International Archive Occupational Environmental Health*, 52: 197 – 208.
37. Nise, G. (1992). Urinary excretion of o-cresol and hippuric acid after toluene exposure in rotogravure printing. *International Archives Occupational Environmental Health*, 63: 377 – 381.
38. Maestri, L., Ghittori, S. and Imbriabu, M. (1997). Determination of specific mercapturic acids as an index of exposure to environmental benzene, toluene and styrene. *Industrial Health*, 35: 489 – 502.
39. Angerer, J., Schildbach, M. and Kramer, A. (1998). S-p-toluylmercapturic acid in the urine of workers exposed to toluene; a new biomarker for toluene exposure. *Archives Toxicology*, 72: 119 – 123.
40. Inoue, O., Seiji, K. and Watanabe T. (1993). Effect of smoking and drinking on excretion of hippuric acid among toluene exposed workers. *International Archives Occupational Environmental Health*, 64: 425 – 430.
41. Kawai, T., Mizunuma, K., Okada, Y., Horiguchi, S. and Ikeda, M. (1996). Toluene itself as the best urinary marker of toluene exposure. *International Archives Occupational Environmental Health*, 68: 289 – 297.
42. Lovreglio, P., Barbieri A., Carrieri, M., Sabatini, L., Fracasso, M.E., Doria, D., Drago, I., Basso, A., D'Errico, M. N., Bartolucci, G.. B., Violante, F. S. and Soleo, L. (2010). Validity of new biomarkers of internal dose for use in the biological monitoring of occupational and environmental exposure to low concentrations of benzene and toluene. *International Archives Occupational Environmental Health*, 83: 341 – 356.
43. Park S. W., Kim N. Y., Yang Y. G, Seo B. and Paeng K. .J. (1998). Toluene Distribution of Glue Sniffers Biological Fluid Samples in Korea. *Journal of Forensic Science*, 43: 888 – 890.
44. Anderson C. E. and Loomis G.. A. (2003). Recognition and Prevention of Inhalant Abuse. *American Academy Family Physician*, 68: 869 – 874.
45. Ameno K., Fuke C., Ameno S., Kirui T., Sogo K. and Ijiri I. (1989). A Fatal Case of Oral Ingestion of Toluene. *Journal Forensic Science International*, 41: 255 – 260.
46. Yamazaki K., Tanaka E. and Misawa S. (1992). Urinary ortho-cresol Concentrations as an Indicator of Toluene Inhalation in Glue Sniffer. *Journal Forensic Science*, 32: 215 – 223.

47. Zuppi C., Rossetti D. V., Vitali A., Vincenzoni F., Giardina B., Castagnola M. and Messana I. (2003). Determination of Urinary Hippuric Acid by Micellar Electrokinetic Capillary Chromatography. *Journal Chromatography B*, 793: 223 – 228.
48. Amorim L. C. A. and Alvarez-Leite E. M. (1997). Determination of o-cresol by Gas Chromatography and Comparison with Hippuric Acid Levels in Urine Sample of Individuals Exposed to Toluene. *Journal Toxicology Environmental Health*, 30: 101 – 107.
49. World Health Organisation (WHO) (2000). Air quality guidelines for Europe. WHO Regional Publications, *European Series, No. 91. 2nd edition*. WHO Regional Office for Europe. Copenhagen.
50. Croes K., McCarthy P. T. and Flanagan R. J. (1994). Simple and Rapid HPLC of Quinine, Hydroxychloroquine, Chloroquine and Desethylchloroquine in Serum, whole Blood and Filter Paper Adsorbed Dry Blood. *Journal Analaytical Toxicology*, 18: 255 – 260.
51. Flanagan R. J., Braithwaite R. A., Brown S. S., Widdop B. and de Wolff F. A. (1995). Basic Analytical Toxicology. World Health Organization, Geneva.
52. Gaffney, G.. W., Schreier, K., Diferrante, N. and Altman, K. I. (1954). The quantitative determination of hippuric acid. *Journal Biology Chemical*, 206: 695 – 698.
53. Umberger, C. J. and Fiorese, F. F. (1963). Colorimetric method of hippuric acid. *Clinical Chemistry*, 9: 191 – 196.
54. Tomokuni, K. and Ogata, M. (1972). Direct colorometric determination of hippuric acid in urine. *Clinical Chemistry*, 18(4): 349 – 351.
55. Yoshida, M., Akane, A., Mitani, T. and Watabiki, T. (2005). Simple colorimetric semi quantitation method of hippuric acid in urine for demonstration of toluene abuse. *Journal of Legal Medicine*, 7(3): 198 – 200.
56. Matsui, H., Kasao, M. and Imamura, S. (1978). High-performance liquid chromatographic determination of hippuric acid in human urine. *Journal of Chromatography*, 145(2): 231 – 236.
57. Bevine, H., Olsson, U., Hemgard, A., Kristensson, J., Palmborg, J. and Sollenberg J. (1990). High Performance Liquid Chromatographic Analysis of Hippuric Acid in Human Blood Plasma. *Journal of Chromatography*, 532: 45 – 53.
58. Kubota, K., Horai, Y., Kushida, K. and Ishizaki, T. (1988). Determination of benzoic acid and hippuric acid in human plasma and urine by high-performance liquid chromatography. *Journal of Chromatography*, 425(1): 67 – 75.
59. Ogata, M. and Taguchi, T. (1987). Quantitation of urinary metabolites of toluene, xylene, styrene, ethylbenzene, benzene and phenol by automated high performance liquid chromatography. *International Archives of Occupational and Environmental Health*, 59(3): 263 – 272.
60. Daneshfar, A., Toulabi, P. and Sahrai R. (2010). Determination of hippuric acid in biological fluids using single drop liquid-liquid-liquid microextraction. *The Royal Society of Chemistry*, 2: 564 – 569.
61. Moein, M. M., El-Beqqali, A., Javanbakht, M., Karimi, M., Akbari-adergani, B. and Abdel-Rehim, M. (2014). On-line detection of hippuric acid by microextraction with a molecularly imprinted polysulfone membrane sorbent and liquid chromatography-tandem mass spectromethy. *Journal of Chromatography A*, 1372: 55 – 62.
62. Buchet, J. P. and Lauwerys, R. R. (1973). Measurement of urinary hippuric and m-methylhippuric acids by gas chromatography. *British Journal of Industrial Medicine*, 30(2): 125 – 128.
63. Kira, S. (1977). Measurement by gas chromatography of urinary hippuric acid and methylhippuric acid as indices of toluene and xylene exposure. *British Journal of Industrial Medical*, 34: 305 – 309.
64. Veuleman, H., Van Vlem, E., Janssens, H. and Masschelein, R. (1979). Exposure to toluene and urinary hippuric acid excretion in a group of heliorotagravure printing workers. *International Archives Occupational Environmental Health*, 44: 99 – 107.
65. Van Roosmalen, P. B. and Drummond, I. (1978). Simultaneous determination by gas chromatography of the major metabolites in urine of toluene, xylenes and styrene. *British Journal Industrial Medical*, 35: 56 – 60.
66. Campbell, L., Wilson, H. K., Samuel, A. M. and Gompertz, D. (1988). Interactions of m-xylene and aspirin metabolism in man. *British Journal Industrial Medical*, 30: 125 – 128.
67. Sanagi, M. M., Salleh, S., Wan Ibrahim, W. A. and Abu Naim, A. (2011). Determination of organophosphorus pesticides using molecularly imprinted polymer solid phase extraction. *Malaysian Journal of Analytical Sciences*, 15(2): 175 – 183.

68. Ahmadi, F., Asgharloo, H., Sadeghi, S., Gharehbagh-Aghababa, V. and Adibi, M. (2009). Post-derivatization procedure for determination of hippuric acid after extraction by an automated micro solid phase extraction system and monitoring by gas chromatography. *Journal of Chromatography B*, 877: 2945 – 2951.
69. Ogata, M., and Taguchi, T. (1986). Quantitative analysis of urinary glycine conjugates by high performance liquid chromatography: excretion of hippuric acid and methylhippuric acids in the urine of subjects exposed to vapors of toluene and xylenes. *International Archives of Occupational and Environmental Health,* 58(2): 121–129.
70. Ogata, M., and Taguchi, T. (1987). Quantitation of urinary metabolites of toluene, xylene, styrene, ethylbenzene, benzene and phenol by automated high performance liquid chromatography. *International Archives of Occupational and Environmental Health,* 59(3): 263 –272.
71. Yacob, A. R. and Zinalibdin M. R. (2010). High Performance Liquid Chromatography Determination of urinary hippuric acid and benzoic acid as indices for glue sniffer urine. *World Academy of Science and Technology,* 38: 973 – 978.
72. Ohashi, Y., Mamiya, T., Mitani, K., Wang, B., Takigawa, T., Kira, S. and Kataoka, H. (2006). Simultaneous determination of urinary hippuric acid, o-, m- and p- methylhippuric acids, mandelic acid and phenylglyoxylic acid for biomonitoring of volatile organic compounds by gas chromatography-mass spectrometry. *Analytica Chimica Acta,* 566: 167 – 171.

MALAYSIAN JOURNAL OF ANALYTICAL SCIENCES
Published by The Malaysian Analytical Sciences Society
ISSN 1394 - 2506

FAST AND SIMPLE FORENSIC RED PEN INK ANALYSIS USING ULTRA-PERFORMANCE LIQUID CHROMATOGRAPHY (UPLC)

(Analisis Forensik Cepat dan Mudah bagi Dakwat Pen Merah menggunakan Kromatografi Cecair Berprestasi Ultra)

Loong Chuen Lee*, Seow Lay Ying, Wan Nur Syazwani Wan Mohamad Fuad, Ab Aziz Ishak, Khairul Osman

Forensic Science Program, School of Diagnostic & Applied Health Sciences,
Faculty of Health Sciences,
Universiti Kebangsaan Malaysia, Jalan Raja Muda Abdul Aziz, 50300 Kuala Lumpur, Malaysia

**Corresponding author: lc_lee@ukm.edu.my*

Received: 28 December 2015; Accepted: 7 March 2016

Abstract

Ultra-performance liquid chromatography (UPLC) is more effective than high performance liquid chromatography in terms of analysis speed and sensitivity. This paper presents a feasibility study on forensic red pen inks analysis using UPLC. A total of 12 varieties of red ballpoint pen inks were purchased from selected stationary shop. For each variety, four different individual pens were sampled to provide intra-variability within a particular variety of pen. The proposed approach is very simple that it only involved limited analysis step and chemicals. A total of 144 chromatograms were obtained from red ink entries extracted with 1.5 mL 80 % (v/v) acetonitrile. Peaks originated from pen inks were determined by comparing the chromatograms of both blank paper and blank solvent against that of ink samples. Subsequently, one-way ANOVA was conducted to discriminate all 66 possible pairs for red pen inks. Results showed that the proposed approach giving discriminating power of 95.45 %. The outcome of the study indicates that UPLC could be a fast and simple approach to red ballpoint inks analysis.

Keywords: forensic ink analysis, ballpoint pen inks, ultra-performance liquid chromatography

Abstrak

Kromatografi cecair berprestasi Ultra (UPLC) adalah lebih berkesan dari kromatografi cecair berprestasi tinggi dari segi kelajuan analisis dan kepekaan. Kertas ini mempersembahkan kajian kebolehlaksanaan pada analisis dakwat pen merah menggunakan UPLC. Sebanyak 12 jenis dakwat pen mata bulat merah dibeli dari kedai alat tulis yang terpilih. Untuk setiap jenis, empat batang pen telah disampel untuk memberi maklumat tentang intra-variasi bagi suatu jenis pen. Pendekatan yang dicadangkan adalah mudah kerana ia hanya melibatkan langkah analisis dan bahan kimia yang terhad. Sejumlah 144 kromatogram telah diperolehi dari dakwat tulisan merah yang diekstrak dengan 1.5 mL 80 % (v/v) asetonitril. Puncak yang berasal dari dakwat pen ditentukan melalui perbandingan antara kromatogram kertas kosong dan pelarut kosong dengan yang diperolehi dari sampel dakwat. Seterusnya, ujian ANOVA sehala telah dijalankan untuk membezalayan kesemua 66 pasangan dakwat pen merah yang terbentuk. Keputusan menunjukkan pendekatan yang dicadangkan memberi 95.45 % kuasa pembezalayan. Hasil kajian ini menunjukkan UPLC dapat dijadikan satu pendekatan yang cepat dan mudah untuk analisis dakwat pen mata bulat merah.

Kata kunci: analisis dakwat forensik, dakwat pen mata bulat, kromatografi cecair prestasi ultra

Introduction

Over recent years, forensic document examination is an important area of forensic science and its contribution towards solving crimes is significant. On one hand, the invention of computer has resulted in reducing usage of writing instruments and paper as a form of proof, agreement and communication. Nevertheless, writing instruments

like ballpoint pen and gel pen are still widely used in documentation [1]. Around 80 % of the questioned documents contain ballpoint pen ink [2]. On the other hand, the forensic analysis of ballpoint pen inks is a frequently encountered at questioned documents examination and its contribution towards solving crimes is significant. For that reason, it is vital to have a fast and simple ink analysis method capable of providing high differentiation power.

Ballpoint pen ink is a complex mixture of different types of chemicals. Inks produced by writing instrument manufacturers are specially formulated depending on their applications. Different kinds of writing instruments have their own writing mechanisms. In addition, characteristics such as color, flow capacity, viscosity and drying time are also taken into account [3]. Therefore, the final composition of inks can be quite complicated. In general, ballpoint pen ink comprises of 50 % solvent, 25 % dyes as well as 25 % resins and other additives [4]. In most cases, ink analysis always focuses on dye components because of their ability to absorb light of different wavelength [5].

Ink analysis aimed at determining the age of a questioned document and identifying the kind of writing instrument/inks used to produce the questioned document. Methods of ink analysis can be divided into destructive and non-destructive. Zieba-Palus and Kunicki reported that 95 % of ballpoint pen can be classified according their varieties via Fourier-transform infrared (FTIR) and Raman spectroscopy [6]. Recently, Lee et al. have proposed a new and non-destructive method for systematic analysis black ballpoint pen inks using micro-ATR-FTIR spectroscopy [7-9]. Nevertheless, non-destructive methods seldom provide satisfactory results. Most of the time, chromatographic techniques such as thin layer chromatography (TLC) and high performance liquid chromatography (HPLC) could assist in further identification of pen ink's source. For example, Djozan et al. successfully differentiate 41 blue ballpoint pens via TLC coupled with image analysis [10]. Feasibility of HPLC for blue ballpoint pen ink classification has been studied as well [11, 12]. While Neumann and Margot have investigated the feasibility of high performance thin layer chromatography (HPTLC) for blue ballpoint pen inks [13, 14].

This study was aimed at exploring advantages of ultra-performance chromatography (UPLC) for forensic ink analysis purpose in terms of simplicity. There were two differences between this paper against two other similar papers published recently [15, 16]. Firstly, this paper present analysis of red ballpoint pen inks that is still very rare being studied. Secondly, the approach proposed here give emphasis on simplicity that we only use chemicals that are readily available in any analytical laboratory and do not apply any advanced statistical techniques such as Principal Component Analysis. In addition, UPLC is well known for its high resolution and faster separation speed [17].

Materials and Methods

Sample preparation

A total of 12 different varieties of red ballpoint pens were selected to be studied. Four different individual pens were sampled for each variety of pens. Table 1 shows the details and identification number of the pen samples. White paper template (Double A premium copy paper, A4 size, 80 gsm, Thailand) was prepared as well. Both pens and paper were brought from a selected stationary shop. Sample pen was prepared using similar methods as described in [16]. Every individual pen was used to write "HUNDRED THOUSAND ONLY" (measured approx. 50 mm x 5 mm) three times on piece of white copy papers. Ink was extracted right after 2 hours of its preparation in the same day to avoid variations introduced by ink ageing process.

UPLC analysis

Ink entry prepared with the red ballpoint pen inks were cut out and eluted with acetonitrile (HPLC grade, Fisher Scientific UK Ltd) and distilled water. All analysis was carried out on Waters® ACQUITY UPLCTM system that consisted of the ACQUITY UPLC Binary Solvent Manager, the ACQUITY UPLC Sample Manager and the Waters 2996 Photodiode Array Detector (PDA) with a low volume flow cell. The ACQUITY UPLC column BEH C18 (2.1 x 50 mm) with 1.7 mm particle size was used to separate the ink components. Injection volumes for all samples were set to 7.5 uL. Two types of mobile phases used were acetonitrile (HPLC grade, Fisher Scientific UK Ltd) and distilled water (solvent B). After several times of trial and error, the time-dependent, gradient elution protocol was established. The mobile phases were run with a flow rate of 0.20 mL/min for a period of eight minutes. Details of gradient elution system were listed in Table 2. To collect as much information as possible, the chromatogram of red

inks were recorded at 205 and 279 nm. All data were acquired and processed using Waters® Empower™ chromatography data software. Chromatograms of the blank paper and blank solvent were also prepared in the same manner as the pen ink samples.

Table 1. Details and identification numbers of each selected varieties of red ballpoint pens. Each variety of pens was assigned with an identification numbers (id no.)

ID No.	Model/Brand	No. of Sample
A1	Bob/Carena	4
B1	XP 243 soft ink xtra fine/Reynolds	4
B2	Popular 240 medium/Reynolds	4
C1	R100 Fine/G'soft	4
C2	BP-GS-56 0.7/G'soft	4
D1	ExtraFinePoint/e-write	4
E1	Fornine 88	4
F1	Round stic Grip fine USA/Bic	4
G1	Kilometrico M/Papermate	4
G2	Kilometrico Fine PT/Papermate	4
G3	Kilometrico 100 LV ink med/Papermate	4
G4	KV2 Fine/Papermate	4

Table 2. Gradient elution system for red ballpoint pen inks; A=80% ACN; B=H_2O

Run Time (min)	Flow rate (mL/min)	% A	% B
Initial	0.20	50.0	50.0
1.00	0.20	80.00	20.0
3.00	0.20	100.00	0.00
4.00	0.20	100.00	0.00
4.50	0.20	50.0	50.00
8.00	0.20	50.0	50.00

Data analysis

As this paper aimed to propose simple analysis protocol to discriminate pen inks, no statistical technique is introduced to the data except one-way ANOVA was applied to determine the discrimination status of pen pairs based on *p*-value. Later, discriminating power (DP) was calculated using the following Equation 1 [9]:

$$DP = 1 - \frac{2M}{n(n-1)} \quad (1)$$

where *M* is the number of non-discriminated pairs of samples and *n* denotes the total number of samples. The DP is a measurement of the selectivity of the method to differentiate the pen inks analyzed [18].

Results and Discussion

Previous studies used to discriminate ballpoint pen inks based on profiling of dye components by chromatographic techniques [13, 14, 19]. Most of the dye components of red ballpoint pen inks have maximum UV-absorption above 500 nm, i.e. rhodamine 6G at 524 nm [20]. However, this study intended to investigate the possibility of discriminating red ballpoint pen inks using information obtained from components other than dyes. Therefore, all of the chromatogram of inks was only scanned between 200 and 500 nm.

Prior to discrimination analysis, all of the chromatograms of ink sample were compared against the chromatogram of blank solvent and blank paper (Figure 1) in order to identify peaks originated from pen inks only. The representative chromatograms for two red pens inks are as shown in Figure 2. A total of 39 peaks obtained from chromatogram scanned at 205 and 279 nm were determined as coming from red ballpoint pen inks. Those identified peaks were most likely due to ink components other than dyes, such as additives that included driers, plasticizers and detergents which are present at very minute amount [16].

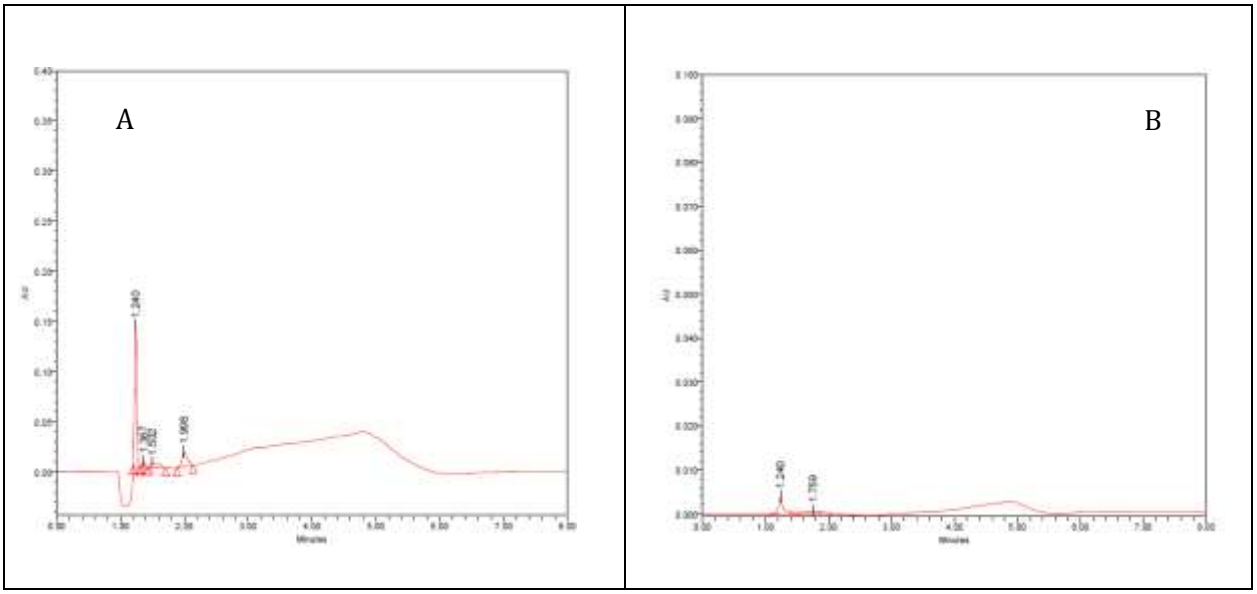


Figure 1. Chromatogram of blank. Solvent blank scanned at 205nm (A) and paper blank scanned at 279nm (B).

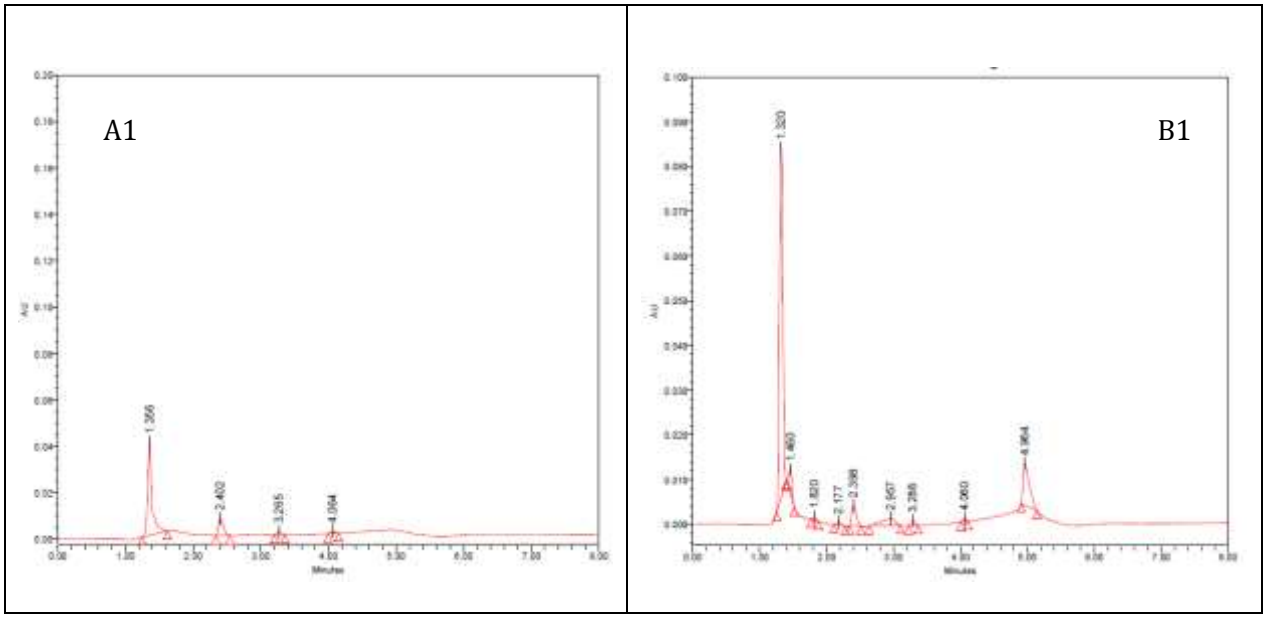


Figure 2. The representative chromatogram of two red ballpoint pen inks, i.e. A1 and B1 scanned at 279 nm.

Since we could not standardize the amount of ink deposited on paper for every ink entry, bias could be introduced if the obtained peak area value is compared directly. To ensure more reliable comparative analysis, the data was normalizing towards a single selected peak to eliminate variations occurred due to uneven initial ink deposition on paper [15]. After careful inspection on all the chromatograms, the first peak (i.e. retention time 1.280 – 1.399) in both chromatograms scanned at 205 and 279 nm was selected to be the normalization factor. It was chosen for the purpose of normalization as its peak is sharp and is the highest in the chromatogram. The peak area value of the other peaks is then divided with the normalization factor.

One-way between groups ANOVA was conducted based on the normalized peak area values. Pen pair that gives *p*-value less than 0.05 is determined to be discriminated pair and pair that give *p*-value more than 0.05 will be labelled as non-discriminated pair. The summary result of the comparative analysis between 66 possible pen-pair is shown by Figure 3. Only three pen-pair cannot be discriminated based on their chromatograms, i.e. B1-F1, B1-E1 and E1-F1. Pen-pairs that cannot be differentiated from each other may have the same or very similar formulation. In other words, this indicates the possibility of purchasing inks from a single ink manufacturer as an inks manufacturer may sell their ink to more than one instrument manufacturers [14]. In brief, the proposed approach gave discrimination power around 95.45 %.

The obtained DP is comparable to other approaches that involved much complicated analytical instrument, i.e. real time mass spectrometry (DART MS) [21] or advanced analysis tools such as image analysis [10]. In this study, differentiation of inks was based purely on the relative peak area of peaks at pre-defined wavelength range. And the objectivity of comparative analysis is secured by applying one-way ANOVA and decision is made based on the *p*-value. The approach proposed here is fast and simple.

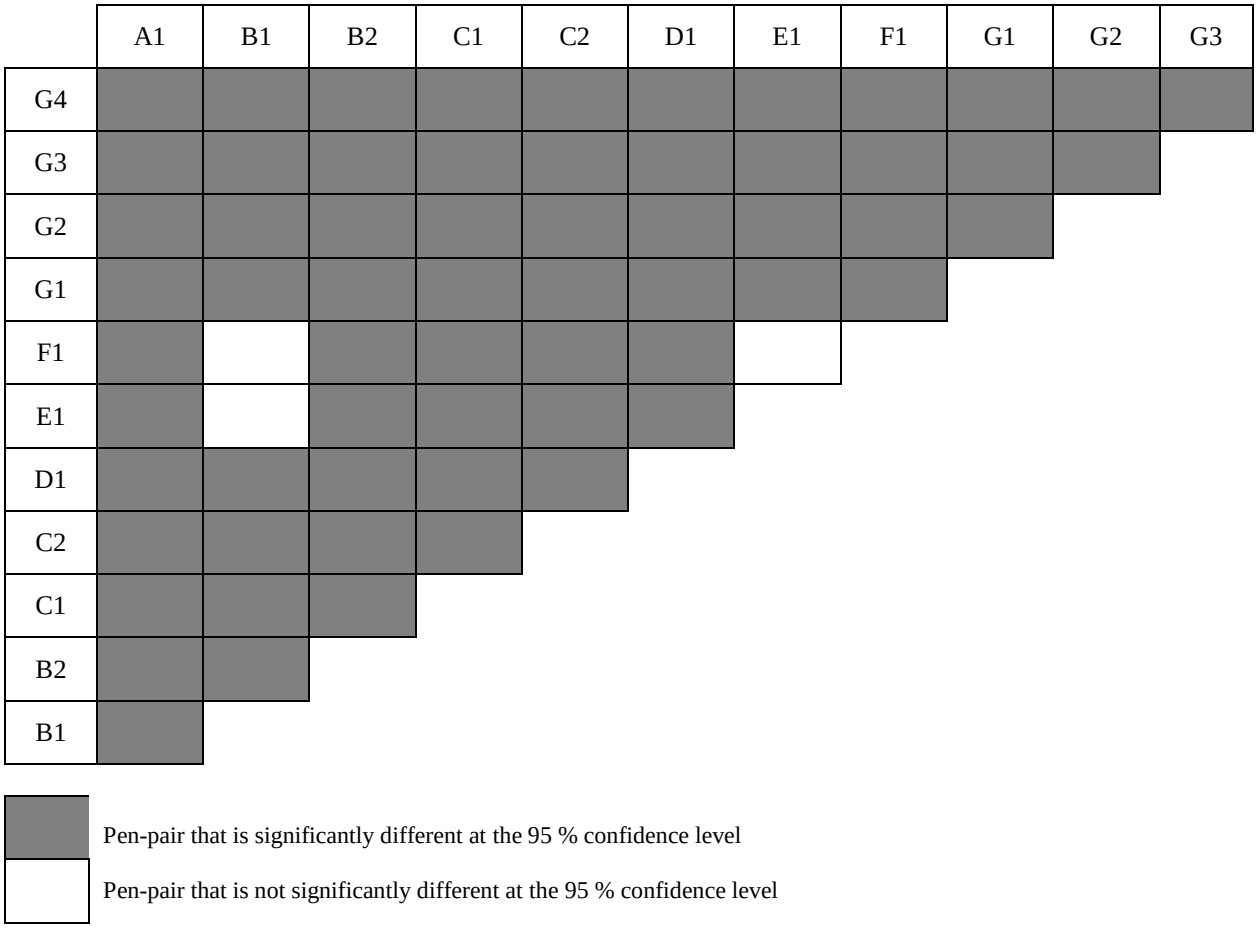


Figure 3. Matrix showing summary result of differentiation of red ballpoint pen inks based on UPLC chromatograms via one way ANOVA analysis

Conclusion

The present study showed that the written extracts from different ballpoint pens can be differentiated at satisfactory level with UPLC coupled with UV/PDA detection. The proposed technique found to be effective as it only involved common chemical, i.e. acetonitrile, and simple statistical techniques, i.e. one-way ANOVA. Besides, composition of minor components in ballpoint pen inks could be as efficient as dye components in classification of pen inks since it was supported by the high level of discriminating power calculated in this study.

Acknowledgement

This work is partially supported by the research grant FRGS/2/2013/ST06/UKM/02/1 and DPP-2015-FSK. Special thanks dedicated to the Ministry of Higher Education Malaysia, and UKM, especially to all the staffs from the forensic science program, UKM, for the support, equipment and facilities provided.

References

1. Blackledge, R. D. (2007). Forensic analysis on the cutting edge: new methods for trace evidence analysis. Hoboken: John Wiley and Sons.
2. Denman, J. A., Skinner, W. M., Kirkbride, K. P. and Kempson, I. M. (2010). Organic and inorganic discrimination of ballpoint pen inks by ToF-SIMS and multivariate statistics. *Applied Surface Science*, 256(7): 2155 – 2163.

3. Coumbaros, J., Kirkbride, K. P., Klass, G. and Skinner, W. (2009). Application of time of flight secondary ion mass spectrometry to the in situ analysis of ballpoint pen inks on paper. *Forensic Science International*, 193: 42 – 46.
4. Weyermann, C. and Spengler, B. (2008). The potential of artificial aging for modelling of natural aging processes of ballpoint ink. *Forensic Science International*, 180: 23 – 31.
5. Senior, S., Hamed, E., Masoud, M. and Shehata, E. (2012). Characterization and Dating of Blue Ballpoint Pen Inks Using Principal Component Analysis of UV–Vis Absorption Spectra, IR Spectroscopy, and HPTLC. *Journal of Forensic Sciences*, 57:1087 – 1093.
6. Zięba-Palus, J. and Kunicki, M. (2006). Application of the micro-FTIR spectroscopy, Raman spectroscopy and XRF method examination of inks. *Forensic Science International*, 158: 164 – 172.
7. Lee, L. C., Othman, M. R., Pua, H., Ishak, A. A. and Ishar, S. M. (2012). Classification and identification of black ballpoint pen inks based on multivariate analysis and infrared spectra. *Problems of Forensic Sciences*, 92: 253 – 264.
8. Lee, L. C., Othman, M. R. and Pua, H. (2012). Systematic Assessment of Attenuated total reflectance Fourier transforms infrared spectroscopy coupled with multivariate analysis for forensic analysis of black ballpoint pen inks. *Malaysian Journal of Analytical Sciences*, 16: 262 – 272.
9. Lee, L. C., Othman, M. R., Pua, H. and Ab Aziz Ishak. (2012). Application of multivariate chemometry for discrimination of black ballpoint on inks based on the IR spectrum. *Malaysian Journal of Forensic Sciences*, 3: 5 – 10.
10. Djozan, D., Baheri, T., Karimian, G. and Shahidi, M. (2008). Forensic discrimination of blue ballpoint pen inks based on thin layer chromatography and image analysis. *Forensic Science International*, 179: 199 –205.
11. Kher, A., Mulholland, M., Green, E. and Reedy, B. (2006). Forensic classification of ballpoint pen inks using high performance liquid chromatography and infrared spectroscopy with principal components analysis and linear discriminant analysis. *Vibrational Spectroscopy*, 40: 270 – 277.
12. Kher, A., Green, E.V. and Mulholland, M.B. (2001). Evaluation of principal components analysis with high-performance liquid chromatography and photodiode array detection for the forensic differentiation of ballpoint pen inks. *Journal of Forensic Sciences*, 46: 878 – 883.
13. Neumann, C., and Margot, P. (2009). New perspectives in the use of ink evidence in forensic science: Part I. Development of a quality assurance process for forensic ink analysis by HPTLC. *Forensic Science International*, 185: 29 – 37.
14. Neumann, C., and Margot, P. (2009). New perspectives in the use of ink evidence in forensic science: Part II. Development and testing of mathematical algorithms for the automatic comparison of ink samples analyzed by HPTLC. *Forensic Science International*, 185: 38 – 50.
15. Lee, L. C., Shandu, K. T. S., Razi, N. S. M., Ishak, A. A. and Osman, K. (2015). Forensic analysis of blue ballpoint pen inks using Ultraviolet-Visible Spectrometer and UPLC. *Malaysian Journal of Analytical Sciences*, 19: 397 – 401.
16. Lee, L. C., Yunus, I. S. M. D, Fuad, W. N. S. W. M., Ishak, A. A. and Osman, K. (2015). Statistical Discrimination of Black Ballpoint Pen Inks using UPLC with PCA. *Journal of Analytical Chemistry*, 70: 374 – 377.
17. Swartz. M. E. (2005). Ultra performance liquid chromatography (UPLC): An introduction and Review. *Journal of Liquid Chromatography & Related Technologies*, 28: 1253 – 1263.
18. Weyermann, C., L. Bucher, P., Majcherczyk, W., Mazzella, Roux, C. and Esseiva, P. (2012). Statistical discrimination of black gel pen inks analyzed by laser desorption/ionization mass spectrometry. *Forensic Science International*, 217: 127 – 133.
19. Neumann, C., Ramotowski, R. and Genessay, T. (2011). Forensic examination of ink by high-performance thin layer chromatography – The United States Secret Service Digital Ink Library. *Journal of Chromatography A*, 1218: 2793 – 2811.
20. Sigma-Aldrich catalog. Online access at [http://www.sigmaaldrich.com/catalog/product/aldrich/201324?lang=en&regio]
21. Roger, W. J. and McClelland, J. F. 2013. Analysis of writing inks on paper using direct analysis in real time mass spectrometry. *Forensic Science International*, 231: 73 – 81.

MALAYSIAN JOURNAL OF ANALYTICAL SCIENCES
Published by The Malaysian Analytical Sciences Society
ISSN 1394 - 2506

PENGGUNAAN KAEDAH PENYINARAN MIKROGELOMBANG DALAM SINTESIS TERBITAN TIOUREA

(An application of Microwave Irradiation Technique in Preparation of Thiourea Derivatives)

Hafizi Ahyak, Atisya Rohadi, Fatimatul Akma Awang Ngah, Bohari Yamin, Siti Aishah Hasbullah*

School of Chemical Sciences and Food Technology,
Faculty of Science and Technology,
Universiti Kebangsaan Malaysia, 43600 UKM Bangi, Selangor, Malaysia

**Corresponding author: aishah80@ukm.edu.my*

Received: 22 January 2016; Accepted: 18 February 2016

Abstrak

Sebatian baru terbitan tiourea, 1-etil-1-(2-hidroksi-etil)-3-naftalen-1-il-tiourea **(3a)** dan 1-(fenil-amino)-3-naftalen-1-il-tiourea **(3b)** telah berjaya disintesis melalui tindak balas antara 1-naftil isotiosianat **(1)** dengan etilena 2-etilaminoetanol **(2a)** dan fenilhidrazina **(2b)** menggunakan kaedah penyinaran mikrogelombang dan kaedah refluks. Peratusan hasil bagi kedua-dua kaedah yang digunakan untuk sebatian **3a** dan **3b** masing-masing adalah **3a** (refluks: 66%, mikrogelombang: 98%) dan **3b** (refluks: 72%, mikrogelombang: 97%). Hasil sintesis dianalisa dengan menggunakan alat spektroskopi FT-Inframerah (FT-IM), Spektroskopi Resonan Magnetik Nuklear (RMN) dan Spektrometri Jisim. Kajian antimikrob juga dilakukan dengan menggunakan *Staphylococcus aureus* dan *Bacillus subtillus* sebagai Gram positif, *Escherichia coli* dan *Salmonella typhimurium* sebagai Gram negatif dan kulat yang digunakan adalah *Aspergillus niger*. Kawalan positif yang digunakan adalah *streptomisin* dan *kanamisin*, manakala kawalan negatif yang digunakan adalah DMSO. Walaubagaimanapun hasil kajian mendapati tiada perencatan yang ketara terhadap pertumbuhan bakteria dan kulat (hanya 6-7mm kawasan perencatan) menggunakan sebatian tiourea ini.

Kata kunci: sebatian tiourea, mikrogelombang, aktiviti antimikrob

Abstract

New thiourea derivatives, 1-ethyl-1-(2-hydroxy-ethyl)-3-naphthalen-1-yl-iourea **(3a)**, 1-(phenyl-amino)-3-naphthalen-1-yl-Tiourea **(3b)** have been synthesized from the reaction of naphthylisothiocyanate with 2-(ethylamino)ethanol **(2a)** and phenylhydrazine **(2b)** using microwave irradiation method. The percentage yield for both method used for compound **3a** and **3b**, respectively **3a** (reflux: 66%, microwave: 98%) and **3b** (refluks: 72%, mikrogelombang: 97%).The compounds were analyzed by using Spectrometer FT-Infrared (FT-IR), Spectrometer Nuclear Magnetic Resonance (NMR) and Mass Spectrometry. Antimicrobial study was also conducted using *Staphylococcus aureus* and *Bacillus subtillus* as Gram positive, *Escherichia coli* and *Salmonella typhimurium* as Gram negative and fungi *Aspergillus niger* is used. The positive control used was streptomycin and kanamycin, while DMSO was used as the negative. However, this study shows no inhibition of bacteria and fungi (6-7mm of inhibition area) using these thiourea compounds.

Keywords: thiourea compound, microvawe, antimicrob activity

Pengenalan

Tiourea adalah sebatian organosulfur yang mempunyai formula $SC(NH_2)_2$. Struktur molekulnya sama seperti urea kecuali kedudukan oksigen digantikan dengan sulfur. Dalam satu kajian terbitan tiourea, kompleks poli(etilena

glikol)–tiourea (PEG.TU) telah menunjukkan sifat mangkin dengan membantu tindak balas untuk menghasilkan produk dalam masa lebih singkat [1]. Selain itu, tiourea juga digunakan sebagai sumber sulfida di mana apabila bertindak balas dengan alkil halida, sebatian tiol dihasilkan. Tiourea juga telah banyak digunakan dalam kajian biologi sebagai racun serangga, racun rumput, anti-bakteria, anti-kulat, penawar penyakit paru-paru, antitiroid, dan pengatur pertumbuhan tumbuhan [2]. Terbitan tiourea juga merupakan blok binaan kimia yang penting dalam bidang kimia dan farmasi [3]. Terdapat juga kajian lepas yang membuktikan keberkesanan tiourea sebagai antimikrob. Tiourea juga mampu bertindak sebagai bahan antimikrob yang baik. Bahan tiourea yang mempunyai gelang benzotiazola mempunyai aktiviti antimikrob yang lebih tinggi berbanding tiourea tanpa gelang benzotiazola [4]. Selain itu, kajian tersebut juga mendapati kehadiran kumpulan pengganti nitro pada gelang benzotiazola dapat meningkatkan aktiviti antimikrobnya.

Sintesis sebatian tiourea dengan menggunakan kaedah refluks merupakan kaedah yang telah lama digunakan. Pada tahun 1940, penggunaan tenaga mikrogelombang dalam proses pemanasan makanan diperkenalkan. Kemudian, pada tahun 1950, inovasi dalam aplikasi teknikal seperti dalam bidang kimia dan industri telah diperkenalkan [5]. Kini dengan adanya kemajuan teknologi, sintesis sebatian ini sudah semakin diperbaharui dengan menggunakan kaedah mikrogelombang. Kaedah mikrogelombang ini bukan sahaja dapat menghasilkan produk dengan cepat, malah dapat meningkatkan ketulenan hasil berbanding kaedah konvensional [6]. Sintesis ini mengambil masa dua jam hingga semalaman [2]. Penggunaan mikrogelombang ini juga dikaitkan dengan konsep 'Kimia Hijau' kerana kaedah ini menggunakan tenaga mikrogelombang untuk tindak balas kimia [7]. Pada tahun 2012, satu kajian untuk sintesis sebatian N-fenil-4-(6-fenilimidazo[2,1-b]tiazol-5-il)tiazol-2-amina turut menggunakan kaedah mikrogelombang [8]. Peratusan produk yang terhasil adalah tinggi iaitu 89–95%. Penggunaan mikrogelombang adalah mempercepatkan transformasi serta tindak balas bahan kimia organik [9,10]. Di dalam kajian ini, dua sebatian terbitan naftalentiourea (**3a** dan **3b**) telah berjaya disintesis melalui bahan pemula amina, 2-(etilamino)etanol **(2a)** dan fenilhidrazina **(2b)** melalui kaedah refluks dan kaedah mikrogelombang. Sifat antimikrobnya juga turut diuji dalam kajian ini.

Bahan dan Kaedah

Bahan kimia

Bahan-bahan kimia berserta pembekal yang digunakan dalam penyelidikan ini adalah 1-1-naftil isotiosianat (Acros), 2-(etilamino)etanol (Sigma Aldrich), fenil hidrazina (Sigma Aldrich), etilena diamina (Sigma Aldrich) dan pelarut organik seperti diklorometana, dimetilsulfoksida dan klorofom yang diperolehi dari syarikat Fisher. Semua bahan kimia dan pelarut digunakan tanpa perlu dilakukan proses penulenan terlebih dahulu.

Instrumentasi

Spektrum Infra Merah direkodkan menggunakan Perkin Elmer FT-IR pada suhu bilik. Sampel disediakan secara kaedah KBr dan dianalisis pada panjang gelombang 400 – 4000 cm^{-1}. ^{1}H NMR and ^{13}C NMR spektrum direkodkan menggunakan spektrometer Bruker Advance (400 MHz) dan tetrametilsilana (TMS) sebagai rujukan. Kaedah pemisahan dan penulenan dilakukan menggunakan kaedah kromatografi lapisan nipis (KLN) di atas gel silika jenama Merck DC Kieselgel 60 F_{254}.

Sintesis tiourea 1-etil-1-(2-hidroksi-etil)-3-naftalen-1-il-tiourea (3a) dan 1-(fenil-amino)-3-naftalen-1-il-tiourea (3b)

Dalam kajian ini, penyediaan sebatian tiourea 1-etil-1-(2-hidroksi-etil)-3-naftalen-1-il-tiourea **(3a)** dan 1-(fenil-amino)-3-naftalen-1-il-tiourea **(3b)** dilakukan dengan menggunakan dua kaedah, iaitu kaedah refluks dan kaedah mikrogelombang. Bagi sintesis sebatian **(3a)**, 2-(etilamino)etanol **(2a)** (0.179g, 2.00 mmol) ditindak balaskan dengan 1-naftil isotiosianat **(1)** (0.370g, 2.00 mmol). Kedua-dua bahan pemula ini dimasukkan ke dalam kelalang dengan kehadiran pelarut diklorometana (DKM) sebanyak 10 ml. Kemudian, campuran tersebut dibiarkan refluks [11] selama semalaman. Setelah kajian kualitatif menggunakan kromatografi lapisan nipis (KLN) menunjukkan semua bahan telah bertindak balas, pelarut DKM akan disejat menggunakan penyejat berputar untuk mendapatkan hasil kasar.

Penyediaan sebatian **(3a)** menggunakan kaedah sinaran mikrogelombang bermula dengan mencampurkan bahan pemula, 2-(etilamino)etanol **(2a)** (0.060g, 0.667 mmol) dan 1-naftil isotiosianat **(1)** (0.123g, 0.667mmol) ke dalam

botol sampel dengan kehadiran pelarut DKM yang sedikit (0.5 ml). Campuran tersebut disinarkan dengan mikrogelombang [12] pada 250W selama 5 minit. Mendakan putih terhasil dan ditentukan melalui analisis KLN.

Kedua-dua kaedah di atas diulangi dengan menggunakan fenilhidrazina **(2b)** (0.216g, 2.00 mmol) bagi menggantikan 2-(etilamino)etanol **(2a)** untuk penyediaan sebatian **(3b).** Kaedah konvensional yang digunapakai adalah kaedah tindak balas biasa iaitu tindak balas penambahan nuklofilik dan kaedah mikrogelombang adalah seperti yang telah dilaporkan oleh Atisya et al. [13].

(3a) Pepejal berwarna putih; takat lebur 114 -116 ^{o}C; FT-IM (KBr, cm^{-1}) 3343, 3291, 1565, 776; ^{1}H NMR (400 MHz, DMSO) δ 1.23 (3H, *t*, J=6.8 Hz, -C*H*$_3$), 3.76 (2H, *t*, J=4.8 Hz, -C*H*$_2$-), 3.82 (2H, *t*, J=5.6 Hz, -C*H*$_2$-), 3.86(2H, *q*, J=6.8 Hz, -C*H*$_2$-), 7.35 (1H, *m*, Ar*H*), 7.47 (3H, *m*, Ar*H*), 7.77 (1H, *m*, Ar*H*), 7.84 (1H, *m*, Ar*H*), 7.89 (1H, *m*, Ar*H*), 9.43 (1H, *s*, -N*H*-); ^{13}C NMR (100 MHz, *d*-DMSO) δ 12.9 (*C*H$_3$), 47.0 (*C*H$_2$), 53.0 (*C*H$_2$), 60.2 (*C*H$_2$), 124.0 (C$_{Ar}$), 124.6 (C$_{kuarternari}$), 126.3 (C$_{Ar}$) 126.6 (C$_{Ar}$), 128.0 (C$_{Ar}$), 128.5 (C$_{Ar}$), 131.1 (C$_{kuarternari}$), 134.1 (C$_{kuarternari}$), 134.3 (C$_{Ar}$) 138.0 (C$_{Ar}$), 182.7 (C=S); MS (ESI) m/z 297.08 [M + Na]$^{+}$.

(3b) Pepejal berwarna putih; takat lebur 189 -193 ^{o}C; FT-IM (KBr, cm^{-1}) 3215, 3169, 1599, 1545, 759; ^{1}H NMR (400 MHz, *d*-DMSO) δ 6.83 (3H, *m*, Ar*H*), 7.22 (1*H*, *m*, Ar*H*), 7.38 (3H, *m*, Ar*H*), 7.74 (4H, *m*, Ar*H*), 7.81 (4H, *m*, Ar*H*), 9.53 (1H, *s*, -N*H*-), 9.87 (1H, *s*, -N*H*-); ^{13}C NMR (100 MHz, *d*-DMSO) δ 113.3 (C$_{Ar}$), 121.6 (C$_{Ar}$), 123.8 (C$_{Ar}$), 126.7 (C$_{Ar}$), 127.4 (C$_{kuarternari}$), 127.9 (C$_{Ar}$), 128.2 (C$_{kuarternari}$), 128.5 (C$_{Ar}$), 129.5 (C$_{kuarternari}$), 129.7 (C$_{Ar}$), 130.8 (C$_{Ar}$), 134.5 (C$_{Ar}$), 134.6 (C$_{kuarternari}$), 135.5 (C$_{Ar}$), 183.3 (C=S); MS (ESI) m/z 316.06 [M + Na]$^{+}$.

Kajian antimikrob sebatian 3a dan 3b

Aktiviti antimikrob diuji menggunakan kaedah penyebaran agar *'agar diffusion method'* [14] dengan menggunakan *Staphylococcus aureus* dan *Bacillus subtillus* sebagai Gram positif, *Escherichia coli* dan *Salmonella typhimurium* sebagai Gram negatif dan kulat yang digunakan adalah *Aspergillus niger*. Kawalan positif yang digunakan adalah S*treptomisin* dan *Kanamisin*, manakala kawalan negatif yang digunakan adalah DMSO.

Stok sebatian tiourea yang telah disintesis disediakan dengan melarutkan 1mg sebatian tiourea ke dalam 1ml pelarut DMSO. Kemudian, 50 µl dan 150 µl dicairkan dalam kelalang isipadu 5ml untuk menghasilkan sebatian tiourea dengan kepekatan 10 µg/ml dan 30 µg/ml masing-masing. Sebanyak 10µl diambil dan diserapkan percakera sampel. Piring agar disebarkan mikrob dan dieramkan pada suhu 37°C selama 24 jam. *Streptomisin*, *Kanamisin* dan DMSO digunakan sebagai agen kawalan positif dan negatif ujian ini dengan menggunakan kaedah yang sama. Selepas 24 jam, diameter kawasan yang tidak ditumbuhi bakteria atau kulat sekitar cakera diukur untuk dibandingkan tahap aktiviti antimikrob dengan agen kawalan anti-bakteria yang digunakan [14, 15].

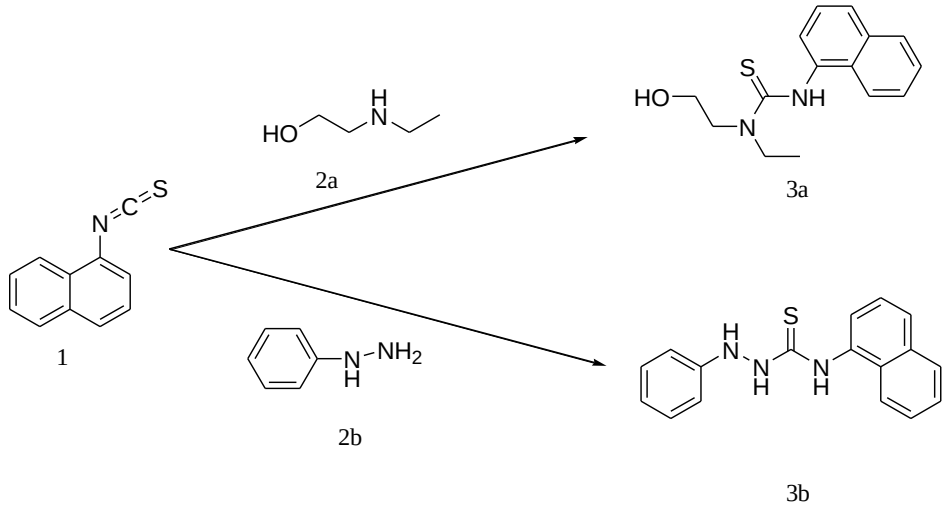
Keputusan dan Perbincangan

Sintesis terbitan tiourea telah berjaya dijalankan melalui tindak balas antara 1-naftil isotiosianat **(1)** dengan beberapa sebatian amina menggunakan kaedah konvensional iaitu kaedah refluks dan juga kaedah mikrogelombang. Tindak balas keseluruhan penghasilan tiourea ditunjukkan pada Rajah 1.

Merujuk kepada pencirian sebatian menggunakan spektroskopi infra merah, terdapat puncak pada 3343 cm^{-1} (OH) dan puncak pada 3291 cm^{-1}(NH) bagi sebatian **3a** dan kehadiran regangan 3215 (NH 1) dan 3169 cm^{-1} (NH 2) bagi sebatian **3b**. Selain itu, ikatan C-N dapat dikenal pasti pada puncak 1565 cm^{-1} dan 1599 cm^{-1} bagi sebatian **3a** dan **3b**. Puncak ikatan C=S pula dapat dilihat pada puncak 776 cm^{-1} dan 759 cm^{-1} bagi sebatian **3a** dan **3b**. Puncak ini adalah penting bagi menunjukkan pembentukan tiourea telah berlaku.

Pencirian ^{1}H NMR bagi sebatian **3a** menunjukkan pada anjakan kimia 3.76 dan 3.82 ppm puncak ini memberikan nilai integrasi 3.27 yang menunjukkan 3 proton –CH$_2$- yang merupakan hidrogen yang terikat kepada karbon pada bahagian etanol sebatian tersebut. Manakala pada anjakan kimia 3.86 ppm pula merupakan proton pada ikatan –CH$_2$- yang bersebelahan dengan –CH$_3$. Ini dapat dibuktikan dengan kewujudan penggandaan spin *quintet* dengan nilai skala penggandingan 6.8 Hz pada anjakan kimia tersebut. Puncak yang penting adalah puncak bagi kumpulan amina yang terbentuk daripada tindak balas antara isotiosianat dan amina yang mana dapat dilihat pada pada anjakan kimia 9.43 ppm. Ini juga disokong oleh spektrum ^{13}C NMR yang menunjukkan terdapat pembentukan

kumpulan C=S yang dibuktikan melalui kehadiran puncak pada anjakan kimia pada 180.7 ppm. Bagi sebatian **3b** pula, terdapat puncak pada anjakan kimia antara 6.83 ppm dan 7.81 ppm yang merupakan puncak bagi kumpulan aromatik. Pada anjakan kimia 9.87 ppm dan 9.53 ppm pula merupakan puncak bagi kumpulan amina. Hidrogen pada amina naftil dijangkakan memiliki anjakan kimia 9.87 ppm manakala pada anjakan kimia 9.53 ppm merupakan puncak pada amina hidrazina. Puncak yang terdapat pada nilai anjakan kimia 183 ppm pula adalah karbon pada ikatan C=S, yang merupakan puncak yang utama bagi sebatian tiourea.



Rajah 1. Sintesis terbitan naftiltiourea 1-etil-1-(2-hidroksi-etil)-3-naftalen-1-il-tiourea **(3a)** dan 1-(fenil-amino)-3-naftalen-1-il-tiourea **(3b)**.

Spektrometri jisim menggunakan mod pengionan elektron (ESI) memberikan puncak sebatian **3a** (274.38 g/mol) bernilai m/z 297.07 merupakan puncak bagi molekul ion $[M+Na]^+$. Begitu juga bagi sebatian **3b** yang mempunyai formula molekul $C_{17}H_{15}N_3S$ (293.39 g/mol) menunjukkan berat ion $[M+Na]^+$ pada nilai m/z 293.38. Ion sodium sebagai ion molekul pseudo biasa digunakan bagi penentuan berat molekul menggunakan mod pengionan elektron. Jadual 1 di bawah menunjukkan peratusan hasil yang diperolehi daripada kaedah refluks dan kaedah mikrogelombang.

Jadual 1. Peratusan hasil kaedah refluks dan kaedah mikrogelombang

Sebatian/ Kaedah	**Peratusan Hasil (%)**	
	Refluks	**Mikrogelombang**
3a	66%	98%
3b	72%	97%

Teknik mikrogelombang menghasilkan pemanasan dalaman yang lebih cekap disebabkan tenaga gelombang mikronya selari dengan molekul-molekul pelarut dan reagen yang terlibat dalam tindak balas. Maka masa tindak balas menjadi lebih cepat [7]. Jadual di atas membuktikan bahawa peratusan hasil daripada kaedah mikrogelombang adalah lebih tinggi berbanding dengan kaedah refluks. Hal ini kerana penggunaan teknik mikrogelombang dapat memberikan hasil tindak balas yang lebih bersih serta dapat mengurangkan pembentukan produk sampingan [16]. Melalui kaedah konvensional pula, peratusan hasil bagi sebatian **3a** dan **3b** adalah masing-masing 66 % dan 72 %. Kaedah ini juga memerlukan masa yang lebih lama bagi suatu tindak balas lengkap. Hal ini disebabkan berlakunya

pemindahan tenaga ke dalam sistem yang mana suhu luar lebih tinggi berbanding suhu di dalam campuran tindak balas [17]. Kebolehulangan tindak balas tidak dijalankan kerana kaedah mikrogelombang telah menghasilkan nilai peratusan yang kuantitatif.

Aktiviti antimikrob

Sebatian tiourea **3a** dan **3b** telah dicirikan dan ujikaji aktiviti antimikrobnya [14] telah dijalankan menggunakan antibiotik *Streptomisin* (10μg/ml) dan *Kanamisin* (30 μg/ml) sebagai kawalan positif dan DMSO sebagai kawalan negatif. Jadual 2 dan Jadual 3 di bawah merupakan hasil daripada kajian yang telah dijalankan:

Jadual 2. Aktiviti antimikrob bagi sebatian terbitan tiourea dan antibiotik (10 μg/ml)

Sebatian	**Bakteria Gram positif (mm)**		**Bakteria Gram negative (mm)**		**Kulat (mm)**
	Staphylococcus aureus	***Bacillus subtilis***	***Escherichia coli***	***Salmonella typhimurium***	***Aspergillus niger***
Antibiotik *streptomisin*	16	17	16	19	10
1-etil-1-(2-hidroksi-etil)-3-naftalen-1-il-tiourea **(3a)**	7	7	6	7	6
1-(fenil-amino)-3-naftalen-1-il-tiourea **(3b)**	6	6	6	7	6

Jadual 3. Aktiviti antimikrob bagi sebatian terbitan tiourea dan antibiotik (30μg/ml)

Sebatian	**Bakteria Gram positif (mm)**		**Bakteria Gram negatif (mm)**		**Kulat (mm)**
	Staphylococcus aureus	***Bacillus subtilis***	***Escherichia coli***	***Salmonella typhimurium***	***Aspergillus niger***
Antibiotik *Kanamisin*	20	20	18	24	24
1-etil-1-(2-hidroksi-etil)-3-naftalen-1-il-tiourea **(3a)**	7	7	6	7	6
1-(fenil-amino)-3-naftalen-1-il-tiourea **(3b)**	6	6	6	7	6

Merujuk pada kedua-dua jadual di atas, aktiviti antimikrob yang dihasilkan oleh sebatian tiourea yang dihasilkan adalah sangat rendah. Keluasan kawasan yang mampu direncat pertumbuhan bakteria dan kulat adalah sekitar enam hingga tujuh milimeter diameter manakala antibiotik pula mampu untuk merencat pertumbuhan bakteria sejauh 10 hingga 24 milimeter diameter. Hasil menunjukkan terbitan tiourea yang dihasilkan tidak bersesuaian untuk dijadikan bahan antimikrob bagi bakteria-bakteria yang diuji. Kehadiran kumpulan penderma elektron atau kumpulan aromatik tanpa kumpulan pengganti penarik elektron menjejaskan aktiviti antimikrob sebatian berkenaan [15]. Sehubungan dengan itu, naftil tanpa kumpulan berfungsi penarik elektron dan kumpulan pengganti lain yang bertindak sebagai penderma elektron kepada kumpulan berfungsi tiourea akan memudaratkan aktiviti antimikrob

tiourea tersebut. Selain itu, beberapa idea juga turut diketengahkan untuk meningkatkan keputusan perencatan bakteria oleh sebatian tersebut seperti meningkatkan kepekatan sebatian yang digunakan dalam merencatkan pertumbuhan mikrob. Terdapat juga cadangan untuk menggunakan kaedah lain yang berkemungkinan lebih efektif dalam menentukan aktiviti antimikrob ini seperti kepekatan perencatan asai minimum.

Kesimpulan

Sebatian 1-etil-1-(2-hidroksi-etil)-3-naftalen-1-il-tiourea (**3a**) dan 1-(fenil-amino)-3-naftalen-1-il-tiourea (**3b**) berjaya disintesiskan dengan menggunakan dua kaedah iaitu kaedah pemanasan secara refluks dan juga kaedah mikrogelombang. Hasil sebatian terbitan tiourea daripada kaedah mikrogelombang membuktikan bahawa peratusan hasil yang diperolehi adalah lebih banyak berbanding kaedah refluks. Jika dibandingkan pada faktor masa, kaedah mikrogelombang juga lebih cepat dan jimat kerana masa yang diperlukan untuk sintesis adalah singkat dan memerlukan pelarut yang paling minima (0.5 – 1.0 ml).

Penghargaan

Kami ingin mengucapkan setinggi-tinggi penghargaan kepada pihak Pusat Pengajian Sains Kimia dan Teknologi Makanan (PPSKTM) Universiti Kebangsaan Malaysia, Pusat Pengurusan Penyelidikan dan Instrumentasi (CRIM), dan juga pihak yang terlibat dalam menjayakan penyelidikan ini. Kajian ini dijalankan dibawah geran penyelidikan FRGS/1/2015/ST01/UKM/02/2 dan PRGS/2/2015/SG01/UKM/02/1.

Rujukan

1. Sanny, V., Suman L. J. and Bir, S. (2010). PEG-embedded Thiourea Dioxide (PEG.TUD) as a Novel Organocatalyst for the Highly Efficient Synthesis of 3,4-dihydropyrimidinones. *Tetrahedron Letters* 51(52): 6897 – 6900.
2. Arslan, H., Demet, S. M., Don, V. and Gun, B. (2009). The Molecular Structure and Vibrational Spectra of N-(2,2-diphenylacetyl)-N′-(236aphthalene-1yl)-thiourea by Hartree–Fock and Density Functional Methods. *Spectrochimica Acta Part A: Molecular and Biomolecular Spectroscopy* 72(3): 561 – 571.
3. Alan R. Katritzky, N. K., Boris V. Rogovoy, J. K. and Tao, H. (2004). Synthesis of Mono- and N, N-Disubstituted Thiourea and N-Acylthioureas. *Heterocyclic*: 1799 – 1805.
4. Saeed, S., Naghmana, R., Peter G. J., Ali, M. and Hussain, R. (2010). Synthesis, Characterization and Biological Evaluation of Some Thiourea Derivatives Bearing Benzothiazole Moiety as Potential Antimicrobial and Anticancer Agents. *European Journal of Medicinal Chemistry* 45(4): 1323 – 1331.
5. Kappe, C. O. and Stadler, A. (2013). Microwaves in Organic and Medicinal Chemistry, John Wiley & Sons.
6. Hayes, B. L. (2004). Recent Advances in Microwave Assisted Synthesis. *Aldrichimica Acta* 37(2): 66 –76.
7. Nguyen, Q. P. B. and Kim, T. H. (2013). Solvent- and Catalyst-free Direct Reductive Amination of Aldehydes and Ketones with Hantzsch Ester: Synthesis of Secondary and Tertiary Amines. *Tetrahedron* 69(24): 4938 – 4943.
8. Kamila, S., Kimberly, M. and Edward R. B. (2012). Microwave-assisted Hantzsch Thiazole Synthesis of N-phenyl-4-(6-phenylimidazo[2,1-b]thiazol-5-yl)thiazol-2-amines from the Reaction of 2-chloro-1-(6-phenylimidazo[2,1-b]thiazol-5-yl)ethanones and Thioureas. *Tetrahedron Letters* 53(37): 4921 – 4924.
9. Gedye, R. N., Smith, F. E., Westaway, K. C., Ali, H., Baldisera, L., Laberge, L. and Rousell, J. (1986). The Use of Microwave Ovens for Rapid Organic Synthesis. *Tetrahedron Letters* 27(3): 279 – 282.
10. Giguere, R. J., Bray, T. L., Duncan, S. M. and Majetich, G. (1986). Application of Commercial Microwave Ovens to Organic Synthesis. *Tetrahedron Letters* 27(41): 4945 – 4948.
11. Khansari, M. E., Wallace, K. D. and Hossain, M. D. (2013). Synthesis and Anion Recognition Studies of Dipodal Thiourea-based Sensor for Anions. *Tetrahedron Letters*: 438 – 440.
12. Nguyen D. T. and Nguyen T. T. M. (2009). Synthesis of N-tetra-O-acetyl-β-D-glucopyranosyl-N'-(4',6'-diarylpyrimidin-2'-yl)thioureas. *Carbohydrate Research* 344: 2399 – 2405.
13. Atisya, R., Hasbullah, S. A. Lazim, A. M., Nordin, R. (2014). Improving the synthesis of spiropyran derivatives using microwave irradiation method. *Heterocycles* 89(4):1017 – 1024.
14. Mohamed, N. A. and Abd El-Ghany, N. A. (2012). Preparation and antimicrobial activity of some carboxymethyl chitosan acyl thiourea derivatives. *International Journal of Biological Macromolecules* 50: 1280 – 1285.

15. Reddy, Y. T. and Reddy, P. N. (2005). Synthesis of 1-(6-methylbenzofuran-2-yl)-3-aryl/[4-(β-substitutedethoxy)phenyl]propenones as marked anti-microbial agents. *Indian Journal of Chemistry* 44:1079 – 1083.
16. Ravichandran, S. and Karthikeyan, E. (2011). Microwave synthesis - A Potential Tool for Green Chemistry. *International Journal of ChemTech Research* 3(1): 466 – 470.
17. Kappe, C. O. (2004). Controlled Microwave Heating in Modern Organic Synthesis. *Angewandte Chemie International Edition* 43: 6250 – 6284.

MALAYSIAN JOURNAL OF ANALYTICAL SCIENCES
Published by The Malaysian Analytical Sciences Society
ISSN 1394 - 2506

TWO ISOLATED CRYSTALLINE SOLIDS FROM THE STEM OF *Entada spiralis* Ridl. (AKAR SINTOK)

(Pemencilan Dua Jenis Pepejal Kristal dari Batang Pokok *Entada spiralis* (Akar Sintok))

Aiza Harun[1]*, Siti Zaiton Mat So'ad[2], Norazian Mohd Hassan[2]

[1]*Faculty of Applied Sciences,*
Universiti Teknologi MARA Pahang, 26400 Bandar Tun Razak Jengka, Pahang, Malaysia
[2]*Kulliyah of Pharmacy,*
International Islamic University Malaysia, Bandar Indera Mahkota, Kuantan Pahang, Malaysia

**Corresponding author: aizaharun@pahang.uitm.edu.my*

Received: 30 November 2015; Accepted: 1 February 2016

Abstract

Entada spiralis Ridl. (Leguminosae) is a woody climber which locally known as 'akar sintok'. The isolation and structure determination of two crystalline solids from active methanol fraction of *E. spiralis* stem bark had been examined. The structure identification of both solids was based on spectroscopic data (^{1}H and ^{13}C NMR, HMQC, HMBC, DEPT135 and MS) along with comparison with literature data. The results revealed that these two crystalline solid sugars isolated from the most active fraction were known as penta-2-acetoxy-β-D-digitoxopyranosyl-(1→2)-fructofuranosyl-(6→4)-β-D-glucopyranosyl-(1→4)-glucopyranosyl-(1→2)-β-D fructofuranosyl-(6→1)-β-D-glucopyranosyl-(4→1)-acetylglucosamine **(1)** and β,D-glucopyranosyl(1→2)-β,D-glucopyranosyl)-(1→3)-β,D-xylopyranosyl(1→4)-α,L-rhamnopyranosyl)-(1→3)-β,D- glucopyranosyl(1→3)-β,D-glucopyranoside **(2)** Thus, this finding can be utilized as a scientific baseline information for further skin disease studies, since both constituents were isolated from moderate antidermatophytic active fraction.

Keywords: *Entada spiralis*, crystalline saponin, glycosides, isolation

Abstrak

Pemencilan dan penentuan struktur dua komponen bersifat kristal dari batang pokok *E. spiralis* yang juga dikenali sebagai akar sintok telah dijalankan. Eksperimen penentuan struktur berdasarkan data – data spektroskopi menggunakan ^{1}H, ^{13}C NMR, HMQC, HMBC, DEPT135 dan spektrometer jisim dan juga perbandingan dengan kajian terdahulu. Hasil analisa spektroskopi yang terperinci menunjukkan kedua – dua kristal tersebut dikenali sebagai penta-2-asetoksi-β-D-digitoxopiranosil-(1→2)-fruktofuranosil-(6→4)-β-D-glukopiranosil-(1→4)-glukopiranosil-(1→2)-β-D fruktofuranosil-(6→1)-β-D-glukopiranosil-(4→1)-acetilglukosamina **(1)** and β,D-glukopiranosil(1→2)-β,D-glukpiranosil)-(1→3)-β,D-xilopiranosil(1→4)-α,L-rhamnopiranosil)-(1→3)-β,D-glukopiranosil(1→3)-β,D-glukopiranosid **(2).** Penemuan ini boleh dijadikan maklumat asas untuk kajian penyakit kulit kerana kedua-dua komponen ini dipencilkan dari fraksi metanol yang bersifat antiderma.

Kata kunci: *Entada spiralis*, kristal saponin, glikosid, pemencilan

Introduction

Medicinal herbs have been consumed traditionally by people throughout the world to cure various diseases long enough before the emerging of modern medicine. Due to their higher content of such valuable chemical compounds, they could be used to prevent microbial invasion. Secondary metabolites produced by plants contain a tremendous source of bioactive compounds such as flavonoid, alkaloid, tannin, saponin and terpenoid. Knowing their

importance, scientific investigation has increased rapidly to overcome the development of resistant pattern of certain microorganisms such as skin disease caused microbes [1].

The structure identification of bioactive constituents from the various types of species of Leguminoceae family had been reported [2-6]. The stem of *E. spiralis* is believed to exhibit antimicrobial properties since it is capable to treat hair problem, itching and body cleansing. Previous phytochemical investigation of other *Entada* species encountered oleanolic acid, echinocystic acid, entagenic acid and acacic acid glycosides Okada et al. [7, 8]. *E. rheedii* Spreng was found to possess saponins [7-10], thiomides [11] and phenylacetic derivatives [12-13]. Investigation also revealed entagenic acid isolated from seed kernels of *E.rheedii* which exhibited moderate cytotoxic potency and antioxidative properties [14]. Phenolic and flavonoid were isolated from the root of *E. Africa* [15], octadecanoic acid from the stem bark of *E. abyssinica* [16] and Entadoiside from kernel nut of *E. phaseoloides* [17].

In this present study, we embark upon isolation and structure identification of two novel crystalline solids from active fractions of *E.spiralis* stem bark.

Materials and Methods

General Experimental Procedures

The general experimental procedures were adapted from Aiza et al. [18]. The ^{1}H Nuclear Magnetic Resonance (NMR) and ^{13}C NMR spectra were recorded in $CDCl_3$, Fourier Transform NMR (FT-NMR) analysis was done using a Cryoprobe on a Bruker Avance 111 600 MHz spectrometer. Tetramethylsilane (TMS) was used as an internal standard in NMR spectrometer analysis. Electronspray ionization mass spectrometer (ESIMS) was performed using a Bruker micrOTOF-Q 86 mass spectrometer operating in positive-ion mode. Vacuum liquid chromatography (VLC) was conducted using silica gel 60 with a 230 – 400 mesh particle size (Merck). Thin layer chromatography (TLC) was performed on Kiesegel 60 F254 (Merck) aluminium support plates developed using chloroform: methanol system. TLC plates were visualized at UV_{366} and UV_{254}.

Fractionation and Isolation

The extraction and fractionation procedures were conducted as previously reported with few modifications [19, 20]. The extraction process involved consecutive soaking with petroleum ether, chloroform and methanol, fractionation process was conducted using vacuum liquid chromatography with the use of several binary solvents to obtain fractions.

Antidermatophytic Evaluation

The antidermatophytic activity of fractions was determined as previously reported by Aiza et al [21]. Generally, all extracts were used against three types of skin diseases dermatophytes namely as *Trychophyton tonsurans*, *Trychophyton mentagrophytes* and *Microsporum gypseum* through disc diffusion method susceptibility testing. The effectiveness of the fractions was evaluated by means of inhibition zone (IZ) measurement around the disk.

Results and Discussion

Compound **(1)** was obtained as white crystalline solid after subjecting methanol extract to vacuum liquid chromatography with an elution system of $CHCl_3$-MeOH (6:4 v/v) to obtain fraction 1 which was previously found to possess moderate antidermatophytic activity [20]. The melting point of white crystalline solid was 187 ^{o}C and two ultra violet (UV) absorption peaks appeared at 228 nm and 280 nm when analyzed with UV VIS-1800 Series (Shimadzu, Japan). The results indicated the absorption of light in the region of 200 – 300 nm, corresponded to the presence of atom with non-bonding orbital such as oxygen and nitrogen. Two peaks observed in the UV spectra were due to the presence of the chromophores, molecules that absorb light with bathochromic effect.

The Electron Spray Ionization Mass Spectrum (ESIMS) of compound **(1)** showed an $[M+H]^+$ ion peak at *m/z* 1905 in accordance with the molecular formula of $C_{78}H_{123}NO_{52}$. The fragment ion peaks were observed on the ESIMS at *m/z* 1049 [M+H-171-172-171-171-171], 365[M+H-171-172-171-171-171-342-342] corresponding, to the consecutive loss of five pentosyls, two hexoxyls (Glc and Fru) and again two hexoxyls (Glc and Fru) respectively. Table 1 and Figure 1 showed the fragmentation of sugar moieties in the whole structure.

Table 1. Fragmentation of ions in compound **(1)** by ESIMS

Mass	Fragmentation of ions
1734	$[M+H] - 171]^+$
1562	$[M+H] - 171\text{-}172]^+$
1391	$[M+H] - 171\text{-}172\text{-}171]^+$
1220	$[M+H] - 171\text{-}172\text{-}171\text{-}171]^+$
1049	$[M+H] - 171\text{-}172\text{-}171\text{-}171\text{-}171]^+$
707	$[M+H] - 171\text{-}172\text{-}171\text{-}171\text{-}171\text{-}342]^+$
365	$[M+H] - 171\text{-}172\text{-}171\text{-}171\text{-}171\text{-}342\text{-}342]^+$

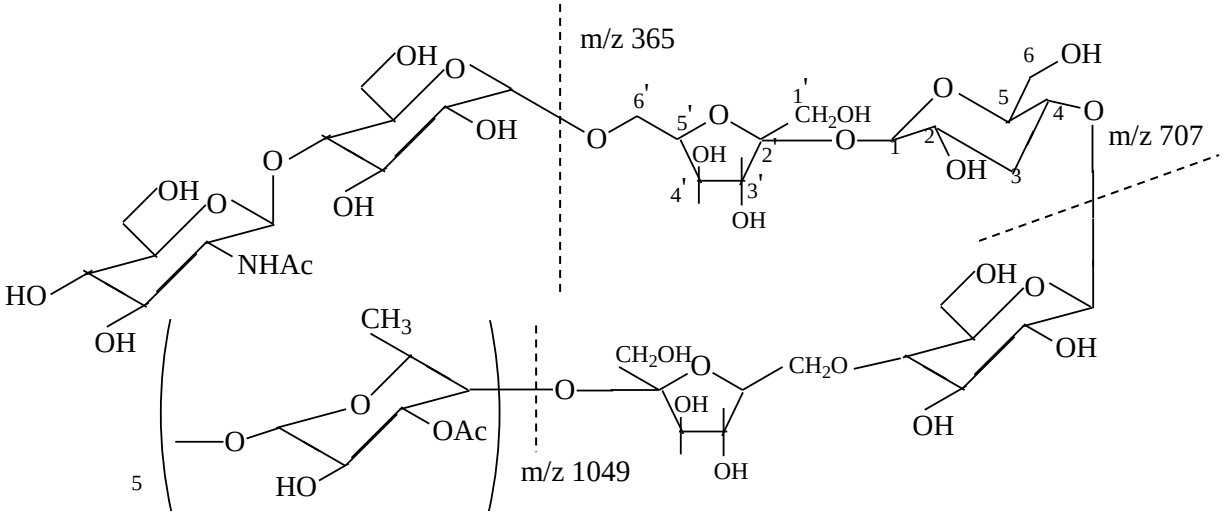


Figure 1. The mass fragmentation of compound **(1)** from *E. spiralis* stem bark

The ^{1}H NMR spectrum of compound **(1)** displayed three sugar anomeric protons at chemical shifts, ppm δ 4.41, 5.18 and 4.80, which indicated the presence of sugar moieties GlcNAc, Glc, acetyl digitoxose, respectively. These values were quite close to those reported in literature. The δ_H for GlcNAc was reported [22] as 4.40 ppm, δ_H 5.44 and δ_H 5.0 for acetyl digitoxose [23]. The proton NMR spectrum furnished nine hydroxyl protons at chemical shifts δ_H 3.14, 3.20, 3.47, 3.49, 3.55, 3.58, 3.68, 3.78 and 3.90, giving direct coupling with nine carbon atoms at δ 70.30, 72.09, 73.27, 60.95, 62.59, 83.01, 73.33, 74.74 and 77.47 ppm, respectively based on HMQC spectrum. The correlation between δ_H 5.18 and chemical shifts of carbon at δ_C 92.21 corresponded to the direct correlation of anomeric proton and anomeric carbon of Glc.

According to ^{13}C NMR spectrum, the chemical shifts at δc 104.49 and δc 92.21 suggested the presence of anomeric carbon for fructose (Fru) and glucose (Glc) respectively, and were quite close to those reported for Fru (δc 104.0) and Glc (δc 93.9) [10, 21]. The high intensity of overlapped peaks indicated more than one sugar present and this was same for absorption peaks of carbon hydroxyl. Thus, it may explain why compound **(1)** showed high molecular weight as displayed in the mass spectrum.

Long range correlations observed in the HMBC spectrum between signals at δ_H 5.18 (Glc-I) and δ_C 104.49 (C2'-Fru) showed three bond correlations between Glc and Fru. The four bond correlation was observed between anomeric proton of GlcNAc δ 4.4 and δc 73.27 (C3-Glc-II) suggested the location GlcNAc in AC1 structure. The anomeric proton of Glc-II (δ_H 5.18) was linked with Fru by four bond correlations at C5'(δ_C 83.01) of Fru. The spectrum also depicted three bond correlations between anomeric proton δ_H 4.80 of acetyldigitoxose moiety and δc 104.49 (C2'-Fru) which showed the linkage to Fru. The two bond correlations can be seen between signal at δ_H 3.90 (C5-glc-I) and δc 62.69 (C6-glc-I), δ_H 3.47 (C3-glc-I) and δc 72.09 (C2-glc-I) and δc 70.30 (C4-glc-I), δ_H 3.14 (C4-glc-I) and δc 73.33 (C3-glc-I), δ_H 3.68 (C3'-Fru) and δc 74.74 (C4'-Fru) and δc 83.01 (C5'-Fru). The three bond correlations were depicted between signal at δ_H 3.68 (C3'-Fru) and δc 83.01 (C5-Fru) and δc 74.74 (C4'-Fru), δ_H 3.49 (C1'-Fru) and δc 73.33 (C3'-Fru), δ_H 5.18 (C1-Glc) and δc 70.30 (C4-Glu), δ_H 3.58 (C5'-Fru) and δc 104.49 (C2'-Fru). The structure of sugar moieties and the HMBC correlation are shown in Figure 2 and 3 respectively. The proton and carbon NMR data of compound (1) in DMSO were summarized in Table 2.

Table 2. ^{1}H NMR (600 MHz) and ^{13}C NMR (150 MHz) data of **AC1** in DMSO

Position	**DEPT**	**^{13}C (δ) (ppm)**	**^{1}H δ (ppm), m**	**HMBC**
Glu				
1	CH	92.21	5.19, m	C2', C4,C5
2	CH	72.09	3.20, m	
3	CH	73.27	3.47, m	C2,C4
4	CH	70.30	3.14, m	C4',C3
5	CH	77.47	3.90, t	C6
6	CH_2	62.59	3.55, m	
Fru				
1'	CH_2	60.95	3.49, m	C3'
2'	C	104.49	-	
3'	CH	73.33	3.68, m	C4',C5'
4'	CH	74.74	3.78, m	C2'
5'	CH	83.01	3.58, m	C2'
6'	CH2	62.51	3.43, m	
GlcNAc				
1	CH		4.41, m	C3
Acetyl digitoxose	CH		4.80, m	C2'

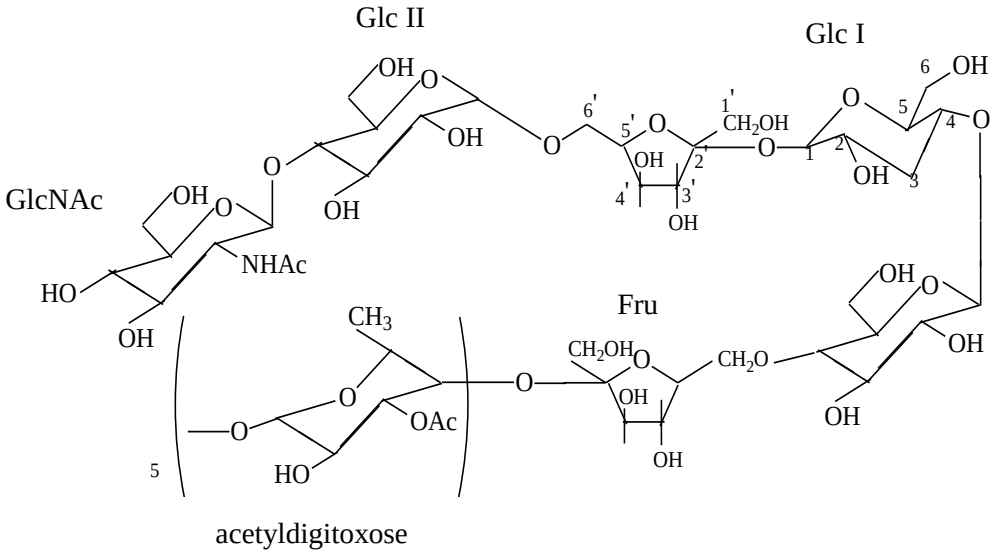


Figure 2. The structure of compound **(1)** from *E. spiralis* stem bark

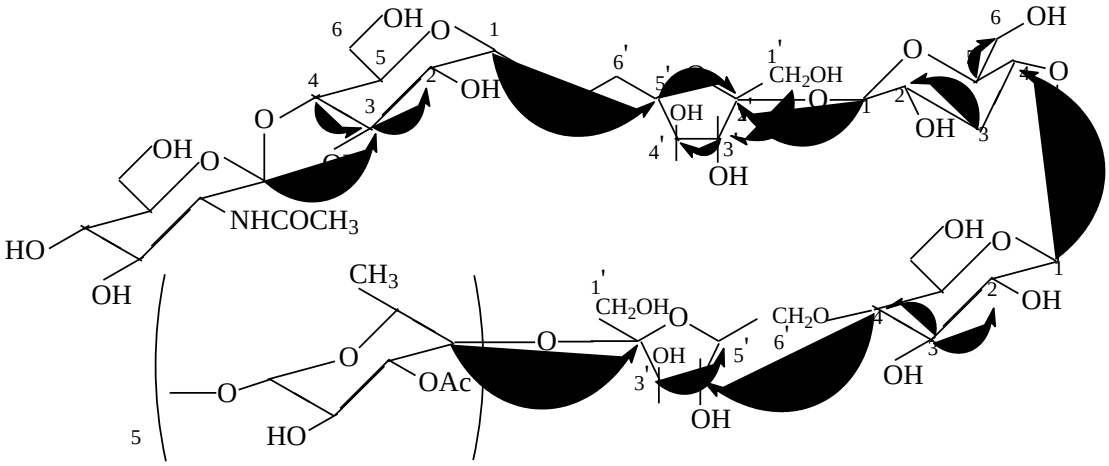


Figure 3. The key HMBC correlation of compound **(1)** from *E. spiralis* stem bark

After gone through an extensive spectroscopic analysis and comparison with literature, compound **(1)** was identified as penta-2-acetoxy-β-D-digitoxopyranosyl-(1→2)-fructofuranosyl-(6→4)-β-D-glucopyranosyl-(1→4)-gluco pyranosyl-(1→2)-β-Dfructofuranosyl-(6→1)-β-D-glucopyranosyl-(4→1)-acetylglucosamine.

Compound **(2)** was isolated as white crystalline solid after subjecting to vacuum liquid chromatography with an elution system of $CHCl_3$-MeOH (7:3 v/v), whereby fraction obtained was found to exhibit moderate antidermatophytic activity. The UV absorption analysis has displayed two absorption peaks at 256 and 280 nm which indicated chromophore of C-O group. The ESIMS displayed $[M+H]^+$ ion peak at *m/z* 922.0135, supported a molecular formula of $C_{35}H_{59}O_{28}$. The fragment ion peaks were observed on the ESIMS at *m/z* 600.5184$[M+H-325]^+$ corresponding to the consecutive loss of two hexosyls. The *m/z* 325.1126 $[M+H-325-278]^+$ referred to the loss of

one pentosyl and again one hexosyl. Further fragmentation ion peak is observed at *m/z* 163.0607 [M+H-325- 278-162]$^{+}$, which showed the loss of another one hexosyl. The mass fragmentation is illustrated in Figure 4.

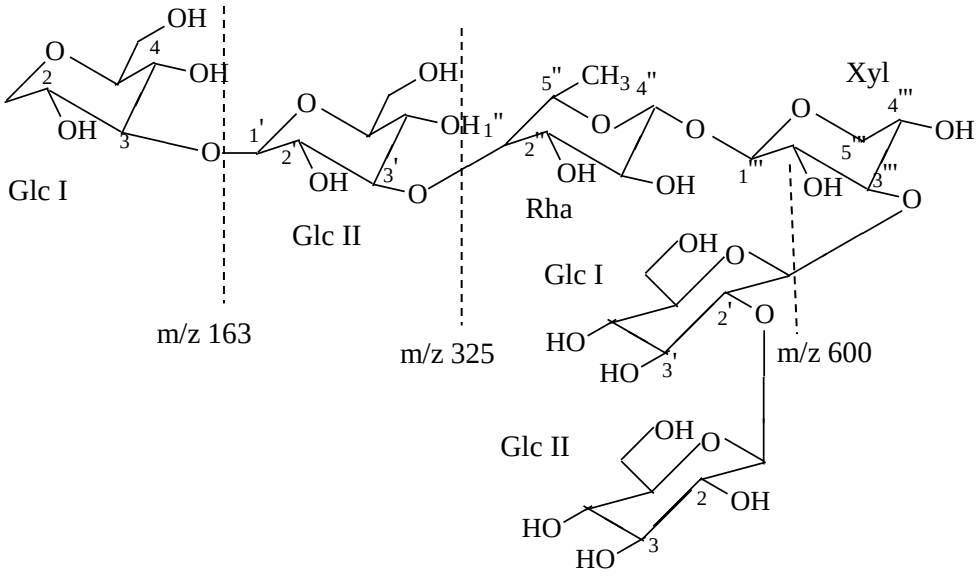


Figure 4. The mass fragmentations of compound **(2)** from *E. spiralis* stem bark

The sequences of the sugar chain were confirmed by HMBC experiments. The cross-peak observed in the HMBC spectrum between anomeric proton at signal δ_H 4.4 (Glc-1) and δ_C 83.02 (C2'), δ_H 5.05 (Rha-1) and δ_C 73.28 (C3'), δ_H 4.78 (Xyl) and δc 73.33 (C4''), δ_H 5.20 (Glc-II) and δ_C 73.28 (C3), showed the location of sugar moieties.

Other correlations with two bond correlations can be observed between proton signal δ_H 3.58 (C2-glc I) and δ_C 73.28 (C3), and δ_H 3.58 (C2'-Glc II) with δ_C 73.28 (C3'-Glc II). Three bond correlations can be seen between proton signal δ_H 3.43 (C5''-Rha) and δc 70.30 (C2''), 3.55 (C5'''-xyl) and δc 74.75 (C4''') and between δ_H 5.20 (C1'-Glc II) and δc 77.48 (C3'''-Xyl). The HMBC correlation is shown in Figure 5 and Table 3 showed the NMR data of compound **(2)**.

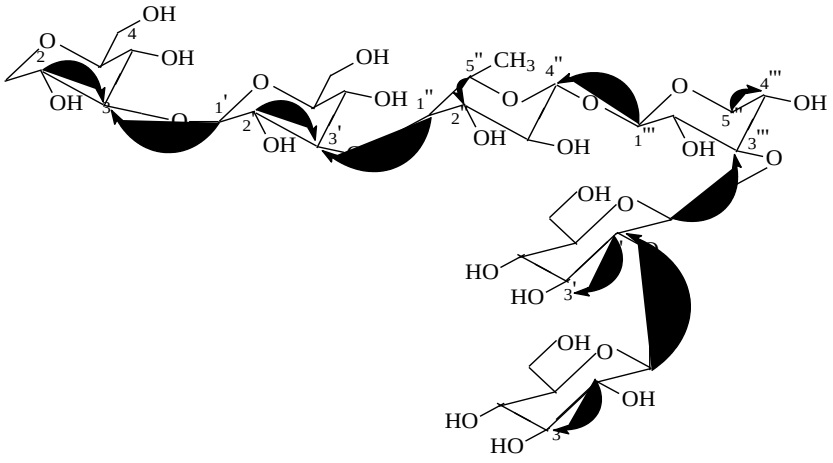


Figure 5. The key HMBC correlation of compound **(2)** from *E. spiralis* stem bark

After went through an extensive spectroscopic analysis and comparison with literature, compound **(2)** was elucidated as β,D-glucopyranosyl(1→2)-β,D-glucopyranosyl)-(1→3)-β,D-xylopyranosyl(1→4)-α,L-rhamno pyranosyl)-(1→3)-β,D-glucopyranosyl(1→3)-β,D-glucopyranoside as shown in Figure 6.

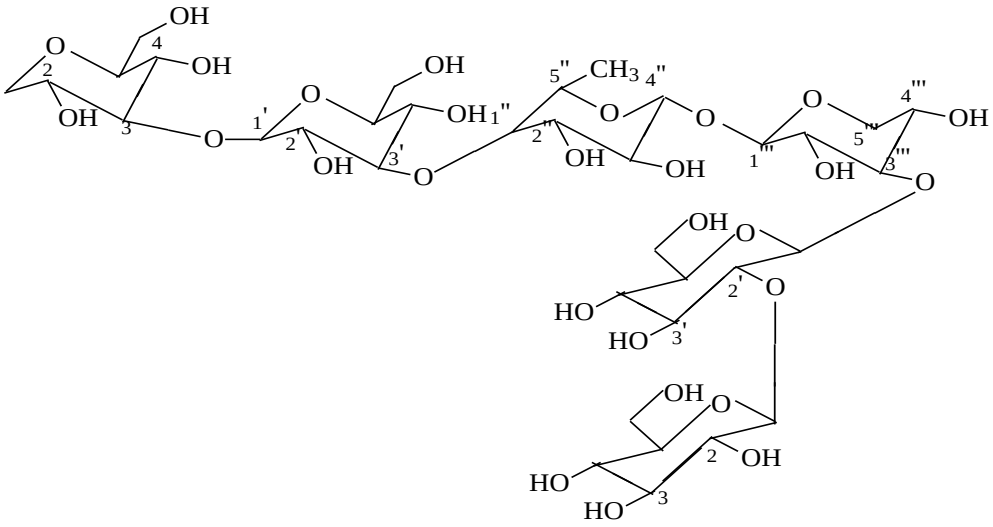


Figure 6. The structure of compound **(2)** from *E. spiralis* stem bark

Table 3. ^{1}H NMR (600 MHz) and ^{13}C NMR (150 MHz) data of compound **(2)** in DMSO

Position	**DEPT**	**^{13}C (δ) (ppm)**	**^{1}H δ (ppm), m**	**HMBC**
Glc I				
1	CH	92.21	4.4, m	C2’
2	CH	83.02	3.58, m	C3’
3	CH	73.28	3.47, m	
4	CH	70.30	3.14, m	
5	CH	77.47	3.90, t	
6	CH_2	62.59	3.55, m	
Glc II				
1’	CH	92.21	5.20, m	C3, C3’’’
2’	CH	83.02	3.58, m	C3’
3’	CH	73.28	3.47, m	
4’	CH	70.30	3.14, m	
5’	CH	77.47	3.90, m	
6’	CH_2	62.51	3.43, m	

Table 3 (cont'd). ^{1}H NMR (600 MHz) and ^{13}C NMR (150 MHz) data of compound **(2)** in DMSO

Position	DEPT	^{13}C (δ) (ppm)	^{1}H δ (ppm), m	HMBC
Rha				
1''	CH	-	5.05, m	C3'
2''	CH	70.30	3.14, m	
3''	CH	72.09	3.20, m	
4''	CH	73.33	3.68, m	
5''	CH	62.51	3.43, m	C2''
6''	CH_3	-	2.5, t	
Xyl				
1'''	CH	104.49	4.78, m	C4''
2'''	CH	74.75	3.78, m	
3'''	CH	77.48	3.90, m	
4'''	CH	70.30	3.14, m	
5'''	CH_2	60.95	3.49, m	C4'''

Conclusion

Two types of crystalline solids from *E.spiralis* stem bark have been successfully isolated and characterized and they were determined as penta-2-acetoxy-β-D-digitoxopyranosyl-(1→2)-fructofuranosyl-(6→4)-β-D-glucopyranosyl-(1→4)-glucopyranosyl-(1→2)-β-Dfructofuranosyl-(6→1)-β-D-glucopyranosyl-(4→1) acetylglu cosamine **(1)** and β,D-glucopyranosyl(1→2)-β,D-glucopyranosyl)-(1→3)-β,D-xylopyranosyl(1→4)-α,L-rhamnopyranosyl)-(1→3)-β,D-glucopyranosyl(1→3)-β,D-glucopyranoside **(2).** Both compounds have been isolated from methanol extract which is antidermatophytic active constituents.

References

1. Mbosso, E. J. T., Ngouela, S., Nguedia, J. C. A., Beng, V. P., Rohmer, M. and Tsamo, E. (2010). In vitro antimicrobial activity of extracts and compounds of some selected medicinal plants from Cameroon. *Journal of Ethnopharmacology*, 128 (2): 476 – 481.
2. Prasad, S. C., Shukla, R., Kumar, A. and Dubey, N. K. (2010) In vitro and in vivo antifungal activity of essential oils of *Cymbopogon martini and Chenopodium ambrosioides* and their synergism against dermatophytes. *Mycoses*, 53 (2): 123 – 129.
3. Silva Silva, G. M., Teles, H. L., Zanardi, L. M., Marx Young, M. C., Eberlin, M. N., Hadad, R., Pfenning, L. H., Costa- Neto, C. M., Castro-Gamboa, I., Da Silva Bolzani, V. and Araujo, A. R. (2006). Cadinane sesquiterpenoids of *Phomopsis cassiae*, an endophytic fungus associated with *Cassia spectabilis*(Leguminosae). *Phytochemistry*, 67 (14): 1964 – 1969.
4. Doughari, J. H. (2006). Antimicrobial activity of *Tamarindus indica* Linn. *Tropical Journal of Pharmaceutical Research* 5 (2): 597 – 603.
5. Duraipandiyan, V. and Ignacimuthu, S. (2007). Antibacterial and antifungal activity of *Cassia fistula* L.: An ethnomedicinal plant. *Journal of Ethnopharmacology* 112 (3): 590 – 594.
6. Khattak, K. F. and Simpson, T. J. (2010). Effect of gamma irradiation on the antimicrobial and free radical scavenging activities of *Glycyrrhiza glabra* root. *Radiation Physics and Chemistry*, 79: 507 –512.
7. Okada, Y., Shibata, S., Ikekawa, T., Javellana, Ana M. J. and Kamo, O. (1987). Entada Saponin III, A saponin Isolated from the bark of *Entada phaseloides. Phytochemistry*, 26 (10): 2789 – 2796.
8. Okada, Y., Shibata, S. and Javellana, A. M. J. (1988). Entada saponin (ES) II and IV from the bark of *Entada phaseloides*. *Chemical and Pharmaceutical Bulletin*, 36: 1264 – 1269.

9. Tapondjou, A. L., Miyamoto, T., Mirjolet, J. F., Guilbaud, N. and Lacaille-Dubois, M. A. (2005). Pursaethosides A-E, Triterpene saponins from *Entada pursaetha*. *Journal of Natural Products*, 68 (8): 1185 – 1190.
10. Ikegami, F., Ohmiya, S., Ruangrungsi, N., Sakai, S. I. and Murakoshi, I. (1987). A second new sulphur-containing amide from *Entada phaseoloides* seeds. *Phytochemistry*, 26 (5): 1525 – 1526.
11. Barua, A. K., Chakrabarty, M. and Datta, P. K.. (1988). Phaseoloidin, a homogentistic acid glucoside from *Entada phaseoloides*. *Phytochemistry*, 27: 3259 – 3261.
12. Dai, J., Kardono, L. B. S. and Tsauri, S. (1991). Phenylacetic acid derivatives and a thiomide glycosides from *Entada phaseoloides. Phytochemistry*, 30: 3749 – 3752.
13. Nzowa, L. K., Barboni, L., Teponno, R. B., Ricciutelli, M., Lupidi, G., Quassinti, L., Bramucci, M. and Tapondjou, L. A. (2010). Rheediinosides A and B, two antiproliferative and antioxidant triterpene saponins from *Entada rheedii*. *Phytochemistry* 71 (2), 254 – 261.
14. Aiza, H., Siti Zaiton, M. S. and Norazian, M. H. (2015). Bioassay guided isolation of an antidermatophytic active constituent from the stem bark of *Entada spiralis* Ridl. *Malaysian Journal of Analytical Sciences* 19 (4): 752 – 759.
15. Tibiri, A., Sawadogo, R. W., Ouedraogo, N., Banzouzi, J.-T., Guissou, I. P. and Nacoulma, G. O. (2010). Evaluation of Antioxidant Activity, Total Phenolic and Flavonoid Contents of *Entada africana* Guill.et Perr. (Mimosaceae) Organ Ectracts, *Research Journal of Medical Sciences* 4(2): 81 – 87.
16. Teke, G. N., Lunga, P. K., Wabo, H. K., Kuiate, J.-R., Vilarem, G., Giacinti, G., Kikuchi, H. and Oshima, Y. (2011). Antimicrobial and antioxidant properties of methanol extract, fractions and compounds from the stem bark of *Entada abyssinica* Stend ex A. Satabie. *BMC Complementary and Alternative Medicine*, 11(1): 57 – 65.
17. Iwamoto, Y., Sugimoto, S., Harinantenaina, L., Matsunami, K. and Otsuka, H. (2012). Entadosides A – D, triterpene saponins and a glucoside of the sulphur-containing amide from the kernel nuts of Entada phaseoloides(L .) Merrill, *Journal Natural Medicine*, 321 – 328.
18. Aiza, H., Siti Zaiton, M. S., Norazian, M. H. and Neni Kartini, C. M. R. (2014). Bioactive Terpenoids from the Stem Bark of Entada spiralis Ridl. (sintok). *Proceeding of the International Conference on Science Technology and Social Science (ICSTSS) 2012. Chapter in Book Springer Science+Business Media Singapore*. 605 – 615.
19. Aiza, H., Siti Zaiton, M.S., Norazian, M.H. and Neni Kartini, C. M. R. (2014b). In-vitro antidermatophytic activity of Methanolic fractions from Entada spiralis Ridl. Stem bark and its bioautographic profile. *Pertanika Journal Science & Technology* 22(1): 113 – 121.
20. Aiza, H, Siti Zaiton, M.S., Norazian, M. H. and Neni Kartini, C. M. R. (2011). *In-vitro* antifungal activity of *Entada spiralis* Ridl. crude extract against dermatophytes of superficial skin disease. *Revelation and Science*, 1 (1), 57 – 61.
21. Yokosuka, A., Kawakam, I. S., Haraguch, I. M. and Mimaki. Y. (2011). Seven new triterpene glycosides from the pericarps of *Stryphnodendron fissuratum*. *Phytochemistry Letters* 4 (3): 259 – 266.
22. Warashina, T. and Noro, T. (2009). 8,14-Secopregnane glycoside from the aerial parts of *Asclepias tuberosa Phytochemistry*, 70 (10): 1294 –1304.
23. Okada, H., Fukushi, E., Yamamori, A., Kawazoe, N., Onodera, S., Kawabata, J. and Shiomi, N. (2010). Novel fructopyranose oligosaccharides isolated from fermented beverage of plant extract. *Carbohydrate Research*, 345 (3): 414 – 418.

MALAYSIAN JOURNAL OF ANALYTICAL SCIENCES
Published by The Malaysian Analytical Sciences Society
ISSN 1394 - 2506

STABILITY INDICATING RP-HPLC METHOD FOR SIMULTANEOUS DETERMINATION OF ASPIRIN AND CLOPIDOGREL IN DOSAGE FORM

(Kestabilan Kaedah KCPT-Indikator bagi Penentuan Serentak Asprin dan Clopidogrel Dalam Bentuk Dos)

Md. Gousuddin*, Pinaki Sengupta, Vijaya Datt Tripathi, Arindam Das

Faculty of Pharmacy,
Lincoln University College, 47301 Petaling Jaya, Selangor, Malaysia

**Corresponding author: Inamdarirfan09@gmail.com*

Received: 13 June 2015; Accepted: 1 February 2016

Abstract

Stability-indicating High Performance Liquid Chromatographic (HPLC) method was developed for simultaneous Aspirin and Clopidogrel, A Phenomenex Gemini C-18, 5 µm column having 250mm x 4.6 mm i.d. in isocratic mode, with mobile phase containing buffer solution 0.3% orthophosphoric acid : acetonitrile (65: 35, v/v). The flow rate was 1 ml/min and effluents were monitored at 266 nm. For linearity seven points calibration curve were obtained in a concentration range from 0.030 –0.120 mg/ml for aspirin and 0.015 – 0.060 mg/ml for clopidogrel with correlation coefficient 0.9999. In the present study stability indicating HPLC method for the combination was tested by degrading the drugs together under various stress conditions like acid hydrolysis, base hydrolysis, oxidation, thermal and photolytic stress which is recommended by ICH guideline.

Keywords*:* revere phase high performance liquid chromatography, stability indicating method, aspirin, clopidogrel

Abstrak

Kestabilan Kaedah Kromatografi Cecair Prestasi Tinggi (KCPT) – indikator telah dibangunkan bagi penentuan serentak Aspirin dan Clopidogrel. Turus Phenomenex Gemini C-18, 250mm x 4.6 mm i.d. diguna dalam mod isokratik, bersama fasa bergerak yang mengandungi larutan penimbal iaitu 0.3% asid orthofosforik : acetonitril. Kadar aliran adalah 1ml/min dan effluent dipantau pada panjang gelombang 266 nm. Tujuh titik lengkung kalibrasi dipilih bagi ujian kelinearan yang diperolehi dari julat 0.030 – 0.120 mg/ml dan 0.015 – 0.060 masing – masing bagi aspirin dan clopidogrel dengan nilai pekali korelasi adalah 0.9999. Dalam kajian ini, kestabilan kaedah KCPT- indikator bagi gabungan analit diuji di bawah pelbagai tekanan seperti hidrolisis asid, hidrolisis bes, pengoksidaan, termal dan tekanan fotolitik seperti yang dicadangkan oleh garis panduan ICH.

Kata kunci*:* kromatografi cecair prestasi tinggi fasa terbalik, kestabilan kaedah indikator, aspirin, clopidogrel

Introduction

Platelet aggregation and thrombus formation play a critical role in the initiation and development of key complications of acute coronary syndromes (ACSs). Antiplatelet therapy and antithrombotic therapy have been demonstrated to favorably modify clinical outcome, and recent trials of revascularization in ACSs have demonstrated a reduction in the frequency of major cardiac events [1 – 12]. Antiplatelet and anti-thrombin have synergistic actions that reduce the risk of spontaneous or revascularization, especially percutaneous coronary intervention (PCI)-related events. Yet, all effective antithrombotic agents also increase the risk of bleeding,

especially bleeding that results from vascular accessor associated with surgery, including coronary artery bypass grafting (CABG). The Clopidogrel in unstable angina to prevent recurrent ischemic Events (CURE) trial demonstrated that the combination of clopidogrel and aspirin was superior to aspirin alone for patients hospitalized with non-ST-elevation ACSs.

Aspirin is chemically acetylsalicylic acid (Figure 1). Its molecular formula is $C_9H_8O_4$ having molecular weight 180 g/mole [14]. It is slightly soluble in water, freely soluble in alcohol, soluble in chloroform and ether, sparingly soluble in absolute ether. Aspirin, one of the first drugs to come into common usage, is still the most widely used drug in the world, is a non-steroidal anti-inflammatory drug that exhibits anti-inflammatory, analgesic and antipyretic activities.

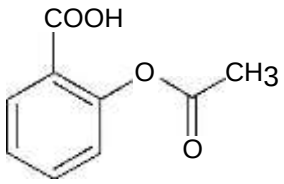


Figure 1. Chemical structure of aspirin

Clopidogrel bisulfate, chemicall y it is [S - (a)(2 - chlorophenyl) - 6,7 - dihydrothieno (3,2-C) pyridine-5 (4H) acetic acid methyl ester sulphate] (Figure 2). The empirical formula of clopidogrel bisulfate is $C_{16}H_{16}ClNO_2S•H_2SO_4$ and its molecular weight is 419.9 g/mole [14]. It is a white to off-white powder. It is practically insoluble in water at neutral pH but freely soluble at pH 1. It also dissolves freely in methanol, dissolves sparingly in methylene chloride and is practically insoluble in ethyl ether. It has a specific optical rotation of about +56°. The structural formula is as follows:

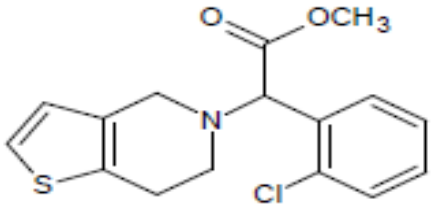


Figure 2. Chemical Structure of clopidogrel

The combination of clopidogrel with aspirin provides enhanced prevention of atherothrombotic events by blocking the platelet aggregation by both ways. (ADP pathway and collagen induced pathway) and it shows a synergistic antiplatelet action in controlling the ischemic events.

Literature reveals that various methods simultaneous determination of aspirin and clopidogrel in pharmaceutical formulation HPTLC [5 – 6]. Various publications are available regarding determination method of aspirin and clopidogrel but most of the methods are applicable to alone aspirin or clopidogrel in pharmaceutical dosage form or in bilogical fluids. Only three methods are reported for the simulteneous determination of apirin and clopidogrel. One is semi-micro column HPLC-UV method for simultaneous determination of clopidogrel metabolite, aspirin and salicylic acid in rat plasma. Second is a spectrophotometric method, which is able to determine aspirin and clopidogrel in combine dosage form and third is simple high performance liquid chromatography, which applicable to routine quality control sample analysis. The separation is performed by high

performance liquid chromatography for reasons of robustness and familiarity of analysts with this technique. To our knowledge, no stability-indicating analytical method for the determination of aspirin and clopidogrel in combine dosage forms has been published.

In the present study stability indicating HPLC method for the combination was tested by degrading the drugs together under various stress conditions like acid hydrolysis, base hydrolysis, and oxidation, thermal and photolytic stress which is recommended by ICH guideline.

Materials and Methods

Pharmacopoeial grade standards of aspirin and clopidogrel bisulphate were provided by Blue Cross laboratory. A tablet containing 150 mg aspirin and 75 mg clopidogrel was commercially available. HPLC grade acetonitrile, methanol and water were obtained from Spectrochem Pvt. Ltd., Mumbai (India). Analytical grade hydrochloric acid, sodium hydroxide pellets, orthophosphoric acid and hydrogen peroxide solution (30 % v/v) were obtained from Ranbaxy Fine Chemical, New Delhi (India).

HPLC instrumentation and conditions

The chromatographic system used to perform development and validation of this assay method was comprised of (SHIMADZU, HPLC) with LC- 20AT (VP series) pump, with software Spinchrom and UV-Visible detector SPD-20A (VP series). Chromatographic analysis was performed on a Phenomenex Luna C8 (250 mm 4.6 mm i.d., 5 µm particle size) column. The mobile phase was consisted of 0.3 % orthophosphoric acid (v/v) - acetonitrile (65:35, v/v). The flow rate of the mobile phase was adjusted to 1.0 ml/min and the injection volume was 20 µl. Detection was performed at 226 nm.

In the presence work, an analytical method based on LC using UV detection was developed and validated for assay determination of aspirin and clopidogrel in tablet formulation. The analytical conditions were selected, keeping in mind the different chemical nature of aspirin and clopidogrel. The development trials were taken by using the degraded sample of each component was done, by keeping them in various extreme conditions.

The column selection has been done on the basis of backpressure, resolution, peak shape, theoretical plates and day-to-day reproducibility of the retention time and resolution between aspirin and clopidogrel peak. After evaluating all these factors, C8 (2) (250 mm 4.6 mm i.d., 5 µm particle size) column was found to be giving satisfactory results. The selection of buffer based on chemical structure of both the drugs.

Preparation of stock solution for stress studies

The degradation samples were prepared by transferring powdered tablets, equivalent to 150 mg aspirin and 75 mg clopidogrel into a 250 ml round bottom flask. Then prepared samples were employed for acidic, alkaline and oxidant media and also for thermal and photolytic stress conditions. After the degradation treatments were completed, the stress content solutions were allowed to equilibrate to room temperature and diluted with mobile phase to attain 0.075 mg/ml of aspirin and 0.0375 mg/ml of clopidogrel concentration.

Results and Discussion

The acidic pH range was found suitable for solubility, resolution, stability, theoretical plates and peak shape of both components. Best results were obtained with 0.3 % orthophosphoric acid solution improved the peak shape of aspirin and clopidogrel. Finally, by fixing 0.3 % orthophosphoric acid (v/v) and mobile phase composition consisting of a mixture of 0.3% orthophosphoric acid (v/v) into ratio 65:35, v/v. Optimized mobile phase proportion was providing good resolution between aspirin and clopidogrel and also for degradation product which is generated during force degradation study. For the selection of organic constituent of mobile phase, acetonitrile was chosen to reduce the longer retention time and to attain good peak shape. Figure 1 and Figure 2 represent the Chromatograms of standard and test preparation respectively.

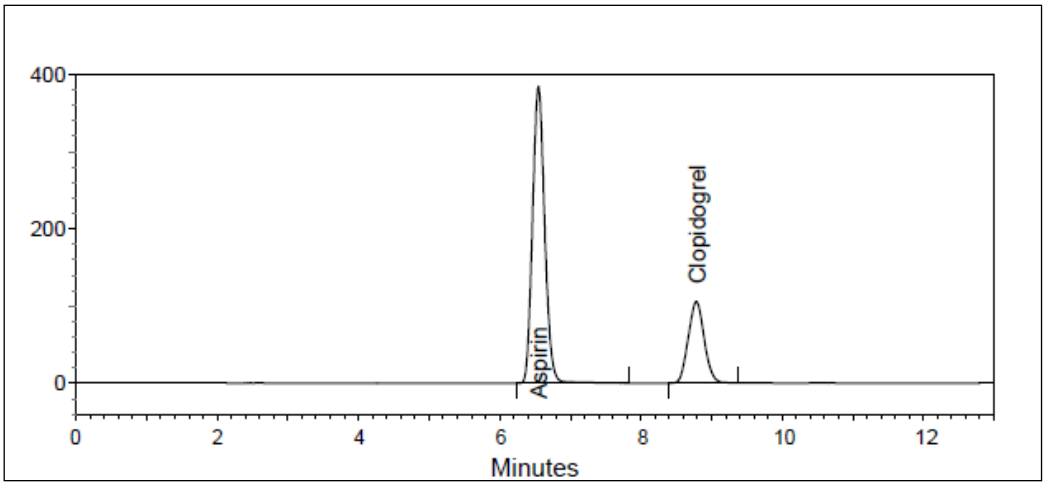


Figure 1. Chromatogram of standard preparation (0.08mg/ml)

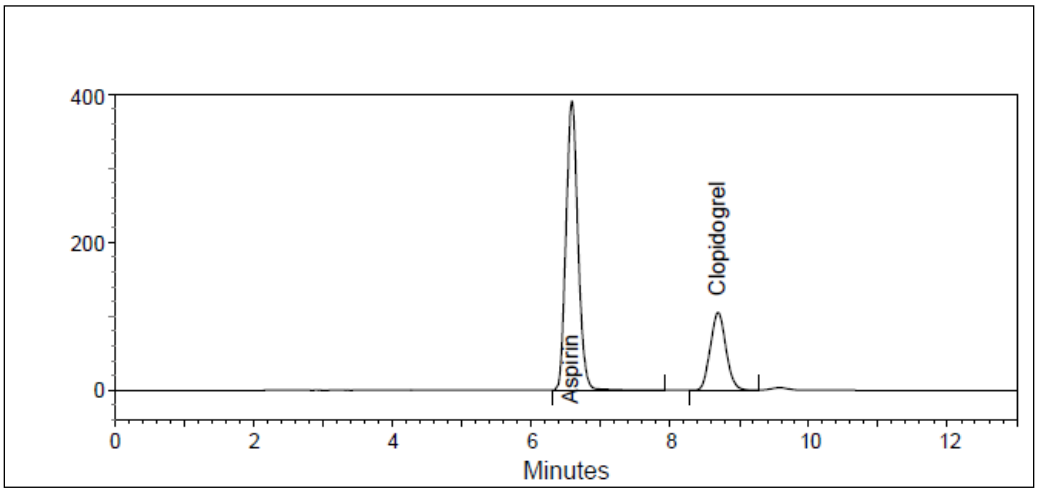


Figure 2. Chromatogram of test preparation (0.08mg/ml)

In order to determine whether the analytical method or assay were stability- indicating, aspirin and clopidogrel combine tablets were stressed under various conditions to conduct forced degradation studies. Regulatory guidance in ICH Q2A, Q2B, Q3B and FDA 21 CFR section 2 11 all require the development and validation of stability-indicating potency assays. Unfortunately, the current guidance documents do not indicate detailed degradation conditions in stress testing. However, the used forced degradation conditions, stress agent concentration and time of stress, were found to effect degradation and not complete degradation of active materials. The discovery of such conditions was based on development trial.

Acidic condition

Acidic degradation study was performed by heating the drug content in 1 N HCl (50 ml) at 80 °C for 1 hour and mixture was neutralized with 1 N NaOH solution. The drug content was found to be degrading up to 16.93 % in acidic condition. Clopidogrel was more susceptible to acid hydrolysis under experimental conditions. In all degradation conditions the drug degrades as observed by by the decreased area in the peak of the drug when

compared with peak area of the same concentration of the undegraded drug, with giving one additional degradation peak at 9.02 min.

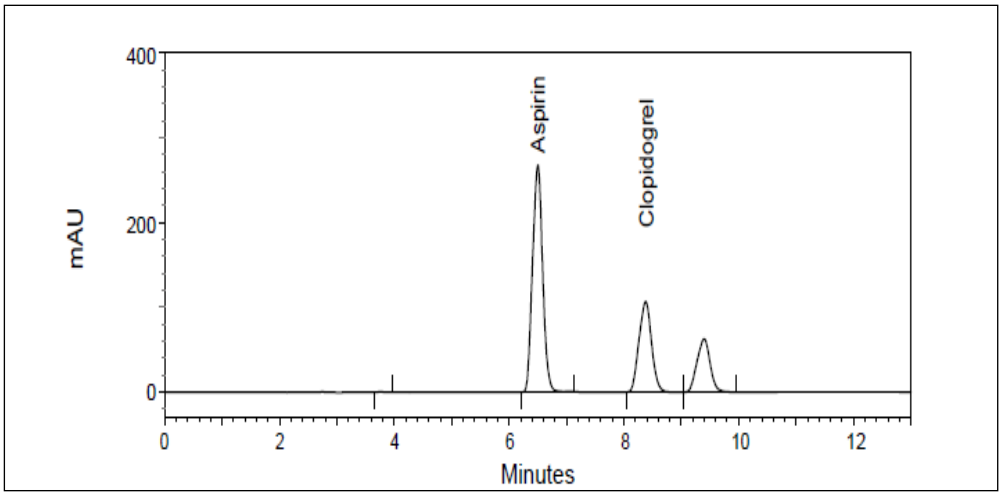


Figure 3. Chromatogram of acidic forced degradation study

Alkaline condition

Alkaline degradation study was performed by heating the drug content in 1 N NaOH (50 ml) at 80 °C for 1 hour and mixture was neutralized with 1 N HCl solutions. In alkali degradation, it was found that around approximately 22 % of the drug was degraded (Figure 4). Aspirin was more susceptible to alkaline hydrolysis under experimental conditions. In all degradation conditions the drug degrades as observed by the decreased area in the peak of the drug when compared with peak area of the same concentration of the undegraded drug, with giving one additional degradation peak at 4.72 min.

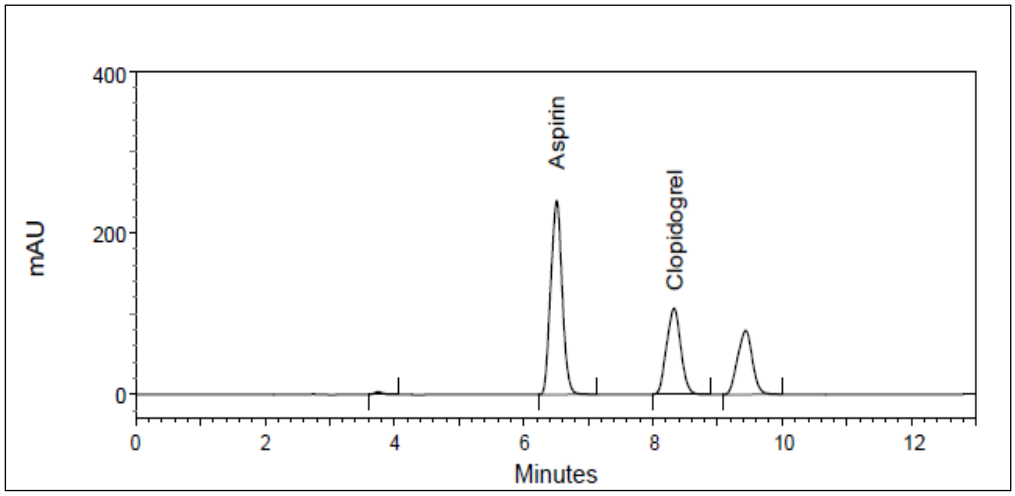


Figure 4. Chromatogram of alkali forced degradation study

Oxidative condition

Oxidation degradation study was performed by heating the drug content it's in initial concentration carried out in 1% v/v hydrogen peroxide no significant changes then will increase into 3% v/v hydrogen peroxide at 80 °C for 30 minutes. In oxidative degradation, it was found that approximately 15.84 % of drug was degraded (Figure 5). .

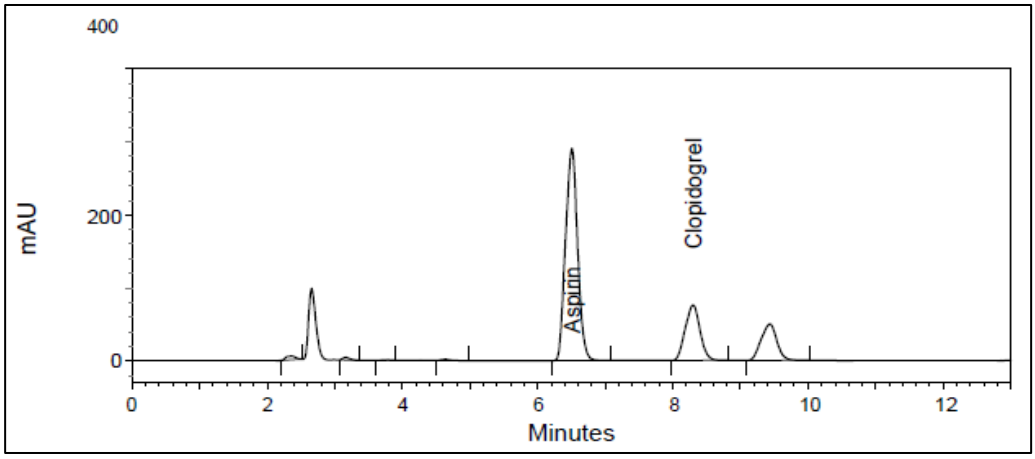
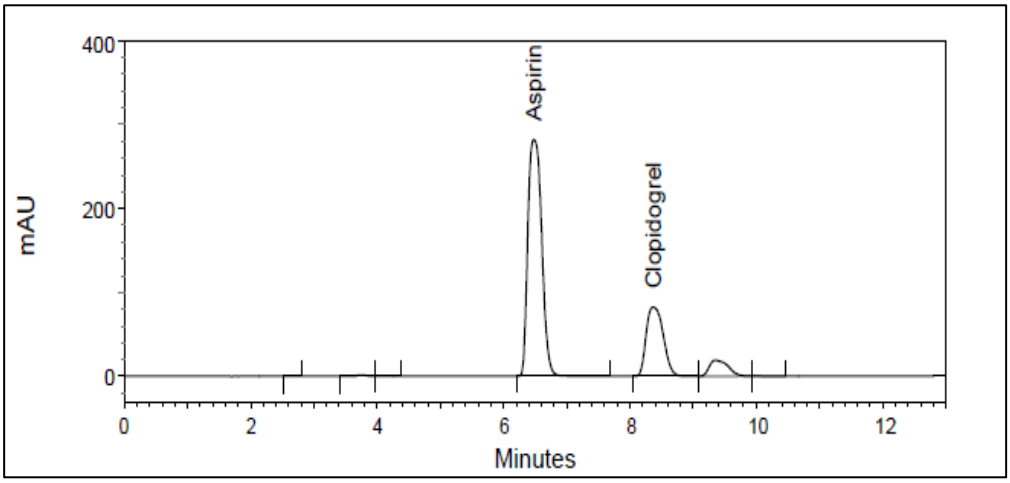


Figure 5. Chromatogram of oxidative forced degradation study

Thermal condition

Thermal degraded samples wherever degradation possible from about 1% to 30%.Preferably, the following stress conditions are was performed by exposing solid drug at 80 °C for 72 hours. Resultant chromatogram of thermal degradation study (Figure 6) indicates that aspirin is found to be slightly stable under thermal degradation condition. Only 7.0 % of drug content was degraded.



.

Figure 6. Chromatogram of thermal degradation study

Photolytic condition

Exposure of drug molecules may produce photolytic degraded products. The rate of photo degradation depends upon the

intensity of incident light and quantity of light absorbed by the drug molecule. Photolytic degradation is carried out by exposing the drug substance (in solid as well as in the solution form) or drug product to a combination of visible and UV light. Photolytic degradation study was performed by exposing the drug above specific photolytic condition. Drug content was found to be more stable than other stress condition stable in UV-light. Aspirin is stable under UV light compare to clopidogrel. (Figure 7).

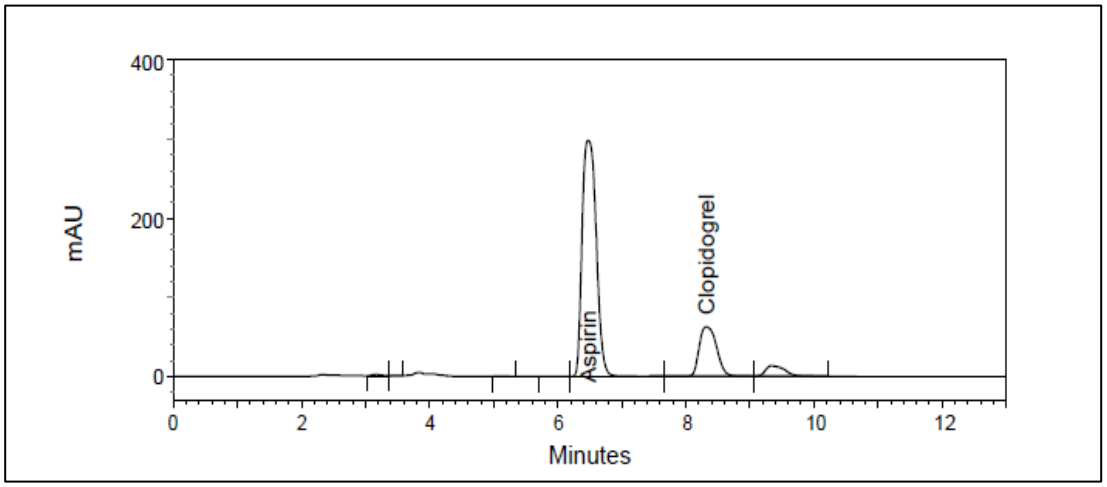


Figure 7. Chromatogram of UV-light degradation study

Linearity

For linearity seven points calibration curve were obtained in a concentration range from 0.030 – 0.120 mg/ml for aspirin and 0.015 – 0.060 mg/ml for clopidogrel, respectively. The response of the drug was found to be linear in the investigation concentration range and the linear regression equation for aspirin was y = 60026378.57x + 51410.11 with correlation coefficient 0.9999 (Figure 8) and for clopidogrel was y = 44544414.03x - 1890.29 with correlation coefficient 0.9999 (Figure 9). Where x is the concentration in mg/ml and y is the peak area in absorbance unit.

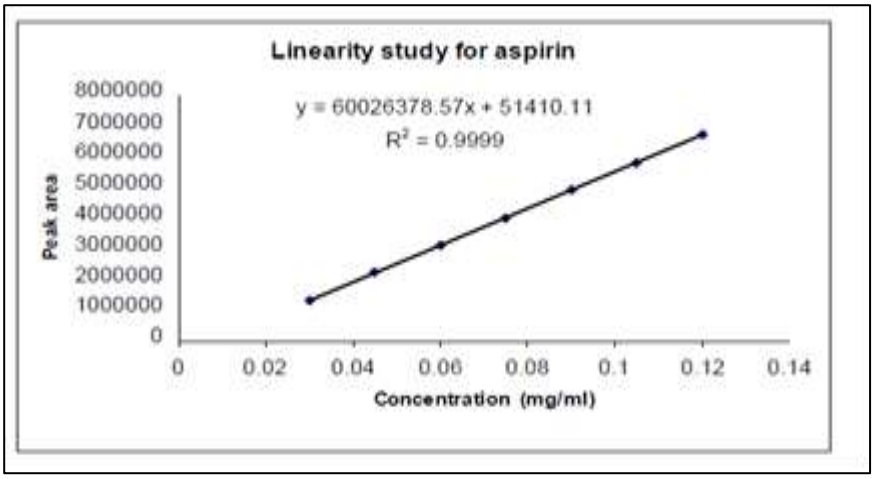


Figure 8. Linearity curve for aspirin

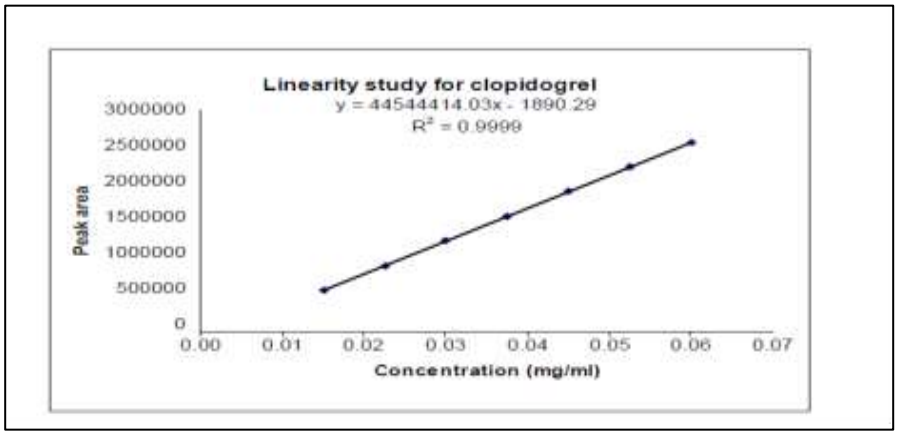


Figure 9. Linearity curve for clopidogrel

Detection and Quantification Limit (LOD and LOQ)

The limit of detection and limit of quantification were evaluated by serial dilutions of aspirin and clopidogrel stock solution in order to obtain signal to noise ratio of 3:1 for LOD and 10:1 for LOQ. The LOD value for aspirin and clopidogrel were found to be 0.05 ppm and 0.15 ppm, respectively and the LOQ value 0.2 ppm and 0.3 ppm, respectively. Chromatogram of LOD study for aspirin and was illustrated in Figure 10.

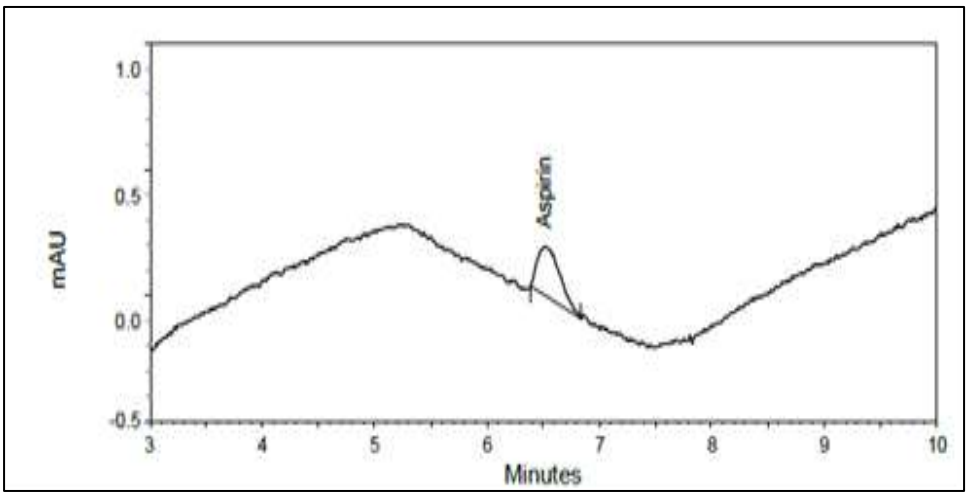


Figure 10. Chromatogram of LOD study of aspirin

Precision

Data obtain from precision experiments are given in Table 1 for intraday and interday precision study for both aspirin and clopidogrel. The RSD values for intraday precision study and interday precision study was < 2.0 % for aspirin and clopidogrel. It was confirmed that the developed method was precise for analysis. Results of precision in this study was summarized in the Table 1 below

Table 1. Results of precision study

Set	Aspirin (%Assay)		Clopidogrel (%Assay)	
	Intraday (n = 6)	**Interday (n = 6)**	**Intraday (n = 6)**	**Intraday (n = 6)**
1	99.1	100.2	99.3	99.6
2	100.0	99.9	98.7	99.6
3	99.6	100.5	98.6	100.1
4	99.5	100.3	99.0	100.1
5	100.3	101.0	100.0	100.6
6	99.1	100.8	99.5	100.7
Mean	99.6	100.5	99.2	100.1
Standard deviation	0.48	0.40	0.53	0.47
% RSD	0.48	0.40	0.53	0.47

Accuracy

Recovery of aspirin and clopidogrel were determined at three different concentration levels. The mean recovery for aspirin was 99.12 – 99.83% and 98.20 – 100.35 % for clopidogrel (Table 2). The result indicating that the method was accurate.

Table 2. Results of accuracy study

Level (%)	Amount Added Concentration (mg/ml)	Amount Found Concentration (mg/ml)	Recovery[a] (%)	RSD[a] (%)
Aspirin				
50	0.03751	0.03721	99.22	0.07
100	0.07497	0.07432	98.12	0.23
150	0.11250	0.11232	99.83	0.05
Clopidogrel				
50	0.01874	0.01840	98.20	0.19
100	0.03748	0.03695	98.59	0.14
150	0.05627	0.05647	100.35	0.24

a Each value corresponds to the mean of three determination

Robustness

The result of robustness study of the developed assay method was established in Table 3 and Table 4, respectively. The result had shown that during all variance conditions, assay value of the test preparation solution was not affected and it was in accordance with that of actual. System suitability parameters were also found satisfactory hence the analytical method would be concluded as robust method.

Table 3. Evaluation data of robustness study of aspirin

	% Assay	System Suitability Parameters		
		Theoretical	Asymmetry	% RSD
Flow 0.9 ml/min	100.5	6460	1.05	0.22
Flow 1.1 ml/min	100.3	5661	1.05	0.09
0.28 % H_3PO_4-ACN (65:35, v/v)	100.0	6117	1.00	0.40
0.32 % H_3PO_4-ACN (65:35, v/v)	99.7	5588	1.02	0.30
0.3% H_3PO_4-ACN (63:37,v/v)	100.2	5475	1.12	0.19
0.3% H_3PO_4-ACN (67:33,v/v)	100.1	5838	1.04	0.20
Column change (different lot)	100.4	5425	1.05	0.34

Table 4. Evaluation data of robustness study for clopidogrel

Robust Conditions	% Assay	System Suitability Parameters			
		Theoretical	Asymmetry	% RSD	Resolution
Flow 0.9 ml/min	98.5	6975	1.07	0.67	5.75
Flow 1.1 ml/min	100.0	5992	1.06	0.39	5.14
0.28 % H_3PO_4-ACN(65:35,v/v)	98.8	6899	1.03	1.03	6.35
0.32 % H_3PO_4-ACN(65:35,v/v)	99.2	6113	1.03	0.69	5.6
0.3% H_3PO_4-ACN(63:37,v/v)	99.5	5850	1.11	0.70	4.31
0.3% H_3PO_4-ACN (67:33,v/v)	99.0	6185	1.04	0.30	5.71
Column change (different lot)	100.0	5996	1.04	0.25	4.97

Conclusion

The method was validated for all validation parameters as per ICH guidelines. The linearity range for aspirin and clopidogrel was 0.030 – 0.120 mg/ml for aspirin and 0.015 – 0.060 mg/ml for clopidogrel with correlation coefficient 0.9999. The % RSD for intra-day precision was < 2%. The developed and validated stability indication HPLC method is found to be linear, accurate, precise, specific and robust, confirming the stability indicating method for the simultaneous estimation of aspirin and clopidogrel.

References

1. Trialists'Collaboration, A. (2002). Collaborative meta-analysis of randomised trials of antiplatelet therapy for prevention of death, myocardial infarction, and stroke in high risk patients. *British Medical Journal*, 324(7329): 71 – 86.
2. Kong, D. F., Califf, R. M., Miller, D. P., Moliterno, D. J., White, H. D., Harrington, R. A. and Topol, E. J. (1998). Clinical outcomes of therapeutic agents that block the platelet glycoprotein IIb/IIIa integrin in ischemic heart disease. *Circulation*, 98(25): 2829 – 2835.
3. Boersma, E., Harrington, R. A., Moliterno, D. J., White, H., Théroux, P., Van de Werf, F. & Simoons, M. L. (2002). Platelet glycoprotein IIb/IIIa inhibitors in acute coronary syndromes: a meta-analysis of all major randomised clinical trials. *The Lancet*, *359* (9302): 189 –198.
4. Yusuf, S., Zhao, F., Mehta, S. R., Chrolavicius, S., Tognoni, G. and Fox, K. K. (2001). Clopidogrel in Unstable Angina to Prevent Recurrent Events Trial Investigators. Effects of clopidogrel in addition to aspirin

in patients with acute coronary syndromes without ST-segment elevation. *New England Journal Medicine*, *345*(7): 494 –502.

5. Mehta, S. R., Yusuf, S., Peters, R. J., Bertrand, M. E., Lewis, B. S. and Natarajan, M. K. (2001). Clopidogrel in Unstable Angina to Prevent Recurrent Events Trial (CURE) Investigators. Effects of pretreatment with clopidogrel and aspirin followed by long-term therapy in patients undergoing percutaneous coronary intervention: the PCI-CURE study. *The Lancet*, *358* (9281): 527 – 533.
6. PURSUIT Trial Investigators. (1998). Inhibition of platelet glucoprotein IIb/IIIa with eptifibatide in patients with acute coronary syndromes. Platelet glycoprotein IIb/IIIa in unstable angina. Receptor suppression using integrilin therapy. *New England Journal Medicine*, 339: 436 – 443.
7. PRISM Study Investigators. (1998). A comparison of aspirin plus tirofiban with aspirin plus heparin for unstable angina. *New England Journal Medicine*, 338 (21): 1498 – 505.
8. GUSTO IV-ACS Investigators. (2001). Effect of glycoprotein IIb/IIIa receptor blocker abciximab on outcome in patients with acute coronary syndromes without early coronary revascularisation: the GUSTO IV-ACS randomised trial. *The Lancet*, 357(9272): 1915 –1924.
9. Ragmin, F. (1999). Fast Revascularisation during InStability in Coronary artery disease (FRISC II) Investigators. Invasive compared with non-invasive treatment in unstable coronary-artery disease: FRISC II prospective randomised multicentre study. *The Lancet*, 354(9180): 708 – 715.
10. Wallentin, L., Lagerqvist, B., Husted, S., Kontny, F., Ståhle, E. and Swahn, E. (2000). Outcome at 1 year after an invasive compared with a non-invasive strategy in unstable coronary-artery disease: the FRISC II invasive randomised trial. *The Lancet*, *356*(9223): 9 –16.
11. Cannon, C. P., Weintraub, W. S., Demopoulos, L. A., Vicari, R., Frey, M. J., Lakkis, N. and Braunwald, E. (2001). Comparison of early invasive and conservative strategies in patients with unstable coronary syndromes treated with the glycoprotein IIb/IIIa inhibitor tirofiban. *New England Journal of Medicine*, *344 (*25): 1879 –1887.
12. Berkowitz, S. D., Granger, C. B., Pieper, K. S., Lee, K. L., Gore, J. M., Simoons, M. and Califf, R. M. (1997). Incidence and predictors of bleeding after contemporary thrombolytic therapy for myocardial infarction. *Circulation*, *95* (11): 2508 – 2516.

MALAYSIAN JOURNAL OF ANALYTICAL SCIENCES
Published by The Malaysian Analytical Sciences Society
ISSN 1394 - 2506

REMOVAL OF MALACHITE GREEN DYE FROM AQUEOUS SOLUTION USING MULTI-WALLED CARBON NANOTUBES: AN APPLICATION OF EXPERIMENTAL DESIGN

(Penyingkiran Malakit Hijau daripada Larutan Akues Menggunakan Karbon Tiub Nano: Aplikasi Reka Bentuk Eksperimen)

Siti Aminah Zulkepli[1], Md Pauzi Abdullah[1, 2]*, Wan Mohd Afiq Wan Mohd Khalik[1]

[1]*School of Chemical Sciences and Food Technology*
[2]*Centre for Water Research and Analysis (ALIR)*
Faculty of Science and Technology
Universiti Kebangsaan Malaysia, 43600 UKM Bangi, Selangor, Malaysia

**Corresponding author: mpauzi@ukm.edu.my*

Received: 11 January 2016; Accepted: 10 March 2016

Abstract

An experimental design methodology was performed in the optimization of removal of malachite green dye by multi-walled carbon nanotubes. A Central Composite Design (2^5) was chosen to develop a mathematical model and determine the optimum condition for adsorption of malachite green by carbon nanotubes. Five experimental factors, namely initial dye concentration, mass of adsorbent, pH, contact time and agitation speed were studied. Maximum adsorption of malachite green was achieved at the suggested optimum conditions: initial dye concentration (20 ppm), weight of adsorbent (0.03 g), pH solution (7) contact time (17 min) and agitation speed (150 strokes per min). The experimental value of adsorption by multi-walled carbon nanotubes were found to be in good agreement with the predicted value (R^2 = 0.922).The experimental equilibrium data were best fitted to isotherm model (Langmuir) and kinetic model (pseudo second-order) respectively. Maximum adsorption by carbon nanotubes at monolayer for malachite green was obtained at 112.36 mg/g while kinetic rate constant was calculated to be 0.0017 g mg^{-1} min^{-1}.

Keywords: carbon nanotubes, adsorption, malachite green, experimental design

Abstrak

Metodologi reka bentuk eksperimen telah dijalankan dalam pengoptimuman penyingkiran pewarna malakit hijau oleh karbon tiub nano multi-dinding. Reka bentuk komposit berpusat (2^5) telah dipilih untuk membentuk satu model matematik dan menentukan kondisi yang optima untuk penjerapan malakit hijau oleh karbon tiub nano. Lima faktor eksperimen yang terdiri daripada kepekatan awal pewarna, berat bahan penjerap, pH larutan, masa sentuhan dan kelajuan goncangan telah dikaji. Malakit hijau telah mencapai penjerapan yang optima oleh karbon tiub nano pada kondisi: kepekatan awal pewarna (20 ppm), berat bahan penjerap (0.03 g), pH larutan (7), masa sentuhan (17 minit) dan kelajuan goncangan (150 strok/minit). Nilai eksperimen untuk penjerapan oleh karbon tiub nano multi-dinding telah mencapai persetujuan yang baik pada nilai jangkaan (R^2 = 0.922). Data eksprimen keseimbangan menunjukkan kesesuaian pada model Langmuir dan model pseudo tertib kedua. Penjerapan maksimum oleh karbon tiub nano pada monolapisan untuk malakit hijau ialah 112.36 mg/g manakala pemalar kadar kinetik ialah 0.0017 g mg^{-1} min^{-1}.

Kata kunci: karbon tiub nano, penjerapan, malakit hijau, reka bentuk eksperimen

Introduction

The wide consumption of dyes in textile industries has produced a large amount of waste in the environment. There are structural varieties of dyes such as acidic, basic, disperse, azo, diazo, metal complex and anthraquinone that have been utilized in industries [1]. Malachite Green (MG) is a N-dimethylated diaminotriphenyl-methane dye that was first introduced during the mid-1933s [2] and is extensively used in aquaculture and dyes industries. MG is a basic dye, readily soluble in water and has been used as a dye in silk, jute, leather, cotton, paper and acrylic industries as well as food colouring agent, food additive, medical disinfectant and anthelmintic [3]. In aquaculture, MG has been used as an effective antifungal and antiprotozoal agent. The fungicidal properties of MG can control fungal attack, protozoan infections and some other diseases in aquatic organisms [4].

Even though MG was not approved by the US Food and Drug Administration, it is still being consumed around the world since it is relatively inexpensive, ready to be used and highly efficacious [5]. The disposal of MG in the environment can cause environmental problems, especially water pollution. MG is classified as a Class II Health Hazard and shows significant health risk to human through consumption of fish that contains MG residue [6]. MG is easily absorbed by fishes after treatment and reduced in the tissues of fish to its colourless metabolite compound known as leucomalachite green (LMG), which is also a suspected mutagen and teratogen [7]. LMG excretes very slow ($t^{1/2}$ ~ 40 days) in certain fatty tissues and this causes the accumulation of LMG in fishes [8]. In addition, MG can cause harm to the aquatic environment; in a way, it is reducing light penetration and photosynthesis [9, 10]. The disposal of dye wastewater without proper treatment is a big challenge since most of the dyes are difficult to eliminate from the environment and dyes are usually hard to biodegrade due to their complex molecular structures [11].

Various techniques have been applied for the removal of MG from wastewater, which included physical, chemical and biological methods. Chemical techniques such as advanced oxidation process consumed more chemical reagent while high cost of chemicals and operation brought about this method as an unattractive option. Meanwhile, biological methods, which include microbial degradation, bioremediation system and fungal discoloration, do not usually achieve a satisfactory elimination of the dyes on a continuous basis and require longer time [9, 12]. Adsorption, which is one of the physical techniques for wastewater treatment, becomes an appealing method in the removal of dyes from wastewater since it offers a simple and easy design, does not contribute to harmful substances, has high efficiency and versatile techniques compared to the others [13].

Recently, carbon nanotubes (CNTs) have been recognized to have a potential to be a superior adsorbent in the adsorption of dye from wastewater because of the unique chemical and physical properties of CNTs. Generally, CNTs are divided into two types, namely single-walled carbon nanotubes (SWCNT) and multi-walled carbon nanotubes (MWCNT). CNTs consist of highly porous and hallow structure, large specific surface area, light mass density and provide a chemically inert surface for physical adsorption. These tremendous morphologies have given an advantage for a good adsorption [14, 15], thus an efficient removal of contaminants. CNTs have been successfully applied to remove numerous contaminants in wastewater such as heavy metals [16, 17], volatile organic compound [18] and dye [10, 15, 19, 20].

Optimization of adsorption studies can be performed by varying experimental factors and conventionally, the classical method has limitations as it only can vary one factor at one time while the other factors are fixed. In addition, it requires a large number of experiments to be performed each time. Meanwhile, the response surface methodology (RSM) is one of the approaches by the researchers to study the interaction of several factors at one time. RSM is a collection of mathematical and statistical techniques in which describing the response to the experimental data fitted in a polynomial equation and the experimental data were achieved by the systematic design [21]. Designing and evaluating experiments by experimental design allows the researchers to optimize the interest factors for the adsorption process and depict the linear, interaction and quadratics effects of all factors involved at the same time. The systematically varied design by RSM also controls and reduces the number of experiments. Beneficially, this made the research become faster, more economical and effective compared to the classical method, which consumes more chemicals and time [21, 22].

In the present study, a central composite design (CCD) has been chosen to be applied in the optimization of MG removal by MWCNTs. The batch experiments under optimized conditions were then tested for isotherm and kinetic model respectively.

Materials and Methods

Reagents and Instruments

Multi-walled Carbon Nanotubes (6 – 9 nm outer diameter, 5 μm in length and >95% purity) were purchased from Sigma-Aldrich (St. Louis, USA) and have been used for adsorption experiment without further purification. The malachite green dye, sodium acetate with analytically graded was purchased from R & M Chemicals (Essex, UK). Acetic acid used for preparation of acidic buffer (Merck, Germany) and for basic buffer, ammonium hydroxide from J. T. Baker (Pennsylvania, USA) and ammonium chloride from Ridel-De Haen (Seelze, Germany) were used. Deionized water was obtained from a Milli-Q EasypureRodi system (Barnstead, USA).

The initial and final concentrations of malachite green were determined by UV-Vis spectrophotometer (Shimadzu Model UV-1650PC) at a wavelength of 617 nm. The pH measurements were carried out by using pH meter (Eutech Model pH 700 series). An agitation effect was performed by shaking water bath (Memmert WNB 22). The cellulose nitrate membrane filter with pore size 0.45 μm produced by Millipore (Merck, Germany) was used for filtering MWCNTs from aqueous solution after adsorption experiment.

Adsorption Experiments

The stock solution of malachite green was prepared by weighing the appropriate mass of malachite green dye salt and dissolved with deionized water. Then, working solutions of malachite green were prepared by diluting volume of stock solution required with deionized water.

In general, the adsorption of malachite green was performed as follows: A specified mass of MWCNTs powder was added into 100 mL of MG solution. The pH of the solution was adjusted with a buffer solution of acetate acid-sodium acetate and ammonium hydroxide-ammonium chloride. Then, each of the solution was shaken in a shaker for a specific time which following the designed experiments (Table 2) and the adsorption experiments were carried out based on central composite design (CCD). The MWCNTs then was filtered using vacuum filter, and the filtrate solution was analyzed to UV-Vis spectrophotometer to determine the final concentration of the dye.

Central Composite Design

A central composite design (2^5) was used to evaluate the implication and influence of variables toward the removal of dye by MWCNTs. The efficiency of malachite green adsorption by MWCNTs was observed by different experimental factors, namely mass of adsorbent, initial concentration of dye, pH of solution, contact time and agitation speed (Table 1). A total of 54 experiments were designed by using Minitab Software version 17 (Minitab Inc., State College, USA). The mathematical relationship between the factors can be approximated by the second order polynomial model as expressed in Eq. 1 [23]:

$$y = \beta_0 + \sum_{i=1}^{5} \beta_i x_i + \sum_{i=1}^{5} \sum_{j=1}^{5} \beta_{ij} x_i x_j + \sum_{i=1}^{5} \beta_{ii} x_i^2 \quad (1)$$

where y is the predicted response (percentage of removal); x_i's are the input variables (mass of adsorbent, initial concentration of dye, pH of solution, contact time and agitation speed) that are known for each experimental run. The parameter β_0 is the model constant; β_i is the linear coefficient; β_{ii} is the quadratic coefficient and β_{ij} is the cross-product coefficient. Generally, CCD consists of three operations which are $2n$ axial run, 2^n factorial run and central run. The CCD in present research is designed based on carrying out 12 axial points, 32 factorial point and 12 replicates at the center (54 experiments) as listed in Table 2. Total of experiments can be calculated by Eq. 2 below:

$$\text{Total number of experiments} = 2n + 2^n + n_c \quad (2)$$

where n is the number of factors, n_c is the number of center points [24].

Table 1. Experimental factors and levels in the CCD

Factors	Levels			Star point $\alpha = \pm 2.00$	
	Low (-1)	Central (0)	High (+1)	-α	+α
(X_1) Mass of adsorbent (g)	0.04	0.06	0.08	0.02	0.10
(X_2) Initial concentration of MG (ppm)	40	60	80	20	100
(X_3) pH of solution	5.5	7	8.5	4	10
(X_4) Contact time (min)	15	20	25	10	30
(X_5) Agitation speed (stroke/min)	60	90	120	30	150

Analysis of variance (ANOVA) was also performed to discriminate the significance of the variables. Interaction between latent experimental factors was visualized using surface plot graph.

Measurement of Dye Concentration

The malachite green removal for each experiment was calculated using the following Eq. 3 [25]:

$$\%\ \text{MG removal} = \frac{(C_0 - C_t)}{C_0} \times 100 \quad (3)$$

where C_0 (mg/L) is the initial concentration of dye, C_t (mg/L) is the concentration at time t. The amount of adsorbed malachite green, Q_e (mg/g) was calculated by using the following Eq. 4 [26]:

$$Q_e = \frac{(C_0 - C_e)V}{m} \quad (4)$$

where C_0 and C_e (mg/L) are the initial dye concentrations and equilibrium dye concentrations in aqueous solution respectively, V (L) is volume of the solution and m (g) is mass of the adsorbent.

Isotherm and Kinetic Study

In identifying the isotherm and kinetics of MG adsorption by MWCNTs, adsorption experiments were performed in 250-mL conical flask with 100 mL of MG solution. The initial concentration of MG was varied in a range from 20 to 60 ppm and the other parameters were kept constant for isotherm experiment. For kinetic study, a series of experiment was carried out with different contact times from adsorption while the others parameters were under optimized condition.

Results and Discussion

Optimization of Adsorption Condition

A total of 54 experiments were run according to the Central Composite Design and their responses are presented in Table 2.

Table 2. Runs order of adsorption experiment by CCD

Runs	X_1	X_2	X_3	X_4	X_5	Removal (%)
1	-1	-1	-1	-1	-1	21.97
2	1	1	-1	-1	-1	53.95
3	1	-1	1	-1	-1	81.57
4	-1	1	1	-1	-1	32.99
5	1	-1	-1	1	-1	80.19
6	-1	1	-1	1	-1	39.58
7	-1	-1	1	1	-1	78.22
8	1	1	1	1	-1	71.34
9	1	-1	-1	-1	1	99.49
10	-1	1	-1	-1	1	52.80
11	-1	-1	1	-1	1	63.05
12	1	1	1	-1	1	96.39
13	-1	-1	-1	1	1	79.44
14	1	1	-1	1	1	88.42
15	1	-1	1	1	1	100.00
16	-1	1	1	1	1	68.30
17	0	0	0	0	0	66.36
18	0	0	0	0	0	67.28
19	0	0	0	0	0	69.19
20	0	0	0	0	0	67.97
21	1	-1	-1	-1	-1	57.83
22	-1	1	-1	-1	-1	36.90
23	-1	-1	1	-1	-1	53.22
24	1	1	1	-1	-1	86.48
25	-1	-1	-1	1	-1	37.11
26	1	1	-1	1	-1	51.75
27	1	-1	1	1	-1	94.83
28	-1	1	1	1	-1	44.26
29	-1	-1	-1	-1	1	65.47
30	1	1	-1	-1	1	80.85
31	1	-1	1	-1	1	100.00
32	-1	1	1	-1	1	63.13
33	1	-1	-1	1	1	99.49
34	-1	1	-1	1	1	70.09
35	-1	-1	1	1	1	92.63
36	1	1	1	1	1	97.24
37	0	0	0	0	0	70.45
38	0	0	0	0	0	72.09
39	0	0	0	0	0	63.62
40	0	0	0	0	0	76.53
41	-2	0	0	0	0	17.25
42	2	0	0	0	0	80.87
43	0	-2	0	0	0	90.49
44	0	2	0	0	0	72.75
45	0	0	-2	0	0	64.28
46	0	0	2	0	0	96.99
47	0	0	0	-2	0	50.19
48	0	0	0	2	0	60.30
49	0	0	0	0	-2	48.64
50	0	0	0	0	2	88.73

Table 3 (cont'd). Runs order of adsorption experiment by CCD

Runs	X_1	X_2	X_3	X_4	X_5	Removal (%)
51	0	0	0	0	0	62.44
52	0	0	0	0	0	68.08
53	0	0	0	0	0	73.59
54	0	0	0	0	0	73.52

An empirical relationship between the response and independent variables was obtained based on results and expressed by the following second-order polynomial Eq. 5:

$$Y = 69.18+14.04X_1 - 4.98X_2+6.99X_3+4.02X_4+12.03X_5 - 4.32X_1^2 +3.81X_2^2+3.57X_3^2 - 2.79X_4^2 - 2.74X_1X_4 - 3.04X_2X_4 -3.52X_3X_5 \quad (5)$$

where Y is the percentage of MG removal, X_1 is mass of adsorbent, X_2 is the initial concentration of MG, X_3 is pH of solution, X_4 is contact time and X_5 is agitation speed. In this equation, only variable X_2 showed negative linearity, whereas the other factors showed positive linearity of the fitted model.

Table 4. Descriptive statistic of ANOVA test for CCD of MG removal by MWCNTs

Source of variation	Degree of freedom	Sum of square	Mean square	*F*-Value	*p*-Value
Model	12	19912.0	1659.34	40.15	**0.001**
Linear					
X_1	1	7880.9	7880.93	190.67	**0.001**
X_2	1	992.8	992.79	24.02	**0.001**
X_3	1	1952.8	1952.76	47.25	**0.001**
X_4	1	646.2	646.22	15.63	**0.001**
X_5	1	5784.9	5784.89	139.96	**0.001**
Square					
X_1*X_1	1	634.8	634.85	15.36	**0.001**
X_2*X_2	1	493.9	493.91	11.95	**0.001**
X_3*X_3	1	432.1	432.06	10.45	**0.002**
X_4*X_4	1	264.5	264.49	6.40	**0.015**
2-Way Interaction					
X_1*X_4	1	240.0	285.19	5.81	**0.021**
X_2*X_4	1	296.4	700.10	7.17	**0.011**
X_3*X_5	1	396.9	261.12	9.60	**0.004**
Error					
Lack-of-Fit	32	1519.5	47.49	2.44	0.079
Pure Error	9	175.1	19.45		
Total SS	53	21606.6			

*Bold value is significant $p<0.05$

To analyze the significance of each variable, analysis of variance (ANOVA) is necessary. ANOVA subdivides the total variation into two parts; variation associated with the model and the variation associated with the experimental error. These will show whether the variation from the model is significant or not when compared to the ones associated with the residual error [27]. To carry out this comparison, the *F*-values were used by calculating the ratio between mean square of the model and the residual error. Meanwhile, the *p*-values were used to check the statistical significance of each coefficient, which in turn is necessary to understand the pattern of the mutual interactions between the test variables. A *p*-value of less than 0.05 in the ANOVA table indicates the statistical significance of an effect at 95% confidence level. The test of significance of regression model for response was evaluated and the result of ANOVA is presented in Table 3.

In this study, all individual experimental factors were significant with p-value<0.05. The p-value of lack-of-fit shows a non-significant value (0.079) which confirms the suitability of the model with the data and the model is significant [24]. The value R^2 predicted is used to measure the how the model fits with the data. A good agreement was shown by the coefficient of determination between R^2 (0.922) and R^2 adjusted (0.899) from the fitted model. In addition to correlation coefficient, the data were also evaluated based on the plots of residual (difference between the observed and the predicted response value).

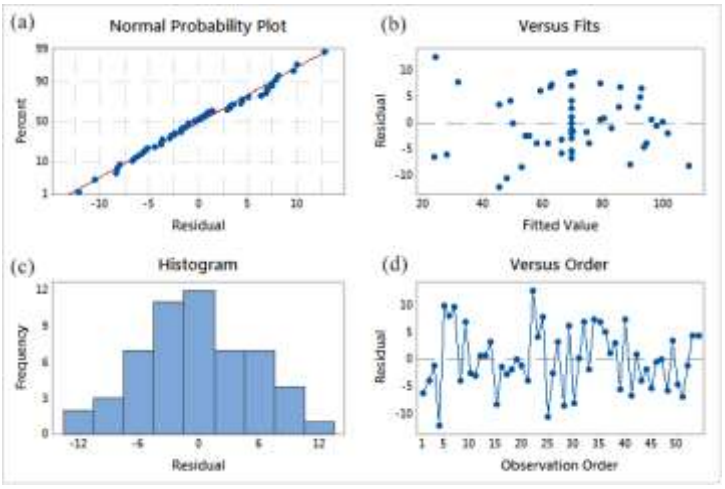


Figure 1. Residual plot for the removal of MG by MWCNTs (a) percentage of removal vs. residual, (b) residual vs. fitted value, (c) frequency vs. residual, (d) residual vs. observation order

Normal probability in Fig. 1(a) plot showed the data followed the straight line, which indicated there is normal distribution and no evidence of non-normality, skewness, outliers or undefined variables. Residuals versus fitted graph (Fig. 1(b)) can explain the consistency of the variance in errors, whereas the residual versus observation order (Fig. 1(c)) is useful in identifying the effect of observation order in inducing the results when the data were collected in a different time sequence. For residual versus fitted graph and residual versus observation order graph in Fig. 1 (d), both of the graphs in this study showed the residuals randomly scattered about zero, thus signified that residuals have constant variance in error terms and data were not affected by the observation order respectively.

The curvature nature of Fig. 2 shows the response surface plots of the removal of MG by MWCNTs confirming strong interaction among latent variables. Fig. 2 (a) and 2 (d) shows the interaction of adsorbent dosage with contact time and agitation speed respectively, in influencing the removal of MG. The increase in percentage of MG removal was observed with the increase amount of adsorbent dosage. As the mass of adsorbent increasing, there are more sites and specific area for adsorption, in which provide more availability for the dye molecules to vacant on the surface of MWCNTs.

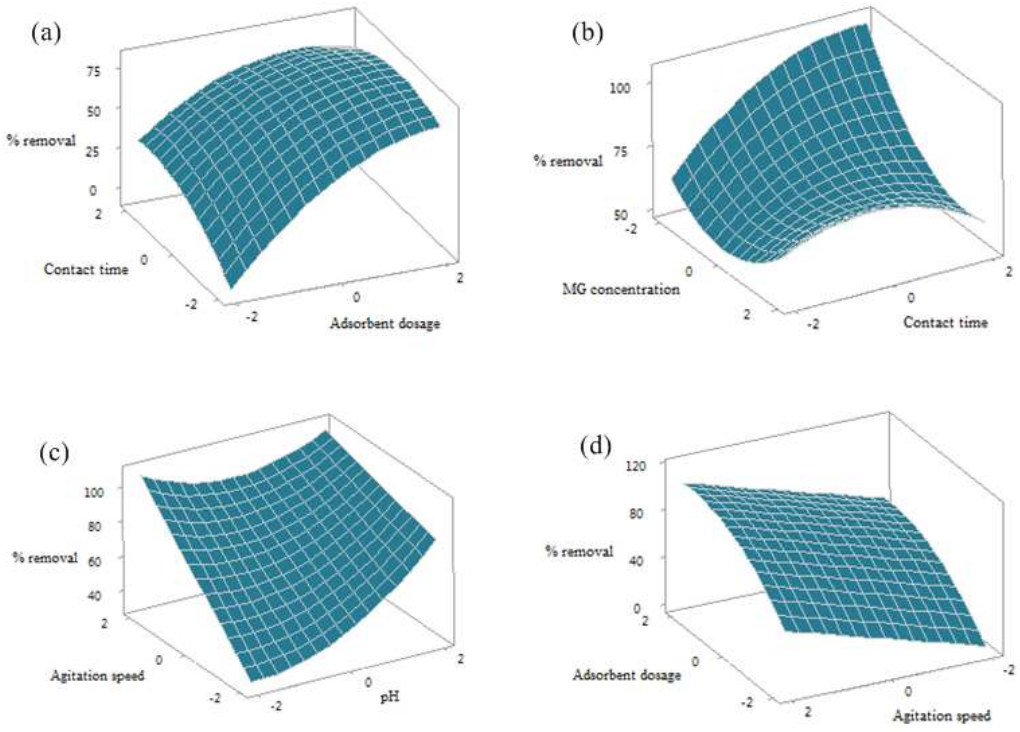


Figure 2. Surface plot for CCD: (a) contact time-adsorbent dosage; (b) initial concentration MG-contact time; (c) agitation speed-pH; (d) adsorbent dosage-agitation speed

The response surface plots shown in Fig. 2 (b) demonstrate the changes in the percentage removal for MG initial with initial MG concentration-contact time interaction. It can be seen that the percentage of MG removal decreased when the concentration of MG increased. At lower dye concentrations, the ratio of solute concentration to adsorbent sites is lower, which increases the rate of dye uptake. However, the yield of adsorption of MG by the MWCNT decrease at higher concentration since there is no vacancy for the adsorption dye on the adsorbent as the adsorbent sites were saturated with dye molecules.

The pH of the system plays important roles in affecting the ability of adsorbent surface for the interaction and dye molecule tendency for binding solid surface [28]. Surface plot in Fig. 2 (c) shows the percentage of MG removal with interaction of pH with agitation speed. The removal of dye was more favourable at higher pH compared to lower pH. This result can be clarified by the fact that at lower pH, the presence of excess H+ ions was competing with MG molecules as a cationic dye to be adsorbed on the surface of MWCNTs. However, on basic condition, the surface of the MWCNTs was enhanced with negatively charge sites and the electrostatic attraction exists between cationic dye molecules and adsorbent site [29]. The effect of contact time was illustrated by the graph in Fig. 2 (a) and 2 (b). Generally, both of surface plot show the removal of MG was increased as the contact time increased, and gradually reaching equilibrium. This is due to a lot of specific surface areas available at initial time, causing the rapid adsorption rate between MG molecules and MWCNTs. However, as the vacancies on the surface of MWCNTs were filled with MG molecules, the adsorption process becomes slower and reached equilibrium.

Another important parameter influencing the rate of adsorption is the speed of agitation. A range of agitation speed from 30 to 150 strokes/min has been studied in the adsorption experiments. As shown in surface plot in Fig. 2 (c) and 2 (d), the percentage of MG removal increased directly with increase of agitation speed. The boundary layer exists between adsorbent particles and solution decreasing as the speed of agitation increasing which results in the

higher of dye uptake by MWCNT. Besides, high agitation speed also increases the distribution of adsorbent in solution [29].

The profile for desirable option with predicted values in the Minitab software was used for the selection of optimum conditions of the dye removal. The profile of desirable responses was chosen after specifying the desirability function (DF) for each dependent variable (removal percentage) by assigning predicted values. The scale in the range from 0.0 (undesirable) to 1.0 (very desirable) was used to achieve a global function (D) that should be maximized to obtain 100% removal by optimizing designed variables. Based on the desirability score of 1.0, maximum removal (99.9%) was achieved at suggested optimum conditions set as: 0.03 g of adsorbent, initial MG concentration of 20 ppm, pH solution of 7, with equilibrium time of 17 minutes and agitation at speed 150 strokes per minute. Three additional experiments were carried out under the optimal conditions, in which a good agreement between the calculated and experimental responses was obtained (99.9 % removal) with 2.17% of RSD value.

Adsorption Isotherm Study

Basically, isotherm analysis was performed to understand the relationship between adsorbate and the surface of adsorbent when the equilibrium is achieved. It gives useful information about mechanism, properties and tendency of adsorbate being adsorbed by the adsorbent. In this study, the data obtained during the equilibrium study were fitted to both Langmuir and Freundlich isotherm models, as a way to evaluate the equilibrium characteristics of the adsorption process.

The most basic of isotherm model was Langmuir isotherm, which assumed that there is no interaction between the adsorbate molecules and the adsorption localized in a monolayer [30]. Langmuir isotherm is expressed by the following Eq. 6:

$$\frac{C_e}{Q_e} = \frac{1}{(K_a Q_m)} + \frac{C_e}{Q_m} \tag{6}$$

where C_e is the concentration of MG at equilibrium (mg L^{-1}); Q_e is the amount of dye adsorbed per mass of MWCNTs (mg g^{-1}); K_L represents the Langmuir constant (L mg^{-1}); and Qm is the theoretical saturation capacity of the monolayer (mg g^{-1}) [23]. The values of Q_m and K_L were calculated from the intercept and slope of the linear plot of C_e/Q_e versus C_e.

The Freundlich model is an empirical equation that assumes heterogeneous adsorption due to the diversity of adsorption sites. The Freundlich isotherm is represented by Eq. 7 below:

$$\ln Q_e = \ln K_F + \frac{1}{n} \ln C_e \tag{7}$$

where Q_e is the amount of dye adsorbed per mass of MWCNTs (mg g^{-1}); C_e is the concentration of MG at equilibrium (mg L^{-1}); K_F (L mg^{-1}) and n are Freundlich constant, which represents the adsorption capacity and the adsorption strength respectively [23]. K_F and 1/n were obtained from the intercept and slope of the linear plot of ln Q_e versus ln C_e. Table 4 summarizes the coefficient of the Langmuir and Freundlich isotherms obtained in this study.

By comparing both Langmuir and Freundlich models, it can be seen clearly that the R^2 values of both models exceeded 0.9, suggesting experimental results fitted well in both of the models. However, as R^2 of Langmuir comparatively higher than Freundlich model, it can be demonstrated that the adsorption is much favourable with Langmuir model. This can be assumed that adsorbed MG molecules formed monolayer coverage on the surface of MWCNTs, and all the adsorption sites.

Table 5. Linear regression of isotherm adsorption and its constant parameter

Isotherm	Linear Regression	Parameter	Value of parameter
Langmuir	y = 0.0089x + 0.0117	Q_m (mg/g)	112.360
		K_a (L/mg)	0.761
		R^2	0.998
Freundlich	y = 0.1198x + 4.2967	*1/n*	0.120
		K_F (L mg/g)	73.457
		R^2	0.933

Another important parameter is separation factor, R_L which is a dimensionless constant that evaluates whether the adsorption is favourable or unfavourable. The R_L equation is represented as follows (Eq. 8):

$$R_L = \frac{1}{(1+K_i C_0)} \quad (8)$$

where K_L is the Langmuir constant (mg L^{-1}) and C_0 is the initial concentration of MG. The value of R_L indicates the type of isotherm to be unfavourable ($R_L > 1$), linear ($R_L = 1$), favourable ($0 < R_L < 1$) or irreversible ($R_L = 0$) [31]. All the values of R_L ranged between 0 and 1 (shown in Fig. 3), denoting that the adsorption of MG onto MWCNTs was favourable. In addition, the R_L values decreased as the initial concentration of MG increased, suggesting that the adsorption process was more favourable at higher concentration [32].

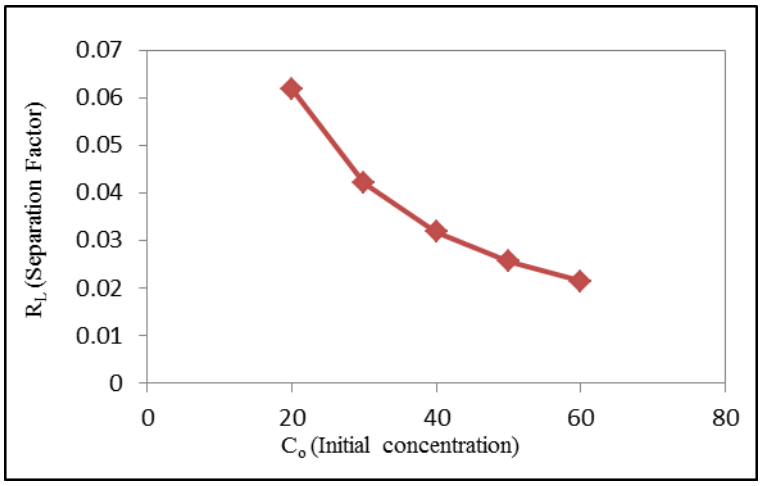


Figure 3. Separation factor, R_L versus initial concentration of MG, C_0 for adsorption of MG by MWCNTs

Adsorption Kinetic Study

Adsorption is a physicochemical process that involves mass transfer of solute from the solution to the surface of the adsorbent [33]. An ideal adsorption is not only having high adsorption capacity, but it also must have high rate of adsorption. Kinetic analysis does not only depict the adsorption rate of the adsorbent but also can provide important information about the mechanism of adsorption on the adsorbent. To elucidate the kinetic properties of the adsorption process of MG on MWCNTs, three most widely use kinetic models were applied, which are the pseudo-first-order, pseudo-second-order and intraparticle diffusion model.

Generally, the pseudo-first-order model is used in explaining the adsorption rate based on the adsorption capacity. The equation of pseudo-first-order is expressed as Eq. 9 below:

$$\log(Q_e - Q_t) = \log Q_e - \frac{k_1 t}{2.303} \quad (9)$$

where Q_e and Q_t are the amount of MG adsorbed per mass of MWCNTs (mg g^{-1}) at equilibrium and time t (min) respectively, and k_1 (min^{-1}) is rate constant of pseudo-first-order model for the adsorption [23]. Values of k_1 and Q_e of pseudo-first-order were obtained from the slope and intercept of plot log ($Q_e - Q_t$) versus t.

For pseudo-second-order, the equation is given as Eq. 10 below:

$$\frac{t}{Q_t} = \frac{1}{k_2 Q_e^2} + \frac{t}{Q_e} \quad (10)$$

where Q_e and Q_t are the amount of dye adsorbed per mass of MWCNTs (mg/g) at equilibrium and time t (min) respectively, and k_2 (g mg^{-1} min^{-1}) is rate constant for pseudo-second-order model of adsorption [23]. For values of k_2 and Q_e of pseudo-second-order, both of the values were obtained from the slope and intercept of plot (t/Q_t) versus t, respectively.

However, pseudo-first-order and pseudo-second-order have their own limitation as both of the models cannot identify the diffusion mechanism of adsorption. Generally, bulk diffusion and adsorption are assumed to be rapid and not rate-determining [31]. Therefore, the kinetic data were also analyzed using the intraparticle diffusion model in describing the diffusion mechanism. This is important in considering the diffusion mechanism between MG molecules and MWCNTs as MWCNTs have porous structure. The intraparticle diffusion model equation is given by Eq. 11 below:

$$Q_t = K_{diff} t^{1/2} + C \quad (11)$$

where k_{diff} is intraparticle diffusion rate constant (mg/g $min^{1/2}$) and C is the intercept. The value of k_{diff} and C value of intraparticle diffusion were obtained from the slope and intercept of plot Q_t versus $t^{1/2}$ [23]. The data from adsorption of MG by MWCNTs at mass of 0.03g were examined and experimental data are presented in Table 5. The best-fit model was selected based on the linear regression correlation coefficient values (R^2).

Table 6. Linear regression of kinetic adsorption and its constant parameter

Model	**Linear regression**	**Parameter**	**Value of parameter**
Pseudo first-order	y = -0.0235x + 1.7648	k_1	0.054
		Q_e (calc)	58.184
		Q_e (exp)	85.700
		R^2	0.916
Pseudo second-order	y = 0.0114x + 0.0746	k_2	0.0017
		Q_e (calc)	87.719
		Q_e (exp)	85.700
		R^2	0.978
Intraparticle diffusion	y = 11.093x + 16.136	k_{diff}	11.093
		C	16.136
		R^2	0.928

Table 5 presents the kinetic parameter for the adsorption of MG by MWCNTs. Both of R^2 values of pseudo-first-order and pseudo-second-order have a good correlation coefficient; however, pseudo-second-order showed a better result as pseudo-second-order has higher R^2 (0.978) compared to pseudo-first-order (0.916). In addition, the value of Q_e (calc) derived from pseudo-second-order is comparatively much closer to Q_e (exp).

For intraparticle diffusion model, the plot of Q_t versus $t^{1/2}$ should give a linear plot if intraparticle diffusion participated in the adsorption and the intraparticle diffusion is the only rate-controlling step if the line of linear regression passes through the origin [34]. Otherwise, there are other mechanisms that also contributed to intraparticle diffusion. The *C* value of intraparticle diffusion is also helpful in boundary thickness; a larger *C* corresponds to a greater boundary layer diffusion effect [31]. Besides, the larger value of the intercept also shows the greater surface adsorption that contributes to the rate-controlling step [33]. The regression (Q_t versus $t^{1/2}$) of MG removal by MWCNTs showed a linear plot; however, the line did not pass through the origin. This indicates that the adsorption involved in intraparticle diffusion was not only rate-controlling step [34].

Conclusion

The present study showed that the MG dye from aqueous solution was successfully removed by MWCNTs and the adsorption condition was efficiently optimized by applying central composite design. The adsorption MG by MWCNT achieved optimum removal in equilibrium time of 17 minutes with 20 ppm of initial dye concentration, 0.03g of mass of MWCNT, pH 7 and agitation speed of 150 strokes/min. Analysis of variance also showed a good coefficient of determination (R^2 = 0.922), ensuring that the model was well-fitted. Central composite design successfully proved the significance of all the experimental factors which affect the rate of the adsorption. The isotherm and kinetic of adsorption were also investigated. For the isotherm model, both Langmuir and Freundlich models were fitted with experimental equilibrium data but the results showed the Langmuir model (R^2=0.998) is best fitted for the concentration range studied. The maximum adsorption capacity of MWCNTs for MG dye was 112.36 mg g^{-1}. The experimental data depicted that the adsorption kinetic of MG by MWCNTs was controlled by pseudo-second-order kinetic model (R^2 =0.978) with rate constant calculated at 0.0017 g mg^{-1} min^{-1}.

Acknowledgement

The authors express their appreciation to Centre for Water Research and Analysis staffs for providing facilities during this study.

References

1. Buthelezi, S.P., Olaniran, A.O., and Pillay, B. (2012). Textile dye removal from wastewater effluents using bioflocculants produced by indigenous bacterial isolates. *Molecules*, 17(12): 14260 - 14274.
2. Sudova, E., Machova, J., Svobodova, Z., and Vesely, T. (2007). Negative effects of malachite green and possibilities of its replacement in the treatment of fish eggs and fish: A review. *Veterinarni Medicina*, 52(12): 527–539.
3. Culp, S. and Beland, F. (1996). Malachite green: A toxicological review. *International Journal of Toxicology*, 15(3): 219-238.
4. Srivastava, S., Sinha, R., and Roy, D. (2004). Toxicological effects of malachite green. *Aquatic Toxicology*, 66(3): 319-329.
5. Culp, S.J., Mellick, P.W., Trotter, R.W., Greenlees, K.J., Kodell, R.L., and Beland, F.A. (2006). Carcinogenicity of malachite green chloride and leucomalachite green in B6C3F1 mice and F344 rats. *Food and Chemical Toxicology*, 44(8): 1204-1212.
6. Hidayah, N., Abu Bakar, F., Nur-Azura, M.S., Mahyudin, N.A., Zaman, M.Z., and Faridah, S. (2013). Detection of malachite green and leuco-malachite green in fishery industry. *International Food Research Journal*, 20(4): 1511-1519.
7. Mitrowska, K., Posyniak, A., and Zmudzki, J. (2007). The effects of cooking on residues of malachite green and leucomalachite green in carp muscles. *Analytica Chimica Acta*, 586(1-2): 420-425.
8. Cho, B.P., Yang, T., Blankenship, L.R., Moody, J.D., Churchwell, M., Beland, F.A., and Culp, S.J. (2003). Synthesis and characterization of N-Demethylated metabolites of malachite green and leucomalachite green. *Chemical Research in Toxicology*, 16(3): 285-294.

9. Derakhshan, M.S. and Moradi, O. (2014). The study of thermodynamics and kinetics methyl orange and malachite green by SWCNTs, SWCNT-COOH and SWCNT-NH_2 as adsorbents from aqueous solution. *Journal of Industrial and Engineering Chemistry*, 20(5): 3186-3194.
10. Madrakian, T., Afkhami, A., Ahmadi, M., and Bagheri, H. (2011). Removal of some cationic dyes from aqueous solutions using magnetic-modified multi-walled carbon nanotubes. *Journal of Hazardous Materials*, 196: 109-114.
11. Aksu, Z. (2005). Application of biosorption for the removal of organic pollutants: A review. *Process Biochemistry*, 40(3-4): 997-1026.
12. Robinson, T., McMullan, G., Marchant, R., and Nigam, P. (2001). Remediation of dyes in textile effluent: A critical on current treatment technologies with a propose alternative. *Bioresource Technology*, 77: 247-255.
13. Wu, C.H. (2007). Adsorption of reactive dye onto carbon nanotubes: Equilibrium, kinetics and thermodynamics. *Journal of Hazardous Materials*, 144(1-2): 93-100.
14. Ren, X., Chen, C., Nagatsu, M., and Wang, X. (2011). Carbon nanotubes as adsorbents in environmental pollution management: A review. *Chemical Engineering Journal*, 170(2-3): 395-410.
15. Gupta, V.K., Kumar, R., Nayak, A., Saleh, T.A., and Barakat, M.A. (2013). Adsorptive removal of dyes from aqueous solution onto carbon nanotubes: A review. *Advances in Colloid and Interface Science*, 193-194: 24-34.
16. Gupta, V.K., Agarwal, S., and Saleh, T.A. (2011). Chromium removal by combining the magnetic properties of iron oxide with adsorption properties of carbon nanotubes. *Water Research*, 45(6): 2207-2212.
17. Li, Y.H., Ding, J., Luan, Z., Di, Z., Zhu, Y., Xu, C., Wu, D., and Wei, B. (2003). Competitive adsorption of Pb^{2+}, Cu^{2+} and Cd^{2+} ions from aqueous solutions by multiwalled carbon nanotubes. *Carbon*, 41(14): 2787-2792.
18. Clément, P., Hafaiedh, I., Parra, E.J., Thamri, A., Guillot, J., Abdelghani, A., and Llobet, E. (2014). Iron oxide and oxygen plasma functionalized multi-walled carbon nanotubes for the discrimination of volatile organic compounds. *Carbon*, 78: 510-520.
19. Kerkez, Ö. and Bayazit, Ş.S. (2014). Magnetite decorated multi-walled carbon nanotubes for removal of toxic dyes from aqueous solutions. *Journal of Nanoparticle Research*, 16(6): 1-11.
20. Yao, Y., Xu, F., Chen, M., Xu, Z., and Zhu, Z. (2010). Adsorption behavior of methylene blue on carbon nanotubes. *Bioresource Technology*, 101(9): 3040-3046.
21. Bezerra, M.A., Santelli, R.E., Oliveira, E.P., Villar, L.S., and Escaleira, L.A. (2008). Response surface methodology (RSM) as a tool for optimization in analytical chemistry. *Talanta*, 76(5): 965-977.
22. Ravikumar, K., Deebika, B., and Balu, K. (2005). Decolourization of aqueous dye solutions by a novel adsorbent: Application of statistical designs and surface plots for the optimization and regression analysis. *Journal of Hazardous Materials*, 122(1-2): 75-83.
23. Roosta, M., Ghaedi, M., Shokri, N., Daneshfar, A., Sahraei, R., and Asghari, A. (2014). Optimization of the combined ultrasonic assisted/adsorption method for the removal of malachite green by gold nanoparticles loaded on activated carbon: experimental design. *Spectrochimica Acta Part A: Molecular and Biomolecular Spectroscopy*, 118: 55-65.
24. Ghaedi, M., Mazaheri, H., Khodadoust, S., Hajati, S., and Purkait, M.K. (2015). Application of central composite design for simultaneous removal of methylene blue and Pb^{2+} ions by walnut wood activated carbon. *Spectrochimica Acta Part A: Molecular and Biomolecular Spectroscopy*, 135: 479-490.
25. Roosta, M., Ghaedi, M., Daneshfar, A., Darafarin, S., Sahraei, R., and Purkait, M.K. (2014). Simultaneous ultrasound-assisted removal of sunset yellow and erythrosine by ZnS:Ni nanoparticles loaded on activated carbon: Optimization by central composite design. *Ultrasonic Sonochemistry*, 21(4): 1441-1450.
26. Ghaedi, M. and Mosallanejad, N. (2014). Study of competitive adsorption of malachite green and sunset yellow dyes on cadmium hydroxide nanowires loaded on activated carbon. *Journal of Industrial and Engineering Chemistry*, 20(3): 1085-1096.
27. Khataee, A.R., Fathinia, M., Aber, S., and Zarei, M. (2010). Optimization of photocatalytic treatment of dye solution on supported TiO2 nanoparticles by central composite design: Intermediates identification. *Journal of Hazardous Materials*, 181(1-3): 886-897.
28. Ghaedi, M., Ansari, A., Habibi, M.H., and Asghari, A.R. (2014). Removal of malachite green from aqueous solution by zinc oxide nanoparticle loaded on activated carbon: Kinetics and isotherm study. *Journal of Industrial and Engineering Chemistry*, 20(1): 17-28.

29. Shirmardi, M., Mahvi, A.H., Hashemzadeh, B., Naeimabadi, A., Hassani, G., and Niri, M.V. (2013). The adsorption of malachite green (MG) as a cationic dye onto functionalized multi walled carbon nanotubes. *Korean Journal of Chemical Engineering*, 30(8): 1603-1608.
30. Gholizadeh, A., Kermani, M., Gholami, M., Farzadkia, M., and Yaghmaeian, K. (2013). Removal efficiency, adsorption kinetics and isotherms of phenolic compounds from aqueous solution using rice bran ash. *Asian Journal of Chemistry*, 25(7): 3871-3878.
31. Farghali, A.A., Bahgat, M., ElRouby, W.M.A., and Khedr, M.H. (2013). Decoration of multi-walled carbon nanotubes (MWCNTs) with different ferrite nanoparticles and its use as an adsorbent. *Journal of Nanostructure in Chemistry*, 3(50): 1-12.
32. Tang, W.W., Zeng, G.M., Gong, J.L., Liu, Y., Wang, X.Y., Liu, Y.Y., Liu, Z.F., Chen, L., Zhang, X.R., and Tu, D.Z. (2012). Simultaneous adsorption of atrazine and Cu (II) from wastewater by magnetic multi-walled carbon nanotube. *Chemical Engineering Journal*, 211-212: 470-478.
33. Bahgat, M., Farghali, A.A., El Rouby, W., Khedr, M., and Mohassab-Ahmed, M.Y. (2012). Adsorption of methyl green dye onto multi-walled carbon nanotubes decorated with Ni nanoferrite. *Applied Nanoscience*, 3(3): 251-261.
34. Khani, M.H. (2011). Uranium biosorption by *Padina* sp. algae biomass: Kinetics and thermodynamics. *Environmental Science Pollution Research*, 18(9): 1593-1605.

MALAYSIAN JOURNAL OF ANALYTICAL SCIENCES
Published by The Malaysian Analytical Sciences Society
ISSN 1394 - 2506

UTILIZATION OF ENCAPSULATED $CACO_3$ IN LIQUID CORE CAPSULES FOR IMPROVING LACTIC ACID FERMENTATION

(Penggunaan Kapsul Berteras Cecair yang Mengandungi $CaCO_3$ untuk Menambah Baik Penapaian Bakteria Asid Laktik)

Boon-Beng Lee *and Nurul Ainina Zulkifli

School of Bioprocess Engineering,
Universiti Malaysia Perlis (UniMAP),
Kompleks Pusat Pengajian Jejawi 3, 02600 Arau, Perlis, Malaysia

**Corresponding author: bblee@unimap.edu.my*

Received: 9 December 2014; Accepted: 9 October 2015

Abstract

Lactic acid bacteria (LAB) have been used for food fermentation due to its fermentative ability to improve and enhance the quality of the end food products. However, the performance of LAB is affected as fermentation time elapsed because the microbial growth is inhibited by its end product, i.e. lactic acid. In this study, a new approach was introduced to reduce the product inhibition effect using $CaCO_3$ which is encapsulated in spherical liquid core capsules of diameter 3.5mm and 3.6 mm produced through extrusion dripping method. The results showed that the pH and lactic acid concentration of LAB fermentation was well maintained by the capsules. The results of the fermentation conducted to control pH and lactic acid concentration using the capsules were better than those of the control set and comparable with that of the free $CaCO_3$ set. In addition, the viable cell concentration of *L. casei shirota* was high at the end of fermentation when the fermentation was conducted using the capsules. The results of this study suggested that the capsules have high potential to be applied for pH and lactic acid level control in LAB fermentation for various productions.

Keywords: calcium carbonate, lactic acid bacteria fermentation, liquid core capsule, pH

Abstrak

Bakteria asid laktik (LAB) telah banyak digunakan untuk penapaian makanan disebabkan oleh keupayaannya untuk meningkatkan dan memperkayakan kualiti produk makanan yang dihasilkan melalui penapaian. Namun, prestasi LAB adalah dipengaruhi oleh hasil penapaian iaitu asid laktik kerana pertumbahan mikrob terencat. Dalam kajian ini, satu kaedah baru diperkenalkan untuk mengurangkan kesan perencatan dengan mengapsulkan $CaCO_3$ di dalam kapsul berteras cecair yang berbentuk sfera dan berdiameter 3.5 mm dan 3.6 mm yang dihasilkan dengan menggunakan kaedah penitisan-penyemperitan. Hasil kajian menunjukkan pH dan kepekatan asid laktik semasa penapaian LAB telah dikawal dengan baik oleh kapsul – kapsul yang dihasilkan. Keputusan kajian yang dijalankan dengan menggunakan kapsul – kapsul untuk mengawal pH dan kepekatan asid laktik adalah lebih baik daripada keputusan kajian yang dijalankan dengan set kawalan, dan setanding dengan set yang menggunakan tanpa $CaCO_3$. Tambahan pula, kepekatan sel hidup bagi *L. casei shirota* adalah tinggi pada akhir penapaian apabila penapaian dijalankan dengan menggunakan kapsul – kapsul. Keputusan daripada kajian ini mencadangkan bahawa kapsul – kapsul yang dihasilkan menpunyai potensi yang tinggi untuk digunakan sebagai kawalan pH dan kepekatan asid laktik dalam pelbagai jenis pengeluaran.

Kata kunci: kalsium karbonat, penapaian bakteria asid laktik, kapsul berteras cecair, pH

Introduction

Lactic acid bacteria (LAB) are one of the microbes used in traditional food fermentation. LAB has been used for the fermentation of dairy and non-dairy products [1, 2]. For example, yogurt, cultured milk, cheese are dairy products that produced from LAB fermentation [2]. LAB is reported to play an important role in a number of Asian fermented non-dairy products such as '*tempoyak*' (acid fermented condiment) [3], "*tapai*" (rice wine) [4], '*kimchi'* (fermented vegetables) [1], "*idli*" in India, "*puto*" in Philippines (steamed bread) [1], "*sikhae*" in Korea and "*burong isda/dalag*" in Philippine (fermented mixture of salted fish and cereals) [1].

LAB has been recognised for their fermentative ability to enhance food safety and nutrients, improve organoleptic quality, as well as increase health related benefits [1, 4]. However, the role of LAB in food fermentation is diminished by the production of its end products, i.e. lactic acid [5, 6]. As the fermentation time elapsed, the concentration of lactic acid in the fermentation broth increased and hence the pH of the broth is consequently increased [5].

In common practice, calcium carbonate or advance instrument like pH controller is used to control the concentration of lactic acid and pH in the fermentation broth. However, the direct addition of calcium carbonate in the fermentation broth is not favorable for the subsequent purification process, and the use of pH controller is limited due to high cost. Therefore, in this research, it is proposed to develop a new approach to control pH during LAB fermentation using liquid core capsules. Liquid core capsules are easy to form at low cost.

Materials and Methods

Liquid core solution and gelation bath preparation

The inner liquid-core solution was prepared by adding 15 g/L of calcium chloride (CaCl2) (R&M Chemical, United Kingdom), 400 g/L of calcium carbonate ($CaCO_3$) (HmbG Chemical, France) and 15 g/L of carboxylmethylcellulose (CMC) (Calbiochem, Germany). The mixture of 15 g/L of alginate (Kimitsu-Kimica, Japan) and 1.5 g/L of Tween-80 (Merck, Germany) was prepared as the gelation bath.

Liquid core capsules formation

Liquid-core capsules were prepared using the extrusion-dripping method. The liquid-core solution was extruded through a hypodermic needle (Terumo, Japan) into the gelation bath. In this study, the outer diameter of the needles used was 0.6 mm and 1.1 mm. After the capsules were formed, the capsules were cured in 5 g/L alginate solution for 1 hour to strengthen the capsules. Then the capsules were washed with distilled water and stored in 15 g/L $CaCl_2$ solution.

Capsule properties characterization

A digital camera (Coolpix S2600, Nikon, Japan) was used to capture the image of 30 capsules. The image was analysed using Sigma ScanPro5 software (SPSS, USA) to determine the diameter, maximum length (Dmax) and minimum length (Dmin) of capsules. The sphericity of the capsules was quantified in term of sphericity factor (SF) using the following equation 1 [7]:

$$SF = (Dmax-Dmin)/(Dmax + Dmin) \quad (1)$$

Lactic acid bacteria fermentation

Lactobacillus casei shirota was selected as the model strain for this study. For each fermentation run, four sets of fermentation flask were prepared. The flask was filled with the de Man, Rogosa and Sharpe (MRS) broth. In which, Flask I was labeled for blank broth as control; Flask II was labeled for the broth with addition of free $CaCO_3$; Flask III and IV was labeled for the broth with addition of two sizes of liquid core capsules that encapsulated $CaCO_3$.

All the experiments were conducted at temperature of about 37 ^oC. The pH of the fermentation broth was measured using a pH meter (Mettler Toledo, Switzerland) at an interval of 4 hours. The lactic acid and glucose content were measured by a reflectometer (Merck, Germany), as per described in the standard procedure [8].

Viable cell concentration determination

The total number of viable cells was determined by the plate counting on the de Man, Rogosa and Sharpe (MRS) agar (Oxoid, UK) incubated at 37°C for 48 hours.

Results and Discussion

Diameter and sphericity of capsules

Table 1 shows the diameter and SF of the liquid core capsules formed from needles with the diameter of 0.6 and 1.1 mm. The diameter of the capsules formed from 0.6 mm needle was smaller than that of capsules formed from 1.1 mm needle. The diameter of the capsule was proportional to the needle diameter because the diameter of the pendant droplet detached from the diameter was also proportional to the needle diameter [7, 9].

Table 1. Diameter and SF of the capsules

Needle diameter, mm	Diameter, mm	Sphericity factor (SF)
0.6	3.53 (±0.09)	0.0261 (±0.002)
1.1	3.62 (±0.04)	0.0648 (±0.006)

Note: The standard error of the measurements was shown in parentheses

The results showed that the capsules formed from the needles were generally spherical as the SF was less than 0.07. Although the capsules were formed using different diameter of needle, the capsules formed were spherical. This is because the capsules were formed from liquid core solution of sufficient viscosity and $CaCl_2$ concentration. The past studies showed that the addition of CMC in the liquid core solution increased the viscosity of the solution and consequently improved the sphericity of the capsules [10, 11]. In general, the concentration of $CaCl_2$ greater than 10 g/L is sufficient to form spherical ca-alginate particles [9]. In this study, the concentration of $CaCl_2$ of 15g/L was used, which is above the suggested critical concentration.

Effect of using encapsulated $CaCO_3$ in monitoring pH of fermentation process

Figure 1 shows the pH of the LAB fermentation broth for different experiment conditions. The pH of the broth in Flask I dropped from pH 5.4 to 3.5 after 40 hours of LAB fermentation, which was the greatest drop among the tested conditions. The results of the capsules (Flask III and Flask IV) were comparable to that of free $CaCO_3$ (Flask II). The pH of the broth was maintained above pH 5.5. Previous study has been reported that $CaCO_3$ has the ability to maintain LAB fermentation broth in the similar range [12]. Even so, LAB fermentation with free $CaCO_3$ (Flask II) showed slightly better results in controlling the pH of the broth. This is because the $CaCO_3$ was free in contact with the lactic acid formed in the medium without any obstacles. Therefore, the $CaCO_3$ can neutralize the acid in more effective way as compared to the $CaCO_3$ in the capsules. The $CaCO_3$ which confined inside the capsules faced diffusion resistance problem as it needed to diffuse through the alginate membrane [11]. As a result, it reacts with the acid at a lesser rate to maintain the pH of the fermentation broth. As shown in Figure 1, there was no apparent difference in the pH control ability between the capsule of 3.5 mm and 3.6 mm.

Lactic acid concentration of fermentation broth

The concentration of lactic acid produced by LAB was monitored and the results are shown in Figure 2. Throughout the 40 hours of fermentation, the concentration of lactic acid in the fermentation broth was increased. The lactic acid concentration in Flask I (control) increased continuously until the end of fermentation at 16.0 g/L. However, the lactic acid concentration in Flask II, III, and IV was maintained by $CaCO_3$ at the level of 10 – 12 g/L. There is no apparent difference was observed between the results of free $CaCO_3$ and encapsulated $CaCO_3$. The free lactic acid in the fermentation broth reacted with $CaCO_3$ to form calcium lactate and hence reduced the concentration of lactic acid in the broth as well as neutralized the pH of the broth (see Figure 1) [13].

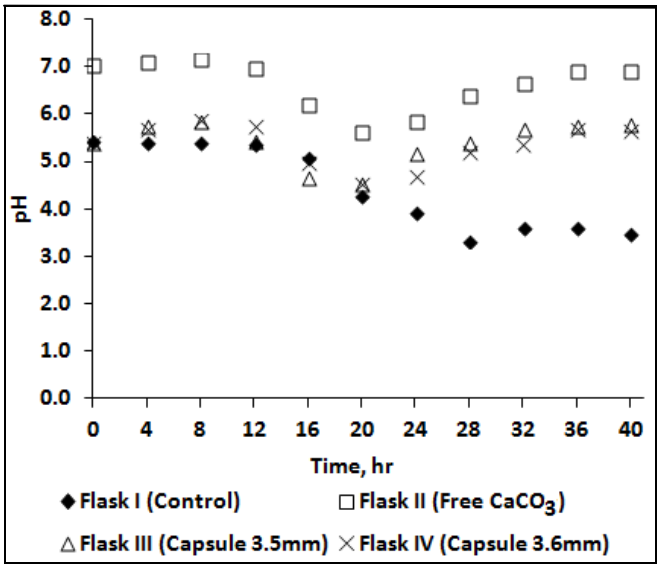


Figure 1. pH of LAB fermentation broth

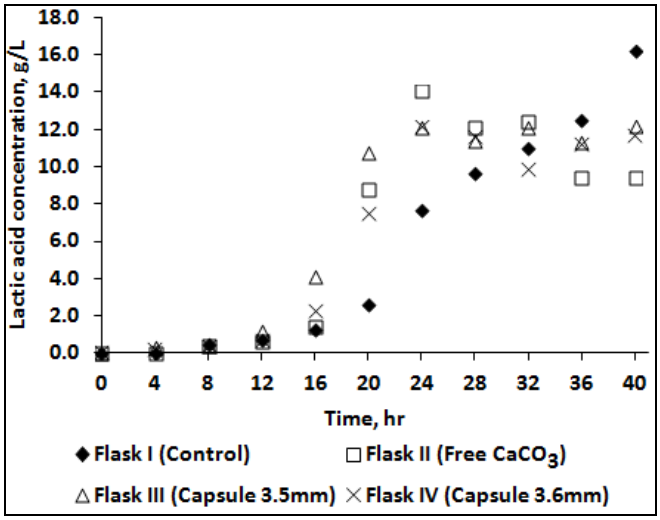


Figure 2. Lactic acid concentration of LAB fermentation broth

Viable cell concentration of LAB

The viable cell concentration of LAB (i.e. *L. casei shirota*) fermentation was at initial and at the end of the fermentation was determined and the results of different experimental conditions were compared, as shown in Table 2. The viable cell concentration of *L. casei shirota* at the end of fermentation was reduced in the case of Flask I (Control) and Flask II (Free $CaCO_3$). The results indicated that the viable cell concentration in LAB fermentation without $CaCO_3$ was reduced because the microbial growth is inhibited by its end-product, lactic acid [5, 6]. In the case of free $CaCO_3$ in Flask II, lower viable cell concentration was obtained at the end of fermentation could be due to the presence of $CaCO_3$ in free form created a less favorable environment for microbial growth. On the other hand, the viable cell concentration of *L. casei shirota* in Flask III and IV was high at the end of fermentation. The results suggested that the liquid core capsules provide a good condition for microbial growth as the pH and lactic acid

concentration were maintained at the desired level and the microbial cell was not in direct contact with the $CaCO_3$.

Table 2. Viable cell concentration of LAB fermentation

Flask number	Initial (0 hr), cfu/ml	End (40 hr), cfu/ml
I	12×10^9	1×10^8
II	18×10^9	5×10^8
III	1×10^9	1×10^9
IV	2×10^9	1×10^9

Note: The results were given based on the average of duplicate sampling

Conclusion

A new approach has been developed to maintain the pH and lactic acid concentration of LAB fermentation at the desired level. Spherical liquid core capsules of diameter of 3.5 mm and 3.6 mm were produced to encapsulate $CaCO_3$ from 0.6 mm and 0.8 mm hypodermic needle, respectively. The results showed that the pH of LAB fermentation was well maintained by the capsules at the desired level of above pH 5.5. Furthermore, the lactic acid concentration of LAB fermentation was averagely 11 g/L during the whole period of fermentation with the use of the liquid core capsules. In general, the results of the fermentation conducted using the capsules were better than that of control and comparable with that of free $CaCO_3$ in maintain the pH and lactic acid level during fermentation. In addition, the viable cell concentration of *L. casei shirota* was high ($> 10^9$ cfu/ml) at the end of fermentation when the fermentation was conducted using the capsules.

Acknowledgement

The authors thank Universiti Malaysia Perlis [the Publication Incentive Grant 2014 (9007-00158)] and the Malaysia Toray Science Foundation (MTSF) [Project no: 9002 – 00015] for providing financial support for this research.

References

1. Rhee, S. J., Lee, J. E. and Lee, C. H. (2001). Importance of lactic acid bacteria in Asian fermented foods. *Microbial Cell Factories*, 10(Suppl 1): S5.
2. Widyastuti, Y., Rohmatussolihat and Febrisiantosa A. (2014). The role of lactic acid bacteria in milk fermentation. *Food and Nutrition Sciences*, 5: 435 - 442.
3. Leisner, J. J., Vancanneyt, M., Lefebvre, K., Vandemeulebroecke, K., Hoste, B., Euras Vilalta, N., Rusul, G. and Swings, J. (2002). *Lactobacillus durianis* sp. nov., isolated from an acid-fermented condiment (tempoyak) in Malaysia. *International Journal of Systematic and Evolutionary Microbiology*, 52: 927 –931.
4. Chiang, Y. W., Chye, F.Y. and Mohd Ismail, A. (2006) Microbial diversity and proximate composition of Tapai, A Sabah's fermented beverage. *Malaysian Journal of Microbiology*, 2(1):1 – 6.
5. Lee, B. B., Tham, H. J. and Chan E. S. (2007) Fed-batch fermentation of lactic acid bacteria to improve biomass production: A theoretical approach. *Journal of Applied Sciences*, 7(15): 2211 – 2215.
6. Hujanen, M., Linko, S., Linko, Y. Y. and Leisola, M. (2001). Optimisation of media and cultivation conditions for L(+)(S)-lactic acid production by *Lactobacillus casei* NRRL B-441. *Applied Microbiology Biotechnology* 56: 126 – 130.
7. Lee, B. B., Pogaku, R and Chan, E. S. (2008). A critical review: Surface and interfacial tension measurement by the drop weight method. *Chemical Engineering Communication*, 195(8): 889 – 924.
8. Serna-Cock L., Camargo-Guarnizo A. F. and Rengifo-Guerrero C. A. (2013). Antimicrobial activity against *Xanthomonas albilineans* and fermentation kinetics of a lactic acid bacterium isolated from the sugar cane crop. *Chilean Journal of Agricultural Research*, 73 (3): 250 – 258.
9. Chan, E. S., Lee, B. B., Pogaku, R. and Poncelet, D. (2009) Prediction models for shape and size of ca-alginate macrobeads produced through extrusion–dripping method. *Journal Colloid Interface Science*, 338(1): 63 – 72.
10. Blandino, A., Macias, M. and Cantero, D. (1999) Formation of calcium alginate capsules: Influence of sodium alginate and $CaCl_2$ concentration on gelation kinetics. *Journal Bioscience and Bioengineering*, 88(6): 686 – 689.

11. Chai, Y., Mei, L-.H., Wu, G-.L., Lin, D-.Q. and Yao, S-.J. (2004) Gelation conditions and transport properties of hollow calcium alginate capsules. *Biotechnology and Bioengineering*, 87(2): 228 – 233.
12. Panesar, P. S., Kennedy, J. F., Gandhi, D. N. and Bunko, K. (2007). Bioutilisation of whey for lactic acid production. *Food Chemistry*, 105:1 –14.
13. Pala, P., Sikder, J., Roy, S. and Giorno, L. (2009) Process intensification in lactic acid production: A review of membrane based processes. *Chemical Engineering and Processing*, 48:1549 – 1559.

MALAYSIAN JOURNAL OF ANALYTICAL SCIENCES
Published by The Malaysian Analytical Sciences Society
ISSN 1394 - 2506

CHEMOMETRIC ANALYSIS OF SELECTED ORGANIC CONTAMINANTS IN SURFACE WATER OF LANGAT RIVER BASIN

(Analisis Kemometrik Bahan Cemar Organik Terpilih dalam Air Permukaan Lembangan Sungai Langat)

Mohamad Rafaie Mohamed Zubir , Rozita Osman, Norashikin Saim*

Faculty of Applied Sciences,
Universiti Teknologi MARA, 40450 Shah Alam, Selangor, Malaysia

**Corresponding author: noras691@salam.uitm.edu.my*

Received: 9 December 2014; Accepted: 9 October 2015

Abstract

Chemometric techniques namely hierarchical agglomerative cluster analysis (HACA), discriminant analysis (DA), principal component analysis (PCA) and factor analysis (FA) were applied to the distribution of selected organic contaminants (polycyclic aromatic hydrocarbons (PAHs), sterols, pesticides (chlorpyrifos), and phenol) to assess the potential of using these organic contaminants as chemical markers in Langat River Basin. Water samples were collected from February 2012 to January 2013 on a monthly basis for nine monitoring sites along Langat River Basin. HACA was able to classify the sampling sites into three clusters which can be correlated to the level of contamination (low, moderate and high contamination sites). DA was used to discriminate the sources of contamination using the selected organic contaminants and relate to the existing DOE local activities groupings. Forward and backward stepwise DA was able to discriminate two and five organic contaminants variables, respectively, from the original 13 selected variables. The five significant variables identified using backward stepwise DA were fluorene, pyrene, stigmastanol, stigmasterol and phenol. PCA and FA (varimax functionality) were used to identify the possible sources of each organic contaminant based on the inventory of local activities. Five principal components were obtained with 66.5% of the total variation. Result from FA indicated that PAHs (pyrene, fluorene, acenaphthene, benzo[a]anthracene) originated from industrial activity and socio-economic activities; while sterols (coprostanol, stigmastanol and stigmasterol) were associated to domestic sewage and local socio-economic activities. The occurrence of chlorpyrifos was correlated to agricultural activities, urban and domestic discharges. This study showed that the application of chemometrics on the distribution of selected organic contaminants was able to trace the sources of contamination in surface water.

Keywords: chemometrics, organic contaminants, chemical markers, Langat River

Abstrak

Teknik kemometriks iaitu Analisis Kelompok Agglomeratif Berhieraki (HACA), Analisis Diskriminan (DA), Analisis Komponen Utama (PCA) dan Analisis Faktor (FA) telah diaplikasi ke atas taburan bahan pencemar organik terpilih (aromatik hidrokarbon polisiklik (PAH), sterol, racun perosak (klorpirifos), dan fenol) untuk menilai potensi penggunaan bahan pencemar organik ini sebagai bahan pengesan di Lembangan Sungai Langat. Sampel air diambil dari bulan Februari 2012 hingga Januari 2013 pada setiap bulan di sembilan stesen pemantauan sepanjang Lembangan Sungai Langat. HACA dapat mengkelaskan kawasan persampelan kepada tiga kelompok yang boleh dikaitkan dengan tahap pencemaran (pencemaran rendah, pencemaran sederhana dan pencemaran tinggi). DA telah digunakan untuk membezakan sumber –sumber pencemaran dengan menggunakan bahan – bahan organik terpilih dan mengaitkannya dengan aktiviti – aktiviti setempat berdasarkan DOE. Analisis Diskriminan Langkah Hadapan dan Belakang masing – masing dapat mendiskriminasikan dua dan lima pembolehubah bahan pencemar organik daripada 13 pembolehubah asal yang dipilih. Lima pembolehubah yang penting adalah fluorena, pyrena, stigmastanol, stigmasterol dan fenol. PCA dan FA telah digunakan untuk mengenalpasti sumber – sumber bagi setiap bahan pencemar organik berdasarkan inventori aktiviti setempat. Lima komponen utama telah diperolehi dengan 66.5 % daripada jumlah variasi. Hasil

daripada FA menunjukkan PAH (pirena, flurena, asenaphtena, benzo[a]antrasena) berpunca dari kegiatan industri dan aktiviti sosio-ekonomi; manakala sterol (coprostanol, stigmastanol dan stigmasterol) daripada kumbahan domestik dan aktiviti – aktiviti sosio-ekonomi setempat. Kehadiran klorpirifos telah dikaitkan dengan aktiviti pertanian, bandar dan pelepasan domestik. Kajian ini menunjukkan bahawa teknik kemometriks yang diaplikasikan ke atas taburan bahan pencemar organik terpilih mampu mengesan punca pencemaran dalam air permukaan.

Kata kunci: kemometriks, bahan pencemar organik, penanda kimia, Sungai Langat

Introduction

Malaysia is a developing country whereby industrialisation and urbanisation becomes the main programme. Due to the rapid growth of industrialisation and urbanisation, Malaysia is facing a number of problems especially water pollution is brought about by discharges of all kinds of effluents, particularly from domestic sewage, industries, and construction sites during dry and wet deposition from the atmosphere. As a result, a wide range of organic contaminants are recognized as enviromentally relevent for their potential adverse effects on human and ecosystem health [1]. Thus, organic contaminants have become one of the rising issues in the field of environmental research. Environmental monitoring studies usually resulted in huge amounts of physical parameters and chemical concentrations collected in various geographical sites, time periods or environmental compartments (surface water, air, sediments and biota) [2].

In order to reveal relevant patterns and sources of variation in these large environmental datasets, chemometric analysis has been proposed [2,4]. Massart et al. [3] defined chemometrics as a chemical discipline that uses mathematics, statistics and formal logic to design or select optimal experimental procedures; to provide maximum relevant chemical data and to obtain knowledge about chemical systems. Chemometric techniques is very useful in tracing the sources and fate of the contaminants in the environment. Application of different pattern recognition techniques to reduce the complexity of large datasets have been proven to give a better interpretation and understanding of pollution source. Chemometric techniques covered three main areas of interest in environmental studies which are quantitative analysis, monitoring for environmental quality assessment and modeling or prediction of toxicology effects [2]. Commonly used chemometric techniques used for clustering are the hierarchical agglomerative cluster analysis (HACA) and principal components analysis (PCA) with factor analysis (FA). The three techiques of chemometric analysis were often used to interpret the data usually the data obtained had multivariate nature also several of variables were correlated [9].

Many studies have used chemometric techniques to identify the sources and distribution of organic (such as PAHs and sterols) or inorganic (such as heavy metal) contaminantions in environmental compartments such as water, air and sediment [4–8]. The application of chemometric techniques would be helpful in the interpretation of complex datasets and gives a better understanding into the sources of contamination. Previous study by Osman et al. [4] reported the application of this techniques provide a more objective interpretation of the results and able to apply organic contaminants as a chemical markers. Thirteen organic contaminants were analyzed which include polycyclic aromatic hydrocarbons (PAHs), sterols, pesticide (chlorpyrifos) and phenol to evaluate as they are potential chemical marker in the Langat River Basin. The dataset covers the period from February 2012 to January 2013 and the water samples were taken at nine monitoring sites provided by Department of Environment (DOE), Malaysia. The applications of chemometric techniques in this study will be able to give valuable information on the distribution and source of contamination of organic contaminants. This approach may reveal the possible sources of organic contaminants along Langat River Basin, Malaysia.

Materials and Methods

Chemicals and reagents

Solvents of gas chromatography (GC) grade or higher (methanol, dichloromethane, n-hexane and acetone) were purchased from Merck (Darmstadt, Germany). Hydrochloric acid (fuming 37% pro analysis) was obtained from Merck (Darmstadt, Germany). Individual standards PAHs; acenaphthene and pyrene were purchased from Dr. Ehrenstorfer GmbH (Augsburg, Germany) and acenaphthylene, fluorene, benzo[a]anthracene and benzo[a]pyrene were obtained from Supelco (Bellefonte, USA). Individual standard of sterols; 5β-cholestan-3-β-ol (coprostanol), 5-cholesten-3β-ol (cholesterol), stigmasterol and stigmastanol were purchased from Sigma-Aldrich (Steinheim,

Germany) while β-sitosterol was purchased from Supelco (Bellefonte, USA). Phenol was purchased from Supelco (Bellefonte, USA). Chlorpyrifos (PESTANAL® 98%) and N,O bis(trimethylsilyl)trifluoroacetamide + trimethylchlorosilane (TMCS), (99:1) were purchased from Sigma-Aldrich (Steinheim, Germany). SPE cartridges, C_{18} (EC) (1000 mg) and LiChrolut (EN 200 mg) were obtained from International sorbent technology (IST) (Mid Glamorgan UK) and Merck (Darmstadt, Germany) respectively.

Instrumentation and equipments

Water samples were extracted using solid phase extraction (SPE) using SPE Vacuum Manifold (Supelco, St. Louis, USA). Water samples were filtered prior to SPE extraction by using 0.45 µm glass fiber filter (Whatman International Ltd Maidstone, England). The pH of sample was measured using Metler Toledo AG, Analytical, (Switzerland) pH meter. Organic contaminants were analysed using gas chromatography (HP6890 series II, Agilent Technologies Palo Alto, CA, USA) with flame ionisation detector (GC-FID) (detection of PAHs sterols), gas chromatography (7890A Agilent Technologies) with electron capture detector (GC-ECD) (detection of chlorpyrifos), gas chromatography (Agilent GC6890/5973MSD) with mass spectrometry detector (GC-MSD) (detection of phenol).

Monitoring sites

Nine monitoring sites (Table 1 and Figure 1) were selected from a list (24 sites) of monitoring sites of the Department of Environmental (DOE), Malaysia. Sampling of water samples was conducted along Langat River Basin from February 2012 to January 2013. The selected monitoring sites represented the sites that experienced domestic sewage discharges, socio-economic and industrial activities.

Table 1. Langat River Basin monitoring sites

River	Station No	Coordinate		Location
		Longitude	Latitude	
Langat	1L01	E 101° 47.030’	N 02° 57.835’	West country Land
Batang Labu	1L02	E 101° 45.014’	N 02° 47.241’	Near Salak Tinggi
Semenyih	1L03	E 101° 50.870’	N 02° 56.772’	Semenyih Town
Batang Benar	1L04	E 101° 49.457’	N 02° 50.898’	Batang Benar village
Rinching	1L05	E 101° 51.765’	N 02° 55.122’	Rinching Ulu village
Balak	1L06	E 101° 46.065’	N 02° 00.934’	Simpang Balak Bridge
Beranang	1L07	E 101° 49.737’	N 02° 53.297’	Bridge at Kampung Kuala Pajam
Buan	1L08	E 101° 47.371’	N 02° 51.874’	Nilai Utara R&R area
Batang Nilai	1L09	E 101° 48.653’	N 02° 48.844’	Infront of Hualon

Extraction of organic contaminants using tandem solid phase extraction (SPE)

Extraction of PAHs, sterols, chlorpyrifos and phenol were done using tandem solid phase extraction procedure [10]. Two cartridges namely, C_{18} and LiChrolut EN were used to extract selected organic contaminants from water samples. PAHs, sterols and chlorpyrifos were extracted using non-polar sorbent (C_{18}) while phenol extracted using polymeric sorbent (LiChrolut EN). The SPE cartridges (C_{18} and LiChrolut EN) were conditioned separately. The C_{18} cartridge (1000 mg) was conditioned by using 10 mL of methanol followed by 6 mL of deionized water without applying vacuum while LiChrolut EN cartridge (200 mg) was conditioned using 10 mL of acetone followed with 3 mL methanol and 3 mL of acidified deionized water (pH 2) and also without applying vacuum. For sample loading, both cartridges C_{18} and LiChrolut EN were arranged in tandem whereby C_{18} cartridge was placed on top of the LiChrolut EN sorbent. Then, one litre (1 L) of water sample was loaded into the column using vacuum manifold at a flow rate of 6 mL min^{-1}. During the process, the column was not allowed to dry. After sample loading, the two

cartridges were separated. Elution of interference and elution of analytes were done separately. Each cartridge was vacuum dried for 30 min before the removal of interference matrix. For C_{18} cartridge, interferences were eluted by using 10 mL deionized water, while for LiChrolut EN cartridge the interferences were removed by using 5 mL 40% aqueous methanol. Both cartridges were vacuum dried. For C_{18} cartridge, the compounds of interest were eluted by gravity. First elution using 6 mL of n-hexane eluted PAHs and chlorpyrifos while second elution using 2×3 mL dichloromethane eluted sterols. For LiChrolut EN cartridge, phenol was eluted by gravity using 2×3 mL dichloromethane. Nitrogen was used to blow down both extract to a final volume of 1 mL for gas chromatographic analysis.

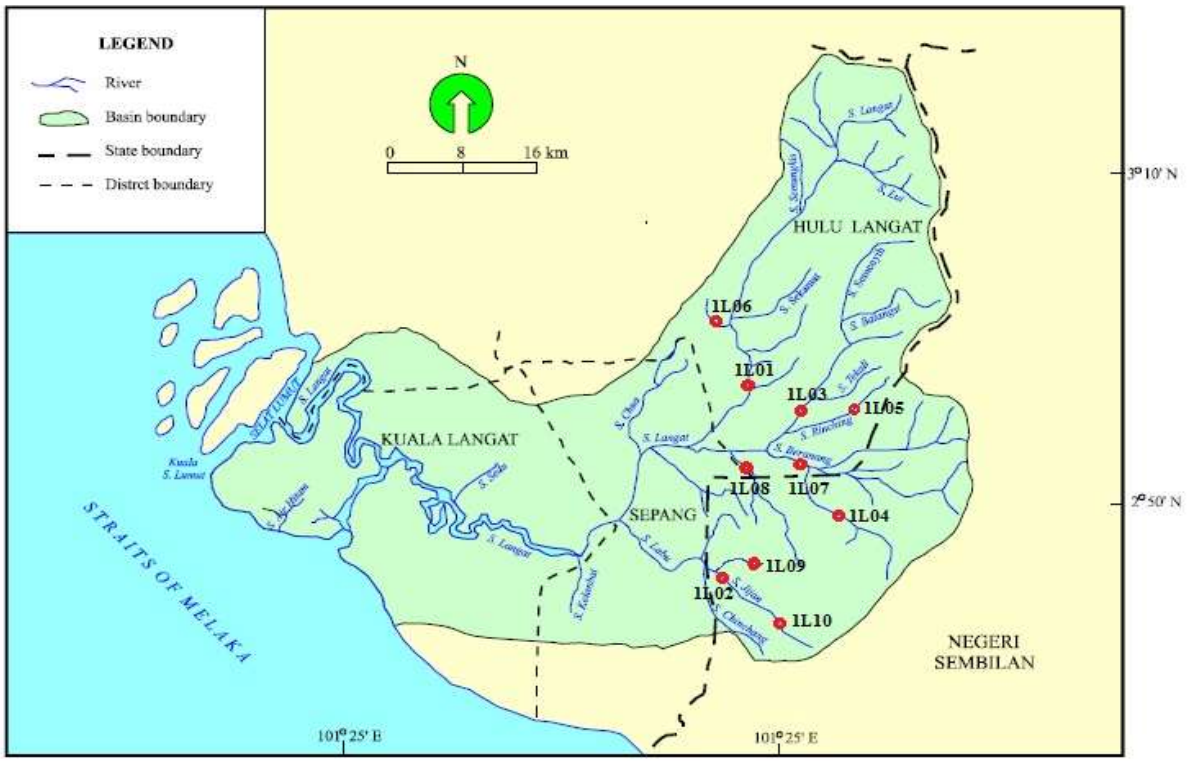


Figure 1. Monitoring sites in Langat River Basin (Source: Juahir *et al.* [13])

Chromatographic analysis

Gas chromatography with flame ionization detector (GC-FID) was used for the separation and quantification of PAHs and sterols. Chlorpyrifos and phenol were analysed using gas chromatography with electron capture detector (GC-ECD) and chromatography with mass spectrometry detector (GC-MSD), respectively [10].

GC-FID analysis

Separation and identification of PAHs and sterols was performed using gas chromatography with splitless injection and flame ionization detector. A 30 m × 0.25 mm id × 0.25 µm film thickness HP5-MS capillary column (Agilent technologies) was used to achieve separation of PAHs and sterols with the following temperature program: initial temperature, 50°C; held for 2 min; increased by 18°C min^{-1} to 250°C, increased by 10°C min^{-1} to 310°C; held for 11 min. The detector temperature was set at 310°C. PAHs quantification was carried out using a five-point calibration plot containing 1.00, 2.00, 3.00, 4.00 and 5.00 mg/L PAH standard mixtures. Sterols quantification was carried out using five-point calibration plot containing 1.00, 2.00, 3.00, 4.00 and 5.00 mg/L sterols standard. Prior to injection, sterols were derivatised by treatment with BSTFA: TMCS, (99:1) at 60°C for one hour.

GC-ECD analysis

Separation of chlorpyrifos was achieved using gas chromatograph equipped with 63 Ni electron capture detectors (GC-ECD). A 30 m × 0.25 mm id × 0.25 µm film thickness HP5-MS capillary column (Agilent technologies) was used for the quantitative analysis of chlorpyrifos. Injection port and detector temperatures were set at 250°C. The injection volume was 1 µL, with 2 min splitless period following the injection. The ECD detector utilized pure N_2 (>99.999%) and the carrier gas and make-up gas was at a controlled constant velocity of 60 mL min^{-1}. The temperature program was set to 150°C for 1 min, then increased by 25°C min^{-1} to 260°C for 8 min. Compounds were identified based on the retention time of the standards and quantified by external standard calibration. Chlorpyrifos quantification was carried out using five-point calibration plot containing 1.00, 2.00, 3.00, 4.00 and 5.00 mg/L chlorpyrifos standard.

GC-MSD analysis

Analysis of phenol was performed with gas chromatography with mass spectrometry detector (GC-MSD). Phenol was separated using a cross-linked fused silica capillary column HP5-MS (30 m × 0.25 mm id × 0.25 µm). The head pressure of the carrier gas (high purity helium) was 50 kPa. The temperature programmed was set at an initial temperature of 50°C, followed by an increased by 10°C min^{-1} to 200°C and held for 15 min. The MS detector was operated in the full scan using the electron impact (EI) ionization mode at 70 eV, scanning from 50-550 mass units at 0.45 s $scan^{-1}$. Phenol was quantified by single point external standard calibration. Prior to injection, phenol were derivatised by treatment with BSTFA: TMCS, (99:1) at 60°C for one hour.

Chemometric analysis

XLSTAT2013 software package was employed in the chemometric application using hierarchical agglomerative cluster analysis (HACA), discriminant analysis (DA) and principal component analysis (PCA) with the factor analysis (FA). These techniques were chosen to interpret and evaluate the organic contaminants dataset along Langat River Basin.

Results and Discussion

Hierarchical agglomerative cluster analysis (HACA)

HACA is a common method to classify variables or cases (observations/samples) into clusters with high homogeneity level within class and high heterogeneity level between classes [5,12]. HACA was performed on the selected organic contaminants data set to evaluate spatial variation among the nine monitoring sites. This analysis resulted in the grouping of sampling stations into three clusters as shown in Figure 2. Cluster 1 formed by five monitoring sites (1L01, 1L02, 1L03, 1L04 and 1L05) represents moderate contamination sites. 1L01, 1L03 and 1L04 monitoring sites located near city area which is experiencing urbanization over the past 15 years as several towns have grown and developed [13]. Possible sources of contaminations of these three monitoring sites are mainly from domestic discharges, and urban discharges. 1L02 and 1L05 monitoring sites located at rural areas but experiencing contamination from socio-economic activities and domestic sewage discharges. Cluster 2, formed by monitoring site (1L09) represents high contamination site located near the city and industrial area. This site is situated in a tributary of Batang Nilai, which carries high pollution flowing through the industrial areas [4]. Cluster 3 represents low contamination sites consisted of three monitoring sites (1L06, 1L07 and 1L08). These sites are located away from municipal discharges and industrial activities and correspond to socio-economic activities except 1L06 monitoring which is experiencing contamination from industrial activities and domestic sewage discharges. This analysis shows that HACA is able to classify the site based on the level of pollution and different possible sources of organic contaminant as the clusters in these groups have similar characteristic. Spatial variations of organic contaminants in water were further evaluated by using discriminant analysis.

Discriminant analysis (DA)

DA was used to discriminate the sources of contamination using the selected organic contaminants and relate the sources to the existing DOE inventory. Figure 3 shows the plot of discriminant functions obtained from water samples and three group's sources of contamination formed. These groups were related to the inventory of local activities provided by DOE, Malaysia and the contamination of Langat River can divide into three sources: domestic sewage/urban discharges, industrial activities and socio-economic activities.

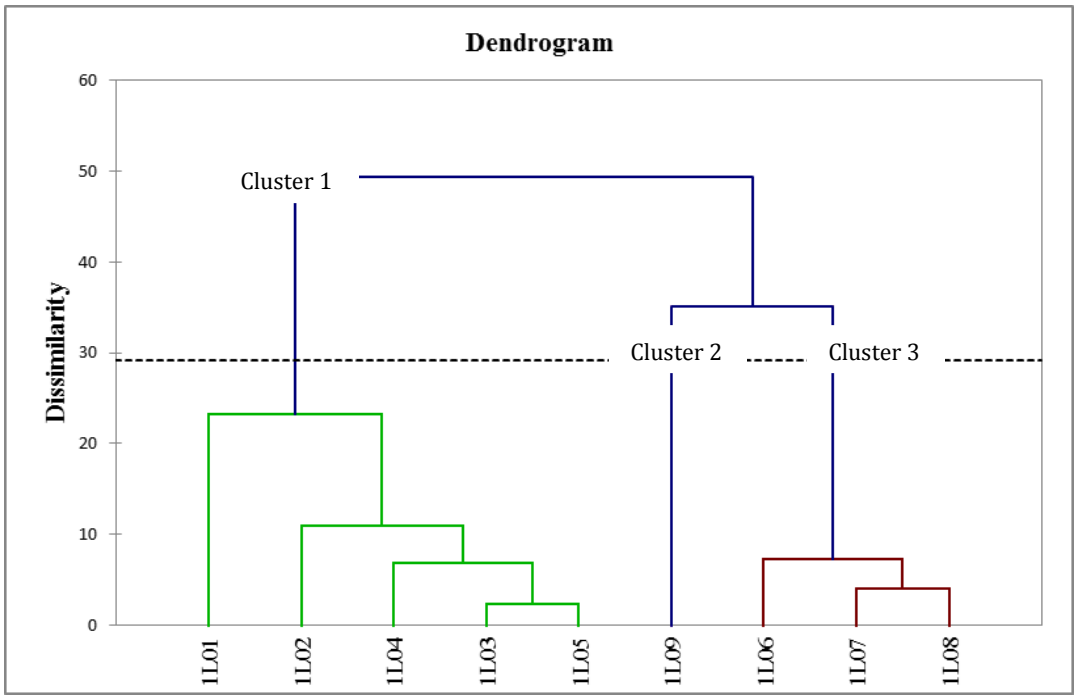


Figure 2. Dendrogram of clustering of monitoring sites according to organic contaminants analysed in water samples of Langat River Basin using Wards' method

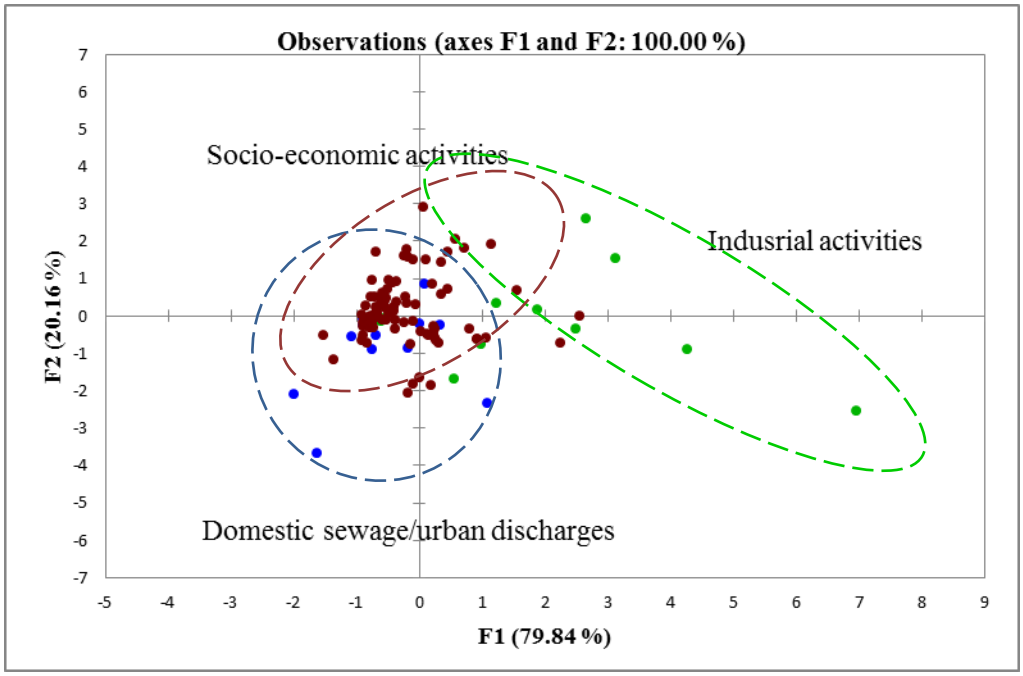


Figure 3. Plot of discriminant functions of water samples datasets

The three groups were treated as dependent variables, while the 13 selected organic contaminants were treated as independent variables. DA was carried out via three modes which are standard, forward stepwise and backward stepwise modes. Classification matrices (CMs) and discriminants functions (DFs) obtained from standard, forward stepwise and backward stepwise mode were tabulated in Table 2 and Table 3, respectively. The standard mode DA was able to discriminate the contamination source to 83.33 % correctly classified with 13 discriminant variables. The forward stepwise mode yielded 80.56 % correctly classified using only two discriminant variables (stigmastanol and stigmasterol), while the percent of cases correctly classified in backward stepwise mode also 79.63 % using only five discriminant variables (fluorene, pyrene, stigmastanol, stigmasterol and phenol). From the result of DA, the five organic contaminants based on backward stepwise DA were chosen as the significant variables to discriminate the sources contamination between the monitoring sites. Fluorene and pyrene were detected at relatively high concentration in the water samples. They were found high at socio-economic activities and industrial area. These contaminants represent the gasoline, coal and vehicular combustion [8,14,15]. Stigmastanol and stigmasterol were detected near domestic sewage area and urban discharges. Both compounds corresponded to faecal contamination and much related to the livestock farming activities [6,11]. Phenol clearly showed high concentration in wastewater of industrial area. This contaminant was associated with industrial activity. Industrial sources of this contaminant were from oil refineries, coal gasification sites and petrochemical units [16].

Table 2. Classification matrix of DA for all data measurements in water samples (n=108) from Langat River

Pollution source	**% Correct**	**Source assigned by DA**		
		Domestic sewage/Urban discharges	**Industrial activities**	**Socio-economic activities**
Standard DA mode				
Domestic sewage/Urban discharges	16.67	2	0	10
Industrial activities	50.00	0	6	6
Socio-economic activities	97.62	0	2	82
Total	**83.33**	**2**	**8**	**98**
Forward DA mode				
Domestic sewage/Urban discharges	0.00	0	0	12
Industrial activities	50.00	0	6	6
Socio-economic activities	96.43	0	3	81
Total	**80.56**	**0**	**9**	**99**
Backward DA mode				
Domestic sewage/Urban discharges	16.67	2	0	10
Industrial activities	50.00	0	6	6
Socio-economic activities	92.86	3	3	78
Total	**79.63**	**5**	**9**	**94**

Table 3. Classification function coefficients for discriminant analysis of organic contaminants in water samples from Langat River Basin (n=108)

Parameters	Standard mode			Forward stepwise mode			Backward stepwise mode		
	DS	IA	SA	DS	IA	SA	DS	IA	SA
Acenaphthylene	-2.345	-4.271	-2.752						
Acenaphthene	22.860	24.500	25.177						
Fluorene	-0.048	-2.395	-1.847				2.350	0.007	0.602
Pyrene	4.508	7.124	6.470				0.530	2.471	1.947
BaA	0.945	1.858	0.630						
BaP	-8.206	-10.950	-10.153						
Coprostanol	-12.844	-13.134	-11.928						
Cholesterol	-6.200	-5.168	-6.001						
Stigmasterol	2.303	5.586	2.541	1.765	5.293	2.461	2.438	6.065	2.928
Stigmastanol	62.518	81.888	65.450	42.867	57.942	43.832	45.460	62.664	46.856
β-sitosterol	0.000	0.000	0.000						
Chlorpyrifos	142.991	144.654	145.780						
Phenol	0.967	1.603	0.378				2.042	2.456	1.387
Constant	-38.678	-50.968	-38.471	-13.102	-23.000	-11.760	-15.637	-26.483	-13.644

DS: Domestic Sewage/Urban discharge, IA: Industrial activities SA: Socio-economic activities BaA=Benzo[a]anthracene; BaP=Benzo[a]pyrene

Principal component analysis (PCA) with factor analysis (FA)

PCA was performed to identify the possible sources of organic contaminants in Langat River Basin. It provides information on the most significant variables, which explains the whole data set by excluding the less significant variables with minimum loss of original information [17]. Five PCs with eigenvalues larger than one were obtained through the analysis. In reference to eigenvalues, only the PCs with eigenvalues greater than one are considered to carry out the FA. Equal numbers of varifactors (VFs) were obtained via factor analysis performed on the PCs and comprised of 66.5% total variance. Table 4 shows the corresponding VFs, variables loadings and explained variance. From the four VFs, VF1 explains 19.9 % from the total variance, showing strong positive loading of coprostanol and moderate loading of stigmastanol. These contaminants were detected from sampling sites associated with domestic sewage, urban discharge and socio-economic activities. Coprostanol and stigmastanol were indicators for faecal contamination [11]. Coprostanol especially is one of general marker of anthropogenic faecal contamination [18]. VF2 explains 16.8% of total variance was dominated by strong positive loading of fluorene and pyrene whereas VF3 accounted for 11.5 % of the total variance, was predominated by moderate loadings of acenaphthene and benzo[a]anthracene. Inputs of the contaminants in VF2 and VF3 can be associated with industrial activities and urban activities along Langat River Basin. As reported by Li et al. [14, 19], the possible sources of pyrene and fluorene were from anthropogenic activities such as combustion. Acenaphthene and benzo[a]anthracene were associated with vehicle exhaust [8]. VF4 and VF5 accounted for 9.9 % and 8.5 % of the total variance, and showing strong positive loading of chlorpyrifos and stigmasterol, respectively. The presence of chlorpyrifos much related to contamination effects of socio-economic activity (agricultural activities such oil plantation) within Langat River Basin [20] whereas presence of stigmasterol usually indicator of faecal contamination and much related to the livestock farming activities along the river basin.

Table 4. Loadings of organic contaminants after varimax rotation (PC extracted 5 factors) of water samples from Langat River Basin

Parameters	**VF1**	**VF2**	**VF3**	**VF4**	**VF5**
Acenaphthylene	-0.382	0.235	0.525	0.426	0.248
Acenaphthene	0.120	-0.124	***0.713***	0.043	-0.207
Fluorene	-0.037	**0.779**	0.309	0.073	-0.011
Pyrene	-0.019	**0.900**	-0.077	-0.051	0.039
Benzo[a]anthracene	0.329	0.131	***0.740***	-0.106	0.173
Benzo[a]pyrene	0.444	0.496	-0.197	0.404	-0.181
Coprostanol	**0.815**	0.011	0.214	-0.047	0.135
Cholesterol	0.344	0.002	0.230	0.257	0.624
Stigmasterol	0.094	0.026	-0.087	0.012	**0.784**
Stigmastanol	***0.688***	-0.058	0.079	0.077	0.160
β-sitosterol	0.000	0.000	0.000	0.000	0.000
Chlorpyrifos	0.011	-0.011	0.004	**0.892**	0.055
Phenol	0.088	0.397	-0.202	0.243	-0.436
Eigenvalue	2.390	2.012	1.377	1.189	1.014
Variability (%)	19.915	16.765	11.471	9.909	8.452
Cumulative (%)	19.915	36.681	48.152	58.060	66.513

(Strong loadings > 0.75 are shown in bold; moderate loadings 0.5-0.75 are in italic bold)

Conclusion

The application of chemometric techniques provides valuable information in assessing the variation of organic contaminants in Langat River Basin. The sources of specific organic contaminants can be explained by correlating the groupings obtained through chemometric approach with local activities identified by DOE. HACA classified the sampling sites into three clusters which can be correlated to the sources of contamination. Forward and backward stepwise DA was able to discriminate two (stigmastanol and stigmasterol) and five (fluorene, pyrene, stigmastanol, stigmasterol and phenol) organic contaminants variables, respectively, from the original 13 selected variables. Result from PCA and FA, shows that the sources of contamination within the Langat River Basin were influenced by industrial, urban and socio-economic activities, represented by selected PAHs (pyrene, fluorene, acenaphthene and benzo[a]anthracene). Sources from domestic and urban discharges were represented by sterols (coprostanol, stigmastanol and stigmasterol). This study shows that the application of chemometric techniques can reveal meaningful information from the datasets of organic contaminant.

Acknowledgement

The authors would like to acknowledge financial support obtained from Organisation for the Prohibition of Chemical Weapons (OPCW), Netherlands and Research Management Institute (RMI) Universiti Teknologi MARA (UiTM).

References

1. Burkhardt, M. R., ReVello, R. C., Smith, S. G. and Zaugg, S. D. (2005). Pressurized liquid extraction using water/isopropanol coupled with solid-phase extraction cleanup for industrial and anthropogenic waste-indicator compounds in sediment. *Analytica Chimica Acta,* 534(1): 89 – 100.
2. Mas, S., de Juan, A., Tauler, R., Olivieri, A. C. and Escandar, G. M. (2010). Application of chemometric methods to environmental analysis of organic pollutants: A review. *Talanta, 80*(3), 1052 – 1067.

3. Massart, D. L., Vandeginste, B., Buydens, L., De Jong, S., Lewi, P. and Smeyers-Verbeke, J. (1997). *Handbook of chemometrics and qualimetrics: Part A*: Elsevier Science Pub Co.
4. Osman, R., Saim, N., Juahir, H. and Abdullah, M. P. (2012). Chemometric application in identifying sources of organic contaminants in Langat river basin. *Environmental Monitoring and Assessment,* 184(2):1001 – 1014.
5. Shrestha, S. and Kazama, F. (2007). Assessment of surface water quality using multivariate statistical techniques: A case study of the Fuji river basin, Japan. *Environmental Modelling & Software,* 22(4): 464 – 475.
6. Saim, N., Osman, R., Sari Abg Spian, D. R., Jaafar, M. Z., Juahir, H., Abdullah, M. P. and Ghani, F. A. (2009). Chemometric approach to validating faecal sterols as source tracer for faecal contamination in water. *Water Research,* 43(20): 5023 – 5030.
7. Dominick, D., Juahir, H., Latif, M. T., Zain, S. M. and Aris, A. Z. (2012). Spatial assessment of air quality patterns in Malaysia using multivariate analysis. *Atmospheric Environment,* 60: 172 – 181.
8. Retnam, A., Zakaria, M. P., Juahir, H., Aris, A. Z., Zali, M. A. and Kasim, M. F. (2013). Chemometric techniques in distribution, characterisation and source apportionment of polycyclic aromatic hydrocarbons (PAHS) in aquaculture sediments in Malaysia. *Marine Pollution Bulletin,* 69(1-2): 55 – 66.
9. Singh, K. P., Malik, A., Mohan, D., Sinha, S. and Singh, V. K. (2005). Chemometric data analysis of pollutants in wastewater – a case study. *Analytica Chimica Acta,* 532(1): 15 – 25.
10. Osman, R., Saim, N. and Abdullah, M. P. (2009). Simultaneously extraction of organic compounds with wide polarity range in water using solid phase extraction technique. *Research Journal of Chemistry and Environment,* 13(3): 7 – 18.
11. Osman, R., Saim, N. and Abdullah, M. P. (2010). Organic Contaminants In Soil/Sediment As A Tracer For Pollution Sources. *Chemical Sciences Journal,* 2010: 1 – 10.
12. McKenna, J. (2003). An enhanced cluster analysis program with bootstrap significance testing for ecological community analysis. *Environmental Modelling & Software, 18*(3): 205 – 220.
13. Juahir, H. (2008). Water Quality Data Analysis and Modeling at Langat River Basin. *PhD dissertation, Universiti Putra Malaysia*.
14. Li, J., Zhang, G., Li, X. D., Qi, S. H., Liu, G. Q. and Peng, X. Z. (2006). Source seasonality of polycyclic aromatic hydrocarbons (PAHs) in a subtropical city, Guangzhou, South China. *Science of Total Environment,* 355(1-3): 145 – 155.
15. Shen, Q., Wang, K. Y., Zhang, W., Zhang, S. C. and Wang, X. J. (2009). Characterization and sources of PAHs in an urban river system in Beijing, China. *Environmental Geochemistry and Health,* 31(4): 453 –462.
16. Dabrowski, A., Podkoscielny, P., Hubicki, Z. and Barczak, M. (2005). Adsorption of phenolic compounds by activated carbon--a critical review. *Chemosphere,* 58(8): 1049 – 1070.
17. Kannel, P. R., Lee, S., Kanel, S. R. and Khan, S. P. (2007). Chemometric application in classification and assessment of monitoring locations of an urban river system. *Analytica Chimica Acta,* 582(2): 390 – 399.
18. Shah, V. G., Dunstan, R. H., Geary, P. M., Coombes, P., Roberts, T. K. and Von Nagy-Felsobuki, E. (2007). Evaluating potential applications of faecal sterols in distinguishing sources of faecal contamination from mixed faecal samples. *Water Research,* 41(16): 3691 – 3700.
19. Li, W. H., Tian, Y. Z., Shi, G. L., Guo, C. S., Li, X. and Feng, Y. C. (2012). Concentrations and sources of PAHs in surface sediments of the Fenhe reservoir and watershed, China. *Ecotoxicology Environment Safety,* 75(1): 198 – 206.
20. Juahir, H., Zain, S., Khan, R., Yusoff, M., Mokhtar, M. and Toriman, M. (2009). Using chemometrics in assessing Langat River water quality and designing a cost-effective water sampling strategy. *Maejo International Journal of Science and Technology,* 3(1): 26 – 42.

MALAYSIAN JOURNAL OF ANALYTICAL SCIENCES
Published by The Malaysian Analytical Sciences Society
ISSN 1394 - 2506

POLYVINYLPYRROLIDONE AS A NEW FLUORESCENT SENSOR FOR NITRATE ION

*(*Polivinilpirolidon Sebagai Sensor Pendafluor Baru Bagi Ion Nitrat*)*

Ing Hua Tang[1], Rita Sundari[2], Hendrik O. Lintang[3], Leny Yuliati[3]*

[1]*Department of Chemistry, Faculty of Science,*
Universiti Teknologi Malaysia, 81310 UTM Johor Bahru, Johor, Malaysia
[2]*The Research Center of Private Universities Coordination, 13360 Jakarta, Indonesia*
[3]*Centre for Sustainable Nanomaterials,*
Ibnu Sina Institute for Scientific and Industrial Research,
Universiti Teknologi Malaysia, 81310 UTM Johor Bahru, Johor, Malaysia

**Corresponding author: leny@ibnusina.utm.my*

Received: 9 December 2014; Accepted: 9 October 2015

Abstract

In this study, non-conjugated polyvinylpyrrolidone(PVP) was investigated for the first time as the potential polymeric material to sense nitrate ions by fluorescence spectroscopy. The PVP was diluted into various concentrations (3-10%) and they were used to sense the nitrate ions in different concentrations (0.1-100 mM). The PVP showed two excitation peaks at 285 and 330 nm due to the presence of C=O and N-C groups, respectively. One strong emission at 400 or 408 nm was observed with the excitation at 285 or 330 nm. The higher value of quenching constant at excitation wavelength of 285 nm indicated that C=O site was more favored for NO_3^- ions sensing than the N-C site. The PVP 7% gave the highest quenching constant; where the K_{SV} value was 9.89×10^{-3} mM^{-1} and 2.44×10^{-3} mM^{-1} for excitation at 285 and 330 nm, respectively. The sensing capability was evaluated in the presence of interference ions (SO_4^{2-}, HCO_3^-, Cl^-, and OH^-). It was observed that the interference ions interacted strongly with the C=O, but weakly with the N-C. Therefore, in the presence of the interference ions, the PVP would be a potential fluorescent sensor when it is excited at 330 nm.

Keywords: polyvinylpyrrolidone; fluorescent sensor; nitrate ions; quenching

Abstrak

Dalam kajian ini, polivinilpirolidon (PVP) yang bersifat bukan konjugat dikaji untuk kali pertama sebagai bahan polimer yang berpotensi untuk mengesan ion nitrat dengan spektroskopi pendaflour. PVP dicairkan kepada kepekatan yang berlainan (3-10%) dan digunakan untuk mengesan ion nitrat dalam kepekatan yang berbeza (0.1-100 mM). PVP menunjukkan dua puncak pengujaan pada 285 and 330 nm dengan kewujudan C=O dan N-C masing-masing. Satu puncak pemancaran yang tinggi pada 400 atau 408 nm diperolehi dengan pengujaan pada 285 atau 330 nm. Pemalar pelidap kejutan dengan nilai yang lebih tinggi pada puncak pengujaan 285 nm menunjukkan bahawa tapak C=O lebih cenderung untuk mengesan ion NO_3^- daripada tapak N-C. PVP 7% memberi pemalar pelidap kejutan yang paling tinggi, dengan nilai K_{SV} 9.89×10^{-3} mM^{-1} and 2.44×10^{-3} mM^{-1} untuk puncak pengujaan pada 285 dan 330 nm masing-masing. Kemampuan pengesanan dinilai dengan kehadiran ion gangguan (SO_4^{2-}, HCO_3^-, OH^-, and Cl^-). Hasil kajian menunjukkan bahawa ion gangguan berinteraksi kuat dengan C=O, tetapi lemah dengan N-C. Oleh itu, dengan kehadiran ion gangguan, PVP berpotensi menjadi pendafluor sensor pada tapak pengujaan 330 nm.

Kata kunci: polivinilpirolidon; pengesan pendaflour, ion nitrat, pelidap kejutan

Introduction

Polymer consisting of repeating units of monomers is highly explored in various fields, owing to its non-toxicity [1], simple fabrication methodology and low cost [2, 3], large surface-to-volume ratio [4] and easy modification [5]. The conjugated polymers have received particular attentions with their wide applications in batteries [6], organic light emitting diodes [2, 4, 7], and sensor [2, 4-6, 8-10], due to their unique metallic and semiconducting properties [4] as well as the fluorescence properties [4, 5, 11]. On the other hand, the non-conjugated polymers are less explored and still poorly understood. To date, the non-conjugated polyvinylpyrrolidone (PVP) is mostly used as a passivator or a capping agent for semiconductor such as ZnS or CdS, with the purpose to reduce the agglomeration and improve the optical property [12]. Some studies reported the application of the PVP as a sensor [14, 15]. Wang *et al*. reported that the PVP can be used as electrochemical sensor for acyclovir molecule [14], while Zhang *et al*. used PVP nanocomposite as a humidity sensor [16]. Since the PVP has been also reported to have photoluminescence property [15], it is worthy to study the possibility to use the non-conjugated PVP as the fluorescence sensor. To the best of our knowledge, there is no investigation on the application of the PVP as the fluorescence sensor. In this study, the PVP is used as the fluorescent sensor for detection of nitrate ions.

The nitrate ions are usually found in fertilizer for agriculture purpose. When the fertilizer is used excessively, the excess nitrate ions in the environmental water system will lead to algae blooms and eutrophication phenomena [17-19]. On the other hand, nitrate ions that are consumed into body may cause methemoglobinemia and the nitrate ions might become the source of carcinogenic *n*-nitrosamines [17, 20]. These are some of the reasons to monitor nitrate ions in the environment. Extensive studies have been explored to detect the nitrate ions using different techniques, such as ion chromatography [18], capillary electrophoresis [3, 20], electrochemical [3, 21-24], and fluorescence spectroscopy [17]. However, the detection limit and linear detection range of existing nitrate ion sensor are still not in satisfactory level [21], and this urges researchers to develop better nitrate sensors.

In this study, the feasibility to develop PVP fluorescence sensor for nitrate ions was examined using different concentrations of PVP and nitrate ions. The favorable sites to interact with the nitrate ions were discussed based on the quenching phenomena. Besides, the selectivity of the PVP to the nitrate ions was evaluated in the presence of other interference ions such as SO_4^{2-}, HCO_3^-, Cl^-, and OH^-.

Materials and Methods

Materials

The PVP solution (K 60, Aldrich, Mw ≈ 160000, 45% in water), sodium nitrate ($NaNO_3$, Merck, 99.5%), sodium sulphate (Na_2SO_4, Fisher Scientific, > 99%), sodium hydrogen carbonate ($NaHCO_3$, Fisher Scientific, 99%), sodium chloride (NaCl, Fisher Chemical, 100.1%), and sodium hydroxide (NaOH, QRëC, 99%) were used as-received without any treatments.

Preparation of PVP

A series of various concentrations of PVP was prepared from the PVP (K 60) by dilution method using deionized water. The prepared solution was shown as x% of PVP, where x showed the concentrations of the PVP (3, 5, 7, and 10%).

Fluorescence, quenching and selectivity test

The fluorescence property and sensing capability of the PVP solutions for detection of nitrate ions were studied using a fluorescence spectroscopy (JASCO, FP-8500) at room temperature. The excitation spectra of the PVP solutions were monitored at emission wavelengths of 400 or 408 nm, while the emission spectra were monitored at the excitation wavelengths of 285 or 330 nm. For quenching test, the PVP solution was exposed to various concentrations of nitrate ions (0.1-100 mM) and the interaction between the emission sites and the nitrate ions was measured. The sensing capability of the PVP was evaluated in the presence of interference ions (SO_4^{2-}, HCO_3^-, Cl^-, and OH^-). The concentration for the nitrate ions and each interference ions was fixed at the concentration of 100 mM.

Results and Discussion

Fluorescence property of PVP

The fluorescence property of the PVP solution was studied by investigating its excitation and emission sites. As shown in Figure 1, all the prepared PVP (3-10%) exhibited two excitation sites at 285 and 330 nm and one emission site at 400 or 408 nm when they were excited at 285 or 330 nm. The excitation at 285 nm would be attributed to the presence of C=O, while the excitation at 330 nm would be corresponded to the presence of N-C in the PVP, similar to the reported one [12]. It was clear that the excitation and emission intensity increased with the increase of the PVP concentrations. The increased intensities were reasonable since they indicated the increased amount of excitation and emission sites of the PVP with the increase of the concentrations. Figure 1 also showed that the intensity of N-C sites was higher than that of C=O sites, suggesting that the N-C sites would be the main excitation sites in the PVP and the N-C sites showed greater fluorescence quantum yield than the C=O site [25].

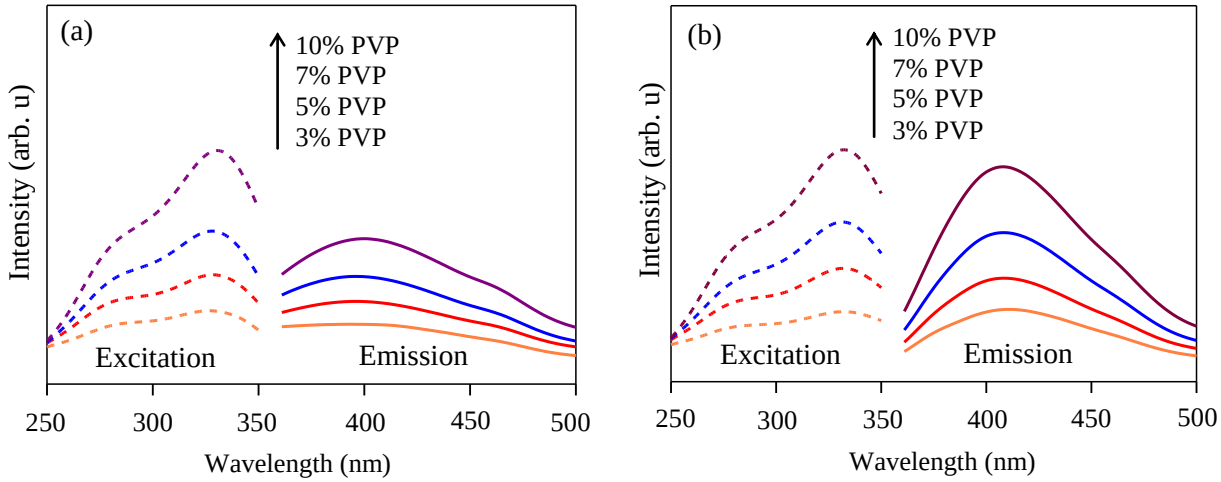


Figure 1. Excitation and emission spectra for 3, 5, 7 and 10% of PVP at (a) C=O and (b) N-C sensing sites

Quenching tests

In order to investigate the performance of the PVP to sense the nitrate ions, the interaction between emission sites and the nitrate ions were evaluated by quenching effect study. The quenching tests were evaluated by monitoring the changes in the emission intensity after addition of various concentrations of nitrate ions (0.1-100 mM). The emission spectra were monitored at two different excitation wavelengths, which were 285 nm and 330 nm. All the 3-10% of PVP showed similar results to each other, in which the emission intensities of the PVP were quenched after addition of the nitrate ions. The results of the quenching tests for the 7% of PVP are shown in Figure 2. The decrease in the emission intensity increased with the increase of nitrate ions concentrations for both emission sites, which were C=O and N-C sites. Among the prepared PVP, the 7% of PVP showed the most quenched intensity, suggesting that the 7% of PVP showed the strongest interaction with the nitrate ions (not shown).

As shown in Figure 2, quenching effects were observed on both C=O and N-C emission sites, suggesting that there were certain interactions between both the emission sites and the nitrate ions. Due to the difference of the charge between the emission sites and the nitrate ions, the most possible interactions between PVP and nitrate ions would be electrostatic interactions. Similar interactions have been proposed for the interactions between nitrates and polypyrrole [22], nitro-containing compounds with polymers [11, 26, 27]. In the presence of the same concentration of nitrate ions, especially at high concentrations, it was obviously observed that the C=O sites were more quenched than the N-C sites. This might be due to the reason that at each C=O can interact with more than one nitrate ions simultaneously and this can be more intense at higher concentration of nitrate ions. Moreover, a slight red shift in

the emission peak wavelength at high concentration of nitrate ions were also observed, suggesting that there was loss of energy through vibrational relation or internal conversion phenomena when the PVP interacted with nitrate ions [25].

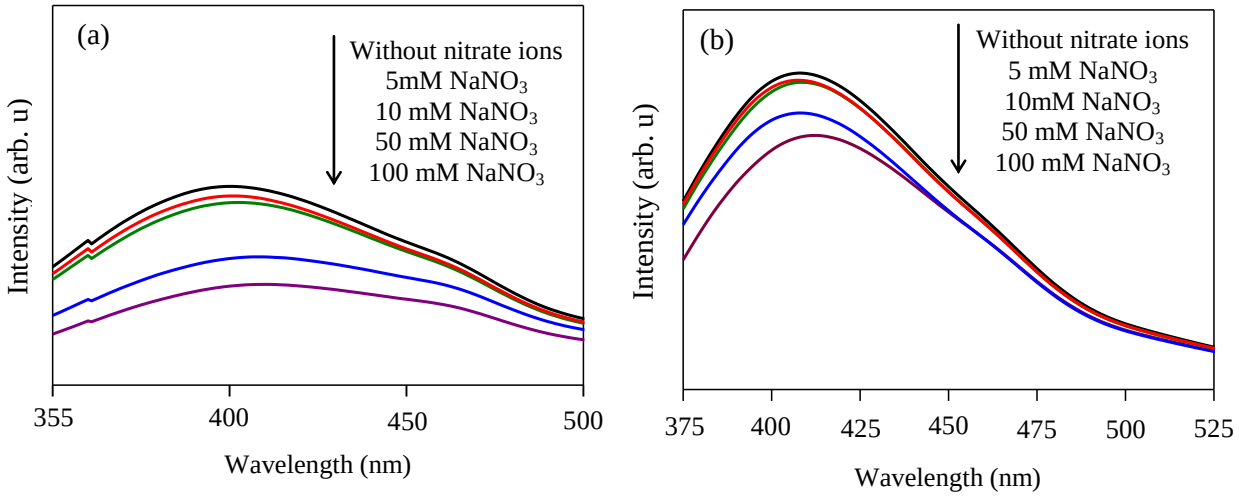


Figure 2. Emission spectra of 7% PVP with the absence and presence of nitrate ions in the 5-100 mM range for C=O sites and N-C sites, monitored at excitation wavelength of (a) 285 nm and (b) 330 nm

The interaction between the emission sites and nitrate ions can be evaluated by using the Stern-Volmer plot. When the illumination intensity and the amount of PVP are maintained to be constant, the relative emission intensity can be expressed as a function of the nitrate ions concentrations, according to the Stern-Volmer equation (Eq. 1),

$$\frac{I_o}{I} = K_{sv}[Q]+1 \quad (1)$$

where I_o and I are fluorescence intensities obtained in the absence and presence of nitrate ions, respectively, Q is the concentration of nitrate ions, and K_{sv} is the Stern-Volmer quenching constant.

Figure 3 shows the Stern-Volmer plots for the 7% of PVP. The plots were linear for both emission sites, suggesting that both C=O and N-C sites acted as the sensing sites for the nitrate ions. The slopes of the Stern-Volmer plots represented the quenching constant (K_{SV}), which values were 9.89×10^{-3} mM^{-1} and 2.44×10^{-3} mM^{-1} for C=O and N-C sites, respectively. The higher value of the K_{SV} for the C=O sites than that for the N-C sites indicated that the C= sites were more favorable to sense nitrate ions than the N-C sites. This might be due to the reasons that the C=O sites have higher polarity than the N-C sites, but with less steric hindrance effect. The higher K_{SV} values obtained on the C=O sites can be observed as well on other PVP with various concentrations, as can be seen in Figure 4. It can be clearly shown that the K_{SV} values increased with the PVP concentrations up to 7%, but decreased when the PVP concentration was 10%. This result clearly suggested that 7% of PVP was an optimum concentration to get the highest quenching efficiency.

Selectivity Tests

The sensing performance of 7% of PVP towards nitrate ions was evaluated with the co-existence of interference ions. The interference ions used in current study were SO_4^{2-}, HCO_3^-, Cl^- and OH^-.The extent of interference was determined according to the equation below (Eq. 2):

$$E = \frac{I_o - I}{I_o} \times 100\% \quad (2)$$

where I_o and I show the fluorescence emission intensity for the 7% of PVP with the presence of nitrate ions only and the presence of both nitrate and interference ions, respectively. The high value of the extent of interference suggested the high interference effect of the ions towards the performance of the 7% PVP for detection of the nitrate ions.

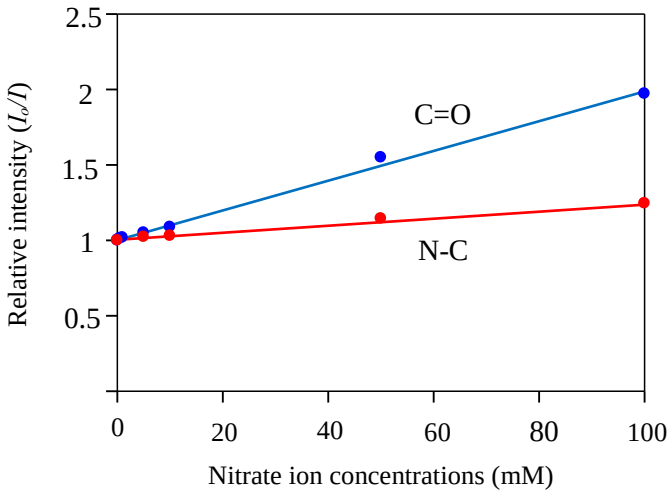


Figure 3. Linear Stern-Volmer plots for 7% PVP at C=O (●) and N-C (●)

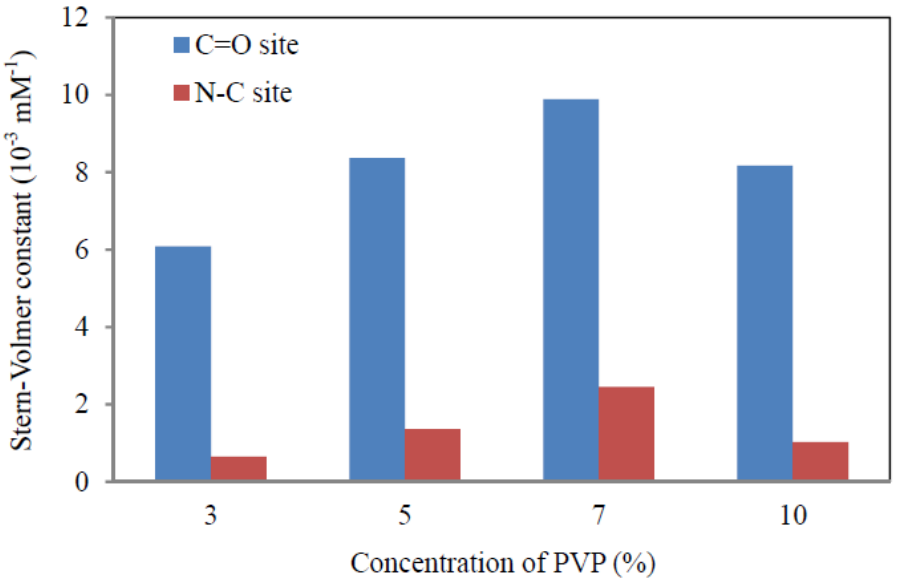


Figure 4. Stern-Volmer constants for nitrate ions detection on PVP with various concentrations for both C=O and N-C sites

The extent of interference for each interference ion was shown in Figure 5. As for the C=O sites, the presence of SO_4^{2-}, HCO_3^-, Cl^-, and OH^- ions gave extent of interferences, which values of 25, 12, 4, and 47%, respectively. This result suggested that the detection of nitrate ions by C=O sites were mostly influenced by OH^-, followed by SO_4^{2-}, HCO_3^-, and Cl^- ions. The high interference effect from OH^- would be caused by the small size and polarity of OH^- ions [27]. Therefore, the 7% of PVP would not be suitable to detect nitrate ions in the presence of OH^- ions. On the other hand, even though the co-existence of polyatom anions such as SO_4^{2-} and HCO_3^- resulted in lower effect than the OH^-, the C=O sites competitively interacted with SO_4^{2-} and HCO_3^-. Therefore, the sensing performance would be affected in the presence of these ions. It is worthy noted that the C=O sites showed much less interaction with Cl^-, suggesting that the C=O sites still could be used to detect the nitrate ions even in the presence of Cl^- ions.

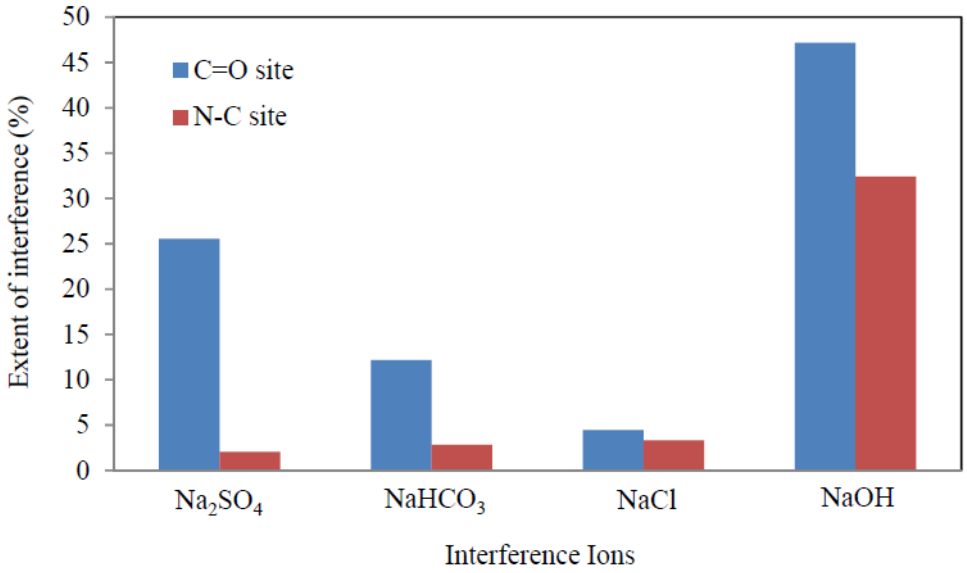


Figure 5. Extent of interferences of ions towards nitrate ions detection on 7% PVP

As for the N-C sites, the presence of SO_4^{2-}, HCO_3^-, Cl^-, and OH^- ions gave extent of interferences, which values of 2, 3, 3, and 32%, respectively. Similar to the C=O sensing sites, the N-C sites were found to be affected by the presence of OH^-. Different from the C=O sites, the performance of the nitrate sensing on the N-C sites were not much influenced by SO_4^{2-}, HCO_3^-, or Cl^- ions. These results suggested that the N-C sensing sites still can selectively interact with nitrate ions in the presence of these interfering ions.

Conclusion

The PVP showed two excitation peaks at 285 and 330 nm and one emission peak at 400 or 408 nm when excited at 285 and 330 nm. Among the prepared PVP, 7% of PVP showed the highest quenching constants toward the nitrate ions. The linear Stern-Volmer plot was observed, suggesting that the PVP can be used as a potential fluorescence sensor for nitrate ions. The C=O sites were found to show much stronger interactions with nitrate ions (four times higher) than the N-C sites, suggesting that the C=O sites were more favorable to sense the nitrate ions. The presence of interference ions were found to affect the fluorescence sensing of nitrate ions differently. As for C=O sites, it can still be used to sense nitrate ions in the presence of Cl^- ions. On the other hand, the N-C sites can selectively sense the nitrate ions in the presence of SO_4^{2-}, HCO_3^-, and Cl^- ions.

Acknowledgement

The work was financially supported by the Ministry of Higher Education (MOHE, Malaysia) and the Universiti Teknologi Malaysia (UTM, Malaysia) through a Tier-1 Research University Grant (cost center code: Q.J130000.2509.06H66). I.H.T acknowledges the support of MyBrain MyPhd scholarship.

References

1. Bourlinos, A. B., Georgakilas, V., Zboril, R., Steriotis, T. A., Stubos, A. K. & Trapalis, C. (2009). Aqueous-phase exfoliation of graphite in the presence of polyvinylpyrrolidone for the water-soluble graphenes. *Solid State Communications*, 149 (47-48): 2172-2176.
2. Harsányi, G. (2000). Polymer films in sensor applications: A review of present uses and future possibilities. *Emerald Insight*, 20 (2): 98-105.
3. Chen, G., Lin, Y. & Wang, J. (2006). Monitoring environmental pollutants by microchip capillary electrophoresis with electrochemical detection. *Talanta*, 68 (3): 497-503.
4. Ozaydin-Ince, G., Coclite, A. M. & Gleason, K. K. (2012). CVD of polymeric thin films: applications in sensors, biotechnology, microelectronics/organic electronics, microfluidics, MEMS, composites and membranes. *Report on Progress in Physics*, 75 (1): 016501
5. Fan, L-J., Zhang, Y. & Jones, W. E. (2005). Design and synthesis of fluorescence "Turn-on" chemosensors based on photoinduced electron transfer in conjugated polymers. *Macromolecules*, 38 (7): 2844-2849.
6. Gangopadhyay, R. & De, A. (2000). Conducting polymer nanocomposites: a brief overview. *Chemistry of Materials*, 12 (3): 608-622.
7. Heeger, A. J. (2001). Semiconducting and metallic polymers: The fourth generation of polymeric materials. *Journal of Physical Chemistry B*, 105 (36): 8475-8491.
8. Vijayakumar, N., Subramanian, E. & Padiyan, D. P. (2012). Conducting polyaniline blends with the soft template poly(vinyl pyrrolidone) and their chemosensor application. *International Journal of Polymer Materials*, 61 (11): 847-863.
9. Akinyeye R. O., Michira, I., Sekota, M., Ahmed, A. A., Tito, D., Baker, P. G. L., Brett, C. M. A., Kalaji, M. & Iwuoha, E. (2007). Electrochemical synthesis and characterization of 1,2-naphthaquinone-4-sulfonic acid doped polypyrrole. *Electroanalysis*, 19 (2-3): 303-309.
10. Liu, S., Wang, L., Luo, Y., Tian, J., Li, H. & Sun, X. (2011). Polyaniline nanofibres for fluorescent nucleic acid detection. *Nanoscale*, 3 (3): 967-969.
11. Sam, M. S., Lintang, H. O., Sanagi, M. M., Lee, S. L. & Yuliati, L. (2014). Mesoporous carbon nitride for adsorption and fluorescence sensor of *n*-nitrosopyrrolidone. *Spectrochimica Acta Part A: Molecular and Biomolecular Spectroscopy*, 124: 357-364.
12. Minh, T. T., Van, B. P., Van, T. D. & Thi, H. N. (2013). The optical properties and energy transition process in nanocomposite of polyvinyl-pyrrolidone polymer and Mn-doped ZnS. *Optical and Quantum Electronics*, 45 (2): 147-159.
13. Nishizawa, S., Kato, Y. & Teramae, N. (1999). Fluorescence sensing of anions via intramolecular excimer formation in a pyrophosphate-induced self-assembly of a pyrene-functionalized guanidium receptor. *Journal of American Chemical Society*, 121 (40): 9463-9464.
14. Wang, P., Gan, T., Zhang, J., Luo, J. & Zhang, S. (2013). Polyvinylpyrrolidone-enhanced electrochemical oxidation and detection of acyclovir. *Journal of Molecular Liquids*, 177:129-132.
15. Thi, T. M., Tinh, L. V., Van, B. H., Ben, P. V. & Trung, V. Q. (2012). The effect of polyvinylpyrrolidone on the optical properties of the Ni-doped ZnS nanocrystalline thin films synthesized by chemical method. *Journal of Nanomaterials*, 2012:1-8.
16. Zhang, J., Shen, G., Wang, W., Zhou, X. & Guo, S. (2010). Individual nanocomposite sheets of chemically reduced graphene oxide and poly(n-vinyl pyrrolidone): Preparation and humidity sensing characteristics. *Journal of Materials Chemistry*, 20 (48): 10824-10828.
17. Taylor, C. J., Bain, L. A., Richardson, D. J., Spiro, S. & Russell, D. A. (2004). Construction of a whole-cell gene reporter for the fluorescent bioassay of nitrate. *Analytical Biochemistry*, 328 (1): 60-66.
18. Ito, K., Takayama, Y., Makabe, N., Mitsui, R. & Hirokawa, T. (2005). Ion chromatography for determination of nitrite and nitrate in seawater using Monolithic ODS columns, *Journal of Chromatography A*, 1083(1-2): 63-67.

19. Smil, V. (1997). Global population and the nitrogen cycle. *Scientific American*, 277: 76-81.
20. Moorcroft, M. J., Davis, J. & Compton, R. G. (2001). Detection and determination of nitrate and nitrite: A review. *Talanta*, 54 (5): 785-803.
21. Tu, X., Gao, Y., Yue, R., Lu, Q., Zhou, Y. & Lu, Z. (2012). An amperometric nitrate sensor based on well-aligned cone-shaped polypyrrole-nanorods. *Analytical Methods*, 4 (12): 4182-4186.
22. Bendikov, T. A. & Harmon, T. C. (2005). A sensitive nitrate ion-selective electrode from a pencil lead. An analytical laboratory experiment. *Journal of Chemical Education*, 82 (3): 439-441.
23. Jang, A., Zou, Z., Lee, K. K., Ahn, C. H. & Bishop, P. L. (2010). Potentiometric and voltammetric polymer lab chip sensors for determination of nitrate, pH, and Cd(II) in Water. *Talanta*, 83 (1): 1-8.
24. Adeloju, S. B. & Sohail, M. (2011). Polypyrrole-based bilayer nitrate amperometric biosensor with an integrated permselective poly-ortho-phenylenediamine layer for exclusion of inorganic interferences. *Biosensors and Bioelectronics*, 26 (11): 4270-4275.
25. Lakowicz, J. R. (2006). *Principles of Fluorescence Spectroscopy*. Springer: New York. 3rd edition.
26. Long, Y., Chen, H., Yang, Y., Wang, H., Yang, Y., Li, N., Li, K., Pei, J. & Liu, F. (2009). Electrospun nanofibrous film doped with a conjugated polymer for DNT fluorescence sensor. *Macromolecules*, 42 (17): 6501-6509.
27. Yang, J.-S., & Swager, T. M. (1998). Fluorescent porous polymer films as TNT chemosensors: Electronic and structural effects. *Journal of American Chemical Society*, 120 (46): 11864-11873.

MALAYSIAN JOURNAL OF ANALYTICAL SCIENCES
Published by The Malaysian Analytical Sciences Society
ISSN 1394 - 2506

OXIDATION OF COMMERCIAL PETRONAS DIESEL WITH TERT-BUTYL HYDROPEROXIDE OVER POLYMOLYBDATE ALUMINA SUPPORTED CATALYST MODIFIED WITH ALKALINE EARTH METALS

(Pengoksidaan Diesel Komersial Petronas dengan Tert-Butil Hidroperoksida bersama Pemangkin Polimolibdenum Diubahsuai dengan Logam Alkali)

Wan Nazwanie Wan Abdullah, Rusmidah Ali*, Wan Azlee Wan Abu Bakar

Department of Chemistry, Faculty of Science,
Universiti Teknologi Malaysia, 81310 UTM Johor Bahru, Johor, Malaysia

**Corresponding author: rusmidah@kimia.fs.utm.my*

Received: 9 December 2014; Accepted: 9 October 2015

Abstract

Due to strict environmental legislation for ultra-low sulfur diesel fuels, increasing technical and operational challenges are imposed to conventional hydrodesulfurization (HDS) technology. Therefore, catalytic oxidative desulfurization (Cat-ODS) has been suggested to be an alternative method to replace a conventional method which is hydrodesulfurization. In this study, catalytic oxidation of commercial diesel was performed using an oil-soluble oxidant, tert-butyl hydroperoxide (TBHP), over polymolybdate supported on alumina MoO_3-PO_4/Al_2O_3 catalyst. A commercial Petronas diesel with 440 ppmw of total sulfur was employed to evaluate the elimination of sulfur compounds. Besides, the percentage of sulfur removal was measured by (GC-FPD). Alkaline earth metals, such as Calcium (Ca), Barium (Ba) and Strontium (Sr) were introduced on the surface of MoO_3-PO_4/Al_2O_3. The results showed that the catalytic activity decreased in the order, Ca/MoO_3-PO_4/Al_2O_3>Sr/MoO_3-PO_4/Al_2O_3> Ba/MoO_3-PO_4/Al_2O_3. The Ca/MoO_3-PO_4/Al_2O_3 catalyst was characterized by XRD and FESEM. XRD results showed that the best catalyst was highly amorphous while FESEM micrograph illustrated an aggregation and agglomeration of various particle sizes. The catalytic activity of Ca/MoO_3-PO_4/Al_2O_3 catalyst with various Ca/Mo ratios were also studied. When the Ca/Mo ratio was 15:85, the sulfur removal was the highest (79%) at 45ºC, 30 min and O/S molar ratio 3.0 with solvent = dimetylformamide (DMF), diesel/solvent ratio = 1.0.

Keywords: Oxidative desulfurization, commercial diesel, tert-butyl hydroperoxide, alkaline earth metals, polymolybdate, dimetylformamide

Abstrak

Disebabkan undang-undang alam sekitar yang ketat untuk bahan api sulfur diesel ultra-rendah, peningkatan cabaran teknikal dan operasi dikenakan kepada hydropenyahsulfuran konvensional teknologi (HDS). Oleh itu, penyahsulfuran oksidatif mengunakan pemangkin (Cat-ODS) telah dicadangkan untuk menjadi satu kaedah alternatif untuk menggantikan kaedah konvensional iaitu hydopenyahsulfuran. Dalam kajian ini, pengoksidaan diesel komersial telah dijalankan menggunakan oksida larut minyak, tert-butil hidroperoksida (TBHP) dan mangkin molibdena berpenyokong alumina, MoO_3-PO_4/Al_2O_3. Diesel komersial Petronas yang mengandungi sulfur 440 ppmw telah digunakan untuk menilai penyahsulfuran. Selain itu, peratusan penyingkiran sulfur telah diukur menggunakan (GC-FPD). Logam alkali, seperti Kalsium (Ca), Barium (Ba) dan Strontium (Sr) telah dicelup pada permukaan MoO_3-PO_4/Al_2O_3 pemangkin. Hasil kajian menunjukkan bahawa aktiviti pemangkin menurun mengikut susunan, Ca/MoO_3-PO_4/Al_2O_3 > Sr/MoO_3-PO_4/Al_2O_3 > Ba/MoO_3-PO_4/Al_2O_3. Pemangkin Ca/MoO_3-PO_4/Al_2O_3 telah dicirikan menggunakan XRD dan FESEM. Keputusan XRD menunjukkan pemangkin yang terbaik adalah sangat amorfus manakala

FESEM mikrograf menggambarkan satu aglomerasi dalam pelbagai saiz zarah. Aktiviti pemangkin Ca/MoO_3-PO_4/Al_2O_3 dengan pelbagai nisbah Ca/Mo telah juga dikaji. Apabila nisbah Ca/Mo adalah 15:85, penyingkiran sulfur adalah tertinggi (79%) pada keadaan optimum: 45ºC, 30 min dan nisbah O/S molar = 3.0 dengan pelarut = dimetilformamida (DMF), nisbah diesel/pelarut = 1.0.

Kata kunci: penyahsulfuran oksidatif, diesel komersial, tert-butil hidroperoksida, logam alkali, polimolibdena, dimetil-formamida

Introduction

Sulfur in transportation fuels is a major source of air pollution. Ultra-deep desulfurization of fuels is a matter of major interest not only because of increasing environmental concern and legal requirements, but also because ultra-low-sulfur fuel is a key requirement for fuel cell applications [1]. In the near future, the requirements for sulfur content in the fuel will become more stringent – with zero sulfur emission from the transport fuel, which calls for the development of advanced technologies for ultra clean fuel. Thus, great efforts have been made todecrease the content of sulfur in diesel oil [2]. HDS can produce lower sulfur level diesel oil, but this technology needs heavy cost in operating and capital. Therefore, oxidative desulfurization (ODS) has been considered as a further new technology for deep desulfurization of light oil [3]. This desulfurization process includes two stages: (i), oxidation in a first step; and (ii), liquid extraction at the end [4]. It is evident that the greatest advantages of the ODS process are low reaction temperature and pressure, and the expensive hydrogen gas is not used in the process. Most of the studies have been concentrated on heterogeneous molybdenum and tungsten supported on alumina. Recently, Wan Abu Bakar et al. [5], reported that MoO_3/Al_2O_3 was an active catalyst for the oxidation of dibenzothiophenic compounds. Therefore, it is interesting to explore the behavior of polymolybdate based catalyst doped with alkaline earth metal as dopant in the ODS reaction of commercial diesel in this paper.

Materials and Methods

Materials

All solvents and reactants were purchased and used without further purification. Phosphomolybdic acid hydrate (Across Organic), magnesium nitrate hexahydrate (Sigma-Aldrich), barium nitrate (Sigma-Aldrich), calcium nitrate tetrahydrate (Sigma-Aldrich) and strontium nitrate (Sigma-Aldrich), λ- Al_2O_3 beads 3-5 mm diameter (Sigma-Aldrich), *tert*-butyl hydroperoxide 70 wt.% in water (Acros Organic), dimethylformamide (MERCK) were used in this research. The fuel tested was a commercial diesel fuel from Petronas, Malaysia with 440 ppmw of sulfur content.

Preparation and characterization of catalysts

Calcium, barium, and strontium-doped MoO_3-PO_4/Al_2O_3 were prepared at ratio 15:85 by dissolving phosphomolybdic acid either with barium nitrate or calcium nitrate tetrahydrate or strontium nitrate in the sufficient volume of water and the solution were used for impregnation of Al_2O_3 (surface area: 292 m^2/g) at room temperature. The wet sample was dried overnight at room temperature before it was calcined at various temperatures for 5 h in air. XRD analysis was conducted by using Siemens D5000 crystalloflex X-Ray diffractometer equipped with 40 kV and 40 mA Cu target (λ CuKα) = 1.54Å) radiation. Using a step scan of 0.050° and a step time of a second per step, data were collected over the range of 2θ from 20° to 80°. FESEM-EDX analysis was accomplished by using Philips XL 40 microscope with energy of 15.9 kV coupled with EDX analyzer and bombarded using electron gun with tungsten filament under 25 kV resolutions to get the required magnification image.

Catalytic oxidative desulfurization

All oxidative desulfurization (ODS) reactions were conducted in a 100 mL round-bottom flask, equipped with a magnetic stirrer and fitted with condenser. In a typical run, the oil bath was first heated and stabilized at a constant temperature (45°C). Then, 10 ml of commercial diesel (440 ppmw) was added to the flask, followed by the addition of sulfur/TBHP in the ratio of 3 and 0.12 g catalyst. The mixture was refluxed for 30 minutes under vigorous stirring at atmospheric pressure. The oxidized diesel was extracted with DMF at ratio diesel/solvent = 1.0. The extraction process was conducted by vigorous stirring for 30 minutes followed by phase separation between diesel

and solvent. The treated diesel was analyzed by gas-chromatography (Agilent 6890N GC) equipped with FPD detector.

Results and Discussion

Catalytic Evaluation: Effect of alkaline earth metal dopants

Malka and Tatibouet [6] reported that Ca was a promoter of MoO_3-PO_4/Al_2O_3 catalyst in the oxidation of methanol. In the present study, several alkaline earth metals were used to modify MoO_3-PO_4/Al_2O_3 catalysts. Figure 1 shows that the activity of catalysts for oxidation of commercial diesel with TBHP decreased in the order: Ca/MoO_3-PO_4/Al_2O_3 >Sr/MoO_3-PO_4/Al_2O_3 > Ba/MoO_3-PO_4/Ba/Al_2O_3. As reported by Chang et al. [7], molybdenum oxide was a typical example of poorly dispersed catalyst, because molybdenum oxide, such as MoO_3, and alumina are considered to have an acidic character, thus weak interaction between molybdenum oxide and alumina is expected. Since alkaline earth metals possess strong basic characters, therefore it is possible to improve the dispersion of MoO_3 on the alumina by the introduction of alkaline earth metals.

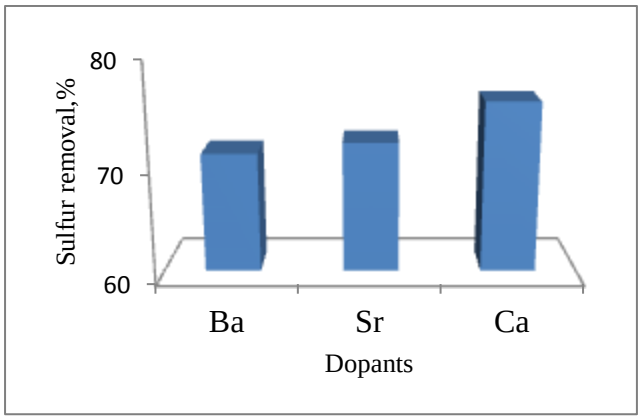


Figure 1. Effect of alkaline earth metal dopants on MoO_3-PO_4/Al_2O_3 catalyst calcined at 500 ºC for 5 h in the ODS reaction of commercial diesel

Effect of calcination temperature

Figure 2 shows the effect of calcination temperatures on Ca/MoO_3-PO_4/Al_2O_3 catalyst, calcined at 400, 500 and 600 ºC. The catalytic activity increase as the calcinations temperature was increased but further increase to 600 ºC would cause the decreasing of catalytic activity. This is because, the calcination temperature of 600 ºC could cause agglomeration of the catalyst particles thus decreasing the surface area consequently produces less active catalyst [8]. The optimum calcinations temperature obtained was 500 ºC.

Effect of Ca loading

The effect of Ca loading was carried out in order to investigate the optimum loading towards the performance of sulfur removal as shown in Figure 3. It clearly showed that an appropriate amount of Ca would increase the catalytic activity of the catalyst. The optimum calcium loading was 15 %. The excessive addition of Ca into the catalyst decreases the sulfur removal. It was due to the excess amount of Ca on the catalyst surface will cause the agglomeration to occur that reduced amount of active size.

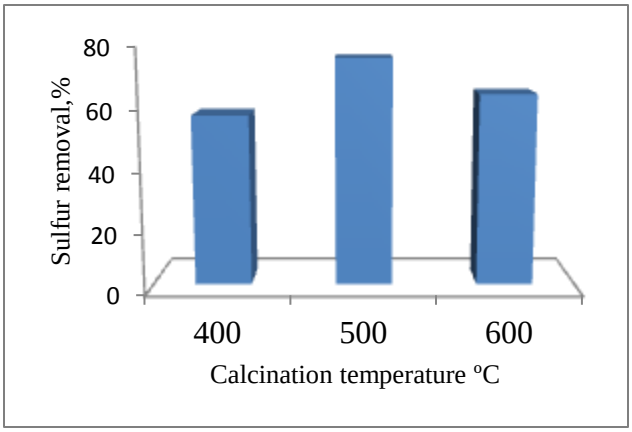


Figure 2. Effect of calcination temperature on Ca/MoO_3-PO_4/Al_2O_3 catalyst in the ODS reaction of commercial diesel

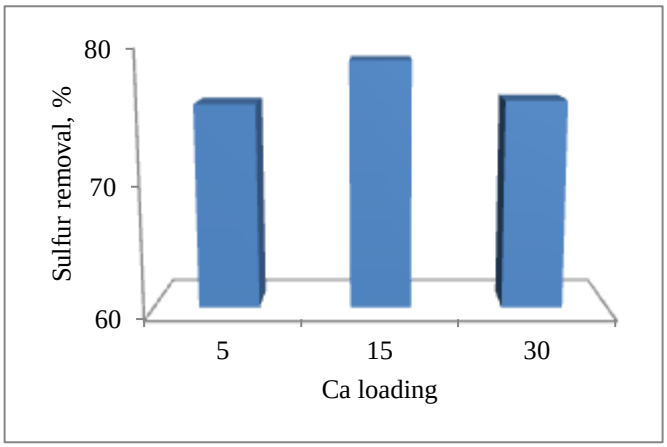


Figure 3. Effect of Ca loading on Ca/MoO_3-PO_4/Al_2O_3 catalyst calcined at 500 ºC for 5 h in the ODS reaction of commercial diesel

Characterization of Catalyst

Table 1 shows the textural properties of the bimetallic oxide catalysts, obtained by EDX analysis. EDX confirmed the presence of Mo, P, and Ca in the catalyst. It can be seen that by increasing the calcination temperatures from 400 to 600 ºC, the composition of Ca element was getting lower. It was probably due to the agglomeration of Mo which will hinder the Ca species, hence decrease the composition of this element and also diminished the catalytic activity. As shown in Figure 4, increase the calcination temperature from 400 to 600 ºC leads to the formation of aggregates and agglomerates with undefined shapes and mixture of larger and smaller particles size.

Table 1. Elemental analysis of the monometallic and bimetallic oxide catalysts

Catalysts	**Calcination T (°C)**	**Loading Mo (wt. %)**	**Loading P (wt.%)**	**Loading Ca (wt.%)**
MoO_3-PO_4/Al_2O_3	500	15	0.63	-
Ca/MoO_3-PO_4/Al_2O_3	400	16.30	2.16	0.5
Ca/MoO_3-PO_4/Al_2O_3	500	15	3.10	0.33
Ca/MoO_3-PO_4/Al_2O_3	600	16	3.3	0.14

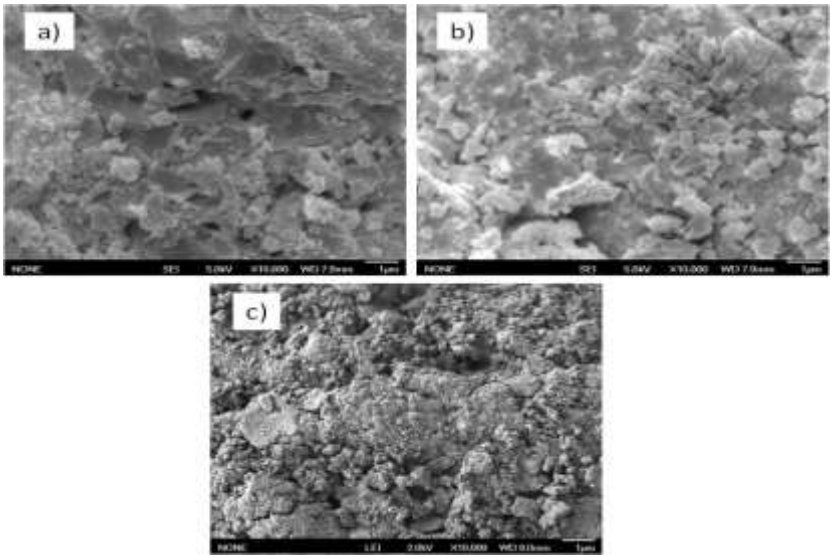


Figure 4. FESEM micrographs of Ca/MoO_3-PO_4 (15:85)/Al_2O_3 calcined at a) 400ºC b) 500ºC c) 600ºC. Magnification 10 k, scale bar 1µm

The XRD diffraction patterns of the Ca/MoO_3-PO_4/Al_2O_3 catalysts (Figure 5) indicate that the catalyst calcined at 500 °C and 700 °C possess amorphous structure which made the molybdenum phase undetectable suggesting the presence of high dispersion monolayer of Mo on the catalyst. This phenomenon could be the reason of higher catalytic activity of Ca/MoO_3-PO_4/Al_2O_3 (15:85) catalyst calcined at 500 ºC .The oxide peak does not appear in the diffractogram probably due to the small particle size of Ca (<4 nm) which is beyond XRD detection limit and low Ca loading in the catalyst as shown in EDX data.

Increasing the calcination temperature at 900 °C led to the formation of crystalline Mo_9O_{26} with new peaks obtained at 2θ value = 21.760° (I_{100}) and 25.85° (I_{60}) which attributed to base centered monoclinic phase. As shown in the diffractogram at 900 °C, the phase was dominated by alumina support which assigned as Al_2O_3 rhombohedral occurred at 2θ = 35.10° (I_{100}), 43.32° (I_{94}), 57.41° (I_{79}), 25.85º (I_{74}). It was claimed by Jones et al. [9] that catalysts calcined at temperatures above 500 °C showed high crystallinity. It was observed that the higher crystallinity and crystallize size of sample was observed at 900 °C than those treated at 500 °C and 700 °C suggesting that sample prepared at high temperature aggregate and agglomerate to form larger particle size with high crystallinity and also showed clear pattern of metal oxide. This results was agreement with our catalytic activity where the increased of calcinations temperature diminished the catalytic activity.

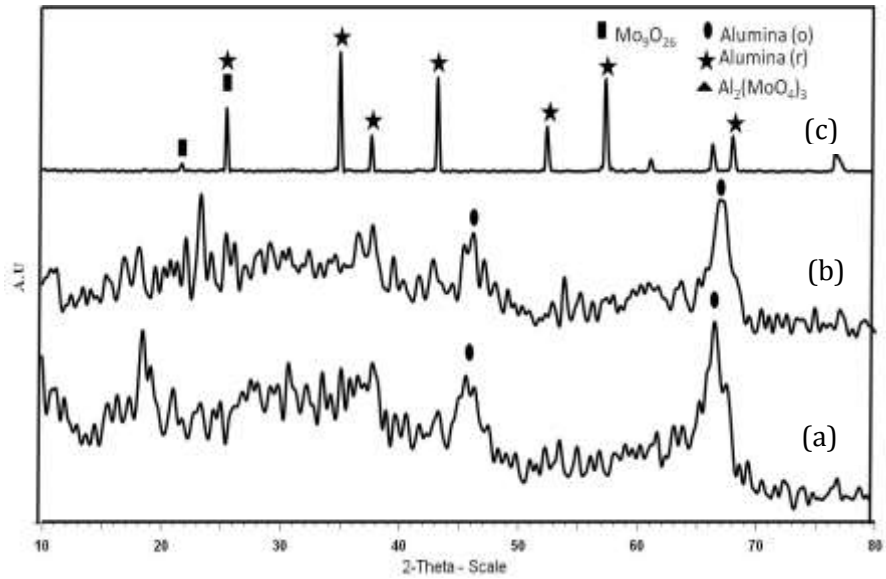


Figure 5. XRD diffractogram patterns of Ca/MoO_3-PO_4/Al_2O_3 calcined at (a) 500°C, (b) 700°C and (c) 900°C.

Mechanistic Study

The proposed peroxidic oxidation mechanism of DBT on Ca/MoO_3-PO_4/Al_2O_3 catalyst with TBHP is shown in Figure 6. The reaction pathway proceeded initially through the nucleophilic attack of TBHP on Ca/MoO_3-PO_4/Al_2O_3 to form species (1). The oxidation process must proceed by nucleophilic attack of the sulfur in the DBT (2) on the positively charged peroxometallic complex (1) to form DBT sulfoxide (3) and regenerated polymolybdate species, respectively. Subsequently, the sulfoxide (3) undergoes further oxidation to form DBT sulfone (4) [2].

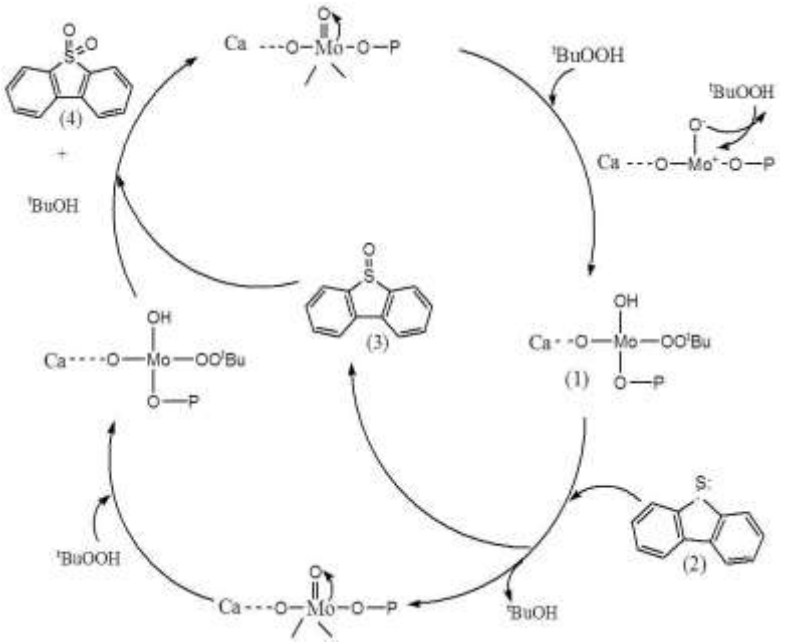


Figure 6. A proposed cyclic mechanism for the oxidation of dibenzothiophene by TBHP in the presence of Ca/MoO_3-PO_4/Al_2O_3 catalyst

Conclusion

Sulfur level in the Malaysia commercial diesel can be reduced from about 440 ppmw to 92 ppmw of sulfur at 45 ºC under mild condition using polymolybdate based catalyst with alkaline earth metal as dopant. Further improvement on MoO_3-PO_4/Al_2O_3 catalyst using different dopants indicated that oxidative desulfurization (ODS) for commercial diesel has been achieved over the Ca/MoO_3-PO_4/Al_2O_3 (15:85) calcined at 500 ºC. The catalyst had good activity in the oxidative desulfurization with TBHP in diesel fuel. These results may indicate that alumina supported polymolybdate based catalyst has the potential to be used as catalyst in Cat-ODS to meet the future regulation of sulfur in diesel fuel.

Acknowledgement

The authors thank the Department of Chemistry, Faculty of Science, Universiti Teknologi Malaysia, Johor as well as to FRGS vot 4F195 for funding the project and Ministry of Higher Education (MOHE).

References

1. Chica, A., Corma, A. and Dómine M. E. (2006). Catalytic oxidative desulfurization (ODS) of diesel fuel on a continuous fixed-bed reactor. *Journal of Catalysis*, 242: 299 – 308.
2. Abdullah, W. N. W., Bakar, W. A. W. A. and Ali, R. (2014). Catalytic oxidative desulfurization of diesel fuel utilizing a polymolybdate alumina supported catalyst: Characterization, catalytic activity and mechanistic study. *Reaction Kinetic Mechanism and Catalyst*, 114:547 – 560.
3. Lifeng, W., Baode, S., Frances, H. Y. and Ralph, T. Y. (2012). Effects of aromatics on desulfurization of liquid fuel by p-complexation and carbon adsorbents. *Chemical Engineering Society*, 73:208 – 217.
4. Tam, P. S., Kittrell, J. R. and Eldridge J. W. (1990). Desulfurization of fuel oil by oxidation and extraction. 1. Enhancement of extraction oil yield. *Industrial & Engineering Chemistry Research*, 29(3): 321 – 324.
5. Wan Abu Bakar, W. A., Ali, R., Abdul Kadir, A. A. and Wan Mokhtar, W. A. (2012). Effect of transition metal oxides catalyst on oxidative desulfurization of model diesel. *Fuel Processing Technology*, 101: 78 – 84.
6. Malka, K. and Tatiboue, J. M. (1998). A two-step preparation of silica-supported calcium-molybdenum catalysts. *Journal of Catalysis*, 175: 204 – 212.
7. Chang, J., Wang, A., Liu, J., Li, X. and Hu, Y. (2010). Oxidation of dibenzothiophene with cumene hydroperoxide on MoO_3/SiO_2 modified with alkaline earth metals. *Catalysis Today*, 149: 122 – 126.
8. Wan Abdullah, W. N., Wan Abu Bakar W. A., Ali R. and Embong Z. (2015). Oxidative desulfurization of commercial diesel catalyzed by tert-butyl hydroperoxide polymolybdate on alumina: Optimization of Box-Behnken design. *Clean Technologies and Environment Policy*, 17: 433 – 441.
9. Jones, C., Cole, K. J., Taylor, S. H., Crudace, M. J. and Hutchings, G. J. (2009). Copper manganese oxide catalysts for ambient temperature carbon monoxide oxidation: Effect of calcination on activity. *Journal of Molecular Catalysis A: Chemical*, 305:121 – 124.

MALAYSIAN JOURNAL OF ANALYTICAL SCIENCES
Published by The Malaysian Analytical Sciences Society
ISSN 1394 - 2506

HYDROGEN PRODUCTION FROM GASIFICATION OF PALM KERNEL SHELL IN THE PRESENCE OF Fe/CeO_2 CATALYSTS

(Penghasilan Hidrogen daripada Pengegasan Isirung Kelapa Sawit dengan Kehadiran Mangkin Fe/CeO_2)

Anita Ramli[1]*, Mas Fatiha Mohamad[2], Suzana Yusup[2], Taufiq Yap Yun Hin[3]

[1]*Department of Fundamental and Applied Sciences*
[2]*Department of Chemical Engineering*
Universiti Teknologi PETRONAS, 32600 Bandar Seri Iskandar, Perak, Malaysia
[3]*Department of Chemistry,*
Universiti Putra Malaysia, 43400 UPM Serdang, Selangor, Malaysia

**Corresponding author: anita_ramli@petronas.com.my*

Received: 24 February 2015; Accepted: 27 October 2015

Abstract

Biohydrogen is a renewable source of clean fuel and energy which can be derived from biomass. One of the suitable candidate as a source of biomass is palm kernel shell (PKS). Our initial work shows that biohydrogen may be produced from PKS in the presence of zeolite supported catalysts. The potential of using cerium oxide (CeO_2) supported catalysts for the production of biohydrogen from PKS is explored in this work using 2.5 – 10 % Fe loading. The catalysts were prepared by incipient wetness impregnation method and calcined at 500 ^oC for 16 h. The physicochemical properties of these catalysts were characterized using BET and XRD. The catalysts were tested in dry and steam gasification of PKS at 700 ^oC using PKS feeding rate of 2 g h^{-1} under N_2 atmosphere with biomass to catalyst ratio of 3:1 (wt/wt). Steam to biomass ratio of 3.5:1 (wt/wt) was used in steam gasification reaction. The gaseous products were analyzed using an on-line gas chromatography equipped with thermal conductivity detectors (TCD) and fitted with Molsieve 5A and Hayesep Q columns. Result shows that 2.5 % Fe/CeO_2 gave the highest hydrogen production in both the dry and steam gasification of PKS.

Keywords: biohydrogen, palm kernel shell, ceria supported catalysts, gasification

Abstrak

Biohidrogen adalah sumber bahan api yang boleh diperbaharui daripada sumber biomas. Isirung kelapa sawit (PKS) merupakan salah satu sumber biomas yang sesuai digunakan umtuk tujuan ini. Kajian awal menunjukkan biohidrogen boleh dihasilkan daripada PKS dengan menggunakan mangkin berpenyokong zeolite. Dalam kajian ini, muatan mangkin 2.5 – 10 % logam Fe berpenyokong cerium oksida (CeO_2) digunakan untuk meningkatkan penghasilan biohydrogen daripada PKS. Pemangkin disediakan menggunakan kaedah pengisitepuan pembasahan permulaan dan dikalsinkan pada suhu 500 ^oC selama 16 jam. Sifat fizikal kimia pemangkin ini dianalisa menggunakan teknik BET dan XRD. Kereaktifan mangkin untuk penghasilan biohidrogen diuji dalam pengegasan kering dan berstim pada suhu 700 ^oC dengan PKS diperkenalkan pada kadar 2g h^{-1} dan nisbah PKS kepada pemangkin adalah 3:1 (wt/wt). Nisbah stim kepada PKS 3.5: 1 (wt/wt) telah ditetapkan dalam eksperimen pengegasan berstim. Gas yang telah dihasilkan telah dianalisa menggunakan kromatograf gas yang dilengkapi pengesan konduktiviti termal (TCD) serta tiub Molsieve 5A dan Hayesep Q. Keputusan kajian menunjukkan penghasilan hidrogen yang maksimum dicapai dengan kehadiran mangkin 2.5 % Fe / CeO_2.

Kata kunci: biohidrogen, tempurung kelapa sawit, mangkin berpenyokong CeO_2, pengegasan

Introduction

The hiking prices of petroleum fuel and growing issues on environmental impact, particularly emission of greenhouse gases draw world's attention to the biomass as an alternative energy. The possible utilization of biomass to produce bio-fuels such as bioethanol and biohydrogen makes biomass a critically important source of sustainable energy future. The production of hydrogen rich gas from renewable biomass is being promoted as the fuel for the future since it has higher engine efficiencies and zero emission.

Biomass can be reformed to hydrogen through gasification technology where it converts lignocellulosic biomass to gaseous products such as H_2, CO, CO_2, CH_4 and light hydrocarbons. Traces amount of char, ash and tar are also produced during biomass gasification. However, the formation of tar and char create severe problems in the operation of gas engine such as corrosion, burning difficulties and internal deposition.

Catalytic gasification of biomass helps to decompose tar and heavy hydrocarbon in the product gas streams at a lower temperature. In fact, the application of catalyst not only functions as tar abatement, but it also plays a significant role in promoting high content of product gases [1]. Despite of having significant activities as water gas shift (WGS) catalysts and in hydrocarbon reforming, Fe-based catalysts also facilitate in biomass steam gasification. This is explained by the capability of Fe to crack tar produced in the product stream which is similar to the capability of dolomite [2].

To avoid catalyst deactivation, different promoters or supports are added to the catalyst precursor. In our previous work, Zeolite Beta (BEA) supported catalysts were used as a catalyst and the result indicated a significant performance in producing H_2 from steam gasification of PKS [3]. This work presents further catalyst development using Cerium Oxide (CeO_2) as the catalyst support due to its redox properties and ability to promote metal-ceria interaction [4]. Tomishige and co-workers [5] investigated various oxide supports and supported metal catalysts for gasification of cellulose at 550 ^oC and reported that the highest yield of CO and H_2 were achieved using CeO_2 as support while the lowest conversion was found on Al_2O_3 and SiO_2. Thus, this work aims to study the effect of Fe loading on CeO_2 on the production of H_2 in dry and steam gasification of PKS.

Materials and Methods

Chemicals and raw materials

Palm kernel shell (PKS), the biomass feedstock for gasification reaction was collected from Felda Nasaruddin Plantation in Perak. The PKS was first dried at 110 ºC for 4 h before they were ground and sieved to 500 µm. The ultimate and proximate analyses of PKS are displayed in Table 1.

Table 1. Ultimate and Proximate analysis of PKS

Ultimate analysis (%)	
C	49.65
H	6.13
N	0.41
S	0.48
O	43.33
Proximate analysis (%wt wet basis)	
Volatile matter	81.03
Fixed carbon	14.52
Ash	4.44

Catalyst loading with range 2.5 – 10 wt% Fe/CeO_2 were prepared using incipient wetness impregnation method with Cerium oxide (CeO_2) as the catalyst support. CeO_2 (Sigma Aldrich, 99.9 %) was first calcined at 500 °C for 16 hr. Next, the required amount of $Fe(NO_3)_3.9H_2O$ (Merck, 98 %) was dissolved in sufficient amount of deionized water followed by addition of CeO_2 to the metal salt solution while stirring. The slurry formed was left for 4 hr and then dried at 120 °C for 16 hr. Finally, the prepared catalysts were calcined at 500 °C for 16 hr. The prepared catalysts were crushed and sieved to <250 µm. The catalysts are denoted as xFe/CeO_2, where x represents the amount of Fe loading e.g. $2.5Fe/CeO_2$ is 2.5wt % of Fe was loaded on cerium oxide.

Characterization of catalysts

N_2 adsorption-desorption isotherm (Micromeritics ASAP 2020) was used to determine the surface area, pore size and pore volume of the catalyst. The samples were degassed in vacuum at 200 °C for 4 hr prior to the measurement. Powder X-Ray Diffraction (XRD) pattern of the catalysts was obtained using a Bruker D8 Advance diffractometer with a radiation sources of Cu-Kα to identify their crystal structures. The reducibility measurement of the catalysts was conducted on a Thermo Electron TPDRO 1100 analyser. The sample was reduced in a stream of 5 $\%H_2/N_2$ at a heating rate of 20 °C to reach a final temperature of 1000 °C.

Gasification of PKS

Both dry and steam gasification reaction of PKS were performed at 700 °C in a two staged reactors. The biomass samples were placed in the first reactor and a catalyst sample was held in placed by quartz wool in the second reactor with biomass to catalyst mass ratio of 3:1. The reactor system was purged with N_2 at 100 ml min^{-1} before both reactors were heated to 700 °C at a heating rate of 150 °C/hr. Then, the PKS was introduced at feeding rate of 2 g hr^{-1} under N_2 atmosphere. Water was introduced by liquid pump when the temperature of the first reactor reached 700 °C, where it was instantly evaporated at the elevated temperature and then carried to the reactor by N_2 flow. The steam to biomass (S/B) ratio was 3.5. The outlet gases passed through a condenser prior to analysis with online gas chromatography (Agilent 7890A) equipped with two thermal conductivity detectors (TCD) and a flame ionization detector (FID). H_2, CO and CO_2 were measured using TCD detectors fitted with Molsieve 5A and Hayesep Q column, while CH_4 and C_2 hydrocarbons were analyzed using FID detector fitted with HP-AL/S and DB-1 columns.

Results and Discussion

Catalysts characterization

The N_2 adsorption- desorption isotherms of the CeO_2 support shows a Type III isotherm according to IUPAC classification system which indicates that the CeO_2 is a non-porous materials. Table 2 shows the BET surface area of the CeO_2 based catalysts. The surface area increases with increasing of Fe loading. This shows that the loading of Fe metal provides additional nucleation sites which contribute to the higher surface area [6].

Table 2. The surface area of Fe/CeO_2 catalysts

Catalysts	**CeO_2**	**$2.5Fe/CeO_2$**	**$5Fe/CeO_2$**	**$7.5Fe/CeO_2$**	**$10Fe/CeO_2$**
Surface area (m^2/g)	4.2	5.0	5.2	5.6	6.4

The X-ray diffractograms of CeO_2 based catalysts are shown in Figure 1. All samples show four significant diffraction peaks at 2θ= 28.6°, 33.1°, 47.6°, 56.4° which correspond to the (111), (200), (220) and (311) planes of cubic CeO_2 (81-0792 JCPDS file). It is observed that the peak heights slightly decrease with increasing loading of Fe on the CeO_2 support. Appearance of a small peak corresponding to the hexagonal hematite iron oxide, Fe_2O_3 (02-0919 JCPDS file) is only detected in $10Fe/CeO_2$ catalyst which indicates that the Fe_2O_3 are finely dispersed on the surface of CeO_2 at lower loading of Fe. However, the absence of diffraction peaks has been suggested to be attributed to the Fe_2O_3 phase where Fe was substituted in the CeO_2 lattice leading to formation of a solid solution of iron-cerium oxide [7].

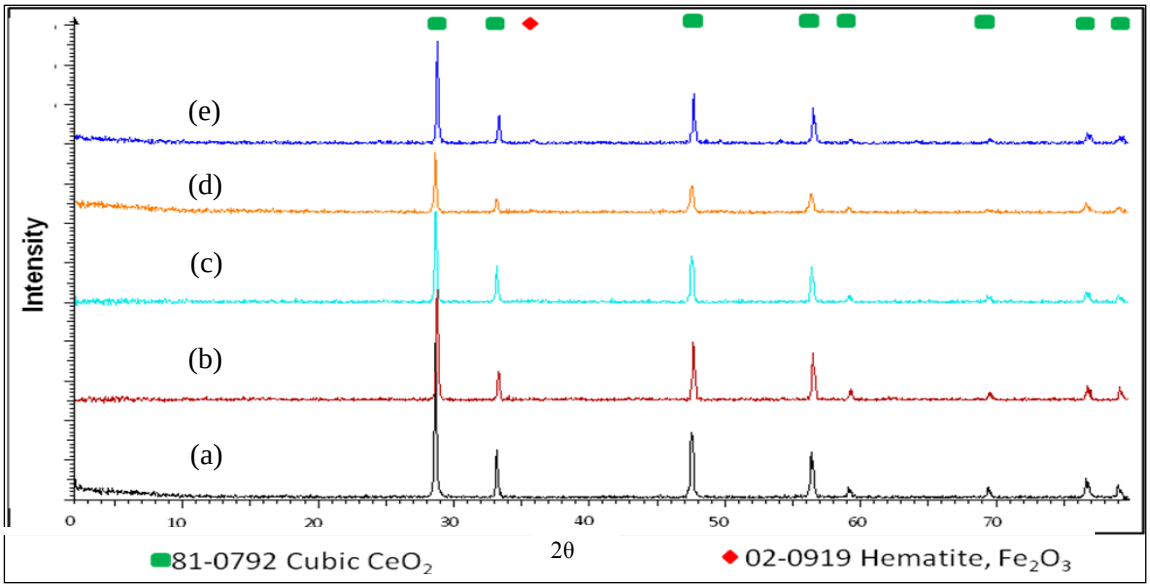


Figure 1. X-Ray diffraction patterns of (a) CeO_2 support, (b) 2.5Fe/CeO_2, (c) 5Fe/CeO_2, (d) 7.5Fe/CeO_2 and (e) 10Fe/CeO_2

Catalytic activity

Figure 2 shows the distribution of gaseous products from dry gasification of PKS in the presence of Fe/CeO_2 catalysts with H_2 as the main products followed by CO_2 and CO while only trace amount of CH_4 was detected. Figure 2 shows that H_2 production is significantly improved when CeO_2 was used as catalyst. Incorporation of 2.5 wt% Fe to the CeO_2 support slightly increased the H_2 production but further increased in Fe loading resulted in reduction in H_2 production. However, it is also observed that increased loading of Fe resulted in an increment in CO_2 and CO produced, which indicates that the PKS undergo oxidation. In addition, the enhanced CO_2 concentration may also contribute from the oxidation of CO to produce CO_2, with reaction path as shown in Eq (1)[8].

$$CO_{ad} + O_{lattice} \rightarrow CO_2 \quad (1)$$

The maximum H_2 yield with the least formation of CO_2 and CO is obtained in the presence of 2.5 wt% Fe for both dry and steam gasification. This result may be explained in term of the formation of cubic ceria-like solid solution as corroborated in XRD pattern. The Fe-O-Ce interaction enables the formation and stabilization of small particles of mixed oxides. As this catalyst reacts, it may provide a larger number of exposed actives sites and result in higher catalytic activity [9]. It is concluded that the interaction between well dispersed Fe species and the good oxygen mobility in the Ce-Fe solid solution promotes the formation of synthesis gas. Therefore, it can be expected that the production of H_2 decreses with increasing of Fe loading.

Both Figures 2 and 3 show that Fe loading higher than 2.5 wt% resulted in a decreased in H_2 production which could be attributed to the lack of Fe-O-Ce interactions. This trend is in agreement with those reported earlier where they proposed that lower catalytic activity of Fe-CeO_2 is due to the diffusion of Fe^{3+} into the lattice structure of Ce^{4+}, resulting in less active sites available for reaction to take place [10].

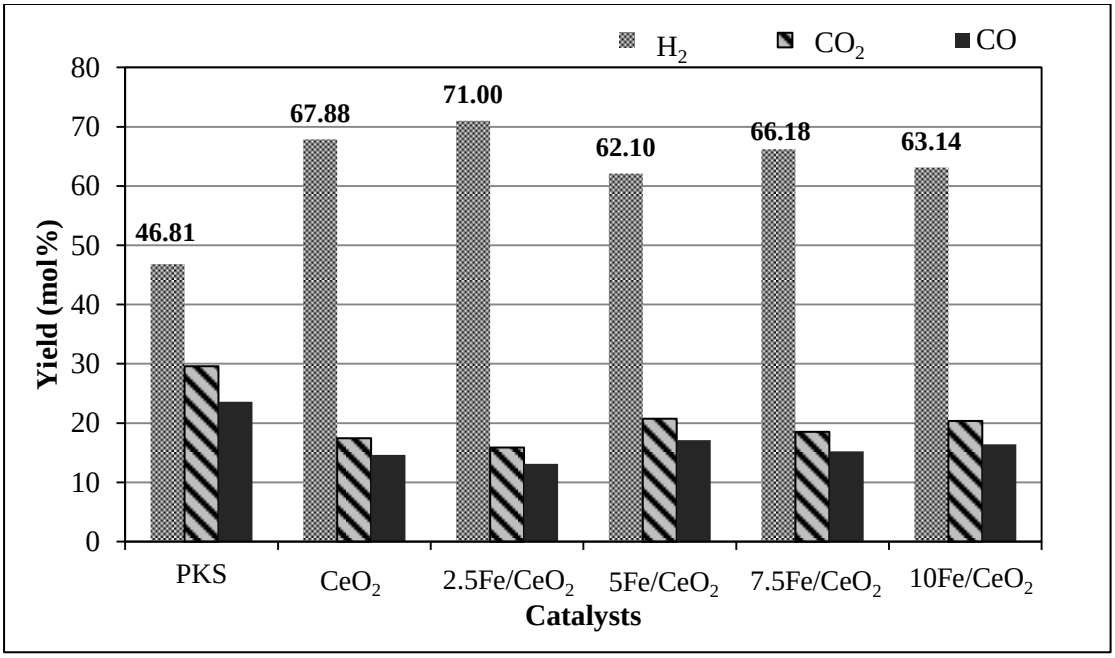


Figure 2. Distribution of gaseous products from dry gasification of PKS

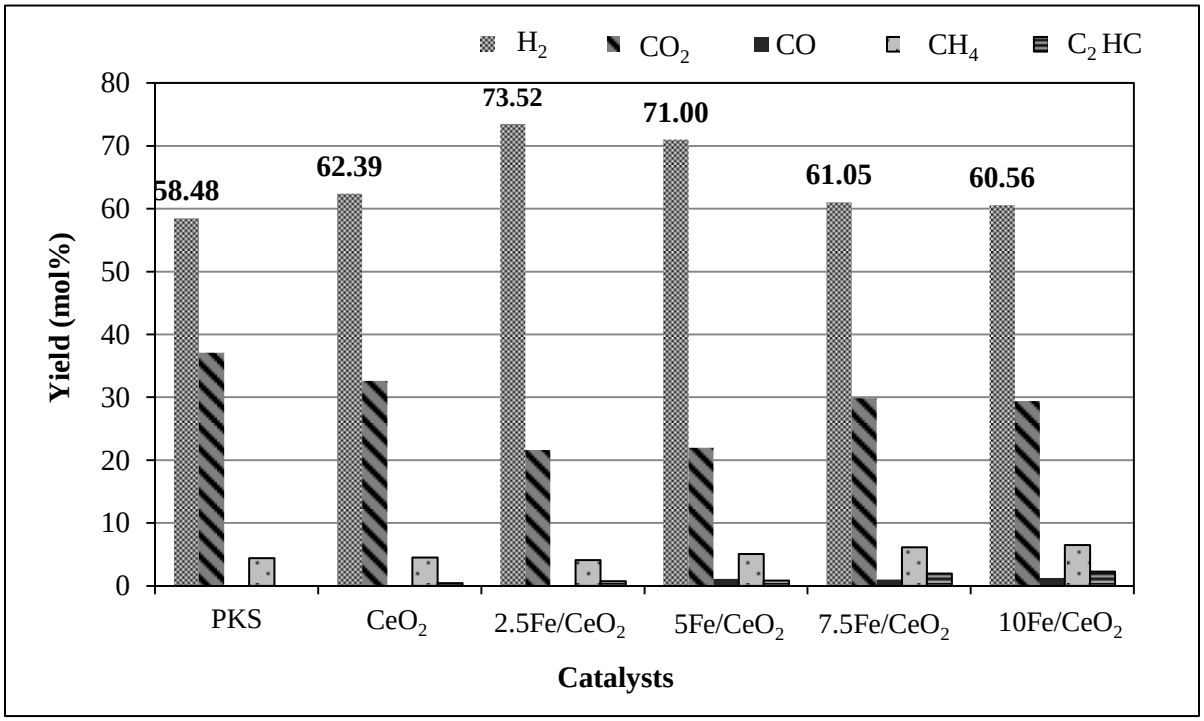


Figure 3. Distribution of gaseous products from steam gasification of PKS

The introduction of steam facilitates further water gas shift reactions to occur in the gasification. It has been suggested that the interaction between carbon deposits from PKS decomposition and the lattice oxygen of CeO_2 would lead to the formation of CO [11] as shown in Eq (2) which then reacts with steam to produce H_2 and CO_2, following the WGS reaction (Eq3).

$$C + O_{lattice} \rightarrow CO \quad (2)$$
$$CO + H_2O \rightarrow H_2 + CO_2 \quad (3)$$

Conclusion

Fe/CeO_2 catalysts with Fe loading of 2.5-10 wt% were successfully prepared and tested in PKS gasification for production of biohydrogen. Nitrogen adsorption-desorption isotherms of these catalysts show that they are Type III materials indicating that the catalysts are nonporous materials. XRD results confirmed the presence of four strong peaks of cubic Ceria and a weak peak of hexagonal hematite iron oxide, Fe_2O_3. The 2.5 wt% Fe/CeO_2 catalyst produced the maximum H_2 yield, 70% with the least formation of CO_2 and CH_4. The H_2 yield increased to 73% in steam gasification of PKS as compared to dry gasification. The favourable catalytic activity in gasification reactions may be correlated to the metal support interaction between iron species and the cubic CeO_2 solid solution. It is concluded that the H_2 yield decreases with increasing of Fe loading.

Acknowledgement

The authors would like to thank Malaysian Ministry of Science, Technology and Innovation (MOSTI) for financial support under National Nanotechnology Directorate and Universiti Teknologi PETRONAS for providing all the necessary facilities.

References

1. Balat, M., Kirtay, E. and Balat. H. (2009). Main routes for the thermo-conversion of biomass into fuels and chemicals. Part 2: Gasification systems *Energy Conversion and Management*, 50: 3158 – 3168.
2. Nordgreen, T., Liliedahl, T. and Sjöström. K. (2006). Metallic iron as a tar breakdown catalyst related to atmospheric fluidized bed gasification of biomass, *Fuel*, 85: 689 – 694.
3. Ramli, A., Misi, S. E. E., Mohamad, M. F. and Yusup. S. (2013). H_2 Production from steam gasification of Palm Kernel Shell in the presence of 5% Ni/BEA and 5% Fe/BEA catalysts, *Advanced Science Letters*, 19: 950 – 954.
4. Kaspar, J., Fornasiero, P. and Graziani. M. (1999). Metallic iron as a tar breakdown catalyst related to atmospheric, fluidised bed gasification of biomass, *Catalysis Today*, 50: 285 – 298.
5. Tomishige, K., Asadullah, M. and Kunimori. K. (2003). Novel catalysts for gasification of biomass with high conversion efficiency, *Catalysis Surveys from Asia*, 7: 219 –223.
6. Pecchi, G., Reyes, P. and Villasenor. J. (2003). Fe supported catalysts prepared by the sol-gel method. Characterization and evaluation in phenol abatement, *Journal of Sol-Gel Science and Technology*, 26: 865 – 867.
7. Reddy, A. S., Chen, C., Chien, S., Lin, C., Lin, K. and Chang. S. (2010). Synthesis and characterization of Fe/ CeO_2 catalysts: epoxidation of cyclohexene, *Journal of Molecular Catalysis A*, 318: 60 – 67.
8. Rao, G. R. and Mishra. B. G. (2003). Structural, redox and catalytic chemistry of ceria based materials, *Bulletin of the Catalysis Society of India*, 2: 122 – 134.
9. Perez-Alonso, F. J., Lopez Granados, M., Ojeda, M., Terreros, P., Rojas, S., Herranz, T., Fierro, J. L. G., Gracia, M. and Gancedo, J. R. (2005). Chemical structures of co-precipitated Fe-Ce mixed oxides, *Chemistry of Materials*, 17: 2329 – 2339.
10. Tang, L., Yamaguchi, D., Burke, N., Trimm, D. and Chiang, K .(2010). Methane decomposition over ceria modified iron catalysts, *Catalysis Communications*, 11: 1215 –1219.
11. Li, K. Z., Wang, H., Wei, Y. And Yan, D. X.(2009). Selective oxidation of carbon using iron-modified cerium oxide, *Journal of Physical Chemistry C*, 113: 15288 – 15297.

MALAYSIAN JOURNAL OF ANALYTICAL SCIENCES
Published by The Malaysian Analytical Sciences Society
ISSN 1394 - 2506

DEVELOPMENT OF CELLULOSE NANOFIBRE (CNF) DERIVED FROM KENAF BAST FIBRE AND IT'S POTENTIAL IN ENZYME IMMOBILIZATION SUPPORT

(Penghasilan Nano-Gentian Selulosa (CNF) diperolehi daripada Gentian Kulit Kenaf dan Potensinya sebagai Penyokong Pemegunan Enzim)

Safwan Sulaiman[1], Mohd Noriznan Mokhtar[1]*, Mohd Nazli Naim[1], Azhari Samsu Baharuddin[1], Mohamad Amran Mohd Salleh[2], Alawi Sulaiman[3]

[1]*Department of Process and Food Engineering*
[2]*Department of Chemical and Environmental Engineering*
Faculty of Engineering,
Universiti Putra Malaysia, 43400 Serdang, Selangor, Malaysia
[3]*Faculty of Plantation and Agrotechnology,*
Universiti Teknologi MARA, 40450 Shah Alam, Selangor, Malaysia

**Corresponding author: noriznan@upm.edu.my*

Received: 24 February 2015; Accepted: 27 October 2015

Abstract

This research mainly focuses on developing a natural cellulose nanofibre (CNF) from kenaf bast fibre and its potential for enzyme immobilization support. CNF was isolated by using a combination between chemical and mechanical treatments such as alkaline process and high-intensity ultrasonication process to increase the efficiency of hemicellulose and lignin removal, and to reduce its size into nano-order. The morphological study was carried out by using scanning electron microscope (SEM), indicating most of CNF diameter in range of 50-90 nm was obtained. The result of chemical analysis shows that cellulose content of raw bast fibre, bleached pulp fibre and CNF are 66.4 %, 83.7 % and 90.0 %, respectively. By decreasing the size of cellulose fibre, it increases the number of (O–H) group on the surface that plays as important role in enzyme immobilization. Covalent immobilization of cyclodextrin glucanotransferase (CGTase) onto CNF support resulted in about 95.0 % of protein loading with 69.48 % of enzyme activity, indicating high immobilization yield of enzyme. The enzymatic reaction of immobilized CGTase was able to produce more than 40 % yield of α-CD. Reusability profile of immobilized CGTase resulted in more than 60 % of retained activity up to 7 cycles. Therefore, the CNF is highly potential to be applied as enzyme immobilization support.

Keywords: cellulose nanofibre (CNF), kenaf, enzyme immobilization; cyclodextrin glucanotransferase (CGTase), chemical and mechanical treatments

Abstrak

Kajian ini memberi tumpuan terutamanya kepada penghasilan nano-gentian selulosa (CNF) semulajadi daripada gentian lapisan kulit kenaf dan potensinya sebagai penyokong pemegunan enzim. CNF dihasilkan dengan menggunakan gabungan antara rawatan kimia dan mekanikal seperti proses alkali dan proses ultrasonikasi berintensiti tinggi untuk meningkatkan kadar kecekapan penyingkiran hemiselulosa dan lignin, dan pengurangan saiz kepada nano. Kajian morfologi menggunakan mikroskop imbasan elektron (SEM), menunjukkan sebahagian besar daripada saiz diameter CNF diperolehi dalam julat 50-90 nm. Hasil kajian analisis kimia menunjukkan bahawa kandungan selulosa daripada gentian mentah, gentian pulpa dan CNF masing-masingnya adalah 66.4 %, 83.7 % dan 90.0 %. Dengan mengurangkan saiz diameter gentian selulosa, ia meningkatkan bilangan kumpulan (O-H) di permukaan sokongan yang mana memainkan peranan yang penting dalam pemegunan enzim. Pemegunan

Siklodektrin Glukanotransferase (CGTase) secara kovalen pada CNF menunjukkan kira-kira 95.0 % muatan protein dengan 69.48 % aktiviti enzim, menunjukkan pemegunan enzim yang tinggi terhasil. Tindak balas berenzim CGTase terpegun juga mampu menghasilkan lebih daripada 40 % pengeluaran α-CD. Kitaran kebolehulangan enzim terpegun menunjukkan lebih daripada 60 % daripada aktivitinya dapat dikekalkan selama 7 kitaran. Oleh itu, CNF sangat berpotensi untuk digunakan sebagai penyokong pemegunan enzim.

Kata kunci: gentian-nano selulosa (CNF), kenaf, pemegunan enzim, siklodektrin glukanotransferase (CGTase), rawatan kimia dan mekanikal

Introduction

Nowadays, billions of tons of natural fibre around the world are considered abundant, inexpensive and readily available. Thus, it becomes more interesting to deal with green environment, energy demand, and financial problems. Kenaf (*Hibiscus cannabinus L.)* is one of the feasible resources of cellulose with economic and ecological advantages. Kenaf consists of two types of fibre, bast and core fibre. Bast refers to outer layer of plant fibre (30 % of dry weight), meanwhile core represents the inner layer of fibre (70 % of dry weight). Bast fibre has been reported possess an excellent mechanical characteristic, which can be an excellent support for enzyme immobilization, as well as alternative to current used of polymer-grafting material support [1]. Bast fibre is one of non-wood lignocellulosic fibres comprises of three major components such as lignin, hemicellulose and cellulose [2]. In fact, cell walls of lignocellulosic fibres consist of basic structural, called as microfibrils. As a result, cellulose microfibrils can actually be considered to be nanofibers, since the definition of a nanofiber is a size <100 nm in one dimension [3]. Cellulose is defined as a linear polymer that consists of both crystalline and amorphous region, while hemicellulose and lignin display a complete amorphous structure [4]. Cellulose chain was bound together by hydrogen bonding, whereas lignin and hemicellulose form a matrix surrounding the CNF. Removal of these matrix by top-down approach techniques (chemical-mechanical treatment) is essential to obtain CNF, as well as to improve the surface morphology for enzyme immobilization [5].

The use of CNF in enzyme immobilization is not only to enhance the performance of enzymatic synthesis, but also to minimize the loss of enzyme activity caused by immobilization due to the presence of large surface area per volume ratio [6]. Large surface area also provides a high number of surface functional group especially (O–H) group on the surface of CNF, which increase the number of the interaction of enzyme onto the CNF support [7]. Covalent interaction is the most stable interaction of enzyme molecules to the support; it can minimize the enzyme leakage from its support into the reaction medium compared to other immobilization techniques [8]. The objective of this work is to study the potential application of CNF from kenaf bast fibre in enzyme immobilization *via* covalent binding.

Materials and Methods

Raw material and chemicals

Kenaf raw bast fibre was a gift from Lembaga Kenaf dan Tembakau Negara (LKTN), Malaysia. All chemicals are technical grade such as sodium hydroxide (NaOH), sodium chlorite ($NaClO_2$), acetic acid (CH_3COOH), aqueous hydrogen peroxide (H_2O_2), anthraquinone (AQ), Bradford reagent (coomasive blue), glutaraldehyde (GA), 1,12-diaminododecane and bovine serum albumin (BSA) (Merck Chemicals and R&M Chemicals, Malaysia). Cyclodextrin glucanotransferase from *B. macerans* (CGTase, EC 2.4.1.19) with activity of 600 U/ml was purchased from Amano Enzyme Inc., Japan. Water soluble potato starch was purchased from Sigma, Malaysia.

Isolation of CNF support

The isolation process of CNF consists of several steps of alkaline process and high-intensity ultrasonication. Kenaf bast fibre was retted by using water and then it was oven-dried overnight. Kenaf bast fibre was then cut into shorter, about 1-2 cm in length. About 20 g of short bast fibre was heated in aqueous solution containing of 15 wt % of NaOH and 0.1 wt % of AQ, using non-stirred pressure vessel (MOC: SS316, Equipment no: 2311, AMAR Equipments PVT. LTD., Mumbai, India), and the process was called as delignification process. The ratio of fibre to liquid was 1:9 and the process was carried out at 180 ^{0}C (40 ± 3 bar) for 30 min. AQ was added in the solution to increase the delignification rate, as well as to preserve the fibres from alkaline degradation [9]. In fact, delignification process is mainly to remove the lignin content in the fibre. The obtained pulp was rinsed using distilled water several times to remove any residual chemical from it. Bleaching process was performed to remove

the residual lignin and hemicellulose, which it involved with three stages of different chemical processes (e.g. $NaClO_2$, CH_3COOH, NaOH, and H_2O_2), according to method disclosed by Jonoobi et al. [10]. After a series of bleaching process, bleached pulp fibre was filtered and rinsed with distilled water until it became neutralized pH. The process was repeated five times until the fibre became white, and kept in a water-swollen condition. In preparation of mechanical treatment, the bleached pulp fibre was soaked in distilled water and sonicated by using high-intensity ultrasonic dismembrator (FB705, Fisher Scientific (M) Sdn. Bhd., Malaysia) at 20 kHz of operating frequency, which equipped with 12.7 mm in diameter size of cylindrical titanium alloy probe. The subsequent ultrasonication was conducted for 30 min to isolate CNF from bleached pulp fibre. The ultrasonic treatment was carried out in an ice/water bath. Ice was maintained throughout the ultrasonication process to avoid overheating [11].

Functionalized support *via* chemical coupling reaction

CNF suspension was freeze-dried. Dried CNF support, about 1 g was coupled with 1 g of 1,12-dodecanediamine in 50 ml of methanol containing 5 g sodium methoxide in a round bottom flask. The reaction mixture was refluxed for 6 hours in a water bath at 80 °C. Then, it was filtered after cooling and washed with distilled water several times to remove any excess chemicals. The CNF–1,12-dodecanediamine derivative was stirred in 40 ml of 0.1 M potassium phosphate buffer (pH 8.0), containing 2.5% (v/v) of GA at 25 °C for 2 hours. The CNF–1,12-dodecanediamine–GA derivative was filtered and washed with the same phosphate buffer to remove the excess GA.

Covalent immobilization of CGTase onto functionalized CNF support

The functionalized support (CNF–1,12-dodecanediamine–GA derivative) was suspended in 2.5 ml of enzyme solution, containing 227.48 U/ml CGTase enzyme and 0.05 M potassium phosphate buffer (pH 6.0). The mixture was gently stirred overnight at 4°C. The unbound enzyme was removed by washing with the same phosphate buffer until there is no enzyme activity detected in the filtrates.

Scanning electron microscopy (SEM)

SEM (S-3400N, Hitachi, Japan) was used to observe the surface morphology of fibre based on the effect of process treatment. The acceleration voltage was set up in range of 5-20kV, and samples were sputter-coated with gold to avoid charging effect during SEM observations. The fibre diameter was measured by using image analyser software. The results were reported as the average values of the data for each set of measurements.

Chemical analysis

The cellulose, hemicellulose and lignin contents of CNF were determined by using Fibertec™2010 Auto Fibre Analysis System (FOSS Analytical AB, Sweden). The analysis was carried out according to its standard procedure based on FOSS manufacturer's manual. Cellulose, hemicellulose and lignin content were determined by using Acid Detergent Fibre (ADF), Neutral Detergent Fibre (NDF) and Acid Detergent Lignin (ADL). The chemical analysis of sample can be calculated by following formula: (a) Hemicellulose = NDF (hemicellulose, cellulose and lignin) – ADF (cellulose and lignin); (b) Cellulose = ADF – ADL (lignin); (c) Lignin = ADL [12].

Protein loading determination

Bradford method is approximately four times more sensitive compared to Lowry assay [13]. Thus, modified Bradford assay was used to determine the amount of protein loaded onto the functionalized CNF [13]. The quantity of immobilized enzyme was measured after the end of the all washing steps at 595 nm. Bovine serum albumin (BSA) was used as a standard protein. The amount of protein content of immobilized enzyme onto support was calculated by using the following formula: amount of protein after immobilization = (amount of protein added) – (amount of unbound protein) [14].

Enzyme activity assay (α-cyclodextrin production and enzyme reusability)

The formation of α-cyclodextrin (α-CD) from soluble starch was determined as follows: 30 mg of immobilized CGTase-CNF support was incubated at 60°C in a shaking water bath with 20 ml 0.05 M phosphate buffer, pH 6.0 (containing with 5 w/v% of water-soluble starch). There were eight samples were incubated for different reaction times (1-8 hours). The enzymatic reaction was stopped by placing each sample in a boiling water bath for 15 min. The supernatant was collected by centrifugation for 10 min (10,000 rpm) and passed through a Millipore filter 0.22

μm. The reaction product of α-CD formation was analysed by using Shimadzu HPLC system (Liquid Chromatograph LC-10AT, Diode Array SPD-M10A, and RID 6A), equipped with a Zorbax Carbohydrate column (L: 150 mm, I.D: 4.6 mm, YMC Co. Ltd., Japan) at 30°C. With injection volume of 20 μl, the sample of α-CD was eluted isocratically with acetonitrile-water (75:25) at a flow rate of 1.0 mL min^{-1}. To measure CGTase activity, the enzymatic reaction was run for 5 min. One enzyme activity unit (U) was defined as the amount of enzyme that liberates 1 μmol/min of α-CD under the assay conditions.

For the reusability analysis, 30 mg of immobilized CGTase-CNF support was incubated with 20 ml of 5% (w/v) water-soluble starch in phosphate buffer (0.05 M, pH 6.0). The reaction process was repeated up to 7 cycles at 60°C for every 1 hour. At the end of each reaction, the supernatant was collected by centrifugation (10,000 rpm) for 5 min and the content of α-CD was analysed as described above. Whereas, the precipitate (immobilized CGTase on CNF) was washed with distilled water. Then, it was re-suspended in 20 ml of freshly prepared substrate to start a new cycle. All results reported are the means of at least three separated experiments.

Results and Discussion

Scanning electron microscopy (SEM) analysis

The aqueous suspensions of the raw bast fibre, bleached pulp fibre and CNF after chemo-mechanical treatments are shown in Figure 1. After the chemical treatments, raw bast fibre turned from brown colour into yellowish colour as bleached pulp fibre, indicating a significant amount of lignin and hemicellulose were removed [11]. After the ultrasonication process, CNF suspension turned white colour and homogenously dispersed in water, indicating the nano-sized fibre was sufficiently dispersed and converted to the highly viscous suspension [15].

The surface morphological of raw bast fibre, bleached pulp fibre and CNF were visualized by using SEM, which images of these samples are also depicted in Figure 1. This study reveals that the surface structure of treated fibre was improved in term of its smoothness, roughness and diameter size. Figure 1(a) shows raw bast fibre composed of microfibre bundle and its surface was covered with other impurities (e.g. hemicellulose, lignin, pectin and waxy substances). The average diameter size of raw bast fibre is in a range of 30-70 μm. After a series of chemical process, raw bast fibre was separated into individual micro-sized cellulose fibre, representing as bleached pulp fibre as shown in Figure 1(b). The average diameter size of bleached pulp fibre was reduced to 5-20 μm. The surface of bleached pulp fibre also found smoother than raw bast fibre and it was reported to be composed of strong hydrogen bonding between cellulosic fibril [16]. Thus, removal the impurities such as lignin and hemicellulose by delignification and bleaching processes could reduce the diameter of fibres, as well as disintegrated the single sized into individual micro-sized cellulose fibres. Figure 1(c) represents the SEM of CNF after passing through the ultrasonication process, display as a cellulosic filament like a long entangled classical web structure. CNF support also represents the combination of chemical and mechanical treatments could strip down the individual micro-sized cellulose fibre from bleached pulp into nano-sized cellulose fibre (average diameter size: 50-90 nm). Thus, further study on the optimization of preparation factors (e.g. concentration of the chemical used, treatment process time and output power of ultrasonication process) is important to increase the yield of nano-sized cellulose fibre as well as to reduce its diameter size.

Chemical composition

Highly cellulose content can be extracted by removal of lignin, hemicellulose and other impurities from raw bast fibre using a series of conventional methods. The changes of chemical composition of raw bast fibre, bleached pulp fibre and CNF were presented in Table 1. Initially, raw bast fibre consisted of around 66.4 %, 18.0 % and 12.6 % of cellulose, hemicellulose and lignin, respectively. During the delignification and bleaching steps, the cellulose content increased up to 83.7 % from raw bast fibre, whereas hemicellulose and lignin decreased to 10.3 % and 5.1 %, respectively. Thus, these major changes were attributed to the chemicals used that employed in process treatment. NaOH, $NaClO_2$, H_2O_2 and CH_3COOH were found efficiently in removing most of lignin and hemicellulose in the fibre [10]. In fact, AQ was added during delignification is to enhance the delignification rate and also to protect the fibers from alkali. Delignification was also carried out under pressure, which contributed to loosen the lignin structure from cellulosic fibre, as well as to increase the degradation rate of lignin in a short period of time. This is because, hemicellulose and lignin formed a matrix surrounding cellulose structure [17]. Removal of hemicellulose and lignin is essential to isolate fibre with high cellulose content. After

ultrasonication, cellulose content in CNF increased up to 90.0 %. Hemicellulose and lignin contents decreased to 6.8 % and 2.4 % respectively. High-intensity of ultrasonication process was able to increase the cellulose content as well as the diameter size of fibre, due to the vibration of water molecules that encourage the dispersion effect of micro-fibre bundles into individual nano-sized cellulose fibres. Nano-order fibre is not only to attribute the increasing of cellulose content on the surface fibre, but also to provide a large surface area per volume ratio. However, variations of these results are corresponding to the result of morphological structure and size of fibres.

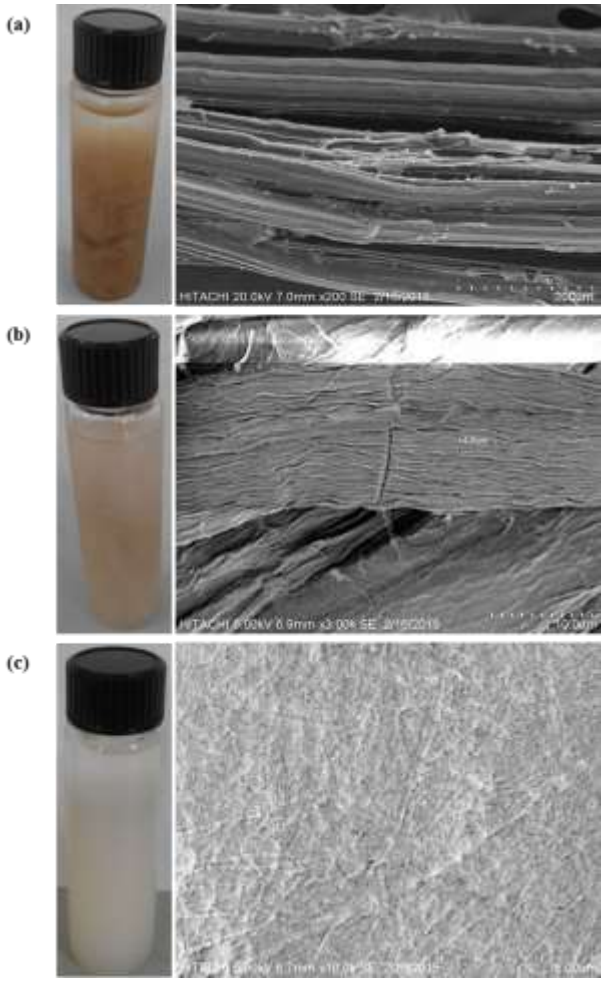


Figure 1. Dispersion states (left) and SEM micrograph (right) of the (a) raw bast fibre (200x), (b) bleached pulp fibre (3000x), (c) CNF.

Table 1. Chemical composition of kenaf bast fibre (based on dry-weight)

Materials	**Cellulose (%)**	**Hemicellulose (%)**	**Lignin (%)**	**Extractive (%)**	**Ash (%)**
Raw bast fibre	66.4 ± 1.1	18.0 ± 1.4	12.6 ± 0.1	1.7 ± 0.2	1.4 ± 0.0
Bleached pulp fibre	83.7 ± 0.3	10.3 ± 0.9	5.1 ± 1.2	0.7 ± 0.3	0.2 ± 0.1
CNF	90.0 ± 0.3	6.8 ± 0.4	2.4 ± 0.2	0.5 + 0.1	0.0 ± 0.0

CGTase immobilization

In this study, CGTase enzyme was immobilized onto CNF support through covalent binding technique. In detail, covalent binding technique represents the CGTase was covalently immobilized *via* chemical coupling agents such as 1,12-dodecanediamine (as spacer arm) and GA (as ligand), representing as one of chemical modification techniques. This technique required two mutual reactive functional groups on CNF support surface and enzyme side to perform essential interaction between functional groups [18]. Chemical coupling agents function as specific linkage or anchor from one side of functional group to other side of functional group, representing as [CGTase enzyme–(ligand–spacer arm)–CNF support], which forms a thin layer on surface CNF support. Chemical coupling agents also permit a very strong binding between target enzyme molecules and CNF support at a specific point of reactive group, as promising the accessibility and flexibility of the interaction [18]. Reactive functional group acts as a platform for the interaction between two end-terminals of the chemical coupling, providing the highest chance to create bio-functionalized linkage with the amino group of enzyme [19].

According to the previous research studies, CNF was reported that consists of mainly (O–H) group on its surface [9–11, 15, 20]. The percentage of immobilization yield is correlated to the interaction of chemical coupling agent onto the surface of CNF. As depicted in Table 2, about 95.0% of immobilization yield of protein binding with 69.48% retained enzyme activity were obtained. The results show high percentage of immobilization yield indicates the successfully of interaction between CGTase molecules and CNF support [18]. High percentage of enzyme activity also contributes to the better performance of enzymatic reaction [14, 21–23].

Table 2. CGTase immobilization onto CNF support

Enzyme added		**Unbound enzyme**		**Immobilized enzyme**		**Immobilization yield**	
Protein(Po) (mg/g support)	**Activity(A) (U/g support)**	**Protein (mg/g support)**	**Activity(U) (U/g support)**	**Protein(P) (mg/g support)**	**Activity(I) (U/g support)**	**Binding (%) (P/Po) x 100**	**Activity (%) I/(A-U) x 100**
30.0	568.7	1.49	119.22	28.51	312.28	95.0%	69.48%

The cyclization activity of immobilized CGTase on CNF support was investigated at temperature of 60 °C, in phosphate buffer (pH 6.0, 0.05 M). The enzymatic reaction of immobilized CGTase converted the soluble starch into mainly α–CD compound. The percentage of α-CD forming for 1 hour shows drastically increased up to 28 % of production yield and gradually increases up to 48 % after 8 hours of reaction time, as presented in Figure 2. Substrate limitation and product inhibition probably effected to the enzymatic reaction of CGTase, indicating stationary line when the reaction process time was extended [24]. Fig. 3 shows the reusability of the 7 cycles of repeated batch process of immobilized CGTase. The result indicated that the residual activity has gradually decreased until 7 cycles. The reusability profile of immobilized CGTase describes the residual activity reduced gradually from cycle 1 to cycle 7, which from 100 % to 66 %. After the fifth cycle, the immobilized enzyme shows a little decreasing on its residual activity. Therefore, the immobilized enzyme is able to maintain in a good yield of forming α–CD even though after 7 cycles. However, both of these results show a good in enzymatic activity either in production of α–CD or reusability of immobilized CGTase on CNF support through covalent interaction. Thus, the CNF support can be applied as a good support structure for enzyme immobilization.

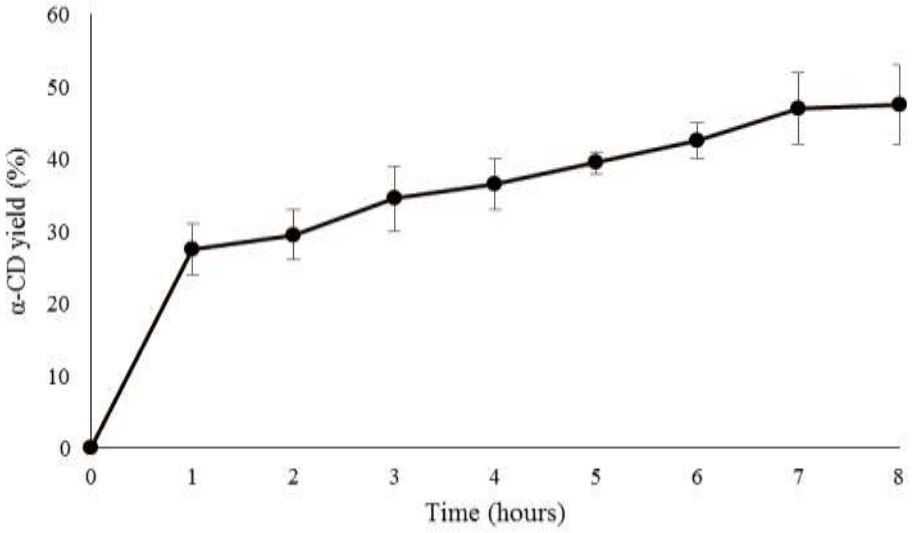


Figure 2. α-CD formation by immobilized CGTase. The immobilized CGTase was reacted in a phosphate buffer (0.05 M, pH 6.0), at temperatures 60 ^{0}C.

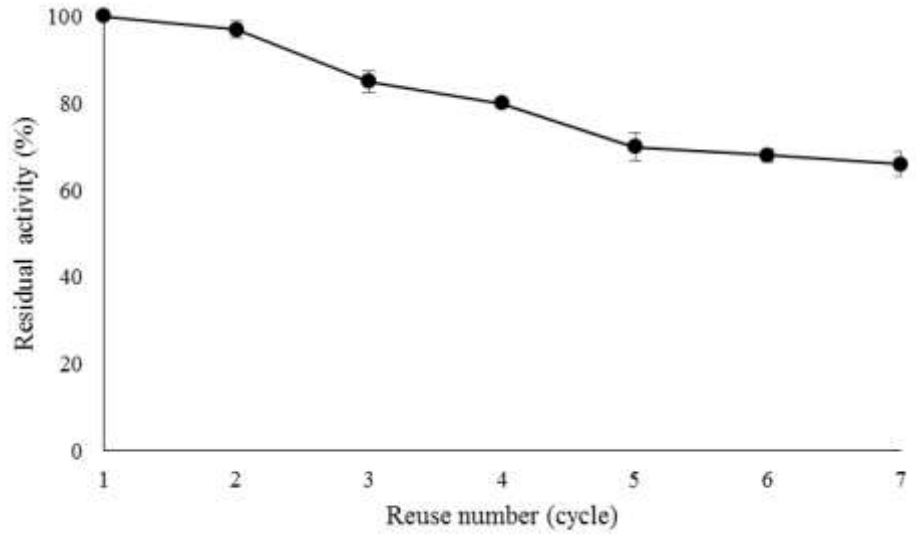


Figure 3. Reusability (repeated batch) of immobilized CGTase. The immobilized CGTase was reacted in a phosphate buffer (0.05 M, pH 6.0), at temperatures 60 ^{0}C.

Conclusion

CNF was successfully isolated from kenaf bast fibres by chemical and mechanical treatments. SEM analysis reveals that CNF has different surface morphology and diameter size which reduction of level roughness and size; attributed to each stage of the treatment processes. Chemical analysis of fibre after each chemical process and high-intensity ultrasonication indicated to the increasing in cellulose content by the decreasing of lignin and hemicellulose contents, also indicated the successfully removal of these impurities. Covalent immobilization of CGTase onto CNF support also reveals a good result in the enzyme assay, which promotes a highly α–CD production and reusability of

enzyme. Thus, CNF support was potential to be applied in enzyme immobilization due to high exposed surface area as well as to provide high cellulose content (e.g. it increases the number of (O–H) group on the surface of CNF for the covalent interaction). Developing of nanobiocatalyst system would benefit for both enzyme and nano-sized support, since the enzyme molecule itself is already in the nano-sized.

Acknowledgement

The authors gratefully acknowledge the financial support by Fundamental Research Grant Scheme (FRGS) from KPM (Grant no. 03-01-14-1426FR) through the Universiti Putra Malaysia and UPM Putra Grant (Grant no. GP-IPS/2014/9438711).

References

1. Faruk, O., Bledzki, A. K., Fink, H.-P. and Sain, M. (2012). Biocomposites reinforced with natural fibers: 2000–2010. *Progess in Polymer Science*, 37(11): 1552 –1596.
2. Li, Y., Mai, Y.-W. and Ye, L. (2000). Sisal fibre and its composites: a review of recent developments. *Composite Science and Technology*, 60(11): 2037 – 2055.
3. Gardner, D. J., Oporto, G. S., Mills, R. and Samir, M. A. S. A. (2008). Adhesion and surface issues in cellulose and nanocellulose. *Journal of Adhesion Science and Technology*, 22(5-6): 545 – 567.
4. Brinchi, L., Cotana, F., Fortunati, E. and Kenny, J. M. (2013). Production of nanocrystalline cellulose from lignocellulosic biomass: Technology and applications. *Carbohydrate Polymer*, 94(1): 154 – 169.
5. Zhang, S. (2003). Fabrication of novel biomaterials through molecular self-assembly. *Nature Biotechnology*, 21(10): 1171 – 1178.
6. Kim, J., Grate, J. W. and Wang, P. (2006). Nanostructures for enzyme stabilization. *Chemical Engineering Science*, 61(3): 1017 – 1026.
7. Kim, J., Grate, J. W. and Wang, P. (2008). Nanobiocatalysis and its potential applications. *Trends Biotechnology*, 26(11): 639 – 646.
8. Cao, L. (2006). Covalent Enzyme Immobilization. In *Carrier-bound Immobilized Enzymes*. Wiley-VCH Verlag GmbH & Co. KGaA (pp. 169–316)..
9. Karimi, S., Tahir, P. M., Karimi, A., Dufresne, A. and Abdulkhani, A. (2014). Kenaf bast cellulosic fibers hierarchy: A comprehensive approach from micro to nano. *Carbohydrate Polymer*, 101: 878 –885.
10. Jonoobi, M., Niska, K. O., Harun, J., Misra, M., Shakeri, A., Misra, M. and Oksman, K. (2009). Chemical composition, crystallinity, and thermal degradation of bleached and unbleached kenaf bast (Hibiscus cannabinus) pulp and nanofibers. *BioResources*, 4(2): 626 – 639.
11. Chen, W., Yu, H., Liu, Y., Chen, P., Zhang, M. and Hai, Y. (2011). Individualization of cellulose nanofibers from wood using high-intensity ultrasonication combined with chemical pretreatments. *Carbohydrate Polymer*, 83(4): 1804 – 1811.
12. Van Soest, P. J., Robertson, J. B. and Lewis, B. A. (1991). Methods for dietary fiber, neutral detergent fiber, and nonstarch polysaccharides in relation to animal nutrition. *Journal of Dairy Science*, 74(10): 3583 – 3597.
13. Bradford, M. M. (1976). A rapid and sensitive method for the quantitation of microgram quantities of protein utilizing the principle of protein-dye binding. *Analytical Biochemistry*, 72(1-2): 248 – 254.
14. Abdel-Naby, M. A., Ismail, A.-M. S., Abdel-Fattah, A. M., and Abdel-Fattah, A. F. (1999). Preparation and some properties of immobilized Penicillium funiculosum 258 dextranase. *Process Biochemistry*, 34(4): 391 – 398.
15. Chen, W., Yu, H. and Liu, Y. (2011). Preparation of millimeter-long cellulose I nanofibers with diameters of 30–80nm from bamboo fibers. *Carbohydrate Polymer*, 86(2): 453 – 461.
16. Abe, K. and Yano, H. (2009). Comparison of the characteristics of cellulose microfibril aggregates of wood, rice straw and potato tuber. *Cellulose*, 16(6): 1017 – 1023.
17. Joonobi, M., Harun, J., Tahir, P. M., Zaini, L. H., SaifulAzry, S. and Makinejad, M. D. (2010). Characteristics of nanofibres extracted from kenaf core. *BioResources*, 5(4): 2556 – 2566.
18. Sulaiman, S., Mokhtar, M. N., Naim, M. N., Baharuddin, A. S. and Sulaiman, A. (2014). A Review: potential usage of cellulose nanofibers (CNF) for enzyme immobilization via covalent interactions. *Applied Biochemistry and Biotechnology*, 175(4): 1817 – 1842.
19. Redeker, E. S., Ta, D. T., Cortens, D., Billen, B., Guedens, W. and Adriaensens, P. (2013). Protein engineering for directed immobilization. *Bioconjugate Chemistry*, 24(11): 1761 – 1777.

20. Chen, W., Yu, H., Liu, Y., Hai, Y., Zhang, M. and Chen, P. (2011). Isolation and characterization of cellulose nanofibers from four plant cellulose fibers using a chemical-ultrasonic process. *Cellulose*, 18(2): 433 – 442.
21. Karim, M. R. and Hashinaga, F. (2002). Preparation and properties of immobilized pummelo limonoid glucosyltransferase. *Process Biochemistry*, 38(5): 809 – 814.
22. Martín, M. T., Plou, F. J., Alcalde, M. and Ballesteros, A. (2003). Immobilization on Eupergit C of cyclodextrin glucosyltransferase (CGTase) and properties of the immobilized biocatalyst. *Journal of Molecular Catalysis B: Enzymatic*, 21(4–6): 299 – 308.
23. Ivanova, V. (2010). Immobilization of cyclodextrin glucanotransferase from Paenibacillus macerans ATCC 8244 on magnetic carriers and production of cyclodextrins. *Biotechnology and Biotechnical Equipment*, 24: 516 – 528.
24. Shahrazi, S., Saallah, S., Mokhtar, M. N., Baharuddin, A. S. and Yunos, K. F. M. (2013). Dynamic mathematical modelling of reaction kinetics for cyclodextrins production from different starch sources using Bacillus macerans cyclodextrin glucanotransferase. *American Journal of Biochemistry and Biotechnology*, 9(2): 195 – 205.

MALAYSIAN JOURNAL OF ANALYTICAL SCIENCES
Published by The Malaysian Analytical Sciences Society
ISSN 1394 - 2506

CHEMICAL PROFILING AND IDENTIFICATION OF ALKALOIDS AND FLAVONOIDS IN *Uncaria lanosa* var. *ferrea* VIA UHPLC-ORBITRAP MS

(Profil Kimia dan Pengenalpastian Alkaloid dan Flavonoid dalam *Uncaria lanosa* var. *ferrea* melalui UHPLC - Orbitrap MS)

Nursyaza Husna Shaharuddin[1, 2], Nor Hadiani Ismail[1, 2], Nurhuda Manshoor[1, 3], Fatimah Salim[1, 2], Rohaya Ahmad[1, 2]*

[1]*Faculty of Applied Sciences,*
Universiti Teknologi MARA, 40450 Shah Alam, Selangor, Malaysia
[2]*Atta-ur-Rahman Institute for Natural Products Discovery*
[3]*Faculty of Pharmacy*
Universiti Teknologi MARA, 42300 Bandar Puncak Alam, Selangor, Malaysia

**Corresponding author: rohayaahmad@salam.uitm.edu.my*

Received: 24 February 2015; Accepted: 27 October 2015

Abstract

Our previous studies on Malaysian *Uncaria* (Rubiaceae) have yielded over 20 compounds including alkaloids and flavonoids with some compounds showing interesting biological activities. In the search of new bioactive compounds from the genus, a phytochemical investigation on *Uncaria lanosa* (Wall.) locally known as “gegambir paya” or “gegambir hitam” was carried out via metabolite profiling. The plant is reported to be used as an infusion for intestine inflammation and a decoction for cleaning wounds and ulcers. Metabolite profiling was carried out using ultrahigh-performance liquid chromatography coupled with orbitrap mass spectrometry detectors (UHPLC-Orbitrap MS). Ten alkaloids and six flavonoids previously isolated from other *Uncaria* species were used as reference compounds. Phytochemical analysis of the stem extracts of the plant found the presence of a flavonoid and three alkaloids whose identities were obtained through the comparison of their mass and fragmentation pattern as well as the retention times of the reference compounds. The developed LC-MS method is expected to lead to a more rapid and reliable approach in discovery of new or novel compounds in *Uncaria* genus. The development of the MS database will also aid in the metabolite profiling of other medicinal plants in natural product research.

Keywords: *Uncaria*, *Uncaria lanosa*, metabolite profiling, UHPLC-Orbitrap MS

Abstrak

Kajian kami sebelum ini ke atas *Uncaria* (Rubiaceae) Malaysia telah menghasilkan lebih 20 sebatian termasuk alkaloid dan flavonoid dengan beberapa sebatian yang menunjukkan aktiviti biologi yang menarik. Dalam usaha mencari sebatian bioaktif baru dari genus ini, siasatan fitokimia ke atas *Uncaria lanosa* (Wall.) yang dikenali sebagai "gegambir paya" atau "gegambir hitam" telah dijalankan melalui profil metabolit. Tumbuhan ini dilapor digunakan sebagai infusi untuk radang usus dan sebagai rebusan untuk membersihkan luka dan ulser. Pemprofilan metabolit telah dijalankan dengan menggunakan kromatografi cecair ultra tinggi dengan pengesan spektrometri jisim orbitrap (UHPLC-Orbitrap MS). Sepuluh alkaloid dan enam flavonoid yang sebelum ini diasingkan daripada spesies *Uncaria* lain telah digunakan sebagai bahan rujukan. Analisis fitokimia ekstrak daripada batang tumbuhan tersebut menemui satu flavonoid dan tiga alkaloid yang dikenalpasti melalui perbandingan jisim, corak fragmentasi serta masa tahanan berbanding sebatian rujukan. Kaedah LC-MS yang dibangunkan dijangka membawa kepada pendekatan yang lebih pantas dan boleh dipercayai dalam penemuan sebatian baru atau novel dalam genus *Uncaria.* Pembangunan pangkalan data MS juga akan membantu pemprofilan tumbuhan ubatan lain dalam penyelidikan produk semulajadi.

Kata kunci: *Uncaria*, *Uncaria lanosa*, profil metabolit, UHPLC-Orbitrap MS

Introduction

Uncaria genus (Rubiaceae) which comprises 34 species worldwide has been used to treat various diseases including treatment of cancer, Parkinson's disease, Alzheimer's disease, chirrhosis, dizziness, hypertension, convulsion, asthma, rheumatism and many other diseases [1, 2]. Fourteen species are available in Malaysia. In our previous studies on Malaysian *Uncaria*, over 20 compounds including alkaloids and flavonoids have been isolated [3]. Some of the tested compounds have shown interesting biological activities. However, isolation of compounds using conventional chromatographic techniques can be tedious and time-consuming and may yield uninteresting or known compounds. In the search of new compounds from the genus, we have carried out a phytochemical investigation on *Uncaria lanosa* Wall which is locally known as "gegambir paya" or "gegambir hitam". The plant is reported to be used as an infusion for intestine inflammation and a decoction for cleaning wounds and ulcers [4]. According to Kam et al. [5], there are 14 species of *Uncaria* identified in Peninsular Malaysia and for Malaysian *Uncaria lanosa* var. *ferrea*, only two alkaloids, isopteropodine and pteropodine have been recorded.

Materials and Methods

Chemicals and raw materials

Stems of *U. lanosa var. ferrea* (Blume) Ridsd. with voucher specimen number HTBP4324 were collected from Pahang, Malaysia and standards were previously isolated from other *Uncaria* species. Ultrapure water was obtained from a PURELAB Ultra Laboratory Water Purification Systems and HPLC grade acetonitrile and methanol were purchased from Merck. Solvents used for fractionation and isolation were of industrial grade and were distilled prior to use.

Sample preparation

Pure compounds previously isolated from *Uncaria* extracts were dissolved separately in methanol. For sample preparation, dried and ground stems of *Uncaria lanosa* was extracted through 3-days maceration with methanol. The mixture was filtered and evaporated off under reduced pressure. The crude extract was further extracted by liquid–liquid extraction using two types of solvents; non-polar solvent (hexane) and medium polar solvent (dichloromethane, DCM). Each mixture was filtered separately and evaporated off under reduced pressure. 1 mg of DCM extract was weighed accurately and dissolved in 1 mL of methanol: water (30:70, v/v). Samples were filtered through a 0.22 µm PTFE filter into 2 ml screw cap vials prior to LC-MS analysis.

Instrumentation

UHPLC-Orbitrap MS was conducted using Thermo Scientific Q Exactive Hybrid Quadrupole – Orbitap Mass Spectrometer with ESI source system, a dual pump, an automatic injector (20 µL loop), a degasser unit and column heater. Data processing was performed using Xcalibur software.

High performance liquid chromatography

Samples were separated using GL Sciences - Inertsil Column C-18 (250 mm x 4.6 mm, i.d., 5µm) at a column temperature 40 °C. Flowrate was 0.6 ml/min and injection volume was 5 µl. After each injection the needle was washed with 100 % ACN. The mobile phase consisted of water containing 0.01 % formic acid (A) and acetonitrile (B). A gradient elution program was used as follows: 5 – 55 % B (0.00 – 30 min) and 55 – 95 % B (30 – 50 min).

Mass spectrometry condition for LC-MS

The LC/MS profiling of the extract and standards were identified using UHPLC-Orbitrap MS. Nitrogen was used as the sheath and auxiliary gas at flow rate of 45 and 25 ml/min, respectively. The optimum source (ESI) condition were: spray voltage 4.5 and 3.7kV for positive and negative respectively, S-Lens RF Level at 55.00, ESI capillary temperature 320 °C and probe heater temperature 30 °C.

Results and Discussion

Four chemical structures of compounds identified in DCM extract of *U. lanosa* var. *ferrea* was illustrated in Figure 1.

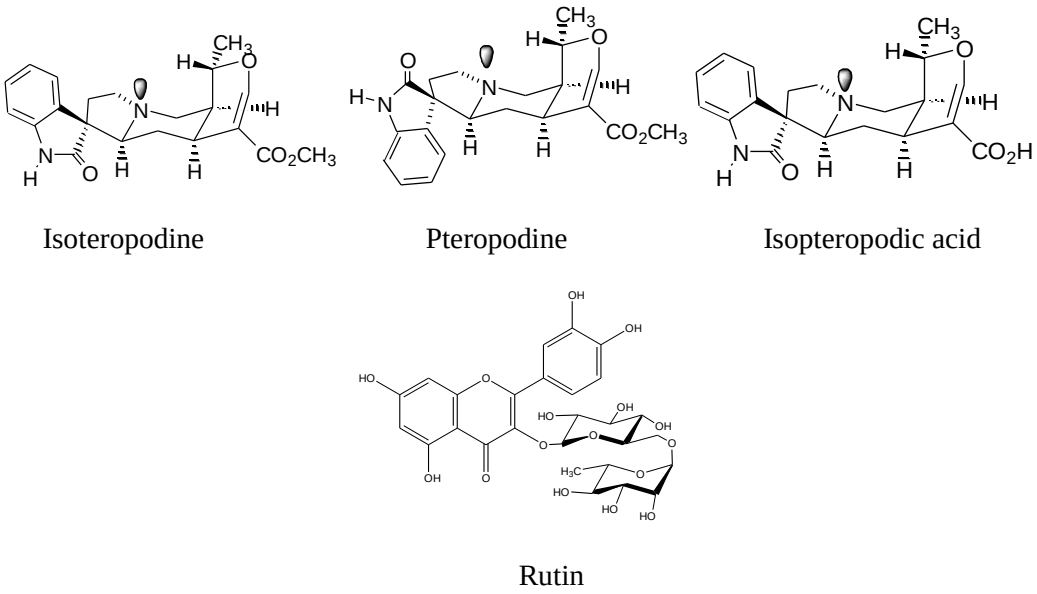


Figure 1. Chemical structures of compounds identified in DCM extract of *U. lanosa* var. *ferrea*

Development of database

The LC-ESI-MS profiles of previously isolated compounds from *Uncaria* species was added into MS database and percent error (ppm) were calculated. The LC-MS spectra of each compound was stored in the MS libary and to be used as reference for the identification of compounds from LC-MS analysis of crude extracts and fractions of *Uncaria* species. The LC-MS profiles are shown in Table 1 and Table 2, respectively.

Table 1. Characterization of reference compound by developed UHPLC-Orbitrap MS method for positive mode

No. of reference compounds	Compound (RT (min))	Proposed formula	Observed mass $[M+H]^+$	Calculated mass $[M+H]^+$	Error (Δ ppm)
1	Catechin (15.18)	$C_{15}H_{14}O_6$	291.08636	291.0868	-1.512
2	Formosaninol (15.19)	$C_{21}H_{26}N_2O_5$	387.19180	387.1920	-0.517
3	(-)Epi-catechin (16.49)	$C_{15}H_{14}O_6$	291.08646	291.0868	-1.168
4	Isoformaninol (16.52)	$C_{21}H_{26}N_2O_5$	387.19180	387.1920	-0.517
5	Rutin (18.27)	$C_{27}H_{30}O_{16}$	611.16058	611.1612	-1.014
6	(-)Epi-afzelechin (18.80)	$C_{15}H_{14}O_5$	275.09158	275.0919	-1.163
7	2-Oxosecologanine (20.31)	$C_{11}H_{15}NO_4$	226.10739	226.1079	-2.256
8	Pteropodine (21.37)	$C_{21}H_{24}N_2O_4$	369.18097	369.1814	-1.165
9	Isopteropodic acid (22.96)	$C_{20}H_{22}N_2O_4$	355.16537	355.1658	-1.211

Table 1 (cont'd). Characterization of reference compound by developed UHPLC-Orbitrap MS method for positive mode

No. of reference compounds	Compound (RT (min))	Proposed formula	Observed mass $[M+H]^+$	Calculated mass $[M+H]^+$	Error (Δ ppm)
10	Rauniticine-allo-acid B(22.97)	$C_{20}H_{22}N_2O_4$	355.16550	355.1658	-0.845
11	Uncariechin (24.88)	$C_{18}H_{14}O_6$	327.08624	327.0868	-1.712
12	Quercetin (27.27)	$C_{15}H_{10}O_7$	303.04993	303.0505	-1.881
13	Isopteropodine (29.83)	$C_{21}H_{24}N_2O_4$	369.18109	369.1814	-0.84
14	Uncarine F (29.92)	$C_{21}H_{24}N_2O_4$	369.18094	369.1814	-1.246
15	Speciophylline (29.98)	$C_{21}H_{24}N_2O_4$	369.18085	369.1814	-1.49
16	Rauniticine-allo-oxindole B (30.01)	$C_{21}H_{24}N_2O_4$	369.18079	369.1814	-1.652
10	Rauniticine-allo-acid B(22.97)	$C_{20}H_{22}N_2O_4$	355.16550	355.1658	-0.845

Table 2. Characterization of reference compound by developed UHPLC-Orbitrap MS method for negative mode

No. of reference compounds	Compound (RT (min))	Proposed formula	Observed mass $[M-H]^-$	Calculated mass $[M-H]^-$	Error (Δppm)
1	Catechin (15.13)	$C_{15}H_{14}O_6$	289.07184	289.0712	2.21
2	Formosanin-17-ol (15.18)	$C_{21}H_{26}N_2O_5$	385.17816	385.1764	4.57
3	(-)Epi-catechin (16.52)	$C_{15}H_{14}O_6$	289.07199	289.0712	2.73
4	Isoformosanin-17-ol (16.53)	$C_{21}H_{26}N_2O_5$	385.17810	385.1764	4.41
5	Rutin (18.26)	$C_{27}H_{30}O_{16}$	609.14783	609.1456	3.66
6	(-)Epi-afzelechin (18.83)	$C_{15}H_{14}O_5$	273.07706	273.0763	2.78
7	Longiflorine	$C_{11}H_{15}NO_4$	-	224.0923	-
8	Pteropodine (21.40)	$C_{21}H_{24}N_2O_4$	367.16754	367.1658	4.74
9	Isopteropodic acid (22.97)	$C_{20}H_{22}N_2O_4$	353.15201	353.1502	5.13
10	Rauniticinic-allo Acid B	$C_{20}H_{22}N_2O_4$	-	353.1502	-
11	Uncariechin (24.87)	$C_{18}H_{14}O_6$	325.07230	325.0712	3.38
12	Quercetin (27.22)	$C_{15}H_{10}O_7$	301.03546	301.0349	1.86
13	Isopteropodine (29.84)	$C_{21}H_{24}N_2O_4$	367.16760	367.1658	4.90
14	Uncarine F (29.91)	$C_{21}H_{24}N_2O_4$	367.16751	367.1658	4.66
15	Speciophylline (30.03)	$C_{21}H_{24}N_2O_4$	367.16751	367.1658	4.66
16	Rauniticine-allo-oxindole B (29.95)	$C_{21}H_{24}N_2O_4$	367.16739	367.1658	4.33

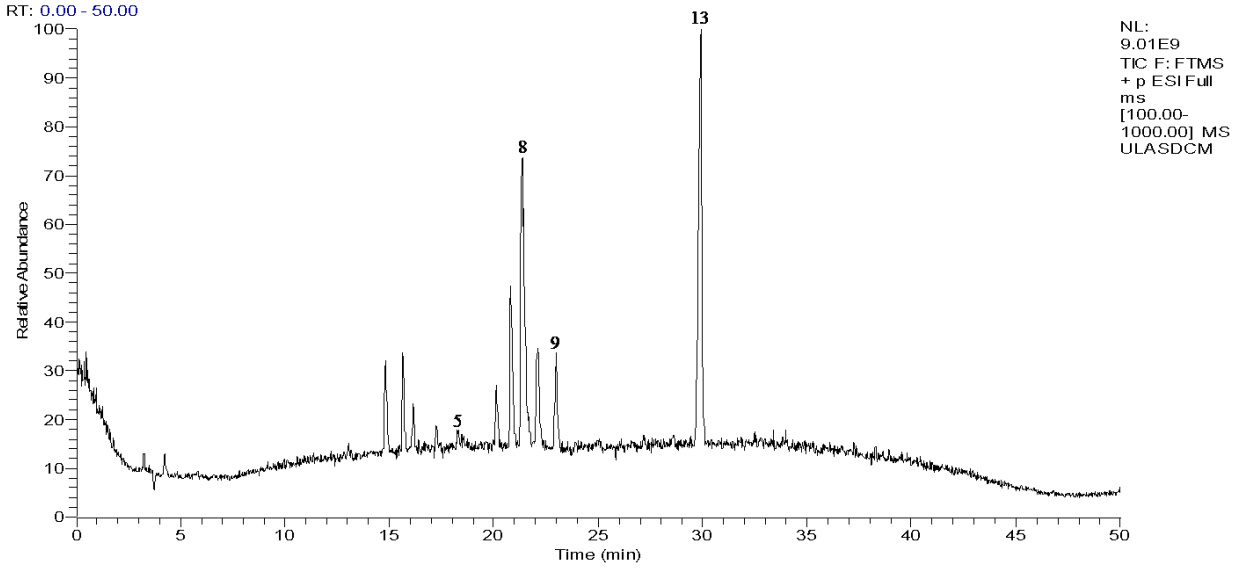


Figure 2**.** Chromatogram of DCM extract of *U. lanosa*; the total ion chromatogram (TIC) in positive mode; the number assigned to the identified peak is according to the number of the reference compound as shown in Table 1

Qualitative analysis of compounds in *Uncaria lanosa* extract

The UHPLC-Orbitrap MS method was employed for the metabolite profiling and identification of the chromatographic peaks of the DCM stem extract of *Uncaria lanosa*. From the analysis, the positive mode affords higher sensitivity for most of the peaks compared to the negative mode. All of the reference compounds can be detected in positive mode but two of the reference compounds cannot be detected in negative mode. Therefore this mode was chosen and applied in the analysis. By comparing the retention time and *m/z* value with the reference compounds, four peaks have been identified, including one flavonoid and three alkaloids which were unambiguously identified as rutin (5), pteropodine (8), isopteropodic acid (9) and isopteropodine (13). The structures of the identified compounds are shown in Figure 1. As shown in Figure 2, peak (5) shows a $[M+H]^+$ ion at 611.16058, peak (8) shows a $[M+H]^+$ ion at 369.18097, peak (9) shows a $[M+H]^+$ ion at 355.16537 and peak (13) shows a $[M+H]^+$ ion at 369.18109. It was found that the Orbitrap MS detection provided accurate molecular weight (±7 ppm). To date, metabolite profiling using mass spectrometry has only been reported for *Uncaria tomentosa* (cat's claw), *Uncaria rhynchophylla* and *Uncaria sinensis* [6 - 9].

Conclusion

In this paper, the proposed UHPLC-Orbitrap MS method was used for the qualitative analysis of alkaloids and flavonoids in *Uncaria lanosa*. Sixteen previously isolated compounds comprising six flavonoids and ten alkaloids were used as standards and were characterized by their retention time and *m/z* values. Four peaks in the extract of *U. lanosa* were identified as rutin, pteropodine, isopteropodic acid and isopteropodine. The developed LC-MS method is expected to lead to a more rapid and reliable approach in the discovery of new or novel compounds from the *Uncaria* genus.

Acknowledgement

This research was supported by Science Fund (MOSTI) (100-RMI/SF 16/6/2 (23/2012). NHS would like to thank to Ministry of Science, Technology and Innovation Malaysia and UiTM for financial support and fellowship award. We also would like to express our appreciation to Thermo Fisher Scientific Malaysia and Technology Park Malaysia for allowing access to UHPLC-Orbitrap MS.

References

1. Heitzman, M. E., Neto, C. C., Winiarz, E., Vaisberg, A. J. and Hammond, G. B. (2005). Ethnobotany, phytochemistry and pharmacology of *Uncaria* (Rubiaceae). *Phytochemistry*, 66: 5 – 29.
2. Zhang, Q., Zhao, J. J., Xu, J., Feng, F. and Qu, W. (2015). Medicinal uses, phytochemistry and pharmacology of the genus *Uncaria*. *Journal of Ethnopharmacology*. 173: 48 – 80.
3. Salim, F., Zain, M. M., Ridzuan, M. S. M., Langat, M. K., Mulholland, D. A. and Ahmad, R. (2013). Flavan-3-ols from the leaves of Malaysian *Uncaria longiflora* var. pteropoda (Miq.) Ridsd. *Phytochemistry Letters.* 6: 236 – 240.
4. Burkill, I. H. (1966). A Dictionary of the Economic Products of the Malay Peninsula. Vols 2. London: Crown Agents to the Colonies. (Reprint 1966, Kuala Lumpur. Ministry of Agriculture and Cooperative). 2236 – 2245.
5. Kam, T., Lee, K. and Goh, S., (1992). Alkaloid distribution in Malaysian *Uncaria. Phytochemistry*, 31: 2031 – 2034.
6. Pavei, C., Kaiser, S., Verza, S. G., Borre, G. L. and Ortega, G. G. (2012). HPLC-PDA method for quinovic acid glycosides assay in Cat's claw (*Uncaria tomentosa*) associated with UPLC/Q-TOF-MS analysis. *Journal of Pharmaceutical and Biomedical Analysis*. 62: 250 – 257.
7. Xie, S., Shi, Y., Wang, Y., Wu, C., Liu, W., Feng, F. and Xie, N. (2013). Systematic identification and quantification of tetracyclic monoterpenoid oxindole alkaloids in *Uncaria rhynchophylla* and their fragmentations in Q-TOF-MS spectra. *Journal of Pharmaceutical and Biomedical Analysis*. 81-82: 56 – 64.
8. Zhang, Y., Yang, W., Yao, C., Feng, R., Yang, M., Guo, D. and Wu, W. (2014). New triterpenic acids from *Uncaria rhynchophylla*: Chemistry, NO-inhibitory activity, and tandem mass spectrometric analysis. *Fitoterapia*. 96: 39 – 47.
9. Tan, S. N., Yong, J. W. H., Teo, C. C., Ge, L., Chan, Y. W. and Hew, C. S. (2011). Determination of metabolites in *Uncaria sinensis* by HPLC and GC–MS after green solvent microwave-assisted extraction. *Talanta*. 83: 891 – 898.

MALAYSIAN JOURNAL OF ANALYTICAL SCIENCES
Published by The Malaysian Analytical Sciences Society
ISSN 1394 - 2506

EFFECT OF PALM OIL FIBER-TiO_2 RATIO IN THE COMPOSITE ON THE REDUCTION OF BTX AND FORMALDEHYDE IN THE AIR

(Kesan Nisbah Serat Kelapa Sawit-TiO_2 dalam Komposit bagi Pengurangan Kandungan BTX dan Formaldehid di Udara)

Nor Rahafza Abdul Manap[1], Roslinda Shamsudin[1]*, Mohd Norhafsam Maghpor[2], Muhammad Azmi Abdul Hamid[1], Azman Jalar[1]

[1]*School of Applied Physics, Faculty of Science and Technology*
Universiti Kebangsaan Malaysia, 43600 UKM Bangi, Selangor, Malaysia
[2]*National Institute of Occupational Safety and Health*
Lot 1, Jalan 15/1, Seksyen 15, 46500 Bandar Baru Bangi, Selangor, Malaysia

**Corresponding author: linda@ukm.edu.my*

Received: 24 February 2015; Accepted: 27 October 2015

Abstract

The effect of palm oil fiber-TiO_2 ratio in the composite on the reduction of benzene, toluene, xylene and formaldehyde in the air is studied. The ratio was set at 1:0, 1:9 and 5:5. The combination of adsorption process by palm oil fiber and photooxidation of volatile organic compounds by titanium dioxide was revealed. The composite were prepared by using mechanical milling technique. The performance of the composite was characterized in terms of percentage of recovery of benzene, toluene and xylene (BTX) using GC/FID and formaldehyde concentration reduction using formaldehyde meter. The results of recovery of the BTX by palm oil fiber/titanium dioxide composite were more than 90%. The palm oil fiber/titanium dioxide composite has successfully reduced the concentration of formaldehyde by up to 66.7%. Therefore, the palm oil mesocarp fiber/titanium dioxide composite produced is able to reduce the concentration of volatile organic compounds.

Keywords: mesocarp fiber, palm oil fiber, titanium dioxide, photocatalyst, photo oxidation, volatile organic compunds

Abstrak

Kesan nisbah serat kelapa sawit-titanium dioksida dalam komposit bagi pengurangan kandungan BTX dan formaldihid dalam udara telah dikaji. Nisbah telah ditetapkan sebagai 1:0, 1:9 dan 5:5. Kombinasi proses penjerapan oleh serat kelapa sawit dan proses oksidasi cahaya sebatian organik meruap oleh titanium dioksida telah dijelaskan. Serbuk komposit serat kelapa sawit-titanium dioksida telah disediakan menggunakan kaedah kisaran mekanikal untuk mendapatkan serbuk komposit. Prestasi komposit telah diuji dari segi nilai peratusan ujian pemulihan benzena, toluena dan xilena (BTX) menggunakan kromatografi gas dengan pengesan pengionan api (GC/FID) dan peratusan pengurangan kepekatan formaldehid menggunakan meter formaldehid. Nilai peratusan ujian pemulihan BTX yang diberikan oleh serbuk komposit melebihi 90%. Serbuk komposit dari serat kelapa sawit dan titanium dioksida telah berjaya mengurangkan kepekatan formaldehid sebanyak 66.7%. Oleh itu, komposit yang dihasilkan dari serat kelapa sawit dan TiO_2 boleh mengurangkan kepekatan sebatian organic meruap dalam udara.

Kata kunci: serat mesokap kelapa sawit, serat kelapa sawit, titanium dioksida, pemangkin cahaya, sebatian organik meruap

Introduction

Indoor air pollution can contribute to many health issues such as headache, dizziness, irritation, cancer and respiratory difficulties [1-4]. The common volatile organic compounds (VOCs) that usually exist in indoor air or a

building are benzene, toluene, isomeric xylene and formaldehyde. These pollutants were from different sources such as incomplete combustion of by-product, construction materials and exhaust emission [2, 5]. In addition to the nature of a new or old building that utilized furniture, paint, adhesive sealants, building materials and floor panels that are recognized as the source of these VOCs [6].

VOCs which can cause various side effects can be trapped and reduced by using adsorbent materials. There are numbers of adsorbent that has been used to treat air pollutants. Local raw minerals such as aluminum oxide (Al_2O_3), silicon dioxide (SiO_2) and titanium dioxide (TiO_2) had been used to remove dimethyl benzene, one of the volatile organic compounds [7]. Whereas nanosilica was used to remove formaldehyde from polluted air [8].

Traditionally, the air pollutants were reduced by increasing the air exchange and controlling the pollutant sources [9]. Recently, photocatalytic oxidation process has been used to remove trace-level organic contaminants in air and has received considerable attention because this technology can be potentially applied in office buildings, factories, labs, homes and cars [10]. TiO_2 is a well-known decomposing agent that has high photo stability, commercial availability, low cost and relatively good activity that uses photocatalytic oxidation process to degrade organic pollutants [11]. In this study, palm oil fiber/TiO_2 composite with different ratio are fabricated to act as adsorbing material using passive sampling technique. The result of percentage of recovery of the prepared composite was compared with the standard percentage value set by National Institute of Occupational Safety and Health (NIOSH). The effect of photocatalyst activity by adding TiO_2 to palm oil fiber was discussed in terms of formaldehyde concentration reduction percentage.

Materials and Methods

Titanium (IV) oxide powder (99.8 % trace metal basis) from Sigma Aldrich, the standard solution of benzene, toluene, pm-xylene and o-xylene were analytical grade with >99% purity, brand Dr Ehrenstorfer. Carbon disulfide with ≤0.001% benzene was purchased from MERCK. Commercial activated charcoal made from coconut shell was purchased from SKC, 1.8 ml glass vial with PTFE lined caps were purchased from Agilent for gas chromatography analysis.

Preparation of composite powder material

Palm oil fibers were washed with distilled water to remove dirt and contaminants. It was dried in the oven at 105 ˚C for 24 hours. Then the palm oil fibers were undergo a series of grinding process; started with grinder (Model, Rocklab grinder TC 40) for 10 minutes and were sieved using rotary sieve (38 micron). It was then ball milled at 600 rpm for 30 minutes. TiO_2 powder together with the palm oil fiber mixture was ball milled at 600 rpm for 30 minutes. Samples were labelled as POFN for 100% palm oil fiber, R1 for 10% titanium dioxide and R5 for 50% titanium dioxide.

Preparation of stock and standard solution

Stock standard solution of toluene, pm-xylene and o-xylene were prepared by adding 1 ml of each standard into 25 ml volumetric flask. Stock standard solution of benzene was done by adding 0.1 ml of standard benzene to 20 ml volumetric flask. Stock solution of formaldehyde was prepared by adding 50 mg of formaldehyde into 100 ml volumetric flask. Then, 5 ml of the stock solution was taken and added into 100 ml volumetric flask to prepare formaldehyde standard solution of 10 ppm.

Recovery test

Carbon disulfide was added into each stock solution to make it either 25 ml or 20 ml solution. Different concentration of standard solution i.e. 8 ppm, 10 ppm and 12 ppm were prepared from stock standard solution. Standard calibration curves for each parameter are performed in Chemstation as stated in instrument manual. 150 mg sample powders with particle size ranges from 47nm to 94.8 nm for palm oil fiber and 62 nm to 111 nm for titanium dioxide were placed in screw cap glass vials and spiked with known amount of benzene, toluene, pm-xylene and o-xylene (BTX) from the standard solution and left in a refrigerator at 4˚C for 24 hours. 1 ml carbon disulfide was added to each vial and immediately closed up. The vials were agitated for 30 minutes and then analysed using gas chromatography with flame ionization detector. A bar chart of recovery percentage was drawn

for comparison purposes. The percentage of recovery was calculated by dividing recovered value with spiked value times by 100.

Formaldehyde test

Stock standard solution and a standard solution of formaldehyde were prepared as above. The formaldehyde solution was heated on a hotplate at 50 ˚C. 10 ml of the standard solution was pipetted into a petri dish and placed inside a 457 x 305 x 305 mm test chamber. The test chamber with 55% relative humidity was set up with a 220-240 V ~ 50/60 Hz 27 Watt lamps. The concentration of formaldehyde was measured by MultiRAE Lite formaldehyde meter. The composite sample was placed inside the test chamber when the formaldehyde meter gave 1 ppm reading on the screen. The light intensity and relative humidity in test chamber maintained as constant.

Results and Discussion

Volatile organic compounds used in this study were toluene, and xylene with three isomers; ortho-, meta-, para-substitution. A good sorbent should be able to desorb all the absorbed analytes [12]. Figure 1 shows that the composite adsorbed all the hazardous VOCs because the obtained value of the percentage of recovery more than 100%. The percentage of recovery for palm oil fiber/titanium dioxide composite powder was calculated using Equation 1 which is given by the area under peak of chromatogram. The amount recovered is the value given by area under peak by gas chromatography as expressed in equation 1 below.

$$\text{Percentage of recovery} = (\text{amount recovered}/\text{amount spiked}) \times 100 \quad (1)$$

As shown in Figure 1(a – c) sample with 100 %, 90 % and 50 % palm oil fiber have more than 100 % recovery of toluene, pm-xylene and o-xylene. For composite powder that was spiked with 8 ppm and 10 ppm of selected analytes, the percentage of recovery ranges from 97 % to 121 %. The increasing number of analytes available that react with the chemical structure and functional group of palm oil fiber gave the highest percentage of recovery, i.e. 203 %. It was found that, the percentage of recovery is very much depending on the heating rate, the gas flow rate and purging time of the gas chromatography [13]. In this study the optimum heating rate and gas flow rate for maximum percentage of recovery was 10 ml/min and 2.0 ml/min, respectively. This finding is in agreement with result studied by Thammakhet and Muneesawang [13] where the optimum heating rate is needed to provide a high percentage of recovery without lowering the adsorption performance of the adsorbent and minimizes the analytes loss. Another possible reason for this observation is contributed by carbon disulfide. Carbon disulfide was used as eluent to elute the compound during the early stage of recovery analysis. When the gaps between double-bonded carbon atoms are similar or greater than Van der Waals separation, direct benzene-benzene polymerization is expected to occur. Due to the carbon disulfide assisted polymerization of the benzene ring in toluene and xylene, high percentage of recovery is obtained similar as reported by Ciabini et al. [14]. In Malaysia, the National Institute of Occupational Safety and Health has set a standard percentage of recovery value. All the adsorbent must meet the 75 % recovery criteria. Result below than 75 % is not accepted.

From the results of recovery for each of the analyte concentration, the palm oil fiber used was able to capture the hazardous volatile organic compounds. All the samples gave a value that exceeds the standard requirement set by NIOSH. The effect of TiO_2 added into the palm oil fiber in term of the formaldehyde reduction is shown in Figure 2. POFN, R1 and R5 samples have successfully reduced the formaldehyde concentration by 62 %, 63 % and 67 % respectively. Photocatalytic degradation by TiO_2 has contributes to better pollutant reducer property of the palm oil fiber composite powder. TiO_2 act as absorbent that absorbed a photon containing energy when it was irradiated by light. The energy that equal or larger than the band gap caused the electron to be excited from the valence band to a conduction band which created vacancy in the valence band. In this reaction, electron hole pair namely, h^+ and e^- are powerful oxidizing and reducing agents respectively [21]. Therefore, formaldehyde is oxidized to carbon dioxide and water according to Equation 2. As report by [15], formaldehyde decomposition rate is depends on humidity, UV light intensity and amount of photocatalyst. Other factors that affecting photocatalytic degradation are adsorption properties and photocatalytic activity of the catalysts [16].

$$HCHO + O_2 \rightarrow CO_2 + H_2O \quad (2)$$

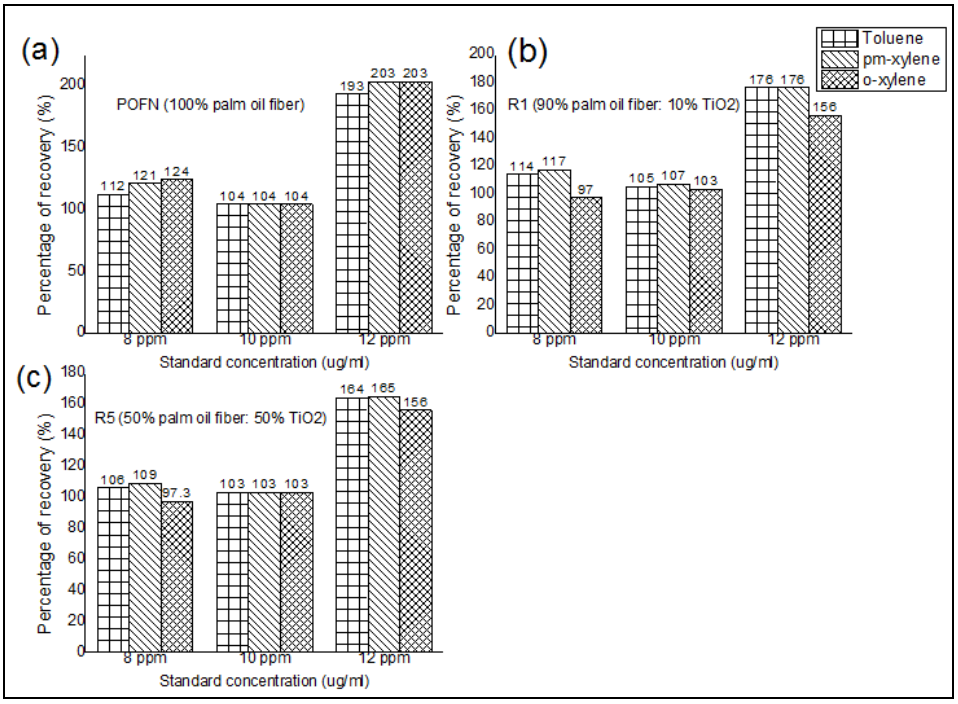


Figure 1. Percentage of recovery of pm-xylene, o-xylene and toluene in Standard 1, Standard 2 and Standard 3 (concentration of 8 ppm for Standard 1, 10 ppm for Standard 2 and 12 ppm for Standard 3) by sample (a) POFN, (b) R1 and (c) R5 after recovery test using carbon disulphide as eluent.

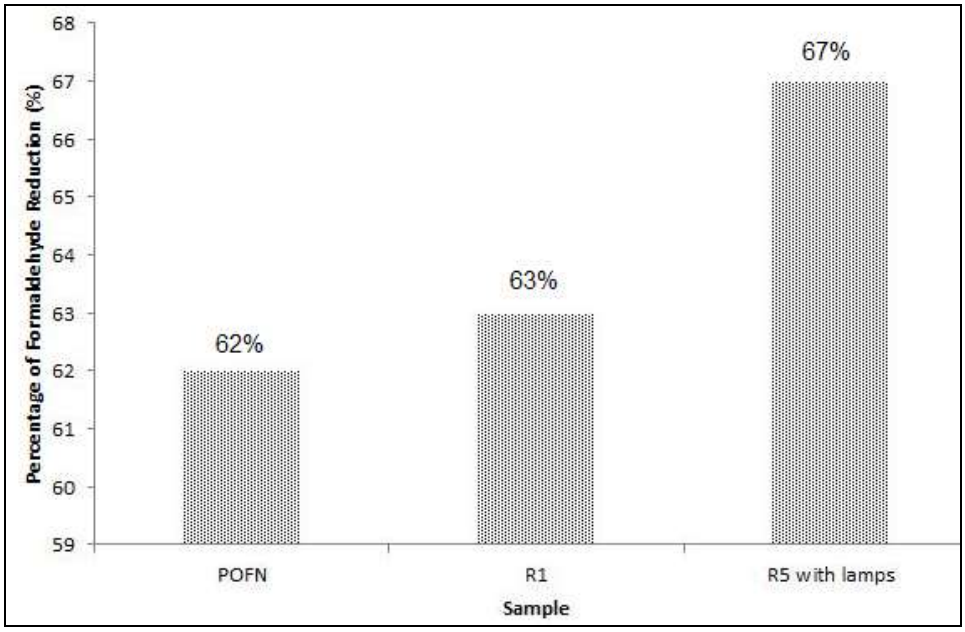


Figure 2. Percentage of formaldehyde concentration reduction by POFN (100% palm oil fiber), R1 (90% palm oil fiber: 10% titanium dioxide and R5 (50% palm oil fiber: 50% titanium dioxide). Only R5 was tested using reading lamps as source of light in the test chamber.

Conclusion

Palm oil fiber/titanium dioxide composite powder has successfully act like commercial activated carbon with percentage of recovery obtained more than 90% as required by the standard method used by NIOSH Malaysia. From the results obtained, a combination between adsorption and photocatalytic process is a promising solution to act as adsorbent and air pollutant reducer. The palm oil fiber/titanium dioxide composite acts as a photocatalyst that oxidized formaldehyde into carbon dioxide and also reduced the concentration of formaldehyde. The capability of the palm oil fiber composite enhance by the amount of the TiO_2 added therefore, the produced palm oil fiber/TiO_2 composite is capable to act as adsorbent and air pollutant reducer, simultaneously.

Acknowledgement

The authors would like to thank to Ministry of Higher Education for supporting this research through ERGS/1/2013/STG05/UKM/02/2 grant. Instrument used in this study has been supported by Makmal Pencirian Struktur Molekul (MPSM), Centre for Research and Instrumentation Management (CRIM), Universiti Kebangsaan Malaysia (UKM). Thank you to National Institute of Occupational Safety and Health Malaysia (NIOSH) for research collaboration and Ministry of Education for financial support through MyBrain15 MyPhD.

References

1. Katsoyiannis, A., Leva, P. and Kotzias, D., (2008). VOC and carbonyl emissions from carpets : A comparative study using four types of environmental chambers. *Journal of Hazardous Materials*, 152: 669–676.
2. Chang, C.T. and Chen, B.Y. (2008). Toxicity assessment of volatile organic compounds and polycyclic aromatic hydrocarbons in motorcycle exhaust. *Journal of Hazardous Materials*, 153: 1262–1269.
3. Wolkoff, P. and Nielsen, G. D. (2010). Non-cancer effects of formaldehyde and relevance for setting an indoor air guideline. *Environmental International*, 36 (7): 788–799.
4. Pala, M., Ugolini, D., Ceppi, M., Rizzo, F., Maiorana, L., Bolognesi, C., Schilirò, T., Gilli, G., Bigatti, P., Bono, R. and Vecchio, D. (2008). Occupational exposure to formaldehyde and biological monitoring of Research Institute workers. *Cancer Detection and Prevention*, 32 (2): 121– 126.
5. Chen, J. and Poon, C. (2009). Photocatalytic construction and building materials: From fundamentals to applications. *Building and Environment*, 44 (9): 1899 – 1906.
6. Sanjuán-herráez, D., De Osa, S., Pastor, A. and De Guardia, M. (2014). Air monitoring of selected volatile organic compounds in wineries using passive sampling and headspace-gas chromatography – mass spectrometry. *Microchemical Journal*, 114: 42–47.
7. Zaitan, H., Korrir, A., Chafik, T. and Bianchi, D. (2013). Evaluation of the potential of volatile organic compound (di-methyl benzene) removal using adsorption on natural minerals compared to commercial oxides. *Journal of Hazardous Materials*, 262: 365–376.
8. Ewlad-Ahmed, A. M., Morris, M. A., Patwardhan, S. V. and Gibson, L. T. (2012). Removal of formaldehyde from air using functionalized silica supports. *Environmental Science and Technology*, 46: 13354 – 13360.
9. Yu, Q. L. and Brouwers, H. J. H. (2009). Indoor air purification using heterogeneous photocatalytic oxidation. Part I: Experimental study. *Applied Catalysis B: Environmental*, 92(3–4): 454 – 461.
10. Zhao, J. and Yang, X. (2003). Photocatalytic oxidation for indoor air purification: A literature review. *Building and Environment*, 38 (5): 645 – 654.
11. Maira, A. J., Yeung, K. L., Lee, C. Y., Yue, P. L. and Chan, C. K. (2000). Size effects in gas-phase photo-oxidation of trichloroethylene using nanometer-sized TiO_2 catalysts. *Journal of Catalysis*, 192 (1): 185 – 196.
12. Tseng, J. Y., Chang, C. Y., Chang, C. F., Chen, Y. H., Chang, C. C., Ji, D. R., Chiu, C. Y. and Chiang, P. C. (2009). Kinetics and equilibrium of desorption removal of copper from magnetic polymer adsorbent. *Journal of Hazardous Materials*, 171 (1–3): 370 – 377.
13. Thammakhet, C. and Muneesawang, V. (2006). Cost effective passive sampling device for volatile organic compounds monitoring. *Atmospheric Environment* 40: 4589 – 4596.
14. Ciabini, L., Santoro, M., Gorelli, F. A., Bini, R., Schettino, V. and Raugei, S. (2007). Triggering dynamics of the high-pressure benzene amorphization. *Nature Materials*, 6: 39 – 43.
15. Quiroz Torres, J., Royer, S., Bellat, J. P., Giraudon, J. M. and Lamonier, J.-F. (2013). Formaldehyde: catalytic oxidation as a promising soft way of elimination. *ChemSusChem*, 6 (4): 578 – 592.
16. Li, F. B., Li, X. Z., Ao, C. H., Lee, S. C. and Hou, M. F. (2005). Enhanced photocatalytic degradation of VOCs using Ln^{3+}-TiO_2 catalysts for indoor air purification. *Chemosphere*, 59 (6): 787 – 800.

MALAYSIAN JOURNAL OF ANALYTICAL SCIENCES
Published by The Malaysian Analytical Sciences Society
ISSN 1394 - 2506

FRACTIONATION OF HEMICELLULOSE FROM RICE STRAW BY ALKALINE EXTRACTION AND ETHANOL PRECIPITATION

(Pemisahan Hemiselulosa daripada Hampas Batang Padi melalui Pengekstrakan Beralkali dan Pemendakan Etanol)

Nur Hazlilla Zulyadi, Sabiha Hanim Saleh*, Siti Halimah Sarijo

School of Chemistry and Environment, Faculty of Applied Sciences,
Universiti Teknologi MARA (UiTM), 40450 Shah Alam, Selangor, Malaysia

**Corresponding author: sabihahanim@salam.uitm.edu.my*

Received: 24 February 2015; Accepted: 27 October 2015

Abstract

Hemicelluloses were extracted from rice straw using alkaline extraction and ethanol precipitation. The effects of different extraction conditions; temperature (45 – 65 °C), pH (4.5 – 6.5), and concentrations of NaOH (0.25 – 1 M) on the hemicellulose yield were investigated. Two hemicelllulosic fractions namely Ha_1 and Ha_2 were obtained by precipitation of alkaline soluble hemicellulose in 0.2 volumes and 4 volumes ethanol, respectively. The Ha_1 and Ha_2 were further characterized to obtain total sugar, monosaccharides and Klason Lignin content. The highest hemicellulose yield for Ha_1 was 4.00 % obtained at 55 °C and pH 5.5 with 0.25 M of NaOH, whereas the highest hemicellulose yield for Ha_2 was 19.88 % obtained at 55 °C and pH 5.5 with 0.5 M of NaOH. This study revealed that hemicellulose yield is dependent on the pH, temperature and concentration of NaOH in the alkaline extraction.

Keywords: hemicelluloses, rice straw, alkaline extraction, ethanol precipitation

Abstrak

Hemiselulosa daripada hampas batang padi telah diekstrak melalui pengekstrakan beralkali dan pemendakan etanol. Kesan perbezaan kondisi pengekstrakan; suhu (45 – 65 °C), pH (4.5 – 6.5), dan kepekatan NaOH (0.25 – 1 M) ke atas hasil hemiselulosa dikaji. Dua pecahan hemiselulosa, Ha_1 and Ha_2 telah diperolehi melalui pemendakan hemisellulosa larut alkali dalam isipadu etanol 0.2 dan 4 masing-masing. Ha_1 and Ha_2 dicirikan oleh jumlah gula, kandungan monosakarida dan Klason Lignin. Hasil hemiselulosa tertinggi untuk Ha_1 adalah 4.00 % yang diperolehi pada suhu 55 °C, pH 5.5 and 0.25 M NaOH, manakala untuk Ha_2 adalah 19.88 % diperolehi pada suhu 55 °C, pH 5.5 and kepekatan 0.5 M NaOH. Kajian ini membuktikan hasil hemisellulosa bergantung kepada pH, suhu dan kepekatan NaOH dalam pengekstrakan beralkali.

Kata kunci: hemiselulosa, hampas batang padi, pengekstrakan beralkali, pemendakan etanol

Introduction

The main cereal crop in the whole wide world is rice, which is being produced in more than 148 million hectares with huge range of ecosystem. The scientific name of paddy is *Oryza sativa*. It is an important cereal crop that produce a lot of residues which is rice straw [1]. Rice straw is the rice plant stalk that is left as waste product on the field after harvesting of the rice grain [2]. A lot of rice straw are disposed by biomass burning that leads to air pollution.Therefore, a lot of research work has been performed to find ways of utilizing these agricultural waste. Hemicellulose is the second most abundant polysaccharide in nature, representing approximately 20-30% of

lignocellulosic biomass [3]. Hemicellulose polymers are complex components in the plants cell wall. With cellulose and lignin, hemicellulose form hydrogen bonds and covalent bond respectively.

The hemicelluloses are used in various industrial applications such as food additives, biodegradable films and in medicinal applications [4]. Various methods were used to isolate hemicellulose from the agricultural waste. Among these methods, alkaline extraction is most widely used. Alkaline solution hydrolyzes the ester linkage between hemicellulose and other components, resulted in isolating hemicellulose in the aqueous media. Usually the isolation of hemicellulose is done by using alkaline solution such as NaOH for softwood and KOH for hardwood [5]. The aim of this study was to optimize the alkaline extraction conditions and ethanol precipitation of hemicelluloses from rice straw. The effects of the concentration of NaOH, temperature and pH on hemicellulose percentage yield were investigated.

Materials and Methods

Materials

Rice straw was obtained from local sources (Perlis, Malaysia). It was dried and cut into small pieces. The straw was ground to pass a 0.08 mm size screen and stored at room temperature. All other chemicals used were of analytical grade unless otherwise stated.

Extraction of hemicelluloses

Extraction of hemicellulose was carried out by mixing the rice straw with 0.25 M sodium hydroxide (NaOH) with ratio of 1:25 (w/v). The mixture was stirred at 400 rpm and heated at constant temperature of 55 °C for 2 hours. After filtration, the pH of the solution was adjusted to pH 5.5 by adding 6 M hydrochloric acid (HCl). Then the mixtures were kept at 4.0 °C for 24 hours. The mixture was then centrifuged at 3500 rpm for 15 minutes. Ethanol 0.2 volumes and 4 volumes containing 10 % of acetic acid were added to the liquid fraction to precipitate Ha_1 and Ha_2 respectively. Both hemicellulose fractions (Ha_1 and Ha_2) were obtained and dried at 40.0 °C for 24 hours. In order to optimize the alkaline extraction conditions, the extraction was carried out at various concentration of NaOH (0.25 M, 0.5 M and 1 M) temperature (45 °C, 55 °C, and 65 °C) and pH (4.5, 5.5 and 6.5).

Analytical method

Total sugar content was measured according to phenol-sulphuric acid method [6]. The hemicellulose fraction with unknown concentration was added with 0.5 mL of 5.0 % phenol solution and the mixture was shaken. A volume of 2.5 mL concentrated H_2SO_4 was quickly added to the mixture (phenol-hemicellulose) and shaken once again. These solutions were then analysed where the absorbance of the mixtures were recorded at 480 nm using UV-Visible spectrophotometer. The hemicelluloses yield (%) was calculated based on total sugar content in the hemicelluloses fraction. The monosaccharides sugar was determined by using a high performance liquid chromatography (HPLC) (Agilent Technologies 1200 Series, Germany) using Aminex HPX 87P column (300 mm x 7.8 mm). The HPLC was equipped with a refractive index detector (G 1362A, Agilent Technologies 1200 Series, Germany) and column oven (Agilent Technologies 1200 Series, Germany). The hemicellulose fraction was filtered through a 0.20 µm nylon syringe filter (Minisart, Sartorius AG, Germany) prior directly injected to the HPLC system. The hemicellulose fractions were eluted using deionised water as the mobile phase at column temperature of 80 °C and a flow rate of 0.5 mL/min. Klason lignin content was determined following TAPPI method T222. The FTIR spectra of the hemicellulose fractions were obtained on a FT-IR spectroscopy (Nicolet 500) using a KBr disc containing 1% finely ground samples. Spectra were recorded between 4000 and 400 cm^{-1} at a resolution of 4 cm^{-1}.

Statistical analysis

ANOVA was used to analyse the data of experiment and Duncan's multiple range test was applied in order to determine the significant difference ($P<0.05$) of samples using Statistical Package for Social Science, Version 10 (SPSS Inc., Illinois). The result was expressed as mean ± SD (standard deviation).

Results and Discussion

Effect of NaOH concentration

Alkaline extraction was carried out to investigate the effects of NaOH concentrations; 0.25 M, 0.5 M and 1 M on hemicellulose yield, while other parameters were fixed as followed : pH 5.5 and temperature 55 °C. As shown in

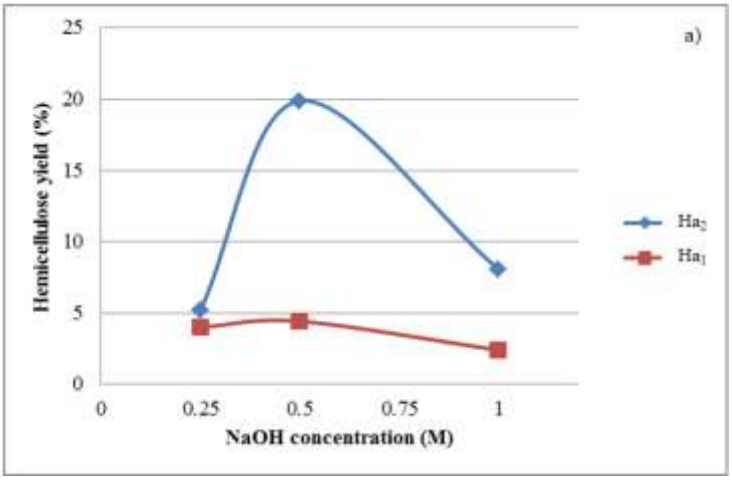
Figure 1 (a), hemicellulose yield for both Ha_1 and Ha_2 increased as NaOH concentration increased from 0.25 M to 0.5 M but then decreased tremendously when the NaOH concentration was increased to 1 M. This indicates that hemicellulose extraction was best performed at mild conditions. Hemicellulose yield for both, Ha_1 and Ha_2 were highest at 0.5 M NaOH concentration. Statistical analysis for Ha_1 showed that there were no significant differences between 0.25 M NaOH and 0.5 M NaOH ($P > 0.05$), while there were significant differences among 0.25 M NaOH and 1 M NaOH. Thus 0.25 M NaOH concentration was chosen for further analysis for Ha_1. On the other hand, the statistical analysis for Ha_2 showed that there were significant differences between 0.25 M, 0.5 M and 1 M NaOH ($P < 0.05$).Therefore, 0.5 M NaOH concentration was chosen for further analysis for Ha_2.

Effect of temperature

The effects of different temperatures (45 – 65 °C) on the yield of hemicellulosic fractions; Ha_1 and Ha_2 were studied while the other parameters were fixed; pH 5.5 with 0.25 M NaOH for Ha_1 and pH 5.5 with 0.5 M NaOH for Ha_2. Statiscal analysis of hemicellulose yield, Ha_1 and Ha_2 showed that the significant difference existence between temperature of 45 °C and 55 °C and among hemicellulose extracted at 55 °C and 65 °C ($P < 0.05$), however there is no significant difference between hemicellulose yield extracted at 45 °C and 65 °C ($P > 0.05$). Based on Figure 1 (b), the best temperature for alkaline extraction was at 55°C which gave the highest hemicellulose yield. The presence of high lignin content hindered the yield of hemicellulose in Ha_1 resulted in lower hemicellulose yield than Ha_2. The hemicellulose yield for both Ha_1 and Ha_2 significantly increased from 45 °C to 55 °C and as temperature of extraction reached 65 °C, the yield of hemicelluloses significantly decreased. The yield of hemicellulose decreased at 65 °C due to less degradation of macromolecular hemicellulose.The minor degradation occurred mainly because of the linkages between glycosyl units were cleaved at high temperature [6].

Effect of pH

pH was another factor which affected the efficiency of hemicellulose extraction. The effect of pH for hemicellulosic fractions, Ha_1 and Ha_2 were studied at different pH (4.5 – 6.5) while the other parameters were fixed; 0.25 M NaOH and temperature of 55 °C for Ha_1 while 0.5 M NaOH and temperature of 55 °C for Ha_2. Statiscal analysis for Ha_1 and Ha_2 showed that the significant difference existence between pH of 4.5 and 5.5 and between pH 5.5 and 6.5, ($P < 0.05$), however there is no significant difference between pH 4.5 and 6.5 ($P > 0.05$). There was an increasing trend in hemicellulose yield from pH 4.5 to 5.5 and decreasing trend from pH 5.5 to 6.5 for both Ha_1 and Ha_2. This indicated that minor degradation occurred when the pH was slightly acidic (pH 4.5) and at neutral condition (pH 6.5). Figure 1 (c) showed that the suitable pH to yield the maximum concentration for both Ha_1 and Ha_2 was at pH 5.5. Thus, pH 5.5 was favorable to isolate hemicellulose from rice straw using alkaline extraction.



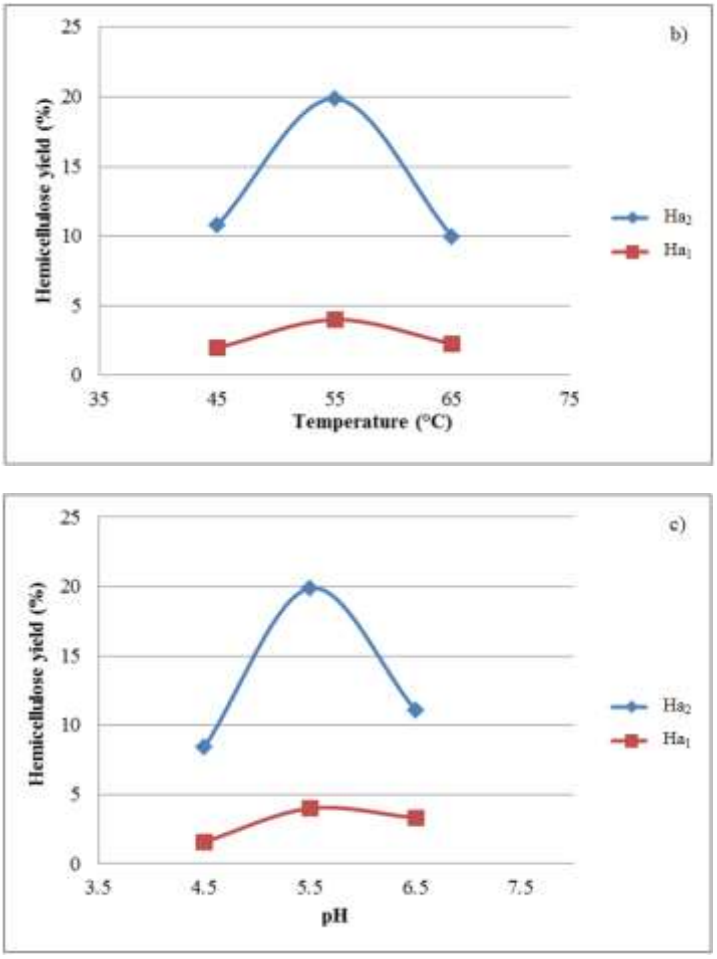


Figure 1. Effects of NaOH concentration (a), temperature (b), and pH (c) on hemicellulose yield (%) Ha_1 and Ha_2.

Klason Lignin content

The Klason lignin content for both hemicellulose fractions, Ha_1 and Ha_2 is shown in Table 1. The result showed that Ha_1 contain more lignin (11.72 %) than Ha_2 (4.22 %). Table 1 showed that as the volume of ethanol decreased (0.2 v) in Ha_1, the Klason lignin content increased and as the volume of ethanol increased (4v) in Ha_2, the Klason lignin content decreased. The increased volume of ethanol (4v) increased the polarity of plant cell wall in Ha_2 exposed it more to the solvent thus promote the lignin removal [7].

Table 1. Monosaccharide composition and Klason Lignin content for Ha_1 and Ha_2

	Glucose (mg/mL)	Arabinose (mg/mL)	Xylose (mg/mL)	Ara/Xyl ratio	Klason Lignin (%)
Ha_1	0.57 ± 0.44	0.10 ± 0.02	0.27 ± 0.02	0.36	11.72 ± 5.07
Ha_2	0.70 ± 0.18	0.96 ± 0.07	0.05 ± 0.05	21.08	4.22 ± 1.32

Data means and standard deviation n=3. Ha_1 represent hemicellulose high lignin prepared by alkaline extraction from rice straw with 0.2v ethanol precipitation. Ha_2 represent hemicellulose low lignin prepared by alkaline extraction from rice straw with 0.4v ethanol precipitation.

Monosaccharide analysis by HPLC

As shown in Table 1, both Ha_1 and Ha_2 composed of glucose, arabinose and xylose. The predominant sugar component for Ha_1 was glucose while for Ha_2 was arabinose. Ha_2 consisted of higher glucose concentration mainly because the presence of glucans which associated with xylans in primary cell wall, which were less associated with lignin. The xylose concentration higher in Ha_1 as compared to Ha_2. The lower amount of arabinose in Ha_1 suggested that the hemicellulose was closely assosiated to the cellulose surface [8]. Hemicellulose fraction, Ha_2 contained higher amount of Ara/Xyl (21.08) whereas Ha_1 showed lower Ara/Xyl ratio (0.36). Higher amount of Ara/Xyl means that the hemicellulose obtained more linear arabinoxylan while lower Ara/Xyl ratio consisted of branched arabinoxylan [9].

FTIR Spectra

Figure 2 shows the FTIR spectra of hemicellulosic fractions (Ha_1, Ha_2) and rice straw within the region of 500 – 4000 cm^{-1} including region 850 – 1200 cm^{-1} which is typical region for hemicellulose [10]. Both hemicellulose fractions show similar features. All of the spectra showed similarity as they all have hemicellulose band (850 –1200 cm^{-1}), which concluded that the alkaline extraction did not change the macromolecular structure of hemicellulose. Absorption band at 1610 cm^{-1} corresponded to the water bending mode presence for only Ha_1 and Ha_2 since hemicellulose have strong affinity towards water whereas, this band could not found in rice straw due to the presence of cellulose which hindered the water affinity [11]. Low intensity absorption band at region 850 – 1200 cm^{-1} in Ha_1 compared to Ha_2 shows low purity of hemicellulose fraction due to the higher lignin content for Ha_1 compared to Ha_2. The absoption band at region between 1126 – 1032 cm^{-1} is a typical band for lignin [12]. Higher intensity absorption band at region 1126 – 1032 cm^{-1} in Ha_1 compared to Ha_2, proved that lignin content was higher in Ha_1. The presence of absorption band at 1710 cm^{-1} in Ha_1 is due to the carboxyl groups as the hydroxyl groups in lignin undergo oxidation [13]. Absorption band at 3049 cm^{-1} is assigned to the C-H in an aromatic vibration as hemicellulose contained a small amount of lignin [10]. Absorption band at 1043 cm^{-1} is due to the C-O-C stretching glycosidic linkages in xylans. And the absorption band at 1740 cm^{-1} refer to acetyl carbonyl. As shown in Figure 2, broad absorption band at 3400 and 2400 cm^{-1} is due to the stretching vibrations of OH and CH respectively and absorption band at 1200 cm^{-1} refer to the stretching vibrations of C-O. The C-H bending vibration shows absoption bands at 1467 and 1427 cm^{-1} while the OH bending vibration shows absoption bands at 1340 cm^{-1} [14].

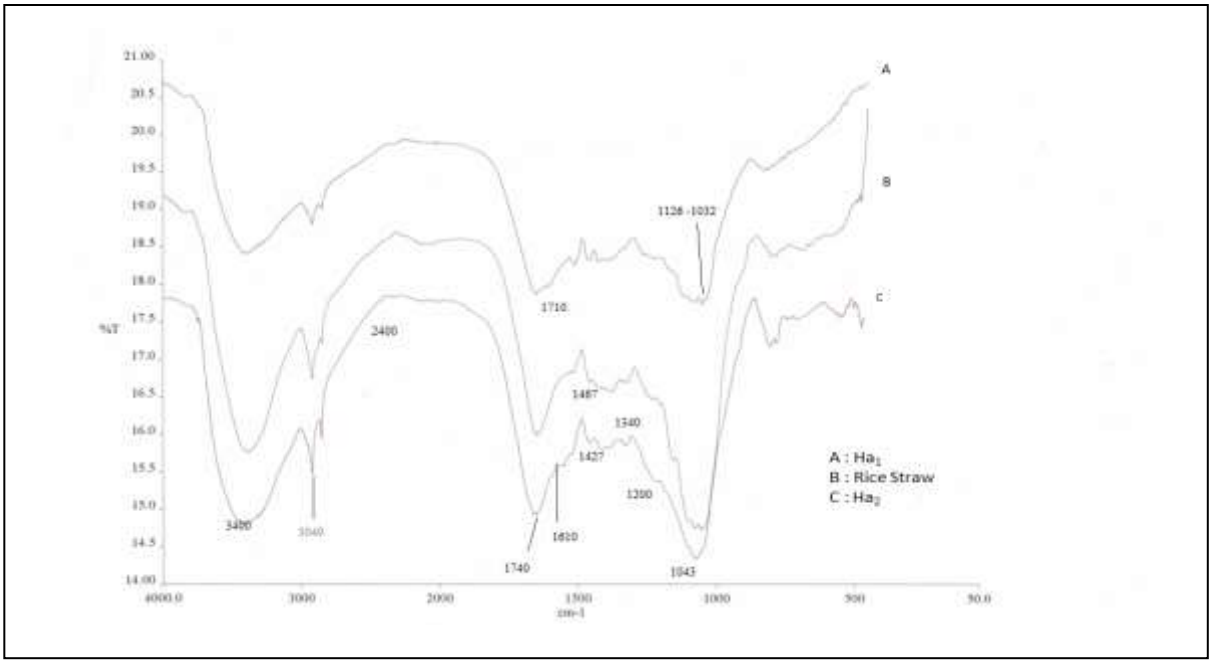


Figure 2. FTIR spectra of Ha_1, Ha_2 and rice straw

Conclusion

This study showed that the maximum hemicellulose percentage yield was obtained by alkaline extraction. The highest hemicellulose yield for Ha_1 was 4.00 % obtained at 55 °C and pH 5.5 with 0.25 M NaOH, whereas the highest hemicellulose percentage yield for Ha_2 was 19.88 % obtained at 55 °C and pH 5.5 with 0. 5M of NaOH. Hemicellulose yield Ha_2 was found to be higher than Ha_1, showing that lignin content affected the percentage yield of hemicellulose.

Acknowledgement

The authors are grateful to the Universiti Teknologi MARA, Malaysia for the financial support of this research by ZAMALAH Sokongan Pasca Siswazah (Postgraduate Supporting Fellowship), 600-RMI/DANA 5/3/PSF (18/2015), and Faculty of Pharmacy, University Teknologi Mara, Puncak Alam for HPLC facilities.

References

1. Sharma, R. K. and Arora, D. S. (2010). Biodegradation of paddy straw obtained from different geographic locations by means of *Phlebia* spp. for animal feed. *Biodegradation*, 22: 143 – 152.
2. Lim, J. S., Abdul Manan, Z., Wan Alwi, S. R. and Hashim, H. (2012). A review on utilisation of biomass from rice industry as a source of renewable energy. *Renewable and Sustainable Energy Reviews*, 16(5): 3084 – 3094.
3. Ebringerová, A., Hromádková, Z., Híbalová, V., Xu, C., Holmbom, B., Sundberg, A., and Willför, S. (2007). Norway spruce galactoglucomannans exhibiting immunomodulating and radical-scavenging activities. *International Journal of Biology Macromolecule*, 42: 1 – 5.
4. Sabiha-Hanim, S. and Siti-Norsafurah, A. M. (2012). Physical properties of hemicellulose films from sugarcane bagasse. *Procedia Engineering*, 42: 1390 – 1395.
5. Peng, P., Peng, F., Bian, J., Xu, F., Sun, R.-C. and Kennedy, J. F. (2011).Isolation and structural characterization of hemicelluloses from the bamboo species Phyllostachysincarnata Wen. *Carbohydrate Polymers*, 86(2): 883 – 890.
6. Bian, J., Peng, F., Peng, X.-P., Xu, F., Sun, R.-C. and Kennedy, J. F. (2012). Isolation of hemicelluloses from sugarcane bagasse at different temperatures: Structure and properties. *Carbohydrate Polymers*, 88(2): 638 – 645.
7. Yang, D., Zhong, L-X., Yuan, T-Q., Peng, X-W. and Sun, R-C. (2013). Studies on the structural characterization of lignin, hemicelluloses and cellulose fractionated by ionic liquid followed by alkaline extraction from bamboo. *Industrial Crops and Products*, 43: 141 – 149.
8. Xiao, B., Sun, X. and Sun, R. (2001). Chemical, structural, and thermal characterizations of alkali-soluble lignins and hemicelluloses, and cellulose from maize stems, rye straw, and rice straw. *Polymer Degradation and Stability*, 74(2): 307 – 319.
9. Egüés, I., Eceiza, A. and Labidi, J. (2013). Effect of different hemicelluloses characteristics on film forming properties. *Industrial Crops and Products*, 47: 331 – 338.
10. Rabetafika, H. N., Bchir, B., Blecker, C., Paquot, M. and Wathelet, B. (2014). Comparative study of alkaline extraction process of hemicelluloses from pear pomace. *Biomass and Bioenergy*, 61: 254 – 264.
11. Kacurakova, M., Belton, P. S., Wilson, R. H. and Hirsch, J. (1998). Hydration properties of xylan-type structure: an FTIR study of xylooligosaccharides. *Journal Science of Food and Agriculture*, 77(1): 38 – 48.
12. Cai, Y., Li, G., Nie, J., Lin, Y., Nie F. and Zhang, J. (2010). Study of the structure and biosynthetic pathway of lignin in stone cells of pear. *Science Horticulturae*, 125()3: 374 – 379.
13. Sun, R. C., Tomkinson, J., Ma, P. L. and Liang, S. F. (2000). Comparative study of hemicelluloses from rice straw by alkali and hydrogen peroxide treatments. *Carbohydrate Polymers*, 42(2): 111 – 122.
14. Kacuráková, M., Ebringerova, A., Hirsch, J. and Horomadkova, Z. (1994). Infrared study of arabinoxylans. *Journal Science of Food Agriculture*, 66 (3): 423 – 427.

MALAYSIAN JOURNAL OF ANALYTICAL SCIENCES
Published by The Malaysian Analytical Sciences Society
ISSN 1394 - 2506

PREPARATION, CHARACTERIZATION AND PERFORMANCE STUDIES OF ACTIVE PVDF ULTRAFILTRATION-SURFACTANTS MEMBRANES CONTAINING PVP AS ADDITIVE

(Penyediaan, Pencirian dan Kajian Prestasi PVDF Aktif Ultraturasan-Surfaktan Membran mengandungi PVP sebagai Bahan Tambahan)

Nur Izzah Md Fadilah and Abdul Rahman Hassan*

Industrial Membrane Technology Laboratory,
Department of Industrial Chemical Technology,
Faculty of Science and Technology,
Universiti Sains Islam Malaysia, 71800 Nilai, Negeri Sembilan, Malaysia

**Corresponding author: abdrahman@usim.edu.my*

Received: 24 February 2015; Accepted: 27 October 2015

The role of surfactants in the formation of active Poly(vinylidene fluoride) (PVDF) ultrafiltration (AUF) membranes was studied. The effect combination of surfactants that are Sodium dodecyl sulfate (SDS)/Tween 80 and Tween 80/Triton X-100 formulations on performance and morphological structures were investigated for the first time. The influence of surfactants blends on the membrane pores was also examined. Experimental data showed that combination of Tween 80/Triton X-100 give the highest BSA permeation flux with a value of 285.51 $Lm^{-2}h^{-1}$. With combination of SDS/Tween 80, the AUF membrane showed the highest protein rejection up to 93 % and 79 % for Bovine Serum Albumin (BSA) and Egg Albumin (EA), respectively. Moreover, membranes characterization demonstrated that the addition of SDS/Tween 80 and Tween 80/Triton X-100 were found to affect the performance, surface morphologies and membrane pores of AUF PVDF membranes.

Keywords: poly(vinylidene fluoride), ultrafiltration, surfactant, protein rejection, morphology

Abstrak

Peranan surfaktan dalam pembentukan ultraturasan PVDF aktif (AUF) membran telah dikaji. Gabungan kesan surfaktan iaitu SDS/Tween 80 dan Tween 80/Triton X-100 formulasi terhadap prestasi dan struktur morfologi telah dikaji buat pertama kali. Pengaruh adunan surfaktan pada liang membran juga diperiksa. Data ujikaji menunjukkan bahawa gabungan Tween 80/Triton X-100 memberikan bacaan penyerapan fluks tertinggi iaitu 285.51 $Lm^{-2}h^{-1}$. Dengan kombinasi SDS/Tween 80, membran AUF menunjukkan protein penolakan tertinggi sehingga 93 % dan 79 % masing – masing untuk Albumin Serum Bovine (BSA) dan Albumin Telur (EA). Selain itu, membran pencirian menunjukkan bahawa penambahan SDS/Tween 80 dan Tween 80/Triton X-100 didapati memberi kesan kepada prestasi, morfologi permukaan dan liang membran AUF PVDF.

Kata kunci: poli(vinylidene fluorida), ultraturasan, surfaktan, penolakan protein, morfologi

Introduction

Membrane technology has been found to be an alternative and attractive approach for separation or filtration because the process is faster, energy efficient and does not involve any phase change. Currently, the application of ultrafiltration (UF) in membrane technology is growing very rapidly in protein separations. The important goal in membrane technology is to control the membrane structure, which affects its performance. Hence, extensive

research has been conducted in attempting to improve the performance of the membrane [1]. Since Loeb and Sourirajan first introduced the phase inversion method, considerable progress has been made for understanding the formation mechanism of asymmetric membranes. The phase inversion process induced by immersion precipitation is a well-known technique to prepare asymmetric polymeric membranes. In that technique, a thin film of polymer solution is cast on to a suitable substrate and subsequently immersed into a coagulation bath. The diffusion exchange of solvent and non-solvent will results in the phase separation and also formation of membrane [2].

The UF membrane structure and performance can be controlled by the casting solution composition, casting condition and coagulation bath composition. Thus, in order to get the membrane with excellent structure and performance, introduction of a suitable additive to the casting solution is a convenient and efficient method [3]. Several researchers have reported on the role of additives in the membranes structure and performance. Some additives have the tendency to form macrovoids, others help in suppressing the macrovoids improving interconnectivity of the pores and resulting in higher porosity in the top layer and sub layer. In this study, Polyvinylpyrolidone (PVP) was used as an additive with combination of surfactants in order to control the membrane performance in the preparation of UF membranes. PVP is known as a non-toxic material which miscibility with membrane and solubility in water as well as solvents make PVP a suitable polymer additive. During the membrane formation process, PVP is added to the polymer solution to promote the formation of micropores [4]. It is assumed that the hydrophilic additive, PVP dissolve in water and the sites where PVP exist become micropores during the phase inversion process. Besides the formation of micropores, it has been generally accepted that the porosity increases and the macrovoid formation disappears as PVP was added to the casting solution [5]. For instance, Xu et al. [6] studied the effect of PVP for different MW on the morphology of polyetherimide hollow fiber and they found that the higher the MW of PVP added, bigger the pores were formed [6]. On the other hand, Wang et al. [7] also found similar finding that the decrease in the concentration of PVP resulted to lower water flux and higher rejection.

Although it appears that a number of works has been reported [5-7] using PVP as additives, there is yet no report regarding the effect of PVP additives with combination of surfactants on the morphology and performance of PVDF membranes. The surfactants need to be introduced in the casting solutions in order to prepare membranes either with good membrane structure (consisting of finger-like, dense top-layer and spongy sub-layer) or penetration properties because the addition of additive is still not versatile enough to prepare the appropriate membrane structure and properties. In this paper, the asymmetric membranes were prepared using polymeric solutions consisting of the PVDF, solvent N-methyl-2-pyrrolidon (NMP) and PVP by classical phase inversion method. By combining of surfactant to the polymeric solutions, the effect of anionic and non-ionic surfactants on morphological and performance of the asymmetric membranes such as pure water permeations and rejections were investigated and discussed.

Materials and Methods

Materials

Poly(vinylidene fluoride) (PVDF, Kynar® from Arkema, MW = 45.00 g/mol, d = 1.78 g/cm3) was obtained in pellet form, which is used as polymer in the preparation of membrane casting solution. N-methyl-2-pyrrolidone (NMP, >99%) (Merck, Darmstadt, Germany, d = 1.00 g/cm^3) was used as the solvent for PVDF. Polyvinylpyrolidone (PVP) (MW = 58000 g/mol, K29-32 from Acros Organics), was used as additive in the dope solution. Sodium dodecyl sulfate (SDS) (MW = 288.37g/mol, Merck Schuchardt OHG, Germany), Triton X-100 (MW = 646.86 g/mol, Fisher Chemical) and Tween 80 (d = 1.060 – 1.090 g/cm^3, Merck Schuchardt OHG, Germany) were used as surfactants in the casting solutions. Other solvents such as ethanol and n-hexane as well as distilled water were used as non-solvent in the coagulant bath. Bovine serum albumin (BSA), MW = 69 kDa and egg albumin (EA), MW = 45 kDa were purchased from Acros Organics, USA, used as the solute for filtration experiments. Disodium phosphate dehydrate ($Na_2HPO_4.2H_2O$) and sodium dihydrogen phosphate ($NaH_2PO_4.H_2O$) were used for the preparation of protein feed solution.

Preparation of membranes

Flat-sheet type PVDF membranes were prepared by the immersion precipitation method at room temperature. The casting solutions were prepared by blending of PVDF and PVP in the presence of different types of surfactant in

NMP under constant stirring for 8h at 60°C. A series of polymer solutions were prepared by various composition and type of surfactants, designated as M-P, M-PST and M-PTT as shown in Table 1. The obtained homogenous solution was allowed to stand for at least 2h to eliminate the air bubbles. Subsequently, the solution was spread uniformly on a glass plate, with the help of a casting knife maintaining a clearance between the knife and the plate. The polymer solutions were cast into thin film (100 µm thick) on glass sheets and then the resulting films were immersed into a water bath immediately and let the precipitation to complete (about 2-4 mins). The colour of the casted films changed from transparent to white immediately after immersion into the coagulation bath and separates out of the glass plate after some-time (3-5s). The formed membranes were immersed into tap water for 1 day. The dry membranes were obtained by soaking with ethanol and n-hexane for 24 hour and 1-3 hours respectively before drying at room temperature. Finally, the sheets were cut into the form of circular disk with diameter of 42 mm to be fitted in the membrane cell for filtration experiments. Two types of phase separation can be distinguished in the membrane preparation process. Firstly, the dry phase inversion takes place in the atmosphere by evaporation of the solvent. Secondly, the wet phase inversion is carried out by immersing the polymer solution film into a coagulation bath of a non-solvent, where an exchange of solvent and non-solvent takes place and the membrane is formed. Hence, in this study, we prepared membranes by a combination of both processes.

Table 1. The composition of dope formulation AUF membranes

Membrane	Total polymer (wt%)	Solvent (wt%)	Additive (wt%)	Surfactants (wt%)		
	PVDF	NMP	PVP	SDS	Triton X-100	Tween 80
M-P	17	80	3	-	-	-
M-PST	17	78	3	1	-	1
M-PTT	17	78	3	-	1	1

Pure water permeation (PWP)

Membranes after compaction were subjected to pure water permeation (PWP) within the range operating pressure of 50 – 300 kPa. The PWP was measured to ensure that the membranes used were stable. The permeability was measured under steady state flow. The PWP in the permeate side was measured at the ambient temperature of 25 ± 1°C. The pure water permeation, J_w was determined using Equation (1).

$$J_W = \frac{Q}{A \times t} \quad (1)$$

where J_w = pure water permeation ($Lm^{-2}h^{-1}$); Q = Volume of permeate (L); A = membrane area (m^2); t = time (h)

Protein rejection studies

Ultrafiltration experiment was conducted in the batch kit cell mentioned to study the influence of the addition of additives and surfactants on solute rejection of the prepared membranes. Bovine serum albumin (BSA, 69 kDa) and egg albumin (EA, 45 kDa) were chosen for the estimation solute rejectio n. The protein solutions was prepared at a concentration of 0.1 wt% in a phosphate buffer (0.5M, pH 7.2) using distilled water and was filtered through each of membranes. During the UF process, the permeate protein concentration were collected over measured time intervals in graduated tubes, and were analyzed for protein content by using UV-Visible spectrophotometer at a wavelength of 280 nm. The percentage rejection was calculated using Equation (2).

$$R(\%) = \left(1 - \frac{C_p}{C_f}\right) \times 100 \quad (2)$$

where R is percentage rejection of protein (%); C_p is concentration of protein in permeate (mg/mL); C_f is concentration of protein in feed (mg/mL).

Membrane Characterization by Morphological Studies

The morphology of the prepared membranes were investigated by microscopic observations which is carried out by a scanning electron microscope (SEM-JEOL JSM-6360LA) to provide the visual information of the top surface as well as cross-sectional morphology of the membranes. The top surface and cross-sectional views of the membranes should be broken in liquid nitrogen and coated with gold by using Auto Fine Coater (JFC-1600). All the SEM images were taken at various magnifications (X400-500). The top of the cross-section photographs presented in this article is the skin layer of the membrane.

Results and Discussion

Ultrafiltration test analysis

Ultrafiltration experiments were performed to explore the performance of PVDF/PVP additives membrane with addition of anionic/non-ionic and non-ionic/non-ionic surfactants. The water flux or pure water permeation (PWP), J_w of prepared membranes was measured to evaluate the influence of membrane composition on the membrane permeability. Figure 1 shows the pressure-dependent fluxes of pure water for the membranes prepared. PWP of all modified membranes were increases gradually with pressure increased up to 300 kPa.

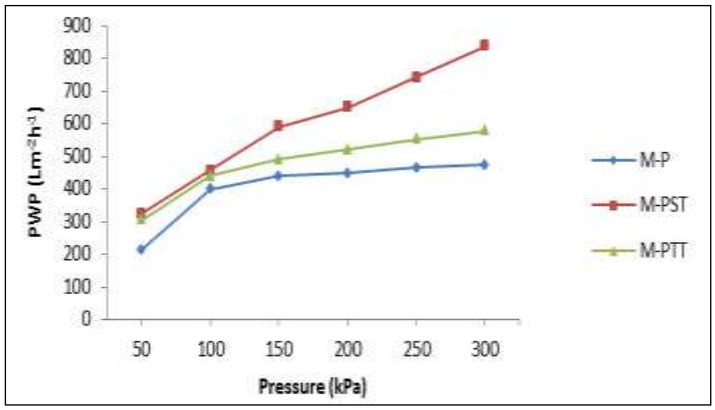


Figure 1. Effect of combination anionic/non-ionic and non-ionic/non-ionic surfactants on pure water permeation (PWP) of PVDF membranes

The combination of anionic and non-ionic surfactants, M-PST exhibited a higher PWP than that of the M-P and M-PTT membranes. From the result obtained, PWP of the M-PST attained a maximum value of 838.11 $Lm^{-2}h^{-1}$, while the minimum value was just 472.39 $Lm^{-2}h^{-1}$ for the M-P at 300 kPa. The water flux variation can be explained as the incorporation of combination anionic with non-ionic surfactants enhanced the hydrophilicity of the membranes which improved the water permeation to a certain extent. In the other hand, the value of PWP for M-PTT was found to be 577.37 $Lm^{-2}h^{-1}$, which is higher than M-P. This is correlates with the combination of both non-ionic surfactants resulted in high hydrophilicity compared to membranes without surfactant.

Protein permeate flux studies

The highest BSA permeate flux (PF) was 285.51 $Lm^{-2}h^{-1}$ for the M-PTT membrane and the minimum BSA-PF was 151.72 $Lm^{-2}h^{-1}$ for the M-P-without surfactant membrane (Figure 2). The highest PF is due to the formation of macrovoids in the sub-layer membrane which is faster rated leaching out during immersion process. Besides, for the combination non-ionic/non-ionic surfactants, interaction between hydrophobic chain and the non-polar sites of the membranes were observed which leading to hydrophilization of the membrane surface and pores [8]. As a result, higher PF for the non-ionic/non-ionic surfactants solution are obtained. In the other hand, the lowest PF may be due

to immiscible phase behaviour of blend composition without surfactant, which predominates due to lower molecular attractive forces between its blend components. During the filtration process, certain protein molecules can be deposited on the membrane surface, which caused an abrupt drop in flux. Additionally, protein molecules can be swept from the surface due to stirring, which resulted in equilibrium between depositions and sweeping [9].

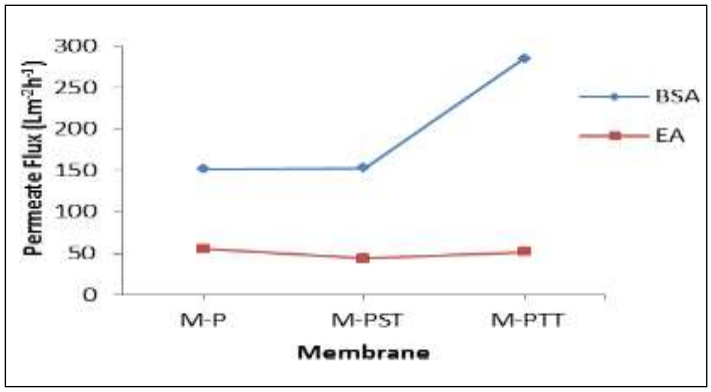


Figure 2. Effect of combination anionic/non-ionic and non-ionic/non-ionic surfactants on permeate flux (PF) of protein BSA and EA

Protein rejection

The performance of the prepared UF membranes is also measured by investigating protein rejection during filtration experiment with macromolecular solute BSA (69kDa) and EA (45kDa) solution as feed. The protein rejection of BSA and EA are illustrated in Figure 3 for all the modified membranes when the feed solution is maintained at pH 7.2, since a change in pH may increase the adsorptive fouling of the membranes. In addition, if the pH of the proteins solution changes, intermolecular forces between protein molecules and membranes will predominate and affect the efficiency of membranes [10]. From the result obtained, the M-PST membrane exhibited higher rejection up to 93 % and 79 % for BSA and EA respectively, compared with other membranes. Higher rejection of BSA may be due to larger solute size of BSA compared with EA. Besides, the M-PTT membrane which combine non-ionic with non-ionic surfactants showed the BSA rejection 90 %, lower than membrane which combine ionic with non-ionic surfactants, may be because of homogeneity between the surfactants in the polymer solution. This will resulted in the formation of aggregate pores in membranes as discussed in SEM analysis.

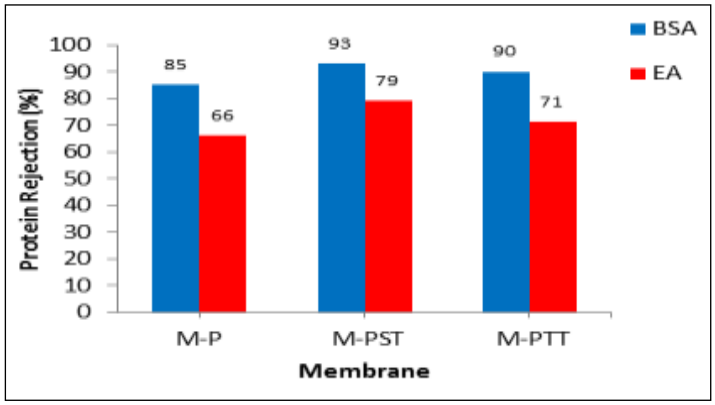
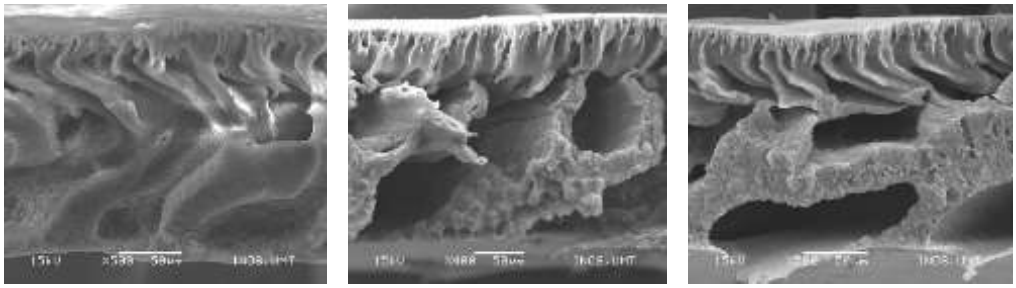


Figure 3. Effect of combination anionic/non-ionic and non-ionic/ non-ionic surfactants on proteins rejection

SEM analysis

Figure 4 shows the SEM images of the cross-section for different membranes prepared with combination of anionic/non-ionic and non-ionic/non-ionic surfactants. The SEM image of M-P membrane as presented in Figure 4 (a) shows the larger (open) finger-like pores formed were influenced by the exchange time between solvent and non-solvent in the coagulation bath [11]. It may be seen from the figures that membranes formed are having short and finger-like structures from the top layer to middle of sub-layer of the membrane. A dense spongy structure also formed beneath the skin layer and porous sub-layer of PVDF membrane. The casting solutions provided from hydrophobic polymers produced sponge-like structures due to delayed phase separation occurred during phase inversion process [12].



(a) M-P (b) M-PST (c) M-PTT

Figure 4. Cross-section SEM micrographs of morphological structure of PVDF membrane prepared withcombination anionic/non-ionic and non-ionic/non-ionic surfactants

The SEM images of M-PST and M-PTT in Figure 4(b) and (c) respectively show the existence of macrovoids in the presence of combination anionic and non-ionic surfactants in the PVDF/NMP blend membranes. Both of these membranes had asymmetric structure consisting of a fine porous selective barrier and a much thicker porous sub-layer. The SEM images in Figure 4(b) and (c) indicate that the combination of small amount SDS/Tween 80 and Triton X/tween 80 respectively in the casting solution can incite macrovoids formation.

A dense top layer and a porous sub-layer that is occupied by closed cell within polymer matrix and finger-like pore as well as interaction of anionic together non-ionic surfactants as shown clearly in Figure 4(b). Obviously, large pores are formed in the sub-layer of the membranes and therefore, it can be explained by miscibility between the added ionic, non-ionic surfactants and the coagulant. The miscibility between surfactant and coagulant plays an important role in the formation process of various sizes of pores. The macrovoids and finger-like pores in the sub-layer can be induced or suppressed by addition of appropriate surfactants, depending on their miscibility with coagulants. The addition of surfactants that have high miscibility with coagulants may be able to extend the formation of finger-like pores and macrovoids. On the other hand, the addition of surfactants with low miscibility with coagulants suppresses the macrovoids formation [13].

Conclusion

This study shows that all the membranes have asymmetric structure as observed from SEM images. It was found out that the combination of small amounts ionic surfactant (i.e. SDS) and non-ionic surfactants (i.e. Tween 80 and Triton X) to the casting solution increases formation of macrovoids and finger-like pores in the sub-layer of the membranes. With this little addition of surfactants to the casting solutions, the thickness of the prepared membranes significantly increases and hence, probably enhanced the PWP to a maximum value of 838.11 $Lm^{-2}h^{-1}$and 93% for BSA protein rejection.

Acknowledgement

The authors are grateful and acknowledge the Ministry of Education of Malaysia and Industrial Membrane Technology Lab, USIM for the support and contribution on this study.Besides, the authors would like to thank the Research Management Centre (RMC), Universiti Sains Islam Malaysia (USIM) to finance the project under the Fundamental Fund.

References

1. Idris, A., Zain, N. M. and Yusof, N. M. (2007). Synthesis, characterization and performance of asymmetric Polyethersulfone (PES) ultrafiltration membranes with polyethylene glycol of different molecular weights as additives. *Desalination*, 207:324 – 339.
2. Zuo, D. Y., Xu, Y. Y., Xu, W. L. and Zou, H. T. (2008). The influence of PEG molecular weight on morphologies and properties of PVDF asymmetric membranes. *Chinese Journal of Polymer Science*, 26: 405 – 414.
3. Zhao, S., Wang, Z., Wei, X., Tian, X., Wang, J., Yang, S. and Wang, S. (2011). Comparison study of the effect of PVP and PANI nanofibers additives on membrane formation mechanism, structure and performance. *Journal of Membrane Science*, 385: 110 – 122.
4. Ismail, A. F. and Hassan, A. R. (2007). Effect of additive contents on the performances and structural properties of asymmetric Polyethersulfone (PES) nanofiltration membranes. *Separation and Purification Technology*, 55: 98 – 109.
5. Jung, B., Yoon, J. K., Kim, B. and Rhee, H. W. (2004). Effect of molecular weight of polymeric additives on formation, permeation properties and hypochlorite treatment of asymmetric polyacrylonitrile membranes. *Journal of Membrane Science*, 243: 45 – 57.
6. Xu, Z. L., Chung, T. S. and Huang, Y. (1999). Effect of polyvinylpyrroli-done molecular weights on morphology, oil/water separation, mechanical and thermal properties of polyetherimide/ polyvinylpyrrolidone hollow fiber membranes. *Journal of Applied Polymer Science*, 74: 2220 – 2233.
7. Wang, D., Li, K. and Teo, W. K. (1999). Preparation and characterization of polyvinylidene fluoride (PVDF) hollow fiber membranes. *Journal of Membrane Science*, 163: 211 – 220.
8. Fernandez, E., Benito, J. M., Pazos, C. and Coca, J. (2005). Ceramic membrane ultrafiltration of anionic and non-ionic surfactant solutions. *Journal of Membrane Science*, 246:1 – 6.
9. Sun, C. (2009). Poly(vinylidene fluoride) membranes: preparation, modification, characterization and applications. University of Waterloo, Waterloo, Ontario, Canada.
10. Arthanareeswaran, G., Thanikaivelan, P., Srinivasn, S., Mohan, D. and Rajendran, M. (2004). Synthesis, characterization and thermal studies on cellulose acetate membranes with additive. *Journal of European Polymer*, 40: 2153 – 2159.
11. Rahimpour, A., Madaeni, S. and Mehdipour-Atei, S. (2008). Synthesis of a novel poly(Amide-Imide) and preparation and characterization of PAI blended Polyethersulfone (PES) membrane. *Journal of Membrane Science*, 311: 349 – 359.
12. Ghasem, N., Al-Marzouqi, M. and Duidar, A. (2012). Effect of PVDF concentration on the morphology and performance of hollow fiber membrane employed as gas-liquid membrane contactor for CO_2 absorption. *Separation and Purification Technology*, 98: 174 – 185.
13. Amirilargani, M., Saljoughi, E. and Mohammadi, T. (2009). Effects of Tween 80 concentration as a surfactant additive on morphology and permeability of flat sheet Polyethersulfone (PES) membranes. *Desalination*, 249: 837 – 842.

MALAYSIAN JOURNAL OF ANALYTICAL SCIENCES
Published by The Malaysian Analytical Sciences Society
ISSN 1394 - 2506

AN EXPERIMENTAL DESIGN METHOD FOR THE EXTRACTION OF EURYCOMANONE FROM TONGKAT ALI (*Eurycoma longifolia*) ROOTS USING PRESSURISED LIQUID EXTRACTION (PLE)

(Kaedah Reka bentuk Eksperimen bagi Pengekstrakan Eurikomanon daripada Akar Tongkat Ali (*Eurycoma longifolia*) Menggunakan Pengekstrakan Cecair Tekanan Tinggi)

Rozita Osman*, Norashikin Saim, Mardiana Saaid, Nor Nasriah Zaini

Faculty of Applied Sciences,
Universiti Teknologi MARA, 40450 Shah Alam, Selangor, Malaysia

**Corresponding author: rozit471@salam.uitm.edu.my*

Received: 24 February 2015; Accepted: 27 October 2015

Abstract

Pressurised liquid extraction (PLE) method was utilised to extract eurycomanone from Tongkat Ali root (*Eurycoma longifolia)* using water as extraction solvent. Optimisation of PLE operating parameters was conducted using three-factor response surface experimental design to evaluate the interactive effects of temperature (90 – 150 ºC), extraction time (10 – 30 min) and pressure (850 – 1700 psi) on the yield of eurycomanone. Online solid phase extraction – high performance liquid chromatography (SPE-HPLC) with a diode array detector (DAD) was used for the separation and detection of this compound. Extraction temperature was found significant in increasing the yield of eurycomanone. Based on maximum yield of eurycomanone, the optimum operating extraction conditions for PLE were set up at temperature (106 ºC), pressure (870 psi) and static time (30 min). The amount of eurycomanone from Tongkat Ali root samples of various sources was analysed using the optimised PLE conditions.

Keywords: pressurised liquid extraction, *Eurycoma longifolia*, eurycomanone, solid phase extraction – liquid chromatography

Abstrak

Kaedah pengekstrakan cecair tekanan tinggi (PLE) telah digunakan untuk mengekstrak eurikomanon daripada akar Tongkat Ali (*Eurycoma longifolia)* menggunakan air sebagai pelarut. Pengoptimuman parameter operasi PLE dijalankan dengan menggunakan reka bentuk eksperimen gerak balas permukaan tiga faktor untuk menilai kesan interaktif suhu (90 – 150 ºC), masa pengekstrakan (10 – 30 min) dan tekanan (850 – 1700 psi) ke atas hasil eurikomanon. Pengekstrakan fasa pepejal-kromatografi cecair tekanan tinggi (SPE-HPLC) dengan pengesan diod (DAD) telah digunakan untuk pemisahan dan pengesanan sebatian ini. Suhu pengekstrakan didapati penting dalam meningkatkan hasil eurikomanon. Berdasarkan hasil maksimum eurikomanon, pengkstrakan optimum untuk PLE, ialah suhu (106 ºC), tekanan (870 psi) dan masa static (30 minit). Amaun eurikomanon daripada pelbagai sampel akar Tongkat Ali telah dianalisis dengan menggunakan keadaan PLE yang telah dioptimumkan.

Kata kunci: pengekstrakan cecair tekanan tinggi, *Eurycoma longifolia*, eurikomanon, pengekstrakan fasa pepejal – kromatografi cecair

Introduction

Eurycoma longifolia or commonly known as Tongkat Ali or pasak bumi is a flowering plant in the family Simaroubaceae, native to Indonesia, Malaysia, Thailand, Vietnam, and Laos. The tree grows up to 12 meters in

height. Various bioactive constituents have been isolated and charaterised from *Eurycoma longifolia*, mostly from roots such as canthin-6-one alkaloids, β-carboline alkaloids, quassinoids, triterpenes, squalene derivatives, biphenylneolignans, eurycolactone, laurycolactone and eurycomalactone [1-5]. Quassinoids form the major bioactive constituents in this plant [6] and are mainly responsible for its bitter taste [1,7]. Eurycomanone (Figure 1), is found in the roots of *Eurycoma longifolia* have been traditionally used for its potential antimalarial, aphrodisiac, anti-diabetic and anti-microbial activities [8]. Among bioactive components of Tongkat Ali, eurycomanone has the highest concentration [9]. Thus, this compound is more commonly used as the marker compound for Tongkat Ali extract quantification [10].

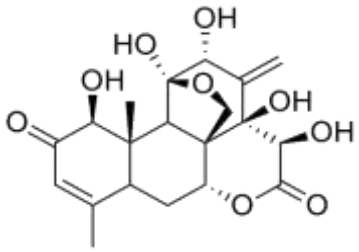


Figure 1. Chemical structure of eurycomanone

Typically, bioactive compounds are isolated using a series of processes beginning with extraction, which involves the transfer of solutes from a solid to a solvent. The ideal extraction system should be quantitative, non-destructive and time saving [11]. Several extraction techniques were reported such as Soxhlet extraction [12] and supercritical fluid extraction [13]. Soxhlet extraction is one of the oldest techniques for isolating metabolites from natural materials. It allows a high yield, but has a number of shortcomings, including long extraction time and large consumption of solvents, cooling water and electric energy. The disposal of waste solvents is also hazardous and very costly. Consequently, there is an increasing demand for new extraction techniques with possibilities for automation, shorter extraction time and lower solvent consumption. Pressurised liquid extraction (PLE), also known under the Dionex trade name accelerated solvent extraction (ASE), is currently attracting interest due to its rapid extraction time (5 – 30 min), a reasonable working temperature that can be optimised to achieve the desired extract, its simplicity, ability to be automated, low cost and its favourable environmental impact because of low solvent use [14]. The technique uses organic solvent or water at elevated temperature and pressure, which drastically improves the speed of the extraction process [15]. The high pressure allows maintaining the solvent in a liquid state at a high temperature. Under these conditions, the solvent has properties favouring the extraction process, and high solvent strength. Traditionally, the optimisation of factors affecting the extraction of active compounds can be achieved by studying each factor separately. However, through the application of chemometric, based on the use of central composite design (CCD) and multilinear regression analysis, an optimisation study that incorporates individual factors and also interactions of extraction temperature, pressure and static time can be obtained efficiently. The aim of this work is to determine an optimised pressurised liquid extraction method using experimental design for the extraction of eurycomanone from Tongkat Ali roots.

Materials and Methods

Plant Material

The roots of *Eurycoma longifolia* were provided by local suppliers. Samples were dried and ground before sieved into the size of 2.4 mm. The ground samples were stored at −20 °C until analysis.

Chemicals

Eurycomanone reference standard was purchased from Chromadex (Irvine, California). Stock standard solution containing 500 µg/mL of eurycomanone was prepared in methanol and kept in amber vials at -4 °C until use. Solvent used for PLE extraction was deionised water. For 2D-HPLC analysis, methanol, acetonitrile of HPLC grade were used, purchased from Merck (Germany).

Pressurised liquid extraction (PLE)

Extractions were done using ASE 350 accelerated solvent extractor (Thermo Scientific Ltd. Camberly, Surrey, UK). The dried and ground roots of *Eurycoma longifolia* (2 g) was accurately weighed into 34 mL extraction cells. The sample cells were then closed and placed into the carousel of the ASE 350 system. Extractions were done using water. The extraction conditions (temperature, pressure and extraction time) were optimised using an experimental design approach based on the marker compound (eurycomanone). The cell was rinsed with water (about 60 % of extraction cell volume). The extract was filtered and kept in a freezer at −20 °C prior to online SPE-HPLC analysis.

Experimental design

The experimental design was generated using Design-Expert version 6.0.4 (Stat Ease Software). The central composite design (CCD) with 5 coded levels; -α, -1, 0, +1 and +α was used. A total of 20 experiments (14 points of factorial design, and 6 center points) were carried out in randomised run order. The level of variables chosen for central composite design was assigned limits as shown in Table 1. The response variable (amount of eurycomanone) was evaluated by using response surface methodology (RSM).

Table 1. Central Composite Design used for the extraction of eurycomanone from Tongkat Ali roots

Coded level	Temperature (°C)	Pressure (Psi)	Extraction time (min)
-α	69.5	560	3
-1	90	850	10
0	120	1275	20
1	150	1700	30
+α	170.5	1990	37

SPE-HPLC separation

Chromatographic separation was performed on a Dionex Ultimate 3000 Liquid Chromatography System on Dionex Ion Pac AG14A (4 x 50 mm), Dionex C_{18} (5µm x 4.6 mm x 50 mm), and Acclaim Polar C18 (5µm x 4.6 mm x 250 mm) columns. The mobile phase comprised of pure water (A), methanol (B) and acetonitrile (C) (0 – 5.7 min: isocratic 70 % A: 30 % C; 5.7 – 8.5 min: gradient elution to 30 % A: 70 % C; 8.5 – 16 min: gradient elution 30 % A: 70 % B to 60 % A: 40 % B; 16 – 19 min: gradient elution 50 % B: 50 % C to 10 % B: 90 % C; 19 – 25 min: isocratic 10 % B: 90 % C), with flow rate kept at 1 mL/min. The column temperature was kept at 37 °C in an oven. Eluted compounds were monitored over a wavelength range of 200 – 400 nm. Figure 2 shows the chromatogram of standard eurycomanone separated using online SPE-HPLC.

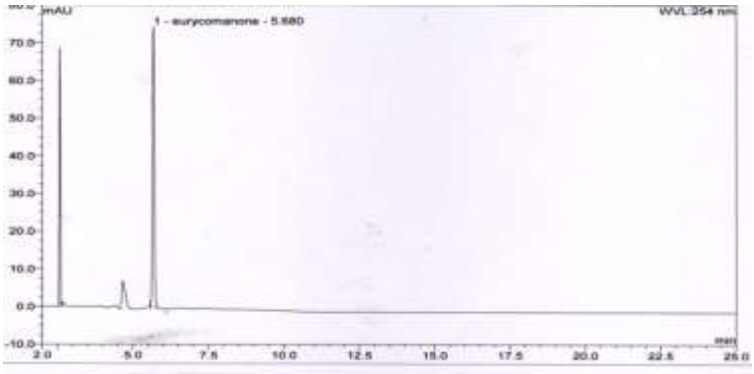


Figure 2. Chromatogram of standard eurycomanone (50 µg/mL)

Results and Discussion

Optimization of PLE operating parameters

Multilinear regression was applied to the results of the central composite design. The results were based on the amount of eurycomanone obtained from the extract as shown in Table 2. The effect of independent variables; extraction temperature (T), extraction time (t) and pressure (P) on the amount of eurycomanone was evaluated by second order (quadratic) and interactive effect (interaction between pairs of variables) (Table 3). The adequacy of the model were determined using model analysis, lack of fit test and coefficient of determination (R^2). ANOVA result showed that the model was significant, $p < 0.05$ ($p = 0.037$) with not significant lack of fit, $p > 0.05$ ($p = 0.0501$). The significance of the equation parameters for each response variable was also assessed by F-ratio at a probability (p) of 0.05. The closer the value of R^2 to unity, the better the empirical model fits the actual data. Criteria for a good fit of a model, the R^2 should be at least 0.80 [16]. In this study, the R^2 was 0.8923. The high value of R^2 (> 0.80) indicates the adequacy of the applied quadratic model.

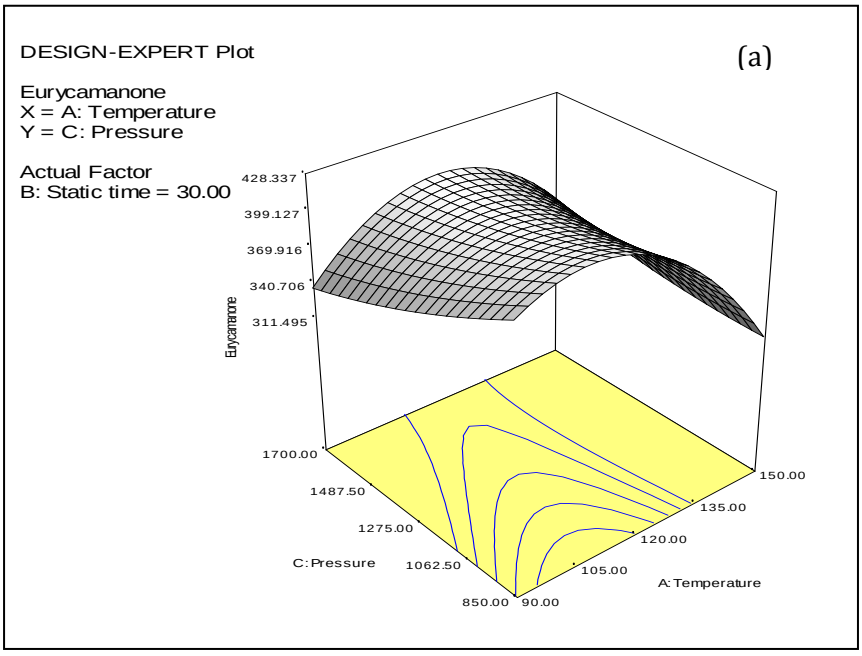
Table 2. Results of the CCD for the analysis of Tongkat Ali Roots

No.	Factor			Compound
	Temperature, T (°C)	Extraction Time, t (min)	Pressure, P (Psi)	Eurycomanone (µg/g)
1	120.0	20.0	1275.0	407.72
2	90.0	10.0	850.0	361.74
3	120.0	20.0	1275.0	406.33
4	150.0	30.0	850.0	286.87
5	90.0	30.0	1700.0	289.38
6	150.0	10.0	1700.0	399.55
7	120.0	20.0	1275.0	382.67
8	120.0	20.0	1275.0	425.03
9	150.0	10.0	850.0	362.56
10	90.0	10.0	1700.0	374.23
11	150.0	30.0	1700.0	363.07
12	90.0	30.0	850.0	390.31
13	69.5	20.0	1275.0	306.33
14	120.0	37.0	1275.0	450.24
15	120.0	20.0	1990.0	390.24
16	170.5	20.0	1275.0	164.76
17	120.0	20.0	1275.0	370.53
18	120.0	20.0	560.0	431.24
19	120.0	20.0	1275.0	370.53
20	120.0	3.0	1275.0	395.75

Table 3. Multilinear Regression Results for analysis of eurycomanone in Tongkat Ali roots

Variable	P value
	Eurycomanone
T	0.1614
t	0.6369
P	0.7850
T^2	**0.0010**
t^2	0.3824
P^2	0.6062
Tt	0.6535
TP	0.1311
tP	0.5532

Variation in extraction temperature (T^2) revealed that the increase in temperature resulted in a higher amount of eurycomanone extracted but reached a maximum value, with no significant further improvement thereafter as shown in Figure 3a and 3b. Pressure (P) and static time (t) were found not significant ($P > 0.05$) in the extraction of eurycomanone from Tongkat Ali root samples.



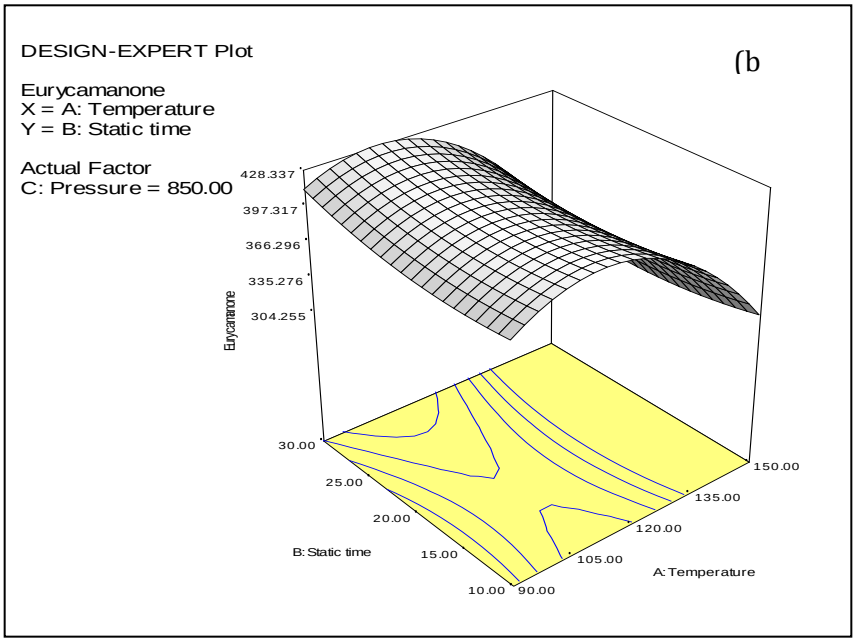


Figure 3. Contour and response surface plot of pressure against temperature (a) and static time against temperature (b) of eurycomanone obtained using Central Composite Design

Extraction temperature has a profound effect of the PLE process as reported by previous researcher [17]. Pressure is a minor variable for the resultant efficiency and it is only required to maintain the extractant in the liquid phase. The SPE-HPLC results obtained from this study indicate that the concentration of the eurycomanone increased significantly ($p < 0.05$) with temperature (Table 1). The results concurred with those reported by Gamiz-Gracia and de Castro [18]. In general, more components are extracted when the temperature is elevated, brought about by increasing solubility.

Analysis of Tongkat Ali Roots

Several sample of Tongkat Ali roots from different sources were extracted using the PLE optimum parameters at temperature of 106 °C, pressure of 850 psi and a static time of 30 min. Figure 4 shows the chromatograms of Tongkat Ali root extracts obtained from different sources.

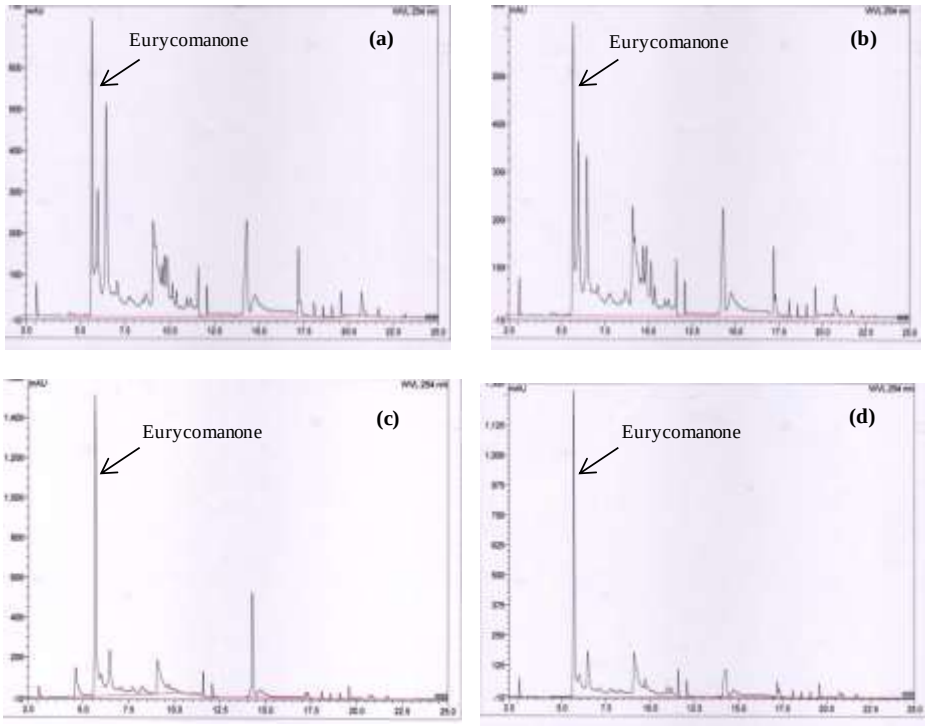


Figure 4. Chromatograms of Tongkat Ali roots of (a) Jengka sample 1(b) Jengka sample 2 (c) Taman Negara sample and (d) Sarawak sample

Figure 5 reveals the amount of eurycomanone extracted from Tongkat Ali root samples obtained from various places in Malaysia. The variation in the amount of eurycomanone in these samples may be due to harvesting age and sources [19].

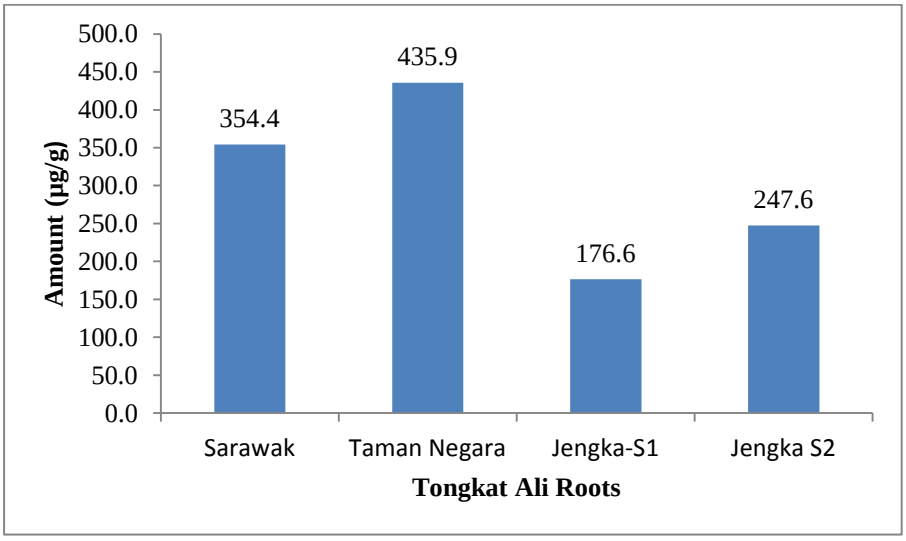


Figure 5. Amount of eurycomanone (µg/g) obtained from Tongkat Ali root samples

Conclusion

Pressurised liquid extraction (PLE) of Tongkat Ali roots was optimised. The PLE method offers important advantages over conventional methods, namely, shorter extraction time (17 min compared to 16 h for Soxhlet extraction), less solvent volumes employed (about 33 mL for PLE compared to 150 mL for Soxhlet extraction) and lower cost (energy cost is higher for Soxhlet extraction) and the possibility of manipulating the composition of the extract by changing the extraction parameters. This extraction method may contribute to the automation in food industry.

Acknowledgement

The authors would like to acknowledge the financial support obtained from Ministriy of Higher Education (600-RMI/FRGS 5/3 (48/2014)) and Research Management Institute (RMI) Universiti Teknologi MARA.

References

1. Bedir, E., Abou-Gazar, H., Ngwendson, J. N. and Khan, I. A. (2003). Eurycomanoside: a new Quassinoids-type glycoside from the roots of *Eurycoma longifolia*. *Chemical Pharmaceutical Bulletin*, 51(11): 1301 – 1302.
2. Ang, H. H., Hitotsuyanagi, Y., Fukaya, H. and Takeya, K. (2002). Quassinoids from *Eurycoma longifolia*. *Phytochemistry*, 59:833 – 837.
3. Morita, H., Kishi, E., Takeya, K., Itokawa, H. and Iitaka, Y. (1993). Squalene derivatives from *Eurycoma longifolia*. *Phytochemistry*, 34:765 – 771.
4. Itokawa, H., Qin, X. R., Morita, H. and Takeya, K. J. (1993). C18 and C19 Quassinoids from *Eurycoma longifolia*. *Journal of Nature Products*, 56: 1766 – 1771.
5. Kardono, L. B. S., Angerhofer, C. K., Tsauri, S., Padmawinata, K., Pezzuto L. M., Kinghorn A. D. J. (1991). Cytotoxic and antimalarial constituents of the roots of *Eurycoma longifolia*. *Journal of Nature Products*, 54:1360 – 1367.
6. Jiwajinda, S., Santisopasri, V., Murakami, A., Kawanaka, M., Kawanaka, H. and Gasquet, M. 2002. In vitro anti-tumor promoting and anti-parasitic activities of the Quassinoids from *Eurycoma longlifolia*, a medical plant in Southeast Asia. *Journal of Ethnopharmacology.*, 82:55 – 58.
7. Chan, K. L., Choo, C.Y., Abdullah, N. R. and Ismail, Z. (2004). Antiplasmodial studies of *Eurycoma longifolia* jack using the Lactare Dehydrogenase assay of Plasmodium Falciparum. *Journal of Ethnopharmacology*. 92: 223 – 227.
8. Bhat, A and Karim, A. A. (2010). Tongkat Ali (*Eurycoma longifolia Jack*): a review on its ethnobotany and pharmacological importance. *Fitoterapia*, 81: 669 – 679.
9. Mohamad, M., Ali, M. W., Ripin, A. and Ahmad, A. (2013). Effect of extraction process parameters on the yield of bioactive compounds from the roots of *Eurycoma longifolia*. *Jurnal Teknologi*. 60:51 – 57.
10. Chan, K. L., Choo, C.Y., Morita, H. and Itokawa, H. (1998). High performance liquid chromatography in phytochemical analysis of *Eurycoma longifolia*. *Planta Medica*, 64(8): 741 – 745.
11. Zhang, S., Bi, H. and Liu, C. (2007). Extraction of bio-active components from *Rhodiola Sachalinensis* under ultrahigh hydrostatic pressure. *Separation and Purification Technol*ogy, 57: 277 – 282.
12. Luque de Castro, M. D. and Garcia, L. E. (1998). Soxhlet extraction of solid materials: an outdated technique with a promising innovative future. *Analytica Chimica Acta*, 369: 1–10.
13. Cheah, E. L. C., Heng, P. W. S. and Chan, L. W. (2010). Optimization of supercritical fluid extraction and pressurized liquid extraction of active principles from Magnolia officinalis using the Taguchi design. *Separation and Purification Technol*ogy, 71: 293 – 301.
14. Ozel, M. Z., Gogus, F. and Lewis, A. C. (2003). Subcritical water extraction of essential oils from Thymbra spicata. *Food Chemistry*, 82: 381 – 386.
15. Ong, E. S. (2004). Extraction methods and chemical standardization of botanicals and herbal preparations. *Journal of Chromatography B*, 812: 23 – 33.
16. Joglekar, A. M. and May, A. T. (1987). Product excellent through design of experiments. *Cereal Foods World*, 32: 857 – 868.
17. Carabias-Martínez, R., Rodríquez-Gonzalo, E., Revilla-Ruiz, P. and Hernandez-Mendez, J. (2005). Pressurized liquid extraction in the analysis of food and biological samples. *Journal of Chromatography A*, 1089: 1 – 17.

18. Gámez-Gracia, L., and Luque de Castro, M. D. (2000). Continuous subcritical water extraction of medicinal plant essential oil: comparison with conventional techniques. *Talanta*, 51: 1179 – 1185.
19. Joshi, K., Chavan, P., Warude, D and Patwardhan, B. (2004). Molecular markers in herbal drug technology. *Current Science*, 87(2): 159 – 165.

MALAYSIAN JOURNAL OF ANALYTICAL SCIENCES
Published by The Malaysian Analytical Sciences Society
ISSN 1394 - 2506

MESOPOROUS SILICA ELECTROCHEMICAL SENSORS FOR THE DETECTION OF ASCORBIC ACID AND URIC ACID

(Sensor Elektrokimia Silika Berliang Meso untuk Pengesanan Asid Askorbik dan Asid Urik)

Hashazirah Mohamad Hassan*, Nurul Barakah Ab Rahman, Mohammad Noor Jalil

School of Chemistry and Environment,
Faculty of Applied Science,
Universiti Teknologi MARA, 40450 Shah Alam, Selangor, Malaysia

**Corresponding author: hashazirah@gmail.com*

Received: 24 February 2015; Accepted: 27 October 2015

Abstract

Mesoporous silica of SBA-15 and SBA-16 were successfully synthesized via the surfactant templating technique using tetraorthosilicate (TEOS) as the silica source and both surfactants, pluronic P123 and F127. Two different modified carbon paste electrodes (MCPE) were fabricated; SBA-15/MCPE and SBA-16/MCPE in compared to unmodified electrode, carbon paste electrode (CPE), for ascorbic acid (AA) and uric acid (UA) determination. Due to the unique properties of mesoporous silica materials, the MCPE fabricated exhibits greater surface enhancement effect, offers better adsorption and increases the response signals of AA and UA towards both MCPEs compared to CPE. The electrochemical behaviours of AA and UA were investigated using cyclic voltammetry. Finally, the electrochemical methods were successfully applied in detection of AA and UA.

Keywords: mesoporous silica, electrochemical sensor, SBA-15, SBA-16, synthesis, electrochemical methods

Abstrak

Mesoporus silika SBA-15 dan SBA-16 telah disintesis dengan jayanya melalui teknik templat surfaktan menggunakan tetraortosilikat (TEOS) sebagai sumber silika dan kedua-dua surfaktan, Pluronic P123 dan F127. Dua elektrod pes karbon yang dimodifikasi (MCPE) yang berbeza, SBA-15/MCPE dan SBA-16/MCPE telah dihasilkan dan dibandingkan dengan elektrod pes karbon yang tidak dimodifikasikan (CPE), untuk penentuan asid askorbik (AA) dan asid urik (UA). Dengan sifat-sifat unik bahan silika, MCPE yang telah difabrikasi mempamerkan peningkatan efek permukaan yang baik, penjerapan yang lebih bagus, dan peningkatan signal respon AA dan UA terhadap kedua-dua MCPE berbanding CPE. Perlakuan elektrokimia AA dan UA telah dikenalpasti dengan menggunakan alat voltametri berkitar. Akhirnya, kaedah elektrokimia telah berjaya diaplikasikan dalam pengesanan AA dan UA.

Kata kunci: silika berliang meso, sensor elektrokimia, SBA-15, SBA-16, sintesis, kaedah elektrokimia

Introduction

Electrochemical sensor is a smart network that acts as an important component in the multifunctional intergrated electrical devices [1]. Electrochemical sensor has been widely discovered in its field of studies. It is commonly used in the detection of favoured molecules [2], hormones [3] or organic compound [4]. AA is an anti-oxidant that influences physiological processes in human body [5]. UA is the primary end product of purine metabolism [6]. AA and UA are considered as important molecules in human metabolism but the improper concentration level of the compounds may lead to various serious diseases. Therefore, the determination of AA and UA in analytical determination and diagnostic research is vital [7]. And to date, various electrochemical methods were developed in

detection of AA and UA utilizing different types of electrodes for example one-dimensional MgO biosensor [8], TiO_2 nanoparticles MCPE [9], Pt nanoparticles supported graphene oxide [10] and reduced grapheme oxide modified electrode [11]. Although there are several research works reported on the determination of AA and UA using mesoporous silica mainly type MCM-41 [12, 13], however, to the best of our knowledge, electrochemical detection of AA and UA using, SBA-15 and SBA-16, has not been reported.

Since the mesoporous silica has been discovered since two decades ago [14], the interest in this field have grown wider and attracted scientist worldwide. Mesoporous silica has large surface area, high pore volume, wide range of pore sizes, and unique mesoporous channels resulting an excellent surface enhancement effect [15, 16], but, its existence in electrochemistry is still very rare [13]. The unique properties of mesoporous silica makes it an excellent component in fabricating electrochemical sensor. With the presence of mesoporous silica, a MCPE provides surface and adsorption enhancement towards the determination of favoured molecules [17-19]. The main objectives of this study was to successfully synthesize the mesoporous silica; SBA-15 and SBA-16 and to build a convenient, cheap, enhanced and sensitive electrochemical method (SBA-15/MCPE and SBA-16/MCPE) for the determination of AA and UA by utilizing the properties of SBA-15 and SBA-16.

Materials and Methods

Chemicals and raw materials

All the chemicals used were of analytical grade and purchased from; Tetraethoxysilane, TEOS (98%, Aldrich), tri-block copolymer Pluronic F127, $EO_{106}PO_{70}EO_{106}$ (Sigma-Aldrich), tri-block copolymer Pluronic P123, $EO_{20}PO_{70}EO_{20}$ (Sigma-Aldrich), Paraffin oil (Biobasic), Graphite powder (<20µm, Aldrich) Hydrochloric acid, HCl (36%, Aldrich), Methanol, CH_4O, Ethanol, C_2H_6O, deionized water, platinum wire, Pt, silver wire, Ag (Sigma-Aldrich), copper wire, Cu, Uric acid, L-Ascorbic acid (vitamin C) (ACS grade, Biobasic), glass tube, epoxy glue.

Instruments

The characterization of the mesoporous materials were investigated using both Rigaku D/max-2500 powder diffractometer with Cu-Kα source (2Θ mode, continuous scanning; 40 kV, 20 mA) and SUPRA 40 FE-SEM from Carl Zeiss AG. Electrochemical measurements were carried out using an Autolab PGSTAT101 potentiostat from Metrohm Autolab B.V. A three-electrode system, consisting of a working electrode (carbon paste electrode (CPE) as well as mesoporous silica modified carbon paste electrode (MCPE), a reference electrode (Ag/AgCl) and a counter electrode (platinum wire).

Synthesis of SBA-15 and SBA-16

The preparation of SBA-15 was adapted from Sayari et al. [20] and minorly modified as follows; 4.0 g of Pluronic P123 was dissolved in 30 ml of deionized water and 120 ml of 2 M HCl in a closed container while stirring at 35 °C for 20 hours. 8.50 g of TEOS was added slowly to the mixture with vigorous stirring for 15 minutes. The mixture was then kept under static condition at constant temperature (35 °C) for 20 hours and transferred to an oven for 24 hours at 90 °C (hydrothermal process). The white precipitation obtained were separated by vacuum filtration. The resulting white solids was then washed with deionized water and dried for 3 days at 45 °. Finally, sample was calcined at 500 °C in air for 6 hours to remove surfactants from mesopores.

The SBA-16 was synthesized according to procedures adapted and minorly modified from Sun & Jun and Boissiere et al. [21, 22]. A amount 2.3 g of Pluronic F127 was dissolved in 0.6 ml concentrated HCl and 103.4 ml methanol with continuous stirring for 2 hours at 35 °C. In a separate beaker, 10.4 ml TEOS, 5.2 ml ethanol and 4.2 ml deionized water were mixed and stirred for 30 minutes at room temperature. The second mixture was slowly added to the first and stirred for an hour at 35 °C. The solution was then kept under static condition for 20 minutes (hydrothermal treatment) at 80 °C. Then, the solution was cooled down at ambient temperature for 4 hours before it was transferred in a closed container and heated for 24 hours at 90 °C to enhance the formation of silica crosslink. Finally, sample was calcined at 500 °C for 10 minutes.

Fabrication of electrochemical sensor

Three types of electrodes were prepared including unmodified carbon paste electrode. The following methods are adapted and slightly modified from Fathirad et al. [23]. The bare carbon paste electrode (CPE) was prepared by

mixing graphite powder with few drops of paraffin oil. While the modified carbon paste electrodes (MCPE) are prepared by mixing 0.85 g of mesoporous silica SBA-15 and 0.15 g graphite powder with the addition of paraffin oil droplets. And the same procedure for SBA-16/MCPE. The pastes were then packed and tightly pressed into the cavity of the glass tubes resulting 3 different electrodes. Electrical contacts are provided by implementing copper wire inside the tube. Finally, the bottom surface of sensors were polished using smooth paper and washed with deionized water.

Analytical procedure

Unless otherwise stated, pH 7.0 phosphate buffer (0.05 M) was used as the supporting electrolyte for both AA and UA. The cyclic voltammetry curves were recorded from 0.0 to 1.0 V per cycle, and oxidation peak currents were individually measured at 0.24 V and 0.79 V.

Results and Discussion

Structural characterization of mesoporous silica

The SEM micrographs shows SBA-15 possessing rod-like shape (Figure 1a) when P123 was used as directing agent with TEOS as the silica source. The production of SBA-16 using Pluronic F127 as surfactant has led the material in forming spherical structure (Figure 1b). SBA-15 and SBA-16 were bind together with graphite powder via the help of paraffin oil (Figure 1c and Figure 1d).

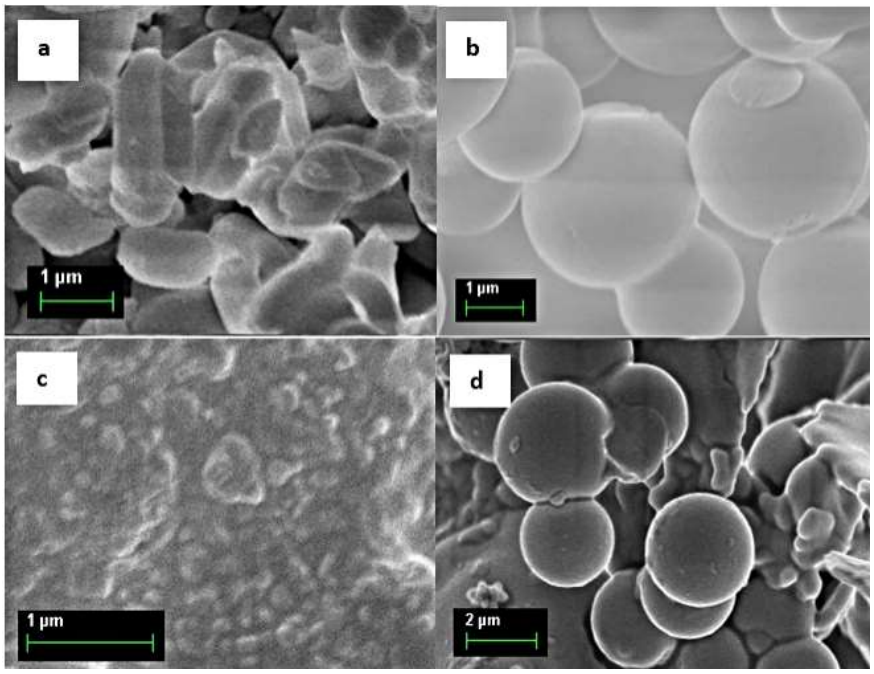


Figure 1. SEM images of SBA-15 and SBA-16. (a) SBA-15 (b) SBA-16 (c) SBA-15/MCPE (d) SBA-16/MCPE

Figure 2 shows X-Ray diffractograms obtained confirm that SBA-15 (diffractogram a) possess hexagonal mesostructure [24, 25] in which it shows three resolved peaks at lower angle 2Θ= 0.5-2.5^{o} which are indexed to (100), (110), and (200) that reflects as the well-ordered mesoporous silica, SBA-15 [26]. As evidence that SBA-16 materials possess a cubic ordering, three peaks of (110), (200), and (211) appears in diffractogram b [27]. The low intensities of peaks shown were discussed previously [28] that this may due to the thickness and roughness of pore walls [29].

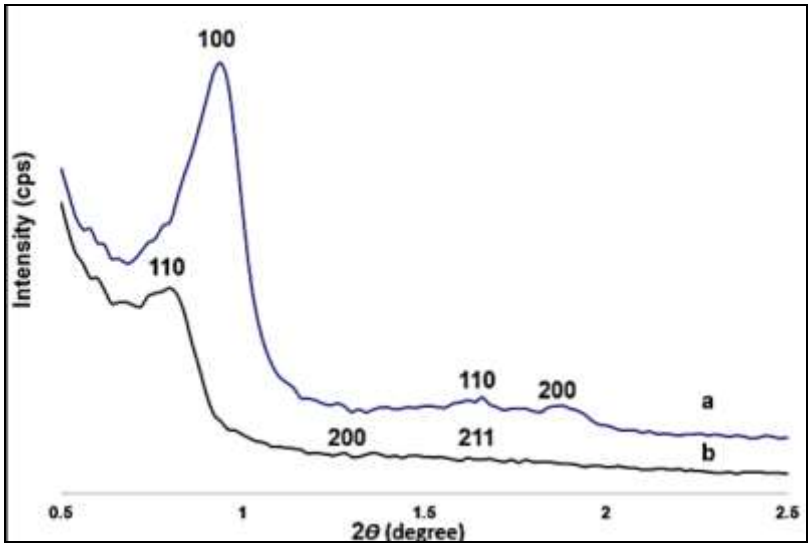


Figure 2. X-Ray diffraction. (A) SBA-15 (B) SBA-16

The electrochemical behaviours

The electrochemical behaviours of AA at three different sensors were studied by using cyclic voltammetry (CV). Figure 3 shows the CV results of $1.0x10^{-3}$ M AA in pH 7 phosphate buffer. During the anodic sweep from 0.00 to 1.00 V, an oxidation peak at unmodified CPE (curve a) is observed at approximately 0.20 V. Reduction peak does not appear which shows that the oxidation of AA is irreversible. When using SBA-15/MCPE (curve b) and SBA-16/MCPE (curve c), the oxidation peaks are greatly enhanced. Curve b shows the oxidation peak of AA at 0.20 V, and the oxidation peak for curve c slightly shifts positively from 0.20 to 0.27 V.

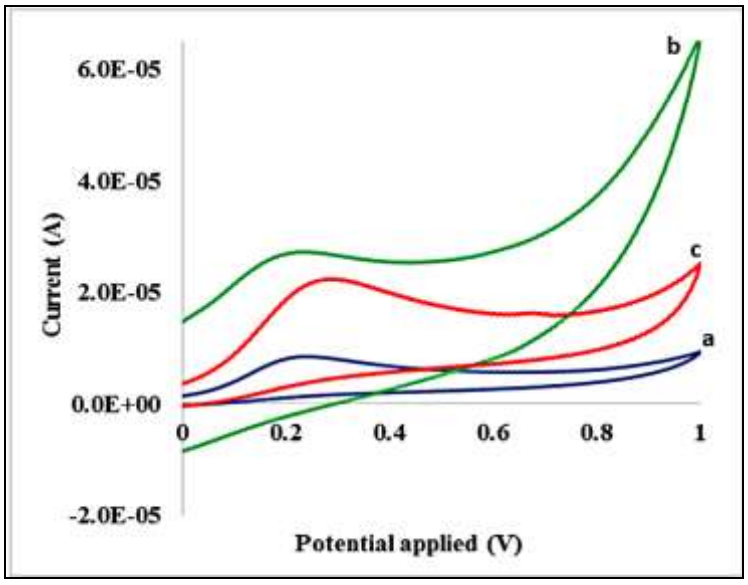


Figure 3. Cyclic voltammograms of $1.0x1^{-3}$M AA in pH 7 phosphate buffer at (a) unmodified CPE (b) SBA-15/MCPE (c) SBA-16/MCPE . Number of cycle: 1. Scan rate: 0.1 V s^{-1}.

Hence, this concludes that both modified sensors possess high efficiency of catalytic activity towards the oxidation of AA, which might be resulted from the short tunnelling distance between AA and porous electrodes. The peak currents of SBA-15/MCPE and SBA-16/MCPE are increased as well which reveals the surface enhancement effect that reflects to the unique properties of mesoporous silica (SBA-15 and SBA-16) consisting large surface are, high pore volume, and good pore network.

Figure 4 shows the CV curves of $1.0x1^{-6}$M UA in pH 7 phosphate buffer at unmodified CPE (curve a), SBA-15/MCPE (curve b) and SBA-16/MCPE (curve c) sensors. During the anodic sweep from 0.20 to 1.00 V, broad oxidation peaks appeared at 0.78 V for both unmodified CPE (curve a) and SBA-16/MCPE (curve c). SBA-16/MCPE sensor slightly enhanced the oxidation peak current. Reduction peak does not appear which concludes that oxidation of UA is reversible. Curve c shows no oxidation and reduction peaks. By comparing both unmodified CPE and SBA-16/MCPE sensor, mesoporous silica (SBA-16) clearly provides the surface enhancement effect towards the detection of UA.

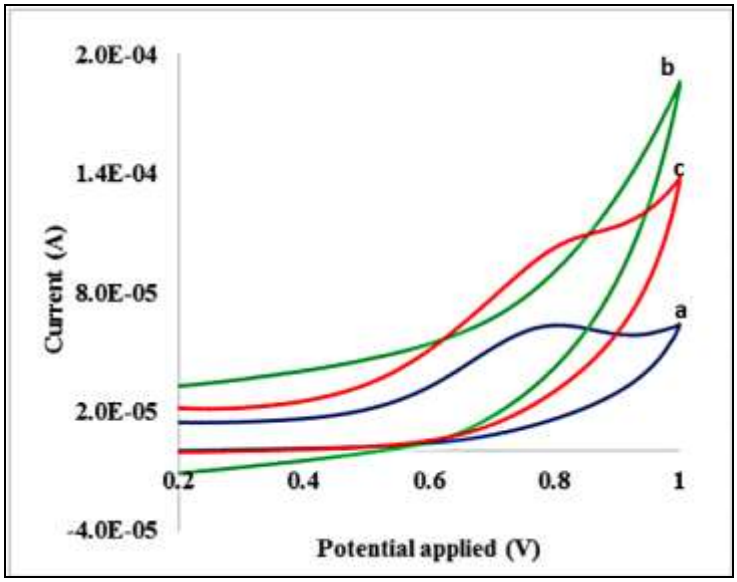


Figure 4. Cyclic voltammograms of $1.0x1^{-6}$M UA in pH 7 phosphate buffer at (a) unmodified CPE (b) SBA-15/MCPE (c) SBA-16/MCPE. Number of cycle: 1. Scan rate: 0.1 V s^{-1}.

Conclusion

Two types of mesoporous silica, SBA-15 and SBA-16 was successfully synthesized using Pluronic P123 and F127 as directing agents with the presence of TEOS as the silica source. SBA-15 and SBA-16 were then used to build two different types of electrochemical sensors (SBA-15/MCPE and SBA-16/MCPE) for the detection of AA and UA. Due to the unique properties that the mesoporous silica possessed, the modified electrodes built exhibit greater surface enhancement towards the determination of AA and UA compared to the unmodified electrode by increasing the oxidation signals. Thus, it can reasonably be concluded that an enhanced, convenient and sensitive electrochemical method was developed to detect AA and UA.

Acknowledgement

The authors would like to thank the Research Management Institute (RMI), Universiti Teknologi MARA (UiTM) for financing the project under the Research Intensive Fund (600-RMI/DANA 5/3/RIF(395/2012) and highly appreciate the facilities provided by the Non-Destructive Biomedical and Pharmaceutical Research Centre of Faculty of Pharmacy from Universiti Teknologi Mara, Puncak Alam in analysing data.

References

1. Cai, W., Lai, T., Du, H. and Ye, J. (2014). Electrochemical determination of ascorbic acid, dopamine and uric acid based on an exfoliated graphite paper electrode: A high performance flexible sensor. *Sensors and Actuators B: Chemical*, 193: 492 - 500.
2. Xu, X., Liu, Z., Zhang, X., Duan, S., Xu, S. and Zhou, C. (2011). β-Cyclodextrin functionalized mesoporous silica for electrochemical selective sensor: Simultaneous determination of nitrophenol isomers. *Electrochimica Acta*, 58: 142 - 149.
3. Mazloum-ardakani, M., Sheikh-mohseni, M. A., Abdollahi-alibeik, M. and Benvidi, A. (2012). Chemical electrochemical sensor for simultaneous determination of norepinephrine , paracetamol and folic acid by a nanostructured mesoporous material. *Sensors and Actuators B*, 172: 380 - 386.
4. Yang, F., Xie, Q., Zhang, H., Yu, S., Zhang, X. and Shen, Y. (2015). Chemical Simultaneous determination of ascorbic acid , uric acid , tryptophan and adenine using carbon-supported $NiCoO_2$ nanoparticles. *Sensors and Actuators B*, 210: 232 - 240.
5. Arrigoni, O. and De Tullio, M. C. (2002). Ascorbic acid: Much more than just an antioxidant. *Biochimica et Biophysica Acta - General Subjects*, 1569(1-3): 1 - 9.
6. Alderman, M. H. (2002). Uric acid and cardiovascular risk. *Current Opinion in Pharmacology*, 2(2): 126 - 130.
7. Wu, D., Li, Y., Zhang, Y., Wang, P., Wei, Q. and Du, B. (2014). Sensitive electrochemical sensor for simultaneous determination of dopamine, ascorbic acid , and uric acid enhanced by amino-group functionalized mesoporous Fe_3O_4 @ Graphene Sheets. *Electrochimica Acta*, 116: 244 - 249.
8. Li, M., Guo, W., Li, H., Dai, W. and Yang, B. (2014). Electrochemical biosensor based on one-dimensional MgO nanostructures for the simultaneous determination of ascorbic acid, dopamine, and uric acid. *Sensors and Actuators B: Chemical*, 204: 629 - 636.
9. Mazloum-Ardakani, M., Sheikh-Mohseni, M. A., Beitollahi, H., Benvidi, A. and Naeimi, H. (2010). Electrochemical determination of vitamin C in the presence of uric acid by a novel TiO_2 nanoparticles modified carbon paste electrode. *Chinese Chemical Letters*, 21 (12): 1471 - 1474.
10. Xu, T.-Q., Zhang, Q.-L., Zheng, J.-N., Lv, Z.-Y., Wei, J., Wang, A.-J. and Feng, J.-J. (2014). Simultaneous determination of dopamine and uric acid in the presence of ascorbic acid using Pt nanoparticles supported on reduced graphene oxide. *Electrochimica Acta*, 115: 109 – 115.
11. Yang, L., Liu, D., Huang, J. and You, T. (2014). Chemical Simultaneous determination of dopamine , ascorbic acid and uric acid at electrochemically reduced graphene oxide modified electrode. *Sensors and Actuators B*, 193: 166 – 172.
12. Sun, D., Zhang, Y., Wang, F., Wu, K., Chen, J. and Zhou, Y. (2009). Electrochemical sensor for simultaneous detection of ascorbic acid, uric acid and xanthine based on the surface enhancement effect of mesoporous silica. *Sensors and Actuators B: Chemical*, 141 (2): 641 - 645.
13. Zeng, Y., Xu, J. and Wu, K. (2008). Electrochemical determination of uric acid using a mesoporous SiO_2-modified electrode. *Microchimica Acta*, 161(1–2): 249 – 253.
14. Beck, J. S., Vartuli, J. C., Roth, W. J., Leonowicz, M. E., Kresge, C. T., Schmitt, K. D., Chu, C. T. W., Olson, D. H. and Sheppard, E. W. (1992). A new family of mesoporous molecular sieves prepared with liquid crystal templates. *Journal of the American Chemical Society*, 114 (27): 10834 – 10843.
15. Hoffmann, F., Cornelius, M., Morell, J. and Fröba, M. (2006). Silica-based mesoporous organic-inorganic hybrid materials. *Angewandte Chemie International Edition*, 45 (20): 3216 - 3251.
16. Sun, D., Xie, X. and Zhang, H. (2010). Surface effects of mesoporous silica modified electrode and application in electrochemical detection of dopamine. *Colloids and Surface B: Biointerfaces*, 75 (1): 88 - 92.
17. Wang, F., Yang, J. and Wu, K. (2009). Mesoporous silica-based electrochemical sensor for sensitive determination of environmental hormone bisphenol A. *Analytica Chimica Acta*, 638 (1): 23 – 28.
18. Zhao, J., Huang, W. and Zheng, X. (2009). Mesoporous silica-based electrochemical sensor for simultaneous determination of honokiol and magnolol. *Journal of Appied. Electrochemistry*, 39 (12): 2415 - 2419.
19. Shimomura, T., Itoh, T., Sumiya, T., Mizukami, F. and Ono, M. (2008). Electrochemical biosensor for the detection of formaldehyde based on enzyme immobilization in mesoporous silica materials. *Sensors and Actuators B: Chemcial*, 135 (1): 268 - 275.
20. Sayari, A. H., Han, B.-H. and Yang, Y. (2004). Simple synthesis route to monodispersed SBA-15 silica rods. *Journal of the American Chemical Sociecty.*, 126 (44): 14348 - 14349.

21. Sun, R.-H. and Jun, W. (2007). The growth mechanism of continuous cubic mesoporous SBA-16 film with a large area of highly ordered pores. *Nanotechnology*, 18(18): 185705.
22. Boissiere, C., Grosso, D., Lepoutre, S., Nicole, L., Bruneau, A. B. and Sanchez, C. (2005). Porosity and mechanical properties of mesoporous thin films assessed by environmental ellopsometric porosimetry. *Langmuir*, 21 (26): 12362 - 12371.
23. Fathirad, F., Afzali, D., Mostafavi, A., Shamspur, T. and Fozooni, S. (2013). Fabrication of a new carbon paste electrode modified with multi-walled carbon nanotube for stripping voltammetric determination of bismuth(III). *Electrochimica Acta*, 103: 206 - 210.
24. Brodie-Linder, N., Dosseh, G., Alba-Simonesco, C., Audonnet, F. and Impéror-Clerc, M. (2008). SBA-15 synthesis: Are there lasting effects of temperature change within the first 10min of TEOS polymerization? *Materials Chemistry and Physics*, 108 (1): 73 - 81.
25. Dos Santos, S. M. L., Nogueira, M. De Souza Gama, J. D. F. Lima, Da Silva Júnior, I. J. and De Azevedo. D. C. S. (2013). Synthesis and characterization of ordered mesoporous silica (SBA-15 and SBA-16) for adsorption of biomolecules. *Microporous and Mesoporous Materials*, 180: 284 - 292.
26. Lin, C.-L., Pang, Y.-S., Chao, M.-C., Chen, B-C., Lin, H. P., Tang, C. Y. and Lin, C.-Y. (2008). Synthesis of SBA-16 and SBA-15 mesoporous silica crystals templated with neutral block copolymer surfactants. *Journal of Physics and Chemistry of Solids*, 69 (23): 415 - 419.
27. Shah, A. T., Ahmad, S., Khan, M. F., Shahzad, K., Tabassum, S. and Mujahid, A. (2014). In situ synthesis of copper nanoparticles on SBA-16 Silica Spheres. *Arabian Journal of Chemistry (In Press)*: 2 - 6.
28. Wang, L., Fan, J., Tian, B., Yang, H., Yu, C., Tu, B. and Zhao, D. (2004). Synthesis and characterization of small pore thick-walled SBA-16 templated by oligomeric surfactant with ultra-long hydrophilic chains. *Microporous and Mesoporous Materials*, 67 (23): 135 – 141.
29. Stevens, W. J. J., Mertens, M., Mullens, S., Thijs, I., Van Tendeloo, G., Cool, P. and Vansant, E. F. (2006). Formation mechanism of SBA-16 spheres and control of their dimensions. *Microporous and Mesoporous Materials*, 93 (1-3): 119 - 124.

MALAYSIAN JOURNAL OF ANALYTICAL SCIENCES
Published by The Malaysian Analytical Sciences Society
ISSN 1394 - 2506

EQUILIBRIUM AND THEMODYNAMIC STUDIES OF ANIONIC DYES REMOVAL BY AN ANIONIC CLAY-LAYERED DOUBLE HYDROXIDE

(Kajian Keseimbangan dan Termodinamik dalam Penyingkiran Pewarna Anionik daripadaTanah Liat Anionik-Dwi Hidroksida Berlapis)

Nesamalar Kantasamy* and Siti Mariam Sumari

School of Chemistry and Environment,
Faculty of Applied Sciences,
Universiti Teknologi MARA, 40450 Shah Alam, Selangor, Malaysia.

**Corresponding author: nesam337@salam.uitm.edu.my*

Received: 24 February 2015; Accepted: 27 October 2015

Abstract

Adsorption isotherm describes the interaction of adsorbates with adsorbent in equilibrium. Equilibrium data was examined using Langmuir and Freundlich isotherm models. Thermodynamic studies were used to evaluate the thermodynamic parameters; heat of enthalpy change (ΔH°), Gibbs free energy change (ΔG°) and heat of entropy change (ΔS°) in order to gain information regarding the nature of adsorption (exothermic or endothermic). Four reactive dyes of anionic type, Acid Blue 29 (AB29), Reactive Black 5 (RB5), Reactive Orange 16 (RO16) and Reactive Red 120 (RR120) were used to obtain equilibrium isotherms at 25 °C, 35 °C, 45 °C and 55 °C. Based on Giles' classification, the isotherm produced were of L2-type, indicating strong dye affinity towards the adsorbent, and with weak competition with the solvent molecules for active adsorption sites. Equilibrium data fitted both Langmuir and Freundlich isotherm models with high correlation coefficient (R^2 > 0.91) indicating the possibility of both homogeneity and heterogeneous nature of adsorption. The negative values of ΔG° indicate the adsorption processes were spontaneous and feasible. The negative values of ΔH° lie between -20 to -75 kJ/mol, suggesting these processes were exothermic and physical in nature. The negative values of ΔS° are indication of decreased disorder and randomness of spontaneous adsorption of reactive dyes on layered double hydroxide as adsorbent.

Keywords: anionic dyes, layered double hydroxides, equilibrium isotherm, thermodynamic parameters

Abstrak

Isoterma penjerapan menerangkan interaksi antara bahan dijerap dan bahan jerap yang berada dalam keseimbangan. Data keseimbangan yang diperolehi dianalisis menggunakan model Langmuir dan Freundlich. Kajian termodinamik digunakan untuk menilai parameter-parameter termodinamik; perubahan haba entalpi (ΔH °), perubahan tenaga Gibbs bebas (ΔG°) dan perubahan haba entropi (ΔS°). Ia bertujuan untuk mendapatkan maklumat mengenai jenis penjerapan (eksoterma atau endoterma). Empat pewarna reaktif jenis anion iaitu, Asid Biru 29 (AB29), Reaktif Hitam 5 (RB5), Reaktif Jingga 16 (RO16) dan Reaktif Merah 120 (RR120) digunakan untuk mendapatkan isoterma keseimbangan pada suhu 25 °C, 35 °C, 45 °C dan 55 °C. Berdasarkan klasifikasi Giles, isoterma yang dihasilkan adalah jenis L2, yakni menandakan bahawa pewarna-pewarna ini mempunyai afiniti tinggi kepada bahan penjerap, dan mempunyai persaingan lemah dengan molekul-molekul pelarut untuk menambat kepada tapak atau permukaan aktif bahan penjerap. Data keseimbangan yang diperolehi didapati sesuai dipadankan dengan model isoterma Langmuir dan Freundlich dengan pekali korelasi yang tinggi (R2 > 0.91), menunjukkan kemungkinan wujud kedua-dua ciri kehomogenan dan heterogen untuk proses penjerapan. Nilai negatif ΔG° menunjukkan proses penjerapan adalah spontan dan boleh dilaksanakan. Nilai negatif ΔH° adalah antara -20 dan -75 kJ/mol, dan ini mencadangkan proses penjerapan adalah eksoterma dan fizikal. Nilai negatif ΔS° adalah petanda penurunan gangguan dan kerawakkan penjerapan spontan pewarna reaktif pada bahan penjerap dwi hidroksida berlapis.

Kata kunci: pewarna anion, dwi hidroksida berlapis, isoterma keseimbangan, parameter termodinamik

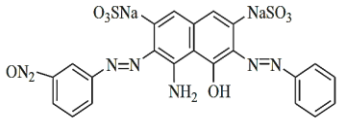
Introduction

Adsorption isotherm used in adsorption studies describes the interaction of adsorbates with adsorbent in equilibrium. It provides insight into adsorption mechanism, surface properties and affinity of adsorbent. Consequently it may be used to compare the properties of different adsorbents quantitatively and explicate the adsorption state of adsorbate on adsorbent surface. Equilibrium data can be analysed using isotherm models such as Langmuir and Freundlich expressions from which equilibrium constants (K_L and K_F) and maximum adsorption capacity (Q_o) can be obtained. The Langmuir adsorption assumes that adsorbate molecules occur on a homogenous surface with a fixed number of adsorption sites. This results in monolayer adsorption without mutual interactions between the adsorbed molecules. The Freundlich model assumes that the dye molecules are adsorbed on the heterogeneous surfaces of the adsorbate which are characterized at different energies. Thermodynamic studies are used to evaluate the thermodynamic parameters; heat of enthalpy change (ΔH°), Gibbs free energy change (ΔG°) and heat of entropy change (ΔS°). These thermodynamic parameters reveal information regarding the nature of adsorption (exothermic or endothermic) and the spontaneity of the adsorption process [1]. If the rate of reaction increases with increase in temperature, the reaction is endothermic. Endothermic adsorption is characterised by increased adsorption capacity and which may involve chemisorption. If an increase in temperature results in decreased adsorption capacity, adsorption is exothermic, which most likely involves physisorption. The objective of this study is to examine and evaluate the adsorption properties of an anionic clay-layered double hydroxide for four anionic dyes (AB29, RB5, RO16 and RR120) in terms of adsorption isotherms and thermodynamic parameters.

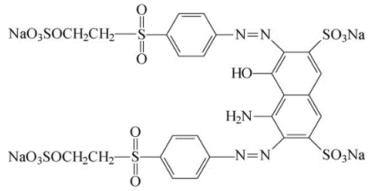
Materials and Methods

Chemicals and raw materials

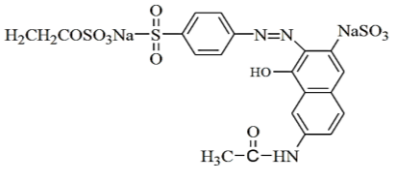
Magnesium nitrate hydrate (Mg $(NO_3)_2.6H_2O$) and Aluminum nitrate hydrate ($Al(NO_3)_2.9H_2O$) (MERCK) were used to synthesise the adsorbent, layered double hydroxide, Mg-Al-NO_3-LDH by co-precipitation procedure followed by hydrothermal treatment as outlined by previous studies [2-4].The adsorbates, anionic dyes, RB5, AB29, RO16 and RR120 (Sigma Aldrich, Germany) were used to obtain four sets of equilibrium isotherms. The structures of the dyes are shown in Fig.1.



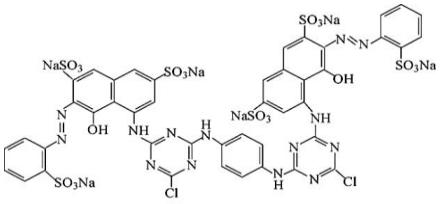
Acid blue 29 (AB29); $C_{22}H_{14}N_6Na_2O_9S$



Reactive Black 5 (RB5); $C_{26}H_{21}N_5Na_4O_{19}S_6$



Reactive Orange 16 (RO16); $C_{20}H_{17}N_3Na_2O_{11}S$



Reactive Red 120 (RR120) ; $C_{44}H_{24}Cl_2N_{14}Na_6O_{20}S$

Figure 1. Chemical structure of anionic dyes

Adsorption Equilibrium

Adsorption equilibrium between adsorbent anionic clay layered double hydroxide ($MgAlNO_3$-LDH) and adsorbates in single dye solution was attained in 24 hours in a water bath shaker operating at 100 rpm and maintained at different temperatures (25 °C, 35 °C, 45 °C and 55°C or 298 K, 308 K, 318 K and 328 K). For comparison purposes the initial pH of all dye solutions were kept constant at pH 5.5 ± 0.5 (using dilute HCl and NaOH) which lies in the range of optimum pH of dyes solutions. A concentration range of 10 – 100 mg/L of single dye solutions was allowed to contact with the adsorbent (0.02 g/50 mL). Based on the equilibrium data of isotherms, the thermodynamic parameters were calculated.

Results and Discussion

Effect of solution temperature on percentage dye removal

The effect of temperature on percentage dye removal for AB29, RB5, RO16 and RR120 are given in Fig. 2 (a)-(d). It was found that the uptake of the dyes by the adsorbent decreased with increasing temperature from 25 °C to 55 °C, indicating energy was released as a result of adsorption. General surface adsorption by anionic dye onto layered double hydroxides can be represented by the expression in equation 1:

$$\text{LDH-surface} + \text{Dye}^- \longrightarrow \text{LDH-Surface}^-/\text{Dye}^- \quad (1)$$

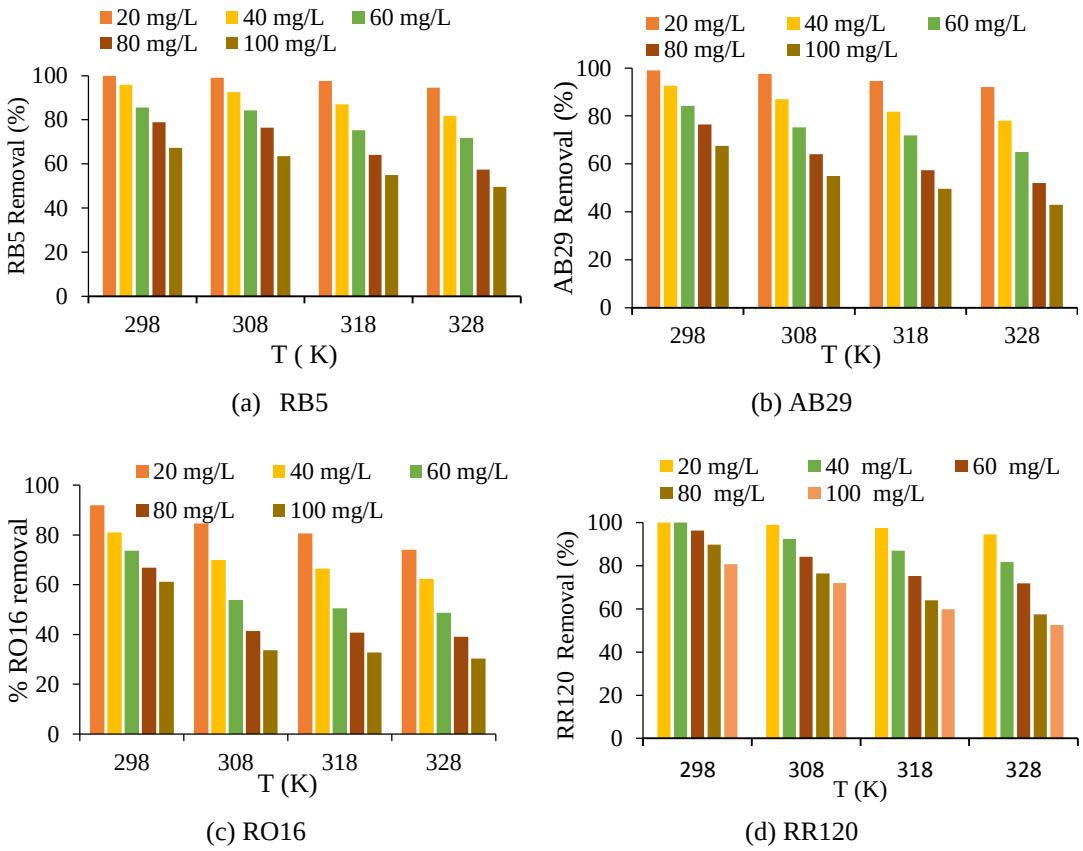


Figure 2. Effect of temperature on percentage removal of anionic dyes by LDH (a) RB5 (b) AB29, (c) RO16 (d) RR120 at different temperatures

This type of adsorption is deemed exothermic in nature [5-7]. This scenario is equivalent to increase in energy content of the system, with a reduction of surface activity [8] and the probability of colliding molecules capturing one another, thus requiring the adsorbent to have more energy [7]. Therefore the resulting reduction in the rate of adsorption may also be explained by the tendency of dye molecules to escape from the solid phase to bulk phase as temperature was increased [9].

The exothermic nature of anionic dye adsorption conforms to most adsorption of dyes including reactive dyes using various adsorbents. Examples from previous studies of exothermic adsorption are the uptake of Remazol Black B by *Rhizopus arrhizus* [8] and RO16 onto AC (A*nanas comosus* (L.)) [10].

Adsorption Isotherm

The relationship between the amount of adsorbate adsorbed on the adsorbent's surface and in liquid state when equilibrium state is achieved at constant temperature is often represented by curves (q_e vs C_e) called adsorption isotherm. Adsorption isotherm is characterized by constants which are functions of surface properties, affinity and adsorption capacity of adsorbents [8]. Fig. 3(a)-(d) shows the adsorption isotherms for RB5, AB29, RO16 and RR120. The shapes of the isotherm give the first diagnostic tool to obtain information about the nature of adsorption. This information is vital for an engineer in order to optimize the design parameters for adsorption system, besides aiding him to establish the most appropriate correlation for equilibrium curves. Auta & Hameed [11] and Giles & Smith [12] classified these isotherms into four main categories: L, S, H and C. Based on the Giles' classification, the isotherms produced correspond to the L-type (sub-group 2 or H). L-type isotherms display concavity toward the abscissa axis and are characteristics of high affinity of adsorbed molecules towards adsorbents. In L-type isotherms, a monolayer formation (plateau) is established. Fig. 3 (a)-(d) indicates that the reactive dyes were effectively removed at lower concentration while higher initial concentrations tend to reach maximum capacity as indicated by the plateau. As such the anionic dyes used in this study can be considered as favourably removed from solutions with low competition from water molecules onto substrates (LDH) until at high solute (dye) concentration when the surface coverage reached maximum [13].

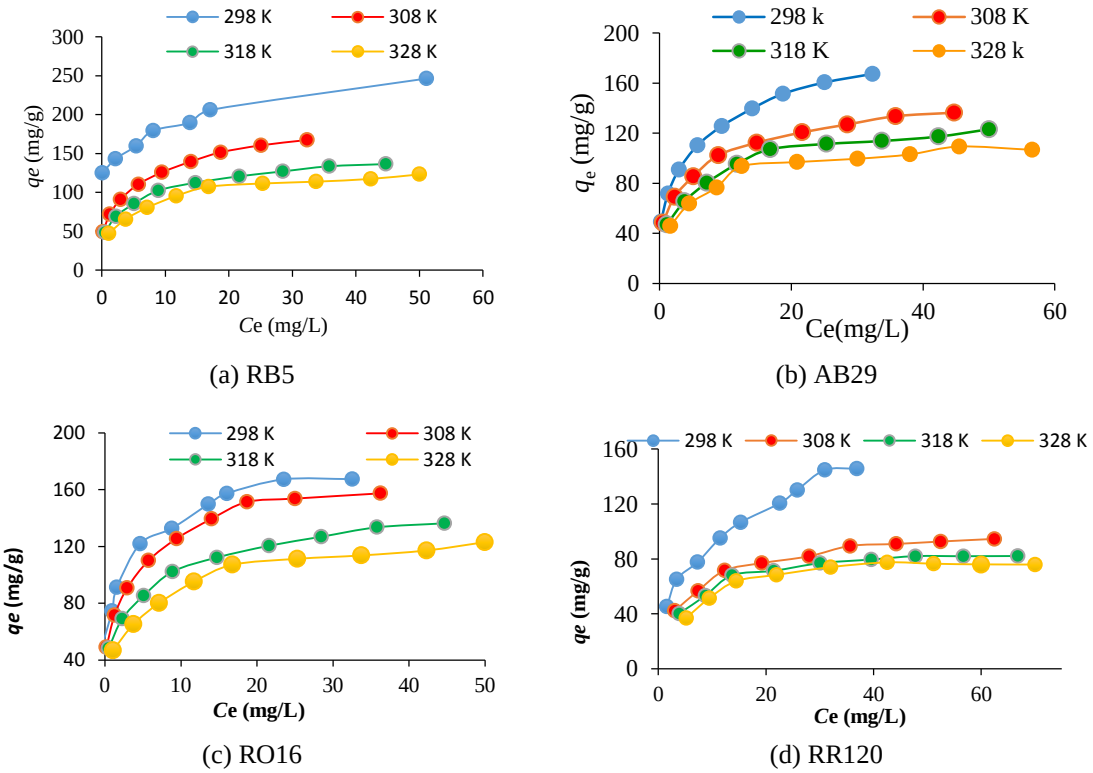


Figure 3. Adsorption isotherms for dyes- LDH (a)-(d): RB5, AB29, RO16, RR120 at different temperatures

Adsorption isotherms modeling

Quantification of dye removal and the use of equilibrium models offer insight into the characterization of these solid surfaces especially on heterogeneity of the adsorbent surface. Two well-known and widely used models, the Freundlich and Langmuir isotherms, have been adopted to explicate dye-clay interaction. To account for the relevance of these two isotherm models, the values of Langmuir and Freundlich parameters correlation coefficients, R^2 at various temperatures together with their respective constants were obtained from the linear plots. The linearised Langmuir equation (1) can be presented graphically in the form of (C_e/q_e) vs C_e in Fig.4 (a)-(d).

$$\frac{C_e}{q_e} = \frac{1}{Q_O K_L} + \frac{C_e}{Q_O} \quad (1)$$

C_e = dye concentration at equilibrium, mg/L; q_e= adsorption capacity at equilibrium, mg/g and Q_o=maximum monolayer capacity (mg/g); K_L = Langmuir constant related to the free energy of adsorption;

The linearized Freundlich equation is given in equation 2

$$\log q_e = \log K_F + \frac{1}{n} \log C_e \quad (2)$$

The Freundlich constant, *n*, reflects both the average binding energy and the energetic heterogeneity of the sorbent binding sites [14]. The constant, K_F indicates adsorption capacity. As shown in Fig. 5, the plot of ln q_e versus ln C_e is employed to determine the value of K_F and n from intercept and slope respectively.

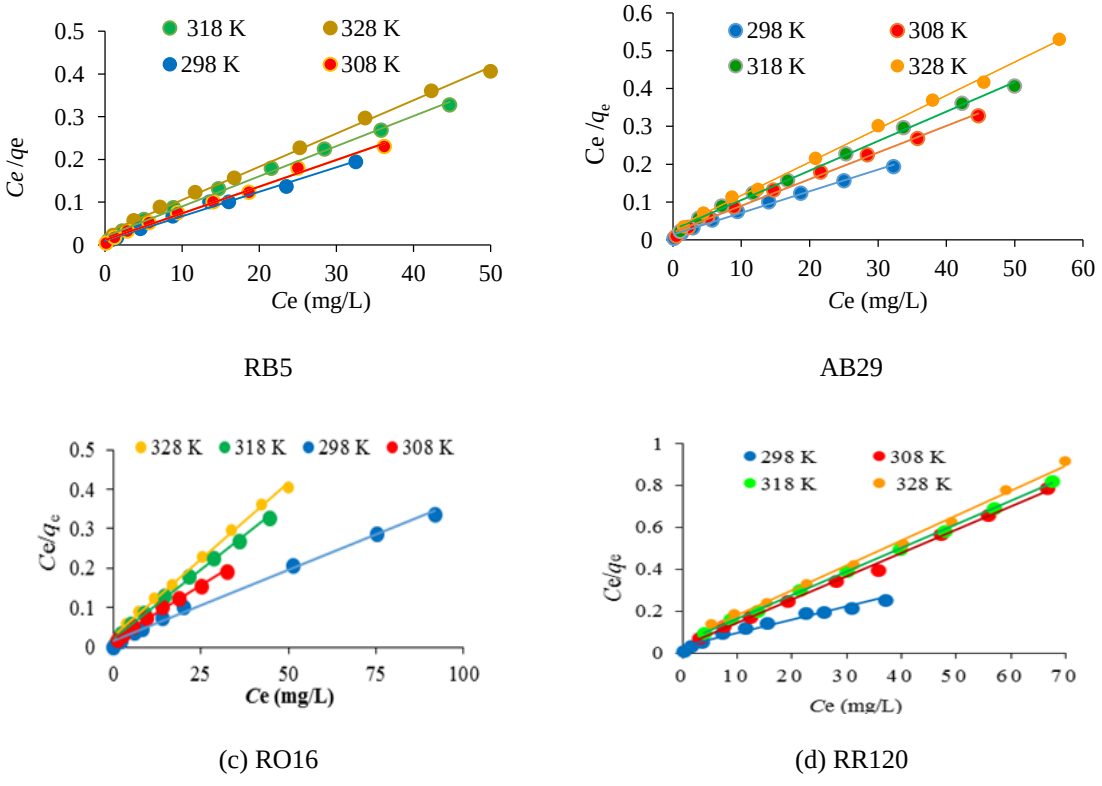


Figure 4. Langmuir isotherm at different temperatures for (a) AB29 (b) RB5 (c) RO16 (d) RR120

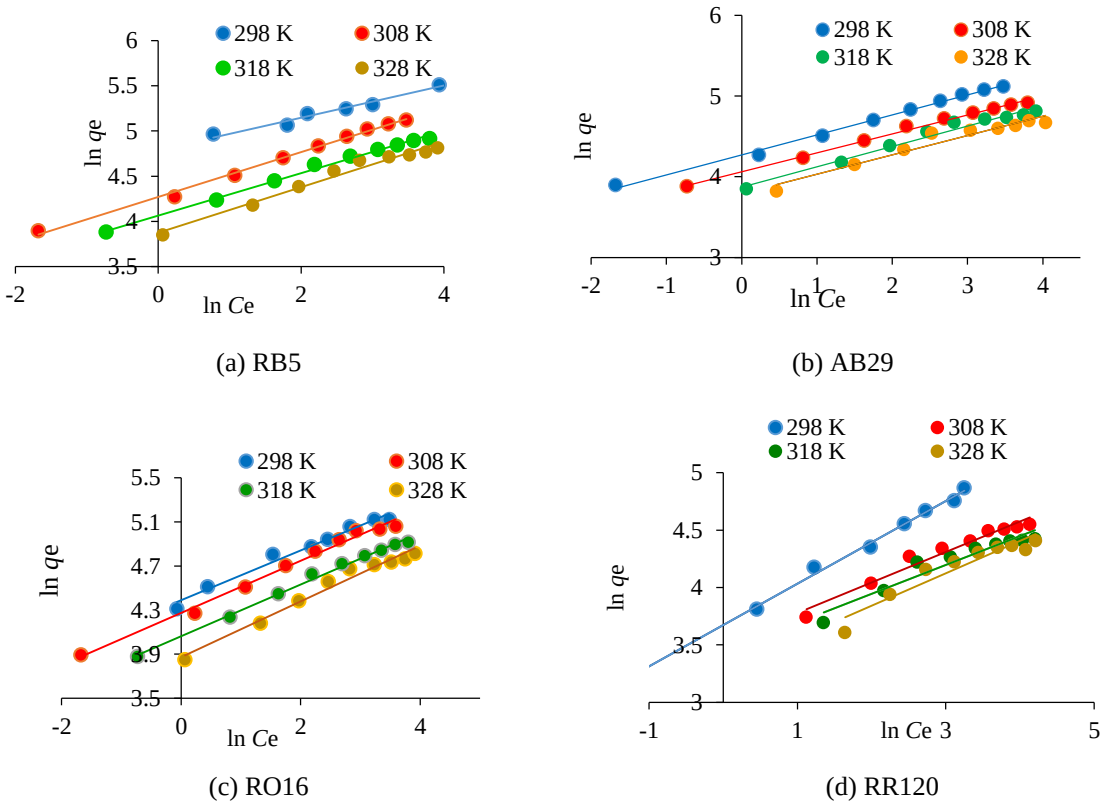


Figure 5. Freundlich isotherm at different temperatures for (a) AB29 (b) RB5 (c) RO16 (d) RR120

The high correlation coefficient values (R^2 = 0.906 - 1.000) for Langmuir and Freundlich (0.91-1.00) models strongly imply the fact that the dye-LDH adsorption closely follows both Langmuir and Freundlich models of adsorption under the present experimental conditions. This finding is not unusual as previous study by Ip *et al* [15] also found that adsorption of RB5 by bamboo activated carbon followed a hybrid of Langmuir and Freundlich equations. The dye binding capacities reflected by maximum monolayer adsorption capacities, Q_o (mg/g) were found to be in the order: RB5 (277.8) > AB29 (186.4) > RO16 (172.4) > RR120 (166.7).

Thermodynamics of adsorption

Analysis of thermodynamic parameters reveals negative values of ΔG°, indicating that the process of adsorption was spontaneous and feasible. The values of negative ΔG° also decreased slightly as temperature was increased from 298K to 328K, showing that the adsorption process was thermodynamically feasible at room temperature but less with higher temperatures. The negative values of enthalpy change, ΔH° confirm the exothermic nature of dye-LDH adsorption system. In this study, the negative values of ΔH° lie between -20 to -75 kJ/mol suggesting the process was physical in nature. The negative values of ΔS° are indication of decreased disorder and randomness of spontaneous adsorption of reactive dyes on the adsorbent.

Conclusion

The high correlation coefficient values (R^2= 0.906 - 1.000) of anionic dyes indicate the adsorption equilibrium data was well described by Freundlich and Langmuir isotherm models suggesting the existence of more than a single mechanism in adsorption of anionic dyes by LDH. In this case the conformity to Langmuir implied homogeneity and second order reaction, meanwhile the compliance to Freundlich indicate the heterogeneity. The adsorption

capacity of RB5, AB29, RO16 and RR120 onto LDH decreased with increasing temperature indicating exothermic adsorption. The affinity of anionic dyes towards LDH followed the order: RB5 > AB29 > RO16 > RR120. Thermodynamically, dye uptake was spontaneous and exothermic and mainly physical in nature.

References

1. Auta, M. and Hameed, B. H. (2012). Modified mesoporous clay adsorbents for adsorption isotherm and kinetics of methylene blue. *Chemical Engineering Journal*, 198: 219 – 227.
2. Reichle, W. T. (1986). Synthesis of anionic clay minerals (mixed metal hydroxides, hydrotalcite). *Solid State Ionic*, 22: 135 – 141.
3. Forano, C., Hibino, T., Leroux, F. and Taviot-Gue' Ho, G. (2006). Layered double hydroxides. *Developments in Clay Science*, 1: 1021 – 1095.
4. Kameda, T., Yamazaki, T. & Yoshioka, T. (2009). Preparation of MgAl layered double hydroxide intercalated with 2, 7-Naphthalene Disulfonate and its selective uptake of aromatic compounds from aqueous solutions. *Bulletin of the Chemical Society of Japan*, 82: 1436 – 1440.
5. Al-Ghouti, M., Khraisheh, M. A. M., Ahmad, M. N. M. and Allen, S. (2005). Thermodynamic behavior and the effect of temperature on the removal of dyes from aqueous solution using modified diatomite. *Journal of Colloid and Interface Science*. 287: 6 – 13.
6. Meroufel, B., Benali, O., Benyahia, M., Benmoussa, Y., and Zenasni, M. A. (2013). Adsorptive removal of anionic dye from aqueous solutions by Algerian kaolin: Characteristics, isotherm, kinetic and thermodynamic studies. *Journal of Material Environmental Science*, 4: 482 – 491.
7. Kobiraj, R., Gupta, N., Kushwaha, A. K. and Chattophadhyaya, M. C. (2012). Determination of equilibrium, kinetic and thermodynamic parameters for the adsorption of the brilliant green dye from aqueous solutions onto eggshell powder. *Indian Journal of Chemical Technology*, 20: 26 – 31.
8. Aksu, Z., & Tezer, S. (2000). Equilibrium and kinetic modelling of biosorption of Remazol Black by *Rhizopus arrhizus* in a batch system: effect of temperature .*Process Biochemistry*, 36*:*431 – 439.
9. Venkatesha, T. G., Viswanatha, R., Arthoba, Y. N. and Chethana, B. K. (2012). Kinetics and thermodynamics of reactive and vat dyes adsorption on MgO nanoparticles. *Chemical Engineering Journal*, 198–199: 1–10.
10. Ramachandran, P., Vairamuthu, R. and Sivakumar, P. (2011). Adsorption isotherms, kinetics, thermodynamics and desorption studies of Reactive orange16 on activated carbon derived from Ananas comosus (L.) Carbon, ARPN. *Journal of Engineering and Applied Sciences.* 6 (11): 15 – 26.
11. Auta, M. & Hameed, B.H. (2011). Optimized waste tea activated carbon for adsorption of Methylene Blue and Acid Blue 29 dyes using response surface methodology. *Chemical Engineering Journal*, 175: 233 – 243.
12. Giles, C. H. & Smith, D. (1974). General treatment and classification of the solute sorption isotherms. *Journal of Colloid and Interface Science*, 47: 755 – 765.
13. Al-Degs, Y. S., El-Barghouthi, M. I., El-Sheikh, A. H. and Walker, G.M. (2008). Effect of solution pH, ionic strength, and temperature on adsorption behavior of reactive dyes on activated carbon. *Dyes Pigments*, 77: 16 – 23.
14. Vega, F. A. I., Covelo, E. F. and Andrade, M.L. (2011). Applying Freundlich, Langmuir and Temkim Models in Cu and Pb Soil Sorption Experiments. *Spanish Journal of Soil Science*, 1(1): 20 – 37.
15. Ip, A. W. M., Bradford, J. P., and McKay, G. (2010). A comparative study on the kinetics and mechanisms of removal of Reactive Black 5 by adsorption onto activated carbons and bone char. *Chemical Engineering Journal*, 57: 434 – 442.

MALAYSIAN JOURNAL OF ANALYTICAL SCIENCES
Published by The Malaysian Analytical Sciences Society
ISSN 1394 - 2506

IDENTIFICATION OF HAZARDOUS EVENTS FOR DRINKING WATER PRODUCTION PROCESS USING MANAGED AQUIFER RECHARGE IN THE NAKDONG RIVER DELTA, KOREA

(Pengenalpastian Kejadian Berbahaya bagi Proses Pengeluaran Air Minuman Menggunakan Akuifer Terkawal Cas Semula dalam Delta Sungai Nakdong, Korea)

Sang-Il Lee and Hyon Wook Ji*

Department of Civil and Environmental Engineering,
Dongguk University, 30, Pildong-ro 1-gil, Jung-gu, Seoul, Korea

**Corresponding author: mousehw@naver.com*

Received: 24 February 2015; Accepted: 27 October 2015

Abstract

Various hazardous events can cause chemical, microbial or physical hazards to a water supply system. The World Health Organization (WHO) and some countries have introduced the hazardous event analysis for identifying potential events which may be harmful to the safety of drinking water. This study extends the application of the hazardous event analysis into drinking water production using managed aquifer recharge (MAR). MAR is a way of using an aquifer to secure water resources by storing freshwater for future use and pumping it whenever necessary. The entire drinking water production process is subjected to the analysis from the catchment area to the consumer. Hazardous event analysis incorporates site-specific data as well as common issues occurring in the process of drinking water production. The hazardous events are classified based on chemical, microbial or physical characteristics. Likelihood and severity values are assigned, resulting in quantitative risk by multiplying them. The study site is located at a coastal area in the delta of the Nakdong River, South Korea. The site has suffered from salt water intrusion and surface water pollution from the water upstream. Nine major hazardous events were identified out of total 114 events from 10 drinking water production processes. These major hazardous events will provide useful information on what to be done to secure the water quality produced by a new water supply method.

Keywords: managed aquifer recharge, hazardous event analysis, drinking water, coastal area

Abstrak

Pelbagai kejadian berbahaya boleh menyebabkan pencemaran kimia, mikrob atau fizikal kepada sistem bekalan air. Pertubuhan Kesihatan Sedunia (WHO) dan beberapa buah negara telah memperkenalkan analisa berbahaya untuk mengenalpasti kejadian yang berpotensi membahayakan keselamatan air minuman. Kajian ini meliputi penggunaan analisa berbahaya dalam pengeluaran air minuman menggunakan akuifer terkawal cas semula (MAR). MAR adalah satu cara menggunakan akuifer untuk mendapatkan sumber air dengan menyimpan air tawar untuk kegunaan masa depan dan mengepam bila-bila masa yang diperlukan. Keseluruhan proses pengeluaran air minuman adalah tertakluk kepada analisa dari kawasan tadahan kepada pengguna. Analisa berbahaya membekalkan maklumat khusus tempat serta isu – isu yang biasa berlaku dalam proses pengeluaran air minuman. Perkara – perkara berbahaya dikelaskan berdasarkan kimia, mikrob atau ciri – ciri fizikal. Kemungkinan dan nilai – nilai ekstrim yang diberikan, menyebabkan risiko kuantitatif dengan mendarabkan mereka. Tapak kajian terletak di kawasan pantai iaitu di delta Sungai Nakdong, Korea Selatan. Tapak tersebut terdedah kepada air masin dan pencemaran air permukaan dari hulu sungai. Sembilan kejadian berbahaya dikenalpasti daripada jumlah 114 yang berlaku dalam 10 proses pengeluaran air minuman. Kejadian berbahaya utama ini akan memberikan maklumat yang berguna mengenai apa yang perlu dilakukan untuk menjamin kualiti air yang dihasilkan dengan kaedah baru bekalan air.

Kata kunci: akuifer caj semula, analisas kejadian berbahaya, air minuman, kawasan pantai

Introduction

Drinking water supplies in coastal areas are exposed to salt water intrusion and pollutants derived upstream, which affects the water quality. In addition, changes in rainfall patterns in relation to climate change also negatively affect the supply of drinking water and cause water resource management issues. In this respect, managed aquifer recharge (MAR) has been introduced to overcome such problems. MAR is a method used to bank or treat water resources using aquifers [1], whereby the water is naturally infiltrated or injected into the aquifer using a pump. This study introduces a method for aquifer storage transfer and recovery (ASTR) of MAR, which entails injecting water into a storage well using a pump and then recovering it from a different well. ASTR has some advantages. First, the use of ASTR delivers a constant supply of fresh water because it uses two different wells: the injection well and the abstraction well (Figure 1). Second, it can be used in saline aquifers because the injected water forms a lens or bubble of fresh water within the saline groundwater [2 - 4]. Third, after the intake and treatment of surface water, a drinking water supply system with ASTR uses aquifers to add natural filtration before supplying water to customers (Figure 2). In comparison with general purification plants, it is able to treat polluted surface water more safely and to decrease the load experienced by purification facilities [1].

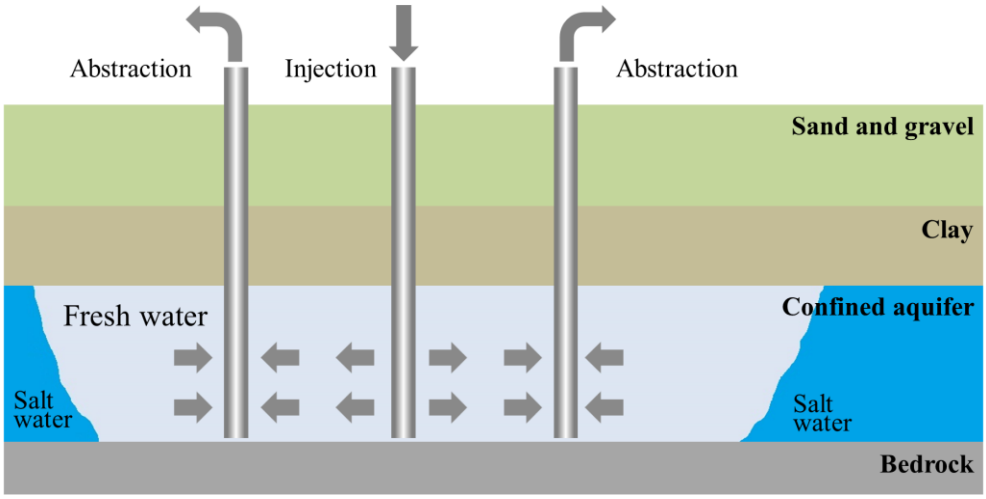


Figure 1. Schematic of ASTR in confined aquifer

Although ASTR is a more enhanced method than that used in general drinking water supply systems, it remains susceptible to multifarious threats such as microbial and chemical agents that can harm public health [5]. Examples of threats may include suspended solid (SS), cyanobacteria, and trihalomethanes (THMs). When the drinking water supply system does not appropriately mitigate these multifarious threats, the health of the consumer can be affected because of the deterioration of the drinking water quality. These multifarious threats are hazards, which are physical, microbial and chemical agents that can bring harm to public health [5]. Hazards below the drinking water standards are harmless to humans and have no inconveniences felt when the water is ingested. However, if such hazards are exponentially increased by any triggers, they can become harmful if consumed. Such triggers are known as hazardous events, and they fail the safety of the drinking water supply system by aggravating hazards [5].

Hazards and hazardous events can be determined using hazard analysis or the identification of critical control points in HACCP, which assesses hazards and establishes control systems to ensure the safety of food [6]. Using hazard analysis, or hazardous event analysis of HACCP, it is possible to prevent water quality accidents, and therefore the application to drinking water supply systems is being expanded globally.

Havelaar [7] adopted the HACCP from the food industry and applied it to drinking water supplies, and attempted to reinforce the safety of drinking water production using a hazard analysis of HACCP. The water qualities of the treatment plant in Iran were improved by applying HACCP [8, 9]. Australian drinking water guidelines [10] and the Water Safety Plan (WSP) [5] of the World Health Organization (WHO) have also accepted HACCP in relation to drinking water production. The WSP has been accepted in economically advanced countries and has also been applied in some regions of Africa that suffer from a shortage of fresh water [11]. In relation to the above examples, it appears that ensuring the safety of drinking water is gradually being considered globally.

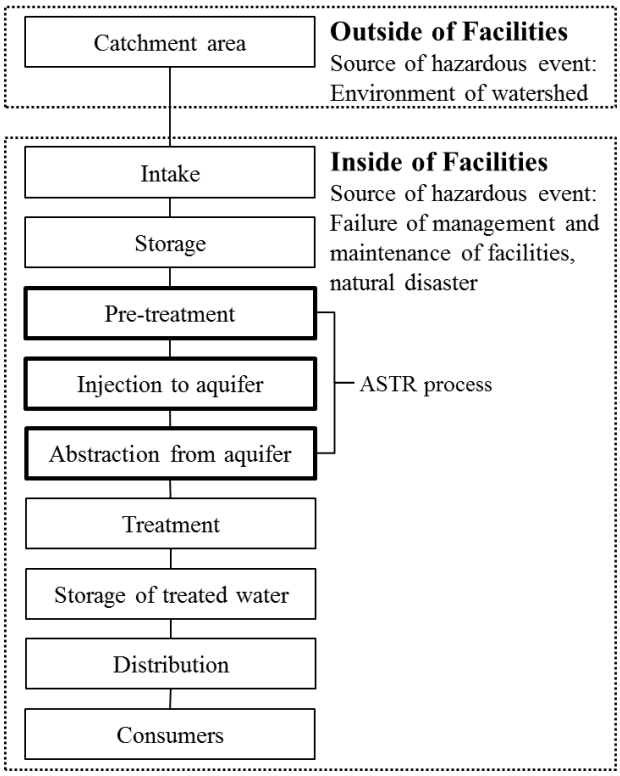


Figure 2. Drinking water supply system using ASTR

This study applied a hazardous event analysis to a drinking water supply system using ASTR, which is widely recognized as being an environment-friendly drinking water supply system [1]. Hazardous event analysis would contribute to restoring the public's lost faith in the safety of drinking water, because it can be used to prevent hazardous events through documenting potential events that could obstruct the achievement of water quality goals.

Materials and Methods

Ten processes of drinking water supply system using ASTR are analyzed (Figure 2). The analysis enables one to evaluate all hazardous events caused by natural and anthropogenic activities such as flood, drought, and the inappropriate maintenance and management of facilities. In this study, although various methods of analysis have previously been introduced by other studies, the analysis table of the WHO is adopted [12].

Hazardous events can be classified as physical, microbial, or chemical [5]. A value between 1 and 5 is then assigned to the likelihood and severity of a hazardous event. The values were given by authors' judgement based on literature review, field survey, and opinion from experts. Table 1 shows the criteria used to determine likelihood and severity.

Risk is then determined by multiplying likelihood and severity and has a risk range of 1 – 25 (Eq. 1). Then the risk rating was categorized, which is classify as low (L, 1—5), medium (M, 6—9), high (H, 10–14), and very high (VH, > 15). Risk ratings of H and VH are considered to be major hazardous events that require effective management.

$$Risk = Likelihood \times Severity \quad (1)$$

Table 1. The criteria for score of likelihood and severity

	Score	Criteria[a]
Likelihood	1	Has not happened in the past and it is highly improbable that it will happen in the future
	2	Is possible and cannot be ruled out completely
	3	Is possible and under certain circumstances could happen
	4	Has occurred in the past and has the potential to happen again
	5	Has occurred in the past and could happen again
Severity	1	Insignificant or no impact
	2	Short term or localized, not health-related non-compliance or aesthetic issues
	3	Widespread aesthetic issues or long-term non-compliance not health-related
	4	Potential long-term health effects
	5	Catastrophic public health impact

[a] modified after Bartram et al. [5]

Study area

The pilot study was conducted on Samrak Park in the Nakdong River estuary, South Korea (Figure 3). This area is experiencing difficulties in the drinking water supply due to following reasons. First, the water quality of the Nakdong River has deteriorated due to the constant inflow of pollutants from upstream metropolitan cities and industrial areas [13]. Second, the ground water is saline water. Third, chemical leakage accidents have occurred in nearby industrial areas. These caused the low level of trust to the drinking water. Although upstream pollutants are contained by the Changnyeong-Haman weir (Figure 3), the public finds it difficult to trust the quality of the drinking water produced by the water purification plant.

Physical, microbial, and chemical clogging of an injection well can occur during the ASTR operation in relation to the various substances contained within surface water. Clogging not only hinders the injection of water, but also leads to the generation of an unpleasant odor, microorganisms, and toxic materials. When clogging occurred, the wells were closed in many cases. To determine whether pre-treatment is necessary to prevent clogging, the pollutant concentration of the injected water (surface water) is checked. There can be various water quality parameters and their concentration levels to be used for checking the clogging possibility. Here we adopted Australian guidelines for ASTR.

Australian guidelines for water recycling instructs that surface water should undergo pre-treatment prior to injection if the water quality is SS > 10 mg/L or TOC > 10 mg/L [14]. Figure 4 shows the results of a water quality analysis at Goopo (Figure 3) nearby Samrak Park. Water quality was changed after building Changnyeong-Haman weir in 2011. TOC of the Nakdong River is lower than 10 mg/L every year. But, SS is higher than 10 mg/L although the weir had an effect of containing SS. Therefore, the river water needs pre-treatment before being injected.

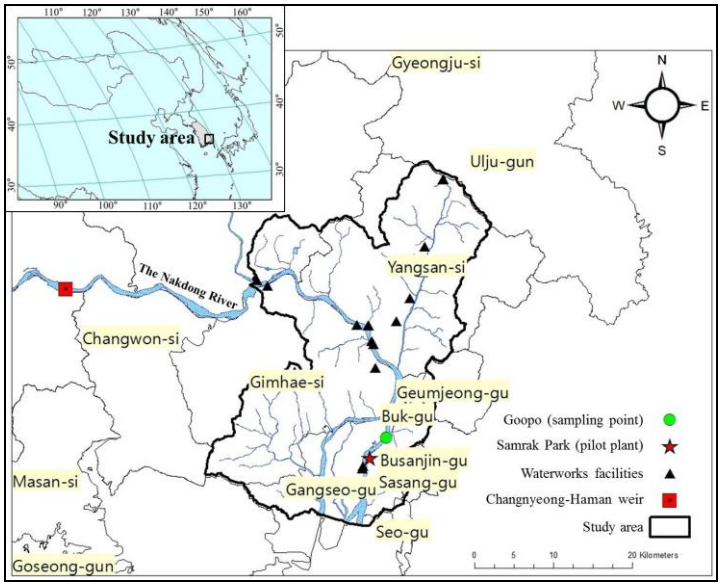


Figure 3. The downstream of the Nakdong River. Study area is at the downstream of Changnyeong-Haman weir. Pilot plant is located at Samrak Park.

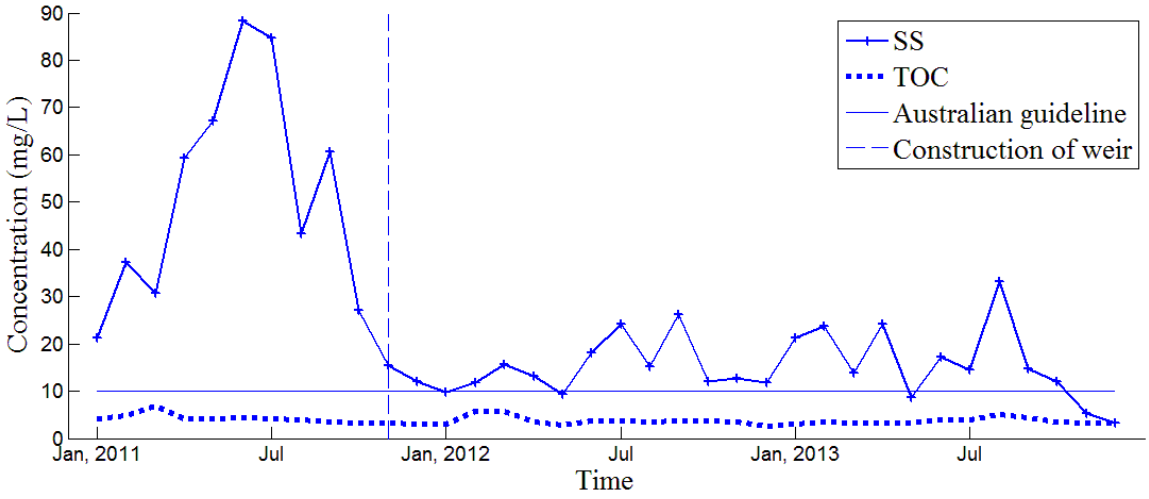


Figure 4. Water quality of the Nakdong River at Goopo (Source: www. water.nier.go.kr)

Results and Discussion

Hazardous events were considered that were unique to the study area and to the special features of ASTR such as pre-treatment, injection to aquifer, and abstraction from aquifer. In this respect, a total of 114 hazardous events were derived from ten processes of the ASTR, and a summary of hazardous events is given in Table 2.

Table 2. The number of hazardous events identified in drinking water supply system using ASTR

Process	No.	Process	No.
Catchment area	25	Abstraction from aquifer	8
Intake	3	Treatment	8
Storage	10	Storage of treated water	15
Pre-treatment	19	Distribution	17
Injection to aquifer	5	Consumers	4

Pollutants that directly flow into a catchment area are exposed to nature. The discharge of wastewater from industrial areas, inflow of chemical fertilizers or animal feces from agricultural and livestock industries, and the inflow of domestic sewage from metropolitan areas are all considered to be hazardous events. Pollutants accumulated on the road and railways flow into the river via surface water flow are also determined to be hazardous events. Hydraulic structures such as weirs, dams, and estuary banks are also considered to be hazardous events because they affect the water quality by interrupting the water flow. Furthermore, because the catchment area is affected by governmental policies, it is possible that an environment could be either polluted by development, or improved by environmental conservation measures or remediation policies.

A catchment area is affected by the weather conditions in addition to anthropogenic activity, and the concentration of pollutants in a river fluctuates in times of flood and drought. Other factors causing hazards are increases in temperature (promoting algal growth), and the development of stratification according to seasonal changes causing anaerobic conditions on the bottom of lakes and rivers.

When surface water is taken from a catchment area to be treated in a confined facility, the water is directly affected by the management and maintenance of aquifers and purification facilities. The malfunction of monitoring devices, the generation of disinfection by-products, power failure, and the corrosion of the equipment are considered to be potential hazardous events.

Although during the process of ASTR the water is exposed to nature within the aquifers, the number of possibly occurring hazardous events is small because the area for the ASTR process is strictly selected and limited in consideration of natural filtration. However, the inflow of outside pollutants and microorganisms through injection wells or abstraction wells, and the possibility of well-clogging are all considered hazardous events, as is the release of heavy metals from the aquifers.

It is possible that when the treated water is distributed to customers, a re-growth of microorganisms in the treated water could occur because there is still some concentration of microorganisms in treated water. The malfunction of pumps and pipe damage are also considered to be hazardous events.

Overall, 114 hazardous events were derived and Table 3 shows the nine major hazardous events that were determined to have risk ratings of ‘High’ and ‘Very High’. Possible hazards were then determined from the hazardous events. Although major hazardous events should be preferentially taken care to reduce risk, it is acknowledged that certain hazardous events cannot be handled by the maintenance facilities and need to be controlled by local or national government.

Table 3. Major hazardous events recorded during this study

Process	Hazardous event	Type†	Likelihood	Severity	Risk	Risk rating‡	Hazards
Catchment area	Illegal release of waste water from restaurants and private waste water treatment plants [15]	M, C	3	5	15	H	Pathogens, nutrients, surfactants, metal, heavy metal, non-biodegradable organics, colour, odor, taste
	Discharge of waste water from factories in the upstream of the Nakdong River (e.g. Eogok Local Industrial Complex) [10, 15]	C	4	5	20	VH	Metal, heavy metal, non-biodegradable organics
	Release by accidents of major chemicals from industrial complex [10, 16]	C	2	5	10	H	Non-biodegradable organics
	Frequent oil leakage accidents [16]	C	2	5	10	H	NAPLs
	Land use (Effects of Busan, Kimhae and Yangsan cities) [10]	M, C, P	5	2	10	H	Pathogens, sulfur oxides, nutrients, turbidity, colour, surfactants, organic matter, oil-contaminant
	Rapid change of river water quality by flood and drought [10]	M, C	3	5	15	H	Pathogens, nutrients, turbidity, colour, algae, toxic material, odor, taste
	Year-round occurrence of eutrophication [7, 10, 17]	M, C	4	5	20	VH	Algae, toxic material, colour, odor, taste
Storage	Rapid growth of cyanobacteria by abnormal high temperature in storage tank [7, 10]	M	2	5	10	H	Algae
Storage of treated water	Regrowth of pathogens or carcinogen (THMs) by inappropriate maintenance of residual chlorine [10]	C	2	5	10	H	Pathogens, disinfection by-products

† M: Microbial, C: Chemical, P: Physical
‡ VH: Very High, H: High

Conclusion

In this study, the entire drinking water system was analyzed from source to tap. The study area was located in the Nakdong River downstream, South Korea. Various pollutants are known to enter the Nakdong River from metropolitan cities and from the industrial areas upstream. In this study, nine major hazardous events with risk ratings equal to or higher than 'High' were classified out of the 114 hazardous events derived. It is considered that the preliminary management of major hazardous events would be effective prevention in relation to water quality accidents in a drinking water supply using ASTR.

Acknowledgement

This research was supported by a grant (code 15AWMP-B066761-03) from AWMP Program funded by Ministry of Land, Infrastructure and Transport of Korean government.

References

1. Dillon P. J. (2005). Future management of aquifer recharge. *Hydrogeology Journal*, 13 (1): 313 – 316.
2. Cederstrom, D. J. (1957) Geology and ground-water resources of the York-James Peninsula. Virginia, US Geological Survey: pp 237.
3. Bakker, M. (2010). Radial Dupuit interface flow to assess the aquifer storage and recovery potential of saltwater aquifers. *Hydrogeology Journal*, 18 (1): 107 – 115.
4. Zuurbier, K.G., Zaadnoordijk, W. J. and Stuyfzand, P. J. (2014). How multiple partially penetrating wells improve the freshwater recovery of coastal aquifer storage and recovery (ASR) systems: A field and modeling study. *Journal of Hydrology* 509 (13): 430 – 441.
5. Bartram J., Corrales L., Davison A., Deere D., Drury D., Gordon B., Howard G., Rinehold A. and Stevens M. (2009). Water Safety Plan Manual: step-by-step risk management for drinking-water suppliers. World Health Organization, Geneva.
6. Codex Alimentarius Commission. (1997). Hazard Analysis and Critical Control Point (HACCP) System and Guidelines for its Application. Annex to the Recommended International Code of Practice – General Principle of Food Hygiene, CAC/RCP 1-1969, Rev. 3.
7. Havelaar A.H. (1994). Application of HACCP to drinking water supply. *Food Control*, 5 (3): 145 – 152.
8. Khaniki G. R. J., Mahdavi M. and Mohebbi M. R. (2009). HACCP application for treatment of drinking water for Germi in Iran. *Journal of Food Agriculture and Environment*, 7 (2): 709 – 712.
9. Tavasolifar A., Bina B., Amin M. M., Ebrahimi A. and Jalali M. (2013). Implementation of hazard analysis and critical control points in the drinking water supply system. *International Journal of Environmental Health Eng*ineering, 1 (3): 1 – 7.
10. National Health and Medical Research Council – Natural Resource Management Ministerial Council, NHMRC – NRMMC (2011). Australian drinking water guidelines. EH52, Canberra.
11. World Health Organization, WHO. (2012). Water safety planning for small community water supplies. World Health Organization.
12. Deere D., Stevens M., Davison A., Helm G. and Dufour A. (2001). Water quality: guidelines, standards and health – assessment of risk and risk management for water-related infectious disease. London, World Health Organization, *IWA Publishing*: pp 257 – 288.
13. Ji H.W., Lee S.-I. and Lee S. J. (2014). Hazardous event analysis for drinking water production by managed aquifer recharge. Proceedings of the 19th IAHR-APD Congress 2014, Hanoi, Vietnam.
14. Natural Resource Management Ministerial Council – Environment Protection and Heritage Council- National Health and Medical Research Council, NRMMC-EPHC-NHMRC (2009). Australian guidelines for water recycling: managing health and environmental risks. Phase 2C: Managed Aquifer Recharge. Biotext, Canberra: pp 45 – 51.
15. Canadian Water and Wastewater Association, CWWA. (2005). Canadian Guidance Document for Managing Drinking Water Systems.
16. Lee J. K., Kim T. O. and Jung Y. J. (2013). Analysis of domestic water pollution accident and response management (in Korean). *Journal of Wetland Research*, 15 (4): 529 –534.
17. Son H. J. (2013) Long-term variations of phytoplankton biomass and water quality in the downstream of Nakdong River (in Korean). *Journal of Korea Society Environment Engineers*, 35 (4): 263 – 267.

MALAYSIAN JOURNAL OF ANALYTICAL SCIENCES
Published by The Malaysian Analytical Sciences Society
ISSN 1394 - 2506

ELECTROCHEMICAL SYNTHESIS OF ORDERED TITANIA NANOTUBES IN MIXTURE OF ETHYLENE GLYCOL AND GLYCEROL ELECTROLYTE

(Sintesis Nanotiub Titania Bertertib Secara Elektrokimia dalam Campuran Elektrolit Etilena Glikol dan Gliserol)

Lim Ying Chin[1]*, Zulkarnain Zainal[2, 3], Zuraida Khusaimi[1], Siti Sarah Ismail[1]

[1]*School of Chemistry and Environment, Faculty of Applied Sciences, Universiti Teknologi MARA, 40450 Shah Alam, Selangor, Malaysia*
[2]*Department of Chemistry, Faculty of Science*
[3]*Advanced Materials and Nanotechnology Laboratory, Institute of Advanced Technology (ITMA) Universiti Putra Malaysia, 43400 UPM Serdang, Selangor, Malaysia*

**Corresponding author: limyi613@salam.uitm.edu.my*

Received: 24 February 2015; Accepted: 27 October 2015

Abstract

The electrolyte chemistry (nature and its composition) plays a critical role in determining the nanotube architecture and its growth process. In the present study, the formation of well-ordered titania nanotubes (TNT) is achieved by electrochemical anodization of titanium substrate in aqueous ethylene glycol-glycerol electrolyte (EG/Gly). The resulted samples were characterized using X-ray Diffraction (XRD) and the morphology changes were monitored by Field Emission Scanning Electron Microscopy (FESEM). Compositional changes of the titania nanotubes (TNT) were determined using Energy Dispersive X-ray Spectroscopy (EDX). The influence of anodization voltage, volume ratio of electrolyte and NH_4F content on the morphology and geometry of titania nanotubes have been investigated. The nature of electrolytes influenced the ordering and uniformity of nanotubes. In addition, nanotubes with various diameters ranging from 62 – 112 nm and lengths of 1.1 – 1.3 μm were obtained by controlling the anodization voltage and volume ratio of EG/Gly. Ultimately, anodization of Ti at 20 V in 1:1 volume ratio of EG/Gly containing 0.25 – 1.0 wt.% NH_4F appears to be an optimum condition for controlling the ordering of nanotubes.

Keywords: titania, nanotube, anodization, glycerol, ethylene glycol

Abstrak

Kimia elektrolit (sifat dan komposisinya) memainkan peranan kritikal dalam menentukan senibina nanotiub dan proses pertumbuhannya. Dalam kajian ini, pembentukan nanotiub titania (TNT) tertertib rapi boleh dicapai melalui penganodan subtrat titanium secara elektrokimia dalam larutan akueus etilena glikol-gliserol (EG/Gly). Pencirian sampel dilakukan menggunakan pembelauan sinar-X (XRD) dan perubahan morfologi pula diawasi menggunakan mikroskopi pengimbasan elektron pancaran medan (FESEM). Perubahan komposisi nanotiub titania ditentukan dengan penyerakan tenaga sinar-X (EDX). Kesan voltan penganodan, nisbah isipadu elektrolit dan kandungan NH_4F ke atas morfologi dan geometri nanotiub titania telah dikaji. Sifat elektrolit mempengaruhi penertiban dan keseragaman nanotiub. Tambahan pula, pelbagai diameter nanotiub berukuran dari 62 – 112 nm dan 1.1 – 1.3 μm panjang dapat dicapai melalui pengawalan voltan penganodan dan nisbah isipadu EG/Gly. Penganodan Ti pada 20V dalam nisbah isipadu 1:1 EG/Gly yang mengandungi 0.25 – 1.0 wt.% NH_4F merupakan keadaan optimum dalam pengawalan penertiban nanotiub.

Kata kunci: titania, nanotiub, penganodan gliserol, etilena glikol

Introduction

Water pollution problem had become a critical issue worldwide. Various methods had been used in order to remove the pollutants for instance; biodegradation, coagulation, adsorption, advanced oxidation process (AOP) and membrane process [1]. Many studies had found that semiconductor materials can photodegrade recalcitrant organic matter under the sunlight illumination using AOP [2,3]. One of them is titania (TiO_2), an inexpensive and photostable semiconductor, which had been studied extensively for the purification of water and air [4,5] due to its high oxidative power. There are three different crystalline structures of titania: anatase, rutile and brookite being anatase and rutile with tetragonal structure and brookite with orthorhombic structure. However, among these crystalline structures, anatase is metastable and is the most photoactive [6]. In this context, titania nanotubes (TNT) have received wide attention from the research community over the last decade because of its wide application in energy conversion and storage, photocatalysis, membrane and sensing. In order to fabricate and functionalize TNT, several methods such as sol-gel method, hydrothermal, and anodization have been used to modify the morphology and functions of TiO_2 [7]. Electrochemical anodization of Ti is one of the promising methods to produce self-organized nanotubes, which is more favorable for electron transport pathways in photoelectrode performance [8]. This method is a simple process that involves connecting the Ti substrate to an anode in electrolyte solution and then applying current/voltage. Other advantages include strong adhesion between oxide layers and the substrate and facile control of the surface morphology [9]. Generally, dilute fluoride anion containing electrolytes is used, with optimization anodization conditions and evaluates the parameters such as pH, water content, fluoride content, anodization voltage, and anodization time on the formation of tubes and resulting geometry [10]. Therefore, in the present work, an attempt is made to fabricate TNT by electrochemical anodization in ethylene glycol and glycerol electrolytes with different anodization parameters such as anodization voltage, volume ratio of ethylene glycol and glycerol and concentration of fluoride ions. The effects of these parameters are studied to observe the impact on the formation and morphology of the TNT.

Materials and Methods

Materials and instruments

Ti foils (0.127 mm, 99.7 % purity) was purchased from Sigma Aldrich and was used as substrate for producing ordered TiO_2 nanotubes film (TNT). Acetone and isopropanol (R&M Chemicals) were used in cleaning of Ti substrate. Ethylene glycol (Fisher, 99.8% p.a), glycerol (Fisher, 98.0% p.a) and ammonium fluoride (Fluka, 98.0%) were used as components for preparation of electrolytes used in anodization process. All reagents were used without further purification. Deionized water (Millipore Alpha Q System, 18.2 MΩ) was used throughout the experiments. Crystalline structure of the TNT films was determined by X-ray diffraction (XRD, Shimadzu D6000) using Cu K_α radiation (λ = 1.5406 Å). The surface morphological and cross sectional features of the films were studied using a field emission scanning electron microscope, FESEM (Zeiss, SUPRA 40 VP, Germany). Quantitative measurements of the geometrical features of TNT were done using image analysis software; Image J. FESEM micrographs were taken from at least three different locations on each sample to ensure the measurements of tube diameter were representatives and to calculate the samples variability (as indicated by the standard deviations). About 100 measurements of tube diameter were taken per sample. The tube length was measured directly from cross section images of mechanically bent samples. An energy dispersive X-ray (EDX) analyzer fitted to the Carl Zeiss FESEM chamber was used to analyze the composition of the as-anodized and calcined TNT films**.**

Preparation of titania nanotubes

The Ti foil was first cut into small rectangle of 1cm × 2cm. Then, it was cleaned by sonicating in acetone, 2-propanol and deionized water for 15 minutes each using an ultrasonicator (Analab Scientific Instruments). After that, the Ti foil was washed with deionized water and then dried at room temperature. The anodization process was conducted in a standard 2-electrode cell in which the Ti foil was served as the anode and the graphite electrode as the cathode. The distance between the two electrodes was fixed at 2 cm. Both electrodes were immersed in electrolyte containing ethylene glycol, glycerol, 50% deionized water and 0.5 wt% NH_4F. The voltage was provided by a DC power supply and the anodization process was carried out at room temperature under continuous stirring. Anodization was carried out at 20 V unless otherwise stated in 1:1 vol.% ethylene glycol and glycerol (herein denoted as EG/Gly) for 60 minutes except for the effect of electrolyte ratio. After anodization, the resulting films were immediately rinsed with deionized water and subsequently dried in air. The as-anodized films were amorphous

initially. To induce crystallinity, the films were annealed at 500 ^{o}C in a Thermolyne 21100 furnace for 2 hours with a heating rate of 2 ^{o}C/min.

Results and Discussion

Effect of voltage

Electrochemical growth of TNT from Ti substrate is considered as a complex reaction, primarily involved three kinds of chemical effect, namely the electric field dissolution (shown as Eq. 1), electric field oxidation (shown as Eq. 2) and chemical dissolution (shown as Eq. 3).

$$Ti \rightarrow Ti^{4+} + 4e^{-} \quad (1)$$

$$H_2O \rightarrow 2H^{+} + O^{2-},\ Ti^{4+} + O^{2-} \rightarrow TiO_2 \quad (2)$$

$$NH_4F \rightarrow NH_4^{+} + F^{-},\ TiO_2 + 6F^{-} + 4H^{+} \rightarrow [TiF_6]^{2-} + 2H_2O \quad (3)$$

At the beginning of anodization, TiO_2 layer is grown due to the electric field dissolution and oxidation. Due to accumulation of electric charge at the interface between TiO_2 and Ti, Ti^{4+} will disrupt the TiO_2 layer and formed nanapores. Consequently, the thickness of TiO_2 layer increases due to electric field dissolution and oxidation, but at the same time, TiO_2 nanopores layer becomes thinner due to chemical dissolution. Growth of nanotubes is believed to be the result of the TiO_2 layer moving forward to the Ti substrate by the effect of oxidation and dissolution continuously. The nanotubes are produced and elongated when the rate of electric field induced dissolution and oxidation of Ti is faster than the rate of chemical dissolution of TiO_2. If the electric field induced oxidation and chemical dissolution are equal, the TiO_2 nanotubes length would remain constant [11].

Figure 1 shows the current density profile of nanotubes formed at different voltage. Generally, current density drops intially followed by a sudden increase and continues to stabilize and reach an equilibrium. The current drop indicates the formation of TiO_2 layer on the Ti as shown in Eq. 2. After the formation of the oxide layer, the current density increases when the fluoride ions attack the TiO_2 layer which lead to the formation of nanotubes as shown in the Equation 3. When the voltage is increased, the electric current also increased until the titania layer is thick enough for electric resistance causing current to decrease. When the dissolution of titania and the formation of the nanotubes start, the current increases again. The electric current remains constant when equilibrium is achieved between the oxide formation and dissolution. From Figure 1, all samples show similar characteristics of the current density where current density increases with increasing voltage.

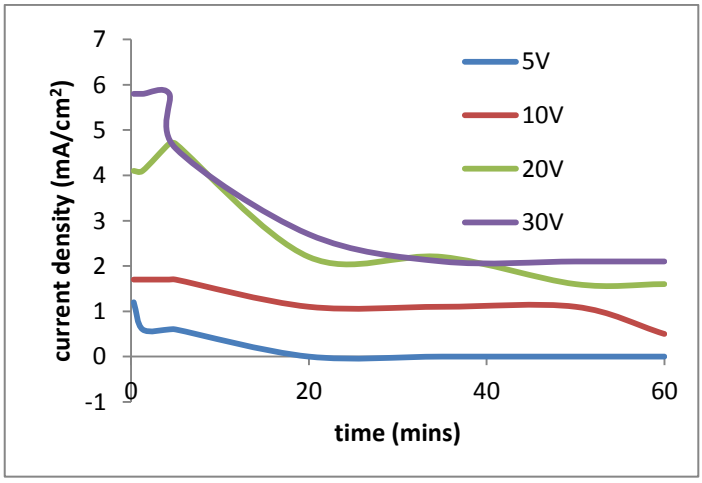


Figure 1. Current density profiles of titania nanotubes formed in 1:1 vol.% of EG/Gly at different voltage

Figure 2 shows the FESEM images of titania nanotubes anodized at different voltages range from 5V to 30V. It can be observed that Ti plate anodized at 5V demostrated porous structure as the voltage supplied was inadequate to form titania nanotubes. Similar observation was applied to the 10V Ti plate where the pore sizes are slightly bigger than that anodized at 5V. At 20 V, well-aligned and unifrom nanotubes can be seen clearly. The tops of the tubes are open and clean. The diameters of these nanotubes are about 86±11 nm with a wall thikcness of 17 ± 5 nm. However, when the applied voltage is too high (30 V), the nanotubes was destroyed or disintegrated, in which few nanotubes can be found among sponge-like structure. This is probably ascribed to electric field induced dissolution and oxidation occur too rapidly. The outer diameter of nanotubes fabricated at 30V is also bigger than that prepared at 20V, which is 122 ± 19 nm as higher voltage can strike out bigger pores leading to increase pore size with increasing voltage.

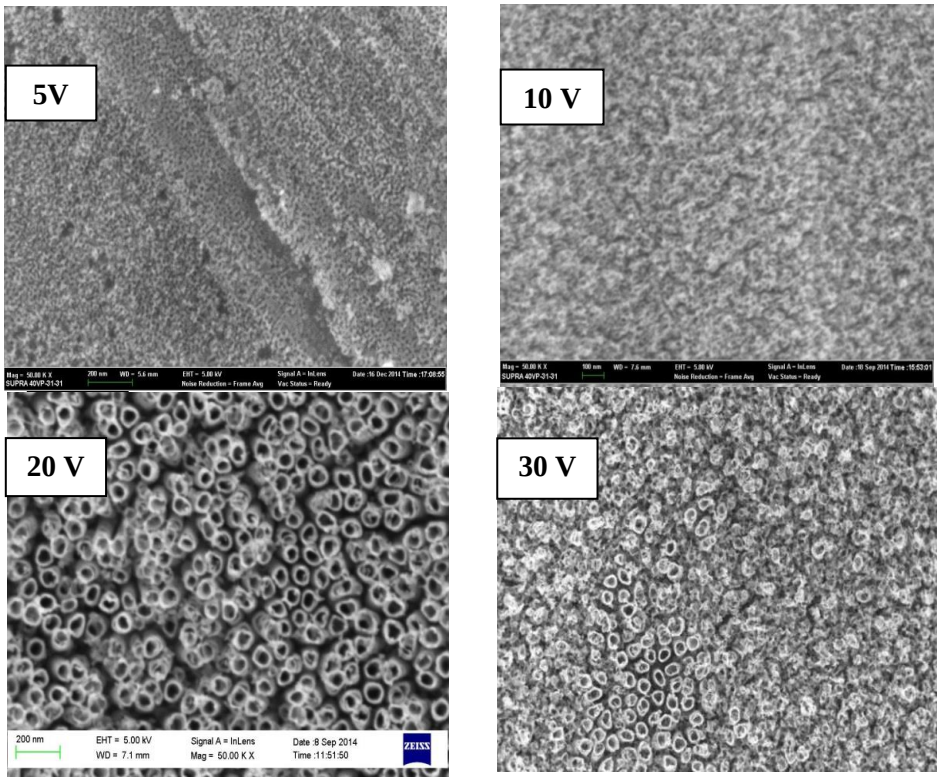


Figure 2. FESEM images showing the formation of titania nanotubes in 1:1 vol.% of ethylene glycol- glycerol for 60 minutes.

Effect of volume ratio of ethylene glycol-glycerol electrolyte

Ethylene glycol and glycerol are organic electrolytes with different viscosity, being the glycerol (945 cP) is more viscous than ethylene glycol (13.5 cP). The viscosity of the electrolyte affects the movement of ions during anodization process and thus resulting in formation of samples with different morphologies. To further compare the effects of electrolyte composition on the nanotubes growth process, mixture of different volume ratio of ethylene glycol and glycerol was explored. Figure 3 shows the FESEM images of titania nanotubes anodized at 20 V in different volume ratio of ethylene glycol and glycerol electrolyte. From Figure 3, it is obvious that equal ratio of both electrolytes gives uniform and clear nanotubes. However, nanotubes tend to clump together with increasing ethylene glycol ratio. In contrast to the observation obtained using different anodization voltage, there is no discernible change in nanotubes diameter as a function of volume ratio of ethylene glycol to glycerol. These nanotubes have a diameter of 85±10 nm with a wall thickness of 17 nm. When the ratio of glycerol is increased,

nanotubes with larger diameter (102 ± 16 nm) were obtained. In addition, higher ratio of glycerol to ethylene yields more compact, uniform and well-aligned nanotubes, indicating the viscosity of the electrolyte has an effect on the uniformity and ordering of nanotubes.

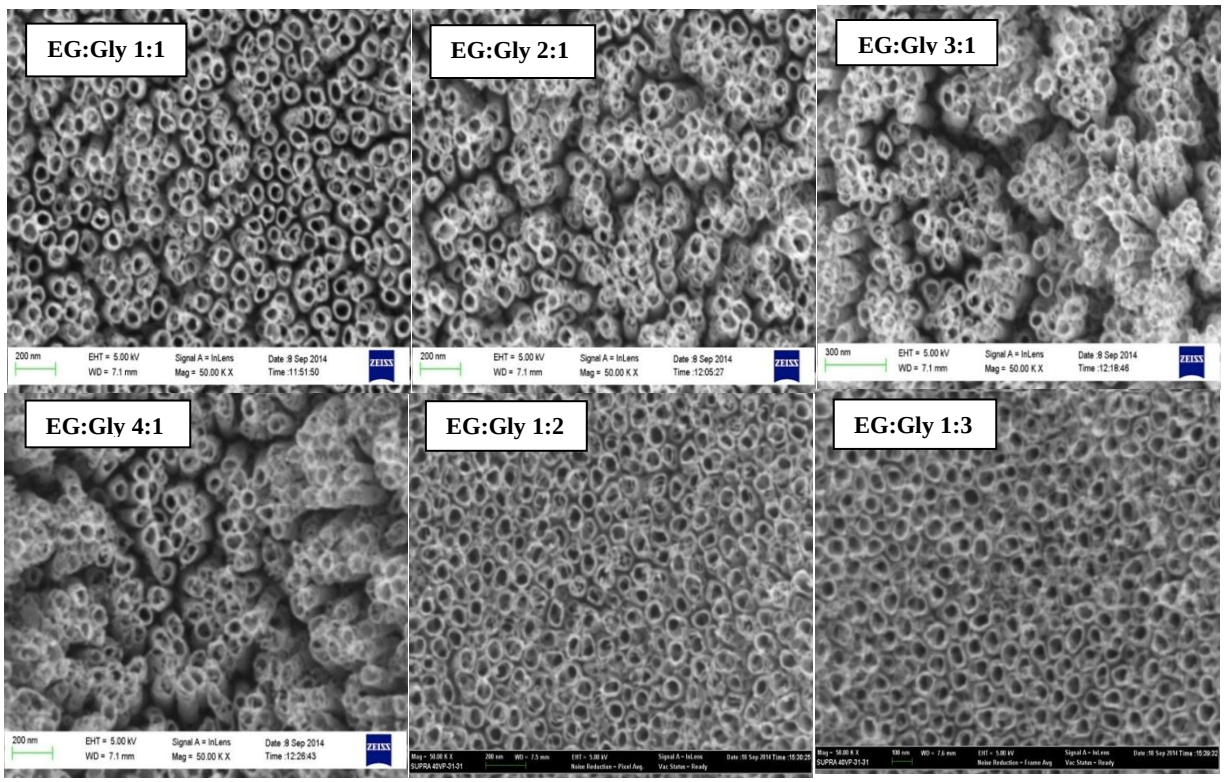


Figure 3. FESEM images of titania nanotubes anodized at 20 V in different ratio concentration of ethylene glycol/ glycerol electrolyte for 60 minutes

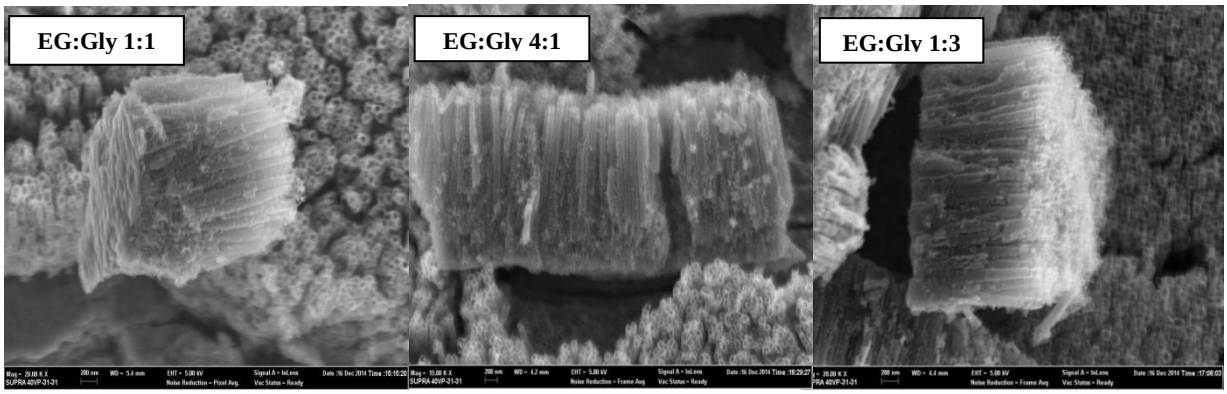


Figure 4. Cross sectional FESEM images of titania nanotubes prepared in different volume ratio of ethylene glycol to glycerol electrolyte.

The lateral view of titania nanotubes with different ratio of EG/Gly in Figure 4 shows that the TiO_2 nanotubes are cylinder-shaped structure and the tubes are packed vertically side by side, and their average length is about 1.1-1.3 μm as shown in Table 1. It seems that the length of nanotubes was not much affected by the ratio composition in the present study where the highest nanotube length was obtained in 1:1 volume ratio of ethylene glycol to glycerol. With addition of water to the electrolyte (50 vol.% in this study), the viscosity of the electrolyte was reduced and thus relatively higher rate of chemical dissolution of TiO2 is expected. This caused the formation of ripples of the side wall of nanotubes as shown in Figure 4.

Table 1. Length measurements of titania nanotubes prepared in different volume ratio of ethylene glycol to glycerol

Ratio concentration (EG:G)	**Length (nm)**
1:1	1320 ± 126
1:3	1112 ± 10
4:1	1275 ± 36

It is interesting to observe the difference of composition of TiO_2 anodized in different volume ratio of ethylene glycol to glycerol. Table 2 shows the EDX result of the as-anodized sample in EG:Gly 1:1 and calcined samples prepared in EG:Gly 4:1 and EG:Gly 1:3, respectively. Apart from the Ti and O, fluorine that originated from NH_4F and carbon from ethylene glycol or/and glycerol was found on the surface of the samples. The as-anodized sample contains higher amount of fluoride ions that act as the pore initiating agent than its calcined counterpart. This is because the fluoride ions were eventually lost during the calcination process. As for the calcined sample prepared in 1:3 EG:Gly, the sample still contain 1.5 wt.% fluorine and but in negligible amount. Same observation was obtained for calcined sample prepared in 1:1 and 4:1 EG:Gly where very little amount of carbon was found in the sample.

Table 2. Elemental composition of titania nanotubes prepared at 20 V in different volume ratio of ethylene glycol to glycerol

Element	**Weight %**			
	As-anodized EG:G 1:1	**Calcined EG:G 1:1**	**Calcined EG:G 4:1**	**Calcined EG:G 1:3**
C	0.91	0.79	1.17	-
O	41.29	35.43	41.65	41.80
F	7.07	1.46	-	1.45
Ti	56.46	56.59	57.18	56.75

The XRD patterns of the titania nanotubes formed in different volume ratio of ethylene glycol to glycerol upon calcination at 500 ^oC are shown in Figure 5. Apparently, a mixture of anatase and rutile was observed for all samples, indicating the electrolyte nature has no effect on the crystal structure of TNT. The diffractions of Ti peaks can be observed at $2\theta = 35.1^o$, 38.6^o, 40.2^o and 53.1^o respectively. The anatase phase can be seen at $2\theta = 25.4^o$, 38.0^o, 48.2^o, 54.0 and 55.2^o corresponding to (101), (004), (200), (105) and (211) plane. Rutile phase was obtained at $2\theta = 44.2^o$ corresponding to (210) plane.

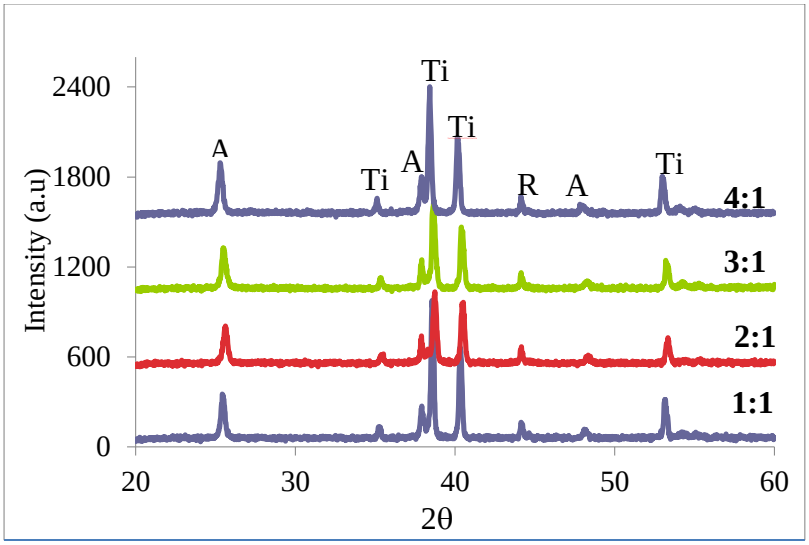


Figure 5. XRD patterns of TNT prepared at 20 V in different concentration ratio of EG:G. A, R and Ti represents anatase, rutile and titanium respectively

Effect of NH_4F concentration

Fluorides ions participate in the chemical dissolution reaction with negligible amount of them were deposited on the surface of TNT. However, most of them form $[TiF_6]^-$ species in electrolyte as shown in Eq. 3 [12]. The presence of fluoride ions is a key factor to activate the pore drilling, which give rise to the formation of highly ordered nanotubes [13,14]. The influence of fluoride ions on the morphology of TNT is schematically presented in Figure 6.

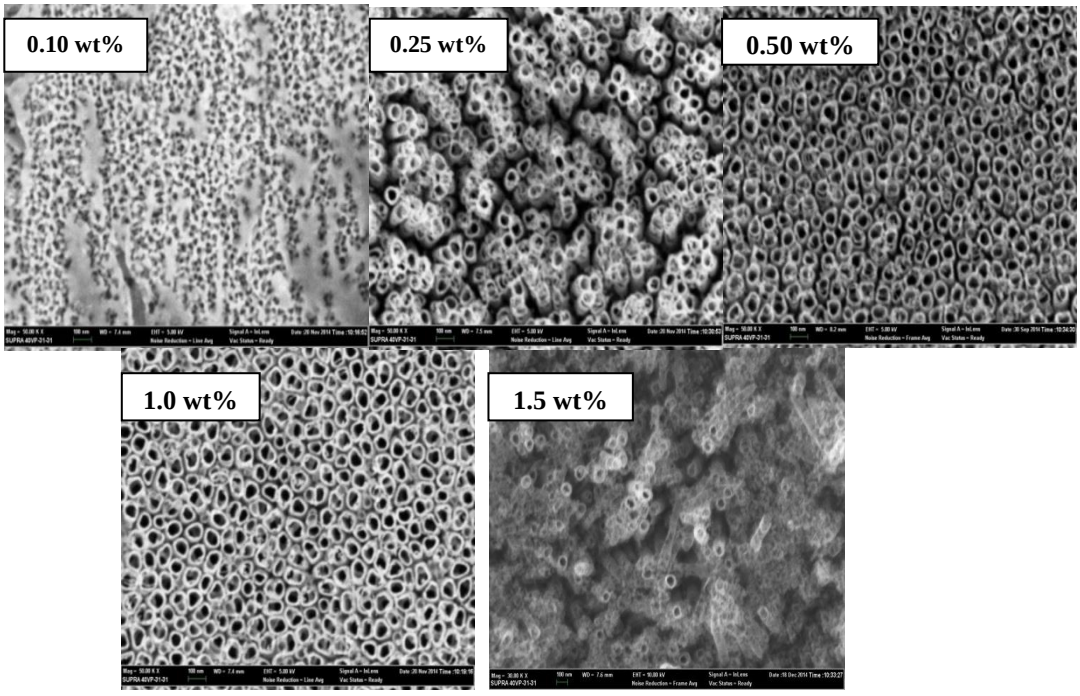


Figure 6. FESEM images of TNT prepared at 20 V in different NH_4F content in 1:1 EG: G for 30 minutes

Apparently, at a NH_4F content of 0.1 wt.%, only an ordered porous TiO_2 film is obtained. This result is attributed to the fact that chemical dissolution rate occurs too slowly to form nanotubes under low F^- content and thus only nanopores is obtained under such condition. Nevertheless, uniform, clean, and well-aligned nanotubes can be formed at NH_4F content of 0.25 wt. % to 1.0 wt.% NH_4F, indicating the amount of NH_4F is adequate for the formation of nanotubes. With increasing concentration of NH_4F to 1.5 wt.%, nanotubes tend to clump together and collapse eventually, ascribed to too rapid chemical etching rate. Table 3 shows the measurements of the nanotube diameter and wall thickness. Nanotubes formed in 1.0 wt. % resulted in bigger diameter and thicker wall, compared to those formed in 0.25 wt.% NH_4F.

Table 3. Measurements of TNT prepared at 20 V in different NH_4F content in 1:1 EG:G for 30 minutes

Concentrations (wt.%)	Outer diameter (nm)	Inner diameter (nm)	Wall thickness (nm)
0.10		porous structure	
0.25	96±14	62±11	17±4
0.50	92±11	57±9	18±5
1.00	112±10	75±4	17±3
1.50		nanotubes collapse	

Conclusion

In summary, TNT was successfully synthesized via electrochemical anodization of Ti in mixture of ethylene glycol and glycerol. Our results revealed that the electrolyte composition affects the morphological features and diameter of TNT. It was found that 20 V is the optimum voltage to form uniform and well aligned nanotubes with a diameter of 86 nm and 1.3 μm in length. A minimum of 0.25 wt.% NH_4F is required to yield an aligned nanotubes. Besides, volume ratio of EG/Gly has no effect on the crystal structure of the TNT formed but does affects the uniformity and ordering of nanotubes.

Acknowledgement

This material is based upon work supported by the Malaysia Toray Science Foundation through S&T research grant no.100-RMI/PRI 16/6/2 (7/2014) and the Ministry of Education through FRGS grant no. 600-RMI/FRGS 5/3 (1/2014). The authors would also like to acknowledge Faculty of Applied Sciences, Universiti Teknologi MARA (UiTM) for the facilities provided.

References

1. Malengreaux, C. M., Léonard, G. M. L., Pirard, S. L., Cimieri, I., Lambert, S. D., Bartlett, J. R. and Heinrichs, B. (2014). How to modify the photocatalytic activity of TiO_2 thin films through their roughness by using additives. A relation between kinetics, morphology and synthesis. *Chemical Engineering Journal*, 243: 537 – 548.
2. Hou, Y., Li, X., Zhao, Q., Quan, X. and Chen, G. (2010). Electrochemically assisted photocatalytic degradation of 4-chlorophenol by $ZnFe_2O_4$− modified TiO_2 nanotube array electrode under visible light irradiation. *Environmental Science & Technology*, 44 (13): 5098 – 5103.
3. Li, Y., Ma, Q., Han, J., Ji, L., Wang, J., Chen, J. and Wang, Y. (2014). Controllable preparation, growth mechanism and the properties research of TiO_2 nanotube arrays. *Applied Surface Science*, 297: 103 – 108.
4. Tekin, D. (2014). Photocatalytic degradation of textile dyestuffs using TiO_2 nanotubes prepared by sonoelectrochemical method. *Applied Surface Science*, 318: 132 – 136.

5. Kumar, S. G. and Devi, L. G. (2011). Review on modified TiO_2 photocatalysis under UV/visible light: selected results and related mechanisms on interfacial charge carrier transfer dynamics. *The Journal of Physical Chemistry A*, 115 (46): 13211 – 13241.
6. Erol, M., Dikici, T., Toparli, M. and Celik, E. (2014). The effect of anodization parameters on the formation of nanoporous TiO_2 layers and their photocatalytic activities. *Journal of Alloys and Compounds*, 604: 66 – 72.
7. Zhang, Y., Yu, D., Gao, M., Li, D., Song, Y., Jin, R., Ma, W. and Zhu, X. (2015). Growth of anodic TiO_2 nanotubes in mixed electrolytes and novel method to extend nanotube diameter. *Electrochimica Acta*, 160: 33 – 42.
8. Nishanthi, S. T., Subramanian, E., Sundarakannan, B. and Padiyan, D. P. (2015). An insight into the influence of morphology on the photoelectrochemical activity of TiO_2 nanotube arrays. *Solar Energy Materials and Solar Cells*, 132: 204 – 209.
9. Komiya, S., Sakamoto, K. and Ohtsu, N. (2014). Structural changes of anodic layer on titanium in sulfate solution as a function of anodization duration in constant current mode. *Applied Surface Science*, 296: 163 – 168.
10. Sánchez-Tovar, R., Lee, K., García-Antón, J. and Schmuki, P. (2013). Formation of anodic TiO_2 nanotube or nanosponge morphology determined by the electrolyte hydrodynamic conditions. *Electrochemistry Communications*, 26: 1 – 4
11. Yao, B. D., Chan, Y. F., Zhang, X. Y., Zhang, W. F., Yang, Z. Y. and Wang, N. (2003). Formation mechanism of TiO_2 nanotubes. *Applied Physics Letters*, 82 (2): 281 – 283.
12. Xue, Y., Sun, Y., Wang, G., Yan, K. and Zhao, J. (2015). Effect of NH_4F concentration and controlled-charge consumption on the photocatalytic hydrogen generation of TiO_2 nanotube arrays. *Electrochimica Acta*, 155: 312 – 320.
13. Liang, Y. Q., Cui, Z. D., Zhu, S. L. and Yang, X. J. (2011). Study on the formation micromechanism of TiO_2 nanotubes on pure titanium and the role of fluoride ions in electrolyte solutions. *Thin Solid Films*, 519 (15): 5150 – 5155.
14. Ku, Y., Chen, Y. S., Hou, W. M. and Chou, Y. C. (2012). Effect of NH_4F concentration in electrolyte on the fabrication of TiO_2 nanotube arrays prepared by anodisation. *Micro & Nano Letters*, 7 (9): 939 –942.

MALAYSIAN JOURNAL OF ANALYTICAL SCIENCES
Published by The Malaysian Analytical Sciences Society
ISSN 1394 - 2506

TEMPERATURE PROGRAMMED REDUCTION AND X-RAY DIFFRACTOMETRY STUDIES OF MoO_3 REDUCTION BY DIFFERENT CONCENTRATIONS OF CARBON MONOXIDE

(Kajian Penurunan Suhu Berprogram dan Pembelauan Sinar-X Terhadap Penurunan MoO_3 Menggunakan Kepekatan Karbon Monoksida Berbeza)

Alinda Samsuri[1, 2]*, Tengku Shafazila Tengku Saharuddin[1], Fairous Salleh[1], Rizafizah Othaman[1], Mohamed Wahab Mohamed Hisham[1], Mohd. Ambar Yarmo[1]

[1]*Catalysis Research Group, School of Chemical Sciences and Food Technology, Faculty of Science and Technology, Universiti Kebangsaan Malaysia, 43600 UKM Bangi, Selangor Darul Ehsan, Malaysia.*
[2]*Centre for Defence Foundation Studies, Universiti Pertahanan Nasional Malaysia, Kem Sungai Besi, 57000 Kuala Lumpur, Malaysia*

**Corresponding author: alindasamsuri@gmail.com*

Received: 24 February 2015; Accepted: 27 October 2015

Abstract

Reduction of molybdenum trioxide, MoO_3 to molybdenum dioxide, MoO_2 by using carbon monoxide, CO has been studied by temperature programmed reduction (TPR) and X-ray diffraction spectroscopy (XRD). The influence of carbon monoxide concentration on the reduction of MoO_3 have been investigated by comparing the reduction behaviour of MoO_3 to MoO_2 with 20 vol.% and 40 vol.% of CO concentration. The XRD results show that by using 20% of CO, reduction to MoO_2 takes place at 700°C in 60 minutes. However, by using 40% of CO, complete reduction to MoO_2 takes place at 700°C in only 30 minutes. Moreover, excess of CO results in the formation of molybdenum carbide, Mo_2C. It is suggested that by using CO, complete reduction from MoO_3 to MoO_2 gives two-steps reduction ($MoO_3 \rightarrow Mo_4O_{11} \rightarrow MoO_2$) with Mo_4O_{11} as an intermediate product. It can be concluded that the reducing behavior of MoO_3 is strongly dependent on the concentration of CO and reaction time.

Keywords: molybdenum trioxide, molybdenum dioxide, molybdenum carbide, carbon monoxide

Abstrak

Penurunan molibdenum trioksida, MoO_3 kepada molibdenum dioksida, MoO_2 dengan menggunakan karbon monoksida, CO telah dikaji menggunakan suhu penurunan berprogram (TPR) dan spektroskopi pembelauan sinar-X (XRD). Kesan kepekatan karbon monoksida terhadap penurunan MoO_3 telah dikaji dengan membandingkan kesan penurunan MoO_3 kepada MoO_2 menggunakan kepekatan karbon monoksida di antara 20 % dan 40 %. Keputusan XRD menunjukkan bahawa dengan menggunakan 20 % kepekatan CO, penurunan kepada MoO_2 berlaku pada suhu 700 °C dalam masa 60 minit. Walau bagaimanapun, dengan menggunakan 40 % kepekatan CO, penurunan lengkap kepada MoO_2 berlaku pada suhu 700 °C dalam masa hanya 30 minit. Selain itu, pendedahan kepada CO berlebihan akan menyebabkan pembentukan molibdenum karbida, Mo_2C. Adalah dicadangkan bahawa dengan menggunakan CO, penurunan lengkap daripada MoO_3 kepada MoO_2 terdiri daripada dua peringkat penurunan ($MoO_3 \rightarrow Mo_4O_{11} \rightarrow MoO_2$) dengan menghasilkan Mo_4O_{11} sebagai produk perantara. Ini boleh disimpulkan bahawa kelakuan penurunan MoO_3 adalah amat bergantung kepada kepekatan CO dan tempoh masa tindak balas.

Kata kunci: molibdenum trioksida, molibdenum dioksida, molibdenum karbida, karbon monoksida

Introduction

Metallic molybdenum offers excellent mechanical, thermal and electric properties and good corrosion resistance and is widely used as an alloying agent for manufacturing steels, cast irons and super-alloys to increase their mechanical strength, hardness, swiftness and resistance to corrosion and wearing [1]. Molybdenum powder is manufactured in two-step process starting from MoO_3. The first step reduction is exothermic in nature that is carried out at lower temperatures and involves transformation of MoO_3 to MoO_2. The second step reduction is endothermic in nature where MoO_2 is further reduced to Mo [2]. The reduction of MoO_3 to MoO_2 is a crucial stage in the production of metallic molybdenum. The reduction of MoO_3 to MoO_2 by using hydrogen consists of two reduction stages, namely $Mo^{6+} \rightarrow Mo^{5+}$ and $Mo^{5+} \rightarrow Mo^{4+}$ [3]. It seems that during the reduction of MoO_3, MoO_3 is first reduced to Mo_4O_{11}, then to MoO_2. Generally, pure molybdenum powders are produced using the well known two-step hydrogen reduction process [4]. The first step occurs in the temperature range of 450 - 650 °C and reduces the input material to MoO_2. The second step reduction is performed in the 1000 - 1100 °C range and this process results the formation of molybdenum metal. Nevertheless, usage of hydrogen as a reducing agent of MoO_3 reduction is expensive. Carbon is also used to reduce MoO_3 at elevated temperature (600 - 1200 °C) [5]. When metal oxides react with carbon, one of the reaction products would be gaseous and could be readily separated from the solid reaction products [6]. Therefore, it would be highly desirable to develop an alternative process to manufacture molybdenum. Reduction of MoO_3 by using CO as reductant was suggested as an alternative process for producing molybdenum. However, currently there are limited number of studies using CO for reduction of MoO_3 to MoO_2. In this study, we report the influence of CO content on the reduction behaviour of MoO_3. The isothermal and non-isothermal temperature programmed reduction (TPR) was performed to investigate the reduction behaviour of MoO_3 to MoO_2 by using CO as a reducing agent and later characterizing by XRD. Reduction of MoO_3 to MoO_2 by CO was suggested to follow two reduction stages which are shown as Equation 1 and Equation 2.

$$4MoO_3 + CO \rightarrow Mo_4O_{11} + CO_2 \quad (1)$$

$$Mo_4O_{11} + 3CO \rightarrow 4MoO_2 + 3CO_2 \quad (2)$$

Materials and Methods

Chemicals and raw materials

Commercial molybdenum trioxide, MoO_3 (AnalaR) powder was obtained from BDH Chemicals Ltd.. The gas mixture of carbon monoxide (CO) in nitrogen (20 and 40 vol % of CO) from Linde Malaysia was used.

Reduction of molybdenum trioxide

The commercially bought MoO_3 powder was calcined to remove impurities at 400 °C for 4 hours in air and then cooled to room temperature before undergo the reduction process by using a Micromeritic Autochem 2920 Chemisorption Analyzer apparatus. The completeness of the reduction of the powder was analysed using a temperature programmed reduction (TPR) method. In this experiment, a mixed gas of 20 % CO in 80 % nitrogen and 40 % CO in 60 % nitrogen was introduced into the apparatus at an effective flow rate of 20 mL/min. Then, temperature was increased from 40 to 700 °C with a heating rate of 10 °C/min and continued with isothermal reduction for 30 and 60 minutes at 700 °C.

Characterization method

The crystal structures of the MoO_3 powder before and after reactions were determined by XRD's Bruker AXS D8 Advance type. The radiation source used was Cu Kα (40 kV, 40 mA) to record the 2θ diffraction angles from 10° to 80° at wavelength ($\lambda = 0.154$ nm). For identification purposes of crystalline phase composition, diffraction patterns obtained were matched with standard diffraction data (JCPDS) file.

Results and Discussion

Thermodynamic Consideration Data

According to the thermodynamic analysis for the reduction of MoO_3 by using CO as a reducing agent to the reaction in Equation 3 and Equation 4, the Gibbs free energy changes due to reaction and the equilibrium composition of the oxides was calculated.

$$MoO_3 + CO \rightarrow MoO_2 + CO_2 \quad (3)$$

$$2MoO_2 + 6CO \rightarrow Mo_2C + 5CO_2 \quad (4)$$

From the calculation, the Gibbs free energy for formation of MoO_2 for reaction Equation 3 is $\Delta G_{(298\ K)}$ = -29.8 kcal/mol which clearly indicates that the reaction is favorable. However, if excess CO is introduced to the reduction system, the formation of Mo_2C will take place according to reaction Equation 4 with the $\Delta G_{(298\ K)}$ = -34.9 kcal/mol which means the reaction is very spontaneous.

Characterization by TPR

The reduction behaviour of MoO_3 to MoO_2 was studied using TPR. Figure 1 shows the TPR profile of non-isothermal reduction of MoO_3 until 700 °C continued with isothermal reduction at 700 °C for 60 minutes by using 20% and 40% of CO in nitrogen. Complete reduction to MoO_2 needs to complete at temperature lower than its melting point (795 °C) since MoO_3 will end up as an alloy fused mass when it is taken to its melting point [5].

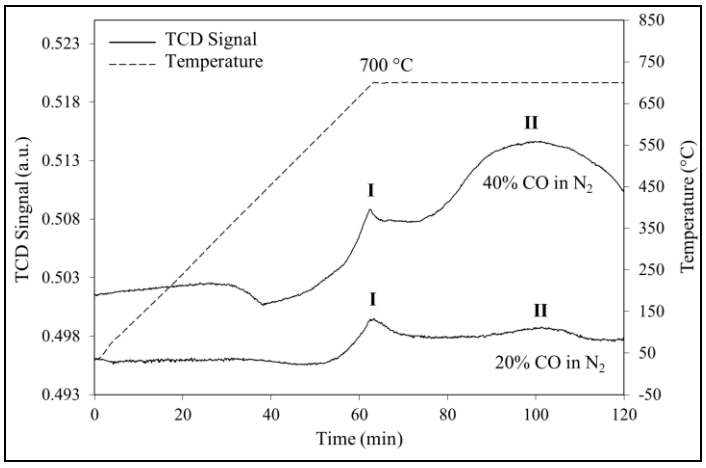


Figure 1. TPR profile of non-isothermal reduction of MoO_3 with 20% and 40% of CO in nitrogen at 40-700 °C and continued with isothermal reduction at 700 °C for 60 minutes.

The TPR profile of MoO_3 represents two reduction events (denoted I and II) which event I owing to peak displayed at early reaction time may regard to the reduction of MoO_3 to Mo_4O_{11}, while event II is subsequent to reduction steps of Mo_4O_{11} to MoO_2. However, with excess of CO supply to the reduction system, it brings to the formation of Mo_2C. The profile monitor CO consumption peaks by using 20 % of CO in nitrogen which started at about 530 °C was pointed to the first stage of reduction (event I) in agreement with Dang et al. [7], as mentioned that the MoO_3 is firstly reduced to Mo_4O_{11}, then to MoO_2. After continuing the reaction with isothermal reduction at 700 °C for 40 minutes, new broad peak is observed due to sample changes that occurred, reflecting to second stage reduction of Mo_4O_{11} to MoO_2.

Then, for the reduction of MoO_3 in 40 % of CO atmosphere, the TPR profile shows two peaks that reflect the two stages of reduction. By increasing concentration of CO to 40 % CO, the reduction peaks are leading to a low temperature to 420 °C, while the second peak can be monitored after 10 minutes, starting off with isothermal reduction at 700 °C. It seems that, the reduction of MoO_3 is observed to occur with a slight shift to lower temperature by increasing the concentration of CO. In addition, it shows that the reducing behaviour of MoO_3 is

strongly dependent on the concentration of CO. The phases formed after the reduction by TPR were analysed by recording XRD pattern of the residual obtained after selected reduction condition.

Characterization by XRD

To investigate the reduction behaviour of MoO_3 by using different concentration of CO, the samples were collected and XRD patterns were measured. The XRD profile obtained in Figure 2 revealed the MoO_3 (JCPDS 74-7383) was not yet reduced to MoO_2 even after flowing with 20 % of CO until 700 °C. It is due to insufficient of CO and heat supply to the reaction. However, by flowing with 40% of CO the XRD patterns showed peaks that identified with MoO_2 phases (JCPDS 76-1807). From the results, the reduction of MoO_3 by using 20% and 40% of CO concentration shows two stages process ($MoO_3 \rightarrow Mo_4O_{11} \rightarrow MoO_2$) in respect to a trace of intermediate Mo_4O_{11} (JCPDS 89-0687) which presence is identified at 700 °C. It is comparable with literature reported by Lalik [8] that suggested formation of Mo_4O_{11} as the earliest product in the reduction of MoO_3.

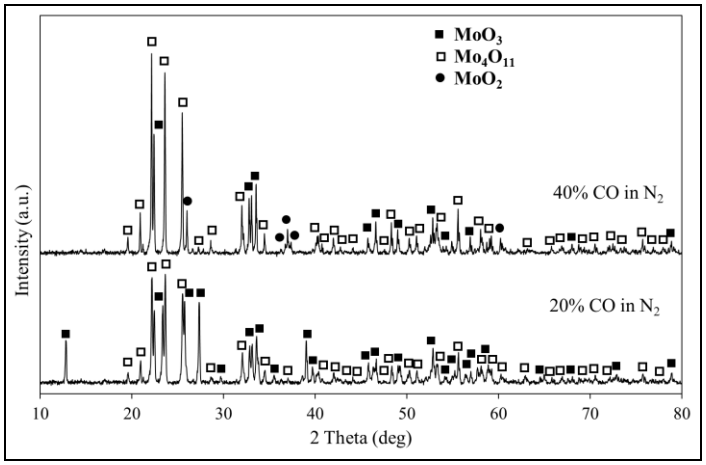


Figure 2. XRD patterns of non-isothermal reduction of MoO_3 with 20 % and 40 % of CO in nitrogen until 700 °C

Since MoO_3 is not completely reduced to MoO_2, isothermal reduction with 20 % and 40 % of CO in nitrogen was conducted at 700 °C for 30 minutes to complete reduction to MoO_2. From the XRD profile obtained in Figure 3, it is seen that by using 20% of CO, the MoO_2 peaks start to appear and MoO_3 peaks nearly disappear. Most of the peaks are intermediate phases of Mo_4O_{11}. However, by using 40 % of CO, the intensity of MoO_2 peaks sharply increase and intermediate phases of Mo_4O_{11} completely disappear. It shows that, reduction to MoO_2 in 20 % of CO concentration required higher heat supply to be accomplished compared by using 40 % of CO. It is seen that the higher concentration of CO will give the higher reduction to MoO_3.

Isothermal reduction at 700 °C was increased to 60 minutes to study the reduction behaviour by excessing the CO supplied. Figure 4 shows the XRD patterns of isothermal reduction for 60 minutes by using 20 % and 40 % of CO. As it is shown, MoO_3 was completely reduced to MoO_2 after isothermal reduction using 20 % of CO at 700 °C for 60 minutes. Figure 4 show the formation of carbide will take place in excess of CO. This was confirmed by the XRD profile of 40 % of CO displayed a decrease in the intensity of the MoO_2 peaks and new formation peaks of Mo_2C (JCPDS 65-8766) when the isothermal reduction prolongs until 60 minutes. This XRD patterns match well to previously reported pattern for processing of Mo_2C [9].

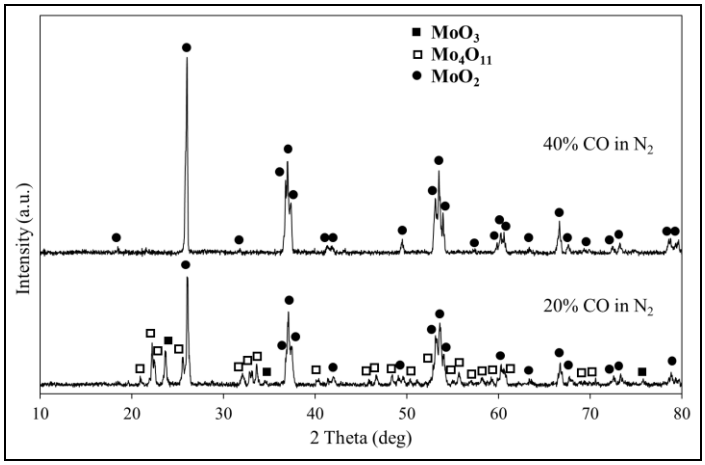


Figure 3. XRD patterns of non-isothermal reduction of MoO_3 with 20 % and 40 % of CO in nitrogen until 700 °C and continued with isothermal reduction at 700 °C for 30 minutes

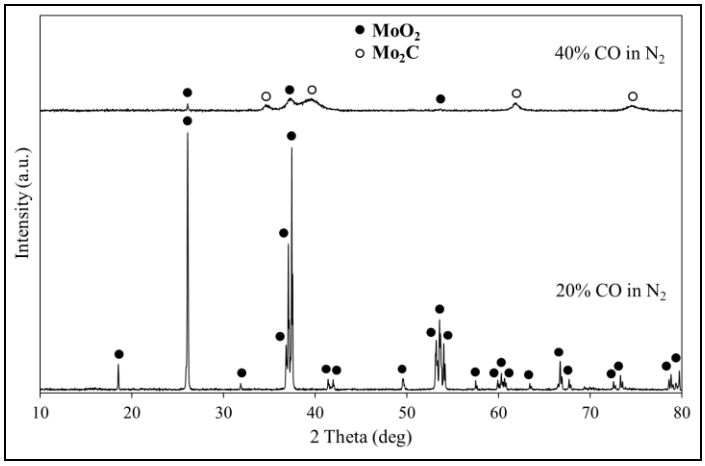


Figure 4. XRD patterns of non-isothermal reduction of MoO_3 with 20% and 40% of CO in nitrogen until 700 °C and continued with isothermal reduction at 700 °C for 60 minutes

Conclusion

In conclusion, the reduction behaviour of MoO_3 by TPR technique and XRD characterization shows that the reduction reaction of MoO_3 is strongly dependent on the concentration of CO and reaction time. The reduction reaction follows the consecutive two-steps mechanism, namely, MoO_3 is firstly reduced to Mo_4O_{11} and then Mo_4O_{11} is reduced to MoO_2. However, if excess of CO is introduced to the system, the formation of Mo_2C will take place.

Acknowledgement

The authors wish to thank the Ministry of Higher Education (MOHE) and Universiti Pertahanan Nasional Malaysia for funding staff's scholarships and also Universiti Kebangsaan Malaysia (UKM) for funding this project under research grant number LRGS/BU/2011/USM-UKM/PG/02, BKBP-FST-K003323-2014, FRGS/2/2013/TK06/ UKM/02/3, ETP-2013-066 as well as the Centre of Research and Innovation Management (CRIM) for the instruments facilities.

References

1. Manukyan, K., Davtyan, D., Bossert, J. and Kharatyan, S. (2011). Direct reduction of ammonium molybdate to elemental molybdenum by combustion reaction. *Chemical Engineering Journal*, 168 (2): 925 – 930.
2. Enneti, R. K. and Wolfe, T. A. (2012). Agglomeration during reduction of MoO_3. *International Journal of Refractory Metals and Hard Materials*, 31: 47 – 50.
3. Wang, J., Ren, Z., Liu, W., Gao, F. and Zhou, M. (2009). Effects of RE_2O_3 doping on the reduction behavior of molybdenum oxide and properties of molybdenum powder. *International Journal of Refractory Metals and Hard Materials*, 27 (1): 155 – 158.
4. Saghafi, M., Heshmati-Manesh, S., Ataie, A. and Khodadadi, A. A. (2012). Synthesis of nanocrystalline molybdenum by hydrogen reduction of mechanically activated MoO_3. *International Journal of Refractory Metals and Hard Materials*, 30 (1): 128 – 132.
5. Saghafi, M., Ataie, A. and Heshmati-Manesh, S. (2011). Effects of mechanical activation of MoO_3/C powder mixture in the processing of nano-crystalline molybdenum. *International Journal of Refractory Metals and Hard Materials*, 29 (4): 419 – 423.
6. Satyajeet Chaudhury, V. V., Mukerjee, S. K. and Vaidya, V. N. (1997). Kinetics and mechanism of carbothermic reduction of MoO_3 to Mo_2C. *Journal Alloys Compounds*, 261: 105 – 113.
7. Dang, J., Zhang, G.-H., Chou, K. C., Reddy, R. G., He, Y. and Sun Y. (2013). Kinetics and mechanism of hydrogen reduction of MoO_3 to MoO_2. *International Journal of Refractory Metals and Hard Materials*, 41: 216 – 223.
8. Lalik, E. (2011). Kinetic analysis of reduction of MoO_3 to MoO_2. *Catalysis Today*, 169: 85 – 92.
9. Claridge, J. B., York, A. P. E., Brungs, A. J., Marquez-Alvarez, C., Sloan, J., Tsang, S. C. and Green, M. L. H. (1998). New Catalysts for the Conversion of Methane to Synthesis Gas : Molybdenum and Tungsten Carbide. *Journal of Catalysis*, 180: 85 – 100.

MALAYSIAN JOURNAL OF ANALYTICAL SCIENCES
Published by The Malaysian Analytical Sciences Society
ISSN 1394 - 2506

CHEMICAL CONSTITUENTS FROM THE LIANAS OF *Gnetum cuspidatum* Blume

(Sebatian Kimia dari Lianas *Gnetum cuspidatum* Blume)

Nik Fatini Nik Azmin[1], Norizan Ahmat[1,2]*, Nik Khairunissa Nik Abdullah Zawawi[1,2]

[1]*Faculty of Applied Sciences,*
Universiti Teknologi MARA, 40450 Shah Alam, Selangor, Malaysia
[2]*Atta-ur-Rahman Institute for Natural Product Discovery,*
Universiti Teknologi MARA, Puncak Alam Campus, 42300 Bandar Puncak Alam, Selangor, Malaysia

**Corresponding author: noriz118@salam.uitm.edu.my*

Received: 24 February 2015; Accepted: 27 October 2015

Abstract

Gnetum is a genus of gymnosperms, the sole genus in the family Gnetaceae with approximately 40 species. Various species has been used for the treatment of rheumatitis, arthritis, bronchitis and asthma in folk medicines. *Gnetum cuspidatum* Blume is known throughout tropical Southeast Asia from Thailand, Vietnam, Cambodia, Malaysia, Sumatra, Java, and Borneo to the Maluku, Sulawesi and New Guinea. In this research work, a methanol extract of the lianas of *Gnetum cuspidatum* was subjected to vacuum liquid chromatography for fractionation. Later, several selective fractions had undergone the repetitive radial chromatography technique for further purification. Four known constituents categorized as stilbene type of compound have been successfully isolated and identified which include resveratrol (1), gnetucleistol C (2), gnetucleistol D (3) and gnemonol M (4). The structures and configuration of the reported compounds were elucidated on the basis of 2D-NMR correlations and comparison with the literature.

Keywords: Gnetaceae, *Gnetum*, *Gnetum cuspidatum*, stilbene

Abstrak

Gnetum merupakan genus gymnosperms, genus tunggal dalam keluarga Gnetaceae dengan kira-kira 40 spesies. Pelbagai spesies telah digunakan untuk rawatan rheumatitis, arthritis, bronkitis dan asma dalam perubatan penduduk tempatan. *Gnetum cuspidatum* Blume dikenali di seluruh tropika Asia Tenggara dari Thailand, Vietnam, Kemboja, Malaysia, Sumatera, Jawa, Borneo dan ke Maluku, Sulawesi dan New Guinea. Satu ekstrak metanol daripada lianas *Gnetum cuspidatum* telah menggunakan vakum kromatografi cecair untuk pemisahan. Kemudian, beberapa pemisahan yang terpilih telah menjalani teknik kromatografi jejarian secara berulang kali untuk penulenan lanjut. Empat sebatian yang dikategorikan sebagai jenis stilbene telah berjaya diasingkan dan dikenalpasti iaitu resveratrol (1), gnetucleistol C (2), gnetucleistol D (3) dan gnemonol M (4). Struktur dan konfigurasi sebatian yang telah dilapor ini berdasarkan korelasi 2D-NMR dan perbandingan dengan kajian literatur.

Kata kunci: Gnetaceae, *Gnetum*, *Gnetum cuspidatum*, stilben

Introduction

The genus *Gnetum* from the family of Gnetaceae comprises approximately 40 species which were found in the tropical lowlands of the world from Northeastern South America, tropical West Africa, and South China to Southeast Asia. The plants are known to contain stilbenoids or oligostilbene and have been ethnobotanically used as folk medicine as well as food [1]. Previously, many studies have been done on several species of *Gnetum* and

revealed various stilbenes and oligostilbenes type of compounds as its major chemical constituents. Interestingly, some of the isolated compounds display multiple bioactivities such as antioxidant, anti-inflammatory and antitumor [2].

In our search for structurally and biological interesting compounds from tropical plants found in Malaysia, the lianas of *Gnetum cuspidatum* has been investigated. *Gnetum cuspidatum* Blume is known throughout tropical Southeast Asia from Thailand, Vietnam, Cambodia, Malaysia, Sumatra, Java, and Borneo to the Maluku, Sulawesi and New Guinea. Previous study revealed the isolation of isorhapontigenin from the stem [3] and two new compounds recently report by Shimokawa et al. [4] known as cuspidan A and cuspidan B from the bark of this plant.

In this study, the methanol extract of the lianas of this plant has led to the isolation of four known stilbenoid compounds, resveratrol (1) [5], gnetucleistol C (2) [6], gnetuclesitol D (3) [7] and gnemonol M (4) [8]. The structures were determined using spectroscopic techniques of 1D and 2D NMR, MS and comparison with previous reports

Materials and Methods

Chemicals and raw materials

All the chemicals used were of analytical grade and purchased from Sigma Chemical Co. (St Louis, Missouri). The lianas of *Gnetum cuspidatum* was collected at Taman Negara, Pahang in August 2011 and identified by Dr Shamsul, a botanist from Universiti Putra Malaysia (UPM), Serdang.

Extraction and isolation of constituents from plant materials

The lianas were air-dried, ground (2 kg) and macerated in methanol which then filtered and concentrated under reduced pressure to obtain crude extract (214.8 g). The crude extract with less tannin (62.60 g) then was subjected to fractionation by using vacuum liquid chromatography (VLC) with various composition of solvent system [n-hexane: EtoAC (7:3, 6:4, 5:5, 3:7, 2:8, 1:9) and EtoAC: MeOH (10:0, 9:1, 8:2)] to yield five major fractions. All pure compounds reported were obtained from one single fraction. Fraction 4 (10.54 g) was subjected to isolation and purification using separation technique of multiple radial chromatography and preparative thin layer chromatography (pTLC) with solvent system of chloroform: methanol (8.5:1.5), and chloroform: acetone (8:2) to yield **1** (1mg), **2** (3.1mg), **3** (6.1mg) and **4** (12.1mg).

Purification and structure elucidation of pure compounds

The structure determination of the constituents isolated from the plants was done using several spectroscopic methods. The ^{1}H-NMR and ^{13}C-NMR were recorded in acetone-D on Bruker 300 Ultrashield NMR spectrometer measured at 300MHz for ^{1}H NMR and 75MHz for ^{13}C NMR. Chemical shifts were reported in ppm (δ) and the coupling constants are given in Hz. The mass spectra were measured on Agilent Technologies LC-MS. Melting point was measured by Fisher Johns 'micro melting point apparatus'.

For purification process to obtain a single constituent, various chromatographic techniques have been applied. Vacuum liquid chromatography (VLC) used silica gel 60, 70 – 230 mesh ASTM (Merck 1.07747), column chromatography using Si-gel Merck 60 (200 – 400mesh) and TLC analysis on pre-coated Si-gel plates Si-gel Merck Kiesel gel 60 F254 0.25mm, 20 x 20 cm while glass supported silica gel 60 F_{254} was used for preparative thin layer chromatography.

Results and Discussion

Four known compounds, resveratrol (1), gnetucleistol C (2), gnetucleistol D (3) and gnemonol M (4) (Figure 1) were successfully isolated from the methanol extract of the lianas of *G.cuspidatum*. The known compounds were elucidated on the basis of NMR (^{1}H and ^{13}C) technique and by comparison of physical and spectroscopic data with values found in the literature. Table 1 displayed all ^{13}C NMR data of the compounds isolated. Resveratrol (1), a naturally occurring stilbene in *Gnetum* plants was obtained as white amorphous powder. ^{1}H NMR (300 MHz, in Acetone-d6) revealed two sets of *ortho*-coupled aromatic protons on a *p*-substituted phenyl moieties (ring B) at δ_H7.40 (2H, d, J = 8.7 Hz, H-2, 6) and δ_H6.82 (2H, d, J = 8.4 Hz, H-3, 5). The spectrum also displayed one set of

meta-coupled aromatic proton δ_H6.53 (2H, d, *J* = 2.4 Hz, H-10, 14) and one *meta*-triplet at δ_H6.26 (1H, t, *J* = 2.1, 2.4 Hz, H-12) on a 1,3,5-trisubstituted benzene ring (ring A). A pair of *trans*-coupled olefinic proton at δ_H6.99 (1H, d, *J* = 16.8 Hz, H-7) /6.90 (1H, d, *J* = 16.2 Hz, H-8) were also observed.

Gnetucleistol C (2) was obtained as an amorphous white powder. The ^{1}H NMR spectrum in acetone-d6 exhibited signals attributable to a methoxy proton at δ_H3.95 (3H,s), an AB_2 system at δ_H6.39 (1H, t, *J* = 2.1 Hz, H-4), δ_H 6.91 (2H, d, *J* = 2.1 Hz, H-2, 6), an ABX system at δ_H6.75 (1H, d, *J* = 8.1 Hz, H-11), δ_H7.12 (1H, dd, *J* = 8.4, 0.9 Hz, H-13), δ_H7.23 (1H, t, *J* = 8.4, 8.1 Hz, H-12), and a doublet at δ_H7.14 (1H, d, *J* = 0.9 Hz, H-8), which display a long-range correlations with the signal of C-1 and C-9. Based on comparison with the ^{1}H and ^{13}C NMR data of gnetifolin A [5], compound **2** was deduced to have a benzofuran skeleton and was categorized under arylbenzofuran monomer type of stilbene.

Gnetuclesitol D (3), also known as 2-methoxyresveratrol was obtained as white amorphous powder. ^{1}H NMR (300 MHz, in Acetone-d6) displayed a single peak at δ_H3.89 (3H, s), showing the existence of an additional substituent which was a methoxy group on carbon 2 of ring B. Signals of one set of *meta*-coupled aromatic protons at δ_H6.53 (2H, d, *J* = 2.4 Hz, H-10, 14) and one *meta*-triplet at δ_H6.27 (1H, d, *J* = 2.1 Hz, H-12) were revealed on ring A. The spectrum also showed an ABX system on a 1,2,4-trisubtituted benzene ring (ring B) at δ_H6.79 (1H, d, *J* = 8.1 Hz, H-6), δ_H (6.99, dd, *J* = 2.1, 8.4 Hz, H-5) and δ_H7.21 (1H, d, *J* = 2.1, H-3). A pair of *trans*-coupled olefinic proton at δ_H7.05 (1H, d, *J* = 16.5 Hz, H-7) /6.89 (1H, d, *J* = 16.2 Hz, H-8) was also shown.

Gnemonol M (4) was obtained as a colorless amorphous powder. The ^{1}H NMR spectrum showed the presence of six sets of H-atoms in ABX systems on two units of 1,3,4-trisubstituted benzene rings at δ_H6.96 (1H, d, J = 1.8 Hz, H-2a)/6.72 (1H, d, J = 8.1 Hz, H-5a)/6.65 (1H, dd, J = 1.8, 8.1 Hz, H-6a); δ_H6.61 (1H, d, J = 2.1 Hz, H-2b)/6.57 (1H, d, J = 8.1 Hz, H-5b)/6.39 (1H, dd, J = 2.1 Hz, 8.1, H-6b). The spectrum also showed four sets of *meta*-coupled H-atoms in AB systems on two units of tetra-substituted benzene rings at δ_H6.54 (1H, d, J = 2.7 Hz, H-14a)/6.06 (1H, d, J = 1.8 Hz, H-12a); δ_H6.44 (1H, d, J = 2.4 Hz, H-14b)/6.16 (1H, d, J = 2.4 Hz, H-12b). Four benzylic methine singlets at δ_H4.20 (H-7a); 3.69 (H-8a); 4.13 (H-8b); 3.77 (H-7b), two signals for methoxyl groups at δ_H3.79 (OMe-3a); 3.64 (OMe- 3b), and phenolic proton at δ_H8.02 was also observed in the spectrum.

Table 1. Spectroscopic data (^{13}C NMR) for compound 1 – 4

No. of carbon	**Compounds**			
	1 δ_C	**2** δ_C	**3** δ_C	**4** δ_C
1	128.9	133.9	129.5	139.0
2	127.8	105.0	147.8	113.0
3	115.5	160.9	109.3	147.6
4	157.4	105.0	146.7	145.5
5	115.5	160.9	120.3	115.2
6	127.8	105.0	115.1	121.4
7	128.2	159.8	128.5	48.5
8	125.9	100.5	126.2	58.7
9	139.9	121.1	139.9	148.0
10	104.7	155.4	104.7	127.8
11	158.8	105.9	158.7	158.6
12	101.8	127.1	101.9	102.8
13	158.8	105.5	158.7	158.6
14	104.7	157.6	104.7	104.2

Table 1 (cont'd). Spectroscopic data (^{13}C NMR) for compound 1 – 4

No. of carbon	Compounds			
	1 δ_C	**2** δ_C	**3** δ_C	**4** δ_C
OCH_3		56.9	55.4	
OCH_3 (3a)				57.3
OCH_3 (3b)				56.9
1b				136.2
2b				112.3
3b				147.6
4b				145.5
5b				115.2
6b				120.9
7b				52.0
8b				51.2
9b				147.2
10b				113.4
11b				157.9
12b				102.8
13b				157.2
14b				105.7

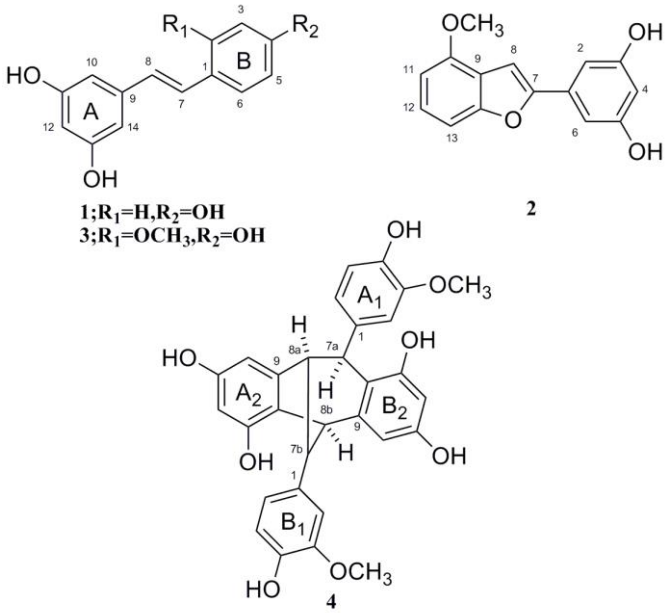


Figure 1. Structure of compound 1 – 4

Conclusion

Four known stilbenoids were successfully isolated and characterized from the methanol extract of the lianas of *Gnetum cuspidatum* Blume. These stilbenoids compounds include resveratrol (1), gnetucleistol C (2), gnetucleistol D (3) and gnemonol M (4). As previous study found that oligostilbenoids from G*netum* displayed diverse pharmacological properties, further detailed on its phytochemical investigation is worth to be explored.

References

1. Medicinal Herb Index in Indonesia. (1995). PT. EISAI Indonesia, Second Edition.
2. Shimizu, K., Kondo, R. and Sakai. K. (2000). Inhibition of tyrosinase by flavonoids, stilbenes and related 4-substituted resorcin. *Planta Medica*, 66: 11–15.
3. Lojanapiwatna, V., Mahaeja, J. and P. Wiriyachitra. (1982). Isolation of (*E*)- 3 ,4, 5-trihydroxy-3'-methoxystilbene from *Gnetum cuspidatum* Bl. *Journal of the Science Society of Thailand*, 8(1): 59 – 63.
4. Shimokawa, Y., Hirasawa, Y., Kaneda, T., Hamid, A., Hadi, A. and H. Morita. (2012). Cuspidans A and B, Two New Stilbenoids from the Bark of *Gnetum cuspidatum. Chemical and Pharmaceutical Bulletin*, 60(6): 790 – 792.
5. Huang, K. S. and Lin, M. (1999). Oligostilbenes from the Roots of *Vitis amurensis. Journal of Asian Natural Products Research*, 2: 21 – 28.
6. Yao, C. S., Lin, M., Liu, X. and Wang, Y. H. (2005). Stilbene derivatives from *Gnetum cleistostachyum*. *Journal of Asian Natural Products Research*, 7: 131 – 137.
7. Yao, C. S., Lin, M., Liu, X. and Wang, Y. H. (2003). Stilbene from *Gnetum cleistostachyum*. *Acta Chimica Sinica*, 61 (8): 1331 – 1334.
8. Ilya, I., Ali, Z., Tanaka, T., Iinuma, M., Furusawa, M., Nakaya, K., Murata, J., Darnaedi, D., Matsuura, N. and Ubukata, M. (2003). Stilbene derivatives from *Gnetum gnemon* Linn. *Phytochemistry*, 62: 601 – 606.

MALAYSIAN JOURNAL OF ANALYTICAL SCIENCES
Published by The Malaysian Analytical Sciences Society
ISSN 1394 - 2506

EFFECT OF SUPPORT MATERIALS ON CATALYTIC ACTIVITY OF NANO RUTHENIUM CATALYST IN HYDROGENOLYSIS OF GLYCEROL

(Kesan Bahan Penyokong Terhadap Aktiviti Pemangkin Nano Ruthenium dalam Hidrogenolisis Gliserol)

Noraini Hamzah[1]* and Mohd Ambar Yarmo[2]

[1]*School of Chemistry and Environmental, Faculty of Science and Technology*
Universiti Teknologi MARA, 40450 Shah Alam, Selangor, Malaysia
[2]*School of Chemical Sciences and Food Technology, Faculty of Science and Technology,*
Universiti Kebangsaan Malaysia, 43600 UKM Bangi, Selangor, Malaysia

**Corresponding author: pnoraini@salam.uitm.edu.my*

Received: 24 February 2015; Accepted: 27 October 2015

Abstract

A series of heterogenous catalysts based on supported ruthenium were prepared from $RuCl_3$ precusor by impregnation method. The effect of support materials (bentonite, TiO_2, Al_2O_3 and SiO_2) on catalytic activity of Ru catalyst for hydrogenolysis of glycerol were investigated under mild reaction condition of 150°C and 20 bar initial hydrogen pressure for 7 hours reaction time and glycerol concentration was 20%(wt). It was found that the type of support material have significant effects on the activity and selectivity of glycerol hydrogenolysis. The order of Ru catalyst activity was Ru/bentonite > Ru/Al_2O_3 ≈ Ru/TiO_2 > Ru/SiO_2. This study showed that bentonite supported Ru catalyst was the most active with glycerol conversion reaching 62.5% compared to other supports. All the tested catalyst exhibited high selectivity to 1,2-propanediol with more than 80%. Characterization of the catalysts was carried out using BET, XPS, FESEM-EDX and TEM to obtain the physicochemical properties of the catalysts.

Keywords: hydrogenolysis, ruthenium, bentonite, 1,2-propanediol, glycerol

Abstrak

Satu siri pemangkin heterogen berasaskan logam ruthenium berpenyokong disediakan daripada prekusor garam $RuCl_3$ menggunakan teknik impregnasi. Kesan bahan penyokong (bentonit, TiO_2, Al_2O_3 dan SiO_2) terhadap aktiviti pemangkin Ru dalam hidrogenolisis gliserol dilakukan pada keadaan tindak balas yang sederhana dengan suhu 150°C, tekanan awal hydrogen 20 bar, masa tindak balas 7 jam dan kepekatan gliserol 20%(wt). Keputusan yang diperolehi menunjukkan jenis bahan penyokong mempunyai kesan signifikan terhadap aktiviti dan pemilihan dalam hidrogenolisi gliserol. Turutan aktiviti pemangkin Ru adalah Ru/bentonit > Ru/Al_2O_3 ≈ Ru/TiO_2 > Ru/SiO_2. Kajian ini menunjukkan pemangkin Ru yang disokong atas bentonit adalah pemangkin yang paling aktif dengan peratus penukaran mencapai 62.5% berbanding dengan penyokong lain. Semua pemangkin yang diuji menunjukkan peratus pemilihan terhadap produk 1,2-propandiol yang tinggi iaitu melebihi 80%. Pencirian pemangkin dilakukan menggunakan alat BET, XPS, FESEM-EDX dan TEM bagi mendapatkan sifat-sifat fizikokimia pemangkin.

Kata kunci: hidrogenolisis, ruthenium, bentonit, 1,2-propanediol, gliserol

Introduction

Glycerol, one of the renewable resources, is obtained as a by-product in hydrolysis of fat, soap-manufacturing process and production of biodiesel [1]. Production of every 9 kg biodiesel, about 1 kg of crude glycerol by-product

is formed [2]. Nowadays, biodiesel derived from vegetable oils and animal fats has received considerable attention. The recent rapid development of biodiesel processes has caused some concern over the oversupply of glycerol in the glycerol market. The glycerol market will likely to be saturated because of limited utilization of glycerol at the present time. It is known that glycerol can be catalytically converted into functionalized and value-added chemical via a variety of reaction routes such as oxidation, hydrogenolysis, dehydration, pyrolysis, steam reforming, etherification, esterification, oligomerization and polymerization [3]. The hydrogenolysis of glycerol produces 1,2-propanediol (1,2-PDO) and ethylene glycol (EG) as a major products with a 4 % annual market growth [4]. Typical uses of 1,2-propanediol are in unsaturated polyester resins, functional fluids, pharmaceuticals, cosmetics, paints and others [5]. Process that can efficiently convert glycerol to a useful compound would be important as an economical and sustainable process. Conversion of glycerol using supported catalyst has been extensively studied by several groups [6-9]. In published papers the effect of various supports (TiO_2, SiO_2, NaY, γ-Al_2O_3 and active –carbon) on Ru catalysts were investigated and found that the support material can influence the metal particles size.

Most of the previous studies have employed solid acid like carbon [2], alumina [10] and silica [8, 11] to be used for supporting the metal catalyst. Bentonite which has surface area about 100 m^2/g is natural clay raw material that has high content of montmorillonite and less amounts of other clay minerals. Previous report have shows that bentonite can be used as support material in catalytic reaction.[12, 13] They found that Ru-Cu bimetallic catalysts supported on clay exhibited 100 % of glycerol conversion and 85 % yield of 1,2-propanediol at 230°C and 8 MPa. Previous study by Yuan et al. claimed that solid base (hydrotalcite and MgO) supported Pt catalysts exhibited the predominant activity and higher 1,2-PDO selectivity than that of solid acids (Al_2O_3, H-ZSM5 and H-Beta)[14].

Since there are only a few studies focus on the application of solid base supported metal catalyst in hydrogenolysis of glycerol, therefore we want to report an efficient solid-base supported Ru catalyst for glycerol hydrogenolysis to 1,2-PDO. In this work, the effect of other support materials (Al_2O_3, SiO_2 and TiO_2) with bentonite material on catalytic performance of ruthenium (Ru) based catalysts in the hydrogenolysis glycerol were investigated. The scope of this study was to investigate the effect of support materials on the structure and physicochemical characteristics of the catalyst as well as the catalytic performance in the glycerol hydrogenolysis reaction.

Materials and Methods

Chemicals

Ruthenium chloride hydrate, $RuCl_3.H_2O$ used as a metal precursor was purchased from Sigma. Aldrich. TiO_2, SiO_2 and Al_2O_3 used as support were purchased from Sigma, Aldrich. The clay mineral used in this work is a calcium-rich bentonite (CaB) was obtained as powder from PT Superintending Company of Indonesia also used as support.

Catalyst preparation

All the supports were calcined in air at 500 °C for 3 hours before used to remove moisture and impurities. About 0.09 gram of $RuCl_3$ was dissolved in acetone and stirred for 15 minutes. Then, approximately 1.8 g of support was added into the resulting solution and sonicated for 1 hour. After that, the mixture was dried in oven at 60 °C overnight. The supported catalyst was calcined in N_2 flow (10 ml/min) at 300 °C for 2 hours and then reduced in H_2 flow (10 ml/min) at 200 °C for 2 hours.

Catalyst characterization

The X-ray photoelectron spectrum (XPS) data of the as-prepared samples were obtained by XPS Ultra from Kratos, UK using 300 W MgK α radiation. The base pressure was about 3 x 10^{-9} mbar. The binding energies were referenced for the C 1s line at 284.5 eV from adventitious carbon. Transmission electron microscope (TEM) images were taken for determination of the particle size with a CM12 instrument (Philips) operated at 200 kV. General morphology information of the samples was examined by FESEM with LEO 1450VP model equipped with energy dispersive X-ray detector (EDX). All the samples were scanning in a high-vacuum mode at 20 kV.

Catalytic reaction

The catalytic hydrogenolysis reactions were carried out in a 50 ml stainless-steel autoclave, PARR reactor equipped with an electronic temperature controller and a mechanical stirrer. Reaction was normally conducted under the following standard conditions: 150°C temperature, 20 bar initial hydrogen pressure, 1.0 g catalyst weight, 23 ml of

20%(wt) aqueous solution of glycerol, 7 h reaction time and at constant stirring speed. Before reaction started, the reactor was flushed three times with N_2 in order to remove oxygen gas and pressurized with H_2 to 20 bar.

Results and Discussion

The physical properties of prepared catalysts by BET nitrogen adsorption isotherm are presented in Table 1. The trend shows that BET surface area of supported catalyst increased following this order: Ru/TiO_2 < Ru/bentonite < Ru/SiO_2 < Ru/Al_2O_3. BET analysis revealed that BET surface area of Ru/bentonite was decreased drastically. It seems that about 65.8% of Ru particle was loaded into the mesoporous of bentonite. This result indicates that pore volume of bentonite was large and much Ru particle could load into pore of bentonite.

The isotherm plot revealed that the catalysts studied exhibited a very much similar types of isotherms, having a mixture of Type III and Type IV (Table 2). The isotherm plot displayed a hysteresis loop which is of the Type H2 according to the IUPAC classification. Type H2 indicating the presence of non-uniformed cylindrical pores.

Table 1. Surface area of supports and supported catalyst

Support	**BET Surface Area (m^2/g)**	**Supported Catalysts**	**BET Surface Area (m^2/g)**
Bentonite	101.3	Ru/bentonite	35.4
TiO_2	8.8	Ru/TiO_2	7.9
SiO_2	130.5	Ru/SiO_2	125.3
AlO_3	155.6	Ru/Al_2O_3	141.4

Table 2. Types of isotherms, porosity, hysteresis and shape of pore for catalysts studied

Catalysts	**Type of isotherms**	**Types of pores**	**Types of hysteresis**	**Shape of Pore**
Ru/bentonite	IV	Mesopore	H2	Non uniform cylindrical pore
Ru/TiO_2	IV	Mesopore	H4	Uniform slit shape
Ru/SiO_2	IV	Mesopore	H4	Uniform slit shape
Ru/Al_2O_3	III and IV	Mesopore and macropore	H3	Non-uniform slit shape

Since XRD analysis did not show any peak related to Ru species except Ru/bentonite, therefore in order to investigate the presence of Ru species on the support, EDX analysis was done. Figure 1 clearly shows the existence of Ru species on the support.

The presence of Ru species was also indicated in the XPS wide scan and the binding energy (B.E) as shown in Table 3. The B.E of 280 and 283 eV is related to the chemical states of Ru^0 and Ru^{n+} respectively [15].

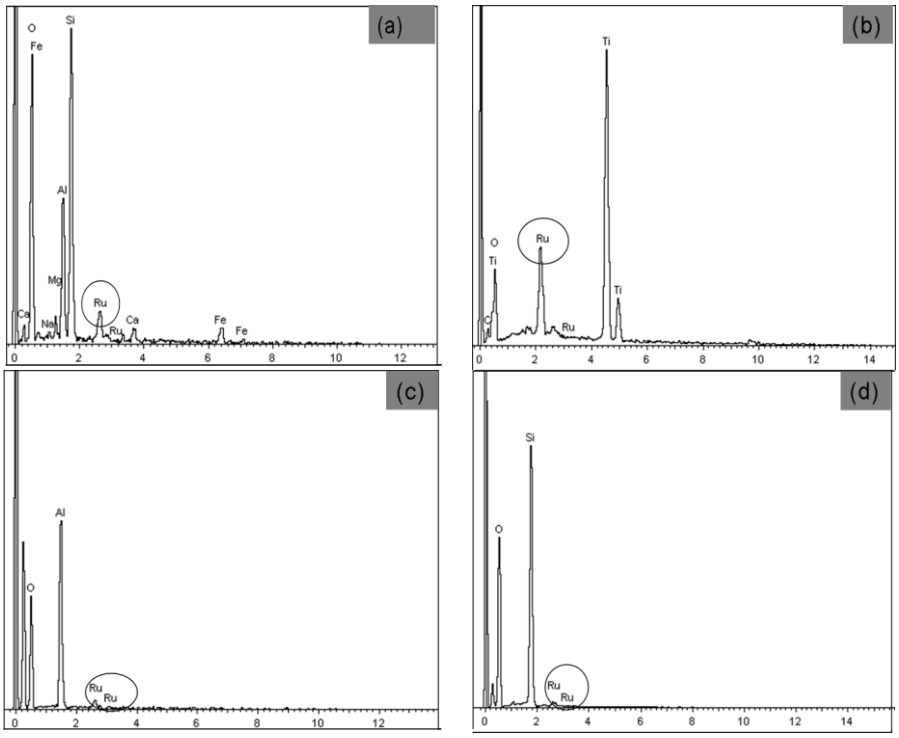


Figure 1. Analysis EDX spectrum of (a) Ru/bentonite, (b) Ru/TiO_2, (c) Ru/Al_2O_3 and (d) Ru/SiO_2

Table 3. XPS data for the supported catalyst

Supported catalyst	**Binding energy (eV)**		
	C 1s	**Ru $3d_{5/2}$**	**Ru $3d_{3/2}$**
Ru/bentonite	284.8	282.0	-
Ru/TiO_2	284.8	281.0	283.3
Ru/SiO_2	284.8	281.5	283.4
Ru/Al_2O_3	284.8	281.7	283.5

Chemical state of the Ru element was investigated via narrow scan and the spectra are shown in Figure 2. Since the binding energy (B.E) of Ru $3d_{5/2}$ (≈ 280 eV) overlapped with that C 1s (≈ 284.5 eV), it was difficult to resolve the small Ru peak out from the large peak of C 1s. The Ru 3d spectra revealed the presence of two different chemical states on the surface (Ru^0 at 281.0 eV and Ru^{4+} at 283.3 eV) except Ru species on bentonite shows chemical state of Ru^0 species only. Previous study have found that B.E of ≈ 283.0 eV was assigned to RuO_2 which is corresponding to Ru^{4+} species.[9] Meanwhile according to [3] the B.E value of Ru^0 species was in the range 280- 281 eV.[9] The presence of Ru^{4+} species indicated the Ru exists as oxide form and this species might be form during calcinations process.

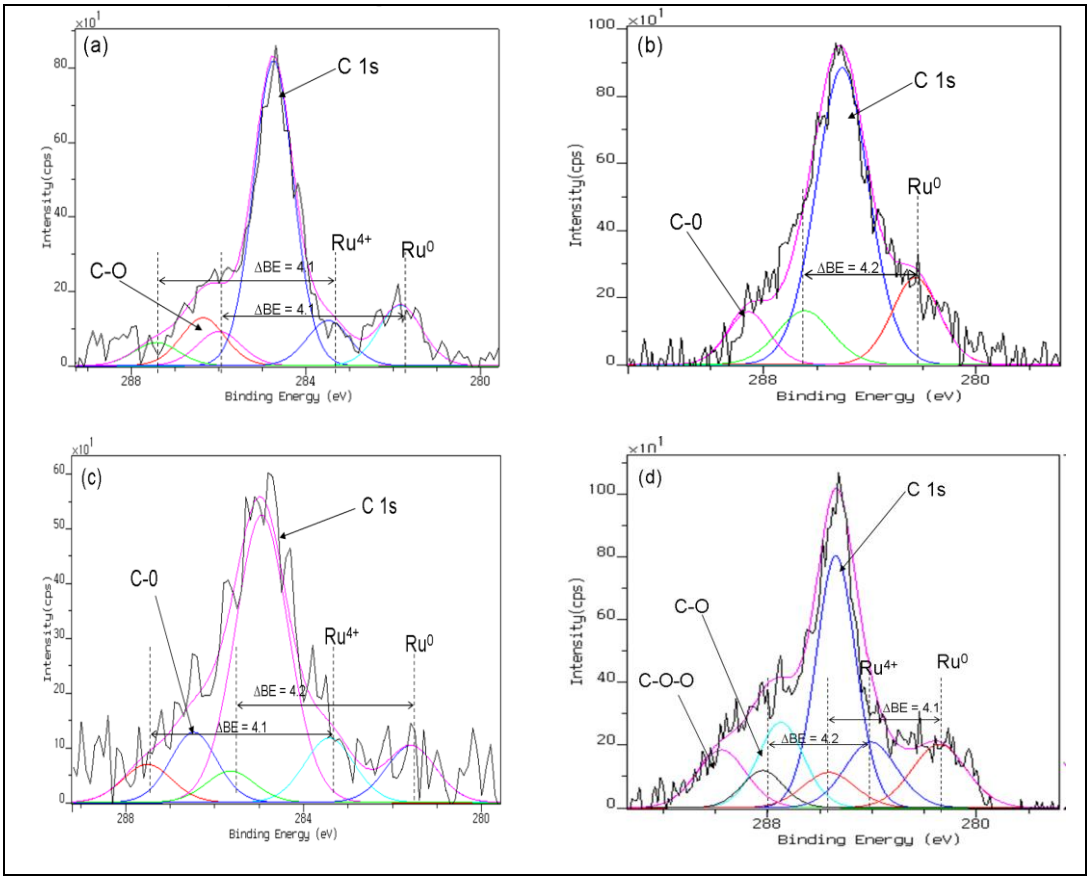


Figure 2. XPS narrow scan of Ru $3d_{5/2}$ for (a) Ru/Al_2O_3, (b) Ru/bentonite, (c) Ru/TiO_2 and (d) Ru/SiO_2

Figure 3 present the morphology of the catalyst analyze by TEM and the average size particle measured by TEM of Ru particle on bentonite, Al_2O_3, SiO_2 and TiO_2 obtained were ≈ 1.5 nm, < 2nm, ≈2 nm and 4-6 nm. This result indicate that particles size of Ru were much smaller on bentonite support than others support and activity of Ru/bentonite was expected was much higher than others catalyst in hydrogenolysis glycerol.

Glycerol hydrogenolysis reaction

The effect of support materials on catalytic of behavior of Ru catalyst for hydrogenolysis glycerol was investigated under mild reaction condition of 150 °C, 20 bar initial hydrogen pressure for 7 hours reaction time. The concentration of aqueous glycerol and catalyst loading used in this study are 20 %(wt) and 5 % respectively. The order of Ru catalyst activity was Ru/bentonite > Ru/Al_2O_3 ≈ Ru/TiO_2 > Ru/SiO_2. Figure 4 shows that Ru/bentonite catalyst was the most active catalyst which gave glycerol conversion reached 62.8 %. Good catalytic of Ru/bentonite is supported by TEM analysis since the average particle Ru/bentonite obtained was the smallest among the catalyst studied. Previous study reported that activity of Ru based catalyst was most active on smaller particle size of Ru.[2] Mapping analysis by FESEM showed that dispersion of Ru particle was also related to the catalytic activity of Ru catalyst. Ru/bentonite which is most active was relatively more dispersed on bentonite support compared to other support. This result indicates that bentonite which has basic property support gave high conversion compared to acidic support (SiO_2, Al_2O_3 and TiO_2). Interestingly, Ru/bentonite also gave high selectivity to 1,2-propanediol (80.1 %) compared to other catalysts which are support on TiO_2, SiO_2 and Al_2O_3.

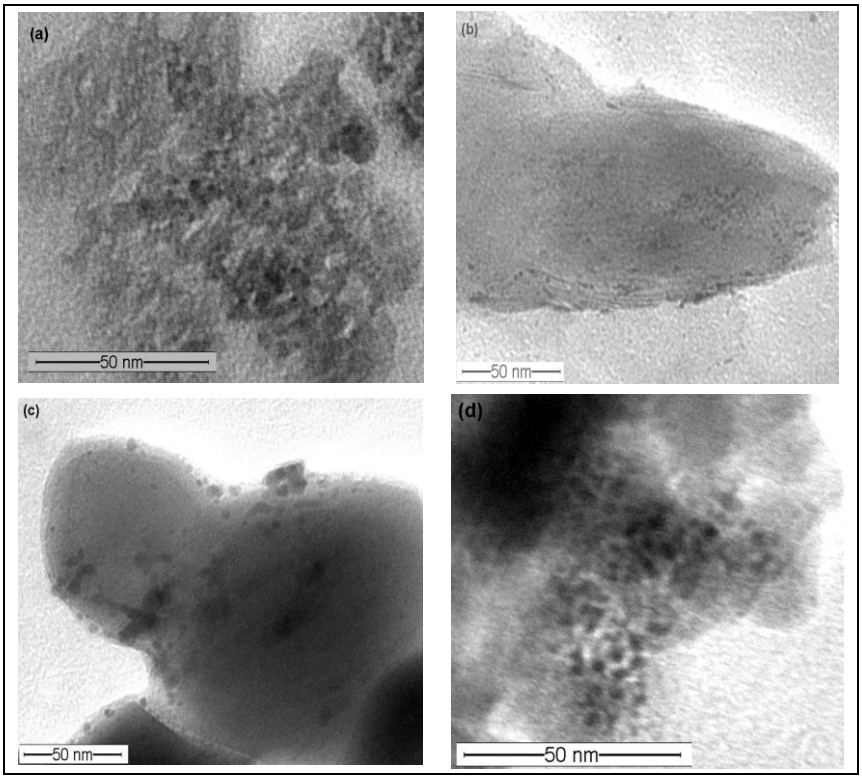


Figure 3. TEM image of (a) Ru/Al_2O_3, (b) Ru/Bentonite, (c) Ru/TiO, and (d) Ru/SiO_2

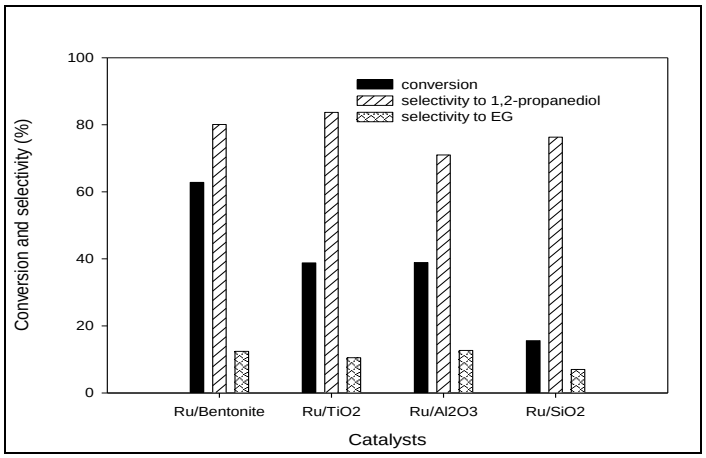


Figure 4. Hydrogenolysis glycerol over Ru-based catalyst at different support

Furthermore, XPS analysis showed that RuO_2 species was reduced to Ru^0 species completely on bentonite compared to other supports. This result indicates that Ru^0 species was the active species that contributes the best

performance of Ru/bentonite catalyst. Surface area of Ru/bentonite analyzed by BET shows moderate BET surface area (35.4 m^2/g) compared to Ru/SiO_2 (131.0 m^2/g) and Ru/Al_2O_3 (141.0). However this does not indicate that the catalyst is not good for hydrogenolysis reaction because BET surface area is not the only factor that contributes to good catalytic activity of the catalyst. Other factors such as types and shapes of pore need to be considered [9].

From the catalytic result, there is a correlation between the types of pores with the activity of the catalyst. The catalyst with Type H2 (non-uniformed cylindrical pore) gave pores which have good catalytic activity with 62.8% conversion. The other catalysts with Type H4 (non-uniformed slit shaped) gave only around 10-35% conversion. As such we can assume that cylindrical pore is an ideal pore shape for hydrogenolysis glycerol reaction. This is because the adsorption and desorption process can easy to takes place in cyclindrical pore during hydrogenolysis glycerol.

Conclusion

It was found that the nature of support material greatly influence the performance of the supported Ru catalyst. A bentonite suppored Ru catalyst (Ru/bentonite) exhibited the predominant activity and selectivity among the test catalyst and in a base-free aqueous solution under lower pressure. To best of our knowledge, Ru/bentonite system catalyst has not been reported yet for hydrogenolysis glycerol. Further study on the acidity and basicity of support has to be carried out.

Acknowledgement

The authors would like to acknowledge the Research Management Institute (RMI), Universtiti Teknologi MARA (UiTM) to finance the project under the FRGS Fund (FRGS/1/2014/STA01/UiTM/02/04).

References

1. Maris, E. P. and Davis, R. J. (2007). Hydrogenolysis of glycerol over carbon-supported Ru and Pt catalysts. *Journal of Catalysis*, 249(2): 328 - 337.
2. Bolado, S., Treviño, R. E., García-Cubero, M. T., and Benito, G. G. (2010). Glycerol hydrogenolysis to 1, 2 propanediol over Ru/C catalyst. *Catalysis Communications*, 12(2): 122 - 126.
3. Balaraju, M., Rekha, V., Prasad, P. S. S., Devi, B. L. A. P., Prasad R. B. N. and Lingaiah N. (2009). Influence of solid acids as co-catalysts on glycerol hydrogenolysis to propylene glycol over Ru/C catalysts. *Applied Catalysis A: General*, 354(1-2): 82 - 87.
4. Balaraju, M., Rekha, V., Sai Prasad P. S., Prasad R. B. N. and Lingaiah N. (2008). Selective hydrogenolysis of glycerol to 1, 2 propanediol over Cu–ZnO catalysts. *Catalysis Letters*, 126(1): 119 - 124.
5. Vasiliadou, E. S., Heracleous, E., Vasalos I. A., and Lemonidou A. A. (2009). Ru-based catalysts for glycerol hydrogenolysis - effect of support and metal precursor. *Applied Catalysis B: Environmental*, 92(1-2): 90-99.
6. Maris, E. P., Ketchie, W. C., Murayama M. and Davis R. J. (2007). Glycerol hydrogenolysis on carbon-supported Pt/Ru and Au/Ru bimetallic catalysts. *Journal of Catalysis*, 251(2): 281- 294.
7. Nakagawa, Y., Shinmi, Y., Koso S. and Tomishige K. (2010). Direct hydrogenolysis of glycerol into 1,3-propanediol over rhenium-modified iridium catalyst. *Journal of Catalysis*, 272(2):191 – 194
8. Huang, L., Zhu, Y., Zheng, H., Ding, G. and Yongwang, Li. (2009). Direct conversion of glycerol into 1,3-propanediol over $Cu\text{-}H_4SiW_{12}O_{40}/SiO_2$ in Vapor Phase. *Chemistry Letters*, 131(1):312 – 320.
9. Feng, J., Fu. H., Wang, J., Li, R., Chen, H. and Li, X. (2008). Hydrogenolysis of glycerol to glycols over ruthenium catalysts: Effect of support and catalyst reduction temperature. *Catalysis Communications*, 9(6): 1458 - 1464.
10. Zhou, Z., Li, X. Zeng, T., Hong, W., Cheng Z. and Yuan, W. (2010). Kinetics of Hydrogenolysis of Glycerol to Propylene Glycol over $Cu\text{-}ZnO\text{-}A_{l2}O_3$ Catalysts. *Chinese Journal of Chemical Engineering*, 18(3): 384 - 390.
11. Shinmi, Y., Koso, S., Kubota, T., Nakagawa. Y. and Tomishige, K. (2010). Modification of Rh/SiO_2 catalyst for the hydrogenolysis of glycerol in water. *Applied Catalysis B: Environmental*, 94(3-4): 318 - 326.
12. Miyazawa, T., Koso, S., Kunimori, K. and Tomishige, K. (2007). Glycerol hydrogenolysis to 1,2-propanediol catalyzed by a heat-resistant ion-exchange resin combined with Ru/C. *Applied Catalysis A: General*, 329: 30 – 35.
13. Jiang, T., Zhou, Y., Liang, S., Liu H. and Han B. (2009) Improved utilisation of renewable resources: New important derivatives of glycerol. *Green Chemistry*, 7: 1000 - 1006.

14. Yuan, Z. Wang, J., Wang, L., Xie, W., Chen, P., Hou Z. and Zheng. X., (2010). Biodiesel derived glycerol hydrogenolysis to 1,2-propanediol on Cu/MgO catalysts. *Bioresource Technology*, 101: 7088 – 7092.
15. Balaraju, M., Rekha, V., Devi, B. L. A. P., Prasad, R. B. N., Prasad P. S. S. and Lingaiah N. (2010). Surface and structural properties of titania-supported Ru catalysts for hydrogenolysis of glycerol. *Applied Catalysis A: General* 384: 107 - 114.

MALAYSIAN JOURNAL OF ANALYTICAL SCIENCES
Published by The Malaysian Analytical Sciences Society
ISSN 1394 - 2506

Moringa oleifera SEED DERIVATIVES AS POTENTIAL BIO-COAGULANT FOR MICROALGAE *Chlorella* Sp. HARVESTING

(Potensi Derivatif Biji *Moringa oleifera* sebagai Bio-Pengental untuk Penuaian Mikroalga *Chlorella* sp.)

Azizah Endut[1,2]*, Siti Hajar Abdul Hamid[1], Fathurrahman Lananan[1], Helena Khatoon[3]

[1]*East Coast Environmental Research Institute*
[2]*Faculty of Innovative Design and Technology*
Universiti Sultan Zainal Abidin, Gong Badak Campus, 21300 Kuala Terengganu, Terengganu, Malaysia
[3]*School of Fishery Science and Aquaculture,*
Unversiti Malaysia Terengganu, 21030 Kuala Terengganu, Terengganu, Malaysia

**Corresponding author: enazizah@unisza.edu.my*

Received: 14 April 2015; Accepted: 30 November 2015

Abstract

Microalgae is an economical and potential raw material of biomass energy, which offer a wide range of commercial potential to produce valuable substances for applications in aquaculture feed, pharmaceutical purposes and biofuels production. However, lack of an economical, efficient and convenient method to harvest microalgae is a bottleneck to boost their full-scale application. Hence, this study was performed to investigate the potentialities of *Moringa oleifera* seed derivatives as an environmentally bio-coagulant to harvest microalgae *Chlorella* sp. biomass from the water column, which acts as a binder to coagulate particulate impurities to form larger aggregates. Results shown *M. oleifera* to have better biomass recovery of 122.51% as compared to 37.08% of alum at similar dosages of 10 $mg \cdot L^{-1}$. In addition, it was found that the zeta potential values of mixed microalgae-coagulant suspension shows positive correlation on the flocculation parameters. For biomass recovery, the correlation for *M. oleifera* protein powder showed the R^2-value of 0.9565 whereas the control chemical flocculant, alum with the R^2-value of 0.7920. It was evidence that *M. oleifera* has a great potential in efficient and economical for environmentally microalgae harvesting and the adaptation of biological harvesting technology especially for the purpose of aquaculture feed in Malaysia.

Keywords: *Chlorella* sp., coagulation-flocculation, isoelectric point, *Moringa oleifera*, zeta potential

Abstrak

Mikroalga merupakan bahan mentah yang murah dan berpotensi untuk tenaga biojisim, yang menawarkan pelbagai peluang pengkomersialan untuk menghasilkan bahan bernilai untuk aplikasi dalam makanan akuakultur, farmaseutikal dan penghasilan bahan bakar bio. Walaubagaimanapun, kekurangan kaedah yang murah, cekap dan mudah untuk penuaian mikroalga merupakan halangan untuk meningkatkan aplikasi teknologi ini dalam skala yang lebih besar. Oleh itu, kajian ini telah dijalankan untuk menyiasat potensi derivatif biji *Moringa oleifera* sebagai bio-penggumpal biojisim mikroalga *Chlorella* sp., yang bertindak sebagai pengikat untuk menggumpalkan zarah enapcemar membentuk agregat yang lebih besar dari kolum air. Keputusan menunjukkan *M. oleifera* mempunyai pemulihan biojisim yang lebih baik iaitu 122.51% berbanding alum iaitu 37.08% pada dos yang sama sebanyak 10 $mg \cdot L^{-1}$. Di samping itu, nilai keupayaan zeta campuran mikroalga dan penggumpal menunjukkan kolerasi positif terhadap parameter penggumpalan. Dalam pemulihan biojisim, kolerasi bagi serbuk protein *M. oleifera* menunjukkan nilai R^2 iaitu 0.9565 manakala penggumpal kimia kawalan, alum mempunyai nilai R^2 iaitu 0.7920. Ini membuktikan bahawa *M. oleifera* mempunyai potensi tinggi untuk penuaian mikroalga yang berkecekapan tinggi dan murah serta penyesuaian teknologi penuaian biologi terutamanya untuk tujuan makanan akuakultur di Malaysia.

Kata kunci: *Chlorella* sp., koagulasi-flokulasi, titik isoelektrik, *Moringa oleifera*, keupayaan zeta

Introduction

The exploration of potential natural coagulant is crucial for sustainability in mass microalgae harvesting. Microalgae harvesting in mass cultivation industry consisting of two stage process involving bulk harvesting and thickening. Bulk harvesting was aimed at the separation of biomass from the bulk suspension using flocculation techniques whereas thickening concentrated the slurry through energy intensive techniques such as centrifugation and filtration [1]. Chemical coagulants normally applied in the bulk harvesting stage. Thus, microalgae harvesting in massive scale would require high amount of chemical flocculants, which is not sustainable for long-term green technology application. Natural coagulant could be investigated for the desired flocculation characteristics similar to chemical flocculants. Plant-based natural coagulant is more environmental friendly and not pose health risks as chemical flocculants such as aluminum and ferric salts. The use of inorganic coagulants such as ferric chloride, $FeCl_3$ and aluminum sulfate, $Al_2(SO_4)_3$ shortly known as alum is proven to be effective for some microalgae flocculation, however it is certainly unacceptable if the harvested biomass is to be used for aquaculture purposes, animal feed or organic fertilizer. It was reported that the major component of alum and acrylamide could lead to human health implications, such as involvement in Alzheimer's disease and the cause of cancers [2]. According to Zheng et al. [3], these flocculants are required in high doses, both are more than 0.75 $g \cdot L^{-1}$ for microalgae harvesting.

In Malaysia, *M. oleifera*, commonly known as *kacang merunggai* is available locally and inexpensive hence making them a viable alternative to chemical coagulant in water and wastewater treatment, which is also possible as bio-flocculants in the microalgae biomass separation process and harvesting [4]. Bio-coagulant from *M. oleifera* was reported to have a high flocculation potential in water treatment, attaining 92 – 97 % flocculation efficiency [5, 6]. Previous study also concluded that *M. oleifera* seeds as a strong candidate as a bio-flocculant for microalgae harvesting at optimal pH range [7]. *M. oleifera* seed active compounds are known as the peptides of molecular weight ranging from 6 to 20 kDa, with an isoelectric pH value between 9 to 10 [6, 8].

Dispersion of microalgae cells in the water column leads to the difference of surface charges between microalgae biomass suspension and chemical ions of the cultivation media. According to Chen et al. [9], the proper reaction mechanisms existing at the colloid surfaces are differential loss ions from the crystal lattice because of the rupture of ionic or covalent bond, adsorption of charged species from the surrounding solution and ionization of chemical groups on the surface. The suspending microalgae cells in the water carried charge, which result in the generation of the electrical-double-layer. In solution, the presence of a net charge on a particle affects the distribution of ions surrounding it, resulting in an increase in the concentration of counter-ions. This region over which this influence extends was referred as electrical-double-layer. Conventionally, this layer is thought of as existing as two separate regions, which are inner region and outer layer. An inner region consists of strongly bound ions to the particle known as stern layer while the outer layer called diffuse layer associated with counter-ions. In the electrophoresis, an electric field is applied to a dispersion of particle, sometimes liquid droplets or even gas bubbles which gives rise to a motion of the charged particles with respect to the bulk liquid [10]. As the particle moves through solution, due to gravity or an applied voltage, the ions move with it. At some distance from the particle there exists a boundary, beyond which ions do not move with the particle. This is known as the surface of hydrodynamic shear, or the slipping plane which exists somewhere within the diffuse layer. During this phenomenon, the potential which is zeta potential do exists at the slipping plane.

The measurements of zeta potential is crucial in determining the stability of a colloidal suspension. Normally in a colloidal system, the dispersion are stable in which particles do not aggregate. The aggregation of particles in suspension depends on the magnitude of the zeta potential. In many instances stable dispersion are required. In other cases, such as water and wastewater treatment, paper manufacturing and oil recovery, unstable dispersion are desired. Stable or unstable dispersion could be produced in a variety of ways, which are by changing the pH of dispersion, addition of electrolyte and addition of coagulant. Generally, zeta potential study was correlated with coagulation-flocculation process. By measuring zeta potential, the isoelectric point (i.e.p.) in a colloidal system could be determined. Isoelectric point is very important from a practical consideration which normally indicated the least stable point in a colloidal system. At this point, the potential energy barrier opposing coagulation disappears,

and it is called the critical coagulation concentration [11]. Effective coagulation process could be performed in order to remove or recover the colloids from its suspended system.

The nature of suspended microalgae and surface charge could make the solid-liquid separation more difficult. However, the determination of zeta potential could lead to the understanding of isoelectric point of a colloidal system and eased explanation of the mechanism and interfacial phenomena occurring during coagulation-flocculation process of microalgae under various coagulants. The aim of this study was to explore the potential use of *M. oleifera* as a novel low cost bio-coagulant for microalgae *Chlorella* sp. harvesting. The interaction of the zeta potential of commercial coagulant which are alum, natural *M. oleifera* seed powder and *M. oleifera* protein powder in harvesting locally isolated freshwater microalgae, *Chlorella* sp. were investigated. The correlation of zeta potential and flocculation ability was explored to explain the interaction between coagulants and microalgae cells in suspended. Selected conditions for coagulation-flocculation were presented, as well as removal and microalgae biomass recovery percentage for different dosage at optimum pH. In this study, the experimental strategy was focused on coagulation-flocculation process corresponding to the profiles of zeta potential with respect to pH for different coagulants used such as alum, *M. oleifera* seed powder and *M. oleifera* protein powder.

Materials and Methods

Study area

Microalgae maintenance and flocculation assays were carried out at the Institute of Tropical Aquaculture, Universiti Malaysia Terengganu, Terengganu. The determination of zeta potential of microalgae suspension and *M. oleifera* seed derivatives were performed at the Civil Engineering Lab, Department of Civil Engineering, Universiti Putra Malaysia, Selangor.

Preparation of alum stock solution

Stock solution of aluminum sulfate (10 $mg \cdot L^{-1}$ Al^{3+}) supplied by Sigma Aldrich was prepared by dissolving 1 g of dry solid in 99 mL of deionized water. The alum powder was totally soluble in the water. A fresh solution was prepared every day for reliable results. In this study, the zeta potential of alum was compared with natural coagulants of *M. oleifera* seed powder and protein powder in harvesting freshwater microalgae, *Chlorella* sp..

Cultivation of freshwater microalgae, *Chlorella* sp.

The inoculum of pure culture of freshwater microalgae, *Chlorella* sp. was obtained from the microalgae culture collections of the Live Feed Culture Lab, Institute of Tropical Aquaculture, Universiti Malaysia Terengganu, Malaysia. *Chlorella* sp. was cultivated in Bold's Basal Medium (BBM) with controlled temperature of 25 ± 2 °C and 24 h illumination at 3350 lumen until late exponential phase in which cell density reached averagely 2.0×10^7 $cells \cdot mL^{-1}$.

Spectrophotometric analysis of *Chlorella* sp. biomass

The *Chlorella* sp. biomass were measured using spectrophotometric colorimetric method to facilitate rapid measurement. Spectrum analysis was performed to determine the peak absorption wavelength for the spectrophotometric colorimetric technique which was at 686 nm. For the establishment of standard calibration curve, *Chlorella* sp. biomass was measured using haemocytometer (Marienfield Neubauer-improved 0.1 mm depth, Germany) and syringe liquid sampler particle system (PMS SLS-2000, USA).

Preparation of *M. oleifera* seed powder

M. oleifera seeds were obtained within the region of Kuala Terengganu, Malaysia. The plant were authenticated by the Faculty of Bioresources and Food Industry, Universiti Sultan Zainal Abidin (UniSZA) Tembila, Terengganu, Malaysia. The plant was deposited at the university herbarium. The collected dry pods were unshelled to obtain the seeds. Pods shells were removed manually and only qualified contaminant-free seeds were selected to be used as coagulant. Then, the seeds consisted of cupule, seed coat and seed kernel were grounded using laboratory mill and sieved through 600 µm stainless steel sieve to obtain homogenous fine powders from each seed structure.

Purification of *M. oleifera* seed protein

The procedures for the purification of *M. oleifera* coagulation polymer were carried out based on Kwaambwa, and Maikokera method [12]. Dried de-oiled *M. oleifera* powder was used for the extraction of coagulant protein polymer. The extraction was performed by adding 3% (w/v) NaCl solution and this suspension was continuously agitated for 12 h in orbital shaker at controlled temperature of 25 ± 2 °C. The extract was filtered with Whatman filter No.44 and further heated in such a way that no white precipitation is formed at the bottom of solution. The heated crude protein extract solution was then poured into the dialysis tube and submerged completely for 12 h with constant temperature of 2 ± 2 °C. After completion of the dialysis procedure, the salt present in the crude brown protein was osmotically extracted into the surrounding water solution leaving white protein extract inside the dialysis tube. Then, the protein was dried at room temperature to form fine protein powder.

Coagulation-flocculation and sedimentation experiments

Coagulants tested in this study included alum, *M. oleifera* seed powder and *M. oleifera* protein powder. Coagulation-flocculation and sedimentation experiments were performed in glass beakers 0.12 m height by 0.09 m diameter (h/D = 1.33) using a 250 mL microalgae volume. Flocculants, previously dissolved in water at concentration 10 $mg \cdot L^{-1}$ were added to the microalgae sample under intense stirring at 150 rpm for 3 minutes to ensure complete solubility of the flocculants. Following that, the stirring was reduced to gentle agitation at 20 rpm for 20 minutes, so as to initiate flocs formation. After that, the suspension was leaved for sedimentation in 20 minutes. When interphases appear, it was clear and 3 mL sample was taken at the top (clear supernatant) for removal efficiency and 3 mL from bottom (saturated *Chlorella* sp. biomass) for biomass recovery. The absorbance of the sample were measured using UV-vis spectrophotometer (Shimadzu UV-1800, Japan). All experiments were carried out in triplicates. Percentage of biomass removal was calculated from the absorbance ratio at clarified zone against the culture absorbance at the beginning of the experiment according to Equation 1:

$$Biomass\ removal\ (\%) = \frac{Abs_{668}\ initial\ culture - Abs_{668}\ clarified\ zone}{Abs_{668}\ initial\ culture} \times 100 \quad (1)$$

Measurements of zeta potential

Methods of measuring zeta potential on a particles dependent both which are the particle and the suspension formulation. In general, the size and concentration of particles are the key parameters that determine which technique is applicable. In this study, zeta potential was measured based on the dispersion concentration of each coagulants which are alum, *M. oleifera* seed powder and *M. oleifera* protein powder in water at room temperature. Zeta potential was not measured directly. Perhaps the most widely used technique for measuring zeta potentials in electrophoresis. By applying an electric field across the sample, charged particles were induced to move. The velocity of particles known as electrophoretic mobility (EM). The electrophoresis measurements were carried out by injecting 25 mL of the aqueous dispersions of each coagulants into the cell of zeta potential instrument (Zeta-Meter System 3.0+, USA) at room temperature. The electrophoresis cell holds the sample for viewing under the microscope. It consists of two electrode chambers connected by an optically polished electrophoresis tube which is 10 cm long and 4 mm in diameter. Zeta potential measurements also was performed on suspending freshwater microalgae, *Chlorella* sp. culture before and after the addition of coagulants in order to investigate the effects of coagulants on its isoelectric point. By directly measuring the electrophoretic mobility of particle in dispersion, the zeta potential was determined using Henry's Equation 2 [13]:

$$\mu = \frac{2\varepsilon_0 \varepsilon_r \zeta f(\kappa r)}{3\eta} \quad (2)$$

where,

μ = electrophoretic mobility
ε_0 = permittivity of a vacuum
ε_r = medium dielectric constant (or permittivity)
ζ = zeta potential
κ = *Debye-Hückle* parameter
r = hydrodynamic radius of particle
η = viscosity of medium
$f(\kappa r)$ = Henry's function

The Henry's function generally has value either 1.5 or 1.0. For the measurements of zeta potential in aqueous solutions of moderate electrolyte concentration, a value of 1.5 is used. In this study, zeta potential was calculated according to the Henry's equation, applying Smoluchowski approximation [14].

Statistical analysis

Zeta potential of *Chlorella* sp., alum, *M. oleifera* seed powder and *M. oleifera* protein powder with respect to pH were recorded in Microsoft Office Excel™ throughout the experimental period. Graphical analyses were performed using Originlab OriginPro 8.6™ whereas the statistical determination involving One-Way ANOVA and post-hoc analysis utilizing Tukey's HSD Test were implemented via Minitab 16™. A confidence level of 95% ($\alpha = 0.05$) was selected in order to strictly determine the significance of between the dosages and types of coagulant used with the dependent parameters on microalgae biomass recovery.

Results and Discussion

Zeta potential analysis

Figure 1 shows the zeta potential values of freshwater microalgae, *Chlorella* sp. biomass and *M. oleifera* seed derivatives suspension in the range of pH 2 to pH 12. Both *M. oleifera* seed powder and *M. oleifera* protein powder zeta potential values decreases from 45.68 and 28.51 mV at pH 2 to the zeta potential values of -38.59 and -15.93 mV at pH 11, respectively. Control coagulant, alum also had decreased zeta potential value as pH increased from pH 2 to pH 12 with the value of 59.64 to -38.40 mV. In addition, *Chlorella* sp. biomass exhibited moderate decrease of the zeta potential value from -24.15 to -49.99 mV at pH 2 to pH 11. As shown in Table 1, *Chlorella* sp., alum and *M. oleifera* protein powder had significant regression with the Boltzmann Sigmoidal Model with the R^2-values of 0.9512, 0.9965 and 0.9549, respectively. Zeta potential values of *Chlorella* sp. and coagulants at various pH fitted with the model were shown in Figure 2.

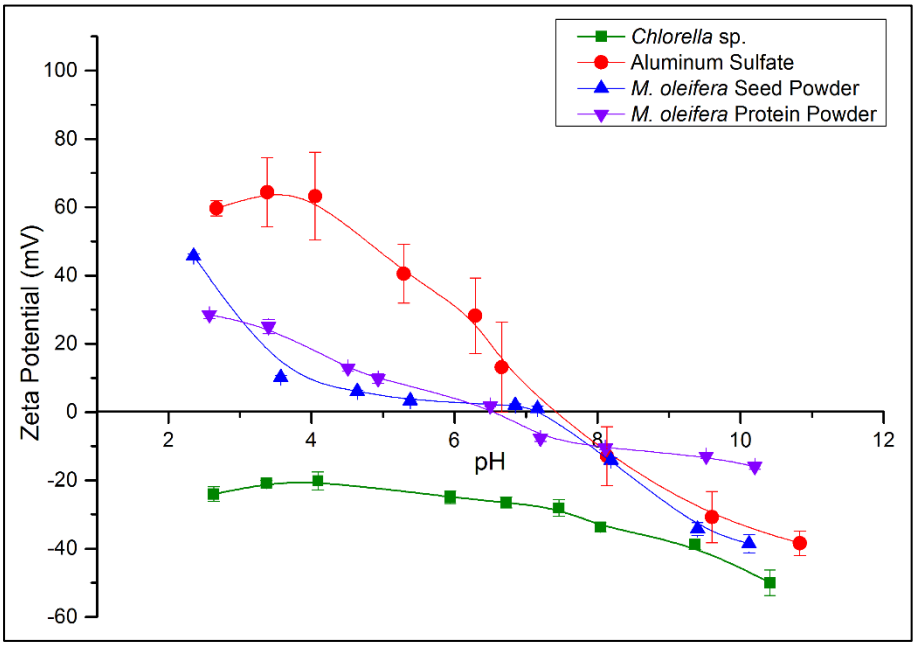


Figure 1. Spline curves of zeta potential values of *Chlorella* sp., aluminum sulfate, *M. oleifera* seed powder and *M. oleifera* protein powder at various pH.

Table 1. Boltzmann sigmoidal parameters of zeta potential at various pH for microalgae, *Chlorella* sp. and several coagulant suspensions

Suspension	Reduced Chi-Square	Adjusted R-Square	Boltzmann Sigmoidal Fit			
			Initial Value, A_1	Final Value, A_2	Centre, X_0	pH Constant, dx
Chlorella sp.	1.1477	0.9512	-19.7754 ± 2.6250	-83.0073 ± 110.0826	10.8864 ± 6.1201	2.0215 ± 1.4815
Aluminum Sulfate	0.1779	0.9965	62.6897 ± 2.2368	-41.5764 ± 3.4869	6.9651 ± 0.1999	1.1466 ± 0.2026
M. oleifera Seed Powder	112.9585	0.6962	411055.3 ± 1.2849 x 10^{10}	-1.7475 ± 7.0051	-8.5312 ± 37406.3888	1.1958 ± 2.5013
M. oleifera Protein Powder	8.8414	0.9549	32.8811 ± 11.2681	-18.9550 ± 5.3989	5.7435 ± 0.6186	1.6050 ± 0.6980

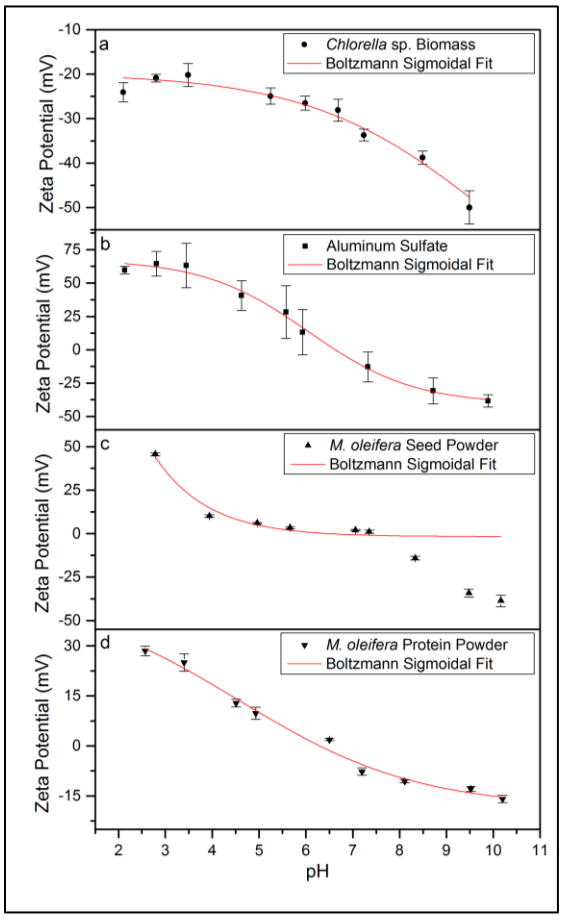


Figure 2. Zeta potential values of *Chlorella* sp. (a), aluminum sulfate (b), *M. oleifera* seed powder (c) and *M. oleifera* protein powder (d) at various pH fitted with Boltzmann Sigmoidal Model.

Through the model fittings, it was found that the initial zeta potential values were respectively -19.78, 62.69 and 32.88 mV for *Chlorella* sp., alum and *M. oleifera* protein powder. Whereas, the predicted final zeta potential values were respectively -83.01, -41.58 and -18.96 mV. The zeta potential of *M. oleifera* seed powder however could not be fitted with the sigmoidal model which yield R^2-value of 0.6962. In order to harvest the *Chlorella* sp. biomass, the coagulants were mixed at various coagulant dosages with the microalgae biomass undergoing flocculation assay and also yielded the mixed suspension zeta potential values and flocculation performance which were removal efficiency and biomass recovery, which were shown in Figure 3 and Figure 4, respectively.

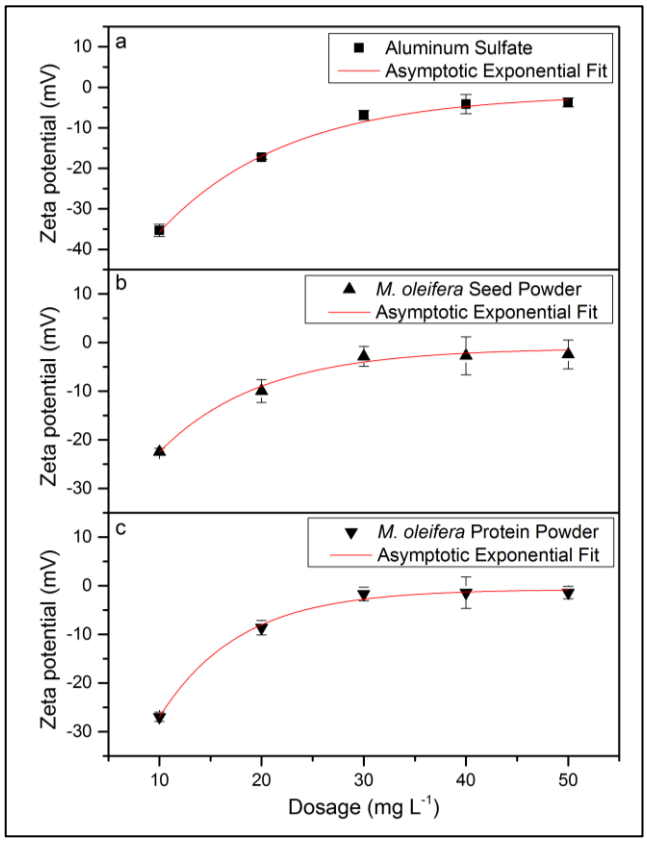


Figure 3. Zeta potential values of *Chlorella* sp. suspension mixed with aluminum sulfate (a), *M. oleifera* seed powder (b), *M. oleifera* protein powder (c) at various coagulant dosages fitted with Asymptotic Exponential Model.

The observed zeta potential values were further analyzed through fitting with the Asymptotic Exponential Model to optimize the coagulant dosage. It was found that the mixed suspension of *Chlorella* sp. with *M. oleifera* protein powder yield the highest i.e.p. of -0.74 mV as compared to -1.13 and -1.62 mV respectively for *M. oleifera* seed powder and alum at the dosage of 50 mg·L^{-1}. Higher i.e.p. values of *M. oleifera* seed protein suggested that it would have better flocculation rate as compared to *M. oleifera* seed powder and alum. In addition, *M. oleifera* protein powder also had the highest response range of 94.50 mV whereas *M. oleifera* seed powder had the lowest zeta potential response range of 58.23 mV as dosage increased from 0 mg·L^{-1} to 50 mg·L^{-1}. Aluminum sulfate showed the highest rate of 0.92 mV per mg·L^{-1} increase of coagulant followed by *M. oleifera* seed powder and seed protein, respectively 0.90 and 0.88 mV per mg·L^{-1}. This value shows that the ζ-potential value of *Chlorella* sp. was highly correlated to the dosage of coagulant used. The addition of dosage cause the value of ζ-potential increase. The

increasing of ζ-potential value indicate the disturbance on the stability of microalgal cells suspension. This is due to the charge neutralization of negatively charged cells with the addition of positively charged coagulants. Same trend was also observed by Muyibi et al. [15] which stated that the gradual decreased in biomass recovery was due to over dosage that led to restabilization of the destabilized suspended solids which previously had agglomerated into flocs.

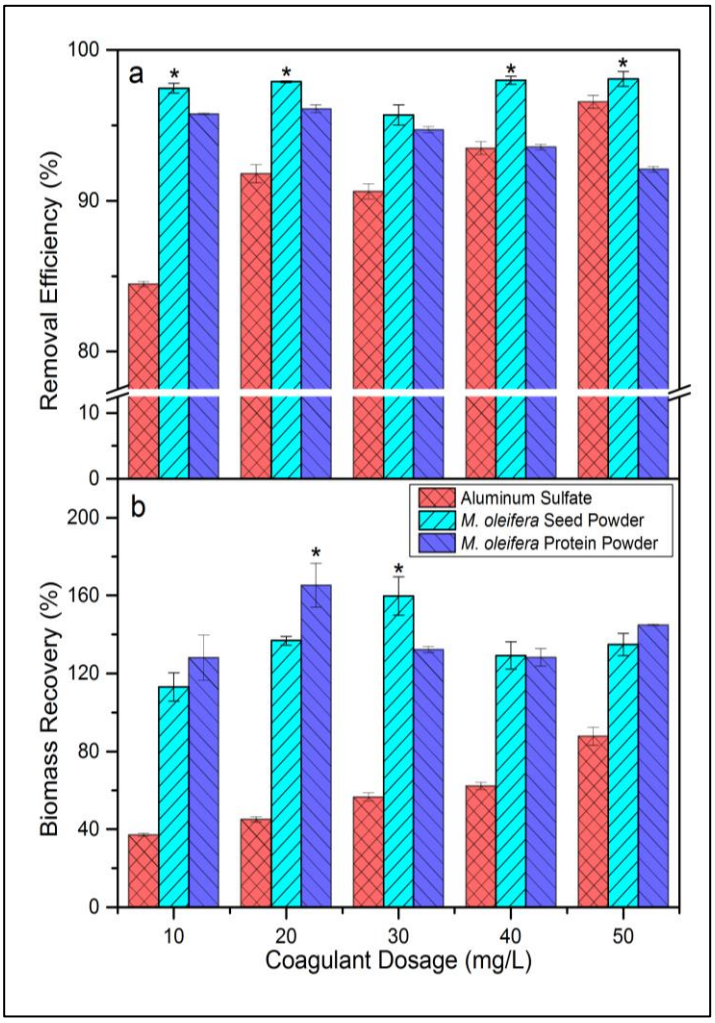


Figure 4. Removal efficiency (a) and biomass recovery (b) of aluminum sulfate, *M. oleifera* seed powder and *M. oleifera* protein powder at various coagulant dosages. Treatment with the significantly highest values was marked with asterisk (*).

Flocculation assays

Flocculation performance of coagulant consisted of removal efficiency and biomass recovery. Removal efficiency is the effectiveness of coagulant in removing the suspended particles from the water column producing a clear supernatant. Meanwhile, biomass recovery is its proficiency in aggregating, settling and compacting the suspended particles at the bottom of the jar test vessel. Figure 4 showed the removal efficiency and biomass recovery of alum, *M. oleifera* seed powder and *M. oleifera* seed derivatives with regards to various coagulant dosage of 10 to 50 $mg \cdot L^{-1}$. *M. oleifera* seed powder achieved significantly highest ($P<0.05$) removal efficiency of above 97% at coagulant dosage of 10, 20, 30, 40 and 50 $mg \cdot L^{-1}$ as compared to other coagulants. The removal efficiency of alum

increased as dosage were increased but *M. oleifera* protein powder showed opposite trend. It could be observed that the maximum removal efficiency for *M. oleifera* protein powder was 96.09% at dosage of 20 $mg \cdot L^{-1}$ and decreased to 92.08% as the dosage increased to 50 $mg \cdot L^{-1}$. *M. oleifera* seed powder however showed consistent removal efficiency among various dosages. All coagulants showed increased biomass recovery as the dosage was increased up to 50 $mg \cdot L^{-1}$. *M. oleifera* protein powder had the significantly highest biomass recovery of 207.46% as compared to other coagulants. *M. oleifera* seed powder, however only showed increased biomass recovery at the dosage of 10 to 30 $mg \cdot L^{-1}$ with the maximum percentage of 159.78%. At the dosage of 40 $mg \cdot L^{-1}$, the biomass recovery decreased at 30.48%. This negative relationship could be explained by the continuous addition of coagulant exceeding the optimum dosage which leads to the formation of excess coagulant residue since all of the available suspended microalgae already formed larger colloids [6].

Table 2 shows the coefficients for Asymptotic Exponential Model with the R^2-value of 1.4443, 0.3026 and 0.4537 for *Chlorella* sp. suspension with aluminum sulfate, *M. oleifera* seed powder and *M. oleifera* protein powder, respectively. In addition, the output of the flocculation assays showed the ability of *M. oleifera* seed extracts not only in harvesting but also concentrate the recovered *Chlorella* sp. biomass for up to 159.78% and 207.46%, respectively for *M. oleifera* seed powder and *M. oleifera* protein powder. The performance of *M. oleifera* seed powder was confirmed by Teixeira et al. [4] which reported its performance in harvesting marine microalgae from cultivation medium with the removal efficiency of more than 90%. Nevertheless, other research involving the investigation on *M. oleifera* protein powder was still lacking.

Table 2. Asymptotic exponential parameters of zeta potential at various pH for mixed suspension of microalgae, *Chlorella* sp. with coagulants.

Microalgae + Coagulants	**Reduced Chi-Square**	**Adjusted R-Square**	**Asymptotic Exponential Fit**		
			Asymptote, a	**Response Range, b**	**Rate, c**
Chlorella sp. + Aluminum Sulfate	1.4443	0.9844	-1.6233 ± 1.7103	75.8976 ± 8.6003	0.9232 ± 0.0096
Chlorella sp. + *M. oleifera* Seed Powder	0.3026	0.9919	-1.1332 ± 1.6076	58.2269 ± 10.3332	0.9046 ± 0.0212
Chlorella sp. + *M. oleifera* Protein Powder	0.4537	0.9952	-0.7401 ± 0.8427	94.5035 ± 14.6837	0.8799 ± 0.0151

Correlation of zeta potential values and flocculation performance

Prior to the correlation analysis, the zeta potential values of mixed suspension of *Chlorella* sp. and coagulants were fitted with the Asymptotic Exponential Model yielding the i.e.p. value (asymptote), zeta potential response range and rate of zeta potential change regarding dosage. Figure 5 shown the correlation of zeta potential and biomass recovery. *M. oleifera* protein powder showed the highest correlation between the zeta potential values and mean biomass recovery with the R^2 value of 0.9565. This was followed by alum and *M. oleifera* seed powder with R^2-value of 0.7920 and 0.7059, respectively. For alum, biomass recovery decreased beyond the dosage of 30 $mg \cdot L^{-1}$ which was inconsistent with the measured zeta potential. Same trend was also observed by Muyibi et al. [5], which stated that the gradual decreased in biomass recovery was due to over dosage that led to restabilization of the destabilized suspended solids which previously had agglomerated into flocs.

Correlation of zeta potential values and flocculation performance involved the use of zeta meter and only jar tests in which only coagulation/flocculation and settling processes were employed. It is therefore recommended that investigations be carried out through pilot plant studies which involves continuous biomass harvesting and various unit operations and processes employed for mass microalgae cultivation. Some studies reported that flocculation of microalgae can occur spontaneously without the need for chemicals, referred to as autoflocculation which can be

induced by increasing the medium pH [16]. According to Harith et al. [17], harvesting efficiency of *Chaetoceros calcitrans* of higher than 90% was achieved by adjusting the culture pH to 10.2 using either NaOH or KOH. The alteration of pH of the culture medium lead to the changes in the zeta potential and hence reduce the colloidal stability. In this study, the addition of coagulant dosage reduce the zeta potential of the microalgae colloidal and increased the biomass recovery percentage. On the other hand, the usage of non-toxic organic polymer, such as polyacrylamide copolymers, chitosan, and cationic starch have been intensively investigated for large-scale applications [18,19]. Unfortunately, they are not economical for microalgae due to its higher price. The coagulant residuals in both algal biomass and harvested water are not only negative for downstream processing but also reduce the possibilities for culture medium recycling.

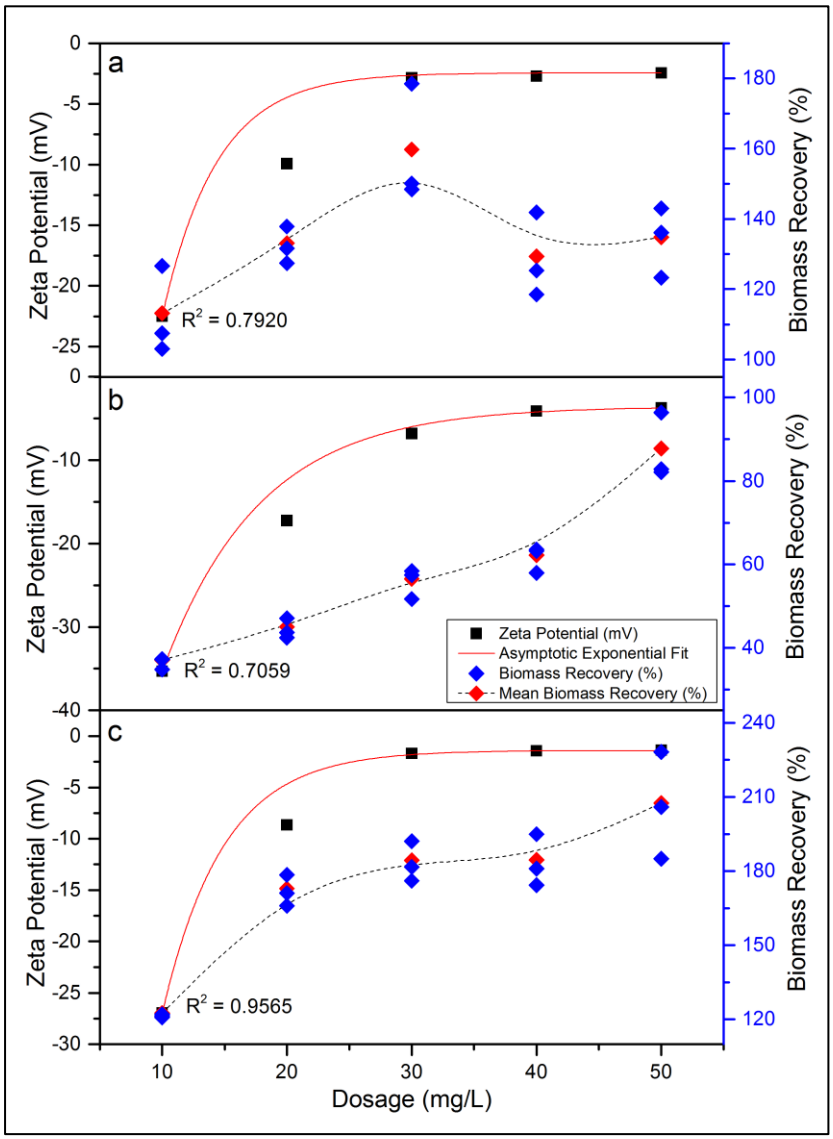


Figure 5. Correlation curves between zeta potential values and biomass recovery of aluminum sulfate (a), *M. oleifera* seed powder (b) and *M. oleifera* protein powder (c).

Conclusion

In addition to the traditional practice of conventional water treatment, *M. oleifera* seed and protein powder as bio-flocculant was proven to be a highly potential alternative to the chemical flocculant in harvesting microalgae *Chlorella* sp. biomass from the culture medium. Indeed, both *M. oleifera* seed derivatives had a higher removal efficiency and biomass recovery as compared to alum even at low dosage. *M. oleifera* seed derivatives were also found to concentrate the density of harvested microalgae to about twofold the initial density. It was also found that the application of the zeta potential determination to predict the flocculation performance of coagulant was probable since both value was highly correlated. Further investigation on the interaction of the zeta potential of *M. oleifera* seed derivatives on the flocculation of different microalgae species is highly recommended. The use of *M. oleifera* seed derivatives as bio-flocculant could assist in lowering the economic cost and providing environmentally-friendly approach for mass microalgae cultivation and the sustainable development of bio-based renewable energy in the future.

Acknowledgement

The authors would like to thank the Ministry of Education of Malaysia for financially support this research under the Fundamental Research Grant Scheme (FRGS), project no. FRGS/1/2014/STWN01/UNISZA/02/2.

References

1. Brennan, L. and P. Owende. (2010). Biofuels from microalgae - A review of technologies for production, processing, and extractions of biofuels and co-products. *Renewable and Sustainable Energy Reviews*, 14(2). 557 – 577.
2. Ahmad, A. L., Yasin, N. M., Derek, C. J. C. and Lim, J. K. (2011). Optimization of Microalgae Coagulation Process using Chitosan. *Chemical Engineering Journal*, 173(3): 879 – 882.
3. Zheng, H. Gao, Z. Yin, J. Tang, X. Ji, X. and Huang, H. (2012). Harvesting of Microalgae by Flocculation with Poly (γ-glutamic acid*). Bioresource Technology*. 112. 212 – 220.
4. Teixeira, C. M. L. L., Kirsten, F. V. and Teixeira, P. C. N. (2012). Evaluation of Moringa oleifera seed flour as a flocculating agent for potential biodiesel producer microalgae. *Journal of Applied Phycology*. 24(3). 557 – 563.
5. Muyibi, S. A. and Evison, L. M. (1995). Moringa Oleifera Seeds for Softening Hardwater. *Water Research*. 29(4): 1099 – 1104.
6. Ndabigengesere, A. and Narasiah, K. S. (1998). Quality of Water Treated by Coagulation using Moringa Oleifera Seeds. *Water Research*. 32(3). 781 – 791.
7. Bilanovic, D., Andargatchew, A., Kroeger, T. and Shelef, G. (2009). Freshwater and Marine Microalgae Sequestering Of CO_2 At Different C And N Concentrations – Response Surface Methodology Analysis. *Energy Conversion and Management*. 50(2). 262 – 267.
8. De Godos, I., Mendoza, J. L., Acién, F. G., Molina, E., Banks, C. J., Heaven, S. and Rogalla, F. (2014). Evaluation of Carbon Dioxide Mass Transfer in Raceway Reactors for Microalgae Culture using Flue Gases. *Bioresource Technology*, 153: 307 – 314.
9. Chen, L., Zhang, G., Wang, L., Wu, W. and Ge, J. (2014). Zeta Potential of Limestone in A Large Range of Salinity. *Colloids and Surfaces A: Physicochemical and Engineering Aspects*, 450: 1 – 8.
10. Moncho, A., F. Martínez-López and Hidalgo-Álvarez, R. (2001). Comparative Study of Theories of Conversion of Electrophoretic Mobility into ζ-potential. *Colloids and Surfaces A: Physicochemical and Engineering Aspects*. 192(1–3). 215 – 226.
11. Ofir, E., Oren, Y. and Adin, A. (2001). Electroflocculation: The Effect of Zeta-potential on Particle Size. *Desalination,* 204(1–3): 33 – 38.
12. Kwaambwa, H. and Maikokera, R. (2007). A Fluorescence Spectroscopic Study of A Coagulating Protein Extracted from Moringa Oleifera Seeds. *Colloids and surfaces B: Biointerfaces*. 60(2): 213 – 220.
13. Hunter, R. J. (2001). Measuring Zeta Potential In Concentrated Industrial Slurries. *Colloids and Surfaces A: Physicochemical and Engineering Aspects*. 195(1–3): 205 – 214.
14. Smoluchowski, M. (1967). Investigation into A Mathematical Theory of the Kinetics of Coagulation of Colloidal Solutions. Physical Chemistry 92:129 – 168.

15. Muyibi, S. A., Abas, S. A. A., Megat Johari, M. M., and Ahmadun, N. F. R. (2003). Enhanced Coagulation Efficiency of Moringa Oleifera Seeds through Selective Oil Extraction. *IIUM Engineering Journal*, 4(1): 1 – 11.
16. Beuckels, A., Depraetere, O., Vandamme, D., Foubert, I., Smolders, E. and Muylaert, K. (2013). Influence of organic matter on flocculation of Chlorella vulgaris by calcium phosphate precipitation. *Biomass and Bioenergy*, 54: 107 – 114.
17. Harith, Z. T., Yusoff, F. M., Mohamed, M. S., Shariff, M., Din, M. and Ariff, A. B. (2009). Effect of different flocculants on the flocculation performance of flocculation performance of microalgae, Chaetoceros calcitrans, cells. *African Journal of Biotechnology*, 8(21): 5971 – 5978.
18. Oh, H. M., Lee, S. J., Park, M. H., Kim, H. S., Kim, H. C., Yoon, J. H., Kwon, G. S and Yoon, B. D. (2001). Harvesting of Chlorella vulgaris using a bioflocculant from Paenibacillus sp. AM49. *Biotechnology Letters*, 23(15): 1229 – 1234.
19. Vandamme, D., Foubert, I., Meesschaert, B. and Muylaert, K. (2010). Flocculation of microalgae using cationic starch. *Journal of Applied Phycology*, 22(4): 525 – 530.

MALAYSIAN JOURNAL OF ANALYTICAL SCIENCES
Published by The Malaysian Analytical Sciences Society
ISSN 1394 - 2506

CHEMICAL AND BIOLOGICAL ANALYSES OF MALAYSIAN STINGLESS BEE PROPOLIS EXTRACTS

(Analysis Kimia dan Biologi Ekstrak Propolis Lebah Kelulut Malaysia)

Nurhamizah Ibrahim[1]*, Nurul Farah Shakila Mohd Niza[1], Muhammad Muslim Mohd Rodi[2], Abdul Jamil Zakaria[2], Zhari Ismail[3], Khamsah Suryati Mohd[1,2]

[1]*School of Agriculture and Biotechnology, Faculty of Bioresources and Food Industry*
[2]*Agriculture Production and Food Innovation Research Institute (AGROPOLIS UniSZA)*
Universiti Sultan Zainal Abidin, Tembila Campus, 22200 Besut, Terengganu, Malaysia
[3]*School of Pharmaceutical Sciences,*
Universiti Sains Malaysia, 11800 Penang, Malaysia

**Corresponding author: caldinamiez@gmail.com*

Received: 14 April 2015; Accepted: 30 November 2015

Abstract

The aim of this study is to evaluate chemical and biological profile of methanol extracts from Malaysian propolis produced by two commonly found stingless bee species, *Heterotrigona itama* (MHI) and *Geniotrigona thoracica* (MGT). Test samples were analyzed for physicochemical parameters such as moisture, fat, crude fibre, crude protein, carbohydrate and ash content. Tests for phytochemical screening by thin layer chromatography of both extracts revealed that presence of terpenoids, flavonoids, phenols and essential oils but steroids, saponin and coumarins only occur in MHI. Both extracts displayed a characteristic profile and vary from each other. Accordingly, MHI possess higher antioxidant activity with an IC_{50} of 15.0 ± 0.21 ug/mL compared to MGT with IC_{50} of 270.0 ± 0.19 ug/mL. MHI showed moderate nitric oxide scavenging activity, while MGT only showed mild inhibition. Antidiabetic activity was determined by α-glucosidase inhibition and found significantly better than that of acarbose (positive control). In conclusion, data gathered in this study revealed that bee species play role in determining the chemical and biological profile of particular propolis and should put into account in decision of further development for propolis.

Keywords: physico-chemical, phytochemical, TLC profiling, antioxidant, antidiabetic

Abstrak

Tujuan kajian ini adalah untuk menilai profil kimia dan biologi ekstrak metanol propolis dari Malaysia yang dihasilkan oleh dua species lebah kelulut yang biasa dijumpai, *Heterotrigona itama* (MHI) dan *Geniotrigona thoracica* (MGT). Sampel telah dianalisis untuk parameter fizikokimia seperti kelembapan, lemak, serat kasar, protein mentah, karbohidrat dan kandungan abu. Pemeriksaan keatas analisis fitokimia menggunakan kromatografi lapisan nipis untuk kedua-dua ekstrak menunjukkan kehadiran terpenoid, flavonoid dan minyak pati tetapi steroid, saponin dan coumarin hanya wujud dalam MHI. Kedua – dua ekstrak menunjukkan profil yang berbeza antara satu sama lain. Sehubungan itu juga, MHI mempunyai aktiviti antioksidan yang lebih tinggi dengan IC_{50} 15.0 ± 0.21 ug/mL berbanding MGT (270.0 ± 0.19 ug/mL). MHI menunjukkan aktiviti perencatan nitrik oksida yang sederhana, sementara MGT menunjukkan perencatan yang sedikit sahaja. Aktiviti antidiabetik telah ditentukan menggunakan perencatan α-glukosida dan didapati lebih baik secara signifikan daripada acarbose (kawalan positif). Kesimpulannya, data yang dikutip dalam kajian ini menunjukkan bahawa spesies lebah memainkan peranan dalam menentukan profil kimia dan biologi propolis tertentu dan perlu dipertimbangkan dalam membuat keputusan untuk pembangunan propolis.

Kata Kunci: fisikokimia, fitokimia, profil KLN, antioksidan, antidiabetik

Introduction

Propolis is a complex resinous substance manufactured by stingless bees and these resins are used to line the inside of nest cavities and reduce the size of hive entrances. The composition of propolis depends on the type of plants accessible to the bees. Propolis has a wide range of biological activities, as antibacterial [1], anti-inflammatory [2], antiulcer [3], antioxidant [4], hepatoprotective [5], and tumoricidal [6] activities and high repellent index against ants [7]. It is generally accepted that bees collect resinous plant materials, produced by a variety of botanical processes, in different parts of plants.

The specificity of local flora is responsible for the chemical composition of propolis [8]. The chemical compositions and biological activities of propolis are attributed to plant sources, geographical area and collecting season [9, 10]. Since bees use the natural available vegetation to create propolis, there is a high variability in the composition of propolis [11]. Propolis has over 150 constituents and its rich in biochemical constituents, including mostly a mixture of polyphenols, flavonoid aglycones, phenolic and ketones [12]. The most studied component was flavonoids and phenolic compounds and they have been reported as the types of antioxidant that possess a strong inhibitory effect against lipid oxidation through radical-scavenging. Besides that, contents of flavonoid and other phenolic substances have been suggested to play a preventative role in the development of cancer and heart disease [13, 14].

In Malaysia, research in propolis has been carried out sparsely. Until now, there are only some preliminary investigations on the composition and biological activity of Malaysian propolis from stingless bee. The present study is an attempt to investigate the physicochemical, preliminary phytochemical, TLC profiling and biological activity of two methanol extracts of propolis that produced from MHI and MGT. Data generate from this study will be a basis of future work on development of Malaysian propolis for health-related products.

Materials and Methods

Chemicals and reagents

DPPH and Folin-Ciocalteu's reagent (Sigma-Aldrich). Sodium carbonate (Na_2CO_3), aluminium chloride ($AlCI_3$), sodium nitrite ($NaNO_2$), and sodium hydroxide (NaOH) were aquired from Merck, Germany. Methanol was used as a solvent for the preparation of samples, toluene, ethyl acetate and formic acid (8: 2: 0.1) used as mobile phase for TLC analysis. All chemicals used were of analytical grade.

Collection and preparation of propolis

Propolis used in this study was collected from AGROPOLIS Apiary, Agriculture Production and Food Innovation Research Institute (AGROPOLIS UniSZA), Universiti Sultan Zainal Abidin. Each sample was cleaned and froze in -20°C, then ground to powder. Propolis extract was prepared by infusing 7 g of crude propolis in 70 mL of 80 % v/v methanol solution for at least 3 days. The extracts were filtered and dried under pressure using rotary evaporator. Crude propolis and extracts were kept cool (-20 °C) prior analysis. Propolis produced by *H. itama* coded as MHI and propolis produced by *G. thoracica* coded as MGT.

Physicochemical analysis

MHI and MGT of propolis were subjected for determination of physicochemical parameters such as moisture, fat, crude fibre, crude protein, carbohydrate and ash content were carried out according to the methods described in pharmacopoeia [17, 18]

Phytochemical screening by Thin Layer Chromatography

MHI and MGT of propolis extracts were screened for the presence of various classes of compounds according to the standard screening method [19] using thin-layer chromatography (TLC) with silica gel G (Merck $60F_{254}$) plates of 0.05 mm thickness. The extracts were dissolved in methanol, while the development of the plate was carried out using mobile systems toluene: ethyl acetate: formic acid (8: 2: 0.1 v/v) for MHI and MGT extracts. After development, the plates were sprayed by various chemical reagents such as anisaldehyde, vanillin-sulphuric acid and iodine for detection of the respective classes of compounds.

DPPH free radical-scavenging activity

The ability of MHI and MGT to scavenge 2,2-diphenyl-1-picrylhydrazyl (DPPH) was determined by DPPH free

radical scavenging activity assay. The scavenging effect of extracts for DPPH was performed based on the method described [20] with a slight modification. Quercetin was used as positive control. One mili Molar of DPPH solution was prepared by diluting 3.94 mg DPPH in 10 mL methanol. 200 µL of standard and sample solution (800, 400, 200,100, 50, 25, 12.5 and 6.25 µg/mL) were added into a 96 well micro plate. Then, 50 µL of 1 mM DPPH solution was mixed into each well and were left at room temperature in the dark place for 30 minutes. After 30 minutes of incubation period, the absorbance was read at 517 nm by Elisa reader spectrophotometer. The blank sample is 200 µL methanol and 50 µL of 1 mM DPPH. All sample extracts were made in triplicate. The ability of different propolis extracts and positive controls to scavenge the DPPH free radical was calculated using the formula, as shown in equation below:

$$\text{Inhibition \%} = [(A_{Blank} - A_{Sample})/ A_{Blank}] \times 100\ \% \quad (1)$$

A_{Blank} is the absorbance of 1 mM of DPPH solution with methanol while A_{Sample} is the absorbance of the propolis sample extracts and positive control solution. The lower absorbance indicates a higher scavenging activity followed by decreasing the intensity of purple to yellow colour. The radical scavenging activities of crude extracts were interpreted via IC_{50} values. The IC_{50} is a concentration that can scavenge the 50 % of DPPH free radical.

Nitric Oxide assay

The nitric oxide (NO) scavenging activity of the extract was measured according to the method described by Ho et al. [21]. 50 µL of propolis extracts were added into 50 µL of 10 M sodium nitroprusside solution in 96-well flat-bottomed plate and then incubated under light at room temperature for 90 min. Finally, an equal volume of Griess reagent (1 % of sulphanilamide and 0.1 % of naphthylethylenediamine in 2.5 % HPO_3) was added to each well to measure the nitrite content immediately at 546 nm. L-ascorbic acid was evaluated as a reference standard. All experiments were carried out in triplicate. The percentage scavenging activity was calculated as described for DPPH assay.

Antidiabetic activity

The enzyme inhibition activity for α-glucosidase was assessed according to the method described by Sancheti et al. [22] with minor modifications to determine the potential of MHI and MGT propolis extract for antidiabetic activity. The reaction mixture contained 50 µL of 0.1 M phosphate buffer (pH 7.0), 25 µL of 0.5 mM 4-nitrophenyl α-D-glucopyranoside, 10 µL of extract sample at various concentrations and 25 µL of α-glucosidase solution (0.2 Unit/mL). This reaction mixture was then incubated at 37 ^{0}C for 30 min. The reaction was terminated by adding 100 µL of 0.2 M sodium carbonate solution. The enzymatic hydrolysis of substrate was monitored by the amount of p-nitrophenol released in the reaction mixture at 410 nm using microplate reader. Individual blanks were prepared for correcting the background absorbance, where the enzymes were replaced with buffer. Controls were conducted in an identical manner replacing the extracts with methanol. Acarbose was used as positive control. All experiments were carried out in triplicates. The inhibition percentage of α-glucosidase was assessed by the following formula:

$$\text{\% Inhibition} = [\ 1 - (\text{sample absorbance} / \text{control absorbance})] \times 100 \quad (2)$$

Statistical analysis

Triplicate determinations, mean and standard deviation were calculated. Calibration curve of standard was obtained for concentration versus absorbance. All data were subjected for analysis using independent variable t-test.

Results and Discussion

Physicochemical evaluation

Bees produce propolis as part of their defense system in order to protect their hive from invaders and microbial attacks. In this study, we collected propolis produced by two different species of stingless bees, *H. itama and G. thoracica* from our Apiary. Even though the location was the same and the distance between hives of these two species is only few meters apart, the physicochemical content such as moisture, fat, crude fibre, protein, soluble extractive and ash content were markedly different as shown in Table 1. MHI contains noticeable high moisture content compared to MGT, ranged from 9.90 – 23.72 %. The lower of moisture content of MGT could prevent bacterial, fungal or yeast growth through storage [23]. The ash values, total ash was found to be in the ranged from

4.11 – 5.99 %, where MGT contain higher value compared to MHI. Ash values used to determine quality and purity of crude samples. It indicates the presence of various impurities like carbonate, oxalate and silicate. MHI had lower percentage of crude fat content in comparison with MGT. However, in contrast, MGT have a lower carbohydrate content but slightly higher in fibre. Meanwhile, protein content of both samples was in close range, 2.17 – 3.87 %. The differences of MHI and MGT physicochemical content might due to vegetation preferences of the bee species [14].

Table 1. Physicochemical analysis of the methanol extracts propolis produced by stingless bees, *H. itama* (MHI) and *G. thoracica* (MGT) (p<0.05)

Parameter	**MHI**	**MGT**
Moisture (%)	23.72 ± 0.62[1]	9.90 ± 11.82
Ash (%)	4.11 ± 0.67	5.99 ± 0.31
Crude fat (%)	21.43 ± 5.39	73.47 ± 2.75
Crude protein (%)	3.80 ± 0.12	2.17 ± 0.15
Crude fibre (%)	44.36 ± 5.07	67.48 ± 1.50
Carbohydrates (%)	49.60 ± 9.19	8.46 ± 10.32

[1]*Each value is the average of three analyses ± standard deviation*

Chemical fingerprint by Thin Layer Chromatography analysis

Propolis is a complex resinous mixture, which contains approximately 50 % resin that composed of flavonoids and related to phenolic acids regarded as the polyphenolic compounds, 30 % wax, 10 % essential oils, 5 % pollen and 5 % various organic compounds [12]. The chemical composition of propolis reportedly depends on the specificity of the local flora at the site collection and also the vegetation preference of stingless bee species. As seen in Table 2, the chemical compositions of propolis were tested by TLC profiling of MHI and MGT in different chemical reagents for detection of the respective classes of compound. There were three reagent used during this step which were iodine, anisaldehyde and also vanillin. TLC plate was stained with iodine vapor to visualize organic compound since iodine has a high affinity for both unsaturated and aromatic compounds such as polycyclic aromatic compounds, phenolic steroid, ester and alkaloids. Anisaldehyde was used to detect aldehyde, phenol, sugar and terpenes compound. When heated, the TLC plate change to light pink color and other functional groups tend to vary with respect to coloration. Vanillin used for the detection of amines, amino acids, higher alcohols, phenols, and essential oils. The plate also visualized by UV light on wavelength 366 nm. The results obtained from determination of the tests illustrated the presence of terpenoids, flavonoids and essential oils were present in both extracts. However, steroids, saponins and coumarins were absence in MGT but presence in MHI. On the other hand, the previous studies by Buenos et al. [24] were showed that the flavonoids were not found on methanol extract but only presence in the ethyl acetate and hexane extracts of propolis. These constituents may contribute to the MHI and MGT propolis therapeutic effect. Overall, from TLC analysis, the chemical composition and chemical fingerprint of propolis produced by *H. itama* are more complex compare to that of *G. thoracica*.

The differences in the phytochemical screening results of propolis might due to the time of harvest, storage, local flora extraction method [25] and the bee species. Besides using TLC method, analytical techniques such as high performance liquid chromatography (HPLC) and gas chromatography (GC), usually coupled to mass spectrometry (MS) were used to obtain molecular weight, structural information and identification [26]. However, the developed TLC method is a straightforward and efficient way for screening propolis samples at preliminary stage and for quality purposes. It is applicable to qualitatively determine biologically active compounds like flavonoids and others constituents in propolis using the specific detection reagent.

Table 2. Phytochemical tests of the methanol extract propolis produced by stingless bees, *H. itama* (MHI) and *G. thoracica* (MGT)

Constituents	Color detected	MHI	MGT	Chemical / Spray reagent
Terpenoids	Pink	+	+	Anisaldehyde
Flavonoids	Blue fluorescence	+	+	Anisaldehyde
Saponins	Dark bluish	+	-	Vanillin-sulphuric acid
Steroids	Bluish green	+	-	Anisaldehyde
Coumarins	Light blue	+	-	UV 365 nm
Essential oils	Red and brown	+	+	Vanillin-sulphuric acid
All compounds	Yellow-brown	+	+	Iodine

Remarks: + ,*detected*; - , *not detect*

DPPH Free Radical Scavenging Activity of MHI and MGT Propolis.

The antioxidant test was conducted to determine the antioxidant potential of propolis extract, using the DPPH scavenging method. The use of DPPH to scavenge radicals has more advantages which easy to use, have high sensitivity and enabled to analyze of large numbers of samples in a short time. In order to measure antioxidant activity, the reduction of DPPH, a stable free-radical was used to evaluate the antioxidant activity of MHI and MGT propolis at concentrations varying from 6.25-800 µg/mL with quercetin as standards. The results show the variation of inhibition percentage. As shown in Figure 1, quercetin has the highest inhibition percentage (antiradical activity) closely followed by MHI while the MGT has the lowest and the differences is statistically significant.

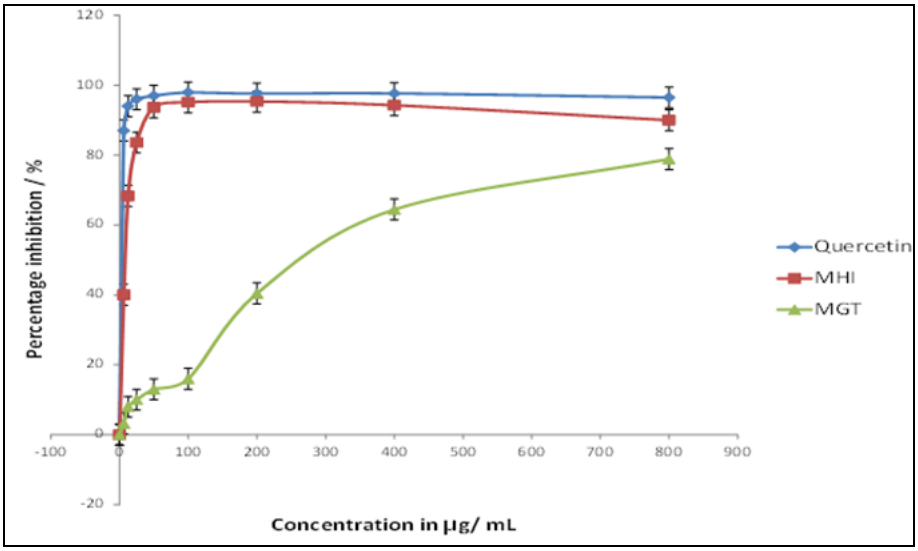


Figure 1. Plot of percentage inhibition against concentration of MHI, MGT and quercetin ($P<0.05$)

The other parameters used for this test is IC_{50} and is defined as the concentration of extract required to capture the DPPH free radical by 50 %. Scavenging activity of MHI is comparable to that of quercetin with IC_{50} of 15 µg/mL and 10 µg/mL, respectively (Figure 2). Meanwhile, MGT only moderately inhibited DPPH scavenging with IC50 of

270 µg/mL (Figure 2). A smaller IC_{50} value of the extract means the higher scavenging activity of the DPPH radical and, therefore, increased activity as an antioxidant. From the results above, propolis produced by MHI shows the higher antioxidant property compared to MGT. The difference in the antioxidant activity might due to the flavonoid content of propolis extracts or other compounds, which are potential antioxidants. As the previous studies by Fuliang et al. [28], the methanol extracts of Peruvian and Netherlands propolis exhibited stronger DPPH free radical scavenging activity than the corresponding water extract. It is due to its phenolic and flavonoid content, which is related to the antioxidant potential. The reasons behind the markedly higher radical scavenging activity exhibited by different types of propolis are probably due to their resin plant origin, climate, and resin collection time by the bees.

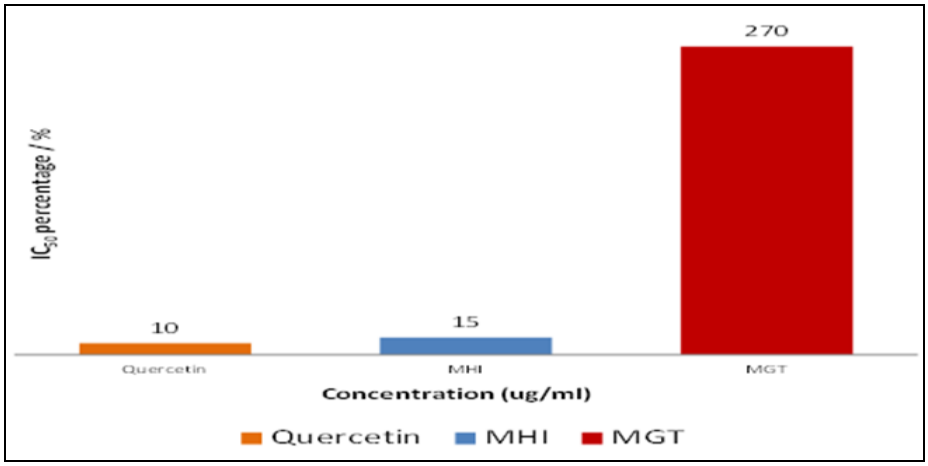


Figure 2. IC_{50} of MHI, MGT and Quercetin by DPPH scavenging method.

Nitric Oxide activity

Nitric oxide is a method to determined the potential of antioxidant that can react with superoxide to form the peroxynitrite anion, which can decompose to produce OH- and NO-. It has also been involved in a variety of biological functions, including neutrotransmission, vescular homeostasis, antimicrobial and antitumor activities. It was based on the principle that sodium nitro-prusside in aqueus solution at physiological pH spontaneously generates nitric oxide which interacts with oxygen to produce nitrite ions that can be estimated using Griess reagent. Scavengers of nitric oxide compete with oxygen leading to reduced production of nitrite ions. Large amounts of NO- may lead to tissue damage [27].

Nitric oxide scavenging activity was performed with MHI and MGT propolis and ascorbic acid as standard compound. The inhibition potential of all samples and standard preparations exhibited dose dependent manner. As shown in Figure 3, ascorbic acid was found more significantly active than both extracts. There is no significant difference between MHI and MGT propolis in the nitric oxide activity. From the graph, it was observed that as concentration increases, the percentage of inhibition scavenging is increasing linearly but constant at 150 µg/mL for all extracts and ascorbic acid (standard preparation). The IC_{50} for ascorbic acid was 30 µg/mL , but there were no scavenging activity at 50 % for MHI and MGT extracts propolis. Previous studies by Myint et al. [27] were found that labdane-type diterpenes, flavonoids and some phenolic compounds possessed potent nitric oxide inhibition activity in water and methanol extracts of Brazilian propolis. That may not be the case for propolis produced by *H. itama* and *G. thoracica*.

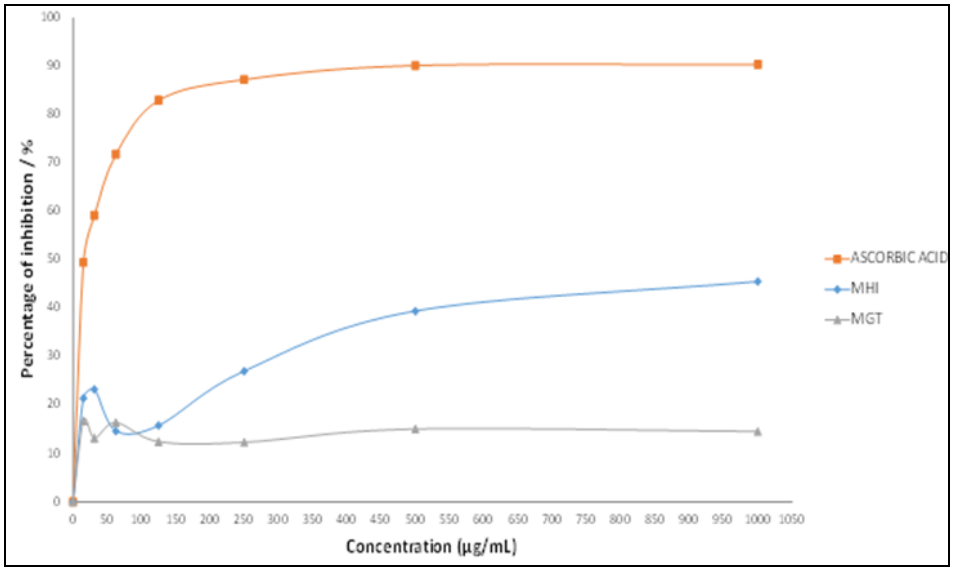


Figure 3. Plot of percentage inhibition against concentration of MHI, MGT and Ascorbic acid (P>0.05)

Antidiabetic activity

In this study, the hypoglycemic potential of both extracts (MHI and MGT) were evaluated by the α-glucosidase inhibition assay. Acarbose was used as positive control. Results were tabulated in Figure 4 and 5 respectively. The IC_{50} was calculated for both extracts and were found significant (P<0.05) than acarbose. These differences in the concentration of propolis extracts may cause the differences in antidiabetic activities between MHI and MGT propolis.The IC_{50} of MHI and MGT were 2.5 µg/mL and 30 µg/mL respectively which were found lower than IC_{50} of acarbose (190 µg/mL). From results, it confirmed that the MHI showed potent antidiabetic potential than MGT and was higher than acarbose (positive control).

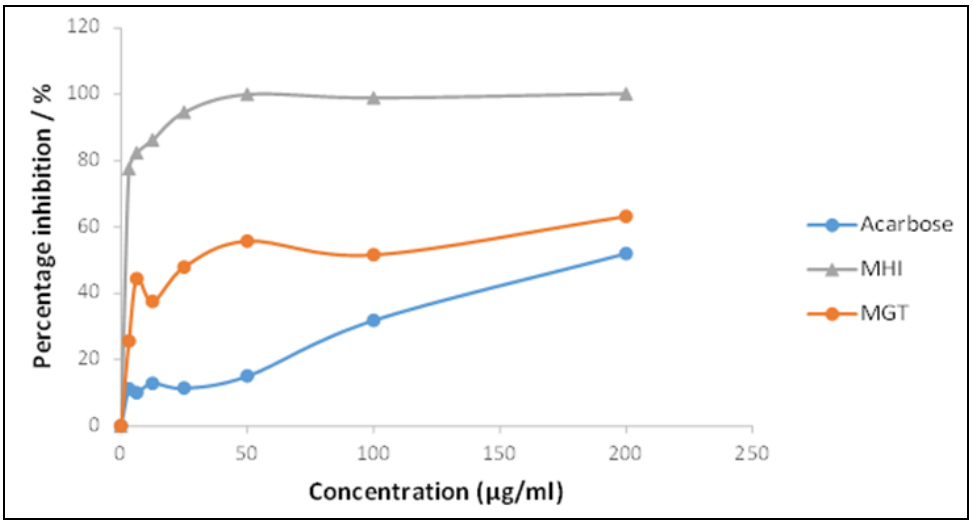


Figure 4. Plot of percentage inhibition against concentration of MHI, MGT and Acarbose (P <0.05)

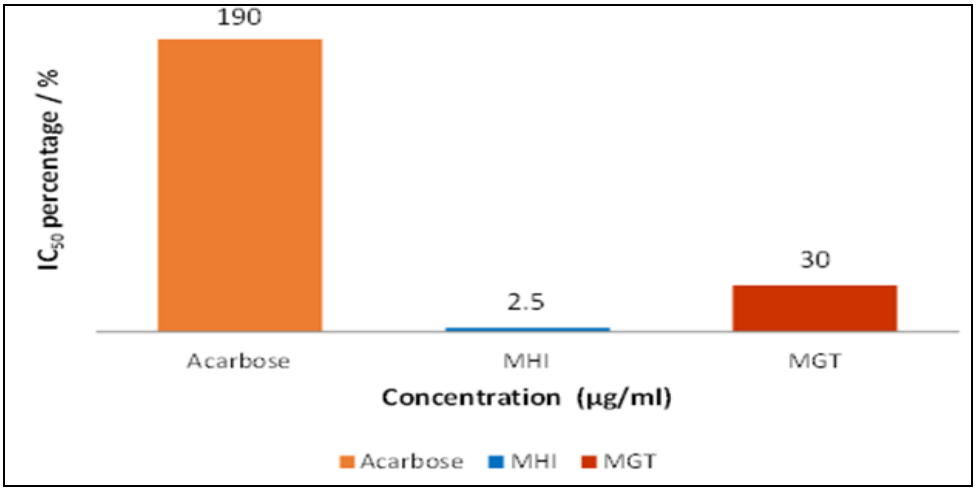


Figure 5. IC_{50} of MHI, MGT and Acarbose by antidiabetic activity

As the previous studies, flavonoids in propolis have an antioxidants activity and are thought to be the compound that is able to lower serum glucose levels through the inhibition of oxidative stress. In addition, the antioxidants activity of propolis can improve insulin receptor signaling in insulin resistant conditions, therefore the insulin sensitivity can be increased [28]. Similarly, result of MHI propolis have higher potential in antioxidant and also antidiabetic activity compare to that of MGT. However, previous reports have demonstrated that a propolis ethanol extract from Brazilian propolis improves insulin sensitivity during the prediabetic and diabetic stages on obese rats [29]. Thus, the chemical composition of propolis was strongly influenced by the source materials, species of bees and also types of the extraction.

Conclusion

From this study, it shows that bee species play role in determining the chemical and biological profile of particular propolis and should put into account in decision of further development for propolis. The data of physicochemical, preliminary phytochemical tests, biological activity and TLC profiling generated in this study will be the basis for authentication, standardization profile and quality control assessment of Malaysian propolis, especially produced by stingless bees, *Heterotrigona itama* and *Geniotrigona thoracia*. Further investigation on identification of marker compounds should be carried out to be use in propolis standardization.

Acknowledgement

This research work was supported by Research Acculturation Collaborative Report (RACE) grant scheme (Code: RR109), under the project Chemical Profiling and Chemometric Analysis of Malaysia Propolis by Ministry of Education Malaysia.

References

1. Souza, R. M., Souza De, M. C., Patitucci, M. L. and Silva, J. F. (2007). Evaluation of antioxidant and antimicrobial activities and characterization of bioactive components of two Brazilian propolis samples using a pKa-guided fraction-ation. *Z Naturforsch*, 62: 801 - 807.
2. Ledon, N., Casaco, A., Gonzalez, R., Merino, N., Gonzalez, A. and Tolon, Z. (1997). Antipsoriatic, anti-inflammatory, and analgesic effects of an extract of red propolis. *Acta Pharmacologica Sinica*, 18(3): 274 -276.
3. Barros, M. P., Lemos. M., Maistro, E. L., Leite, M. F., Sousa, J. P., Bastos, J. K. and Andrade, S. F. (2008). Evaluation of antiulcer activity of the main phenolic acids found in Brazilian Green Propolis. *Journal of Ethnoparmacology*, 120: 372 - 377.

4. Teixeira, É. W., Message, D., Negri, G., Salatino, A. and Stringheta, P. C. (2010). Seasonal variation, chemical composition and antioxidant activity of Brazilian propolis samples. *Evidence-Based Complementary and Alternative Medicine*, 7(3): 307 - 315.
5. Basnet, P., Matsushige, K., Hase, K., Kadota, S. and Namba, T. (1996). Four di-O-caffeoyl quinic acid derivatives from propolis. Potent hepatoprotective activity in experimental liver injury models. *Biological and Pharmaceutical Bulletin*, 19:1479 - 1484.
6. Suzuki, I., Hayashi, I., Takaki, T., Groveman, D. S. and Fujimiya, Y. (2002). Anti-tumor and anticytopenic effects of aqueous extracts of propolis in combination with chemotherapeutic agents. *Cancer Biotherapy and Radiopharmaceuticals*, 17: 553-560.
7. Duangphakdee, O., Koeniger, N., Deowanish, S., Hepburn, H. R. and Wongsiri, S. (2009). Ant repellent resins of honeybees and stingless bees. *Insectes sociaux*, 56: 333 - 339.
8. Righi, A. A., Negri, G. and Salatino, A. (2013). Comparative chemistry of propolis from eigght Brazilian localities. *Evidence-Based Complementary and Alternative Medicine* 2013: 1 - 15..
9. Popova, M., Bankova, V., Bogdanov, S., Tsvetkova, I., Naydenski, C., Marcazzan, G. L. and Sabatini, A. G. (2007). Chemical characteristics of poplar type propolis of different geographic origin. *Apidologie*, 38: 306 - 311.
10. Sforcin, J. M. and Bankova, V. (2011). Propolis: Is there a potential for the development of drugs? *Journal of Ethnopharmacology*, 133: 253 - 260.
11. Simone-Finstrom, M. and Spivak, M. (2010). Propolis and bee health: the natural history and significance of resin use by honey bees. *Apidologie*, 41: 295 - 311.
12. Marcucci, M. C. (1995). Propolis: chemical composition, biological properties and the therapeutic activity. *Apidologie*, 26: 83 - 99.
13. Markham, K. R., Mitchell, K. A., Wilins, A. L., Daldy, J. A. and Lu, Y. (1996). HPLC and GC-MS identification of the major organic constituents in New Zealand propolis. *Phytochemistry*, 42: 205 - 211.
14. Bankova, V., Castro De, S. & Marcucci, M. (2000). Recent advances in chemistry and plant origin. *Apidologie*, 31: 3 – 15.
15. Chen, Y. W., Wu, S. W., Ho, K. K, Lin, S. B., Huang, C. Y. and Chen, C. N. (1998). Characterization of Taiwanese propolis collected from different locations and seasons. *Journal Science and Food Agriculture*, 88: 412 - 419.
16. Popova, M., Chen, C. N., Chen, P. Y., Huang, C. Y. & Bankova, V. (2010). A validated spectrophotometric method for quantification of prenylated flavonones in Pacific propolis from Taiwan. *Phytochemical Analysis*, 21: 186 - 191.
17. The Siddha Formulary of India.(1992). Part-I. Department of ISM & H, Ministry of Health & Family Welfare. Government of India. New Delhi.
18. World Health Organisation (1998). Quality Control Methods of Medicinal Plant Materials.Geneva.
19. Trease, G. E. and Evans, W. C. (1983). Textbook of Pharmacognosy. 12th edn. Balliese Tindall and Company Publisher, London. pp. 343 - 383.
20. Brand-Williams, W., Cuvelier, M. E. and Berset, C. (1995). Use of free radical method to evaluate antioxidant activity. *LWT-Food science and Technology* 28: 25 - 30.
21. Ho, S. C., Tang, Y. L., Lin, S. M. and Liew, Y. F. (2010). Evaluation of peroxynitrite scavenging capacities of several commonly used fresh spices. *Food Chemistry*, 119: 1102 - 1107.
22. Sancheti, S., Sancheti, S. and Seo, S. Y. (2010). Evaluation of antiglycosidase and anticholinesterase activities of Boehmeria nivea. *Pakistan Journal of Pharmaceutical Sciences*, 23: 236 - 240.
23. Emmanuel, T., Alfred, N. T., Pierre, B., Paul, S., Forche, P. A., Joseph, T. M., Nestor, F. F. T. and Robert, N. (2014). Phytochemical screening, antioxidant activity, total polyhenols and flavonoids content of different extracts of propolis from Tekel (Ngaoundal, Adamawa region, Cameroon). *Journal of Phytopharmacology*, 3(5): 321 - 329.
24. Buenos, M. I., Cunha, I. B. S., Marcucci, M. C. and Marassi, M. (1997). Evidence of lead contamination in propolis by X-Ray fluroscence analysis. In the International Apicultural Congress of Apimondia. The Centenary Congress Apimondia Publishing House, Bucharest, Romania.
25. Bankova, V. (2005). Chemical diversity of propolis and the problem of standardization. *Journal of Ethnopharmacology*, 100: 114-117.

26. Pandey, M. K., Singh, G. N., Sharma Rajeev Kr and Sneh Lata. (2012). Standardization of Yakrit Plihantak Churna: An Ayurvedic Poly herbal formulation. *International Journal of Pharmaceutical Sciences and Research*, 3 (1): 171 - 176.
27. Myint, M. T., Aljun, H. B., Yasuhiro, T. and Kiyoshi, M. (2003). Inhibitors of nitric oxide (NO) production in murine macrophage-like J774.I cells from Brazillian propolis. *Journal Tradional Medicine*, 20: 22 - 29.
28. Fuliang, H. U., Hepburn, H. R., Xuan, H., Chen, M., Daya, S. and Radloff, S. E. (2005). Effects of propolis on blood glucose, blood lipid and free radicals in Rats with diabetes mellitus. *Pharmacology Research*, 51:147 – 52.
29. Tasleem, A., Bhawana, S., Anjum, G., Vijay, K. and Rajesh, D. (2014). Anti-diabetic agents from medicinal plants: A review. *Chemistry Biology Letters*, 1(1): 1 - 13.

MALAYSIAN JOURNAL OF ANALYTICAL SCIENCES
Published by The Malaysian Analytical Sciences Society
ISSN 1394 - 2506

CHARACTERIZATION OF $CaCO_3$ MICROSPHERES FABRICATED USING DISTILLED WATER

(Pencirian $CaCO_3$ Mikrosfera Difabrikasi Menggunakan Air Suling)

Intan Nabila Sabri[1], Nadiawati Alias[2], Abdul Manaf Ali[2], Javeed Shaikh Mohammed[1]*

[1]*Faculty of Innovative Design and Technology,*
Universiti Sultan Zainal Abidin, Gong Badak Campus, 21300 Kuala Terengganu, Terengganu, Malaysia
[2]*Faculty of Bioresources and Food Industry,*
Universiti Sultan Zainal Abidin, Besut Campus, 22200 Tembila, Terengganu, Malaysia

**Corresponding author: javeedsm@unisza.edu.my*

Received: 14 April 2015; Accepted: 30 November 2015

Abstract

Calcium carbonate ($CaCO_3$) microspheres (μ-spheres) are widely used as inorganic templates (or cores) for fabricating nano-engineered microcapsules. Deionized water is commonly used in the fabrication of $CaCO_3$ μ-spheres using precipitation reaction between calcium chloride ($CaCl_2$) and sodium carbonate (Na_2CO_3) solutions under vigorous stirring. However, in the current work distilled water was used throughout the experiments. Furthermore, two simple fabrication approaches, namely membrane filtration and centrifugation approaches, were used in order to understand the effect of different experimental factors on the size and shape of $CaCO_3$ μ-spheres. For the membrane filtration approach, the experimental factors tested included mixing procedure of solutions, stirring speeds, drying techniques, and types of filter paper used. For the centrifugation approach, the experimental factors tested included mixing procedure of solutions, stirring speeds, centrifugation times, drying techniques, and quantity of washing agents used. The size measurements and shape of the $CaCO_3$ μ-spheres were investigated using compound microscopy. Scanning electron microscopy (SEM) was used to observe the fine surface morphological details of the $CaCO_3$ μ-spheres. Overall results indicate that the centrifugation approach can yield better $CaCO_3$ μ-spheres as compared to the membrane filtration approach in terms of narrow size distribution and uniform spherical shape. The fabricated $CaCO_3$ μ-spheres can be used as inorganic templates for fabricating nano-engineered microcapsules.

Keywords: $CaCO_3$ microspheres, scanning electron microscopy (SEM), compound microscopy

Abstrak

Kalsium karbonat ($CaCO_3$) mikrosfera (μ-sfera) digunakan secara meluas sebagai templat bukan organik (atau teras) untuk memfabrikasi mikrokapsul nano-kejuruteraan. Air ternyahion lazim digunakan dalam fabrikasi $CaCO_3$ μ-sfera dengan menggunakan tindak balas pemendakan antara larutan kalsium klorida ($CaCl_2$) dan natrium karbonat (Na_2CO_3) dengan pengacauan yang laju. Namun begitu, dalam kerja-kerja semasa air suling telah digunakan sepanjang eksperimen. Dua teknik fabrikasi yang ringkas, iaitu teknik penapisan membran dan pengemparan telah digunakan untuk memahami kesan faktor eksperimen yang berbeza terhadap saiz dan bentuk $CaCO_3$ μ-sfera. Bagi teknik penapisan membran, faktor – faktor eksperimen yang diuji termasuk prosedur pencampuran larutan, kelajuan pengacauan, teknik pengeringan, dan jenis kertas penapis yang digunakan. Bagi teknik pegemparan, faktor – faktor eksperimen yang diuji pula termasuk prosedur pencampuran larutan, kelajuan pengacauan, masa pengemparan, teknik pengeringan, dan kuantiti agen pembasuhan yang digunakan. Ukuran saiz dan bentuk $CaCO_3$ μ-sfera telah dikaji dengan menggunakan mikroskopi sebatian. Mikroskopi elektron pengimbasan (SEM) digunakan untuk meneliti morfologi permukaan halus $CaCO_3$ μ-sfera. Keputusan kajian menunjukkan bahawa teknik pengemparan mampu menghasilkan $CaCO_3$ μ-sfera lebih baik berbanding teknik penapisan membran dari segi taburan saiz yang kecil dan berbentuk sfera yang seragam. Rekaan $CaCO_3$ μ-sfera boleh digunakan sebagai templat bukan organik untuk fabrikasi mikrokapsul nano-kejuruteraan.

Kata kunci: $CaCO_3$ microsfera, mikroskop elektron pengimbasan (SEM), mikroskopi sebatian

Introduction

Calcium carbonate ($CaCO_3$) microspheres (μ-spheres) have been extensively used as core templates to fabricate nano-engineered microcapsules for drug delivery applications [1, 2]. $CaCO_3$ cores can be easily fabricated and can also be easily dissolved by using ethylenediaminetetraacetic acid (EDTA) after the layer-by-layer (LbL) multilayer self-assembly process [3]. Several different approaches have been used to fabricate $CaCO_3$ μ-spheres or co-precipitated protein-$CaCO_3$ μ-spheres in the nm-μm size range [1, 4–10]. The membrane filtration and centrifugation approaches are two simple and low-cost approaches for fabricating $CaCO_3$ μ-spheres. The membrane filtration approach is based on pressure-driven separation of microspheres from the solution [11]. A vacuum pump can aid in applying pressure (lower than the atmospheric pressure) to the filtration equipment for faster separation. The centrifugation approach is based on centrifugal force-driven sedimentation of microspheres in the solution [12].

Deionized water (with resistivity of 18 MΩ·cm) is commonly used in the fabrication of $CaCO_3$ μ-spheres using precipitation reaction between calcium chloride ($CaCl_2$) and sodium carbonate (Na_2CO_3) solutions under vigorous stirring. However, in the current work distilled water was used throughout the experiments. Furthermore, the easy-to-use membrane filtration and centrifugation approaches were tested in the current work in order to achieve uniformly-shaped $CaCO_3$ μ-spheres with narrow size distribution. Mixing procedure of solutions, stirring speeds, drying techniques, types of filter paper, and centrifugation times are some of the experimental factors that need to be evaluated for their potential to influence the formation of uniformly-shaped and monodispersed $CaCO_3$ μ-spheres [13–15]. Limited details are available in literature regarding the influence of mixing procedure of solutions, stirring speeds, drying techniques, types of filter paper, and centrifugation times on the formation of uniformly-shaped and monodispersed $CaCO_3$ μ-spheres using distilled water. Therefore, the aim of the current work was to gain further knowledge about the influence of experimental factors in preparing uniformly-shaped $CaCO_3$ μ-spheres with narrow size distribution. The knowledge gained from the current work can be used to prepare $CaCO_3$ microtemplates using distilled water for the fabrication of nano-engineered microcapsules.

Materials and Methods

Chemicals

Calcium chloride ($CaCl_2$) (Fisher Scientific UK Ltd., Loughborough, UK), Sodium carbonate (Na_2CO_3) (Nacalai Tesque Inc., Kyoto, Japan) and acetone (RCI Labscan Ltd., Bangkok, Thailand) were purchased and used.

Fabrication of $CaCO_3$ μ-spheres

Two different fabrication approaches, namely membrane filtration and centrifugation approaches, were used in order to prepare uniformly-shaped $CaCO_3$ μ-spheres with a narrow size distribution. In both approaches, precipitation reaction between $CaCl_2$ and Na_2CO_3 solutions was used. The experiments were carried out at room temperature unless specified otherwise.

Membrane filtration approach

The $CaCO_3$ μ-spheres were fabricated by precipitation reaction between $CaCl_2$ and Na_2CO_3 solutions as reported by Petrov et al. [1] with slight modification. Briefly, 20 mL of 0.33 M solutions of $CaCl_2$ and Na_2CO_3 were mixed under vigorous stirring at 900 rpm for 30 s at room temperature. After the stirrer was stopped, the reaction mixture was left without stirring for 10 min. Subsequently, the precipitated $CaCO_3$ μ-spheres were collected and thoroughly washed with 100 mL of distilled water three times followed by acetone one time using membrane filtration system equipped with a filter paper. Finally, the μ-spheres were dried.

Two different mixing procedures, four different stirring speeds, two different drying techniques, and two types of filter paper were carried out in order to understand the effect of these experimental factors on the morphology and size distribution of $CaCO_3$ μ-spheres. The two mixing procedures of solutions used were: Na_2CO_3 solution was added rapidly (directly) to $CaCl_2$ solution and Na_2CO_3 solution was added drop-by-drop (one drop per second) to $CaCl_2$ solution. The four stirring speeds of magnetic stirrer used were: 300 rpm, 600 rpm, 900 rpm, and 1200 rpm

for 30 s at room temperature. The two drying techniques used were: drying in air for 24 h, and drying in oven at 50 °C for 60 min. The two types of filter papers used were: Smith filter paper AO336 with 15-20 μm pore size (Smith Scientific Ltd., UK) and Whatman filter paper with 11 μm pore size (GE Healthcare UK Ltd., UK).

Centrifugation approach

The $CaCO_3$ μ-spheres were fabricated by precipitation reaction between $CaCl_2$ and Na_2CO_3 solutions as reported by Volodkin et al. [16, 17] with slight alteration. Briefly, 20 mL of 0.33 M solutions of $CaCl_2$ and Na_2CO_3 were mixed under vigorous stirring at 900 rpm for 30 s at room temperature. After the stirrer was stopped, the reaction mixture was left without stirring for 10 min. Subsequently, centrifugation washing steps with distilled water for four times were conducted in order to eliminate the unreacted species [18]. The $CaCO_3$ μ-spheres were then washed by centrifugation with acetone twice. Finally the μ-spheres were dried.

Two different mixing procedures, four different stirring speeds, two different drying techniques, two different centrifugation times and two different quantities of washing agents were carried out in order to understand the effect of these experimental factors on the morphology and size distribution of $CaCO_3$ μ-spheres. In the case of first, second, and third experimental factors, parameters similar to the membrane filtration were used. The two centrifugation times (at 1000 rpm) used were: 1 min and 5 min. The two quantities of washing agents (distilled water and acetone) used were: 25 mL and 40 mL.

Characterization of $CaCO_3$ μ-spheres

The shape and size measurements of the $CaCO_3$ μ-spheres were investigated using a compound microscope (Nikon ECLIPSE E100) at 4x, 10x, 40x, and 100x magnification. Powder samples of $CaCO_3$ μ-spheres were used for the compound microscopy experiments. The compound microscope was equipped with Dino-eye (Microscope Eye-Piece Camera) to take the images and DinoCapture 2.0 software to measure the diameters of $CaCO_3$ μ-spheres. The fine surface morphological details of the $CaCO_3$ μ-spheres were observed using a scanning electron microscope (SEM) (JSM-6360 LA JEOL, US).

Data analysis

The statistical analysis to determine the mean and standard deviation of the diameters of $CaCO_3$ μ-spheres was done using SPSS software. Histograms overlaid with a normal distribution curve showing the size distribution of $CaCO_3$ μ-spheres was also done using the same software.

Results and Discussion

For most applications, narrow size distribution and uniform shape of $CaCO_3$ μ-spheres are highly desirable characteristics. In order to achieve the desired μ-sphere characteristics, the experimental factors related with the preparation of μ-spheres using distilled water were studied. For the membrane filtration approach, the experimental factors tested included mixing procedure of solutions, stirring speeds, drying techniques, and types of filter paper used. For the centrifugation approach, the experimental factors tested included mixing procedure of solutions, stirring speeds, centrifugation times, drying techniques, and quantity of washing agents used. The results from the different experimental factors tested (under membrane filtration and centrifugation approaches) in order to understand their influence on the formation of $CaCO_3$ μ-spheres are presented and discussed in terms of shape and size distribution of the μ-spheres in the following sections.

Effect of mixing procedure of solutions

Figures 1a and 1c show the $CaCO_3$ μ-spheres obtained from the rapid addition mixing procedure of solutions that produced spherical shaped μ-spheres. The average size of μ-spheres was 5.93 ± 0.72 μm and 5.33 ± 0.95 μm for membrane filtration and centrifugation approaches, respectively. Compound microscopy results show that the $CaCO_3$ μ-spheres formed clusters when using drop-by-drop addition mixing procedure of solutions (Figures 1b, 1d). The reaction mixture should be mixed rapidly (reactive precipitation) and then left undisturbed for certain time. The solutions were left undisturbed for around 10 min in order to allow the crystal nucleation and growth of $CaCO_3$. The histograms in Figure 2 show that both approaches produced narrow size distributions of $CaCO_3$ μ-spheres; with a positively skewed distribution for the membrane filtration approach.

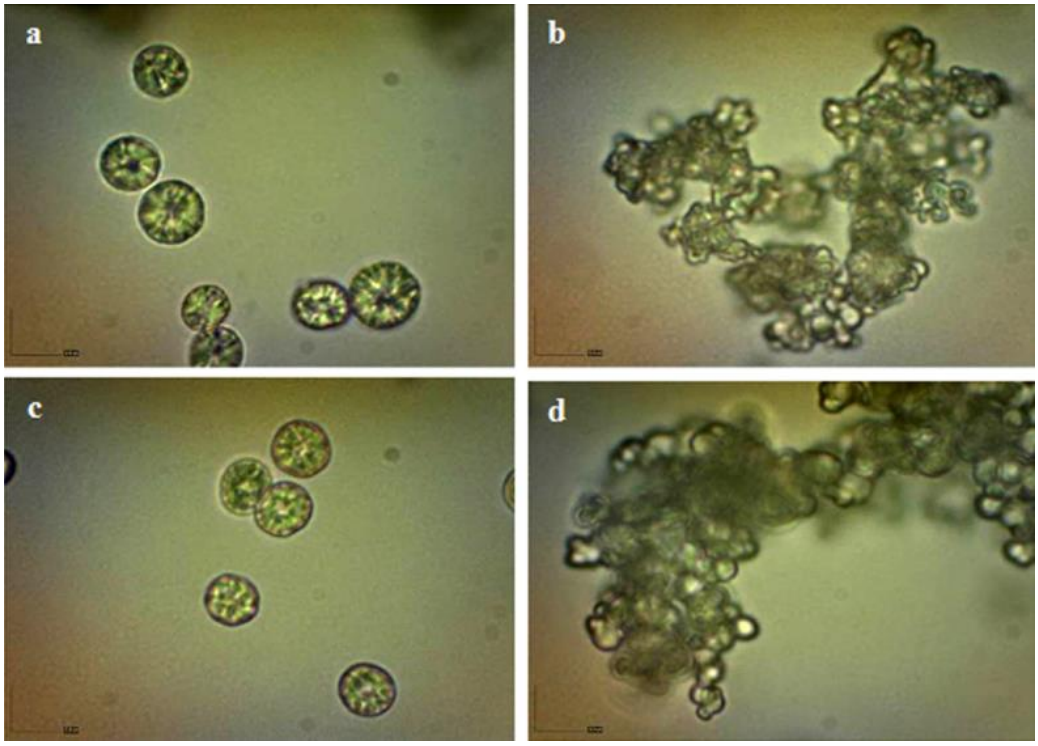


Figure 1. Microscope images of $CaCO_3$ µ-spheres fabricated using different mixing procedures of solutions (a, c) Na_2CO_3 was added directly to $CaCl_2$ and (b, d) Na_2CO_3 was added drop-by-drop to $CaCl_2$. Membrane filtration approach (a, b) and centrifugation approach (c, d) (100x magnification, scale bars indicate 5 µm)

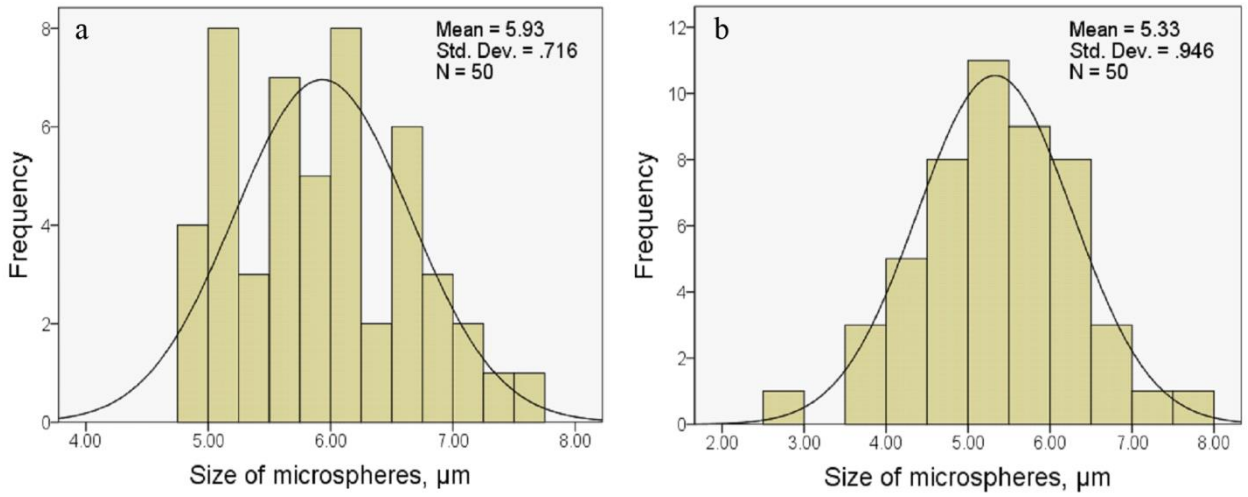


Figure 2. Histograms showing size distribution for $CaCO_3$ µ-spheres fabricated using rapid addition mixing procedure of solutions (a) membrane filtration approach and (b) centrifugation approach

Effect of stirring speed

Compound microscopy images show that the $CaCO_3$ μ-spheres obtained using stirring speeds of 300, 600, and 900 rpm have a mixture of calcite and spherical shapes (Figures 3a, 3b, 3c, 3e, 3f, and 3g). As shown by representative images, it was observed that non-uniform sizes and shapes of $CaCO_3$ μ-spheres were obtained at lower stirring speeds. Uniform shaped $CaCO_3$ μ-spheres were achieved at a stirring speed of 1200 rpm (Figures 3d, 3h), with the average sphere diameters of 4.98 ± 0.57 μm and 7.27 ± 0.78 μm for membrane filtration and centrifugation approaches, respectively. Histograms in Figure 4 show that both approaches produced narrow size distribution of $CaCO_3$ μ-spheres; with a negatively skewed distribution for the centrifugation approach. The results indicate that stirring speed has an effect on the shape and size of the μ-spheres and that higher stirring speed yields better size distribution and spherical $CaCO_3$ μ-spheres, similar to previously reported work [14].

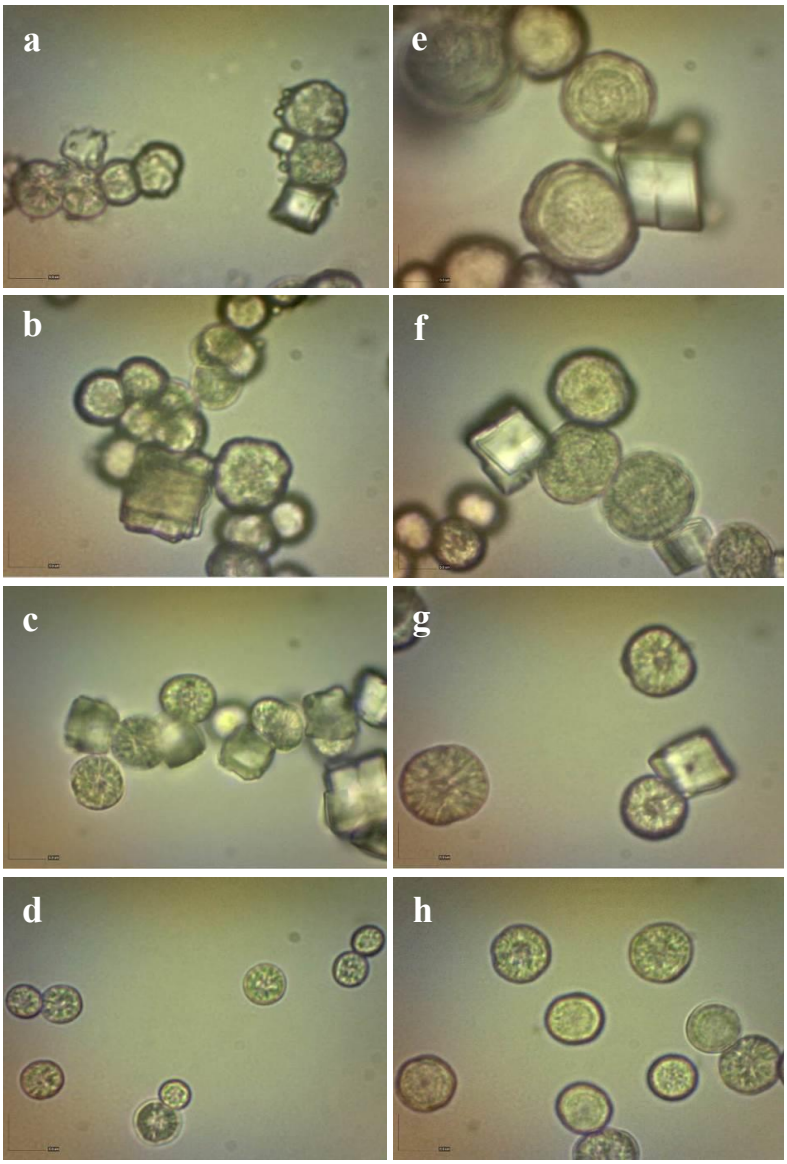


Figure 3. Microscope images of $CaCO_3$ μ-spheres fabricated using different stirring speeds (a, e) 300 rpm, (b, f) 600 rpm, (c, g) 900 rpm and (d, h) 1200 rpm. Membrane filtration approach (a to d) and centrifugation approach (e to h) (100x magnification, scale bars indicate 5 μm)

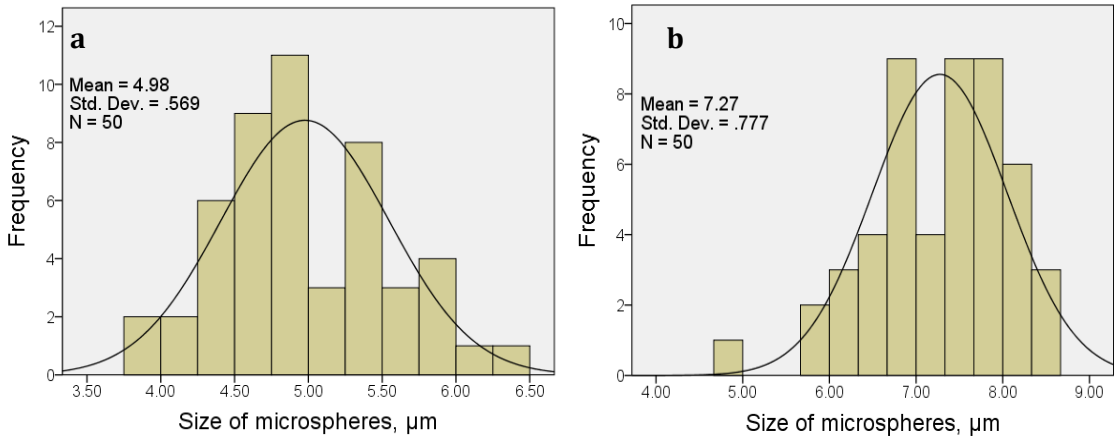


Figure 4. Histograms showing size distribution for $CaCO_3$ µ-spheres fabricated using a stirring speed of 1200 rpm (a) membrane filtration approach and (b) centrifugation approach

Effect of drying technique

The purpose of drying the $CaCO_3$ µ-spheres was to remove physically adsorbed water or acetone from the µ-spheres. Figures 5a and 5c show that spherical shaped $CaCO_3$ µ-spheres were obtained when dried in air. $CaCO_3$ µ-spheres obtained by drying in oven at 50 °C had spherical and calcite shapes (Figures 5b, 5d). The average size of µ-spheres was 6.64 ± 1.64 µm and 5.33 ± 0.95 µm for membrane filtration and centrifugation approaches, respectively. Histograms in Figure 6 show that centrifugation approach produced narrow size distribution of $CaCO_3$ µ-spheres, whereas the membrane filtration approach has a bimodal distribution. The drying technique also influenced the final quantity of $CaCO_3$ µ-spheres. It was observed that the $CaCO_3$ µ-spheres dried in air were heavier than those dried in oven. With the membrane filtration approach, the average weight of $CaCO_3$ µ-spheres obtained by drying in air was 0.95 ± 0.04g and by drying in oven was 0.58 ± 0.13g. Similar results were obtained with the centrifugation approach, where the average weight of $CaCO_3$ µ-spheres by drying in air was 0.50 ± 0.19g and by drying in oven was 0.43 ± 0.15g. Overall, the results indicate that membrane filtration approach yields more quantity of $CaCO_3$ µ-spheres compared to the centrifugation approach, and drying at room temperature provides spherical shaped $CaCO_3$ µ-spheres.

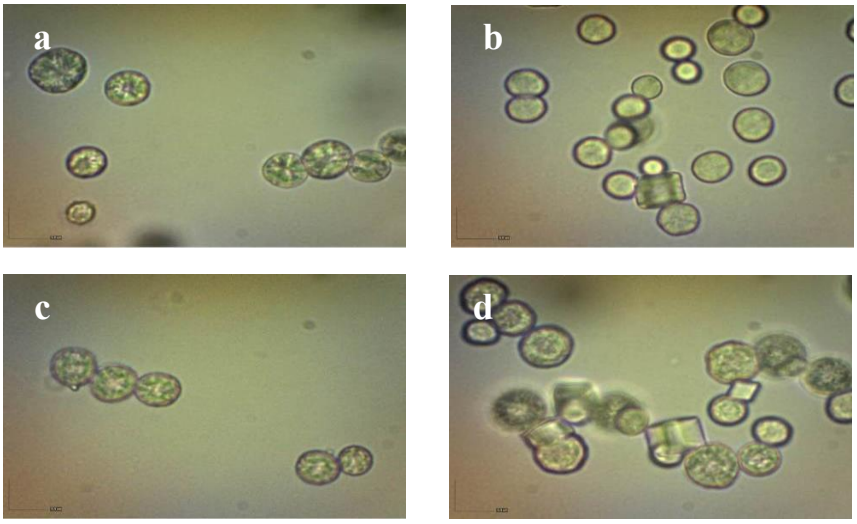


Figure 5. Microscope images of $CaCO_3$ µ-spheres fabricated using different drying techniques (a, c) dried in air and (b, d) dried in oven at 50 °C. Membrane filtration approach (a, b) and centrifugation approach (c, d) (100x magnification, scale bars indicate 5 µm)

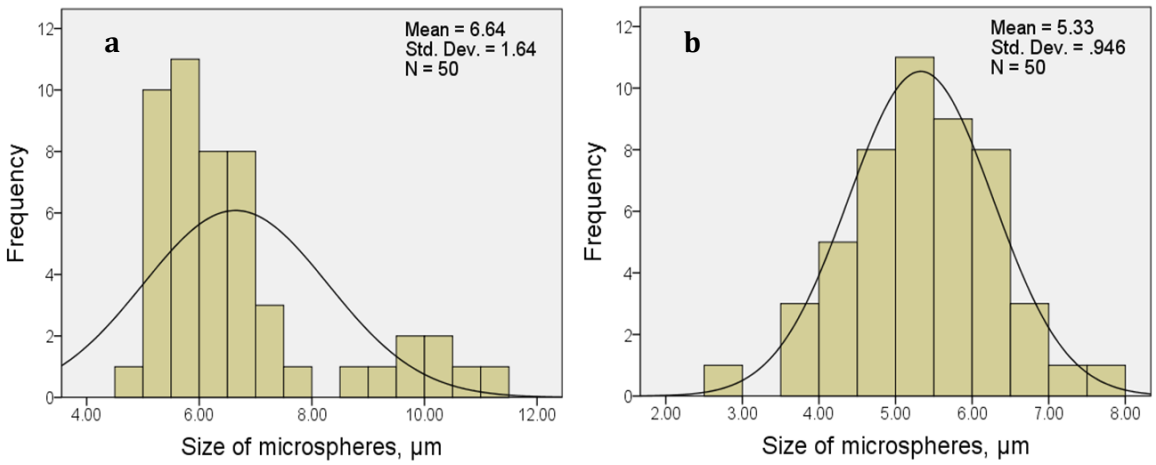


Figure 6. Histograms showing size distribution for $CaCO_3$ µ-spheres fabricated by drying in air (a) Membrane filtration approach and (b) centrifugation approach

Effect of type of filter paper

Figure 7 shows the effect of using different brands of filter paper that have different pore sizes. Compound microscope images show that $CaCO_3$ µ-spheres obtained by using Smith filter paper (with 15-20 µm pore size) had spherical shape and better size distribution (Figure 7a).

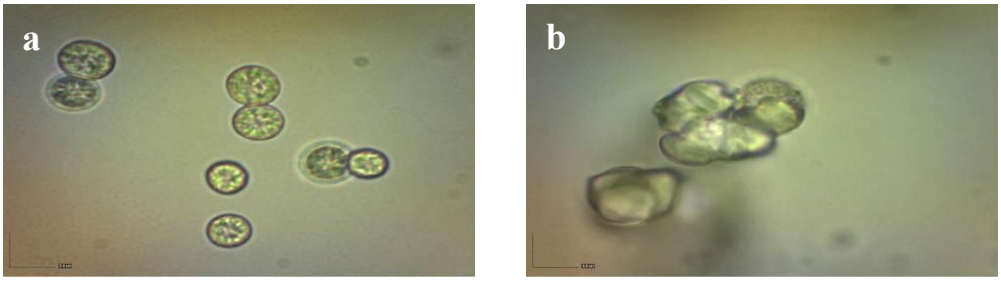


Figure 7. Microscope images of $CaCO_3$ µ-spheres fabricated using different types of filter paper in membrane filtration approach (a) Smith filter paper and (b) Whatman filter paper (100x magnification, scale bars indicate 5 µm)

Images of $CaCO_3$ µ-spheres obtained using Whatman filter paper had irregular particles (Figure 7b). The average size of the µ-spheres was 4.98 ± 0.57 µm by using smith filter paper. Histogram in Figure 8 shows that using membrane filtration system equipped with the smith filter paper yielded a narrow distribution of $CaCO_3$ µ-spheres. The results depict that the smith filter paper used here is more suitable to produce $CaCO_3$ µ-spheres.

Effect of centrifugation time

For centrifugation washing step at 1000 rpm for 1 min, uniform spherical $CaCO_3$ µ-spheres were obtained (Figure 9a); at 1000 rpm for 5 min, agglomeration (clustering) of the $CaCO_3$ µ-spheres was observed (Figure 9b). The average size of the µ-spheres was 5.14 ± 0.68 µm for centrifugation time of 1 min. Histogram in Figure 10 shows a narrow distribution of $CaCO_3$ µ-spheres obtained for centrifugation time of 1 min. The results indicate that a shorter centrifugation time results in spherical shapes and narrow size distribution of $CaCO_3$ µ-spheres.

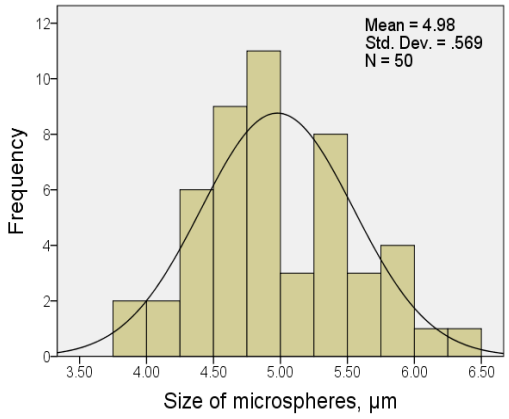


Figure 8. Histogram showing size distribution for $CaCO_3$ µ-spheres fabricated using Smith filter paper

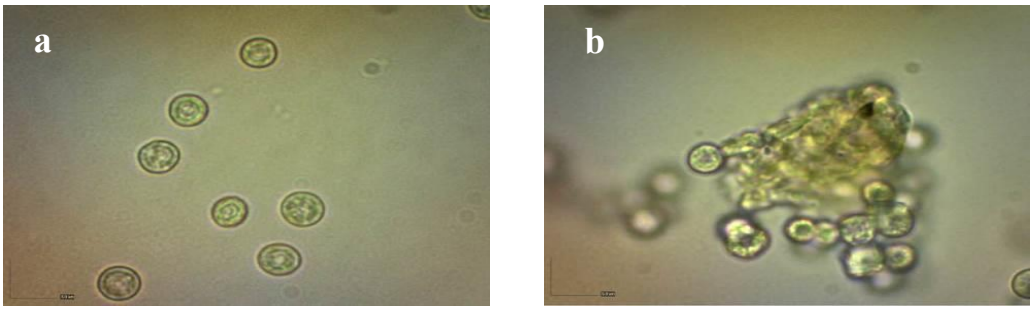


Figure 9. Microscope images of $CaCO_3$ µ-spheres fabricated using different times (a) 1 min, (b) 5 min centrifugation at 1000 rpm (100x magnification, scale bars indicate 5 µm)

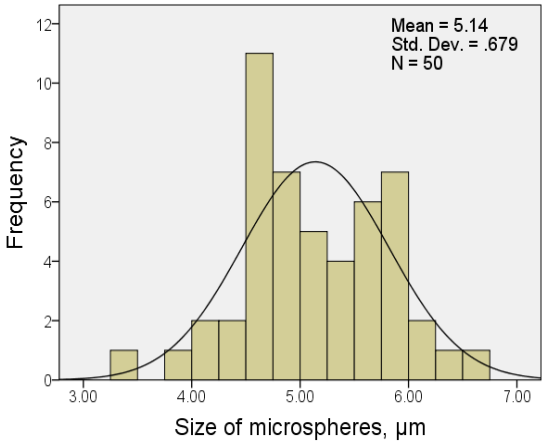


Figure 10. Histogram showing size distribution for $CaCO_3$ µ-spheres fabricated by centrifugation at 1000 rpm for 1 min

Effect of quantity of washing agents

Before drying, the μ-spheres were washed with distilled water and acetone for several times in order to eliminate the unreacted species. Figure 11a shows that spherical μ-spheres with average diameter of 4 ± 0.52 μm were obtained by using 25 mL of washing agents. Figure 11b shows that cauliflower-shaped $CaCO_3$ μ-spheres [19] were obtained by using 40 mL of washing agents. The results might be a consequence of the capacity of the centrifuge tube used; 25 mL of washing agents appeared to be suitable with 50 mL centrifuge tubes used in this study. Histogram in Figure 12 shows narrow distribution of $CaCO_3$ μ-spheres obtained using 25 mL of washing agents.

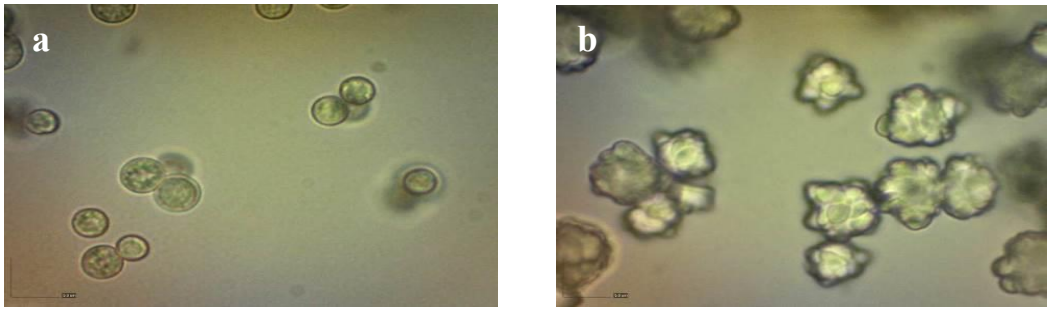


Figure 11. Microscope images of $CaCO_3$ μ-spheres fabricated using different quantity of centrifugation washing agents (a) 25 mL and (b) 40 mL of distilled water and acetone (100x magnification, scale bars indicate 5 μm)

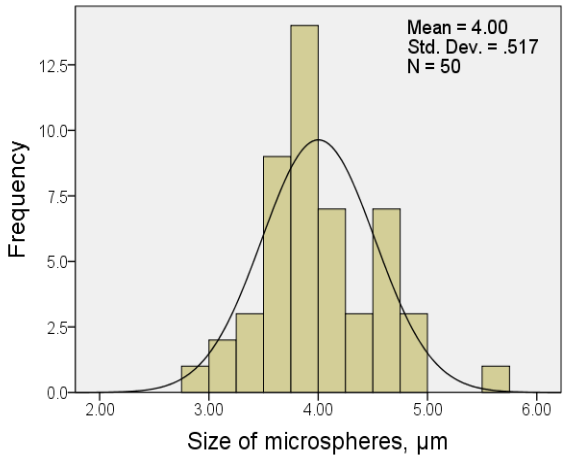


Figure 12. Histogram showing size distribution for $CaCO_3$ μ-spheres fabricated using 25 mL of centrifugation washing agents

Table 1 summarizes the results obtained for the $CaCO_3$ μ-spheres from all the experiments conducted to evaluate the influence of different experimental factors. For each fabrication approach, the experimental factors that yielded the best results were used to fabricate a new set of $CaCO_3$ μ-spheres. For membrane filtration approach (microscopy images shown in Figure 13a) the fabrication conditions used were direct mixing, stirring speed of 1200 rpm, drying in air, and Smith filter paper, whereas for centrifugation approach (microscopy images shown in Figure 13b) the fabrication conditions used were direct mixing, stirring speed of 1200 rpm, drying in air, centrifugation time of 1 min, and 25 mL of centrifugation washing agent. The average size of μ-spheres was 5.14 ± 0.68 μm and 4.81 ± 1.51 μm for centrifugation and membrane filtration approaches, respectively. Based on the final weight of $CaCO_3$ μ-

spheres, membrane filtration approach produced more quantity (average weight of 0.77 ± 0.16g) than centrifugation approach (average weight of 0.59 ± 0.07g). Histograms in Figure 14 show that the centrifugation approach yields better size distribution compared to the membrane filtration approach which has a bimodal distribution. SEM micrographs in Figure 15 show the spherical shaped $CaCO_3$ μ-spheres. The higher magnification micrographs clearly show the typical surface morphology of $CaCO_3$ μ-spheres.

Table 1. Summary of influence of experimental factors on $CaCO_3$ microsphere shape and size

Factor		**Figure**	**Weight (g)**	**Structure/Shape**	**Particle size (μm)**
Mixing procedure of solutions	Rapidly (directly)	1a	0.94	Spherical[a]	5.93 ± 0.72
		1c	0.72	Spherical[a]	5.33 ± 0.95
	Drop-by-Drop	1b	1.06	Agglomeration	-[b]
		1d	0.25	Agglomeration	-[b]
Stirring speeds (rpm)	300	3a	0.71	Calcite, Cluster	-[b]
		3e	0.59	Calcite, Cluster	-[b]
	600	3b	0.75	Calcite, Cluster	-[b]
		3f	0.60	Calcite, Cluster	-[b]
	900	3c	0.70	Calcite, Cluster	-[b]
		3g	0.62	Calcite, Cluster	-[b]
	1200	3d	0.80	Spherical[a]	4.98 ± 0.57
		3h	0.63	Spherical[a]	7.27 ± 0.78
Drying technique	Air	5a	0.95	Spherical[a]	6.64 ± 1.64
		5c	0.50	Spherical[a]	5.33 ± 0.95
	Oven (50°C)	5b	0.58	Spherical[a], Calcite	-[b]
		5d	0.43	Spherical[a], Calcite, Cluster	-[b]
Type of filter Paper	Smith		0.80	Spherical[a]	4.98 ± 0.57
	Whatman		0.90	Irregular particles	-[b]
Centrifugation time	1000 rpm, 1 min.		0.56	Spherical[a]	5.14 ± 0.68
	1000 rpm, 5 min.		0.66	Spherical[a], Agglomeration	-[b]
Centrifugation washing agents	25 mL		0.41	Spherical[a]	4 ± 0.52
	40 mL		0.37	Cauliflower-shaped	-[b]

[a]Nearly spherical
–[b]Clustered or agglomeration structure (data not analysed)

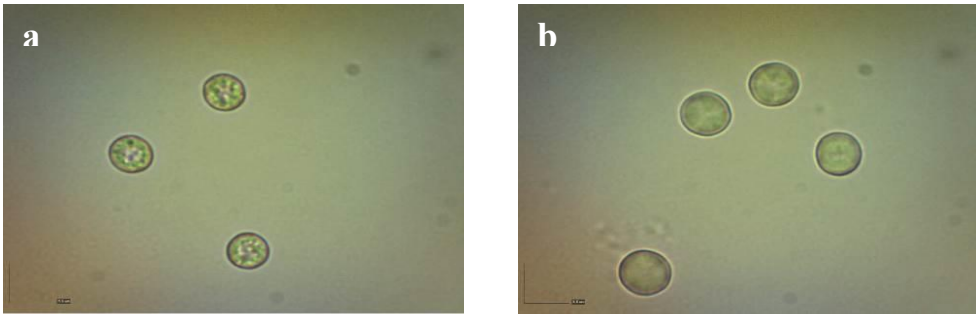


Figure 13. Microscope images of $CaCO_3$ µ-spheres fabricated using (a) membrane filtration approach and (b) centrifugation approach (100x magnification, scale bars indicate 5 µm)

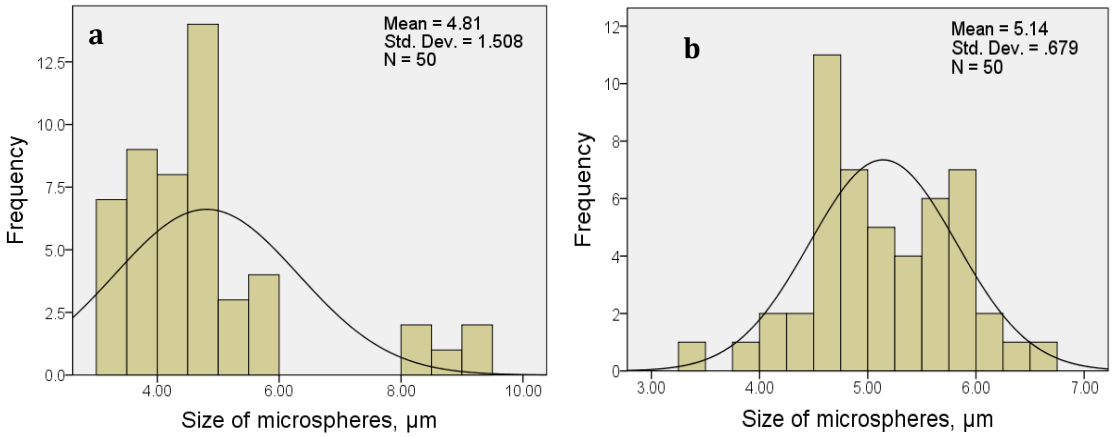


Figure 14. Histograms showing size distribution for $CaCO_3$ µ-spheres fabricated using (a) Membrane filtration approach and (b) centrifugation approach

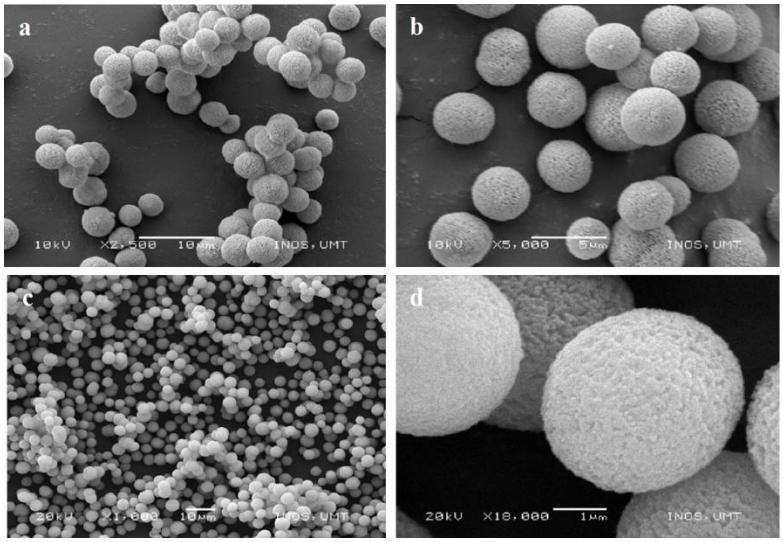


Figure 15. SEM images of $CaCO_3$ µ-spheres (a, b) taken using 10kV, and (c, d) taken using 20kV

Overall, the results indicate that the centrifugation approach can yield better $CaCO_3$ μ-spheres as compared to the membrane filtration approach in terms of uniform spherical shape and narrow size distribution of μ-spheres. These two are the desired characteristics for the $CaCO_3$ μ-spheres that would be used as templates for fabricating nano-engineered microcapsules.

Conclusion

Fabrication of $CaCO_3$ μ-spheres using precipitation reaction between $CaCl_2$ and Na_2CO_3 solutions was carried out using membrane filtration and centrifugation approaches by varying different experimental factors that have important roles in the formation of $CaCO_3$ μ-spheres; with distilled water used throughout the experiments. Better size distribution of $CaCO_3$ μ-spheres was obtained through direct mixing procedure of solutions, 1200 rpm of stirring speed, and drying in air for both the approaches. Also, better size distribution of $CaCO_3$ μ-spheres was obtained through using Smith filter paper in the case of the membrane filtration approach and at 1000 rpm for 1 min centrifugation time, using 25 mL of washing agents in the case of the centrifugation approach. Overall, our results indicate that the centrifugation approach can yield better $CaCO_3$ μ-spheres as compared to the membrane filtration approach in terms of uniform spherical shape and narrow size distribution of μ-spheres. The knowledge from this study will be used to prepare $CaCO_3$ μ-spheres that will act as templates for fabricating nano-engineered microcapsules.

Acknowledgement

This work was supported by Ministry of Higher Education (MOHE), Malaysia under the Fundamental Research Grant Scheme (FRGS), Grant no.: FRGS/1/2014/TK04/UNISZA/02/1.

References

1. Petrov, A. I., Volodkin, D. V. and Sukhorukov, G. B. (2005). Protein-calcium carbonate coprecipitation: A tool for protein encapsulation. *Biotechnology Progress*, 21: 918 – 925.
2. De Temmerman, M.-L., Demeester, J., De Vos, F. and De Smedt, S. C. (2011). Encapsulation performance of layer-by-layer microcapsules for proteins. *Biomacromolecules*, 12: 1283 – 1289.
3. Chapel, J.-P. and Berret, J.-F. (2012). Versatile electrostatic assembly of nanoparticles and polyelectrolytes: Coating, clustering and layer-by-layer processes. *Current Opinion in Colloid and Interface Science*, 17: 97 – 105.
4. Shimpi, N. and Mishra, S. (2010). Synthesis of nanoparticles and its effect on properties of elastomeric nanocomposites. *Journal of Nanoparticle Research*, 12: 2093 – 2099.
5. Mishra, S. and Shimpi, N. (2005). Comparison of nano $CaCO_3$ and flyash filled with styrene butadiene rubber on mechanical and thermal properties. *Journal of Scientific & Industrial Research*, 64: 744 - 751.
6. Gumfekar, S., Kunte, K., Ramjee, L., Kate, K. and Sonawane, S. (2011). Synthesis of CaCO 3–P (MMA–BA) nanocomposite and its application in water based alkyd emulsion coating. *Progress in Organic Coatings*, 72: 632 – 637.
7. Kirboga, S. and Oner, M. (2013). Effect of the experimental parameters on calcium carbonate precipitation. *Chemical Engineering Transactions*, 32: 2119 – 2124.
8. Tai, C. Y. and Chen, C. (2008). Particle morphology, habit, and size control of $CaCO_3$ using reverse microemulsion technique. *Chemical Engineering Science*, 63: 3632 – 3642.
9. Hanafy, N. A. N., De Giorgi, M. L., Nobile, C., Rinaldi, R. and Leporatti, S. (2015). Control of colloidal $CaCO_3$ suspension by using biodegradable polymers during fabrication. *Beni-Suef University Journal of Basic and Applied Sciences*, 4: 60 – 70.
10. Kitamura, M., Konno, H., Yasui, A. and Masuoka, H. (2002). Controlling factors and mechanism of reactive crystallization of calcium carbonate polymorphs from calcium hydroxide suspensions. *Journal of Crystal Growth*, 236: 323 – 332.
11. Koris, A. and Vatai, G. (2002). Dry degumming of vegetable oils by membrane filtration. *Desalination*, 148: 149 – 153.
12. Majekodunmi, S. O. (2015). A review on centrifugation in the pharmaceutical industry. *Annals of Biomedical Engineering*, 5: 67 – 78.
13. Trippa, G. and Jachuck, R. (2003). Process intensification: precipitation of calcium carbonate using narrow channel reactors. *Chemical Engineering Research and Design*, 81: 766 –772.

14. Prabu, S. B., Karunamoorthy, L., Kathiresan, S. and Mohan, B. (2006). Influence of stirring speed and stirring time on distribution of particles in cast metal matrix composite. *Journal of Materials Processing Technology*, 171: 268 – 273.
15. Kowalczyk, B., Lagzi, I. and Grzybowski, B. A. (2011). Nanoseparations: Strategies for size and/or shape-selective purification of nanoparticles. *Current Opinion in Colloid and Interface Science*, 16: 135 – 148.
16. Volodkin, D. V., Petrov, A. I., Prevot, M. and Sukhorukov, G. B. (2004). Matrix polyelectrolyte microcapsules: new system for macromolecule encapsulation. *Langmuir*, 20: 3398 – 3406.
17. Volodkin, D. V., Larionova, N. I. & Sukhorukov, G. B. (2004). Protein encapsulation via porous $CaCO_3$ microparticles templating. *Biomacromolecules*, 5: 1962 – 1972.
18. Lee, S., Park, J.-H., Kwak, D. and Cho, K. (2010). Coral mineralization inspired $CaCO_3$ deposition via CO_2 sequestration from the atmosphere. *Crystal Growth & Design*, 10: 851 – 855.
19. Ouhenia, S., Chateigner, D., Belkhir, M., Guilmeau, E. & Krauss, C. (2008). Synthesis of calcium carbonate polymorphs in the presence of polyacrylic acid. *Journal of Crystal Growth*, 310: 2832 –2841.

MALAYSIAN JOURNAL OF ANALYTICAL SCIENCES
Published by The Malaysian Analytical Sciences Society
ISSN 1394 - 2506

EMULSION LIQUID MEMBRANE TECHNOLOGY IN ORGANIC ACID PURIFICATION

(Teknologi Emulsi Membran Cecair dalam Penulenan Asid Organik)

Norela Jusoh[1], Norasikin Othman[1,2]*, Nur Alina Nasruddin[1]

[1]*Department of Chemical Engineering, Faculty of Chemical and Energy Engineering*
[2]*Centre of Lipids Engineering & Applied Research (CLEAR), Ibnu Sina Institute for Scientific and Industrial Research*
Universiti Teknologi Malaysia, 81310 UTM Johor Bahru, Johor, Malaysia

**Corresponding author: norasikin@cheme.utm.my*

Received: 14 April 2015; Accepted: 30 November 2015

Abstract

Emulsion Liquid Membrane (ELM) process have shown a great potential in wide application of industrial separations such as in removal of many chemicals, organic compounds, metal ions, pollutants and biomolecules. This system promote many advantages including simple operation, high selectivity, low energy requirement, and single stage extraction and stripping process. One potential application of ELM is in the purification of succinic acid from fermentation broth. This study outline steps for developing emulsion liquid membrane process in purification of succinic acid. The steps include liquid membrane formulation, ELM stability and ELM extraction of succinic acid. Several carrier, diluent and stripping agent was screened to find appropriate membrane formulation. After that, ELM stability was investigated to enhance the recovery of succinic acid. Finally, the performance of ELM was evaluated in the extraction process. Results show that formulated liquid membrane using Amberlite LA2 as carrier, palm oil as diluent and sodium carbonate, Na_2CO_3 as stripping agent provide good performance in purification. On the other hand, the prepared emulsion was observed to be stable up to 1 hour and sufficient for extraction process. In conclusion, ELM has high potential to purify succinic acid from fermentation broth.

Keywords: emulsion liquid membrane, purification, succinic acid, formulation, stability

Abstrak

Proses emulsi membran cecair (ELM) telah menunjukkan potensi yang hebat dalam pelbagai aplikasi pemisahan perindustrian seperti pembuangan pelbagai bahan kimia, sebatian organik, ion logam, bahan pencemar, dan molekul biologi. Sistem ini menawarkan banyak kelebihan termasuk operasi yang mudah, sangat selektif, keperluan tenaga yang rendah, dan proses pengekstrakan dan pelucutan dalam satu peringkat. Satu potensi aplikasi ELM adalah dalam proses penulenan asid succinic daripada larutan penapaian. Kajian ini menggariskan beberapa langkah untuk membangunkan proses emulsi membran cecair dalam penulenan asid sussinik. Langkah – langkah tersebut termasuklah formulasi cecair membran, kestabilan ELM, dan pengekstrakan asik sussinik menggunakan ELM. Beberapa pembawa, pelarut, dan agen pelucutan telah ditapis untuk mencari rumusan membran yang sesuai. Selepas itu, kestabilan ELM dikaji untuk meningkatkan perolehan asid sussinik. Akhir sekali, prestasi ELM dinilai dalam proses pengekstakan. Keputusan menunjukkan bahawa rumusan cecair membran menggunakan Amberlite LA2 sebagai pembawa, minyak kelapa sawit sebagai pelarut dan natrium karbonat, Na_2CO_3 sebagai agen pelucutan memberikan prestasi yang baik dalam proses penulenan. Disamping itu, emulsi diperhatikan stabil sehingga 1 jam dan ini mencukupi untuk proses pengekstrakan. Kesimpulannya, ELM berpotensi tinggi untuk mnulenkan asid sussinik daripada proses penapaian.

Kata kunci: emulsi membran cecair, penulenan, asid sussinik, formulasi, kestabilan

Introduction

Two fluid phases can be separated by a barrier called membrane which allow the selective permeation of solute through the barrier [1]. Membrane extraction utilizes either a porous or nonporous polymeric membrane to provide a selective barrier between the feed and the receiving phase. Instead of using solid as membrane material, it is also possible to use liquid as a membrane. Liquid membrane technology is widely applied in different potential area like wastewater treatment, textile industries, electroplating, pulp and paper, pharmaceutical, mining, semiconductor, dairy, food and beverage processing, biotechnology industries, and tanning and leather industries [2-4].

The liquid membrane extraction or commonly known as emulsion liquid membrane (ELM) was introduces as an alternative technique to the liquid-liquid extraction and to the separation by solid polymeric membranes. Basically, ELM is double emulsion produced by emulsifying two immiscible liquid phase (i.e. water droplet in oil or vice versa). Then, the resulting emulsion is dispersed into another external feed phase containing solute to be recovered or removed. The driving force of the solute transport through the membrane is simply the concentration gradient.

ELM offers numerous advantages because of high transport efficiency, economical, relatively low energy consumption, and high extraction efficiency due to large mass transfer surface area available. Besides, ELM also one of the most efficient techniques for separation and concentration process for low concentration of solute [5]. In addition, ELM process involve combination of extraction and stripping process [6]. This combination can remove the equilibrium limitation between the organic and aqueous phase. Besides, with the use of appropriate carrier for transport mechanism, specific molar recognition can be achieved.

An ELM process includes four main steps: (1) emulsification, (2) dispersion and extraction, (3) settling, and (4) demulsification (breaking of the emulsion). In the first step, emulsion is prepared by emulsifying internal phase and membrane phase. Then, the prepared emulsion is dispersed into the external feed phase containing solute to be extracted. After that, settling process is allowed to occur to separate emulsion and feed solution. Then, the membrane phase is recovered by demulsification process.

One potential application of ELM is in the purification of succinic acid from fermentation broth. Generally, succinic acid fermentation broth contains many components especially acetic acid as major by-product. Therefore, in this study, an ELM process was developed for selective separation of succinic acid from simulated solution. Important aspects regarding the ELM process is its formulation in terms of the emulsification procedure, the choice of surfactants, carrier, stripping agent and diluent, which decide whether the process is successful or not. Besides that, stability also plays an important role for successful ELM process. The emulsion should be stable enough to resist leakage during extraction, but not too stable so that the emulsion can easily demulsified.

This paper will present the investigation of liquid membrane component selection, stability study and several parameter of succinic acid extraction such as stripping agent concentration, carrier concentration and treat ratio.

Materials and Methods

Materials

Amberlite LA2 as carrier was obtained from Merck Company. Amberlite LA2 used, was mixture of straight-chain secondary amine mixture (374 g/mol). Trioctylamine (TOA) (>93 % assay) and tridodecylamine (TDA) (>95 % assay) were purchased from Merck. Kerosene as diluent was purchased from Sigma Aldrich. Palm oil, also as diluent used in this study was ordinary cooking oil (BURUH) acquired from supermarket. Sodium hydroxide (NaOH) (98 % assay) was purchased form J.T. Baker, while Sodium carbonate, Na_2CO_3 (99.5 % assay) was purchased from Merck. Sorbitan Monooleate (Span 80) (with more than 60 % oleic acid composition) as surfactant was purchased from Sigma Aldrich. Polyethylene glycol sorbitan monooleate (Tween 80) and Cocamide diethanolamine (DEA) was purchased from Sigma Alderich and Chemicalland21 respectively. In addition, succinic acid (SA) (99.0 % assay) and acetic acid (AA) (99.7 % assay) were purchased from Sigma Aldrich and J.T. Baker, respectively. All these solutions and reagents were used directly as received without further purification.

Methods

In formulation, ELM components including carrier, diluent and stripping agent was screened by liquid-liquid extraction process. The experiment was conducted by mixing an equal volume of organic solution and with simulated aqueous feed solution at 320 rpm using mechanical shaker. The solution was then poured carefully into separating funnel for phase separation. Sample of aqueous phase at the bottom was taken for succinic and acetic acid concentration measurement. Similar procedures was repeated for screening diluent and stripping agent. Extraction and stripping performance was evaluated using Equation 1 and 2 respectively.

The selected formulation was then used to study ELM stability. An equal volume of liquid membrane and stripping solution was emulsified at 5000 rpm using homogenizer. The emulsion formed was transferred into measuring cylinder and then stored at room temperature. The volume of different phase separated was recorded as a function of time. Similar procedure was repeated for different parameter.

In extraction study, the prepared emulsion was dispersed into feed phase of simulated succinic acid solution. The mixture was then agitated at 600 rpm for 3 minutes using a motor stirrer. The mixture was then separated in separating funnel. The aqueous phase at the bottom was taken for analysing. The performance of extraction was evaluated using Equation 1.

$$Amount\ extract\ (g/l)\ =\ \frac{[A]_{i(aq)} - [A]_{f(aq)}}{[A]_{i(aq)}} \tag{1}$$

$$Amount\ strip\ (g/l) = [A]_{fs(aq)} \tag{2}$$

where, $[A]_{i(aq)}$ is the initial acid concentration in external aqueous phase (g/l); $[A]_{f(aq)}$ is the acid concentration in aqueous extrenal phase after extraction (g/l); $[A]_{fs(aq)}$ is the acid concentration in aqueous stripping phase after stripping (g/l).

Besides that, distribution ratio (D) and separation factor (α) for the extraction of succinic and acetic acid were determined using Equation 3, 4, and 5.

$$D_{SA} = \frac{[SA]_{org}}{[SA]_{aq}} \tag{3}$$

$$D_{AA} = \frac{[AA]_{org}}{[AA]_{aq}} \tag{4}$$

$$\alpha_{\frac{SA}{AA}} = \frac{D_{SA}}{D_{AA}} \tag{5}$$

where D_{SA} is the distribution ratio of succinic acid; D_{AA} is the distribution ratio of acetic acid; $\alpha_{SA/AA}$ is the separation factor of succinic over acetic acid.

Results and Discussion

ELM formulation for Succinic Acid

The experimental results for liquid membrane component screening are shown in Table 1. The first parameter in liquid membrane formulation is carrier screening. The selection of suitable carrier is very crucial for the ELM system to perform well and selectively form complex with desired solute. Secondary or tertiary amine are generally typical carrier for carboxylic acid [6]. In this study, TOA, TDA and Amberlite LA2 from amine group were used to extract succinic acid. The current study clearly shows that Amberlite LA2 gives the best performance for succinic acid extraction (19.98 g/l) compared to TOA (10.99 g/l) and TDA (3.20 g/l). This is due to the Amberlite LA2 is one of the secondary amine, while TOA and TDA are both tertiary amine. Secondary amine can easily form complex with succinic acid and form ammonium salt. The process of complex formation involved the ion pair

association between the acid radical and the alkylammonium cation. Since Amberlite LA2 is a secondary amine, it can easily react with acid radical by losing the H bonding. This finding in line with the results found by Ricker (1978) who reported that the secondary amine shows better extractability compared to tertiary amine. Besides, highest value of separation factor was obtained using Amberlite LA2 as the carrier. This means that Amberlite LA2 not only can extract high amount of succinic acid, but it also selectively forms complex with succinic acid over acetic acid. Therefore, the use of Amberlite LA2 was preferred for the ELM formulation to separate succinic and acetic acid and used in the following section.

Table 1. Results of liquid membrane component screening

Parameters	**Variables**	**SA extract (g/l)**	**AA extract (g/l)**	**Selectivity,** $\alpha_{SA/AA}$
Carrier	TOA	10.99	1.40	2.15
	TDA	3.20	0.48	8.48
	Amberlite LA2	19.98	0.42	23.81
Kerosene/palm oil %	100/0	18.45	0.07	134.73
	70/30	20.89	0.70	17.79
	50/50	20.11	0.42	27.73
	30/70	22.22	0.28	57.82
	0/100	21.39	0.41	34.10
		SA stripped (g/l)		
Stripping agent	NaOH	7.58	-	-
	Na_2CO_3	16.34	-	-

The influence of diluents on separation of succinic and acetic acid also tabulated in Table 1. The present study shows that similar amount of succinic acid was extracted using different composition of kerosene and palm oil between 18 – 22 g/l of succinic acid. The results indicate that the composition of kerosene and palm oil did not give much effect on succinic acid extraction. Nevertheless, there was a really large different on the selectivity of succinic acid, where kerosene gives the best selection of succinic acid with 134.73 separation factor value. However, kerosene is not environmentally friendly and the toxicity effect of kerosene will be harmful to human. Hence, it is highly desirable to replace it with another material, such as palm oil. According to the results in Table 1, the combination of 30/70 kerosene to palm oil also leads to high separation factor (57.82) followed by a comparatively separation factor using pure palm oil (34.10). The 30/70 kerosene to palm oil provide larger separation factor, but the combination can complicate the extraction process and kerosene is still being used although in a small proportion. Therefore pure palm oil is selected as possible diluent in this study. This is because the valuable property in palm oil over kerosene seen as renewable, nontoxic and readily available. Hence, pure palm oil is considered as diluent in next study.

In the ELM system, the succinic acid extraction is governed by pH difference between the external feed and internal receiving phase. Therefore, alkaline solution such as NaOH and Na_2CO_3 were screened in this study as stripping agent for succinic acid extraction. The results indicate there is almost no acetic acid stripped in the process due to very small amount of acetic acid is extracted in the loaded organic phase. The amount of succinic acid stripped using Na_2CO_3 is 16.34 g/l compared to NaOH which is only 7.59 g/l. This is because Na_2CO_3 dissociates, and forms 2 moles of sodium ion in comparative to NaOH that gives only 1 mol. Therefore, more succinic acid will be stripped using Na_2CO_3. The result of this study seems to be consistent with other research, who reported that Na_2CO_3 show better performance than NaOH in stripping process of succinic acid [8].

ELM stability study: *Effect of organic to internal ratio*

Organic to internal phase ratio is important in order to achieve optimal emulsion stability. Table 2 represents stability of prepared emulsion showing various stage of phase separation. The most unstable emulsion was formed by 1/1 organic to internal ratio where the internal droplets dispersion did not last long and about 27 % of aqueous phase was separated just within 10 minutes. This is because the nature property of the palm oil and the existing natural surface-active agent called stearin influence the oil/water interface and modify the structure of the interfacial film and hence affect its stability [9]. Therefore, less droplets was formed for 1/1 ration. Increasing the ratio of O/I to 3/1 cause increasing in emulsion stability due to increase in the membrane phase layer around the internal droplets [10]. Besides, increasing the organic fraction will also increase the surfactant content in the emulsion, results in better droplet formation, increase mechanical resistance of the membrane and prevent coelescence of the dispersed droplet. Thus, more stable emulsion with greater amount of droplets was formed. Hence, 3/1 of O/I ratio is highly preferable to produce a stable emulsion.

Table 2. Effect of organic to internal ratio on emulsion stability

O/I ratio	Aqueous phase separated (%)		
	10 min	30 min	60 min
1:1	26	36	40
2:1	10	16	30
3:1	0	1	5

Effect of homogenizer speed

Application of mechanical energy can make one of the liquid breaks into droplets and disperse in the other and form emulsion. The influence of homogenizer speed on the performance of water in oil emulsion stability was presented in Table 3. Result indicates that the water in oil emulsion stability significantly increase as increasing homogenizer speed from 5000 to 7000 rpm. This is because increasing the homogenizer speed produce higher number of droplets with greater interfacial area, thus stabilize the emulsion. A study by Sulaiman et al. [11] also found that higher homogenizer speed increase emulsion stability. Further increase the speed to 9000 shows that the stability is lower than that of 7000 rpm. This is due to the droplets tend to coalesce among each other, thus enlarging their size which leading to the breakage of the droplet. At 12000 rpm homogenizer speed, a highly viscous, "mayonnaise-like" emulsion was formed. The reason for this is due to foaming mechanism, where air-bubbles are incorporated into the emulsion phase, and lead to a more rigid system. Therefore, homogenizer speed at 7000 rpm is preferable in this study in producing stable emulsion.

Table 3. Effect of homogenizer speed on emulsion stability

Homogenizer speed (rpm)	Aqueous phase separated (%)		
	10 min	30 min	60 min
5000	0	0.96	7.69
7000	0	0.96	3.85
9000	0	0.96	5.77
12000	0	0.96	0.96

Effect of emulsifying time

Table 4 demonstrate the effect of emulsification time on water in oil emulsion stability. For 3 minutes emulsification time, about 2 % of aqueous phase was separated from the emulsion in 10 minutes storage. This indicates that short emulsifying time produce unstable emulsion because of the organic membrane and aqueous internal solution was not well homogenized. Additions of emulsification time to 5 minutes produce more stable emulsion, where it starts to break after 30 minutes. This is due to smaller internal droplets formed, thus leading to stable emulsion because smaller droplets take more time to coalesce [12]. However, an extending the emulsification time up to 10 minutes and above decrease the stability of water in oil emulsion due to high shear exposure and causing emulsion breakage. The breakage phenomena because of prolonged emulsification time also observed by Othman et al. [13]. Thus, 5 minutes emulsification time is sufficient for the production of most stable emulsion.

Table 4. Effect of emulsifying time on emulsion stability

Emulsifying time (min)	**Aqueous phase separated (%)**		
	10 min	**30 min**	**60 min**
3	2	15	21
5	0	0.96	3.85
10	2	15	20
15	4	13	21
20	0	15	22

Effect of surfactant blend

Surfactant blend have synergistic effects in enhancing emulsion stability. Compared to individual emulsifiers, appropriate surfactant combination produce a greatly enhanced emulsion stability [9]. Basically, the addition of a co-surfactant can further reduce interfacial tension, also through adsorbing in the w/o interface thereby minimizing the repulsion of the hydrophilic head-groups of the surfactants, which contributes to a more efficient packing of the surfactants at the interface and reduces water droplet size. Result shows better stability was observed when HLB is increased. This indicate that Span 80 is compatible with Tween 80. This is due to similarity structure between both surfactant, since Tween 80 is a derivative from Span 80. Due to the compatibility structure, the film of Span 80 be better solvent for the Tween 80 on the mixed film, therefore form a phase that resist breakage. Hence, the emulsion is more stable. Figure 4 shows emulsion at HLB 8 and HLB 15 remain unseparated. However, emulsion at HLB 15 using only Tween 80 favours oil in water emulsion. Thus, combination of Span 80 and Tween 80 at HLB 8 will be considered for the next experiment.

Table 5. Effect of surfactant blend on emulsion stability

HLB	**Aqueous phase separated (%)**		
	10 min	**30 min**	**60 min**
4.3	0	18	20
5	0	0	4
6	0	17	20
7	0	12	18
8	0	0	0
15	0	0	0

ELM extraction study

The experimental results for succinic acid extraction efficiency are shown in Table 6. Effect of stripping agent concentration is shown in Table 6 varying from 0.01 to 2M of Na_2CO_3. The amount of succinic acid extracted increase when stripping agent concentration was increase from 0.01 to 0.5 M. The highest succinic acid extracted was 31.5 g/L. This is because of the tendency of the internal phase to strip succinic acid was increased and this delays the accumulation of succinic complex in the membrane layer. Further increase in Na_2CO_3 concentration reduces succinic acid extraction performance. This might be due to leakage of the succinic acid extracted and internal stripping agent through the membrane to the external. On the other hand, highest selectivity was obtained when using 0.50 M Na_2CO_3. It shows that at this stripping agent concentration, high amount of succinic acid was extracted. Furthermore, the system favors succinic acid than acetic acid to be extracted. Hence, 0.5 M Na_2CO_3 was selected as the best stripping agent concentration in this process.

Table 6. Results on succinic acid extraction

Parameters	Variables	Amount of succinic acid extracted (g/l)	Amount of acetic acid extracted (g/l)	Selectivity $\alpha_{SA/AA}$
Na_2CO_3 (M)	0.01	2.12	2.21	0.20
	0.10	2.51	2.96	0.18
	0.50	31.54	1.75	15.02
	1.00	9.19	2.45	1.08
	2.00	3.49	2.98	0.26
Amberlite LA2 (M)	0.005	7.79	3.63	0.50
	0.05	33.79	3.96	15.79
	0.50	31.97	3.11	14.24
	1.00	18.38	2.48	3.16
Treat ratio	1:1	32.45	1.38	43.95
	1:2	33.57	3.72	16.34
	1:3	33.79	0.57	184.83
	1:4	35.02	4.29	21.94
	1:5	28.47	0.76	41.28

Besides that, Table 6 also shows effect of carrier concentration on succinic acid extraction. Succinic acid was slightly extracted when 0.005 M of Amberlite LA2 was used. This indicates amount of carrier was insufficient for extraction process. Increasing the Amberlite LA2 concentration to 0.05 increase the succinic acid extraction up to 33.8 g/L from 40g/L succinic acid solution. An increased in succinic acid extraction occur due to the fact that the concentration of carrier in the organic membrane phase phenomenologically increases the solute concentration at the interface and thus increasing the driving force for extraction. However, the extraction performance was reduced when Amberlite concentration increased beyond 0.05M. This is due to excess of free carrier in the organic membrane phase. The excessive concentration of carrier cause higher viscosity of membrane, thus reduce the mass transfer of solute into the internal phase. On the other hand, highest selectivity at 15.79 was obtained at 0.05 M Amberlite LA2 concentration, which means succinic acid is the most favorable compared to acetic acid under this condition. Therefore, 0.05 M Amberlite LA2 was chosen as the optimum carrier concentration due to highest amount of succinic acid extracted and highest selectivity.

This study also varies treat ratio from 1:1 to 1:5. The amount of succinic acid extracted was slightly increased from treat ratio 1:1 to 1:4. At high treat ratio (1:1 to 1:2), larger mass transfer area can be obtained because higher number of emulsion globule was formed. However, with the help of surfactant hydration, this condition cause

continuous water movement into the internal aqueous phase and leads to emulsion breakage. This breakage therefore reduce succinic acid extraction at high treat ratio. This results is in line with Sulaiman et al. [11], who reported emulsion breakage occur at high treat ratio. Further reducing the treat ratio to 1:5 reduce the succinic acid extraction performance because of the reduction in the dispersibility of the emulsion. This cause smaller mass transfer surface area. As a result, the extraction efficiency shows a decreasing trend. Besides that, succinic acid extraction also may be reduced due to the emulsion breakage, owing to the increasing osmotic pressure difference between the external and ELM phase. Despite the highest succinic acid extracted when treat ratio 1:4 is applied, result of shows that the value is smaller than selectivity in treat ratio 1:3. This indicates that more acetic acid also extracted in the system. In addition, the emulsion breakage also higher compared to 1:3. Hence, 1:3 of treat ratio was selected as optimum condition.

Conclusion

The finding of this study provides an approach for selective extraction of succinic acid toward acetic acid. It can be concluded the best liquid membrane was formulated using Amberlite LA2 as carrier, palm oil as diluent, and Na_2CO_3 as stripping agent. Besides, all the parameter has shown a significant effect on the stability of water in palm oil emulsion. The most stable emulsion was recorded at 7000 rpm homogenizer speed, 5 minute emulsification time, and 3 % (w/v) span 80, and HLB value of 8 with combination of Span 80 and Tween 80. Meanwhile, up to 33.9 g/L succinic acid was extracted under promising conditions which are 0.5 M Na_2CO_3, 0.05 M Amberlite LA2, and 1:3 treat ratio.

Acknowledgement

The authors would like to acknowledge the Ministry of Higher Education (MOHE), Universiti Teknologi Malaysia (RU Research Grant; GUP: Q.J130000.2544.04H47, and Centre of Lipids Engineering and Applied Research (CLEAR) for financial support to make this research possible.

References

1. Ho, W. S. and Kamalesh, K. S. (1992). *Membrane Handbook*. New York: Chapman & Hall.
2. Othman, N., Noah, N. F. M., Harruddin, N., Abdullah, N. A. and Bachok, S. K. (2014). Selective extraction of palladium from simulated liquid waste solution by emulsion liquid membrane process using D2EHPA as a mobile carrier. *Jurnal Teknologi*. **69**(9): 1 - 4.
3. Ooi, Z.-Y., Harruddin, N. and Othman, N. (2015). Recovery of kraft lignin from pulping wastewater via emulsion liquid membrane process. *Biotechnology Progress*. **31**(5): 1305 - 1314.
4. Araki, T. and H. Tsukube (1990). *Liquid Membranes: Chemical Applications*. Boca Raton, FL: CRC Press.
5. Othman, N., H. Mat, and M. Goto (2005). Selective extraction of silver from liquid photographic waste. *Solvent Extraction Research and Development* **12**: 27 - 34.
6. Hong, Y., Hong, W. and Han, D. (2001). Application of reactive extraction to recovery of carboxylic acids. *Biotechnology and Bioprocess Engineering.* **6**(6): 386 - 394.
7. Ricker, N. L. (1978). Recovery of Carboxylic Acids and Related Organic Chemicals from Wastewater by Solvent Extraction. University of California: Berkeley.
8. Lee, S. C. (2011). Extraction of succinic acid from simulated media by emulsion liquid membranes. *Journal of Membrane Science*. **381**(1–2): 237 - 243.
9. Chow, M. C. and Ho, C. C. (1996). Properties of palm-oil-in-water emulsions: Effect of mixed emulsifiers. *Journal of the American Oil Chemists' Society*. **73**(1): 47 - 53.
10. Jilska, M. P. and Geoff, W. S. (2008). Use of Emulsion Liquid Membrane Systems in Chemical and Biotechnological Separations, in *Handbook of Membrane Separations*. CRC Press. pp. 709 - 740.
11. Sulaiman, R. N. R., Othman, N. and Amin, N. A. S. (2014). Emulsion liquid membrane stability in the extraction of ionized nanosilver from wash water. *Journal of Industrial and Engineering Chemistry*. **20**(5): 3243 - 3250.
12. Sabry, R., Hafez, A., Khedr, M. and El-Hassanin, A. (2007). Removal of lead by an emulsion liquid membrane: Part I. *Desalination*. **212**(1–3): 165 - 175.
13. Othman, N., Mili, N., Idris, A. and Zailani, S. N. (2012). Removal of Dyes from Liquid Waste Solution: Study on Liquid Membrane Component Selection and Stability. *Sustainable Membrane Technology for Energy, Water, and Environment.* pp. 221-229.

MALAYSIAN JOURNAL OF ANALYTICAL SCIENCES
Published by The Malaysian Analytical Sciences Society
ISSN 1394 - 2506

THE POTENTIAL OF COCONUT SHELL POWDER (CSP) AND COCONUT SHELL ACTIVATED CARBON (CSAC) COMPOSITES AS ELECTROMAGNETIC INTERFERENCE (EMI) ABSORBING MATERIAL

(Potensi Serbuk Tempurung Kelapa (CSP) dan Karbon Teraktif Tempurung Kelapa (CSAC) Sebagai Bahan Penyerap Gangguan Elektromagnatik)

Siti Nurbazilah Ab. Jabal[1], Yew Been Seok[1]*, Wee Fwen Hoon[2]

[1]*Faculty of Innovative Design and Technology,*
Universiti Sultan Zainal Abidin, Kampus Gong Badak, 21300 Kuala Terengganu, Terengganu, Malaysia
[2]*Embedded Computing Research Cluster, School of Computer and Communication Engineering,*
Universiti Malaysia Perlis, Jalan Kangar-Alor Star, Taman Pertiwi Indah Seriab, 01000 Kangar, Perlis, Malaysia

**Corresponding author: bseokyew@unisza.edu.my*

Received: 14 April 2015; Accepted: 30 November 2015

Abstract

Agriculture waste is potentially useful as an alternative material to absorb and attenuate electromagnetic interference (EMI). This research highlights the use of coconut shell powder (CSP) and coconut shell activated carbon (CSAC) as raw materials with epoxy resin and amine hardener composite to absorb microwave signals over frequency of 1 – 8 GHz. In order to investigate the suitability of these raw materials as EMI absorbing material, carbon composition of the raw materials is determined through CHNS Elemental Analysis. The surface morphology of the raw materials in term of porosity is investigated by using TM3000 Scanning Electron Microscope (SEM). The complex permittivity of the composites is determined by using high temperature dielectric probe in conjunction with Network Analyzer. From the result, the Carbon% of CSP and CSAC is 46.70% and 84.28% respectively. In term of surface morphology, the surface porosity of CSP and CSAC is in the range of 2 µm and 1µm respectively. For the dielectric properties, the dielectric constant and the dielectric loss factor for CSP and CSAC is 4.5767 and 64.8307and 1.2144 and 13.8296 respectively. The materials more potentially useful as substitute materials for electromagnetic interference (EMI) absorbing are discussed.

Keywords: agricultural wastes, dielectric properties, carbon composition

Abstrak

Sisa pertanian mempunyai potensi untuk digunakan sebagai bahan alternatif untuk menyerap atau melemahkan gangguan elektromagnatik (EMI). Kajian ini menekankan kepada penggunaan serbuk tempurung kelapa (CSP) dan karbon teraktif tempurung kelapa(CSAC) sebagai bahan mentah dengan campuran resin epoksi dan komposit penguat amina untuk menyerap gelombang mikro dalam frekuensi 1 – 8 GHz. Bagi mengkaji kesesuaian bahan mentah sebagai bahan penyerap gelombang mikro, komposisi karbon dalam bahan mentah ditentukan mengunakan analisis unser CHNS. Liang permukaan bahan mentah pula dikaji mengunakan mikroskop pengimbas elektron TM3000 (SEM). Ketelusan kompleks bagi bahan campuran diukur menggunakan prob dielektrik suhu tinggi dan alat analisis rangkaian. Daripada keputusan yang diperolehi, peratusan karbon dalam CSP dan CSAC adalah sebanyak 46.70 % dan 84.28 %. Manakala dari segi liang permukaan pula, keliangan CSP dan CSAC masing – masing berada dalam lingkungan 2um dan 1um.Bagi sifat dielektrik, pemalar dielektrik untuk CSP dan CSAC masing – masing adalah 4.5767 dan 64.8307. Bagi pembelauan dielektrik, nilai untuk CSP dan CSAC masing – masing adalah 1.2144 dan 13.8296. Isu bahan yang lebih berpotensi untuk digunakan sebagai bahan penyerap gangguan elektromagnatik (EMI) dibincangkan.

Kata kunci: sisa pertanian, sifat dielektrik, komposisi karbon

Introduction

Recently, researchers have focused to identify the agricultural wastes (organic materials) as a new absorbing material. Agricultural waste is made up of organic compounds from living plant like oil palm shell, rice husk, and coconut shell. Many natural substances (agricultural wastes) are used as base materials to make activated carbon. The most common being used in absorbing material are sugarcane, rice husk, ground nut shell, oil palm shell, coconut shell, corncobs, durian shell, soybean oil cake [1-6]. At present, coconut wastes are used in horticultural and agricultural applications [7]. Carbon is the main element to absorb unwanted electromagnetic signals [8-12].

The French chemist Antoine-Alexandre-Brutus Bussy who in a 1822 is the first publication suggested that porosity was important to the adsorptive properties of activated carbons. Optical microscopy and scanning electron microscopy (SEM) have demonstrated enormous potential for use in the study and characterization of activated carbons because of their ability to directly view the micro-structure of activated carbons [13,14]

Dielectric properties are the main characteristic that determines a material to absorb energy. The dielectric properties (ε) are derived from transmission line theory [15-17] and are expressed as complex permittivity, shown in Equation 1:

$$\varepsilon = \varepsilon' - j\varepsilon'' \tag{1}$$

where ε is define as dieletric properties, ε' is define dieletric constant and ε'' define as dieletric loss factor.

Dielectric constant (ε') is the real part of the complex permittivity whereas the imaginary part of the complex permittivity is called the dielectric loss factor (ε'').The dielectric constant and dielectric loss factor effect the ability of a material to act as microwave absorber. The dielectric constant defines the ability of a material to store the microwave energy while the dielectric loss factor defines the ability of a material to convert and dissipate the stored microwave energy to heat. In other words, microwave absorber prefers materials that possess higher thermal conductivity because when the thermal conductivity increases, the ability of these materials to dissipate heat also increase.

In this paper, the potential of CSP and CSAC with epoxy resin and amine hardener composite will be investigated.

Materials and Methods

Material preparation

For the coconut shell source, it was economically important to use a readily available agricultural waste by product. To manufacture coconut shell powder, the shells of fully matured nuts are first cleaned of the adhering pithy matter. The matured coconut shells were taken from Kuala Ibai, Terengganu, Malaysia. The coconut shell is sanded using sanding machine in order to get the coconut shell powder. The readymade CSAC powder was bought from Tan Meng Keong Sdn. Bhd company, Perak Darul Ridzuan, Malaysia.

Material characterisation

The carbon composition of the CSP and CSAC is determined by using ultimate analyses through CHNS Elemental Analysis. The CHNS elemental analysers provide a means for rapid determination of carbon, hydrogen, nitrogen and sulphur in organic matrices [18,19]. In order to investigate the surface morphology of CSP and SCAC materials in term of porosity, sample was investigated by using TM3000 Scanning Electron Microscope. For SEM measurements, the samples were prepared by coated with a thin layer of platinum [5-20].

Composite preparation

The raw material was mix with epoxy resin matrix and the composites were prepared in weight ratio 80: 20 (80 % for raw material, 20 % of epoxy resin). Sample 1, the CSP composites were stirred by using IKA RW20 Digital Stare for 1 hour. Sample 2 was prepared in similar manner but using CSAC. The mixture was poured in 30mm x

30mm x 5 mm rectangular planner moulds. Fabrication of sample 1 can be done through the steps summarized in Figure 1 below.

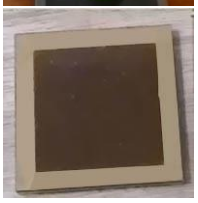
Step 1		Sanding process of matured and cleaned coconut shell
Step 2		Collection of coconut shell powder
Step 3		The coconut shell powder mixing with resin and hardener in weight ratio 80:20
Step 4		The coconut shell powder composites were stirred by using IKA RW20 Digital Stirer for 1hour
Step 5		The composite were filled and fabricate using mould.

Figure 1. Fabrication of composite sample

Dielectric Properties Measurement

Several popular measurement techniques are the transmission line techniques (waveguide, coaxial and free-space), impedance, dielectric probe and cavity methods [21]. Amongst these techniques, high temperature dielectric probe techniques are chosen to determine of the complex permittivity of the coconut shell powder and coconut shell activated carbon polymer composite dielectric properties measurement. The high temperature dielectric probe is performed by contacting the probe into the samples. The high temperature probe measurement procedure, which is done by contacting the probe to a flat surface of a sample, is shown in Figure 2. The fields at the probe end "fringe" into the material and change as they come into contact with the MUT.

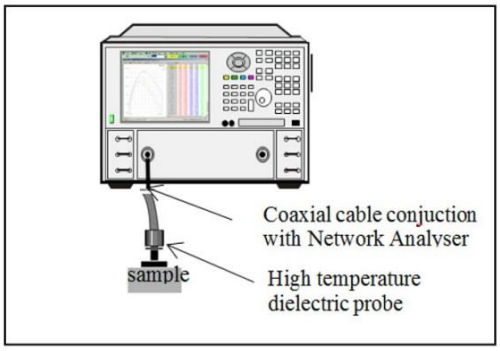


Figure 2. Measurement techniques for CSP and CSAC composites: High Temperature Dielectric Probe Technique

Results and Discussion

Carbon composition

The carbon composition of the CSP and CSAC is determined through CHNS Elemental Analysis. The CHNS Elemental Analysis determines the percentages of Carbon, Hydrogen, Nitrogen and Sulphur [22]. The result of elemental analysis of CSP and CSAC is presented in Table 1.

Table 1. The CHNS Elemental Analysis of CSP and CSAC

Material	Total Mass (mg)	Carbon		Hydrogen		Nitrogen		Sulphur		Oxygen
		%	mg	%	mg	%	mg	%	mg	(by diff)
CSP	2.0120	46.70	0.94	3.174	0.064	0.171	0.003	1.036	0.021	48.92
CSAC	2.0140	84.28	1.697	0.478	0.010	0.222	0.005	1.084	0.022	13.94

As presented in Table 1, the carbon % of CSP and CSAC is 46.70 % and 84.28 % respectively. The CSP has lower carbon content compare to CSAC. The high composition of carbon in the coconut shell as presented from the elemental analysis indicates a good precursor material for porous carbon [23].

CSAC have higher carbon content compared to CSP because to produce activated carbon from coconut shells, the overall process utilizes the pyrolysis of coconut shells into char, followed by steam activation in a fluidized bed reactor (FBR). The resulting activated carbon is 97% pure.

Surface Morphology

SEM morphologies in Figure 3 and Figure 4 shown reveal details of activated porosity development of CSP and CSAC.

The most important property of the activated carbon is its adsorptive capacity, which in general is proportional to the surface area [24, 25]. Carbon's highly porous nature provides a large surface area for absorption. The application of activated carbon in absorption processes mainly depends on the surface chemistry and pore structure of porous carbon [26]. While, Li et al. said that activated carbon having porous structure and high surface area where the pore structure is importance for optimal performance for absorbing material [27]. CSAC is an excellent quality high surface area material [28].

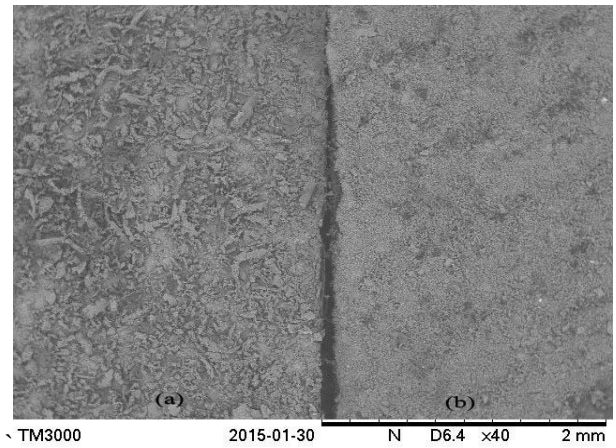
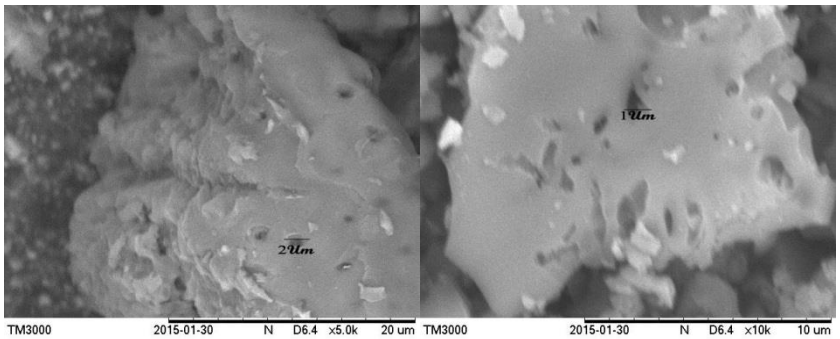


Figure 3. SEM morphology on composite surface (a) CSP; (b) CSAC



(a) (b)

Figure 4. SEM morphology on particle porosity (a) CSP; (b) CSAC

In Figure 4, presence of mesopores is detected in CSP and CSAC where the porosity is in the range of 2um and 1um respectively.

Dielectric Properties

The result of dielectric properties of CSP and CSAC over frequency of 1-8 GHz is presented in Table 2.

Figure 5 (a) and (b) show the dielectric properties that were measured from CSP and CSAC composites. The dielectric constant and dielectric loss factor vary when the frequency increased from 1GHz to 8GHz. It can be observed that the dielectric properties of the CSAC composite are higher compared to the CSP composite. This is due to the high carbon composition in the CSAC compared to the raw CSP.

Table 2. Dielectric properties for CSP and CSAC

Frequency (GHz)	Sample Composite	Dielectric Properties		
		Dielectric Constant (ε')	Dielectric Loss Factor (ε'')	Loss Tangent ($\tan\delta$)
1	CSP	5.1244	0.5200	0.1015
	CSAC	64.8307	18.0791	0.2789
2	CSP	5.0726	0.7029	0.1386
	CSAC	60.8409	14.7596	0.2426
3	CSP	4.8108	0.7497	0.1558
	CSAC	58.6587	13.6022	0.2319
4	CSP	4.8539	0.8508	0.1753
	CSAC	57.5637	13.6078	0.2364
5	CSP	4.6504	0.9517	0.2046
	CSAC	56.1002	13.7901	0.2459
6	CSP	4.5765	1.0525	0.2300
	CSAC	54.9361	13.7144	0.2497
7	CSP	4.4164	1.1331	0.2566
	CSAC	54.2399	14.0169	0.2584
8	CSP	3.1100	1.2144	0.3905
	CSAC	52.0081	13.8296	0.2659

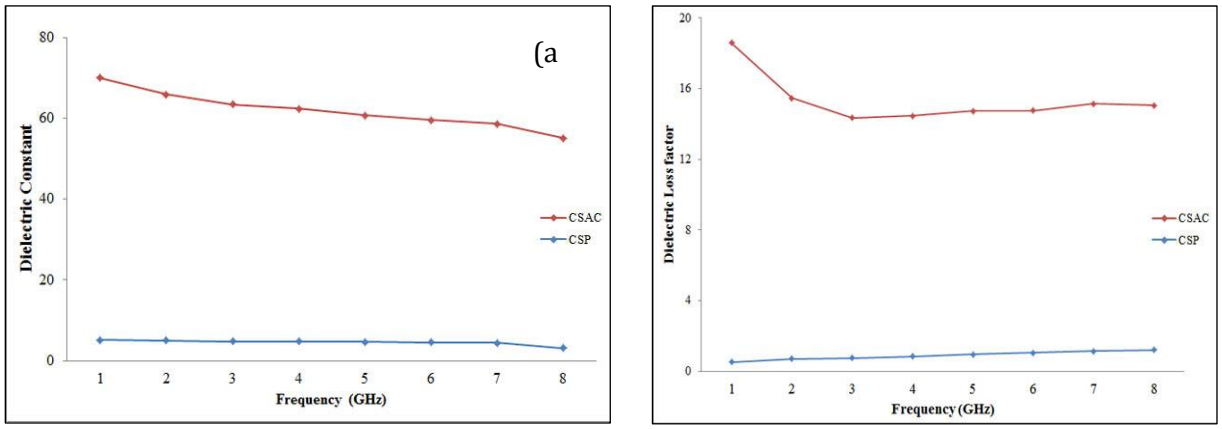


Figure 5. (a) Dielectric constant of CSP and CSAC; (b) Dielectric loss factor of CSP and CSAC

Conclusion

From this experiment, we investigate the potential of CSP and CSAC composites as EMI absorbing material in term of carbon composition, surface morphology and dielectric properties. Both CSP and CSAC composites show desirable potential to be used as EMI absorbing material, in term of carbon as dominant element, mesopores porosity and thermal conductivity. From the result, CSAC composite possess better carbon composition, surface morphology and thermal conductivity compared to CSP composite.

Acknowledgement

The authors would like to thank to UniSZA for supporting this research and MOHE for providing research grant (RAGS/1/2014/TK06/UNISZA//1), UniMAP for providing the facilities for measurement purpose, by means of Agilent E8362B P-series Network Analyser and TM3000 Scanning Electron Microscope and Universiti Malaya for providing the CHNS Elemental Analyser for measurement purpose.

References

1. Salleh M. K. M., Yahya M., Awang Z., Muhamad W. N. W., Mozi A.M. and Yaacob N. (2011). Single layer coconut shell – based microwave absorber. *IEEE TENCON:* pp 1110 – 1113.
2. Sivakumar, K. and Mohan, N. K. (2010). Performance analysis of downdraft gasifier for agriwaste biomass materials. *Indian Journal of Science and Technology*, 3: 58 – 60.
3. Daud, W. M. A. W. and Ali, W. S. W. (2004). Comparison on pore development of activated carbon produced from palm shell and coconut shell. *Bioresource Technology*, 93: 63 – 69.
4. Cobb, A., Warms, M., Maurer, E. P. and Chiesa, S. (2012). Low-tech coconut shell activated charcoal production. *International Journal for Service Learning in Engineering,* 7: 93 –104.
5. Chandra, T. C., Mirna, M. M., Sunarso, J., Sudaryanto, Y. and Ismadji, S. (2009). Activated carbon from durian shell: preparation and characterization. *Journal of Taiwan Institute Chemical Engineering.* 40: 457 – 462.
6. Tay, T., Ucar, S. and Karagoz, S. (2009). Preparation and characterization of activated carbon from waste biomass. *Journal of Hazardous Materials,* 165: 481 – 485.
7. Cresswell, G., (2011). Coir dust a proven alternative to peat. *Cresswell Horticulrutal Services (Report):* 1 – 13.
8. Yusof, A. A. (2004). Thesis The development of microwave absorber from oil palm shell carbon.
9. Yusof, A. A., Ali, W. K. W., Rahman, T. A. and Ani F. N. (2005). Microwave and reflection properties of palm shell carbon-polyester conductive composite absorber. *Jurnal Teknologi*, 42: 59 – 74.
10. Zahid, L., Malek, M. F. B. A., Nornikman, H., Mohd Affendi, N. A., Ali, A., Hussin, N., Ahmad B. H. and Abdul Aziz, M. Z. A. (2013). Development of pyramidal microwave absorber using sugar cane bagasse (SCB). *Progress in Electromagnetics Research*, 137: 687 – 702.
11. Menéndez, J. A., Arenillas, A., Fidalgo, B., Fernández, Y., Zubizarreta, L., Calvo, E. G. and Bermúdez, J. M. (2010). Microwave heating processes involving carbon materials. *Fuel Processing Technology*, 91: 1 – 8.
12. Information from Biofuels Research Infrastructure for Sharing Knowledge (BRISK), Database for biomass and waste, Retrived from https://www.ecn.nl/phyllis2/
13. Achaw, O-W. and Afrane, G. (2008). The evolution of pore structure of coconut shells during the preparation of cocnut shell-based activated carbons. *Microporous and Mesoporous Materials,* 112: 284 – 290.
14. Mfanacho, S. M., Hemang, P. and Manocha, L. M. (2010). Enhancement of microporosity through physical activation. *PRAJÑĀ - Journal of Pure and Applied Sciences*, 18: 106 – 109.
15. Saini, P., Arora, M. and Ailton, D.S.G. (2012). Microwave absorption and EMI shielding behaviour of nanocomposites based on intrinsically conducting polymers, graphene and carbon nanotubes. In Chapter 3. Crotia: InTech Publishing: pp 1 – 42.
16. Li, S., Chen, S., Anwar, S., Lu, W., Lai, Y., Chen, H., Hou, B., Ren, B, F. and Gu, B. (2012). Applying Effective Medium Theory in Characterizing Dielectric Constant of Solids. *Progress in Electromagnetics Research*. 35: 145 –153.
17. Micheli, D., Apollo, C., Pastore, R., Morles, R.B., Marchetti, M., Gradoni, G. edited by Reddy, B. (2011). Electromagnetic characterization of composite materials and microwave absorbing modelling in Chapter 16. InTech Publishing: pp 359 – 384.
18. Thompson, M. (2008). CHNS Elemental Analysers (Analytical Methods Committee). Royal Chemical Society: pp 1 – 2.
19. Meena, P. L., Saxena, R. and Sharma, N. (2014). A rapid analytical method using flow injection preconcentration of zinc on dithizone impregnated on amberlite XAD-2 and its determination in water samples by FAAS. *International Journal of Agriculture and Food Science Technology,* 5: 287 – 296.
20. Koboski, K. R., Nelsen, E. F. and Hampton, J. R. (2013). Hydrogen evolution reaction measurements of dealloyed porous NiCu. *Nanoscale Research Letters*, 8: 528 – 535.
21. Hoon, W. F., Jack, S. P., Malek, M. F. A. and Hasssan, N. (2012). Alternatives for pcb laminates: dielectric properties' measurements at microwave frequencies in Chapeter 5. InTech Publishing.

22. Chakma, S., Vaishya, R. C. and Yadav, A. K. (2015). Modeling chemical compositions of municipal solid waste. *Environmental Geotechnics (Article in Press)*: September 11, 2015
23. Cazetta, A. L., Vargas, A. M. M., Nogami, E. M., Kunita, M. H., Guiherme, M. R., Martins, A. C., Silva, T. L., Moraes, J. C. G. and Almeid, V. C. (2011). NaOH activated carbon of high surface area produced from coconut shell: kinetics and equilibrium studies from the methylene blue adsorption. *Chemical Engineering Journal*, 174: 117 – 125.
24. Demiral, H., Demiral, I., Karabacakoglu, B. and Tumsek. F. (2011). Production of activated carbon from olive bagasse by physical activation. *Chemical Engineering Research and Design*, 89: 206 – 213.
25. Nasria, N. S., Jibrila, M., Zaini, M .A. A., Mohsin, R. Daduma, H. U. and Musa, A. M. (2014). Synthesis and characterization of green porous carbons with large surface area by two step chemical activation with KOH. *Jurnal Teknologi*. 67(4): 25 – 28.
26. Bhatnagar, A., Hogland, W., Marques, M. and Sillanpaa, M. (2013). An overview of the modification methods of activated carbon for its water treatment applications. *Chemical Engineering Journal*, 219: 499 – 511.
27. Iqbaldin, M. M., Khudzir, I., Azlan, M. M., Zaidi, A. G., Surani, B. and Zubri, Z. (2013). Properties of coconut shell activated carbon. *Journal of Tropical Forest Science*, 25: 497 – 503.
28. Atwater, J. E. and Jr. R.R. Wheeler. (2004). Microwave permittivity and dielectric relaxation of a high surface area activated carbon. *IEEE Electrical Insulation Magazine,* 17(2): 66 – 66.

MALAYSIAN JOURNAL OF ANALYTICAL SCIENCES
Published by The Malaysian Analytical Sciences Society
ISSN 1394 - 2506

ANALYSIS OF SEASONAL SOIL ORGANIC CARBON CONTENT AT BUKIT JERIAU FOREST, FRASER HILL, PAHANG

(Analisis Kandungan Karbon Organik Tanah Secara Bermusim Di Hutan Bukit Jeriau, Fraser Hill, Pahang)

Ahmad Adnan Mohamed[1,2], Sahibin Abd. Rahim[2], David Allan Aitman[2], Mohd Khairul Amri Kamarudin[1,3]*

[1]*East Coast Environmental Research Institute (ESERI), Universiti Sultan Zainal Abidin, Gong Badak Campus, 21300 Kuala Terengganu, Terengganu, Malaysia.*
[2]*School of Environmental and Natural Resources Science, Faculty of Science and Technology, Universiti Kebangsaan Malaysia, 43600 UKM Bangi, Selangor, Malaysia*
[3]*Faculty of Innovative Design and Technology, Universiti Sultan Zainal Abidin, Gong Badak Campus, 21300 Kuala Terengganu, Terengganu, Malaysia*

**Corresponding author: mkhairulamri@unisza.edu.my*

Received: 14 April 2015; Accepted: 30 November 2015

Abstract

Soil carbon is the carbon held within the soil, primarily in association with its organic content. The total soil organic carbon study was determined in a plot at Bukit Jeriau forest in Bukit Fraser, Pahang, Malaysia. The aim of this study is to determine the changing of soil organic carbon between wet season and dry season. Soil organic carbon was fined out using titrimetric determination. The soil organic carbon content in wet season is 223.24 t/ha while dry season is 217.90 t/ha. The soil pH range in wet season is between 4.32 to 4.45 and in dry season in 3.95 to 4.08 which is considered acidic. Correlation analysis showed that soil organic carbon value is influenced by pH value and climate. Correlation analysis between clay and soil organic carbon with depth showed positively significant differences and clay are very much influenced soil organic carbon content. Correlation analysis between electrical conductivity and soil organic carbon content showed negative significantly difference on wet season and positively significant different in dry season.

Keywords: organic carbon, Fraser's Hill, forest, soil

Abstrak

Karbon tanah adalah nama generik bagi karbon yang wujud di dalam tanah, terutamanya dalam pencampuran kandungan organiknya. Satu kajian kandungan karbon organik di dalam tanih telah ditentukan di satu plot berukuran 1 hektar persegi di Hutan Simpan Bukit Jeriau, Bukit Fraser, Pahang, Malaysia. Tujuan kajian ini adalah untuk menentukan perbezaan kandungan karbon organik dalam tanah antara musim basah dan musim kering. Kandungan karbon organik ditentukan dengan menggunakan kaedah pentitratan.Jumlah kandungan karbon organik pada musim basah adalah sebanyak 223.24 t/ha manakala pada musim kering pula sebanyak 217.90 t/ha. Julat pH pada musim basah adalah 4.32 hingga 4.45 manakala pada musim kering adalah dari 3.95 hingga 4.08, dalam lingkungan berasid. Nilai pH pada musim kering mengalami penurunan. Analisis korelasi mendapati nilai pH dan iklim memberi kesan kepada kandungan karbon organik. Ujian korelasi antara lempung dengan kandungan karbon organik menunjukkan terdapat pebezaan signifikan positif. Ini menunjukkan kandungan lempung mempengaruhi kandungan karbon organik dalam tanih. Ujian korelasi kekonduksian elektrik dengan kandungan karbon organik menunjukkan perbezaan signifikan yang negatif pada persampelan musim basah manakala perbezaan signifikan positif pada musim kering.

Kata kunci: karbon organik, Bukit Fraser, hutan, tanih

Introduction

Organic are the terms use to describe the materials that associated with or derived from living organisms. The amount of organic matter in soil is often used as an indicator of the potential sustainability in a soil system. Soil organic matter are playing important part in nutrient cycle and repairing soil structure. Organic carbon in soil is important to ensuring good health in soil environment and critical in supplying the needs of the ecosystem [1,2]. Recently, research on soil organic carbon becoming important because of terrestrial organic carbon is critical factor to understanding carbon emission in which can causing climate change [3]. Organic carbon in soil are part of soil organic component, including others important elements such as hydrogen, oxygen and nitrogen. Organic in soil is derived from plants and animals that gradually decomposes. Soils constitute a significant reservoir of carbon (C) in both organic and mineral forms and can play an important global role, by mitigating or contributing carbon to the atmosphere [4,5]. Globally, soils contain more than two thirds of the total C stored in vegetation and almost twice the amount in the atmosphere while forest soils (including peaty soils) contain approximately 69 % of the total forest C pool [6]. With a small change in soil organic carbon, it can show a significant change for CO2 in atmosphere [7]. Carbon absorbance into the soil is a way that can decrease carbon accumulation in atmosphere which can lower the risks of climate changes. From that, the result show where soil organic carbon is very important to predict the effects and brings on global environment [8,9]. Field survey are a good ways to evaluate soil organic carbon including in the high altitude area such as Fraser Hill.

Carbon stored form the organic carbon in soil is highly sensitive to land use changes [10,11]. Organic carbon contain in soil are decrease with decreasing of organic matter inputs, while it increasing in organic carbon oxidation cause of aggregates disruption, and increasing the aeration. Many factors can indicate the stabilization of organic carbon in soil, the important factors are clay content, pH, hydrology, climate, and organic matter inputs. Some of these factors are fixed and depended on soil characteristics while some are depended on climate and land use management. Soil organic carbon storage are controlled by balanced from input from vegetation and decomposition output [12,13]. Organic carbon storage in soil are high in high altitude are because of high in carbon concentration (organic carbon per area) [14]. With unique climate and less human activity, Fraser Hill are ideal place to run a research on determine the soil organic carbon for the higher altitude area. Research on soil organic carbon changes are important for us to understand the relationship of its content in forest and their changes effect on global in the future [15].

Materials and Methods

Study area

Fraser Hill is very popular as a highland vacation and situated on 1500 m from sea level. This area is located on Titiwangsa range in Peninsular Malaysia which is formed by igneous formation activities from late Triassic to early Jurassic [2,15]. Annual rainfall distribution is 2624 mm with average 208 wet days. The area receives 20mm to 410mm of rainfall each month, typically low during the first quarter, and very high during the last quarter of the year. The temperature is cool, ranging from 18 °C – 22 °C annually with high humidity ranging from 85 – 95 % every month. The surrounding vegetation is lower montane forest [16]. Study site is one hectare plot located in Jeriau Forest, Fraser Hill, Pahang (Figure 1).

Soil samplings were done on one hectare plot (100m x 100m) where it has been divided into 9 subplots. To represent both dry and wet season, the soil sample was taken once for each season. The dry and wet season was determined using annual average rainfall at the nearest station and Malaysia annual rainfall data. Soil samples were taken from each subplot (Figure 2) by profile deep from 0 – 20 cm, 20 – 40 cm, 40 – 60 cm, 60 – 80 cm, and 80 – 100 cm. Research plot were located at 03°43’ 33.5” N, 101° 43’ 076” E to 03° 43’ 34.3” N, 101° 43’ 07.0” E and 03° 43’ 32.7” N, 101°43’ 05.6” E to 03° 43’ 32.9” N, 101°43’ 06.3” E. Each soil sample was taken to laboratory to be air dried and sieved using 2 mm sieve. Samples were then ready for analysis.

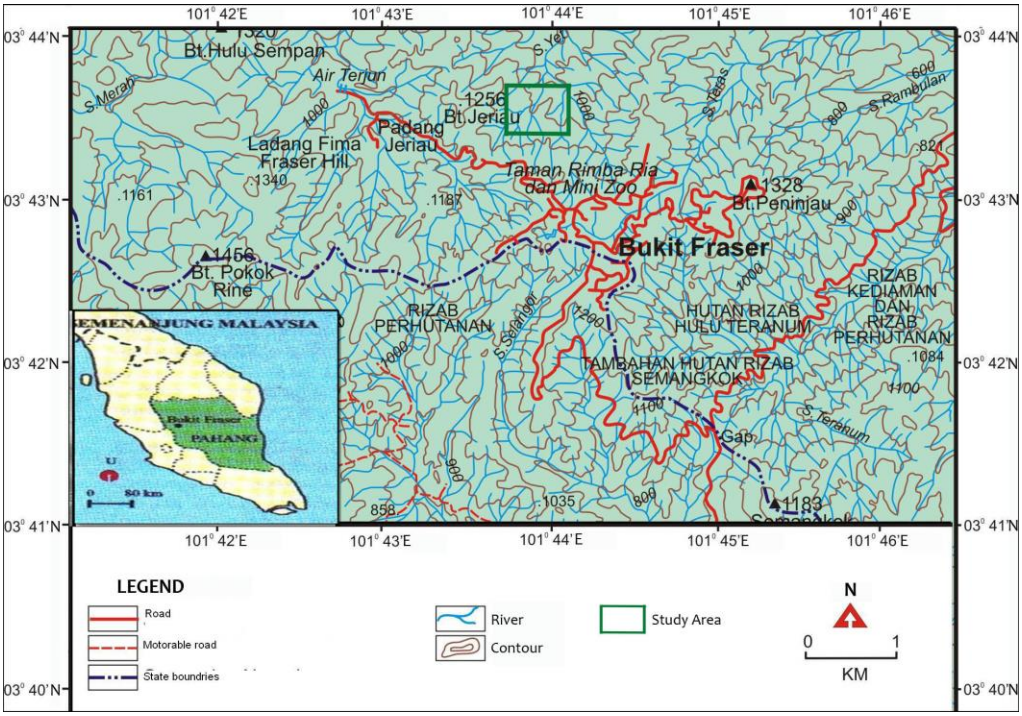


Figure 1. The map of study area

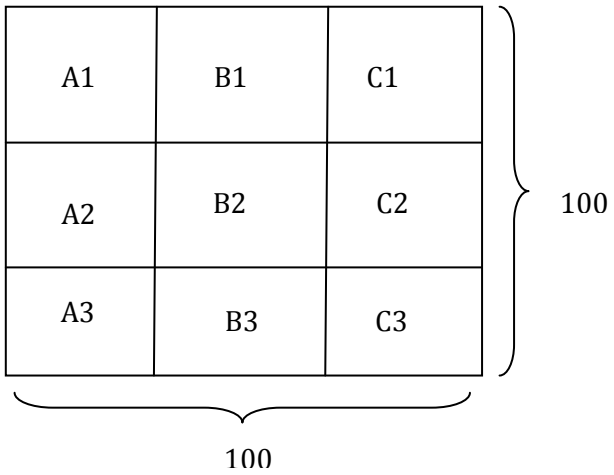


Figure 2. Research plot and subplots

Soil particle size distribution

20g soil are inserted into 600 ml beaker. Then, 50 ml of hydrogen peroxide (H^2O^2 - 30vol.) are pouring into it and heated on the sand bath with the temperature 60 – 70 °C until the mixture become less than 100 ml. Then, samples were transferred into Erlenmeyer flask and 5% sodium hexametaphosphate (20 ml) were added before shaking it in a period of 2 hour on reciprocating shaker. Then, the samples were transferred into 1000 ml beaker with the adding of water. Sub-sample size < 20µm and < 2µm were collected using pipette. The remaining samples were transferred into 600 ml beaker and the samples are slowly being washed until it's clear. The remaining was inserted into oven

overnight at 105 °C. The samples when through sieved to determine the size and weighed to determine the soil particles distributions.

Measurement of pH and conductivity

Determinations of pH were using soil: water ratio of 1:1.2.5 [17]. pH value were read with pH meter that has been calibrated [18]. Soil electrical conductivity was determined using saturated gypsum extract. The remaining of filtered of mixtures were determined using conductivity meter which has been calibrated.

Determination of organic carbon content

Soil organic carbon was determined using Walkley & Black method [19]. An amount 0.5g soil sample were weighed and inserted into 500 ml Erlenmeyer flask. Then, 10 ml of Potassium Dichromate, 1.0 N $K_2Cr_2O_7$ were inserted and shake to mix it. Then, 20 ml sulphuric acid, H_2SO_4 (98 %) was poured into the mixture. The mixtures were left for 30 minutes to cool it. After that, 3 g of sodium fluoride (NaF) were added with 100 ml of distilled water. Ten drop of ferroin indicator were added which made the mixtures turned into orange solution. The mixtures were titrated with 0.5 N ammonium sulphate, until it turned into bright green [18]. The totals of FAS were recorded. The same operations were used to determine blank value with no sample was added. The formula to calculate the content of organic carbon in soil expressed as equation 1 below:

$$\text{Carbon content (KC)} = B \times A \times D \times C \quad (1)$$

where as KC is define as carbon content in ton, B is define as soil bulk density, (g^{cm-3}), A is define as area (m^2), D is define as soil depth (m) and C is percentage (%) of carbon organic.

Results and Discussion

Soil particle size distributions in study area were dominated by sandy and clayey soil (Table 1). Sand content on soil surface (0 – 20cm) were range from 39 % to 56 % with average value is 49 %. Soil texture becoming more sandy and less clayey with the increasing the depth. With sandier texture, water movements are high compare to clayey texture. According to Bationo and Buerkert [20], clay and silt type play an important role in the stabilization of organic compounds and small variations in soil texture could have large effects on soil organic carbon. With increasing clay content, it can decreased carbon output because of its stabilization effect on soil organic carbon.

Table 1. Soil particles size distribution

Sample	Depth (cm)	Sand (%)	Clay (%)	Silt (%)	Texture
A1	0 – 20	45	36	19	Sandy caly
	20 – 40	49	30	22	Sandy clay loam
	40 – 60	48	24	29	Sandy clay loam
	60 – 80	47	18	35	Loam
	80 – 100	64	11	25	Loamy sand
A2	0 – 20	48	34	18	Sandy clay loam
	20 – 40	53	32	15	Sandy clay loam
	40 – 60	59	27	14	Sandy clay loam
	60 – 80	69	15	16	Loamy sand
	80 –100	66	13	21	Loamy sand

Table 1 (cont'd). Soil particles size distribution

Sample	Depth (cm)	Sand (%)	Clay (%)	Silt (%)	Texture
A3	0 – 20	54	36	10	Sandy clay
	20 – 40	57	14	29	Loamy sand
	40 – 60	71	10	19	Loamy sand
	60 – 80	71	8	21	Loamy sand
	80 –100	72	8	20	Loamy sand
B1	0 – 20	42	39	19	Silty clay loam
	20 – 40	44	40	16	Silt
	40 – 60	51	32	17	Sandy clay loam
	60 – 80	53	27	19	Sandy clay loam
	80 –100	51	23	27	Sandy clay loam
B2	0 – 20	54	36	10	Sandy clay
	20 – 40	49	36	16	Sandy clay
	40 – 60	47	37	16	Sandy clay
	60 – 80	52	37	11	Sandy clay
	80 – 100	59	32	10	Sandy clay loam
B3	0 – 20	39	36	26	Sandy clay
	20 – 40	41	40	19	Sandy clay
	40 – 60	46	35	19	Sandy clay loam
	60 – 80	49	32	20	Sandy clay loam
	80 – 100	52	27	21	Sandy clay loam
C1	0 – 20	54	35	12	Loam
	20 – 40	49	31	19	Loam
	40 – 60	54	30	17	Loamy sand
	60 – 80	65	14	21	Sandy clay loam
	80 –100	78	7	15	Loamy sand
C2	0 – 20	46	35	19	Loam
	20 – 40	52	32	16	Loamy sand
	40 – 60	57	29	14	Loamy sand
	60 – 80	66	16	18	Loamy sand
	80 – 100	79	5	15	Loamy sand
C3	0 – 20	56	33	11	Loamy sand
	20 – 40	58	16	26	Sandy clay loam
	40 – 60	71	10	19	Sandy clay loam
	60 – 80	71	8	21	Sandy clay loam
	80 – 100	70	11	19	Loamy sand

According to Table 2, soil organic carbon content were decreasing with increasing soil depth with the highest soil organic carbon content in depth of 0 – 20 cm for both seasons. The percentage of organic carbon content in wet seasons were higher than dry season at the depth 0 – 20 cm and 20 – 40 cm, while at the depth 40 – 60 cm, 60 – 80 cm, and 80 – 100 cm the percentage of soil organic carbon were higher in dry season. These differences were attributed to differences in belowground allocation of biomass among vegetation types, and tree dominated systems had higher inputs of organic matter than other types at the surface of the soil [21]. There was obvious changing in soil organic carbon concentration until 60 cm depth. After 60 cm depth, soil organic carbon concentration slowly reduces until 100 cm depth. The difference in soil organic carbon concentration at this depth is due to vegetation and hydrology [22]. Water moving downwards carries dissolved organic carbon to deeper soil horizons, where it is preserved from complete mineralization, gradually the transported compounds are reabsorbed to soil particles and contribute to carbon storage deeper in the soil profile. The difference of soil organic carbon content between both seasons is 5.33t/ha (Figure 3).

Table 2. The average soil organic carbon content with depth

Depth (cm)	% OC Wet season	Bulk density (gm^{-3})	TOC, (t/ha)	% OC Dry season	Bulk density, (gm^{-3})	TOC, (t/ha)
0 – 20	4.93	1.04	102.54	4.18	1.03	86.38
20 – 40	2.95	1.04	61.36	2.78	1.03	57.41
40 – 60	1.31	1.03	26.99	1.72	1.03	35.44
60 – 80	1.05	1.04	21.84	1.14	1.03	23.53
80 –100	0.51	1.03	10.51	0.74	1.02	15.14
		Total	223.24		Total	217.90

% OC = percentage of organic carbon in soil; TOC = Total organic carbon

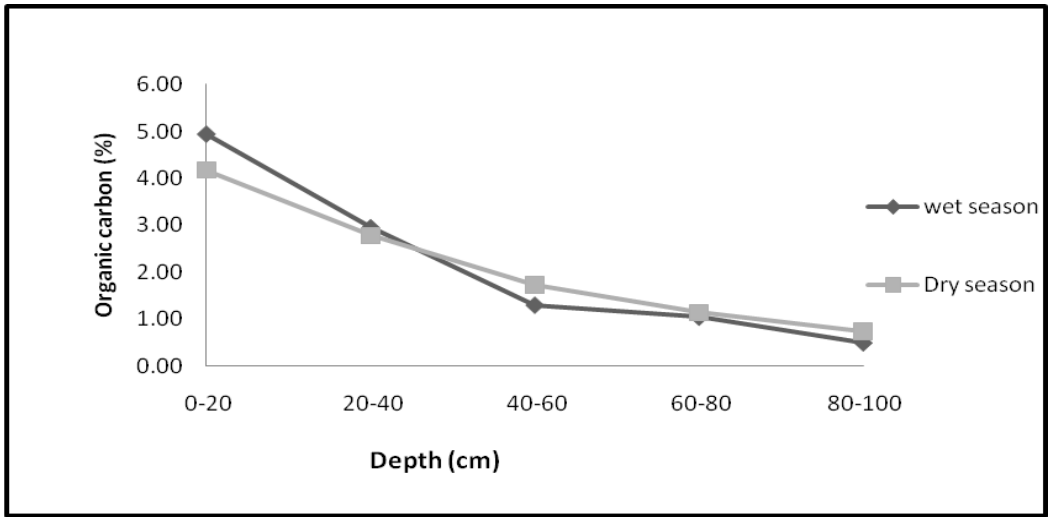


Figure 3. Seasonal soil organic carbon content with depth

Correlation analysis between clay and organic carbon content were significant different on both seasons. Wet season were positively significant at 0.01 (n = 30, r = 0.594**), while on dry season also positively significant at 0.01 (n = 45, r = 0.688**). Soil organic carbon concentration were high at upper soil profile and become lesser at the deep profile. Particle size distribution analysis showing clay content increase with depth. Carbon content and status in the

soil are closely associated with clay and silt contents and clay type, which influences the stabilization of organic carbon [20]. Increasing clay content can provide the stabilization of organic carbon in soil and slowing down decomposition process by microbes [11,23]. In this study, soil organic carbon concentrations were high at high clay area. High clay content can increase plant productivity through water holding capacity in which adding carbon input into the soil [24].

Figure 4 show the value of pH versus depth on both seasons. pH values were stable on both seasons at all station. On dry season pH value were ranging from 3.95 – 4.08 and during wet season it ranging from 4.32 –4.45. Relatively, pH values were lower at depth 0 cm to 40 cm. From 40 cm to 100 cm deep, the changing values were low on both seasons. pH value are related to decomposition of organic matter in which it can affect pH value and also increase organic carbon content in soil. This is also related with the low organic carbon concentration in deeper soil profile, meaning soil organic carbon content increase with decreasing pH value. Correlation analysis between pH and soil organic carbon on dry season were negatively significant at 0.015 (n = 45, r = - 0.378*). There is no significantly different on wet season.

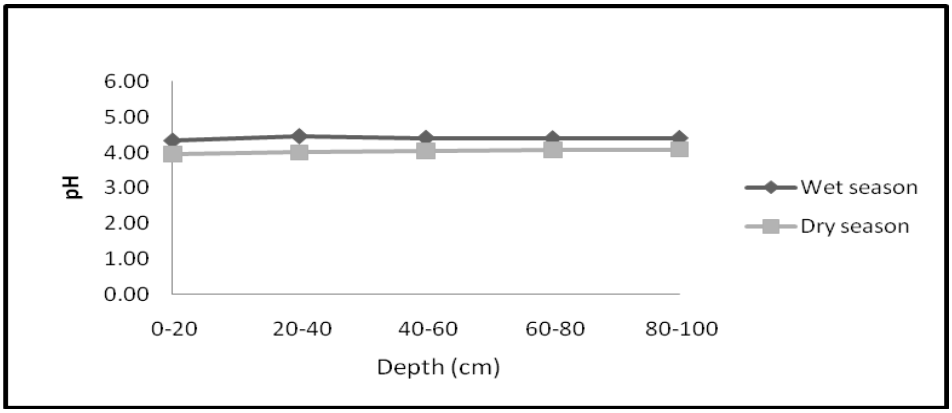


Figure 4. An average of pH value in soil samples

Electrical conductivity (Figure 5) values were stable at every depth on both seasons. During wet season, the highest electrical conductivity was measured at 0 – 20 cm deep with the value 2.65mS/cm and lowest value was 2.52mS/cm at 60 – 80cm deep. During the dry season, highest electrical conductivity value was 2.56mS/cm at 0 – 20 cm deep and at depth of 40 – 60cm the lowest value recorded at 2.33m^S/cm. Electrical conductivity in soil are influenced by soil texture (especially clay), water content and soil water holding capacity, dissolved ion in soil capillary. Soil electrical conductivity value increased with increasing of clay content and water content. According to Officer et. al. [25], the soil zone with high electrical conductivity value are high in clay and organic material content. Correlation analysis between electrical conductivity and soil organic carbon content on wet season showing significantly positive at 0.05 (n = 45, r = 0.315*) and on dry season were significantly negative at 0.01 (n = 45, r = - 0.583**). It showed that electrical conductivity influenced by the value of soil organic carbon content. Correlation analysis between electrical conductivity with pH showing negatively significant on dry season at 0.05 (n = 45, r = - 0.353*) but on wet season, there is no significantly different. It means on dry season, salt content in soil have small influence on pH value but not in wet season.

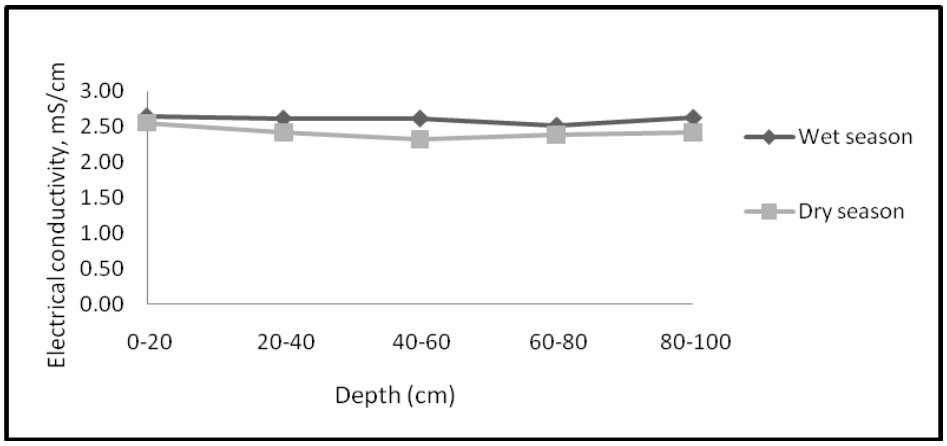


Figure 5. Measurement of electrical conductivity in soil samples

Conclusion

Soil organic carbon content were slightly higher in wet season compared to dry season with the different value of 5.34 t/ha. Soil organic carbon content is decreasing with depth on both seasons. The value of soil organic carbon decreasing drastically from high organic matter in higher soil profile and lower in deeper soil profile. pH value in dry season were acidic than wet season. Soil electrical conductivity values were stable and not much significantly different on both seasons. The average soil electrical conductivity value on wet season is 2.61m^S/cm and during dry season is 2.42m^S/cm.

Acknowledgement

The authors want to thank to Fraser Hill Research Centre, Faculty of Science and Technology, Universiti Kebangsaan Malaysia for the equipment. This research was funded by UKM-GUP-ASPL-07-05-004. The authors also thankful to East Coast Environmental Research Institute (ESERI), University Sultan Zainal Abidin for this work.

References

1. Toriman, M.E, Gasim, M. B., Yusop, Z., Shahid, I., Mastura, S. A. S., Abdullah, P., Jaafar, M., Abd Aziz, N. A., Kamarudin, M. K. A., Jaafar, O., Karim, O., Juahir, H. and Jamil, N. R. (2012). Use of 137Cs activity to investigate sediment movement and transport modeling in river coastal environment. *American Journal of Environmental Sciences*, 8 : 417 – 423.
2. Kamarudin, M. K. A., Toriman, M. E., Rosli, M. H., Juahir, H., Azid, A., Mohamed Zainuddin, S. F., Abdul Aziz, N. A. and Sulaiman, W. N. A. (2015). Analysis of meander evolution studies on effect from land use and climate change at upstream reach of Pahang River, Malaysia. *Mitigation and Adaptation Strategies for Global Change*, 20:1319 – 1334.
3. Velmurugan, A., Gopal K., Dadhwal, V. K. Kumar, S., Swarnam, T. P. and Saha, S.K.(2009). Harmonizing soil organic carbonestimates in historical and current data. *Current Science*, 97(4): 12 – 22
4. Azid, A., Che Hasnam, C. N., Juahir, H., Amran, M. A., Toriman, M. E., Kamarudin, M. K. A., Mohd Saudia, M. S., Gasim, M. B. and Mustafa, A. D. (2015). Coastal erosion measurement along Tanjung Lumpur to Cherok Paloh, Pahang during the northeast monsoon season. *Jurnal Teknologi*, 74 (1): 27 – 34.
5. Kamarudin, M. K. A., Toriman, M. E., Sarifah A., S. M, Idris, M., Jamil, N. R. and Gasim, M. B. (2009). temporal variability on lowland river sediment properties and yield. *American Journal of Environmental Sciences*, 5(5): 657 – 663.
6. Zerva, A. and Maurizio M. (2005). Carbon stock changes in a peaty gluey soil profile after afforestation with Sitka spruce (Picea sitchensis). *Annals Forest Science*, 62: 873 – 880.
7. Thornley J. H. M. and Cannell, M. G. R. (2001). Soil carbon storage response to temperature: an hypothesis. centre for ecology & hydrology, Bush Estate, Penicuik, Midlothian, *UK Annals of Botany*, 87: 591 – 598.

8. Sahibin, A. R., Mohd. Nizam, M.S. and Izzat Hidayat, I. (2004/05). Physico-chemical characteristics of soil at Sg. Cheruai in the national park at Merapoh Pahang. *Journal Wildlife and Parks,* 22: 145 - 152.
9. Steinbeiss, S., Temperton, V. M. and.Gleixner, G. (2007). Mechanisms of soil carbon storage in experimental grasslands. *Biogeosciences Discuss.*, 4, 3829 – 3862.
10. Abdullah, N. M., Toriman, M. E., Md Din, H., Abd Aziz, N. A., Kamarudin, M. K. A., Abdul Rani, N. S., Ata, F. M., Saad, M. H., Abdullah, N. W., Idris, M. and Jamil, N. R. (2013). Influence of spatial and temporal factors in determining rainfall interception at dipterocarp forest canopy, Lake Chini, Pahang. *Malaysian Journal of Analytical Sciences,* 17 (1): 11 – 23.
11. Yuanhe, Y., Ngyun, F., Yanhong, T., Chengjun, J., Chengyang Z., Jinsheng H. and Biao Z. (2008). Storage, patterns and controls of soil organic carbon in the Tibetan grasslands. *Global Change Biology* 14: 1592 – 1599
12. Veldkamp, E., Becker, A., Schwendenmann, L., Clark. D. A, and Schult-Bisping. H (2003). Substantial labile carbon stocks and microbial activity in deeply weathered soils below a tropical wet forest. *Global Change Biology,* 9: 1171 – 1184.
13. Steinbeiss, S., Temperton, V. M. and Gleixner, G. (2007). Mechanisms of soil carbon storage in experimental grasslands. *Biogeosciences Discuss,* 4: 3829 – 3862.
14. D'bek-Szreniawska, M. and Balashov, E (2007). Seasonal changes in labile organic matter, mineral nitrogen, and N_2O emission in a loamy sand Orthic Luvisol cultivated under three management practices. *International Agrophysics* , 21: 127 – 132.
15. Zulfahmi, A. R., Jasni, Y., Sahibin, A. R. Gasim, M. B. and Ramlan, O. (2002). Preliminary survey of landslide occurrences along main road of gap-Fraser's Hill, Pahang. *Proceedings of the Regional Symposium on Environment and Natural Resources,* 1: 745 – 751.
16. Noraini M.T. (2002). The use of selected geo-materials for erosion and sediment control at Fraser's Hill. *Proceedings of the Regional Symposium on Environment and Natural Resources,* 1: 305 – 312.
17. Metson, A. J. (1956). Methods of chemical analysis for soil survey samples. Bulletin of the New Zealand Department of Industrial Research. No. 12.
18. Rowell, D.L. (1994). Soil science: method and applications. Singapore: Longman Singapore Publishers (Pte) Ltd.
19. Avery, B. W. and Bascomb, C. L. (1982). Soil survey laboratory methods. Soil Survey Technical Monograph No. 6. Harpenden.
20. Bationo A. and Buerkert A. (2001). Soil organic carbon management for sustainable land use in the Sudano-Sahelian West Africa. *Nutrient Cycling in Agroecosystems* 61:131 – 142.
21. Richard V. Pouyat, Ian D. Yesilonis Nancy E. Golubiewski. (2009). A comparison of soil organic carbon stocks between residential turf grass and native soil. *Urban Ecosyst,* 12:45 – 62
22. Reese, R. E. and Moorhead, K. K.. (1996). Spatial characteristics of soil pro:perties along an elevational gradient in a Carolina Bay wetland. *Soil Science Society American Journal,* 60: 1273 – 1277.
23. Zhuang, Q., Li, Q., Jiang, Y., Liang, W. and Steinberger, Y. (2005). Vertical distribution of soil organic carbon in agrosystems of Songliao Plain along a latitudinal gradient. *American-Eurasian Journal of Agriculture and Environment Science,* 2(2): 127 – 132.
24. Henry. M., Valentini. R., and Bernoux. M (2009). Soil carbon stocks in ecoregions of Africa. *Biogeosciences Discussions,* 6: 797 – 823.
25. Officer, S. J., Kravchenko, A., Bollero, G. A., Sudduth, K. A., Kitchen, N. R. and Wiebold. W. J. (2004). Relationships between soil bulk electrical conductivity and the principal component analysis of topography and soil fertility values. *Plant and Soil,* 258: 269 – 280.

Malaysian Journal of Analytical Sciences Vol 20 No 3 2016

Articles 7-16 are selected papers from the "International Conference on Applied Science and Technology (ICASIT 2015) for Chemistry and Environment Symposium, 24-26 February 2015, Grand Lexis, Port Dickson, Negeri Sembilan, Malaysia; organised by Faculty of Applied Science, Universiti Teknologi MARA, Shah Alam, Selangor, Malaysia."

Guest Editor: Rohaya Ahmad

Articles 17-23 are selected papers from the "International Conference on Applied Sciences and Industrial Technology (ICASIT 2015) for Food Science Symposium, 24-26 February 2015, Grand Lexis, Port Dickson, Negeri Sembilan, Malaysia; organised by Faculty of Applied Science, Universiti Teknologi MARA, Shah Alam, Selangor, Malaysia."

Guest Editor: Noorlaila Ahmad

Articles 24-30 are selected papers from the "International Conference on Fuel Cell and Hydrogen Technology 2013 (ICFCHT 2013), 7-10 October 2013, Inna Garuda Hotel, Convention Business, Yogyakarta, Indonesia; organised by Agency for the Assessment and Application of Technology (BPPT), Universiti Kebangsaan Malaysia (UKM) and Universiti Teknologi Malaysia (UTM)."

Guest Editor: Edy Herianto Majlan

Page

1. OPTIMIZATION OF ACTIVATED CARBON PREPARATION FROM SPENT MUSHROOM FARMING WASTE (SMFW) VIA BOX–BEHNKEN DESIGN OF RESPONSE SURFACE METHODOLOGY (Penyediaan Secara Optimum Arang Teraktif daripada Sisa Tanaman Cendawan Terpakai (SMFW) Melalui Reka Bentuk Box-Behnken dari Kaedah Gerak Balas Permukaan) 461
Nurul-Shuhada Md-Desa, Zaidi Ab Ghani, Suhaimi Abdul-Talib, Chia-Chay Tay

2. ADSORBENT FROM WASTE AND NATURAL DEPOSITS FOR PARAQUAT REMOVAL IN WATER (Penjerap daripada Sisa Industri dan Semulajadi untuk Penyingkiran Paraquat di dalam Air) 469
Nur Fatin Zakaria, Zaiton Abdul Majid, Zainab Ramli, Jafariah Jaafar, Azmi Aris, Juhaizah Talib, Rusmidah Ali

3. TAILORING PEPTIDOMIMETICS ANTIFREEZE PROTEIN FROM EXOTIC ANTARCTIC MARINE (Pengubahsuaian Protein Antibeku Peptidomimetik daripada Hidupan Eksotik Marin Antartika) 477
Mohd Basyaruddin Abdul Rahman, Azren AidaAsmawi, Emilia Abdulmalek, Abu Bakar Salleh, Bimo Ario Tejo

4. CORROSION INHIBITION OF Q235A STEEL IN ACID MEDIUM USING ISATIN DERIVATIVES: A QSAR STUDY (Perencatan Kakisan Keluli Q235A di dalam Medium Asid Menggunakan Terbitan Isatin: Satu Kajian QSAR) 484
Abdo M. Al-Fakih, Madzlan Aziz, Hassan H. Abdallah, Hasmerya Maarof, Rosmahaida Jamaludin, Bishir Usman

5. BIOMONITORING OF HEAVY METALS USING INTERTIDAL MOLLUSKS IN EAST JOHOR COASTAL WATERS (Biopemerhatian Logam Berat Menggunakan Moluska Intertidal di Perairan Pantai Johor 491

Timur)
Mohd Mokhlesur Rahman, Fuad Miskon, Kamaruzzaman Yunus, Noor Azhar M. Shazili

6. NITROGEN USE EFFICIENCY IN MR219-4 AND MR219-9 RICE MUTANT LINES UNDER DIFFERENT WATER POTENTIALS AND NITROGEN LEVELS USING 15N ISOTOPIC TRACER TECHNIQUE 500
(Kecekapan Penggunaan Nitrogen dalam Padi Titisan Mutan MR219-4 dan MR219-9 di bawah Potensi Air dan Aras Nitrogen yang Berbeza Menggunakan Teknik Isotop Penyurih 15N)
Ahmad Nazrul Abd Wahid, Sahibin Abdul Rahim, Khairuddin Abdul Rahim, Abdul Rahim Harun

7. THE EFFECT OF CTAB AND SDS SURFACTANT ON THE MORPHOLOGY AND PERFORMANCE OF LOW PRESSURE ACTIVE REVERSE OSMOSIS MEMBRANE 510
(Kesan Surfaktan CTAB dan SDS Terhadap Morfologi dan Prestasi Membran Osmosis Berbalik Aktif Bertekanan Rendah)
Nurul Syuhada Mohd Ali and Abdul Rahman Hassan

8. EVALUATION OF HEAVY METAL CONCENTRATIONS IN WILD AND CULTIVATED *Hemibagrus* sp. USING PRINCIPAL COMPONENT ANALYSIS 517
(Penilaian Kepekatan Logam Berat dalam *Hemibagrus* sp. dari Habitat Semulajadi dan Kolam Ternakan Menggunakan Kaedah Analisis Komponen Utama)
Nor Shahirul Umirah Idris, Sharifuddin Md.Zain, Kah Hin Low, Ahmad Firdaus Kamaruddin, Kaharudin Md. Salleh

9. XYLOOLIGOSACCHARIDES PRODUCTION FROM OIL PALM FROND BY *Trichoderma longibrachiatum* XYLANASE 525
(Penghasilan Xilooligosakarida daripada Pelepah Kelapa Sawit Menggunakan Xilanase *Trichoderma longibrachiatum*)
Sabiha Hanim Saleh, Siti Normah Mohd Damanhuri Shah, Khalilah Abdul Khalil, Aishah Bujang

10. INFLUENCE OF CHROMIUM ON THE REDUCTION BEHAVIOR OF FERRIC OXIDE BY USING CARBON MONOXIDE: TEMPERATURE PROGRAMMED REDUCTION AND KINETIC STUDIES 531
(Pengaruh Kromium Terhadap Kelakuan Penurunan Ferik Oksida dengan Menggunakan Karbon Monoksida: Kajian Penurunan Suhu Berprogram dan Kinetik)
Tengku Shafazila Tengku Saharuddin, Alinda Samsuri, Fairous Salleh, Mohammad Bin Kassim, Rizafizah Othaman, Mohamed Wahab Mohamed Hisham, Mohd Ambar Yarmo

11. SYNTHESIS AND CHARACTERIZATION OF MESOPOROUS SILICA MCM-41 AND SBA-15 FROM POWER PLANT BOTTOM ASH 539
(Sintesis dan Pencirian Silika Mesoporos MCM-41 dan SBA-15 daripada Debu Bawah Loji Janakuasa)
Nurul Barakah Ab Rahman, Hamizah Md. Rasid, Hashazirah Mohammad Hassan, Mohammad Noor Jalil

12. PHYTOCHEMICAL STUDY ON THE STEM BARK OF *Mallotus leucodermis* Hook F. 546
(Kajian Fitokimia ke atas Kulit Ranting *Mallotus leucodermis* Hook F.)
Aiza Syuhada Mohd Yusoff, Norizan Ahmat, Humera Naz

13. FITTING STATISTICAL DISTRIBUTIONS FUNCTIONS ON OZONE CONCENTRATION DATA AT COASTAL AREAS 551
(Penyesuaian Fungsi Taburan Statistik pada Data Kepekatan Ozon di Kawasan Pesisiran Pantai)
Muhammad Yazid Nasir, Nurul Adyani Ghazali, Muhammad Izwan Zariq Mokhtar, Norhazlina

Suhaimi

14. COMPARATIVE COLUMN STUDIES OF CHEMICALLY MODIFIED ION EXCHANGE RESIN WITH AGGLOMERATED ADSORBENTS FOR FLUORIDE REMOVAL 560
(Kajian Perbandingan Turus Resin Penukaran Ion Terubahsuai dengan Penjerap Teraglomerat bagi Penyingkiran Fluorida)
Sivasankari Chandasekaran and Arulanantham Arthanas

15. QUANTIFICATION OF CATECHIN IN LEAVES AND STEMS OF MALAYSIAN *Uncaria gambir* (HUNTER) ROXB. BY HPLC-DAD 567
(Kuantifikasi Catechin dalam Daun dan Batang *Uncaria gambir* (Hunter) Roxb. dari Malaysia Menggunakan KCPT-PSD)
Nurliayana Ibrahim, Nurul Zulaikha Mohd Yusoff, Rohaya Ahmad

16. ISOLATION OF ACETYL ALEURITOLIC ACID FROM *Pimeleodendron griffithianum* (Euphorbiaceae) 573
(Pemisahan Asid Asetil Aleuritolik Daripada *Pimeleodendron griffithianum* (Euphorbiaceae))
Rosmawati Abdul Aziz and Norizan Ahmat

17. IMMOBILISED METAL AFFINITY CHROMATOGRAPHY (IMAC) BEADS FOR LYSOZYME SEPARATION: SYNTHESIS AND CHARACTERIZATION STUDY 578
(Kromatografi Afiniti Logam Dipegun (IMAC) untuk Pemisahan Lysozim: Sintesis dan Kajian Pencirian)
Fatin Mohd Nasir, Sofiah Hamzah, Amirah Hamzah, Nora'aini Ali, Marinah Mohd Ariffin

18. EFFECTS OF DIFFERENT GRINDING METHODS ON MORPHOLOGICAL, TEXTURAL PROPERTIES AND PASTING PROFILES OF MR220 RICE FLOUR 585
(Kesan Kaedah Pengisaran yang Berbeza terhadap Morfologi, Sifat Tekstur dan Profil Pempesan Tepung Beras MR220)
Noorlaila Ahmad, Asmeda Rajab, Norziah Mohd Hani

19. BITTERNESS AND PHYSICHOCHEMICAL PROPERTIES OF ANGELWING CLAM (Pholas orientalis) HYDROLYSATE 594
(Kepahitan dan Ciri – Ciri Fizikokimia Hidrolisat Mentarang (Pholas orientalis))
Normah Ismail and Nurul Fasihah Razak

20. CHEMICAL CHANGES IN SHORTFIN SCAD (*Decapterus macrosoma*) AT CHILLED (4 °C) AND FROZEN (-18 °C) STORAGE 601
(Perubahan Kimia dalam Ikan Selayang (*Decapterus macrosoma*) pada Penyimpanan Suhu Dingin (4 °C) dan Sejuk Beku (-18 °C))
Fazilah Fazilin Juhari, Norizzah Abd. Rashid, Cheow Chong Seng, Anida Yusoff, Emilia Azrina Mohd Bakri

21. ANTIOXIDANT ACTIVITY, COLOUR AND MINERAL CONTENT OF HERBAL TEA PREPARED FROM *Cosmos caudatus* LEAVES AT DIFFERENT MATURITY STAGES 607
(Aktiviti Antioksida, Warna dan Kandungan Mineral di dalam Teh Herba daripada Daun *Cosmos caudatus* pada Peringkat Kematangan yang Berbeza)
Dian Nashiela Fatanah, Noriham Abdullah, Nooraain Hashim, Azizah Abd Hamid

22. EFFECT OF EDIBLE LIPID-CHITOSAN FILM FORMING DISPERSION ON POSTHARVEST LIFE OF GUAVA STORED AT CHILLED TEMPERATURE 618
(Kesan Serakan Filem Lipid-Kitosan Ke Atas Jangka Hayat Jambu yang Disimpan Pada Suhu Sejuk)
Nurul Adilla M. Loai, Halimahton Zahrah Mohamed Som, Zaibunnisa Abdul Haiyee

23. QUALITY PARAMETERS OF *Curcuma longa* L. EXTRACTS BY SUPERCRITICAL FLUID EXTRACTION (SFE) AND ULTRASONIC ASSISTED EXTRACTION (UAE) 626
(Parameter Kualiti Ekstrak *Curcuma longa* L. daripada Pengekstrakan Cecair Supergenting (SFE) dan Pengekstrakan Ultrasonik Berbantu (UAE))
Zaibunnisa Abdul Haiyee, Siti Hafsah Mohd Shah, Khudzir Ismail, Nooraain Hashim, Wan Iryani Wan Ismail

24. CONDUCTIVITY AND THERMAL STABILITY OF SOLID ACID COMPOSITES $CsH_2PO_4/NaH_2PO_4/SiO_2$ 633
(Konduktiviti dan Kestabilan Terma Asid Pepejal Komposit $CsH_2PO_4/NaH_2PO_4/SiO_2$
Norsyahida Mohammad, Abu Bakar Mohamad, Abdul Amir Hassan Kadhum, Loh Kee Shyuan

25. FABRICATION OF Y-TZP FOR DENTAL CROWNS APPLICATIONS BY COMBINING SLIP CASTING AND COLD ISOSTATIC PRESSING 642
(Pembangunan Y-TZP untuk Aplikasi Korona Gigi melalui Penggabungan Kaedah Penuangan Buburan dan Penekanan Isostatik Sejuk)
Chin Chuin Hao, Andanastuti Muchtar, Che Husna Azhari, Masfueh Razali, Mohamed Aboras

26. EFFECT OF USING PITAYA PEEL AS DYE-SENSITIZER AND DYE MOLECULES IN ELECTROLYTE FOR PHOTOELECTROCHEMICAL REACTION 651
(Kesan Penggunaan Kulit Buah Naga Sebagai Pemeka-Pewarna dan Molekul Pewarna di dalam Elektrolit bagi Tindak Balas Fotoelektrokimia)
Siti Nur Hidayah Jaafar, Lorna Jeffery Minggu, Khuzaimah Ariffin, Mohammad B. Kasssim, Wan Ramli Wan Daud

27. EFFECT OF PROCESS PARAMETERS ON THE SYNTHESIS OF POLYPYRROLE BY THE TAGUCHI METHOD 660
(Kesan Pembolehubah Proses Terhadap Sintesis Polipirola Menggunakan Kaedah Taguchi)
Rika Sri Utami, Ifa Puspasari, Loh Kee Shyuan, Abu Bakar Mohamed, Sagir Alva

28. THERMAL PROPERTIES AND CONDUCTIVITY OF NAFION-ZIRCONIA COMPOSITE MEMBRANE 670
(Sifat Terma dan Konduktiviti Membran Komposit Nafion-Zirkonia)
Siti Rahmah Mokhtaruddin, Abu Bakar Mohamad, Kee Shyuan Loh, Abdul Amir Hasan Kadhum

29. PREPARATION OF MEMBRANE ELECTRODE ASSEMBLY FOR HIGH PERFORMANCE OF FORMIC ACID FUEL CELL 678
(Penyediaan Himpunan Membran Elektrod untuk Sel Fuel Asid Formik Berprestasi Tinggi)
Norraihanah Mohamed Aslam, Mohd Shahbudin Masdar, Siti Kartom Kamarudin

30. CRITICAL POWDER LOADING AND RHEOLOGICAL PROPERTIES OF POLYPROPYLENE/GRAPHITE COMPOSITE FEEDSTOCK FOR BIPOLAR PLATE APPLICATION 687
(Beban Serbuk Kritikal dan Sifat Reologi Bahan Suapan Komposit Polipropilena/Grafit untuk Aplikasi Plat Dwi kutub)
Iswandi, Jaafar Sahari, Abu Bakar Sulong, Teuku Husaini

Malaysian Journal of Analytical Sciences, Vol 20 No 3 (2016): 461 - 468
DOI: http://dx.doi.org/10.17576/mjas-2016-2003-01

MALAYSIAN JOURNAL OF ANALYTICAL SCIENCES
Published by The Malaysian Analytical Sciences Society
ISSN 1394 - 2506

OPTIMIZATION OF ACTIVATED CARBON PREPARATION FROM SPENT MUSHROOM FARMING WASTE (SMFW) VIA BOX–BEHNKEN DESIGN OF RESPONSE SURFACE METHODOLOGY

(Penyediaan Secara Optimum Arang Teraktif daripada Sisa Tanaman Cendawan Terpakai (SMFW) Melalui Reka Bentuk Box-Behnken dari Kaedah Gerak Balas Permukaan)

Nurul-Shuhada Md-Desa[1], Zaidi Ab Ghani[2], Suhaimi Abdul-Talib[3], Chia-Chay Tay[2]*

[1]*Faculty of Applied Sciences*
Universiti Teknologi MARA, 40450 Shah Alam, Selangor, Malaysia
[2]*Faculty of Applied Sciences,*
Universiti Teknologi MARA, 02600 Arau, Perlis Malaysia
[3]*Faculty of Civil Engineering*
Universiti Teknologi MARA, 40450 Shah Alam, Selangor, Malaysia

**Corresponding author: taychiay@perlis.uitm.edu.my*

Received: 9 December 2014; Accepted: 22 March 2016

Abstract

This study focuses on activated carbon preparation from spent mushroom farming waste (SMFW) via chemical activation using Box-Behnken design (BBD) of Response Surface Methodology (RSM). Potassium hydroxide (KOH) functions as activating reagent and it plays an important role in enhancing the activated carbon porosity. Three input parameters and two responses were evaluated via this software generated experimental design. The effects of three preparation parameters of impregnation ratio, activation time and activation temperature as well as two responses of carbon yield and iodine number were investigated. The optimum conditions for preparing activated carbon from SMFW was found at SMFW: KOH impregnation ratio of 0.25, activation time of 30 min and activation temperature of 400 ^{o}C which resulted in 28.23 % of carbon yield and 314.14 mg/g of iodine number with desirability of 0.994. The predicted results were well corresponded with experimental results. This study is important in economical large scale SMFW activated carbon preparation for application study of adsorption process for metal treatment in wastewater with minimum chemical and energy input.

Keywords: activated carbon, spent mushroom farming waste, Box-Behnken design, response surface methodology

Abstrak

Kajian ini memfokuskan penyediaan arang teraktif daripada sisa tanaman cendawan terpakai melalui reka bentuk box-behnken (BBD) dari kaedah gerak balas permukaan (RSM). Potasium hidroksida (KOH) berperanan sebagai agen pengaktifan dan penting untuk meningkatkan liang arang teraktif. Tiga parameter input dan dua respon telah dinilai oleh perisian ini yang dihasilkan oleh rekabentuk eksperimen. Kesan daripada penyediaan tiga parameter iaitu nisbah pemadatan, masa pengaktifan dan suhu pengaktifan serta dua respon iaitu hasil arang teraktif dan nilai iodin telah disiasat. Keadaan optimum dalam penyediaan arang teraktif telah didapati pada nisbah SMFW: KOH iaitu 0.25, tempoh pengaktifan selama 30 min dan suhu pengaktifan 400 °C, di mana ia menghasilkan jumlah maksimum arang teraktif sebanyak 28.23 % dan nilai iodin yang boleh diterima iaitu sebanyak 314.14 mg/g dengan ketepatan 0.994. Keputusan yang telah diramalkan adalah seiring dengan keputusan eksperimen. Kajian ini adalah penting dalam penyediaan arang teraktif secara berskala besar dengan ekonomi daripada sisa tanaman cendawan terpakai untuk kajian proses penjerapan terhadap rawatan logam dalam air sisa dengan input bahan kimia dan tenaga yang minimum.

Kata kunci: karbon teraktif, sisa tanaman cendawan terpakai, reka bentuk Box-Behnken, kaedah gerak balas permukaan

Introduction

Activated carbon (AC) is a carbonaceous material with large surface area and high porosity. The surface area and pore size distribution are important factors in determination of AC performance. The macropores act as the entrance to the AC, while the mesopores and micropores responsible for adsorption process determined by iodine number. Iodine number is important parameter to indicate the quality of carbon porosity by measuring the amount of iodine adsorbed (in milligrams) by 1 g of carbon using standard method of ASTM D4607-94. On the other hand, the percentage yield in activated carbon preparation plays a major role in continuous supply for application.

Generally, optimization of AC preparation is via traditional method. However, response surface methodology (RSM) has been found to be a useful tool to optimize AC preparation. Box–Behnken design (BBD) is one of RSM method with an independent quadratic design. It does not contain an embedded factorial or fractional factorial design. In this design, the treatment combinations are at the midpoints of edges of the process space and at the center. The BBD is favourable due to its less number of experiments with variable parameter consuming less time.

Most of the study had reported in multiple input parameters such as impregnation ration (IR), activation time and activation temperature. Precusors from agricultural wastes such as flamboyant (*Delonix regia*) pods [1], *Prosopisafricana* seed hulls [2], *Borassus aethiopum* shells [3] and coconut husk [4] have been studied. Spent mushroom farming waste (SMFW) is a low cost agricultural based material, abundantly available and is a renewable resource. The SMFW consists of sawdust and rice husk majorly. Previous study using sawdust as AC by Foo & Hameed [5] and Moodley et al.[6] and rice husk as AC by Khan et al.[7], Chen et al.[8], Kumagai et al.[9] and Ding et al.[10] have generated highly porous carbonaceous carbon. These reports showed that both components of sawdust and rice husk are suitable as a potential precursor. Thus, SMFW has been selected as precursor for this study as there is lack of literature study on utilization of sawdust and rice husk combination medium of SMFW AC preparation and application.

The aim of this study is to optimize SMFW AC preparation parameters of impregnation ratio (IR) between KOH and SMFW, activation time and activation temperature. The analysis involve multiple responses of percentage yield and iodine number via BBD of RSM method.

Materials and Methods

Materials

Spent mushroom farming waste (SMFW) used for preparation of activated carbon was provided by C&C Mushroom Cultivation Farm, Johor, Malaysia.

Characterization of the activated carbon

The AC surface morphology was analyzed using Field Emission Scanning Electron Miscroscope (FESEM) of ZEISS Supra 40VP at voltage of 5 kV and 12000 magnifications. The Fourier Transform Infrared (FTIR) spectra were analyzed using Series 100 PerkinElmer Fourier Transform Infra-Red (FTIR) spectroscopy in the range of 400 – 4000 cm^{-1} for surface functional groups identification. Thermogravimetric analyzer (TGA) TA Model SDT Q600 V8.3, under nitrogen gas atmosphere with heating condition following the ASTM D2974 was conducted.

Activated carbon preparation via Box-Behnken Design

The preparation of AC from SMFW was accomplished using sodium hydroxide (KOH) as activating agent. The SMFW was impregnated with the KOH for 24 hours respectively. The slurry was then dried at 80 ^{0}C for 24 hours. The impregnate precursor was carbonized in furnace. The produced char was washed with hydrochloric acid and distilled water to remove residual KOH and dried at 80 ^{0}C. Finally, the prepared AC was sieved to size of 150 micrometer and kept in drying cabinet prior to use. The experiments were applied using parameter set by BBD of RSM method. The variables studied were (i) $x1$, KOH: SMFW impregnation ratio; (ii) $x2$, activation time and (iii) $x3$, activation temperature. The experimental sequence was randomized in order to minimize the effects of the uncontrolled factors [3]. The two responses were carbon yield (Y_1) and iodine number (Y_2). Each response was used to develop an empirical model which correlated the response to the three activated carbon preparation parameters.

The percentage of activated carbon yield was calculated as equation (1). Iodine test was conducted according to ASTM D4607method and calculation as shown in equation (2) below:

$$\text{Percentage yield (\%)} = \frac{\text{Weight of activated carbon}}{\text{Weight of dried SMFW}} \text{ x } 100 \quad (1)$$

$$\frac{X}{M} = \frac{[A-(DF)(B)(S)]}{M} \quad (2)$$

where X/M is defined as iodine adsorbed per gram of carbon (mg/g), A is defined as normality of iodine solution × 12693, DF is defined as dilution factor (2.2), B is defined as normality of sodium thiosulfate solution × 126.93, S is defined as sodium thiosulfate used for every titration (mL) and M is defined as weight of activated carbon used.

Results and Discussion

Characterization of the activated carbon

The SEM image of SMFW AC is shown in Figure 1. The SMFW AC has a rough surface with different size of pores. The large irregular structure of pores in the AC external surface indicated the macropores with linkage of mesopores and micropores rooting inside the internal structure of AC. Formation of the pores corresponded to the formation of metallic potassium (K) through activation process using KOH as activating agent. Intercalation of K in the carbon structure widened the existing pores and developed new porosity essential for adsorption process.

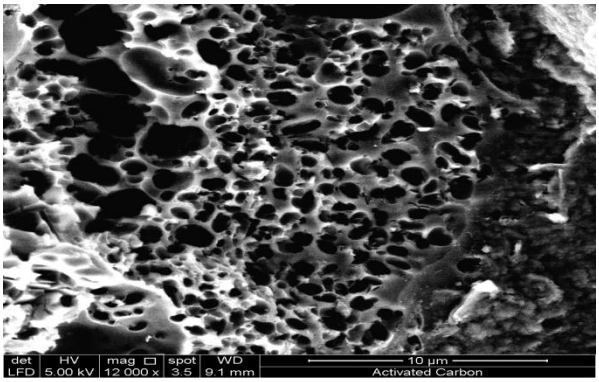


Figure 1. SEM image of SMFW activated carbon

Figure 2 shows the FTIR image of SMFW AC to determine the AC surface chemistry of functional groups. From the spectra, the band at 3405 cm^{-1} was attributed to the hydrogen bond between –OH in the AC surface or –OH in water molecule [11]. Besides, band at 1384 cm^{-1} was attributed to stretching vibration of C-N bond [12] and band at 1714 cm^{-1} was attributed to the C=O stretching bond of ketone [13]. The N-H stretch bond at band 3500 cm^{-1} represented amine group in the AC.

Figure 3 demonstrates the TGA/DTG curve thermogravimetry (TG) of AC and its derivatives represented by green line and blue line respectively. The TGA curve showed three phases of AC weight loss. The first stage was the moisture elimination of 3.4 % below temperature of 200 ^{0}C. Next, second stage weight loss of 26 % was due to the degradation of hemicelluloses, cellulose and lignin occurred at temperature 200 – 500 ^{0}C [14]. According to the previous study by Yang et al. [15], hemicelluloses started to degrade at 220 ^{0}C and completed at 315 ^{0}C while degradation of cellulose occurred between 315 – 390 ^{0}C. Stronger structure of lignin degraded in a wider temperature range than the other two components. The third stage involved weight loss according to the weight loss of 51.2 % volatile matter at temperature 500 – 900 ^{0}C. The same results have been reported in literature by Gao et al. [14], Zhang et al. [16] and Domingueza et al. [17]. The DTG curve of Figure 4 shows a significant change occurred due to the weight loss of AC starting of the degradation of hemicelluloses, cellulose and lignin. This was

explained by the fact that hemicelluloses and cellulose compounds have the structure of branching chain of polysaccharides without aromatic compound, which are easily volatilized. Meanwhile, lignin consists of various –O- and C-C functional groups and aromatic structural units [18].

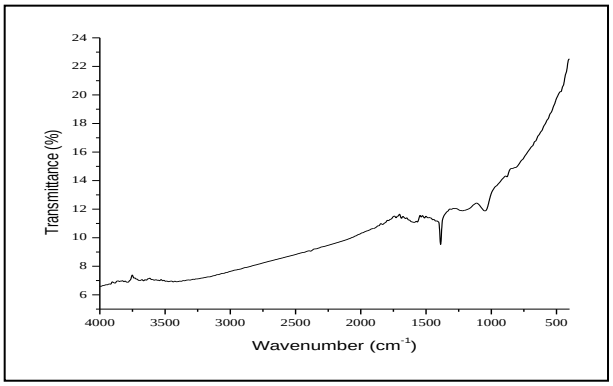


Figure 2. FTIR image of SMFW AC

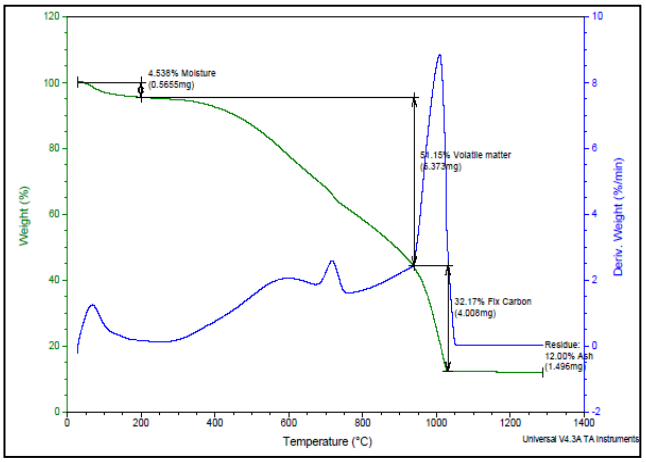


Figure 3. TGA/DTG image of SMFW AC

Optimization of parameters on carbon yield

Figure 4 (a – c) illustrate the 3-D response surface plots of percentage yield on AC as a function of three process parameters of impregnation ratio, activation time and activation temperature.

Figure 4 (a) shows the effect of impregnation ratio and activation time on the percentage yield. There are only little effect of time on yield. However, decreasing of yield with increasing ratio was observed which was due to increase of the carbon burn-off. Increased the impregnation ratio has resulted increased the weight loss of releasing the volatile matter from the intensifying dehydration and elimination reactions [4]. This is supported by Muthanna et al.[19] using Siris seed pods. Figure 4 (b) shows the effect of impregnation ratio and activation temperature on the percentage yield. When the ratio and temperature increased, the percentage yield of carbon was decreased. This was due to higher elimination of tars in the pores. Sentorun-Shalaby et al. [20] reported that at higher activation temperature, activation of apricot stones became more extensive and resulted in a lower solid yield with a more

widened porous structure. Figure 4 (c) shows the effect of activation time and activation temperature on the percentage yield. As the temperature increased, the percentage yield of carbon was decreased. Meanwhile, activation time did not have significant effect on the percentage yield since heating duration of AC only affect it's surface area. This is supported by Tan et al. [4] study on coconut husk AC.

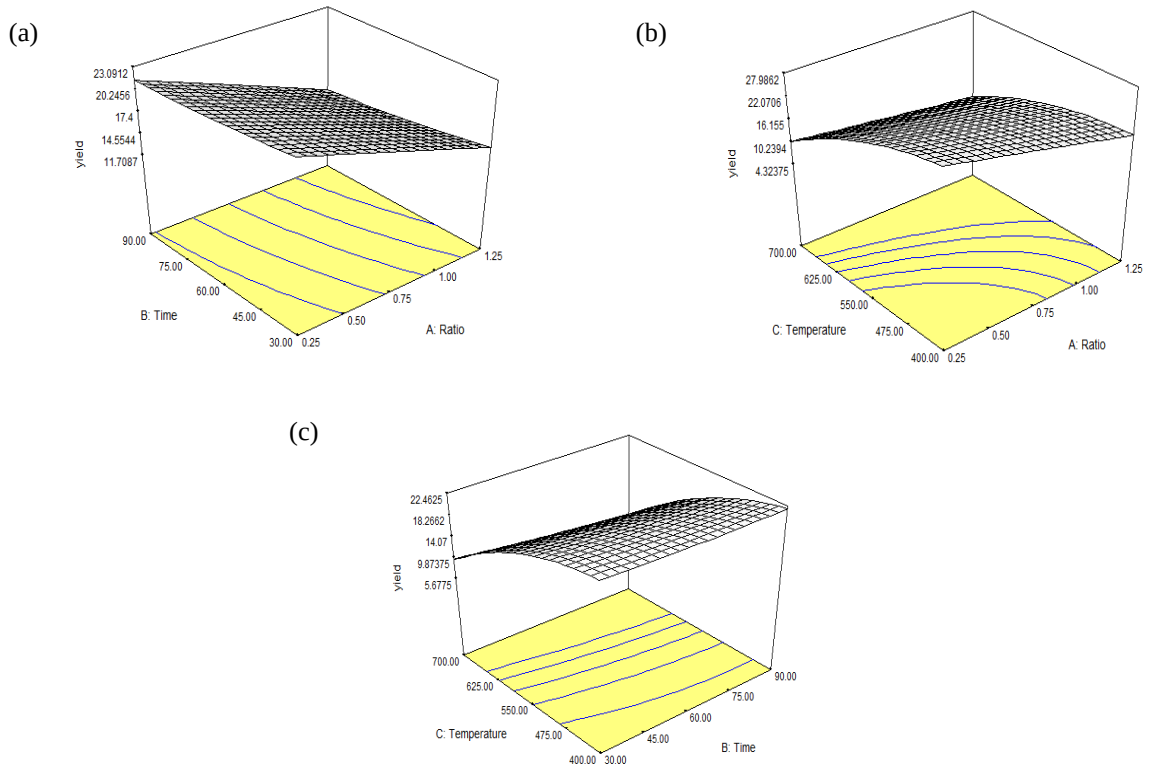


Figure 4. (a) Response for the effect of ratio KOH: SMFW and activation time on percent yield, (b) Response for the effect of ratio KOH: SMFW and activation temperature on percent yield and (c) Response for the effect of activation time and activation temperature on percent yield

Optimization of parameter on iodine number

Figure 5(a – c) illustrate the 3-D response surface plots of iodine number for AC as a function of three process parameters of impregnation ratio, activation time and activation temperature. Figure 5(a) shows the effect of impregnation ratio and activation time on the iodine number of the prepared AC. The iodine number increased with increased of the impregnation ratio. The impregnation ratio plays an important role in the formation of pores and promotes catalytic oxidation simultaneously. The KOH served to increase porosity of AC, thus resulted the raised in iodine number. This is supported by Abechi et al. [21] using KOH-kernel shell. Figure 5(b) shows the effect of impregnation ratio and activation temperature on the iodine number of prepared AC. As the activation temperature and impregnation ratio increased, the value of iodine number was increased. High temperature would increase the C–KOH reaction rates, thus resulting in increasing devolatilization and development of the pore structure in the char. Muthanna et al. [19] reported similar observation using AC from Siris seed pods. Figure 5(c) shows the effect of activation time and activation temperature on the iodine number of carbon. Since both the activation time and activation temperature increased, the value of iodine number was also increased. Tham et al.[22] reported that longer activation time had generated more micropores and mesopores in the AC produced from durian shell.

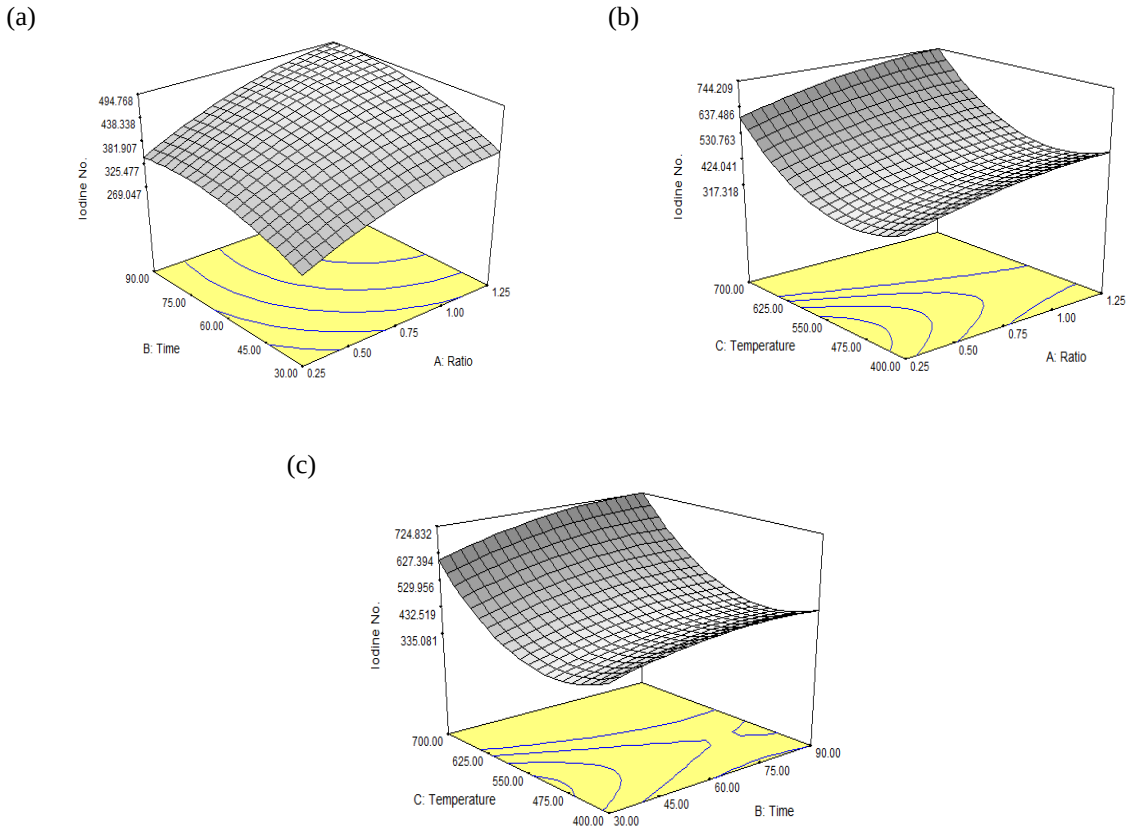


Figure 5. (a) Response for the effect of ratio KOH: SMFW and activation time on iodine number, (b) Response for the effect of ratio KOH: SMFW and activation temperature on iodine number, and (c) Response for the effect of activation time and activation temperature on iodine number.

Comparisons between experimental data and predicted data of Box-Behnken design

Final empirical models in terms of coded factors for carbon yield (Y_1) and iodine number (Y_2) are shown in equation (3) and (4), respectively.

$$Y_1 = 17.48 - 4.56xx1 - 1.13xx2 - 7.27xx3\text{-}0.045xx1^2 + 0.26xx2^2 - 2.83xx3^2 - 0.30xx1xx2 + 1.55xx1xx3 - 0.84\ xx2xx3 \quad (3)$$

$$Y_2 = 433.10 + 66.64xx1 + 45.65xx2 + 120.13xx3 - 26.86xx1^2 - 33.10xx2^2 + 144.64xx3^2 + 8.20xx1xx2 + 6.56xx1\ xx3 + 14.11xx2xx3 \quad (4)$$

Figure 6 shows the comparison between the experimental and predicted value of percentage yield and iodine number of AC. It was observed that there were good agreement between the experimental and predicted values of percentage yield and iodine number, which indicated the excellent reliability of the model with high R^2 of 0.9804 and 0.9333 respectively.

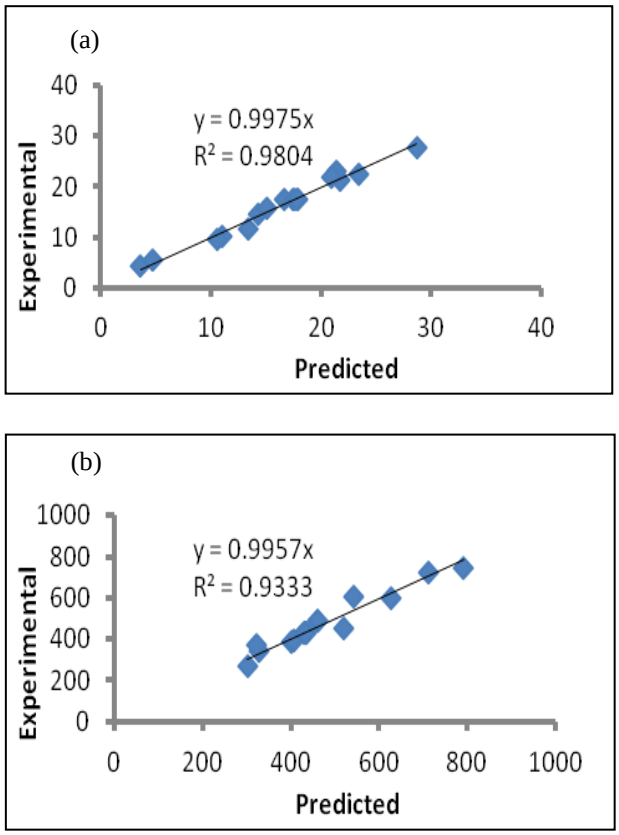


Figure 6. (a) Relationship between actual and predicted value of percentage yield of activated carbon, and (b) Relationship between actual and predicted value of iodine number of activated carbon.

Conclusion

Preparation of AC via Box-Behnken design of Response Surface Methodology was evaluated. The analysis of percentage yield and iodine number using this method generated optimum condition of impregnation ratio, activation time and activation temperature at 0.25, 30.04 min and 400 ^{0}C respectively. Experimental result was well fitted to predicted result with high R^2 of 0.9804 for percentage yield of AC and 0.9333 for iodine number. This method is applicable for industrial practice in AC production which involves multiple input and responses with minimum chemical and energy input, contribute on green technology.

Acknowledgement

The authors acknowledge the research grant RAGS, provided by the MOHE (RAGS/2013/UiTM/SG01/4), C&C Mushroom Cultivation Farm Sdn. Bhd. and also Universiti Teknologi MARA for supporting the facility.

References

1. Vargas, A. M. M., Garcia, C. A., Reis, E. M., Lenzi, E., Costa, W. F. and Almeida, V. C. (2010). NaOH-activated carbon from flamboyant (*Delonix regia*) pods: Optimization of preparation conditions using central composite rotatable design. *Chemical Engineering Journal*, 162 (1): 43 – 50.
2. Garba, Z. N. and Rahim, A. A. (2014). Process optimization of $K_2C_2O_4$-activated carbon from Prosopis africana seed hulls using response surface methodology. *Journal of Analytical and Applied Pyrolysis*, 107: 306 – 312.
3. Garba, Z. N., Abdul Rahim, A. and Hamza, S. A. (2014). Potential of Borassus aethiopum shells as precursor for activated carbon preparation by physico-chemical activation; optimization, equilibrium and kinetic studies. *Journal of Environmental Chemical Engineering*, 2(3): 1423 – 1433.

4. Tan, I. A. W., Ahmad, A. L. and Hameed, B. H. (2008). Preparation of activated carbon from coconut husk: optimization study on removal of 2,4,6-trichlorophenol using response surface methodology. *Journal of Hazardous Materials*, 153(1-2): 709 –717.
5. Foo, K. Y. and Hameed, B. H. (2012). Mesoporous activated carbon from wood sawdust by K_2CO_3 activation using microwave heating. *Bioresource Technology*, 111: 425 – 432.
6. Moodley, K., Singh, R., Musapatika, E. T., Onyango, M. S. and Ochieng, A. (2011). Removal of nickel from wastewater using an agricultural adsorbent, *Water SA*, 37(1): 41 – 46.
7. Yahaya, E. M., Faizal, M., Mohamed, P., Abustan, I. and Azmier, M. (2010). Effect of preparation conditions of activated carbon prepared from rice husk by $ZnCl_2$ activation for removal of Cu (II) from aqueous solution. *International Journal of Engineering Technology* 10 (6): 1– 5.
8. Chen, Y., Zhu, Y., Wang, Z., Li, Y., Wang, L., Ding, L. and Guo, Y. (2011). Application studies of activated carbon derived from rice husks produced by chemical-thermal process – a review. *Advances in Colloid and Interface Science* 163(1): 39 – 52.
9. Kumagai, S., Sato, M. and Tashima, D. (2013). Electrical double-layer capacitance of micro- and mesoporous activated carbon prepared from rice husk and beet sugar. *Electrochimica Acta*, 114: 617 –626.
10. Ding, L., Zou, B., Gao, W., Liu, Q., Wang, Z., Guo, Y. and Liu, Y. (2014). Adsorption of Rhodamine-B from aqueous solution using treated rice husk-based activated carbon. *Colloids and Surfaces A: Physicochemical and Engineering Aspects*, 446: 1 – 7.
11. Yao, X., Liu, J., Gong, G., Jiang, Y. and Xie, Q. (2013). Preparation and modification of activated carbon for benzene adsorption by steam activation in the presence of KOH. *International Journal of Mining Science and Technology*, 23(3): 395 – 401.
12. ElShafei, G. M. S., ElSherbiny, I. M., Darwish, A. S., and Philip, C. A. (2014). Silkworms' feces-based activated carbons as cheap adsorbents for removal of cadmium and methylene blue from aqueous solutions. *Chemical Engineering Research and Design*, 92(3): 461 – 470.
13. Pezoti Junior, O., Cazetta, A. L., Gomes, R. C., Barizão, É. O., Souza, I. P. A. F., Martins, A. C. and Almeida, V. C. (2014). Synthesis of $ZnCl_2$-activated carbon from macadamia nut endocarp (Macadamia integrifolia) by microwave-assisted pyrolysis: Optimization using RSM and methylene blue adsorption. *Journal of Analytical and Applied Pyrolysis*, 105: 166 –176.
14. Gao, Y., Yue, Q., Gao, B., Sun, Y., Wang, W., Li, Q. and Wang, Y. (2013). Preparation of high surface area-activated carbon from lignin of papermaking black liquor by KOH activation for Ni(II) adsorption. *Chemical Engineering Journal*, 217: 345 – 353.
15. Yang, H., Yan, R., Chen, H., Lee, D. H. and Zheng, C. (2010). Characteristic of hemicellulose, cellulose and lignin pyrolysis. *Fuel*, 86(12): 1781 – 1788.
16. Zhang, M., Resende, F. L. P., Moutsoglou, A. and Raynie, D. E. (2012). Pyrolysis of lignin extracted from prairie cordgrass, aspen and kraft lignin by Py-GC/MS and TGA/FTIR. *Journal of Analytical and Applied Pyrolysis*, 98: 65 – 71.
17. Dominguez, J. C., Oliet, M., Alonso, M. V., Gilarranz, M. A. and Rodriguez, F. (2008). Thermal stability and pyrolysis kinetics of organosolv lignins obtained from Eucalyptus globulus. *Industrial Crops and Products*, 27(2): 150 – 156.
18. Sharma, R. K., Wooten, J. B., Baliga, V. L., Lin, X.,Chan, W. G. and Hajaligol, M.R. (2004). Characterization of chars from pyrolysis of lignin. *Fuels*, 83(11): 1469 – 1482.
19. Muthanna, J. A. and Samar K. T. (2013). Microporous activated carbon from Siris seed pods by microwave-induced KOH activation for metronidazole adsorption. *Journal of Analytical and Applied Pyrolysis*, 99: 101 – 109.
20. Şentorun-Shalaby, Ç., Uçak-Astarlıogˇlu, M. G., Artok, L. and Sarıcı, Ç. (2006). Preparation and characterization of activated carbons by one-step steam pyrolysis/activation from apricot stones. *Microporous and Mesoporous Materials*, 88(1): 126 – 134.
21. Abechi, S. E., Gimba, C. E., Uzairu, A. and Dallatu, Y. A. (2013). Preparation and Characterization of Activated Carbon from Palm Kernel Shell by Chemical Activation. *Research Journal of Chemical Science*, 3(7): 65 – 61.
22. Tham, Y. J., Shamala, D. A., Nur Hidayah, A. L., Ahmad, M. A. and Puziah, A. L. (2010). Effect of activation temperature and heating duration on physical characteristics of activated carbon prepared from agricultural waste. *Environment Asia*, 3: 143 –148.

Malaysian Journal of Analytical Sciences, Vol 20 No 3 (2016): 469 - 476
DOI: http://dx.doi.org/10.17576/mjas-2016-2003-02

MALAYSIAN JOURNAL OF ANALYTICAL SCIENCES
Published by The Malaysian Analytical Sciences Society
ISSN 1394 - 2506

ADSORBENT FROM WASTE AND NATURAL DEPOSITS FOR PARAQUAT REMOVAL IN WATER

(Penjerap daripada Sisa Industri dan Semulajadi untuk Penyingkiran Paraquat di dalam Air)

Nur Fatin Zakaria[1], Zaiton Abdul Majid[1]*, Zainab Ramli[1], Jafariah Jaafar[1], Azmi Aris[2,3], Juhaizah Talib[2,3], Rusmidah Ali[1]

[1]*Department of Chemistry, Faculty of Science*
[2]*Department of Environmental Engineering, Faculty of Civil Engineering*
[3]*Institute of Environmental and Water Resource Management,*
Universiti Teknologi Malaysia, 81310 Johor Bharu, Johor, Malaysia

**Corresponding author: zaiton@kimia.fs.utm.my*

Received: 9 December 2014; Accepted: 21 March 2016

Abstract

Studies on the removal of frequently used herbicide for controlling broad-leafed weeds, Paraquat Dichloride (PQ) has been carried out intensively. Waste from steelmaking industries (Electric Arc Furnace (EAF) slag) and natural zeolite (clinoptilolite) were used as the starting materials. Preparation of an adsorbent involved two steps, namely extraction iron oxide (IO) from slag and precipitation of IO onto clinoptilolite. Characterization of NZIC were done using Fourier Transform Infrared spectroscopy (FTIR), Scanning Electron Microscopy (SEM), single-point Brunauer Emmett Teller (BET) surface area analysis, Vibrating Sample Magnetometer (VSM) and pH at zero point charge (pHzpc). The NZIC showed a lower magnetic saturation at 8.13 emu/g compared to maghemite at 29.5 emu/g. The BET surface area of NZIC was 146.29 m^2/g, larger compared to the individual surface area of clinoptilolite and maghemite which are 37.84 and 17.84 m^2/g respectively. Adsorption of PQ onto clinoptilolite and NZIC were investigated using a batch experiment. Surface characteristic of NZIC was investigated by pHzpc experiment showing that at pH 8.2 its electric surface charge is zero. Optimum parameters for adsorption of PQ in water were found at pH 12 with 0.01 g/10 mL of NZIC and equilibrium time of 20 minutes. Desorption experiment revealed that NZIC have a good recovery in repetitive usage for PQ removal in water.

Keywords: waste, clinoptilolite, iron oxide, paraquat, adsorption

Abstrak

Kajian ke atas penghapusan racun rumpai yang sering digunakan untuk mengawal tumbuhan berdaun besar, Paraquat Diklorit (PQ) telah dijalankan secara intensif. Sisa daripada industri keluli dan zeolit asli (klinoptilolit) telah digunakan sebagai bahan mentah. Elektrik relau arka (EAF) sanga mengandungi logam oksida berharga seperti oksida besi (IO) yang merangkumi 37% (w/w) sanga. Kajian ini memberi tumpuan untuk mengekstrak IO dan pemendakan ke atas klinoptilolit. Penyediaan Zeolit-Besi Oksida Komposit (NZIC) melibatkan dua langkah mudah iaitu pengekstrakan IO dari sanga EAF dan pemendakan IO ke atas klinoptilolit. Pencirian NZIC telah dilakukan dengan menggunakan Fourier Transform Inframerah Spektroskopi (FTIR), Imbasan Elektron Mikroskopi (SEM), analisis kawasan permukaan Brunauer Emmett Teller (BET), Vibrating Sample Magnetometer (VSM) dan pH di caj titik sifar (pHzpc). NZIC menunjukkan ketepuan magnet yang rendah iaitu pada 8.13 emu/g berbanding maghemite dengan ketepuan magnet 29.5 emu/g. Kawasan permukaan BET untuk NZIC adalah 146.29 m^2/g, lebih besar berbanding dengan kawasan permukaan individu klinoptilolit dan maghemite, 37.84 dan 17.84 m^2/g masing-masing. Penjerapan PQ ke atas klipnotilolit dan NZIC telah disiasat menggunakan eksperimen kumpulan. pHzpc untuk NZIC adalah pada pH 8.2 di mana caj permukaannya adalah seimbang. Parameter optimum untuk penjerapan PQ dalam air didapati pada pH 12 dengan 0.01 g/10 mL NZIC dan keseimbangan masa iaitu 20 minit. Eksperimen penyaherapan menunjukkan NZIC mempunyai kadar pemulihan yang baik dalam penggunaan berulang-dalam penyingkiran PQ di dalam air.

Kata kunci: sisa, klinoptilolit, ferum oksida, paraquat, penjerapan

Introduction

Paraquat (1,1'-dimethyl-4,4'-bipyridinium) is a highly effective herbicide used to control weeds and grass in agricultural area. Commonly, farmers tend to spray the diluted herbicides to the plant area and eventually the excess PQ may reach the source of fresh water by leaching from soil. Paraquat (PQ) is hydrophilic compound and it is highly soluble in water. Paraquat is classified as toxic to human and environment. The maximum concentration level (MCL) of PQ in drinking water is 20 µg/L according to United States Environmental Protection Agency (USEPA). Hence, efficient method for pesticides removal in water is constantly being researched. Various techniques has been research including adsorption [1, 2] and advanced oxidation process (AOP) via catalyst and Fenton [3-5]. Adsorption is considered a feasible method for pesticides removal due to its simplicity, cost-effectiveness and high removal.

The use of agricultural and industrial waste as precursors in the preparation of adsorbent constantly studied. In this study, electric arc furnace (EAF) slag and clinoptilolite were used as the starting materials for the production of an adsorbent. Natural zeolite namely clinoptilolite is a cation exchanger and have high selectivity properties. The selectivity and size exclusion of zeolite offers more effective removal of PQ. The performance of synthetic and natural zeolite in removing contaminants is not much different [6]. Zeolites also reduce the effect of NOM in adsorption of contaminant in real water sample [7].

The EAF slag is a highly available material from steel-making industry wastes and comprised of many valuable metal oxides such as Zinc (Zn), Iron (Fe), Calcium (Ca), Copper (Cu) and Manganese (Mn) [8]. Numerous works have been reported on the recovery of these valuable materials from slag. For example, Saufi [8] extracted Fe to use to enhance its carbon nanotube (CNT). On the other hand, Shawabkeh [9], Fallman [10] and Orhan [11] studied on maximizing Zinc, Chromium and Barium recovery from slag. In this work, iron was extracted from EAF slag and precipitated onto clinoptilolite to produce an adsorbent for the removal of PQ in water.

Materials and Methods

Raw material

Electric arc furnace slag was collected from Antara Steel Mills (M) Sdn.Bhd and clinoptilolite was purchased from Shafzan Feed and Fertilizer. Both raw materials were ground and sieved to a particle size of 75 µm prior to use. Clinoptilolite was first activated by agitating in 2M sodium chloride (NaCl) solution [12]. Paraquat standard was purchased from Fluka Analytical and used without further purification. Stock solution of PQ was prepared by dissolving standard paraquat in double distilled water. The working solution of PQ was prepared by series of dilution from the stock solution prepared.

Preparation of Natural Zeolite-Iron Oxide Composite (NZIC)

The NZIC was prepared via two simple steps. First, iron oxide (IO) was extracted from EAF slag, followed by the precipitation of iron (hydr)oxide onto clinoptilolite. Powdered EAF slag was added to ammonium chloride (NH_4Cl) solution and the mixtures were refluxed for 2 hours. A desired amount of clinoptilolite was added to the filtrate solution to make a 3 to 1 amount of clinoptilolite to iron oxide. Concentrated sodium hydroxide (NaOH) was added dropwise to the filtrate with an aid of sonication. The mixture was stirred for another 2 hours until homogenous suspension was obtained. Synthesized product was filtered, washed and dried overnight in an oven at 70˚C. Final product was calcined in a box furnace at 500°C for two hours at a temperature rate of 10 ˚C/min.

Characterization of NZIC

Fourier Transform Infra-red (FTIR) spectroscopy (Perkin Elmer, Spectrum One) was used to analyse the functional groups found in the clinoptilolite and NZIC prepared at a spectral range of 4000 cm^{-1} to 400 cm^{-1}. The morphology of clinoptilolite, maghemite and NZIC were observed using Scanning Electron Microscopy (SEM) (Phenom G2 Pro). Effect of surface area of clinoptilolite, maghemite and NZIC were studied using single-point Brunauer Emmett Teller (BET) surface area analysis. Magnetic properties of maghemite and NZIC were analysed using Vibrating

Sample Magnetometer (VSM) at room temperature. Zero point charge (zpc) of NZIC was determined by pH at zero point charge (zpc) experiment [13].

Removal of Paraquat in water by NZIC

Adsorption experiment for study on effect of time, adsorbent dosage and pH in paraquat removal by NZIC were conducted in a batch mode study. The experiment take place in thermostat orbital shaker (Lab Companion) and experiments were repeated to ensure the reproducibility of the result is obtained. Adsorption and desorption experiment were done using 10 mg/L PQ standard solution followed by desorption with distilled water. Initial and final concentration of PQ was quantified using calibration curve of PQ standard, analysed by UV-Vis spectrophotometry (UV-Vis-Perkin Elmer Lambda25 Spectrophotometer) at maximum absorption wavelength of 257 nm.

Results and Discussion

Characterization of NZIC

Fourier Transform Infra-red

Spectra of clinoptilolite, maghemite and NZIC in Figure 1 showed an intense peak at 1028 cm^{-1} indicates the presence of internal vibration of tetrahedral Si-O and Al-O. At 450 cm^{-1} band showed the vibration of O-Al-O or O-Si-O bonds. The existence of in-plane-bending vibration of water (H_2O) and OH bending in clinoptilolite and maghemite observed at 1637 cm^{-1} and 3447 cm^{-1} respectively were due to moisture in the sample preparation. Low band at wavenumber of 600 and 790 cm^{-1} found at spectrum of maghemite and NZIC were attributed to the characteristics band of iron oxide [14].

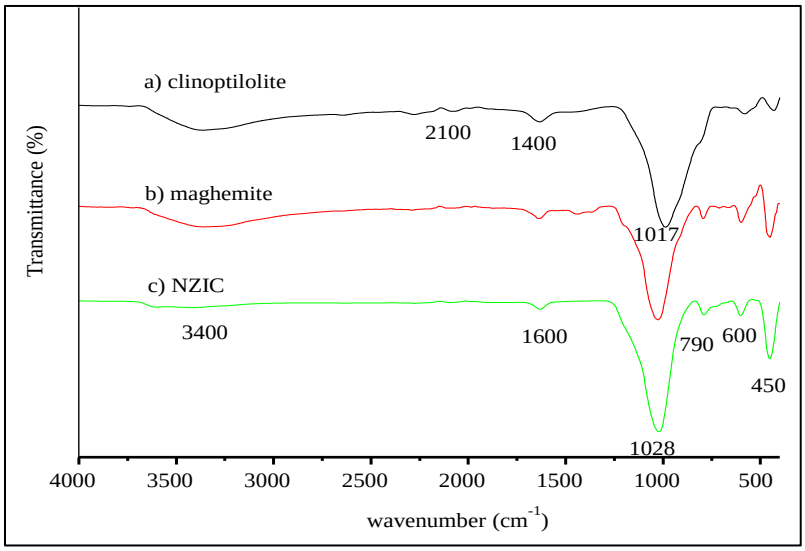


Figure 1. IR spectra of a) clinoptilolite, b) maghemite, and c) NZIC

Scanning Electron Microscopy micrograph

SEM images of clinoptilolite, maghemite and NZIC were shown in Figure 2. Micrograph in Figure 2a showed an irregularly shaped of clinoptilolite. Maghemite poses a prismatic and flake-like shape as observed in Figure 2b. Maghemite was scattered around clinoptilolite in Figure 2c showing the effective effect of dispersive by sonication in preparation of NZIC procedure.

Magnetic saturation

Figure 3a showed the hyteresis loop for maghemite and NZIC analysed by VSM at room temperature indicate curve for paramagnetism materials. Magnetic saturation of maghemite and NZIC were 29.55 and 8.13 emu/g respectively. Magnetic curve of maghemite and NZIC showed small loop indicating the remaining of magnetic reflux in the sample eventhough magnetic force is zero. Figure 3b suggested that NZIC in water was attracted effectively when external magnetic field was introduced. The decreasing effect of magnetic saturation in NZIC sample was due to small amount of maghemite in per gram of NZIC as well as the presence of non-magnetic material, clinoptilolite in NZIC..

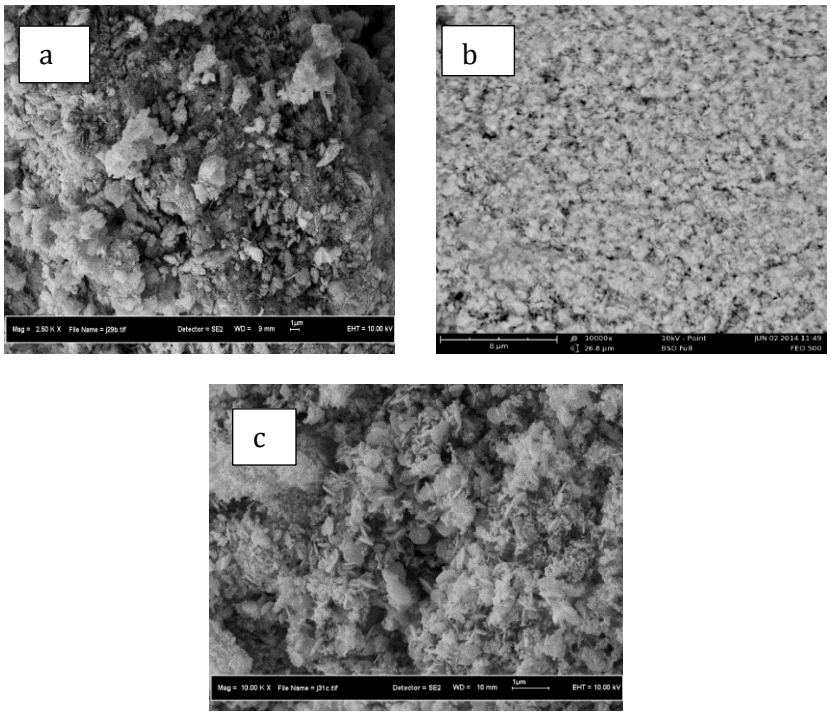
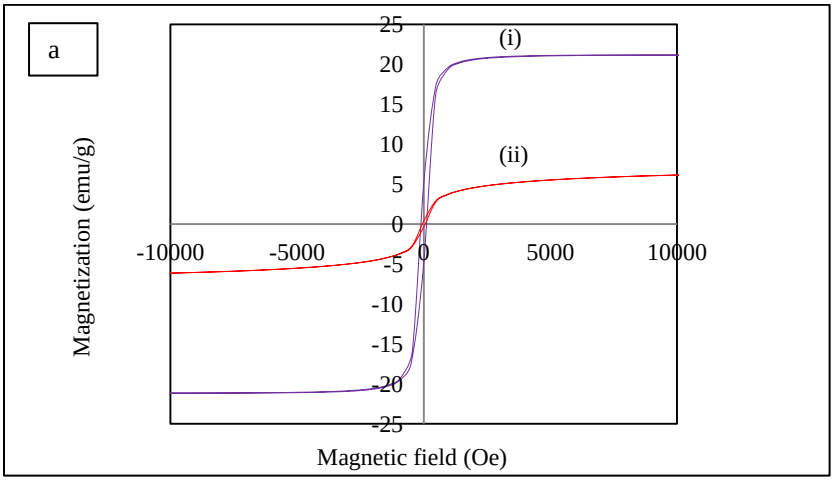


Figure 2. Micrograph of a) clinoptilolite, b) maghemite, and c) NZIC



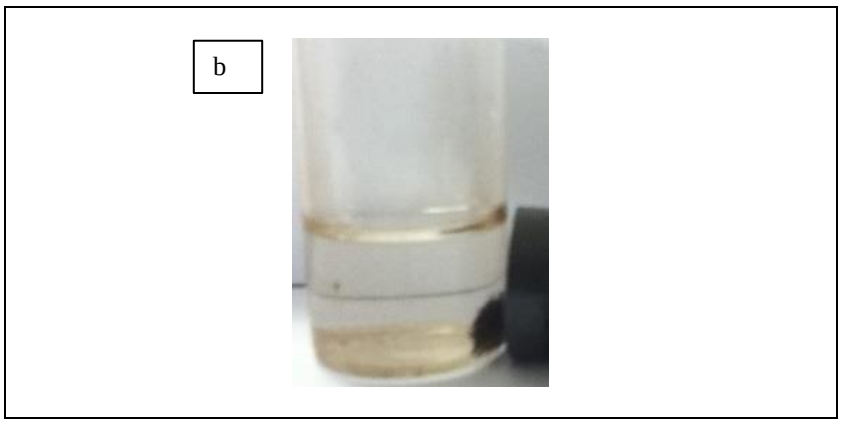


Figure 3. a) Magnetization curve of i) maghemite and ii) NZIC at 300 K, and b) magnetic attraction of NZIC towards external magnetic application

Surface area

The surface areas of raw materials, clinoptilolite and EAF slag as well as maghemite and NZIC were presented in Table 1. Iron oxide showed a small surface area due to the agglomeration effects and its mutual magnetic attraction. By modification of maghemite with clinoptilolite, the surface area increase almost four fold. The larger surface area of an adsorbent, then the bigger active site available for adsorption to take place.

Table 1. Surface area of clinoptilolite, EAFS, iron oxide and NZIC

Sample	**Clinoptilolite**	**Raw EAFS**	**Maghemite**	**NZIC**
Surface area, m^2/g	37.84	3.02	9.62	146.29

pH at zero point charge

The pH at zero point charge (pH_{zpc}) for NZIC was determined by mixing 0.15 g NZIC in 0.01 M concentration of NaCl and varying the pH of the solution from pH 2-13. After 24 hours agitation, the resulting mixtures were analysed for its pH. The plot of initial and final pH in Figure 4 showed an intersection of the two curves at pH 8.2. At this point, the NZIC surface charge is considered neutral. The adsorption of PQ depends on the pH of solution as PQ exists in its cationic form in water. At lower pH, surface of NZIC was saturated with hydronium ions (H_3O^+), thus high competition of these positively charge paraquat (PQ^+) and H_3O^+ decreased the adsorption of PQ.

Paraquat removal by NZIC

Figure 5 shows the plots of PQ removal by clinoptilolite, maghemite and NZIC against time. Adsorption of PQ by clinoptilolite and NZIC (3:1) were rapid at first and reached plateau after 20 minutes contact time. The equilibrium time of PQ removal was attained at the 20th minutes. From the graph in Figure 5, maghemite showed a very low adsorption, means that maghemite was not a good adsorbent. Although the surface area of NZIC was higher than clinoptilolite, but, the removal of paraquat by clinoptilolite was slightly higher than NZIC. As observed in Figure 5, low removal of PQ is observed despite a high surface area of NZIC. This is due to the existence of maghemite in NZIC.

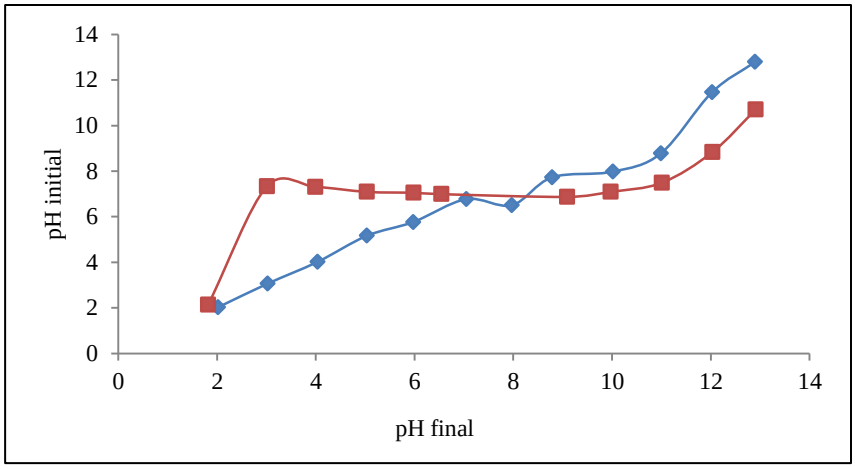


Figure 4. The pH at zero point charge of NZIC

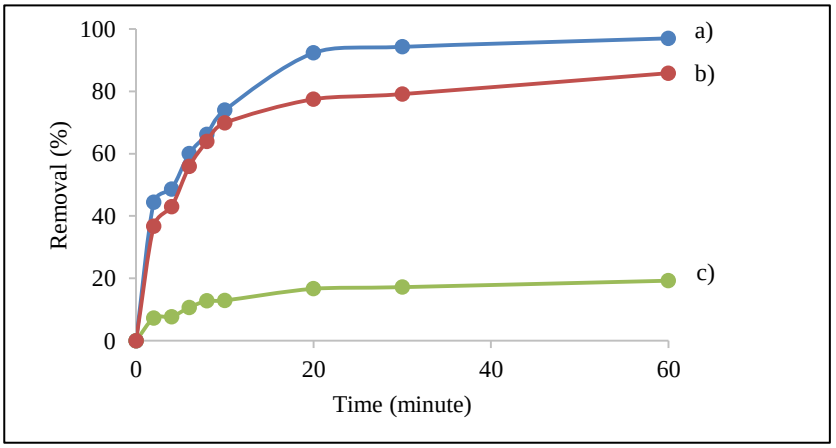


Figure 5. Comparison on the PQ removal by a) clinoptilolite, b) maghemite and c) NZIC (initial PQ concentration = 10 mg/L, Adsorbent dosage = 0.01 g, pH = neutral)

Plot in Figure 6 indicates that paraquat uptake increased with increasing pH. Maximum PQ uptake was obtained at pH 12. The removal of PQ is highly dependent on initial solution pH. This condition interrelated with the nature of PQ in water. The pK_a value of cationic PQ is 9 – 9.5 [14]. At higher pH than pH_{zpc}, higher concentration of hydroxide ions (OH^-) was present on NZIC surface. Hence, NZIC acquired a negatively surface charge at higher pH and cationic PQ easily attached to the surface of NZIC via attraction force.

Figure 7 shows that NZIC have a good recovery of PQ in desorption experiment. At first adsorption-desorption experiment, 99% of PQ was adsorbed and desorbed into the solution. The performance of PQ removal after second and third time repetitive usage was decreased to 86%. This small decreasing in percentage removal of PQ showed that the stability of these adsorbent for repetitive usage.

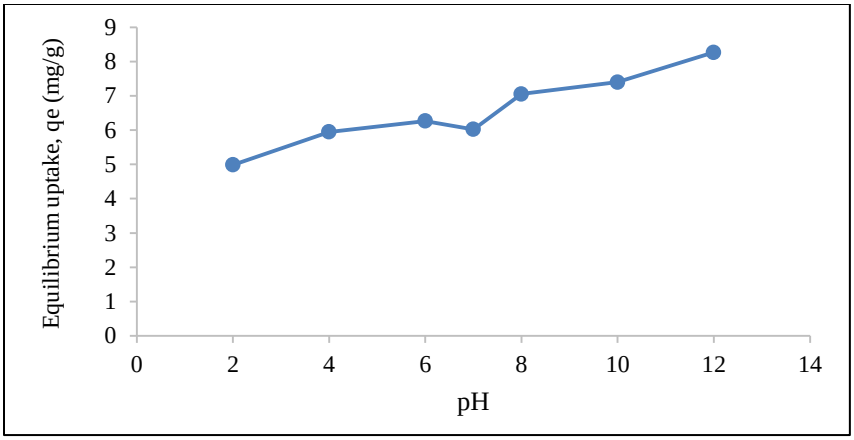


Figure 6. Effect of pH on PQ uptake by NZIC (initial PQ concentration = 10 mg/L, Adsorbent dosage = 0.01 g, pH=12)

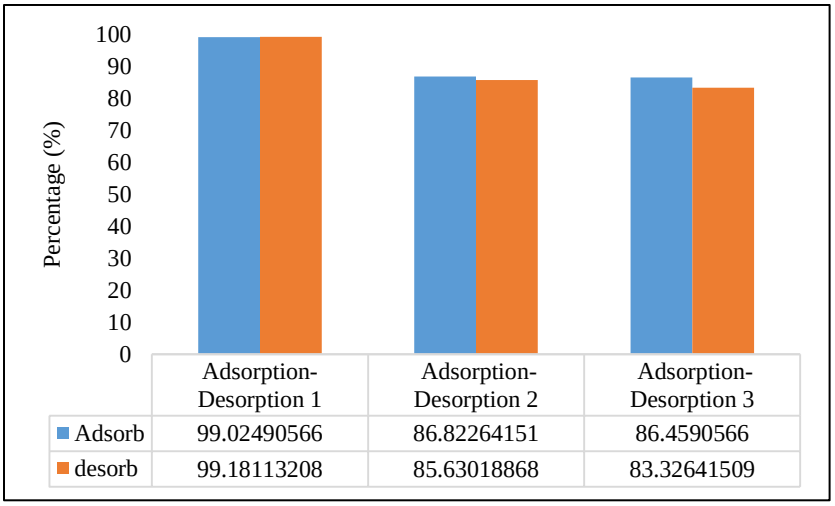


Figure 7. Repetitive adsorption of PQ onto NZIC (initial PQ concentration = 10 mg/L, Adsorbent dosage = 0.01 g, pH = 12)

Conclusion

Preparation of NZIC was done by extraction of iron oxide (IO) from slag and precipitation of IO onto clinoptilolite. Magnetization analysis of NZIC revealed the ability of maghemite in NZIC as a magnetic separator when external magnetic field was applied. Preliminary study showed that clinoptilolite have higher removal percentage of paraquat (96%) compared to NZIC (86%) due to nature of maghemite which is not a good adsorbent. Optimum parameters for adsorption of 10 mg/L PQ in water were found at pH 12 with 0.01 g of NZIC with equilibrium time of 20 minutes. Desorption experiment demonstrate that NZIC as a stable adsorbent for repetitive usage for PQ adsorption.

Acknowledgement

We would like to express our gratitude to Universiti Teknologi Malaysia, Institute of Environmental and Water Resource Management (IPASA) and Ministry of Higher Education (MOHE) for the financial support given under Long Term Research Grant, 4L810 and 4L812 and Fundamental Research Grant, 4F234.

References

1. Rahman, I. A., Sing, Y.Y., Bari, M. F. and Saad, B. (2015). Adsorption of paraquat by treated and untreated rice husks studied by flow injection-analysis. *Research Journal of Chemistry and Environment* 9 (1): 13 – 18.
2. Hsu, S.-T. and Pan, T.-C. (2007). Adsorption of paraquat using methacrylic acid-modified rice husk. *Bioresource Technology*, 98 (18): 3617 – 3621.
3. Ali, R. and Hassan, S. H. (2008). Degradation studies on paraquat and malathion using TiO_2/ZnO based photocatalyst. *Malaysian Journal of Analytical Sciences*, 12 (1): 77 – 87.
4. Santos, M. S. F., Alves, A. and Madeira, L. M. (2011). Paraquat removal from water by oxidation with Fenton's reagent. *Chemical Engineering Journal*, 175: 279 – 290.
5. Oliveira, C., Gruskevica, K., Juhna, T. and Tihomirova, K. (2014). Removal of paraquat pesticide with Fenton reaction in a pilot scale water system. *Drinking Water Engineering Science*, 7: 11 – 21.
6. Nah, I. W., Hwang, K.-Y., Jeon, C. and Choi, H. B. (2006). Removal of Pb ion from water by magnetically modified zeolite. *Mineral Engineering*, 19 (14): 1452 – 1455.
7. Ridder D. J. (2012). Adsorption of organic micropollutants onto activated carbon and zeolites. Water Management Academic Press, Netherlands
8. Mohd Saufi bin Rosmi. (2010). Synthesis of high quality of CNT via decomposition of acethylene on unsupported catalyst derived from industrial waste". Thesis Bachelor of Science, University Teknologi Malaysia.
9. Shawabkeh, R. A. (2010). Hydrometallurgical extraction of Zinc from Jordanian electric arc furnace dust. *Hydrometallurgy*, 104 (1): 61 – 65.
10. Fallman, A.-M. (2000). Leaching of Chromium and Barium from steel slag in laboratory and field tests- a solubility controlled process? *Waste Management*, 20 (2-3): 149 –154.
11. Orhan, G. (2005). Leaching and cementation of heavy metals from electric arc furnace dust in alkaline medium. *Hydrometallurgy*, 78 (3-4): 236 – 245.
12. Pode, V., Popovici, E., Pode, R. and Georgescu, V. (2007). Magnetic properties of an adsorbent based on modified natural zeolite. *Revue Roumaine Chimie*, 52 (10): 983 – 989.
13. Faria, P. C. C., Orfão, J. J. and Pereira, M. F. (2004). Adsorption of anionic and cationic dyes on activated carbons with different surface chemistry. *Water Research*, 38 (8): 2043 – 2052.
14. Tantriratna, P., Wirojanagud, W., Neramittagapong, S., Wantala, K. and Grisdanurak, N. (2011). Optimization for UV-Photocatalytic degradation of paraquat over titanium dioxide supported on rice husk silica using Box-Behnken Design. *Indian Journal of Chemical Technology*, 18: 363 – 371.

Malaysian Journal of Analytical Sciences, Vol 20 No 3 (2016): 477 - 483
DOI: http://dx.doi.org/10.17576/mjas-2016-2003-03

MALAYSIAN JOURNAL OF ANALYTICAL SCIENCES
Published by The Malaysian Analytical Sciences Society
ISSN 1394 - 2506

TAILORING PEPTIDOMIMETICS ANTIFREEZE PROTEIN FROM EXOTIC ANTARCTIC MARINE

(Pengubahsuaian Protein Antibeku Peptidomimetik daripada Hidupan Eksotik Marin Antartika)

Mohd Basyaruddin Abdul Rahman[1, 2]*, Azren AidaAsmawi[1,2], Emilia Abdulmalek[1,2], Abu Bakar Salleh[1], Bimo Ario Tejo[3]

[1]*Enzyme and Microbial Technology Research Centre (EMTech)*
[2]*Department of Chemistry, Faculty of Science*
Universiti Putra Malaysia, 43400 UPM Serdang, Selangor, Malaysia.
[3]*Center for Infectious Diseases Research,*
Surya University, Jalan Boulevard Gading Serpong Blok O/1,
Scientia Business Park, Tangerang 15810, Indonesia

**Corresponding author: basya@upm.edu.my*

Received: 9 December 2014; Accepted: 22 March 2016

Abstract

Antifreeze proteins (AFPs) are synthesized by various cold-adapted organisms to enable them to survive in subzero environment. The unique role of AFPs recently attracted enormous interest to develop them as commercial products. In this work, we have studied the antifreeze activity of short helical protein fragments (peptides) instead of the entire antifreeze protein of Antarctic yeast *Glaciozyma antarctica*. Several short peptide segments were designed according to amino acid sequence of helical region of AFP-1 *G.antarctica*, which are assumed to be involved in its antifreeze activity. We have demonstrated that short peptide segments derived from yeast AFP possess antifreeze activity and result in modification of the ice crystals growth rates and habits. This strategy has enabled the preparation of short AFP with high antifreeze activity in large amount of quantities at a low cost further opens the chance of developing the commercial potentials of AFPs.

Keywords: Antarctic yeast, antifreeze protein (AFP), *Glaciozyma antarctica*, ice recrystallization inhibition (IRI)

Abstrak

Protein antibeku (AFPs) disintesis oleh pelbagai adaptasi-sejuk organisma untuk membolehkan ia bertahan di persekitaran suhu bawah takat beku. Peranan unik AFPs telah menarik minat yang besar bagi tujuan produk komersil. Di dalam kajian ini, kami telah mengkaji aktiviti protein antibeku berlingkar yang pendek (peptida) daripada protein antibeku Antartika yis *Glaciozyma antarctica*. Beberapa segmen peptida pendek direka mengikut jujukan asid amino berlingkar AFP-1 *G.antarctica*, yang dianggap terlibat dalam aktiviti antibeku. Kami telah menunjukkan bahawa segmen – segmen peptida pendek yang diperolehi daripada yis AFP mempunyai aktiviti antibeku dan menyebabkan pengubahsuaian kadar pertumbuhan dan tabiat hablur ais. Strategi ini telah membolehkan penyediaan AFP pendek dengan aktiviti antibeku yang tinggi dalam jumlah kuantiti besar pada kos yang rendah seterusnya membuka peluang untuk membangunkan potensi komersial AFPs.

Kata kunci: yis Antartika, protein antibeku (AFP), *Glaciozyma antarctica*, perencatan penghabluran ais (IRI)

Introduction

The effect of sub-zero temperatures on organisms can cause extensive damage due to the presence of ice crystals. If freezing persists, intracellular water passes into extracellular spaces and leads to cell dehydration. Despite this,

various species such as plants, fish, insect, bacteria and fungi are able to survive in the coldest and most southerly continent of the world, Antarctica, where it was once thought conditions would render it uninhabitable. DeVries [1] and his colleagues [2] were the first to reveal the mechanisms through which species of a thriving marine inhabiting the polar oceans at freezing temperatures are able to survive. Although these species have high levels of salt ions as compared to temperate species, the presence of these ions accounted for only about half of the observed water freezing point depression in their body fluid. From the analyses, it is clear that the primary defense in these organisms is attributed to a class of highly specialized biomolecules known as antifreeze proteins or AFPs [3].

Antifreeze activity has been speculated to be a result of ice recrystallization inhibition process. AFPs inhibit the growth of ice crystals by binding to ice surfaces and disrupt the normal propagation of the ice crystal by restricting the growth in the areas where AFPs cover the ice surface [4]. This leads to a curvature of the surface of the ice crystal, increasing the ratio of the surface area to volume, and resulting in a ratio which is no longer thermodynamically supportive of spontaneous ice growth. The potential for an ice crystal to grow is therefore arrested by this mechanism [5]. Most exciting is that AFPs are now leading to promising commercial applications such as improving the texture of ice-cream [6], extending the half-life of frozen dough [7] and as far as cryosurgery [8]. Another interesting development in the application of AFPs is their potential for the cryopreservation of cells, tissues and membranes from damage at low, but not freezing temperatures [9].

There are five types of AFPs which have already been identified: AFP type I, II, III and IV. Type I AFPs are known as amphipathic α-helical structure with alanine-rich sequence sized between 3.3 kDa to 9 kDa -R, type II AFPs with molecular mass ranging from 11 kDa to 24 kDa exists as large globular proteins comprising multi-cysteine residue in their structure [10-12], type III AFPs are recognized as β-sandwich globular proteins with molecular weight around 6 kDa [13-16], type IV AFPs are rich with glutamate (E) or glutamine (Q) residues in sequence form a bundle of with α-helical [17], while type V AFPs were recently reported and known as hyperactive proteins isolated from insects [18].

Instead of using an antifreeze protein, this study will focus on application of the peptide segments of AFP. Because of the simpler structure of antifreeze peptides over antifreeze proteins, it can be used as “molecular tools” to investigate each sequence in peptide structure which performs a function in the antifreeze protein [19]. The α-helical structures are believed to play a major role in inhibiting of ice crystal in Type-I AFPs, and this require the binding of hydrophobic face helices with water crystals [20]. These facts led us to design and study antifreeze activity of short peptides isolated from Antarctic yeast, *Glaciozyma Antarctica* that produced an 18 kDA of AFP I. The predicted three-dimensional structure of AFP I display several α-helical conformations in its structure expected to have biological activity as their native protein.

Materials and Methods

Peptides

Peptide 1, peptide 1m, peptide 2, peptide 3, peptide 4 and peptide 4m, were bought from GL Biochem, Shanghai, China. Each peptide was supplied HPLC purified >90% purity and was used without further purification. The molecular weight of each peptide was analyzed using ESI LC-MS.

Peptide design

Four peptides namely peptide 1, 2, 3 and 4 were derived from α-helical regions in the predicted structure of *G. antarctica* AFP-1. Further modifications were made in peptides 1 and 4 by introducing salt bridges in their structure to improve their α-helical conformation. A scrambled peptide was designed based on the systematic scrambling of peptide 1m and was used as a negative control. Their sequences are shown in Table 1. Structure of the design peptides were then predicted using online server; PEP-FOLD [21]. The basic principle behind PEP-FOLD is that the three dimensional model is built based on the concept of hidden Markov model (HMM) derived structural alphabet (SA) of 27 four amino acids letters. The SA letter profiles of each peptide sequences were first predicted and subsequently assembled with the fragments according to the sOPEP coarse-grained force field.

Table 1. List of peptide used in this work

Peptide	Sequence
1	MRSNFHPLAASFIVRCAFLHSRRFT
1m	QRSNFHPLAASFIVRCAFEHSRRFT
2	RRFTDSLFQLLSSLISLTSAATAID
3	TGNVGLSPGLSTALTGFTLVPVEDH
4	VKGRIDAPDFPSSPAILGQAATDVVAAWKS
4m	VKGRIDAPDFPSSPAILGKAATDVVAAWKS
Scrambled	QSSFHNTRFAEHFARALSPRIVCFR

Antifreeze activity determination

Ice crystals growth in 30 % sucrose solution was studied using a temperature-controlled freezing stage (Model THM 600 Linkham Scientific Instrument, UK) connected with a temperature controller unit (Model TMS 94, Linkham Scientific Instrument, UK). The freezing stage was incorporated on top of the conventional microscope stage (Olympus BX51, USA). In ice recrystallization experiment, 1.5 µL mixture of 1 mM peptide solution and 30 % sucrose (1:1 ratio) was sandwiched between two microscope glass coverslip. The sample was added inside the freezing stage and the temperature was adjusted from 20°C to – 40°C at the rate of 100°C/min. The temperature of the sample was then slowly increased from – 40°C to – 6°C at the rate 10°C/min and was maintained for 3 hours. The irruptive of ice recrystallization phase was occurred, generating a very fine of ice nuclei with different size in different sample. A reduce number and growth of ice crystals size in peptide solution after 3 hours incubation period would be indicative of the peptide efficiency in inhibiting ice crystal growth [23]. The sample microscopic images were captured at the end of incubation period at 100x magnification. The mean size of the ice crystals formed was calculated using the Cell^F software.

Results and Discussion

The ability of Antarctica yeast *Glaciozyma antarctica* to survive in freezing temperature is believed by employing antifreeze proteins. Currently, only AFP-1 gene sequence has been successfully characterized and expressed from the yeast [22]. The large antifreeze protein (AFP) from this *antarctica* yeast shows very low homology as compared to other AFP genes [23]. Interestingly, the predicted three-dimensional structure of AFP-1 sequence shows the presence of several α-helical conformations in its structure. Garner and Harding [20] put forward the idea to design small structured peptides with antifreeze properties and suggested that the α-helical structures which contained both hydrophilic and hydrophobic region are important and may responsible for the antifreeze activity [24].

Peptides 1, 2, 3 and 4 were designed representing the helices presence in the AFP-1 while peptide 1m and 4m were modified version of peptide 1 and 4. The solubility of peptides 1, 1m, 3, 4 and 4m in an unbuffered solution at pH 5.0 was good. However, peptide 2 was dropped from this study due to poor insolubility in water. Modification were made in peptides 1 and 4 sequences and produced peptides 1m and 4m to improve helical structure formation by the use of lactam bridges, which might form at positions either *i, i*+4 or *i, i*+7 between basic and acidic residues. In addition, peptide solubility in water will increase in the presence of more basic and acidic amino acids in the peptide sequence. Besides, it has been recently reported that, reducing the helicity content of AFP results a reduction of the antifreeze activity [24]. Therefore, through the amino acids sequence alterations, the fixed α-helical structures of modified peptides are predicted to be more stable and consequently exhibit higher antifreeze activity.

The three dimensional structure of peptides are predicted to exists as single, amphipathic, α-helix by PEP-FOLD. The prediction can only provide an indication of how certain peptide conforms in an aqueous solution. According to the results, peptide 1m is structurally predicted being more straightforward helix, while both peptides 3 and 4m are structurally less straightforward since there are slightly helical twist can be seen in their structure. As shown in Figure 1, the cross-section view of 3D conformation clearly shows the amino acid distribution in the peptides structure. All peptides have hydrophobic face in their structure. A clear distinct region of hydrophilic and flat

hydrophobic region may be observed in peptide 1m (Figure 2). Although the exact mechanism which attributed to the action of antifreeze by these peptides is remain elusive, it is expected that it may follow a mechanism similar to that of antifreeze activity of type-1 AFPs as found in organisms that live in freezing temperatures [25]. It is well accepted that flat-faced proteins in hydrophobic region may contribute to the binding mechanism of these proteins to ice crystals [20].

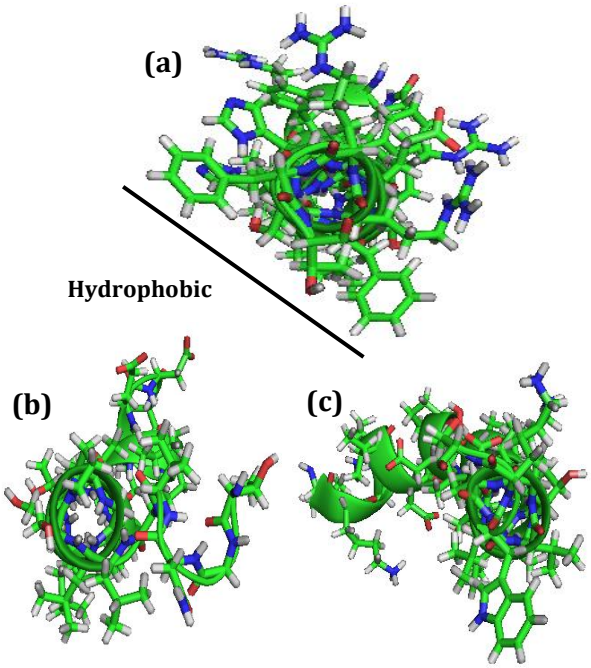


Figure 1. Cross-section view of 3D conformation of (a) peptide 1m, (b) peptide 3 and (c) peptide 4m, using PEP-FOLD and PyMOL showing hydrophobic region. Carbon: green, hydrogen: white, nitrogen: blue, oxygen: red, sulphur: yellow.

Throughout this work, to ensure on the accuracy of antifreeze activity determination, all peptide samples used were dissolved in unbuffered solution at pH 5.0, as salt presence in a solution would elevate the antifreeze activity due to its ability to reduce the freezing point [26]. In this work, to obtain a quantitative estimation of antifreeze activity, ice recrystallization inhibition (IRI) was investigated by observing the ice crystals size after 3 hours of incubation time at – 6°C at low peptides concentration. Figure 2 and Table 2 show IRI results for 1 mM of designed peptide. To investigate the ability of the peptides in ice growth inhibition, the results were compared with a negative control, namely scrambled peptide. The results obtained show that, all five designed peptides could not completely arrest the ice crystal growth. Nevertheless, by comparing IRI results of negative control, diminutive ice crystal size can be clearly seen. The designed peptides demonstrated moderate growth of ice crystals growth. The order of antifreeze activity of peptides at 1 mM concentration based on the size of ice crystal growth was found to be highest in modified peptide 1m and peptide 4m followed by peptide 1, peptide 4 and peptide 3. Interestingly, both modified peptide (peptides 1m and 4m) able to arrest ice growth better than their original peptide (peptides 1 and 4) due to the mutations of Leu19Glu and Gln19Lys in their sequence.

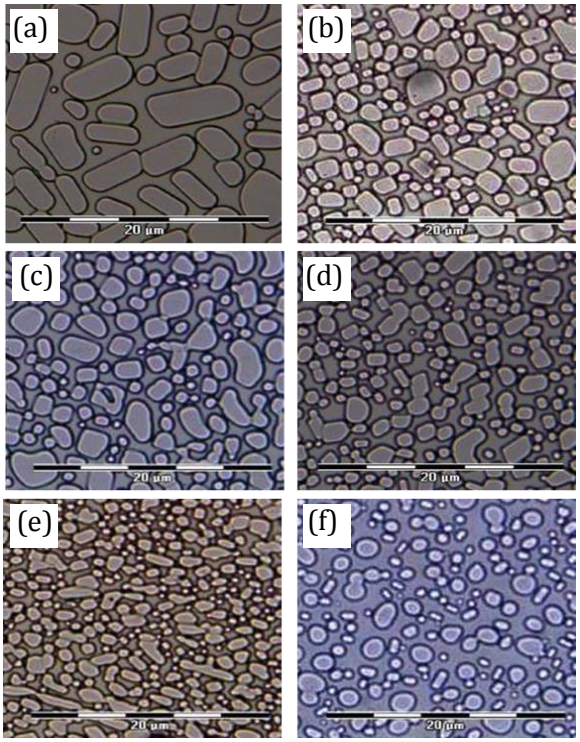


Figure 2. Ice recrystallization inhibition (IRI) of 1 mM peptide assays results. The growth of ice crystals were observed after 3 h incubation at the temperature of -6 °C. (a) scrambled peptide, (b) peptide 1, (c) peptide 3, (d) peptide 4, (e) peptide 4m, (f) peptide 1m.

Table 2. Mean of ice crystal size in 30% sucrose solution containing peptide

Sample	**Mean ice crystal diameter ± SD (µm)**
30% sucrose + 1 mM peptide 1	6.37 ± 2.61
30% sucrose + 1 mM peptide 3	9.27 ± 4.61
30% sucrose + 1 mM peptide 4	7.66 ± 2.94
30% sucrose + 1 mM peptide 1m	4.50 ± 2.42
30% sucrose + 1 mM peptide 4m	5.57 ± 2.21
30% sucrose + 1 mM scrambled peptide	17.22 ± 3.42

The results reported here appear to support the hypothesis that short helical fragments of antifreeze protein should be able to mimic the biological activity of its parent protein by modifying the ice crystals growth and habit. The short designed peptides appear to have similar adaptability which required for antifreeze activity. It was also evident that the hydrophobicity and straightforwardness of helical peptide were crucial for their ice crystal modification capabilities [3]. In this respect, modified peptides (peptide 1m and 4m) possessing a high degree of helicity due to the formation of salt bridges between acidic residues and basic residues exhibited the greatest inhibitory activity than less helical peptide.

Conclusion

As a conclusion, our results proved that a well-conserved α-helical with distinctive hydrophobic and hydrophilic region in the peptide structure, reinforcing the antifreeze activity. The antifreeze activity was found to be peptide 1m > peptide 4m > peptide 1 > peptide 4 > peptide 4. The success of our strategy of using short segments of yeast AFP may enhance potential to develop applications using the short antifreeze peptide properties via routine design and synthesis in cost-effective commercial production.

Acknowledgement

The authors thank the Malaysian Ministry of Science, Technology and Innovation (MOSTI) for financial support to the Malaysian Genome Institute (02-05-20-SF11113) and Universiti Putra Malaysia.

References

1. DeVries, A. L. (1971). Glycoproteins as biological antifreeze agents in antarctic fishes. *Science* 172: 1152 – 1155.
2. Scholander, P. F., Van Dam, L., Kanwisher, J. W., Hammel, H. T. and Gordon, M. S. (1957). Supercooling and osmoregulation in arctic fish. *Journal of Cellular and Comparative Physiology*, 49: 5 – 24.
3. Sicheri, F. and Yang, D. S (1995). Ice-binding structure and mechanism of an antifreeze protein from winter flounder. *Nature* 375: 427 – 431.
4. Davies P. L., Baardsnes, J., Kuiper, M. J. and Walker, V. K. (2002). Structure and function of antifreeze proteins. *Philosophical Transactions of the Royal Society of London B: Biological Sciences* 357: 927 – 935.
5. Nutt, D. R. and Smith, J. C. (2008). Dual function of hydration layer around an antifreeze protein revealed by atomic molecular dynamics simulations. *Journal American Chemical Soc*iety 130: 13066 -13073.
6. Regand, A. and Goff, H. D. (2006). Ice recrystallization inhibition in ice cream as affected by ice structuring proteins from winter wheat grass. *Journal of Dairy Science*, 89: 49 – 57.
7. Zhang, C., Zhang, H. and Wang, L. (2007). Effect of carrot (*Daucus carota*) antifreeze proteins on the fermentation capacity of frozen dough. *Food Research International* 40: 763 – 769.
8. Muldrew, K., Rewcastle, J., Donnell, B. J., Saliken, J. C., Liang, S., Goldie, S., Olson, M., Baissalov, R. and Sandison, G. (2001). Flounder antifreeze peptides increase the efficacy of cryosurgery. *Cryobiology* 42: 182 – 189.
9. Fuller, B. J. (2004). Cryoprotectants: the essential antifreezes to protect life in the frozen state. *CryoLetters* 25: 375 – 388.
10. Ng, N. F., Trinh, K. Y. and Hew, C. L. (1986). Structure of an antifreeze polypeptide precursor from the sea raven Hemitripterus americanus. *Journal of Biological Chemistry* 261: 15690 – 15695.
11. Ng, N. F. and Hew C. L. (1992). Structure of an antifreeze polypeptide from the sea raven. Disulfide bonds and similarity to lectin-binding proteins. *Journal of Biological Chemistry* 267: 16069 – 16075.
12. Chao, H., Davies, P. L., Skyes, B. D. and Sonnichsen, F. D. (1993). Use of proline mutants to help solve the NMR solution structure of type III antifreeze protein. *Protein Science* 2: 1411 – 1428.
13. Jia, Z., DeLuca, C. I. and Davies, P. L. (1995). Crystallization and preliminary X-ray crystallographic studies on Type III antifreeze protein. *Protein Science* 4: 1236 – 1238.
14. DeLuca, C. I., Chao, H., Sonnichsen, F. D., Skyes, B. D. and Davies, P. L. (1996). Effect of type III antifreeze protein dilution and mutation on the growth inhibition of ice. *Biophysical Journal* 71: 2346 –2355.
15. Sonnichsen, F. D., DeLuca, C. I., Davies, P. L. and Sykes, B. D. (1996). Refined solution structure of type III antifreeze protein: hydrophobic groups may be involved in the energetics of the protein-ice interaction. *Structure* 4: 1325 – 1337.
16. Deng, G., Andrews, D. W. and Laursen, R. A. (1997). Amino acid sequence of a new type of antifreeze protein, from the longhorn sculpin Myoxocephalus octodecimspinosis. *FEBS Letters* 402: 17 – 20.
17. Liou, Y. C., Davies, P. L. and Jia, Z. (2000). Crystallization and preliminary X-ray analysis of insect antifreeze protein from the beetle Tenebrio molitor. *Acta Crystallographica Section D: Biological Crystallography*. 56: 354 – 356.
18. Kun, H. and Mastai, Y (2007). Activity of short segments of Type I antifreeze protein. *Biopolymers* 88: 807 – 814.
19. Harding, M. M., Ward, L. G. and Haymet, A. D. (1999). Type I 'antifreeze' proteins. Structure-activity studies and mechanisms of ice growth inhibition. *European Journal of Biochemistry* 264: 653 – 665.

20. Maupetit, J., Derreumaux, P. and Tuffery, P. (2009). PEP-FOLD: an online resource for de novo peptide structure prediction. *Nucleic Acids Res*earch 37: 498 – 503.
21. Rahman, M. B., Zulkifli, M. F., Murad, A. M., Mahadi, N. M., Basri, M., Zahman, R. N. Z. and Salleh, A. B. (2008). *Ab-Initio* protein structure prediction of *Leucosporidium antarcticum* antifreeze proteins using I-TASSER simulations. *1st WSEAS International Conference on Biomedical Electronics and Biomedical Informatics*, Rhodes, Greece.
22. Fairley, K., Westman, B. J., Pham, L. H., Haymaet, A. D., Harding, M. M. and Mackay, J. P. (2002). Type I shorthorn sculpin antifreeze protein: Recombinant synthesis, solution conformation, and ice growth inhibition studies. *Journal Biology Chem*istry 277: 24073 – 24080.
23. Hashim, H. N. F., Bharudin, I., Nguong, D. L. S., Bakar, F. D. A., Nathan, S., Rabu, A., Kawahara, H., Ilias, R. M., Najimudin, M., Mahadi, N. M. and Murad, A. M. A. (2013). Characterization of Afp1, an antifreeze protein from the psychrophilic yeast *Glaciozyma antarctica* PI12. *Extremophiles* 17: 63 – 73.
24. Park, K. S., Jung, W. S., Kim, H. J. and Shin, S. Y. (2010). Determination of the minimal sequence required for antifreeze activity of type I antifreeze protein (AFP 37). *Bulletin Korean Chemical Society* 31: 3791 – 3793.
25. Jia, Z. and Davies, P. L. (2002). Antifreeze proteins: An unusual receptor-ligand interaction. *Trends in Biochemical Sciences* 27: 101 – 106.
26. Fan, Y., Liu, B., Wang, H., Wang, S. and Wang, J. (2002). Cloning of an antifreeze protein gene from carrot and its influence on cold tolerance in transgenic tobacco plants. *Plant Cell Rep*orts 21: 296 – 301.

Malaysian Journal of Analytical Sciences, Vol 20 No 3 (2016): 484 - 490
DOI: http://dx.doi.org/10.17576/mjas-2016-2003-04

MALAYSIAN JOURNAL OF ANALYTICAL SCIENCES
Published by The Malaysian Analytical Sciences Society
ISSN 1394 - 2506

CORROSION INHIBITION OF Q235A STEEL IN ACID MEDIUM USING ISATIN DERIVATIVES: A QSAR STUDY

(Perencatan Kakisan Keluli Q235A di dalam Medium Asid Menggunakan Terbitan Isatin: Satu Kajian QSAR)

Abdo M. Al-Fakih[1,2], Madzlan Aziz[1]*, Hassan H. Abdallah[3], Hasmerya Maarof[1], Rosmahaida Jamaludin[1], Bishir Usman[1]

[1]*Department of Chemistry, Faculty of Science, University Technology Malaysia, 81310 UTM Johor Bahru, Johor, Malaysia*
[2]*Department of Chemistry, Faculty of Science, Sana'a University, Sana'a, Yemen*
[3]*Department of Chemistry, College of Education, Salahaddin University, Erbil, Iraq*

**Corresponding author: madzlan@utm.my*

Received: 9 December 2014; Accepted: 22 March 2016

Abstract

Quantitative Structure-Activity Relationship (QSAR) study was performed on 10 isatin derivatives which were reportedly used as corrosion inhibitors. Dragon software was used to calculate the molecular descriptors. Partial least square (PLS) method was used to run the regression analysis between the descriptors and the corrosion inhibition efficiencies (IE) of the inhibitors. A predictive QSAR model was developed with a correlation coefficient (r^2_{cal}) of 0.9676. The model validity was assessed through internal and external validation. The results show that cross-validation regression coefficient (r^2_{cv}) and prediction regression coefficient (r^2_{pred}) are 0.8163 and 0.9189, respectively. The model was used to predict the IE for ten isatin derivatives. The results confirm a good stability and predictive ability of the model. Dragon-based descriptors provide a very good description of the corrosion inhibition properties of the inhibitors. The results of the QSAR study were found to be consistent with the experimental data.

Keywords: QSAR modeling study, corrosion inhibition, isatin derivatives, partial least square

Abstrak

Kajian hubungan aktiviti-struktur kuantitatif (QSAR) dilaksanakan ke atas 10 terbitan isatin yang dilaporkan diguna sebagai perencat kakisan. Perisian Dragon digunakan untuk mengira pemerihal molekul. Kaedah kuasa dua terkecil separa (PLS) digunakan untuk melaksanakan analisis regresi antara pemerihal dan keberkesanan perencatan kakisan (IE) terhadap perencat kakisan. Ramalan model QSAR dibangunkan dengan pekali kolerasi (r^2_{cal}) bernilai 0.9676. Kesahan model dinilai melalui pengesahan dalaman dan luaran. Keputusan menunjukkan bahawa pekali regresi kesahan-silang (r^2_{cv}) dan pekali regresi ramalan (r^2_{pred}) adalah masing-masingnya 0.8163 dan 9189. Model tersebut digunakan untuk meramal IE bagi 10 terbitan isatin. Keputusan mengesahkan kestabilan dan kemampuan ramalan yang baik terhadap model. Pemerihal berasaskan Dragon memberi penerangan yang baik tentang sifat perencatan kakisan bagi perencat-perencat kakisan. Keputusan kajian QSAR ini adalah konsisten dengan data eksperimen.

Kata kunci: kajian pemodelan QSAR, perencatan kakisan, terbitan isatin, kuasa dua terkecil separa

Introduction

Steel is the main constructional material and has several types with variety of mechanical properties. It has extensive applications in industries because of its low cost and excellent mechanical properties [1-3]. However, it is prone to corrosion and raises a serious concern since it costs a huge loss in properties and safety problems [4]. Therefore, prevention of corrosion or at least reduction in its rate has been widely studied. Heterocyclic organic compounds containing nitrogen, sulfur, oxygen or phosphorous in their molecular structures are the most reported inhibitors of the steel corrosion especially in acidic corrosive media [5, 6]. The performance of the corrosion inhibitors is based on their adsorption onto metal surface. The adsorption of the inhibitors forms a protected film and reduces the corrosion rate [7]. Many experimental and theoretical studies have been done to study the efficiency of many corrosion inhibitors. However, experimental measurements are costly and time consuming. Therefore, theoretical methods have become more desirable since they may overcome disadvantages of running experiments [8, 9]. For example, quantitative structure activity relationship (QSAR) is a modeling technique which is applied in many disciplines of chemistry [10].

In QSAR modeling, molecular descriptors are calculated based on the molecular structures of the compounds. The traditional method is to calculate the descriptors using quantum chemical calculations. In addition, other techniques such as Molconn-Z, CODESSA and Dragon software are used to calculate molecular descriptors [11]. A number of 4885 molecular descriptors can be calculated using Dragon software [12]. Multiple linear regressions (MLR) and partial least square (PLS) are the most applied regression methods in QSAR modeling. Various variable selection methods such as stepwise regression (RS), genetic algorithms (GA), genetic algorithme-partial least square (GA-PLS) [13, 14], and interval partial linear square (IPLS) [15, 16], were proposed to specify the most relevant variables.

This study aims to develop a reliable QSAR model using data of newly synthesized isatin derivatives as corrosion inhibitors for Q235A steel in 3 M HCl. Apart from quantum chemical calculations, Dragon software was used in this work to calculate molecular descriptors based on the molecular structures.

Materials and Methods

Dataset

The dataset consists of ten isatin derivatives used as corrosion inhibitors of Q235A steel in acid medium (Table 1) [17]. The corrosion inhibition efficiency sorted in decreasing order from 70.4 to 15.9 %. The dataset was split into 70 % training set and 30 % test set.

Table 1. Inhibition efficiencies and molecular structures of isatin derivatives collected from Ref. [17]

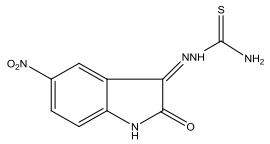
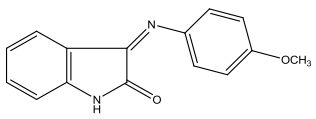
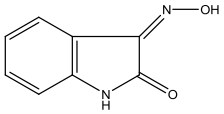
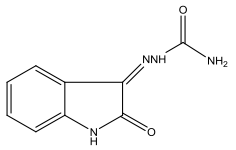
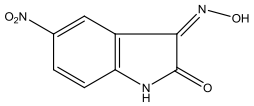
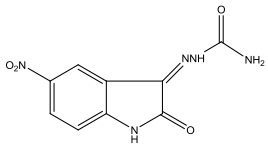
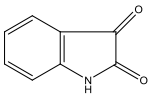
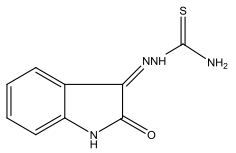
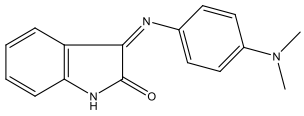
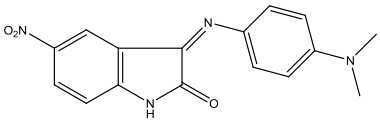
No.	Structure	Inhibition efficiency, IE (%)
Training set		
1		67.7
2		66.8

Table 1 (cont'd). Inhibition efficiencies and molecular structures of isatin derivatives collected from Ref. [17]

No.	Structure	Inhibition efficiency, IE (%)
3		61.9
4		56.6
5		35.7
6		23.5
7		15.9
Test set		
8		70.4
9		61.0
10		18.3

Calculation of descriptors and variable selection

Prior to descriptors calculation, molecular structures of the inhibitors were drawn with the Chem3D software and optimized using the MM2 followed by the Molecular Orbital Package (MOPAC) module. The Dragon software Version 6.0 [12], was used to calculate the descriptors using the optimized structures. The total number of the calculated descriptors was 2754. A variable selection was applied. One of the highly correlated descriptors pairs with $R \geq 0.90$ was randomly excluded. Descriptors with at least one missing value were then excluded yielding a reduced set of 227. Then descriptors with more than 90% equal values or with zero values were manually eliminated yielding a final set of 165 descriptors. The final set of descriptors was subjected to variable selection using IPLS selection method. The IPLS method was used to select a subset of variables. The selected variables subset could produce reliable models with better prediction ability compared to the use of all dataset variables. The variable selection and models building were performed using PLS Toolbox 6.2 (Eigenvector Research Inc.) in Matlab 7.6.0.324 (R2008a).

Statistical evaluation of the QSAR models

The QSAR model was evaluated in terms of its stability and predictive ability using several statistical parameters. The statistical parameters included correlation coefficient (r^2_{cal}), cross-validation regression coefficient (r^2_{cv}), prediction regression coefficient (r^2_{pred}), root-mean-square error of calibration (RMSEC), root-mean-square error of cross-validation (RMSECV), and root-mean-square error of prediction (RMSEP).

Results and Discussion

IPLS-based model

A set of three significant descriptors were selected from the final set (165 descriptors) using IPLS selection method. The descriptors were used to develop QSAR models. The selected descriptors are HATS3u, R3s and De. The HATS3u (Leverage-weighted autocorrelation of lag3/unweighted) descriptor is a type of GETAWAY descriptors. The R3s (R maximal autocorrelation of lag 3/weighted by I-state) descriptor is also one of GETAWAY descriptors. GETAWAY descriptors are 3D geometrical descriptors which calculated from atomic Cartesian coordinate's values. GETAWAY descriptors were designed to match the 3D-molecule geometry, relatedness of atom, and chemical information [18]. The De (D total accessibility index/weighted by Sanderson electronegativity) descriptor is one of WHIM (weighted holistic invariant molecular) descriptors. WHIM descriptors are molecular descriptors based on statistical indices calculated on the projections of the atoms along principal axes. WHIM descriptors are developed to extract 3D molecular information related to molecular size, shape, symmetry, and atom distribution with respect to invariant reference frames [19,20]. Table 2 shows the correlation matrix of the selected descriptors. It is clear that there is no inter-correlation between the descriptors. Several QSAR models were developed using PLS regression and the best model was selected based on statistical parameters. The best IPLS-based model for modeling the inhibition efficiency of isatin derivatives as a function of a set of three significant descriptors is presented by the Equation (1). The correlation coefficients r^2_{cal}, r^2_{cv}, and r^2_{pred} of the model are 0.9676, 0.8163, and 0.9189, respectively. The values of root-mean-square errors RMSEC, RMSECV, and RMSEP are lower than that of other developed models by the same method. This is an indication of higher prediction ability of the proposed model.

$$\text{IE}\,\% = 61.3368 + 63.4336(\text{De}) + 112.0971(\text{HATS3u}) - 14.7415\,(\text{R3s}) \quad (1)$$

whereas r^2_{cal} = 0.9676, r^2_{cv} = 0.8163, r^2_{pred} = 0.9189, RMSEC = 3.5874, RMSECV = 8.8106 and RMSEP = 18.3132

Table 2. Inter-correlation matrix of descriptors presents the model

Descriptor	De	HATS3u	R3s
De	1		
HATS3u	-0.249	1	
R3s	-0.289	0.230	1

Outliers detection

Detecting and then removing outliers is to enhance the prediction ability of the model. The possibility of the existence of outliers in the dataset was studied by plotting of standardized residuals against predicted values (Figure 1). A compound was considered as an outlier when the standardized residual was greater than 2 or less than -2 [21]. Figure 1 shows the outlier plot of the model. Only one compound has standardized residual higher than 2 which was excluded as an outlier.

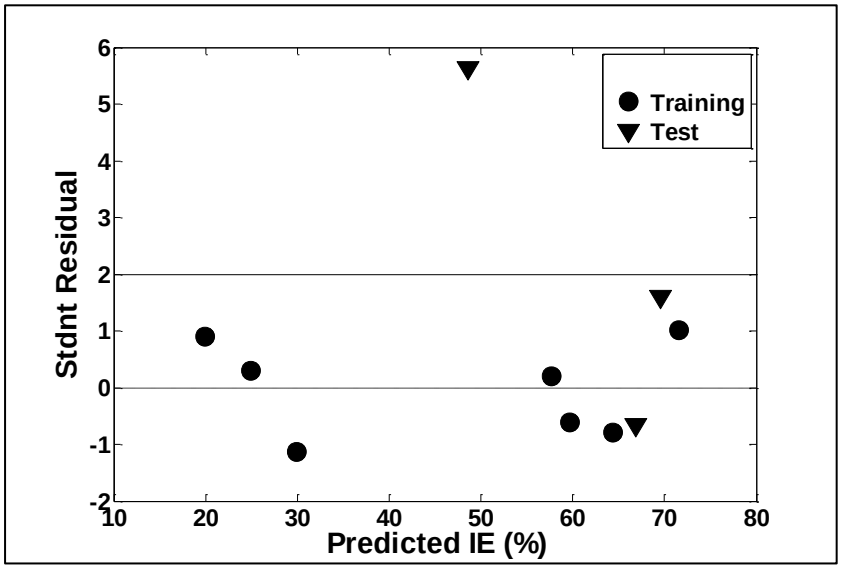


Figure 1. Plot of standardized residual versus predicted values

Model interpretation

Significant descriptors (i.e. HATS3u, R3s and De) were found to be useful to build reliable QSAR models. The proposed QSAR model was used to predict the corrosion inhibition efficiency (IE %) of the dataset compounds. Figure 2 displays a plot of predicted against the experimental values. The plot shows that the QSAR model has a high correlation coefficient. This indicates a good correlation between the experimental and predicted values. According to the statistical parameters, the developed model has high r^2_{cal} and r^2_{cv} of 0.9676 and 0.8163, respectively. Furthermore, the values of RMSEC, RMSECV are lower than that of other developed models by the same method. The result indicates high stability and predictive ability of the proposed model.

Model validation

The stability and predictive power of the model were validated using both internal and external validation. Internal validation was carried out using cross-validation leave-one-out. Internal validation provides internal check on the model. The cross-validation regression coefficient r^2_{cv} is 0.8163. The external validation was conducted by the prediction of test set efficiencies. The predicted efficiencies are in a good agreement with the experimental values. The prediction regression coefficient r^2_{pred} is 0.9189. The results indicate a high ability of the model to predict corrosion inhibition efficiency of new structurally relevant compounds. Further validation was performed to check the robustness of the model using a Y-randomization test. The training set was shuffled several times. The PLS regression was performed to each randomized dataset. The obtained values of r^2_{cal} ranged from 0.0418 to 0.2896. The low r^2_{cal} values indicate that the model is not due to a chance correlation.

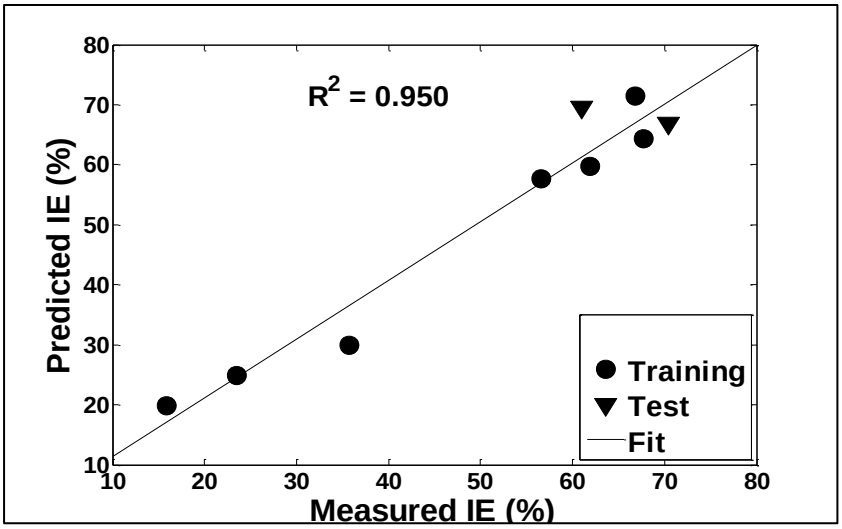


Figure 2. Plot of predicted and measured IE (%)

Conclusion

Dragon software was used to calculate the molecular descriptors. A QSAR model was built using PLS regression method. According to the statistical assessment and validation results, the proposed model reveals high stability and predictive power. Three significant descriptors (i.e. R3s, HATS3u and De) were used to develop a QSAR model. The descriptors contributed significantly to describe the corrosion inhibition properties of the inhibitors. Therefore, the use of Dragon software provides more opportunities to enrich the corrosion area with new descriptors. The computational methods used in this study are useful for developing predictive QSAR models with potent ability to predict and design novel and potential corrosion inhibitors.

Acknowledgement

The authors gratefully acknowledge the Ministry of Higher Education of Malaysia (MOHE), the Research Management Center (RMC) at the University Technology Malaysia (UTM), and the grant with VOT No. 4F257. The authors would like to show appreciation to Dr. Mohamed Noor Hasan for his kind permission to use the Dragon software and computational laboratory, Faculty of Science, University Technology Malaysia. We also acknowledge the financial support given by Sana'a University, Sana'a, Yemen.

References

1. Abdallah, M., Helal, E. A. and Fouda, A. S. (2006). Aminopyrimidine derivatives as inhibitors for corrosion of 1018 carbon steel in nitric acid solution. *Corrosion Science*, 48 (7): 1639 - 1654.
2. Badr, G. E. (2009). The role of some thiosemicarbazide derivatives as corrosion inhibitors for C-steel in acidic media. *Corrosion Science*, 51 (11): 2529 – 2536.
3. Pavithra, M. K., Venkatesha, T.V., Punith Kumar, M. K. and Tondan, H. C. (2012). Inhibition of mild steel corrosion by Rabeprazole sulfide. *Corrosion Science*, 60: 104 – 111.
4. Musa, M., Rodhi, M. N. M., Najmiddin Yaakob, N., Hamid, K.H.K. and Idris. J. (2013). Development of bio-based paint by using methyl esters from palm oil for corrosion inhibitor. *Malaysian Journal of Analytical Sciences*, 17 (1): 30 – 37.
5. Raja, P. B., Qureshi, A. K., Abdul Rahim, A., Osman, H. and Awang, K. (2013). Neolamarckia cadamba alkaloids as eco-friendly corrosion inhibitors for mild steel in 1M HCl media. *Corrosion Science*, 69: 292 – 301.
6. Kamal, N. K. M., Fadzil, A. H., Kassim, K., Rashid, S. H. and Mastuli, M. S. (2014). Synthesis, characterization and corrosion inhibition studies of o,m,p-decanoyl thiourea derivatives on mild steel in 0.1 M H_2SO_4 solutions. *Malaysian Journal of Analytical Sciences*, 18 (1):21 – 27.

7. Solmaz, R. (2014). Investigation of adsorption and corrosion inhibition of mild steel in hydrochloric acid solution by 5-(4-Dimethylaminobenzylidene)rhodanine. *Corrosion Science*, 79: 169 – 176.
8. Zhao, H., Zhang, X., Ji, L., Hu, H. and Li, Q. (2014). Quantitative structure–activity relationship model for amino acids as corrosion inhibitors based on the support vector machine and molecular design. *Corrosion Science*, 83: 261 – 271.
9. Zhang, J., Liu, J., Yu, W., Yan, Y., You, L. and Liu, L. (2010). Molecular modeling of the inhibition mechanism of 1-(2-aminoethyl)-2-alkyl-imidazoline, *Corrosion Science*, 52 (6): 2059 – 2065.
10. Khaled, K.F. (2011). Modeling corrosion inhibition of iron in acid medium by genetic function approximation method: A QSAR model. *Corrosion Science*, 53 (11): 3457 – 3465.
11. Bababdani, B.M. and Mousavi, M. (2013). Gravitational search algorithm: A new feature selection method for QSAR study of anticancer potency of imidazo[4,5-b]pyridine derivatives. *Chemometrics and Intelligent Laboratory Systems*, 122: 1 – 11.
12. Talete srl. (2010), Dragon (software for molecular descriptor calculation), version 6.0. Milano, Italy: Talete. http://www.talete.mi.it/
13. Riahi, S., Ganjali, M.R., Norouzi, P. and Jafari, F. (2008). Application of GA-MLR, GA-PLS and the DFT quantum mechanical (QM) calculations for the prediction of the selectivity coefficients of a histamine-selective electrode. *Sensors and Actuators B: Chemical*, 132 (1): 13 – 19.
14. Soltani, S., Abolhasani, H., Zarghi, A. and Jouyban, A. (2010). QSAR analysis of diaryl COX-2 inhibitors: Comparison of feature selection and train-test data selection methods. *European Journal of Medicinal Chemistry*, 45 (7): 2753 – 2760.
15. Chen, Q., Jiang, P. and Zhao, J. (2010). Measurement of total flavone content in snow lotus (Saussurea involucrate) using near infrared spectroscopy combined with interval PLS and genetic algorithm. *Spectrochimica Acta Part A: Molecular and Biomolecular Spectroscopy*, 76 (1): 50 – 55.
16. Abrahamsson, C., Johansson, J., Sparén, A. and Lindgren, F. (2003). Comparison of different variable selection methods conducted on NIR transmission measurements on intact tablets. *Chemometrics and Intelligent Laboratory Systems*, 69: 3 – 12.
17. Chen, G., Su, H.-J., Song, Y.-P., Gao, Y., Zhang, J., Hao, X.-J. and Zhao, J.-R. (2013). Synthesis and evaluation of isatin derivatives as corrosion inhibitors for Q235A steel in highly concentrated HCl. *Research on Chemical Intermediates*, 39 (8): 3669 – 3678.
18. Consonni, V., Todeschini, R., Pavan, M. and Gramatica, P. (2002). Structure/Response Correlations and Similarity/Diversity Analysis by GETAWAY Descriptors. 2. Application of the Novel 3D Molecular Descriptors to QSAR/QSPR Studies. *Journal of Chemical Information and Computer Sciences*, 42(3): 693 – 705.
19. Pourbasheer, E., Aalizadeh, R., Ganjali, M. R., Norouzi, P. and Shadmanesh, J. (2014). QSAR study of ACK1 inhibitors by genetic algorithm–multiple linear regression (GA–MLR). *Journal of Saudi Chemical Society*, 18(5): 681 – 688.
20. Todeschini, R., Bettiol, C., Giurin, G., Gramatica, P., Miana, P. and Argese, E. (1996). Modeling and prediction by using WHIM descriptors in QSAR studies: submitochondrial particles (SMP) as toxicity blosensors of chlorophenols. *Chemosphere*, 33(1): 71 –79.
21. Melagraki, G. and Afantitis, A. (2013). Enalos KNIME nodes: Exploring corrosion inhibition of steel in acidic medium. *Chemometrics and Intelligent Laboratory Systems*, 123: 9 – 14.

Malaysian Journal of Analytical Sciences, Vol 20 No 3 (2016): 491 - 499
DOI: http://dx.doi.org/10.17576/mjas-2016-2003-05

MALAYSIAN JOURNAL OF ANALYTICAL SCIENCES
Published by The Malaysian Analytical Sciences Society
ISSN 1394 - 2506

BIOMONITORING OF HEAVY METALS USING INTERTIDAL MOLLUSKS IN EAST JOHOR COASTAL WATERS

(Biopemerhatian Logam Berat Menggunakan Moluska Intertidal di Perairan Pantai Johor Timur)

Mohd Mokhlesur Rahman[1]*, Fuad Miskon[2], Kamaruzzaman Yunus[2], Noor Azhar M. Shazili[3]

[1]*Department of Pharmacy, Faculty of Pharmacy*
[2]*Department of Biotechnology, Faculty of Science*
International Islamic University Malaysia, 25200 Kuantan, Pahang, Malaysia
[3]*School of Marine and Environmental Sciences,*
Universiti Malaysia Terengganu, 21030 Kuala Terengganu, Terengganu

**Corresponding author: mdrahman@iium.edu.my*

Received: 9 December 2014; Accepted: 6 April 2016

Abstract

Interspecies, inter-tissue and interspatial dissimilarities of trace metals in particular body parts of *Saccostrea cucullata*, *Thais clavigera* and *Nerita chameleon* from the east Johor coastal waters were compared. Metals of interest includes Pb, Cd, Zn, Cu, Mn, Co, Se and Sr. Bivalve mollusk *S. cucullata* evidenced to be a worthy bioindicator for Zn and Cu while the two gastropod molluscs, *T. clavigera* for Cd and Se, and *N. chameleon* for Pb, Mn and Sr. The prominent concentration of metals originate in *T. clavigera* may be the outcome of biomagnification transfer from the *S. cucullata* on which they feed while for *N. chameleon*, it might be resulting from their herbivorous feeding behavior on algae on rocks which they graze. The metal accumulation patterns indicate consistent enrichment of essential metals in soft tissue. Values of operculum to tissue ratio (OTR) and shell to tissue (STR) higher than unity in *T. clavigera* indicate that operculum had higher affinities for Pb, Mn and Se while shell had higher affinities for Co and Sr. In *N. chameleon*, values of OTR and STR higher than unity displayed that operculum and shell had similar higher affinities for Co and Sr and Cd, Co and Sr, respectively. Significant interspatial variations ($p< 0.05$ and $p< 0.01$) in trace metals were noted. Assessment of metal concentration with maximum permissible limits of toxic metals in food shown the values were well within safety levels, except for Zn in *S. cucullata* that need to be monitored.

Keywords: heavy metals, intertidal mollusks, body parts, safety level

Abstrak

Perbezaan logam surih antara spesis, antara tisu dan antara kawasan dalam bahagian badan tertentu *Saccostrea cucullata*, *Thais clavigera* dan *Nerita chameleon* dari perairan pantai Johor timur telah dikaji. Logam yang menjadi perhatian termasuklah Pb, Cd, Zn, Cu, Mn, Co, Se dan Sr. Moluska bivalvia *S. cucullata* terbukti berpotensi menjadi bioindikator bagi Zn dan Cu manakala kedua-dua moluska gastropoda, *T. clavigera* bagi Cd dan Se, dan *N. chameleon* bagi Pb, Mn dan Sr. Kepekatan logam yang menonjol dari *T. clavigera* kemungkinan terhasil dari pemindahan biomagnifikasi dari *S. cucullata* yang dimakan manakala bagi *N. chameleon*, ia berkemungkinan terhasil dari tabiat pemakanan secara herbivor ke atas alga di atas batu. Corak pengumpulan logam menunjukkan kepekatan logam perlu yang konsisten dalam tisu lembut. Nilai ratio operculum kepada tisu (OTR) dan ratio kulit ke tisu (STR) lebih tinggi dari paduan dalam *T. clavigera* menunjukkan operculum mempunyai affiniti yang tinggi bagi Pb, Mn dan Se manakala kulit pula mempunyai affiniti yang tinggi bagi Co dan Sr. Dalam *N. chameleon*, nilai OTR dan STR lebih tinggi dari paduan menggambarkan bahawa operculum dan kulit mempunyai persamaan affiniti yang tinggi bagi Co dan Sr dan Cd, Co dan Sr, masing-masing. Variasi antara kawasan yang signifikan ($p<0.05$ and $p<0.01$) dalam logam surih telah dicatatkan. Pemeriksaan kepekatan logam dengan tahap maksimum yang dibenarkan bagi logam berat menunjukkan nilai masih lagi di bawah tahap selamat, kecuali Zn dalam *S.cucullata* yang perlu diberi perhatian.

Kata kunci: logam berat, intertidal moluska, bahagian badan, had selamat

Introduction

Heavy metals in the aquatic system can be naturally formed by the slow leaching from soil to water, typically at low levels in the parts per billion ranges and producing serious effects on social health [1]. They remains in solution for a long time before being removed to the sediments of the sea floor, a route of reverse weathering, which removal mechanisms consist of inorganic precipitation and reactions between dissolved materials and solid particles, as well as biological process like bioaccumulation of bacteria and phytoplankton and larger organisms [2]. Although many metals were recognized to have vital biological roles in low concentration, e.g. Cu, Zn, Mn, Fe; all these elements have the potential to be toxic to certain organisms above threshold concentration. Specific metal might alter into the persistent force of the metallic compounds with high toxicity, which leads to bioaccumulation in the organism's body, being magnified in the food chain and eventually threatening social health.

Much attention has been paid to the capability of marine organisms, especially molluscs to accumulate metallic toxicants from the marine environment where it lives. Goldberg [3] was the first to initiate the ``Mussel Watch Program" in which the bivalves were used as a surveillance tool of coastal pollution. Biomonitoring is a scientific technique in evaluating environment health based on sampling and analysis of an individual organism's tissue and fluids. This method, which comprises human contacts to natural and synthetic chemicals, takes advantage of the facts that chemicals that have entered the organisms leave indicators reflecting this exposure. Compared with other invertebrate groups like arthropods and especially vertebrates, molluscs exhibit only a limited ability to excrete pollutants directly via their kidneys or other excretory organs and tissues, to metabolize organic chemicals, and physiologically to inactivate toxic heavy metals such as by the formation of and binding to metallothioneins [4]. As a consequence, molluscs achieve higher bioaccumulation factors for many toxicants than other groups. Observing of heavy metal contamination and bioavailabilities by the diverse parts of molluscs is remarkable since it might lessen the imprecisions of defining the heavy metal levels by using the total soft tissues [5].

The use of bioindicator organisms to study heavy metal pollution in the Malaysian environment has acknowledged extensive attention. Bivalves and gastropod were frequently used by a number of researchers while fishes were primarily used for health concern related to fish consumption by human. Since the molluscs are accessible along the coastal areas of Peninsular Malaysia and are easily collected, it can therefore be suggested to be good monitoring agents for chemicals pollution. The objectives of this study were to discover the heavy metals bioavailability in selected body parts of *S. cucullata*, *T. clavigera* and *N. chameleon* from rocky shore sites along the coastal waters of the east Johor and to provide an insight in their safety levels for human and environment monitoring. Data of *S. cucullata* was acquired from a study by Fuad et al. [6] for comparison.

Materials and Methods

Study Area

Table 1 and Figure 1 displayed map of sampling locations, coordinates and species collected for this study. Five sampling sites with the abundant numbers of *S. cucullata*, *T. clavigera* and *N. chameleon* population on natural rocky structures were sampled. Not all species were present in sufficient numbers at all sites. *S*amples of relatively same size were hand collected during low tide. All samples were placed in plastic bags, sealed, labeled and stored at 4 – 6 °C during transportation to the laboratory where the samples were rinsed with running Mili-Q water (18.2 Ω) to remove sediment and salt particles prior to store frozen.

After allometric parameter measurement and tissue extraction, extracted tissues were freeze-dried before being weighed again in order to evaluate the water content and conversion factor. Freeze-dried samples were then minced to a homogenous powder and kept at room temperature until analysis. Please note that only soft tissue was extracted from rock oyster.

The analytical procedure was based on Shazili et al. method [7] with little modification. Measurement was carried out using Inductive Coupled Plasma Mass Spectrometry (ICP-MS) Elan 9000 in its standard configuration. Results

were quantified via an external calibration curve generated from the responses obtained from multiple dilutions of a multi-element calibration standard that was prepared from multi-element standards stock solution (Merck). The results were blank corrected and expressed as μg g^{-1} dry weight. Glassware used was immersed in 10% nitric acid (HNO_3) solution in advance for contamination prevention.

Table 1. Sampling locations, coordinates and species collected from east Johor coastal waters

No	Sampling location	Coordinate	Species collected
1	Sungai Rengit	N 01^0 20.985', E 104^0 13.256'	*S. cucullata*, *T. clavigera*, *N. chameleon*
2	Batu Layar	N 01^0 26.673', E 104^0 17.673'	*S. cucullata*, *N. chameleon*
3	Tanjung Balau	N 01^0 36.794', E 104^0 15.558'	*S. cucullata*, *T. clavigera*, *N. chameleon*
4	Sedili Kechil	N 01^0 50.617', E 104^0 08.957'	*S. cucullata*, *T. clavigera*, *N. chameleon*
5	Mersing	N 02^0 25.764', E 103^0 50.870'	*S. cucullata*, *T. clavigera*, *N. chameleon*

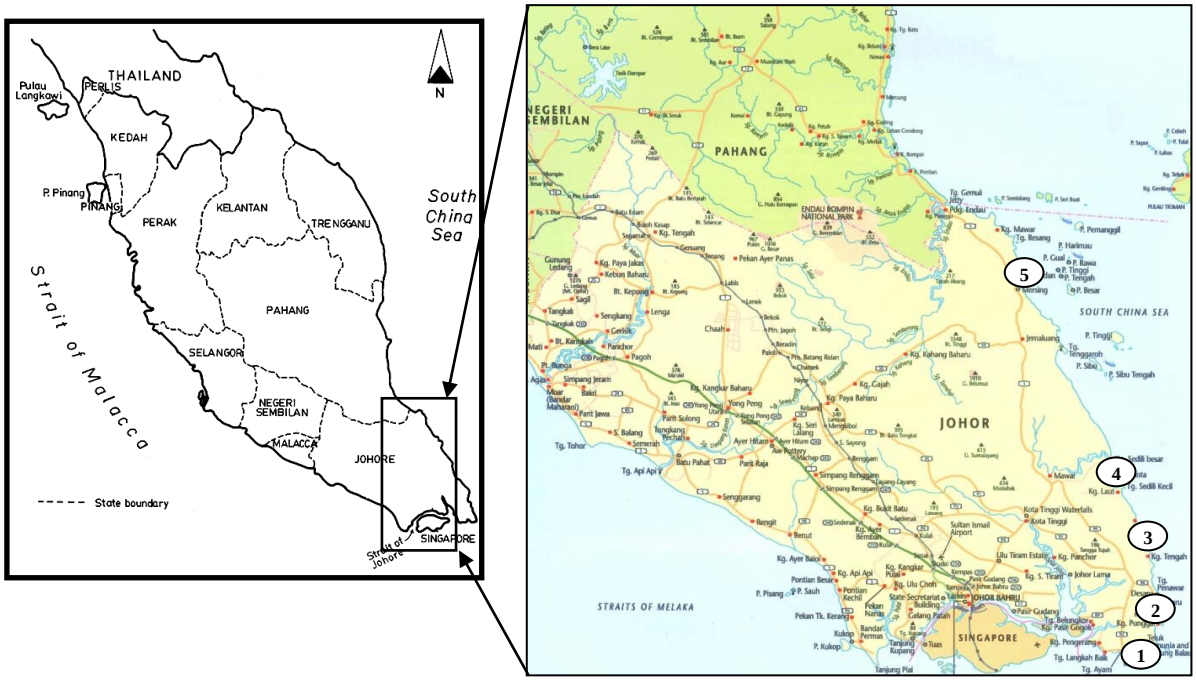


Figure 1. Map showing sampling locations at east Johor coastal waters. Sites are specified in Table 1

The quality of method used was confirmed in a separate comparative study using a standard reference material, Lobster Hepatopancreas TORT-2. Recoveries were as follows: 113.57 % (Pb), 97.31 % (Cd), 85.56 % (Cu), 86.54 % (Zn), 81.80 % (Mn), 96.53 % (Co), 88.59 % (Se) and 82.60% (Sr). One-way ANOVA was employed among assessment of variation between content of analyzed metals concentration in different sites. All comparisons were made at least at the 95% ($p< 0.05$) and 99% ($p< 0.01$) level of significance

Results and Discussion

The different studied species within the same location and the same species from different locations showed variations in their ability to concentrate trace elements. A comparison among species indicates that even closely

related species from the same location might have significantly different accumulated element concentrations as well as interspatial variability. The fact that sampled organisms inhabits common localities but different feeding behavior indirectly shows a function of the preferences for a certain size and nature of food particles and the detoxifying mechanism that each species has. The differences in accumulation of the metals may arise from species-specific feeding habits as uptake of metals via food plays an important role.

According to Table 2, there are significant differences in concentrations of Pb, Cd, Cu, Zn, Mn, Co and Se among sampling locations ($p< 0.05$) but no significant differences were found for Sr ($p> 0.05$) in *S. cucullata.* While for *T. clavigera*, there are significant differences ($p< 0.05$) in Pb, Zn and Co concentrations among locations in the soft tissue and Zn, Se and Sr in the shell. However, no significant differences were found for all studied metals among locations in the operculum. The interspatial distribution on metals shows no similar pattern among body parts.

Table 2. Concentrations of Pb, Cd, Cu, Zn, Mn, Co, Se and Sr (µg g^{-1} dry weight) in soft tissue, operculum and shell of *S. cucullata, T. clavigera* and *N. chameleon* (mean and standard deviation) from East Johore coastal waters

Site	Pb	Cd	Cu	Zn	Mn	Co	Se	Sr
S. cucullata								
1	1.19±0.17	1.79±0.26	211.5±35.27	2253.1±459.6	10.92±7.17	0.23±0.08	3.05±0.30	89.37±86.4
2	0.98±1.31	2.49±0.36	226.2±47.70	1114.7±247.0	4.39±2.79	0.08±0.02	3.85±0.95	49.02±11.4
3	0.85±0.38	2.24±0.13	256.4±12.7	5277.3±843.3	4.03±1.58	0.42±0.05	6.83±1.20	45.89±1.13
4	0.35±0.19	4.37±0.71	212.4±29.3	5190.6±1510.0	5.30±2.54	0.29±0.05	6.46±0.20	168.7±161.4
5	1.02±0.22	2.84±0.39	166.1±54.5	810.3±245.1	5.12±2.31	0.20±0.05	3.08±0.17	80.65±38.0
Average	0.88±0.32	2.75±0.99	214.52±32.57	2929±2171	5.95±2.83	0.25±0.13	4.65±1.85	86.72±49.61
T. clavigera								
	Soft tissue							
1	0.43±0.06	3.73±1.40	192.2±120.0	308.8±79.02	2.86±0.49	0.29±0.30	5.88±2.02	34.98±6.55
3	0.21±0.02	4.15±1.24	148.1±58.9	868.8±262.3	4.30±0.40	0.31±0.08	7.69±1.08	48.71±9.71
4	0.21±0.06	4.65±1.82	157.3±71.6	374.8±106.0	6.06±3.71	0.09±0.07	5.19±3.08	34.91±30.02
5	0.49±0.41	5.00±1.50	215.9±86.1	238.1±8.08	6.60±2.62	0.10±0.02	7.16±1.56	42.11±11.01
Average	0.33±0.15	4.38±0.56	178.36±31.42	447.61±286.27	4.96±1.71	0.20±0.12	6.48±1.15	40.18±6.62
	Operculum							
1	0.63±0.16	0.16±0.11	13.64±1.53	15.83±4.71	9.10±4.38	0.09±0.03	34.97±8.63	10.26±1.97
3	0.71±0.08	0.19±0.01	23.73±10.92	26.83±3.92	12.33±2.66	0.22±0.03	53.73±8.72	18.29±10.29
4	0.43±0.03	0.23±0.14	19.93±3.60	28.29±8.13	9.03±2.50	0.07±0.03	39.19±10.7	7.74±2.00
5	1.04±1.04	0.39±0.03	20.37±3.51	25.09±5.94	9.26±2.02	0.10±0.02	31.86±7.79	10.92±7.85
Average	0.70±0.26	0.24±010	19.42±4..21	24.01±5.61	9.93±1.60	0.12±0.07	39.93±9.67	11.80±4.54
	Shell							
1	0.19±0.03	0.29±0.17	1.47±0.75	2.70±0.62	1.63±0.65	0.70±0.07	8.33±3.63	1343.6±39.04
3	0.14±0.01	0.36±0.51	1.63±0.70	3.90±0.66	0.94±0.08	0.58±0.02	3.89±0.94	1216.9±30.02
4	0.17±0.10	2.24±3.65	3.06±1.65	6.07±2.20	0.85±0.80	0.58±0.13	2.78±0.11	1306.9±126.2
5	0.16±0.04	0.17±0.03	3.20±1.94	3.65±0.59	0.59±0.12	0.57±0.05	2.22±0.44	1258.3±62.01
Average	0.16±0.02	0.77±0.02	2.33±0.99	4.08±0.91	1.00±1.43	0.61±0.45	4.31±0.06	1281.42±2.77
N. chameleon								
	Soft tissue							
1	3.98±1.88	0.36±0.28	86.33±22.25	62.61±8.83	29.14±8.83	0.45±0.13	3.41±0.8	223.7±141.1
2	3.92±0.87	0.83±0.45	37.98±9.57	61.42±11.39	21.67±6.67	0.32±0.09	3.10±0.53	151.0±60.29
3	2.24±0.74	2.35±4.78	16.06±14.51	63.39±12.14	22.92±6.82	0.34±0.08	2.45±0.97	143.7±73.99
4	2.62±0.29	0.23±0.16	19.93±1.88	69.33±9.52	17.28±6.44	0.29±0.02	4.24±0.88	127.8±36.02
5	3.37±0.95	15.59±22.41	55.59±11.86	62.91±16.93	20.90±2.89	0.30±0.04	3.29±0.98	71.84±32.70
Average	3.22±0.78	3.87±6.61	43.18±28.81	63.93±3.10	22.38±4.32	0.34±0.06	3.30±0.64	143.61±54.48

Table 2 (cont'd). Concentrations of Pb, Cd, Cu, Zn, Mn, Co, Se and Sr (μg g^{-1} dry weight) in soft tissue, operculum and shell of *S. cucullata*, *T. clavigera* and *N. chameleon* (mean and standard deviation) from East Johore coastal waters

Site	Pb	Cd	Cu	Zn	Mn	Co	Se	Sr
	Operculum							
1	1.02±0.23	0.05±0.02	1.14±0.36	2.49±1.81	4.52±1.29	0.32±0.08	1.40±0.20	2485.7±128.5
2	0.95±0.27	0.05±0.02	0.49±0.56	2.07±1.05	2.76±0.65	0.39±0.04	1.22±0.38	2164.7±131.6
3	1.56±1.28	0.57±0.87	1.12±0.86	3.97±1.82	6.47±1.83	0.52±0.12	1.06±0.67	2446.1±245.1
4	1.57±0.47	0.06±0.03	0.90±0.10	4.42±2.09	6.65±2.62	0.43±0.02	1.81±0.18	2500.4±93.77
5	1.19±0.23	0.03±0.01	1.92±0.39	3.56±3.10	8.77±2.78	0.44±0.02	1.56±0.55	2445.0±81.41
Average	1.37±0.16	0.16±0.23	2.93±4.12	4.83±3.10	6.40±2.23	0.42±0.07	1.48±0.33	2355.28±151.6
	Shell							
1	0.63±0.30	0.03±0.01	1.66±2.30	5.82±2.77[c]	8.75±3.80	0.89±0.15	0.76±0.21	1676.6±186.8
2	1.12±2.11	3.29±8.98	1.78±3.10	5.52±6.04	4.77±1.52	0.80±0.11	1.09±0.22	1319.0±149.4
3	0.35±0.23	1.58±2.18	0.83±0.91	2.94±0.95	8.11±4.20	0.74±0.10	1.11±0.27	1199.3±99.27
4	0.15±0.05	1.48±3.13	0.25±0.15	3.16±1.16	5.06±1.65	0.66±0.11	1.04±0.32	1091.8±65.51
5	0.24±0.07	0.93±0.99	1.24±1.35	3.66±2.83	9.16±3.85	0.61±0.07	0.94±0.16	1134.8±65.64
Average	0.50±0.39	1.46±1.19	1.15±0.62	4.22±1.36	7.17±2.09	0.74±0.11	0.99±0.14	1284.29±235.4

In *N. chameleon,* significant differences ($p< 0.05$) among concentrations of all studied metals between locations were found in the soft tissue of *N. chameleon*, except Cd. There were significant differences ($p< 0.05$) between Pb, Cd, Mn, Co, Se and Sr concentrations in operculum of *N. chameleon* among sampling locations. No correlation was found for Cu and Zn. Significant differences ($p< 0.05$) were found only for Zn, Mn and Co concentrations in shell of *N. chameleon* between sampling locations.

Interspecies

A point to be made on the significance of accumulated trace metal concentrations among species is the potential for metals to be transferred along food chains. The elevated concentration of metals found in *T. clavigera* may be the result of biomagnification transfer from the rock oysters on which they feed while for *N. chameleon*, it might be derived from their herbivorous feeding behaviour on algae on rocks which they graze. Predatory gastropod, *T. clavigera* and prey *S. cucullata* have been acknowledged to have food chain relationships by several studies [8, 9]. Therefore, the levels of heavy metals in this predatory organism could be derived as a result of transfer from the rock oysters [10, 11]. It may obtain significant amounts of metals from the dietary source if the prey has high metals content. Also, field evidence suggests that dietary exposure is the dominant route for *Thais* to accumulate metals [12]. In this case, it is concluded that food (*S. cucullata)* probably is the most important source for metals in *T. clavigera*.

The metal accumulation pattern of Zn and Cu within studied organisms presented a decreasing pattern of *S. cucullata* > *T. clavigera* > *N. chameleon* (Table 2). Zn and Cu concentrations in the studied bivalve are much higher than gastropods by about 6 – 27 times. Zn and Cu are emphasized as they evidently proved to being essential in living organisms in the functioning of metabolic processes and associated with many enzymatic proteins functions [13-14]. Filter feeders are acknowledged to have high proportion of permeable surfaces and thus have been proven to take up metals at high rates [15].

T. clavigera in this study evidently accumulates the highest concentration of Cd and Se with the sequence of *T. clavigera* > *S. cucullata* > *N. chameleon*. The high concentration of Cd within *T. clavigera* is well documented by several studies. This neogastropod is able to accumulate Cd very efficiently from the food without any noxious effect [16], and even in unpolluted waters, neogastropod accumulate Cd at high concentration. Se metal is one of interest because it is classified as both an essential elements for organisms [17] and toxic at elevated levels [18]. It is suggested that this metal has a high potential of biomagnifications during transfer to top predator. Studies by Underwood [19] had shown that there were differences in the type of feeding between grazing species and type of food ingested by these species as well as differences in digestion and feeding mechanisms.

The result highlighted that Sr, which is considered as a non-essential element, is distributed differently in soft tissue of *N. chameleon* compared with the other elements (Table 2). Distribution of Sr within soft tissue in other literature was sparse as they commonly focused on the incorporation of Sr and Mg together with other trace metals as well within the shell [20, 21]. Despite a few differences, the pattern of metal occurrences is in agreement with studies by Ruelaz-Inzunza & Paez-Osuna [22] and Amin et al. [23] that indicate approximately the same pattern of essential metals enrichment.

Inter tissue

Referring to Table 2, metal accumulations in soft tissue, operculum and shell of *T. clavigera* vary in magnitude but generally showed similar patterns of accumulation for certain metals. The Zn and Cu accumulation pattern was in the sequence of soft tissue > operculum > shell; Cd soft tissue > shell > operculum; Se, Mn and Pb operculum > soft tissue > shell; and Co and Sr shell > soft tissue > operculum. While in *N. chameleon*, Pb, Cd, Zn and Mn concentrations was found in the sequence of soft tissue > operculum > shell; for Cu and Se, soft tissue > shell > operculum; Co shell > operculum > soft tissue; and Sr operculum > shell > soft tissue. The results indicated that most metals were accumulated in soft tissue compared to operculum and shell.

In order to evaluate the relationship between the operculum, shell and soft tissue with the concentrations of the metals studied, the ratio in body parts of *T. clavigera* and *N. chameleon* was computed (Table 3). Values of operculum to tissue ratio (OTR) and shell to tissue (STR) higher than unity in *T. clavigera* indicate that operculum had higher affinities for Pb, Mn and Se while shell had higher affinities for Co and Sr. Meanwhile, values of OTR and STR higher than unity in *N. chameleon* display that operculum and shell had similar higher affinities for Co and Sr, with addition of Cd for shells. The high concentration of these metals in operculum and shell could probably be due to the fact that the crystalline structures of the operculum and shell matrix had a higher capacity for incorporation in the soft tissue.

Table 3. Mean ratios and standard deviation of operculum metals to soft tissue metals (OTR) and shell metals to soft tissue metals (STR) in *T. clavigera* and *N. chameleon*

Species	Ratio	Pb	Cd	Cu	Zn	Mn	Co	Se	Sr
T. clavigera	OTR	2.28 ±0.85	0.05 ±0.02	0.11 ±0.04	0.07 ±0.03	2.23 ±0.92	0.69 ±0.29	6.23 ±1.36	0.29 ±0.07
	STR	0.56 ±0.22	0.17 ±0.21	0.01 ±0.01	0.01 ±0.01	0.25 ±0.22	4.11 ±2.28	0.69 ±0.49	32.68 ±6.39
N. chameleon	OTR	0.46 ±0.19	0.15 ±0.12	0.06 ±0.04	0.08 ±0.05	0.29 ±0.12	1.29 ±0.34	0.45 ±0.04	18.98 ±9.14
	STR	0.15 ±0.09	2.24 ±2.84	0.03 ±0.02	0.07 ±0.02	0.32 ±0.08	2.20 ±0.21	0.31 ±0.09	9.78 ±3.39

Permissible limits

To safeguard public health, maximum acceptable concentrations of toxic contaminants have been established in various countries, including Malaysia. Most of safety levels established was expressed on a wet weight basis. Therefore, metal concentrations for each species in this study have been calculated into wet weight basis using conversion factor for comparison with permissible limits set by Malaysia and other different countries (Table 4).

Table 4. Maximum permissible limits on heavy metals (in µg g^{-1}) for food safety set by different countries based on wet weight basis of soft tissue

	Pb	**Cd**	**Cu**	**Zn**
Shellfish molluscs				
European Community	1.5 [24]	1 [24]		
Hong Kong	6 [25]	2 [25]		
Australia	2 [26]	2 [26]	30 [27]	
USA	1.7 [28]	3.7 [28]		
Malaysia	2 [29]	1 [29]	30 [29]	100 [29]
This study				
S. cucullata	0.24	0.41	34.69*	332.98*
T. clavigera	0.13	1.10*	32.52*	73.70
N. chameleon	0.77	0.55	8.18	14.34

[24] European Community (CE, 2006), [25] Hong Kong Environmental Protection Department (HKEPD, 1997), [26] Food standards Australia New Zealand Authority (FSANZ, 1996), [27] Australian Government, 2006, [28] Food and Drug Administration of the United States (USFDA, 1990), [29] Malaysian Food Regulation Fourteen Schedule (1985), *Values that exceed the permissible limits set by Malaysian Food Regulation Fourteen Schedule

The results of this study indicate that Zn concentrations in rock oyster *S. cucullata* are higher than the food security limits. Thus, *S. cucullata* is considered unsafe for consumption in conjunction with high Zn concentration, as concentrations are approximately three times higher than safety limits. The high levels of Zn may pose a serious problem as *S. cucullata* is one of important food source that consumed in Malaysia [30].

Conclusion

The present work has provided a synoptic survey of metals distribution in selected species in rocky shore areas along the east Johor coastal waters. The bivalve mollusc, *S. cucullata* and the two gastropod molluscs *T. clavigera* and *N. chameleon* possessed high potential as cosmopolitan bioindicators for trace metal. These species have the necessary prerequisites of bioindicators: they are easy to identify and to sample, are available throughout the year, and are widely abundant in almost all rocky shore areas.

Interspecies variation among studied species indicated that certain species are proven to be good bioindicators of certain metals. Inter-tissue variation of metal concentrations lead to the conclusion that essential metals like Zn, Cu, Se and Mn are highly accumulated in soft tissue compare with operculum and shell as a result of having an important role in metabolism. Ratio calculation on body parts indicates high affinities of certain metals in operculum and shell of *T. clavigera* and *N. chameleon*, indicating that these body parts are also able to serve as bioindicator tissue as an alternative to the commonly used soft tissue. Particular significant metal pair correlation indicates that metal accumulation in specific body part might be affected by the other metal in the pairing. Consistent enrichment of essential metals over non-essential metals is also observed.

From the present status, it may be concluded that *S. cucullata* is unsafe for human consumption in conjunction with high Zn concentration, which was approximately three times higher than the safety limits set by Malaysian Food Regulations 1985 Fourteen Schedule and also with the limits set by other countries. Due to the importance of oyster as seafood and its ability to accumulate pollutants, sustained and continued monitoring of metals in *S. cucullata* may be important in avoiding future health risk issues related to their consumption.

References

1. Zhou, Q., Zhang, J., Fu, J., Shi, J. and Jiang, G. (2008). Biomonitoring: An appealing tool for assessment of metal pollution in the aquatic ecosystem. *Analytica Chimica Acta*, 606 (2): 135 – 150.

2. Shazili, N. A. (2004). Metals in the Marine Environment. KUSTEM Inaugural Lecture. Kolej Universiti Sains dan Teknologi Malaysia (KUSTEM).
3. Goldberg, E. D. (1978). The mussel watch - A first step in global marine monitoring. *Marine Pollution Bulletin*, 6(7): 111 – 114.
4. Legierse, K. C. H. M., Sijm, D. T. H. M., Leeuwen, C. J. V., Seinen, W. and Hermens, J. L. M. (1998). Bioconcentration kinetics of chlorobenzenes and the organophosphorus pesticide chloration in the pond snail *Lymneaestagnalis*- a comparison with the guppy *Poeciliareticulata*. *Aquatic Toxicology*, 41: 301 – 323.
5. Yap, C. K., Ismail, A., Edward, F. B., Tan, S. G. and Siraj, S. S. (2006). Use of different soft tissues of *Perna viridis* as biomonitors of bioavailability and contamination by heavy metals (Cd, Cu, Fe, Pb, Ni and Zn) in a semi- enclosed intertidal water, the Johore Straits. *Toxicological and Environmental Chemistry*, 88(4): 683 – 695.
6. Fuad, M. M., Shazili, N. A. M and Faridah, M. (2013). Trace metals and rare earth elements in Rock Oyster *Saccostrea cucullata* along the east coast of Peninsular Malaysia. *Aquatic Ecosystem Health and Management*, 16(1): 78 – 87.
7. Shazili, N. A. M, Azlisham, M. and Vedamanikam, V. J., 2009. Concentrations of cadmium, manganese, copper, zinc and lead in the tissues of the oyster (*Crassostrea iradalei*) obtained from Setiu Lagoon, Terengganu, Malaysia. *Toxicological and Environmental Chemistry*, 91(2): 251 – 258.
8. Blackmore, G. (2000). Field evidence of metal transfer from invertebrate prey to an intertidal predator, *Thais clavigera* (Gastropoda: Muricidae). *Estuarine, Coastal and Shelf Science*, 51(2): 127 – 139.
9. Blackmore, G. and Wang, W.-X. (2004). The transfer of cadmium, mercury, methylmercury, and zinc in an intertidal rocky shore food chain. *Journal of Experimental Marine Biology and Ecology*, 307(1): 91 – 110.
10. Jeng, M-. S., Jeng, W-. L., Hung, T-. C., Yeh, C-. Y., Tseng, R-. J., Meng, P-. J. and Han, B-.C. (2000). Mussel Watch: A review of Cu and other metals in various marine organisms in Taiwan, 1991-98. *Environmental Pollution*, 110(2): 207 – 215.
11. Shazili, N. A., Husain, M. L., Rashid, M. K. A., Yaakob, R., Shamsuddin, A. A. and Razali, M. S., (1995). Trace metal contents in the fish and bivalves from East Coast Malaysia, International Seminar on Marine Fisheries Environment 1995. Eastern Marine Fisheries Development Center and Japan International Cooperation Agency, Rayong, Thailand, pp. 199-208.
12. Blackmore, G. and Morton, B. (2001). The interpretations of body trace metal concentrations in Neogastropods from Hong Kong. *Marine Pollution Bulletin*, 42(11): 1161 – 1168.
13. Amiard, J. C., Triquet, C. A., Charbonnier, L., Mesnil, A., Rainbow, P. S., and Wang, W. (2008). Bioaccessibility of essential and non-essential metals in commercial shellfish from Western Europe and Asia. *Food and Chemical Toxicology*, 46(6): 2010 – 2022.
14. Yap, C. K., Hisyam, M. N. D., Edward, F. B., Cheng, W. H. and Tan, S. G. (2010). Concentrations of heavy metal in different parts of the gastropod, *Faunus ater*, collected from intertidal areas of Peninsular Malaysia. *Pertanika Journal of Tropical* Agricultural Science**,** 33(1): 45 – 60.
15. Blackmore, G. (2001). Interspecific variation in heavy metal body concentrations in Hong Kong marine invertebrates. *Environmental Pollution*, 114(3): 303 – 311.
16. Cheung, M.-S., Fok, E. M. W., Ng, T. Y. T., Yen, Y. F. and Wang, W. X. (2006). Subcellular cadmium distribution, accumulation and toxicity in a predatory gastropod, *Thais clavigera*, fed different prey. *Environmental Toxicology and Chemistry*, 25: 174 – 181.
17. Jolley, D. F., Maher, W. A. and Kyd, J. (2004). Selenium accumulation in the cockle *Anadara trapezia*. *Environmental Pollution*, 132: 203 – 212.
18. Peters, G. M., Maher, G. M., Krikowa, F., Roach, A. C., Jeswani, H. K., Barford, J. P., Gomes, V. G. and Reible, D. D. (1999). Selenium in sediments, pore waters and benthic infauna of Lake Macquire, New South Wales, Australia. *Marine Environmental Research*, 47: 491 – 508.
19. Underwood, A. J. (1974). The reproduce cycles and geographical distribution of some common Eastern Australian prosobranch (Mollusca: Gastropoda). *Australian Journal of Marine and Freshwater Research*, 25: 63 – 88.
20. Cravo, A., Foster, P., Ameida, C., Company, R., Cosson, R. P. and Bebianno, M. J. (2007). Metals in the shell of *Bathymodiolus azoricus* from a hydrothermal vent site on the Mid-Atlanctic Ridge. *Environment International*, 33: 609 – 615.

21. Foster, P. and Cravo, A. (2003). Minor elements and trace elements in the shell of marine gastropods from a shore in tropical East Africa. *Water, Air and Soil Pollution*, 145: 53 – 65.
22. Ruelas-Inzunza, J. R. and Paez-Osuna, F. (2000). Comparative bioavailability of trace metals using three filter-feeder organisms in a subtropical coastal environment (Southeast Gulf of California). *Environmental Pollution*, 107: 437 – 444.
23. Amin, B., Ismail, A., Arshad, A., Yap, C.K. and Kamarudin, M.S. (2006). A comparative study of heavy metal concentrations *Neritalineata* from the intertidal zone between Dumai, Indonesia and Johor, Malaysia. *Journal of Coastal Development*, 10: 19 – 32.
24. Commission Europeénne, CE (2006). Regulation (CE) No. 1881/2006 of 19 December 2006 setting maximum levels for certain contaminants in foodstuffs. Official Journal of the European Union, L 364/5 du 20 December 2006.
25. Hong Kong Environmental Protection Department, (1997). Marine water quality in Hong Kong in 1997. Government Printer Hong Kong.
26. Food Standards Australia New Zealand Authority, FSANZ (1996). Food Standard for Australia and New Zealand.
27. Australian Government (2006). The Maximum Residual Limit Standard.
28. Food and Drug Administration of the United States, USFDA (1990). US Food and Drug Administration Shellfish Sanitation Branch, Washington, DC.
29. Malaysian Food Regulation (1985). Fourteenth Schedule Malaysian law on food and drugs. Malaysian Law Publishers.
30. Yap, C. K., Mohd Ruszaidi, S. and Cheng, W. H. (2010). Different tissues of rock oyster *Saccostrea cucullata* as biomonitors of trace metal bioavailabilities in the Penang coastal waters, Malaysia. *Research Journal of Chemistry and Environment*, 14(3): 17 – 21.

Malaysian Journal of Analytical Sciences, Vol 20 No 3 (2016): 500 - 509
DOI: http://dx.doi.org/10.17576/mjas-2016-2003-06

MALAYSIAN JOURNAL OF ANALYTICAL SCIENCES
Published by The Malaysian Analytical Sciences Society
ISSN 1394 - 2506

NITROGEN USE EFFICIENCY IN MR219-4 AND MR219-9 RICE MUTANT LINES UNDER DIFFERENT WATER POTENTIALS AND NITROGEN LEVELS USING ^{15}N ISOTOPIC TRACER TECHNIQUE

(Kecekapan Penggunaan Nitrogen dalam Padi Titisan Mutan MR219-4 dan MR219-9 di bawah Potensi Air dan Aras Nitrogen yang Berbeza Menggunakan Teknik Isotop Penyurih ^{15}N)

Ahmad Nazrul Abd Wahid[1, 2]*, Sahibin Abdul Rahim[1], Khairuddin Abdul Rahim[2], Abdul Rahim Harun[2]

[1]*Environmental Science Programme,*
School of Environmental and Natural Resource Science, Faculty of Science and Technology,
Universiti Kebangsaan Malaysia, 43600 UKM Bangi, Selangor, Malaysia
[2]*Agrotechnology and Bioscience Division,*
Malaysian Nuclear Agency, 43000 Kajang, Bangi, Selangor, Malaysia

**Corresponding author: a_nazrul@nuclearmalaysia.gov.my*

Received: 3 August 2015; Accepted: 29 March 2016

Abstract

This study was conducted to evaluate the nitrogen use efficiency of rice mutant lines of MR219, viz. MR219-4 and MR219-9, developed under rice radiation mutagenesis programme for adaptability to aerobic conditions, grown under conditions of varying water potentials and nitrogen levels in a shade house. Direct ^{15}N isotopic tracer method was used in this study, whereby the ^{15}N labeled urea fertilizer was utilized as a tracer for nitrogen nutrient uptake by the test crops. ^{15}N isotope presence in the samples was determined by using emission spectrometer analysis and percentage of total nitrogen was determined by using Kjeldahl method. ^{15}N atom access values of the samples were to determine the efficiency of N use by the mutant varieties. In this work, the data of yield components, viz. grain yield, plant biomass, plant height and 1000 grain weight, and nitrogen components viz, total N, % nitrogen derived from labeled fertilizer (% Ndff), % nitrogen derived from soil (% Ndfs), nitrogen uptake, fertilizer nitrogen use and nitrogen use efficiency were obtained. Results from this study showed a significant difference to the nitrogen component and yield when there is a change in the rate of fertilizer and water potential. However, varietal factor does not show any significant differences.

Keywords: mutant lines of rice, aerobic condition, water potentials, ^{15}N isotopic tracer, nitrogen use efficiency

Abstrak

Kajian ini telah dijalankan untuk menilai keberkesanan penggunaan nitrogen padi garisan mutan dari MR219, iaitu MR219-4 dan MR219-9, yang dibangunkan di bawah program mutagenesis untuk penyesuaian ke keadaan aerob dan ditanam dalam keadaan potensi air dan aras nitrogen yang berbeza di dalam rumah teduhan. Kaedah isotop penyurih ^{15}N secara terus telah digunakan dalam kajian ini, di mana baja urea berlabel isotop ^{15}N digunakan sebagai penyurih untuk pengambilan nutrien nitrogen oleh tanaman ujian. Kehadiran isotop ^{15}N dalam sampel ditentukan dengan analisis spektrometer pelepasan dan peratusan jumlah nitrogen di dalam sampel ditentukan dengan menggunakan kaedah Kjeldahl. Nilai akses Atom ^{15}N yang terkandung dalam sampel akan digunakan dalam penentuan keberkesanan penggunaan nitrogen dalam baja melalui formula pengiraan tertentu. Melalui kajian ini, data daripada komponen hasil (hasil bijirin, berat biojisim, ketinggian tumbuhan dan 1000 berat bijirin) dan komponen nitrogen (jumlah nitrogen, % Ndff, % Ndfs, pengambilan nitrogen, penggunaan baja nitrogen dan kecekapan penggunaan nitrogen) telah diperolehi. Hasil daripada kajian ini telah menunjukkan terdapat perbezaan yang ketara terhadap komponen nitrogen dan hasil tanaman apabila terdapat perubahan faktor kadar baja dan potensi air. Walaubagaimanapun, faktor varieti tidak menunjukkan apa – apa perbezaan yang ketara.

Kata kunci: titisan mutan padi, keadaan aerob, potensi air, isotop penyurih ^{15}N, kecekapan penggunaan nitrogen

Introduction

Malaysia's rice production is presently focused in the major irrigated rice areas in Peninsular Malaysia, contributing to 85 % of the national rice production. The main method of rice cultivation in Malaysia is through flooding. This type of cultivation consumes a very high amount of water, where about 3000 litre of water are used to produce 1 kg of rice [1]. Over 80 % of the freshwater resources in Asia are used for irrigation and about half the amount is consumed for rice [2]. In Malaysia, rice is grown in two seasons where the first season is between August to February, meanwhile the second season is between March to July. Water demands during the first season are less worrying because the rainy season is likely to occur, however during the second season, low rainfall and drought are likely to occur thus the high demand of water is crucial. Rice field will experience drought due to a short supply of water by declining rainfall and dam water level. Globally climate change due to global warming is said to contribute to the water shortage in rice production. Increase in freshwater scarcity has threatened the sustainability of irrigated rice ecosystems [3].

For strategic water management and utilization purposes, the traditional submerged rice cultivation system is gradually moving toward a system where rice is grown in low water input and aerobic conditions while maintaining high productivity. Aerobic cultivation is a planting system where rice is grown in well-drained, non-puddle, and non-saturated soils. In aerobic rice systems, fields remain unsaturated throughout the season. Crop yields are on average only 1000 to 2000 kg/ha) because of adverse environmental conditions (poor soils, little rainfall, weeds), low use of external inputs, and low yield potential of upland rice cultivars [4]. Evidence from studies showed that aerobic rice used only 50 % of the water compared with the lowland rice [5]. The aerobic cultivation can reduce the total water usage by 27 – 51 % and increase water productivity by 32 – 88% [6]. Most countries that suffer from water shortages have been using aerobic cultivation method in their rice farming system. Therefore, steps have been taken including the production of various types of new cultivars is suitable for planting in their aerobic condition. Through a radiation-induced mutation breeding project (IRPA 01-01-03-000/PR0068/0504) using the high yielding and good quality rice MR 219, Malaysian Nuclear Agency (Nuclear Malaysia), in collaboration with Malaysian Agricultural Research and Development Institute (MARDI) and Universiti Putra Malaysia (UPM), discovered an advanced mutant line MR 219-4 and MR 219-9 varieties.

Nitrogen is one of the essential macronutrients for rice growth and becomes the main factors to be considered for developing high-yielding rice cultivar [7]. Nitrogen (N) requirements of the rice plant are supplied from soil and fertilizer. Due to the acute shortage of nitrogen in the soil mostly, nitrogenous fertilizer must be used to meet the needs of the plant. In flooded rice ecosystems, some reports said that nitrogen fertilizer used for rice crops have been lost partly through different mechanisms including ammonia volatilization, denitrification, leaching and run by water [8, 9]. Nitrogen losses can cause environmental problems such as pollution of the atmosphere, aquatic systems and ground water in a bowl. Nitrogen use efficiency is generally low with normally less than 30 – 40 % of the applied N took up by flooded rice [10 – 12]. This situation challenges the researchers to develop the strategies to increase nitrogen use efficiency in rice production. Increasing of nitrogen use efficiency offers the greatest economic benefits to farmers and countries. Nitrogen use efficiency may be defined as yield per unit input. In agriculture, this is usually related to the input of nitrogen fertilizer, whereas in scientific literature the nitrogen use efficiency is often expressed as fresh weight or product yield per content of nitrogen. Thus, nitrogen use efficiency can be defined as nitrogen absorbed by a plant to growth and gave yield [13]. Nitrogen use efficiency of crops can be improved by adopting adequate management practices. The usage of N fertilizers with an adequate amount, form, and methods of application are important management strategies of this element [14].

Although Malaysia has produced aerobic rice varieties and rice adaptable to low water inputs, including MR219-4 and MR219-9, information on nitrogen use efficiency (NUE) of these new lines is negligible. In Malaysia, aerobic rice cultivation is a recent development and there are only a handful of agencies who conducted tests on this rice. In addition to using minimal water, aerobic rice research purposes in Malaysia also aims to improve the effectiveness use of nitrogen in the aerobic rice ecosystem. The previous report stated that changes in water management of flood

conditions to aerobic conditions affecting the availability and forms of nitrogen present in the soil [15]. Change in water management can have a significant impact on the availability of nutrient intake by plants and lost in the environment [16]. There are few reports that have indicated the use of nitrogen fertilizer on dry land is more efficient [17] and nitrogen application improved rice plant growth under continuous aerobic rice cropping, but for phosphorus (P) and potassium (K) and other micronutrients had a little or no effect [18]. Improvement of nitrogen use efficiency is an essential pre-requisite for expansion of crop production into marginal lands with low nutrient availability. Nitrogen use efficiency depends on the ability to efficiently take up the nutrient from the soil, but also on transport, storage, mobilization, usage within the plant, and even on the environment.

The only direct means of measuring nitrogen use efficiency from the applied fertilizer is through the use of isotopes. In nitrogen efficiency study, a labelled fertilizer ^{15}N is added to the soil and the amount of nitrogen that a plant has taken up is determined. In this way, different nitrogen fertilizer practices (placement, timing, sources, etc.) were studied [19]. Isotopic studies using ^{15}N labelled plant materials have been useful in estimating crop N uptake [20 – 22].

The objective of this study is to examine the effects of nitrogen levels and water potentials on yield components and to evaluate the nitrogen use efficiency on MR 219-4 and MR 219-9 mutant lines under different water potential and different nitrogen availability. This data can be used as a reference to farmers or any party who wish to develop and implement aerobic rice industry in this country. Through this study, the added value will be assigned to MR 219-4 and MR 219-9 rice mutant lines.

Materials and Methods

Study location

Aerobic rice cultivation exercise was carried out in a paddy shield house in Malaysian Nuclear Agency. The shade house provided some control on environmental factors, including rain shelter facilities.

Rice varieties

Two types of mutant lines rice varieties namely MR219-4 and MR219-9 were used in this experiment. Both varieties are produced by mutation induction using gamma irradiation on MR219 variety (parent). Mutation induction was carried out by exposure of plant organs such as seeds or biological entity to ionizing radiation that can penetrate the tissue cells so that the heritage elements of the chromosome and the process causes the physical changes to the plants [23].

Soil types

The soil used in this experiment is sandy loam texture with a bulk density of 1.45 g/cm^3. Water retention curve analysis of this soil has been done using pressure plate method. The curve shown in Figure 1 indicated that available water capacity calculated between 10 to 1500 kPa for this soil is about 18 % (w/w).

Experimental design and crop management

Rice mutants MR219-4 and MR219-9 were planted on loam soil through measuring plot 3 m^2 (3m x 1m). Aerobic rice seeds are sown manually at 2 cm depth and covered with soil. Three watering regimes and three nitrogen levels in a completely randomized block design with three replicates treatment were carried out. Aerobic rice were grown for 110 days under three water potentials, (i) Field capacity from 0 to 40 DAS and saturated from 41 to 110 DAS [ST], (ii) Field capacity from 0 to 110 DAS [FC], and (iii) Field capacity from 0 to 40 DAS and 70% of field capacity from 41 to 110 DAS [SS]. DAS is standing for days after sowing. Nitrogen in the form of ^{15}N-labeled urea (5.20 % atom excess) was applied in three rates; none (0 kg N ha^{-1}), moderate (60 kg N ha^{-1}) and high (120 kg N ha^{-1}) in three splits at 7 days after emergence, 35 days after emergence and 60 days after emergence, respectively. Basal fertilizers of phosphorus from triple superphosphate (TSP) at 60 kg P_2O_5 ha^{-1} and potassium from muriate of potash (MOP) at 60 kg K_2O ha^{-1} were applied at 15 days and 65 days after emergence. A tensiometer, an instrument that directly measured soil moisture continuously was installed. Soil moisture was measured and observed daily.

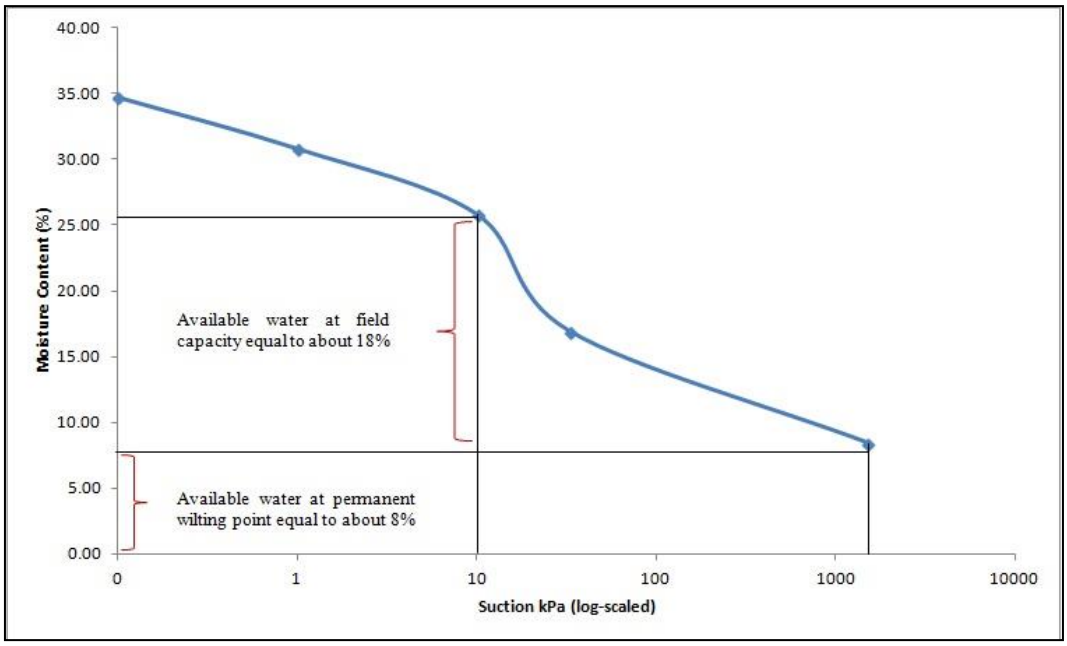


Figure 1. Soil water retention curve for soil moisture content

Plant sampling and analysis

Paddy plants were sampled after 110 days when the aerobic rice has matured and ripened. Harvesting and sampling were done on a 1 m x 0.5 m area (0.5 m^2). Total plant biomass was weighed to obtain the overall fresh weight. Plant parts such as straw, leaf and grain were separated and measured the fresh weight. Straw, leaf, and grain samples were oven dried at 70 to 80 ^oC for three days after which they were weighed and finely milled for further analysis.

Total nitrogen content in straw, leaf and grain was extracted by Kjeldahl digestion followed by steam distillation and subsequently ^{15}N content was analyzed using emission spectrometer [24]. Percentage of ^{15}N abundance was transformed into atom percentage ^{15}N excess by subtracting the natural abundance (0.3663 atom % N) from the percentage of N abundance of the sample.

Kjeldahl digestion method

The Kjeldahl digestion is a method for determination of nitrogen content in rice samples. The Kjeldahl method consist of three main steps; (i) Digestion, where the decomposition of nitrogen in plants samples utilizing a concentrated acid solution. This part was accomplished by boiling a homogeneous sample in concentrated sulphuric acid. The end result is an ammonium sulphate solution. (ii) Distillation, where adding an excess base to the acid digestion mixture to convert NH_4^+ to NH_3, followed by boiling and condensation of the NH_3 gas in a receiving solution and (iii) Titration to quantify the amount of ammonia in the receiving solution.

Emission spectrometer analysis

Emission spectrometer is an analytical instrument that be used to determine ^{15}N isotope tracer in rice samples. Samples were concentrated in liquid forms. An approximately 25 µL of samples were put in a glass capsule and placed in an emission spectrometer syringe. Emission spectrometer is equipped with a data acquisition unit which stores the data and automatically converts the measured to the actual value.

Nitrogen components calculation

After the data were obtained from analysis of samples, the following calculations as expressed in equation 1 – 6 were utilised [19].

$$\% Ndff = \frac{atom\ \%\ 15\text{N}\ excess\ \text{plant}}{atom\ \%\ 15\text{N}\ excess\ \text{fertilizer}}\ x\ 100 \quad (1)$$

where *Ndff* is nitrogen derived from fertilizer.

$$\% Ndfs = 100 - \% Ndff \quad (2)$$

where *Ndfs* is define as nitrogen derived from soil and *Ndff* is define as nitrogen derived from fertilizer.

$$\text{Dry Matter Yield (kg/ha)} = \text{FW (kg)} \times \frac{10000\ (\text{m}^2/\text{ha})}{\text{area harvested}\ (\text{m}^2)} \times \frac{\text{SDW (kg)}}{\text{SFW (kg)}} \quad (3)$$

where FW is fresh weight per area harvested. Meanwhile SDW and SFW are subsample dry and fresh weight, respectively.

$$\text{Nitrogen Yield (kg/ha)} = \text{Dry Matter Yield (kg/ha)} \times \frac{\%\ \text{Total N}}{100} \quad (4)$$

$$\text{Fertilizer Nitrogen Yield (kg/ha)} = \text{Nitrogen Yield (kg/ha)} \times \frac{\%\ \text{Ndff}}{100} \quad (5)$$

$$\%\ \text{NUE} = \frac{\text{Fertilizer Nitrogen yield}}{\text{Rate of Nitrogen application}} \times 100 \quad (6)$$

where NUE is nitrogen use efficiency. Nitrogen use efficiency is a quantitative measure of the actual uptake of fertilizer nutrient by the plant in relation to the amount of nutrient added to the soil as fertilizer. A common form of expression of fertilizer use efficiency is plant recovery of the added fertilizer.

Statistical analysis

Analysis of variance (ANOVA) for variables that was used for testing treatment differences (water and nitrogen treatments and independent T-Test to compare mean between two varieties) was carried out. Correlation analysis was used to evaluate the relationship between nitrogen rates and grain yield. General linear model was used to test the interaction between treatments.

Results and Discussion

Total Nitrogen

Total Nitrogen (Total N) is the sum of nitrate (NO^3), nitrite (NO^2), organic nitrogen and ammonia (all expressed as N). It can be measured in the laboratory using Kjeldahl method. Figure 2 shows the differences in total N contained in plant parts of aerobic rice variety under different nitrogen fertilizer application levels and water potentials. It shows there is no significant different in MR219-4 and MR219-9 rice lines in terms of total N on three plant parts (straw, leaf and grain) with different nitrogen levels and water potentials ($p > 0.05$). It means total N in all parts of aerobic rice are not affected by a varietal factor. However, an analysis of ANOVA test shows nitrogen application levels give a clear significant difference or effect on the total N content in plant parts ($p < 0.05$) but water potentials remain do not have a significant effect on total N in paddy plants. Referring to Figure 2, it also shows that most cases a total N in the straw is higher than leaf and grain. Pirmoradian et al. [25] reported similar finding in this study were increasing of nitrogen levels has significantly affected the total N content in the rice straw and leaf.

Yield components

The experimental results for analysis of variance for yield components such as grain yield, biomass, plant height and weight of 1000 grains are summarized in Table 1. Water potentials and nitrogen levels gave significance effects to the yield components except for 1000 grain weight, where there was apparently no effect by nitrogen treatments. The varietal factor does not show any significant effect of the yield components. It means, there are no

significant different between MR219-4 and MR219-9 in terms of yield components. The significant interactions occurred for total biomass weight and 1000 grain weight with the main treatments factors such as water and nitrogen was included. However, the other interaction effects do not have a significant different to all yield components. From this table, we can conclude that water and nitrogen factors have very importance roles to the yield components in aerobic rice ecosystem.

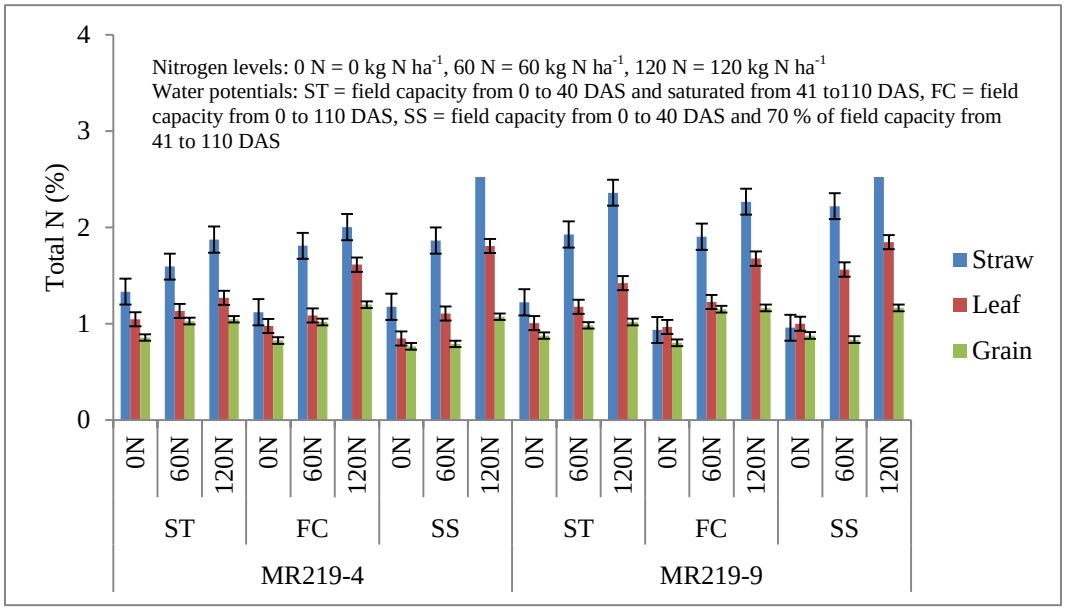


Figure 2. The differences in total N in plant parts of MR219-4 and MR219-9 mutant lines under different nitrogen levels and water potentials. Error bars denote standard errors.

Table 1. Analysis of variance effect of the treatments on the yield components

Source of Variations[a]	Levels of Significance[b]			
	Grain Yield (kg ha^{-1})	Total Biomass Weight (kg ha^{-1})	Plant Height (cm)	1000-grain Weight (g)
W	**	**	**	**
N	**	**	**	NS
V	NS	NS	NS	NS
W x N	NS	**	NS	**
W x V	NS	NS	NS	NS
N x V	NS	NS	NS	NS
W x N x V	NS	NS	NS	NS

[a] W = Water potential, N = Nitrogen rates and V = Variety, [b] Levels of significance indicated: NS = Not significant, ** = Significance at $p \leq 0.05$

The importance of nitrogen to the aerobic rice yield under different water potentials was illustrated in Figure 3 and 4 respectively. Finding study showed that nitrogen level factors have a very strong and significance relationship with the grain yield of both varieties despite the differences in soil water potentials.

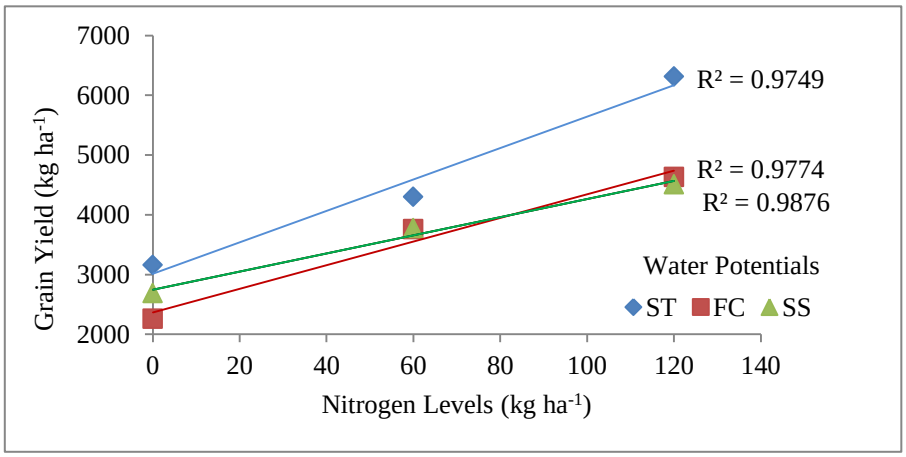


Figure 3. The relationship between nitrogen fertilizer levels on MR219-4 mutant line under different water potentials

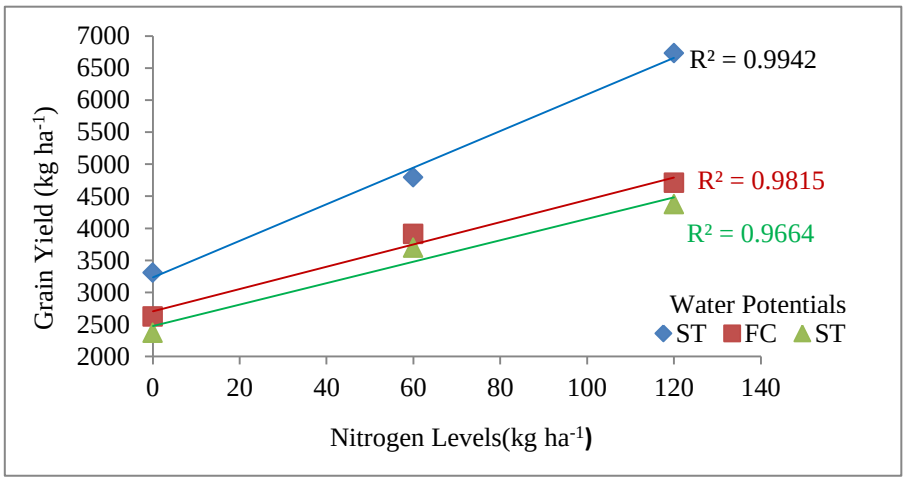


Figure 4. The relationship between nitrogen fertilizer levels on MR219-9 mutant line under different water potentials

Nitrogen components

The experimental results for analysis of variance for nitrogen components such as nitrogen derived from fertilizer (*Ndff*), nitrogen derived from soil (*Ndfs*), nitrogen uptake (NU), fertilizer nitrogen yield (FNY), and nitrogen use efficiency (NUE) were summarized in Table 2. The result clearly showed that only nitrogen level treatments give the significant effect to the percentage of *Ndff* and *Ndfs* but not on the water potential treatments. However, both nitrogen level and water potential treatments are displayed a significant effect to the NU, FNY and NUE. Nayak et al. [26] also found a similar result related to nitrogen levels effect on NU and FNY where increasing the rates of

nitrogen fertilizer application cause a significant effect to NU and FNY. Mannan et al. [27] found NU and FNY on rice crop is lower under water stressed compared to none stressed condition, similar to this study where NU and FNY on both rice varieties is lower under inadequate water supply condition. This study also showed that there are significant interactions between water and nitrogen that influence only the NU and NUE but not FNY. However, the other interaction effects do not have a significant different at all nitrogen components. Both varieties MR219-4 and MR219-9 also found not have significant different with each other at all nitrogen components.

Table 2. Analysis of variance effect of the treatments on the nitrogen components

Source of Variations [a]	Levels of Significance[b]				
	% Ndff	% Ndfs	NU	FNY	NUE
W	NS	NS	**	**	**
N	**	**	**	**	**
V	NS	NS	NS	NS	NS
W x N	NS	NS	**	NS	**
W x V	NS	NS	NS	NS	NS
N x V	NS	NS	NS	NS	NS
W x N x V	NS	NS	NS	NS	NS

[a] W = Water potential, N = Nitrogen rates and V = Variety, [b] Levels of significance indicated: NS = Not significant, ** = Significance at $p \leq 0.05$

Nitrogen use efficiency (NUE)

Nitrogen use efficiency (NUE) for MR219-4 and MR219-9 rice mutant lines, shown in Figure 5 depict the influence of nitrogen application rates on both rice varieties under different water potentials. The result clearly indicated a significant difference of NUE between different water potentials and nitrogen levels. Water treatment at field capacity from 0 to 110 days [FC] showed higher NUE than other water potentials for both varieties. This study also showed that at FC water regime with nitrogen level 60 kg N ha^{-1}, N was utilized more than 50% to produce yield. These results indicated that the use of absorbed nitrogen from soil at the level of 60 kg N ha^{-1} at FC level is more efficient than others. It also proved that changes in water level in the soil can influence the intake of nitrogen by plants. At field capacity 0 to 40 days and saturated from 40 to 110 days [ST] water potential the NUE is slightly lower than FC. Stagnant water conditions at ST level may have caused some nitrogen fertilizer loss through leaching and water runoff.

In this study, nitrogen dynamics data on varieties MR219-4 and MR219-9 rice mutant lines was obtained. Initial data for this crop is very important as aerobic rice cultivation for these varieties is still in the initial stage in Malaysia. However, this study was only made in the shade house where environmental factors were controlled. In future work, studies on the nitrogen dynamics for this crop using isotope techniques can be extended up to the farm level.

The nitrogen use efficiency is affected by several factors, but in most cases for a given irrigation management and water regime, the nitrogen fertilizer rate is the main source of variation, especially with regard to the nitrogen uptake issue. Avoiding over fertilization is the utmost means to match a high use efficiency and economic return of nitrogen fertilizer with limited environmental risks from nitrogen losses. This study has shown that use of high nitrogen rates does not mean that the efficiency of nitrogen use by plants is also high. Farmers in Malaysia should wisely control the use of nitrogen fertilizer on their crops. Excessive use of fertilizers will certainly increase the cost of farming besides doesn't necessarily increase rice production. Apart from the increase in expenditure high nitrogen application is also detrimental to the environmental health issue.

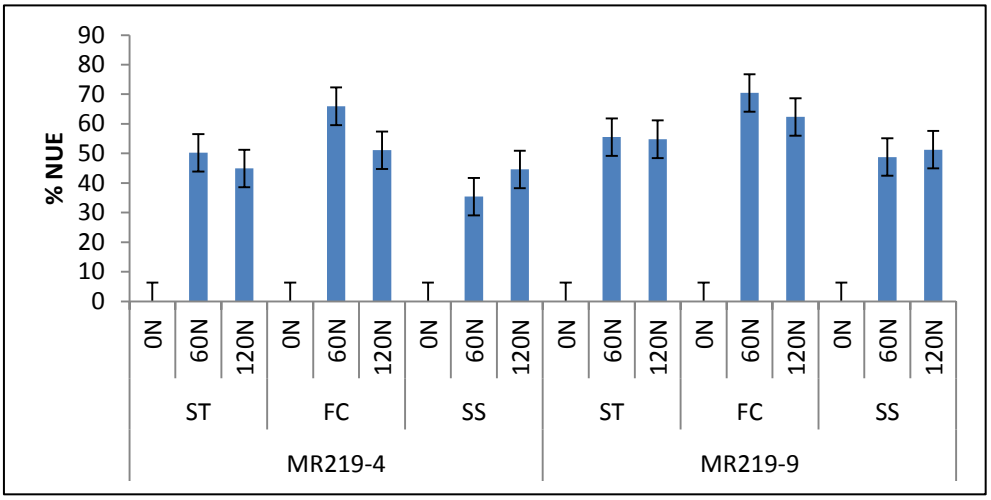


Figure 5. The influence of nitrogen level on nitrogen use efficiency (NUE) on MR219-4 and MR219-9 mutant lines under different water potentials. Error bars denote standard errors.

Conclusion

The present study highlighted the nitrogen use efficiency at a different range of nitrogen levels under different water potentials. In this work, we can conclude that nitrogen and water are affecting yield and nitrogen components on aerobic rice MR219-9 and MR219-4 ecosystem. It clearly shows that nitrogen and water level of application are very important inputs in the aerobic rice industry. Increasing nitrogen rates application may increase the yield but in some water condition, nitrogen use efficiency is low despite high fertilizer rates. Nitrogen use efficiency is optimum at field capacity for 60 Kg N ha^{-1} treatment. Change in soil water potential from flood to aerobic condition is proven to give a good improvement in the efficiency of nitrogen fertilizer uptake. Both aerobic rice MR219-4 and MR219-9 mutant lines exhibit no significant differences in terms of yield and nitrogen components.

Acknowledgement

The first author would like to acknowledge the Government of Malaysia for the scholarship granted to pursue his M.Sc. study at the Faculty of Science and Technology, The National University of Malaysia, Bangi. The present research is funded by MOSTI ScienceFund Grant: 06-03-01-SF0203. The work presented in this paper has been carried out at the Malaysian Nuclear Agency, Bangi, Kajang, Selangor. The capable technical assistance by Latiffah Norddin, Abdul Razak Ruslan and Hazlina Abdullah is deeply appreciated.

References

1. Sariam, O., Khanif, Y. M. and Zahrah, T. (2002). Rice growth and nitrogen uptake as influenced by water management. *Malaysian Journal of Soil Science*, 6: 1 – 11.
2. Dawe, D., Seckler, D. and Barker, R. (1998). Water supply and research for food security in Asia. *Proceeding of the workshop on increasing water productivity and efficiency in rice-based system*, IRRI, Los Banos Philippines.
3. Tuong, T. P. and Bouman, B. A. M. (2003). Rice production in water-scarce environments. In water productivity in agriculture: Limits and opportunities for improvement. *Eds. J W Kijne, R Barker, D Molden*: 53 – 67.
4. Priyanka, S., Jitesh, B. and Babu, S. (2012). Aerobic rice, a new approach of rice cultivation. *International Journal of Research in BioSciences*, 1(1): 1 – 6.
5. Sheng, C. C., Kimi, S., Man, A. and Hussain, Z. P. (2012). Aerobic rice: producing more rice with less water. http://www.mancid.org.my/index.php?mod=publication&task=detail&nid=1 [6 Mac 2014].
6. Bouman, B. A. M. (2005). Rice and water. *Advances in Agronomy*, 92: 187 – 237.

7. Duan, Y. H., Zhang, Y. L., Ye, L. T., Fan, X. R., Xu, G. H. and Shen, Q. R. (2007). Responses of rice cultivars with different nitrogen use efficiency to partial nitrate nutrition. *Annals of Botany*, 99: 1153 – 1160.
8. Choudhury, A. T. M. A. and Kennedy, I. R. (2005). Nitrogen fertilizer losses from rice soils and control of environmental pollution problems. *Communications in Soil Science and Plant Analysis*, 36: 1625 – 1639.
9. Dobermann, A. and Fairhurst, T. (2000). Rice: nutrient disorders and nutrient management. *Handbook Series*, pp. 147 – 149.
10. Craswell, E. T. and Vlek, P. L. G. (1979). Fate of nitrogen fertilizer applied to wetland rice. *In: Nitrogen and rice*, pp. 175 – 192.
11. Abou Seeda, M., Soliman, S. and Khater, A. (1994). The assessment of nitrogen balance under flooding and saturation circumstances using N-15. *Second Arab Conference on the Peaceful Uses of Atomic Energy*, pp. 709 – 721.
12. De Datta, S. K. (1986). Improving nitrogen fertilizer efficiency in lowland rice in tropical Asia. *Fertilizer Research*, 9: 171 – 186.
13. Janssen, B. H. (1998). Efficient use of nutrients: an art of balancing. *Field Crops Research*, 56: 197 – 201.
14. Tayefe, M., Gerayzade, A., Amiri, E. & Zade, A. N. (2011). Effect of nitrogen fertilizer on nitrogen uptake, nitrogen use efficiency of rice. *International conference on biology, environment and chemistry*, pp. 470 – 473.
15. Savant, N. K. and De Datta, S. K. (1982). Nitrogen transformation in wetland rice soils. *Advance in Agronomy*, 35: 241 – 302.
16. Jing, X., Van, R. H., Shaobing, P., Bouman B. A. M., Romeo, M. V., Lixiao, N., Jianliang, H. and Kehui, C. (2009). Improvement in nitrogen availability, nitrogen uptake and growth of aerobic rice following soil acidification. *Soil Science and Plant Nutrition*, 55 (5): 705 – 714.
17. Brian, D. (2010). Nitrogen for rice. *IREC Farmer's Newsletter – Large Area*, 183: 35 – 37.
18. Nie, L., Peng. S. and Bouman B. A. M. (2008). Alleviation of soil sickness cause by aerobic monocropping: growth response of aerobic rice to nutrient supply. *Field Crops Research*, 107: 129 – 136.
19. IAEA. (2001). Use of isotopes and radiation methods in soil and water management and crop nutrition. *Training Course*, 14: 21 – 96.
20. Azam, F., Simmons, F. W. and Mulvaney, R. L. (1993). Mineralization of N from plant residues and its interaction with native soil N. *Soil Biology and Biochemistry*, 25: 1787 – 1792.
21. Jensen, E. S. (1994). Availability of nitrogen in 15N-labelled mature pea residues to subsequent crops in the field. *Soil Biology and Biochemistry*, 26: 465 – 472.
22. Vanlauwe, B., Swift, M. J. and Merckx, R. (1996). Soil litter dynamics and N use in a leucaena (*Leucaena leucocephala* Lam. (De Witt) alley cropping system in southwestern Nigeria. *Soil Biology and Biochemistry*, 28: 739 – 749.
23. Abdul Rahim, H. and Andullah M. Z. (2012). Padi sinaran gama. *Dewan Kosmik Majalah Sains dan Teknologi*, 20 (10): 10 – 13.
24. IAEA. (2001). Use of isotopes and radiation methods in soil and water management and crop nutrition. *Training Course*, 14: 1 – 20.
25. Pirmoradian, N., Sepaskhah, A. and Maftoun, M. (2004). Deficit irrigation and nitrogen effects on nitrogen use efficiency and grain protein of rice. *Agronomic EDP Sciences*, 24: 143 – 153.
26. Nayak, B. R., Pramnik, K., Panigraphy, N., Dash, A. K. and Swain, S. K. (2015). Yield, nitrogen uptake and nitrogen use efficiency indices of aerobic rice (*Oryza sativa* L.) under various irrigation regimes and nitrogen levels. *International Journal of Bioresources*, 1(2): 8 – 13.
27. Mannan, M. A., Bhuiya, M. S. U., Akhand, M. I. M. and Zaman, M. M. (2012). Growth and yield of basmati and traditional aromatic rice as influenced by water stress and nitrogen level. *Journal of Science Foundation*, 10(2): 52 – 62.

Malaysian Journal of Analytical Sciences, Vol 20 No 3 (2016): 510 - 516
DOI: http://dx.doi.org/10.17576/mjas-2016-2003-07

MALAYSIAN JOURNAL OF ANALYTICAL SCIENCES
Published by The Malaysian Analytical Sciences Society
ISSN 1394 - 2506

THE EFFECT OF CTAB AND SDS SURFACTANT ON THE MORPHOLOGY AND PERFORMANCE OF LOW PRESSURE ACTIVE REVERSE OSMOSIS MEMBRANE

(Kesan Surfaktan CTAB dan SDS Terhadap Morfologi dan Prestasi Membran Osmosis Berbalik Aktif Bertekanan Rendah)

Nurul Syuhada Mohd Ali and Abdul Rahman Hassan*

Industrial Membrane Technology Lab (IMTL), Department of Industrial Chemical Technology,
Faculty of Science and Technology,
Islamic Science University of Malaysia, 71800 Nilai, Negeri Sembilan, Malaysia

*Corresponding author: abdrahman@usim.edu.my

Received: 24 February 2015; Accepted: 27 October 2015

Abstract

This study reported on the preparation of newly low pressure active reverse osmosis (LPARO) membrane by phase inversion technique. The effect of cetyl trimethylammonium bromide (CTAB) and sodium dodecyl sulphate (SDS) as surfactants on performance and morphological structure were examined. Using brackish water as a sample, the membrane performance was evaluated in terms of pure water permeation (PWP), flux and salt rejection. Experimental data revealed that at 2.0 wt. % of SDS, the LPARO membrane achieved the optimum performance and produced the finest membrane.

Keywords: low pressure reverse osmosis, surfactant, morphology, performance, brackish water

Abstrak

Kajian ini melaporkan mengenai penyediaan membran osmosis songsang aktif bertekanan rendah (LPARO) dengan teknik fasa penyongsangan. Kesan setil trimetilammonium bromida (CTAB) dan natrium dodekil sulfat (SDS) sebagai surfaktan terhadap prestasi dan struktur morfologi telah diselidik. Dengan menggunakan air payau sebagai contoh, prestasi membran telah dinilai dari segi penyerapan air tulen (PWP), penyingkiran fluks dan garam. Data eksperimen menunjukkan bahawa pada 2.0 wt . % SDS, membran LPARO berjaya mencapai prestasi yang optimum dan menghasilkan membran yang terbaik.

Kata kunci: osmosis songsang bertekanan rendah, surfaktan, morfologi, prestasi, air payau

Introduction

Asymmetric membranes are prepared by phase inversion via immersion precipitation [1]. In this process, it involves the conversion of a homogeneous polymer solution consisting of two or more components to a two-phase system, the solid polymer rich phase and the liquid polymer poor phase. The solid phase forms the membrane structure while the liquid phase forms the membrane pores [2]. The successive solidification of the phase separated solution leads to a porous, asymmetric structure. The morphology and performance of membranes depend strongly on the thermodynamics as well as kinetics of the phase inversion process [3].

One option for controlling the membrane formation process is introducing an additive in the casting solution. PVP is a well-known additive that can increase the viscosity of the polymer solution. Several studies were done on the

effect of PVP as additive on the morphology and performance of membranes. Han and Nam [4] studied the variation of thermodynamic and rheological properties in PSF casting solution by adding PVP. Jung et. al [5] investigated the effect of molecular weight of polymeric additives on formation, permeation properties and hypochlorite treatment of asymmetric polyacrylonitrile (PAN) membranes. The results indicated that the top layer of the membrane and suppression of macrovoid formation strongly depends upon the molecular weight of PVP. Besides that, Fontananova et. al [6] and Curcio et. al [7] reported that PVP was an effective permeation flux promoter, and the thermodynamic effect played a dominant role during the flat-sheet membrane formations of both polyvinylidine fluoride (PVDF) homopolymer and PVDF-HFP copolymer. Also, the preparation, morphology and performance of cellulose acetate (CA)/polyvinylpyrrolidone (PVP) blend asymmetric membranes has been studied by Saljoughi and Mohammadi [8]. It was found out that initial addition of PVP to the cast film solution (from 0 to 3 wt. %) results in increasing macrovoids formation, meanwhile further addition of PVP (from 3 to 6 wt. %) results in suppression of macrovoids.

Addition of surfactant as one of the materials necessary for membrane making formulation can be one of the effective strategies to produce high performance membrane with high selectivity. The effects of surfactants as additive in the process of membrane fabrication were reported in other studies [9-13]. Sodium dodecyl sulphate (SDS) was added as additive into polysulfone (PSF) casting solution for gas separation and as gelatin media on the formation of polyethersulfone (PES) membranes by Yamasaki et. al [9] and Alsari et. al [10], respectively. The effects of temperature and concentration of cationic surfactant, which is cetyl trimethylammonium bromide (CTAB) in the formation of asymmetric nanofiltration membrane is reported by Mulijani et. al [11]. The result indicated that the formation of membrane pore increases as the addition of CTAB increases. Saedi et. al [12] investigated the effect of three types of surfactant including SDS, CTAB and Triton X-100 on the structure and performance of PES membrane for carbon dioxide separation from methane. The result demonstrated that the addition of surfactants in the casting solution increases the formation of macrovoids and large finger-like pores in the sub-layer of PES membranes. The effect of CTAB and Triton X-100 on the surface morphology and nitrophenols separation using CA nanofiltration membrane was investigated by Ghaemi et. al [13]. Addition of surfactants as additive resulted in membranes with superior pure water flux, permeation and rejection in comparison to CA membrane.

Materials and Methods

Chemicals and raw materials

Polysulfone (PSF (Udel-P1700) (Solvay) was used as polymer, while N-methyl-2-pyrrolidone (NMP) (Merck) was used as non-solvent for membrane preparation. Polyvinylpyrrolidone, (PVP, K29-32) (Acros Organics) was used as additive. Cetyl trimethylammonium bromide (CTAB) (EMD Chemicals) and Sodium Dodecyl Sulphate (SDS) (Fisher Scientific UK) were used as cationic and anionic surfactant for addition in the casting solution. Ethanol and n-hexane (Merck) were used as the coagulation bath. Sodium chloride, NaCl (Merck) was used for the salt rejection test.

Membrane preparation

Homogeneous dope solution of the PSF dissolved in NMP was prepared using PVP as additive, and different surfactants which are CTAB as cationic surfactant and SDS as anionic surfactant by stirring for 8 hours at room temperature. The stirring process was fixed at 300 rpm. The solution was poured and cast on glass plate using casting knife with thickness of 150 µm. Then, the membrane was moved into water for immersion precipitation. The immersion precipitation was carried out at room temperature. In order to ensure complete phase separation, the membrane was immersed in water for 24 hours. Then, the membrane was immersed in ethanol for 24 hours and n-hexane for 3 hours to ensure all the solvents is completely removed. As the final stage, membrane was dried for 24 hours.

Membranes morphological characteristics

The cross-section of the prepared low pressure reverse osmosis (LPARO) membranes was investigated using scanning electron microscopy. Samples of the membranes were fractured cryogenically in liquid nitrogen and mounted on the sample stubs with double-surface tape. After the samples were sputtered with gold by an automatic gold coater (JFC 1600), they were scanned by employing a JEOL JSM 6360LA Scanning Electron Microscopy (Tokyo, Japan) under magnification of 500x to 5000x with potentials 15kV.

Reverse osmosis performance evaluation

Reverse osmosis performance in terms of pure water permeation (PWP) and salt rejection for the LPARO membranes were tested using lab-scale cross flow filtration apparatus with circular filtration cell having an effective area of 1.38×10^{-3} m^2. To begin with, the circular membrane coupons loaded in the filtration cells were pressured at 5 bar with deionized water for at least 30 minutes for compaction. Desalination tests were then carried out at operating pressure of 5 bar with aqueous solution containing 2000 ppm of NaCl represent brackish water. The PWP was determined by measuring the permeate volume collected over a certain period in terms of liter per square meter per hour (L/m^2h) and calculated through the following equation 1:

$$J_w = \frac{Q}{A \times \Delta t} \quad (1)$$

where J_w is the volumetric PWP, A is the effective area of the membrane for permeation, and Q is the volume of permeation over a time interval (Δ t). The salt rejection was evaluated using the following equation 2:

$$R = \left(1 - \frac{C_p}{C_f}\right) x100 \quad (2)$$

in which C_p and C_f are the salt concentrations in permeate and feed, respectively. The salt concentration was determined by measuring the electrical conductivity of the salt solution using a conductivity meter (CON 700, Eutech Instruments).

Results and Discussion

Effect of CTAB as cationic surfactant on the performance of PSF membrane

Figure 1 shows that the presence of CTAB in the casting solution increases the PWP values with the maximum value of 1 wt. % CTAB. Increasing CTAB concentration more than 1 wt. % resulted in decreasing the PWP. This might due to the high viscosity of casting solution that prevents the penetration of non-solvent and weaken the macrovoids formation, hence lead to low permeability of membrane.

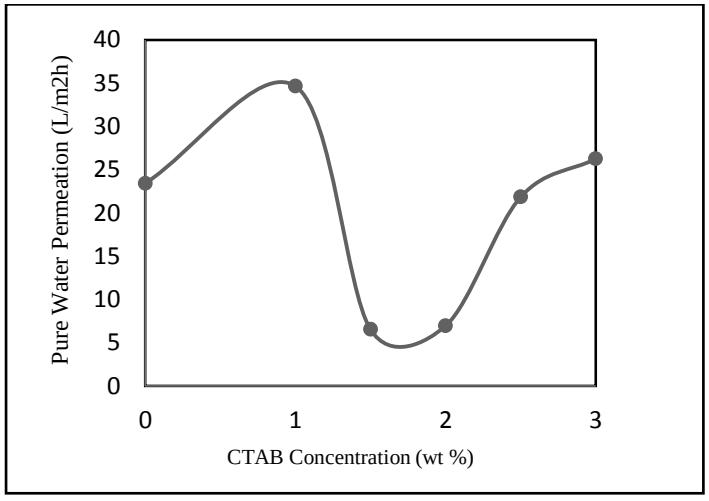


Figure 1. Effect of CTAB concentration on pure water permeation

The effect of CTAB concentration on brackish water flux and salt rejection of membrane prepared from PSF/NMP/PVP/CTAB system is shown in Figure 2. The brackish water flux increases as CTAB surfactant introduced in the casting solution, reaches the maximum at 1 wt. % concentration of CTAB which is 32.48 L/m^2h. The salt rejection improves from 77.8 % (without CTAB) to 81.1 % in the presence of 2 wt. % of CTAB in the

casting solution. As the CTAB concentration increased more than 2 wt. %, the salt rejection gradually decreased. The cross-sectional morphology of the prepared membrane with CTAB (Figure 5b) justify the high PWP and brackish water permeation in the presence of CTAB due to the formation of large finger-like pore in the sub-layer of membranes.

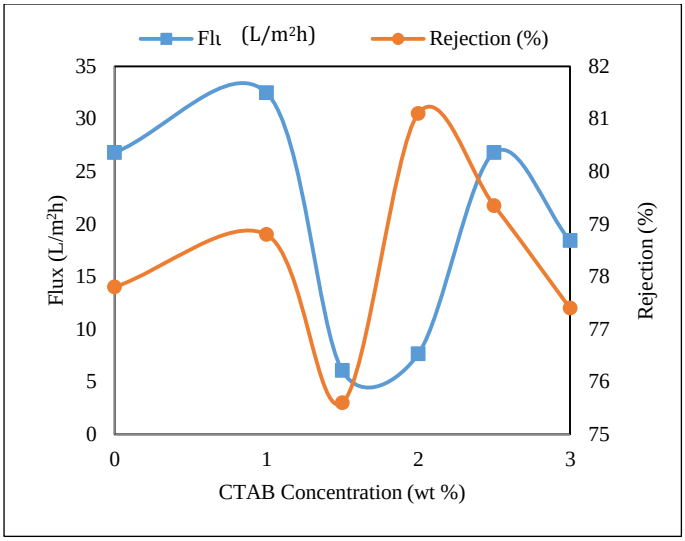


Figure 2. Effect of CTAB on brackish water flux and salt rejection

Effect of SDS as anionic surfactant on the performance of PSF membrane

To investigate the effect of anionic surfactant as additive in the casting solution, sodium dodecyl sulphate (SDS) was selected as strong anionic surfactant. Figure 3 show the effect of SDS concentration on PWP for the prepared membrane. The PWP increases gradually by increasing the SDS concentration in the casting solution, and reaches the maximum value for the concentration of 2.5 wt. % SDS, then decreases afterwards. This corresponds with the finding of Rahimpour et al. [3].

The effect of SDS on brackish water flux and salt rejection are shown in Figure 4. The obtained results demonstrated that the addition of SDS in the casting solution enhance the brackish water flux and salt rejection. On the other hand, as the concentration of SDS increases more than 2.5 wt. %, the brackish water flux and salt rejection decreases.

Most surfactants have a long hydrophobic alkali and a hydrophilic ionic group (polar group) in their structure. Rahimpour et al. [3] reported when the surfactant enters in aqueous media the ionic head tends to water while the non-polar tail tends to absorb on solid surface, air or organic phase. The alkali chain can join to polymer matrix when it comes near to hydro-carbonic structure of polymer but the hydrophilic but the hydrophilic and polar portion leave freely. The accumulation of polar groups in polymer structure results in repulsion between polymer chains and consequently increases the porosity of membrane by forming an open structure. When concentration of the surfactant increase, the non-polar tail of surfactant molecules settle beside one another and form micelles with polar groups in outer surface and non-polar groups inside the micelles in addition to the polymer surfactant complex. These free micelles deteriorate the membrane structure and decrease the membrane performance [11].

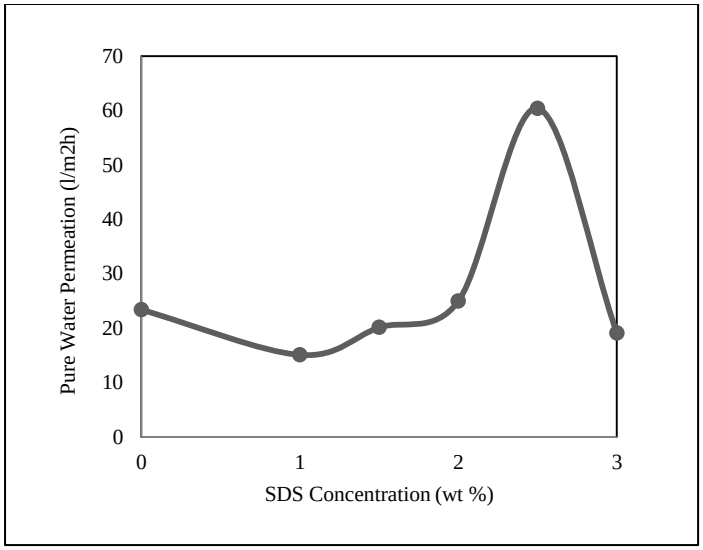


Figure 3. Effect of SDS concentration on pure water permeation

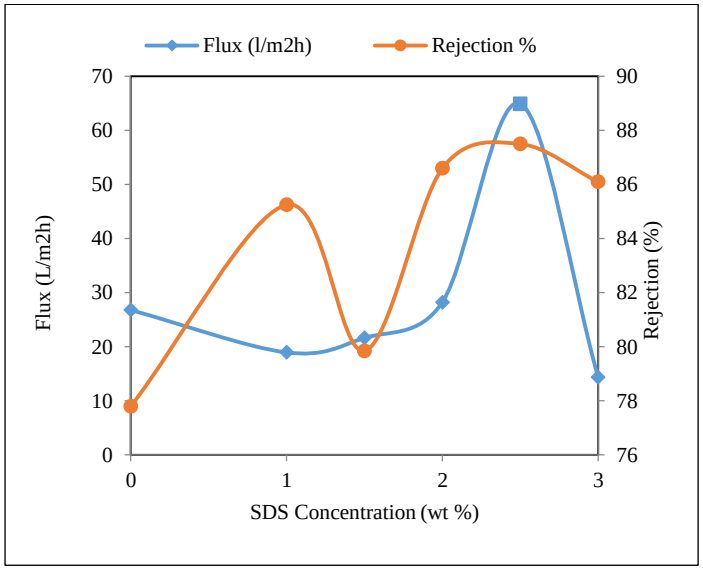
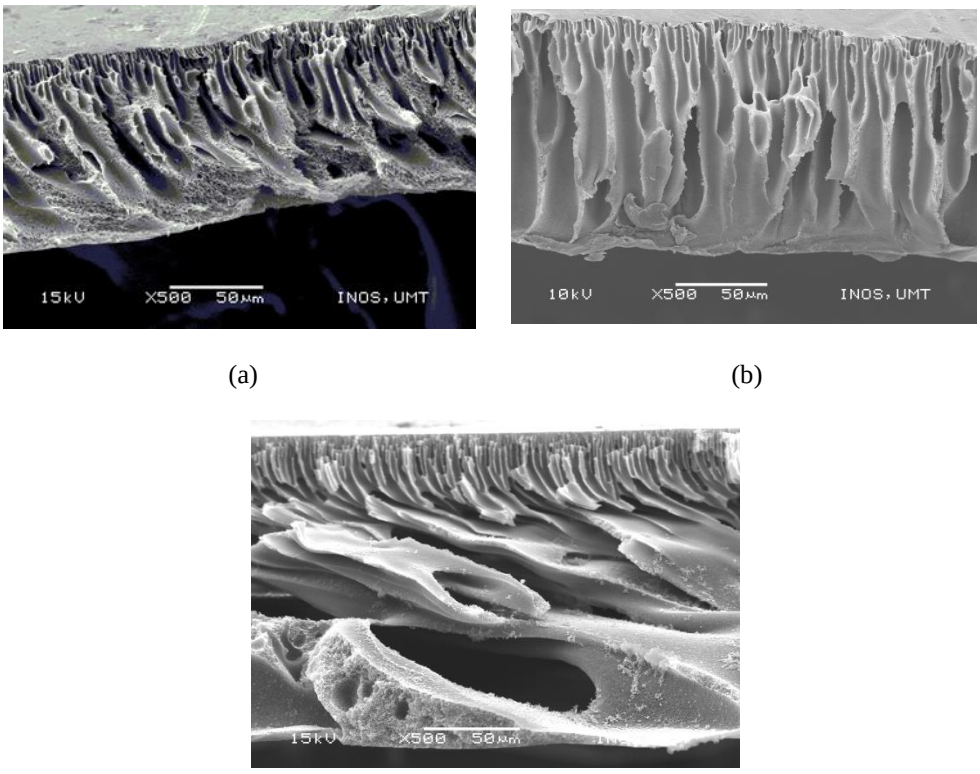


Figure 4. Effect of SDS on brackish water flux and salt rejection

Effect of surfactants on the morphology of the PSF membrane

The scanning electron microscopy (SEM) images were taken to determine the effect of CTAB and SDS as surfactants on the surface morphology of the LPARO membranes. SEM photograph of cross section of membranes, prepared from PSF membrane without surfactant, with CTAB and SDS as shown in Figure 5(a), 5(b) and 5(c), respectively. Asymmetric structure of the membranes consists of a dense top layer, a porous sub-layer that is occupied by closed cell within polymer matrix, and finger-like pores. The SEM images indicate that the addition of CTAB in the casting solution lead to formation of large finger-like pores in sub-layer of membranes. There is evident correlation between the miscibility of surfactant in the coagulant and the formation process of various pores.

Addition of an appropriate surfactants leads to induction or suppression of the macrovoids and finger-like pores in the sub-layer [3]. Although there is low miscibility between CTAB and NMP, CTAB is classified as hydrophilic surfactant that has high miscibility in water. If the added surfactant to the casting solution has high miscibility with the coagulant, it resulting in formation of finger-like pores and macrovoids via decreasing the surface tension and subsequently decrease in the demixing time [12].



(a) (b)

(c)

Figure 5. SEM cross-sectional images of prepared PSF membranes (a) without surfactant, (b) with CTAB and (c) with SDS

Meanwhile, SDS as hydrophilic surfactant can affect membrane morphology and porosity of sub layer in three manners which are (i) enhancement in macrovoid formation and increasing the membrane porosity by increasing solvent–nonsolvent mixing affinity and increasing demixing rate via distribution of SDS molecules as free molecules in NMP and formation of free micelles, (ii) enhancement in membrane free volume and membrane porosity and macrovoid formation via formation of polymer–surfactant complexes, (iii) decreasing sub layer porosity by decreasing demixing rate via increasing casting solution viscosity [12]. The SEM images indicated that the addition of small amount of SDS in the casting solution enhanced macrovoids formation. The high porosity of sub-layer of membranes prepared with SDS can be responsible for high performance of membranes.

Conclusion

This study has demonstrated that the addition of surfactants in the casting solution increases the formation of macrovoids and large finger-like pores in the sub-layer of LPARO membranes. This enhance the pure water permeation, brackish water flux with slight decrease in salt rejection. Surfactant concentration plays an important

role in the membrane morphology and performance. The obtained result revealed that at 2.0 wt. % of SDS, the LPARO membrane achieved the optimum performance and produced the finest membrane.

Acknowledgement

The authors would like to thank to Ministry of Education (MOE), Malaysia through Exploratory Research Grant Scheme (USIM/ERGS-FST-33-50113) for their financial assistance and support.

References

1. Strathmann. H. and Koch. K. (1977). The formation mechanism of phase-inversion membranes. *Desalination*, 21: 241 – 255.
2. Yuxin, M., Fengmei, S., Jun, M., Miaonan. W., Jun, Z. and Congjie, G. (2011). Effect of PEG addiive on the morphology and performance of polysulfone ultrafiltration membranes. *Desalination*, 272: 51 – 58.
3. Rahimpour, A., Madaeni, S. S. and Mansourpanah, Y. (2007). The effect of anionic, non-ionic and cationic surfactants on morphology and performance of polyethersulfone ultrafiltration membranes for milk concentration. *Journal of Membrane Science*, 296: 110 – 121.
4. Han, M. J. and Nam. S. T. (2002). Thermodynamic and rheological variation in polysulfone solution by PVP and its effect in the preparation of phase inversion membrane. *Journal of Membrane Science*, 202: 55 – 61.
5. Jung, B. Yoon, J. K., Kim, B. and Rhee, H. (2004). Effect of molecular weight of polymeric additives on formation, permeation properties and hypochlorite treatment of asymmetric PAN membranes. *Journal of Membrane Science*, 243: 45 – 57.
6. Fontananova, E., Jansen, J. C., Cristiano, A., Curcio, E. and Drioli, E. (2006). Effect of additives in the casting solution on the formation of PVDF membranes. *Desalination*, 192: 190 – 197.
7. Curcio, E., Fontananova, E., Di Profio, G. and Drioli, E. (2006). Influence of the structural properties of poly (vinylidene fluoride) membranes on the heterogeneous nucleation rate of protein crystals. *The Journal of Physical Chemistry B*, 110(25): 12438 – 12445.
8. Saljoughi, E. and Mohammadi, T. (2009). Cellulose acetate (CA) / polyvinylpyrrolidone (PVP) blend asymmetric membranes: Preparation, morphology and performance. *Desalination*. 249: 850 – 854.
9. Yamasaki, A., Tyagi, R. K., Fouda, A. E., Jonnason, K. and Matsuura, T. (2000). Effect of SDS surfactant as an additive on the formation of asymmetric polysulfone membranes for gas separation in: Pinnau, I., Freeman, B.D. (Eds.), *Membrane Formation and Modification*, Chapter 6.
10. Alsari, A. M., Khulbe, K. C. and Matsuura, T. (2001). The effect of sodium dodecyl sulfate solutions as gelation media on the formation of PES membranes. *Journal of Membrane Science*, 188(2): 279 – 293.
11. Mulijani, S., Budianto, E. and Hikam, M. (2010). Formation and Characterization of Asymetric Nanofiltration Membrane: Effect of Temperature and Surfactant as a Template. *ASEAN Journal on Science & Technology For Development*, 27: 21 – 29.
12. Saedi, S., Madaeni, S. S., Shamsabadi, A. A. and Mottaghi, F. (2012). The effect of surfactants on the structure and performance of PES membrane for separation of carbon dioxide from methane. *Separation and Purification Technology*, 99: 104 – 119.
13. Ghaemi, N., Madaeni, S. S., Alizadeh, A., Daraei, P., Zinatizadeh, A. A. and Rahimpour, F. (2012). Separation of nitrophenols using cellulose acetate nanofiltration membrane: Influence of surfactant additives. *Separation and Purification Technology*, 85: 147 – 156.

Malaysian Journal of Analytical Sciences, Vol 20 No 3 (2016): 517 - 524
DOI: http://dx.doi.org/10.17576/mjas-2016-2003-08

MALAYSIAN JOURNAL OF ANALYTICAL SCIENCES
Published by The Malaysian Analytical Sciences Society
ISSN 1394 - 2506

EVALUATION OF HEAVY METAL CONCENTRATIONS IN WILD AND CULTIVATED *Hemibagrus* sp. USING PRINCIPAL COMPONENT ANALYSIS

(Penilaian Kepekatan Logam Berat dalam *Hemibagrus* sp. dari Habitat Semulajadi dan Kolam Ternakan Menggunakan Kaedah Analisis Komponen Utama)

Nor Shahirul Umirah Idris[1, 2, 3]*, Sharifuddin Md.Zain[1], Kah Hin Low[1], Ahmad Firdaus Kamaruddin[4], Kaharudin Md. Salleh[5]

[1]*Environmental Research Group, Department of Chemistry, Faculty of Science*
[2]*Institute of Graduate Studies*
University of Malaya, 50603 Kuala Lumpur, Malaysia
[3]*Faculty of Earth Science,*
Universiti Malaysia Kelantan Kampus Jeli, Karung Berkunci No.100, 17600 Jeli, Kelantan, Malaysia
[4]*East Coast Environmental Research Institute (ESERI),*
Universiti Sultan Zainal Abidin, Gong Badak Campus, 21300 Kuala Terengganu, Terengganu, Malaysia
[5]*Fisheries Research Institute, Freshwater Fisheries Research Division,*
Glami Lemi, 71650 Titi, Jelebu, Negeri Sembilan, Malaysia

**Corresponding author: shahirulumirah@gmail.com*

Received: 24 February 2015; Accepted: 27 October 2015

Abstract

In the present study, the concentration of Cr, Cd, Cu, Zn, Pb, and As in various tissues of *Hemibagrus* sp. from two different habitat were determined with microwave assisted digestion-inductively coupled plasma-mass spectrometry. The objective of this research was to determine the differences between wild and cultivated in terms of heavy metal accumulation in muscle, liver and gills tissues. The metals accumulation pattern relating types of tissue and elements as well as fish habitats were revealed by principal component analysis. The results revealed that variation in metal accumulation pattern is strongly dependent on the type of tissues. The results suggested that Cu, Zn, and Pb are highly associated with liver tissue while Cr and As with muscle and gills. The differences in heavy metal accumulation observed between wild and cultivated *Hemibagrus* sp. were probably due to the differences in their environmental conditions.

Keywords: principal component analysis, pattern recognition, heavy metal, fish, farmed

Abstrak

Kepekatan Cr, Cd, Cu, Zn, Pb, dan As dalam pelbagai tisu *Hemibagrus* sp. dari dua habitat yang berlainan adalah ditentukan dengan pencernaan bantuan gelombang mikro-plasma gadingan teraruh-jirim spektrometri. Objektif kajian ini adalah untuk menentukan perbezaan antara ikan dari habitat semulajadi dan kolam ternakan dari segi pengumpulan logam berat dalam tisu, hati, dan insang. Corak pengumpulan logam berkaitan jenis tisu dan elemen kajian serta habitat ikan ditunjukkan oleh analisis komponen utama. Keputusan menunjukkan bahawa perubahan dalam corak pengumpulan logam adalah bergantung kepada jenis tisu. Keputusan kajian mencadangkan bahawa elemen Cu, Zn, dan Pb adalah berkaitan dengan organ hati manakala elemen Cr dan As adalah berkaitan dengan tisu dan insang. Perbezaan dalam pengumpulan logam berat di antara *Hemibagrus* sp. dari habitat liar dan kolam ternakan adalah mungkin disebabkan oleh perbezaan dalam keadaan persekitaran mereka.

Kata kunci: Analisis komponen utama, corak taburan, logam berat, ikan, kolam ternakan

Introduction

The rapid development of agriculture and industrialization has resulted in increasing of metal pollution in the aquatic ecosystems, which are significantly hazardous for fish and human [1]. Significant quantities of contaminant elements are discharged into river, which can be strongly accumulated and biomagnified along water, sediment and aquatic food chain, thus resulting in sublethal effects or death in fish populations [2-4]. Fish are commonly situated at top of the aquatic food chain and normal metabolism of fish may accumulate large amounts of certain metals from food, water and sediment [5]. Commonly, fish is known to be nutritious with essential proteins, polyunsaturated fatty acids and liposoluble vitamins [6]. Nevertheless, levels of metals in fish are of particular interest due to their high potential to enter and accumulate in food chains [7, 8]. Even low concentrations of these elements have damaging effects to humans and animals because there is no good mechanism for their elimination from the body [9]. On the other hand, fish can be regarded as a good bioindicator because it is easily sampled and found in abundant population, with the potential to accumulate metals and has a long life span with an optimum size for analysis [10]. In this study, heavy metal (Cr, Cd, Cu, Zn, Pb) of *Hemibagrus* sp. in certain tissues (gill, liver, muscle) from wild and cultivated habitat are compared. Accumulation pattern relating tissue and elements and the underlying structure related to their origins and tissues were evaluated with principal component analysis (PCA). The aim of PCA is finding the similarities and differences between *Hemibagrus* sp. of different habitats based on ICP-MS measurement so as to create classification and identification of key discriminants that distinguish between samples.

Materials and Methods

The slaughtered *Hemibagrus* sp. was donated in June 2012 by a local fisherman and local fish farmer. The samples originated from the Selangor River and the cultivated pond located at Taman Agroteknologi Pertanian Bistari Jaya, Kuala Selangor, Selangor (Figure 1). The samples were stored in 20˚C freezer and the length and weight were recorded before dissection. The tissues of muscle, gills, and liver samples were freezing dried (CHRiST, Germany) and the homogenized with a mortar and pestle. Dried samples were kept in amber jars in a desiccator before microwave digestion.

Laboratory procedure

Ultra-Pure Water (UPW) with resistivity more than 18 MΩ was obtained from the PURELAB® UHQII system (ELGA®, UK). 65 % nitric acid and 30 % hydrochloric acid solution were of Suprapur ® quality (Merck, Germany). The dogfish liver (DOLT-4) (NRCC, Canada) certified reference material (CRM) for trace metals were used to evaluate the analytical performance of the methods. The tissue samples were analysed according to the method described by Low et al. [11] in which microwave-assisted digestion (MAD) were carried out in a CEM Mar Xpress Microwave Accelerated Reaction System (CEM, Corporation, Matthews, NC, USA). Dried samples (0.25g) was weighted directly in each 55mL self-regulating pressure control PFA® vessel and digested with a reagent consists of 2.50 mL of 65 % HNO_3, 0.50 mL of 30 % HCI and 7 mL UPW. Under microwave power of 800W, the microwave temperature was ramped to 185˚C in 10.5 min and held for 14.5 min. After digestion, the sample was cooled before being transferred to a 50 mL polypropylene volumetric flask and the volume was made up to the mark with UPW. Diluted sample solutions were stored in polyethylene vials below 8˚C and analysed by ICP-MS [12].

Statistical analysis

Principal component analysis (PCA) was conducted to transform the original data matrix (composed of 120 samples and 5 variables) into a product of two matrices, one which contains information about metal concentrations (loading matrix) and the other about the samples (score matrix). All statistical calculations were performed using the software package JMP version 9.0.



Figure 1. Location of sampling sites, letter S denotes to samples from wild, letter AP denotes cultivated fish.

Results and Discussion

Certified reference materials of dogfish liver (DOLT-4) were used to check the accuracy of MAD-ICP-MS method. The elemental concentrations determined in the standard reference materials were in a good agreement with the certified values (Table 1).

Table 1. Analysis of certified reference materials

		Cr	Cu	Zn	Pb	Cd	As
DOLT -4	Certified values	-	31 ± 1	116 ± 6	0.16 ± 0.04	24 ± 0.8	9.7 ± 0.6
(mg kg^{-1})	Amount detected	-	32 ± 2	118 ± 7	0.16 ±0.04	28 ± 1.6	9.6 ± 0.3
	Recovery / %	-	102 ± 6	102 ± 5	100 ± 6	116 ± 4	99 ± 3

95 % confidence intervals , n = 7, Note : - not certified

Morphometric data of *Hemibagrus* sp. from wild and cultivated samples are summarized in Table 2. Condition factor (CF) was calculated by the ratio of weight/length which is commonly used as an index of fish health, while hepatosomatic index (HSI) is defined as the ratio of liver weight to body weight that reflects the energy reserve in fishes[13]. Samples obtained from the cultivated pond were generally smaller than those caught from Selangor River. Although there are differences in size variation, there were no substantial differences noted in the effect of metal concentration in studied tissues [14].

Table 2. Biometric parameters for *Hemibagrus sp.* from different habitat

Biometric Parameter	**Habitat**	
	Aquaculture	**Wild**
Location	N 03˚25.046 E 101˚ 21.203	N 03˚21.883 E 101˚ 18.728
Condition factor (CF)	0.8 ± 0.2	0.7 ± 0.0
Hepatosomatic index (HSI)	0.7 ±0.2	0.7 ±0.1

95% confidence intervals, n = 20

Mean concentrations of heavy metals in the muscle, liver, and gills of wild and cultivated *Hemibagrus* sp. are presented in Table 3. Chromium, cadmium, copper, zinc, and lead were selected as the analyte elements. There are significant differences ($p<0.001$) concentrations obtained in different organs. The results have demonstrated that liver tissues generally contained higher concentrations of Cd, Cu, Zn, and Pb for both habitats except for higher Cr concentrations in the gill tissues. This result is also in a good agreement with Fernandes et al [15], where metal concentrations of Cu, Zn, and Pb were higher in liver than other studied tissues. Essential metals such Cu and Zn are needed in fish metabolism, while others such as Pb and Cr have no functional in biological systems. Our study showed that tissue of wild *Hemibagrus* sp. contained significantly higher content ($p < 0.001$) of Pb and As, while tissue of farmed *Hemibagrus* sp. had significantly higher contents ($p < 0.05$)of Cu. However, all metals may cause harmful effects on fish depending on their concentrations [16]. Overall metal concentrations are generally found to be higher in liver compared to other studied tissues regardless of the sample origins.

The accumulation pattern of metals varies greatly depends on the species as well type of tissues. Previous report by Begum et al. [17], showed that the liver appeared to be the main storage of heavy metal, while the muscle tissue with the lowest level. Yet, Mormede and Davies [18], suggested that the liver is the target organ, which functions to detoxify and accumulate [19], while muscles are at most concern to humans because it is the main tissues of human diet [20]. Based on permissible level limits for the muscle meat of fish, all metal studied were below the permissible level recommended by Malaysian Food Regulation and USEPA risk based concentrations. For a better understanding, PCA was conducted to evaluate the distribution of metals in the studied tissues. PCA is usually discussed in terms of loadings and scores since they complement each other. The scree test proposed by Cattell [21] suggest that with only the first two PCs accounted for 74% of the total variability of associated metal concentrations in tissues studies and 3 distinct clusters can be revealed (Figure 2). The model demonstrated that Cluster I is made up of liver tissues, Cluster II composed of scores of gill tissues, while the scores of muscle tissues are grouped in

Cluster III. The variation of these clusters, are totally associated with the type of tissues regardless their habitats. The variation of metal accumulation trends depends on the studied tissues. Combination of the results from Figure 2 and Table 3 suggest that the total metals accumulation is liver > gill > muscle.

Table 3. The concentration of heavy metals in freeze dried *Hemibagrus* sp.

	Tissue (mg kg^{-1})	**Cr**	**Cu**	**Zn**	**Pb**	**Cd**	**As**
Aquaculture	Muscle	0.3±0.0	1.2±0.2	33.0±3.8	0.2±0.1	< LoD	0.3±0.0
	Liver	0.3±0.1	(1.4±0.2) x 10^2	(1.8±0.2) x 10^2	1.2±0.3	< LoD	0.1±0.0
	Gill	0.4±0.1	2.9±0.4	56.1±4.1	0.2±0.0	< LoD	0.6±0.1
Natural	Muscle	0.3±0.0	0.8±0.1	22.8±1.0	< LoD	< LoD	2.3±0.5
	Liver	0.3±0.0	79.3±6.8	(1.5±0.1) x 10^2	5.0±0.6	< LoD	0.4±0.1
	Gill	0.4±0.0	1.6±0.1	49.8±3.0	0.9±0.1	< LoD	0.9±0.1

All reported values are referred to dry base, 95% confidence intervals, n = 20, LoD – Limit of Detection (Pb < 0.03 mg kg^{-1})

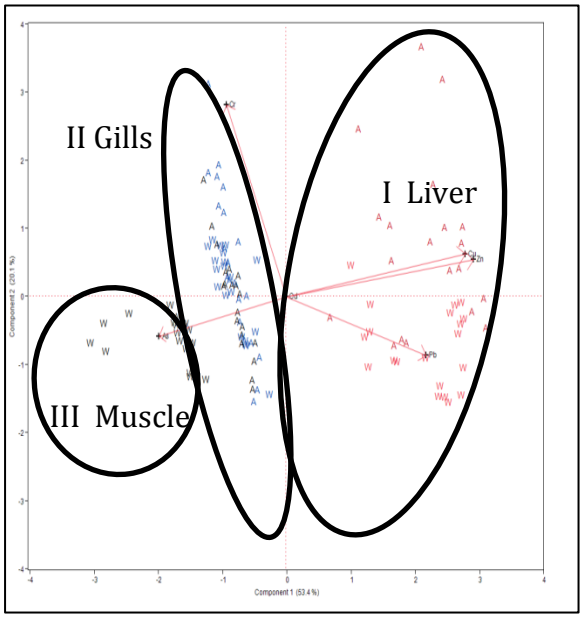


Figure 2. PCA bi-plot for all samples (n = 120). The letter A denotes aquacultured fish, letter W denotes to wild fish.

Based on Figure 2, it is noticed that the scores of liver sample (Cluster I) in PC1 axis was spread in the region with positive loadings of Pb, Cu and Zn. High variation of these metals makes liver samples stand out more from others on the right-hand side of the scores plot. These observations are consistent with the findings reported by [22], that higher metal accumulation in liver tissues are due to the greater binding tendency of the metals with oxygen carboxylate, amino groups, nitrogen, and/or sulphur of the mercapto group in the metallothionein protein.

PCA bi-plot for liver samples demonstrates two clusters (Figure 3) were obtained. The liver samples from cultivated *Hemibagrus* sp. have positive scores on PC1 than wild *Hemibagrus* sp. which explained 52 % of the total variance

and have positive loadings of Cr, Cu, and Zn. The gills (Cluster II) and muscle samples (Cluster III) are discriminated from liver samples with negative score on PC1. Nevertheless, Cluster II and Cluster III overlap with high score of Cr and As. In fact, Cluster III mainly consists of two sub-clusters which can be distinguished by the magnitude of score on PC1 (53% of total variance). Similar trend was observed in gills samples, where the bi-plot also indicates 2 distinct cluster (Figure 4) (which explained 73% of the total variances. These results also demonstrated that cultivated *Hemibagrus* sp. from Selangor River accumulated high metal concentrations than wild *Hemibagrus* sp.

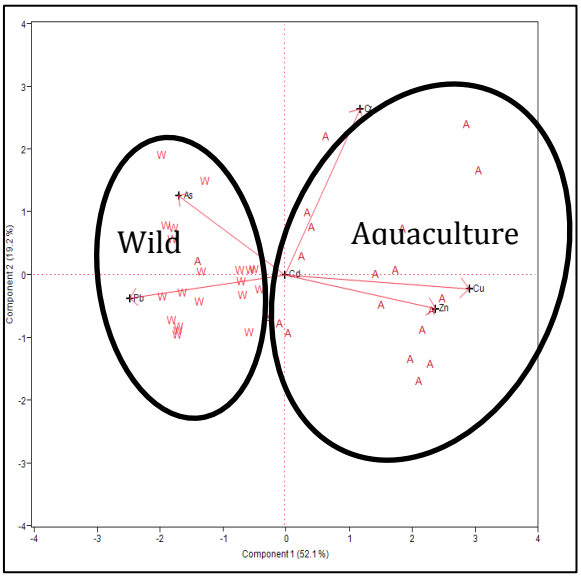


Figure 3. PCA bi-plot for liver samples (n = 40).The letter A denotes aquacultured fish, letter W denotes to wild fish.

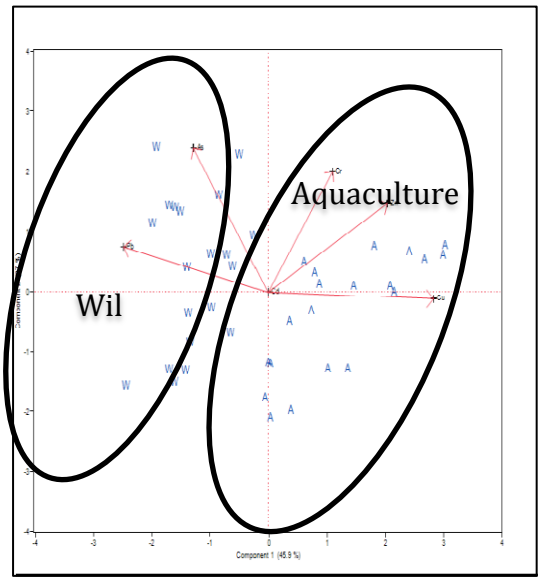


Figure 4. PCA bi-plot for gills samples (n = 40). The letter A denotes aquacultured fish, letter W denotes to wild fish.

Refer to PCA bi-plot for muscle sample (Figure 5), it was demonstrated that two discrete cluster are separated by PC1 (75% of total variance), which high positive loadings of Cu, Zn, and Pb for cultivated fish while negative loading of Cr and As for wild fish. According to the Malaysian Food Act 1983 and Food Regulations 1985 [23], accumulation of heavy metal in muscle samples are below the permissible level.

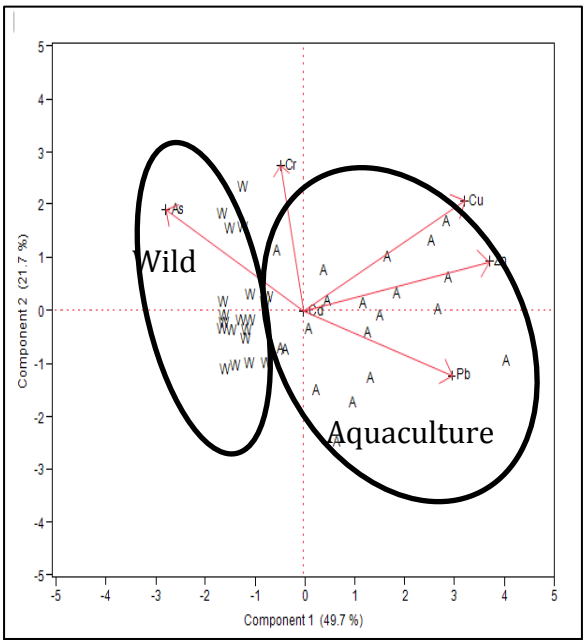


Figure 5. PCA bi-plot for muscle samples (n = 40). The letter A denotes aquacultured fish, letter W denotes to wild fish.

Conclusion

The results of the study show that PCA can identify patterns in our data, where PCA provides a way to visualize the clustering pattern among different organs of *Hemibagrus* sp from two different habitats, and easily identifies which metals contribute most to these variation. It also demonstrates the similar clustering tendencies related to the origin of the samples. The results revealed Cu, Zn, and Pb highly associated with liver tissues while Cr and As with muscle and gills. This suggests that the differences in accumulation of heavy metals between two habitats were probably due to the differences in their environmental conditions.

Acknowledgement

The authors gratefully acknowledge the financial assistance for this work from the Malaysian Ministry of Science, Technology, and Innovation (ER010-2011A) and Freshwater Fisheries Research Division for technical support during sampling.

References

1. Uluturhan, E. and Kucuksezgin, F. (2007).Heavy metal contaminants in Red Pandora (Pagellus erythrinus) tissues from the Eastern Aegean Sea, Turkey. *Water Research*, 41(6): 1185 - 1192.
2. McGeer, J. C., Szebedinszky, C., McDonald, D.G., and Wood, C.M. (2000).Effects of chronic sublethal exposure to waterborne Cu, Cd or Zn in rainbow trout. 1: Iono-regulatory disturbance and metabolic costs. *Aquatic Toxicology*, 50(3): 231 - 243.

3. Almeida, J. A., Diniz, Y. S., Marques, S. F. G., Faine, L. A., Ribas, B. O., Burneiko, R. C. and Novelli, E. L. B. (2002).The use of the oxidative stress responses as biomarkers in Nile tilapia (Oreochromis niloticus) exposed to in vivo cadmium contamination. *Environment International*, 27(8): 673 - 679.
4. Xu, Y. J., Liu, X. Z. and Ma, A. J. (2004).Current research on toxicity effect and molecular mechanism of heavy metals on fish. *Marine Science*, 28(10): 67 - 70.
5. Yilmaz, F., Özdemir, N., Demirak, A. and Tuna, A. L. (2007).Heavy metal levels in two fish species *Leuciscus cephalus* and *Lepomis gibbosus*. *Food Chemistry*, 100(2): 830 - 835.
6. Gratwicke, B. and Speight, M. R. (2005).The relationship between fish species richness, abundance and habitat complexity in a range of shallow tropical marine habitats. *Journal of Fish Biology*, 66(3): 650 - 667.
7. Jarić, I., Višnjić-Jeftić, Z., Cvijanović, G., Gačić, Z., Jovanović, L., Skorić, S., and Lenhardt, M., (2011).Determination of differential heavy metal and trace element accumulation in liver, gills, intestine and muscle of sterlet (Acipenser ruthenus) from the Danube River in Serbia by ICP-OES. *Microchemical Journal*, 98(1): 77 - 81.
8. Burger, J. and Gochfeld, M. (2005).Heavy metals in commercial fish in New Jersey. *Environmental Research*, 99(3): 403 - 412.
9. Chen, Y., Wang, C., and Wang, Z. (2005).Residues and source identification of persistent organic pollutants in farmland soils irrigated by effluents from biological treatment plants. *Environment International*, 31(6): 778 - 783.
10. Batvari, B. P. D., Kamala-Kannan, S., Shanthi, K., Krishnamoorthy, R., Lee, K. J. and Jayaprakash, M., (2008).Heavy metals in two fish species (*Carangoidel malabaricus* and *Belone stronglurus*) from Pulicat Lake, North of Chennai, Southeast Coast of India. *Environmental Monitoring and Assessment*, 145(1-3): 167 - 175.
11. Low, K. H., Zain, S. M., and Abas, M. R. (2012).Evaluation of microwave-assisted digestion condition for the determination of metals in fish samples by inductively coupled plasma mass spectrometry using experimental designs. *International Journal of Environmental Analytical Chemistry*, 92(10): 1161 - 1175.
12. Low, K.H., Zain, S.M., and Abas, M.R., 2011.Evaluation of metal concentrations in red tilapia (*Oreochromis spp*) from three sampling sites in Jelebu, Malaysia using principal component analysis. *Food Analytical Methods*, 4(3): 276 - 285.
13. Dethloff, G. M. S., C. J. (2000).*Condition factor and organo-somatic indices.* U.S. Geological Survey,Information & Technology Report, USGS/BRD-2000-2005.
14. Anno, G. H., Young, R. W., Bloom, R. M. and Mercier, J. R (2003).Pose response relationship for acute ionizing radiation lethality. *Health Physics*, 84: 565 - 575.
15. Fernandes, C., Fontaínhas-Fernandes, A., Cabral, D. and Salgado, M. A. (2008).Heavy metals in water, sediment and tissues of Liza saliens from Esmoriz-Paramos lagoon, Portugal. *Environmental Monitoring and Assessment*, 136(1-3): 267 - 275.
16. Roméo, M., Siau, Y., Sidoumou, Z., and Gnassia-Barelli, M. (1999).Heavy metal distribution in different fish species from the Mauritania coast. *Science of the Total Environment*, 232(3): 169 - 175.
17. Begum, A., Mustafa, A. I., Amin, M. N., Chowdhury, T. R., Quraishi, S. B., and Banu, N. (2013).Levels of heavy metals in tissues of shingi fish (*Heteropneustes fossilis*) from Buriganga River, Bangladesh. *Environmental Monitoring and Assessment*, 185(7): 5461 - 5469.
18. Mormede, S. and Davies, I. M. (2001). Heavy metal concentrations in commercial deep-sea fish from the rockall trough. *Continental Shelf Research*, 21(8-10): 899 - 916.
19. Uysal, K., Köse, E., Bülbül, M., Dönmez, M., Erdoğan, Y., Koyun, M., Ömeroğlu, Ç., and Özmal, F., (2009).The comparison of heavy metal accumulation ratios of some fish species in Enne Dame Lake (Kütahya/Turkey). *Environmental Monitoring and Assessment*, 157(1-4): 355 - 362.
20. Shah, A. Q., Kazi, T. G., Arain, M. B., Jamali, M. K., Afridi, H. I., Jalbani, N., Baig, J. A. and Kandhro, G. A. (2009).Accumulation of arsenic in different fresh water fish species - potential contribution to high arsenic intakes. *Food Chemistry*, 112(2): 520 - 524.
21. Cattell, R. B. (1966).The scree test for the number of factors. *Multivariate Behavioral Research*, 1(2): 245 - 276.
22. Al-Yousuf, M. H., El-Shahawi, M. S. and Al-Ghais, S. M. (2000).Trace metals in liver, skin and muscle of *Lethrinus lentjan* fish species in relation to body length and sex. *Science of the Total Environment*. 256(2-3): 87 - 94.
23. Ministry of Health Malaysia (1995).*Malaysian Food Act 1983 and Food Regulation 1985*. Kuala Lumpur.

Malaysian Journal of Analytical Sciences, Vol 20 No 3 (2016): 525 - 530
DOI: http://dx.doi.org/10.17576/mjas-2016-2003-09

MALAYSIAN JOURNAL OF ANALYTICAL SCIENCES
Published by The Malaysian Analytical Sciences Society
ISSN 1394 - 2506

XYLOOLIGOSACCHARIDES PRODUCTION FROM OIL PALM FROND BY *Trichoderma longibrachiatum* XYLANASE

(Penghasilan Xilooligosakarida daripada Pelepah Kelapa Sawit Menggunakan Xilanase *Trichoderma longibrachiatum*)

Sabiha Hanim Saleh[1]*, Siti Normah Mohd Damanhuri Shah[1], Khalilah Abdul Khalil[2], Aishah Bujang[3]

[1]*School of Chemistry and Environment*
[2]*School of Biology*
[3]*School of Food Science and Technology*
Faculty of Applied Sciences,
Universiti Teknologi MARA, 40450 Shah Alam, Selangor Malaysia

**Corresponding author: sabihahanim@salam.uitm.edu.my*

Received: 24 February 2015; Accepted: 27 October 2015

Abstract

Oil palm fronds containing rich hemicellulose are low cost resources that could be potentially converted into valuable products such as xylooligosaccharides. The main objective of this study was to investigate the production of xylooligosaccharides from OPF hemicelluloses using *Trichoderma longibrachiatum* xylanase. The OPF hemicellulose extracted by alkaline extraction was hydrolysed by xylanase at pH 4.6, temperature 40 °C, hemicellulose substrate concentration 2 % (w/v) and enzyme concentration 2 U/ml for different period of time from 0 to 48 hours to produce xylooligosaccharides. The hydrolysate obtained from enzymatic hydrolysis was further purified through ultrafiltration using 10 kDa molecular weight cut off membranes. The highest total of xylobiose and xylotriose was found to be 21.91 mg/mL and obtained at 8 hours of hydrolysis time. After ultrafiltration step, xylooligosaccharides mixture were obtained in the permeate and retentate. The highest xylobiose (56.64g/100g) and xylotriose (45.80g/100g) were found in retentate and permeate, respectively.

Keywords: xylooligosaccharides, oil palm frond, ultrafiltration, enzymatic hydrolysis, xylanase

Abstrak

Pelepah kelapa sawit yang kaya dengan hemisellulosa adalah sumber kos rendah yang berpotensi untuk ditukarkan kepada produk bernilai seperti xilooligosakarida. Objektif utama kajian ini adalah untuk menyiasat penghasilan xilooligosakarida daripada hemisellulosa pelepah kelapa sawit menggunakan enzim xilanase *Trichoderma longibrachiatum*. Hemisellulosa yang diekstrak daripada pelepah kelapa sawit menggunakan alkali, dihidrolisis menggunakan enzim xilanase pada pH 4.6, suhu 40 °C, kepekatan hemiselulose 2 % (w/v) dan kepekatan enzim 2U/ml umtuk tempoh masa berbeza dari 0 hingga 48 jam untuk menghasilkan xilooligosakarida. Hidrolisat yang diperoleh daripada hidrolisis enzimatik kemudiannya ditulenkan melalui ultrafiltrasi menggunakan membran yang berat molekulnya 10 kDa. Jumlah tertinggi xilobios dan xilotrios adalah 21.91 mg/mL yang diperoleh pada masa hidrolisis 8 jam. Setelah ultrafiltrasi, campuran xilooligosakarida diperoleh dalam 'permeate' dan 'retentate'. Kandungan tertinggi xilobios (56.64g/100g) dan xilotrios (45.80g/100g) ditemui di dalam 'retentate' dan 'permeate'.

Kata kunci: xilooligosakarida, pelepah kelapa sawit, ultrafiltrasi, hidrolisis enzimatik, xilanase

Introduction

Oil palm fronds (OPF) generated the most of waste among the other biomass with 54.17 million tons and 54.24 million tons from oil palm industry in Malaysia for year 2010 and 2011, respectively [1]. The OPF is available daily throughout the year when the palms are pruned during the harvesting of bunches of fresh fruit. It is composed of hemicelluloses, cellulose and lignin. Hemicellulose extracted by alkaline extraction can be used as starting material for xylooligosaccharides (XOs) production. XOs are sugar oligomers made up of xylose unit. XOs can be used as ingredients of functional foods, cosmetics, pharmaceuticals or agricultural products [2]

Enzymatic method is more preferable to produce XOs compared to other methods, because it does not produce undesirable component or high amount of monomers and does not require special equipment [3]. Enzymatic production of xylooligosaccharides performed by xylanase having high endoxylanase and low β-xylosidase activity besides present of others side group enzyme removal include α-arabinofuranosidases, acetylxylan esterase, and α-glucuronidase [4]. Membrane separations, such as ultrafiltration and nanofiltration have been shown to be very promising methods for refining and concentrating several oligosaccharides [3]. Membrane technologies have been applied successfully in conjugation with enzymatic hydrolysis following steam hydrolysis for processing XOs.

Previous study used *Trichoderme viride* xylanase to produce XOs from OPF. However the result showed that the yield of XOs was only 25.64% [5]. Since there is also no purification step was performed in the previous study, thus in the present work, xylanase from *Trichoderma longibrachiatum* was used for enzymatic hydrolysis due to a few reports on their ability to produce high yield of XOs [6-8] following by ultrafiltration step. Therefore, the main objective of this study was to investigate the production of XOs mixture from alkaline extracted oil palm fronds hemicellulose using *Trichoderma longibrachiatum* and ultrafiltration.

Materials and Methods

Raw material

Oil palm frond (OPF) samples used in this study were obtained from local farmers in Perak, Malaysia. The samples were chipped, ground and sieved into fibers with width and length of 0.5 mm and 3 to 8 mm, respectively, and then stored at room temperature prior to use. All chemicals used were of analytical grade unless otherwise stated.

Hemicellulose extraction

Hemicellulose extraction from OPF was conducted according to the method reported by Anis [9] with some modifications. An amount of 50 g sample of oil palm frond chips were soaked in 3 M potassium hydroxide (KOH) with the solid to liquid ratio of 1:10, stirred at 40 °C and 400 rpm with mechanical heat stirrer (HS-30D, WiseStir) for 4 hours. Then, the crude hemicellulose was filtered. The filtrate was acidified with 50 % (v/v) acetic acid to pH 4.8 ± 0.1 and allowed to stand for 24 hours at 4 °C. The extracts were centrifuged (Centrifuged 5702, Eppendorf) at 3500 rpm for 15 min and filtered. The precipitate was washed with 50 mL of 95 % (v/v) ethanol to eliminate acid residue from the sample before dried in an oven (UFB 500, Memmert) at 40 °C for 4 hours. The supernatant was then added with four volumes of 95 % ethanol and was kept for overnight. Hemicellulose in the form of pellet was obtained from precipitate after centrifuged, while the supernatant was discarded. Finally, the pellet was dried in the oven and used as a hemicellulose source.

Enzymatic hydrolysis

A volume of 1 mL of 2 U/mL of xylanase from *T. longibrachiatum* (Sigma, USA) was added to 10 mL of 2 % (w/v) alkaline extracted hemicellulose solution from OPF in 0.05 M citrate buffer at pH 4.6. The mixture was incubated at 40 °C with mild shaking in an incubator shaker (IKA® KS 4000i Control, China). Enzymatic hydrolysis was carried out at pH 4.6, temperature 40 °C, hemicellulose concentration 2 % (w/v) and enzyme concentration 2 U/ml. This hydrolysis was conducted from 0 to 48 hours. Periodically, samples were taken out and the enzymatic reaction was stopped by boiling for 5 min before the samples were subjected to analyses. The hydrolysate obtained at optimal time was further used for purification step using ultrafiltration [10]. XOs contents were determined using HPLC.

Purification of hydrolysate using Ultrafiltration

Purification process was carried out using an Amicon Stirred Ultrafiltration Cell, Model 8400 (Millipore-Amicon, Bedford, MA) pressurized by nitrogen gas. A volume of 50 mL of hydrolysate obtained from hemicellulose

hydrolysis was passed through the ultrafiltration system with 10 kDa molecular weight cut off (MWCO) membrane. The operating condition allowed membrane operating pressure 55 psi at room temperature. The filtration was stopped when approximately 40 mL of permeate was collected. The total sugar in retentate and permeate after ultrafiltration process was determined by phenol/sulfuric acid method. The XOs content was determined by HPLC.

Total sugar analysis

Total sugar content in hydrolysate was measured by using the phenol-sulfuric acid method [11]. An amount of 1 mL of 5 % (w/v) phenol solution and 5 mL of 98 % concentrated sulfuric acid were added to 1 mL of hydrolysate. The mixture was mixed well and kept at room temperature for 10 minutes for color development before being cooled in the water bath (Memmert, Germany) at 25 °C for 20 minutes. The absorbance was measured at wavelength 480 nm by UV spectrophotometer (Perkin Elmer Precise, 35 Lambda, USA). The amount of total sugar was expressed as mg/mL alkaline extracted hemicellulose (pellet).

Monosaccharides determination by HPLC

The content of monosaccharides in the XOs-containing liquor from ultrafiltration process was determined by HPLC (Agilent Technologies 1200 Series, Germany) using Aminex HPX 87P column (300 mm x 7.8 mm). The HPLC was equipped with a refractive index detector (G 1362A, Agilent Technologies 1200 Series, Germany) and column oven (Agilent Technologies 1200 Series, Germany). The sample was filtered through a 0.20 µm nylon syringe filter (Minisart, Sartorius AG, Germany) prior to direct injection into HPLC. The sample was eluted using deionised water as the mobile phase at column temperature of 80 °C and a flow rate of 0.5 mL/min.

Xylooligosaccharides determination by HPLC

XOs were analyzed by HPLC (Agilent Technologies 1200 Series, Germany) equipped with a refractive index detector (G 1362A, Agilent Technologies 1200 Series, Germany), and column oven (Agilent Technologies 1200 Series, Germany). A volume of 2 mL of hydrolysate obtaining from ultrafiltration was filtered through a 0.20 µm nylon syringe filter (Minisart, Sartorius AG, Germany). A 20 µL volume of the filtered sample was injected into HPLC. The sample was eluted using deionised water as the mobile phase. The BioRad-Aminex HPX 42A column (300 mm x 7.8 mm) was used at 80 °C and a flow rate of 0.5 mL/min. Concentration of XOs was measured using an average peak areas compared to the mixture of XOs standards and expressed as mg/mL XOs. Standard calibration curve was plotted based on peak areas against concentration of XOs standards.

Results and Discussion

Monosaccharides Composition of Hemicellulose

The monosaccharide compositions of OPF hemicellulose were xylose, arabinose and glucose. Xylose was the major component with 46.67 % (w/w) found in the OPF hemicellulose indicating the existence of xylan as the main polysaccharides [12], followed by a small amount of arabinose and glucose with 11.01 % (w/w) and 9.01 % (w/w), respectively. Xylose probably originated from the backbone of the hemicellulose [13], while arabinose and glucose came from the side chain [14]. This result is in accordance with the finding reported by Fazilah et al. [15] using similar raw materials.

Enzymatic hydrolysis of OPF

Table 1 shows the enzymatic hydrolysis of OPF for a period of time from 0 to 48 hours using 2 U/mL xylanase concentrations with 2 % (w/v) OPF hemicellulose substrate at pH 4.6 and 40 °C. HPLC analysis indicated that OPF hemicellulose is hydrolysed to xylose and a variety of XOs fractions, which are xylobiose, xylotriose, xylotetraose, xylopentaose and xylohexaose.

During the initial 2 hours, the concentration of xylobiose decreased as much as to 42 % from 7.24 ± 0.44 mg/mL to 4.19 ± 0.06 mg/mL, and the concentration of xylotriose decreased slightly from 8.93 ± 0.16 mg/mL to 8.32 ± 0.47 mg/mL, which corresponds to 7 %. However, the concentration of xylobiose and xylotriose increased rapidly at 8 hours. The highest total of xylobiose and xylotriose was 21.91 mg/mL at hydrolysis time of 8 hours. Further increase in the time from 8 to 24 hours significantly decrease ($p < 0.05$) the xylobiose and xylotriose concentrations.

In the present study, XOs in the range of xylobiose to xylohexaose except xylotetraose were produced by *Trichoderma longibrachiatum* xylanase in all hydrolysis time. This result was in accordance with the study reported by Akpinar et al. [3] for the production of XOs from cotton stalk using *Aspergillus niger* xylanase. The absence of xylotetraose in all hydrolysis time was due to its immediate hydrolysis into smaller oligosaccharides once it was produced. The concentration of xylopentaose increased from 0 to 2 hours, whereas the concentration of xylohexaose increased from 0 to 8 hours. Further increase the hydrolysis time from 8 to 24 hours did not significantly increase the xylopentaose and xylohexaose.

Table 1. Concentration of Xylose and XOs at different time of hydrolysis

Sugars (mg/mL)	**Hydrolysis Time (hour)**				
	0	**2**	**8**	**24**	**48**
Xylose	0.04 ± 0.01^{a}	1.74 ± 0.05^{b}	8.46 ± 0.32^{c}	17.78 ± 0.90^{d}	23.79 ± 0.33^{e}
Xylobiose	7.24 ± 0.44^{c}	4.19 ± 0.06^{b}	9.70 ± 0.04^{d}	3.25 ± 0.59^{a}	3.77 ± 0.42^{b}
Xylotriose	8.93 ± 0.16^{c}	8.32 ± 0.47^{bc}	12.21 ± 0.59^{d}	0.86 ± 0.67^{a}	7.19 ± 1.12^{b}
Xylotetraose	n.d	n.d	n.d	n.d	n.d
Xylopentaose	3.69 ± 0.13^{a}	9.31 ± 0.11^{c}	6.45 ± 0.51^{b}	5.98 ± 0.25^{b}	5.96 ± 0.11^{b}
Xylohexaose	3.85 ± 0.03^{a}	3.02 ± 0.45^{a}	7.05 ± 0.09^{b}	7.18 ± 0.49^{b}	6.90 ± 0.15^{b}
Xylobiose + Xylotriose (Total)	16.17	12.51	21.91	4.11	10.96

Results are presented as means ± standard deviation (n=3), Mean values followed by different superscript letters in a row are significantly different ($p < 0.05$), n.d: not detected.

Table 1 also shows that extending the reaction time to 48 hours did not significantly increase the production of XOs, but instead produced high amount of xylose. The amount of xylose increased drastically after 2 hours. These results were corroborated with the yield of the XOs, which decreased after 8 hours due to a small amount of XOs was hydrolysed into monosaccharides, thus could also inhibit the production of XOs [16]. The concentration of xylose also increased drastically when the reaction time increased. The concentration of Xylose rose up to 23.79 mg/mL when hydrolysis time increased to 48 hours. The result showed that increasing hydrolysis time resulted in higher xylose production.

Purification of OPF XOs by Ultrafiltration

It can be seen that the composition of permeate with molecular weight of 10 kDa MWCO membrane exhibited higher content of xylotriose , followed by xylopentaose, xylohexaose and xylobiose (Table 2) . The xylobiose composition in the initial feed decreased from 27.40 g/100 g to 10.64 g/100 g, whereas xylotriose composition increased from 34.47 g/100 g to 45.80 g/100 g when passing through 10 kDa MWCO membrane. It was found that xylobiose was decreased by 61%, while xylotriose was increased by 33% in the permeate. In addition, xylopentaose and xylohexaose composition in the permeate increased slightly from initial feed with 22 % and 7 %, respectively.

Both xylopentaose and xylohexaose composition decrease in the retentate by 33 % and 38 %, respectively. Other than that, xylobiose composition in the retentate increased significantly ($p < 0.05$) from 27.40 g/100 g to 56.64 g/100 g. This result showed that the composition of xylobiose in the retentate was higher compared to in permeate. However, xylotriose decrease significantly ($p < 0.05$) from 34.47 g/100 g to 18.73 g/100 g in the retentate. The initial feed containing XOs was fractionated with 10 kDa MWCO membrane, clearly showed that the permeate

fraction containing XOs ranging from xylobiose to xylohexaose. In contrast, the retentate fraction containing XOs is ranging from xylobiose to xylohexaose. However, Akpinar et al. [3] found that ultrafiltration with 10 kDa MWCO membrane successfully retained mainly high molecular weight oligosaccharides in the retentate. The presence of low molecular weight oligosaccharides in retentate may be due to fouling mechanism. Fouling mechanism caused by blocking of pore in high cut-off membrane by big molecules, so that transportation of small molecules was hindered. Membrane selection is also very important in order to reduce fouling problem [17].

Table 2. Total sugar concentration and composition of permeate and retentate at 8 hours of hydrolysis.

XOs	**Initial feed amount (Total sugar, mg/ml)**	**Composition of feed (g/100g)**	**Composition of permeate of MWCO 10 kDa membrane (g/100g)**	**Composition of retentate of MWCO 10 kDa membrane (g/100g)**
Total	35.42	100.00	100.00	100.00
Xylobiose	9.70±0.04	27.40^{b}	10.64^{a}	56.64^{c}
Xylotriose	12.21±0.59	34.47^{b}	45.80^{c}	18.73^{a}
Xylotetraose	0.00	0.00	0.00	0.00
Xylopentaose	6.45±0.51	18.22^{b}	22.23^{c}	12.25^{a}
Xylohexaose	7.05±0.09	19.92^{b}	21.33^{c}	12.38^{a}

Mean ± standard deviation of at least duplicate determinations. Mean values followed by different superscript letters in a row are significantly different ($p < 0.05$).

Conclusion

The highest total of xylobiose and xylotriose was found to be 21.91 mg/mL and obtained at 8 hours of hydrolysis time. After ultrafiltration step, mostly xylooligosaccharides mixture were obtained in the permeate and retentate. The highest xylobiose (56.64 g/100 g) and xylotriose (45.80 g/100 g) were found in retentate and permeate respectively.

Acknowledgement

The authors are grateful to the Ministry of Education Malaysia, Research Management Institute (RMI), Universiti Teknologi MARA for the financial support under the Exploratory Research Grant Scheme (ERGS):600-RMI/ERGS 5/3 (8/2012) and Faculty of Pharmacy, UiTM Puncak Alam for using HPLC equipment.

References

1. Ofori-Boateng, C. and Lee, K.T. (2013). Response surface optimization of ultrasonic-assisted extraction of carotenoids from oil palm (*Elaeis guineensis* Jacq.) fronds. *Food Science and Nutrition*, 1 (3): 209 – 221.
2. Vázquez, M. J., Alonso, J. L., Domínguez, H. and Parajó, P. C. (2000). Xylooligosaccharides: manufacture and application. *Trends in Food Science and Technology*, 11: 387 – 393.
3. Akpinar, O., Ak, O., Kavas, A., Bakir, U. and Yilmaz, L. (2007). Enzymatic production of xylooligosaccharides from cotton stalks. *Journal of Agricultural and Food Chemistry*, 55: 5544 – 5551.
4. Carvalho, A. F. A., Neto, P. O., Silva, D. F. and Pastore, G. M. (2013). Xylooligosaccharides from lignocellulosic materials: Chemical structure, health benefits and production by chemical and enzymatic hydrolysis. *Food Research International*, 51: 75 - 85.

5. Sabiha-Hanim, S., Nor, M. A. M. and Rosma, A. (2011). Effect of autohydrolysis and enzymatic treatment on oil palm (*Elaeis guineensis* Jacq.) frond fibres for xylose and xylooligosaccharides production. *Bioresource Technology*, 102: 1234 – 1239.
6. Royer, J. C. and Nakas, J. P. (1991). Purification and characterization of two xylanases from *Trichoderma longibrachiatum*. *European Journal of Biochemistry*, 202: 521 – 529.
7. Chen, C. S., Chen, J. L. and Lin, T. Y. (1997). Purification and characterization of a xylanase from *Trichoderma longibrachiatum* for xylooligosaccharide production. *Enzyme and Microbial Technology*, 21: 91 – 96.
8. Akpinar, O. and Bostanci, S. (2009). Xylooligosaccharide production from lignocellulosic wastes with *Trichoderma longibrachiatum* xylanase. *Journal of Food, Agriculture & Environment*, 7 (1): 70 – 74.
9. Anis. M. (2000). Extraction and functional properties of oil palm biomass. Doctoral dissertation, Universiti Sains Malaysia, Penang, Malaysia
10. Akpinar, O., Erdogan, K. and Bostanci, S. (2009). Enzymatic production of xylooligosaccharides from selected agricultural wastes. *Food and Bioproducts Processing*, 87: 145 – 151
11. Dubois, M., Gillies, K. A., Hamilton, J. K., Rebers, P. A. and Smith, F. (1956). Colorimetric method for determination of sugars and related substances. *Analytical Chemistry*, 28(3): 350 – 357.
12. Ruiz, H. A., Cerquira, M. A., Silva, H. D., Rodríguez-Jasso, R. M., Vicente, A. A. and Teixeira, J. A. (2013). Biorefinery volarization of autohydrolysis wheat straw hemicellulose to be applied in a polymer-blend film. *Carbohydrate Polymers*, 92: 2154 – 2162.
13. Luo, Q., Peng, H., Zhou, M., Lin, D., Ruan, R., & Wan, Y., Zhang, J. and Liu Y. (2012). Alkali extraction and physicochemical characterization of hemicelluloses from young bamboo (*Phyllostachys pubescens* mazel). *Bioresources*, 7(4): 5817 – 5828.
14. Bian, J., Peng, F., Peng, P., Xu, F. and Sun, R-C. (2010). Isolation and fractionation of hemicelluloses by graded ethanol precipitation from *Caragana korshinskii*. *Carbohydrate Research*, 345*:* 802 – 809.
15. Fazilah, A., Azemi, M. N. M., Karim, A. A., and Norakma, M. N. (2009*).* Physicochemical properties of hydrothermally treated hemicellulose from oil palm frond. *Journal of Agricultural and Food Chemistry*, 57: 1527 – 1531.
16. Akpinar, O., Gunay, K., Yilmaz, Y., levent, O. and Bostanci, S. (2010). Enzymatic process and antioxidant activity of agricultural waste autohydrolysis liquors. *Bioresources*, 5(2): 699 – 711.
17. Gullón, P., González-Muñoz, M. J., Domínguez, H. and Parajó, J. C. (2008). Membrane processing of liquors from *Eucalyptus globulus* autohydrolysis. *Journal of Food Engineering*, 87: 257 – 265.

Malaysian Journal of Analytical Sciences, Vol 20 No 3 (2016): 531 - 538
DOI: http://dx.doi.org/10.17576/mjas-2016-2003-10

MALAYSIAN JOURNAL OF ANALYTICAL SCIENCES
Published by The Malaysian Analytical Sciences Society
ISSN 1394 - 2506

INFLUENCE OF CHROMIUM ON THE REDUCTION BEHAVIOR OF FERRIC OXIDE BY USING CARBON MONOXIDE: TEMPERATURE PROGRAMMED REDUCTION AND KINETIC STUDIES

(Pengaruh Kromium Terhadap Kelakuan Penurunan Ferik Oksida dengan Menggunakan Karbon Monoksida: Kajian Penurunan Suhu Berprogram dan Kinetik)

Tengku Shafazila Tengku Saharuddin[1]*, Alinda Samsuri[1,2], Fairous Salleh[1], Mohammad Bin Kassim[1], Rizafizah Othaman[1], Mohamed Wahab Mohamed Hisham[1], Mohd Ambar Yarmo[1]

[1]*School of Chemical Science and Food Technology, Faculty of Science and Technology*
Universiti Kebangsaan Malaysia, 43600 UKM Bangi, Selangor, Malaysia
[2]*Centre for Defence Foundation Studies,*
Universiti Pertahanan Nasional Malaysia, Kem Sungai Besi, 57000 Kuala Lumpur, Malaysia

**Corresponding author: tengkushafazila@gmail.com*

Received: 24 February 2015; Accepted: 27 October 2015

Abstract

This study was undertaken to investigate the effect of chromium on the reduction behaviour of ferric oxide with carbon monoxide (10 %, v/v) in nitrogen as a reductant. Ferric oxide was impregnated with 3 % chromium to produce chromium-doped ferric oxide (Cr-Fe_2O_3). The reduction behaviour and the kinetic studies of Cr-Fe_2O_3 and Fe_2O_3 have been studied by temperature programmed reduction (TPR) and the phases formed of partially and completely reduced samples were characterized by X-ray diffraction spectroscopy (XRD). Meanwhile, the activation energy values were calculated from the Arrhenius equation using Wimmer's method. TPR results indicate that the reduction of Cr-Fe_2O_3 proceeded in two reduction steps ($Fe_2O_3 \rightarrow Fe_3O_4 \rightarrow Fe$), while, Fe_2O_3 proceeded in three reduction steps ($Fe_2O_3 \rightarrow Fe_3O_4 \rightarrow FeO \rightarrow Fe$) with doped ferric oxide showed a large shifted towards lower temperature. The complete reduction of ferric oxide to metallic Fe occur at 700 °C compared to the undoped ferric oxide (900 °C). The XRD pattern showed that the diffraction peaks of Cr-Fe_2O_3 are more intense compare to Fe_2O_3, indicating that the improvement on the crystallinity of the characteristic peaks of Fe_2O_3 with no additional peak observed meaning that the chromium particles loaded on the ferric oxide were well dispersed. Furthermore, additional of 3 % chromium on ferric oxide gives larger surface area and decrease in the activation energy up to 12.39 % regarding to transition phases of $Fe_2O_3 \rightarrow Fe_3O_4$ during the reduction process may also led to the increase in the rates of ferric oxide reduction.

Keywords: temperature programmed reduction, kinetic, reduction, ferric oxide, chromium, carbon monoxide

Abstrak

Kajian ini dijalankan untuk melihat pengaruh kromium pada kelakuan penurunan ferik oksida di mana karbon monoksida (10%, v/v) di dalam nitrogen digunakan sebagai agen penurunan. Serbuk ferik oksida yang didopkan pada kromium (Cr-Fe_2O_3) disintesis menggunakan kaedah impregnat. Kelakuan penurunan dan kinetik oleh Cr-Fe_2O_3 and Fe_2O_3 dikaji menggunakan teknik suhu penurunan berprogram (TPR) dan fasa - fasa yang terbentuk bagi separa dan penurunan penuh dicirikan menggunakan teknik pembelauan sinar X (XRD) sementara nilai - nilai tenaga pengaktifan dikira daripada persamaan Arrhenius dan kaedah Wimmer. Profil TPR menunjukkan bahawa penurunan ferik oksida yang didopkan kromium melalui dua langkah tindak balas penurunan ($Fe_2O_3 \rightarrow Fe_3O_4 \rightarrow Fe$) manakala ferik oksida yang tidak didopkan melalui tiga langkah tindak balas penurunan ($Fe_2O_3 \rightarrow Fe_3O_4 \rightarrow FeO \rightarrow Fe$). Suhu proses penurunan tamat beranjak kepada suhu yang lebih rendah iaitu 700 °C dan proses penurunan tamat pada suhu (900 °C). Difraktogram XRD terhadap Cr-Fe_2O_3 menunjukkan peningkatan pada kehabluran puncak Fe_2O_3 berbanding ferik oksida yang tidak didopkan dengan tiada puncak tambahan diperhatikan dimana ia

menjelaskan bahawa zarah kromium yang dimuatkan pada ferik oksida telah tersebar dengan baik. Di samping itu, tambahan sebanyak 3 % kromium pada ferik oksida memberikan kawasan permukaan yang lebih besar dan pengurangan tenaga pengaktifan sehingga 12.39 % bagi peralihan fasa $Fe_2O_3 \rightarrow Fe_3O_4$ serta juga membawa kepada peningkatan kepada kadar proses penurunan ferik oksida tersebut.

Kata kunci: penurunan suhu berprogram, kinetik, penurunan, ferik oksida, kromium, karbon monoksida

Introduction

Reduction of ferric oxide was a subject of numerous studies due to the importance of iron and steel in the current and future technologies [1]. The iron and ferric oxide are nontoxic and cheap materials give them as an important chosen material in the catalysis field [2, 3]. As a catalyst, the reduction behaviour and the degree of reduction of the iron species were highly important in such catalysis and previous studies, reaction temperature of ferric oxide reduction was determined using thermodynamics [4, 5] and experimental [1, 6]. The reduction process of Fe_2O_3 involves different mechanism depending on temperature, particle size, concentration reduction gas used and additives to the Fe_2O_3 [7-9]. Reduction by carbon monoxide generally involves two-steps reduction can be described as equation 1 and 2 follows [7-9]:

$$3Fe_2O_3 + CO \rightarrow 2Fe_3O_4 + CO_2 \qquad \Delta H_r = -47.2\ kJmol^{-1} \qquad (1)$$

$$Fe_3O_4 + 4CO \rightarrow Fe + 4CO_2 \qquad \Delta H_r = -13.6\ kJmol^{-1} \qquad (2)$$

Meanwhile three steps reduction is additional of another two subsequent steps from the final process of Fe_3O_4 directly reduce to metallic iron (equation 3 and 4) as describe below:

$$Fe_3O_4 + CO \rightarrow 3FeO + CO_2 \qquad \Delta H = 19.4\ kJmol^{-1} \qquad (3)$$

$$FeO + CO \rightarrow Fe + CO_2 \qquad \Delta H = -11.5\ kJmol^{-1} \qquad (4)$$

Briefly, equations (1) and (2) are responsible for the two-step reduction and whereas a sequence of equations (1), (3) and (4) represents the three-step reduction. Furthermore, the thermodynamic calculations based on the Gibbs free energy change due to reaction and the equilibrium composition of the oxides for the equations above indicate that equation (1), (3) and (4) are spontaneous with ΔG between -102.3 to +9.61 $kJmol^{-1}$ at temperature 300 °C to 900 °C. While, the reduction process for equation (2) is thermodynamically more favourable at rather lower temperatures (below 500 ^{0}C, ΔG<+20 $kJmol^{-1}$). In addition, chromium as an additive to the ferric oxide has been explored widely for their improved catalytic activity due to the unique performance to the role of chromium in stabilizing the ferric oxide against sintering. To enhance the reduction performance of ferric oxide, the addition of other metal additives was considered. In this study we report the reduction behavior of the addition of chromium species into ferric oxides catalyst. The temperature programme reduction was performed to investigate the non-isothermal reduction behaviour of Cr doped ferric oxide by comparing to none doped species. Moreover, the kinetic studies were also carried out to calculate the activation energy of the reduction process using different heating rate.

Materials and Methods

Chemicals and raw materials

Iron (III) oxide (99%) was obtained from Sigma Aldrich Chemical Company and chromium (III) nitrate from R&M Chemicals. Gas mixture CO/N_2 (10% CO) was obtained from Linde.

Catalyst preparation

The Cr doped ferric oxide was prepared by impregnating Fe_2O_3 powder with aqueous solution containing chromium cation additives. The amount of chromium added was adjust to be 3 wt% in Fe_2O_3. The Fe_2O_3 powder was directly impregnated into 50 ml distilled water corresponding metal cation additives in the above proportion and stirred vigorously for 2 hours at room temperature. The impregnated sample was dried at 110 °C overnight and subsequently calcined at 600 °C in the furnace for 3 hours.

Characterization studies

Temperature programmed reduction (TPR) measurements was conducted using a Micromeritic Autochem 2920 Chemisorption Analyzer apparatus; a feed of 10 % CO in N_2 at a flow rate of 20 mL min^{-1} (Standard Temperature and Pressure, STP) was used as reducing gas. An amount 50 mg of samples were heated up to 900 °C, at a rate of 10 °C min^{-1}. For the kinetic study, different heating rate (10, 13, 15 °C min^{-1}) were applied to the samples. The reduction kinetics of doped ferric oxides is an essential point that deserves investigation. There are numerous models in the literature for the estimation of the kinetic parameters and in this study Wimmers's method [11] was chosen and it describes the correlation between shifts in T_{max} with the heating rate. In this method, the activation energy can be calculated from TPR data by using equation (5) below:

$$\ln (\Psi/T_{max}) = -E_a/RT_{max} + \ln (AR/E_a) + C \quad (5)$$

The activation energy is achieved from the shift of rate maximum temperature (T_{max}) against the heating rate (Ψ). If a straight line graph is obtained from the plot of ln (Ψ/T_{max}) versus 1/ (T_{max}), the slop is E_a/R which R is the gas constant. To investigate the role of Cr in the reduction behaviour of Fe_2O_3, the samples were collected and XRD patterns were measured. Samples were collected according to the TPR pattern when the reduction of Cr-Fe_2O_3 is assumed to be finished at 700 °C. Meanwhile, undoped Fe_2O_3 was also collected at 700 °C for the comparison purposes. The carbon monoxide consumption was monitored using a thermal conductivity detector (TCD). Phase characterization was carried out by X-ray diffraction (XRD) Bruker AXS D8 Advance type with X-ray radiation source of Cu Kα (40 kV, 40 mA) to record the 2θ diffraction angle from 10 – 80 degree at wavelength (λ = 0.154 nm). For identification purposes of crystalline phase composition, diffraction patterns obtained were matched with Joint Committee on Powder Diffraction Standards (JCPDS) files. Physical surface analysis (Brunauer–Emmett–Teller, BET) of nitrogen adsorption at 77 K (liquid nitrogen) was conducted using a Micromeritics ASAP 2010 instrument to obtain the adsorption isotherm of each sample. The calcined sample of Cr-Fe_2O_3 and Fe_2O_3 were degassed at 350 °C for 6 h before the BET surface area analyses were done. The Brunauer–Emmett–Teller (BET) surface area were calculated from the isotherms.

Results and Discussion

Isotherm adsorption of N_2

The result indicates that the impregnation of Fe_2O_3 with chromium nitrate (5.90 m^2/g) shows the BET surface area was a little larger than undoped Fe_2O_3 (4.67 m^2/g) manifesting that Cr could also prevent the aggregation of particles. Moreover, Hu et al. [11] mentioned that specific surface area was also an important factor as higher specific surface area usually results in more unsaturated surface coordination sites exposed to the gas which may result in the increasing of the reducibility performance of the ferric oxide in this study.

Crystallinity effect by XRD

Figure 1 shows the XRD patterns of Cr-Fe_2O_3 and undoped Fe_2O_3 before reduction in CO in nitrogen (10%, v/v). The XRD patterns obtained for both sample are identical to the Fe_2O_3 phase (ferric oxide, JCPDS 74-6271). The 2θ Fe_2O_3 main peaks reveal the presence of contribution at about 24.2, 33.2, 35.7, 40.9, 49.5, 53.5, 57.2, 62.4, 64.2, 72.4 and 75.7 °. The diffraction peaks were shifted to higher 2θ positions which is mainly due to the interference of the Cr element changed the lattice constant of the Fe_2O_3. This can be attributed to the small atomic radius of Fe (0.126 nm) compared to those of Cr (0.128 nm) that gave changed to the lattice parameters and lattice spacing. Furthermore, the diffraction peaks of freshly prepared Cr-Fe_2O_3 showed an improvement in the crystallinity of the characteristic peaks of Fe_2O_3 when loaded with Cr. Furthermore, no additional peak observed in the XRD patterns showing that the chromium particles loaded on the ferric oxide were well dispersed.

From the observation in Figure 2, Cr-Fe_2O_3 gives only metallic Fe diffraction peaks (iron, JCPDS 65-4899) at 700 ^{0}C, while undoped Fe_2O_3 still consist of the remaining crystalline phases of Fe_3O_4 (3,1,1), Fe_3O_4 (4,4,0) (magnetite, JCPDS 71-6336) and crystallite phases of FeO (1,1,1) and FeO (2,2,0) (wustite, JCPDS 80-0686). Fe_2O_3 showed a complete reduction to metallic Fe when the reduction temperature reached 900 ^{0}C. To further investigate the mechanism involved in the reduction process of Cr-Fe_2O_3 and undoped Fe_2O_3, samples were collected at various temperatures (400, 500, 600 and 700 ^{0}C) and detailed characterization using XRD were shown in Figure 3 and Figure 4, respectively. At temperature 400 ^{0}C and 500 ^{0}C the XRD patterns show strong diffraction peaks of

magnetite and a growth of metallic iron phases. By increasing the reduction temperature to 600 ^{0}C, undoped Fe_2O_3 started to display a formation of metastable FeO with crystallite phases of FeO (1,1,1), (2,0,0), (2,2,0), (3,1,1) and (2,2,2) (wustite, JCPDS 80-0686). The reduction of Fe_3O_4 to FeO proceeded at higher temperature >570 ^{0}C while FeO was also reduced to Fe, simultaneously (Fig.4). For Cr-Fe_2O_3, FeO was not detected in the XRD patterns for the whole reduction process as the addition of chromium inhibits FeO phases to occur. This indicated that the formation of metastable FeO phase was not only affected by the reduction temperature but also depended on the nature of the sample itself, which in this case the involvement of chromium element in the structure of ferric oxide enhance it reducibility.

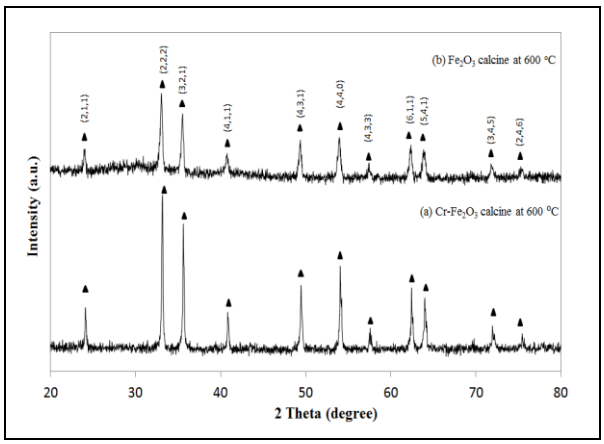


Figure 1. XRD diffractogram of (a) Cr-Fe_2O_3 calcined at 600 ^{0}C, and (b) fresh Fe_2O_3 calcined at 600 ^{0}C. (▲) Fe_2O_3

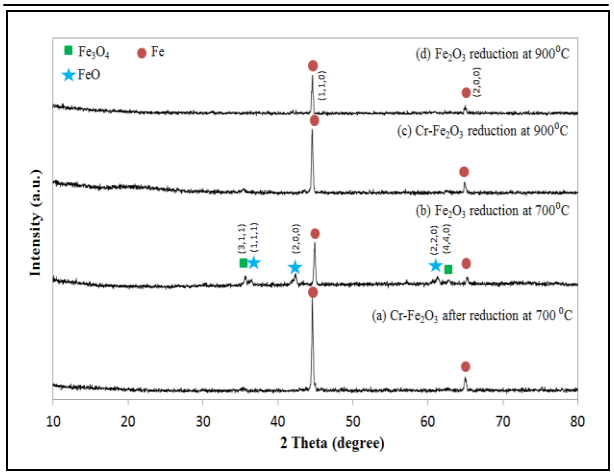


Figure 2. XRD diffractogram of (a) Cr-Fe_2O_3 and (b) Fe_2O_3 after reduction by CO at 700 ^{0}, (c) Cr-Fe_2O_3 and (d) Fe_2O_3 after reduction by CO at 900 ^{0}C. (■) Fe3O4, (★) FeO and (●) metallic Fe

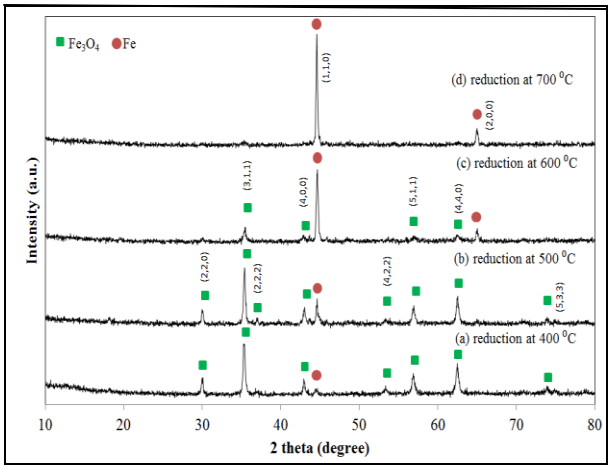


Figure 3. XRD diffractogram of Cr-Fe_2O_3 after reduction by CO at 400 ^{0}C, 500 ^{0}C, 600 ^{0}C, 700 ^{0}C. (■) Fe_3O_4 and (●) metallic Fe

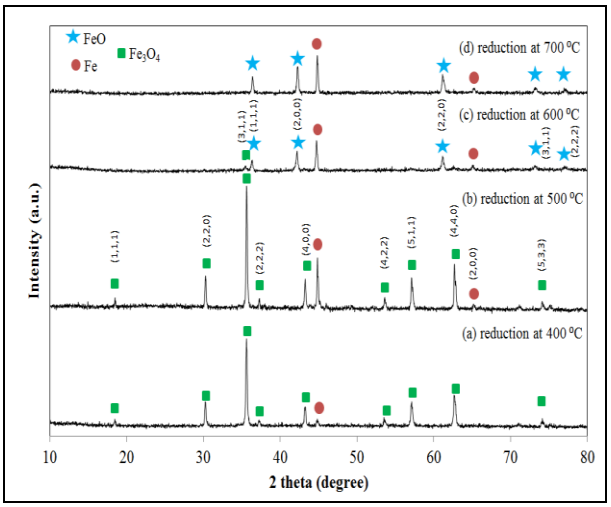


Figure 4. XRD diffractogram of Fe_2O_3 after reduction by CO at 400 ^{0}C, 500 ^{0}C, 600 ^{0}C, 700 ^{0}C. (■) Fe_3O_4, (★) FeO and (●) metallic Fe

Chemical properties by TPR analysis

The TPR patterns for non-isothermal reduction of Cr-Fe_2O_3 and undoped Fe_2O_3 by CO in nitrogen (10 %, v/v) is shown in Figure 5. The TPR profiles of undoped Fe_2O_3 represented 3 reduction events (denoted I, II and III) which event I represent to peak displayed at lower temperature exhibited the reduction of $Fe_2O_3 \rightarrow Fe_3O_4$. Meanwhile, the second peak (event II) was related to the reduction of $Fe_3O_4 \rightarrow$ FeO and the last peak (event III) was attributed to the reduction of FeO to metallic Fe. Three reduction events of Fe_2O_3 reflected by 3 peaks around 361 °C (I), 509 °C (II) and 807 °C (III) as display in Figure 5., showing three-steps reduction route of Fe_2O_3 to Fe through Fe_3O_4 and FeO as an intermediate and for Cr-Fe_2O_3, the temperature for the peak obtained for event I is 353 °C and for higher temperature, the peaks were observed overlaping to each other with a shoulder at 507 °C and a peak at 591 °C. The higher temperature shoulder of Cr-Fe_2O_3 may refer to the Fe_3O_4 to complete the reduction process by forming a better crystallite of Fe_3O_4 as indicated in the XRD results and another peak may refer to further reduction of Fe_3O_4 to metallic Fe. The absence of FeO throughout the reduction process of Cr-Fe_2O_3 attributed to two-steps of

reduction ($Fe_2O_3 \rightarrow Fe_3O_4 \rightarrow$ metallic Fe). Furthermore, the addition of Cr to ferric oxide enhance the reducibility of the ferric oxide to metallic Fe by shifted the peaks to lower temperature and completed at 700 ^{0}C which was lower than undoped Fe_2O_3 (900 °C) as also confirmed by XRD analysis.

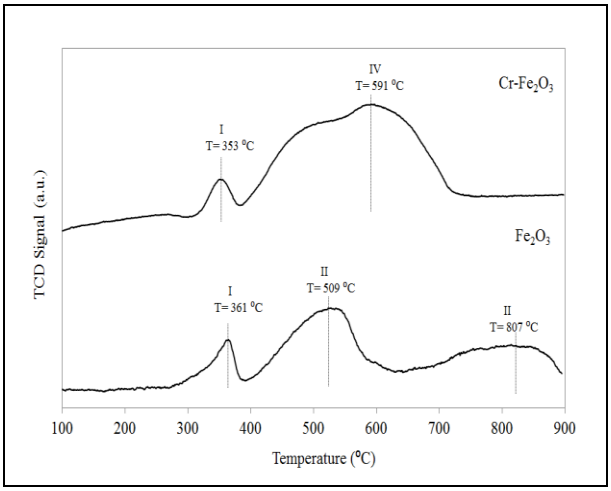


Figure 5. TPR profile of Fe_2O_3 and Cr-Fe_2O_3

Activation energy (Ea) effect

To evaluate the activation energy of Cr-Fe_2O_3 and undoped Fe_2O_3 a TPR measurement with various heating rates (10, 13 and 15 ^{0}C/min) were carried out. The results showed that by increasing the heating rate, the peaks showing a maximal temperature were shifted to higher temperature as shown in Figure 6.

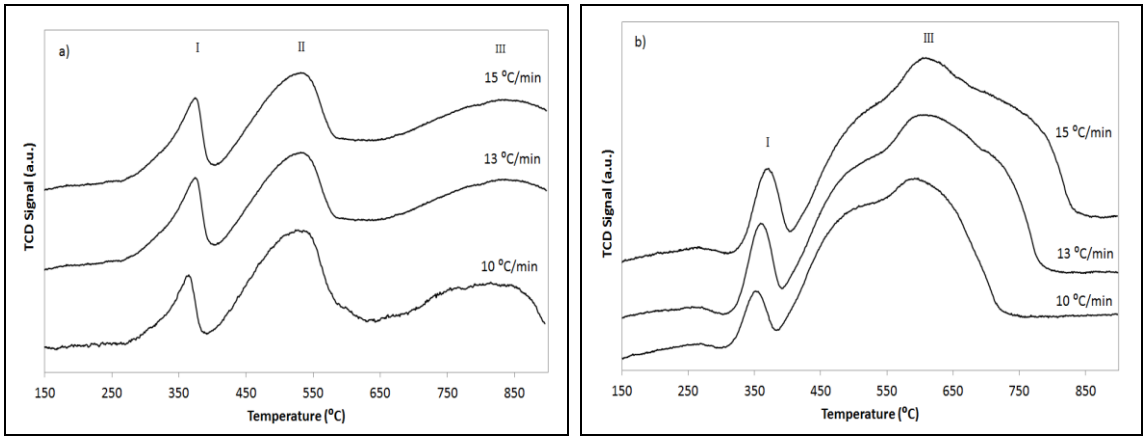


Figure 6. TPR profiles of (a) Fe_2O_3 and (b) Cr-Fe_2O_3 reduction by carbon monoxide with heating ramp of 10 °C/min, 13 °C/min and 15 °C/min

To describe the process, we considered that during the TPR analysis, 3 reduction steps involve for undoped Fe_2O_3 and 2 reduction steps for Cr-Fe_2O_3. The processes were described below with the rate constant of K_I, K_{II}, K_{III} and K_{IV}.

Fe_2O_3: $Fe_2O_3 \xrightarrow{K_I} Fe_3O_4 \xrightarrow{K_{II}} FeO \xrightarrow{K_{III}} Fe$

Cr-Fe_2O_3: $Fe_2O_3 \xrightarrow{K_I} Fe_3O_4 \xrightarrow{K_{IV}} Fe$

The E_a for undoped Fe_2O_3 and Cr-Fe_2O_3 by referring to their transition phase were shown in Table 1. The results suggest that by adding Cr metal into ferric oxide, the Ea value decrease by 12.39 % for the reduction step of $Fe_2O_3 \rightarrow Fe_3O_4$ that lower the reduction temperature. This also in agreement with previous work by Ryu et. al. (2008) [12] with addition of metal additive in their case is Ru metal, played an important role on lowering the reduction temperature which also due to a decrease of activation energy according to $Fe_2O_3 \rightarrow Fe_3O_4$ course in H_2 reducing atmosphere. Nevertheless, Ea value regarding to other transition phases could not be compared since both samples involved a different mechanism in the reduction process. Moreover, Cr-Fe_2O_3 which gives two reduction steps with transition phase of $Fe_2O_3 \rightarrow Fe_3O_4$ display an E_a value of 123.7 kJ mol^{-1} and $Fe_3O_4 \rightarrow$ Fe give a value of 89.0 kJ mol^{-1}. For undoped Fe_2O_3 three values of Ea were calculated, first transition of $Fe_2O_3 \rightarrow Fe_3O_4$ give a value of 141.2 kJ mol^{-1}, second and third transition of $Fe_3O_4 \rightarrow$ FeO and FeO $\rightarrow$ Fe give Ea value of 82.5 kJ mol^{-1} and 100.3 kJ mol^{-1}, respectively.

Table 1. The E_a of Fe_2O_3 and Cr-Fe_2O_3 according to the transition phase

Sample	**E_a^I (kJ mol^{-1})**	**E_a^{II} (kJ mol^{-1})**	**E_a^{III} (kJ mol^{-1})**	**E_a^{IV} (kJ mol^{-1})**
	$Fe_2O_3 \rightarrow Fe_3O_4$	**$Fe_3O_4 \rightarrow FeO$**	**$FeO \rightarrow Fe$**	**$Fe_3O_4 \rightarrow Fe$**
Cr-Fe_2O_3	123.7	n.d.	n.d.	89.0
Fe_2O_3	141.2	82.5	100.3	n.d.

Note: n.d. = not detected.

Referring to Table 1, it has been seen that the activation energy for reduction steps of $Fe_2O_3 \rightarrow Fe_3O_4$ is higher compare to the other transition phases. The values were unpredicted but somehow was similar to the activation energy obtained by Munteanu et al. [13] for reduction of fresh α-Fe_2O_3 by 10% hydrogen in argon with the reduction steps of $Fe_2O_3 \rightarrow Fe_3O_4$ give 139.2 kJ mol^{-1} and $Fe_3O_4 \rightarrow$ FeO and FeO $\rightarrow$ Fe were 77.3 and 85.7 kJ mol^{-1}, respectively [13].

Conclusion

The kinetics and reduction behaviour of chromium doped Fe_2O_3 and undoped Fe_2O_3 were investigated and compared using TPR technique and characterized by XRD and BET. The data obtained from XRD evidenced the presence of well dispersed chromium particles loaded on the ferric oxide and promotes better crystallinity of the Fe_2O_3 leads to the effect on enhancing the reduction process by lowering the reduction temperature of Fe_2O_3 to metallic Fe which has been completed at 700 °C compare to undoped Fe_2O_3 (900 °C). The reducing path of ferric oxide was found to be dependent on the doped element as Cr doped ferric oxide favours complete reduction to metallic iron without formation of intermediate FeO. Thus, addition of chromium element give a two-steps reduction ($Fe_2O_3 \rightarrow Fe_3O_4 \rightarrow$ metallic Fe) and undoped ferric oxide preferentially reduced through wüstite formation with three-steps reduction ($Fe_2O_3 \rightarrow Fe_3O_4 \rightarrow FeO \rightarrow$ metallic Fe). Furthermore, better reducibility of Cr-Fe_2O_3 is also due to the higher in surface area and the decrease of the activation energy regarding to transition phases of $Fe_2O_3 \rightarrow Fe_3O_4$ during the reduction process by carbon monoxide compare to undoped one.

Acknowledgement

The author wish to thank Ministry of Higher Education (MOHE) for funding this project under research grant number BKBP-FST-K003323-2014, FRGS/2/2013/TK06/UKM/02/3, ETP-2013-066, TD-2014-024 & Centre of Research and Innovation Management CRIM-UKM for instruments facilities.

References

1. Pineau, A., Kanari, N. and Gaballah, I. (2007). Kinetics of reduction of iron oxides by H_2, *Thermochimica Acta*, 456(2): 75 – 88.
2. Li, K., Haneda, M., Gu, Z., Wang, H. and Ozawa, M. (2013). Modification of CeO_2 on the redox property of Fe_2O_3. *Materials Letters*, 93: 129 – 132.
3. Monazam, E. R., Breault, R. W. and Siriwardane, R. (2014). Reduction of hematite (Fe_2O_3) to wüstite (FeO) by carbon monoxide (CO) for chemical looping combustion,*Chemical Engineering Journal*, 242: 204 – 210.
4. Pickles, C. A. (2008). Thermodynamic analysis of the separation of zinc and lead from electric arc furnace dust by selective reduction with metallic iron. *Separation and Purification Technology*, 59: 115 – 128.
5. Longbottom, R. and Kolbeinsen, L. (2008). Iron ore reduction with CO and H_2 gas mixtures – thermodynamic and kinetic modelling. *Proceedings of 4th Ulcos Seminar*, October:1 – 13.
6. Colombo, U., Gazzarrini, F. and Lanzavecchia, G. (1967). Mechanisms of iron oxides reduction at temperatures below 400 °C. *Materials Science Engineering*, 2(3):125 – 135.
7. Jozwiak, W. K., Kaczmarek, E., Maniecki, T. P., Ignaczak, W. and Maniukiewicz, W. (2007). Reduction behavior of iron oxides in hydrogen and carbon monoxide atmospheres. *Applied Catalysis A: General*, 326(1): 17 – 27.
8. Leith, I. R. and Howden, M. G. (1988). Temperature-programmed reduction of mixed iron-manganese oxide catalysts in hydrogen and carbon monoxide. *Applied Catalysis*, 37:75 – 92.
9. Khan A. and Smirniotis, P. G. (2008). Relationship between temperature-programmed reduction profile and activity of modified ferrite-based catalysts for WGS reaction. *Journal of Molecular Catalysis A: Chemical* 280: 43 – 51.
10. Mondal, K., Lorethova, H., Hippo, E., Wiltowski, T. and Lalvani, S. B. (2004). Reduction of iron oxide in carbon monoxide atmosphere - reaction controlled kinetics. *Fuel Processing Technology*, 86(1): 33 –47.
11. Hu, C., Gao, Z. and Yang, X. (2007). Facile synthesis of single crystalline α-Fe_2O_3 ellipsoidal nanoparticles and its catalytic performance for removal of carbon monoxide, *Materials Chemistry and Physics*, 104 (2–3): 429 – 433.
12. Ryu, J. C., Lee, D. H., Kang, K. S., Park, C. S., Kim, J. W. and Kim, Y. H. (2008). Effect of additives on redox behavior of iron oxide for chemical hydrogen storage, *Journal of Industrial and Engineering Chemistry*, 14(2): 252 – 260.
13. Munteanu, G., Illieve, L. and Andreeva, D. (1997). Kinetic parameters obtained from TPR data for ol-Fe_2O_3 and Au/o~-Fe_2O_3 systems, *Thermochimica Acta*, 291:171 – 177.

Malaysian Journal of Analytical Sciences, Vol 20 No 3 (2016): 539 - 545
DOI: http://dx.doi.org/10.17576/mjas-2016-2003-11

MALAYSIAN JOURNAL OF ANALYTICAL SCIENCES
Published by The Malaysian Analytical Sciences Society
ISSN 1394 - 2506

SYNTHESIS AND CHARACTERIZATION OF MESOPOROUS SILICA MCM-41 AND SBA-15 FROM POWER PLANT BOTTOM ASH

(Sintesis dan Pencirian Silika Mesoporos MCM-41 dan SBA-15 daripada Debu Bawah Loji Janakuasa)

Nurul Barakah Ab Rahman*, Hamizah Md. Rasid, Hashazirah Mohammad Hassan, Mohammad Noor Jalil

School of Chemistry and Environment,
Faculty of Applied Sciences,
Universiti Teknologi MARA, 40450 Shah Alam, Selangor, Malaysia

**Corresponding author: barakahrahman@gmail.com*

Received: 24 February 2015; Accepted: 27 October 2015

Abstract

Silica was extracted from power plant bottom ash by alkali fusion method and used to synthesize MCM-41 and SBA-15. As comparison, MCM-41 and SBA-15 were synthesized by using tetraethylorthosilicate (TEOS) as pure silica source. All synthesized MCM-41 and SBA-15 were characterized using X-ray Diffraction (XRD) and nitrogen adsorption to determine the formation of hexagonal pores, Field Emission Scanning Electron Micrograph (FESEM) was used to observe their morphology while Fourier Transform Infrared Spectroscopy (FTIR) was used to obtain the functional group and removal of surfactant after calcinations. XRD results confirmed bottom ash MCM-41 (BA MCM-41), pure SBA-15 (PSBA-15) and bottom ash SBA-15 (BA SBA-15) have well-ordered mesostructures. N_2 adsorption of pure MCM-41 (PMCM-41), PSBA-15 and BA SBA-15 indicated type IV isotherm while BA MCM-41 exhibit type III isotherm. According to FESEM analyses, the particle morphology of bottom ash mesoporous silica was different from those prepared using pure chemical. Morphology of PMCM-41 and PSBA-15 showed rod like particle while BA MCM-41 and BA SBA-15 exhibited agglomerated particle. PMCM-41, PSBA-15 and BA SBA-15 shows ordered hexagonal, high surface area and narrow pore distribution.

Keywords: mesoporous silica, MCM-41, SBA-15

Abstrak

Silika telah diekstrak daripada abu bawah loji janakuasa melalui kaedah gabungan alkali dan digunakan untuk sintesis MCM-41 dan SBA-15. Sebagai perbandingan, MCM-41 dan SBA-15 telah disintesis dengan menggunakan tetraetilortosilika (TEOS) sebagai sumber silika tulen. Semua MCM-41 dan SBA-15 yang telah disintesis dicirikan menggunakan kaedah pembelauan Sinar X (XRD) dan penjerapan nitrogen untuk menentukan pembentukan liang heksagon, mikroskopi elektron pengimbasan pancaran medan (FESEM) digunakan untuk memerhati morfologi manakala Spektroskopi Inframerah Tranformasi Fourier (FTIR) digunakan untuk mengenalpasti kumpulan berfungsi dan penyingkiran surfaktan selepas pengkalsinan. Keputusan XRD membuktikan debu MCM-41 (BA MCM-41), SBA-15 tulen (PSBA-15) dan debu SBA-15 (BA SBA-15) mempunyai mesostruktur yang teratur. Penjerapan N_2 oleh MCM-41 (PMCM-41), PSBA-15 dan BA SBA-15 menunjukkan isoterma jenis IV manakala isoterma jenis III bagi BA MCM-41. Berdasarkan analisis FESEM, morfologi zarah silika mesoporos daripada debu bawah loji janakuasa adalah berlainan berbanding yang disediakan menggunakan bahan kimia tulen. Morfologi PMCM-41 dan PSBA-15 menunjukkan zarah jenis rod manakala BA MCM-41 dan BA SBA-15 wujud sebagai zarah bercampur. PMCM-41, PSBA-15 dan BA SBA-15 mempunyai struktur heksagon yang seragam, luas permukaan yang tinggi dan taburan liang yang kecil.

Kata kunci: silika mesoporos, MCM-41, SBA-15

Introduction

In year 1990s, the researchers of Mobil Corporation discovered MCM-41 molecular sieves can be synthesized by using an inorganic silicate species and organic template [1]. Tetraethylorthosilicate (TEOS) and sodium silicate (Na_2SiO_3) were the sources of silicon used by researchers to synthesize mesoporous silica [2]. The features of MCM-41 are high pore volume with large uniform pore size (14-100Å), high specific surface area which give advanced advantages over zeolites and have many applications in material sciences, chemistry and biology [3, 4]. MCM-41 exhibit hexagonal packed rod-shaped micelle structure, cubic shape for MCM-48 and MCM-50 in lamellar form [4]. The pore size of MCM-41 and MCM-48 can be controlled and widely used as an adsorbent, support and catalyst [5]. Santa Barbara Amorphous-15 (SBA-15) has same features as MCM-41 but their specific surface area and pore volume smaller than M41S materials with thicker pore walls [6]. Fly ash has a high recycling rate and can be use in various parts of recycling systems while 79 % of bottom ash thrown and only 21 % was used in asphalt or in construction. Researchers had considerable interest in conversion of coal bottom ash and fly ash into zeolites or mesoporous silica materials as MCM-41, MCM-48 and SBA-15 [7]. Recently preparation of mesoporous materials from natural waste such as coal fly ash have been reported [8 -11]. Limited reports have addressed in converting coal bottom ash into mesoporous silica [7, 12]. Chandrasekar et al. [12] synthesized mesoporous MCM-41, SBA-15 and SBA-16 from supernatant derived from coal bottom ash. They used additional sodium metasilicate in synthesis of SBA-15 and SBA-16.

In this country, there have been no reports thus far in synthesis of mesoporous silica using natural waste like coal bottom ash as silica source. This research aims to extract silica from lower grade bottom ash and mesoporous materials which are MCM-41 and SBA-15 were synthesized using extracted silica. Instead of using expensive reagent, a cheaper silica source can be used to minimize the high production cost of porous silica materials. Then the mesoporous materials were characterized by X-ray Diffraction (XRD), N_2 adsorption desorption, Field Emission Scanning Electron Micrograph (FESEM) and Fourier Transform Infrared Spectroscopy (FTIR) analyses

Materials and Methods

Chemicals and raw materials

All the chemicals used were commercial reagent grade and purchased from Merck and Sigma-Aldrich. Coal bottom ash was obtained from Tanjung Bin Power Plant in Pontian, Johor, Malaysia.

Alkali fusion and silicate extraction

Bottom ash was ground to powder with a mesh size of less than 200 μm by using a commercial mixing grinder. The finely ground ash was mix with NaOH powder at 1:1.2 weight ratio with the sample. The mixture of ash and NaOH was fused in a furnace at 550 $^{\circ}$C for one hour. The obtained fused mass was cooled to room temperature and ground again to obtain a fine powder with mesh size less than 100 μm. The fine powder of fused mixture was mixed with distilled water at 1:4 ratios and stirred for 24 hours. The solution was centrifuged and filtered. The supernatant will be used for the synthesis of mesoporous silica [12].

Synthesis of MCM-41

An amount 1.2 g of cetyltrimethylammonium bromide (CTABr) was dissolved in 15 g of water and 1.0 g of ammonium hydroxide (NH_4OH). The solution was stirred for 30 minutes. Next, 40 mL of bottom ash supernatant was slowly added to the homogeneous solution under stirring and stirring maintained for 2 hour. The synthesis pH was adjusted to 10 using dilute acetic acid. Then the stirring was continued for another 30 minutes. The gel product was heated in an oven at 100 $^{\circ}$C for 48 hours. The solid product was filtered, washed and dried at 100 $^{\circ}$C. The product was calcined at 550 $^{\circ}$C for 8 hours. For comparison, pure MCM-41 was synthesized by using TEOS as silica source same as previous procedure [12].

Synthesis of SBA-15

Template for synthesis of SBA-15 is amphiphilic triblock polymer of Pluronic P123 ($EO_{20}PO_{70}EO_{20}$). An amount 4.0 g of P123 was dissolved in 30 mL of deionised water and 120 mL of 2 M HCl and was stirred at 35 ^{0}C for 20 hours. Then, an amount 8.5 g of bottom ash supernatant was slowly added under vigorous stirring for 15 minutes. The mixture was kept under static conditions at the same temperature (35 $^{\circ}$C) for 20 hours. The milky mixture was

transferred to an oven at 90 °C for 24 hours. For comparison, a pure SBA-15 was synthesized by using TEOS as silica sources same as previous procedure. The solid products were filtered, washed and dried at 45 °C for 72 hours. The products were calcined at 500 °C for 6 hours [13].

Characterization studies

X-Ray Diffraction (XRD) patterns of the synthesized samples were determined by using Rigaku D/max-2500 powder diffractometer with Cu-Kα source (λ = 1.5418 Å, 40 kV, 40 mA). N_2 adsorption isotherm and BET surface area were obtained at 77K on a Micromeritics ASAP 2010 Volumetric Adsorption Analyzer. Carlzeiss Supra 40 VP Field Emission Scanning Electron Microscopy (FESEM) was used to characterize the particle size and morphology of mesoporous silica synthesized. Functional groups and removal of surfactant in samples were analyzed from FTIR spectra obtained by using Perkin-Elmer Spectrum One FTIR spectrometer.

Results and Discussion

X-Ray Diffraction (XRD*)*

The XRD pattern of bottom ash MCM-41 (BA MCM-41) (Figure 1a) exhibits an intense (100) signal and three higher order reflections of (110), (200) and (210) planes which confirm the sample is well-defined hexagonal MCM-41[14]. Pure SBA-15 (PSBA-15) in (b) shows three well resolved diffraction peaks which are corresponding to the (100), (110) and (200), indicating hexagonal symmetry with the *p6mm* space group. As a comparison, the XRD pattern of BA SBA-15 in (c) indexed an intense (100) peak while the other two peaks (110) and (200) were not resolved as well as those in pure SBA-15 [12, 15].

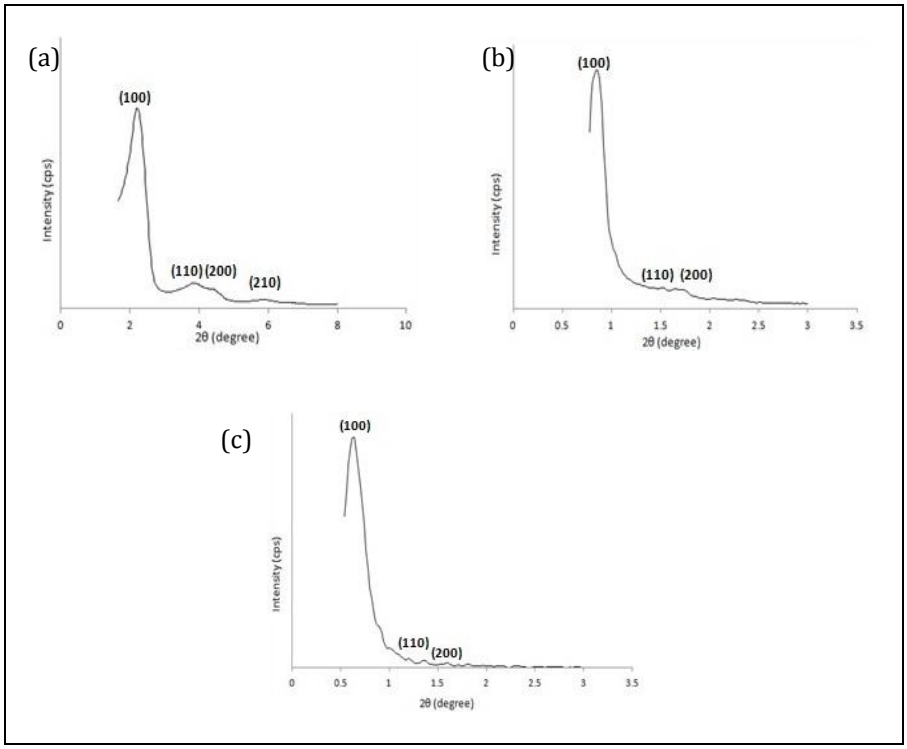


Figure 1. XRD patterns of (a) BA MCM-41, (b) PSBA-15 and (c) BA SBA-15

Nitrogen adsorption desorption

Figure 2 shows the nitrogen adsorption isotherms of calcined MCM-41 and SBA-15 synthesized from bottom ash and TEOS. PMCM-41 in (a) featured hysteresis loops with the sharp adsorption and desorption branches, which

exhibit type IV isotherm [16]. The adsorption branches of PMCM-41 located at P/P_0 from 0.4 to 0.5. Figure 2a inset shows the pore size distributions (PSDs) for PMCM-41 sample, indicate maxima of 47.75 Å. BA MCM-41 (Figure 2b) shows type III isotherm which attributed to the adsorption on macroporous materials [13]. Nitrogen isotherms for PSBA-15 (Figure 2c) and BA SBA-15 (Figure 2d) shows hysteresis loop at P/P_0 from 0.44 to 0.98 and 0.74 to 0.98 respectively. The both isotherms were similar to those reported in the literatures which are type IV. The sharpness of adsorption branches indicate the narrow pore size distribution[17]. Table 1 presents a summary of physicochemical of calcined mesoporous silica synthesized from bottom ash and pure chemical. The specific surface area (S_{BET}) of PMCM-41 was 561.39 m^2/g with a pore volume of 0.406 cm^3/g whereas the corresponding values of BA MCM-41 were 5.25 m^2/g and 0.00477 cm^3/g, respectively. PSBA-15 has 509.41 m^2/g surface area and 0.497 cm^3/g pore volume. The surface area and pore volume of BA SBA-15 decrease to 71.40 m^2/g and 0.204 cm^3/g respectively.

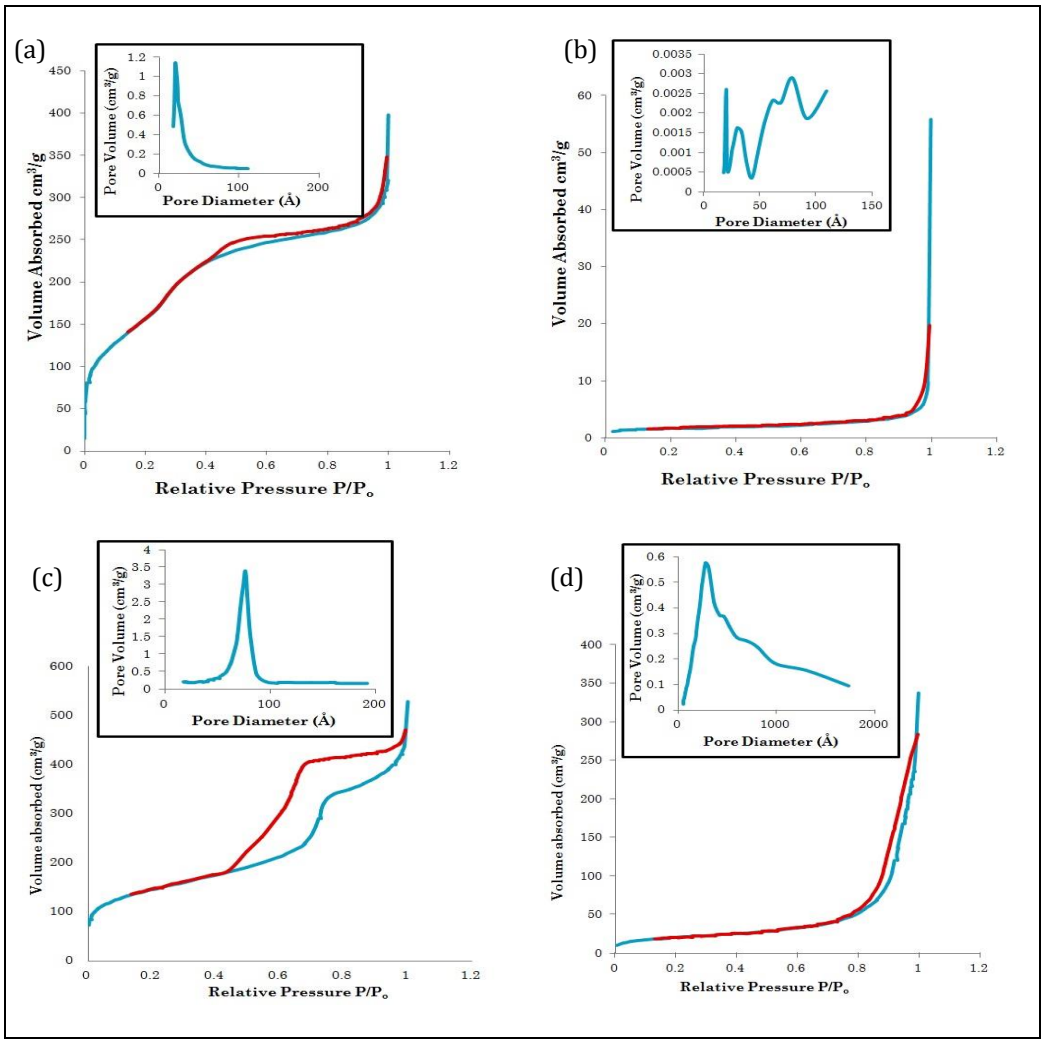


Figure 2. Nitrogen adsorption isotherms and pore size distributions (inset): (a) PMCM-41, (b) BA MCM-41, (c) PSBA-15 and (d) BA SBA-15

Table 1. Physicochemical of calcined mesoporous silica synthesized from bottom ash and pure chemical

Types of mesoporous silica	S_{BET} (m^2/g)	V_p (cm^3/g)	D_{pore} (Å)
PMCM-41	561.39	0.406	47.75
BA MCM-41	5.25	0.00477	1009.32
PSBA-15	509.41	0.497	84.71
BA SBA-15	71.40	0.204	315.65

Field Emission Scanning Electron Micrograph (FESEM)

Figure 3 displays the FESEM micrograph of all synthesized mesoporous silica materials. PMCM-41 (a) and PSBA-15 (c) shows rod like. Particle morphology of BA MCM-41 and BA SBA-15 exhibit agglomerated particles of 1 to 3 μm in diameter [16].

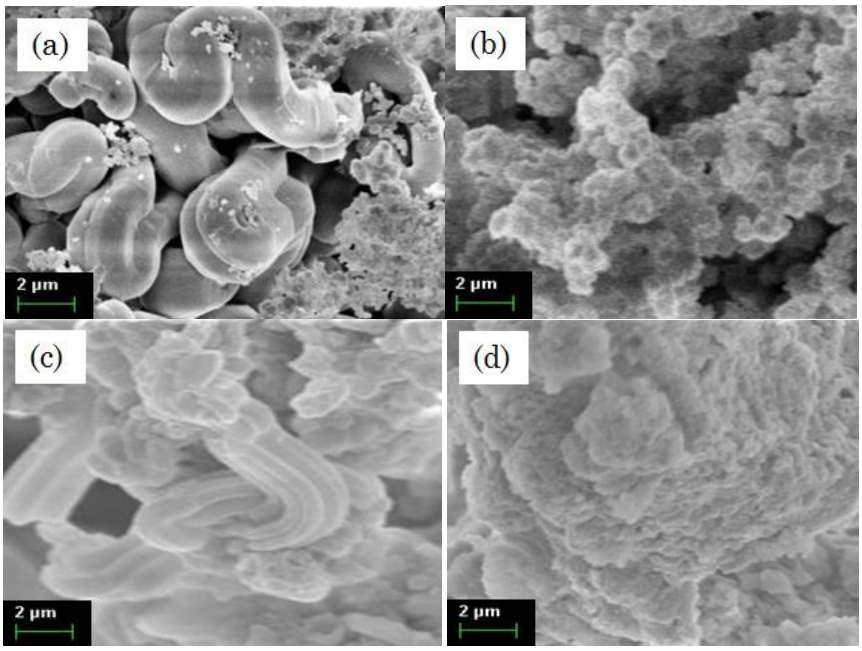


Figure 3. Morphology of: (a) PMCM-41, (b) BA MCM-41, (c) PSBA-15 and (d) BA SBA-15

Fourier Transform Infrared (FTIR)

The infrared spectrum of synthesized materials in the region of 4000 – 400 cm^{-1} recorded at ambient condition with KBr technique shown in Figure 4 (a) and (b), respectively. For calcined MCM-41 (Figure 4a: (ii), (iv)) and calcined SBA-15 (Figure 4b: (ii), (iv)), the bands around 2920 cm^{-1} and 2850 cm^{-1} assigned for the long chain of alkyl group of surfactant molecules were disappeared after calcinations due to the removal of surfactants. The FTIR spectra of MCM-41 and SBA-15 shows the intense bands at 1097.43 - 1067.25 cm^{-1} attributes for asymmetric stretching Si-O-Si bonds while 806.63 – 792.92 cm^{-1} bands indicates the symmetric stretching Si-O-Si bonds. The bands at 965.75 – 941.68 cm^{-1} and 474.69 – 466.46 cm^{-1} accounts for the stretching and bending vibrations of surface $Si\text{-}O^-$ groups [18].

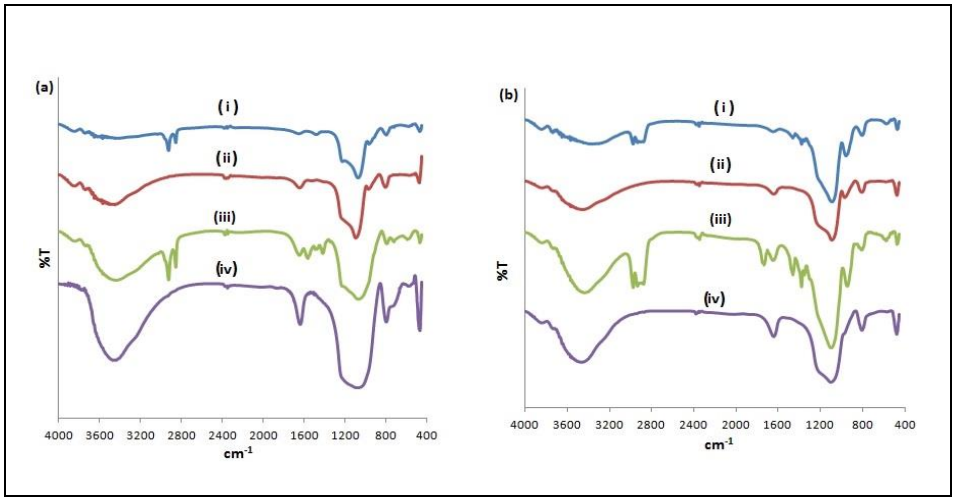


Figure 4. (a) IR spectra of MCM-41: (i) Uncalcined PMCM-41, (ii) Calcined PMCM-41, (iii) Uncalcined BA MCM-41 and (iv) Calcined BA MCM-41; and (b) IR spectra of SBA-15: (i) Uncalcined PSBA-15, (ii) Calcined PSBA-15, (iii) Uncalcined BA SBA-15 and (iv) Calcined BA SBA-15.

Conclusion

Characterization results indicated PMCM-41, PSBA-15 and BA SBA-15 were successfully synthesized. They exhibited ordered hexagonal, high surface area and narrow pore distributions. According to N_2 adsorption desorption analyses, the porous structure of BA MCM-41 was destroyed after calcinations. The synthesis of SBA-15 by using silica source from bottom ash supernatant was better than MCM-41. MCM-41 and SBA-15 synthesized from pure chemical was superior compared to those syntheses from bottom ash supernatant.

Acknowledgement

The authors would like to thank the Ministry of Higher Education (MOHE) for financing the project under the Fundamental Research Grant Scheme no: 600-RMI/FRGS 5/3 (59/2013). Special thanks to Tanjung Bin Power Plant Pontian Johor for the supplied coal bottom ash and highly appreciation to Faculty of Applied Sciences and Faculty of Pharmacy Universiti Teknologi MARA (UiTM) for facilities in completing this research.

References

1. Zhao, X. S., Lu, G. Q. (Max) and Millar, G.J. (1996). Advances in mesoporous molecular sieve MCM-41. *Industrial and Engineering Chemical Research* 35 (7): 2075 - 2090.
2. Liou, T.-H. (2011). A green route to preparation of MCM-41 silicas with well ordered mesostructure controlled in acidic and alkaline environments. *Chemical Engineering Journal*, 17: 1458 - 1468
3. Huang, L., Huang, Q., Xiao, H., and Eić, M. (2007). Effect of cationic template on the adsorption of aromatic compounds in MCM-41. *Microporous and Mesoporous Materials*, 98(1-3): 330 - 338.
4. Vartuli, J. C., Roth, W. J. and Degnan, T. F. (2008). Mesoporous materials (MS41S): From discovery to application, in *Dekkar Encyclopedia of Nanoscience and Nanotechnology*: 1797 - 1811.
5. Tatsumi, T., Koyano, K. A., Tanaka, Y. and Nakata, S. (1999). Mechanical Stability of Mesoporous Materials, MCM-48 and MCM-41. *Journal of Porous Materials*, 6: 13 - 17.
6. Andersson, J, and J Rosenholm, (2008). Mesoporous silica : an alternative diffusion controlled drug delivery system. *Topics in Tissue Engineering*: 1 - 19.
7. Park, J. E., Youn, H. K., Yang, S. T, and Ahn, W. S. (2012). CO_2 capture and MWCNTs synthesis using mesoporous silica and zeolite 13X collectively prepared from bottom ash. *Catalysis Today*, 190: 15 - 22.

8. Majchrzak-Kuceba, I. and Nowak, W. (2011). Characterization of mesoporous materials derived from polish fly ashes. *International Journal of Mineral Processing.* 101: 100 - 111.
9. Hui, K. S., and Chao, Y. H. (2006). Synthesis of MCM-41 from coal fly ash by a green approach: Influence of synthesis pH. *Journal of Hazardous Materials*, 137: 1135 - 1148.
10. Halina, M., Ramesh, S., Yarmo, M. A. and Kamarudin, R.A. (2007). Non-hydrothermal synthesis of mesoporous materials using sodium silicate from coal fly ash. *Materials Chemistry and Physics*, 101: 344 – 351.
11. Chang, H. L., Chun, C. M., Aksay, I. A. and Shih, W. H. (1999). Conversion of fly ash into mesoporous aluminosilicate. *Industrial & Engineering Chemistry Research* 38: 973 - 977.
12. Chandrasekar, G., You, K. S., Ahn, J. W. and Ahn, W.S. (2008). Synthesis of hexagonal and cubic mesoporous silica using power plant bottom ash. *Microporous and Mesoporous Materials.* 111: 455 -462.
13. Jalil, M. N., (2011). The preparation and characterization of mesoporous films for electrochemical applications. Ph.D. Thesis. University of Manchester, United Kingdom: pp 249.
14. Ng, E-P, Goh, J-Y, Ling, T. C., and Mukti, R. R. (2013) .Eco-friendly synthesis for MCM-41 nanoporous materials using the non-reacted reagents in mother liquor. *Nanoscale Research Letters*, 8(1): 120.
15. Du, G., Lim, S., Pinault, M., Wang, C., Fang, F., Pfefferle, L. and Haller, G., (2008). Synthesis, characterization, and catalytic performance of highly dispersed vanadium grafted SBA-15 catalyst. *Journal of Catalysis*, 253(1): 74 - 90.
16. Ahmad, A., Rasid, H. M. and Kassim, K. (2013). Physicochemical properties of CuO_2 (acac)2 supported on functionalized MCM41 containing thiourea ligand. *International Journal of Chemical Engineering and Applications*, 4(1): 6 - 10.
17. Kruk, M. and Jaroniec, (2000). Characterization of the porous structure of SBA-15. *Chemistry Material*, 12: 1961 - 1968.
18. Fonseca, L. C., Faez, R., Camilo, F. F. and Bizeto, M. A. (2012). Evaluation of the doping process of polyaniline produced inside the mesopores of a sulfonic acid grafted MCM-41. *Microporous and Mesoporous Materials* 159: 24 - 29.

Malaysian Journal of Analytical Sciences, Vol 20 No 3 (2016): 546 - 550
DOI: http://dx.doi.org/10.17576/mjas-2016-2003-12

MALAYSIAN JOURNAL OF ANALYTICAL SCIENCES
Published by The Malaysian Analytical Sciences Society
ISSN 1394 - 2506

PHYTOCHEMICAL STUDY ON THE STEM BARK OF *Mallotus leucodermis* Hook F.

(Kajian Fitokimia ke atas Kulit Ranting *Mallotus leucodermis* Hook F.)

Aiza Syuhada Mohd Yusoff [1], Norizan Ahmat [1, 2]*, Humera Naz[2]

[1]*Department of Chemistry, Faculty of Applied Sciences, Universiti Teknologi MARA, 40450 Shah Alam, Selangor, Malaysia*
[2]*Atta ur Rahman Institute for Natural Products Discovery, Universiti Teknologi MARA, 42300 Bandar Puncak Alam, Selangor, Malaysia*

**Corresponding author: noriz118@salam.uitm.edu.my*

Received: 24 February 2015; Accepted: 27 October 2015

Abstract

The stem barks of *Mallotus leucodermis* Hook F. (Euphorbiaceae) was studied for its chemical constituents. The air dried and pulverized of stem bark of *M. leucodermis* (1.3 kg) was extracted successively with acetone for three days at room temperature yielding 66.0 g of crude extract. The crude extract was fractionated using vacuum liquid chromatography (VLC) to afford six fractions. Fraction 6 was further washed and recrystallized to afford bergenin (1). Fraction 3 was subjected to multiple purification using radial chromatography ($CHCl_3$: acetone) with different ratio 9:1, 8:2, 6:4 and 5:5 to yield a flavonoid compound, epicatechin (2). These compounds were elucidated based on spectroscopic analysis (Ultra Violate, Infra-Red, Mass Spectrometry and Nuclear Magnetic Resonance) as well as comparison with literatures.

Keywords: Euphorbiaceae, *Mallotus*, bergenin, epicatechin

Abstrak

Kulit ranting *Mallotus leucodermis* Hook F. (Euphorbicaeae) telah dikaji untuk sebatian kimianya. Kulit ranting *M. leucodermis* (1.3 kg) yang telah dikeringkan dan dikisar, direndamkan dalam aseton selama tiga hari pada suhu bilik bagi memperolehi 66.0 g bahan ekstrak. Fraksinasi telah dilakukan ke atas ekstrak tersebut dgn menggunakan hampagas kromatografi cecair dan menghasilkan enam fraksi. Fraksi 6 telah dicuci beberapa kali dan dihablurkan semula untuk menghasilkan bergenin (1). Manakala fraksi 3 ditulenkan beberapa kali menggunakan radial kromatografi untuk mendapatkan sebatian flavonoid, epicatechin (2). Dua sebatian tulen ini dikenal pasti berdasarkan analisis spektroskopi (Ultralembayung, Inframerah, Spektrometri Jisim and Resonans Magnet Nukleus) dan juga perbandingan data.

Kata kunci: Euphorbiaceae, *Mallotus*, bergenin, epicatechin

Introduction

Mallotus leucodermis Hook F., is a species under genus of *Mallotus* from Euphorbiaceae family. Euphorbiaceae is also commonly known as spurge family. The family of Euphorbiaceae consists of 283 genera and 7300 species which have been distributed in tropical region around the world. The main genus of Eurphobiaceae family consist of *Euphorbia*, *Phyllantus*, *Mallotus*, *Macaranga* and many more [1]. *Mallotus* is a genus of shrubs, trees and climbers with approximately 150 species were distributed in tropical and sub-tropical regions of Asia [2]. The genus of *Mallotus* belongs to the Malphighiales order, the Euphorbiaceae family, Acalyphoideae subfamily, Acalypeae pro parte and Rotterinae subtribe [3]. Research on *Mallotus* species revealed that this genus were very rich with active

compounds such as flavonoids, phenolic compounds, terpenoids and phloroglucinol derivatives [5]. Moreover, the pharmaceutical research has found that some of chemical constituents of *Mallotus* have the capability to possess several biological activities such as antioxidant, anti-inflammatory, antimicrobial, antiviral, cytotoxic and antitumor activities [3]. Therefore, the outcomes from this study will improve and enhance the application of natural product in the development of drug discovery.

Some species of the genus of *Mallotus* in Malaysia are used as traditional medicines. The roots of *M. paniculatus* are boiled and drunk after child birth, the leaves of *M. macrostachyus* are used as an antidote against snake poison whereas the roots and fruits of *M. barbatus* are used against muscle stiffness [2]. *Mallotus leucodermis* Hook f., is also commonly known as "balik angin bopeng" in Malaysia, is used to treat skin complaints [4]. In this study, two compounds namely bergenin (1) and epicatechin (2) have been isolated from the stem bark of *Mallotus leucodermis*. The structure elucidation of these two compounds will be discussed according to NMR (1D and 2D) analysis and also by the comparison with the literature data.

Materials and Methods

Chemicals and plant materials

The industrial grade solvent was used for extraction of sample while the analytical grade solvents such as acetone, chloroform ($CHCl_3$), ethyl acetate (Ea), hexane (Hex), and methanol (MeOH), were used in the isolation and purification of compounds. The stem bark of *M. leucodermis* Hook f., was collected from Kuala Keniam, Pahang National Park.

Extraction procedure

Air dried and pulverized stem bark of *M. leucodermis* (1.3 kg) was successively extracted with 95 % acetone for 72 hours at room temperature. The extract was then filtered and evaporated to dryness under reduced pressure using rotary evaporator. The maceration was repeated three times to obtain optimum yield of crude extract. The crude extract (124.6 g) was subjected to removal of tannin by using diethyl ether yielded less tannin crude extract 67.8 g.

Fractionation and isolation

The crude extract was subjected to vacuum liquid chromatography (VLC) over silica gel eluted with hexane: ethyl acetate (3:7 – 1:9) and $CHCl_3$: acetone (7:3 – 3:7) to yield several fractions. All fractions were spotted on thin layer chromatography (TLC) plate and the similar patterns of separation were combined together into six fractions (F1 – F6). The last fraction from VLC was further purified by repeated washing using acetone and methanol to give white crystal ML1 (0.66 g). Fraction 3 (800 mg) was then subjected to radial chromatography on silica coated plate with $CHCl_3$: acetone (9:1 – 5:5) to give seven subfractions. Subfraction 7 (F3.7) was further purified by radial chromatography (RC) using $CHCl_3$: acetone (8:2, 6:4, 5:5) and washing method to give ML2 (17 mg).

Structure elucidation

The pure compounds were identified by using NMR spectroscopy on a Bruker AC 300 instrument, UV-Vis spectrophotometer, Infra-red, FTIR and gas chromatography – mass spectrometry, GC-MS. The spectra were measured on the spectrometers. Structures identified after analysis of the data obtained from spectra.

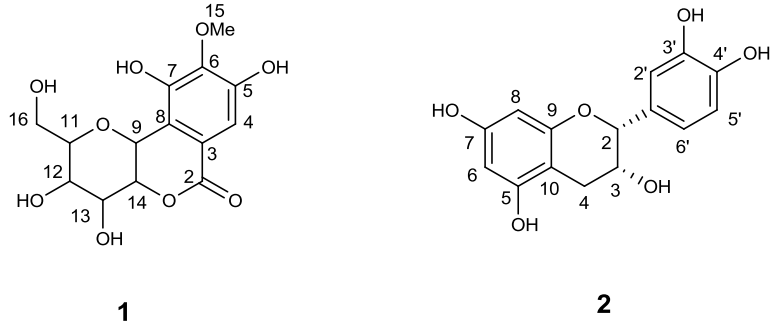
Results and Discussion

Structural elucidation of isolated compounds

The isolated compounds were characterized and identified via 1D and 2D NMR spectroscopy and by comparison with literature data. The structures of these pure compounds were shown in Figure 1.

The pure compound ML1 is a white crystals, isolated from VLC and recrystallized in methanol. Compound ML1 gave a $[M]^+$ at m/z 328 in the EI-mass spectrum, which corresponds to the molecular formula $C_{14}H_{16}O_9$. The melting point for this compound is consistent with the reported melting point of bergenin which is 236 – 238 °C [6]. The ^{1}H NMR spectrum showed a signal for an aromatic proton at δ_H 6.99 (1H, s) and a signal for methoxy protons at δ_H 3.77 (3H, s). The ^{13}C APT spectrum showed the total of 14 resonances representing 14 carbons. The carbonyl group signal appeared at downfield region, δ 163.8 (C-2) whereas the signal for methoxy carbon appeared at δ 60.3 (C-15). The methylene carbon (C-16) showed a signal at δ_C 61.5 while the five peaks of methine carbons in glucose

ring appeared at δ_C 71.3 (C-12), 72.5 (C-9), 74.1 (C-13), 80.2 (C-14) and 82.2 (C-11). Table 1 summarised the ^1H and ^{13}C NMR data for ML1 in comparison with the literature data. Based on the spectral data and comparison with literature [7] and [8], ML1 was determined to be a bergenin.



1 **2**

Figure 1. Structure of isolated compounds (1) bergenin and (2) epicatechin

Bergenin is a colourless crystalline polyphenol, which contains five hydroxyl groups that played an important role in its pharmacological activity [5]. This compound is reported in literature to exhibit various biological activities such as antifungal, antiulcer, burn wound healing effects and also immunomodulatory [6]. Bergenin was previously isolated from *Mallotus philippinensis*, *Mallotus japonicus*, and *Bergenial crassifolia* [5].

Table 1. The comparison of ^1H and ^{13}C NMR for ML1 with the literature data

No.	δH	*δH	δC	**δC
1	-	-	-	-
2	-	-	163.8	164.6
3	-	-	118.5	118.2
4	6.99 (1H, s)	6.99 (1H, s)	109.9	109.9
5	9.76 (1-OH, s)	9.75 (1-OH, s)	151.4	151.1
6	-	-	141.0	141.1
7	8.45 (1-OH, s)	8.45 (1-OH, s)	148.5	148.2
8	-	-	116.4	116.1
9	4.98 (1H, d, J= 10.8 Hz)	4.99 (1H, d, J= 10.5 Hz)	72.5	73.1
10	-	-	-	-
11	3.58 (1H, t, J=8.1 Hz)	3.57 (1H, t, J= 8.8 Hz)	82.2	81.9
12	3.22 (1H, ddd, J= 8.1, 5.1 Hz)	3.20 (1H, ddd, J= 8.8, 6.6 Hz)	71.1	70.7
13	3.67 (1H, ddd, J=5.4,3.3,5.4Hz)	3.65 (1H, ddd, J=8.8,5.6,5.6Hz)	74.1	74.4
14	4.00 (1H, dd, J=10.2, 9.6 Hz)	4.00 (1H, dd, J= 10, 9.6 Hz)	80.2	80.2
15	3.77 (3H, s)	3.78 (3H, s)	60.3	59.8
16	3.83 (1H, dd, J= 10.8 Hz)	3.84 (1H, dd, J= 11.6, 4.4 Hz)	61.5	61.5

* ^1H (400 MHz, DMSO-d_6) [7]
**^{13}C (500 MHz, CD_3OD-d_4) [8]

The pure compound ML2 was obtained as yellow powder, after several purification using RC eluted with $CHCl_3$: acetone (9:1 – 5:5). Compound ML2 gave a $[M]^+$ at m/z 313.2 in the EIMS, corresponding to the molecular formula $C_{15}H_{14}O_6$. The melting point obtained 224-226 °C which is acceptable with the literature melting point of epicatechin [9]. The 1H NMR spectrum showed a broad singlet peak at δ_H 4.88 (1H, s, H-2) which indicate a cis-orientation between H-2 and H-3. An ABD system was observed at region by protons at δ_H 6.81 (d_o), 6.83 (d_m) and 7.06 (dd). The spectrum also revealed two doublets at δ_H 6.04 (H-8) and δ_H 5.93 (H-6) which were indicated as proton with meta-subtitution in ring A. The ^{13}C APT spectrum showed the total of 15 resonances representing 15 carbons. The methylene carbon (C-4) showed a signal at very upfield region at δ_C 28.1 whereas the signal at δ_C 78.5 represents C-2. The total of seven signals of quarternary carbons at δ_C 157.0, 157.2, 156.6, 99.6, 131.7, 144.9 and 145.1 representing as C-5, C-7, C-9, C-10, C-1', C-3', and C-4', respectively.

Table 2 summarized the ^1H and ^{13}C NMR data for ML2 in comparison with the literature data. Based on the spectral data and comparison with literature [10], ML2 was confirmed to be an epicatechin. Epicatechin is a flavan-3-ol, a type of natural phenol and antioxidant. It belongs to the family of flavonoids. This major flavanol in food is known to possess antioxidant, antiulcer and anti-inflammatory [7].

Table 2. The comparison of ^1H and ^{13}C NMR for **ML2** with the literature data

No.	***δ*H**	****δ*H**	***δ*C**	****δ*C**
1	-	-	-	-
2	4.88 (1H, s)	4.88 (1H, s)	78.5	79.1
3	4.21 (1H, m)	4.24 (1H, m)	66.1	66.6
4β	2.72 (1H, dd, J=16.5, 3.6 Hz)	2.72 (1H, dd, J=16.7, 3.5 Hz)	28.1	28.5
4α	2.89 (1H, dd, J=16.5, 4.5 Hz)	2.87 (1H, dd, J=16.7, 4.5 Hz)		
5	-	-	156.7	157.0
6	5.93 (1H, d, J= 1.5 Hz)	5.96 (1H, d, J=2.3 Hz)	95.3	96.1
7	-	-	156.7	157.2
8	6.04 (1H, d, J= 1.5 Hz)	6.06 (1H, d,J= 2.3Hz)	94.8	95.4
9	-	-	156.2	156.6
10	-	-	98.9	99.6
1'		-	131.3	131.7
2'	7.06 (1H, s)	7.05 (1H, s)	114.4	115.1
3'	-	-	144.5	144.9
4'	-	-	145.6	145.1
5'	6.83 (2H, m)	6.83 (2H, m)	114.6	115.1
6'			118.4	119.1

*(300 MHz, acetone-d_6) [10].

Spectroscopic data

Bergenin (**1**): $C_{14}H_{16}O_9$, white crystals (0.66 g), m.p 236-238 °C. ESI-MS (positive mode) m/z 328.0 $[M+Na]^+$. ^1H NMR (DMSO-d_6, 300 MHz) δ: 3.22 (1H, ddd, J=8.1 Hz, 5.1 Hz, H-12), 3.58 (1H, t, J=8.1 Hz, H-11), 3.67 (1H, ddd, J=5.4Hz, 3.3Hz, 5.4Hz, H-13), 3.77 (3H, s, OCH_3), 3.83 (1H, dd, J=10.8Hz, H-16), 4.00 (1H, dd, J=10.2Hz, 9.6Hz, H-14), 4.98 (1H, d, J=10.5Hz, H-9), 6.99 (1H, s, H-4). 13C NMR (DMSO-d_6, 300 MHz) δ: 163.8 (C-2), 151.4 (C-5), 148.5 (C-7), 141.0 (C-6), 118.5 (C-3), 116.4 (C-8), 109.9 (C-4), 82.2 (C-11), 80.2 (C-14), 74.1 (C-13), 72.5 (C-9), 71,1 (C-12), 60.3 (C-15), 61.5 (C-16).

Epicatechin (**2**): $C_{15}H_{14}O_6$, yellowish powder (17 mg), m.p. 224-226 °C. ESI-MS (positive mode) m/z 313.2 $[M+Na]^+$, 291.2 $[M+H]^+$. ^{1}H NMR (Acetone-d_6, 300MHz) δ: 2.72 (1H, dd, J= 16.5 Hz, 3.6 Hz, H-4β), 2.89 (1H, dd, J= 16.5 Hz, 4.5 Hz, H-4α), 4.21 (1H, m, H-3), 4.88 (1H, s, H-2), 5.93 (1H, d, J= 1.2 Hz, H-6), 6.04 (1H, d, J= 1.5 Hz, H-8), 6.83 (2H, m, H-5', H-6'), 7.06 (1H, s, H-2'). ^{13}C NMR (Acetone-d_6, 300MHz) δ: 28.5 (C-4), 66.6 (C-3), 79.1 (C-2), 95.4 (C-8), 96.1 (C-7), 99.6 (C-10), 115.1 (C-2'), 115.5 (C-5'), 119.1 (C-6'), 131.2 (C-1'), 144.9 (C-3'), 145 (C-4'), 156.6 (C-9), 157.0 (C-5), 157.2 (C-7).

Conclusion

The isolation and identification of bergenin (**1**) and epicatechin (**2**) from the stem bark of *Mallotus leucodermis* Hook f., was the first ever to be reported from this plants. These compounds were elucidated based on spectroscopic analysis (UV-Vis, Infra-Red, Mass Spectra and Nuclear Magnetic Resonance) as well as comparison with literatures.

Acknowledgement

The authors would like to thank Professor Dr Mohd Nazip Suratman, the botanist and lecturer from Universiti Teknologi MARA Shah Alam for his contribution in identifying the plant species. The authors are also grateful to Faculty of Applied Sciences (UiTM) for providing lab facility during this study.

References

1. Thakur, H. A. and Patil, D. A. (2011). Taxonomic and phylogenetic assessment of the Euphorbiaceae: A review. *Journal of Experimental Sciences*, 2 (3):37 - 46.
2. Sierra, S. E. C., Welzen, P.C. and Slik, J. W. F. (2005). A taxonomic revision of Mallotus section philippinensis (former section Rottlera-Euphorbiaceae) in Malesia and Thailand. *Blumea*, 50 : 221 - 248.
3. Riviere C., Hong V. N. T., Hong Q. T., Chataigne G., Hoai N. N., Dejaegher B., Tistaert C., Kim T. N. T., Heyden, Y. V., Van, M. C. and Quetin-Leclercq, J. (2010). Mallotus species from Vietnamese mountainous areas: phytochemistry and pharmacological activities. *Phytochemical Review*, 9: 217 -253.
4. Faridah, H. and Nurulhuda, H. (1999). The use of medicinal plant species by the temuan tribe of Ayer Hitam Forest, Selangor, Peninsular Malaysia. *Pertanika Journal of Tropical Agriculture Sci*ence, 22 (2):85 - 94.
5. Patel, D., Patel, K., Kumar, R., Gadewar, M., and Tahilyani, V. (2012). Pharmacological and analytical aspects of bergenin: A concise report. *Asian Pacific Journal of Tropical Disease*, 2 (2): 163 - 167.
6. Nasser, J. A., Yaacob, W. A., Din, L. B., Yamin, B. M, and Latip, J. (2009). Isolation of atranorin, bergenin and goniothalamin from *Hopea Sangal*. *Journal of Engineering and Applied Sciences*, 4 (1): 92 - 95.
7. Jimenez, R., Duarte, J., and Perez-vizcaino, F. (2012). Epicatechin: Endothelia funtion and blood pressure. *Journal of Agriculture and Food Chemistry*, 60(36): 8823 - 8830.
8. Nunomura, R. C. S., Oliveira, V. G. and Nunomura, S. M. (2009). Characterization of bergenin in *Endopleura uchi* bark and its anti-inflammatory activity. *Journal of Brazilian Chemical Society*, 20 (6): 1060 - 1064.
9. Wei, X. H., Yang, S. J., Liang, N., Hu, D.Y., Jin, L. H., Xue, W. and Yang, S., (2013). Chemical constituents of Caesalpinia decapetala (Roth) Alston. *Molecules*, 18 (1):1325 - 1336.
10. Lu, Y. and Foo, L.Y. (1999). The polyphenol constituents of grape pomace. *Food Chemistry*, 65: 1 - 8.

Malaysian Journal of Analytical Sciences, Vol 20 No 3 (2016): 551 - 559
DOI: http://dx.doi.org/10.17576/mjas-2016-2003-13

MALAYSIAN JOURNAL OF ANALYTICAL SCIENCES
Published by The Malaysian Analytical Sciences Society
ISSN 1394 - 2506

FITTING STATISTICAL DISTRIBUTIONS FUNCTIONS ON OZONE CONCENTRATION DATA AT COASTAL AREAS

(Penyesuaian Fungsi Taburan Statistik pada Data Kepekatan Ozon di Kawasan Pesisiran Pantai)

Muhammad Yazid Nasir*, Nurul Adyani Ghazali, Muhammad Izwan Zariq Mokhtar, Norhazlina Suhaimi

School of Ocean Engineering,
Universiti Malaysia Terengganu, 21030 Kuala Terengganu,Terengganu, Malaysia

**Corresponding author: muhammad.yazidnasir@gmail.com*

Received: 24 February 2015; Accepted: 27 October 2015

Abstract

Ozone is known as one of the pollutant that contributes to the air pollution problem. Therefore, it is important to carry out the study on ozone. The objective of this study is to find the best statistical distribution for ozone concentration. There are three distributions namely Inverse Gaussian, Weibull and Lognormal were chosen to fit one year hourly average ozone concentration data in 2010 at Port Dickson and Port Klang. Maximum likelihood estimation (MLE) method was used to estimate the parameters to develop the probability density function (PDF) graph and cumulative density function (CDF) graph. Three performance indicators (PI) that are normalized absolute error (NAE), prediction accuracy (PA), and coefficient of determination (R^2) were used to determine the goodness-of-fit criteria of the distribution. Result shows that Weibull distribution is the best distribution with the smallest error measure value (NAE) at Port Klang and Port Dickson is 0.08 and 0.31, respectively. The best score for highest adequacy measure (PA: 0.99) with the value of R^2 is 0.98 (Port Klang) and 0.99 (Port Dickson). These results provide useful information to local authorities for prediction purpose.

Keywords: ozone concentration, coastal area, statistical distributions, goodness-of-fit, performance indicator

Abstrak

Ozon merupakan salah satu pencemar yang banyak menyumbang kepada masalah pencemaran udara. Maka kajian tentang ozon adalah penting untuk dijalankan. Objektif kajian ini adalah mencari taburan statistik yang terbaik untuk mewakili data kepekatan ozon. Tiga fungsi taburan yang digunakan dalam kajian ini adalah Gaussian songsang, Weibull dan Lognormal telah dipilih bagi menentukan taburan statistik yang terbaik untuk mewakili data taburan ozon per jam pada tahun 2010 di Port Dickson dan Port Klang. Kaedah penganggar kebolehjadian maksimum (MLE) telah digunakan untuk mengira parameter yang membentuk graf fungsi taburan kebarangkalian (PDF) dan fungsi taburan kumulatif (CDF). Tiga penunjuk prestasi (PI) iaitu ralat mutlak dinormalkan (NAE), kejituan ramalan (PA) dan pekali penentuan (R^2) telah digunakan untuk menguji prestasi kriteria taburan yang terbaik. Hasil kajian menunjukkan taburan Weibull adalah yang terbaik untuk mewakili data kepekatan ozon dengan nilai ukuran ralat terkecil (NAE) di Port Klang dan Port Dickson masing-masing ialah 0.08 dan 0.031. Skor terbaik juga terhasil untuk pengiraan kejituan tertinggi (PA: 0.99) dengan nilai R^2 di kedua-dua tempat ialah 0.98 (Port Klang) dan 0.99 (Port Dickson). Hasil kajian ini membekalkan maklumat penting kepada penguatkuasa tempatan untuk tujuan ramalan kepekatan pada masa akan datang.

Kata kunci: Kepekatan ozon, pesisir pantai, taburan statistik, penyesuaian terbaik, penunjuk prestasi

Introduction

Ozone is one of air pollutant that exists in the atmosphere. Ozone is known as strong photochemical oxidants and one of the major problems originating from air pollution in urban areas [1]. Ozone formation at ground level was

originated by the ozone precursor which is Nitrogen oxides (NO_x) and Volatile Organic Compounds (VOC_s) has comes mainly from vehicles emission. The ozone concentration trend change when the emissions of its precursor change [2]. The ozone concentration that exists at ground level may be harmful to living organism especially human. Ozone was also known as the major contributing factor on chronic disease and mortality [3].

Ozone was expected to be existing at coastal site by the influence of the geographical structure of the site and others parameters. These secondary pollutants were affected by the continental and maritime wind as well as the sea breeze [4,5]. The diurnal ozone coastal has been investigated by Nair et al. [6], state that the ozone mixing ratio increase during early morning and reach maximum at 1100 hour and start decreasing after 1600 hour. However, the pattern has secondary peak appearing about 1900 hour shows the ozone is closely associate with the circulation pattern from sea-breeze to land breeze. Other studies found that ship emission also give a significant impact to the ozone flocculation. The impact of ships emission to ozone concentration at coastal site up to 15 ppb and about 5 ppb at location 2 km from that coastal site [7]. Hence, this study of ozone concentration is important to predict ozone exceedances to assess and monitor the air quality.

There are many statistical approaches used to study the ozone concentration such as probability distribution, multiple linear regression and artificial intelligence. Among that, probability distribution has been widely used by researcher to predict the air pollutant concentration [8,9]. This study will focus on three distributions namely Lognormal, Weibull and inverse Gaussian distribution for prediction purposes. Those distributions being used for certain parameter to form their own shape and characteristic [10]. These parameters were commonly determined by using few techniques such as maximum likelihood estimator (MLE), method of moment (MOM) and least square error. However, MLE method is preferable in parameter estimation cause its efficiency and good theoretical properties [11].

The two-parameter Weibull distribution (scale (σ) and shape (λ)) is widely used in data analysis because of its flexibility in modeling. There are numerous papers and books dealing with various aspects of Weibull modeling, inference, applications, as well as parameter estimation [12]. The others competitor of Weibull distribution is Lognormal distribution which also good in most cases significant fit in seasonal and meteorological characterizations of daily data [13]. It was known that 2-parameter log-normal distribution (location (μ) and scale (σ)) give the best description of annual mean daily sulphur dioxide concentration for a wide range of ambient level. The others competitor of the Weibull and Log-normal distribution in modelling asymmetric data from various scientific fields is Inverse Gaussian distribution. In reliability and life testing, the inverse Gaussian distribution is particularly useful in situations where early failures dominate [14]. Inverse Gaussian consists of two identical parameters which is location (μ) parameter and scale (σ) parameter. It is a two-parameter family of continuous probability distribution [15].

The first aim of this study is to determine the goodness-of-best fit distribution data representing ozone concentration by using distribution function method. The second aim of this study is to determine the best distribution for ozone concentration level at Port Dickson and Port Klang by using three performance indicators namely normalized absolute error (NAE), prediction accuracy (PA), and coefficient of determination (R^2).

Materials and Methods

Study area

Two sites were selected for this study, Port Dickson and Port Klang as illustrated in Figure 1.

Site 1 (Port Dickson) is located 1 km from sea and it has large contributions to the local economy in oil and gas sector. It has two refineries that have been operating by Shell Refining and Petron Company which expected to contribute with air pollution problem. According to Department of Environment Malaysia (DoE) [16], Port Dickson was recorded 7 days unhealthy during 2012 which means that the air quality in Port Dickson needs to be investigated. Site 2 (Port Klang) has the main business in marine-based activity. A lot of ships docked here for export and import purposes. Highly shipping emission and traffic congestions were observed here due to truck involvement was expected to trigger the ozone formation, thus lead to high ozone concentration. Malaysian

Department of Environment (DOE) [16] stated that Port Klang had 13 unhealthy days on 2012 which represents third highest in Klang Valley based from the annual Environment Quality Report.

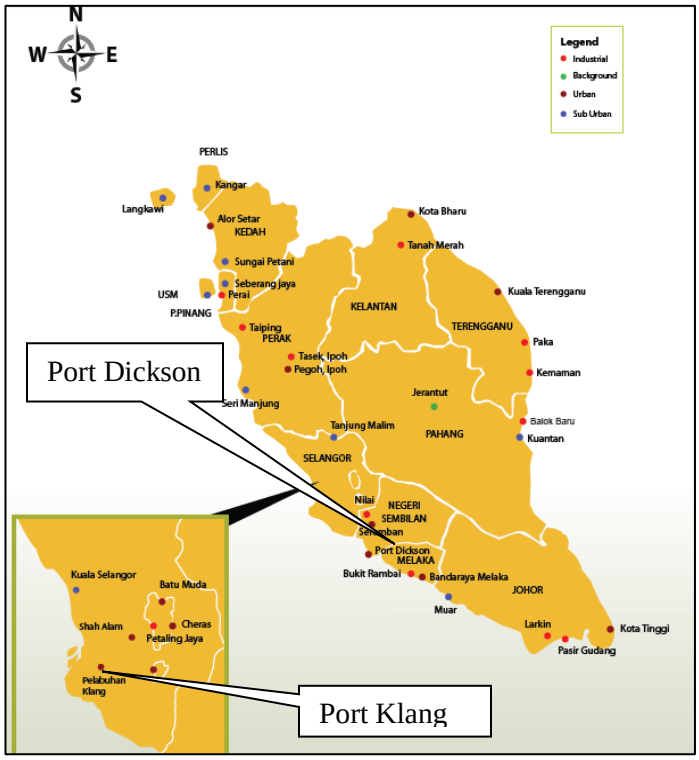


Figure 1. Description of the selected study area (Source: EQR 2012).

Probability distribution

Probability distribution is mathematical form to construct theoretical and idealization of real data set [17]. The probability density function (PDF) and cumulative density function (CDF) were used to estimate the probability of the exceedences of ozone based on Malaysian Ambient Air Quality Guideline (MAAQG). The PDF plot was used to identify the skewness of the distribution and it plot by using the value of parameter estimation [18]. The derivation of PDF was used for prediction of exceedences [19] and the CDF was used to determine the probability of air pollutant concentration [20]. Table 1 shows the PDF and the parameter estimation used [21].

Weibull distribution

The formula used for parameter estimation that was given by Lu [9]:

$$f(x) = \left(\frac{\lambda}{\sigma}\right)\left(\frac{x}{\sigma}\right)^{\lambda-1} \exp\left[-\left(\frac{x}{\sigma}\right)^{\lambda}\right]$$

The cumulative distribution function takes the form as

$$F(x) = 1 - \exp\left[-\left(\frac{x}{\beta}\right)^{\alpha}\right]$$

where $x \geq 0$, α = shape parameter, β = scale parameter.

β was obtain by

$$\frac{\left(\sum_{i=1}^{n}(x_i^{\sigma}\ln x_i)\right)}{\left(\sum_{i=1}^{n}x_i^{\sigma}\right)}-\left(\frac{1}{\sigma}\right)-\left(\frac{1}{n}\right)\left(\sum_{i=1}^{n}\ln x_i\right)=0$$

and α was then calculated using following equation

$$\lambda=\left(\frac{1}{n}\sum_{i=1}^{n}x_i^{\hat{x}}\right)^{\frac{1}{\sigma}}$$

Table 1. Probability density function and its parameter estimates

Distribution	Probability Density Function	Parameter Estimates
Weibull	$f(x)=\left(\frac{\lambda}{\sigma}\right)\left(\frac{x}{\sigma}\right)^{\lambda-1}\exp\left[-\left(\frac{x}{\sigma}\right)^{\lambda}\right]$	$\frac{\left(\sum_{i=1}^{n}(x_i^{\sigma}\ln x_i)\right)}{\left(\sum_{i=1}^{n}x_i^{\sigma}\right)}-\left(\frac{1}{\sigma}\right)-\left(\frac{1}{n}\right)\left(\sum_{i=1}^{n}\ln x_i\right)=0$; $\lambda=\left(\frac{1}{n}\sum_{i=1}^{n}x_i^{\hat{x}}\right)^{\frac{1}{\sigma}}$
gnormal	$f(x)=\frac{1}{x\lambda\sqrt{2\Pi}}\exp\left[-\frac{1}{2}\left(\frac{\ln(x)-\sigma}{\lambda}\right)^2\right]$	$\sigma=\frac{1}{n}\sum_{i=1}^{n}\ln(x_i)$; $\mu=\sqrt{\frac{1}{n}\sum_{i=1}^{n}[\ln(x_i)-\sigma]}$
Inverse gaussian	$\left(\frac{\sigma}{2\pi x^3}\right)^{\frac{1}{2}}\exp(-\frac{\sigma(x-\mu)^2}{2\mu^2 x})$	$\mu=\bar{x}$; $\sigma=\frac{n-1}{\sum_{i=1}^{n}\left(\frac{1}{x_i}-\frac{1}{\bar{x}}\right)}$

*μ is the location parameter, σ is the scale parameter, λ is the shape parameter, n is the total number of data

Lognormal Distribution

Lognormal was used to fit the ozone concentration data. Lognormal distribution with probability density function is given by Lu [9]:

$$f(x)=\frac{1}{x\lambda\sqrt{2\Pi}}\exp\left[-\frac{1}{2}\left(\frac{\ln(x)-\sigma}{\lambda}\right)^2\right]$$

The cumulative density function form for normal distribution is

$$f(x)=\frac{1}{2\Pi}\int_{-\infty}^{\frac{\ln(x)-\sigma}{\alpha}}e^{-\frac{x^2}{2}}\,dt$$

σ is obtain by solution below

$$\sigma=\frac{1}{n}\sum_{i=1}^{n}\ln(x_i)$$

and α by using solution below

$$\lambda = \sqrt{\frac{1}{n}\sum_{i=1}^{n}[\ln(x_i) - \sigma]}$$

Inverse Gaussian distribution
The probability density function (pdf) for Inverse Gaussian distribution given by Tweedie [15] is:

$$\left(\frac{\sigma}{2\pi x^3}\right)^{\frac{1}{2}} \exp\left(-\frac{\sigma(x-\mu)^2}{2\mu^2 x}\right)$$

where λ is scale parameter and μ is location parameter. The parameter estimation used is:

$$\sigma = \frac{n-1}{\sum_{i=1}^{n}\left(\frac{1}{x_i} - \frac{1}{\bar{x}}\right)}$$

for shape parameter, and

$$\mu = \bar{x}$$

for location parameter.

Performance indicator
The performance indicators used for this study were NAE, PA, and R^2 to identify the best distribution. The best distribution were selected by range of value that closest to 1 for adequacy measure (PA and R^2) and the value closest to zero for error measure (NAE). Table 2 shows three equations used for the performance indicator [22].

Table 2. Performance indicator equation

Indicators	**Equation**
Normalize absolute error	$\frac{\sum_{i=1}^{n} Abs(P_i - O_i)}{\sum_{i=1}^{n} O_i}$
Prediction of accuracy	$\frac{\sum_{i=1}^{N}(P_i - \bar{O})^2}{\sum_{i=1}^{N}(O_i - \bar{O})^2}$
Coefficient of determination	$\left(\frac{\sum_{i=1}^{N}(P_i - \bar{P})(O_i - \bar{O})}{NS_{pred}S_{obs}}\right)^2$

* N = Number of observations, P_i = Predicted values, O_i = Observed values, $\bar{P}$ = Mean of the predicted values, $\bar{O}$ = Mean of the observed values, S_{pred} = Standard deviation of the predicted values, S_{obs} = Standard deviation of the observed values

Results and Discussion

Ozone concentration data

The ozone concentration data collected over a year period 2010 from January to December by DOE Malaysia and managed by private company Alam Sekitar Malaysia Sdn Bhd (ASMA). The ozone concentration was measured by ASMA using Teledyne Ozone Analyzer Model 400 A UV Absorption [23]. The data was collected every hour and the unit measurement is part per million (ppm). All descriptive statistic ozone concentration for Port Klang and Port Dickson is run by using IBM SPSS statistic 20 analytical and MATLAB r2014a computational software. Table 3 is the descriptive statistic of ozone concentration result from the software used in this study.

Table 3. Descriptive statistics of ozone concentrations

Descriptive	Port Klang (ppm)	Port Dickson (ppm)
Maximum	0.123	0.140
Mean	0.020	0.026
Median	0.014	0.022
Standard Deviation	0.018	0.019
Skewness	1.321	1.013

From Table 3, the maximum value of ozone concentration recorded in Port Dickson was higher than Port Klang. However, measurements at both sites were exceeding the MAAQG (0.1ppm). The mean value of both sites was greater than median indicated there was high concentration recorded during period of study. The result also shows positively skewed to the right for Port Klang (sk = 1.321) and Port Dickson (sk = 1.013) explicate that the right tails of data is longer and higher concentration has been occurred.

Parameter estimation

Table 4 shows the parameter estimation values for Port Dickson and Port Klang, respectively. From the table, the shape parameter (λ) is higher than scale parameter (σ) for Weibull distributions indicate higher ozone concentration has occurred at both sites. The Lognormal parameter shows higher ozone concentration has occured which indicate by the scale parameter (σ) is higher than location parameter (μ). The inverse Gaussian parameter also show the location or mean parameter (μ) is higher than shape parameter (λ) which indicates high ozone concentration was occurred during this period.

Table 4. Parameter estimation for Port Dickson and Port Klang

Distribution	Site	Parameter	
Weibull	Port Dickson	σ= 0.029	λ= 1.418
	Port Klang	σ= 0.021	λ= 1.098
Lognormal	Port Dickson	μ= -3.963	σ= 0.901
	Port Klang	μ= -4.386	σ= 1.036
Inverse Gaussian	Port Dickson	μ= 0.026	λ= 0.019
	Port Klang	μ= 0.020	λ= 0.012

The location parameter (μ), the scale parameter (σ) is the shape parameter, λ.

Probability distribution graph

From the parameter estimation, the CDF graph can be plotted to estimate goodness-of-fit of data. CDF graph for all distribution used were plotted to determine the best goodness-of-fit and the result were found to be Weibull distribution. Figure 2, shows the Weibull CDF plot of Port Dickson and Port Klang, respectively. The observation line was underestimates at approximately 0.038 ppm before it fitted again with theoretical line between 0.04 ppm and 0.06 ppm for Port Dickson site. Meanwhile, observation line was overestimates at 0.08 until 0.02 ppm then underestimate between 0.02 ppm and 0.06 ppm before it fitted again with theoretical line at 0.07 ppm for Port Klang site. Figure 3 shows the PDF plot of Weibull distribution depicted as it skewed to the right. The result also showed that the mode for Port Dickson site is approximately about 0.012 ppm and Port Klang site is approximately 0.008 ppm.

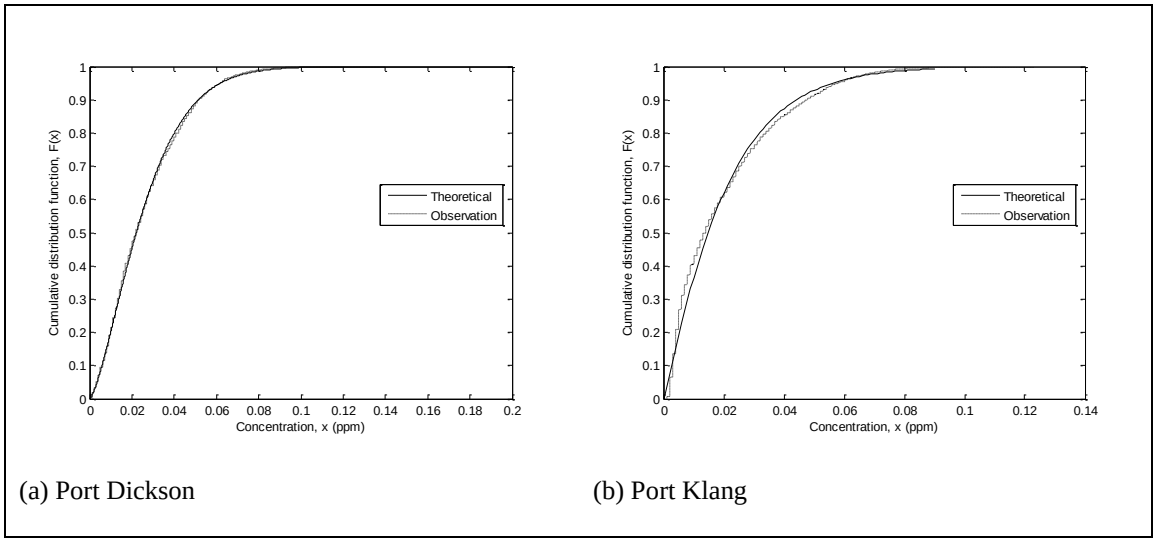


Figure 2. Weibull distribution CDF plot for Port Dickson and Port Klang

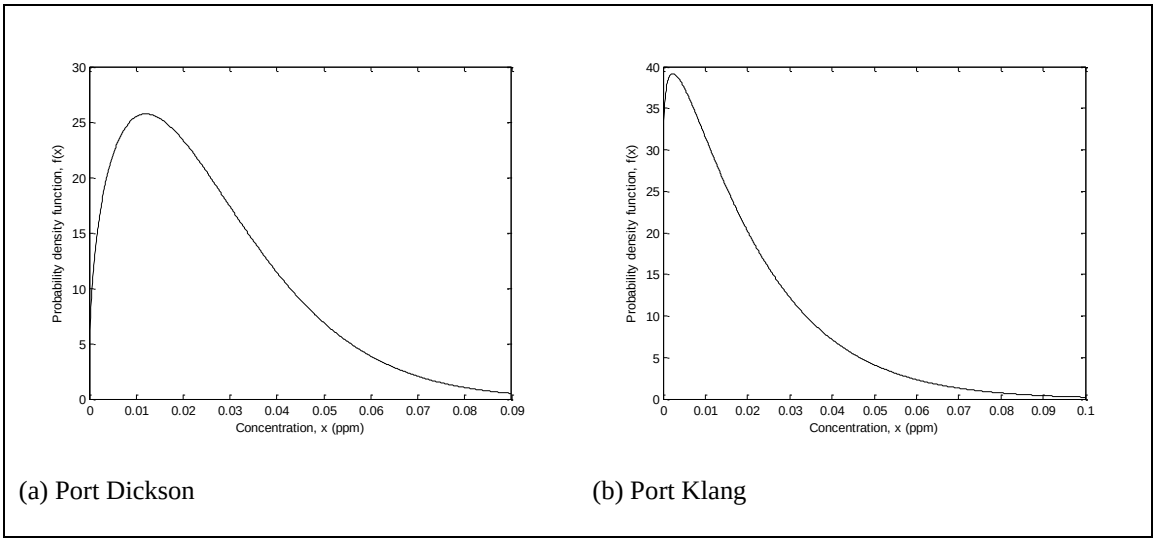


Figure 3. Weibull distribution PDF plot for Port Dickson and Port Klang

Performance indicators

Table 5 shows the best performance for both sites is Weibull distribution that computes by using computational MATLAB software.

The best result for adequacy measure PA and R^2 at Port Dickson is 0.99 and 0.98, respectively. Meanwhile, Weibull distribution scores the best for adequacy measure (PA = 0.99 and R^2 = 0.99) and error measure (NAE = 0.08) at Port Klang site. Thus the Weibull distribution can be used for prediction purposes at both sites.

Table 5. Descriptive of performance indicator

Distribution	Site	NAE	PA	R^2
Weibull	Port Dickson	0.309	0.992*	0.984*
	Port Klang	0.077*	0.993*	0.986*
Lognormal	Port Dickson	0.205*	0.911	0.829
	Port Klang	0.203	0.886	0.786
Inverse Gaussian	Port Dickson	0.264	0.921	0.849
	Port Klang	0.213	0.923	0.852

*best distribution

Conclusion

The descriptive of ozone concentrations in Port Dickson and Port Klang were statistically investigated. This study concluded the best distribution to represent ozone concentration at Port Dickson and Port Klang were found to be Weibull distribution. This distribution performs the best goodness-of-fit data from CDF graph plotted. This distribution also shows best performance indicator with highest score in NAE with smallest error measure (value closest to zero) for Port Klang. It is also scored well in PA and R^2 with highest adequacy measure (value closest to 1) for both sites.

Acknowledgement

Authors would like to thank the Ministry of Higher Education that was funded this study under Fundamental Research Grant Scheme 2013. Last but not least, DoE Malaysia for their permission to utilize the air quality data for this study and Universiti Malaysia Terengganu for their financial support.

References

1. Ghazali N. A., Ramli N. A., Yahaya A. S., Md Yusof N. F. F., Sansuddin N. and Al Madhoun W. A. (2010). Tr ansformation of nitrogen dioxide into ozone and prediction of ozone concentrations using multiple linear regres sion techniques. *Environmental Monitoring and Assessment*, 165: 475 – 489.
2. Munir S, Chen H, and Ropkins K (2012). Modelling the impact of road traffic on ground level ozone concentrat ion using a quantile regression approach. *Atmospheric Environment*, 60: 283 – 291.
3. Yang, W. and Omaye, S., (2009). Air pollutants, oxidative stress and human health. *Research/Genetic tox icology and Environmental Mutagenesis*, 674: 45-54.
4. Shan W., Zhang J., Huang Z. and You L. (2010). Characterizations of ozone and related compounds under the influence of maritime and continental winds at a coastal site in the Yangtze Delta, nearby Shanghai. *Atmospheric Research*, 97: 26 – 34.
5. Donev E., Zeller K. and Avramov A., (2002). Preliminary background ozone concentration in the mountain and coastal areas of Bulgaria. *Environment Pollution*, 117: 281 – 286.
6. Nair P. R., Chand D., Lal S., Modh K. S., Naja M., Parameswaran K., Ravindran S. and Venkataramani S. (2002). Temporal variations in surface ozone at Thumba (8.6^{o}N, 77°E)- a tropical coastal site in India. *Atmospheric Environment*, 36:603 – 610.

7. Song S. K., Shon Z. H., Kim Y. K., Kang Y. H., Oh I. B. and Jung C.H. (2010). Influence of ship emissions on ozone concentrations around coastal areas during summer season. *Atmospheric Environment*, 44: 713 – 723.
8. Lu, H. C., (2000). The statistical characters of PM_{10} concentration in Taiwan area. *Atmospheric Environment*, 36: 491 – 502.
9. Lu, H. C., (2003). Estimating the Emission Source Reduction of PM_{10} in Central Taiwan. *Chemosphere*, 54: 805-814.
10. Forbes C., Evan M., Hastings N. and Peacock B., (2011). Statistical Distributions. 4th Edition. John Wiley & sons. New Jersey.
11. Zerda I. (2012). An experimental comparison of popular estimation method for the Weibull, Gamma, and Gompertz distributions. *Schedae Informaticae*, 20: 67 – 82.
12. Zhibin T., (2009). A new approach to MLE of Weibull distribution with interval data. *Reliability Engineering and System Safety*, 94: 394 – 403.
13. Hadley A. and Toumi R., (2003). Assessing changes to the probability distribution of sulphur dioxide in the UK using a lognormal model. *Atmospheric Environment*, 37: 1461 – 1474.
14. Chikara R. S. and Folks J. L., (1989). The inverse Gaussian distribution: Theory methodology and applications. Marcel Dekker. New York.
15. Tweedie M. C. K. (1957). Statistical properties of inverse Gaussian distribution. I. *The Annal of Mathematical Statistics*, 362 – 367.
16. Department of Environment, Ministry of Natural Resources and Environment (2012). Malaysia Environmental Quality Report 2012; ISSN 0127-6433.
17. Wilks D. S. (2011). Statistical methods in the atmospheric sciences. 3rd Edition. Elsevier. USA.
18. Alshangiti, A.M., Kayid, M. and Alarfaj, B. (2014). A new family of Marshall–Olkin extended distribution. *Journal of Computational and Applied*, 271: 369 – 379.
19. Hamid, H. A., Yahaya, A. S., Ramli N. A., and Ul-Saufie, A. Z. (2013). Finding the best statistical distribution model in PM_{10} concentration modeling by using lognormal distribution. *Journal of Applied Science*, 13 (2): 294 – 300.
20. Sansuddin, N., Ramli, N. A., Yahaya, A. S., Yusof, N. F. F. M., Ghazali, N. A. and Madhoun, W. A. A. (2011). Statistical analysis of PM_{10} concentrations at different locations in Malaysia. *Environment Monitoring and Asse ssment*, 180: 573 – 588.
21. Sharma, P., Sharma, P., Jain, S. and Kumar, P., (2013). An intergrated statistical approach for evaluating the exceedance of criteria pollutants in the ambient air of megacity Delhi. *Atmospheric Environment*, 70: 7 – 17.
22. Yahaya, A. S. Ramli, N. A. Ul-Saufie, A. Z., Hamid, H. A., Ahmat, H. and Mohtar, Z. A. (2013). Predicting CO concentrations levels using probability distributions. *International Journal of Engineering and Technology*, 3: 900 – 905.
23. Banan N, Latif M. T., Juneng L. and Ahamad F., (2013). Characteristics of surface ozone concentrations at stations with different backgrounds in the Malaysia Peninsula. *Aerosol and Air Quality Research*, 13: 1090 – 1106.

Malaysian Journal of Analytical Sciences, Vol 20 No 3 (2016): 560 - 566
DOI: http://dx.doi.org/10.17576/mjas-2016-2003-14

MALAYSIAN JOURNAL OF ANALYTICAL SCIENCES
Published by The Malaysian Analytical Sciences Society
ISSN 1394 - 2506

COMPARATIVE COLUMN STUDIES OF CHEMICALLY MODIFIED ION EXCHANGE RESIN WITH AGGLOMERATED ADSORBENTS FOR FLUORIDE REMOVAL

(Kajian Perbandingan Turus Resin Penukaran Ion Terubahsuai dengan Penjerap Teraglomerat bagi Penyingkiran Fluorida)

Sivasankari Chandasekaran[1]* and Arulanantham Arthanas[2]

[1]*Department of Chemistry,*
Government College of Technology, Coimbatore 641 013, India
[2]*Department of Chemistry,*
Sri Sakthi Institute of Engineering and Technology, Coimbatore 641 062, India

**Corresponding author: sivasankarigct@gmail.com*

Received: 24 February 2015; Accepted: 27 October 2015

Abstract

The present study is aimed to prepare three different granular adsorbents and applying on fluoride removal in column operations. Commercially available powdered adsorbents activated alumina (PAA) and tri-calcium phosphate (PTCP) is agglomerated to obtain granular polymer agglomerated alumina (GPAA) and granular polymer agglomerated tri-calcium phosphate (GTCP). Agglomeration was carried out using powdered adsorbents with neutral and non-toxic polymer Poly (vinyl acetate) to granular form of 20 – 50 mesh size. Plain Amberlite IRA 400 anion exchange resin (PR) was chemically modified (CMR) through phosphorylation by alum impregnation and investigated for fluoride removal as a third adsorbent. Column studies were carried out using 1.5 cm diameter columns to find out the suitability of the material for large scale applications. Solutions containing 5 mg L^{-1} of fluoride adjusted to pH 7.0 were allowed to percolate through the column at known flow rates. Under optimum conditions of flow rate 10 mL min^{-1} and bed height of 31 cm (25 g) of GPAA, 36 cm (20 g) of GTCP and 42 cm (20 g) of CMR respectively. The amount of fluoride removed were 1.948 mg g^{-1}, 2.1005 mg g^{-1}, and 2.3325 mg g^{-1} of the respective adsorbent. The effects of co-existing anions were also studied in column experiments. Column regeneration studies were also carried out for all the adsorbents with $Al_2(SO_4)_3$ solutions. The cyclic regeneration experiments indicated that all the three adsorbents could be completely regenerated and used for repeated cycle. Ground water sample was collected from a village in Dharmapuri district of South India. The defluoridation capacity of the wet resin (6.80 mg g^{-1}) was found to be three times more than dried resin. CMR potentially can be the best adsorbent for fluoride removal.

Keywords: defluoridation, agglomeration, poly vinyl acetate, granular adsorbents, column studies

Abstrak

Matlamat kajian ini adalah untuk menyediakan tiga penjerap berbutir yang berbeza dan diaplikasikan untuk penyingkiran fluorida dalam operasi turus. Penjerap komersial serbuk teraktif alumina (PPT) dan tri-kalsium fosfat (PTCP) digumpalkan untuk mendapatkan polimer berbutir alumina (GPAA) dan polimer berbutir tri-kalsium fosfat (GTCP). Penggumpalan telah dijalankan dengan menggunakan penjerap serbuk poli polimer (vinil asetat) neutral dan tidak toksik kepada bentuk berbutir dari 20-50 saiz sirat. Amberlit kosong IRA 400 anion resin pertukaran (PR), telah diubahsuai secara kimia (CMR) melalui kaedah pemfosforilan mengunakan impregnasi alum, dan diuji untuk penyingkiran fluorida sebagai penjerap ketiga. Kajian turus telah dilakukan dengan menggunakan 1.5 cm diameter turus bagi mengetahui kesesuaian bahan untuk aplikasi skala besar. Larutan fluorida yang berpekatan 5 mg L^{-1} dan pH 7.0 dibiarkan meresap melalui turus pada kadar aliran yang telah dikenalpasti. Di bawah keadaan

optimum, kadar aliran ialah 10 mL min $^{-1}$ dan ketinggian dasar masing – masing ialah 31 cm (25 g) GPAA, 36 cm (20 g) GTCP dan 42 cm (20 g) CMR. Jumlah fluoride yang disingkirkan ialah 1,948 mg g^{-1}, 2,1005 mg g^{-1}, dan 2,3325 mg g^{-1} mengikut bahan penjerap masing-masing. Kesan anion sedia ada juga dikaji dalam eksperimen turus. Kajian pengunaan semula turus turut dijalankan untuk semua penjerap menggunakan larutan $Al_2(SO_4)_3$. Eksperimen penghasilan semula kitaran menunjukkan bahawa ketiga-tiga penjerap boleh dihasilkan semula sepenuhnya dan digunakan untuk kitaran berulang. Sampel air bawah tanah telah dikumpulkan dari sebuah kampung di daerah Dharmapuri, India Selatan. Kapasiti penyingkiran fluorida oleh resin basah (6.80 mg g^{-1}) telah didapati tiga kali lebih tinggi daripada resin kering. CMR berpotensi menjadi penjerap yang terbaik untuk penyingkiran fluorida.

Kata kunci: penyingkiran fluorida, penggumpalan, poli vinil asetat, penjerap berbutir, kajian turus

Introduction

It is well known that trace elements are essential and beneficial to organism in minute concentrations, as they play a significant role in many metabolic processes. But they would be toxic when their concentrations exceed the permissible levels. Fluoride, a typical trace element is distributed in rock, soil and water. The safe limit of fluoride in drinking water level in between 0.7 mg L^{-1} to 1.5 mg L^{-1} but harmful once it exceeds to 1.5 mg L^{-1} which is the World Health Organization limit being followed in most of the nation's [1]. Fluoride in minute quantity is an essential component for normal mineralization of bones and formation of dental enamel [2]. However its excessive intake may result in slow, progressive crippling scourge known as fluorosis.

Defluoridation is the only practicable option to overcome the problem of excessive fluoride in drinking water, where alternate source is not available. Adsorption technique retains a major place in defluoridation research and practice because of its greater accessibility and lower cost. Several adsorbent materials have been tried in the past to find out an efficient and economical defluoridating agent. Activated carbons, low cost waste materials, alum impregnated materials, mineral based adsorbents, activated alumina, tri-calcium phosphate and ion-exchange resins etc. are different adsorbent materials reported. Activated alumina is regarded as an excellent and widely used adsorbent for defluoridation. Tri-calcium phosphate is another adsorbent that has gel structure and better characteristics than that of activated alumina [3]. Both the adsorbents show increased adsorption capacity in the powder form as the surface area and consequently more number of active sites are exposed.

However, the adsorbents in the powdered form are not suitable for continuous column operations as they produce pressure drop. It was decided to agglomerate the above powdered adsorbents into granular form so that the adsorbents could be profitably used in column operations without loss in their capacity for fluoride removal. A suitable method could be agglomeration using a cheap, readily available and non-toxic polymer. Polyvinyl acetate was found to be a better choice as it is soluble in simple organic solvents but insoluble in aqueous medium. Apart from the preparation of granular adsorbents from powdered activated alumina and tri-calcium phosphate by agglomeration it was also decided to prepare a superior adsorbent for fluoride removal and compare its fluoride removal capacity with other two adsorbents. The better choice would be to chemically modify readily available granular ion exchange polymer resin so that its physical characteristics could be retained, simultaneously improving its capacity, pH tolerance and selectivity towards fluoride in the presence of common anions.

Materials and Methods

Defluoridation materials

Commercially available acidic powdered activated alumina (PAA) and powdered tri-calcium phosphate (PTCP), and solid poly vinyl acetate were used for agglomeration. Granular polymer agglomerated alumina (GPAA) was prepared by thoroughly mixing one part by weight of Poly (vinyl acetate) in minimum quantity of acetone and 2.5 parts by weight of finely powdered activated alumina till a semi-solid mass was obtained. Large volume of water was poured into it in one lot with vigorous stirring. It was found that this approach was effective to cover the aluminium oxide powder by polymer. The agglomerated product was separated and pressed between two glass plates into a sheet of 2 – 3 mm thickness. The sheet was washed with water dried overnight at room temperature and then cut to 20 – 50 mesh size for detailed examination. Polymer agglomerated granular tri-calcium phosphate (GTCP) was also prepared by the same method used for the preparation GPAA. Chemically modified resin (CMR) was prepared by phosphorylation of Amberlite IRA 400 anion exchange resin followed by alum impregnation.

Initially the resin was washed with distilled water and dried at room temperature for few hours. An amount of 50 g of this resin was treated with 100 mL of concentrated phosphoric acid and heated in the hot air oven at a temperature of 160 ± 1ºC for 12 hours. The material removed from the oven was washed with distilled water to remove excess acid. The sample was then soaked in 1% aluminium sulphate solution; the pH was adjusted to 3.0 – 3.5 and left soaked for 12 hours. At the end of this period, the resin was separated, washed to remove excess of Al(III) ions and then dried at 100 ± 5 ºC.

Reagents and standard solutions

Fluoride stock solution was prepared by dissolving 2.21 g pure of anhydrous sodium fluoride (Sd fine-chemicals Ltd) in 1000 mL distilled water in a plastic volumetric flask and all working solutions were prepared by appropriate dilution of stock solution with distilled water. The Total Ionic Strength Adjustment Buffer (TISAB) was prepared according to a recommended procedure [4]. Fluoride ion concentration was estimated by Orion Ion meter (EA 920 model).

Column experiments

Powder activated alumina (PAA) and powder tri-calcium phosphate (PTCP) developed pressure drops in the course of column experiments. To overcome the problem of pressure drop, GPAA, GTCP were used and their fluoride removal behaviors were compared with that of CMR. Column experiments were carried out using 70 cm long and 1.5 cm diameter. Teflon column packed with the materials under study, to a predetermined height. As the fluoride concentration of untreated drinking water usually lies below 5 mg L^{-1} and pH remains in the range of 6.5 to 8.5, solutions containing 5 mg L^{-1} of fluoride adjusted to pH 7.0 were allowed to percolate through the column at known flow rates. Each batch of the effluent (1000 mL) was separately collected and analyzed for fluoride content using Orion ion meter. Percolation of fluoride solution was stopped when the concentration of fluoride in the effluent exceeded the permissible limit of 1.5 mg $L^{-1.}$ In order to find out the optimum flow rate, the fluoride solutions were allowed to flow through the column of constant bed height at separate flow rates from 7, 10, 12 and 15 mL min^{-1}. The effluent was analyzed until breakthrough (1.5 mg L^{-1}) occurred and the capacity of the adsorbents in each instance was established. In order to find out the optimum bed height for maximum removal of fluoride, experiments were conducted using varying amount of each adsorbents to fill up the column to different bed heights, and percolating the fluoride solution at optimum flow rate.

Effects of co-existing anions

The effect of co-existing anions (Cl^-, SO_4^{2-}, HCO_3^- and PO_4^{3-}) on fluoride removal efficiency of the adsorbents were also studied using column experiments with fluoride solution of 5 mg L^{-1} and varying anions concentration from 50 mg L^{-1} to 200 mg L^{-1}. All the experiments were conducted using GPAA, GTCP and CMR with already established optimum flow rates and bed heights. Each batch of the effluents (1000 mL) were separately collected and analyzed for fluoride content.

Column regeneration studies

Regeneration of the column was done by percolating sufficient volume of aluminium sulphate solution of predetermined concentrations through the exhausted bed of adsorbents. In order to find out the efficiency of the adsorbents after regeneration, experiments were performed using columns containing 25 g of GPAA, 20 g each of GTCP and CMR. Fluoride solution containing 5 mg L^{-1} was allowed to percolate through the column at 10 mL min^{-1} till the break point. The volume of aluminium sulphate solution used was measured in terms of number of bed volumes. Since the desorption of fluoride from the adsorbent bed is a slow process, the exhausted column was washed with three bed volumes of aluminium sulphate solution at a flow rate of 5 mL min^{-1} and one bed volume of aluminium sulphate solution was left in contact with the adsorbent for 12 hours.The solution was then drained out and the column was washed thoroughly with water to render it free from aluminium (III). The capacity of the regenerated adsorbents was determined after conducting the defluoridation experiments under optimum conditions. Attrition loss of all the three adsorbents was found out by the usual procedure [5].

Application of CMR for defluoridation of real water sample

In order to find out the suitability of the adsorbent for large scale applications for removal of fluoride from ground water, experiments were conducted using 20 g of wet CMR. The water used for the experimental purposes was

collected from Dharmapuri district of Tamilnadu in South India. Water sample was analyzed for its characteristics as presented in Table 1. The capacity of CMR under wet condition for real water sample was determined as per the procedure discussed in column studies.

Table 1. Characteristics of the real water sample

Characteristics of the water sample	**Concentration (mg L^{-1}) except pH**
pH	7.98
Alkalinity	96 as $CaCo_3$ equivalent
Total hardness	161 as $CaCo_3$ equivalent
Chloride	109
Sulphate	42
Fluoride	3.3

Results and Discussion

Influence of flow rate

The capacities at various flow rates obtained for GPAA, GTCP and CMR are summarized in Table 2. It was found that the fluoride removal is almost constant 1.694 ± 0.03 mg g^{-1} for GPAA, 1.86 ± 0.02 mg $g^{-1}$for GTCP and 2.36 ± 0.03 mg g^{-1} for CMR up to flow rates 12 mL min^{-1}. At a higher flow rate of 15 mL min^{-1} the fluoride removal was found to be drastically reduced to 1.165 mg g^{-1}, 1.506 mg g^{-1} and 1.9175 mg g^{-1} for the respective adsorbents. It may be concluded that at lower flow rates the fluoride ions have sufficient time to reach the reaction sites and get adsorbed. At higher flow rates there is a reduced interaction between the fluoride and the adsorbent and hence there was a rapid fall in the capacity of adsorbents for fluoride. Therefore, in all subsequent experiments, a flow rate of 10 mL/min was employed for all the three adsorbents.

Table 2. The capacities of various flow rates obtained for GPAA, GTCP and CMR

Adsorbents	**Fixed bed heights (cm)**	**Capacities at various flow rate (mg g^{-1})**			
		7 mL (min^{-1})	**10 mL (min^{-1})**	**12 mL (min^{-1})**	**15 mL (min^{-1})**
GPAA	25	1.697	1.694	1.693	1.165
GTCP	27	1.868	1.868	1.846	1.507
CMR	42	2.390	2.333	2.328	1.918

Influence of bed height

The bed height is another important parameter that determines the capacity of any adsorbent. The effect of variation of fluoride removal capacity by unit weight of all the three adsorbents, at the fixed flow rate of 10 mL min^{-1} was summarized in Table 3.

It was found that the minimum bed heights for maximum fluoride removal, in terms of unit weight of adsorbents are 31 cm (25 g) for GPAA 36 cm (20 g) for GTCP and 42 cm (20 g) for CMR. Therefore the fluoride removal capacities by unit weight of all the three adsorbents can be reported as 1.95 mg g^{-1} for GPAA, 2.10 mg g^{-1} for GTCP and 2.33 mg g^{-1} for CMR. The results obtained are summarized in Table 4. Therefore the optimum bed heights maintained for further experiments are 31 cm for GPAA, 36 cm for GTCP and 42 cm for CMR.

Table 3. The capacities of various bed heights obtained for GPAA, GTCP and CMR

Adsorbents	Fed flow rate (mL min^{-1})	Various bed height (cm)	Adsorption capacities (mg g^{-1})
GPAA	10	19 (15 g)	1.309
		25 (20 g)	1.695
		31 (25 g)	1.948
		37 (30 g)	1.950
GTCP	10	18 (10 g)	1.848
		27 (15 g)	1.868
		36 (20 g)	2.099
		45 (25 g)	2.140
CMR	10	21 (10 g)	1.896
		31.5 (15 g)	2.185
		42.0 (20 g)	2.333
		52.5 (25 g)	2.331

Table 4. The results obtained for GPAA, GTCP and CMR

Adsorbents	Flow rate (mL^{-1})	Bed heights (cm)	Capacities of the adsorbents (mg g^{-1})
GPAA	10	31	1.948
GTCP	10	36	2.099
CMR	10	42	2.333

Effect of common anions on the removal of fluoride on GPAA, GTCP and CMR

From the results (Table 5), it was observed that the presence of chloride has no significant effect on the efficiency of the adsorbents up to 200 mg L^{-1}. The presence of sulphate found to affect the efficiency of the adsorbents to a small extent. For GPAA the fluoride removal capacity was found to be reduced to 95.2 %, 87.5 %, 66.5 % and 45.7 % and in case of GTCP it was found to be reduced to 99.6 %, 92.7 %, 78.6 % and 67.3 % for respectively for 50 mg L^{-1},100 mg L^{-1}, 150 mg L^{-1} and 200 mg L^{-1} of SO_4^{2-} ion concentration. Presence of sulphate has no significant effect on fluoride removal capacity of CMR within the tested concentration range of 50 mg L^{-1} to 200 mg L^{-1}. The bicarbonate interference showed significant reduction of fluoride removal due to the change in pH as well as the competing effect of this co-ion for the active sites of the adsorbents [6]. For the presence of bicarbonate concentration 50 mg L^{-1}, 100 mg L^{-1},150 mg L^{-1} and 200 mg L^{-1} the fluoride removal capacity was found to be reduced to 77.7 %, 67.5 %, 48.7 % and 38.6 % respectively for GPAA and 80.2 %, 44.7 %, 32.8 % and 22.4 % respectively for GTCP.

The presence of bicarbonate has no significant effect on the fluoride removal capacity of CMR up to a concentration of 200 mg L^{-1}. The other ion PO_4^{3-} interferes with the sorption of fluoride at the elevated concentrations due to the preferential adsorption of PO_4^{3-} over activated alumina and tri-calcium phosphate. The fluoride removal efficiency of GPAA decreased to 69.9 %, 44.8 %, 26.4 % and 18.4 % for 50 mg L^{-1}, 100 mg L^{-1},150 mg L^{-1} and 200 mg L^{-1} of PO_4^{3-} and for GTCP it was reduced to 79.8 %, 33.2 %, 21.1 % and 10.6 %. It was noted that, the affinity sequence for anion adsorption on these two adsorbents were in the order $PO_4^{3-} > HCO_3^- > SO_4^{2-} > Cl^-$. These results agreed

with the reported defluoridation property of activated alumina [7].The presence of ion PO_4^{3-} found to significantly interfere with the adsorption of fluoride over CMR and the fluoride removal efficiency of the adsorbent decreased to 78.4 %, 60.0 %, 48.7 % and 39.5 % for 50 mg L^{-1}, 100 mg L^{-1}, 150 mg L^{-1} and 200 mg L^{-1} of PO_4^{3-} ion. From the results it was observed that bicarbonate, sulphate and chloride have no significant effect on fluoride removal capacity of CMR. The phosphate alone showed negative effect on CMR that to a lesser extent compared to the other two adsorbents. These characteristics of CMR suggest the fact that the adsorbent is selective for fluoride removal. Similar types of results were reported by Viswanathan and Meenakshi [8].

Table 5. Effect of common anions on the removal of fluoride on GPAA, GTCP and CMR

Adsorbents	Anions	Concentration of solution (%)			
		200 mg L^{-1}	150 mg L^{-1}	100 mg L^{-1}	50 mg L^{-1}
GPAA			Negligible		
GTCP	Cl^-		Negligible		
CMR			Negligible		
GPAA		38.6	48.7	67.5	77.7
GTCP	SO_4^{2-}	22.4	32.8	44.7	80.2
CMR			Negligible		
GPAA		38.6	48.7	67.5	77.7
GTCP	HCO^{3-}	22.4	32.8	44.7	80.2
CMR			Negligible		
GPAA		18.4	26.4	44.8	69.9
GTCP	PO_4^{3-}	10.6	21.1	33.2	79.8
CMR		39.5	48.7	60.0	78.4

Column regeneration

From the column regeneration studies, it was established that 0.25 %, 0.5 % and 1.0 % solutions of $Al_2(SO_4)_3$ was adequate for the complete regeneration of GPAA, GTCP and CMR. The cyclic defluoridation and subsequent regeneration with aluminium sulphate indicated the potential usefulness of the adsorbents for nearly 8 cycles without significant loss of adsorption capacity. The attrition loss was only around 5 %, for GPAA and GTCP, and 4 % for CMR even after 8 cycles. After 8 cycles, the adsorbents were withdrawn from the column, washed, air dried and weighed to find out its loss. It was noticed that there was no significant loss of all the three adsorbents [9].

It was surprising to note that the fluoride removal capacity of CMR was increased three fold after first regeneration and remained nearly the same, cycle after cycle. Hence, it could be established that the regeneration is not only complete but also has introduced new sites for adsorption of fluoride. The reason for this phenomenon may be due to the replacement of γ- AlOOH present on the dried resin by $-Al(H_2O)_3(OH)_3$ during regeneration under wet condition. This was also verified by fluoride column adsorption studies using freshly prepared wet CMR without drying. Hence, the following mechanism was proposed.

$$-Al(H_2O)_3(OH)_3 + 3F^- \longrightarrow Al(H_2O)_3(F_3) + 3OH^-$$

$$-Al(H_2O)_3(OH)_3 \text{ (under wet condition)} \longrightarrow AlOOH \text{ (Dry)} + 4H_2O$$

$$\text{-AlO-OH (under dry condition)} + F^- \xrightarrow{105 \pm 5^oC} \text{- AlO-F} + OH^-$$

Similar phenomenon has been observed for removal of fluoride using alum impregnated coconut shell carbon in wet condition [10].

Application of CMR

The defluoridation capacity of the wet resin for real water sample was calculated to be 6.8 mg g^{-1}. From the results, it is evident that the capacity of the adsorbent remained unaffected when applied to ground water containing fluoride. The attrition loss of CMR was found to be only around 4 %, even after 8 cycles of adsorption and regeneration.

Conclusion

Aluminium sulphate solution was found to be the best regenerent for regeneration of all the three adsorbents after saturation with fluoride. Complete regeneration could be achieved with 0.25 %, 0.5 % and 1.0 % aluminium sulphate solution in the case of GPAA, GTCP and CMR respectively. Column studies have clearly demonstrated that the unit capacity of CMR for adsorption of fluoride was found to be higher than that of other adsorbents GPAA and GTCP. The application of CMR to fluoride bearing waste water showed considerable adsorption capacity. In column regeneration studies, it could be seen that the capacity of GPAA and GTCP for the removal of fluoride remained nearly the same, cycle after cycle showing that the regeneration was complete and the capacity of the adsorbents were retained. The cyclic defluoridation and subsequent regeneration experiments indicated the potential usefulness of the GPAA, GTCP and CMR for nearly 8 cycles without significant loss of sorption capacity. But the fluoride removal capacity of CMR was increased three fold after first regeneration and remained nearly the same, cycle after cycle. It may be pointed out that chemically modified resin (CMR) is superior to other two adsorbents with respect to the removal of fluoride. A ground water sample collected from a village in Dharmapuri district of South India was tested for fluoride removal. The results showed that the defluoridation capacity of the wet resin was 6.80 mg g^{-1}, which leads to the conclusion that CMR could be a better adsorbent for fluoride removal from drinking water.

References

1. World Health Organization, WHO (1984), Guidelines for Drinking water Quality: Health Criteria and Supporting Information, World Health Organization, Geneva, Switzerland, Vol. II.
2. Bell, M. C. and Ludwig, T. G. (1970). The supply of fluoride to man: ingestion from water, in: Fluorides and Human Health, WHO Monograph Series 59, World Health Organization, Geneva.
3. Adler, H., Klein, G. and Lindsay F. K. (1938). Removal of fluorides from potable water by Tri-calcium phosphate. *Industrial and Engineering Chemistry*, 30 (2): 163 – 165.
4. Kemer, B., Ozdes, D., Gundogdu, A., Bulut, N., Duran, C. and Soyla, M. (2009). Removal of fluoride ions from aqueous solution by waste mud. *Journal of Hazardous Materials*, 168: 888 – 894.
5. Ragunathan J. and Krishnamoorthy S. (1984). Studies on resorcinol formaldehyde cationic resins. *Journal of Indian Chemical Society*, 61(10): 911 – 914.
6. Kagne, S., Jagtap, S., Dhawade, P., Kamble, S. P., Devotta, S. and Rayalu, S. S. (2008). Hydrated cement: A promising adsorbent for the removal of fluoride from aqueous solution. *Journal of Hazardous Materials*, 154: 88 – 95.
7. Tang, Y., Guan, X., Su, T., Gao, N. and Wang, J. (2009). Fluoride adsorption onto activated alumina: Modeling the effects of pH and some competing ions. *Colloids and surfaces A: Physicochemical Engineering Aspects*, 337: 33 – 38.
8. Viswanathan, N. and Meenakshi S. (2009). Role of metal ion incorporation in ion exchange resin on the selectivity of fluoride. *Journal of Hazardous Materials*, 162: 920 – 930.
9. Nur, T., Loganathan, P., Nguyen, T. C., Vigneswaran, S., Singh, G and Kandasamy, J. (2014). Batch and column adsorption and desorption of fluoride using hydrous ferric oxide: solution chemistry and modeling. *Chemical Engineering Journal*, 247: 93 – 102.
10. Arulanantham, A., Ramakrishna, T. V. and Balasubramanian, N. (1992). Studies on fluoride removal by coconut shell carbon. *Indian Journal of Environmental Protection*, 12(7): 531 – 536.

Malaysian Journal of Analytical Sciences, Vol 20 No 3 (2016): 567 - 572
DOI: http://dx.doi.org/10.17576/mjas-2016-2003-15

MALAYSIAN JOURNAL OF ANALYTICAL SCIENCES
Published by The Malaysian Analytical Sciences Society
ISSN 1394 - 2506

QUANTIFICATION OF CATECHIN IN LEAVES AND STEMS OF MALAYSIAN *Uncaria gambir* (HUNTER) ROXB. BY HPLC-DAD

(Kuantifikasi Katekin dalam Daun dan Batang *Uncaria gambir* (Hunter) Roxb. dari Malaysia Menggunakan KCPT-PSD)

Nurliayana Ibrahim[1], Nurul Zulaikha Mohd Yusoff[1], Rohaya Ahmad[1, 2]*

[1]*Faculty of Applied Sciences,*
Universiti Teknologi MARA, 40450 Shah Alam, Selangor, Malaysia
[2]*Atta-ur-Rahman Institute for Natural Products Discovery (AuRins),*
Universiti Teknologi MARA, 43600 Bandar Puncak Alam, Selangor, Malaysia

**Corresponding author: rohayaahmad@salam.uitm.edu.my*

Received: 24 February 2015; Accepted: 27 October 2015

Abstract

Recently, we reported the isolation of a novel flavonoid named uncariechin along with epicatechin and epiafzelechin from the leaf extract of *Uncaria longiflora* variety *pteropoda* (Miq.) Ridsd. of the family *Rubiaceae*. Continuing our investigation on the *Uncaria* genus, the identification and quantification of its phytoconstituents was carried out. The species of particular interest is the Malaysian *Uncaria gambir*. This species is distributed mainly in Malaysia and Indonesia and has been cultivated for the flavonoid catechin in Indonesia. Hence, the objective of this study is to determine the quantity of catechin in hexane (Hx), dichloromethane (DCM) and methanol (MeOH) extracts in both stem and leaf parts of the plant via HPLC-DAD. Our findings indicate that catechin is present in higher amounts in the MeOH extract [8.64 % (leaves); 5.12 % (stems)] compared to the DCM extract [0.77 % (leaves); 0.92 % (stems)] with no catechin found in the hexane extract. This is the first report of the quantification of catechin from Malaysian *U. gambir* using HPLC-DAD. The method can be used for the quantification of flavonoids from other *Uncaria* and related genus and is useful for targeted isolation of interest flavonoids.

Keywords: *Uncaria gambir*, catechin, flavonoid, HPLC-DAD

Abstrak

Kami telah melaporkan pengasingan satu flavonoid novel iaitu unkariekin bersama-sama dengan epikatekin dan epiafzelekin daripada ekstrak daun *Uncaria longiflora* var. *pteropoda* (Miq.) Ridsd. yang tergolong dalam famili *Rubiaceae.* Lanjutan terhadap penyelidikan genus ini, pengenalpastian fitokonstituen serta kuantifikasinya telah dijalankan, khususnya terhadap species *Uncaria gambir* dari Malaysia. Spesies ini banyak dijumpai di Malaysia dan Indonesia dan telah ditanam di Indonesia untuk flavonoid katekin. Maka, objektif penyelidikan ini adalah penentuan kuantiti katekin dalam ekstrak heksana (Hx), diklorometana (DCM) dan metanol (MeOH) dari batang dan juga daun *Uncaria gambir* dengan menggunakan KCPT-PSD. Hasil penyelidikan mendapati bahawa katekin banyak dijumpai di dalam ekstrak metanol [8.64 % (daun); 5.12 % (batang)] berbanding di dalam ekstrak diklorometana [0.77 % (daun); 0.92 % (batang)] tetapi tidak dikesan dalam ekstrak heksana. Ini merupakan laporan pertama bagi kuantifikasi katekin daripada *U. gambir* tempatan melalui KCPT-PSD. Kaedah ini boleh digunakan untuk kuantifikasi flavonoid dari spesies *Uncaria* lain dan genus berkaitan, malah berguna untuk pengasingan flavonoid sasaran.

Kata kunci: *Uncaria gambir*, katekin, flavonoid, KPCT-PSD

Introduction

The Uncaria genus comes from family of *Rubiaceae* and has been known for their medicinal and therapeutic properties. This genus represents 34 species which is widely distributed in tropical regions and about 14 species are available in Malaysia [1]. The most popular among local *Uncaria* species is *Uncaria gambir*. Malaysian *Uncaria* species have been reported to have antioxidant properties due to their flavonoids [2]. Catechin is a flavonoid frequently used as a chemical marker in the analysis of flavonoids in *Uncaria*. The choice of catechin as a marker flavonoid is due to its abundance in *Uncaria gambir* [3]. Previous studies on the quantification of flavonoids from crude extracts showed that five flavonoids are present in *Uncaria gambir* which are (-)-epigallocatechin, (-)-gallocatechin, (+)-catechin hydrate, (-)-epicatechin and (-)-epicatechin gallate [4]. Quantification of catechin on *Uncaria gambir* especially Malaysian *Uncaria gambir* has not been reported. There has been some report on the quantification of catechin in the leaves of *Uncaria gambir* collected from West Sumatera but no report has been found on the stems and leaves of Malaysian *Uncaria gambir*.

Thus, the objectives of this study are to obtain HPLC profiles and to quantify the amount of catechin in hexane, dichloromethane and methanol extracts of leaves and stems of *Uncaria gambir*. This study provides beneficial information regarding catechin content in the leaves and stems of Malaysian *Uncaria gambir* and knowledge on quantification of flavonoids by High Performance Liquid Chromatography (HPLC).

Materials and Methods

Chemicals and raw materials

The reference compound catechin was purchased from Sigma-Aldrich (India). The purity of the reference compound was over 95 %. HPLC-grade acetonitrile was purchased from RCL Labscan Limited (Bangkok, Thailand). HPLC-grade methanol and formic acid 98 % pure were purchased from Merck (Darmstadt, Germany). HPLC-grade hexane and HPLC-grade dichloromethane were purchased from Merck (USA) and Fisher Scientific (UK). Ultra-pure water, 18 MΩ-cm resistances, filtered through a 0.2 μm filter by Thermo Scientific (referred to here as deionized water). Trifluoroacetic acid (TFA), 99 % pure was purchased from Merck (Hohenbrunn, Germany).

Uncaria gambir was collected from Bukit Diman, Ajil, Terengganu, Malaysia. Voucher specimens (HTBP 4320) were deposited at the Herbarium Taman Botani, Putrajaya, Malaysia.

Preparation of reference and sample solutions for quantification and identification

Standard catechin was accurately weighed and dissolved in 0.05 % formic acid in 70 % methanol to make a stock solution with a concentration of 1.0 mg/ml. Appropriate volumes of the stock standard was added into the appropriate volume of 0.05 % formic acid in 70 % MeOH to prepare a mix working standard. The mixed standard was stored at 4 ^{o}C in the dark.

For sample preparation, dried leaves and stems of *U. gambir* were ground into fine powder. The finely ground plants materials were accurately weighed and macerated individually with MeOH for 72 hours at room temperature. The solvent was evaporated off under reduced pressure. A 10 g of crude methanolic *Uncaria gambir* extract (stems and leaves) was dissolved in H_2O: MeOH (1:1) and was put in a separatory funnel. The mixture was then subjected to liquid – liquid partitioning using Hx and DCM to yield Hx, DCM and MeOH extracts after solvent evaporation. The weight of the extracts was recorded. The extracts were stored at 4 ^{o}C until they were subjected to HPLC analysis.

For quantification, an amount 1.0 mg of each extracts was accurately weighed and dissolved in 1.0 ml of 0.05 % formic acid in 70 % MeOH. The solutions were then filtered through a 0.2 μm membrane filter before being injected into HPLC for analysis.

HPLC-DAD quantitative analysis

HPLC quantitative analysis was performed on an Agilent series 1200 LC system (Agilent Technologies, USA) equipped with a quaternary solvent delivery system, an on-line degasser, a diode-array detector (DAD) system performing the wavelength scanning from 190 to 400 nm, an injector with 20 μL sample loop and a column

compartment. Separation was carried out using a Zorbax Eclipse XDB-C18 column (250 mm x 4.6 mm, i.d. 5 μm), from Agilent Technologies (USA). Column temperature was maintained at 25 ^{o}C. Elution was conducted using mobile phase A (0.1 % TFA in 5 % acetonitrile) and mobile phase B (0.1 % TFA in acetonitrile) with a gradient elution program at a flow rate of 0.8 mL/min. The following gradient was applied: 0-10 min 88-82 % A, 10-15 min 82 % A, 15-30 min 50 % A. The UV absorbance was monitored at wavelength of 280 nm. The solvents for the mobile phases were filtered through a 0.45 μm membrane filter. 10 μL of each sample and standard was injected manually to the HPLC system. The data were processed with Agilent ChemStation software (Agilent Technologies, USA).

Method validation

Linearity was measured at six concentration levels for each standard. Each solution was tested in triplicates. Calibration curves were constructed by plotting the peak area versus concentration of each standard. Acceptability of linearity data was determined by the correlation coefficient, r^2. Limits of detection (LOD) and quantification (LOQ) for each standard were calculated based on linear regression method. Accuracy was determined by analyzing the percentage recovery for the catechin flavonoid in the *U. gambir* leaf extract by spiking the raw material with reference standards at three levels. Three replicates were performed for each analysis. Variations of all the tests were expressed in terms of relative standard deviation (% RSD).

Results and Discussion

Validation of HPLC method

The HPLC method for quantification was validated and the results are summarized in Tables 1 – 2, respectively. As seen in Table 1, the calibration curve demonstrated good linearity with $r^2 \geq 0.981$. The LODs and the LOQs were found to be 2 mg/L and 6 mg/L, respectively, showing good sensitivity of the method. The recovery test represented in Table 2 which ranged from 80.1-88.1 % showed good accuracy of the method.

Table 1. Figure of merits of catechin

Analyte	Concentration range (mg/L)	Regression equation	Correlation coefficient (r^2)	Limit of detection (mg/L)	Limit of quantification (mg/L)
Catechin	2 – 100	y = 8.7935x + 22.615	0.981	2	6

Table 2. Recovery of catechin

Analyte	Concentration level (mg/L)	Percent recovery (%)
Catechin	25	88.10 ± 1.13
	50	80.10 ± 0.71
	75	82.30 ± 0.71

Quantification of flavonoids

Catechin was successfully determined and quantified from the hexane, dichloromethane and methanol leaf and stem extracts of Malaysian *U. gambir* using the developed HPLC-DAD method. The chromatogram of the leaf and stem extract is shown in Figure 1 and Figure 2, respectively. The identity of the peaks was determined by comparison of the UV-vis spectra and the retention times with the authentic standard. The purity of the peak was ascertained by the singularity of the peak component.

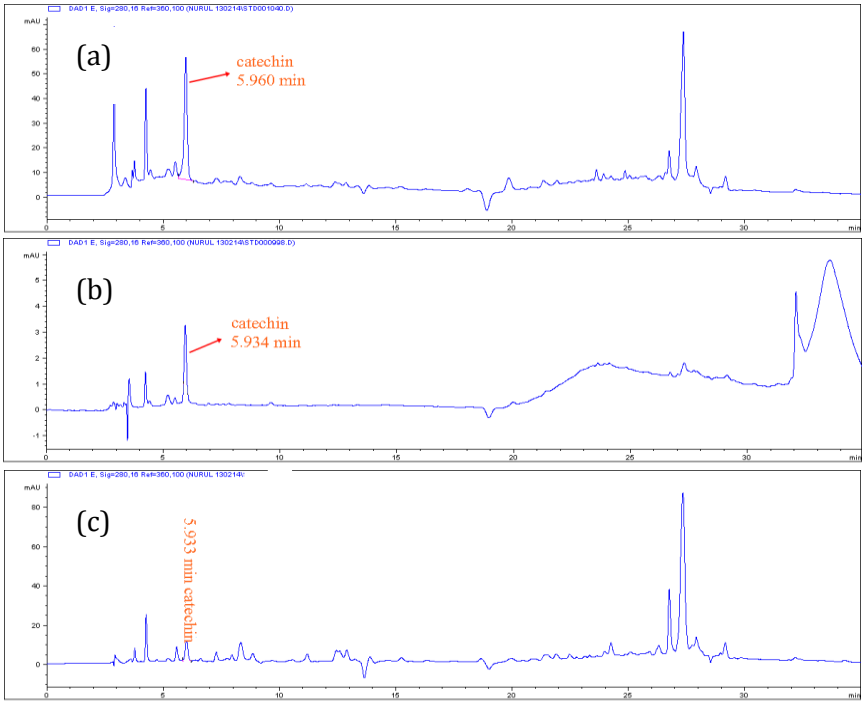


Figure 1. HPLC chromatograms *of U. gambir*: (a) MeOH extract (b) Hx extract and (c) DCM extract of the leaves

Quantification of catechin was performed using the external standard method. The relationship between the amount of standard solution (concentration) and detector responses (peak area) were plotted to construct the calibration curve. The data was fitted by linear least squares to determine response equation.

Recently, a study done by Amir et al. [5] on *U. gambir* collected in Indonesia found that the estimated total flavonoid content of this plant using the aluminium chloride colorimetric method to be 5.82 ± 2.23 mg rutin equivalents (RE)/g dry weight. In addition, the catechin content of four sub-species of Indonesian *U. gambir* known as gambir cubadak, gambir udang, gambir riau mancik and gambir riau gadang had been earlier determined by HPLC [6]. They had found that the catechin content of the respective sub-species was 104.5, 101.2, 99.4 and 108.5, 104.5 µg/ml, respectively. However, the initial concentration of the extract was not specified. Hence, the content of catechin in µg/mg could not be determined for comparison.

As far as our knowledge, the quantification of the catechin in *Uncaria gambir* from the Malaysian population has not yet been determined by HPLC methods. The contents of catechin obtained in each leaf and stem extracts are shown in Table 3 and Table 4, respectively. Catechin was present in higher amounts in the MeOH extract compared to Hx and DCM extracts. It was suggested that polar compounds in plant matrix would be easier to extract with more polar solvent such as MeOH. The amount of catechin present in MeOH leaf extract was 86.35 mg/g while in MeOH stem extract was 51.20 mg/g. The DCM extract showed that reasonable amounts of catechin can be extracted from the leaves and stems with 7.71 mg/g and 9.19 mg/g, respectively. This is because DCM is a moderately polar compound, thus it has the ability of 'like dissolve like' between the polar compounds. The Hx extract indicated that the amount of catechin cannot be quantified since the peak area was below limit of quantification. Furthermore, by comparing stems and leaves of *Uncaria gambir*, the amount of catechin present in leaf extracts are higher than in the stem extracts with an average amount of 94.06 g/kg and 60.39 g/kg plant material correlating to 9.406 % and 6.039 %, respectively.

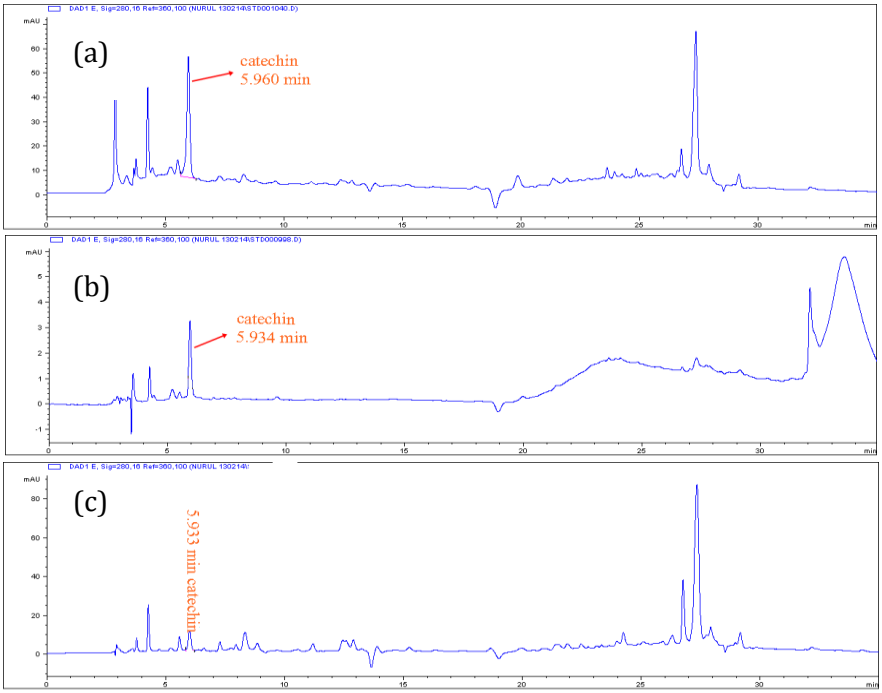


Figure 2. HPLC chromatograms *of U. gambir*: (a) MeOH extract (b) Hx extract and (c) DCM extract (C) of the stems

Table 3. Contents of catechin in leaf extract of *U. gambir* (mg/g)

Sample	Retention times (min)	Area (mAU* s)	Amount of catechin (mg/g)	Percentage of catechin (%)
MeOH extract	6.027 ± 0.020	782.3 ± 3.5	86.35 ± 0.35	8.635
DCM extract	5.942 ± 0.070	90.4 ± 1.4	7.71 ± 0.16	0.771
Hx extract	5.913 ± 0.050	11.0 ± 0.8	N/A	N/A

± is standard deviation value, N/A is non-applicable (below the limit of quantification)

Table 4. Contents of catechin in stem extract of *U. gambir* (mg/g)

Sample	Retention times (min)	Area (mAU* s)	Amount of catechin (mg/g)	Percentage of catechin (%)
MeOH extract	5.901 ± 0.0800	473.05 ± 1.06	51.20 ± 0.14	5.120
DCM extract	5.918 ± 0.110	103.40 ± 1.06	9.19 ± 0.12	0.919
Hx extract	5.920 ± 0.020	22.60 ± 0.49	N/A	N/A

± is standard deviation value, N/A is non-applicable (below the limit of quantification)

Conclusion

A HPLC-DAD method was successfully developed and validated for the analysis of catechin in Malaysian *U. gambir*. The developed LC method is proven to be an efficient, selective and rapid analytical method for the quantification of catechin in the hexane, dichloromethane and methanol leaf and stem extracts of the plant. Catechin can be found in each of the three extracts in different amounts. This is the first report on the quantification of flavonoids from Malaysian *U. gambir*. The method can be used for the quantification of flavonoids from other *Uncaria* and related genus and useful for targeted isolation of interest flavonoids.

Acknowledgement

We wish to thank the Ministry of Science, Technology and Innovation Malaysia (MOSTI) for the research grant (02-01-01-SF 0563) under E-Science fund and Universiti Teknologi MARA (UiTM) for providing us with facility.

References

1. Risdale C. E. (1978). A revision of *Mitragyna* and *Uncaria* (*Rubiaceae*). *Blumea*, 24: 43 – 100.
2. Salim, F., Zain, M. M., Ridzuan, M. S. M., M., Langat, K., Mulholland, D. and Ahmad, R. (2013). Flavan-3-ols from the leaves of Malaysian *Uncaria longiflora* var. *pteropoda* (Miq.) Ridsd. *Phytochemistry Letters*, 6: 236 – 240.
3. Taniguchi, S., Kuroda, K., Doi, K., Inada, K., Yoshikado, N., Yoneda, Y., Tanabe, M., Shibata, T., Yoshida, T. and Hatano, T. (2007). Evaluation of gambir quality based on quantitative analysis of polyphenolic constituents. *Yakugaku Zasshi*, 127 (8): 1291 – 1300.
4. Kassim, M. J., Hussin, M. H., Achmad, A., Hazwani, D., Kim, S. T. and Hamdan H. S. (2011). Determination of total phenol, condensed tannin and flavonoid contents and antioxidant activity of *Uncaria gambir* extracts. *Majalah Farmasi Indonesia*, 22(1): 50 – 59.
5. Amir, M., Mujeeb, M., Khan, A., Ashraf, K., Sharma, D. and Aqil M. (2012). Phytochemical analysis and in vitro antioxidant activity of *Uncaria gambir*. *International Journal of Green Pharmacy*, 6: 67 –72.
6. Anggraini, T., Tai, A., Yoshino, T. and Itani T. (2011). Antioxidative activity and catechin content of four kinds of *Uncaria gambir* extracts from West Sumatra, Indonesia. *African Journal of Biochemistry Research*, 5: 33 – 38.

Malaysian Journal of Analytical Sciences, Vol 20 No 3 (2016): 573 - 577
DOI: http://dx.doi.org/10.17576/mjas-2016-2003-16

MALAYSIAN JOURNAL OF ANALYTICAL SCIENCES
Published by The Malaysian Analytical Sciences Society
ISSN 1394 - 2506

ISOLATION OF ACETYL ALEURITOLIC ACID FROM *Pimeleodendron griffithianum* (Euphorbiaceae)

(Pemisahan Asid Asetil Aleuritolik Daripada *Pimeleodendron griffithianum* (Euphorbiaceae))

Rosmawati Abdul Aziz[1, 2]* and Norizan Ahmat[1, 2]

[1]*Faculty of Applied Sciences,*
Universiti Teknologi MARA, 40450 Shah Alam, Selangor, Malaysia
[2]*Atta-ur-Rahman Institute for Natural Product Discovery,*
Universiti Teknologi MARA, Puncak Alam Campus, 42300 Bandar Puncak Alam, Selangor, Malaysia.

**Corresponding author: rosmawatiaa@perlis.uitm.edu.my*

Received: 24 February 2015; Accepted: 27 October 2015

Abstract

Pimeleodendron griffithianum, locally known as Perah ikan is available in Thailand, Peninsular Malaysia and Sumatra. The plant can be found in wet forest, secondary forest, pole forest, semi-swamps, and along logging roads or on hill slopes. In Malaysia, the stem of *P. griffithianum* being used as commercial timber. So far, no chemical constituents have been reported from *P. griffithianum*. In this study, a phytochemical study was conducted on the stem bark of *P. griffithianum*. The stem bark was obtained from Sungai Siput, Perak. The cleaned, chopped and dried stem-bark was extracted using acetone for several times. The separation of the components was carried out using vacuum liquid chromatography (VLC) followed by recrystallization method. The structure of the pure compound was elucidated by spectroscopic methods including nuclear magnetic resonance (NMR), ultraviolate – visible (UV-Vis) and comparison with literature. One compound (1) was isolated and identified as acetyl aleuritolic acid. This compound was reported for the first time from this plant.

Keywords: *Pimeleodendron griffithianum*, Euphorbiaceae, acetyl aleuritolic acid

Abstrak

Pimeleodendron griffithianum, yang dikenali sebagai pokok Perah ikan oleh penduduk tempatan didapati di Thailand, Semenanjung Malaysia dan Sumatra. Pokok ini dapat ditemui di dalam hutan lembap, hutan sekunder, semi-paya dan di sepanjang jalan pembalakan atau di cerun bukit. Di Malaysia, batang pokok ini lazimnya digunakan sebagai kayu komersial. Setakat ini tidak ada laporan direkodkan mengenai bahan kimia yang ditemui daripada pokok ini. Dalam penyelidikan ini, satu kajian fitokimia telah dijalankan ke atas kulit batang *P. griffhianum*. Kulit batang pokok *P.griffithianum* diperolehi dari Sungai Siput, Perak. Kulit pokok yang telah dibersihkan, dipotong-potong kecil dan dikeringkan, diekstrak menggunakan aseton untuk beberapa kali. Pengasingan komponen dilakukan menggunakan kaedah kromatografi cecair vakum (VLC) diikuti dengan proses penghabluran semula. Struktur kimia sebatian tulen dijelaskan dengan kaedah spektroskopi termasuk spektroskopi resonans magnet nukleus (NMR), ultralembayung (UV) dan perbandingan dengan data literatur. Satu sebatian (1) yang dipisah dikenal pasti sebagai asid asetil aleuritolik. Sebatian ini dilaporkan buat kali pertama bagi tumbuhan ini.

Kata kunci: *Pimeleodendron griffithianum*, Euphorbiaceae, asid asetil aleuritolik

Introduction

Malaysia is known for its lush tropical rain forest. The natural resources of tropical rainforest in Malaysia bring many benefits to the country. Among them is supplying food resources to local community, timber, rattan and

bamboo. Forests are not only a source of food supply and construction, but also a source of valuable medicinal plants. Forest plants in Malaysia contain many medicinal properties in the production of medicines. The tropical rain forests are chemically and biologically diverse resources as they synthesize various chemicals as defense agents against pests, diseases and predators. Euphorbiaceae is among the largest flowering plant families consisting of a wide variety of vegetative forms some of which are plants of great importance. The family is very diverse in range, comprises of all sorts of plants ranging from large woody trees through climbing habit to simple weed that grows prostrate to the ground. Euphorbiaceae is comprised of five subfamilies, 49 tribes, 317 genera and about 8000 species [1].

Pimeleodendron is a small genus in the Euphorbiaceae. Its distribution ranges from Peninsular Thailand to the Solomon Islands and tropical East Australia, Peninsular Thailand, Malay Peninsula, Sumatra, Borneo, Sulawesi, Lesser Sunda Islands, Moluccas, New Guinea, Solomon Islands, and NE Australia. *Pimeleodendron* comprises five species which are *P. amboinicum*, *P. griffithianum*, *P. macrocarpum*, *P. zoanthogyne* and *P. dispersum* [2]. Some species of this genus are economically important since they provide food, medicine, or varnish for local people. The wood of *P. macrocarpum* is used in house construction. In Sumatra, the fruit of *P. griffithianum* is used for seasoning. In eastern Malay Peninsula *P. amboinicum* furnishes edible seeds, which taste like hazelnuts; its bark being used as a purgative; the juice of the leaves, used in a mixture, cleans the mouths of children, and acts as a gentle purgative (adults can eat the leaves without purging) while the latex serves as a varnish. People in the Solomon Islands drink an infusion of the bark of *P. amboinicum* as a remedy for fever [2].

Pimeleodendron griffithianum (P. griffithianum) is one of the species in the genus *pimeleodendron*. This plant is locally known as Perah ikan. It is a mid-canopy tree up to 30 m tall. The bark is light brown, rugose, glabrous, and the inner bark is light brown about 2 mm thick with pale yellow sap. It is distributed in Thailand, Peninsular Malaysia, Sumatra, Borneo and Philippines. The plant usually found in wet forest, secondary forest, and pole forest, semi-swamps, and along logging roads or on hill slopes [2]. In Malaysia, *P. griffithianum* is found in over hill dipterocarp forest. The plant was used mainly as commercial timber. The timber being used for general light or temporary construction, interior trim, lining, shelving, joinery, furniture, mouldings, tool handle for non-impact purposes and plywood [3]. It also be used as edible fruit [4] while in Sumatra, the fruit of *P. griffithianum* is used for seasoning [2]. There is very limited information available regarding the uses of *P. griffithianum*. Currently, there is no chemical constituents have been reported from *P. griffithianum.*

Materials and Methods

Instrumentation

The NMR spectra were recorded on a Bruker AV300 NMR spectrometer 1D-NMR (^{1}H-NMR, ^{13}C-APT) and 2D-NMR (HMQC, HMBC and COSY) with TMS as internal standard and $CDCI_3$ as solvent. UV spectra were determined using UV-Vis spectrophotometer LAMBDA 35 Perkin Elmer. Silica gel 60 G (Merck 7747) was used for vacuum liquid chromatography. TLC were performed on pre-coated silica gel 60 F_{254} plates (Merck 5554) and visualized under UV light and by spraying with Cerium sulphate reagent followed by heating.

Plant collection

Fresh stem bark was collected from Sungai Siput, Perak. The stem bark was cleaned, chopped and dried under shade at room temperature until completely dry (5.60 kg). Then, it was ground to coarse powder using mechanical grinder (5.05 kg).

Extraction and isolation

The extract of the *P. griffithianum* was obtained by taking 4 kg of the powder, macerated with 5 liter of acetone in a container covered with aluminum foil and left to macerate overnight. The solvent was then filtered and evaporated under reduced pressure to obtain crude extract (207.6 g) [5]. The crude extract was then dissolved in 200 ml methanol and added with 2 L diethyl ether to precipitate tannin constituents. Decantation and evaporation of MeOH-dietyl ether soluble fraction gave crude extract that contain less tannin [6]. Crude extract obtained from this process (187.6 g) was used for further isolation and purification.

The extract which contain less tannin was fractionated by vacuum liquid chromatography (VLC) eluted with hexane: chloroform: ethyl acetate from 10:0:0 to 8:0:2. The fractionation produced 16 fractions. Fraction 10 was observed as green crystal with the mass of 138.0 mg. This fraction was washed several times with hexane. From the recrystallization processes, compound (1) was obtained as white needles (10.1 mg). The compound was detected by TLC profile and confirmed by $CeSO_4$ reagent. The compound (1) was characterized using NMR, UV-Vis and comparison with previous data.

Results and Discussion

Compound (1): Crystallized as white needles; showed maximum absorption of λ($CHCI_3$) 242.22 nm. It indicated that the compound did not contain chromophore. ^{13}C APT NMR spectrum ($CDCI_3$) of compound (1) displayed 32 carbon resonances; they are nine quartenary carbons (C) at δ_C 29.3 (C-20), 37.3 (C-13), 37.6 (C-4), 37.9 (C-10), 39.0 (C-8), 51.5 (C-17), 160.5 (C-14), 184.2 (C-28) and 171.0 (C-1'), five methine groups (CH) at δ_C 41.9 (C-18), 49.2 (C-9), 55.3 (C-5), 81.0 (C-3), 117.0 (C-15), ten methylene groups (CH_2) at δ_C 17.3 (C-11), 18.7 (C-6), 23.4 (C-2), 30.7 (C-22), 31.3 (C-16), 33.6 (C-21), 35.6 (C-8), 37.3 (C-1), and 40.7 (C-7) and eight methyl group (CH_3) at δ_C 16.6 (C-25), 16.6 (C-24), 21.3 (C-2'), 22.5 (C-27), 26.2 (C-26), 27.9 (C-23), 28.6 (C-3) and 31.8 (C-29). ^{1}H NMR (300 MHz, $CDCI_3$) δ_H: 0.84 (H-23, s, 3H), 0.87 (H-24 s, 3H), 0.90 (H-27, H-30, s, 3H), 0.92 (H-29 ,s, 3H), 0.94 (H-25, H-26 ,s, 3H), 2.03 (H-2', s, 3H), 4.45 (H-3, dd, *J* = 6.54, 9.18 Hz, 1H), 5.50 (H-15, dd, *J* = 3.19, 7.77 Hz, 1H). The ^{1}H and ^{13}C NMR assignments are given in Table 1.

The presence of thirty-two resonances showed a pentacyclic triterpene skeleton. The signals at δ_C 184.25 and 171.02 indicate the presence of carboxylic acid and acetoxy carbonyl function. Position of acetoxy group was determined from HMQC spectrum, which revealed that protons were found to be related with C-3 and it can be recognized from HMBC spectrum of quaternary carbon at acetoxy group. Position of carboxylic acid group was determined from HMBC spectrum, which revealed that carbon on carbonyl groups and C-17 were found correlate to protons at C-16 and C-22. The double bond (C=C) showed deshielding condition at δ_C 160.5 and 116.8, which is a typical C14-C15 double bond of taraxerane skeleton. Position of this double bond was clearly determined from the HMBC spectrum, which revealed that H-15 correlate to C-15 and recognized with carbon C-14. ^{1}H NMR spectrum showed a characteristic singlet at δ_H 2.03 assigned to acetoxy protons, a doublet doublet proton at 5.50 (*J* = 7.77 and 3.19 Hz) indicating a proton on the trisubstituted double bond adjacent to methylene function. Another doublet of doublet proton resonated at δ_H 4.45 (*J* = 9.18 and 6.54 Hz) assigned to the ubiquitous 3 α methane proton germinate to the acetoxy function of triterpene skeleton. Seven tertiary methyls appeared as singlets in the region δ_H 0.84 – 0.94. The above data of ^{1}H NMR and ^{13}C APT NMR for the compound (1) was identical with the reported data of that acetyl aleuritolic acid [7 - 10]. The structure of acetyl aleuritolic acid is shown in Figure 1.

Table 1. ^{1}H and ^{13}C NMR assignments of compound (1)

Position of C	**δ_C**	**δ_H**	**APT**
1	37.3	1.04,1.62	CH_2
2	23.4	1.61, 1.65	CH_2
3	80.9	4.45 (1H, dd, J= 6.54, 9.18 Hz)	CH
4	37.7	-	C
5	55.5	0.88	CH
6	18.7	1.48, 1.58	CH_2
7	40.7	1.27, 1.99	CH_2
8	39.0	-	C
9	49.0	1.44	CH
10	37.9	-	C
11	17.3	1.44, 1.62	CH_2

Table 1 (cont'd). ^{1}H and ^{13}C NMR assignments of compound (1)

Position of C	δ_C	δ_H	APT
12	33.3	1.60, 1.80	CH_2
13	37.3	-	C
14	160.5	-	C
15	116.8	5.5 (1H, dd, J = 3.19, 7.77 Hz)	CH
16	31.3	1.91, 2.36	CH_2
17	51.5	-	C
18	41.3	2.26 (1H, dd, J= 13.70, 2.70 Hz)	CH
19	35.3	1.06, 1.23	CH_2
20	29.3	-	C
21	33.6	1.05, 1.15	CH_2
22	30.7	1.44, 1.72	CH_2
23	27.9	0.84 (3H,s)	CH_3
24	16.6	0.87 (3H,s)	CH_3
25	15.6	0.94 (3H,s)	CH_3
26	26.2	0.94 (3H,s)	CH_3
27	22.5	0.90 (3H,s)	CH_3
28	184.3	-	C
29	31.8	0.92 (3H,s)	CH_3
30	28.6	0.90 (3H,s)	CH_3
1'	171.0	-	C
2'	21.3	2.03 (3H,s)	CH_3

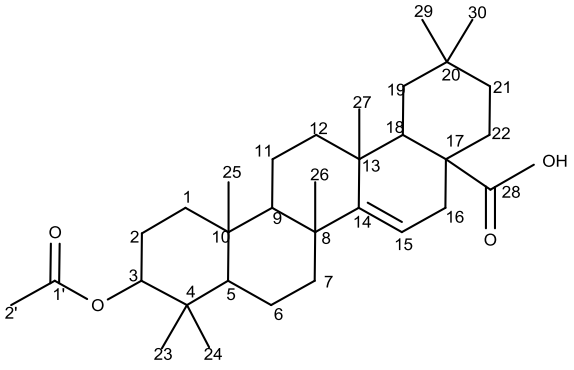


Figure 1. The chemical structure of acetyl aleuritolic acid

Conclusion

Acetyl aleuritolic acid was successfully isolated from the stem bark of *P. griffithianum*. This compound is reported for the first time from this plant. The structure of the pure compound was elucidated by spectroscopic methods including nuclear magnetic resonance (NMR), ultraviolate – visible (UV-Vis) and comparison with literature.

Acknowledgement

We thank to the Faculty of Applied Sciences, Universiti Teknologi MARA, Shah Alam for providing the laboratory facilities to carry out this research. The authors also would like to thanks to Mrs. Zuriati, and Miss Faeza from Sekolah Kebangsaan Pos Piah, and Mr. Azman, one of the local resident in Sungai Siput, Perak for his assistance during the stem bark collection of *P. griffithianum*.

References

1. Mwine, J. T. and Van Damme, P. (2011). Why do Euphorbiaeceae tick as medicinal plants? A review of Euphorbiaceae family and its medicinal features. *Journal of Medicinal Plants Research*, 5(5): 652 - 662.
2. Djarwaningsih, T. (2004). Revision of Pimeleodendron (Euphorbiaceae) in Malesia. *Blumea - Biodiversity, Evolution and Biogeography. Plants*, 49(2): 407 - 423.
3. MTC Wood Wizard, Perah ikan. (2012). Online access from www.mtc.com.my.
4. Eswani, N., Abd, K., Nazre, M., Noor, A. G. A., and Ali, M. (2010). Medicinal plant diversity and vegetation analysis of logged over Hill Forest of Tekai Tembeling Forest Reserve, Jerantut, Pahang. *Journal of Agricultural Science*, 2(3): 189 - 210.
5. Jones, W. P. and Kinghorn, A. D. (2005). Extraction of plant secondary metabolites. *Natural Products Isolation, Method in Biotechnology* 20: 323 - 351.
6. Wibowo, A., Ahmat, N., Hamzah, A. S., Ismail, N. H., Ahmad, R., and Jaafar, F. M. (2012). Resveratrol oligomers from the stem bark of *Dryobalanops aromatica*. *Biochemical Systematics and Ecology*, 40: 62 - 64.
7. McLean, S., Perpick-Dummont, M., Reynolds, W. F., Jacobs, H. and Lachmansing, S. S. (1987). Unambiguous structural and nuclear magnetic resonance spectral characterization of two triterpenoids of Maprounea guianensis by two-dimensional nuclear magnetic resonance spectroscopy. *Canadian Journal of Chemistry*, 6(7): 2519 - 2525.
8. Prabowo, W. C., Wirasutisna, K. R. and Insanu, M. (2013). Isolation and characterization of 3-acetyl aleuritolic acid and scopoletin from stem bark of *Aleurites Moluccana* (L.) willd. *International Journal of Pharmaceutical Science*, 5(3): 851 - 853.
9. Agidew, E., Reneela, P. and Deyou, T. (2013). Phytochemical investigation of *Sapium ellipticum*. *Journal of Natural Product Plant Resource*, 3(5): 1 - 6.
10. Viswanadh, G. S., Ramaiah, P. A., Laatsch, H. and Maskey, R. (2006). Chemical constituents of the heartwood and barks of *Homonoia riparia*. *Journal of Tropical Medicinal Plants*, 7(2): 267 - 273.

Malaysian Journal of Analytical Sciences, Vol 20 No 3 (2016): 578 - 584
DOI: http://dx.doi.org/10.17576/mjas-2016-2003-17

MALAYSIAN JOURNAL OF ANALYTICAL SCIENCES
Published by The Malaysian Analytical Sciences Society
ISSN 1394 - 2506

IMMOBILISED METAL AFFINITY CHROMATOGRAPHY (IMAC) BEADS FOR LYSOZYME SEPARATION: SYNTHESIS AND CHARACTERIZATION STUDY

(Kromatografi Afiniti Logam Dipegun (IMAC) untuk Pemisahan Lysozim: Sintesis dan Kajian Pencirian)

Fatin Mohd Nasir[1], Sofiah Hamzah[1]*, Amirah Hamzah[1], Nora'aini Ali[1], Marinah Mohd Ariffin[2]

[1]*School of Ocean Engineering*
[2]*School of Marine Science and Environment*
Universiti Malaysia Terengganu, 21030 Kuala Terengganu, Terengganu, Malaysia

**Corresponding author: sofiah@umt.edu.my*

Received: 24 February 2015; Accepted: 27 October 2015

Abstract

Immobilized metal affinity chromatography (IMAC) has been established as a highly specific chromatographic technique for the production of enzymes and proteins including lysozyme. This study aimed to prepare and characterize the IMAC beads for lysozyme separation. Silica gel served as chromatographic matrix which has been coated with chitosan layer and crosslinked with glutaraldehyde (GTA-CTS-SiO_2) since it is very convenient to promote fixation. Various IMAC ligands were immobilized by chelating 1500 mg/l Cu^{2+}, Zn^{2+}, Fe^{2+}, Fe^{3+} and Al^{3+} ions, respectively on GTA-CTS-SiO_2. IMAC which was immobilized with 1200mg/l Cu^{2+} exhibited the maximal immobilization capacity (27.08mg/g) of within 30 minutes incubation time. This fundamental study can be a momentous pathway to develop an efficient chromatographic system for lysozyme separation in the future**.**

Keywords: silica gel, chitosan, glutaraldehyde, metal ions, copper (II) ion

Abstrak

Kromatografi afiniti logam dipegun (IMAC) telah diperlihatkan sebagai satu teknik kromatografi yang sangat spesifik untuk pengeluaran enzim dan protein termasuk lysozim. Kajian ini bertujuan untuk menyediakan dan mencirikan manik IMAC bagi tujuan pemisahan lysozim. Gel silika berperanan sebagai sokongan kepada kromatografi yang telah dilapisi dengan lapisan kitosan dan diaktifkan dengan glutaraldehid (GTA-CTS-SiO_2) kerana kesesuaiannya yang berupaya menggalakkan lekatan. Beberapa ligan IMAC dengan kepekatan 1500mg/l (Cu^{2+}, Zn^{2+}, Fe^{2+}, Fe^{3+} dan Al^{3+} ion) telah dipegunkan pada GTA-CTS-SiO_2. IMAC yang dipegunkan dengan kepekatan 1200mg/l Cu^{2+} menunjukkan penjerapan kapasiti yang maksimum (27.08 mg) dalam tempoh 30 minit masa pengeraman. Kajian asas ini boleh menjadi satu anjakan dalam langkah membangunkan sistem kromatografi yang berkesan untuk pengasingan lysozim pada masa akan datang.

Kata kunci: gel silika, kitosan, glutaraldehid, ion logam, ion kuprum (II)

Introduction

Currently lysozyme has been commercially become as an important enzyme used due to the high specificity, selectivity and efficiency function in the industries. Potent bacteriostatic and bactericidal properties of lysozyme give a huge impact as an antimicrobial agent [1] for the human body and as the food preservative especially in

extension shelf life in food industries. Small amount of lysozyme makes the process of purification becomes challenge and intricate especially for the large scale production. Conventionally, separation of lysozyme has been obtained by several techniques such as ion exchange chromatography, ultrafiltration and affinity chromatography. However rigorous limitations occur including lengthy steps, complicated and expensive for large scale production has hampered the applications. Separation technique for protein by Immobilized Metal Affinity Chromatograph (IMAC) has established [2] due to the ligand stability, high adsorption capacity, mild elution condition, simple regeneration and low cost [3]. Selection of IMAC solid chromatographic matrix to entrap metal ions for the best serve as affinity ligands for various proteins such a critical attention in order to meet the requirement of high efficiency and fast flow operation. Conventional supports for IMAC are based on soft gel that coating with dextran and agarose give the compressible and restricted low flow rate in chromatography operations [4]. Upgrading matrix with porous silica as an ideal IMAC support which has high mechanical resistance, insolubility and available for long shelf life inorganic materials. To achieve the maximum protein adsorption, surface of silica beads are modified by coating with a hydrophilic and functional natural polymer. According to Wu et al, silica beads cross-linked with chitosan indicate convenient matches for metal ion adsorption [5].

Chitosan (CTS) is widely used for the hydrophilic modification due to its biocompatibility, biodegradability, chemical innertness, high mechanical strength and non-toxic material [6]. Besides, amino and hydroxyl groups in chitosan molecules supplied active reaction sites for the various functional ligands, therefore it considered as an excellent matrix for IMAC. However, chitosan required a cross-linker to modify chemical structure and textural properties by linking at the amine or the hydroxyl sites. Glutaraldehyde (GTA) is the best chosen cross-linker for chitosan which has a porous network that could improve adsorption properties and helped to form quaternary structure on the surface of the materials, thus increase the content of protonated amino groups [7] as well as improved the chemical stability of chitosan in acidic solution [8]. Practically, IMAC is depend on the formation of coordinate bonds between immobilized metal ions such as Cu^{2+}, Zn^{2+}, Ni^{2+}, and Fe^{2+} with the functional groups of exposed amino acids on the surface of the target protein [9].

Inspired by previous researches, we have prepared IMAC beads with porous silica based characterized by chitosan-glutaraldehyde modified polymer. ATR-FTIR was analysed to determine the binding of chitosan and crosslinking agent onto the silica beads. Then, modificated silica beads were studied the immobilized various metal ions sorption and the evaluation of optimum metal ion in different concentration by ICP-OES.

Materials and Methods

Chemicals and materials

Silica gels (70-230 mesh size) were obtained by Merck Millipore. Chitosan as a modified polymer and glutaraldehyde were purchased by Sigma Aldrich. Glacial acetic acid, sodium hydroxide, hydrochloric acid, dimethylsulphoxide (DMSO), copper (II) sulfate, calcium sulfate, iron (II) sulfate, iron (III) sulfate and zinc sulfate were analytical grade reagents commercially available and used without further purification.

Preparation of chitosan coated silica beads

Preparation of Chitosan-coated silica beads (CTS-SiO_2) was according to Shi et al. [8] with some modification. Chitosan powder (5 g) was added into 250 ml of 1M acetic acid and dissolved by magnetic stirring for several minutes at room temperature and finally, the prepared chitosan solution was stored in a Schott bottle at room temperature. Initiate with treated 50 g of silica beads with 20 % of hydrochloric acid for 8 hours in incubator shaker at room temperature to obtain high adsorptive property of porous silica beads. The beads were rinsed with distilled water to remove the residual of hydrochloride inside silica beads and dried at 40 ^{o}C in oven. Prior to the surface coating, treated silica beads were immersed again into distilled water for 2 hours in order to wet the pore surface. An amount 10 g of silica beads were immersed into the chitosan solution and the flask containing the mixture was placed in the incubator shaker for the process of surface coating reaction at room temperature with 100 rpm for 72 hours. Subsequently, immersed chitosan coated silica beads with dimethylsulphoxide (DMSO) for one hour to enhance polarity of the surface. Coated beads were then added into sodium hydroxide (NaOH) solution (pH 8) for 2 hours to ensure solidify and fix the coating layer in the incubator shaker at 25 ^{o}C.

Beads activation and ligand immobilization

CTS-SiO_2 beads were cross-linking with glutaraldehyde which can be form a Schiff's base for chitosan. CTS-SiO_2 beads were incubated in incubator shaker for 30 minutes in reacting solution containing 50 v/v % (25 % glutaraldehyde in 0.1M NaCl and 0.1M sodium acetate-acetic acid buffer pH 7.4) at room temperature. After adjusting pH to 6.0 by adding acetic acid, the flask was sealed and reaction was allowed to continue for 16 hours in the incubator at 25 ^{o}C. When the reaction achieved, the excess GTA was removed by washing the beads with distilled water.

Activated silica beads (GTA-CTS-SiO_2) were reacted with 0.1M of five metal ions; $CuSO_4$, $FeSO_4$, $Al_2(SO_4)^3$, $Fe(SO_4)^3$ and $ZnSO_4$ respectively for 20 hours in incubator shaker (100 rpm) at room temperature. The adsorbent were then rinsed with distilled water before storage or usage for the lysozyme adsorption. Prepared beads hereafter are called immobilized metal affinity chromatography (IMAC) beads. IMAC is operated based on the affinity adsorption between the metal-binding amino acids in the side chains of the proteins such as histidine, lysine, glutamic acid and etc as well as the metal ions including Cu^{2+}, Fe^{3+}, Fe^{2+}, Al^{3+} and Zn^{2+} chelated by chelating ligand immobilized on the solid supports. The optimum metal ion immobilization has been chosen and verified the best concentration of metal ion before further studies with the evaluation performance of lysozyme adsorption.

IMAC characterization

Prepared IMAC beads were characterized in terms of morphology and the structure were observed using Scanning Electron Microscope (SEM), while the presence of elements has been analyzed by inductively coupled plasma optical emission spectrometry (ICP-OES) and the determination of functional groups for modified beads by using Attenuated Total Reflectance Fourier Transform Infra-Red Spectroscopy (ATR-FTIR).

Adsorption studies

After the metals concentration analysis using the ICP-OES, the amount of elements (Cu^{2+},Fe^{3+},Fe^{2+},Al^{3+} and Zn^{2+}) immobilized on the beads, P(mg/g), were approximately calculated using the following equation 1:

$$P\ (mg/g) = V\ (Co - Ce) / W_D \quad (1)$$

where Co (mg/l) is the initial elements concentration; Ce (mg/l) is the final elements concentration after adsorption; V is the volume of the elements solution used; and W_D (g) is the weight of beads.

Results and Discussion

IMAC characterization

IMAC beads were achieved in several stages including treating silica beads with hydrochloric acid, chitosan coating, cross-linking with glutaraldehyde and metal chelating. Chitosan mechanism interaction with silica beads been established [10] and the glutaraldehyde cross-linking could exhibit high operational stability of chitosan beads was coated [11]. Amination of the residue epoxy groups of could recover the loss of primary amino group during cross-linking with glutaraldehyde [12]. Hydrophilic characteristics of activated beads were improved the tendency of matrix for metal ion immobilization in the final stage of IMAC preparation. The surface morphologies of silica bead treated with hydrochloric acid is shown in Figure 1(a). The treated silica beads displayed smooth and channel like surface. The surface morphologies of silica beads modified with chitosan-glutaraldehyde represented in Figure 1(b) covered with a layer of rough surface as well as Figure 1(c) presented the rough and highly porous surface structure which can exhibit surface area and reducing the mass transfer resistance and facilitated the diffusion of protein molecules.

The ATR-FTIR spectra of native and modified silica beads are represented in Figure 2. The large broad stretching band around 3400 cm^{-1} corresponds to the associated O-H stretching vibration of the hydroxyl groups and adsorbed water which means the hydrophilic character of the porous silica shown in Figure 2(a). The peaks at around 800 and 566 cm^{-1} are attributed to the typical symmetric and bending vibration of Si-O-Si in support framework of silica beads, respectively [13].

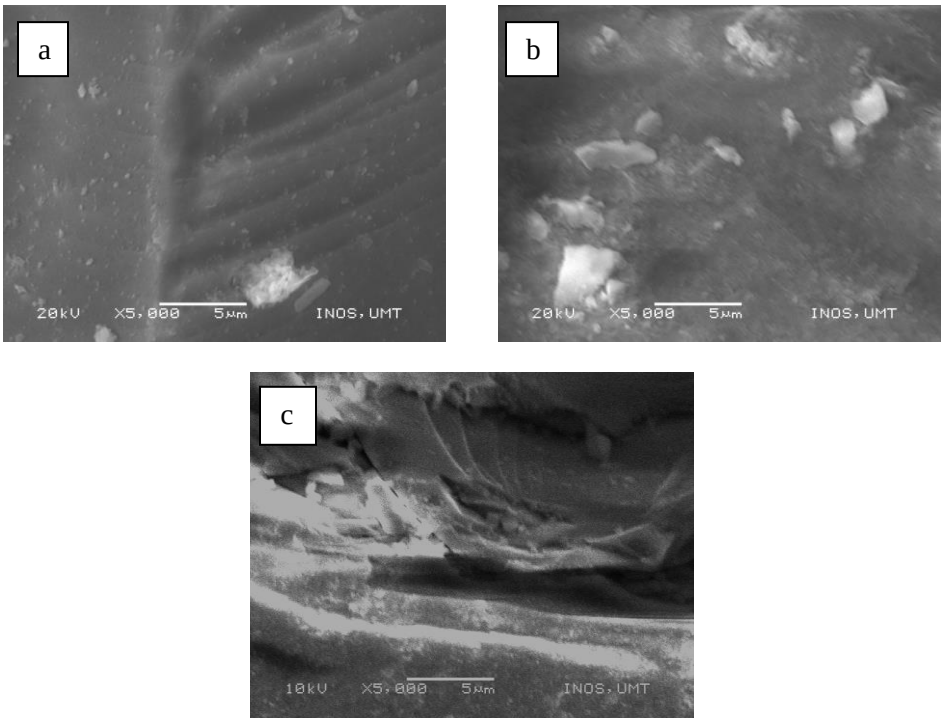


Figure 1. SEM micrograph of (a) silica bead treated with hydrochloric acid (b) modified silica beads with chitosan glutaraldehyde (c) IMAC absorbent

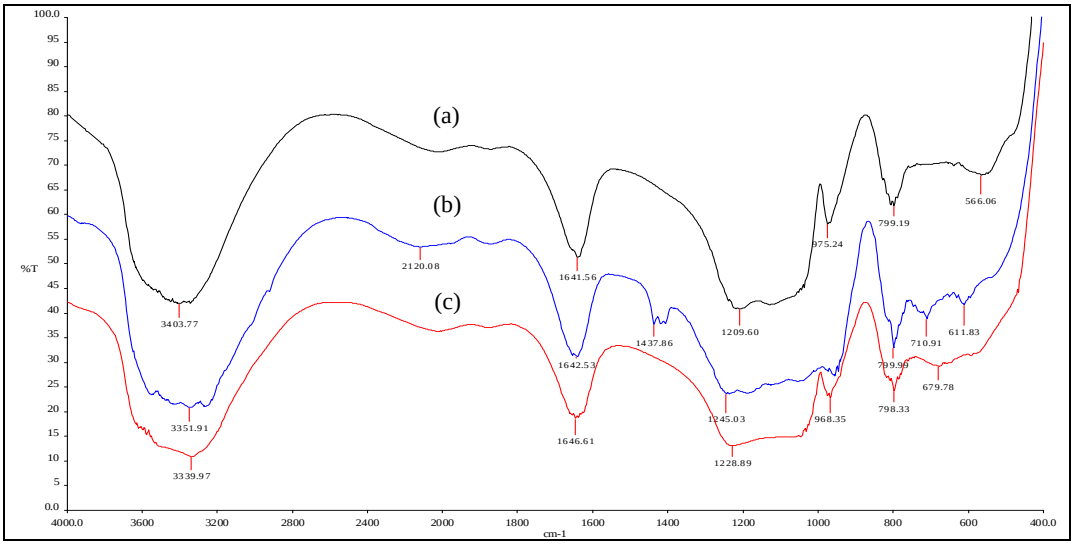


Figure 2. ATR-FTIR spectra (a) silica beads (b) chitosan coated beads (c) GTA-CTS-SiO_2

The band around 975 cm^{-1} from free silanol groups of silica disappeared or weakened after the modification (Figure 2(b)). The stretching vibration around 1640 cm^{-1} represent the C=N in amine reaction between amino groups in

silica and chitosan and aldehyde groups in glutaraldehyde [14]. The chitosan cross-linked with glutaraldehyde (Figure 2(c)) illustrated peaks at 968 and 1200 cm^{-1} assigned to saccharide structure. Hence, all peaks summarized the characterization of chitosan and glutaraldehyde for IMAC support.

Immobilization capacity of metal ion onto IMAC matrix

According to the IMAC separation concept, the use of metal ions that covalently bound chelating compound on a solid chromatographic matrix serves as affinity ligands that were vital to entrap optimum target proteins. Immobilization capacities studies of several kinds of metal ions were investigated in order to choose the most excellent metal ion among them. The chosen of metal ions; Cu^{2+}, Fe^{2+}, Fe^{3+}, Al^{3+} and Zn^{2+} ions rather than Ni^{2+} which is usually used in IMAC technique and has higher binding affinity for protein because of the leaking Ni^{2+} ions could cause human carcinogenic even in trace amount [15]. In this study, the GTA-CTS-SiO_2 beads were used as IMAC supports and immobilization of ligand (metal ion) displayed in Figure 3.

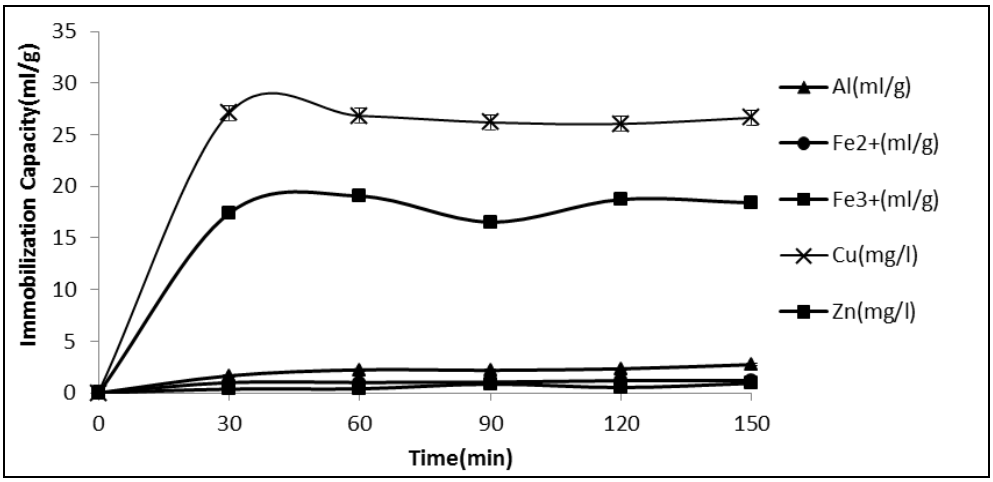


Figure 3. Immobilization capacity of metal ions

The capacity of Fe^{3+}, Fe^{2+} and Al^{3+} ions adsorption is the lower than surfactant modified chitosan beads. Those metal ions might not suitable for the chitosan coated beads adsorption. Fe^{3+} and Al^{3+} have been used for *Ortho*-phosphoserine (OPS) chelating compounds for immobilization in IMAC [16]. The adsorption capacities for Zn^{2+} is lower than Cu^{2+} otherwise still give high adsorbent amount. The maximal adsorption achieved at 30 minutes of incubation time. Obviously, Cu^{2+} is the high immobilized metal ion towards the GTA-CTS-SiO_2 with the maximal capacity 28.07 mg/g within the optimum time incubation, 30 minutes. The apparent affinity of a protein for a metal chelate depends strongly on metal ions involved in coordination. To fulfil the requirement of high protein adsorption onto the IMAC beads, the particular concentration of metal ion need to be obtained.

The principle of IMAC towards the immobilization of protein on IMAC beads were mainly through the coordination between metal ions with electron donating side chain of residues such as histidine and crysteine hence known as important factors in determining the absolute concentration of immobilized metal ion [17].

Based on the calculated values which is analysed by ICP-OES, the optimum concentration amount that ideal to the IMAC beads is 1200 mg/l with maximal adsorption amount 286.11 mg/g (Figure 4). It shown that efficient ligand immobilization could be achieved when 1200 mg/l ligand were utilized. An increased of ligand concentration up to 1500 mg/l tend to the formation of precipitation due to the excess of Cu(II) and also effected the adsorption of further protein. This optimum concentration of ligand provided higher surface area and accessible for lysozyme to bind. The lower concentration of glutaraldehyde was maintained to give the sufficient amount of free amino groups of Cu^{2+} interaction on the chitosan beads as well as yielded better adsorption capacity. The glutaraldehyde method

was served high endurance for the ligand immobilization [18]. Furthermore, Cu^{2+} adsorption was performed excellent at neutral pH to avoid the formation of Cu^{2+} hydroxide which could affect the adsorption capacity for the further protein recovery.

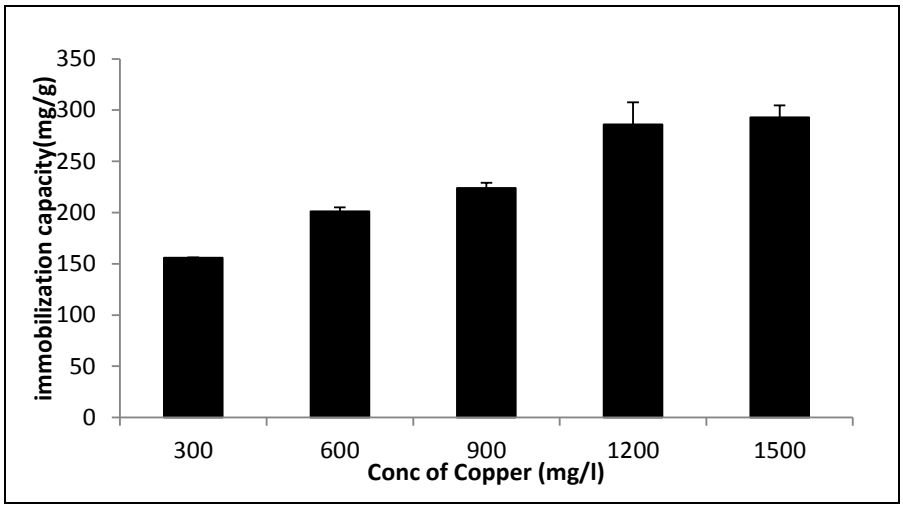


Figure 4. Immobilization capacity on different concentration of copper (II) ion

Conclusion

Preparation and characterization of IMAC beads were successfully performed by modification of silica beads with chitosan and glutaraldehyde as activated cross-linked. The morphology of modified polymer and IMAC absorbent was visualized by SEM and followed with the ATR-FTIR analysis, which was verified the presence of chitosan, glutaraldehyde and Cu^{2+} onto the IMAC surface. Maximum immobilization capacity of metal ion obtained using Cu^{2+} at 1200 mg/l and this finding could be used for further application of lysozyme adsorption.

Acknowledgement

The authors would like to express a high gratitude to Ministry of Higher Education Malaysia for the funding of this research (ERGS 55097) and University Malaysia Terengganu (UMT) for all supports and contribution.

References

1. Evrim, B. A., Nalan, T., Candan, N. and Adil, D. (2007). Use of magnetic poly(glycidyl methacrylate) monosize beads for the purification of lysozyme in batch system. *Journal of Chromatography*, 853(1-2): 105 – 113.
2. Mooney, J. T., Fredericks, D. P., Hearn and Milton T. W. (2013). Application of an IMAC cassette for the purification of N-terminally tagged proteins. *Separation and Purification Technology*, 120: 265 –274.
3. Arnold F. H. (1991). Metal affinity separations: a new dimension in protein processing. *Biotechnology*, 9 (2): 151– 156.
4. Gaberc-Porekar, V. and Menart, V. (2001). Perspectives of immobilized-metal affinity chromatography. *Journal Biochemical and Biophysical Methods*, 49 (1-3): 335 – 360.
5. Wu, F., Zhu, Y. and Jia Z. (2006). Preparation of dye–ligand affinity chromatographic packing's based on monodisperse poly (glycidylmethacrylate-coethylenedimethacrylate) beads and their chromatographic properties. *Journal Chromatography A*, 1134(1–2): 45 – 50.
6. Tan, T. W., Xu, W. J. and Zhang, S. R. (1997). The synthesis of chitosan coated affinity chromatography absorbent. *Ion Exchange Adsorption*. 13: 141 – 146.
7. Rose, D., Jöris, J., Hackermüller, J., Reiche, K., Li, Q. and Stadler, P. F.(2008). Duplicated RNA genes in teleost fish genomes. *Journal of Bioinformatics and Computational Biology*, 6(6): 1157 – 1175.

8. Shi, Q-H, Tian, Y, Dong, X-Y, Bai, S. and Sun. Y. (2003). Chitosan-coated silica beads as immobilized metal affinity support for protein adsorption. *Biochemical Engineering Journal*, 16: 317 – 322.
9. Xi, F. N. and Wu, J. M. (2004). Macroporous chitosan layer coated on non-porous silica gel as a support for metal chelate affinity chromatographic adsorbent. *Journal Chromatography* A, 1057: 41 – 47.
10. Singla, A. K. and Chawla, M. (2001). Chitosan: some pharmaceutical and biological aspects – an update. *Journal of Pharmacy and Pharmacology*, 53: 1047 – 1067.
11. Lee, Y. M., Nam, S. Y. and Woo, D. J. (1998). PV performance of β–chitosan membrane for water/alcohol mixtures. *Journal of Polymer Engineering*, 18(12): 131 – 146.
12. Altun, G. D and Cetinus, S. A. (2007). Immobilization of pepsin on chitosan beads. *Food Chemistry* 100: 964 – 971.
13. Qu, R., Zhang,Y., Qu, W., Sun, C., Chen, J., Ping, Y., Chen, H. and Niu, Y. (2013). Mercury adsorption by sulfur- and amidoxime-containing bifunctional silica gel based hybrid materials. *Chemical Engineering Journal*, 219: 51 – 61.
14. Cetinus, S. A., Sßahin, E. and Saraydin, D., (2009). Preparation of Cu(II) adsorbed chitosan beads for catalase immobilization. *Food Chemistry*, 114: 962 – 969.
15. Bal, W., Liang, R., Lukszo, J., Lee, S. H., Dizdaroglu, M. and Kasprzak, K. S. (2000). Ni(II) specifically cleaves the C-Terminal tail of the major variant of histone H2A and forms an oxidative damage-mediating complex with the cleaved-off octapeptide. *Chemistry Research Toxicology*, 13(7): 616 – 624.
16. Zachariou, M, Traverso, I. and Hearn, M. T. (1993). High-performance liquid chromatography of amino acids, peptides and proteins. CXXXI. O-phosphoserine as a new chelating ligand for use with hard Lewis metal ions in the immobilized-metal affinity chromatography of proteins. *Journal of Chromatography*, 646(1): 107 – 120.
17. Sun, J., H. Ma, Y. Liu, Y. Su, W. Xia and Yang, Y. (2012). Improved preparation of immobilized trypsin on superparamagnetic nanoparticles decorated with metal ions. *Colloids Surfaces A: Physicochemical Engineering Aspects*, 414: 190 – 197.
18. Guo, W. and Ruckenstein, E. (2003). Crosslinked glass fiber affinity membrane chromatography and its application to fibronectin separation. *Journal Chromatography B*,795: 61 – 72

Malaysian Journal of Analytical Sciences, Vol 20 No 3 (2016): 585 - 593
DOI: http://dx.doi.org/10.17576/mjas-2016-2003-18

MALAYSIAN JOURNAL OF ANALYTICAL SCIENCES
Published by The Malaysian Analytical Sciences Society
ISSN 1394 - 2506

EFFECTS OF DIFFERENT GRINDING METHODS ON MORPHOLOGICAL, TEXTURAL PROPERTIES AND PASTING PROFILES OF MR220 RICE FLOUR

(Kesan Kaedah Pengisaran yang Berbeza terhadap Morfologi, Sifat Tekstur dan Profil Pempesan Tepung Beras MR220)

Noorlaila Ahmad[1]*, Asmeda Rajab[1], Norziah Mohd Hani[2]

[1]*Department of Food Technology, Faculty of Applied Sciences, Universiti Teknologi MARA, 40450 Shah Alam, Selangor, Malaysia*
[2]*Food Technology Department, School of Industrial Technology, Universiti Sains Malaysia, 40450 Minden, Penang, Malaysia*

**Corresponding author: dnoorlaila@salam.uitm.edu.my*

Received: 24 February 2015; Accepted: 27 October 2015

Abstract

Three different grinding techniques (dry, semi-wet, and wet) were employed in rice flour production. Investigation on the effects of the grinding techniques on starch damage percentage, particle size distribution, pasting profiles, morphological and textural properties of rice flours produced were evaluated. Wet grinding resulted in significantly ($p< 0.05$) has lower percentage of damaged starch (3.24 %) than other grinding methods. Morphological studies (microscopy and particle size analysis) have reflected significant differences among rice flours granule shapes. The granules displaying different shapes of polygonal, round and angular forms, with some as an individual granule while others tend to attached together. Wet grinding technique also yielded flour that exhibit significantly ($p< 0.05$) with higher gel hardness (16.62 g). Pasting profiles showed that pasting temperature for rice flour produce using these three grinding methods varied between 80.15 – 80.42 °C. Results revealed that the three grinding techniques clearly affected the physicochemical properties of rice flour. The results from this study play an important role in the selection criteria of rice flour with desirable pasting and textural properties for manufacturing rice-based product.

Keywords: Grinding techniques, particle size, pasting profiles, rice flour, starch damage

Abstrak

Tiga jenis teknik pengisaran (kering, separa basah, dan basah) telah digunakan dalam penghasilan tepung beras. Kajian ke atas kesan teknik pengisaran pada peratusan kerosakan kanji, taburan saiz partikel, profil pempesan, sifat morfologi dan tekstur tepung beras yang dihasilkan telah dianalisa. Pengisaran basah menyebabkan peratusan kanji rosak ($p< 0.05$) lebih rendah secara signifikan (3.24 %) berbanding kaedah – kaedah pengisaran lain. Kajian morfologi (mikroskopi dan analisis saiz zarah) telah menunjukkan perbezaan yang signifikan antara tepung beras dari segi saiz dan bentuk granul yang terhasil. Granul memaparkan bentuk berlainan seperti poligon, bulat dan bentuk bersudut, samada wujud sebagai granul sendirian ataupun berkluster. Teknik pengisaran basah juga menghasilkan perbezaan yang signifikan ($p< 0.05$) berbanding teknik pengisaran lain dari segi kekerasan gel yang lebih tinggi (16.62 g). Profil pempesan menunjukkan suhu pempesan untuk tepung beras yang dihasilkan menggunakan ketiga – tiga kaedah pengisaran berada dalam julat antara 80.15 – 80.42 °C. Hasil kajian dengan jelas menunjukkan bahawa tiga teknik pengisaran memberi kesan kepada ciri – ciri fizikokimia tepung beras. Hasil kajian ini sangat penting dalam menentukan kriteria tepung beras berdasarkan sifat dan sifat tekstur yang dikehendaki untuk pembuatan produk berasaskan beras.

Kata kunci: Teknik pengisaran, saiz partikel, profil pempesan, tepung beras, kerosakan kanji

Introduction

Rice (*Oryza sativa* L.) has been consumed by humans for almost 5000 years. Rice is a staple food for Malaysians, with current intake of rice is approximately 2.8 million tons [1]. The rice paddy will be milled in order to obtain white or brown rice grains. Rice flour is widely used to produce many kinds of food; hence it is crucial to produce flour with fine size particle for applications in various types of food products. Rice has been shown to vary widely in its cooking [2] and eating quality [3], depending on variety and type of rice.

Grinding is a unit operation widely used in the food industry. In developing countries, it is the common method for food powder processing [4]. In general, grinding is one part of a larger set of operations involved in the process of size reduction [5]. Dry grinding uses no water, need few manpower, and thus require low cost in production. While semi-wet grinding consume small amount of water for the soaking process and use one particular machine. As compared to dry and semi-wet grinding process, wet grinding involved usage of more than one machine, more manpower and more water thus generate higher cost as compared to others.

Flour characteristics as result from grinding process, such as particle size and damaged starch level; determine its suitability for specific end-products [6, 7]. When starch is heated continuously in excess water with stirring, starch granules swell irreversibly, accompanied by leaching of amylose and possibly solubilisation of amylopectin, resulting in the formation of paste. To a certain extent, the starch pasting behaviour determines rice cooking quality and functionality, since starch is the main component in rice [8].

This study aim to investigate the effect of different grinding practices in rice utilization, and filling the gap by providing specific information on physicochemical properties and pasting profiles of rice flour from Malaysian variety which is still lacking. The information is essential for predicting their functionality and subsequent end-use in foods. In addition, the present study were conducted to compare the performance of the dry grinding, semi-wet grinding, and wet grinding processes in order to improve the eating quality of rice or for selection of specific behavior/characteristic by using the appropriate grinding method.

Materials and Methods

Raw material

Malaysian rice variety of MR220 was obtained from Malaysian Agricultural Research and Development Institute (MARDI) Pulau Pinang, Malaysia. This rice variety was grown from genes seeds obtained from cross breeding of parents MR151 and MR137. Rice paddy was harvested at maturity, cleaned, dehulled and milled to obtain milled rice grains. Only whole rice grain without any physical damage or insect infestation was selected for analysis. The chemicals were obtained from the commercial scientific suppliers. The assay kit of damaged starch content was purchased from Megazyme International Ltd. (Ireland).

Grinding machines

For dry and semi-wet grinding process, a hammer mill (Rotary Type CNS, Taiwan) was used. For wet grinding, hammer mill and stone mill (Wet Grain Grinder, WGG 254, Malaysia) were used.

Rice flour preparation

Sample was prepared using three different grinding techniques. In the dry grinding technique, the rice grains obtained were directly ground into rice flour for two cycles using the hammer mill. In the semi-wet grinding technique, rice grains were soaked in water for 8 hours at rice to water ratio of 1:1 (w/v). The excess water was then drained and the rice grains were allowed to dry at room temperature before grinding with the hammer mill. In the wet grinding technique, rice grains were ground using stone mill with excess water after subjected to soaking for 8 hours at rice to water ratio of 1:1 (w/v). The slurry obtained was filtered pressed and the semi dried residue was collected. The dried sample was reground using hammer mill. All flour samples were dried in a cabinet dryer to obtain moisture content of less than 15 % prior to the analysis. Flour samples were sieved through a 100 mesh sieve (Retsch, Germany) and packed in air tight plastic container until further use.

Starch damage determination
The damaged starch content in the flour samples was determined using the starch damage assay kit by Megazyme International Ireland in accordance with the approved method 76-31 of the American Association of Cereal Chemists (AACC) [9].

Particle size distribution
The particle size distribution and average particle size of rice flour samples were analyzed by using the Mastersizer (Malvern Instrument, UK) fitted with Scirocco 2000 unit for the dry samples at a refractive index of 1.54. The equipment was equipped with a laser beam for detection.

Scanning electron microscopy
The microstructure of rice flour was observed using a scanning electron microscope (SEM, JSM-6610, JEOL, Tokyo, Japan). The rice flour sample was coated with platinum and dispersed on a SEM specimen stub with double-sided conductive tape. The SEM was operated at an accelerated voltage of 10 kV.

Pasting profiles
The pasting profiles of rice flour were evaluated using the Rapid Visco Analyzer (RVA, Newport Scientific, Australia) following the AACC method 61-02 [10]. Parameters including pasting temperature (PT), peak viscosity (PV), final viscosity (FV), breakdown viscosity (BV), setback viscosity (SB), trough (T) and peak time were calculated from the pasting curve assisted by the Thermocline software program for Windows (TCW).

Gel texture
The gelatinized mixture in the canister, after the RVA measurement was being used to measure gel hardness. The paddle was removed immediately and the paste in the canister was covered by parafilm and left at room temperature for 1 hour to allow formation of a solid gel. Texture of the gel was then determined using a TA-XT2 texture analyser (Stable Micro Systems, Surrey, UK). Gel in the canister (with a dimension of 37 mm in diameter and 20 mm in height) was compressed at a speed of 1.0 mm/s to a distance of 10.0 mm with a stainless steel punch probe 6.0 mm in diameter. The maximum force peak in the TPA profile represented the gel hardness [11].

Statistical analysis
Values were expressed as mean with standard deviation of triplicate determinations. Data was analyzed by analysis of variance (ANOVA) using Statistical Analysis System (SAS) [12]. Differences among samples were considered significant at $p< 0.05$.

Results and Discussion

Means of damaged starch content, average particle size and gel hardness of dry, semi-wet and wet ground flours were summarized in Table 1. The damaged starch levels for the rice flour samples varied from 3.24 % to 13.07 %. Wet grinding process produced flour with significantly ($p< 0.05$) lowest percentage of damaged starch while dry ground flour exhibits the highest. The high percentage of damaged starch in dry ground flour is likely attributable to damage produced by the shears force and the heat during grinding [13] as the rice grains were directly ground as it is, whereby the hammer mill pressed the grains against an abrasive ring at high rotating speed to break the grain structure. In addition, high damaged starch also due to the higher grain hardness of dry grinding technique compared to others since there is no soaking step in the process that eventually provides softening effect to the rice kernels [14]. Starch damage profoundly changes starch granule structure and it influences functional properties of starch [15].

Particle size of flour, measured as the mean particle diameter, is a critical factor in determining the flour's usefulness and application in further processing [16]. Figure 1 shows the particle size distributions of dry, semi-wet and wet ground flour samples. The curves showed two distinct types among the rice flour samples: dry and semi-wet ground vs wet ground flour. Dry and semi-wet ground flours showed unimodal distributions while wet ground flour displayed bimodal distributions. The wet ground flour showed to distinct peaks consisted of two particle types, with size of 2-20 µm and 20-106 µm. Significant differences were found ($p< 0.05$) in the average flour particle diameter for each sample (Table 1). Average particle size of flours ranged from 9.70 to 51.44 µm, with wet ground

flour composed of the finest average particle size as compared to others. Though dry ground rice flour yield flour with smaller average particle size when compared with semi-wet ground flour, but the former exhibit significantly ($p< 0.05$) highest damaged starch. This is supported by Nishita and Bean [17] that claimed in dry milling, a high percentage of damaged starch was associated with finer particles. Nevertheless, the average particle size of dry ground rice flour obtained in this study was smaller (39.4 µm) than findings reported by Hossen et al.[18] of hammer-milled flour (72.3 – 141.2 µm), due to different manners in the technique. Noomhorn et al. [19] claimed that the starch granules of smaller rice particles are more resistant to swelling than those of larger particles and thus affecting the RVA measurement [20, 21] as it caused a decrease in peak viscosity. The peak viscosity of fine wet ground flour was significantly ($p< 0.05$) lower as compared to others, confirming the reports of Bryant et al. [22].

Table 1. Starch damage contents, average particle size distribution and gel hardness of dry, semi-wet and wet ground rice flours

Grinding Process	Starch Damage (%)	Average Particle Size (um)	Gel Hardness (g)
Dry Grinding	13.07±0.03[a]	39.37±0.14[b]	13.65±0.05[b]
Semi-Wet Grinding	4.85±0.03[b]	51.44±0.13[a]	13.70±0.11[b]
Wet Grinding	3.24±0.03[c]	9.70±0.17[c]	16.62±0.07[a]

Mean values with the same superscript letters within a column are not significantly different at $p > 0.05$

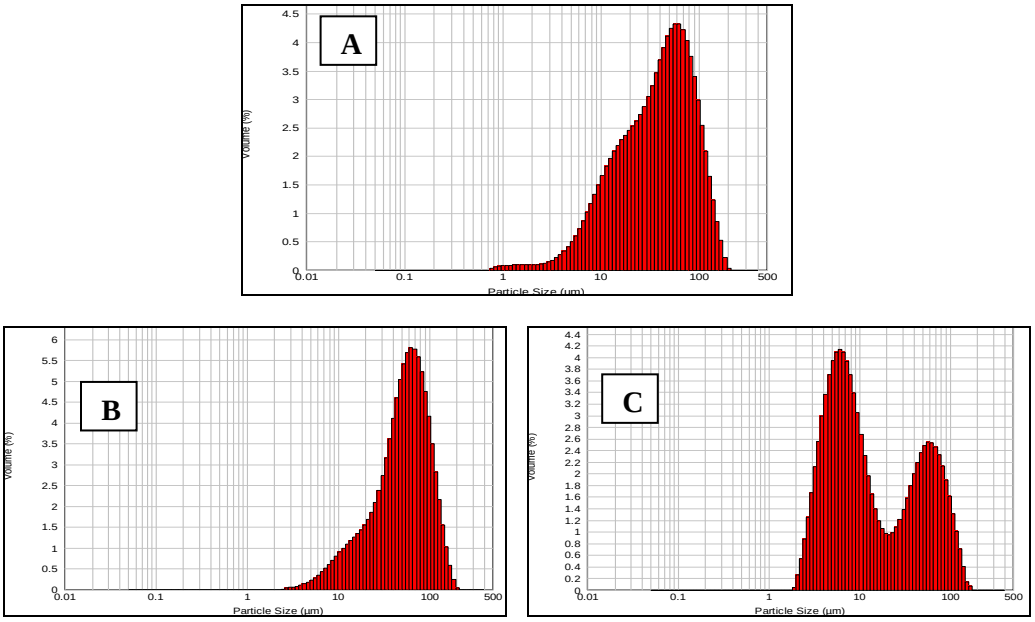


Figure 1. Particle size distributions of dry (A), semi-wet (B) and wet (C) ground rice flours

Scanning electron microscopy was used to observe the submicroscopic shape and surface characteristic of flour particles (Figure 2). Scanning electron micrographs of all flours showed irregular pentagonal or hexagonal shaped particles with protein matrix. Wet ground flour contains more free starch granules and smaller particles, plus more material adheres to the starch granules. On the other hand, some damaged granules were viewed in the dry ground

flour. As observed by Santhi and Poongodi [23], rice consists of several polyhedral starch granules in a single amyloplast and rice starch granules are the smallest of the starch grains produced by plants (3.8 µm) [24].

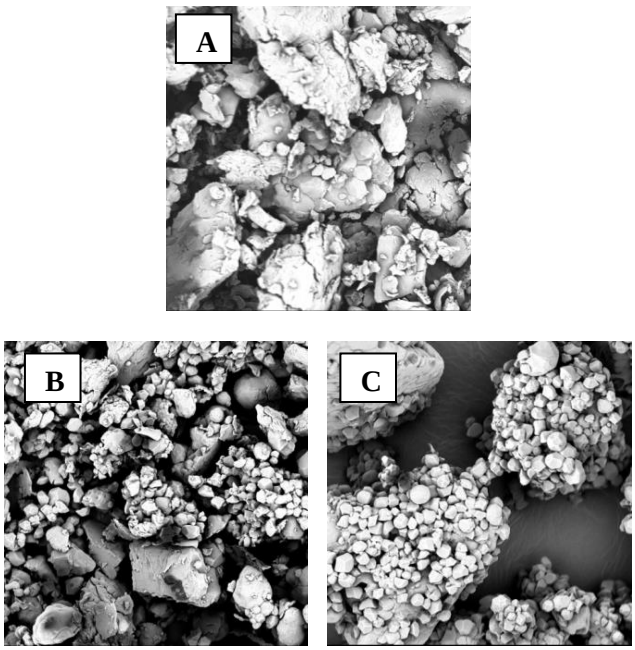


Figure 2. Microscopic structure of dry (A), semi-wet (B) and wet (C) ground rice flours

Hardness was derived from texture profile analysis curve with the starch gel from wet ground flour showed the highest hardness (16.62 g), whereas there is no significant difference ($p>0.05$) between dry and semi-wet ground flour samples. Starches that exhibit harder gels tend to have higher amylose content and longer amylopectin chains [25]. It is also associated with starch gel retrogradation, along with the crystallisation of amylose in a short time which leads to harder gels [26]. Miles et al. [27] also claimed that rigidity of starch gel is highly dependent on retrogradation of gelatinised starch granules, syneresis of water and crystallisation of amylopectin. Therefore, presence of certain level of soluble carbohydrates from wet ground flour could enhance starch gel retrogradation that would give rise to harder gels [28].

Pasting property is one of the most important properties that influence quality and aesthetic considerations in the food industry as they affect texture and digestibility as well as the end use of starch-based food commodities [29]. Pasting profile results from a complex interaction of the test material and water, affected by temperature and time, and it was performed using the rapid visco analyzer (RVA). The plot of viscosity of the flour samples against heating time was shown in Figure 3. Significant differences were found ($p< 0.05$) at each parameter of the RVA curve, except the pasting temperature (Table 2).

Peak viscosity is an index of the ability of starch-based food to swell freely before their physical breakdown [30]. The value ranged from 2777.67 – 2834.67 centipoise (cP). Dry ground flour had significantly ($p< 0.05$) highest peak viscosity followed by semi-wet and wet ground flour. High peak viscosity indicates high starch content [31] and is an indicative that the flour may be suitable for products requiring high gel strength and elasticity [32, 33] The peak viscosity of wet ground flour was significantly low ($p< 0.05$) compared to other samples and this indicates that the carbohydrate components of wet ground flour will not breakdown easily and quickly like the other samples until it is cooked properly [34].

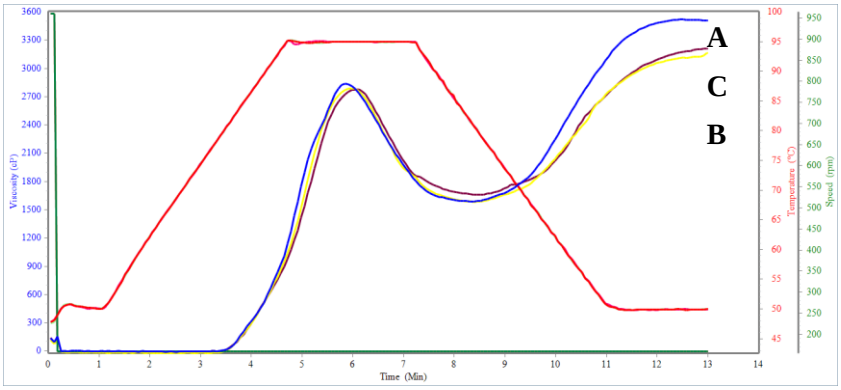


Figure 3. Pasting profiles of dry (A), semi-wet (B) and wet (C) ground rice flours

Table 2. Pasting profiles of dry, semi-wet and wet ground rice flours

Pasting Viscosity (cP)	Dry Grinding	Semi-Wet Grinding	Wet Grinding
Peak Viscosity	2834.67±6.51^{a}	2798.67±10.12^{b}	2777.67±6.51^{c}
Trough	1602.00±13.75^{ab}	1582.00±45.00^{b}	1656.67±9.71^{a}
Breakdown	1232.67±17.24^{a}	1216.67±45.63^{a}	1121.00±16.09^{b}
Final Viscosity	3548.67±44.19^{a}	3153.00±8.19^{b}	3195.00±22.52^{b}
Setback	1946.67±37.86^{a}	1571.00±39.96^{b}	1538.33±13.61^{b}
Pasting Temperature (°C)	80.37±0.45^{a}	80.42±0.54^{a}	80.15±0.57^{a}

Mean values with the same superscript letters across the row are not significantly different at $p > 0.05$

The ability of paste to resist breakdown during cooling is indicated by trough viscosity [35]. Trough is the minimum viscosity value in the constant temperature phase of the pasting profile [31]. The value ranged between 1582.00 – 1656.67 cP; with sample of semi-wet flour having the lowest value and wet ground flour having the highest value. Breakdown viscosity measured the starch paste resistance to heat and shear [8], while setback viscosity exhibited the tendency of starch pastes to retrograde, which is an index of starch retrogradation [36]. The breakdown value ranged from 1121.00 to 1232.67 cP while the setbacks ranged from 1538.33 to 1946.67 cP. Referring toTable 2, breakdown of dry and semi-wet ground flour was similar ($p > 0.05$), but was significantly ($p < 0.05$) higher than wet ground flour. The rate of the breakdown is dependent on temperature, shear stress applied to the system, and the nature of the starch tested [37]. Decrease in breakdown would cause less amylose molecules leached out into the matrix during cooking. Ultimately this could result in reduced retrogradation of amylose molecules [38]. High values in breakdown and low values in setback of semi-wet ground flour are indicative of high cooking quality since neither the cooked rice retrogrades nor becomes stiff upon cooling [39].

Final viscosity is commonly used to define the quality of particular starch-based flour, since it indicates the ability of the flour to form a viscous paste after cooking and cooling [35]; measure as the change in the viscosity after holding cooled starch at 50 °C [40]. It also represents the re-association of starch granules especially amylose during cooling time after gelatinization and the formation of gel network [41]. The final viscosity value recorded from this study ranged from 3153.00 to 3548.67 cP. Final viscosity, as well as setback viscosity values of dry ground flour were significantly ($p < 0.05$) higher than semi-wet and wet ground flour. The lower final viscosity of flours displayed the extension of the effect on the amylose chains, which might lose the ability to retrograde during

cooling due to their fragmentation [42], in this case, may due to mechanism involved in hammer mill when rice grains subjected to semi-wet grinding process.

Pasting temperature is the temperature at which the viscosity of the starch pastes begins to rise; indicates the minimum temperature required in cooking the sample [43].The pasting temperature ranged between 80.15 ^{o}C and 80.42 ^{o}C. There were no significant differences ($p > 0.05$) in pasting temperature among all the samples. These values are comparatively low as compared with values having been reported in a number of rice pasting studies e.g., 86 °C in long grain [44] and 90 – 95 °C in cryomilled and hammer milled rice [30, 35]. The attainment of the pasting temperature is essential in ensuring swelling, gelatinization and subsequent gel formation during processing [11]. Lower pasting temperatures were found to be associated with faster particle swelling and higher peak viscosity [45] while higher pasting temperatures indicates higher water binding capacity, higher gelatinization tendency and lower swelling properties of starch based flour due to high degree of association between starch granules [46]. The difference in damaged starch content and particle size distribution between flours is reported to affect the RVA profile [47]. Damaged starch granules can absorb water, swell and leach out amylose and amylopectin, which causes an increase in the viscosity of starch [48].

Conclusion

Dry, semi-wet and wet grinding techniques involved in rice flour production significantly ($p < 0.05$) affects the percentage of damaged starch, average particle size distribution, gel hardness and pasting profiles parameters except the pasting temperature. Wet grinding process exhibit flour of lowest amount of damaged starch granules 3.24 % with finest average particle size of 9.70 um. Flour samples had similar pattern of viscosity curves, but samples of dry ground flour showed significantly ($p < 0.05$) higher final viscosity. Overall, the findings suggest that wet grinding process can be regarded as the potential flour grinding practice since it produces flour with lowest starch damage, and finest average particle size as compared to others. Nevertheless, grinding method to be considered in producing the flour and to be utilized in rice based food products is depending on the specific uses.

Acknowledgement

The authors thank Universiti Teknologi MARA, Research Management Institute Universiti Teknologi MARA, Universiti Sains Malaysia and Malaysian Agricultural Research and Development Institute for the support and assistance throughout this research.

References

1. Wahab, A. G. and Rittgers, C. (2014). *Global Agricultural Information Network Report MY4001* – Grain & Feed Annual, Malaysia. (No.: MY4001), pp 1-5.
2. Hossain, M. S., Singh, A. K. and Fasih-uz-Zaman. (2009). Cooking and eating characteristics of some newly identified inter sub-specific (*Indica/Japonica*) Rice Hybrids. *Science Asia*, 35: 320 – 325.
3. Bhattacharya, K. R. (2009). Physicochemical basis of eating quality of rice. *Cereal Foods World*, 54 (1): 18 - 28.
4. Song, S. –H., Lee, M. –G., Lee, H. –J. and Yoon, W. –B. (2014). Analysis of grinding kinetics to control the effect of rice flour particle size on the yield of alcohol and glucose during fermentation. *International Journal of Food Science & Technology:* 1 – 8.
5. Djantou, E. B., Mbofung, C. M., Scher, J. and Desobry, S. (2007). A modelling approach to determine the effect of pre-treatment on the grinding ability of dried mangoes for powder production (*Mangifera indica* var kent). *Journal of Food Engineering*, 80: 668 – 677.
6. Pauly, A., Pareyt, B., Fierens, E. and Delcour, J. A. (2013). Wheat (*Triticum aestivum* L. and *T. turgidum* L. ssp**.** *durum*) kernel hardness: ii. implications for end-product quality and role of puroindolines therein. *Comprehensive Reviews in Food Science & Food Safety*, 12 (4): 427 – 438.
7. Winger, M., Khouryieh, H., Aramouni, F. and Herald, T. (2014). Sorghum flour characterization and evaluation in gluten-free flour tortilla. *Journal of Food Quality*, 1 – 12.
8. Kong, X., Zhu, P., Sui, Z. and Bao, J. (2015). Physicochemical properties of starches from diverse rice cultivars varying in apparent amylose content and gelatinisation temperature combinations. *Food Chemistry*, 172: 433 – 440.

9. American Association of Cereal Chemists. (2000). AACC Method 76-31. In Approved Methods of AACC, 10th Ed., St. Paul, MN.
10. American Association of Cereal Chemists. (2000). AACC Method 61-02. In Approved Methods of AACC, 10th Ed., St. Paul, MN.
11. Hasjim, J., Li, E. and Dhital, S. (2013). Milling of rice grains: effects of starch/flour structures on gelatinization and pasting properties. *Carbohydrate Polymer,* 92: 682 – 690.
12. Statistical Analysis System. (2002). *SAS: User's Guide Statistics*, (Version 9.13). SAS Institute, Inc., Cary, NC.
13. Hossen, M. S., Sotome, I., Takenaka, M., Isobe, S., Nakajima, M. and Okadome, H. (2011). Effect of particle size of different crop starches and their flours on pasting properties. *Japan Journal of Food Engineering,* 12 (1): 29 – 35.
14. Ngamnikom, P. and Songsermpong, S. (2011). The effects of freeze, dry, and wet grinding processes on rice flour properties and their energy consumption. *Journal of Food Engineering,* 104: 632 – 638.
15. Cai, L., Choi, I., Hyun, J.–N. and Jeong, B.–K. (2014). Influence of bran particle size on bread baking quality of whole grain wheat flour and starch retrogradation. *Cereal Chemistry,* 91 (1): 65 – 71.
16. Patwa, A., Malcolm, B., Wilson, J. and Ambrose, R. P. K. (2014). Particle size analysis of two distinct classes of wheat flour by sieving. *American Society of Agricultural & Biological Engineers,* 57 (1): 151 – 159.
17. Nishita, K. D. and Bean, M. M. (1982). Grinding methods: their impact on rice flour properties. *Cereal Chemistry,* 59 (1): 46 – 49.
18. Hossen, M. S., Sotome, I., Takenaka, M., Isobe, S., Nakajima, M. and Okadome, H. (2011). Starch damage and pasting properties of rice flours produced by dry jet grinding. *Cereal Chemistry,* 88 (1): 6 – 11.
19. Noomhorn, A., Kongseree, N. and Apintapong, N. (1997). Effect of aging on the quality of glutinous rice crackers. *Cereal Chemistry,* 74: 12 – 15.
20. Bryant, R. J., Kadan, R. S., Champagne, E. T., Vinyard, B. T. and Boykin, D. (2001). Functional and digestive characteristics of extruded rice flour. *Cereal Chemistry,* 78: 131 – 137.
21. Park, J. H., Kim, D. C., Lee, S. E., Kim, O. W., Kim, H., Lim, S. T. and Kim, S. S. (2014). Effects of rice flour size fractions on gluten free rice bread. *Food Science Biotechnology,* 23 (6): 1875 – 1883.
22. Song, J. Y. and Shin, M. S. (2007). Effects of soaking and particle sizes on the properties of rice flour and gluten-free rice brad. *Food Science Biotechnology,* 16: 759 – 764.
23. Santhi, K. and Poongodi, V. T. (2014). Physical and functional characteristics of milling fractions of indian kavun pigmented brown rice (*oryza sativa* l.). *International Journal of Agricultural & Food Science,* 4 (2): 78 – 83.
24. Zhongkai, Z., Kevin, R., Stuart, H. and Chris, B. (2002). Composition and functional properties of rice. *International Journal Food Science Technology,* 37: 849 – 868.
25. Wang, L., Xie, B., Shi, J., Xue, S., Deng, Y., Wei, Y. and Tian, B. (2010). Physicochemical properties and structure of starches from chinese rice cultivars. *Food Hydrocolloids,* 24: 208 – 216.
26. Mir, S. A. and Bosco, S. J. D. (2014). Cultivar difference in physicochemical properties of starches and flours from temperate rice of Indian Himalayas. *Food Chemistry,* 157: 448 – 456.
27. Miles, M. J., Morris, V. J., Orford, P. D. and Ring, S. G. (1985). The roles of amylose and amylopectin in the gelation and retrogradation of starch. *Carbohydrate Research,* 135: 271 – 281.
28. Chang, S. M. and Liu, L. C. (1991). Retrogradation of rice starches studied by differential scanning calorimetry and influence of sugars, NaCl and lipids. *Journal of Food Science,* 56: 564 – 566.
29. Onabanjo, O. O. and Ighere Dickson, A. (2014). Nutritional, functional and sensory properties of biscuit produced from wheat-sweet potato composite. *Journal of Food Technology Research,* 1 (3): 111 – 121.
30. Adebowale, A. A., Sanni, L. O. and Onitilo, M. O. (2008). Chemical composition and pasting properties of tapioca grit from different cassava varieties and roasting method. *African Journal of Food Science,* 2: 77 – 82.
31. Adegunwa, M. O., Ganiyu, A. A., Bakare, H. A. and Adebowale, A. A. (2014). Quality evaluation of composite millet-wheat chinchin. *Agriculture & Biology Journal of North America,* 5 (1): 33 – 39.
32. Regena, J. K. and Chen, Z. (2009). Physic-chemical properties of peanut meal flour as affected by processing methods. *Journal of Biochemistry,* 34: 229 – 243.
33. Ikegwu, O. J., Okechukwu, P. E. and Ekumankana, E. O. (2010). Physic-chemical and pasting characteristics of flour and starch from achi (*brachystegiaeunycoma)* seed. *Journal of Food Technology,* 8 (2): 58 – 66.
34. Obadina, A. O., Babatunde, B. O. and Olotu, I. (2014). Changes in nutritional composition, functional, and sensory properties of yam flour as a result of presoaking. *Food Science & Nutrition,* 1 – 6.

35. Adebowale, A. A., Adegoke, M. T., Sanni, S. A., Adegunwa, M. O. and Fetuga, G. O. (2012). Functional properties and biscuit making potentials of sorghum-wheat flour composite. *American Journal of Food Technology*, 7: 372 – 379.
36. Liang, X. and King, J. M. (2003). Pasting and crystalline property differences of commercial and isolated rice starch with added amino acids. *Journal of Food Science*, 68: 832 – 838.
37. Newport Scientific. (1998). *Interpretation*. In Applications Manual for the Rapid Visco Analyzer, Australia, Newport Scientific Pty. Ltd., pp 13 – 16.
38. Sharma, R., Oberoi, D. P. S., Sogi, D. S. and Gill, B. S. (2009). Pasting and crystalline property differences of commercial and isolated rice starch with added amino acids. *Journal of Food Processing & Preservation*, 33: 401 – 414.
39. Asante, M. D., Offei, S. K., Gracen, V. Adu-Dapaah, H., Danquah, E. Y., Bryant, R. and McClung, A. (2013). Starch physicochemical properties of rice accessions and their association with molecular markers. *Starch / Starke*, 65: 1022 – 1028.
40. Danbaba, N., Ukwungwu, M. N., Maji, A. T., Ndindeng, S. A., Jiya, A. G., Danfulani, S. and On, E. N. (2014). End-use quality of upland *NERICA* rice (*Oryza sativa* L) as affected by the addition of sweet cassava (low cyanide, *Manihotesculenta*) flour. *International Journal of Agriculture & Forestry*, 4 (3): 237 – 245.
41. Chanapamokkhot, H. and Thongngam, M. (2007). The chemical and physicoc-chemical properties of sorghum starch and flour. *Journal of Natural Science*, 41: 343 – 349.
42. Martinez, M. M., Calvino, A., Rosell, C. M. and Gomez, M. (2014). Effect of different extrusion treatments and particle size distribution on the physicochemical properties of rice flour. *Food Bioprocess Technology*, 7: 2657 – 2665.
43. Kaur, S., Singh, N., Sodhi, N. S. and Rana, J. C. (2009). Diversity in properties of seed and flour of kidney bean germplasm. *Food Chemistry*, 117: 282 – 289.
44. Chung, H., Liu, Q., Huang, R., Yin, Y. and Li, A. (2010). Physicochemical properties and in vitro starch digestibility of cooked rice from commercially available cultivars in Canada. *Cereal Chemistry*, 87 (4): 297 – 304.
45. Offia-Olua, B. I. (2014). Chemical, functional and pasting properties of wheat (*Triticumspp*)-walnut (*Juglansregia*) flour. *Food & Nutrition Sciences*, 5: 1591 – 1604.
46. Liu, L., Herald, T. J., Wang, D., Wilson, J. D., Bean, S. R. and Aramouni, F. M. (2012). Characterization of sorghum grain and evaluation of sorghum flour in a Chinese egg noodle system. *Journal of Cereal Science*, 55: 31 – 36.
47. Ashida, K. (2014). Properties of floury rice mutant and its utilization for rice flour. *Japan Agricultural Research Quarterly*, 48 (1): 51 – 56.
48. Barrera, G. N., Bustos, M. C., Iturriaga, L., Flores, S. K., Leon, A. E. and Ribotta, P. D. (2013). Effect of damaged starch on the rheological properties of wheat starch suspensions. *Journal of Food Engineering*, 116: 233 – 239.

Malaysian Journal of Analytical Sciences, Vol 20 No 3 (2016): 594 - 600
DOI: http://dx.doi.org/10.17576/mjas-2016-2003-19

MALAYSIAN JOURNAL OF ANALYTICAL SCIENCES
Published by The Malaysian Analytical Sciences Society
ISSN 1394 - 2506

BITTERNESS AND PHYSICHOCHEMICAL PROPERTIES OF ANGELWING CLAM (*Pholas orientalis*) HYDROLYSATE

(Kepahitan dan Ciri – Ciri Fizikokimia Hidrolisat Mentarang (*Pholas orientalis*))

Normah Ismail* and Nurul Fasihah Razak

Department of Food Technology, Faculty of Applied Sciences,
Universiti Teknologi MARA, 40450 Shah Alam, Selangor, Malaysia

**Corresponding author: norismel@salam.uitm.edu.my*

Received: 24 February 2015; Accepted: 27 October 2015

Abstract

Protein hydrolysates from angelwing clam were obtained by enzymatic hydrolysis using bromelain. The bitterness of hydrolysates was evaluated based on the degree hydrolysis (DH), sensory analysis, molecular weight distribution and functional group. By using 3 % of enzyme substrate ratio bromelain resulted in high DH value at 12.57 % when angelwing clam was hydrolysed for 2 hours. Sensory analysis showed that angelwing hydrolysate was bitter. Angelwing hydrolysate had molecular weight below 50 kDa. The lower molecular weight indicated that the protein has been degraded into smaller peptide chains which contribute to bitter taste. Moreover, the high peak of amine group in angelwing hydrolysate (3385.6 cm^{-1}) suggested that bitterness exists. Angelwing hydrolysate had higher protein content, lower fat content and had good water holding capacity than the flesh. This result suggested that angelwing hydrolysate could be useful as food ingredient even though bitter taste developed after the hydrolysis. Thus, debittering should be considered in order to pave the way for full utilization of angelwing clam hydrolysate as a food ingredient.

Keywords: angelwing clam, sensory, hydrolysate, bromelain, bitterness, physicochemical properties

Abstrak

Hidrolisat protein daripada kerang mentarang diperolehi daripada hidrolisis proses menggunakan enzim bromelain. Kepahitan hidrolisat dinilai berdasarkan tahap hidrolisis (DH), analisis deria, pengedaran berat molekul dan kumpulan berfungsi. Dengan menggunakan 3 % daripada nisbah substrat enzim bromelain menyebabkan nilai DH tinggi pada 12.57 % apabila kerang mentarang telah dihidrolisiskan selama 2 jam. Analisis deria menunjukkan kerang mentarang hidrolisat adalah pahit. Hidrolisat kerang mentarang mempunyai berat molekul di bawah 50 kDa. Berat molekul yang rendah menunjukkan bahawa protein yang telah dipecahkan kepada rantaian peptida yang lebih kecil menyumbang kepada rasa pahit. Selain itu, kumpulan amina yang mempunyai puncak yang tinggi dalam mentarang hidrolisat (3385.6 cm^{-1}) menunjukkan bahawa kepahitan wujud. Hidrolisat kerang mentarang mempunyai kandungan protein yang lebih tinggi, kandungan lemak yang lebih rendah dan mempunyai keupayaan pegangan air yang lebih baik daripada daging. Hasil keputusan ini menunjukkan bahawa kerang mentarang hidrolisat boleh dimanfaatkan sebagai bahan makanan walaupun rasa pahit hadir selepas hidrolisis. Oleh itu, penyah-pahitan perlu dipertimbangkan untuk membuka jalan kepada penggunaan penuh kerang mentarang hidrolisat sebagai bahan makanan.

Kata kunci: mentarang, *Pholas orientalis*, hidrolisat, bromelain, kepahitan, ciri-ciri fizikokimia

Introduction

Angelwing clam (*Pholas orientalis)* is a marine bivalve found worldwide in countries such as France, Canada, Mexico, Japan, Australia, India, Papua New Guinea, Malaysia and Philippine [1]. In Malaysia, angelwing clam is

abundantly found in Perlis, Kuala Kedah, Kuala Limau, Yan, Penaga, Telok Ayer Tawar and Kuala Selangor [2]. Protein hydrolysate is well-known protein rich by product that can be utilized as functional ingredients in food systems [3]. According to Jin et al. [4] marine bivalves protein hydrolysate has good functionalities such as high in solubility, water holding capacity, oil holding capacity and surface hydrophobicity. Besides, these marine bivalves protein hydrolysate has high nutritive value such as all essential amino acids that make it suitable to be multifunctional food ingredients. Zhou et al. [5] studies showed that bivalve mollusks such as scallop and abalone protein hydrolysate possessed a significant antioxidant ability that can replace the synthetic antioxidant.

The degree of bitterness that developed during hydrolysis are associated with the level of hydrophobic amino acids and the release of bitter taste peptides [6, 7]. The size of peptide and lower molecular weight peptides are considered crucial to the sensation of bitterness [8].Therefore, the aim of this study was to investigate the development of bitter flavour in angelwing hydrolysate produced by bromelain.

Materials and Methods

Raw materials

Angelwing clam was purchased from Pantai Remis, Selangor, Malaysia. The clam was placed in ice and transported to the laboratory. Upon arrival the flesh was separated manually, washed and then stored at -20 ^{0}C. Bromelain (1.5 AU/g) was obtained from Novozymes.

Preparation of angelwing clam protein hydrolysates

Angelwing hydrolysate was prepared according to the methods by Normah and Fazlika [9] with some modification. An amount of 500 g angelwing clam flesh was mixed with 531.33 mL of distilled water and then minced. The mixture was transferred into 1 L beaker which was then placed in a water bath. The water bath was set at 45 ºC and the pH of the mixture was adjusted to 6. Once the temperature and pH were constant, bromelain was added at 3 % enzyme substrate ratio and the hydrolysis was performed for two hours. The mixture was continuously stirred at 200 rpm. The pH was kept constant throughout the hydrolysis by the addition of 1 N NaOH. At the end of the two hour hydrolysis, the reaction was terminated by heating at 90 ˚C for 15 minutes in a water bath. The mixture was then centrifuged (Hettich ZENTRIFUGEN, UNIVERSAL 320R) at 10000 rpm at 4˚C for 20 minutes. The supernatant was collected and freeze dried using SANYO-Biomedical freeze dryer.

Degree of hydrolysis

The percentage of solubilized protein in 10 g trichloroacetic acid (TCA), in relation to the total protein content of the sample was measured by the method of Silvestre et al. [10] with modification. After hydrolysis, 20 mL of protein hydrolysate was added to 20 mL of 20 % (w/v) TCA to produced 10 % TCA soluble material. The mixtures were left to stand for 30 minutes to allow precipitation followed by centrifugation at 7800 g for 15 minutes (Hettich ZENTRIFUGEN, UNIVERSAL 320R). Soluble protein content in 10 % TCA and total protein content was detected by Lowry method. The DH is calculated as formula equation 1:

$$\mathrm{DH} = \frac{\text{soluble protein content in 10 g TCA (mg)}}{\text{Total protein content (mg)}} \text{ x } 100 \quad (1)$$

Evaluation of bitter taste

The intensity of the bitter taste was conducted according to methods Nilsang et al. [7]. Samples were evaluated by 10 trained panelists who have been trained for three weeks using caffeine solution. Different concentrations of caffeine solutions at 0 to 1500 ppm were prepared and presented to panelists. Panelists were instructed to rate the bitterness by marking a point on a 15 cm line scale. After each tasting, they were asked to rinse their mouth with 10% v/w citrus water and twice with warm water.

Determination of molecular weight distribution by Sodium Dodecyl Sulfate Polyacrylamide Gel Electrophoresis (SDS-PAGE)

An approximately 1 g of samples was mixed with 10 mL deionized water and then filtered using membrane filter with pore size 0.45µm. An amount 6.5 µL of the solution was mixed with 2.5 µL NuPAGE®LDS sample Buffer (4X) and 1µL NuPAGE® Reducing Agent (10X). The mixture was heated at 70 ºC for 10 minutes. 15µL sample was loaded into each well of the SDS-PAGE system comprising of 12 % resolving gel and 5 % stacking gel.

Benchmark™ protein ladder with the range of 220 to 4.6 kDa was used as a marker. Electrophoresis was performed using the XCell Surelock electrophoresis cell (Bio-Rad laboratories, Hercules, CA, USA). Electrophoresis was run for 50 minutes at 100-125 mA/gel. After the running process, the gels were washed with 100 mL of ultrapure water. Then, the gel was stained using Coomassie Brilliant Blue dye and heated in a microwave oven at 180 °C for one minute. The gel was shaken again in the orbital shaker for about 2 minutes. The process was repeated twice. The gels were destained using ultrapure water and shaken with orbital shaker for another 30 minutes.

Functional group analysis

The functional group analysis in samples was performed using Thermo Nicolet, Avatar 370a Fourier Transform Infer-Red Spectrophotometer (FTIR). This analysis was determined according to Normah et al. [6] with slight modification. The angelwing sample was ground using agate mortar until the particle size became so small (approximately 2.5 micron) that the surface of the solid appears shiny. An amount 0.08 g of powdered potassium bromide (KBr) was added and the mixture was ground for about 30 seconds. The mixture was scraped into the middle and ground for another 15 seconds. The sample and KBr should be finely ground to avoid the mixture from scattering the infrared radiation excessively. The mixture was then placed in an evacuable mold and subjected to a pressure of 10 to 20MPa. Perkin Elmer Spectrum Software was used to control the spectrometer and data were collected over a wavenumber range of 4000 – 400 cm^{-1} with resolution of 4 cm^{-1} and collection spectra of 16.

Determination of fat content

The extraction and determination of the fat content from the minced muscle or the hydrolysate sample were performed using the Soxhlet extraction method [11].

Protein concentration

Protein concentration was determined using the Lowry method based on the modified procedure of Hartree [12].

Water holding capacity

Water holding capacity (WHC) was determined using the centrifugation method according to Diniz and Martin [13].The samples (0.5 g) of hydrolysate was dissolved in 20 mL water in centrifuge tubes and dispersed with a vortex mixer for 30s. The dispersion was allowed to stand at room temperature for 6 hours, and subsequently centrifuged at 2800 g for 30 min. The supernatant was filtered through Whatman filter paper No. 1 and the volume recovered was accurately measured. The difference between the initial volume of distilled water added to the protein sample and the volume of the supernatant were determined. The results were reported as mL of water absorbed per gram of protein sample (Equation 2).

$$\text{WHC}\left(\frac{\text{ml}}{\text{g}}\right) = \frac{\text{Initial Volume of Distilled Water} - \text{Volume of supernatant (ml)}}{\text{Weight of Hydrolysate (g)}} \quad (2)$$

Results and Discussion

Degree of hydrolysis (DH)

Hydrolysis at pH 6, E/S 3% and at the duration of 2 hours produced 12.57 % degree of hydrolysis by using bromelain. DH has been shown to be affected by the percent and type of enzyme used during the hydrolysis. Increasing the enzyme substrate ratio increased the DH as reported by Haslaniza et al. [14]. By increasing the enzyme concentration, the released peptides were further hydrolysed into amino acid and smaller peptide. According to Bhaskar et al. [15] degree of hydrolysis was higher at elevated temperatures as the degree of hydrolysis increased at increasing hydrolysis time and temperature. Besides, enzyme at given pH also affect the DH percentage as the optimum pH for higher rate of hydrolysis by using bromelain was at pH 6 to 7 [16].

Evaluation of bitter taste

Quantitative descriptive analysis (QDA) was carried out by ten trained panelists and the result is presented in Figure1a. The scores of bitterness using a 15-cm QDA line scale was 0.47 for the flesh, 9.49 for angelwing hydrolysate and 8.37 for caffeine reference solution. Angelwing hydrolysate was significantly ($p < 0.05$) bitter compared to the reference solution. The angelwing hydrolysate taste mildly bitter when produced using bromelain.

The bitter taste perceived in angelwing hydrolysate was due to the high amount of enzyme (E/S %) used that contribute to the increased of DH [7]. This result was also supported by Seo et al. [17] where the small amount of S/E% at 0.5 % bromelain used could gave a bitter taste to soy protein hydrolysate. According to Imelda [18] samples showed hydrolysis with different proteases had varying level of bitterness, where alcalase and protamex showed high level of bitterness within 1500 to 2000 ppm caffeine.

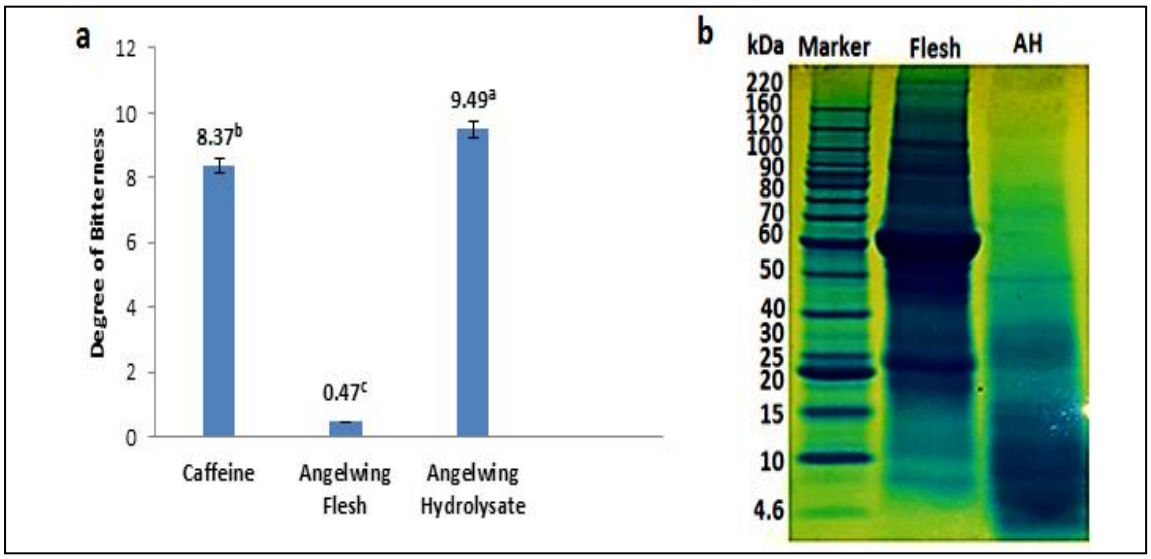


Figure 1. a) Degree of bitterness in caffeine solution, angelwing clam flesh and hydrolysate obtained by Quantitative Descriptive Analysis (QDA) where a, b, c (superscript) are significantly different ($p < 0.05$) and b) Electrophoresis patterns of angelwing clam flesh and hydrolysates produced at pH 6, 45◦C for 2 hours by using bromelain.

Molecular weight distribution of angelwing flesh and hydrolysate

The electrophoresis patterns of angelwing flesh and hydrolysate are shown in Figure 1b. The flesh consists of many clear bands ranging from 9 to 220 kDa compared to angelwing hydrolysate where clear bands were found very distinctly below 50 kDa. The absence of high molecular weight bands above 50 kDa and the fade bands were at 90, 80 and 60 kDa showed that bromelain is capable of degrading most of the larger protein. According to Jefferey et al. [19] the smaller the peptide, the bitter is the hydrolysate. As shown in Figure 2, angelwing hydrolysate had thick bands at 4.6 kDa and below compared to the flesh. This suggested that the bitterness was perceived after the hydrolysis. This result was in line with sensory analysis. According to Kristinsson and Rasco [20], molecular weight with protein below 10 kDa contributed to the bitterness of hydrolysate. While Jeffery et al. [19] stated that bitterness develops when small to medium-sized of hydrophobic peptides <18 kDa were produced after hydrolysis process. This was also supported in previous study by Normal et al. [6], where green muscle hydrolysate produced using alcalase had molecular weight of <3 kDa were bitter. In this study, angelwing hydrolysate had bands below 15kDa that indicated the hydrolysate has smaller peptide compared to the flesh that contribute to bitterness.

Functional group analysis

The peak ranges between 3500 – 3200 cm^{-1} in Figures 2 represent the N-H of amine group. The functional group of angelwing hydrolysate showed high peak at 3385.6 cm^{-1} while the flesh showed a peak at 3305.65cm^{-1}. According to Agrawal and Chiddarwar [21] the functional groups that are usually present in the bitter drugs were amine group. Therefore, this result is in accordance with the sensory analysis which showed that angelwing hydrolysate was bitter due to the presence of the high peak of N-H groups. Besides, Figure 2 showed angelwing hydrolysate has peak bands at 1640 cm^{-1} while the flesh has a peak bands at 1654 cm^{-1} which attributed to the carbonyl (C=0) stretch

vibration centered approximately between 1650 cm^{-1} – 1540 cm^{-1}[22]. These bands indicated the presence of functional compounds strong amide I and II in protein amide group (-$CONH_2$) which this amides of carboxylic acid ($RCONH_2$) were bitter [23].

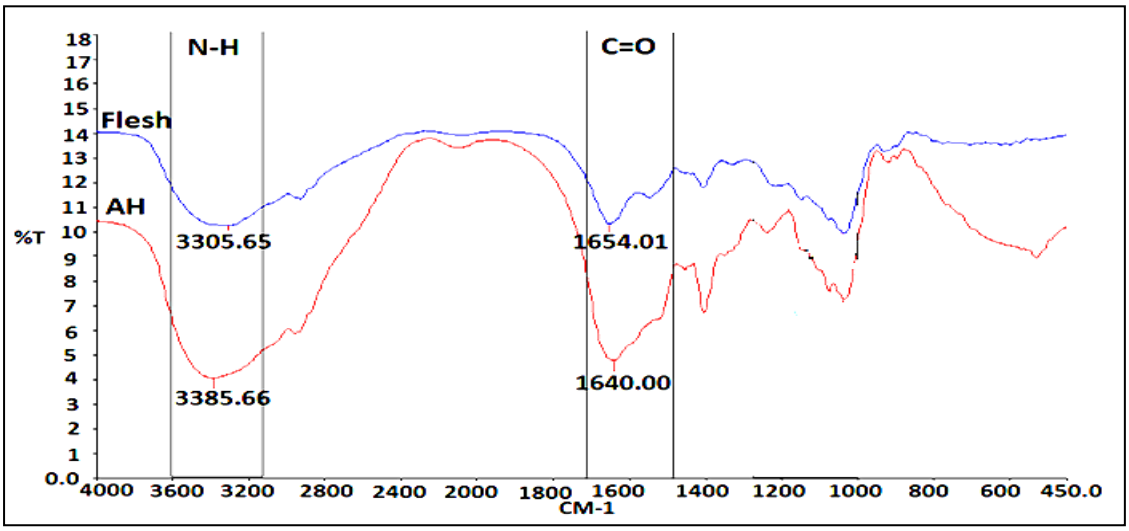


Figure 2. FTIR spectrums of angelwing clam flesh and hydrolysate (AH) produced at pH 6, 45 °C for 2 hours by using bromelain

Protein, fat and water holding capacity

Hydrolysis of angelwing clam increased the protein concentration in hydrolysate. Table 1, showed the hydrolysate contain 74.41% protein, which increased the protein content to 48.28 % more than the flesh. These results were in line with DH where angelwing hydrolysate had high DH (12.10 %).Previous study stated that the higher DH gave higher protein content [24]. This is because protein that solubilized during hydrolysis contained in the layer of supernatant compared to its precipitate.

Table 1. The properties of angelwing clam flesh and hydrolysate produced at pH 6, 45◦C for 2 hours by using bromelain

The properties of sample [a]	Flesh	Angelwing hydrolysate
Protein content (%)	25.91±0.19	74.41±0.35
Fat content (%)	6.43±0.09	3.43±0.11
Water holding capacity (ml/g)	-	4.60±0.25

[a]Mean ± SD from triplicate determination.

Fat content in the angelwing flesh (6.43 %) was higher compared to the hydrolysate (3.43 %). As the hydrolysis proceeds, the muscle cell membranes tended to roundup and form insoluble vesicles leading to the removal of membrane structured lipid [25]. The insoluble fraction (vesicles) was separated from the soluble hydrolysate in the form of pellet by centrifugation and removed prior to spray-drying [26]. Thus higher DH lead to higher fat removal.

The water-protein interaction is important factor for functional properties of proteins in food systems [27]. In this studies water holding capacity on powdered angelwing hydrolysate was 4.60 ml/g (Table 1). According to Amiza et

al. [25] water holding capacity increased with an increased in degree of hydrolysis. Besides, at higher hydrolysis, polar groups such as COOH and NH_2 increased thus gave significant effects on water absorption and tend to exert better water-holding capacity [22]. In this study the functional group analysis showed that NH group peak was higher in angelwing hydrolysate compared to the flesh thus support the finding by Kristinsson and Rasco [28]. Water holding capacity of partly unfolded and hydrolysed proteins is greater than that of the native proteins due to an increase in surface area to mass ratio with an exposure of some previously buried hydrophobic groups [29, 26]. Low-molecular weight peptides from high extent of enzymatic hydrolysis also appeared to be more effective in water-holding capacity than larger size peptides as smaller fragments of peptides are possibly more hydrophilic [30].

Conclusion

Angelwing hydrolysate has a potential to be good source of food ingredient. However the uses of bromelain in the preparation of angelwing hydrolysate resulted in bitter taste. Thus, further studies may need to be carried out using simple technique of debittering which can enhance the application of angelwing hydrolysate in the food industry.

Acknowledgement

The authors would like to thank for all the laboratory staff of Food Technology Department and facilities provided from Faculty of Applied Science, Universiti Teknologi Mara (UiTM), Shah Alam Campus.

References

1. Berthou, P., Poutiers, J. M., Goulletquer, P. and Dao, J.C. (2009). Shelled molluscs, in fisheries and agricultural from encyclopedia of life support systems (EOLSS), Developed under the Auspices of the UNESCO, Eolss Publishers, Oxford, UK, 1-19.
2. Bee Wah, N. (2009). Biological aspect and development of larvae and juvenile of the angelwing clam *Pholas orientalis* (Gmeline, 1971). Georgetown, Penang: Universiti Sains Malaysia, MSc Thesis, 1-24.
3. Herpandi, N., Huda, A., Rosma, A. and Wan Nadiah, W. A. (2012). Degree of hydrolysis and free tryptophan content of skipjack tuna (*Katsuwonus pelamis*) protein hydrolysates produced with different type of industrial proteases. *International Food Research Journal*, 19(3): 863 – 867.
4. Jin, W-G., Wu, H-T., Zhu, B-W. and Ran, X-Q. (2012). Functional properties of gelation-like protein hydrolysates from scallop (*Patinopecten yessoensis*) male gonad. *European Food Research and Technology*, 234(5): 863 – 872.
5. Zhou, D-Y., Zhua, B-W., Qiao, L., Wua, H-T., Lia, D-M., Yanga, J-F. and Murata, Y. (2012). In vitro antioxidant activity of enzymatic hydrolysates prepared from abalone (*Haliotis discus hannai Ino*) viscera. *Food and Bioproducts Processing*, 90: 148 – 154.
6. Normah, I., Siti Hafsah, M. S. and Nurul Izzaira, A. (2013). Bitterness of green mussel (*Perna viridis*) hydrolysate as influenced by the degree of hydrolysis. *Food Research International Journal*, 20(5): 2261 – 2268.
7. Nilsang, S., Lertsiri, S., Suphantharika, M. and Assavanig, A. (2005). Optimization of enzymatic hydrolysis of fish soluble concentrate by commercial proteases. *Journal Food Engineering*, 70(4): 571 – 578.
8. Ramos de Armas, R., Diaz, H. G., Molina, R., Gonzalez, M. P. and Uriarte, E. (2004). Stochastic based descriptors studying peptides biological properties: modelling the bitter tasting threshold of peptides. *Biorganic and Medicinal Chemistry*, 12: 4815 – 4822.
9. Normah, I. and Nurfazlika Nashrah M. P. (2013). Evaluation on the properties of mentarang (*Pholas orientalis*) protein hydrolysate. *Journal of Tropical Agricultural Science*, 36 (2): 199 – 210.
10. Silvestre, M. P. C., Morais, H. A., Silva, V. D. M. and Silva, M. R. (2013). Degree of hydrolysis and peptide profile of whey proteins using pancreatin. *Journal of the Brazilian Society for Food and Nutrition*, 38(3):278 – 290.
11. AOAC. (2005). Official methods of analysis of international (16th ed.). Washington, DC: Association of Official Analytical Chemist.
12. Hartree, E. F. (1972). Determination of proteins: A modification of the lowry method that give a linear photometric response. *Analytical Biochemistry*, 48: 422 – 427.
13. Diniz, F. M. and Martin, A. M. (1997). Effects of the extent of enzymatic hydrolysis on functional properties of shark protein hydrolysate. *Lebensmittel Wissenschaft and Technologies*, 30: 266 – 272.

14. Haslaniza, H., Maskat, M. Y. and Wan Aida, W. M. (2010). The effects of enzyme concentration, temperature and incubation time on nitrogen content and degree of hydrolysis of protein precipitate from cockle (*Anadara granosa*) meat wash water. *International Food Research Journal* 17: 147 – 152.
15. Bhaskar, N., Benila, T., Radha, C. and Lalitha, R. G. (2008). Protein hydrolysate from visceral waste proteins of catla (*Catla catla*): Optimization of hydrolysis conditions for a commercial neutral protease. *Bioresource Technology*, 99 (10): 4105 – 4111.
16. Himonides, A. T.**,** Taylor, A. K. D. and Morris, A. J. (2011). A study of Enzymatic Hydrolysis of Fish Frames Using Model System. *Food and Nutrition Sciences*, 2: 575 – 585.
17. Seo, W. W. H., Lee, H. G. and Baek, H. H. (2008). Evaluation of bitterness in enzymatic hydrolysates of soy protein isolate by taste dilution analysis. *Journal of Food Science*, 73: 41 – 46.
18. Imelda, W.Y.C. (2007). Bitterness in enzymatically-produced hydrolysates of commercial shrimp (*Pandalopsis dispar*) processing waste. Kelowna, Canada: University of British Columbia, MSc thesis, 15 –185.
19. Jeffery, R. B., Mary, B., Charlotte, B., Marie, S., Kristen, H., Mark, E. J. and James, L. S. (2002). Contribution of *Lactococcus lactis* cell envelope proteinase specificity to peptide accumulation and bitterness in reduced-fat cheddar cheese. *Applied and Environmental Microbiology*, 68(4): 1778 – 1785.
20. Kristinsson, H. G. and Rasco, B. A. (2000). Fish protein hydrolysates: Production, biochemical and functional properties. *Critical Reviews in Food Science and Nutrition*, 40: 43 – 81.
21. Agrawal, V. A. and Chiddarwar, A. P. (2010). Taste abatement techniques to improve palatability of oral pharmaceuticals: A Review. *International Journal of Pharmaceutical Research Development*, 2: 1 – 10.
22. Oliver, C. M., Kher, A., McNaughton, D. and Augustin, M. A. (2009). Use of FTIR and mass spectrometry for characterization of glycated caseins. *Journal Dairy Research*, 76: 105 – 110.
23. Charalambous, G. and Inglett, G. (2012). Instrumental analysis of food, Recent progress Vol 1. Academic Press. Inc., Fifth Avenue, New York, 315 – 316.
24. Dalgleish, D. G. and Hunt J. A. (1995). Protein-protein interactions in Food Materials, in Gaonkar, A.G. editor. Ingredient interactions effect on food quality. Marcel Dekker, Inc, 199 – 205.
25. Amiza, M. A., Ow, Y. W. and Faazaz A. L. (2013). Physicochemical properties of silver catfish (*Pangasius* sp.) frame hydrolysate. *International Food Research Journal*, 20(3):1255 – 1262.
26. Shahidi, F., Han, X. Q. and Synowiecki, J. (1995). Production and characteristics of protein hydrolysates from capelin. *Food Chemistry*, 53: 285 – 293.
27. Kelfala Foh, M. B., Amodou, I., Mabel Foh, B., Kamara, M. T. and Xia, W. (2010). Functionality and antioxidant properties of tilapia (*Oreochromis niloticus*) as influenced by the degree of hydrolysis. *International Journal of Molecular Science*, 11 (4): 1851 – 1869.
28. Kristinsson, H. G. and Rasco, B. A. (2000). Biochemical and functional properties of Atlantic salmon (*Salmo salar*) muscle proteins hydrolyzed with various alkaline proteases. *Journal of Agricultural & Food Chemistry*, 48(3): 657 – 666.
29. Damodaran,S., Parkin, K. L. and Fennema, O. R. (2007). Fennema's food chemistry in amino acids, peptides and proteins. (4th edition). CRC Press Taylor and Francis Group, Boca Raton, 321 – 430.
30. Cumby, N., Zhong, Y., Naczk, M. and Shahidi, F. (2007). Antioxidant activity and water-holding capacity of canola protein hydrolysates. *Journal of Food Chemistry*, 109: 144 – 148.

Malaysian Journal of Analytical Sciences, Vol 20 No 3 (2016): 601 - 606
DOI: http://dx.doi.org/10.17576/mjas-2016-2003-20

MALAYSIAN JOURNAL OF ANALYTICAL SCIENCES
Published by The Malaysian Analytical Sciences Society
ISSN 1394 - 2506

CHEMICAL CHANGES IN SHORTFIN SCAD (*Decapterus macrosoma)* AT CHILLED (4 °C) AND FROZEN (-18 °C) STORAGE

(Perubahan Kimia dalam Ikan Selayang (*Decapterus macrosoma*) pada Penyimpanan Suhu Dingin (4 °C) dan Sejuk Beku (-18 °C))

Fazilah Fazilin Juhari, Norizzah Abd. Rashid*, Cheow Chong Seng, Anida Yusoff, Emilia Azrina Mohd Bakri

Department of Food Technology, Faculty of Applied Sciences,
Universiti Teknologi MARA, 40450 Shah Alam, Selangor, Malaysia

**Corresponding author: norizzah850@salam.uitm.edu.my*

Received: 24 February 2015; Accepted: 27 October 2015

Abstract

The aim of this study was to determine the chemical changes in muscle tissue of shortfin scad during storage at chilled (4 °C) and frozen (-18 °C) conditions for 18 days. The chemical changes were monitored every three days for Thiobarbituric acid (TBA), Peroxide value (PV), Total Volatile Base Nitrogen (TVBN) and Trimethylamine (TMA) content. Results show that there was a significant difference ($p<0.05$) in peroxide and TBA values between chilled and frozen shortfin scad starting from day 3. The highest PV values occured in chilled and frozen shortfin scad at day 12 (1.57 mEq/kg and 1.13 mEq/kg, respectively), and then decreased due to decomposition of hydroperoxides to secondary products such as aldehydes, alcohols and ketones. In contrast, TBA reached the highest values at day 15 for both chilled and frozen shortfin scad. For TVBN content, only the chilled sample shows significant increased ($p<0.05$) with storage time. The TVBN values declined significantly ($p<0.05$) for frozen shortfin scad. The TMA values for both chilled and frozen shortfin scad increased during storage. However, the TMA values increased at a faster rate in chilled compared to frozen shortfin scad. Based on the PV, TBA, TVBN and TMA values, chilled shortfin scad undergoes spoilage at a faster rate compared to the frozen shortfin scad.

Keywords: shortfin scad, thiobarbituric acid, peroxide value, total volatile base nitrogen, trimethylamine

Abstrak

Matlamat kajian ini adalah untuk menentukan perubahan kimia dalam tisu otot ikan selayang semasa penyimpanan pada suhu dingin (4 °C) dan sejuk beku (-18 °C) selama 18 hari. Perubahan kimia dipantau setiap tiga hari melalui ujian Asid Tiobarbiturik (TBA), Nilai Peroksida (PV), Jumlah Bes Nitrogen Meruap (TVBN) dan Trimetilamina (TMA). Hasil kajian menunjukkan terdapat perbezaan ketara ($p<0.05$) nilai peroksida dan nilai TBA antara ikan selayang yang disimpan pada suhu dingin dan sejuk beku bermula dari hari ketiga. Nilai PV tertinggi bagi ikan selayang berlaku pada hari ke 12 (masing-masing 1.57 mEq/kg dan 1.13 mEq/kg) bagi penyimpanan suhu dingin dan sejuk beku, dan kemudian menurun disebabkan penguraian hidroperoksida kepada produk sekunder seperti aldehid, alkohol dan keton. Sebaliknya, TBA mencapai nilai tertinggi pada hari ke 15 untuk ikan selayang yang disimpan pada kedua–dua suhu. Bagi nilai TVBN, hanya sampel dingin menunjukkan peningkatan ketara ($p <0.05$) bagi masa penyimpanan. Nilai TVBN menurun dengan ketara ($p<0.05$) bagi ikan selayang yang disejukbekukan. Nilai TMA untuk ikan selayang yang didingin dan disejukbeku meningkat semasa penyimpanan. Walau bagaimanapun, nilai TMA ikan selayang meningkat pada kadar yang lebih cepat dalam suhu dingin berbanding suhu sejuk beku. Berdasarkan nilai PV, TBA, TVBN dan TMA, ikan selayang yang disimpan pada suhu dingin mengalami kerosakan pada kadar yang lebih cepat berbanding dengan ikan selayang yang disimpan pada suhu sejuk beku.

Kata kunci: ikan selayang, asid tiobarbiturik, nilai peroksida, jumlah bes nitrogen meruap dan trimetilamina

Introduction

Fish is an important source of protein and is increasingly marketed due its health benefit to consumer [1]. Even though fish contains high nutritional content, it is very perishable. Fish is susceptible to biochemical, microbiological, and physico-chemical changes because of the high protein content, essential amino acids and unsaturated fatty acids that can reduce the quality of fish during storage [2].

Lipid oxidation is one of the main causes for the decline in fish quality [3]. The process of oxidation occurs at the double bond and resulted in the formation of short-chain fatty acid, aldehyde or ketone compounds, giving rise to rancidity which can cause a decrease in the quality of fish [4]. Lipid hydroperoxides which is the primary product of lipid oxidation are generally considered not to have a flavour impact. Secondary oxidation compounds, such as aldehydes and ketones derived from breakdown of hydroperoxides and are responsible for rancid flavour and odour [5].

Total volatile base nitrogen (TBVN) and trimethylamine is a general term which includes the measurement of trimethylamine (produced by spoilage bacteria), dimethylamine (produced by autolytic enzymes during frozen storage), ammonia (produced by the deamination of amino-acids and nucleotide catabolites) and other volatile basic nitrogenous compounds associated with fish spoilage. The TVBN is a good indicator in fish quality assessment [6].Chemical analysis has been used to measure the amount of breakdown product derived from enzymatic, bacterial or oxidation activity. Among these, trimethylamine, hypoxanthine, ammonia, formaldehyde and several other breakdown products should be determined in order to evaluate the fish quality [7].

Hence, the objective this study was to determine the chemical changes in muscle tissue of shortfin scad which was monitored based on the thiobarbituric acid, peroxide value, total volatile base nitrogen and trimethylamine contents during storage at chilled (4 °C) and frozen (-18 °C) conditions for 18 days.

Materials and Methods

Raw materials

Shortfin scad was purchased from wet market, Kuala Pilah, Negeri Sembilan, Malaysia and placed in boxes filled with ice and brought to laboratory immediately. Shortfin scad with average weight of 65 – 85 g was eviscerated and cleaned prior to storage in plastic containers. The fish was then stored at chilled (4 °C) and frozen (-18 °C) storage conditions for 18 days and subjected to chemical analysis such as peroxide value, thiobarbituric acid, total volatile base nitrogen and trimethylamine every three days.

Chemical analysis

All the chemicals used were of analytical grade and were obtained from CHEMOLAB Supplies, Seri Kembangan, Selangor, Malaysia.

Peroxide value (PV)

Extraction of the fish oil was done according to method proposed by Razak et al. [8]. Fish oil was extracted using mixture of chloroform and methanol (1:1) followed by evaporation of the solvent. The PV value of fish oil was determined according to AOAC guideline [9]. The results were expressed in terms of milliequivalent of free iodine per kg of lipid.

Thiobarbituric acid (TBA)

The TBA was determined according to Tokur et al. [10] using distillation method. An amount 10 gram of fish muscle was homogenised with 0.2 N hydrochloric acid and distilled using distillation unit (behr Labor-Technik GmbH, Germany). Five mililiter of distillate was pipetted into test tube and 5 mL of TBA reagent was added. The sample was heated in boiling water for 35 minutes and was allowed to cool immediately. The absorbance of the pink solution was read at 538 nm using a single beam spectrophotometer (Genesys 20 Thermo Scientific, USA). The absorbance was measured against a corresponding blank. The results were expressed as mg malonaldehyde per kg sample.

Total Volatile Base Nitrogen (TVBN) and Trimethylamine (TMA)

The TVBN and TMA were determined according to Sallam et al. [11]. An amount 100 g of fish muscle was homogenised with 200 mL 7.5 % (v/v) aqueous trichloroacetic acid solution and centrifuge at 3000 rpm for 5 minutes. The supernatant was filtered through Whatman No.1 filter paper. The TVBN was measured by distillation method. Accurately, 25 mL of fish extracts and 5 mL of 10 % (w/v) sodium hydroxide was poured into Kjedahl flask and distilled for 3 minutes. The distillate was collected into conical flask containing 15 mL of 4 % (v/v) boric acid and 0.04 mL methyl red and bromocresol green indicator. The titration was allowed to run against aqueous 0.05 M sulfuric acid solution. The same experimental procedure of TVBN was used for TMA analysis. The difference in TMA analysis is the addition of 20 mL of 35 % (v/v) formaldehyde into Kjedahl flask. The results were expressed as mg nitrogen per hundred g of sample and calculated using equation 1 [6]:

$$\text{TVBN/TMA} = \frac{14\ (\text{g/mol}) \times a \times b \times 300}{\text{Volume of filtrate}} \quad (1)$$

where, a is defined as volume (mL) of sulfuric acid and b is defined as normality of sulfuric acid

Statistical analysis

All the analysis was performed in triplicate and data were expressed as mean ± standard deviation. Data were analysed using SPSS 15.0. Duncan's multiple-range test was used to determine the difference between means. A significant difference was considered at the level of $p<0.05$.

Results and Discussion

Figure 1 shows the changes of PV, TBA, TVBN and TMA in shortfin scad muscle during chilled (4 °C) and frozen (-18 °C) storage. A significant increased ($p<0.05$) in PV was observed in shortfin scad muscle up to 12 days at both chilled and frozen conditions (Figure 1a). The initial PV was 0.38 mEq/kg and reached up to 1.54 mEq/kg and 1.15 mEq/kg for shortfin scad stored and chilled and frozen temperature, respectively. The decreased in PV was noticeable at day 15 for both conditions. Chaijan et al. [12] reported the decreased in PV occurred with extended storage time due to decomposition of hydroperoxide into aldehydes. The same trend was reported when sardine was stored at 0 °C up to 15 days. From the results, PV increase slowly at both conditions. The release of non-heme iron in fish muscle during prolonged chilled and frozen storage might influence the oxidation process in the fish muscle [12]. Based on Orak et al. [13] the accepted PV to indicate good quality of fish is below 2 mEq/kg. The PV was used to determine the formation of primary oxidation products during the storage period of fish [14]. Lipid oxidation is a process by which molecular oxygen reacts with unsaturated lipids to form lipids peroxide [7].

Thiobarbituric acid (TBA) was used to determine fat oxidation based on total malonaldehyde in fish muscle which is a by-product of lipid oxidation. Figure 1b shows there was significant differences ($p<0.05$) between chilled and frozen shortfin scad started from day 3 where TBA value in chilled condition was 3.05 mg malonaldehyde/kg, while for frozen was 0.25 mg malonaldehyde/kg. The TBA values in shortfin muscle increased from day 12 to day 15 at both storage conditions. The TBA increased from 4.01 mg malonaldehyde/kg to 5.46 mg malonaldehyde/kg at chilled and from 0.69 mg malonaldehyde/kg to 1.06 mg malonaldehyde/kg at frozen storage but decreased at day 18 (4.68 and 0.46 mg malonaldehyde/kg, respectively). The decreased in TBA values might be as a result from interaction of malonaldehyde with other components of fish muscle [13]. The TBA value increased during storage due to breakdown of primary fat oxidation product to secondary oxidation which produce rancid odour [2]. These same trend was reported by Kilinc et al. [15] for sardine when stored at chilled and frozen temperatures. The maximum level of TBA value indicating good quality of frozen fish is 5mg malonaldehyde/kg [15]. Malonaldehyde and fat oxidation are not stable and very reactive towards protein content and amino acid in fish muscle [2]. The TBA value revealed an increase rate of lipid oxidation during chilled condition. It is also important to note that TBA value may not reveal the actual rate of lipid oxidation since malonaldehyde can interact with other components of fish body such as amines, nucleosides and nucleic acid, proteins, amino acids of phospholipids, or other aldehydes that are end products of lipid oxidation and this interaction may vary greatly with species of fish [5].

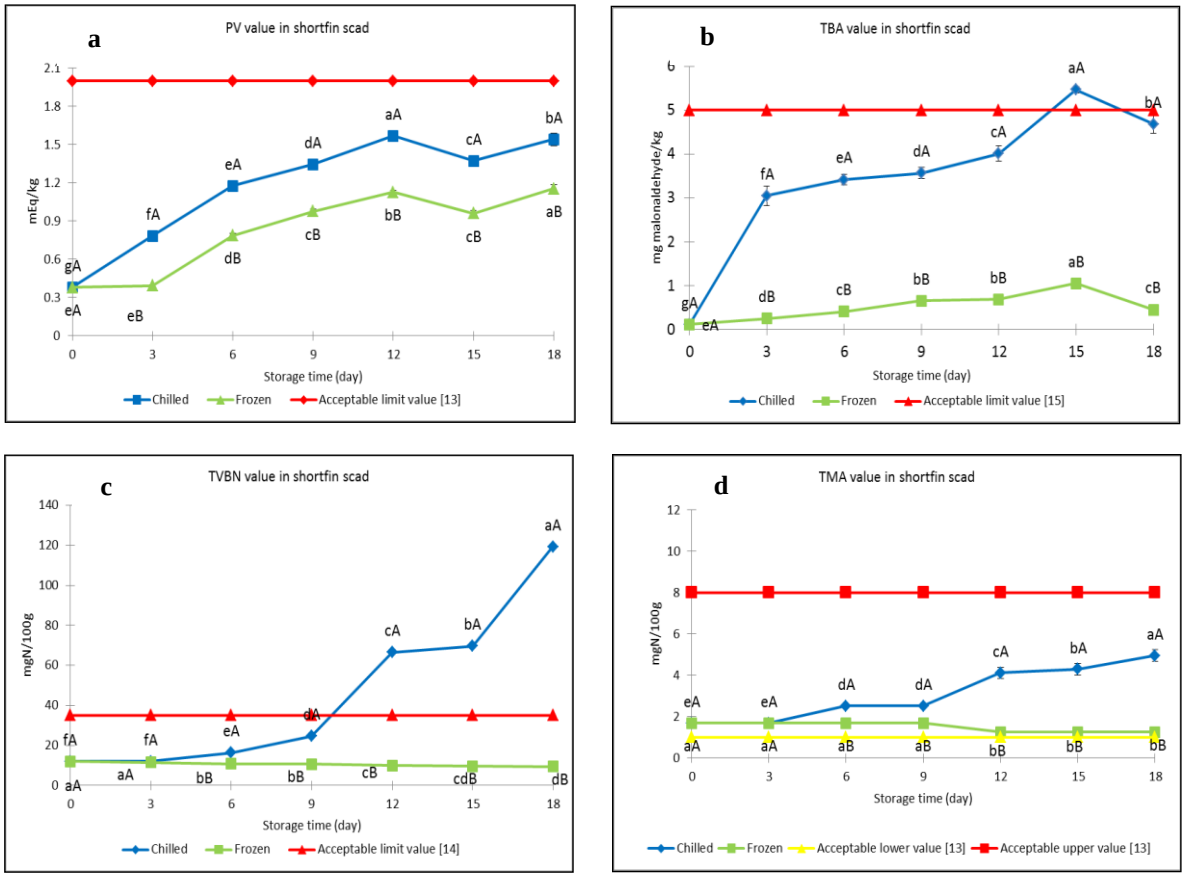


Figure 1. Changes in PV, TBA, TVBN and TMA for shortfin scad muscle at chilled (4 °C) and frozen (-18 °C) storage conditions for 18 days. *Values are expressed as mean (A, B) and (a, b, c) marked with different letters were significantly different at the level of $p<0.05$. Lower case letter indicate the effect of storage period of shortfin scad by day while upper case letter indicate the effect of storage condition at chilled (4°C) and frozen (-18 °C).

Figure 1c indicates there was significant differences ($p<0.05$) in TVBN between chilled and frozen shortfin scad started from day 3 up to day 18. The TVBN value in chilled condition increased rapidly from 11.95 mgN/100 g to 119.37 mgN/100 g and started to reach the upper limit at day 12, which was 66.55 mgN/100 g. This increased trend may be due to the production of amines by autolytic processes. The increment in TVBN in fish muscles during chilled condition is generally associated with activity of microorganisms during later stages of deterioration. This increase may be attributed essentially to ammonia produced from bacterial catabolism of nitrogen-containing compounds [6]. The TVBN are indices of the spoilage level of fish during the storage period [13, 15] and are affected by fish species [6, 16]. Based Ozyurt et al. [14] the TVBN value shall be less than 35mgN/100g to indicate the good quality for fishery product. Furthermore, Ozyurt et al. [14] reported that the TVBN value of red mullet at chilled condition increased from 26.19 mgN/100 g at day 8 to 47.18 mgN/100 g at day 11 of storage. For frozen condition TVBN value decreased slowly from 11.95 mgN/100 g to 9.33 mgN/100 g. Frozen fish quality can be determined from the amounts of TVBN, which is a product of proteolytic changes in fish meat. This decreased trend may due to prevention of changes in fish muscle caused by proteolysis. This same trend was reported by Jezek and Buchtova [17] that throughout the storage period of silver carp, no significant differences ($p>0.05$) in TVBN concentrations were found, and the TVBN concentration ascertained after 12 months of frozen storage was decreased from 15.99 mgN/100 g to 15.73 mgN/100 g. Hence frozen storage of fish is a reliable technique for prevention of changes in fish muscle caused by proteolysis.

Figure 1d reveals that there was significant difference ($p<0.05$) between chilled and frozen shortfin scad started from day 6 for TMA values. The TMA at chilled condition increased slowly from 1.68 mgN/100 g to 4.95 mgN/100 g during storage. For frozen shortfin scad, no significant difference ($p>0.05$) in TMA values was observed. The TMA values from day 0 to day 9 remained unchanged (1.68 mgN/100 g). The TMA value started to increase at day 12 ($p<0.05$) which was 1.25 ± 0.00 mgN/100g and also remained unchanged until day 18 ($p>0.05$). Temperature is very important in influencing TMA value. Natseba et al. [18] indicated that freezing inhibit bacterial activity and TMA accumulation. The TMA formation is due to activity of bacterial enzymatic decomposition of trimethylamine oxide (TMAO) and this occurs to a significant level only during logarithmic phase microbial growth [13]. The level of TMA in fish muscle depends on the species of fish and storage conditions [19]. According Orak et al. [13] TMA must be between 1 mg/100 g and 8 mg/100g to indicate good quality of fish.

Conclusion

The rate of chemical changes in muscle tissues of chilled and frozen shortfin scad differ significantly throughout 18 days of storage. Frozen storage delayed the spoilage of the fish due to oxidative and microbial activities compared to chilled storage. Hence, frozen storage is a reliable technique to preserve the quality of shortfin scad fish.

Acknowledgement

The authors would like to thank the European Commission (EU Grant no. 289282) for providing financial aid and Universiti Teknologi MARA (UiTM) for technical support and facilities.

References

1. Nurnadia, A. A., Azrina, A. and Amin, I. (2011). Proximate composition and energetic value of selected marine fish and shellfish from the West Coast of Peninsular Malaysia. *International Food Research Journal,* 18, 137-148.
2. Rosari, M. I., Ma'arut, W. F., and Agustini, T. W. (2014). Pengaruh ekstrak kasar buah mahkota dewa (Phaleria macrocarpal) sebagai antioksidan pada fillet ikan bandeng *(Chanos chanos forsk)* segar. *Jurnal Pengolahan dan Bioteknologi Hasil Perikanan,* 3(2), 34-43.
3. Azhar, K. F. and Nisa, K. (2006). Lipid and their oxidation in Seafood. *Journal of The Chemical Society of Pakistan,* 28(3): 289-305.
4. Yuanita, L. (2006). Oksidasi asam lemak daging sapi dan ikan pada penggunaan natrium c tripolifosfat pemasakan dan penyimpanan. *Jurnal Ilmu Dasar,* 7(2): 194-200.
5. Simeonidou, S., Govaris, A., and Vareltzis, K. (1998). Quality assessment of seven Mediterranean fish species during storage on ice. *Food Research International,* 7: 479-484.
6. Zeway, A. L. A. (2013). Microbiological and chemical changes of nile tilapia *(Oreochromis niloticus L.)* fillet during ice storage: effect of age and sex. *Advance Journal of Food Science and Technology,* 5(10): 1260-1265.
7. Bouriga, N., Selmi, S., Faure, E. and Trabelsi, M. (2008). Changes in proximate composition and lipid quality of atherina (*Atherina Sp.*) during sun drying process. *Bulletin Institute National Science Technology* 35: 69-72.
8. Razak, Z. K. A., Basri, M., Dzulkefly, K., Razak, C. N. A. and Salleh, A. B. (2001). Extraction and characterization of fish oil from monopterus albus. *Malaysian Journal of Analytical Science,* 7(1): 217-220.
9. Association of Official Analytical Chemist, AOAC. (1990). Official Methods of Analysis of the Association of Official Analytical Chemists (15 edition). Washington D.C
10. Tokur, B., Korkmaz, K. and Ayas, D. (2006). Comparison of two thiobarbituric acid (TBA) method for monitoring lipid oxidation in fish. *E.U. Journal of Fisheries & Aquatic Sciences,* 23(3-4): 331 – 334.
11. Sallam, K. I. (2007). Chemical, sensory and shelf life evaluation of sliced salmon treated with salts of organic acids. *Food Chemistry,* 101(2): 592-600.
12. Chaijan, M., Benjakul, S., Visessanguan, W. and Faustman, C. (2006). Changes of lipids in sardine (*Sardinilla gibbosa*) muscle during iced storage. *Food Chemistry,* 99: 83-91.
13. Orak, H. and Kayisoglu, S. (2008). Quality changes in whole, gutted and filleted three fish spesies *(Gadus euxinus, Mugil cephalus, Engraulis encrasicholus)* at frozen storage period (-26°C). *ACTA Scientiarum Polonorum Technologia Alimentaria,* 7(3): 15-25.

14. Ozyurt, G., Kuley, E., Ozkutuk, S. and Ozogul, F. (2009). Sensory, microbiological and chemical assessment of the freshness of red mullet (*Mullus barbatus*) and goldband goatfish (*Upeneus moluccensis*) during storage in ice. *Food Chemistry*, 114(2): 505 – 510.
15. Kilinc, B., Cakli, S. and Kisla, D. (2003). Quality changes of sardine (*Sardina pilchardus*) during frozen storage. *E.U. Journal of Fisheries & Aquatic Sciences*, 20: 139 – 146.
16. Fan, W., Sun, J., Chen, Y., Qiu, J., Zhang, Y. and Chi, Y. (2009). Effect of chitosan coating on quality and shelf life of silver carp during frozen storage. *Food Chemistry*, 115(1): 66 – 70.
17. Jezek, F. and Buchtova, H. (2011). Monitoring of physicochemical changes in frozen fish muscle tissue. *Agriculturae Conspectus Scientificus*, 76(3): 201 – 204.
18. Natseba, A., Lwalinda, I., Kakura, E., Muyenja, C. K. and Muyong, J. H. (2005). Effect of pre freezing icing duration on quality changes in frozen nile perch *(Lates nitoticus)*. *Food Research International*, 35: 469 – 474.
19. Robertson, G. L. (2010). Food packaging and shelf life: A practical Guide. Boca Raton: CRC Press.

Malaysian Journal of Analytical Sciences, Vol 20 No 3 (2016): 607 - 617
DOI: http://dx.doi.org/10.17576/mjas-2016-2003-21

MALAYSIAN JOURNAL OF ANALYTICAL SCIENCES
Published by The Malaysian Analytical Sciences Society
ISSN 1394 - 2506

ANTIOXIDANT ACTIVITY, COLOUR AND MINERAL CONTENT OF HERBAL TEA PREPARED FROM *Cosmos caudatus* LEAVES AT DIFFERENT MATURITY STAGES

(Aktiviti Antioksida, Warna dan Kandungan Mineral di dalam Teh Herba daripada Daun *Cosmos caudatus* pada Peringkat Kematangan yang Berbeza)

Dian Nashiela Fatanah[1], Noriham Abdullah[1,2]*, Nooraain Hashim[1], Azizah Abd Hamid[3]

[1]*Department of Food Science and Technology, Faculty of Applied Sciences*
[2]*Malaysia Institute of Transportation (MITRANS)*
Universiti Teknologi MARA, 40450 Shah Alam, Selangor, Malaysia
[3]*Department of Food Science, Faculty of Food Science and Technology,*
Universiti Putra Malaysia, 43400 UPM Serdang, Selangor, Malaysia

**Corresponding author: noriham985@salam.uitm.edu.my*

Received: 24 February 2015; Accepted: 27 October 2015

Abstract

In recent years, increasing consumption of herbal tea is a worldwide trend because of their refreshing taste, positive potential health effect, convenience, abundant resources and also cheaper in price. However, different maturity stages of plants being used as raw material could affect the antioxidant activity, colour and mineral content in herbal tea. Thus, this present study was aimed at determining antioxidant activity, colour and mineral content of herbal tea prepared from *Cosmos caudatus* (*C. caudatus*) leaves at three different maturity stages namely young, mature and old. All prepared herbal tea were analysed for total phenolic content (TPC), total flavonoid content (TFC), ferric reducing antioxidant power (FRAP), 2-2-diphenyl-1-picrylhydrazyl (DPPH) radical scavenging assay, colour and mineral content. The results demonstrated that herbal tea prepared from young leaves had strong ($p< 0.05$) antioxidant activity compared to mature and old leaves for all assays tested. Pearson's correlation coefficient also revealed that TPC and TFC exhibited a strong positive correlation with reducing power but negatively correlated with DPPH scavenging activity indicating that these compounds are major contributors to the antioxidant activity. In fact, the darker ($p< 0.05$) colour of *C. caudatus* herbal tea prepared from young leaves relates to their higher antioxidant activity as compared to mature and old leaves. However, *C. caudatus* herbal tea prepared from old leaves showed significantly higher in mineral content compared to mature and young leaves. Hence, it can be concluded that, as maturity increased, antioxidant activity and colour in *C. caudatus* herbal tea decreased and *vice-versa* for mineral content.

Keywords: herbal tea, *Cosmos caudatus,* maturity, antioxidant activity, colour, mineral content

Abstrak

Pada masa kini, peningkatan pengambilan teh herba menjadi ikutan terkini di seluruh dunia kerana rasa yang menyegarkan, mempunyai potensi yang positif terhadap kesihatan, sumber yang mudah didapati dan harga yang murah. Walaubagaimanapun, penggunaan sumber bahan mentah daripada tumbuh-tumbuhan pada peringkat kematangan yang berbeza mempengaruhi aktiviti antioksida, warna dan kandungan mineral di dalam teh herba. Oleh itu, kajian ini bertujuan untuk menentukan aktiviti antioksida, warna dan kandungan mineral di dalam teh herba yang dihasilkan daripada daun *Cosmos caudatus (C. caudatus)* pada tiga peringkat kematangan iaitu daun muda, matang dan tua. Semua sampel teh herba telah dianalisa untuk menentukan jumlah kandungan fenol (TPC), jumlah kandungan flavonoid (TFC), ujian penurunan ferik (FRAP), pemerangkapan radikal bebas 2-2-difenil-1-1pikrilhidrazil (DPPH), warna dan kandungan mineral. Keputusan menunjukkan bahawa, teh herba dihasilkan daripada daun muda mempunyai aktiviti antioksida yang tinggi ($p< 0.05$) berbanding dengan daun matang dan tua untuk semua asai diuji.

Pekali korelasi Pearson juga menunjukkan bahawa TPC dan TFC mempunyai korelasi positif yang kuat dengan pengurangan kuasa tetapi mempunyai korelasi negatif yang kuat terhadap aktiviti pemerangkapan DPPH, menunjukkan bahawa sebatian-sebatian ini merupakan penyumbang utama kepada aktiviti antioksida. Malah, warna teh herba yang dihasilkan daripada daun *C. caudatus* muda yang lebih gelap ($p< 0.05$), menunjukkan tahap aktiviti antioksida yang tinggi berbanding daun matang dan tua. Walaubagaimanapun, teh herba yang dihasilkan daripada daun *C. caudatus* tua menunjukkan kandungan mineral yang tinggi berbanding daun matang dan muda. Kesimpulannya, semakin meningkat kematangan daun, aktiviti antioksida dan warna semakin berkurang dan adalah sebaliknya bagi kandungan mineral.

Kata kunci: teh herba, *Cosmos caudatus,* kematangan, aktiviti antioksida, warna, kandungan mineral

Introduction

Increasing consumption of herbal tea is a worldwide trend because people believed that supplementation of human diet with herbal provides beneficial effects to their health [1]. Herbal tea has been used for health care and diseases prevention for thousands of years in many countries [2]. Moreover, numerous epidemiological studies link herbal tea consumption to a reduction in cardiovascular diseases, cholesterol levels, diabetes, arthritis, osteoporosis and dental carries [3]. Besides giving negligible side effects and mild in action, herbal tea is easy to prepare, richer in resources and cheaper in price [4]. Herbal tea can be prepared with fresh or dried flowers, leaves, seeds or roots, generally by pouring boiling water over the plant parts and letting them to steep for a few minutes [5]. In Malaysia, there are abundant herbal teas produced by Small Medium Enterprise (SME) industry such as misai kucing *(Orthosiphon stamineus)* tea, kacip fatimah *(Labisia pumila)* tea, sabung nyawa *(Gynura procumbens)* tea, kaca beling *(Strobilanthes crispa)* tea, ginger *(Zingiber officinale)* tea and lemongrass *(Cymbopogon)* tea.

Cosmos caudatus (*C. caudatus*) or commonly known as ulam raja by the Malay society has been developed in tea form because of its potential health-promoting properties. *C. caudatus* is used traditionally to reduce body heat, improving blood circulation, as an anti-aging agent, strengthening bone marrow (because of high calcium content), to treat infection associated with pathogenic microorganisms and to promote fresh breath [6]. These beneficial health properties have been attributed to the antioxidant content in *C. caudatus* plant particularly a number of proanthocyanidins that exists as dimers through hexamers, quercetin glycosides, chlorogenic, neo-chlorogenic acid and (+)-catechin [7]. With extremely high antioxidant activity, *C. caudatus* is believed to reduce oxidative stress because these compounds may have direct contribution in the defence against oxidative stress and could be considered to be active metabolites involved in the antioxidant activity in herbs [8]. From the nutritional point of view, other valuable components in herbs like minerals are also major contribution of health properties in *C. caudatus* plant. In fact, it has been established that deficiency of several minerals might induced phenolics and flavonoids content accumulation and supplementation of some minerals might promote antioxidant content [9]. However, maturation stages constitute an important factor in influencing antioxidant activity, chemical composition and mineral content of the *C. caudatus* plant. Usage of young leaves for herbal tea preparation might cause yield losses due to premature stages but usage of mature or old leaves could also possibly results in leaves senescence.

Therefore, this present study is designed to determine antioxidant activity, colour and mineral content of herbal tea prepared from *C. caudatus* leaves at different maturity stages since to the best of our knowledge antioxidant activity, colour and mineral content of these types of tea have not yet been reported.

Materials and Methods

Chemicals

Folin-Ciocalteu reagent, sodium carbonate (Na_2CO_3), sodium nitrite ($NaNO_2$), aluminium chloride ($AlCl_3$), ferric chloride ($FeCl_3$) and sodium hydroxide (NaOH), concentrated nitric acid (HNO_3), hydrogen peroxide (H_2O_2) and Inductively Coupled Plasma (ICP) multi-element standard solution IV were purchased from Merck, Germany. Gallic acid, quercetin, trolox, 2-4-6-tripyridyl-s-triazine (TPTZ), 2-2-diphenyl-1-picrylhydrazyl (DPPH) and ascorbic acid were supplied by Sigma-Aldrich Chemie, Germany. Sodium acetate was purchased from R & M Chemicals, U.K while glacial acetic acid was purchased from Friendemann Schmidt Chemicals, U.K.

Raw material collection and selection

The fresh leaves of 8-week-old *C. caudatus* plant were collected from Durian Tunggal, Malacca, Malaysia. The leaves were divided into 3 groups, classified as young leaves, mature leaves and old leaves as shown in Figure 1. The 8-week-old *C. caudatus* plant was selected based on the previous findings from Mediani et al. [8] where they reported that 8-week-old plant consist higher antioxidant activity compared to 10 and 12-week-old *C. caudatus* plant. Young leaves were selected from the first four tiers where the leaves are still tender, newly emerged and not attaining full expansion. Mature leaves are located at the middle part of *C. caudatus* plant where the leaves are fully developed while old leaves are located at the lower part of the plant and the leaves had showed initial sign of senescence. Mature leaves were selected between the fifth to eighth tiers and old leaves were selected starting from ninth tier and above.

Sample preparation

Each stage of *C. caudatus* leaves was prepared according to the normal procedure of herbal tea preparation by Small Medium Enterprise (SME) industry in Malaysia. The leaves at different maturity stages were dried at 50 °C for 8 hours in cabinet dryer until constant weight. *C. caudatus* herbal tea powder was prepared according to method described by Gião et al. [10] with some modifications. The dried leaves were ground using centrifugal mill, which were then sieved into 1to 2 mm mesh size. Two grams of ground leaves were collected and packed in a sachet of tea bag. The tea bag of *C. caudatus* herbal teas with different maturity stages were infused in 200 mL boiling distilled water for 3 minutes according to method as suggested by Horžić et al. [3]. The infused herbal teas were filtered through a Whatman filter paper No. 41 prior to further analyses.



Figure 1. Selection of 8-week-old *C. caudatus* leaves based on maturity. (A) Young leaves (B) Mature leaves (C) Old leaves

Antioxidant content and antioxidant activity: *Total phenolic content (TPC)*

The total phenolic content in herbal tea sample was determined by using the Folin-Ciocalteu assay [11]. Accurately, 0.5 mL Folin-Ciocalteu reagent, 1.5 mL 7.5 % sodium carbonate and 7.9 mL distilled water were introduced in a test tube containing 0.1 mL sample/standard. The solution was mixed thoroughly and allowed to stand for 2 hours in a dark place. The absorbance at 765 nm was read by using UV-VIS Spectrophotometer (Helios Zeta, Thermo Fisher Scientific, USA). The TPC of herbal tea sample was expressed as mg of gallic acid equivalents (mg GAE)/ml of tea sample.

Total flavonoid content (TFC)

The total flavonoid content was analysed according to method as described by Singh et al. [12]. Accurately 1 mL of sample/standard was diluted with 4 mL distilled water then 0.3 mL 5 % sodium nitrate solution and 0.3 mL 10 % aluminium chloride were added. The mixture was kept for 5 minutes. Then, 2 mL of 1M sodium hydroxide were added to the mixture and the mixture was vortexed thoroughly. The absorbance was measured at 510 nm using Helios Zeta UV-VIS Spectrophotometer. This was calculated as mg of quercetin equivalents (mg QE)/ml of tea sample.

Ferric reducing antioxidant power (FRAP)

The FRAP assay was carried out by the method of Deetae et al. [13]. FRAP reagent was freshly prepared by mixing 300 mM acetate and glacial acetic acid buffer (pH 3.6), 20 mM ferric chloride and 10 mM TPTZ was made to 40 mM HCl at a ratio of 10:1:1. Briefly, 0.1 mL sample/standard was mixed with 3 mL FRAP reagent and 3 mL distilled water. The mixture was incubated in the dark place at 37 °C for 8 minutes and the absorbance at 595 nm was then read using Helios Zeta UV-VIS Spectrophotometer. The total antioxidant activity of samples were determined against a standard of known FRAP value and was expressed as µM of trolox equivalent (µM TE)/ml of tea sample.

2-2-diphenyl-1-picrylhydrazyl (DPPH) radical scavenging assay

The DPPH assay was performed according to procedure as described by Nuengchamnong and Ingkaninan [14]. Accurately, 0.1 mL sample/standard was mixed with 2.9 mL of 0.05 mM DPPH in methanol and incubated in the dark at room temperature for 30 minutes. The absorbance of the sample/standard was measured using Helios Zeta UV-VIS Spectrophotometer at 515 nm where methanol was used as blank.

Colour

The colour of *C. caudatus* herbal tea was determined using a CR-400 Chroma Meter (Konica Minolta, Minolta Co., Osaka, Japan) according to Marete et al. [15] method. The Hunter L, a, b Colour Scale was used with L*, a*, b*, C and h^o axes expressing the lightness, redness-greenness, blueness-yellowness, chroma and hue angle respectively. Hue angle is defined by as a colour wheel with red-purple at an angle of 0^0, yellow at 90^0, bluish-green at 180^0 and blue at 270^0.

Mineral content

The mineral content determination was performed based on Pytlakowska [16] procedure. In determining the concentration of selected elements (Ag, Al, Ba, Ca, Cd, Cr, Cu, Fe, K, Mg, Mn, Na, Pb and Zn) in herbal tea, the prepared infused herbal tea was evaporated to near dryness. To the solid residue, 5 mL of concentrated HNO_3 solution and 5 mL of 30 % H_2O_2 solution were added, and sample was again evaporated to near dryness. Then, the residue was dissolved in 10 mL hot water, filtered and filled up to 25 mL with deionized water. Measurements were carried out using the Inductively Coupled Plasma-Optical Emission Spectroscopy (ICP-OES) (Optima 5300 DV, Perkin Elmer Inc., USA) based on the following parameter: autosampler model – AS-93 plus, sample flow rate – 1.5 mL/min, plasma gas flow rate – Ar, 15 l/min, auxiliary gas flow rate – Ar, 0.2 l/min, nebulizer gas flow rate – Ar, 0.65 l/min, back pressure – 75kPa and using both axial and radial plasma view.

Statistical analysis

All experiments were run in triplicates. Statistical analyses were conducted with the Statistical Analysis System (SAS) 9.1.3 software package. Analyses of variance were performed by ANOVA procedures. Significant differences ($p < 0.05$) were determined by least square means comparison.

Results and Discussion

Antioxidant content and antioxidant activity

The results for antioxidant activity for *C. caudatus* herbal tea prepared from three different maturity stages are presented in Table 1. The highest TPC and TFC were obtained from *C. caudatus* herbal tea prepared from young leaves and the values of TPC and TFC ranged from 66.30 to 18.38 mg GAE/ml herbal tea and 203.22 to 72.24 mg GAE/ml herbal tea respectively. In line the declined in TPC and TFC values, FRAP values also significantly decreased as maturity of *C. caudatus* leaves used to prepare herbal tea progressed with the values ranging from 502.21 to 239.18 µM TE/ml herbal tea. In contrast to FRAP values, the IC_{50} values of DPPH scavenging activity increased as maturity of *C. caudatus* leaves increased indicating that young leaves had strong antioxidant activity compared to mature and old leaves. The IC_{50} values of *C. caudatus* herbal tea prepared from young leaves, mature leaves and old leaves were 1055.37, 1409.99 and 2408.84 µg/ml respectively.

Table 1. Antioxidant activity in herbal tea prepared from *C. caudatus* leaves at different maturity stages. Values are expressed as mean ± standard deviation. Means with different letters are significantly different ($p < 0.05$)

Herbal tea sample	Assay			
	TPC (mg GAE/ml herbal tea)	TFC (mg QE/ml herbal tea)	FRAP (µM TE/ml herbal tea)	DPPH (µg/ml)
Young leaves	66.30 ± 5.20^{a}	203.22 ± 15.90^{a}	502.21 ± 21.18^{a}	1055.37 ± 42.38^{c}
Mature leaves	36.55 ± 2.77^{b}	124.55 ± 6.22^{b}	332.00 ± 8.81^{b}	1409.99 ± 103.17^{b}
Old leaves	18.38 ± 2.46^{c}	72.24 ± 3.04^{c}	239.18 ± 19.19^{c}	2408.84 ± 365.36^{a}

In previous study of antioxidant activity by Mediani et al. [8] and Siddiqui et al. [17], they believed that, the reduction of antioxidant activity with the advanced maturity might be contributed to the conversion of phenolics and flavonoids to other secondary metabolites such as sugar by enzyme action. The declining of secondary metabolites in mature and old leaves reduced the ability of plant defense systems to neutralise the overproduction of ROS which stimulates by aging process, eventually cause senescence of plant tissues. This is supported by Sreelatha and Padma [18], where they observed the components of both the enzymatic and the non-enzymatic antioxidant system correlates well with oxidative stress during senescence and plant development. Another possible reason could be due to the stoppage of new biosynthesis of the secondary metabolites during maturation [19]. In contrast, most of these new biosynthesis are took place at the early stages of plant growth which provide highest phenolic and flavonoid compounds in young leaves to react with ROS produced [20]. The ROS will be chelated and disengaged by the antioxidant in young leaves from participating in the initiation of oxidative stress [17] where the ROS will be converted to a more stable products and the radical chain reaction will be terminated [21]. Therefore, this will provide protection of plant tissues against pests and disease [22].

Interrelationship between antioxidant activity (FRAP and DPPH) with TPC and TFC using Pearson's correlation coefficient are shown in Table 2. The correlations between antioxidant activity with TPC and TFC are mainly due to their redox properties, hydrogen donors and singlet oxygen quenchers [18]. From the table, it revealed that FRAP had strong correlation with TPC and TFC with the values are $R = 0.9967$ and $R = 0.9980$ respectively while DPPH shows negative correlation with TPC ($R = -0.9224$) and TFC ($R = -0.9288$). This is in agreement with study by Baros et al. [23], where they highlighted the negative correlation between DPPH with TPC and TFC reflected that the sample with highest antioxidant content exhibited higher antioxidant activity and lower IC_{50} while sample with lowest antioxidant content exhibited lower antioxidant activity and higher IC_{50}. Therefore, from correlations, phenolic and flavonoid compounds might contribute to the antioxidant activity in *C. caudatus* herbal tea prepared from leaves at three different maturity stages. According to Villa-Rodríguez et al. [24] phenolics and flavonoids had been devoted to their antioxidant activity due to their ability to reduce *in vitro* free radical formation and to

scavenge free radicals which are responsible for inhibiting or preventing the deleterious consequences of oxidative stress [18].

Table 2. Pearson's correlation coefficient (R) between antioxidant activities of *C. caudatus* herbal tea prepared from leaves at different maturity stages

	FRAP	**DPPH**
TPC	0.997 ± 0.0018^{a}	-0.922 ± 0.058^{a}
TFC	0.998 ± 0.0024^{a}	-0.929 ± 0.060^{a}

Colour

Correlations between colour (L* - lightness, a* - redness/greenness, b* - yellowness/blueness, C - Chroma intensity, h^{o} - hue angle tonalities) of *C. caudatus* herbal tea prepared from leaves at three different maturity stages with antioxidant activity were significantly strong (Table 3). As expected, *C. caudatus* herbal tea prepared from young leaves has significantly darker and yellower (L* - 37.39, h^{o} – 97.46) than mature (L* - 36.48, h^{o} – 98.04) and old leaves (L* - 35.26, h^{o} – 99.45) since herbal tea prepared from young leaves has significantly highest antioxidant activity. It also showed that as maturity of *C. caudatus* leaves used to prepared herbal tea increased, the C value decreased significantly from 7.31 to 4.42. From the results in Table 3, colour of *C. caudatus* herbal tea prepared from three different maturity stages give negative value for a* and positive value for b* which contributed to greenness and yellowness characteristic.

These findings is corroborated by Alves et al. [25] where they confirmed that index of antioxidant power had influenced by colour of the sample in which generally they found their light-coloured honeys have lower antioxidant activity while their dark-coloured honeys have huge amount of antioxidant activity. Similar results have been reported by others literatures, for examples Harbourne et al. [11] found that the meadowsweet extracts were significantly darker and redder than willow extract due to higher total phenolic content in meadowsweet extracts while Schwarz et al. [26] found that the increase of red and yellow tonalities of Sherry wines present an extraordinarily high antioxidant activity. Marete et al. [15] believed that, the dark colour of sample is possibly due to higher total phenolic content in the sample. Futhermore, Alvarez-Suarez [27] explained that the colour intensity of sample is related to pigments such as flavonoids and carotenoids. In fact, the increasing of the colour intensity seems to be related to an increase of the concentration of these compounds. Therefore, the results of this study seem to confirm that antioxidant activity is directly affecting *C. caudatus* herbal tea colour.

Table 3. The colour values of herbal tea prepared from *C. caudatus* leaves at different maturity stages. Values are expressed as mean ± standard deviation. Means with different letters are significantly different ($p < 0.05$)

Herbal tea sample	**Colour**				
	Lightness (L*)	**Greenness (a*)**	**Yellowness (b*)**	**Chroma (C)**	**Hue angle (h^{o})**
Young leaves	35.25 ± 0.20^{c}	-0.95 ± 0.06^{c}	7.25 ± 0.08^{a}	7.31 ± 0.07^{a}	97.46 ± 0.53^{b}
Mature leaves	36.48 ± 0.15^{b}	-0.82 ± 0.04^{b}	5.79 ± 0.19^{b}	5.85 ± 0.16^{b}	98.04 ± 0.47^{b}
Old leaves	37.39 ± 0.28^{a}	-0.73 ± 0.03^{a}	4.36 ± 0.17^{c}	4.42 ± 0.18^{c}	99.45 ± 0.62^{a}

Mineral content

Most people believed that consumption of herbal tea can enhance human health. Hence, determination of mineral content is also important in herbal tea due to their responsibilities in providing medicinal and nutritional properties. According to Tokalıoğlu [28], the quantitative estimation of various mineral content is important in determining the effectiveness of the medicinal plants used in herbal tea preparation in treating various diseases and also to

understand their pharmacological action. Therefore this study involved the evaluation of some important macroelements (Ca, K, Mg and Na) and microelements (Ag, Al, Ba, Cd, Cr, Cu, Fe, Pb and Zn) in *C. caudatus* herbal tea prepared from three different maturity stages and results are shown in Table 4. Interestingly, among all the *C. caudatus* herbal tea samples, *C. caudatus* herbal tea prepared from old leaves had significantly higher minerals like Ca, Mg, Na (macroelements) and Ba, Cd, Cr, Cu, Mn (microelements) compared to mature and young leaves. However, for K (macroelements) Ag, Al, Fe, Pb, Zn (microelements) there were no significant difference among samples.

Table 4**.** Mineral content of *Cosmos caudatus* herbal tea sample prepared from leaves at different maturity stages. Values are expressed as mean ± standard deviation. Means with different letters are significantly different ($p<0.05$)

	Mineral (µg/ml of tea)	**Herbal tea prepared from young leaves**	**Herbal tea prepared from mature leaves**	**Herbal tea prepared from old leaves**
macro elements	Ca	13.5958 ± 0.9019^{c}	31.4583 ± 1.0670^{b}	51.0042 ± 4.6142^{a}
	K	94.5375 ± 1.7852^{a}	96.4208 ± 9.1021^{a}	98.6583 ± 5.1247^{a}
	Mg	8.3117 ± 0.2564^{b}	9.3179 ± 0.2905^{b}	13.6108 ± 1.0186^{a}
	Na	0.5463 ± 0.0055^{c}	0.6070 ± 0.0343^{b}	0.6830 ± 0.0253^{a}
microelements	Ag	0.0035 ± 0.0006^{a}	0.0035 ± 0.0001^{a}	0.0045 ± 0.0007^{a}
	Al	0.0310 ± 0.0035^{a}	0.0311 ± 0.0024^{a}	0.0318 ± 0.0010^{a}
	Ba	0.0052 ± 0.0003^{c}	0.0076 ± 0.0002^{b}	0.0149 ± 0.0021^{a}
	Cd	0.0073 ± 0.0006^{b}	0.0070 ± 0.0010^{b}	0.0011 ± 0.0020^{a}
	Cr	0.0321 ± 0.0031^{b}	0.0394 ± 0.0044^{ab}	0.0433 ± 0.0036^{a}
	Cu	0.0313 ± 0.0024^{b}	0.0319 ± 0.0004^{b}	0.0388 ± 0.0036^{a}
	Fe	0.0458 ± 0.0007^{a}	0.0454 ± 0.0044^{a}	0.0500 ± 0.0022^{a}
	Mn	0.0310 ± 0.0018^{b}	0.0675 ± 0.0012^{a}	0.0730 ± 0.0046^{a}
	Pb	0.0012 ± 0.0006^{a}	0.0011 ± 0.0012^{a}	0.0012 ± 0.0006^{a}
	Zn	0.0534 ± 0.0027^{a}	0.0533 ± 0.0083^{a}	0.0534 ± 0.0012^{a}

This result might be due to the location of old leaves in which they are located near to the roots, where generally, the roots contain the highest levels of elements followed by vegetative tissues [28]. This is because the plants readily assimilate the elements through the roots, which will dissolved in water and occur in ionic forms [29]. Another possible reason is that, the growth of tissues plants also profoundly influence the minerals absorption, in which as tissues mature, volume of water uptake by cell increased which may dilute the internal concentration of minerals, thus increase absorption activity [30]. This is supported by Flowers and Yeo [31] where they reported that the volume of mature cell increase with time, providing mineral-storage capacity at constant concentration. However, some authors believed that, the decrement in concentration of mineral content might be directly related to

the accumulation of antioxidant content in plants. Sulaiman et al. [32] reported that an imbalance of minerals in plants would change the content of flavonoids, a proven antioxidant compounds. For example, as found by some researchers, the deficiency of several minerals such as K, Mg, and Mn induced the flavonoid accumulation in plants [5, 32]. Therefore, this study revealed that, as maturity of *C. caudatus* leaves used to prepared herbal tea increased, it may increase some of mineral content due to decrement in antioxidant activity.

Table 5. Dietary Reference Intake (DRI) and percentage contribution of herbal tea prepared from *C. caudatus* leaves prepared from different maturity stages per 200 ml in a day

Mineral		**Recommended Dietary Allowances, RDA / Adequate Intake, AI (19 – 50 years old)(mg)**	**Percentage contribution of *C. caudatus* herbal tea per 200 ml in a day (%)**
Macro elements	Ca	Men = 1000* Women = 1000*	Men = 0.22 – 1.02 Women = 0.22 – 1.02
	K	Men = 4700 Women = 4700	Men = 0.40 – 0.42 Women = 0.40 – 0.42
	Mg	Men = 400 Women = 310	Men = 0.41 – 0.68 Women = 0.54 – 0.88
	Na	Men = 1500 Women = 1500	Men = 0.007 – 0.009 Women = 0.007 – 0.009
Micro elements	Ag	Men = na Women = na	Men = na Women = na
	Al	Men = na Women = na	Men = na Women = na
	Ba	Men = na Women = na	Men = na Women = na
	Cd	Men = na Women = na	Men = na Women = na
	Cr	Men = 35* Women = 25*	Men = 18.29 – 24.86 Women = 25.60 – 34.80
	Cu	Men = 900 Women = 900	Men = 0.70 – 0.87 Women = 0.70 – 0.87
	Fe	Men = 8 Women = 18	Men = 0.12 – 0.13 Women = 0.05 – 0.06
	Mn	Men = 2.3* Women = 1.8*	Men = 0.27 – 0.63 Women = 0.34 – 0.81
	Pb	Men = na Women = na	Men = na Women = na
	Zn	Men = 11 Women = 8	Men = 0.10 Women = 0.13

Note : Ordinary type represents source from [33] while bold type represents source from [34], Italic type represents the unit in µg, Value with asterisk (*) represent Adequate Intake (AI), na = not available

Macroelements (Ca, K, Mg and Na) were detected in highest concentration in all three *C. caudatus* herbal tea samples compared to microelements. This is because bioavailability of the elements depends on the bonding with the constituents of the soil [29]. In addition, as confirmed by Devlin and Witham [30] that Ca, K, Mg and Na are major elements that contributed to the plant growth. Nevertheless, the contribution of mineral content in herbal tea

on the average dietary intake must be taken into consideration. The consumption rate of *C. caudatus* herbal tea should be under strict control and should not exceed Dietary Reference Intake (DRI) since exceeding some of these minerals might cause toxicity. Based on the results obtained, none of the macro and microelements was exceed the DRI based on Recommended Dietary Allowances (RDA) or Adequate Intake (AI) as in Table 5 [33,34]. Besides, the toxic elements such as Ag, Al, Ba, Cd and Pb were detected in low concentration. Therefore, depending on the mineral content in *C. caudatus* herbal tea prepared from three different maturity stages, these herbal tea may be a good source of essential minerals.

Conclusion

In conclusion, usage of *C. caudatus* leaves for tea production at different maturity stages, affects the antioxidant activity, colour and mineral content of herbal tea. *C. caudatus* herbal tea prepared from young leaves possessed significantly strong antioxidant activity compared to mature and old leaves in all assays tested. Strong positive Pearson's correlations between reducing power with TPC and TFC, and strong negative Pearson's correlation between DPPH scavenging activity with TPC and TFC showed that phenolic and flavonoid compounds are major contributions to the antioxidant activity in *C. caudatus* herbal tea at all maturity stages studied. The darker colour of *C. caudatus* herbal tea prepared from young leaves compared to other two leaves relates to the high phenolic and flavonoid content in young leaves. In contrast, *C. caudatus* herbal tea prepared from old leaves exhibited significantly high in Ca, Mg, Na for macro elements and Ba, Cd, Cr, Cu Mn for microelements compared to mature and young leaves.

Acknowledgement

The authors would like to thank Universiti Teknologi MARA (UiTM) for their technical and financial support.

References

1. Quispe, C., Viveros-Valdez, E. and Schmeda-Hirschmann, G. (2012). Phenolic constituents of the chilean herbal tea *Fabiana imbricata* R. et P. *Plant Foods for Human Nutrition*, 67(3): 242–246.
2. Zhao, J., Deng, J. W., Chen, Y. W. and Li, S. P. (2013). Advanced phytochemical analysis of herbal tea in China. *Journal of Chromatography A*, 1313: 2 – 23.
3. Horžić, D., Komes, D., Belščak, A., Ganić, K. K., Iveković, D. and Karlović, D. (2009). The composition of polyphenols and methylxanthines in teas and herbal infusions. *Food Chemistry*, 115(2): 441 – 448.
4. Tschiggerl, C. and Bucar, F. (2012). The volatile fraction of herbal teas. *Phytochemistry Reviews*, 11(2–3): 245 – 254.
5. Whittaker, A., Vazzana, C., Vecchio, V. and Benedettelli, S. (2009). Evaluation of direct and indirect effects of flavonoids, mineral elements and dry weight on antiradical scavenging activity in leaf material of field-grown *Trifolium pratense* cultivars using path analysis. *Field Crops Research*, 113: 1 – 11.
6. Amna, O. F., Nooraain, H., Noriham, A., Azizah, A. H. and Husna, R. N. (2013). Acute and oral subacute toxicity study of ethanolic extract of *Cosmos caudatus* leaf in sprague dawley rats. *International Journal of Bioscience, Biochemistry and Bioinformatics*, 3(4): 301 – 305.
7. Shui, G., Leong, L. P. and Wong, S. P. (2005). Rapid screening and characterisation of antioxidants of *Cosmos caudatus* using liquid chromatography coupled with mass spectrometry. *Journal of Chromatography B*, 827(1): 127 – 138.
8. Mediani, A., Abas, F., Ping, T. C., Khatib, A. and Lajis, N. H. (2012). Influence of growth stage and season on the antioxidant constituents of *Cosmos caudatus*. *Plant Foods for Human Nutrition*, 67(4): 344 – 350.
9. Rehecho, S., Hidalgo, O., Cirano, M. G. D., Navarro, I., Astiasarán, I., Ansorena, D., Yolanda, R. and Isabel, M. (2011). Chemical composition, mineral content and antioxidant activity of *Verbena officinalis* L . *LWT - Food Science Technology*, 44(4): 875 – 882.
10. Gião, M. S., Pereira, C. I., Fonseca, S. C., Pintado, M. E. and Malcata, F. X. (2009). Effect of particle size upon the extent of extraction of antioxidant power fom the plants *Agrimonia eupatoria*, *Salvia sp.* and *Satureja montana*. *Food Chemistry*, 117(3): 412 – 416.
11. Harbourne, N., Marete, E., Jacquier, J. C. and O'Riordan, D. (2009). Effect of drying methods on the phenolic constituents of meadowsweet *(Filipendula ulmaria)* and willow *(Salix alba)*. *LWT - Food Science Technology*, 42(9): 1468 – 1473.

12. Singh, V., Guizani, N., Essa, M. M., Hakkim, F. L and Rahman, M. S. (2012). Comparative analysis of total phenolics, flavonoid content and antioxidant profile of different date varieties *(Phoenix dactylifera L .)* from Sultanate of Oman. I*nternational Food Research Journal,* 19(3): 1063 – 1070.
13. Deetae, P., Parichanon, P., Trakunleewatthana, P., Chanseetis, C. and Lertsiri, S. (2012). Antioxidant and anti-glycation properties of thai herbal teas in comparison with conventional teas. *Food Chemistry,* 133(3): 953 – 959.
14. Nuengchamnong, N. and Ingkaninan, K. (2010). On-line HPLC–MS–DPPH assay for the analysis of phenolic antioxidant compounds in fruit wine: *Antidesma thwaitesianum Muell. Food Chemistry,* 118(1): 147 – 152.
15. Marete, E. N., Jacquier, J. C. and O'Riordan, D. (2009). Effects of extraction temperature on the phenolic and parthenolide contents, and colour of aqueous feverfew *(Tanacetum parthenium)* extracts. *Food Chemistry,* 117(2): 226 – 231.
16. Pytlakowska, K., Kita, A., Janoska, P., Połowniak, M. and Kozik, V. (2012). Multi-element analysis of mineral and trace elements in medicinal herbs and their infusions. *Food Chemistry,* 135(2): 494 – 501.
17. Siddiqui, M.W., Momin, C. M., Acharya, P., Kabir, J., Debnath, M. K. and Dhua, R. S. (2012). Dynamics of changes in bioactive molecules and antioxidant potential of capsicum chinense *Jacq. cv. Habanero* at nine maturity stages. *Acta Physiologiae Plantarum* 35(4): 1141 – 1148.
18. Sreelatha, S. and Padma, P. R. (2009). Antioxidant activity and total phenolic content of *Moringa oleifera* leaves in two stages of maturity. *Plant Foods for Human Nutrition,* 64(4): 303 – 311.
19. Fawole, O. A. and Opara, U. L. (2013). Changes in physical properties, chemical and elemental composition and antioxidant capacity of pomegranate *(cv. Ruby)* fruit at five maturity stages. *Science Horticulture (Amsterdam).,* 150: 37 – 46.
20. Menichini, F., Loizzo, M. R., Bonesi, M., Conforti, F., Luca, D. D., Statti, G. A., Cindio, B. D., Menichini, F. and Tundis, R. (2011). Phytochemical profile, antioxidant, anti-inflammatory and hypoglycemic potential of hydroalcoholic extracts from *Citrus medica L. cv Diamante* flowers, leaves and fruits at two maturity stages. *Food Chemistry and Toxicology,* 49(7): 1549 – 1555.
21. Oh, J., Jo, H., Cho, A. R., Kim, S.-J. and Han, J. (2013). Antioxidant and antimicrobial activities of various leafy herbal teas. *Food Control,* 31(2): 403 – 409.
22. Shuib, N. H., Shaari, K., Khatib, A., Kneer, R., Zareen, S., Raof, S. M., Lajis, N. H. and Neto, V. (2011). Discrimination of young and mature leaves of *Melicope ptelefolia* using ^{1}H NMR and multivariate data analysis. *Food Chemistry,* 126(2): 640 – 645.
23. Barros, L., Queiro, B., Ferreira, I. C. F. R. and Baptista, P. (2007). Total phenols, ascorbic acid , β-carotene and lycopene in portuguese wild edible mushrooms and their antioxidant activities. *Food Chemistry,* 103: 413– 419.
24. Villa-Rodríguez, J. A., Molina-Corral, F. J., Ayala-Zavala, J. F., Olivas, G. I. and González-Aguilar, G. A. (2011). Effect of maturity stage on the content of fatty acids and antioxidant activity of 'hass' avocado. *Food Research International,* 44(5): 1231 – 1237.
25. Alves, A., Ramos, A., Gonçalves, M. M., Bernardo, M. and Mendes, B. J. (2013). Antioxidant Activity, quality parameters and mineral content of portuguese monofloral honeys. *Journal of Food Composition and Analysis,* 30(2): 130 –138.
26. Schwarz, M., Rodríguez, M. C., Guillén, D. A. and Barroso. C. G. (2012). Evolution of the colour, antioxidant activity and polyphenols in unusually aged sherry wines. *Food Chemistry,* 133: 271 – 276.
27. Alvarez-Suarez, J. M., Tulipani, S., Díaz, D., Estevez, Y., Romandini, S., Giampieri, F., Damiani, E., Astolfi, P., Bompadre, S. and Battino, M. (2010). Antioxidant and antimicrobial capacity of several monofloral cuban honeys and their correlation with color, polyphenol content and other chemical compounds. *Food Chemistry Toxicology,* 48(8–9): 2490 – 2499.
28. Tokalıoğlu, Ş. (2012). Determination of trace elements in commonly consumed medicinal herbs by ICP-MS and multivariate analysis. *Food Chemisty,* 134(4): 2504 – 2508.
29. Başgel, S. and Erdemoğlu, S. B. (2006). Determination of mineral and trace elements in some medicinal herbs and their infusions consumed in Turkey. *Science of Total Environment,* 359(1–3): 82 – 89.
30. Devlin, R. M. and Witham, F. H. (1983). Plant physiology. *Willard Grant Press, Boston,* pp. 96 -129.
31. Flowers, T. J. and Yeo, A. R. (1992). Tertiary level biology: solute transport in plants. *Thomas Press, New Delhi, India,* pp. 137.

32. Sulaiman, S. F., Sajak, A. A. B., Ooi, K. L. and Seow, E. M. (2011). Effect of solvents in extracting polyphenols and antioxidants of selected raw vegetables. *Journal of Food Composition and Analysis*, 24(4–5): 506 – 515.
33. The National Academies. Dietary reference intakes: elements dietary reference intakes: elements. (2001). Downloaded from www.nap.edu.
34. Ministry of Health Malaysia. Recommended nutrient intakes for Malaysia: A Report of the technical working group on nutritional guidelines. (2005). Downloaded from http://www.moh.gov.my/images/gallery/rni/insert.pdf.

Malaysian Journal of Analytical Sciences, Vol 20 No 3 (2016): 618 - 625
DOI: http://dx.doi.org/10.17576/mjas-2016-2003-22

MALAYSIAN JOURNAL OF ANALYTICAL SCIENCES
Published by The Malaysian Analytical Sciences Society
ISSN 1394 - 2506

EFFECT OF EDIBLE LIPID-CHITOSAN FILM FORMING DISPERSION ON POSTHARVEST LIFE OF GUAVA STORED AT CHILLED TEMPERATURE

(Kesan Serakan Filem Lipid-Kitosan Ke Atas Jangka Hayat Jambu yang Disimpan Pada Suhu Sejuk)

Nurul Adilla M. Loai, Halimahton Zahrah Mohamed Som*, Zaibunnisa Abdul Haiyee

Faculty of Applied Sciences,
Universiti Teknologi MARA, 40450 Shah Alam, Selangor, Malaysia

**Corresponding author: halimah@salam.uitm.edu.my*

Received: 24 February 2015; Accepted: 27 October 2015

Abstract

An edible lipid-chitosan film forming dispersion (FFD) was developed to delay ripening of guava. Four percent (v/v) of palm stearin (PS) and palm kernel olein (PKOo) in ratios of 0:100, 25:75, 50:50, 75:25 and 100:0 were added to a chitosan solution base and applied on guava by dipping technique. Surface appearance, weight loss, firmness, carbon dioxide, oxygen and ethylene concentrations were evaluated every 3 days during 31 days of storage at chilled temperature (5±2 °C). An application of FFD on guava significantly ($p < 0.05$) delayed chilling injury, reduced weight loss, maintained firmness, slowed down respiration and ethylene production as compared to uncoated guavas. PS:PKOo (75:25) coating was able to form compatible blends and showed good moisture and gas barrier properties when applied on guava surface, resulting in increased postharvest life of guava.

Keywords: guava, film forming dispersion, chitosan, palm stearin, palm kernel olein

Abstrak

Serakan filem lipid-kitosan yang boleh dimakan telah dihasilkan untuk melambatkan proses jambu untuk ranum. Empat peratus (v/v) stearin sawit dan olein isirong sawit dengan nisbah 0:100, 25:75, 50:50, 75:25 and 100:0 telah ditambah ke dalam larutan kitosan dan diaplikasikan ke atas jambu dengan menggunakan teknik celupan. Permukaan buah, kehilangan berat, kekerasan, kepekatan gas karbon dioksida, oksigen dan etilena telah dikaji setiap 3 hari sepanjang 31 hari penyimpanan di dalam suhu sejuk (5±2 °C). Penggunaan salutan ke atas jambu telah melambatkan kerosakan buah, mengurangkan kehilangan berat, mengekalkan kekerasan, melambatkan proses respirasi dan penghasilan etilena jika dibandigkan dengan jambu yang tidak disalut. Salutan PS:PKOo (75:25) telah menghasilkan campuran yang sesuai dan menunjukkan sifat-sifat penghalang air dan gas yang baik apabila diaplikasikan ke atas permukaan jambu dan telah meningkatkan jangka hayat jambu.

Kata kunci: jambu, serakan lapisan filem, kitosan, stearin sawit, olein isirong sawit

Introduction

Guava is an excellent source of vitamin C and is grown for both the domestic and exports markets. However, guava ripens rapidly during transportation and storage, thus often requiring rapid shipment in order to prolong postharvest life and decrease its respiration rate. Many postharvest diseases such as anthracnose, mucor rot and aspergillus rot can also limit the commercialisation of guava. Although refrigeration can increase the shelf life of guava, it adds cost and may cause chilling injury. Thus, coating the fresh fruit appears to be a cheaper alternative to preserve guava.

Materials that can be used to make edible coating includes polysaccharides [1], proteins [2] and lipids [3], or a combination of these materials [4]. Most hydrophilic films are excellent gas, aroma and lipid barriers with good mechanical properties, while hydrophobic films have high moisture resistance with poor mechanical properties. Improved film or coating performance can be obtained when hydrophilic and hydrophobic compounds are mixed.

Chitosan as a coating material has good antimicrobial [4] and gas barrier properties [5] with its tough and flexible film [6]. To date, there is no research data on the study of functional properties of chitosan based dispersion incorporated with palm stearin and palm kernel olein (PKOo). It can thus be combining with palm stearin and PKOo to provide moisture barrier properties, as PKOo has limited application because of excessive foaming due to medium-short chain fatty acids [7]. Results obtained from this study can be used to assess the potential of lipid-chitosan coating, besides diversifying the use of palm stearin and PKOo.

Materials and Methods

Chemicals and raw materials

Raw materials used were guava, chitosan, palm kernel olein and palm stearin. Refined, bleached and deodorised medium-hard palm stearin (IV: 33, SMP: 54) and palm kernel olein (IV: 24, SMP: 25) were obtained from Cargill Specialty Fats (M) Sdn. Bhd, Pelabuhan Klang, Malaysia. Guavas (*Psidium guajava* L.) at maturity index 2 were obtained from FAMA Chui Chak, Bidor, Perak, Malaysia. High molecular weight chitosan, with a deacetylation degree of 85 % was purchased from Saintifik Zener Sdn. Bhd, Kuala Lumpur, Malaysia. Glacial acetic acid (99.5 %), glycerol and Tween 80 were supplied by Merck Sdn Bhd, Petaling Jaya, Selangor, Malaysia.

Preparation of film forming dispersion (FFD)

An amount 3 g of chitosan was dispersed in an aqueous solution of glacial acetic acid (0.75 % v/v), at 40 °C. Tween 80 at 0.1 % (v/v) and 0.5 % of glycerol were added and the FFD was shaken by using an orbital shaker at 350 rpm, 65 °C. After 8 hours, palm stearin and palm kernel olein were added at 4 % (v/v) in ratios of 0:100, 25:75, 50:50, 75:25 and 100:0 to the chitosan solution. These mixtures were then emulsified at room temperature using a high speed homogeniser at 13500 rpm for 4 minutes [8].

Coating application

Guavas of uniform size, shape and colour and without any signs of mechanical damage or fungal decay were selected. The fruits were washed and immersed in 10 mg/L of sodium hypochlorite solution for 5 minutes and then drained prior to coating. The fruits were dipped in the FFD for 15 seconds [9] while control samples were dipped in distilled water. Fruits were allowed to dry at ambient temperature on trays, and were stored at chilled temperature (5 ± 2°C) and 80 – 95 % relative humidity for 31 days. Temperature and relative humidity were measured by using a Temperature and RH logger (HOBO U12 – O13) [10].

Physicochemical analyses

Physicochemical analyses of guava were performed at 1, 4, 7, 10, 13, 16, 19, 22, 25, 28, and 31 days of storage.

Determination of surface appearance

Guavas samples were assessed by visual inspection on overall appearance, colour changes and acceptability at 1, 4, 7, 10, 13, 16, 19, 22, 25, 28, and 31 days of storage. Pictures of guavas were captured by using a digital camera (Canon IXUS HS115). Guava that showed any sign of fungal development was considered decayed [11].

Determination of weight loss

Weight loss was determined by weighing the samples on a laboratory digital balance (A & D HF-300, Japan) after air-drying the FFD and thereafter at 1, 4, 7, 10, 13, 16, 19, 22, 25, 28, and 31 days of storage. Results were expressed as percentage loss of moisture based on the original mass [12].

Determination of firmness retention

Firmness of guava was determined by using a TA-XT2i Texture Analyzer (Stable Microsystems, Surrey, UK) equipped with a compression cell of 10 kg and a cylindrical and flat acrylic probe of 1 cm in diameter, 10 mm/s crosshead speed, a 1 N force and a 75 % strain to penetrate the fruit. Determination was performed at three different

parts of guavas. Results were expressed as percentage of firmness retention (compression force at storage time was compared to force on day 1) [13].

Determination of gas concentrations

Carbon dioxide and ethylene concentrations were measured by enclosing each fruit in a 0.5 L plastic jar, hermetically sealed with a rubber stopper for one hour. One milliliter of the atmosphere in the plastic jar was withdrawn into a gas tight syringe. Carbon dioxide and ethylene concentrations were quantified using a Gas Chromatograph (Agilent 78990A) equipped with Thermal Conductivity Detector (TCD) and Flame Ionization Detector (FID), respectively. Column and detector temperatures were 55 ˚C and 180 ˚C, respectively. The carrier gas was helium at a flow rate of 50 ml/min. Results from the means of triplicate determinations were expressed in ppm (10). Oxygen concentration was analysed in the same headspace gas by using a carbon dioxide and oxygen analyzer (Mocon Pac Check 200). Results from the means of triplicate determinations were expressed as percentage of oxygen [14].

Statistical analysis

SPSS for Windows Evaluation (version 15.0) was used for all statistical analyses. Analysis of variance and Duncan multiple comparisons were performed at 5 % confidence level.

Results and Discussion

Surface appearance

The overall acceptability of fruit was evaluated based on the appearance of fruit skin. The results obtained on the visual appearance of guavas are shown in Figure 1. The uncoated guava showed sign of chilling disorder at day 13 with the chilling injury becoming more prominent as storage progressed. Lipid-chitosan coating (PS:PKOo 75:25) delayed the chilling injury of guava by shifting the chilling disorder to day 22 of storage. The coating delayed disease development and retarded the ripening process. The intensification of chilling injury during storage of guava was also observed by Gonzalez-Aguilar et al [15]. Meanwhile, Vargas et al [9] reported that surface moisture loss could be responsible for the darker colour of fruits's skin.

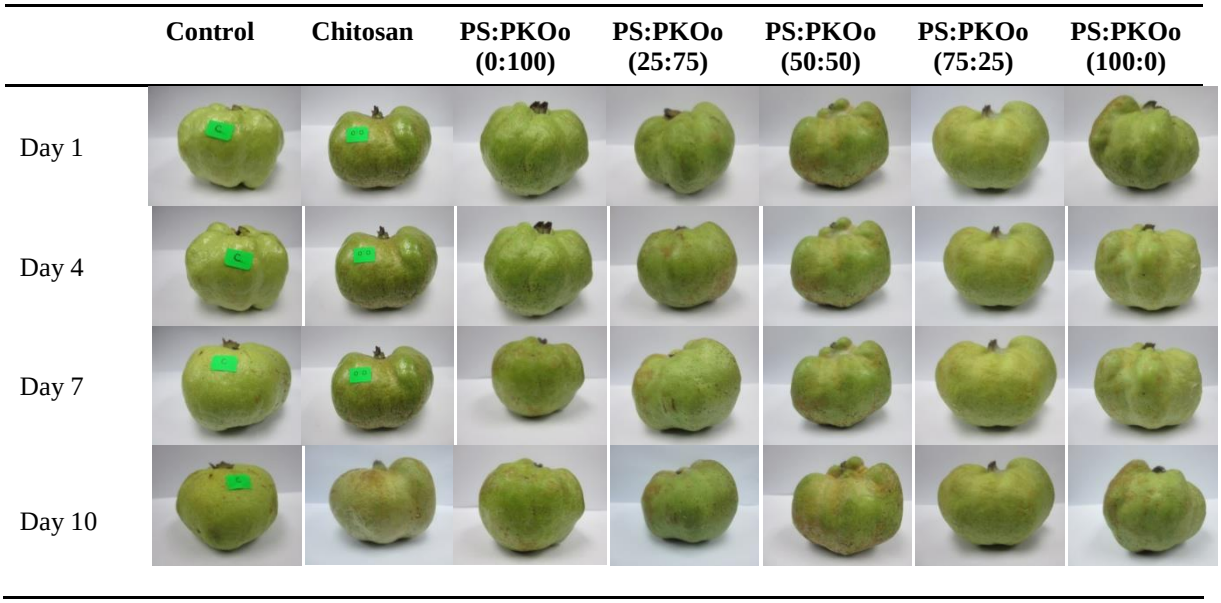


Figure 1. Appearance of seedless guavas stored at chilled temperature

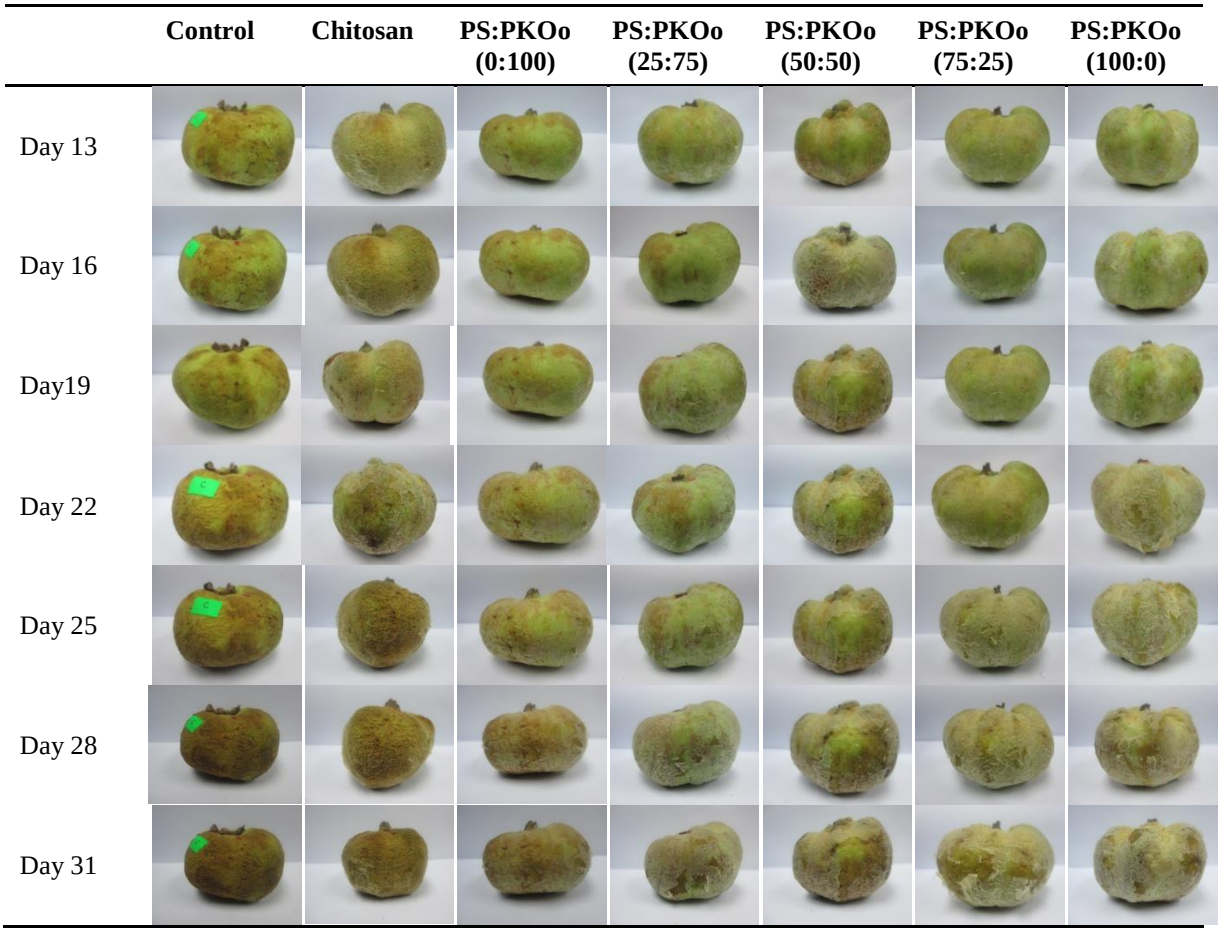


Figure 1 (cont'd). Appearance of seedless guavas stored at chilled temperature

Weight loss

Figure 2 shows the increases in weight loss of both coated and uncoated guavas. The results obtained showed that chitosan coating significantly reduced the weight loss of guava. Similar results were also observed with chitosan coating on sliced mango fruit at chilled temperature [5]. In this study, lipid-chitosan coatings exhibited smaller weight loss as compared to chitosan coating, with PS:PKOo (75:25) coated guava showing the lowest percentage of weight loss. This phenomenon happened probably due to the optimum interaction of PS and PKOo with chitosan during the drying process.

In this study, lipid-chitosan coatings showed good moisture barrier properties due to the combination of PS and PKOo. The lipids gave better protection on moisture loss of the seedless guava hence slowing down the weight loss of fruits. These results agreed with the findings of other researchers who reported that coatings made from lipids have good water vapour barrier properties. This is because lipids are not miscible with water, hence water is retained and shrinkage of fruits is prevented [16].

Firmness retention

Results on firmness retention of guavas are shown in Figure 3. Firmness of guava coated with chitosan coating decreased slower compared to uncoated guava because the chitosan coating provided the barrier to gases in the fruit. Lipid-chitosan coating could retain the firmness of guava better than chitosan coating alone, because the incorporation of lipid into chitosan coating was able to provide both moisture and gas barrier properties. PSPKOo

(75:25) coating appeared to be the best formulation in preventing the loss of water vapour and maintained the firmness of seedless guavas. Yaman and Bayoundurh [17] reported that the decrease of oxygen and increase in carbon dioxide concentrations reduced the activity of enzyme that is responsible for texture loss, hence allowing the retention of fruit firmness.

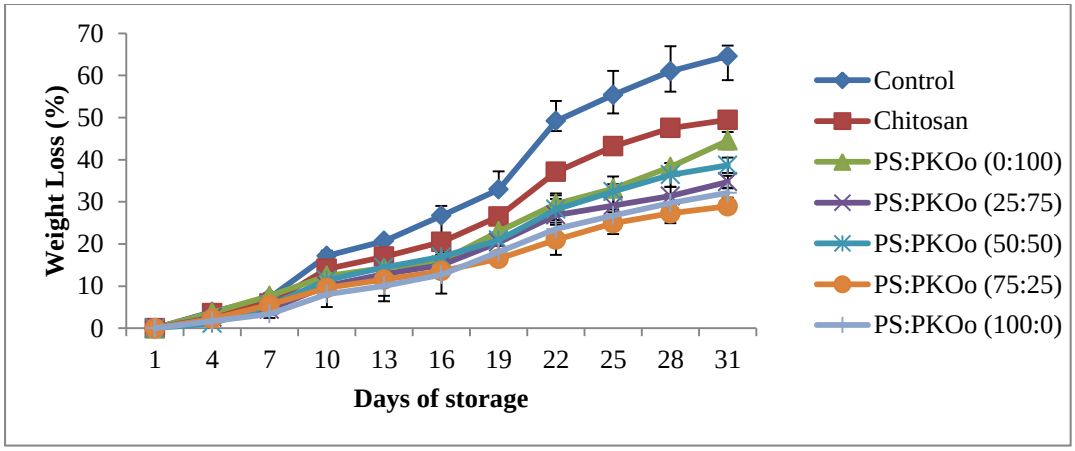


Figure 2. Weight loss of seedless guavas during storage at chilled temperature

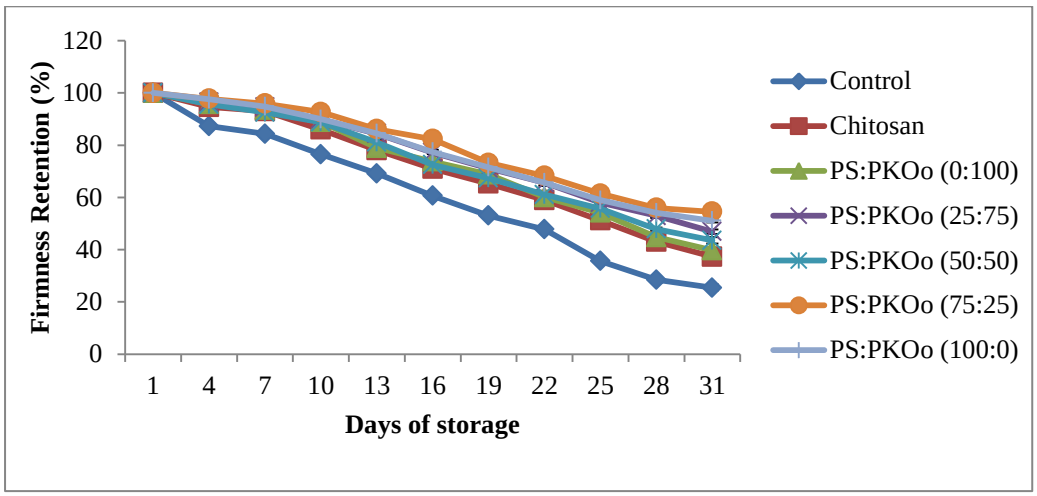


Figure 3. Firmness retention of seedless guavas during storage at chilled temperature

Ethylene concentration

Figure 4 shows the ethylene production of guavas during storage at chilled temperature. Chilled storage is one of the methods used to delay fruit maturation by reducing respiration and synthesis of ethylene, which cause maturation. The ethylene production during ripening of guava exhibited a typical climacteric pattern of respiration for climacteric fruits. The uncoated guava reached the climacteric peak at day 13 while chitosan coated guava reached the climacteric peak after day 16.

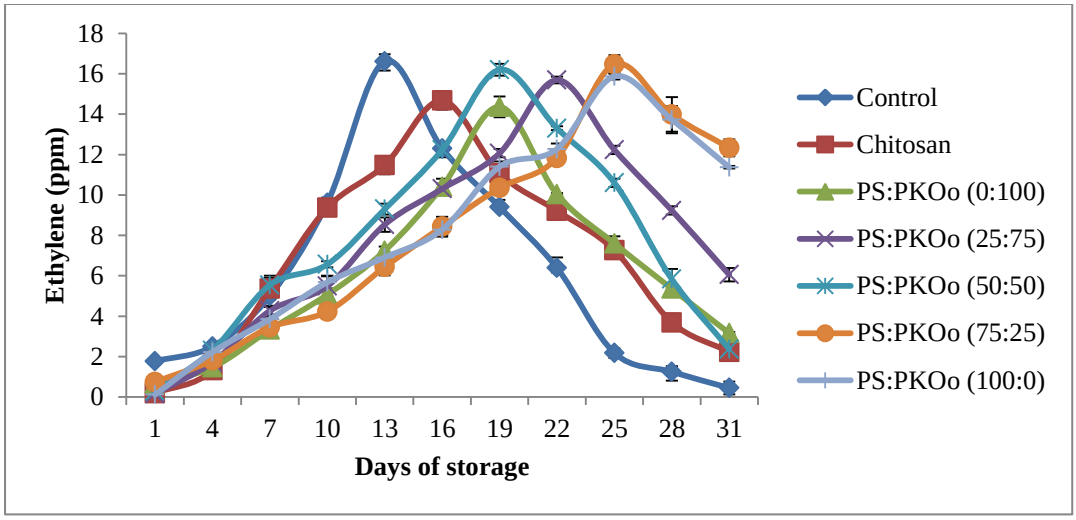


Figure 4. Ethylene concentration of seedless guavas during storage at chilled temperature

The amount of ethylene release for guavas that were coated with chitosan coating, PS:PKOo (0:100), PS:PKOo (25:75), PS:PKOo (50:50), PS:PKOo (75:25) and PS:PKOo (100:0) increased with storage time and reached the highest values of 14.67 ppm, 14.36 ppm, 15.69 ppm, 16.20 ppm, 16.47 ppm and 15.87 ppm, respectively. Ethylene production decreased gradually after reaching the climacteric peaks. The decrease in ethylene concentration was probably due to the emergence of chilling injury on the fruit surface. Guavas that were coated with PS:PKOo (75:25) and PS:PKOo (100:0) shifted the climacteric peak of uncoated guava from day 13 to day 25. The results showed that both coatings showed greater gas barrier properties compared to the other coatings.

Carbon dioxide and oxygen concentrations

Figure 5 presents the concentration of carbon dioxide throughout chilled storage of guava. Coated guavas showed significantly lower amount of carbon dioxide than the uncoated guavas during chilled storage.

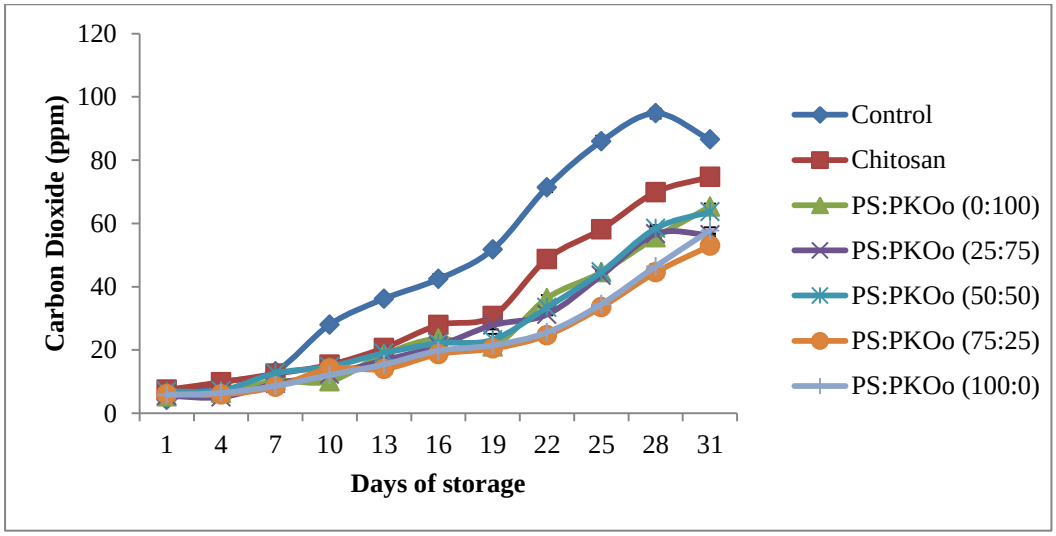


Figure 5. Carbon dioxide concentration of seedless guavas during storage at chilled temperature

Application of lipid-chitosan coatings could control the production of carbon dioxide by the guava, with PS: PKOo (75:25) coating showing the lowest amount of carbon dioxide throughout the 31 days of storage. All the guavas showed increases in carbon dioxide concentration which agrees with the increase in the metabolic activity of guava. Carbon dioxide in internal tissue of fruits should be decreased to control the ripening process [18]. Carbon dioxide concentration is related to tissue senescence and cell breakdown [19]. The reduced rate of respiration in coated guava might be correlated with a delayed senescence and reduced susceptibility to decay. Hence, the chitosan-lipid coatings can be used to modify the internal atmosphere, thereby delaying the ripening of fruits.

As the amount of carbon dioxide is important to be decreased, the amount of oxygen surrounding the fruit should be maintained in order to control fruit ripening. The results of oxygen concentration (Figure 6) showed that all coatings had significantly prevented the decline of oxygen concentration surrounding the coated guavas ($P < 0.05$) indicating a delay in fruit ripening as compared to the control. This indicates that coating acted as an oxygen barrier that limited the acceleration of aerobic respiration. According to Singh and Pal [14], the increase in oxygen concentration in storage atmosphere accelerated the loss of green colour in guava.

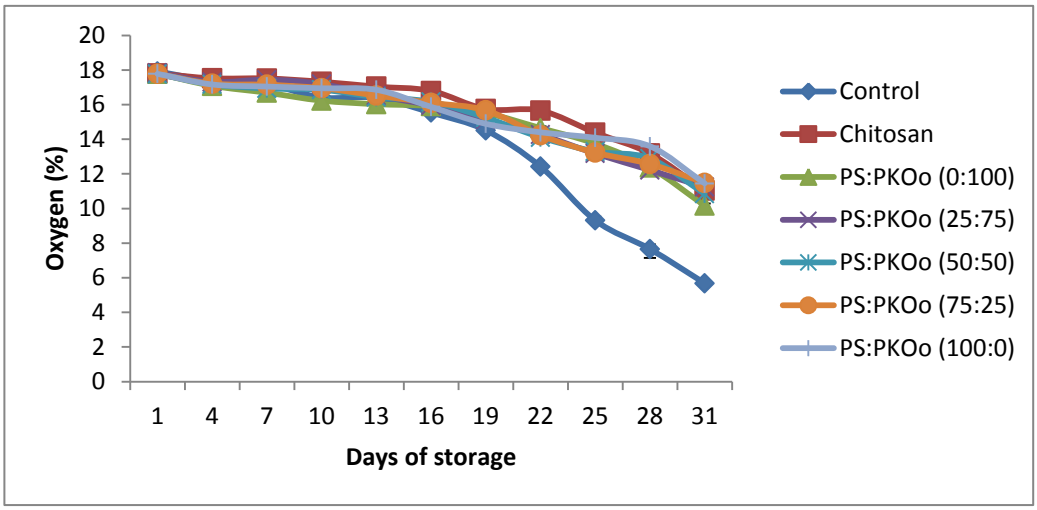


Figure 6. Oxygen concentration of seedless guavas during storage at chilled temperature

Conclusion

Application of edible lipid-chitosan coating was able to improve the quality and shelf-life of seedless guavas throughout 31 days of storage at chilled temperature. Results showed that the edible lipid-chitosan coating reduced the weight loss and increased the firmness retention. The coatings decreased ethylene and oxygen concentrations indicating a delay in fruit ripening as compared to the control. Application of lipid-chitosan coating showed beneficial effects on guava as it slowed the increases in carbon dioxide concentration of fruits. Overall, PSPKOo 75:25 was the best coating formulation as it showed good moisture and gas barrier properties. Hence, PS and PKOo showed potential to be used as cheap sources of edible coating.

Although the FFD in this study was found to have good moisture and gas barrier properties, chemical degradation of FFD could occur during storage. In order for this FFD to be used in commercial applications, future research is necessary to find methods to protect the FFD from degradation during storage. Incorporation of other types of lipids such as fatty acids or palm olein can be used as alternative lipids to improve FFD properties. Sensory evaluation can also be conducted to determine the perception of consumers towards the appearance and overall acceptability of coated fruits.

Acknowledgement

We thank the Ministry of Higher Education of Malaysia for the financial support (600-RMI/ST/FRGS 5/3 Fst (31/2010) and Universiti Teknologi MARA for giving us the opportunity to conduct this research.

References

1. Zahedi, Y., Ghanbarzadeh, B. and Sedaghat, N. (2010). Physical properties of edible emulsified films based on pistachio globulin protein and fatty acids. *Journal of Food Engineering*, 100(1): 102 – 108.
2. Gennadios, A., Weller, C. L. and C. H. and Gooding, C. H. (1994). Measurements errors in water vapour permeability of highly permeable, hydrophilic edible films, *Journal of Food Engineering*, 21: 395 – 409.
3. Hernandez, E. (1994). Edible coatings from lipids and resins. In J. M. Krochta, E. A. Baldwin and M. O. NisperosCarriedo (Ed.), Edible Coatings and Films to Improve Food Quality. Lancaster, Pennsylvania: Technomic Publishing Company, Inc. pp. 279 – 303.
4. Barbara, B., Donatella, P. and Alessandro, S. (2006). Development and application of polysaccharide - lipid edible coating to extend shelf life of dry bakery products. *Journal of Food Engineering*, 76: 280 – 290.
5. Chien, P. J., Sheu, F. and Yang, F. H. (2007). Effects of edible chitosan coating on quality and shelf life of sliced mango fruit. *Journal of Food Engineering*, 78: 225 – 229.
6. Kaplan, D. L., Mayer, J. M., Ball, D., McCassie, J., Allen, A. L. and Stenhouse, P. (1993). Fundamental of biodegradable polymer. In Ching, C., Kaplan D., and Thomas E. (eds.). Biodegradable Polymers and Packaging. Lancaster: Technomic Publishing. pp. 1 – 42
7. Norizzah, A. R., Chong, C. L., Cheow, C. S. and Zaliha, O. (2004). Effects of chemical interesterification on physicochemical properties of palm stearin and palm kernel olein blends. *Food Chemistry*, 86: 229 – 235.
8. Vargas, M., Albors, A., Chiralt, A., and González-Martínez, C. (2009). Characterization of chitosan-oleic acid composite films. *Food Hydrocolloids*, 23: 536 – 547.
9. Vargas, M., Albors, A., Chiralt, A., and González-Martínez, C. (2006). Quality of cold-stored strawberries as affected by chitosan-oleic acid edible coatings. *Postharvest Biology and Technology*, 41: 164 – 171.
10. Martínez-Romero, D., Alburquerque, N., Valverde, J. M., Guillèn, F., Castello, S., Valero, D. and Serrano, M. (2006). Postharvest sweet cherry quality and safety maintenance by Aloe vera treatment: a new edible coating. *Postharvest Biology and Technology*, 39: 93 – 100.
11. Abd. Rashid, N., Amin Zaki, E. N. and Mohd Som, H. Z. (2009). Application of water-based and lipid-based stearin wax coatings to improve the quality and shelf-life of seedless guavas (*Psidium guajava* L.). Paper presented at World Congress on oils & fats and 28th ISF Congress 2009. Sydney, Australia.
12. Maftoonazad, N. and Ramaswamy, H. S (2005). Postharvest shelf-life extension of avocados using methyl-cellulose-based coating. *LWT Food Science and Technology*, 38: 617 – 624.
13. Tanadu-Palmu, P. S. and Grosso, C. R. F. (2005). Effect of edible wheat gluten-based films and coatings on refrigerated strawberry (Fragariaananassa) quality. *Postharvest Biology and Technology*, 36: 199 – 208.
14. Singh, S. P., Pal, R. K. (2008). Response of climacteric-type guava (*Psidiumguajava* L.) to posthrvest treatment with 1-MCP. *Postharvest Biology andTechnol*ology, 47: 307 – 314.
15. Gonzalez-Aguilar, G. A., Tiznado-Hernandez, M. E., Zavaleta Gatica, R. and Martinez Tellez, M. A., (2004). Methyl jasmonate treatments reduce chilling injury and activate the defense response of guava fruits. *Biochemical Biophysic Research Communinaction*, 313: 694 – 701.
16. Morillon, V., Debeaufort, F., Blond, G., Capelle, M. and Voilley, A. (2002). Factors affecting the moisture permeability of lipid-based edible films: a review. *Critical Review in Food Science and Nutrition*, 42: 67 –89.
17. Yaman, O. and Bayoundurh, L. (2002). Effects of an edible coating and cold storage on shelf-life and quality of cherries. *Journal of Food Engineering*, 35: 146 – 150.
18. Nurul Hanani, M. Z., Halimahton Zahrah, M. S. and Zaibunnisa, A. H. (2012). Application of palm stearin-chitosan edible coating on star fruits (*Averrhoacarambola* L.) *Malaysian Journal of Analytical Sciences*, 16(3): 325 – 334.
19. Pastor, C., Sanchez-Gonzalez, L., Marcilla, A., Chiralt, A., Chafer, M. and Gonzalez-Martinez, C. (2011). Quality and safety of table grapes coated with hydroxypropylmethylcellulose edible coatings containing propolis extract. *Postharvest Biology and Technology*, 36: 69 – 75.

Malaysian Journal of Analytical Sciences, Vol 20 No 3 (2016): 626 - 632
DOI: http://dx.doi.org/10.17576/mjas-2016-2003-23

MALAYSIAN JOURNAL OF ANALYTICAL SCIENCES
Published by The Malaysian Analytical Sciences Society
ISSN 1394 - 2506

QUALITY PARAMETERS OF *Curcuma longa* L. EXTRACTS BY SUPERCRITICAL FLUID EXTRACTION (SFE) AND ULTRASONIC ASSISTED EXTRACTION (UAE)

(Parameter Kualiti Ekstrak *Curcuma longa* L. daripada Pengekstrakan Cecair Supergenting (SFE) dan Pengekstrakan Ultrasonik Berbantu (UAE))

Zaibunnisa Abdul Haiyee[1]*, Siti Hafsah Mohd Shah[1], Khudzir Ismail[1], Nooraain Hashim[1], Wan Iryani Wan Ismail[2]

[1]*Faculty of Applied Sciences,*
Universiti Teknologi MARA, 40450 Shah Alam, Selangor, Malaysia
[2]*Faculty of Pharmacy,*
Universiti Teknologi MARA, 42300 Puncak Alam, Selangor, Malaysia

**Corresponding author: nisha@salam.uitm.edu.my*

Received: 24 February 2015; Accepted: 27 October 2015

Abstract

Turmeric is one of the prominently use herbal plants due to its diverse beneficial effects especially in Indian medicine. The rhizome part of the turmeric contains valuable compounds which have been said to owe its antimicrobial effects, anti-cancer, anti-inflammatory and enhance wound healing. Due to its short-life span and perishable properties, the conversion of the rhizome into turmeric extract is desirable. Several methods have been used for extraction such as Soxhlet extraction and pressurized liquid extraction (PLE). However, these techniques are tedious, laborious, time consuming and involves the usage of toxic organic solvent, of which safeness of the end product is doubtful. In this study, a rapid, reliable and green extraction method of supercritical fluid extraction (SFE) and ultrasonic assisted extraction (UAE) were used. SFE without modifier has resulted in 0.0006 mg/100 g of curcuminoids concentration and 5.62 % of yield (dry weight basis). UAE using ethanol was able to produce significantly the highest yield (6.40 %, dry weight basis) and the highest curcuminoids concentration (0.1020 mg/100 g). However, SFE was able to produce extract that contain significantly higher major volatile compounds; tumerone, ar-turmerone and curlone. Therefore, this study proves that both extraction methods were able to produce high quality turmeric extract.

Keywords: Supercritical fluid extraction, Ultrasonic assisted extraction, percentage yield, curcuminoids, volatile compounds

Abstrak

Kunyit merupakan tumbuhan herba yang terkenal disebabkan kebaikannya yang pelbagai terutamanya dalam perubatan masyarakat India. Bahagian rizom kunyit mengandungi sebatian berkhasiat yang dipercayai mempunyai kesan antimikrobial, anti-kanser, anti-keradangan dan juga mempercepatkan kadar penyembuhan luka. Disebabkan kitar hidup yang singkat dan ciri mudah rosak yang terdapat pada kunyit, maka penukaran rizom kunyit kepada ekstrak kunyit adalah amat wajar. Beberapa kaedah pengekstrakan telah digunakan seperti pengekstrakan Soxhlet dan pengekstrakan cecair bertekanan (PLE). Bagaimanapun, kaedah-kaedah tersebut amat rumit, sukar, mengambil masa yang lama serta melibatkan penggunaan pelarut organik bertoksik yang menyebabkan keraguan terhadap tahap keselamatan produk iaitu ekstrak kunyit. Di dalam kajian ini, kaedah pengekstrakan yang pantas, dipercayai serta mesra alam iaitu pengekstrakan cecair supergenting (SFE) dan pengekstrakan ultrasonik berbantu (UAE) telah digunakan. SFE tanpa bahan pengubahsuai telah menghasilkan 0.0006 mg/100 g kepekatan kurkuminoids dan 5.62 % hasil ekstrak kunyit (berdasarkan berat kering). UAE menggunakan etanol telah menghasilkan hasil ekstrak yang ketara tinggi (6.40 %, berdasarkan berat kering) dan nilai kepekatan kurkuminoids tertinggi iaitu 0.1020 mg/100 g. Walaubagaimanapun, SFE telah menghasilkan ekstrak yang mengandungi sebatian meruap yang

signifikan tingginya iaitu tumerone, ar-turmerone dan curlone. Maka, kajian ini membuktikan bahawa kedua-dua kaedah berupaya menghasilkan produk ekstrak kunyit yang berkualiti tinggi.

Kata kunci: Pengekstrakan cecair supergenting, Pengekstrakan ultrasonik berbantu, peratusan hasil, kurkuminoids, sebatian meruap

Introduction

Turmeric (*Curcuma longa* L.) is an economically important plant for the production of turmeric based products. It is well known worldwide as one of the major source of drug both in modern and traditional system of medicine for possessing number of biomolecules credited with myriad of therapeutic activities [1]. The extract of turmeric rhizome consisting of a light (volatile oil) fraction and a heavy (non volatile) fraction of yellowish-brown colour [2]. Ar-tumerone is the marker compound in turmeric oil which contributes to its camphory note [3,4] while curcumin, demethoxycurcumin and bisdemethoxycurcumin and the non-volatile compounds of turmeric acts as colouring agent [2].

Currently, there are several extraction techniques have been used to extract turmeric oils and bioactive components from plant such as Soxhlet distillation, hydrodistillation, solid-liquid extraction and blending. Some of the disadvantages of using these techniques are long extraction time, large consumption of toxic organic solvents and low percentage of oil yield. Supercritical fluid extraction (SFE) and ultrasonic assisted extraction (UAE) are recent techniques that can overcome the shortcomings of traditional methods. SFE has advantages such as environmental friendly as it does not use toxic organic solvent, able to select thermally labile compounds under mild conditions and has a shorter time. Other than SFE, UAE is also one of the alternative methods to replace conventional extraction processes [5]. In most previous literatures, UAE has been known as a tool that assists in the extraction of medicinal compounds or different vegetal materials [6]. It has many advantages such as it can improve extraction efficiency, extraction rate and reduce extraction temperature [7]. UAE also utilizes the ultrasound during extraction that can disrupt the biological cell wall, and thus facilitating the release of contents [8].

In this present work, the efficiency of SFE and UAE techniques on the extraction of *Curcuma longa* L. extract been compared based on the percentage yield, curcuminoids concentration and volatile components.

Materials and Methods

Chemicals and raw materials

Ethanol used for GC-MS and UV-Visible spectrophotometer was of analytical grade and purchased from Merck Sdn. Bhd (Selangor, Malaysia). Fresh turmeric rhizomes (*Curcuma longa* L.) were bought from a local cultivator in Selangor, Malaysia.

Preparation of dried turmeric powder

Fresh turmeric rhizomes were cleaned with water and sliced about 3 mm thick and air-dried at room temperature until the moisture content reached to 10 – 15 % as reported by Zaibunnisa et al. [9]. Samples were then ground and sieved to 2 mm size and were put into sealed plastic bags at chilled temperature until further analysis.

Determination of moisture content

The moisture content of dried turmeric rhizome was determined using AOAC method [10].

Extraction methods

Supercritical Fluid Extraction (SFE)

Extractions were carried out using supercritical carbon dioxide (SC-CO_2) laboratory scale extraction system (TST, Ltd., Taiwan). Turmeric sample was extracted with supercritical carbon dioxide in a continuous-flow extractor. For the first cycle, sample (211 g) of the dried turmeric powder was accurately weighed and packed inside 1 L extraction vessel and fixed into extraction oven. Incoming and outgoing tubes were attached at the bottom and upper part of the vessel, respectively. Liquid CO_2 from the cylinder was passed, delivered and compressed to 22.5 Mpa by air compressor and heated up to the supercritical condition. For the second cycle, similar process was done, but, for the second cycle, organic modifier (ethanol) was introduced into the system by mixing 211 grams of sample

with 50 mL of ethanol before putting it inside the vessel. Operating temperature was set to 40 °C for each cycles. The temperature was measured using a thermocouple device. Both extraction cycles; with and without modifier, were conducted at similar pressure and temperature. The extract was collected in a glass vial and kept for further analysis.

Ultrasonic Assisted Extraction (UAE)

Ultrasonic assisted extraction was performed in an ultrasonic water bath with temperature control. Dried turmeric powder (50 grams) were placed in two glass beaker and mixed with 400 mL water and ethanol, respectively. Samples were exposed to ultrasonic waves for pre-defined time periods (15 minutes) consecutively at 40 °C with frequency about 40 kHz until extraction fully completed. The extracts were collected, filtered and dried using rotary evaporator for further analysis.

Extraction yield

The weight of the extracts were obtained and used for the calculations of the percentage yield as carried out by Zaibunnisa et al. [9].

Curcuminoids concentration

The curcuminoids concentration in the turmeric extract was determined by spectrophotometric method according to Haiyee et al. [11]. Turmeric extract (0.002 g) was dissolved with 10 mL of 95 % ethanol. The absorbance was measured at 425 nm using 95 % ethanol as blank. Curcuminoids concentration in the sample was quantified using standard calibration curve of pure curcumin, concentration of 0.25, 0.50, 0.75, 1.00 and 1.25 ppm. Triplicate analysis were carried out for each treatment.

Volatile compounds

The volatiles were analyzed using Agilent Technologies 6890N Network GC system equipped with an Agilent Technologies 5973 Inert Mass Selective Detector and Agilent 7683 Series Injector [9]. A HP-5MS column was used. GC-MS detection was done using an electroionization system with ionization energy of 70 eV in the 50 to 550 a.m.u. mass range. Column temperature was increased from 60 °C to 325 °C at the rate of 10 °C/min. Initial and final time were 6 minutes and 10 minutes, respectively. Helium was used as the carrier gas, at a flow rate of 1.0 mL/min in splitless mode. Identification of the compounds was done by comparing their relative retention indices and mass spectral fragmentation pattern with those of NIST data inbuilt library provided along with instrument [9].

Results and Discussion

Extraction yield

Percentage yield of *Curcuma longa* L. extract obtained from different extraction methods are shown in Table 1 below.

Table 1. Percentage yields of turmeric extract obtained from different extraction techniques

Extraction techniques	**Yield (%)**	
Ultrasonic assisted extraction	Ethanol 6.40 ± 0.80^{a}	Water 4.72 ± 0.66^{b}
Supercritical fluid extraction	Without modifier 5.62 ± 0.19^{a}	With modifier 5.21 ± 0.46^{a}

Data shown as mean ± S.D. from triplicate determinations, Superscript $^{a\ b}$ within row showed significant differences at (p<0.05)

Generally, extraction using ultrasonic assisted extraction (UAE) were able to produce higher yield compared with supercritical fluid extraction (SFE). Ethanol and water have been chosen as the extraction solvents for ultrasonic study due to the fact that they are safer in handling as compared to other organic solvents like methanol and acetone.

For ultrasonic assisted extraction, with ethanol resulted in significantly higher yield compared to with water. This is due to the function of ethanol that acts as a liquid which received the ultrasonic waves with high intensity and forms bubbles or cavities [7]. This acoustic cavitation, when triggered close to solid surfaces like dried turmeric powder will make the cavity collapse and thus produces high-speed jets of liquid that impact strongly to the solid surface [7] of dried turmeric powder. Eventually, it will lead to pitting and errosion [7] of the dried turmeric surface and easier for the materials being extracted out from the plant matrices. However, the yield obtained from UAE with water was lower which might be due to insolubility of some turmeric compounds in water.

Since SFE only extracting the volatiles, the yield obtained was significantly lower than UAE. This probably due to extraction can be done without the usage of modifier as the carbon dioxide used in the SFE itself will be able to extract out all compounds at supercritical point whereby the temperature and pressure set has reaches the critical point. This was also supported by previous research done by Chang et al. [5], which reported that the use of supercritical carbon dioxide was possible without the addition of co-solvents. Carbon dioxide have been widely used as extracting solvent for SFE as it is non-toxic, available abundantly, non-explosive, can be removed easily from the final extract without leaving a solvent residue [7] and the most important is the low viscosity of carbon dioxide enables it to penetrate into the matrix of the analyte to reach the material being extracted and extract out the material selectively [7]. Additionally, Daneshvand et al. [7] reported that the most effective factors for SFE were pressure and extraction time. The addition of modifier in SFE method did not have an apparent effect to the process since the result showed only slight differences between SFE, with or without modifier. The volume of modifier added to the dried sample might be too little for the modifier to aid in the extraction process. Chang et al. [5] supported this claimed by stated that larger solvent volume can dissolve target components more effectively and thus increase the extraction yield.

Curcuminoids content

The curcuminoids concentration was higher in UAE in comparison to SFE as shown in Table 2.

Table 2. Curcuminoids concentrations (mg/100g) in the extracts obtained from SFE and UAE

Extraction techniques	**Curcuminoids concentration (mg/100g)**	
Ultrasonic assisted extraction	Ethanol 0.1020 ± 0.0013^{a}	Water 0.0014 ± 0.0012^{b}
Supercritical fluid extraction	Without modifier 0.0006 ± 0.0002^{a}	With modifier 0.0005 ± 0.0002^{a}

Data shown as mean ± S.D. from triplicate determinations, All values were standardised to 100 g of turmeric extract, Superscript $^{a\,b}$ within row showed significant differences at ($p<0.05$)

Extraction using UAE has affected to the high concentration of curcuminoids since the fascinating role of UAE is it can avoids degradation of bioactive compounds by quenching of radical in aqueous system and also its ability to achieve targeted hydroxylation of polyphenolics like curcuminoids by potential use of the radical sonochemistry [12]. Results also indicated that curcuminoids concentration is the highest when extracted using UAE with ethanol which was 0.1020 mg/100g. These results correlate well with the findings by Wakte et al. [13] and Li et al. [14] which reported that ethanol gave the highest curcuminoids content among different extraction solvents as more compounds will be dissolved in a polar organic solvent.

Carbon dioxide, the non-polar extracting solvent for SFE causes curcuminoids to only slightly soluble in it. The non-polarity and poor solvation power of SFE-CO_2 causes the failure to quantitate extraction of polar analytes from solid matrices [7]. Although SFE can alter carbon dioxide properties to behave either as a polar or non-polar solvent depending on pressure and temperature employed [7], by subjecting it to the supercritical fluid state and extract certain classes of compounds easily [15], however, it can be concluded that the temperature and pressure used in this study might be not sufficient enough to fully extracted the targeted curcuminoids based on the result presented.

According to Herrero *et al*., [16], the solubility of target compounds in supercritical fluid is strongly influenced by the properties of solvent such as density whereby the properties of solvent are greatly influenced by pressure and temperature.

Volatile compounds composition

Traditionally, volatile compounds of turmeric extract were obtained by hydrodistillation techniques which require long extraction times and causes heat-sensitive volatile compounds easily be destroyed [17]. While solvent extraction of plant materials causes safety hazards in term of the toxic solvent residue in the extract and also may lead to oxidation of aroma of the volatile compounds, especially in the presence of air [17].

The chemical components present in the turmeric extract were identified and presented in Table 3, according to their order of elution from a HP-5MS column. Compounds identification was based on NIST library.

Table 3. Volatile compounds of *Curcuma longa* L. identified from turmeric extract

Volatile compounds	Extraction techniques			
	SFE (modifier)	SFE	UAE (Ethanol)	UAE (Water)
	Relative proportion (area %)			
β-cymene	0.58	n.d.	n.d.	n.d.
β-caryophyllene	n.d.	0.23	n.d.	n.d.
ar-curcumene	0.70	0.55	0.33	n.d.
α-zingiberene	1.15	2.09	1.26	n.d.
ar-turmerone	21.50	10.84	6.84	n.d.
Turmerone	36.14	45.68	33.87	n.d.
Curlone	22.30	21.27	13.92	n.d.
Cuparene	n.d.	0.55	n.d.	n.d.
β-bisabolane	0.21	0.28	0.17	n.d.
β-sesquiphellandrene	1.38	1.74	1.01	n.d.
β-farnesene	0.60	1.74	n.d.	n.d.

n.d. = not-detected

Ten compounds were identified in turmeric extract obtained from SFE, nine compounds for SFE with modifier and seven compounds for UAE with ethanol while no compound was detected for UAE with water. Major compounds found using those techniques were ar-turmerone, turmerone and curlone, while the minor compounds presented using those methods were α-zingiberene, β-sesquiphellandrene, ar-curcumene and β-bisabolane, except for SFE with and without modifier, of which β-farnesene was also detected. In addition, β-cymene was also detected in the extract of SFE with modifier.

The result for this current studies is in accordance with the result obtained from Singh et al. [18] which studied the chemical compositions of four different species of turmeric and they found out that the rhizome of *C. longa* contain mostly sesquiterpinoids and its major constituents are ar-turmerone, β- bisabolene, ar-turmerol, zingiberene, β-caryophyllene while 1,8-cineole was not present. Some volatile compounds such as 1,8-cineole was not present in the extract and this might be due to its low boiling point as well as high volatility characteristics which resulted in their loss during sample preparation like cutting and grinding steps [19] and post-treatment of the extract such as solvent removal using rotary evaporator. Though the major compounds found were similar among them, the composition of each volatile compound was differed based on the percentage area. This is in agreement with the report from Li et al. [14], which stated that different extraction methods gives variation in the contents of volatile compounds.

Most of the compounds for SFE extract show higher percentage area composition than SFE with modifier extract, for instance, SFE contains 45.68 % of turmerone while SFE with modifier extract contains only 36.14 % of turmerone. For UAE technique, only UAE with ethanol reported the presence of volatile compounds but in small percentage area as compared to SFE extract. It is clearly show that SFE will be able to produce more volatile compounds with high percentage area. Extraction techniques that uses organic solvent like ethanol contains lacks of volatile compounds composition due to the losses of the compounds during evaporation process of the solvents [3]. UAE using water as extracting solvent shows the absence of volatile compound since removing of water by evaporation takes longer time and requires high boiling point of water which leads to the losses of more volatile compounds than UAE with ethanol because ethanol was evaporated faster than water. Acoustic cavitation of UAE during vibration also has the probability to cause the loss of light fraction of volatile compounds from dried turmeric material.

Conclusion

Ultrasonic assisted extraction (UAE) was able to produce worthy *Curcuma longa* L. extract in term of high percentage yield and high curcuminoids content. While supercritical fluid extraction (SFE) was also able to produce worthy *Curcuma longa* L. extract based on the volatile compounds present. Both techniques have been chosen as no toxic organic solvent involves in the extraction. In this regard, it can be concluded that a selection of extraction techniques to obtain turmeric extract is dependent on the proposed use of the extracts whether it is based on percentage yield of oleoresin, curcuminoids concentration or volatile compounds composition.

Acknowledgement

The authors would like to thank Universiti Teknologi MARA (UiTM) and the Ministry of Higher Education for technical support and Fundamental Research Grant Scheme (600-RMI/FRGS 5/3 (149/2013)) for funding this study.

References

1. Singh, S., Joshi, R. K. and Nayak, S. (2013). Identification of elite genotypes of turmeric through agroclimatic zone based evaluation of important drug yielding traits. *Industrial Crops and Products*, 43: 165 – 171.
2. Braga, M. E. M., Leal, P. F., Carvalho, J. E. and Meireles, M. A. A. (2003). Comparison of yield, composition and antioxidant activity of turmeric (*Curcuma longa* L.) extracts obtained using various techniques. *Journal of Agricultural & Food Chemistry*, 51: 6604 – 6611.
3. Began, G., Goto, M., Kodama, A. and Hirose, T. (2000). Response surfaces of total oil yield of turmeric (*Curcuma longa*) in supercritical carbon dioxide. *Food Research International*, 33: 341 – 345.
4. Haiyee, Z. A., Saim, N., Said, M., Illias, R. M., Mustapha, W. A. W. and Hassan, O. (2009). Characterization of cyclodextrin complexes with turmeric oleoresin. *Food Chemistry*, 114: 459 – 465.
5. Chang, L-H., Jong, T-T., Huang, H-S., Nien, Y-F. and Chang, C-M. J. (2006). Supercritical carbon dioxide extraction of turmeric oil from *Curcuma longa* Linn and purification of turmerones. *Separation and Purification Technology*, 47: 119 – 125.
6. Vinatoru, M. (2001). An overview of the ultrasonically assisted extraction of bioactive principles from herbs. *Ultrasonics Sonochemistry*, 8: 303 – 313.
7. Daneshvand, B., Ara, K. M. and Raofie, F. (2012). Comparison of supercritical fluid extraction and ultrasound-assisted extraction of fatty acids from quince (*Cydonia oblonga* Miller) seed using response surface methodology and central composite design. *Journal of Chromatography A*, 1252: 1 – 7.
8. Wang, L. and Weller, C. L. (2006). Recent advances in extraction of nutraceuticals from plants. *Trends in Food Science & Technology*, 17: 300 – 312.
9. Zaibunnisa, A. H., Norashikin, S., Mamot, S. and Osman. H. (2009). An experimental design approach for the extraction of volatile compounds from turmeric leaves (*Curcuma domestica*) using pressurised liquid extraction (PLE). *LWT - Food Science and Technology*, 42(1): 233 – 238.
10. Official Method of Analysis, AOAC 17th edn. (2000). Moisture in Spices / I.S Specification No I.S 1797- 1985. *Methods of Test for Spices and Condiments*.
11. Zaibunnisa, A. H. (2009). Inclusion complexes of turmeric oleoresin with β and γ-cyclodextrin. *Ph.D. Thesis*, Universiti Kebangsaan Malaysia.

12. Gilda, S., Kanitkar, M., Bhonde, R. and Paradkar, A. (2010). Activity of water-soluble turmeric extract using hydrophilic excipients. *LWT - Food Science and Technology*, 43(1): 59 – 66.
13. Wakte, P. S., Sachin, B. S., Patil, A. A., Mohato, D. M., Band, T. H. and Shinde, D. B. (2011). Optimization of microwave, ultra-sonic and supercritical carbon dioxide assisted extraction techniques for curcumin from *Curcuma longa*. *Separation and Purification Technology*, 79: 50 – 55.
14. Li, S., Yuan, W., Deng, G., Wang, P., Yang, P. and Aggarwal, B. B. (2011). Chemical Composition and Product Quality Control of Turmeric (*Curcuma longa* L.). *Pharmaceutical Crops*, 2: 28 – 54.
15. Allawzi, M., Al-Otoom, A., Allaboun, H., Ajlouni, A. and Nseirat, F. A. (2011). CO_2 supercritical fluid extraction of Jordanian oil shale utilizing different co-solvents. *Fuel Processing Technology*, 92(10): 2016 – 2023.
16. Herrero, M., Castro-Puyana, M., Mendiola, J. A. and Ibañez, E. (2013). Compressed fluids for the extraction of bioactive compounds. *TrAC Trends in Analytical Chemistry*, 43: 67 – 83.
17. Sovilj, M. N., Nikolovski, B. G. and Spasojević, M. Đ. (2011). Critical review of SFE of selected spice plant materials. *Macedonian Journal of Chemistry and Chemical Engineering*, 30(2): 197 – 220.
18. Singh, G., Singh, O. P. and Maurya, S. (2002). Chemical and biocidal investigations on essential oils of some Indian *Curcuma* species. *Progress in Crystal Growth and Characterization of Materials*, 45: 75 – 81.
19. Gounder, D. K. and Lingamallu, J. (2012). Comparison of chemical composition and antioxidant potential of volatile oil from fresh, dried and cured turmeric (*Curcuma longa*) rhizomes. *Industrial Crops and Products*, 38: 124 – 131.

Malaysian Journal of Analytical Sciences, Vol 20 No 3 (2016): 633 - 641
DOI: http://dx.doi.org/10.17576/mjas-2016-2003-24

MALAYSIAN JOURNAL OF ANALYTICAL SCIENCES
Published by The Malaysian Analytical Sciences Society
ISSN 1394 - 2506

CONDUCTIVITY AND THERMAL STABILITY OF SOLID ACID COMPOSITES $CsH_2PO_4/NaH_2PO_4/SiO_2$

(Konduktiviti dan Kestabilan Terma Asid Pepejal Komposit $CsH_2PO_4/NaH_2PO_4/SiO_2$)

Norsyahida Mohammad[1], Abu Bakar Mohamad[1, 2], Abdul Amir Hassan Kadhum[2], Loh Kee Shyuan[1]*

[1]*Fuel Cell Institute*
[2]*Department of Chemical and Process Engineering, Faculty of Engineering and Built Environment*
Universiti Kebangsaan Malaysia, 43600 UKM Bangi, Selangor, Malaysia

**Corresponding author: ksloh@ukm.edu.my*

Received: 5 February 2016; Accepted: 22 April 2016

Abstract

Solid acid composites $CsH_2PO_4/NaH_2PO_4/SiO_2$ with different mole ratios of CsH_2PO_4 and NaH_2PO_4 to SiO_2 were synthesized and characterized. Preliminary infrared measurements of CsH_2PO_4 and its composites indicated that hydrogen bonds breaking and formation were detected between 1710 to 2710 cm^{-1}, while the rotation of phosphate tetrahedral anions occurred between 900 and 1200 cm^{-1}. The superprotonic transition of $CsH_2PO_4/NaH_2PO_4/SiO_2$ composite was identified at superprotonic temperatures between 230 and 260 °C, under atmospheric pressure. This study reveals higher conductivity values for composites with higher CsH_2PO_4 (CDP) content. Solid acid composite CDP 613 appeared as the composite with the highest conductivity that is 7.2 x 10^{-3} S cm^{-1} at 230 °C. Thermal stability of the solid acid composites such as temperature of dehydration, melting and decomposition were investigated. The addition of NaH_2PO_4 lowers the dehydration temperature of the solid acid composites.

Keywords: solid acid, conductivity, thermal analysis, caesium dihydrogen phosphate, fuel cell

Abstrak

Asid pepejal komposit $CsH_2PO_4/NaH_2PO_4/SiO_2$ dengan nisbah mol CsH_2PO_4 kepada SiO_2 dan NaH_2PO_4 kepada SiO_2 yang berbeza telah disintesis dan dicirikan dalam ujikaji ini. Pencirian awal sinar inframerah menunjukkan bahawa pemecahan dan pembentukan ikatan hidrogen dikesan antara 1710 cm^{-1} dan 2710 cm^{-1}, manakala putaran anion tetrahedron fosfat berlaku diantara 900 cm^{-1} dan 1200 cm^{-1}. Fasa peralihan berkonduktiviti tinggi bagi asid pepejal komposit $CsH_2PO_4/NaH_2PO_4/SiO_2$ telah dikenal pasti antara suhu 230 hingga 260 °C, di bawah tekanan atmosfera. Nilai kekonduksian proton adalah lebih tinggi bagi komposit yang mempunyai kandungan CsH_2PO_4 (CDP) yang lebih tinggi. Asid pepejal komposit CDP 613 telah muncul sebagai komposit dengan kekonduksian tertinggi iaitu 7.2 x 10^{-3} S cm^{-1} pada suhu 230 °C. Kestabilan terma asid pepejal komposit seperti suhu dehidrasi, takat lebur dan penguraian telah dikenal pasti melalui analisis termogravimetri dan kalorimeter imbasan perbezaan. Penambahan NaH_2PO_4 merendahkan suhu dehidrasi asid pepejal komposit.

Kata kunci: asid pepejal, kekonduksian, analisa terma, sesium dihidrogen fosfat, sel bahanapi

Introduction

Solid acids emerged as a potential solid electrolyte for fuel cell applications due to its high proton conductivity, also known as superprotonic conductivity as the conductivity values increases by 2 to 3 orders of magnitude at intermediate temperatures between 100 to 250 °C, accompanied by phase transition [1]. Solid acids are defined by the basic chemical formula $M_aH_b(XO_4)_c$ where M is a monovalent or divalent metal cation, XO_4 is a tetrahedral oxy-anion, and a, b, c are integers [2]. Solid acids caesium dihydrogen phosphate, CsH_2PO_4 (CDP) and caesium

hydrogen sulphate, $CsHSO_4$ (CHS) have high conductivity values of 2.2 x 10^{-2} S cm^{-1} at 240 °C [3, 4] and 10^{-2} S cm^{-1} at 141 °C [1], respectively. They are comparable to Nafion®, a perfluorosulfonic acid polymer with conductivity value ranging from 9 x 10^{-3} S cm^{-1} to 1.2 x 10^{-1} S cm^{-1} [1, 5] between 80 °C and 100 °C [6], which has been commercialized for application in proton exchange membrane fuel cells (PEMFC), direct methanol fuel cell(DMFC) [7] and micro DMFC [8] due to its stability and robustness.

The disadvantage of Nafion membrane is that humidification is needed during operation of the fuel cell, hence limit the operating temperature to about 100 °C. This escalates the issues of catalyst inefficiency and intolerance to carbon monoxide associated with PEMFC working at low temperatures. Therefore, solid acid emerged as a potential alternative to Nafion as it is able to operate without hydration at higher temperatures, which lowers the operating costs and eliminate the issues of catalyst inefficiency due to carbon monoxide poisoning associated with PEMFC working at low temperatures [9].

It has been found that solid acids with sulphates (SO_4) and selenates (SeO_4) gradually decompose in hydrogen-rich surroundings [10], producing H_2S and H_2Se that are poison to the Pt catalyst at the anode [11, 12] and is further accelerated by the presence of anode catalyst [1]. CHS reacts in hydrogen-rich surroundings to produce H_2S such as in Equation 1.

$$2CsHSO_4 + 4H_2 \rightarrow Cs_2SO_4 + 4H_2O + H_2S \quad (1)$$

Studies have been focusing on CDP [3, 4, 13, 14] due to its stability in hydrogen-rich surroundings. Solid acid is mixed with another solid acid and/or a hygroscopic oxide to produce a solid acid composite with higher conductivity values and improved thermal properties and stability. Two or more solid acids are mixed to widen the temperature range of superprotonic conductivity and induce superprotonic conductivity in solid acids without superprotonic conductivity at atmospheric pressure [15]. Martsinkevich and Ponomareva [16] in the study of CDP partially substituted with sodium dihydrogen phosphate, NaH_2PO_4 (SDP) found that mixed salt solid acid $Cs_{1-x}Na_xH_2PO_4$ with x value up to 0.2 increases the low temperature conductivity of CDP up to 2 orders of magnitude. This study investigates the effect of adding SDP into the CDP/SiO_2 composite. Addition of hygroscopic oxides such as silica (SiO_2), ZrO_2, TiO_2 and Al_2O_3 produces solid acid composites which are more robust and less brittle [2, 15]. The hydrophilic property of SiO_2 enhance proton conductivity of the solid acid composite CDP/SiO_2 [17, 18] and the structure of SiO_2 matrix in the composites of CDP/Al_2O_3 [15] and CDP/SiP_2O_7 [19] enhance the thermal stability of the composites.

Studies on CDP composites include synthesis and characterization of CDP/SiO_2 such as phase transition and proton transport characteristics [20], effects of different types of silica material [18] and different models of protonic conductivity at the ionic salt and oxide interface [21]. In this study, we investigate the properties of solid acid composite $CsH_2PO_4/NaH_2PO_4/SiO_2$, such as the conductivity of the composite via electrochemical impedance spectroscopy, functional groups identification via Fourier-transform infrared spectroscopy and thermal stability via thermogravimetric analysis and differential scanning calorimetry.

Materials and Methods

CDP was synthesized by mixing stoichiometric amounts of caesium carbonate, Cs_2CO_3 (ReagentPlus®, ≥ 99% Sigma Aldrich) and phosphoric acid H_3PO_4 (≥85 wt% in H_2O, Sigma Aldrich) according to the following reaction (Equation 2):

$$Cs_2CO_3 + 2H_3PO_4 \rightarrow 2CsH_2PO_4 + CO_2 + H_2O \quad (2)$$

In CDP synthesis, measured amount of Cs_2CO_3 was dissolved in distilled water. Surfactant powder, Cetyltrimethylammoniumbromide, CTAB (BioXtra®, ≥ 99 % Sigma Aldrich) was dissolved in ethanol separately and added to the Cs_2CO_3 solution to reduce water surface tension and hence assist particle dispersion. The mixture was then stirred for 10 minutes until clear solution was produced. Phosphoric acid was added, drop-wise into the mixture with continuous stirring for another 10 minutes. Acetone is added excessively to the mixture while stirring for another 30 minutes and the solution is vacuum-filtered to produce CDP in the form of white precipitate. The

white precipitate is washed several times by mixing with excess acetone and vacuum-filtered to remove remaining surfactants. The synthesized CDP is dried at 130 °C for 24 hours to eliminate absorbed water and grinded to produce powdered CDP.

Solid acid composites $CsH_2PO_4/NaH_2PO_4/SiO_2$ of different molar ratios as tabulated in Table 1 were synthesized via the sol gel method, the similar method used synthesize electrolyte of a solid oxide fuel cell[22]. The synthesized CDP and NaH_2PO_4, SDP (ReagentPlus®, ≥ 99 % Sigma Aldrich) powders were mixed prior addition to tetraethyl orthosilicate, TEOS solution. TEOS solution was prepared by mixing TEOS (Reagent Grade®, 98 % Sigma Aldrich) with ethanol, water and hydrochloric acid (1 mol L^{-1}, Merck) in mole ratio of 1:8:30:0.05. The solid acid and TEOS mixture was stirred until all powders were dissolved. The mixture was kept at 40 °C for 24 hours and further dried at 150 °C for 15 hours to produce white precipitate solid acid composite, $CsH_2PO_4/NaH_2PO_4/SiO_2$. The resultant precipitate was then grinded to produce fine solid acid composite powders.

Table 1. Solid acid composites synthesized

Solid acid sample	**CsH_2PO_4:NaH_2PO_4:SiO_2 molar ratio**
CDP 631	6:3:1
CDP 721	7:2:1
CDP 811	8:1:1
CDP 613	6:1:3
CDP 523	5:2:3
CDP 433	4:3:3

Solid acid CDP and its composites were characterized via electrochemical impedance spectroscopy, Fourier-transform infrared spectroscopy, thermogravimetric analysis and differential scanning calorimetry. The solid acids were tested for its protonic conductivity via electrochemical impedance spectroscopy (EIS). The pure CDP and its composite powders were pressed into pellets of 1 mm thickness and 13 mm diameter by uniaxially pressing at 3 tonnes cm^{-2} at room temperature for 1 minute. The pellets were calcined at 260 °C for 1 hour in air, painted with silver (Ag) suspension and heat-treated to improve contacts of the surfaces to the current collector, prior to assembly in the pellet holder for impedance measurements. The pellet was sandwiched between two square platinum meshes which acts as the current collector, placed inside a metal pellet holder with ceramic lining and connected to an Autolab impedance analyser. The impedance readings were taken in air at 180 °C, 210 °C, 230 °C 250 °C and 260 °C with frequency of 1.0 x 10^{-2} to 1.0 x 10^{6} Hz and current of 0.01A. The measured data was analyzed using the Nova software package where the proton conductivity value was determined from the impedance data plotted on real and imaginary axes, Z' and -Z'' respectively, known as Nyquist plot. The curve was fitted using the equivalent circuit as in Figure 1. The proton conductivity value, σ for pure CDP and $CsH_2PO_4/NaH_2PO_4/SiO_2$ composites were calculated using the resistance value, R and is given by the following Equation 3:

$$\text{Conductivity, } \sigma \text{ (S cm}^{-1}) = {}^{1/R(\Omega)}\Big/_{A(cm^2)/l(cm)} \quad (3)$$

Fourier-transform infrared spectroscopy (FTIR) is used to identify functional groups that are present in the solid acid materials. Solid acid samples were mixed with grounded KBr with solid acid to KBr weight ratio of 1 to 300 and pressed into a pellet for FTIR measurements. The spectrum was collected via Perkin-Elmer 125 spectrometer between 200 and 4000 cm^{-1} wavenumbers at room temperature.

Thermal stability of the solid acid materials were measured via thermogravimetric analysis (TGA) and differential scanning calorimetry (DSC). Solid acid decomposition is identified by measuring mass loss as a function of temperature via TGA analysis. DSC measurements display endothermic or exothermic peaks that appear during

heating of the solid acid, which are usually related to the phase transition of solid acid. Both TGA and DSC tests were run simultaneously using STA 449 F3 Netzsch simultaneous TGA-DSC between 30 °C and 600 °C with heating rate of 5 °C min^{-1} under nitrogen flow.

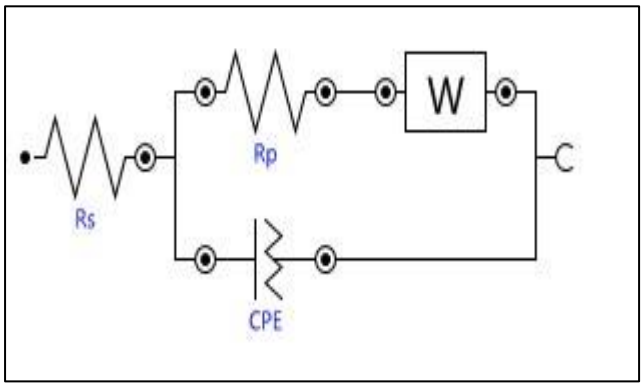


Figure 1. The equivalent circuit used to analyze the impedance data

Results and Discussion

Proton conductivity of $CsH_2PO_4/NaH_2PO_4/SiO_2$ composites

The Nyquist plot for each CDP composite has a similar pattern to the plot for CDP 613 at various temperatures as shown in Figure 2. The semi-circle of the fitted plot represents the impedance of the bulk of the solid acid electrolyte and the straight line represents the semi-infinite diffusion behaviour of the solid-gas interface of the solid acid electrolyte. The conductivity of CDP 613 increases as temperature increases from 180 °C to 210 °C and 230 °C where the conductivity is the highest. However, as temperature is increased to 250 °C and 260 °C, the conductivity drops slightly, indicating that the optimum temperature with highest conductivity value is at 230 °C for CDP 613.

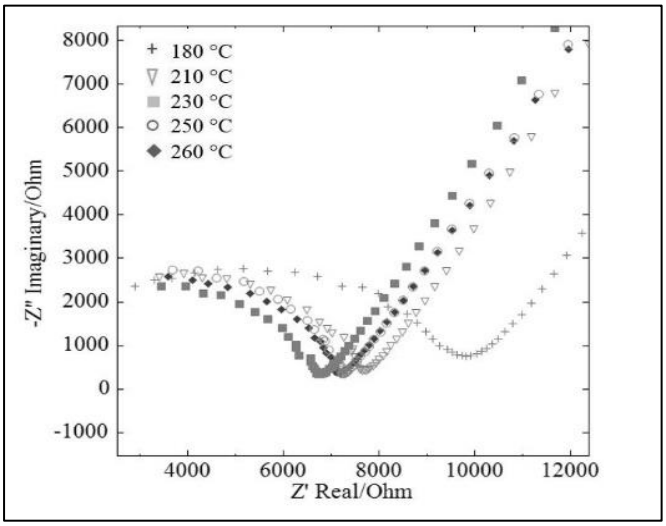


Figure 2. The impedance measurement of CDP 613 at 180 °C, 210 °C, 230 °C, 250 °C and 260 °C plotted in Nyquist plot.

Conductivity measurements were conducted for all CDP composites at 180°C, 210°C, 230°C, 250°C and 260°C. The highest conductivity values of pure CDP and its composites are tabulated in Table 2. It was found that the superprotonic conductivity of pure CDP occurs at about 230 °C with conductivity value of 1.9 x 10^{-2} S cm^{-1}, comparable to proton conductivity value of 2.2 x 10^{-2} S cm^{-1} at 240 °C obtained by Haile et al. [3]. Solid acid composite CDP 613 has the highest conductivity value of 7.2 x 10^{-3} S cm^{-1} at about 230 °C compared to other composites. The conductivity of CDP 613 composite is lower than the conductivity of pure CDP at the same temperature. The presence of SiO_2 which is non-conductive, slightly reduces the conductivity of solid acid composites, due to the imperfect interconnections between the solid acid and SiO_2 [15].

Table 2. The highest conductivity value for each solid acid

Solid acid	**Highest conductivity value, σ (S cm^{-1})**	**T_{sp} (°C)**
CDP [3]	2.2 x 10^{-2}	240
CDP (pure)	1.9 x 10^{-2}	230
CDP 631	5.0 x 10^{-3}	230
CDP 721	1.7 x 10^{-3}	250
CDP 811	8.5 x 10^{-4}	250
CDP 613	7.2 x 10^{-3}	230
CDP 523	2.0 x10^{-3}	260
CDP 433	2.6 x 10^{-3}	250

In previous work by Boysen [2], it was found that SDP alone melts without reaching the superprotonic phase. A recent study by Marsinkevich [16] highlights the effect of adding SDP up to 20 % of CDP/SDP composite, where conductivity increases by 2 orders of magnitude around 160 °C to 200 °C compared to pure CDP. In this study, we found that the addition of SDP into the CDP/SiO_2 composites increases the conductivity value of composites with 10 % SiO_2 that are CDP 631, CDP 721 and CDP 811, whilst reducing the temperature where superprotonic conductivity of the composites occur. The conductivity of $Cs_{1-x}Na_xH_2PO_4$ composite increases by 2 orders of magnitude with x values up to 0.2 at 160 °C to 200 °C, lower than the superprotonic temperature of pure CDP that is 240 °C [16]. This is associated with the structural order-disorder movements caused by Cs^+ and Na^+ cations coexisting within the lattice of the solid acid composites.

Structure and thermal stability of $CsH_2PO_4/NaH_2PO_4/SiO_2$ composites

The infrared spectra of CDP is shown in Figure 3 where well separated peaks were observed at 2710 cm^{-1}, 2310 cm^{-1} and 1710 cm^{-1} which are assigned to the stretching of oxygen-hydrogen bonds in and out of planes also known as the 'ABC bonds of OH', while the strong absorption bands between 900 cm^{-1} and 1200 cm^{-1} were attributed to the internal vibrations of $H_2PO_4^-$ oxyanion that are the vibrations of two main groups PO_2 and $P(OH)_2$. The PO_2 stretching modes result in more intense bands compared to the $P(OH)_2$ stretching modes. The wavelength of PO_2 stretching modes are due to PO_2 symmetric and asymmetric stretching measured at 941 cm^{-1} and 1070 cm^{-1} respectively. Weaker bands of $\delta_{P\text{-}O\text{-}H}$ in-plane bending and $\gamma_{P\text{-}O\text{-}H}$ out-of-plane bending are identified at 1130 cm^{-1} and 1213 cm^{-1} respectively and is comparable to the bands of CDP nanoparticles that are 1140 cm^{-1} and 1185 cm^{-1} respectively [23]. The generated Cs···O-H bond is represented by the peaks within 300 cm^{-1} to 500 cm^{-1} region. The IR spectra of CDP and its composites measured in this work is compared to previous works as in Table 3.

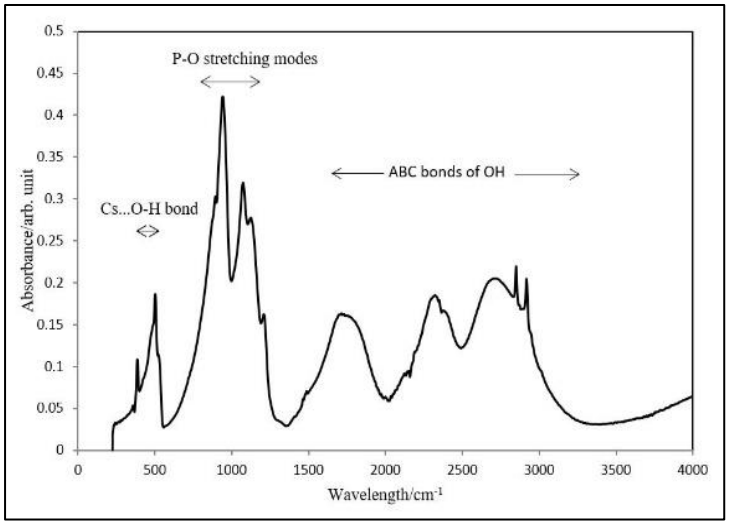


Figure 3. The FTIR absorbance bands for CDP.

Table 3. The comparison of functional groups present in solid acid materials

Solid acid sample	Reference	Wavelength (cm^{-1})					
		Cs …O-H bond	P-O_2 stretching		O-H stretching		
			symmetric	asymmetric			
CDP (pure)	This study	502	941	1070	1710	2310	2710
CDP nanoparticles	[23]	490	940	1070	1650	2300	2650
CDP	[18]	N/A	950	1100	1700	2300	2700

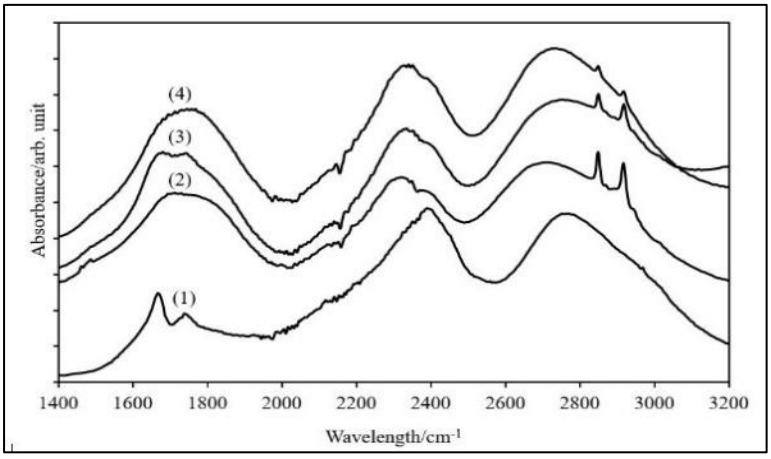


Figure 4. Infrared spectra of (1) sodium dihydrogen phosphate, (2) caesium dihydrogen phosphate, (3) CDP 811 composite and (4) CDP 631 composite.

The FTIR measurement conducted for CDP composites found that the addition of SDP into the solid acid composite did not produce any obvious change in the pattern of the absorbance bands for ABC bonds of OH, as depicted in Figure 4 for CDP 631 and CDP 811. However, it increases the frequency of the absorbance bands slightly, indicating lengthening of P-O¨H and shortening of P-O bonds. This is similar to the trend observed by Martsinkevich and Ponomareva [16].

The DSC measurements for CDP and its composites are presented in Figure 5. Decomposition occurs in these solid acids according to the following dehydration pathway (Equation 4) [24-26]:

$$CsH_2PO_4 \rightarrow Cs_2H_2P_2O_7 \rightarrow CsPO_3 \quad (4)$$

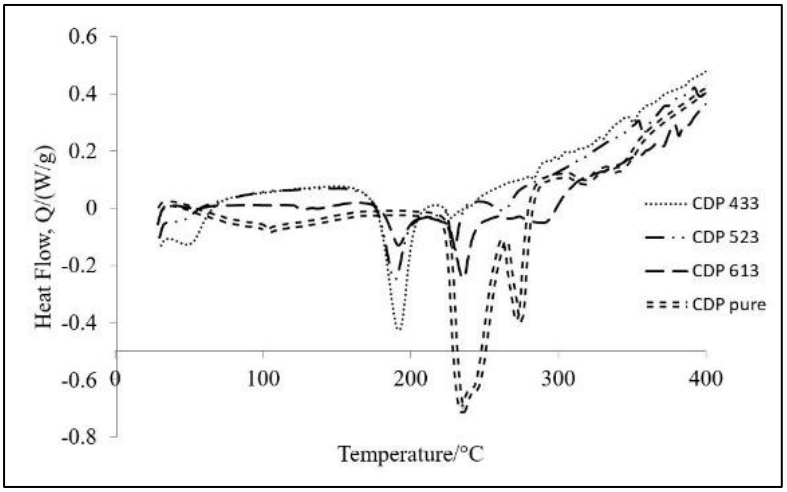


Figure 5. DSC curves for CDP and its composites.

The first reaction pathway ($CsH_2PO_4 \rightarrow Cs_2H_2P_2O_7$) occurs over temperature range of 220 °C to 260 °C due to thermal decomposition of CDP to form another compound, dicaesium dihydrogen pyrophosphate $Cs_2H_2P_2O_7$. This is followed by the formation of $CsPO_3$ around temperature range of 265 °C to 285 °C. At about 320 °C, decomposition occurs. This is in agreement with the findings by Hosseini et al. [24]. The CDP composites that are CDP 433, CDP 523 and CDP 613 with different ratios of SDP and SiO_2 shows two distinctive peaks in DSC measurements at lower temperatures around 190 °C and 230 °C as compared to the DSC curve of pure CDP. The first reaction pathway of the composite producing $Cs_2H_2P_2O_7$ occurs over temperature range of 175 °C to 210 °C followed by the formation of $CsPO_3$ around temperature range of 220 °C to 255 °C, both occurrence at lower temperature than pure CDP.

The lower temperature dehydration of CDP composites may be associated with the presence SDP in the composite. DSC analysis of SDP revealed three distinctive peaks at 60 °C, 210 °C and 345 °C as in Figure 6. It is noteworthy that due to the hygroscopic nature of the solid acid, the first peak at 60 °C represent the release of water molecules at the surface of the solid acids during the DSC measurement. This is supported by thermal analysis of SDP [16], where dehydration peaks were identified at 208 °C and 280 °C. Similarly, prior studies indicated that SDP undergo dehydration at a lower temperature such as at 169 °C [27] and 200 °C [2]. Therefore, by adding SDP into the solid acid composites, dehydration occurs at a lower temperature than pure CDP.

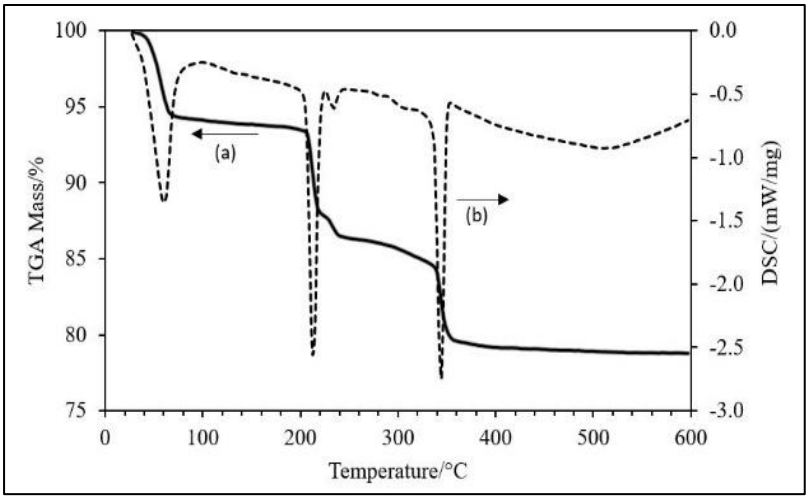


Figure 6. TGA (a) and DSC (b) curves for solid acid NaH_2PO_4, SDP

Conclusion

Conductivity measurements revealed solid acid composite CDP 613 as the composite with the highest conductivity that is 7.2 x 10^{-3} S cm^{-1} at about 230 °C compared to the other composites. This conductivity value is lower than the conductivity of pure CDP due to the defective interconnections between the solid acid and the non-conductive SiO_2 particles. The addition of SDP into the CDP/SiO_2 composites increases the conductivity of composites whilst reducing the temperature at which the superprotonic transition occur. Thermal analysis showed earlier onset of dehydration for CDP/SDP/SiO_2 composites compared to pure CDP, which is most likely due to the presence of SDP which has lower dehydration and melting point. The mechanism of proton transport within CDP was confirmed to occur by breaking and formation of hydrogen bonds and rotation of the phosphate tetrahedron anions, as identified via the FTIR analysis where distinctive peaks were observed from 1710 to 2710 cm^{-1} and 900 to 1200 cm^{-1} respectively.

Acknowledgement

The authors gratefully acknowledge the financial support by the Malaysian Ministry of Higher Education (MOHE) through the Exploratory Research Grant Scheme (ERGS/1/2012/TK07/UKM/01/1) and the Universiti Kebangsaan Malaysia (UKM) through University Research Grant (DLP-2013-038).

References

1. Dupuis, A.-C. (2011). Proton exchange membranes for fuel cells operated at medium temperatures: Materials and experimental techniques. *Progress in Materials Science*, 56(3): 289 - 327.
2. Boysen, D. A. (2004). Superprotonic solid acids: structure, properties, and applications (PhD Dissertation), California Institute of Technology. Retrieved from http://resolver.caltech.edu/CaltechETD:etd-05282004-155105
3. Haile, S. M., Chisholm, C. R. I., Sasaki, K., Boysen, D. A. and Uda, T. (2006). Solid acid proton conductors: from laboratory curiosities to fuel cell electrolytes. *Faraday Discussions*, 134: 17 - 39.
4. Taninouchi, Y.-K., Uda, T., Awakura, Y., Ikeda, A. and Haile, S. M. (2007). Dehydration behavior of the superprotonic conductor CsH_2PO_4 at moderate temperatures: 230 to 260 °C. *Journal of Materials Chemistry*, 17(30): 3182 - 3189.
5. Alberti, G., Casciola, M., Pica, M., Tarpanelli, T. and Sganappa, M. (2005). New preparation methods for composite membranes for medium temperature fuel cells based on precursor solutions of insoluble inorganic compounds. *Fuel Cells*, 5(3): 366 - 374.
6. Peighambardoust, S. J., Rowshanzamir, S. and Amjadi, M. (2010). Review of the proton exchange membranes for fuel cell applications. *International Journal of Hydrogen Energy*, 35(17): 9349 - 9384.

7. Jaafar, J., Ismail, A. F., Matsuura, T. and Norddin, M. N. A. M. (2013). Stability of SPEEK-triaminopyrimide polymer electrolyte membrane for direct methanol fuel cell application. *Sains Malaysiana*, 42(11): 1671 - 1677.
8. Hashim, N., Kamarudin, S. K. and Daud, W. R. W. (2010). Design and development of micro direct methanol fuel cell (μDMFC) for portable application. *Sains Malaysiana*, 39(6): 1015 - 1023.
9. Haile, S. M., Boysen, D. A., Chisholm, C. R. I. and Merle, R. B. (2001). Solid acids as fuel cell electrolytes. *Nature*, 410: 910 - 913.
10. Unnikrishnan, S. (2009). Micromachined dense palladium electrodes for thin-film solid acid fuel cells. (PhD Dissertation), University of Twente, Enschede. Retrieved from http://doc.utwente.nl/68765/
11. Haile, S. M. (2003). Materials for fuel cells, in Materials Today. Elsevier Science Ltd.
12. Merle, R. B., Chisholm, C. R. I., Boysen, D. A. and Haile, S. M. (2002). Instability of sulfate and selenate solid acids in fuel cell environments. *Energy & Fuels*, 17(1): 210 - 215.
13. Botez, C. E., Hermosillo, J. D., Zhang, J., Qian, J., Zhao, Y., Majzlan, J., Chianelli, R. R. and Pantea, C. (2007). High-temperature phase transitions in CsH_2PO_4 under ambient and high-pressure conditions: A synchrotron x-ray diffraction study. *The Journal of Chemical Physics*, 127(19): 194701 -194706.
14. Baranov, A. I., Khiznichenko, V. P. and Shuvalov, L. A. (1989). High temperature phase transitions and proton conductivity in some kdp-family crystals. *Ferroelectrics*, 100(1): 135 - 141.
15. Baranov, A. I., Grebenev, V. V., Khodan, A. N., Dolbinina, V. V. and Efremova, E. P. (2005). Optimization of superprotonic acid salts for fuel cell applications. *Solid State Ionics*, 176(39–40): 2871 - 2874.
16. Martsinkevich, V. V. and Ponomareva, V. G. (2012). Double salts $Cs_{1-x}M_xH_2PO_4$ (M = Na, K, Rb) as proton conductors. *Solid State Ionics*, 225(0): 236 - 240.
17. Otomo, J., Minagawa, N., Wen, C.-j., Eguchi, K. and Takahashi, H. (2003). Protonic conduction of CsH_2PO_4 and its composite with silica in dry and humid atmospheres. *Solid State Ionics*, 156(3–4): 357 - 369.
18. Ponomareva, V. G. and Shutova, E. S. (2007). High-temperature behavior of CsH_2PO_4 and CsH_2PO_4–SiO_2 composites. *Solid State Ionics*, 178(7–10): 729 - 734.
19. Matsui, T., Kukino, T., Kikuchi, R. and Eguchi, K. (2005). An intermediate temperature proton-conducting electrolyte based on a CsH_2PO_4/SiP_2O_7 composite. *Electrochemical and Solid-State Letters*, 8(5): 256 - 258.
20. Otomo, J., Ishigooka, T., Kitano, T., Takahashi, H. and Nagamoto, H. (2008). Phase transition and proton transport characteristics in CsH_2PO_4/SiO_2 composites. *Electrochimica Acta*, 53(28): 8186 - 8195.
21. Naidoo, S. (2004). Cesium Hydrogen Sulphate and Cesium Dihydrogen Phosphate Based Solid Composite Electrolyte for Fuel Cell Application. University of the Western Cape.
22. Panuh, D., Muchtar, A., Muhamad, N., Majlan, E.H. and Daud, W. R. W. (2014). $Sm_{0.2}Ce_{0.8}O_{1.90}$ (SDC)/ $Y_{0.25}Bi_{0.75}O_{1.5}$ (YSB) bilayered electrolytes for intermediate solid oxide fuel cells. *Sains Malaysiana*, 43(11): 1769 - 1774.
23. Hosseini, S., Wan Daud, W.R., Badiei, M., Kadhum, A. A. H. and Mohammad, A. B. (2011). Effect of surfactants in synthesis of CsH_2PO_4 as protonic conductive membrane. *Bulletin of Materials Science*, 34(4): 759 - 765.
24. Hosseini, S., Mohamad, A., Kadhum, A. and Wan Daud, W. R. (2010). Thermal analysis of CsH_2PO_4 nanoparticles using surfactants CTAB and F-68. *Journal of Thermal Analysis and Calorimetry*, (1): 197 - 202.
25. Boysen, D. A., Haile, S. M., Liu, H. and Secco, R. A. (2003). High-Temperature Behavior of CsH_2PO_4 under both ambient and high pressure conditions. *Chemistry of Materials*, 15(3): 727 - 736.
26. Hosseini, S. (2009). Synthesis of proton conducting membrane using cesium dihydrogen phosphate nanoparticles for the fabrication of membrane electrode assembly for fuel cell. Universiti Kebangsaan Malaysia.
27. Gupta, L. C., Rao, U. R. K., Venkateswarlu, K. S. and Wani, B. R. (1980). Thermal stability of CsH_2PO_4. *Thermochimica Acta*, 42(1): 85 - 90.

Malaysian Journal of Analytical Sciences, Vol 20 No 3 (2016): 642 - 650
DOI: http://dx.doi.org/10.17576/mjas-2016-2003-25

MALAYSIAN JOURNAL OF ANALYTICAL SCIENCES
Published by The Malaysian Analytical Sciences Society
ISSN 1394 - 2506

FABRICATION OF Y-TZP FOR DENTAL CROWNS APPLICATIONS BY COMBINING SLIP CASTING AND COLD ISOSTATIC PRESSING

(Pembangunan Y-TZP untuk Aplikasi Korona Gigi melalui Penggabungan Kaedah Penuangan Buburan dan Penekanan Isostatik Sejuk)

Chin Chuin Hao[1], Andanastuti Muchtar[1,2]*, Che Husna Azhari[1], Masfueh Razali[3], Mohamed Aboras[1]

[1]*Department of Mechanical and Materials Engineering, Faculty of Engineering and Built Environment*
[2]*Fuel Cell Institute*
Universiti Kebangsaan Malaysia, 43600 UKM Bangi, Selangor, Malaysia.
[3]*Periodontology Department, Faculty of Dentistry,*
Universiti Kebangsaan Malaysia, Jalan Raja Muda Abdul Aziz, 50300 Kuala Lumpur, Malaysia.

**Corresponding author: muchtar@ukm.edu.my*

Received: 5 February 2016; Accepted: 22 April 2016

Abstract

Yttria-stabilized tetragonal zirconia polycrystalline (Y-TZP) is a popular material for dental restoration because of its outstanding mechanical properties and biocompatibility. Cold isostatic pressing (CIP) and slip casting are among several consolidation methods for Y-TZP. These methods produce Y-TZP with high mechanical properties. This study aims to enhance the mechanical properties of Y-TZP by combining slip casting and CIP. Y-TZP samples were fabricated using CIP, slip casting, and their combination. Subsequently, the green bodies of the samples were sintered at 1600 °C. Their mechanical properties (density and hardness) were tested and their microstructures were scrutinized under a scanning electron microscope. Compared with the other two methods, the combined method significantly improved the mechanical properties of Y-TZP. In addition, the combined method also produced a compact and homogeneous microstructure. Therefore, the combination of slip casting and CIP is recommended in the production of Y-TZP with high mechanical properties for dental crown applications.

Keywords: cold isostatic pressing, slip casting, colloidal processing

Abstrak

Polikristal tetragon zirkonia yang distabilkan dengan yttria (Y-TZP) merupakan bahan restorasi pergigian yang popular disebabkan sifat mekanik dan bioserasi yang baik. Kaedah penekanan isostatik sejuk (CIP) dan penuangan buburan adalah kaedah pengukuhan yang lazim digunakan untuk Y-TZP. Kedua-dua kaedah ini berupaya menghasilkan Y-TZP yang bersifat mekanik tinggi. Kajian ini bertujuan meningkatkan sifat mekanik Y-TZP melalui gabungan penuangan buburan dan CIP. Sampel Y-TZP dihasilkan melalui kaedah penuangan buburan, CIP dan gabungan kedua-dua kaedah tersebut. Seterusnya, jasad anum yang terhasil disinter pada suhu 1600 ˚C. Sifat mekanik sampel Y-TZP (ketumpatan dan kekerasan) diuji dan mikrostruktur juga diteliti di bawah mikroskop elektron imbasan. Kaedah gabungan didapati meningkatkan sifat mekanik Y-TZP dengan ketara. Selain itu, mikrostruktur yang padat dan homogen juga diperolehi. Justeru, gabungan kaedah penuangan buburan dan CIP dicadangkan untuk penghasilan Y-TZP yang bersifat mekanik tinggi dalam aplikasi korona gigi.

Kata kunci: penekanan isostatik sejuk, penuangan buburan, pemprosesan berkoloid

Introduction

Tetragonal zirconia polycrystalline partially stabilized by 3 mol% of yttria (3Y-TZP) is well known for its superior mechanical properties among other dental ceramics [1, 2]. Piconi et al. [3] remarked that Y-TZP has high flexural strength (> 900 MPa, four-point bending), high fracture toughness (approximately 10 $MPa.m^{1/2}$) and high hardness (12-14 GPa). The outstanding mechanical properties of Y-TZP are associated with the transformation toughening mechanism that involves phase transformation from tetragonal (*t*) to monoclinic (*m*) [4]. Given this mechanism, Y-TZP possesses adequate mechanical properties for clinical use as fixed prostheses when subjected to high stresses. Meanwhile, the excellent biocompatibility and optical properties of Y-TZP make it a suitable material for aesthetic and metal-free dental restoration [5, 6]. Recently, Y-TZP has been extensively applied in dental crown applications because it offers better aesthetics and biocompatibility compared with metal restoration [4, 5].

Most advanced ceramics, including Y-TZP, are processed through powder metallurgy methods, in which ceramic powders are compacted and undergo densification under elevated temperatures. Every procedure during ceramic processing (powder preparation, consolidation, and densification) can introduce detrimental heterogeneities, such as agglomerates and defects, which remain and exacerbate after sintering [7]. These heterogeneities may form large pores or flaws in the microstructure during densification and deteriorate the mechanical properties of the final products [8, 9]. Hence, minimizing the possibility of heterogeneity formation and achieving the desired spatial distribution phases (including pores) in green bodies is crucial [7].

There are many forming methods of ceramics such as micro-powder injection molding, pressing and sol-gel [10-12]. Uniaxial pressing, cold isostatic pressing (CIP), and hot isostatic pressing (HIP) are among several consolidation processes that involve pressing in ceramic processing. Pressing is a dry-forming technique in ceramic processing that is known for producing critical parts in near net shape [13]. Compared with traditional methods such as uniaxial pressing, CIP can pressurize the powder compact from all directions. Thus, CIP produces green compacts with relatively high density and uniform packing using inexpensive tooling [14, 15].

Colloidal processing methods such as slip casting and tape casting have recently emerged as popular consolidation methods for ceramics. Colloidal processing methods have a great potential to offer high-quality green bodies with a high packing factor, thereby providing excellent mechanical properties for the final products [16-18]. Colloidal processing methods are highly recommended for submicron ceramic powder because submicron particles tend to agglomerate owing to their high specific surface area [17]. These agglomerates are invariably detrimental to the mechanical properties of ceramics. Colloidal processing controls the interparticle forces of ceramic particles through three mechanisms namely electrostatic, steric and electrosteric [7]. This method can effectively minimize the agglomeration of particles and thus improve the quality of green bodies. However, a suspension with excellent colloidal stability and rheological properties is required for a successful colloidal processing [19].

Slip casting and CIP are known for producing Y-TZP with excellent mechanical properties. This study aims to improve the mechanical properties of Y-TZP for dental crown applications by combining both slip casting and CIP.

Materials and Methods

Materials

Y-TZP nanopowder partially stabilized with 3 mol% of Y_2O_3 (US Research Nanomaterials Inc., Houston, USA) was used in this study. This powder has a BET specific surface area of 30 m^2/g and a true density of 5.89 g/cm^3. The transmission electron micrograph (TEM) of the as-received powder in Figure 1 shows that the primary particle size of the powder was approximately 20 nm. Polyethyleneimine (PEI, Sigma–Aldrich) with an average molecular size of 50,000 was employed as a dispersant agent in colloidal processing.

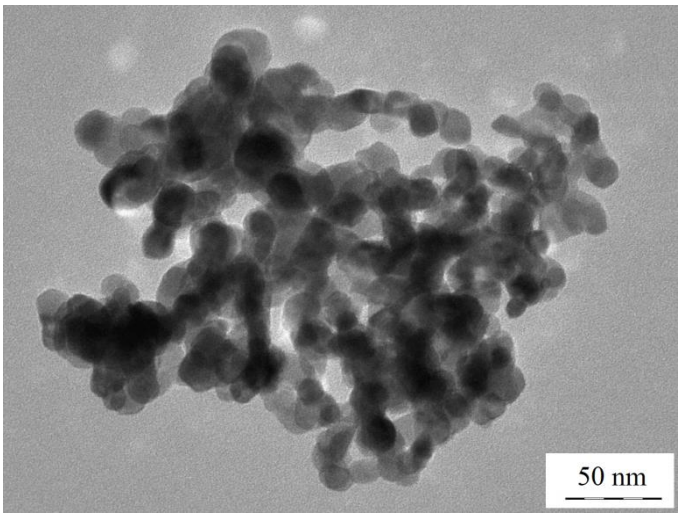


Figure 1. TEM image of the as-received Y-TZP powder

Fabrication of Green Body

A Y-TZP suspension with 30 wt.% powder loading was prepared. The dispersing medium was distilled water. The suspension was added with 0.4 wt.% of 0.005 M PEI, thoroughly mixed using a magnetic stirrer for 45 min, and then ultrasonicated for 15 min to break the agglomerates. A HNO_3 solution was used to adjust the pH of the suspension to pH 2. The PEI amount and pH used in suspension preparation are optimized parameters from a previous study [20]. Slip casting was used to fabricate green bodies. The Y-TZP suspension was poured into a 15 mm-diameter Teflon mold placed on top of a plaster of Paris block, which was then left for consolidation at room temperature. After 24 h, the green bodies were carefully extracted from the mold.

For CIP, approximately 0.6 g of Y-TZP powder was measured and pressed into cylindrical disc shape through uniaxial pressing (Carver 4369, USA) in a 13 mm-diameter mold (#3619, Carver, USA). The powder was pressed at 25 MPa and 10 s dwell time. Subsequently, the Y-TZP disc was subjected to CIP (Riken Seiki Co. Ltd., Japan) at 200 MPa for 1 min.

Combined method of slip casting and CIP was also used to fabricate green bodies. Y-TZP green bodies were first produced using slip casting method with the same procedures and parameters discussed previously. Then, the slip-casted green bodies were subjected to CIP at 200 MPa for 1 min.

Sintering method

The green bodies were sintered at 1600 °C by a two-step sintering method in a high-temperature furnace (VMK-1800, Linn High Therm, Germany). The sintering profile is shown in Figure 2. The green bodies were initially heated to 600 °C at a rate of 3 °C/min and maintained for 45 min. Next, the green bodies were further heated to 1600 °C, with a soaking time of 2 hours.

Sample characterization

The sintered densities of the Y-TZP samples were measured with a density meter (Newclassic MS, Mettler Toledo, Columbus, OH, USA) by applying Archimedes' immersion method. A field-emission scanning electron microscope, FESEM (Hitachi SU8000, Hitachi, Tokyo, Japan) was used to observe the microstructure of the Y-TZP samples. Before the examination, the sample surface was prepared by grinding using silicon carbide paper (600, 800, and 1200 grit) and then polishing with diamond paste (3 and 1 µ grit sizes). After surface preparation, thermal etching at 1200 °C was conducted on the samples so that the grain boundaries can be observed clearly under the FESEM machine. During etching, the temperature increased to 1200 °C at a rate of 20 °C/min and maintained for 1 h. Then, the temperature decreased to room temperature at the same rate. The Vickers hardness machine (EW422-

DAT, Eseway, Bowers Group, Camberly, UK) was used to examine the hardness of the Y-TZP samples. The Vickers hardness test was performed in accordance with ASTM C 1327-03 (Standard Test Method for Vickers Indentation Hardness of Advanced Ceramics). Six indentations were rendered on the prepared surface of the Y-TZP samples at 0.2 kgf load and 10 s dwell time, and the average values were obtained. Similar procedures of surface preparation in the morphological test were also employed in this test. Finally, X-Ray diffraction (XRD, D8 Advance, Bruker, Billerica, MA, USA) was performed to observe the phase changes in Y-TZP after sintering.

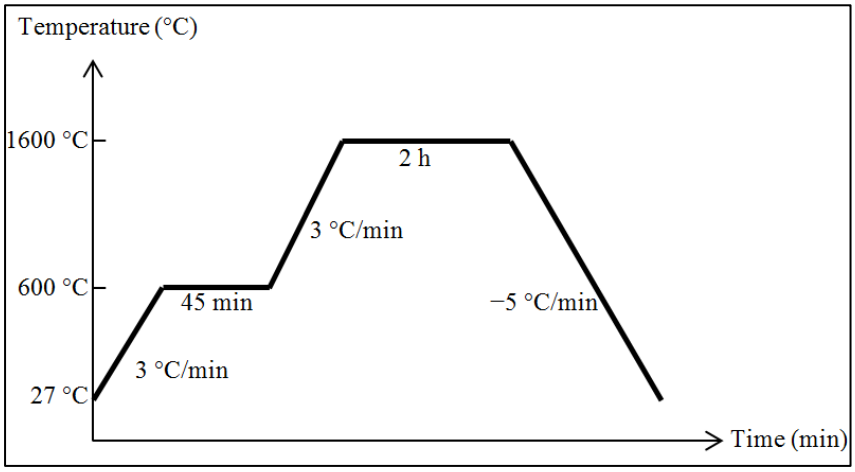


Figure 2. Sintering profile of Y-TZP samples

Results and Discussion

Sintered density

The sintered densities of the Y-TZP samples fabricated through different methods are shown in Figure 3. The sintered density of the Y-TZP sample fabricated through CIP was 98% of the theoretical density of Y-TZP (6.1 g/cm^3). Meanwhile, the sample processed with slip casting had the lowest sintered density, i.e., 92% of the theoretical density. The highest density of 99% was observed in the sample fabricated with the combination of slip casting and CIP.

Density is correlated with porosity, which is undesirable in ceramic processing because it deteriorates the mechanical strength of a ceramic body. The samples fabricated by CIP and the combined method achieved full densification (> 98 %). The full densification of grains has been proven in many studies [18, 20] to yield high mechanical properties in Y-TZP. This result can be attributed to the high powder packing factor of the green bodies. The powder packing factor of a green body determines its quality. Inadequate packing of powder granules before sintering often results in irregularities such as pores and agglomerates after sintering which lead to low mechanical properties. Hence, high powder packing factor usually yields high sintered density. A consolidation process in ceramic processing must be carefully controlled to eradicate irregularities that deteriorate the mechanical properties of the final product. The density test results showed that the Y-TZP green bodies produced using CIP and the combined method had better powder packing than those produced using slip casting. This result indicates that the two methods are more suitable for consolidation than slip casting. Moreover, the CIP method significantly increased the density of slip-casted Y-TZP from 92 % to 99 %.

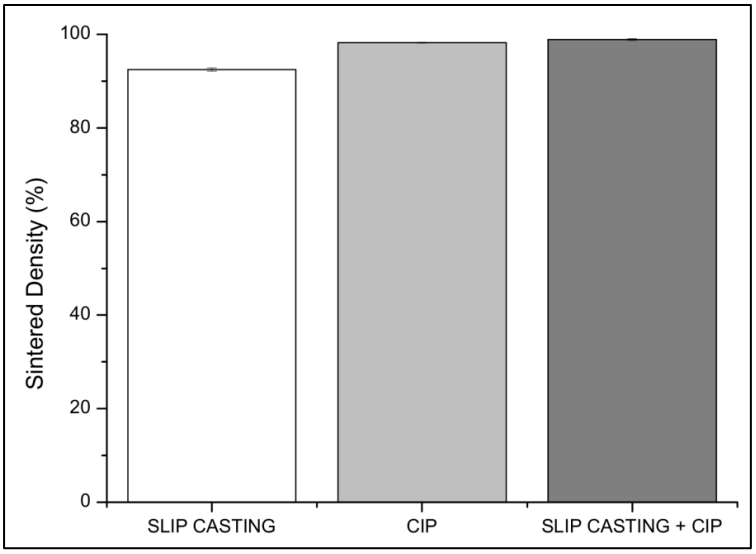


Figure 3. Relative sintered densities of Y-TZP samples

Morphological analysis

The scanning electron micrograph of the samples in Figure 4 shows that CIP produced a more compact and less porous microstructure compared with slip casting. This finding is corresponding to the density test results, in which the CIP sample showed a higher density than the slip casting sample. Average grain sizes of 614 and 569 nm were recorded in CIP and slip casting samples, respectively. However, the combined method produced a highly homogeneous and compact microstructure with an average grain size of 517 nm. This compact and fine microstructure favors the production of Y-TZP samples with promising mechanical strength. Chin et al. [20] reported a smaller average grain size of 486 nm in the Y-TZP sample fabricated via slip casting method and a hardness of 10 GPa. In the present study, a higher hardness value was achieved with the combined method of slip casting and CIP (hardness test results will be discussed in following section) although the average grain size is larger compared to that of Chin et al. [20]. This is attributed to the compact microstructure with extremely low porosity yielded via the combined method in this study.

The microstructure of the CIP sample exhibited excessive grain growth primarily because uniaxial pressing and CIP cannot eliminate the agglomerates inherited from the raw Y-TZP powder. Ceramic powders in submicron size generally appear in the form of agglomerates, which are formed by bonded primary particles. Agglomeration always occurs because fine particles tend to reduce their surface energy [21]. These agglomerates, if left untreated, will persist until the end of processing and bring undesired sintered characteristics, such as high porosity, exaggerated grain growth, and flaws [22]. Coarse grains brought about by exaggerated grain growth in CIP samples (refer to Fig. 4b) are very detrimental to the mechanical properties because large grains are highly vulnerable to trans-granular cleavage, in which the crack propagates across the grain. Muchtar and Lim [23] also explained that trans-granular cleavage is not likely to occur in fine grains. Hence, a ceramic body with fine grain size is more resistant to trans-granular fracture and possesses higher mechanical properties.

The combined method of slip casting and CIP yielded the most desired microstructure, which is compact and homogeneous because most agglomerates had been eliminated during colloidal processing. CIP further enhanced powder packing. Consequently, a nonporous homogeneous microstructure was obtained.

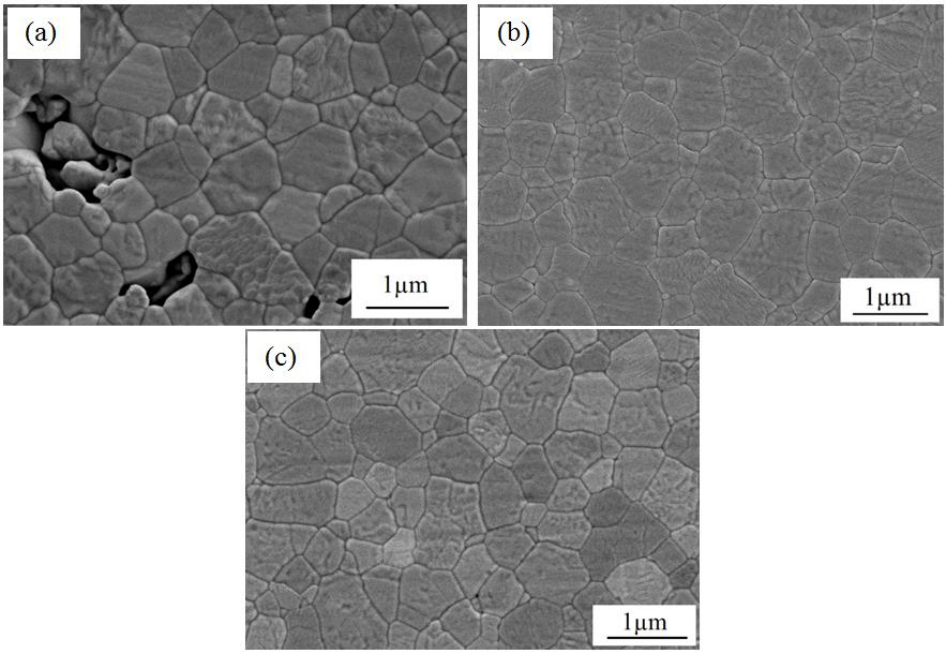


Figure 4. SEM images of Y-TZP samples fabricated through (a) slip casting, (b) CIP and (c) slip casting + CIP

Hardness

The materials of the crown should have high hardness values to prevent failure of the dental crown. The Vickers hardness of the samples fabricated with different methods is shown in Figure 5. The hardness of the CIP sample was slightly higher than that of the slip casting sample. However, CIP considerably improved the hardness of the slip-casted Y-TZP sample. Thus, the combined method yielded the highest hardness of 14.4 GPa. This is comparable to the highest hardness value of Y-TZP reported by Piconi et al. [3] which is 14 GPa. This result proves the effectiveness of CIP in improving the mechanical properties of slip-casted Y-TZP. The high hardness value of the sample fabricated by the combined method is ascribed to its compact and homogeneous microstructure. As stress concentrators that promote crack propagation, pores deteriorate the mechanical properties of the final products [18]. Thus, a compact microstructure can ensure favorable mechanical properties. A homogeneous and fine microstructure is also effective in impeding trans-granular fracture that usually results in low mechanical properties.

X-Ray Diffraction (XRD)

The XRD results in Figure 6 reveal a portion of monoclinic zirconia in the Y-TZP sample fabricated by CIP. This result can be attributed to the high stress level subjected to the Y-TZP powder during uniaxial pressing. *t-m* phase transformation can be triggered by high stress level and exaggerated grain growth. Previous studies [24-26] reported that the grain size threshold for spontaneous *t-m* transformation is approximately 1 μm. Coarse grains > 1 μm in size were found in the microstructure of the CIP sample (Fig. 4b). Thus, this morphology encouraged the formation of monoclinic zirconia. The existence of the monoclinic phase is highly undesirable in dental crown applications because it poses the problem of low temperature degradation (LTD). LTD deteriorates the mechanical properties of Y-TZP at a fast rate in oral circumstance. Therefore, LTD limits the efficiency of Y-TZP in dental crown applications. Slip casting offers extra phase stability to the tetragonal phase because it produces the monophase of tetragonal zirconia. The combined method also offers good tetragonal phase stability because only a negligible amount of monoclinic zirconia was detected.

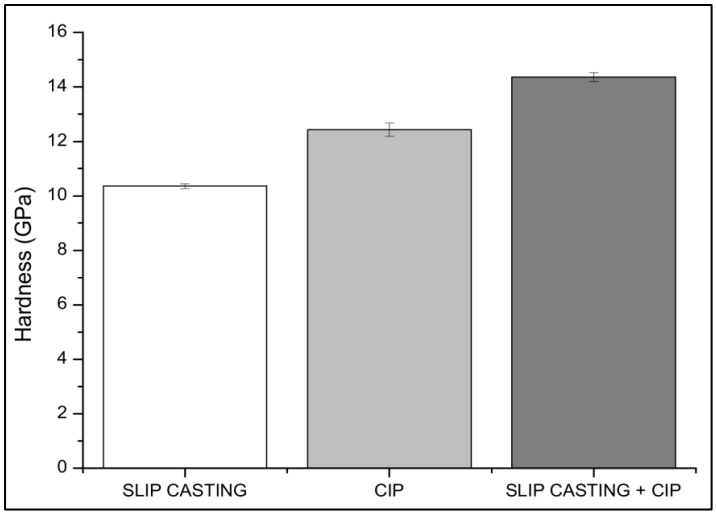


Figure 5. Hardness of Y-TZP samples

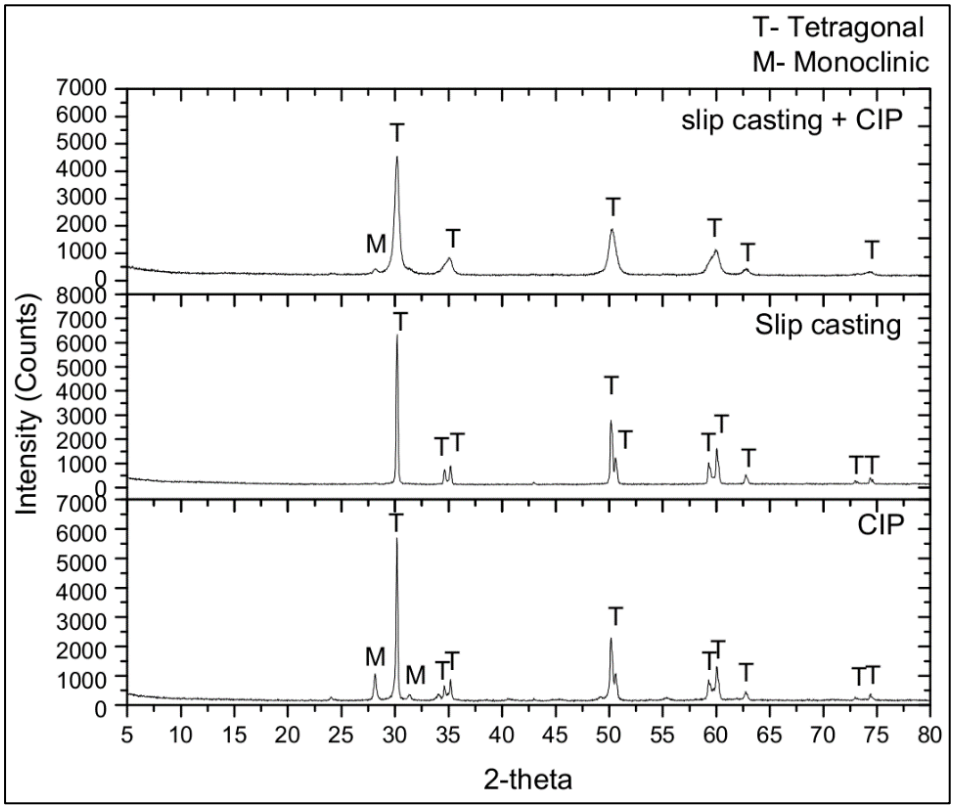


Figure 6. XRD results of Y-TZP samples processed with different methods

Conclusion

Both slip casting and CIP can produce Y-TZP with high mechanical properties. The CIP method offers better mechanical properties than the slip casting method. However, CIP method also encourages the formation of monoclinic zirconia, which can potentially jeopardize the mechanical properties of the final products. The combined method of slip casting and CIP is proven to be a better alternative processing route for Y-TZP. This method significantly enhances the mechanical properties of Y-TZP, for example, there was approximately 20 % improvement in the hardness of Y-TZP fabricated via the combined method. This method also offers favorable tetragonal stability.

Acknowledgement

This work was supported by the Universiti Kebangsaan Malaysia (UKM) and the Ministry of Science, Technology and Innovation, Malaysia through the research sponsorship of DLP-2015-007 and FRGS/1/2013/SG06/UKM/01/1. The authors would like to acknowledge the support of the Centre for Research and Instrumentation Management (CRIM), UKM, and SIRIM for their excellent testing equipment.

References

1. Vleugels, J., Yuan, Z. X. and Van Der Biest, O. (2002). Mechanical properties of Y_2O_3/Al_2O_3-coated Y-TZP ceramics. *Journal of the European Ceramic Society,* 22 (6): 873 - 881.
2. Xu, T., Vleugels, J., Van Der Biest, O., Kan, Y. and Wang, P. (2006). Phase stability and mechanical properties of TZP with a low mixed Nd_2O_3/Y_2O_3 stabiliser content. *Journal of the European Ceramic Society,* 26 (7): 1205 - 1211.
3. Piconi, C., Condo, S. G. and Kosmač, T. (2014). Chapter 11 - Alumina- and zirconia-based ceramics for load-bearing applications. *Advanced Ceramics for Dentistry,* 219 - 253.
4. Ozturk, O., Uludag, B., Usumez, A., Sahin, V. and Celik, G. (2008). The effect of ceramic thickness and number of firings on the color of two all-ceramic systems. *The Journal of Prosthetic Dentistry,* 100 (2): 99 - 106.
5. Manicone, P. F., Rossi, I. P. and Raffaelli, L. (2007). An overview of zirconia ceramics: basic properties and clinical applications. *Journal of Dentistry,* 35 (11): 819 - 826.
6. Persson, C., Unosson, E., Ajaxon, I., Engstrand, J., Engqvist, H. and Xia, W. (2012). Nano grain sized zirconia–silica glass ceramics for dental applications. *Journal of the European Ceramic Society,* 32 (16): 4105 - 4110.
7. Lewis, J. A. (2000). Colloidal processing of ceramics. *Journal of the American Ceramic Society,* 83 (10): 2341 - 2359.
8. Briscoe, B. J., Khan, A. U. and Luckham, P. F. (1998). Stabilising zirconia aqueous suspensions using commercial polyvalent electrolyte solutions. *Journal of the European Ceramic Society,* 18 (14): 2169 - 2173.
9. Rafferty, A., Alsebaie, A. M., Olabi, A. G. and Prescott, T. (2009). Properties of zirconia-toughened-alumina prepared via powder processing and colloidal processing routes. *Journal of Colloid and Interface Science,* 329 (2): 310 - 315.
10. Zakaria, H., Muhamad, N., Sulong, A. B., Ibrahim, M. H. I. and Foudzi, F. (2014). Moldability characteristics of 3 mol% yttria stabilized zirconia feedstock for micro-powder injection molding process. *Sains Malaysiana,* 43 (1): 129 - 136.
11. Osman, N., Ibarahim, N., Ishak, M. A. M. and Hassan, O. H. (2014). Characterization of cerate-zirconate ceramics powder prepared by three different methods: A comparative study. *Sains Malaysiana,* 43 (9): 1373 - 1378.
12. Ani, S. M., Muchtar, A., Muhamad, N. and Ghani, J. A. (2013). Characterisation of mixing uniformity and rheological properties of alumina-zirconia powder for ceramic injection moulding. *Sains Malaysiana,* 42 (9): 1311 - 1317.
13. Ng, L. S., Loh, N. L. and Boey, F. Y. C. (1997). Cold-hot isostatic pressing of Mar M200 superalloy powders. *Journal of Materials Processing Technology,* 67 (1-3): 143 - 149.
14. Henderson, R. J., Chandler, H. W., Akisanya, A. R., Barber, H. and Moriarty, B. (2000). Finite element modelling of cold isostatic pressing. *Journal of the European Ceramic Society,* 20 (8): 1121 - 1128.
15. Mouzon, J., Glowacki, E. and Odén, M. (2008). Comparison between slip-casting and uniaxial pressing for the fabrication of translucent yttria ceramics. *Journal of Materials Science,* 43 (8): 2849 - 2856.

16. Rafferty, A., Alsebaie, A. M., Olabi, A. G. and Prescott, T. (2009). Properties of zirconia-toughened-alumina prepared via powder processing and colloidal processing routes. *Journal of Colloid and Interface Science*, 329 (2): 310 - 315.
17. Rami, M.-L., Meireles, M., Cabane, B. and Guizard, C. (2009). Colloidal stability for concentrated zirconia aqueous suspensions. *Journal of the American Ceramic Society*, 92: 50 - 56.
18. Amat, N. F., Muchtar, A., Ghazali, M. J. and Yahaya, N. (2014). Suspension stability and sintering influence on yttria-stabilized zirconia fabricated by colloidal processing. *Ceramics International*, 40 (4): 5413 - 5419.
19. Liu, Y. and Gao, L. (2003). Deflocculation study of aqueous nanosized Y–TZP suspensions. *Materials Chemistry and Physics*, 78 (2): 480 - 485.
20. Chin, C. H., Muchtar, A., Azhari, C. H., Razali, M. and Aboras, M. (2015). Optimization of pH and dispersant amount of Y-TZP suspension for colloidal stability. *Ceramics International*, 41 (8): 9939 - 9946.
21. Balakrishna, P., Narasimha Murty, B. and Anuradha, M. (2009). A New process based agglomeration parameter to characterize ceramic powders. *Journal of Nuclear Materials*, 384 (2): 190 - 193.
22. Trunec, M. and Maca, K. (2014). Chapter 7 - Advanced ceramic processes. *Advanced Ceramics for Dentistry*, 123 - 150.
23. Muchtar, A. and Lim, L. C. (1998). Indentation fracture toughness of high purity submicron alumina. *Acta Materialia*, 46 (5): 1683 - 1690.
24. Lange, F. F. (1982). Transformation toughening. *Journal of Materials Science*, 17 (1): 240 - 246.
25. Bravo-Leon, A., Morikawa, Y., Kawahara, M. and Mayo, M. J. (2002). Fracture toughness of nanocrystalline tetragonal zirconia with low yttria content. *Acta Materialia*, 50 (18): 4555 - 4562.
26. Zhang, Y. (2014). Making yttria-stabilized tetragonal zirconia translucent. *Dental Materials*, 30 (10): 1195 - 1203.

Malaysian Journal of Analytical Sciences, Vol 20 No 3 (2016): 651 - 659
DOI: http://dx.doi.org/10.17576/mjas-2016-2003-26

MALAYSIAN JOURNAL OF ANALYTICAL SCIENCES
Published by The Malaysian Analytical Sciences Society
ISSN 1394 - 2506

EFFECT OF USING PITAYA PEEL AS DYE-SENSITIZER AND DYE MOLECULES IN ELECTROLYTE FOR PHOTOELECTROCHEMICAL REACTION

(Kesan Penggunaan Kulit Buah Naga Sebagai Pemeka-Pewarna dan Molekul Pewarna di dalam Elektrolit bagi Tindak Balas Fotoelektrokimia)

Siti Nur Hidayah Jaafar[1], Lorna Jeffery Minggu[1]*, Khuzaimah Ariffin[1], Mohammad B. Kasssim[1, 2], Wan Ramli Wan Daud[1, 3]

[1]*Fuel Cell Institute*
[2]*School of Chemical Sciences and Food Technology, Faculty of Science and Technology*
[3]*Department of Chemical and Process Engineering, Faculty of Engineering and Built Environment, Universiti Kebangsaan Malaysia, 43600 UKM Bangi, Selangor, Malaysia*

**Corresponding author: lorna_jm@ukm.edu.my*

Received: 5 February 2016; Accepted: 22 April 2016

Abstract

Natural dye sensitizer in photoelectrochemical shows a great potential in improving the efficiency of metal oxide semiconductor especially Titanium dioxide (TiO_2) due to its prominent in absorbing visible light and also low cost. In this work, the effect of using pitaya peel as natural dye sensitizes to TiO_2 has been studied through characterizations analysis and PEC test. The bare TiO_2 thin films were fabricated on Fluorine-doped tin oxide (FTO) glass substrate by doctor blade method meanwhile dye-sensitized TiO_2 thin films prepared by immersion of TiO_2 in the dye extracts. The fabricated thin films were characterized with Scanning Electron Microscopy (SEM), X-ray difractometer (XRD), UV-Vis spectrophotometer and photoelectrochemical analysis. The surface of TiO_2 was porous and uniform meanwhile dye particles could not been observed due to very small size. The energy band gap of dye-sensitized TiO_2 from the UV-Vis spectrum is 2.1 eV which is smaller than bare TiO_2 (3.7 eV). Meanwhile, photoactivities of dye-sensitized TiO_2 has the highest compared to bare TiO_2 photoelectrodes which is 127µA/cm^2 in 6.25% v/v of pitaya dye in the electrolyte.

Keywords: titanium dioxide, dye-sensitizers, betalains, photoelectrochemical cell, water splitting

Abstrak

Pemeka-pewarna semulajadi di dalam fotoelektromia (PEC) menunjukkan potensi yang bagus untuk meningkatkan keupayaan semikonduktor logam oksida terutamanya titanium dioksida (TiO_2) disebabkan kemampuannya untum menyerap cahaya nampak dan kos yang rendah. Di dalam penyelidikan ini, kesan menggunakan kulit buah naga sebagai pemeka-pewarna semulajadi terhadap TiO_2 telah dikaji melalui pencirian dan analisis fotoelektrokimia. Filem nipis TiO_2 asli telah dihasilkan melalui kaedah Doctor blade di atas kepingan kaca bersalut FTO (Stanum oksida terdop fluorin) manakala filem nipis TiO_2 dengan pewarna-pemeka telah dihasilkan dengan merendam TiO_2 ke dalam larutan ekstrak pewarna. Filem nipis yang telah terbentuk telah melalui beberapa analisis pencirian iaitu, Mikroskopi Elektron Imbasan (SEM), Difraktometer Pembelauan Sinar-X (XRD), Spektrofotometer Ultralembayung dan Cahaya Nampak **(**UV-Vis**)** dan juga ujian fotoelektrokimia. Permukaan TiO_2 adalah berliang dan seragam manakala zarah pewarna tidak dapat dilihat disebabkan saiznya yang terlalu kecil. Jurang tenaga filem nipis TiO_2 dengan pewarna-pemeka adalah lebih rendah iaitu 2.1 eV jika dibandingkan dengan TiO_2 asli (3.7 eV). Manakala, fotoaktiviti bagi fotoelektrod TiO_2 dengan pewarna-pemeka adalah lebih tinggi daripada TiO_2 asli dengan 127µA/cm^2 di dalam kepekatan 6.25% v/v pewarna di dalam elektrolit.

Kata kunci: titanium dioksida, pemeka-pewarna, betalain, sel fotoelektrokimia, pembelahan air

Introduction

The hydrogen gas production by using solar energy is deliberated as one of the most significant sustainable and clean energy technologies [1]. Photoelectrochemical (PEC) water splitting is the most promising method in generating hydrogen gas. Metal oxide semiconductor such as TiO_2, SnO_2, and WO_3 is widely studied as having a great potential as photoelectrodes in PEC system [2]. Nonetheless, TiO_2 semiconductor is more favorable due to its good stability in thermal and chemical properties, inexpensive and non-toxic [3]. However, TiO_2 is characterized by its wide band gap of 3.2 eV (anatase phase) and required Ultra-Violet (UV) irradiation which only absorb small fraction (< 10 %) of the sunlight energy [3, 4]. An improvement of TiO_2 semiconductor can be achieved by using dye sensitizer plays as a main role in absorbing light energy in production of hydrogen [4]. Dye sensitizer has been widely studied caused by its great potential as sunlight harvester and improved PEC efficiency by increased light absorption in solar spectrum to visible light range [5]. The advantages of dye sensitizer includes low cost, minimal and simple fabrication process [6]. However, dye-sensitizer should have strong attachment to the surface of metal oxide semiconductor to achieved higher efficiency in PEC system [7]. Other than that, recombination also influenced the photocurrent generation in PEC reaction. Yet, the electron injection of dyes sensitizer is very fast while the back reaction is slow, hence the rate of recombination believed to be very small [8].

Synthetic dyes such as ruthenium complexes may offer high efficiency in PEC however, due to its expensive cost and rarity as well as toxic materials, substantially lead to the use natural dye as sensitizer [9]. Up till now, various natural dyes pigments from plants and fruits has been utilized such as anthocyanins, betalains, chlorophyll and carotenoids because of their low cost in extraction process while having good light absorption in visible region [10-13]. Among all of the natural dye pigments, betalains is the most suitable candidate as a sensitizer to TiO_2 photoelectrode as its having essential anchoring group that can attached efficiently onto TiO_2 surface which is carboxyl group [14].

Red pitaya fruit is one of the new focuses for dye-sensitizers as it rich in betalains pigment. Betalain can be found in both peel and flesh of the fruit and also can be divided into the red-violet betacyanins and yellow-orange betaxanthins group that promise variants in colour. However, in this study focused more on pitaya peel as it is a leftover product especially in beverage industries. The deep purple colour observed in pitaya peel contributes by at least seven known betalain that have identical maximum light absorption (λ_{max}) namely betanin, isobetanin, betanidin, isobetanidin, phyllocactin, and bougainvilllein-r-I [15]. The advantage of betalains possess over other pigments is its anchor group that adsorb efficiently onto atoms of semiconductor. The study of betalain dye molecules bonding to the TiO_2 subtrate has been reported previously. They suggested that ability of betalain's anchor group, carboxyl is the key factors to an efficient PEC reaction [16].

So far, the literature study work on pitaya peel dye in PEC water splitting is still barely known [17]. Thus, our research particular interest is the uses of natural pitaya peel dye molecules as light harvester sensitizer and also finding the influence of dye molecules added in liquid electrolyte.

Materials and Methods

Dye pigment extraction

Pitaya peel was macerated with double distilled water in a blender until completely homogenized in room temperature. The mixture is filtered by using vacuum filter to extract the dye and stored at 20 ºC prior to analysis. Any contact of the dye extract to the light was inhibited to avoid change in colour.

Fabrication of thin films

Prior to fabrication process, Fluorine-doped Tin Oxide (FTO) glasses were cleaned using ultrasonicator by immersed into three different solvent sequentially; ethanol (Merck), acetone (Merck) and single distilled water for 5 minutes each at 30 ºC. After that, the cleaned FTO glasses were dried at room temperature. In the meantime, TiO_2 paste was prepared using nanoparticles powder of titanium dioxide P25 Degussa (Sigma Aldrich) mixed with double distilled water at ratio 1:3 of mass (g) to volume (ml). Then, the paste was stirred by using spatula to ensure

homogenous mixture. The TiO_2 paste was coated on top of FTO glass by Doctor Blade method and the thickness of thin films were controlled by taping the scotch tape at sides of FTO glass. Later, TiO_2 thin film were calcined and sintered in a furnace at 450 ºC for 2 hours with constant heating of 5 ºC/min. The preparation is carried out in duplicates to prepare TiO_2 with dye sensitizer thin films.

After cooling down, the sintered TiO_2 thin film was soaked into a container filled with pitaya peel dye up to 24 hours in room temperature and dark condition to allow the adsorption of the dye molecules as a sensitizer. Later, the non-adsorbed materials on TiO_2 with dye sensitizer thin film were removed by distilled water. The thin film stored at 0ºC for further analysis and any contact with light is prevented to keep its colour stability.

Characterization and Photoelectrochemical (PEC) test of thin films

All of thin films prepared were characterizes using X-ray diffraction measurement, XRD (Bruker D8 Advance diffractometer) with CuKα radiation in determining its structure and crystallinity. The percentage of the anatase and rutile crystalline phase was determined using following Equation 1 [18]:

$$\text{Anatase (\%)} = \frac{1}{1+1.265\left(\frac{I_{rutile}}{I_{anatse}}\right)} \text{ x } 100\% \quad (1)$$

where $I_{anatase}$ and I_{rutile} are the intensities at highest peak of anatase and rutile phase respectively for TiO_2. Menawhile, the size of crystal can be measured by using Scherrer Equation 2 [19]:

$$D = \frac{K\lambda}{\beta \cos \theta} \quad (2)$$

where K is the crystal shape factor (0.9), λ is the wavelength of x-ray (CuKα1 = 0.15406 nm), β is full width at half the maximum intensity (rad) and θ is diffraction angle.

The morphology, grain sizes, and thickness of the thin films were studied with scanning electron microscope, SEM (Zeiss AM10). Meanwhile, the light absorption of thin films was measured by UV-Vis spectrophotometer (PerkinElmer Lambda 35). Light absorption of thin film can be calculated using following Equation 3:

$$T = e^{-\alpha d} \quad (3)$$

where T is normalised transmittance, α is the absorption coefficient, *d* is the thickness of the film (cm). Besides that, the optical absorption coefficient is corresponding to the energy band gap (E_g) determined by using the Tauc formula (Equation 4):

$$Ah\nu = B(h\nu - E_g)^n \quad (4)$$

where A is a absorption coefficient, B is a constant; E_g is optical band gap energy of the film and n is the exponent. For crystalline semiconductors, n is ½, 3/2, 2, and 3 when the transition is direct allowed, direct forbidden, indirect allowed and indirect forbidden respectively.

For the study of photoelectrochemical (PEC) activity, FTO glass coated with thin films were assembled with copper wire as described by Minggu et al [20] to form photoelectrodes. A PEC cell set-up with optical window was used with three electrodes system which consists of a working electrode (fabricated photoelectrodes), a counter electrode (platinum electrode) and a reference electrode (Saturated Calomel Electrode) whereas double distilled water with dye as electrolyte. Beforehand, the electrolyte was purged with nitrogen gas for 30 minutes. The analysis was carried out under 100mWcm^{-2} Xenon full arc lamp as light source with Ametek Versastat 4. The initial and final potential was set to -0.5V and 1.5V respectively where the scan rate is 0.05V/s.

Results and Discussion

Morphological analysis

The images of surface and cross sectional morphology for bare TiO_2 and TiO_2 with dye sensitizer thin films can be observed using Scanning Electron Microscopy (SEM) as shown in Figure 1. The surface of TiO_2 thin film demonstrates porous with good uniformity which can be benefit to support dye adsorption [21]. The thickness of bare TiO_2 has been measured from cross-sectional image which is approximately 6 µm meanwhile dye-sensitized TiO_2 is approximately 8 µm which is 2 µm thicker than the bare TiO_2. Dye particles were not clearly visible on the surface and cross-sectional of TiO_2 with dye sensitized thin films due to very small size of dye molecule. Besides that, the particles size of TiO_2 is almost in the same size and agglomerated with 40 nm in average.

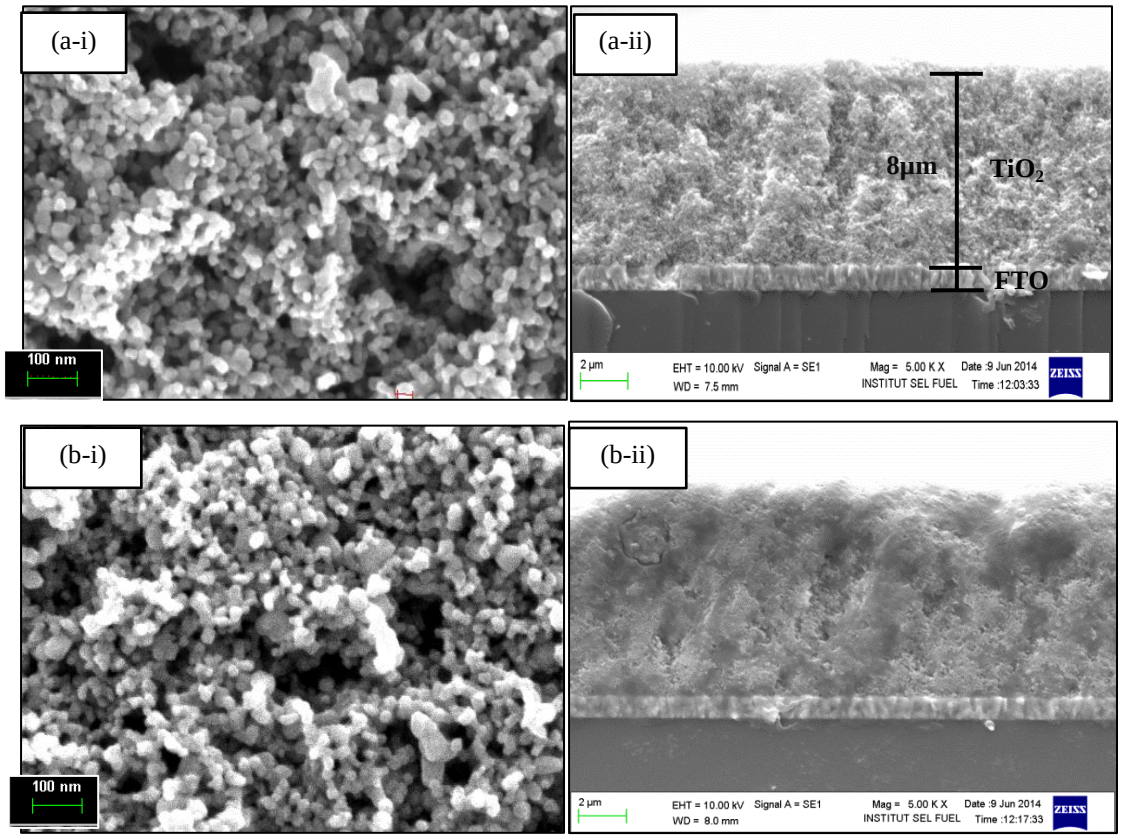


Figure 1. SEM images of (a) bare TiO_2 and (b) dye-sensitized TiO_2 thin films for its (i) surface and (ii) cross sectional respectively

Crystalline structure of thin films

Figure 2 shows the X-Ray Diffraction (XRD) pattern of TiO_2 and dye-sensitized TiO_2 thin films deposited onto FTO surface. The P25 Degussa TiO_2 nanoparticles contain 74 % anatase and 26 % rutile with average crystallite size of 20 nm obtained from Equation (1) and (2), respectively. Anatase peaks were observed at 2θ of 25.43°, 48.15° and 54.70° where correspondingly located at plane (101), (200) and (105) which in agreement with reported by Hamadanian et al. [21]. Meanwhile, the strongest peak of rutile appears at 27.55° at plane (110). In general, anatase phase is phocatalytically more active compared to rutile due to low rate of eletron-hole recombination [22]. Besides, the addition of dye sensitizer on TiO_2 thin films did not change the percentage of the anatase and rutile crystalline phase. However a new diffraction peak was exhibited at 2θ of 26.64° due to the present of mineral salts in dye

which later form crystal phase. In addition, there is increment in intensity of TiO_2 peaks which suggest that the crystallinity of TiO_2 is improved with adsorption of dye particles to TiO_2 crystal lattice.

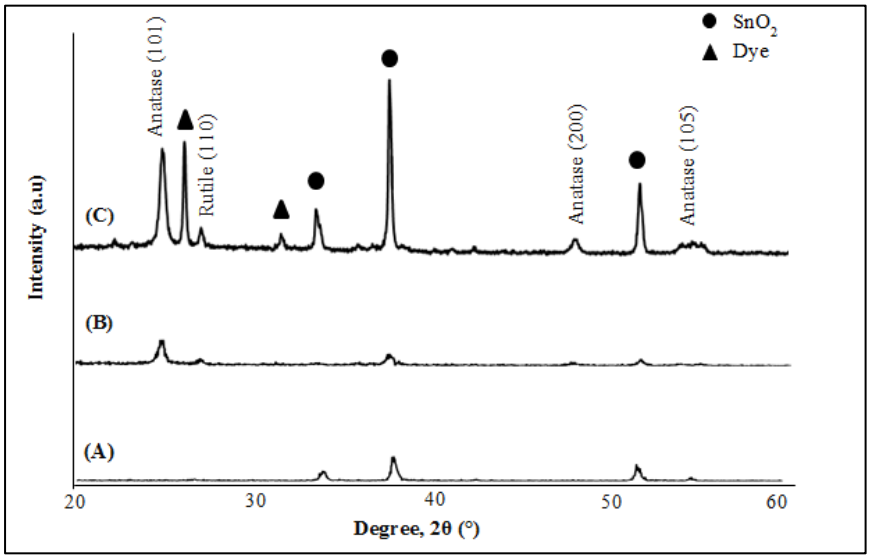


Figure 2. X-Ray Diffraction (XRD) pattern of (A) FTO, (B) TiO_2 and (C) dye-sensitized TiO_2 thin films deposited onto FTO

Optical light absorption and band edge analysis

Measurement of optical light absorption and band edge of pitaya peel dye and thin films has been done using UV-Visible spectrophotometer. The visible light makes majority of solar spectrum at wavelength range between 400 nm and 800 nm. Generally, the natural pitaya peel extracts contains mixture of several group pigments of betalain. In this study, the maximum light absorption (λ_{max}) for betalain pigments at about 546 nm as shown in Figure 3 which almost same as characteristic absorption of betacynanin, one of the red violet betalain group [23]. It shows that they have good light absorption at visible light portion and can utilize more photon energy. From the equation (3) and (4) shown in Section 2.3, the energy band gap, E_g of pitaya peel dye is 2.1 eV which include in the range of ideal band gap for PEC($1.23\ eV < E_g < 3.0\ eV$).

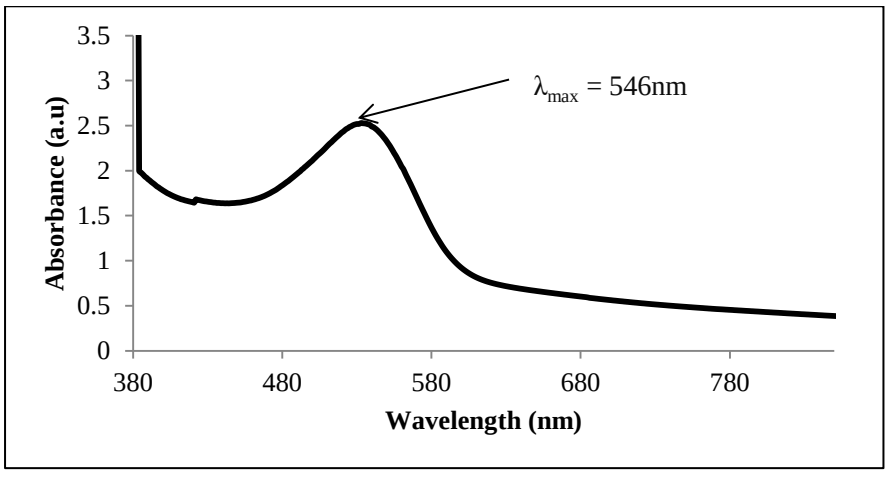


Figure 3. UV-Vis spectrum of pitaya peel dye pigment

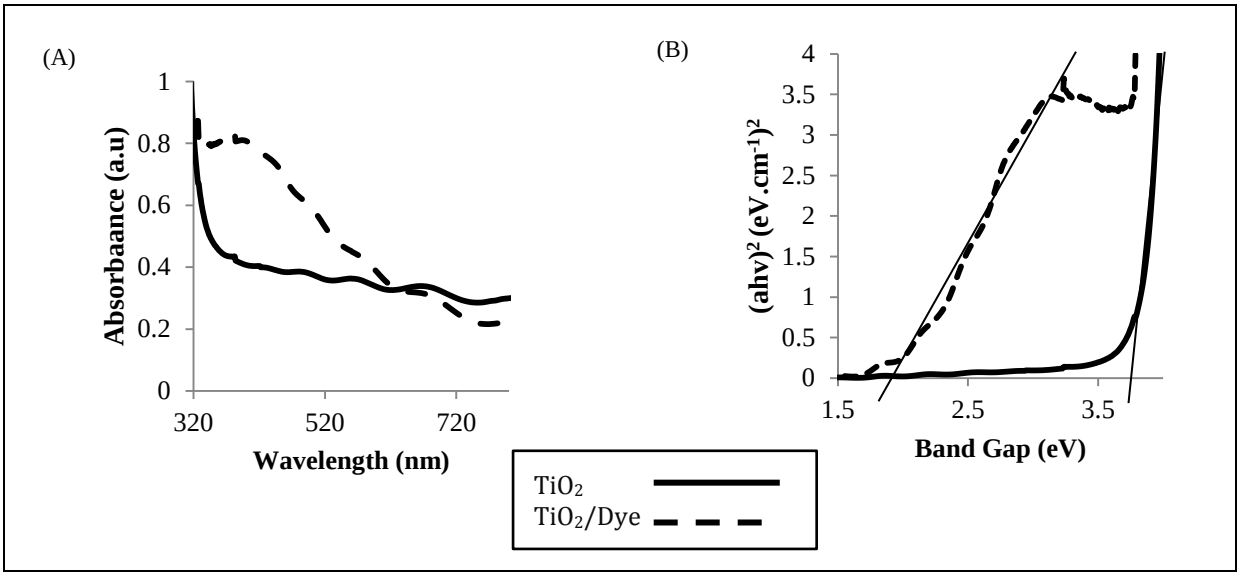


Figure 4. Optical light absorption (A) and direct allowed transition band gap (B) of bare TiO_2 and dye-sensitized TiO_2 thin films respectively

Photoelectrochemical analysis

Figure 5 shows measurement of photocurrent density for bare TiO_2 and dye-sensitized TiO_2 photoelectrodes in different concentration of dye in water electrolyte. The highest photocurrent density achieved by bare TiO_2 are by 6.25% and 12.5% v/v concentration of pitaya peel dye in the electrolyte which is 93 $\mu A/cm^2$ as shown in Figure 5 (A). However, the increased concentration of dye in electrolyte has decreased the photocurrent density with 66 $\mu A/cm^2$ at 100% v/v concentration of dye. In the meantime, the lowest photocurrent for bare TiO_2 is 43 $\mu A/cm^2$ without the addition of dye molecule electrolyte (0% v/v). From the Figure 5(B), dye-sensitized TiO_2 shows the increment in photocurrent density compared to bare TiO_2 where the highest photocurrent gained is 127 $\mu A/cm^2$ in 6.25% v/v concentration of pitaya peel dye in the electrolyte. Meanwhile, zero adding of dye molecule (0% v/v) has produced the lowest photocurrent which is around 52 $\mu A/cm^2$.

From the result, the present of dye-sensitizer layer on top of TiO_2 film has enhanced the production of photocurrent. This is due to the betalain molecules in pitaya peel dye-sensitizer has improved the light absorption of TiO_2 thus reducing the band gap. Besides that, functional group of carboxylic acid in betalains have forms a reversible binding with high equilibrium binding constant between TiO_2 surface and dye molecules in order to establish bonds and attached efficiently [24]. In dye-sensitized TiO_2 photoelectrode, the absorption of photon energy cause the electron transfer from highest occupied molecular orbital (HOMO) to lowest unoccupied molecular orbital (LUMO) following dihydropyridinie which attached on carboxyl group of dye-sensitizer. This caused photoexcitation dye state coupled electronically with an acceptor states in conduction band TiO_2 and lead to fast electron injection and increased photocurrent generation [10, 16, 25].

In the other hand, water is a poor electrolyte [26] and proven in this study as having the lowest photocurrent density for both bare TiO_2 and TiO_2 with dye sensitizer (0% v/v). However, the addition of dye molecules in electrolyte has shown increment in the photocurrent generation for both photoelectrodes. This may due to degradation of dye in electrolyte has made it as an electron donor to fill-up holes leaved by photoexcited electrons. Moreover, for dye-sensitized TiO_2 photoelectrode, dye-added molecules in the electrolyte has reduce driving force of desorption of the dye from TiO_2 surface hence increase its stability in water [27].

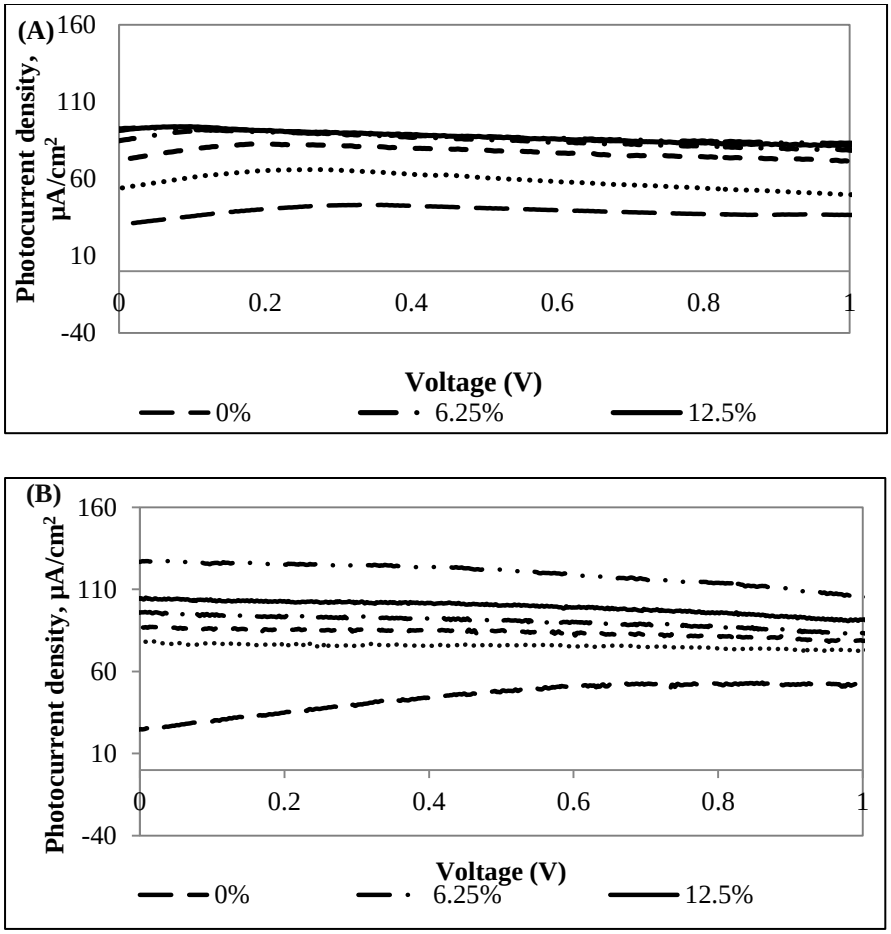


Figure 5. Performance of photocurrent density of (A) bare TiO_2 and (B) TiO_2 with dye sensitizer on different concentrations of pitaya peel dye in electrolyte

Conclusion

In this work, dye-sensitized TiO_2 was successfully fabricated using pitaya peel dye. There is no significant change in morphological studies of dye-sensitized TiO_2 thin film compare to bare TiO_2 due to its very fine of dye particle size. However, the crystallinity of TiO_2 has improved by the present of dye's crystal structure without change its phase. Besides, the light absorption dye-sensitized TiO_2 also has extended into visible light region. By using pitaya peel as dye-sensitizer has shown an increment in photocurrent generation in water splitting reaction. Furthermore, additional of dye molecules also has influenced photocurrent density where dye-sensitized TiO_2 photoelectrodes with 6.25% v/v of dye in electrolyte has the highest photocurrent density with 127µA/cm^2 under the Xenon lamp.

Acknowledgement

The authors would like to thank Universiti Kebangsaan Malaysia for providing the facilities and research grant (DIP-2012-27) and (GUP-2013-068).

References

1. Jeng, K.T., Liu, Y.C., Leu, Y.F., Zeng, Y.Z., Chung, J.C. and Wei, T.Y. (2010). Membrane electrode assembly-based photoelectrochemical cell for hydrogen generation. *International Journal of Hydrogen Energy,* 35(20): 10890 - 10897.

2. Ng, K. H., Minggu, L. J., Jumali, M. H. and Kassim, M. (2012). Fotoelektrod tungsten trioksida terdop nikel untuk tindak balas pembelahan air fotoelektrokimia. *Sains Malaysiana,* 41(7): 893 – 899.
3. Manoharan, K. and Venkatachalam, P. (2015). Photoelectrochemical performance of dye sensitized solar cells based on aluminum-doped titanium dioxide structures. *Materials Science in Semiconductor Processing,* 30: 208 – 217.
4. Al-Bat'hi, S. A. M., Alaei, I. and Sopyan, I. (2013). Natural photosensitizers for dye sensitized solar cells. *International Journal of Renewable Energy Research,* 3(1): 138 - 143.
5. Mark Lee, W. F., Minggu, L. J. and Kassim, M. (2012). Sifat foto-kimia kompleks molibdenum ditiolena. *Sains Malaysiana,* 41(5): 597 – 601.
6. Zhang, J., Jarboui, A., Vlachopoulos, N., Jouini, M., Boschloo, G. and Hagfeldt, A. (2015). Photoelectrochemical polymerization of EDOT for solid state dye sensitized solar cells: role of dye and solvent. *Electrochimica Acta,* 179: 220 - 227.
7. Calogero, G., Yum, J.-H., Sinopoli, A., Di Marco, G., Gratzel, M. and Nazeeruddin, M. K. (2012). Anthocyanins and betalains as light-harvesting pigments for dye-sensitized solar cells. *Solar Energy,* 86: 1563 – 1575.
8. Tennakone, K., Jayaweera, P. V. V. and Bandaranayake, P. K. M. (2003). Dye-sensitized photoelectrochemical and solid-state solar cells: charge separation, transport and recombination mechanisms. *Journal of Photochemistry and Photobiology A: Chemistry,* 158: 125 – 130.
9. Torchani, A., Saadaoui, S., Gharbi, R. and Fathallah, M. (2015). Sensitized solar cells based on natural dyes. *Current Applied Physics,* 15: 307 - 312.
10. Calogero, G., Di Marco, G., Caramori, S., Cazzanti, S., Argazzic, R. and Bignozzi, C.A. (2009). Natural dye senstizers for photoelectrochemical cells. *Energy & Environmental Science,* 2: 1162 -1172.
11. Khan, M. A., Khan, S. M. M., Mohammed, M. A., Sultana, S., Islam, J. M. M. and Uddin, J. (2012). Sensitization of nanocrystalline titanium dioxide solar cells using natural dyes: Influence of acids medium on coating formulation. *American Academic & Scholarly Research Journal,* 4 (5): 1 - 10..
12. Shanmugam, V., Manoharan, S., Anandan, S. and Murugan, R. (2013). Performance of dye-sensitized solar cells fabricated with extracts from fruits of ivy gourd and flowers of red frangipani as sensitizers. *Spectrochimica Acta Part A: Molecular and Biomolecular Spectroscopy,* 104: 35 - 40.
13. Liao, C. H., Huang, C. W. and Wu, J. C. S. (2012). Hydrogen production from semiconductor-based photocatalysis via water splitting. *Catalysts,* 2: 490 - 516.
14. Zhang, D., Lanier, S. M., Downing, J. A., Avent, J. L., Lum, J. and McHale, J. L. (2008). Betalain pigments for dye-sensitized solar cells. *Journal of Photochemistry and Photobiology A: Chemistry,* 195: 72 – 80.
15. Rebecca, O. P. S., Zuliana, R., Boyce, A. N. and Chandran, S. (2008). Determining pigment extraction effieciency and pigment stability of dragon fruit (*Hylocereus polyrhizus*). *Journal of Biological Sciences,* 8(7): 1174 - 1180.
16. Oprea, C. I., Dumbrava, A., Enache, I., Georgescu, A. and Gîrtu, M. A. (2012). A combined experimental and theoretical study of natural betalain pigments used in dye-sensitized solar cells. *Journal of Photochemistry and Photobiology A: Chemistry,* 240: 5 - 13.
17. Jamilah, B., Shu, C. E., Kharidah, M., Dzulkifly, M. A. and Noranizan, A. (2011). Physico-chemical characteristics of red pitaya (*Hylocereus polyrhizus*) peel. *International Food Research Journal,* 18: 279 - 286.
18. Spurr, R.A. and Myers, H. (1957). Quantitative analysis of anatase-rutile mixtures with an X-Ray diffractometer. *Analytical Chemistry,* 29(5): 760 - 762.
19. Scherrer, P. (1918). Bestimmung der Grösse und der inneren Struktur von Kolloidteilchen mittels Röntgenstrahlen. *Nachr. Ges. Wiss. Göttingen,* 26: 98 - 100.
20. Minggu, L. J., Daud, W. R. W. and Kassim, M. (2010). An overview of photocells and photoreactors for photoelectrochemical water splitting. *International Journal of Hydrogen Energy,* 35: 5233 - 5244.
21. Hamadanian, M., Safaei-Ghomi, J., Hosseinpour, M., Masoomi, R. and Jabbari, V. (2014). Uses of new natural dye photosensitizers in fabrication of high potential dye-sensitizedsolarcells (DSSCs). *Materials Science in Semiconductor Processing,* 27: 733 - 739.
22. Kusmierek, E. and Chrzescijanska, E. (2015). Application of TiO2–RuO2/Ti electrodes modified with WO3 in electro- and photoelectrochemical oxidation of Acid Orange 7 dye. *Journal of Photochemistry and Photobiology A: Chemistry,* 302: 59 – 68.

23. Woo, K. K., Ngou, F. H., Ngo, L. S., Soong, W. K. and Tang, P. Y. (2011). Stability of betalain pigment from red dragon fruit (*Hylocereus polyrhizus*). *American Journal of Food Technology,* 6(2): 140 - 148.
24. Hug, H., Bader, M., Mair, P. and Glatzel, T. (2014). Biophotovoltaics: Natural pigments in dye-sensitized solar cells. *Applied Energy,* 115: 216 – 225.
25. Mark Lee, W. F., Ng, K. H., Minggu, L. J., Umar, A. A. and Kassim, M. (2012). Penentuan aras jalur tenaga kompleks tungsten nitrosilditiolena. *Sains Malaysiana,* 41(4): 439 - 444.
26. Grimes, C. A., Varghese, O. K. and Ranjan, S. *Light, Water, Hydrogen: The Solar Generation of Hydrogen by Water Photoelectrolysis*. 2008: Springer Science+Business Media.
27. Heo, N., Jun, Y. and Park, J. H. (2013). Dye molecules in electrolytes: new approach for suppression of dye-desorption in dye-sensitized solar cells. *Scientific Reports,* 3: 1712.

Malaysian Journal of Analytical Sciences, Vol 20 No 3 (2016): 660 - 669
DOI: http://dx.doi.org/10.17576/mjas-2016-2003-27

MALAYSIAN JOURNAL OF ANALYTICAL SCIENCES
Published by The Malaysian Analytical Sciences Society
ISSN 1394 - 2506

EFFECT OF PROCESS PARAMETERS ON THE SYNTHESIS OF POLYPYRROLE BY THE TAGUCHI METHOD

(Kesan Pembolehubah Proses Terhadap Sintesis Polipirola Menggunakan Kaedah Taguchi)

Rika Sri Utami[1], Ifa Puspasari[1], Loh Kee Shyuan[1]*, Abu Bakar Mohamed[1, 2], Sagir Alva[3]

[1]*Fuel Cell Institute*
[2]*Department of Chemical and Process Engineering, Faculty of Engineering and Built Environment*
Universiti Kebangsaan Malaysia, 43600 UKM Bangi, Selangor, Malaysia
[3]*Mechanical Engineering Department, Engineering Faculty,*
Mercu Buana University, 11650 Jakarta, Indonesia

**Corresponding author: ksloh@ukm.edu.my*

Received: 5 February 2016; Accepted: 22 April 2016

Abstract

Polypyrrole is a conductive polymer that is widely used in electrochemical applications. To identify the effects of different parameters on the synthesis of polypyrrole, an experimental design based on an orthogonal array L_9 (3^4) proposed by Taguchi was applied. The parameters investigated were the oxidant type, molar ratio of oxidant: pyrrole, reaction time and dopant concentration, whereas the response variables observed were the yield, particle size and conductivity. Field Emission Scanning Electron Microscope (FESEM) characterization was used to study the morphology characteristics of the polypyrrole particles. Based on the signal-to-noise (S/N) ratio and the results of analysis of variance (ANOVA), the molar ratio of oxidant: pyrrole and the oxidant type significantly affected the yield and conductivity of the synthesized polypyrrole particles.

Keywords: design of experiment, conductive polymer, yield, particle size, conductivity

Abstrak

Polipirola merupakan polimer konduktif yang digunakan secara meluas dalam aplikasi elektrokimia. Bagi tujuan mengenal pasti kesan-kesan parameter yang berbeza pada sintesis polipirola, reka bentuk eksperimen berdasarkan ortogon L_9 (3^4) yang dicadangkan oleh Taguchi telah digunakan. Parameter yang dikaji ialah jenis oksidan, nisbah molar oksidan: pirola, masa tindak balas dan kepekatan pendopan, manakala pemboleh ubah sambutan yang diperhatikan adalah jumlah hasil, saiz zarah dan kekonduksian. Pencirian FESEM telah digunakan untuk mengkaji morfologi zarah polipirola. Berdasarkan nisbah isyarat-hingar (S/N) dan hasil analisis varians (ANOVA), nisbah molar oksidan: pirola dan jenis oksidan memberi kesan yang ketara kepada hasil dan kekonduksian dari sintesis polipirola.

Kata kunci: reka bentuk eksperimen, polimer konduktif, jumlah hasil, saiz zarah, kekonduksian

Introduction

Conducting polymers, such as polyaniline (PAni), polypyrrole (PPy), and polythiophene (PTh), have found many industrial applications due to their unique characteristics, such as the dual function of ionic and electronic conductivity, large surface area and good mechanical properties [1-4]. Among the conductive polymers, PPy has attracted much attention because of its high conductivity [5], good environmental stability [6], electrocatalytic activity [7] and ease of synthesis [8]. Therefore, it has been widely used in electrochemical applications (e.g., as an

electrode material, in electrochemical energy storage [9], as a catalyst support in fuel cells [10], in supercapacitors [11] and in solar cells [12].

Polypyrrole can be synthesized by an electrochemical method [13], chemical oxidative polymerization [14], the reactive self-degradation template method [15], and micro emulsion polymerization [16]. Among the methods of PPy synthesis, the chemical oxidative polymerization method is extensively used because it is cheap, fast, and easy to scale up [17]. Several parameters have been reported to influence the chemical polymerization of PPy such as temperature, polymerization time [18], oxidant species [19], dopant type and dopant concentration [20]. However, prior studies have only examined the effect of one parameter individually and kept the other parameters constant. The Design of Experiments (DOE) method can be used to simultaneously evaluate the parameters for the synthesis of PPy, and this design also reduces the number of experiments.

An experimental design using the Taguchi approach has been implemented by numerous investigators to study the effect of different parameters on the synthesis of polymer particles. For example, a study by Hajian et al. [12] applied the Taguchi method to investigate several factors in the synthesis of polyvinyl butyral. Another study by Shahbazian et al. [1] reported the influence of five operating variables on the polymerization of vinyl chloride using the Taguchi method. The variables studied were temperature, water to monomer weight ratio, concentration of initiator and emulsifier, and agitation speed. The effect of each factor was comprehensively discussed, and the relative optimum condition was also determined. Ashassi-Sorkhabi and Bagheri [21] applied the Taguchi method to optimize the factors affecting the sonoelectrochemical synthesis of the PPy-SiN nanocomposite. The factors investigated were current density, synthesis time and amount of nanoparticles.

In this study, the Taguchi method was used to investigate the effects of (A) oxidant type, (B) molar ratio of oxidant:pyrrole, (C) time and (D) dopant concentration on the chemical synthesis of PPy. The response variables observed included the yield, particle size and conductivity.

Materials and Methods

The synthesis of PPy was carried out using the chemical oxidative polymerization method [22]. A certain amount of TsOH was added to 100 mL double-distilled water in a 250 mL round-bottom flask and stirred for 15 min. Fresh pyrrole (1.0 mL, 14.4 mmol) was added to the above solution, and the mixture was stirred for 45 min at room temperature to obtain a dark solution. An oxidant was added dropwise to the above mixture. Then, the mixture was stirred for a certain amount of time. The black products were filtered and washed repeatedly with ethanol and distilled water until the filtrate was colourless, and then the products were dried under vacuum at room temperature for 24 h.

The particle size of the samples was obtained using a particle sizer analyzer (Malvern Zeta sizer, model Nano zs/ZEN 3600). The conductivity of the samples was measured using Electrochemical Impedance Spectroscopy (EIS) over a frequency range of 10^2 to 10^4 Hz with 10 mv at room temperature using a two point probe cell. The morphologies and chemical composition of the samples were characterized using Field Emission Scanning Electron Microscopy (FE-SEM) coupled with Energy Dispersive X-Ray Spectroscopy (EDX) (ZEISS, Germany).

In this work, a Taguchi L_9 orthogonal array was used to study the effect of different parameters and determine the optimal conditions. Four factors at three levels were used in this design of experiment, as presented in Table 1 and Table 2, respectively. The response variables observed were yield, particle size and conductivity.

Table 1. Parameters and levels used in this experiment

Parameters		**Levels**		
		1	**2**	**3**
A	Oxidant type	APS	$FeCl_3$	H_2O_2
B	Molar ratio of oxidant: pyrrole	1 : 1	3 : 1	5 : 1
C	Time (h)	1	8	24
D	Dopant concentration (M)	0.01	0.05	0.1

Table 2. Experimental layout using a L_9 orthogonal array

Exp. No.	**A** **Oxidant type**	**B** **Molar ratio**	**C** **Time (h)**	**D** **Dopant concentration (M)**
1	1	1	1	1
2	1	2	2	2
3	1	3	3	3
4	2	1	2	3
5	2	2	3	1
6	2	3	1	2
7	3	1	3	2
8	3	2	1	3
9	3	3	2	1

The S/N (signal-to-noise) is a quality indicator that is used to evaluate the effect of changing particular parameter on the process performance. Generally, there are three categories of performance characteristics in the analysis of the S/N ratio [23-26].

Type S (smaller is better):

$$S/N_S = -10 \log \left[\frac{\sum_{i=1}^{n}(yi^2)}{n}\right] \quad (1)$$

Type B (Bigger is better):

$$S/N_B = -10 \log \left[\frac{\sum_{i=1}^{n}\left(\frac{1}{yi^2}\right)}{n}\right] \quad (2)$$

and Type N (nominal is better):

$$S/N_N = 10 \log \frac{\left(\frac{1}{n}\right)(((\sum_{i=1}^{n} yi)^2/n) - (\sum_{i=1}^{n} yi^2 - ((\sum_{i=1}^{n} yi)^2/n)/n-1))}{(\sum_{i=1}^{n} yi^2 - ((\sum_{i=1}^{n} yi)^2/n)/n-1} \quad (3)$$

where n is the number of replicates and yi is the response variable at ($i = n$).
In this study, the S/N ratio was selected according to the criterion that smaller is better for particle size and bigger is better for both yield and electronic conductivity.

Results and Discussion

Morphology of the polypyrrole particles

The FE-SEM morphology for the PPy particles obtained in this experiment was presented in Figure 1. As shown in Figure 1, all the PPy particles exhibited agglomerates of various sizes depending on the synthesis parameters.

Table 3 shows the chemical composition of the PPy particles as obtained by EDAX. The results confirmed that the presence of sulfur originated from the dopant (TSOH). The presence of chlorine and iron elements from experiments no. 4 to no. 6 may come from $FeCl_3$, which was doped into the PPy/TSOH particles as the oxidant.

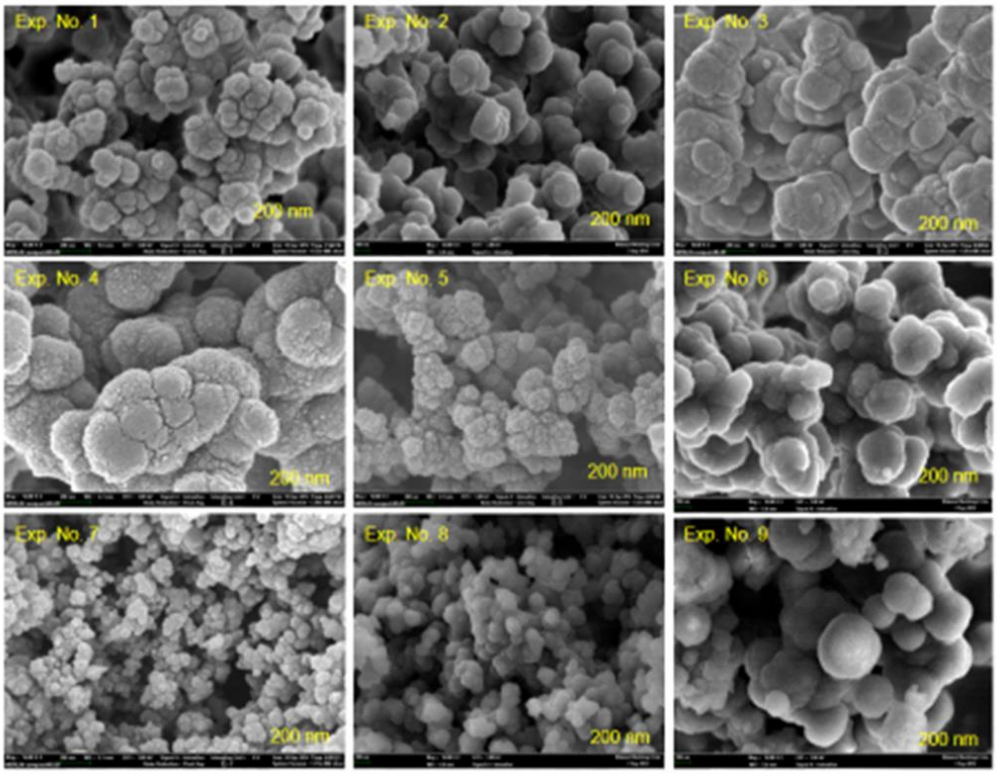


Figure 1. FESEM images of the samples

Table 3. Chemical composition in weight percent as obtained by EDAX

Experiment	Weight (%)					
	C	N	O	S	Cl	Fe
1	68.24	8.67	20.32	2.77	-	-
2	61.98	14.04	18.97	5.00	-	-
3	75.47	1.71	13.91	8.90	-	-
4	63.39	14.44	16.37	3.56	1.86	0.18
5	72.17	1.54	20.31	3.64	1.90	0.44
6	70.96	2.54	11.94	6.78	3.66	4.11
7	60.87	13.03	22.10	4.01	-	-
8	66.65	0.70	31.95	0.70	-	-
9	60.76	12.65	22.19	4.41	-	-

Taguchi experimental design analysis

The Taguchi method was used to identify the optimal conditions and to select parameters that have the most influence on the yield, particle size and electronic conductivity of polypyrrole. The results of the measurement and S/N ratio values of the Taguchi method are shown in Table 4. As shown in Table 4, the smallest particle size (0.394 µm) was found in experiment no. 1, whereas the highest yield (0.69 g) and electronic conductivity (0.730 S/cm) were found in experiments no. 3 and no. 6, respectively.

Table 4. Experimental measured value and S/N ratio for yield, particle size and electronic conductivity of polypyrrole particles

No.	Yield		Particle Size		Electronic conductivity	
	Raw data (g)	S/N ratio (dB)	Raw data (µm)	S/N ratio (dB)	Raw data (S/cm)	S/N ratio (dB)
1	0.09	-20.92	0.394	8.09	0.085	-21.41
2	0.34	-9.37	0.481	6.36	0.270	-11.37
3	0.69	-3.22	0.675	3.42	0.043	-27.33
4	0.07	-23.10	1.574	-3.94	0.660	-3.61
5	0.22	-13.15	0.430	7.33	0.230	-12.77
6	0.43	-7.33	0.772	2.25	0.730	-2.73
7	0.01	-40.00	0.965	0.31	0.014	-37.08
8	0.20	-13.98	0.675	3.41	0.029	-30.75
9	0.49	-6.20	1.059	0.50	0.030	-30.46

The mean S/N ratio for each parameter level is summarized in Table 5. As shown in Table 5, the molar ratio of oxidant: pyrrole (76.91 %) has the highest value for yield and the oxidant type (82.62 %) has the highest value for electronic conductivity. Therefore, it can be concluded that the molar ratio of oxidant: pyrrole and oxidant type are the parameters that are significant and affect the yield and electronic conductivity, respectively. In contrast, all the parameters were found almost equally to affect the particle size (Table 5).

Table 5. Mean S/N ratio for yield, particle size, and electronic conductivity

Factor	A	B	C	D
Parameter	Oxidant type	Molar ratio	Time	Dopant concentration
Yield				
Level 1 (dB)	-11.17	-28.00	-14.08	-13.42
Level 2 (dB)	-14.53	-12.17	-12.89	-18.90
Level 3 (dB)	-20.06	-5.58	-18.79	-13.43
ρ (%)	11.67	76.91	5.65	5.78
Particle Size				
Level 1 (dB)	5.96	1.49	4.58	5.31
Level 2 (dB)	1.88	5.70	0.97	2.98
Level 3 (dB)	1.41	2.06	3.69	0.96
ρ (%)	31.67	26.49	17.88	23.95
Electronic Conductivity				
Level 1 (dB)	-20.04	-20.70	-18.30	-21.54
Level 2 (dB)	-6.37	-18.30	-15.15	-17.06
Level 3 (dB)	-32.76	-20.17	-25.72	-20.56
ρ (%)	82.62	0.76	13.99	2.63

Figure 2 displays the graphs for (a) yield, (b) particle size and (c) electronic conductivity. As shown in Figure 2 (a), the optimum levels for each of the parameters are A1, B3, C3, and D3. Therefore, based on the graph, the optimum conditions for maximizing the yield are an oxidant type of APS, a molar ratio of oxidant:pyrrole of 5:1, a polymerization time of 24 hours and a dopant concentration of 0.1 M. Figure 2 (b) displays the optimum levels for decreasing particle size, which are as follows: A1, B2, C1, and D1, i.e., an oxidant type of APS, a molar ratio of oxidant: pyrrole of 3:1, a polymerization time of 1 hour and a dopant concentration of 0.01 M. Finally, to maximize the electronic conductivity (Figure 2 (c)), the optimum conditions are at A2, B3, C2, and D2, i.e., an oxidant type of $FeCl_3$, a molar ratio of oxidant: pyrrole of 5:1, a polymerization time of 8 hours and a dopant concentration of 0.05 M.

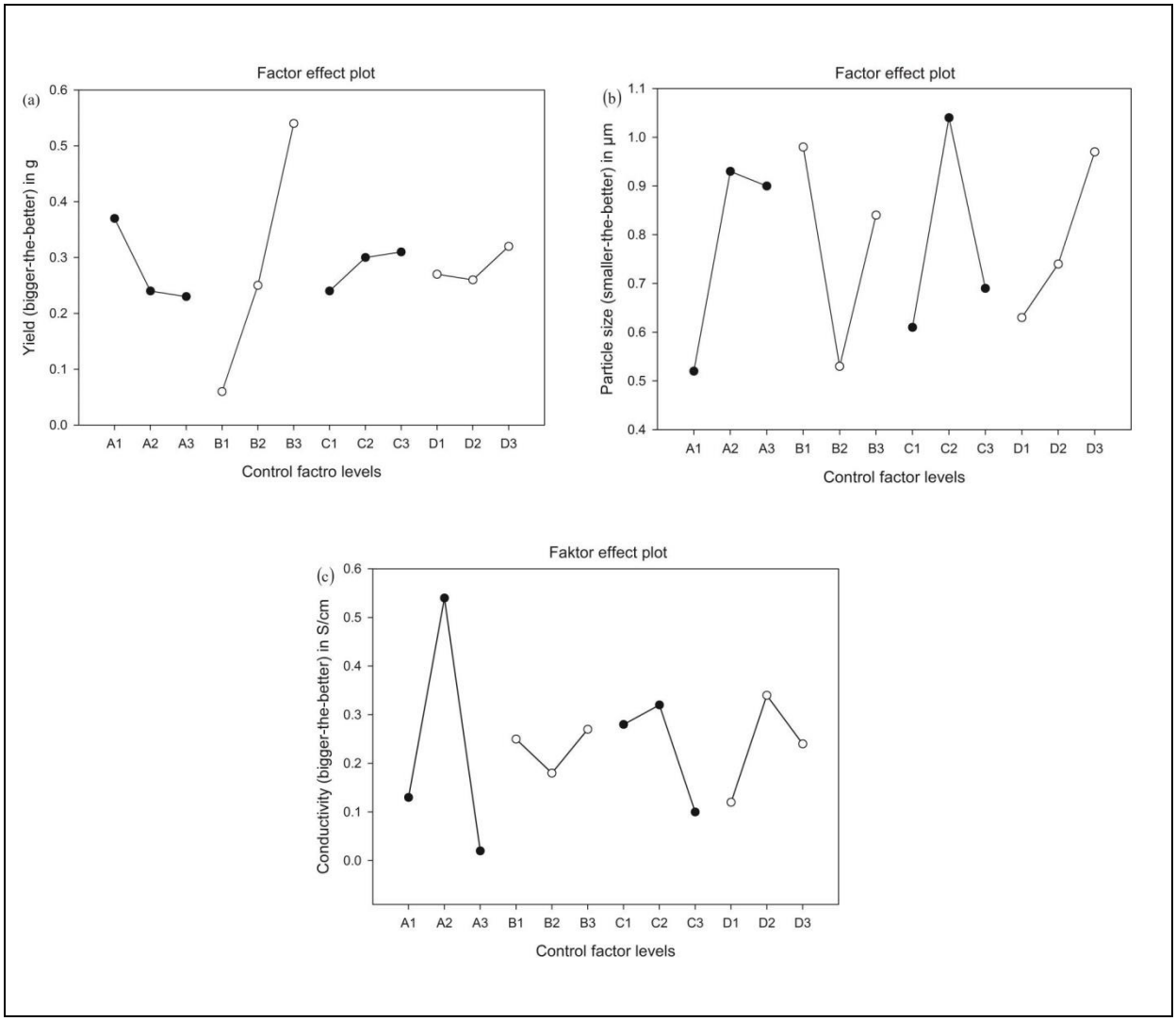


Figure 2. Graph for (a) yield, (b) particle size, and (c) electronic conductivity

In addition to S/N ratio, the variance analysis (ANOVA) was performed to investigate which process parameters significantly affect the response variables. The results of the ANOVA for yield, particle size and electronic

conductivity are presented in Table 6. As shown in Table 6, the order of significance of the factors for yield is as follows: B> A> D> C, whereas for particle size and electronic conductivity the order is: A> B> D> C and A> C> D> B, respectively.

Table 6. The ANOVA table of yield, particle size, and electronic conductivity for selected factorial model

Factor	Yield				Particle size				Electronic conductivity			
	S	***ϕ***	***V***	***F***	***S***	***ϕ***	***V***	***F***	***S***	***ϕ***	***V***	***F***
A	121	2	60	6	38	2	19	16	1045	2	523	41
B	797	2	398	38	31	2	16	13	10	2	5	0
C	59	2	29	3	21	2	11	9	177	2	88	7
D	60	2	30	3	28	2	14	12	33	2	17	1
Total	1036	8			119	8			1265	8		

Additional experiments at level A2, B3, C1, and D2 were conducted to confirm the Taguchi method. The results of the experiments as well as the prediction are shown in Table 7. There are good agreements between the predicted and experimental results for the yield, particle size and electronic conductivity. Thus, the synthesis process for the polypyrrole particles can be improved using the Taguchi method.

Table 7. Results of the confirmation for yield, particle size and electronic conductivity

	Level	Yield		Particle size		Electronic conductivity	
		Yield (g)	S/N ratio (dB)	Particle size (μm)	S/N ratio (dB)	E. Conductivity (S/cm)	S/N ratio (dB)
Prediction	A2B3C1D2	0.43	-7.33	0.771	2.26	0.73	-2.73
Experiment	A2B3C1D2	0.40	-7.96	0.725	2.79	0.77	-2.27

Effects of process parameters on the synthesis of the polypyrrole particles

Three types of oxidants were used to study their effects on pyrrole polymerization. All the solid products observed from the different types of oxidants were dark in colour. From the results of the Taguchi analysis shown in Figure 2, when APS was used, the products obtained the highest yield (0.37 g) and smallest particle size (0.52 μm), whereas when $FeCl_3$ was used, the highest conductivity (0.54 S/cm) was obtained. When H_2O_2 was used as the oxidant, it produced the lowest yield (0.23 g) and conductivity (0.02 S/cm) and the larger particles size (0.90 μm). The PPy synthesized using APS as the oxidant produced a higher yield than $FeCl_3$ and H_2O_2 because APS has more oxidizability towards the pyrrole monomers than the other oxidants [19, 27]. The high conductivity obtained with $FeCl_3$ as the oxidant compared to APS and H_2O_2 is due to the presence of iron ions. This result is in agreement with the previous work by Lascelles et al. [28]. They also found that the synthesis of polypyrrole silica particles using $FeCl_3.6H_2O$ produces a significantly higher conductivity than $(NH_4)_2S_2O_8$ and H_2O_2.

The effects of the molar ratio of oxidant to pyrrole on the yield, particle size and electronic conductivity are shown in Figure 2 (a-c). The product yield increased from 0.06 g to 0.54 g as the molar ratios of oxidant to pyrrole increased from 1:1 to 5:1. The same observation was also found by Li et al. [27] for the polymerization of PPy using APS as the oxidant. They also noted that the amount of oxidant required to produce sufficient PPy particles is at least equal to the monomer (molar ratio of oxidant/monomer higher than 1). From Figure 2 (b), when the molar ratios increased from 1:1 to 5:1, the particle size of PPy decreased first from 0.98 μm to 0.53 μm and then increased

again (0.84 µm). This is consistent with the finding of Li et al. [27]. They emphasized that at a lower concentration of oxidant, less Py radicals are formed, the polymerization process is slow, and thus smaller particles are formed. When the oxidant concentration is too high, more monomers are oxidized into radicals, and the particle size increases. The amount of oxidant also influenced the electronic conductivity of the PPy. Figure 2 shows that as the molar ratio increased from 1:1 to 5:1, the conductivity decreased first from 0.25 S/cm to 0.18 S/cm and then increased with a maximum of 0.27 S/cm at a molar ratio of 5:1.

Figure 2 also shows the influence of polymerization time on the synthesis of the PPy particles. The yield of the PPy particles increased from 0.24 g to 0.31 g when the polymerization time increased from 1 to 24 h. The same trend were also observed by Omastova et al. [29] and Pina et al. [11] for the pyrrole polymerization using silver nitrate and gold as the dopant, respectively. From their studies, the yield increased from 0.394 g to 4.939 g and 1 % to 99 % when the polymerization time increased from 24 to 168 hours and 8 to 72 hours, respectively. Thus, the longer the reaction time, the more PPy particles formed. Figure 2 also shows that as the polymerization time increased from 1 h to 24 hours, the particle size increased first from 0.61 µm to 1.04 µm and then decreased to approximately 0.69 µm, whereas the electronic conductivity increased from 0.28 S/cm to 0.32 S/cm and decreased after a polymerization time of 24 hours (0.10 S/cm).

When TsOH as a dopant into the polymerization was introduced, the yield increased from 0.27 g to 0.32 g as the dopant concentration increased. This is because the TsOH acted as both dopant and template at the higher concentration. Upadhyay and Kumar [15] showed that the yield of the sample increased from 43.12 % to 58.63 % with an increase in CTAB (dopant) concentration from 1 mM to 3 mM. They also observed that the particle size increased from 0.63 µm to 0.97 µm when the concentration of dopant (TsOH) increased. However, the conductivity of the PPy particles was found to increase from 0.12 S/cm to 0.34 S/cm when the dopant concentration was increased from 0.01 M to 0.05 M. Upon further increase in the dopant concentration, the conductivity decreased to 0.24 S/cm. Yang and Liu [30] observed a similar trend for the polymerization of PPy with the addition of PHMPS as the dopant. Their results showed that the conductivity of the samples increased when the feeding ratio of PHMPS was increased from 1 to 10 wt % and subsequently decreased. Several other investigators also reported the same observation [14-15, 22, 31].

Conclusion

In this study, an orthogonal Taguchi L9 array was used to investigate the effects of the synthesis parameters on the polymerization of pyrrole. The parameters studied were oxidant type, molar ratio of oxidant: pyrrole, time and dopant concentration. The results showed that the molar ratio of oxidant: pyrrole and the oxidant type significantly affected the yield and electronic conductivity, respectively. As the molar ratios of oxidant to pyrrole increased from 1:1 to 5:1, the product yield also increased from 0.06 g to 0.54 g. Additionally, when using $FeCl_3$ as the oxidant, the highest conductivity (0.54 S/cm) was obtained compared with APS and H_2O_2.

Acknowledgement

This work was supported by the Universiti Kebangsaan Malaysia and the Malaysia Ministry of Higher Education (MOHE) with research grants of GGPM-2013-044, DIP-2014-002 and FRGS/2/2013/UKM/02/3.

References

1. Shahbazian, A., Navarchian, A. H. and Pourmehr, M. (2009). Application of Taguchi method to investigate the effects of process factors on the performance of batch emulsion polymerization of vinyl chloride. *Journal of Applied Polymer Science*, 113 (5): 2739-2746.
2. Al-Dulaimi, A. A., Hashim, S. and Khan, M. (2011). Corrosion protection of carbon steel using polyaniline composite with inorganic pigments. *Sains Malaysiana*, 40 (7): 757-763.
3. Izzuddin, I., Jumali, M. H. H., Yahaya, M. and Salleh, M. M. (2012). New hybridization approach of titanium organometallic: PANI thin films as room temperature gas sensors. *Sains Malaysiana*, 41 (8): 1017-1021.
4. Juamli, M. H. H., Ramli, N., Izzuddin, I., Salleh M. M. and Yahaya, M. (2011). Influence of PANI additions on methanol sensing properties of ZnO thin films. *Sains Malaysiana*, 40 (3): 203-208.

5. Khan, A. A. and Paquiza, L. (2011). Electrical behavior of conducting polymer based 'polymeric–inorganic'nanocomposite: Polyaniline and polypyrrole zirconium titanium phosphate. *Synthetic Metals*, 161 (9): 899-905.
6. Qi, K., Qiu, Y., Chen, Z. and Guo, X. (2012). Corrosion of conductive polypyrrole: Effects of environmental factors, electrochemical stimulation, and doping anions. *Corrosion Science*, 60: 50-58.
7. Ghamouss, F., Brugère, A., Anbalagan, A. C., Schmaltz, B., Luais, E. and Tran-Van, F. (2013). Novel glycerol assisted synthesis of polypyrrole nanospheres and its electrochemical properties. *Synthetic Metals*, 168: 9-15.
8. Kim, D. K., Oh, K. W., Ahn, H. J. and Kim, S. H. (2008). Synthesis and characterization of polypyrrole rod doped with p-toluenesulfonic acid via micelle formation. *Journal of Applied Polymer Science*, 107 (6): 3925-3932.
9. Karaca, E., Pekmez, N. Ö. and Pekmez, K. (2014). Galvanostatic deposition of polypyrrole in the presence of tartaric acid for electrochemical supercapacitor. *Electrochimica Acta*, 147: 545-556.
10. Yuan, X., Ding, X.-L., Wang, C.-Y. and Ma, Z.-F. (2013). Use of polypyrrole in catalysts for low temperature fuel cells. *Energy & Environmental Science*, 6 (4): 1105-1124.
11. Pina, C. D., Falletta, E., Faro, M. L., Pasta, M. and Rossi, M. (2009). Gold-catalysed synthesis of polypyrrole. *Gold Bulletin*, 42 (1): 27-33.
12. Hajian, M., Koohmareh, G. A. and Rastgoo, M. (2010). Investigation of factors affecting synthesis of polyvinyl butyral by Taguchi method. *Journal of Applied Polymer Science*, 115 (6): 3592-3597.
13. Tam, P. D. and Hieu, N. V. (2011). Conducting polymer film-based immunosensors using carbon nanotube/antibodies doped polypyrrole. *Applied Surface Science*, 257 (23): 9817-9824.
14. Yang, C., Wang, X., Wang, Y. and Liu, P. (2012). Polypyrrole nanoparticles with high dispersion stability via chemical oxidative polymerization in presence of an anionic–non-ionic bifunctional polymeric surfactant. *Powder Technology*, 217: 134-139.
15. Upadhyay, J. and Kumar, A. (2013). Structural, thermal and dielectric studies of polypyrrole nanotubes synthesized by reactive self degrade template method. *Materials Science and Engineering: B*, 178 (15): 982-989.
16. Hazarika, J. and Kumar, A. (2013). Controllable synthesis and characterization of polypyrrole nanoparticles in sodium dodecylsulphate (SDS) micellar solutions. *Synthetic Metals*, 175: 155-162.
17. Yuan, X., Kong, H.-C., He, Y.-J., Ma, Z.-F., Yang, Y. and Li, Q. (2014). Effects of composition on electrochemical properties of a non-precious metal catalyst towards oxygen reduction reaction. International *Journal of Hydrogen Energy*, 39 (28): 16006-16014.
18. Karami, H. and Nezhad, A. R. (2013). Investigation of pulse-electropolymerization of conductive polypyrrole nanostructures. *International Journal of Electrochemical Science*, 8: 8905-8921.
19. Liao, Y., Wang, X., Qian, W., Li, Y., Li, X. and Yu, D.-G. (2012). Bulk synthesis, optimization, and characterization of highly dispersible polypyrrole nanoparticles toward protein separation using nanocomposite membranes. *Journal of Colloid and Interface Science*, 386 (1): 148-157.
20. Paramo-García, U., Ibanez, J. & Batina, N. (2013). AFM analysis of polypyrrole films synthesized in the presence of selected doping agents. *International Journal of Electrochemical Science*, 8: 2656-2669.
21. Ashassi-Sorkhabi, H. and Bagheri, R. (2014). Sonoelectrochemical synthesis, optimized by Taguchi method, and corrosion behavior of polypyrrole-silicon nitride nanocomposite on St-12 steel. *Synthetic Metals*, 195: 1-8.
22. Wang, Y., Yang, C. and Liu, P. (2011). Acid blue AS doped polypyrrole (PPy/AS) nanomaterials with different morphologies as electrode materials for supercapacitors. *Chemical Engineering Journal*, 172 (2-3): 1137-1144.
23. Hung, S.-L., Wen, T.-C. and Gopalan, A. (2002). Application of statistical design strategies to optimize the conductivity of electrosynthesized polypyrrole. *Materials Letters*, 55 (3): 165-170.
24. Taguchi, G. (1990). Introduction to Quality Engineering: Designing Quality into Products and Processes, Asian Productivity Organization, Tokyo.
25. Bendell, A., Disney, J. & Pridmore, W. A. (1989). Taguchi Methods: Applications in World Industry. IFS Publications, UK.
26. Taguchi, G. (1962). Tables of orthogonal arrays and linear graphs. Maruzen, Tokyo.
27. Li, X.-G., Li, A., Huang, M.-R., Liao, Y. and Lu, Y.-G. (2010). Efficient and scalable synthesis of pure polypyrrole nanoparticles applicable for advanced nanocomposites and carbon nanoparticles. The *Journal of Physical Chemistry C*, 114 (45): 19244-19255.

28. Lascelles, S., McCarthy, G., Butterworth, M. and Armes, S. (1998). Effect of synthesis parameters on the particle size, composition and colloid stability of polypyrrole–silica nanocomposite particles. *Colloid and Polymer Science*, 276 (10): 893-902.
29. Omastová, M., Mosnáčková, K., Fedorko, P., Trchová, M. and Stejskal, J. (2013). Polypyrrole/silver composites prepared by single-step synthesis. *Synthetic Metals*, 166: 57-62.
30. Yang, C. and Liu, P. (2010). Water-dispersed polypyrrole nanoparticles via chemical oxidative polymerization in the presence of a functional polyanion. *Reactive and Functional Polymers*, 70 (10): 726-731.
31. Wang, X., Yang, C., Li, H. and Liu, P. (2013). Synthesis and electrochemical performance of well-defined flake-shaped sulfonated graphene/polypyrrole composites via facile in situ doping polymerization. *Electrochimica Acta*, 111: 729-737.

Malaysian Journal of Analytical Sciences, Vol 20 No 3 (2016): 670 - 677
DOI: http://dx.doi.org/10.17576/mjas-2016-2003-28

MALAYSIAN JOURNAL OF ANALYTICAL SCIENCES
Published by The Malaysian Analytical Sciences Society
ISSN 1394 - 2506

THERMAL PROPERTIES AND CONDUCTIVITY OF NAFION-ZIRCONIA COMPOSITE MEMBRANE

(Sifat Terma dan Konduktiviti Membran Komposit Nafion-Zirkonia)

Siti Rahmah Mokhtaruddin[1, 2], Abu Bakar Mohamad[1, 2]*, Kee Shyuan Loh[1], Abdul Amir Hasan Kadhum[1, 2]

[1]*Fuel Cell Institute*
[2]*Department of Chemical and Process Engineering, Faculty of Engineering and Built Environment*
Universiti Kebangsaan Malaysia, 43600 UKM Bangi, Selangor, Malaysia

**Corresponding author: drab@ukm.edu.my*

Received: 5 February 2016; Accepted: 22 April 2016

Abstract

The application of composite membranes for high temperature polymer electrolyte membrane fuel cell has attracted interests. Nafion-metal dioxide composite membranes are considered among the research niche. In this study, Nafion membranes and Nafion-zirconia composite membranes with 1, 3 and 5 wt. % of hydrous zirconia were prepared accordingly. All membranes were characterized by quantitative analysis techniques such as thermogravimetry analyse, diffraction scanning calorimetry and Fourier transform infrared. All composite membranes showed high glass transition temperatures and improved water retention properties, compared to the Nafion membrane. The composite membrane with 3 wt. % of zirconia showed the highest thermal resistance at 90°C.

Keywords: high temperature PEM, glass transition temperature, conductivity, composite membrane, Nafion-zirconia

Abstrak

Penggunaan membran komposit dalam operasi sel bahanapi membran penukar proton pada suhu tinggi semakin mendapat perhatian pengkaji. Membran komposit Nafion-logam dioksida adalah antara bidang kajian dalam kumpulan ini. Bagi kajian ini, membran Nafion dan membran komposit Nafion-zirkonia dengan 1, 3, dan 5 wt. % telah disediakan. Kesemua membran dicirikan menggunakan teknik analisis kuantitatif seperti analisis termogravimetri, kalorimetri imbasan kerbedaan dan Fourier inframerah. Kesemua membran komposit mempunyai suhu peralihan kaca yang tinggi dan keupayaan penahanan air yang lebih baik berbanding membran Nafion. Membran komposit dengan 3 wt. % zirkonia menunjukkan ketahanan suhu tinggi pada suhu operasi 90°C.

Kata kunci: PEM suhu tinggi, suhu peralihan kaca, konduktiviti, membran komposit, Nafion-zirkonia

Introduction

Fuel cells are electrochemical devices which convert the energy from the reaction of fuel and oxygen into electric energy continuously with water and CO_2 as the byproducts [1]. Polymer electrolyte membrane fuel cell (PEMFC) is one of the fuel cell types, for temperature ranging from 60 - 100 °C. Nafion membranes are the most commonly used polymer electrolytes in PEMFC application as it has excellent chemical, mechanical and electrochemical properties as well as high proton conductivity at ambient temperature and high humidity condition. This water-based electrolyte needs to be kept in a hydrated condition for the best performance and a maximum conductivity of 0.083 S/cm at 100% relative humidity (RH) [2].

However, the membrane tends to shrink at low humidity and swells under excess water conditions due to its molecular structure. The ionic groups form clusters of 2 – 4 nm in diameter, which are connected by narrow channels; the size of these clusters is proportional to the water level in the membrane, which can explain the shrink-swell behavior of the polymer [3]. Therefore, developing membranes with good stability for both thermal and mechanical properties is desirable. Many methods have been developed to produce composite membranes, including incorporating hygroscopic metal oxides such as SiO_2 [4], TiO_2 [5] and ZrO_2 [6] into the Nafion polymer structure. Incorporating a hydrophilic, inorganic material into the perfluorinated polymer is an alternative way to increase the binding energy of water [7]. The membrane strength and performance increased, as the organic polymer formed strong interaction with the inorganic component having large specific area [8].

In this study, a series of Nafion-ZrO_2 composite membranes with 1, 3 and 5 wt. % of hydrous zirconia loading were prepared with the purpose of increasing the thermal resistance of membrane, thus increasing the proton conductivity of the membrane. The hygroscopic property of zirconia was expected to improve the thermal strength of the membrane by increasing the glass transition temperature.

Materials and Methods

Materials

The 5 wt. % Nafion solution (EW 1100) and Nafion 115 were purchased from DuPont, USA. Zirconium (IV) oxychloride octahydrate ($ZrOCl_2.8H_2O$), ammonium solution (NH_4OH), dimethylformamide (DMF), sulfuric acid (H_2SO_4, 98 %) and hydrogen peroxide (H_2O_2, 30 %) were all purchased from Aldrich. Deionized water was used as the solvent in all experiments.

Preparation of the Nafion-ZrO_2 composite membrane

Nafion solution was evaporated at room temperature to obtain solid Nafion. The solid Nafion was then dissolved in DMF and stirred for two hours. Meanwhile, the hydrous zirconia was prepared via film casting process according to the method proposed by Chuah et al [9]. $ZrOCl_2.8H_2O$ was dissolved in distilled water. Dilute aqueous ammonia was added drop-wise to the solution with vigorous stirring until the pH of the solution reached 10. The obtained precipitate was washed with distilled water several times to remove the chloride ions before being oven-dried at 100°C for 12 hours. Matrices of 1, 3 and 5 wt% of Nafion-ZrO_2 were mixed in a DMF solution. Subsequently, the mixture was casted onto a container and heated at 80°C for 2 hours, before the temperature was increased to 110°C for six hours to enhance the polymer strength and remove excess solvent. After that, the recast composite membrane was detached from the container and washed with a 3 wt % H_2O_2 and 0.5 M H_2SO_4 solution. These samples were labeled as NZ01, NZ03 and NZ05 according to the loading of 1 wt%, 3 wt% and 5 wt% of hydrous zirconia, respectively. A similar method was used to prepare the recast Nafion.

Characterization of the Nafion-ZrO_2 composite membrane

The infra-red spectra of the composite membranes (NZ01, NZ03 and NZ05) were recorded to detect the functional groups chemical change in the polymer as compared to pure Nafion membrane. A Thermo Fisher Scientific FTIR (Nicolet 6700) spectrophotometer was used in the analyses.

The DSC spectra of the prepared composite membranes were obtained using a DSC 1 Star System (Mettler Toledo). Membrane samples were cut and weighed to 0.25 g in an aluminum crucible. Measurements were performed over the temperature range of 30 – 300 °C with a heating rate of 20 °C /min under nitrogen gas.

The ionic conductivity of the membranes was measured with a potentiostat (Autolab, PGSTAT 128N) in the frequency range between 1 mHz and 100 kHz. The membrane samples were immersed for 30 minutes in de-ionized water at the desired temperature before being placed on electrode cells for measurements. The measurement was carried out at room temperature and at 90 °C in order to study the effect of operating temperature and compositions of the inorganic compound embedded in the polymer matrix towards conductivity at 90 °C. The graph of the negative imaginary impedance versus the real impedance was plotted for each set of data. The bulk impedance R_b of the samples was determined from the curve and thus, the ionic conductivity, σ, was calculated using Equation 1.

$$\sigma = t/(R_b * A) \quad (1)$$

where, *t* is the sample thickness (cm), *A* is the effective contact area of the film and the electrode (cm^2) and R_b is the bulk resistance (Ω).

Results and Discussion

Structure analysis

Figure 1 shows the FTIR spectra of recast Nafion; NZ01, NZ03, NZ05 composite membranes; and hydrous zirconia. The peaks at 3455.03 – 3428 cm^{-1} are assigned to the bending vibrations of water molecules and the OH stretching mode of the adsorbed water [10]. It is observed that the broad peak of the -OH peak increases with the addition of the zirconia composition. The peaks at 1198.28 cm^{-1}, 1198.25 cm^{-1} and 1198.32 cm^{-1} are attributed to the $-CF_2-CF_2-$ vibration, as reported by Zhai et al. [11]. The $–SO_3-$ peaks appear at 1059.26 cm^{-1}, 1058.19 cm^{-1} and 1055.21 cm^{-1}. The IR spectra of NZ01, NZ03 and NZ05 are similar to that of recast Nafion, except for the appearance of a small peak near 1500 cm^{-1}, indicating the existence of hydrous zirconia molecules in the composite membranes. The peak that appears around 1530.49 – 1520.22 cm^{-1} indicates the Zr-OH bending vibrations. Peaks at 514.28 cm^{-1} and 513.72 cm^{-1} show the Zr-O vibrations, which are overlapped by the transmittance peaks of the Nafion [12]. As mentioned by Pan et al., the overlapping peaks suggest that the addition of zirconia does not affect the crystallinity or the molecular structure of the Nafion membrane [6].

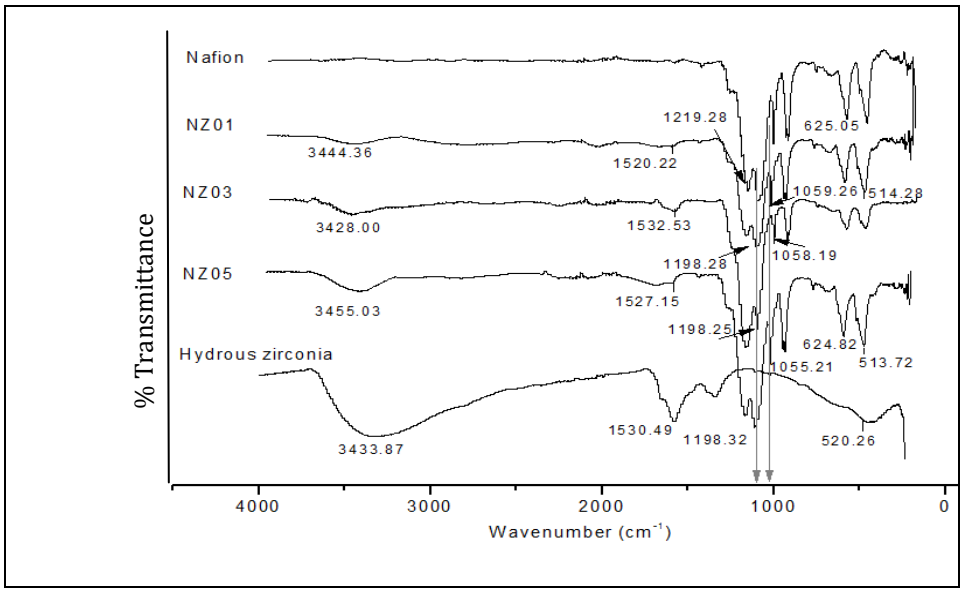


Figure 1. FTIR spectra of Nafion and Nafion-ZrO_2 composite membranes

Thermal properties

The results obtained from thermal gravimetric analysis (TGA) is shown in Figure 2. The TGA curves show a three step degradation, which is the loss of physically and chemically bound water (below 200 °C), the decomposition of sulfonic acid groups or desulfonation (250 – 400 °C) and main chain degradation (400 –800°C) [13]. As expected, recast Nafion degrades faster than the composite membranes in all three degradation steps.

The magnified portion of the graph shows the first part of the degradation. Low of mass loss (<6 %) is shown for the composite membranes at this temperature range. The degradation of the Nafion membrane was caused by the breakage of the perfluorinated backbone and the side-chains in the membrane. The desulfonation of the membrane starts at approximately 280 °C for the recast Nafion membrane, whereas it begins higher for the composite membranes, at the temperatures of 300 °C for NZ01 and NZ03, 280 °C for NZ05, which indicates the breaking of

C-S bonds. NZ05 has the lowest desulfonation temperature among the composite membranes, which is similar to the recast Nafion.

For the third step of the degradation, it is clearly seen that the Nafion decomposes at a lower temperature than the composite membranes. Iwai and Yamanishi [14] have reported that cations with larger ionic radii show higher thermal stability when reacted with Nafion and Zirconia is a metal oxide with large molecular radius. Therefore, the composite membranes have higher thermal retention as a higher temperature is needed to activate the energy barrier and break the bond.

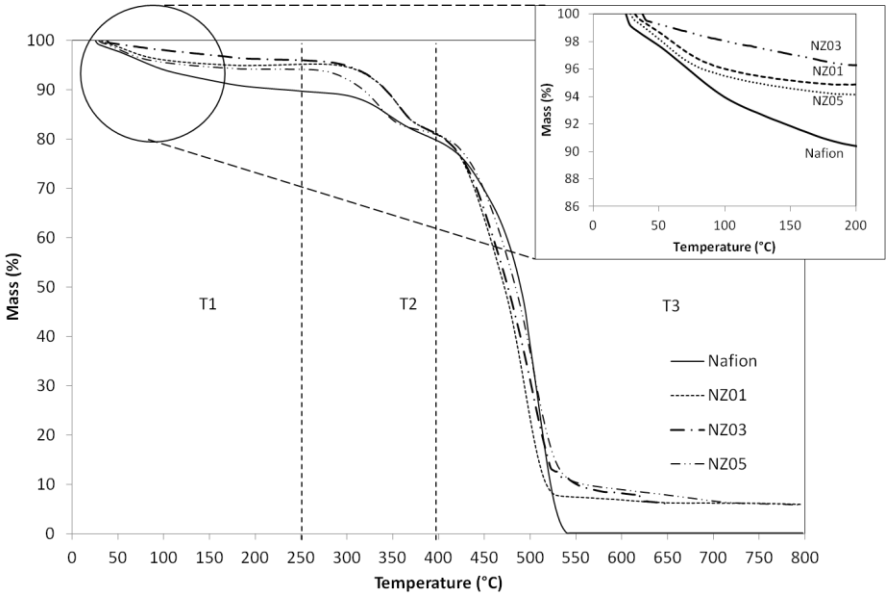


Figure 2. TGA curves for Nafion and composite membranes. T1: Water loss, T2: desulfonation, T3: main chain degradation.

Figure 3 shows that an endothermic peak appears at approximately 70 – 90 °C, which increases up to 3 wt. % of hydrous zirconia content, indicating the enhanced water retention. These broad peaks (ranging from 50 – 140 °C) caused by the structural change in the membrane cluster as shown in the FTIR spectrum. The composite membranes show different behavior than Nafion membrane as temperature increases. This observation is consistent with the report by Sacca et al [2], where zirconia functions well as a hygroscopic compound in improving the water content in the membrane, although the pattern shows a decrease for NZ05. At the desulfonation phase, the recast Nafion degraded slower than the Nafion membrane, as they have amorphous zirconia to resist the degradation. A broad exothermic peak appears at approximately 350 °C for all composite membranes, which is attributed to the dehydroxylation of the hydrous zirconia with increasing temperature. The exothermic event is then followed by another weight loss due to main chain degradation. The exothermic peak with weight change is assigned to the releasing of hydroxyl groups at a high temperature, resulting in the formation and crystallization of the amorphous zirconia [15]. Another two peaks of crystallization appear at approximately 450 °C and 550 °C, indicating another phase change in the hydrous zirconia.

From Figure 3, it is seen that Nafion had loss almost 10 % of mass at 300 °C but the NZ01 and NZ03 composite membranes had retain more than 95 % of their weight while NZ05 had 8 % mass loss at the same temperature. Above 300 °C, all membranes decompose rapidly as the membranes starts losing their sulfonyl chain in the Nafion matrix. However, the temperature shifted for the composite membranes, due to the nature of the hygroscopic inorganic component; increasing water content in the composite membrane [16]. Thermal degradation of Nafion

membrane occurs at 308 °C; whereas the degradation temperature shifted to 333 °C for both NZ01 and NZ03, and at 317 °C for NZ05. Shao has reported that the increment of degradation temperature is due to the addition of metal oxide (such as SiO_2, TiO_2, ZrO_2) into the Nafion matrix as the inorganic compound is temperature tolerant filler [17].

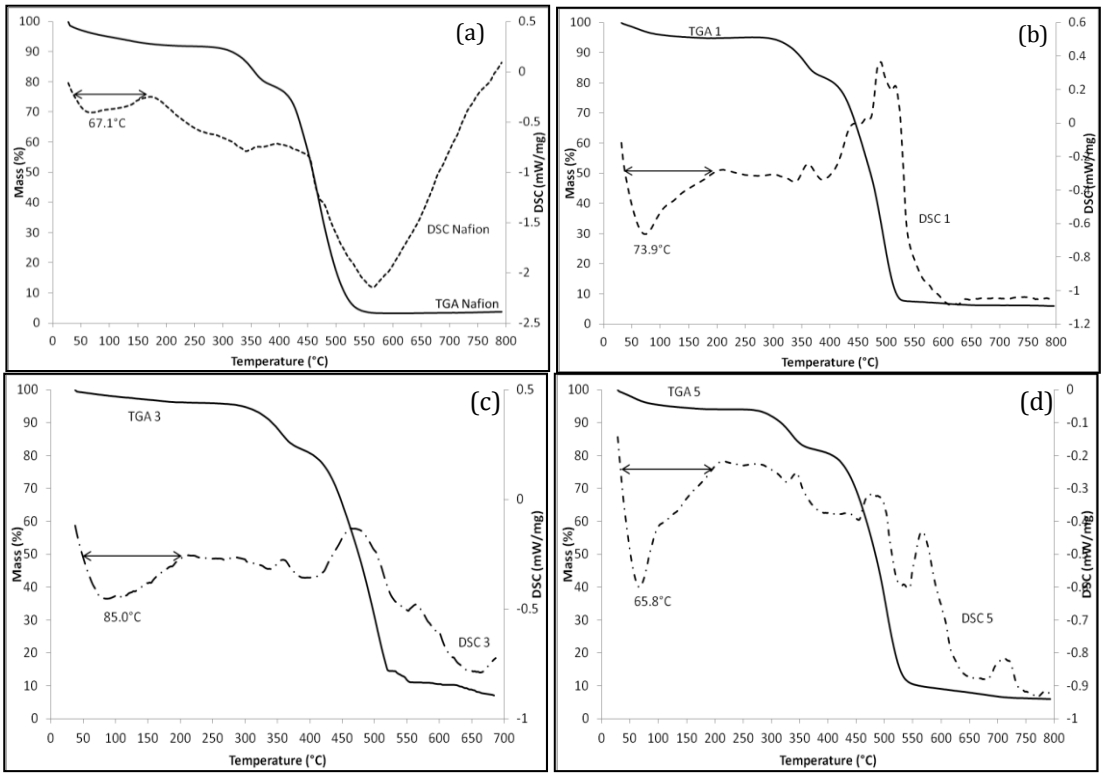


Figure 3. TG and DSC curves of composite membranes, taken at 10°C/min, under N_2, for (a) Nafion, (b) NZ01, (c) NZ03, (d) NZ05.

As for the glass transition temperature (T_g), another test was conducted using differential scanning calorimetry (DSC). The related results are shown in Table 1, increased in the sequence of: Recast Nafion < NZ05 < NZ01 < NZ03. It is seen that the T_g value of Nafion membrane is observed at 117.73 °C, which is lower than the T_g of the composite membranes. Whilst, NZ03 has the highest T_g = 171.50 °C, indicating the strength of the membrane to resist high temperature is improved. Incorporation of the amorphous zirconia particles into Nafion polymer matrix would improve the thermal stability and increase the T_g [18]. The occupied inorganic particles resulting on more energy needed for starting segmental motions, which would increase the T_g value. However, the T_g value decreases for NZ05, despite having the same thickness with NZ03 composite membrane. Probably, the presence of excessive inorganic particles has weakened its structure by forming a brittle membrane [2].

Membrane conductivity

Figure 4 shows the typical impedance curves of four different membranes. Fundamentally, all depicted spectra consist of two arcs, one each for low and high frequency. The basic circuit of a circle is R(RQ), as depicted below the plotted graph. The graph shows the increasing diameter of the arcs within the composition, except for NZ05 which represent increase conductivity.

Table 1. Thermal properties of recast Nafion and composite membranes

Membrane	Thickness (µm)	Residue (%)	Glass transition temperature (Tg)
Nafion	127.00	3.64	117.73
NZ01	107.07	6.01	139.62
NZ03	121.47	6.02	145.28
NZ05	122.97	5.89	141.33

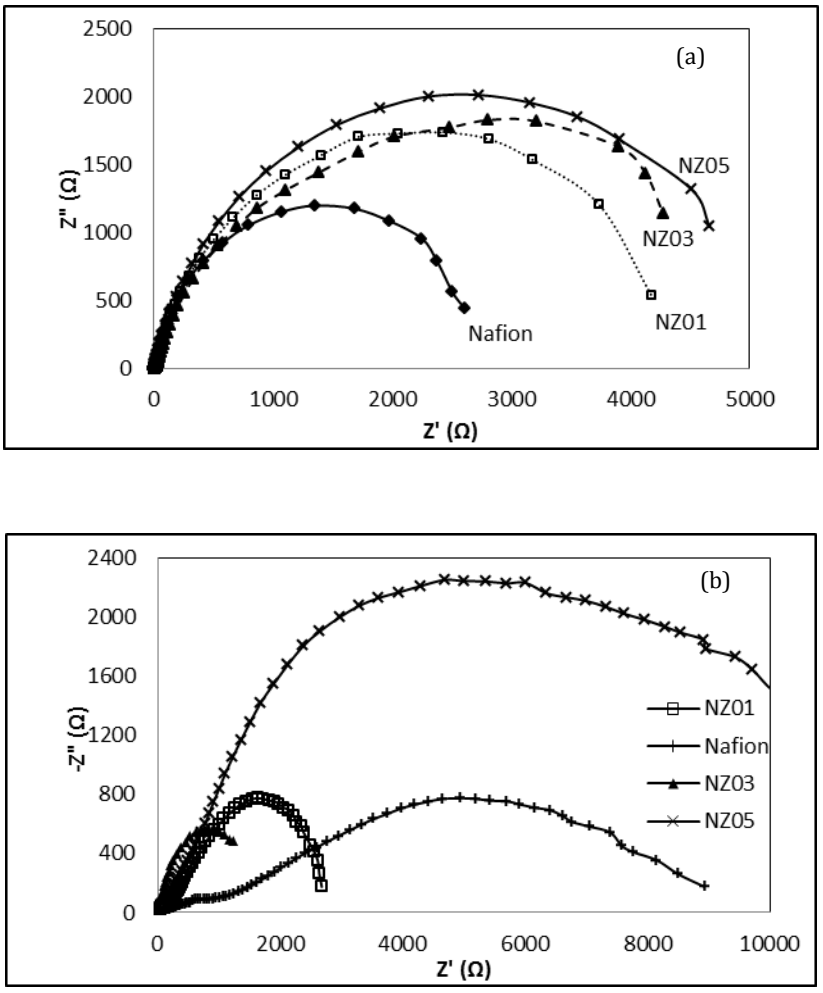


Figure 4. Impedance curves of Nafion and the composite membranes (a) room temperature and (b) at 90°C

The equivalent circuit that is presented in Figure 4 provides a good fitting for these responses. Each circuit consists of two sets of resistor-capacitor pairs. The calculated conductivity of the Nafion membrane at room temperature is 8.32×10^{-3} S/cm. From the obtained data, the ionic conductivity of the composite membranes ranges from 1.41×10^{-2}

S/cm to 1.62 x 10^{-2} S/cm. These values increase proportionally with the zirconia composition, which is consistent to the results reported by Uma [19].

Impedance curves for the Nafion and the composite membranes at 90 °C were shown in Figure 4b. The circle diameters for NZ01 and NZ03 are smaller than the Nafion membrane and the NZ05 composite membrane. A decreased diameter results in higher conductivity. Compared to the value for room temperature measurements, NZ01 and NZ03 at 90°C have circles in smaller diameter, indicating good conduction of the membranes. As the temperature increases, the conductivity is also increases [20]. The calculated conductivity increases from 0.014 to 0.042 S/cm for NZ03 and increased from 0.014 to 0.022 S/cm for NZ01. On the contrary, the conductivity is decreased for the Nafion and the NZ05 composite membrane. For the commercial Nafion, the plotted arcs have the same equivalent circuit (two arcs) as at room temperature but with larger diameter, resulting in a lower conductivity. This effect is caused by the weak thermal resistance of Nafion, as a result of which the membrane starts to shrink at a temperature near 100 °C [21].

Conclusion

In this study, Nafion-ZrO_2 composite membranes were prepared through film casting process and characterized for their structure, morphology, thermal stability and conductivity. The Nafion membrane exhibited lower conductivity than the composite membranes at room temperature under fully hydrated conditions. Despite an increase in temperature, the conductivity of the composite membranes improves. This effect is due to the hygroscopic properties of hydrous zirconia, which has an optimal content of 3 wt. %. Whenever excess hydrous zirconia is used, the conductivity decreases and it affects the *in situ* performance of the membrane in the membrane electrode assembly (MEA) due to the increase in the particle size. Through understanding that the composite membrane has an improved water uptake and conductivity at room temperature and at 90 °C, further investigation will be conducted in the future to explore the effect of hydrous zirconia on the performance at moderate temperature (100 °C).

Acknowledgement

The authors gratefully thank the financial support from the Universiti Kebangsaan Malaysia (UKM) through research grants UKM-GUP-BTT-07-30-188 and UKM-AP-TK-05-2009. The National Science Fellowship awarded to Siti Rahmah Mokhtaruddin is also acknowledged.

References

1. Raharjo, J., Muchtar, A., Daud, W. R. W., Muhamad, N. and Majlan, E. H. (2012). Pencirian fizikal dan terma komposit seramik elektrolit SDC-$(Li/Na)_2CO_3$. *Sains Malaysiana*, 41(1): 95 – 102.
2. Saccà, A., Gatto, I., Carbone, A., Pedicini, R. and Passalacqua, E. (2006). ZrO2–Nafion composite membranes for polymer electrolyte fuel cells (PEFCs) at intermediate temperature. *Journal of Power Sources*, 163(1): 47 – 51.
3. Ramani, V., Kunz, H. R., and Fenton, J. M. (2005). Stabilized heteropolyacid/Nafion® composite membranes for elevated temperature/low relative humidity PEFC operation. *Electrochimica Acta*, 50(5): 1181 – 1187.
4. Dresch, M. A., Isidoro, R. A., Linardi, M., Rey, J. F. Q., Fonseca, F. C. and Santiago, E. I. (2013). Influence of sol–gel media on the properties of Nafion–SiO_2 hybrid electrolytes for high performance proton exchange membrane fuel cells operating at high temperature and low humidity. *Electrochimica Acta*, 94(0): 353 – 359.
5. Zhengbang, W., Tang, H. and Pan, M. (2011). Self-assembly of durable Nafion/TiO_2 nanowire electrolyte membranes for elevated-temperature PEM fuel cells. *Journal of Membrane Science*, 369(1-2): 250 – 257.
6. Pan, J., Zhang, H., Chen, W. and Mu, P. (2010). Nafion–zirconia nanocomposite membranes formed via in situ sol–gel process. *International Journal of Hydrogen Energy*, 35(7): 2796 – 2801.
7. Hammami, R., Ahamed, Z., Charradi, K., Beji, Z., Ben Assaker, I., Ben Naceur, J., Auvity, B., Squadrito, G. and Chtourou, R. (2013). Elaboration and characterization of hybrid polymer electrolytes Nafion–TiO_2 for PEMFCs. *International Journal of Hydrogen Energy*, 38(26): 11583 - 11590.
8. Thiam, H. S., Daud, W. R. W., Kamarudin, S. K., Mohamad, A. B., Kadhum, A. A. H., Loh, K. S. and Majlan, E. H. (2013). Nafion/Pd-SiO_2 nanofiber composite membranes for direct methanol fuel cell applications. *International Journal of Hydrogen Energy*, 38(22): 9474 – 9483.

9. Chuah, G. K., Jaenicke, S., Cheong, S. A., and Chan, K. S. (1996). The influence of preparation conditions on the surface area of zirconia. *Applied Catalysis A: General* 145(1–2): 267 – 284.
10. Yang H. N., Lee D. C., Park S. H. and Kim W. J. (2013). Preparation of Nafion/various Pt-containing SiO_2 composite membranes sulfonated via different sources of sulfonic group and their application in self-humidifying PEMFC. *Journal of Membrane Science*, 443: 210 – 218.
11. Zhai, Y., Zhang, H., Hu. J. and Yi, B. (2006). Preparation and characterization of sulfated zirconia (SO_4^{2-}/ZrO_2)/Nafion composite membranes for PEMFC operation at high temperature/low humidity. *Journal of Membrane Science*, 280(1–2): 148 – 155.
12. Sarkar, D., Mohapatra, Deepak, Ray, S., Bhattacharyya, S., Adak, S. and Mitra, N. (2007). Synthesis and characterization of sol–gel derived ZrO_2 doped Al_2O_3 nanopowder. *Ceramics International*, 33(7): 1275 – 1282.
13. Wu, C. M., Xu, T., W. and Yang, W. H. (2004). Synthesis and characterizations of new negatively charged organic–inorganic hybrid materials: effect of molecular weight of sol–gel precursor. *Journal of Solid State Chemistry*, 177(4–5): 1660 – 1666.
14. Iwai, Y. and Yamanishi, T. (2009). Thermal stability of ion-exchange Nafion N117CS membranes. *Polymer Degradation and Stability*, 94(4): 679 – 687.
15. Gong-Yi Guo, Yu-Li Chen and Wei-Jiang Ying. (2004). Thermal, spectroscopic and X-ray diffractional analyses of zirconium hydroxides precipitated at low pH values. *Materials Chemistry and Physics*, 84(2–3): 308 – 314.
16. Yu, S., Zuo, X., Bao, R., Xu, X., Wang, J. and Xu, J. (2009). Effect of SiO_2 nanoparticle addition on the characteristics of a new organic–inorganic hybrid membrane. *Polymer*, 50(2): 553 – 559.
17. Shao, Z-G., Joghee, P. and Hsing, I-M. (2004). Preparation and characterization of hybrid Nafion–silica membrane doped with phosphotungstic acid for high temperature operation of proton exchange membrane fuel cells. *Journal of Membrane Science*, 229(1–2): 43 – 51.
18. Jalani, N. H., Dunn, K. and Datta, R. (2005). Synthesis and characterization of Nafion®-MO_2 (M=Zr, Si, Ti) nanocomposite membranes for higher temperature PEM fuel cells. *Electrochimica Acta*, 51(3): 553 – 560.
19. Uma, T. and Nogami, M. (2007). Fabrication and performance of Pt/C electrodes for low temperature H_2/O_2 fuel cells. *Journal of Membrane Science*, 302(1-2): 102 – 108.
20. Ahmad A., Isa, K. B. Md. and Osman, Z. 2011. Conductivity and structural studies of plasticized polyacrylonitrile (PAN) – lithium triflate polymer electrolyte films. *Sains Malaysiana*, 40 (7): 691 – 694.
21. Wang, K., McDermid, S., Li, J., Kremliakova, N., Kozak, P., Song, C., Tang, Y., Zhang, J. and Zhang, J. (2008). Preparation and performance of nano silica/Nafion composite membrane for proton exchange membrane fuel cells. *Journal of Power Sources*, 184(1): 99 – 103.

Malaysian Journal of Analytical Sciences, Vol 20 No 3 (2016): 678 - 686
DOI: http://dx.doi.org/10.17576/mjas-2016-2003-29

MALAYSIAN JOURNAL OF ANALYTICAL SCIENCES
Published by The Malaysian Analytical Sciences Society
ISSN 1394 - 2506

PREPARATION OF MEMBRANE ELECTRODE ASSEMBLY FOR HIGH PERFORMANCE OF FORMIC ACID FUEL CELL

(Penyediaan Himpunan Membran Elektrod untuk Sel Bahanapi Asid Formik Berprestasi Tinggi)

Norraihanah Mohamed Aslam[1], Mohd Shahbudin Masdar[1,2]*, Siti Kartom Kamarudin[1,2]

[1]*Fuel Cell Institute*
[2]*Department of Chemical and Process Engineering, Faculty of Engineering and Built Environment*
Universiti Kebangsaan Malaysia, 43600 UKM Bangi, Selangor, Malaysia

**Corresponding author: shahbud@ukm.edu.my*

Received: 5 February 2016; Accepted: 22 April 2016

Abstract

This study is focused on development of membrane electrode assembly (MEA) for direct formic acid fuel cell (DFAFC). The effects of the backing layer, the loading of the gas diffusion layer (GDL), the carbon structures and the electrolyte membrane types, and fuel concentrations on the DFAFC's performance are investigated. Two types of backing layer are used in either a carbon paper (CP) or carbon cloth (CC) form, and three different types of carbon structures, carbon black (CB), carbon nanofiber (CNF) and carbon nanotube (CNT), are studied. A single cell DFAFC is tested to obtain the performance of the MEA, including the open circuit potential (OCP), current density, and power density. From the results, carbon paper indicates a much better performance than carbon cloth and gas diffusion layer (GDL) with 1 mg cm^{-2} loading shows a uniform surface morphology under scanning electron microscopy (SEM) and records a higher power density than 2.5 mg cm^{-2}. Moreover, it is found that the power density increases with increase of the formic acid concentration up to an optimum concentration. However, the optimum fuel concentrations are different for each type of carbon structure. The highest power density is obtained using a combination of CNT and electrolyte membrane of Nafion 117 at 18.36 mW cm^{-2} using 10 M fuel concentration.

Keywords: electrode; performance, microporous, characteristic, direct formic acid fuel cell

Abstrak

Kajian in tertumpu kepada pembangunan himpunan membran elektrod (MEA) untuk asid formik sel bahanapi langsung (DFAFC). Kesan lapisan sokongan, kandungan lapisan resapan gas (GDL), struktur karbon and jenis membran elektrolit, serta kepekatan bahan api terhadap prestasi DFAFC diselidiki. Dua jenis lapisan sokongan sama ada kertas karbon mahupun kain karbon, dan tiga jenis struktur karbon; karbon hitam (CB), nano-serat karbon (CNF) dan nano-tiub karbon (CNT) digunakan dalam kajian ini. Sel tunggal DFAFC diuji untuk memperoleh prestasi MEA termasuk keupayaan litar terbuka (OCP), ketumpatan arus dan ketumpatan kuasa. Berdasarkan hasil kajian, kertas karbon menunjukkan prestasi yang lebih baik berbanding kain karbon. Manakala, GDL dengan kandungan 1 mg cm^{-2} menunjukkan morfologi permukaan yang seragam di bawah mikroskop pengimbas elektron (SEM) dan merekodkan ketumpatan kuasa yang lebih tinggi berbanding 2.5 mg cm^{-2}. Sementara itu, ketumpatan kuasa meningkat dengan peningkatan kepekatan asid formik sehingga kepekatan optimum. Ketumpatan kuasa yang tertinggi diperoleh melalui kombinasi CNT dan membran elektrolit Nafion 117 pada nilai 18.36 mW cm^{-2} menggunakan kepekatan bahan api 10 M.

Kata kunci: elektrod, prestasi, mikroporos, pencirian, asid formik sel bahanapi langsung

Introduction

A fuel cell is a source of renewable energy which excludes the combustion process. Hence it does not release any harmful pollution as a side-product of the reaction. Direct formic acid fuel cell (DFAFC) is one of the fuel cell type which has a higher open circuit potential (OCP), at 1.40 V, than the proton exchange membrane fuel cell (PEMFC) (1.23 V) and direct methanol fuel cell (DMFC) (1.18 V). Therefore, the DFAFC has a high potential to be commercialized as a microfuel cell due to its high output power compared to other liquid fuel cells like DMFC [1] and it is the most suitable technology to replace the battery.

The membrane electrode assembly (MEA) is the heart of a fuel cell, where the main electrochemical reaction takes place and produces electricity. Hence, it is the most crucial part of the fuel cell as well as the direct formic acid fuel cell (DFAFC) [2]. Currently, there are a lot of studies focusing on the optimizing the MEA for the fuel cell [3-5]. However, the conventional characteristics of an anode may not be suitable for the DFAFC due to its formic acid properties. As a result, formic acid fuel presents the difficulty of mass transport constraints through absorption media in the anode, which is usually in a hydrophobic condition [6]. For instance, the Nafion content in the GDL will increase the proton transport moving towards the cathode [7]. The mass transport constraints on the anode depend on the nature of the anode absorption media and formic acid concentrations. This constraint is due to the hygroscopic nature of formic acid in the absorption of hydrophobic media [8]. Therefore, it is necessary to develop a good anode as well as anode absorption media and MEA, including the formulation and the types of materials to overcome the mass transport constraints at the DFAFC's anode.

Based on Sharma and Pollet [9], CB is a conventional catalyst support used for the platinum (Pt) catalyst and Pt alloys in the research and commercialization of fuel cells. However, the use of CB is constrained by problems such as the presence of sulfur impurities and pores that trap microporous nanoparticle catalyst. This means that the active site of reaction cannot be reached by the reactants, resulting in deterioration of the catalytic activity. Zainoodin et al. conducted a study on the effects of the porous layer structure at the anode on the performance of DMFCs. They used three types of carbon powder structures; CB, mixtures of CB and CNF, and CNF. From the results, it was found that the CNF structure recorded a higher performance for methanol concentration in the range of 2 to 5 M [10]. This explains the impact of high electrical conductivity and good use of the catalyst in CNF as the GDL for DMFCs.

Generally, the fuel of formic acid has better compatibility with Nafion membrane [1] than methanol in DMFCs. However, formic acid also has a certain limit of concentration to prevent a high fuel crossover from the anode to the cathode, and this reduces the DFAFC performance. Besides the fuel concentration, Jeong et al. reported that the thickness of the membrane also influences the crossover of formic acid, which affects the performance [11]. On the other hand, Kim et al. found that Nafion 117 was the best electrolyte membrane for 12 M formic acid, with 84 mW cm^{-2} power density generated at 0.43 V [1].

In this study, the MEA is developed for the use of DFAFC. The effects of the backing layer, the loading of GDL, the carbon structures and the electrolyte membrane types, and fuel concentrations on the passive DFAFC's performance are investigated. The characterization of the electrode was analyzed, including the morphology structure, hydrophobicity level and electrical conductivity, and will be discussed on the basis of DFAFC performance.

Materials and Methods

Fabrication of anode's diffusion layer and MEA

Homogeneous carbon ink was prepared by ultrasonication of the carbon with 5 % Nafion solution and isopropyl alcohol. The ink was coated on the backing layer to make the GDL and dried in an oven at 80° C for about an hour. At the anode side, two types of backing layer, i.e. carbon paper (CC) and carbon paper (CP), and three different carbon structures were used (shown in Table 1) and two GDL loadings were investigated at 1.0 mg cm^{-2} and 2.5 mg cm^{-2}. For the cathode, CP with 2.5 mg cm^{-2} CB loading was used throughout the study. Meanwhile, for the catalyst layer, 8 mg cm^{-2} catalyst loading of palladium (Pd) black (Alfa Aesar) was used as catalyst at the anode side, while platinum (Pt) black was used at the cathode side. For the electrolyte membrane, Nafion 117 (DuPont) and NRE 212 (DuPont) were used and the active area for the MEA was 4.84 cm^2. For the MEA preparation, the

anode and cathode were then assembled by the hot-pressed process with the electrolyte membrane at 135 °C and 50 kg cm^{-2} for 3 minutes.

Table 1. Properties of carbon powder

Carbon structure	Specification	Manufacturer
Carbon black (CB)	Purity > 99% Relative density 1.7-1.9 g cm^{-3} at 20^0C	Cabot
Carbon vaporised growth nanofiber (CNF)	Outer diameter 200-600 nm Length 5-50 µm Purity >95.0%	Cheaptubes
Multiwall carbon nanotube (CNT)	Outer diameter 100-150 µm Length 20 µm Purity ≥95	Sigma- Aldrich

Characterization of anode and single cell DFAFC operation

The physicochemical properties and surface morphology of the GDL were observed with a contact angle measurement (KRÜSS Drop Shape Analysis by Fischer) and SEM (ZEISS), respectively. Contact angle measurements were done by using deionized water, methanol fuel (0.5 – 2 M) and formic acid fuel (0.5 – 6 M). SEM images were taken before the catalyst layers were coated onto the GDL. Meanwhile, the electrical conductivity test for the backing layer with different GDL was conducted by using the four point probes technique (Jandel Model RM3) to measure electrical resistivity towards the plane of the GDL. As a result, the through plane electrical conductivity of the GDL can be calculated by applying 5 mA current.

The electrochemical reaction for a half-cell as well as single cell DFAFC was measured and studied based on cyclic voltammetry (CV) and current–voltage (I–V) testing using WonATech potentiostat (WMPG1000). The CV test involved three electrodes, which are Ag/AgCl as reference electrode, and platinum wire as counter electrode, while the working electrode used for the measurement was the anode prepared with different carbon structures with active area of 1 cm^2. For the electrolyte of the half-cell reaction, 0.5 M H_2SO_4 was added to 0.5 M formic acid to maintain a constant pH and stabilize the reference electrode potential. The scan rate for this electrochemical measurement was set at 50 mV s^{-1} in the range of 0.02 to 1.2 V and the electrochemical surface area (ECSA) was determined via CV analysis. For a single cell DFAFC, the cell was operated passively at 25 ºC with ambient pressure by injecting a formic acid solution at 5 ml with a certain concentration from 4 M to 16 M into the reservoir under ambient conditions.

Results and Discussion

Effect of backing layer and GDL loading

The contact angle surfaces for the backing layer for a series of different concentrations of methanol and formic acid are shown in Figure 1. At this measurement, both commercial CC and CP were used without the GDL coated and had the same Teflon loading of 20 wt.%. From the figure, it is clear that different levels of hydrophobicity were obtained at different liquid fuel concentrations. For instance, the contact angle is very similar, at 92°, using 2 M methanol and 6 M formic acid.

In the case of the hydrophobicity profile, the contact angle for carbon cloth and carbon paper with a solution of methanol decreased significantly with the decrease in the methanol concentration gradient from 0.5 M to 2 M. However, for formic acid, the contact angle decreased with increasing formic acid concentration from 0.5 M to 3 M for both backing layers, while there was a significant decrease from 3 M to 6 M especially for carbon paper, as shown in Figure 1. The contact angle between the formic acid and carbon cloth is observed to be higher than with carbon paper. A similar tendency of the contact angle decreasing with the increasing concentration of formic acid was also obtained in previous studies by Uhm et al. [8].

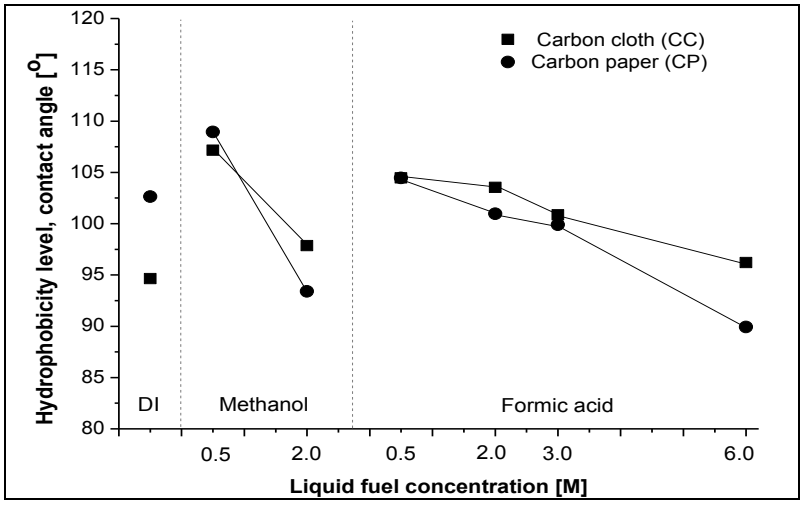


Figure 1. Hydrophobicity level for carbon support without GDL in different fuel concentrations

Nevertheless, the values of the contact angles for all backing layers with liquid fuel concentrations are greater than 90°, which indicates a hydrophobic surface layer of support. Chen et al. reported that a static contact angle between 0° and 90° was hydrophilic while a contact angle greater than 90° was hydrophobic [12]. The wetting of porous solids also involves a contact angle phenomenon but it is complicated by the presence of a porous architecture that can be seen in the next section and shows the surface of the GDL. Konduru stated that a high reading of the contact angle and a rough surface on the carbon support and GDL restrict the accuracy of the contact angles [13]. In the case of formic acid fuel, Uhm et al. reported that the hydrophobicity level in the direct liquid fuel cell (DLFC) could control the liquid fuel transport to a certain extent for the reaction process and hence affected the performance of the cell [6]. Therefore, measuring the hydrophobicity level for different liquid fuel types and concentrations shows that the DMFC and DFAFC should have a different GDL or electrode structure to prevent the mass transport limitation of the fuel. Therefore, it is important to maintain the hydrophobicity level at the optimum condition in the GDL.

The GDL requires good electrical conductivity to support the catalyst and to ensure a good contact between the catalyst and ionomer material, which has an ionic contact with the electrolyte membrane [10]. Figure 2 shows the measurement data of electrical conductivity for different GDL structures, i.e., different backing layers and carbon structures, with 2.5 mg cm^{-2} carbon loading. From the figure, the backing layer without GDL provided a high conductivity. However, it has a drawback in terms of durability and this affects the water management in the electrode in order to prevent the flooding phenomenon. It was found that the GDL structure with CNT has the highest electrical conductivity compared with other microporous layers for both CP and CC at 1.25 S cm^{-1} and 1.46 S cm^{-1}, respectively. However, the electrical conductivity of the CB and CNF is still within the range of appropriate electrical conductivity of GDL, between 0.40 S cm^{-1} and 1.64 S cm^{-1} [14]. CNT has higher conductivity due to its unique structural, mechanical and electrical properties and also has a high aspect ratio to form a network of conductive tubes [15].

Moreover, it was observed that the electrical conductivity of the carbon cloth was higher than that of carbon paper. It was suggested that the carbon cloth with its highly porous structure provided a good support to build a uniform layer of GDL, and hence higher electrical conductivity was obtained. Figure 3 shows the performance of the DFAFC using different types of backing layer and GDL loading at the anode using 4 M formic acid. In general, the power density for carbon cloth is lower than for carbon paper with the same structural carbon. This might be influenced by coarse structure in the carbon cloth's surface. The performance of each carbon support with different carbon structures with 2.5 mg cm^{-2} loading is low.

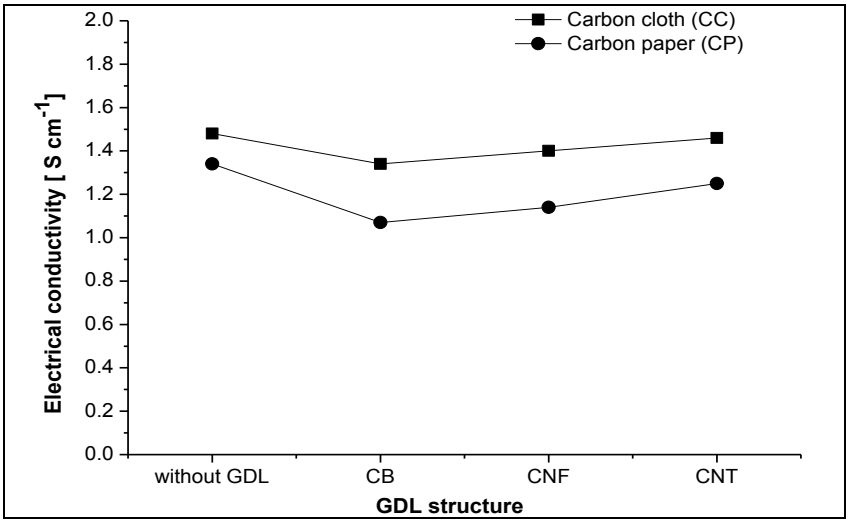


Figure 2. Electrical conductivity for different structures of GDL

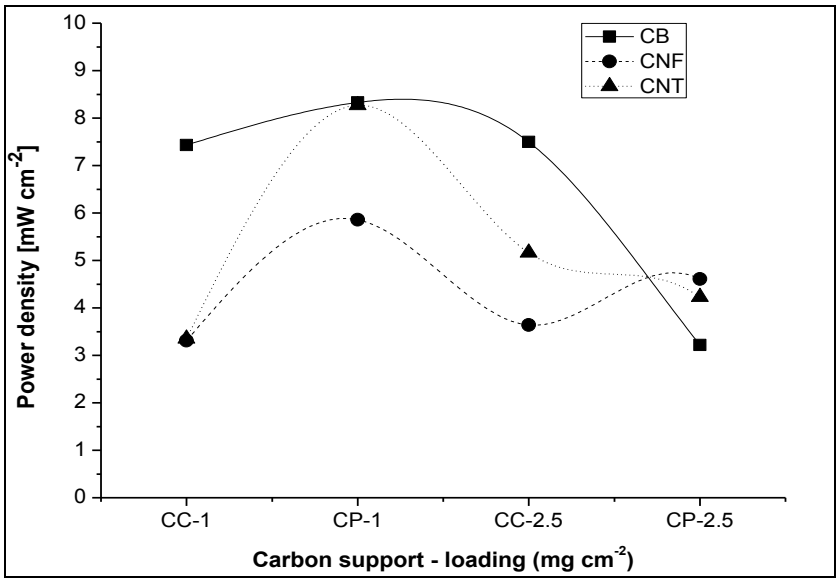


Figure 3. DFAFC performances for different types of carbon and loading at 4 M formic acid

From the observation, the microstructure layer with CP as support with a loading of 1.0 mg cm^{-2} (CP-1) recorded the highest power density. The porous structure of carbon cloth causes all the ink of the carbon to diffuse to the carbon support. This phenomenon prevents the GDL surface giving good support as a catalyst layer. This explains the maximum power density obtained by the carbon loading of 2.5 mg cm^{-2} of carbon black compared to other microstructures (CNF and CNT) with carbon cloth. As the size of the nanostructure particles decreases, they tend to agglomerate during the ultrasonication process, which hinders the absorption of fuel to react with the catalyst. Therefore, it is easier for the CB to achieve the homogeneous level compared to the other carbon powder. Hence, the high loading (2.5 % mg cm^{-2}) of CNF and CNT is not preferable for this application.

However, CNF and CNT with 1.0 mg cm^{-2} loading at the CC diffuse more easily due to the pore size. Hence, using CP that requires a loading of 1.0 mg cm^{-2} is preferable because it offers good diffusion for the catalyst to react with the formic acid as fuel. From the results, carbon powders achieve higher performance for all layers of the microstructure. CP with a loading of 1.0 mg cm^{-2} microstructure for both CB and CNT recorded high performances, at 8.15 mW cm^{-2} and 8.27 mW cm^{-2}, respectively. From the results acquired, carbon paper as the support layer will provide a better performance with a loading of 1.0 mg cm^{-2} than with 2.5 mg cm^{-2}. Therefore, CP with a loading of 1 mg cm^{-2} was used as the backing layer for the following study to fabricate the anode.

Effect of carbon structure, electrolyte membrane and fuel concentrations

Figure 4 shows the image of the anode's GDL morphology structure through SEM using different carbon structures at the carbon paper: a) without GDL; b) CB; c) CNF), and d) CNT. As seen in Fig. 4, different structures can be observed with different carbon structures or without the GDL. By comparing the morphology, it is clear that the CP without a microporous layer of GDL has a surface layer of coarse fibers compared with a GDL.

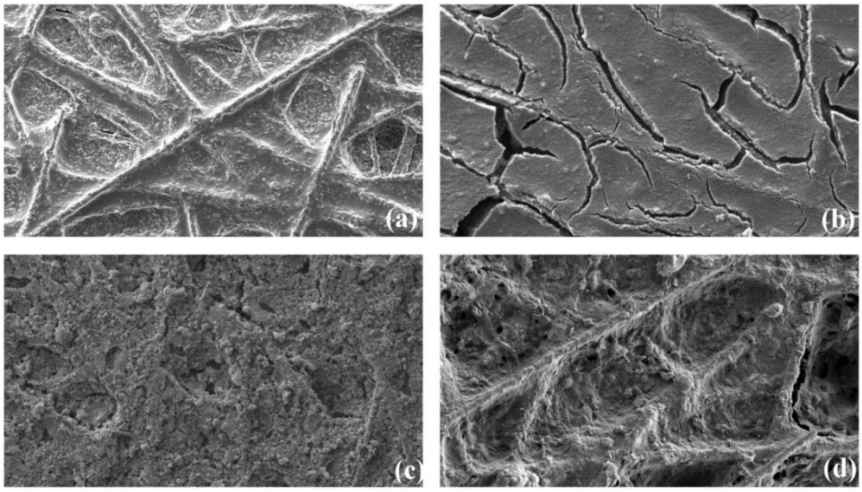


Figure 4. SEM images of CP support with GDL loading 1.0 mg cm^{-2} for (a) without GDL, (b) CB, (c) CNF and (d) CNT at 200 X magnification and a scale of 100 µm

The structure of the GDL with CB gives a smoother surface than without a microporous layer support. However, the GDL with CB (Figure 4 (b)) results in a cracking layer which increases the loss of the catalyst because it may be adsorbed on the cracked microporous layer. Figure 4 (c) and (d) shows that the dispersion of carbon ink CNF and CNT is more even. The CNT structure in Figure 4 (d) presents some of the carbon fiber from the carbon paper due to the smaller size of CNT compared to CNF, as previously mentioned in Table 1. The smooth surface ensures good GDL contact with the catalyst layer, but also nanostructured carbon can be used to improve the electrical properties and structure of the GDL [16] for the DFAFC.

Figure 5 shows the CV test on the anode with different GDL-Pd coatings for carbon paper as a backing layer with 1.0 mg cm^{-2} GDL loading. From Figure 5, the peak of the reaction, recorded at 0.6 – 0.75 V, may be associated with the rate of reaction on the Pd catalyst layers with different adsorption. The electrochemical surface area (ECSA) values for CB-Pd, CNF-Pd and CNT-Pd are 12.81 cm^2 mg^{-1}, 21 cm^2 mg^{-1} and 23.58 cm^2 mg^{-1} respectively. It can be seen that the rate of reaction with a CNT anode as the absorption layer is higher than with the CB and CNF, achieving a current density of 22.3 mA cm^{-2} with the same pattern of curves. Smaller ECSA value for CB indicating lower electrocatalytic activity towards formic acid reaction compared to CNT as catalyst support.

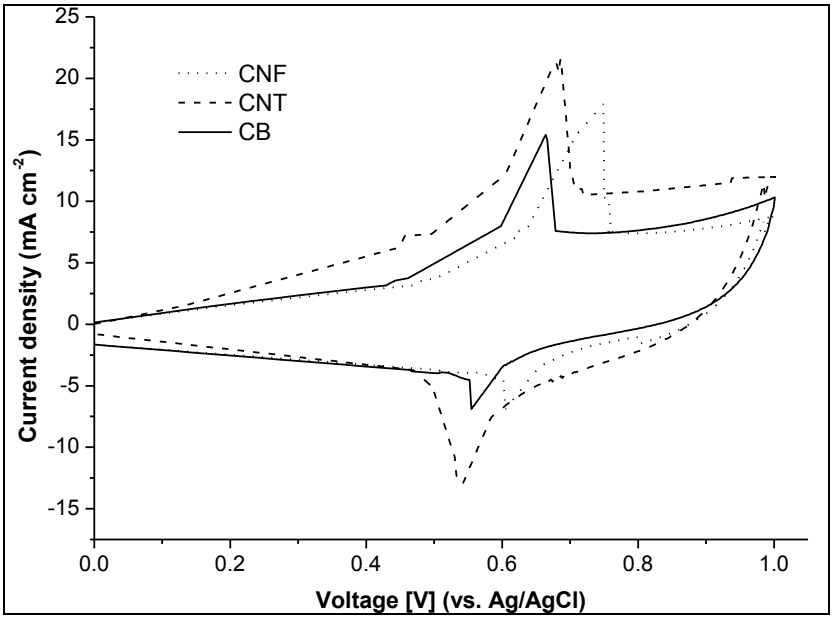


Figure 5. Cyclic voltammetry for anode with different structures of GDL

The CB carbon structure that is commonly used has the problem of elemental sulfur impurities and pores that trap microporous nanoparticles and degrade the catalyst activity. In addition, it is also thermochemically unstable, which inhibits the DFAFC's ability to curb erosion events on the carbon support, which deteriorates when in contact with the catalyst support [9].

Figure 6 shows the maximum power density obtained for different types of membrane and carbon structure. The different in electrode structures (by using different carbon material) would affect the MEA, and hence affect the cell performance. These indicate the different between current and power densities (shown in the Fig. 5 and Fig. 6, respectively) for different carbons used are due to the different in their carbon properties. The CNT showed a highest performance of current and power density compared to that CB and CNF. In general, the polarization curve profile for DFAFCs is similar, where the samples obtained show lower performance, i.e., maximum power density, at low fuel concentrations, and increase with concentration until the optimum concentration. From Fig. 6 it can be seen that the optimum concentration for the DFAFC for every sample is 10 M, whereas only one sample, N117-CP-CNF, achieved the maximum power density on a formic acid concentration of 13 M. The performance drops after the optimum concentration is achieved.

At low concentrations, formic acid cannot accommodate fuel operation at a high current density due to the presence of the mass transport limit [17]. The formic acid concentration of 10 M is the optimum concentration acquired, which matches the results of studies by past researchers [1, 17, 18]. However, when the concentration increases from the optimum concentration and above until 16 M, the DFAFC performance will decrease due to low catalyst activity and the occurrence of fuel flux crossing [1, 18]. The decline in performance at high formic acid concentrations may also be caused by the very nature of formic acid, which is hydrophilic and thus dries the layer near the membrane, which can inhibit proton transfer [19]. Meanwhile, Nafion 117 membrane gives a much higher performance overall, with a range of 10.43 mW cm^{-2} to 18.36 mW cm^{-2} compared to NRE 212 membrane with a range of 6.77 mW cm^{-2} to 8.91 mW cm^{-2}. As the NRE 212 membrane thickness is very similar to Nafion 112 membrane, the finding by Rhee et al. that the rate of crossing for Nafion 112 is higher compared to Nafion 117 indicates the same cause of the decline of performance in this study [19]. For a cell that uses CNF carbon structure as the GDL with NRE 212 membrane, the optimum concentration that is acquired by this cell is different from the use of N117, which is 10 M, like the optimum concentration achieved by other MEAs. The highest maximum power

density that is achieved for MEAs is 7.67 mW cm^{-2} for the 10 M and the lowest is 4.10 mW cm^{-2} for the 4 M of formic acid fuel.

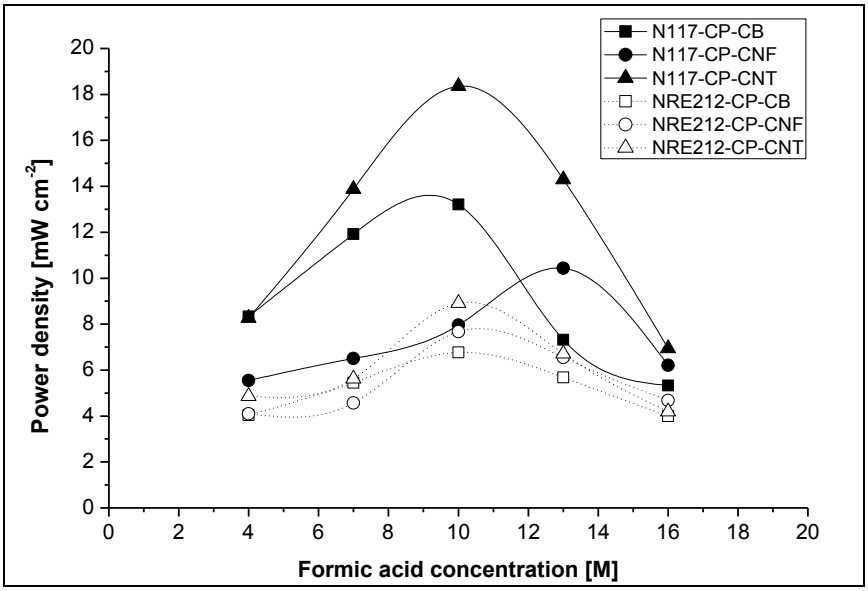


Figure 6. Single cell performance with different MEA combinations for 4–16 M formic acid

Overall, single cell performance using N117 electrolyte membrane gives a higher performance compared to the use of NRE 212 membrane. The decline in performance with the use of NRE 212 membrane is the same as found in research by Tsujiguchi et al., who state that formic acid flux is the highest compared to N115 and N117 membrane [20]. This further reinforces the main reason for the decline in performance that occurs when using NRE 212 membrane. According to Park et al., the diffusion layer can increase the overall performance of the catalyst and fuel cell depending on its structure [21].

Conclusion

The effects of the backing layer, carbon structures, carbon loading and membrane thickness on DFAFC performance were investigated in order to fabricate high performance of MEA. The maximum power density of 18.36 mW cm^{-2} was obtained by using the combination of CP as carbon support with a 1.0 mg cm^{-2} CNT layer and N117 as the electrolyte membrane at 10 M formic acid. High ECSA values for CNT as catalyst support for Pd in CV testing indicate that CNT have high potential to reduce the loading of catalyst usage due to the improve catalyst utilization. Hence, it can give a good support for efficient catalyst utilization as well as reduce the cost. Therefore, a good and thorough understanding of electrode structure and electrochemical properties is needed in order to increase the performance and durability of passive DFAFCs for mobile power sources.

Acknowledgement

This study was supported partially by ERGS/1/2011/TK/UKM/03/17 and FRGS/1/2013/TK07/UKM/02/1 from the Ministry of Higher Education, Malaysia and GUP-2014-069, DLP-2013-026 from Universiti Kebangsaan Malaysia.

References

1. Kim, H. S., Morgan, R. D., Gurau, B. and Masel, R. I. (2009). A miniature direct formic acid fuel cell battery. *Journal of Power Sources*, 188(1): 118 – 121.

2. Miesse, C. M., Jung, W. S., Jeong, K.-J., Lee, J. K., Lee, J., Han, J., Yoon, S. P., Nam, S. W., Lim, T.-H. and Hong, S.-A. (2006). Direct formic acid fuel cell portable power system for the operation of a laptop computer. *Journal of Power Sources*, 162(1): 532 – 540.
3. Ahmad, M. M., Kamarudin, S. K. and Daud, W. R. W. (2010). Design of and optimal micro direct methanol fuel cell for portable applications. *Sains Malaysiana* 39(3):467 – 472.
4. Hashim, N., Kamarudin, S.K. and Daud, W. R. W. (2010). Design and development of micro direct methanol fuel cell. *Sains Malaysiana*, 39(6): 1015 – 1023
5. Jaafar, J, Ismail, A. F., Matsuura, T. and Mohd Nordin, M. N. A. (2013). Stability of SPEEK-triaminopyrimide polymer electrolyte membrane for direct methanol fuel cell application. *Sains Malaysiana*, 42(11):1671 – 1677.
6. Uhm, S., Chung, S. T. and Lee, J. (2008). Characterization of direct formic acid fuel cells by impedance studies: in comparison of direct methanol fuel cells. *Journal of Power Sources*, 178(1): 34 – 43.
7. Kim, S., Han, J., Kwon, Y., Lee, K.-S., Lim, T.-H., Nam, S. W. and Jang, J. H. (2011). Effect of nafion ionomer and catalyst in cathode layers for the direct formic acid fuel cell with complex capacitance analysis on the ionic resistance. *Electrochimica Acta*, 56(23): 7984 – 7990.
8. Uhm, S., Lee, J. K., Chung, S. T. and Lee, J. (2008). Effect of anode diffusion media on direct formic acid fuel cells. *Journal of Industrial and Engineering Chemistry*, 14(4): 493 – 498.
9. Sharma, S. and Pollet, B. G. (2012). Support materials for PEMFC and DMFC electrocatalysts - A review. *Journal of Power Sources*, 208(0): 96 – 119.
10. Zainoodin, A. M., Kamarudin, S. K. and Daud, W. R. W. (2010). Electrode in direct methanol fuel cells. *International Journal of Hydrogen Energy*, 35(10): 4606 – 4621.
11. Jeong, K-J, Miesse, C. M., Cho,i J-H., Lee, J., Han, J. and Yoon, S. P. (2007). Fuel crossover in direct formic acid fuel cells. *Journal of Power Sources*, 168: 119 – 125.
12. Chen, W.-H., Ko, T.-H., Lin, J.-H., Liu, C.-H., Shen, C.-W. and Wang, C.-H. (2011). Influences of gas diffusion layers with pitch-based carbon coated in polymer electrolyte membrane fuel cell. *International Journal of Electrochemical Science*, 6: 2192 – 2200.
13. Konduru, V. (2010). Static and dynamic contact angle measurement on rough surfaces using sessile drop profile analysis with application to water management in low temperature fuel cells. Michigan Technological University.
14. Litster, S. and Mclean, G. (2004). PEM fuel cell electrodes. *Journal of Power Sources*, 130(1): 61 – 76.
15. Choi, J. and Zhang, Y. (2015). Properties and applications of single-, double- and multi-walled carbon nanotubes. Sigma Aldrich. Access online [26 May 2015].
16. Sundarrajan, S., Allakhverdiev, S. I. and Ramakrishna, S. (2012). Progress and perspectives in micro direct methanol fuel cell. *International Journal of Hydrogen Energy*, 37(10): 8765 – 8786.
17. Zhu, Y., Ha, S. Y. and Masel, R. I. (2004). High power density direct formic acid fuel cells. *Journal of Power Sources*, 130(1-2): 8 – 14.
18. Ha, S., Dunbar, Z. and Masel, R. I. (2006). Characterization of a high performing passive direct formic acid fuel cell. *Journal of Power Sources*, 158(1): 129 – 136.
19. Rhee, Y.-W., Ha, S. Y. and Masel, R. I. (2003). Crossover of formic acid through Nafion® membranes. *Journal of Power Sources*, 117(2): 35 – 38.
20. Tsujiguchi, T., Iwakami, T., Hirano, S. and Nakagawa, N. (2014). Water transport characteristics of the passive direct formic acid fuel cell. *Journal of Power Sources*, 250: 266 – 273
21. Park, S., Lee, J-W. and Popov, B. N. (2006). Effect of carbon loading in microporous layer on PEM fuel cell performance. *Journal of Power Sources*, 163:357 – 363.

Malaysian Journal of Analytical Sciences, Vol 20 No 3 (2016): 687 - 696
DOI: http://dx.doi.org/10.17576/mjas-2016-2003-30

MALAYSIAN JOURNAL OF ANALYTICAL SCIENCES
Published by The Malaysian Analytical Sciences Society
ISSN 1394 - 2506

CRITICAL POWDER LOADING AND RHEOLOGICAL PROPERTIES OF POLYPROPYLENE/GRAPHITE COMPOSITE FEEDSTOCK FOR BIPOLAR PLATE APPLICATION

(Beban Serbuk Kritikal dan Sifat Reologi Bahan Suapan Komposit Polipropilena/Grafit untuk Aplikasi Plat Dwikutub)

Iswandi[1,2,3], Jaafar Sahari[1,2], Abu Bakar Sulong[1,2], Teuku Husaini[1]*

[1]*Fuel Cell Institute*
[2] *Department Mechanical and Materials Engineering, Faculty of Engineering and Built Environment*
Universiti Kebangsaan Malaysia, 43600 UKM Bangi, Selangor, Malaysia
[3]*Department Mechanical Engineering,*
Institut Teknologi Medan, Medan, Indonesia

**Corresponding author: t_husaini_st@yahoo.com*

Received: 5 February 2016; Accepted: 22 April 2016

Abstract

Bipolar plate is one of the key parts in the fuel cell technology with the advantages of a higher electrical conductivity and mechanical properties are high. Injection molding is one of the manufacturing method that being used in the manufacture of bipolar plates. The critical powder loading and rheological properties of the feedstock are an important factor in the process of injection molding in the manufacturing process of bipolar plate. The critical powder loading feedstocks with a mixture of polypropylene and graphite have been conducted with the torque method test. The appropriate critical powder loading the using a graphite filler material was produced with the composition of 75 % the weight of an optimum load and 25 % weight of polypropylene. The rheological studies have also been carried out using capillary test for determining critical loading powder by increasing the viscosity of the feedstock. The test results showed that the rheological properties of the feedstock with optimum powder loading to exhibit pseudoplastic properties are suitable for injection molding process with the n less than one.

Keywords: injection molding, polymer composite, bipolar plate, fuel cell

Abstrak

Plat dwikutub adalah salah satu bahagian utama pada teknologi sel bahanapi dengan kelebihan sifat kekonduksian elektrik dan mekanik yang tinggi. Pengacuan suntikan adalah salah satu kaedah pembuatan yang digunakan dalam pembuatan plat dwikutub. Pembebanan serbuk genting dan sifat reologi bahan suapan adalah faktor penting dalam proses pengacuan suntikan semasa proses pembuatan plat dwikutub. Pembebanan serbuk genting bahan suapan dengan campuran polipropilina dan grafit telah pun dijalankan dengan kaedah ujian nilai tork. Pembebanan serbuk genting yang sesuai menggunakan bahan suapan grafit telah dihasilkan dengan komposisi 75 % berat yang merupakan beban optimum dan 25 % berat polipropilena. Kajian reologi juga telah dijalankan menggunakan ujian rerambut bagi menentukan beban serbuk genting dengan peningkatan nilai kelikatan bahan suapan. Keputusan ujian sifat reologi didapati bahawa bahan suapan dengan beban serbuk optimal mempamerkan sifat pseudoplastik yang sesuai bagi proses pengacuanan suntikan dengan nilai *n* kurang daripada 1.

Kata kunci: pengacuan suntikan, komposit polimer, plat dwikutub, sel bahanapi

Introduction

Conductive polymer composite (CPC) materials generally comprise a mixture of polymers and conductive fillers, such as carbon-based and metallic fillers. Conductive materials contribute to the improvement of electrical and mechanical properties (e.g., critical load) of a material, particularly for carbon-based materials, such as graphite (G), carbon black (CB), carbon nanotubes, and carbon fiber (CF) [1 – 3]. One of the applications of CPC is the bipolar plate, which requires high electrical conductivity for electron mobility. The properties of CPC materials favor their application in the manufacture of bipolar plates. Among various carbon-based fillers, graphite is the optimal material type because of its chemical stability [4], corrosion resistance [4], lightness [5 – 8], and high electrical conductivity [9]. Achieving the required properties when such materials are utilized depends on the manufacturing method. Compression and injection molding are two of the most commonly used methods to fabricate bipolar plates. Injection molding has an advantage over compression molding when used for mass production; injection molding has better factor cycle time and compact ability during production than compression molding. Several factors, such as process parameters, contribute to the success of the manufacturing process. However, the most important factors are the characteristics that correspond to the properties of the feedstock. Feedstock injection molding is a balanced blend of filler powder and binder matrix. Three important factors influence powder loading injection molding; these three factors are the rheological properties of a good feedstock for production, mechanical properties of the materials, and tight dimensional control and limited distortion [10].

A number of studies have been conducted to determine the load range of the feed for the powder filler material. Generally, ceramic powder carbon-based filler is the material used; it is injected at a load range of 50 % to 55 % by volume. Previous studies [11 – 13] have indicated that the appropriate critical load could be up to 65 % by volume. Other studies have reported the use of alumina powder as filler at feedstock composition of 80.5 wt.% filler (50 % by volume) [14]. Feedstock with different types of metals as fillers are commonly injected during powder loading at 56 % [15, 16] to 60 % by volume [17, 18]. Injection of fillers such as G, CB, and CF has also been successfully conducted at filler composition of up to 60 % by weight [19]. The load volume of feedstock refers to critical filler loads in the feedstock up to the maximum that can be injected. An increase in the volume load of feedstock affects feedstock viscosity [20]. Relative changes in viscosity influence critical powder loading. Feedstock viscosity is highly dependent on particle size, particle size distribution, solid loading, and specific surface area [21]. A study has demonstrated through modeling that powder load is influenced by particle size distribution [22]. Studying the critical powder loading feedstock of polypropylene (PP)/G is necessary to determine the maximum powder load of G fill in the appropriate feedstock injection molding process. A detailed investigation of the maximum powder loading of this feedstock has never been conducted.

The current study investigates the critical powder load by using mixer torque variations and analyzing the viscosity behavior of G feedstock. Rheological analysis with various G fillers was conducted on the composition of the feedstock to determine the feedstock's pseudo-plastic nature and mold reliability.

Materials and Methods

A matrix polypropylene (PP) (injection molding grade, impact copolymer SM 240) with a melting point of 160 °C to 170 °C, density of 0.9 g cm^{-1}, and MFR of 10 g/10 min was utilized. PP allows for balance between stiffness and impact resistance. PP was purchased from Polypropylene Malaysia Sdn. Bhd. Natural G was obtained from Asbury of 3243 (99 % purity, 44 μm average normal powder size, 3 m^2 gr^{-1} surface area, 27.8 S cm^{-1} electrical conductivity, and 2.31 kg m^{-3} density); the technical aspects of the utilized natural G were provided by the supplier. The morphology of the G powder was observed with a scanning electron microscope (SEM; Zeis EVO MA10). The morphology of graphite filler is important to know the effects that occur during the test (Figure 1).

Figure 1 show that the morphology of natural graphite flakes has different shapes and sizes. Shaped pieces of G particles have better electrical properties than others in the form of a sphere [23, 24]. The process of mixing the powder and testing the critical powder loading (G and binder PP) was performed with an internal mixer (Haake Remix Roller rotor type 600R with Haake Polylab TM programming). The PP melt was mixed in a chamber at a volume of 50 cm^3 and filler composition of 60 wt. % to 80 wt. % of graphite. The mixing parameters were 200 ºC and 50 rpm for 2 hours. The experimental torque values were observed and found to be unstable [24]. Feedstock viscosity was measured with a Shimadzu capillary rheometer (CFT 500D) with a capillary diameter (*D*) of 0.1 cm,

length (*L*) of 1 cm, and *L*/*D* of 10 at 160 ^{o}C. The measurement was done at a temperature of melts viscosity of the feedstock with a given load and power passing through the capillary.

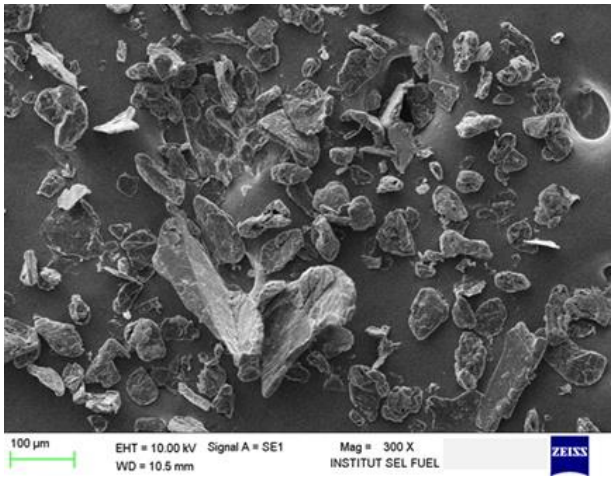


Figure 1. Morphology of graphite powder

Results and Discussion

Critical powder loading was determined by observing the changes in the value of the torque variations (critical solid loadings) of the G feedstock. Generally, with the increase in filler material content during the process, torque slowly increased during mixing until an unstable condition was reached. The results in (Figure 2) show an increase in torque blending at 80 wt. % of the powder filler. The blending process became uncertain after this increase. Torque did not reach a steady state and fluctuated instead. These results indicate that the critical load mix was approximately 75 wt. % of the filler powder. These results are similar to those of ceramic-based materials and metals reported in [13] at 80.5 wt. % of filler. In this study the critical powder loading test has been carried out three times the test at between 139 minutes to 142 minutes. Based on observations of time tests showed phenomenal torque value changes are likely the same, at 80 % by weight graphite. This situation showed that the increase in the torque tends to depend on the content of graphite powder filler. The feedstock includes G filler with different particle sizes. The particle size distribution was shown in (Figure 3), which illustrates the variations in particle size and percentage of different feedstock. The differences in particle size were divided into small-sized [d(0.1): 18.85 µm], mean- or mid-sized [d(0.5): 56.43 µm], and large-sized [d(0.9): 127.08 µm].

Particle sizes have a significant impact on critical powder load, where the amount of large particles that result in high critical loading filler is large [10, 25]. The consolidation of particles with various sizes in the feed material affects density. In particular, the composition of the dominant particle size in the feedstock material has a significant effect on density. Small particles can be added to fill the empty spaces between large particles to increase density [17, 18]. The particle size of the powder filler affects the determination of density and maximum aspect ratio of the feedstock [26]. During the blending process, the powder particles are arranged according to shape and size to achieve a stable level because neither the blending process nor excessive pressure can force particles to enter a dense compound [27, 28]. High packing densities can be achieved if the particle size is not uniform [27, 28]. The gap that forms between coarse particles because of restructuring allows the entry of a large number of fine particles, thereby contributing to the density of the random feedstock. Critical powder loading is also influenced by particle size, and density affects size variation, as shown in the feedstock schematic in (Figure 3). Based on SEM observation on the composition of 75 % by weight graphite was found that the structure of graphite flakes form more compact. This condition is known of the composition of the particles homogeneously mixed to form a bond between the particle size large, medium and small. The other factor is the flakes particles very easily formed a solid

structure as shown in (Figure 4). In a simple illustration of the bond between the graphite particles with different sizes are shown in (Figure 5).

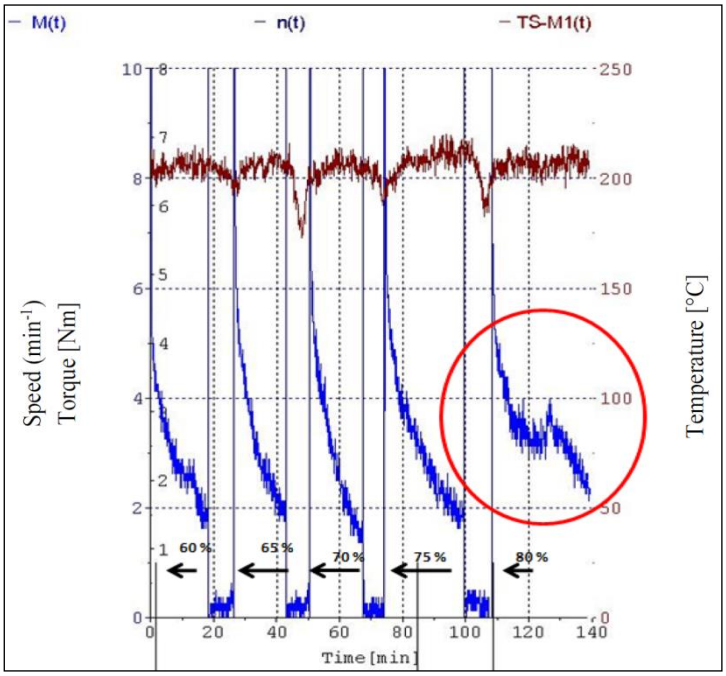


Figure 2. Effect of power loading on torque and temperature

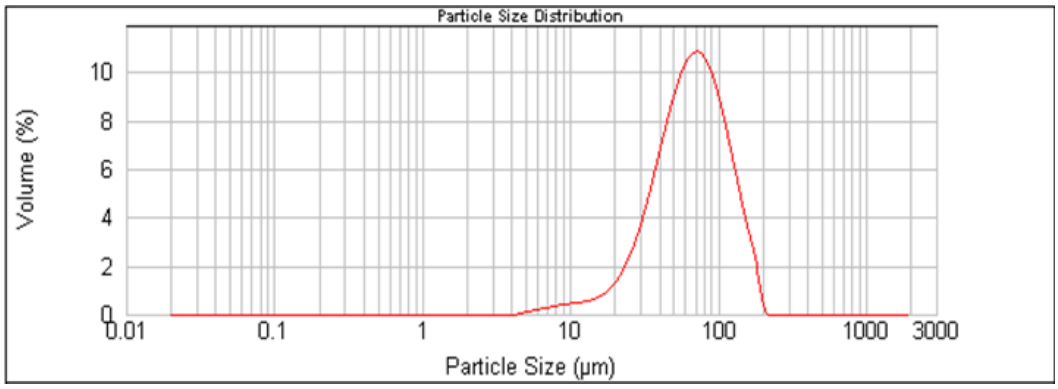


Figure 3. Particle size distribution of graphite

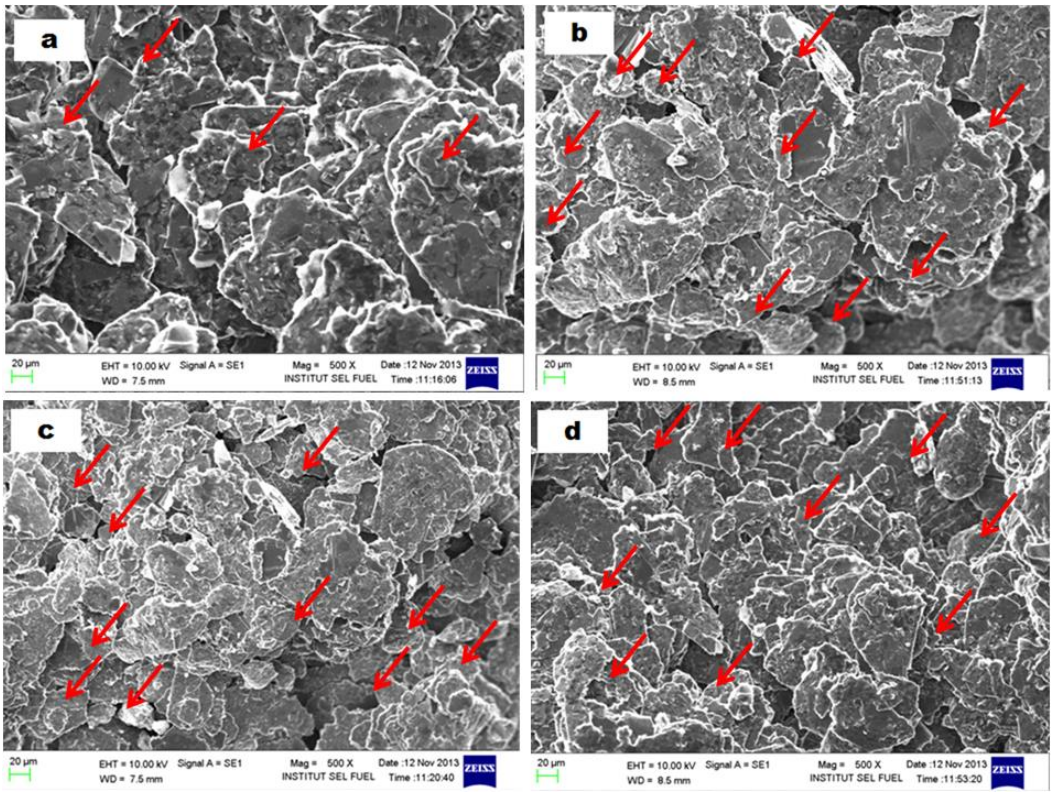


Figure 4. SEM of G feedstock (a) 60 wt.%, (b) 65 wt.%, (c) 70 wt.%, and (d) 75 wt.%

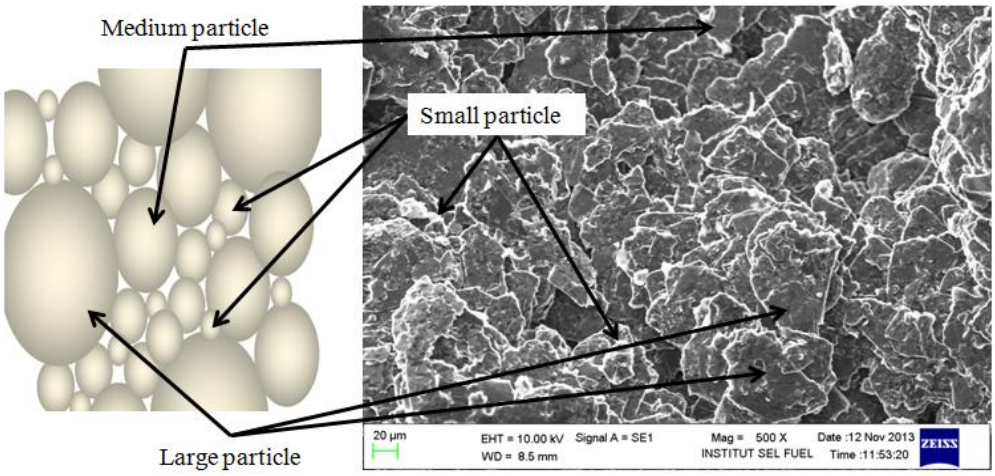


Figure 5. Schematic of different graphite particle sizes

The results of the viscosity test indicated an increase in viscosity versus the shear rate at the maximum filler powder content of 75 wt. % (Figure 6). The increase in viscosity was inversely proportional to the increase in shear rate.

This finding is consistent with that of previous studies [17, 18] and thus reveals that the materials that are pseudo-plastic using the PIM process.

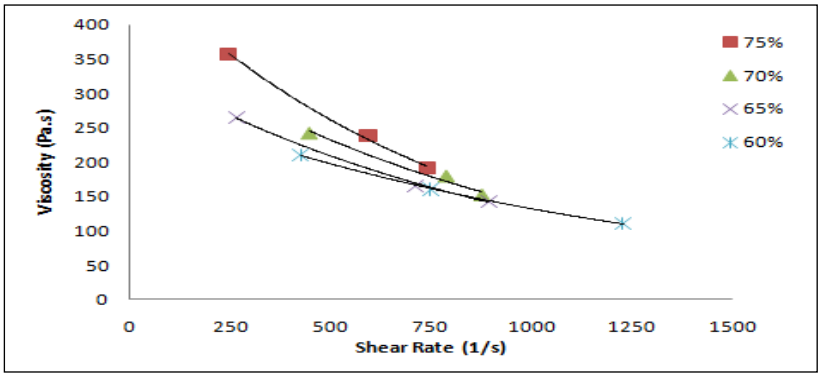


Figure 6. Feedstock viscosity versus shear rate at different powder loadings

The increase in feedstock viscosity was also affected by the increase in surface area, which occurred because of the increase in small particle variations in the filler. The improved composition of small particles simultaneously increased the surface area and caused agglomeration, which increased feedstock viscosity. The agglomeration in the feedstock fine powder formed a bond between the powders. This phenomenon occurs naturally because of the force of attraction between the surfaces of particles with varying strengths. The agglomeration of small particles in the feedstock is difficult to overcome [29]. Previous studies on critical powder loading using G do not exist; nevertheless, this phenomenon shows similarities with the viscosity of ceramic feedstock because the use of solid powder materials and polymers as ceramic composite has the same characteristics as mixed feedstock. Studies that dealt with this phenomenon reported that the increase in surface area in feedstock containing ZrO_2 and polymer ethylene-vinyl acetate copolymer grade at feedstock composition of 20 vol. % to 50 vol.% ceramic powder has an impact on lowering the activation energy flow [29]. High shear rate at low powder load shows more polymer components than filler components. Viscosity and shear rate suitable for injection molding have already been reported in numerous studies. Studies recommend maximum viscosity of 1,000 Pa.s and shear rate in the range of 100 s^{-1} to 100,000 s^{-1} [27, 29]. The results of rheological studies on feedstock PP/G in the present study indicate viscosity at 80 Pa.s. The shear rate is below the level allowed for injection molding processing (1,700 s^{-1}). The test results show that feedstock viscosity and shear rate are generally within the range suitable for injection molding. The variations in viscosity caused by temperature at different powder loadings are shown in (Figure 7). A high load is required when the powder has high viscosity. Viscosity decreased when the feedstock temperature increased. By contrast, an increase in viscosity reduced the shear rate, as shown in (Figure 6). The increase in viscosity is anticipated because of the increase in powder filler content consisting of fine powder agglomeration. Devaluation of viscosity occurs when the percentage content of fine powder is low. Increasing the coarse powder content reduces feedstock agglomeration [30, 31]. Changing on the different powder loading results in a change in feedstock shear rate. Similar conditions were observed during injection molding, wherein shear rate was applied to the material at a given pressure value. The ratio between the filler and matrix polymer powder is significant to the success of the current and subsequent processes.

High powder loading makes it easy to control the dimensions. An extremely high powder loading (very small binder matrix) produces a mixture with remarkably high viscosity, which could complicate the injection molding process [10, 27]. The critical composition of the powder mixture can be achieved by reducing the concentration of the polymer matrix. Reduction of the polymer matrix concentration also sets the highest filler powder loading. When the powder loading exceeds the critical limit, the viscosity of the mixture becomes extremely high [32]. The results of the mean flow index behavior, *n*, for all compositions show that all feed materials exhibit a pseudo-plastic behavior (Table 1.). The value of *n* indicates the uniformity of the flow of a mixture in the capillary during testing

[30, 31]. The decrease in the viscosity of pseudo-plastic materials with the increase in shear rate was noticeable at a low powder load. The n value was less than 1, which indicates that the feed material exhibits shear thinning. A feedstock should have an *n* value of less than 1 during injection molding [29].

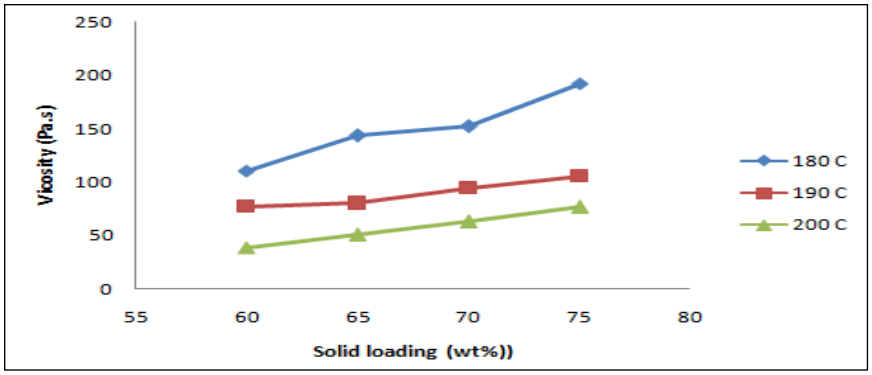


Figure 7. Relationship between feedstock viscosity and different powder loading temperatures

Table 1. Rheological properties of feedstock at a filler content of 60 wt. % to 75 wt. %

Feedstock wt. %	Temperature	E (kJ/mol)	*n* value	α
60	180	93.412	0.377	501.83
	190	93.412	0.415	616.35
	200	93.412	0.301	1610.85
65	180	92.731	0.295	440.70
	190	92.731	0.348	727.32
	200	92.731	0.323	1196.08
70	180	78.937	0.521	331.49
	190	78.937	0.285	796.74
	200	78.937	0.444	932.04
75	180	82.146	0.331	352.30
	190	82.146	0.312	660.47
	200	82.146	0.366	837.11

The ability of feedstock containing high G filler to flow during injection molding is indicated by the value of n, which should be small. The effect of increasing load on the feedstock powder through injection can be obtained by developing the relationship between particle and particle bonding in the composite. The value of *n* is obtained with Equation (1) [27, 29] as follows:

$$\tau - \tau_y = k(\gamma)^n \quad (1)$$

The calculation of the n value and moldability α shown in Table 1., where n is the average resulting from the composition of 60 wt. % to 75 wt. % of G filler, shows that n is smaller or less than 1. This situation proves that the feedstock is pseudoplastic and that qualified feedstock can be injected because of flow ability. The determination of moldability index value (α) is an important method to predict the suitability of an material for the injection molding

process as shown in Table 1. The result of the calculation shows that the largest value at 200 °C for each weight percent graphite filler. It means the larger values of moldability, the more easily feedstock was provided by the injection molding process [18, 27]. The activation energy (E) of a feedstock is strongly related to its viscosity [33]. An improvement in viscosity significantly affects the rate of increase of the activation energy value. This relationship occurs because of the different particle sizes arranged in the feedstock. In this study, a parallel increase in viscosity was observed with the addition of the filler material into the feedstock. The difference in the composition of fine- and large-sized particles contributed to the changes in viscosity. Another factor that affected the increase in viscosity was the content and composition of small particles. These results are consistent with the findings on microstructures because viscosity increased in a parallel manner with the increase in G filler content at a composition of 60 wt. % to 75 wt. %.

The composition of in-sized particles also improved when density was increased, resulting in an increase in viscosity. The obtained SEM images show an increase in small-sized particle content in the feedstock. Studies on the effect of size on viscosity have shown that a feedstock mixture with fine-sized particles has a higher melting point than that with large-sized particles. Different particle sizes also influence the temperature of the process; fine-sized particles are more likely to increase the temperature of the process compared with rough-sized particles [30, 31]. The differences in the activation energy values (shown in Table 1) are due to the thermal expansion between the components of the material; this expansion occurred because of differences in particle size and agglomeration in the fine particles. This phenomenon occurred at 60 wt. % and 65 wt. % of graphite. Furthermore, activation energy was affected by the decrease and increase in G content (wt. %). Graphite powder dispersion between small and large particle sizes was evenly distributed. Nevertheless, agglomeration should occur between particle dispersion on small particle sizes to increase the activation energy, as shown at 70 wt. % G and 75 wt. % of graphite. This condition will increase the interaction among various particle sizes so that feedstock viscosity can increase. The viscosity of the obtained feedstock was still acceptable because the injection provided G dispersion in a uniform feedstock, which resulted in an improved particle distribution network and electrical conductivity between the particle surface and various particle sizes. The mechanical properties of the composite materials were increased by the dispersion of particles with different sizes, which filled the gaps, thereby increasing density.

The microstructures of the feedstock are shown in Figure 4. Compaction with particle sizes was parallel to the increase in filler content in the feedstock from 60 wt. % to 75 wt. %. The improvement of G filler composition with different particle sizes indicated the potential for increased density. These results are supported by studies on the microstructures shown in (Figure 4) and indicate an increase in the content of small-sized particles that appeared to be more dispersed in the feedstock. The increase in the amount of small-sized particles significantly affected feedstock viscosity, as shown by the red arrows in (Figure 4(d)). The SEM observation shows the difference of the shape and size of particles in the presence of polypropylene as a binder, a white coat over the form of graphite. The decrease in filler content resulted in a decline in the dispersion of small-sized particles. The decrease in the amount of small-sized particles in the filler content is shown in (Figure 4(a)), which shows the composition of the filler content to be 60 wt. % of graphite. These results are consistent with those obtained by Bobek et al. [34], who found that high packing densities can be achieved when particle size is not uniform. The variations in particle size are also shown in the schematic of particle size in (Figure 5).

The particle dispersion conditions in the blending process provide the opportunity to form porosity. An increase in porosity occurs when the filler content in the feedstock decreases slightly, instead of porosity reduction in feedstock occurring because of filler content increase. The increase in filler content with filler size variation denotes the possibility of small particles filling the gaps in the feedstock and ultimately reducing porosity. Dispersion of particles different sizes also showed homogeneous up to contribute to an increase in viscosity, in which the homogeneous properties is the important properties of the feedstock [35].

Conclusion

This study showed that a suitable feedstock composition determined by fitting should involve balance between the powder filler and binder matrix, particularly during injection molding. Critical solid loading of 75 wt. % was found to be the optimal composition of the powder and binder; it affected the stability of the injection molding process. At the maximum critical load of 75 wt. % of the filler, torque stability remained normal. At 80 wt. % composition,

torque became unstable. This situation suggests that an increase in maximum viscosity and is unsuitable for injection molding. High viscosity was caused by the density of the filler content compared with polymeric materials that serve as a binder in the filler. The differences in the size and composition of the powder particles increased viscosity significantly because solid particles increased the density of the feedstock powder. An improvement in density and viscosity affected the injection molding parameters such as injection pressure and flow of the feedstock.

Acknowledgement

The authors gratefully acknowledge the financial support provided for this work by the Malaysian Ministry of Higher Education under contract numbers DIP-2012-05, ERGS/1/2011/TK/UKM/01/20 and FRGS/1/2013/TK04/UKM/01/2.

References

1. Dicks, A. L. (2006). The role of carbon in fuel cells. *Journal of Power Sources*, 156(2): 128 – 141.
2. Heo, S. I., Oh, K. S., Yun, J. C., Jung, S. H., Yang, Y. C., and Han, K. S. (2007). Development of preform moulding technique using expanded graphite for proton exchange membrane fuel cell bipolar plates. *Journal of Power Sources*, 171(2): 396 – 403.
3. Dweiri, R. and Sahari, J. (2007). Electrical properties of carbon-based polypropylene composites for bipolar plates in polymer electrolyte membrane fuel cell (PEMFC). *Journal of Power Sources*, 171(2): 424 – 432.
4. Liao, S. H., Yen, C. Y., Weng, C. C., Lin, Y. F., Ma, C. C. M., Yang, C. H., Tsai, M. C., Yen, M. Y., Hsiao, M. C., Lee, S. J., Xie, X. F. and Hsiao, Y. H. (2008). Preparation and properties of carbon nanotube/polypropylene nanocomposite bipolar plates for polymer electrolyte membrane fuel cells. *Journal of Power Sources*, 185(2): 1225 – 1232.
5. Derieth, T., Bandlamudi, G., Beckhaus, P., Kreuz, C., Mahlendorf, F., and Heinzel, A. (2008). Development of highly filled graphite compounds as bipolar plate materials for low and high temperature PEM fuel cells. *Journal of New Materials for Electrochemical Systems*, 11(1): 21 – 29.
6. Lee, J. H., Jang, Y. K., Hong, C. E., Kim, N. H., Li, P., and Lee, H. K. (2009). Effect of carbon fillers on properties of polymer composite bipolar plates of fuel cells. *Journal of Power Sources*, 193(2): 523 – 529.
7. Guo, N., and Leu, M. C. (2012). Effect of different graphite materials on the electrical conductivity and flexural strength of bipolar plates fabricated using selective laser sintering. *International Journal of Hydrogen Energy*, 37(4): 3558 – 3566.
8. Taherian, R., Golikand, A. N. and Hadianfard, M. J. (2011). The effect of mold pressing pressure and composition on properties of nanocomposite bipolar plate for proton exchange membrane fuel cell. *Materials & Design*, 32(7): 3883 – 3892.
9. Planes, E., Flandin, L., and Alberola, N. (2012). Polymer composites bipolar plates for PEMFCs. *Energy Procedia*, 20: 311 – 323.
10. Agote, I., Odriozola, A., Gutierrez, M., Santamarıa, A., Quintanilla, J., Coupelle, P. and Soares, J. (2001). Rheological study of waste porcelain feedstocks for injection moulding. *Journal of the European Ceramic Society*, 21(16), 2843 – 2853.
11. Reddy, J. J., Ravi, N. and Vijayakumar, M. (2000). A simple model for viscosity of powder injection moulding mixes with binder content above powder critical binder volume concentration. *Journal of the European Ceramic Society*, 20(12): 2183 – 2190.
12. Baojun, Z., Xuanhui, Q., and Ying, T. (2002). Powder injection molding of WC–8% Co tungsten cemented carbide. *International Journal of Refractory Metals and Hard Materials*, 20(5), 389 – 394.
13. Krauss, V. A., Pires, E. N., Klein, A. N., and Fredel, M. C. (2005). Rheological properties of alumina injection feedstocks. *Materials Research*, 8(2): 187 – 189.
14. Loh, N. H., Tor, S. B. and Khor, K. A. (2001). Production of metal matrix composite part by powder injection molding. *Journal of Materials Processing Technology*, 108(3): 398 – 407.
15. Loebbecke, B., Knitter, R. and Haußelt, J. (2009). Rheological properties of alumina feedstocks for the low-pressure injection moulding process. *Journal of the European Ceramic Society*, 29(9): 1595 –1602.
16. Mighri, F., Huneault, M. A. and Champagne, M. F. (2004). Electrically conductive thermoplastic blends for injection and compression molding of bipolar plates in the fuel cell application. *Polymer Engineering & Science*, 44(9): 1755 – 1765.

17. Ahn, S., Park, S. J., Lee, S., Atre, S. V. and German, R. M. (2009). Effect of powders and binders on material properties and molding parameters in iron and stainless steel powder injection molding process. *Powder Technology*, 193(2): 162 – 169.
18. Khakbiz, M., Simchi, A. and Bagheri, R. (2005). Analysis of the rheological behavior and stability of 316L stainless steel–TiC powder injection molding feedstock. *Materials Science and Engineering: A*, 407(1): 105 – 113.
19. Hanemann, T. (2008). Influence of particle properties on the viscosity of polymer–alumina composites. *Ceramics International*, 34(8): 2099 – 2105.
20. Wan, W., Yang, J., Zeng, J., Yao, L. and Qiu, T. (2014). Effect of solid loading on gelcasting of silica ceramics using DMAA. *Ceramics International*, 40(1): 1735 – 1740.
21. Subbanna, M. and Kapur, P. C. (2002). Role of powder size, packing, solid loading and dispersion in colloidal processing of ceramics. *Ceramics International*, 28(4): 401 – 405.
22. Jie, Z., Yan-wen, Z. O. U. and Jun, H. E. (2005). Influence of graphite particle size and its shape on performance of carbon composite bipolar plate. *Journal of Zhejiang University Science A*, 6(10): 1080 – 1083.
23. Iswandi, Sahari, J. and Sulong, A. B. (2011, June). Effects of different particles sizes of graphite on the engineering properties of graphites/polypropylene composites on injection molding application. *Key Engineering Materials*, 471: 109 – 114.
24. Thomas-Vielma, P., Cervera, A., Levenfeld, B. and Várez, A. (2008). Production of alumina parts by powder injection molding with a binder system based on high density polyethylene. *Journal of the European Ceramic Society*, 28(4), 763 – 771.
25. Zakaria, H., Muhamad, N., Sulong, A. B. and Ibrahim, I. (2014). Moldability characteristics of 3 mol% yttria stabilized zirconia feedstock for micro-powder injection molding process. Sains Malaysiana, 43(1): 129 – 136.
26. Kalyon, D. M., Birinci, E., Yazici, R., Karuv, B. and Walsh, S. (2002). Electrical properties of composites as affected by the degree of mixedness of the conductive filler in the polymer matrix. *Polymer Engineering & Science*, 42(7): 1609 – 1617.
27. Karatas, C., Kocer, A., Ünal, H. I. and Saritas, S. (2004). Rheological properties of feedstocks prepared with steatite powder and polyethylene-based thermoplastic binders. *Journal of Materials Processing Technology*, 152(1): 77 – 83.
28. German, R. M. and Bose, A. (1997). Injection molding of metal and ceramic. Metal Powder Industries Federation. New Jersey: John Wiley & Sons.
29. Aggarwal, G., Smid, I., Park, S. J. and German, R. M. (2007). Development of niobium powder injection molding. Part II: Debinding and sintering. *International Journal of Refractory Metals and Hard Materials*, 25(3): 226 – 236.
30. Olhero, S. M. and Ferreira, J. M. F. (2004). Influence of particle size distribution on rheology and particle packing of silica-based suspensions. *Powder Technology*, 139(1): 69 – 75.
31. Han, C.D. (2007). Rheology and processing of polymeric materials. *Polymer Processing*, Vol. 2. Oxfort University Press.
32. Trunec, M. and Hrazdera, J. (2005). Effect of ceramic nanopowders on rheology of thermoplastic suspensions. *Ceramics International*, 31(6): 845 – 849.
33. Amin, S. Y. M., Muhamad, N., Jamaludin, K. R., Fayyaz, A. and Yunn, H. S. (2014). Characterization of the feedstock properties of metal injection-molded WC-Co with palm stearin binder system. *Sains Malaysiana*, 43(1), 123 – 128.
34. Bobek, J., Seidl, M., Lenfeld, P., BČhálek, L. and Ausperger, A. (2011). Rheology of composites with nature vegetal origin fibers. *International Journal of Mechanical, Aerospace, Industrial, Mechatronic and Manufacturing Engineering*, 5(10): 1956 – 1959.
35. Hassan, N., Ahmad, S., Muhamad, N., Omar, M. A. and Hassan, N. A. (2013). Thermoplastic natural rubber (TPNR) as a backbone polymer for metal injection molding. *Sains Malaysiana*, 42(12): 1787 –1791.

Malaysian Journal of Analytical Sciences Vol 20 No 4 2016

Articles 11-17 are selected papers from the "International Conference on Applied Sciences and Industrial Technology (ICASIT 2015) for Food Science Symposium, 24-26 February 2015, Grand Lexis, Port Dickson, Negeri Sembilan, Malaysia; organised by Faculty of Applied Science, Universiti Teknologi MARA, Shah Alam, Selangor, Malaysia."

Guest Editor: Noorlaila Ahmad

Articles 18-22 are selected papers from the "International Conference on Applied Science and Technology (ICASIT 2015) for Chemistry and Environment Symposium, 24-26 February 2015, Grand Lexis, Port Dickson, Negeri Sembilan, Malaysia; organised by Faculty of Applied Science, Universiti Teknologi MARA, Shah Alam, Selangor, Malaysia."

Guest Editor: Rohaya Ahmad

Articles 23-32 are selected papers from the "International Conference on Fuel Cell and Hydrogen Technology 2013 (ICFCHT 2013), 7-10 October 2013, Inna Garuda Hotel, Convention Business, Yogyakarta, Indonesia; organised by Agency for the Assessment and Application of Technology (BPPT), Universiti Kebangsaan Malaysia (UKM) and Universiti Teknologi Malaysia (UTM)."

Guest Editor: Edy Herianto Majlan

Page

1. EFFECTS OF IRGAROL-1051 ON FATTY ACID PROFILE OF SOLITARY CORALS, *Fungia fungites* AFTER ACUTE EXPOSURE 697
(Kesan Irgarol-1051 terhadap Profil Asid Lemak Karang Solitari, *Fungia fungites* selepas Pendedahan Akut)
Zainudin Bachok, Marinah Mohd Ariffin, Mohammed Ali Sheikh, Noor Azhar Mohamed Shazili, Hassan Rashid Ali

2. A FLUORESCENCE PHOSPHATE SENSOR BASED ON POLY(GLYCIDYL METHACRYLATE) MICROSPHERES WITH ALUMINIUM-MORIN 704
(Sensor Fosfat Berpendarfluor Berasaskan Mikrosfera Poli(Glisidil Metakrilat) dengan Aluminium-Morin)
Amalina Ahmad, Norhadisah Mohd Zaini, Normazida Rozi, Nurul Huda Abd Karim, Siti Aishah Hasbullah, Lee Yook Heng, Sharina Abu Hanifah

3. PREPARATION AND CHARACTERIZATION OF Cu-Fe/TiO_2 PHOTOCATALYST FOR VISIBLE LIGHT DEEP DESULFURIZATION 713
(Penyediaan dan Pencirian Fotokatalis Cu-Fe/TiO_2 untuk Proses Nyahsulfur Di Bawah Cahaya Tampak)
Hayyiratul Fatimah Mohd Zaid, Chong Fai Kait, Mohamed Ibrahim Abdul Mutalib

4. DETERMINATION OF PRAZOSIN AND SIMVASTATIN IN LANDFILL LEACHATE USING LIQUID CHROMATOGRAPHY-TIME OF FLIGHT-MASS SPECTROMETRY 726
(Penentuan Prazosin dan Simvastatin di dalam Larut Lesap Mengunakan Kromatografi Cecair-Masa Penerbangan-Spektrometri Jisim)
Zainab Haider Mussa, Fouad Fadhil Al-Qaim, Md Pauzi Abdullah, Mohamed Rozali Othman

5. SPECTROSCOPIC CHARACTERIZATION OF COPPER(II)-BASED TETRAPEPTIDES 735
(Pencirian Spektroskopik Kuprum(II) Tetrapeptida)

Mohd. Basyaruddin Abdul Rahman, Sharifa Zaithun Begum, Mohamed Ibrahim Mohamed Tahir, Haslina Ahmad, Emilia Abdul Malek

6. SYNTHESIS AND ANTIMICROBIAL ACTIVITIES OF ELEVEN N-SUBSTITUTED MALEIMIDES 741
(Sintesis dan Kajian Antimikrob Terhadap Sebelas Terbitan Maleimida)
Tang Sook Chin, Fatin Ilyani Nasir, Nurul Izzaty Hassan

7. IDENTIFICATION OF VOLATILE SECONDARY METABOLITES FROM AN ENDOPHYTIC MICROFUNGUS *Aspergillus nomius* KUB105 751
(Pengenalpastian Metabolit Sekunder Meruap daripada Kulat Mikro Endofitik *Aspergillus nomius* KUB105)
Lateef Adebola Azeez, Sepiah Muid, Bolhassan Mohamad Hasnul

8. SYNTHESIS, CHARACTERIZATION AND DNA BINDING ACTIVITY OF A POTENTIAL DNA INTERCALATOR 760
(Sintesis dan Pengikatan DNA oleh Sebatian Interkalasi DNA Yang Berpotensi)
Siti Norain Harun, Yaakob Razak, Haslina Ahmad

9. SEPARATION AND RADIOLOGICAL IMPACT ASSESSMENT OF THORIUM IN MALAYSIAN MONAZITE PROCESSING 770
(Pengasingan dan Penilaian Impak Radiologi Torium dalam Pemprosesan Monazit di Malaysia)
Wadeeah M. Al-Areqi, Che Nor Aniza Che Zainul Bahri, Amran Ab. Majid, Sukiman Sarmani

10. ADSORPTION OF ANIONIC DYES FROM AQUEOUS SOLUTIONS BY CALCINED AND UNCALCINED Mg/Al LAYERED DOUBLE HYDROXIDE 777
(Penjerapan Pewarna Ionik daripada Larutan Akues Menggunakan Mg/Al Lapisan Dwi-Hidroksida Berkalsin dan Tanpa Kalsin)
Siti Mariam Sumari, Zaini Hamzah, Nesamalar Kantasamy

11. CHEMICAL CHANGES OF SHORT-BODIED MACKEREL (*Rastrelliger brachysoma*) MUSCLE AT CHILLED AND FROZEN STORAGE 793
(Perubahan Kimia ke atas Tisu Otot Ikan Kembung Bertubuh Pendek (*Rastrelliger brachysoma*) Pada Penyimpanan Suhu Dingin dan Sejuk Beku)
Emilia Azrina Mohd Bakri, Norizzah Abd Rashid, Cheow Chong Seng, Anida Yusoff, Fazilah Fazilin Juhari

12. ISOLATION AND PURIFICATION OF LYSOZYME FROM ALBUMIN: EFFECT OF ALBUMIN CONCENTRATION, pH AND IONIC STRENGTH OF BUFFER SOLUTION 799
(Pemisahan dan Penulenan Lisozim dari Albumin: Kesan Kepekatan Albumin, pH dan Kekuatan Ionik Larutan Penimbal)
Amirah Hamzah, Sofiah Hamzah, Fatin Mohd Nasir, Marinah Mohd Ariffin

13. PREPARATION AND PHYSICOCHEMICAL PROPERTIES OF OCTENYL SUCCINIC ANHYDRIDE (OSA) MODIFIED SAGO STARCH 806
(Penyediaan dan Sifat Fizikokimia Oktenil Suksinat Anhidrat (OSA) Modifikasi Kanji Sagu)
Nur Farhana Zainal Abiddin, Anida Yusoff, Noorlaila Ahmad

14. SENSORY CHARACTERISTICS OF MUD CLAM (*Polymesoda erosa*) HYDROLYSATE 812
(Ciri–ciri Deria Hidrolisat Lokan (*Polymesoda erosa*))
Normah Ismail and Noorasma Mustakim

15. NUTRITIONAL COMPOSITION AND COLOUR ANALYSIS OF CHOLESTEROL-REDUCED EGG YOLK POWDER 820

(Komposisi Nutrisi dan Analisis Warna Serbuk Kuning Telur Rendah-Kolesterol)
Fauziah Che In, Zaibunnisa Abdul Haiyee, Osman Hassan, Wan Aida Wan Mustapha

16. DETERMINATION OF OPTIMUM CONDITION OF LEUCINE CONTENT IN BEEF PROTEIN HYDROLYSATE USING RESPONSE SURFACE METHODOLOGY 829
(Penentuan Keadaan Optimum bagi Kandungan Leusina di dalam Protein Hidrolisat Daging Menggunakan Kaedah Gerak Balas Permukaan)
Siti Roha Ab Mutalib, Zainal Samicho, Noriham Abdullah

17. CHARACTERISATION OF CATFISH (*Clarias batrachus*) OIL: β-CYCLODEXTRIN INCLUSION COMPLEX 838
(Pencirian Kompleks Rangkuman Minyak Ikan Keli (*Clarias batrachus*): β-siklodekstrin)
Zaibunnisa Abdul Haiyee, Nor Izzatul Adyani Yahya, Norizzah Abd Rashid, Dzulkifly Mat Hashim

18. ISOLATION OF FLAVONOLS FROM THE STEMS OF MALAYSIAN *Uncaria cordata* var. *ferruginea* (BLUME) RIDSD. 844
(Pemisahan Flavonol dari batang *Uncaria cordata* var. *ferruginea* (Blume) Ridsd. Malaysia)
Nur Hakimah Abdullah, Fatimah Salim, Rohaya Ahmad

19. CHARACTERIZATION OF HEMICELLULOSES FROM OIL PALM EMPTY FRUIT BUNCHES OBTAINED BY ALKALINE EXTRACTION AND ETHANOL PRECIPITATION 849
(Pencirian Hemisellulosa Daripada Tandan Kosong Kelapa Sawit Diperolehi dari Pengekstrakan Alkali dan Pemendakan Etanol)
Maizatul Akhmar Mohd Nasir and Sabiha Hanim Saleh

20. IMMOBILIZATION OF HIGHLY EFFECTIVE PALLADIUM CATALYST ONTO POLY(4-VINYLPYRIDINE): SYNTHESIS AND CHARACTERIZATION 856
(Pemegunan Mangkin Paladium yang Efektif ke atas Poli(4-vinilpiridina): Sintesis dan Pencirian)
Siti Kamilah Che Soh, Intan Shafinass Kassim, Siti Aminah Jusoh, Mustaffa Samsuddin

21. MODELLING DISTRIBUTION FUNCTION OF SURFACE OZONE CONCENTRATION FOR SELECTED SUBURBAN AREAS IN MALAYSIA 863
(Permodelan Fungsi Taburan Kepekatan Permukaan Ozon di Kawasan Sub-Bandar yang Terpilih di Malaysia)
Muhammad Izwan Zariq Mokhtar, Nurul Adyani Ghazali, Muhammad Yazid Nasir, Norhazlina Suhaimi

22. SYNTHESIS AND CHARACTERIZATION OF BISCOUMARIN AND BENZOPYRANO DICOUMARIN DERIVATIVES 870
(Sintesis dan Pencirian Terbitan Biskumarin dan Benzopirano Dikumarin)
Nik Khairunissa' Nik Abdullah Zawawi, Muhammad Taha, Norizan Ahmat, Nor Hadiani Ismail

23. EFFECTS OF FUEL CONCENTRATIONS, CATALYST LOADINGS AND ACTIVATION ON THE PERFORMANCE OF DIRECT FORMIC ACID FUEL CELL (DFAFC) STACK 877
(Kesan Kepekatan Bahan Api, Kandungan Mangkin dan Pengaktifan ke atas Prestasi Susunan Sel Bahan Api Asid Formik Langsung (DFAFC))
Mohd Shahbudin Masdar, Nurulain Ngah, Norraihanah Mohamed Aslam, Dedikarni Panuh, Siti Kartom Kamarudin, Wan Ramli Wan Daud

24. SYNTHESIS AND CHARACTERISATION OF CHITOSAN-CELLULOSE BIOCOMPOSITE MEMBRANE FOR FUEL CELL APPLICATIONS 885
(Sintesis dan Pencirian Membran Biokomposit Kitosan-Selulosa untuk Aplikasi Sel Bahan

Api)
Nur Fatin Ab. Rahman, Kee Shyuan Loh, Abu Bakar Mohamad, Abdul Amir Hassan Kadhum, Kean Long Lim

25. TiO_2 DOPED WITH Fe_2O_3 FOR PHOTOELECTROCHEMICAL WATER SPLITTING ELECTRODE: EXPERIMENTAL AND DENSITY FUNCTIONAL THEORY STUDY 892
(TiO_2 Di Dop Bersama Fe_2O_3 untuk Elektrod Pembelahan Molekul Air Secara Fotoelektrokimia: Eksperimen dan Kajian Teori Fungsi Ketumpatan)
Khuzaimah Arifin, Hasmida Abdul Kadir, Lorna Jeffery Minggu, Wan Ramli Wan Daud, Mohammad B. Kassim

26. STUDY OF HYDROGEN CONSUMPTION BY CONTROL SYSTEM IN PROTON EXCHANGE MEMBRANE FUEL CELL 901
(Kajian Penggunaan Hidrogen oleh Sistem Kawalan dalam Sel Bahan Api Membran Penukaran Proton)
Ros Emilia Rosli, Edy Herianto Majlan, Siti Afiqah Abd. Hamid, Wan Ramli Wan Daud, Ramizi Mohamed, Teuku Husaini, Dedi Rohendi

27. EFFECT OF LONG TIME OXYGEN EXPOSURE ON POWER GENERATION OF MICROBIAL FUEL CELL WITH ENRICHED MIXED CULTURE 913
(Kesan Terhadap Penjanaan Kuasa Sel Bahan Api Mikrob dengan Kultur Campuran yang Diperkaya Melalui Pendedahan pada Oksigen untuk Jangka Masa Lama)
Mimi Hani Abu Bakar, Neil F Pasco, Ravi Gooneratne, Kim Byung Hong

28. FABRICATION AND CHARACTERIZATION OF Fe-DOPED TUNGSTEN TRIOXIDE PHOTOELECTRODES IN AQUEOUS MEDIUM USING TUNGSTIC ACID AND FERROCENE AS STARTING MATERIALS 923
(Pembuatan dan Pencirian Fotoelektrod Tungsten Trioksida Terdop Fe Dalam Medium Akueus Dengan Asid Tungstik dan Ferosin Sebagai Bahan Permulaan)
Ng Kim Hang, Nurul Akmal Jaafar, Lorna Jeffery Minggu, Mohammad bin Kassim

29. PROTON EXCHANGE MEMBRANE FUEL CELL/SUPERCAPASITOR HYBRID POWER MANAGEMENT SYSTEM FOR A GOLF CART 931
(Sistem Pengurusan Kuasa Hibrid Sel Bahan Api Membran Penukaran Proton/Superkapasitor untuk Kereta Golf)
Siti Afiqah Abd. Hamid, Ros Emilia Rosli, Edy Herianto Majlan, Wan Ramli Wan Daud, Ramizi Mohamed, Teuku Husaini, Ramli Sitanggang

30. MOLECULAR AND ELECTRONIC STRUCTURES OF A NEW RUTHENIUM-TUNGSTEN BIMETALLIC COMPLEX USING DENSITY FUNCTIONAL THEORY CALCULATIONS 946
(Struktur Molekul Dan Elektronik Kompleks Dwilogam Rutenium-Tungsten Berdasarkan Pengiraan Teori Fungsi Ketumpatan)
Khuzaimah Arifin, Wan Ramli Wan Daud, Mohammad B. Kassim

31. ENERGY MANAGEMENT STRATEGY FOR A FUEL CELL/ULTRACAPASITOR/BATTERY HYBRID SYSTEM FOR PORTABLE APPLICATIONS 955
(Strategi Pengurusan Tenaga bagi Sistem Hibrid Sel Bahan Api/ Ultrakapasitor/Bateri untuk Aplikasi Mudah Alih)
Siti Afiqah Abd. Hamid, Edy Herianto Majlan, Ros Emilia Rosli, Wan Ramli Wan Daud, Ramizi Mohamed, Teuku Husaini, Ramli Sitanggang

32. STRUCTURAL STUDY OF REDUCED GRAPHENE OXIDE/POLYPYROLE COMPOSITE AS METHANOL SENSOR IN DIRECT METHANOL FUEL CELL 965
(Kajian Struktur Komposit Grafin Oksida Terturun/Polipirol Sebagai Sensor Metanol Dalam Sel Bahan Api Metanol Langsung)

Malaysian Journal of Analytical Sciences, Vol 20 No 4 (2016): 697 - 703
DOI: http://dx.doi.org/10.17576/mjas-2016-2004-01

MALAYSIAN JOURNAL OF ANALYTICAL SCIENCES
Published by The Malaysian Analytical Sciences Society
ISSN 1394 - 2506

EFFECTS OF IRGAROL-1051 ON FATTY ACID PROFILE OF SOLITARY CORALS, *Fungia fungites* AFTER ACUTE EXPOSURE

(Kesan Irgarol-1051 terhadap Profil Asid Lemak Karang Solitari, *Fungia fungites* selepas Pendedahan Akut)

Zainudin Bachok[1,2]*, Marinah Mohd Ariffin[1], Mohammed Ali Sheikh[3], Noor Azhar Mohamed Shazili[2], Hassan Rashid Ali[3]

[1]*School of Marine and Environmental Sciences*
[2]*Institute of Oceanography and Environment*
Universiti Malaysia Terengganu, 21030 Kuala Terengganu, Terengganu, Malaysia
[3]*Tropical Research Centre for Oceanography, Environment and Natural Resources,*
The State University of Zanzibar, P. O. Box 146, Zanzibar-Tanzania

**Corresponding author: zainudinb@umt.edu.my*

Received: 14 March 2016; Accepted: 23 May 2016

Abstract

The short term exposure (4 days) was done to *Fungia fungites* using different concentration of Irgarol to establish the health effects of this species by measuring their fatty acid composition. It was done by comparing fatty acid composition of the fresh, control and exposed groups. The results indicated that, fresh and control samples of *F. fungites* were not significant different ($p > 0.05$) and dominated by Saturated Fatty Acids (SAFA) followed by Polyunsaturated Fatty Acids (PUFA) and the Monounsaturated Fatty Acids (MUFA). However, trends of other tested groups (20, 100 and 500 µg/L) were significant different ($p < 0.05$), with species suffered more as the dose of chemicals increased. For example, α-Linolenic acid (C18:3ω3) was not detected in *F. fungites* which exposed in this biocide at 100 and 500 µg/L whereas C20:5ω3 was not detected in all exposed groups. These ecotoxicological data proved that Irgarol may affect the fatty acids composition of coral reef organisms even if exposed at the low levels of this biocide.

Keywords: Irgarol, booster biocides, fatty acids composition, *Fungia fungites*, coral reef organisms

Abstrak

Pendedahan jangka pendek (4 hari) telah dilakukan ke atas *Fungia fungites* menggunakan kepekatan Irgarol yang berbeza untuk membangunkan kesan kesihatan spesies tersebut dengan mengambilkira komposisi asid lemak mereka. Ianya telah dilakukan dengan membandingkan komposisi asid lemak bagi kumpulan segar, kawalan dan yang telah didedahkan. Keputusan menunjukkan bahawa, sampel segar dan kawalan *F. fungites* tidak berbeza secara bererti ($p > 0.05$) dan didominasi olah Asid Lemak Tepu (SAFA) diikuti oleh Asid Lemak Tidak Tepu Poli (PUFA) dan Asid Lemak Tidak Tepu Mono (MUFA). Walaubagaimanapun, corak bagi kumpulan lain yang diuji (20, 100 and 500 µg/L) adalah berbeza secara bererti ($p < 0.05$), dengan spesies mengalami sengsara yang lebih apabila dos bahan kima ditingkatkan. Misalnya asid lemak α-Linolenat (C18:3ω3) tidak dikesan dalam *F. fungites* yang terdedah dengan biosid peransang ini pada 100 and 500 µg/L manakala C20:5ω3 tidak dikesan dalam semua kumpulan yang terdedah. Data ekotoksikologi ini membuktikan bahawa Irgarol berkemungkinan menjejaskan komposisi asid lemak organisma terumbu karang sungguhpun jika terdedah pada tahap yang rendah oleh biosid ini.

Kata kunci: Irgarol, biosid perangsang, komposisi asid lemak, *Fungia fungites*, organisma terumbu karang

Introduction

Irgarol-1051 is one among the commonly used alternative antifouling chemical after the prohibition of tri-butyltin (TBT) by International Maritime Organization (IMO) [1, 2]. It was reported that, Irgarol-1051 is very effective in prevention of attachments of biofoulings in recreational boats and yachts [3, 4]. In addition, the Irgarol is considered as a photosystem II inhibitor, which prevents photosynthesis and block conversion of excitation energy into chemical energy [5]. It has been broadly detected in aquatic ecosystems [6–10]. The significant concentrations of Irgarol have been also reported in coastal sediments [11–13]. Numbers of studies have demonstrated the impacts of Irgarol on marine organisms such as corals. For example, Owen et al. [7] reported that 60 ng/L of Irgarol reduced ^{14}C incorporation in the *Madracis mirabilis*, while 63 ng/L reduced net photosynthesis of intact corals. Moreover, 50 ng/L reduced photosynthetic efficiency (F0/Fm0) of *Seriatopora hystrix* [5]. It is also revealed that 1000 ng/L of Irgarol significantly reduced the photosynthesis rate of *G. fascicularis* and 100 ng/L reduced the settlement of coral larvae [4, 10]. The concerns on toxicity nature of Irgarol-1051 to marine habitats lead some countries such as Denmark, UK and Sweden to restrict the use of Irgarol as an antifouling paint to the boats under 25 m [14]. Studies on detection and distribution have reported the level of Irgarol 1015 in the coastal waters of Asian countries, for example, Singapore [15] and Malaysia [2], however, very little is known about its impact to corals in this region. To our knowledge only the study by Ali et al. [16] has reported the effects of Irgarol to the fatty acid composition of Asian Sea-bass (*Lates calcarifer*) from Malaysia. This study therefore presents the ecotoxicological data on the impact of Irgarol-1051 in the *F. fungites* by measuring fatty acid composition after exposed at different doses for four days in laboratory.

Materials and Methods

Sample collection

Fresh corals (*F. fungites*) were taken from Bidong Island, Terengganu Malaysia. The corals were acclimatized for 2 weeks in well aerated holding polyethylene tanks (500 L), containing natural seawater with a salinity of 30 ppt, under a natural photoperiod 12:12 hours (light: dark) cycle. The water in the tank was passed through a 1-mm filter, treated with UV-sterilized and refilled daily. The coral was not fed at all.

Chemical

A stock solution of 1000 mg/L Irgarol was prepared by using acetone and the working concentrations were made up by spiked the required concentrations to the sea water.

Experimental procedures

F. fungites were acclimatized for two weeks in the laboratory before the acute exposure tests to Irgarol for 96 hours. Water quality characteristics were measured daily: dissolved oxygen (DO) 7.2 ± 0.5 mg/L, and pH 7.69 ± 0.2, but the temperature was automatically controlled to 27 $^{\circ}C$ using cooling chiller throughout the whole experiment duration. After the two weeks acclimatization period, corals were transferred into different experimental tanks containing three litres of water and exposed to test concentrations of 20, 100, and 500 µg/L of Irgarol in three replicates for 96 hours. The control and acetone (check-up tanks) were kept for the sake of comparison. After four days (96 hours), the tissue of the coral were removed by using water pick and taken to the laboratory for fatty acid analysis.

Analytical procedure

Tissues of *F. fungites* coral were taken as samples for fatty acid composition analysis. The one step method [17] was used in this experiment to combine extraction and esterification processes using a single tube. Three replicates of each tissue samples (200 – 300 mg) were mixed with 4 mL of hexane and 1 mL of internal standard solution in a 50 mL centrifuge tube. After adding 2mL of 14% BF_3 in methanol and a magnetic stirring bar, the head space of tube was flushed with nitrogen gas and then closed tightly with a Teflon-lined screw-cap. The capped tube was heated on a hot plate at 100 °C for 120 min under continuous stirring. After cooling to room temperature, 1 mL of hexane was added followed by 2 mL of distilled water. The tube was then shaken vigorously for 1 min and centrifuged for 3 min at 2500 rpm (650 ×g). Of the two phases which formed, the upper phase was hexane layer containing the FAMEs. Finally, approximately 1 – 2 mL of the hexane layer was transferred using a Pasteur pipette into a clean sample vial to be injected into the GC-FID for FAME analysis.

Fatty acid concentrations (C_{FA}, mg/g of dry sample) were calculated by comparing the peak area of fatty acid in the sample with the peak area of internal standard as equation (1) follows:

$$C_{FA} = {}^{A_S}/_{A_{IS}} \times {}^{C_{IS}}/_{W_S} \quad (1)$$

where A_S = peak area of fatty acid in the sample in chromatogram, A_{IS} = peak area of internal standard in chromatogram, C_{IS} = concentration of internal standard (mg) and W_S = weight of sample (g). Qualitatively (as a percentage), composition of individual fatty acids were calculated by comparing the peak area of each fatty acid with the total peak area of all fatty acids in the sample.

Gas chromatography conditions

The FAMEs were separated and quantified using a gas chromatograph (GC 14-B Shimadzu) equipped with flame ionization detector. Separation was performed with an FFAP-polar capillary column (30 m × 0.32 mm internal diameter, 0.25 µm film thickness). Purified hydrogen was used as a carrier gas. After injection at 60 °C, the oven temperature was raised to 150 °C at a rate 40 °C min^{-1}, then to 230 °C at 3 °C min^{-1}, and finally held constant for 30 min. The flame ionization was held at 240 °C. FAME peaks were identified by comparing their retention times with those of authentic standards (Supelco Inc.). Fatty acids were designated as an n:pωx, where n is the number of carbon atoms in the aliphatic chain, p is the number of double bonds and x is the position of the first double bond from the terminal methyl group. The analytical precision for samples was generally < 5 % for total amounts and major components of FAMEs.

Results and Discussion

Fatty acid composition

The fatty acid results were calculated and presented as mean ± standard deviation (Table 1). Significant differences among the mean value of treatments were treated by One-way Analysis of Variance (ANOVA) followed by Least Significant Different (L.S.D). Two-way Analysis of Variance was used to support one way Analysis of Variance to get the F-probability interactions between chemicals, concentrations and / or species. Duncan's multiple range test (p <0.05) were calculated.

Fatty acid composition data for acute exposure of the *F. fungites* in Irgarol are presented in Table 1. The corals were dominated by SAFA 27.4 ± 6.17 (54.3 %), 23.8 ± 5.04 (49 %) and 23.2 ± 6.33 (50.6 %) mg/g dry weight, followed by PUFA 20.5 ± 5.48 (40.6 %), 23.2 ± 6.67 (47.8 %) and 20.9 ± 6.31 (45.8 %) mg/g dry weight and last is MUFA 2.25 ± 1.14 (5.06 %), 1.15 ± 0.69 (3.21 %) and 1.65 ± 0.74 (3.61 %) mg/g dry weight of fresh, control and acetone samples respectively.

In this study, *F. fungites* samples exposed with 20, 100 and 500 µg/L Irgarol have the same trend as fresh, control and acetone samples of SAFA > PUFA > MUFA (Figure 1). It was noted that SAFA, PUFA and MUFA are reduced as the dose of Irgarol increased in tested species. It is also interesting to note that in *F. fungites* (Figure 1), MUFA groups contributed less in the total FA among all exposed groups. The behavior of some groups of corals organisms to show different trends as in fresh and control samples can be justified by the fact that the activities in these groups were affected not only by the chemicals but also the ability of the individual organism to fight the toxic behavior of the used chemical.

Saturated fatty acids (SAFA)

The *F. fungites* are relatively enriched in Saturated Fatty Acids (SAFA) and the total SAFA are not significant different (p > 0.05) between fresh and control groups, however the other groups and individual SAFA were significant difference (p < 0.05) in this species (Table 1). Palmitic acid (C16:0) was found dominant in all SAFAs of the *F. fungites* (Table 1) and showed a significant difference (p < 0.05) between the samples. SAFA is pronounced more in average in *F. Fungites* (Figure 1). It was also reported that palmitic acid was the predominant in SAFA group as found in freshwater channel catfish (*Ictalurus punctatus*) (19.2 %) [18], and in freshwater rainbow trout (*Oncorhynchus mykiss*) (21.3 %) [19]. The fresh water species domination on SAFA fatty acids is also reported in the study conducted by Jabeen and Chaundhry [20].

Table 1. Fatty acid composition (mg/g) dry weight of tissue samples of *Fungia fungites* (mushroom) after 96 hours acute exposure test. Values are means ± standard deviation (SD) for n=3.

Fatty Acids	Fresh	Control	Acetone	Irgarol		
				20µg/L	100µg/L	500µg/L
SAFA						
C14:0	$2.05^{a} \pm 0.58$	$1.57^{b} \pm 0.08$	$1.40^{b} \pm 0.16$	$1.41^{b} \pm 0.08$	$1.58^{b} \pm 0.13$	$1.60^{b} \pm 0.13$
C16:0	$15.9^{a} \pm 1.39$	$13.2^{bc} \pm 1.53$	$15.2^{ab} \pm 1.77$	$14.1^{ab} \pm 1.64$	$11.4^{c} \pm 1.20$	$6.25^{d} \pm 0.61$
C18:0	$5.27^{a} \pm 0.34$	$5.15^{a} \pm 0.18$	$3.84^{ab} \pm 0.44$	$4.39^{a} \pm 1.01$	$3.69^{ab} \pm 0.47$	$4.46^{a} \pm 0.97$
C20:0	$4.21^{a} \pm 0.15$	$3.89^{ab} \pm 0.61$	$2.76^{c} \pm 0.11$	ND	$3.44^{bc} \pm 0.31$	ND
MUFA						
C16:1	$2.55^{a} \pm 0.45$	$1.55^{c} \pm 0.18$	$1.65^{bc} \pm 0.08$	$1.78^{bc} \pm 0.13$	$1.41^{c} \pm 0.61$	$1.56^{bc} \pm 0.07$
C17:1	ND	ND	ND	ND	ND	ND
C18:1ω9	ND	ND	ND	ND	ND	ND
C20:1	ND	ND	ND	ND	ND	ND
PUFA						
C18:3ω6	$3.03^{bc} \pm 0.12$	$3.30^{b} \pm 0.22$	$2.28^{c} \pm 0.19$	$2.29^{c} \pm 0.29$	$6.15^{a} \pm 0.25$	$2.84^{bc} \pm 1.05$
C18:3ω3	$13.7^{bc} \pm 1.07$	$16.4^{a} \pm 0.76$	$15.1^{ab} \pm 0.86$	$11.7^{d} \pm 1.04$	0.00	0.00
C20:3ω3	$1.24^{cd} \pm 0.30$	$2.04^{a} \pm 0.14$	$1.06^{d} \pm 0.07$	$1.45^{bcd} \pm 0.19$	$1.01^{d} \pm 0.11$	$2.29^{a} \pm 0.26$
C20:5ω3	$2.54^{a} \pm 0.08$	$1.46^{b} \pm 0.25$	$2.55^{a} \pm 0.23$	ND	ND	ND
C22:6ω3	ND	ND	ND	ND	ND	ND
ΣSAFA	$27.4^{a} \pm 6.17$	$23.8^{ab} \pm 5.04$	$23.2^{ab} \pm 6.33$	$19.9^{b} \pm 6.39$	$20.1^{b} \pm 4.37$	$12.3^{cd} \pm 2.85$
ΣMUFA	$2.55^{a} \pm 1.14$	$1.55^{c} \pm 0.69$	$1.65^{bc} \pm 0.74$	$1.78^{bc} \pm 0.80$	$1.41^{c} \pm 0.80$	$1.56^{bc} \pm 0.70$
ΣPUFA	$20.5^{ab} \pm 5.48$	$23.2^{a} \pm 6.67$	$20.9^{ab} \pm 6.31$	$15.4^{c} \pm 4.92$	$7.2^{d} \pm 2.67$	$5.1^{d} \pm 1.43$
ΣFA	$50.4^{a} \pm 5.04$	$48.5^{a} \pm 5.18$	$45.8^{ab} \pm 5.18$	$37.1^{b} \pm 4.58$	$28.7^{c} \pm 3.30$	$19.0^{d} \pm 2.02$

SAFA: Saturated fatty acids; MUFA: Monounsaturated fatty acids; PUFA: Polyunsaturated fatty acids; Means within rows followed by the same superscript(s) are not significant different ($p > 0.05$); ND – Not detected

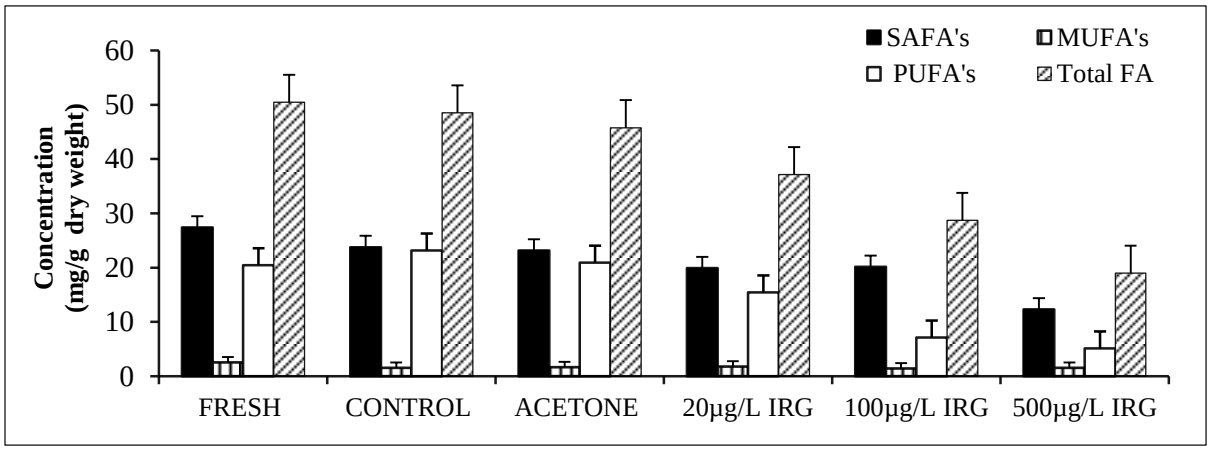


Figure 1. Fatty acid concentration of different classes and total fatty acid (mg/g dry weight) from tissues of Fungia fungites after exposed at different concentrations of Irgarol. Values are mean ± S.D, n = 3.

Mono unsaturated fatty acids (MUFA)

The ΣMUFA for *F. fungites* were significant difference in fresh, control, acetone and other exposed concentrations (Table 1). It is observed that MUFA contribution is less in total fatty acids in *F. fungites* (Table 1). This is due to the fact that, only palmitoleic acid (C16:1) was observed in the GC-FID where the rest of MUFA were below the detectable limit. In fact, Ho and Paul [21] found about 8 % only of oleic acid in total fatty acid in Asian sea bass. However, Steiner-Asiedu et al. [22] found that freshwater tilapia (*Tilapia* sp.) had significantly higher oleic acid levels than flat sardine (*Sardinella*) and sea bream (*Dentex*). The level of oleic acid in American freshwater channel catfish flesh was also reported higher; about 50 % [23] compared to less than 1% in sardine and sea mullet [24].

Polyunsaturated fatty acids (ΣPUFA)

The sum of Polyunsaturated Fatty Acids (ΣPUFA) in *F. fungites* was not significantly different among fresh, control and acetone samples ($p > 0.05$). α-Linolenic acid (C18:3ω3) was dominant PUFA in *F. fungit*es (66.8 % fresh sample) (see Figures 1 & 2). The rest of the PUFA in this species have less contribution. The higher levels of omega 3 and 6 in this species was not surprising because seawater organisms obtain their omega-3 and 6 FA from oceanic plankton [16, 25] or are fed fishmeal containing these FA [26].

Individual fatty acids were not detected in some exposed groups which differed with fresh and control groups (Figure 2). For example, α-Linolenic acid (C18:3ω3) was not detected in *F. fungites* exposed in this biocide at 100 and 500 µg/L whereas C20:5ω3 was not detected in all exposed groups (Figure 2). As expected, individual fatty acids in 500 µg/L exposure groups were much affected than the rest of the groups in *F. fungites* (Figure 2). The results show an inverse relationship between the dose of chemical used and activities of the *F. fungites* in the tanks. It is clear that, as the concentration of the Irgarol increased in different exposed tanks there was a decrease in activities of *F. fungites.*

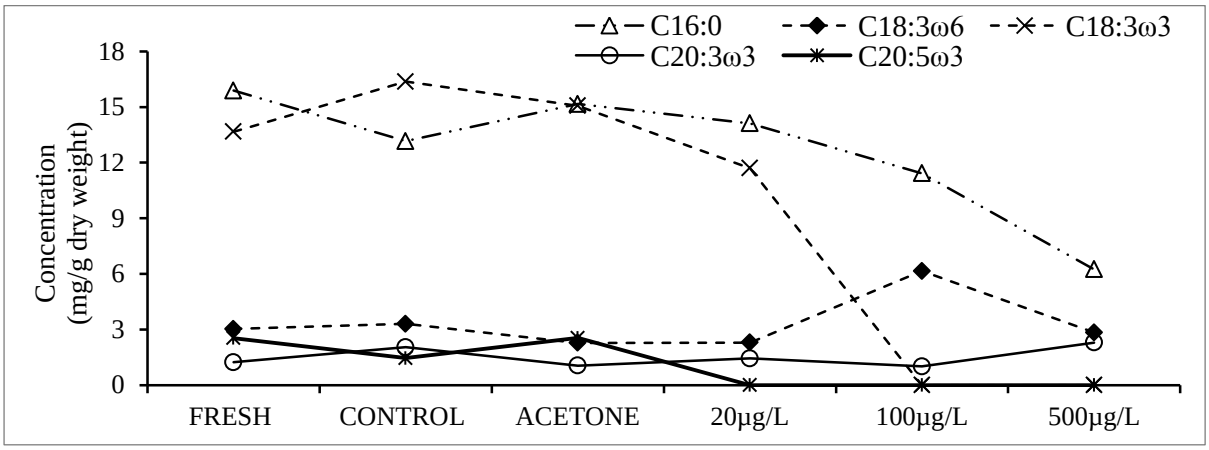


Figure 2. Individual Fatty acid concentrations of *Fungia fungites* exposed at different doses of Irgarol.

Conclusion

This paper explains the toxicological responses of *F. fungites* upon exposure to different concentrations of Irgarol in laboratory experiments. It can be concluded that; acute exposure of *F. fungites* (96 hours) to different concentrations of Irgarol had shown significant impact to the fatty acid composition. Fresh, control and all exposed samples of *F. fungites* were in trend of SAFA > PUFA > MUFA, however the exposed samples suffer more as the dose of Irgarol increased. The results of this study reveal that Irgarol is toxic and reduce the fatty acid composition of the coral even at the low level of exposure (20µg/L) and for a short period of time (96 hours). There is a need of further researches to be conducted in this area of specialization so as to understand more effects of these new antifouling chemicals to marine organisms as well as in coral reef using different species.

Acknowledgement

We sincerely acknowledge the Ministry of Education of Malaysia (MOE) for providing fund to support conducting this study using Fundamental Research Grant Scheme (FRGS/1/2011/STWN/UMT/02/3) and Higher Centre of Excellent (HiCOE) program. We also acknowledge University of Malaysia Terengganu (UMT) special Institute of Oceanography and Environment (INOS), School of Marine and Environmental Sciences, and the State University of Zanzibar (SUZA) for their support in conducting this research.

References

1. Gatidou, G., Thomaidis, N. S. and Zhou, J. L. (2007). Fate of Irgarol 1051, diuron and their main metabolites in two UK marine systems after restrictions in antifouling paints. *Environment International*, 33(1): 70 – 77.
2. Ali, H. R., Arifin, M. M., Sheikh, M. A., Mohamed Shazili, N. A. and Bachok, Z. (2013). Occurrence and distribution of antifouling biocide Irgarol-1051 in coastal waters of Peninsular Malaysia. *Marine Pollution Bulletin*, 70(1-2): 253 – 257
3. Gardinali, P. R., Plasencia, M., Mack, S. and Poppell, C. (2002). Occurrence of Irgarol 1051 in coastal waters from Biscayane Bay, Florida, USA. *Marine Pollution Bulletin*, 44: 781 – 788.
4. Knutson, S., Downs, C. A. and Richmond, R. H. (2012). Concentrations of Irgarol in selected marinas of Oahu, Hawaii and effects on settlement of coral larval. *Ecotoxicology*, 21(1): 1 – 8.
5. Jones, R. J. and Heyward, A. J. (2003). The effects of produced formation water (PFW) on coral and isolated symbiotic dinoflagellates of coral. *Marine and Freshwater Research*, 54(2): 153 – 162.
6. Tolosa, I., Readman, J. W., Blaevoet, A., Ghilini, S., Bartocci, J. and Horvat, M. (1996). Contamination of Mediterranean (Cite d'Azur) coastal waters by organotins and Irgarol 1051 used in antifouling paints. *Marine Pollution Bulletin*, 32(4): 335 – 341.
7. Owen, R., Knap, A., Toaspern, M. and Carbery, K. (2002). Inhibition of coral photosynthesis by the antifouling herbicide Irgarol 1051. *Marine Pollution Bulletin*, 44(7): 623 – 632.
8. Okamura, H., Aoyama, I., Ono, Y. and Nishida, T. (2003). Antifouling herbicides in the coastal waters of western Japan. *Marine Pollution Bulletin*, 47: 59 – 67.
9. Sapozhnikova, Y., Wirth, E., Schiff, K., Brown, J. and Fulton, M. (2007). Antifouling pesticides in the coastal waters of Southern California. *Marine Pollution Bulletin*, 54(12): 1972 – 1978.
10. Sheikh, M. A., Higuchi, T., Fujimura, H., Imo, T. S., Miyagi, T. and Oomori, T. (2009). Contamination and impacts of new antifouling biocide Irgarol-1051 on subtropical coral reef waters. *International Journal of Environmental Science and Technology*, 6(3): 353 – 358.
11. Biselli, S., Bester, K., Hühnerfuss, H. and Fent, K. (2000). Concentrations of the antifouling compound Irgarol 1051 and of organotins in water and sediments of German North and Baltic Sea marinas. *Marine Pollution Bulletin*, 40(3): 233 – 243.
12. Boxall, A. B. A., Comber, S. D., Conrad, A. U., Howcroft, J. and Zaman, N. (2000). Inputs, monitoring and fate modelling of antifouling biocides in UK estuaries. *Marine Pollution Bulletin*, 40(11): 898 – 905.
13. Kitada, Y., Kawahata, H., Suzuki, A. and Oomori, T. (2008). Distribution of pesticides and bisphenol a in sediments collected from rivers adjacent to coral reefs. *Applied Catalysis B: Environmental*, 82(3-4): 163 –168.
14. Thomas, K. V., McHugh, M. and Waldock, M. (2002). Antifouling paint booster biocides in UK coastal waters: Inputs, occurrence and environmental fate. *Science of the Total Environment*, 293(1-3): 117 – 127.
15. Basheer, C., Tan, K. S. and Lee, H. K. (2002). Organotin and Irgarol-1051 contamination in Singapore coastal waters. *Marine Pollution Bulletin*, 44(7): 697 – 703.
16. Ali, H. R., Arifin, M. M., Sheikh, M. A., Mohamed Shazili, N. A. and Bachok, Z. (2015). Toxicological studies of Irgarol-1051 and its effects on fatty acid composition of Asian sea-bass, *Lates calcarifer*. *Regional Studies in Marine Science*, 2: 171 – 176.
17. Abdulkadir, S. and Tsuchiya, M. (2008). One-step method for quantitative and qualitative analysis of fatty acids in marine animal samples. *Journal of Experimental Marine Biology and Ecology*, 354(1): 1– 8.
18. Sathivel, S., Prinyawiwatkul, W., Grimm, C. C., King, J. M. and Lloyd, S. (2002). FA composition of crude oil recovered from catfish viscera. *Journal of the American Oil Chemists' Society*, 79(10): 989 – 992.
19. İbrahim Haliloğlu, H., Bayır, A., Necdet Sirkecioğlu, A., Mevlüt Aras, N. and Atamanalp, M. (2004). Comparison of fatty acid composition in some tissues of rainbow trout (*Oncorhynchus mykiss*) living in seawater and freshwater. *Food Chemistry*, 86(1): 55 – 59.

20. Jabeen, F. and Chaudhry, A. S. (2011). Chemical compositions and fatty acid profiles of three freshwater fish species. *Food Chemistry*, 125(3): 991 – 996.
21. Ho, B. T. and Paul, D. R. (2009). Fatty acid profile of Tra Catfish (*Pangasius hypophthalmus*) compared to Atlantic Salmon (*Salmo solar*) and Asian Seabass (*Lates calcarifer*). *International Food Research Journal*, 16(4): 501 – 506.
22. Steiner-Asiedu, M., Julshamn, K. and Lie, Ø. (1991). Effect of local processing methods (cooking, frying and smoking) on three fish species from Ghana: Part I. Proximate composition, fatty acids, minerals, trace elements and vitamins. *Food Chemistry*, 40(3): 309 – 321.
23. Nettleton, J. A., Allen, W. H., Klatt, L. V., Ratnayake, W. M. N. and Ackman, R. G. (1990). Nutrients and chemical residues in one-to two-pound Mississippi farm-raised channel catfish (*Ictalurus punctatus*).*Journal of Food Science*, 55(4): 954 – 958.
24. Ackman, R. G. (1994). Seafood lipids. In Shahidi, F. and Botta, J. R. (Eds). Seafoods: Chemistry, Processing, Technology and Quality. Glasgow: Chapman and Hall p. 34 – 48.
25. Steffens, W. (1997). Effects of variation in essential fatty acids in fish feeds on nutritive value of freshwater fish for humans. *Aquaculture*, 151: 97 – 119.
26. Henderson, R. J. (1996). Fatty acid metabolism in freshwater fish with particular reference to polyunsaturated fatty acids. *Archives of Animal Nutrition*, 49(1): 5 – 22.

Malaysian Journal of Analytical Sciences, Vol 20 No 4 (2016): 704 - 712
DOI: http://dx.doi.org/10.17576/mjas-2016-2004-02

MALAYSIAN JOURNAL OF ANALYTICAL SCIENCES
Published by The Malaysian Analytical Sciences Society
ISSN 1394 - 2506

A FLUORESCENCE PHOSPHATE SENSOR BASED ON POLY(GLYCIDYL METHACRYLATE) MICROSPHERES WITH ALUMINIUM-MORIN

(Sensor Fosfat Berpendarfluor Berasaskan Mikrosfera Poli(Glisidil Metakrilat) dengan Aluminium-Morin)

Amalina Ahmad[1], Norhadisah Mohd Zaini[1], Normazida Rozi[1], Nurul Huda Abd Karim[1], Siti Aishah Hasbullah[1], Lee Yook Heng[1], Sharina Abu Hanifah[1,2]*

[1]*School of Chemical Sciences and Food Technology*
[2]*Center for Water Research and Analysis*
Faculty of Science and Technology,
Universiti Kebangsaan Malaysia, 43600 UKM Bangi, Selangor, Malaysia

**Corresponding author: sharina@ukm.edu.my*

Received: 8 December 2015; Accepted: 11 March 2016

Abstract

The performance of new phosphate sensor was investigated using fluorescence spectrometer in the form of immobilized Al-morin on poly(glycidyl methacrylate) (pGMA) microspheres. pGMA microspheres that were synthesized by using suspension photopolymerization exhibited spherical-shaped morphology with diameters from 1.5 to 5.3 µm. The studies were carried out at pH 5 and the ratio of aluminium (III) chloride hexahydrate to morin was 3:1 (v/v). At pH 5, $H_2PO_4^-$ was measured at 548 nm emission wavelength. The relative fluorescence intensity was inversely proportional to $H_2PO_4^-$ concentrations. The linear range was observed between 6.6 – 58.8 µmol/L with detection limit (LOD) of 0.7 µmol/L. Ion interference study demonstrated that Al-morin was highly selective towards $H_2PO_4^-$.

Keywords: phosphate sensor, polymer microspheres, aluminium-morin, fluorescence

Abstrak

Prestasi sensor fosfat baru telah dikaji dengan menggunakan spektrometer pendarfluor dalam bentuk Al-morin terpegun pada mikrosfera poli(glisidil metakrilat) (pGMA). Mikrosfera pGMA yang disintesis dengan menggunakan pemfotopolimeran ampaian mempamerkan morfologi berbentuk sfera dengan diameter 1.5 hingga 5.3 µm. Kajian telah dijalankan pada pH 5 dan nisbah aluminium (III) klorida heksahidrat kepada morin adalah 3: 1 (v/v). Pada pH 5, $H_2PO_4^-$ diukur pada gelombang pancaran 548 nm. Keamatan pendarfluor relatif adalah berkadar songsang dengan kepekatan H_2PO_4- Julat linear diperhatikan antara 6.6 – 58.8 µmol/L dengan had pengesanan (LOD) pada 0.7 µmol/L. Kajian gangguan ion menunjukkan Al-morin adalah sangat selektif kepada $H_2PO_4^-$.

Kata kunci: sensor fosfat, polimer mikrosfrera, aluminium-morin, pendafluor

Introduction

Phosphorus can be divided into organic phosphate and inorganic phosphate. Phosphate ions that move freely in water known as orthophosphate (P_i) which is an inorganic phosphate [1]. High phosphate content in water can cause eutrophication. Eutrophication is the excess nutrients in aquatic ecosystems that bring to an excess algae growth and cause water and environmental problem [2]. Thus, monitoring phosphate in drinking water is vital to ensure that water quality follows the standard. The maximum concentration of phosphate recommended by World Health

Organization (WHO) is 1 mgL^{-1}[3]. Besides, the determination of phosphate concentrations in body fluids is necessary to diagnose hyperparathyroidism, hypertension [4], vitamin D deficiency, mineral and bone disorder, kidney failure [5] and Franconia syndrome [6, 7].

Optical sensor is a device that converts light rays into electronic signals [8]. Fluorescence, luminescence, chemiluminescence and UV–visible spectrophotometers are commonly applied instruments in optical sensors [3]. Fluorescence method is widely used because it is highly sensitive, easy to operate, response rapidly and less costly [9]. Phosphate has known to quench aluminium-morin (Al-morin) fluorescence intensity. During 1950's, Al-morin has been used to detect trace amount of fluoride ion and indirectly phosphate was determined to be an interfering ion [10]. Previously, Hong et al. [11] reported that Al-morin immobilized on PVA/PVC plasticized composite membrane based on sandwich configuration has been used in phosphate detection. This technique had improved the indicator leaching problem however produced narrow linear range of phosphate detection (11.0 – 51.4 µmol/L). In order to overcome its limitation, Lin et al. [12] claimed that Al-morin immobilized on pretreated PVC membrane is more sensitive as it produces wider linear range (44.1 – 110.2 µmol/L).

In this work, phosphate sensor was developed by immobilizing Al-morin onto poly(glycidyl methacrylate) (pGMA) microspheres which were synthesized by suspension photopolymerization technique. High surface area of pGMA microspheres is suitable for Al-morin immobilization matrix in order to increase the reaction site for phosphate detection. The microspheres are also a water-insoluble polymer, causing it to be applicable in phosphate sensing. All characterizations of immobilized Al-morin phosphate sensors were analyzed by fluorimetric method.

Materials and Methods

Apparatus and reagent

Chemicals including morin hydrate (98%, MP Biomedicals LLC), aluminium (III) chloride hexahydrate ($AlCl_3.6H_2O$) (99 %, Systerm), glycidyl methacrylate (97 %, Sigma Aldrich), ethylene glycol dimethacrylate (9 8%, Sigma Aldrich), polyvinyl alcohol (98 %, Sigma Aldrich), 2,2-dimethoxy-2-phenylacetophenone (99 %, Sigma Aldrich), potassium dihydrogen phosphate (99 %, Systerm), potassium carbonate (K_2CO_3) (99 %, Sigma Aldrich), potassium acetate (CH_3COOK) (99 %, Sigma Aldrich), potassium chloride (KCl) (99 %, Sigma Aldrich), potassium fluoride (KF) (99 %, Sigma Aldrich), potassium nitrate (KNO_3) (99 %, BDH Chemicals Ltd), potassium sulfate (K_2SO_4) (99 %, Sigma Aldrich) and ethanol (95 %, Sigma Aldrich) were used as received.

The surface of microspheres was observed using Zeiss LEO 1450VP Scanning Electron Microscope (SEM). Infrared spectra of the microspheres were recorded by Fourier Transform Infrared spectrometer (Perkin Elmer) using attenuated total reflection (ATR-FTIR) spectrometry method. Response of Al-morin complex on fluorescence intensity was measured by Perkin Elmer Fluorescence Spectrometer at 548 nm emission wavelength.

Synthesis of Al-morin complex

A concentration of 23.2 µmol/L Morin solution was prepared in ethanol and 16.6 µmol/L aluminium (III) chloride hexahydrate ($AlCl_3.6H_2O$) in deionized water. Al-morin complex was formed by mixing $AlCl_3.6H_2O$ with Morin in 3:1 (v/v). The formation of Al-morin was then confirmed when the fluorescence emission of Al-morin was determined to be at wavelength 510 nm as reported in the literature [12].

Synthesis of poly(glycidyl methacrylate) (pGMA) microspheres

An mount of 1 ml of glycidyl methacrylate (GMA), 1 ml of ethylene glycol dimethacrylate (EGDMA), 5 ml of 1% polyvinyl alcohol (PVA) and 1.6 % (w/w) of 2,2-dimethoxy-2-phenylacetophenone (DMPP) were placed in a vial. The mixture was sonicated within 15 minutes. The suspension was transferred into a petri dish and photocured under continuous nitrogen flow for 10 minutes. The microspheres were collected by centrifugation at 2000 rpm for 10 minutes. They were then left to dry at room temperature. pGMA microspheres were characterized by Scanning Electron Microscope (SEM) and Attenuated Total Reflectance-Fourier-transform Infrared (ATR-FTIR) spectrometer.

Immobilization of Al-morin onto pGMA microspheres

An amount of 20 – 30 % (v/v) of Aluminium-Morin (Al-morin) complex was added into the mixture of GMA monomer, 1 ml ethylene glycol dimethylacrylate (EGDMA), 5 ml of 1% polyvinyl alcohol (PVA) and 1.6% (w/w) of 2,2-dimethoxy-2-phenylacetophenone (DMPP) in a vial. The mixture was sonicated within 15 minutes then it was transferred into a petri dish for photocuring procedure under continuous nitrogen flow for 10 minutes. The microspheres were collected by centrifugation at 2000 rpm for 10 minutes and dried at room temperature. pGMA/Al-morin microspheres were characterized by SEM and ATR-FTIR.

pH analysis

The optimum pH for Al-morin to react with 110.2 µmol/L dihydrogen phosphate ($H_2PO_4^-$) was studied. pGMA/Al-morin microspheres were soaked in pH 1 buffer solution before they were next soaked into phosphate solution prepared at pH 1 for 5 minutes as reported previously [13]. These steps were repeated for analyzing the same concentration of phoshate solution at pHs ranging from 1 to 7. Fluorescence intensity before and after Al-morin reacts with phosphate were recorded by calculating the relative of fluorescence intensity at 548 nm.

Effect of phosphate concentration

pGMA/Al-morin microspheres were soaked in dihydrogen phosphate ($H_2PO_4^-$) solution prepared at pH 5 buffer with concentrations ranging from 0.7 – 124.9 µmol/L for 5 minutes. They were initially soaked at pH 5 buffer to remove the unreacted monomer. The fluorescence intensity of immobilized Al-morin before and after reacting with phosphate for each concentration was measured at 548 nm.

Effect of interference ions

Interference study was carried out by preparing a fixed concentration of $H_2PO_4^-$ (110.2 µmol/L) in the presence of common anions including carbonate (CO_3^{2-}), acetate (CH_3COO^-), chloride (Cl^-), fluoride (F^-), nitrate (NO_3^-) and sulfate (SO_4^{2-}). Each anion at the same concentration as $H_2PO_4^-$ was prepared. Fluorescence intensity of pGMA/Al-morin microspheres soaked in the analyte containing $H_2PO_4^-$ and interference ions were recorded at 548 nm.

Results and Discussion

Characterization of Al-morin immobilized onto pGMA

Morphology of pGMA microspheres

pGMA microspheres were used as a matrix to immobilize Al-morin complex. High surface area of these microspheres makes it possible to act as a matrix with good physical properties and these microspheres are chemically stable. pGMA microspheres were prepared using a rapid synthesis method, which is suspension photopolymerization. The droplets of monomer mixtures form pGMA at room temperature in the presence of DMPP. The polymerization process was terminated by the removal of the ultraviolet (UV) light source. The schematic polymerization of GMA is presented in Figure 1.

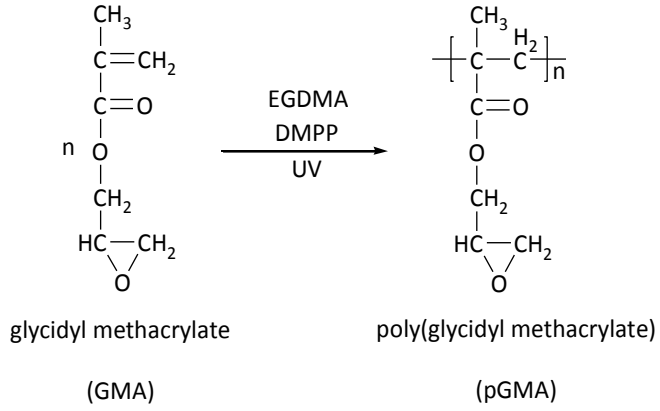


Figure 1. Polymerization of GMA microspheres

The spheres produced by this approach varied in size from 1.5 to 5.3 µm and are polydisperse. The size maintains even after Al-morin was immobilized onto pGMA microspheres. This observation might be due to the entrapment of chemical doping technique used to immobilize Al-morin which did not involve any chemical bonding. The presence of Al-morin causes pGMA/Al-morin microspheres to exhibit rougher surface compared to pGMA. The roughness of the microspheres surface has provides higher surface area [14]. SEM micrographs of pGMA microspheres and pGMA/Al-morin are presented in Figure 2.

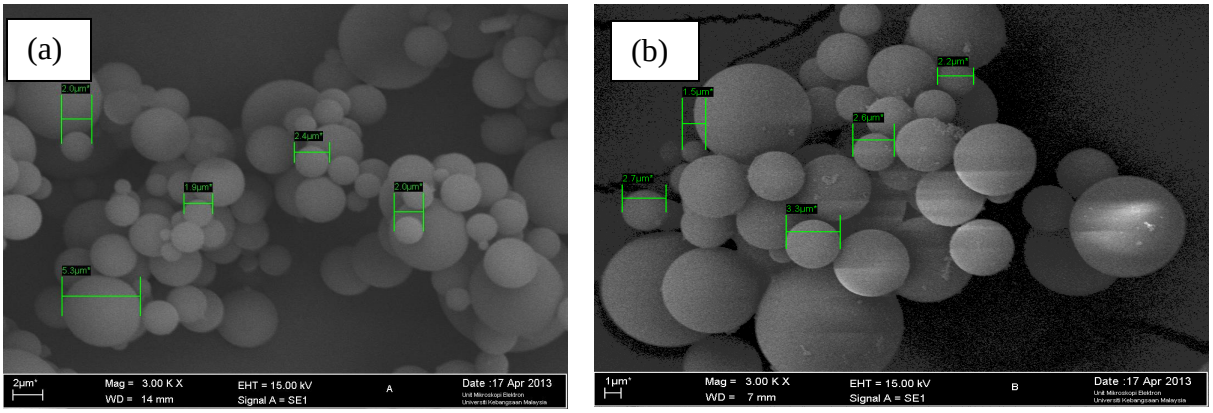


Figure 2. Surface morphology of microspheres (A) pGMA and (B) pGMA with Al-morin

Spherical matrix is capable to maximize the surface area of sensor reagent and reduce the response time by allowing the analyte to penetrate through the matrix [15]. This shows that pGMA provides high surface area for phosphate detection and increases the chemisensor sensitivity. Microspheres optical chemisensor can reduce sample volume, increase sensitivity, shorten response time and reduce detection limit [16].

ATR-FTIR spectra of pGMA/Al-morin

ATR-FTIR spectra of pGMA and pGMA/Al-morin microspheres are shown in Figure 3. Both types of pGMA spectra have recorded a strong band at 1721 cm^{-1} (pGMA) and 1722 cm^{-1} (pGMA/Al-morin) due to C=O vibrations. Furthermore, bands of 843 cm^{-1} and 905 cm^{-1} correspond to the epoxy groups. No additional peak can be seen between pGMA and pGMA/Al-morin bands. This result confirms that the pGMA and Al-morin involved entrapment method which does not involve any chemical bonding between Al-morin complex and the GMA polymer.

Optimization of pGMA/Al-morin

pH analysis

Figures 4 shows graph of fluorescence intensity versus pH that was measured at 548 nm respectively. pH 5 was determined to be the optimum pH for pGMA/Al-morin to react with $H_2PO_4^-$. Mohr and Wolfbeis [17] have reported that $H_2PO_4^-$ is the predominant form of phosphate at pH 5. At pH <5, low fluorescence intensity could be related to the protonation of $H_2PO_4^-$ to form H_3PO_4 resulting in a poor ability of $H_2PO_4^-$ to interact with Al-morin. Furthermore at pH >5, gradual decrease in fluorescence intensity is observed which may be due to hydroxide ions interference and formation of other form of phosphate ions [18].

Effect of phosphate concentrations

Morin (2',3,4',5,7-pentahydroxyflavone) is brown in colour when dissolves in ethanol and turn to light yellow solution as it is diluted. Free morin is weakly fluorescent and it becomes stronger as it forms a complexe with aluminium [19]. However, the fluorescence of Al-morin complex quenches distinctly when phosphate is introduced into the system [12]. The proposed reaction between Al-morin with $H_2PO_4^-$ is shown in Figure 5.

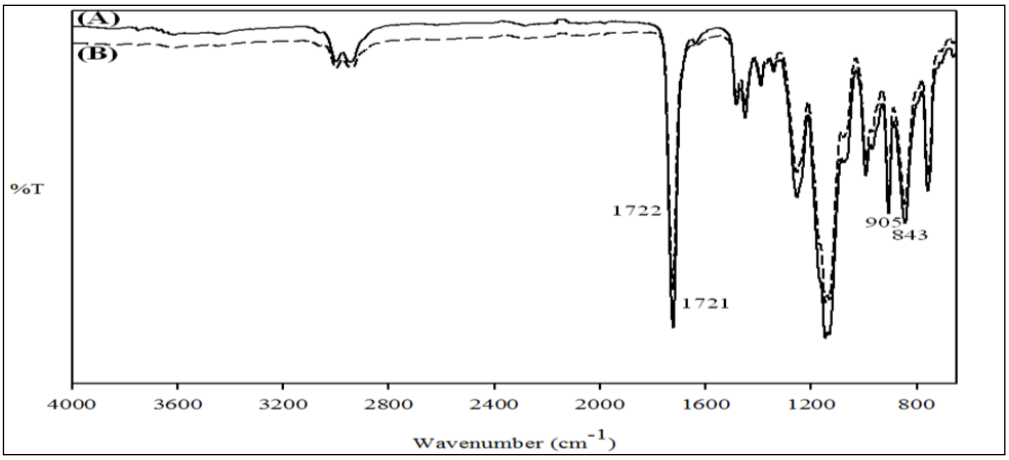


Figure 3. ATR-FTIR spectra of (A) pGMA and (B) pGMA/Al-morin microspheres

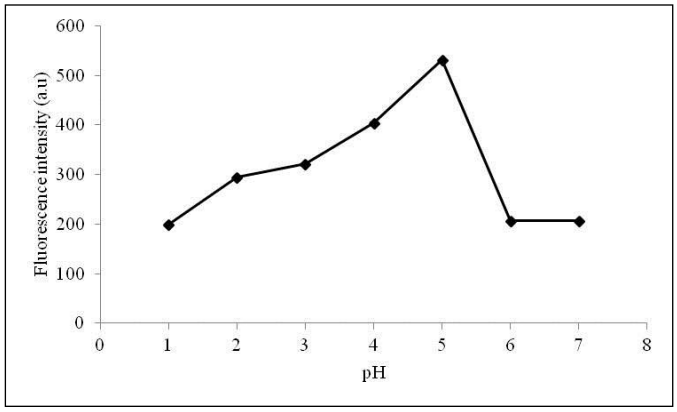


Figure 4. Effect of pH on pGMA/Al-morin with $H_2PO_4^-$

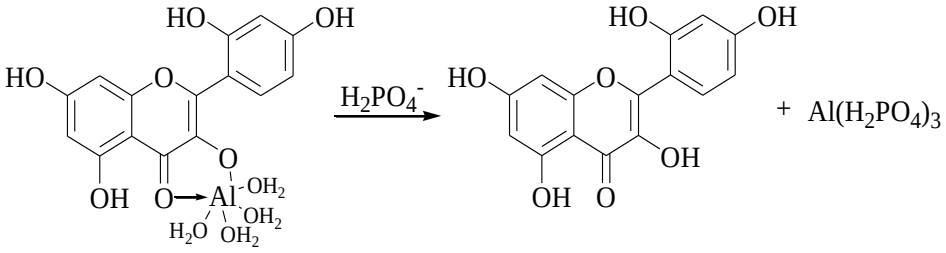


Figure 5. Proposed chemical reaction of Al-morin with phosphate anion.

Study on the effect of phosphate concentration was carried out at pH 5 to investigate the ability of immobilized Al-morin in detecting $H_2PO_4^-$ at various concentrations. The pGMA/Al-morin microspheres was allowed to react with

$H_2PO_4^-$ at a fixed concentration within 5 minutes before analyzing by fluorescence spectrometer. Figure 6 shows the fluorescence intensity of pGMA/Al-morin reached equilibrium at 124.9 µmol/L $H_2PO_4^-$ with the linearity from 6.6 to 58.8 µmol/L (inset) and a detection limit as low as 0.7 µmol/L. This sensor produced higher range of phosphate concentration compared to poly(vinyl chloride) and poly(vinyl alcohol) based membrane may be due to larger surface area provided by pGMA microspheres [11, 12, 20].

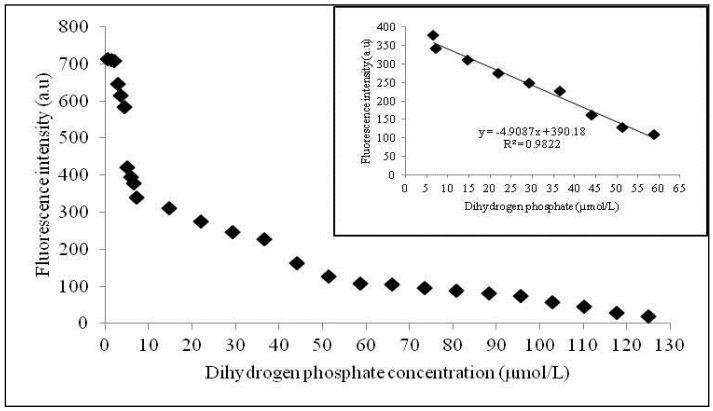


Figure 6. Calibration curve and linear range (inset) of pGMA/Al-morin based sensor towards different phosphate concentrations at pH 5.

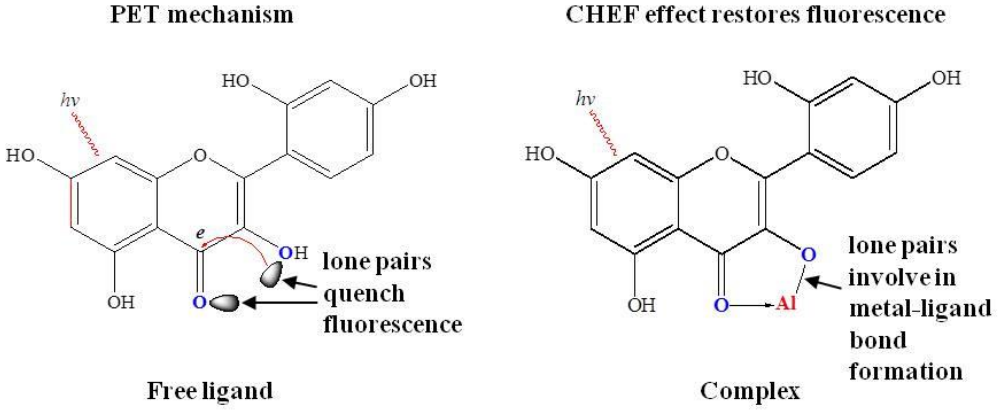


Figure 7. PET and CHEF effects on morin complexation.

The relative fluorescence intensity is inversely proportional to $H_2PO_4^-$ concentrations. The quenching of fluorescence could be further explained in Figure 7 [21]. It is possibly an example of CHEF (Chelation-Enhanced Fluorescence) and PET (Photoinduced Electron Transfer) phenomenons. CHEF effect is related to the photoinduced electron transfer (PET) mechanism. In the PET mechanism, exciting radiation induces electrons in the free ligand to transfer from the lone pairs on donor atoms (O-donors) to the π-system of the fluorophores and resulting in fluorescence quenching. These same lone pairs which involve in bonds formation with metal ions reduce the PET quenching effect. This occurrence leads to the CHEF effect, where metal ions can be detected by the increment of fluorescence intensity [22]. In this case, introducing $H_2PO_4^-$ to the system reduces the fluorescence intensity as aluminium detaches from morin by forming aluminium dihydrogenphosphate, $Al(H_2PO_4)_3$. This is due to poor fluorescence of non-chelating morin. Simultaneously, PET involves explaining about this phenomenon. Lone pairs

on morin O-donor atoms are no longer chelated with metal ion thus leading to increase PET quenching effect and indirectly reduce the fluorescence intensity.

Effect of Ions Interference

According to Table 1, pGMA/Al-morin was highly selective for $H_2PO_4^-$ over other anions which were commonly present in water samples such as CO_3^{2-}, CH_3COO^-, Cl^-, F^-, NO_3^- and SO_4^{2-}. The higher affinity for $H_2PO_4^-$ over other anions may be caused by the presence of appropriately spaced cationic charges, Al^{3+} [23]. All the interfering ions do not affect much on the detection of $H_2PO_4^-$ because the percentage of interference was less than 10% [24 – 26].

Table 1. Percentage of ion interference of immobilized Al-morin at pH 5.

Ion interference	**Percentage of interference (%)**
Carbonate, CO_3^{2-}	1.51
Acetate, CH_3COO^-	0.52
Chloride, Cl^-	5.43
Floride, F^-	0.00
Nitrate, NO_3^-	2.74
Sulfate, SO_4^{2-}	1.58

Performance of pGMA microspheres in the present study and PVC based membranes for immobilizing Al-morin is summarized in Table 2. It is clearly seen that pGMA/Al-morin has improved phosphate sensor performance compared to polyvinyl alcohol/ polyvinyl chloride/ aluminium-morin (PVA/PVC/Al-morin) composite membrane [11] and PVC/Al-morin matrix membrane [12] for $H_2PO_4^-$ detection. pGMA/Al-morin microspheres serves as a useful matrix for rapid phosphate measurement as the response time was recorded within 5 minutes.

Table 2. Summary of Al-morin phosphate sensor performances.

Parameters	**pGMA/Al-morin micropsheres**	**PVA/PVC/Al-morin membrane[a]**	**PVC/Al-morin membrane[b]**
pH	5	4	5
Dynamic range (µmol/L)	0.7 – 124.9	3.7 – 73.5	7.3 – 132.3
Linear range (µmol/L)	6.6 – 58.8	11.0 – 51.4	44.1 – 110.2
Limit of detection (µmol/L)	0.7	0.1	0.1

[a] [11] [b] [12]

Conclusion

A convenient method for preparing pGMA/Al-morin microspheres for the development of optical phosphate sensor has been highlighted. pGMA/Al-morin microspheres have the ability to detect phosphate within a short time, high selectivity and able to measure phosphate concentrations at wider linear range caused by high surface area of the microspheres.

Acknowledgement

The authors would like to extend their gratitude towards Universiti Kebangsaan Malaysia for providing research facilities that was used in this research. This work was supported by the UKM grants DPP-2015-064 and ICONIC-2013-004.

References

1. Kramer, M. (2008). Protein engineering of pyruvate oxidase from *Lactobacillus plantarum* for application in biosensors. Thesis Diss. Naturwissenschaften, Eidgenössische Technische Hochschule ETH Zürich, Nr. 17765.
2. Carpenter, S. R. (2005). Eutrophication of aquatic ecosystems: biostability and soil phosphorus. *Proceedings of the National Academy of Sciences of the United States of America*, 102(29): 10002 – 10005.
3. Lawal, A. T. and Adeloju, S. B. (2013). Progress and recent advances in phosphate sensors: A review. *Talanta*, 114: 191 – 203.
4. Kumar, R. (2009). Phosphate sensing. *Current Opinion in Nephrology and Hypertension*, 18(4): 281 – 284.
5. Slatopolsky, E. (2011). The intact nephron hypothesis: the concept and its implications for phosphate management in CKD-related mineral and bone disorder. *Kidney International*, 79: 3 – 8.
6. Engblom, S. O. (1998). The phosphate sensor. *Biosensors and Bioelectronics*, 13(9): 981 – 994.
7. Kawasaki, H., Sato, K., Ogawa, J., Hasegawa, Y. and Yuki, H. (1989). Determination of inorganic phosphate by flow injection method with immobilized enzymes and chemiluminescence detection. *Analytical Biochemistry*, 182(2): 366 – 370.
8. Ahuja, D. and Parande, D. (2012). Optical sensors and their applications. *Journal of Scientific Research and Reviews*, 1(5): 60 – 68.
9. Noh, J. Y., Hwang, I. H., Kim, H., Song, E. J., Kim, K. B. and Kim, C. (2013). Salicylimine-based colorimetric and fluorescent chemosensor for selective detection of cyanide in aqueous buffer. *Bulletin Korean Chemical Society*, 34(7): 1985 – 1989.
10. Willard, H. H. and Horton, C. A. (1952). Fluorometric determinations of traces of fluoride. *Analytical Chemistry*, 24(5): 862 – 865.
11. Xie, Z. H., Lin, X. C. and Chen, G. N. (2003). Novel phosphate-sensitive fluorescent composite matrix. *Chemical Research Chinese Universities*, 19(2): 201 – 205.
12. Lin, X., Wu, X., Xie, Z. and Wong, K. Y. (2006). PVC matrix membrane sensor for fluorescent determination of phosphate. *Talanta*, 70(1): 32 – 36.
13. Ahmad, A., Hanifah, S. A., Hasbullah, S. A., Suhud, K., Zaini, N. M. and Heng, L. Y. (2014). Phosphate sensor based on immobilized aluminium-morin in poly(glycidyl methacrylate) microspheres. *AIP Conference Proceedings*, 1614(1): 486 – 491.
14. Denizli, A., Garipcan, B., Karabakan, A. and Senoz, H. 2005. Synthesis and characterization of poly(hyroxyethyl methacrylate-*N*-methacryloyl-(L)-glumatic acid) copolymer beads for removal of leads ions. *Materials Sciences and Engineering Journal C*, 25(4): 448 – 454.
15. Peper, S., Tsagkatakis, I. and Bakker, E. 2001. Cross-linked dodecyl acrylate microspheres: novel matrices for plasticizer-free optical ion sensing. *Analytica Chimica Acta* 442(1): 25 – 33.
16. Xu, C., Wygladacz, K., Qin, Y., Retter, R., Bell, M. and Bakker, E. 2005. Microsphere optical ion sensors based on doped silica gel templates. *Analytica Chimica Acta* 537(1): 135 – 143.
17. Mohr, G. J. and Wolfbeis, O. S. 1995. Optical sensing of anions via polarity-sensitive dyes: a bulk sensor membrane for nitrate. *Analytica Chimica Acta* 316(1995) 239 – 246.
18. Chandra, S., Raizada S. and Sharma, S. 2012. Highly selective monohydrogen phosphate anion sensor for $[CrL](NO_3)_3$. *Journal of Chemical and Pharmaceutical Research* 4(8): 3769 – 3777.
19. Mulon, J. B., Destandau, É., Alain, V. and Bardez, É. 2005. How can aluminium(III) generate fluorescence? *Journal of Inorganic Biochemistry* 99(2005): 1749 – 1755.
20. Ulianas, A., Heng, L. Y., Hanifah, S. A. and Ling, T. L. (2012). An electrochemical DNA microbiosensor based on succinimide-modified acrylic microspheres. *Sensors* 12: 5445 – 5460.
21. Williams, N. J., Gan, W., Reibenspies, J. H. and Hancock, R. D. (2009). Possible steric control of the relative strength of chelation enhanced fluorescence for zinc(II) compared to cadmium(II): Metal ion complexing properties of tris(2-quinolylmethyl)amine, a crystallographic, UV-visible, and fluorometric study. *Inorganic Chemistry*, 48: 1407 – 1415.

22. De Silva, A. P., Gunaratne, H. N., Gunnlaugsson, T., Huxley, A. J., McCoy, C. P., Rademacher, J. T. and Rice, T. E. (1997). Signaling recognition events with fluorescent sensors and switches. *Chemistry Reviews,* 97(5): 1515 – 1566.
23. Kaur, S., Hwang, H., Lee, J. T. and Lee, C. H. (2013). Displacement-based, chromogenic calix [4] pyrrole-indicator complex for selective sensing of pyrophosphate anion. *Tetrahedron Letters*, 54(29): 3744 – 3747.
24. Neri, T. S., Carvalho, D. C., Alves, V. N. and Coelho, N. M. (2015). Noteworthy method for direct determination of Sb^{III} and total inorganic antimony in natural waters. *Journal of the Brazilian Chemical Society*, 26(5), 985 – 991.
25. Zhang, Y., Hu, Y., Wilson, G. S., Moatti-Sirat, D., Poitout, V., and Reach, G. (1994). Elimination of the acetaminophen interference in an implantable glucose sensor. *Analytical Chemistry*, 66(7): 1183 – 1188.
26. Edwards, H. A. (1982). Ion concentration and activity in the haemolymph of *Aedes aegypti* larvae. *Journal of Experimental Biology*, 101(1): 143 – 151.

Malaysian Journal of Analytical Sciences, Vol 20 No 4 (2016): 713 - 725
DOI: http://dx.doi.org/10.17576/mjas-2016-2004-03

MALAYSIAN JOURNAL OF ANALYTICAL SCIENCES
Published by The Malaysian Analytical Sciences Society
ISSN 1394 - 2506

PREPARATION AND CHARACTERIZATION OF Cu-Fe/TiO_2 PHOTOCATALYST FOR VISIBLE LIGHT DEEP DESULFURIZATION

(Penyediaan dan Pencirian Fotokatalis Cu-Fe/TiO_2 untuk Proses Nyahsulfur Di Bawah Cahaya Tampak)

Hayyiratul Fatimah Mohd Zaid[1], Chong Fai Kait[1]*, Mohamed Ibrahim Abdul Mutalib[2]

[1]*Department of Fundamental & Applied Sciences*
[2]*Department of Chemical Engineering*
Universiti Teknologi PETRONAS, 32610 Seri Iskandar, Perak., Malaysia

**Corresponding author: chongfaikait@petronas.com.my*

Received: 17 August 2015; Accepted: 23 May 2016

Abstract

A photooxidative system for deep desulfurization of model diesel fuel was explored. Nanoparticles of anatase titania (TiO_2) were synthesized via sol-gel hydrothermal method. The TiO_2 was further modified with bimetallic Cu-Fe using wet-impregnation method followed by calcination process in order to extend the activity region of the photocatalyst to visible-light. A series of bimetallic 2.2 wt% Cu-Fe/TiO_2 photocatalysts with different Cu:Fe mass compositions were characterized for their physical, chemical and optical properties using X-ray diffraction (XRD), field emission scanning electron microscopy (FESEM), high resolution transmission electron microscopy (HRTEM), diffuse reflectance UV-visible spectroscopy (DR-UV-Vis), Fourier Transform Infrared Spectroscopy (FTIR) and Brunauer–Emmett–Teller (BET) surface area analysis. The performance of the photocatalysts was evaluated for photooxidation of dibenzothiophene (DBT) as the sulfur species from model oil in the presence of hydrogen peroxide, H_2O_2 under 500 W visible light illumination. The highest sulfur conversion of 82.36 % was observed for photocatalyst with 10:1 Cu:Fe mass composition.

Keywords: photocatalyst, titania, oxidation, desulfurization, visible light, copper-iron

Abstrak

Sistem fotopengoksidaan untuk proses nyahsulfur daripada model minyak diesel dikaji. Nanopartikel titania (TiO_2) dengan fasa anatas disediakan menggunakan kaedah hidrotermal sol-gel. Pengubahsuaian dengan dwilogam Cu-Fe dilakukan terhadap TiO_2 menggunakan kaedah impregnasi basah diikuti dengan proses pengkalsinan untuk melanjutkan aktiviti fotokatalis ke bahagian cahaya tampak. Siri fotokatalis dwilogam 2.2 wt% Cu-Fe/TiO_2 dengan komposisi jisim Cu:Fe yang berlainan dicirikan untuk menentukan sifat-sifat fizikal, kimia dan optik menggunakan pembelauan sinar-X (XRD), pemancaran medan mikroskopi imbasan elektron (FESEM), mikroskopi transmisi elecktron beresolusi tinggi (HRTEM), spektroskopi pantulan resapan ultraungu-tampak (DR-UV-Vis), spektroskopi transformasi Fourier inframerah (FTIR) dan analisis luas permukaan Brunauer–Emmett–Teller (BET). Kajian terhadap fotopengoksidaan dibenzothiophene (DBT) sebagai spesis sulfur di dalam model minyak menggunakan fotokatalis tersebut dilakukan dalam kehadiran hidrogen peroksida, H_2O_2 di bawah sinaran cahaya tampak 500 W. Prestasi tertinggi penukaran sulfur yang tercapai adalah 82.36 %, daripada fotokatalis yang mempunyai komposisi jisim untuk Cu:Fe sebanyak 10:1.

Kata kunci: fotokatalis, titania, pengoksidaan, nyahsulfur, cahaya tampak, kuprum-besi

Introduction

Energy production is one of the most pressing issues of the modern world. The main task of modern refinery is to efficiently produce high yields of valuable products. Gasoline, diesel and non-transportation fuel comprises 75 - 80 % of refinery products. Environmental restrictions regarding the quality of transportation fuels produced and the emissions from the refinery itself are currently the most important issues, as well as the most costly to meet. Sulfur species represent one of the most common impurities in crude oil [1]. The distribution of the sulfur species mainly depend on the origin of the petroleum, type and volume of different stream feeding into the diesel pool. Diesel feeds contain a large number of individual sulfur species, such as dibenzothiophene (DBT) and alkyl derivatives [2].

Sulfur species are undesirable in the refining process as they tend to deactivate some catalysts used in the crude oil processing and cause corrosion problems in pipelines, pumping and refining equipment. Naturally occurring residual sulfur species in fuels will lead to the emission of sulfur oxide gases during combustion. These gases react with water in the atmosphere to form sulfates and acid rain which can damage buildings, destroy automotive paint finishes, acidifies soil and ultimately lead to destruction of forest and various other ecosystems. Sulfur emission also causes respiratory problems, heart diseases, asthma and contributes to the formation of atmospheric particulates. Automobiles are also adversely affected by the presence of sulfur species in the fuels, as the sulfur species have a profound effect on the efficacy of catalytic converters [3].

The current industrial method for removal of sulfur species from fuels is known as hydrodesulfurization (HDS), which operates at high temperature and pressure. This makes HDS a very costly option for deep desulfurization. In addition, HDS is not effective in removing refractory heterocyclic sulfur species such as DBT and its derivatives, especially 4,6-dimethyldibenzothiophene (4,6-DMDBT) [4, 5]. Oxidative desulfurization (ODS) [6, 7], extractive desulfurization (EDS) [8, 9], adsorptive desulfurization [10, 11] and biodesulfurization (BDS) [12, 13] are other desulfurization techniques that have the potential to produce ultra clean fuel. In ODS, the sulfur species are oxidized to sulfone by chemical reaction using oxidants such as hydrogen peroxide (H_2O_2), nitric acid, ozone, air and others.

Recently, research has focused on investigating the desulfurization of sulfur species via photocatalysis [14, 15] utilizing radiation energy. Titanium dioxide (TiO_2) based photocatalysis has been widely employed in environmental purification to decompose organic compounds in air and wastewater since this method can be conducted under mild reaction conditions [16]. Moreover, TiO_2 is inert to chemical corrosion, has a strong oxidizing power (with UV light) and is cost effective [17]. The successful application of photocatalysis in deep desulfurization process has been reported previously to remove thiophenes and derivatives of benzothiophene (BT) and DBT, which are the model sulfur species in gasoline [18, 19], light oil [14, 20] and diesel [21]. The results indicated that photodesulfurization has displayed higher activity compared to the conventional HDS in removing refractory DBT derivatives such as 4-methyldibenzothiophene (4-MDBT) and 4,6-DMDBT [14].

As reported by Matsuzawa et al. [22], DBT and 4,6-DMDBT in acetonitrile are photooxidized to 5-oxide (sulfoxide) and 5,5-dioxide (sulfone) using TiO_2. The application of this photochemical oxidation to desulfurization as been realized in some literatures [22, 23] using oil-water and oil-polar solvent two phase systems. The desulfurization of light oil to a sulfur content of less than 0.05 wt% has been achieved successfully. However, ultraviolet (UV) irradiation was found to be essential to oxidize DBTs and the desulfurization hardly progresses at wavelength, $\lambda > 400$ nm. Therefore, there is a need to develop a photocatalyst system that enables the use of renewable energy resources such as sunlight which provides cleaner and more efficient removal of sulfur species from petroleum fuel oils. Incorporation of transition metal onto TiO_2 structure could produce photocatalyst that displays activity in visible light. Iron (Fe) and copper (Cu) have received much attention as metal dopants as these metals are cheap and abundant in supply. A great deal of research has been conducted using Cu or Fe doped TiO_2, but co-doped Cu and Fe onto TiO_2 is rarely reported. Liu et al. [24] and Zhang [25] degraded organic dye pollutants, Reactive Black 5 (RB 5) and Methyl Orange (MO) in wastewater under UV [24] and visible light [25] radiation, respectively. They showed that co-doped Cu and Fe onto TiO_2 displayed significant enhancement in photodegradation of the organic dye pollutants compared to the un-doped TiO_2.

This paper focused on the synthesis and characterization of Cu-Fe/TiO_2 photocatalysts for the photooxidation of sulfur species in model oil under visible light radiation. Further treatment to the model oil is required in order to

remove the oxidized sulfur species and also the residual sulfur species in order to complete the deep desulfurization process. Example of such treatment is extraction using eutectic ionic liquids which was reported in a separate work [26].

Materials and Methods

Materials and reagents

Titanium tetraisopropoxide, TTIP ($Ti(OC_3H_7)_4$) (Merck, 97 %), *n*-heptane (C_7H_{16}) (Fisher, 99 %), anhydrous iron(III) chloride ($FeCl_3$) (Merck, 98 %), copper(II) chloride dihydrate ($CuCl_2.2H_2O$) (Merck, 99 %), dibenzothiophene, DBT ($C_{12}H_8S$) (Merck, 98 %) and dodecane ($C_{12}H_{26}$) (Merck, 98 %) were used without further purification.

Synthesis of TiO_2

Nanoparticle TiO_2 was synthesized using a method modified from that reported by Khan et al. [27]. An amount 27 mL of titanium tetraisopropoxide (TTIP) was added into 100 mL of *n*-heptane as a solvent. The mixture was stirred at 300 rpm for 2 hours. This was followed by drop wise addition of 7.98 mL distilled water to the mixture, giving a molar ratio of 1:5 for TTIP:H_2O. The mixture was left to age for 72 hours at room temperature. The obtained sol was transferred to a 100 mL teflon-lined autoclave vessel and was heated to 240 ^oC for 12 hours. The resulting precipitate was dried in the oven at 70 ^oC for 12 hours. After drying, the raw TiO_2 was calcined in a furnace at 500 ^oC in ambient air for 1 hour. The calcination process was carried out to remove any residual organic substance and also as an activation process to transform the hydroxides into anatase TiO_2.

Preparation of Cu-Fe/TiO_2

A series of 2.2 wt% Cu-Fe/TiO_2 photocatalysts with different Cu:Fe mass composition (10:1, 9:2 and 8:3) was prepared using wet impregnation method. $CuCl_2.2H_2O$ and $FeCl_3$ were used as metal precursors. Predetermined amounts of $CuCl_2.2H_2O$ and $FeCl_3$ salts were dissolved in distilled water with continuous stirring. The required amount of TiO_2 support was added into the metal salt solution. The suspension was stirred for 1 hour before the solvent was evaporated in a water bath at 80 ^oC and further dried in an oven at 120 ^oC for 18 hours. The raw photocatalysts were ground into fine powder and then calcined at 500 ^oC for 1 hour (10 $^oC \cdot min^{-1}$ ramping). The temperature selected was adopted from previous reported method [26]. The denotation of the photocatalysts was: xCuyFe, where 'x' represents the amount of Cu and 'y' represents the amount of Fe in which 'x' + 'y' = 11. For example, 10Cu1Fe refers 2.2 wt% Cu-Fe/TiO_2 photocatalyst with 10:1 Cu:Fe mass composition. Monometallic Cu/TiO_2 and Fe/TiO_2 photocatalysts with 2.2 wt% metal loading, denoted as Cu and Fe, respectively, were also prepared for comparison purposes.

Characterization of photocatalysts

The X-ray diffraction (XRD) patterns of the calcined TiO_2 and also the prepared Cu-Fe/TiO_2 photocatalysts were recorded using Bruker D8 Advance with CuKα radiation (40 kV, 40 mA) at 2θ angles from 2 to 80° and a scan speed of 4 $^oC \cdot min^{-1}$ to determine the active TiO_2 phase present. Morphology of the photocatalysts were examined using field emission scanning electron microscopy (FESEM, Supra55VP) coupled with energy dispersive X-ray analysis (EDX) and high resolution transmission electron microscopy (HRTEM, Zeiss Libra 200). The light absorption properties of the photocatalysts were recorded using diffuse reflectance UV-visible spectroscopy (DR-UV-Vis) where the Shimadzu Spectrometer 3150 was equipped with an integrated sphere assembly in which $BaSO_4$ was used as the reference material. Tauc Plot, derived from DR-UV-Vis spectrum was employed to determine the band gap energy of the photocatalysts. The BET surface area of the photocatalysts was determined using surface analyzer (Tristar II 3020). Fourier Transform Infrared (FTIR) spectra of the photocatalysts were scanned from 4000 to 450 cm^{-1} at 1.2 cm^{-1} resolution using Perkin Elmer Spectrophotometer. The surface area and pore volume were calculated using the Brunauer-Emmett-Teller (BET) method, and pore size distribution was determined from the desorption branch of the desorption isotherm by the Barrett-Joyner-Halenda (BJH) method.

Photooxidative deep desulfurization process

The photooxidation process involved suspending the photocatalyst in model oil containing 100 ppm dibenzothiophene (DBT) as the model sulfur species in dodecane. Photooxidation was carried out in a glass photoreactor positioned below the light source (500W halogen lamp, λ >400 nm) at a distance 15 cm from the lamp.

The model oil was mixed with 1 $g \cdot L^{-1}$ of photocatalyst. H_2O_2 with a molar ratio of 4:1 (H_2O_2:S) was added and the suspension was stirred in the dark for 30 min to achieve adsorption-desorption equilibrium between DBT in the model oil and the photocatalyst. Subsequently, photooxidation process occurred under visible light illumination. The photooxidation process was monitored by periodic sampling where the photocatalyst was separated from the model oil by filtration prior to analysis using GC-SCD (Agilent 7890A gas chromatograph coupled with Agilent 355 sulfur chemiluminescence detector). The DB-1 J & W 123-1033 (30 m x 320 um x 1 um) column was maintained at 325^oC with helium as carrier gas flowing at 1.1 $mL \cdot min^{-1}$. The auto sampler was in split mode (300 ^oC, 6.16 psi, 50:1 split ratio at 55 $mL \cdot min^{-1}$, split flow 50 $mL \cdot min^{-1}$, septum purge flow 3 $mL \cdot min^{-1}$) and injection volume of 1.0 µL. The detector settings were: burner at 800 ^oC (to ensure complete sulfur combustion), dual plasma controller at 250 – 400 torr, 65 sccm of air flow rate, 40 sccm of H_2 flow rate and 20 – 30 $mL \cdot min^{-1}$ at 3 – 6 psi of ozone flow rate. The efficiency in converting sulfur species to oxidized sulfur species in the model oil was calculated using equation (1):

$$\text{Sulfur conversion (\%)} = \frac{S_i - S_f}{S_i} \times 100\ \% \qquad (1)$$

where, S_i and S_f refer to the initial and final concentrations of sulfur species (DBT) in model oil.

Results and Discussion

X-ray diffraction

The effect of Cu:Fe mass composition on the crystallite phase and crystallinity of the photocatalysts was analyzed. Figure 1 display the XRD patterns of Cu-Fe/TiO_2 with different Cu:Fe mass composition (10:1, 9:2 and 8:3). The photocatalysts were calcined at 500 ^oC for 1 hour prior to analysis. All the samples displayed the typical anatase TiO_2 crystal structure with peaks at 2θ of 25.3°, 38.0°, 48.3°, 54.8°, 55.8° and 62.6° corresponding to (101), (004), (200), (105), (211) and (204) phases, respectively [27, 28]. The preferred orientation corresponding to the phase (101) is observed in all the samples. Both monometallic TiO_2 (Cu and Fe) and bimetallic Cu-Fe/TiO_2 photocatalysts displayed high intensity for the diffraction peak at 2θ = 25.3^o. This indicates larger crystallite size compared to bare TiO_2. There was no indication of the presence of Cu, Fe or Cu-Fe species in all the XRD patterns. This may be due to the presence of highly dispersed Cu and Fe species and also low metal content [29], which are below the detection limit of the equipment [30]. In order for the metal to be detectable by XRD analysis, the concentration of metals should be higher than 5wt% [31]. However, the presence of the incorporated metals can be confirmed from EDX mapping that will be discussed in later section. No peaks attributed to the rutile phase could be detected. This may be due to the calcination temperature, as the transition from anatase to rutile phase normally occurs at temperature above 600 ^oC.

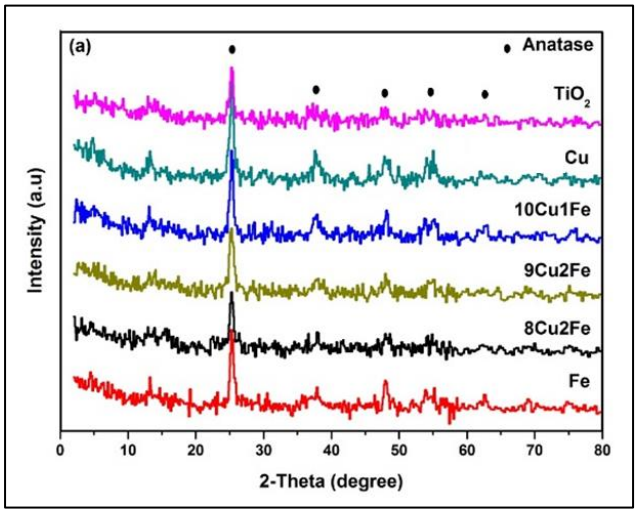


Figure 1. XRD patterns of TiO_2, Cu, 10Cu1Fe, 9Cu2Fe, 8Cu3Fe and Fe

The dominant peak at 25.3° (101) was used to estimate the crystallite size of the photocatalyst using Debye Scherrer's equation [32]. The average crystallite sizes for the photocatalysts are listed in Table 1. The estimated crystallite size for TiO_2 was 11.50 nm. Monometalic Fe showed larger crystallite size compared to monometallic Cu. For the bimetallic photocatalysts, as the composition of Cu decreased, the average crystallite size also showed a decreasing trend. Higher Fe content led to smaller crystallite size in the bimetallic system. Incorporating both Cu and Fe metals decreases the crystallite size compared to single doping. This could be caused by restrained grain growth in the presence of both Cu and Fe, which in turn led to smaller crystallite size at certain mass composition. Similar trend was reported by Kim and Kang [33] where incorporation of both Cu and Ag produced smaller crystallites compared to single doped photocatalyst.

Table 1. Crystallite and particle sizes of photocatalysts from different analysis methods

Sample	Average Crystallite Size (nm)	Particle Size Range (nm)	
	XRD	FESEM	HRTEM
TiO_2	11.50	10.39 – 15.79	10.88 – 16.24
Cu	18.22	17.78 – 19.04	18.03 – 26.11
10Cu1Fe	17.42	17.34 – 17.61	13.51 – 20.67
9Cu2Fe	17.34	17.21 – 17.58	12.92 – 21.01
8Cu3Fe	17.06	16.92 – 17.12	13.04 – 19.17
Fe	19.92	19.84 – 20.11	11.61 – 22.37

Field Emission Scanning Electron Microscopy

FESEM micrographs of photocatalysts at different Cu:Fe mass composition are shown in Figure 2 (a-f). The particles were spherical in shape with slight agglomeration observed for all the photocatalysts. As the Cu:Fe mass composition decreased from 10:1 to 9:2 and 8:3, the average particle size decreased from 17.53, 17.43, and 17.20 nm, respectively. The particles of TiO_2 were small compared to the metal doped photocatalysts with particle size ranging from 10.39 – 15.79 nm (average particle size of 11.39 nm). The average particle size of monometallic Cu and Fe were 18.44 and 20.12 nm, respectively, comparable to the trend observed on the average crystallite sizes from XRD analysis. Detailed particle size distribution as provided in Table 1. No localized metal particles were detected, indicating high metallic dispersion of Cu and Fe on TiO_2. This observation is in agreement with the results obtained from XRD analysis.

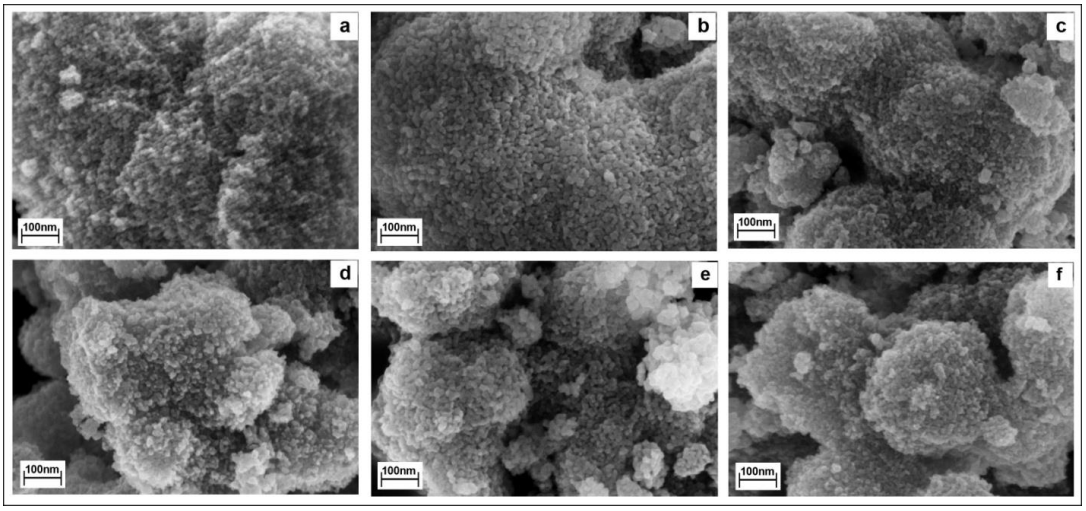


Figure 2. FESEM micrographs of (a) TiO_2, (b) Cu, (c) 10Cu1Fe, (d) 9Cu2Fe, (e) 8Cu3Fe and (f) Fe (100 kX magnification)

Figure 3 shows the EDX mapping of 10Cu1Fe. The elements that were mapped were displayed as colored spots in the images. Cu and Fe metal dopants were uniformly distributed on the TiO_2 surface. As mentioned before, the presence of Cu and Fe metals were not detected from XRD analysis because of the well dispersed small crystallite size of the metal species on TiO_2 [32, 34]. The highly dispersed metal particles on TiO_2 led to better activity thus further enhances the photocatalytic activity [35]. Similar mapping images were obtained for other photocatalysts, showing that the preparation method has successfully incorporated Cu and Fe onto the TiO_2 surface.

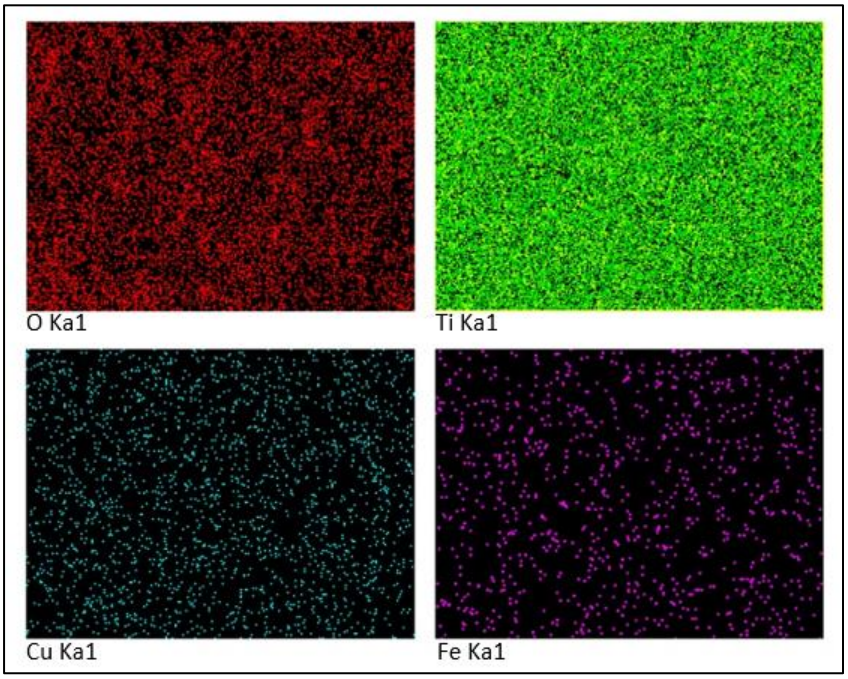


Figure 3. EDX and mapping images of 10Cu1Fe

High Resolution Transmission Electron Microscopy

HRTEM analysis was carried out to determine the detailed morphology of the photocatalyst. Image processing analysis of HRTEM micrographs was used to refine the microstructures for more accurately analyzed single grains and grains boundaries. Figure 4 (a-f) shows the HRTEM micrographs of Cu-Fe/TiO_2 photocatalysts at different Cu:Fe mass compositions. All micrographs showed good crystallite morphology of the particles with mixtures of spherical and polygonal shapes [36]. TiO_2 has the most polygons and as the Fe content increased, the particles became more spherical. The estimated particle sizes of the photocatalysts are tabulated in Table 1. These particle size distribution are in good agreement with the data extracted from FESEM analysis. HRTEM micrographs of the photocatalysts showed agglomeration of particles. This is possible due to high content of surface hydroxyl groups contributing towards the hydrophilic properties [37].

Brunauer-Emmett-Teller

Isotherm plot of 10Cu1Fe is shown in Figure 5. The plot shows Type IV isotherm with hysteresis loop indicating mesoporous structure. The inflection points showed P/Po range of 0.6 – 1.0. The other photocatalysts also displayed similar isotherm. The pore distribution of the photocatalysts was determined by BJH method. Cu-Fe/TiO_2 photocatalysts are mesoporous with an average pore diameter (4V/A) of 13.76, 13.30 and 14.06 nm for 10u1Fe, 9Cu2Fe and 8Cu3Fe, respectively. The BET surface area of the materials for 10u1Fe, 9Cu2Fe and 8Cu3Fe were 49.99, 42.11 and 45.33 m^2/g, respectively, which was comparable.

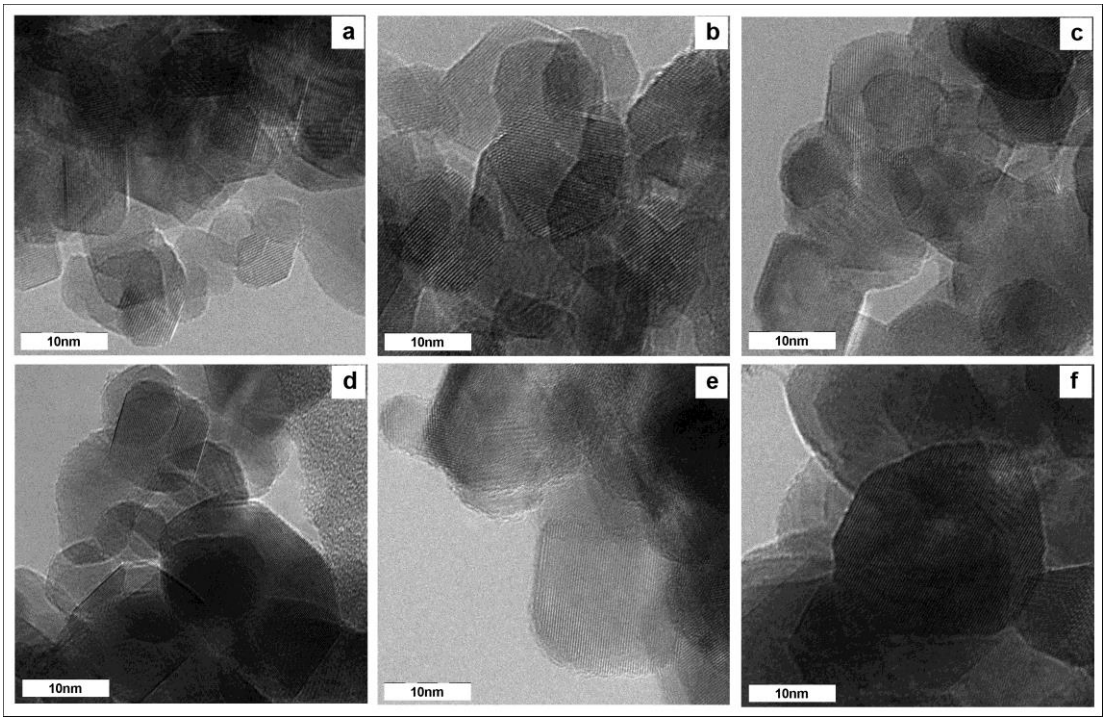


Figure 4. HRTEM micrographs of (a) TiO_2, (b) Cu, (c) 10Cu1Fe, (d) 9Cu2Fe, (e) 8Cu3Fe and (f) Fe

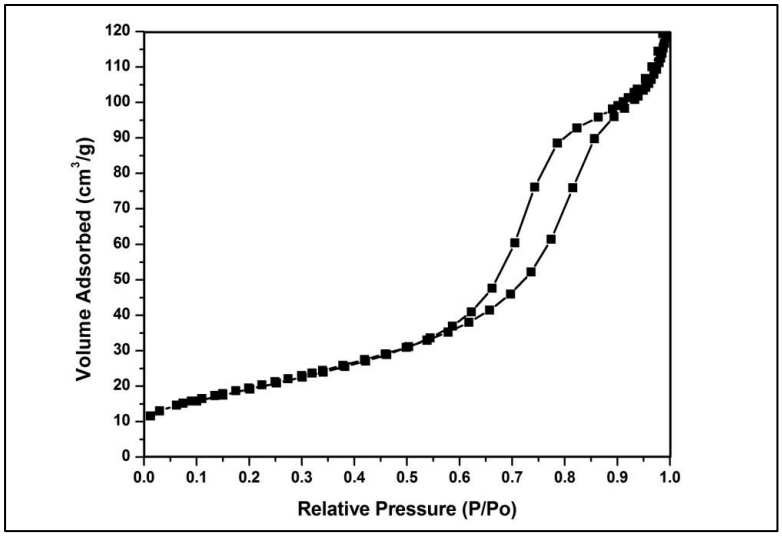


Figure 5. N_2 adsorption-desorption isotherm of 10Cu1Fe

Fourier Transform Infrared Spectroscopy

Figure 6 exhibits the FTIR transmission spectra of Cu-Fe/TiO_2 with different Cu:Fe mass composition with additional 7Cu4Fe. For all the spectra, the broad band around 3400 cm^{-1} was attributed to O-H stretching, and the peak near 1600 cm^{-1} to H-O-H bending [38]. These peaks might be due to the physically adsorbed water. The broad band observed between 400 – 900 cm^{-1} corresponds to the Ti-O stretching vibrations [39]. FTIR is not a suitable

technique to detect the presence of Cu, Fe or Cu-Fe species since the metal–O vibrations are not IR-active. However, these species were detected using EDX.

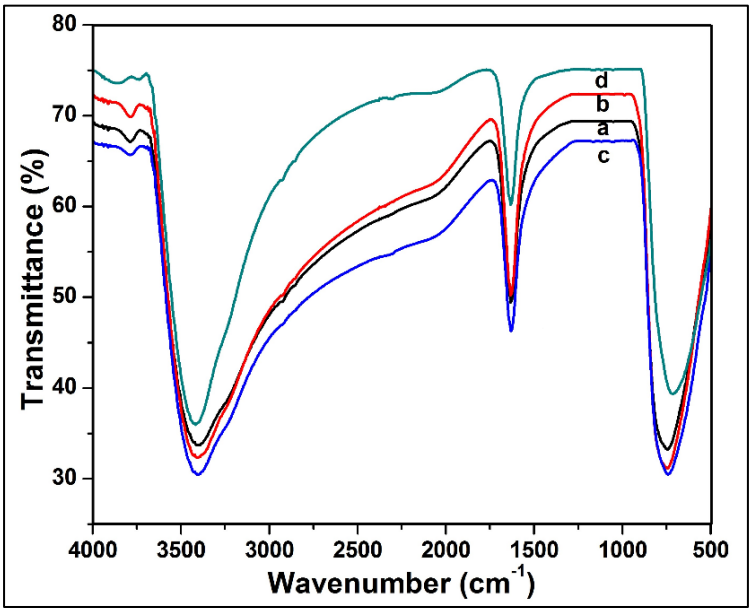


Figure 6. FTIR spectra of (a) 10Cu1Fe, (b) 9Cu2Fe, (c) 8Cu3Fe and (d) 7Cu4Fe

Diffuse Reflectance UV-Visible Spectroscopy

The DR-UV-Vis spectra of the photocatalysts are depicted in Figure 7. The absorption spectrum for TiO_2 shows an absorption edge at 400 nm corresponding to the band gap of 3.09 eV. The absorption band at 323 nm is generally related to the electronic excitation from the valence band O 2p electron to conduction band Ti 3d orbital indicating that Ti is in the form of tetrahedral Ti^{4+} species [40]. All Cu-Fe co-doped photocatalyst shows considerable shift of the absorption edge towards visible region compared to TiO_2. In general, as the Fe content increases, the absorption in the visible region (400 – 780 nm) also increases. It has been generally accepted that the metal dopants introduces a new energy level into the band gap of TiO_2 which is close and above the valence band. Thus, the charge transfer from the valence band to the conduction band from the new energy level requires lower photon energy at lower wavelength [41]. TiO_2 sample doped with Cu-Fe doped TiO_2 sample showed substantial and broader absorption shoulder up to 800 nm. The extended absorption of metal doped TiO_2 samples into the visible region has been explained in terms of excitation of electrons of dopant ion to TiO_2 conduction band. For example, the enhanced absorption observed for the metal doped TiO_2 samples doped with Fe, Cu and Cu-Fe in visible region can be considered to involve excitation of 3d electrons of dopant ion to TiO_2 conduction band according to their respective energy levels [42]. The enhancement of light absorption in the visible region provides a possibility for improving the photocatalytic performance of TiO_2 under visible light irradiation. Doping with Cu-Fe could create sub band states in the band gap of TiO_2 which can then be easily excited to produce more electron-hole pairs under visible light irradiation, hence resulting in higher photocatalytic performance compared to undoped TiO_2. Moreover, a decrease in the band gap energy together with an enhanced absorption intensity of all doped TiO_2 can be seen from the UV-Vis results. This pheonomenon could be due to many factors such as morphology, crystallite size, phase structure and amount of metal loadings [43].

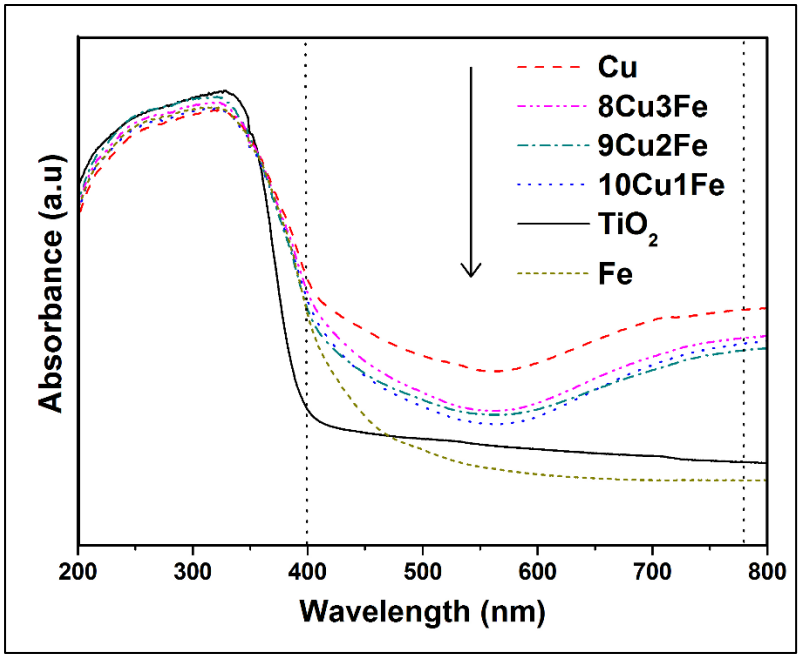


Figure 7. DR-UV-Vis spectra of TiO_2, Cu, 10Cu1Fe, 9Cu2Fe, 8Cu3Fe and Fe

In order to determine the band gap energy of the photocatalyst, reflectance [F(R)] spectra using Kubelka-Munk formalism and Tauc plot was employed for each synthesized photocatalyst [44]. Using the Tauc plot of $[F(R).hv]^n$ vs. hv where hv is the photon energy and n = ½ for direct band gap of the photocatalyst, the linear region of the plot was extrapolated to intersect the photon energy axis to deduce the band gap energy of the respective photocatalyst. The band gap of bare TiO_2 was 3.09 eV and upon incorporation of Cu, Fe or Cu-Fe, the band gap values were reduced. The band gap for Cu was 2.70 eV. The incorporation of Cu and Fe at 10:1 mass composition gave the highest reduction to the band gap (2.69 eV). As the Fe content increases, the band gaps slowly increases from 2.72 to 2.73 eV for 9Cu2Fe and 8Cu3Fe, respectively, indicating some synergistic effect [43]. The band gap for Fe was the highest, 2.82 eV. The blue shift in the absorption of photocatalysts suggested that the dopants successfully generate lower energy level between the valence and conduction bands [45]. The estimated band gap energy of metal doped TiO_2 was lower compared to that of TiO_2 P25 (3.2 eV) [46]. Decreasing band gap energy increases the absorbance in the visible region and indicates that the electron-hole pairs can be generated with metal doping on the TiO_2, which can be attributed to the charge transfer between metal ions and TiO_2 [34].

Photocatalytic performance

The mass composition of metals in the bimetallic photocatalyst plays a significant role in the photocatalytic activity [47]. Figure 8 displays the photooxidative efficiency for DBT conversion of model diesel using the photocatalysts with different Cu:Fe mass composition. The highest DBT conversion was 82.36 % displayed by 10Cu1Fe. It is noteworthy that the monometallic photocatalysts displayed the lowest DBT conversion of 18.95 % for Fe and 54.88 % for Cu compared to the bimetallic photocatalysts. This observation is similar to studies reported by Liu et al. [24] and Zhang [25], where the photocatalytic activity of Cu-Fe co-doped TiO_2 was higher than that of undoped or singly doped photocatalyst.

The formation of electron-hole pairs ($e_{cb}^- - h_{vb}^+$) are important in the photooxidation of DBT. During photooxidation process, the electrons (e_{cb}^-) in the valence band were excited by photons from the light energy. Excited electrons migrate to the conduction band leaving holes in the valence band. Both the electrons (e_{cb}^-) and the holes (h_{vb}^+) can react with entities in the system to produce hydroxyl radicals (•OH) with an oxidation potential of 2.8 V. By incorporating Cu and Fe metals, the recombination rate of $e_{cb}^- - h_{vb}^+$ pairs can be reduced by trapping

these charges. The electrons can be trapped by Cu^{2+} ions to form Cu^{+} or CuO. The potential of Cu^{2+}/Cu^{+} (0.17 V) and Cu^{+}/CuO (0.52 V) are thermodynamically feasible since an electron trapper could provide better separation between the electrons and holes compared to TiO_2 (–0.2 V) alone. Because of this, more holes are available for the photooxidation process. On the other hand, Fe^{3+} can become a trapper for both the electrons and holes simultaneously forming Fe^{2+} and Fe^{4+}, respectively. This is possible due to the energy levels of Fe^{3+}/Fe^{4+} and Fe^{2+}/Fe^{3+} that lie above the valence band and below the conduction band of TiO_2. Theoretically, the stability of Fe^{2+} and Fe^{4+} are lower compared to Fe^{3+} which has a half-filled $3d^5$ orbital configuration. Hence, Fe^{2+} can easily release the trapped electron to be oxidized back to Fe^{3+} which then migrates to the surface to initiate photocatalytic reaction. Fe^{4+} can be reduced to Fe^{3+} by donating the trapped holes to combine with the surface OH groups to give •OH. When the Cu:Fe mass composition were 9:2 and 8:3, the DBT conversion were 74.58 and 75.24 %, respectively.

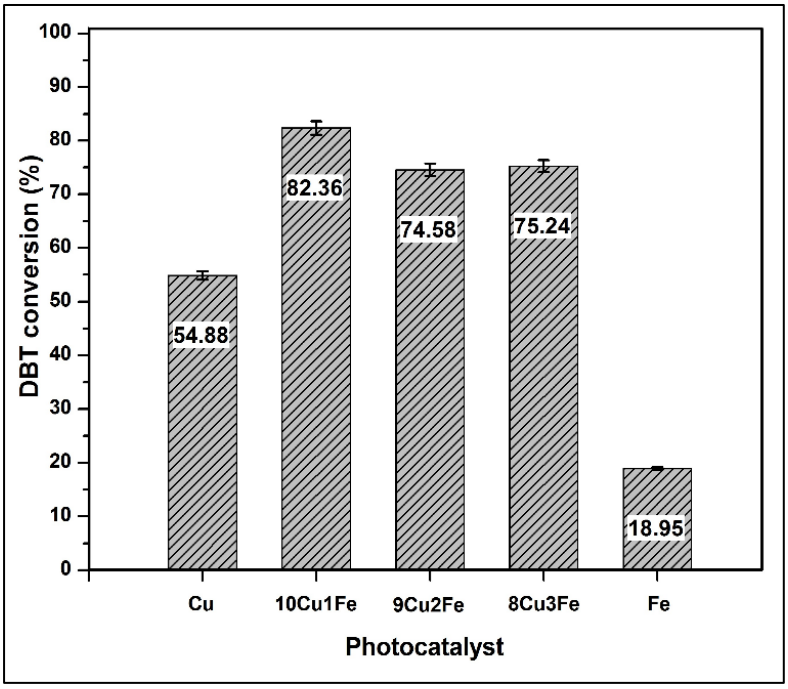


Figure 8. DBT conversion using Cu, 10Cu1Fe, 9Cu2Fe, 8Cu3Fe and Fe

Conclusion

The incorporation of Cu-Fe onto TiO_2 nanoparticles was able to reduce the band gap from 3.09 to as low as 2.69 eV for photocatalyst with Cu:Fe 10:1 mass composition. The lowering of band gap is an indication of shifting of the absorption edge to visible light region, which is important for photocatalysts to harvest energy from the free and abundant sunlight. The presence of bimetallic Cu-Fe co-catalyst was able to enhance the photoactivity of TiO_2 under visible light illumination. Photodegradation of 100 ppm DBT in model diesel using 10Cu1Fe in the presence of H_2O_2 has led to 82.36 % DBT conversion. Although the photocatalyst displayed good DBT degradation, the oxidized sulfur species which are retained in the model oil need to be removed. An integrated photodegradation-extraction system is required to photooxidize the sulfur species followed by removal of the oxidized compounds.

Acknowledgement

The authors extend their utmost gratitude for the financial support and research facilities provided by Yayasan UTP, MyPhD and FRGS from the Ministry of Education, Malaysia; and the Centre of Research in Ionic Liquid (CORIL), Universiti Teknologi PETRONAS.

References

1. Srivastava, V. C. (2012). An evaluation of desulfurization technologies for sulfur removal from liquid fuels. *RSC Advances*, 2: 759 – 783.
2. Zhang, J., Zhao, D. S. and Wang, J. L. (2009). Photocatalytic oxidation of dibenzothiophene using TiO_2/bamboo charcoal. *Journal of Materials Science*, 44: 3112 – 3117.
3. Maricq, M. M., Chase, R. E., Xu, N. and Laing, P. M. (2002). The effects of the catalytic converter and fuel sulfur level on motor vehicle particulate matter emissions: Light duty diesel vehicles. *Environmental Science & Technology*, 36: 283 – 289.
4. Campos-Martin, J. M., Capel-Sanchez, M. C., Perez-Presas, P. and Fierro, J. L. G. (2010). Oxidative processes of desulfurization of liquid fuels. *Journal of Chemical Technology and Biotechnology*, 85: 879 – 890.
5. Jiang, Z., Lu, H., Zhang, Y. and Li, C. (2011). Oxidative desulfurization of fuel oils. *Chinese Journal of Catalysis*, 32(5): 707 – 715.
6. Lina, Y., Jian, L., Xingdong, Y., Shen, J. and Yutai, Q. (2007). One step non-hydrodesulfurization of fuel oil: catalyzed oxidation adsorption desulfurization over HPWA-SBA-15. *Journal of Molecular Catalysis A: Chemical*, 262: 114 – 118.
7. Lu, H., Deng, C., Ren, W. and Yang, X. (2014). Oxidative desulfurization of model diesel using $[(C_4H_9)_4N]_6Mo_7O_{24}$ as a catalyst in ionic liquids. *Fuel Process Technology*, 119: 87 – 91.
8. Ban, L. L., Liu, P., Ma, C. H. and Dai, B. (2013). Deep extractive desulfurization of diesel fuel by $FeCl_3$/ionic liquids. *Chinese Chemistry Letters*, 24:755 – 758.
9. Rodriguez-Cabo, B., Rodriguez, H., Rodil, E., Arce, A. and Soto, A. (2014). Extractive and oxidative–extractive desulfurization of fuel with ionic liquids. *Fuel*, 117: 882 – 889.
10. Li, W. L., Tang, H., Liu, Q., Xing, J., Li, Q., Wang, D., Yang, M., Li, X. and Liu, H. (2009). Deep desulfurization of diesel by integrating adsorption and microbial method. *Biochemical Engineering Journal*, 44: 297 – 301.
11. Kim, H., Ma, X., Zhou, A. and Song, C. (2006). Ultra-deep desulfurization and denitrogenation of diesel fuel by selective adsorption over three different adsorbents: a study on adsorptive selectivity and mechanism. *Catalysis Today*, 111:74 – 83.
12. Dinamarca, M. A., Ibacache-Quiroga, C., Baeza, P., Galvez, S., Villarroel, M., Olivero, P. and Ojeda, J. (2010). Biodesulfurization of gas oil using inorganic supports biomodified with metabolically active cells immobilized by adsorption. *Bioresource Technology*, 101: 2375 – 2378.
13. Fatemeh, D. D., Manouchehr, V. and Abed, A. Z. (2010). Biodesulfurization of dibenzothiophene by newly isolated rhodococcus erythropolis strain. *Bioresource Technology*, 101:1102 – 1105.
14. Hirai, T., Ogawa, K. and Komasawa, I. (1996). Desulfurization process for dibenzothiophenes from light oil by photochemical reaction and liquid-liquid extraction. *Industrial and Engineering Chemical Research*, 35: 586 – 589.
15. Shiraishi, Y., Hirai, T. and Komasawa, I. (2002). TiO_2-mediated photocatalytic desulfurization process for light oils using an organic two-phase system. *Journal of Chemical Engineering of Japan*, 35: 489 – 492.
16. Huang, Y., Ho, W., Ai, Z., Song, X., Zhang, L. and Lee, S. (2009). Aerosol-assisted flow synthesis of B-doped, Ni doped and B–Ni-codoped TiO_2 solid and hollow microspheres for photocatalytic removal of NO. *Applied Catalysis B*, 89:398 – 405.
17. Liu, G. Q., Jin, Z. G., Liu, X. X., Wang, T. and Liu, Z. F. (2006). Anatase TiO_2 porous thin films prepared by sol-gel method using CTAB surfactant. *Journal of Sol-Gel Science and Technology*, 41: 49 – 55.
18. Ibrahim, A., Xian, S. B. and Wei, Z. (2003). Desulfurization of FCC gasoline by solvent extraction and photooxidation. *Petroleum Science and Technology*, 21: 1555 – 1573.
19. Zhao, D., Li, F., Han, J. and Li, H. (2007). Photochemical oxidation of thiophene by O_2 in an organic two-phase liquid-liquid extraction system. *Petroleum Chemistry*, 47: 448 – 451.
20. Shiraishi, Y., Hirai, T. and Komasawa, I. (1999). Identification of desulfurization products in the photochemical desulfurization process for benzothiophene and dibenzothiophene from light oil using an organic two-phase extraction system. *Industrial and Engineering Chemical Research*, 38: 3300 –3309.
21. Song, C. (2003). An overview of new approaches to deep desulfurization for ultra-clean gasoline, diesel and jet fuel. *Catalysis Today*, 86: 211 – 263.

22. Matsuzawa, S., Tanaka, J., Sato, S. and Ibusuki, T. (2002). Photocatalytic oxidation of dibenzothiophene in acetonitrile using TiO_2: effect of hydrogen peroxide and ultrasound irradiation. *Journal of Photochemistry and Photobiology A*, 149: 183 – 189.
23. Shiraishi, Y., Hirai, T. and Komasawa, I. (2001). Photochemical desulfurization and denitrogenation process for vacuum gas oil using an organic two-phase extraction system. *Industrial and Engineering Chemical Research*, 40: 293 – 303.
24. Liu, J, Zhang, Z, Yang, L, Zhang, Y, Deng S. (2011). The degradation of reactive black wastewater by Fe/Cu co-doped TiO_2. *International Journal of Chemistry*, 3: 87 – 92.
25. Zhang, D. (2010). Enhanced photocatalytic activity for titanium dioxide by commodification with copper and iron. *Transition Metal Chemistry*, 35: 933 – 938.
26. Zaid, H. F. M., Chong, F. K. and Mutalib, M. I. A. (2014). Integrated photooxidative–extractive desulfurization system for fuel oil using Cu, Fe and Cu–Fe/TiO_2 and eutectic based ionic liquids: effect of calcination temperature and duration. *AIP Conference Proceedings*, 1621: 231 – 237.
27. Khan, M. A., Akhtar, M. S. and Yang, O. B. (2010). Synthesis, characterization and application of sol–gel derived mesoporous TiO_2 nanoparticles for dye-sensitized solar cells. *Sol Energy*, 84: 2195 – 2201.
28. Vijayalakshmi, R. and Rajendran, V. (2012). Synthesis and characterization of nano-TiO_2 via different methods. *Archives Applied Science Research*, 4:1183 – 1190.
29. Kim, D. S. and Kwak, S. Y. (2007). The hydrothermal synthesis of mesoporous TiO_2 with high crystallinity, thermal stability, large surface area, and enhanced photocatalytic activity. *Applied Catalysis A: General*, 323: 110 – 118.
30. Yu, J., Zhao, X. and Zhao, Q. (2000). Effect of surface structure on photocatalytic activity of TiO_2 thin films prepared by sol–gel method. *Thin Solid Films*, 379: 7 – 14.
31. Wu, Y., Zhang, J., Xiao, L. and Chen, F. (2009). Preparation and characterization of TiO_2 photocatalysts by Fe^{3+} doping together with Au deposition for the degradation of organic pollutants. *Applied Catalysis B: Environment*, 88: 525 – 532.
32. Yoong, L. S., Chong, F. K. and Dutta, B. K. (2009). Development of copper-doped TiO_2 photocatalyst for hydrogen production under visible light. *Energy*, 34: 1652 – 1661.
33. Kim, A. Y. and Kang, M. (2012). Effect of Al-Cu bimetallic components in a TiO_2 framework for high hydrogen production on methanol/water photo-splitting. *International Journal of Photoenergy*, 2012:1-9.
34. Nurlaela, E., Chong, F. K., Dutta, B. K. and Riaz N. (2010). Bimetallic Cu–Ni/TiO_2 as photocatalyst for hydrogen production from water. *International Conference on Fundamental and Applied Sciences (ICFAS2010).* Kuala Lumpur, Convention Center, KL.
35. Zhu, J., Chen, F., Zhang, J., Chen, H. and Anpo, M. (2006). Fe^{3+}–TiO_2 photocatalysts prepared by combining sol–gel method with hydrothermal treatment and their characterization. *Journal of Photochemistry and Photobiology A: Chemistry*, 180: 196 – 204.
36. Lu, C. H., Wu, W. H. and Kale, R. B. (2008). Microemulsion-mediated hydrothermal synthesis of photocatalytic TiO_2 powders. *Journal of Hazardous Materials*, 154: 649 – 654
37. Aeroxide and Aeroperl. (2005). Technical information (1243) for Aeroxide and Aeroperl titanium Dioxide as photocatalyst; Bulletin No. 1-1243-0:1-14.
38. Li, D., Haneda, H., Hishita, S. and Ohashi, N. (2005). Visible-light driven nitrogen-doped TiO_2 photocatalysis: Effect of nitrogen precursors on their photocatalysis for decomposition of gas-phase organic pollutants. *Materials Science and Engineering B*, 52: 843 – 850.
39. Yan, X., He, J., Evans, D. G., Zhu, Y. and Duan, X. (2004). Preparation, characterization and photocatalytic activity of TiO_2 formed from mesoporous precursor. *Journal of Porous Materials*, 11:131 – 139.
40. Fuerte, A., Hernandez-Alonso, M. D., Maira, A. J., Martinez-Arias, A., Fernandez-Garcia, M., Conesa, J. C., Soria, J. and Munuera, G. (2002). Nanosize Ti-W mixes oxides: Effect of doping level in the photocatalytic degradation of toluene using sunlight type excitation. *Journal of Catalysis*, 212: 1 – 9.
41. Cao, H., Lin, X., Zhan, H., Zhang, H. and Lin J. (2013). Photocatalytic degradation kinetics and mechanism of phenobarbital in TiO_2 aqueous solution. *Chemosphere*, 90: 1514 – 1519.
42. Nahar, M. S., Hasegawa, K. and Kagaya, S. (2006). Photocatalytic degradation of phenol by visible light-responsive iron-doped TiO_2 and spontaneous sedimentation of the TiO_2 particles. *Chemosphere*, 65: 1976 – 1982.

43. Li, H., Zhang, Y., Wang, S., Wu, Q. and Liu, C. (2009). Study on nanomagnets supported TiO_2 photocatalysts prepared by a sol–gel process in reverse microemulsion combining with solvent-thermal technique. *Journal of Hazardous Materials*, 169: 1045 – 1053.
44. Murphy, A. B. (2007). Band-gap determination from diffuse reflectance measurements of semiconductor films, and application to photoelectrochemical watersplitting. *Solar Energy Materials Solar Cells*, 91: 1326 – 1337.
45. Wu, D., Long, M., Cai, W., Chen, C. and Wu, Y. (2010). Low temperature hydrothermal synthesis of N-doped TiO_2 photocatalyst with high visible-light activity. *Journal of Alloys and Compounds*, 502: 289 – 294.
46. Yalçin, Y., Kiliç, M. and Çinar, Z. (2010). Fe^{+3}-doped TiO_2: a combined experimental and computational approach to the evaluation of visible light activity. *Applied Catalysis B: Environment*, 99: 469 – 477.
47. Singto, S., Sorapong, P., Yoshikazu, S. and Susumu, Y. (2005). Photocatalytic activity of titania nanocrystals prepared by surfactant-assisted templating method – Effect of calcination conditions. *Materials Letters*, 59: 2965 – 2968.

Malaysian Journal of Analytical Sciences, Vol 20 No 4 (2016): 726 - 734
DOI: http://dx.doi.org/10.17576/mjas-2016-2004-04

MALAYSIAN JOURNAL OF ANALYTICAL SCIENCES
Published by The Malaysian Analytical Sciences Society
ISSN 1394 - 2506

DETERMINATION OF PRAZOSIN AND SIMVASTATIN IN LANDFILL LEACHATE USING LIQUID CHROMATOGRAPHY-TIME OF FLIGHT-MASS SPECTROMETRY

(Penentuan Prazosin dan Simvastatin di dalam Larut Lesap Mengunakan Kromatografi Cecair-Masa Penerbangan-Spektrometri Jisim)

Zainab Haider Mussa[1,2], Fouad Fadhil Al-Qaim[1,3]*, Md Pauzi Abdullah[1,4], Mohamed Rozali Othman[1,4]

[1]School of Chemical Sciences and Food Technology, Faculty of Science and Technology, Universiti Kebangsaan Malaysia, 43600 UKM Bangi, Selangor, Malaysia
[2]Faculty of Pharmacy
[3]Department of Chemistry, Faculty of Sciences for Women University of Babylon, PO Box 4, Hilla, Iraq
[4]Centre for Water Research and Analysis (ALIR), Faculty of Science and Technology, Universiti Kebangsaan Malaysia, 43600 UKM Bangi, Selangor, Malaysia

**Corresponding author: fouadalkaim@yahoo.com*

Received: 13 January 2016; Accepted: 27 March 2016

Abstract

Human pharmaceuticals have been shown to occur in considerably high amounts in sewage treatment plant (STP) effluents and surface waters. So far there is no data available on the occurrence of prazosin and simvastatin in leachate sample in Malaysia. Thus, this study is the first report to analysis of prazosin and simvastatin in leachate samples by using solid phase extraction-liquid chromatography-time of flight-mass spectrometry (SPE-LC-TOF-MS). The proposed method included isolation and reconstitute procedure. The linearity range was achieved at 1.5 - 3000 µg/L and 0.8 – 125 µg/L for prazosin and simvstatin, respectively with a determination coefficient (R^2) > 0.99. The limit of quantification (LOQ) for prazosin and simvastatin was calculated at 2.1 and 0.5 ng/L in deionised water (DIW), meanwhile it was recorded at 3.5 and 2.4 ng/L for prazosin and simvastatin in effluent sample, respectively. Two pharmaceutical compounds were detected in the leachate samples: prazosin and simvastatin at concentrations levels of 3850 and 415 ng/L, respectively.

Keywords: prazosin, simvastatin, leachate, solid phase extraction, pharmaceutical pollution

Abstrak

Farmaseutikal manusia telah hadir di dalam effluen loji sisa rawatan dan air permukaan. Sehingga kini, tiada data kajian yang merekodkan kehadiran prazosin dan simvastatin dalam sampel larut lesap di Malaysia. Maka, kajian ini merupakan laporan pertama tentang analisis terhadap prazosin dan simvastatin di dalam sampel larut lesap mengunakan pengekstrakan fasa pepejal-kromatografi cecair-masa penerbangan-spekrometri jisim (SPE-LC-TOF-MS). Kaedah yang dibangun meliputi langkah pemisahan dan nilai isian semula. Julat kelinearan dicapai antara 1.5 – 3000 µg/L dan 0.8 – 125 µg/L masing – masing bagi prazosin dan simvastatin dengan nilai pekali (R^2) > 0.99. Had kuantifikasi (LOQ) bagi prazosin and simvastatin dihitung pada aras 2.1 dan 0.5 ng/L di dalam air ternyahion manakala direkod masing-masing pada aras 3.5 dan 2.4 ng/L di dalam sampel efluen. Dua jenis sebatian farmaseutikal ini dikesan in dalam sampel larut lesap pada aras kepekatan masing-masing adalah 3850 and 415 ng/L.

Kata kunci: prazosin, simvastatin, larut lesap, pengekstrakan fasa pepejal, pencemaran farmaseutikal

Introduction

The occurrence of pharmaceutical in the aquatic environment has been recognized as one of the emerging issues in environmental chemistry. The widespread presence in the aquatic environment can be explained by their extensive use in medical practice and incomplete removal in wastewater treatment plants (WWTPs) [1]. These compounds present in the environment at trace levels (ng/L - µg/L), hence it is known as micro pollutants. For this reason, in the past century, their detection was infeasible due to lack of sophisticated analytical technique. In recent years, advancements in analytical methods have contributed to the detection of over 100 active agents in pharmaceutical products in different environmental matrices [2, 3]. Scientific research studies conducted in Malaysia and worldwide have reported widespread occurrence of pharmaceuticals in surface water, influent and effluent sewage treatment plants and hospitals [4 – 7]. The reason may related to several ways which are participated to introduce the pharmaceuticals to surface water such as insufficiently treated sewage effluents, production residues, improper disposal of expired medications and unused drugs and accidental spillage during manufacturing and distribution [8].

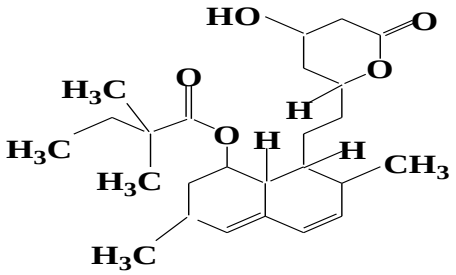
In leachate samples, the detection of pharmaceuticals has never been studied except few reported papers [9, 10]. Landfills may be sources of a large number of organic compounds known as emerging contaminants (ECs and/or EDCs) such as pharmaceuticals, pesticides, fertilizers and others. Pharmaceutical compounds may occur in concentration of approximately 8.1 mg/kg in typical municipal solid waste. In landfills, these compounds may be degraded/metabolized, adsorbed to solids or dissolved in leachate. Release of these chemicals in the environment may affect public health on humans, animals and ecosystem.

Liquid chromatography - tandem mass spectrometry [LC-MS/MS] is one of the most popular analytical methods used to analyse pharmaceutical residues in water samples due to its versatility, specificity and selectivity. Other different approaches have been tried, including gas chromatography-mass spectrometry (GC-MS), voltammetry, potentiometry and LC-Uv as reviewed in previous studies [11, 12]. In Malaysia, simvastatin has been detected less than limit of detection (LOD) [13] while in Canada; it has been detected in 0.001 µg/L [14]. The differences in concentrations of simvastatin in treated wastewaters between different countries generally reflect different usage patterns, per-capita water consumption, and treatment processes.

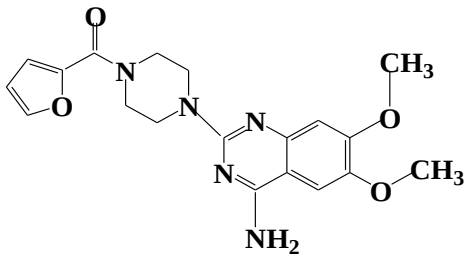
The aim of this study is to determine the amount of prazosin and simvastatin in raw leachate, post-biological and post-charcoal adsorption treatment using liquid chromatography-time of flight/mass spectrometry.

Materials and Methods

Prazosin (PRZ) (CAS no.19237-84-4), simvastatin (SMV) (CAS no. 79902-63-9) were obtained from Sigma-Aldrich (USA). Figure 1 shows the chemical structure of these pharmaceuticals with molecular weight. Deionized water (DIW) used was supplied by EASYPure RODI (USA). Acetone, acetonitrile and methanol (HPLC grade) were purchased from Sigma-Aldrich (USA). Formic acid (FA) was supplied by Merck (Germany). Methyl Tertiary Butyl Ether (MTBE) was supplied by J. T. Baker (USA). The cartridges used for solid phase extraction (SPE) were (Oasis HLB 3 cm^3, 60 mg purchased from Waters (USA).



Simvastatin (SMV), 418 g/mol



Prazosin (PRZ), 383 g/mol

Figure 1. Chemical structures of the studied compounds

Site description and sampling activities

The leachate samples namely raw, biological and physico-chemical treated samples used in this study were collected from Jeram sanitary landfill leachate. Jeram sanitary landfill leachate is located in an oil palm plantation near Kuala Selangor Malaysia as shown in Figure 2. It is roughly rectangle in shape and occupied 64.7 hectares. Jeram sanitary landfill has been in operation by Worldwide Holdings since January 2007. This landfill is designed with a capacity to hold 6 million tons of waste. Currently, approximately 2000 tons of solid waste is disposed of at the landfill every day, and to date 4.1 million tons of waste has been added to the landfill [15].

All samples were collected in 1L amber glass bottles with Teflon lined caps to ensure sample integrity using a stain steel bucket previously rinsed with distilled water and methanol. The bottles head spaces were kept to a minimum by filling the bottles to the top. The bottles were rinsed once with sample and filled to the top on the second sampling. Disposable gloves were used to prevent any personal care products from contaminating the sample bottles, then immediately transported to the laboratory. Samples were filtered through a 0.7 µm GF/G filter from Whatman (UK) to remove suspended solids and stored at 4 ^{o}C in order to keep the wastewater characteristics unchanged.

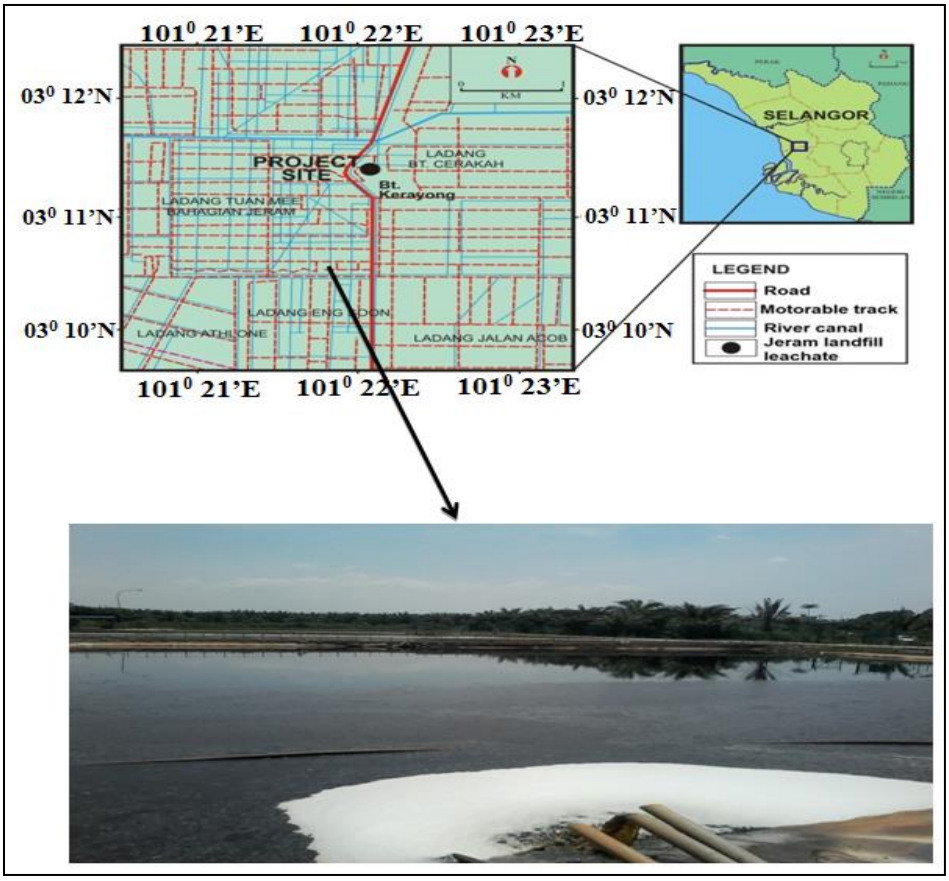


Figure 2. Map to describe location area

Method extraction of Prazosin and Simvastatin

Solid phase extraction procedure used in this study has been described in our previous paper [7]. In summary, the Oasis HLB cartridges (3 cm^3, 60 mg) were preconditioned with 2 mL MTBE, 2 mL of MeOH and 2 mL of deionized water at a flow rate of 1 mL/min. After the conditioning step, an aliquot of 250 mL of sample (after biological and charcoal treatment) were loaded into the cartridge. In case of raw leachate, 10 mL was diluted to 250 mL with deionised water because of its high complexity. Samples were passed through the cartridges at a flow rate of 9.0 mL/min and then, rinsed with 2 mL of deionized water prior to elution. After that, the cartridges were vacuum dried for 25 min to remove excess water. The pharmaceutical compounds were subsequently eluted into 12 mL glass tubes by sequentially passing 5×1 mL MTBE, 2×1 mL acetone–MeOH (21:9, v/v), and 3×1 mL acetone–MeOH (9:21, v/v). The combined eluents were evaporated to dryness under a gentle stream of N_2 gas. Dry extracts were reconstituted with 500 µL MeOH–DIW (10:90, v/v) and then transferred to 250 µL deactivated glass insert with polymer feet inserted in amber glass vials from Agilent Technologies (USA). The extract (30 µL) was automatically injected into LC–ESI–TOF/MS system for analysis.

The LC analysis was performed using a Dionex Ultimate 3000/LC 09115047 (USA) system equipped with a vacuum degasser, a quaternary pump, an auto sampler and a UV-Vis diode array detector. Chromatography was performed on a Thermo Scientific C18 (250 mm × 2.1 mm, i.d.: 5 µm) column. The injection volume was 30 µL. Simvastatin and prazosin were analysed in positive ion (PI) mode and eluted off from the column using mobile phase consisting of (A) 0.1 % FA in DIW and (B) ACN-MeOH (3:1, v/v) at 0.3 mL/min. The elution started at 5 % B and was then linearly increased to 60 % B over 3 min, further increased to 97 % B for 3 min and then kept isocratic for 5 min. Next, the elution was returned to its starting conditions over 11.1 min and allowed to equilibrate for 5 min prior to the next run.

The mass spectrometry was carried out on a TOF instrument (Bruker/Germany) equipped with a Z-spray electrospray interface. The results were obtained with the following settings: MS capillary voltages, 4000/3500 (PI/NI); collision energy for prazosin and simvastatin, 10 eV; drying-gas flow rate, 8.0 L/min; drying gas temperature, 190 °C; set capillary, 4000 V; set end plate offset −500 V; set collision cell RF, 250 Vpp and nebuliser pressure, 4.0 bar. Two adduct ions, namely $[M+H]^+$ for prazosin and $[M+Na]^+$ for simvastatin, were observed using TOF/MS analysis in positive-ion mode. The TOF results were collected between *m/z* 50 – 600. All analytes were acquired using an independent reference spray via the LockSpray interference to ensure accuracy and reproducibility; mixture of sodium hydroxide and formic acid was used as the lock mass *m/z* 90.9766 – 974.8132. The accurate mass was calculated using software Daltonic Analysis incorporated in the instrument.

Quality control

Recoveries of the studied pharmaceuticals were determined by initially spiking the samples with a standard mixture of prazosin and simvastatin (10 µg/L). Six replicates of samples were then enriched using Oasis HLB SPE. Instrumental quantification limits (IQLs) are defined as the lowest concentration with a signal to noise ratio (S/N) of 10. This parameter was estimated by analyzing the standard of decreasing concentration. The LOQ was calculated based on the level of IQLs spiked in each compound using Equation (1), as reported by Vieno et al. [16].

$$LOQ = \frac{IQL \times 100}{Rec\ (\%) \times CF} \quad (1)$$

where IQL is the instrumental quantification limit (ng/L), Recovery (%) is the absolute recovery of the analyte at the IQL spiking level in the corresponding matrix, and *CF* is the concentration factor (1000).

Selectivity of the proposed method was investigated by analyzing the chromatograms obtained from the individual standards, standard mixture, and solvent. Robustness of the method was studied by changing the flow rate of mobile phases (0.29 – 0.31 mL/min), location of instrument (Lab1 and Lab2), and volume of injection (10 – 40 µL).

Results and Discussion

Quality control analysis

Table 1 shows the linearity, limit of quantification (LOQ), instrumental quantification limit and recovery of prazosin and simvastatin obtained using the developed method.

Table 1. Method validation parameters

Compound	Linearity Range (µg/L)	Equation	R^2	IQL (µg/L)	LOQ[a] ng/L	LOQ[b] ng/L	R%[c]
PRZ	1.5 – 3000	Y = 2311.4X – 2485	0.999	1.5	2.1	3.5	66
SMV	0.8 – 125	Y = 14930.1X – 49270	0.997	0.8	0.5	2.4	62

[a] Deionized water, [b] STP effluent, [c] Recovery using STP effluent

It was observed that same retention time was obtained under all the conditions, indicating that the method was robust (Table 2). Thus, it was reliable to perform for analysis of real samples especially high complexity such as leachate samples.

Table 2. Effect of injection volume, lab movement and mobile phase on the robustness of LC method

Figure of Merit	Value	PRZ	SMV
Volume injection (µL)	10 µL	6.95	11.57
	20 µL	6.97	11.58
	30 µL	6.96	11.56
	40 µL	6.95	11.58
Instrument place	Lab1	6.95	11.59
	Lab2	6.93	11.57
Flow rate (mL/min)	0.29	7.11	11.87
	0.30	6.94	11.58
	0.31	6.76	11.29
	Mean	6.95	11.58
	SD	0.09	0.15
	RSD%	1.3	1.4

Lab 1 and Lab 2: Instrument has been moved from place to place.

TOF screening and confirmation

Measuring environmental contaminants in complex matrices is difficult because the analyte signals can be altered by interferences that are present in the real sample together with analytes. To increase the selectivity of TOF measurements, a narrow accurate mass interval was used to reconstruct the chromatographic traces. Extracted ion chromatograms (XICs) were typically extracted using a 20 mDa mass window for prazosin and simvastatin (Figure 3).

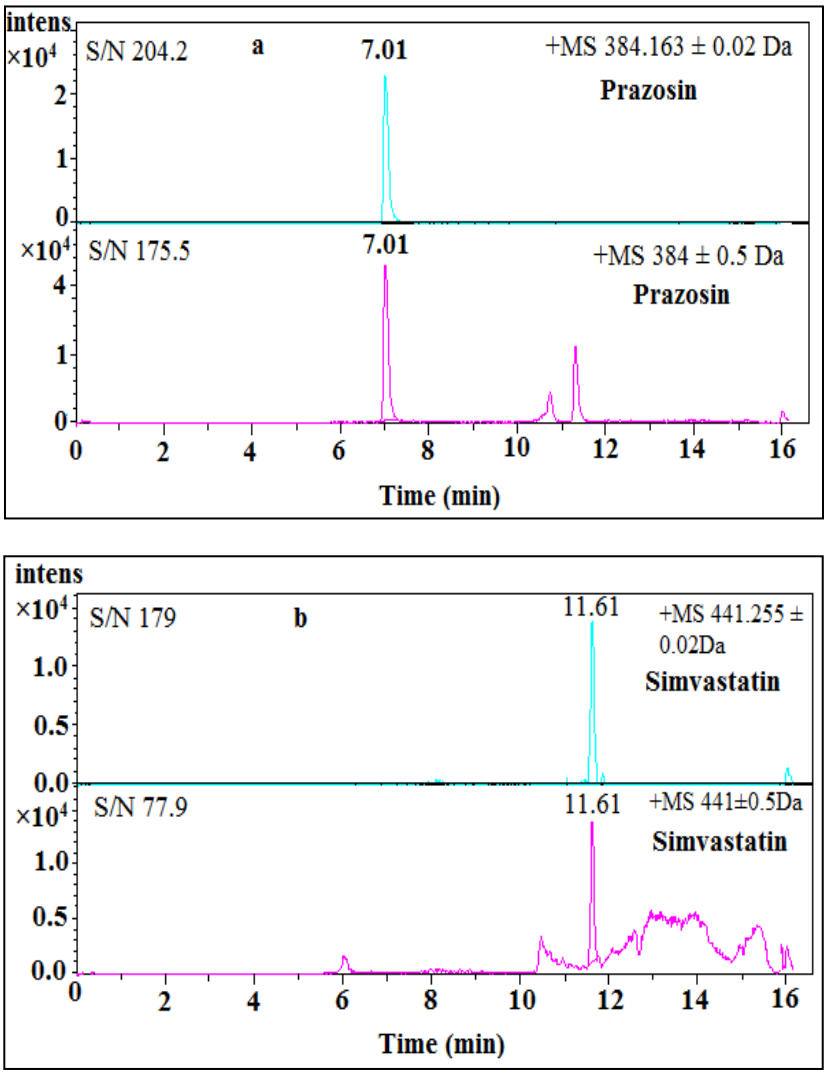


Figure 3. Enhanced selectivity of the LC–TOF/MS analysis corresponding to reconstruct ion chromatogram of (a) prazosin (*m/z* 384) and (b) simvastatin (*m/z* 441) in leachate sample with varying mass windows

Accurate mass data for the molecular ions were processed using Bruker Daltonics Data Analysis software, which provided the elemental formula and mass errors (i.e. differences between the accurate masses and the theoretical values), prazosin was selected as an example (Figure 4). The exact mass measurements and mass errors obtained in the TOF mode for molecular ions are listed in Table 3. The errors obtained were 1.56 and 0.2 ppm for prazosin and simvastatin, respectively.

Analysis of prazosin and simvastatin in real samples

The proposed method was applied to real samples to determine prazosin and simvastatin in raw leachate, post-biological and post-charcoal adsorption treatment leachate. Prazosin and simvastatin were detected and quantified in the raw leachate and treated leachate. Prazosin was commonly used for treatment of hypertension, symptomatic benign prostatic hyperplasia, and severe congestive heart failure [17]. It was detected in surface water and wastewater in the previous study conducted by Al-Qaim et al. [5]. In this study, prazosin was found in raw leachate at relatively high concentration 3850 ng/L while it was detected in leachate samples after biological and charcoal

treatment at concentration 98 and 94 ng/L, respectively which is observed less concentration compared with raw leachate 40 fold-times. It showed that prazosin was persistent as it can be detected after treatment even at low concentration as shown in Figure 5.

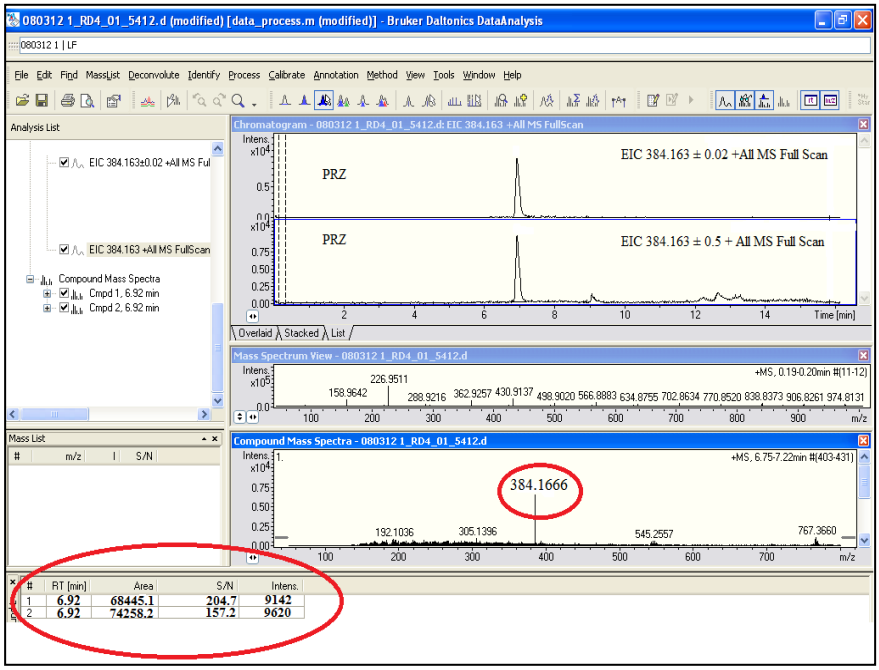


Figure 4. Daltonic data analysis software of prazosin

Table 3. Retention times and accurate mass measurements of molecular ions of target compounds in a standard solution

Peak No.	Compound	Ret. (min)	Elemental Composition	Experimental Mass (*m/z*)	Theoretical Mass (*m/z*)	Error (mDa)	Error (ppm)
1	PRZ	6.95	$[M+H]^+$ $C_{19}H_{22}N_5O_4$	384.1660	384.1666	0.6	1.56
2	SMV	11.59	$[M+Na]^+$ $C_{25}H_{38}NaO_5$	441.2611	441.2612	0.1	0.2

Simvastatin being used in the treatment of primary hypercholesterolemia and it is effective in reducing total and LDL-cholesterol as well as plasma triglycerides and apolipoprotein B [17]. Previously, it was detected in surface water, effluent sewage treatment plants and hospital in Malaysia [7]. Finding study indicates that high concentration of simvastatin (415 ng/L) was detected in raw leachate sample. Other compartment such as biological and physico-chemical (charcoal adsorption) treatments were able to reduce the concentration of samvastatin to 12 and 10.4 ng/L, respectively. However, detection of simvastatin and prazosin in raw leachate may be due to disposal direct of these compounds as a solid form. In the light of these results, the biological and charcoal adsorption treatment processes are insufficient to remove these two compounds as they were detected in treated leachate as well as surface water.

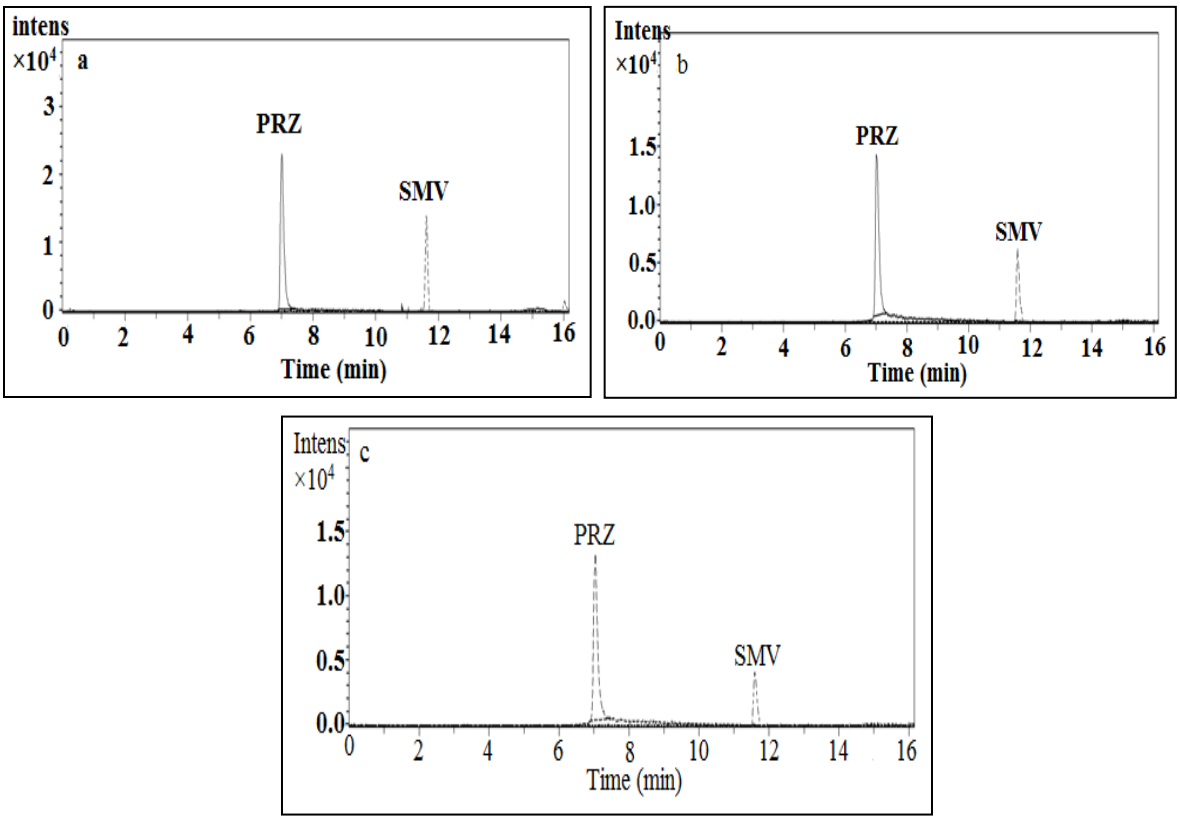


Figure 5. Extracted ionic chromatogram (EIC in PI mode) for prazosin and simvastatin in (a) raw leachate, (b) sample leachate post biological treatment and (c) sample leachate post charcoal adsorption.

Conclusion

The occurrence of prazosin and simvastatin in the leachate after biological and physico-chemical treatments showed that the difficulties are involved in treating this type of samples. Prazosin was persistent compounds as it can be detected after treatment even at low concentration. The detection of trace amounts of prazosin and simvastatin in complex sample indicated that LC-TOF/MS instrument is a powerful technique and very accurate for the analysis pharmaceuticals in water samples.

Acknowledgement

The authors thank Mr. Alefee for providing the LC-TOF/MS facilities to perform this study and the ALIR staff for providing ultra-pure water and facilities for leachate sampling. Special thanks to the staff of Jeram sanitary landfill company for given the permission in collecting leachate samples. This work was financially supported by UKM-DLP-2012-024, UKM-AP-2011-21, BKP-FST-K001671 and FRGS-1-2013-ST01-UKM-01-1.

References

1. Moldovan, Z. (2006). Occurrences of pharmaceutical and personal care products as micropollutants in rivers from Romania. *Chemosphere*, 64 (11): 1808 – 1817.
2. Koreje, K. O., Demeestere, K., Wispelaere, P., Vergeynst, L., Dewulf, J. and Langenhove, H. V. (2012). From multi-residue screening to target analysis of pharmaceuticals in water: Development of a new approach based on magnetic sector mass spectrometry and application in the Nairobi river basin, Kenya. *Science of the Total Environment*, 437: 153 – 164.

3. Petrović, M., Škrbić, B., Živančev, J., Ferrando-Climent, L. and Barcelo, D. (2014). Determination of 81 pharmaceutical drugs by high performance liquid chromatography coupled to mass spectrometry with hybrid triple quadrupole-linear ion trap in different types of water in Serbia. *Science of the Total Environment*, 468-469: 415 – 428.
4. Al-Odaini, N. A., Zakaria, M. P., Yaziz, M. I., Surif, S. and Abdulghani, M. (2013). The occurrence of human pharmaceuticals in wastewater effluents and surface water of Langat river and its tributaries, Malaysia. *International Journal of Environmental Analytical Chemistry*, 93 (3): 245 – 264.
5. Al-Qaim, F. F., Abdullah, M. P., Othman, M. R., Latip, J. and Afiq, W. M. (2013). Development of analytical method for detection of some pharmaceuticals in surface water. *Tropical Journal of Pharmaceutical Research*, 12 (4): 609 – 616.
6. Al-Qaim, F. F., Abdullah, M. P., Othman, M. R., Latip, J. and Afiq, W. (2014). A validation method development for simultaneous LC-ESI-TOF/MS analysis of some pharmaceuticals in Tangkas river-Malaysia. *Journal of the Brazilian Chemical Society*, 25 (2): 271 – 281.
7. Al-Qaim, F. F., Abdullah, M. P., Othman, M. R., Latip, J. and Zakaria, Z. (2014b). Multi-residue analytical methodology-based liquid chromatography-time-of-flight-mass spectrometry for the analysis of pharmaceutical residues in surface water and effluents from sewage treatment plants and hospitals. *Journal of Chromatography A*, 1345: 139 – 153.
8. Gómez, M. J., Petrović, M., Fernández-Alba, A. R. and Barceló, D. (2006). Determination of pharmaceuticals of various therapeutic classes by solid-phase extraction and liquid chromatography-tandem mass spectrometry analysis in hospital effluent wastewaters. *Journal of Chromatography A*, 1114 (2): 224 – 233.
9. Joseph, L., Zaib, Q., Khan, I. A., Berge, N. D., Park, Y. G., Saleh, N. B. and Yoon, Y. (2011). Removal of bisphenol A and 17α-ethinyl estradiol from landfill leachate using single-walled carbon nanotubes. *Water Research*, 45 (13): 4056 – 4068.
10. Andrews, W. J., Masoner, J. R. and Cozzarelli, I. M. (2012). Emerging contaminants at a closed and an operating landfill in Oklahoma. *Groundwater Monitoring & Remediation*, 32 (1): 120 – 130.
11. Mohamed, F. F., Abdullah, M. P., Othman, M. R. and Zakeria, Z. B. (2012). SPE-LC-Mass spectrometry analysis for basic pharmaceuticals with different therapeutic classes in aquatic environment. *Journal of Applied Sciences Research*, 8 (4): 2124 – 2132.
12. Al-Qaim, F. F., Abdullah, M. P. and Othman, M. R. (2012). Analysis of different therapeutic classes using liquid chromatography-mass spectrometry in the aquatic environment: a review. *International Journal of Pharmacy and Pharmaceutical Science*, 4: 3 – 11.
13. Al-Odaini, N. A., Zakaria, M. P., Yaziz, M. I. and Surif, S. (2010). Multi-residue analytical method for human pharmaceuticals and synthetic hormones in river water and sewage effluents by solid-phase extraction and liquid chromatography–tandem mass spectrometry. *Journal of Chromatography A*, 1217 (44): 6791 – 6806.
14. Miao, X. S. and Metcalfe, C. D. (2003). Determination of cholesterol-lowering statin drugs in aqueous samples using liquid chromatography–electrospray ionization tandem mass spectrometry. *Journal of Chromatography A*, 998 (1): 133 – 141.
15. Jeram Landfill. Access online http://fishguy85.blogspot.my/2012/12/jeram-landfill.html in February 2013.
16. Vieno, N. M., Tuhkanen, T. and Kronberg, L. (2006). Analysis of neutral and basic pharmaceuticals in sewage treatment plants and in recipient rivers using solid phase extraction and liquid chromatography-tandem mass spectrometry detection. *Journal of Chromatography A*, 1134 (1-2):101 – 111.
17. Drugbank. Open Data Drug and Drug Target Database. Access online http://www.drugbank.ca/ in November 2014.

Malaysian Journal of Analytical Sciences, Vol 20 No 4 (2016): 735 - 740
DOI: http://dx.doi.org/10.17576/mjas-2016-2004-05

MALAYSIAN JOURNAL OF ANALYTICAL SCIENCES
Published by The Malaysian Analytical Sciences Society
ISSN 1394 - 2506

SPECTROSCOPIC CHARACTERIZATION OF COPPER(II)-BASED TETRAPEPTIDES

(Pencirian Spektroskopik Kuprum(II) Tetrapeptida)

Mohd. Basyaruddin Abdul Rahman[1,2]*, Sharifa Zaithun Begum[1], Mohamed Ibrahim Mohamed Tahir[2], Haslina Ahmad[1,2], Emilia Abdul Malek[1,2]

[1]*Enzyme and Microbial Technology Research*
[2]*Department of Chemistry, Faculty of Science*
Universiti Putra Malaysia, 43400 UPM Serdang, Selangor, Malaysia

**Corresponding author: basya@upm.edu.my*

Received: 17 August 2015; Accepted: 7 May 2016

Abstract

Five different histidine and aspartic acid based tetrapeptides were designed using LOMETS and PyMol. They were chemically synthesized following the solid phase Fmoc-peptide synthesis protocols and were analysed using the reverse-phase High Performance Liquid Chromatography (HPLC) C_{18} analytical column for the purity. The peptides were further analysed by Liquid Chromatography Mass Spectrometry (LCMS) to see if the desired peptides were synthesized systematically. Copper(II) acetate monohydrate was bound to the peptides and the best molar ratio for the binding of these metal salts to peptides was 2:1. These observations were monitored through several spectroscopic techniques. The first physical observations for the successful synthesis of metallopeptides were the colour change, the melting/decomposition points and the solubility of these metallopeptides. Due to the visible colour change of the peptides to metallopeptides, UV-Visible spectroscopy and UV-Fluorescence spectroscopy were used as a qualitative analysis tests and the results were in agreement with other researchers' data from similar researches.

Keywords: copper(II), histidine, aspartic acid, tetrapeptides, spectroscopic

Abstrak

Lima tetrapeptida berbeza yang mempunyai histidine dan asid aspartik direkabentuk oleh LOMETS dan PyMol. Tetrapeptida ini disintesis mengikut skim fasa pepejal peptida dan dianalisis menggunakan fasa sonsang Kromatografi Cecair Berprestasi Tinggi (HPLC) C_{18} turus analisis untuk mengetahui keaslian peptida. Kesemua peptida ini dianalisis mengunakan Kromatografi Cecair-Spektrometer Jisim (LC-MS) untuk mengkaji sintesis peptida secara sistematik. Kuprum(II) asetat monohidrat terikat kepada peptida dan nisbah mol yang terbaik untuk mengikat garam logam ini kepada peptida adalah 2:1. Cerapan ini telah dipantau melalui beberapa teknik spektroskopi. Pemerhatian fizikal pertama untuk logam peptida yang berjaya disintesis ialah perubahan warna, takat lebur/penguraian dan kebolehlarutan peptida logam ini. Oleh kerana perubahan warna yang nyata dalam dari peptida kepada logam peptida, spektroskopi Ultralembayung-tampak (UV-Vis) dan spektroskopi Ultralembayung-Pendafluor (UV-Fluorescence) digunakan sebagai ujian analisis kuantatif dan data yang diperolehi adalah setara dengan perolehan data bagi penyelidikan yang serupa.

Kata kunci: Kuprum(II), histidin, asid aspartik, tetrapeptida, spektroskopi

Introduction

Metallopeptides that are easier and cheaper to synthesise when compared to metalloproteins have caught the attention of many researchers. Metallopeptides, synthesized from metal salt and peptides, are known as *pseudo*-proteins. They imitate the applications of large proteins especially in the industrial field of catalysis as well as in biological applications [1]. Metallopeptides are hybrid structures that combine peptides and metal and in this project, the transition metal copper(II) was used, that has various roles when used as biological probes [2]. The purpose of inserting a metal, particularly a transition metal is to increase the stability of short chain peptides, to provide the active site for various organic catalytic reactions (by behaving like an enzyme), to act as an antimicrobial agent in peptides that have no antimicrobial properties, to improve the anticancer properties of peptides and also to proliferate normal cells, amongst others [3].

The industrial applications of metallopeptides are applicable only when there is an understanding on its synthesis, for instance, the stability of the copper(II)-tetrapeptides will be understood only when data is available on the structure and geometry of copper(II) binding to the peptide. After confirming the stability of the metallocomplex, they can be applied as a catalyst or in biological assays. In this project, copper(II) acetate was bound to tetrapeptides containing metal binding amino acids; histidine and aspartic acid. Sulphur containing amino acids, though they are also metal binding amino acids were not used as they can be hazardous when applied in biological applications. In this research, the confirmation of the binding of metal to side chain of a particular amino acid in the peptides through UV-Visible spectroscopy and UV-Fluorescence is discussed. A brief discussion on how these two spectroscopic techniques can help in predicting the geometry of the copper(II) peptides is outlined, whether they form square planar, tetrahedral or octahedral complexes.

Materials and Methods

Five peptides were designed (P1: (Fmoc)NH-HAAD, P2: (Fmoc)NH-HAFD, P3: (Fmoc)NH-HAVD, P4: NH_2-AGHD, P5: NH_2-PGHD), synthesized and purified. They were characterized by High Performance Liquid Chromatography-Ultraviolet detector (HPLC-UV) for its purity and Liquid Chromatography-Mass Spectroscopy (LC-MS) for confirmation of the formation of peptides by its molecular weight. Copper(II) acetate monohydrate was bound to these five peptides in a 2:1 mole ratio.

Synthesis of metallopeptides

Copper(II) acetate monohydrate ($Cu(CH_3COO)_2.H_2O$ (189mg, 2 mol) was dissolved in deionized water (~10mL until all has dissolved) and heated in a water bath. In a separate test tube, the peptides P1-3 (300 mg) were dissolved in a mixture of deionized water and acetonitrile (20 mL and 10 mL respectively). Except for P4 and P5, these peptides were dissolved in deionized water only (20 mL) as the other three peptides had an FMOC group (hydrophobic group). The metal salt solution (cooled to room temperature) was added dropwise into the peptide solution with constant stirring at 40 – 60 °C. The resultant solution was stirred until the solution changed color and a precipitate was observed. After the precipitate was formed, the stirring was continued for another 1 – 2 hours to ensure that the reaction was completed (No further observation). The precipitate was vacuum-filtered and washed with cold deionized water and dried with acetone [4]. The final product was analyzed and characterized biophysically using UV-Vis and UV-Fluorescence spectroscopy. The product was purified through crystallization.

UV-Visible spectroscopic analysis of Cu(II)-tetrapeptides and its parent peptides

Peptides (10mM) and metallopeptides (5 – 10 mM) were dissolved in 5 mL of water and 10 mL of KH_2PO_4 buffer [11.11 mM] separately and were placed into 1 cm path length rectangular quartz cuvettes. The UV-Vis wavelength range was set from 200 – 1000 nm with fast scanning speed. The average of three scan readings were taken and plotted.

UV-Fluorescence spectroscopic analysis of Cu(II)-tetrapeptides and its parent peptides

Peptides (10mM) and metallopeptides (5-10mM) prepared for UV-Vis were used for UV- fluorescence as well. The samples were placed in a fluorescent cuvette. The scanning wavelength was set from 250 – 650 nm. The excitation wavelength was set to 280 nm. The slit width was 5 nm and the spectrum recorded was an average of three scans at fast speed.

Results and Discussion

Five histidine and aspartic acid based tetrapeptides that were designed computationally had proven random secondary structure and were synthesized and analyzed by HPLC and LC-MS as shown in Table 1. Their physical observations and their % yields are also mentioned.

Table 1. Physical observations, solubility in water and % yields of peptides

No.	Peptides	Morphology of solid	Solubility in water	% yield
P1	(Fmoc)NH-HAAD	White clumps	Hydrophilic	74.0
P2	(Fmoc)NH-HAFD	Whitish-yellow powder	Hydrophobic	74.2
P3	(Fmoc)NH-HAVD	White powder	Hydrophilic	83.1
P4	NH_2-AGHD	White powder	Hydrophilic	69.9
P5	NH_2-PGHD	White powder	Hydrophilic	65.6

Fmoc- Fluorenylmethyloxycarbonyl chloride

The purity of all these peptides was above 80% and they were not purified further. Copper(II) acetate-tetrapeptides (% yields: 50 – 65%) were analyzed by UV-Visible and UV-Fluorescence spectroscopy and the results are discussed in the sections below.

UV-Visible spectral analysis

One of the distinctive features of successful binding is the colour of the metallopeptide (refer to Figure 1). Colour is always associated with d-d transitions, ligand-metal charge transfer (LMCT) and metal-ligand charge transfer (MLCT). This analysis points out where and to what intensity these bands appear and are shown in Table 2.



Figure 1. Copper(II) based tetrapeptides (2, 4, 6, 8 and 10)

The results are in agreement with other reported data that d-d transitions have absorptions at the said wavelength with molar absorptivity in the range of about 2 – 3 $Lcm^{-1}mol^{-1}$ [5] and the charge transfer bands (CT bands) for copper bound peptides normally have similar or lower molar absorptivity than that of d-d transition bands and appear in the range of 400 – 600 nm [6].

No charge transfer bands and only a weak d-d transition band were observed in MP5 probably due to the low concentration of metallopeptide. All the metal salts were expected to bind to the imidazole ring of histidine. This was observed in both the UV-Vis and UV-Fluorescence spectra. According to Boka et al., copper and zinc binds to

the nitrogen (C=N) in the imidazole ring of histidine in the range of 250 – 300 nm giving rise to a strong sharp peak with high absorbance. However, it was also mentioned that copper also binds to the carboxylate side chain of aspartic acid and henceforth, the values are shifted further right (higher wavelength) due to the acidic nature of the metallopeptides [7], as observed in this study.

Table 2. d-d transition, LMCT and MLCT transitions of metallopeptides

Metallopeptides[a]	**Wavelength/nm (log ε/ $Lcm^{-1}mol^{-1}$)**	**Assignment**
MP1 (Cu-P1-Cu)	714 (2.04)	d-d transition
	458 (1.98)	charge transfer
	239 (3.84)	bound to histidine
MP2 (Cu-P2-Cu)	708 (1.60)	d-d transition
	530 (1.72)	charge transfer
	268 (3.74)	bound to histidine
MP3 (Cu-P3-Cu)	737 (2.17)	d-d transition
	648 (2.23)	charge transfer
	270 (3.85)	bound to histidine
MP4 (Cu-P4-Cu)	747 (2.31)	d-d transition
	518 (1.25)	charge transfer
	307 (2.60)	bound to histidine
MP5 (Cu-P5-Cu)	749 (1.16)	d-d transition
	-	no charge transfer
	264 (1.93)	bound to histidine

UV-Fluorescence spectral analysis

UV-Fluorescence measures the intensity of light emitted during the relaxation process when a particular substance absorbs UV radiation. These substances are termed as chromophores. The imidazole ring, -CONH, COOH, and cyclic compounds are important chromophores in peptides. The shift in the wavelength and intensity of fluorescence emitted by these chromophores can be due to the presence of metal and other chromophores that are added into the system [8]. For instance, the presence of copper(II) binding to the nitrogen in the imidazole ring of His or to the COOH of the Asp resulted in quenching due to the formation of new bonds or electrostatic forces of attraction. Similarly, when copper(II) acetate was used to bind to peptides, the presence of acetate, a chromophore, could affect the peptide system. Either, an extra band was observed further down the wavelength or the intensity of the existing band increased [9], as observed in Figure 2.

In most cases, addition of any metal into peptide or protein results in the quenching of its parent peptide as observed in the range of 600 – 650 nm [10]. Just like the UV-vis spectra, a strong signal was observed in the range of 285 – 340 nm (Figure 2). This was due to the presence of the imidazole ring of histidine [7]. In some of the metallopeptides, quenching was observed in this range. For the case of P4 and P5, the absence of Fmoc group at the N-terminal made them unstable and hence such emittance bands were observed. As for the copper(II) complexes of these two peptides (Figure 3), due to the positions of histidine and aspartic acid side by side, and the free N-terminal as a possible candidate for binding of one of the copper(II) ions also led to different results compared to MP1-3.

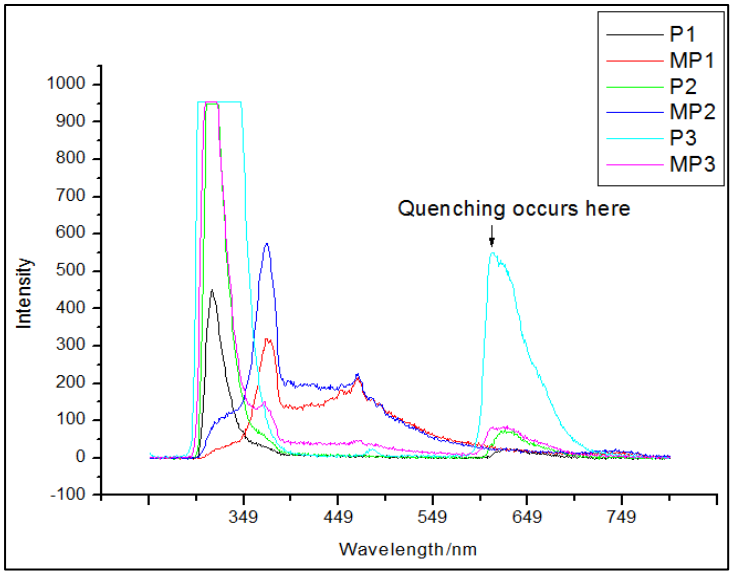


Figure 2. UV-Fluorescence spectra of P1-P3 and its copper(II) complexes

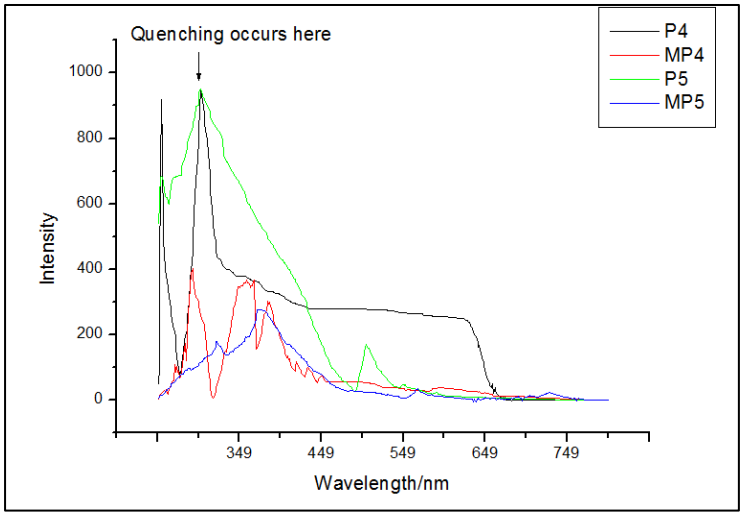


Figure 3. UV-Fluorescence spectra of P4, P5 and its copper(II) complexes

Conclusion

Based on the data reported in this work, it can be concluded that copper(II) acetate bound to the imidazole ring of histidine and at carboxylate of aspartic acid (one copper(II) at each amino acid) for all the peptides. The UV-Fluorescence shows the existence of the acetate (CH_3COO) ion in the complex. From the color of copper-peptides (blue), it was also concluded that water was bound to the complex.. Hence, for each copper(II) complex, the geometry is predicted to be a square planar or tetrahedral. To confirm the structure and the geometry, single crystal X-ray diffraction needs to be carried out but suitable crystals have not yet been obtained.

Acknowledgement

We gratefully acknowledge the Fundamental Grant Research Scheme (FGRS 5524292) entitled "Rational Design of Peptide Chiral Catalyst Based on Aldo-Ketoreductase for asymmetric Aldol reaction", the Faculty of Science, UPM and Malaysian Genome Institute for providing laboratory services and facilities.

References

1. Ming, L. J. (2010). Metallopeptides from drug discovery to catalysis. *Journal of Chinese Chemical Society,* 57*:* 285 – 299.
2. Ball, Z. T. and Zaykov, A. N. (2011). A general synthesis of dirhodium metallopeptides as MDM2 ligands. *Chemical Communications*, 47: 10927 – 10929.
3. Tay, W. M (2010). Metallopeptides as model systems for the study of Cu(II)-dependent oxidation chemistry, Thesis University of South Florida.
4. Sambasivan, R. and Ball, Z. T. (2010). Metallopeptides for asymmetric dirhodium catalysis. *Journal of the American Chemical Society.* 132: 9289 – 9295.
5. Karavelas, T., Mylonas, M., Malandrinos, G., Plakatouras, J. C., Hadjiliadis, N., Mlynarz, P. and Kozlowski, H. (2005). Coordination properties of Cu(II) and Ni(II) ions towards the C-terminal peptide fragment -ELAKHA- of histone H2B. *Journal of Inorganic Biochemistry.* 99(2): 606 – 615.
6. Neupane, K. P, Aldous, A. R. and Kritzer, J. A. (2013). Macrocyclization of the ATCUN motif controls metal binding and catalysis. *Inorganic Chemistry*. 52(5): 2729 – 2735.
7. Boka, B., Myari, A., Sovago, I. and Hadjiliadis, N. (2004). Copper(II) and zinc(II) complexes of the peptides Ac-HisValHis-NH_2 and Ac-HisValGlyAsp-NH_2 related to the active site of the enzyme CuZnSOD. *Journal of Inorganic Biochemistry*. 98(1): 113 – 122.
8. Penner, M. H. (2010). Ultraviolet, visible and fluorescence spectroscopy. In *Food Analysis, 4th Ed*., Suzanne Nielsen, Ed. Springer.
9. Goulding, A.M. (2010). Biochemical applications of DsRed-Monomer utilizing fluorescence and metal-binding affinity. Unpublished doctoral dissertation, Purdue University, Indianapolis, Indiana.
10. Deo, S.K., Rahimi, Y., Goulding, A., Shrestha, S., Mirpuri, S. (2008). Mechanism of copper induced fluorescence quenching of red fluorescent protein, DsRed. *Biochemical and Biophysicsal Research Communication.* 370(1): 57 – 61.

Malaysian Journal of Analytical Sciences, Vol 20 No 4 (2016): 741 - 750
DOI: http://dx.doi.org/10.17576/mjas-2016-2004-06

MALAYSIAN JOURNAL OF ANALYTICAL SCIENCES
Published by The Malaysian Analytical Sciences Society
ISSN 1394 - 2506

SYNTHESIS AND ANTIMICROBIAL ACTIVITIES OF ELEVEN *N*-SUBSTITUTED MALEIMIDES

(Sintesis dan Kajian Antimikrob Terhadap Sebelas Terbitan Maleimida)

Tang Sook Chin, Fatin Ilyani Nasir, Nurul Izzaty Hassan*

School of Chemical Sciences and Food Technology,
Faculty of Science and Technology,
Universiti Kebangsaan Malaysia, 43600 UKM Bangi, Selangor, Malaysia

**Corresponding author: drizz@ukm.edu.my*

Received: 13 January 2016; Accepted: 4 April 2016

Abstract

The antimicrobial activities of eleven maleimide derivatives were tested in this study. Out of the eleven samples, *N*-(4-fluorophenyl) maleimide, *N*-(4-chlorophenyl) maleimide and *N*-(4-bromophenyl) maleimide were synthesized by reacting maleic anhydride with 4-fluorophenylaniline, 4-chlorophenylaniline and 4-bromophenylaniline, respectively in the presence of acetic acid, by refluxing overnight. Crystals were successfully obtained after the products were recrystallized with different mixture of solvents. Their chemical structures were confirmed by infrared spectroscopy (IR), ^{1}H and ^{13}C Nuclear Magnetic Resonance (NMR) and melting point determination. Subsequently, all the samples were screened for their biological activity using disc diffusion method. The bacteria chosen for this study were Gram-negative *Escherichia coli*, Gram-positive *Bacillus subtilis* and yeast *Saccharomyces cerevisae*. Positive control for bacteria was streptomycin and nystatin for the yeast. **M1** to **M6** compounds gave remarkable result at low concentrations whereas **M8, M9** and **M11** compounds are mostly inactive up to a high concentration. In contrast, the unsubstituted maleimide, **M7** was highly reactive towards both bacteria and yeast at low and high concentrations.

Keywords: *N*-substituted maleimide, antimicrobial, disc diffusion

Abstrak

Kajian antimikrob terhadap sebelas terbitan *N*-maleimida telah diuji dalam kajian ini. Tiga daripada sebelas sebatian maleimida yang diuji, iaitu *N*-(4-florofenil)maleimida, *N*-(4-klorofenil)maleimida dan *N*-(4-bromofenil)maleimida telah disintesis melalui tindakbalas maleik anhidrida dengan 4-florofenilanilina, 4-klorofenilanilina and 4-bromofenilanilina secara berasingan dalam kehadiran asid asetik, diikuti dengan refluks semalaman. Mendakan tidak berwarna telah diperolehi setelah penghabluran semula dilakukan ke atas hasil sintesis. Pencirian struktur sebatian dilakukan melalui kaedah spektroskopi Infra Merah (IR), ^{1}H dan ^{13}C Resonans Magnet Nukleus (NMR) dan penentuan takat lebur. Seterusnya, kajian antimikrob bagi kesemua sebelas sampel dilakukan melalui kaedah resapan cakera. Bakteria yang digunakan dalam kajian ini ialah *Escherichia coli* dan *Bacillus subtilis* manakala yis yang digunakan ialah *Saccharomyces cerevisae.* Kawalan positif untuk bakteria ialah *streptomisin* dan *nystatin* untuk yis. Sebatian **M1** ke **M6** mencatatkan keaktifan yang baik pada kepekatan rendah. Sebatian **M8**, **M9** dan **M11** kebanyakannya tidak menunjukkan keaktifan walaupun kepekatan dos ditingkatkan. Berbeza pula dengan sebatian **M7**, iaitu maleimida yang tidak mempunyai sebarang kumpulan gantian yang menunjukkan keaktifan yang tinggi terhadap kedua-dua bakteria dan yis pada kepekatan rendah dan tinggi.

Kata kunci: maleimida *N*-gantian, antimikrob, kaedah resapan cakera

Introduction

Microbe resistance has been a challenge for health practitioner and the pharmaceutical industry. The prescription of antibiotics are reported to be related to bacterial resistance. The most commonly found drug-resistant bacteria in hospitals are methicilin-resistant *Staphylococcus aureus* (MRSA) and *Pseudomonas aeruginosa* [1]. The resistance towards various drugs and medicines shown by bacteria and fungi has also become the main reason for failure in chemotherapy of infectious diseases. Therefore, the need for a novel anti microbe agent is highly desirable.

Recently, researchers are focusing on bacterial and fungal enzymes that are responsible for catalysing important biochemical reactions in microbe cells. Biologically active compounds capable of deactivating these enzymes and block the metabolic pathway of these bacteria and fungi selectively in human body are potential novel antimicrobial drugs [2]. Many biologically active compounds including most of the antibiotics are enzyme inhibitors. Compounds that are active towards the thiol group are able to inhibit cysteine protease and other proteins containing important cysteins. Maleimides for instance, portrayed the ability to inhibit cysteine protease and *N*-ethylmaleimide specifically, acts spontaneously and fast with the sulphydryl group.

Cyclic imides such as succinimides, maleimides, phthalimides and their derivatives have an imide ring and the –CO-N(R)-CO- structure that gives them neutrality and hydrophobicity. Previous studies have shown that various kinds of biological activities such as antibacterial, antifungal and antitumor are related to these compounds and their derivatives as shown in Table 1 [3]. Maleimide compounds in specific have shown antifungal and antibacterial properties [4], ability to inhibit Protein Kinase C and antitumor property [5], and analgesic activity [6]. Li research group mentioned about the antifungal activity of simple compounds with dimethylmaleimide structure against *Botrytis cinerea,* which revealed that natural products containing maleimide structure has high biological activity while non-natural products having maleimide structure also shows antifungal activity [7].

Table 1. Antimicrobial activity of *N*-substituted maleimide

Types of Maleimide	**Types of Microbe**		
	E. coli	***B. subtilis***	***S. cerevisiae***
N-(4-chlorophenyl) maleimide	-	-	MIC: 3.90 µg/mL [10]
N-(4-florophenyl) maleimide	-	-	MIC: 3.90 µg/mL [10]
N-(4-bromophenyl) maleimide	MIC: 128 µg/mL [2]	MIC: 64 µg/mL [2]	MIC: 1.0 µg/mL [2]
			MIC: 7.81 µg/mL [10]
N-(2-methylphenyl) maleimide	-	-	MIC: 7.81 µg/mL [10]
N-(4-methylphenyl) maleimide	-	-	MIC: 3.90 µg/mL [10]
N-(*tert*-butyl) maleimide	MIC: 32 µg/mL [2]	MIC: 2.0 µg/mL [2]	MIC: 2.0 µg/mL [2]
N-methylmaleimide	-	-	MIC: 7.81 µg/mL [2]

Studies have also reported that some of the maleimide derivatives that is biologically active is neither haemolytic nor cytotoxic towards the human cancer cell, which indicated the selectivity of action of maleimides towards fungal pathogen [8]. Zentz et al. has reported that *N*-substituted maleimides, *N*-(*tert*-butyl)maleimide in particular shows antibacterial properties towards *Escherichia coli*. [9].

Maleimide compounds are Michael acceptors prone to be attacked at the double bond in the maleimide ring, by nucleophilic species such as the thiol group as shown in Figure 1. The maleimides react specifically on biological molecules containing thiol group and form stable conjugate protein through thioether bond [11]. The thioether bond formed has strong C-S bond which is often irreversible and cannot be reduced by reducing agents. This reaction takes place specifically at pH 6.5 – 7.5. in alkaline condition when pH exceeds 8.5, hydrolysis of maleimide to maleimic acid is prone to take place [12].

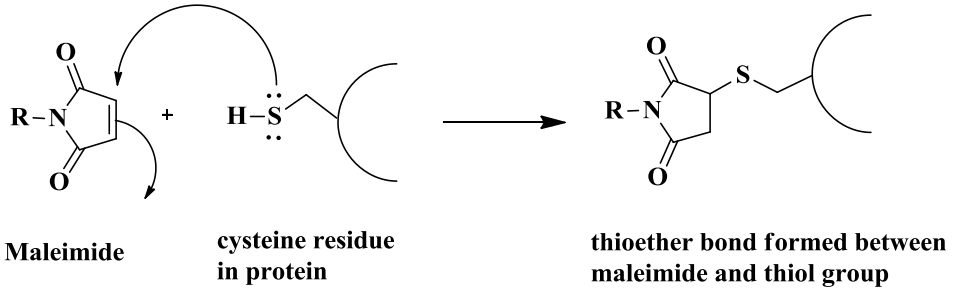


Figure 1. Reaction between maleimide and thiol group

Many types of active protein and enzymes can be found on bacteria cell membrane. When these enzymes react with foreign substances such as drugs, their enzyme activity will change and subsequently inhibit its growth [13].

In this study, we focused on *N*-substituted maleimides, which refer to any maleimide compounds that has substituent groups such as alkyl or halides attached to the nitrogen atom in the maleimide ring. Since biological activitiy of each maleimide derivatives varies from one another, the structure activity relationship display distinct properties that will affect the reactivity of different maleimide compounds. Some of the factors responsible for the different reactivities of maleimide compounds are the presence of aryl group on the nitrogen atom in the maleimide ring [5], the length of alkyl chain on the alkylphenyl group attached to the nitrogen atom in the maleimide ring [7], the lipophilicity and bulkiness of the compound molecule [2] and the presence of any substituents on the maleimide ring [14].

In view of this, 11 samples of *N*-substituted maleimides (**M1** to **M11**) have been tested on three different microbes, namely *Escherichia coli* (Gram negative), *Bacillus subtilis* (Gram positive) and *Saccharomyces cerevisiae* through the disc diffusion method to study the inhibition ability of these samples.

Materials and Methods

Synthesis of *N*-(2-methylphenyl)maleimide (M1)

Maleic anhydride (44.0 mmol) was reacted with *o*-toluidine (42.3 mmol) by dissolving the mixture in THF (50 mL). The reaction mixture was stirred overnight at room temperature (RT) under nitrogen atmosphere. The precipitate formed was filtered and used in next reaction without further purification. The reaction mixture (1.71 mmol) was suspended in dry acetonitrile (40 mL) before the addition of zinc bromide (1.71 mmol) and HMDS (8.55 mmol) and heated at 90 °C for 2 hours before it was allowed to cool to RT and filtered. Subsequently, water (25 mL) was added and acidified with 1M HCl until pH 1. The mixture was washed with ethyl acetate (3 x 50 mL) and the organic layer was dried over anhydrous $MgSO_4$, filtered and concentrated *in vacuo* to obtain black solution. The solution was recrystallized to yield colourless crystalline solid (35%).

Synthesis of N-(3-methylphenyl)maleimide (M2)

Maleic anhydride (44.0 mmol) was reacted with *m*-toluidine (42.3 mmol) by dissolving the mixture in THF (50 mL). The reaction mixture was stirred overnight at RT under nitrogen atmosphere. The precipitate formed was filtered and used in next reaction without further purification. The reaction mixture (1.71 mmol) was suspended in dry acetonitrile (40 mL) before the addition of zinc bromide (1.71 mmol) and HMDS (8.55 mmol) and heated at 90 °C for 2 hours before it was allowed to cool to RT and filtered. Subsequently, water (25 mL) was added and acidified with 1M HCl until pH 1. The mixture was washed with ethyl acetate (3 x 50 mL) and the organic layer was dried over anhydrous $MgSO_4$, filtered and concentrated *in vacuo* to yield yellowish crystalline solid (28%).

Synthesis of *N*-(4-methylphenyl)maleimide (M3)
Maleic anhydride (44.0 mmol) was reacted with *p*-toluidine (42.3 mmol) by dissolving the mixture in THF (50 mL). The reaction mixture was stirred overnight at RT under nitrogen atmosphere. The precipitate formed was filtered and used in next reaction without further purification. The reaction mixture (1.71 mmol) was suspended in dry acetonitrile (40 mL) before the addition of zinc bromide (1.71 mmol) and HMDS (8.55 mmol) and heated at 90 °C for 2 hours before it was allowed to cool to RT and filtered. Subsequently, water (25 mL) was added and acidified with 1M HCl until pH 1. The mixture was washed with ethyl acetate (3 x 50 mL) and the organic layer was dried over anhydrous $MgSO_4$, filtered and concentrated *in vacuo* to obtain yellow powder. The solution was recrystallized to yield yellow needle-like crystalline solid (84%).

Synthesis of *N*-(4-florophenyl)maleimide (M4)
Maleic anhydride (9.0 mmol) was reacted with equimolar of 4-fluoroaniline by dissolving the mixture in 50 mL acetic acid at RT. The reactants are stirred for 6.5 hours. The resulting suspension was refluxed overnight for 17.5 hours at 130 °C and then cooled to room temperature. The resulting solution of maleimide was extracted with ethyl acetate (3 x 50 mL). Extracts were combined and recrystallized (40%).

Synthesis of *N*-(4-chlorophenyl)maleimide (M5)
Maleic anhydride (7.84 mmol) was reacted with equimolar of 4-chloroaniline by dissolving the mixture in 50 mL acetic acid at RT. The reactants are stirred for 5.5 hours at 130 °C and then cooled to room temperature. The resulting solution of maleimide was extracted with ethyl acetate (3 x 50 mL). Extracts were combined and recrystallized (45%).

Synthesis of *N*-(4-bromophenyl)maleimide (M6)
Maleic anhydride (5.81 mmol) was reacted with equimolar of 4-bromoaniline by dissolving the mixture in 50 mL acetic acid at RT.The reactants are stirred for 5.5 hours at 130 °C and then cooled to room temperature. The resulting solution of maleimide was extracted with ethyl acetate (3 x 50 mL). Extracts were combined and recrystallized (51%).

Synthesis of 1-(3,5-bis(trifloromethyl)phenyl)-3-(4-(3-(2,5-dioxo-2H-pirol-1(5H)-yl)phenetyl)phenyl)urea (M8)
4'-ethylene dianiline (1.08 g, 5.1 mmol) in dry CH_2Cl_2 (20 mL) was slowly reacted with 3,5-dimethyl phenylisocyanate (0.5 g, 3.4 mmol) at −5°C and allowed to stir at ambient temperature for 16 hours. The solvent was removed under reduced pressure. The residue was then purified by column chromatography (CH_2Cl_2:EtOAc, 8:1). The product was obtained as yellow solid was dissolved in THF (10 mL) before reacted with maleic anhydride (82 mg, 0.84 mmol). The reaction mixture was stirred at ambient temperature under a Ar atmosphere for 3 hours. The precipitate was filtered and the compound obtained (460 mg, 98%) was carried out to the next step without further purification. The acid derivative (0.20 g, 0.35 mmol) was dissolved in dry CH_3CN (10 mL) and refluxed for 1 hour after the subsequent addition of $ZnBr_2$ (80 mg, 0.35 mmol) and hexamethyldisilazone (0.38 mL, 1.77 mmol). The reaction mixture was filtered and the filtrate was reduced to 10%. The solution was acidified with 0.5M HCI until pH 1 and extracted into CH_2CI_2. The organic layer were combined and dried over $MgSO_4$. The solvent was evaporated *in vacuo* to give the maleimide **M8** as yellow solid (78%).

Synthesis of 1-(4-(4-(2,5-dioxo-2H-pirol-1(5H)-yl)phenetyl)phenyl)-3-(3,5-dimethylphenyl)urea (M9)
A solution of 3,5-dimethylbenzoic acid (2.0 g, 13.3 mmol) in toluene (50 mL) and thionyl chloride (1.1 mL, 14.6 mmol) was heated to reflux at 80 °C for 16 h. The excess thionyl chloride was distilled off by the azeotropic distillation with toluene under reduced pressure, affording 3,5-dimethylbenzoyl chloride as brownish oil quantitatively. The product was used in the next step without further purification. The acid derivative (2.24 g, 13.3 mmol) in dry CH2Cl2 (20 mL) was added dropwise over 1.5 h to a solution of 4,4'-ethylenedianiline (6.20 g, 29.2 mmol) and Et_3N (3.7 mL, 26.6 mmol) in dry CH_2Cl_2 (50 mL) at ambient temperature under N_2 atmosphere. The reaction mixture was stirred at ambient temperature for 16 hours. The organic phase was washed successively with sat. solution of $NaHCO_3$ and brine, dried over $MgSO_4$ and concentrated by evaporation under reduced pressure. The residue was purified by column chromatography (Hexane:EtOAc, 2:1), affording a yellow solid. The solid (0.5 g, 1.45 mmol) was treated with maleic anhydride (0.14 g, 1.45 mmol) in THF (15 mL) and stirred at ambient

temperature under N_2 atmosphere for 3 hours. The yellow precipitate (66%) was filtered and carried out to the next step without further purification. The acid derivative obtained (0.34 g, 0.78 mmol) was dissolved in dry CH_3CN (20 mL) and refluxed for 2 h after the subsequent addition of $ZnBr_2$ (0.18 g, 10.78 mmol) and hexamethyldisilazone (0.83 mL,3.91 mmol). The reaction mixture was filtered and the filtrate was reduced to 10%. The solution was acidified with 0.5M HCl until pH 1 and extracted into CH_2Cl_2. The organic layers were combined and dried over $MgSO_4$. The solvent was evaporated to give the desired product as yellow crystalline solid (96%).

Synthesis of 2-(4-(2,5-dioxo-2H-pirol-1(5H)-yl)phenyll) acetic acid (M10)
Maleic anhydride (6.05 g, 40 mmol, 1 eq) and 4-aminophenyl acetic acid (3.92 g, 40 mmol, 1 eq) were dissolved in acetic acid (200 mL) and stirred under N_2 at RT for 2 hours before refluxing for 2 hours. The solvent was then evaporated under vacuum and the residue was dissolved in 5% acetic acid in CH_2Cl_2. The solution was passed through a plug of silica eluted with 5% acetic acid in CH_2Cl_2. The fractions containing product as identified by tlc were combined and the solvent removed under vacuum. The residue was then purified by recrystallisation by using chloroform to yield the product as a yellow powder (36%).

Synthesis of 3,5-dimethyl-N-(4-(2,5-dioxo-2H-pirol-1(5H)-yl)phenyl)benzamide (M11)
Cyanuric fluoride (0.85 mL, 10.1 mmol) was added dropwise to a solution of 3,5-dimethylbenzoic acid (1.52 g, 10.1 mmol) and dry pyridine (0.82 mL, 10.1 mmol) in dry CH_2Cl_2 (40 mL) at 0 °C under a N_2 atmosphere. The reaction mixture was stirred at 0 °C for 20 min and then at ambient temperature for a further hour. The reaction mixture was diluted with CH_2Cl_2. The organic layer was washed with saturated NaCl solution, dried ($MgSO_4$) and the solvent was removed by evaporation under reduced pressure to afford a yellow solid (100%). The solid (1.52 g, 10.0 mmol) was then dissolved in dry CH_2Cl_2 (40 mL) was added dropwise (over 4 h) to a solution of 1,4phenylenediamine (3.26 g, 30.1 mmol) in dry CH_2Cl_2 (60 mL), under a N_2 atmosphere. The reaction mixture was stirred at ambient temperature overnight, and then diluted with CH_2Cl_2. The organic layer was washed successively with saturated $NaHCO_3$ solution and saturated NaCl solution, dried ($MgSO_4$) and concentrated by evaporation under reduced pressure. The residue was purified by column chromatography (SiO_2, gradient from 100:0 to 95:5 CH_2Cl_2/MeOH) to give a yellow solid (80%). The solid (0.95g, 3.95 mmol) obtained was dissolved in acetic acid (70 mL) to react with maleic anhydride (388 mg, 3.96 mmol). The reaction mixture was stirred at ambient temperature under a N_2 atmosphere for 6 h, and then heated to reflux for 16 h. The solvent was removed by evaporation under reduced pressure. The residue was purified by column chromatography (SiO2, gradient from 100:0 to 98:2 $CHCl_3$/MeOH) to give a yellow solid (66%).

Antimicrobial screening
All samples were tested using disc diffusion method against *Escherichia coli* (Gram negative), *Bacillus subtilis* (Gram positive) and *Saccharomyces cerevisiae*. The samples were prepared in two concentrations, 1.0 µg/µL (10 µg/disc) and 2.0 µg/µL (20 µg/disc) by dissolving the solid samples in appropriate solvent. The positive control for the bacteria was streptomycin at 10 µg/disc while nystatin at 20 µg/disc was used as positive control for the yeast. Nutrient agar and potato dextrose agar were prepared by dissolving the premixed powder in water following with heating and auto-clave. The dissolved solution was then poured on petri dishes, allowed to dry and ready to be used. The bacteria cultures were then spread on the surface of the Nutrient Agar (NA) and yeast cultures on Potato Dextrose Agar (PDA). Subsequently, the discs were impregnated with (10 µg/disc) and (20 µg/disc) test samples and then placed on the surface of the agar media. Experimental plates of bacteria cultures were incubated at 37 °C for 18 to 21 hours whereas the experimental plates of yeast cultures were incubated for 48 hours at 30 °C. The antimicrobial activity was the determined by measuring the diameter of inhibition zone (IZ) and compared with positive control.

Results and Discussion

Characterization study: N-(2-methylphenyl)maleimide (M1)
M.p. = 150.6-150.8 °C; ^{1}H NMR (400 MHz, $CDCl_3$): $^\delta$H 7.34 (1H, d, *J* = 6.20 Hz, Ar*H*), 7.33 (1H, d, *J* = 6.24 Hz, Ar*H*) , 7.29 (1H, d, *J* = 7.72 Hz, Ar*H*), 7.10 (1H, d, *J* = 7.68 Hz, Ar*H*), 6.85 (2H, s, Ar*H*), 2.15 (3H, s, CH_3); ^{13}C NMR (100 MHz; $CDCl_3$) $^\delta$C 169.7 (*C*=O), 136.6 (*C*=*C*), 134.5 (q, 131.3 (Ar*C*), 130.0 (Ar*C*), 129.5 (Ar*C*), 128.8 (Ar*C*), 126.9 (q, 17.9 (*C*H_3); MS (EI) m/z 187.2 (M^+, 100 %); IR ν_{max} (KBr) cm-1: 2929.45 cm^{-1} (sp^3 CH), 1702.31 cm^{-1} (C=O), 1029.23 cm^{-1} (C-N).

N-(3-methylphenyl)maleimide (M2)
^{1}H NMR (400 MHz, $CDCl_3$): $^{\delta}$H 7.34 (1H, t, *J* = 7.70 Hz, Ar*H*), 7.17 (1H, d, *J* = 7.72 Hz, Ar*H*), 7.11 (1H, d, *J* = 8.44 Hz, Ar*H*), 7.11 (1H, d, *J*= 8.44 Hz, Ar*H*), 6.80 (2H, s, Ar*H*), 2.37 (3H, s, CH_3); ^{13}C NMR (100 MHz; $CDCl_3$) $^{\delta}$C 169.7 (*C*=O), 139.3 (Ar*C*), 134.2 (q, 131.1 (Ar*C*), 129.0 (Ar*C*), 128.9 (Ar*C*), 126.9 (q, 123.4 (Ar*C*), 21.4 (*C*H_3); MS (EI) m/z 187.2 (M^+, 100 %); IR ν_{max} (KBr) cm-1: 2922.57 cm^{-1} (sp^3 CH), 1705.59 cm^{-1} (C=O), 1033.45 cm^{-1} (C-N).

***N*-(4-methylphenyl)maleimide (M3)**
M.p. = 150.5-150.7 °C; ^{1}H NMR (400 MHz, d-Acetone): $^{\delta}$H 7.27 (2H, d, *J* = 8.08 Hz, Ar*H*), 7.22 (2H, d, *J* = 8.44 Hz, Ar*H*), 7.00 (2H, s, Ar*H*), 2.35 (3H, s, CH_3); ^{13}C NMR (100 MHz; d-Acetone) $^{\delta}$C 169.8 (*C*=O), 137.4 (Ar*C*), 134.4 (q, 129.5 (Ar*C*), 129.3 (Ar*C*), 126.5 (q, 20.0 (*C*H_3); MS (EI) m/z 187.1 (M^+, 100 %); IR ν_{max} (KBr) cm-1: 3450.67 cm^{-1} (OH), 2967.11 cm^{-1} (sp^3 CH), 1702.41 cm^{-1} (C=O), 1041.54 cm^{-1} (C-N).

***N*-(4-florophenyl)maleimide (M4)**
M.p. = 151.8 –153.2 °C; ^{1}H NMR (400.1 MHz, d_6-Acetone): $^{\delta}$H 7.45-7.39 (2H, m; 2xAr*H*), 7.28-7.22 (2H, m, 2×Ar*H*), 7.03 (2H, s, Ar*H*); ^{13}C NMR (100.6 MHz, d_6-DMSO): $^{\delta}$C 169.7 (*C*=O), 161.6 (*C*F), 134.5 (Ar*C*H), 128.7 (Ar*C*H), 128.3 (Ar*C*-N), 115.6 (Ar*C*H).

***N*-(4-chlorophenyl)maleimide (M5)**
M.p. = 106.7 –108.5 °C; ^{1}H NMR (400.1 MHz, d_6-Acetone): $^{\delta}$H 7.53-7.51 (2H, m; 2xAr*H*), 7.43-7.41 (2H, m, 2×Ar*H*), 7.04 (2H, s, Ar*H*); ^{13}C NMR (100.6 MHz, d_6-DMSO): $^{\delta}$C 169.4 (*C*=O), 134.6 (Ar*C*H), 132.6 (Ar*C*-N), 131.1 (Ar*C*-Cl), 128.9 (Ar*C*H), 128.0 (Ar*C*H); ^{19}F NMR (376.5 MHz, d_6-DMSO) : $^{\delta}$F 115.6 (Ar*C*-F).

***N*-(4-bromophenyl)maleimide (M6)**
M.p. = 101.5 –103.9 °C; ^{1}H NMR (400.1 MHz, d_6-Acetone): $^{\delta}$H 7.68-7.65 (2H, m; 2xAr*H*), 7.38-7.35 (2H, m, 2×Ar*H*), 7.04 (2H, s, Ar*H*); ^{13}C NMR (100.6 MHz, d_6-DMSO): $^{\delta}$C 169.4 (*C*=O), 134.6 (Ar*C*H), 131.9 (Ar*C*H), 131.5 (Ar*C*-N), 128.3 (Ar*C*H), 120.6 (*C*-Br).

1-(3,5-bis(trifloromethyl)phenyl)-3-(4-(3-(2,5-dioxo-2H-pirol-1(5H)-yl)phenetyl)phenyl)urea (M8)
M.p. = 205.3 – 208.3 °C; ^{1}H NMR (300.1 MHz, d_6-DMSO) : $^{\delta}$H 9.36 (1H, s; N*H*), 8.89 (1H, s, N*H*), 8.13 (2H, s; 2×Ar*H*), 7.61 (1H, s; Ar*H*), 7.39 (2H, d, $^{3}J_{HH}$ 8.4 Hz; 2×Ar*H*), 7.33 (2H, d, $^{3}J_{HH}$ 8.4 Hz; 2×Ar*H*), 7.22 (2H, d, $^{3}J_{HH}$ 8.4 Hz; 2×Ar*H*), 7.18 (2H, d, $^{3}J_{HH}$ 8.4 Hz; 2×Ar*H*), 7.16 (2H, s; 2×C*H*), 2.94 – 2.82 (4H, m; 2×CH_2); ^{13}C NMR (75.5 MHz, d_6-DMSO): $^{\delta}$C 170.0 (*C*=O), 152.4 (*C*=O), 142.0 (Ar*C*), 141.3 (Ar*C*), 136.8 (Ar*C*), 135.5 (Ar*C*), 134.6 (Ar*C*H), 130.7 (q, $^{2}J_{CF}$ 32.7 Hz, Ar*C*), 129.3 (Ar*C*), 128.8 (Ar*C*H), 128.7 (Ar*C*H), 126.6 (*C*H), 123.3 (q, $^{1}J_{CF}$ 272.3 Hz, CF_3), 119.0 (Ar*C*H), 117.8 (m; Ar*C*H), 114.2 (m, Ar*C*H), 36.7 (*C*H_2), 36.3 (*C*H_2) ; ^{19}F NMR (376.5 MHz, d_6-DMSO) : $^{\delta}$F −62.2 (ArC*F*$_3$); MS (ES^-) *m/z* 546 ([M−H]$^-$, 100); HRMS (ES^-) *m/z* calculated for $C_{27}H_{18}N_3O_3F_6$ [M−H]$^-$ 546.1252, found 546.1257.

1-(4-(4-(2,5-dioxo-2H-pirol-1(5H)-yl)phenetyl)phenyl)-3-(3,5-dimethylphenyl)urea (M9)
M.p. = 229.3 –231.4 °C; ^{1}H NMR (400.1 MHz, $CDCl_3$): $^{\delta}$H 7.81 (1H, s; N*H*), 7.57 – 7.54 (2H, m; 2×Ar*H*), 7.46 (2H, s; 2×Ar*H*), 7.29 – 7.27 (2H, m; 2×Ar*H*), 7.25 – 7.22 (2H, m; 2×Ar*H*), 7.19 – 7.17 (3H, m; 3×Ar*H*), 6.84 (2H, s; 2×C*H*), 2.97 – 2.89 (4H, m; 2×CH_2),2.38 (6H, s; 2×CH_3); ^{13}C NMR (100.6 MHz, $CDCl_3$): $^{\delta}$C 169.8 (*C*=O), 166.1 (*C*=O), 141.8 (Ar*C*), 138.6 (Ar*C*), 137.7 (Ar*C*), 136.2 (Ar*C*), 135.2 (Ar*C*), 134.3 (*C*H), 133.5 (Ar*C*H), 129.4 (Ar*C*H), 129.2 (Ar*C*), 129.1 (Ar*C*H), 126.1 (Ar*C*H), 124.9 (Ar*C*H), 120.4 (Ar*C*H), 37.7 (*C*H_2), 37.3 (*C*H_2), 21.4 (*C*H_3); MS (ES^+) *m/z* 447 ([M+Na]$^+$, 75), 479 (100); HRMS (ES^+) *m/z* calculated for $C_{27}H_{24}N_2O_3Na$ [M+Na]$^+$ 447.1685, found 447.1674.

2-(4-(2,5-dioxo-2H-pirol-1(5H)-yl)phenyll) acetic acid (M10)
M.p. = 160.0 –162.0 °C; ^{1}H NMR (400.1 MHz, d_6-DMSO): $^{\delta}$H 12.07 (1H, s, CO_2*H*), 7.36 (2H, d, $^{3}J_{HH}$ = 8.5 Hz, 2×Ar*H*), 7.26 (2H, d, $^{3}J_{HH}$ = 8.5 Hz 2×Ar*H*), 7.18 (2H, s, 2×C*H*), 3.63 (2H, s, CH_2); ^{13}C NMR (100.6 MHz, d_6-DMSO): $^{\delta}$C 172.5 (CO_2H), 169.3 (*C*=O), 134.7 (Ar*C*-N), 134.6 (*C*H), 130.0 (Ar*C*), 129.9 (Ar*C*H), 126.6 (Ar*C*H),

40.1 (*C*H_2); MS (EI^+) *m/z* 254 ($[M+Na]^+$, 100); HRMS (EI^+) *m/z* calculated for $C_{12}H_9NO_4$ $[M+Na]^+$ 254.0429, found 254.0434.

3,5-dimethyl-N-(4-(2,5-dioxo-2H-pirol-1(5H)-yl)phenyl)benzamide (M11)
^{1}H NMR (300.1 MHz, $CDCl_3$): $^{\delta}$H = 7.86 (1H, s, NH), 7.79–7.74 (2H, m, ArH), 7.47 (2H, s, ArH), 7.37–7.32 (2H, m, ArH), 7.19 (1H, s, ArH), 6.85 (2H, s, ArH), 2.39 (6H, d, J = 0.5 Hz, CH_3); ^{13}C NMR (75.5 MHz, $CDCl_3$): $^{\delta}$C = 169.7 (*C*=O), 166.2 (*C*ONH), 138.8 (Ar*C*), 137.9 (Ar*C*), 134.8 (Ar*C*), 134.4 (Ar*C*H), 133.8 (Ar*C*H), 127.2 (Ar*C*), 126.9 (Ar*C*H), 124.9 (Ar*C*H), 120.6 (Ar*C*H), 21.4 (*C*H_3); MS (ES^+): m/z (%) = 321 ($[M+H]^+$, 100), 375 (70); HRMS (ES^+): m/z calc. for $[M+H]^+$ $C_{19}H_{17}N_2O_3$ 321.1239, found 321.1237.

The structure of the 11 maleimide compounds as shown in the following Table 2.

Table 2. Structure of eleven *N*-substituted maleimides

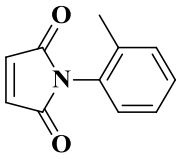
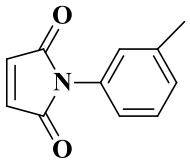
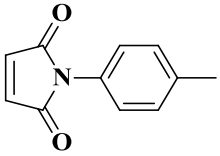
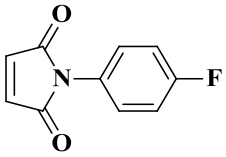
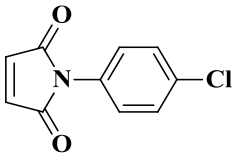
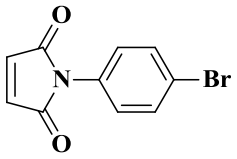
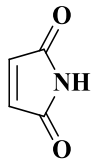
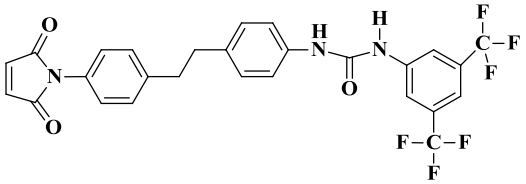
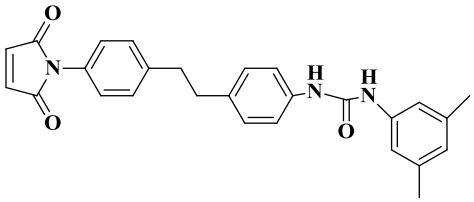
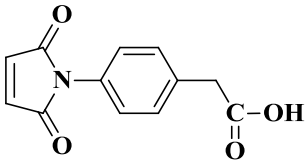
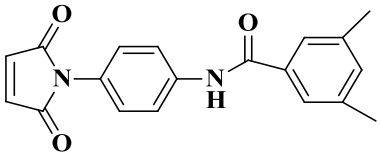
	Name of Compound	Structure	Yield (%)
M1	*N*-(2-methylphenyl)maleimide		35%
M2	*N*-(3- methylphenyl)maleimide		28%
M3	*N*-(4- methylphenyl)maleimide		84%
M4	*N*-(4-florophenyl)maleimide		40%
M5	*N*-(4-chlorophenyl)maleimide		45%
M6	*N*-(4-bromophenyl)maleimide		51%

Table 2 (cont'd). Structure of eleven *N*-substituted maleimides

	Name of Compound	Structure	Yield (%)
M7	Maleimide		*commercial available
M8	1-(3,5-bis(trifloromethyl)phenyl)-3-(4-(3-(2,5-dioxo-2H-pirol-1(5H)-yl)phenetyl)phenyl)urea		78%
M9	1-(4-(4-(2,5-dioxo-2H-pirol-1(5H) yl)phenetyl)phenyl)-3-(3,5-dimethylphenyl)urea		96%
M10	2-(4-(2,5-dioxo-2H-pirol-1(5H)-yl)phenyll) acetic acid		36%
M11	3,5-dimethyl-N-(4-(2,5-dioxo-2H-pirol-1(5H)-yl)phenyl)benzamide		66%

The *N*-substituted maleimides **M1** to **M11** were tested against two bacterial strains and a yeast. The biological screening activity of the studied compounds were determined by disc diffusion method. Data shown in Table 3 indicate that all compounds exhibited notable antibacterial and antifungal activity except **M8**, **M9** and **M11**.

According to Table 3, the reactivity of **M1**, **M2** and **M3** toward all three microbes tested were positive, showing inhibition zone ranging from 9 mm to 21 mm for sample concentration up to 20 µg/disc. Whereas, the inhibition zone for **M4**, **M5** and **M6** were around 10 mm, except for **M5** at 20 µg/disc showed 18 mm inhibition zone on the yeast, *Saccharomyces cerevisiae*. Surprisingly, **M4** which showed inhibition towards *Escherichia coli* at 10 µg/disc, became inactive when the concentration double up to 20 µg/disc. On the other hand, unsubstituted maleimide, **M7** is very reactive towards *Saccharomyces cerevisiae*. **M8** possess a trifluoromethane moiety which is often used to increase the biological stability of a drug. Nonetheless, our finding indicated that samples **M8** to **M11** are generally unreactive, except that **M10** showed a small inhibition zone of 9 mm towards *Saccharomyces cerevisiae*.

Generally, most of the samples were biologically active against the yeast *Saccharomyces cerevisiae* compared to *Escherichia coli* and *Bacillus subtilis*. It is also noted that the biological reactivity of the samples does not directly proportional to the dosage concentration. This might be due to the reason that maleimide compounds only show optimum biological reactivity at optimum dosage. Hence, any concentrations beyond the optimum range would have no effect against the microbes tested. Fascinatingly, maleimides substituted with methyl phenyl group are among the most reactive compounds tested. Their inhibition zone is comparable to that of the positive control.

Table 3. Biological activity of *N*-substituted maleimide towards three microbes

Compound	**Inhibition Zone (mm)**					
	Escherichia coli		***Bacillus subtilis***		***Saccharomyces cerevisiae***	
	10 µg/disc	**20 µg/disc**	**10 µg/disc**	**20 µg/disc**	**10 µg/disc**	**20 µg/disc**
M1	15	15	10	15	21	18
M2	11	13	11	12	15	19
M3	10	11	9	10	12	14
M4	10	-	10	11	10	10
M5	9	12	11	12	15	18
M6	8	10	10	10	12	10
M7	22	25	21	25	30	29
M8	-	-	-	-	-	-
M9	-	-	-	-	-	-
M10	-	-	-	-	-	9
M11	-	-	-	-	-	-
Negative control	-	-	-	-	-	-
Streptomycin 10 µg	16	NA	15	NA	NA	NA
Nystatin 20 µg	NA	NA	NA	NA	NA	-

Note: Experiments are done in triplicate to rule out experimental bias or random error.

In addition, unsubstituted maleimide was more reactive towards the microbes compared to the *N*-substituted maleimide since the maleimide core itself is the main active centre which possess good biological activites [15]. Thus, it is apparent that the introduction of bulky substituents at the *N* position of the maleimide ring had different influence on the biological activities. A possible explanation is that maleimide and derivatives could inactivate some enzymes in the microbes. With change in the polarity and chain length of *N*-phenyl substituents, their capacity to bind to eznyme differs and therefore also had different influence on biological activities.

Conclusion

In conclusion, the present work has demonstrated that unsubstituted maleimide was most reactive while simple *N*-phenyl substituted maleimide exhibit potential activity against the tested microbes. Nevertheless, bulky *N*-phenyl substituted maleimides were biologically inactive with rapid decreasing action towards the microbe when more complex moieties inserted. This might be explained by the nitrogen–carbon distances betweeen the two rings which play an important role in the antimicrobial activities of these compounds. Furthermore, steric hindrance might affect inhibition activity. For further investigation, more sensitive antimicrobe screening method such as dilution method should be used to evaluate the potential of maleimide derivatives against different types of microbes. Structural optimisation of these compounds are underway.

Acknowledgement

The authors would like to thank Universiti Kebangsaan Malaysia, for the research grant GUP-2014-016, DIP-2015-015 and facilities provided by PPSKTM and everyone who has helped in this research.

References

1. Beović, B. (2006). The issue of antimicrobial resistance in human medicine. *International Journal of Food Microbiology*, 112(3): 280 – 287.
2. Salewska, N., Boros-Majewska, J., Łcka, I., Chylińska, K., Sabisz, M., Milewski, S. and Milewska, M. J. (2012). Chemical reactivity and antimicrobial activity of n-substituted maleimides. *Journal of Enzyme Inhibition and Medicinal Chemistry*, 27(1): 117 – 124.
3. Prado, S. R. T., Cechinel-Filho, V., Campos-Buzzi, F., Corrêa, R., Cadena, S. M. C. S. and De Oliveira, M. B. M. (2004). Biological evaluation of some selected cyclic imides: mitochondrial effects and in vitro cytotoxicity. *Zeitschrift fur Naturforschung - Section C Journal of Biosciences*, 59(9-10): 663 –672.
4. Bansode, T. N., Shelke, J. V. and Dongre, V. G. (2009). Synthesis and antimicrobial activity of some new n-acyl substituted phenothiazines. *European Journal of Medicinal Chemistry*, 44(12): 5094 –5098.
5. Ye, Q., Cao, J., Zhou, X., Lv, D., He, Q., Yang, B. and Hu, Y. (2009). Synthesis and evaluation of novel 7-azaindazolyl-indolyl-maleimide derivatives as antitumor agents and protein kinase C inhibitors. *Bioorganic & Medicinal Chemistry*, 17(13): 4763 – 4772.
6. Mahle, F., Da Rosa Guimarães, T., Vergilina Meira, A., Corrêa, R., Bella Cruz, R. C., Bella Cruz, A., Nunes, R. J., Cechinel-Filho, V. and De Campos-Buzzi, F. (2010). Synthesis and biological evaluation of n-antipyrine-4-substituted amino-3-chloromaleimide derivatives. *European Journal of Medicinal Chemistry*, 45(11): 4761 – 4768.
7. Li, W., Fan, Y., Shen, Z., Chen, X. and Shen, Y. (2012). Antifungal activity of simple compounds with maleic anhydride or dimethylmaleimide structure against Botrytis Cinerea. *Journal of Pesticide Science*, 37(3): 247 – 251.
8. Sortino, M., Cechinel Filho, V., Corrêa, R. and Zacchino, S. (2008). N-Phenyl and N-Phenylalkyl-maleimides acting against candida spp.: time-to-kill, stability, interaction with maleamic acids. *Bioorganic and Medicinal Chemistry*, 16(1): 560 – 568.
9. Zentz, F., Valla, A., Le Guillou, R., Labia, R., Mathot, A. G. and Sirot, D. (2002). Synthesis and antimicrobial activities of n-substituted imides. *Farmaco*, 57(5): 421 – 426.
10. Sortino, M., Garibotto, F., Cechinel Filho, V., Gupta, M., Enriz, R. and Zacchino, S. (2011). Antifungal, cytotoxic and sar studies of a series of n-alkyl, n-aryl and n-alkylphenyl-1,4-pyrrolediones and related compounds. *Bioorganic & Medicinal Chemistry*, 19(9): 2823 – 2834.
11. Xu, H., Baidoo, K. E., Wong, K. J. and Brechbiel, M. W. (2008). A novel bifunctional maleimido chx-a″ chelator for conjugation to thiol-containing biomolecules. *Bioorganic and Medicinal Chemistry Letters*, 18(8): 2679 – 2683.
12. Hayworth, D. (2014). Sulfhydryl-reactive crosslinker chemistry. http://www.piercenet.com/method/ sulfhydryl-reactive-crosslinker-chemistry [4 April 2014].
13. Ye, X., Li, X., Yuan, L., Ge, L., Zhang, B. and Zhou, S. (2007). Interaction of houttuyfonate homologues with the cell membrane of gram-positive and gram-negative bacteria. *Colloids and Surfaces A: Physicochemical and Engineering Aspects*, 301(1–3): 412 – 418.
14. López, S. N., Castelli, M. V., De Campos, F., Corrêa, R., Cechinel Filho, V., Yunes, R. A., Zamora, M. A., Enriz, R. D., Ribas, J. C., Furlán, R. L. E. and Zacchino, S. A. (2005). In Vitro antifungal properties, structure-activity relationships and studies on the mode of action of n-phenyl, n-aryl, n-phenylalkyl maleimides and related compounds. *Arzneimittel-Forschung/Drug Research*, 55(2): 123 – 132.
15. Xiao-Long, C., Li-Jun,Z., Fu-Ge, L., Yong-Xian, F.,Wei-Ping, W., Bao-Ju, L. and Yin-Chu, S. (2015). Synthesis and antifungal evaluation of a series of maleimides, *Pest Management Science*; 71: 433 – 440.

Malaysian Journal of Analytical Sciences, Vol 20 No 4 (2016): 751 - 759
DOI: http://dx.doi.org/10.17576/mjas-2016-2004-07

MALAYSIAN JOURNAL OF ANALYTICAL SCIENCES
Published by The Malaysian Analytical Sciences Society
ISSN 1394 - 2506

IDENTIFICATION OF VOLATILE SECONDARY METABOLITES FROM AN ENDOPHYTIC MICROFUNGUS *Aspergillus nomius* KUB105

(Pengenalpastian Metabolit Sekunder Meruap daripada Kulat Mikro Endofitik *Aspergillus nomius* KUB105)

Lateef Adebola Azeez[1,2]*, Sepiah Muid[1], Bolhassan Mohamad Hasnul[1]

[1]*Department of Plant Science and Environmental Ecology, Faculty of Resource Science and Technology, Universiti Malaysia Sarawak, 94300 Kota Samarahan, Sarawak, Malaysia*
[2]*Department of Plant Biology, Faculty of Life Science, University of Ilorin, Nigeria*

**Corresponding author: lateef.aa@unilorin.edu.ng*

Received: 12 August 2015; Accepted: 9 May 2016

Abstract

Microfungi are a highly diverse group of micro-organisms and important components of the ecosystem with great potential for diverse metabolite production. During a survey of microfungi on leaves in a National Park in Sarawak, an uncommon endophytic microfungus *Aspergillus nomius* was encountered. The metabolite production of this microfungus was investigated by growing it in a liquid basal medium for 2 weeks. Gas Chromatography - Mass Spectrometry (GC-MS) and Fourier Transform Infrared (FTIR) profiling of the secondary metabolites produced by this microfungus in the liquid medium revealed the presence of 46 different secondary metabolites. The metabolites include saturated hydrocarbons, alkyl halides, alcohols and an unsaturated hydrocarbon. Majority of the metabolites produced were saturated hydrocarbons. Tetracosane, Icosane and 10-Methylicosane were the most abundant metabolites identified while heptadecane and 2,4-dimethylundecane were the least abundant respectively. This study is the first GC-MS and FTIR report of secondary metabolites from *A. nomius*. The results from this study confirm the ability of microfungi to produce diverse metabolites, including saturated hydrocarbons.

Keywords: *Aspergillus nomius*, endophytic fungi, gas chromatography, hydrocarbons, secondary metabolites

Abstrak

Kulat mikro adalah kumpulan yang pelbagai daripada organisma kecil dan merupakan komponen penting dalam ekosistem dengan potensi besar dalam penghasilan pelbagai metabolit. Kulat mikro endofitik yang jarang dijumpai, iaitu *Aspergillus nomius* telah ditemui semasa kaji selidik kulat mikro atas daun yang dijalankan di Taman Negara, Sarawak. Penghasilan metabolit oleh kulat mikro ini telah dikaji dengan menumbuhkankannya dalam medium cecair asas selama dua minggu. Penghasilan sebanyak 46 metabolit sekunder oleh kulat mikro ini telah disahkan melalui penggunaan Kromatografi Gas – Spektrometri Jisim (GC-MS) dan profil (FTIR). Metabolit yang terhasil termasuklah hidrokarbon tepu, alkil halida, alkohol dan hidrokarbon tidak tepu. Kebanyakan metabolit yang dihasilkan adalah hidrokarbon tepu. Tetrakosana, Ikosana dan 10 Metilikosana adalah metabolit yang paling banyak dikenal pasti manakala heptadekana dan 2,4-dimetilundekana adalah yang paling sedikit. Kajian ini merupakan kajian pertama penghasilan metabolit sekunder dari *A. nomius* melalui penggunaan GC-MS dan FTIR. Hasil kajian ini mengesahkan kebolehan kulat mikro untuk menghasilkan pelbagai metabolit termasuklah hidrokarbon tepu.

Kata kunci: *Aspergillus nomius*, kulat endofitik , kromatografi gas, hidrokarbon, metabolit sekunder

Introduction

Fungal secondary metabolites are important natural products from fungi. There are many undiscovered volatile organic compounds produced by fungi. The high diversity of fungi with many species yet to be discovered, coupled with the relatively insufficient research on fungal metabolites puts fungi as a promising source of useful compounds for biotechnological, pharmacological, medicinal, agricultural and industrial applications. There are over 5.1 million fungal species in the world as estimated by Blackwell [1] and only few have been studied for their secondary metabolites production [2, 3].

Fungal secondary metabolites are organic compounds that are not involved in the normal growth and development of the fungi [4]. Unlike the primary metabolites, secondary metabolites does not play a key role in the survival of an organism and are frequently produced in high amounts during an organism's transition from active phase of growth to stationary phase [5]. These metabolites are involved in different biological processes in their host such as defence against predators; diseases; parasites; bio-control of pathogens and for communication between micro-organisms and their environment [6, 7]. Fungal metabolites have been useful as anti-cancer drugs, anti-oxidants, anti-viral, immunosuppressive and immunomodulatory compounds [8–11].

Recently, Strobel et al. [12] discovered the production of biodiesel by the microfungus *Gliocladium roseum*. They discovered that *G. roseum* produced an array of chemical compounds which include saturated hydrocarbons such as undecane, alcohols such as 2-Octanol and other compounds classified as esters and acids. In addition, about 270 secondary metabolites were identified from the liquid culture of *Trichoderma harzianum* with some compounds identified for the first time from *T. harzianum* [13]. Considering the high diversity of fungi [1], many species are yet to be studied for their secondary metabolites as compared to the few published reports [3,2].

This study was aimed to identify the volatile secondary metabolites produced in liquid culture of an endophytic microfungus, *Aspergillus nomius* KUB105, isolated during a microfungal survey using Gas Chromatography-Mass Spectrometry (GC-MS) and Fourier Transform Infrared (FTIR).

Materials and Methods

Isolation and identification of the Microfungus

A. nomius KUB105 fungus was isolated during a survey of microfungi on leaves of Belian tree (*Eusideroxylon zwageri*) collected from Kubah National Park, Sarawak, Malaysia. The leaf samples collected were processed for endophytic microfungal isolation [14], plated on 3 % Malt Extract Agar (MEA) and incubated at room temperature. *A. nomius* was then isolated and identified from segments of the leaf samples after seven days. This microfungus was identified based on its microscopic and cultural morphological characteristics in addition to molecular identification to confirm the identity of the microfungus.

Molecular identification of *A. nomius* KUB105: Total genomic DNA extraction

Isolates of *A. nomius* KUB105 was grown on Potato Dextrose Agar (PDA) and incubated at room temperature (27 ± 2 ℃) for three days before harvesting for DNA extraction. Mycelia of the isolates (about 500 – 700 mg) were scraped from the surface of the culture media using sterilized razor blades into a 2 mL eppendorf tube. The total genomic DNA was extracted using the CTAB method [15].

The extracted DNA was verified for successful extraction by gel electrophoresis and if successful, the sample is used immediately for Polymerase Chain Reaction (PCR) or stored at 4 °C for further use. The internal transcribed spacer (ITS) gene regions of the total genomic DNA were amplified by PCR using the primer pairs ITS 5 (5′-GGAAGTAAAAGTCGTAACAAGG-3′) and ITS 4 (5′-TCCTCCGCTTATTGATATGC-3′) [16] in a SensQuest lab cycler. A PCR mixture of 25 µL total volume was used. The master mix contains 5 µL of 5 × Mg free-PCR buffer, 2 µL of $MgCl_2$, 0.5 µL of dNTPs, 1.5 µL of each primers, 0.15 µL of Fementas Taq DNA polymerase and 12.85 µL of double-sterilised distilled water (ddH_2O) and 1.5 µL of DNA template including a tube for control reaction with ddH_2O as template instead of DNA. The PCR programme was set at initial denaturation of 2 min at 94 °C, followed by 35 cycles of 94 °C for 1 min, 55 °C for 1 min, 72 °C for 1 min and final extension of 72 °C for 10 min. The PCR products were gel electrophoresed as described for genomic DNA detection above using 2 µL of

PCR products and 2 µL of DNA marker. Successful PCR products were sent to a private sequencing company (1st-Base, Asia) for both forward and reverse primer sanger sequencing.

The sequences obtained from the sequencing company were confirmed to belong to the proposed microfungi using BLAST-n on the GenBank website [17]. SeqTrace version 0.9.0 software [18] was used to obtain a consensus sequence from the forward and reverse sequences. The sequence obtained was submitted to the GenBank to obtain an accession number. Similar reference sequences were downloaded from GenBank for phylogenetic analysis following a similarity search. Sequences were aligned using T-coffee alignment software [19] and manually adjusted using AliView Version 1.17-beta1 [20] where necessary. Phylogenetic analysis was done using MEGA 5.0 [21].

Cultivation of *A. nomius* KUB 105 for metabolite production

A. nomius KUB105 was initially grown on solidified 3 % MEA at 27 ± 2 °C for 3 days to produce mycelial inoculum for the liquid culture. A liquid basal medium was used for the growth of this microfungus for secondary metabolites extraction using the method proposed by McMullin et al. [22]. The basal medium contained, per litre: 10.00 g glucose, 2.00 g peptone, 0.30 g KH_2PO_4, 0.30 g $MgSO_4$, 0.20 g $CaCl_2$, 0.20 mg $FeSO_4$, 0.10 mg $CuSO_4$, 0.5 mg pyridoxine, 0.5 mg niacin and 0.3 mg $ZnSO_4$. All chemicals were of analytical grade. An amount of 30 mL of the basal medium was poured in 100 mL conical flask and autoclaved for 15 min at 121 °C. After cooling, agar plugs of *A. nomius* were aseptically cut with a 5 mm cork borer into the autoclaved basal medium, sealed with aluminium foil and incubated in a stationary condition for 2 weeks at 27 ± 2 °C with alternating 12 hours darkness and light. Three replicates were prepared.

Extraction and identification of secondary metabolites

After 2 weeks of growth, the liquid culture was filtered using Whatmanns No. 1 filter paper (90 mm diameter) to separate the mycelium from the filtrate. The cell free crude filtrate was then extracted by liquid-liquid extraction method. 30 mL of ethyl acetate was added to the culture filtrate, mixed together and the extraction process was left overnight to ensure maximum extraction. 15 mL of hexane was then added to the ethyl acetate extract. This is to allow the metabolites to be extracted into hexane, since the hexane extract will be injected into the GC-MS. The solvents were then cleaned up using a silica-gel column chromatography. The remaining solvent (hexane) was then carefully evaporated at 40 °C until only 2 mL of the solvent remained. 2 mL of the hexane extract was then used for Gas Chromatography-Mass Spectrometry (GC-MS) analysis. The basal medium hexane extract without the microfungus was also processed to serve as a control.

The secondary metabolites from the hexane extract were identified by a GC-MS (Shimadzu, Japan) equipped with a (QP2010 plus) mass selective detector. The ionization energy used was 70 eV. Preliminary identification was done with a non-polar capillary column (BP5) 30 m × 0.25 mm × 0.25 mm. The oven program had an initial temperature of 50 °C for 5 min, then a 10 °C/min run to 260 °C with a final hold at 260 °C for 10 min. The injector temperature was kept at 280 °C (splitless) and detector temperature was at 280 °C. The carrier gas was purified Helium (99.99 %) at a linear flow rate of 1 mL/min. The MS detector was operated at 280 °C and the scan range was from 40 to 500 m/z.

All detected compounds were putatively identified by mass spectral database search of the National Institute of Standards and Technology (NIST) followed by matching of the mass spectral data. Fourier Transform Infrared Spectroscopy (FTIR) analysis was also done to show the different functional groups present in our sample using a Thermo scientific Nicolet iS50 FTIR machine. Spectral shifts obtained were interpreted with reference to shifts in the peaks of the various functional groups.

Results and Discussion

Identification of the microfungus

The cultural characteristics of the isolates used in this study were similar to those of microfungi in the *Aspergillus flavus* section which includes *A. flavus*, *A. parasiticus* and *A. nomius*. The colony observe colour was green (which indicates the matured spores) with white colour at the margins (the young spores), the reverse side was creamish to light cream-brown (Figure 1). The mycelia reached about 8 cm diameter in seven days and is aerial. The mycelium

is septate with a globus terminal head conidiophore having spores arranged radially in chains and the spore surface is rough. However, in this study, *A. nomius* is different from other members of the *A. flavus* section by having a uniseriate conidial head and a rough conidia (as seen by Scanning electron microscopy, result not shown in this paper) and by its molecular identification (Figure 2) with accession number KR737578.

A. nomius also have an indeterminate sclerotia and a lower optimum temperature for growth as compared to the other species in the *A. flavus* section [23].

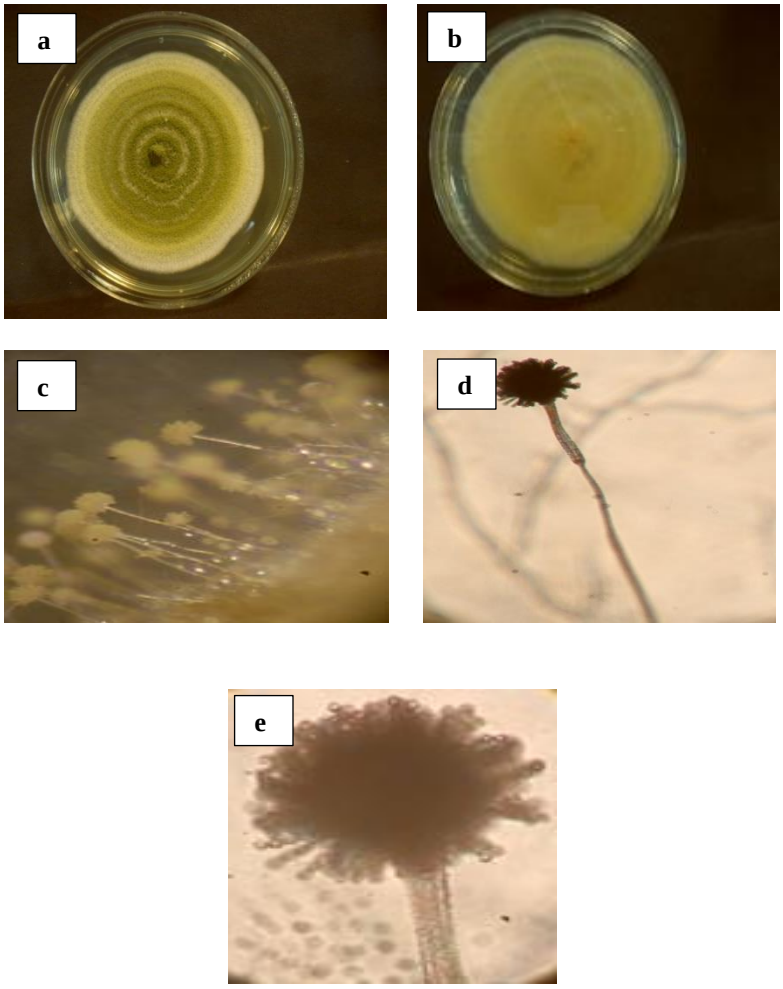


Figure 1. *Aspergillus nomius*: (a) cultural morphology, observe surface; (b) reverse surface; (c) conidiophores with conidial head on PDA; (d-e) conidial heads

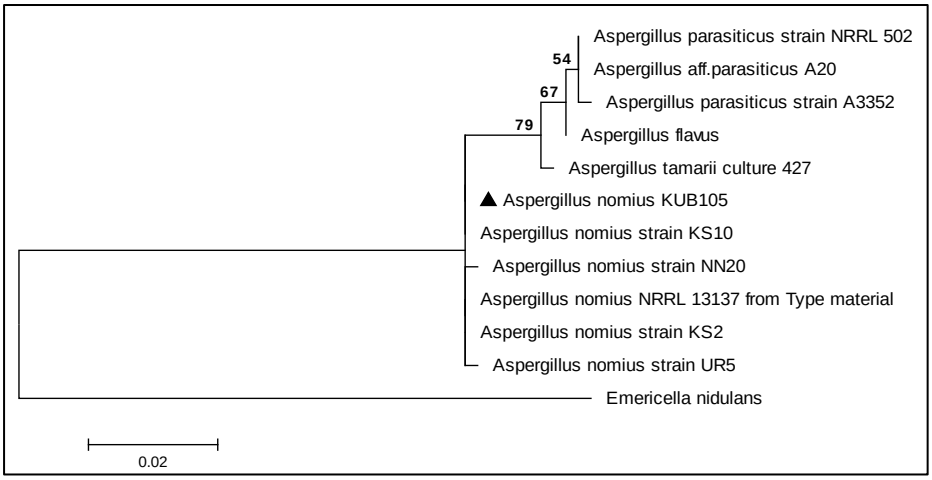


Figure 2. Molecular phylogenetic analysis by Maximum Likelihood method for identification of *A. nomius* KUB105 (KR737578) performed using MEGA5.1

Identification of metabolites from culture filtrate of *A. nomius* KUB105

After subtraction of the compounds in the control, GC-MS chromatograms of hexane extract of *A. nomius* (Figure 3) revealed 46 metabolites identified with reference to NIST mass spectral database which corresponds to each compound's identity. The identified metabolites include 43 saturated hydrocarbons, one alcohol, one ester & one chloro-hydrocarbon (alkyl halide) compounds. Tetracosane was the most abundant compound produced by *A. nomius* KUB105 with the highest peak area, while normal heptadecane and 2,4-Dimethylundecane were the least abundant (Table 1).

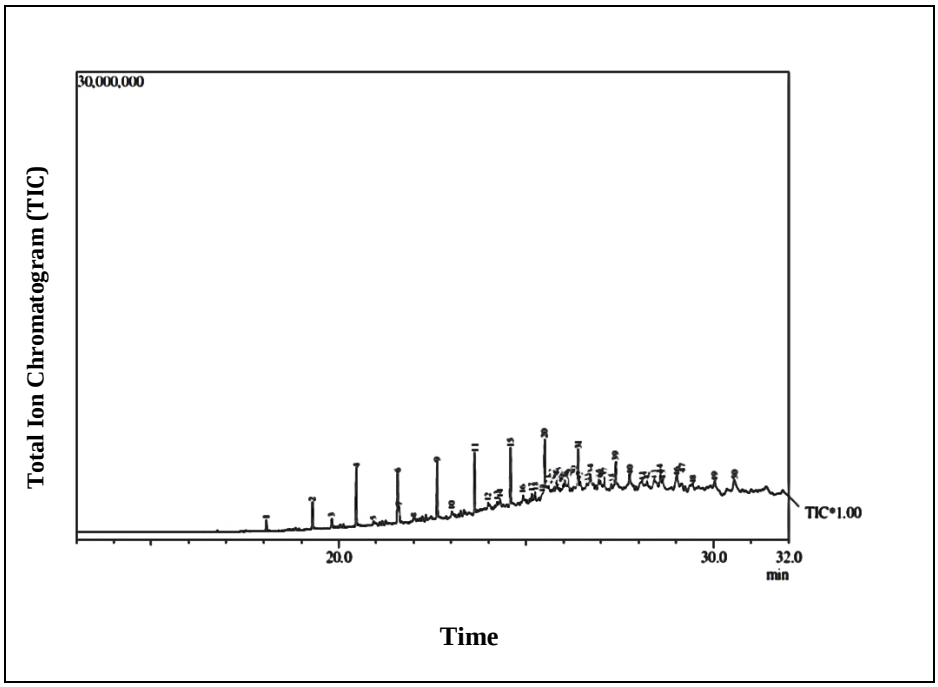


Figure 3. GC-MS chromatogram of secondary metabolites from culture of *A. nomius* KUB105

Table 1. List of various secondary metabolites identified from culture of *A. nomius* by GC-MS

Number	Family	Metabolite Name	Structure/ Formula	Retention Time (min)	Abundance (%)
1	Alkane	n-Pentadecane	$C_{15}H_{32}$	18.07	0.78
2		n-Hexadecane	$C_{16}H_{34}$	19.30	1.95
3		2,6,10-Trimethylpentadecane	$C_{18}H_{38}$	19.82	1.03
4		2,6-Dimethylheptadecane	$C_{19}H_{40}$	20.45	4.52
5		n-Nonadecane	$C_{19}H_{40}$	20.93	0.99
6		Octadecan	$C_{18}H_{38}$	21.57	4.13
7		Pristane	$C_{19}H_{40}$	21.61	1.18
8		Henicosane	$C_{21}H_{44}$	22.62	4.13
9		6-Propyltridecane	$C_{16}H_{34}$	23.01	0.83
10		Icosane	$C_{20}H_{42}$	23.63	4.71
11		Normal-heptadecane	$C_{17}H_{36}$	23.99	0.68
12		2-Methylicosane	$C_{21}H_{44}$	24.23	0.75
13		3-Methylicosane	$C_{21}H_{44}$	24.31	1.45
14		10-Methylicosane	$C_{21}H_{44}$	24.58	4.62
15	Alkane	n-Octacosane	$C_{28}H_{58}$	24.92	1.33
16		2-Methylnonadecane	$C_{20}H_{42}$	25.15	1
17		3-Methyltetradecane	$C_{15}H_{32}$	25.24	1.32
18		Pentadecylcyclohexane	$C_{21}H_{42}$	25.43	1.2
19		n-Tetracosane	$C_{24}H_{50}$	25.49	5.76
20	Ester	n-Heptadecyl acetate	$C_{19}H_{38}O_2$	25.61	3.8
21	Alkene	Neodene	$C_{20}H_{40}$	25.69	1.06
22	Alkane	2,6,10,15-Tetramethylheptadecane	$C_{21}H_{44}$	25.74	1.69
23		9-Methylnonadecane	$C_{20}H_{42}$	25.81	2.69
24		2,5-Dimethyltridecane	$C_{15}H_{32}$	25.88	0.76
25		2,4-Dimethylundecane	$C_{13}H_{28}$	25.92	0.68
26		4-Methyltetradecane	$C_{15}H_{32}$	25.99	1.55
27		7-Hexylicosane	$C_{26}H_{54}$	26.04	1.84
28		11-Decyltetracosane	$C_{34}H_{70}$	26.13	2.38
29		1-Cyclopentyldecane	$C_{15}H_{30}$	26.26	1.26
30		2,6,10,14-Tetramethylhexadecane	$C_{20}H_{42}$	26.44	1.17
31		8-Hexylpentadecane	$C_{21}H_{44}$	26.71	2.73
32		11-(1-Ethylpropyl)	$C_{26}H_{54}$	26.93	1.3
33		2-Methyloctadecane	$C_{19}H_{40}$	26.99	1.22
34		7-Hexyldocosane	$C_{28}H_{58}$	27.09	1.78
35	Alcohol	2-Hexyl-1-decanol	$C_{16}H_{34}O$	27.27	0.82
36	Alkane	n-Heptacosane	$C_{27}H_{56}$	27.39	2.87
37		n-Tetratetracontane	$C_{44}H_{90}$	27.76	2.21

Table 1 (cont'd). List of various secondary metabolites identified from culture of *A. nomius* by GC-MS

Number	Family	Metabolite Name	Structure/ Formula	Retention Time (min)	Abundance (%)
38		9-Octyldocosane	$C_{30}H_{62}$	28.09	2.05
39		3-Methylheptadecane	$C_{18}H_{38}$	28.23	1.08
40		n-Tetratriacontane	$C_{34}H_{70}$	28.41	2.52
41		(1-Propyldecyl)cyclohexane	$C_{19}H_{38}$	28.64	1.14
42	Alkyl halide	1-Chloroheptacosane	$C_{27}H_{55}Cl$	29.01	3.53
43	Alkane	Untriacontane	$C_{31}H_{64}$	29.17	1.47
44	Alkyl halide	1-Chloroicosane	$C_{20}H_{41}Cl$	29.44	2.23
45	Alkane	11-Butyldocosane	$C_{26}H_{54}$	30.02	1.18
46		11,20-Didecyltriacontane	$C_{50}H_{102}$	30.55	2.85

Most of these hydrocarbons have also been reported by [24–26], and [27] from culture extracts of *Aspergillus flavus*, *A. niger*; *A. ochraceus*, *A. niger* and *A. carbonarius* respectively. However, these metabolites are reported for the first time from culture extracts of *A. nomius* using GC-MS.

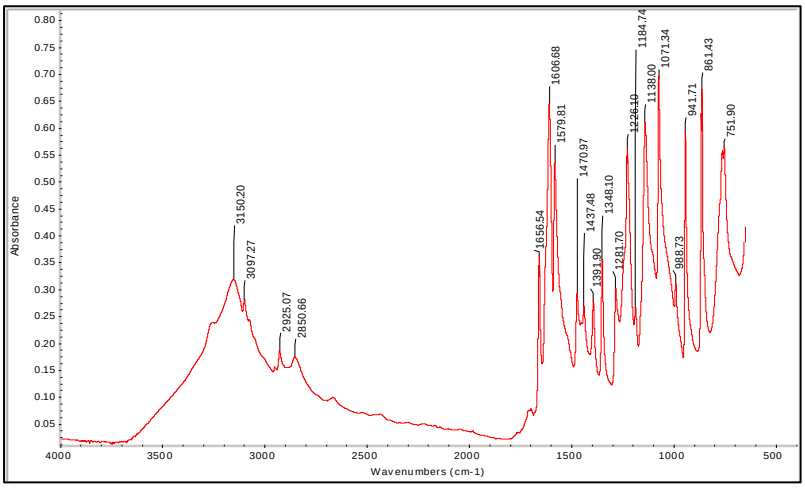


Figure. 4. The FTIR spectrum of the crude extract from liquid culture of *A. nomius* with bands extending from 550 – 4000 cm^{-1}.

The analysis of the FTIR spectrum indicates the presence of hydrocarbons and alcohol in the extract. The peak obtained at 751.90 cm^{-1} (Figure. 4) shows the presence of a C-Cl functional group which can be attributed to 1-Chloroicosane identified by the GC-MS analysis (see Table 1). The numerous peaks obtained between 861.43 to 1656.54 cm^{-1} shows the abundance of C-H functional groups which can be attributed to the saturated hydrocarbon (alkane) compounds [28] produced by the microfungus. Peaks at 2850.66 to 3150.20 cm^{-1} indicates the presence of O-H functional groups matching with 2-Hexyl-1-decanol and n-Heptadecyl acetate identified by the GC-MS. The spectrum from the FTIR further corroborates the spectral identifications obtained by GC-MS analysis.

Saturated hydrocarbons are the main ingredients of diesel fuel [12] and the identification of these compounds from culture filtrate of *A. nomius* and other microfungi indicates a close involvement of microfungi in the formation of these compounds through decomposition of certain organic and inorganic matter. Industrial application of the processes involved in the production of these hydrocarbon secondary metabolites coupled with the high diversity and easy growth potentials of microfungi can be a promising option to finding more sources of renewable energy production.

Conclusion

Our results have shown that saturated hydrocarbons are the major metabolites produced by *A. nomius* KUB105 grown for 2 weeks on a liquid basal medium (as described) at 27 ±2 ^{o}C. The findings in this study further support the claim by other researchers about microfungal hydrocarbon-metabolite production. Also, this study has been able to make the first report of the secondary metabolites produced by *A. nomius* KUB105 identified by GC-MS and FTIR analysis. Further study on the large scale production and purification of these secondary metabolites are necessary to fully utilize these compounds.

Acknowledgement

The First author thanks Universiti Malaysia Sarawak for the scholarship awarded. The authors are also grateful to Sarawak Forestry Corporation and the Sarawak Government.

References

1. Blackwell, M. (2011). The fungi: 1, 2, 3 ... 5.1 million species? *American Journal of Botany*, 98 (3): 426 – 438.
2. Strobel, G. A. and Daisy, B. (2003). Bioprospecting for microbial endophytes and their natural products. *Microbiology and Molecular Biology Reviews*, 67 (4): 491 – 502.
3. Strobel, G. A. (2014). The use of endophytic fungi for the conversion of agricultural wastes to hydrocarbons. *Biofuels*, 5(4): 447 - 455.
4. Tamano, K. (2014). Enhancing microbial metabolite and enzyme production: current strategies and challenges. *Frontiers in Microbiology*, 5: 718 - 723.
5. Agostini-Costa, T. da S., Silveira, D., Bizzo, H. R., Gimenes, M. A., and Vieira, R. F. (2012). *Secondary Metabolites*. INTECH Open Access Publisher.
6. Netzker, T., Fischer, J., Weber, J., Mattern, D. J., König, C. C., Valiante, V.,Schroeckh, V. and Brakhage, A. A. (2015). Microbial communication leading to the activation of silent fungal secondary metabolite gene clusters. *Frontiers in Microbiology*, 6: 299 – 302.
7. Vinale, F., Sivasithamparam, K., Ghisalberti, E. L., Marra, R., Barbetti, M. J., Li, H., Woo, S. L. and Lorito, M. (2008). A novel role for *Trichoderma* secondary metabolites in the interactions with plants. *Physiological and Molecular Plant Pathology*, 72 (1–3): 80 – 86.
8. Pandi, M., Rajapriya, P. and Manoharan, P. T. (2013). Extraction and characterization of taxol: an anticancer drug from an endophytic and pathogenic fungi. *Laboratory Protocols in Fungal Biology*, 523 –527.
9. Li, S. Y., Shi, L. J., Ding, Y., Nie, Y. and Tang, X. M. (2015). Identification and functional characterization of a novel fungal immunomodulatory protein from *Postia placenta*. *Food and Chemical Toxicology: An International Journal Published for the British Industrial Biological Research Association*, 78: 64 – 70.
10. Marson Ascêncio, P. G., Ascêncio, S. D., Aguiar, A. A., Fiorini, A. and Pimenta, R. S. (2014). Chemical Assessment and Antimicrobial and Antioxidant Activities of Endophytic Fungi Extracts Isolated from *Costus spiralis* (Jacq.) Roscoe (Costaceae). *Evidence-Based Complementary and Alternative Medicine*, 2014: 1 – 10.
11. Mizerska-Dudka, M., Jaszek, M., Błachowicz, A., Rejczak, T. P., Matuszewska, A., Osińska-Jaroszuk, M., Stefaniuk, D., Janusz, G., Sulej, J. and Kandefer-Szerszeń, M. (2015). Fungus *Cerrena unicolor* as an effective source of new antiviral, immunomodulatory, and anticancer compounds. *International Journal of Biological Macromolecules*, 79: 459 – 468.
12. Strobel, G. A., Knighton, B., Kluck, K., Ren, Y., Livinghouse, T., Griffin, M., Spakowicz, D. and Sears, J. (2008). The production of myco-diesel hydrocarbons and their derivatives by the endophytic fungus *Gliocladium roseum* (NRRL 50072). *Microbiology*, 154 (11): 3319 – 3328.
13. Siddiquee, S., Cheong, B. E., Taslima, K., Kausar, H., and Hasan, M. M. (2012). Separation and identification of volatile compounds from liquid cultures of *Trichoderma harzianum* by GC-MS using three different capillary columns. *Journal of Chromatographic Science*, 50 (4): 358 – 367.

14. Rakotoniriana, E. F., Munaut, F., Decock, C., Randriamampionona, D., Andriambololoniaina, M., Rakotomalala, T., Rakotonirina, E. J., Rabemanantsoa, C., Cheuk, K. S., Ratsimamanga, U., Mahillon, J., El-Jaziri, M., Quetin-Leclercq, J. and Corbisier, A. M. (2008). Endophytic fungi from leaves of *Centella asiatica*: occurrence and potential interactions within leaves. *Antonie van Leeuwenhoek*, 93 (1–2): 27 – 36.
15. Murray, M. G., and Thompson, W. F. (1980). Rapid isolation of high molecular weight plant DNA. *Nucleic Acids Research*, 8 (19): 4321 – 4325.
16. White, T. J., Bruns, T., Lee, S., and Taylor, J. (1990). Amplification and direct sequencing of fungal ribosomal RNA genes for phylogenetics in PCR protocols: A guide to methods and applications. *Academic Press, New York, USA.*, 315 – 322.
17. National Center for Biotechnology Information (NCBI). (2015). BLAST: Basic Local Alignment Search Tool. Access online http://blast.ncbi.nlm.nih.gov/Blast.cgi [Retrieved May 7, 2016]
18. Stucky, B. J. (2012). SeqTrace: A graphical tool for rapidly processing DNA sequencing chromatograms. *Journal of Biomolecular Techniques*, 23 (3): 90 – 93.
19. Di Tommaso, P., Moretti, S., Xenarios, I., Orobitg, M., Montanyola, A., Chang, J.-M.,Taly, J-F, Notredame, C. (2011). T-Coffee: a web server for the multiple sequence alignment of protein and RNA sequences using structural information and homology extension. *Nucleic Acids Research*, 39 (Web Server issue), W13-17.
20. Larsson, A. (2014). AliView: a fast and lightweight alignment viewer and editor for large datasets. *Bioinformatics (Oxford, England)*, 30 (22): 3276 – 3278.
21. Tamura, K., Peterson, D., Peterson, N., Stecher, G., Nei, M., and Kumar, S. (2011). MEGA5: Molecular evolutionary genetics analysis using maximum likelihood, evolutionary distance, and maximum parsimony methods. *Molecular Biology and Evolution*, 28 (10): 2731 – 2739.
22. McMullin, D. R., Nsiama, T. K., and Miller, J. D. (2014). Secondary metabolites from *Penicillium corylophilum* isolated from damp buildings. *Mycologia*, 106 (4): 621 – 628.
23. Kurtzman, C. P., Horn, B. W., & Hesseltine, C. W. (1987). *Aspergillus nomius*, a new aflatoxin-producing species related to *Aspergillus flavus* and *Aspergillus tamarii*. *Antonie van Leeuwenhoek*, 53 (3): 147 – 158.
24. De Lucca, A. J., Boue, S. M., Carter-Wientjes, C. and Bhatnagar, D. (2012). Volatile profiles and aflatoxin production by toxigenic and non-toxigenic isolates of *Aspergillus flavus* grown on sterile and non-sterile cracked corn. *Annals of Agricultural and Environmental Medicine*, 19 (1): 91 – 98.
25. Fiedler, K., Schutz, E., and Geh, S. (2001). Detection of microbial volatile organic compounds (MVOCs) produced by moulds on various materials. *International Journal of Hygiene and Environmental Health*, 204: 111 – 121.
26. Siddiquee, S., Azad, S. A., Abu Bakar, F., Naher, L. and Vijay Kumar, S. (2012). Separation and identification of hydrocarbons and other volatile compounds from cultures of *Aspergillus niger* by GC–MS using two different capillary columns and solvents. *Journal of Saudi Chemical Society*, 19 (3): 243 – 256.
27. Sinha, M., Sørensen, A., Ahamed, A. and Ahring, B. K. (2015). Production of hydrocarbons by *Aspergillus carbonarius* ITEM 5010. *Fungal Biology*, 119 (4): 274 – 282.
28. Devi, N. N. and Prabakaran, J. J. (2014). Bioactive metabolites from an endophytic fungus *Penicillium* sp. isolated from *Centella asiatica*. *Current Research in Environmental & Applied Mycology*, 4 (1): 34 – 43.

Malaysian Journal of Analytical Sciences, Vol 20 No 4 (2016): 760 - 769
DOI: http://dx.doi.org/10.17576/mjas-2016-2004-08

MALAYSIAN JOURNAL OF ANALYTICAL SCIENCES
Published by The Malaysian Analytical Sciences Society
ISSN 1394 - 2506

SYNTHESIS, CHARACTERIZATION AND DNA BINDING ACTIVITY OF A POTENTIAL DNA INTERCALATOR

(Sintesis dan Pengikatan DNA oleh Sebatian Interkalasi DNA Yang Berpotensi)

Siti Norain Harun, Yaakob Razak, Haslina Ahmad*

Faculty of Science,
Universiti Putra Malaysia, 43400 UPM Serdang, Selangor, Malaysia

**Corresponding author: haslina_ahmad@upm.edu.my*

Received: 17 August 2015; Accepted: 23 May 2016

Abstract

A novel complex, $[Ru(dppz)_2(p\text{-MOPIP})]^{2+}$ (dppz = dipyrido-[3,2-a:20,30-c]phenazine, *p*-MOPIP = 2-(4-methoxyphenyl) imidazo[4,5-f][1,10]phenanthroline) has been synthesized and characterized by elemental analysis, ^{1}H Nuclear Magnetic Resonance spectroscopy, mass spectrometry, Fourier Transform Infrared analysis, Ultra Violet visible and fluorescence spectroscopy. Herein, the complex was designed by adding *p*-MOPIP as an intercalating ligand and dppz as the ancillary ligand. The DNA binding properties of the complex with Calf Thymus DNA (CT-DNA) were investigated using spectroscopic methods. The UV-visible absorption band observed at 460 nm corresponded to the metal-to-ligand charge transfer (MLCT) while bands at 358 and 281 nm corresponded to intra-ligand (IL) π-π* transitions of the ligand scaffold in *p*-MOPIP and dppz. The intrinsic binding constant, K_b for this complex was 1.67 x 10^6 M^{-1} and this suggested that this complex, $[Ru(dppz)_2(p\text{-MOPIP})]^{2+}$ bound to DNA *via* the intercalative mode. Interestingly, the interaction of this complex with CT-DNA also had a 'molecular light switch' effect.

Keywords: ruthenium, DNA binding, molecular light switch

Abstrak

Satu kompleks baru, $[Ru(dppz)_2(p\text{-MOPIP})]^{2+}$ (dppz = dipyrido-[3,2-a:20,30-c]fenazin, *p*-MOPIP = 2-(4-metoksifenil) imidazo[4,5-f][1,10]fenantrolina) telah dihasilkan dan dianalisis dengan menggunakan analisis elemen, spektroskopi resonans magnet nukleus (^{1}H NMR), spektrometri jisim, analisis inframerah tranformasi Fourier (FTIR), spektroskopi ultra-lembayung dan pendafluor. Penyediaan kompleks telah dilakukan dengan menambah *p*-MOPIP sebagai ligan interkalasi dan dppz sebagai ligan sisi. Ciri-ciri ikatan DNA bagi kompleks ini dengan *Calf Thymus* DNA (CT-DNA) telah dianalisis dengan menggunakan kaedah spektroskopik. Jalur pada 460 nm merujuk kepada caj metal-kepada-ligan (*MLCT*), manakala jalur pada 358 dan 281 nm dikaitkan dengan peralihan π-π* intra-ligan (IL) bagi ligan *p*-MOPIP dan dppz. Nilai pemalar ikatan, K_b ialah 1.67 x 10^6 M^{-1} dan keputusan eksperimen mencadangkan pengikatan berlaku melalui mod interkalasi. Menariknya, kompleks ini juga menunjukkan kesan 'suis cahaya molekul'.

Kata kunci: ruthenium, pengikatan DNA, suis cahaya molekul

Introduction

Ruthenium, as other transition metals, generally have the electronic configuration where the 4d sub-shells are partially filled [1], allowing it to form different sorts of complexes that are suitable for various applications including as anticancer drugs, biosensors, in catalysis and others. Ruthenium complexes have properties that make them active biologically [2]. One of the properties is ligand exchange, where ruthenium(II) and ruthenium(III)

complexes having similar exchange kinetics to those of platinum(II) complexes [3], thus, are able to display similar biological effects as platinum(II) drugs. Additionally, ruthenium has a wide range of accessible oxidation states [4], for instance, ruthenium(II), ruthenium(III) or ruthenium(IV). The reduction and oxidation (redox) potential of metal complexes can be modified and exploited by varying the ligands to improve the effectiveness of ruthenium based drugs in the pharmaceutical industry [5]. Ruthenium(II) complexes with d^6 configuration are predominantly are octahedral and diamagnetic [6]. Recently, researchers have been more focused on the ruthenium(II) polypyridyl complexes due to their photoluminescence which makes them stable and also suitable as DNA probes.

Previously, the development of classical ruthenium drugs was based on the capability of ruthenium to bind with DNA *via* some of the nitrogen atoms of nucleic bases. The interaction between transition metal complexes and nucleic acids were studied extensively in order to develop drugs that could react and bind to nucleic bases. The most important characteristics of ruthenium(II) complexes are that their intercalating ligand must possess extended and planar aromatic structures which is able to stack and insert between the base pairs of the DNA double helix. The intercalating ligand plays an important role in order to make the interaction with DNA happen.

The modification of polypyridyl ligands would allow fine tuning of the configuration and electronic structures of ruthenium(II) polypyridyl complexes therefore, varying the DNA binding properties of these complexes. Nowadays, the researchers are more interested in the complexes that contain one intercalating ligand and two ancillary ligands due to their stability, strong DNA affinity, photochemical properties and various other applications. Ruthenium complexes with stable, inert, coordinatively saturated and water soluble properties are the most ideally suited and extremely valuable as non-covalent probes of both structural and functional aspects of nucleic acid chemistry [7].

Thus, the objective of this study is to synthesis, characterization and evaluate the DNA binding activity of a potential DNA intercalator based on novel complex, $[Ru(dppz)_2(p\text{-}MOPIP)]^{2+}$.

Materials and Methods

Materials

All the chemicals and solvents in this experiment are at least of analytical grade and used as received from the suppliers unless stated otherwise. The reagents used without purification are as follows: ruthenium(III) chloride hydrate, 4-methoxybenzaldehyde, 1,10-phenanthroline, sodium bromide, sodium hydrogen carbonate, magnesium sulfate, ammonium acetate, *o*-phenylene diamine, lithium chloride (LiCl), potassium hexaflorophosphate (KPF_6) and tetra-*N*-butylammoniumchloride. The solvents are listed as follows: nitric acid, sulphuric acid, chloroform, methanol, glacial acetic acid, aqueous ammonia, dimethylformamide, toluene, acetonitrile and ethylene glycol.

Instrumentation

The elemental analysis of the complex was carried out by using Leco CHNS-932 Elemental Analyzer. The nuclear magnetic resonance (NMR) spectra was recorded at room temperature in deuterated acetonitrile (CD_3CN) by using JEOL ECX500 FT NMR 500 MHz spectrometer with tetramethylsilane (TMS) as the internal standard for ^1H. Electrospray Ionization Mass Spectrometry (ESI-MS) of the complex was performed on a triple stage quadrupole Finnigan TSQ7000 mass spectrometer with a diverted inject valve where the spectra recorded were in the scanning range of 50 – 2200 *m/z* ratio. The Infrared absorption spectra were measured by using Perkin Elmer 100 series FT-IR Spectrometer in the range 4000 – 200 cm^{-1}. UV-Visible spectra were recorded over the range of 200 – 600 nm on Shimadzu H.U.V.1650 PC UV-Visible spectrophotometer using quartz cells of 10 mm path length. Emission spectra were recorded over the range 500 – 850 nm using an excitation wavelength of 460 nm on a Shimadzu RF-5301 PC spectrofluorometer at room temperature.

Preparation of the precursor ligand and complex

The precursor ligand, 1,10-phenanthroline-5,6-dione was prepared according to literature [8] and recrystallized in methanol. The precursor ligand was later used to prepare dipyrido[3,2-a:2',3'-c]phenazine (dppz) [9] and 2-(4-methoxylphenyl)imidazo[4,5-f][1,10]phenanthroline (*p*-MOPIP) [10] by following literature methods.

Synthesis of $Ru(dppz)_2Cl_2$

$Ru(dppz)_2Cl_2$ was prepared according to an established method [11]. A mixture of 0.2 g (1.0 mmol) $RuCl_3.3H_2O$, 0.55 g (2.0 mmol) dppz, 0.22 g of LiCl, and 30 mL of DMF was refluxed for 8 hours. The dark solution was stirred in 100 mL of chilled acetone and then kept in the freezer overnight. The crude product was collected by filtration and washed with water. The dried crude product was a fine dark purple powder. Yield: 0.623 g (80.1%), MS, *m/z*: 703 [M^+- 2Cl] ; ^{1}H NMR 500 MHz (CD_3CN, δ ppm): 9.50 (d, 4H), 9.17 (d, 4H), 8.38 (dd, 4H), 8.04 (dd, 4H) and 7.92 (d, 4H) ; IR (ν, cm^{-1}) :3057.49 (sp^2 C-H), 1631.00 (C=N), 1581.31 (C=C), 1073.58 (C-N) and 327.32 (Ru-Cl).

Synthesis of $[Ru(dppz)_2$*p*-MOPIP$_2]^{2+}$

A mixture of 0.034g (0.10 mmol) *p*-MOPIP, 0.08g (0.10 mmol) of $[Ru(dppz)_2Cl_2]^{2+}$ was dissolved in 10 ml of ethylene glycol and refluxed for 4 hours under nitrogen. Upon cooling, concentrated KPF_6 solution was added into the dark solution. Once the precipitation was complete, the solution was filtered by using a grade-4 crucible followed by washing with water. The crude product was purified by column chromatography by using neutral alumina with a 1:1 ratio of acetonitrile and toluene. The orange-red band was collected and analyzed. The final product was a fine dark orange solid. Yield: 0.08g (62.5%); Found: C, 53.2; H, 2.67; N, 13.2 (calculated for $C_{56}F_{12}H_{34}N_{12}OP_2Ru$: C, 52.4; H, 3.0; N, 13.1); MS, *m/z*: 1136.9 [M^+- PF_6^-] and 993.2 [M^+- $2PF_6^-$], ; ^{1}H NMR (CD_3CN, δ ppm): 9.65 (d, 6H, *J*=6.87 Hz), 9.05 (d, 4H, *J*=8.02 Hz), 8.43 (m, 6H), 8.23 (dd, 4H, *J*=3.44 Hz), 8.15 (d, 2H, *J*=9.16 Hz), 7.82 (m, 4H), 7.69 (dd, 2H, *J*=5.73 Hz), 7.20 (d, 2H, *J*=9.16 Hz) and 3.88 (s, 3H) ; IR (*v*, cm^{-1}) :3386.03 (secondary N-H), 2954.87 (sp^3 C-H), 1458.91 (C=C), 1354.91 (C=N), 1022.27 (C-N) and 811.44 (Ar *para*-subs.)

UV-Visible titration

The interaction of ruthenium(II) complex, $[Ru(dppz)_2$(*p*-MOPIP)$]^{2+}$ with CT-DNA was analyzed using UV-Vis spectroscopy. The UV-Vis titration of the complex in a buffer was performed at room temperature using a fixed concentration of the complex with increasing concentration of DNA. The concentration of the $[Ru(dppz)_2$(*p*-MOPIP)$]^{2+}$ solution was 15 μM while the concentration of DNA titrated varied from 0 to 86 μM. The complex-DNA solution was allowed to incubate for10 minutes before the spectra were recorded. The titration processes were repeated several times until no more changes were observed in the spectra which indicated that the binding saturation was achieved. The changes in the concentration of the ruthenium(II) complex due to dilution at the end of each titration were negligible.

Emission titration

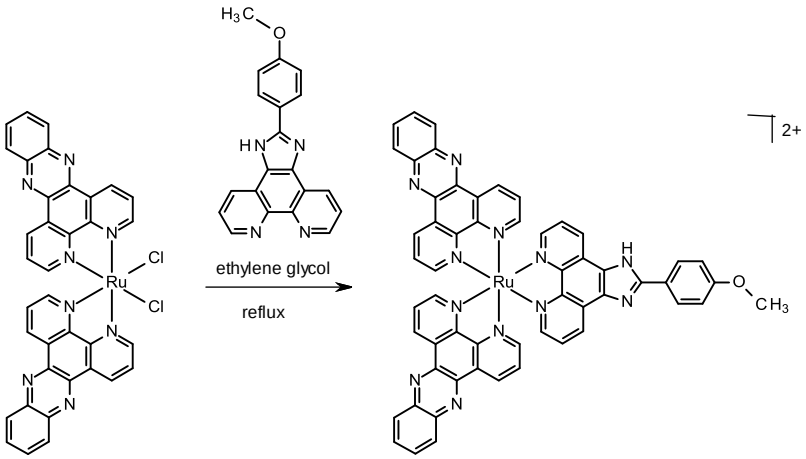
The intrinsic fluorescence emission spectra of the complex in Tris-buffer was carried out by using a fixed ruthenium(II) concentration to which increments of the DNA stock solution were added. Ruthenium-DNA solution was allowed to incubate for 5 minutes before the emission spectra were recorded. The excitation wavelength was set at 460 nm.

Viscosity measurements

Viscosity measurements were carried out with an Cannon Flask viscometer, suspended vertically and immersed in a water bath with a constant temperature of 25℃. The flow time was measured with a digital stopwatch and each sample was tested three times to obtain the average flow time. Data were represented as $(\eta/\eta_0)^{1/3}$ *versus* binding ratio, 1/R where η is the viscosity of DNA in the presence of the complex. Specific viscosity values were calculated by the equation $\eta = (t - t_0)/t_0$, where t and t_0 represent flow time of the DNA solution and the blank buffer, respectively.

Results and Discussion

The reaction of $[Ru(dppz)_2Cl_2]$ with *p*-MOPIP in a ratio 1:1 treated with potassium fluorophosphate resulted in formation of $[Ru(dppz)_2$p-MOPIP$]^{2+}$ in PF_6 salt (Scheme 1). The purified complex was obtained as an orange-red fine solid with 62.5% yield. Conversion to chloride salts was done with the treatment of the complex in acetonitrile solution with tetra-*N*-butylammoniumchloride. The complex in PF_6 salt was easily soluble in acetonitrile while as a chloride salt, it was soluble in water.



Scheme 1. Preparation of $[Ru(dppz)_2p\text{-MOPIP}]^{2+}$

Electrospray ionization mass spectrometry (ESI-MS) in acetonitrile showed a peak at *m/z* 1136.9 for $[M^+]$ while the intense peak at *m/z* 496.1 served as the base peak for $[M^{2+}]$. The ^{1}H NMR spectrum of $[Ru(dppz)_2p\text{-MOPIP}]^{2+}$ (Figure 1) in deuterated acetonitrile were properly defined and integrated. There are nine signals which corresponded to the protons of dppz and *p*-MOPIP ligands in the complex. The resonance at 9.65 ppm corresponded to the proton attached to the carbon adjacent to a coordinated nitrogen atom in the aromatic ring while the proton attached to the neighboring oxygen atom was shielded at 7.20 ppm. The proton signal for the methyl group was observed at 3.88 ppm as a singlet peak. Unfortunately, the signal that corresponded to the proton directly attached to nitrogen atom in *p*-MOPIP was not observed in the spectrum, probably due to fast exchange chemistry of the active proton in the imidazole ring or it was obscured by the nitrogen quadrapole broadening property [12]. However, the presence of NH was confirmed by the IR spectrum.

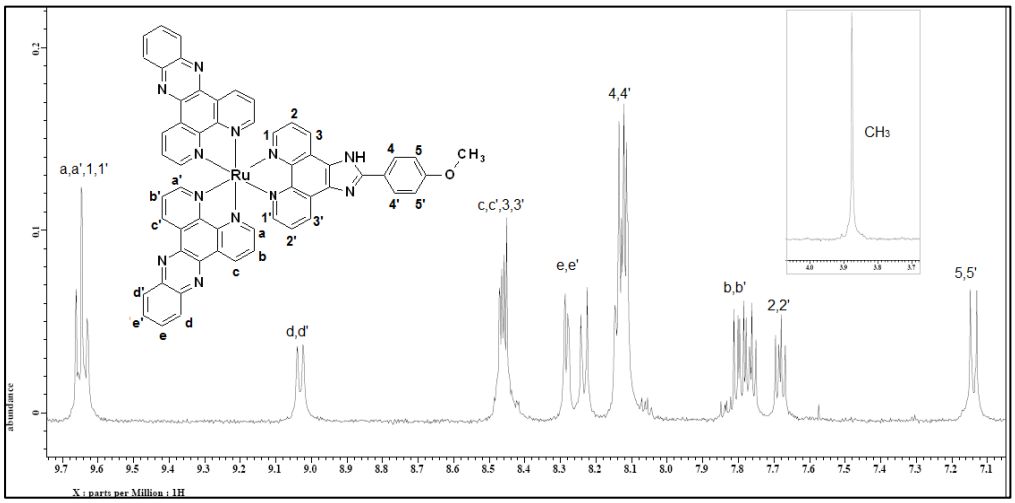


Figure 1. ^{1}H NMR spectrum of $[Ru(dppz)_2p\text{-MOPIP}]^{2+}$

The IR spectrums of the complex were recorded in the region of 4000 – 280 cm^{-1} and the data is summarized in Table 1. A broad and strong peak which gives information on secondary amine group of imidazole *v*(N-H) was

observed at 3386 cm^{-1}. The carbon-nitrogen bonds absorptions *v*(C=N) and *v*(C-N) were at 1638 and 1354 cm^{-1}, respectively. The stretching frequency of *v*(C-O) at 1022 cm^{-1} were indicative of the O-CH_3 group. In addition, a strong out of plane *v*(C-H) bending frequency appeared at 811 cm^{-1} indicating that the substitution in the aromatic phenyl referred to the *para*-position. The accumulated MS, NMR and IR data supported by elemental analysis was consistent with the proposed structure and composition of the complex.

Table 1. IR data of $[Ru(dppz)_2p\text{-}MOPIP]^{2+}$

v	**Wave number (cm^{-1})**	**Intensity**
(N-H)	3386	strong, broad
(sp^3 C-H)	2954	strong, sharp
(C=N)	1638	medium, sharp
(C=C)	1458	strong, sharp
(C-N)	1354	strong, sharp
(C-O)	1022	medium
Para subs ring	811	medium

The UV-Visible absorption spectrum for $[Ru(dppz)_2p\text{-}MOPIP]^{2+}$ was recorded in acetonitrile, with a concentration of 10 µM at room temperature. Through comparison to related molecules [8, 9], the bands centered at around 281 nm (ε = 66600 M^{-1} cm^{-1}) and 358 nm (ε = 17400 M^{-1} cm^{-1}) were assigned to intra-ligand $\pi \rightarrow \pi^*$ transitions in the scaffold. The lowest energy band at 460 nm (ε = 10200 M^{-1} cm^{-1}) was attributed to the metal-to-ligand charge transfer (MLCT) transition of the $Ru(d_\pi) \rightarrow$ ligand. The luminescence spectra of the complex upon MLCT excitation was performed at room temperature and the excitation wavelength was set at 460 nm. Figure 2 displays the emission spectra of complex in acetone (**blue**) and water (**red**) at room temperature to show the effect of the protic solvent on the complex. The complex displayed high luminescence in acetonitrile but almost no emission in water probably due to the presence of the dppz ligands in the complex. In an aqueous environment, the free electron on the nitrogen of the phenazine ring can form hydrogen bonds with water molecules [13,14]. As a result, the excited-state luminescence was quenched [15, 16]. This property is advantageous in DNA-binding studies using an aqueous buffer, where the complex binds to DNA, and the dppz ligands were protected from water, thus intense luminescence could be observed. This phenomenon has been termed as the 'molecular light switch' effect [17].

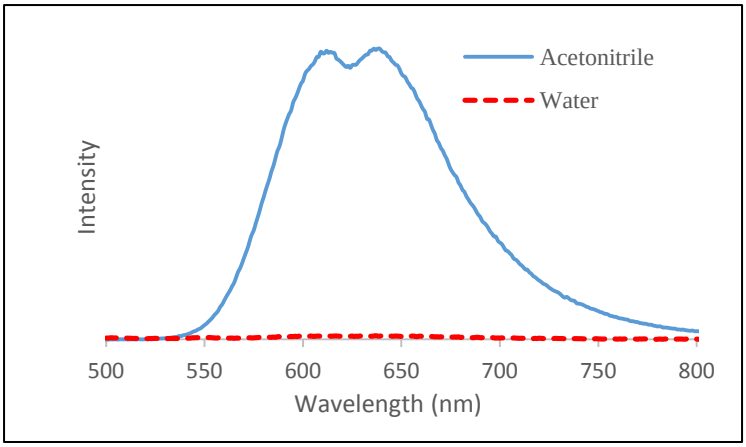


Figure 2. Luminescence spectra of $[Ru(dppz)_2p\text{-}MOPIP]^{2+}$ in acetonitrile and water

DNA-binding studies

The interaction of the ruthenium(II) complex, $[Ru(dppz)_2(p\text{-MOPIP})]^{2+}$ with CT-DNA was analyzed using UV-Vis spectroscopy. The UV-Vis titration of the complex in a buffer was performed at room temperature using a fixed concentration of the complex with increasing concentration of DNA.

The concentration of the $[Ru(dppz)_2(p\text{-MOPIP})]^{2+}$ solution was at 15 μM while the concentration of DNA varried from 0 to 86 μM. The complex-DNA solution was allowed to incubate for 10 minutes before the spectra were recorded in order to allow the interaction between DNA and the complex. The titration processes were repeated several times until no more changes were observed in the spectra indicating that the binding saturation was achieved. The changes in the ruthenium(II) complex concentration due to dilution at the end of each titration were too small and thus were negligible [18]. The absorption spectrum of complex with increasing concentration of CT-DNA is shown in Figure 3.

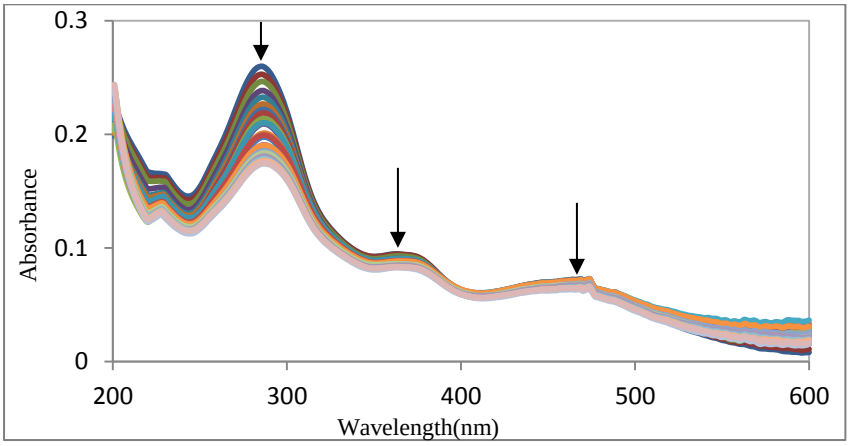


Figure 3. Absorption spectra of ruthenium(II) complex in Tris-HCl buffer upon addition of CT-DNA. [Complex] = 15μM, [DNA]= 0-86 μM

The arrows showed the absorbance changing upon the increase in DNA concentration. Normally, the hypochromic and bathochromic effects are seen during the binding process which is due to the perturbation of the metal centred MLCT band and the ligand centred π-π* band of the complex [19]. For this case, although there was no obvious red shift, hypochromicities was observed. The hypochromicities in the absorption bands for $[Ru(dppz)_2(p\text{-MOPIP})]^{2+}$ complex by the addition of CT-DNA in aqueous buffer was 29 %. This hypochromism effect has been attributed to the presence of synergic non-covalent interactions: electrostatic, groove or intercalation binding along the outside of DNA helix, and often the extent of hypochromism was parallel to the intercalative binding strength [20].

There were three well resolved bands at 284 nm, 363 nm and 474 nm. The absorption bands decreased with higher concentration of CT-DNA which fit a characteristic feature of CT-DNA binding interaction. The ultraviolet bands at 284 nm and 363 nm correlated to the intra-ligand π-π* transition [19]. The lowest energy bands at 474 nm was assigned to the MLCT transitions pf $Ru(d_\pi) \rightarrow$ ligand according to the other related ruthenium (II) complexes [21].

In order to quantitatively illustrate the DNA binding strength of the complex, the intrinsic binding constant, K_b of complex with CT-DNA was determined by monitoring the changes of absorbance at 284 nm while increasing the concentration of DNA according to the following equation 1 [22]:

$$[DNA]/(\varepsilon_a - \varepsilon_f) = [DNA]/(\varepsilon_b - \varepsilon_f) + 1/K_b(\varepsilon_b - \varepsilon_f) \quad (1)$$

where [DNA] is the concentration of CT-DNA in base pairs, the apparent absorption coefficient, ε_a, ε_f and ε_b correspond to $A_{observed}$/[Ru], the extinction coefficient for the free ruthenium complex and the extinction coefficient for the free ruthenium complex in the fully bound form, respectively .

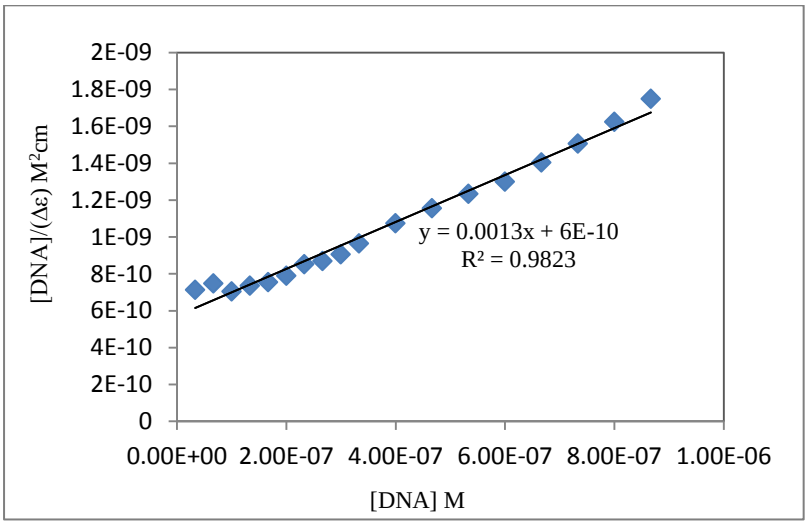


Figure 4. [DNA]/(Δε) vs [DNA] for the titration of DNA with the ruthenium(II)complex

K_b was determined by the ratio of slope to the intercept and the value obtained was 1.67 x 10^6 M^{-1}. By comparing with other similar ruthenium(II) complexes that contained *p*-MOPIP as ligand, this value was greater compared to $[Ru(bpy)_2(p\text{-MOPIP}]^{2+}$ and $[Ru(phen)_2(p\text{-MOPIP})]^{2+}$ where the value of K_b were 5.0 x 10^5 M^{-1} and 0.20 x 10^5 M^{-1} [10, 13], respectively. This signified that $[Ru(dppz)_2(p\text{-MOPIP})]^{2+}$ bound more tightly to DNA compared to those complexes. In this case, the ancillary ligand dppz might have played an important influence suggesting that the high DNA binding affinity was relative to the dimension of π-conjugated aromatic area of ancillary ligands. This was mainly induced by the extended-aromatic structure of the ancillary ligand which was dppz that increased the action between the complexes and DNA. The dppz itself might also react with DNA consequently giving a higher value of binding constant as mentioned before.

The K_b value was consistent with previous report by Sun et al. [23] on a closely related compound consisting of two dppz ligands in one system, $[Ru(dppz)_2(L^1)]^{2+}$, (L^1=5,5'-di(1-(trimethylammonio)methyl)-2,2'-dipyridyl cation) showed the effect of the intercalating ligand in DNA binding, with K_b values at 0.58 x 10^6 M^{-1}. The distinct structure of *p*-MOPIP which comprised of an extended aromatic area assisted $[Ru(dppz)_2(p\text{-MOPIP})]^2$ to bind strongly to DNA through intercalation compared to $[Ru(dppz)_2(L^1)]^{2+}$ where L^1 contained longer alkyl groups in the ligand. The binding affinity of $[Ru(dppz)_2(p\text{-MOPIP})]^{2+}$ was improved by bis-intercalation due to presence of more than one intercalating ligand in one system, namely *p*-MOPIP and two sites of dppz [8,14].

The intrinsic fluorescence emission spectra of complex in Tris buffer was carried out by using a fixed ruthenium(II) concentration to which increments of the DNA stock solution were added. Ruthenium-DNA solution was allowed to incubate for 10 minutes before the emission spectra were recorded. The excitation wavelength was set at 460 nm.

In the emission spectra (Figure 5), the arrow showed the emission intensity changes upon increasing the DNA concentration. The concentrations of the ruthenium(II) complex and CT-DNA were 30 μM and 0-200 μM, respectively. The interaction of the complex with DNA shows increased emission intensity in buffer solution. However, the emission changes were not so pronounced even after excess addition of DNA because of solvent quenching and enhancement of emission intensity when bound intercalatively to DNA. This implied that the

ruthenium(II) complex could strongly interact with DNA and be protected by DNA efficiently. In other words, the hydrophobic environment inside the DNA helix reduced the accessibility of solvent water molecules to the complex and the complex mobility was restricted at the binding site [24], leading to a decrease of the vibrational modes of relaxation. Increase in emission was an indication of intercalation between CT-DNA and the complex.

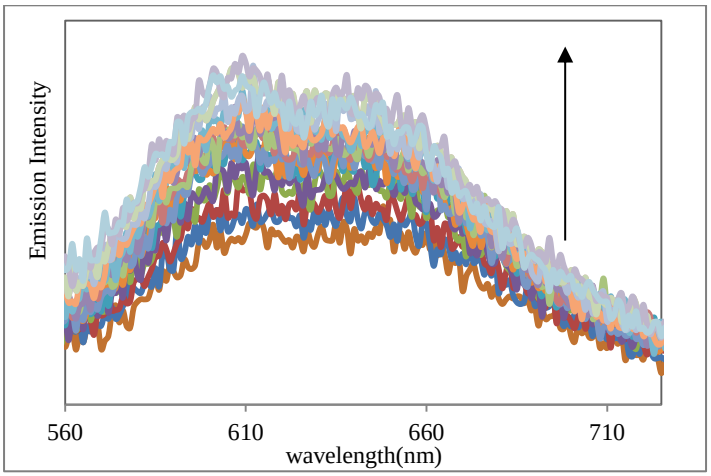


Figure 5. The emission spectra of the ruthenium(II) complex in buffer in the presence of increasing amounts of CT-DNA, [Ru]= 30μM, [DNA] = 0 - 200μM

This result also revealed the selective nature of $[Ru(dppz)_2(p\text{-MOPIP})]^{2+}$ as a molecular switch, responding sensitively to the suitable changes in the structure of the helix, a phenomenon called the 'molecular light switch' effect, due to presence of the dppz ligands.

In order to elucidate the binding mode of $[Ru(dppz)_2(p\text{-MOPIP})]^{2+}$, viscosity measurements were carried out by keeping a constant concentration of CT-DNA and varying the concentration of the complex. Viscosity measurements provided reliable evidence to study the mode of interaction. Electrostatic or groove binding generally had no significant consequence on the viscosity of DNA, whereas classical intercalation affects the lengthening of DNA helix as base pairs are separated to accommodate foreign molecules, therefore, increasing the viscosity of DNA [25]. As shown in Figure 6, with continuing addition of $[Ru(dppz)_2(p\text{-MOPIP})]^{2+}$ to CT-DNA solution, the viscosity of CT-DNA increased. This result validated the hypothesis that $[Ru(dppz)_2(p\text{-MOPIP})]^{2+}$ bound to DNA *via* intercalation. This result was in agreement with other previous reports on ruthenium(II) polypyridyl complexes [10, 26].

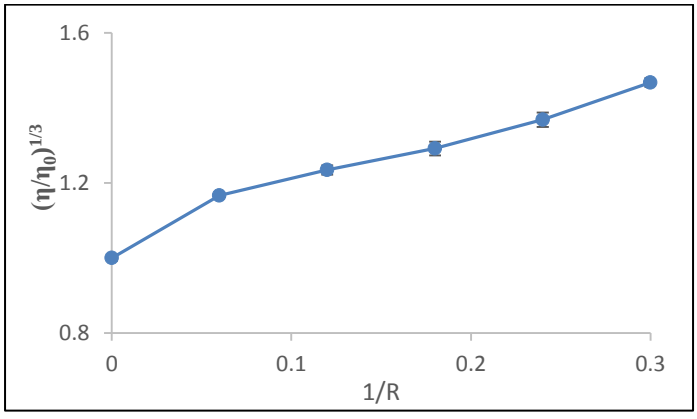


Figure 6. Effect of increasing concentration of $[Ru(dppz)_2(p\text{-MOPIP})]^{2+}$ on the viscosity of CT-DNA

Conclusion

In this study, a novel complex $[Ru(dppz)_2(p\text{-MOPIP})]^{2+}$ has been synthesized. The structure and composition was supported by analysis *via* ^{1}H-NMR, mass spectrometry, elemental analysis, FT-IR, and UV-Vis spectroscopy. The binding properties of CT-DNA with the complex were studied by UV-Vis titration and viscosity measurements showed that the interaction occurred *via* intercalation mode giving the intrinsic binding constant of $K_b = 1.67 \times 10^6$ M^{-1}. $[Ru(dppz)_2(p\text{-MOPIP})]^{2+}$ was bound more tightly than similar related complexes. From the comparison, it was clear that the extended aromaticity of the ancillary ligand influenced the binding strength of ruthenium(II) complex to DNA. In the luminescence titration, it was found that the $[Ru(dppz)_2(p\text{-MOPIP})]^{2+}$ was a highly sensitive spectroscopic reporter of double-helical DNA. Whereas in aqueous solution, the luminescence was detectable only when $[Ru(dppz)_2(p\text{-MOPIP})]^{2+}$ intercalated in the nucleic acid structure and was perhaps shielded by DNA. Therefore, $[Ru(dppz)_2(p\text{-MOPIP})]^{2+}$ was concluded that served as a true 'molecular light switch' for the DNA structures. The stark contrast between the 'off' and 'on' states of $[Ru(dppz)_2(p\text{-MOPIP})]^{2+}$ made this complex useful for the quantitative study of DNA and other non-polar microenvironments, a significant outcome for the design of novel intercalator reagents. However, the details of binding of complex with the sequence of DNA is not clear yet and further studies are required.

Acknowledgement

The authors gratefully acknowledge the Government of Malaysia for financial aid through Fundamental Research Grant Scheme (FRGS) project 01-01-14-1466FR. The authors would like to extend our thanks to those directly and indirectly involved in this project.

References

1. Balzani,V., Juris, A., Venturi, M., Campagna, S. and Serroni, S. (1996). Luminescent and redox-active polynuclear transition metal complexes. *Chemical Reviews*, 96 (2): 759 – 834.
2. Clarke, M. J. (2003). Ruthenium metallopharmaceuticals. *Coordination Chemistry Reviews*, 236 (1–2): 209 – 233.
3. Brabec, V. and Nováková, O. (2006). DNA binding mode of ruthenium complexes and relationship to tumor cell toxicity. *Drug Resistance Update.*, 9 (3): 111 – 22.
4. Allardyce, C. S. and Dyson, P. J. (2001). Ruthenium in medicine : Current clinical uses and future prospects. *Platinum Metal Reviews*, 45 (2): 62 – 69.
5. Allardyce, C. S., Dorcier, A., Scolaro, C. and Dyson, P. J. (2005). Development of organometallic (organo-transition metal) pharmaceuticals. *Applied Organometallic Chemistry*, 19(1): 1–10.
6. Stephenson, T. and Wilkinson, G. (1966). Carboxylatoruthenium chlorides. *Journal of Inorganic Nuclear Chemistry*, 28: 2285 – 2291.
7. Maheswari, P. U., Rajendiran, V., Palaniandavar, M., Parthasarathi, R. and Subramanian, V. (2006). Synthesis, characterization and DNA binding properties of rac-$[Ru(5,6\text{-dmp})_2(dppz)]^{2+}$ - enantiopreferential DNA binding and co-ligand promoted exciton coupling. *Journal of Inorganic Biochemistry*, 100(1): 3 – 17
8. Zhong, V., Huang, H., He, A. and Zhang, H. (2008). Synthesis and luminescent properties of novel polymeric metal complexes with bis(1,10-phenanthroline) group. *Dye Pigment*, 77 (3): 578 – 583.
9. Hiort, C., Lincoln, P. and Norden, B. (1993). DNA binding of DELTA- and LAMBDA-$[Ru(phen)_2dppz]^{2+}$. *Journal of The American Chemical Society*, 115 (9): 3448 – 3454.
10. Liu, J., Zheng W., Shi, S., Tan, C., Chen, J., Zheng, K. and Ji, L. (2008). Synthesis, antitumor activity and structure-activity relationships of a series of Ru(II) complexes. *Journal of Inorganic Biochemistry*, 102 (2): 193 – 202.
11. Sullivan, B. P., Meyer, T. J. and Salmon, D. J. (1978). Mixed phosphine 2,2'-bipyridine complexes of ruthenium. *Inorganic Chemistry*, 17 (12): 3334 – 3341.
12. Devi, C. S., Kumar, D. A., Singh, S. S., Gabra, N., Deepika, N., Kumar, Y. P. and Satyanarayana, S. (2013). Synthesis, interaction with DNA, cytotoxicity, cell cycle arrest and apoptotic inducing properties of ruthenium(II) molecular 'light switch' complexes. *European Journal of Medicinal Chemistry* 64: 410 – 421.
13. Huang, H-L., Liu, Y-J., Zeng, C-H., Yao, J-H., Liang, Z-H., Li, Z-Z. and Wu, F-H. (2010). Studies of ruthenium(II) polypyridyl complexes on cytotoxicity in vitro, apoptosis, DNA-binding and antioxidant activity. *Journal of Molecular Structure*, 966(1–3): 136 – 143.

14. Lan Jin, P. Y. (1997). Synthesis and DNA binding studies of Co(III) mixed-ligand complex containing dipyrido. *Polyhedron*, 16 (19): 3395 – 3398.
15. Lakowicz, J. (2007). Quenching of fluorescence. *Principles of fluorescence spectroscopy*, 277 – 330.
16. Zeglis, B. M., Pierre, V. C. and Barton, J. K. (2007) Metallo-intercalators and metallo-insertors. *Chemical Communicatios (Cambridge)*,7345 (44): 4565 – 4579.
17. Friedman, A. E., Kumar, C. V., Turro, N. J. and Barton, J. K. (1991). Luminescence of ruthenium(II) polypyridyls: Evidence for intercalative binding to Z-DNA. *Nucleic Acids Research*, 19 (10): 2595 –2602.
18. Yu, Q., Liu, Y., Wang, C., Sun, D., Yang, X., Liu, Y. and Liu, J. (2012). Chiral ruthenium(II) polypyridyl complexes: Stabilization of G-Quadruplex DNA, inhibition of telomerase activity and cellular uptake. *PLoS One*, 7 (12): 1 – 13.
19. Ahmad, H. (2009). Kinetically locked metallomacrocycles as self-assembled hosts for biomolecules. Ph.D Thesis.
20. Shi, S., Yao, T., Geng, X., Jiang, L. and Liu, J. (2009). Synthesis, characterization, and DNA binding of chiral complexes D - and L - [$Ru(bpy)_2(pyip)]^{2+}$. *Chirality*, 283: 276 – 283.
21. Liu, J., Mei, W. J., Lin, L. J., Zheng, K. C., Chao, H., Yun, F. C. and Ji, L. N. (2004). Electronic effects on the interactions of complexes $[Ru(phen)_2(p\text{-}L)]^{2+}$ (L=MOPIP, HPIP, and NPIP) with DNA. *Inorganica Chimica Acta*, 357(1): 285 – 293.
22. Srishailam, A., Kumar, Y. P., Venkat Reddy, P., Nambigari, N., Vuruputuri, U., Singh, S. S. and Satyanarayana, S. (2014). Cellular uptake, cytotoxicity, apoptosis, DNA binding, photocleavage and molecular docking studies of ruthenium(II) polypyridyl complexes. *Journal of Photochemistry and Photobiology B: Biology*, 132: 111 – 123.
23. Sun, J., An, Y., Zhang, L., Chen, H., Han, Y., Wang, Y., Mao, Z. and Ji, L. (2011). Studies on synthesis, characterization, and G-quadruplex binding of Ru(II) complexes containing two dppz ligands. *Journal of Inorganic Biochemistry*, 105 (2): 149 – 154.
24. Xu, L., Zhong, N.-J., Xie, Y.-Y., Huang, H.-L., Jiang, G.-B. and Liu, Y.-J. (2014). Synthesis, characterization, in vitro cytotoxicity, and apoptosis-inducing properties of ruthenium(II) complexes. *PLoS One*, 9 (5): e96082.
25. Rehman, S. U., Yaseen, Z., Husain, M. A., Sarwar, T., Ishqi, H. M. and Tabish, M. (2014). Interaction of 6 mercaptopurine with calf thymus DNA - Deciphering the binding mode and photoinduced DNA damage. *PLoS One*, 9(4): 1–11.
26. Shi, S., Liu, J., Li, J., Zheng, K-C., Huang, X-M., Tan, C-P., Chen, L-M. and Ji, L-N. (2006). Synthesis, characterization and DNA binding of novel chiral complexes delta- and lambda-$[Ru(bpy)_2L]^{2+}$ (L = o-mopip and p-mopip). *Journal of Inorganic Biochemistry*, 100(3): 385 – 395.

Malaysian Journal of Analytical Sciences, Vol 20 No 4 (2016): 770 - 776
DOI: http://dx.doi.org/10.17576/mjas-2016-2004-09

MALAYSIAN JOURNAL OF ANALYTICAL SCIENCES
Published by The Malaysian Analytical Sciences Society
ISSN 1394 - 2506

SEPARATION AND RADIOLOGICAL IMPACT ASSESSMENT OF THORIUM IN MALAYSIAN MONAZITE PROCESSING

(Pengasingan dan Penilaian Impak Radiologi Torium dalam Pemprosesan Monazit di Malaysia)

Wadeeah M. Al-Areqi*, Che Nor Aniza Che Zainul Bahri, Amran Ab. Majid, Sukiman Sarmani

Nuclear Science Program, School of Applied Physics,
Faculty of Science and Technology,
Universiti Kebangsaan Malaysia, 43600 UKM Bangi, Selangor, Malaysia

**Corresponding author: walareqi@yahoo.com*

Received: 2 November 2015; Accepted: 6 April 2016

Abstract

The processing of mineral monazite to produce thorium (Th) and rare earth elements may create a radiological impact if the processing and residue are not properly or safely managed. Malaysian Atomic Energy Licensing Board (AELB) categorized monazite as a radioactive material because the concentration of thorium in the mineral is higher than 1Bq/g. Therefore, the current study aimed to determine the separation percentage of thorium from Malaysian monazite and to assess the radiological impact of thorium during various stages involved in the processing. In this study, monazite was digested by hot sulphuric acid followed by selective precipitation of thorium using ammonia. Neutron Activation Analysis (NAA) and Inductively Coupled Plasma Mass Spectrometry (ICP-MS) techniques were used to determine thorium. The result of the study showed that the average concentration of thorium in Malaysian monazite ore was 17,990.5 ± 1,239.3 ppm. After digestion, 46.56 % of thorium was recovered and about 97.68 % of thorium was separated as thorium hydroxide from the obtained sulphate leach solution. The study also indicated that less than 3% of Thorium entered in the rich rare earth elements filtrate during the separation. The calculated maximum dose that could be received by workers and public from the monazite ore were 61.91 ± 4.27 mSv/y and 54.24 ± 3.73 mSv/y respectively. However, during the processing of 25 g the monazite ore, the worker and public will receive a lower dose in the range of 0.01 – 0.72 and 0.01 – 0.63mSv/y respectively. Based on the results, useful suggestions on how to improve thorium recovery and how to minimize the radiological impact as a whole are provided.

Keywords: thorium, monazite, radiological impact, separation, dose

Abstrak

Pemprosesan mineral monazit untuk menghasilkan torium (Th) dan unsur nadir bumi boleh menyebabkan impak radiologi sekiranya pemprosesan dan residu tidak diuruskan dengan baik. Lembaga Perlesenan Tenaga Atom Malaysia (AELB) telah mengkategorikan monazit sebagai bahan beradioaktif kerana kepekatan torium dalam mineral adalah tinggi iaitu melebihi 1Bq/g. Oleh itu, tujuan utama kajian ini adalah untuk menentukan peratus pengasingan torium daripada bijih monazit dan menilai impak radiologi torium dalam beberapa peringkat yang terlibat dalam pemprosesan. Dalam kajian ini, asid sulfurik telah digunakan untuk menghadam monazit dan diikuti dengan pemendakan terpilih torium menggunakan ammonia. Teknik Analisis Pengaktifan Neutron (NAA) dan Induktif Plasma Pendua – Spektrometri Jisim (ICP-MS) telah digunakan untuk menentukan kandungan torium. Hasil kajian menunjukkan purata kepekatan torium dalam bijih monazit Malaysia adalah 17,990.5 ± 1,239.3 ppm. Selepas penghadaman, peratus mendapatkan torium adalah 46.56 % dan 97.68 % torium telah diasingkan sebagai torium hidroksida daripada larutan larut lesap sulfat. Kajian juga menunjukkan kurang daripada 3 % torium terdapat dalam turasan unsur nadir bumi semasa pengasingan. Dos maksimum yang boleh diterima oleh pekerja dan orang awam daripada bijih monazit telah dikira dan masing – masing adalah 61.91 ± 4.27 mSv/y dan 54.24 ± 3.73 mSv/y. Walau bagaimanapun, semasa pemprosesan bijih monazit, pekerja dan orang awam akan menerima dos yang rendah iaitu masing – masing dalam julat 0.01 –

0.72 dan 0.01 – 0.63mSv/y. Berdasarkan hasil kajian ini, cadangan penambah baikan dalam mendapatkan torium dan bagaimana untuk meminimumkan impak radiologi secara menyeluruh dapat disediakan.

Kata kunci: torium, monazit, impak radiologi, pengasingan, dos

Introduction

Mineral processing industries containing natural radionuclides contribute to radiation exposure to the public and workers with significant doses. The radiation exposure during mineral processing industries can occur on the mining, transportation, or at any stage of mineral processing for generating the products, wastes and by-products [1]. In Malaysia, Naturally Occurring Radioactive Materials (NORM) are mainly found in scales and sludge from the oil and gas industries, iron oxide and red gypsum from the processing of ilmenite and thorium hydroxide in particular from the processing of xenotime and monazite. Other NORM are tin slag produced from the smelting of tin, ilmenite, zircon, and monazite produced from the processing of tin tailing (amang) [2, 3]. These activities are regulated and controlled under the Atomic Energy Licensing Act, 1984 (Act 304).

Malaysia implemented 1 Bq/g for naturally occurring radionuclides from ^{238}U and ^{232}Th decay series in raw material and waste as the control limit of activity concentrations. It stated the annual dose limit for the members of the public and workers from the activity concentration of radionuclides must be below the control limits which are unlikely to exceed 1 mSv/y and 20 mSv/y, respectively [4, 5]. There are two sources of thorium existing in Malaysia namely rare earth minerals and rare earth elements production residue. For instance, Malaysian monazite containing thorium ranged between 6.5 – 7.5 % and the average thorium concentrations in xenotime were 1.5 % [6]. The residue from Asian Rare Earth (ARE) contains 36 % of thorium meanwhile Water Leach Purification (WLP) residue generating from Lynas Advanced Materials Plant (LAMP) containing 0.17 % of thorium with total dose contribution of Th-232, Ra-228, U-238 and Ra-226 for workers and public 3.90 and 0.20 mSv/y, respectively [3, 6, 7]. Practically, the processing of monazite for rare earth production will produce a significant amount of thorium that needs to be managed safely to prevent the public concern and environmental impacts.

Typically, thorium is extracted from its minerals with either hot sulphuric acid or hot strong alkali, converted into thorium nitrate and extracted with tributyl phosphate (TBP) in kerosene for final purification of the thorium [4, 5, 11]. Chemically, monazite is phosphate of thorium and rare earths besides small uranium content. It is particularly rich in the light REEs. Digestion of monazite mineral can be used hot concentrated sulphuric acid or hot alkali. In typical acid process, cracking monazite mineral is performed at >230 ºC as shown in the following equation 1:

$$Th_3 (PO_4)_4 + 6H_2SO_4 \rightarrow 3Th (SO_4)_2 + 4H_3PO_4 \quad (1)$$

In the acid process, thorium and REEs which are water soluble salts in monazite sulphuric solution are filtrated, and thorium is separated from these REEs by reducing the acidity to precipitate thorium as thorium hydroxide usually in the selective precipitation. Moreover, ammonia is used at about pH 1.05. Nitric acid may dissolve thorium hydroxide precipitate. Produced thorium nitrates in acid solutions are widely used to extract thorium into organic solvents. For purification of thorium from impurities, solvent extraction commonly using tributyl phosphate TBP in kerosene is achieved by a multi-stage extracting and stripping process [10 – 14].

In strong alkali digestion, insoluble thorium hydroxide is produced in thorium cake which is easily dissolved in acid as illustrated by the following equation 2:

$$Th_3 (PO_4)_4 + 12NaOH \rightarrow 3Th (OH)_4 + 4Na_3 PO_4 \quad (2)$$

Thorium is purified by solvent extraction in nitric acid media [14 – 16]. Pure thorium nitrate can be converted into thorium peroxide or thorium oxalates which are calcinated at 800 ºC in a furnace to produce high purity thorium oxide [17, 18]. Previous studies separated thorium from the rare earth residue and RE ores in order to minimize the environmental impact of thorium radioactivity and to produce thorium for future nuclear fuel [3, 8, 9].

In the present study, the separation percentage of thorium from Malaysian monazite and the improvement on thorium separation were studied. Radiological impact assessment of thorium was discussed for the whole scenario of Th separation, and it was suggested to minimize the radiological impact as well.

Materials and Methods

Separation of thorium

Malaysian monazite sample was collected from Syarikat Leong Sin Nam, Kempari, Perak and it was grinded to obtain fine powder. In preparing the samples for gamma spectrometry (HPGe), sample together with standard reference material namely (IAEA soil-375) were stored for 4 weeks in sealed plastic containers to re-establish the secular radioactive equilibrium. The specific activities of the natural radionuclides ^{232}Th and ^{238}U were measured for a period of 12 hours by HPGe γ-ray spectrometry. The ^{232}Th specific activity was determined from Ac-228 (911.1 keV) and Tl-208 (583.2 keV) respectively. In addition, the ^{238}U specific activity was assessed using Bi-214 (1764.49 keV).

In preparing the samples for the instrumental neutron activation analysis (INAA), approximate 0.05 g of monazite sample and 0.4 g standard reference material (IAEA 312N) were placed in high-purity polyethylene irradiation vials and sealed by heat sealing process. Triplicates were prepared for each sample. Then, the samples, standard reference materials and standard solution were irradiated for 1 hour in the rotary rack (RR) facility of the TRIGA Mark II reactor at Malaysian Nuclear Agency. The measurements were carried out using a HPGe detector (GC3018) and the analysis of photo peaks were performed using Genie-2000 software (Canberra Inc.).The samples were measured for 1 hour at different cooling times which ranged from 2 days to 4 weeks and measured at 4 cm distances from the detector.

Monazite leach sulphuric acid solution

The digestion of monazite and the selective precipitations of thorium were performed on glass beakers and the measurements of pH were carried out using EUTECH instruments pH700. The thorium concentrations in the aqueous solutions were determined using ICP-MS -ELAN 9000 (PerkinElmer SCIEX).There are two main parts of the process: Digestion of monazite with hot sulphuric acid and dissolving with water to produce monazite leach sulphate solution and separation of thorium from REEs and U by selective precipitation using ammonia and produce thorium precipitate as shown in Figure 1.

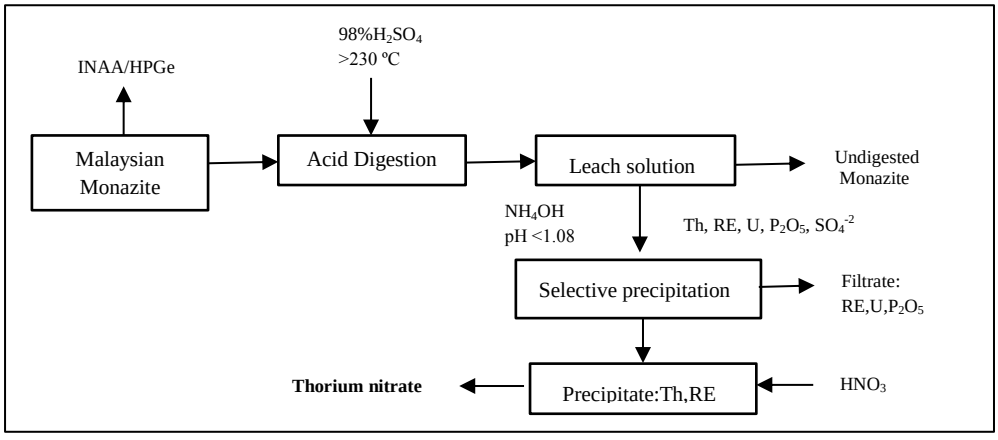


Figure 1. Simplified flowchart for sulphuric acid digestion of Malaysian monazite and recovery of thorium

Digestion of Malaysian monazite

The monazite leach solution used in this study was prepared by digesting approximately 25 g of monazite in 75 ml of 98 % sulphuric acid at 200 °C for 3 hours as digestion time using the glass beakers on the stirring hot plate. Then,

the mixture was cooled to room temperature, adding 200 mL water to dissolve the metal sulphates, and filtering to produce a clear solution.

Selective precipitation of thorium with ammonia

The monazite leach solution contains thorium, rare earths, and uranium with other impurities. Reduction of the acidity of sulphate leach solution at a pH of 1: 05 can precipitate thorium and leave the rare earths and uranium in the solution [10, 14]. In this part, 100 mL of leach solution was used and the selective precipitation for thorium was carried out at pH 1.08 – 1.89 using ammonia. The thorium rich precipitate was filtrated and dissolved in nitric acid to form thorium concentrate solution. ICP-MS used for determination of metal concentrations in the monazite leach solution, thorium concentrate and RE filtrate solutions. Triplicate procedures were performed and separation percentage of thorium from monazite leach solution was calculated.

Radiological impact assessment

Thorium concentrations were determined in Malaysian monazite ore and in each stage of the chemical process to produce the thorium nitrate. Radiological impact was assessed based on the magnitude of radiation hazard and effective dose rates. All the data on the activity concentrations of thorium in each stage of process was obtained from converting the thorium concentration into ppm to Bq/g. The Annual Effective Doses Equivalent for public and workers were estimated using equation (3) as recommended by UNSCEAR 2000 [19].

$$\text{Annual Effective Dose Equivalent (mSv/y)} = \text{Dose rate at 1m (nGy/h)} \times \text{time (h/y)} \times \text{occupancy factor} \times \text{conversion factor (Sv/Gy)} \times 10^{-6} \quad (3)$$

where Dose rate is define as activity of Th (Bq/kg) x conversion factor for Th (0.604 $nGyh^{-1}/Bqkg^{-1}$), Time for public is define as 365 days x 24 hours = 8760 hours and working time for worker is define as 2000 hours. Occupancy factor for outdoor activity is 0.2 and conversion factor is 0.7 Sv/Gy.

Results and Discussion

Thorium and uranium in Malaysian monazite were determined via the NAA and gamma ray spectroscopy. The mean concentrations of thorium and uranium in Malaysian monazite are presented in Table 1. The activity concentrations of thorium and uranium were 15258.14 ± 28.71 ppm (62.41 ± 0.05 Bq/g) and 1445.68 ± 19.38 ppm (17.98 ± 0.24 Bq/g) respectively by gamma spectroscopy. Mean concentrations of thorium and uranium via the NAA were 17,990.52 ± 1,239.3 ppm (73.58 ± 5.07 Bq/g) and 637.29 ± 25.8 (2.61 ± 0.11 Bq/g) ppm, respectively. In addition, the relative error of the INAA for analysis of ^{232}Th and ^{238}U in IAEA 312N was determined and they were calculated as 4.59 % and 9.64 %, respectively. Because the concentration of thorium obtained from NAA was more accurate, it was used for the following calculations of the thorium separation and radiological impact assessment. The study indicated that the different results between these two techniques could be due to radioactive equilibrium, homogeneity problems or gamma rays interferences.

Table 1. Mean concentration of thorium and uranium (ppm) measured in Malaysian Monazite by NAA and Gamma ray spectroscopy

Element	NAA		γ- ray spectroscopy		AELB*
	ppm	Bq/g	ppm	Bq/g	Bq/g
Th-232	17,990.52 ± 1,239.3	73.58 ± 5.07	15258.14 ± 28.71	62.41 ± 0.05	1
U-238	637.29 ± 25.8	2.61 ± 0.11	1445.68 ± 19.38	17.98 ± 0.24	1

*The limit control is imposed by Atomic Energy Licensing Board

As seen from the results presented in Table 1, Malaysian monazite ore was rich with thorium compared to uranium. Moreover, the thorium concentration was much higher than the AELB control limit, and therefore, Malaysian monazite was classified as the radioactive mineral. The low level of uranium in Malaysian monazite does not cause

serious radiological hazard into the environment and public while thorium has a great concern due to its high level concentrations of ore and residue.

Separation of thorium

The study on digestion of Malaysian monazite showed that it could be achieved about 46.56 % of thorium recovery under the previously mentioned parameters and significant amount of thorium was left in the undigested monazite residue. Thorium recovery can be improved if the multi-stage digestion process is required. As a result of this, thorium will decrease in the residue and then reduce the hazard of radioactivity too. At high temperature (< 230 ºC) used in chemical digestion processing, the thorium is converted into refractory and insoluble form (thorium pyrophosphate) and subsequently removed it completely from the residue [8, 20 – 22]. In this study, the temperature was used less than 230 ºC to avoid forming insoluble thorium form. Table 2 shows thorium separation from sulphate leach solution and thorium recovery from Malaysian monazite.

Table 2. Thorium separation from sulphuric leach solution (pH 1.08 – 1.84 by 13.4 M NH_4OH)

Stage of Chemical Extraction Process	**Th Concentration (ppm)**	**Th Recovery* (%)**	**Th Separation (%)**
Monazite ore by NAA	17,990.52 ± 1,239.3		
Sulphuric leach solution	837.61 ± 11.7	46.56	
Selective precipitation			
Sulphuric leach solution in 100 mL	837.61 ± 11.7		
Thorium precipitate	260.10 ± 0.10		
Rich- RE filtrate	7.76 ± 2.93		97.68

*Thorium recovery percentage was calculated using 25 g of Malaysian monazite

The results of this separation showed that most of thorium was separated from the monazite sulphate solution by selective precipitation at pH 1.08 – 1.84 using ammonia. The percentage of the thorium separation obtained in this study was almost 97.68 % and only less than 3% of total thorium was left in the rich rare earth filtrate as shown in Table 2. Furthermore, the different pH and concentration of ammonia as a precipitant were affected the separation percentage results. The obtained thorium precipitate contained only a small amount of rare earth elements which was co-precipitated during the reduction of the acidity. Subsequent purification of thorium precipitated by solvent extraction is required to extract the thorium nitrate from rare-earth elements and other impurities.

Radiological impact assessment

Based on the high concentration of thorium in the Malaysian monazite ore samples (17,990.52 ± 1,239.3 ppm), the risk assessment performed indicates the thorium was responsible for the high risk. The average annual effective doses equivalent received by workers and public from Malaysian monazite were calculated to be 61.91 ± 4.27 mSv/y and 54.24 ± 3.73 mSv/y, respectively. These values are over 3 times for workers and 54 times for public of the annual dose limit.

Table 3 shows the annual effective dose equivalent for public and workers during the processing of 25 g Malaysian monazite. As previously mentioned the radiological risk of Th in each step of the monazite processing depends on distribution of thorium during the processing, whatever the purpose of separation is and whether separating thorium as a product or removing it from the residue in order to produce REEs. From Table 3, it is apparent that the annual effective doses equivalent received by public and worker resulting from 25 g of monazite ore were 1.36 and 1.56 mSv/y, respectively. The dose for public was higher than AELB requirement.

Table 3. Annual Effective Dose Equivalent for public and workers (mSv/y) during the processing of (25 g) Malaysian monazite

Stage of Process	Total content of Th (mg)	Activity of Th (Bq)	Annual Effective Dose Equivalent for public (mSv/y)	Annual Effective Dose Equivalent for worker (mSv/y)
Monazite ore (25 g)	449.76	1839.53	1.36	1.56
Sulphuric leach solution (250 mL)	209.40	856.46	0.63	0.72
Undigested monazite (residue)	240.36	983.07	0.73	0.83
Sulphuric leach solution in 100 mL	83.76	342.58	0.25	0.29
Thorium precipitate	26.01	106.38	0.08	0.09
Rich- RE filtrate	1.94	7.93	0.01	0.01

The results also show that single - stage digestion process decreased the dose to be become the half of the initial raw monazite. Several process stages are required for achieving the minimal thorium in the residue as well as improvement of the experiment parameters.

Undigested monazite residue may cause slightly radiological risk with the annual effective dose equivalent for public 0.73and 0.83m Sv/y for workers, therefore, it is required to manage safely especially whenever using large amount of monazite. However, during the processing of the monazite ore, the worker and public received lower dose in the range 0.72 – 0.01 and 0.63 – 0.01 mSv/y respectively. It may be seen that the radiological risk in the final stages was much less than the recommended value because thorium content was completely separated during the process.

From this scenario, it was indicated that the radiological risk decreases from the initial until the final process if the separation of thorium is well performed and safely managed. Moreover, comparing the radiological impact assessment of our study with LAMP, it can be seen that LAMP reported that maximum dose rates received by workers and pubic resulting from operation of the plant were 5.61 mSv/y and 0.002 mSv/y, respectively. These doses are below AELB requirement and those reported in our study. The present study showed that Malaysian monazite processing caused a significant radiological impact on workers and public.

Conclusion

The results of the current study showed that it was possible to achieve about 46.56 % of thorium recovery by signal stage digesting monazite with hot sulphuric acid and separation percentage of thorium from REEs in monazite leach solution was 97.68 % using selective precipitation by ammonia. The optimum parameters of separation were stated. It can be figured out that most of thorium was separated during ammonia precipitation and co-precipitated few amount of REEs. Improvement of the separation was required for several flows. The calculated maximum doses that could be received by workers are 61.91 ± 4.27 mSv/y and public 54.24 ± 3.73 mSv/y from the Malaysian monazite ore which were high than the control limits. However, the lower dose in the range of 0.01 – 0.72 and 0.01 – 0.63 mSv/y respectively was received by the worker and public during the processing of monazite. The results of the effective dose showed that a regulatory control is required to save the public and workers from these types of activities.

Acknowledgement

The authors would like to thank the grant project with reference number FRGS/2013/ST01/UKM/01/2, UKM-GUP-2012-083 and FP0214D052-2.4DSTIN for sponsorship, great thank to MTCP scholarship, Malaysia Nuclear Agency and Nuclear Science Program, UKM.

References

1. Pontedeiro, E. M., Heilbron, P. F. L and Cotta, R. M. (2007). Assessment of the mineral industry NORM/TENORM disposal in hazardous landfills. *Journal of Hazardous Materials*, 139: 563 – 568.
2. Omar, M. (2010). NORM processing in Malaysia: An overview nuclear Malaysia/L/2010/11.1
3. Al-Areqi, W. M, Ab. Majid, .A. and Sarmani, S. (2015). Thorium: Issues and prospects in Malaysia. *AIP conference proceedings* 1659: 1 – 7.
4. IAEA. (2011). Radiation protection and safety of radiation sources: International basic safety standards, GSR Part 3.Access online http://www-pub.iaea.org/MTCD/publications/PDF/Pub1578_web-57265295.pdf
5. The Atomic Energy Licensing (Radioactive Waste Management) Regulations (2011). http://www.ecolex.org/details/legislation/atomic-energy-licensing-radioactive-waste-management-regulations-2011-lex-faoc107766/
6. The Academy of Sciences Malaysia (2013). Revitalising of rare earth mineral programme in Peninsula Malaysia as a strategic industry, The Academy of Sciences Malaysia (ASM) study report 1/2013.
7. Radiological impact assessment (2011). Radiological impact assessment of Lynas Advanced Materials Plant 2011: Executive Summary. Access online 4 November 2011.
8. Al-Areqi, W. M, Ab. Majid, A. and Sarmani, S. (2014). Digestion study of water leach purification (WLP) residue for possibility of thorium extraction. *Malaysian Journal of Analytical Sciences*, 18(1): 221 – 225.
9. Al-Areqi, W. M, Ab. Majid, A. and Sarmani, S. (2014). Separation of thorium (IV) from lanthanide concentrate (LC) and water leach purification (WLP) residue. *AIP conference proceedings* 1614: 482.
10. Vijayalakshmi, R., Mishra, S. L., Singh, H. and Gupta, C. K. (2001). Processing of xenotime concentrate by sulphuric acid digestion and selective thorium precipitation for separation of rare earths. *Hydrometallurgy*, 61: 75 – 80.
11. Crouse D. J. and Brown K. B. (1959). Recovery of thorium, uranium, and rare earths from monazite sulfate liquors by amine extraction (AMEX) process, USA: Oak Ridge National Laboratory, pp 5 – 66.
12. Wang L., Y. Yu, X. Luang, Z. Long and D. Cui. (2013). Toward greener comprehensive utilization of bastnaesite: Simultaneous recovery of cerium, fluorine, and thorium from bastnaesite leach liquor using HEH(EHP) . *Chemical Engineering Journal*, 215-216: 162 – 167.
13. Amaral, J.C.B.S. and Morais, C. A. (2010).Thorium and uranium extraction from rare earth elements in monazite sulphuric acid liquor through solvent extraction. *Minerals Engineering*, 23:498 – 503.
14. Wickleder, M. S. Fourest, B. and Dorhout, P. K. (2010). The chemistry of the actinide and transactinide Elements, Chapter three: Thorium pp 52.
15. Ali, A. M. I, El-Nadi, Y. A, Daoud, J. A. and Aly, H. F. (2007). Recovery of thorium (IV) from leached monazite solutionsusing counter-current extraction. *International Journal of Mineral Processing*, 8: 217 – 223.
16. Hughes, K. C. and Singh, R. (1980). The isolation of thorium from monazite by solvent extraction. *Hydrometallurgy*, 6: 25 – 33.
17. Balakrishna, P., Varma, B. P., Krishnan, T. S., Mohan, T. R. R. and Ramakrishnan, P. (1988). Thorium oxide: calcination, compaction and sintering. *Journal of Nuclear Materials*, 160: 88 – 94.
18. Abrao, A., Alves de Freitas, A. and Sequeira de Carvalho, F. M. (2001). Preparation of highly pure thorium nitrate via thorium sulfate and thorium peroxide. *Journal of Alloys and Compounds*, 323–324: 53 – 56.
19. UNSCEAR (2000). Sources and effects of ionizing radiation. united nations scientific committee on the effects of atomic radiation. Report to the general assembly with annexes. United Nations Publication, New York.
20. IAEA (2011). Radiation protection and NORM residue management in the production of rare earths from thorium containing minerals, Safety reports series No. 68.
21. Cardarelli, F. (2008). Materials Handbook: A Concise Desktop Reference, 2nd Edition.
22. Zhu, Z., Pranolo, Y. and Cheng, C. Y. (2015). Separation of uranium and thorium from rare earths for rare earth production – A review. *Minerals Engineering*, 77: 185 – 196.

Malaysian Journal of Analytical Sciences, Vol 20 No 4 (2016): 777 - 792
DOI: http://dx.doi.org/10.17576/mjas-2016-2004-10

MALAYSIAN JOURNAL OF ANALYTICAL SCIENCES
Published by The Malaysian Analytical Sciences Society
ISSN 1394 - 2506

ADSORPTION OF ANIONIC DYES FROM AQUEOUS SOLUTIONS BY CALCINED AND UNCALCINED Mg/Al LAYERED DOUBLE HYDROXIDE

(Penjerapan Pewarna Ionik daripada Larutan Akues Menggunakan Mg/Al Dwi-Hidroksida Berlapis Berkalsin dan Tanpa Kalsin)

Siti Mariam Sumari*, Zaini Hamzah, Nesamalar Kantasamy

Faculty of Applied Sciences,
Universiti Teknologi MARA, 40450 Shah Alam, Selangor, Malaysia

**Corresponding author: sms21vic@gmail.com*

Received: 9 December 2015; Accepted: 6 May 2016

Abstract

The uptake of Acid Blue 29 (AB29), Reactive Orange 16 (RO16) and Reactive Red 120 (RR120) from aqueous solutions by calcined (CLDH) and uncalcined Mg/Al layered double hydroxide (LDH) has been investigated. The adsorption process was conducted in a batch mode at 25 °C. Anionic dye removal was more efficient using the CLDH rather than LDH. The adsorption process by CLDH involved reconstruction and hydration of the calcined LDH and intercalation of AB29, RO16 and RR120. Physical characterization using X-Ray Diffraction (XRD), Scanning Electron Microscopy (SEM) and Fourier Transform Infrared (FTIR) were used to ascertain the 'memory effect' phenomenon that is structural reconstruction to regain its original LDH after rehydration. To gain insight into the mechanism of adsorption by CLDH, the pseudo-first order (PFO) and pseudo-second order (PSO) and intraparticle diffusion (IPD) kinetic models were used to analyse experimental data. Based on the correlation coefficient (R^2), the PSO has better fitting (R^2 = 0.987 – 1.00) compared to PFO (R^2 = 0.867 –0.990). Furthermore the values of maximum adsorption capacity, (q_e) calculated from PSO model are consistent with the experimental q_e indicating that the experimental kinetic data for AB29, RO16 and RR120 adsorption by CLDH are suitable for this model. Recycling of the adsorbent, in cycles of calcination-reconstruction process promised a possibility of regeneration of CLDH.

Keywords: calcined, adsorption capacity, reconstruction, memory effect, regeneration

Abstrak

Penyingkiran pewarna Acid Blue 29 (AB29), Reactive Orange 16 (RO16) dan Reactive Red 120 (RR120) daripada larutan akues menggunakan Mg/Al dwi-hidroksida berlapis berkalsin (CLDH) dan tanpa kalsin (LDH) telah dilakukan menggunakan kaedah berkelompok pada suhu 25 °C. Penjerapan bahan pewarna menggunakan CLDH didapati lebih berkesan berbanding LDH. Penjerapan bahan pewarna oleh CLDH berlaku melibatkan proses penghidratan dan penstrukturan semula CLDH dan juga apitan AB29, RO16 dan RR120. Pencirian fizikal pada bahan penjerap yang diperolehi dengan menggunakan kaedah Pembelauan Sinar-X (XRD), Mikroskopi Imbasan Elektron (SEM) dan Spektroskopi Inframerah Transformasi Fourier (FTIR) telah digunakan untuk mengenalpasti fenomena 'kesan memori', iaitu proses penstrukturan semula kepada LDH selepas berlaku penghidratan. Cerapan lebih lanjut mengenai mekanisme proses penjerapan ini, model-model kinetik pseudo tertib pertama (PFO), pseudo tertib kedua (PSO) dan resapan intrapartikel (IPD) telah digunakan untuk menganalisis data ujian. Berdasarkan nilai pekali korelasi (R^2), model PSO didapati lebih sesuai (R^2 = 0.99 – 1.00) berbanding PFO (R^2 = 0.85 – 0.99). Fakta ini diperkukuhkan lagi dengan nilai kapasiti penjerapan maksimum, (q_e) hasil pengiraan menggunakan PSO yang didapati konsisten dengan q_e ujian ($q_{e,\ expt.}$) untuk AB29, RO16 dan RR120. Kitaran semula bahan penjerap melalui beberapa siri kitaran pengkalsinan-penstrukturan semula juga didapati dapat menjanjikan penjanaan semula CLDH.

Kata kunci: berkalsin, kapasiti penjerap, penstrukturan semula, kesan memori, penjanaan semula

Introduction

Dyehouse effluent usually contain various types of dye classes such as azo, anthraquinone, triphenylmethane,etc. Most of them are synthetic aromatic benzenoid compounds with potential toxic, mutagenic and carcinogenic properties, endangering human health and environment [1]. Generally, they are difficult to treat by conventional water treatment as they are structurally stable to biodegradation [2, 3].The most efficient colour removal from aqueous solution has been attributed to adsorption, which largely employs activated carbon (AC) as adsorbent. Since AC is commercially costly for large scale production and difficult to regenerate, alternative adsorbents are being sought. A positively charged anionic clay known as layered double hydroxide (LDH), with an empirical formula $[M^{II}_{1-x}M^{III}_{x}(OH)_2]^{x+}[A^{n-}_{x/n}\cdot mH_2O]^{x-}$, where M^{II} = Zn, Mg, Co, Ni and M^{III} = Al, Fe, Cr, Ga, etc., A^{n-} = CO_3^{2-}, NO_3^-, Cl^-, SO_4^{2-} [4, 5] is known for its versatile applications as well as excellent adsorbent for anionic species in aqueous solution.

Calcination of LDHs at temperature 400 – 700 °C can decompose LDH containing carbonate or nitrate to release CO_2 or NO_x gas with end products containing a solid mixture of Mg–Al oxide, which can revert to the original structure (reconstruction) of LDH upon rehydration [1, 6]. This phenomenon, well known as 'memory effect' was responsible for enhanced uptake of anionic dye removal by CLDH in comparison to its precursor LDH. The objective of this study is to investigate the kinetic behaviour of AB29, RO16 and RR120 adsorption by CLDH in comparison to its precursor LDH, while at the same time to assess the possibility of regeneration of the adsorbent. Kinetic parameters are important pre-requisites for eventual design of water treatment processes employing the use of adsorbents such as LDH/CLDH. XRD, FTIR and SEM were used to characterize the adsorbents before and after dye adsorption by CLDH. Kinetic models, Lagergren's pseudo-first order [7], Ho's pseudo-second order [8] and intraparticle diffusion [9] were used to gain understanding of the adsorption mechanism of by CLDH.

Therefore, desorption or calcination study was undertaken to evaluate the prospect of regeneration and reuse of the adsorbent.

Materials and Methods

Preparation of adsorbent LDH by co-precipitation method

Synthesis of layered double hydroxide (LDH) of the formula, $[M^{2+}_{1-x}M^{3+}_{x}(OH)_2]A^{n-}_{x/n}.mH_2O$ with M^{2+} = Mg^{2+}, M^{3+}=Al^{3+} and interlayer anion, A^{n-} = NO_3^- was conducted by coprecipitation procedure followed by hydrothermal treatment as outlined by several authors [10 – 12], with slight modification. A solution of $Mg(NO_3)_2.6H_2O$ and $Al(NO_3)_3.9H_2O$ with molar ratio of Mg/Al:4/1 were allowed to mix with 1M NaOH by drop wise addition of NaOH at a rate of 1 mL/min, stirring the mixture all the time using a magnetic stirrer, while keeping N_2 gas bubbling in the solution mixture throughout the coprecipitation process. This was to minimize the inclusion of CO_2 in the solution. The N_2 addition was allowed to continue until the solution's pH reading reached 10.0 ± 0.5 in a 1L beaker. The resulting heavy slurry was poured into stoppered glass bottles, and then aged in a thermostated oil bath shaker operating at 70 °C, 100 rpm for 24 hours duration. Once the resulting white precipitate was cooled, it was washed several times with distilled water until the pH reached 7 – 8, to get rid of excess alkali, after which the solid was separated out by vacuum filtration. The final white solid, named layered double hydroxide (LDH) was dried (80 °C, 24 hours) before being ground and sieved.

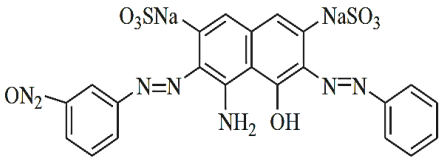
Preparation of calcined LDH

Calcination of the synthesized LDH was carried out by heating LDH at a designated temperature (100, 200, 300, 400, 500, 600 and 700 °C) in a furnace (Lenton, UK) for 8 hours. The calcined product (henceforth referred to as CLDH100, CLDH200, etc.) was stored in a desiccator prior to characterization and adsorption studies. The calcined product (CLDHs) were subjected to contact time experiment to study which CLDH (CLDH100, CLDH200, CLDH300, etc.) gave the highest percentage of dye removal and adsorption capacity, and consequently selected for adsorption by CLDH in comparison with its precursor LDH. In carrying out this experiment for a particular dye, the dosage and volume (*W*/*V*) were kept constant.

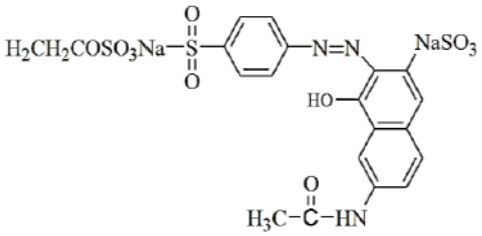
Preparation of adsorbates

Aqueous stock solutions (1000 mg/L) of RR120, RO16 and AB29 were prepared, from which diluted solutions were obtained for batch adsorption analysis. The chemical structures and physical properties of the three dyes are shown in Figure 1.

C.I Name	Acid blue 29 (AB29)
C.I No	20460
Formula Weight	616.49
Class	Diazo
λ_{max}	602 nm
Mol. Formula	$C_{22}H_{14}N_6Na_2O_9S$



C.I Name	Reactive Orange 16
C.I No	17757
Formula Weight	617.53
Class	Azo
λ_{max}	494 nm
Mol. Formula	$C_{20}H_{17}N_3Na_2O_{11}S$



C.I Name	Reactive Red 120
C.I No	25810
Formula Weight	1469.43
Class	Azo, Triazine
λ_{max}	532 nm
Mol. Formula	$C_{44}H_{24}Cl_2N_{14}Na_6O_{20}S$

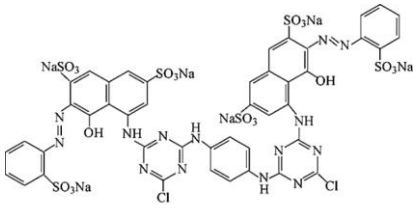


Figure 1. Chemical structures and physical properties of AB29, RO16 and RR120

Adsorption by calcined LDH (CLDH) and uncalcined LDH

The adsorption of AB29, RO16 and RR120 by LDH and CLDH was conducted in a batch mode in duplicates using initial concentration ranging from 50 to 100 mg/L with a constant dose of 0.2 g/L adsorbent at 25 ± 1°C in a thermostated water bath shaker, operating at 100 rpm. Since a previous separate experiment had shown that maximum removal for anionic and acidic dyes occurred at mild acidic pH, the batch adsorption of dyes under study was conducted at the pH of natural solutions without pH adjustment since the dyes are weakly acidic (5.6 – 6.6). This would be cost saving procedure since no extra cost for chemicals would be necessary. At the end of predetermined contact time (0 – 1440 min), the solution was filtered using 0.45 µm cellulose nitrate syringe filter (Whatman) so the remaining dye left in the solution can be measured using UV-Vis spectrophotometer (Secoman UVIKON SL/XS (M8307) at the wavelength of maximum absorption of each dye (Figure 1).

Adsorption data obtained were analysed for amount of dye adsorbed by the LDH and CLDH in terms of adsorption capacity (q_t, mg/g) and percentage dye removal (%) using the Equation (1) and (2), respectively

$$\text{Adsorption capacity, } q_t \text{ (mg/g)} = \frac{(C_0 - C_t)V}{W} \quad (1)$$

$$\text{Dye removal (\%)} = \frac{(C_0 - C_t)}{C_0} \text{ x } 100 \quad (2)$$

where, q_t is adsorption capacity in mg/g, C_o and C_t are initial and final dye concentrations (mg/L) after treatment for certain period of time, t; V is the volume of each dye solution (L) and W is the weight of adsorbent (g). At equilibrium time t_e, q_t=q_e.

Kinetic modeling

The data obtained from these experiments were used to evaluate the kinetic parameters. To gain insight into the mechanism of adsorption by LDH and CLDH, pseudo-first order (PFO) (Equation 3a), pseudo-second order (PSO) (Equation 4a) and intra-particle diffusion models (IPD) (Equation 5) were applied.

Pseudo-first order (PFO) model

The linear expression based on Lagergren's PFO rate equation [7] is represented by Eq. (3a):

$$\log(q_e - q_t) = \log q_e - \frac{k_1 t}{2.303} \quad (3a)$$

The initial rate h_1 (mg/g. min), at t=0 is defined by the following expression:

$$h_1 = k_1 q_e \quad (3b)$$

A linear plot of log(q_e -q_t) versus t enables the determination of k_1 (1/min) and q_e from the gradient and intercept of the plot.

Pseudo-second order (PSO) model

The linear expression for Ho's PSO rate equation [8] is represented by Equation (4a):

$$\frac{t}{q_t} = \frac{1}{k_2 q_e^2} + \frac{t}{q_e} \quad (4a)$$

The initial rate h_2 (mg/g. min), at t=0 is defined by the following equation:

$$h_1 = k_2 q_e^2 \quad (4b)$$

A linear plot of t/q_t versus t enables the determination of k_2 (g/mg.min) and q_e, from the intercept and the slope.

Intraparticle diffusion (IPD) model

The possibility of IPD resistance affecting adsorption was explored by using the Weber-Morris IPD model [9] is represented by Equation (5):

$$q_t = k_p t^{0.5} + C \quad (5)$$

where k_p(g/mg.min) is the intraparticle diffusion rate constant and C. By plotting q_t versus $t^{0.5}$, the values of k_p was calculated from the slope. The value of constant C can be found from the intercept and is a measure of the thickness of boundary layer. Hence, the higher value of C, the greater the effect of boundary layer [13]. Based on IPD theory, the plot is linear if intraparticle diffusion is involved in the adsorption process. Additionally, if these lines pass through the origin then intra particle diffusion is the rate controlling step [14,15].

Desorption and regeneration

The residue after initial adsorption (0 cycle) by CLDH was thermally treated at its calcination temperature and the final product (regenerated CLDH) was again subjected to dye adsorption (1st cycle). This process was repeated until

the 4th cycle when the percentage removal of dye became less than 25 – 30 %. The reusability of regenerated adsorbent was based on percentage dye removal calculated for each cycle using Equation 2.

Characterization

Powder X-Ray Diffraction (PXRD) is a technique used to characterize the crystallite size (grain size), crystallographic structure, and the preferred orientation in polycrystalline or powdered solid samples. The X-ray diffraction (XRD) patterns of LDHs and CLDHs before and after adsorption were recorded using a PanAlytical (Germany) diffractometer under the following conditions: 40 kV, 25 mA, Ni-filtered Cu-Kα radiation (λ = 1.542 Å) and scanning rate of 2θ/min in the range of 10 – 70 °C. The XRD patterns enable the elucidation of basal spacings (d-spacings) of LDHs and CLDHs at pre or post adsorption of dye and give some indications of any change in crystallographic structure. Microstructural examination of LDH and CLDH was carried out using a Carl Zeiss SMT-Supra 40VP (Germany) scanning electron microscope (SEM) to study surface morphologies. The specific surface area of LDH and CLDH was obtained from adsorption/desorption isotherm of liquid N_2 at -196 °C following the standard Brunauer, Emmett and Teller (BET) method using using Micromeritics surface area analyser (USA).

Results and Discussion

Calcination temperature of Mg/Al LDH

Figure 2 shows the results based on a preliminary investigation on percentage of dye removal using LDH calcined at various temperatures (200 – 700 °C). It is obvious that dye removal percentage was highest with LDH calcined at 500 °C (CLDH500). Upon calcination, LDH was transformed to aluminium and magnesium oxides by the loss of interlayer anions, causing the adsorption of dye to increase in the temperature range 200 –500 °C, reaching the highest at 500 °C, corresponding to complete or almost complete decomposition of interlayer nitrate (Equation 6). Until this stage, the process was reversible; it was able to reconstruct its original LDH structure (memory effect) by incorporating anions such as water or anionic dyes or others (Equation 7). Above 500 °C, CLDH was transformed into a spinel which lost the property of reconstruction and reversibility, resulting in the observed decrease in dye adsorption. Other researchers using calcined Mg/Al-LDH to remove pollutants had also used the same temperature (500 °C) to obtain calcined LDH [16 – 18]. Based on this result, subsequent adsorption experiment was conducted using CLDH500.

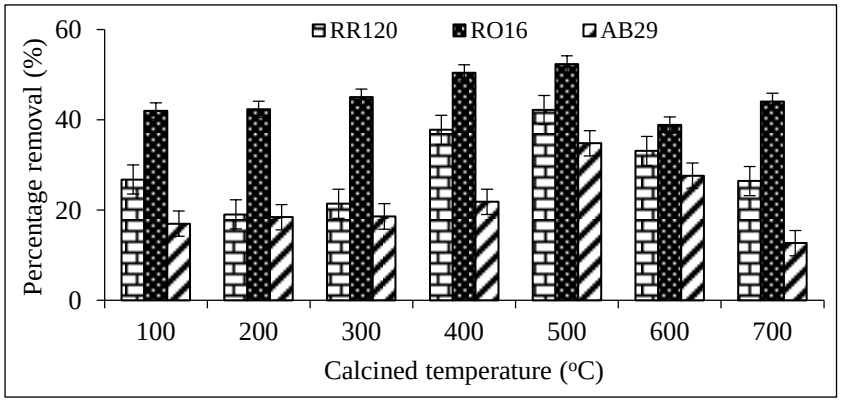


Figure 2. Percentage of dye removal by CLDHs calcined at different temperatures

Decomposition:

$$Mg_{1-x}Al_x(OH)_2(NO_3)_{x/2}.mH_2O \xrightarrow{500\ ^oC} Mg_{1-x}Al_xO_{1+x/2} + (x/2\ NO_2) + (m+1)H_2O \quad (6)$$

Regeneration:

$$Mg_{1-x}Al_xO_{1+x/2} + (x/n)A^{n-} + (m + 1 + (x/2) + y)H_2O \longrightarrow Mg_{1-x}Al_x(OH)_x(A^{n-})_{x/n}.mH_2O + xOH^- \quad (7)$$

Characterization of calcined and uncalcined LDH

X-Ray diffraction

The XRD pattern of precursor LDH in Figure 3(a) consists of three intense lines at low 2θ angle equivalent to diffraction by planes (003), (006) and (009) [7]. These sharp and symmetric peaks indicate the formation of a single well crystallized $MgAlNO_3$. The interlayer distance or (d_{003}) and (d_{006}) of LDHs corresponding to 8.01 Å and 3.99 Å, are due to basal reflections of crystal lattice, indicating successive layer stacking of the brucite-like lamellar sheets of hydrotalcite-like LDHs (ICSD collection code 086655). These values, together with other non- basal spacings at 1.54 Å (d_{110}) and 1.51 Å (d_{113}) are consistent with typical XRD pattern of LDH as reported by several authors [1, 3, 19 – 21]

Calcination up to 500 °C led to the progressive loss of physiosorbed water molecules, then the interlayer water and finally water from dehydroxylation of the brucite layer. The dehydration process was accompanied by the loss of interlayer anion leading to the collapse of the lamellar structure of LDH with the formation of mixed metal oxides $MgO\text{-}AI_2O_3$. As implied in the XRD pattern in Figure 3(b), the layered structure of the original LDHs has been destroyed in CLDH500 (CLDH) as evident from the significant absence of d_{006} and d_{003} peaks. Instead broad diffraction peaks appeared suggesting low structural order with almost total decomposition of the original LDHs with elimination of most interlayer nitrate anions and water. The XRD patterns of CLDH now resemble that of rock salt MgO whose reflection has shifted to higher angle due to the presence of Al^{3+} in in $Mg_{(1-x)}Al_xO_{(1+x/2)}$ [17]. No separated phases for Al^{3+}cations (Al_2O_3) were observed, indicating that these cations were dispersed in the MgO matrix solid solution [19], which is capable of being restored to LDH when rehydrated [5]. These observations were consistent with CLDH patterns cited in the literatures [1, 3, 17]. Figures 3(c – e) also shows that the diffraction patterns of dye- loaded CLDHs displaying peaks corresponding to (d_{003}) and (d_{006}) which are similar to the original LDH's XRD pattern. However the resulting peaks were broadened and with decreased peak intensity. This implies some reduction in crystallinity as a result of calcinations, rehydration and structural reconstruction which have occurred [21]. Due the 'memory effect', the CLDH was able to reconstruct and regain its original LDH when rehydrated [5].

After reconstruction, the basal spacings, notably (d_{003}) were observed to have increased in the dye-loaded CLDH (8.55 Á, 8.47 Á and 8.86 Á), indicating some increase in the interlayer distance. Theoretically, the increase in basal spacing (d_{003}) and (d_{006}) may indicate some dyes were intercalated into the spacing. Being bigger molecule than nitrate, the dye intercalated in the interlayer spacing was expected to result in an increase of the basal spacing or gallery height of the lamellar LDH. However, since the increase was not significantly large, it considered that total intercalation has indeed taken place [5]. The structural reconstruction property, called 'memory effect' forms the basis of regeneration for adsorbent LDH and the main mechanism of dye adsorption by CLDH though surface adsorption is presumed to have taken place as well [19]. This should be possible as surface area of calcined LDH has been reported to increase compared to its precursor LDH. On the basis of larger surface area of CLDH relative to LDH, it is fair to assume that CLDH offers better adsorption efficiency than its precursor.

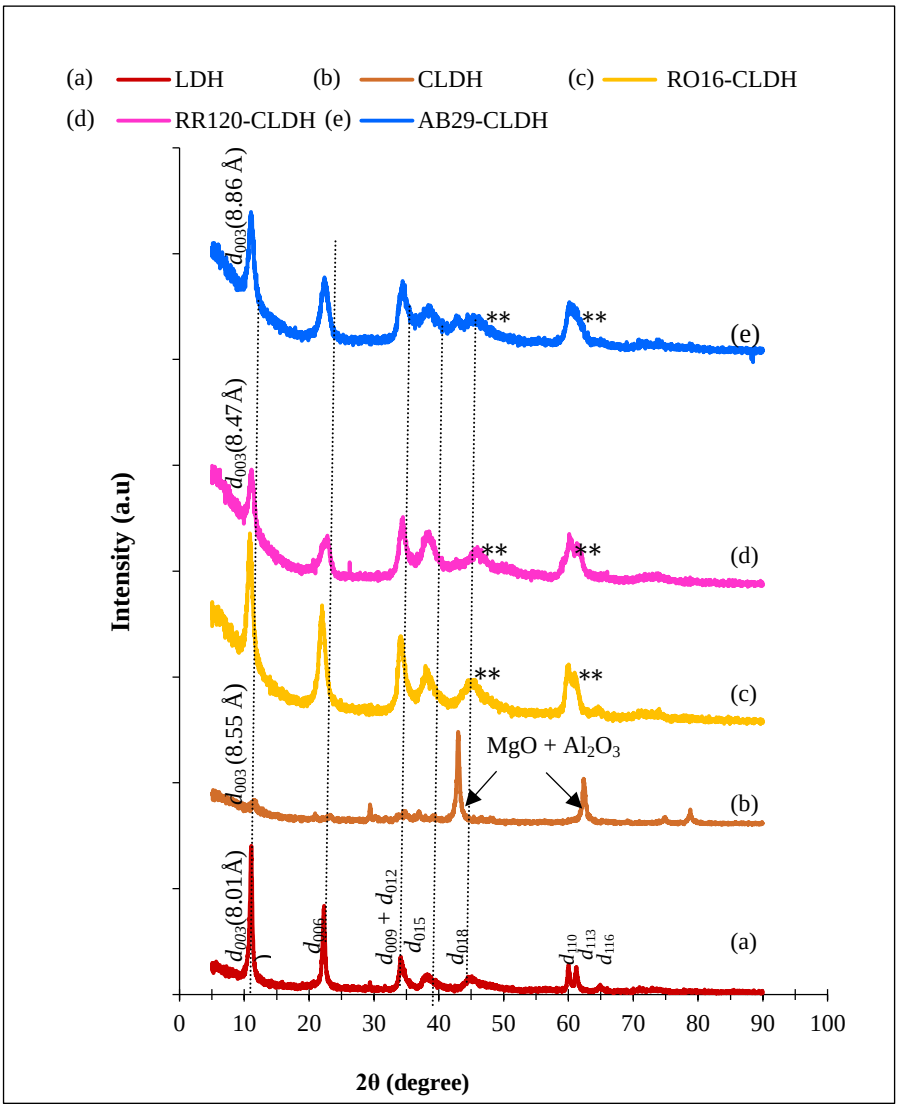


Figure 3. X-Ray Diffraction for LDH, CLDH and Dye loaded CLDH

Scanning electron microscopy

The textural properties of the LDH, CLDH and dye-loaded CLDHs have been investigated by scanning electron microscopy, as shown in Fig. 4 (a – e). It can be seen that the LDH image presents thin irregular aggregates of hexagonal platelets while CLDH resembles bigger platelets with rounded edges, with some still retaining the hexagonal-shaped of precursor LDH materials that were still retained in the CLDH product. This observation was understandable since both LDH and CLDH gave the same N_2 adsorption-desorption analysis results [21]. It has been reported that during thermal decomposition of LDH, the evolution of gas such as CO_2 (from carbonate) or NO/NO_2 (NO_x) from nitrate took place through fine pores at the brucite-like ($Mg(OH)_2$) layers, inducing the creation of channels and chimneys, which account for the increase surface area for calcined LDH. Since adsorption is a surface phenomenon, increase in surface area would enhance adsorption by CLDH. In the current study, the BET surface area for CLDH was found to be 121.58 m^2/g compared to 82.74 m^2/g for uncalcined LDH. Closer examination on SEM images in Fig.4 (a – e) reveals that dye materials have been incorporated onto the CLDH.

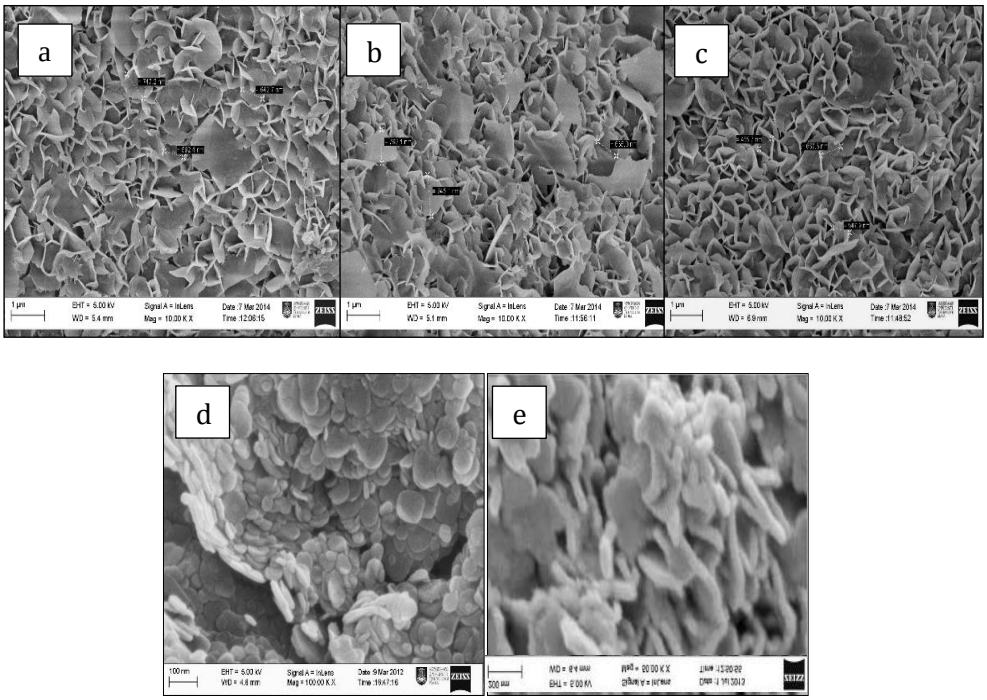


Figure 4. SEM images of (a) AB29-CLDH, Mag.:10K, (b) RO16-CLDH, Mag.:10 K, (c) RR120-CLDH, Mag.:10K, (d) LDH, Mag.: 100 K and (e) CLDH, Mag.: 50 K

Infrared spectra

The FTIR spectra of LDH, CLDH and dye-loaded CLDHs are presented in Figure 5. The LDH spectrum resembles that of other hydrotalcite-like phases with NO_3^- as the interlayer anions. The broad band at 3455 –3500 cm^{-1}, with a weak shoulder near 3100 cm^{-1} is due to the interlayer water molecules and the H-bonded stretching vibration respectively [7, 22, 23]. The weak peak at 1637 cm^{-1} may be assigned to the H_2O bending vibration of interlayer water, while the strong peak at 1384 cm^{-1} is attributed to the vibration of nitrate species. The bands in the range of 500 – 700 cm^{-1} are indicative of metal–oxygen–metal stretching [23].

Figure 5 shows the absorption bands of dye-loaded CLDH. It may be not plausible to exactly quantify the amount of NO_3^- the LDH or CLDH by FT-IR spectroscopy, but the reduced intensity of the nitrate peaks with reference to the broad band at 3450 cm^{-1} and at 1637 cm^{-1} after dye uptake indicate that anion exchange between NO_3^- ion and dye molecules did take place. The absorption band at around 1421 cm^{-1} in CLDH is indicative of the presence of CO_3^{2-} in the interlayer. The presence of CO_3^{2-} as an impurity may be difficult to avoid under the prevailing experimental conditions with the readiness of CLDH to take up moisture containing CO_2. The expected intercalation of dye in the CLDH interlayer may also be discerned by the presence of absorption band in the region around 1200 cm^{-1} which can be attributed to C-H bending vibration of aromatic dye molecules. The band occurring between 1450 cm^{-1} and 1380 cm^{-1} corresponds to the stretching mode of an azo-compound. The presence of sulfate S=O stretching vibration bands at around 1000 –1250 cm^{-1} and 1065 cm^{-1} due to sulfonic group in the dyes' structures were also observed. The result indicated that the dyes had existed on the surface of the CLDH after adsorption.

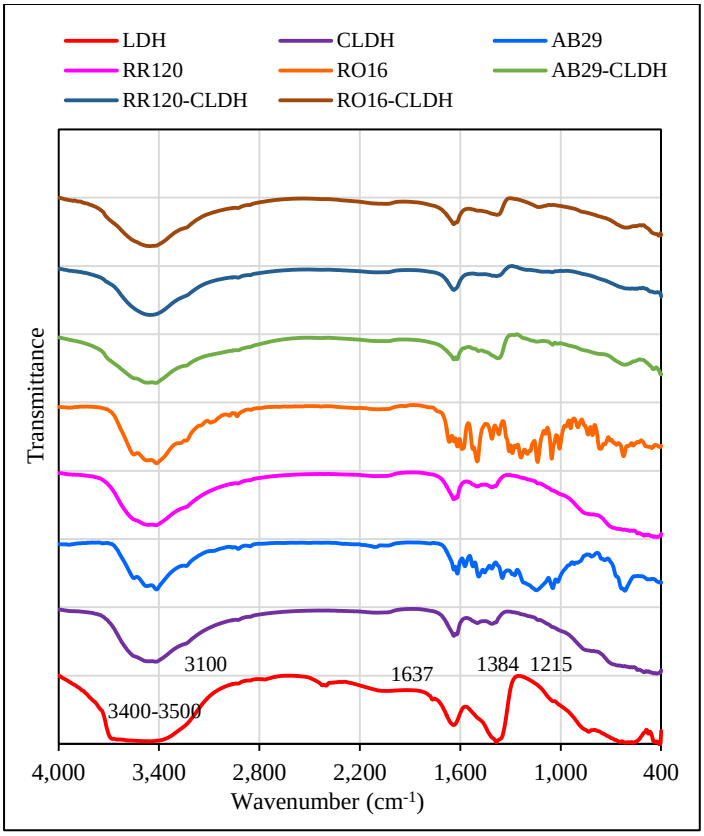


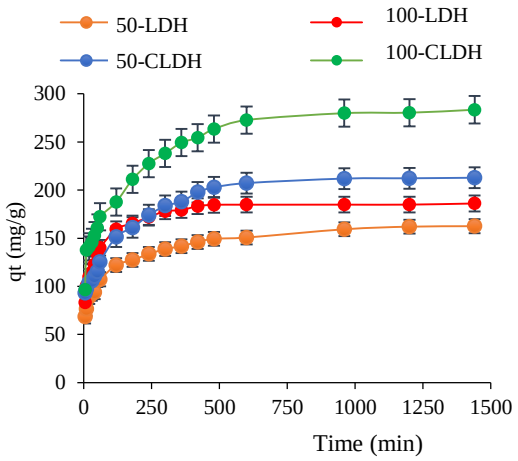
Figure 5. FTIR spectra of LDH, CLDH, dyes and dye-loaded CLDH, respectively

Effect of contact time and initial dye concentrations

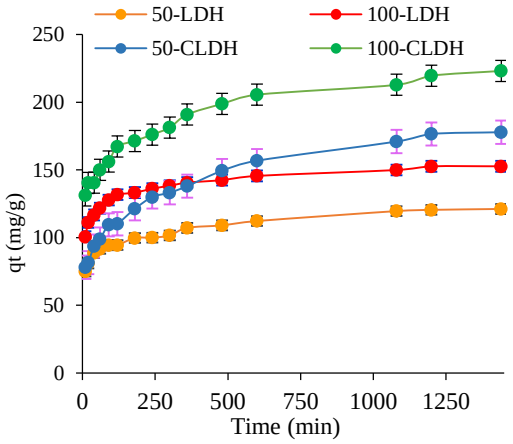
The effect of contact time on and initial concentrations on dye removal by CLDH was compared with dye removal by LDH. The results for AB29, RO16 and RR120 are depicted in Figure 6 (a – c) for adsorption capacity, q_t, mg/g. Figure 6 shows that adsorption capacity increased with increased contact time until equilibrium was attained and thereafter remained almost unchanged after contact time of approximately 150 –180 min. For both LDH and CLDH, the adsorption capacity of dye increased rapidly within the first 10 – 20 min, after which the rate of adsorption decreased with time until it gradually approached a plateau due to the continuous decrease in the concentration driving force.

The time curves of dye removal for concentrations 50 – 100 mg/L in Figure 6 (a – c) are smooth and continuous indicating the possibility of a monolayer formation on adsorbent surface [16][23]. As Figure 6 (a – c) depict, the maximum adsorption capacity by CLDH and LDH decreased with increasing initial dye concentration as the number of moles of dye competing for the available surface area of the adsorbent which was fixed for a constant adsorbent dose, increased [16]. The most significant observation in this experiment was the enhanced dye uptake, both in terms of percentage dye removal and adsorption capacity by CLDH over its precursor LDH for any given initial dye concentration. Examples of this elevated dye removal by CLDH over its precursor LDH are highlighted for 50 and 100 mg/L dye concentration for AB29, RO16 and RR120 in Table 1, which shows the values of q_t (mg/g). Calculation for (dye uptake by CLDH/dye uptake by LDH) ratio reveals that the increase was between 150 – 200 %. The increase uptake by CLDH was attributed largely to the 'memory effect' phenomenon which is synonym with structural reconstruction by calcined LDH to its original layered structure when exposed to aqueous solution containing ions such as simple inorganic ions (eg. CO_3^{2-}, SO_4^{2-}, SeO_3^{2-}, CO_3^{2-}, NO_3^-, Cl^-) or polar organic molecules [5]. Among the three dyes, AB29 exhibit the highest dye uptake followed by RO16 and RR120, the same

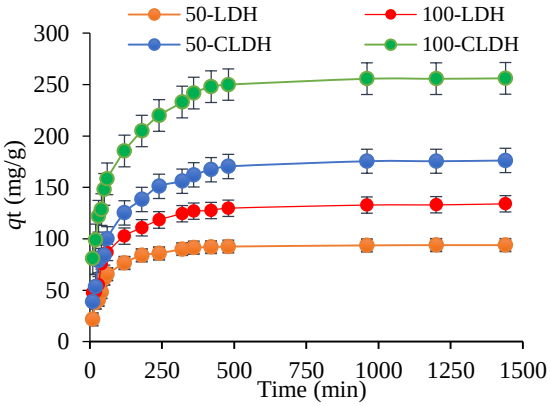
trend as uptake by pristine LDH. This trend is reflective of binding capacity of these dyes towards the adsorbent LDH and CLDH.



(a) AB29



(b) RO16



(c) RR120

Figure 6. Effect of contact time and initial dye concentrations on adsorption capacity in adsorption by LDH and CLDH on anionic dyes (a)AB29, (b) RO16 and (c) RR120

Kinetic of adsorption

The kinetic parameters for PFO, PSO and IPD kinetic models for dye-LDH and dye-CLDH obtained using experimental data for Figure 6 are summarised in Tables 2, 3 and 4, respectively. It is apparent that the values of correlation coefficient (R^2) are mostly quite high (> 0.9) for PFO, PSO and IPD models. Based on the correlation coefficient (R^2), it can be seen that PSO have better fitting (R^2 = 0.99 – 1.00) than PFO (R^2 = 0.85 –0.99). Furthermore the values of q_e calculated ($q_{e,alc}$) from PSO model are more consistent with the experimental q_e ($q_{e,expt.}$), indicating that the experimental kinetic data for AB29, RO16 and RR120 adsorption by LDH and CLDH are suitable for this model. Similar finding was obtained by [17] on Reactive Orange 10 adsorption by CLDH. In addition, the values of ($q_{e,\ calc}$) and q_e ($q_{e,expt.}$) shows that maximum adsorption capacities are higher for CLDH than

those by LDH. The results are consistent with CLDH being a more efficient adsorbent than LDH as dye scavenger from solution. The order of adsorption affinity for adsorbent is reflected from the values of the adsorption capacities. It can be seen that the order of affinity of adsorbent for dyes under study is AB29 >RO16 > RR120. This trend was obeyed by systems, dye-LDH and dye-CLDH.

Table 1. Comparison between dye uptake by LDH and CLDH in terms of adsorption capacity, ($q_{t,expt}$) at t=24 h, T=25 ^{o}C, W/V=0.2g/L for AB29, RO16 and RR120, respectively

Dye	**Adsorbent**	**Concentration**	
		50 mg/L	**100 mg/L**
		qt (mg/g)	**qt (mg/g)**
AB29	LDH	162.501	186.100
	CLDH	212.830	283.506
RO16	LDH	121.160	152.655
	CLDH	177.858	268.140
RR120	LDH	96.338	133.979
	CLDH	176.155	256.074

To understand this trend, factors that influence dye binding capacity to adsorbent have to be considered. These factors include the characteristics and chemistry of the dye such as molecule structure, molecular weight, spatial and steric effect, all of which exert influence on the adsorption onto adsorbent either singly or in concert with other factors present in the aqueous environment. In this case AB9 and RO16, having smaller size than RR120 would be more unhindered during adsorption compared to the bulkier RR120 in terms of spatial and steric effect, even though RR120 has six sulfonic groups (SO_3^-) compared to two in AB29 and RO16. As a result RR120 would have less mobility in attaching itself to adsorbent, even though the sulfonic groups render negative charge to the RR120, thus enhancing the dye ability to attach itself onto positively-charged adsorbent. In terms of negative charges, AB29 would be expected to have similar binding capacity. The fact that acid dye AB29 displayed better binding capacity than vinylsulphone reactive dye RO16 is probably due to a side reaction of RO16 in water. The vinylsulphone group ($-CH_2CH_2SO_2$ -) in RO16 is electron attracting group which induces electron deficiency on the terminal carbon atom, initiating a nucleophilic (addition reaction) attack by electron rich hydroxyl ion, OH^- from water. This hydrolysis can be represented by the reaction:

$$\text{Dye-}SO_2CH = CH_2 + \text{H-OH} \longrightarrow \text{Dye-}SO_2\text{-}CH_2\text{-CH2-OH} \quad (8)$$

As a result of this hydrolysis, RO16 is less available for binding sites on LDH/CLDH with an overall reduction in binding capacity of RO16.

The resulting IPD linear plots of q_t versus $t^{0.5}$ (not shown) show the existence of two or three-staged linear curves, none of which pass through the origin. This is an indication that IPD was not the sole rate limiting step. Moreover, the existence a two or three-linear phases for each concentration implies that most likely the adsorption process involved more than one rate equation.

Table 2. Pseudo-first order and pseudo-second-order kinetic parameters for dye-LDH system for AB29, RO16 and RR120, W/V= 0.2 g/L, T=25°C

AB29-LDH		**Pseudo first-order**				**Pseudo second-order**			
Co (mg/L)	$q_{e,expt}$ **(mg/g)**	$q_{e,\ calc}$ **(mg/g)**	$k_1 \times 10^{-3}$ **(1/min)**	$h_1 \times 10^{-1}$ **(mg/g.min)**	R^2	$q_{e,\ calc}$ **(mg/g)**	$k_2 \times 10^{-4}$ **(mg/g min)**	h_2 **(mg/g.min)**	R^2
50	162.500	122.462	4.836	5.923	0.988	156.250	1.74	5.970	0.998
100	186.100	156.315	4.145	6.480	0.990	188.679	3.17	11.274	0.994
RO16-LDH		**First-order kinetic**				**Second-order kinetic**			
Co (mg/L)	$q_{e,expt}$ **(mg/g)**	$q_{e,\ calc}$ **(mg/g)**	$k_1 \times 10^{-3}$ **(1/min)**	$h_1 \times 10^{-3}$ **(mg/g.min)**	R^2	$q_{e,\ calc}$ **(mg/g)**	$k_2 \times 10^{-4}$ **(mg/g min)**	h_2 **mg/g.min**	R^2
50	121.160	18.621	2.764	2.533	0.944	106.383	6.38	7.225	0.992
100	152.655	35.278	2.533	2.764	0.946	185.185	3.36	11.534	0.999
RR120-LDH		**First-order kinetic**				**Second-order kinetic**			
C_o (mg/L)	$q_{e,expt}$ **(mg/g)**	$q_{e,\ calc}$ **(mg/g)**	$k_1 \times 10^{-3}$ **(1/min)**	$h_1 \times 10^{-1}$ **(mg/g.min)**	R^2	$q_{e,\ calc}$ **(mg/g)**	$k_2 \times 10^{-4}$ **(g/mg min)**	$h_2 \times 10^{-3}$ **(mg/g min)**	R^2
50	96.338	57.610	8.291	4.78	0.982	96.154	3.553	3.286	1.000
100	133.979	79.177	6.448	5.11	0.983	136.986	2.132	4.002	1.000

Table 3. Pseudo-first order and pseudo-second-order kinetic parameters for dye-CLDH system for AB29, RO16 and RR120, W/V = 0.2 g/L, T = 25 ^{o}C

AB29-CLDH		**Pseudo first-order**				**Pseudo second-order**			
Co (mg/L)	$q_{e,expt}$ **(mg/g)**	$q_{e,\ calc}$ **(mg/g)**	$k_1 \times 10^{-3}$ **(1/min)**	$h_1 \times 10^{-1}$ **(mg/g.min)**	R^2	$q_{e,\ calc}$ **(mg/g)**	$k_2 \times 10^{-5}$ **(g/mg min)**	h_2 **(mg/g min)**	R^2
50	212.83	103.514	4.606	5.719	0.946	250.000	8.84	5.525	0.998
100	283.506	141.254	2.303	3.253	0.991	333.333	6.34	7.042	0.998
RO16-CLDH		**Pseudo first- order**				**Pseudo second-order**			
Co (mg/L)	$q_{e,expt}$ **(mg/g)**	$q_{e,\ calc}$ **(mg/g)**	$k_1 \times 10^{-3}$ **(1/min)**	$h_1 \times 10^{-1}$ **(mg/g.min)**	R^2	$q_{e,\ calc}$ **(mg/g)**	$k_2 \times 10^{-5}$ **(g/mg min)**	$h_2 \times 10^{-3}$ **(mg/g min)**	R^2
50	177.858	105.196	3.224	2.423	0.965	181.818	7.944	2.631	0.994
100	268.140	111.764	3.224	3.603	0.958	277.778	7.840	6.050	0.999
RR120-CLDH		**Pseudo first-order**				**Pseudo second-order**			
Co (mg/L)	$q_{e,expt}$ **(mg/g)**	$q_{e,\ calc}$ **(mg/g)**	$k_1 \times 10^{-3}$ **(1/min)**	h_1 **(mg/g.min)**	R^2	$q_{e,\ calc}$ **(mg/g)**	k_2 **x10-10^{-4} (g/mg min)**	h_2 **x (mg/g min)**	R^2
50	176.155	97.275	4.376	0.4256	0.938	181.818	3.6	3.824	1.000
100	256.074	168.578	6.909	1.1647	0.992	344.828	0.58	11.136	1.000

The calculated values of IPD rate constant, k_p, C and the R^2 values summarized in Table 4 were obtained through fitting the experimenal data at second linear portion of Equation (3)[24]. The correlation coefficients for IPD diffusion model obtained are between 0.746 and 0.979. The R^2-values are quite high and some are close to unity

indicating the validity of application of this model. The values of IPD rate constant, k_p decreased with decreasing initial dye concentration which provided the driving force in overcoming the resistance due to mass transfer [24] and was found to be correlated with the initial dye concentration. The values of *C* give an idea about the thickness of the boundary layer, i.e. the larger the intercept the greater is the boundary layer effect (mass resistance), and the greater is the contribution of the surface adsorption in the rate limiting step[25]. In conclusion the adsorption mechanism of dye uptake by LDH is quite a complex process and cannot be explained by a single kinetic model alone, but could have involved more than single type of kinetic mechanism, all of which may be operating simultaneously [26][27].

Table 4. Intraparticle diffusion constants at different initial dye concentrations at 25 ^{o}C for dye-LDH and dye-CLDH system for AB29, RO16 and RR120; *W*/*V* = 0.2 g/L, T = 25°C

Dye		**Intraparticle diffusion model**			**Dye**		**Intraparticle diffusion model**		
LDH	**C_o mg/L**	**k_p (mg/g.min$^{0.5}$)**	**C**	**R^2**	**CLDH**	**C_o mg/L**	**k_p (mg/g.min$^{0.5}$)**	**C**	**R^2**
AB29	50	1.710	107.401	0.892	AB29	50	4.396	104.172	0.983
	100	1.333	151.071	0.746		100	6.209	127.031	0.974
RO16	50	0.4251	91.001	0.955	RO16	50	2.929	77.801	0.965
	100	0.8052	123.98	0.973		100	2.643	132.03	0.952
RR120	50	2.608	83.250	0.985	RR120	50	4.095	83.252	0.979
	100	2.302	77.438	0.957		100	6.073	122.76	0.978

Mechanisms of adsorption by CLDH

Results on dye removal had shown that CLDH exhibited better efficiency than its precursor LDH in removing anionic dyes from solution. The resulting calcined LDH (CLDH) has higher specific surface areas compared to its precursor LDH. Since adsorption is a surface phenomenon, this could be a major factor accounting for the significant increase in the anionic dye affinity for CLDH. During calcination process, fine pores and channels were generated as H_2O vapor and NO_2/NO gas were evolved, resulting in the creation of chimneys and channels in the particles, which ultimately resulted in the increase in specific surface area and smaller pores in the mesoporous CLDH particles.

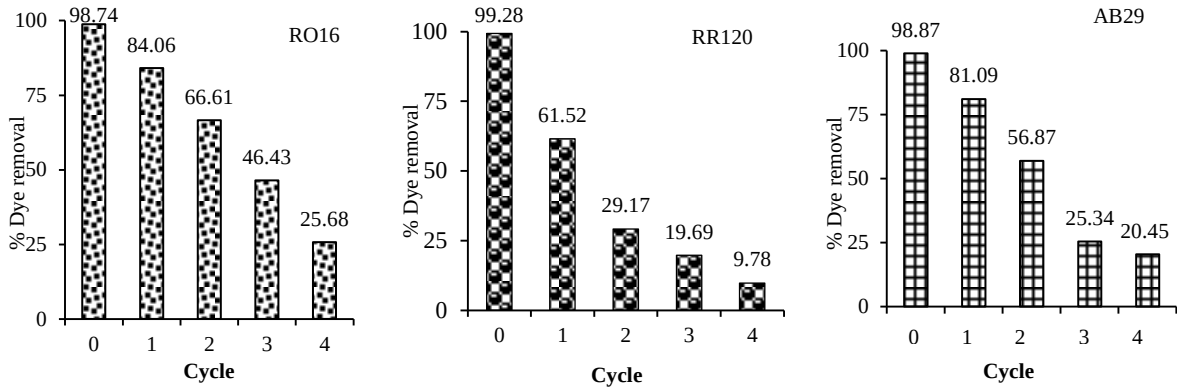
The diffactograms of calcined materials shown in Figure 3 show that the CLDH displayed its 'memory effect' by reconstructing to its former LDH structure as evident through the re-emergence of (003) and (006) reflections. This is further supported by the observed of somewhat broadened, less symmetrical peaks with reduced intensity in comparison to the original LDH, indicating less ordered platelet–like structure and crystallinity [5], typical of post adsorption products following rehydration and reconstruction. It has been postulated that intercalation via reconstruction had played a role in this process of adsorption by CLDH according to Eq. (8), given the relatively slow increase in dye adsorption as dye concentration was increased (Figure 6). This 'memory effect' may be construed as a reconstruction reaction expressed as expressed by the preceding Equation (8) [21].

It may be concluded that under prevailing conditions, external surface adsorption appeared to be the main mechanism in the adsorption. Furthermore, the peaks corresponding to MgO in CLDH still remained in all CLDH products, indicating that reconstruction was not complete.

Regeneration and recyclability

Regeneration of adsorbent for possible reuse gives an advantage commercially and economically to an adsorbent. The results from four cycles of regeneration were obtained from calcination-hydration process whereby the adsorbed dyes was combusted during calcination, followed by rehydration of the regenerated adsorbent LDH in the

dye solution. As shown in Figure 7, the thermally treated LDHs, exhibited progressive loss in percentage dye removal after each cycle. This percentage loss varied for each dye. After four cycles the efficiency has been reduced to almost 10 – 25 %, and may be regarded as uneconomical for further regeneration. A possible reason for the reduced efficiency is the reduced crystallinity of adsorbent, after undergoing repeated calcination-hydration process [28].



Co= 50 mg/L; *W*/*V*= 0.1 g/50 mL, 25 ^{o}C

Figure 7. Regeneration of CLDH after adsorption by RO16, RR120 and AB29

Conclusion

The adsorption of AB29, RO16 and RR120 was much more efficient by CLDHs than LDHs. Similarly, the adsorption capacities of CLDHs were much higher than that of its precursor LDHs. The affinity towards dye removal follows the order: AB29 > RO16 > RR120. Therefore CLDHs may be recommended for use in sequestering higher concentration of anionic dyes, while LDHs may be more appropriately used for low concentrations. The kinetics of adsorption of anionic dyes was well described by PSO reaction while PFO reaction and IPD kinetics may have contributed to the overall mechanism of dye uptake. Reconstruction of LDH via rehydration and intercalation was evident from X-ray diffraction and FTIR spectroscopy analysis. Recycling and reuse of LDH/CLDH was possible, until the fourth cycle when this is no longer economical. For better performance, only the second and third cycle may be considered when the percentage dye removal could still be maintained at 50 – 66 % for these dyes.

References

1. El Gaini, L. Lakraimi, M., Sebbar, E., Meghea, A., and Bakasse, M. (2009). Removal of indigo carmine dye from water to Mg–Al–CO3-calcined layered double hydroxides. *Journal of Hazardous Materials*, 161: 627 – 632.
2. Lazaridis, N. K., Karapantsios, T. D. and Georgantas, D. (2003). Kinetic analysis for the removal of a reactive dye from aqueous solution onto hydrotalcite by adsorption. *Water Research*, 37: 3023 – 3033.
3. Abdelkader, N. B-H., Bentouami, A. Derriche, Z., Bettahara, N., de Menorval, L-C. Chemical. (2011). Synthesis and characterization of Mg–Fe layer double hydroxides and its application on adsorption of Orange G from aqueous solution. *Engineering Journal*, 169: 231 – 238.
4. Das, J., Das, D. K. M. and Parida, K. M. (2006). Preparation and characterization of Mg–Al hydrotalcite-like compounds containing cerium, *Journal of Colloid and Interface Science*, 301: 569 –574.
5. Auxilio, A. R., Andrews, P. C., Junk, P. C. and Spiccia, L. (2009). The adsorption behavior of C.I. Acid Blue 9 onto calcined Mg–Al layered double hydroxides. *Dyes and Pigments*, 81: 103 – 112.

6. Das, J., Das, D. K. M. and Parida, K. M. (2006). Preparation and characterization of Mg–Al hydrotalcite-like compounds containing cerium, *Journal of Colloid and Interface Science*, 301: 569 –574.
7. Lagergren, S. (1898). About the theory of so called adsorption of soluble substances. K. Sven. Vetenskapsakad. Handl., Band 24, 1 – 39.
8. Ho, Y. S. (2006). Review of second-order models for adsorption systems. *Journal of Hazardous Materials*, 136: 681 – 689.
9. Weber, W. J. and Morris, J. C. (1963). Kinetics of Adsorption on Carbon from Solution. *Journal of the Sanitary Engineering Division*, 89(2): 31 – 60.
10. Reichle, W. T. (1986). Synthesis of anionic clay minerals (mixed metal hydroxides, hydrotalcite). *Solid State Ionics*, 22: 135 – 141.
11. Forano, C., Hibino, T., Lerouxa, F. C. and Taviot-Gue, H. (2006). Layered double hydroxides. *Developments in Clay Science*, 1: 1021 – 1095.
12. Kameda, T., Yamazaki, T. and Yoshioka, T. (2009). Preparation of MgAl layered double hydroxide intercalated with 2,7-Naphthalene Disulfonate and its selective uptake of aromatic compounds from aqueous solutions. *Bulletin of the Chemical Society of Japan*, 82: 1436 – 1440.
13. Mahmoodi, N. M., Hayati, B. and Arami, M. (2012). Kinetic, equilibrium and thermodynamic studies of ternary system dye removal using a biopolymer. *Industrial Crops and Products*, 35: 295 – 301.
14. Senthilkumaar, S., Kalaamani, P., Porkodi, K., Varadarajan, P. R. and Subburaam, C. V. (2006). Adsorption of dissolved reactive red dye from aqueous phase onto activated carbon prepared from agricultural waste. *Bioresource Technology*, 97: 1618 – 1625.
15. Yu, L. and Luo, Y. (2014). The adsorption mechanism of anionic and cationic dyes by Jerusalem artichoke stalk-based mesoporous activated carbon. *Journal of Environmental Chemical Engineering*, 2: 220 – 229.
16. Das, J., Das, D. K. M. and Parida, K. M. (2006). Preparation and characterization of Mg–Al hydrotalcite-like compounds containing cerium. *Journal of Colloid and Interface Science*, 301: 569 –574.
17. Bouhent, M. M., Derriche, Z., Denoyel, R., Prevot, V., and Forano, C. (2011). Thermodynamical and structural insights of orange II adsorption by MgRAlNO3 layered double hydroxides. *Journal of Solid State Chemistry*, 184: 1016 – 1024.
18. Bouraada, M., Belhalfaoui, F. and Ouali, M. S. (2009). Sorption study of an acid dye from an aqueous solution on modified Mg–Al layered double hydroxides. *Journal of Hazardous Materials*, 163: 463 –467.
19. Extremera, R., Pavlovic, I., Pérez, M. R., and Barriga, C. (2012). Removal of acid orange 10 by calcined Mg/Al layered double hydroxides from water and recovery of the adsorbed dye. *Chemical Engineering Journal*, 213: 392 – 400.
20. Zhu, M-X., Li, Y-P., Xie, M. and Xin, H-Z. (2005). Sorption of an anionic dye by uncalcined and calcined layered double hydroxides: A case study. *Journal of Hazardous Materials*, 120: 163 – 171.
21. Ni, Z. M., Xia, S. J., Wang, L. G., Xing, F. F. and Pan, G. X. (2007). Treatment of methyl orange by calcined layered double hydroxides in aqueous solution: Adsorption property and kinetic studies. *Journal of Colloid and Interface Science*, 316: 284 – 291.
22. Crepaldi, E. L., Tronto, J., Cardoso, L. P. and Valim, J. B. (2002). Sorption of terephthalate anions by calcined and uncalcined hydrotalcite-like compounds. *Colloids and Surfaces A: Physicochemical and Engineering Aspects*, 211: 103 –114.
23. Ferreira, O. P., Alves, O. L., Gouveia, D. X., Filho, A. G. S., de Paiva, J. A. C. and Filho, J. M. (2004). Thermal decomposition and structural reconstruction effect on Mg–Fe-based hydrotalcite compounds. *Journal of Solid State Chemistry*, 177: 3058 – 3069.
24. Naveen, N., Saravanan, P., Baskar, G. and Sahadevan, R. (2011). Equilibrium and kinetic modeling on the removal of Reactive Red 120 using positively charged Hydrilla verticillata. *Journal of the Taiwan Institute of Chemical Engineers*, 42: 463 – 469.
25. Kobiraj, R., Gupta, N., Kushwaha, A. K. and Chattophadhyaya, M. C. (2012). Determination of equilibrium, kinetic and thermodynamic parameters for the adsorption of the brilliant green dye from aqueous solutions onto eggshell powder. *Indian Journal of Chemical Technology*, 20: 26 – 31.
26. Greluk, M. and Hubicki, Z. (2010).Kinetics, isotherm and thermodynamic studies of Reactive Black 5 removal by acid acrylic resins. *Chemical Engineering Journal* 162: 919 – 926.

27. Baccar, R., Blánquez, P., Bouzid, J., Feki, M., Attiya, H. and Sarrà, M. (2013). Modelling of adsorption isotherms and kinetics of a tannery dye onto an carbon prepared from an agricultural by-product activated carbon prepared from an agricultural by-product. *Fuel Processing Technology*, 106: 408 – 415.
28. Ulibarri, M. A., Pavlovic, I.. Barriga, C. Hermos´ın and Cornejo, M. C. (2001). Adsorption of anionic species on hydrotalcite-like compounds: effect of interlayer anion and crystallinity, *Applied Clay Science*, 18: 17 – 27.

Malaysian Journal of Analytical Sciences, Vol 20 No 4 (2016): 793 - 798
DOI: http://dx.doi.org/10.17576/mjas-2016-2004-11

MALAYSIAN JOURNAL OF ANALYTICAL SCIENCES
Published by The Malaysian Analytical Sciences Society
ISSN 1394 - 2506

CHEMICAL CHANGES OF SHORT-BODIED MACKEREL (*Rastrelliger brachysoma*) MUSCLE AT CHILLED AND FROZEN STORAGE

(Perubahan Kimia ke atas Tisu Otot Ikan Kembung Bertubuh Pendek (*Rastrelliger brachysoma*) Pada Penyimpanan Suhu Dingin dan Sejuk Beku)

Emilia Azrina Mohd Bakri, Norizzah Abd Rashid*, Cheow Chong Seng, Anida Yusoff, Fazilah Fazilin Juhari

Department of Food Technology,
Faculty of Applied Sciences,
Universiti Teknologi MARA, 40450 Shah Alam, Selangor, Malaysia

**Corresponding author: norizzah850@salam.uitm.edu.my*

Received: 24 February 2015; Accepted: 27 October 2015

Abstract

This study was carried out to evaluate the chemical changes in short-bodied mackerel during chilled (4 °C) and frozen (-18 °C) storage for 18 days. The chemical changes were monitored at three days interval using Peroxide Value (PV), Thiobarbituric Acid (TBA), Total Volatile Base Nitrogen (TVBN) and Trimethylamine (TMA) tests. The PV of both chilled and frozen mackerel significantly increased ($p < 0.05$) with storage time and the rate was significantly higher in chilled than frozen mackerel. Based on the results, the chilled and frozen mackerel started to become rancid at day 15 and day 18, respectively. Similar trend was observed for TBA value, where the malonaldehyde content significantly increased ($p < 0.05$) for both chilled and frozen mackerel with storage time, and the rate of increase was higher in chilled than frozen mackerel. The TVBN and TMA of chilled mackerel increased significantly during storage time, but the values declined in frozen mackerel which might be due to inhibitory effects of freezing on the bacterial activities and hence avoid accumulation of TMA. Based on the chemical analyses, chilled mackerel spoiled rapidly compared to frozen mackerel.

Keywords: short-bodied mackerel, thiobarbituric acid, peroxide value, total volatile base nitrogen, trimethylamine

Abstrak

Kajian ini telah dijalankan untuk menilai perubahan kimia dalam tisu otot ikan kembung bertubuh pendek semasa penyimpanan pada suhu dingin (4 °C) dan suhu sejuk beku (-18 °C) selama 18 hari. Perubahan kimia telah dipantau selang tiga hari menggunakan ujian Nilai Peroksida (PV), Asid Tiobarbiturik (TBA), Jumlah Bes Nitrogen Meruap (TVBN) dan Trimetilamina (TMA). Nilai Peroksida ikan kembung pada kedua-dua suhu dingin dan sejuk beku meningkat dengan ketara ($p < 0.05$) semasa penyimpanan dan kadar peningkatan PV lebih ketara bagi ikan kembung yang disimpan pada suhu dingin berbanding suhu sejuk beku. Berdasarkan keputusan yang diperolehi, ikan kembung pada suhu dingin dan sejuk beku masing – masing menjadi tengik pada hari ke 15 dan ke 18 penyimpanan. Pola yang sama diperolehi bagi nilai TBA, di mana kandungan malonaldehid meningkat dengan ketara ($p < 0.05$) bagi kedua-dua ikan kembung pada suhu dingin dan suhu sejuk beku semasa penyimpanan, dan kadar kenaikan malonaldehid adalah lebih tinggi terhadap ikan kembung pada suhu dingin. Nilai TVBN dan TMA ikan kembung pada suhu dingin meningkat dengan ketara semasa penyimpanan. Walau bagaimanapun kedua-dua nilai ini menurun bagi ikan kembung sejuk beku disebabkan kesan perencatan sejuk beku terhadap aktiviti bakteria dan seterusnya mengelakkan pengumpulan TMA. Berdasarkan analisis kimia ini, ikan kembung dingin rosak lebih cepat berbanding dengan ikan kembung sejuk beku.

Kata kunci: Ikan kembung bertubuh pendek, asid tiobarbiturik, nilai peroksida, jumlah bes nitrogen meruap, trimetilamina

Introduction

Fish is one of the most highly perishable food products [1] due to high concentrations of free amino acids and volatile bases [2]. In addition, fish is highly susceptible to oxidative rancidity due to large amount of phospholipids containing polyunsaturated fatty acids. Sallam [3] reported that there is a complex process of deterioration occurs in fish which are physical, chemical and microbiological reactions degrading the quality of fish thereby may cause approval or rejection after prolonged storage.

Oxidative rancidity is an autoxidation or hydrolysis process of fats into short-chain aldehydes and ketones and is responsible for rancid flavor and odour. When this process occurs in food, it may result in food rejection even though the food had been held under chilled or frozen storage. Nowadays, Total Volatile Base Nitrogen (TVBN) and Trimethylamine (TMA) are widely used to determine the quality of fish and are very good indicators to measure the trimethylamine, dimethylamine, ammonia and other basic nitrogenous compounds which were produced by spoilage bacteria, autolytic enzyme at frozen temperature, deamination of amino-acids and nucleotide catabolites that are associated with fish spoilage.

Monitoring fish quality is important in many food industries to produce high quality product when fish was used as one of the ingredients. Hence, the objective of this study was to evaluate the chemical changes in muscle tissue of short-bodied mackerel based on PV, TBA, TVBN and TMA tests during 18 days of storage at chilled (4 °C) and frozen (-18 °C) temperature.

Materials and Methods

Sample preparation

Short-bodied mackerel (*Rastrelliger brachysoma*) with average size of 15 to 20 cm and weight of 50 to 100 g were bought fresh from wet market, Kuala Pilah, Negeri Sembilan, Malaysia. The fish were placed in boxes with ice and immediately delivered to the laboratory. Short-bodied mackerel were eviscerated and cleaned before packed in the plastic containers. Then, samples were stored at chilled (4 °C) and frozen (-18 °C) temperature for 18 days and were analysed for PV, TBA, TVBN and TMA every 3 days.

Chemical analyses

All the chemicals used were of analytical grade and were obtained from CHEMOLAB Supplies, Seri Kembangan, Selangor, Malaysia.

Peroxide value (PV) test

Peroxide value of short-bodied mackerel was determined according to method described by AOAC [4] and oil was extracted based on method proposed by Razak et al [5]. The results were determined in terms of miliequivalent of peroxides per kg of fish.

Thiobarbituric acid (TBA) test

The TBA was measured according to the method of Tokur et al [6]. Ten gram of fish was mixed with 100 mL of 0.2 M hydrochloric acid and homogenised prior to distillation (Behr Labor-Technik GmbH, Germany). Approximately within 5 minutes, 50 mL of distillate was collected. An amount 5 mL of distillate was pipetted into test tube and 5 mL of TBA reagent was added. The sample was heated for 30 minutes and was allowed to cool immediately under running tap water. Blank was prepared using distilled water. A pink colour solution was produced and the colour absorbance was measured using a single beam spectrophotometer (Genesys 20 Thermo Scientific, USA) at 538 nm. The spectrophotometric results were multiplied by a constant value of 7.8 and the TBA values were expressed as mg malonaldehyde per kg fish.

Total Volatile Base Nitrogen (TVBN) and Trimethylamine (TMA) test

The TVBN and TMA were measured by distillation method according to method reported by Orak and Kayisoglu [7]. The fish extract was prepared by homogenising 100 g of sample with 200 mL of 7.5 % (v/v) aqueous trichloroacetic acid solution, after which the solution was filtered through Whatman No.1 filter paper. An amount 25 mL of filtrate was poured into a distillation tube followed by 5 mL of 10 % (w/v) aqueous sodium hydroxide solution and distilled for 3 minutes. Distillate was collected in 15 mL of 4 % (v/v) boric acid that contained 0.04

mL indicator (methyl red and bromocresol green) until final volume was up to 50 mL and then titrated with 0.05 M sulfuric acid. For TMA measurement, the same experimental procedure was carried out as in TVBN and the only difference was the addition of 20 mL of 35 % (v/v) formaldehyde to the distillation tube. The amount of TVBN and TMA were calculated from the volume of 0.05 M sulfuric acid used for titration and the results were expressed in mg N/100g of fish. The following formula equation 1 was used [8]:

$$\text{TVBN or TMA (mg N per 100 g)} = \frac{14(\text{g/mol}) \times a \times b \times 300}{\text{Volume of filtrate}} \quad (1)$$

where, a is defined as volume (mL) of sulfuric acid, b is defined as molarity of sulfuric acid

Statistical analysis

All analyses were carried out in triplicate. Statistical analysis of data was carried out using analysis of variance (ANOVA) and the analytical procedure of Scientific Package of Social Science (SPSS) 15.0. Duncan's multiple-range test was used to determine the differences among mean values between storage conditions and storage time at $p < 0.05$.

Results and Discussion

Figure 1 indicated the PV of both chilled and frozen mackerel significantly increased ($p < 0.05$) with storage time and generally the rate was significantly higher in chilled than frozen mackerel. The chilled and frozen mackerel started to become rancid as the PV were beyond the acceptable limit at day 15 (2.10 mEq/kg) and day 18 (2.28 mEq/kg), respectively. According to Orak and Kayisoglu [7], the acceptable limit for peroxide value was 2.0 mEq/kg. Fish oil is one of the highly unsaturated oils where peroxides initially formed are unstable and can react quickly to form secondary oxidation products [9]. Therefore, PV measurement alone is not a parameter reliable in measuring the oxidation of fish oil and for this reason the PV should be used in conjunction with other methods such as TBA test.

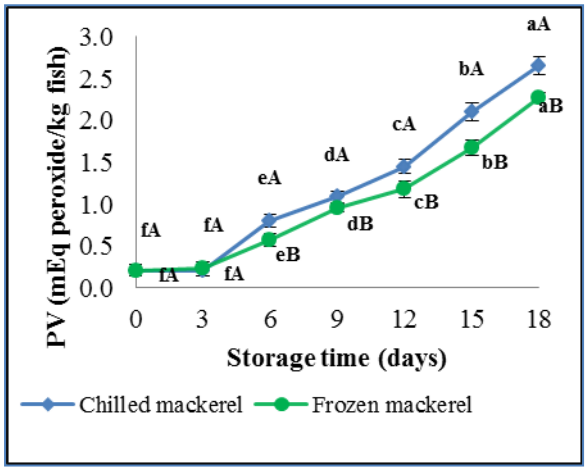


Figure 1. Changes in Peroxide Value of short-bodied mackerel in chilled and frozen storage for 18 days. Values are expressed as mean (A, B) and (a, b, c) marked with different letters were significantly different at $p < 0.05$. Lower case letters indicate the effect of storage time on short bodied-mackerel while upper case letters indicate the effect of storage conditions.

The TBA value is widely used as an indicator for the degree of lipid oxidation according to Tokur et al. [6]. The TBA number is a measurement of malonaldehyde (MDA), which is a by-product of lipid oxidation. The MDA

content was significantly increased ($p < 0.05$) with storage time for both chilled and frozen mackerel, and the rate of increase was higher in chilled than frozen mackerel (Figure 2). Similar phenomenon was reported by Boran et al. [2] where the PV and TBA in fish oils extracted from horse mackerel, shad, garfish and golden mullet were increased with increasing storage time for both storage temperatures. The increasing of the TBA values during frozen storage also has been demonstrated by Rosari et al. [10] where with longer storage days, the TBA values were increased slowly but still not reaching the rejection limit at day 18 for milkfish.

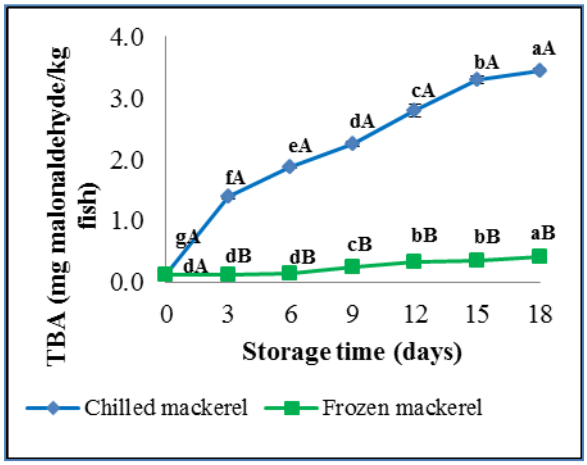


Figure 2. Changes in Thiobarbituric acid (TBA) of short-bodied mackerel in chilled and frozen storage for 18 days. Values are expressed as mean (A, B) and (a, b, c) marked with different letters were significantly different at $p < 0.05$. Lower case letters indicate the effect of storage time on short bodied-mackerel while upper case letters indicate the effect of storage conditions.

The TVBN is a term that includes measurement of trimethylamine, dimethylamine, ammonia and other volatile compound associated with fish spoilage, which increases as spoilage progresses. Figure 3 showed the TVBN of chilled mackerel increased significantly ($p < 0.05$) during storage time, but the values for frozen mackerel declined slowly. A similar pattern of increasing in TVBN values for the control has been reported by Sallam [3] during shelf life evaluation of sliced salmon at chilled condition. According to Raouf et al. [11], this trend was due to the denaturation of muscle protein by surviving microorganisms. On the other hand, the decrement of TVBN values in frozen mackerel may due to the fact that low temperature caused the bacteria become inactive and hence slower the rate of deterioration. The acceptable limit for TVBN that had been stipulated by literatures [7, 12] was 35 mgN/100g sample. Hence, in this study the chilled mackerel had reached the maximum limit at day 9 with TBVN value of 69.91 mgN/100g.

Changes in TMA levels were shown in Figure 4 where similar pattern had been demonstrated in TVBN results for both chilled and frozen mackerel. Trimethylamine (TMA) is usually used to determine the quality of fish because it is rapidly accumulated in the fish muscle under chilled condition. The TMA is always related to the pungent odour occurred in fish muscle and in this study, only chilled mackerel gave pungent odour while frozen mackerel still maintain the fishy odour until the day 18. For chilled mackerel, the TMA values were significantly increased ($p < 0.05$) during storage period while for frozen mackerel the values decreased slowly. The acceptable limit for TMA was 8 mgN/100g as indicated by Orak and Kayisoglu [7], and remarkably in this study, the chilled mackerel reached maximum acceptable limit at day 6 (8.31 mgN/100g). For frozen short-bodied mackerel, similar trend was reported by Orak and Kayisoglu [7] for filleted gray mullet where the TMA values were not significantly affected by storage time. This trend could be due to inhibitory effects of freezing on the bacterial activities and hence avoid accumulation of TMA in the muscle.

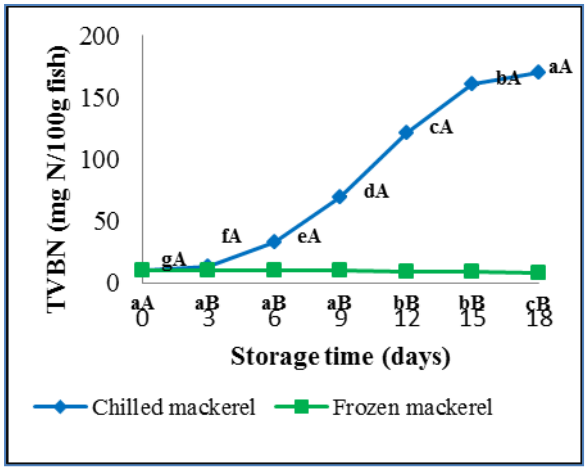


Figure 3. Changes in Total Volatile Base Nitrogen (TVBN) of short-bodied mackerel in chilled and frozen storage for 18 days. Values are expressed as mean (A, B) and (a, b, c) marked with different letters were significantly different at $p < 0.05$. Lower case letters indicate the effect of storage time on short bodied-mackerel while upper case letters indicate the effect of storage conditions.

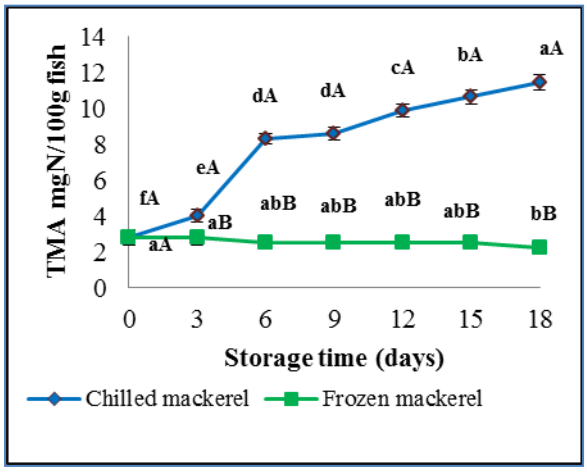


Figure 4. Changes in Trimethylamine (TMA) of short-bodied mackerel in chilled and frozen storage for 18 days. Values are expressed as mean (A, B) and (a, b, c) marked with different letters were significantly different at $p < 0.05$. Lower case letters indicate the effect of storage time on short bodied-mackerel while upper case letters indicate the effect of storage conditions.

Conclusion

There were significant differences in the rate of chemical changes for both chilled and frozen mackerel during 18 days of storage. Frozen mackerel had a slower rate of deterioration than chilled mackerel in terms of oxidative rancidity and microbial activity. Therefore, frozen temperature (-18 °C) can be used in food industry to prolong the shelf life of fish and hence could produce high quality finished products.

Acknowledgement

The researchers would like to thanks the European Commission (EU Grant no. 289282) for the financial support and Universiti Teknologi MARA for the technical facilities.

References

1. Sallam, K. I., (2007). Antimicrobial and antioxidant effect of sodium acetate, sodium lactate, and sodium citrate in refrigerated sliced salmon. *Journal of Food Control*, 18 (5): 566 – 576.
2. Boran, A. G. K., Karac, A. M. B. H. and Boran, B. M. (2006). Changes in the quality of fish oils due to storage temperature and time. *Food Chemistry*, 98: 693 – 698.
3. Sallam, K. I. (2007). Chemical, sensory and shelf life evaluation of sliced salmon treated with salts of organic acids. *Food Chemistry*, 101 (2): 592 – 600.
4. Association of Official Analytical Chemists, AOAC (1990), Official methods of analysis of the Association of Official Analytical Chemists. 15 ed. Washington D.C: Association of Official Analytical Chemist.
5. Razak, Z. K. A., Basri, M., Dzulkefly, K., Razak, C. N. A. and Salleh, A. B. (2001). Extraction and characterization of fish oil from *Monopterus albus*. *Malaysian Journal of Analytical Sciences*, 7 (1): 217 – 220.
6. Tokur, B., Korkmaz, K. and Ayas. D. (2006). Comparison of two thiobarbituric acid (TBA) method for monitoring lipid oxidation in fish. *EU Journal of Fish and Aquatic Sciences*, 23 (3-4): 331 – 334.
7. Orak, H. and Kayisoglu, S. (2008). Quality changes in whole, gutted and filleted three fish species (*Gadus euxinus, Mugil cephalus, Engraulis encrasicholus)* at frozen storage period (-26 °C). *Acta Scientiarum Polonorum Technologia Alimentaria*, 7 (3): 15 – 25.
8. Zeway, A. L. A. (2013). Microbiological and chemical changes of nile tilapia (*Oreochromis niloticus L.)* fillet during ice storage: Effect of age and sex. *Advance Journal of Food Science and Technology*, 5(10): 1260 – 1265.
9. Saeed, S. and Howell, K. N. (2002). Effect of lipid oxidation and frozen storage on muscle proteins of Atlantic mackerel (*Scomber scombrus*). *Journal of the Science of Food and Agriculture*, 82: 579 – 586.
10. Rosari, M. I., Ma'arut, W. F. and Agustini, T. W. (2014). Pengaruh ekstrak kasar buah mahkota dewa (*Phaleria macrocarpal*) sebagai antioksidan pada fillet ikan bandeng (*Chanos chanos forsk*) segar. *Jurnal Pengolahan dan Bioteknologi Hasil Perikanan*, 3 (2): 34 – 43.
11. Raouf, M., Saloua, S. and Insaf, B. (2009). Quality changes of the mediterranean horse mackerel (*Trachurus mediterraneus*) during chilled storage: The effect of low-dose gamma irradiation. *Radiation Physics and Chemistry*, 78 (4):288 – 292.
12. Ojagh, S. M., Rezaei, M., Razavi, S. H. and Hosseini, S. M. H., (2010). Effect of chitosan coatings enriched with cinnamon oil on the quality of refrigerated rainbow trout. *Food Chemistry*, 120:193 –198.

Malaysian Journal of Analytical Sciences, Vol 20 No 4 (2016): 799 - 805
DOI: http://dx.doi.org/10.17576/mjas-2016-2004-12

MALAYSIAN JOURNAL OF ANALYTICAL SCIENCES
Published by The Malaysian Analytical Sciences Society
ISSN 1394 - 2506

ISOLATION AND PURIFICATION OF LYSOZYME FROM ALBUMIN: EFFECT OF ALBUMIN CONCENTRATION, pH AND IONIC STRENGTH OF BUFFER SOLUTION

(Pemisahan dan Penulenan Lisozim dari Albumin: Kesan Kepekatan Albumin, pH dan Kekuatan Ionik Larutan Penimbal)

Amirah Hamzah[1], Sofiah Hamzah[1]*, Fatin Mohd Nasir[1], and Marinah Mohd Ariffin[2]

[1]*School of Ocean Engineering*
[2]*School of Marine Science and Environment*
Universiti Malaysia Terengganu, 21030 Kuala Terengganu, Terengganu, Malaysia

**Corresponding author: sofiah@umt.edu.my*

Received: 24 February 2015; Accepted: 27 October 2015

Abstract

The low content of lysozyme in albumin makes its purification process becomes complicated and challenge either in lab or industrial scale system. This study aimed to investigate the parameters influencing the purification performance lysozyme from chicken egg white (CEW) namely initial concentration of albumin, pH and ionic strength of buffer solution. Immobilized metal affinity chromatography (IMAC) beads were prepared using chitosan-coated silica beads which then crosslinked with glutaraldehyde (GTA) and reacted with metal ion copper (Cu) for metal ion immobilization to be used as purification tools. The prepared beads were characterized in term of morphology and structure using scanning electron microscope (SEM). Column chromatographic has been utilized for evaluation performance of IMAC for lysozyme separation. Optimum recovery obtained using 20 mg/ml CEW concentration at pH 7, with 0.05 M ionic strength. The finding of this study exhibited a good pathway to design an affinity system for lysozyme purification either from chicken egg white or other sources in the future.

Keywords: lysozyme, chicken egg white, purification, pH, ionic strength, affinity chromatography

Abstrak

Kandungan lisozim yang rendah di dalam albumin membuatkan proses penulenan menjadi semakin rumit dan mencabar sama ada sistem di makmal atau industri. Kajian ini bertujuan untuk mengoptimumkan parameter yang mempengaruhi prestasi penulenan lisozim dari albumin iaitu kepekatan awal albumin, pH dan kekuatan ionik larutan penimbal. Kromatografi affiniti logam pegun telah disediakan dengan menggunakan silika yang bersalut kitosan yang kemudiannya diaktifkan menggunakan glutaraldehid (GTA) serta bertindak balas dengan ion logam kuprum bagi pemegunan ion logam (kuprum) untuk digunakan sebagai alat penulenan. Pencirian silika telah dilakukan dari segi morfologi dan struktur dengan menggunakan mikroskop elektron pengimbas (SEM). Kolum kromatografi digunakan untuk menilai prestasi IMAC bagi pemisahan lisozim. Penghasilan yang optimum diperolehi dengan menggunakan 20 mg/ml kepekatan putih telur pada pH 7 dengan kekuatan ionik sebanyak 0.05 M. Hasil kajian ini menunjukkan cara yang baik untuk mereka bentuk sistem affiniti untuk penulenan lisozim sama ada daripada sumber putih telur atau sumber lain pada masa akan datang.

Kata kunci: lisozim, albumin, penulenan, pH, kekuatan ionik, kromatografi affiniti

Introduction

For many decades, chicken egg white (albumin, abbreviation as CEW) have been used as the subject of study for chemical, biochemical and food technological research because of the importance in human for food supply and also the potential use in biotechnology processes. Chicken egg white is the cheapest source for production of enzyme such as lysozyme using protein fractionation. Industrial application often restricted by the difficulty of recovery and reuse of the enzyme as well the lack of long-term operational stability. In order to overcome the problems, techniques that been applied in the laboratories for the separation of lysozyme from chicken egg white protein which are centrifugation, electrophoresis and chromatography [1]. Moreover, the isolation and purification process of the lysozyme becomes complicated and challenges due to the low content of the lysozyme in the chicken egg white. It is required to apply the effective and large scale protein purification process for lysozyme purification [2]. For the reason, a large quantity of the raw materials from chicken egg white needed in order to get the rational amount of pure lysozyme.

Protein separation and purification using immobilized metal affinity chromatography (IMAC) silica beads has become a powerful technique due to the inexpensive cost, ease of preparation as well high adsorption capacity [3]. The optimize purification conditions are needed to achieve both high yield and purity of the enzyme [4]. Thus, the important parameters of the physico-chemical environment of the feed solution that affect the separation process of lysozyme from chicken egg white such as pH of buffer solution, ionic strength and initial chicken egg white concentration that have been studied using affinity column chromatography as an alternative separation technique which is can be fine tuned to achieve high productivity in protein separation process. However, for the enzyme activity of the lysozyme, it was indicated using *Micrococcus lysodeikticus* as the substrate. The addition of *M. lysodeikticus* to the lysozyme solution in order to detect the enzyme activity that causes the decrease in the optical density. One lysozyme unit was defined as the amount of enzyme causing a decrease of 0.001 per minute in the absorbance at 450 nm where the suspension of 1 mg/ml *M. Lysodeikticus* as the substrate in 1 ml reaction mixture.

Thus, the aim of this research is to provide a new efficient and low cost technique for industrial manufacturing of purified lysozyme from raw chicken egg white using IMAC bead.

Materials and Methods

Chemicals and Materials

All materials used during the conduct of research are of analytical grades. Lysozyme and chicken egg white are purchased from Sigma Chemical Company. All other chemicals were guaranteed or analytical grade reagents commercially available and used without further purification.

Immobilized metal affinity chromatography beads preparation

In this study, chitosan-coated silica beads which then crosslinked with glutaraldehyde (GTA) and reacted with metal ion copper (Cu) for metal ion immobilization been used as IMAC support. Preparation of chitosan-coated silica beads was according to Shi et al. [5] with some modification. Silica gel were washed with 20 % hydrochloric acid solution for 8 hours and been dried at 40 °C before immersed into distilled water to wet the pore surface. Then, the silica gel was immersed into chitosan solution (0.1 wt. % in acetic acid pH 5) for 72 hours for surface coating. The chitosan-coated silica gel then added to NaOH solution for 2 hours and being washed with distilled water before crosslinking the beads with glutaraldehyde (GTA) for 16 hours in incubator shaker. The activated chitosan-silica beads were reacted with metal ion ($CuSO_4$) for 24 hours and kept in the distilled water for storage and been called immobilized metal affinity chromatography (IMAC) beads. Then, the IMAC beads were characterized using scanning electron microscope (SEM) for the morphology and structure study. The IMAC samples were coated with gold before transferred under microscope.

Lysozyme purification from chicken egg white and activity measurements

Chromatographic studied were carried out on IMAC beads using affinity column chromatography according to Ai et al. [6] with some modification. Thus, for the study of the feed solution, there were three factors being identified for the purification process of the lysozyme such as pH of buffer solution, ionic strength and initial CEW concentration. The optimize purification conditions are needed to achieve both high yield and purity of the enzyme as well. The column was equilibrated with 50 mL of phosphate buffer solution. Chicken egg white solution prepared with the

same buffer solution was bumped into the column at a constant volume velocity of 1.0 mL/min for five hours. When the adsorption of the CEW was saturated, the column been washed with 50 mL of same buffer solution to eliminate unbound proteins. The lysozyme adsorbed on the column was eluted by using a mixture solution of 0.3 M imidazole and 0.25 M NaCl in 0.01 M phosphate buffer (pH 6.0). The final lysozyme concentration in elution medium was determined spectrophotometrically using Bradford method [7].

Determination of total protein

The detection and quantitation of the total protein has been detected using Bradford assay method [7] while bovine serum albumin (BSA) has been used as the standard. Different dilutions of BSA standard solutions were prepared by mixing BSA stock solution (1 mg/mL) and phosphate buffer. The absorbance and concentration were analyzed using UV –Vis spectrophotometer at 595 nm by dissolving every 100 µL sample with 3mL Bradford reagent. The absorbance against protein concentration was plotted to obtain a standard calibration curve. The analysis was repeated using the lysozyme obtained from CEW as the sample.

Lysozyme activity measurement

Lysozyme activity was determined by its lytic action on *Micrococcus lysodeikticus* cell suspended in the phosphate buffer. One lysozyme unit was defined as the amount of enzyme causing a decrease of 0.001 per minute at 25 °C and pH 7.0 in the absorbance at 450 nm where the suspension of 2.9 mL of *M. Lysodeikticus* as the substrate mixed with 0.1 mL of diluted lysozyme.

Results and Discussion

IMAC characterization

IMAC beads have been used as one of the successful processes for isolation and purification of the proteins as well enzymes. It was immobilized with 0.1M concentration of metal ions and high amount of enzyme loading can be applied to obtain high yield of lysozyme recovery. Thus, the process also allow for the easy product elution and metal ions regeneration [3].

Figure 1 shows the surface morphology of (a) silica gel and (b) IMAC adsorbent using scanning electron microscope (SEM) with 5000x enlargement. The silica have uneven surface that made it easier to bind with chitosan, glutaraldehyde activator and metal ion copper (Cu^{2+}) as the IMAC adsorbent. The silica that being crosslinked using glutaraldehyde to stabilize the surface of silica for metal ion immobilization [8]. It also provided the best surface area for the enzyme binding and eluted during affinity chromatography of the lysozyme from CEW.

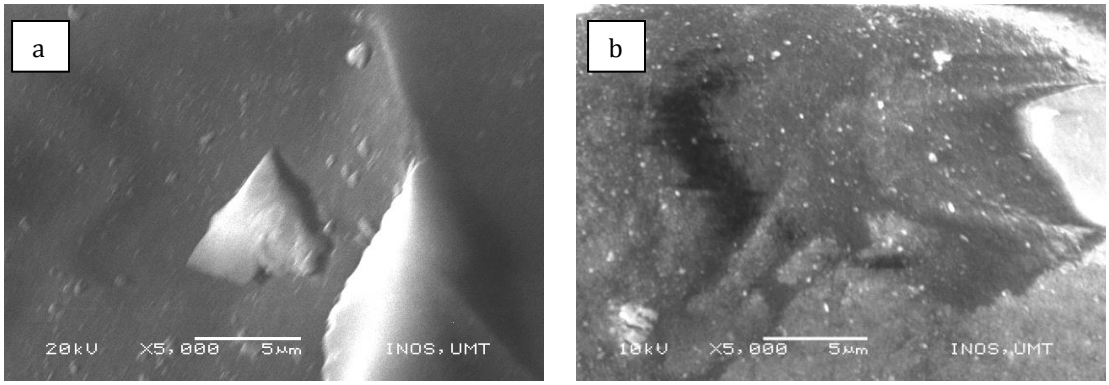


Figure 1. Surface morphology of (a) Silica gel and (b) IMAC adsorbent

Effect of CEW solution concentration, pH and ionic strength of buffer solution

The content of the lysozyme in chicken egg white was about 3.4 % [9] making its purification process becomes complicated. There are some factors that influenced the performance of the lysozyme from CEW which were concentration of the CEW solution, pH and ionic strength of buffer solution. The effects of CEW concentration on

lysozyme separation and purification from IMAC beads was studied using CEW concentration ranged from 5mg/mL to 25 mg/mL of CEW in buffer solution. The results obtained displays in Figure 2 (a) and (b) and there was a remarkable change in the purity of lysozyme even there were only slight difference in the yield obtained.

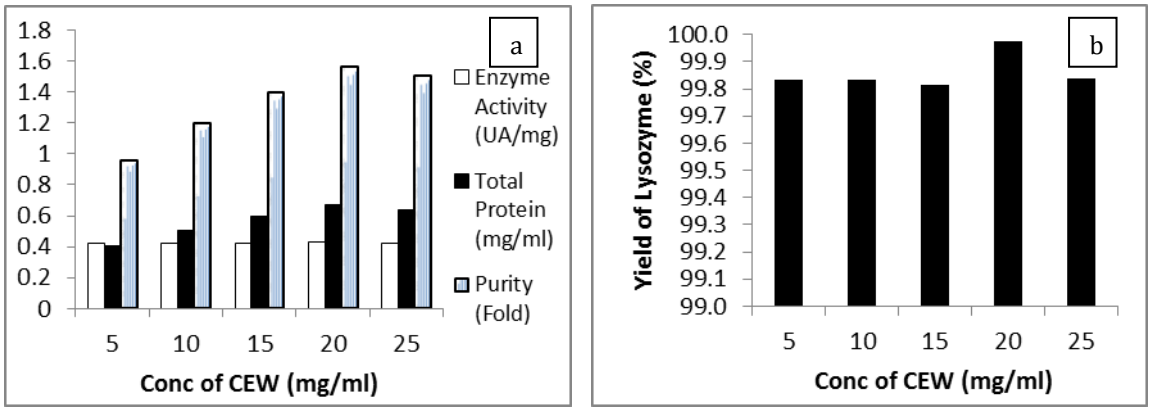


Figure 2. Affinity column chromatography with different concentration of CEW solution (a) enzyme activity, total protein, purity of lysozyme and (b) yield of lysozyme

The highest lysozyme recovery (99.97 %) obtained using 20 mg/mL initial concentration of CEW where the specific activity of lysozyme and total protein concentration in the feed solution were assayed at 0.42 UA/mg and 0.67 mg/ml as well with 1.56 of purification fold. This promising result was due to the equilibrium phase of the CEW concentration at 20 mg/mL and the further increase of initial concentration (25 mg/mL) did not improve the separation performance since all the active site of IMAC beads had been bound with lysozyme.

The increasing of the CEW concentration from 5mg/mL to 20 mg/mL had been promoting the adsorption of enzyme from the surface of IMAC beads and gave higher recovery (yield) of lysozyme. While the concentration of CEW was about 5 mg/mL, the specific activity of lysozyme was also 0.42 UA/mg but the recovery of lysozyme was about 99.81 %. Overall, the initial concentration used in this study promoted very outstanding result when more that 99 % lysozyme can be recovered. This finding can be explained due to the cooperative effect of different interaction mechanisms such as hydrogen bonding, electrostatics and hydrophobic cause by the buffer in the CEW and IMAC beads as well [10].

Figure 3 shows the effects of pH of the buffer solution on the adsorption capacity of lysozyme onto IMAC beads, whereas the best recovery occurred at pH 7 when the specific activity of lysozyme and total protein concentration in the feed solution were about 0.41 UA/mg and 0.33 mg/ml with 0.81 purification fold. At this rate, pH 7 had promoted very high yield recovery of lysozyme which about 99.85 %. The pH of buffer solution provide great effect for the recovery of the lysozyme from CEW since the changes of the solution pH can be altered the electrical charge on the lysozyme as well. The isoelectric point (IEP) of lysozyme was around 11 and at pH value below the IEP, the lysozyme adsorbed was clearly higher than at pH values above the IEP. At pH 7, lysozyme would be cationic since this pH was below than its isoelectric point. This pH 7 was served as a good environment for the lysozyme with the help of electrostatic interaction that has been predominant for recovery of the enzyme from CEW.

At pH 5, the purification capacity of lysozyme was the lowest which about 0.38 UA/mg of lysozyme specific activity with its yield were 95.23 %. This result indicated that the capability of lysozyme coordination with the IMAC beads was not necessarily suitable in acidic condition. This occurrence might result from the protonation of electron donor group in lysozyme molecule, leading to decreasing coordination ability with metal ions [11]. Furthermore, lower performance at the pH approaches IEP of lysozyme at pH 9 was due to the instability

occurrence. This result can be explained as the percentage of HPO_4^{2-} and PO_4^{3-} in buffer solution which acquired a relative higher metal coordinating ability compared to HPO_4^-. This condition would compete with lysozyme for metal binding and increased in alkali condition [12]. Due to lysozyme isoelectric point which at pH 11, lysozyme specific activity just about 0.43 UA/mg and its yield that has been recovered from IMAC beads was about 99.01%. This result might be explained due to the protein aggregation [13] since the lysozyme surface net charge was zero, thus there were no electrostatic repulsive force being effective between the lysozyme molecules at this pH.

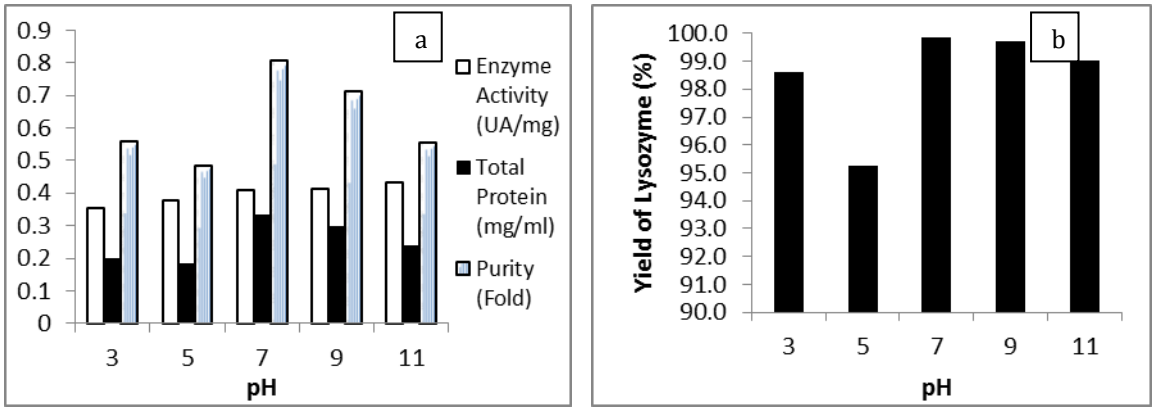


Figure 3. Affinity column chromatography with different pH of buffer solution (a) enzyme activity, total protein, purity of lysozyme and (b) yield of lysozyme

The effect of ionic strength was studied using the CEW solution with a fixed pH 7 since the previous observation determined that pH 7 successfully promoted the best recovery of lysozyme. Since the IMAC beads were highly charged with electrolyte, the effects of ionic strength on lysozyme separation and purification from CEW was studied using addition of NaCl from 0.01M to 0.09M. The results obtained were displayed in Figure 4 (a) and (b) where there was a significant change in the lysozyme recovery through the change in ionic strength of the buffer solution. For the effects of ionic strength, the results that been achieved the best when NaCl was 0.05 M with the 0.33 UA/mg lysozyme specific activity and 0.29 mg/ml of total protein concentration in the feed solution. While the yield of the lysozyme was about 99.24 % with 0.89 purification fold. It was due to the high lysozyme being eluted from CEW.

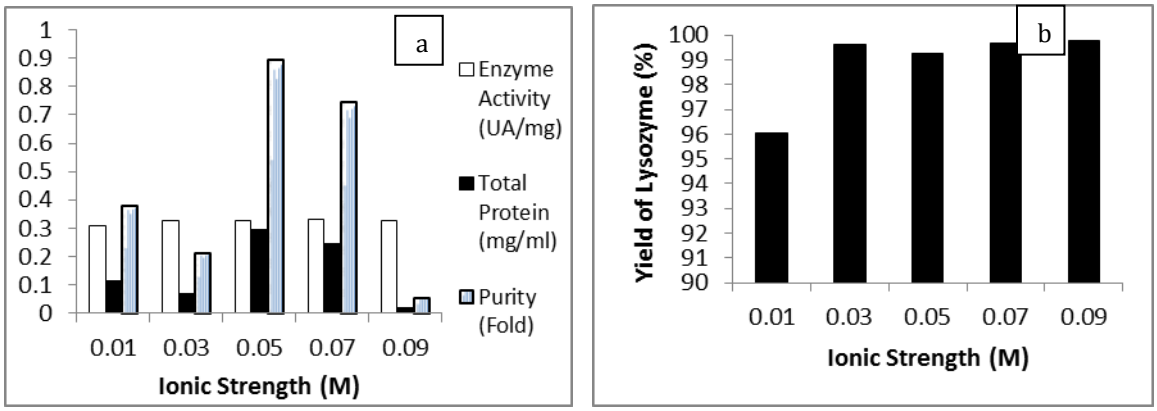


Figure 4. Affinity column chromatography with different ionic strength of buffer solution (a) enzyme activity, total protein, purity of lysozyme and (b) yield of lysozyme

Otherwise, when the NaCl was at 0.03 M, the specific activity of lysozyme was about 0.32 UA/mg and 0.06 mg/ml of total protein concentration in the feed solution. Meanwhile the yield of the lysozyme was obtained at 99.6 %. Although the yield of lysozyme when the NaCl concentration about 0.03 M higher than the concentration at 0.05 M, but the purification fold was just 0.21. It shows that the concentration of 0.05 M NaCl have the highest purity rather than concentration of 0.03 M. The increasing of the NaCl concentration from 0.01M to 0.05M had been encouraged the recovery of the enzyme from the surface of IMAC beads. Then, the hydrophobic interactions among them become strong. Furthermore, the addition of NaCl more than 0.05M caused the recovery capacity to reduce since the ionic strength had affects the chelating bonding of lysozyme on both metal affinity carriers [14]. Besides, in high ionic strength buffer, protein solubility usually reduces which were salt-out effect due to the decreasing activity of water and the neutralization of surface charge. These conditions also assist the formation of protein aggregates, leading to the decrease in lysozyme adsorption onto IMAC beads and reduce the purification of the lysozyme itself.

Conclusion

The process developed using IMAC beads allows the recovery and purification of the lysozyme from chicken egg white (CEW) with high recovery capacity of matrix at low cost and high efficiency. This study proved that concentration of CEW, pH and ionic strength of buffer solution significantly influenced the purification process of the lysozyme from CEW. The most optimum lysozyme recovery was at 20 mg/mL of CEW concentration in buffer solution at pH 7 and ionic strength of 0.05M. Affinity chromatography using IMAC beads was a potential alternative for industrial purposes.

Acknowledgement

The authors would like to express their sincere gratitude to the Ministry of Education, for the grant of the Exploratory Research Grant Scheme (ERGS) and high appreciation to School of Ocean Engineering and Central Laboratory, University Malaysia Terengganu for the cooperation and support.

References

1. Muller, A., Daufin, G. and Chaufer, B. (1999). Ultrafiltration modes of operation of α-lactalbumin from acid casein whey. *Journal of Membrane Science*, 153: 9 – 21.
2. Wan, W. H., Lub, J. R., and Cui, Z. F. (2006). Separation of lysozyme from chicken egg white using ultrafiltration. *Separation and Purification Technology*, 48: 133 – 142.
3. Yilmaz, M., Bayromoğlu, G. and Arica, M. Y. (2005). Separation and purification of lysozyme by Reactive Green 19 immobilised membrane affinity chromatography. *Food Chemistry*, 89: 11 – 18.
4. Shin, H. S. and Cha, H. J. (2003). Statistical optimization for immobilized metal affinity purification of secreted human erythropoietin from Drosophila S2 cells. *Protein Expression and Purification*, 28: 331 – 339.
5. Shi, Q. H., Tian, Y., Dong, X. Y., Bai, S. and Sun, Y. (2003). Chitosan-coated silica beads as immobilized metal affinity support for protein adsorption. *Biochemical Engineering Journal*, 16: 317 – 322.
6. Lu, A. X., Liao, X. P., Zhou, R. Q. and Shi, B. (2007). Preparation of Fe(III)-immobilized collagen fiber for lysozyme adsorption. *Colloids and Surfaces A: Physicochemical Engineering Aspects*, 301: 85 – 93.
7. Kruger, N. J. (2002). The protein protocols handbook, second edition: the Bradford method for protein quantitation. *Humana Press*, pp.15 – 21.
8. Guo, W. and Ruckenstein, E. (2003). Separation and purification of horseradish peroxidise by membrane affinity chromatography. *Journal Membrane Science*, 211: 101 – 111.
9. Ghosh, R., Sudarshana, S. S. and Cui, Z. F. (2000). Lusozyme separation by hollow-fibre ultrafiltration. *Biochemical Engineering Journal*, 6: 19 – 24.
10. Evrim, B. A. and Adil, D. (2006). Monosize poly(glycidyl methacrylate) beads for dye-affinity purification of lysozyme. *International Journal of Biological Macromolecules*, 38: 99 – 106.
11. Sun, Y., Liu, Y., Li, Y., Lv., M., Li, P., Xu, H. and Wang, L. (2011). Preparation and characterization of novel curdlan/chitosan blending membranes for antibacterial applications. *Carbohydrate Polymers*, 84: 952 – 959.
12. Hamzah, S., Nasir, F. M and Hamzah, A. (2014). Lysozyme adsorption onto immobilised metal affinity chromatographic adsorbent: effect of pH and ionic strength. *International Journal of Applied Engineering Research*, 9: 17783 – 17792.

13. Gustafsson, C., Thorn, C. and Holmberg, K. (2011). A comparison of lipase and trypsin eccapsulated in mesoporous materials with varying pore sizes and pH conditions. *Colloids and Surfaces B: Biointerfaces*, 87: 464 – 471.
14. Muller, C.H., Agarwal, G.P., Melin, T. and Vintgens, T. (2003). Study of UF of single and binary protein solution in a thin spiral channel module. *Journal of Membrane Science*, 227: 51 – 69.

Malaysian Journal of Analytical Sciences, Vol 20 No 4 (2016): 806 - 811
DOI: http://dx.doi.org/10.17576/mjas-2016-2004-13

MALAYSIAN JOURNAL OF ANALYTICAL SCIENCES
Published by The Malaysian Analytical Sciences Society
ISSN 1394 - 2506

PREPARATION AND PHYSICOCHEMICAL PROPERTIES OF OCTENYL SUCCINIC ANHYDRIDE (OSA) MODIFIED SAGO STARCH

(Penyediaan dan Sifat Fizikokimia Oktenil Suksinat Anhidrat (OSA) Modifikasi Kanji Sagu)

Nur Farhana Zainal Abiddin, Anida Yusoff*, Noorlaila Ahmad

Department of Food Science and Technology,
Faculty of Applied Sciences,
Universiti Teknologi MARA, 40450 Shah Alam, Selangor, Malaysia

**Corresponding author: anida@salam.uitm.edu.my*

Received: 24 February 2015; Accepted: 27 October 2015

Abstract

Starch from sago (*Metroxylon sagu*) was esterified with octenyl succinic anhydride (OSA) in order to regulate its shortcoming by adding amphiphilic properties. The objective of this work is to determine the physicochemical properties of native sago and OSA sago starches. The OSA sago starch was produced according to the optimum condition generated via response surface methodology (RSM) with 5.00 % OSA at pH 7.20 and a reaction time of 9.65 hours. The esterified sago starch gives a degree of substitution (DS) value of 0.012. The physicochemical properties of OSA sago starch was determined by measuring the amylose content, laser diffraction particle size analyzer, scanning electron microscopy (SEM) and Fourier transform infrared (FT-IR). The amylose content for OSA sago starch was found to be reduced after esterification reaction. The particle size of OSA sago starch was found to increase significantly ($p < 0.05$) compared to their native starches. Scanning electron microscopy (SEM) revealed that OSA starch developed slightly rough surface and their edges lost some definition. FT-IR spectroscopy shows that there was appearance of new absorption correspond to ester carbonyl group (1717 cm^{-1}) and carboxylate RCOO- (1569 cm^{-1}). This study showed that the physicochemical properties of modified starches were influenced not only by DS but also on the botanical origin of the starches.

Keywords: physicochemical properties, sago starch, octenyl succinic anhydride, esterification

Abstrak

Kanji daripada sagu (*Metroxylon sagu*) telah diesterifikasi dengan oktenil suksinat anhidrat (OSA) sebagai usaha untuk mengawal kelemahan dengan menambah sifat amfifilik. Objektif kajian ini adalah untuk menentukan sifat – sifat fizikokimia kanji sagu asli dan OSA kanji sagu. OSA kanji sagu disediakan mengikut keadaan optima berdasarkan kaedah gerak balas permukaan (RSM) dengan 5.00 % OSA pada pH 7.20 dan masa tindak balas selama 9.65 jam. Esterifikasi kanji sagu memberikan nilai darjah pengantian (DS) sebanyak 0.012. Ciri – ciri fizikokimia OSA kanji sagu ditentukan dengan mengira kandungan amilosa, saiz partikel laser pembelauan analisis, mikroskop imbasan elektron (SEM) dan Fourier transformasi inframerah (FT-IR). Kandungan amilosa untuk OSA kanji sagu didapati berkurangan selepas tindak balas esterifikasi. Saiz partikel OSA kanji sagu didapati meningkat dengan ketara ($p < 0.05$) berbanding saiz kanji sagu asli. Mikroskop imbasan elektron (SEM) menunjukkan bahawa OSA kanji sagu menghasilkan permukaan sedikit kasar dan kehilangan beberapa sisi definisi. FT-IR spektroskopi menunjukkan bahawa terdapat kemunculan penyerapan baru yang bersesuaian dengan kumpulan ester karbonil (1717 cm^{-1}) dan RCOO- karboksilik (1569 cm^{-1}). Kajian ini menunjukkan bahawa ciri – ciri fizikokimia kanji diubahsuai bukan hanya dipengaruhi oleh DS tetapi juga berdasarkan pada asal usul botanikal kanji tersebut.

Kata kunci: sifat-sifat fizikokimia, kanji sagu, oktenil suksinat anhidrat, esterifikasi

Introduction

Starch is a carbohydrate polymer which comprised of amylose and amylopectin chains and has been widely used as a functional ingredient in food and non-food application [1]. In order to meet specific requirements, the native starches were chemically modified to improve its properties which require disruption of hydrogen bonding [2]. Chemical modification can be achieved by different types such as esterification, etherification, cross-linking and grafting of starch. Sago starch, like other starch, exhibit hydrophilic nature which is the main constraint that limit the usability of starch. Esterification of starch with octenyl succinic anhydride (OSA) impart an amphiphilic nature by the addition of hydrophobic chain into the starch backbone and broaden their potential uses in the food industry [3]. The succinylated starch tends to swell in cold water, having more stable pasting and gelatinisation properties also giving the derivative surface activity and colloid protector properties [4].

There are a number of methods that can be used to characterize starch, which could be used to identify the unique properties of modified starch. Scanning electron microscopy (SEM) has been used to study the morphology of the starch granules by giving a clear visual variation in size and shape of starch granule [5]. Laser diffraction particle size analyzer has been used to study the particle size by characterize the granule diameter, as the size of starch can influence the rate and efficiency of the chemical modification [6]. The presence of carbonyl group in the starch backbone can be confirmed by FT-IR spectroscopy. The introduction of this group indicate that the succinylation have been successfully made into the starch [7]. The amylose content of starch before and after modification can be as one of the sign to recognize the extent of modification by determining the degree of substitution. Amylose content also has been found to have a significant correlation with the size and shape of the starch granules [8].

Thus, the objective of the present study was to characterize the physicochemical properties of both native and OSA sago starch using different type of instruments.

Materials and Methods

Chemicals and raw materials

Food grade sago starch was purchased from Nee See Ngeng & Sons Sago Industries Sdn. Bhd (Sarawak, Malaysia). The starch was used without any further treatment. Octenyl succinic anhydride (OSA) (Lot# J1097009-A) was donated by Dixie Chemical Company, Pasadena, Texas, USA. Other chemicals used in this study were of analytical grade.

Preparation of OSA starches

OSA sago starch was prepared according to the optimum condition generated by response surface methodology (RSM). The starch was treated according to condition at 5.00 % OSA concentration, pH 7.20 and reaction time of 9.65 hours as reported in our earlier work [9]. The preparation step and calculation of degree of substitution (DS) of OSA sago starch was determined using the method from [10] by using the formula equation 1 and 2 below:

$$\text{OSA substitution (\%)} = \frac{(V_{\text{blank}} - V_{\text{sample}}) \text{ x } 0.1 \text{ x } N \text{ x } 100}{W} \quad (1)$$

where V_{blank} is defined as the volume of HCl required for blank titration, V_{sample} is defined as volume of HCl required to titrate the sample, W is defined as the weight (g) of sample and N is the normality of the HCl solution.

$$\text{DS} = \frac{162 \text{ x OSA substitution (\%)}}{21\,000 - [209 \text{ x OSA substitution (\%)}]} \quad (2)$$

where 162 is defined as molecular weight of the glucose unit, 21 000 is defined as 100 x molecular weight of octenyl succinyl group and 209 is molecular weight of octenyl succinyl group minus the molecular weight of hydrogen atom.

Characterization of OSA starches: ***Amylose content***

The amylose content of starches was estimated following the modification by Ratnayake et al. [11] from the method of McGrance et al. [12]. Starch (20 mg, dry basis) was dissolved in 8 mL of 90 % DMSO. The slurry was vigorously mixed for 20 min and volume to 25 mL in a volumetric flask. The diluted solution (1 mL) was taken out and mixed with deionized water then placed in water bath at 85 °C for 15 min. The vials were left to cool at ambient temperature before make up the volume to 25 mL in a volumetric flask. The diluted solution (1 mL) was taken out and mixed with deionized water (40 mL) and iodine solution (5 mL). The volume of the mixture was adjusted to a final value of 50 mL. Then, the solution was allowed to stand for at least 15 min and the absorbance was read at 600 nm by using UV-VIS spectrophotometer. A standard curve of amylose was plotted in order to determine the amylose content of native and OSA starches.

Particle size of starch

Particles size of OSA sago starch was measured by static multi-angle light scattering method using Mastersizer Hydro 2000 (Malvern Instrument, Malvern, UK) equipped with Scirocco Dry Powder Feeder. An amount 2 g of native and OSA starches were added into the feeder and the OSA sago starch was measured three times. An average droplet sizes were characterized in terms of Sauter mean diameter d_{32}.

Scanning electron microscopy

The microstructure of starch granule and their surfaces after modification with OSA was examined with scanning electron microscopy (SEM). The air-dried starch powders were stuck on double-sided adhesive tape on a specimen holder and then coated with gold in vacuum evaporator. The samples were analyzed using scanning electron microscope (Leo Supra 50VP Field Emission SEM, Carl Zeiss SMT, Germany). The samples were measured at a magnification of 2000x.

Fourier transfer infrared (FT-IR) spectroscopy

FT-IR spectra of native and OSA starches were performed using Perkin Elmer Spectrum One FT-IR spectrophotometer (Massachusetts, USA). The starch samples were dried at 105 °C for 12 hours to remove any moisture. The dried sample was finely grind with KBr in a ratio of 1: 70 (w/w) and scanned over a wavenumber range from 400 to 4000 cm^{-1} with a resolution of 4 $cm^{-1.}$

Statistical analysis

All tests were performed in triplicate. Analysis of variance (ANOVA) was performed using the Duncan multiple range tests to compare treatments means. Significance was defined at $p < 0.05$.

Results and Discussion

Amylose content for native and OSA starches

Table 1 shows the amylose content for native and modified starches after being esterified with OSA. Normally, botanical origin will influence the amount of amylose in the starch where waxy starches contain less than 15 % amylose, regular starch 20 – 35 % amylose and high amylose starch have more than 40 % amylose [13]. The amylose content of native sago starch and OSA sago starch were 30.18 % and 25.27 %, respectively. This result was supported by Ahmad et al. [14] which reported that the amylose content of native sago starch was in the range of 24 – 30 %. According to the amylose content, sago starch can be categorized as a regular starch.

From the result, there was a significant ($p < 0.05$) decrease in amylose content in treated starch. Amylose is located at the amorphous region while amylopectin is in crystalline lamellae. The amorphous region is more accessible than crystalline domains which explain that substitution occur preferentially at amylose chains [15]. As amorphous region is easily accessible, OS group might distribute and disrupt at this region more than in crystalline domains, which explain the reduction of amylose content in esterified starches [16].

Particle size distribution and morphology of starches

The results for particle size analysis are shown in Table 1. The particle size of native sago starch was 29.05 µm. This agreed with the result from [17] which state that the particle size of native sago granules was between 5 to 65 µm and the average was 30 – 31 µm. The particle size of esterified starch shows a significant increased ($p < 0.05$)

when compared to their native state. Structural disorder happens as OS groups incorporate with native starch, making the granule to swell to a greater extent and increase the particle size [18].

Table 1. Effect of octenyl succinylation on DS, amylose content and particle size of starches

Sample	Degree of substitution (DS)	Amylose content (%)	Particle size (µm)
Native sago starch	-	30.18 ± 0.71^{a}	29.05 ± 0.09^{b}
OSA sago starch	0.012 ± 0.00	25.27 ± 0.36^{b}	29.89 ± 0.23^{a}

Values are mean ± standard deviation. Mean within each column with different superscripts letter are significantly different at $p < 0.05$.

Figure 1 shows the SEM image of native and OSA sago starch. Scanning electron microscopy revealed sago starch consists of oval granules with smooth surfaces and non-visible pores [14, 19]. There is an only slight difference in shape of OSA sago starch from their original shape. However, the surface of OSA starch was observed to be rough and their edges lose some definition. The addition of NaOH to maintain the alkaline condition during esterification process might result in surface gelatinization, thus contribute to rough appearance on the surface of OSA starch granules [6]. This observation also could be associated with granule swelling and distruption of starch particles during reaction [20].

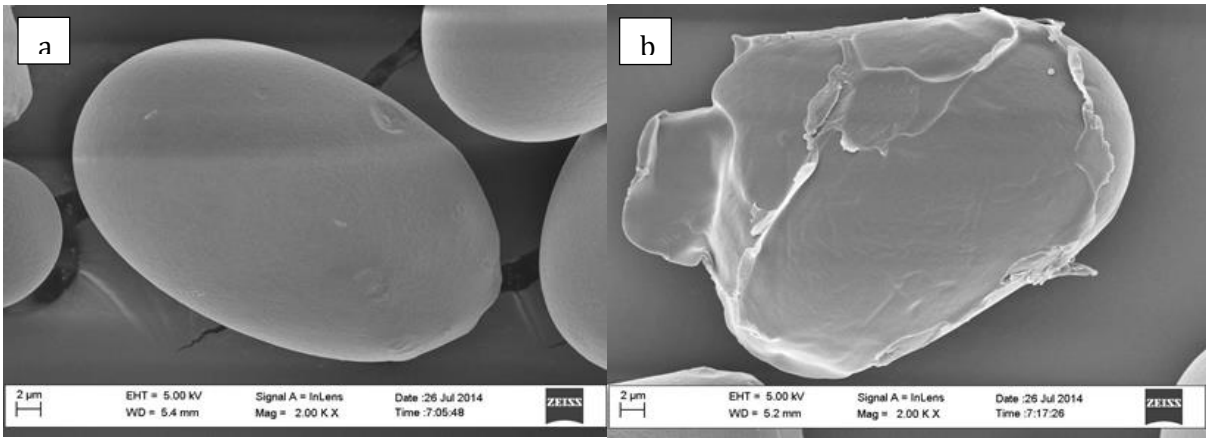


Figure 1. Scanning electron micrographs of a) native sago starch and b) OSA sago starch at 2000x magnification

Fourier transfer infrared (FT-IR) spectroscopy

Fourier transform infrared spectroscopy (FT-IR) was used to detect the presence of OSA groups after esterification. The FT-IR spectra of native and OSA starches are shown in Figure 2. The extremely broad band at 3400 cm^{-1} is resulting from vibration of hydroxyl group (O-H) whereas the band at 2924 cm^{-1} is characteristics of C-H stretching vibration of glucose unit. Compared with native starch, two absorption bands were observed at 1569 cm^{-1} and 1717 cm^{-1} which correspond to assymetric stretch of vibration of a carboxyl group and C=O stretching vibration of an ester group, respectively [21]. The peak at 1647 cm^{-1} was due to tightly bound water present in the starch [22]. The intensity of absorption bands at 1569 cm^{-1} and 1717 cm^{-1} was reported to increase with increasing DS [23].

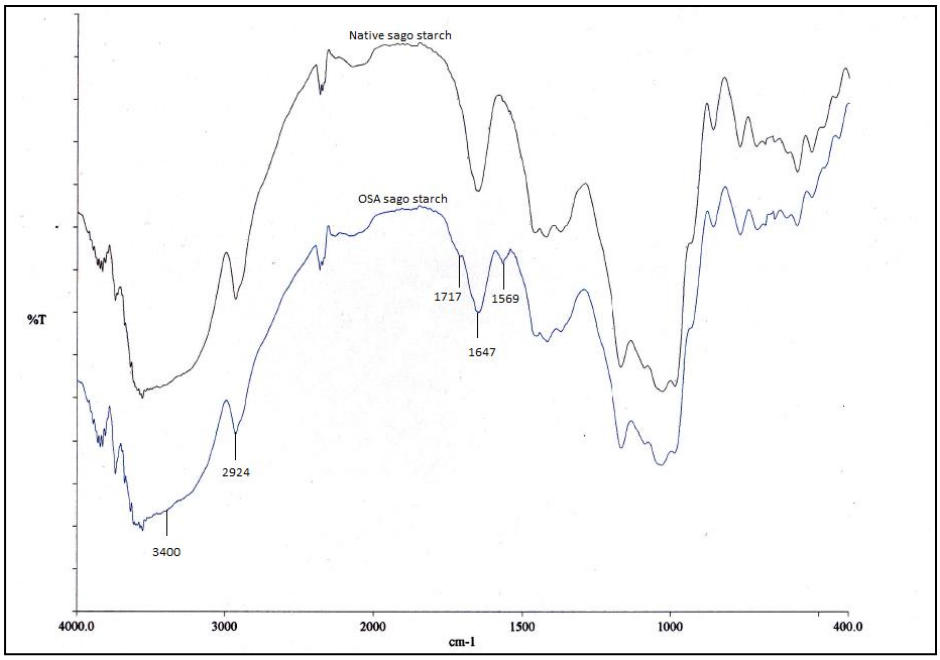


Figure 2. FT-IR spectra for native and OSA sago starches

Conclusion

Our results have shown that the physicochemical properties of native sago starch have been altered after being esterified with OSA. SEM image illustrated that there is only a slight change in the surface of the esterified starch, but does not bring any visible pores or crack on the starch surfaces. Particle size of starch granules was found to increase significantly ($p < 0.05$), which correspond to swelling activity. The amylose content of starch decreased after esterification, indicating that the modification occurred primarily in the amorphous regions and disrupt the linearity of amylose chains. FT-IR spectroscopy confirmed the existence of carbonyl group through absorption bands at 1569 cm^{-1} and 1717 cm^{-1}. The esterification of sago starch with OSA will add the hydrophobic chain to the originally hydrophilic starch molecule hence the modified starch obtains surface active properties which will be useful in stabilizing emulsion. The stabilizing and emulsifying properties of OSA sago starch need further study.

Acknowledgement

The authors would like to thank Universiti Teknologi MARA (600-RMI/ERGS 5/3 (2/2013)) and Ministry of Higher Education Malaysia for the facilities and financial support.

References

1. Steeneken, P. A. M. and Woortman, A. J. J. (2008). Surface effects in the acetylation of granular potato starch. *Carbohydrate Research*, 343(13): 2278 – 2284.
2. Chang, P. R., Qian, D., Anderson, D. P. and Ma, X. (2012). Preparation and properties of the succinic ester of porous starch. *Carbohydrate Polymers*, 88: 604 – 608.
3. Segura-Campos, M., Chel-Guerrero, L. and Betancur-Ancona, D. (2010). Effects of octenylsuccinylation on functional properties of lima bean (*Phaseolus Lunatus*) starch. *Journal of Food Process Engineering*, 33(4): 712 – 727.
4. Segura-Campos, M., Chel-Guerrero, L. and Betancur-Ancona, D. (2008). Synthesis and partial characterization of octenylsuccinic starch from *Phaseolus Lunatus*. *Food Hydrocolloids,* 22(8): 1467 – 1474.
5. Singh, N., Singh, J., Kaur, L., Sodhi, N. S. and Gill, B. S. (2003). Morphological, thermal and rheological properties of starches from different botanical sources. *Food Chemistry*, 81(2): 219 – 231.

6. Singh, J., Kaur, L. and McCarthy, O. J. (2007). Factors influencing the physico-chemical, morphological, thermal and rheological properties of some chemically modified starches for food applications – A review. *Food Hydrocolloids*, 21(1): 1 – 22.
7. Wang, J., Su, L. and Wang, S. (2010). Physicochemical properties of octenyl succinic anhydride-modified potato starch with different degrees of substitution. *Journal of the Science of Food and Agriculture*, 90(3): 424 – 429.
8. Kaur, L., Singh, N. and Sodhi, N. S. (2002). Some properties of potatoes and their starches II. Morphological, thermal and rheological properties of starches. *Food Chemistry*, 79(2): 183 – 192.
9. Zainal Abiddin, N. F., Yusoff, A. and Ahmad, N. (2015). Optimisation of reaction conditions of octenyl succinic anhydride (OSA) modified sago starch using response surface methodology (RSM). *International Food Research Journal*, 22(3): 930 – 935.
10. Bhosale, R. and Singhal, R. (2006). Process optimization for the synthesis of octenyl succinyl derivative of waxy corn and amaranth starches. *Carbohydrate Polymers*, 66(4): 521 – 527.
11. Ratnayake, W. S., Hoover, R., Shahidi, F., Perera, C. and Jane, J. (2001). Composition, molecular structure, and physicochemical properties of starches from four field pea (*Pisum sativum* L.) cultivars. *Food Chemistry*, 74(2): 189 – 202.
12. McGrance, S. J., Cornell, H. J. and Rix, C. J. (1998). A simple and rapid colorimetric method for the determination of amylose in starch products. *Starch-Stärke*, 50(4): 158 – 163.
13. Tester, R. F., Karkalas, J. and Qi, X. (2004). Starch-composition, fine structure and architecture. *Journal of Cereal Science*, 39(2): 151 – 165.
14. Ahmad, F. B., Williams, P. A., Doublier, J-L., Durand, S. and Buleon, A. (1999). Physico-chemical characterisation of sago starch. *Carbohydrate Polymers*, 38(4): 361 – 370.
15. van der Burgt, Y. E. M., Bergsma, J., Bleeker, I. P., Mijland, P. J. H. C., van der Kerk-van Hoof, A., Kamerling, J. P. and Vliegenthart, J. F. G. (2000). Distribution of methyl substituents im amylose and amylopectin from methylated potato starches. *Carbohydrate Research*, 325(3): 183 – 191.
16. Nor Nadiha, M. Z., Fazilah, A., Bhat, R. and Karim, A. A. (2010). Comparative susceptibilities of sago, potato and corn starches to alkali treatment. *Food Chemistry*, 121(4): 1053 – 1059.
17. Kaur, B., Fazilah, A. and Karim, A. A. (2011). Alcoholic-alkaline treatment of sago starch and its effect on physicochemical properties. *Food and Bioproducts Processing*, 89(4): 463 – 471.
18. Bello-Flores, C.A., Nuñez-Santiago, M. C., Martín-Gonzalez, M. F., BeMiller, J. N. and Bello-Pérez, L. A. (2014). Preparation and characterization of octenylsuccinylated plantain starch. *International Journal of Biological Macromolecules*, 70: 334 – 339.
19. Karim, A. A., Nadiha, M. Z., Chen, F. K., Phuah, Y. P., Chui, Y. M. and Fazilah, A. (2008). Pasting and retrogradation properties of alkali-treated sago (*Metroxylon sagu*) starch. *Food Hydrocolloids*, 22(6): 1044 – 1053.
20. Wang, X., Li, X., Chen, L., Xie, F., Yu, L. and Li, B. (2011). Preparation and characterisation of octenyl succinate starch as a delivery carrier for bioactive food components. *Food Chemistry*, 126(3): 1218 – 1225.
21. Hui, R., Qi-he, C., Ming-liang, F., Qiong, X. and Guo-qing, H. (2009). Preparation and properties of octenyl succinic anhydride modified potato starch. *Food Chemistry*, 114(1): 81 – 86.
22. Chi, H., Xu, K., Xue, D., Song, C., Zhang, W. and Wang, P. (2007). Synthesis of dodecenyl succinic anhydride (DDSA) corn starch. *Food Research International*, 40(2): 232 – 238.
23. Zhang, B., Huang, Q., Luo, F-X., Fu, X., Jiang, H. and Jane, J-l. (2011). Effects of octenylsuccinylation on the structure and properties of high-amylose maize starch. *Carbohydrate Polymers*, 84(4): 1276 –1281.

Malaysian Journal of Analytical Sciences, Vol 20 No 4 (2016): 812 - 819
DOI: http://dx.doi.org/10.17576/mjas-2016-2004-14

MALAYSIAN JOURNAL OF ANALYTICAL SCIENCES
Published by The Malaysian Analytical Sciences Society
ISSN 1394 - 2506

SENSORY CHARACTERISTICS OF MUD CLAM (*Polymesoda erosa*) HYDROLYSATE

(Ciri–ciri Deria Hidrolisat Lokan (*Polymesoda erosa))*

Normah Ismail* and Noorasma Mustakim

Department of Food Technology,
Faculty of Applied Sciences,
Universiti Teknologi MARA, 40450 Shah Alam, Selangor, Malaysia

**Corresponding author: norismel@salam.uitm.edu.my*

Received: 24 February 2015; Accepted: 27 October 2015

Abstract

Mud clam (*Polymesoda erosa*) was hydrolysed using two different microbial enzymes; alcalase and flavourzyme. The volatile compounds, amino acids and molecular weight associated with umami and bitter taste in mud clam hydrolysate were determined by head space solid phase micro-extraction gas chromatography (HS-SPME-GCMS), High performance liquid chromatography (HPLC) and sodium dodecyl sulphate polyacrylamide gel electrophoresis (SDS-PAGE). The characteristics of hydrolysates produced using alcalase and flavourzyme were compared. In total, eighteen, seven and six volatile compounds were identified in the flesh, alcalase hydrolysate and flavourzyme hydrolysate, respectively. 2-piperidinone volatile compound content which is associated with bitterness was 6.79 % in alcalase hydrolysate and 3.78 % in flavourzyme hydrolysate. SDS-PAGE results showed that alcalase hydrolysate contains smaller peptide (<52 kDa) compared to flavourzyme hydrolysate (<126 kDa). In addition, sensory analysis using quantitative descriptive analysis (QDA) showed that flavourzyme hydroysate was the least bitter but elicited more umami taste compared to alcalase hydrolysate. Further treatments are still needed to enhance umami taste and to remove bitter taste in mud clam hydrolysate.

Keywords: mud clam hydrolysate, volatile compounds, amino acids, molecular weight, sensory

Abstrak

Lokan (*Polymesoda erosa)* telah dihidrolisiskan menggunakan dua microbial enzim yang berbeza; alcalase dan flavourzyme. Sebatian meruap, asid amino dan berat molekul yang dikaitkan dengan umami dan rasa pahit di dalam hidrolisat lokan ditentukan oleh ruang kepala pepejal mikro fasa kromatografi gas (HS-SPME-GCMS), cecair kromatografi berprestasi tinggi (HPLC) dan elektroforesis gel sodium dodekil sulfat poliakrimida (SDS-PAGE). Ciri – ciri hidrolisat dihasilkan menggunakan alcalase dan flavourzyme dibandingkan. Secara keseluruhan, lapan belas, tujuh dan enam sebatian meruap telah dikenal pasti dalam masing – masing pada isi lokan, hidrolisat alcalase dan hidrolisat flavourzyme. Kandungan sebatian meruap; 2-piperidinone yang dikaitkan dengan kepahitan adalah 6.79 % pada hidrolisat alcalase dan 3.78 % pada hidrolisat flavourzyme. Keputusan SDS-PAGE menunjukkan hidrolisat alcalase mengandungi peptida yang lebih kecil (<52 kDa) berbanding hidrolisat flavourzyme (<126 kDa). Di samping itu, analisis deria menggunakan kuantitatif deskriptif analisis (QDA) menunjukkan bahawa hidrolisat flavourzyme adalah yang paling kurang pahit dan memberi rasa umami yang lebih berbanding hidrolisat alcalase. Penambahbaikan lanjut masih diperlukan untuk meningkatkan rasa umami dan untuk menghilangkan rasa pahit dalam hidrolisat lokan.

Kata kunci: hidrolisat lokan, sebatian meruap, asid amino, berat molekul, deria

Introduction

Mud clam (*Polymesoda erosa)* is one of the edible bivalve species. Recently, the utilization of bivalve species becomes famous due to its high protein content and delicacy in coastal areas. Hydrolysate can be useful in food applications especially for flavour enhancer [1, 2]. Hydrolysate refers to proteins that are broken down into peptide of various sizes [3]. Flavour is defined as sensations arising from the integration of signal produced as consequence of smell and taste [4]. According to Su et al. [1], the hydrolysate produced from hydrolytic enzymes can enhance the flavour of the protein hydrolysate because it increases the amount of amino acids and low molecular weight peptides that possess unique taste properties including sweet, sour and bitter tastes. The types of protease and protein substrate affect the functional and flavour profile of the protein hydrolysate [5]. Volatile compounds in protein hydrolysate of various species have been identified by several researchers using different techniques of sample preparation and methods of analysis [6]. In this study, volatile compound was extracted by using headspace solid phase micro-extraction (HS-SPME). This method was claimed to have no solvent interference and consumed less time for sample preparation. Amino acids have the most variation in taste and the effect of amino acids and peptides on food taste has been researched extensively [1, 7].The amino acid compositions is important in protein hydrolysate because it contributes to the nutritional value besides influencing the functional properties and flavour of the hydrolysate [7, 8].There were several studies conducted on protein hydrolysate [9]. However, information on volatile compounds, amino acids, molecular weight and sensory related to the flavour of mud clam protein hydrolysate were limited.

Therefore, the aim of this study is to identify the volatile compounds, amino acid, molecular weight that contribute to the flavour of mud clam hydrolysate by using head space solid phase micro-extraction gas chromatography-mass spectrometry (HS-SPME-GC-MS), High performance liquid chromatography (HPLC) and sodium dodecyl sulphate polyacrylamide gel electrophoresis (SDS-PAGE). The sensory analysis using quantitative descriptive analysis (QDA) was conducted. The bitter and umami flavour of the hydrolysates produced by alcalase or flavourzyme were compared.

Materials and Methods

Raw materials

Mud clam (*Poymesoda erosa*) was bought from a supplier in Kuala Selangor and immediately placed in ice and transported to the laboratory. Upon arrival, the flesh was separated manually and then washed.

Enzymes

Alcalase is a bacterial endopeptidase produced by *Bacillus licheniformis*. Alcalase 2.4 L has a declared activity of 2.4 Anson Units (AU) g−1. Flavourzyme 500 L with declared activity of 500 Leucine Amino Peptidase Units per gram (LAPU/g) is a fungal protease/peptidase complex produced by submerged fermentation of a selected strain of *Aspergillus oryzae*. These two enzymes were obtained from Novozyme (Bagsvaerd, Denmark).

Preparation of mud clam (*Polymesoda erosa*) hydrolysate

Protein hydrolysate was prepared according to the method by Normah et al. [10]. An amount of 453 g flesh and 619 g distilled water was mixed and homogenized in a blender. The mixture was incubated in a circulated water bath. The pH of the mixture was adjusted to pH 8.5 and maintained constant during hydrolysis using 4.0 N of NaOH. Once the pH and temperature (60 °C) has stabilized, alcalase at enzyme-substrate ratio of 3 % was added and the hydrolysis continued for 2 hours. The mixture was continuously stirred using a stirring propeller throughout the hydrolysis period. At the end of hydrolysis, the enzymatic reaction was terminated by placing the samples in a water bath at 90 °C for 15 min. This was followed by centrifugation at 10 000 rpm, 4 °C for 20 min. Supernatant obtained was freeze-dried using the SANYO-Biomedical freeze dryer (ALPHA 1-4 (MARTIN CHRIST)). This procedure was repeated using Flavourzyme 500 L with condition at 55 °C and pH 7. The powdered hydrolysate was stored in -20 °C for further analysis.

Headspace solid-phase micro-extraction (HS-SPME)

One gram of hydrolysate sample was placed into a 15 mL headspace vial and pre-equilibrated for 15 min at 50 °C in thermostatic water bath with vial capped using a silicon septum. Afterward, stainless steel needle, PolydimethylSiloxane (PDMS) fibre was pushed through the vial septum. The fibre was pushed out of the housing

and exposed to the headspace at 55 °C for 30 min extraction time. After extraction, the fibre was pulled into the housing and the SPME device was removed from the vial and inserted into the injection port of GC for thermal desorption of the analysis.

Gas chromatography- mass spectrometry (GC-MS)
GC-MS analysis was performed using Agilent GC-MS (Santa Clara, CA, USA). The sample was desorbed in the injection port at 250 °C for 2 minutes in splitless mode. HP-5MS analytical capillary column (29 m x 250 µm x 0.25 µm, Agilent) and helium gas at a constant flow rate of 0.8 mL/min was used. The oven temperature was programmed at an initial temperature of 40 °C for 2 min followed by an increase of 5 °C/min to 150 °C (held for 5 min) and finally at 10 °C/min to 220 °C (held for 10 min). MS operating conditions (electron impact ionization mode) were an ion source temperature of 200 °C, ionization voltage of 70 eV and mass scan range of m/z 33 – 450 at 2.76 scans/s.

Volatile compound identification
The chromatography peak identification was carried out by comparing their mass spectra with those of the bibliographic data of known compounds from the Wiley 6 library (Hewlett-Packed Co., Palo Alto, CA) and NIST 98 library (Hewlett-Packed Co., Palo Alto, CA) mass spectral database on the basis of the criterion similarity (SI)>800 (the highest value is 1,000). Results are presented as the percent area (%).

Amino acid analysis
An amount of 0.1 grams mud clam hydrolysate or flesh was hydrolysed using 6 N HCl at 110 °C for 24 hours and derivatised using phenyl isothiocyanate prior to AccQ Tag HPLC analysis. The total amino acid was analysed by the AccQTag method using an AccQ Tag column (3.9 x 150 mm) at a flow rate of 1 mL/min equipped with fluorescence detector. The mobile phase used was AccQTaq Eluent A consists of 100 mL Eluent A and 1000 mL deionized water while AccQ Tag Eluent B consists of 60 % acetonitrile and 40 % deionized water. The total running time per injection was 50 minutes.

Sodium dodecyl sulphate polyacrylamide gel electrophoresis (SDS-PAGE)
SDS PAGE was used to determine the molecular weight of the mud clam flesh and mud clam hydrolysate. An amount of 0.1 g of powdered sample was dissolved in 10 mL deionized water and then filtered using membrane filter with pore sizes 0.45 µm. Filtered solution at 6.5µL was mixed with 2.5 µL NuPAGE®LDS sample Buffer (4X) and 1µL NuPAGE® Reducing Agent (10X). The mixture was heated at 70 °C for 10 minutes in water bath. Ten µL sample was loaded into each well of the SDS-PAGE system comprising of 12 % resolving gel and 5 % stacking gel. Benchmark™ protein ladder is used as a standard marker at the range of 175 to 9 kDa.

Electrophoresis was performed using the XCellSurelock electrophoresis cell (Bio-Rad laboratories, Hercules, CA, USA). Electrophoresis was run for 50 minutes at 100 – 125 mA/gel. After the running process, the gels were washed with 100 mL of ultrapure water. Then, the gel was stained using staining solution containing Coomassie Brilliant Blue dye and heated in a microwave oven at 180 °C for one minute. The gel was shaken again in the orbital shaker for about 2 minutes. The process was repeated twice. The gel were destained using Ultrapure water and shaken with orbital shaker for another 30 minutes.

Identification of bitter and umami taste
Sensory evaluation for bitterness and umami taste of mud clam hydrolysate was conducted using qualitative descriptive analysis (QDA). Ten panellists were trained for three weeks by using caffeine and monosodium glutamate (MSG) solution to represent the bitter and umami taste. Different concentrations of caffeine solutions (0.05 – 2.00 %) and MSG solutions (1 to 200 mM) were prepared and presented to the panellists. The lowest concentration that the panellist could perceive was identified and this concentration was used as the reference to evaluate the degree of bitterness and umaminess of mud clam hydrolysates. A 15 cm scale anchored from ‘none to strong bitterness’ was used for the evaluation. Mud clam hydrolysate (2.5 % (w/v)) were prepared and presented to the panellists.

Statistical analysis

The data obtained was analysed using the Analysis of Variance (ANOVA) to determine significance at 5 % level. Duncan Multiple Range Test (DMRT) was used to identify differences between means. Two sample t-tests were used to compare the mean values. Values were expressed as means ± standard deviations. The significant difference between two means was obtained when t value < p value 0.05.The statistical program used was SPSS software (Version 16.0) for Windows (SPSS Inc. Chicago, IL).

Results and Discussion

Volatile compound analysis

Savoury taste in seafood product is important to give a higher degree of acceptability among customer. This taste is dependent on the composition of volatile compounds. The number of compounds detected and identified were eighteen, seven and six for mud clam flesh, alcalase hydrolysate and flavourzyme hydrolysate, respectively (Table 1). Two different types of volatile alcohol (2-furanmethanol and benzyl alcohol) were only detected in the flesh and flavourzyme hydrolysate. According to Jin et al. [11], alcohols do not affect the flavour of food unless they are present in large amount because of their high threshold values. Mud clam flesh contains higher percent of hydrocarbon compound compared to the hydrolysate. Nor Qhairul Izzreen and Vijaya Ratnam [12] stated that high percentage of hydrocarbon in seafood is very common. Esters are produced by esterification with alcohols and carboxylic acid. According to Jin et al. [11], the content of esters increased slightly in fish processed products. Esters of low molecular weight greatly affect the sweet, fruity and candy-like flavour of salted and fermented anchovies [13]. Nitrogen- containing compound such as pyrazines were reported to have nutty, roasted or toasted aroma in most foods [8, 14]. 2,5 dimethylpyrazine compound was higher (4.09 %) in flavourzyme hydrolysate compared to those in alcalase hydrolysate (1.01 %). These compounds were the predominant aroma active compound in cooked shrimp, crab and seaweed [6, 15, 2]. Fatty acid are considered important compound in seafood flavour [2]. Fatty acid such as 2-propenoic acid, tetradecanoic acid and hexadecanoic acid was only identified in mud clam flesh as shown in Table 1.

Table 1. Major volatile compounds in mud clam flesh, alcalase hydrolysate and flavourzyme hydrolysate

Volatile compounds	Percent area (%)		
	Mud clam flesh	Alcalase hydrolysate	Flavourzyme hydrolysate
2-Furanmethanol	1.84	n.d.	n.d.
Benzyl Alcohol	n.d.	n.d.	15.10
Hexadecanoic acid, methyl ester	1.80	48.96	n.d.
Octadecanoic methyl ester	n.d.	16.61	n.d.
1,2-Benzenedicarbocylicacid, diisooctyl ester	0.99	n.d.	26.62
2-Propenoic acid	0.74	n.d.	n.d.
Tetradecanoic acid	20.51	n.d.	n.d.
n-hexadecanoic acid	33.28	n.d.	n.d.
4H-Pyran-4-one, 2,3-dihydro-3, 5-dihyroxy-6-methyl	4.52	n.d.	6.68
Cyclopentasiloxane, decamethyl	1.83	2.17	3.87
Heptadecane	0.97	0.27	n.d.
Octadecane	1.48	0.13	n.d.
Cyclopentadecane	1.57	n.d.	n.d.

n.d. = not detectable

Table 1 (cont'd). Major volatile compounds in mud clam flesh, alcalase hydrolysate and flavourzyme hydrolysate

Volatile compounds	Percent area (%)		
	Mud clam flesh	Alcalase hydrolysate	Flavourzyme hydrolysate
Nonadecane	2.18	n.d.	n.d.
Eicosane	2.63	n.d.	n.d.
Docasane	2.51	n.d.	n.d.
Heneicosane	3.73	n.d.	n.d.
Cholesta-3,5-diene	4.33	n.d.	n.d.
Tetracosane	2.87	n.d.	n.d.
Hexacosane	2.15	n.d.	n.d.
2,5 dimethylpyrazine	n.d.	1.01	4.09
2-Piperidinone	n.d.	6.79	3.78

n.d. = not detectable

According to Natta et al. [2], fatty acids were not found due to thermal degradation of lipids. 2-piperidinone is from amide group which caused bitter flavour was presence in both hydrolysates. The flavourzyme hydrolysate gave significantly lower content of 2-piperidinone (3.78 %) compared to alcalase hydrolysate (6.79 %). This finding was in agreement with amino acid and sensory analysis which indicated that alcalase hydrolysate has significantly higher degree of bitterness compared to flavourzyme hydrolysate. These compounds were also found in fermented castor oil bean [16].

Amino acids content

The amino acids content in mud clam flesh and hydrolysates is shown in Table 2. The total amino acids were 75.23 %, 62.37 % and 47.66 % for alcalase hydrolysate, flavourzyme hydrolysate and mud clam flesh, respectively. The amino acids grouping based on their taste characteristic as described by Tseng et al. [17] are shown in Table 2. The bitter amino acid was predominant taste in those three samples. Alcalase hydrolysate contains highest amount of bitter like amino acids (46.76 %) followed by flavourzyme hydrolysate (37.79 %) and mud clam flesh (30.4 %). The MSG-like amino acids (aspartic acid and glutamic acid) were 5.06 % in alcalase hydrolysate followed by mud clam flesh with 3.45 % and flavourzyme hydrolysate which is 3.28 %. This result was in agreement with sensory data in which alcalase hydrolysate gave higher bitter taste compared to flavourzyme hydrolysate. According to Zhang and Tao [7] who studied on the final taste characteristic of five different types of soy sauce revealed that the balance and interaction between different taste components in amino acid gave different taste to every sauce.

Sodium dodecyl sulphate polyacrylamide gel electrophoresis (SDS-PAGE)

The molecular weight distributions of mud clam flesh and mud clam hydrolysates are shown in Figure 1. More intense bands with wide molecular weight range were observed in mud clam flesh compared to both hydrolysates. This showed that both enzymes are capable of breaking the protein into the smaller peptides. Mud clam hydrolysate produced from alcalase has lower molecular weight (<52 kDa) compared to flavourzyme hydrolysate (<126 kDa). Therefore, alcalase hydrolysate was bitterer than flavourzyme hydrolysate which is in line with sensory analysis.

Table 2. Total amino acids content ($g100g^{-1}$) in mud clam flesh, alcalase and flavourzyme hydrolysate based on their taste characteristic

Amino acid	Mud clam flesh	Alcalase hydrolysate	Flavourzyme hydrolysate
MSG-like*			
Asp	0.15±0.01	0.96±0.02	0.42±0.01
Glu	3.30±0.40	4.10±0.38	2.86±0.91
Total	3.45	5.06	3.28
Sweet*			
Ala	2.21±0.93	1.86±0.53	1.43±0.31
Gly	2.64±0.94	1.71±0.51	2.09±0.21
Ser	1.38±0.29	3.57±0.14	5.14±0.10
Thr	1.21±0.20	2.79±0.47	1.41±0.33
Total	7.44	9.93	10.07
Bitter*			
Arg	2.84±0.52	5.29±0.83	2.09±0.21
His	4.10±0.96	5.69±0.91	3.81±0.88
Ile	1.60±0.50	2.45±0.56	1.01±0.67
Leu	1.61±0.52	4.89±0.42	5.98±0.86
Met	1.72±0.41	3.71±0.32	0.68±0.59
Phe	17.18±0.11	21.56±0.41	23.12±0.40
Val	1.35±0.10	3.17±0.59	1.10±0.02
Total	30.4	46.76	37.79
Tasteless*			
Cys	0.47±0.56	6.54±0.70	7.38±0.88
Lys	2.02±0.91	2.97±0.86	1.58±0.92
Pro	3.62±0.39	2.72±0.23	1.14±0.06
Total	6.11	12.23	10.1

Values are expressed as means ± standard deviation from triplicate determinations, *Amino acids grouping based on taste as described by [17].

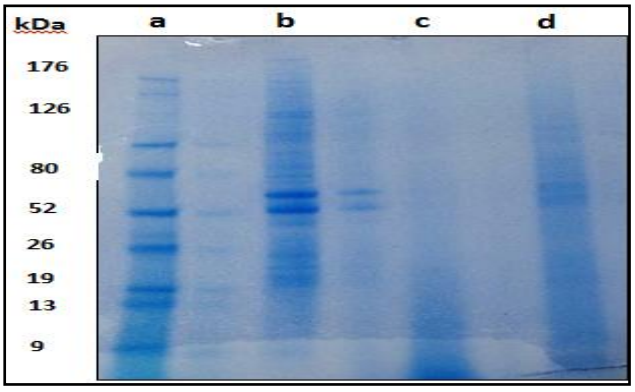


Figure 1. Molecular weight distributions of (a) protein marker, (b) mud clam flesh, (c) alcalase hydrolysate and (d) flavourzyme hydrolysate.

Identification of degree of bitterness and umami taste

The bitterness and umami taste of mud clam hydrolysate were evaluated using caffeine and monosodium glutamate (MSG) solutions. The score for bitterness using 15-cm line scale with anchor from 'none' to 'very strong' for alcalase hydrolysate was 6.60, 3.56 for flavourzyme hydrolysate and 9.66 for caffeine solution.

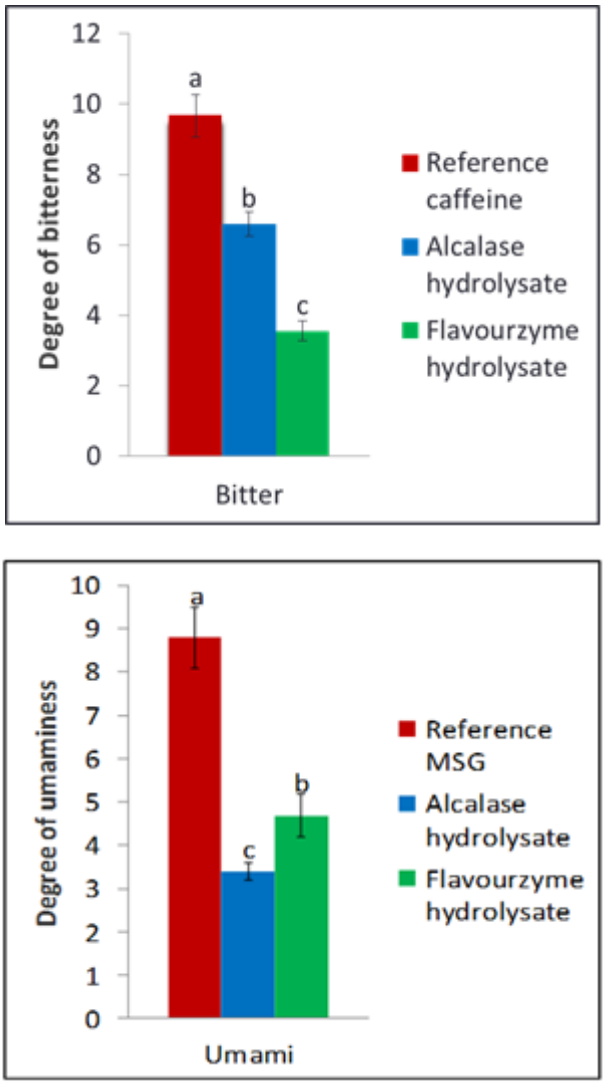


Figure 2. Degree of bitterness and umaminess of mud clam hydrolysates. Values are expressed as means ± standard deviation. Different letters indicate significant different at $p < 0.05$

This result revealed that the bitterness of the hydrolysates and caffeine solution were in the following order: flavourzyme hydrolysate <alcalase hydrolysate < caffeine reference solution. This result was in agreement with total amino acids content in which alcalase hydroysate had higher amount of bitter taste amino acids compared to flavourzyme hydrolysate. For umami taste, the reference monosodium glutamate (MSG) degree of umaminess was significantly higher ($p < 0.05$) compared to alcalase and flavourzyme hydrolysate (Figure 2). Flavourzyme

hydrolysate was perceived to be slightly more umami than alcalase hydrolysate by the panellists which could be associated with higher content of the sweet amino acids.

Conclusion

Volatile compound (2-piperidinone) that contributes to bitter taste was identified in hydrolysate. Alcalase hydrolysate has higher bitter like amino acid content compared to those of flavourzyme. The sensory analysis also suggested that flavourzyme hydrolysate was less bitter than alcalase hydrolysate. Both hydrolysates showed lower umami value than the reference umami solution. Further treatment of mud clam protein hydrolysate is needed to reduce the bitter taste and to enhance the umami taste in order to give more acceptable product.

Acknowledgement

The authors would like to thank for all the laboratory staff of Food Technology Department and facilities provided from the Faculty of Applied Sciences, Universiti Teknologi MARA (UiTM), Shah Alam campus.

References

1. Su, G., Cui, C., Zheng, L., Yang, B., Ren, J. and Zhao, M. (2012). Isolation and identification of two novel umami and umami-enhancing peptides from peanut hydrolysate by consecutive chromatography and MALDI-TOF/TOF MS. *Food Chemistry*, 135: 479 – 485.
2. Natta, L., Orrapun, S. and Orapin, K. (2014). Seafood-like flavour obtained from the enzymatic hydrolysis of the protein by-products of seaweed (*Gracilaria sp.). Food Chemistry*, 158: 162 – 170.
3. Adler-Nissen, J. (1986). Enzymic hydrolysis of food proteins. New York: Elsevier Applied Science Publishers.
4. Laing, D. G. and Jinks, A. (1996). Flavour perception mechanisms. *Trends in Food Science and Technology*, 7: 387 – 389.
5. McCarthy, A., O'Callaghan, Y. and O'Brien, N. (2012). Protein hydrolysates from agricultural crops - bioactivity and potential for functional food development. *Agriculture*, 3(1): 112 – 130.
6. Morita, K., Kubota, K. and Aishima, T. (2001). Sensory characteristics and volatile components in aromas of boiled prawns prepared according to experimental designs. *Food Research International*, 34: 473 – 481.
7. Zhang, Y. and Tao, W. (2009). Flavour and taste compounds analysis in Chinese solid fermented soy sauces. *African Journal of Biotechnology*, 8(4): 673 – 681.
8. Oh, K. S, Kang, S. T and Ho, C. T. (2001). Flavour constituents in enzyme hydrolysates from shore swimming crab and spotted shrimp. *Journal Korean Society of Food Science and Nutrition*, 30: 787 – 795.
9. Sathivel, S., Bechtel, P. J., Babbitt, J., Smiley, S., Crapo, C. and Reppond, K. D. (2003). Biochemical and functional properties of herring (*Clupea harengus*) byproduct hydrolysates. *Food Chemistry and Toxicology*, 68: 2196 – 2200.
10. Normah, I., Siti Hafsah, M. S. and Nurul Izzaira, A. (2013).Bitterness of green mussel (*Perna viridis*) hydrolysate as influenced by the degree of hydrolysis. *International Food Research Journal*, 20(5): 2261 – 2268.
11. Jin, Y. P., Ye, J. K. and Yang, B. L. (2014). Analysis of headspace volatile compounds in cold-stored and freeze-dried krill *Eupausia superb. Fish Aquatic Science*, 17(2): 189 – 195.
12. Nor Qhairul Izzreen, M. N. and Vijaya Ratnam, R. (2011).Volatile compound extraction using solid phase micro extraction coupled with gas chromatography mass spectrometry (SPME-GCMS) in local seaweeds of *Kappaphycus alvarezii*, *Caulerpa lentillifera* and *Sargassum polycystem*. *International Food Research Journal*, 18(4): 1449 – 1456.
13. Cha, Y. J., Cho, W. J and Jeong, E. J. (2006). Comparison of volatile flavour compounds in commercial crab-like flavorants by analyzing methods. *Journal of Life Sciences*, 16: 1243 – 1249.
14. Ahn, J. S., Cho, W. J., Jeong, E. J. and Cha, Y. J. (2006). Reaction technology for making natural crab like flavoran from snow crab processing by-products. *Journal Korean Fish Society*, 39: 437 – 440.
15. Yu, H. Z. and Chen, S. S. (2010). Identification of characteristic aroma-active compounds in steamed mangrove crab (*Scylla serrata*). *Food Research International*, 43: 2081 – 2086.
16. Ojinnaka, M. C. and Ojimelukwe, P. C. (2013). Study of the volatile compounds and amino acid profile in *Bacillus* fermented castor oil bean condiment. *Journal of Food Research*, 2: 191 – 203.
17. Tseng, Y. H., Lee, Y. L., Li, R. C. and Mau, J. L. (2005). Non-volatile flavour components of *Ganoderma tsugae*. *Food Chemistry*, 90: 409 – 415.

Malaysian Journal of Analytical Sciences, Vol 20 No 4 (2016): 820 - 828
DOI: http://dx.doi.org/10.17576/mjas-2016-2004-15

MALAYSIAN JOURNAL OF ANALYTICAL SCIENCES
Published by The Malaysian Analytical Sciences Society
ISSN 1394 - 2506

NUTRITIONAL COMPOSITION AND COLOUR ANALYSIS OF CHOLESTEROL-REDUCED EGG YOLK POWDER

(Komposisi Nutrisi dan Analisis Warna Serbuk Kuning Telur Rendah-Kolesterol)

Fauziah Che In[1], Zaibunnisa Abdul Haiyee[1]*, Osman Hassan[2], Wan Aida Wan Mustapha[2]

[1]*Faculty of Applied Sciences,*
Universiti Teknologi MARA, 40450 Shah Alam, Selangor, Malaysia
[2]*School of Chemical Science and Food Technology, Faculty of Science and Technology,*
Universiti Kebangsaan Malaysia, 43600 UKM Bangi, Selangor, Malaysia

**Corresponding author: nisha@salam.uitm.edu.my*

Received: 24 February 2015; Accepted: 27 October 2015

Abstract

Dietary cholesterol should be limited to less than 200 mg/day. A single large egg yolk contains approximately 275 mg of cholesterol. Thus, consumption of a single egg yolk exceeds the recommended daily intake of cholesterol. This study was focused on determination of the effect of addition of increasing amount of β-cyclodextrin (β-CD) to encapsulate cholesterol in egg yolk. The quality of cholesterol-reduced egg yolk powder was evaluated by determining its nutritional composition and colour analysis. Increasing amount of β-CD (0 – 15 mM) was added in liquid egg yolk and the encapsulated cholesterol in the form of precipitate was removed. The supernatant was dried and the end product; cholesterol-reduced egg yolk powder (CREYP) was analyzed for moisture content, total lipid, fatty acids content, protein and colour. There were no significant difference ($p > 0.05$) in term of total solid content. However, protein content of CREYP was significantly ($p < 0.05$) reduced up to 7 mM β-CD and no further significant reduction was noticed with further addition of β-cyclodextrin. The appearance of the powder became lighter in colour as validated using chromameter; L*, a*, b*, C* and h^o values. The results obtained from this study indicate that cholesterol can be successfully removed from egg yolk. However, slight reduction in protein content was observed. Nutritional composition of CREYP was minimally affected with the removal of encapsulated cholesterol. Therefore, cholesterol-reduced egg yolk powder can be utilized as an essential ingredient in any egg yolk based products.

Keywords: cholesterol, β-cyclodextrin, egg yolk, nutritional composition

Abstrak

Pengambilan kolesterol dalam diet seharusnya tidak melebihi 200 mg/sehari. Sebiji kuning telur mengandungi hampir 275 mg kolesterol. Maka, pengambilan sebiji kuning telur telah melebihi kadar cadangan diet seharian kolesterol. Kajian ini memfokuskan kepada kesan penambahan kuantiti β-siklodekstrin (β-CD) untuk pengkapsulan kolesterol dalam kuning telur. Kualiti serbuk kuning telur kurang-kolesterol di analisis dengan menentukan komposisi nutrien dan analisis warna. Peningkatan kuantiti β-siklodekstrin (β-CD) (0 – 15 mM) ditambahkan ke dalam kuning telur dan pengkapsulan kolesterol di dalam bentuk mendakan dibuang. Supernatan dikeringkan dan hasil produk (serbuk kuning telur kurang-kolesterol) yang terhasil dianalisa untuk jumlah kandungan kelembapan, jumlah lipid, asid lemak, protein dan warna. Tiada perbezaan yang signifikan ($p > 0.05$) dalam jumlah kandungan pepejal. Walaubagaimanapun, kandungan protein kuning telur kurang-kolesterol berkurang secara signifikan ($p < 0.05$) bagi penambahan 7 mM β-CD dan tiada pengurangan yang signifikan dengan peningkatan penambahan β-CD. Serbuk kuning telur menunjukkan pengurangan warna seperti dibuktikan menggunakan kromameter; bacaan L*, a*, b*, C* dan h^o. Keputusan menunjukkan bahawa kolesterol telah berjaya dibuang daripada kuning telur. Walaubagaimanapun, pengurangan sedikit kandungan protein diperhatikan. Kesan pengurangan pengkapsulan kolesterol ke atas komposisi nutrisi serbuk kuning telur kurang-kolesterol adalah sedikit. Maka, serbuk kuning telur kurang-kolesterol dapat digunakan sebagai bahan ramuan penting di dalam mana – mana produk berasaskan kuning telur.

Kata kunci: kolesterol, β-siklodekstrin, kuning telur, komposisi nutrisi

Introduction

Egg yolk contains approximately 50 % of solids. The major constituents of the solid matter in egg yolk are lipids (65 – 70 % on dry basis) and proteins (30 % on dry basis), consisting of proteins in solution referred to as livetin, lipoprotein particles including high-density lipoproteins (HDLs), low-density lipoproteins (LDLs), and phosvitin [1]. Each constituent of yolk possesses special physical and chemical characteristics responsible for its own functional properties. Thus, yolk represents a major source of active principles usable in medical, pharmaceutical, cosmetic and biotechnological industries [2].

Nowadays foods not only intended to provide necessary nutrients, but also to prevent nutrition-related diseases and improve physical and mental well-being of the consumers [3]. It can be assumed that cholesterol-lowering and cholesterol-free products or those containing phystosterol esters, which are considered to lower the cholesterols level, will gain increasing relevance in the coming years [3]. Food companies have developed many methods to reduce cholesterol in food, such as short-path and vacuum molecular distillation, blending in vegetable oils, extraction by organic solvents, cholesterol degradation by cholesterol oxidases, and removal by supercritical carbon dioxide extractions. However, the cost of these are non-selective methods is high, and when cholesterol removed, flavor and nutritional components are removed as well [3, 4, 5]. This was agreed by Heshmati and Khodadadi, [6] where these methods are not applicable to all edible products. For example, *cis* fatty acid isomers are converted to atherogenic trans isomers during vacuum steam distillation method, aromatic and carcinogenic solvents may remain in the food after utilization, and a substantial capital investment and operating costs are required for carbon dioxide extraction procedure [7]. Moreover, the usage of solvents may present health risk or are so harsh that the restoration of the egg texture is impossible [8]. Vegetable oil extraction processes able to achieve substantial removal of cholesterol however, the amount of fresh oil needed for cholesterol extraction, usually 4 – 25 (wt/wt) times more than the egg yolk makes such processes impractical and uneconomical because after extraction such oil must be discarded [8]. Even though there is an improvement in the recyclability of the oil used, still the amount of oil used is in huge amount.

Encapsulation using cyclodextrins (CDs) is a method that has been used during the last few years in the cosmetics, drug and food industries for many purposes. Their molecular structure and shape made CDs to have the ability to act as molecular containers by entrapping guest molecules in their internal cavity [3]. Cyclodextrin can bind to various kinds of low molecule compounds into its cave structure, thereby stabilising the low molecule organic compounds by the inclusion effect [9]. The hydrophobic cavity forms inclusion complexes with a wide range of guest molecules. Non-covalent bonds are formed or broken during the complex formation and in aqueous solution, the complexes readily dissociate remaining the released molecules in equilibrium with the molecules bound within CD cavity [3]. The internal cavity which is hydrophobic allows the cyclodextrins to complex molecules such as aromatic alcohols, fatty acids and their esters and cholesterol.

Fresh eggs in liquid form are also difficult to transport because of their bulkiness, fragility, and highly perishable nature [10]. Therefore egg in powder form, able to overcome this problem. This study is therefore aimed at determining the effects of addition of β-cyclodextrin on the nutritional composition of cholesterol-reduced egg yolk powder dried using oven drying.

Materials and Methods

Materials

Fresh eggs were purchased from local market in Shah Alam, Malaysia. β-CD (purity 99.5%) was purchased from the Sigma Chemical Company (St. Louis, MO, USA). Chloroform-absolute alcohol, hexane (Ph. Eur., GC grade, Merck, Germany) and ethanol (Ph. Eur., Merck, Germany) were used in this study. Purified water (Milli QUV plus water system, Millipore, Molsheim, France) was also been used.

Preparation of cholesterol-reduced egg yolk: *Formation of inclusion complex*

Cholesterol was removed from egg yolk by formation of egg yolk cholesterol:β-cyclodextrin inclusion complex (EYCβIC) following the method used by Awad et al. [11] with some modifications. The egg yolk pH and ^{o}Brix were adjusted to 10.5 and 2.9, respectively with continuous stirring using homogenizer (IKA Ultra Turrax T25 Homogenizer, UK) at 210 ± 10 rpm. The egg yolk was placed in a laboratory shaking water bath (100 rpm, 1 hour, 50 ^{o}C). Diluted egg yolk (5 g) was mixed with increasing amounts of β-CD (0 – 15 mM) with continuous mixing using a vortex mixer (Laboratory equipment, VELP, Italy) at 1600 rpm for 10 minutes. The treated egg yolk was placed in a shaking water bath (100 rpm, 20 min, 50 ^{o}C) and cooled to 8 – 10 ^{o}C for 1 hour and centrifuged at 5000 rpm at 5 ^{o}C for 15 min (Hettich Universal 320, Benchtop centrifuge, Germany). Insoluble β-CD-cholesterol inclusion complex in the form of sediment was separated from the supernatant. The pH of the supernatant was adjusted back to pH 6.0. The supernatant were oven dried (44 ^{o}C, 4 hours) for production of cholesterol-reduced egg yolk powder.

Compositional analysis

Moisture content

The moisture content of the samples were determined in triplicate by drying under vacuum oven at 98 – 100 °C according to the method as described by AOAC, 1975 [12].

Total lipid

Lipids were extracted from the egg yolks using the standard method [13]. According to this method, approximately 4 g well mixed egg yolk was weighed into a 100 mL volumetric flask and 25 mL chloroform-absolute alcohol were added (1:1) the solvent was mixed very slowly from pipette. It was shaken constantly until proteins were coagulated. An additional 60 – 65 mL mixed solvent was added and let stand for 1 hour, shaken every 5 min. At the end of the time it was diluted to volume with mixed solvent and the mixture was let stand until clear. The mixture was then filtered very slowly (filtrate should be clear), solvent was evaporated and egg yolk lipid was obtained. The total lipid content of the samples was evaluated in triplicate.

Cholesterol determination

The supernatant (1 mL) were placed in screw-capped glass tubes (15 x 180 mm). The samples were saponified [14]. The extracts were redissolved in 1 mL of hexane and stored at -20 °C until analysis. The total cholesterol was determined using gas chromatography [15]. The percentage of cholesterol reduction was calculated using the equation given below:

$$\text{Cholesterol reduction (\%) at 15 mM} = \frac{(\text{amount of cholesterol at 0 mM} - \text{amount of cholesterol at 15 mM}) \times 100}{\text{amount of cholesterol at 0 mM}} \quad (1)$$

Fatty acids determination

FAMEs were prepared according to the method as described by Zara et al. [16] with some modifications. FAME analysed were performed on gas chromatograph (Perkin Elmer). Fatty acid methyl esters were separated on a capillary column (HP-5 MS; Agilent 0.25 mm x 30 m 0.25 µm) equipped with an auto-sampler. The initial temperature of 50 °C was held for 3 min, increased to 180 °C at 10 °C min, increased to 220 °C at 5 °C /min and held for 10 min. The column temperature was elevated to 230 °C at 5 °C/min and held at the final temperature for 3 min. Helium was used as the carrier gas at a flow rate of 3.0 mL/min. The detector was set at 240 °C. Fatty acid methyl esters were identified by comparison with retention times of standard mixture. The fatty acid content of egg yolk was calculated using the following formula equation 2 [17, 18]:

$$\text{Concentration (mg/g)} = \frac{\text{Peak area of a given fatty acid} \times \text{concentration of IS (mg/mL) peak area of IS}}{\text{Weight of sample (g)}} \quad (2)$$

IS is defined as internal standard.

Protein determination

The Kjeldahl method of nitrogen analysis was conducted to calculate the protein content [13]. The protein content of liquid egg yolk treated from 0 – 15 mM addition of β-CD was determined in triplicate.

Colour determination

Colour values (L*, a*, b*, C*, h^o) of EY powder treated from treatment of liquid egg yolk with 0 – 15 mM addition of β-CD were measured in triplicate using Chromameter CR-400.

Statistical analysis

Mean values from the three separate experiments or replicate analysis were reported. The statistical significance of observed differences among three treatment means evaluated by analysis of variance (ANOVA) and the comparison of means were carried out by Duncan's multiple range test ($p < 0.05$) by using SPSS 10 for Windows.

Results and Discussion

Moisture content

Moisture content is important in food quality and preservation. Moisture content is expressed as dry basis. Dry basis of moisture content is defined as the ratio of water weight to the dried weight of sample [19]. The moisture content of the egg yolk powder with the addition of increasing amount of β-cyclodextrin was shown in Table 1. Moisture content of the dried egg yolk powder obtained in this study was in the range of 2.4 – 2.7 %. Previous researcher suggested the optimum moisture content for egg yolk powder should be within the range of 2 – 4 %, low enough to extend the shelf life in an environment of low humidity [10].

Table 1. Moisture content of cholesterol-reduced egg yolk powder

Concentration of β-cyclodexrin (mM)	**0**	**1**	**3**	**5**	**7**	**11**	**13**	**15**
Moisture content (g/100 g egg yolk powder)	2.5 ± 0.66[a]	2.4 ± 0.35[a]	2.6 ± 0.48[a]	2.4 ± 0.35[a]	2.6± 0.11[a]	2.5 ± 0.09[a]	2.7 ± 0.11[a]	2.7 ± 0.10[a]

Means within the same row with different letters differ significantly ($p < 0.05$).

Total lipid

The lipid content in egg yolk are principally triglycerides (65 %, w/w), phospholipids (28 %, w/w), cholesterol (5 %, w/w) [20] and were exclusively associated with lipoproteins assemblies [21]. The concentration of lipid in the dried cholesterol-reduced egg yolk powder showed in Figure 1. The reduction of total lipid was from 55 to 48 g/100gm egg yolk powder. Our previous work has shown and proven that certain fraction of cholesterol molecules was included into β-CD cavity which confirmed the formation of inclusion complex and finally in accomplishment of the reduction of cholesterol in egg yolk [22]. Since cholesterol molecules are part of egg yolk lipids, the total lipid contents of egg yolk powder were expected to be slightly reduced. There were no significant differences ($p > 0.05$) in total lipid content as increased in the addition of β-CD concentration.

The reduction of total lipids should be due to removal cholesterol through encapsulation. Egg yolk consists mainly of 68 % low-density lipoproteins (LDL), 16 % high-density lipoproteins (HDL), 10 % livetins and 4 % phosvitins [23]. Cholesterols which were situated in the large spherical of LDL particles, probably the reason why total lipids were reduced along with cholesterol extraction.

The cholesterol removal process such as stirring, separation and centrifugation during separation of cholesterol: β-CD inclusion complexes may affect the decreasing of total lipid content of egg yolk. These results correlated with the study by Kim et al. [24]. Furthermore, Ha et al. [25] suggested that the free fatty acids in food may be reduced because they are trapped in β-CD cavities molecule.

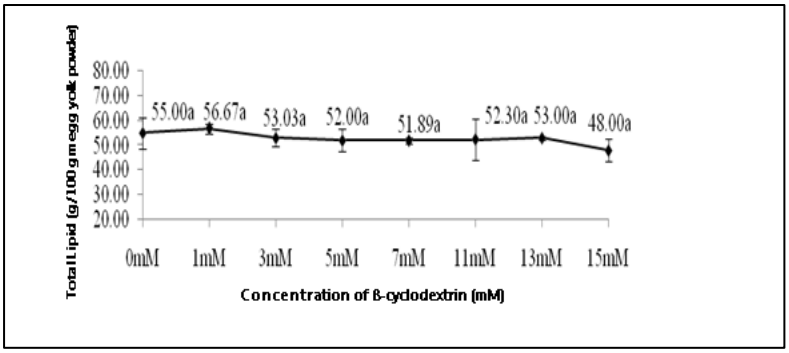


Figure 1. Total lipid content of cholesterol-reduced egg yolk powder

Cholesterol reduction

Increasing amounts of β-cyclodextrin (β-CD) were added to optimize the weight ratio for maximal cholesterol removal from the egg yolk. The concentrations of cholesterol remaining in the supernatant after removal of the pellet inclusion complexes were shown in Figure 2. The curve shows a gradual decrease in the concentration of cholesterol in the egg yolk as the concentration of added β-CD (mM) increased, which is in agreement with the findings of the previous study [26]. At 0 mM β-CD, cholesterol content was 12.51 mg/gm, whereas as 1 mM, 3 mM, 5 mM, 7 mM, 11 mM and 13 mM β-CD were recorded at 10.72, 6.14, 4.36, 3.87, 2.02 and 1.14 mg/gm cholesterol content respectively. Cholesterol-reduced egg yolk powder at 15 mM β-CD was lower than at 0 mM β-CD ($p < 0.05$). At 15 mM β-CD with 0.24 mg/gm cholesterol content left resulted in 98 % cholesterol was extracted from the 5 gm supernatant.

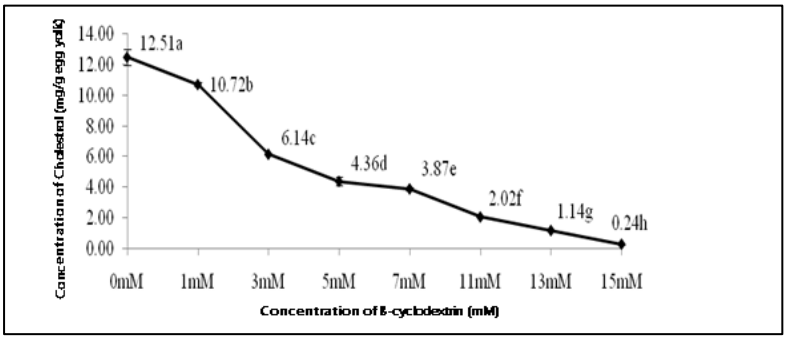


Figure 2. Cholesterol contents of cholesterol-reduced egg yolk powder. Data are expressed as means ± SD. Value with different letters indicates significant difference at $p < 0.05$.

Fatty acids determination

Fatty acids were prepared from different concentration of increasing β-CD concentrations according to the method as described by Zara et al. [16]. Among the different fatty acids tested (Table 2), there were no difference ($p > 0.05$) was observed as increasing β-CD concentrations for linolenic acid (C18:3) with 0.86 ± 0.13^a, 0.56 ± 0.34^a , 0.56 ± 0.46^a , 0.30 ± 0.10^a and 0.48 ± 0.04^a (mg/g fatty acids) for 0 mM (control), 3 mM, 7 mM, 11 mM and 15 mM β-CD concentrations respectively (Table 2). Arachidonic acid (C20:4 (n-6)) showed significant different with the highest β-CD concentrations (15 mM), with fatty acids content of 5.51 ± 0.03^a, 5.39 ± 0.07^a, 5.69 ± 0.09^a, 5.42 ± 0.14^a and 1.67 ± 0.33^b for 0 mM (control), 3 mM, 7 mM, 11 mM and 15 mM β-CD concentrations respectively.

Table 2. Fatty acids content of cholesterol-reduced egg yolk powder

Fatty acids	Concentration β-CD (mM)				
	0	3	7	11	15
Myristic acid C14:0	2.02 ± 0.14^{a}	1.90 ± 0.01^{ab}	1.81 ± 0.08^{bc}	1.69 ± 0.03^{c}	1.45 ± 0.03^{d}
Palmitoleic acid C16:1	22.42 ± 2.87^{a}	24.81 ± 0.51^{a}	16.56 ± 1.89^{b}	22.45 ± 0.93^{a}	20.12 ± 1.57^{b}
Palmitic acid C16:0	118.92 ± 8.40^{b}	133.16 ± 0.72^{a}	118.68 ± 2.04^{b}	105.27 ± 4.35^{c}	48.09 ± 0.62^{d}
Linolenic acid (C18:3)	0.86 ± 0.13^{a}	0.56 ± 0.34^{a}	0.56 ± 0.46^{a}	0.30 ± 0.10^{a}	0.48 ± 0.04^{a}
Oleic acid C18:1 (n-9)	217.8 ± 3.89^{a}	220.62 ± 1.88^{a}	222 ± 1.41^{a}	186.11 ± 5.81^{b}	69.97 ± 1.03^{c}
Linoleic acid C18:2 (n-6)	20.1 ± 0.04^{ab}	18.77 ± 0.40^{b}	24.31 ± 1.71^{a}	18.2 ± 3.59^{b}	18.38 ± 0.20^{b}
Stearic acid C18:0	33.84 ± 2.17^{a}	33.79 ± 0.63^{a}	35.16 ± 0.69^{a}	35.02 ± 0.67^{a}	12.08 ± 0.04^{b}
Arachidonic acid C20:4 (n-6)	5.51 ± 0.03^{a}	5.39 ± 0.07^{a}	5.69 ± 0.09^{a}	5.42 ± 0.14^{a}	1.67 ± 0.33^{b}
EPA C20:5 (n-3)	1.07 ± 0.04^{b}	1.21 ± 0.04^{a}	1.14 ± 0.04^{ab}	0.45 ± 0.05^{c}	0 ± 0.00^{d}
DHA C22:6 (n-3)	1.48 ± 0.16^{ab}	1.71 ± 0.03^{a}	1.30 ± 0.02^{ab}	0.68 ± 0.68^{bc}	0.21 ± 0.10^{c}

Means within the same row with different letters differ significantly ($p < 0.05$).

Whereas for 15 mM β-CD concentration, there was totally lost in EPA as 0 mM (control) having lower EPA content. However, other fatty acids; myristic acid (C14:0), palmitoleic acid (C16:1), palmitic acid (C16:0), oleic acid (C18:1 (n-9)), linoleic acid (C18:2 (n-6)), EPA (C20:5 (n-3)), and DHA (C22:6 (n-3)) resulted in difference in decreasing of fatty acids content ($p < 0.05$) as increasing β-CD concentrations. These results were same as reported by Awad et al. [27]. The changes in concentration of C18:1 (n-9), C18:2 (n-6) and C16:0 might be due to changes in the relatively concentrations of triglycerides and phospholipids, which are composed of different fatty acids [27]. The major fatty acids of triglycerides are oleic acids and palmitic acid. Therefore as the β-CD concentrations were increased, all the fatty acids of the egg yolk powder being tested were decreased.

Protein quantification

The egg yolk protein content was significantly decreased ($p < 0.05$) as cholesterol being reduced with increasing β-CD concentrations from 0 to 15 mM (Figure 3). Protein content in the egg yolk was significantly reduced as β-CD concentration increased up to 7 mM. There was no significant difference with further addition of β-CD. Smith et al. [28] reported that protein reduction of 9.2 % with 89.2 % cholesterol reduction in liquid egg yolk using β-CD which proven better reduction of cholesterol with 98% reduction of cholesterol with almost less than 9 % protein reduction in this study.

Cyclodextrins molecular structure is unique with hydrophilic exterior properties and hydrophobic in central of its cavities. These properties allow them to form non-covalent inclusion complexes by encapsulating of variety of 'guest' molecules into the 'host' which refer to their central cavities through associate and dissociating process. Kim et al. [24] and Kwak et al. [30] reported the protein reduction in milk after removal of cholesterol. It was confirmed that the protein content of cream was reduced during reduction of cholesterol by 4 –10 % β-CD due to entrapment of amino acids in β-CD cavities [29].

Maskooki et al. [31] reported that, the outer surface of β-CD macromolecules has affinity to absorb the negative charges that cover the protein surfaces. Subsequently, parts of protein together with β-CD:cholesterol inclusion complexes leave during centrifugation and separation process. Thus, cholesterol reduction processing such as mixing, separation, and centrifugation may affect decrease of total protein content of egg yolk.

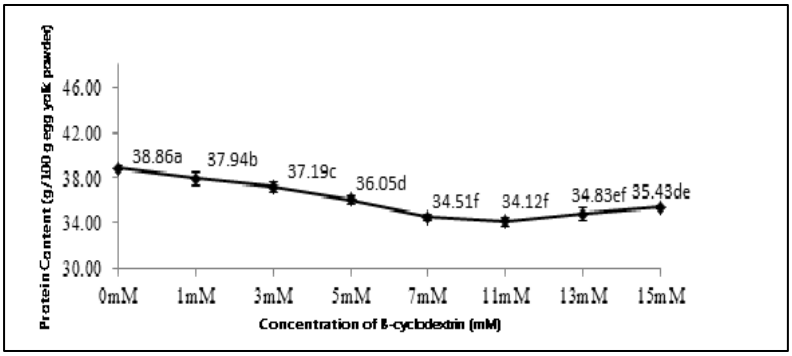


Figure 3. Protein contents of cholesterol-reduced egg yolk powder

Colour determination

The colour analysis of the egg yolk powder produced from the reduction of cholesterol by β-CD: cholesterol inclusion complexes was confirmed by the data obtained (Table 3) from the instrumental analysis using Minolta Chroma Meter CR-300 (Japan) to detect the lightness (L*), redness (a*) and yellowness (b*), saturation, (C*) and hue angle (h^o) values of egg yolk powder. L* value represents lightness (negative towards black, positive towards white), a* value is the red-greenness colour scale (negative towards green, positive towards red) whereas b* value represents blue-yellow colour scale (negative towards blue, positive towards yellow).

The lightness (L*), redness (a*) and yellowness (b*), Chroma (C*) and hue angle (h^o) of egg yolk powder were significantly different with direct correlation with increasing addition amount of β-CD concentrations as cholesterol being reduced.

Table 3. Colour values of cholesterol-reduced egg yolk powder

Egg yolk powder	*L	a*	b*	C*	h^o
0 mM	72.55 ± 0.03^{h}	1.83 ± 0.09^{a}	39.40 ± 0.07^{a}	39.42 ± 0.07^{a}	87.57 ± 0.18^{f}
1 mM	73.06 ± 0.06^{g}	1.48 ± 0.13^{a}	38.49 ± 0.04^{b}	38.50 ± 0.03^{b}	87.88 ± 0.04^{e}
3 mM	73.70 ± 0.15^{f}	1.29 ± 0.07^{c}	36.57 ± 0.04^{c}	36.25 ± 0.22^{c}	88.09 ± 0.11^{de}
5 mM	74.34 ± 0.29^{e}	1.08 ± 0.03^{de}	34.62 ± 0.06^{d}	34.57 ± 0.20^{d}	88.24 ± 0.14^{d}
7 mM	79.53 ± 0.10^{d}	1.13 ± 0.16^{cd}	33.37 ± 0.15^{e}	33.41 ± 0.19^{e}	89.74 ± 0.02^{c}
11 mM	80.68 ± 0.19^{c}	0.95 ± 0.14^{ef}	32.69 ± 0.21^{f}	31.57 ± 0.14^{f}	89.80 ± 0.14^{c}
13 mM	82.47 ± 0.15^{b}	0.86 ± 0.08^{f}	31.70 ± 0.07^{g}	30.71 ± 0.15^{g}	90.03 ± 0.03^{b}
15 mM	83.74 ± 0.12^{a}	0.43 ± 0.41^{g}	28.42 ± 0.07^{h}	28.11 ± 0.03^{h}	92.03 ± 0.19^{a}

Means within a column with different letters differ significantly ($p < 0.05$).

Increasing amount of β-CD concentrations resulted in production of egg yolk powder with reduced in yellow colour. This was proven as the L-values of egg yolk powder was increased showing that the egg yolk powder turn to much lighter colour. Decreasing of redness (a*) and yellowness (b*) intensity colour of egg yolk powder correlate with reduction of yellowness of yolk and finally makes the egg yolk powder became greener and bluer as increased in the addition of β-CD. The colour of egg yolk is attributed to fat-soluble carotenoids (xanthophylls; including lutein, zeaxanthin, β-cryptoxanthin and minor amounts β-carotene) [32]. It appeared that the lightness (L*), redness (a*) and yellowness (b*), were influenced by β-CD concentrations additions with the reduction of cholesterol. Lipid-soluble pigments of egg yolk probably were being trapped by β-CD cavities during the cholesterol removal process.

Chroma (C*) is a measure of intensity or saturation and calculated as $[(a^*)^2 + (b^*)^2]^{1/2}$ and represents saturation whereas h° represents hue angle which is derived from the two coordinates a* and b* and determined as $\tan^{-1} b^*/a^*$ [33]. Hue angle (h°) is expressed on a 360° grid where 0° = bluish-red, 90° = yellow, 180° = green and 270° = blue [34]. Egg yolk powder with yellow coloured sample going from thick yellow to light yellow (towards green) when h^o values was increased as βCD addition also was increased. Whereas C* values of egg yolk powder showed that as egg yolk pigment concentrations reduced, the C* values lessened.

The yellow-orange colour of yolk is due to carotenoid pigments, primarily xanthophylls with minor amount of carotene [31]. Awad et al. [27] reported that β-carotene concentrations of egg yolk powder treatment with β-CD were lower than those of untreated egg yolk powder. Except for problems with colour, these results suggest that CD can be used to produce a low cholesterol egg product with functional properties similar to those of the original liquid egg yolk.

Conclusion

Cholesterol has been successfully reduced from egg yolk using β-CD with minimal depletion of nutritional composition of egg yolk powder. Utilization of cholesterol-reduced egg yolk powder in food can be beneficial to food industry in production of healthy and nutritious products even minimizing the cost of loss in industry due to spoilage and improper handling of native egg yolk.

Acknowledgement

The authors would like to thank the Universiti Teknologi MARA, Shah Alam Malaysia for the financial support.

References

1. Li-Chan, E. C. Y., Powrie, W. D. and Nakai, S. (1995). The chemistry of eggs and egg products. In W. J. Stadelman & O. J. Cotterill (Eds.), Egg science and technology. New York: Food Products Press, pp: 105 – 175.
2. Laca, A., Sáenz, M. C., Paredes, B. and Díaz, M. (2010). Rheological properties, stability and sensory evaluation of low-cholesterol mayonnaises prepared using egg yolk granules as emulsifying agent. *Journal of Food Engineering*, 97: 243 – 252.
3. Santos, C. D., Buera, M. P. and Mazzobre, M. F. (2011). Phase solubility studies and stability of cholesterol/β-cyclodextrin inclusion complexes. *Journal of Science Food and Agriculture*, 91: 2551 –2557.
4. Han, E. M., Kim, S. H., Ahn, J. and Kwak, H. S. (2008). Comparison of cholesterol reduced cream cheese manufactured using crosslinked b-cyclodextrin to regular cream cheese. *Asian–Australasian Journal of Animal Sciences*, 21(1): 131 – 137.
5. Han, E.-M., Kim, S.-H., Ahn, J. and Kwak, H.-S. (2005). Cholesterol removal from homogenized milk with crosslinked β-cyclodextrin by adipic acid. *Asian–Australasian Journal of Animal Sciences*, 18 (12): 1794 – 1799.
6. Heshmati, A., and Khodadadi, I. (2009). Reduction of cholesterol in beef suet using lecithin. *Journal of Food Composition and Analysis* 22: 684 – 688.
7. Hettinga, D., (2005). Butter. In: Shahedi, F. (Ed.), Edible oil and fat products: Edible oils. 6th ed. Bailey's industrial oil and fat products, John Wiley and Sons, Inc., New York, pp. 15 – 17.
8. Zeidler, G. (1995). Method for removal of cholesterol and fat from liquid egg yolk with recovery of free cholesterol as a by-product. US PATENT 5, 468 511.
9. Zaibunnisa, A. H., Saim, N., Said, Ilias, R., Wan, A. and Hassan. (2009). Characterisation of cyclodextrin complexes with turmeric oleoresin. *Journal of Food Chemistry*, 114: 459 – 465.
10. Frazier, W. C. and Westhoff, D. C. (1988). Food Microbiology. 2nd ed. McGraw- Hill Publisher Inc., New Delhi, India.
11. Awad, A. C. and Smith, D. M. (1996). Method for reduction of cholesterol in egg materials. US International Patent, 5, 484, 624.
12. Association of official analytical chemists (AOAC), Official methods of analysis. (1975). Washington, DC.
13. Association of official analytical chemists (AOAC), official methods of analysis. (1990). 15th ed. Association of official analytical chemists, Arlington, VA.

14. Kim, S. H., Ahn, J. and Kwak, H. S. (2004). Crosslinking of β-Cyclodextrin on cholesterol removal from milk. *Archives of Pharmacal Research*, 27 (11): 1183 – 1187.
15. Zaibunnisa, A. H., Noarashikin, S., Mamot, S. and Osman, H. (2009) .An experimental design approach for the extraction of volatile compounds from turmeric leaves (*Curcuma domestica*) using pressurized liquid extraction (PLE), *Journal of Food Science and Technology,* 42: 233 – 238.
16. Zara, R. F., Bonafé, E. G., Martin, C. A., Souza, N. E. D., Muniz, E. C. and Visentainer, J. V. (2012). *American Journal of Analytical Chemistry*, 3: 288 – 294.
17. Wang, Y., Sunwoo, H., Cherian, G. and Sim, J. S. (2000). Fatty acid determination in chicken egg yolk: A comparison of different methods. *Poultry Science Journal,* 79:1168 – 1171.
18. Meynier, A., Leborgne, C., Viau, M., Schuck, P., Guichardant, M., Rannou, C. and Anton, M. (2014). n-3 fatty acid enriched eggs and production of egg yolk powders: An increased risk of lipid oxidation?. *Food Chemistry*, 153: 94 – 100.
19. Chen, C. (2003). Evaluation of air oven moisture content determination methods for rough rice. *Biosystems Engineering Journal*, 86(4): 447 – 457.
20. All`egre, P., Moulin, B., Gleize, G., Pieroni, F. and Charbit. (2006). Cholesterol removal by nanofiltration: Applications in nutraceutics and nutritional supplements. *Journal of Membrane Science*, 269:109 – 117.
21. Anton, M. (2007). Composition and structure of hen egg yolk. In R. Huopalahti, R. Lo´pez-Fandin˘o, M. Anton, & R. Schade (Eds.), Bioactive egg compounds, Springer, pp. 1– 6.
22. Fauziah, C. I., Zaibunnisa, A. H. Osman, H. and Wan, A. W. M. (2013). Thermal analysis and surface morphology study of cholesterol:β-cyclodextrin inclusion complex. *Advanced Materials Research*, 812: 221 – 225.
23. McCully, K. A., Mok, C. C. and Common, R. H. (1962). Paper electrophoresis characterization of proteins and lipoproteins of hen's yolk. *Canadian Journal of Biochemistry and Physiology,* 40: 937 –952.
24. Kim, S-H., Han, E-M., Ahn, J. and Kwak, H-S. (2005). Effect of crosslinked-cyclodextrin on quality of cholesterol-reduced cream cheese. *Asian–Australasian Journal of Animal Sciences* 18(4): 584 – 589.
25. Ha, H. J., Jeon, S. S., Chang, Y. H., and Kwak, H. S. (2009). Entrapment of milk nutrients during cholesterol removal from milk by crosslinked β-cyclodextrin. *Korean Journal for Food Science of Animal Resources*, 29(5): 566 – 572.
26. Williams, R. O., Mahaguna, V. and Sriwongjanya, M. (1998). Characterization of an inclusion complex of cholesterol and hydroxypropyl-β-cyclodextrin. *European Journal of Pharmaceutics and Biopharmaceutics.* 46: 355 – 360.
27. Awad, A. C., Bennink, M. R., and Smith, D. M. (1997). Composition and functional properties of cholesterol reduced egg yolk. *Poultry Science Journal*, 76: 649 – 653.
28. Smith, D. M., Awad, A. C., Bennink, M. R. and Gill, J. L. (1995). Cholesterol reduction in liquid egg yolk using β-cyclodextrin. *Journal of Food Science*, 60(4): 691 – 694.
29. Ha, H. J., Lee, J. E., Chang, Y. H. and Kwak, H-S. (2010). Entrapment of nutrients during cholesterol removal from cream by crosslinked β-cyclodextrin. *International Journal of Dairy Technology*, 63(1): 119 – 126.
30. Kwak, H. S., Jung, C. S., Shim, S. Y. and Ahn, J. (2002). Removal of cholesterol from cheddar cheese by β-cyclodextrin. *Journal of Agricultural and Food Chemistry,* 50(25): 7293 – 7298.
31. Maskooki, A. M., Beheshti, S. H. R., Valibeigi, S. and Feizi, J. (2013). Effect of cholesterol removal processing using β-cyclodextrin on main components of milk. *International Journal of Food Science,* 2013: 1 – 6.
32. Li-Chan, E. C. Y. and Kim, H. O. (2008). Structure and chemical composition of eggs. In Y. Mine (Ed.), Egg bioscience and biotechnology, New Jersey: John Wiley & Sons Inc., pp. 1 – 96.
33. Bianchi, M., Petracci, M. and Cavani, C. (2006). Processing, products and food safety. The influence of genotype, market live weight, transportation, and holding conditions prior to slaughter on broiler breast meat colour. *Poultry Science*, 85:123 – 128.
34. Wrolstada, R. E., Dursta R. W. and Lee, J. (2005). Tracking colour and pigment changes in anthocyanin products. *Trends in Food Science & Technology*, 16: 423 – 428.

Malaysian Journal of Analytical Sciences, Vol 20 No 4 (2016): 829 - 837
DOI: http://dx.doi.org/10.17576/mjas-2016-2004-16

MALAYSIAN JOURNAL OF ANALYTICAL SCIENCES
Published by The Malaysian Analytical Sciences Society
ISSN 1394 - 2506

DETERMINATION OF OPTIMUM CONDITION OF LEUCINE CONTENT IN BEEF PROTEIN HYDROLYSATE USING RESPONSE SURFACE METHODOLOGY

(Penentuan Keadaan Optimum bagi Kandungan Leusina di dalam Protein Hidrolisat Daging Menggunakan Kaedah Gerak Balas Permukaan)

Siti Roha Ab Mutalib, Zainal Samicho*, Noriham Abdullah

Programme of Food Science and Technology,
Faculty of Applied Sciences,
Universiti Teknologi MARA, 40450 Shah Alam, Selangor, Malaysia

**Corresponding author: zainal147@salam.uitm.edu.my*

Received: 24 February 2015; Accepted: 27 October 2015

Abstract

The aim of this study is to determine the optimum condition of leucine content in beef hydrolysate. Beef hydrolysate was prepared by enzymatic hydrolysis using bromelain enzyme produced from pineapple peel. Parameter conditions such as concentration of bromelain, hydrolysis temperature and hydrolysis time were assessed to obtain the optimum leucine content of beef hydrolysate according to experimental design which was recommended by response surface methodology (RSM). Leucine content in beef hydrolysate was determined using AccQ.Tag amino acid analysis method using high performance liquid chromatography (HPLC). The condition of optimum leucine content was at bromelain concentration of 1.38 %, hydrolysis temperature of 42.5 °C and hydrolysis time of 31.59 hours with the predicted leucine content of 26.57 %. The optimum condition was verified with the leucine value obtained was 26.25 %. Since there was no significant difference ($p > 0.05$) between the predicted and verified leucine values, thus it indicates that the predicted optimum condition by RSM can be accepted to predict the optimum leucine content in beef hydrolysate.

Keywords: leucine, enzymatic hydrolysis, bromelain, response surface methodology

Abstrak

Matlamat kajian ini adalah untuk menentukan keadaan optimum kandungan leusina di dalam hidrolisat daging lembu. Hidrolisat daging lembu telah disediakan secara hidrolisis enzim menggunakan enzim bromelin yang dihasilkan daripada kulit nanas. Keadaan parameter seperti kepekatan bromelin, suhu hidrolisis dan masa hidrolisis telah dinilai untuk mendapatkan kandungan leusina yang optimum dari hidrolisat daging lembu mengikut reka bentuk eksperimen yang disyorkan oleh kaedah gerak balas permukaan (RSM). Kandungan leusina di dalam hidrolisat daging lembu telah ditentukan dengan menggunakan kaedah analisis AccQ.Tag asid amino menggunakan kromatografi cecair prestasi tinggi (HPLC). Keadaan optimum kandungan leusina didapati pada kepekatan bromelin 1.38 %, suhu hidrolisis 42.50 ºC dan masa hidrolisis 31.59 jam dengan kandungan leusina yang diramalkan adalah 26.57 %. Keadaan optimum telah disahkan di mana nilai leusina diperolehi adalah 26.25 %. Oleh kerana tiada perbezaan yang signifikan ($p > 0.05$) antara nilai leusina yang diramalkan dan disahkan, maka ia menunjukkan bahawa keadaan optimum yang diramalkan oleh RSM boleh diterima dan digunakan untuk meramalkan kandungan leusina yang optimum dalam hidrolisat daging lembu.

Kata kunci: leusina, hydrolisis enzim, bromelin, kaedah gerak balas permukaan

Introduction

Beef consumption has decreased in the last decades due to negative health images [1]. Many studies deal with the opportunities of enhancing the beneficial fatty acids such as increasing the *n*-3 polyunsaturated fatty acids and conjugated linoleic acids (CLA) and reducing saturated fatty acids (SFA) in beef. In addition, limited knowledge is known about the alteration of other nutritional ingredients such as amino acid composition in beef [2, 3]. Meat and meat products are good sources of protein for human consumption. These proteins are well balanced in amino acid and contain all essential amino acids that human cannot synthesize. However, certain people are advised not to consume beef due to health problems. According to Bjoern et al. [4] several essential amino acids such as leucine and phenylalanine or non-essential amino acids such as arginine and glutamine, have shown to directly stimulate insulin secretion from pancreatic beta-cells, resulting in beneficial therapeutic effects in patients with type 2 diabetes.

One of the methods for protein recovery from this meat protein is production of protein hydrolysate through enzymatic hydrolysis. It is widely employed to improve nutritional and functional properties of meat protein. In the effort of attempting to hydrolyse beef protein by using controlled enzymatic hydrolysis process, many factors have to be considered. One of the important factors is the choice of enzymes since different enzymes have different specific activities and optimal working parameters. There were many commercial proteases have been reported to be used for the hydrolysis of beef protein such as alcalase, flavorzyme, bromelain and papain [5 – 7]. However, bromelain is the most preferred to be used in enzymatic hydrolysis as it is proven to give the highest total yield of α-amino groups compared to other proteases such as papain and alcalase [6].

Bromelain enzyme is endopeptidase enzyme. It is related to the family of cysteine protease C1 and has a single chain, glycosylated amino acid cysteine with seven bridges and probably three disulfides [8]. The mechanism of action of cysteine protease to cleave peptide bonds through a double-displacement pathway involving general acid-base formation and hydrolysis of an acyl-thiol intermediate. The initial step in catalytic process involves noncovalent binding of the free enzyme and the substrate to form the complex. This is followed by the acylation of the enzyme with the formation and release of the first product, the amine R`-NH2. In the next deacylation step, the acyl-enzyme reacts with a water molecule to release the second product, with the regeneration of free enzyme [8].

Under standard condition, proteases hydrolysed peptide bond. Bromelain cleave glycol, anayl and leucyl bonds [9]. At pH6, bromelain hydrolysed ethyl ester of L-leuicne, L-arginine, L-glycine, L-phenylalanine, L-tyrosine, L-lysine and L-glycine [10]. In the process of enzymatic hydrolysis, factors such as pH, time, enzyme to substrate level and temperature will influence enzymatic activity. In this context, the main goal of enzymatic hydrolysis of beef was to obtain the maximum leucine content in flank cut of beef. Studying the effect of these hydrolysis parameters on leucine content contribute to the understanding of the protein hydrolysate released. Optimization is one of the methods to find a best alternative from a specified set of alternatives. It is the modern statistically derived experimental designs that are viewed as a way to achieve this purpose.

Response surface methodology (RSM) has been effective in the optimization and monitoring of food processes [11]. Response surface methodology is an empirical modeling technique and was used to estimate the relationship between a set of controllable experimental factors and observed results [12]. A multiple regressions analysis technique that is included in the RSM was performed to determine all the coefficients of linear (X_1, X_2, X_3), quadratic (X_1 X_1, X_2 X_2, X_3 X_3) and interaction (X_1X_2, X_1X_3, X_2X_3) terms to fit a full response surface model for the responses. The goodness of fit of the regression model was defined by determining the coefficient R^2 and adjusted R^2 (multiple correlation coefficient, R), which provides a measure of how much variability in the observed response values can be explained by the experimental factors and their interaction [13]. The lack-of-fit test measures the variation of data with regards to the fitted model and is one of the important aspects of a reduced model. If the model does not fit the data well, the lack-of-fit test will be significant. A model should be rejected if the results showed any significance in the lack-of-fit test [14] Patel et al. [15] testified that an insignificant lack-of-fit indicates a good model. The F value for the lack-of-fit can be obtained by dividing the lack-of-fit mean square by its pure error mean square.

The objective of this study was to determine optimal enzymatic hydrolysis parameter (bromelain concentration, hydrolysis temperature and hydrolysis time) of flank cut of beef to obtain the optimum leucine content by using RSM. Additionally, the degree of hydrolysis and amino acid composition of the optimum beef protein hydrolysate prepared using the optimized hydrolysis conditions were determined.

Materials and Methods

Chemicals and raw materials

All chemicals used were purchased from Sigma Chemical Co. (St Louis, Missouri). Peel of pineapple index 2, variety N36 were obtained from Peninsula Plantation Sdn Bhd, Simpang Renggam, Johor, Malaysia and flank cut of beef were obtained from a slaughter house in MZR Livestock (M) Sdn. Bhd, Rantau Panjang, Klang, Selangor, Malaysia.

Optimisation of enzymatic hydrolysis condition

The optimum enzymatic hydrolysis conditions of flank cut of beef was determined by response surface methodology (MINITAB Software Version 15). The three test variables chosen were bromelain concentration, hydrolysis temperature and hydrolysis time as shown in Table 1. The experiment was optimized by using three-factors, five levels central composite design (CCD). The central composite design composed of 20 treatments including 2^3 factorial points, six axial points (α ±1.68) and six replicates of the central point. The design of experiments and dependent variable values was presented in Table 2.

Table 1. Coded and uncoded variables used in optimisation experiment

Parameter	Code	-1.68	-1	0	1	1.68
Bromelain concentration (% w/w)	X_1	0.5	1.0	1.5	2.0	2.5
Hydrolysis temperature (°C)	X_2	40	42.5	45	47.5	50
Hydrolysis time (hours)	X_3	24	30	36	42	48

Enzymatic hydrolysis of beef

The protein hydrolysate of the beef was produced through enzymatic hydrolysis using bromelain from pineapple peel extract. Clarified pineapple peel extract were purified using cation exchange chromatography to produce purified bromelain. Then the purified bromelain undergo the desalting process whereby this process was carried out by using the diafiltration process. Desalted bromelain was dried using vacuum freeze dryer to produce powdered bromelain. This bromelain powder was used for enzymatic hydrolysis of beef. The enzymatic hydrolysis process was carried out based on Haslaniza et al. [6] method. Two gram (2g) flank cut of beef was placed in 100 mL conical flask. Then, 50 mL of distilled water was added. The mixture was then hydrolysed in the oven (95 °C) for 20 minutes followed by cooling to room temperature condition. The pH of the mixture was adjusted to pH 6 using 4N NaOH. Then, enzyme bromelain at different concentrations (0.5, 1.5 and 2.5% (w/w)) were added followed by the addition of 2 mL of 0.1M L-Cysteine as a catalyst. The mixture was incubated at 200 rpm in an incubator shaker with temperature (40 – 50 °C) and time (24 – 48 hours) according to the experimental design as shown in Table 2. After that, the samples were heated at 95 °C for 15 min to deactivate the enzyme. The protein hydrolysate sample was centrifuged at 7800 x g for 15 min in order to separate any impurities from hydrolysate. The clear supernatants were frozen at -20 °C before the freeze drying process.

Determination of amino acid

The beef protein hydrolysate was hydrolysed using 5 mL 6N HCl at 110 °C for 24 hours. The amino acid content was analysed according to AccQ.Tag Amino acid analysis method [7] using HPLC equipped with a Waters 410 Scanning Flourescence and AccQ Tag column (3.9 x 150 mm). AccQ Tag Eluent A (19 % sodium acetate) and AccQ Tag Eluent B (60 % acetonitrile acid) was used as the mobile phase (flow rate = 1 mL/min). The column temperature was set at 36 ºC. The HPLC system was run by concentration gradient in the process of analysing amino acid.

Table 2. Experimental design by MINITAB Software

Run No	Factors			Response (Leucine %)	
	X_1	X_2	X_3	Predicted	Experimental
1	1	42.5	30	23.618	23.587
2	2	42.5	30	25.399	25.406
3	1	47.5	30	11.751	11.753
4	2	47.5	30	12.046	11.997
5	1	42.5	42	12.219	12.210
6	2	42.5	42	21.300	21.241
7	1	47.5	42	16.030	15.966
8	2	47.5	42	23.448	23.422
9	0.5	45	36	20.840	20.942
10	2.5	45	36	25.452	25.579
11	1.5	40	36	26.570	26.662
12	1.5	50	36	21.699	21.836
13	1.5	45	24	19.762	19.833
14	1.5	45	48	19.699	19.857
15	1.5	45	36	24.418	24.579
16	1.5	45	36	24.682	24.579
17	1.5	45	36	24.852	24.579
18	1.5	45	36	24.762	24.579
19	1.5	45	36	24.550	24.579
20	1.5	45	36	24.667	24.579
R^2 = 99.94%, Adjusted R^2 = 99.89%					

Determination of degree hydrolysis and nitrogen content

The degree of hydrolysis was calculated according to the percentage of trichloroacetic acid (TCA) ratio method as described by Haslaniza et al. [6]. After enzymatic hydrolysis, 20 mL of beef protein hydrolysate was added into 20 mL of 20 % (w/v) TCA to produce 10 % TCA soluble material. The mixture was left to stand for 30 minutes to allow precipitation, and then followed by centrifugation at 7800 x g for 15 minutes. The degree of hydrolysis (DH) was calculated using the following formula equation 1:

$$\% \text{ DH} = \frac{\text{Soluble N in TCA 10\% (w/v)}}{\text{Total N in beef}} \times 100 \quad (1)$$

where DH is defined as degree hydrolysis and TCA is defined as trichloroacetic acid.

The nitrogen content in supernatant, powdered beef hydrolysate and flank cut of beef was determined using CHNS elemental analyser. Before the analysis, all the samples were dried for 1 hour in oven at 110 ^{o}C.

Statistical analysis

The results from CCD was assessed using multi linear regression [16] using an equation 2 below:

$$Y = b_0 + b_1A + b_2B + b_3C + b_4A^2 + b_5B^2 + b_6C^2 + b_7AB + b_8AC + b_9BC \quad (2)$$

where Y represents the predicted response, b_0 is the value for the fixed response at the central point of the experiment, b_1, b_2 and b_3 are linear coefficients, b_4, b_5 and b_6 are quadratic coefficients, and b_7, b_8, and b_9 are cross-product or interaction coefficients.

The R^2 value and the lack of fit value were determined. After the multifactor analysis of variance and the second-order model prediction determinations, the optimal enzymatic hydrolysis conditions were obtained by the desirability function approach. The response surface plots were developed to represent a function of two test variables while keeping the other test variable at the optimal value.

For the verification value, the experimental value of response (leucine) was compared to the predicted value of response (leucine). Data were analysed using t-test method using SPSS 20. A significant difference was considered at the level of $p < 0.05$.

Results and Discussion

Optimization of enzymatic hydrolysis of beef

A central composite design was performed to study the combined effect of three factors (bromelain concentration, hydrolysis temperature and hydrolysis time) on the response, leucine content (%). The predicted and experimental results of the 3-factors, 5-levels central composite design was presented in Table 2. The determination of coefficient (R^2) was 99.94%, which suggested that this quadratic model was appropriately to represent the real relationships among the chosen hydrolysis parameters. The closer the R^2 value to one, the better the fitting of the empirical model with the actual data and the better the correlation between experimental and predicted values [16].

The adjusted R^2 was a corrected value for R^2 after the elimination of unnecessary model terms. If there are many non-significant terms included in the model, the adjusted R^2 would be smaller than R^2. In this present study, it is found that the adjusted R^2 is high and very close to the R^2. Respective values for adjusted R^2 and R^2 were 99.89 % and 99.94 %. The high values of adjusted R^2 and R^2 indicate a high dependence and correlation between the observed values and the predicted values of response.

The effect of experimental variables on the linear, quadratic and interaction terms were tested for adequacy and fitness by analysis of variance (ANOVA). The summary of the results obtained are shown in Table 3. By using lack-of-fit and correlation coefficient determination (R^2), the adequacy of the model can be revealed. The significance of the equation parameter for test variables was assessed by F ratio at a probability (p) of 0.05. The F value predicts the quality of the entire model while considering all design factors all at once.

Table 3. ANOVA test for optimisation of leucine content in protein hydrolysate treated with bromelain

Source	DF	Seq SS	Adj SS	Adj MS	F	P	Status
Regression	9	431.421	431.421	47.936	1921.790	0.000	Significant
Linear	3	112.002	5.027	1.676	67.180	0.000	Significant
Square	3	170.656	170.656	56.885	2280.580	0.000	Significant
Interaction	3	148.764	148.764	49.588	1988.030	0.000	Significant
Residual Error	10	0.249	0.249	0.025			
Lack of fit	5	0.131	0.131	0.026	1.110	0.456	Not significant
Pure Error	5	0.118	0.118	0.024			
Total	19	431.670					

DF = degree of freedom, Seq SS = sequential sum of square, Adj SS = adjusted sum of square, Adj MS = adjusted mean square, F = fischer, P = probability

The p value is the probability of the factors having very little or insignificant effect on the response. A larger F value signifies a better fit of the RSM model to the experimental data [17]. Datta et al. [18] reported that an F value with a low p value indicates the high significance of the regression model. However, the p value should be lower than 0.05 for the model to be statistically significant [15]. Based on reports by literatures [17, 18, 15] the regression model found in this study was highly significant as denoted by the large F and low p value of 1921.79 and 0.000, respectively. From Table 3, it was observed that the quadratic (square) and interaction factors were highly significant compared to linear factors as indicated by the large F values of 2280.58 and 1988.03 with a low p value of 0.000, each. In this study, the lack of fit model showed a non-significant result ($p > 0.05$) with a p value of 0.456. Thus, the insignificant p value indicates that the model is good and fits well with the experimental data.

Overall, the analysis of variance suggested that the predicted quadratic model for enzymatic hydrolysis conditions of flank beef cut was statistically valid. The second-order polynomial model equation for the optimisation of leucine in beef hydrolysate treated with bromelain is illustrated as follows:

$$Y = 204.095 + 12.988X_1 - 5.103X_2 - 3.124X_3 - 5.271X_1^2 - 0.053X_2^2 - 0.131X_3^2 - 0.315X_1X^2 + 0.601\ X_1X^3 + 0.260X_2X^3$$

where X_1= concentration of bromelain, X_2 = hydrolysis temperature, X_3= hydrolysis time.

Based on Table 4, it was found that the optimum conditions for the target goal with a bromelain concentration of 1.38 % (% w/w), hydrolysis temperature of 42.5 °C and hydrolysis time of 31.59 hours as well as for the minimum goal with a bromelain concentration of 1 % (% w/w), hydrolysis temperature of 47.5 °C and hydrolysis time of 30 hours were feasible to be carried out. Meanwhile, the optimum condition for the maximum goal with a bromelain concentration of 1.93 % (% w/w), hydrolysis temperature of 42.5 °C and hydrolysis time of 38.48 hours was not feasible to be carried out. This is in accordance with the optimum conditions for the target and minimum goals being located in the white area or in the feasible region based on the overlaid contour plots obtained. Meanwhile, the optimum condition for the maximum goal is located in the grey area or non-feasible region. However, the optimum condition for the target goal was chosen because the response value was higher compared to the optimum condition for the minimum goal.

Condition for optimum response

The optimum conditions of enzymatic hydrolysis of flank cut of beef were 1.38% (% w/w) for bromelain concentration, 42.5°C for hydrolysis temperature and 31.59 hours for hydrolysis time.

The Dimension (2D) contour and (3D) surface plots for leucine content in protein hydrolysate treated with bromelain at a feasible optimum condition are shown in Figures 1 and 2, respectively. The shape of the contour plot (circular or elliptical) indicates whether the mutual interaction between test variables is significant or not. A circular contour plot indicates that the interaction between related test variables is negligible. In contrast, an elliptical contour plot indicates that the interaction between related test variables is significant [19]. In this study, results revealed that the contour plot was elliptical, indicating that there is a significant interaction effect between bromelain concentration, hydrolysis temperature and hydrolysis time on the leucine content in protein hydrolysate.

Validation for the optimum condition of leucine content in protein hydrolysate treated with bromelain was performed and the results are 26.25 % and 26.57 % for validation and predicted response, respectively. The suitability of the model equation for predicting the optimum response value was evaluated for the optimum condition of leucine content under conditions where the bromelain concentration is 1.38 %, hydrolysis temperature is 42.5 °C and hydrolysis time is 31.59 hours. Optimisation using actual experimental values was tested using the t-test (SPSS). There was no significant difference ($p > 0.05$) between predicted and verified values. Thus, indicating that the model was significant and can be used to predict the optimisation of leucine content in protein hydrolysate.

Table 4. Comparison values of target and predicted responses for different optimum conditions and experiment feasibilities

Goal		Lower	Target	Upper	Optimum condition			Predicted Response (FITS)	F/NF
					X_1	X_2	X_3		
Target	Leucine (%)	11.751	26.569	26.570	1.38	42.5	31.59	26.5699	F
	FITS 1	11.753	26.661	26.662					
Maximum	Leucine (%)	11.751	26.570	26.570	1.93	42.5	38.48	28.3081	NF
	FITS 1	11.753	26.662	26.662					
Minimum	Leucine (%)	11.751	11.751	26.570	1.00	47.5	30.00	11.7528	F
	FITS 1	11.753	11.753	26.662					

X_1= bromelain concentration (% w/w), X_2= hydrolysis temperature (ºC), X_3= hydrolysis time (hours), FITS= predicted response (%), F= feasible, NF= not feasible

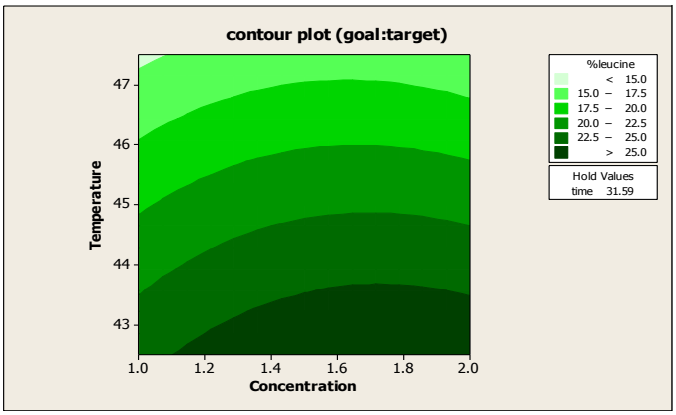


Figure 1. Contour plot of leucine in protein hydrolysate treated with bromelain at a feasible optimum condition, with a bromelain concentration of 1.38 %, hydrolysis temperature of 42.5 °C and hydrolysis time of 31.59 hours (holding value: hydrolysis time at 31.59 hours)

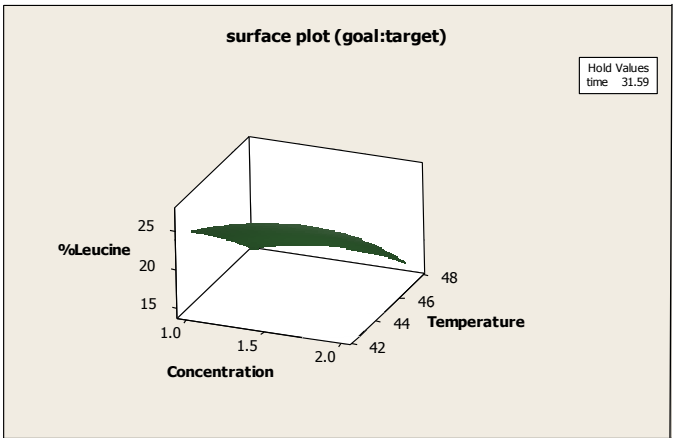


Figure 2. Surface plot of leucine in protein hydrolysate treated with bromelain at a feasible optimum condition with a bromelain concentration of 1.38%, hydrolysis temperature of 42.5°C and hydrolysis time of 31.59 hours (holding value: hydrolysis time at 31.59 hours)

Leucine content, nitrogen content and degree hydrolysis

It was found that leucine content was significantly high in the treated beef compared to untreated flank beef cut. The difference is due to the characteristics of bromelain which contains protease and is able to release more amino acid in treated beef than in untreated beef [20]. Stein et al. [21] carried out an enzymatic hydrolysis of Atlantic cod viscera using different types of enzymes (actinidin, alcalase, bromelain, neutrase, papain and protamex). They found that bromelain gave the highest total yield of the alpha amino group, signifying that the highest amount of peptide bonds could be broken in the reaction.

Table 5. Degree of hydrolysis, comparison of leucine and nitrogen content in flank cuts and beef hydrolysate before and after treatment

Analysis	Flank cut of beef	Flank cut of beef hydrolysate
Leucine	2.277 ± 0.003^{b}	5.453 ± 0.003^{a}
Nitrogen	$13.22\ \%^{b}$	$15.16\ \%^{a}$
Degree of hydrolysis	-	61.73 %

Means within each row was significantly different at $p < 0.05$.

It was found that the nitrogen content in the flank cuts and beef hydrolysate were 13.22 % and 15.16 %, respectively (Table 5). These results corresponds to previous findings by Haslaniza et al. [6] who discovered that cockle meat that went through an enzymatic hydrolysis using a bromelain concentration of 1.5 % had a higher nitrogen content compared to raw cockle meat. The degree of hydrolysis (DH) was determined for the optimum condition of protein hydrolysate. DH refers to the percentage of enzymatically hydrolysed peptide bonds compared to the original peptide bonds in raw materials, representing a number of peptide bonds being degraded during the reaction. DH can be simplified as the percentage of cleaved peptide bonds. In this present study, DH was calculated according to the percentage of trichloroacetic acid ratio. High DH indicates a high level of protein hydrolysed into smaller peptides and free amino acids [7]. Based on this study, it was found that the percentage of the degree of hydrolysis (DH) was 61.73 %, indicating a high DH of beef protein hydrolysis using the bromelain enzyme.

Conclusion

The leucine content of protein hydrolysate from flank cut of beef was significantly affected by the hydrolysis conditions including enzyme concentration, temperature and time. According to the model, the optimum hydrolysis parameters were 1.38 % (w/w) of bromelain concentration, hydrolysis temperature of 42.5 °C and hydrolysis time of 31.59 hours. Based on the optimum hydrolysis condition, the protein hydrolysate was obtained at higher amount of leucine and degree of hydrolysis.

Acknowledgement

Special thanks to Ministry of Higher Education, Malaysia for funding this project under Fundamental Research Grant Scheme [600-RMI/ST/FRGS/Fst(32/2010)] and also Peninsula Plantation Sdn Bhd, Simpang Renggam, Johor, Malaysia for supplying pineapple for this project.

References

1. Cordts, A., Nitzko, S. and Spiller, A. (2014). Consumer response to negative information on meat consumption in Germany. *International Food and Agribusiness Management Review*, 17: 83 – 106.
2. Scollan, N., Hocquette, J. F., Nuernberg, K. and Dannenberger, D. (2006). Innovation in beef production systems that enhance the nutritional and health value of beef lipids and their relationship with meat quality. *Meat Science,* 70: 17 – 33.
3. Hollo, G., Nuernberg, K. and Hollo, I. (2007). Effect of feeding on the composition of longissmus muscle of hungarian grey and the holsteh friesian bulls. *Arch Tierz Dummersturf,* 50(6): 575 – 586.

4. Bjoern, A. M., Schrader, H. and Ritter, D. R. (2010). Selective amino acid deficiency in patients with impaired glucose tolerance and type 2 diabetes. *Regulatory Peptide,* 160: 75 – 80.
5. Murna, M., Novi, S. and Fahrizal, Z. (2012). Production of protein hydrolysates from fish byproduct prepared by enzymatic hydrolysis. *International Journal of the Bioflux Society,* 5(1): 36 – 39.
6. Haslaniza, H., Maskat, M. Y., Wan Aida, W. M. and Mamot, S. (2010). The effects of enzyme concentration, temperature and incubation time on nitrogen content and degree of hydrolysis of protein precipitate from cockle (*Anadara granosa*) meat wash water. *International Food Research Journal,* 17: 147 – 152.
7. Apiwatanapiwat, W., Vaithanomsat, P., Somkliang, P. and Malapant, T. (2009). Optimization of protein hydrolysate production process from *Jatropha curcas* cake. *International Journal of Chemical and Biological Engineering* 2(3): 161 – 164.
8. Fernandes, H. P., Cesar, C. L. and Barjas-Castro, M. D. L. (2011). Electrical properties of the red blood cell membrane and immunohematological investigation. *Revista Brasileira de Hematologia e Hemoterapia,* 33(4): 297 – 301.
9. Bhattacharyya, B. K. (2008). Bromelain: An overview. *Natural Product Radiance,* 4: 359 – 363.
10. Boyer, P. D. (1997). The enzymes: Hydrolysis other C-N bonds, phosphate ester. *The enzymes* (3 ed.): Academic press.
11. Wangtueai, S. and Noomhorm, A. (2009). Processing optimization and characterization of gelatin from lizardfish (*Saurida spp*.) scales. *LWT – Food Science and Technology,* 42: 825 – 834.
12. Gomes, N., Teixeira, J. A. and Belo, I. (2011). Empirical modelling as an experimental approach to optimize lactone production. *Catalysis Science & Technology,* 1: 86 – 92.
13. Sudamalla, P., Saravanan, P. and Matheswaran, M. (2012). Optimisation of operating parameters using response surface methodology for adsorption of crystal violet by activated carbon prepared from mango kernel. *Sustainable Environment Research,* 22: 1 – 7.
14. Siti Nadiah, S., Noorlaila, A., Mohd Zahid, A., Norziah, M. H. and Normah, I. (2013). Optimization of hydrocolloids and maltodextrin addition on roselle-based fruit leather using two-level full factorial design. *International Journal of Bioscience, Biochemistry and Bioinformatics,* 3(4): 387 – 391.
15. Patel, S., Kothari, D. and Goyal, A. (2011). Enhancement of dextransucrase activity of *Pediococcus pentosaceus* SPAm1 by response surface methodology. *Indian Journal of Biotechnology,* 10: 346 – 351.
16. Zaibunnisa, A. H., Norashikin, S., Mamot, S. and Osman, H. (2009). An experimental design approach for the extraction of volatile compounds from turmeric leaves (*Curcuma domestica*) using pressurized liquid extraction (PLE). *LWT Food Science Technology,* 42: 233 – 238.
17. Panwal, J. H., Viruthagiri, T. and Baskar, G. (2011). Statistical modeling and optimization of enzymatic milk fat splitting by soybean lecithin using response surface methodology. *International Journal of Nutrition and Metabolism,* 3: 50 – 57.
18. Datta, D. and Kumar, S. (2012). Modeling and optimisation of recovery process of glycolic acid using reactive extraction. *International Journal of Chemical Engineering and Applications,* 3: 141 – 146.
19. Mannan, S., Fakhru'l-Razi, A. and Md Zahangir, A. (2007). Optimization of process parameters for the bioconversion of activated sludge by *Penicillium corylophilum*, using response surface methodology. *Journal of Environmental Sciences,* 19: 23 – 28.
20. Harckova, M., Rusnakova, M. and Zemonovic, J. (2002). Enzymatic hydrolysis of defatted soy flour by three different proetease and their effect on the functional properties of resulting protein hydrolysates. *Czech Journal Food Science,* 20(1): 7 – 14.
21. Stein, I. A., Svein, J. H., Vincent, G. H., and Eijsinka. (2005). Enzymatic hydrolysis of Atlantic cod (*Gadus morhua* L.) viscera. *Process Biochemistry,* 40: 1957 – 1966.

Malaysian Journal of Analytical Sciences, Vol 20 No 4 (2016): 838 - 843
DOI: http://dx.doi.org/10.17576/mjas-2016-2004-17

MALAYSIAN JOURNAL OF ANALYTICAL SCIENCES
Published by The Malaysian Analytical Sciences Society
ISSN 1394 - 2506

CHARACTERISATION OF CATFISH (*Clarias batrachus*) OIL: β-CYCLODEXTRIN INCLUSION COMPLEX

(Pencirian Kompleks Rangkuman Minyak Ikan Keli (*Clarias batrachus*): β-siklodekstrin)

Zaibunnisa Abdul Haiyee[1]*, Nor Izzatul Adyani Yahya[1], Norizzah Abd Rashid[1], Dzulkifly Mat Hashim[2]

[1]*Food Technology Programme, Faculty of Applied Sciences,*
Universiti Teknologi MARA, 40450 Shah Alam, Selangor, Malaysia
[2]*Halal Products Research Institute,*
Universiti Putra Malaysia, Putra Infoport, 43400 UPM Serdang, Selangor, Malaysia

**Corresponding author: nisha@salam.uitm.edu.my*

Received: 24 February 2015; Accepted: 27 October 2015

Abstract

Catfish is a cheap source of essential omega-3 fatty acids especially eicosapentaenoic acid (EPA) and docosahexaenoic acid (DHA). Catfish oil was extracted and clean-up using pressurised liquid extraction (PLE) from the viscera of catfish (*Clarias batrachus*). However, the characteristics of catfish oils are sticky, strong fishy odour and can easily be oxidised with short shelf-life. In this study, catfish oil was converted into powder by formation of inclusion complex with β–cyclodextrin. Inclusion complex was prepared by using co-precipitation and kneading methods and compared with physical mixture. The inclusion complex formed were characterised by using field emission scanning electron microscopy (FESEM), differential scanning calorimeter (DSC) and fourier transform infrared spectroscopy (FTIR). FESEM images revealed that inclusion complex using co-precipitation and kneading methods has smaller in crystal sizes and appeared as different morphology compared to physical mixture. DSC proved that co-precipitation method was able to form new solid phase due to shifting of melting point to-higher temperature (145.22 °C). FTIR supported the result by proving strengthening of carbonyl group (C=O). Therefore, co-precipitation method was able to successfully produce inclusion complex of catfish oil, β-cyclodextrin.

Keywords: catfish oil, β-cyclodextrin, co-precipitation, kneading, physical mixture

Abstrak

Ikan keli merupakan sumber murah yang mengandungi asid lemak omega-3 terutama asid eikosapentaenoik **(**EPA) dan a**sid** dokosaheksaenoik (DHA). Minyak ikan keli telah diekstrak dan disulingkan dengan menggunakan pengekstrakan cecair tekanan tinggi (PLE) daripada visera ikan keli (*Clarias batrachus*). Walau bagaimanapun, ciri – ciri minyak ikan keli adalah melekit, bau hanyir yang kuat, mudah teroksida dengan mempunyai jangka hayat yang terhad. Dalam kajian ini, minyak ikan keli telah ditukarkan menjadi serbuk melalui pembentukan kompleks rangkuman dengan β-siklodekstrin (BCD). Kompleks rangkuman telah dihasilkan dengan menggunakan teknik ko-pemendakan dan penggulian serta dibandingkan dengan campuran fizikal. Kompleks rangkuman telah dicirikan dengan menggunakan mikroskop elektron imbasan medan (FESEM), kalorimeter imbasan kebezaan (DSC) dan spektrofotometer infra merah transformasi fourier (FTIR). Hasil kajian daripada imej FESEM menunjukkan bahawa pembentukan kompleks rangkuman menggunakan teknik ko-pemendakan dan penggulian mempunyai saiz kristal yang kecil dan muncul sebagai morfologi yang berbeza dibandingkan dengan campuran fizikal. DSC membuktikan ko-pemendakan mampu menghasilkan fasa baru kerana takat pencairan berubah dari yang asal ke suhu yang lebih tinggi (145.22 ºC). FTIR mendokong keputusan melalui bukti penegangan kumpulan karbonil dan C=O telah digunakan untuk rangkuman. Oleh itu, kaedah ko-pemendakan membuktikan kaedah yang paling sesuai untuk merangkum minyak ikan keli menggunakan β-siklodekstrin.

Kata kunci: minyak ikan keli, β-siklodekstrin, ko-pemendakan, penggulian, campuran fizikal

Introduction

The walking catfish, *Clarias batrachus* represents a cheap priced food fish and a great deal of attention is now being paid for popularization of its mass culture [1, 2]. Recently, catfish have high demand in marketplace since catfish contribute a lot of nutritional value to human and other industry. Every year a considerable amount of total catch is discarded as processing leftovers and that include trimmings, fins, frames, head, skin and viscera. Some of the by-products are utilized, but the main bulk is dumped into waste, creating both disposal and pollution problems. Annual discard is estimated to be about 25 % of the total production of capture [3]. Most of the oil in catfish is found in the viscera, which contain approximately 33 % fats or other lipids which could be converted into edible oil [4]. The oil extracted from fish is rich in polyunsaturated fatty acids (PUFAs) especially those of the omega-3 family, mainly eicosapentaenoic acid (EPA; C20:5n-3) and docosahexaenoic acid (DHA; C22:6n-3). The importance of PUFAs in human health and nutrition is well recognized in preventing cardiovascular diseases, Alzheimer's disease and psoriasis [4, 5].

One of the major drawbacks of oils containing a high amount of omega-3 PUFA such as fish oils is their susceptibility to oxidation which involves the formation of toxic products such as peroxides or volatile compounds which contribute to undesirable off flavours [5]. Encapsulation is a technology of packing solid, liquid or gaseous materials in miniature sealed capsules for release at controlled rates using desired released triggers [6]. Some researchers have reported that the encapsulation of fish oil significantly retards lipid oxidation. It can also mask the objectionable odours caused by volatile oxidation products and enhance the odor of fish oil enriched products [5]. Cyclodextrin has been extensively used in areas such as pharmaceutical, cosmetic and food industries because it is inexpensive and non-toxic. Using the molecular inclusion method, cyclodextrin can solubilise and stabilise active compounds on the molecular scale. Cyclodextrin can form solid phases by self-assembly. This process depends on the solubility, temperature, pH, molecular weight and chemical nature of guest materials [6].

In this study, microencapsulation of catfish oil with β-cyclodextrin (BCD) will be used to overcome this problem. Two methods can be used to produce inclusion complex namely co-precipitation, and kneading [7]. Physical mixture product will usually act as a control [8]. Characterisation of the encapsulated products was performed to confirm formation of inclusion complex. The inclusion complex formed were characterised using Fourier Transform Infrared Spectroscopy (FTIR), Field Emission Scanning Electron Microscopy (FESEM) and Differential Scanning Calorimeter (DSC). The resultant water soluble fish oil in powdered form has many applications such as food, pharmaceutical and medical fields. In addition, results from this study will be useful for future research that involves other fish oils that contain high PUFAs especially DHA and EPA.

Materials and Methods

Materials

The β-cyclodextrin (BCD) (purity: 99.5 %) was purchased from the Sigma Chemical Company (St. Louis, MO, USA). All solvents were of analytical grade. Ethanol (ACS Reagent, Ph Eur Merck, Germany) were of pharmaceutical grade and the water was deionised using a Milli-QUV device (Millipore, Molsheim, France).

Sample preparation

Fresh catfish viscera were obtained from local supplier in Kajang, Selangor. The samples were kept in plastics bags and transported in an insulated container to the laboratory. Upon arrival at the laboratory, the sample was washed under running tap water. The samples were ground with a commercial blender for 10 minutes and kept at -20 °C in the freezer until further use. Prior to PLE extraction method; samples were dried using freeze dryer at -50 °C for 5 days. The dried samples were freezed at -20 °C until needed for extraction.

Pressurised liquid extraction

Extractions were done using ASE 200 accelerated solvent extractor (Dionex Ltd. Camberley, Surrey, UK). Catfish oil was extracted using n-hexane with predetermined optimised conditions (Design Expert 6.0.4, Stat Ease Software): temperature of 96 °C, pressure of 15,140 kPa and static time of 17 min. The extract was evaporated to dryness using a rotary evaporator.

Inclusion complex
The inclusion complex of catfish oil: BCD (1:8) was prepared using the kneading and co-precipitation methods. The kneading method and physical mixture as control were as reported by Zhang et al. [7]. The method for co-precipitation was referring to method by Waleczek et al. [8].

Characterisation of the inclusion complex: ***Differential scanning calorimetry (DSC)***
DSC analyses were carried out using Perkin Elmer DSC1 STAR System. An amount 5 mg sample was placed in aluminium pans and heated at 10°C/min in the temperature range of 0 °C to 300 °C. The measurements were carried out under dry nitrogen at a flow rate of 50 mL/min [8].

Fourier transform infrared spectroscopy (FTIR)
The FTIR spectra of catfish oil, BCD, their physical mixture and the inclusion complex were measured between 4000 and 400 cm^{-1} using a Perkin Elmer Model GX FTIR spectrophotometer (Waltham, MA, USA), with 16 scans at a resolution of 1 cm^{-1}. The KBr disk method was used for the solid samples [8].

Field emission scanning electron microscopy (FESEM)
The surface morphology of the dried samples was examined using a scanning electron microscope, Model Supra 40VP (GEMINI). Prior to analysis, the samples were attached to SEM aluminium stubs via 2-sided adhesive tape. The attached powder was then sputter coated for 50 s at a beam current of 0 mA to obtain a 15 nm layer of gold-palladium alloy and was then examined using a scanning electron microscope operating at 5 Kv [8].

Statistical analysis
A one-way analysis of variance (ANOVA) and Duncan's Multiple Range test ($p < 0.05$) were used to establish the significance of differences in analysis data. The analyses were performed using SPSS 16.0 for Windows software.

Results and Discussion

Differential scanning calorimetry (DSC)
The thermal behaviour of catfish oil with β-cyclodextrin (BCD) inclusion complex was studied using Differential Scanning Calorimetry (DSC). The thermograms of pure BCD and catfish oil-BCD physical mixture, kneading, co-precipitation and pure catfish oil, were represented in Figure 1.

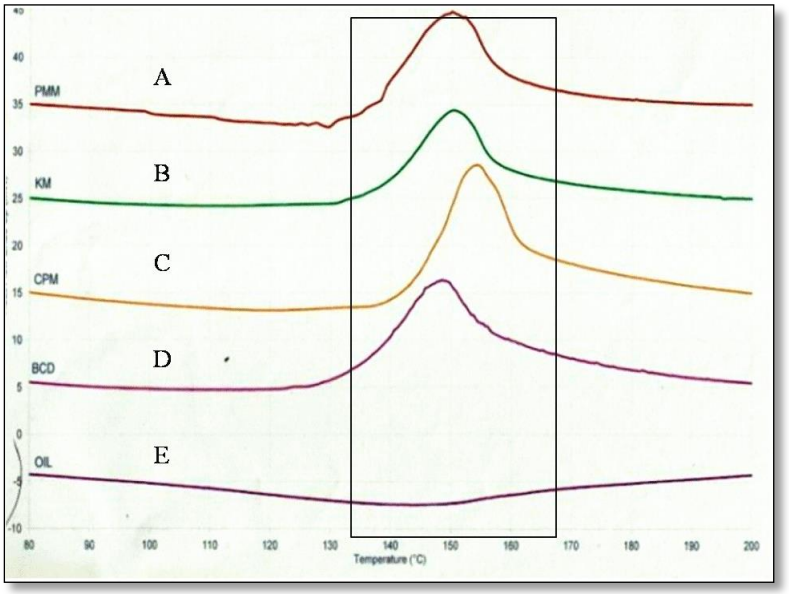


Figure 1. DSC thermograms of physical mixture (PMM) (A), kneading (KM) (B), co-precipitation (CPM) (C), β-cyclodextrin (BCD) (D) and catfish oil (Oil) (E)

Table 1. Data obtained from DSC thermograms.

	T_{Onset} (°C)	T_{Peak} (°C)	T_{Endset} (°C)
Catfish oil (Oil)	92.31 ± 0.05	143.60 ± 0.12	175.39 ± 0.05
β-cyclodextrin (BCD)	139.10 ± 0.11	148.47 ± 0.05	158.50 ± 0.03
Co-precipitation method (CM)	145.22 ± 0.08	154.18 ± 0.05	163.81 ± 0.15
Kneading method (KM)	139.07 ± 0.05	150.31 ± 0.01	159.15 ± 0.02
Physical mixture method (PMM)	138.01 ± 0.04	149.99 ± 0.07	159.36 ± 0.01

Fourier transform infrared spectroscopy (FTIR)

The complexation between catfish oil and BCD was further investigated by using FTIR and the spectra obtained were shown in Figure 2. FTIR is a useful technique used to confirm the formation of an inclusion complex [10].

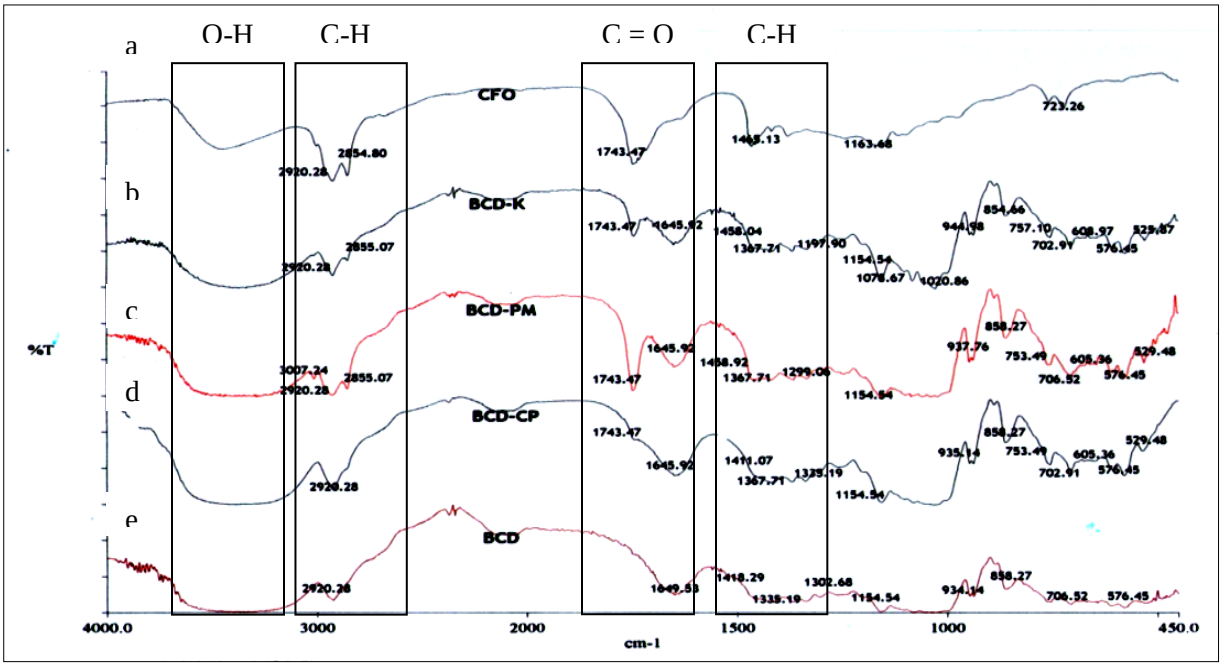


Figure 2. FTIR spectrum of catfish oil (CFO) (a), kneading (BCD-K) (b), physical mixture (BCD-PM) (c), β- co-precipitation (BCD-CP) (d), and β-cyclodextrin (BCD) (e)

Overall, catfish oil bands were masked from cyclodextrin as the main component of complexes formation. Generally, the stretching region of hydroxyl group, -OH was shown at the band range of 3600 – 3200 cm^{-1}. The band at 3400 cm^{-1} indicates the presence of hydroxyl group in the catfish oil. The presence of water in BCD resulted in the presence of broad peak of O-H which masks the presence of –OH in catfish oil.

A few bands of alkanes (C-H) are shown at 2930 – 2800 cm^{-1}. The C-H peak appeared at 2920 cm^{-1} and 2855 cm^{-1} can be observed in the catfish oil and 2920 cm^{-1} for BCD. Inclusion complex band formed by co-precipitation method were shifted to higher wavenumber indicate that the conjugation in catfish oil was reduced in the presence of BCD. This result indicates C-H been used for inclusion complex. The band for carbonyl group

(C=O) peaks appeared at the band range of 1650 – 1620 cm^{-1}. The FTIR studies indicated that a cyclodextrin complex was formed with guest molecules possessing carbonyl group [12].

The intensity of this band appeared reduced for co-precipitation, kneading and physical mixture methods. This indicated that carbonyl group been used for complexation. A few bands of alkanes (C-H) were shown at 1300 – 1512 cm^{-1}. The wavenumber for catfish oil was noticed at 1465 cm^{-1} and 1418 cm^{-1} for BCD. The intensity of this band appeared reduced for co-precipitation and kneading. This indicated that C-H group also been used for complexation. A stronger interaction of inclusion complex might be seen in co-precipitation process due to almost similar peak to the pure BCD compared to kneading and physical mixture.

Field emission scanning electron microscopy (FESEM)
FESEM provides qualitative information on study of pure substance and complexes formation by different methods of preparation. In recent study, FESEM observation was done in collaboration with DSC and FTIR to verify the occurrence of BCD-catfish oil complexes formation. This helps to assess existence of any products during the process [8]. The FESEM images of pure BCD, catfish oil; co-precipitation, kneading and physical mixture products at 2500 times magnification are shown in Figure 3.

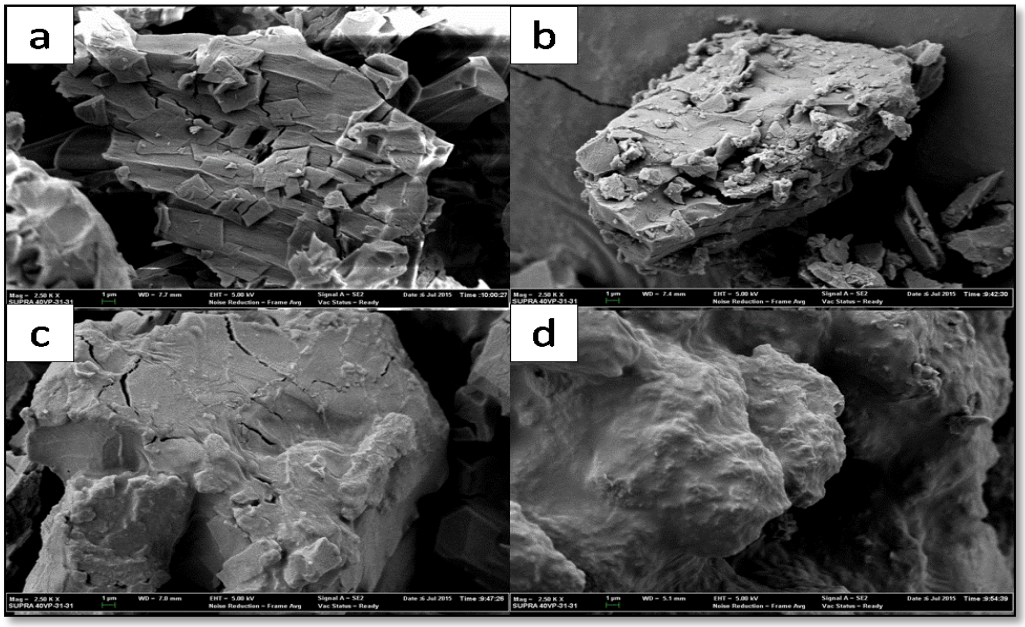


Figure 3. FESEM illustration of (a) β-cyclodextrin (BCD), (b) co-precipitation, (c) kneading and (d) physical mixture at magnification x 2500

Particle size for BCD as shown in Figure 3 (a) was appeared bigger than other samples. It due to the commercial pure BCD was well structured, plated and parallelogram shape. The shape of kneaded complexes as shown in Figure 3 (c) appear quite different from the co-precipitation complexes (Figure 3 (b)). The products appears as irregular and clumping to each other. The drastic change of the particles shape and aspects in the co-precipitation sample were indicative of the presence of a new solid phase, leading us to suggest the existence of a single phase. Previous study by Reddy et al. [11] reported similar findings for a cyclodextrin: celecoxib system. Physical mixture of BCD with catfish oil (Figure 3 (d)) forms sticky and clumps to each other. This appearance as big oily agglomerates was clearly seen under SEM observation. Furthermore, the oiliness of structure can be seen on the surface of the complexes. Thus, an inclusion complex may not formed for BCD using this physical mixture method. This finding supported by Zaibunissa et al. [12] which stated that the new solid phase of oleoresin and cyclodextrins

formed using the co-precipitation method appeared as a crystal structure which was completely different from the original morphology of its pure compounds.

Conclusion

The interaction between C-H and BCD resulted in the formation of an inclusion complex. The formation of the inclusion complex was investigated and confirmed using DSC, FTIR and FESEM analysis. The results obtained from this study will be very useful for producing odourless catfish oil powder from cheap source. Kneading and physical mixture were able to form loose interaction inclusion complex. However, co-precipitation was the chosen method for the potential of future study.

Acknowledgement

The authors would like to acknowledge financial support of Universiti Teknologi MARA and Ministry of Higher Education for the Exploratory Research Grant Scheme (ERGS) (ERGS/1/2011/STG/UITM/01/10). Laboratory facilities for the utilisation of pressurised liquid extraction (PLE), fourier transform infrared spectroscopy (FTIR), differential scanning calorimetry (DSC) and field emission scanning electron microscope (FESEM) in Forensic Chemistry Laboratory, Universiti Teknologi MARA are kindly appreciated.

References

1. Nayak, S., Solanki, H. U. and Dwivedi, R. M. (2003). Utilization of IRS P4 ocean colour data for potential fishing zone- a cost benefit analysis. *Indian Journal of Marine Sciences*, 32 (3): 244 − 248.
2. Malaysia Department of Fisheries (2004). *Perangkaan Perikanan Tahunan 2004*. Access from http://www.dof.gov.my/index.php/pages/view/111
3. Tacon, A. G. J. and Metian, M. (2008). Global overview on the use of fish meal and fish oil in industrially compounded aquafeeds: trends and future prospects. *Aquaculture*, 285: 146 − 158.
4. Simopoulus, A. P., Leaf, A. and Salem, N. (1999). Essentiality of and recommended dietary intakes for omega-6 and omega-3 fatty acids. *Annals Nutrition and Metabolism*, 43: 127 – 131.
5. Haraldsson, G .G., Kristinsson, B., Sigurdardottir, R., Gudmundsson, G.G. and Breivik, H. (1997). The preparation of concentrates of eicosapentaenoic acid and docosahexaenoic acid by lipase-catalyzed transesterification of fish oil with ethanol. *Journal of the American Oil Chemist's Society*, 74: 1419 − 1424.
6. Choi, M. J., Ruktanonchai, U., Min, S. G., Chun, J. Y. and Soottitantawat, A. (2010). Physical characteristics of fish oil encapsulated by β-cyclodextrin using an aggregation method or polycaprolactone using an emulsion–diffusion method. *Food Chemistry*, 119 (4): 1694 − 1703.
7. Zhang, A., Liu, W., Wang L. and Wen, Y. (2005). Characterization of Inclusion Complexation between Fenoxaprop-*p*-ethyl and Cyclodextrin. Journal of Agricultural and Food Chemistry, ***53*** (18): 7193 – 7197.
8. Waleczek, K. J., Marques, C., Hempel, B. and Schmidt, P. C. (2003). Phase solubility studies of pure (2)-a-bisabolol and camomile essential oil with b-cyclodextrin. *European Journal of Pharmaceutics and Biopharmaceutics*, 55: 247 – 251.
9. Zaibunnisa, A. H., Siti Rashima, R. and Nur Ain, A.H. (2011). Stabilization of curcumin with γ-cyclodextrin: phase solubility study and its characterisation. *2nd International Conference on Biotechnology and Food Science IPCBEE*, 7: 9 − 13.
10. William III, R. O., Mahaguna, V. and Sriwongjany, M. (1998). Characterization of an inclusion complex of cholesterol with hydroxyproopyl-β-cyclodextrins. *European Journal of Pharmaceutics and Biopharmaceutics*, *46*: 355 − 360.
11. Reddy, M. N., Rehana, T., Ramakrishna, S., Chowdary, K. P. R. and Diwan, P. V. (2004). β-cyclodextrin complexes of celecoxib: molecular modelling, characterization, and dissolution studies. *AAPS Pharmaceutical Sciences*, 6(1): 1 − 9.
12. Zaibunnisa, A. H., Norashikin, S., Mamot, S., Rosli, M. I., Wan A, W. M. and Osman, H. (2009). Characterization of cyclodextrin complexes with turmeric oleoresin. *Food Chemistry*. 114: 459 − 465.

Malaysian Journal of Analytical Sciences, Vol 20 No 4 (2016): 844 - 848
DOI: http://dx.doi.org/10.17576/mjas-2016-2004-18

MALAYSIAN JOURNAL OF ANALYTICAL SCIENCES
Published by The Malaysian Analytical Sciences Society
ISSN 1394 - 2506

ISOLATION OF FLAVONOLS FROM THE STEMS OF MALAYSIAN *Uncaria cordata* var. *ferruginea* (BLUME) RIDSD.

(Pemisahan Flavonol dari batang *Uncaria cordata* var. *ferruginea* (Blume) Ridsd. Malaysia)

Nur Hakimah Abdullah[1], Fatimah Salim[2,3], Rohaya Ahmad[1,2]*

[1]*Faculty of Applied Science,*
Universiti Teknologi MARA, 40450, Shah Alam, Selangor, Malaysia
[2]*Atta– ur– Rahman Institute for Natural Products Discovery,*
Universiti Teknologi MARA Kampus Puncak Alam, 42300 Bandar Puncak Alam, Selangor, Malaysia
[3]*Center of Foundation Studies,*
Universiti Teknologi MARA, Dengkil Campus, 43800 Dengkil, Selangor, Malaysia

**Corresponding author: rohayaahmad@salam.uitm.edu.my*

Received: 24 February 2015; Accepted: 27 October 2015

Abstract

Continuing our interest in the genus, a phytochemical investigation on *Uncaria cordata* var. *ferruginea* collected from Hutan Pasir Raja, Malaysia has been carried out. Two flavonols known as quercetin and kaempferol were isolated from the methanolic stem extract of this plant along with other phenolic compounds and terpenes. The two flavonols are reported for the first time from this species. The structure of the compounds were elucidated on the basis of spectroscopic data, mostly 1D-NMR, 2D-NMR as well as comparison with literature.

Keywords: flavonoid, flavonol, kaempferol, quercetin, *Uncaria cordata*

Abstrak

Dalam meneruskan minat kami terhadap genus ini, satu kajian fitokimia ke atas *Uncaria cordata* var. *ferruginea* yang diambil dari Hutan Pasir Raja, Malaysia telah dijalankan. Dua flavonol dikenali sebagai quercetin dan kaempferol telah diasingkan daripada ekstrak metanol bahagian batang tumbuhan ini bersama sebatian fenolik lain dan terpena. Kedua-dua flavonol ini dilaporkan buat pertama kali daripada spesies ini. Struktur sebatian telah dielusidasi berdasarkan data spektroskopi, terutamanya 1D-NMR, 2D-NMR dan juga perbandingan dengan kajian literatur.

Kata kunci: flavonoid, flavonol, kaempferol, quercetin, *Uncaria cordata*

Introduction

The genus *Uncaria* (Rubiaceae) is well known for centuries among medicinal practitioners due to its medicinal properties and ability in healing various diseases such as diarrhea, dysentery, fevers, diabetes and others. Many studies have been carried out scientifically for its pharmacological activities on *Uncaria* species [1]. For example, *Uncaria tomentosa* which is widely explored has been proven to have anticancer, anti-inflammatory and other biological properties. A biological study on five species of Malaysian *Uncaria* including *Uncaria longiflora* var. *pteropoda, Uncaria acida, Uncaria lucida, Uncaria callophylla* and *Uncaria cordata* have indicated that they are rich sources of antioxidants and potential anti-diabetic agents which may be used in the prevention and control of type II diabetes [2].

Uncaria is amongst the genera known for its alkaloid content. Previously, we have reported the isolation of two new heteroyohimbine-type oxindole alkaloids, namely rauniticine-*allo*-oxindole B and rauniticinic-*allo* acid B along with five of their stereoisomers including four pentacyclic oxindole alkaloids, isopteropodine, pteropodine, uncarine F and isopteropodic acid from Malaysian *Uncaria longiflora* var. *pteropoda* [3 – 5]. In contrast, the non-alkaloid constituents have not been widely reported from *Uncaria* genus. Lately, the isolation of flavonoids and other chemical constituents present in *Uncaria* have gained more interest. The flavonoids reported from the genus are mostly isolated from *Uncaria gambir* particularly flavane derivatives including flavan-3-ols and their dimers [6]. Recently, we have reported the isolation of a novel flavonoid, (-)-2*R*, 3*R*-3,5,4'-trihydoxyflavan-[6,7:5",6"]-2"-pyranone named uncariechin, along with (-)-*epi*afzelechin and (-)-*epi*catechin from the methanol extract of the leaves of *Uncaria longiflora* var. *pteropoda* [7]. Therefore, continuing our interest on the phytochemicals from *Uncaria*, the isolation of two flavonols, quercetin (**1**) and kaempferol (**2**) from the stems of Malaysian *Uncaria cordata* var. *ferruginea* was reported in this study.

Materials and Methods

General

Column chromatography packed with Sephadex LH-20 was carried out and flavonoids were detected on thin layer chromatography (TLC) stained with aluminium chloride ($AlCl_3$) reagent. A positive result was indicated by the observation of yellow spots visualized under UV light at 365 nm. Mass spectra were measured on an Agilent 1100 Series Technologies HPLC-TOF LC/MS, where the analysis for compound **1** was run in the positive mode, while compound **2** was analysed in the negative mode. The ultraviolet (UV) spectra were obtained in methanol on a Shimadzu UV-Vis 160i. The infrared (IR) data was recorded on a Perkin Elmer model FT-IR spectrometer as KBr disks. ^{1}H and ^{13}C-NMR data for compound **1** was obtained in acetone-d_6 on Bruker 600 Ultrashield NMR spectrometer measured at 600 and 150 MHz, respectively while ^{1}H-NMR and ^{13}C-NMR data for compound **2** was obtained in MeOD on Bruker 500 Ultrashield NMR spectrometer measured at 500 and 125 MHz, respectively.

Plant material

Stems of *Uncaria cordata* var. *ferruginea* was collected from Hutan Pasir Raja, Terengganu in December 2011 and was identified by Dr. Shamsul Khamis (Universiti Putra Malaysia). The voucher specimens were deposited at the Herbarium of Institute of Bioscience, Universiti Putra Malaysia.

Extraction and isolation of compounds

Stems of Malaysian *Uncaria cordata* var. *ferruginea* were cut into small pieces, air-dried and ground into fine powder. The finely ground stems were then weighed and soaked in methanol for 72 hours at room temperature. The solvent was evaporated off under reduced pressure by using a rotary evaporator. Then the extract was dissolved with methanol and water (1:1) before being subjected to liquid-liquid partitioning using chloroform and ethyl acetate. The ethyl acetate fraction (9.8 g) was further fractionated using a column packed with Sephadex LH-20 employing $CHCl_3$: MeOH (9:1) as the solvent system to give four sub-fractions. Based on their TLC profiles, flavonoids were detected in sub-fractions f2 and f4 by using aluminium chloride reagent. Repeated column chromatography of these two sub-fractions using Sephadex LH-20 successfully yielded compound **1** and compound **2**.

Results and Discussion

Compound **1** was isolated as a yellow amorphous solid with melting point 316 °C. The mass spectrum of this compound showed a molecular ion $[M+H]^+$ peak at m/z 303 which corresponded to the molecular formula $C_{15}H_{10}O_7$. Its UV absorptions maxima at 295, 338 and 385 nm were found to be in agreement with a flavonol-type compound [7]. The IR spectrum displayed absorption bands at 3411, 1665 and 1615 cm^{-1} indicating the presence of functional groups of OH, C=O and C=C aromatic, respectively. The ^{1}H NMR spectrum of compound **1** showed the characteristic signals of flavonoid-type compound with ABX system. In A-ring system, two doublet peaks of *meta*-coupled aromatic protons present at δ 6.28 (1H, d, J = 2.4 Hz) and at δ 6.54 (1H, d, J = 2.4 Hz) were assigned as H-6 and H-8, respectively. The rest of proton signals belonging to the ring-B system appeared at δ 7.01 (1H, d, J = 8.4 Hz, H-5'), 7.72 (1H, dd, J = 8.4, 2.4 Hz, H-6') and 7.85 (1H, d, J = 2.4 Hz, H-2'). Its COSY spectrum showed the H-H correlation indicating H-5' and H-6' to be neighbouring protons. Its ^{13}C NMR spectrum showed the presence of 15 carbon signals which were typical of a flavonol skeleton. The most downfield signal at δ 175.67 was attributed

to carbonyl C-4 due to electron withdrawing oxygen and anisotropic effects. In addition, five oxyaryl carbons observed at δ 135.85, 144.97, 147.51, 161.45 and 164.16 were attributed to C-3, C-3', C-4', C-5, and C-7. Four quaternary carbons at δ 103.23, 122.86, 146.05 and 156.90 were assigned as C-10, C-1', C-2 and C-9, respectively. The rest of the signals at δ 93.57, 98.29, 114.87, 115.34 and 120.56 were subsequently determined as aromatic methine carbons C-8, C-6, C-2', C-5' and C-6', respectively which are confirmed by HMQC correlations. All carbon assignments were further confirmed by HMBC and NOESY correlations. In short, the characterization of compound **1** is given below.

Pale yellow amorphous solid, wt: 3.2 mg; MS *m/z* = 303 $[M+H]^+$, $C_{15}H_{10}O_7$; UV (MeOH) λ_{max} nm: 295, 338, 385; IR (KBr) υ_{max} cm^{-1}: 3411 (free OH), 1665 (C=O), 1615 (C=C aromatic); ^1H NMR (Acetone-d_6, 600 MHz) δ ppm : 12.19 (1H, br s, OH), 7.85 (1H, d, *J* = 2.0 Hz, H-2'), 7.72 (1H, dd, *J* = 8.5, 2.0 Hz, H-6'), 7.01 (1H, d, *J* = 8.5 Hz, H-5'), 6.54 (1H, d, 2.0 Hz, H-8), 6.28 (1H, d, 2.0 Hz, H-6); ^{13}C NMR (Acetone-d_6, 150 MHz) δ ppm : 175.67 (C=O), 164.16 (C-7), 161.45 (C-5), 156.90 (C-9), 147.51 (C-4'), 146.05 (C-2), 144.97 (C-3'), 135.85 (C-3), 122.86 (C-1'), 120.56 (C-6'), 115.34 (C-5'), 114.87 (C-2'), 103.23 (C-10), 98.29 (C-6), 93.57 (C-8). Thus, based on the 1D and 2D NMR spectral data, as well as comparison with the literature [8], compound **1** was identified as quercetin.

Compound **2** was isolated as yellow amorphous powder with melting point 277°C. Its mass spectrum showed a molecular ion $[M-H]^-$ peak at *m/z* 285 which corresponds to the molecular formula $C_{15}H_{10}O_6$. Its UV absorptions at 310 and 380 nm were indicative of a flavonol-type compound. The IR spectrum displayed absorption bands at 3324, 1660 and 1614 cm^{-1}which were due to the functional groups of OH, C=O, and C=C aromatic, respectively. The ^1H NMR spectrum of this compound showed proton signals of a typical flavonol-type compound with ABX system (6-8 ppm). For the A-ring protons, two doublet peaks observed at δ 6.18 (1H, d, *J* = 2 Hz) and at δ 6.39 (1H, d, *J* = 2 Hz) were assigned as H-6 and H-8, respectively. Both of these protons were *meta*-coupled as indicated by their coupling constant value. In the B-ring system, proton signals appeared as a pair of doublet of doublets at δ 6.90 (2H, dd, *J* = 7, 2 Hz, H-3', H-5') and at δ 8.09 (2H, dd, *J* = 7, 2 Hz, H-2', H-6'). These protons were *ortho*-coupled based on their *J* values and were adjacent to each other as was evident from the COSY spectrum. Its ^{13}C NMR spectrum exhibited 13 carbons signal attributed to 15 carbons with the peak at δ 129.27 representing equivalent carbons C-2' and C-6' and the peak at δ 114.89 representing equivalent carbons C-3' and C-5'. A very downfield signal at δ 175.95 was attributed to carbonyl C-4 due to electron withdrawing oxygen and anisotropic effect. In addition, four oxyaryl carbons observed at δ 135.72, 159.13, 161.10 and 164.17 were attributed to C-3, C-4', C-5 and C-7, respectively. Four quaternary carbons at δ 103.14, 122.33, 146.62 and 156.84 were then assigned as C-10, C-1', C-2 and C-9, respectively. The rest of the carbon signals observed at δ 93.07 (C-8), 97.86 (C-6), 114.89 (C-3', C-5'), and 129.27 (C-2', C-6') were methine carbons. The carbon assignments were confirmed by HMQC and HMBC data. The characterization of compound **2** is given below.

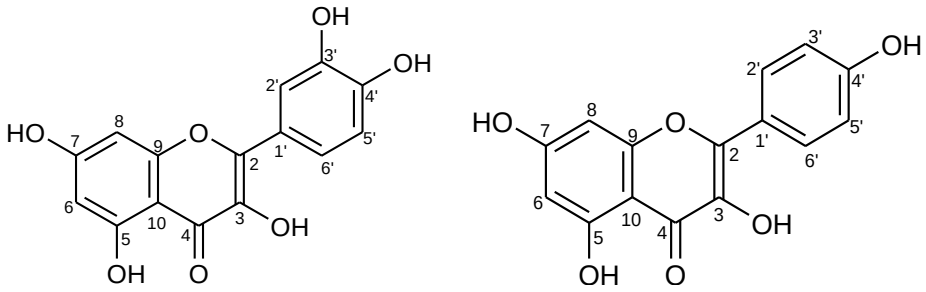
Pale yellow amorphous solid, wt: 1.3 mg; MS *m/z* = 285 $[M-H]^-$, $C_{15}H_{10}O_7$; UV (MeOH) λ_{max} nm: 310, 380; IR (KBr) υ_{max} cm^{-1}: 3324 (free OH), 1660 (C=O) 1614 (C=C aromatic);^1H NMR (MeOD, 500 MHz) δ ppm : 8.09 (2H, dd, *J* = 8.9, 2.0 Hz, H-2',H-6'), 6.90 (2H, dd, *J* = 8.9, 2.0 Hz, H-3', H-5'), 6.39 (1H, d, *J* = 2.0 Hz, H-8), 6.18 (1H, d, *J* = 2.0 Hz, H-6); ^{13}C NMR (MeOD, 150 MHz) δ ppm : 175.95 (C=O), 164.17 (C-7), 161.10 (C-5), 159.13 (C-4'), 156.84 (C-9), 146.62 (C-2), 135.72 (C-3), 129.27 (C-2', C-6'), 122.33 (C-1'), 114.89 (C-3', C-5'), 103.14 (C-10), 97.86 (C-6), 93.07 (C-8). On the basis of spectral data and comparison with literature [9], compound **2** was identified as 3,4',5,7-tetrahydroxyflavone or kaempferol.

Table 1 shows the ^{13}C NMR data compounds **1** and **2** along with literature values. Figure 1 shows the structure of the flavonoids.

Table 1. ^{13}C NMR data for compounds 1 and 2

Compound 1			Compound 2		
Position	**δ_C (ppm)**	**δ_C (ppm) in MeOD[a]**	**Position**	**δ_C (ppm)**	**δ_C (ppm) in DMSO[b]**
2	146.05	147.8	2	146.62	147.3
3	135.85	137.3	3	135.72	136.0
4	175.67	177.4	4	175.95	176.4
5	161.45	162.4	5	161.10	161.2
6	98.25	99.4	6	97.86	98.7
7	164.16	165.6	7	164.17	164.4
8	93.57	94.5	8	93.07	94.0
9	156.90	158.3	9	156.84	156.7
10	103.23	104.5	10	103.14	103.5
1’	122.86	124.0	1’	122.33	122.1
2’	114.87	116.1	2’	129.27	130.0
3’	144.97	146.2	3’	114.89	115.9
4’	147.51	148.7	4’	159.13	159.7
5’	115.34	116.3	5’	114.89	115.9
6’	120.56	121.5	6’	129.27	130.0

[a][8], [b][9]



1 **2**

Figure 1. Structure of flavonols isolated from the stems of Malaysian *Uncaria cordata* var. *ferruginea*: (**1**) Quercetin, (**2**) Kaempferol

Conclusion

Phytochemical study of the methanolic stem extract of Malaysian *Uncaria cordata* var. *ferruginea* has led to the isolation of two flavonols, quercetin and kaempferol along with other phenolic compounds and terpenes. The structure of the compounds was elucidated on the basis of spectroscopic data. The presence of other non-alkaloidal constituents should be further explored in order to justify their chemotaxonomic significance in the *Uncaria* genus.

Acknowledgement

We wish to thank the Ministry of Science, Technology and Innovation Malaysia (MOSTI) for research grant under E-Science Fund (02-01-01-SF0563) as well as Universiti Teknologi MARA for the facilities provided.

References

1. Heitzman, M. E., Neto, C. C., Winiarz, E., Vaisberg, A. J. and Hammond, G. B. (2005). Ethnobotany, phytochemistry and pharmacology of *Uncaria* (Rubiaceae). *Phytochemistry*, 66: 5 – 29.
2. Ahmad, R., Hashim, M. H., Noor, M. Z., Ismail, N. H., Salim, F., Lajis, N. H. and Shaari, K. (2011). Antioxidant and antidiabetic potential of Malaysian *Uncaria*. *Research Journal of Medicinal Plant*, 5 (5): 587 – 595.
3. Salim, F. and Ahmad, R. (2010). Isopteropodic acid from Malaysia *Uncaria longiflora* var. *pteropoda*. *World Applied Sciences Journal*, 10 (11): 1334 – 1337.
4. Salim, F. and Ahmad, R. (2011). Alkaloids from Malaysian *Uncaria longiflora* var. *pteropoda*. *Biochemical Systematics and Ecology*, 39 (2): 151 – 152.
5. Salim, F., Ismail, N. H., Awang, K. and Ahmad, R. (2011). Rauniticine-*allo*-oxindole B and Rauniticinic-*allo* acid B, new heteroyohimbine-type oxindole alkaloids from the stems of Malaysian *Uncaria longiflora* var. *pteropoda*. *Molecules*, 16: 6541 - 6548.
6. Andre, N., Wang, X., He, Y., Pan, G., Kojo, A. and Liu, Y. (2013). A review of the occurrence of non-alkaloid constituents in *Uncaria* species and their structure-activity relationships. *American Journal of Biomedical and Life Sciences*, 1 (4): 79 – 98.
7. Salim, F., Zain, M. M., Ridzuan, M. S. M., Langat, M., Mullholand, D. and Ahmad, R. (2013). Flavan-3-ols from the leaves of Malaysian *Uncaria longiflora* var. *pteropoda* (Miq.) Ridsd. *Phytochemistry Letters*, 6: 236 – 240.
8. Jash, S. K., Roy, R. and Gorai, D. (2014). Bioactive constituents from *Bauhinia variegata* Linn. *International Journal of Pharmaceutical and Biomedical Research*, 5 (2): 51 – 54.
9. Li, S. G., Dong, X. X., Shan, Y. J., Liang, Z. M., Xun, L. L. and Yuan, J. Q. (2011). Non-alkaloid components from *Uncaria sinensis* (Oliv.) Havil. and their chemotaxonomic significance. *Journal of Medicinal Plants Research*, 5 (19): 4962 – 4967.

Malaysian Journal of Analytical Sciences, Vol 20 No 4 (2016): 849 - 855
DOI: http://dx.doi.org/10.17576/mjas-2016-2004-19

MALAYSIAN JOURNAL OF ANALYTICAL SCIENCES
Published by The Malaysian Analytical Sciences Society
ISSN 1394 - 2506

CHARACTERIZATION OF HEMICELLULOSES FROM OIL PALM EMPTY FRUIT BUNCHES OBTAINED BY ALKALINE EXTRACTION AND ETHANOL PRECIPITATION

(Pencirian Hemisellulosa Daripada Tandan Kosong Kelapa Sawit Diperolehi dari Pengekstrakan Alkali dan Pemendakan Etanol)

Maizatul Akhmar Mohd Nasir and Sabiha Hanim Saleh*

School of Chemistry and Environment,
Faculty of Applied Sciences,
Universiti Teknologi MARA, 40450 Shah Alam, Selangor, Malaysia

**Corresponding author: sabihahanim@salam.uitm.edu.my*

Received: 24 February 2015; Accepted: 27 October 2015

Abstract

Hemicelluloses from oil palm empty fruit bunches were extracted using alkaline extraction and fractionated by ethanol precipitation. Extraction of hemicellulose from oil palm empty fruit bunches were carried out with different KOH concentration (1 M, 3 M, 5 M), temperature (30 °C, 40 °C, 50 °C) and time (2 hours, 4 hours, 6 hours). The alkaline extraction produced two hemicellulosic fractions namely precipitate (HA) and alkali soluble hemicelluloses (HB). The alkali soluble hemicelluloses were then sub-fractionated by precipitation in 0.2 and 4 volumes ethanol for obtaining HB1 and HB2, respectively. Three hemicellulosic fractions (HA, HB1 and HB2) were further characterized in the form of total sugar, monosaccharides and Klason Lignin content. The optimal alkaline extraction was obtained at temperature of 40 °C, 3 M KOH concentration and extraction time 4 hrs. It was found that the alkaline extraction and ethanol precipitation is the suitable method to maximize the hemicelluloses yield.

Keywords: oil palm empty fruit bunches, alkaline extraction, hemicellulose

Abstrak

Hemisellulosa daripada tandan kosong kelapa sawit telah dieskstrak menggunakan pengesktrakan alkali dan terpisah oleh pemendakan etanol. Pengesktratan hemisellulosa daripada tandan buah kepala sawit dijalankan dengan pelbagai kepekatan KOH (1 M, 3 M, 5 M), suhu (30 °C, 40 °C, 50 °C) dan masa (2 jam, 4 jam, 6 jam). Pengesktrakan alkali menghasilkan dua pecahan hemisellulosa iaitu mendakan (HA) dan hemisellulosa yang larut alkali (HB). Hemisellulosa yang larut alkali masing- masing kemudiannya di sub-pisahkan oleh pemendakan dalam isipadu etanol 0.2 dan 4 masing-masing bagi menghasilkan HB1 dan HB2. Tiga pecahan hemisellulosa (HA, HB1 dan HB2) selanjutnya dicirikan oleh jumlah gula, kandungan monosakarida dan Klason Lignin. Pengesktrakan alkali optimum telah diperolehi pada suhu 40 °C, KOH 3 M dan masa 4 jam. Secara kesimpulannya pengesktrakan alkali dan pemendakan etanol merupakan kaedah yang sesuai untuk memaksimumkan hasil hemisellulosa.

Kata kunci: tandan kosong kelapa sawit, pengesktratan alkali, hemisellulosa

Introduction

Oil palm (*Elaeis guineensis)* were originated from West Africa and currently is one of the leading perennial oleaginous food crops cultivated widely in Malaysia, Indonesia and Thailand [1, 2]. Malaysia alone produce 47 %

oil palm which can be considered as second largest producer and exporter of oil plam. According to Idris et al. [3] oil palm cultivation in Malaysia covered more than 3.88 million hectares of land and operates more than 368 palm mills. Eventhough, palm oil industry has boosted the national economy in Malaysia, it also generated abundant of by-products. For every tonne of palm oil produced from fresh fruit bunch (FFB), approximately 1 tonne of oil palm empty fruit bunch (EFB), 0.7 tonnes of palm fibers, 0.3 tonnes of palm kernels and 0.3 tonnes of palm shells were generated in palm oil mills during the processing of palm oil from FFB [4]. Out of these by-products, EFB considered the biggest biomass waste and if not handled properly, would pose a severe environmental menace. Part of EFB is either incinerated for burn ash or recyled back to the plantation as mulching or used as solid fuel in the boilers to generate steam and electricity for the mills [5]. Increasing the utilization of this biomass is necessary and one such possibility would be to extract hemicelluloses to convert them to highly value-added products such as biodegradable film. The EFB biomass contains cellulose, hemicelluloses and lignin. It is estimated that EFB biomass comprised of 24 % hemicellulose which known as a valuable in pulp additives [6] and natural barrier for packaging film [7].

Hemicelluloses are the second most abundant polysaccharides in nature. Hemicelluloses, which are found in wood together with cellulose and lignin, give the best combination of mechanical support and transport properties. It is difficult to separate hemicelluloses from cellulose and lignins due to the component in lignocelluloses are bound tightly together without significant modification to its structure [8]. This could be among the main explanation why the material properties of hemicelluloses have not been exploited. Many treatments have been done to extract hemicelluloses from the plant such as steam explosion and ultra-filtration, heat treatment, classical alkaline extraction, ultrasound extract assistant and organosolv process. But among this processes, alkaline extraction has been the most promising method to accomplish complete utilization of lignocelluloses with minimal harm to the environment [9].

The purpose of the present work is to optimize the alkaline extraction conditions and ethanol precipitation of EFB on the yield of hemicelluloses. The effect of KOH concentration, temperature and time on hemicelluloses yield was investigated. The chemical properties of hemicelluloses fractions were examined in detail by means of sugar analysis and Klason Lignin. Furthermore, FT-IR was used to determine the chemical structure of sample.

Materials and Methods

Material

Oil palm EFB was obtained from a local palm oil factory in Johor, Malaysia. It was first soaked with distilled water overnight to remove dirt. Then EFB was oven-dried at 105 °C overnight to avoid fungus growth. Finally, dried EFB were ground to pass a 0.08 mm size screen using a mill blade. The samples were stored in the plastic bag prior to use. All chemicals used were of analytical grade unless otherwise stated. Xylose, glucose and arabinose were used as a standard for monosaccharide determination.

Hemicelluloses extraction

The extraction of hemicelluloses was carried out according to the method reported by Anis [10] with some modification. Oil palms EFB were soaked in different concentrations (1 – 5 M) KOH solution for different soaking time (2 – 6 hours) and at different temperatures (30 – 50 °C) with solid liquid ratio of 1:10. After extraction, the crude hemicelluloses was collected by filtration, acidified with 50 % acetic acid until pH 4.7 – 5.0 and allowed to stand for 24 hours at 4°C. The mixture was centrifuged at 3000 rpm for 15 min and the precipitates were washed with 95 % ethanol to remove the residual acid. The precipitate was dried in an oven at 60 °C for 24 hours to evaporate the ethanol and was designated as hemicelluloses (HA). The supernatant were successively sub-fractionated by graded ethanol volume solutions of 0.2V and 4V. Then both supernatant were centrifuged at 3000 rpm for 15 min. After centrifuged, the precipitates were dried in an oven at 60 °C for 24 hours to evaporate the ethanol. The precipitate obtained from the supernatant was designated as hemicelluloses B1 (0.2 volumes) and B2 (4 volumes). Hemicelluloses yield in solid extract were quantified by determining the total sugar content.

Hemicellulose characterization

Total sugar content was measured according to phenol-sulphuric acid method [11]. The total sugar content was evaluated using UV-Vis spectrophotometer (Perkin Elmer, USA) at 480 nm. Deionized water was used as a blank.

Klason lignin content in the hemicellulosic fractions was determined following TAPPI method T222. The monosaccharides content of hemicellulose fraction analysis was performed by acid hydrolysis. The hemicelluloses fraction was pre-hydrolyzed with 1.5 mL of 72 % H_2SO_4, before diluting the samples with 40 mL of distilled water and autoclaving them at 121°C for 1 hour. The samples were neutralized using $CaCO_3$ to pH 5.5 – 6.0.

The monosaccharides sugar was determined by high performance liquid chromatography (HPLC) (Agilent Technologies 1200 Series, Germany) using Aminex HPX 87P column (300 mm x 7.8 mm). The HPLC was equipped with a refractive index detector (G 1362A, Agilent Technologies 1200 Series, Germany) and column oven (Agilent Technologies 1200 Series, Germany). The sample was filtered through a 0.20 µm nylon syringe filter (Minisart, Sartorius AG, Germany) prior directly injected to the HPLC system. The sample was eluted using deionised water as the mobile phase at temperature of 80 °C with a flow rate of 0.5 mL/min [12]. The FT-IR spectra were obtained at a resolution of $4cm^{-1}$ using potassium bromide (KBr) pellet technique. The spectra were recorded between 500 and 4000 cm^{-1}.

Statistical analysis
Statistical analyses were performed using the software SPSS 16.0 program, via one way analysis of variance (ANOVA). Tukey's multiple range test was applied to determine the significantly different ($P < 0.05$) samples.

Results and Discussion

Effect of concentration of KOH on the hemicelluloses yield
To investigate the effect of KOH concentration on hemicelluloses yield, different KOH concentration (1 M, 3 M and 5 M) were used for extraction at 40 °C for 4 hours. Alkali extraction was found to have the most efficient method for isolating large amounts of hemicellulose polysaccharides. Hydroxyl ions cause swelling of cellulose, hydrolysis of ester linkage and disruption of storage linkages, such as intermolecular hydrogen bonds between hemicelluloses and cellulose, bring a portion of hemicellulose material into solution [13]. As shown in Figure 1a, the yield of hemicelluloses; HA (3.46 % to 4.67 %), HB1 (8.97 % to 7.43 %) and HB2 (17.32 % to 29.37 %) increased from 1 M to 3 M. Hemicelluloses yield increased with increasing of KOH concentration, however up to 5M KOH, the yield of all hemicelluloses fractions decreased indicating that appreciable amounts of hemicelluloses were leached out. It was found that HB2 has higher hemicelluloses yield compared to HA and HB1. Therefore, 3 M KOH was chosen for the following experiments.

Effect of temperature on the hemicelluloses yield
The hemicelluloses yield obtained at different temperature are shown in Figure 1b. It was observed that all hemicelluloses fractions increased after temperature 30 °C. The yields of hemicelluloses increased from 2.3 % to 4.7 %, 13.7 % to 24.4 % and 10.9 % to 29.4 % for HA, HB1 and HB2 respectively. Hemicellulose has a finite solubility in cold alkaline temperatures, but presumably, warm alkaline solutions lead to enhance hemicelluloses degradation; above 40 °C further extraction was occurred. It shows that high temperature is necessary for extracting hemicellulose in order to help the process of penetrating the lignified cell wall [14]. However at 50 °C, hemicellulose yield for HA (4.7 % to 2.6 %), HB1 (24.4 % to 8.5 %) and HB2 (29.3 % to 26.9 %) were decreased. Hemicellulose yield decreased at 50 °C due to degradation of hemicellulose by end-wise peeling reactions [15]. Therefore, a reaction temperature of 40 °C was considered as an optimum temperature for all hemicelluloses fractions.

Effect of time on the hemicelluloses yield
The effect of time on hemicelluloses yield during alkaline extraction was examined after an ideal concentration and temperature were obtained. Extraction periods of 2, 4 and 6 hrs were used at 40 °C and 3 M KOH. As observed from Fig. 1c), an increasing of extraction time from 2 hours to 4 hours, the hemicellulose yield were increased for HA and HB2. Both hemicellulosic fractions, HA and HB2 have higher hemicelluloses yield at 4 hours extraction. The results indicated that increasing extraction time may enhance the yield of hemicellulose. This is in accordance with other research finding [16]. Hydrolytic cleavage may degrade polysaccharides and induces the change of polysaccharides molecule structure at elevated time [17]. Therefore, the period of time 4 hours was chosen as an ideal time for the following experiments to save time and energy.

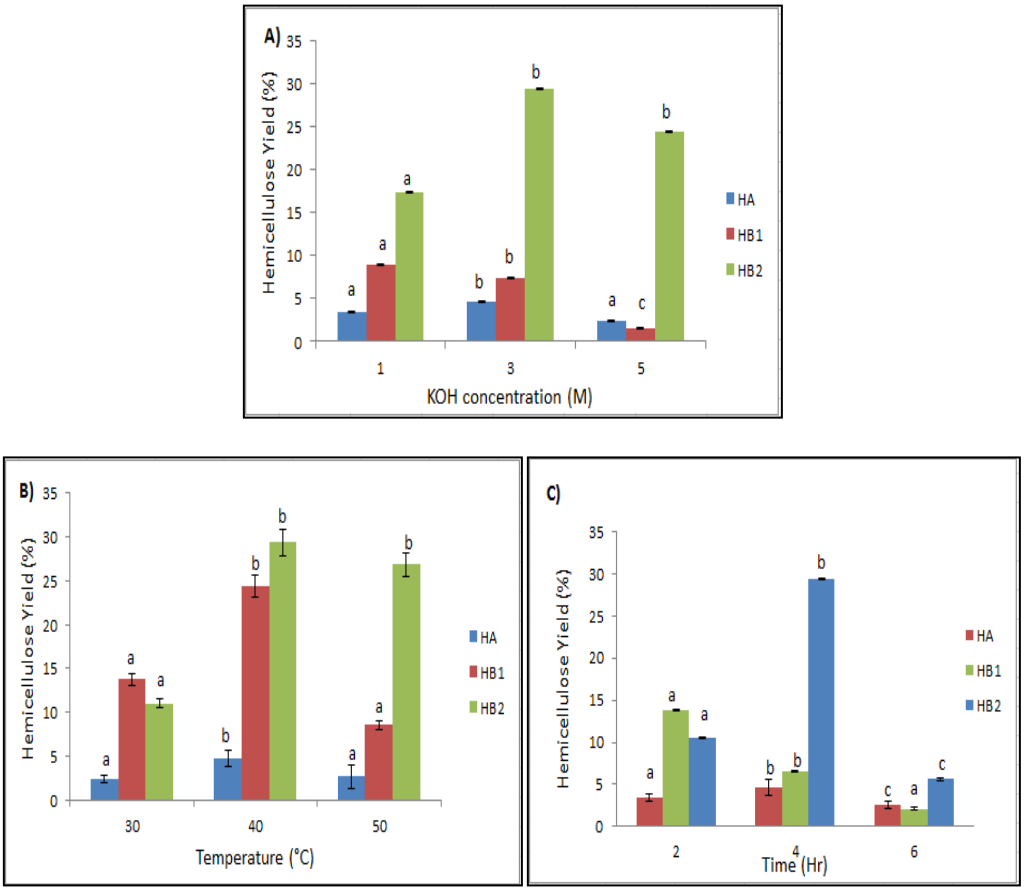


Figure 1. Effect of KOH concentration (a), temperature (b) and time (c) on the hemicelluloses yield (%). Letters (a - c) represent statistical comparisons made between different samples (HA, HB1 and HB2). Means with different letters indicate statistically significant difference from each other ($p < 0.05$).

Characterization:

Fourier transform infrared analysis

Figure 2 displays the FTIR spectra of untreated EFB, HA1, HB1 and HB2, recorded as the transmittance (%) versus wavenumber in the range of 500-4000 cm^{-1}. The O-H and aliphatic C-H stretching frequencies can be seen in region from 4000 to 1900 cm^{-1} [18]. Stretching band at 3440 cm^{-1} is attributed for O-H stretching band which corresponds to hydroxyl groups on anhydrogalactose bonds, this band showed a decrease in the intensity of HA spectra with alkaline treatment. This is due to the removal of –OH groups by reaction with KOH. HB1 and HB2 showed similar characteristics because they were also subjected to alkaline treatment. The band at 2941 cm^{-1} is attributed to C-H stretching vibration in cellulose and hemicellulose. The absorption at 1575 – 1665 cm^{-1} in all spectra is associated with water, since the hemicelluloses has strong affinity for water [19]. Untreated EFB has characteristic of ring vibrations overlapped with stretching vibrations of C-OH side groups and the C-O-C glycosidic bond vibration band at 1200 – 1000 cm^{-1} [20]. The disappearance peak observes at 1277 cm^{-1} in HA, HB1 and HB2 sample suggested that lignin was removed during alkaline extraction. This peak represents C-O linkage in guiacyl aromatic methoxy groups [21]. Combination of deformation of syringyl and cellulose was assigned at 1165 cm^{-1} band. The decrease in intensity at wavenumber 1165 cm^{-1} was greater than that at wavenumber 1277 cm^{-1} after alkaline extraction. This suggests that syringyl was more solubilized by alkaline extraction than guaicyllignin [22]. Band at ~1035 cm^{-1} is responsible for typical of xylan-rich polysaccharides which indicated a dominant xylan of the hemicellulosic

fractions [23]. Bands at 1420, 1360 and 1052 cm^{-1} are indication of hemicelluloses existence in the sample. In addition with band at 900 $cm^{-1}$is a characteristic of β-glycosidic linkage between the monosaccharide units, indicating β-linked hemicelluloses [23]. These spectral changes are characteristics of hemicellulose, which further demonstrates the removal of lignin.

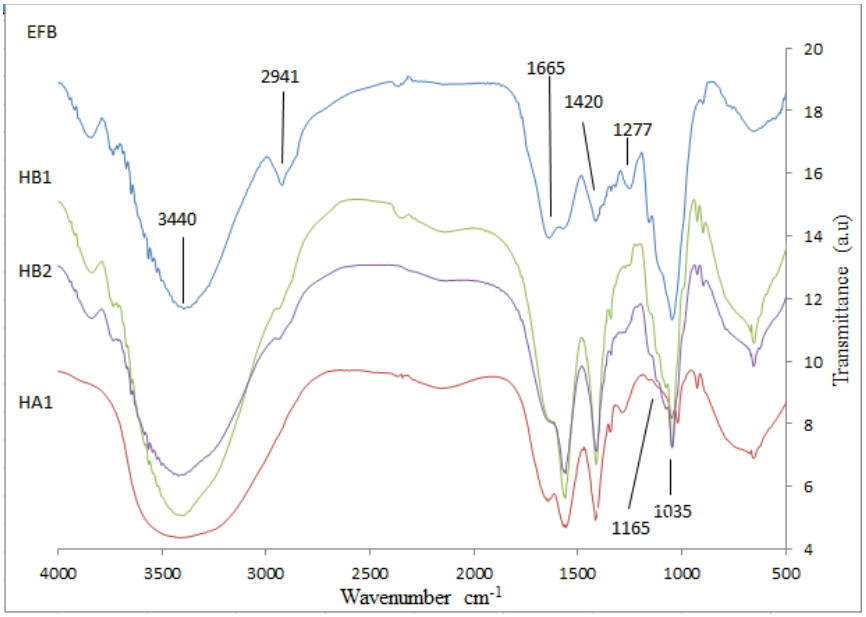


Figure 2. FTIR spectra of EFB, HA, HB1 and HB2

Klason lignin content

It was observed that a significant reduction in lignin content of HA has been achieved as compared to the original untreated OPEFB through the alkaline extraction process (Table 1). Treatment using KOH permitted the swelling of the particles that resulted in easy lignin degradation. It proved that alkaline extraction can significantly breaks the bonds between lignin and hemicelluloses [24]. After alkali extraction, the lignin content of HB1 and HB2 were decreased. This is in accordance with the finding reported by Zhao et al. [25].

Table 1. Monosaccharide compositions and lignin content in untreated EFB and hemicellulosic fractions

Sample	Monosaccharide Compositions (mg/ml)				Lignin Content (%)
	Glucose	Xylose	Arabinose	Ratio Xyl/Ara	
Untreated EFB	-	-	-	-	24.50 ± 0.01
HA	0.051 ± 0.033	0.490 ± 0.017	0.142 ± 0.027	3.456	12.06 ± 0.05
HB1	nd	0.546 ± 0.105	0.119 ± 0.004	4.591	8.96 ± 0.05
HB2	0.277 ± 0.043	1.130 ± 0.042	4.131 ± 0.023	0.273	6.08 ± 0.03

nd = not detected. Each data point were average at least two replicate measurements

Monosaccharide analysis by HPLC

The neutral monosaccharides composition content of the three precipitated hemicellulosic fractions; HA, HB1 and HB2 are shown in Table 1. Sugar analysis of hemicellulosic fractions showed that the two predominant monosaccharides in EFB were xylose and arabinose. It is suggested that the fraction may be a mixture of xylan with a small amount of arabinoxylans-type polysaccharides [26, 27]. The degrees of linearity or branching of hemicellulosic polymers were indicated by the ratio of xylose to arabinose (Xyl/Ara). A low Xyl/Ara ratio suggest that a short-chain polymer with a large amount of branching with other monosaccharide constituents. As shown in the Table 1, the ratio of Xyl/Ara gradually increased from 3.456 to 4.591. These result indicated that the hemicellulosic fractions released in alkaline extraction and ethanol precipitation has more linear structures [28].

Conclusion

This study presented extraction of hemicellulose from empty fruit bunches with various conditions. The hemicelluloses yield of HB2 was found to be higher than HA and HB1. As conclusion, alkaline extraction and ethanol precipitation are suitable methods for extracting hemicelluloses from oil palm empty fruit bunches.

Acknowledgement

The authors are grateful to the Ministry of Education Malaysia, Research Management Institute (RMI), Universiti Teknologi MARA for the financial support under the Fundamental Research Grant Scheme (FRGS):600-RMI/FRGS 5/3 (58/2013) and Faculty of Pharmacy, UiTM Puncak Alam for using HPLC equipment.

References

1. Mohammed, M. A. A., Salmiaton, A., Wan Azlina, W. A. K. G., Mohammad Amran, M. S., Fakhru'l-Razi, A. and Taufiq-Yap, Y. H. (2011). Hydrogen rich gas from oil palm biomass as a potential source of renewable energy in Malaysia. *Renewable and Sustainable Energy Reviews*, 15(2): 1258 – 1270.
2. Chiew, Y. L. and Shimada, S. (2013). Current state and environmental impact assessment for utilizing oil palm empty fruit bunches for fuel, fiber and fertilizer – A case study of Malaysia. *Biomass and Bioenergy*, 51: 109 – 124.
3. Idris, S. S., Rahman, N. A., Ismail, K., Alias, A. B., Rashid, Z. A. and Aris, M. J. (2010). Investigation on thermochemical behaviour of low rank Malaysian coal, oil palm biomass and their blends during pyrolysis via thermogravimetric analysis (TGA). *Bioresource Technology* (101):4584 – 4592.
4. Chang, S. H. (2014). An overview of empty fruit bunch from oil palm as feedstock for bio-oil production. *Biomass and Bioenergy*: 1 – 8.
5. Malaysian Palm Oil Board (2015). Oil palm planted area by category. Access online http://www.mpob.gov.my/en/home [February 2015].
6. Ferrer, A., Rosal, A., Valls, C., Roncero, B. and Rodriguez, A. (2011). Modeling hydrogen peroxide bleaching of soda pulp from oil-palm empty fruit bunches. *Bioresources*, 6 (2): 1298 – 1307.
7. Hartman, J., Albertsson, A-C., SöderqvistLindblad, M. and Sjöberg, J. (2006). Oxygen barrier materials from renewable sources: material properties of softwood hemicellulose-based films. *Journal Applied Polymer Sciences* 100: 2985 – 2991.
8. Sun J. X., Sun X. F., Sun R. C. and Su Y.Q. (2004). Fractional extraction and structural characterization of sugarcane bagasse hemicelluloses. *Carbohydrate Polymer* 56:195 – 204.
9. Zhu Ryberg, Y. Z., Edlund, U. and Albertsson, A-C. (2011). Conceptual approach to renewable barrier film design based on wood hydrolysate. *Biomacromolecules*, 12: 1355 – 1362.
10. Anis, M. (2000), Isolation and functional properties of oil palm trunk and frond hemicelluloses. Penang, Malaysia: Universiti Sains Malaysia, Phd Thesis.
11. Abbott, T. P., Nelsen, T. C. and Kleiman, R. (1995). Seed surface gums content using the Dubois carbohydrate analysis. *Industrial Crops Production* 4:185 – 192.
12. Norsyabilah, R., Hanim, S. S., Nor Suhaila, M. H. Noraishah, A. and Siti Kartina, A. K. (2013). Subcritical water extraction of monosaccharides from oil palm fronds hemicelluloses. *Malaysian Journal of Science* 17 (2): 272 – 275.
13. Sun, X. F., Sun, R. C., Fowler, P. and Baird, M. S., (2005). Extraction and characterization of original lignin and hemicelluloses from wheat straw. *Journal Agriculture and Food Chemistry*, 2(53): 860 − 870.

14. Mosier, N., Wyman, C., Dale, B., Elander, R., Lee, Y. Y., Holtzapple, M. and Ladisch, M. (2005). Features of promising technologies for pretreatment of lignocellulosic biomass. *Bioresource Technology*, 96(6): 673 – 686.
15. Hojie, A., Grondahl, M. and Tommeraas, K. (2005). Isolation and characterization of physiochemical and material properties of arabinoxylans from barley husks. *Carbohydrate Polymers* 61: 266 – 275.
16. Sabiha Hanim, S., Norsyabilah, R., Nor Suhaila, M. H., Noraishah, A. and Siti Kartina, A. K. (2012). Effect of temperature, time and pressure on the hemicelluloses yield extracted using subscritical water extraction. *Procedia Engineering* (42): 562 – 565.
17. Azhar, S., Henriksson, G., Theliander, H. and Lindstrom, M. K. (2015). Extraction of hemicelluloses from fiberized spruce woods. *Carbohydrate Polymers*, 117: 19 – 24.
18. Moshiul Alam, A. K. M., Beg, M. D. H., Reddy Prasad, D. M., Khan, M. R. and Mina, M. F. (2012). Structures and performances of simultaneous ultrasound and alkali treated oil palm empty fruit bunch fiber reinforced poly(lactic acid) composites. *Composites Part A: Applied Science and Manufacturing*, 43(11):1921 – 1929.
19. Peng, F., Bian, J., Ren, J.-L., Peng, P., Xu, F. and Sun, R. C. (2012). Fractionation and characterization of alkali-extracted hemicelluloses from peashrub. *Biomass and Bioenergy*, 39: 20 – 30.
20. Alriols, M. G., Tejado, A., Blanco, M., Mondragon, I. and Labidi, J. (2009). Agricultural palm oil tree residues as raw material for cellulose, lignin and hemicelluloses production by ethylene glycol pulping process. *Chemical Engineering Journal*, 148(1): 106 – 114.
21. Fan, S-P., Zakaria, S., Chia, C.-H., Jamaluddin, F., Nabihah, S., Liew, T-K. and Pua, F-L. (2011). Comparative studies of products obtained from solvolysis liquefaction of oil palm empty fruit bunch fibres using different solvents. *Bioresource Technology*, 102(3): 3521 – 3526.
22. Isroi, Ishola, M. M., Millati, R., Syamsiah, S., Cahyanto, M. N., Niklasson, C. and Taherzadeh, M. J. (2012). Structural changes of oil palm empty fruit bunch (OPEFB) after fungal and phosphoric acid pretreatment. *Molecules*, 17(12): 14995 – 5002.
23. Junli, R., Xinwen, P., Linxin, Z., Feng, P. and Runcang, S. (2012). Novel hydrophobic hemicelluloses: Synthesis and characteristic. *Carbohydrate Polymers*, 89(1): 152 – 157.
24. Jayabal, S., Sathiyamurthy, S., Loganathan, K. T. and Kalyanasundaram, S. (2012). Effect of soaking time and concentration of NaOH solution on mechanical properties of coir – polyester composites, 35(4): 567 – 574.
25. Zhao, X., Cheng, K. and Liu, D. (2009). Organosolv pretreatment of lignocellulosic biomass for enzymatic hydrolysis. *Applied Microbiology and Biotechnology*, 82(5): 815 – 827.
26. Peng, P., Peng, F., Bian, J., Xu, F., Sun, R. C. and Kennedy, J. F. (2011). Isolation and structural characterization of hemicelluloses from the bamboo species *Phyllostachysincarnata Wen*. *Carbohydrate Polymers*, 86: 883 – 890.
27. Thomsen, M. H., Thygesen, A. and Thomsen, A. B. (2008). Hydrothermal treatment of wheat straw at pilot plant scale using a three-step reactor system aiming at high hemicellulose recovery, high cellulose digestibility and low lignin hydrolysis. *Bioresource Technology*, 99(10): 4221 – 4228.
28. Peng, F., Peng, P., Xu, F. and Sun, R. C. (2012). Fractional purification and bioconversion of hemicelluloses. *Biotechnology Advances* 30(4): 879 – 903.

Malaysian Journal of Analytical Sciences, Vol 20 No 4 (2016): 856 - 862
DOI: http://dx.doi.org/10.17576/mjas-2016-2004-20

MALAYSIAN JOURNAL OF ANALYTICAL SCIENCES
Published by The Malaysian Analytical Sciences Society
ISSN 1394 - 2506

IMMOBILIZATION OF HIGHLY EFFECTIVE PALLADIUM CATALYST ONTO POLY(4-VINYLPYRIDINE): SYNTHESIS AND CHARACTERIZATION

(Pemegunan Mangkin Paladium yang Efektif ke atas Poli(4-vinilpiridina): Sintesis dan Pencirian)

Siti Kamilah Che Soh[1]*, Intan Shafinass Kassim[1], Siti Aminah Jusoh[1], Mustaffa Samsuddin[2, 3]

[1]*Analytical & Environmental Chemistry Program, School of Marine and Environmental Sciences, Universiti Malaysia Terengganu, 21030 Kuala Terengganu, Terengganu, Malaysia*
[2]*Department of Chemistry, Faculty of Science*
[3]*Ibnu Sina Institute for Fundamental Science Studies*
Universiti Teknologi Malaysia, 81310 Johor Bahru, Johor, Malaysia

**Corresponding author: sitikamilah@umt.edu.my*

Received: 24 February 2015; Accepted: 27 October 2015

Abstract

A commonly known weakness of homogeneous catalysts is the difficulty to recover the active catalyst from the product. Due to the disadvantage, the designing of supported catalyst has been approached to overcome the separation difficulty of the palladium-based homogeneous catalyst. New polymer supported N_2O_2 metal complex was successfully immobilized by mixing of poly(4-vinylpyridine) with palladium(II) complex in the presence of ethyl acetate as solvent. Then, the reaction was stirred for 72 hours at room temperature to form corresponding P_4VP-Pd catalyst. The properties of immobilized catalyst were characterized by various techniques such as fourier transform infrared (FTIR), thermogravimetric (TGA), X-ray diffraction (XRD), scanning electron microscopy/energy dispersive X-ray (SEM/EDX) and inductively coupled plasma-optical emission (ICP-OES) spectroscopy.

Keywords: immobilized catalyst, palladium(II) complex, poly(4-vinylpyridine)

Abstrak

Satu kelemahan penggunaan mangkin homogen adalah umum diketahui bahawa kesukaran untuk memperoleh kembali mangkin yang aktif daripada hasil produk. Oleh kerana kelemahan ini, reka bentuk mangkin berpenyokong telah diperkenalkan untuk mengatasi kesukaran pemisahan mangkin homogen berasaskan logam paladium. Kompleks logam N_2O_2 berpenyokong polimer baru telah berjaya dipegunkan dengan mencampurkan poli(4-vinilpiridina) dengan kompleks paladium(II) dengan kehadiran etil asetat sebagai pelarut. Kemudian, campuran tindak balas dikacau selama 72 jam pada suhu bilik untuk menghasilkan mangkin P_4VP-Pd. Sifat – sifat mangkin yang berjaya dipegunkan telah dicirikan dengan pelbagai teknik spektroskopi antaranya infra merah transformasi fourier (FTIR), analisis termogravimetrik (TGA), pembelauan sinar-X (XRD), mikroskopi elektron imbasan/ sinar-X tenaga tersebar (SEM/EDX) dan spektroskopi pancaran optik-aruhan (ICP-OES).

Kata kunci: mangkin terpegun, kompleks paladium(II), poli(4-vinilpiridina)

Introduction

Historically, the homogeneous catalysts have been developed to be used in industry earlier than heterogeneous catalyst. Homogeneous catalyst offered a several number of advantages to the researchers. It was found the homogeneous catalyst having transition metal complexes exhibited high selectivity and activity [1]. Despite of its advantages, the homogeneous catalyst is not commonly used as heterogeneous catalyst due to its difficulties to recover. These was proven when Dunnewijk et al. [2] reported that homogeneous catalyst is not widely used in chemical industry because the catalyst is difficult to recover and the catalysts also suffer from corrosion problems and product contamination [2]. Moreover, the homogeneous metal catalyst such as palladium is expansive to afford, toxic and suffered from prohibited drawbacks deactivation of poor conversion [3] Therefore, due to these reason there is a need to use the most applicable catalyst which is heterogeneous catalyst where the metal is heterogenized on a polymer support [4]. Other than that, heterogeneous catalyst offered easy recovery of catalyst from the reaction mixture by simple filtration and can be reused for several times [5].

One of the reasons palladium is commonly used in research because palladium is one of the most versatile of the transition metals and can formed coordination with electron donor atoms such as nitrogen and oxygen [6]. Due to these reason, Evangelisti et al. [7] discovered that the development of heterogeneous Schiff base a phosphine-free palladium catalyst which is economic and its environmental points of view have been done [7]. Schiff base is a compound which consists of nitrogen analogue of an aldehyde or ketone in which carbonyl group (C=O) have been replaced with an imine or azomethine group. The Schiff base compounds or also known as azomethines are very easy to be prepared from relatively inexpensive material and these selective ligands are sensitive towards most of the metal ions [8 – 10].

Polymers have been widely explored as immobilised material for supported catalyst [11]. In this research, poly(4-vinylpyridine) (P_4VP) has emerged as an interesting approach for catalyst support to the Schiff base metal complex. P_4VP has gained interest due to its stability towards high temperature resistance, hardness, impact strength, and its transparency can be precisely controlled through the metallocene structure.

In this present paper, the synthesis and characterization of the poly(4-vinylpyridine) supported palladium(II)-Schiff base complex which highly potential as heterogeneous catalyst for carbon-carbon bond formation were reported.

Materials and Methods

Materials

All of the reagents which included chemicals, materials and solvent are analytical grade and commercially purchased from standard suppliers (Aldrich and Fluka) were used without further purification. All reactions were carried out under an ambient atmosphere and no special precaution was taken to exclude air or moisture during synthesis work-up.

Synthesis of N,N'-bis(3,5-di-tert-butylsalicylidene)-propane-1,3-diamine

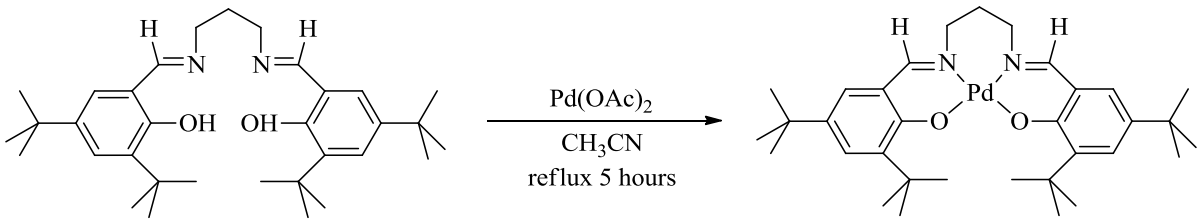
The N_2O_2-Schiff base ligand was synthesized according to the literature methods [12, 13]. The spectroscopic characterizations of these ligands were in agreement with literature values.

Synthesis of N,N'-bis(3,5-di-tert-butylsalicylidene)-propane-1,3-diaminepalladium(II) complex

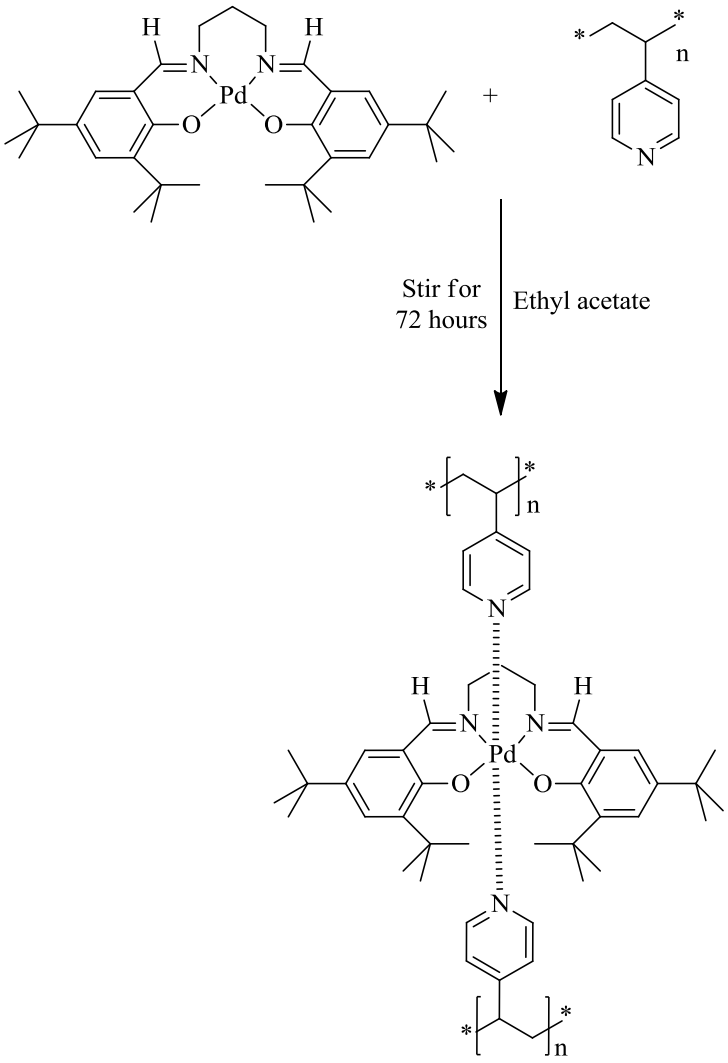
The Pd(II) complex (Scheme 1) was synthesized following standard method [14]. The complex was prepared by treating an equivalent molar amount of the corresponding ligand with $Pd(OAc)_2$ in acetonitrile. The spectroscopic data (^1H, ^{13}C NMR and FTIR) of this complex are in agreement with those reported recently by Soh et al. [15] .Yield: 88%. Melting point: 375-376 °C. CHN elemental analysis (%): Experimental: C, 55.60; H, 6.53; N, 3.82. Calculated for $C_{33}H_{48}N_2O_2Pd$ requires: C, 64.85; H, 7.92; N, 4.58

Synthesis of Poly(4-vinylpyridine) supported Pd(II) complex

The poly(4-vinylpyridine) (0.8 g) was loaded into round bottom flask containing complex (0.8 g) with ethyl acetate as a solvent. The solution was stirred for 72 hours at room temperature (Scheme 2). The resultant solid catalyst was filtered off and washed with ethyl acetate two times followed by acetone. The residue was dried in air for 24 hours.



Scheme 1. Synthesis of N,N'-bis(3,5-di-tert-butylsalicylidene)-propane-1,3-diaminepalladium



Scheme 2. Synthesis of poly(4-vinylpyridine) supported Pd(II) complex

Results and Discussion

Synthesis of N_2O_2 Schiff Base ligand and Palladium(II) complex

The Schiff base ligand N,N'-bis(3,5-di-tert-butylsalicylidene)-propane-1,3-diamine was obtained yellow solid in high yield through condensation reaction between 3,5-di-tert-butyl-2-hydroxybenzaldehyde with 1,3-diaminopropane. The resulting ligand was further treated with palladium(II) acetate in order to form metal complex. The synthesis of the Schiff base palladium(II) complex is shown in Scheme 1.

Synthesis of Poly(4-vinylpyridine) supported Pd(II) complex

The outline for synthesizing of P_4VP-Pd(II) complex was presented in Scheme 2. The N_2O_2 palladium(II) complex was then immobilized onto poly(4-vinylpyridine) solid support in order to obtain heterogeneous catalyst of P_4VP-Pd(II) complex. The immobilized P4VP-Pd(II) complex was well characterized by FTIR, TGA, XRD, SEM-EDX and ICP-OES. The amount of metal present determined by ICP-OES suggested 0.361 mmol/g palladium loading onto supported palladium complex.

FTIR spectrum (Figure 1) showed the important bands of P_4VP-Pd(II) complex are located at 1610.73 cm^{-1}, 3401.29 cm^{-1}, and 1456.16 cm^{-1} due to stretching vibration of ν(C=N), ν(N-H) and ν(C=C). The thermal stability curves of P_4VP and its supported Pd(II) complex are presented in Figure 2 were carried out at a heating rate of 10 °C min^{-1} in nitrogen over a temperature range of 30-700 °C. TGA data demonstrated that P_4VP and P_4VP-Pd(II) complex degraded at considerably high temperature. P_4VP-Pd(II) complex was stable up to 330 °C and above this temperature it undergo decomposition process.

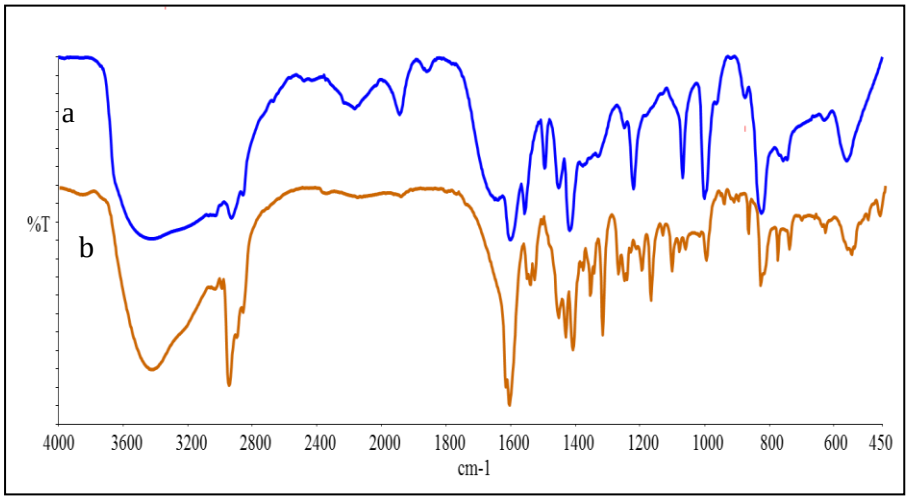


Figure 1. The FTIR spectrum for (a) P_4VP and (b) P_4VP Pd(II) complex

The surface morphological features of each sample of P_4VP and P_4VP-Pd(II) complex were observed using SEM (Figure 3) equipped with energy dispersive X-ray spectroscopy (EDX) (Figure 3). The morphology of P_4VP shows as compact and lumps surface. Meanwhile, the morphology of P_4VP-Pd(II) complex has changed and small like particles are observable through the specimen. This could be due to the existence of palladium crystallite. The EDX data (Figure 4) clearly supported the presence of palladium metal on the surface of polymeric chain of poly(4-vinylpyridine).

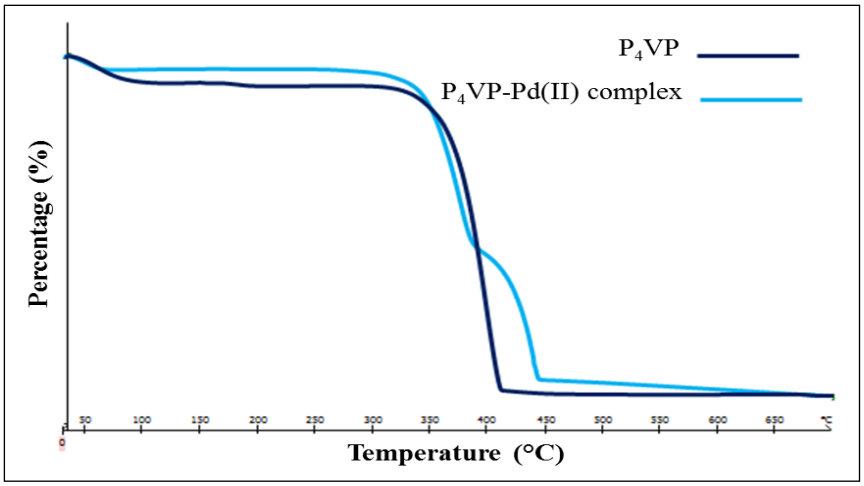


Figure 2. The TGA curves of the supported catalysts and free P_4VP

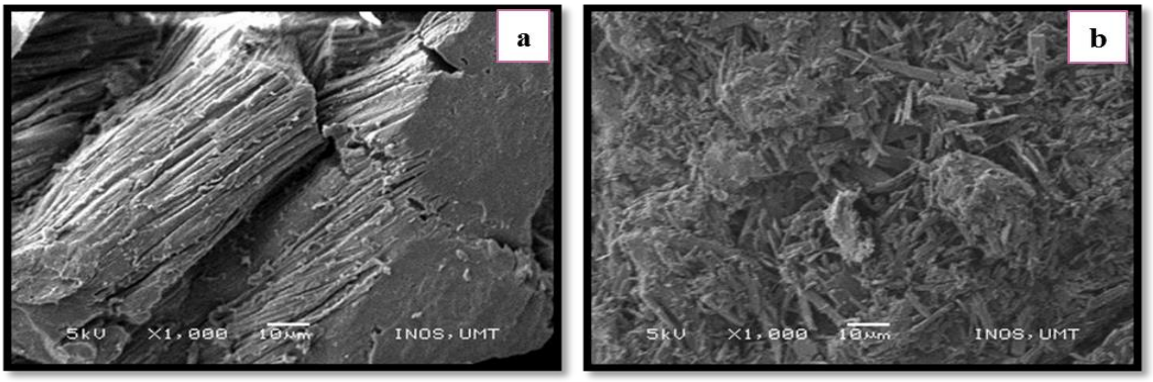


Figure 3. SEM image of the (a) P_4VP and (b) P_4VP-Pd(II) complex

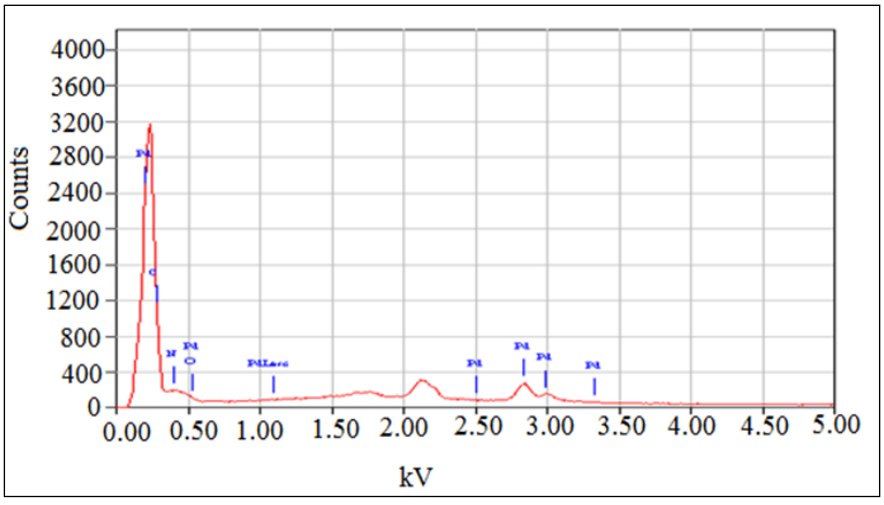


Figure 4. The EDS profile for supported P_4VP-Pd(II) complex

Powdered X-ray diffraction study is regularly used to assess the quality and structural ordering of P_4VP and supported catalyst (Figure 5). XRD pattern showed that the P_4VP support is amorphous nature with no characteristic XRD peaks is observed. The diffractogram of P_4VP-Pd(II) complex showed dramatic changes compared to P_4VP structure due to the represent of crystalline phase and indicated that the palladium complex which is incorporated with P_4VP matrix.

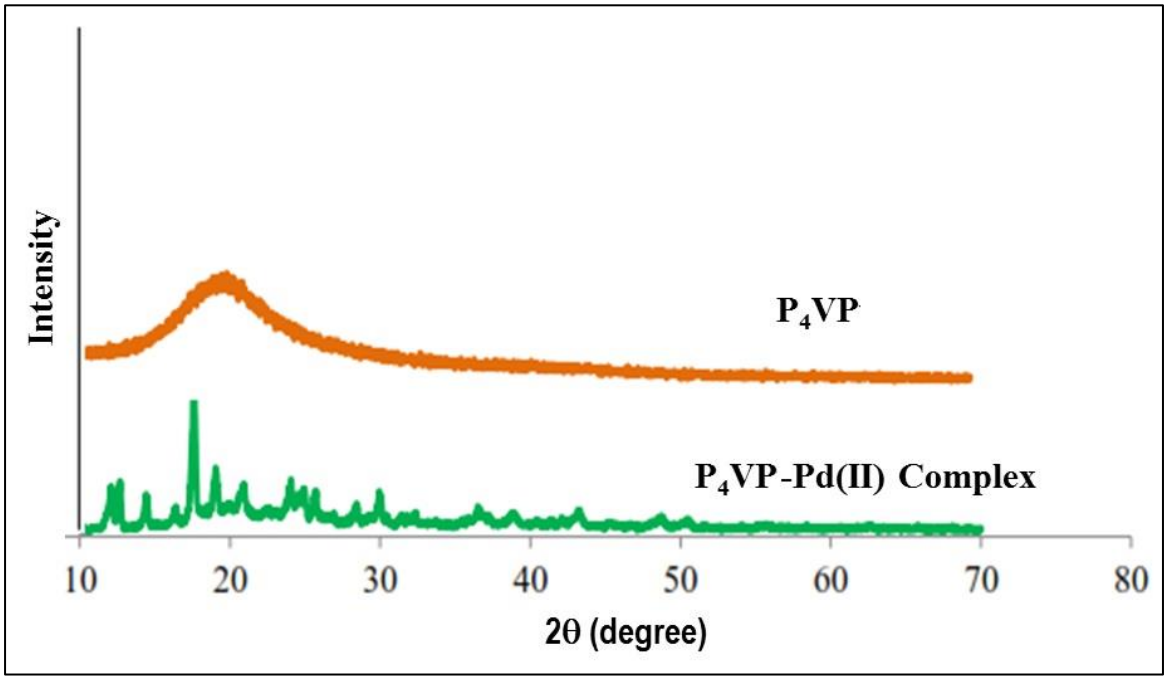


Figure 5. The XRD pattern for free P_4VP and its supported P_4VP-Pd(II) catalyst

Conclusion

In conclusion, Pd(II) complex was successfully immobilized onto P_4VP solid support and characterized via several of spectroscopic and analytical technique. The ease and simple preparation, stability towards air and moisture will make this immobilized catalyst as an ideal supported catalyst for C-C bond formation.

Acknowledgement

The author would like to thank the Ministry of Higher Education and Universiti Malaysia Terengganu for the financial support through the RAGS Vote No. 57095 and Universiti Malaysia Terengganu for providing research facilities.

References

1. Kulkarni, S., Alurkar, M. and Kumar. A. (1996). Polymer supported with Schiff base functional group with cobaltous palmitate as oxidation catalyst for cyclohexane. *Applied Catalysis A: General*, 142(2): 243 – 254.
2. Dunnewijk, J., Bosch, H., and de Haan, A. B. (2004). Reverse flow adsorption: Integrating the recovery and recycling of homogeneous catalyst. *Separation and Purification Technology,* 40 (3):317 – 320.
3. Daniel, S., Rao, P. P., Nandakumar, M. and Rao, T. P. (2005). Synthesis of heterogenous phosphine-free palladium based catalyst assemblies via solid phase extraction and their characterization. *Materials Chemistry and Physics*, 90(1): 99 – 105.
4. Augustine, R. L., Goel, P., Mahata, N., Reyes, C. and Tanielyan, S. K. (2004). Anchored homogeneous catalysts: high turnover applications. *Journal of Molecular Catalysis A: Chemical*, 216(2):189 – 197.

5. Tyrrell, E., Whiteman, L. and Williams, N. (2011). The synthesis and characterization of immobilized palladium carbene complexes and their applications to heterogeneous catalysis. *Journal of Organometallic Chemistry*, 22: 3465 – 3472.

6. Petruci, J., and Cardoso, A. A. (2013). A new palladium chelate compound for determination of sulfide. *Microchemical Journal*, 106: 368 – 372.
7. Evangelisti, C., Panziera, N., Pertici, P., Vitulli, G., Salvadori, P., Battocchio, C. and Polzonetti, G. (2009). A readily prepared, highly reusable and active polymer-supported molybdenum carbonyl Schiff base complex as epoxidation catalyst. *Inorganic Chemistry Communication*, 10(8): 914 – 917.
8. Emregul, K. C., Duzgun, E. and Atakol, O. (2006). The application of some polydentate Schiff base compounds containing aminic nitrogen as corrosion inhibitors for mild steel in acidic media. *Corrosion Science*, 48 (10): 3243 – 3260.
9. Cimerman, Z., Galic, N. and Bosner, B. (1997), The Schiff bases of salicylaldehyde and aminopyridines as highly sensitive analytical reagents. *Analytica Chimica Acta*, 343(2): 145 – 153.
10. He, Y. and Cai, C. (2011). Polymer-supported macrocyclic Schiff base palladium complex: An efficient and reusable catalyst for Suzuki cross-coupling reaction under ambient condition. *Catalysis Communication* 12(7): 678 – 683.
11. Zhongmin, D. and Zhibin, Y. (2015). Heterogeneous palladium catalyst constructed with cross-linked hyperbranched poly(phenylacetylene) as polymer support: A reusable highly active PPM-level catalyst for multiple cross-coupling reactions, *Applied Catalysis A: General*., 489: 61 – 71.
12. Selvakumar, J., Varghese, B., Raghunathan, V. S. and Nagaraja, K. S. (2007). 2,2'-[1,1'-(Propane-1,3-diyl)bis(nitriloethylidyne)]diphenol, *Acta Crystallographica Section E Structure Reports Online* 63: 1924 – 1925.
13. Fonseca, J., Martinez, J., Cunha-Silva, L., Magalhaes, A. L., Duarte, M. T. and Freire, C. (2010). Insights into electronic and structural properties of novel Pd(II) *Salen*-type complexes. *Inorganica Chimica Acta*, 363(14): 4096 – 4107.
14. Fan, Y., You, W., Huang, W., Liu, J. L. and Wang, Y. N. (2010). Salen-type nickel(II), palladium(II) and copper(II) complexes having chiral and racemic camphoric diamine components. *Polyhedron*, 29(3): 1149 – 1155.
15. Soh, S. K. C. and Shamsuddin, M. (2013). Tetradentate N_2O_2 chelated palladium(II) complexes: Synthesis, characterization, and catalytic activity towards Mizoroki-Heck reaction of aryl bromides. *E-Journal of Chemistry*, 2013: 1 – 8.

Malaysian Journal of Analytical Sciences, Vol 20 No 4 (2016): 863 - 869
DOI: http://dx.doi.org/10.17576/mjas-2016-2004-21

MALAYSIAN JOURNAL OF ANALYTICAL SCIENCES
Published by The Malaysian Analytical Sciences Society
ISSN 1394 - 2506

MODELLING DISTRIBUTION FUNCTION OF SURFACE OZONE CONCENTRATION FOR SELECTED SUBURBAN AREAS IN MALAYSIA

(Permodelan Fungsi Taburan Kepekatan Permukaan Ozon di Kawasan Sub-Bandar yang Terpilih di Malaysia)

Muhammad Izwan Zariq Mokhtar, Nurul Adyani Ghazali*, Muhammad Yazid Nasir, Norhazlina Suhaimi

School of Ocean Engineering,
Universiti Malaysia Terengganu, 21030 Kuala Terengganu, Terengganu, Malaysia

**Corresponding author: nurul.adyani@umt.edu.my*

Received: 24 February 2015; Accepted: 27 October 2015

Abstract

Ozone is known as an important secondary pollutant in the atmosphere. The aim of this study is to find the best fit distribution for calculating exceedance and return period of ozone based on suburban areas; Perak (AMS1) and Pulau Pinang (AMS2). Three distributions namely Gamma, Rayleigh and Laplace were used to fit 2 years ozone data (2010 and 2011). The parameters were estimated by using Maximum Likelihood Estimation (MLE) in order to plot probability distribution function (PDF) and cumulative distribution function (CDF). Four performance indicators were used to find the best distribution namely, normalized absolute error (NAE), prediction accuracy (PA), coefficient of determination (R^2) and root mean square error (RMSE). The best distribution to represent ozone concentration at both sites in 2010 and 2011 is Gamma distribution with the smallest error measure (NAE and RMSE) and the highest adequacy measure (PA and R^2). For the 2010 data, AMS1 was predicted to exceed 0.1 ppm for 2 days in 2011 with a return period of one occurrence per 179 days. However, AMS2 do not exceed MAAQG limit (0.1 ppm) based on both 2010 and 2011. From the results, the exceedance and return period can be used as a guidance to overcome future air pollution problem.

Keywords: ozone, performance indicators, probability distribution function, return period, cumulative distribution function

Abstrak

Ozon dikenali sebagai pencemar sekunder yang paling penting di atmosfera. Matlamat kajian ini adalah untuk mengenalpasti taburan yang terbaik dalam mengira jumlah kepekatan yang melepasi had yang ditetapkan dan tempoh kembali untuk ozon berdasarkan kawasan sub-bandar; Perak (AMS1) dan Pulau Pinang (AMS2). Pembolehubah-pembolehubah telah dianggarkan melalui penggunaan penganggar kebolehjadian maksimum (MLE) untuk plot fungsi taburan kebarangkalian (PDF) dan fungsi taburan kumulatif (CDF). 4 penunjuk prestasi telah digunakan untuk mencari taburan terbaik antaranya, ralat mutlak dinormalkan (NAE), kejituan ramalan (PA), pekali penentuan (R^2) dan punca min ralat kuasa dua (RMSE). Taburan terbaik yang mewakili kepekatan ozon di kedua-dua tempat adalah taburan Gamma dengan nilai ukuran ralat yang terkecil (NAE dan RMSE) dan nilai ukur kadaran yang terbesar (PA dan R^2). Data bagi tahun 2010, AMS1 dijangkakan akan melepasi had 0.1 ppm dalam masa 2 hari pada tahun 2011 dengan tempoh kembali satu kejadian dalam masa 179 hari. Walaubagaimanapun, AMS2 tidak melebihi had MAAQG (0.01 ppm) untuk kedua-dua tahun 2010 dan 2011. Berdasarkan hasil kajian, didapati jumlah kepekatan yang melepasi had yang ditetapkan dan tempoh kembali boleh digunakan sebagai panduan untuk mengatasi masalah pencemaran udara pada masa akan datang.

Kata kunci: ozon, penunjuk prestasi, fungsi taburan kebarangkalian, fungsi taburan kumulatif, tempoh kembali

Introduction

Owing to the burgeoning development of infrastructure in all areas in Malaysia including suburban areas, surface ozone occurrence is very likely. The higher entropic emissions such as heating emission from building and the unfavourable dispersion conditions can initiate the temperate climate of high air pollution [1]. The precursors of surface ozone are contributed by anthropogenic and natural sources. Anthropogenic sources such as deforestation, logging, fuel combustion, biomass burning, industrial causes and marine emission [2]. The examples of natural sources are nitrogen cycle, sea salt aerosol, cud-chewing animal waste and atmospheric lightning [2]. The ozone (O_3) can irritate lung airways and cause inflammation much like sunburn [3]. In Malaysia, many studies applied statistical distribution on particulate matter (PM_{10}) but less in ozone (O_3). Most of the studies on ozone use different method which are multiple linear regressions (MLR), variation and correlation between parameters such as reported in previous studies [4, 5], but there are lack of studies applying statistical distribution on ozone.

The aim of this study is to find the best fit distribution for determining exceedance and return period of ozone in AMS1 and AMS2 via statistical distribution. Three distributions namely Gamma, Rayleigh and Laplace were used to fit 2 years ozone data (2010 and 2011).

Materials and Methods

Study area

Both sites selected in this study were shown in Figure 1. The coordinate of AMS1 is 3°41’17.00’’ N and 101°31’11.79’’ E. AMS1 situated at Tanjung Malim district. Surrounded by many residential and construction areas, contained partly of Lebuhraya Utara-Selatan (main highway in Malaysia) can catalyse the ozone formation. The coordinate of AMS2 is 5°21’38.12’’ N and 100°17’55.74’’ E. AMS2 located at an education based centre in Pulau Pinang and congested with resident areas and traffics including Pulau Pinang bridge which is connected with the mainland.

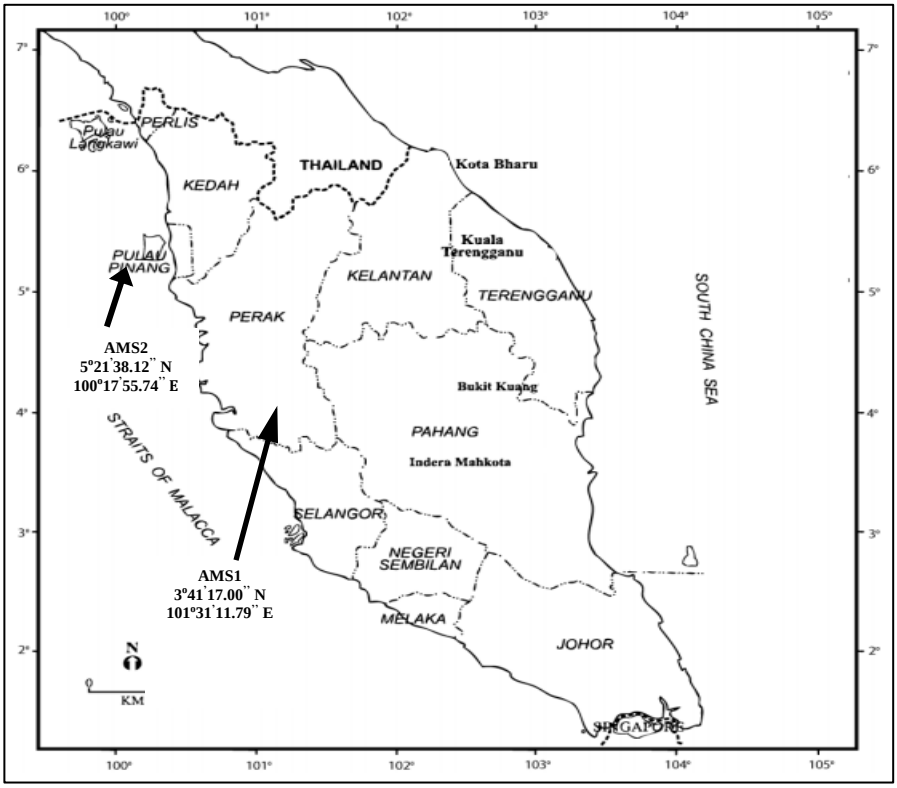


Figure 1. Map of Malaysia Peninsula (site location and its description [6])

Instrumentation and data collection

The hourly O_3 data is procured from both sites in year 2010 and 2011 which were owned from Department of Environment Malaysia (DoE) and managed by Alam Sekitar Sdn. Bhd (ASMA). The data are subjected to standard quality control processes and quality assurance procedures [7]. ASMA applied Beer-Lambert law to measure low range surface ozone concentration by using Teledyne Ozone Analyzer Model 400E UV Absorption [7]. Those best fit distribution, best distribution, exceedance and return period were obtained by analysing selected distributions via MATLAB R2014a. Statistical Package for Social Science version 19 (SPSS) was implemented to identify descriptive statistics for both stations.

Probability distribution and performance indicator

The parameters for the distributions were estimated by maximum likelihood estimation (MLE). The Gamma distribution is comprised of Chi-Squared, Erlang and Exponential distribution. It has scale and shape parameter in which growing rate of shape parameter signifies the large dataset [8]. Laplace distribution is known as double exponential distribution because of its CDF pattern [8]. It has location and scale parameter in which increasing number of scale parameter epitomizes heavier tail and lower kurtosis in PDF figure. Rayleigh distribution has scale parameter only which is simplified from Weibull distribution [8]. The formulas are as shown in Table 1. The formulas for the performance indicators are tabulated in Table 2.

Table 1. Each distribution with respective probability distribution function (PDF), cumulative distribution function (CDF) and maximum likelihood estimation (MLE)

Distribution	PDF and CDF	MLE parameter
Gamma	PDF: $f\left(x; a, B\right) = \frac{1}{\Gamma(a)B^a} x^{a-1}\exp\left(-x/B\right)$ (1) CDF: $\frac{1}{\Gamma(a)}\gamma(a, \frac{x}{B})$ $a > 0, B > 0$ (3)	Scale Parameter: $\hat{a} = \bar{x}/\hat{B}$ (2) Shape Parameter : $log\hat{a} - \varphi(\hat{a}) = \left[\bar{x}/(\prod_{i=1}^{n} x_i)\,\hat{}\,\frac{1}{n}\right]$ (4)
Rayleigh	PDF: $f(x; a) = \frac{x}{a^2} e^{\frac{-x^2}{2a^2}}$ (5) CDF: $1 - e^{\frac{-x^2}{2a^2}}$ $a > 0$ (7)	Scale Parameter : $a = \left(\left(\frac{1}{2n}\sum_{i=1}^{n} x_i^2\right)\right)\hat{}\,\frac{1}{2}$ (6)
Laplace	PDF: $f(x; \mu, \lambda) = \frac{1}{2\lambda} e\left(-\frac{\lvert x-\mu\rvert}{\lambda}\right)$ (8) CDF: $\begin{cases} \frac{1}{2} e\left(\frac{x-\mu}{\lambda}\right) \; if \; x < \mu \\ 1 - \frac{1}{2} e\left(\frac{-x-\mu}{\lambda}\right) \; if \; x \geq \mu \end{cases}$ (10)	Scale Parameter: $\frac{1}{n}\sum_{i=1}^{n}\lvert x_i - \mu\rvert$ (9) Location Parameter: Median (11)

Notation: μ is the scale parameter for Laplace distribution, a is the scale parameter for Gamma and Rayleigh distribution, λ is the location parameter and B is the shape parameter [8].

Table 2. The formula and best value for each performance indicator

Type	Performance Indicator	Formula	Best Value
Error Measure	Normalized Absolute Error (NAE)	$NAE = \frac{1}{\sum_{i=1}^{N}(O_i)}\sum_{i=1}^{N}\lvert P_i - O_i\rvert$ (12)	Near 0
	Root Mean Square Error (RMSE)	$RMSE = \sqrt{\left(\frac{1}{N-1}\right)\sum_{i=1}^{N}(P_i - O_i)\hat{}2}$ (13)	Near 0
Adequacy Measure	Prediction Accuracy (PA)	$PA = \sum_{i=1}^{N}\left[\frac{(P_i-\bar{P})(O_i-\bar{O})}{(N-1)\sigma_P\sigma_O}\right]$ (14)	Near 1
	Coefficient of Determination (R^2)	$R^2 = \left[\frac{1}{N}\frac{\sum_{i=1}^{N}(P_i-\bar{P})(O_i-\bar{O})}{\sigma_P\sigma_O}\right]$ (15)	Near 1

Exceedance and return period

Actual exceedance can be obtained by calculating the cases number exceeding the threshold of Malaysia Ambient Air Quality Guideline (MAAQG) limit and dividing this number by the number of available data [12]. Predicted exceedance can be determined by using the data collected from both actual and previous years [12]. Thus, the formula of exceedance is written in equation 16 below [9].

Exceedance: $P\{X > 0.1\} = 1 - P\{X \leq 0.1\} = 1 - F(0.1)$ (16)

Return period is a time period to calculate how many days the ozone data exceed the standard. The formula of return period is stated as below [9].

Return Period: $\frac{1}{P\{X>0.1\}} \times 365\ days$ (17)

Results and Discussion

The description statistic for AMS1 and AMS2 were shown in Table 3. The skewness showed positive numbers that define the occurrence of extreme events and high ozone emissions. These results showed that the ozone distributions are skewed to the right represent most data is concentrated on the left of the PDF plots with few high values. The mean, median, skewness and kurtosis were increasing for both sites from 2010 until 2011, indicating growing air pollution problem.

Table 3. The descriptive statistic for both sites

Data parameters	AMS1		AMS2	
	2010	2011	2010	2011
Maximum	0.127	0.165	0.086	0.089
Mean	0.018	0.019	0.019	0.020
Standard Deviation	0.018	0.021	0.014	0.015
Median	0.011	0.012	0.015	0.017
Skewness	1.13	1.6	0.9	1.005
Kurtosis	3.76	6.03	3.18	3.55

Table 4 shows that the parameter estimates are different when dissimilar statistical distributions models were applied via Maximum Likelihood Estimation (MLE). All shape parameter (a) in Gamma and Rayleigh distribution and scale parameter (λ) in Laplace distribution were less than 0.5 for both sites in 2 years. These showed that the PDF plot for all distributions had high and sharp central peak (represent high ozone concentration) and the tails are long and fat (represent few high values). The scale parameters (B) were greater than shape parameters (a) in Gamma distribution. The scale parameters (λ) were larger than location parameter (μ) in Laplace distribution. From the results, these parameters showed higher concentration for both sites in 2011 compared to 2010.

Table 4. MLE parameter estimates for both sites

Data parameters for distributions	AMS1		AMS2	
	2010	2011	2010	2011
Gamma	a=0.019 B=0.95	a=0.017 B=1.12	a=0.019 B=0.994	a=0.013 B=1.656
Rayleigh	a=0.018	a=0.020	a=0.017	a=0.018
Laplace	μ=0.011 λ=0.014	μ=0.011 λ=0.015	μ=0.015 λ=0.011	μ=0.017 λ=0.012

From the parameter estimates, CDF and PDF for Gamma, Rayleigh and Laplace distribution were plotted. Among these distributions, Gamma was the best fitted distribution as shown in Figure 2 for both sites from 2010 until 2011. PDF plots for both sites in 2010 and 2011 are positively skewed and the densities were lower meaning that ozone concentration had risen. Long tail recorded in both PDF plots indicated the presence of extreme value. The CDF plot was used to indicate the best distribution that fit the ozone concentration data. Observational line in CDF plot for AMS1 in 2010 fit at 0.044 ppm with theoretical line. Meanwhile, for AMS1 in 2011, the observational line fit at 0.02 ppm. The observational line in CDF plot for AMS2 in 2010 fitted to theoretical line at 0.04 ppm and for AMS2 in 2011, most of ozone concentration data fit to the theoretical line.

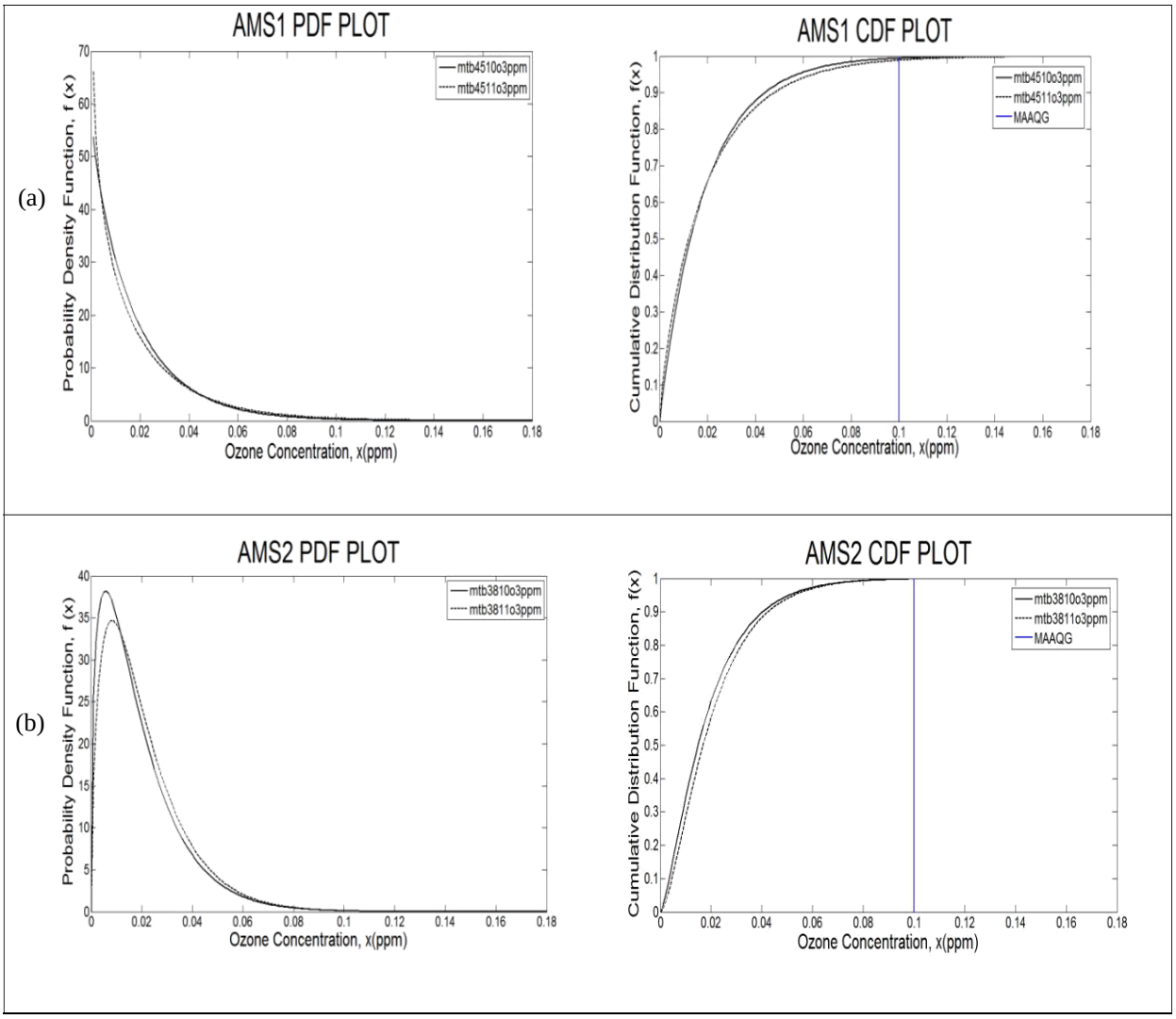


Figure 2. Gamma distribution PDF and CDF plots for both sites in 2010 and 2011 with MAAQG limit

The role of performance indicator is to determine the best fit distribution. NAE and RMSE were in error measure category which decides the smallest value gives the best fit. The R^2 and PA were categorized in adequacy measure which indicates the closer value to 1 gives the best fit. The result shows that the Gamma distribution is the best for both sites from 2010 to 2011 as shown in Table 5.

Table 5. The performance indicators for ozone concentration in both sites

Performance Indicator	Sites (Year)	Gamma Distribution	Rayleigh Distribution	Laplace Distribution	Best Distribution
NAE (near to 0)	AMS1 (2010)	0.151	0.405	0.361	Gamma
	AMS1 (2011)	0.181	0.496	0.410	
	AMS2 (2010)	0.150	0.223	0.206	
	AMS2 (2011)	0.054	0.198	0.197	
RMSE (near to 0)	AMS1 (2010)	0.005	0.009	0.008	Gamma
	AMS1 (2011)	0.006	0.011	0.008	
	AMS2 (2010)	0.004	0.005	0.012	
	AMS2 (2011)	0.002	0.005	0.013	
R^2 (near to 1)	AMS1 (2010)	0.950	0.939	0.790	Gamma
	AMS1 (2011)	0.989	0.919	0.784	
	AMS2 (2010)	0.943	0.980	0.851	
	AMS2 (2011)	0.982	0.980	0.858	
PA (near to 1)	AMS1 (2010)	0.975	0.969	0.889	Gamma
	AMS1 (2011)	0.994	0.959	0.886	
	AMS2 (2010)	0.971	0.990	0.923	
	AMS2 (2011)	0.991	0.990	0.926	

Table 6 shows that the predicted exceedances were underestimated for AMS1 from 2010 to 2011. However, the differences between predicted and actual days were small for both years. The gap of more than 1-day difference for AMS1 which is surrounded by residential areas showed that there was a few of consistent high hourly ozone detection in 2010. For 2011, the gap was below 1-day difference showed that there was detection of greater amount of consistent high hourly ozone concentration. From the result, the decreasing of difference between predicted and actual exceedances showed that the ozone concentration had become worsen from 2010 to 2011.

Table 6. The exceedance probability and return period of AMS1 for 2010 and 2011

	Elements	AMS1	
		2010	2011
	Probability ≤ 0.1 ppm	0.9944	0.9938
	Exceedance Probability > 0.1 ppm	5.6×10^{-3}	6.2×10^{-3}
Return Period	Predicted Exceedances (day)	2	2.3
	Actual Exceedances (day)	0.3	2.7
	Difference of predicted and actual exceedances (day)	1.7	0.4

Conclusion

This study shows Gamma distribution is the best fit distribution for both suburban-based sites in 2010 and 2011. Both sites show the mean are greater than median indicating the observation data are positively skewed in all three distributions. For the 2010 data, AMS1 was expected to surpass 0.1 ppm for 2 days in 2011 with a return period of one occurrence per 179 days. For the 2011 data, AMS1 was expected to surpass 0.1 ppm for 2.3 days in 2012 with a return period of one occurrence per 159 days. The results showed the ozone concentration at AMS1 became worsen from 2010 to 2011. AMS2 do not have data that exceed 0.1 ppm for both years, therefore no exceedance and return period need to be considered.

Acknowledgement

The authors would like to thank to Ministry of Higher Education of Malaysia for funding FRGS grant 59314, University Malaysia Terengganu for supporting this project and Department of Environment Malaysia (DoE) for providing the O_3 data on 2010 and 2011 to complete this study.

References

1. Yusof, N. F. F. M., Ramli, N. A., Yahaya, A. S., Sansuddin, N., Ghazali, N. A. and Madhoun, W. A. (2010). Monsoonal differences and probability distribution of PM_{10} concentration. *Environmental Monitoring and Assessment*, 163: 655 – 667.
2. Wallace, J. M. and Hobbs, P.V. (2006). Atmospheric Science. *Academic Press Publication*, 2: 153 – 198.
3. Ramli, N. A., Ghazali, N. A. and Yahaya, A. S. (2010). Diurnal fluctuations of ozone concentrations and its precursors and prediction of ozone using multiple linear regressions. *Malaysia Journal of Environmental Management*, 11(2): 57 – 69.
4. Banan, N., Latif, M.T. and Juneng, L. (2013). An assessment of ozone levels in typical urban areas in the Malaysian Peninsular. *International Journal of Environmental, Earth Science and Technology*, 7(2): 61 – 64.
5. Ahamad, F., Latif, M.T., Tang, R., Juneng, L., Dominick, D. and Juahir, H. (2014). Variation of surface ozone exceedance around Klang Valley, Malaysia. *Journal of Atmospheric Research*, 139: 116 – 127.
6. Ismail, A. S., Latif, M. T., Azmi, S. Z., Juneng, L. and Jemain, A. A. (2010). Variation of surface ozone recorded at the eastern coastal region of the Malaysian Peninsula. *American Journal of Environmental Sciences*, 6(6): 560 – 569.
7. Department of Environment, Ministry of Natural Resources and Environment (2012). Malaysia environmental quality report. ISSN 0127 – 6433.
8. Forbes, C., Evans, M., Hastings, N. and Peacock, B. (2010). Statistical Distributions. Wiley, 4: 109 – 176.
9. Noor, N. M., Tan, C., Ramli, N. A., Yahaya, A. S. and Yusof, N. F. F. M. (2011). Assessment of various probability distributions to model PM_{10} concentration for industrialized area in Peninsula Malaysia: A case study in Shah Alam and Nilai. *Australian Journal of Basic and Applied Sciences*, 5(12): 2796 – 2811.
10. Lu, H.C. (2003). Estimating the emission source reduction of PM_{10} in Central Taiwan. *Journal of Chemosphere*, 54: 805 – 814.
11. Ul-Saufie, A. Z., Yahaya, A. S., Ramli, N. A. and Hamid, H.A. (2012). Robust regression models for predicting PM_{10} concentration in an industrial area. *International Journal of Engineering and Technology*, 2(3): 364 – 370.
12. Sansuddin, N., Ramli, N. A., Yahaya, A. S., Yusof, N. F. F. M., Ghazali, N. A. and Madhoun, W. A. A. (2011). Statistical analysis of PM_{10} concentrations at different locations in Malaysia. *Environmental Monitoring Assessment*, 180: 573 – 588.

Malaysian Journal of Analytical Sciences, Vol 20 No 4 (2016): 870 - 876
DOI: http://dx.doi.org/10.17576/mjas-2016-2004-22

MALAYSIAN JOURNAL OF ANALYTICAL SCIENCES
Published by The Malaysian Analytical Sciences Society
ISSN 1394 - 2506

SYNTHESIS AND CHARACTERIZATION OF BISCOUMARIN AND BENZOPYRANO DICOUMARIN DERIVATIVES

(Sintesis dan Pencirian Terbitan Biskumarin dan Benzopirano Dikumarin)

Nik Khairunissa' Nik Abdullah Zawawi[1,2], Muhammad Taha[1,2], Norizan Ahmat[1,2]*, Nor Hadiani Ismail[1,2]

[1]*Faculty of Applied Sciences,*
Universiti Teknologi MARA, 40450 Shah Alam, Selangor, Malaysia
[2]*Atta-ur-Rahman Institute for Natural Product Discovery,*
Universiti Teknologi MARA, Puncak Alam Campus, 42300 Bandar Puncak Alam, Selangor, Malaysia

**Corresponding author: noriz118@salam.uitm.edu.my*

Received: 24 February 2015; Accepted: 27 October 2015

Abstract

The wide-ranging biological activities of 4-hydroxycoumarin have stimulated considerable interest in this class of compounds, and various biscoumarin derivatives have been synthesized. Recently, a number of methods have been reported for the synthesis of biscoumarin by the reaction of 4-hydroxycoumarin and various aldehydes in the presence of catalysts. In the present study, a new series of biscoumarin and benzopyrano dicoumarin were synthesized and physically characterized by nuclear magnetic resonane (^{1}H and ^{13}C NMR), fourier transform infrared spectroscopy (FTIR), mass spectrometry (MS) and melting point.

Keywords: synthesis, 4-hydroxycoumarin, biscoumarin, benzopyrano, nuclear magnetic resonane

Abstrak

Aktiviti biologi yang meluas daripada 4-hydroksikumarin telah merangsang minat yang besar di dalam kelas sebatian ini dan pelbagai terbitan biskumarin telah disintesis. Baru-baru ini, beberapa kaedah telah dilaporkan bagi sintesis biskumarin melalui tindak balas 4-hidroksikumarin dan pelbagai aldehid dengan kehadiran pemangkin. Dalam kajian ini, satu siri baru biskumarin dan benzopyrano dikumarin telah disintesis dan telah dicirikan secara fizikal oleh resonans magnet nukleus (^{1}H dan ^{13}C NMR), spektroskopi infra merah transformasi Fourier (FTIR), spektrometri jisim (MS) dan pengukuran takat lebur .

Kata kunci: sintesis, 4-hidroksikumarin, biskumarin, benzopirano, resonans magnet nukleus

Introduction

Significant properties and wide-ranging biological activities of 4-hydroxycoumarin have stimulated considerable interest in this class of compounds, and various biscoumarin derivatives have been synthesized. Biscoumarin, the bridge substituted dimers of 4-hydroxycoumarin, have enormous potential as anticoagulants [1, 2], antidiabetic [3], urease inhibitors [4], anticancer [5], antibacterial [6]. A number of biscoumarin have also been found to significantly inhibit c-Met phosphorylation in BaF3/TPR-Met and EBC-1 NSCLC cell lines [7]. Recently, a number of methods have been reported for the synthesis of biscoumarin by reaction of 4-hydroxycoumarin and various aldehydes in the presence of various catalysts such as tetrabutylammonium bromide [8], molecular iodine [9], [bmin] BF4 [10], SO_3H-functionalized ionic liquid [11], sodium dodecyl sulfate [12], piperidine [4], n-dodecylbenzene sulfonic acid (DBSA) [13], nano silica chloride [14], ruthenium (III) chloride hydrate [15] and Zn (proline)2 [16]. Benzopyrano dicoumarin are a derivative of biscoumarin resulting from the removal of a water

molecule. Both compounds are reported to possess versatile activities through chemical modifications (different substituents on the aromatic ring) [4,17].

Therefore, in the present study a new series of biscoumarin and benzopyrano dicoumarin were synthesized and physically characterized by Nuclear Magnetic Resonane (^{1}H and ^{13}C NMR), Fourier Transform Infrared Spectroscopy (FTIR), Mass Spectrometry (MS) and measurement of melting point.

Materials and Methods

Instrumentation

Infrared spectra were recorded on a Spectrum One FTIR Spectrometer (Perkin Elmer), using KBr discs and values were signified in cm^{-1}. The ^{1}H NMR and ^{13}C NMR spectra were measured on Bruker 500 Ultrashield Plus NMR (500 MHz) in DMSO-*d*6 as solvent, using tetramethylsilane (TMS) as an internal standard, and chemical shifts are expressed as ppm. HR-ESI-MS were determined on Agilent 6224 TOF-LC/MS using negative mode at Faculty of Pharmacy, UiTM Puncak Alam, Malaysia.

General procedure for the synthesis of compounds 1 – 18

Biscoumarin analogs 1 – 16 and benzopyrano dicoumarin 17 – 18 were synthesized by stirring the mixture of 6-Cl-4-hydroxycoumarin (1 mmol) and substituted aromatic aldehyde (0.5 mmol) in water and 10 mmol triethyl ammonium bromide (TEAB) [3]. The reaction mixture was refluxed for 24 hours. Completion of reaction was monitored by periodic TLC. After completion of reaction, the product was filtered and then washed with distilled water affording a pure product in high yields. The structures of compounds 1 – 18 were characterized by using different spectroscopic techniques namely Nuclear Magnetic Resonanes (^{1}H and ^{13}C NMR), Fourier Transform Infrared Spectroscopy (FTIR), Mass Spectrometry (MS) and melting point.

Results and Discussion

Characterization study: 3,3'-(o-tolylmethylene)bis(6-chloro-4-hydroxy-2H-chromen-2-one) (1)

Yield; 0.23g (84%). m.p. 227 °C. IR(KBr) (ν_{max}, cm^{-1}): 3076, 1668, 1610, 1560, 1115, 1175. ^{1}H NMR (500 MHz, DMSO) δ 7.77 (d, *J* = 2.5 Hz, 2H), 7.54 (dd, *J* = 8.8, 2.5 Hz, 2H), 7.32 (d, *J* = 8.8 Hz, 2H), 7.25 (d, *J* = 4.0 Hz, 1H), 7.19 (t, *J* = 5.5 Hz, 1H), 7.02 (s, 2H), 6.08 (s, 1H, Ar_3CH), 2.08 (s, 3H, CH_3). ^{13}C NMR (126 MHz, DMSO) δ 166.5, 164.0, 151.4, 140.6, 136.1, 131.1, 130.6, 128.6, 127.7, 125.9, 125.4, 123.6, 121.4, 118.2, 104.4, 36.12. EI-MS: 493.0255 (M^-, 1).

3,3'-((2-chlorophenyl)methylene)bis(6-chloro-4-hydroxy-2H-chromen-2-one) (2)

Yield; 0.24g (86%). m.p. 225 °C. IR(KBr) (ν_{max}, cm^{-1}): 3277, 1668, 1618, 1567, 1176, 1116. ^{1}H NMR (500 MHz, DMSO) δ 7.77 (d, *J* = 2.5 Hz, 2H), 7.63 (d, *J* = 8.0 Hz, 1H), 7.54 (dd, *J* = 8.7, 2.6 Hz, 2H), 7.37 (d, *J* = 7.5 Hz, 1H), 7.32 (d, *J* = 8.7 Hz, 2H), 7.27 (dd, *J* = 7.5, 1.3 Hz, 1H), 7.25 – 7.09 (m, 2H), 6.13 (s, 1H, Ar_3CH). ^{13}C NMR (126 MHz, DMSO) δ 166.3, 163.8, 151.4, 139.9, 133.1, 131.2, 130.7, 129.9, 127.8, 127.8, 126.6, 123.6, 121.4, 118.2, 104.0, 36.7. EI-MS: 512.9706 (M^-, 1).

3,3'-(p-tolylmethylene)bis(6-chloro-4-hydroxy-2H-chromen-2-one) (3)

Yield; 0.23g (84%). m.p. 280°C. IR(KBr) (ν_{max}, cm^{-1}): 3026, 1671, 1619, 1567, 1177. ^{1}H NMR (500 MHz, DMSO) δ 7.76 (d, *J* = 2.6 Hz, 2H), 7.56 (dd, *J* = 8.7, 2.6 Hz, 2H), 7.34 (d, *J* = 8.8 Hz, 2H), 6.98 (s, 4H), 6.21 (s, 1H, Ar_3CH), 2.23 (s, 3H, CH_3). ^{13}C NMR (126 MHz, DMSO) δ 166.3, 164.6, 151.5, 138.5, 134.4, 131.3, 128.9, 127.7, 127.0, 123.6, 121.4, 118.2, 104.8, 36.3, 21.0. EI-MS: 493.0252 (M^-, 1).

3,3'-((3-hydroxyphenyl)methylene)bis(6-chloro-4-hydroxy-2H-chromen-2-one) (4)

Yield (0.24 g) 86%. m.p. 292 °C. IR(KBr) (ν_{max}, cm^{-1}): 3077, 1657, 1618, 1564, 1169. ^{1}H NMR (500 MHz, DMSO) δ 7.77 (d, *J* = 2.4 Hz, 2H), 7.55 (dd, *J* = 8.7, 2.4 Hz, 2H), 7.41 (dd, *J* = 13.1, 5.3 Hz, 1H), 7.32 (d, *J* = 8.7 Hz, 2H), 7.25 (t, *J* = 7.9 Hz, 1H), 7.17 (dd, *J* = 12.8, 6.4 Hz, 1H), 7.03 (t, *J* = 7.4 Hz, 1H), 6.98 (dd, *J* = 10.6, 8.6 Hz, 1H), 6.30 (s, 1H, Ar_3CH). ^{13}C NMR (126 MHz, DMSO) δ 166.5, 163.9, 151.4, 131.2, 130.3, 127.7, 123.8, 123.7, 121.5, 118.2, 115.5, 115.3, 103.8, 32.5. HR-EI-MS: 495.0043 (M^-, 1).

3,3'-(m-tolylmethylene)bis(6-chloro-4-hydroxy-2H-chromen-2-one) (5)
Yield (0.23 g) 84%. m.p. 243 °C. IR(KBr) (ν_{max}, cm^{-1}): 3014, 1668, 1618, 1565, 1181. ^{1}H NMR (500 MHz, DMSO) δ 7.76 (d, *J* = 2.4 Hz, 2H), 7.55 (dd, *J* = 8.7, 2.5 Hz, 2H), 7.33 (d, *J* = 8.7 Hz, 2H), 7.06 (t, *J* = 7.7 Hz, 1H), 6.90 (m, 3H), 6.22 (s, 1H, Ar_3CH), 2.19 (s, 3H, CH_3). ^{13}C NMR (126 MHz, DMSO) δ 166.5, 164.6, 151.5, 141.8, 137.1, 131.2, 128.2, 127.7, 127.7, 126.3, 124.3, 123.7, 121.6, 118.2, 104.7, 36.6, 21.7. EI-MS: 493.0257 (M^-, 1).

3,3'-((2-nitrophenyl)methylene)bis(6-chloro-4-hydroxy-2H-chromen-2-one) (6)
Yield (0.20 g) 78%. m.p. 244°C. IR(KBr) (ν_{max}, cm^{-1}): 3084, 1676, 1616, 1563, 1479, 1440, 1367, 1257, 1176, 1119, 1070. ^{1}H NMR (500 MHz, DMSO) δ 7.71 (d, *J* = 2.5 Hz, 2H), 7.57 (d, *J* = 7.9 Hz, 1H), 7.55 (dd, *J* = 8.8, 2.6 Hz, 2H), 7.51 (td, *J* = 8.0, 1.0 Hz, 1H), 7.37 (dd, *J* = 15.2, 7.8 Hz, 2H), 7.32 (d, *J* = 8.7 Hz, 2H), 6.45 (s, 1H). ^{13}C NMR (126 MHz, DMSO) δ 166.7, 163.5, 151.5, 150.0, 135.0, 132.1, 131.3, 130.0, 127.7, 127.3, 124.4, 123.6, 121.2, 118.3, 103.3, 34.5. HR-EI-MS: 523.9945 (M^-, 1).

3,3'-((2-fluorophenyl)methylene)bis(6-chloro-4-hydroxy-2H-chromen-2-one) (7)
Yield (0.24 g) 86%. m.p. 201°C. IR(KBr) (ν_{max}, cm^{-1}): 3080, 1660, 1615, 1565, 1489, 1452, 1253, 1116, 977, 760. ^{1}H NMR (500 MHz, DMSO) δ 7.77 (d, *J* = 2.4 Hz, 2H), 7.55 (dd, *J* = 8.7, 2.4 Hz, 2H), 7.32 (d, *J* = 8.7 Hz, 2H), 7.25 (t, *J* = 7.9 Hz, 1H), 7.17 (dd, *J* = 12.8, 6.4 Hz, 1H), 7.03 (t, *J* = 7.4 Hz, 1H), 6.98 (dd, *J* = 10.6, 8.6 Hz, 1H), 6.30 (s, 1H). ^{13}C NMR (126 MHz, DMSO) δ 166.5, 163.9, 151.4, 131.2, 130.3, 127.7, 123.8, 123.6, 121.5, 118.2, 115.5, 115.3, 103.8, 32.5. HR-EI-MS: 497.0005 (M^-, 1).

3,3'-(pyridin-2-ylmethylene)bis(6-chloro-4-hydroxy-2H-chromen-2-one) (8)
Yield (0.21 g) 80%. m.p. 309°C. IR(KBr) (ν_{max}, cm^{-1}): 3155, 2837, 1648, 1606, 1534, 1455, 1349, 1205, 1168, 1032, 947, 765. ^{1}H NMR (500 MHz, DMSO) δ 8.62 (d, *J* = 5.4 Hz, 1H), 8.42 (t, *J* = 7.6 Hz, 1H), 7.90 (d, *J* = 8.1 Hz, 1H), 7.85 (dd, *J* = 6.6, 5.0 Hz, 1H), 7.74 (d, *J* = 2.5 Hz, 2H), 7.61 (dd, *J* = 8.8, 2.5 Hz, 2H), 7.39 (d, *J* = 8.8 Hz, 2H), 6.48 (s, 1H). ^{13}C NMR (126 MHz, DMSO) δ 167.7, 163.9, 151.8, 131.9, 127.9, 123.9, 121.3, 118.5, 101.6, 37.2. HR-EI-MS: 480.0047 (M^-, 1).

3,3'-((3-chlorophenyl)methylene)bis(6-chloro-4-hydroxy-2H-chromen-2-one) (9)
Yield (0.24 g) 86%. m.p. 222°C. IR(KBr) (ν_{max}, cm^{-1}): 3079, 1654, 1614, 1563, 1475, 1440, 1341, 1298, 1253, 1181, 1071, 978, 785. ^{1}H NMR (500 MHz, DMSO) δ 7.78 (s, 2H), 7.56 (dd, *J* = 8.7, 2.5 Hz, 2H), 7.34 (d, *J* = 8.8 Hz, 2H), 7.20 (dd, *J* = 21.6, 7.9 Hz, 2H), 7.08 (d, *J* = 5.3 Hz, 2H), 6.25 (s, 1H).^{13}C NMR (126 MHz, DMSO) δ 166.6, 164.5, 151.5, 134.6, 133.3, 131.4, 130.2, 127.8, 126.8, 126.0, 125.7, 123.7, 121.3, 118.3, 104.1, 36.6. HR-EI-MS: 512.9709 (M^-, 1).

3,3'-((3-fluorophenyl)methylene)bis(6-chloro-4-hydroxy-2H-chromen-2-one) (10)
Yield (0.26 g) 90%. m.p. 238°C. IR(KBr) (ν_{max}, cm^{-1}): 3079, 1654, 1615, 1563, 1485, 1440, 1256, 1183, 1104, 1072, 813, 789. ^{1}H NMR (500 MHz, DMSO) δ 7.77 (d, *J* = 2.0 Hz, 2H), 7.56 (dd, *J* = 8.7, 1.9 Hz, 2H), 7.34 (d, *J* = 8.7 Hz, 2H), 7.22 (dd, *J* = 14.6, 7.5 Hz, 1H), 6.91 (dd, *J* = 28.3, 17.6 Hz, 2H), 6.83 (s, 1H), 6.25 (s, 1H).^{13}C NMR (126 MHz, DMSO) δ 166.7, 164.4, 151.5, 131.3, 127.7, 123.7, 123.2, 121.5, 118.3, 104.2, 36.7. HR-EI-MS: 497.0006 (M^-, 1).

3,3'-((3-nitrophenyl)methylene)bis(6-chloro-4-hydroxy-2H-chromen-2-one) (11)
Yield (0.25 g) 88%. m.p. 248°C. IR(KBr) (ν_{max}, cm^{-1}): 3075, 1657, 1611, 1563, 1529, 1348, 1104, 977, 818, 793. ^{1}H NMR (500 MHz, DMSO) δ 8.01 (d, *J* = 7.5 Hz, 1H), 7.88 (s, 1H), 7.76 (d, *J* = 2.4 Hz, 2H), 7.65 – 7.53 (m, 3H), 7.51 (t, *J* = 7.9 Hz, 1H), 7.36 (d, *J* = 8.7 Hz, 2H), 6.33 (s, 1H). ^{13}C NMR (126 MHz, DMSO) δ 167.0, 164.3, 151.6, 134.2, 131.5, 129.9, 127.8, 123.7, 121.5, 121.5, 121.0, 118.3, 103.7, 36.9. HR-EI-MS: 523.9949 (M^-, 1).

3,3'-(pyridin-3-ylmethylene)bis(6-chloro-4-hydroxy-2H-chromen-2-one) (12)
Yield (0.21 g) 80%. m.p. 376°C. IR(KBr) (ν_{max}, cm^{-1}): 3446, 3062, 2594, 2147, 1685, 1610, 1537, 1389, 1179, 1123, 1012, 815. ^{1}H NMR (500 MHz, DMSO) δ 8.78 – 8.61 (m, 2H), 8.37 (d, *J* = 8.1 Hz, 1H), 7.93 (dd, *J* = 7.9, 5.9 Hz, 1H), 7.74 (d, *J* = 2.5 Hz, 2H), 7.59 (dd, *J* = 8.7, 2.6 Hz, 2H), 7.36 (d, *J* = 8.8 Hz, 2H), 6.38 (s, 1H). ^{13}C NMR (126 MHz, DMSO) δ 167.2, 164.0, 151.7, 145.1, 142.5, 140.9, 139.8, 131.6, 127.8, 127.1, 123.7, 121.4, 118.4, 102.7, 35.2. HR-EI-MS: 480.0049 (M^-, 1).

3,3'-((4-chlorophenyl)methylene)bis(6-chloro-4-hydroxy-2H-chromen-2-one) (13)
Yield (0.22 g) 82%. m.p. 277°C. IR(KBr) (ν_{max}, cm^{-1}): 2929, 1668, 1566, 1492, 1340, 1302, 1252, 1179, 1117, 1097, 1071, 821, 789, 758. ^{1}H NMR (500 MHz, DMSO) δ 7.75 (d, *J* = 2.1 Hz, 2H), 7.55 (dd, *J* = 8.7, 2.3 Hz, 2H), 7.33 (d, *J* = 8.7 Hz, 2H), 7.22 (d, *J* = 8.3 Hz, 2H), 7.10 (d, *J* = 8.2 Hz, 2H), 6.21 (s, 1H).
^{13}C NMR (126 MHz, DMSO) δ 166.7, 164.5, 151.5, 140.9, 131.3, 130.2, 129.0, 128.2, 127.8, 123.7, 121.5, 118.2, 104.3, 36.3. HR-EI-MS: 512.9709 (M^-, 1).

3,3'-((4-nitrophenyl)methylene)bis(6-chloro-4-hydroxy-2H-chromen-2-one) (14)
Yield (0.24 g) 86%. m.p. 285°C. IR(KBr) (ν_{max}, cm^{-1}): 3067, 1644, 1570, 1512, 1483, 1440, 1331, 1252, 1118.^{1}H NMR (500 MHz, DMSO) δ 8.06 (d, *J* = 8.8 Hz, 2H), 7.75 (d, *J* = 2.5 Hz, 2H), 7.57 (dd, *J* = 8.8, 2.6 Hz, 2H), 7.36 (dd, *J* = 10.9, 8.9 Hz, 4H), 6.32 (s, 1H).^{13}C NMR (126 MHz, DMSO) δ 167.0, 164.3, 151.6, 151.0, 145.9, 131.4, 128.4, 127.8, 123.7, 123.6, 121.5, 118.3, 103.8, 37.3. HR-EI-MS: 523.9953 (M^-, 1).

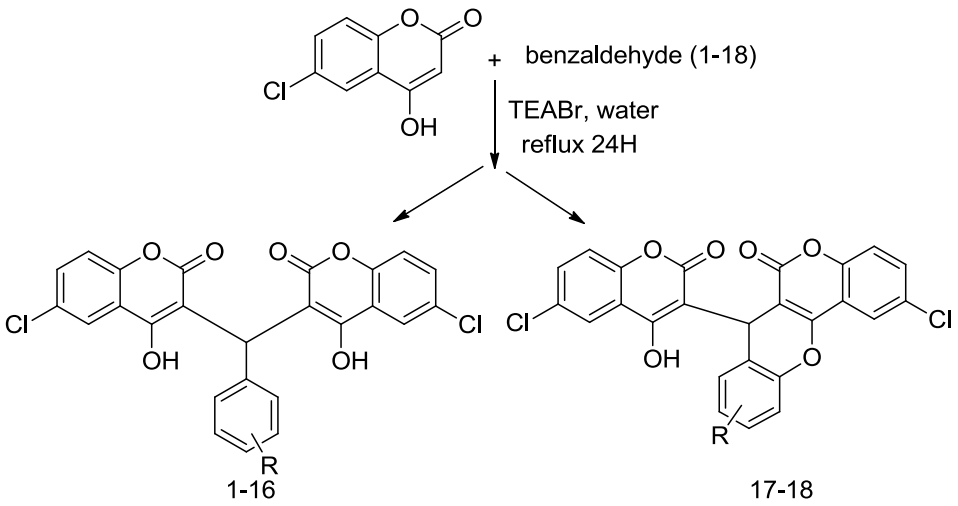
3,3'-((4-hydroxyphenyl)methylene)bis(6-chloro-4-hydroxy-2H-chromen-2-one) (15)
Yield (0.21 g) 80%. m.p. 358°C. IR(KBr) (ν_{max}, cm^{-1}): 3083, 1717, 1663, 1614, 1564, 1299, 1241, 1177, 1118. ^{1}H NMR (500 MHz, DMSO) δ 7.76 (d, *J* = 2.5 Hz, 2H), 7.54 (dd, *J* = 8.7, 2.5 Hz, 2H), 7.32 (d, *J* = 8.7 Hz, 2H), 6.88 (d, *J* = 8.3 Hz, 2H), 6.57 (d, *J* = 8.5 Hz, 2H), 6.15 (s, 1H). ^{13}C NMR (126 MHz, DMSO) δ 166.3, 164.6, 155.3, 151.4, 131.6, 131.1, 128.0, 127.7, 123.6, 121.6, 118.2, 115.1, 105.0, 35.9. HR-EI-MS: 495.0046 (M^-, 1).

3,3'-(pyridin-4-ylmethylene)bis(6-chloro-4-hydroxy-2H-chromen-2-one) (16)
Yield (0.25 g) 88%. m.p. 349°C. IR(KBr) (ν_{max}, cm^{-1}): 3446, 1673, 1608, 1390, 1246, 1205, 1124, 1052. ^{1}H NMR (500 MHz, DMSO) δ 8.66 (d, *J* = 4.7 Hz, 2H), 7.80 (d, *J* = 4.7 Hz, 2H), 7.74 (s, 2H), 7.60 (d, *J* = 7.9 Hz, 2H), 7.38 (d, *J* = 8.5 Hz, 2H), 6.41 (s, 1H).^{13}C NMR (126 MHz, DMSO) δ 167.32, 164.08, 151.75, 141.88, 131.75, 127.87, 125.57, 123.78, 121.33, 118.44, 102.51, 38.15. HR-EI-MS: 480.0050 (M^-, 1).

2-chloro-7-(6-chloro-4-hydroxy-2-oxo-2H-chromen-3-yl)-10,11-dihydroxychromeno[4,3-b]chromen-6(7H) -one (17)
Yield (0.24 g) 86%. m.p. 375°C. IR(KBr) (ν_{max}, cm^{-1}): 3291, 1676, 1608, 1568, 1488, 1422, 1371, 1199. ^{1}H NMR (500 MHz, DMSO) δ 9.32 (s, 1H), 9.14 (s, 1H), 8.58 (d, *J* = 2.4 Hz, 1H), 8.03 (s, 1H), 7.73 (dd, *J* = 8.8, 2.5 Hz, 1H), 7.63 (dd, *J* = 8.8, 2.2 Hz, 1H), 7.48 (d, *J* = 8.8 Hz, 1H), 7.36 (d, *J* = 8.7 Hz, 1H), 6.57 (d, *J* = 8.3 Hz, 1H), 6.45 (d, *J* = 8.2 Hz, 1H), 5.64 (bs, 1H). ^{13}C NMR (126 MHz, DMSO) δ 160.6, 151.3, 151.2, 146.2, 133.5, 132.5, 132.1, 130.4, 129.1, 128.7, 128.5, 123.3, 118.9, 118.8, 118.4, 117.9, 116.0, 113.0, 27.3. HR-EI-MS: 508.9840 (M^-, 1).

2-chloro-7-(6-chloro-4-hydroxy-2-oxo-2H-chromen-3-yl)-9-hydroxychromeno[4,3-b]chromen-6(7H)-one (18)
Yield (0.23 g) 84%. m.p. 310°C. IR(KBr) (ν_{max}, cm^{-1}): 3306, 1695, 1614, 1568, 1473, 1423, 1386, 1206. ^{1}H NMR (500 MHz, DMSO) δ 9.79 (s, 1H), 8.12 (d, *J* = 2.4 Hz, 1H), 8.04 (d, *J* = 1.1 Hz, 1H), 7.74 (dd, *J* = 8.8, 2.5 Hz, 1H), 7.64 (dd, *J* = 8.8, 2.3 Hz, 1H), 7.50 (d, *J* = 8.8 Hz, 1H), 7.37 (d, *J* = 8.7 Hz, 1H), 6.98 (d, *J* = 8.4 Hz, 1H), 6.77 (d, *J* = 2.2 Hz, 1H), 6.59 (dd, *J* = 8.4, 2.3 Hz, 1H), 5.62 (bs, 1H). ^{13}C NMR (126 MHz, DMSO) δ 160.51, 157.87, 155.73, 151.25, 151.03, 150.10, 132.58, 132.18, 129.56, 129.17, 128.51, 122.4, 119.0, 118.8, 118.3, 115.8, 113.6, 103.4, 28.7. HR-EI-MS: 492.9892 (M^-, 1).

In this work, a new series of biscoumarin and benzopyrano dicoumarincoumarin were synthesized (Scheme 1) in moderately good yields by Claisen condensation according to a previous report [3]. The formation of biscoumarin 1–16 were prompted with aldol condensation of 6-Cl-4-hydroxycoumarin (2 mmol) and substituted aromatic aldehydes linker (1 mmol) followed by dehydration of the aldol product to give a chromone. Subsequent *in situ* reaction of the chromone with another 6-Cl-4-hydroxycoumarin present in excess gave dimeric coumarin derivatives 1–16 bearing an aryl substituent in the central methylene linker [6]. In contrast, the chromone derivatives containing an *ortho*-substituted phenyl moiety gave fused benzopyrano dicoumarin 17-18 under spontaneous cyclization and removal of water. The structures of compounds 1 – 18 (Table 1) were characterized by using different spectroscopic techniques such as ^{1}H, ^{13}C NMR, FTIR, Mass Spectroscopy and melting point.



Scheme 1. Synthesis of biscoumarin (1-16) and benzopyrano dicoumarin derivatives (17-18)

Table 1. Aldehyde substituents of compound (1-18)

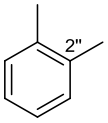
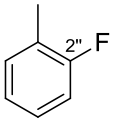
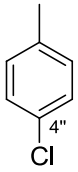
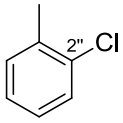
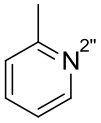
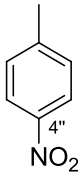
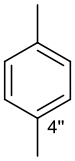
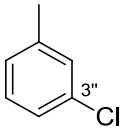
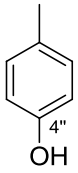
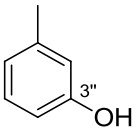
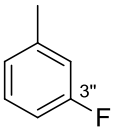
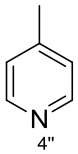
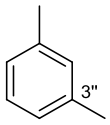
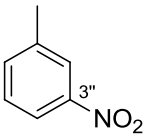
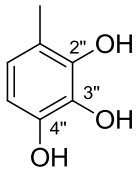
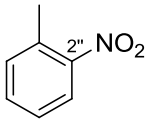
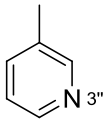
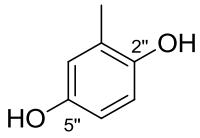
Comp. No	R	Comp. No	R	Comp. No	R
1		7		13	
2		8		14	
3		9		15	
4		10		16	

Table 1 (cont'd). Aldehyde substituents of compound (1-18)

Comp. No	R	Comp. No	R	Comp. No	R
5		11		17	
6		12		18	

The ^{1}H NMR spectra of biscoumarin derivatives 1 – 16 showed characteristic of sharp singlet peak at δ 6.08–6.48 assigned to a methine proton, a bridge substituted dimers of 4-hydroxycoumarin. In the ^{13}C NMR spectra, this methine carbon appeared at δ 38.2 – 32.5. The hydroxyl protons of 4-hydroxycoumarin were not observed in the ^{1}H NMR spectra. Benzopyrano dicoumarin of compound 17 – 18 were form when benzaldehyde having 2-hydroxy substituent was allowed to react with 4-hydroxycoumarin under the same reaction conditions. In the ^{1}H NMR spectra, the methine was shifted to a more upfield region (δ 5.62 – 5.64) and appeared as a broad singlet peak compared to methine of biscoumarin. We thus turned our attempt to characterize this compound by means of other spectroscopic methods. The mass spectra of both compounds showed a molecular ion peak at m/z 508.9840 and 492.9892, respectively, which is in accordance with a cyclization reaction by the removal of one water molecule from the corresponding biscoumarin. However, IR spectra of both compounds showed similar characteristic absorption bands at 1600 – 1700 cm^{-1} and 2900 – 3500 cm^{-1} due to carbonyl and OH group, respectively.

Conclusion

In conclusion, a series of new 6-chloro-4-hydroxy substituted biscoumarin and benzopyrano dicoumarin derivatives of compound (1-18**)** were synthesized in moderately good yield and characterized by using different spectroscopic techniques such as ^{1}H, ^{13}C Nuclear Magnetic Resonanes (NMR), fourier transform infrared spectroscopy (IR), mass spectrometry (MS) and melting point. A further study to investigate the potential pharmacological activity is in progress.

Acknowledgement

The authors would like to acknowledge the Ministry of Education Malaysia and Universiti Teknologi MARA for the financial support under ERGS grant 600-RMI/ERGS /5/3/ (4/2013).

References

1. Appendino, G., Cravotto, G., Tagliapietra, S., Ferraro, S., Nano, G. M., Palmisano, G. (1991). The chemistry of coumarin derivatives synthesis of 3-Alkyl-4-Hydroxycoumarins by reductive fragmentation of 3,3'-alkylidene-4,4'-dihydroxybis[coumarins]. *Helvetica Chimica Acta*, 74: 1451 – 1458.
2. Manolov, I., Maichle-Moessmer, C., Danchev, N. (2006). Synthesis, computational study and cytotoxic activity of new 4-hydroxycoumarin derivatives. *European Journal of Medicinal Chemistry,* 41 (4): 882 – 890.
3. Khan, K. M., Rahim, F., Wadood, A., Kosar, N., Taha, M., Lalani, S., Khan, S., Fakhri, M. I., Junaid, M., Rehman, W., Khan, M., Perveen, S., Sajid, M. and Choudhary, M. I. (2014). Synthesis and molecular docking studies of potent a-glucosidase inhibitors based on biscoumarin skeleton. *European Journal of Medicinal Chemistry*, 81:245 – 252.
4. Khan, K. M., Iqbal, S., Lodhi, M. A. and Maharvi, G. M. (2004). Biscoumarin: new class of urease inhibitors: Economical synthesis and activity. *Bioorganic and Medicinal Chemistry,* 12(8): 1963 – 1968.

5. Talhi, O., Schnekenburger, M., Panning, J., Diana, Pinto, G. C., Fernandes, J. A., Almeida Paz, F. A., Jacob, C., Diederich, M. and Silva, A. M. S. (2014). Bis(4-hydroxy-2H-chromen-2-one): synthesis and effects on leukemic cell lines proliferation and NF-jB regulation. *Bioorganic and Medicinal Chemistry,* 22: 3008 – 3015.
6. Qu, D., Li, J., Yang, X. H., Zhang, Z. D., Luo, X. X., Li, M. K. and Li, X. (2014). New biscoumarin derivatives: synthesis, crystal structure, theoretical study and antibacterial activity against *Staphylococcus aureus. Molecules,*19 (2): 19868 – 19879.
7. Xu, J., Ai, J., Liu, S., Peng, X., Yu, L., Geng, M. and Nan, F. (2014). Design and synthesis of 3,3'-biscoumarin-based c-Met inhibitors. *Organic and Biomolecular Chemistry,* 12: 3721 – 3734.
8. Khurana, J. M. and Kumar, S. (2009). Tetrabutylammonium bromide (TBAB): a neutral and efficient catalyst for the synthesis of biscoumarin and 3,4-dihydropyrano[*c*]chromene derivatives in water and solvent free conditions. *Tetrahedron Letters,* 50 (28): 4125 – 4127.
9. Kidwai, M., Bansal, V., Mothsra, P., Saxena, S., Somvanshi, R. K., Day, S. and Singh, T. P. (2007). Molecular iodine: a versatile catalyst for the synthesis of bis (4-hydroxycoumarin) methanes in water. *Journal Molecular Catalysis A,* 268(1-2): 76 – 81.
10. Khurana, J. M. and Kumar, S. (2010). Ionic Liquid: an efficient and recyclable medium for the synthesis of octahydroquinazolinone and biscoumarin derivatives. *Monatshefte fur Chemie,* 141(5): 561 – 564.
11. Li, W., Wang, Y., Wang, Z., Dai L. and Wang, Y. (2011). Novel SO_3H-functionalized ionic liquids based on benzimidazolium cation: efficient and recyclable catalysts for one-pot synthesis of biscoumarin derivatives. *Catalysis Letters* 141(11): 1651 – 1658.
12. Mehrabi, H. and Abusaidi, H. (2010). Synthesis of biscoumarin and 3,4-dihydropyrano[*c*]chromene derivatives catalyzed by sodium dodecyl sulfate(SDS) in neat water. *Journal Iranian Chemical Society,* 7(4): 890 – 894.
13. Pawar, B., Shinde, V. and Chaskar, A. (2013). N-dodecylbenzene sulfonic acid (DBSA) as a novel bronsted acid catalyst for the synthesis of bis(indolyl) methanes and bis(4- hydroxyl coumarin-3-yl)methanes in water. *Green Sustainability Chemistry,* 3: 56 – 60.
14. Karimian, R., Piri, F., Safari, A. A., Davarpanah, S. J. (2013). One-pot and chemoselective synthesis of bis(4-hydroxycoumarin) derivatives catalyzed by nano silica chloride. *Journal Nanostructure Chemistry,* 3: 52 – 57.
15. Tabatabaeian, K., Heidari, H., Khorshidi, A., Mamaghani, M. and Mahmoodi, N. O. (2012). Synthesis of biscoumarin derivatives by the reaction of aldehydes and geneous catalyst. *Journal Serbian Chemical Society,* 77(4): 407 – 413.
16. Siddiqui, Z. N., Forooq, F. (2011). Zn (Proline)2: a novel catalyst for the synthesis of dicoumarols. *Catalysis Science Technology,* 1: 810 – 816.
17. Hamdi, N., Puerta, M. C. and Valerga, P. (2008). Synthesis,structure,antimicrobialand antioxidant investigations of dicoumarol and related compounds. *European Journal of Medicinal Chemistry,* 43: 2541 – 2548.

Malaysian Journal of Analytical Sciences, Vol 20 No 4 (2016): 877 - 884
DOI: http://dx.doi.org/10.17576/mjas-2016-2004-23

MALAYSIAN JOURNAL OF ANALYTICAL SCIENCES
Published by The Malaysian Analytical Sciences Society
ISSN 1394 - 2506

EFFECTS OF FUEL CONCENTRATIONS, CATALYST LOADINGS AND ACTIVATION ON THE PERFORMANCE OF DIRECT FORMIC ACID FUEL CELL (DFAFC) STACK

(Kesan Kepekatan Bahan Api, Kandungan Mangkin dan Pengaktifan ke atas Prestasi Tindanan Sel Bahan Api Asid Formik Langsung (DFAFC))

Mohd Shahbudin Masdar[1, 2]*, Nurulain Ngah[1], Norraihanah Mohamed Aslam[2], Dedikarni Panuh[2], Siti Kartom Kamarudin[1,2], Wan Ramli Wan Daud[1,2]

[1]*Department of Chemical and Process Engineering, Faculty of Engineering & Built Environment*
[2]*Fuel Cell Institute*
Universiti Kebangsaan Malaysia, 43600 UKM Bangi, Selangor, Malaysia

**Corresponding author: shahbud@ukm.edu.my*

Received: 5 February 2016; Accepted: 22 April 2016

Abstract

An air-breathing stack for a direct formic acid fuel cell (DFAFC) was designed, fabricated and evaluated. The DFAFC stack consisted of six cells arranged in a hexagonal arrangement and each single cell contained a pair of stainless steel current collectors, a membrane electrode assembly (MEA) and a cathode end-plate. A fuel reservoir was located at the center which supplied formic acid supply to the anode of each cell. The effects of fuel concentration, palladium (Pd) loading at the anode and activation on DFAFC performance and long term operation were evaluated. DFAFC stack performance increased with increasing fuel concentration and a stable power up to 200 mW at 2.4 V was achieved for passive and ambient conditions at a 7 M fuel concentration. Catalyst loading had a slight effect on DFAFC performance, where 4 mg cm^{-2} Pd loading was best for 7 M fuel operation. During long-term operation, the DFAFC stack could be operated for 27 hours without adding more fuel and less than a 20 % reduction in performance during operation. MEA reactivation with deionized water technique was required for immediate recovery of stack performance.

Keywords: stack, activation, passive direct formic acid fuel cell, membrane electrode assembly

Abstrak

Tindanan pasif udara bagi sel bahan api asid formik langsung (DFAFC) direka bentuk, difabrikasi dan diuji. Tindanan DFAFC mengandungi enam sel yang dibentuk secara susunan heksagon. Setiap sel mempunyai sepasang pengumpul arus, himpunan membran elektrod (MEA) dan plat penghujung katod. Takungan bahan api ditempatkan di tengah yang mana akan membekalkan asid formik ke setiap sel. Kesan kepekatan bahan api, kandungan palladium (Pd) di anod dan pengaktifan terhadap prestasi dan jangka masa panjang DFAFC dikaji. Prestasi tindanan DFAFC meningkat dengan peningkatan kepekatan bahan api dan kuasa yang stabil sehingga 200 mW dicapai pada 2.4 V dan 7 M kepekatan bahan api dalam keadaan pasif dan persekitaran. Kandungan mangkin mempunyai kesan minimum terhadap prestasi DFAFC yang mana kandungan Pd 4 mg cm^{-2} merupakan kandungan terbaik bagi pengoperasian 7 M kepekatan asid formik. Sepanjang pengoperasian jangka masa panjang, tindanan DFAFC boleh beroperasi selama 27 jam tanpa menambah bahan api di dalam takungan dan kurang daripada 20 % pengurangan prestasi tindanan. Pengaktifan MEA menggunakan teknik nyahion air diperlukan bagi pemulihan segera prestasi tindanan DFAFC.

Kata kunci: tindanan, pengaktifan, sel bahan api asid formik langsung pasif, himpunan membran elektrod

Introduction

With respect to direct liquid fuel cells (DLFCs), a direct formic acid fuel cell (DFAFC) is a promising alternative to direct methanol fuel cell (DMFC) and direct ethanol fuel cell (DEFC) cells. The main advantages of DFAFC are a relatively high electro-catalytic oxidation rate [1, 2] and low crossover rate for the fuel [3 – 5] and has the potential to replace batteries in electronic devices [6]. Based on previous work, a Pd-based catalyst was used as the DFAFC anode due to better cell performance compared to other precious metals such as platinum (Pt). However, a disadvantage of electro-catalytic anodes is their activity decreases or they are rapidly deactivated with operation time. To address these issues, Zhu et al. reported a palladium DFAFC anode which could be recovered by applying a potential of 1.2V versus dynamic hydrogen electrode (DHE) to the anode for a few seconds [1], while Tsujiguchi et al. used a water-wash technique to reactivate the electrode [7].

Furthermore, one of the major issues for a DFAFC is the mass transport limitation of the anode electrode due to the hygroscopic characteristic of formic acid. Then, it would affect the hydrophobicity; for better gas transport, or even hydrophilicity characteristics in the electrode, specifically in diffusion layer. Therefore, the electro-structure of the anode electrode requires proper design with respect to Teflon or Nafion content as well as carbon or catalyst loading. Currently, there are a lot of studies focusing on the optimizing the MEA for the fuel cell [8 – 10]. Rice et al. discussed the constraints to formic acid mass transport to the anode side might be due to Nafion ® within the catalyst layer, Teflon on carbon cloth, or both [11]. Oedegaard et al. showed that without Teflon-loading, the membrane electrode assembly (MEA) had a maximum current density of 173 mA cm^{-2}, while at 15 wt. % and 30 wt. % Teflon-loading, 137 mA cm^{-2} and 125 mA cm^{-2} were observed, respectively [12]. Kim et al. reported that higher catalyst loading was needed at lower temperatures (i.e. 30 ^{o}C), while low catalyst loading was suitable for high-temperature operation, (i.e. 70 ^{o}C) [13]. These data indicated the anode side of the DFAFC has significant mass transfer limitations depending on the anode media diffusion properties and operating parameters such as temperature and fuel concentrations.

Review of published literature indicates researchers have focused on a single cell DFAFC either in passive, semi-passive or active modes in order to improve performance. However, little has been published on the development of a DFAFC stack [6, 14]. In reality, passive-mode DFAFCs are more attractive, since they eliminate auxiliary devices such pumps for feeding fuel or a blower to supply air, and a simplified stack configuration for a passive DFAFC is highly desirable for portable applications.

In this study, an air-breathing stack for a direct formic acid fuel cell (DFAFC) was designed, fabricated and evaluated. The effects of catalyst loading, fuel concentrations, and MEA reactivation will be addressed on the basis of stack performance.

Materials and Methods

DFAFC stack design

The DFAFC fuel cell stack consisted of six single cells, and each single fuel cell consisted of current collector plates, gaskets, membrane electrode assembly (MEA) and the end plate. Six single cells were combined to form a hexagon with the fuel reservoir located in the center of the stack, which allowed the formic acid fuel to be supplied passively to each cell (Figure 1). The dimensions of the polycarbonate stack holder, including fuel reservoir, were 143 mm x 124 mm x 30 mm stainless steel (SS, 316L), 1 mm in thickness was used as the current collector plate. Polycarbonate (5 mm thickness) was used as the end plate for each cell and silicone rubber was used as a gasket. At the top of the stack, the cover and holder were constructed from acrylic material (3 mm), and two 3.0 mm circular holes were located in the cover to release any CO_2 formed by the anode reaction. The plate had 12 small 3.1 mm holes which allowed passage of stainless steel bolts used to hold the cell components together. The overall weight of the stack was 560 g, without formic acid fuel.

MEA fabrication

A membrane electrode assembly (MEA) with an active area of 2.0 cm^2 was fabricated using the conventional brush painting technique. Commercial carbon fibre paper (E-TEK, USA) was used as a backing layer with a 2.0 mg cm^{-2} of carbon black loading serving as a diffusion layer at the anode and cathode. Pd-black and Pt-black (Johnson-

Matthey) were used as the catalyst at the anode and cathode, respectively. These catalysts were mixed with isopropyl alcohol and a Nafion solution 5 wt% (Wako Pure Chemical Industries, Ltd.) to produce catalyst ink which was used to prepare the catalyst layer for the anode and cathode electrodes. Catalyst loading was fixed at 10 mg cm^{-2} for the cathode, while loading was 6, 8 and 10 mg cm^{-2} at the anode. The MEA was assembled by sandwiching the NRE 212 electrolyte membrane (DuPont™) between the anode and the cathode and hot pressing at 135°C and 4 MPa for 3 min.

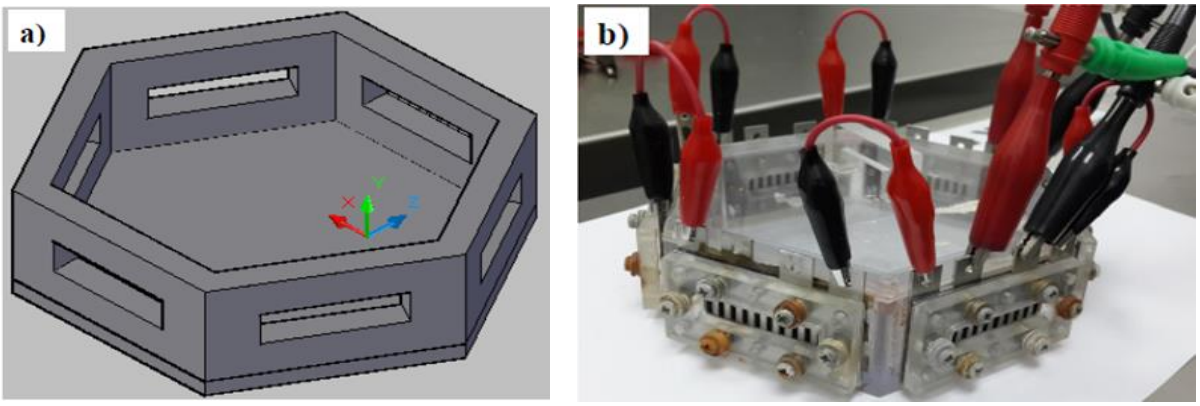


Figure 1. DFAFC fuel cell stack developed in this study: (a) stack holder and (b) fuel reservoir of the DFAFC stack during performance testing

DFAFC stack operation and long term performance

To activate the MEAs, the stack was flushed with pure hydrogen (H_2) gas at 500 ml min^{-1} for one hour (pre-treatment mode). The DFAFC stack was then operated at ambient room conditions at various fuel concentrations and Pd loadings (for the MEA). Formic acid solution (2 to 10 M, 150 mL) was added to the reservoir and the cathode exposed to ambient air. Each cell (1 – 6) was connected in series in order to measure the performance of stack during operation and power generation was conducted at a 2.4 V for 2 hours. The electrochemical performance of the cell was measured using a Potentiostat/Galvanostat WMPG1000 model (WonATech, Korea) though only one cell of cell 1 could be measured due to a limited channel to measure the electrochemical performance and will be represented the performance profile for each single cell. Long-term performance testing (over 24 hours) was also conducted and after a certain time (nearly 27 hours), the cell was refueled, with or without reactivation of the MEAs by the water-washing technique. During washing, the cell or stack was washed several times (more than three times) using deionized water to eliminate or reduce adsorption of any impurities (such as carbon monoxide, CO).

Results and Discussion

Power profiles and effect of fuel concentration on performance

Figure 2 shows the power profiles obtained over 120 min for cell 1, while Figure 3 shows the power profiles for the direct formic acid fuel cell (DFAFC) using 10 mg cm^{-2} Pd loading at the anode and formic acid concentrations varying from 2M to 10M. For all the cases in Figure 2 and Figure 3 (single cell or stack), at the beginning of cell operation, power values were unstable with largely decreasing from initial by two or three times larger than a stable power obtained before became nearly stable with time.

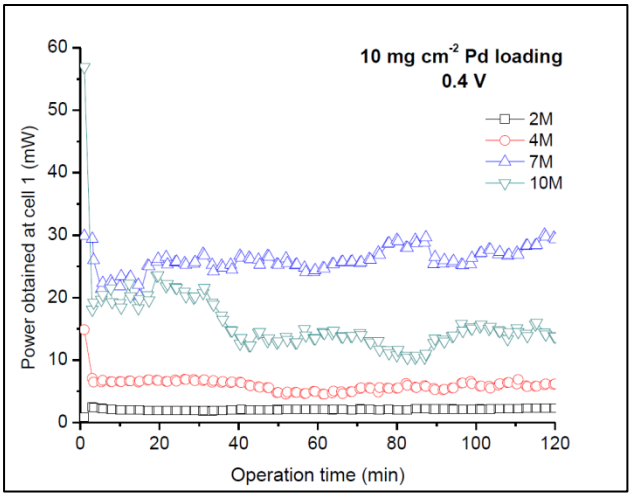


Figure 2. DFAFC power profiles for cell 1 at 10 mg cm^{-2} Pd loading at anode and different formic acid concentrations

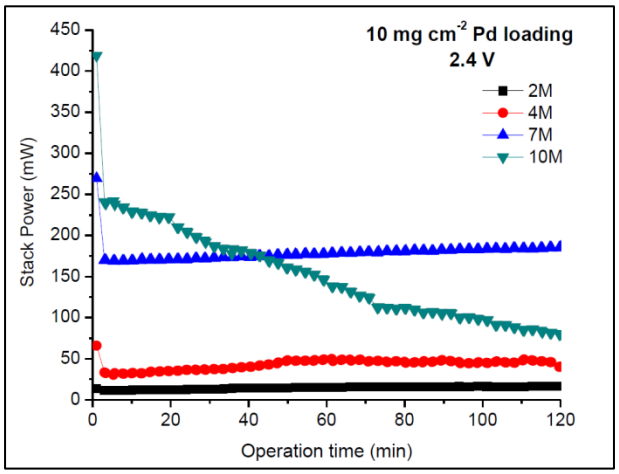


Figure 3. DFAFC power profiles for stack at 10 mg cm^{-2} Pd loading at anode and different formic acid concentrations

The unstable power could be related to the conditions of cell 1 and due to mass transport limitations at the anode or water flooding at the cathode at high concentrations (7 M and 10 M). When fueled with 10 M formic acid, the power profile for the DFAFC stack rapidly decreased over 120 min from 240.8 mW to 80.5 mW. This could be due to high formic acid crossover from the anode to the cathode which directly affected the electrochemical DFAFC reaction, and decreased stack performance.

The power values measured at 60 min (Figures 2 and 3) are summarized in Table 1. The power obtained either from cell 1 or the stack increased as the formic acid concentration in the reservoir was increased from 2 M up to 7 M giving power values of 15.03 mW, 49.36 mW and 178.06 mW at 2M, 4M and 7M formic acid, respectively. These data indicated the 7 M concentration yielded the highest output, while operation at 10 M decreased stack performance (150.85 mW). This trend of increased DFAFC performance as formic acid concentrations increased (to a certain concentration limit) was similar to previous studies [1, 4]. Increasing fuel concentration could enhance

formic acid mass transfer in terms of flux from the diffusion layer into the anode catalyst layer. For example, at a low formic acid concentration, mass transfer of formic acid was slow and directly can be influenced to no sufficient formic acid flux to maintain a stable electron movement for formic acid oxidation at anode.

Table 1. Stable power obtained at 60 min for cell 1 and stack using different formic acid concentrations

Formic Acid Concentration (M)	Stable power at 60 min operation (mW)	
	Cell 1	Stack
2	2.08	15.03
4	4.52	49.06
7	24.64	178.06
10	14.33	150.85

Moreover, the trend could have contributed to the thermal effect of the stack. In general, fuel crossover increased as the fuel concentration increased, which contributed to increasing stack temperature due to the direct cathode reaction. Therefore, the electrochemical reaction at the anode would be improved with increased stack temperature (Table 1) at 7 M formic acid. Furthermore, at high concentrations (such as 10 M), mass transfer of formic acid was not the rate-controlling power generation step, though it could be controlled by the electrode reaction due to high formic acid crossover from the anode to the cathode rather than fuel supply to the anode.

Effect of anode catalyst loading on stack performance

To ensure the relationship between fuel mass transports and stack performance, membrane electrode assemblies (MEAs) with different Pd catalyst loadings at the anode layer were tested in the DFAFC stack. Figure 4 shows the DFAFC stack power output capacity profile at different catalyst loadings when 7M formic acid was used as fuel. For all the cases shown in Figure 4, the power profiles were similar to each other and similar to the trend seen in Figure 3.

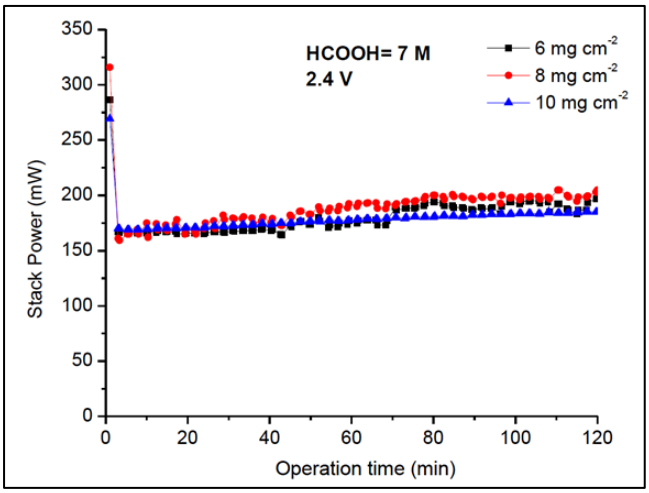


Figure 4. DFAFC power profiles at different anode catalyst loadings using a 7M concentration of formic acid

The power values obtained at 60 min are summarized in Figure 5, and additional data obtained from measurements at 2 M, 4 M and 10 M formic acid and 6, 8 and 10 mg cm^{-2} Pd loadings at the anode are presented. For all Pd loadings, the power increased linearly with increasing formic acid concentrations up to 7 M and decreased when

using 10 M, which were due to the rate controlling step (fuel mass transfer) at the anode. Meanwhile, the trend differed when Pd loading was compared to operation at different fuel concentrations. For an example, at 6 mg cm^{-2} Pd loading, the power obtained over during stable 60 min was always lower or similar to that 8 and 10 mg cm^{-2}, respectively.

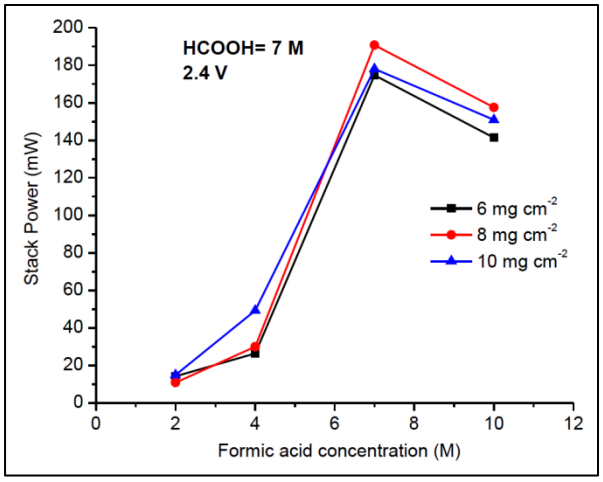


Figure 5. Stable power for the DFAFC stack at 1 h operation at various anode catalyst loadings using different concentrations of formic acid

For the power obtained at low concentrations (2 M and 4 M), high Pd loading (10 mg cm^{-2}) was dominant, while 8 mg cm^{-2} was dominant at 7 M and 10 M formic acid concentrations. These profiles could be related to the limitations in proton transfer through the electrolyte membrane. Kim et al. also linked the effect of catalyst layer thickness to proton transport through the Nafion membrane [13]. In this study, high catalyst loading would have resulted in increasing the thickness of the catalyst layer, and protons would need to be transported a greater distance (compared to the shorter distance at a low catalyst loading), which directly affected power generation. At this stage, design and optimization of the Nafion content of the catalyst layer at the anode could be important for proton transport. These results indicated the essential role of proper catalyst loading, as well as the importance of optimizing anode electrode fabrication, to enhancing anode mass transfer limitations.

Long term operation with and without reactivation

To explore the long-term operation of a DFAFC stack and the effect of reactivation by the water-washing technique, the stack was operated in two modes. Figure 6 shows the long-term performance testing for a DFAFC stack using 7 M formic acid with/without reactivation of the MEA with deionized water. In the first stage, the stack was operated nearly 27 hours after pre-treatment of MEAs (using pure H_2), while in second stage, fresh fuel (7M) was added to the fuel reservoir after the reactivation (or not) of MEA.

During the first stage (first 27 hours of operation) (Figure 6), stack power generation was similar and these data were good for comparison between first and second stages regions. The data showed that decreasing stack power over time (during the first 27 hours) was due to dilution of the formic acid fuel (i.e. fuel consumption for anode reaction). By focusing on the first stage region, the power produced by the DFAFC stack was nearly stable over the 27 hours of operation and the calculated reduction in performance was 20 %. These data suggested the DFAFC stack evaluated in this study had good stability for over a one-day period in a free-air breathing environment and could be used to power very low power electronic devices.

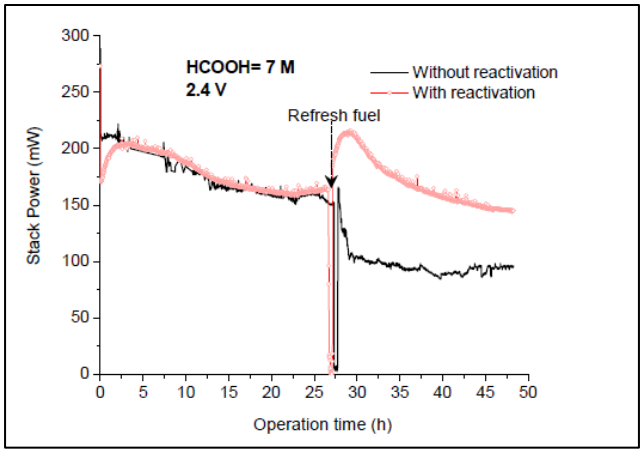


Figure 6. Long-term performance testing of the DFAFC stack using a 7 M concentration of formic acid, with and without membrane electrode assembly (MEA) reactivation with deionized water

In the second stage, when the MEAs were reactivated, the profiles and the magnitude of power produced were similar to the first stage. Without reactivation, the power increased slightly within five minutes of operation before significantly dropping to 80 mW and becoming stable, which could be due to deactivation of the Pd catalyst at the anode. Based on a literature review, deactivation of the Pd catalyst is due to adsorbed intermediates which form during the oxidation of formic acid at the anode (especially CO species) [3, 7]. Using a simple water-washing technique for MEA reactivation could eliminate or remove the poisoning species present at the anode catalyst layer. Therefore, MEA reactivation was an important step for DFAFC to recover their performance.

Conclusion

An air-breathing DFAFC stack with six cells was developed and evaluated in this study. The effect of formic acid concentration was investigated and 7 M formic acid yielded the best performance. The stable power achieved by the DFAFC stack was 200 mW and 2.4 V (16.7 mW cm^{-2}) using the optimum concentration. Catalyst loading indicated optimization of electrode fabrication was important to power generation. Proper catalyst loading (8 mg cm^{-2}) was achieved when the stack was operated at the optimum concentration (7 M) of formic acid. Furthermore, MEA reactivation was needed for long term operation to recover the electro-activity of the catalyst layer, while the performance and stability of DFAFC could be maintained by refueling with formic acid, and a high energy density could be achieved.

Acknowledgement

A part of this study was supported by FRGS/1/2013/TK 07/UKM/02/1 from Ministry of Education, Malaysia and GUP-2014-069, DLP-2013-026 from Universiti Kebangsaan Malaysia.

References

1. Zhu, Y., Khan, Z. and Masel, R. I. (2005). The behavior of palladium catalysts in direct formic acid fuel cells. *Journal of Power Sources*, 139: 15 – 20.
2. Cai, W., Liang, L., Zhang, Y., Xing, W. and Liu, C. (2013). Real contribution of formic acid in direct formic acid fuel cell: Investigation of origin and guiding for micro structure design. *International Journal of Hydrogen Energy*, 38: 212 – 218.
3. Baik, S. M., Han, J., Kim, J. and Kwon, Y. (2011). Effect of deactivation and reactivation of palladium anode catalyst on performance of direct formic acid fuel cell (DFAFC). *International Journal of Hydrogen Energy*, 36: 14719 – 14724.
4. Zhu, Y., Ha, S.Y. and Masel, R. I. (2004). High power density direct formic acid fuel cells. *Journal of Power Sources*, 130: 8 – 14.

5. Aslam, N. M., Masdar, M. S. and Kamarudin, S. K. (2013). Effect of different types of microporous layer toward the performance of direct formic acid fuel cell. *Jurnal Teknologi (Sciences & Engineering)*, 65: 41 – 45.
6. Cai, W., Yan, L., Li, C., Liang, L., Xing, W. and Liu C. (2012). Development of a 30 W class direct formic acid fuel cell stack with high stability and durability. *International Journal of Hydrogen Energy, 3*7: 3425 – 3432.
7. Tsujiguchi, T., Hirano, S., Iwakami, T. and Nakagawa, N. (2013). The performance degradation of a passive direct formic acid fuel cell and its improvement by a hydrophobic filter. *Journal of Power Sources,* 223: 42 – 49.
8. Ahmad, M. M., Kamarudin, S. K. and Daud, W. R. W. (2010). Design of and optimal micro direct methanol fuel cell for portable applications. *Sains Malaysiana,* 39(3): 467 – 472.
9. Hashim, N., Kamarudin, S. K. and Daud, W. R.W. (2010). Design and development of micro direct methanol fuel cell. *Sains Malaysiana,* 39(6):1015 – 1023.
10. Jaafar, J, Ismail, A. F., Matsuura, T. and Mohd Nordin, M. N. A. (2013). Stability of SPEEK-triaminopyrimide polymer electrolyte membrane for direct methanol fuel cell application. *Sains Malaysiana,* 42(11):1671 – 1677.
11. Rice, C., Ha, S., Masel, R. I., Waszczuk, P., Wieckowski, A. and Barnard, T. (2002). Direct formic acid fuel cells. *Journal of Power Sources,* 111: 83 – 89.
12. Oedegaard, A., Hebling, C., Schmitz, A., Møller-Holst, S. and Tunold, R. (2004). Influence of diffusion layer properties on low temperature DMFC. *Journal of Power Sources,* 127: 187 – 196.
13. Kim, J. S., Yu, J. K., Lee, H. S., Kim, J. Y., Kim, Y. C., Han, J. H., Oh, I. H. and Rhee, Y. W. (2005). Effect of temperature, oxidant and catalyst loading on the performance of direct formic acid fuel cell. *Korean Journal of Chem Engineering*, 22: 661 – 665.
14. Ping, H., Yiliang, Z., Shijun, L., Jianhuang, Z., Xueyi, L. and Wei, C. (2011). A 4-cell miniature direct formic acid fuel cell stack with independent fuel reservoir: Design and performance investigation. *Journal of Power So urces*, 196(14): 5913 – 5917.

Malaysian Journal of Analytical Sciences, Vol 20 No 4 (2016): 885 - 891
DOI: http://dx.doi.org/10.17576/mjas-2016-2004-24

MALAYSIAN JOURNAL OF ANALYTICAL SCIENCES
Published by The Malaysian Analytical Sciences Society
ISSN 1394 - 2506

SYNTHESIS AND CHARACTERISATION OF CHITOSAN-CELLULOSE BIOCOMPOSITE MEMBRANE FOR FUEL CELL APPLICATIONS

(Sintesis dan Pencirian Membran Biokomposit Kitosan-Selulosa untuk Aplikasi Sel Bahan Api)

Nur Fatin Ab. Rahman[1], Kee Shyuan Loh[1]*, Abu Bakar Mohamad[1,2], Abdul Amir Hassan Kadhum[1,2], Kean Long Lim[1]

[1]*Fuel Cell Institute*
[2]*Department of Chemical and Process Engineering*
Universiti Kebangsaan Malaysia, 43600 UKM Bangi, Selangor, Malaysia

**Corresponding author: ksloh@ukm.edu.my*

Received: 5 February 2016; Accepted: 22 April 2016

Abstract

In this work, proton exchange membranes (PEMs) based on chitosan (CS) and cellulose (CL) have been prepared using a solution-casting technique with sulfosuccinic acid (SSA) as an ionic cross linker. The characteristics of these CS-CL biocomposite membranes were studied using scanning electron microscopy (SEM), Fourier transform infrared spectroscopy (FTIR), electrochemical impedance spectroscopy (EIS) in addition to the measurement of the water uptake rate (WUR) and the ion exchange capacity (IEC). The results indicate that the amount of SSA used in this study played a significant role in the proton conduction of the membrane. The proton conductivity of a cross-linked CS-CL membrane was on the order of 10^{-5} S cm^{-1}, which is greater than the proton conductivity of a pure CS membrane.

Keywords: proton exchange membranes, chitosan, cellulose, biocomposite, membrane

Abstrak

Dalam kajian ini, membran penukaran proton (PEM) berasaskan kitosan (CS) dan selulosa (CL) telah disediakan dengan menggunakan teknik tuangan larutan bersama dengan asid sulfosusinik (SSA) yang berfungsi sebagai pemaut silang ion. Sifat membran biokomposit CS-CL ini dikaji menggunakan mikroskopik pengimbas elektron (SEM), spektroskopi inframerah transformasi Fourier (FTIR), spektrometer elektrokimia impedans (EIS) sebagai tambahan kepada pengukuran kadar penyerapan air (WUR) dan kapasiti penukaran ion (IEC). Keputusan menunjukkan bahawa jumlah SSA digunakan dalam kajian ini memainkan peranan penting dalam pengangkutan proton di dalam membran. Kekonduksian proton untuk CS-CL bertaut silang membran yang diperoleh adalah di dalam lingkungan 10^{-5} S cm^{-1}, iaitu lebih tinggi berbanding dengan kekonduksian proton membran CS tulen.

Kata kunci: membran penukaran proton, kitosan, selulosa, biokomposit, membran

Introduction

Recently, fuel cells have been recognised as a prime candidate for new energy resources and have been extensively studied as an alternative to limited fossil fuel resources. Fuel cells have received attention, as they are efficient, clean and eco-friendly power sources [1, 2]. Extensive research has been undertaken to develop and prepare a new membrane to prevent a deficiency in currently used perfluorinated membranes (Nafion). This effort includes an expanded search of natural polymers that could produce biopolymer and biocomposite membranes with valuable properties. The use of natural polymer-based membranes became a focus when environmental concerns motivated

the use of renewable resources for producing clean energy and sustainable consumption and production with the goal to maintain or even improve quality of life [3, 4].

Among all natural polymers, chitosan (CS) and cellulose (CL) are the most important and abundantly available renewable resources on the earth. CS and CL possess many attractive properties such as biodegradable, biocompatible and non-toxic [5, 6]. Both CS and CL have similar molecular structure except for the group attached to the C2 atom. In this configuration CS has a primary amine ($-NH_2$) group, whereas CL has a hydroxyl (-OH) group that can be modify [7].

In this study, CS-CL biocomposites with various amount of sulfosuccinic acid (SSA) were prepared using the casting method to improve their properties as well as the conductivity of the membrane. The main purpose of this research was to develop the biopolymer material for electrolyte membrane.

Materials and Methods

The following chemicals were reagent grade and obtained from Sigma-Aldrich: chitosan (CS) powder (low molecular weight), α-cellulose (CL) powder, acetic acid (glacial 100 % anhydrous for analysis), dimethyl sulfoxide (DMSO) ($H_2O \leq 0.005\%$), and sulfosuccinic acid (SSA) (70 wt. % in H_2O). Deionised water was used during the preparation of the acetic acid solution.

Pre-weighed CS powder was added to 1.0 wt. % aqueous acetic acid solution and was stirred vigorously to form a 1.0 wt. % CS solution. CL (0.18 g) was dissolved in the DMSO using an ultrasonic stirrer. Both the CS and CL solutions were mix together at a weight ratio of 1: 0.18 and were stirred vigorously using a magnetic stirrer for several hours at room temperature. The CS-CL solutions were mixed with various amounts of SSA (0.05 and 0.10 M SSA, labelled as CA05 and CA10, respectively. The mixtures were then continuously stirred and were poured into a petri dish and left to dry at room temperature for 48 hours to form a thin membrane layer. Finally, the biocomposite membranes were dried in an oven at 70 °C for several hours to remove the solvents. The membrane thickness was in the range of 25 – 26 µm.

The surface morphology of the CS-CL biocomposite membranes was characterised using SEM with Carl Zeiss EVO MA10 model at a voltage of 15 kV. The membranes were freeze-fractured with liquid nitrogen to expose the edge of the membrane and sputter coated with a thin layer of gold before SEM analysis. The infrared spectra of the membranes were recorded with a model Nicolet 6700 Thermo FTIR spectrophotometer in the wavenumber range of 400 to 4000 cm^{-1} at a resolution of 4 cm^{-1}.

The water uptake rate of the CS-CL membranes was measured by immersing the membrane samples into deionised water at various temperatures (25, 50, 70, and 90 °C) for 2 hours. Then, the membranes were bolted dry with tissue paper and were immediately weighted to determine the initial wet weight. The samples were then maintained in an oven at 120 °C for 2 hours. The procedure was repeated three times until satisfactory reproducibility was obtained. The water uptake values were calculated according to Equation 1:

$$\text{Water uptake } (\%) = \frac{(\text{Wwet} - \text{Wdry})}{\text{Wdry}} \times 100 \quad (1)$$

where W_{wet} and W_{dry} are the wet weight and the dry weight of the membrane, respectively [8].

The IEC values of the membrane sample were determined using a titration method. The sample were immersed in a 1.0 M NaCl solution for 2 hours followed by titration with a 0.01 M NaOH solution using phenolphthalein as an indicator [9]. The IEC values were calculated from the titration data using Equation 2:

$$\text{IEC } (\text{mmol g}^{-1}) = \frac{(\text{VNaOH} \times \text{MNaOH})}{\text{Wdry}} \times 10 \quad (2)$$

where V_{NaOH} and M_{NaOH} are the consumed volume (mL) and molar concentration of the NaOH solution, respectively. W_{dry} is the weight of the dry membrane.

The proton conductivity of the CS-CL membranes was measured using electrochemical impedance spectroscopy between 10^{-1} to 10^{5} Hz using a Metrohm Autolab potentiostat (PGSTAT128N) equipped with a FRA2 module. The type of cell configuration used in this test is two-electrode AV impedance method in ambient air with relative humidity. The proton conductivity, σ, was calculated using the Equation 3:

$$\sigma = \frac{L}{R\ X\ A} \tag{3}$$

where σ (S cm^{-1}) is the membrane conductivity, L (cm) is the thickness of the membrane inside the conductivity cell, A (cm^2) is the geometric area of the membrane, and R (Ω) is the bulk resistance calculated from the high-frequency intercept on the real axis of the complex impedance plot [10].

Results and Discussion

The morphology of the CS-CL membranes is shown in Figure 1 and represents the cross-sections and the surface of the biocomposite membranes. The cross-sectional micrographs (a) and (b) display the two-phase separation. The CL fibres were visible but well distributed at the bottom of the membranes. These observations provide evidence that the CL fibres were deposited at the bottom layer of the dried membrane after the homogenised biocomposite solution was cast into the petri dish and allowed to dry completely. The phase separation of CS and CL was apparent for all blends indicating that a non-homogenous membrane was obtained. Both biopolymer membranes were brittle. Where, the CS-Cl blend in this study has demonstrated poor miscibility between CS and CL in the samples. Therefore, in this study, CL acted as the filler in the CS membrane used to improve the mechanical strength of the biocomposite membrane. The surface structure of the polymeric blend membranes has a rough structure compared with the morphology of the CS blend membranes reported by Khan et al. [11]. According to his report, CL appeared as shiny white dots in the CS, which could correspond to transverse sections of the CL.

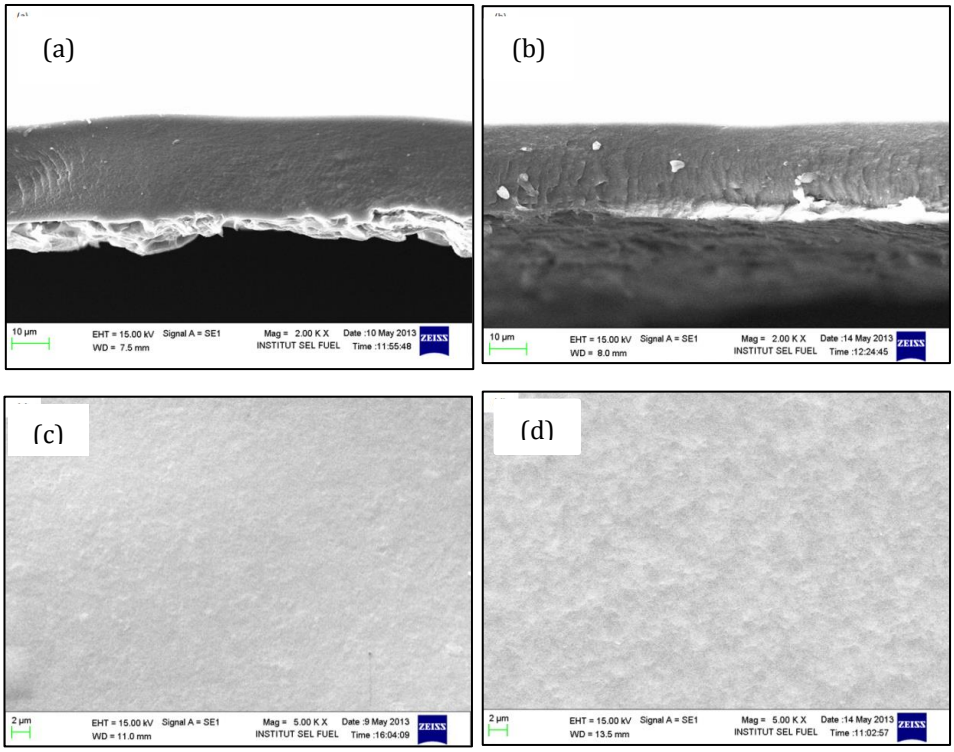


Figure 1. SEM images of the cross section (a) CA05, (b) CA10, and the surface of (c) CA05, (d) CA10 biocomposite membranes.

The FTIR spectrum (Figure 2) of CS, CL and the biocomposite CS-CL membranes with different amount of SSA were compared to investigate the interconnected structural network formed from linking the functional groups in the membranes. For the CS and CL spectrums, which act as the "control"; there are peaks similar to peaks reported by different authors in the literature [12 – 14]. The CS spectrum showed the presence of absorption bands at 3355, 2874, 1650, 1587, 1429, 1376, 1150 and 1069 cm^{-1}. The band observed at 3355 cm^{-1} is due to O-H stretching, which overlaps with the NH- stretching in the same region [11, 14]. The peaks at 2874 cm^{-1} correspond to C-H stretching. The absorption bands at 1429 cm^{-1} and 1376 cm^{-1} could be assigned to the C-H and O-H vibration and CH_3-bending vibrations. The characteristic bands of CS and CL were observed in the spectra of the biocomposite membranes. The spectrum of both the CL and CS showed similar bands with the exception of the absorption bands at 1650 and 1587 cm^{-1}, which correspond to characteristic of –C=O stretching (amide I) and –NH bending (amide II), respectively, as shown in the structure of CS.

The same absorption bands can also be seen from the CA05 and CA10 membranes with slightly significant differences at 1650 to 1646 cm^{-1} and at 1585 to 1579 cm^{-1}. The basic characteristics of CS were also shown in the CA05 and CA10 membranes, which had bands at 1154 cm^{-1} and 1155 cm^{-1} due to the anti-symmetric stretching of the C-O-C bridge. The bands at 1022 and 1029 cm^{-1} were the skeletal vibrations involving C-O stretching. Indeed, a band observed in that region is assigned to the amide group of the CS polysaccharide structure [15]. From the CA05 and CA10 spectra, a new band was being observed in the range from 1350 to 1000 cm^{-1}, which represents C-N interactions. Moreover, the absorption bands near 1250 cm^{-1} indicate the presence of the sulfonic acid group caused by the introduction of SSA. Therefore, from the FTIR spectrum of the samples, the cross linking reaction occurs primarily between the amine group in the chitosan and the carboxylic group in the SSA [16]. There was likely no interaction occurs between CS and CL functional group. These interactions are more towards a physical interaction rather than chemical interactions.

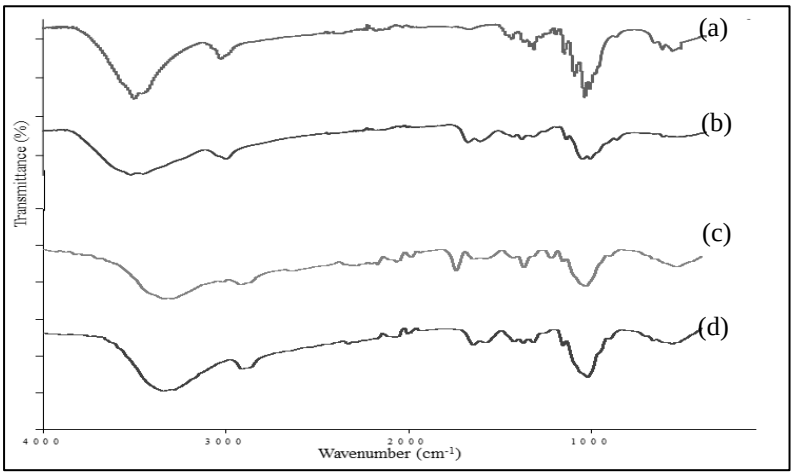


Figure 2. The IR spectra of (a) cellulose (b) chitosan (c) CA05 and (d) CA10.

Table 1 shows the results of water uptake for Nafion 212, CA05 and CA10 membranes. When considering the water uptake properties, the transport of protons in the sulfonated polymer membranes is greatly affected by the presence of water molecules [17]. The membrane water uptake has been determined at four different temperatures. Table 1 shows the trend that the water uptake of the biocomposite membranes increased with an increased temperature, which is similar to the Nafion membrane. As a result, water uptake of the cross-linked CS-CL was found to be multiple times greater than the Nafion 212 in the temperature range between 25 and 90 °C. The CA05 and CA10 membranes possessed greater hydrophilic characteristic compared with the Nafion membrane due to the presence of three polar functional groups. CS is highly capable of forming a hydrogen bond with water and trapping water in its

structure [8]. This result is in contrast with the Nafion membranes, which have both hydrophilic and hydrophobic zones and contain polar hydrophobic (C-F bonds) and polar functional groups (C-O-C linkages). The concentration of the cross-linking agent also influenced the water uptake capacity of the membranes. The CS-CL membrane that contained 0.05 M SSA exhibited greater water uptake than the membranes that contained 0.10 M SSA. With an increase in the concentration of SSA, the membranes became more rigid and structurally compact, and this may have caused the free volume of water molecules retain in the structure to decrease.

Table 1. The water uptake rate of membranes in various temperatures

Temperature (°C)	Water uptake (%)		
	Nafion 212	CA05	CA10
25	9.0	64	34
50	11.8	71	54
70	16.0	87	61
90	16.3	104	78

Table 2 shows the IEC values of Nafion and the CS-CL biocomposite membranes. The IEC value is the opposite of the water uptake results. The IEC values for Nafion 212 and CA10 membranes decreased due to an increase in the condition temperature. Rhim et al. has reported that at low operating temperature resulted in more cation exchangeable sites due to the unreacted carboxylic acid groups in the SSA [16]. Conversely, the CA05 membrane, IEC increased with an increase in the temperature. This result could be attributed to the increment of charge carriers and closely related to the rigidity of the molecule structure. An increase in the IEC values (interpreted as an increase in the number of sulfonic acid groups within the polymer matrix) will not necessarily increase the water uptake values. Therefore, the amount of cross linker added to a polymer electrolyte membrane is not a dominant factor of the increase in the proton conductivity [16]. It can be concluded that the degree of cross linking in the membranes affected significantly their proton conductivities.

The proton conductivity measurements were carried out to study the effect of cross-linking and the temperature of the operating system on the electrical properties of the CS-CL membranes. The conductivity of the CS-CL membranes has shown in Table 3. As seen in Table 2 and Table 3, the conductivity of the membranes followed a similar trend with the IEC, as it is believed that increasing the amount of SSA in the membrane could lead to significant improvement in the proton conductivity of the membrane due to the increase in proton carriers by the sulfonic acid group ($-SO_3^-H^+$). Even though the conductivity of the CS-CL membranes in this study has a lower value than other membranes, the conductivity is still an improvement compared with a pure CS membrane. There is potential to obtain greater proton conductivity through modification of the CS structure.

Table 2 The ion exchange capacity of the membranes in various temperatures.

Temperature (°C)	Ion exchange capacity (mmol/g)		
	Nafion 212	CA05	CA10
25	1.57	0.49	2.00
50	1.47	0.69	2.04
70	1.18	0.74	1.25
90	1.41	1.22	1.03

Table 3. Ionic conductivity of the membranes at room temperature condition

Membranes	**Proton conductivity (S cm^{-1})**
Nafion 212	5.96×10^{-3}
CA05	2.30×10^{-5}
CA10	4.73×10^{-5}

Conclusion

CS-CL biocomposite polymers cross-linked with various amount of SSA have been prepared and evaluated as a potential polymer electrolyte membrane for fuel cell applications. CL has been shown to be filler that strenghthens biocomposite membrane. Further study will be focusing on conductivity using different types of ionic crosslinker agent. Specifically, SSA has improved the proton conductivity of the CS membrane from ~10^{-9} to ~10^{-5} by introducing a cross linking agent and an ionic carrier in the biocomposite membrane. The proton conductivity was found to be dependent on the concentration of the ionic cross linker.

Acknowledgement

The authors gratefully acknowledge the financial support provided for this work by the Universiti Kebangsaan Malaysia through the Research Universiti Grants GUP-2011-374, DLP-2013-038, and DIP-2014-002.

References

1. Higashihara, T. Matsumoto, K. and Ueda, M. (2009). Sulfonated aromatic hydrocarbon polymers as proton exchange membranes for fuel cells. *Polymer*, 50: 5341 – 5357.
2. Lee, D. C., Yang, H. N., Park, S. H. and Kim, W. J. (2014). Nafion/graphene oxide composite membranes for low humidifying polymer electrolyte membrane fuel cell. *Journal of Membrane Science*, 452: 20 – 28.
3. Vilaplana, F., Strömberg, E. and Karlsson, S. (2010). Environmental and resource aspects of sustainable biocomposite. *Polymer of Degradation and Stability*, 95: 2147 – 2161.
4. Pereda, M., Amica, G. and Marcovich, N. E. (2012). Development and characterization of edible chitosan/olive oil emulsion films. *Carbohydrate Polymers*, 87: 1318 – 1325.
5. Kaco, H., Zakaria, S., Razali, N. F., Chia, C. H., Zhang, L. and Jani, S. M. (2014). Properties of cellulose hydrogel from Kenaf core prepared via pre-cooled dissolving method. *Sains Malaysiana*, 43(8): 1221 – 1229.
6. Wirach Taweepreda. (2014). Dynamic mechanical and dielectric properties of modified surface chitosan/natural rubber latex. *Sains Malaysiana*, 43(2): 241 – 245.
7. Zakaria, S., Chia, C. H., Ahmad, W. H. W., Kaco, H., Chook, S. W. and Chan, C. H. (2015). Mechanical and antibacterial properties of paper coated with Chitosan. *Sains Malaysiana*, 44(6): 905 – 911.
8. Ma, J., Sahai, Y. and Buchheit, R. G. (2012). Evaluation of multivalent phosphate cross-linked chitosan biopolymer membrane for direct borohydride fuel cells. *Journal of Power Sources*, 202: 18-27.
9. Thiam, H. S., Daud, W. R. W., Kamarudin, S. K., Mohamad, A. B., Kadhum, A. A. H., Loh, K. S. and Majlan, E. H. (2012). Nafion/Pd-SiO_2 nanofiber composite membranes for direct methanol fuel cell applications. *International Journal of Hydrogen Energy*, 38: 9474 – 9483.
10. Ma, J., Choudhury, N. A., Sahai, Y. & Buchheit, R. (2011). A high performance direct borohydride fuel cell employing cross-linked chitosan membrane. *Journal of Power Sources*, 196: 8257 – 8264.
11. Khan, A., Khan, R. A., Salmieri, S., Tien, C. L., Riedl, B., Bouchard, J., Chauve, G., Tan, V., Kamal, M .R. and Lacroix, M. (2012). Mechanical and barrier properties of nanocrystalline cellulose reinforced chitosan based nanocomposite films. *Carbohydrate Polymers*, 90: 1601 – 1608.
12. Pavia, D. L., Lampman, G. M. and Kriz, G. S. (2001). Introduction to spectroscopy: A Guide for students of organic chemistry. United States: Thomson Learning, Inc.
13. Yin, J., Luo, K., Chen, X. and Khutoryanskiy, V. V. (2006). Miscibility studies of the blends of chitosan with some cellulose ethers. *Carbohydrate Polymers*, 63: 238 – 244.
14. Stefanescu, C., Daly, W. H. and Negulescu, I. I. (2012). Biocomposite films prepared form ionic liquid solutions of chitosan and cellulose. *Carbohydrate Polymers*, 87: 435 – 443.

15. Ávila, A., Bierbrauer, K., Pucci, G., López-González, M. and Strumia, M. (2012). Study of optimization of the synthesis and properties of biocomposite films based on grafted chitosan. *Journal of Food Engineering,* 109: 752 – 761.
16. Rhim, J., Park, H., Lee, C., Jun, J., Kim, D. and Lee, Y. (2004). Crosslinked poly(vinyl alcohol) membranes containing sulfonic acid group: proton and methanol transport through membranes. *Journal of Membrane Science,* 238: 143 – 151.
17. Ahmad, H., Kamarudin, S. K., Hasran, U. A. and Daud, W. R. W. (2010). Overview of hybrid membranes for direct methanol fuel cell applications. *International Journal of Hydrogen Energy,* 35: 2160 – 2175.

Malaysian Journal of Analytical Sciences, Vol 20 No 4 (2016): 892 - 900
DOI: http://dx.doi.org/10.17576/mjas-2016-2004-25

MALAYSIAN JOURNAL OF ANALYTICAL SCIENCES
Published by The Malaysian Analytical Sciences Society
ISSN 1394 - 2506

TiO_2 DOPED WITH Fe_2O_3 FOR PHOTOELECTROCHEMICAL WATER SPLITTING ELECTRODE: EXPERIMENTAL AND DENSITY FUNCTIONAL THEORY STUDY

(TiO_2 Di Dop Bersama Fe_2O_3 untuk Elektrod Pembelahan Molekul Air Secara Fotoelektrokimia: Eksperimen dan Kajian Teori Fungsi Ketumpatan)

Khuzaimah Arifin[1*], Hasmida Abdul Kadir[1,3], Lorna Jeffery Minggu[1], Wan Ramli Wan Daud[1,2], Mohammad B. Kassim[1,3]

[1]*Fuel Cell Institute*
[2]*Department of Chemical and Process Engineering*
[3]*School of Chemical Sciences and Food Technology, Faculty of Science and Technology*
Universiti Kebangsaan Malaysia, 43600 UKM Bangi, Selangor, Malaysia

**Corresponding author: khuzaim@ukm.edu.my*

Received: 5 February 2016; Accepted: 22 April 2016

Abstract

Various modifications of the titanium dioxide thin films have been done in fulfilling the photoelectrode requirements for photoelectrochemical water splitting reaction. In this study, surface passivation of TiO_2 by hematite-Fe_2O_3 was reported. Electrodeposition technique was used to deposit the Fe_2O_3 onto the TiO_2/FTO film with variation of time. X-ray diffraction (XRD), Scanning Electron Microscope (SEM) and UV-Vis spectroscopic analyses were used to characterize the electrode. Plane-wave-based pseudopotential density functional theory (DFT) calculations were used to analyze the electronic structure and charge potential at the surface of the electrode. The photocurrent measurement showed that current density of TiO_2/Fe_2O_3 electrode was higher than the TiO_2/FTO under the same illumination intensity of 100 $mWcm^{-2}$. The highest current density was produced by 5 minutes electrodeposition of Fe_2O_3, which also shifted the absorption to visible region at the threshold wavelength of 518 nm.

Keywords : titanium dioxide, iron(III) oxide, passivation layer, band gap

Abstrak

Pelbagai pengubahsuaian titanium dioksida filem nipis telah dilakukan untuk memenuhi keperluan fotoelektrod bagi tindak balas fotoelektrokimia pembelahan molekul air. Dalam kajian ini, dilaporkan pempasifan permukaan TiO_2 dengan bijih besi-Fe_2O_3. Teknik pengelektroenapan digunakan untuk mendepositkan Fe_2O_3 ke TiO_2/FTO filem dengan pelbagai masa pengelektroenapan. Analisis XRD, SEM dan UV-Vis spektroskopi telah digunakan untuk mencirikan elektrod. pengiraan teori fungsi ketumpatan (DFT) berasaskan planar gelombang pseudopotential telah digunakan untuk menganalisis struktur elektronik dan potensi caj di permukaan elektrod. Pengukuran arusfoto menunjukkan bahawa ketumpatan arus TiO_2/Fe_2O_3 elektrod adalah lebih tinggi daripada TiO_2/FTO bawah keamatan pencahayaan yang sama, 100 $mWcm^{-2}$. Ketumpatan semasa tertinggi dihasilkan oleh 5 minit pengelektroenapan Fe_2O_3, yang mana penyerapan beralih ke kawasan yang boleh dilihat pada panjang gelombang ambang 518 nm.

Kata kunci: titanium dioksida, ferum (III) oksida, lapisan pasif, sela jalur

Introduction

Hydrogen has been considered as an alternative fuel to replace fossil fuels for many years. It is used in fuel cell technology to generate electricity where water molecule is the only byproduct [1]. Hydrogen is plentiful in the universe, obtained via extraction off water molecule, an element, which is abundant and cheap; however requires a lot of energy to extract it. One of the promising method to produce hydrogen from water molecule is through photoelectrochemical (PEC) reaction that utilizes sunlight energy [2]. The system uses inexpensive metal oxide photoelectrode without the expense of electrolyzer, which leads to a further reduction in the cost of hydrogen delivery. The concept was first demonstrated by Honda and Fujishima in 1972 and since then, its science has influenced many followers [3].

PEC cell is a type of an electrolytic cell, where the sunlight is absorbed by the photoelectrode to generate current that is used to drive an electrochemical reaction. Generally, photoelectrode is an n or a p-type semiconductor electrode, which flows the electrons generated by the light induced chemical reactions initiated at its surface. Several photoelectrode requirements that must be fulfilled for direct PEC water splitting to occur are listed in Table 1. The band gap of photoelectrode semiconductor must be at least 1.5 eV, higher than the effective redox potential of water, which is about 1.23 – 1.4 eV [4,5].

Table 1. Main PEC water-splitting requirements [4]

Condition	**Requirement**
PEC water-splitting	$H_2O_{(liquid)} + 2h\upsilon \rightarrow ½O_{2(gas)} + H_{2(gas)}$
Minimum potential	$E°_{H_2O}(25\ °C)_{min} = 1.229$ eV
Practical potential (+overpotential & losses)	$E°_{H_2O}(25\ °C)_{prac} = 1.6 - 2.0$ eV $E_{bandgap} > E°_{H_2O}$
Utilization of sunlight	UV > hυ (Vis) > IR $h\upsilon \geq E_{bandgap}$
Bandedges	$C_{band\ edge} < E°_{H2/H^+}$ $V_{band\ edge} > E°_{O2/H2O}$

Concurrently, the semiconductor's conduction band (CB) must be higher than the reduction potential of water, whle its valence level (VB) must be lower than the oxidation potential of water. The focus of recent PEC research are mostly on developing photoelectrode materials that meet with the criteria besides high efficiencies, low-cost, long-term usages and non-photocorrosion of materials [3].

Titanium dioxide (TiO_2) is reported as the most promising photoelectrode [6]. This material has several advantages for photochemistry and photo-electrochemistry including low cost, widely available, non-photocorrosion and nontoxic. However, TiO_2 photocatalytic has large band gaps that limit its absorption of solar radiation to just 4 %, which is of UV spectrum. Numerous attempts have been made to expand the TiO_2 photoanode absorption spectrum to longer wavelengths: through doping TiO_2 with various metals and anions, use a dye-sensitizer molecule [7] and also morphology modifications of nano-scaled TiO_2, namely spheres, wires, rods and tubes [8, 9]. Significant experimental results are also observed by a surface passivation layer of TiO_2 with various metal oxide [10, 11]. Surface passivation layers electrode is a type of junction electrode, which comprises two or more layers of semiconductors. The surface passivation layers provide an alternative low energy route for charge transfer through catalytically active sites. In addition, surface passivation layers can reduce corrosion and improve chemical or photochemical stability of photoelectrode when immersed in an electrolyte [3,12].

In designing the passivation layer, it is important to consider the band positions of the metal oxides (Figure 1). For wide band gap semiconductor, TiO_2 should be combined with a narrow band gap metal oxide: WO_3 [13], Cu_2O

[14], CdTe [15] and CdS [16], that can absorb visible light. Here, investigation TiO_2 passivated by hematite-Fe_2O_3 is reported. Fe_2O_3 is one of prospective material for PEC. It is a photoactive material and absorbs visible light, however is poor in conductivity and has a CB energy below the reduction potential of hydrogen ion [11].

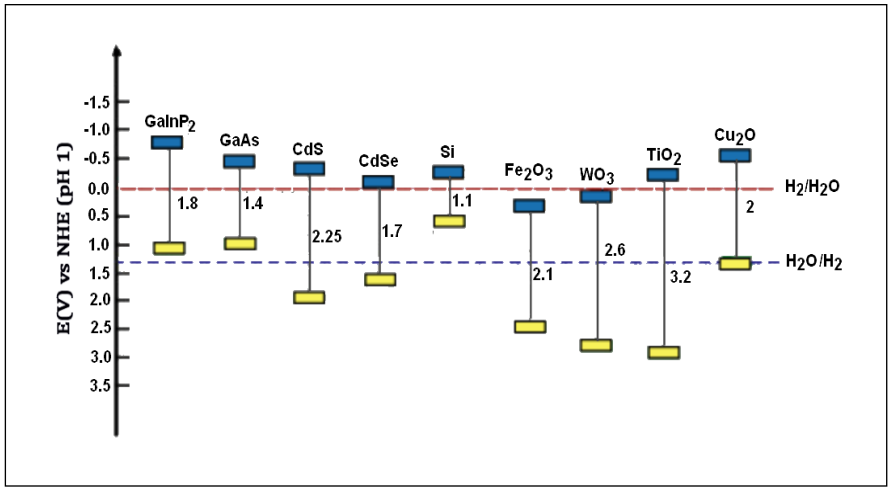


Figure 1. Bandgap and band edges of some semiconductor materials compared with a redox potential of water molecules

In this study, the Fe_2O_3 was electrodeposited on the TiO_2/ FTO thin film by variation of time. The Fe_2O_3/TiO_2/FTO multilayer film system was characterized by X-ray diffraction (XRD), Scanning Electron Microscope (SEM) and Uv-vis spectroscopy. PEC performance was measured by calculating its I-V under UV–vis light illumination.

Materials and Methods

Photoelectrode preparation

The TiO_2 electrodes were prepared using commercial colloidal TiO_2 powder (Degussa P25) by doctor-blading onto fluorine-doped tin oxide (FTO) glass plates. The 1 g TiO_2 powder was ground with 1 ml dipolyethylene glycol 300 (Merck), Triton-X and double-distilled water to form homogenous paste. The paste was smeared onto a clean FTO glass. Then, the TiO_2/FTO was dried at room temperature for a few minutes and was heated in a furnace at 450 ^oC for 2 hours with ramping rate of 5 $^oC\ s^{-1}$. Afterward, the Fe_2O_3 was deposited onto the TiO_2/FTO using electrodeposition method for 5 minutes, in which the iron sulfate ($FeSO_4$) was used as the starting material. The process was carried out using a potentiostat (VersaSTAT 4, Ametek), connected to a working electrode (TiO_2/FTO), counter electrode (Pt) and reference electrode (Saturated Calomel Electrode, SCE). The samples were calcined in a furnace at 500 ^oC for 60 minutes with heating rate of 1 $^oC\ s^{-1}$. Characterization of thin films was done using X-Ray diffraction (Bruker D8 Advance) via Cu Kα radiation. Morphology of the thin film was characterized using scanning electron microscopy (Zeiss AM10).

Photoelectrochemical analysis

The PEC analysis was conducted based on previous study [17]. The analyses were carried out using Ametek Versastat 4 on the TiO_2 and TiO_2 deposited by Fe_2O_3 at different times. The 450 W full arc Xenon light source at an intensity of 100 $mWcm^{-2}$ was used to irradiate the electrodes. The electrolyte in this experiment was 0.5 M Na_2SO_4, and it was purged with nitrogen gas for 30 min before the tests. The scan rate was set to 0.01 $V\ s^{-1}$.

Computational method

Density functional theory (DFT) calculations were carried out using the $DMol^3$ code in Materials Studio 5.5 from Accelrys. Geometry of the bulk molecule was optimized in a double-numeric-plus polarization (DNP) basis, set

using three different functional methods: PWC, PW91 and PBE. Self-consistent field (SCF) method was used for calculating the electronic structure; all core electrons were treated as being polarizable and Hartree-Folk (RHF) spin-restricted mode. TDDFT calculations were conducted on the ground state in spin-restricted mode.

Results and Discussion

X-ray diffraction (XRD) patterns of the TiO_2 and TiO_2/Fe_2O_3 on the FTO films are shown in Figure 2. The TiO_2 anatase (101) phase was observed at 25.35°, while rutile (110) phase appered at 27.40° (Figure 2b). The peaks for α-Fe_2O_3 (104) appeared at 33.50°, while α-Fe_2O_3(110) at 35.50° (Figure 2c) (JCPDS file no. 01-077-9926). All TiO_2 and Fe_2O_3 peaks were observed at TiO_2/Fe_2O_3 composite pattern (Figure 2d). Diffractogram pattern of the TiO_2 produced is similar with TiO_2 pattern that was reported by Vlasa et al. [18].

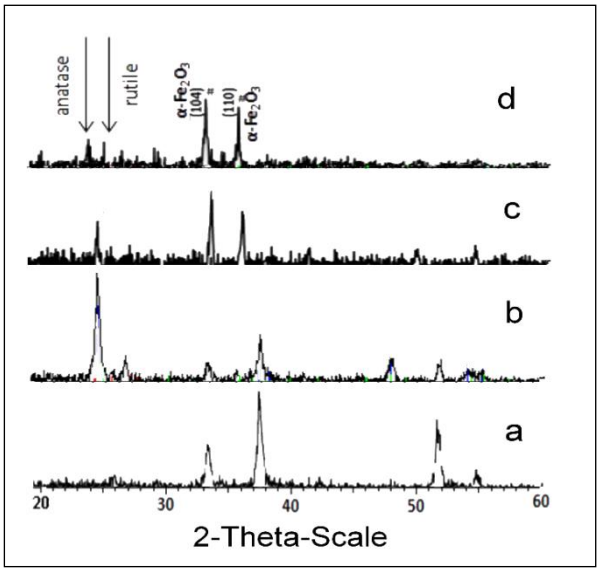


Figure 2. X-ray diffraction for (a) FTO (b) TiO_2 and (c) Fe_2O_3 and (d) TiO_2/Fe_2O_3

The surface morphology by scanning electron microscopic (SEM) image of TiO_2/Fe_2O_3 on an FTO glass substrate is shown in Figure 3. The image clearly shows flower-like shape on the surface of TiO_2 substrate (B), which is similar to a previous study [19]. The duration of deposition time changed the shape of Fe_2O_3; at 3 minutes, the flower-like shape changed to a spiny and globular structure (C) and then turned to fine particles that scattered randomly onto TiO_2 surface at 5 minutes (D). The presence of Fe was confirmed by EDX analysis (Table 2). The number of Fe did not automatically increased with time of deposition; however, the shape of Fe was: at 5 minutes of deposition time, the Fe shape became clotted and the TiO_2 surface became exposed. The thickness of TiO_2/Fe_2O_3 layer on the FTO substrate based on SEM images was obtained around 10-15 μm.

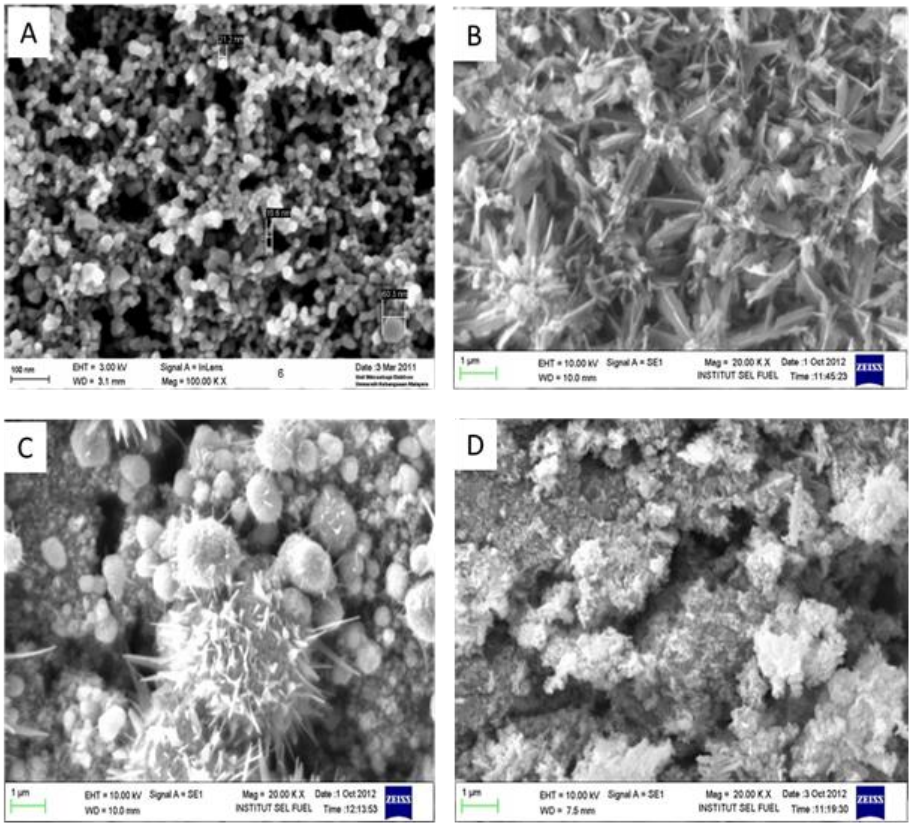


Figure 3. Surface morphology of (a) TiO_2 and (b) TiO_2/Fe_2O_3 on FTO films

Table 2. Element percentage of Fe, Ti and O based on EDX analysis

Element	Percentage (%) of element		
	TiO_2-Fe_2O_3 (1 min)	**TiO_2-Fe_2O_3 (3 min)**	**TiO_2-Fe_2O_3 (5 min)**
Ferrum (Fe)	57.0	29.8	16.3
Titanium (Ti)	55.6	42.8	18.6
Oxygen (O)	28.2	27.4	24.4

The optical characterizations of TiO_2 and TiO_2 doped Fe_2O_3 are shown in Figure 4. The band gaps were determined from reflectance spectra of the films using the following formula equation 1[5]:

$$E_g\ (eV) = 1240/\lambda_g\ (nm) \quad (1)$$

where, E_g and λ_g are the band gap energy and the absorption wavelength threshold of the doping material, respectively. In Figure 4, the band gap of TiO_2 was found to be 3.44 eV with the threshold wavelength at 360 nm. On the other hand, band gap of the TiO_2 doped with Fe_2O_3 was 2.39 eV with the threshold wavelength at 518 nm. The TiO_2/Fe_2O_3 film absorption was shifted to visible light, caused by excitation of electrons in the 3d shell of Fe to conduction band of TiO_2 [20].

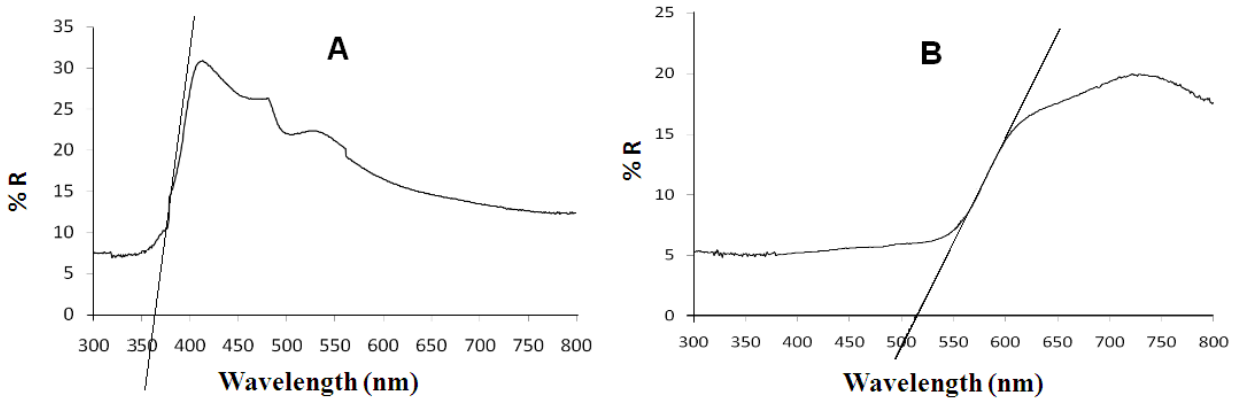


Figure 4. Reflection (R) spectra of TiO_2 (**A**) and TiO_2 doped Fe_2O_3 (5 min) (**B**) electrodes

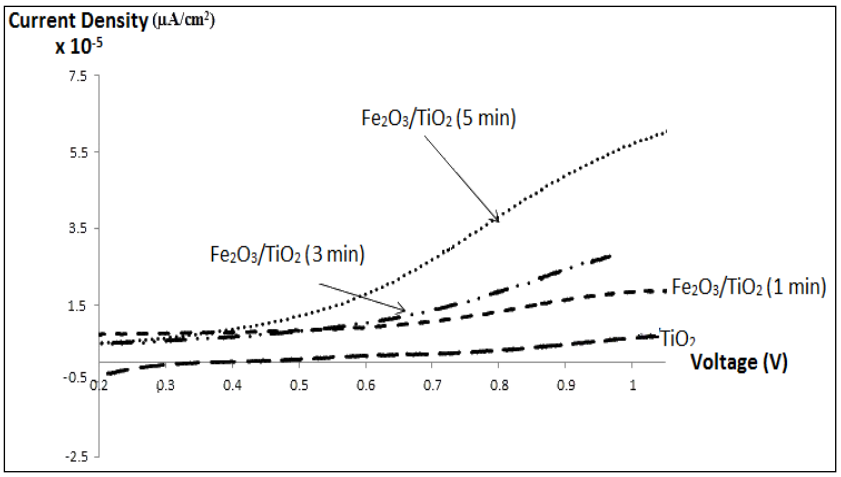


Figure 5. Current density-voltage (V/SCE) characteristics for Fe_2O_3/TiO_2 at different duration of electrodeposition proses

Photocurrent density was measured using three electrodes in 0.5 M Na_2SO_4 electrolyte under a Xenon lamp (100 mW cm^{-2}) irradiation. The applied voltage bias was measured againts SCE as the reference, and the values of photocurrent are shown in Figure 5. The current density of undoped TiO_2 was low compared with TiO_2 doped with Fe_2O_3. In addition, the deposition time of Fe_2O_3 onto TiO_2 surface contributed to the increase of current density. The highest photocurrent was measured at 5 minutes deposition of Fe_2O_3, which was about 55 µA cm^{-2} at 1.0 V bias potential. The current density of TiO_2 without Fe_2O_3 is 7 µAcm^{-2} and TiO_2/Fe_2O_3 at 1 and 3 minutes are 28 µAcm^{-2} and 29 µAcm^{-2}, respectively. This is probably due to the reduction of electron-hole recombination on TiO_2 doped with Fe_2O_3. Kim et al. found similar result, where the passivation layer of TiO_2 with Fe_2O_3 as photo-absorber on FTO film showed 3.5 times higher photocurrent densities for water splitting under UV-vis light illumination than the Fe_2O_3/FTO or TiO_2/FTO films [11].

Theoretical investigation started with the optimization of the bulk structure of TiO_2 and Fe_2O_3 in three kinds of functional methods. The average length of Ti-O and Fe-O are shown in Table 3. Calculated bond length of the Ti-O in these three methods gave similar results, which was about 1.92 Å. The calculated bond length of the Fe-O in

PWC was about 0.03 Å smaller than the calculated PW91 and PBE, which was about 1.96 Å. All calculated bond lengths of the Ti-O and Fe-O were in normal range [16]. The band gap of TiO_2 and Fe_2O_3 in these three methods were similar at about 0.076 Ha (2.06 eV) and 0.03 Ha (0.81 eV), respectively (Figure 6). Although the calculated band gaps were smaller than the experimental data, it is aceptable since the calculations were in atomic level.

Table 3. Bond length (Å) of the optimized structure in three different functional method calculation.

Bulk	**LDA-PWC**	**GGA-PW91**	**GGA-PBE**
Ti-O	1,923	1,927	1,927
Fe-O	1,939	1,960	1,960

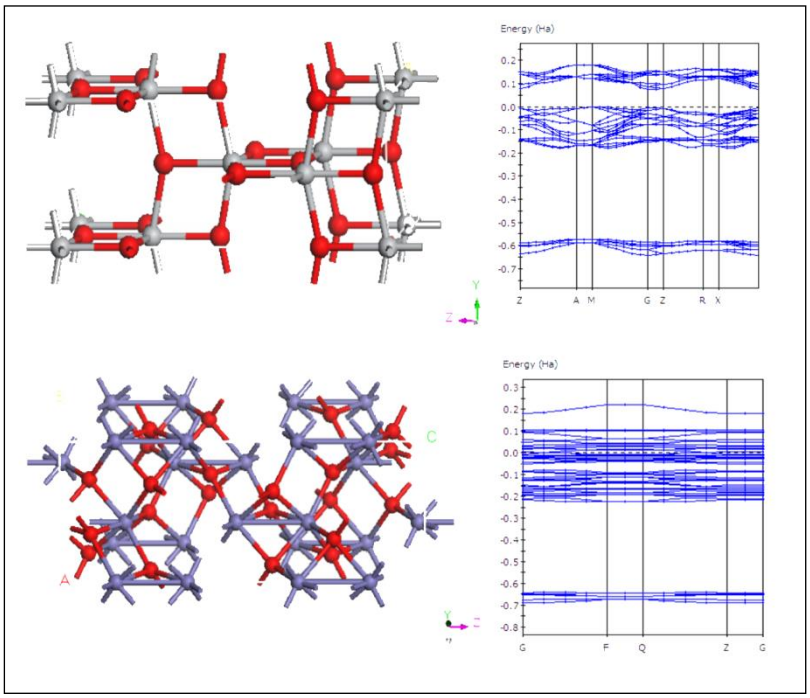


Figure 6. Molecular structure and electronic structure of TiO_2 (101), Fe_2O_3 (104) and composite TiO_2/Fe_2O_3

The optimized bulk structures of TiO_2 and Fe_2O_3 were used to form TiO_2 (101) and Fe_2O_3 (104) phases, which were then re-optimized further. The molecular structure of TiO_2 (101)/Fe_2O_3 (104) bilayer is shown in Figure 7. The electronic structure of the bilayer can not be determined easily since the increasing atomic number causes overlapping of the electronic orbitals. Nevertheless, band gap of the composite can be determined from the calculation of HOMO-LUMO energy gaps (0.70 eV), which is smaller than the monolayer oxides bad gaps; an indication of the charge transfer improvement in the system. Also shown in Figure 7 the potential electrophilic charge of the composite surface, where the potential of both oxides are similar. The more positive charge was found around Fe atoms, where supposedly the location of oxygen atom oxidation.

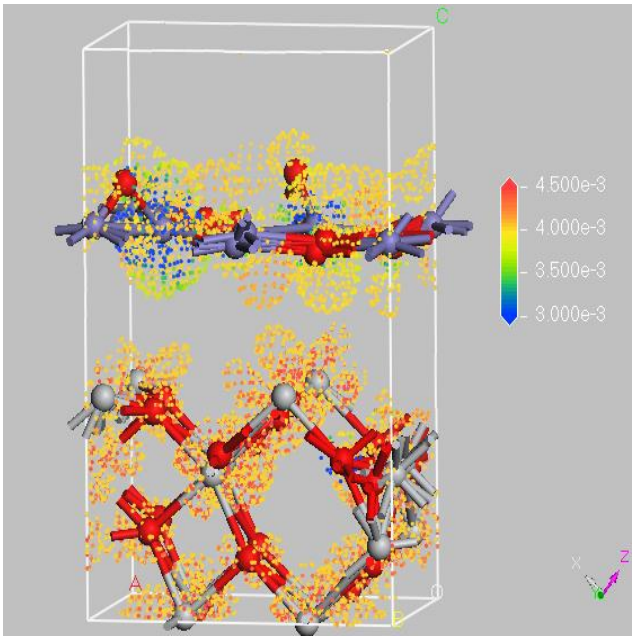


Figure 7. Molecular structure and electrophilic charge of TiO_2 (101)/Fe_2O_3 (104) composite

Conclusion

Surface passivation layer of TiO_2/Fe_2O_3 for use in the PEC water splitting application was successfully fabricated. $FeSO_4$ was used as the starting material and electrodeposition technique was used to deposit the iron molecule onto TiO_2 thin film. The measurements from photocurrent and reflection spectrum showed that Fe_2O_3 increased the performance of TiO_2 electrode. The maximum photocurrent was obtained from 5 minutes electrodeposition of Fe_2O_3 on TiO_2/FTO film. The TiO_2/Fe_2O_3 composite structure was built based on DFT calculations. The potential charges of the composite surface were successfully determined.

Acknowledgement

The authors would like to acknowledge Universiti Kebangsaan Malaysia for sponsoring this project under UKM-GUP-2011-369 and UKM-AP-TK-05-2009 research grants.

References

1. Arifin, K., Majlan, E.H., Daud, W. R.W. and Kassim, M.B. (2012). Bimetallic complexes in artificial photosynthesis for hydrogen production: A review. *International Journal of Hydrogen Energy*, 37: 3066 – 3087.
2. Currao, A. (2007) Photoelectrochemical water splitting. *Chimia*, 61: 815 – 819.
3. Liu, R., Zheng, Z., Spurgeon, J. and Yang, X. (2014). Enhanced photoelectrochemical water-splitting performance of semiconductors by surface passivation layers. *Energy and Environmental Science*, 7: 2504 – 2517.
4. Minggu, L. J., Daud, W. R.W. and Kassim, M. B. (2010). An overview of photocells and photoreactors for photoelectrochemical water splitting. *International Journal of Hydrogen Energy*, 3(35): 5233 – 5244.
5. Arifin, K., Daud, W. R.W. and Kassim, M.B. (2013). Optical and photoelectrochemical properties of a TiO_2 thin film doped with a ruthenium-tungsten bimetallic complex. *Ceramics International*, 39: 2699 – 2707.
6. Fujishima, A., Zhang, X. and Tryk, D.A. (2008). TiO_2 photocatalysis and related surface phenomena. *Surface Science Reports*, 63: 515 – 582.
7. Arifin, K., Daud, W. R.W. and Kassim, M.B. (2014). A novel ruthenium-tungsten bimetallic complex dye-sensitizer for photoelectrochemical cells application. *Sains Malaysiana*, 43(1): 95 – 101.

8. Ni, M., Leung, M. K. H., Leung, D.Y.C. and Sumathy, K. (2007). A review and recent developments in photocatalytic water-splitting using TiO_2 for hydrogen production. *Renewable and Sustainable Energy Review,* 11: 401 – 425.
9. Lin, F. and Boettcher, S.W. (2013). Adaptive semiconductor/electrocatalyst junctions in water-splitting photoanodes. *Nature Materials*, 13: 81 – 86.
10. Cao, C., Hu, C., Shen, W., Wang, S., Tian, Y. and Wang, X. (2012). Synthesis and characterization of TiO_2/CdS core–shell nanorod arrays and their photoelectrochemical property. *Journal of Alloys and Compounds* 523: 139 – 145.
11. Kim, B-R., Oh, H-J., Yun, K-S., Jung, S-C., Kang, W. and Kim, S-J. (2013). Effect of TiO_2 supporting layer on Fe_2O_3 photoanode for efficientwater splitting. *Progress in Organic Coatings,* 76:1869 – 1873
12. Fitzmorris, R. C. and Zhang, J. Z. (2015). Recent advances in metal oxide-based photoelectrochemical hydrogen production. In: Andrews D.L., editors. Photonics, Volume 2: Nanophotonic Structures and Materials, Canada, John Willey & Son. pp 346 – 358.
13. Smith, W., Wolcott, A., Fitzmorris, R. C., Zhang, J. Z. and Zhao, Y. (2011). Quasi-core-shell TiO_2/WO_3 and WO_3/TiO_2 nanorod arrays fabricated by glancing angle deposition for solar water splitting. *Journal of Material Chemistry,* 21**:** 10792 – 10800.
14. Minggu, L. J., Ng, K. H., Kadir, H. A. and Kassim, M. B. (2014). Bilayer n-WO_3/p-Cu_2O hotoelectrode with photocurrent enhancement in aqueous electrolyte photoelectrochemical reaction. *Ceramics International,* 40: 16015 – 16021.
15. Wang, Q., Yang, X., Chi, L. and Cui, M. (2013). Photoelectrochemical performance of CdTe sensitized TiO_2 nanotube array photoelectrodes. *Electrochimica Acta,* 91: 330 – 336.
16. Zhong, M., Shi, J., Xiong, F., Zhang, W. and Li, C. (2012). Enhancement of photoelectrochemical activity of nanocrystalline CdS photoanode by surface modification with TiO_2 for hydrogen production and electricity generation. *Solar Energy,* 86: 756 – 763.
17. Hang, N. K., Minggu, L.J. and Kassim, M.B. (2013). Gallium-doped tungsten trioxide thin film photoelectrodes for photoelectrochemical water splitting. *International Journal of Hydrogen Energy*, 38: 9585 – 9591.
18. Vlasa, A., Varvara, S., Pop, A., Bulea, C. and Muresan, L.M. (2010). Electrodeposited Zn–TiO_2 nanocomposite coatings and their corrosion behavior. *Journal of Applied Electrochemistry*, 40: 1519 –1527.
19. Zanganeh, S., Torabi, M., Kajbafvala, A., Zanganeh, N., Bayati, M.R., Molaei, R., Zangar, H.R. and Sadrnezhaad, S. K. (2010). CVD fabrication of carbon nanotubes on electrodeposited flower-like Fe nanostructures. *Journal of Alloys & Compounds,* 507: 494 – 497.
20. Khan, M. A., Woo, S. I. and Yang, O-B. (2008). Hydrothermally stabilized Fe(III) doped titania active under visible light for water splitting reaction. *International Journal of Hydrogen Energy,* 33: 5345 –5351.

Malaysian Journal of Analytical Sciences, Vol 20 No 4 (2016): 901 - 912
DOI: http://dx.doi.org/10.17576/mjas-2016-2004-26

MALAYSIAN JOURNAL OF ANALYTICAL SCIENCES
Published by The Malaysian Analytical Sciences Society
ISSN 1394 - 2506

STUDY OF HYDROGEN CONSUMPTION BY CONTROL SYSTEM IN PROTON EXCHANGE MEMBRANE FUEL CELL

(Kajian Penggunaan Hidrogen oleh Sistem Kawalan dalam Sel Bahan Api Membran Penukaran Proton)

Ros Emilia Rosli[1], Edy Herianto Majlan[1]*, Siti Afiqah Abd. Hamid[1], Wan Ramli Wan Daud[1], Ramizi Mohamed[2], Teuku Husaini[1], Dedi Rohendi[3]

[1]*Fuel Cell Institute*
[2]*Department of Electrical and System Engineering, Faculty of Engineering & Built Environment*
Universiti Kebangsaan Malaysia, 43600 UKM Bangi, Selangor, Malaysia
[3]*Department of Chemistry, Faculty of Mathematics and Sciences,*
Sriwijaya University, 30662 Inderalaya, Palembang, Indonesia

**Corresponding author: edy@ukm.edu.my*

Received: 5 February 2016; Accepted: 22 April 2016

Abstract

Efficient operation results from a proper control strategy. In the operation and performance of a Proton Exchange Membrane Fuel Cell (PEMFC), the hydrogen gas flow rate is one of the most essential control parameter in addition to operating pressure, water management, temperature and humidity. This is because of the high cost and amount of energy are required to produce the purity hydrogen gas. In this paper, a Proportional Integral Derivative (PID) feedback control system is used to control the hydrogen flow rate. A strategy is adapted to balance the hydrogen use based on the loading requirements, especially during start-ups and sudden power demands. This system is implemented using National Instrument (NI) devices powered by the LabVIEW program. This is due to its simplicity and customization flexibility for measuring, processing and recording data. Designed structure allows the real-time implementation of a robust control law that is able to address the related nonlinearities and uncertainties without incurring a heavy computational load for the controller algorithm. While it facilitating a fast sampling rate according to the needs of the power system. Test results from the controller show that the new fuel control system provides good performance by reducing the amount of wasted hydrogen gas compared with that of the previous open loop system by 30 % to over 80 % saved by the varied load. This improvement is beneficial for any PEMFC that experiences fluctuating power demand, especially for vehicle applications.

Keywords: PEM fuel cell, proportional integral derivative, reactant controller, LabVIEW, national instrument

Abstrak

Operasi yang cekap terhasil dari strategi kawalan yang baik. Dalam operasi dan prestasi Fuel Cell Membran Penukaran Proton (PEMFC), kadar aliran gas hidrogen adalah salah satu parameter kawalan yang paling penting selain dari tekanan operasi, pengurusan air, suhu dan kelembapan. Ini kerana kos yang tinggi dan jumlah tenaga dikehendaki untuk menghasilkan gas hidrogen berketulenan tinggi. Dalam kertas kerja ini, sistem kawalan Perkadaran, Kamiran dan Perbezaan (PID) suap balik digunakan untuk mengawal kadar aliran hidrogen. Strategi disesuaikan untuk mengimbangi penggunaan hidrogen berdasarkan keperluan bebanan, terutamanya pada permulaan dan permintaan kuasa secara tiba-tiba. Sistem ini dilaksanakan dengan menggunakan peranti instrumen nasional (NI) yang dikuasakan oleh program LabVIEW. Ini kerana ia ringkas dan fleksibel untuk mengukur, pemprosesan dan rakaman data. Struktur yang direka bentuk membolehkan pelaksanaan masa sebenar hukum kawalan yang mantap yang mampu menangani keadaan yang tidak linear dan tidak menentu tanpa memerlukan pengiraan yang sukar untuk algoritma pengawal. Sambil itu, ia memudahkan kadar pensampelan yang cepat mengikut keperluan sistem kuasa. Hasil ujian dari pengawal menunjukkan bahawa sistem kawalan sel fuel yang baru memberikan prestasi yang baik dengan

mengurangkan jumlah gas hidrogen yang terbazir berbanding sistem gelung terbuka dengan pengurangan sebanyak dari 30 % hingga 80 % pada variasi beban. Peningkatan ini memberi manfaat kepada mana-mana PEMFC yang mengalami permintaan kuasa turun naik, terutama untuk aplikasi kenderaan.

Kata kunci: Sel bahan api PEM, perkadaran, kamiran dan perbezaan (PID), pengawal bahan reaktan, LabVIEW, instrument nasional

Introduction

The proton exchange membrane fuel cell (PEMFC) generates energy from chemical sources to produce electrical energy efficiently and directly via an electrochemical reaction between the hydrogen and oxidant as the reactant. It has drawn enormous Research and Development (R&D) interest because its high energy density makes it the most viable candidate for use in the transportation, stationary power and portable device sectors [1]. PEMFC have the characteristics of low operating temperature, low noise, low weight, low corrosion, small volume and fast start-up capability, thus resulting in high energy density and quick start features.

However, the commercialization of this technology is still hampered by many challenges such as cutting costs, improving performance and increasing durability. Although those issues could be solved primarily by material selection, PEMFC performance relies mostly on design and operation of a fuel cell system. That includes a balance of plant, power converters and their control systems. System that commonly use are the humidity, reactant pressure, reactant flow rate, water, temperature and power electronics management systems [2, 3]. Every system plays a role in the design that will determine the correct amount of material that must be supplied for proper function and better electricity generation.

In this paper, study will focus on reactant system where the parameter should be considered for high performance; pressure, flow rate and stoichiometric ratio. To supply the reactant source three mode can be used; the dead-end mode, the flow-through mode and the recycling mode [4]. For the pressure factor, the amount supplied is depending on the size of stack. A higher value can increase the kinetics reaction in the electrochemical process. Thus, result in a higher power density and greater stack efficiency. Even so too high pressure will cause damage on the membrane electrode assembly (MEA) components. In the other hand, at low supplied pressure may result in a lower net available power. Therefore, its value should be sufficient in order to produce a required power and maintain the durability of fuel cell [5, 6]. Danzer et al. [7] prevent starvation issue of their stack operated at transient condition. They adjust the oxidant fuel by designing a controller that supplied a minimum pressure.

The flow rate and stoichiometric ratio are closely related. Higher flow rates cause the stoichiometric ratio and power production to become high as well because additional reactants are available for the reaction. However, this will reduce the energy production efficiency because more reactants are supplied but did not react and are wasted. Usually this happen when the fuel is supplied at a fixed and high stoichiometric ratio in orders to maintain the desired current density [8, 9]. But if the stoichiometric ratio is too low, will result in low performance [10, 11]. But problems often arise when the imposed loading varies and the supplied reactants are insufficient to produce the needed power. Zhou et al. [12] studies the behavior of fuel cell under fuel starvation condition. At different stoiciometric ratio and loading variation, they observe after unsatisfactory condition, the carbon corrosion issues arise.

This problem requires serious attention, especially in vehicle and load variation applications, because this complex phenomenon may cause a transient power issue that leads to performance degradation, damage to the electrode and electrolyte surface and shorter fuel cell life [13]. To solve this problem, a reactant controller should be implemented to control the flow rate supplied to the fuel cell stack. This is done to ensure an educate supply of reactant can be consume by fuel cell and generate the required power needed in both normal and transient operation mode. Flow control chosen to be control since it is critical parameter at uncertainties. This overview shows that a more efficient hydrogen-air supply management system is required for better PEMFC system operation to increase the efficiency of the reactant used.

In this paper, we focus on implementing a hydrogen fuel controller in which the design of a feedback control system using the PID controller was carried out to manipulate the supply to the fuel cell. But the fan speeds are maintained at a specific power for reduction of system complexity. A sufficient flow rate based on performance is determined to obtain the required reactant supply and to prevent excessive fuel consumption. This implementation can be broadly used in many applications that address load variation, such as electric vehicles in which the power demand is impulsive rather than constant.

Materials and Methods

System setup

PEMFC stack from Horizon Fuel Cell Technologies was used in this study. The open cathode stack was supplied with 99.99 % pure hydrogen gas that stored in compressed gas cylinder. The hydrogen gas flows inside the stack using a dead-end mode; every 10 seconds, the end valve was opened to release the existing gas for purging action. An axial fan are used to supply the oxygen source (air) using the flow-through mode. The overall setup tables for the experiment shown in Figure 1. This fuel cell can generate a variable power demand with a maximum rated value of 100 W (±14.4 V at ±7.2 A) and consists of 24 MEA cells with a total electrode area of 45 cm². The measurement of the stack performances are being varied using the DC electronic load and recorded by the NI data logger and LabVIEW program.

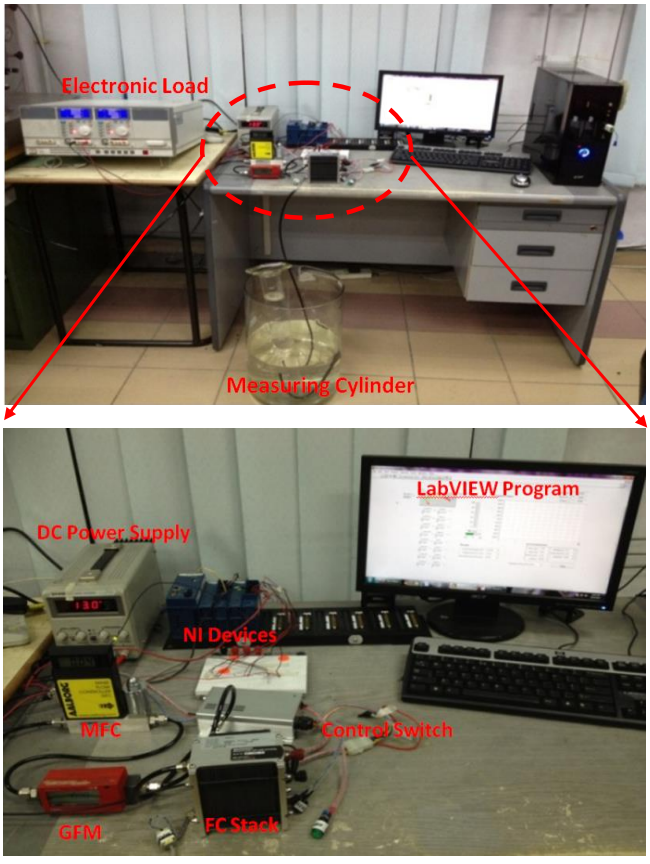


Figure 1. Overall table setup for testing PEMFC commercial stack

Fuel cells often use open loop system (OLS) shown Figure 2. In which hydrogen was supplied directly to the stack from compressed hydrogen gas stored in a cylinder tank in which the pressure are manually controlled with a pressure regulator. The procedures to operate the commercial stack with the OLS are based on flow diagram as in Figure 3. In this situation we need to make sure that the source of reactant are sufficient by supplying the flow rate in excess amount to avoid starvation problem.

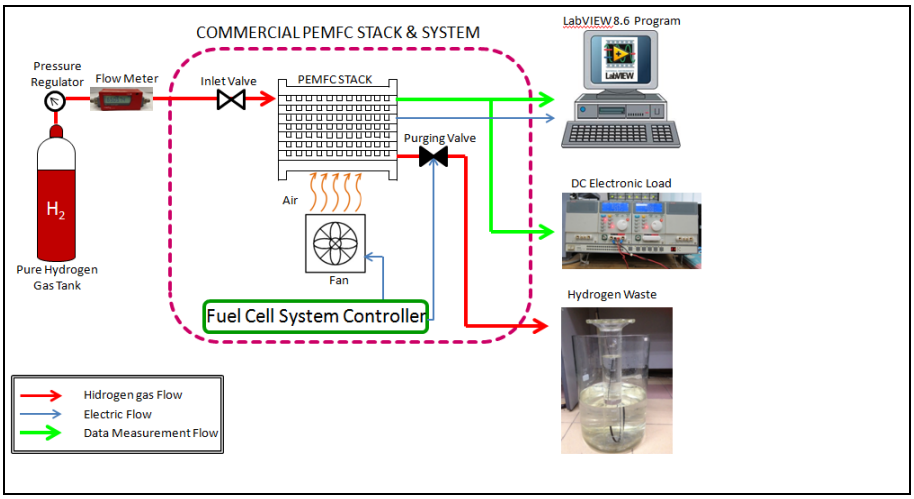


Figure 2. Flow diagram of operating the fuel cell stack using an Open Loop System (OLS)

However, the OLS system has the disadvantage where it will lead to starvation or waste of resources reactant when the flow rate is not controlled. Therefore, a hydrogen control system using PID control is built to reduce this problem. The application of controller functions in a manner similar to an automatic control system known as closed loop system (CLS). To see the hydrogen consumption difference for both systems; OLS without any modification and CLS with PID controller implemented used to manage the hydrogen flow rate when PEMFC generating the power.

An electrical circuit diagram build for the hydrogen flow rate control system shown in Figure 4. Electrical connection is made between 100 W commercial fuel cell stack, the DC power supply to turn on electronic equipment, mass flow controller (MFC) for the determination of the output and input current to change the flow rate of hydrogen, NI device (CFP-AIO-600) as connective reaction programmed in LabVIEW software and DC electronic load to monitor the voltage and power produce and also applied current load.

Control techniques

The PID controllers are used to improve fuel cell performance by regulating the amount of hydrogen using control element that exists in the LabVIEW program. The controller can provide control actions designed for the specific process requirements. The general form of PID is express as equation 1:

$$u(t) = K_p e(t) + K_I \int e(t)dt + K_D \frac{d}{dt} e(t) \quad (1)$$

where the signal input (u) of the controller is equivalent to the increase in the proportion of (K_P) times the magnitude of the error plus the integral increase (K_i) times the integral of the error plus the increase in the difference (K_d) times the error difference.

For CLS, specific amounts of hydrogen are adjusted to a sufficient value by increasing and decreasing the delivery via a current control mode. This mode is based on the power required to maintain the stack output voltage, and this concept is vital to providing an efficient amount of power output and reducing hydrogen waste. To control this process, the signal must be subjected to these algorithms. The process begins by measuring the fuel cell system voltage output using a compact field point (cFP) hardware tool (read signal). The control program built using LabVIEW was used to measure the parameters, log the data, record the outputs and analyze the data to be applied to the fuel cell stack on a real-time basis. The results were subsequently passed to the cFP hardware tool (write signal) for implementation. A programmable electronic load was used to generate a pulse current load profile. These sequences were maintained and continued as the signal was sent out (control) and received (feedback) to analyze the system power.

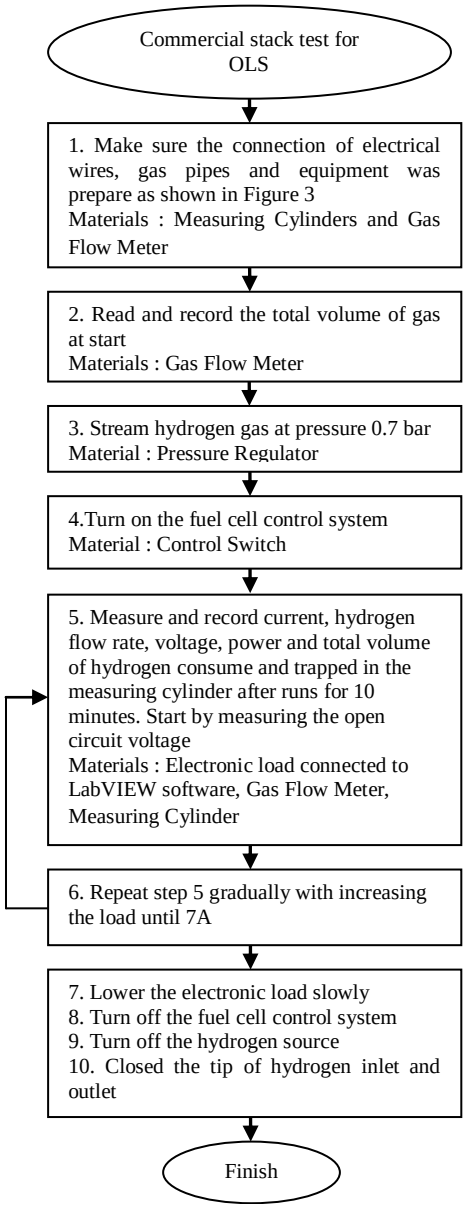


Figure 3. Flow chart of operating OLS

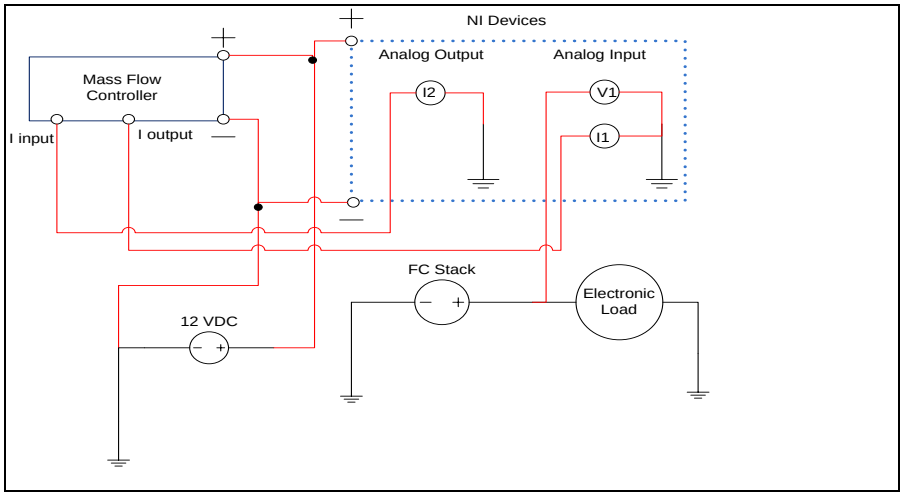


Figure 4. Hydrogen control system electrical circuit

In the CLS, adjustments are enacted using a hydrogen mass flow controller (MFC) functions to control the amount of hydrogen flow. The MFC is controlled by measurement and supply of a signal through the NI devices (cFP-AIO-600) based on the program built using LabVIEW. The setup of the system is shown in Figure 5.

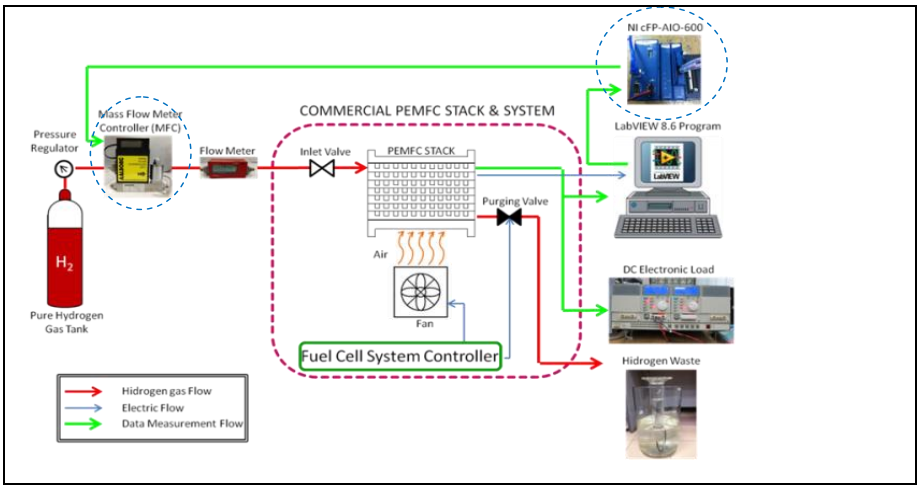


Figure 5. Flow diagram of the CLS

The NI module was placed between the fuel cell system and the computer (LabVIEW) to convert the analog input to a digital output for cFP measurements and control actions. A voltage range between 14 V (minimum voltage) up to 24 V (open circuit voltage) was determined to maintain suitable flow rates. The voltage was measured and the signal was logged using the NI analog input and subsequently sent to the LabVIEW controller program for processing. The required flow rate was automatically chosen using the PID program. The signal was sent back using the NI analog output current to control the MFC valve flow rate. The program reactions are based on PID changes that produce an operating signal that manipulates the flow rate of the hydrogen reactant to maintain the stack output voltage.

The flow rates required were determined from the OLS results and aimed to conserve hydrogen based on the loading demand to maintain the fuel cell stack voltage. Eight sets of voltage ranges were fixed to comply with the different flow rates at the transient conditions. The detailed voltage ranges, flow rates and MFC output currents are listed in Table 1. The procedures to operate the CLS are also listed as in Figure 6. The developed PID controller program details structure are shown in the block diagram in Figure 7.

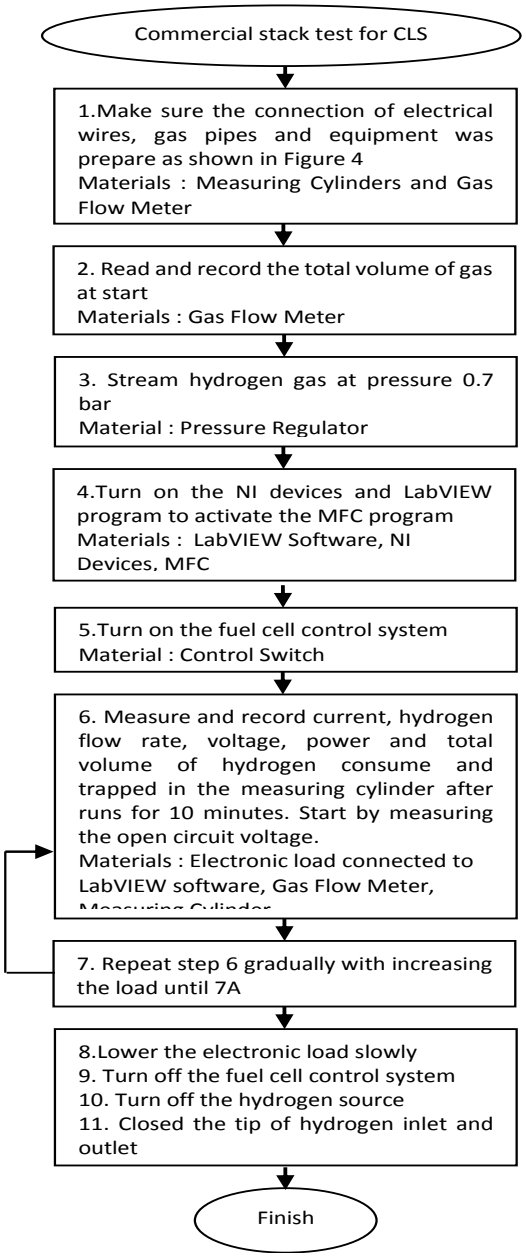


Figure 6. Flow diagram of the CLS

Table 1. Voltage range options at different hydrogen flow rates for controller calibration

Range Option	Stack Voltage Range (V)	Hydrogen Flow Rates (l/min)	cFP AIO 600 Output Current to MFC (A)
1	24.0 – 22.0	0.01	0.0044
2	22.0 – 20.0	0.35	0.0046
3	20.0 – 18.5	0.52	0.0049
4	18.5 – 18.0	0.72	0.0052
5	18.0 – 17.4	0.83	0.0054
6	17.4 – 16.5	0.98	0.0057
7	16.5 – 15.5	1.23	0.0061
8	15.5 – 14.0	1.41	0.0064

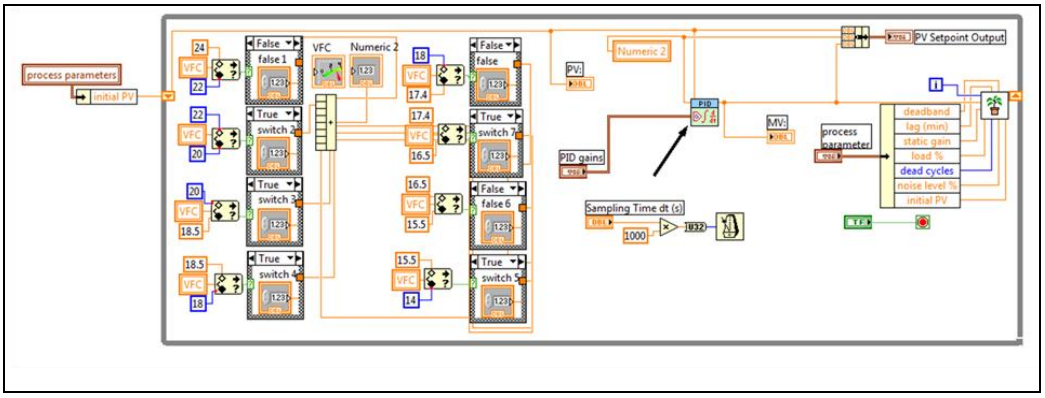


Figure 7. Block diagram interface of the PID control system

Results and Discussion

Stack performance in different systems

As the main part of this study, a flow rate controller was implemented for more reliable operation using CLS. The strategies used then were compared with the OLS and controller used by Kim et al. [14]. Kim et al. using a PEM fuel cell stack can power up to 150-W and implement a closed-loop method controller. The effects on the fuel cell system performance in response to hydrogen reactant control were analyzed. Figure 8 shows the performance comparison between them, where Figure 8a indicates that the implementations of controlled hydrogen flow rates are able to satisfy the power demand.

The performance response at different loadings shows the values of the hydrogen consumption rates are affected. Where, as the power stack demand is increasing, the hydrogen flow rates consumed also increase, but the value consumed different depends on the system used. In Figure 8b, can be observe that the demand of hydrogen are lower request by the CLS compared to the two other system. Therefore, it is necessary to consider hydrogen control management in the fuel cell design in order to reduce hydrogen usage. After ensuring control of the hydrogen supply does not affects the power performance, the impact of hydrogen consumption and wasted (purged out) will further studied for both the OLS and CLS processes.

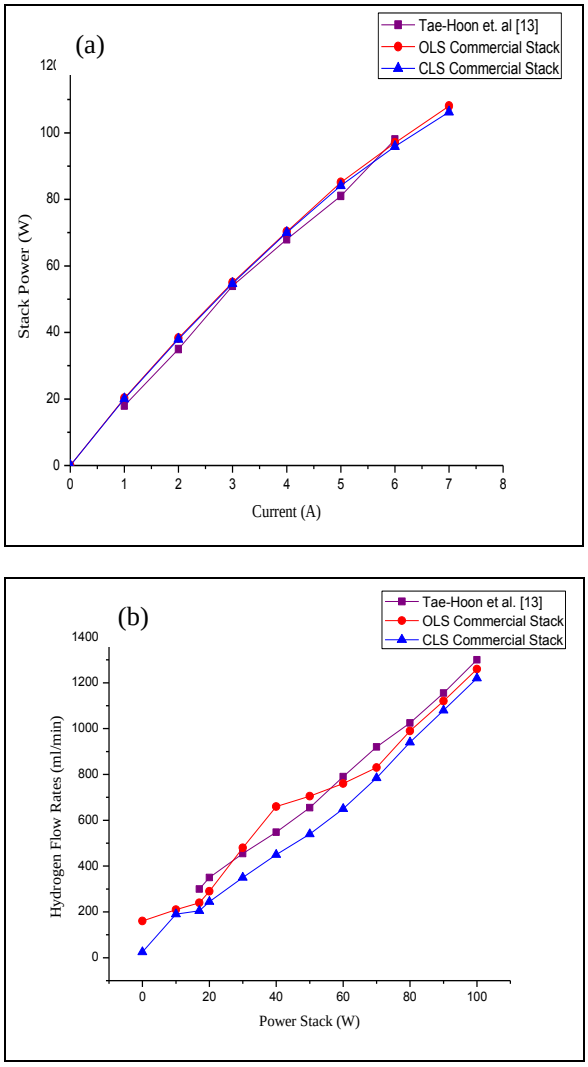


Figure 8. Characteristics of (a) stack power and (b) hydrogen flow rate under various loading values at different stack conditions

Control system impact in hydrogen consumption

The data of overall performance shows that the amount of hydrogen consumes are directly proportional to the load demand. Figures 9 indicate that the volumes of hydrogen that flowed into the stack were consumed and were subsequently purged out of the fuel cells every 10 minutes differed with respect to the loading value.

An increase in loading also increased the amount of hydrogen that entered the fuel cell; for the OLS in Figure 9, almost 2 liters of hydrogen was wasted at low currents from the OCV until a current of 4 A was reached because of the purging condition. However, the amount of wasted hydrogen decreased as the loading increased, which indicates that additional hydrogen reacts at a higher demand. Between 5 A and 7 A, the purging value increased to greater than 2 liters. The CLS showed an almost identical pattern to that previously discussed for the OLS. The load and hydrogen influx were positively correlated, but the influx was limited by the controller. Thus, the purged amounts of hydrogen were smaller compared with those of the OLS, and thus, the CLS constitutes an improvement by gradually and appropriately allowing hydrogen to enter the fuel cell. Hydrogen purged out recorded between 30% to over 80% have been successfully saved depends on the applied load.

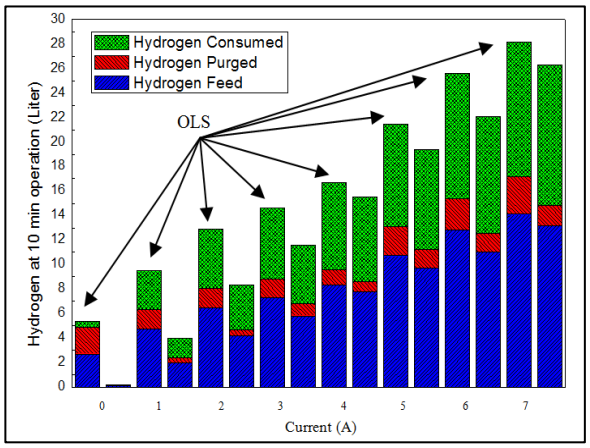


Figure 9. Total hydrogen consumption for OLS and CLS configuration

Transient loading effect

The study continues with an application of a variable load to observe the effect on the performance and use of hydrogen flow control and to determine whether it can produce effective results for the active load current changes. The load current for this stack can vary depending on the load demand, from 0 A to 7 A, and the changes cover all of the stack operations. In this implementation, the patterns in the current changes are set to distinguish the results from the system used. Figure 10 shows the change in current fluctuations applied manually via an electronic load. These changes cover nearly the entire fuel cell stack operating conditions.

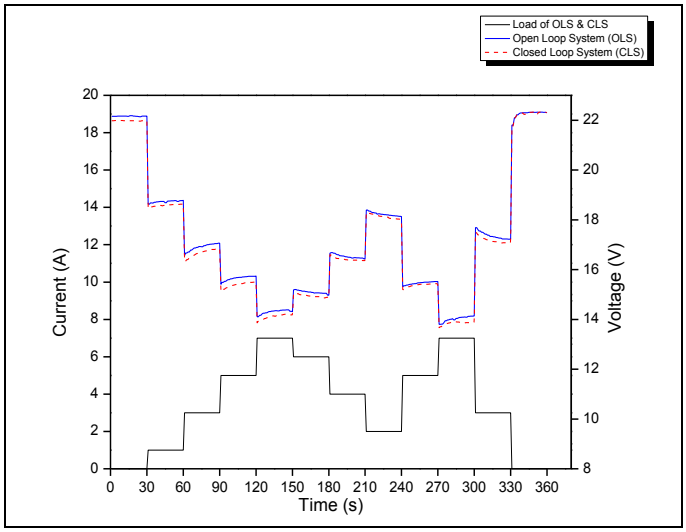


Figure 10. Stack performance at variation loading for OLS and CLS vs. time

The performance of load variation at both conditions operate at 360 second can be observed in Figure 10. The amount of hydrogen flow used by the commercial stack for the OLS is 4.90 liters with 1.30 liters wasted. However, for the CLS condition, only 4.20 liters were used and 0.67 liters were released into the atmosphere. This result shows that almost 50% of the hydrogen waste has been eliminated. The designed controller produced more optimal

power efficiency in terms of fuel consumption. This result shows that the new system improved the fuel cell system efficiency in terms of fuel consumption and cost effectiveness by reducing the waste of hydrogen resources released into the atmosphere.

Conclusion

The impact of hydrogen consumption in both the open-loop and closed-loop operations was compared to validate the proposed design. The controlled flow rates mimicked those of the OLS, and this system was most beneficial at the purging condition. The power performance of the CLS control system result was the same as that of the previously established OLS. The implementation effectively controlled the hydrogen flow rate under active current load variations such that minimal amounts of hydrogen were wasted while accommodating the needs of the reaction. Although this experiment used small-scale and commercialized fuel cells, with short time of operation indicated that the CLS improved the fuel cell hydrogen efficiency and cost effectiveness by reducing waste, which constitutes a significant benefit to the commercial fuel industry. The newly proposed fuel cell control system is also able to accommodate transient load demands. A sufficient hydrogen supply maintains fuel cell performance, reduces fuel waste and prevents MEA damage. If this condition is applied to higher power fuel cells or is implemented for longer durations, additional hydrogen can be conserved.

Acknowledgement

The authors gratefully acknowledge their thanks to Universiti Kebangsaan Malaysia for their financial support provided through a University Research Grants; UKM-AP-TK-08-2010, DIP-2012-05 and AP-2013-010.

References

1. Wang, J. (2015). Barriers of scaling-up fuel cells: Cost, durability and reliability. *Energy*, 80(0): 509 -521.
2. Bizon, N. (2011). Nonlinear control of fuel cell hybrid power sources: Part I - Voltage control. *Applied Energy*, 88(7): 2559 - 2573.
3. Thanapalan, K., Fan, Z., Premier, G., Maddy, J. and Guwy, A. (2011). Control-oriented PEM fuel cell system modeling and repetitive controller design. *2nd International Conference on Intelligent Control and Information Processing, 2:* 1055 - 1060.
4. Barbir, F. (2005) *PEM Fuel Cells: Theory and practice*. Academic Press Sustainable World, ed. R. C.Dorf. California: Elsevier. 433.
5. Garcia-Gabin, W., Dorado, F. and Bordons, C. (2010). Real-time implementation of a sliding mode controller for air supply on a PEM fuel cell. *Journal of Process Control*, 20(3): 325 - 336.
6. Kim, Y. S., Kim, S. I., Lee, N. W. and Kim, M. S. (2015). Study on a purge method using pressure reduction for effective water removal in polymer electrolyte membrane fuel cells. *International Journal of Hydrogen Energy*, 40(30): 9473 - 9484.
7. Danzer, M. A., Wittmann, S. J. and Hofer, E. P. (2009). Prevention of fuel cell starvation by model predictive control of pressure, excess ratio, and current. *Journal of Power Sources*, 190(1): 86 - 91.
8. Sekine, F., Eguchi, M., Kobayashi, Y. and Tsutsumi, Y. (2010). Measuring method for flow rate distribution between cells in a polymer electrolyte fuel cell stack. *Journal of Power Sources*, 195(18): 5971 - 5974.
9. Tae-Hoon, K., Sang-Hyun, K., Wook, K., Jong-Hak, L. and Woojin, C. (2010). Development of the novel control algorithm for the small proton exchange membrane fuel cell stack without external humidification. *Applied Power Electronics Conference and Exposition (APEC) Twenty-Fifth Annual IEEE*: 2166 - 2173
10. Yousfi-Steiner, N., Moçotéguy, P., Candusso, D. and Hissel, D. (2009). A review on polymer electrolyte membrane fuel cell catalyst degradation and starvation issues: Causes, consequences and diagnostic for mitigation. *Journal of Power Sources*, 194(1): 130 - 145.
11. Rosli, R. E., Majlan, E. H., Wan Daud, W. R. and Hamid, S. A. A. (2012). Hydrogen rate manipulation of proton exchange membrane fuel cell (PEMFC) stack using feedback control system. *IEEE International Conference on Power and Energy (PECon)*: 553 - 557.
12. Zhou, F., Andreasen, S. J. and Kær, S. K. (2015). Experimental study of cell reversal of a high temperature polymer electrolyte membrane fuel cell caused by H_2 starvation. *International Journal of Hydrogen Energy*, 40(20): 6672 - 6680.
13. Varigonda, S. & Kamat, M. (2006). Control of stationary and transportation fuel cell systems: Progress and opportunities. *Computers & Chemical Engineering*. 30(10–12): 1735 - 1748.

14. Kim, T.-H., Kim, S.-H., Kim, W., Lee, J.-H., Cho, K.-S., Park, K.-W. and Choi, W. (2010). Development of the novel control algorithm for the small proton exchange membrane fuel cell stack without external humidification. *Journal of Power Sources*, 195(18): 6008 - 6015.

Malaysian Journal of Analytical Sciences, Vol 20 No 4 (2016): 913 - 922
DOI: http://dx.doi.org/10.17576/mjas-2016-2004-27

MALAYSIAN JOURNAL OF ANALYTICAL SCIENCES
Published by The Malaysian Analytical Sciences Society
ISSN 1394 - 2506

EFFECT OF LONG TIME OXYGEN EXPOSURE ON POWER GENERATION OF MICROBIAL FUEL CELL WITH ENRICHED MIXED CULTURE

(Kesan Terhadap Penjanaan Kuasa Sel Bahan Api Mikrob dengan Kultur Campuran yang Diperkaya Melalui Pendedahan pada Oksigen untuk Jangka Masa Lama)

Mimi Hani Abu Bakar[1, 2, 3]*, Neil F Pasco[2], Ravi Gooneratne[3], Kim Byung Hong[1,4,5]

[1]*Fuel cell Institute,*
Universiti Kebangsaan Malaysia, 43000 UKM Bangi, Selangor, Malaysia
[2]*Lincoln Ventures Ltd,*
PO Box 133, Lincoln, Christchurch 7640, New Zealand
[3]*Lincoln University, PO Box 84, Lincoln, 7647, New Zealand*
[4]*Korea Institute of Science & Technology,*
Seongbuk-ku, Seoul 136-792, Korea
[5]*State Key Laboratory of Urban Water Resource & Environment,*
Harbin Institute of Technology, Harbin 150090, China

**Corresponding author: mimihani@ ukm.edu.my*

Received: 5 February 2016; Accepted: 22 April 2016

Abstract

In this study, we are interested in the effect of long time exposure of the microbial fuel cells (MFCs) to air on the electrochemical performance. Here, MFCs enriched using an effluent from a MFC operated for about eight months. After 30 days, the condition of these systems was reversed from aerobic to anaerobic and vice versa, and their effects were observed for 11 days. The results show that for anaerobic MFCs, power generation was reduced when the anodes were exposed to dissolved oxygen of 7.5 ppm. The long exposure of anodic biofilm to air led to poor electrochemical performance. The power generation recovered fully when air supply stopped entering the anode compartment with a reduction of internal resistance up to 53%. The study was able to show that mixed facultative microorganism able to strive through the aerobic condition for about a month at 7.5 ppm oxygen or less. The anaerobic condition was able to turn these microbes into exoelectrogen, producing considerable power in relative to their aerobic state.

Keywords: microbial fuel cell, aerobic, oxygen exposure, wastewater

Abstrak

Dalam kajian ini, kami berminat untuk mengesan prestasi elektrokimia sel bahan api mikrob (MFC) terhadap pendedahan jangka masa panjang kepada udara. Di sini, MFC diperkaya menggunakan efluen daripada MFC yang telah beroperasi selama kira – kira lapan bulan. Selepas 30 hari, keadaan sistem ini telah diterbalikkan dari aerobik untuk anaerobik dan sebaliknya, dan kesannya diperhatikan selama 11 hari. Keputusan menunjukkan bahawa untuk MFC anaerobik, penjanaan kuasa telah berkurangan apabila anod terkena oksigen terlarut 7.5 ppm. Pendedahan jangka masa panjang biofilem anod kepada udara membawa kepada prestasi elektrokimia yang rendah. Penjanaan kuasa pulih sepenuhnya apabila bekalan udara berhenti memasuki ruangan anod dengan pengurangan rintangan sehingga 53 %. Kajian ini dapat menunjukkan bahawa mikroorganisma fakultatif campuran dapat hidup melalui keadaan aerobik selama sebulan pada 7.5 ppm oksigen atau kurang. Keadaan anaerobik mampu mengubah mikrob ini kepada eksoelektrogen, seterusnya menghasilkan kuasa yang tinggi berbanding dengan apabila berada di dalam keadaan aerobik.

Kata kunci: sel bahan api mikrob, aerobik, pendedahan oksigen, air sisa

Introduction

A microbial fuel cell (MFC) system is a bioenergy converter that utilizes bacteria to generate electricity through bacterial metabolic pathway [1]. These bacteria are known as exoelectrogens and could transfer electrons to anode electrode. Oxygen and nitrate are preferred electron acceptor over the anode reducing power generation in their presence in the anolyte. Tests on the impact of oxygen in air on anaerobic MFCs had been done on both single cell culture, such as from the genus *Shewanella* [2, 3], *Escherichia coli (E. coli)* [4] and mixed bacterial cultures from anaerobic wastewater treatment streams [5, 6]. It was shown that the dissolved oxygen in anolyte reduces the capability of certain bacteria to transfer electrons to external anode. Kim et al. [7] in their research on biosensor, found that *Shewanella putrefaciens* completely loss its electrochemical activity within three hours of exposure to air, while Biffinger et al. [8] found that *Shewanella oneidensis* work well as exoelectrogen in the presence of oxygen. Wang et al. [4] discovered that *E. coli* had about 61- 68 % decreased in capability to reduce external mediator, hexacyanidoferrate (III) $[Fe(CN)_6]^{3-}$ in anaerobic MFC when oxygen is presence. In the case of mixed culture, Liu et al. [5] found that the diffusion of oxygen to the anolyte from the catholyte would lead to 21- 50 % loss of substrate to aerobic oxidation by bacteria, which translates as the loss of generated electricity through the MFC.

A more detail work was done by Li et al. [3] on the response of *Shewanella decolorationis* with oxygen within six days of changing the flowing of argon gas and air into the MFCs to create alternate condition of aerobic and anaerobic. They discovered that in contact with oxygen, *S. decolorationis* reduced more NAD to NADH, which in turns increase in charge production. However, the dissolved oxygen (DO) in the anolyte increased aerobic respiration and biomass production that leads to current reduction in MFCs. There are not many studies reported on aerobic effect towards the anodic biofilm of MFCs [9]. Though available findings pointed out the short term adverse effect of oxygen on generation of current by bacteria in MFCs, to our knowledge there are no reports that show long term oxygen exposure on anolyte in MFC.

Therefore, this study aims to analyse the effect of long-duration exposure towards oxygen on the electrochemical performance of enriched multi-cultured bacteria in MFCs. In this work, effluent from an air-cathode MFC operated for about eight months was used as inocula for aerobic and anaerobic MFCs. After 30 days, the conditions of the system were changed by swapping between the nitrogen and air. This turned the aerobic into anaerobic and anaerobic into aerobic and were let to acclimatize in their new condition for 11 days. The electrochemical performance of the MFCs before and after the gas swapping were compared in view of maximum power density (P_{max}), current density (I_{max}) at P_{max} and internal resistance (R_{int}) accomplished within the systems.

Materials and Methods

Chemicals

Chemicals were of analytical grade. Peptone was purchased from Merck (Darmstadt, Germany). Yeast extract was purchased from Scharlau (Barcelona, Spain). Ammonium chloride (NH_4Cl) and sodium acetate anhydrous (CH_3.COONa) was purchased from AnalaR®, BDH Laboratory Supplies (Poole, England). Di-sodium hydrogen orthophosphate anhydrous (Na_2HPO_4) and potassium chloride (KCl) were purchased from Fisher Scientific UK Ltd. (Leicestershire, UK). Sodium dihydrogen orthosphosphate ($NaH_2PO_4.H_2O$) was purchased from LabServTM, Biolab (Aust) Ltd. (Victoria, Australia). All analytical solution was made using distilled water unless otherwise stated.

Inoculum, buffers, reagents and media

Effluent from an air cathode MFC inoculated with sludge collected from Bromley Wastewater treatment plant and operated about eight months using acetate as the electron donor was used to inoculate air-cathode MFCs used in this study. The basal medium was prepared by dissolving 0.31 g/L NH_4Cl, 3.12 g/L $NaH_2PO_4 \cdot 2H_20$, 4.58 g/L Na_2HPO_4, and 0.13 g/L KCl in phosphate buffer (50 mM, pH 7.0) [10, 11]. The acetate medium was made by dissolving 1 g/ L CH_3 COONa, 1 g/ L peptone of casein and 2 g/ L yeast extract in the basal medium [12]. The medium was autoclaved at 121 ^oC for 15 min prior to use.

MFC air-cathode construction

The study utilized single chambered air-cathode MFCs as described in Weld & Singh [13]. The reactor was constructed using three machined polycarbonate pieces with O-rings and steel bolts. The internal volume was 19.2 mL (Figure 1). The middle polycarbonate had its top equipped with three holes: two big holes of ø 1.8 cm and ø 1.0 cm for batch mode feeding and reference electrode respectively and one small hole of ø 0.4 cm for gas inlet. The anode chamber was separated from an air cathode by using cation exchange membrane (Ultrex) from BASF Fuel Cell Inc. (Somerset, NJ. USA).

The air-cathode and the anode were 4 cm × 4 cm of 10% Pt-carbon cloth (Fuel Cell Earth LLC, Stoneham, MA) covered with a layer of 4 cm × 4 cm plain carbon cloth (Fuel Cell Earth LLC, Stoneham, MA) and 4 cm × 4 cm plain carbon cloth respectively. The cathode was fastened to the exterior wall of the Ultrex membrane with a nickel strip, acted as current collector and also used to grip the anode.

Operation

Here, 2 % (v/v) of anolyte (OD_{600} of 2.85) from an eight month old MFC was incubated in acetate media for 24 h at 150 rpm and 24 °C. Each six new MFCs were filled with 0.4 mL of the incubated culture and topped up with acetate media. Two of the MFCs were bubbled with nitrogen to create anaerobic condition, the other two were bubbled with air to create aerobic condition, while two more were made as control, free from flowing of gas to create natural anaerobic condition. Except for the controlled MFCs, the anodes of gassed MFCs were poised at potential of +200 mV (vs. Ag/AgCl) for seven days and operated in controlled temperature of 28 °C. From the eighth day onwards, the anode poising was discontinued and the MFCs were connected to external resistors of 1,000 Ω.

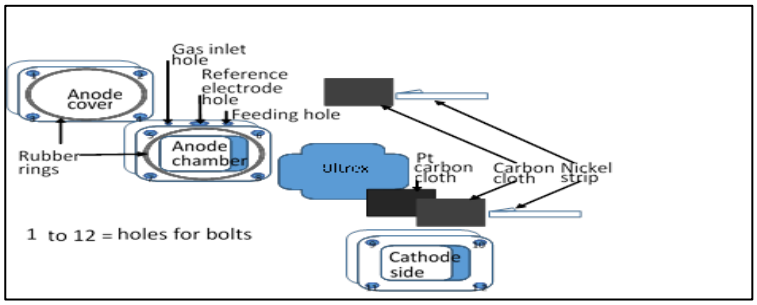


Figure 1. MFC used in this study

Analytical methods and calculation

Cell voltage (*E*) across the external resistor and cell current generated from the anode fixed potential poised were measured every twice a day using a Digitech QM 1326 multimeter or every 30 s to 30 min using a four channel Quadstat 164 potentiostat (eDAQ Pty Ltd, NSW, Australia) and continuous recording using an e-corder 1621 (eDAQ Pty Ltd, NSW, Australia) data acquisition system. Current (*I*) and power (*P*) were calculated using the Ohm's law (Equation 1 and 2):

$$I = \frac{E}{Rext} \quad , \; I_{density} = \frac{I}{Anode\ area} \tag{1}$$

$$P = I\ x\ E \quad , P_{density} = \frac{P}{Anode\ area} \tag{2}$$

where *E* represents circuit's potential and R_{ext} represents circuit external resistance, with the current density, $I_{density}$ and power density, $P_{density}$ normalized by the projected area of the anode [14].

Dissolved oxygen concentration in the anolyte was determined before the gas swapping activity from the aerobic MFCs as 7.5 ppm, using HQ40d portable multi-parameter meter (pH/ conductivity/ dissolved oxygen/ ORP/ ISE)

(Hach Company, Colorado, US). The polarization curve and the power density curves were produced by using method in Luo et al. [14] and Watson and Logan, [15] to obtain the open circuit voltage (OCV), P_{max}, I_{max} and R_{int} of the system. In this study, the polarization curves were obtained using multiple resistors (820 kΩ to 18 kΩ), with each resistance changed in decreasing order after every pseudo steady-state achieved or not more than 20 min intervals (which ever comes first) over a complete fed batch cycle. Analysis was conducted once the voltage output was stabilised after replenishing the media. The analysis was done for two consecutive cycles to ensure that the voltage response was unchanged with successive cycles.

Results and Discussion

Current density shows that once the anode poising was discontinued, only anaerobic MFCs show high current density with total daily average from day-8 till day-25 of 38.26 ± 0.13 mA/ m^2 and lowest by aerobic MFCs of 2.08 ± 0.01 mA/ m^2 while the control gave an average of 20.65 ± 0.28 mA/ m^2 (Figure 2). As soon as the MFC characterisation started (day 23, 24 and 25), the aerobic MFCs began to show significant in current density (t-test, $p<0.05$), which is higher than anaerobic MFCs with total daily average from day-26 till day-30 of 70.93 ± 0.19 and 67.49 ± 0.32 mA/ m^2 respectively. For the control system, there was not much increase in current density recorded after day-26, 30.69 ± 0.68 mA/ m^2.

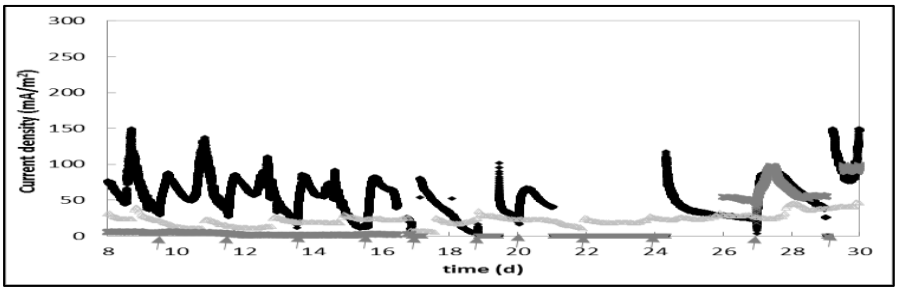


Figure 2. Biocatalytic current generation compared between aerobic and anaerobic environment.The air-cathode MFCs: anode chamber bubbled with nitrogen (◆), anode chamber bubbled with air (x) and control (▲). The frequency of batch feeding mode was in daily average (represented by ↑)(n=2).

The poising of the anode was to allow consistent control of the biofilm electrode potential, by making the electrode as the sole electron acceptor [16]. The reason of nitrogen bubbling into the anode compartment was to accelerate the anaerobic condition in the system simultaneously increase the MFC electrochemical performance. The control MFCs were solely depending on the bacteria in the anode chamber to create anaerobic environment by gradually consuming the soluble oxygen in the anolyte [17]. The current density generated by the control MFCs was almost 2-fold less than that generated by nitrogen bubbled MFCs. The high mass of bacteria inoculated in the anode compartment of the control MFCs, capable to consume oxygen available in the chamber for a short time. When the condition became suitable for anaerobic bacteria to survive and perform anodophilic transfer, then only current density started to gain pace. A similar situation was observed by Hutchinson et al. [18], who stated the importance of having the anode compartment free of diffused oxygen from the cathode esspecially during startup. In this study, feeding was done manually through a designated cavity at the top of the MFC reactor. This action might allow air to seep into the control MFCs, while for the anaerobic MFCs, the pressure created by the nitrogen bubbled MFC kept the air out during feeding. Therefore, the nitrogen bubbled MFCs could generate high current without the interference of air. In contrast, air bubbled MFCs remained at much lower current density than the control MFCs during the gassing period.

The characterisation of the MFCs for power and polarization curves, appeared to increase the current intensity of the aerobic and the anaerobic MFCs. From the Ohm's law in equation 1, new voltage at the electrodes can be obtained through changing the R_{ext}. During the characterisation analysis, the R_{ext} applied had values larger than the fixed R_{ext} used for the MFCs' operation. The large R_{ext} values were necessary to obtain the standard MFC characterisation and

polarization curves. This might attributed to the moment surged in current intensity once the MFC characterisation was stopped and the system were again connected to the fixed $R_{ext,}$ which had much lower value. Similar incident was experienced by Aelterman et al. [19], in their studies on the effect of R_{ext} ranges towards MFCs current generation. They found that the current intensity of their MFCs increased by 3.29-fold when they changed the R_{ext} from 50 to 10.5 Ω. However, further study is necessary to identify reason on how the aerobic increased in current density by one fold more than the anaerobic after characterisation analysis was done.

The switching of gasses between air and nitrogen began on day-33 until day 44. The total daily average current calculated for the 11 days after gas swapping did not show any significant in current density (t-test, p >0.05) between before (day-26 to 30) and after gas swapping for each MFC conditions (day-33 to 44): 49.89 ± 0.19 mA/ m^2(nitrogen gassed MFCs) and 74.81 ± 0.18 mA/ m^2 (aerated MFCs) (Figure 3).

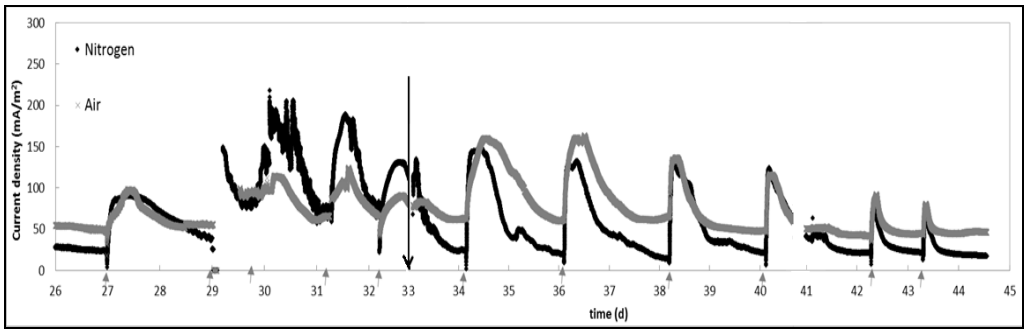


Figure 3. Effect of gas swapping (↓) between the aerobic and anaerobic MFCs. The frequency of batch feeding mode was in average every two days (represented by ↑)(n=2)

However, when looking at the individual daily average in current density (Table 1), there seems to be clear decreasing trend for the anaerobic MFCs from the beginning of the swapping till day-43. For aerobic MFCs, the effect of nitrogen bubble seems evidenced within the first four days after gas swapping and the anaerobic effect slowly became reduced and stabilized at about 50 mA/ m^2. Further study would need to be carried out to understand this phenomenon.

The impact of the gas swapping before and after can be observed through the polarization and the power curves. Comparisons done on the OCV from the polarization curves between the aerobic and anaerobic MFCs before and after the gas swapping (Figure 4a), which was about 20 days apart and the control, shows that the aerobic MFCs possessed 2.3 fold higher OCV than before the gas swapping (150 mV, vs. Ag/ AgCl), and 1.2 fold higher OCV than both the anaerobic (before and after gas swapping) and the control MFCs (300 mV, vs. Ag/ AgCl)(Figure 4a). The OCV zone is known as the activation loss zone and refers to the electron transfers reaction at the electrode surface. The OCV is the highest voltage produced in an MFC, measured in the absence of current and take into consideration various potential losses as follows (Equation 3 and 4)[20, 21].

$$OCV = E_{cell} + IR_{int} \tag{3}$$

$$E_{cell} = E_{emf} - (\sum \eta_a + |\sum \eta_c| + IR_{\Omega}) \tag{4}$$

where the E_{cell} is the measured cell voltage, IR_{int} is the sum of all internal losses of the MFC, $\sum \eta_a$ and $|\sum \eta_c|$ represents the overpotentials of the anode and cathode respectively. The overpotential of the anode and cathode reflect the influence of slow kinetics of heterogenous electron transfer, which is the movement of electrons between a chemical species and a solid-state electrode, together with ohmic resistance and concentration

gradients [22]. E_{emf} is the cell electromotive force from the differece of cathode potential, E_{cat} to anode potential, E_{an} , and IR_{Ω} represents the sum of all ohmic losses.

Table 1. Daily average current calculated after gas swapping (± standard error of mean) (n=2)

Day	**Anaerobic MFCs bubbled with air (mA/ m^2)**	**Aerobic MFCs bubbled with nitrogen (mA/ m^2)**
26 – 30 $_{\text{(before gas swap)}}$	70.93 ± 0.19	67.49 ± 0.32
Gas swapping dates:		
33 – 34	53.40 ± 0.58	71.92 ± 0.16
35 – 36	33.89 ± 0.17	85.28 ± 0.39
36 $_{\text{(feed)}}$ – 37	82.84 ± 0.69	124.66 ± 0.59
37 – 38	30.68 ± 0.17	69.21 ± 0.17
38 $_{\text{(feed)}}$ – 39	74.19 ± 0.75	87.11 ± 0.53
39 – 40	30.70 ± 0.08	50.43 ± 0.04
40 $_{\text{(feed)}}$ – 41	69.36 ± 0.54	72.69 ± 0.44
41 $_{\text{(feed)}}$ – 42	31.66 ± 0.16	47.88 ± 0.07
42 $_{\text{(feed)}}$ – 43	33.08 ± 0.29	52.23 ± 0.25
43 $_{\text{(feed)}}$ – 44	28.49 ± 0.23	49.15 ± 0.17

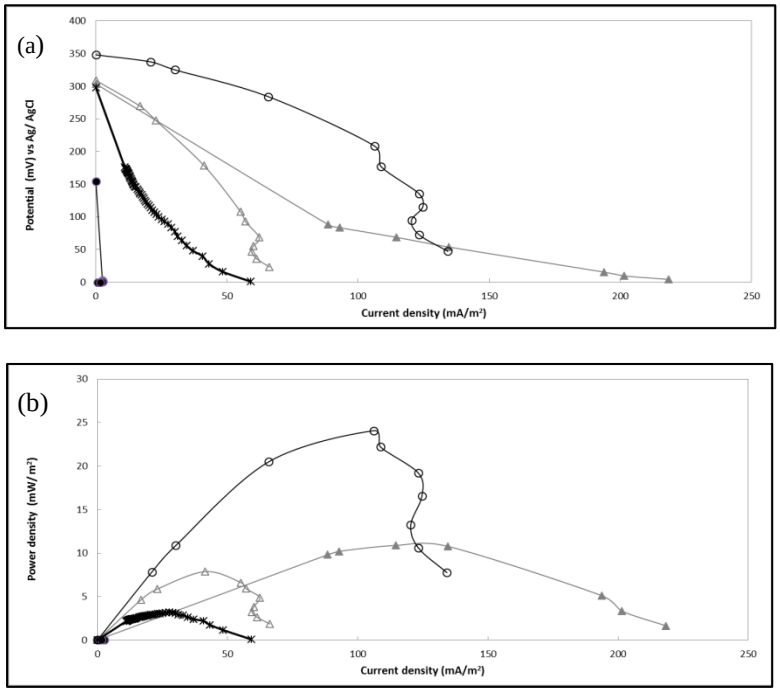


Figure 4. Polarization (a) and power density (b) curves recorded. Symbols in the figure represent anaerobic MFCs before (△) and after (△) gas switching and aerobic MFCs before (●) and after (○) gas switching as well as controls (x)(n=2).

Hence, apart from the low concentraiton of oxygen in air (ca. 21%), the reduced in OCV could be attributed to factors, such as potential generated by the exoelectrogen that formed the anodic biofilm, diffused oxygen into the anode compartment that interrupts the anodic biofilm and inefficient oxygen reduction reaction (ORR) occurs at the cathode site [23]. Ideally, an OCV of an air-cathode MFC should be around +621 mV (vs. Ag/AgCl) (+820 mV, vs. SHE) when pure oxygen is used. The 820 mV is based on the potential of redox couple between pure oxygen and water (½ O2/ H_2O, $2e^-$) [24]. However when air is used at the cathode side, OCV obtained are much lower than the ideal. In an MFC study done by Li et al. [25] using anaerobic wastewater as inoculum in a 75.6 mL dual chambered MFC with air bubbled in deionized catholyte, OCV was within the range of +419 to +489 mV (vs. Ag/ AgCl). In other study done by Khan et al. [26] using anaerobic digester from palm oil waste as inoculum in 20 mL single chamber air-cathode, found that the OCV also dependent on the catalyst applied onto the cathode, which could ranged from +385 to +626 mV (vs. Ag/ ACl). In this study, however, the high OCV recorded for the aerobic MFCs after the anolyte was continously bubbled with nitrogen for 11 days, might have increased the population of the exoelectrogens in the anode compartment, thus reduce the overpotential of the anode and the internal losses in the MFC.

From the MFC characterisations (Table 2), positive changed were seen on the aerobic MFCs where the P_{max} increased by more than 1,000- fold, increased in I_{max} by 42-fold, once the air in the anolyte was replaced with nitrogen. The change in the anaerobic MFCs after the nitrogen bubble replaced with air was small, about 1.4- fold of decreased in P_{max} along with a slight decreased in I_{max} by 2.8-fold. This increase in both I_{max} and P_{max} for the aerobic MFCs after the gas swapping shows that when MFCs were in the aerobic state, the exoelectrogens were already there, and these became active once the environment turned to anaerobic. Exoelectrogens are believed to be facultative bacteria that could survive in both conditions, aerobic and anaerobic [27]. In the air bubbling anode chamber, the small number of exoelectrogenic bacteria near the anode still survive because concentration of oxygen lessen with the increasing depth of biofilm; while the centre is already anaerobic [28]. Diffused oxygen is consumed in the outer layers of biofilm, providing favourable conditions for growth of facultative and strict anaerobes in the deep layers of the biofilm [29]. Similar to oxygen, substrate diffusion also decrease with the increase of biofilm mass depth from bulk fluid to the interior biofilm [30].

Table 2. Details obtained from MFC electrochemical characterizations

MFC	P_{max} **(mW/ m^2)**	I_{max} **(mA/ m^2)**	R_{int} **(kΩ)**
Anaerobic- before gas swap	10.88 ± 8.33	114.61 ± 49.97	30.55 ± 0.00
Anaerobic- after gas swap (aerobic condition)	7.87 ± 2.13	41.29 ± 5.35	226.40 ± 2.45
Aerobic- before gas swap	0.02 ± 0.02	2.50 ± 2.25	50.92 ± 0.00
Aerobic- after gas swap (anaerobic condition)	24.07 ± 4.06	106.22 ± 11.20	107.79 ± 3.89
Control	2.91 ± 2.52	31.09 ± 17.94	2.41 ± 0.00

Although both the P_{max} and the I_{max} showed expected results with the swapping of gasses, the R_{int} for aerobic MFCs showed an increment of 2.1-fold after the gas swapping. Comparison between the R_{int} of aerobic and anaerobic MFCs after the gas swapping however shows that the nitrogen replacing the air in aerobic MFCs, reduced its R_{int} lower than that of anaerobic MFCs. This effect can be seen clearly in the power curves where the curve of aerobic MFCs after the swapping was not symmetrical as the power curve of the anaerobic MFCs (Figure 4b). Based on Logan et al. [20], the symmetric nature of the power density curve obtained from the MFC characterisation analysis, which was also seen in this study represents a high R_{int} in an MFC mostly due to the ohmic resistance (R_{Ω}) at the point of P_{max}. R_{Ω} is derived from any material that creates resistance in the system, such as substrates, bacteria, gap between electrodes, loose contacts between components, and low ionic conductivity in the substrate. The continuous air bubbling in the anode chamber probably helped with the growth of aerobic microbes due to a direct reduction of

oxygen in the cell to increase biomass production. Although increase in biomass means increase in the NADH production, which leads to increase in electrons production, most of these electrons however will be consumed for biomass before able to generate electricity [3]. This could be the reason for the high R_{int} observed from aerobic MFCs before the gas swapping with very poor I_{max} and P_{max} [24].

Although this study was able to culture exoelectrogen from aerobic sludge originated from trickling filter, the electrochemical performance was way too low from results that have been reported in other publications, which is no less than 100 mW/m^2. According to Rahimnejad et al. and Haslett et al [31, 32], the performance of MFCs are commmonly associated with the following: 1) Substrates oxidation in the anode compartment, 2) Microorganism used for inoculum, 3) Mediator, 4) Permeabililty of cation exchange membrane (if any), 5) Electrode material and their surface area, 6) Electron acceptor at the cathode chamber, 7) Electron trasport pathway to anode surface, 8) Overpotential at the electrodes, 9) External load applied, 10) Distance between electrodes, 11) Mass transport, and 12) Operational temperature [31, 32]. For instance Feng et al. [33] analysed the effect of acid modified carbon fiber brush in 28 mL air-cathode MFC having 20% inoculum from domestic wastewater with external load of 1 kΩ, achieved P_{max} of 1,370 mW/ m^2. Watson and Logan [15] adapted similar MFC design with an increased of inoculum concentration upto 50%, different type of microorganism and used a non modified carbon fiber brush, had achieved 1.6 fold lower P_{max} than the later. Santoro et al. [34] on the other hand with completely different MFC design, used 4.6 fold more volume and non modified carbon cloth for anode and cathode, only achieved 268 mW/m^2 of P_{max}. To identify the reason of poor electrochemical performance in this study and to reduce such high R_{int}, the variables affecting the performance of MFCs listed above need to be analyzed and compare them with those having similar MFC designs.

Conclusion

The goal of this study was to analyse the effect of long-duration exposure towards oxygen in air through gas swapping on the electrochemical performance of enriched multi-cultured bacteria in air-cathode MFCs. The results showed that prolong exposure in 7.5 mg/L (ppm) of dissolved oxygen MFCs for a month on the enriched multi-cultured bacteria culture, makes the bacteria electrochemically inactive and produced low power and current generation. This however is not permanent since it could easily and quickly be rectified with improvements up to 100 % in P_{max} and I_{max} and a reduction in R_{int} of up to 53 %, when introduced into an anaerobic environment. Future studies could be carried out to gain a more in-depth understanding on electrochemical performance of MFCs before and after gas swapping, and also understanding of its effect on microbial community in the biofilm and half-wave redox potential ($E_{1/2}$). Further research can also be carried out on electrode polarization and the effect of different oxygen concentration ranges on MFC performance.

Acknowledgement

This work was supported by funding from Ministry of Higher Education of Malaysia (MoHE), Universiti Kebangsaan Malaysia (UKM), Lincoln University, Canterbury, New Zealand and lab facility from Lincoln Agritech Ltd, Christchurch, New Zealand.

References

1. Rittmann, B. E. (2006). Microbial ecology to manage processes in environmental biotechnology. *Trends in Biotechnology*, 24(6): 261 - 266.
2. Kim, H. J., Park, H. S., Hyun, M. S., Chang, I. S., Kim, M. and Kim, B. H. (2002). A mediator-less microbial fuel cell using a metal reducing bacterium, Shewanella putrefaciens. *Enzyme and Microbial Technology*, 30(2): 145 - 152.
3. Li, S.-L., Freguia, S., Liu, S. M., Cheng, S. S., Tsujimura, S., Shirai, O. and Kano, K. (2010). Effects of oxygen on Shewanella decolorationis NTOU1 electron transfer to carbon-felt electrodes. *Biosensors and Bioelectronics*, 25: 2651 - 2656.
4. Wang , Y.-F., Cheng, S. S., Tsujimura, S., Ikeda, T. and Kano, K. (2006). E. coli-catalyzed bioelectrochemical oxidation of acetate in the presence of mediators. *Bioelectrochemistry*, 69(1): 74 - 81.
5. Liu, H., Cheng, S. and Logan, B. E. (2005). Production of electricity from acetate or butyrate using a single-chamber microbial fuel cell. *Environmental Science & Technology*, 39(2): 658 - 662.

6. Kim, B. H., Park, H. S., Kim, H. J., Kim, G. T., Chang, I. S., Lee, J. and Phung, N. T. (2004). Enrichment of microbial community generating electricity using a fuel-cell-type electrochemical cell. *Applied Microbiol Biotechnology*, 63(3): 672 – 681.
7. Kim, B., Ikeda, T., Park, H. S., Kim, H. J., Hyun, M. S., Kano, K., Takagi, K. and Tatsumi, H. (1999). Electrochemical activity of an Fe(III)-reducing bacterium, Shewanella putrefaciens IR-1, in the presence of alternative electron acceptors. *Biotechnology Techniques*, 13(7): 475 - 478.
8. Biffinger, J. C., Byrd, J. N., Dudley, B. L. and Ringeisen, B. R. (2008). Oxygen exposure promotes fuel diversity for Shewanella oneidensis microbial fuel cells. *Biosensors and Bioelectronics*, 23(6): 820 - 826.
9. Mohan, S. V., Velvizhi, G., Modestra, J. A., and Srikanth, S. (2014). Microbial fuel cell: Critical factors regulating bio-catalyzed electrochemical process and recent advancements. *Renewable and Sustainable Energy Reviews*, 40: 779 - 797.
10. Kim, J. R., Min, B. and Logan, B. E. (2005). Evaluation of procedures to acclimate a microbial fuel cell for electricity production. *Applied Microbial Biotechnology*, 68: 23 - 30.
11. Rader, G.K. and Logan, B. E. (2010). Multi-electrode continuous flow microbial electrolysis cell for biogas production from acetate. *International Journal of Hydrogen Energy*, 35(17): 8848 - 8854.
12. Atlas, R. M. (2005). Handbook of microbiological media. Second Edition ed. Acetate agar, Fluorida: Taylor & Francis Group.
13. Weld, R. J. and Singh, R. (2011). Functional stability of a hybrid anaerobic digester/microbial fuel cell system treating municipal wastewater. *Bioresource Technology*, 102(2): 842 - 847.
14. Luo, Y., Zhang, F., Wei, B., Liu, G., Zhang, R. and Logan, B. E. (2011). Power generation using carbon mesh cathodes with different diffusion layers in microbial fuel cells. *Journal of Power Sources*, 196(22): 9317 - 9321.
15. Watson, V.J. and Logan, B. E. (2011). Analysis of polarization methods for elimination of power overshoot in microbial fuel cells. *Electrochemistry Communications*, 13(1): p. 54-56.
16. Babauta, J., Renslow, R., Lewandowski, Z. and Beyenal, H. (2012). Electrochemically active biofilms: facts and fiction. A review. *Biofouling*, 28(8): 789 - 812.
17. Ringeisen, B. R., Ray, R. and Little, B. (2007). A miniature microbial fuel cell operating with an aerobic anode chamber. *Journal of Power Sources*, 165: 591 - 597.
18. Hutchinson, A. J., Tokash, J. C. and Logan, B. E. (2011). Analysis of carbon fiber brush loading in anodes on startup and performance of microbial fuel cells. *Journal of Power Sources*, 196(22): 9213 -9219.
19. Aelterman, P., Versichele, M., Marzorati, M., Boon, N. and Verstraete, W. (2008). Loading rate and external resistance control the electricity generation of microbial fuel cells with different three-dimensional anodes. *Bioresource Technology*, 99: 8895- 8902.
20. Logan, B. E., Hamelers, B., Rozendal, R., Schröder, U., Keller, J., Freguia, S., Aelterman, P., Verstraete. W. and Rabaey, K. (2006). Microbial fuel cells: Methodology and technology. *Environmental Science & Technology*, 40(17): 5181 - 5192.
21. Osman, M. H., Shah, A. A. and Walsh, F. C. (2010). Recent progress and continuing challenges in bio-fuel cells. Part II: Microbial. *Biosensors and Bioelectronics*, 26(3): 953 - 963.
22. Tayhas, G., Palmore, R. and Whitesides, M. G. (1994). Chapter 14: Microbial and enzymatic biofuel cells, in Enzymatic conversion of biomass for fuels production. American Chemical Society: Massachusetts.
23. Cheng, S., Liu, H. and Logan, B. E. (2006). Increased power generation in a continuous flow MFC with advective flow through the porous anode and reduced electrode spacing. *Environmental Science & Technology*, 40(7): 2426 - 2432.
24. Logan, B. E. (2008). Mechanism of electron transfer, in *Microbial Fuel Cell*. John Wiley & Sons, Inc: New Jersey. pp. 13.
25. Li, X.M., Cheng, K. Y., Selvam, A. and Wong, J. W (2013). Bioelectricity production from acidic food waste leachate using microbial fuel cells: Effect of microbial inocula. *Process Biochemistry*, 48(2): 283 - 288.
26. Khan, M.R., Chan, K. M., Ong, H. R., Cheng, C. K. and Rahman, W. (2015). Nanostructured pt/mno2 catalysts and their performance for oxygen reduction reaction in air cathode microbial fuel cell. *International Journal of Electrical, Computer, Electronics and Communication Engineering*, 9(3): 295 - 301.
27. Lefebvre, O., Shen, Y., Tan, Z., Uzabiaga, A., Chang, I. S. and Ng, H. Y. (2011). A comparison of membranes and enrichment strategies for microbial fuel cells. *Bioresource Technology*, 102(10): 6291 - 6294.

28. Cunningham, A.B., Lennox, J. E. and Ross, R. J. (2014). The Biofilms Hypertextbook: Intermediate level. Chapter 2: Biofilm formation and growth 2001-2008; Section 3: Biofilm development]. Available from: http://biofilmbook.hypertextbookshop.com/public_version/contents/chapters/chapter002/section003/blue/page003.html [Access online 19 September 2014].
29. Pastorella, G., Gazzola, G., Guadarrama, S. and Marsili, E. (2012). Biofilms: Applications in bioremediation, in Microbial Biofilms: Current research and applications, G. Lear and G.D. Lewis, Editors, Horizon Scientific Press: UK. : 73 - 98.
30. Dirckx, P. (1997). Biofilm structure with labels, Biofilm.jpg, Center for Biofilm Engineering: Montana.
31. Rahimnejad, M., Ghoreyshi, A. A., Najafpour, G. and Jafary, T. (2011). Power generation from organic substrate in batch and continuous flow microbial fuel cell operations. *Applied Energy*, 88(11): 3999 -4004.
32. Haslett, N. D. (2012). Development of a eukaryotic microbial fuel cell using Arxula adeninivorans, in Department of Agricultural Sciences. Lincoln University. pp. 245.
33. Feng, Y., Yang, Q., Wang, X. and Logan, B. E. (2010).Treatment of carbon fiber brush anodes for improving power generation in air-cathode microbial fuel cells. *Journal of Power Sources*, 195(7): 1841 - 1844.
34. Santoro, C. Lei, Y., Li, B. and Cristiani, P. (2012). Power generation from wastewater using single chamber microbial fuel cells (MFCs) with platinum-free cathodes and pre-colonized anodes. *Biochemical Engineering Journal*, 62: 8 - 16.

Malaysian Journal of Analytical Sciences, Vol 20 No 4 (2016): 923 - 930
DOI: http://dx.doi.org/10.17576/mjas-2016-2004-28

MALAYSIAN JOURNAL OF ANALYTICAL SCIENCES
Published by The Malaysian Analytical Sciences Society
ISSN 1394 - 2506

FABRICATION AND CHARACTERIZATION OF Fe-DOPED TUNGSTEN TRIOXIDE PHOTOELECTRODES IN AQUEOUS MEDIUM USING TUNGSTIC ACID AND FERROCENE AS STARTING MATERIALS

(Pembuatan dan Pencirian Fotoelektrod Tungsten Trioksida Terdop Fe Dalam Medium Akueus Dengan Asid Tungstik dan Ferosin Sebagai Bahan Permulaan)

Ng Kim Hang [1], Nurul Akmal Jaafar[1], Lorna Jeffery Minggu [1]*, Mohammad bin Kassim[1,2]

[1]*Fuel Cell Institute*
[2]*School of Chemical Sciences and Food Technology, Faculty of Science and Technology*
Universiti Kebangsaan Malaysia, 43600 UKM Bangi, Selangor, Malaysia

**Corresponding author: lorna_jm@ukm.edu.my*

Received: 5 February 2016; Accepted: 22 April 2016

Abstract

Different compositions of Fe-doped tungsten trioxide thin films were synthesized on fluorine-doped tin oxide (FTO) glass substrate by sol-gel method, with ferrocene and tungstic acid as starting materials. The synthesized thin films was characterized with X-ray diffraction (XRD), scanning electron microscope (SEM), UV/Vis spectrophotometer and photoelectrochemical (PEC) analysis. The results show that the surface morphology of the thin films became rough and the grain size increased along with the concentration of Fe. Monoclinic structure of tungsten trioxide was obtained for all doped and undoped WO_3 and red-shift can be observed from UV-vis spectrum. Band gap reduced from 2.74 eV of undoped WO_3 thin films to 2.60 eV of 20 % Fe-doped WO_3 thin films. Photoactivities of all Fe-doped WO_3 are higher than undoped thin films. The highest photoactivities contributed by 5 % Fe-doped WO_3 films with photocurrent densities measured was 0.148 mA/cm^2, which is 3 times higher compared to undoped WO_3.

Keywords: Fe-doped WO_3, direct water splitting, photoelectrochemical cell, photoanode

Abstrak

Filem nipis tungsten trioksida terdop Fe berbagai komposisi telah disediakan di atas kaca substrat FTO (fluorine-doped tin oxide) dengan kaedah sol-gel, dengan menggunakan ferosin dan asid tingstik sebagai bahan pemula. Filem nipis yang terhasil kemudiannya dicirikan dengan pembelauan sinar X (XRD), mikroskopi elektron pengimbasan (SEM), UV/Vis spektrofotometer dan analisis fotoelektrokimia. Keputusan menunjukkan bahawa morfologi permukaan filem nipis menjadi kasar dan saiz butiran bertambah dengan penambahan kepekatan Fe. Tungsten trioksida yang berstruktur monoklinik telah dihasilkan dan anjakan merah telah diperhatikan di dalam spectrum UV-vis. Jurang tenaga telah berkurang dari 2.74 eV (WO_3 tulen) kepada 2.60 eV (20 % Fe-dop WO_3). Fotoaktiviti WO_3 terdop Fe adalah lebih tinggi berbanding WO_3 tulen. Fotoaktiviti yang tertinggi dicatatkan oleh filem 5 % WO_3 terdop Fe dengan ketumpatan fotoarus 0.148 mA/cm^2. Ia adalah 3 kali ganda lebih tinggi berbanding WO_3 tulen.

Kata kunci: Fe-dop WO_3, pembelahan air secara langsung, sel fotoelektrokimia, fotoanod

Introduction

Hydrogen is a potential energy replacing current used of fossil fuel because it is renewable and environmentally friendly energy where the product of its consumption is only water and heat compared to fossil fuel which emit

carbon based gases. Thus, hydrogen is a promising future energy [1, 2]. However, most of hydrogen production is via steam reforming which also consumes fossil fuels. In 1972, Fujishima and Honda first reported photocatalytic water splitting using semiconductor material TiO_2 in 1972 [3]. Since then, photocatalytic water splitting using semiconductor catalysts received much interest from scientific community due to its potential to convert sunlight energy into chemical energy (hydrogen gas). The process of water splitting involves the excitation of electrons from the valence band during illumination. The excited electrons then moved to conduction band leaving holes in valence band. The holes on the semiconductor catalyst surface will oxidize water to produce oxygen gas and hydrogen ions while the excited electrons in conduction band moves towards the cathode to reduce the hydrogen ions into hydrogen gas [4]. The energy in excess of the band gap energy will be dissipated as heat. In practice, a semiconductor with a band gap of 1.70 eV [5] which is greater than the energy required for water splitting reaction (1.23 eV), can utilize maximum absorption of energy for PEC reactions [6,7]. There are several important criteria to be considered in selecting the semiconductor catalyst such as (1) favorable band edge position, (2) stability in harsh environments, (3) small band gap, and (4) photocorrosion resistance. However semiconductor catalyst that satisfy all of these criterial has yet to be found. Therefore several modifications on this photocatalyst was introduced such as fabrication of nanostructures, layered/junction, noble metal loading, and doping (anion or cation) [8-10]. In this paper, doping are our main interests because it is an alternatives approach to decrease the bandgap of semiconductor materials [11].

Tungsten trioxide (WO_3) is a good candidate in electrochromic, photochromic and sensoring applications [12 -17] and is one of the semiconductors which have the potential in water splitting when induced by sunlight. However, WO_3 has a large band gap of 2.8 eV where it can only absorb < 450 nm wavelength in the solar spectrum. In order to reduce the band gap, WO_3 was synthesized via different methods [18-21]. The narrow band gap of 2.20 - 2.80 eV helps in absorption of ultraviolet region and blue region of visible light in solar spectrum [22-25]. Furthermore, WO_3 has been investigated with the aim of improving catalyst activity and stability in the irradiated aqueous environment [26-29]. Tungsten trioxide powders prepared from various W precursors has been studied by Bamwenda and Arakawa [30]. They found that the WO_3 using tungstic acid as precursor has the lowest light absorption in long wavelength region, but it has the highest crystallinity level and photoactivity. On the other hand, iron nitrate has been used as dopant for Fe-doped TiO_2 thin film [31] and Fe-doped WO_3 powder photocatalyst [32]. Band gap of Fe-doped TiO_2 reduced from 3.30 eV to 2.89 eV when 0.2 at. % of Fe is added. Photocurrent density of 0.2 at.% Fe-doped TiO_2 is much higher than undoped TiO_2. The 10 % Fe-doped WO_3 photocatalyst is able to evolve more hydrogen gas under laser illumination compared to undoped WO_3. Apart from the nitrate salt, ferrocene is another Fe source that has been studied in various applications. Saremi Yarahmadi et al. [33] found that the thin films prepared using ferrocene has increased the optical absorption due to higher packing density, and improved the measured photocurrent density.

In this paper, we aim to prepare Fe-doped WO_3 photoelectrodes with ferrocene as the Fe source and tungstic acid as the WO_3 precursor. Photoactivity performance of the thin film photoanode was studied as well. The film properties are discussed herein.

Materials and Methods

Fe-doped WO_3 was fabricated via sol-gel method on the fluorine-doped tin oxide (FTO) glass using starting material made of Tungstic acid, H_2WO_4 (Sigma-Aldrich), ammonia aqueous (Merck, 28-30%), ferrocene (Sigma-Aldrich) and PEG 300 (Merck). Other chemicals involved in this fabrication were of analytic purity grades and distilled de-ionized water. The starting material was prepared by adding the tungstic acid into aqueous ammonia which formed 0.4 M ammonium tungstate solution. The excess ammonia from the solution was eliminated by heating. The ferrocene and PEG 300 were then added into the ammonium tungstate solution which resulted in the desired ratio of W to Fe (W:Fe = x:1-x, where x = 1, 0.95, 0.9, 0.85 or 0.8). Before the fabrication process, the FTO glass was cleaned using ultrasonic cleaner by immersing the FTO glass into three different beakers containing acetone, ethanol, and iso-propanol for 5 minutes in each beaker sequentially. The cleaned FTO glass was then coated with ferrocene-ammonium tungstate solution by doctor blading method, which formed thin films on the FTO glass. The as-deposited thin films were calcined and sintered in furnace at 500°C for 30 minutes with constant heating rate of 5 $^{o}Cs^{-1}$.

The calcined thin films were characterized using X-ray diffraction measurement, XRD (Bruker D8 Advance diffractometer) with CuKα radiation, to determine the structure and crystalinity of thin films, scanning electron microscope, SEM (Zeiss AM10) to determine its morphology, grain size and thickness of the thin films, and UV-Vis spectrophotometer (PerkinElmer Lambda 35) to measure the absorption of the thin films. Meanwhile, the band gaps of the thin films were estimated from the UV-Vis absorption spectrum and by utilizing the Tauc formula. Photoelectrodes were prepared by attaching copper wire to the FTO glass as described by Minggu et al. [34]. The photoelectrochemical (PEC) tests of the photoelectrodes prepared was carried out in a conventional three electrodes system, which consists of working electrode (photoelectrode), counter electrode (platinum wire), and reference electrode (SCE) whereas, 0.5 M Na_2SO_4 was used as the electrolyte. Prior to PEC analysis, the electrolyte was purged with nitrogen gas for 30 minutes. The scan rate was set to be 0.01 Vs^{-1}. The photoelectrochemical (PEC) analyses were carried out by using Ametek Versastat 4 with 450W full arc Xenon lamp source.

Results and Discussion

SEM analysis

Figure 1 shows SEM micrographs of undoped WO_3 and Fe-doped WO_3 on FTO glass. The morphology of undoped WO_3 is different from the WO_3 thin film prepared by Yagi et al. [35] using similar method. In their study, tungstic acid was dissolved in ammonia aqueous and PEG was added but the film produced was covered with micro-scale plates. This morphological difference might be caused by the much higher molecular weight of PEG they used (PEG 20000 was used in their study). This plate-like feature can also be observed in WO_3 thin film produced from tungstic hexaethoxide/PEG annealed in 300°C [36]. The organic residue causes the degradation in porosity and finally it forms plate. Therefore, spherical surface feature observed in this paper suggested that the organic compounds used were successfully eliminated. Morphological differences among the doped WO_3 thin films can be noticed by comparing the micrographs in Figure 1.

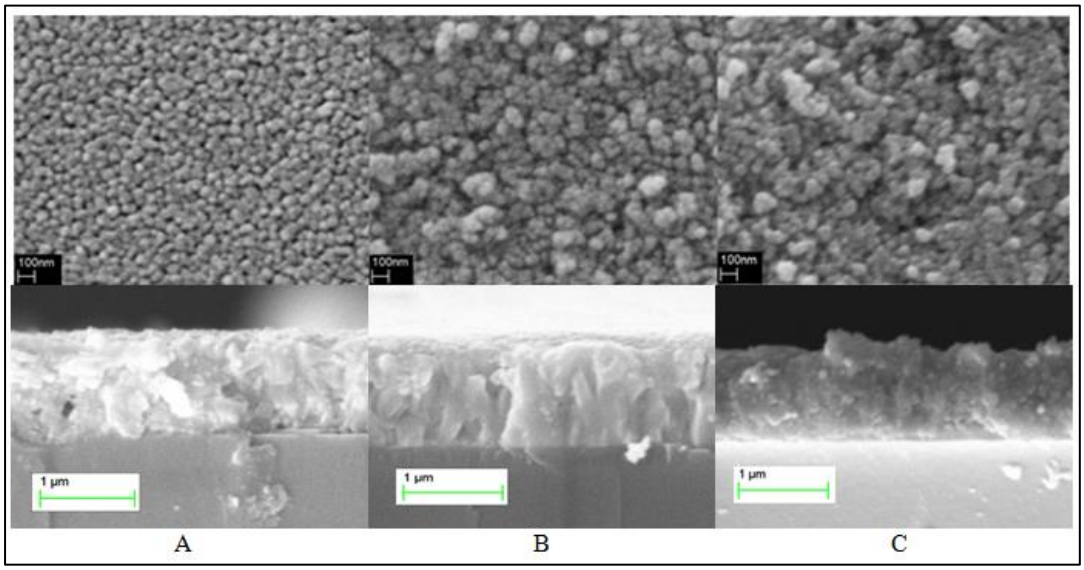


Figure 1. SEM image of (A) undoped, (B) 10% and (C) 20% Fe-doped WO_3 thin films

By comparing Fe-doped WO_3 with the undoped WO_3 thin films, it is noticed that surface of the Fe-doped WO_3 is rough. The presence of Fe would lead to agglomeration of the WO_3 particles. Therefore, the grain size of the Fe-doped WO_3 is increasing as the Fe content increases [37]. From cross section, the thickness of the films are approximately 1 µm. Taking account of the fluorine-tin oxide layer 900 nm, the actual thickness of undoped and Fe-doped WO_3 is around 100 nm.

XRD analysis

All thin films of different Fe concentration of Fe-doped WO_3 and undoped WO_3 thin films were subjected to X-ray diffraction measurement. The XRD pattern in Figure 2, which are in agreement with the Joint Committee on Powder Diffraction Standards (JCPDS) file no. 01-083-0950, displayed strongest peak at 24.4º, which corresponding to (2 0 0) plane of the annealed WO_3 thin films. This peak shows that the thin films were all of monoclinic, polycrystalline WO_3 structure. The XRD pattern of each thin films was coincident with undoped WO_3, which suggested well incorporation of Fe into WO_3 lattice. Furthermore, additional peaks that were not detected from the patterns shown, indicates that the crystalline structure of WO_3 thin films was not affected by Fe-doping with various concentration. Besides, the increment in intensity of the WO_3 peaks can also be observed. This suggested that the crystallinity of WO_3 is improved as the crystal defects disappear when Fe particle was added to the WO_3 crystal lattice [30]. The increased in crystallinity is due to reduce nucleation centre density which favors crystal grains growth [38]. High crystalline WO_3 was obtained for 20% Fe-doped WO_3 and this effect can also be observed on Fe-doped TiO_2 [31]. The main peak was shifted to lower lattice parameters due to the size of ionic radii of Fe^{2+} (0.064 nm) [39], which was larger than W^{6+} (0.060) [40]. The shifted peak also suggested that Fe^{2+} had successfully replaced some of the W^{6+} in bulk WO_3 lattice and thus, Fe-doped WO_3 was successfully synthesized.

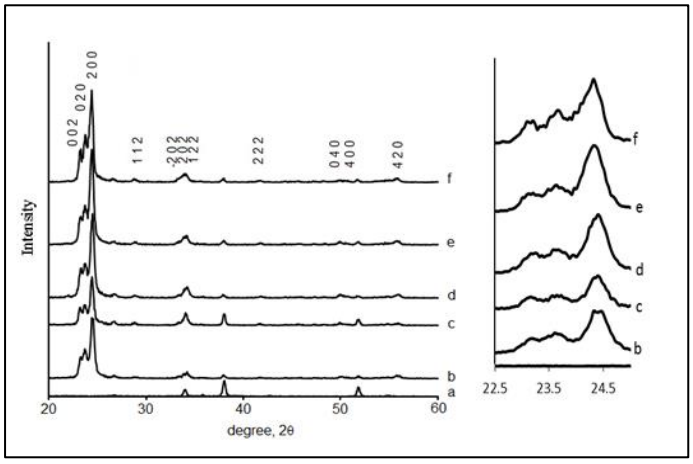


Figure 2. XRD pattern of (a) FTO, (b) undoped, (c) 5%, (d) 10%, (e) 15% and (f) 20% Fe-doped WO_3 thin films

The average crystallite size of each thin films was estimated using the Scherrer equation by referring to the XRD pattern. The crystallite size of undoped WO_3 was found to be 17 nm, estimated based on (200) peak, which is in agreement with previous study [34]. The crystallite size remains almost the same for all the doped thin films of 5 %, 10 %, 15 %, and 20 % Fe-doped WO_3. However, from the SEM measurement, the particle size is found to be larger, which is due to the agglomeration of the particle with only slight growth of crystal [41]. This indicates that the doping of Fe to WO_3 does not alter the crystallite size.

Optical charaterization

Figure 3 shows the UV-vis absorption spectra of the undoped and Fe-doped WO_3 thin films. From the Figure, it is observed that the spectrums are shifted to higher wavelength, which is also known as the red-shift in light absorption. The red shift shows that the band gap of Fe-doped WO_3 thin films was reduced compared to the undoped sample. To estimate the optical band gap, E_g of the thin films, equation (1) and (2) below were used [42]

$$T = e^{-\alpha d} \quad (1)$$

$$\alpha h\nu = B(h\nu - E_g)^n \quad (2)$$

From equation (1), α is the optical absorption coefficient, T is measured spectral transmittance, and d is thickness of the film (cm). Meanwhile from equation (2), B is a constant, n is the exponent where, n = 1/2, 3/2, 2, and 3 when the transition is direct allowed, direct forbidden, indirect allowed and indirect forbidden, respectively for crystalline semiconductors. The band gap of the thin films was estimated by plotting $(-InT)^{1/2}$ against energy (hν) for undoped and Fe-doped WO_3 thin films, assuming the materials are indirect semiconductors. The band gap of the undoped WO_3 is 2.74 eV and it is in agreement with previous studies [22-26]. Meanwhile, the band gap of the doped thin films was decreased to 2.60 eV as the concentration of Fe increased up to 20%. This band gap reduction was attributed to the doping of Fe into the WO_3 lattice, as shown in XRD pattern.

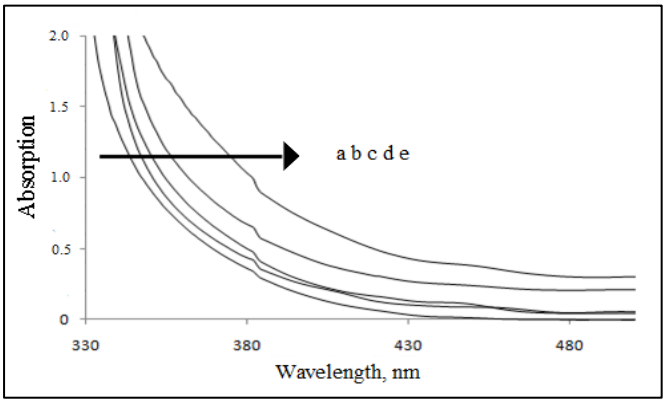


Figure 3. UV-Vis spectrum of (a) undoped, (b) 5%, (c) 10%, (d) 15% and (e) 20% Fe-doped WO_3 thin films

PEC analysis

The photocatalyst of undoped and Fe-doped WO_3 thin film performance was studied by measuring the photocurrent densities by applying potential (0 V to 1.5 V) in 0.5 M Na_2SO_4 as electrolyte, under full arc xenon lamp irradiation (100 $mWcm^{-2}$). The photocurrents are calculated by subtracting the measured currents under light irradiation with the respective dark currents. Figure 4 shows the photocurrent density of undoped and Fe-doped WO_3 thin films.

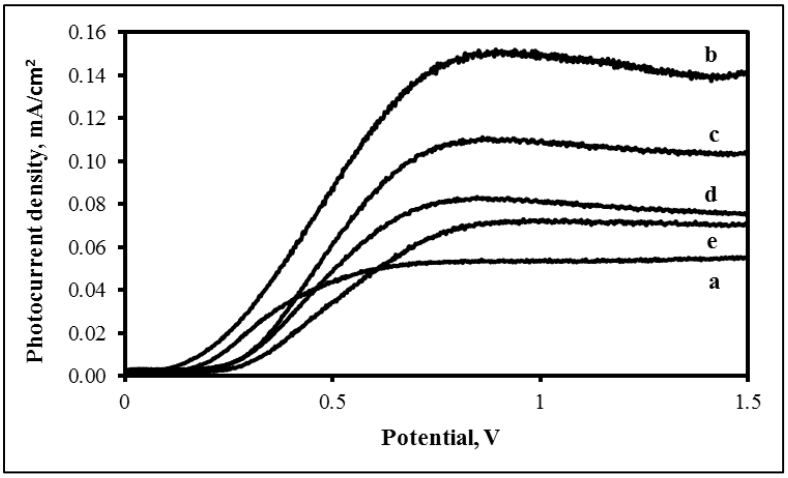


Figure 4. PEC analysis of (a) undoped, (b) 5%, (c) 10%, (d) 15% and (e) 20% Fe-doped WO_3 thin films

Figure 4 shows that the photocurrents produced by Fe-doped WO_3 photoelectrodes are higher compared to the undoped WO_3 under the same bias potential of 0.8 V. This indicates that under the same irradiation of 100 $mWcm^{-2}$ with the same bias potential of 0.8 V, the flow of photoexcited electrons of Fe-doped WO_3 electrode are more than the electron flow of the undoped WO_3 electrode via external circuit towards the cathode. As the electron leaving, the photoexcited holes remains at the surface of the photoelectrodes, which eventually drives the oxidation reaction. The high photoactivity with Fe-doped electrode was due to the Fe particles in WO_3 lattice act as electron acceptors, which helps in charge separation and thus, contributes to the improvement of photocurrent in Fe-doped WO_3. However, we observed that the photocurrent saturation potential of Fe-doped WO_3 were higher than the undoped WO_3. A high potential was needed to achieve the highest photocurrent production. This might be due to the rapid recombination rate in iron oxide as it has short carrier diffusion length of 2-4 nm [21].

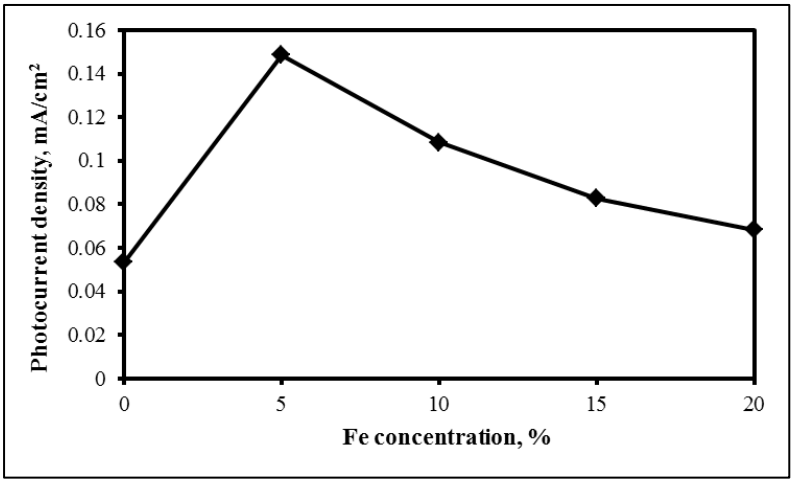


Figure 5. Photocurrent density versus Fe concentration of 0 %, 5 %, 10 %, 15 % and 20 % at 0.8 V vs SCE

The photogenerated charges (electron-holes) are easily separated by supplying bias to the PEC system and the reduction and oxidation reaction (process of splitting of water and generation of hydrogen) occurs at physically different electrode. Hence, surface recombination is not the main contribution of photogenerated charges recombination. However, the main contribution is from the recombination that occurs during the electron flows through photocatalyst films and the movement of holes towards the electrode-water interface which is known as volume recombination [43]. Comparing among the Fe-doped WO_3 thin films, the photocurrent density of the sample with 5% of Fe is the highest and it is decreasing with the increase in concentration of Fe in the thin films (Figure 5). This is because of the grain size of the sample increases as the concentration of Fe increases, causing the volume recombination of electron-hole pair increases. Therefore, in this study, 5% fe-doped WO_3 electrode exhibits the best water splitting capability than the others under xenon light irradiation.

Conclusion

In this paper, we have described the fabrication of WO_3 doped with different concentration of Fe and undoped WO_3 thin films via sol-gel method, using ferrocene and tungstic acid as starting materials. The XRD result of thin films with different Fe concentration has shown that all WO_3 thin films are in monoclinic form and also shows the Fe particles are successfully incorporated into WO_3 lattice. The Fe-doped WO_3 thin films show red-shift in UV-vis absorption spectra which corresponding to band gap reduction. Also, photoelectrohemical analysis shows that thin films of 5 % Fe-doped WO_3 produce the highest photocurrent under the full arc xenon lamp irradiation. The photocurrent of 5 % Fe-doped WO_3 is 3 times higher compared to undoped WO_3.

Acknowledgement

The authors would like to acknowledge Universiti Kebangsaan Malaysia for sponsoring this project under UKM-GUP-BTT-07-30-189.

References

1. Ab Hamid, N. Z., Md Jahim, J., Anuar, N. and Khalid, S. (2012). Hydrogen production via *rhodobacter sphaeroides* NCIMB 8253. *Sains Malaysiana*, 41(12): 1587 – 1593.
2. Wun Fui, M. L., Minggu, L. J. and Kassim, M. B. (2012). Photo-chemical properties of molybdenum dithiolene. *Sains Malaysiana*, 41:597 – 601.
3. Fujishima, A. and Honda, K. (1972). Electrochemical photolysis of water at a semiconductor. Electrode *Nature* 238: 37 – 38.
4. Ni, M., Leung, M. K. H., Leung, D. Y. C. and Sumathy, K. (2008). A review and recent developments in photocatalytic water-splitting using TiO_2 for hydrogen production. *Renewable and Sustainable Energy Reviews*, 11: 401 – 425.
5. Weber, M. F. and Dignam, M. J. (1986). Splitting water with semiconducting photoelectrodes-efficiency considerations. *International Journal of Hydrogen Energy*, 11: 225 – 232.
6. Bolton, J. R, Strickler, S. J. and Connolly, J. S. (1985). Limiting and realizable efficiencies of solar photolysis of water. *Nature*, 316: 495 – 500.
7. Murphy, A. B., Barnes, P. R. F., Randeniya, L. K., Plumb, I. C., Grey, I. E., Horne, M. D. and Glasscock, J. A. (2006). Efficiency of solar water splitting using semiconductor electrodes. *International Journal of Hydrogen Energy*, 31:1999 – 2017.
8. Li, Y., Yu, H., Zhang, C., Fu, L., Li, G., Shao, Z. and Yi, B. (2013). Enhancement of photoelectrochemical response by au modified in TiO_2 nanorods. *International Journal of Hydrogen Energy* 36: 14374 – 14380.
9. Minggu, L. J., Ng, K. H., Kadir, H. A. and Kassim, M. B. (2014). Bilayer n-WO_3/p-Cu_2O photoelectrode with photocurrent enhancement in aqueous electrolyte photoelectrochemical reaction. *Ceramics International*, 40: 16015 – 16021.
10. Rahman, G. and Joo, O. S. (2012). Photoelectrochemical Water Splitting at Nanostructured α-Fe_2O_3 Elecrodes. *International Journal of Hydrogen Energy* 37: 13989-13997.
11. Pung, S. Y., Ong, C. S., Mohd Isha, K. and Othman, M. H. (2014). Synthesis and characterization of Cu-doped ZnO nanorods. *Sains Malaysiana*, 43(2): 273 – 281.
12. Gavrilyuk, A. I. (1999). Photochromism in WO_3 thin films. *Electrochimica Acta* 44: 3027 – 3037.
13. He, T. and Yao, J. N. (2006). Photochromism in composite and hybrid materials based on transition-metal oxides and polyoxometalates. *Progress in Materials Science*, 51: 810 – 879.
14. Kawasaki, H., Ueda, T., Suda, Y. and Ohshima, T. (2004). Properties of metal doped tungsten oxide thin films for NO_x gas sensors grown by PLD method combined with sputtering process. *Sensors and Actuators B*, 100: 266 – 269.
15. Monk, P. M. S., Akhtar, S. P., Boutevin, J. and Duffield, J. R. (2001). Toward the tailoring of electrochromic bands of metal–oxide mixtures. *Electrochimica Acta* 46: 2091 – 2096.
16. Svensson, J. S. E. M. and Granqvist, C. G. (1985). Electrochromic coatings for smart windows. *Solar Energy Materials*, 12: 391 – 402.
17. Teowee, G., Gudgel, T., McCarthy, K., Agrawal, A., Allemand, P. and Cronin, J. (1999). User Controllable Photochromic (UCPC) Devices. *Electrochimica Acta*, 44: 3017 – 3026.
18. Avellaneda, C. O. and Bulhões, L. O. S. (2003). Photochromic properties of WO_3 and WO_3:X (X=Ti, Nb, Ta and Zr) thin films. *Solid State Ionics*, 165: 117 – 121.
19. Finlason, A. P., Ward, E., Tsaneva, V. N. and Glowacki, B. A. (2005). Bi_2O_3–WO_3 compounds for photocatalytic applications by solid state and viscous processing. *Journal of Power Sources* 145: 667 – 674.
20. Karuppasamy, K. M. and Subrahmanyam, A. (2008). The electrochromic and photocatalytic properties of electron beam evaporated vanadium-doped tungsten oxide thin films. *Solar Energy Materials and Solar Cells*, 92: 1322 – 1326.
21. Memar, A., Phan, C. M. and Tade, M. O. (2012). Influence of surfactants on Fe_2O_3 nanostructure photoanode. *International Journal of Hydrogen Energy*, 37: 16835 – 16843
22. Scarminio, J., Urbano, A. and Gardes, B. (1999). The Beer-Lambert Law for electrochromic tungsten oxide thin films. *Materials Chemistry and Physics*, 61: 143 – 146.

23. Sivakumar, R., Jayachandran, M. and Sanjeeviraja, C. (2004). Studies on the effect of substrate temperature on (VI–VI) textured tungsten oxide (WO_3) thin films on glass, SnO_2:F substrates by PVD:EBE technique for electrochromic devices. *Materials Chemistry and Physics*, 87: 439 – 445.
24. Su, L., Wang, H. and Lu, Z. (1998). All-solid-state electrochromic window of prussian blue and electrodeposited WO_3 film with poly(ethylene oxide) gel electrolyte. *Materials Chemistry and Physics*, 56: 266 – 270.
25. Tong, M., Dai, G. and Gao, D. (2001). WO_3 thin film sensor prepared by sol–gel technique and its low-temperature sensing properties to trimethylamine. *Materials Chemistry and Physics*, 69: 176 – 179.
26. Enesca, A., Duta, A. and Schoonman, J. (2007). Study of photoactivity of tungsten trioxide (WO_3) for water splitting. *Thin Solid Films*, 515: 6371 – 6374.
27. Gavrilyuk, A. I. (2009). Application of WO_3 thin films for enhancement of photolysis in AgCl. *Solar Energy Materials and Solar Cells*, 93: 1885 – 1895.
28. Hong, S. J., Jun, H., Borse, P. H. and Lee, J. S. (2009). Size effects of WO_3 nanocrystals for photooxidation of water in particulate suspension and photoelectrochemical film systems. *International Journal of Hydrogen Energy*, 34: 3234 – 3242.
29. Su, L., Dai, Q. and Lu, Z. (1999). Spectroelectrochemical and photoelectrochemical studies of electrodeposited tungsten trioxide films. *Spectrochimica Acta Part A*, 55: 2179 – 2185.
30. Bamwenda, G. R. and Arakawa, H. (2001). The visible light induced photocatalytic activity of tungsten trioxide powder. *Applied Catalysis A*, 210: 181 – 191.
31. Sigh, A. P., Kumari, S., Shrivastav, R., Dass, S. and Satsangi, V. R. (2008). Iron doped nanostructured TiO_2 for photoelectrochemical generation of hydrogen. *International Journal of Hydrogen Energy* 33: 5363 – 5368.
32. Hameed, A., Gondal, M. A. and Yamani, Z. H. (2004). Effect of transition metal doping on photocatalytic activity of WO_3 for water splitting under laser illumination: role of 3d-orbitals. *Catalysis Communication*, 5: 715 – 719.
33. Saremi-Yarahmadi, S., Tahir, A. A., Vaidhyanathan, B. and Wijayantha, K. G. U. (2008). Fabrication of nanostructured α-Fe_2O_3 electrodes using ferrocene for solar hydrogen generation. *Material Letters*, 53: 523 – 526.
34. Minggu, L. J., Daud, W. R. W. and Kassim, M. B. (2010). An overview of photocells and photoreactors for photoelectrochemical water splitting. *International Journal of Hydrogen Energy* 35: 5233 – 5244.
35. Yagi, M., Maruyama, S., Sone, K., Nagai, K. and Norimatsu, T. (2008). Preparation and photoelectrocatalytic activity of a nano-structured WO_3 platelet film. *Journal of Solid State Chemistry*, 181: 175 – 182.
36. Solarska, R., Alexander, B. D. and Augustynski, J. (2006). Electrochromic and photoelectrochemical characteristics of nanostructured WO_3 films prepared by a sol-gel method. *Comptes Rendus Chimie*, 9: 301 – 306.
37. Ng, K. H., Minggu, L. J., Jumali, M. H. H. and Kassim, M. B. (2012). Fotoelektrod tungsten trioksida terdop nikel untuk tindak balas pembelahan air fotoelektrokimia. *Sains Malaysiana*, 41(7): 893 – 899
38. Upadhyay, S. B., Mishra, R. K. and Sahay, P. P. (2014). Structural and alcohol response characteristics of Sn-doped WO_3 nanosheets. *Sensors and Actuators B: Chemical* 193: 19 – 27.
39. Boudjemaa, A. and Trari, M. (2010). Photo-catalytic hydrogen production over Fe_2O_3 based catalysts. *International Journal of Hydrogen Energy*, 35: 7684 – 7689.
40. Łącz, A. and Pasierb P. (2013). Synthesis of $BaCe_{1-x}Y_xO_{3-\delta}$-$BaWO_4$ composite protonic conductors. *Journal of Thermal Analysis and Calorimetry*, 113: 405-412.
41. Sun, Y., Murphy, C. J., Reyes-Gil, K. R., Reyes-Garcia, E. A., Thornton, J. M., Morris, N. A. and Raftery, D. (2009). Photoelectrochemical and structural characterization of carbon-doped WO_3 films prepared via spray pyrolysis. *International Journal of Hydrogen Energy*, 34: 8476 – 8484.
42. Redecka, M., Rekas, M., Trenczek-Zajac, A. and Zakrzewska, K. (2008). Importance of the band gap energy and flat band potential for application of modified TiO_2 photoanodes in water photolysis. *Journal of Power Sources*, 181: 46 – 55.
43. Suk, J. H., Jun, H., Borse, P. H. and Lee, J. S. (2009). Size effects of WO_3 nanocrystals for photooxidation of water in particulate suspension and photoelectrochemical film systems. *International Journal of Hydrogen Energy*, 34: 3234 – 3242.

Malaysian Journal of Analytical Sciences, Vol 20 No 4 (2016): 931 - 945
DOI: http://dx.doi.org/10.17576/mjas-2016-2004-29

MALAYSIAN JOURNAL OF ANALYTICAL SCIENCES
Published by The Malaysian Analytical Sciences Society
ISSN 1394 - 2506

PROTON EXCHANGE MEMBRANE FUEL CELL/SUPERCAPASITOR HYBRID POWER MANAGEMENT SYSTEM FOR A GOLF CART

(Sistem Pengurusan Kuasa Hibrid Sel Bahan Api Membran Penukaran Proton/Superkapasitor untuk Kereta Golf)

Siti Afiqah Abd. Hamid[1], Ros Emilia Rosli[1], Edy Herianto Majlan[1]*, Wan Ramli Wan Daud[1], Ramizi Mohamed[2], Teuku Husaini[1], Ramli Sitanggang[3]

[1]*Fuel Cell Institute*
[2]*Department of Electrical and System Engineering, Faculty of Engineering & Built Environment, Universiti Kebangsaan Malaysia, 43600 UKM Bangi, Selangor, Malaysia*
[3]*Department of Chemical Engineering, Faculty of Industrial Engineering, Universitas Pembangunan Nasional "Veteran" Yogyakarta, Yogyakarta 55283, Indonesia*

**Corresponding author: edy@ukm.edu.my*

Received: 5 February 2016; Accepted: 22 April 2016

Abstract

This paper presented the transformation of a golf cart system powered lead acid battery into an environmental friendly hybrid vehicle. The design developed by using an advantage contributes by the uprising alternative power source candidate which is Proton Exchange Membrane Fuel Cell (PEMFC) and the maintenance free energy storage device, a supercapacitor (SC). The fuel cell (FC) stack was an in house manufactured with 450 W (36 V, 12.5 A) power, while the SC was from Maxwell Technologies (48 V, 165 F). This two power sources were controlled by the mechanical relay, meanwhile the reactant (hydrogen) are control by mass flow controller (MFC) both signaled by a National Instrument (NI) devices. The power management controller are programmed in the LabVIEW environment and then downloaded to the NI devices. The experimental result of the power trend was compared before and after the transformation with the same route to validate the effectiveness of the proposed power management strategy. The power management successfully controls the power sharing between power sources and satisfies the load transient. While the reactant control managed to vary the hydrogen mass flow rate feed according to the load demand in vehicular applications.

Keywords: proton exchange membrane fuel cell, supercapacitor, hybrid, power management strategy

Abstrak

Kertas kerja ini membentangkan tentang transformasi sistem kereta golf dikuasakan oleh bateri asid plumbum kepada kenderaan hibrid yang mesra alam. Reka bentuk ini dibangunkan dengan menggunakan kelebihan yang disumbangkan oleh sumber kuasa alternatif iaitu Sel Bahan Api Membran Penukaran Proton (PEMFC) bersama peranti penyimpanan tenaga tanpa penyelenggaraan, Superkapasitor (SC). Tindanan Sel Bahan Api (FC) telah dibina sendiri dengan kuasa 450 W (36 V, 12.5A) manakala SC adalah dari Teknologi Maxwell (48V, 165F). Kedua-dua sumber kuasa ini dikawal menggunakan geganti mekanikal, sementara itu bahan tindak balas (hidrogen) dikawal menggunakan meter pengawal aliran (MFC) yang kedua-dua diisyaratkan dengan menggunakan peranti Instrumen Nasional (NI). Pengawal pengurusan kuasa diprogramkan di dalam persekitaran LabVIEW dan kemudiannya dimuat turun kepada peranti NI. Hasil eksperimen trend kuasa telah dibandingkan sebelum dan selepas transformasi dengan laluan yang sama untuk mengesahkan keberkesanan strategi pengurusan tenaga yang dicadangkan. Pengurusan kuasa ini berjaya mengawal perkongsian kuasa di antara sumber kuasa dan memenuhi kehendak beban fana. Manakala kawalan bahan tindak balas berjaya mengurus kadar aliran hidrogen mengikut permintaan beban dalam aplikasi kenderaan.

Kata kunci: sel bahan api membran penukaran proton, superkapasitor, hibrid, strategi pengurusan kuasa

Introduction

Today, with increasing number of vehicles on the road that used internal combustion engine (ICE), concerns about the inability to supply sufficient fossil fuels is increasing because the failure to discover new oil sites and the impact of pollution produced are more serious [1]. As a consequence, much interest in new solutions to replace ICEs powered vehicles has increased steadily [2].

Nowadays the hybrid system technology becoming new phenomena in transportation area. These technologies are developed to help reduce the pollution made by ICEs vehicles. The interest in the hybrid vehicle has open new aspects to optimize its performance. The component of hybrid power sources are such as petrol, diesel engines, electric motor/generator units, batteries (BTs), SCs and FCs. The first commercial hybrid vehicle was introduced by Toyota in 1997 named Prius, and many more coming to the market from other vehicle manufactured throughout the world such as Honda, Hyundai, Lexus, BMW, Mercedes-Benz and many more. This type of vehicle used BT as the auxiliary source. However, BT has its own limitation. When the life time of BT depend on the reactant material and electrodes. Moreover, once energy stored is depleted, the BT needs to be recharged and if the performance degrades, the BT will be replaced with new ones. So, using BT produce wastage that involve time and cost.

Currently, the world is seeking for a more reliable power source where FC as an alternative energy is one of the best candidates. This technology offer variety of advantages over existing power sources and based on its specific characteristics where the reactants source is not limited, efficient energy, light in weight, fuel flexibility, and ability to provide power to the range of diverse applications [3-5]. FC technology generates power through an electrochemical reaction between hydrogen and oxygen. The process emitting zero pollutants gases, greenhouse gases, and hazardous waste make it an environmentally friendly, quiet and considered a green energy source of power generator [6, 7]. There are various types of FCs, one of it is Proton Exchange Membrane Fuel Cell (PEMFC). This type of FC is the most popular choice and highly sought after development of this technology in recent years. It is much more compatible towards vehicle, portable and stationary applications. This is evidenced by some of the world's great enterprises were using or developing this technologies such as Horizon Fuel Cell, Ballard Power Systems, Power Energy, Daimler-Chrysler, General Motors, Honda, Toyota and many more.

Many interest to build a FC car since it is a green car with zero pollutants as the result of an electrochemical process in FC that produces electric with only water and heat as byproduct compared to conventional ICE automobiles that emit carbon dioxide and volatile organic compounds that do not burn. However, FC is known to have a slow dynamic response to load changes that many have agreed FCs alone might not be sufficient to satisfy the load demands in vehicular applications [8-11]. The slow dynamic response of FC will lead to more serious problem like permanent cell damage, system stall, or reduced the cell lifetime. This is due to fast load demand that cause fuel starvation where it happen when a high voltage is drop in a short time. The hybridization of FC with energy storage devices that is SC or also known as Ultracapacitor (UC) are claim much helpful by the researchers where it minimize the size of this power generator and increase it efficiency by storing the regenerative braking energy from the vehicle [7, 11-19]. SCs are well known with it characteristic of fast charge and fast discharge without damaging its structure. SC also have more life cycle compare to BT, thus less wastage.

However, due to it fast discharge characteristic, this device need to combine with power generator (such as ICE or FC) before it can apply to vehicle. This combination (hybrid) SCs and FCs are being examine by several researchers with various control strategy to support FCs [9, 12, 16, 20, 21]. Eren et al. [21] studied fuzzy logic based supervisory controller of FC/UC hybrid for vehicular power system. Lin and Weng [16] studied the adaptive optimal-control method of a FC/UC hybrid power system. While Ates et al. [12] studied the energy management based on combined neural network-wavelet transform of FC/UC hybrid for vehicular application. Thounthong et al. studied the energy management based on differential flatness control of FC/SC hybrid sources [17] and a DC link voltage regulation FC/SCs hybrid power sources for vehicular application. Erdinc et al. [22] studied the wavelet-fuzzy logic based load sharing and control algorithm of FC/UC hybrid for vehicular application. In contrary to the

other positive results achieved in the literature of PEMFC with SC/UC vehicles hybridization, reference in [14, 19] claims that this combination are rarely used because of the high power train cost.

Another characteristic of FC are the current produced fluctuate due to the change in load and input reactants [23, 24]. Reviews from various studies indicate that the performance of PEMFC is very dependent on the conditions of operation, in which the voltage generation depending on the dependent variable to be controlled. Among the important factors for power generation from the FC is design of balance of plant (BOP). BOP works to supply the right amount of power to the right place and at the time required. BOP can improve the electrochemical reaction in PEMFC and ensure operational stability even in times of uncertainty interrupt its capability. Therefore, it will improve the performance and durability of PEMFC [25, 26]. The BOP often built in PEMFC based on humidity system, water management, operating temperature, pressure and the appropriate flow rate response [27-33]. Every parameter plays their own role where the design will determine the correct amount need to be supply function to result in better generation of electricity. Here, the focus is the reactant mass flow rates where the hydrogen amount to be supply are the biggest concern for power generation. The fuel management is design with the controller to prevent the occurrence of unsatisfactory fuel supply that will limit the ability of FC to deliver the power being request from load.

With nearby growing era of FCs in transportation sector, it is very important to understand this technology in its applications. In this paper, development, manufacturing and car assembly of the PEMFC as a power generator are done with hybridization with SC as the secondary power supply. To avoid the high cost and complex control system, golf cart are used as a prototype FC car using DC 3 kW electric motor. The power management of this hybrid FC car and reactant control system are done using LabVIEW program and applied using NI devices.

Materials and Methods

Fabrication of PEMFC stack

Two stacks with 40 cells each built consists of end plates, current collectors, bipolar plates, gas diffusion layer, membrane electrode assemblies (MEA), and sealants that are sandwiched together. Bipolar plates used instead of single plates in this stack to reduce the FC size. The flow fields are engraved using a computer numerical control (CNC) machine. The stacks built are connected in series to obtain higher voltage value. Flow field pattern and size of the bipolar plate (anode and cathode) are designed and produce an output power of 450 W at 36 VDC. The PEMFC stack is designed based on the FC open cathode system with air as cooling system. For the anode side, the flow shape build with the serpentine flow but for cathode, straight flow are engraved. The size of both plate are 30 cm length and 11 cm width, with the plate area 330 cm^2. The material of bipolar plate is a mixture of graphite and carbon materials.

The MEA as the heart of FC consists of three main components namely gas diffusion layer (GDL), membrane and catalyst layer. The performance of FC is much depends on the good electrode and electrolyte (MEA) composition and research to improve the performance of both materials are necessary for the successful manufacturing process. A fabrication, characterization and performance tests of nano catalyst platinum-ruthenium-nickel/carbon (Pt-Ru-Ni/C) done to improve the performance of MEA. Nano materials are potential for increasing performance of FC through the nano impact. Production of Pt-Ru-Ni/C catalyst in this research is expected to increase carbon monoxide (CO) tolerance caused by the oxidation of CO or low CO adsorption process. Developments are focus on the design and manipulation of materials structures at the atomic or molecular level to provide a more effective catalyst. This composite can be used to overcome problems such as high production costs, corrosion and CO poisoning of the electrode, thus can improve the durability, stability and performance of the FC. For electrode, the anode and cathode electrodes used carbon fiber paper as gas absorption distribution layer and catalyst platinum/carbon (Pt/C) as an electrochemical reaction layer. GDL are made from carbon paper, while for the membrane, Nafion^{TM} being used as a proton exchange membrane. Method of manufacturing GDL and catalyst layer are by spraying method. The main ingredient of catalyst is Pt/C with 0.3 mg cm^{-2}. The three components are pressed at 350°C for three minutes before merge to become MEA. The thickness of each MEA produced was around 0.23 mm. Figure 1 shows the PEMFC stack built.

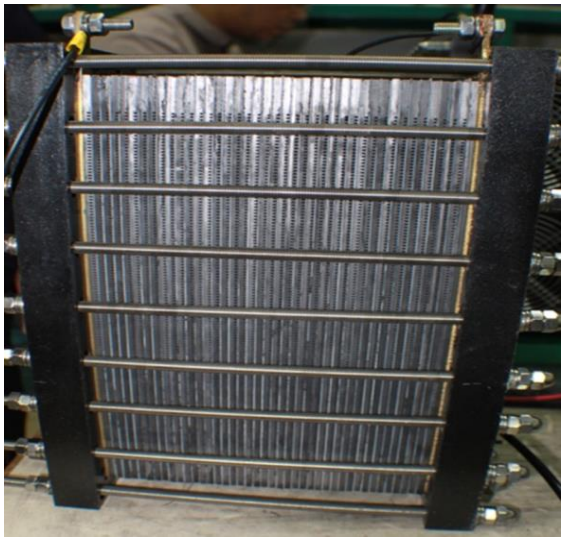


Figure 1. Fabrication of single stack open cathode PEMFC

Balance of plant (BOP)

The PEMFC performance relies mainly on the design and operation of a FC system that includes the BOP and power converters as well as their control systems. The complexity of the FC requires many studies on the design and operation of these units. This PEMFC system used pure hydrogen that stored in cylindrical pressurized tank with 7.2 m³ capacity flowed in FC stack with pressure control using a pressure regulator. The hydrogen flow are using continuous mode, but it supplied based on request load. The reactant control system build [34] are used to ensure the gases entering the stack is sufficient with the amount of power produced. Otherwise for oxygen in cathode sides, fans are used to blow source of oxygen from the air. Eight fans powered with 24 V, 0.5 A each is used and the fan speed applied at the maximum rate to ensure the air flow is sufficient for the reaction at the cathode as well as to cool the stack. The flow diagram of reactant controller is shown in Figure 2.

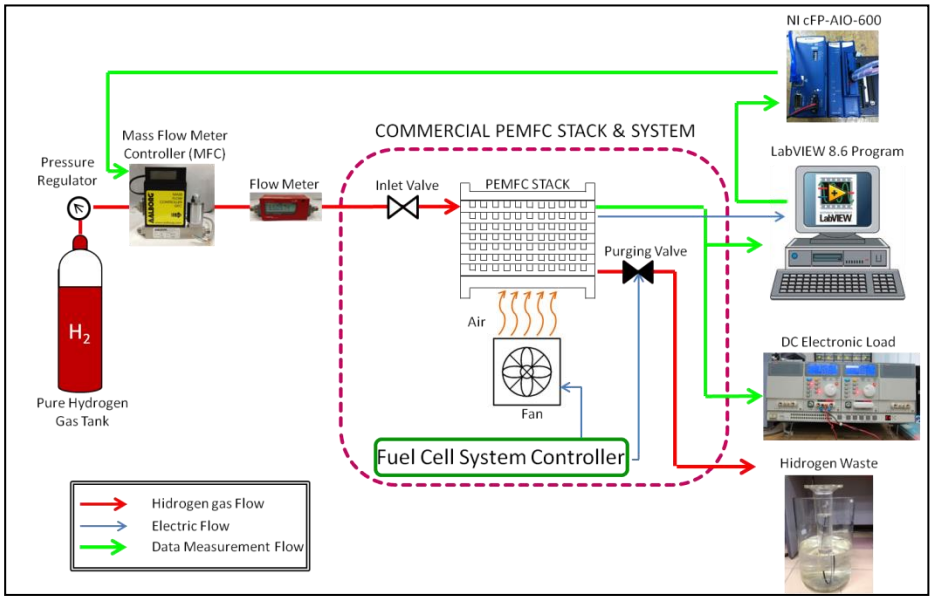


Figure 2. Flow diagram reactant controller of PEMFC stack

NI-cFP-AIO-600 is one of standard products from NI that provides precise data acquisition. It used in this experiment to measure and monitor the input voltage, current, power and to control the gas flow via the output current. It consists of four analog voltage or current input channels with 11 input ranges up to ±36 V or ±24 mA and four analog current output channels ranging from 0 to 20 or 4 to 20 mA without over-ranging. The NI module placed between FC system and a computer (LabVIEW) to convert the analog input to a digital output for the cFP measurements and controlling actions. Voltage ranges to maintain suitable flow rates was determined. This voltage measured and the signal logged using the NI analog input (NI-cFP-AIO-600 – voltage input-channel 1) and sent to LabVIEW controller program to be processed. The required flow rate will automatically choose using the PID program. The signal then sent back using the NI analog output current (NI-cFP-AIO-600 - current output-channel 3) to control the MFC valve flow rate. The program react are based on the PID changes that can produce an operating signal that manipulates the flow rate of the hydrogen reactant to maintain stack output voltage. The PID controller program developed as shown in the front panel on Figure 3 and the detail of the structure is shown in the block diagram in Figure 4.

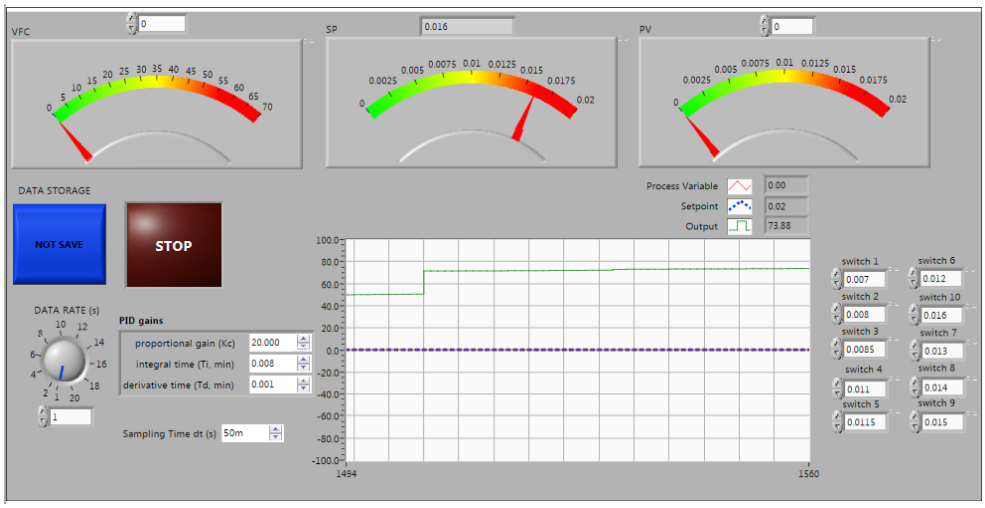


Figure 3. Front panel interface of PID control system for reactant control

Golf Cart specification after transformation

A golf cart serves as the vehicle prototype. Originally, the BTs used in the golf cart as the power generator, then it was replaced with FC and SC. The space required are to place the hydrogen storage tanks, FC stack, SC, and power management system. Figure 5 showed the modification done to the golf cart during this study. Power management system unit is designed for 3 kW power to control the golf cart motor. This unit are integrated with a FC system that control the amount of hydrogen into the FC stack conducted in accordance with the power requirements. The Global Positioning System (GPS) and collection or storage of data is designed and installed in this prototype car using seagull devices, NI devices and LabVIEW program.

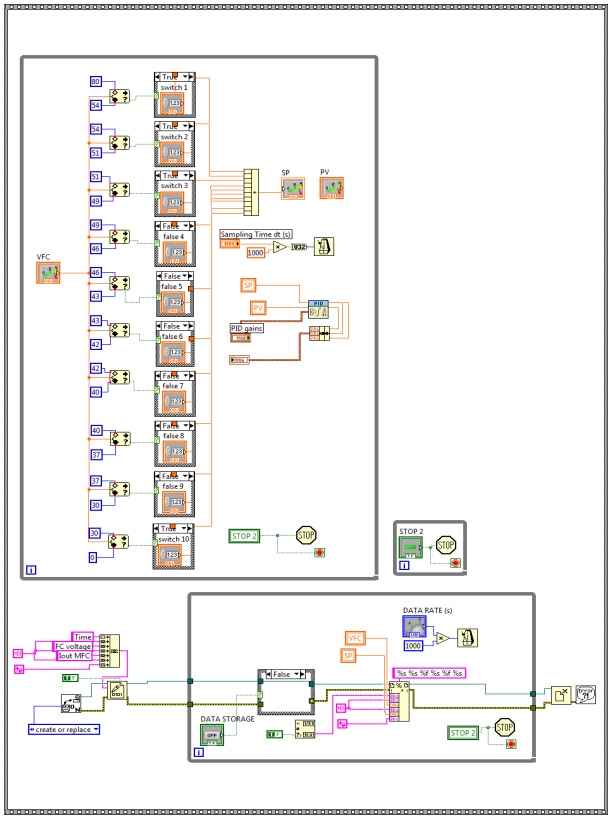


Figure 4. Block diagram interface of PID control system for reactant control



Figure 5. Prototype golf cart after modification

The SC model BMOD0165 from Maxwell Technologies used as the auxiliary power source in this hybrid system are with a rated voltage of 48 V and rated capacitance of 165 F. Its features are compact, rugged, fully enclosed splash proof design was the main points that make this SC the primary choice. The benefit of choosing SC rather than BTs was because it provide over 1,000,000 duty cycles which is a thousand times more than average BTs.

All components built are assembled and tested on a golf cart, and the system was constructed and equipped with manual and automatic hydrogen flow valve functions. The manual function was prepared as a safety precaution to avoid severe circumstances that could occur during testing, and also used as the start-up function for the electronic components in the cart. After all required electronic parts are functioning, the valve switch to automatic valve to control the hidrogen mass flow rate during speed changing or load demand, and changes in the stack voltage reading will vary the hydrogen flow rate according to the programmed control structure. The flow diagram for hydrogen is displayed in Figure 6.

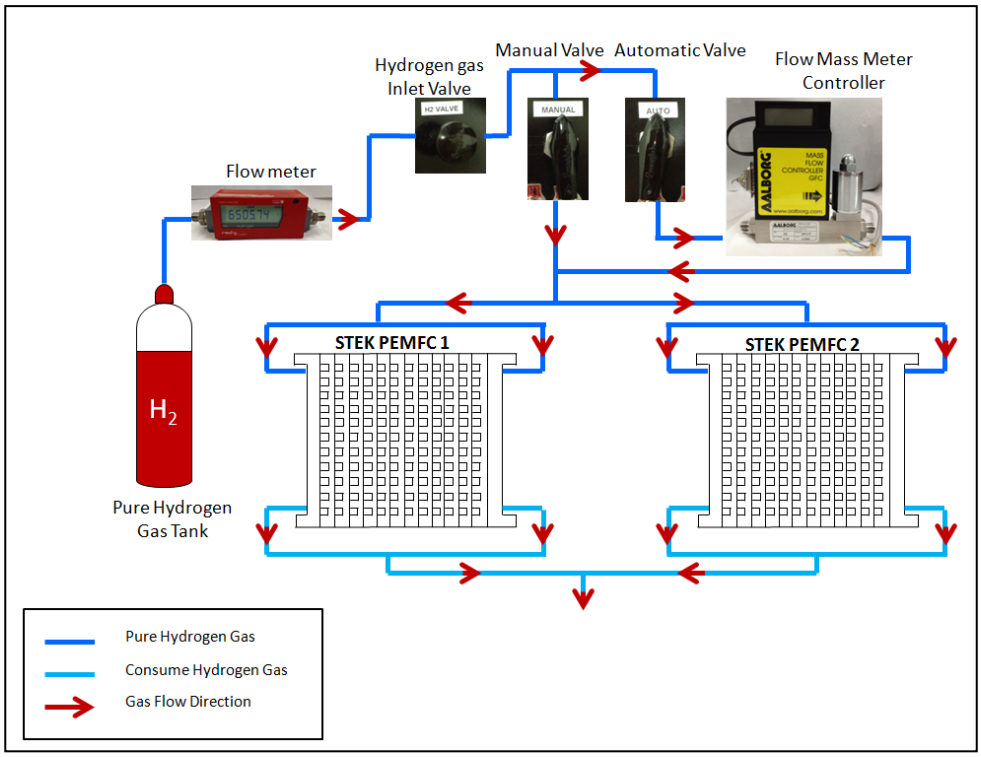


Figure 6. The flow diagram of hydrogen on a golf cart

Power management strategies of hybrid vehicle

The hybrid system combines the FC and the SC to run the golf cart. The FC in this system serves as the primary power source to satisfy the load and to charge the SC. In contrast, the SC acts as the auxiliary power source to supply any load amount that exceeds the capability of the FC. This power management system contains two components, one of which is the controller circuit unit and the other is the power controller device. These two components are related to one another through the controller circuit, which carries out the power management strategy programmed in the power controller device.

The focuses of this study are design and developed the controller circuit unit. This unit includes power relays, recovery diodes, and a DC/DC converter. This system uses the power relay as a switch to allow power flow for discharging or charging the SC. The power relay required a supply of 12 V voltage and 417 mA current to function.

The relay chosen was model G9EA1B from OMRON, which is capable of allowing a 100 A maximum switching current suitable for the golf cart system. The recovery diode is a 150UR series from International Rectifier and functions as a blocking device to ensure that the current flows only in one direction, as directed by the diode. The objective is to decide when to charge and when to discharge the SC as programmed in the controller. The DC/DC converter is a voltage stabilizer device. As the load demand increase, the FC output voltage will decrease. This phenomenon is well understood as a characteristic of FC technologies, but application devices will not tolerate this situation because they require a stable operating voltage within a certain tolerance. The golf cart must be supplied with 48 V, which is also the output voltage of DC/DC converter used in this system and the input voltage for converter are from FC.

The power management strategy is programmed in the LabVIEW software that will be integrated with the cFP device. In this application, extensive palette of functions and tools connected by strings are used to meet the strategy objective. The block diagram of the power management strategy are shown in Figure 7. The power management strategy used in the golf cart is based on voltage regulation, and the control strategy is described below:

1) If the load voltage is greater than 48 V and the SC voltage is greater than or equal to 48 V, the excess power from the FC will be supplied directly to the motor.
2) If the load voltage is greater than 48 V and the SC voltage is less than 48V, the excess FC power will charge the SC.
3) If the load voltage is less than 48 V, the SC will discharge to meet the load power demand.

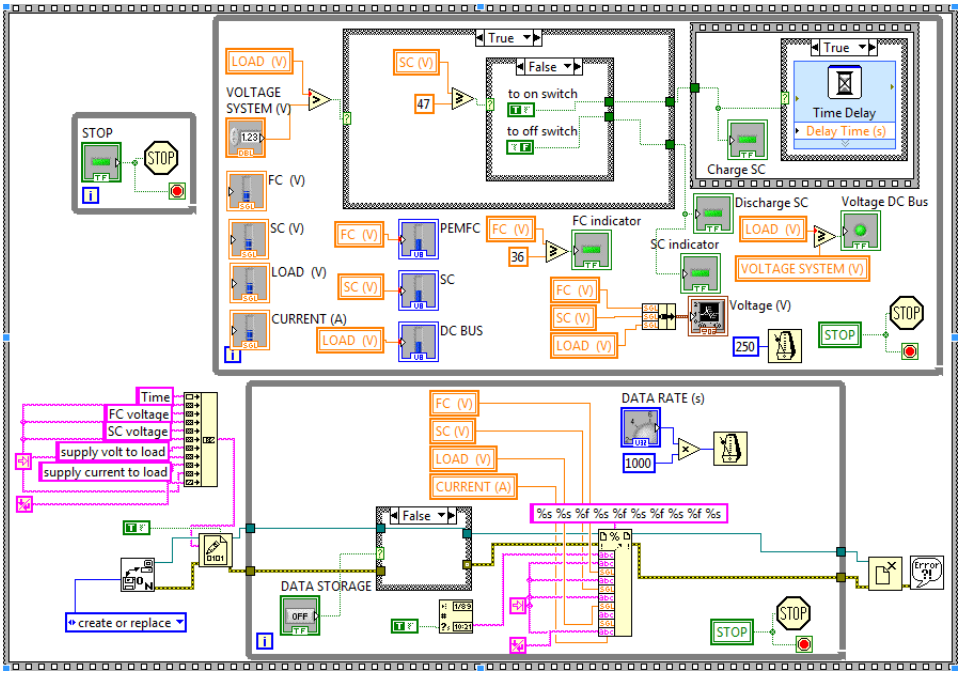


Figure 7. Block diagram of power management program

Results and Discussion

Performance test of the prototype FC hybrid cars done in and outside the laboratory. FC system performance testing in the laboratory will use the FC system performance test. For test outside the laboratory, prototype FC cars are designed and manufactured with equipment to be able to record and store the data needed for doing performance test.

Electric golf cart – before transformation

The performance test of the golf cart before transformation was done on a route around UKM in the Figure 8. The test was done to check the performance of the golf cart with BT system. The speed, current drawn from BT, voltage of the system and the resultant power of the golf cart are recorded during the route. This result (Figure 9) was a benchmark to compare with the new hybrid system proposed. The golf cart power requirement and the capability of golf cart are discovering during this test. The highest altitude the golf cart climb was around 110 m above sea level, the maximum speed of the golf cart can be move by this motor are around 20 km/h throughout the test. The highest current draws are 77.13 A during climbing up slopes. The voltage are fluctuates from 44 V to 54 V maximum due to discharge and charge of BTs during the course, but the average voltage of 48 V are required to run the golf car motor that being set by the motor controller. The power consumption extract from this test was not more than 4 kW.

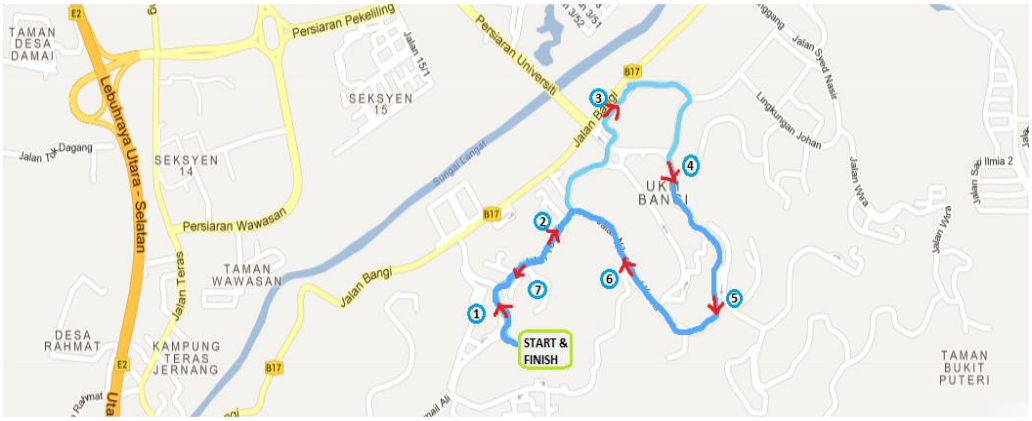


Figure 8. Route map of on road test

Hybrid golf cart – after transformation

In laboratory testing

The development of the reactant system was applied towards the stack as in Figure 2 and the system was tested in the laboratory using electronic load 3311D to change the value of the load variations. Test results are shown in the Figure 10 where the polarization curve plotted shows that the highest amount of power can be drawn from the FC stack is around 380 W. The flow rate of hydrogen change with the increasing load in Figure 11, this prove that controlling of hydrogen flow rate amount are essential in order to supply sufficient reactant amount to have a good power performance. In Figure 12, the graph show the voltage fluctuation as the test done resultant form the LabVIEW program measurement, the setpoint current programmed function well as the voltage change to satisfy the current output getting from the controller.

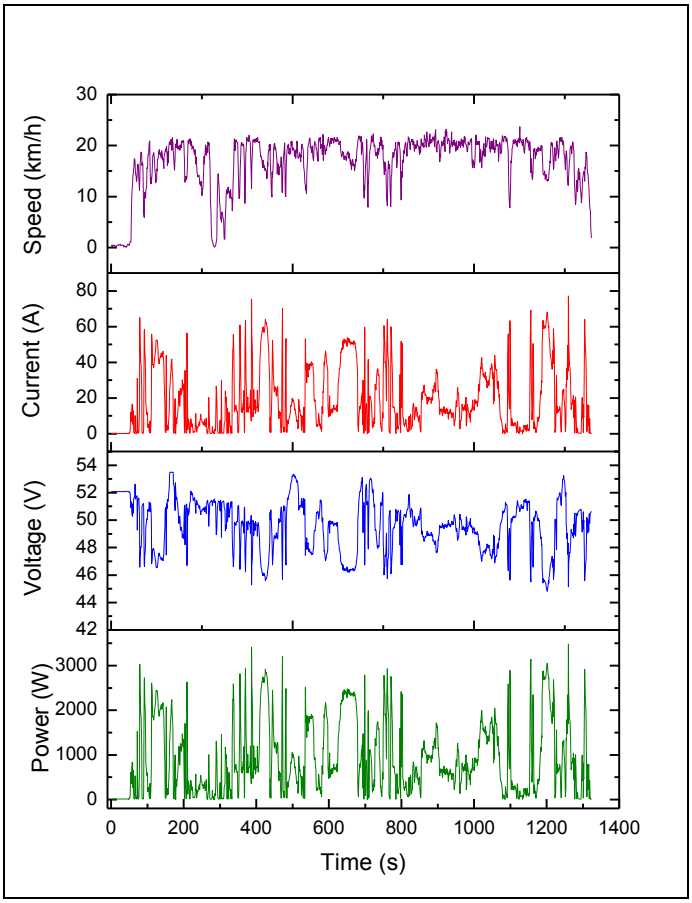


Figure 9. Measurement of speed, current, voltage and power response during on road testing using BT as power generator

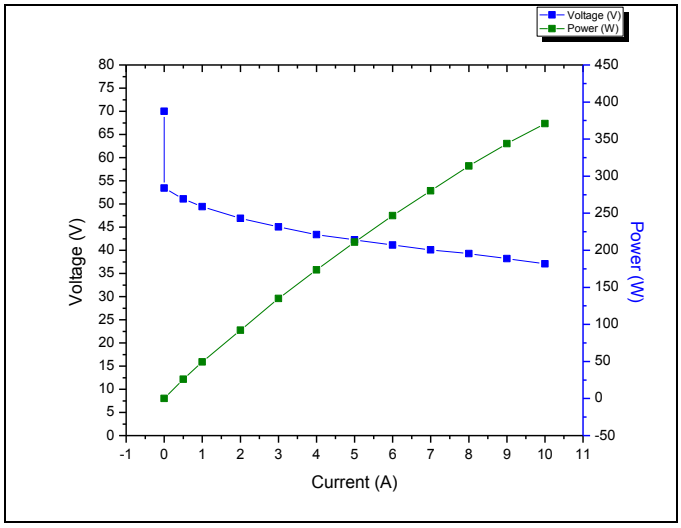


Figure 10. Polarization curve of power and voltage changes on the current towards fabricate FC stack

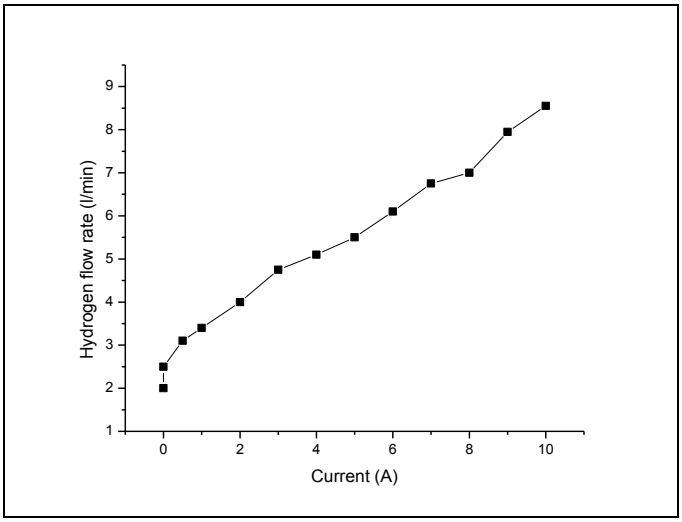


Figure 11. Hydrogen gas flow rate changes with variation of load

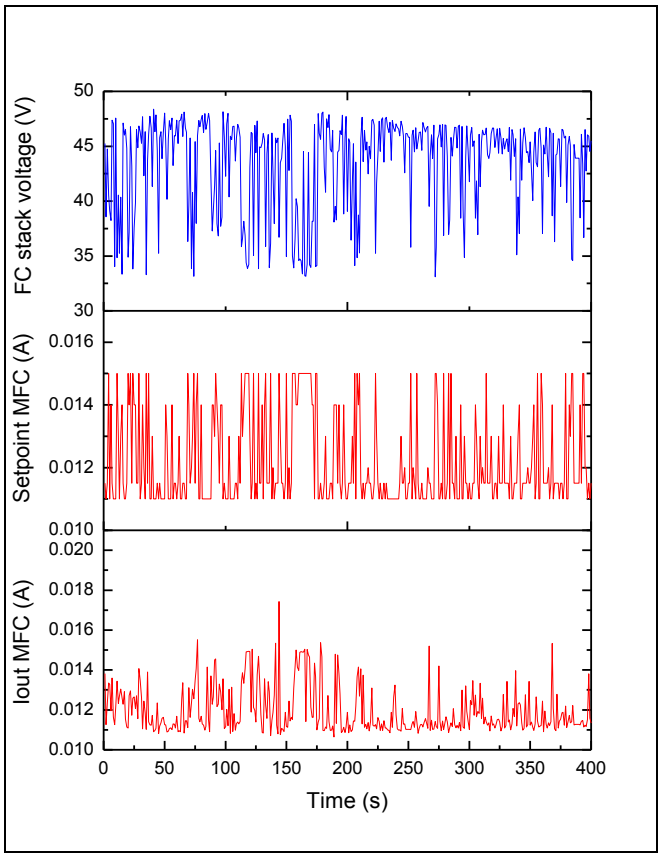


Figure 12. Measurement of voltage variation with change response of current setpoint andoutput form mass flow controller

On road testing

For on road tests, the reactant control system built was applied to the FC stack, and FC are as the primary source and the power management system used to control the FC stack and SC for golf cart to replace the six pieces of 8 V lead-acid BTs connected in series before. The on road tests after transformation are done with the same route before. The test objective was to make sure the hybrid system work and the power management system flow are working as they are programmed. This new power management system was working as programmed but due to existence of slope in the route, the SC discharge rapidly and worst depleted. The speeds are maintaining not more than 15 km/h so it can sustain throughout the test. The new hybrid golf car was worked successfully with the power sources helping each other to serve the load demand. Due to reduce in weight of golf cart as described in Table 1, the current consumption drawn also reduced. Their average currents are 17 A. The resultant powers are also decrease and there are not fluctuate so much as before. The results are shown as in Figure 13.

Table 1. Weight and volume comparison of the transformation of the FC/SC hybrid system with the BT system

		BT	**FC/SC hybrid**
BT (6 unit)	Weight (kg)	174	-
	Volume (m^3)	0.0809	-
FC (2 stack)	Weight (kg)	-	26
	Volume (m^3)	-	0.0441
SC	Weight (kg)	-	14.2
	Volume (m^3)	-	0.0152
Total	Weight (kg)	174	40.2
	Volume (m^3)	0.0809	0.0593

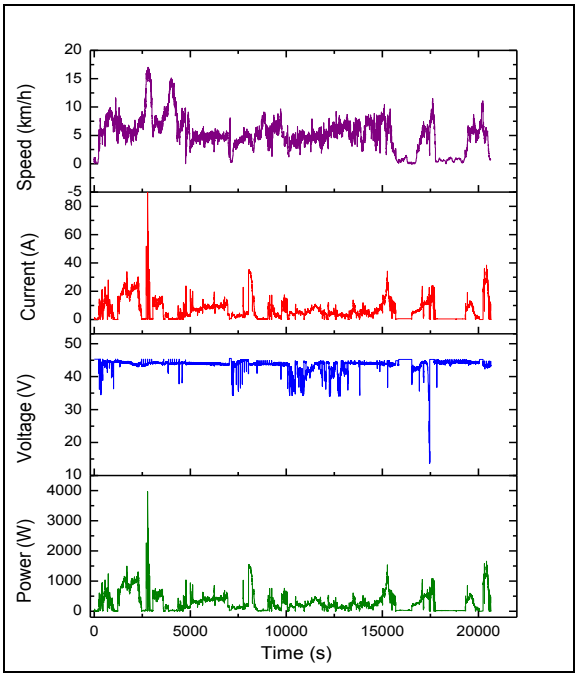


Figure 13. Measurement of speed, current, voltage and power response during on road testing using FC and SC as power generator

From Figure 14, the voltages of the golf cart power source are shown. The FC stacks are successfully maintaining the operating voltage with the help from DC/DC converter. As we can see from the second graph, SC voltage begin to depleted at 700 s. FC voltage from 700 s onward fluctuations rapidly as it try to charge the SC. The SC voltage begins to increase at 1500 s and the FC voltage fluctuation reduces a bit. The graph proves that the power management is working as the strategyprogram in LabVIEW. Moreover, the last graph shows the resultant voltage from FC and SC. A SC can advance the load, following the characteristics of the main sources by providing a stronger power response to the changes in system load. During essential steps in the load, the SC provides the energy balance needed during load transition periods. Adding energy storage (SC) to the power generator (FC) systems improves power quality and efficiency. The graphs clearly proof the function of having SC as the auxiliary power source.

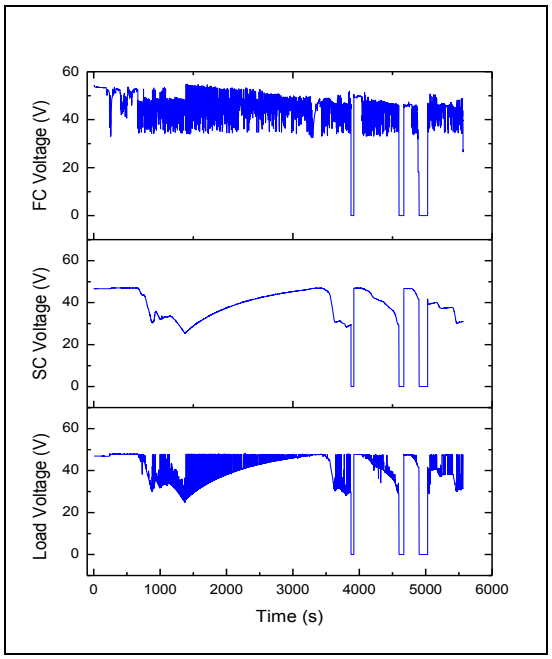


Figure 14. Measurement of FC, SC and load voltage

Conclusion

The transformation of the commercialize electric golf cart powered by the conventional lead acid BT done by replacing the power generator to more environment friendly power source that is PEMFC and SC. This hybrid vehicle development includes from the PEMFC manufacturing process, to the reactant controller of the FC stack, as well as the hybrid power management controller. The PEMFC build consist of two stacks connected in series to add up their equivalent voltage to be sufficient with the motor. The reactant controller is focus on the flow rate of the hydrogen supply to adjust with the requested load power in order to meet the reaction requirement and reduce from excess waste to atmosphere. The power management controller manages the power flow of the FC and SC to meet the load demand. The controller program work successfully and satisfy the required load and the use of PEMFC and SC in hybrid vehicle appear to be environmentally benign and sustainable option to overcome the environment pollution made by ICE vehicles.

Acknowledgement

The authors gratefully acknowledge their thanks to Universiti Kebangsaan Malaysia for their financial support provided through a University Research Grants; UKM-AP-TK-08-2010, DIP-2012-05 and AP-2013-010.

References

1. Chen, B. (2009). Ultracapacitor boosted fuel cell hybrid vehicle, elecrical engineering. Thesis Msc: pp. 130.
2. Erdinc, O., Vural, B. and Uzunoglu M. (2009). A wavelet-fuzzy logic based energy management strategy for a fuel cell/battery/ultra-capacitor hybrid vehicular power system. *Journal of Power Sources*, 194(1): 369 – 380.
3. El-Sharkh, M.Y., Rahman, A. and Alam, M.S. (2004). Neural networks-based control of active and reactive power of a stand-alone PEM fuel cell power plant. *Journal of Power Sources*, 135(1-2): 88 – 94.
4. Thanapalan, K. K. T., Williams, J. G., Liu, G. P., and Rees, D. (2008). Modelling of a PEM fuel cell system. *Proceeding of the 17th World Congress - The International Federation of Automatic Control*, Seoul, Korea.
5. Shen, M., Meuleman, W. and Scott K. (2003). The characteristics of power generation of static state fuel cells. *Journal of Power Sources*, 115(2): 203 – 209.
6. Shen, M. and Scott, K. (2005). Power loss and its effect on fuel cell performance. *Journal of Power Sources*, 148: 24 – 31.
7. Uzunoglu, M. and Alam, M. S. (2007). Dynamic modeling, design and simulation of a PEM fuel cell/ultra-capacitor hybrid system for vehicular applications. *Energy Conversion and Management*, 48(5): 1544 – 1553.
8. Jeong, K. S., Lee, W. Y. and Kim, C. S. (2005). Energy management strategies of a fuel cell/battery hybrid system using fuzzy logics. *Journal of Power Sources*, 145(2): 319 – 326.
9. Thounthong, P., Raël, S. and Davat, B. (2006). Control strategy of fuel cell/supercapacitors hybrid power sources for electric vehicle. *Journal of Power Sources*, 158(1): 806 – 814.
10. Bernard, J., Hofer, M., Hannesen, U., Toth, A., Tsukada, A., Büchi, F. N. and Dietrich, P. (2011). Fuel cell/battery passive hybrid power source for electric powertrains. *Journal of Power Sources*, 196(14): 5867 – 5872.
11. Erdinc, O. and Uzunoglu, M. (2010). Recent trends in PEM fuel cell-powered hybrid systems: Investigation of application areas, design architectures and energy management approaches. *Renewable and Sustainable Energy Reviews*, 14(9): 2874 – 2884.
12. Ates, Y., Erdinc, O., Uzunoglu, M. and Vural, B. (2010). Energy management of an FC/UC hybrid vehicular power system using a combined neural network-wavelet transform based strategy. *International Journal of Hydrogen Energy*, 35(2): 774 – 783.
13. Caux, S., Hankache, W., Fadel, M. and Hissel, D. (2010). On-line fuzzy energy management for hybrid fuel cell systems. *International Journal of Hydrogen Energy.* 35(5): 2134 – 2143.
14. Fernandez, L. M., Garcia, P., Garcia, C. A. and Jurado, F. (2011). Hybrid electric system based on fuel cell and battery and integrating a single dc/dc converter for a tramway. *Energy Conversion and Management*, 52(5): 2183 – 2192.
15. Khaligh, A. and Zhihao, L. (2010). Battery, ultracapacitor, fuel cell, and hybrid energy storage systems for electric, hybrid electric, fuel cell, and plug-in hybrid electric vehicles: state of the art. *IEEE Transactions on Vehicular Technology*, 59(6): 2806 – 2814.
16. Lin, W.S. and Zheng, C.H. (2011). Energy management of a fuel cell/ultracapacitor hybrid power system using an adaptive optimal-control method. *Journal of Power Sources*, 196(6): 3280 – 3289.
17. Thounthong, P., Pierfederici, S., Martin, J. P., Hinaje, M. and Davat, B. (2010). Modeling and control of fuel cell/supercapacitor hybrid source based on differential flatness control. *IEEE Transactions on Vehicular Technology*, 59(6): 2700 – 2710.
18. Torreglosa, J. P., Jurado, F., García P. and Fernández, L. M. (2011). Application of cascade and fuzzy logic based control in a model of a fuel-cell hybrid tramway. *Engineering Applications of Artificial Intelligence*, 24(1): 1 – 11.
19. Fernandez, L. M., Garcia, P., Garcia, C. A., Torreglosa, J. P. and Jurado, F. (2010). Comparison of control schemes for a fuel cell hybrid tramway integrating two dc/dc converters. *International Journal of Hydrogen Energy*, 35(11): 5731 – 5744.
20. Payman, A., Pierfederici, S. and Meibody-Tabar, F. (2008). Energy control of supercapacitor/fuel cell hybrid power source. *Energy Conversion and Management*, 49(6): 1637 – 1644
21. Eren, Y., Erdinc, O., Gorgun, H., Uzunoglu, M. and Vural, B. (2009). A fuzzy logic based supervisory controller for an FC/UC hybrid vehicular power system. *International Journal of Hydrogen Energy*, 34(20): 8681 – 8694.

22. Erdinc, O., Vural, B., Uzunoglu, M. and Ates, Y. (2009). Modeling and analysis of an FC/UC hybrid vehicular power system using a wavelet-fuzzy logic based load sharing and control algorithm. *International Journal of Hydrogen Energy*, 34(12): 5223 – 5233.
23. Sakhare, A., Davari, A. and Feliachi, A. (2004). Fuzzy logic control of fuel cell for stand-alone and grid connection. *Journal of Power Sources*, 135(1-2): 165 – 176.
24. Ke, J., Xinbo, R., Mengxiong, Y. and Min, X. (2008). Power management for hybrid fuel cell system. *IEEE* in *Power Electronics Specialists Conference:* 504 – 509.
25. Bizon, N. (2011). Nonlinear control of fuel cell hybrid power sources: Part I - Voltage control. *Applied Energy*, 88(7): 2559 – 2573.
26. Thanapalan, K., Fan, Z., Premier, G., Maddy, J. and Guwy, A. (2011). Control-oriented PEM fuel cell system modeling and repetitive controller design. *2nd International Conference on Intelligent Control and Information Processing (ICICIP)*, 2: 1055 – 1060.
27. Li, F., Li, D. & Yang, R. (2009) A Dynamic Model of PEM Fuel Cell Stack System for Real Time Simulation. *Power and Energy Engineering Conference:* 1 – 5
28. Lu-Ying, C., Diong, B. and Gemmen, R.S. (2004). An improved small-signal model of the dynamic behavior of PEM fuel cells. *IEEE Transactions on Industry Applications*, 40(4): 970 – 977.
29. Caponetto, R., Fortuna, L. and Rizzo. A. (2005). Neural network modelling of fuel cell systems for vehicles. *10th IEEE Conference on Emerging Technologies and Factory Automation ETFA, 1*: 6.
30. Tae-Hoon, K. and Woojin, C. (2009). Control system design for the small proton exchange membrane fuel cell stack. *31st International Telecommunications Energy Conference:* 1 – 6.
31. Hou, Y., Shen, C., Yang, Z. and He, Y. (2012). A dynamic voltage model of a fuel cell stack considering the effects of hydrogen purge operation. *Renewable Energy*, 44: 246 – 251.
32. Chen, D., Li, W. and Peng, H. (2008). An experimental study and model validation of a membrane humidifier for PEM fuel cell humidification control. *Journal of Power Sources*, 180(1): 461 – 467.
33. Ye, Q., Cui, H. and Deng, M. (2010). Design of a 100W fuel cell test system. *Power and Energy Engineering Conference (APPEEC):* 1 – 4.
34. Rosli, R. E., Majlan, E. H., Wan Daud, W. R. and Hamid, S. A. A. (2012). Hydrogen rate manipulation of proton exchange membrane fuel cell (PEMFC) stack using feedback control system. *IEEE International Conference on Power and Energy (PECon):* 553 – 557.

Malaysian Journal of Analytical Sciences, Vol 20 No 4 (2016): 946 - 954
DOI: http://dx.doi.org/10.17576/mjas-2016-2004-30

MALAYSIAN JOURNAL OF ANALYTICAL SCIENCES
Published by The Malaysian Analytical Sciences Society
ISSN 1394 - 2506

MOLECULAR AND ELECTRONIC STRUCTURES OF A NEW RUTHENIUM-TUNGSTEN BIMETALLIC COMPLEX USING DENSITY FUNCTIONAL THEORY CALCULATIONS

(Struktur Molekul Dan Elektronik Kompleks Dwilogam Rutenium-Tungsten Berdasarkan Pengiraan Teori Fungsi Ketumpatan)

Khuzaimah Arifin[1]*, Wan Ramli Wan Daud[1,2], Mohammad B. Kassim[1,3]

[1]*Fuel Cell Institute*
[2]*Department of Chemical and Process Engineering*
[3]*School of Chemical Sciences and Food Technology, Faculty of Science and Technology*
Universiti Kebangsaan Malaysia, 43600 UKM Bangi, Selangor, Malaysia

**Corresponding author: khuzaim@ukm.edu.my*

Received: 5 February 2016; Accepted: 22 April 2016

Abstract

A potential dye sensitizer material for solar cell composed of a ruthenium-(4, 4'dimethyl-2, 2′-bipyridine)-isothiocyanato-tungsten-[bis-(phenyl-1, 2-ethilenodithiolenic)] bimetallic complex structure was successfully developed using Density Functional Theory (DFT) calculations. The optimal structure was realized by calculations using the generalized gradient approximation (GGA) framework in a double numeric plus polarization (DNP) basis set using the following three functional methods: Becke-Pardew (BP), Becke-Lee-Yang-Parr (BLYP) and Perdew-Burke-Ernzerhof (PBE). The PBE calculation gave a structure with bond lengths and angles that approximated the experimental data. The restricted-spin calculation of PBE found that BM has 339 molecular orbitals in which the highest occupied molecular orbital (HOMO) and lowest unoccupied molecular orbital (LUMO) are located at orbital numbers 312 and 313, respectively. The HOMO was delocalized over the $W(S_2C_2)$ ring, the ruthenium metal center and the thiocyanate bridging ligand. In contrast, the LUMO was found mainly at the bipyridyl ligand with a small contribution from the ruthenium metal center. Electron excitation from the HOMO → LUMO occurred at 2964 nm with an excitation energy of 0.42 eV, which is depicted by the charge transfer from one metal to another (intervalence charge transfer, IVCT) or as a manifestation of the NCS bridging ligand.

Keywords: density functional theory, bimetallic, thiocyanate, bridging ligand

Abstrak

Pembangunan struktur molekul kompleks dwilogam rutenium-(4,4'dimetil-2,2′-bipiridina)-isotiosianat-tungsten[bis-(fenil-1,2-etilenoditiolena)] (BM) telah dilakukan menggunakan kaedah pengkomputeran Teori Fungsi Ketumpatan (DFT) berdasarkan data yang diperoleh dari eksperimen. Untuk mendapatkan struktur yang optimum, pengiraan telah dilakukan dengan menggunakan pendekatan gradien menyeluruh (GGA) dengan set asas pengutuban tambahan gandaan angka (DNP) pada tiga kaedah fungsian; Becke-Pardew (BP), Becke-Lee-Yang-Parr (BLYP) dan Perdew–Burke–Ernzerhof (PBE). Pengiraan menggunakan fungsian PBE menghasilkan struktur dengan panjang dan sudut ikatan yang paling mendekati nilai eksperimen. Hasil pengiraan spin terhad dengan PBE mendapati bahawa kompleks BM memiliki 339 orbital molekul, di mana orbital molekul berisi tertinggi (HOMO) dan orbital molekul tak berisi terendah (LUMO) masing-masing berada pada orbital molekul 312 dan 313. Orbital HOMO kompleks dwilogam BM didapati dinyah setempat pada gelang $W(S_2C_2)$, logam pusat Ru serta ligan penghubung NCS. Sebaliknya, orbital LUMO sebahagian besarnya berada pada ligan bipiridil dengan sedikit sumbangan dari logam pusat Ru. Tenaga pengujaan elektron dari HOMO → LUMO wujud sebagai puncak penyerapan pada 2964 nm

dengan tenaga pengujaan 0.42 eV yang berpadanan dengan peralihan cas daripada logam kepada logam (peralihan cas antara velensi, IVCT) yang menyokong peranan NCS sebagai ligan titian.

Kata kunci: teori fungsi ketumpatan, kompleks dwilogam, thiosianat, ligan penghubung

Introduction

Computational chemistry investigations have been used in many fields, such as in solar cell material development [1], batteries [2], sensors [3] and thermoelectric materials [4]. The investigation can be used to identify the structure and properties of the crystal and bulk molecule as well as the thin film surface; it can also be used to model the chemical reactions on the structure surface for a more detailed understanding [5, 6]. The computational chemistry methods and the ability of each method to analyze the structure and predict the properties of molecules have been widely discussed, including the density functional theory (DFT) method. The DFT method has been used to successfully and accurately study various properties of molecules in the ground state, including transition metal complex molecules.

The ruthenium-(4,4'dimethyl-2,2′-bipyridine)-isothiocyanato-tungsten-[bis-(phenyl-1,2-ethilenodithiolenic)] bimetallic complex, abbreviated BM, was successfully synthesized, and its properties were investigated as a potential dye sensitizer molecule for TiO_2 [7, 8]. Because the acquisition of a suitable BM single crystal for X-ray diffraction studies has been unsuccessful, in this study, the theoretical development of the BM molecular structure was investigated. DFT analysis used for in-depth studies was performed on the optimized molecular structure. The development of the molecular structure using a theoretical calculation is similar in principal to the X-ray diffraction refinement of a single crystal molecule, which defines the most stable structure at the lowest energy or stationary state. The molecular orbital configuration and the optical properties of the lowest energy BM structure were reported for various parameter calculations.

Materials and Methods

Computational details

The molecular structure and density functional theory (DFT) calculations were performed using Microsoft visualizer and the $DMol^3$ module in Bolivia Materials Studio 7.0 software. All of the calculations were performed using the self-consistent field (SCF) method on a spin polarization system with the multiplicity set to auto for all of the core electron treatments. The SCF is a repetition of Hatree Fock calculations on all of the electrons until the effective electrostatic field does not further change or converges. For the DFT calculation, an approximation should be performed because an energy function is not precisely known. In this study, the generalized gradient approximation (GGA) was used with varying correlation functional methods, such as Pardew Backe (BP), Beckie (B), gradient-corrected correlation of Lee-Yang-Parr (LYP) and the exchange correlation Perdew-Burke-Ernzerhof (PBE) [9,10,11]. Double numerical plus polarization (DNP), which is comparable to 6-31G ** of the Gaussian basis set was used [12]. The entire geometry optimization process in this study was performed with fine quality. The geometry optimization was reiterated until the structure reached its lowest energy state.

Vibrational frequency analysis was used to confirm the energy state of the structure in every geometry optimization process. The absence of imaginary frequencies in the optimization results indicates that the structures are already in a stationary state [13]. In addition, the comparison results of vibration frequency analysis calculations with experimental FTIR analysis results were used as supplementary information for the confirmation of the molecular structure. The result was quality examined by comparing the bond lengths and angles of the calculation results with a similar molecular structure that has been reported. Analysis of the molecular orbital calculations and the optical properties was performed on the optimized structures of the molecule using the time dependence of the density functional theory (TD-DFT) method [14].

Results and Discussion

Molecular structure

The molecular structure of BM was constructed from two octahedral precursors. The molecular structures of the precursors were derived from X-ray single crystal data of similar molecules with ligand modification (Figure 1). Both of the precursor structures were optimized to the stationary state and placed adjacent to each other with the

thiocyanate ligands of ruthenium-[bis(4,4'-dimethyl-2,2′-bipyridyl)-isothiocyanato], abbreviated as M1 complex, and the carbonyl ligands of the tungsten dithiolene carbonyl complex $[W(S_2C_2Ph_2)_2(CO)_2]$ (M2) facing each other. The carbonyl ligands of complex M2 were then removed, and each S atom on the –NCS– ligands of complex M1 was connected to the tungsten atom of complex M2, forming double –NCS– bridging ligands. The bond lengths of W–S and S–Ru were arranged to approach normal lengths. The BM structure was then optimized several times until no imaginary frequencies were found using various parameters.

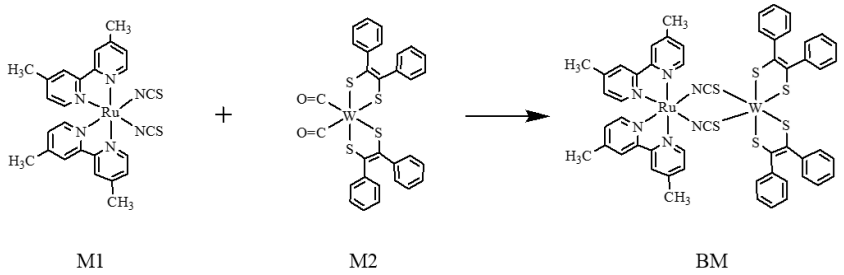


Figure 1. The reaction scheme for preparation of BM

To ensure that the complex structure agreed with the experimental data, the frequency vibration spectra were compared with FTIR experimental data (Figure 2). Although the peaks of the harmonic vibration frequency spectra calculation and those from the FTIR experiment were not exactly in the same position, the important peaks, such as N–H, C–C aromatic, and –NCS, among others, were present in both of the spectra. Most of the peaks of the spectrum calculation appeared at a lower energy of approximately 200 cm^{-1} compared with the FTIR experimental peak frequencies. This result is because the environmental factors of the experiment cannot be perfectly modeled, such as the presence of residual solvent molecules that might affect the experimental spectrum. In this study, the optimization calculation was processed under vacuum conditions. The optimized structure of BM is similar to the bimetallic complex with the double thiocyanate ligand structure reported by Eran et al. [15]. Eran has reported a homobimetallic complex of Pt connected to double thiocyanate ligands in which each Pt was connected to –S and N– of the thiocyanate.

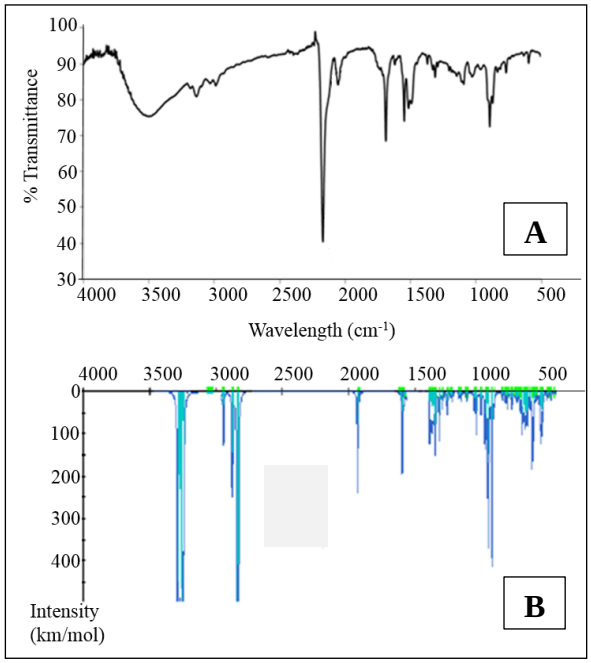
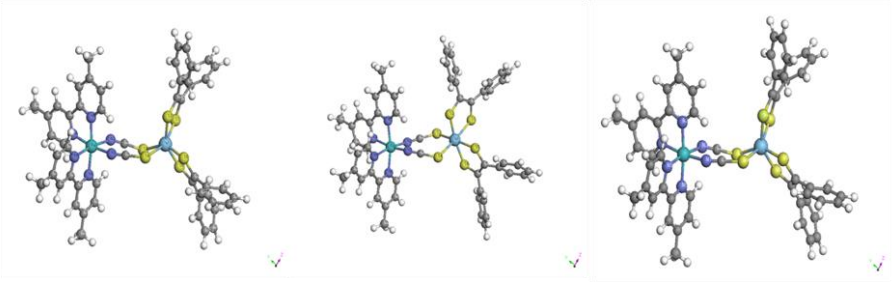


Figure 2. Comparison of FTIR experiment (A) and harmonic vibrational frequencies spectrum (B) of BM

The BM was optimized using three different GGA functionals, which produced a slightly different geometrical structure (Figure 3). The total energy consumption during the optimization process and the band gap energy produced are listed in Table 1. All of the optimized structures have two metals in the center of the perpendicular plane. All of the bipyridine and dithiolene ligands chelated each metal center, which distorted the octahedral structure. The optimized structure of BM using BLYP and PBE resulted in a similar structure in which the geometry of the W metal center was more closely distorted to trigonal prismatic. The W-S bond length of the BLYP calculation result was generally longer than that of the BP and PBE results. All of the bond length and angle calculation results are summarized in Table 2.



BLYP BP PBE

Figure 3. The optimize molecular structure of BM using three different GGA functionals calculation

Table 1. Energy calculation for structural optimization of two isomers of BM at three different DFT functional calculations

GGA Functional	Energy Optimization (Ha)	E-HOMO (eV)	E-LUMO (eV)	Band gap energy (eV)
BLYP	-24538.44	-3.527	-3.125	0.402
BP	-24540.34	-4.575	-3.236	1.339
PBE	-24534.05	-3.671	-3.288	0.383

Table 2. Comparison of selected bond lengths (Å) and angles (°) of optimized BM geometries using three DFT functional calculations

Bond Length (Å)	GGA			Bond Length (Å)	GGA		
	BLYP	BP	PBE		BLYP	BP	PBE
W-S(1)	2.388	2.427	2.406	S(5)-C(37)	1.766	1.764	1.749
W-S(2)	2.432	2.417	2.413	S(6)-C(46)	1.765	1.766	1.756
W-S(5)	2.406	2.416	2.414	Ru-N(1)	2.114	2,085	2.076
W-S(6)	2.405	2.413	2.399	Ru-N(2)	2.126	2.098	2.099
W-S(3)	2.699	2.599	2.617	Ru-N(3)	2.128	2.113	2.099
W-S(4)	2.675	2.647	2.601	Ru-N(4)	2.125	2.097	2.091
S(3)-C(2)	1.703	1.666	1.657	Ru-N(5)	2.127	2.097	2.090
S(4)-C(1)	1.752	1.665	1.661	Ru-N(6)	2.138	2.113	2.109
S(1)-C(9)	1.766	1.760	1.752	N(1)-C(1)	1.181	1.181	1.182
S(2)-C(10)	1.761	1.760	1.748	N(2)-C(2)	1.184	1.183	1.186

Table 2 (cont'd). Comparison of selected bond lengths (Å) and angles (°) of optimized BM geometries using three DFT functional calculations

Bond Angle (°)				**Bond Angle (°)**			
S(1)-W-S(2)	79.25	79.76	79.48	C(1)-N(1)-Ru	153.61	151.67	152.00
S(5)-W-S(6)	79.92	80.16	80.15	C(2)-N(2)-Ru	151.25	149.19	143.73
S(3)-W-S(4)	92.44	95.61	94.31	N(1)-Ru-N(2)	81.19	79.62	80.66
S(1)-W-S(5)	120.17	113.8	117.5	N(3)-Ru-N(4)	77.39	77.87	78.12
S(1)-W-S(6)	85.78	84.63	85.93	N(5)-Ru-N(6)	77.30	77.89	78.04
S(1)-W-S(3)	82.65	83.22	84.08	N(1)-Ru-N(6)	89.20	89.49	90.13
S(2)-W-S(4)	79.10	84.29	82.62	N(1)-Ru-N(5)	94.67	93.53	93.59
S(2)-W-S(5)	95.89	87.67	80.77	N(1)-Ru-N(3)	96.74	96.02	94.69
S(4)-W-S(5)	83.86	74.26	76.32	N(2)-Ru-N(3)	89.61	90.49	89.71
S(2)-W-S(3)	105.89	87.67	129.8	N(2)-Ru-N(4)	97.11	95.33	95.48
S(3)-W-S(6)	78.22	77.40	78.60	N(3)-Ru-N(5)	97.77	97.39	97.93
S(4)-W-S(6)	103.83	113.4	118.1	N(4)-Ru-N(5)	88.02	92.19	91.07
S(3)-W-S(5)	158.21	154.0	149.0	N(2)-Ru-N(6)	97.11	94.77	94.71
S(1)-W-S(4)	156.81	155.0	154.9	N(1)-Ru-N(4)	174.11	172.13	171.93
S(2)-W-S(6)	174.56	161.6	147.1	N(2)-Ru-N(5)	171.77	170.09	170.93
C(1)-S(4)-W	111.41	115.5	113.7	N(3)-Ru-N(6)	172.51	172.98	173.92
C(2)-S(3)-W	112.77	115.7	112.8				
Torsian angle (°)				**Torsian angle (°)**			
Ru-N(1)-C(1)-S(4)	138.93	173.9	157.8	W-S(3)-C(1)-N(2)	173.89	178.32	152.48
Ru-N(2)-C(2)-S(3)	146.95	142.7	97.3	W-S(4)-C(2)-N(1)	126.83	171.24	156.20

The bond angle of S–W–S in the chelating ligands from the BLYP calculation is 79.25º and 79.92º, and the bond angle of S–W–S on the NCS bridging ligands is 78.22° to 174.56°, while the bond angle of S–W–S between the 5-membered ring WS_2C_2 is 92.44º. Overall, the distorted octahedron of the tungsten metal is between 5.4° and 11.78°. The double bridging ligands –SCN– that connect the tungsten and ruthenium metals form an 8-membered W–$(SCN)_2$–Ru ring, with a W–S bond length of 2.388 Å and 2.432 Å. Umakoshi et al. have reported the molecule structure of the tungsten bimetallic complex, which is connected to a sulfur atom with a W–S bond length of 2.329 Å to 2.322 Å [16]. Meanwhile, the C–S bond length in the bridging ligand is 1.703 and 1.752 Å, which is shorter than the C–S bond length in the WS_2C_2 rings. However, both of the C–S bonds have lengths in normal range [17]. The two bipyridyl ligands and the two thiocyanate ligands that connect to the ruthenium metal center result in a distorted octahedral geometry with a distorted angle of 5.89 - 8.23°. Both of the bipyridyl ligands are perpendicular to the main plane of the eight-membered rings of W-$(SCN)_2$-Ru. The Ru–N bond length calculation result is between 2.123-2.138 Å, which is 3.8% longer than the experimental result reported [17]. Meanwhile, the N–Ru–N angle calculation result is between 77.30° and 81.19°.

The molecular structure from the PBE functional calculation results obtained was similar to the BLYP structure; however, the bond lengths and angles are more uniform and closer to the experimental results that have been reported. The W-S bond length is 2.399 - 2.414 Å, and the bond length of the W–S of bridging ligands is 2.602 and 2.617 Å. The S–W–S bond angles of PBE are similar to those obtained with the BLYP calculation results. The Ru–N bond lengths of PBE are shorter than the BLYP calculation result, with the average bond length of 2.09 Å, which is approximately 2% longer than the experimental results [18].

Moreover, the calculations with the BP functional method resulted in a structure with longer bond lengths than the PBE calculation results but slightly shorter than those in the BLYP. The distorted octahedral geometry of the BP calculation result is smallest compared with the BLYP and PBE calculation results. Overall, the PBE method result is considered closest to the experimental value compared with BLYP and BP. For further study, the characterization calculation is only performed with the PBE functional method.

Orbital molecular configuration

Most of the orbital configurations of the monometallic complex molecules have been well described, such as the complex of cis-bis(4,4'-dicarboxylate-2,2'-bipyridine)diisothiocyianate-ruthenium (II) (N3), whose HOMO comes from the Ru metal and isothiocyanate ligand, while its LUMO is mostly derived from bipyridine aromatic rings [19]. In contrast to monometallic complexes, the electronic distribution and molecular orbital configuration of bimetallic complexes have seldom been reported because there are many molecular orbitals involved in the bimetallic complex, causing the orbitals to become irregular and creating difficulty in defining the position of the HOMO and LUMO. Recently, the use of the DFT method, which can describe the molecular orbital configuration of a molecule composed of more than 500 atoms, has led to the successful description of the molecular orbital configuration of large complexes, which contributes to the knowledge of these compounds.

The molecular orbital configuration of the BM bimetallic complex with the PBE calculation results is displayed in Figure 4. There are 339 molecular orbitals involved in the BM bimetallic complex in which the HOMO and LUMO are located at the orbital numbers of 312 and 313, respectively. The HOMO of the BM bimetallic complex is located along the $W(S_2C_2)$ ring with a portion at the ruthenium metal and the –NCS– bridging ligands. The LUMO is located in the bipyridyl and ruthenium metal. The BM complex has overlap energies, as shown in Fig. 4, in which HOMO and HOMO-1, HOMO-2 and HOMO-3, HOMO-4 and HOMO-5, as well as LUMO and LUMO+1, among others, lie at the same energies. This phenomenon always occurs at the *C1* molecular symmetry due to the repetitive unit and dimeric nature of the complex [20]. The molecular orbital of LUMO+1 up to LUMO+4 also fully lies in the bipyridine ligands and the ruthenium metal center, while all of LUMO+5 and LUMO+6 lies at the tungsten metal and the SCN bridging ligands. Meanwhile, HOMO-1 to HOMO+4 are primarily spread over the tungsten metal, along with the dithiolene ligand with some at ruthenium and the NCS bridging ligands, while HOMO-5 and HOMO-6 lie along the two metal centers and the bridging ligands.

The LUMO to LUMO+2 band gap energy is smaller than that of HOMO to HOMO-2, indicating that it is easier to reduce than to oxidize the BM complex. Furthermore, oxidation occurs more easily on tungsten metal because the HOMO and HOMO-1 are mostly lying at the tungsten and the dithiolene ligands. Reduction occurs more easily at bipyridine and the ruthenium metal. This result is compatible with the cyclic voltammetry analysis results that have been previously reported [7]. The HOMO-LUMO band gap energy calculation using PBE (0.383 eV) was found as the smallest compared with the band gap energy from the BLYP (0.402 eV) and BP (1.339 eV) methods.

Optical properties

The optical properties of the bimetallic complex were studied from the TD-DFT calculation using the PBE functional of the GGA method. Using this technique, the optical properties, which are difficult to identify experimentally, could be easily solved. Table 3 summarizes the 12 lowest singlet and triplet excitations under vacuum. The lowest excitation energy of the singlet state is the excitation of an electron from the HOMO to the LUMO, which lies at the 312 $\rightarrow$ 313 molecular orbital. This excitation appears as an absorption peak at 2964 nm with an energy of 0.42 eV, which is absorption of ^{1}MMCT. This absorption is wider than that of the two constituent complexes. The highest oscillator strength is the excitation of the 310 $\rightarrow$ 314 orbitals (HOMO-3 $\rightarrow$ LUMO), which is the excitation of ^{1}MLCT at an absorption wavelength of 847 nm with a 1.46 eV excitation energy. While at the triplet state (^{3}MMCT), the electron excitation of HOMO $\rightarrow$ LUMO occurs at a lower energy wavelength, with an energy of 0.39 eV. Table 3 shows that the twelfth position of excitation of the lowest singlet and triplet in the bimetallic complex molecular excitation is derived from metal to metal and metal to ligand. The calculations results show that the BM absorbs light energy up to the near IR region. These results also agree with the experimental results in which the absorption of light of the bimetallic complex BM was higher than the monometallic complexes (M1 & M2) and N3 commercial sensitizer [7].

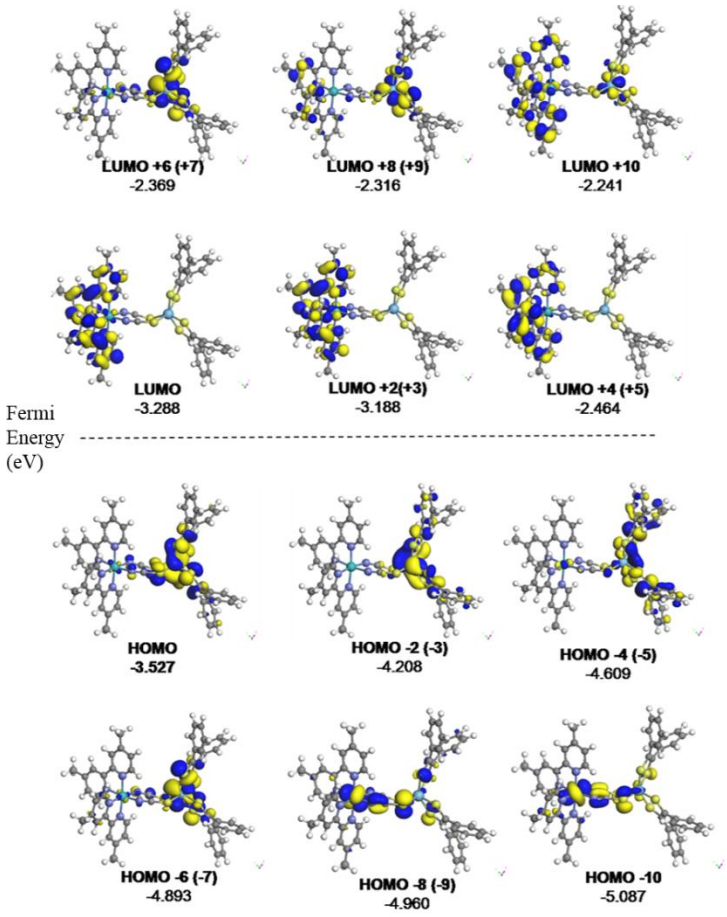


Figure 4. Molecular orbital configuration of BM

Table 3. Summary of 12 lowest singlet TDDFT excitations energies for optical transitions of BM in vacuum

Singlet		**Overlap %**	**Excitation**			**Oscilator strength**
From	**To**		**eV**	**Nm**	**Ha**	
312	→ 313	0.19	0.42	2964	0.015370	0.009184
312	→ 314	0.19	0.50	2475	0.018411	0.004193
311	→ 313	0.10	0.97	1272	0.035811	0.000440
311	→ 314	0.12	1.07	1163	0.039175	0.005050
312	→ 315	0.11	1.22	1017	0.044806	0.000296
312	→ 316	0.64	1.34	928	0.049115	0.000337
310	→ 313	0.13	1.40	883	0.051610	0.006453
312	→ 317	0.61	1.43	868	0.052498	0.006724
310	→ 314	0.15	1.46	847	0.053778	0.014428
312	→ 318	0.47	1.54	806	0.056517	0.006252
312	→ 319	0.26	1.58	785	0.058034	0.000703
312	→ 320	0.14	1.61	771	0.059124	0.013394

Table 3 (cont'd). Summary of 12 lowest singlet TDDFT excitations energies for optical transitions of BM in vacuum

Triplet From To	Overlap %	Excitation eV	Nm	Ha	Oscilator strength
312 → 313	0.19	0.39	3176	0.014347	0.0
312 → 314	0.19	0.48	2585	0.017628	0.0
311 → 313	0.10	0.97	1278	0.035643	0.0
311 → 314	0.12	1.06	1171	0.038918	0.0
312 → 315	0.11	1.21	1021	0.044616	0.0
312 → 316	0.64	1.22	1018	0.044771	0.0
310 → 313	0.13	1.29	961	0.047400	0.0
312 → 317	0.61	1.33	932	0.048888	0.0
310 → 314	0.15	1.42	874	0.052117	0.0
312 → 318	0.47	1.43	866	0.052628	0.0
312 → 319	0.26	1.55	802	0.056782	0.0
312 → 320	0.14	1.57	788	0.057822	0.0

Conclusion

The geometrical structure of the BM bimetallic complex was successfully modeled using the DFT calculation technique with the DMol^3 Material Studio software package. This technique can be used to build the molecular structure, although it was unsuccessful at growing a quality crystal for X-ray single crystal analysis. The bond lengths and angles of the calculation results using the PBE functional of the GGA method had the most similar appearance to the experimental data. From the calculation result, 339 molecular orbitals were involved in the complex in which the HOMO and LUMO orbitals were located at orbital numbers 312 and 313, respectively. The band gap energy between the HOMO and LUMO was 0.383 eV. The HOMO of the complex was mostly derived from the W(S_2C_2) rings with a portion from the Ru metal and the NCS bridging ligands. The LUMO was primarily derived from the bipyridyl ligands and the Ru metal. The optical properties of the complex analysis from the TD-DFT calculation shows that the electronic absorption of the complex can reach up to 2964 nm and is wider compared with the absorption area of the monometallic complex starting materials, which is 902 nm for *cis*-$W(S_2C_2Ph_2)_2(CO)_2$ (M2) and 1652 nm for *cis*-[$Ru(dmbpy)_2NCS_2$] (M1).

Acknowledgement

The authors would like to acknowledge the Universiti Kebangsaan Malaysia for sponsoring this project under the UKM-GUP-07-30-190 and FRGS/1/2015/SG01/UKM/03/1 research grants.

References

1. Guo, P., Ma, R., Guo, L., Yang, L., Liu, J., Zhang, X., Pan, X. and Dai, S. (2010). Theoretical study on the electronic absorption spectra and molecular orbitals of ten novel ruthenium sensitizers derived from N3 and K8**.** *Journal of Molecular Graphics and Modelling*, 29: 498 – 505.
2. Islam, M. S. and Fisher, C. A. J. (2014). Lithium and sodium battery cathode materials: computational insights into voltage, diffusion and nanostructural properties. *Chemical Society Reviews*, 43: 185 – 204.
3. Mehmood, F. and Pachter, R. (2014). Density functional theory study of chemical sensing on surfaces of single-layer MoS2 and graphene. *Journal of Applied Physics*, 115: 164302.
4. Khan, W., Reshak, A. H., Ahmad, K. R. and Alahmed, Z. A. (2014) Magnetic and thermoelectric properties of three different atomic ratio of Bi/Mn in $BiMn_2O_5$: DFT approach. *Journal of Magnetism and Magnetic Materials*, 369: 234 – 242.
5. Shariatinia, Z. and Shahidi, S. (2014). A DFT study on the physical adsorption of cyclophosphamide derivatives on the surface of fullerene C_{60} nanocage**.** *Journal of Molecular Graphics and Modelling*, 52: 71 – 81.

6. Young, D. C. (2001). Computational chemistry: A practical guide for applying techniques to real-world problems, John Wiley & Sons, Inc., New York.
7. Arifin, K., Daud, W. R. W. and Kassim, M.B. (2013). Optical and photoelectrochemical properties of a TiO_2 thin film doped with a ruthenium-tungsten bimetallic complex. *Ceramics International* 39: 2699 –2707.
8. Arifin, K., Daud, W. R. W. and Kassim, M. B. (2014) A novel ruthenium-tungsten bimetallic complex dye-sensitizer for photoelectrochemical cells application. *Sains Malaysiana,* 43 (1): 95 – 101.
9. Becke, A. D. (1988). Density-functional exchange-energy approximation with correct asymptotic behavior. *Physical Review*, 38: 3098 – 3100.
10. Parr, R. G. and Yang, W. (1989). Density-functional theory of atoms and molecules, Oxford Univ. Press, Oxford.
11. Perdew, J. P., Burke, K., and Ernzerhof, M. (1996). Generalized gradient approximation made simple. *Physical Review Letters*, 77: 3865.
12. Sokolov, A. N., Atahan-Evrenk, S., Mondal, R., Akkerman, H. B., Sánchez-Carrera, R. S., Granados-Focil, S. J., Schrier, S. C., Mannsfeld, B., Zoombelt, A. P., Bao, Z. and Aspuru-Guzik, A. (2011). From computational discovery to experimental characterization of a high hole mobility organic crystal. *Nature Communications*, 2: 437 – 445.
13. Wilson, G. J. and Will, G. D. (2010). Density-functional analysis of the electronic structure of tris-bipyridyl Ru(II) sensitisers. *Inorganic Chimica Acta* 363(8): 1627 – 1638.
14. Delley, B. (2010). Time dependent density functional theory with $DMol^3$. *Journal of Physics: Condensed Matter*, 22: 384208.
15. Eran, B. B., Singer, D., Pickardt, J. and Praefcke, K. (2001). Thiocyanato-bridged platinum heterocycles: structure and properties of disc-like metallomesogens. *Journal of Organometallic Chemistry*, 620: 249 -255.
16. Umakoshi, K., Nishimoto, E., Sokolov, M., Kawano, H., Sasaki, Y. and Onishi, M. (2000). Synthesis, structure, and properties of sulfido-bridged dinuclear tungsten(V) complex of dithiolene, $(Pr_4N)_2[W_2(m\text{-}S)_2\{S_2C_2(CO_2Et)_2\}_4]$. *Journal of Organometallic Chemistry*, 611: 370 - 375.
17. Allen, F. H., Kennard, O., Watson, D. G., Brammer, L., Orpen, A. G. and Taylor, R. J. (1987). Tables of bond lengths determined by X-Ray and neutron diffraction. Part 1. Bond lengths in organic compounds, *Journal of the Chemical Society, Perkin Transactions 1*, 112: 1 - 19.
18. Arifin, K., Daud, W. R. W. and Kassim, M. B. (2014). A DFT analyses for molecular structure, electronic state and spectroscopic property of a dithiolene tungsten carbonyl complex. *Spectrochimica Acta Part A: Molecular and Biomolecular Spectroscopy*. 124: 375 – 382.
19. Nazeeruddin, M. K., Angelis, F. D., Fantacci, S., Selloni, A., Viscardi, G., Liska, P., Ito, S., Takeru, B. and Grätzel, M. (2005). Combined experimental and DFT-TDDFT computational study of photoelectrochemical cell ruthenium sensitizers. *Journal of the American Chemical Society*, 127: 16835 – 16847.
20. Rabias, I., Howlin, B. J., Provata, A. And Theodorou, D. (2000). Modelling of structural and vibrational properties of poly(p-phenylene) and polypyrrole using molecular orbital methods. *Molecular Simulation* 24: 95 – 105.

Malaysian Journal of Analytical Sciences, Vol 20 No 4 (2016): 955 - 964
DOI: http://dx.doi.org/10.17576/mjas-2016-2004-31

MALAYSIAN JOURNAL OF ANALYTICAL SCIENCES
Published by The Malaysian Analytical Sciences Society
ISSN 1394 - 2506

ENERGY MANAGEMENT STRATEGY FOR A FUEL CELL/ULTRACAPASITOR/BATTERY HYBRID SYSTEM FOR PORTABLE APPLICATIONS

(Strategi Pengurusan Tenaga bagi Sistem Hibrid Sel Bahan Api/ Ultrakapasitor/Bateri untuk Aplikasi Mudah Alih)

Siti Afiqah Abd. Hamid[1], Edy Herianto Majlan[1]*, Ros Emilia Rosli[1], Wan Ramli Wan Daud[1], Ramizi Mohamed[2], Teuku Husaini[1], Ramli Sitanggang [3]

[1]*Fuel Cell Institute*
[2]*Department of Electrical and System Engineering, Faculty of Engineering & Built Environment Universiti Kebangsaan Malaysia, 43600 UKM Bangi, Selangor, Malaysia*
[3]*Department of Chemical Engineering, Faculty of Industrial Engineering, Universitas Pembangunan Nasional "Veteran" Yogyakarta, Yogyakarta 55283, Indonesia*

**Corresponding author: edy@ukm.edu.my*

Received: 5 February 2016; Accepted: 22 April 2016

Abstract

A proton exchange membrane (PEM) fuel cells (FCs) with ultracapacitor (UC) and battery (BT) hybrid system has fast transient response compare to stand alone FCs. This hybrid system is promising candidates for environmentally friendly alternative energy sources. An energy management system design and control strategy was introduced in this study. The energy management strategy FC/UC/BT hybrid system model has been developed and the control strategy was programmed in the LabVIEW™ environment and implemented using National Instrument (NI) devices. The energy management strategy is able to manage the energy flow between the main power source (FCs) and auxiliary sources (UC and BT). To control the hybrid system and achieved proper performance, a controller circuit was developed with the three energy sources aligned in parallel to deliver the requested power. The developed model demonstrates the proportion power from the FC, UC and BT under various load demand. Experimental results demonstrate that FC/UC/BT hybrid system operated automatically with the varying load condition. The experimental results are presented; showing that the proposed strategy utilized the characteristic of both energy storage devices thus satisfies the load requirement.

Keywords: proton exchange membrane fuel cell, ultracapacitor, battery, hybrid energy system, energy management strategy

Abstrak

Sistem hibrid sel bahan api (FC) membran penukaran proton (PEM) dengan ultrakapasitor (UC) dan bateri (BT) mempunyai tindak balas yang lebih cepat berbanding FC sahaja. Sistem hibrid adalah salah satu sumber tenaga alternatif mesra alam yang amat berpotensi. Satu reka bentuk sistem pengurusan tenaga dan strategi kawalan telah diperkenalkan dalam kajian ini. Model strategi pengurusan tenaga sistem hibrid FC/UC/BT telah dibangunkan dan strategi kawalan telah diprogramkan dalam perisian LabVIEW™ dan dilaksanakan dengan menggunakan peranti instrument Nasional (NI). Strategi pengurusan tenaga ini mampu untuk menguruskan aliran tenaga di antara sumber kuasa utama (FC) dan sumber kuasa tambahan lain (UC dan BT). Untuk mengawal sistem hibrid dan mencapai prestasi yang sewajarnya, litar pengawal telah dibangunkan dengan tiga sumber tenaga sejajar selari untuk menyediakan permintaan kuasa. Model yang dibangunkan menunjukkan keseimbangan jumlah kuasa daripada FC, UC dan BT di bawah pelbagai permintaan beban. Keputusan eksperimen menunjukkan bahawa sistem hibrid FC/UC/BT beroperasi secara automatik dengan keadaan beban yang berbeza-beza. Keputusan eksperimen dibentangkan,

menunjukkan bahawa strategi yang dicadangkan memanfaatkan ciri kedua-dua sumber kuasa tambahan dengan itu memenuhi keperluan beban.

Kata kunci: Sel bahan api membran penukaran proton, ultrakapasitor, bateri, sistem tenaga hibrid, strategi pengurusan tenaga

Introduction

Research in the field of alternative/renewable energy sources increasingly become the focus of many researchers, in an attempt to find a novel and environmentally friendly energy source that does not rely on fossil fuels, to replace internal combustion engines for use in vehicles. This research, besides ensuring energy supplies for the future, it may also reduce the pollution caused by fossil fuels. As an alternative to the internal combustion engine, fuel cell technology has advantages in many aspects that make it the preferred choice of researchers [1-5]. PEMFC is one that has been applied widely, from a stand-alone system and a hybrid system, especially in vehicle applications, power units, and electronic devices mobile. A stand-alone PEMFC system unfortunately cannot satisfy the sudden load variation in vehicles due to its slow dynamic response. The voltage decreases drastically and this situation evidently harmful to the PEMFC [6]. Most electronic devices and vehicles require a stabilized power source and fast transient response. Combining a PEMFC with an auxiliary power source would improve the operational efficiency and dynamic response of the system and extend the PEMFC lifetime. The auxiliary energy source usually uses an energy storage device that can store the excess energy from the PEMFC (charge) and support the load demand when needed (discharge). This system includes power electronics and a controller for the energy management system. The concept of hybrid technology was widely embraced for the conventional internal combustion engine (ICE) to minimize the peak power possible for acceleration, allow for optimal operational efficiency [7], recapture kinetic energy when braking (regenerative braking), and, more importantly, conserve fuel. In the literature [8-11], the preferred energy storage devices for PEMFCs are BTs and UCs because they have their own unique characteristics. BTs can charge rapidly and have excellent energy density [12] and a higher specific energy than UCs, thus supplying extra power for a longer period of time. And the key advantage of UCs is their ability to charge and discharge for almost an unlimited number of cycles, have relatively high power densities and long lifetimes, are cheaper and environmentally safe, can be operated at high or low temperatures without maintenance, and can deliver high power/currents in a short time without incurring structural damage [12].

The energy management strategy and controller are important factors in hybridizing PEMFCs and energy storage devices. In the past, researchers extensively studied hybrid system technologies using various control strategies to manage the energy distribution between the FC and auxiliary energy source. The strategy for each system, which can affect the system performance, was developed based on a certain objective (for example, the fuel consumption) within the constraints of the device used (BT state of charge limits, power limits, etc.) [13]. Hybrid systems capture the best features of each energy resource and can provide stable and quality electricity.

Materials and Methods

Basically, in active hybrid, several configurations can be used to achieve power sharing in PEMFC hybrid systems. Uzunoglu and Alam developed the simplest parallel operating structure for vehicle applications, which was direct integration by Honda [14]. The auxiliary power source is directly connected in line between the FC and the load as shown in Figure 1. This configuration is quite attractive because it does not require a high-power DC/DC converter, and thus, the complexity, cost, weight, and volume of the system are significantly reduced. Therefore, we modified the direct integration configuration to include three energy sources.

After choosing an appropriate system configuration, the components should be selected carefully. Our objective was to design a low-cost system with a simple configuration that did not involve a complex mathematical algorithm and that had an easy-to-follow circuit arrangement. The system uses an active hybrid with one buck DC/DC converter directly integrated into the system. The power demand of the electronic load is satisfied by the combination of the FC, UC and BT. The resultant load current and output power can be expressed in equation 1 and 2 as given below:

$$I_L = I_{FC} + I_{UC} + I_{BT} \quad (1)$$

$$P_L = V_L I_L \quad (2)$$

where I_L is load current, I_{FC} is FC current, I_{UC} is UC current and I_{BT} is BT current. While P_L is load power and V_L is load voltage respectively.

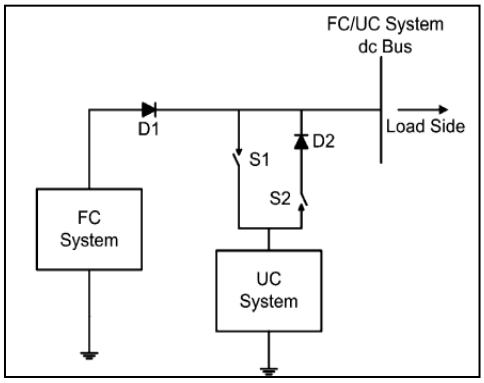


Figure 1. PEMFC/UC hybrid power system [14]

Energy management system controller

National Instruments Compact Field Point (cFP) is the energy management system controller. The power control is based on the output voltage from each energy source and the resulting load voltage. The strategy is programmed using the LabVIEW™ software and then implemented using the cFP devices combined with the controller circuit. The input and output modules used in this work were cFP-RLY-425 (relay module) and cFP-AI-102 (analog input module for the voltage). This relay module was used to control the power of the mechanical relay in the controller circuit. Approximately 5 W were required to turn on the mechanical relay in the controller circuit with a rated voltage of 12 V and a rated current of 417 mA. The cFP-AI-102 module on the other hand acts as a voltage indicator to the controller program in LabVIEW™. The PEMFC, BT, UC, and load voltages and currents were also measured using this device.

Controller circuit

The controller circuit (Figure 2) is the electrical board that links the energy sources, controller device, and electronic devices to the load. To give the specific load requirements for this study, the DC electronic load is employed. The controller circuit consists of four mechanical relays, three diodes, four DC buses, and a 12 V DC/DC converter. The mechanical relay serves as the switch to allow power to flow from the UC and/or BT to support the FC or to charge and discharge the UC and BT. The diode acts as a blocking device to prevent the power from flowing in the wrong direction. The voltage drop from the diode is only 0.7 V, which is negligible. Moreover, the DC bus is a connecting bar where all the power sources connect to the DC/DC converter for ease of plugging into and out of the power source. The DC/DC converter is the voltage regulator that maintains the voltage output from the DC bus at 12 V. This controller circuit manages the power transfer between these three power sources.

Energy storage device

UC and BT energy storage devices are used in the proposed hybrid system. These two energy sources are combined with a PEMFC to be in line with the power generator unit. In this study, we use 350 F, 2.5 V Boostcap UCs from Maxwell Technologies. For the experiment, a nominal voltage of 12 V is required; therefore, six single 350 F, 2.5 V Boostcap UCs are connected in series. The equivalent series capacitance is 58.333 F. As the UCs discharge, their voltage drops. To manage the UC charging, the voltage limits for the controller circuit program were set to 12 V, as suggested by the manufacturer.

A 12 V, 5A H nanogel BT (model YTZ5S-BS, Koyoko) are used for the second energy storage device. It is a plug-and-play product, meaning no acid or BT water needs to be added. The manufacturer suggests that the BT voltage remain at 12.5V or higher to maintain its excellent mode operation. The charging settings are 13 V – 15 V and 0.8 A - 1.2 A. In this work, the BT is charged by the power output from the DC/DC converter, which is limited to a maximum of 12 V.

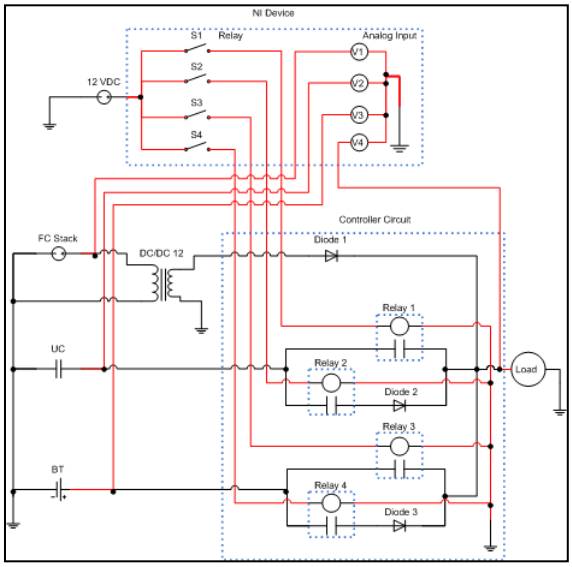


Figure 2. Controller's electrical circuit of the energy management system

PEMFC stack

The advantages of using PEMFC are the simplicity, high efficiency, lightweight design, smaller size, ease of integration and use, few peripherals, and good reliability. In this work, a model H-100 PEMFC manufactured by Horizon Technology is used. This PEMFC is an open-cathode FC with 24 cells stacked together. The nominal voltage capacity of the PEMFC stack is 14.4 V at a current of approximately 7.2 A and typically capable of producing 100 W at a rated power. The stack efficiency at 14.4 V is 40%, as stated in the manufacturer's manual.

Energy management strategy

Currently, energy management is an absolute necessity. FCs sometimes supplies more energy than necessary, and the excess energy should be used to charge the auxiliary energy source. Occasionally, the FC does not supply enough energy. Then, the auxiliary energy source is partially depleted, but the power demand is high, making it necessary to satisfy the load demand rather than charge the auxiliary energy source. The energy management strategy proposed in this paper is described below and was based on voltage regulation:

a) The system measures the load voltage. If the load voltage is greater than 12 V, then the system measures the UC voltage to determine if it is also greater than 12 V. The system charges the UC if the voltage is below 12 V. If the UC voltage is 12 V or higher, the system checks the BT voltage and charges the BT if its voltage is below 12 V. If all voltages are at least 12 V, the excess energy is delivered to the load only.
b) If the measured load voltage is less than 10 V, both the UC and BT switches are opened to supply the needed energy. Otherwise, if the load voltage is between 10 V and 12 V, only the UC switch is opened because the UC can charge and discharge quickly.

Test bench

The test bench setup as in Figure 3 consists of the three energy sources (PEMFC, UC and BT), controller device, and circuit described previously. The controller device requires a computer to monitor the performance of the hybrid system and the DC electronic load, which is the load demand. The electronic load was programmed to act as the current load to replicate the current required on most application devices. The load profile used in this study is based on one from the literature [15] to prove that this configuration and energy management strategy can satisfy the load profile.

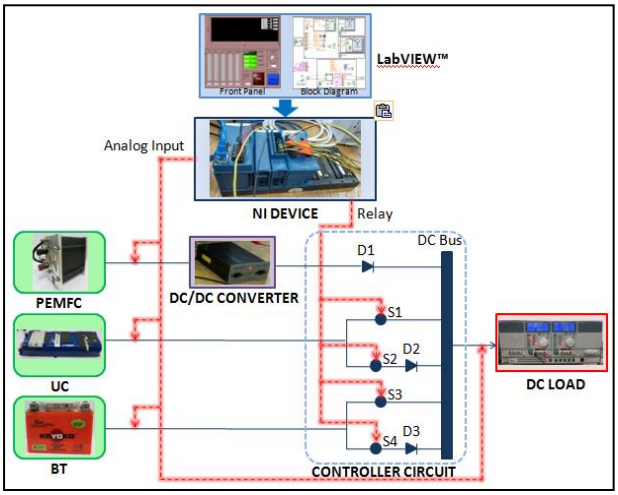


Figure 3. Diagram of the PEMFC/UC/BT hybrid energy management system.

Results and Discussion

In this study, the load profile used is a series of step signals to represent the load-required power presented in Figure 4a. The load profile can be used to represent the power consumed in most electronic applications. The controller is then manage the load sharing between FC, UC and BT. Initially, the step power starts at 1.1 W, which is the power required to start most electronic devices. The power increases to 3.3 W at 31 s and rises to 43 W at 61 s, then decreases to 22 W at 91 s. At 121 s, the power increases again to 43 W. The system begins to overload at 151 s when the power increases to 60 W, and the peak power of about 65 W is reached at 153 s. The power slowly decreases to 53 W at 211 s and further decreases to 37 W at 241 s. Then, the system increases the power demand to 43 W at 271 s and to 57 W at 301 s. The power then decreases to 6.7 W at 331 s and goes to 1.1 W at 361 s. The performance of the developed energy management strategy of PEMFC/UC/BT hybrid system, FC, UC, BT and load power, voltage and current as a function of time are illustrated in Figure 4 until Figure 6.

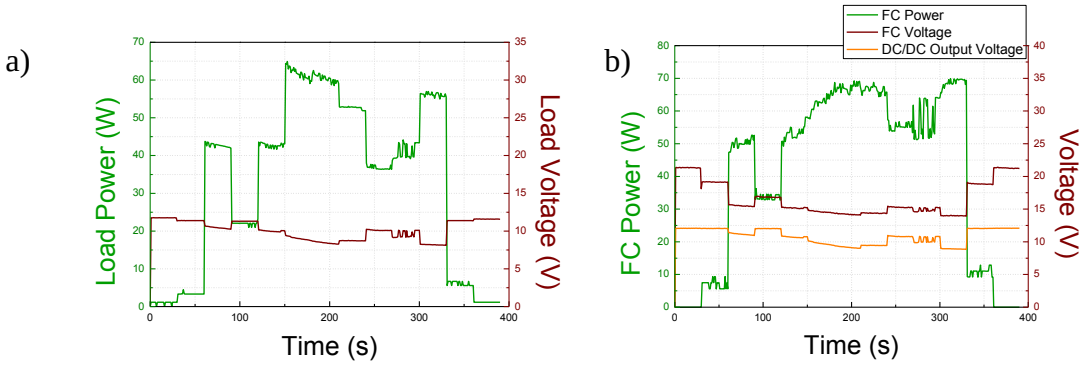


Figure 4. Power and voltage of a) Load and b) Fuel Cell

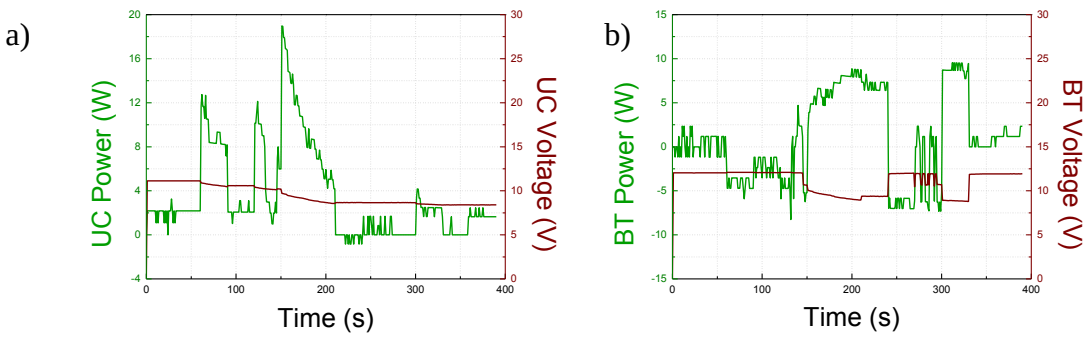


Figure 5. Power and voltage of a) Ultracapasitor and b) Battery

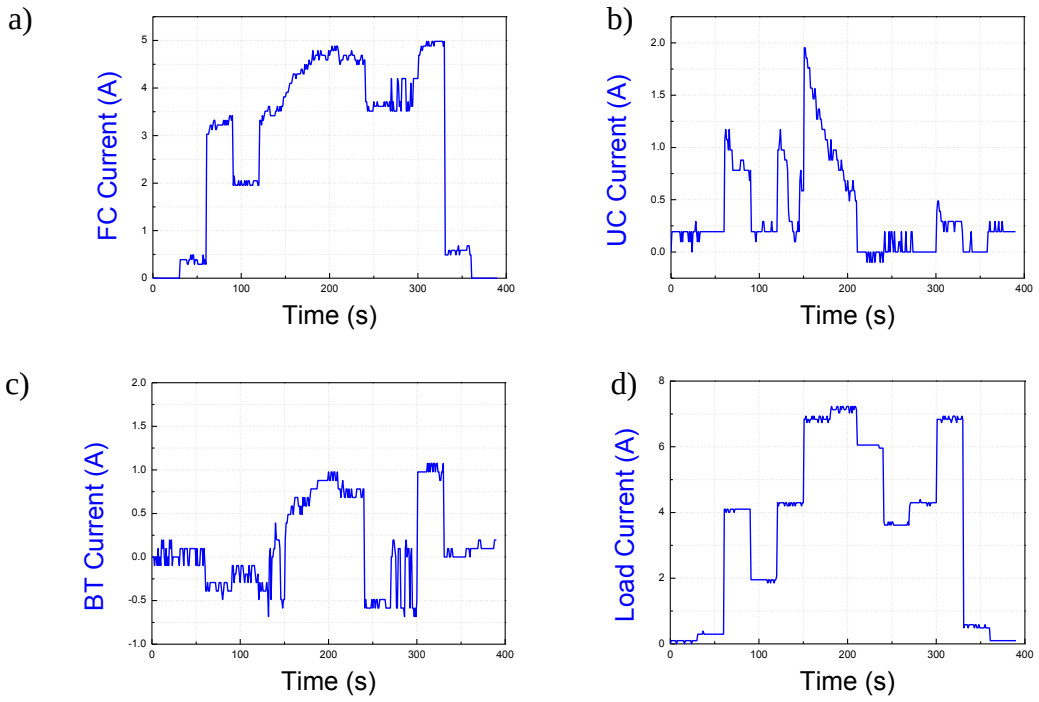


Figure 6. Current of a) Fuel Cell; b) Ultracapasitor; c) battery and d) Load

The FC, however, needs to be regulated by the DC/DC converter to ensure that the output power was constant at 12 V. The efficiency of the FC power was reduced by 15 % due to the DC/DC converter, and the input voltage is between 14 V and 24 V. If the FC voltage is lower than 14 V, the DC/DC converter output is considerably less than 12 V, and the UC or BT is required to supply the remaining needed power. The FC system successfully maintained the output voltage above 14 V, but due to the high load demand between 151 to 240 s and between 301 to 330 s illustrate in Figure 6a where the current draw from FC are near to 5 A, the system voltage at the DC bus fell below 10 V. The resulting FC voltage decreases as the power increases, as shown in Figure 4b is due to the basic characteristic of FC. However, its support the load demand base portion without facing a crucial transient changes.

The maximum power generated by the FC is approximately 69 W when the load at peak power about 60 W. On contrarily, the load profile used in literatures [12, 14] research are based on urban dynamometer driving schedule (UDDS) drive cycle. Thus, the power demand varied all the time. Both research are in hybrid system for FC, only differ with the energy storage unit. In [12] the energy storage unit are the same with this paper, which combine UC and BT. While in study reported by Uzunoglu and Alam [14], it used only UC as the energy storage unit. In Figure 7a and 7b show the FC output power of both system and clearly present that the combination of UC and BT greatly reduce the transient power demand face by FC.

The energy stored in the UC is depleted between 151 s to 390 s, as shown by the decrease in the voltage during this period in Figure 5a. The energy strategy dictates that the UC provide the necessary energy to the system by discharging and high current draw from UC as in Figure 6b. The UC then starts to charge for a short while then discharge until end of experiment (as mentioned before, UC only can support power for a short time) after 241 s. In contrast, the BT begins to discharge at 141 s. In the meantime, the BT charges and discharges as the current demand changes and support FC longer to satisfied the load, this utilize the BT characteristic of high energy densities. The details are presented in Figure 5b for BT power and voltage while in Figure 6c the current draw presented. This result provides good advantages in commercializing FC with the help of hybrid system. While decreasing the size and cost of the FC, the hybrid system also prevent the FC from operate in fuel starvation situation.

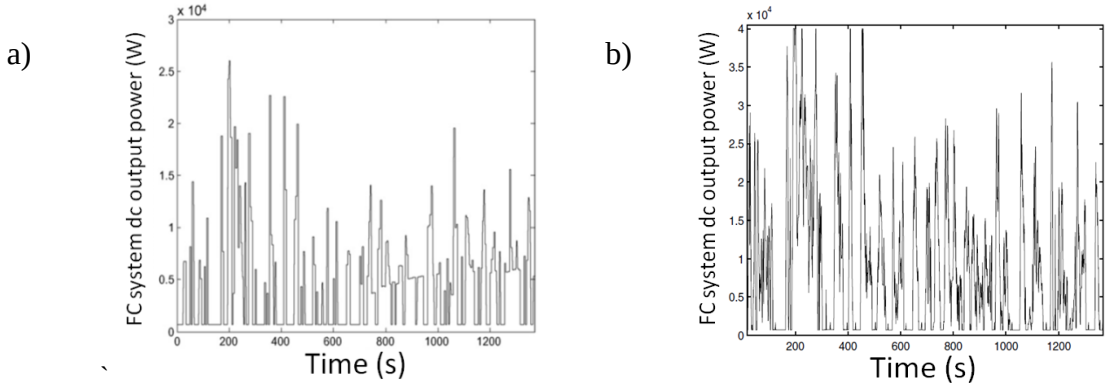


Figure 7. The FC output power variation according to UDDS of a) FC/UC/BT hybrid system [12] and b) FC/UC hybrid system [14].

The hybrid energy management system directs the flow of energy from the energy source to the load system successfully. As shown by the resulting current of the hybrid system in Figure 6d. The system on the other hand did not maintain the operating voltage at 12 V (Figure 4a). The single DC/DC converter however was not sufficient for this system, and an additional DC/DC converter is needed to stabilize the UC and/or BT voltage output, making the system more costly.

The test was continued further by increasing the current step by 0.5 A for every 30 s to determine the maximum operating current of this system. The objective of development a PEMFC/UC/BT hybrid system was to develop a system that utilizes a PEMFC as the primary energy source to supply DC power to electronic devices. Accordingly, the output of the PEMFC/UC/BT hybrid system is recorded at the DC bus. The system was predicted to supply a constant 12 V voltage despite the changing current. The current step profile used for this test is shown in Figure 8a. The current was increased by 0.5 A every 30 s. Figure 8b shows the DC bus voltage output of the system, which was a constant 12 V for 180 s. This system is thus a good working supply system for the operation of electronic devices. This test demonstrates that the PEMFC/UC/BT hybrid energy management system can handle up to a 2.5 A current load. However, the DC bus output begins to decrease after 180 s because of the DC/DC converter used. The 12 V DC/DC converters can receive an input voltage between 14 V and 24 V to produce a constant 12 V voltage with an efficiency of approximately 90%. Lower input values result in a much lower voltage because the efficiency

of the DC/DC converter can drop to 30%. The output power of this hybrid system is also shown in Figure 8b and demonstrates that this system can provide up to 30 W for an electronic application.

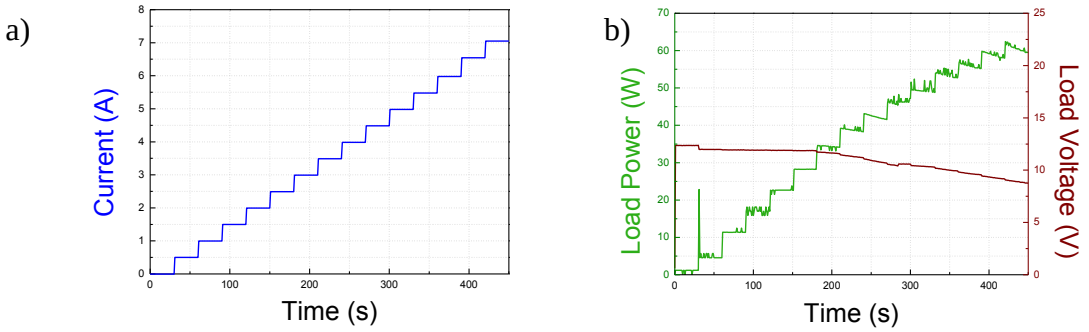


Figure 8. Result of step load for a) current and b) power and voltage

These results indicate that this hybrid energy source is an environmentally friendly energy source that can supply a constant, stable 12 V voltage up until 2.5 A current load compare to 1.5 A in literature [15]. Yan Zhang et al. [15] who also developed an energy management strategy but using only BT as the energy storage unit. Despite using an in-house manufacturing PEMFC, their energy management system, which utilized a simulation developed with the Simulink software, worked well up to a current of 1.5 A, as shown in Figure 9. Due to the unstable voltage output shown in Figure 10a and the limitations of the FC output voltage, the portable PEMFC-BT power system did not produce more than 18 W of power (Figure 10b). The results presented here show that the PEMFC/UC/BT hybrid energy management system is more capable of supplying power and stable than the PEMFC-BT or PEMFC/UC hybrid system.

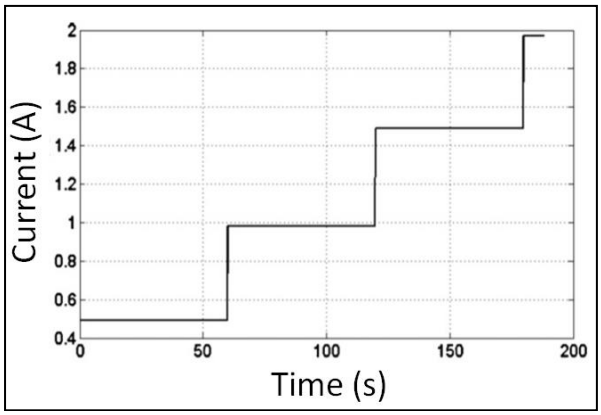


Figure 9. Current step input in PEMFC-BT hybrid system study [15]

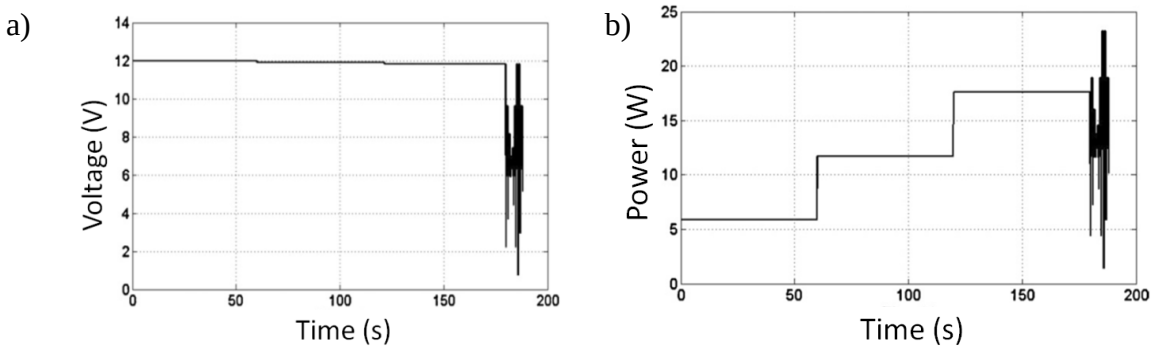


Figure 10. a) Voltage and b) power output of PEMFC-BT hybrid system [15]

Conclusion

The results of this research convincingly show the benefits of PEMFC hybrid systems. The energy management strategy successfully fulfilled the system requirements during peak power demand, charging and discharging the auxiliary energy sources. This new energy controller is easy to develop, low-cost with few electronic components and employ in the management of the energy sources. This hybrid system did not require full FC power to meet the load demand; the UC and BT helped to reduce the requirements on the FC. In other words, the FC stack is more cost-effective when used in a hybrid system. The transient response of the hybrid system was improved because the auxiliary energy source overcame the limitations of the FC. This system is also more portable compared to that in an electric vehicle because the BT in an electric vehicle must be charged by plugging it into an external energy source, while in hybrid system used FC.

Acknowledgement

The authors gratefully acknowledge financial support from UKM for Grant UKM-AP-TK-08-2010 and DIP-2012-05.

References

1. Baharuddin, N. A., Rahman, H. A., Muchtar, A., Abu Bakar, S. and Huda, A. (2014). Kesan masa pengendapan dan saiz elektrod lawan dalam penghasilan katod komposit LSCF-SDC karbonat untuk SOFC. *Sains Malaysiana*, 43(4): 595 - 601.
2. Juhana Jaafar, Ismail, A. F., Matsuura, T. and Mohd Norddin, M. N. A. (2013). Stability of SPEEK-triaminopyrimide polymer electrolyte membrane for direct methanol fuel cell application. *Sains Malaysiana*, 42(11): 1671 - 1677.
3. Ahmad, A. A., Othman, R., Yusof, F. and Wahab, M. F. A. (2014). A Hybrid enzymatic zinc-air fuel cell. *Sains Malaysiana*, 43(3): 459 - 465.
4. Arifin, K., Wan Ramli Wan, D. and Mohammad, K. (2014). A novel ruthenium-tungsten bimetallic complex dye-sensitizer for photoelectrochemical cells application. *Sains Malaysiana*, 43(1): 95 - 101.
5. Panuh, D., Muchtar, A., Norhamidi, M., Majlan, E. H. and Wan Ramli. W. D. (2014). Elektrolit dwi lapisan Sm0.2Ce0.8O1.90 (SDC)/ Y0.25Bi0.75O1.5 (YSB) untuk sel fuel oksida pepejal bersuhu sederhana. *Sains Malaysiana*, 43(11): 1769 - 1774.
6. Taniguchi, A., Akita, T., Yasuda, K. and Miyazaki, Y. (2004). Analysis of electrocatalyst degradation in PEMFC caused by cell reversal during fuel starvation. *Journal of Power Sources*, 130(1-2): 42 - 49.
7. Van Vliet, O. P. R., Kruithof, T., Turkenburg, W. C. and Faaij, A. P. C. (2010). Techno-economic comparison of series hybrid, plug-in hybrid, fuel cell and regular cars. *Journal of Power Sources*, 195(19): 6570 - 6585.
8. Burke, A. F. (2007). Batteries and ultracapacitors for electric, hybrid, and fuel cell vehicles. *Proceedings of the IEEE*, 95(4): 806 - 820.
9. Hwang, J. J. and Chang, W. R. (2012). Characteristic study on fuel cell/battery hybrid power system on a light electric vehicle. *Journal of Power Sources*, 207: 111 - 119.

10. Khaligh, A. and Zhihao, L. (2010). Battery, ultracapacitor, fuel cell, and hybrid energy storage systems for electric, hybrid electric, fuel cell, and plug-in hybrid electric vehicles: State of the art. *IEEE Transactions on Vehicular Technology*, 59(6): 2806 - 2814.
11. Schaltz, E., Khaligh, A. and Rasmussen, P. O. (2008). Investigation of battery/ultracapacitor energy storage rating for a fuel cell hybrid electric vehicle. *Vehicle Power and Propulsion Conference:* 1- 6.
12. Erdinc, O., Vural, B. and Uzunoglu, M. (2009). A wavelet-fuzzy logic based energy management strategy for a fuel cell/battery/ultra-capacitor hybrid vehicular power system. *Journal of Power Sources*. 194(1): 369 - 380.
13. Bernard, J., Hofer, M., Hannesen, U., Toth, A., Tsukada, A., Büchi, F. N. and Dietrich, P. (2011). Fuel cell/battery passive hybrid power source for electric powertrains. *Journal of Power Sources*, 196(14): 5867 - 5872.
14. Uzunoglu, M. and Alam, M. S. (2007). Dynamic modeling, design and simulation of a PEM fuel cell/ultra-capacitor hybrid system for vehicular applications. *Energy Conversion and Management*, 48(5): 1544 - 1553.
15. Zhang, Y. and Zhou, B. (2011). Modeling and control of a portable proton exchange membrane fuel cell–battery power system. *Journal of Power Sources*, 196(20): 8413 - 8423.

Malaysian Journal of Analytical Sciences, Vol 20 No 4 (2016): 965 - 970
DOI: http://dx.doi.org/10.17576/mjas-2016-2004-32

MALAYSIAN JOURNAL OF ANALYTICAL SCIENCES
Published by The Malaysian Analytical Sciences Society
ISSN 1394 - 2506

STRUCTURAL STUDY OF REDUCED GRAPHENE OXIDE/POLYPYRROLE COMPOSITE AS METHANOL SENSOR IN DIRECT METHANOL FUEL CELL

(Kajian Struktur Komposit Grafin Oksida Terturun/Polipirol Sebagai Sensor Metanol Dalam Sel Bahan Api Metanol Langsung)

Mumtazah Atiqah Hassan[1], Siti Kartom Kamarudin[1, 2]*, Kee Shyuan Loh[1]

[1]*Fuel Cell Institute*
[2]*Department of Chemical and Process Engineering, Faculty of Engineering and Built Environment*
Universiti Kebangsaan Malaysia, 43600 UKM Bangi, Selangor, Malaysia

**Corresponding author: ctie@ukm.edu.my*

Received: 5 February 2016; Accepted: 22 April 2016

Abstract

Density functional theory (DFT) computations were performed on the optimized geometric and electronic properties of reduced graphene oxide/polypyrrole (rGO/PPy) composite in comparison with pure graphene and graphene oxide structures. Incorporation of both reduced GO (rGO) and PPy will form a good composite which have advantages from both materials such as good mechanical strength and excellent electrical conductivity. These composite would be very suitable in fabrication of methanol sensor in direct methanol fuel cell (DMFC). The HOMO-LUMO energy (eV) was also calculated. These computational calculations provide a theoretical explanation for the good performance of rGO/PPy composite as electrode materials in methanol sensor.

Keywords: graphene, structure, polypyrrole, direct methanol fuel cell, density functional theory

Abstrak

Pengiraan teori fungsi ketumpatan (DFT) telah dilakukan ke atas ciri-ciri optimum geometri dan elektronik oksida komposit grafin terturun/polipirol (rGO/PPy) berbanding dengan grafin tulen dan grafin oksida. Gabungan kedua-dua GO terturun (rGO) dan PPy akan membentuk komposit yang baik yang mempunyai kelebihan dari kedua-dua bahan seperti kekuatan mekanikal dan kekonduksian elektrik yang sangat baik. Komposit ini menjadi sangat sesuai dalam pembuatan sensor metanol dalam sel bahan api metanol langsung (DMFC). Tenaga HOMO-LUMO (eV) juga telah dikira. Pengiraan ini memberikan penjelasan teori untuk prestasi baik rGO/PPy komposit sebagai bahan elektrod dalam sensor metanol.

Kata kunci: grafin, struktur, polipirol, sel bahan api metanol langsung, teori fungsi ketumpatan

Introduction

Direct Methanol Fuel Cell (DMFC) is a potential device as a source of mobile power which provides advantages such as high energy density, low pollution, fast starting time, lightweight and more compact compare to rechargeable battery and other types of fuel cells. It is also easy to use. DMFC is capable of converting chemical energy directly between the reaction of methanol and oxidant (air or oxygen) into electrical energy [1, 2]. The overall reaction for methanol oxidation is given as Eq. 1 below [3]:

$$CH_3OH + H_2O \longrightarrow CO_2 + 6e^- + 6H^+ \text{ (anode)} \quad (1)$$

The reaction for the fuel-cell-based sensor expressed as Eq. 2 below:

$$5O_2 + 6e^- + 6H^+ \longrightarrow 3H_2O \text{ (cathode)} \quad (2)$$

A constraint to the fuel cell is the fuel cell performance itself in terms of efficiency and low power density due to the low electro-catalyst activity. In addition, the constrains faced by toxicity in the anode as a result of the absorption of the intermediate products, such as carbon monoxide and high methanol crossover through Nafion membranes [4]. The objective of this paper is to investigate the optimized rGO and graphene structure as well as to determining their energy bands.

Polymer composites have showed significant potentials in development of various application areas like electronic devices, supercapacitor, rechargeable electrode and sensors. The usage of carbon based materials such as graphene, carbon black, single wall carbon nanotubes, carbon nanofibres instead of silicate compound layer or synthetic clay are states to be useful in enhancing the electrical and thermal conductivity [5 – 7].

Graphene oxide (GO) is one of the member in carbon based materials. GO is chemically modified form of graphene that contains oxygen functional groups such as epoxides, alcohols, and carboxylic acids which contributes to more reactive GO. Sharing the same atomically thin structural framework as graphene, it provide alternative for graphene which is complicated to produce. It recently emerged as a solution-processable material for large-area electronics because it can be deposited readily and uniformly on a variety of substrates. GO contains saturated sp3 carbon atoms bound to oxygen, which makes it an insulator. Transition to a semiconductor through chemical or thermal removal of oxygen allows it to be reduced incrementally so that the electrical conductivity can be tuned over several orders of magnitude [8].

While, conducting polymers such as polypyrrole (PPy) have high conductivity, are lightweight, low in cost, flexible and environmentally friendly but, as electrode materials, the degradation during cycling might happened where the volume of the polymer changes due to the insertion/deinsertion of counter ions [9]. Incorporation of graphene oxide in a conducting polymer matrix leads to the formation of nanocomposites which own advantages from both components. This advantages would be every useful in fabricating the methanol sensor in DMFC. The rGO/PPy composite electrode shows larger specific capacitance, higher rate performance, and better charge–discharge stability [10]. The rGO/PPy composite also provide large surface area which increases the binding sites [11]. According to Chandra and Kim, the PPy component of the composite is effectively lessen the swelling/shrinkage of polymer chains which solve the problem of the usage of PPy.

In this paper, the density functional theory (DFT) is applied to study on optimizing the structure of rGO/PPy composite and to examine the effect on incorporating the PPy as a composite with rGO. The energy of graphene, GO and rGO/PPy in applying the composite as methanol sensor electrode are also compared.

Materials and Methods

Calculation details

The spin-restricted DFT calculation was performed using DMol3 package. All results were obtained by PBE functional the exchange -correlation function within the generalized gradient approximation (GGA). In terms of numerical basis sets, double numerical plus polarization (DNP) was chosen within DFT semi-core pseudopots due to its reasonable accuracy in energy calculation. A lateral 5x3 cell was selected as the pure graphene. In the geometrical optimization, all structures were relaxed until the total energy were converged to 1.0×10^{-4} Hatree. The maximum force converged to less than 2×10^{-2} Hartree/Å, and the maximum displacement convergence was 5×10^{-2} Å. All structures were fully optimized without any symmetry constraint. Figure 1 show the structures of graphene and rGO of Min and Chang et al. [12] and Bagri et al. [13] respectively.

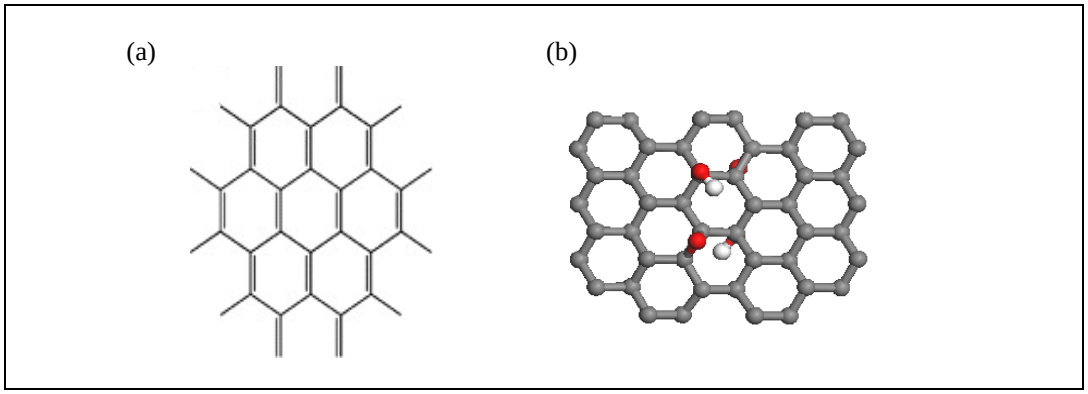


Figure 1. Min and Chang model structure of graphene (a) and Bagri et al. structure of graphene oxide (b)

Results and Discussion

Figure 2 shows the optimized structure of pure graphene based on structure proposed by Min and Chang. It consists of 42 atoms of carbon. The use of hydrogen atoms in terminating the boundaries of graphite cluster model is a good choice for simulation purposes [14].

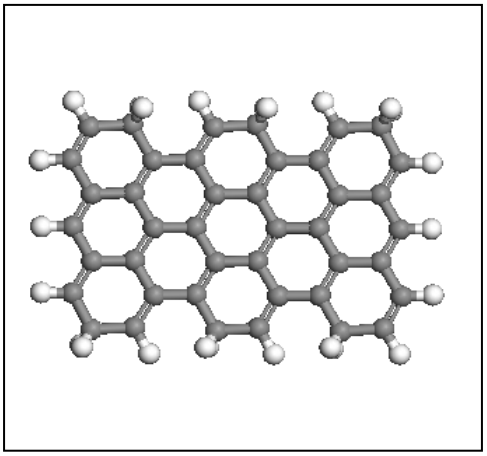


Figure 2. The modelled optimized structure of graphene

For graphene, the calculation is done in two different basis set, DSPP and all-electron basis set to determine which give the lowest value. The calculated value of DSPP, which is -1597.89 Ha is taken into consideration due to diverging that occur when using all-electron basis set. The optimized rGO is shown in Figure 3. The calculated properties of optimized rGO structure were compared with the graphene structure. The total energy of optimized rGO is -2051.3074 Ha.

From Table 1, the both value were compared. The optimized rGO have lower total energy than graphene. This proves that optimized rGO is more stable than graphene. Liu et al. [15] stated that the edge defects arising from the epoxide and carbonyl groups caused the electrical conductivity of functionalized graphene oxide is several orders of magnitude lower than graphene. The electronic properties of rGO, the highest occupied molecular orbital (HOMO)

and lowest unoccupied molecular orbital (LUMO) were also calculated. Result shows that, rGO also has lower HOMO-LUMO energy. This showed that graphene has higher binding energy compared to rGO.

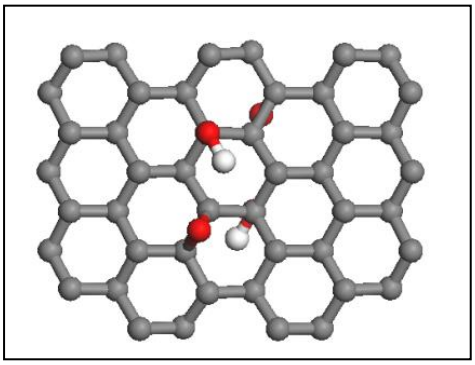


Figure 3. The optimized structure of rGO

Table 1. The comparison of Graphene and rGO

Molecular Structure	**HOMO – LUMO (eV)**	**Total Energy (Ha)**
Graphene	-1.094	-1613.348
rGO	-0.087	-2051.909

The optimized structure of rGO/PPy is calculated using the same method as the structure before. Figure 4 showed the structure of PPy, which consists of 10 monomers of pyrole. The calculation were done in three different postition of attachement of PPy on GO; at C-C bond, C-O bond (i.e. replacing the H atom from hydroxyl) and N-C bond. Based on DFT calculations, only rGO/PPy with C-C bond linking both structure converge. Table 2 below show the results obtained.

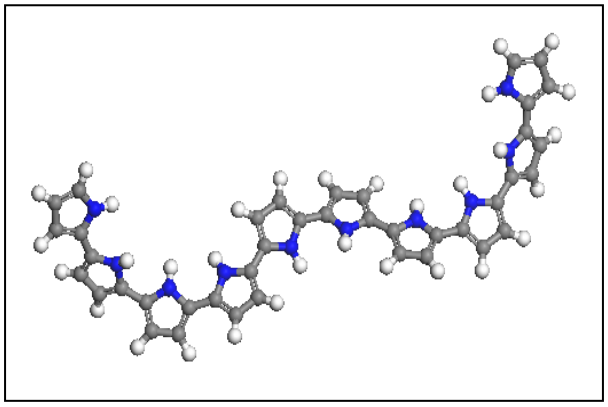


Figure 4. The optimized structure PPy with 10 monomers of pyrole

Table 2. Comparison between the optimized structure

Optimized Molecular Structure	HOMO – LUMO (eV)	Total Energy (Ha)
rGO	-0.087	-2051.909
PPy (10 monomers)	-2.094	-2091.038
rGO/PPy (C-C)	-0.145	-4106.005

From Table 2, the lowest energy structure is rGO/PPy composite at C-C bond which is -4106.005 Ha compared to the other structures. More negative the energy, more stable the structure. This proves that, the rGO/PPy composite possess stability which can be applied as electrode material. The HOMO-LUMO calculation was also done to the structure. The rGO/PPy possesses -0.145 eV which is slightly greater than rGO. Supposedly, the expected value for rGO/PPy is greater than rGO. Due to high eV for PPy, slightly greater energy needed to bind these two materials. Nevertheless, the data obtained is satifactory in giving early conclusion that rGO/PPy is stable to be applied as electrode materials in methanol sensor in DMFC. Further investigation on the binding on both materials is needed.

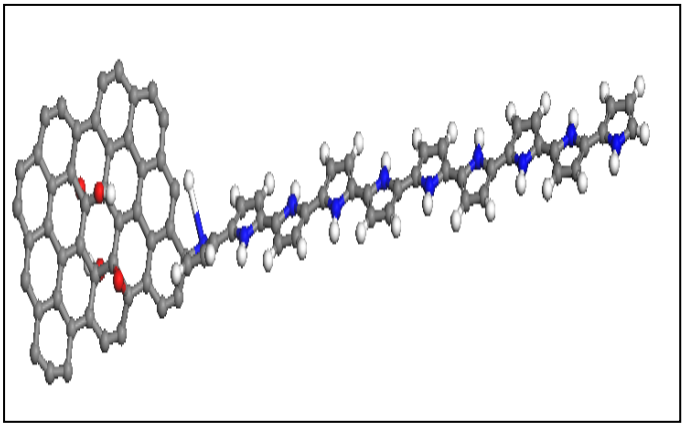


Figure 5. Optimize structure of rGO/PPy composite

Conclusion

In summary, DFT calculations were successfully applied to determine the lowest energy structure of rGO/PPy. In order to obtain the best result comparison of ideal graphene and rGO are made. It showed that rGO possess more stability than graphene in term of binding energy and also total energy. This is important to prepare rGO as the base in incoporation of polymer matrix, which in this case is PPy. Final optimized rGO/PPy structure is when the C atom of PPy matrix is attached at the C atom of rGO. The HOMO-LUMO calculated for GO/PPy optimized structure is -0.145 eV which is higher binding energy than the rGO but lower than graphene. The optimized rGO-PPy is good enough to be applied as electrode material of the methanol sensor but futher calculation should be made.

Acknowledgement

The authors would like to thank Universiti Kebangsaan Malaysia for the financial support given through GUP-2014-071 and Ministry of Higher Education, Malaysia (MOHE) through MyBrain15 (MyMaster) scholarship.

References

1. Basri, S., Kamarudin, S. K., Daud, W. R. W. and Ahmad, M. M. (2010). Non-linear optimization of passive direct methanol fuel cell (DMFC). *International Journal of Hydrogen Energy*, 35: 1759 – 1768.

2. Hashim, N., Kamaruddin S. K. and Daud W. R. W (2010). Design and development of micro direct methanol fuel cell (μdmfc) for portable application. *Sains Malaysiana*, 39(6): 1015 – 1023.
3. Hassan, M. A., Kamaruddin, S. K., Loh, K. S. and Daud, W. R. W. (2014). Sensors for direct methanol fuel cell. *Renewable and Sustainable Energy Reviews*, 40: 1060 – 1069.
4. Ahmad, M. M, Kamarudin, S. K. and Daud W. R. W. (2010). Design of an optimal micro direct methanol fuel cell for portable applications. *Sains Malaysiana*, 39(3): 467 – 472.
5. Bora, C., and Dolui, S. K. (2012). Fabrication of polypyrrole/graphene oxide nanocomposites by liquid /liquid interfacial polymerization and evaluation of their optical, electrical and electrochemical properties. *Polymer*, 53(4): 923 – 932.
6. Potts, J. R., Dreyer, D. R., Bielawski, C. W. and Ruoff, R. S. (2011). Graphene-based polymer nanocomposites. *Polymer*, 52(1): 5 – 25.
7. Karamdel, J., Damghanian, M., Razaghian, F., Dee, C. F., and B. Yeop Majlis (2010). Dependence of band structure and carrier concentration of metallic (13,13) and semiconducting (13,0) single wall carbon nanotube on temperature. *Sains Malaysiana*, 39(4): 615 – 620.
8. Dreyer, D. R., Park, S., Bielawski, C. W. and Ruoff, R. S. (2010). The chemistry of graphene oxide. *Chemical Society Reviews*, 39(1): 228 – 240.
9. Saner, B., Gürsel, S. A. and Yürüm, Y. (2013). Layer-by-layer polypyrrole coated graphite oxide and graphene nanosheets as catalyst support materials for fuel cells. *Fullerenes, Nanotubes and Carbon Nanostructures*, 21(3): 233 – 247.
10. Liu, G., Zhuang, X., Chen, Y., Zhang, B., Zhu, J., Zhu, C.-X., Neoh, K-G. and Kang, E.-T. (2009). Bistable electrical switching and electronic memory effect in a solution-processable graphene oxide-donor polymer complex. *Applied Physics Letters*, 95(25): 253301.
11. Chandra, V., and Kim, K. S. (2011). Highly selective adsorption of Hg^{2+} by a polypyrrole–reduced graphene oxide composite. *Chemical Communications*, (47): 3942 – 3944.
12. Bagri, A., Mattevi, C., Acik, M., Chabal, Y. J., Chhowalla, M. and Shenoy, V. B. (2010). Structural evolution during the reduction of chemically derived graphene oxide. *Nature Chemistry*, 2(7): 581 –587.
13. Qi, X., Guo, X. and Zheng, C. (2012). Density functional study the interaction of oxygen molecule with defect sites of graphene. *Applied Surface Science*, 259: 195 – 200.
14. Huh, D. S., Basavaraja, C. and Jung, K. W. (2012). Polypyrrole/graphene oxide composites with improved conductivity and solubility. *Plastic Research Online*, 50: 10 – 11.
15. Liu, Y., Zhang, Y., Ma, G., Wang, Z., Liu, K. and Liu, H. (2013). Ethylene glycol reduced graphene oxide/polypyrrole composite for supercapacitor. *Electrochimica Acta*, 88: 519 – 525.

Malaysian Journal of Analytical Sciences Vol 20 No 5 2016

Articles 13-22 are selected papers from the "Malaysia Polymer International Conference 2015 (MPIC 2015), 10-11 June 2015, Palm Garden Hotel, IOI Resort, Putrajaya; organised by Polymer Research Center, Faculty of Science and Technology, Universiti Kebangsaan Malaysia."

Guest Editor: Ishak Ahmad

Articles 23-29 are selected papers from the "UniSZA Research Conference 2015 (URC 2015), 14-16 April 2015, Universiti Sultan Zainal Abidin, Gong Badak Campus, Kuala Terengganu, Terengganu; organised by Centre For Research and Innovation Management (CRIM) UniSZA."

Guest Editor: Mohd Khairul Amri Kamarudin

		Page
1.	NEW INDOLIZIDINE ALKALOIDS FROM PSYCHROPHILIC YEAST *Glyciozyma antarctica* PI12 (Alkaloid Indolizidin Baharu daripada Yis Psikrofilik *Glyciozyma antarctica* PI12) *Andi Rifki Rosandy, Wickneswary Nadarajah, Muntaz Abu Bakar, Cheah Yoke Kqueen, Mohd. Ikram Mohd. Said, Laode Muhammad Ramadhan Al Muqarrabun, Rozida Khalid*	971
2.	IMMOBILIZATION OF TYROSINASE IN NANOCRYSTALLINE CELLULOSE/CHITOSAN COMPOSITE FILM FOR AMPEROMETRIC DETECTION OF PHENOL (Pemegunan Tyrosinase dalam Filem Komposit Selulosa Nanokristalin/Kitosan untuk Pengesanan Amperometrik bagi Fenol) *Fariza Aina Abd Manan, Jaafar Abdullah, Nur Nadziera Nazri, Izyan Nadira Abd Malik, Nor Azah Yusof, Ishak Ahmad*	978
3.	DETERMINATION OF OPTIMUM CONDITIONS AND STABILITY STUDY OF BIOSURFACTANT PRODUCED BY *Bacillus subtilis* UKMP-4M5 (Penentuan Keadaan Optimum dan Kajian Kestabilan Biosurfaktan yang Dihasilkan oleh *Bacillus subtilis* UKMP-4M5) *Ummul Khair Mohd Syahriansyah and Ainon Hamzah*	986
4.	OPTIMIZATION PARAMETER FOR THERMOELECTRIC PROPERTIES OF ZnO USING RESPONSE SURFACE METHODOLOGY (Pengoptimuman Parameter Untuk Sifat Termoelektrik ZnO Menggunakan Kaedah Gerak Balas Permukaan) *Lim Joon Hoong, Yeoh Cheow Keat, Abdullah Chik, Teh Pei Leng*	1001
5.	SINTESIS DAN PENCIRIAN HIDROGEL BERASASKAN KANJI DARIPADA UBI GADONG DENGAN MENGGUNAKAN TEKNIK RADIASI GAMMA (Synthesis and Characterization of Starch-Based Hydrogel by using Gamma Radiation Technique) *Boo Wei Ping dan Azwan Mat Lazim*	1011
6.	FABRIKASI BIOSENSOR DNA PORSIN BERASASKAN KOMPLEKS RUTENIUM BIPIRIDINA (Fabrication of Porcine DNA Biosensor Based on Ruthenium Bipyridine Complex) *Nurul Izni Abdullah Halid, Emma Izzati Zakariah, Lee Yook Heng, Nurul Huda Abd Karim, Haslina Ahmad, Siti Aishah Hasbullah*	1020
7.	PREPARATION AND CHARACTERIZATIONS OF POLY(ANILINE-co-m-AMINOBENZOIC	1033

ACID)/POLYSTYRENE COMPOSITE NANOFIBERS AND FILMS
(Penyediaan dan Pencirian Poli(Anilina-ko-m-Asid Aminobenzoik)/Polistirena Komposit Fiber Nano dan Filem)
Fatimah Syahidah Mohamad and Norizah Abdul Rahman

8. FREE FATTY ACIDS SEPARATION FROM MALAYSIAN HIGH FREE FATTY ACID CRUDE PALM OIL USING MOLECULAR DISTILLATION 1042
(Pemisahan Asid Lemak Bebas daripada Minyak Sawit Mentah Berasid Lemak Bebas Tinggi Melalui Penyulingan Molekul)
Murad Awadh Bahadi, Abd-Wali Japir, Jumat Salimon

9. PERFORMANCE OF EGZrO_2-EGFe_2O_3/HY AS PHOTOCATALYST AND ITS EFFICACY IN DECOLORIZATION OF DYE-CONTAMINANTS 1052
(Keupayaan EGZrO_2-EGFe_2O_3/HY sebagai Fotomangkin dan Keberkesanannya Dalam Penyahwarnaan Bahan Cemar Pewarna)
Muhammad Farhan Hanafi, Norzahir Sapawe, Mohd Zulkhairi Abdul Rahim, Nurul Nabihah Rahman, Abu Hassan Abd Rahman, Asimi Ana Ahmad

10. ASSESSMENT OF ANTIOXIDANT ACTIVITY AND TOTAL PHENOLIC CONTENT FROM GREEN COFFEE *Robusta Sp.* BEANS 1059
(Penilaian Aktiviti Antioksidan dan Kandungan Jumlah Fenolik dari Biji Kopi *Robusta Sp.* Hijau)
Raseetha Siva, Noratikah Rajikin, Zaibunnisa Abdul Haiyee, Wan Iryani Wan Ismail

11. EFFECTS OF RAIN pH, SOIL ORGANIC MATTER, CATION EXCHANGE CAPACITY AND TOTAL LEAD CONTENT IN SHOOTING RANGE SOIL ON THE CONCENTRATION OF LEAD IN LEACHATE 1066
(Kesan pH Hujan, Jirim Organik Tanah, Kapasiti Tukaran Kation dan Kandungan Plumbum di dalam Tanah Lapang Sasar ke atas Kepekatan Plumbum di dalam Air Larut Lesap)
Soon Kong Yong, Siti Norazieyana Mohd Zin, Madinah Jaafar Mad Ariff

12. EFFECT OF pH ON THE PHYSICOCHEMICAL PROPERTIES AND REDUCIBILITY OF MoVTeNbOx CATALYSTS 1073
(Kesan pH Terhadap Sifat Fizikokimia dan Kebolehturunan Mangkin MoVTeNbOx)
Syazwani Mohd Noor, Irmawati Ramli, Taufiq Yap Yun Hin, Norhazlin Zainuddin

13. EFFECT OF MULTI WALLED CARBON NANOTUBES ON THERMAL CONDUCTIVITY OF POLYLACTIC ACID NANOCOMPOSITE 1084
(Kesan Penambahan Nanotiub Karbon Berbilang Dinding Ke Atas Kekonduksian Terma Polilaktik Asid Nanokomposit)
Adilah Mat Ali, Sahrim Hj Ahmad, Mou'ad A. Tarawneh

14. PREPARATION AND CHARACTERIZATION OF EPOXIDISED NATURAL RUBBER (ENR)/POLY (VINYLIDENE FLUORIDE) (ENR/PVDF) COMPOSITE MEMBRANE 1090
(Penyediaan dan Pencirian Membran Komposit Getah Asli Terepoksida (ENR) / Poli (Vinilinida Fluorida) (PVDF) (ENR/PVDF)
Norliyana Mod, Farah Hannan Anuar, Rizafizah Othaman

15. THERMAL BEHAVIORS OF OIL PALM EMPTY FRUIT BUNCH FIBER UPON EXPOSURE TO ACID-BASE AQUEOUS SOLUTIONS 1095
(Perilaku Terma Serabut Tandan Kosong Sawit Selepas Rawatan Larutan Akueus Asid-Alkali)
Nur Syakilla Hassan and Khairiah Haji Badri

16. ZETA POTENTIAL AND ENVIRONMENTAL SCANNING ELECTRON MICROSCOPY ANALYSIS IN DEPROTEINISATION OF NATURAL RUBBER LATEX 1104
(Analisis Keupayaan Zeta dan Pengimbas Persekitaran Mikroskopi Elektron di dalam Penyahprotein Lateks Getah Asli)
Nurulhuda Abdullah, Asrul Mustafa, Mok Kok Lang

17. THERMAL CHARACTERISTICS OF MICROCRYSTALLINE CELLULOSE FROM OIL PALM BIOMASS 1112
(Sifat Terma Mikrokristal Selulosa Daripada Biojisim Tandan Kosong Sawit)
Fatin Afifah Ahmad Kuthi, Nor Rabbi'atul 'Adawiyah Norzali, Khairiah Haji Badri

18. LATEX PARTICLES MORPHOLOGY OF EPOXIDISED AND HIGH AMMONIA NATURAL RUBBER LATEX FROM ELECTRON MICROSCOPY TECHNIQUES 1123
(Morfologi Partikel Lateks Bagi Lateks Getah Asli Terepoksi dan Lateks Getah Asli Kandungan Tinggi Ammonia daripada Teknik-Teknik Mikroskopi Elektron)
Norhanifah Mohd Yazid, Fatimah Rubaizah Mohd Rasdi, Asrul Mustafa

19. SYNTHESIS OF BIO-BASED HYDROGEL FROM EPOXIDIZED PALM OIL CATALYZED BY FLUOROANTIMONIC ACID HEXAHYDRATE 1129
(Sintesis Hidrogel Berasaskan Bio Daripada Minyak Sawit Terepoksidasi Bermangkinkan Asid Fluoroantimonik Heksahidrat)
Wan Nurhayati Wan Tajulruddin, Abdul Razak Rahmat, Rohah Abd Majid

20. VIBRATION EXPOSURE ANALYSIS OF POLYDIMETHYLSILOXANE REINFORCED SILICA DERIVED RICE HUSK ASH 1138
(Kajian Pendedahan Getaran Terhadap Polidimetilsiloksana yang Diperkuat Silika Dari Abu Sekam Padi)
Mohd Azham Azmi, Mohd Syahmi Muin @ Marsayid, Shahruddin Mahzan, Sufizar Ahmad, Hariati Taib

21. NEW PROCESS DEPROTENISED NATURAL RUBBER (PUREPRENA™): RAW RUBBER, PROCESSABILITY AND BASIC PHYSICAL PROPERTIES 1145
(Proses Baru Getah Asli Nyah Protein (Pureprena™): Getah Mentah, Kebolehprosesan dan Sifat Fizikal)
Rohaidah Abd Rahim, Teku Zakwan Zaeimoedin, Ahmad Khairul Muhamad and Siti Salina Sarkawi

22. PLASTICIZING POLY(LACTIC ACID) USING EPOXIDIZED PALM OIL FOR ENVIRONMENTAL FRIENDLY PACKAGING MATERIAL 1153
(Pemplastikan Poli(laktik asid) Menggunakan Minyak Kelapa Sawit Terepoksi untuk Bahn Pembungkus Mesra Alam)
Fathilah Binti Ali, Raina Awale Jama, Hanan Fakhruldin, Hazleen Anuar

23. MONTHLY ANALYSIS OF PM10 IN AMBIENT AIR OF KLANG VALLEY, MALAYSIA 1159
(Analisis PM10 Bulanan di dalam Udara di Lembah Klang, Malaysia)
Mohd Asrul Jamalani, Ahmad Makmom Abdullah, Azman Azid, Mohammad Firuz Ramli, Mohd Rafee Baharudin, Mahmud Mohammed Bose, Rashieda Elawad Elhadi, Khaleed Ali Ahmed Ben Youssef, Azadeh Gnadimzadeh, Danladi Yusuf Gumel

24. KLASIFIKASI SEDIMEN MENGGUNAKAN TEKNIK ENVIROMETRIK: SATU KAJIAN KES DI SUNGAI PAHANG, MALAYSIA 1171
(Sediment Classification using Envirometric Technique: A Study Case in Pahang River, Malaysia)
Frankie Marcus Ata, Mohd Khairul Amri Kamarudin, Mohd Ekhwan Toriman, Mohd Saupi Mohd Zin, Nur Hishaam Sulaiman, Norjima Abd Wahab, Sarif Mohd Nasir, Jamaluddin

Mohamad Saad

25. PHYTOCHEMICAL SCREENING, TOTAL FLAVONOID AND PHENOLIC CONTENT ASSAYS OF VARIOUS SOLVENT EXTRACTS OF TEPAL OF Musa paradisiaca 1181
(Penyaringan Fitokimia, Jumlah Asai Kandungan Flavonoid dan Fenolik Pelbagai Ekstrak Pelarut Tepal Musa paradisiaca)
U.S. Mahadeva Rao, Muhammad Abdurrazak, Khamsah Suryati Mohd

26. IN VITRO NITRIC OXIDE SCAVENGING AND ANTI INFLAMMATORY ACTIVITIES OF DIFFERENT SOLVENT EXTRACTS OF VARIOUS PARTS OF Musa paradisiaca 1191
(Aktiviti Pemerangkapan Nitrik Oksida dan Anti-Radang Secara In Vitro oleh Ekstrak Pelarut Berbeza dari Pelbagai Bahagian Musa paradisiaca)
U.S Mahadeva Rao, Bashir Ado Ahmad, Khamsah Suryati Mohd

27. ANTIULCER ACTIVITY OF Musa paradisiaca (BANANA) TEPAL AND SKIN EXTRACTS IN ULCER INDUCED ALBINO MICE 1203
(Aktiviti Antiulser dari Ekstrak Jantung dan Kulit Musa paradisiaca (Pisang) pada Tikus Albino Teraruh Ulser)
U.S Mahadeva Rao, Bashir Ado Ahmad, Khamsah Suryati Mohd, Thant Zin

28. A STUDY OF MICROBE AIR LEVELS IN SELECTED ROOMS OF A HOSPITAL CULTIVATED ON TWO CULTURE MEDIAS 1217
(Kajian Tahap Mikrob dalam Udara yang Di Kultur Pada Dua Media Kultur di dalam Bilik Hospital Terpilih)
Che Noraini Che Hasnam, Hafizan Juahir, Azman Azid, Mohammad Azizi Amran, Fazureen Azaman, Ahmad Dasuki Mustafa, Zarizal Suhaili, Sukri Md. Ismail, Khairul Affendi Yusof, Cik Fatimah Nadia Che Hasnam

29. SALTWATER INTRUSION ANALYSIS IN EAST COAST OF TERENGGANU USING MULTIVARIATE ANALYSIS 1225
(Analisis Pencerobohan Air Masin di Kawasan Pantai Timur, Terengganu Menggunakan Analisis Multivariat)
Norsyuhada Hairoma, Muhd Barzani Gasim, Azman Azid, Haniff Muhamad, Nur Hishaam Sulaiman, Zuriati Khairuddin, Ahmad Dasuki Mustafa, Fazureen Azaman, Muhammad Azizi Amran

Malaysian Journal of Analytical Sciences, Vol 20 No 5 (2016): 971 - 977
DOI: http://dx.doi.org/10.17576/mjas-2016-2005-01

MALAYSIAN JOURNAL OF ANALYTICAL SCIENCES
Published by The Malaysian Analytical Sciences Society
ISSN 1394 - 2506

NEW INDOLIZIDINE ALKALOIDS FROM PSYCHROPHILIC YEAST *Glyciozyma antarctica* PI12

(Alkaloid Indolizidin Baharu daripada Yis Psikrofilik *Glyciozyma antarctica* PI12)

Andi Rifki Rosandy[1], Wickneswary Nadarajah[1], Muntaz Abu Bakar[1], Cheah Yoke Kqueen[2], Mohd. Ikram Mohd. Said[1], Laode Muhammad Ramadhan Al Muqarrabun[3], Rozida Khalid[1]*

[1]*School of Chemical Science and Food Technology, Faculty of Science and Technology, Universiti Kebangsaan Malaysia, 43600 UKM Bangi, Selangor, Malaysia*
[2]*Department of Biomedical Sciences, Faculty of Medicine and Health Sciences, Universiti Putra Malaysia, 43400 UPM Serdang, Selangor, Malaysia*
[3]*Atta-ur-Rahman Institute for Natural Product Discovery, Universiti Teknologi MARA, Puncak Alam Campus, 43200 UiTM Puncak Alam, Selangor, Malaysia*

**Corresponding author: rozidakhalid@ukm.edu.my*

Received: 2 March 2016; Accepted: 10 May 2016

Abstract

Two alkaloid compounds: namely *3-(1-aminoethyl)tetrahydro-1H-pyrrolo[1,2-d][1,2,4]oxadiazine-1,4(3H)-dione* (**1**) and *tetrahydro-1H-pyrrolo[2,1-c][1,4]oxazine-1,3(4H)-dione* (**2**) was isolated from *Glyciozyma antarctica* (*PI12*), a psychrophilic yeast. The isolated compounds were isolated by Radial Chromatography and Thin Layer Chromatography techniques. The chemical structures were elucidated by Ultraviolet-visible, Infrared, Nuclear Magnetic Resonance and Mass Spectroscopy.

Keywords: *Glyciozyma antarctica* PI12, alkaloids, yeast, psychrophiles

Abstrak

Dua sebatian alkaloid: *3-(1-aminoetil)tetrahidro-1H-pirrolo[1,2-d][1,2,4]oksadiazin-1,4(3H)-dion* (**1**) and *tetrahidro-1H-pirrolo[2,1-c][1,4]oksazin-1,3(4H)-dion* (**2**) telah diasingkan daripada *Glyciozyma antarctica* PI12, sejenis yis psikrofilik. Sebatian-sebatian telah diasingkan menggunakan teknik Kromatografi Pepejal dan teknik Kromatografi Lapisan Nipis. Struktur-struktur kimia telah dicirikan dengan menggunakan Ultra-Lembayung, Infra-Merah, Resonans Magnet Nukleus dan Spektroskopi Jisim.

Kata kunci: *Glyciozyma antarctica* PI12, alkaloid, yis, psikrofil

Introduction

Since the 1960s, bioactive secondary metabolites have been isolated and structurally characterized from eubacteria, archaea, and fungi, microorganisms that have adopted strategies to grow in extreme terrestrial environments. The isolation and bioactivity of these molecules from the following extremophiles has been described such as thermophiles, psychrophiles, acidophiles, alkaliphiles, halophiles, xerophiles, epi- or endophytes, as well as metallotolerant, radioresistant, and unclassifiable microorganisms. Secondary metabolites often play an important role in defense systems of different organisms [1]. Humans use secondary metabolites as medicines, flavorings, and recreational drugs. Microbial secondary metabolites include antibiotics, pigments, toxins, effector of ecological competition and symbiosiss, pheromones, enzyme inhibitors, immunomodulating agents, receptor antagonists and

agonist, pesticides, antitumor agents and growth promoters of animals and plants. They have a major effect of the health, nutrition and economics of our society [2].

Scientist used the term "psychrophiles" to refer to microorganisms that grow optimally in extremely cold temperatures ranging from 15 °C or below (e.g. −20 °C in sea ice) to a maximum temperature of 20 °C [3]. Roughly 80 % of our planet's biosphere is at temperatures below 5 °C, which includes most of the world's oceans (70 % of the Earth's surface), sea ice, Antarctica, parts of North America and Europe, the deep-sea, mountain regions, as well as the mesosphere and stratosphere [4]. Thus, most microorganisms on Earth can be considered to be psychrophiles. *Glaciozyma antarctica* PI12 (previously known as *Leucosporidium antarcticum*) is a psychrophilic yeast strain which was isolated from a marine environment in Antarctica [5, 6]. Recently, Turchetti et al. [7] have proposed to reclassify this yeast from *Leucosporidium antarcticum* to *Glyciozyma antarctica*. Besides, *Glyciozyma antarctica* has also been isolated from various locations in Antarctica [8, 9]. Turkiewicz et al. [10] reported that *Glyciozyma antarctica* 171 has an optimum growth temperature at around 15 ^{0}C and is able to tolerate higher temperatures up to 20 ^{0}C. So far, the chemical constituents of this species have not been studied.

This paper describes the isolation and detailed characterization of new derivatives indolizidine alkaloid, 3-(1-aminoethyl)tetrahydro-1H-pyrrolo[1,2-d][1,2,4]oxadiazine-1,4(3H)-dione (**1**) and tetrahydro-1H-pyrrolo[2,1-c][1,4]oxazine-1,3(4H)-dione (**2**).

Materials and Methods

Material

Glyciozyma antarctica PI12 was isolated from sea ice collected in the vicinity of Case Station (66°21'25"S, 110°37'09"E), Antarctica. It was identified based on its LSU rRNA and ITS sequences which have been deposited in the GenBank database under accession number JX896855 and JX986956. *Glyciozyma antarctica* PI12 was routinely cultivated in yeast peptone dextrose (YPD) broth (Difco) medium.

Culturing material

The culturing of *Glyciozyma antarctica* PI12 was conducted in collaboration with the Malaysia Genome Institute [11]. The psychrophilic yeast, *Glyciozyma antarctica* PI12 was originally isolated from Casey sea ice research station located in Antarctica. Initially, 10 µL of the *Glyciozyma antarctica's* glycerols stock was sub-cultured on the YPD agar with 50 µg/mL of Ampicillin and 50 µg/mL Kanamycin at 12 °C until a single colony is obtained. Next, a starter culture of *Glyciozyma antarctica* PI12 was prepared by inoculated a single colony of *Glyciozyma antarctica* PI12 from the agar plate into 10 mL of YPD medium (50 mL falcon tube) with 50 µg/ml of Ampicillin and 50 µg/ml Kanamycin. It is then cultured at 12 °C at 180 rpm until mid-log phase (OD600: 1.0 to 1.8) (5 days). Thirdly, a fix amount (10^{6} yeast cells/ml) of starter culture was inoculated into 50 mL of YPD medium (3 flasks of 250 mL of conical flask was used) with two antibiotics and then cultured at 12 °C at 180 rpm until mid-log phase (OD600: 1.0 to 1.8) (8 days). After the yeast culture has reached to the mid-log phase (OD600: 1.0 to 1.8), the flask with the yeast culture were exposed separately to -18 °C, 0 °C and 12 °C (without shaking) for 48 hours. Finally, the yeast culture was harvested by pouring them to a 50 mL falcon tube and centrifuged at 3000 rpm for 10 min at 4 °C. The supernatant and the pellet were collected.

Extraction and isolation

An amount of 200.7 mg n-butanol extract of *G. antarctica* PI12 was subjected to Radial Chromatography (RC) with 1 mm thickness silica gel on a round glass plate and eluted with the mixtures of dichloromethane and methanol with increasing polarity (Starting from DCM/Me-OH, 9.6:0.4). The eluents that showed the same profile on thin layer chromatography (TLC) chromatogram were combined to give three fractions (I-III). Purification of fraction I (1-4) (29.7 mg) was carried out using RC with silica gel plate of 0.5 mm thickness eluted with DCM and Me-OH (9.2:0.8) in 5 % polarity increment to yield compound **1** (4 mg). Purification of fraction II (5-7) (48.8 mg) was conducted utilizing another RC with silica gel plate of 0.5 mm thickness. Elution with DCM and Me-OH (8.4:1.6) produced compound **2** (12.5 mg).

Compound identification

Structures of pure compounds were determined based on the spectral data recorded on Shimadzu UV-260 spectrophotometer, Frontier Perkin-Elmer FTIR/NIR spectrophotometer and Bruker NMR 700 MHz Cryo-Probe instrument that included 1-D and 2-D NMR. HR-ESI-MS were recorded by using LCMS-Ultra Performance liquid Chromatography (UPLC), Brand Waters. The isolation was then carried out by radial chromatography using round glass plates of the Merck Kieselgel 60 PF254 (art. no. 7749) and profile was analyzed using smaller pieces from aluminium sheets 20 x 20 cm of the Merck TLC silica gel 60 F254 of 0.25 mm thickness (art. no. 5554) and then detected under UV light (254 nm) or by $CeSO_4$ spraying reagent followed by heating.

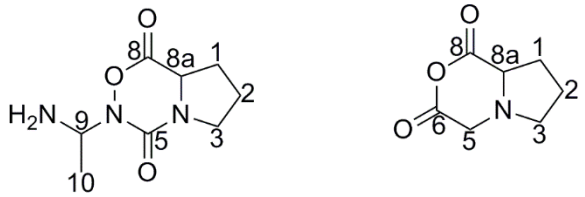
Results and Discussion

Characterization study

3-(1-aminoethyl)tetrahydro-1H-pyrrolo[1,2-d][1,2,4]oxadiazine-1,4(3H)-dione (**1**) is white amorphous solid. HR-ESI-MS $[M+H]^+$ at *m/z*: 200.2132 (calc. for $C_8H_{14}N_3O_3$ 200.2151). IR $\bar{\upsilon}_{max}$ (ATR) cm^{-1}: 3357, 2108, 1647, 1318-1238 and 1087. ^1H NMR (MeOD, 700 MHz) δ_H (ppm) and ^{13}C NMR (MeOD, 175 MHz) δ_C (ppm) are tabulated in Table 1.

Tetrahydro-1H-pyrrolo[2,1-c][1,4]oxazine-1,3(4H)-dione (**2**) is clear crystal. HR-ESI-MS $[M+H]^+$ at *m/z*: 156.1508 (calc. for $C_7H_{10}NO_3$ 156.1592). IR $\bar{\upsilon}_{max}$ (ATR) cm^{-1}: 3191, 1640, 1453, 1332, 1294-1217, 1110, 1004, 922-764. ^1H NMR (MeOD, 700 MHz) δ_H (ppm) and ^{13}C NMR (MeOD, 175 MHz) δ_C (ppm) are tabulated in Table 2.

The structure (Figure 1) elucidation of the compounds were conducted using several spectroscopic methods including mass spectrometer, UV, FT-IR, NMR 1D and 2D (HMQC, HMBC, COSY, and NOESY), and by comparison with reported data.



1 **2**

Figure 1. Chemical structures of isolated compounds **1** and **2**

3-(1-aminoethyl)tetrahydro-1H-pyrrolo[1,2-d][1,2,4]oxadiazine-1,4(3H)-dione **(1)**

Compound **1** was isolated as white amorphous. The molecular formula is $C_8H_{13}N_3O_3$, generated using HR-ESI-MS $[M + H]^+$ ion at *m/z*: 200.2132 (calc. for $C_8H_{14}N_3O_3$ 200.2151). The FTIR spectral data displays broad absorbance peak at 3357 representing primary amine ($-NH_2$), overtone (weak) at 2108 cm^{-1} and tertiary amine at 1318 cm^{-1}, 2985 and 2881 cm^{-1} representing the C-H (aliphatic cyclic). The presence of carbonyl group is characterized by absorbance bands, i.e. C=O stretch at 1647 cm^{-1} indicated that the carbonyl group linked with the tertiary amide. Furthermore, that tertiary amide is characterized by absorbance at 1318 and 1087 cm^{-1}.

The ^{13}C spectrum reveals that the compound contains 8 carbons consisting of one methyl, three methylenes, two methines and two quaternary carbons. The most highly deshielded signals at δ_C 170.1 (C-8) and 165.0 (C-5) were attributed to carbonyl group linked with tertiary amide and another one was from ester group. Two signal of methines at δ_C 58.8 (C-8a) provide information of the presence of an *1H-pyrrolo* carbon that linked with a quarternary carbon C-8 and a tertiary amine, while the other one (C-9) linked with an equivalent proton methyl and a primary amine. Three shielded carbons (C-1, C-2 and C-3) represent the existence of a pyrrolidine framework in the molecule. The Double Bond Equivalent (DBE) value of $C_8H_{13}N_3O_3$ is 4, indicating that the compound consists of two double bonds as carbonyls group and two ring of derivative indolizidine alkaloid as main structure. Meanwhile, 10 proton signals representing 13 protons appeared in the ^1H-NMR spectrum. Ten of the signals came

from the four signals, one each from a methyl group at H-10 (1.45, *d*, *J*= 7) bind with a methine proton at H-9 (δ_H 4.05) are *quartet*, while a primary amine bind this methine at C-9. Furthermore, the other methine at (δ_H 4.26) is triplet, indicating it is adjacent to a methylene at C-1. Meanwhile, the other two saturated methylenes form pyrrolidine skeleton in the molecule.

The structure is confirmed using 2D NMR (Table 1). The HMBC experiment shows H-8a has correlation with C-1, and H-1 with C-2 and C-3. Proton methine H-9 has correlations with C-10, while all methine protons have correlation with the carbonyl carbons, confirming the position of C-5 and C-8. In COSY spectrum, H-2 shows strong coupling with H-1 and H-3, while H-9 show strong coupling with methyl proton at H-10 (Fig. 2 (a)).

Table 1. NMR data of 3-(1-aminoethyl)tetrahydro-1H-pyrrolo[1,2-d][1,2,4]oxadiazine-1,4(3H)-dione (**1**)

No	**APT (ppm)**	**HSQC (*mult.*, *J* in Hz) ΣH**	**HMBC**	**H-H Cosy**	**H-H Noesy**
1	28.2	2.35 (*m*)ax1H 1.97 (*m*)eq 1H	C-8a; C-3 C-8a; C-3; C-2	H-8a; H-2	H-2eq; H-3ax; H8a$_{(ax)}$
2	21.8	2.04 (*m*)ax 1H 1.95 (*m*)eq 1H	C-1 C-1; C-3; C-8a	H-1; H-3	H-1eq; H8a$_{(ax)}$
3	44.8	3.62 (*m*)ax 1H 3.51 (*m*)eq 1H	C-2 C-1; C-2	H-2 H-2	H-2eq: H-1ax
5	165.0	-	-	-	-
8	170.1	-	-	-	-
8a	58.8	4.26 (*t*, *J*= 7)ax 1H	C-1; C-8	H-1	H-1eq; H-2ax
9	50.4	4.05 (*Ψm*)eq 1H	C-1; C-5; C-10	H-10	H-10eq
10	18.6	1.45 (*d*, *J*= 7)eq 3H	C-5; C-8; C-9	H-9	H-1ax; 9-NH$_2$; H-9eq
9-NH$_2$	-	4.60 (*br-s*)eq 2H	-	-	-

According to Silverstein et al. [12], the vicinal coupling constant between an axial H with another axial H ranges from 6 to 10 Hz, while the vicinal coupling constant between an equatorial H with an axial H is around 0 to5 Hz. The relative configuration of the sole chiral carbon (C-8a) was observed using Nuclear Overhauser Effect Spectroscopy (NOESY) experiment which describes the H–H correlation through space (Figure 2(b)). From the NOESY spectrum, it was observed that carbon methine at C-8a in pyrrolidine skeleton bind one proton in the axial position with coupling constant value *J* = 7 Hz. Since H-8a$_{(ax)}$ generates cross peak with H-2$_{ax}$, which means they are in the same orientation. According to Karplus curve, if a proton has correlation with another proton in the same orientation, indicating they are in the eclipse position (dihedral angel of 0^0). Then, methyl group at C-10 binds three *geminal* protons, has *doublet* splitting and *J* value is 7 Hz, indicating that H-10 is in axial position/eclipse position (dihedral angel of 0^0) toward H-9.



(a) (b)

Figure 2. Compound **1**; 2D correlation NMR; (a) HMBC (⟶) & COSY (━), (b) NOESY

Tetrahydro-1H-pyrrolo[2,1-c][1,4]oxazine-1,3(4H)-dione **(2)**

Compound **2** was isolated as a clear crystal. The molecular formula $C_7H_9NO_3$ was generated using HR-ESI-MS [M + H]$^+$ ion at *m/z* 156.1532 (calc. for $C_7H_{10}NO_3$ 156.1592). The UV spectrum indicated that there was no conjugated double bond in the molecule; this was deducted by the presence of only one absorbance band at 203 nm. The FT-IR spectral data presence of carbonyl group was indicated by a strong stretching band of C=O at 1640 cm^{-1} and the vibration band at 1004 cm^{-1} indicated the C-O bending representing an ester group. The C-C(=O)-O asymmetrical stretching vibration was indicated by absorbance band at 1294 cm^{-1}. The Csp^3-H stretching band appeared at 2956-2889 cm^{-1}, while absorption bands at 1453 cm^{-1} indicated the asymmetrical bending vibrations of Csp^3-H of the methylene groups. A tertiary amine was detected in this compound at 1332 cm^{-1}.

The presence of functional groups is supported by NMR analysis of 1-D (^{1}H and APT experiment of ^{13}C-NMR) and 2-D (HSQC, HMBC, H-H COSY and H-H NOESY) data. The APT experiment data showed the presence of 7 carbon signals representing two quaternary, one methine and four methylenes carbons. The DBE value of four indicated that this compound was an indolizidine alkaloid containing two double bonds. The most deshielded carbons at δ_C 170.5 and 165.0 ppm was indicated as an asymmetrical carbonyl group. Three saturated non-equivalent methylenes signals at δ_C 27.9 (C-1), 21.9 (C-2) and 44.9 (C-3) are attributed to pyrrolidine ring in this molecule, while another methylene signal at δ_C 45.5 ppm (C-5) indicated the presence of a methylene existed between carbonyl and tertiary amine. Furthermore, methine carbon at δ_C 58.4 ppm (C-8a) is the specific of methine signal of indolizidine alkaloid for this molecule. Meanwhile, 9 proton signals representing 9 protons appeared in the ^{1}H-NMR spectrum as shown in Table 2. Eight of the signals came from the three methylenes proton, one each from isolated methylene at H-5 binds carbonyl and tertiary amine and another three non-equivalent methylenes at H-1, H-2 and H-3, forming a basic pyrrolidine ring. An aminated methine proton, H-8a$_{(ax)}$ (δ_H 4.25, *Ψt*, *J*= 7.0) are *pseudo doublet*, indicating that C-8a is adjacent to a methylene group (C-1).

The structure of **2** was confirmed using 2D NMR including HMBC, COSY and NOESY. The HMBC spectrum revealed a strong correlation between methine (C-8a) and the carbonyl carbon (C-8) as well as between C-8a and saturated non-equivalent methylene group (C-1). This indicated that the methine group as *chiral* position. The correlations between H-5 and C-8a as well as between H-5 and C-6 confirmed the position of the isolated methylene in the molecule as described in Figure 2(a). NOESY spectrum revealed correlation between H-8a$_{(ax)}$ and H-1ax as well as between H-8a$_{(ax)}$ and H-2ax confirming the position of the chiral group in the molecule (Figure 3(b)).



(a) (b)

Figure 3. Compound **2**; 2D correlation NMR; (a) HMBC (⟶) & COSY (▬), (b) NOESY

Table 2. NMR data of tetrahydro-1H-pyrrolo[2,1-c][1,4]oxazine-1,3(4H)-dione (**2**)

No	^{13}C (ppm)	HSQC (*mult.*, *J* in Hz,) ΣH	HMBC	H-H Cosy	H-H Noesy
1	27.9	2.34 (*t*, *J*= 7)ax 1H 1.99 (*t*, *J*= 7)eq 1H	C-2; C-3; C-8a C-2; C-8a; C-8	H-8a$_{(ax)}$ H-3	H-3ax H-2eq; H-8a$_{(ax)}$
2	21.9	2.04 (*m*)ax 1H 1.95 (*m*)eq 1H	C-1; C-3; C-8a; C-8 C-1; C-3; C-8a	H-3 H-3	H-8a$_{(ax)}$ H-1eq; H-3eq
3	44.9	3.57 (*Ψt*, *J*= 7)ax 1H 3.54 (*Ψt*, *J*= 7)eq 1H	C-2; C-1; C-8a; C-6 C-2; C-1; C-8a; C-6	H-2 H-1	H-1ax; H-5eq: H-8a$_{(ax)}$ H-2eq
5	45.5	4.13 (*Ψd*, *J*= 16.8)ax1H 3,77 (*d*, *J*= 16.8)eq 1H	C-8a; C-6; C-3; C-8 C-8a; C-6; C-3; C-8	H-5 H-5	- H-3ax
6	165.0	-	-	-	
8	170.5	-	-	-	
8a	58.4	4.25 (*Ψt*, *J*= 7.0)ax 1H	C-1; C-8	H-1; H-1	H-1eq; H-2ax; H-3ax

Conclusion

The phytochemical investigation of the psycrophilic yeast *Glyciozyma antarctica* PI12 resulted in the isolation of new derivatives indolizidine alkaloid named 3-(1-aminoethyl)tetrahydro-1H-pyrrolo[1,2-d][1,2,4]oxadiazine-1,4(3H)-dione (**1**) and tetrahydro-1H-pyrrolo[2,1-c][1,4]oxazine-1,3(4H)-dione (**2**). To the best of our knowledge, this is the first report for both of compounds from this species. In addition, these compounds contributed to the small yet expending database of secondary metabolites from psychrophiles.

Acknowledgement

Authors would like to thank the School of Chemical Sciences and Food Technology, Faculty of Science and Technology, Universiti Kebangsaan Malaysia (UKM); Malaysia Genome Institute for providing research facilities and also would like to express our gratitude to the LPDP (Indonesia Endowment Fund for Education) and the Ministry of Science and Technology for financial support through research grants of 02-05-20-SF0007 and GGPM-2013-076, respectively.

References

1. Stamp, N. (2003). Out of the quagmire of plant defense hypotheses. *The Quarterly Review of Biology*, 78: 23 – 55.
2. Davati, N. and Najafi, M. B. H. (2013). Overproduction strategies for microbial secondary metabolites: A review. *International Journal of Life Science & Pharma Research*, 3: 23 – 37.
3. Morita, R.Y. (1975). Psychrophilic bacteria. Bacteriological Reviews, 39: 144 – 167.
4. De Maayer, P., Anderson, D., Cary, C. and Cowan, D. A. (2014). Some like it cold: Understanding the survival strategies of psychrophiles. *EMBO Reports*, 15: 508 – 517.
5. Fell, J. W., Statzell, A., Hunter, I. L. and Phaff, H. J. (1969). *Leucosporidium* genus, the heterobasidiomycetous stage of several yeasts of the genus *Candida. Antonie van Leeuwenhoek*, 35: 433 – 462.
6. Fell, J. W. (1974). Heterobasidiomycetous yeasts *Leucosporidium* and *Rhodosporidium.* Their systematics and sexual incompatibility systems. *Transactions of the Mycological Society of Japan*, 15: 316 – 323.
7. Turchetti, B., Thomas-Hall, S. R., Connell, L. B., Branda, E., Buzzini, P., Theelen, B., Müller, W. H. and Boekhout, T. (2011). Psychrophilic yeasts from antarctica and european glaciers: description of *Glaciozyma* genus, *Glaciozyma martinii* species and *Glaciozyma watsonii* species. *Extremophiles*, 15: 573 – 586.
8. Donachie, S. P. (1995). Ecophysiological description of marine bacteria from Admiralty Bay (Antarctica), and the digestive tracts of selected Euphausiidae. Ph. D. Thesis. Department of Antarctic Biology, Polish Academy of Sciences, Warsaw.

9. Connell, L., Redman, R., Craig, S., Scorzetti, G., Iszard, M. and Rodriguez, R. (2008). Diversity of soil yeasts isolated from South Victoria land, Antarctica. *Microbial Ecology,* 56: 448 – 459.
10. Turkiewicz, M., Pazgier, M., Donachie, S. P. and Kalinowska, H. (2005). Invertase and α-glucosidase production by the endemic Antarctic marine yeast *Leucosporidium antarcticum*. *Polish Polar Research*, 26: 125 – 136.
11. Boo, S. Y., Wong, M. V. L., Rodrigues, K. F., Najimudin, N., Murad, A. M. A. and Mahadi, N. M. (2013). Thermal stress responses in Antarctic yeast, *Glaciozyma antarctica* PI12, characterized by real-time quantitative PCR. *Polar Biology*, 36: 381 – 389.
12. Silverstein, R. M., Webster, F. X. and Kiemle, D. J. (2005). Spectrometric identification of organic compounds. 7th ed. Hoboken, NJ: Wiley.

Malaysian Journal of Analytical Sciences, Vol 20 No 5 (2016): 978 - 985
DOI: http://dx.doi.org/10.17576/mjas-2016-2005-02

MALAYSIAN JOURNAL OF ANALYTICAL SCIENCES
Published by The Malaysian Analytical Sciences Society
ISSN 1394 - 2506

IMMOBILIZATION OF TYROSINASE IN NANOCRYSTALLINE CELLULOSE/CHITOSAN COMPOSITE FILM FOR AMPEROMETRIC DETECTION OF PHENOL

(Pemegunan Tyrosinase dalam Filem Komposit Selulosa Nanokristalin/Kitosan untuk Pengesanan Amperometrik bagi Fenol)

Fariza Aina Abd Manan[1], Jaafar Abdullah[1,2]*, Nur Nadziera Nazri[1], Izyan Nadira Abd Malik[1], Nor Azah Yusof[1,2], Ishak Ahmad[3]

[1]*Department of Chemistry, Faculty of Science*
[2]*Institute of Advanced Technology*
Universiti Putra Malaysia,43400 UPM Serdang, Selangor, Malaysia
[3]*School of Chemical Sciences and Food Technology, Faculty of Sciences and Technology,*
Universiti Kebangsaan Malaysia, 43600 UKM Bangi, Selangor, Malaysia

**Corresponding author: jafar@upm.edu.my*

Received: 17 August 2015; Accepted: 17 June 2016

Abstract

Nanocrystalline cellulose (NCC)/chitosan composite for immobilization of tyrosinase enzyme for the determination of phenol have been developed. The NCC/Chitosan composite film on screen printed carbon electrode (SPCE) was prepared by using drop casting technique. Characterization of the modified SPCE surface was investigated by using Transmission Electron Microscopy (TEM) and Fourier Transform Infrared (FTIR), respectively. Chronoamperometric (CA) technique is used to perform the electrochemical measurements. The detection of phenols by the developed system is derived on the direct electrochemical reduction of quinones produced by enzymatic reaction. The results demonstrated that the maximum response was observed at ratio of NCC/chitosan of 1 to 1 (v/v), tyrosinase concentration of 10 mg/mL and pH buffer of 7, respectively. It was found that the developed system gave linear response in the phenol concentration range of 0.39 – 7.74 µM (slope = 28.316, R^2 = 0.9808) with the detection limit of 0.38 µM. The reproducibility of the system was also estimated and the Relative Standard Deviation (RSD) was found to be at 4.27 %.

Keywords: nanocrystalline cellulose, nanocomposite, immobilization, electrochemical, phenol

Abstrak

Komposit selulosa nanokristalin/kitosan untuk pemegunan enzim tirosinase bagi penentuan fenol telah dibangunkan. Filem komposit NCC/Chitosan di atas elektod karbon skrin bercetak (SPCE) telah disediakan melalui kaedah penyalutan acuan. Pencirian permukaan SPCE dimodifikasi dikaji menggunakan Mikroskop Elektron Transmisi (TEM) dan Transformasi Fourier Inframerah (FTIR). Teknik kronoamperometri (CA) digunakan untuk menjalankan pengukuran elektrokimia. Pengesanan fenol oleh sistem yang dibangunkan ini adalah berasaskan penurunan langsung elektrokimia oleh kuinon yang dihasilkan daripada tindak balas enzim. Keputusan menunjukkan bahawa rangsangan maksimum diperhatikan pada nisbah NCC/kitosan adalah 1 kepada 1 (v/v), kepekatan tirosinase 10 mg/mL dan larutan penimbal pada pH 7. Didapati bahawa sistem yang dibangunkan memberi rangsangan linear dalam julat kepekatan fenol 0.39-7.74 µM (kecerunan = 28.316, R^2 = 0.9808) dengan had pengesanan 0.38 µM. Kebolehulangan sistem juga telah dianggarkan dan nilai sisihan piawai relatif (RSD) yang diperolehi ialah 4.27 %.

Kata kunci: selulosa nanokristalin, nanokomposit, pemegunan, elektrokimia, fenol

Introduction

Nanocrystalline cellulose (NCC) is a unique and sustainable nanomaterial obtained through acid hydrolysis of native cellulose, it has remarkable physical properties, such as biocompatibility, biodegradability and low toxicity as it originating from natural resources raw materials [1]. NCC has been studied to have a rigid rod-shape structure with 5 – 10 nm in diameter and 10 – 100 nm in length [2]. It can be extracted from native cellulose which is found in plants, animals and bacteria that composed of the nanoscaled structure material. Since nanocellulose is a natural nanoscaled material, it possesses varied characteristics different from traditional materials, as well as special morphology and geometrical dimensions like crystallinity, high specific surface area, rheological properties, liquid crystalline behaviour, alignment and orientation, mechanical reinforcement, barrier properties and surface chemical reactivity [1]. NCC is an attractive material for drug delivery excipients [3], support for immobilization of protein [4,5] and for applications of nanocomposite [4] because of its properties for instance high surface area, high aspect ratio, high and specific stiffness and strength, and low toxicity. Depending on the origin and method of extraction, the nano-dimensional cellulose might be in the form of rods, spheres, and have network morphology with an extremely high surface to volume ratio [6]. The presence of –OH groups on the NCC surface allow it to undergo further surface modification to alter its hydrophobicity, serve as a stable matrix that is compatible for widespread bioapplications, specifically in enzyme immobilization, antimicrobial and medical materials, green catalysis, biosensing and controlled drug delivery [5].

Chitosan is a natural biopolymer product found in the exoskeleton of crustaceans, in fungal cell wall and other biological materials. Chitosan is natural linear polysaccharide made primarily of glucosamine repeating units, partially deacetylated derivative of chitin and the second most abundant natural polysaccharide after cellulose [7]. Its properties of biodegradability, non-toxicity, biocompatibility, high mechanical strength and good adhesion make it a promising matrix for enzyme immobilization. In spite of its biodegradability, it has numerous reactive amino acid and hydroxyl groups that allows chemical modification possibilities, formation of a large variety of functional derivatives which are commercially available or can be made available through graft reactions and ionic interactions [8, 9]. The reaction of chitosan is considerably more versatile than cellulose as there is the presence of NH_2 groups.

Recently development of biosensor system with better sensitivity, selectivity and rapid detection is the key important step and gain much attention from many researchers. Among of that is the selection of new material for enzyme immobilization which offers good electronic properties, biocompatible, stable and easily accessible by the analyte and large surface area. However, it is difficult to find a single material that contains all these important characteristics. The use of composite materials made of two and more components has gotten increasing interest as a way to achieve adequate sensitivity and stability for biosensors development.

In this work, we explored the utilization of nanocrystalline cellulose (NCC) in combination with chitosan for biosensing application. The nanostructure of NCC could provide high surface to volume ratio and high surface activity, and thus possess unique advantages over other conventional materials in terms of enzyme immobilization and signal transduction. These biomaterials could preserve enzyme activity due to the desirable microenvironment and enhance the direct electron transfer between the enzyme active sites and the electrode.

Materials and Methods

Reagents

All chemicals used in this experiment were of analytical grade. Sodium phosphate dibasic, sodium phosphate monobasic, phenol and tyrosinase were obtained from Sigma Aldrich and Fluka (Switzerland). Sodium hydroxide was from Merck (Germany). Acetic acids and potassium chloride were obtained from R&M chemicals (United Kingdom). Chitosan powder was purchased from Chito-Chem (Malaysia) Sdn Bhd. Nanocrystalline cellulose (NCC) powder was acquired from Universiti Kebangsaan Malaysia. Deionized water was used throughout the experiment.

Preparation of NCC colloidal suspensions and chitosan solution

An amount 1 mg/mL or 0.1% (w/v) of NCC suspension was prepared by dissolving 0.025 g of NCC powder in 25 ml deionized water followed by sonication for 3 min. 1.0 % (w/v) of chitosan solution was prepared by dissolving

1.0 g of chitosan powder in 100 mL of acetic acid (1%, v/v). The viscous chitosan solution was stirred overnight at room temperature by using magnetic stirrer.

Immobilization of tyrosinase into NCC/Chitosan composite on SPCE

Preparation of NCC/Chitosan mixture was carried out by varying the ratio of NCC/Chitosan in the range of 1:3 to 3:1 (v/v). For immobilization of tyrosinase, 20 µL of NCC/Chitosan mixture with different ratio was mixed with 10 µL of tyrosinase (40 mg/mL) in eppendorf tube and stirred gently until homogeneous solution was obtained. Then 2 µL of the prepared mixture was deposited and spread onto SPCE. It was kept at 4 °C for drying process for overnight. All electrodes are stored at 4 °C prior to use.

Study the performance of NCC/Chitosan/tyrosinase composite electrode

An electrochemical measurement was performed by using Autolab potentiostat (Netherlands) controlled by GPES software connected to a PC and screen printed carbon electrode (Quasense, Thailand). Chronoamperometry method was used to record current-time activity. Two-electrode system was employed in this work with NCC/Chitosan/tyrosinase as a working electrode and an AgCl served as the reference/counter electrode.

Characterization of the SPCE modified with NCC/chitosan/tyrosinase composite was carried out using Transmission Electron Microscopy (TEM) and Fourier Transform Infrared (FTIR), respectively.

Results and Discussion

The morphology characterization of the composite film

Figure 1a depicts the TEM image of NCC showing agglomerated rod-like nanocrystals, ranging approximately 10 – 30 nm in diameter and corresponding length of about 100-300 nm. Similar observations were also reported by previous researchers which the NCC obtained was highly crystalline nanometer sized rod-like particle ranging from 50 – 60 nm that is obtained as a stable aqueous colloidal suspension [4,7]. Fig. 1b illustrates the image of NCC/chitosan with ratio of 1 to 1 (v/v). As can be seen the NCC/Chitosan appeared like a shiny dot which correspond to the transverse sections of the cellulose nanocrystals [10]. Fig. 1c exhibits the uniform distribution of tyrosinase on the NCC/Chitosan composite films.

FTIR analysis attempted to characterize the effect of NCC incorporation with chitosan and also to determine NCC-chitosan and NCC-chitosan-tyrosinase interactions from the infrared bands and related shifts. Fig. 2 shows the FTIR spectra recorded for NCC, chitosan, NCC-chitosan, and NCC-chitosan-tyrosinase. In the FTIR spectra of pure NCC film (Fig. 2a), the absorption band between 3600 and 3200 cm^{-1} which is related to the O-H stretching vibrations. The broad peak recorded at 3348 cm^{-1} may be attributed to the O-H vibrations because of the intramolecular hydrogen bonding [11]. The bands of absorption between 3000-2800 cm^{-1} and 1500-1250 cm^{-1} indicated the functional group of C-H and $C-H_2$ stretching and bending vibration, respectively [12]. The adsorption of C-H stretching was obtained at 2915 cm^{-1} and the strongest band across NCC spectra is at 1447 cm^{-1} which assigned to $C-H_2$ stretching. Other bands between 800-650 cm^{-1} originated from O-H out of plane bending vibrations. The position of the peaks of chitosan film spectrum is similar to those described by Cao et al. [13]. The absorption peaks of the chitosan film in Fig.2b are due to the stretching of intra- and intermolecular O-H and CH_2OH vibrations at 3500-3250 cm^{-1}, overlapped with stretching $-NH_2$ (3500-3400 cm^{-1}) and –NH secondary amides vibrations (3300-3280 cm^{-1}). The band between 2960-2870 cm^{-1} corresponds to symmetric and asymmetric C-H vibrations. Amide at 1557 cm^{-1} was also been observed.

There are some differences can be observed in FTIR spectra of chitosan films in Fig. 2c because of the incorporation of NCC to the chitosan matrix. A broad peak appeared at 3287 cm^{-1}, which was not present in the control chitosan film. The band intensity 3287 cm^{-1} increased suggesting hydrogen bonding which occurred between chitosan and NCC [14]. Band at 1569 cm^{-1} and 1397 cm^{-1}, their intensity was increased after NCC addition due to the bending of C-H and –OH group. Furthermore, a drastic increased was observed in the intensity of the absorption band at 1063 cm^{-1} due to incorporation of NCC which refer to C-H stretching vibration of C-O. An incorporation of tyrosinase enzyme in NCC-chitosan film (Fig. 2d) caused no changes in intensity of band spectra of NCC-chitosan which a broad peak appeared at 3286 cm^{-1}. Also, there was a decrease in intensity of bands at

1642 cm^{-1} might be attributed to the amide I vibrations indicating that tyrosinase had been successfully attached on the membranes consisting of NCC/chitosan film.

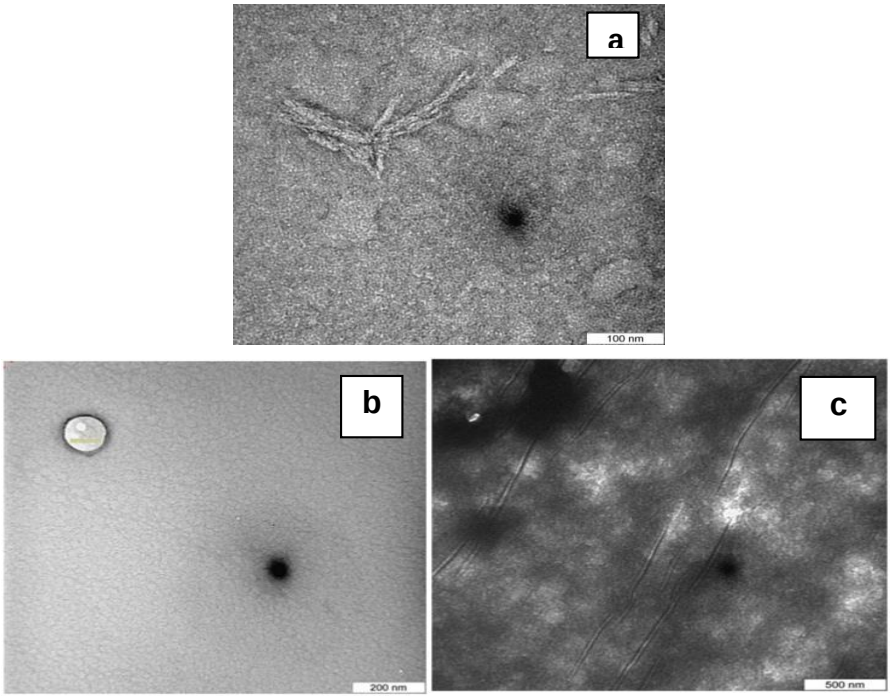


Figure 1. TEM images of (a) NCC, (b) NCC/Chitosan, (c) NCC/Chitosan/ tyrosinase

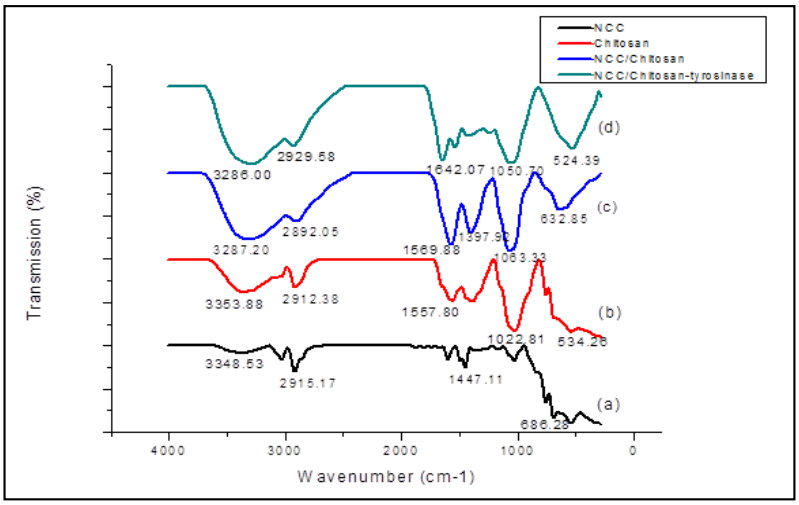
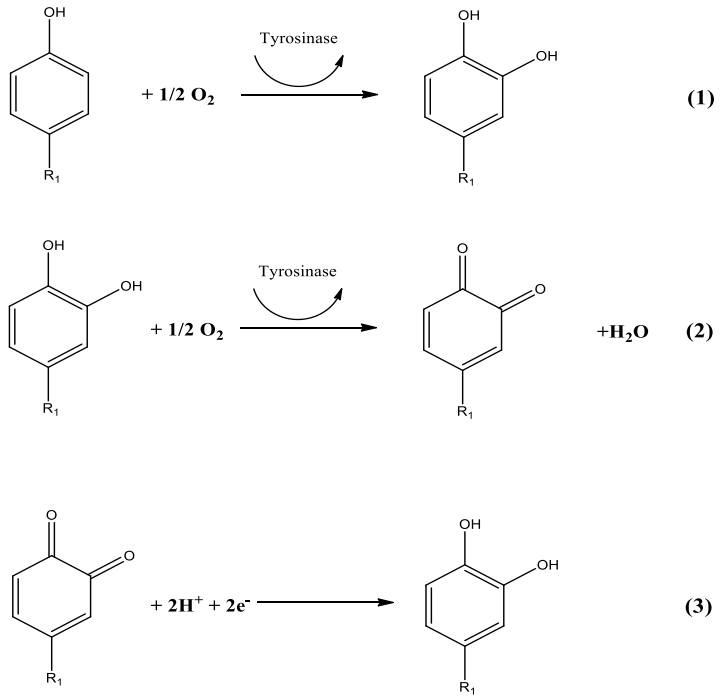


Figure 2. FTIR spectra of films based on NCC (a), chitosan (b), NCC/chitosan (c), and NCC/chitosan/ tyrosinase (d)

Principal of detection of phenol

In this work, the electrochemical measurements were performed using chronoamperometric technique. The electrochemical experiments were carried out with two-electrode system with NCC/Chitosan/tyrosinase on carbon electrode as a working electrode and an AgCl served as the reference/counter electrode. Tyrosinase is a copper containing enzyme, which catalyzes the oxidation of phenol group to o-quinone is commonly used in the detection of phenolic compounds. The oxidation of phenols by tyrosinase can be presented according to the following reactions:



The oxidation of phenol by tyrosinase has two steps: phenol is oxidized to catechol (o-benzenediol), which is consequently oxidized (by tyrosinase) to o-quinone [15]. The liberated quinone species catalytically oxidized by tyrosinase is electrochemically reduced and the reaction can be measured at low potential. Thus, this provides the additional advantages of the enzymatic/electrochemical recycling of the substrate, giving rise to signal amplification. In this work, effect of applied potential was investigated in the range of 0.0 V to -0.6 V and the optimum response of the immobilized tyrosinase in NCC/Chitosan composite film was observed at - 0.3 V vs AgCl. Thus, applied potential of - 0.3 V was chosen for further study.

Optimization parameter

Effect of ratio NCC/Chitosan on the sensing response was evaluated in this work by employing various ratios such as NCC, 1:3, 1:1, 3:1 and chitosan, respectively. As shown in Figure 3, the ratio of NCC/Chitosan of 1:1 (v/v) gave maximum current response. This shows that the NCC/Chitosan composite with composition of 1:1 gave relatively higher protein loading which might be attributable to the abundant active –OH groups and highly surface area of the NCC that contribute to the cross-linking of tyrosinase onto the composite film. However, pure NCC film gave the lowest current response due to the high solubility in water and hydrophilic character of NCC which caused the NCC to be easily detached from the surface of electrode and dissolved in buffer solution.

The zeta potentials of the NCC and chitosan were also evaluated to characterize the surface charge density of the material. The zeta potential was investigated at different pH value. It was observed that the zeta potential value at

pH 3, 7, 9 were -27.50, -14.37, -16.78 for NCC and +36.87, +12.78, -4.04 for chitosan, respectively. Remarkably, NCC and chitosan carried opposite surface charges at the pH range from 3 to 7, indicated in this range electrostatic attraction occurred. In a previous work, NCC and chitosan film was also prepared via electrostatic self-assembly due to electrostatic interaction between negatively charged NCC and positively charged chitosan [16].

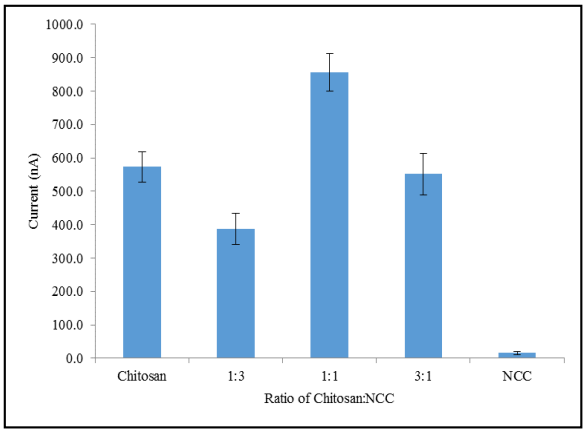


Figure 3. The effect of ratio of NCC/chitosan

The effect of a different amount of tyrosinase loading on the sensor response was also examined. As depicted in Figure 4, upon increasing the concentration, the biosensor response increased steeply to reach a maximum value when 10 mg/mL of enzyme concentration was utilized. Further increased in enzyme concentration, the sensor response decreased and thus concentration of 10 mg/mL was subsequently used for enzyme immobilization.

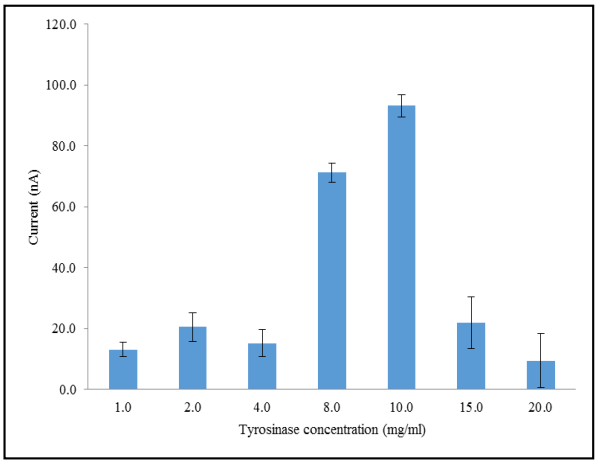


Figure 4. Effect of enzyme concentration used towards the response of the sensor

Influence of pH of the working buffer was also investigated by using 50 mM phosphate and acetate buffer. The buffering system covered over the range of pH 7.0 to 9.0. As shown in Figure 5, the sensor response increased drastically from pH 5.0 to 7.0. The optimum response was observed at pH 7.0. This indicates that the immobilization of enzyme does not alter its pH response characteristics [17]. Therefore, pH 7.0 was chosen for further studies.

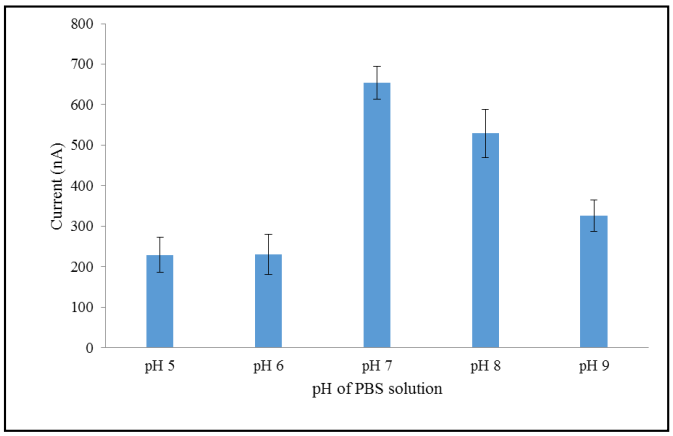


Figure 5. Influence of pH on the response of the immobilized tyrosinase in NCC/Chitosan composite film

Analytical performance

The dynamic range of the developed biosensor towards different phenol concentration was studied from the concentration range of 0.39 µM to 100 µM (Figure 6). The response was monitored by predicting the current of the composite films produced, which is proportional to the phenol concentration. As shown, a linear response of the biosensor was observed in the phenol concentration range of 0.39-7.74 µM (slope = 28.316, R^2 = 0.9808) with the detection limit of 0.379 µM. The reproducibility of the biosensor was estimated from the response of the electrode at 50 µM phenol. The relative standard deviation (R.S.D) obtained was 4.27 % (n = 10). This result shows a remarkable reproducibility of the proposed biosensor.

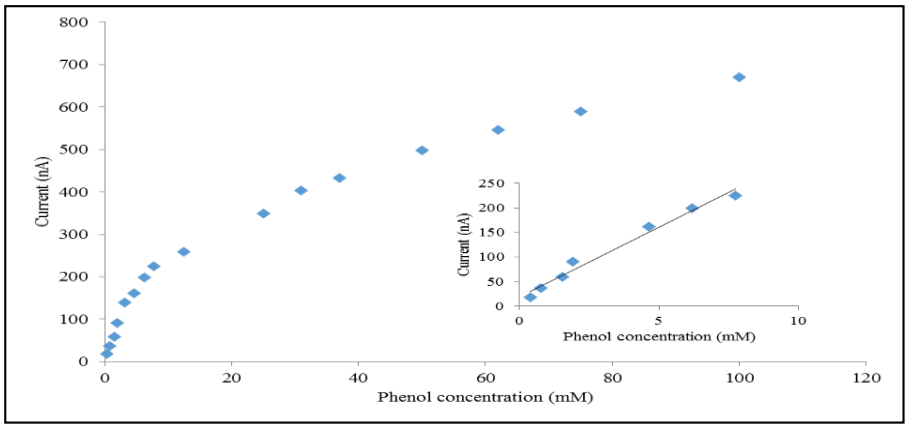


Figure 6. The dynamic calibration range of the sensor towards different concentration of phenol. Inset is the linearity range of the sensor

Conclusion

An amperometric biosensor based on the immobilized tyrosinase enzyme in a NCC/chitosan composite film has been successfully developed for the detection of phenol. The biosensor permits an attractive alternative to existing analysis methods in order to determine phenolic compounds as they offer advantages for instance minimal preparation of sample, good selectivity, better sensitivity, reproducibility, quick response time and easily for continuous analysis. The effect of immobilization of enzyme into nanocomposites material and its stabilization for

sensing application have been extensively determined. The nanocomposites showed significant improvement in performance of the biosensors which is promising for developing dependable enzyme-biosensors which has good potential use in quantitative determination of phenolic compunds in industrial applications.

Acknowledgement

The authors are grateful for the financial support provided by the Malaysian Government through its Ministry of Education under Fundamental Research Grant Scheme (FRGS/1/2012/SG01/UPM/02/1).

References

1. Lin, N. and Dufresne, A. (2014). Nanocellulose in biomedicine: Current status and future prospect. *European Polymer Journal*, 59: 302 – 325.
2. Revol, J.-F., Bradford, H., Giasson, J., Marchessault, R. H. and Gray, D. G., (1992). Helicoidal self-ordering of cellulose microfibrils in aqueous suspension. *International Journal of Biological Macromolecules*, 14: 170 – 172.
3. Zhang, X., Huang, J., Chang, P. R., Li, J., Chen, Y., Wang, D. and Chen, J. (2010). Structure and properties of polysaccharide nanocrystal-doped supramolecular hydrogels based on cyclodextrin inclusion. *Polymer*, 51 (19): 4398 – 4407.
4. Mahmoud, K. A., Male, K. B., Hrapovic, S. and Luong, J. H. (2009). Cellulose nanocrystal/gold nanoparticle composite as a matrix for enzyme immobilization. *ACS applied materials & interfaces, 1* (7), 1383 – 1386.
5. Lam, E., Male, K. B., Chong, J. H., Leung, A. C. W. and Luong, J. H. T. (2012). Applications of functionalized and nanoparticle-modified nanocrystalline cellulose. *Trends in Biotechnology*, 30(5), 283 – 290.
6. Hamad, W. (2006). On the development and applications of cellulosic nanofibrillar and nanocrystalline materials. *The Canadian Journal of Chemical Engineering*, 84 (5): 513 – 519.
7. Khan, A., Khan, R. A., Salmieri, S., Le Tien, C., Riedl, B., Bouchard, J. and Lacroix, M. (2012). Mechanical and barrier properties of nanocrystalline cellulose reinforced chitosan based nanocomposite films. *Carbohydrate Polymers*, 90 (4): 1601 – 1608.
8. Abdullah, J., Ahmad, M., Heng, L. Y., Karuppiah, N. and Sidek, H. (2006). Chitosan-based tyrosinase optical phenol biosensor employing hybrid nafion/sol–gel silicate for MBTH immobilization. *Talanta*, 70 (3), 527 – 532.
9. Dutta, P. K., Dutta, J. and Tripathi, V. (2004). Chitin and chitosan: Chemistry, properties and applications. *Journal of Scientific and Industrial Research*, 63 (1): 20 – 31.
10. Azizi Samir, M. A. S., Alloin, F. and Dufresne, A. (2005). Review of recent research into cellulosic whiskers, their properties and their application in nanocomposite field. *Biomacromolecules*, 6 (2): 612 – 626.
11. Li, Q. and Renneckar, S. (2011). Supramolecular structure characterization of molecularly thin cellulose I nanoparticles. *Biomacromolecules*, 12 (3): 650 – 659.
12. Nikonenko, N., Buslov, D., Sushko, N. and Zhbankov, R. (2005). Spectroscopic manifestation of stretching vibrations of glycosidic linkage in polysaccharides. *Journal of Molecular Structure*, 752 (1), 20 – 24.
13. Cao, X., Dong, H. and Li, C. M. (2007). New nanocomposite materials reinforced with flax cellulose nanocrystals in waterborne polyurethane. *Biomacromolecules*, 8 (3), 899 – 904.
14. Khan, R. A., Salmieri, S., Dussault, D., Uribe-Calderon, J., Kamal, M. R., Safrany, A., and Lacroix, M. (2010). Production and properties of nanocellulose-reinforced methylcellulose-based biodegradable films. *Journal of Agricultural and Food Chemistry*, 58 (13): 7878 – 7885.
15. Švitel, J. and Miertuš, S. (1998). Development of tyrosinase-based biosensor and its application for monitoring of bioremediation of phenol and phenolic compounds. *Environmental Science & Technology*, 32 (6): 828 – 832.
16. Cao, S. L., Li, X. H., Lou, W. Y. and Zong, M. H. (2014). Preparation of a novel magnetic cellulose nanocrystal and its efficient use for enzyme immobilization. *Journal of Material Chemistry B*, (2): 5522 – 5530.
17. Wang, G., Xu, J.-J., Ye, L.-H., Zhu, J.-J. and Chen, H.-Y. (2002). Highly sensitive sensors based on the immobilization of tyrosinase in chitosan. *Bioelectrochemistry*, 57 (1): 33 – 38.

Malaysian Journal of Analytical Sciences, Vol 20 No 5 (2016): 986 - 1000
DOI: http://dx.doi.org/10.17576/mjas-2016-2005-03

MALAYSIAN JOURNAL OF ANALYTICAL SCIENCES
Published by The Malaysian Analytical Sciences Society
ISSN 1394 - 2506

DETERMINATION OF OPTIMUM CONDITIONS AND STABILITY STUDY OF BIOSURFACTANT PRODUCED BY *Bacillus subtilis* UKMP-4M5

(Penentuan Keadaan Optimum dan Kajian Kestabilan Biosurfaktan yang Dihasilkan oleh *Bacillus subtilis* UKMP-4M5)

Ummul Khair Mohd Syahriansyah and Ainon Hamzah*

School of Biosciences and Biotechnology, Faculty of Science and Technology,
Universiti Kebangsaan Malaysia, 43600 UKM Bangi, Selangor Darul Ehsan, Malaysia

**Corresponding author: ainonh@gmail.com*

Received: 29 January 2016; Accepted: 17 June 2016

Abstract

Bacillus subtilis UKMP-4M5 was isolated from a hydrocarbon contaminated site which was found to be the most potential biosurfactant producer. Isolates were grown in a mineral salt medium (MSM) supplemented with sunflower oil (1% v/v) as the main carbon source. Screening was based on both qualitative (oil spreading technique) and quantitative (emulsification index and surface tension measurement) methods. *B. subtilis* UKMP-4M5 produced the highest oil displacement activity with and emulsification index of 17%. It also reduced surface tension of culture medium from 58.95 to 41.75 mN/m. *B. subtilis* UKMP-4M5 produced biosurfactant with surface tension measurement of 32.7 ± 0.66 mN/m using 2% (v/v) palm oil and 0.5% (w/v) yeast extract as carbon and nitrogen sources respectively. The tested biosurfactant exhibited excellent thermal (up to 120 °C) and pH (6.0 – 8.0) stability as well as high tolerance for varying salt concentrations (1 – 5% w/v) in terms of surface tension reducing ability. This suggests potential applications in fields such as enhanced oil recovery, bioremediation, and the food industry.

Keywords: *Bacillus subtilis,* biosurfactant, palm oil, surface tension

Abstrak

Bacillus subtilis UKMP-4M5 yang dipencilkan dari kawasan yang tercemar dengan hidrokarbon didapati paling berpotensi sebagai penghasil biosurfaktan. Pencilan dihidupkan di dalam medium garam mineral (MSM) yang ditambahkan dengan 1% (i/i) minyak bunga matahari sebagai sumber karbon utama. Penyaringan adalah berdasarkan kepada kedua-dua kaedah kualitatif (teknik penyebaran minyak) dan kuantitatif (indeks emulsifikasi dan ukuran ketegangan permukaan). *B. subtilis* UKMP-4M5 merekodkan aktiviti sesaran minyak yang tertinggi dengan indeks emulsifikasi sebanyak 17%. Ia juga merendahkan ketegangan permukaan kultur medium dari 58.95 mN/m ke 41.75 mN/m *B. subtilis* UKMP-4M5 menghasilkan biosurfaktan dengan ukuran ketegangan permukaan 32.7 ± 0.66 mN/m menggunakan 2% (i/i) minyak kelapa sawit dan 0.5% (b/i) ekstrak yis masing-masing sebagai sumber karbon dan nitrogen. Biosurfaktan yang diuji menunjukkan kestabilan yang amat baik pada suhu (sehingga 120 °C) dan pH (6.0 – 8.0) serta toleransi yang tinggi pada kepekatan garam yang berbeza (1 – 5% b/i) dari segi keupayaannya merendahkan ketegangan permukaan. Ini mencadangkan potensi aplikasinya dalam industri seperti peningkatan perolehan minyak, bioremediasi dan industri makanan.

Kata kunci: *Bacillus subtilis,* biosurfaktan, minyak kelapa sawit, ketegangan permukaan

Introduction

Biosurfactants are amphiphilic molecules containing hydrophobic and hydrophilic moieties. They are produced by a variety of microorganisms such as yeasts, fungi, and bacteria. A majority of these molecules are produced by

bacteria which are able to interact between two immiscible interfaces, such as water-oil or water-air phases. *Bacillus subtilis,* for example, produces lipopeptide surfactin, a powerful biosurfactant that can reduce surface tension of water from 72 mN/m to 27 mN/m at a concentration of 0.05% [1]. Other lipopeptide biosurfactants synthesised by *Bacillus sp*. include iturin [2] and fengycin [3].

Many organisms produced biosurfactants which metabolise water-immiscible substrates such as hydrocarbons and vegetable oil, thus increasing bioavailability and allowing for their adsorption, emulsification, and dispersion. Furthermore, the ability to reduce surface tension is a major characteristic of a surfactant which has potential applications in many consumer and industrial products such as shampoos, detergents, and toothpaste. Other potential applications include enhanced oil recovery, bioremediation, pharmaceuticals, cosmetics, and food-related industries. In comparison with the current widely used chemical surfactants, biosurfactants offer several advantages such as lower toxicity, higher biodegradability, and effectiveness at extreme temperatures and pH values [1].

Although promising, biosurfactants in general cannot compete with their chemically synthesised counterparts in the surfactant market mainly due to their high production costs. Thus the attention is now geared to the need for cost-effective processes and the use of inexpensive substrates, as these can reduce overall production costs up to 30% [1]. Optimisation of culture conditions for maximum biosurfactant production would also be among the strategies employed by researchers for the purpose of cost reduction. Studies on the biosurfactant production by *Bacillus* sp. have been performed using water-soluble substrates such as glucose [4] and glycerol [5] as well as water immiscible substrates such as diesel oil [6]. Other substrates such as molasses were also used for the production of biosurfactants by *Bacillus subtilis* [7]. Others have reported the optimization of culture conditions such as pH and temperature on bacterial cell growth which in turn affecting biosurfactant production [8].

Identification of a newly-found bacterium strain capable of producing a biosurfactant combined with use of cheap substrates for growth medium could give a promising future to biosurfactant to become economically competitive in the surfactant industry. Therefore, the objectives of this study were to screen and identify potential biosurfactant-producing bacteria, determine the best culture conditions for increased production of biosurfactants, and carry out a stability study of the biosurfactant produced.

Materials and Methods

Bacterial culture

Twenty five bacterial isolates were obtained from culture collection in Microbiology laboratory, School of Biosciences and Biotechnology, Faculty of Science and Technology, Universiti Kebangsaan Malaysia.

Preparation of standard inoculum

The amount of bacteria was standardized as described by Hamzah et al. [9] in order to obtain the same number of bacteria for all the tests.

Screening methodology for biosurfactant production

Approximately 10% (v/v) of standard inoculum from each isolate were grown in a 250 mL Erlenmeyer flask containing 50 mL of mineral salt medium (MSM) [10] supplemented with 1% (v/v) sunflower oil as a carbon source. The pH value of the medium was adjusted to 7.0 and the cultures were incubated in shaking condition at 150 rpm, 37 °C for 5 days. Biosurfactant production was tested from the cell-free culture supernatant obtained via centrifugation at 15000 rpm for 20 mins at 4 °C (RC5C Sorvall Centrifuge Instrument, USA).

Screening of biosurfactant producer

Potential biosurfactant producing bacteria were screened via both qualitative (oil spreading technique) and quantitative (emulsification index and surface tension measurement) methods. In the oil spreading technique, the test method was carried out according to Yousseff et al. [11]. Tapis crude oil (15 μL) was added to a Petri dish containing 50 mL of distilled water. Then, 10 μL of cell-free culture supernatant was dropped onto the surface of oil. Formation of a clear zone indicates the presence of biosurfactant. The diameter of oil displaced was measured in cm.

The emulsification index was determined according to Cooper and Goldenberg [12]. Cell-free culture supernatant and Tapis crude oil (1:1, v/v) were mixed in a test tube and vortexed at high speed for 2 min. After 24 h of incubation at room temperature, the emulsification index (% E_{24}) was determined. Isolates that give high emulsification index indicates high emulsification activity of the biosurfactant produced.

The surface tension of cell-free culture supernatant was measured using a tensiometer (Surface Tensiomat, Fisher Scientific, USA) following the Du Nouy ring method [13]. An isolate that is able to reduce surface tension < 40 mN/m is regarded as the potential biosurfactant producer [14]. Sodium dodecyl sulphate (SDS) and MSM only were used as positive and negative controls, respectively. The selected potential biosurfactant producers will be used for identification.

Identification of biosurfactant-producing bacteria
Potential biosurfactant-producing bacteria were identified based on morphological (including Gram reaction) and biochemical characteristics. Isolates were further identified by 16S rDNA analysis. Bacterial DNA was extracted via a nucleic acid extraction kit (Macherey-Nagel, Germany) according to manufacturer's instruction and amplified by polymerase chain reaction (PCR) using universal primers (p16Sf: 5'–AGAGTTTGATCCTGGCTCAG-3'; p16Sr: 5'-GGTTACCTTGTTACGACTT-3'). The PCR products were purified with a PCR purification kit (Macherey-Nagel, Germany) and sent for sequencing analysis to First Base Laboratories Sdn. Bhd. The resulting sequences were compared with sequences in the GenBank database of NCBI using the BLAST network service.

Determination of the best carbon and nitrogen sources for biosurfactant production
The best carbon and nitrogen sources for increased biosurfactant production by the test bacteria was determined by the lowest surface tension value of the cell-free culture supernatant. Different types of carbon and nitrogen sources were evaluated for production of biosurfactants, followed by determining the optimum concentration of each source. For the following experiments, 10% (v/v) of standard inoculum was inoculated in a 250 mL Erlenmeyer flask containing 50 mL MSM. pH of the medium was adjusted to (7.0). The broth cultures were incubated with shaking condition at 150 rpm, 37 °C for 5 days. Production of biosurfactant was monitored by determining the surface tension value of the cell-free culture supernatant, via du Nouy ring method using a tensiometer. Measurements were performed in triplicate.

Five different carbon sources, namely crude oil, glycerol, molasses, palm oil, and palm oil mill effluent (POME) were used at 1% (v/v) added to MSM for for increased production of biosurfactant. The best carbon source will be selected based on the lowest surface tension value and used for determining optimum concentration, which may range from 0.5 to 3% (v/v).

Four nitrogen sources (ammonium chloride (NH_4Cl), ammonium nitrate (NH_4NO_3), peptone and yeast extract) were evaluated for increased production of biosurfactant, maintaining equal amount of total nitrogen in each media at 24.21%. For the evaluation of the most optimum nitrogen concentration, the selected nitrogen source was varied from 0.1 to 0.8% (w/v). The selected carbon and nitrogen sources at their optimum concentration will be used in the subsequent experiments.

Stability studies
Stability studies were carried out using extracted biosurfactant which was carried out via acid precipitation followed by solvent extraction method [7].

To study the effects of pH on biosurfactant activity, equal volumes of extracted biosurfactant (1% w/v in distilled water) and buffer solution were mixed and adjusted to pH 2 – 5 using citrate-phosphate buffer, pH 6 – 8 using phosphate buffer, and pH 9 – 12 using carbonate-bicarbonate buffer solutions and incubated for 30 min. at room temperature before measuring surface tension using a tensiometer.

For the thermal stability study, extracted biosurfactant was used to prepare biosurfactant solutions (1% w/v) in 0.1 M phosphate buffer solution (pH 7). Test tubes containing biosurfactant solutions were incubated at different

temperatures (10, 20, 30, 40, 50, 60, 70, 80, 90, 100 °C) for 1 hour, then autoclaved at 121 °C for 15 min. Test solutions were allowed to cool to room temperature before measuring surface tension.

A stability study at different salinity levels was performed by adding extracted biosurfactant (1% w/v) into sodium chloride (NaCl) solution at different concentrations (2 – 10% w/v). Surface tension was determined after incubation for 1 hour at room temperature.

Statistical analysis

The results are represented as the mean ± standard deviation from at least three replicates. One-way analysis of variance was performed on surface tension data to determine the significant differences in the values obtained. All statistical analyses were performed using SPSS (version 14.0).

Results and Discussion

Screening of biosurfactant production

Three analytical methods were selected for screening of biosurfactant production due to their advantages in terms of simplicity, low cost, and quick implementation. Of 25 isolates screened, five isolates (3M17, 6M1, 10M2, 1M13 & 4M5) showed occurrence of clearing zone by the oil spreading technique indicating potential biosurfactant production (Table 1). Isolate 4M5 scored the most positives results by producing the largest diameter of clearing zone of > 1.5 cm, emulsification index of 17% and the lowest surface tension value at 41.75 ± 0.54 mN/m.

The oil spreading technique is one of the common method used for detecting biosurfactant production [11]. This technique is more sensitive for biosurfactant detection in the cell-free culture supernatant than other screening methods such as drop collapse [15] and blood haemolysis [16]. The oil spreading technique depends on the decrease in water-oil interfacial tension due to the presence of biosurfactant regardless of its structures [17]. Of five isolates positive for oil spreading technique, it was found that isolate 4M5 produced the largest diameter of clearing zone of more than 1.5 cm, suggesting high biosurfactant concentration in the culture medium. Thavasi et al. [18] showed potential biosurfactant producers produced diameter of clearing zone of ≥0.5 cm. Karthik et al. [19], employing oil spreading technique as one of their screening methods, reported a potential biosurfactant-producing microorganism produced diameter of clearing zone in the range of 0.9 – 2.0 cm, whereas poor biosurfactant producers produced 0.1 – 0.2 cm.

Emulsification index (E_{24}) was employed to investigate the emulsifying properties of biosurfactant. Crude oil was used as the hydrophobic substrate, for isolates capable of releasing surfactant and emulsifying crude oil may have potential application in bioremediation processes of contaminated areas with crude oil. Table 1 showed no emulsification ($E_{24} = 0$) when distilled water (negative control) was mixed with crude oil, indicating no surfactant or surfactant-like molecules that may influence the results present in the system. The assumption is that if the cell-free culture supernatant contains biosurfactant, it will then emulsify hydrophobic substrates and maintain stable emulsions for at least 24 hours [20], consequently this method gives just an indication of the presence of biosurfactant. Of 25 isolates screened, only isolates 4M5 and Sf-S5-3 were able to form and maintain stable emulsions with E_{24} of 17% and 8% respectively, while all other isolates that showed negative in oil spreading technique had $E_{24} = 0$ (Table 1).

Emulsification index (17%) by isolate 4M5 was found to be lower by 30% compared to *Pseudomonas aeruginosa* [16] and 36% compared to *Serratia sp* [21] used for selection of biosurfactant producers. Karthik et al. [19] reported that an emulsification index ranging from 5.0 – 75% was indicative of biosurfactant producers by marine actinobacteria such as *Streptomyces, Nocardiopsis* and *Rhodococcus sp*. Isolate Sf-S5-3 on the other hand, may produce an extracellular compound, also known as a bioemulsifier that has emulsifying activity, but it could not effectively reduce the surface tension of culture media, as the diameter of the clearing zone was negative and surface tension value of isolate Sf-S5-3 was 55.5 mN/m.

Table 1. Comparison of three methods for biosurfactant producer

Bacterial isolates	Oil spreading technique	Surface tension (mN/m)	Emulsification index (% E_{24})
SDS (1% w/v)	+++	32.078 ± 0.95	81.67
Distilled water	-	72.0 ± 0.21	0
MSM only	-	58.95 ± 0.3	0
10M2	+	50.18 ± 0.62	0
3M16	-	52.84 ± 0.55	0
3M17	+	51.08 ± 0.53	0
6M1	+	50.98 ± 0.42	0
4M5	+++	41.75 ± 0.54	17.04
5M7	-	57.8 ± 0.3	0
7M4	-	55.23 ± 0.87	0
1M13	+	49.78 ± 1.70	0
7M22	-	53.70 ± 1.01	0
SF-S11-47	-	55.17 ± 1.11	0
SF-S11-26	-	49.49 ± 0.86	0
SF-S5-9	-	56.60 ± 1.35	0
SF-S5-30	-	54.05 ± 0.43	0
SF-S5-3	-	55.50 ± 0.84	8.33
SF-S10-12	-	48.99 ± 0.42	0
SF-S8-13	-	57.33 ± 1.35	0
SF-S2-5	-	57.95 ± 0.05	0
LF-S11-9	-	53.18 ± 1.24	0
60	-	55.63 ± 0.51	0
19	-	55.27 ± 1.12	0
8	-	53.00 ± 0.61	0
7	-	53.60 ± 0.72	0
6	-	50.00 ± 0.2	0
5	-	54.37 ± 0.72	0
4	-	56.00 ± 1.98	0

Oil spreading technique '-' clear zone diameter <0.5cm '+' clear zone diameter 0.5-0.9cm; '++' clear zone diameter 1.0-1.5 cm; '+++' clear zone diameter >1.5cm

Quantitative analysis using surface tension measurement additionally supported the biosurfactant production potential of isolate 4M5. It was able to reduce the surface tension of culture medium from 58.95 to 41.75 mN/m. This value is much closer to the surface tension value of 40 mN/m, which was recommended for selection of biosurfactant producer [14]. All other isolates showed surface tension measurements of > 45 mN/m.

A lot of studies related to screening of potential biosurfactant producers rely on surface tension measurement due to its reliability and accuracy in quantifying soluble biosurfactant in the culture medium [15]. Thavasi et al. [18] obtained surface tension values ranging between 30.8 - 38.75 mN/m for potential biosurfactant producers among *Bacillus* species. Surface tension value above 45 mN/m is regarded as negative for biosurfactant production [22].

Since the cell-free culture supernatant of isolate 4M5 was the only isolate that satisfied all three screening methods, it was then selected for identification, determination of the best carbon and nitrogen sources for biosurfactant production and stability studies. Production of extracellular biosurfactant is advantageous from an industrial point of view because product recovery process can be simplified, therefore becoming more economical [23].

Several studies have shown that the use of vegetable oils as the only source of carbon and energy stimulate biosurfactant production by microorganisms. *Pseudomonas* spp. were reported to produce higher amount of biosurfactant when using sunflower oil compared to other vegetable oil such as olive and corn oil [24], with some strains recorded surface tension value of < 40 mN/m [25]. Ferraz et al. [26] found that *Serratia marcescens* produced biosurfactant with surface tension value of 29.75 mN/m, while biosurfactant from *Enterococcus* strains recorded 68% reduction in surface tension of culture media [27] when using sunflower oil as the carbon substrate. Vegetable oil contains fatty acids that undergo modification for incorporation into surface active products [28]. Main fatty acid content in sunflower oil is linoleic acid (60%) [26], thus suggesting that this fatty acid was responsible for stimulating biosurfactant production by isolate 4M5.

Identification of biosurfactant-producing bacteria

Gram staining of isolate 4M5 showed that it is a Gram positive, rod-shaped bacterium. The colonies on nutrient agar were cream-coloured, flat, and circular with diameter between 5 – 6 mm. Biochemical tests revealed that isolate 4M5 is motile, hydrolysed starch and able to break down hydrogen peroxide suggesting the presence of the enzyme catalase. Isolate 4M5 fermented glucose but not sucrose or lactose and able to utilise citrate as its sole carbon source for growth. Biochemical test results for isolate 4M5 were negative for oxidase enzyme, indole, and H_2S production (Table 2). All of these features strongly indicate that isolate 4M5 is *Bacillus subtilis*. This was further confirmed by analysis of 16S rRNA gene sequences (1212 bp) by BLAST database. The BLAST analysis showed 99% similar identity with *B. subtilis*. Isolate 4M5 is now designated *Bacillus subtilis* UKMP-4M5.

Table 2. Characteristics of isolate 4M5

Test	Results	Test	Results
Gram reaction	+	Shape	rod
Motility	+	Catalase	+
Growth at		Starch hydrolysis	+
20 ºC	−	Methyl red	+
30 ºC	+	Vogues-Proskauer	+
50 ºC	+	H_2S production	−
60 ºC	−	Indole	−
Triple Sugar Iron	K/A	Simmon's citrate	+

+ = positive, − = negative, K/A = alkaline slant/acidic butt

The majority of Gram-positive bacteria capable of producing biosurfactant are from the *Bacillus* sp. often which was isolated from oil reservoir [29] or soil sample contaminated with petroleum [30]. The genus is reported to produce different types of lipopeptide biosurfactants, such as surfactin, lichenysin, gramicidins and polymyxins. *Bacillus subtilis*, for example, has been reported to produce three types of lipopeptides, namely surfactin, iturin and fengycin [1, 2].

Determination of the best carbon and nitrogen source for biosurfactant production

Production of biosurfactant by *B. subtilis* UKMP-4M5 has been found to be induced by carbon sources. All five types of carbon sources tested showed a reduction in surface tension of a culture medium (Figure 1). Surface tension values obtained were ranged from 39.7 – 51.7 mN/m indicating production of extracellular surface active

compounds by *B. subtilis* UKMP-4M5 using different carbon sources. There is no significant difference in surface tension value between palm oil and POME. Palm oil was chosen as the best carbon source for biosurfactant production based on the lowest surface tension value at 39.7 ± 1.23 mN/m, compared to POME which recorded a higher surface tension value at 43.0 ± 0.84 mN/m.

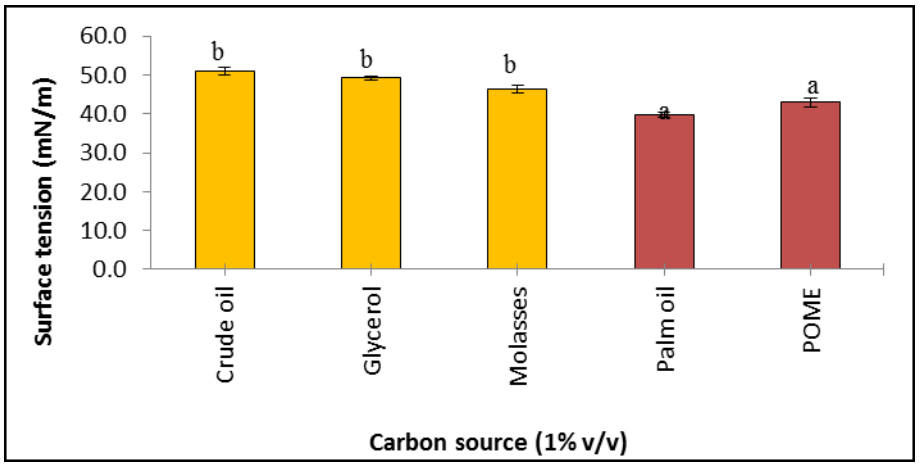


Figure 1. Effect of different carbon sources on the production of biosurfactant by *B. subtilis* UKMP-4M5. All values are mean of three replicates ± SD. The letters a and b indicate significant differences ($p < 0.05$) among different carbon sources.

Production of biosurfactant by *B. subtilis* had been reported utilizing mainly water-soluble substrates such as glucose [4], sucrose [31] and glycerol [5]. This is probably due to single-phase fermentation pathway using water-soluble substrate is simpler and thus preferred by microbes than biphasic fermentation [32]. The present study however, showed the ability of *B. subtilis* UKMP-4M5 to produce biosurfactant using various types of carbon sources. Although no experiments on cell growth towards different carbon substrates were conducted, *B. subtilis* strains were reported to be able to grow and subsequently produce biosurfactants on various carbon substrates tested such as POME [33], glycerol [5], palm oil [34], molasses [7] and crude oil [35]. In the present study, when palm oil was used as a carbon substrate, *B. subtilis* UKMP-4M5 produced biosurfactant with the lowest surface tension value (39.7 mN/m) compared to the other carbon substrates used. This suggests that *B. subtilis* UKMP-4M5 is a lipase positive. This enzyme might be responsible for hydrolysing vegetable oils to produce long chain fatty acids, the important precursors for biosurfactant synthesis [36]. Furthermore, at the same concentrations, vegetable oil can generate more energy than glucose. Other studies have also shown that the use of palm oil as carbon source induced biosurfactant production by *B. subtilis* PT2 [34] and *P. aeruginosa* FR [37]. A study by Li et al. [36] demonstrated that palm oil was the best carbon source for *P. aeruginosa* GIM32 produced the highest yield of rhamnolipid (30.4 g/L). The use of palm oil as carbon source is advantageous from industrial point of view since it is inexpensive substrates and abundantly available so it can drastically decrease the biosurfactant production cost. Alternative carbon sources from industrial byproducts such as POME can also be effectively used for biosurfactant production by *B. subtilis* UKMP-4M5 since it produces low surface tension values with no significant difference with palm oil. Nevertheless, palm oil produced the lowest surface tension value (39.7 mN/m) compared to POME (43.0 mN/m). Crude oil was found to be the least preferred carbon source for biosurfactant production. Crude oil in general contains various components such as saturated hydrocarbons, aromatic compounds, and heavy metals [38] that probably not suitable for enzyme synthesis necessary for biosurfactant production. Haddad et al. [32] reported that crude oil did not support the growth of *B. subtilis* HOB2, thus resulting in a high surface tension value for the culture medium, while Jazeh et al. [35] reported the use of crude oil as carbon substrate supported the growth of *B. subtilis* and subsequently production of biosurfactant.

Palm oil was then used to study the biosurfactant production by *B. subtilis* UKMP-4M5 at various concentrations (0.5 – 3% v/v). Figure 2 displayed that the highest biosurfactant activity was at 2% (v/v) palm oil concentration, with the lowest surface tension value of 35.89 ± 0.71 mN/m. Further increases in the concentration of palm oil resulted in a significant increase in surface tension measurements.

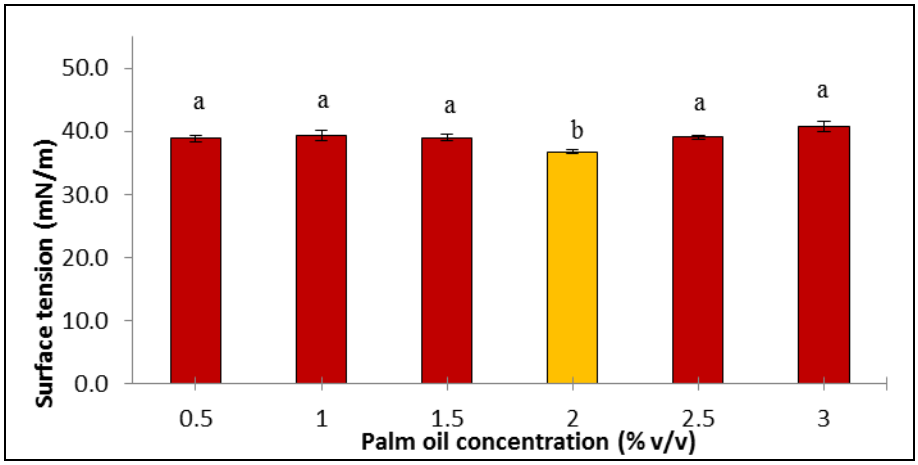


Figure 2. Effect of different concentrations of palm oil on the production of biosurfactant by *B. subtilis* UKMP-4M5. All values are mean of three replicates ± SD. The letters a and b indicate significant differences ($p < 0.05$) among different concentration of palm oil.

Pornsunthorntawee et al. [34] also reported in their study that optimum concentration of palm oil for biosurfactant production by *B. subtilis* PT2 was 2% (v/v) with maximum surface tension reduction of about 43%. This value is comparable to the percentage obtained in the present study, which was a 40% surface tension reduction from negative control (surface tension value of 58.89 mN/m). *P. aeruginosa* was also found to produce biosurfactant when using 2% (v/v) palm oil as carbon source with surface tension value of 30 mN/m [39]. Other researchers demonstrated the use of 5% (v/v) palm oil as an optimum concentration for maximum production of biosurfactant (30.4 g/L) by *P. aeruginosa* [37].

Medium constituents such as nitrogen source also affect the production of biosurfactants by *B. subtilis* UKMP-4M5. In this study, there was no significant difference between yeast extract and ammonium chloride in terms of surface tension reduction (Figure 3). Nevertheless, yeast extract was chosen to be the best nitrogen source as it produced the lowest surface tension value (35.02 ± 0.25 mN/m) compared to ammonium chloride (36.77 ± 0.71 mN/m).

A study by Pereira et al. [31] also showed yeast extract was found to be the best nitrogen source for optimum biosurfactant production by *B. subtilis* #309 with surface tension value of 28.73 ± 0.3 mN/m. A study by Fontes et al. [40] found that the use of yeast extract in combination with ammonium sulphate were the best nitrogen sources for optimum production of biosurfactant by *Yarrowia lipolytica* (surface tension value of 21.1 mN/m and E_{24}=60.4%). For inorganic nitrogen, ammonium chloride was shown to be a better source of nitrogen as opposed to ammonium nitrate for biosurfactant production by *B. subtilis* UKMP-4M5, though a study by Fonseca et al. [41] showed that ammonium nitrate was the best inorganic nitrogen source for biosurfactant production by *B. subtilis* YRE207. Besides growth, nitrogen plays an important role in biosurfactant production, especially in the lipopeptide biosurfactant as a peptide structure [42].

Effect of different yeast extract concentration (0.1 – 0.8% w/v) for biosurfactant production by *B. subtilis* UKMP-4M5 was investigated. An increase in the concentration of yeast extract increases the production of biosurfactant as

evidenced from reduction in surface tension of culture medium (Figure 4). Although there was no significant difference in the surface tension values for yeast extract concentration between 0.3 – 0.6% (w/v); the lowest surface tension value at 33.6 ± 0.33 mN/m was recorded when 0.5% (w/v) yeast extract was used. Therefore 0.5% (w/v) of yeast extract was chosen to be the best concentration for biosurfactant production rather than 0.3% (w/v) of yeast extract (higher surface tension value recorded at 35.9 ± 1.1 mN/m). An increase in the concentration of yeast extract beyond 0.6% (w/v) resulted in the increase of surface tension values significantly, indicating less biosurfactant production by the test bacterium.

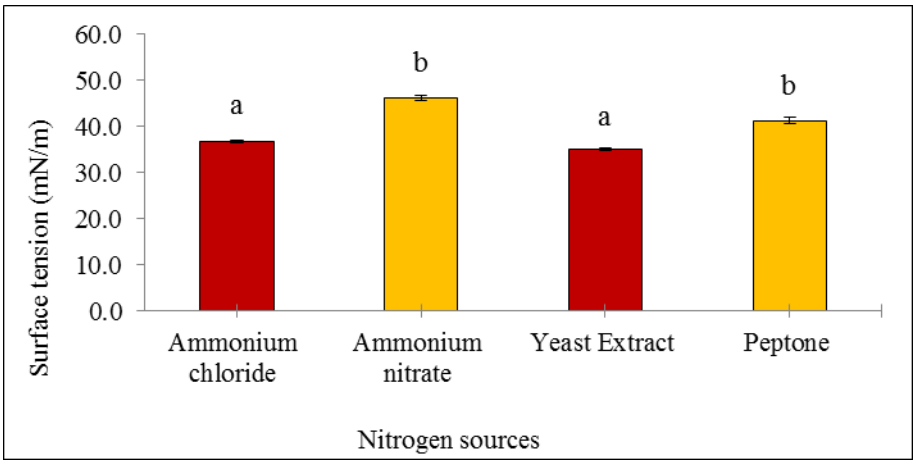


Figure 3. Effect of different nitrogen sources on the production of biosurfactant by *B. subtilis* UKMP-4M5. All values are mean of three replicates ± SD. The letters a and b indicate significant differences ($p < 0.05$) among different nitrogen sources.

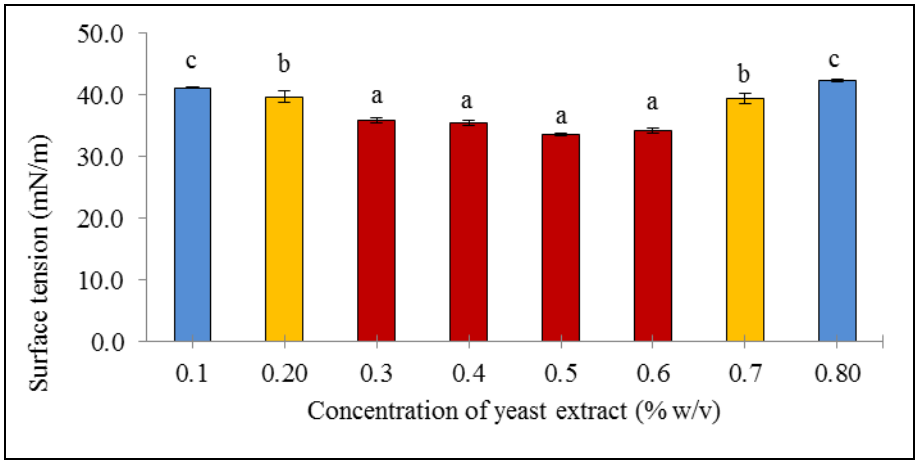


Figure 4. Effect of different concentrations of yeast extract on the production of biosurfactant by *B. subtilis* UKMP-4M5. All values are mean of three replicates ± SD. The letters a, b, and c indicate significant differences ($p < 0.05$) among concentrations of yeast extract.

Bacillus subtilis UKMP-4M5 was found to produce biosurfactant with the lowest surface tension value of 35.02 ± 0.25 mN/m when using 0.5% (w/v) yeast extract. Similar results were shown by Vedaraman & Venkatesh [43] whereby the use of 0.5% (w/v) yeast extract was optimum for surfactin production (983 mg/L) by *B. subtilis* MTC2423. Rashedi et al. [44] reported in their study that the use 0.5% (w/v) yeast extract in combination with 0.5% (w/v) soy flour were the best nitrogen sources for optimal production of rhamnolipid (3.7 g/L) by *P. aeruginosa*. A study by Nalini et al. [6] reported the use of 0.3% (w/v) yeast extract was optimal for biosurfactant production by *Bacillus sp* grown in a glucose-containing medium, while Pereira et al. [31] used 0.2% (w/v) yeast extract for biosurfactant production by *B. subtilis* #309 when grown in sucrose-containing medium. Fontes et al. [32] on the other hand, used a combination of 0.05% (w/v) yeast extract and 10 g/L ammonium sulphate to obtain optimum production of biosurfactant by *Y. lipolytica*, with surface tension value of 20.9 mN/m and emulsification index of 73.1%. The present study showed 0.3% (w/v) yeast extract was enough to produce biosurfactant with significant reduction in the surface tension value; however, 0.5% (w/v) produced the lowest surface tension value. The increase in surface tension value with further increase in yeast extract concentration (beyond 0.6% w/v) may be due to nitrogen-limiting conditions no longer being a factor in biosurfactant biosynthesis. Some studies reported that biosurfactant production is more efficient under nitrogen-limiting conditions [36].

The best conditions for biosurfactant production by *B. subtilis* UKMP-4M5 were using 2% (v/v) palm oil and 0.5% (w/v) yeast extract as carbon and nitrogen sources respectively as it produced the lowest surface tension value at 33.6 ± 0.33 mN/m.

Stability studies

Biosurfactant activity was tested over a range of pH values (2 – 12). Results showed the activity of biosurfactant was greatly affected by changes in pH. Low biosurfactant activity was detected at extreme pH; 2 to 4 and above 10 (Figure 5). Surface tension values remained relatively stable between pH 6 to 8 with no significant difference; however the lowest surface tension value was achieved at pH 6. The result also showed that highly acidic pH caused a greater reduction in surface activity than highly alkaline pH (surface tension value of 38.77 mN/m at pH 2 as opposed to 36.9 mN/m at pH 12).

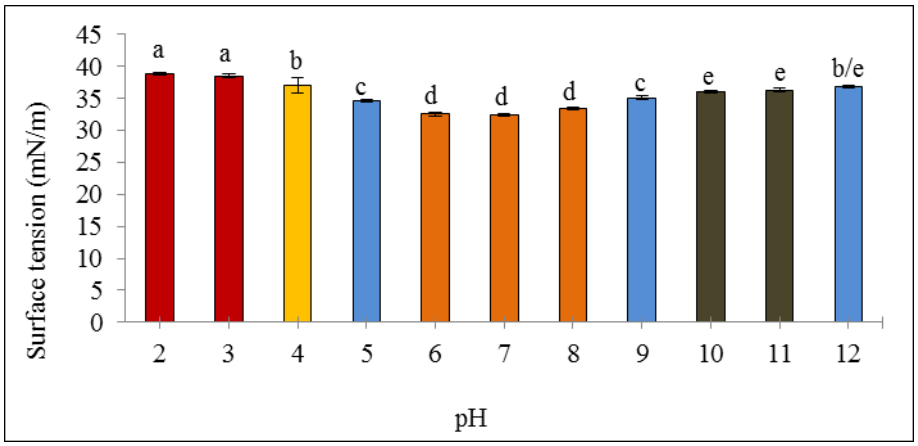


Figure 5. Effect of pH on biosurfactant activity produced by *B. subtilis* UKMP-4M5. All values are mean of three replicates ± SD. The letters a, b, c, d, and e indicate significant differences ($p < 0.05$) among different pH.

pH values between 2 to 4 showed a significant decrease in biosurfactant activity as shown by the increase in surface tension values. These results are in accordance with those reported by Vaz et al. [45], whereby biosurfactant stability from *B. subtilis* EG1 was found to be unstable by acidic pH. Abdel-Mawgoud et al. [7] also reported similar findings in their study in which surfactin activity started to decrease at pH < 5, samples become turbid due partial precipitation of biosurfactant in acidic conditions. The test biosurfactant showed better stability at alkaline

than acidic conditions, as shown by lower surface tension values when incubated in alkaline conditions as compared to acidic conditions. Similar results reported by El-Sersy [8] indicated that biosurfactant from *B. subtilis* N10 was found to have high surface activity predominantly in the alkaline condition, pH between 6.0-12. Abdel-Mawgoud et al. [7] reported that surfactin from *B. subtilis* was soluble in aqueous solutions at pH values higher than 5.0 with optimum solubility at pH 8.0-8.5. This could be due to the acidic nature of surfactin, as the presence of two carboxylic groups from glutamic and aspartic acid residues confers an anionic nature [7]. Similar results had been reported for biosurfactant production from other microorganisms such as *P. aeruginosa* [14], which was stable at a wide range of pH between 6.0-10.0, whereas stability of biosurfactant from *Nocardiopsis* sp. was found to be stable between pH 8 – 12 [46].

Thermal stability of biosurfactant was investigated over a wide temperature range (10 – 100 °C) for 1 hour and cooled to room temperature. Results showed that the biosurfactant from *B. subtilis* UKMP-4M5 exhibited excellent surface activity with no significant difference ($p > 0.05$) of the temperature tested (Figure 6). Surface activity remained relatively stable with surface tension values between 32.47 – 33.10 mN/m even after exposure to high temperature (100 °C). Interestingly, the test biosurfactant retained its surface activity even after autoclaving, with a negligible increase in surface tension value (0.67 mN/m) before and after autoclaving (Figure 7), suggesting that no degradation occurred.

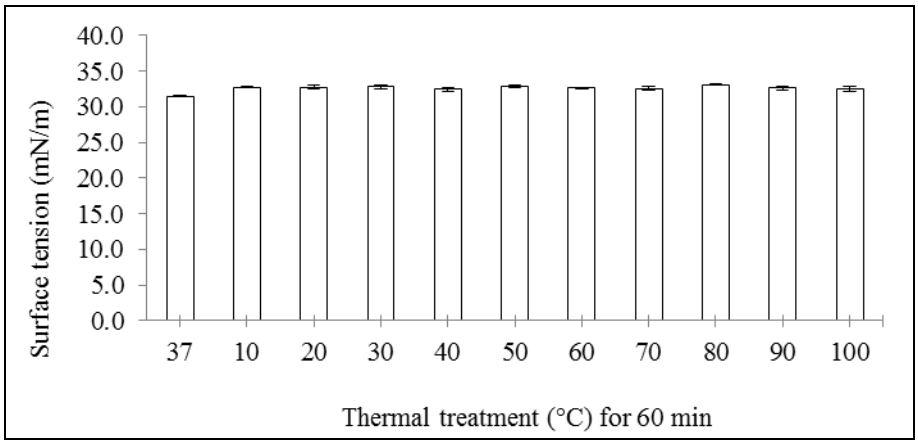


Figure 6. Effect of temperature on biosurfactant activity produced by *B. subtilis* UKMP-4M5. All values are mean of three replicates ± SD.

Thermal stability studies of biosurfactant from *B. subtilis* UKMP-4M5 indicated that the surfactant was thermostable, as heating up to 100 °C caused no significant effect on the biosurfactant performances. The high thermal stability of the test biosurfactant is on par with other synthetic surfactants such as linear alkylbenzene sulfonate (LAS) and alkylpolyglucoside [45], but superior to sodium dodecyl sulphate, which exhibits a significant loss of activity at temperatures above 70 °C [46]. Interestingly, the test biosurfactant retained its surface activity even after autoclaving at 121 °C for 20 min, suggesting its potential application in food, pharmaceutical and cosmetic industries where heating to achieve sterility are important. Biosurfactants from *B. subtilis* have been reported to exhibit excellent thermal stability. Surfactin for example showed no change in surface tension value before and after heating treatment at 100 °C, though slight increase was observed at 121 °C for 10 min. This may be due to precipitation of heat-dependent substances such as proteins contaminating the surfactin solution which might have been co-extracted during the extraction steps [7]. Haddad et al. [32] investigated the stability of biosurfactant from a *B. subtilis* strain at 100 °C at different exposure time. The authors reported that no interference on the surface activity could be found, thus corroborating the results obtained in the current study. Results from the current study have thus illustrated the stability of biosurfactant produced by *B. subtilis* UKMP-4M5 at high temperatures which may be encountered in oil fields.

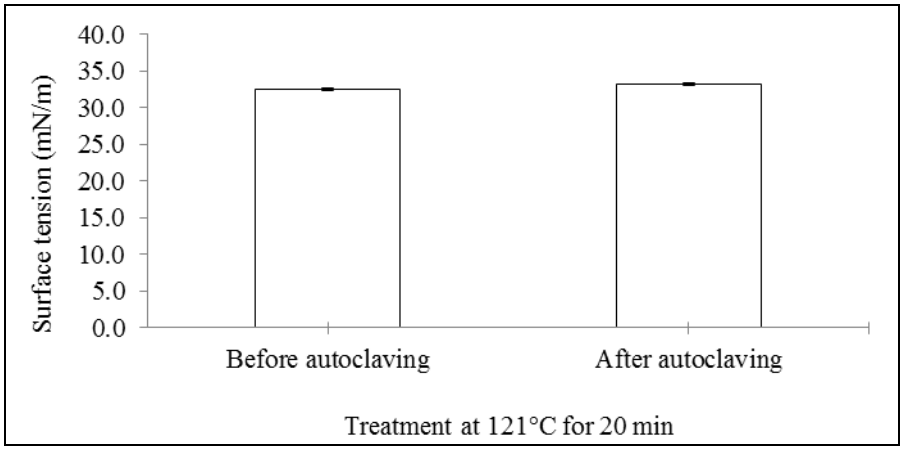


Figure 7. Effect of autoclaving on biosurfactant activity produced by *B. subtilis* UKMP-4M5. All values are mean of three replicates ± SD.

The effect of different NaCl concentrations (1 – 15% w/v) on biosurfactant activity from *B. subtilis* UKMP-4M5 was studied to evaluate its potential application in bioremediation of contaminated marines. Figure 8 shows that the changed in surface tension value of the tested biosurfactant was not significant between 1 – 5% (w/v) NaCl concentrations. Optimum stability of biosurfactant was observed at 3% (w/v) NaCl with the lowest surface tension value at 33.18 mN/m.

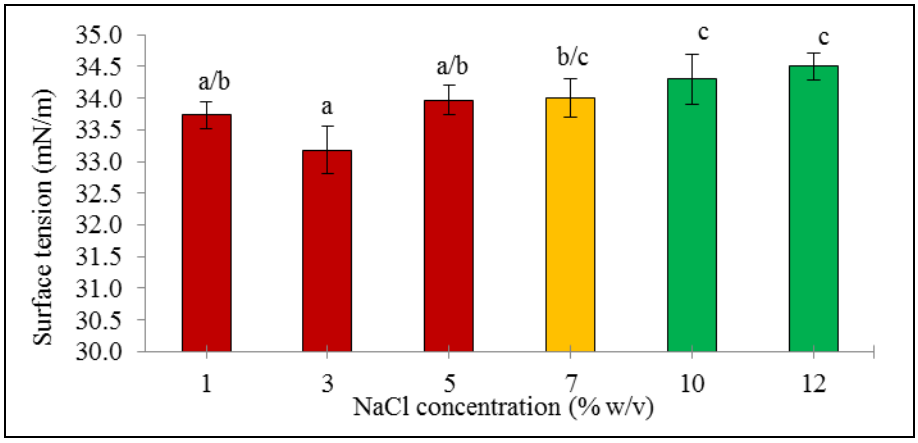


Figure 8. Effect of NaCl concentration on biosurfactant activity produced by *B. subtilis* UKMP-4M5. All values are mean of three replicates ± SD. The letters a, b, and c indicate significant differences ($p < 0.05$) among NaCl concentrations

The addition of NaCl in the range tested had a weak effect on the surface tension of biosurfactant produced by *B. subtilis* UKMP-4M5. Stability of biosurfactant from *B. subtilis* had been reported to be excellent in the presence of NaCl up to 20% (w/v) [8]. Ghojavand et al. [29], who reported that NaCl concentration, did not affect the surface activity of biosurfactant from *B. subtilis* PTCC 1696, the highest surface tension value recorded at 34 mN/m at 20% (w/v) NaCl. Similarly, Haddad et al. [32] reported that 25% (w/v) NaCl concentration showed only slight variation in the surface tension value (4 mN/m) of biosurfactant from *B. subtilis* HOB2. The stability of the biosurfactant

obtained from the present study is shown to be superior to other strain of *B. subtilis* which was reported to be losing its surface activity (surface tension value at 45 mN/m) when level of NaCl reached 11% (w/v) [5]. These findings have revealed that the tested biosurfactant had a high level of tolerance to ionic strength, and is thus an excellent candidate if compared with chemical surfactants for use in bioremediation of contaminated marine environments. Chemical surfactants, however, are deactivated by 2 – 3% salt concentrations [47].

Conclusion

In the present study, a bacterial isolate identified as *B. subtilis* UKMP-4M5 was found to be the most potential biosurfactant producer. This isolate can produce biosurfactant using 2% (v/v) palm oil with addition of yeast extract with low surface tension value. The semi purified biosurfactant is thermostable to extreme temperatures. Furthermore, the test biosurfactant has proved to be robust and stable over huge ranges of pH and salinity. Thus, the biosurfactant has great potential for commercial use in industries such as enhanced oil recovery, bioremediation, and food-related industries as an alternative to the synthetic surfactants. Further work is required to fully characterise the biosurfactant to better predict its potential applications.

Acknowledgement

The authors would like to express gratitude to Universiti Kebangsaan Malaysia for providing grant UKM-ST-06-FRGS0098-2009.

References

1. Muthusamy, K., Gopalakrishnan, S., Ravi, T. K. and Sivachidambaram, P. (2008). Biosurfactants: Properties, commercial production and application. *Current Science,* 94(6): 736 – 747.
2. Kim, P. I. I., Ryu, J., Kim, Y. H. and Chi, Y-T. (2010). Production of biosurfactant lipopeptides iturin A, fengycin, and surfactin A from *Bacillus subtilis* CMB32 for control of *Colletotrichum gloeosporioides*. *Journal of Microbiology and Biotechnology*, 20(1): 138 – 145.
3. Lee, S-C., Kim, S-H., Park, I-H., Chung, S-Y., Chandra, M. S. and Choi, Y-L. (2010). Isolation, purification, and characterization of novel fengycin S from *Bacillus amyloliquefaciens* LSC04 degrading crude oil. *Biotechnology and Bioprocess Engineering*, 15: 246 – 253.
4. Chander, C. R. S., Lohitnath, T., Kumar, D. J. M. and Kalaichelvan, P. T. (2012). Production and characterization of biosurfactant from *Bacillus subtilis* MTCC441 and its evaluation to use as bioemulsifier for food bio-preservative. *Advances in Applied Science Research,* 3(3): 1827 – 1831.
5. Simmai, A., Rukadee, O., Sohbon, V. and Manerat, S. (2012). Biosurfactant production by *Bacillus subtilis* TD4 and *Pseudomonas aeruginosa* SU7 grown on crude glycerol obtained from biodiesel production plant as sole carbon source. *Journal of Scientific and Industrial Research,* 71: 396 – 406.
6. Nalini, S., Parthasarathi, R. and Thandapani, C.M. (2013). Isolation, screening and characterization of bio-surfactant produced by *Bacillus* sp. from automobile oil contaminated soil. *International Journal of Pharmaceutical & Biological Archives*, 4(1): 130 – 135.
7. Abdel-Mawgoud, A. M., Aboulwafa, M. M. and Hassouna, N. A. H. (2008). Characterization of surfactin produced by *Bacillus subtilis* isolate BS5. *Applied Biochemistry and Biotechnology,* 150(3): 289 – 303.
8. El-Sersy, N.A. (2012). Plackett-Burman design to optimize biosurfactant production by marine *Bacillus subtilis* N10. *Romanian Biotechnological Letter*, 17(2): 7049 – 7064.
9. Hamzah A., Rabu, A., Azmy, R. F. H. R. and Yussoff, N. A. (2010). Isolation and characterization of bacteria degrading sumandak and South and Angsi oils. *Sains Malaysiana*, 39(2): 161 – 168.
10. Zajic, E. and Supplison, B. (1972). Emulsification and degradation of "Bunker C" fuel oil by microorganisms. *Biotechnology and Bioengineering,* 14: 331 – 334.
11. Youssef, N. H., Duncan, K. E., Nagle, D. P., Savage, K. N., Knapp, R. M. and Mcinerney, M. J. (2004). Comparison of methods to detect biosurfactant production by diverse microorganisms. *Journal of Microbiological Methods,* 56: 339 – 347.
12. Cooper, D. and Goldenberg, B. (1987). Surface-active agents from two *Bacillus* species. *Applied Environmental Microbiology,* 53(2): 224 – 229.
13. Bodour, A. A. and Miller-Maier, R. M. (1998). Application of a modified drop-collapse technique from surfactant quantitation and screening of biosurfactant-producing microorganisms. *Journal of Microbiological Methods,* 32: 273 – 280.

14. Techaoei, S., Lumyong, S., Prathumpai, W., Santiarwarn, D. and Leelapornspisid, P. (2011). Screening characterization and stability of biosurfactant produced by *Pseudomonas aeruginosa* SCMU106 isolated from soil in Northern Thailand. *Asian Journal of Biological Sciences,* 4(4): 340 – 351.
15. Hamzah, A., Sabturani, N. and Radiman, S. (2013). Screening and optimization of biosurfactant production by the hydrocarbon-degrading bacteria. *Sains Malaysiana,* 42(5): 615 – 623.
16. Varjani, S. J., Rana, D. P., Bateja, S., Sharma, M. C. and Upasani, V. N. (2014). Screening and identification of biosurfactant (bioemulsifier) producing bacteria from crude oil contaminated sites of Gujarat India. *International Journal of Innovative Research in Science, Engineering and Technology*, 3(2): 9205 – 9213.
17. Morikawa, M., Hirata, Y. and Imanaka, T. (2000). A study on the structure-function relationship of lipopeptide biosurfactant. *Biochemical and Biophysics Acta*, 1488(3): 211 – 218.
18. Thavasi, R., Sharma, S. and Jayalakshmi, S. (2011). Evaluation of screening methods for the isolation of biosurfactant producing marine bacteria. *Journal of Petroleum and Environmental Biotechnology.* S1: 1 – 6.
19. Karthik, L., Kumar, G. and Rao, K.V.B. (2010). Comparison of methods and screening of biosurfactant producing marine *actinobacteria* isolated from Nicobar marine sediment. *The IIOAB Journal*, 9(2): 34 – 38.
20. Shoeb, E., Ahmed, N., Akhter, J., Badar, U., Siddiqui, K., Ansari, F. A., Waqar, M., Imtiaz, S., Akhtar, N., Shaikh, Q. A., Baig, R., Butt, S., Khan, S., Khan, S., Hussain, S., Ahmed, B. and Ansari, M. (2015). Screening and characterization of biosurfactant-producing bacteria isolated from the Arabian Sea coast of Karachi. *Turkish Journal of Biology*. 39: 210 – 216.
21. Nishanthi, R., Kumaran, S., Palani, P., Chellaram, C., Anan, T. P. and Kannan, V. (2011). Screening of biosurfactants from hydrocarbon degrading bacteria. *Journal of Ecobiotechnology*. 2(5): 47 – 53.
22. Viramontes-Ramos, S., Portillo-Ruiz, M. C., Ballinas-Casarrubias, M. L., Torres-Munoz, J.V., Rivera-Chavira, B. E. and Nevarez-Moorillon, G.V. (2010). Selection of biosurfactant/bioemulsifier-producing bacteria from hydrocarbon-contaminated soil. *Brazilian Journal of Microbiology,* 41: 668 – 675.
23. Safary, A., Ardakani, M. R., Suraki, A. A., Khiavi, M. A. and Motamedi, H. (2010). Isolation and characterization of biosurfactant producing bacteria from Caspian Sea. *Biotechnology,* 9(3): 378 – 382.
24. Cerqueira dos Santos, S., Fernandez, L. G., Rossi-Alva, J. C. and de Abreu Roque, M. R. (2010). Evaluation of substrates from renewable-resources in biosurfactants production by *Pseudomonas* strains. *African Journal of Biotechnology*, 9(35): 5704 – 5711.
25. Haba, E., Espuny, M. J., Busquets, M. and Manresa, A. (2000). Screening and production of rhamnolipids by *Pseudomonas aeruginosa* 47T2 NCIB 40044 from waste frying oils. *Journal of Applied Microbiology*. 88: 379 – 387.
26. Ferraz, C., De Araujo, A. A. and Pastore, G. M. (2002). The influence of vegetable oils on biosurfactant production by *Serratia marcescens*. *Applied Biochemistry and Biotechnology*, 98(1): 841 – 847.
27. Jadhav, M., Kagaikar, A., Jadhav, S. and Govindwar, S. (2011). Isolation, characterization and antifungal application of a biosurfactant produced by *Enterobacter* sp. MS16. *European Journal of Lipid, Science and Technology*, 113(11): 1347 – 1358.
28. Banat, I. M., Satpute, S. K., Cameotra, S. S., Patil, R. and Nyayanit, N. V. (2014). Cost effective technologies and renewable substrates for biosurfactants' production. *Frontier in Microbiology*, 5: 697 – 715.
29. Ghojavand, H., Vahabzadeh, F., Roayaei, E. and Shahraki, A. K. (2008). Production and properties of a biosurfactant obtained from a member of the *Bacillus subtilis* group (PTCC 1696). *Journal of Colloid and Interface Science*. 324: 172 – 176.
30. Joshi, S. J., Suthar, H., Yadav, A. K., Kingurao, K. and Nerurkar, A. (2013). Occurrence of biosurfactant producing *Bacillus* spp. in diverse habitats. *ISRN Biotechnology*, 2013: 1 – 6.
31. Pereira, J. F. B., Gudina, E. J., Costa, R., Vitorino, R., Teixeira, J. A., Coutinho, J. A. P. and Rodrigues, L. R. (2013). Optimization and characterization of biosurfactant production by *Bacillus subtilis* isolates towards microbial enhanced oil recovery applications. *Fuel*, 111: 259 – 268.
32. Haddad, N. I. A., Wang, J. and Mu, B. (2009). Identification of a biosurfactant producing strain: *Bacillus subtilis* HOB2. *Protein and Peptide Letters.* 16: 7 - 13.
33. Abas, M. R., Kader, A. J. A., Khalil, M. S., Hamid, A. A. and Isa, M. H. M. (2013). Production of surfactin from *Bacillus subtilis* ATCC 21332 by using treated palm oil mill effluent (POME) as fermentation media. *International Conference on Food and Agricultural Sciences*, 55: 87 – 93.
34. Pornsunthorntawee, O., Arttaweeporn, N., Paisanjit, S., Somboonthanate, P., Abe, M., Rujiravanit, R. and Chavadej, S. (2008). Isolation and comparison of biosurfactants produced by *Bacillus subtilis* PT2 and

Pseudomonas aeruginosa SP4 for microbial surfactant-enhanced oil recovery. *Biochemical Engineering Journal,* 42: 172 – 179.

35. Jazeh, G., Forghani, F. and Oh, D-H. (2012). Biosurfactant production by *Bacillus sp*. isolated from petroleum contaminated soils of Sirri Island. *American Journal of Applied Sciences*, 9(1): 1 – 6.
36. Li, A-H., Xu, M-Y., Sun, W. and Sun, G-P. (2010). Rhamnolipid production by *Pseudomonas aeruginosa* GIM 32 using different substrates including molasses distillery wastewater. *Applied Biochemistry and Biotechnology,* 163(5): 600 – 611.
37. Oliveira, F.J.S., Vazquez, L., Campos, N.P. and Franca, F.P. (2007). Biosurfactant production by *Pseudomonas aeruginosa* RF using palm oil. *Applied Biochemistry and Biotechnology*, 129 – 132: 727 – 737.
38. Abalos, A., Vinas, M., Sabate, J., Manresa, M. A. and Solanas, A. M. (2004). Enhanced biodegradation of Casablanca crude oil by a microbial consortium in presence of a rhamnolipid produced by *Pseudomonas aeruginosa* AT10. *Biodegradation*, 15: 249 – 260.
39. Thaniyavarn, J., Chongchin, A., Wanitsuksombut, N., Thaniyavarn, S., Pinphanichakarn, P., Leepipatpiboon, N., Morikawa, M. and Kanaya, S. (2006). Biosurfactant production by *Pseudomonas aeruginosa* A41 using palm oil as carbon source. *Journal of General Applied Microbiology*, 52: 215 – 222.
40. Fontes, G. C., Amaral, P. F. F., Nele, M. and Coelho, M. A. Z. (2010). Factorial design to optimize biosurfactant production by *Yarrowia lipolytica*. *Journal of Biomedicine and Biotechnology,* 2010: 1 – 8.
41. Fonseca, R. R., Silva, A. J. R., De Franca, F. P., Cardoso, V. L. and Servulo, E. F. C. (2007). Optimizing carbon/nitrogen ratio for biosurfactant production by a *Bacillus subtilis* strain. *Applied Biochemistry and Biotechnology.* 137(1): 471 – 486.
42. Nawawi, W. M. W., Jamal, P. and Alam, M. Z. (2010). Utilization of sludge palm oil as a novel substrate for biosurfactant production. *Bioresource Technology*, 101: 9241 – 9247.
43. Vedaraman, N. and Venkatesh, N. (2011). Production of surfactin by *Bacillus subtilis* MTCC 2423 from waste frying oils. *Brazilian Journal of Chemical Engineering.* 28(02): 175 – 180.
44. Rashedi, H., Azadi, M. M., Jamshidi, E. and Bonakdarpour, B. (2006). Production of rhamnolipids by *Pseudomonas aeruginosa* growing on carbon sources. *International Journal of Environmental Science and Technology,* 3(3): 297 – 303.
45. Vaz, D. A., Gudina, E. J., Alameda, E. J., Teixeira, J. A. and Rodrigues, L. R. (2012). Performance of a biosurfactant produced by a *Bacillus subtilis* strain isolated from crude oil samples as compared to commercial chemical surfactants. *Colloids and Surfaces B:Biointerfaces*, 89: 167 – 174.
46. Khopade, A., Biao, R., Liu, X., Mahadik, K., Zhang, L. and Kokare, C. (2012). Production and stability studies of the biosurfactant isolated from marine *Nocardiopsis* sp. B4. *Desalination.* 285: 198 – 204.
47. Bognolo, G. (1999). Biosurfactants as emulsifying agents for hydrocarbons. *Colloids Surfaces A: Physicochemical Engineering Aspects.* 152(1): 41 – 52.

Malaysian Journal of Analytical Sciences, Vol 20 No 5 (2016): 1001 - 1010
DOI: http://dx.doi.org/10.17576/mjas-2016-2005-04

MALAYSIAN JOURNAL OF ANALYTICAL SCIENCES
Published by The Malaysian Analytical Sciences Society
ISSN 1394 - 2506

OPTIMIZATION PARAMETER FOR THERMOELECTRIC PROPERTIES OF ZnO USING RESPONSE SURFACE METHODOLOGY

(Pengoptimuman Parameter Untuk Sifat Termoelektrik ZnO Menggunakan Kaedah Gerak Balas Permukaan)

Lim Joon Hoong*, Yeoh Cheow Keat, Abdullah Chik, Teh Pei Leng

School of Materials Engineering,
Universiti Malaysia Perlis, 02600 Jejawi, Perlis, Malaysia

**Corresponding author: jhlim07@gmail.com*

Received: 5 January 2016; Accepted: 23 May 2016

Abstract

The effect of Al dopants and sintering temperature on thermoelectric properties of ZnO was studied using the response surface method. The design of experimental work was performed with the response surface method used to determine the significant level of factors which are sintering temperature in the range of 800 – 1000 °C and Al dopants in the range of 0 – 4 wt.%. The thermoelectric properties of Al-doped ZnO were enhanced with increasing Al dopants and slightly decreased when increasing sintering temperature. Additional phase $ZnAl_2O_4$ was detected for 3 wt.% and 4 wt.% Al-doped ZnO pellets as the sintering temperature increased to 1000 °C. The presence of $ZnAl_2O_4$ phase slightly decreased the electrical conductivity compared to single ZnO phase samples. The optimum parameter values for this study was Al dopant (4 wt.%) and sintering temperature (800 °C). The effect of Al doping to the band structure of ZnO was studied using first-principles based on density functional theory (DFT). The calculated band structure of ZnO and Al doped ZnO shows that ZnO is a direct band gap semiconductor. The calculated band gap of ZnO (0.749 eV) become smaller with the concentration of Al doping increased to 4 wt.% (0.551 eV). The trend of the calculated band gap of Al-doped ZnO was in agreement with the electrical conductivity test results which increased with increasing Al content. However, it must be noted that the software predictions do not take into account the presence of additional $ZnAl_2O_4$ phases. The presence of these extra phases may lead to even lower electrical conductivity.

Keywords: Al-doped ZnO, response surface method, sintering temperature, thermoelectric, electronic band structure

Abstrak

Kesan Al dop dan suhu pembakaran ke atas termoelektrik ZnO dikaji dengan menggunakan kaedah gerak balas permukaan. Reka bentuk kerja eksperimen telah dilakukan dengan kaedah gerak balas permukaan untuk menentukan aras signifikan suhu pembakaran pada julat 800 – 1000 °C dan Al dop dalam lingkungan 0 – 4% berat. Sifat – sifat termoelektrik Al-dop ZnO telah dipertingkatkan dengan peningkatan Al dop dan pensinteran suhu. Fasa tambahan $ZnAl_2O_4$ dikesan bagi 3% berat dan 4% berat Al-dop ZnO bila suhu pembakaran meningkat daripada 800 °C hingga 1000 °C. Kekonduksian elektrik menurun dengan kehadiran fasa $ZnAl_2O_4$ berbanding sampel fasa ZnO tunggal. Nilai – nilai parameter optimum untuk kajian ini adalah Al pendopan (4% berat) dan suhu pensinteran (800 °C). Kesan Al doping kepada struktur jalur ZnO dikaji menggunakan prinsip pertama berdasarkan teori fungsi ketumpatan. Struktur jalur yang dikira pada ZnO dan Al dop ZnO menunjukkan bahawa ZnO adalah semikonduktor jurang jalur terus. Dengan Al dop, jurang jalur ZnO (0.749 eV) menjadi lebih kecil dengan peningkatan kepekatan Al dop pada 4 wt.% (0.551 eV). Trend jurang jalur yang dikira pada ZnO Al-didopkan adalah selari dengan keputusan ujian kekonduksian elektrik yang meningkat dengan peningkatan kandungan Al. Walau bagaimanapun, ia perlu diambil perhatian bahawa ramalan perisian tidak mengambil kira kehadiran fasa $ZnAl_2O_4$ tambahan. Kehadiran kedua – fasa tambahan boleh membawa kepada kekonduksian elektrik yang lebih rendah.

Kata kunci: Al dop ZnO, kaedah gerak balas permukaan, suhu pembakaran, termoelektrik, struktur jalur elektronik

Introduction

Thermoelectric materials could potentially convert heat into electricity through thermoelectric power [1]. The efficiency of energy conversion depends on the thermoelectric figure of merit of the material. Based on the figure of merit, these materials must have the unique combination of high electrical conductivity, high Seebeck coefficient and low thermal conductivity [2]. Seebeck coefficient (S) of a material is the voltage generated between two points in the material per unit temperature difference between these points [3].

Zinc oxide (ZnO) is an II-VI compound semiconductor with a wide direct band gap at room temperature [4]. It is a widely used material in various application such as gas sensors, varistors, UV resistive coatings, piezoelectric devices, surface acoustic wave devices and transparent conductive oxide electrodes [5,6]. The main drawback of ZnO as thermoelectric materials is due to the low electrical conductivity at room temperature. The electrical conductivity can be increased by special heat treatment and doping of specific impurities into the crystal lattice. In the hexagonal close packed lattice of the ZnO wurtzite structure, half of the tetrahedral holes and all of the octahedral holes are empty, providing further possible dopant sites [7]. A dopant ion introduced to modify the electronic properties of a material needs to be incorporated into the crystal structure of the host material (either in lattice sites or interstitially). ZnO can even be made to exhibit metallic conductivity as for transparent electrode similar to Indium tin oxide glass. In general, 0.5 – 1% addition of trivalent cations such as aluminium (Al) and chromium (Cr) decrease the resistivity of ZnO approximately 10 orders of magnitude [8]. Jimenez-Gonzalez et al. [9] explains the increase in the conductivity of ZnO when Al is introduced as a dopant, in terms of donor behaviour from Al. Al has one valence electron more than Zn, substitution of Al for the Zn atom or Al occupation of the interstitial sites increases the concentration of charge carriers present in the material.

The properties of ZnO are related to the composition and phase formation. The conductivity properties of ZnO can be tailored by controlling the deviation from stoichiometry and doping [10]. Therefore, it is necessarily to understand the effect of the individual dopant element to the electrical properties and phase formation of ZnO. In this work, the effect of Al dopant (0 – 4 wt.%) and sintering temperature (800 – 1000 ^{o}C) on the thermoelectric properties were studied using the response surface methodology. The band structure of ZnO with different Al contents are calculated by first principles method based on Density Functional Theory (DFT) as a comparison for the electrical conductivity.

Materials and Methods

Chemical and reagent

Analytical grade ZnO powder and Al_2O_3 powder were used as the starting materials for the preparation of pellet samples. The properties of ZnO and Al_2O_3 were shown in Table 1.

Table 1. Properties of ZnO, Al_2O_3, Fe_2O_3 and CuO (HmbG Chemicals)

Properties	Zinc oxide	Alumina
Molecular formula	ZnO	Al_2O_3
Molar mass, g/mol	81.408	375.134
Appearance	white solid	white solid
Density, g/cm^3	5.606	3.95 – 4.1

Experimental procedure

Appropriate amounts of ZnO and Al_2O_3 powder were mixed using the solid state method to prepare 0, 1, 2, 3 and 4 wt.% Al-doped ZnO. The samples were shaped into pellets of 5 mm of thickness and 15 mm in diameter. All

samples were compacted using a cold hydraulic press machine at 75MPa for 10min. The green compact was sintered in furnace (Model HT4-1600-SIC) at different sintering temperature 800 °C, 900 °C and 1000 °C for 4 hours with heating rate of 10 °C/min. The synthesized samples were characterized by X-ray diffraction analysis (Shimadzu XRD 2000). The electrical conductivity of the samples was determined by the two-probe method. The current voltage measurements were carried out using a Keithley's source measure unit (Model SMU 236). The thermal conductivity of the samples was determined based on Fourier's law. The Seebeck coefficient was measured by using differential method [11] at room temperature.

Response surface methodology

Response surface methodology is a statistical method used to improve and optimize process. The response surface methodology has the advantages to evaluate multiple processing parameters and reduced the number of experimental trials. The experimental results were evaluated by the dependent variables of thermoelectric efficiency using Design Expert 8 [12] with surface response model. The results are obtained with the experimental design that was aimed at identifying the best levels of the Al doping (0 – 4 wt.%) and sintering temperature (800 – 1000 °C). The analysis of variance (ANOVA) is a statistical technique for the purpose of testing hypotheses on the parameters of the model. A 3-factor, 3-level factorial Box–Behnken design (BBD) was employed to investigate the effects of selected variables. BBD which is a widely used form of response surface methodology, specially made to require only 3 levels, coded as –1, 0, and +1. BBD is an independent, rotatable or nearly rotatable quadratic design (contains no embedded factorial or fractional factorial design) in which the treatment combinations are at the midpoints of the edges of the process space and at the centre.

Computational method

The ABINIT program was used to perform the band structure calculations. ABINIT is an open source program that used to compute band structure and ground state properties. The band structures of Al doped ZnO was calculated based on the DFT Kohn-Sham equations with GW computations. The GW method is a Green function technique that obtained the electron self-energy and provides an accurate determination of the quasiparticle excitation energies [13]. The k-point parameter was 3 x 3 x 1 Monkhorst-Pack. The cut off energy was set to be 816 eV (30 hartree). The ideal ZnO has a wurtzite structure at normal temperatures and pressures. The primitive cell parameters for ideal ZnO were determined as α = 3.2005 Å, c/α = 1.6131 and u = 0.3792. The parameters used in ABINIT were optimized with a convergence criterion 0.01 eV to calculate self-energy for the band gap.

Results and Discussion

XRD analysis

Based on Figure 1(a), all the samples peaks for 0, 1, 2, 3 and 4 wt.% Al-doped ZnO were identified as the plane reflection for wurtzite phase of ZnO according to the JCPDS data file (No. 36-1451). The XRD pattern of Al-doped ZnO sintered at 900 °C was indicated in Figure 1(b). Based on the test results, all the peaks for 0, 1, 2, 3 and 4 wt.% Al-doped ZnO matched the JCPDS data file (No.36-1451) as the plane reflection for wurtzite phase of ZnO. There was additional phase $ZnAl_2O_4$ that matched the JCPDS data file (No.05-0669) detected for 4 wt.% Al-doped ZnO sintered at 900 °C. From the test results show in Figure 1(c), additional phase $ZnAl_2O_4$ was detected for 3 wt.% and 4 wt.% Al-doped ZnO with the sintering temperature increased to 1000 °C. The existence of secondary phase $ZnAl_2O_4$ may reduce the electrical conductivity of the sample [14].

Electrical conductivity

Based on the analysis of variance (ANOVA) for electrical conductivity as shown in Table 2, the Model F-value of 404.80 implies the model was significant. The Prob > F values of less than 0.05 may indicate that Al dopants and sintering temperature have significant effects on the electrical conductivity of the samples.

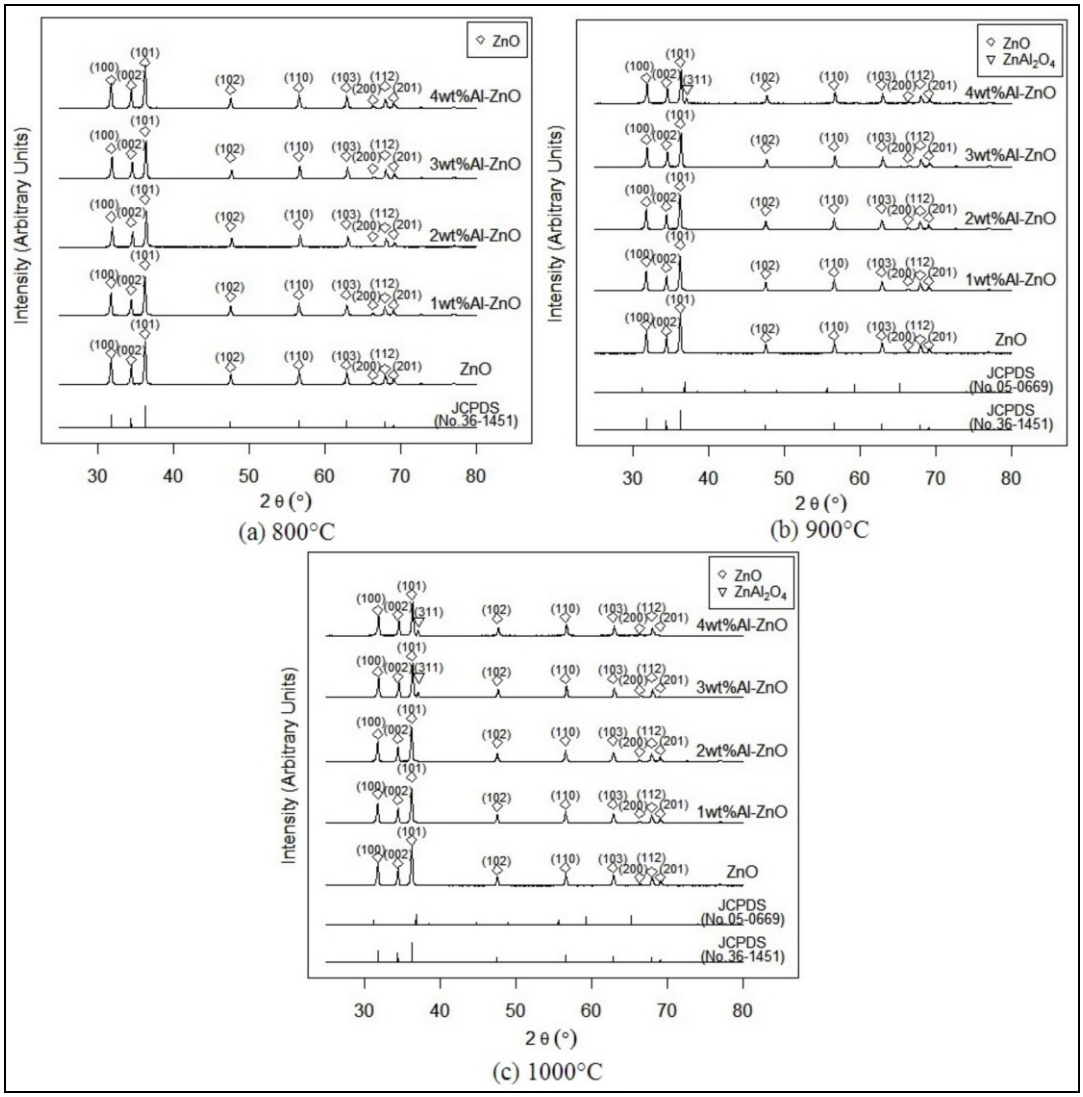


Figure 1. XRD pattern of Al-doped ZnO sintered at (a) 800 °C (b) 900 °C (c) 1000 °C

Table 2. Analysis of variance for electrical conductivity

Source	**Sum of Squares**	**Df**	**Mean Square**	**F value**	**p-value Prob > F**
Model	8219.08	5	1643.82	404.80	< 0.0001
A-Al dopants	7360.83	1	7360.83	1812.63	< 0.0001
B-Sintering temperature	14.18	1	14.18	3.49	0.0245
AB	12.31	1	12.31	3.03	0.1157
A^2	831.35	1	831.35	204.72	< 0.0001
B^2	0.41	1	0.41	0.100	0.7591
Residual	36.55	9	4.06		
Cor Total	8255.62	14			

Figure 2 show the 3D plot for electrical conductivity profile in accordance to the response surface model. The highest peak electrical conductivity for ZnO was achieved with 4wt.% Al dopants sintered at temperature 800 °C. Based on results shown in Figure 2, increasing the concentration of Al dopant caused a significant increase in the electrical conductivity. This might due to the Al dissolved in the ZnO crystal lattice acts as donor [15]. For example, the electrical conductivity of bulk pellets was increased significantly from 9.95 S/cm (pure ZnO) to 37.39 S/cm, 59.38 S/cm, 69.26 S/cm and 71.49 S/cm as the dopant increased to 1, 2, 3 and 4 wt.% respectively. The electrical conductivity for 4 wt.% Al-doped ZnO sintered in air at 1000 °C (70.98 S/cm) and 900 °C (71.49 S/cm) were slightly lower compared to 800 °C (71.87 S/cm). This might due to the existence of $ZnAl_2O_4$ phase as shown in Figure 1. The $ZnAl_2O_4$ phase believed to induce oxygen vacancies that lead to low conductivity. The formation of this phase may cause the resistivity increase in the samples [16].

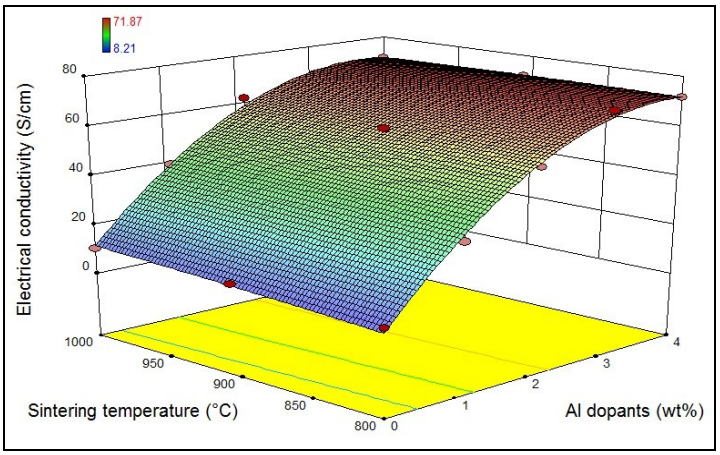


Figure 2. 3D response surface plot for electrical conductivity of Al-doped ZnO

Band structure

The electronic band structure for ZnO calculated using DFT was shown in Figure 3. The band structure shows that ZnO is direct band gap material with the valence band maximum (VBM) and the conduction band minimum (CBM) at G. The calculated band gap at point G is 0.749 eV for ZnO. Low band gap might be due to the lower exchange correlation between electrons made by the DFT-GW function.

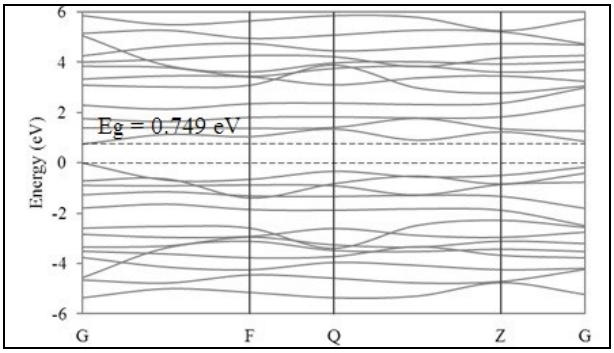


Figure 3. Electronic band structure of pure ZnO

Figure 4(a)-(d) shows the calculated band structure of 1 wt.% Al-ZnO, 2 wt.% Al-ZnO, 3 wt.% Al-ZnO and 4 wt.% Al-ZnO respectively, the corresponding band gap are 0.684 eV, 0.619 eV, 0.557 eV and 0.551eV. The band gap values of Al doped ZnO are smaller than pure ZnO shown in Figure 3. The band gap of Al doped ZnO becomes smaller with increasing Al doping content. This may due to increase of carrier concentration and enhancement of conduction [19]. As shown from Figure 4(a)-(d), The CBM and VBM are all located in the G point, it indicated that Al doped ZnO is a direct band gap semiconductor. The electrical conductivity test results were similar to the calculated band gap. The band gap becomes smaller with the amounts of Al doping increased that resulting an increase in electrical conductivity. This emphasized that a reduction of the band gap would increase the intrinsic (without defects) conductivity of ZnO. It shifts the intrinsic defect states to energies inside the conduction band.

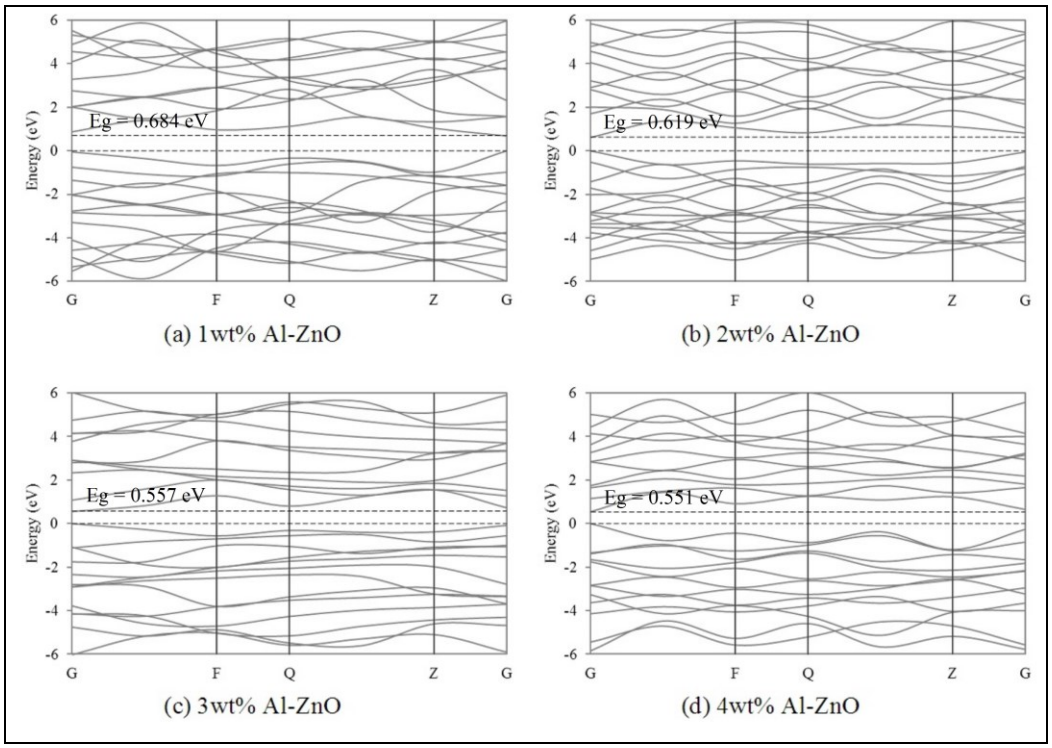


Figure 4. Electronic band structure of Al doped ZnO

Thermal conductivity

Table 3 show the analysis of variance (ANOVA) output used to estimate the variation due to each factor. The Model F-value of 51477.35 implies the model was significant. Values of "Prob > F" less than 0.05 indicate the model terms are significant. The ANOVA indicates that changing the sintering temperature and Al dopants may have a significant effect on the thermal conductivity of the samples.

The highest peak thermal conductivity for ZnO was achieved for pure ZnO sintered at 800°C. Based on results shown in Figure 5, increasing the amount of Al dopants caused a decrease in the thermal conductivity of the samples. The thermal conductivity of ZnO was 34.59 W/mK reduced to 33.21 W/mK, 31.82 W/mK, 30.44 W/mK and 29.05 W/mK with the Al doping increased to 1, 2, 3 and 4 wt% respectively. The reduction of thermal conductivity might due to the Al dopant suppress the lattice thermal conductivity of ZnO materials [20]. The thermal conductivity of the ZnO pellets decreased slightly when increasing the amount of Al dopants. The wurtzite ZnO has a high intrinsic thermal conductivity due to its strong covalent bonding and light atoms. The decrease in the thermal conductivity might be due to a phonon scattering caused by increased ZnO crystal lattice disorder when

Al dopants were added.

Table 3. Analysis of variance for thermal conductivity

Source	Sum of Squares	Df	Mean Square	F value	p-value Prob > F
Model	83.85	5	16.77	51477.35	< 0.0001
A-Al dopants	56.42	1	56.42	1.732E+005	< 0.0001
B-Sintering temperature	26.67	1	26.67	81852.09	< 0.0001
AB	0.099	1	0.099	305.12	< 0.0001
A^2	9.524E-006	1	9.524E-006	0.029	0.8680
B^2	0.67	1	0.67	2062.67	< 0.0001
Residual	2.932E-003	9	3.258E-004		
Cor Total	83.86	14			

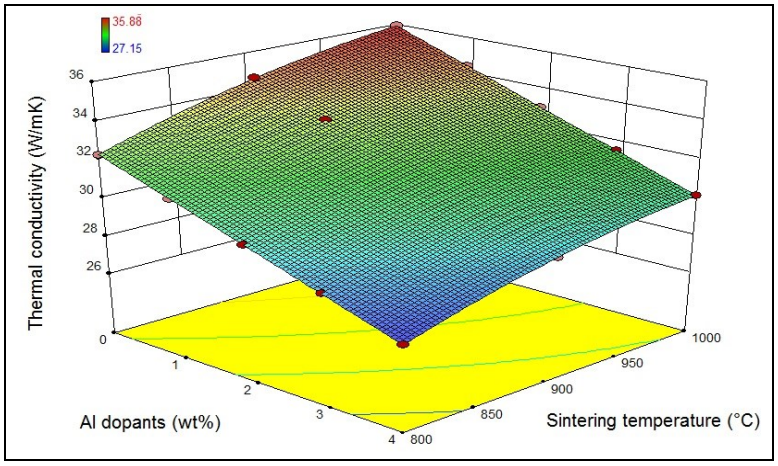


Figure 5. 3D response surface plot for thermal conductivity of Al-doped ZnO

Seebeck coefficient

Based on the analysis of variance for Seebeck coefficient as shown in Table 4, the Model F-value of 370.54 implies the model was significant. The Prob > F values below 0.05 may indicate that the sintering temperature and Al dopants have a significant effect on the Seebeck coefficient.

Figure 6 show a 3D plot curvilinear profile in accordance to the response surface model for the Seebeck coefficient. The highest peak Seebeck coefficient for ZnO was achieved for pure ZnO sintered at 1000 °C. Based on results shown in Figure 6, an increase in the Al doping concentration caused a decrease in the Seebeck coefficient of the bulk pellets. This might due to the Al dissolved in the ZnO crystal lattice acts as donor that improved the electrical conductivity and carrier concentration [21]. The negative sign of the Seebeck values was used to indicate the samples were n-type semiconductors. The magnitude of Seebeck coefficient for ZnO was 50.22 μV/K decreased to 49.22 μV/K, 48.71 μV/K, 48.21 μV/K and 47.95 μV/K with the Al dopant increased to 1, 2, 3 and 4 wt.% respectively.

Table 4. Analysis of variances for Seebeck coefficient

Source	Sum of Squares	Df	Mean Square	F value	p-value Prob > F
Model	16.48	5	3.30	370.54	< 0.0001
A-Al dopants	10.33	1	10.33	1160.46	< 0.0001
B-Sintering temperature	5.63	1	5.63	632.19	< 0.0001
AB	4.805E-003	1	4.805E-003	0.54	0.4811
A^2	0.40	1	0.40	44.54	< 0.0001
B^2	0.13	1	0.13	14.99	0.0038
Residual	0.080	9	8.898E-003		
Cor Total	16.56	14			

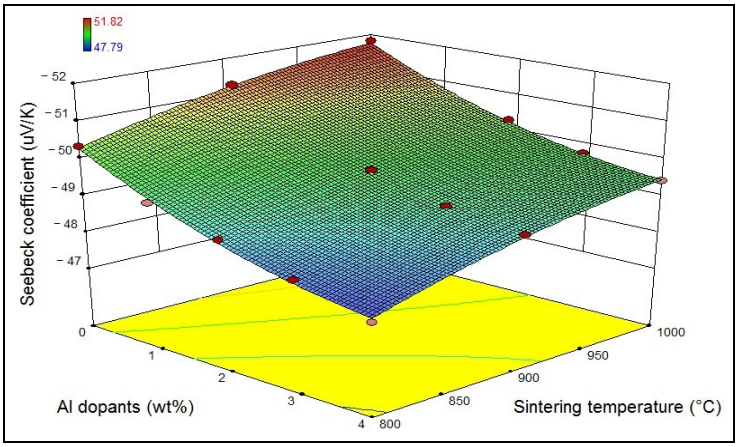


Figure 6. 3D response surface plot for Seebeck coefficient of Al-doped ZnO

Thermoelectric figure of merit

The thermoelectric figure of merit calculated from the measured values of electrical conductivity, Seebeck coefficient and thermal conductivity was shown in Figure 7. Higher figure of merit values (0.61) was observed for 4 wt.% Al-doped ZnO pellet sintered at 800 °C. The figure of merit for Al-doped ZnO was improved by doping Al. The figure of merit for 4 wt.% Al-doped ZnO sintered at 800 $^{\circ}$C was higher (Z ~ 0.58 x10^{-6}) due to high electrical conductivity and low thermal conductivity was obtained when increasing Al. The figure of merit for Al-doped ZnO (Al > 3 wt.%) was decreased when increasing sintering temperature. This was due to the formation of $ZnAl_2O_4$ phase at higher sintering temperature that lead to the reduction of electrical conductivity [22]. The presence of $ZnAl_2O_4$ phase was observed to reduce the figure of merit compared to single ZnO phase samples. This indicated the additional $ZnAl_2O_4$ phases had a deleterious effect on the thermoelectric properties.

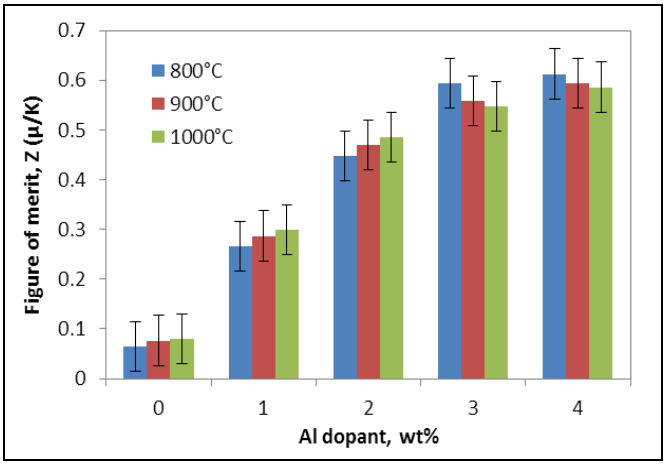


Figure 7. Figure of merit of Al-doped ZnO

Conclusion

Thermoelectric properties of ZnO were improved with increasing the amount of Al dopants. The thermoelectric figure of merit for 4 wt.% Al-doped ZnO (0.61) yielding a 10 times enhancement compared to the pure ZnO (0.06). The electrical conductivity of Al-doped ZnO was increased with increasing the amount of Al dopants. The Seebeck coefficient and thermal conductivity were decreased for Al-doped ZnO with increasing the amount of Al dopants. Thermoelectric properties of Al-doped ZnO were decreased with increasing the sintering temperature due to the additional phase $ZnAl_2O_4$. The thermoelectric figure of merit for 4 wt.% Al-doped ZnO (0.61) with lower sintering temperature (800 °C) was higher compared to the 4 wt.% Al-doped ZnO (0.58) sintered at higher temperature (1000 °C). Based on the analysis of variance, the sintering temperature and Al dopants have a significant effect to the thermoelectric properties of Al doped ZnO. Based on the response surface, the optimum values for this study were Al dopant (4 wt.%) and sintering temperature (800 °C). By using the first principles method based on DFT, the band structure of ZnO and Al doped ZnO were calculated. The band structure calculation of Al doped ZnO was investigated to provide a reference values for the electrical conductivity. Based on the DFT calculation, ZnO is a direct band gap. The band gap getting narrow as the concentration of Al doping increased from 1wt.% (0.684 eV) to 4 wt.% (0.551 eV) compare to pure ZnO (0.749 eV).

Acknowledgement

The financial support of Fundamental Research Grant Scheme (FRGS) grant no 9003-00392 is gratefully acknowledged.

References

1. Tritt, T. M. (2011). Thermoelectric phenomena, materials, and applications. *Annual Review of Materials Research*, 41(1):433 – 448.
2. Cheng, H., Xu, X. J., Hng, H. H. and Ma, J. (2009). Characterization of Al-doped ZnO thermoelectric materials prepared by RF plasma powder processing and hot press sintering. *Ceramics International*, 35(8):3067 – 3072.
3. Goldsmid, H. (2010). Application of the transverse thermoelectric effects. *Journal of Electronic Materials*, 1:1 – 6.
4. Huang, M. H., Mao, S., Feick, H., Yan, H., Wu, Y., Kind, H., Weber, E., Russo, R. and Yang. P. (2001). Room-temperature ultraviolet nanowire nanolasers. *Science*, 292:1897 – 1899.
5. Ried, R. P., Kim, E., Hong, D. M. and Muller, R. S. (1993). Piezoelectric microphone with on-chip CMOS circuit. *Journal of Microelectromechanical Systems*, 2: 111 – 120.
6. Ito, Y., Kushida, K., Sugawara, K. and Takeuchi, H. (1995). A 100-Mhz ultrasonic transducer array using ZnO thin films. *IEEE Transaction on Ultrasonic, Ferroelectric and Frequency Control*, 42: 316 – 323.

7. Burdett, J. K., Price, G. D. and Price, S. L. (1982). Role of the crystal field theory in determining the structures of spinels. *Journal of the American Chemical Society*, 104(1): 92 – 95.
8. Yan, X. D., Han, J., Chen, R. Q., Gao, W., Metson, J. and Zou., C. W. (2009). Study of a nitrogen-doped ZnO film with synchrotron radiation. *Applied Physics Letters*, 94: 171903.
9. Jimenez-Gonzalez, A. E., Jose A., Urueta, S. and Suarez-Parra, R. (1998). Optical and electrical characteristics of aluminum-doped ZnO thin films prepared by sol-gel technique. *Journal of Crystal Growth*, 192: 430 – 438.
10. Look, D. C. (2001). Recent advances in ZnO materials and devices. *Materials Science and Engineering* B, 80(1-3): 383 – 387.
11. Ravinder, D. (1999). Thermoelectric power studies of zinc substituted copper ferrites. *Journal of Alloys and Compounds*, 291(1-2): 208 – 214.
12. Inc.Stat-Ease. (2007). Design Expert Software, Educational Version 7.0.3, Wiley Publishing.
13. Gonze, X., Amadon, B., Anglade, P. M., Beuken, J. M., Bottin, F. and Boulanger, P. (2009). ABINIT: first-principles approach to material and nanosystem properties. *Computer Physical Communication*, 180: 2582 – 2615.
14. Takagi, Y., Ito, M., Majima, K., Nagai, H., and Katsuyama, S. (2002). Thermoelectric properties of $(Zn1_yMg_y)1_xAl_xO$ ceramics prepared by the polymerized complex method. *Journal of Applied Physics,* 92: 1391 – 1398.
15. Qu, X., Wang, W., Lv, S., and Jia, D. (2011). Thermoelectric properties and electronic structure of Al-doped ZnO. *Solid State Communications*, 151(4): 332 – 336.
16. Han, J., Mantas, P. Q., and Senos, A.M.R. (2001). Effect of Al and Mn doping on the electrical conductivity of ZnO. *Journal of the European Ceramic Society*, 21(10-11): 1883 – 1886.
17. Zhang, M., Zhang, C. H. and Shen, J. (2011). First-principles calculation of electronic structure of $Mg_xZn1\text{-}_xO$ codoped with aluminium and nitrogen. *Chinese Physics B*, 20: 017101.
18. Yang, P., Zhao, Y. and Yang, H. (2015). Investigation on optoelectronic performances of Al, N codoped ZnO: First-principles method. *Ceramics International*, 41: 2446 – 2452.
19. Li, P., Deng, S. H., Li, Y. B., Huang, J., Liu, G. H. and Zhang, L. (2011). Aluminum and nitrogen impurities in Wurtzite ZnO: first-principles studies, *Physica B*, 406: 3125 – 3129.
20. Ozgur, U., Ya, Liu, C., Teke, A., Reshchikov, M. A., Dogan, S., V., Avrutin, Cho, S. J. and Morkoc, H. (2005). A comprehensive review of ZnO materials and devices. *Journal of Applied Physics*, 98(4): 1 –103.
21. Bhan, R. and Dhar, V. (2004). Carrier density approximation for non-parabolic and highly degenerated HgCdTe semiconductors. *Semiconductor Science and Technology*, 19(3): 413 – 416.
22. Cheng, H., Xu, X. J., Hng, H. H. and Ma, J. (2009). Characterization of Al-doped ZnO thermoelectric materials prepared by RF plasma powder processing and hot press sintering. *Ceramics International*, 35(8): 3067 – 3072.

Malaysian Journal of Analytical Sciences, Vol 20 No 5 (2016): 1011 - 1019
DOI: http://dx.doi.org/10.17576/mjas-2016-2005-05

MALAYSIAN JOURNAL OF ANALYTICAL SCIENCES
Published by The Malaysian Analytical Sciences Society
ISSN 1394 - 2506

SINTESIS DAN PENCIRIAN HIDROGEL BERASASKAN KANJI DARIPADA UBI GADONG DENGAN MENGGUNAKAN TEKNIK RADIASI GAMMA

(Synthesis and Characterization of Starch-Based Hydrogel by using Gamma Radiation Technique)

Boo Wei Ping dan Azwan Mat Lazim*

Program Sains Kimia, Pusat Pengajian Sains Kimia dan Teknologi Makanan,
Fakulti Sains dan Teknologi,
Universiti Kebangsaan Malaysia, 43600 UKM Bangi, Selangor, Malaysia

**Pengarang utama: azwanlazim@ukm.edu.my*

Received: 13 August 2015; Accepted: 11 April 2016

Abstrak

Hidrogel berasaskan kanji daripada ubi gadong dengan menggunakan teknik radiasi gamma telah disintesis dan pencirian terhadapnya telah dilakukan bagi mendapatkan hidrogel yang terbaik. Hidrogel berasaskan kanji ini dihasilkan dengan menggunakan asid akrilik (AA) sebagai monomer dan kanji ubi gadong sebagai ko-monomer. Teknik radiasi gamma telah digunakan sebagai agen penaut silang. Isipadu ubi gadong yang berlainan digunakan untuk menghasilkan hidrogel dengan nisbah asid akrilik (AA) kepada ubi gadong. Hidrogel dengan nisbah 4:1 dan 5:2 telah disintesis. Tindak balas yang terlibat ialah pempolimeran radikal bebas dengan menggunakan radiasi gamma. Ujian pengembangan telah dilakukan untuk menguji sensitiviti hidrogel terhadap perubahan pH. Analisis morfologi hidrogel dilakukan dengan menjalani analisis Mikroskopi Pengimbasan Elektron (SEM). Analisis struktur kimia hidrogel ditentukan oleh Spektroskopi Inframerah (IR). Pembelauan Sinar X (XRD) dijalankan bagi menunjukkan hidrogel mengandungi komponen amorfus. Kalorimetri Pengimbasan Perbezaan (DSC) dan Analisis Gravimetri Terma (TGA) dijalankan bagi menunjukkan kestabilan terma hidrogel yang disintesis. Ujian pembengkakan telah dijalankan di dalam larutan penimbal pH 3, 5, 7, 9 dan 12 pada suhu bilik. Dalam larutan penimbal 7, 9 dan 12, didapati bahawa hidrogel bernisbah 5:2 mempunyai nilai yang lebih tinggi berbanding dengan hidrogel bernisbah 4:1. Manakala di dalam larutan penimbal pH 3 dan 5 pula, hidrogel bernisbah 4:1 mempunyai nilai pengembangan yang lebih tinggi berbanding hidrogel bernisbah 5:2. Puncak pada Spektrum Inframerah membuktikan kehadiran kumpulan berfungsi –OH daripada kanji berkurangan kerana telah digunakan dalam proses pempolimeran. Daripada termogram DSC dan TGA dapat diperhatikan bahawa nilai peralihan kaca, Tg untuk hidrogel bernisbah 5:2 lebih tinggi berbanding dengan hidrogel bernisbah 4:1.

Kata kunci: hidrogel, kanji, ubi gadong, teknik radiasi gamma

Abstract

Starch-based hydrogel is synthesized using gamma radiation. The hydrogel is then characterized to obtain the best ratio of hydrogel. Starch-grafted-acrylic acid hydrogels is produced using acrylic acid as monomer and starch from gadong tuber as co-monomer. Gamma radiation is used as cross-linking agent. Different volume of starch is used to produce hydrogels with different ratios of acrylic acid (AA) to starch. Hydrogels with ratio of 4:1 and 5:2 are synthesized. The reaction involved in the synthesis of hydrogel was a free radical polymerization. Swelling test for the starch-based hydrogel is carried out to observe the ability of hydrogel respond to the environmental change. Scanning Electron Microscope (SEM) is used to determine the morphology of hydrogel. The analysis of chemical structure is determined using the Infrared Spectrometer (IR). X-Ray Diffraction (XRD) is used to determine the present of amorphous component in the hydrogel. Differential Scanning Calorimetry (DSC) and Thermogravimetric Analysis (TGA) are used to determine the thermal stability of the hydrogel. Swelling test for this hydrogel is carried out in 5 different pH buffer solution with pH 3, 5, 7, 9 and 12 at a room temperature. In the buffer solution of pH 7, 9 and

12, the hydrogel with ratio 5:2 shows high value of swelling percentage compare to the hydrogel with ratio 4:1. However, in the buffer solution of pH 3 and 5, the hydrogel with ratio 4:1 swells more compare to the hydrogel with ratio 5:2. The peak showed in the IR proved that the present of the carboxyl group in the hydrogel after the polymerization process. From the thermogram of DSC and TGA, the hydrogel with ratio 5:2 showed higher value of glass transition compared to the hydrogel with ratio 4:1.

Keywords: hydrogel, starch, ubi gadong, gamma radiation technique

Pengenalan

Hidrogel adalah rangkaian polimer tiga dimensi yang bersifat hidrofilik di mana ia boleh memerangkap dan mengekalkan sekurang-kurangnya 20 % kandungan air di dalam jaringannya [1]. Hidrogel yang mengandungi lebih daripada 90 % air dikenali sebagai bahan penyerap berkeupayaan tinggi dan mempunyai sifat biokeserasian yang baik. Ia juga mempunyai ciri-ciri keserupaan fisiokimia dengan matrik ekstrasel dari segi komposisinya serta sifat mekanikalnya [2]. Dewasa ini, aplikasi hidrogel adalah amat luas, terutamanya dalam industri seperti pemakanan, biobahan, pertanian, dan rawatan air [3].Oleh itu, pelbagai kaedah telah dikaji bagi penghasilan hidrogel. Namun demikian, penggunaan polimer sintetik seperti polivinil alkohol (PVA), polivinil pirolidon (PVP), poli(nisopropilakrilamida) dan poliakrililik asid dalam penghasilan hidrogel adalah mahal memandangkan ia melibatkan proses sintesis kimia yang rumit. Selain itu, polimer sintetik dan terbitan polisakarida ini merupakan bahan yang tidak boleh diperbaharui dan tidak mudah terbiodegradasi [1,4].

Penghasilan hidrogel menggunakan kanji pada masa kini mendapat perhatian yang serius daripada para pengkaji yang disebabkan oleh kos penghasilan yang rendah dan mesra alam. Kanji merupakan sumber yang boleh diperbaharui dan boleh didapati dengan mudah. Menurut Eichhom et al. [5] kanji dijangkakan akan menjadi bahan utama sumber kimia pada masa hadapan. Permintaan terhadap produk yang mesra alam dan juga produk bioserasi kini kian meningkat. Ini kerana penggunaan bahan berasaskan sumber asli boleh mengurangkan pencemaran terhadap alam sekitar. Selain daripada bahan penyerap bioserasi boleh diuraikan dan digunakan oleh mikroorganisma serta tumbuhan.

Dalam kajian yang dijalankan ini, teknik sinaran gamma telah digunakan dalam proses mensintesis hidrogel. Penghasilan biobahan menggunakan teknik radiasi telah mendapat tempat dalam penyelidikan di negara ini. Pushpamalar [6] melaporkan bahawa hidrogel yang dihasilkan melalui taut silang secara radiasi telah digunakan sebagai pembalut luka untuk pesakit di Hospital Navi 411. Justeru, penggunaan sinaran gamma telah dibuktikan selamat digunakan dalam industri perubatan. Penggunaan teknik gamma ini bukan sahaja dapat menggantikan penggunaan bahan kimia sebagai petaut silang yang secara umumnya bertoksik malahan teknik sinaran gamma ini juga turut dapat menjimatkan masa [7].

Bahan dan Kaedah

Sintesis hidrogel

Ubi gadong yang baru digali dibersihkan dengan air, dikupas dan dipotong kecil. Kemudian, ubi tersebut dikisar dengan menggunakan pengisar elektronik dan dikeringkan menjadi serbuk. Serbuk ubi gadong dilarutkan dengan menggunakan air suling dan natrium hidroksida yang berkepekatan 1.0 M. Kemudian, asid akrilik dicampurkan ke dalam larutan ubi dan campuran dipindah ke dalam piring petri. Sampel kemudian didedahkan pada radiasi gamma iaitu 40 kGy dengan menggunakan penyinar sel gamma model Gammacell 220. Hidrogel yang telah dihasilkan kemudiannya dikeringkan di dalam ketuhar pada suhu 45 °C selama 24 jam. Proses penyingkiran bahan kimia berlebihan dilakukan dengan merendam sampel hidrogel di dalam air suling dan dikeringkan di dalam ketuhar. Kaedah ini diulang dengan menggunakan nisbah asid akrilik kepada kanji yang berbeza iaitu 4:1 dan 5:2.

Ujian pembengkakan

Kuasa pembengkakan, hidrogel diuji dengan merendamkan sampel hidrogel di dalam larutan pH yang berbeza iaitu pH 3, 5, 7, 9, dan 12 pada suhu bilik. Berat sampel hidrogel ditimbang dan dicatatkan pada setiap lima minit selama satu jam. Peratus pembengkakan hidrogel dikira dengan menggunakan persamaan 1 berikut.

$$\%S = \frac{M_0 - M}{M_0 \times 100\%} \quad (1)$$

S ialah peratus pembengkakan, M_o dalah jisim asal hidrogel (g) dan M adalah jisim hidrogel yang mengalami pembengkakan pada masa t (min).

Spektroskopi inframerah (IM)
Spektroskopi inframerah (IM) digunakan untuk menentukan kumpulan berfungsi yang hadir dalam struktur molekul. Prinsip spektroskopi inframerah adalah berdasarkan kepada perubahan tenaga yang disebabkan oleh peralihan molekul daripada aras tenaga getaran atau putaran ke aras tenaga yang lain. Dalam penentuan kumpulan berfungsi dalam hidrogel, spektroskopi inframerah untuk jumlah pantulan teratenuat (ATR-FTIR) dengan model Perkin Elmer telah digunakan. Imej dicerap pada panjang nombor gelombang di antara 4000 – 650 cm^{-1}.

Kalorimetri pengimbasan perbezaan (DSC)
Kalorimetri pengimbasan perbezaan digunakan untuk menentukan titik kritikal terma seperti takat lebur, haba spesifik entalpi dan suhu peralihan kaca dan merupakan kaedah yang cepat dalam penentuan sifat terma bahan polimer [8].

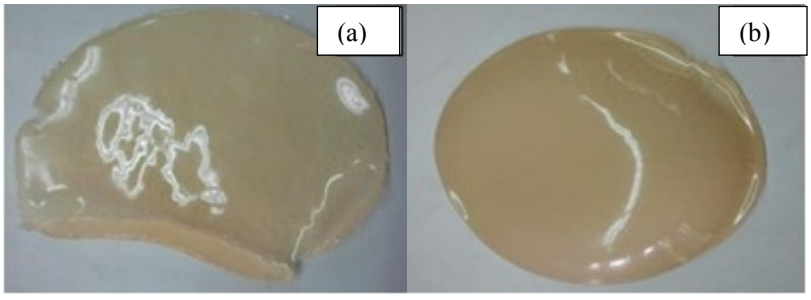
Analisis gravimetri terma (TGA)
Analisis gravimetri terma digunakan bagi mengukur jumlah dan kadar perubahan jisim sampel dalam keadaan suhu yang terkawal. Sampel dipanaskan dengan kehadiran nitrogen dan udara sintetik pada kadar haba yang tetap manakala perbezaan jisim diukur. Jisim yang kurang menunjukkan bahawa berlakunya degradasi sampel. Justeru teknik ini sesuai untuk analisis kerencaman daripada bahan-bahan multi-komponen atau campuran, kestabilan terma, kestabilan oksidatif, anggaran hayat produk, kinetik penguraian, kesan atmosfera reaktif terhadap bahan-bahan, kandungan pengisi bahan dan kelembapan serta kandungan meruap.

Pembelauan sinar-X
Pembelauan sinar-X sesuai digunakan untuk menganalisis ciri-ciri polimer dan kompositnya dalam keadaan struktur pepejalnya dan digunakan dalam aplikasi pengenalan sampel, penghabluran polimer, tekanan berbaki dan juga analisis tekstur.

Mikroskopi Pengimbasan Elektron (SEM)
Mikroskopi pengimbasan electron digunakan untuk menganalisis topografi permukaan sampel, komposisi, serta kekonduksian elektrik. Magnifikasi SEM boleh mencapai julat antara 10 hingga 500,000 kali. SEM merupakan satu teknik yang sesuai untuk melihat morfologi hidrogel [9].

Keputusan dan Perbincangan

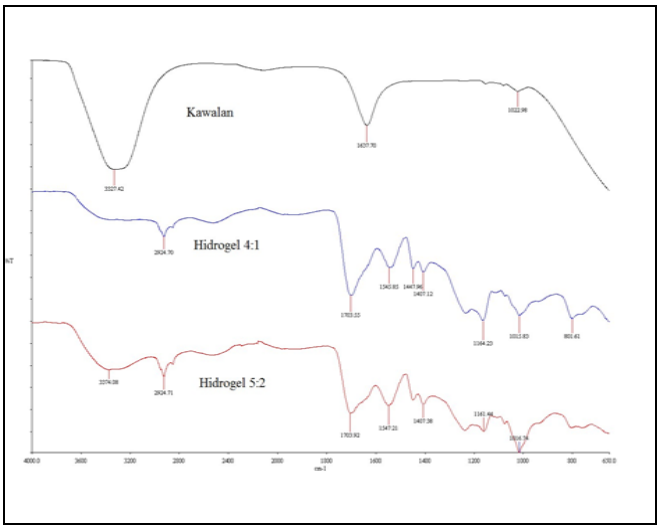
Sintesis hidrogel
Dalam kajian ini, hidrogel berasaskan ubi gadong telah berjaya disintesis dengan menggunakan nisbah ubi gadong kepada asid akrilik yang berbeza iaitu 4:1 dan 5:2. Rajah 1 menunjukkan hidrogel yang telah berjaya disintesis. Hidrogel yang dihasilkan mempunyai tekstur yang lembut dan elastik seperti getah. Warna hidrogel adalah sedikit kekuningan dan tidak mempunyai sifat lut cahaya.



Rajah 1. Hidrogel dengan nisbah 4:1 (a) manakala hidrogel dengan nisbah 5:2 (b)

Analisis spektroskopi inframerah

Dalam Rajah 2, dapat diperhatikan bahawa kedua – dua hidrogel mempunyai puncak yang sama tetapi berlainan keamatan. Perbezaan antara keamatan spektrum menunjukkan penggunaan nisbah asid akrilik dengan ubi gadong yang berbeza. Manakala bagi sampel pemalar pula hanya menunjukkan beberapa puncak sahaja. Hal ini kerana, asid akrilik tidak dimasukkan ke dalam sampel pemalar dan memberikan perbezaan yang ketara antara spektrum hidrogel bernisbah 4:1 dan 5:2.



Rajah 2. Perbandingan spektrum inframerah untuk hydrogel bernisbah 4:1, 5:2 dan sampel pemalar

Spektrum inframerah untuk kedua-dua hidrogel 4:1 dan 5:2 menunjukkan puncak penyerapan masing-masing pada sekitar 3370 dan 3374 cm^{-1} yang mewakili kumpulan hidroksi (–OH) pada kanji. Puncak sekitar 2500cm^{-1} pada kedua-dua spektrum hidrogel adalah disebabkan oleh getaran regangan daripada puncak lebar –OH. Selain itu, puncak sekitar 2924 cm^{-1}dapat dilihat dan ia merupakan kesan daripada regangan $–CH_2$ tidak simetri dari kumpulan $–CH_2OH$ di dalam kanji ubi gadong [10]. Seterusnya, puncak 1703 cm^{-1} yang terdapat pada kedua-dua hidrogel menunjukkan getaran peregangan C=O kumpulan –COOH daripada asid akrilik. Puncak pada julat 1750 – 1400 cm^{-1} membuktikan bahawa wujudnya kumpulan karboksil di dalam hidrogel selepas pempolimeran. Kedua-dua hidrogel turut memberikan puncak pada 1164 cm^{-1} bagi hidrogel bernisbah 4:1 dan 1161 cm^{-1} pada hidrogel bernisbah 5:2 menunjukkan wujudnya peregangan C-O-C ikatan eter kanji [11]. Dapat diperhatikan dengan memperbandingkan ketiga-tiga puncak spektrum ini, puncak spektrum bagi kedua-dua hidrogel dengan sampel pemalar menunjukkan perbezaan yang ketara terutamanya pada puncak sekitar 3300 cm^{-1} iaitu puncak bagi –OH. Ini membuktikan berlakunya pembentukan hidrogel kerana keamatan puncak spektrum tersebut mengurang dengan ketara.

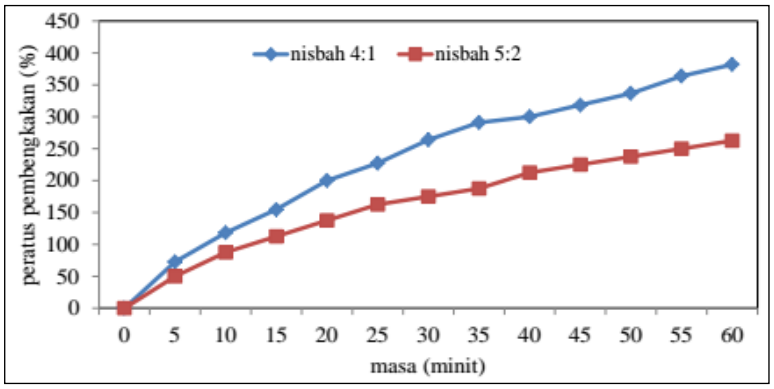
Pembengkakan hidrogel dalam larutan penimbal pH 3

Rajah 3 menunjukan peratus pembengkakan hidrogel di dalam larutan penimbal pH 3 selama satu jam. Nilai peratus pembengkakan bagi hidrogel dengan nisbah 4:1 menunjukkan pembengkakan yang lebih tinggi iaitu sebanyak 382 % berbanding hidrogel dengan nisbah 5:2 iaitu hanya 263 % sahaja.

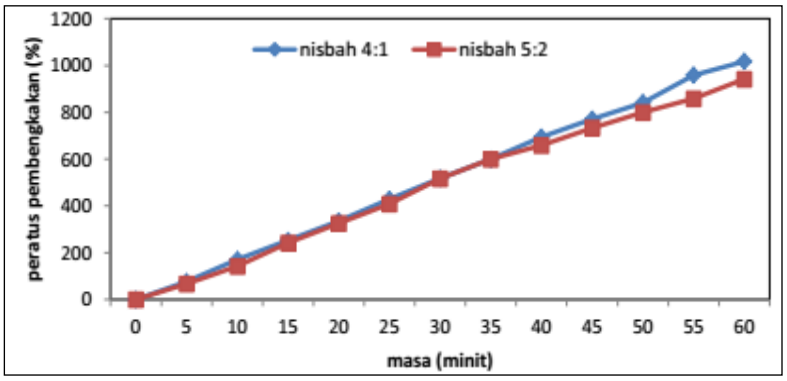
Pembengkakan hidrogel dalam larutan penimbal pH 5

Pada pH 5, dapat diperhatikan bahawa peratus pembengkakan bagi kedua-dua jenis hidrogel tidak mempunyai perbezaan yang ketara seperti yang ditunjukkan pada Rajah 4. Peratus pembengkakan bagi hidrogel dengan nisbah

4:1 mencapai nilai pembengkakan 1018 % manakala bagi hidrogel dengan nisbah 5:2 pula mencapai 942 %. Dapat diperhatikan, hidrogel 4:1 masih mempunyai keupayaan menyerap air yang lebih baik berbanding dengan hidrogel 5:2 di dalam larutan penimbal pH 5.



Rajah 3. Graf peratus pembengkakan hidrogel di dalam larutan penimbal pH 3



Rajah 4. Graf peratus pembengkakan hidrogel di dalam larutan penimbal pH 5

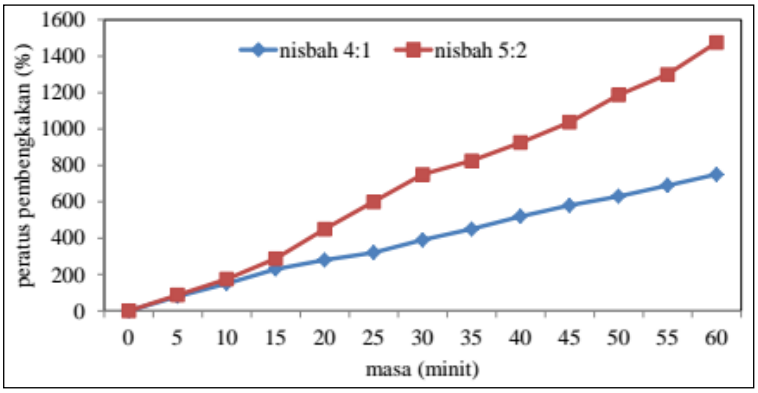
Pembengkakan hidrogel dalam larutan penimbal pH 7

Hidrogel dengan nisbah 5:2 mula menunjukkan keupayaan penyerapan yang baik iaitu dengan nilai peratus pembengkakan sebanyak 1475 % manakala hidrogel bernisbah 4:1 dengan nilai peratus pembengkakan sebanyak 750 % dalam larutan penimbal pH 7. Pada awal ujian, dapat diperhatikan peratus pembengkakan bagi kedua – dua hidrogel tidak mempunyai perbezaan yang ketara, namun selepas 15 minit hidrogel dengan nisbah 5:2 menyerap air dengan kadar yang jauh lebih cepat berbanding dengan hidrogel bernisbah 4:1. Ini bermakna, pada larutan penimbal pH 7, hidrogel bernisbah 5:2 lebih efisien dalam keupayaan penyerapan air berbanding dengan hidrogel bernisbah 4:1. Rajah 5 menunjukkan perbezaan peratus pembengkakan antara hidrogel bernisbah 4:1 dan 5:2 di dalam larutan penimbal pH 7.

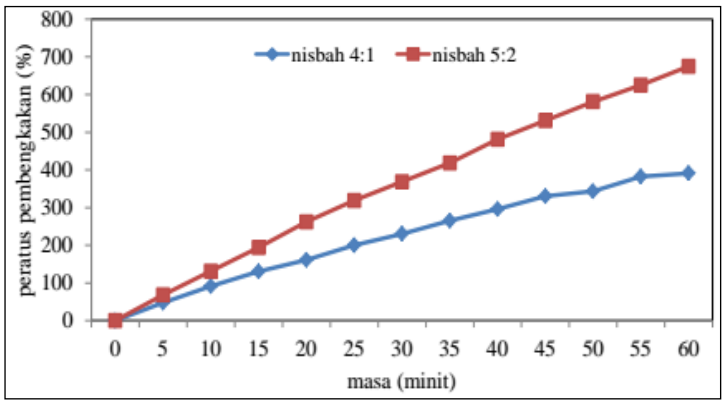
Pembengkakan hidrogel dalam larutan penimbal pH 9

Bagi larutan penimbal pH 9 pula, hidrogel dengan nisbah 5:2 masih lagi mendominasi iaitu dengan nilai peratus pembengkakan sebanyak 675 % dan hidrogel bernisbah 4:1 hanya mencapai nilai peratus pembengkakan sebanyak 391 % sahaja. Rajah 6 menunjukkan kadar pembengkakan bagi hidrogel dengan nisbah 5:2 adalah lebih tinggi

berbanding dengan hidrogel dengan nisbah 4:1. Perbezaan kadar pembengkakan dapat diperhatikan dari awal ujian sehingga ke akhir ujian.



Rajah 5. Graf peratus pembengkakan (%) hidrogel di dalam larutan penimbal pH 7



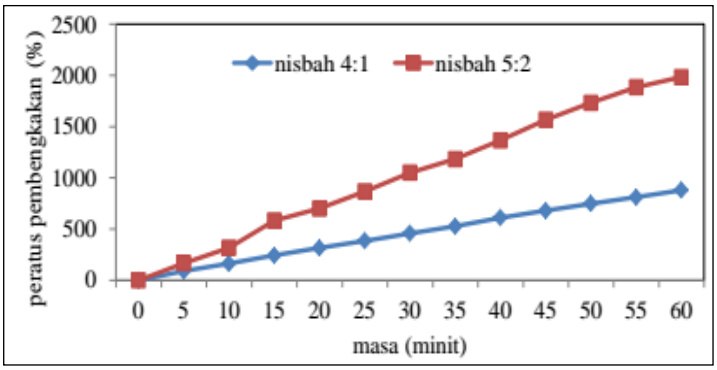
Rajah 6. Graf peratus pembengkakan (%) hidrogel di dalam larutan penimbal pH 9

Pembengkakan hidrogel dalam larutan penimbal pH 12

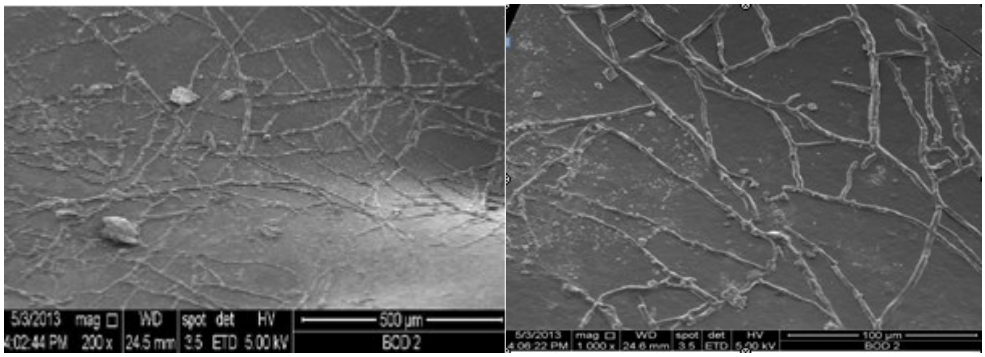
Dalam larutan penimbal pH 12, dapat diperhatikan pada Rajah 7, hidrogel dengan nisbah 5:2 mempunyai nilai peratus pembengkakan sebanyak 1983 % berbanding dengan hidrogel bernisbah 4:1 yang hanya mencapai nilai peratus pembengkakan sebanyak 879 % sahaja. Ini menunjukkan bahawa pada larutan penimbal pH 12, hidrogel 5:2 jauh lebih baik berbanding dengan hidrogel 4:1 dalam keupayaannya menyerap air.

Analisis mikroskopi pengimbasan elektron

Rajah 8 menunjukkan morfologi bagi permukaan hidrogel dengan nisbah 5:2 yang telah dihasilkan berdasarkan kepada imej mikrograf, hidrogel dengan nisbah 5:2 mempunyai kerapuhan yang baik di mana tiada berlakunya peretakan di atas permukaan hidrogel [12].



Rajah 7. Graf peratus pembengkakan (%) hidrogel di dalam larutan penimbal pH 12



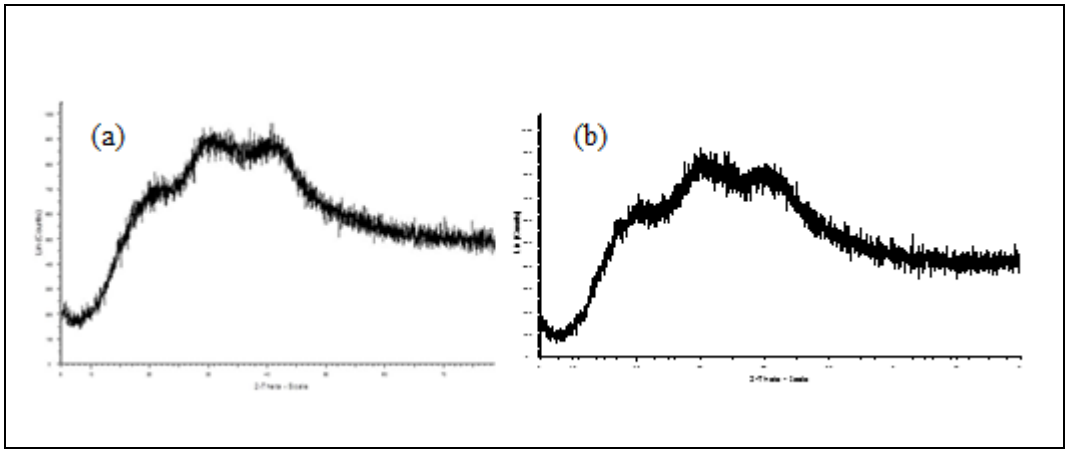
Rajah 8. Mikrograf bagi hidrogel dengan nisbah 5:2 (a) dan hidrogel dengan nisbah 5:2 pada pembesaran 100 µm

Analisis pembelauan sinar-X

Rajah 9 menunjukkan difraktogram pembelauan sinar X yang telah dijalankan bagi menentukan peratusan penghabluran hidrogel. Kedua-dua hidrogel memberikan puncak spektrum yang sama kerana berlakunya taut silang. Ketiga-tiga puncak ini membuktikan terdapatnya pembentukan kristal yang membuktikan berlakunya taut silang antara hidrogel. Perbandingan antara kedua-dua difraktogram tersebut, hidrogel dengan nisbah 4:1 memberikan spektrum dengan puncak keamatan yang lebih tinggi berbanding dengan hidrogel yang bernisbah 5:2. Spektrum yang menunjukkan puncak yang luas dan lebar disebabkan hidrogel mengandungi komponen amorfus. Manakala puncak spektrum yang tajam menunjukkan peratus penghabluran yang lebih tinggi. Peratus penghabluran yang terlalu tinggi boleh mendorong kepada peningkatan kadar kerapuhan hidrogel.

Analisis kalorimetri pengimbasan pembezaan-analisis gravimetri terma (DSC-TGA)

Jadual 1 menunjukkan perbezaan nilai peralihan gelas bagi hidrogel dengan nisbah 4:1 dan 5:2. Dalam analisis kalorimetri pengimbasan pembezaan (DSC), nilai peralihan gelas bagi hidrogel dengan nisbah 4:1 adalah dalam julat 125 – 175 °C manakala bagi hidrogel 5:2 pula, nilai peralihan gelas berjulat antara 175 – 200 °C. Bagi analisis gravimetri terma (TGA) pula, kadar kehilangan berat maksimum berlaku pada julat 125 – 175 °C bagi hidrogel 4:1 manakala 175 – 200 °C bagi hidrogel 5:2. Hidrogel 5:2 mempunyai kestabilan terma yang lebih baik berbanding hidrogel 4:1. Hal ini disebabkan oleh perbezaan kandungan serbuk ubi gadong dalam hidrogel. Menurut Halib et al. [13], struktur kanji mempunyai banyak kumpulan hidroksil di mana kumpulan ini akan membentuk ikatan hidrogen dengan air dan menyebabkan nilai peralihan kaca tinggi. Justeru, hidrogel 5:2 lebih stabil berbanding hidrogel dengan nisbah 4:1. Puncak yang terhasil pada keluk DSC bagi kedua – dua hidrogel berkemungkinan disebabkan oleh peralihan fasa yang berkaitan dengan pembentukan dan pemutusan jaringan struktur kompleks kanji [14].



Rajah 9. Difraktogram bagi hidrogel dengan nisbah 4:1 (a) manakala hidrogel dengan nisbah 5:2 (b)

Jadual 1. Perbandingan termogram bagi kedua – dua hidrogel

Nisbah hidrogel	Nilai Peralihan Gelas	
	DSC (℃)	TGA (℃)
4:1	125 – 175	125 – 175
5:2	175 – 200	175 – 200

Kesimpulan

Hidrogel berasaskan serbuk ubi gadong telah berjaya disintesis dengan menggunakan teknik radiasi gamma. Hidrogel dengan nisbah 5:2 di dapati mempamerkan ciri – ciri yang baik berbanding hidrogel 4:1. Hidrogel dengan nisbah 5:2 mempamerkan peratus pembengkakan yang tinggi pada pH 7, 9 dan 12. Analisa DSC dan SEM menunjukkan ciri – ciri hidrogel yang baik manakala keputusan TGA menunjukkan hidrogel dengan nisbah 5:2 lebih stabil secara termodinamiknya berbanding dengan hidrogel bernisbah 4:1.

Penghargaan

Penulis ingin mengucapkan terima kasih kepada UKM kerana memberi peluang penyelidikan dijalankan menggunakan geran KOMUNITI-2014-010 dan GUP-2014-079

Rujukan

1. Nadia, H., Amin, M. C. I. M. and Ahmad, I. (2010). Unique stimuli responsive characteristics of electron beam synthesised bacterial cellulose/acrylic acid composite. *Journal of Applied Polymer Science*,116(5): 2920 – 2929.
2. Hoare, T. R. and Kohane, D. S. (2008). Hydrogels in drug delivery: Progress and challenges. *Polymer*, 49(8): 1993-2007.
3. Chang, C. and Zhang, L. (2010). Cellulose-based hydrogels: Present status and application prospects. *Carbohydrate Polymers*,84(1): 40 – 53.
4. Maran, J. P., Sivakumar, V., Sridhar, R. and Immanuel, V. P (2013). Development of model for mechanical properties of Tapioca Starch based edible films. *Industrial Crops and Products*, 42: 159 – 168.
5. Eichhorn, S. J., Young, R. J. and Davies, G. R. (2005). Modeling crystal and molecular deformation in regenerated cellulose fibers. *Biomacromolecules*, 6(1): 507 – 513.
6. Pushpamalar, V., Langford, S. J., Ahmad, M., Hashim, K. and Lim, Y. Y. (2012). Preparation of carboxymethyl sago pulp hydrogel from sago waste by electron beam irradiation and swelling behavior in water

and various pH media. *Journal of Applied Polymer Science*, 128(1): 451 – 459.
7. Francis, S, Mitra, D., Dhanawade, B. R., Lalitvarshney and Sabharwal, S. (2009). Gamma radiation synthesis of rapid swelling super porous polyacrylamide hydrogels. *Radiation Physics and Chemistry*,78(11): 951 – 953.
8. Pielichowski, K. and Njuguna, J. (2005). Thermal degradation of polymeric materials. United Kingdom: Rapra Technology Limited.
9. Gulrez, S. K. H., Al-Assaf, S. and Phillips, G. O. (2011). Hydrogels: Methods of preparation, characterization and applications. *Progress in Molecular and Environmental Bioengineering*, INTECH Open Access Publisher.
10. Zhao, Q. S., Ji, Q. X., Xing, K., Li, X. Y., Liu, C. S. and Chen, X. G. (2009). Preparation and characteristics of novel porous hydrogel films based on chitosan and glycerophosphate. *Carbohydrate Polymers*, 76: 410 – 416.
11. Mohd. Amin, M. C. I. and Ahmad, N. (2012). Synthesis and characterisation of thermo- and pH-responsive bacterial cellulose/arylic acid hydrogels for drug delivery. *Carbohydrate Polymers*, 88: 465 – 473.
12. Theiss, D., Schmidt, T., Dorschner, H., Reichelt R. and Arndt, K.F. (2005). Filled temperature-sensitive poly(vinyl methyl ether) hydrogels. *Journal of Applied Polymer Science*, 98: 2253 – 2265.
13. Halib, N., Mohd. Amin, M. C. I and Ahmad, I. (2012). Physiochemical properties and characterisation of nata de coco from local food industries as a source of cellulose. *Sains Malaysiana*, 41(2): 205 – 211.
14. Pourjavadi, A. and Zohuriaan-Mehr, M. J. (2002). Modification of carbohydrate polymers via grafting in air. 2. ceric-initiated graft copolymerization of acrylonitrile onto natural and modified polysaccharides. *Starch-Starke*, 54: 482 – 488.

Malaysian Journal of Analytical Sciences, Vol 20 No 5 (2016): 1020 - 1032
DOI: http://dx.doi.org/10.17576/mjas-2016-2005-06

MALAYSIAN JOURNAL OF ANALYTICAL SCIENCES
Published by The Malaysian Analytical Sciences Society
ISSN 1394 - 2506

FABRIKASI BIOSENSOR DNA PORSIN BERASASKAN KOMPLEKS RUTENIUM BIPIRIDINA

(Fabrication of Porcine DNA Biosensor Based on Ruthenium Bipyridine Complex)

Nurul Izni Abdullah Halid[1], Emma Izzati Zakariah[1], Lee Yook Heng[1], Nurul Huda Abd Karim[1], Haslina Ahmad[2], Siti Aishah Hasbullah[1]*

[1]*Pusat Pengajian Sains Kimia dan Teknologi Makanan, Fakulti Sains dan Teknologi, Universiti Kebangsaan Malaysia, 43600 UKM Bangi, Selangor, Malaysia*
[2]*Jabatan Kimia, Fakulti Sains, Univesiti Putra Malaysia, 43400 Serdang, Selangor, Malaysia*

**Pengarang utama: aishah80@ukm.edu.my*

Received: 17 February 2016; Accepted: 9 June 2016

Abstrak

Biosensor DNA elektrokimia bagi pengesanan jujukan DNA porsin berasaskan kompleks rutenium (II) sebagai label aktif redoks telah dibangunkan. Sistem biosensor difabrikasi berdasarkan elektrod bercetak skrin (SPE) terubahsuai dengan zarah nano emas (AuNPs) sebagai transduser yang dipegunkan bersama mikrosfera poli (n-butilakrilat-N-akriloksisuksnimida) dan jujukan DNA prob terikat melalui ikatan kovalen. Kompleks interkalator rutenium (II), $[Ru(bpy)_2PIP]^{2+}$ dan (bpy = bipiridina, PIP = 2-fenillimidazo[4,5-f[1,10-fenantrolina] digunakan dalam pengesanan DNA porsin. Pengukuran dan pengoptimuman biosensor telah dilakukan dengan menggunakan voltammetrik siklik (CV) dan voltammetrik denyutan pembezaan (DPV). Interaksi antara $[Ru(bpy)_2PIP]^{2+}$ dengan beberapa jenis jujukan DNA telah dikaji iaitu, i) bebenang tunggal DNA prob, ii) selepas penghibridan DNA sasaran dan iii) selepas penghibridan dengan DNA bukan sasaran. Keputusan menunjukkan bahawa interaksi antara $[Ru(bpy)_2PIP]^{2+}$ dengan DNA sasaran yang telah terhibrid memberikan rangsangan yang paling tinggi. Prestasi biosensor adalah dipengaruhi oleh beberapa faktor antaranya ialah kepekatan $[Ru(bpy)_2PIP]^{2+}$ dan DNA prob, masa pemegunan dan penghibridan DNA prob, pH, kekuatan ion, kepekatan larutan penimbal dan suhu juga dikaji untuk menilai prestasi biosensor. Hasil kajian menunjukkan kepekatan kompleks $[Ru(bpy)_2PIP]^{2+}$ dan DNA prob, masing-masing adalah 50 µM dan 2 µM. Masa yang optimum bagi pemegunan DNA prob dan penghibridan DNA sasaran adalah 7 jam dan 60 minit. Keadaan optimum bagi pH, kekuatan ion, kepekatan larutan penimbal dan suhu, masing-masing adalah pH 7.0, 1.0 M NaCl, 0.05 M potassium fosfat pada suhu 25°C. Julat linear bagi kepekatan DNA sasaran yang berbeza adalah antara 1.0×10^{-13} M to 1.0×10^{-8} M. Kajian ini adalah yang pertama melaporkan tentang penggunaan $[Ru(bpy)_2PIP]^{2+}$ bagi pengesanan DNA porsin

Kata kunci: biosensor, DNA porsin, kompleks rutenium bipiridina

Abstract

Electrochemical DNA biosensor for detection of porcine oligonucleotides based on ruthenium (II) as label redox complex has been developed. The system of biosensor is based on the modified screen printed carbon electrode (SPE) with goldnanoparticles (AuNPs) as transducer immobilized with poly(n-butylacrylate-N-acryloxysuccinimide) microsphere and porcine DNA probe sequences was attached onto it via the covalent bond. The ruthenium(II) complex, $[Ru(bpy)_2PIP]^{2+}$ PIP = 2-phenylimidazo[4,5-f[1,10-phenanthroline] intercalator has been been used to determine prcine DNA. The biosensor was measured and optimized by cyclic voltammetry (CV) and differential pulse voltammetry (DPV). The interaction of $[Ru(bpy)_2PIP]^{2+}$ with various DNA with different sequences, i) single stranded probe DNA, ii) after hybridization with its complementary DNA and iii) after hybridization with mismatch complementary DNA were studied. The results indicated that the interaction of $[Ru(bpy)_2PIP]^{2+}$ with hybridized complementary DNA gave the highest response. Thus, development of porcine DNA biosensor and influences of many factors such as $[Ru(bpy)_2PIP]^{2+}$ complex and DNA probe concentration, DNA probe immobilization and hybridization

time, pH, ionic strength, buffer concentration and temperatures were also studied to evaluate the performance of biosensor. The concentration of $[Ru(bpy)_2PIP]^{2+}$ complex and DNA probe were found to be optimal at 50 μM and 2 μM, respectively. The optimal time for DNA probe immobilization and hybridization were 7 hours and 60 minutes, accordingly. The optimal condition of pH, ionic strength, buffer concentration and temperatures were at pH 7.0, 1.0 M NaCl, 0.05 M of Na-phosphate buffer and 25 °C, respectively. The linear range of different concentration complementary DNA was within the range between 1.0×10^{-13} M to 1.0×10^{-8} M. This study was first reported the used of $[Ru(bpy)_2PIP]^{2+}$ for detection of porcine oligonucleotides

Keywords: biosensor, porcine DNA, ruthenium bypyridine complex

Pengenalan

Asid deoksiribonukleik (DNA) merupakan suatu bahan biomolekul yang penting dalam organisma sebagai asas kepada ekspresi gen [1]. DNA membawa maklumat genetik organisma dan maklumat yang wujud dalam DNA adalah lebih banyak daripada protein disebabkan oleh kemerosotan kod genetik yang berlaku apabila DNA mengalami perubahan bentuk daripada DNA kepada protein [2]. Pada masa kini, pengesanan DNA adalah satu bidang yang menarik minat penyelidik kerana aplikasinya yang meluas dalam bidang klinikal, forensik, farmaseutikal dan pemprosesan makanan [3]. Selain daripada itu, penggunaan DNA dalam bidang biosensor mempunyai pelbagai manfaat seperti kebolehannya dalam pengesanan molekul secara semulajadi [4]. Pengesanan urutan-urutan spesifik dalam asid nukleik dengan menggunakan kaedah biosensor ini dapat mengatasi masalah penyediaan sampel yang rumit, kaedah analisis yang memakan masa yang lama, penggunaan bahan kimia yang berbahaya dan instrumentasi yang mahal [5].

Biosensor DNA secara elektrokimia memberikan hasil yang menarik kerana teknik elektrokimia mempunyai kelebihan mengatasi alat yang sedia ada. Kebiasaannya, teknik elektrokimia yang digunakan oleh penyelidik ialah transduksi voltammetri siklik (CV) dan voltammetri pembezaan denyutan (DPV) sebagai alat menganalisis interaksi larutan penunjuk redoks dengan DNA. Teknik elektrokimia ini juga ringkas dan mempunyai kos yang rendah [6]. Kaedah pengesanan penghibridan DNA berdasarkan kepada penggunaan penunjuk redoks menawarkan cara yang lebih menarik dan digemari para penyelidik berbanding pengesanan secara label bebas. Maka, pembangunan penunjuk elektrokimia yang lebih peka adalah penting untuk digunakan dalam biosensor DNA [3]. Kompleks logam polipiridil seperti ruthenium(II), rhodium(II), kuprum(II) dan sebagainya sering digunakan di dalam interaksi DNA bagi menghasilkan prob DNA elektrokimia, pemecahan kimia dan reagen biomedikal. Kini, kompleks ruthenium(II) pula telah digunakan secara meluas dalam kajian pengikatan DNA disebabkan oleh kestabilannya dari segi kimia, elektrokimia, geometri dan enantiomer serta kepekaan sifat – sifat fotofizikalnya kepada interaksi pengikatan dengan DNA [7]. Hal ini dilapor dengan kajian literatur yang dilakukan oleh Arockiasamy et al. [8] bahawa keupayaan kompleks logam polipiridil seperti ruthenium(II) mempunyai sifat pengikatan yang baik sebagai interkalator pada DNA.

Penggunaan kaedah – kaedah konvensional bagi pengesanan DNA seperti tindak balas rantai pempolimeran (PCR) dan southern blot mempunyai kekurangan seperti penyediaan sampel yang rumit, prosedur analisis yang banyak dan memakan masa yang lama serta instrumentasi mahal. Oleh kerana itu, kaedah biosensor DNA yang lebih praktikal ini mampu mengatasi masalah yang dihadapi pada kaedah-kaedah konvensional. Pembangunan biosensor DNA menghasilkan alat yang kecil, mudah alih, berkos rendah dan mudah dikendalikan [9].

Bahan dan Kaedah

Bahan kimia

Bahan kimia yang digunakan di dalam eksperimen ini seperti 1, 10 –fenontralina, ruthenium (III) klorida, 2, 2-bipiridina, benzaldehid, DNA sintetik porsin, DNA sasaran, DNA sintetik bos Taurus, DNA sintetik gallus didapati daripada Sigma Aldrich. kepekatan asid sulfurik 30% dan kepekatan asid nitric 10% dibeli daripada Sigma Aldrich dan garam natrium klorida dan garam natrium hidroksida daripada Fluka. Air nyahion yang digunakan diperoleh daripada daripada alat penyahion (Milipore).

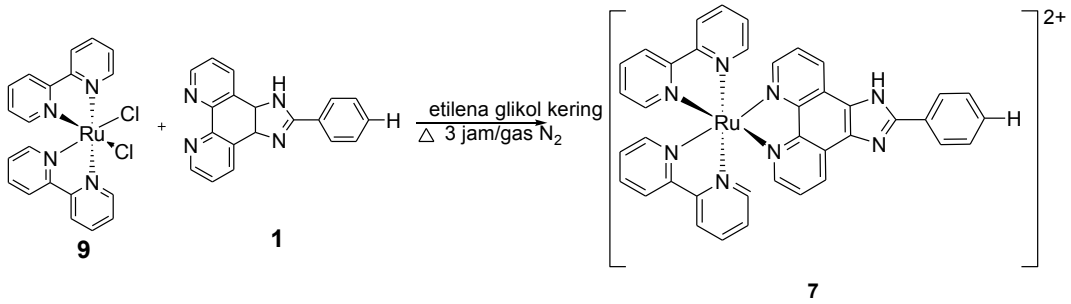
Pengukuran fizikal

Spektrum NMR (^1H and ^{13}C NMR) bagi kompleks ruthenium direkod menggunakan Bruker /AVANCE III 600 MHz Fourier 600 MHz. Spektrum Inframerah direkodkan menggunakan dis KBr (FTIR Perkin-Elmer GX Model).

Alat potentiostat Autolab dilengkapi dengan peranti *General Purpose Electrochemical System (GPES)* digunakan untuk pengukuran keupayaan biosensor.

Sintesis dan pencirian kompleks $[Ru(bpy)_2PIP]^{2+}$

Kompleks logam polipiridil $[Ru(bpy)_2PIP]^{2+}$ adalah tindak balas antara rutenium bipiridina diklorida dengan ligan pembantu, PIP, 2-fenilimidazo[4,5-f[1,10-fenantrolina] seperti yang dilaporkan oleh Li et al [10]. Gambarajah umum penyediaan kompleks ini ditunjukkan pada Rajah 1.1 di bawah.



Rajah 1. Sintesis penghasilan komples $[Ru(bpy)_2PIP]^{2+}$

Penyediaan elektrod bercetak skrin (SPE) terubah suai

Pemegunan zarah nano emas (AuNPs) dan mikrosfera poli(n-butilakrilat-N-akriloksisuksimida)

Elektrod karbon bercetak skrin (SPE) diubahsuai dengan pemendapan 0.1 mg zarah nano emas (AuNPs) dan 0.1 mg mikrosfera poli(n-butilakrilat-N-akriloksisuksimida) ke atas SPE. 0.1 mg zarah nano emas (AuNPs) yang telah dilarutkan methanol itu dikeringkan selama 20 minit. Mikrosfera akrilik yang digunakan di dalam kajian ini adalah seperti yang dilakukan oleh Ulianas et al [11].

Pencirian larutan $[Ru(bpy)_2PIP]^{2+}$

Kajian voltammetri siklik (CV) terhadap larutan $[Ru(bpy)_2PIP]^{2+}$

Elektrolit yang digunakan ialah 0.05 M larutan penimbal K-fosfat pH 7.0. Kajian voltammetri siklik bagi larutan penunjuk redoks $[Ru(bpy)_2PIP]^{2+}$ pada kepekatan 30 µM dijalankan dengan menggunakan kadar imbasan 100 mV/s. Kitaran voltammetrik siklik diimbas pada julat keupayaan 0.85 V hingga 1.2 V. Kajian voltammetri siklik dijalankan dalam keadaan statik.

Pencirian interaksi antara $[Ru(bpy)_2PIP]^{2+}$ dengan DNA porsin terpegun

Kesan kepekatan DNA prob

Kesan kepekatan DNA prob dikaji dengan memegunkan pelbagai kepekatan DNA prob (1.0, 2.0, 3.0, 4.0, 5.0 µM) ke atas SPE yang telah terubah suai dengan AuNPs dan mikrosfera akrilik. SPE terubah suai direndamkan di dalam larutan yang mengandungi prob DNA dan 0.05 M larutan penimbal K-fosfat pH 7.0.

Kesan masa pemegunan dan penghibridan DNA

Kajian kesan masa pemegunan DNA prob dilakukan pada sela masa 1 jam sehingga 24 jam manakala kajian terhadap masa penghibridan DNA sasaran dilakukan dengan pelbagai masa penghibridan antara 0.5 hingga 3.0 jam. Pemegunan 5.0 µM DNA prob dilakukan dalam larutan penimbal K-fosfat 0.05M (pH 7.0) manakala penghibridan dengan 2.0 µM DNA sasaran di dalam 0.05 M penimbal Na-fosfat (pH 7.0) yang juga mengandungi 30 µM larutan penunjuk redoks $[Ru(bpy)_2PIP]^{2+}$ dan kekuatan ion Na^+ 1.5 M.

Kesan pH dan kepekatan penimbal terhadap penghibridan DNA

Kajian kesan pH dilakukan dengan menyediakan larutan DNA sasaran 2.0 µM dalam larutan penimbal Na-fosfat 0.05 M pada pH yang berbeza (6.0 hingga 8.0). Kesan kepekatan penimbal pula dilakukan dengan menyediakan 2.0

μM larutan DNA sasaran dalam penimbal Na-fosfat pada pH 7.0 dengan kepekatan penimbal yang berlainan (0.02 M hingga 0.25 M). Proses penghibridan DNA sasaran dilakukan dengan kehadiran 30 μM $[Ru(bpy)_2PIP]^{2+}$ dan 1.5 M Na^+ ion.

Kesan kekuatan ion terhadap penghibridan DNA
Kesan kekuatan ion dikaji dengan menyediakan larutan 2.0 μM DNA sasaran dalam penimbal Na-fosfat 0.05 M (pH 7.0) yang mengandungi 30 μM $[Ru(bpy)_2PIP]^{2+}$ dan kekuatan ion yang berbeza iaitu 0.05 M hingga 2.0 M.

Kebolehasilan biosensor DNA
Kajian kebolehasilan terhadap interaksi 30 μM $[Ru(bpy)_2PIP]^{2+}$ dengan DNA sasaran ditentukan dengan melakukan pengukuran arus puncak secara berturutan dengan menggunakan lima SPE yang sama keadaan. SPE yang telah terubah suai itu mengandungi kuantiti AuNPs, mikrosfera akrilik, kepekatan prob dan DNA sasaran, masa pemegunan dan penghibridan DNA serta kepekatan larutan penimbal fosfat dan kekuatan ion Na^+

Keselektifan biosensor DNA pada DNA sasaran
Kajian keselektifan biosensor DNA sasaran porsin diuji dengan menggunakan jenis – jenis DNA sasaran yang berbeza iaitu DNA gallus (ayam), DNA bos taurus (daging lembu) dan DNA bukan sasaran porsin manakala DNA prob porsin dijadikan sebagai pengosong.

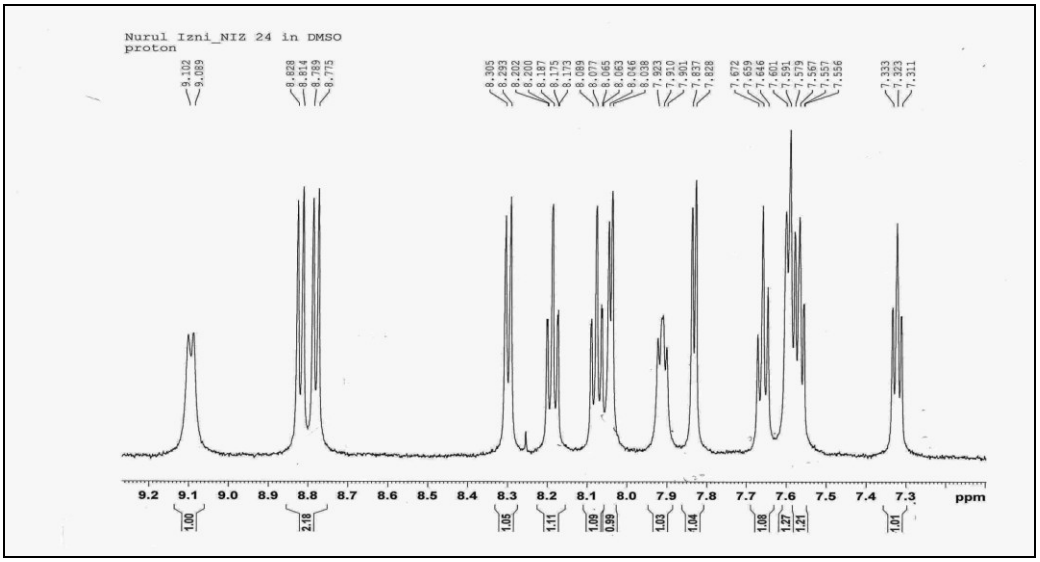
Julat rangsangan linear
Pelbagai kepekatan DNA sasaran daripada 1.0×10^{-13} μM sehingga 1.0×10^{-5} μM telah digunakan bagi menentukan julat rangsangan linear.

Keputusan dan Perbincangan

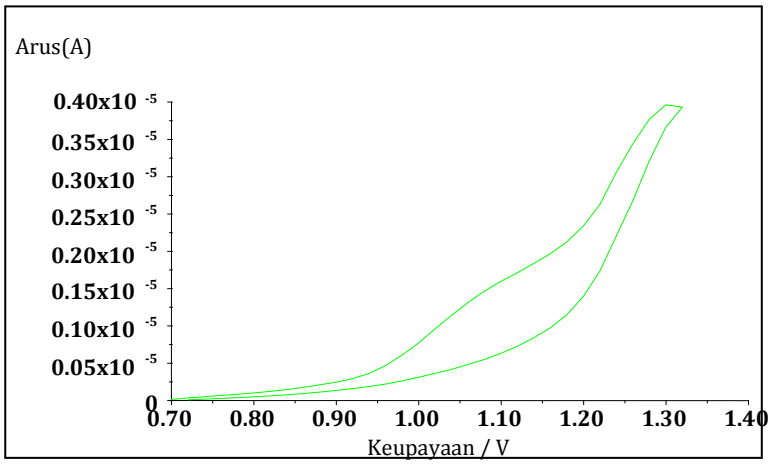
Sintesis dan pencirian kompleks ruthenium (II), $[Ru(bpy)_2PIP]^{2+}$
Analisis spektroskopi inframerah bagi kompleks $[Ru(bpy)_2PIP]^{2+}$ dilakukan bagi mengenal pasti kumpulan berfungsi yang terdapat pada kompleks ruthenium (II) ini. Data NMR (^1H dan ^{13}C) adalah bersamaan dengan data yang didapati pada kajian literatur. Spektroskopi infra merah menunjukkan kewujudan ligan 2-fenilimidazo[4,5-f[1,10-fenantrolina] dalam kompleks $[Ru(bpy)_2PIP]^{2+}$. Di dalam spektrum ini, terdapat jalur penyerapan pada 3369.77 cm^{-1} yang berpunca daripada regangan N-H pada kumpulan imidazol dalam ligan. Ciri – ciri gelang 2,2-bipiridina dalam kompleks logam $[Ru(bpy)_2PIP]^{2+}$, iaitu regangan –N=C aromatik, regangan C=C aromatik, getaran C-N aromatik dan bengkokkan =C-H (luar satah) juga dapat dikesan masing-masing pada 2373.61 cm^{-1}, 1604 cm^{-1}, 1314.5 cm^{-1} dan 763.1 cm^{-1}.

Pencirian kompleks $[Ru(bpy)_2PIP]^{2+}$ dengan menggunakan kaedah spektroskopi resonans magnet nukleus (RMN) ^1H dan ^{13}C (Rajah 2) dilakukan dengan melarutkan sampel dalam pelarut dimetilsulfoksida terdeuterat. Anjakan kimia bagi pelarut dimetilsulfoksida terdeuterat dapat dilihat pada spektrum RMN ^1H masing-masing pada 2.50 dan 3.50 ppm. Spektrum RMN ^1H menunjukkan terdapat lapan isyarat proton yang dapat dikesan pada julat 7.32 – 8.00 ppm. Isyarat dalam julat 7.32 hingga 8.00 ppm adalah dikenalpasti daripada proton-proton yang terdapat pada gelang benzena, 1,10-fenantrolina dan 2,2-bipiridina dalam kompleks $[Ru(bpy)_2PIP]^{2+}$.

Sifat voltammetri siklik larutan penunjuk redoks, $[Ru(bpy)_2PIP]^{2+}$
Rajah 3 menunjukkan voltammetrik siklik bagi 1 mM $[Ru(bpy)_2PIP]^{2+}$ dalam larutan penimbal K-fosfat pada pH 7.0 menggunakan SPE yang tidak diubahsuai. Keupayaan puncak anodik (E_{pa}) dan keupayaan puncak katodik (E_{pc}) dapat dilihat pada voltammogram siklik masing-masing pada 1.0 V dan 1.1 V dan nilai ini adalah menyamai keupayaan yang dilaporkan dalam kajian – kajian lepas oleh Erdem et al. [12] dan Johnston et al. [13].



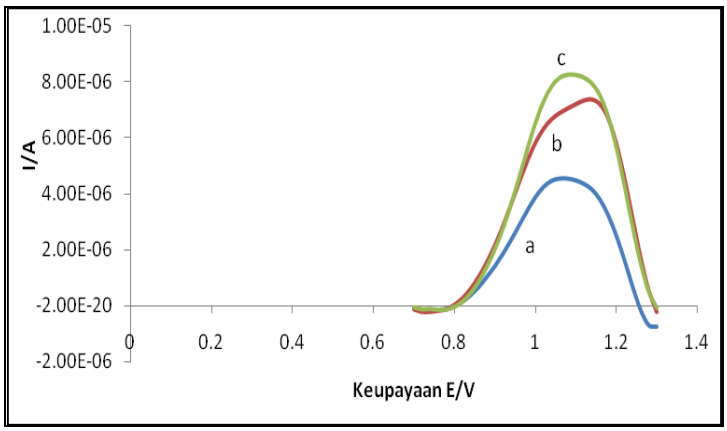
Rajah 2. Data spektroskopi RMN ^{1}H bagi kompleks ruthenium $[Ru(bpy)_2PIP]^{2+}$



Rajah 3. Voltammogram siklik bagi 1.0 mM $[Ru(bpy)_2PIP]^{2+}$ pada kadar imbasan 50 mV/s dalam larutan penimbal 0.05 M K-fosfat, elektrod rujukan Ag/AgCl, 3M KCl

Kajian voltammetri pembezaan denyutan (DPV) bagi $[Ru(bpy)_2PIP]^{2+}$ dengan DNA

Disebabkan oleh isyarat yang kurang jelas ditunjukkan daripada voltammogram siklik di atas, kajian interaksi antara kompleks ruthenium(II) ini dengan pelbagai DNA dikaji dengan menggunakan voltammetri pembezaan denyutan (DPV) kerana DPV lebih sensitif dan peka berbanding CV. Rajah 4 menunjukkan interaksi antara $[Ru(bpy)_2PIP]^{2+}$ dengan a) prob DNA porsin sahaja, b) DNA bukan sasaran selepas penghibridan dan c) DNA sasaran porsin selepas penghibridan. Daripada hasil kajian interaksi di atas, terdapat peningkatan arus DPV apabila kompleks $[Ru(bpy)_2PIP]^{2+}$ berinteraksi dengan baik secara interkalasi dengan DNA prob yang mengalami penghibridan dengan DNA sasarannya. Ini menyokong dapatan kajian yang telah dilakukan pada kajian sebelum ini oleh Xiong and Ji [14] di mana melaporkan bahawa kebanyakan kompleks logam polipiridil ruthenium(II) berinteraksi dengan DNA secara interkalasi.



Rajah 4. Voltammogram pembezaan denyutan (DPV) bagi interaksi antara $[Ru(bpy)_2PIP]^{2+}$ dengan a) prob DNA sahaja (bebenang tunggal), b) DNA bukan sasaran selepas penghibridan dan c) DNA sasaran selepas penghibridan

Pembangunan biosensor DNA porsin berdasarkan elektrod bercetak skrin (SPE) terubahsuai zarah nano emas (AuNPs), mikrosfera akrilik dan interkalator, $[Ru(bpy)_2PIP]^{2+}$

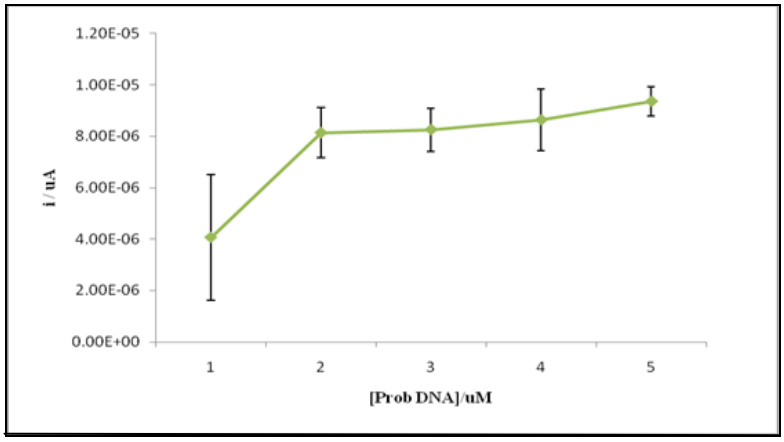
Kaedah bagi penyediaan SPE terubahsuai AuNPs-mikrosfera akrilik ini adalah seperti yang telah dijelaskan pada bahagian bahan dan kaedah. Kehadiran kumpulan berfungsi NH pada DNA adalah bagi membentuk ikatan kovalen kepada mikrosfera akrilik suknimida yang digunakan. Ini membuatkan mikrosfera akrilik itu seolah –olah memegang DNA prob dalam keadaan tegak, memudahkan proses penghibridan DNA sasaran dan interkalator menyelit ke dalam pasangan-pasangan bes DNA. Rangsangan biosensor DNA porsin diuji dengan voltammetrik siklik (CV) dan voltammetrik pembezaan denyutan (DPV) pada keupayaan 0.85 V sehingga 1.10 V di dalam larutan penimbal K-fosfat pada pH dan kepekatan tertentu.

Kesan kepekatan prob DNA porsin

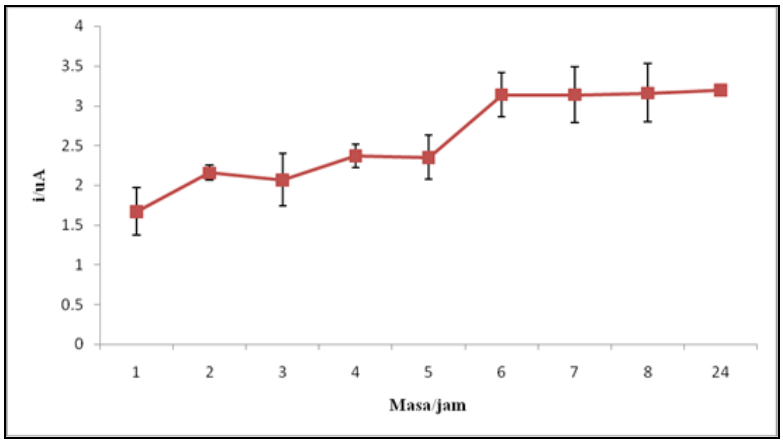
Rajah 5 menunjukkan kesan kepekatan prob DNA yang terpegun pada SPE yang terubahsuai dengan 0.025 mg zarah nanoemas (AuNPs) dan 0.1 mg mikrosfera akrilik terhadap rangsangan biosensor DNA porsin. Rangsangan DPV bagi interkalator $[Ru(bpy)_2PIP]^{2+}$ meningkat pada kepekatan prob DNA 1.0 µM sehingga 2.0 µM, kemudian selepas itu tiada perubahan ketara pada rangsangan yang dihasilkan sehingga kepekatan prob DNA 5 µM. Peningkatan rangsangan ini adalah disebabkan oleh peningkatan kepekatan prob DNA yang terpegun di atas SPE kerana semakin tinggi kepekatan prob DNA yang digunakan, semakin tinggi peluang prob DNA terpegun di atas SPE. Peningkatan kuantiti prob DNA yang terpegun pada bahan penyokong jika kepekatan prob DNA ditingkatkan adalah sama seperti yang dilaporkan oleh kajian – kajian lepas [15] yang menggunakan elektrod karbon berkaca (GCE) dan [16] elektrod emas terubahsuai sebagai tapak pemegunan prob DNA. Hasil kajian ini mendapati bahawa kepekatan prob DNA porsin yang optimum ialah 2.0 µM.

Kesan masa pemegunan prob DNA porsin

Dalam tindak balas kimia, masa tindak balas memberi kesan terhadap kuantiti hasil tindak balas. Oleh itu, kajian kesan masa pemegunan dan penghibridan perlu dijalankan seperti yang pernah dilaporkan oleh Ping et al [17]. Ini bertujuan untuk menentukan masa optimum pemegunan prob DNA dan penghibridan DNA sasaran. Rajah 6 menunjukkan kesan masa pemegunan 2.0 µM prob DNA porsin terhadap SPE terubahsuai.



Rajah 5. Kesan kepekatan prob DNA terhadap rangsangan biosensor DNA. Penghibridan dilakukan dalam larutan penimbal Na-fosfat 0.05 M pada pH 7.0 yang mengandungi 1 M NaCl dan $[Ru(bpy)_2PIP]^{2+}$



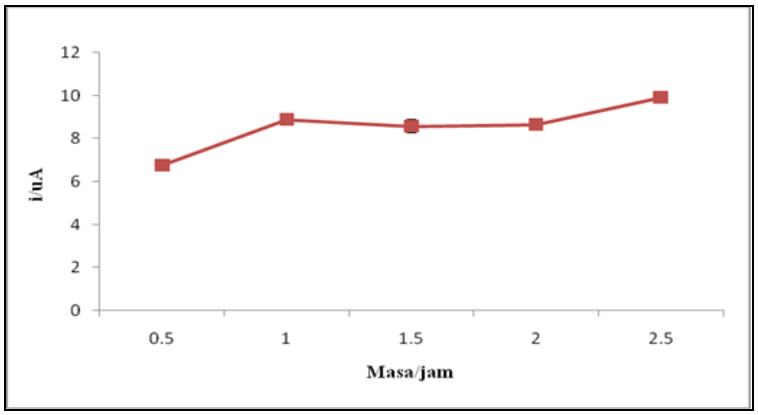
Rajah 6. Kesan masa pemegunan 2 µM prob DNA porsin ke atas SPE-AuNPs-mikrosfera terhadap rangsangan biosensor. Pemegunan dilakukan dalam 0.05 M penimbal K-fosfat pH 7.0 manakala penghibridan pula dilakukan dalam penimbal Na-fosfat 0.05 M pH 7.0 yang mengandungi 1.0 M NaCl dan 30 µM $[Ru(bpy)_2PIP]^{2+}$

Peningkatan rangsangan DPV interkalator $[Ru(bpy)_2PIP]^{2+}$ direkodkan berlaku pada 1 jam sehingga 6 jam prob DNA dipegunkan ke atas mikrosfera akrilik. Ini kerana berlakunya peningkatan kuantiti prob DNA yang terpegun ke atas SPE terubahsuai (SPE-AuNPs-mikrosfera). Selepas 6 jam, didapati tiada perubahan yang ketara pada arus DPV dan ia menjadi malar sehingga mencapai 24 jam. Ini menunjukkan bahawa semua tapak pemegunan mikrosfera akrilik (0.1 mg) telah terpegun dengan prob DNA (2 µM) pada masa pemegunan 6 jam. Oleh itu, tiada penambahan kuantiti prob DNA yang terpegun direkodkan selepas 6 jam sehingga jam ke 24. Hasil kajian mendapati masa yang optimum bagi pemegunan prob DNA pada permukaan mikrosfera akrilik adalah 6 jam.

Kesan masa penghibridan DNA sasaran porsin

Rajah 7 pula menunjukkan kesan masa penghibridan DNA terhadap rangsangan biosensor. Masa penghibridan DNA daripada 0.5 sehingga 1 jam telah meningkatkan penghibridan DNA, namun setelah masa penghibridan dipanjangkan sehingga 2.5 jam, rangsangan DPV $[Ru(bpy)_2PIP]^{2+}$ tidak menunjukkan peningkatan yang ketara. Ini

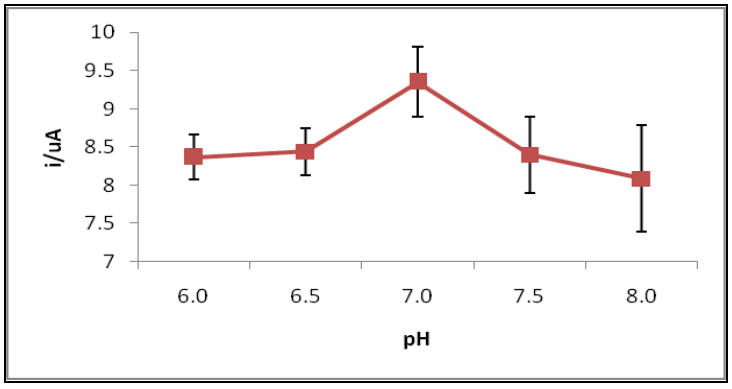
kerana pada 1 jam penghibridan semua prob DNA yang terpegun ke atas SPE-AuNPs-mikrosfera oleh DNA sasaran. Hasil kajian ini mendapati bahawa masa optimum bagi penghibridan DNA sasaran adalah optimum setelah 1 jam.



Rajah 7. Kesan masa penghibridan DNA sasaran porsin terhadap rangsangan biosensor. Penghibridan dilakukan dalam 0.05 M penimbal Na-fosfat pH 7.0 yang mengandungi 1.5 M NaCl dan 30 µM $[Ru(bpy)_2PIP]^{2+}$

Kesan pH dan kepekatan larutan penimbal terhadap penghibridan DNA

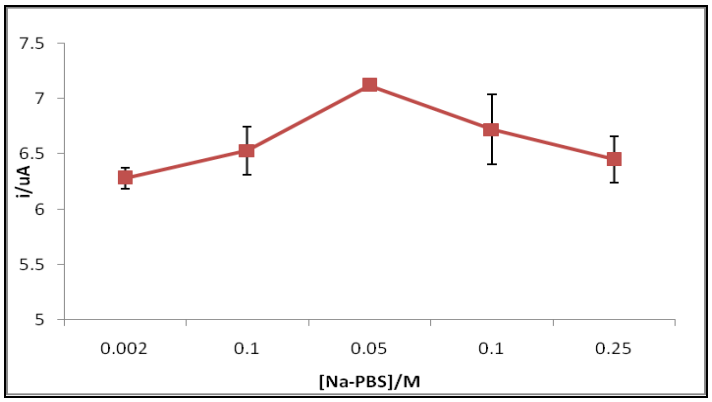
Rajah 8 menunjukkan kesan pH terhadap rangsangan biosensor DNA. Arus DPV $[Ru(bpy)_2PIP]^{2+}$ meningkat daripada pH 6.0 sehingga 7.0 dan kemudian menurun sehingga pH 8.0. Peningkatan rangsangan biosensor DNA ini menunjukkan bahawa penghibridan DNA sasaran semakin meningkat dengan peningkatan pH di dalam larutan. Sebaliknya penurunan rangsangan DPV $[Ru(bpy)_2PIP]^{2+}$ menunjukkan kuantiti penghibridan DNA semakin kurang pada julat 7.5 hingga 8.0. Ini menjelaskan bahawa kadar tindak balas penghibridan DNA boleh dipengaruhi oleh pH larutan seperti yang dilaporkan oleh kajian literatur [18]. Pada keadaan berasid berlaku tindak balas pemprotonan rantai fosfodiester DNA. Pemprotonan rantai fosfodiester akan menurunkan kelarutan molekul DNA [19]. Kelarutan yang menurun boleh mengganggu dan menurunkan kadar tindak balas penghibridan DNA.



Rajah 8. Kesan pH terhadap penghibridan DNA porsin. Penghibridan dilakukan dalam penimbal 0.05 M Na-fosfat yang mengandungi 1.5 M NaCl dan 30 µM $[Ru(bpy)_2PIP]^{2+}$

Rajah 9 pula adalah rangsangan biosensor DNA porsin dengan pelbagai kepekatan penimbal. Rangsangan DPV $[Ru(bpy)_2PIP]^{2+}$ meningkat daripada 0.002 M sehingga 0.05 M dan kemudian mulai merosot. peningkatan

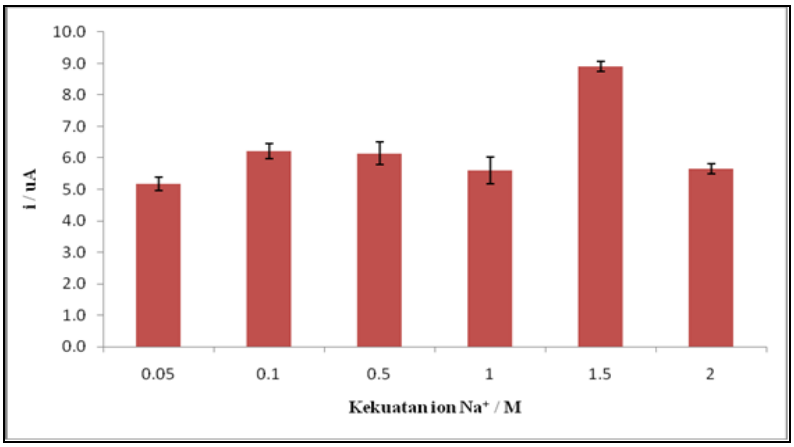
rangsangan DPV $[Ru(bpy)_2PIP]^{2+}$ menunjukkan berlakunya peningkatan kuantiti penghibridan DNA. Ini disebabkan oleh meningkatnya kuantiti ion Na^+ (kekuatan ion) jika kepekatan penimbal meningkat. Hasil kajian ini mendapati bahawa kepekatan penimbal Na-fosfat 0.05 M adalah optimum untuk penghibridan DNA porsin.



Rajah 9. Kesan kepekatan penimbal terhadap penghibridan DNA. Penghibridan dilakukan dalam pelbagai kepekatan penimbal Na-fosfat pH 7.0 yang mengandungi 1.5 M NaCl dan 30 µM $[Ru(bpy)_2PIP]^{2+}$

Kesan kekuatan ion terhadap penghibridan DNA sasaran porsin

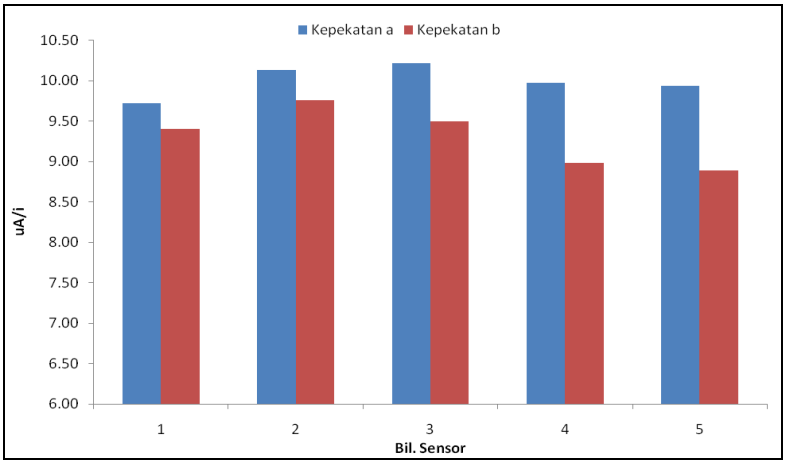
Kajian kesan kekuatan ion terhadap penghibridan DNA sasaran telah dilakukan dengan pelbagai kepekatan ion Na^+ daripada 0.05 M sehingga 2.0 M di dalam larutan penimbal Na-fosfat 0.05 M pada pH 7.0. Rajah 10 menunjukkan kesan kekuatan ion terhadap rangsangan biosensor. Rangsangan DPV $[Ru(bpy)_2PIP]^{2+}$ meningkat jika kekuatan ion meningkat dari 0.05 M hingga 1.5 M. Kekuatan ion berkesan menurunkan penolakan elektrostatik molekul DNA dan memberi kesan terhadap penghibridan DNA. Kadar tindak balas penghibridan meningkat dengan bertambahnya kepekatan garam. Kepekatan garam yang tinggi boleh menstabilkan bebenang dubel DNA (dsDNA) [20]. Kekuatan ion yang didapati daripada hasil kajian ini mencapai keadaan optimum pada 1.5 M ion Na^+ dalam larutan penimbal Na-fosfat 0.05 M dengan nilai pH 7.0.



Rajah 10. Kesan kekuatan ion Na+ terhadap penghibridan DNA. Penghibridan dilakukan dalam penimbal 0.05 M Na-fosfat pada pH 7.0 yang mengandungi 30 µM $[Ru(bpy)_2PIP]^{2+}$

Kebolehasilan biosensor DNA porsin

Rajah 11 menunjukkan rangsangan DPV $[Ru(bpy)_2PIP]^{2+}$ untuk setiap kepekatan DNA sasaran. Ia menjelaskan tiada perbezaan yang ketara prestasi setiap biosensor dengan nilai RSD, masing-masing ialah 1.93 % dan 3.97 % (n = 5) bagi kepekatan 1 x 10^{-5} (a) dan 1 x 10^{-9} (b) µM. Nilai RSD yang diperolehi di dalam kajian ini adalah lebih rendah berbanding dengan kajian yang dilaporkan oleh kajian literatur seperti Erdem et al. [12] dan Wang et al. [21] iaitu masing-masing mencapai 10.13 % dan 10.12 %. Hal ini membuktikan bahawa interaksi antara kompleks logam $[Ru(bpy)_2PIP]^{2+}$ dengan DNA adalah lebih baik daripada kajian literatur yang menggunakan penunjuk redoks, $[Ru(bpy)_3]^{2+}$ dan $[Co(phen)_3]^{3+}$.



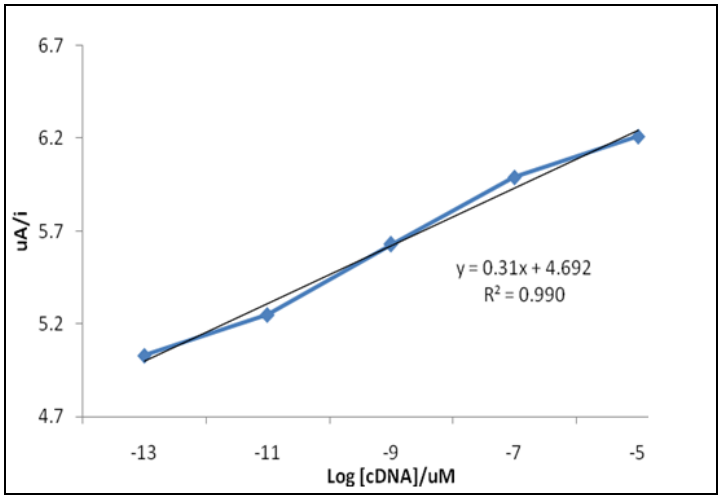
Rajah 11. Kebolehasilan biosensor DNA porsin dengan pelbagai kepekatan DNA sasaran dengan masa penghibridan selama 1 jam pada suhu bilik

Julat rangsangan linear bagi biosensor DNA porsin

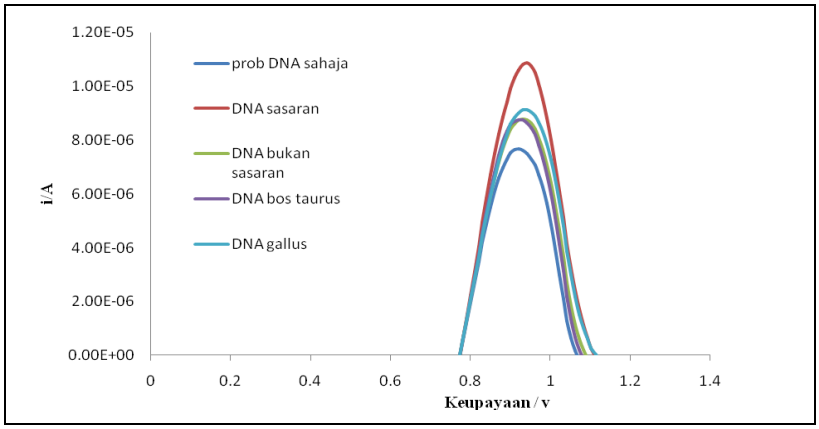
Hasil kajian mendapati rangsangan DPV $[Ru(bpy)_2PIP]^{2+}$ berkadar terus dengan kepekatan DNA sasaran pada julat kepekatan 1 x 10^{-13} sehingga 1 x 10^{-5} µM (Rajah 12). Menurut Kerman et al. [6] rangsangan biosensor DNA ini dengan menggunakan kompleks logam ini mempunyai had pengesanan yang baik. Hasil yang lebih baik ini adalah disebabkan oleh sifat hidrofobik dan peningkatan luas satah permukaan struktur 2,2-bipiridina dan 1,10-fenantrolina yang terdapat pada kompleks ruthenium ini. Ia meningkatkan sifat keafinan kompleks logam $[Ru(bpy)_2PIP]^{2+}$ berinteraksi dengan DNA.

Keselektifan biosensor DNA pada DNA sasaran

Rajah 13 menunjukkan rangsangan DPV bagi interaksi antara $[Ru(bpy)_2PIP]^{2+}$ dengan prob DNA porsin tanpa penghibridan, DNA bukan sasaran, DNA bos taurus (daging), DNA gallus (ayam) dan DNA sasaran porsin. Setiap satu DNA sasaran yang diuji mempunyai jujukan DNA yang berbeza. Hasil kajian menunjukkan bahawa rangsangan DPV yang paling tinggi terhasil daripada interaksi antara $[Ru(bpy)_2PIP]^{2+}$ tersebut dengan penghibridan DNA sasaran yang berpadanan dengan prob porsin itu. Manakala, didapati rangsangan DPV bagi penghibridan DNA prob dengan DNA bukan sasaran, DNA gallus (ayam) dan DNA bos taurus (daging) adalah lebih rendah daripada penghibridan dengan DNA sasaran (cDNA) dan interaksi kompleks $[Ru(bpy)_2PIP]^{2+}$ dengan prob DNA sahaja tanpa dihibrid menunjukkan rangsangan DPV yang paling rendah. Namun begitu, perbezaan rangsangan DPV antara penghibridan dengan DNA sasaran (cDNA) dengan DNA bukan sasaran yang lain tidak begitu ketara iaitu masing – masing, 10.9 uA (100%) dengan 8.74 uA hingga 9.12 uA (80 – 83.67 %). Hal ini menunjukkan biosensor DNA ini tidak dapat menghasilkan hasil keselektifan yang baik.



Rajah 12. Kesan pelbagai kepekatan DNA sasaran terhadap rangsangan biosensor DNA porsin. Penghibridan dilakukan dalam larutan penimbal K-fosfat 0.05 M pada pH 7.0 yang mengandungi 30 µM larutan $[Ru(bpy)_2PIP]^{2+}$ dan 1.5 M NaCl.

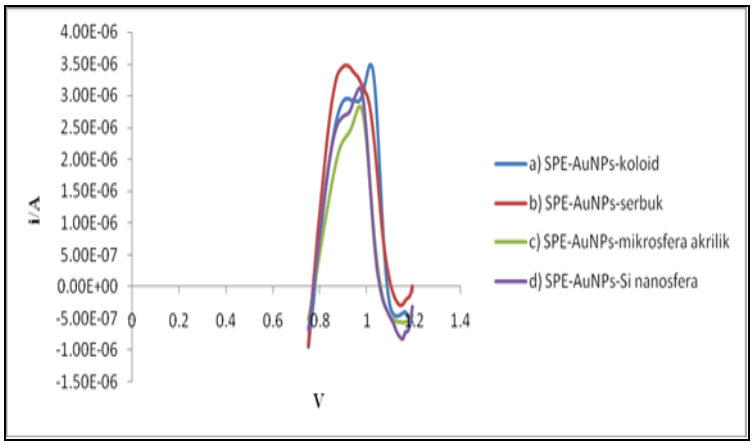


Rajah 13. Keselektifan biosensor DNA terhadap DNA sasaran porsin dan pelbagai jenis DNA tidak berpadanan. Penghibridan dilakukan dalam larutan penimbal K-fosfat 0.05 M pH 7.0 yang mengandungi 30 µM $[Ru(bpy)_2PIP]^{2+}$ dan 1.5 M NaCl

Hal ini berlaku dijangkakan kerana berlaku deposit kompleks $[Ru(bpy)_2PIP]^{2+}$ ke dalam permukaan karbon elektrod skrin bercetak (SPE) semasa proses penghibridan prob DNA dengan DNA sasaran (cDNA). Apabila kompleks logam ruthenium tersebut telah diserap terlebih dahulu ke dalam permukaan elektrod, maka apabila penghibridan DNA berlaku atau tidak, ia tetap memberikan rangsangan pada arus DPV kerana redoks berlaku dengan kehadiran kompleks logam $[Ru(bpy)_2PIP]^{2+}$ iaitu dioksidakan kepada $[Ru(bpy)_2PIP]^{3+}$ dan diturunkan kembali kepada $[Ru(bpy)_2PIP]^{2+}$.

Justeru itu, kajian diteruskan dengan mengubahsuai permukaan elektrod iaitu daripada menggunakan mikrosfera akrilik suksinimida ditukar kepada menggunakan silika nanosfera (SiO_2). Signifikan pengubahsuaian ini adalah kerana SiO_2 yang mempunyai cas positif, di mana ia akan menolak tarikan dengan kompleks interkalator $[Ru(bpy)_2PIP]^{2+}$.

Rajah 14 menunjukkan rangsangan DPV bagi $[Ru(bpy)_2PIP]^{2+}$ pada elektrod yang terubahsuai yang berbeza-beza iaitu, a) SPE yang dipegunkan dengan 50 µL zarah nanoemas (AuNPs) koloid, b) SPE yang dipegunkan dengan 20 µL (1 mg/350 µL EtOH), c) SPE yang dipegunkan dengan mikrosfera akrilik 10 µL (1 mg/1000 µL EtOH) dan d) SPE yang dipegunkan dengan 2 µL (6 mg/500 µL EtOH). Ini bagi mengkaji punca sebenar deposit kompleks ruthenium (II) ke atas elektrod. Walau bagaimanapun, hasil kajian mendapati tiada perbezaan signifikan terhadap rangsangan DPV $[Ru(bpy)_2PIP]^{2+}$ pada SPE yang terubahsuai. Justeru itu, ia dapat disimpulkan bahawa penggunaan SiO_2 juga tidak dapat menyelesaikan masalah ini. Maka, kajian lanjutan perlu dilakukan bagi memastikan pembangunan biosensor DNA porsin ini mampu menghasilkan keselektifan yang tinggi. Kajian masa hadapan yang boleh dilakukan adalah dengan memberi tumpuan kepada fabrikasi biosensor sendiri. Kajian lanjutan menggunakan beberapa elektrod juga adalah wajar. Walaubagaimanapun, hasil kajian ini telah membuktikan bahawa penggunaan ruthenium kompleks memberikan rangsangan yang tinggi dalam pengesanan DNA porsin.



Rajah 14. Rangsangan DPV bagi $[Ru(bpy)_2PIP]^{2+}$ pada SPE terubahsuai berlainan

Kesimpulan

Secara keseluruhannya, hasil kajian menunjukkan bahawa elektrod skrin bercetak (SPE) yang telah terubahsuai dengan menggunakan zarah nanoemas dan mikrosfera akrilik yang dihubungkan dengan voltammetri pembezaan denyutan (DPV) adalah sesuai untuk mengesan DNA porsin pada kepekatan rendah. Kaedah ini adalah mudah, kebolehpercayaannya tinggi dan memerlukan penggunaan sampel yang kecil. Kelebihan utama biosensor DNA ini adalah ia tidak memerlukan penggunaan bahan kimia beracun dan modifikasi asid nukleik. Selain itu, pengesanan DNA terpegun pada permukaan elektrod juga dapat dilakukan dengan cepat.

Penghargaan

Pengarang ingin mengucapkan ribuan terima kasih kepada Universiti Kebangsaan Malaysia kerana menyediakan fasiliti penyelidikan. Penyelidikan ini mendapat sokongan dan dana daripada Kerajaan Malaysia melalui Kementerian Pengajian Tinggi melalui geran e-science fund 02-01-02-SF1212 dan FRGS/1/2015/ST01/UKM02/2.

Rujukan

1. Zhai, J., Cui, H. and Yang, R. (1997). DNA based biosensors. *Biotechnology Advances,* 15(1): 43 – 58.
2. Wolf, C., Burgener, M., Hübner, P. and Lüthy, J. (2000). PCR-RFLP analysis of mitochondrial DNA: differentiation of fish species. *LWT-Food Science and Technology,* 33(2): 144 – 150.
3. Zhang, S., Tan, Q., Li, F. and Zhang, X. (2007). Hybridization biosensor using diaquabis [N-(2-pyridinylmethyl) benzamide-κ 2 N, O]-cadmium (II) dinitrate as a new electroactive indicator for detection of human hepatitis B virus DNA. *Sensors and Actuators B: Chemical,* 124(2): 290 – 296.

4. Ferancová, A., Bucková, M., Korgová, E., Korbut, O., Gründler, P., Wärnmark, I., Štepán, R., Barek, J., Zima, J. and Labuda, J. (2005). Association interaction and voltammetric determination of 1-aminopyrene and 1-hydroxypyrene at cyclodextrin and DNA based electrochemical sensors. *Bioelectrochemistry,* 67(2): 191 – 197.
5. Erdem, A., Kerman, K., Meric, B., Akarca, U. S. and Ozsoz, M. (2000). Novel hybridization indicator methylene blue for the electrochemical detection of short DNA sequences related to the hepatitis B virus. *Analytica Chimica Acta,* 422(2): 139 – 149.
6. Kerman, K., Ozkan, D., Kara, P., Meric, B., Gooding, J. J. and Ozsoz, M. (2002). Voltammetric determination of DNA hybridization using methylene blue and self-assembled alkanethiol monolayer on gold electrodes. *Analytica Chimica Acta,* 462(1): 39 – 47.
7. Richards, A. D. and A. Rodger (2007). Synthetic metallomolecules as agents for the control of DNA structure. *Chemical Society Reviews,* 36(3): 471 – 483.
8. Arockiasamy, L. D., Radhika, S., Parthasarathi, R. and Unni Nair, B (2009). Synthesis and DNA-binding studies of two ruthenium (II) complexes of an intercalating ligand. *European Journal of Medicinal Chemistry,* 44(5): 2044 – 2051.
9. Ozsoz, M., Erdem, A., Kara, P., Kerman, K. and Ozkan, D. (2003). Electrochemical biosensor for the detection of interaction between arsenic trioxide and DNA based on guanine signal. *Electroanalysis,* 15 (7): 613 – 619.
10. Li, J., Xu, L.-C., Chen, J.-C., Zheng, K.-C. and Ji, L.-N. (2006). Density functional theory/time-dependent DFT studies on the structures, trend in DNA-binding affinities, and spectral properties of complexes [Ru (bpy) 2 (p-R-pip)] 2+(R=-OH,-CH3,-H,-NO2). *The Journal of Physical Chemistry A,* 110(26): 8174 – 8180.
11. Ulianas, A., Lee, Y. H., Hanifah, S. A. and Tan. L. L. (2012). An electrochemical DNA microbiosensor based on succinimide-modified acrylic microspheres. *Sensors,* 12(5): 5445 – 5460.
12. Erdem, A., Kerman, K., Mer˙ic¸ B., Ozkan, D., Kara, P. and Ozsoz, M. (2002). DNA biosensor for Microcystis spp. sequence detection by using methylene blue and ruthenium complex as electrochemical hybridization labels. *Turkish Journal of Chemistry,* 26(6): 851 – 862.
13. Johnston, D. H., Katherine, C. G. and Thorp, H. H. (1995). Electrochemical measurement of the solvent accessibility of nucleobases using electron transfer between DNA and metal complexes. *Journal of the American Chemical Society,* 117 (35): 8933 – 8938.
14. Xiong, Y. and Ji, L.-N. (1999). Synthesis, DNA-binding and DNA-mediated luminescence quenching of Ru (II) polypyridine complexes. *Coordination Chemistry Reviews,* 185: 711 – 733.
15. Alferdo, D. L. E. M., Maria, B. G. G and Agustin, C. G. (2007). DNA hybdridization sensor based on aurothiomalate electroactive label on glassy carbon electrodes. *Biosensor and Bioelectronics,* 22: 1048 – 1054.
16. Loaiza, O. A., Campuzano, S., Pedrero, M. and Pingarron, J. M. (2007). DNA sensor based on an *Escherichia col lac* Z gen prob immobilization at sel-assembled monolayres-modified gold electrodes. *Talanta* 73: 838 – 844.
17. Ping, D., Hongzia, L. and Wei, C. (2009). Construction of DNA sandwich electrochemical biosensor with nano PbS and nanoAu tags on magnetic microbeads. *Biosensor and Bioelectronics,* 24: 3223 –3228.
18. Hames, B. B. and Higgins, S. J (1985). Nucleic acid hybridisation-a practical approach. *Oxford University Press*.
19. Metzenberg, S (2007). Working with DNA. *USA: Taylor & Francis. California State University Northridge.*
20. Lucarelli, F., Marazza, G., Turner, A.P.F and Mascini, M. (2004). Carbon and gold electrodes as electrochemical transducers for DNA hybridization sensors. *Biosensors and Bioelectronics,* 19: 515 –530
21. Wang, J. Cai, X., Rivas, G. and Shiraishi, H. (1996). Stripping potentiometric transduction of DNA hybridization process. *Analytica Chimica Acta,* 326: 141 – 147.

Malaysian Journal of Analytical Sciences, Vol 20 No 5 (2016): 1033 - 1041
DOI: http://dx.doi.org/10.17576/mjas-2016-2005-07

MALAYSIAN JOURNAL OF ANALYTICAL SCIENCES
Published by The Malaysian Analytical Sciences Society
ISSN 1394 - 2506

PREPARATION AND CHARACTERIZATIONS OF POLY(ANILINE-*co*-*m*-AMINOBENZOIC ACID)/POLYSTYRENE COMPOSITE NANOFIBERS AND FILMS

(Penyediaan dan Pencirian Poli(Anilina-*ko*-*m*-Asid Aminobenzoik)/Polistirena Komposit Fiber Nano dan Filem)

Fatimah Syahidah Mohamad and Norizah Abdul Rahman*

Department of Chemistry,
Universiti Putra Malaysia, 43400 Serdang, Selangor, Malaysia

**Corresponding author: a_norizah@upm.edu.my*

Received: 17 August 2015; Accepted: 17 June 2016

Abstract

In this research, a simple method was used to synthesize poly(aniline-*co*-*m*-aminobenzoic acid) also known as P(ANI-*co*-*m*-ABA) composite polystyrene (PS) nanofibers by using *in situ* chemical polymerization technique. The copolymer was polymerized on electrospun PS nanofibers mats with varied monomers solution concentration and the polymerization time. P(ANI-*co*-*m*-ABA) was also polymerized on PS films were prepared for comparison. The conductivity of the composites was studied and the result showed addition of graphene (GP) into the composites improved the conductivity of the composites. The composites of P(ANI-*co*-*m*-ABA)/PS nanofibers and films were characterized by Fourier transform infra-red (FTIR), thermogravimetric analysis (TGA) and ultraviolet visible (UV-vis) spectroscopy. Surface morphology of the composite was studied by scanning electron microscopy (SEM).

Keywords: poly(aniline-*co*-*m*-aminobenzoic acid), nanofibers, electrospinning

Abstrak

Dalam kajian ini, satu cara mudah telah digunakan untuk sintesis poli(anilina-*ko*-*m*-asid aminobenzoik) atau diringkas sebagai P(ANI-*co*-*m*-ABA) komposit polistirena (PS) fiber nano dengan menggunakan teknik pempolimeran kimia *in situ*. Pempolimeran kopolimer telah dijalankan ke atas PS fiber nano pada kepekatan monomer dan masa pempolimeran yang berbeza. P(ANI-*co*-*m*-ABA) juga menjalani proses pempolimeran ke atas filem PS sebagai perbandingan. Konduktiviti komposit telah dikaji dan keputusan menunjukkan dengan penambahan grafin (GP) ke dalam filem PS, bacaan konduktiviti elektrik telah meningkatkan. Komposit P(ANI-*co*-*m*-ABA) dan fiber nano PS telah dicirikan dengan menggunakan spektroskopi inframerah transformasi Fourier (FTIR), analisis termogravimetri (TGA) dan spektroskopi ultraungu nampak (UV-vis). Morfologi komposit juga telah dikaji dengan menggunakan mikroskopi elektron imbasan (SEM).

Kata kunci: poli(anilina-*ko*-*m*-asid aminobenzoik), fiber nano, putaran elektro

Introduction

PANI is one of the most studied conducting polymers due to its high electronic conductivity, redox and ion-exchange properties, excellent environmental stability and ease of preparation from common chemicals. The utilization of homopolymer PANI in industrial and technological application is hampered by its poor processability and miscibility due to low solubility [1]. The synthesizing copolymer of aniline and substituted aniline with

carboxylic acid is one of the attempts that have been made in order to increase its processability. Acid functionalize PANI such as P(ANI-*co*-*m*-ABA) was prepared chemically by adding the aniline with co-monomer, in this case is *m*-aminobezoic acid (*m*-ABA). The incorporation of functional group (COOH) into polymer backbone gives different properties from those of PANI in terms of lower conductivity with increasing solubility [2].

Meanwhile, PS nanofiber have received attention due to their unique properties such as low density, large surface area to mass, and high pore volume with controllable pore size [3]. In recent years, PS nanofibers have been fabricated by electrospinning technique. The electrospun PS nanofibers have a good macromolecular orientation along the fibers direction, which is produced by stretching of the polymer jet during electrospinning. The high molecular orientation of polymer molecules in the electrospun nanofibers enhances their mechanical properties (e.g. higher elastic modulus and strength) as compared to bulk material [4]. Therefore, the composite of P(ANI-*co*-*m*-ABA) and PS nanofiber can enhace the properties of both polymers.

GP is known for its very low weight and great efficiency in conduction of both and electricity [5]. Due to graphene's exceptional thermal, mechanical and electrical properties, it stands out as the most promising candidate to be a major filling agent for composite applications. GP nanocomposites at very low loading show substantial enhancements in their multifunctional aspects, compared to conventional composites and their materials. This not only makes the material lighter with simple processing, but also makes it stronger for various multifunctional applications. The remarkable properties of GP are able to improve the physicochemical qualities of the host matrix upon distribution [6].

The aim of this study is to prepare the poly(aniline-co-m-aminobenzoic acid) composite polystyrene (PS) nanofibers by using in situ chemical polymerization technique and characterize their physical and chemical properties.

Materials and Methods

Materials

Aniline was purchased from Fischer Chemical. The aniline was purified by distillation and hermetically sealed in the absence of light. The co-monomers, *m*-ABA, and oxidizing agent, APS ($(NH_4)_2S_2O_2$) with purity 97 % was supplied by Merck Schuchardt OHG. Solvents used namely dimethyl-formamide (DMF) and tetrahydrofuran (THF) were purchased from the Fischer Chemical.

Preparation of PS nanofibers

Electrospinnable solutions was obtained by dissolving 0.2 g of PS in THF/DMF (1:1) Then, the PS solution was filled in a 5 mL syringe attached with a blunt steel needle of 0.8 mm inner diameter. A square box covered with aluminium foil was placed 10 cm away from the needle tip as counter electrode. Electrospinning was carried out at room temperature in a horizontal spinning configuration, using the applied voltages 8 kV, driven by a high voltage power with a flow rate of 1 mL/h. The aluminum foil was placed over the counter electrode as collecting substrate.

Preparation of PS and PS/GP films

The preparation of PS/graphene film was similar to the preparation of PS nanofibers. An amount 10 wt. % of PS thin film was prepared by stirring 0.2 g of PS in 2 mL of THF/DMF (1:1) using a magnetic bar until PS completely dissolved. The polymer solution was poured into the petri dish and left for air dried overnight. Then, the thin PS film was cut into 5 cm x 1cm. PS/graphene film was prepared using 10 wt. % PS solution added with 15 mg of graphene powder and stirred until the whole mixture homogenously mixed together. The solution was poured into the petri dish and left for air dried overnight. The thickness of PS and PS/graphene films were measured using vernier caliper.

Preparation of PS/P(ANI-*co*-*m*-ABA) composite via *in-situ* polymerization

The PS nanofibers and film were cut into 5cm x 1cm and put in the aniline and/or *m*-ABA solution for *in situ* polymerzation. The P(ANI-*co*-*m*-ABA) was synthesized at fixed ratio of aniline to *m*-ABA 1:1. APS (3.65 g) in 50 mL of 1M HCl was added dropwise into 100 ml of 1M HCl containing aniline (1.46 mL) and *m*-ABA (1.100 g) at room temperature. The solution was stirred and left for 24 hours. The concentration of monomers (aniline and *m*-ABA) in HCl was varied from 0.5 M to 1.5 M to obtain thin P(ANI-*co*-*m*-ABA) coated on PS film or nanofibers.

The time of polymerization was also altered, 24 hours, 48 hours and 72 hours. After that, polymer composite was rinsed using deionized water and dried in oven at 40 ºC for a day.

Characterization of composite polymer

The morphologies of the products were investigated with a JEOL XL30S field emission scanning electron microscope (SEM). The samples for SEM were mounted on aluminium studs using adhesive graphite tape and sputter-coated with gold before analysis. Infrared spectra were measured in the range 200 – 2000 cm^{-1} on PANI pellets made with KBr at a Perkin Elmer 1600 FTIR spectrophotometer, taking 10 scans at a resolution of 4 cm^{-1}. Two-probe resistivity and hall voltage measurements with the model Kethley 2611-SMU is used to determine the resistivity of the sample. Two-point probe technique is used to measure the conductivity of the polymer. The sample is put on the holder and two probes was stick on the sample. A graph of current against voltage was plotted throughout this technique. Thermal gravimetric analysis (TGA) Mettler Toledo Star SW 7.01 was used. The sample was purged with nitrogen gas with a flow rate of 50 ml/min and the sample was heated from ambient temperature to 700 °C with heating rate 10° C/min.

Results and Discussion

Spectroscopic study of PS/P(ANI-*co*-*m*-ABA) composite film

Figure 1 and 2 show the UV-Vis spectra of the P(ANI-*co*-*m*-ABA) with different monomers concentrations and polymerization times. The UV-Vis spectra as shown in figure 1 and 2 display two main absorption peaks at 225 – 325 nm and 465 – 565 nm. The first peak contributed to π→ π* transition and significant to extended conjugation in polymer chain [7]. The copolymer undergoes blue shifted as the concentration of monomers used in the polymerization lower due to the less conjugated property and belongs high energy. The second peak in between 465 – 565 nm attributed to the transition of exciton of quinine due to the inter- and intrachain charge transfer [8]. The hypsochromic shift in copolymer is due to the carboxylic interruption in polymer chain as mentioned before, in which give implication to its conductivity property. The behavior of copolymer that proved in this UV-Vis is in agreement with the conductivity measurement results in which suggest that higher concentrations of monomers will decrease the conductivity property in copolymer.

In P(ANI-*co*-*m*-ABA) there is hypsochromic shift and hypochromic shift display due to the incorporation of *m*-ABA into backbone of parent structure. This phenomenon can be explained by the increasing of steric repulsion between adjacent groups as consequences of carboxylic acid group from *m*-ABA substituent addition that lead to the twisting of the polymer chain. Indirectly, this situation will lower the degree of co-planarity and interrupt the conjugation of the polymer rings, as well as increase the transition energy.

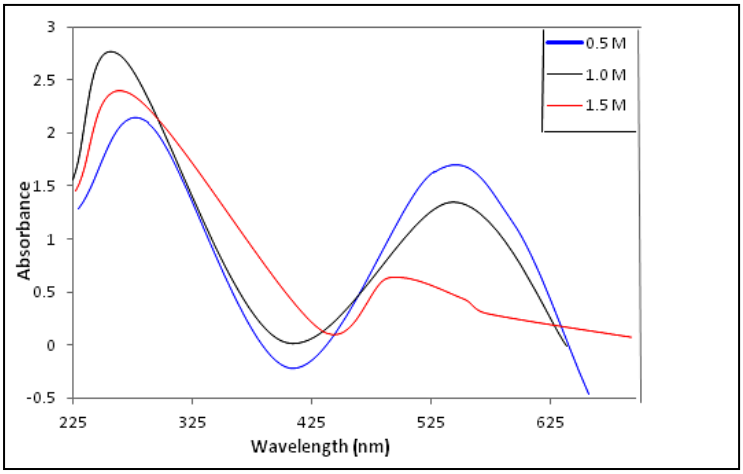


Figure 1. UV-Vis spectra of P(ANI-*co*-*m*-ABA) synthesized with monomers concentrations of 0.5 M, 1.0 M and 1.5 M, respectively

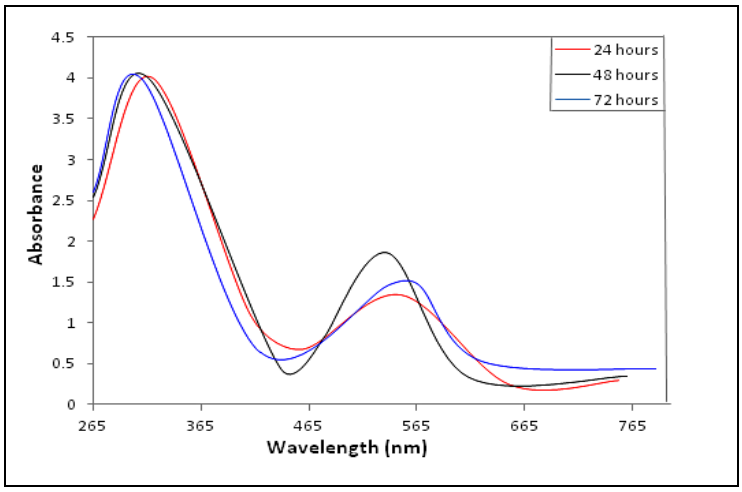


Figure 2. UV-Vis spectra of P(ANI-*co*-*m*-ABA) at 24, 48 and 72 hours

Figure 3 and Figure 4 show FT-IR spectra of composite film of the copolymer at different concentrations of monomers and polymerization time. As shown in the spectra of all samples the peaks are approximately presented at 700, 1000, 1250, 1490, 1570 cm^{-1}. The main peaks at 1490 cm^{-1} can be associated with C=N and C=C stretching vibrations of quinone and benzene rings in PANI chains. The peaks at 1250 cm^{-1} are attributed to the C-N stretching mode and the vibration of C-H in benzene ring. The peak at 1000 cm^{-1} is due to quinonoid unit of doped PANI. These related peaks confirm the successfully formation of PANI at different monomers ratios. The carbonyl group, C=O can be observed in the region in between 1500 cm^{-1} to 1600 cm^{-1}. The FT-IR results confirming the incorporation of *m*-ABA into polymer backbone due to copolymerization of aniline and *m*-ABA, thus proving that there is carboxylic group presence in the polymer structure. Both of the spectra in Figure 3 and Figure 4 assign the bands in between 650 – 750 cm^{-1} and 500 cm^{-1} in which indicates the presence of N-H bending, C-H bending in-plane and out-plane respectively [9]. The FTIR spectra of PS/P(ANI-*co*-*m*-ABA) composite nanofibers is not shown here because it is very similar to PS/P(ANI-*co*-*m*-ABA) composite film.

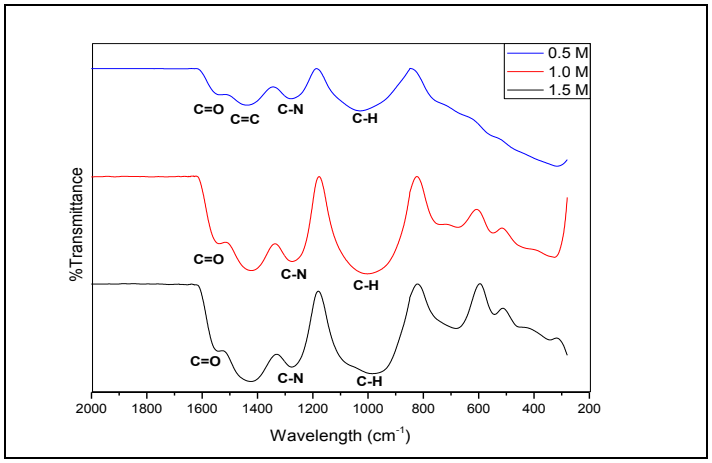


Figure 3. FTIR spectra of PS/P(ANI-*co*-*m*-ABA) film at different concentrations of monomer

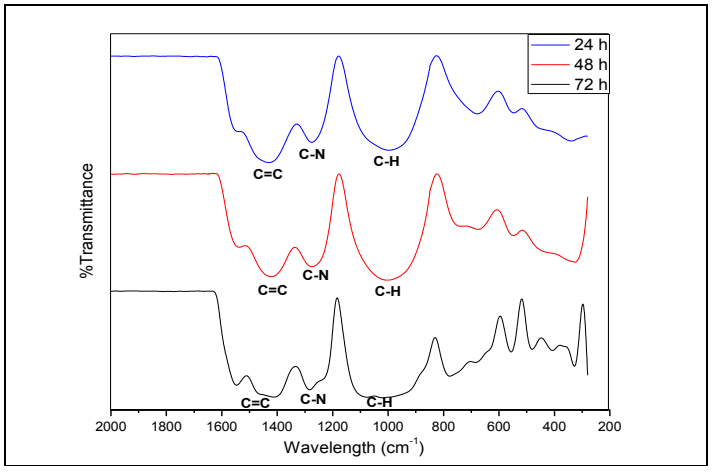


Figure 4. FTIR spectra of PS/P(ANI-*co*-*m*-ABA) composite film at different polymerization times

Thermal study of the P(ANI-*co*-*m*-ABA)/PS composite nanofiber

Figure 5 and Figure 6 represent the TGA thermograms for P(ANI-*co*-*m*-ABA)/PS at different polymerization times and different concentrations of monomers, respectively. Figure 5 and Figure 6 shows three degradation steps of PS/P(ANI-*co*-*m*-ABA) composite nanofibers**.** The composite shows a weight loss of 7 – 8 % up to 100 ℃, a weight loss of 22 % from 100 – 450 ℃ and a weight loss of 40 % from 450 – 800 ℃. Our data are found in good agreement with the data reported in literature [10, 11] which confirms the reliability of our results. When P(ANI-*co*-*m*-ABA) was polymerized onto PS nanofiber at different monomer concentration and polymerization time, a different thermal behaviour with respect to the parent polymer, i.e. PANI are shown in figures below. Thermogram suggests that weight loss mainly occurs in two steps. First step corresponds to the loss of water molecules, slow removal of oligomers and loss of impurities up to 120 ℃ with a total weight loss of 6 % at ratio concentration of monomer to monomer 0.5 M, up to 150 ℃ with a weight loss of 9 % in 1.0 M and up to 100 ℃ with a weight loss of 12 % in 1.5 M. Second weight loss is due to the expulsion of oxidizing agent, ammonium persulphate (APS).

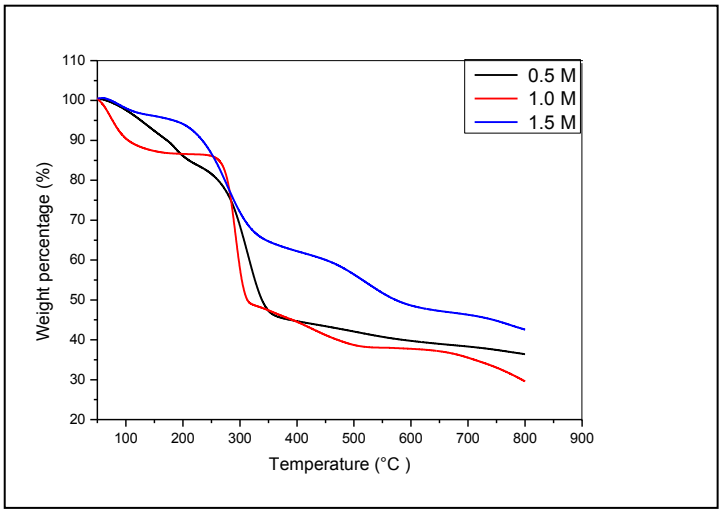


Figure 5. TGA thermograms of P(ANI-*co*-*m*-ABA)/PS composite nanofibers at different concentrations of monomers

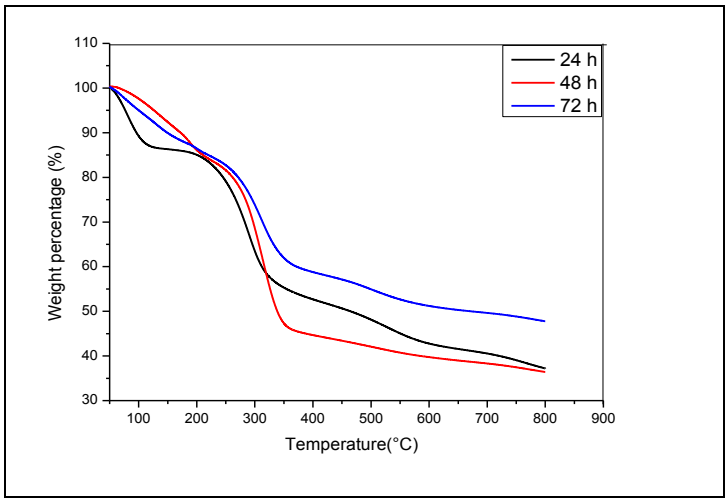


Figure 6. TGA thermograms of P(ANI-*co*-*m*-ABA)/PS composite nanofibers at different polymerization times

For P(ANI-*co*-*m*-ABA)/PS at 0.5 M and 1.5 M, the weight losses of polymer had occurred at 200 °C to 350 °C whereas for P(ANI-*co*-*m*-ABA)/PS at 1.0 M, it occurred at 270 °C to 330 °C. Third step corresponds to the degradation of polymeric backbone and polystyrene ions in the range of 300 – 400 ℃ (weight loss of ca. 13 %) in 0.5 M, in the range of 300 – 500 ℃ (weight loss ca. 25 %) in 1.0 M, and in the range of 140 – 360 ℃ (weight loss of ca. 38 %) in 1.5 M. Thus, the thermal stabilities of all the composites are considerably less than that of polyaniline. This may be attributed to the decreased chain length and presence of bulky groups in the composites. PS shows a negligible weight loss up to 350 ℃ and a continuous weight loss (ca. 15 %) is observed up to 650 ℃, which is possibly due to the degradation of PS in its thermogram. The explanation for thermograms of P(ANI-*co*-*m*-ABA)/PS at different polymerization time is almost similar to the explanation for P(ANI-*co*-*m*-ABA)/PS with different concentration. From figure 6, initial weight loss occurred because the water loss whereas the second weight loss happened because of expulsion of APS and then degradation of P(ANI-*co*-*m*-ABA).

Surface morphology of the composite film and nanofibers

Figure 7(a) and (b) show the surface morphology of the PS/GP films before and after coated with copolymer respectively. Based on the results from thermal analysis, PS/P(ANI-co-m-ABA) composite films and nanofibers were prepared using 0.5 M concentration of monomers and 24 hours' polymerization time. Figure 7(a) shows the PS film before undergoes *in situ* polymerization. There are pores presences on the surface of PS films due to the presence of air bubble inside the films. The other reasons of formation of holes on the surface of PS films may be due to the solvent DMF evaporate slowly to the surrounding during drying process. While Figure 7(b) shows the image of PS films after being coated with copolymer. The presence of copolymer can be seen as the surface of the PS film become rough and the absence of the pores is because the pores are fully covered by the copolymers. The Figure 7(b) also shown that P(ANI-*co*-*m*-ABA) has been completely and uniformly coated the surface of PS films.

Figure 8(a) and (b) show SEM images of 10 % and 15 % PS nanofibers before coated with copolymer. PS nanofibers appear to be long, thin and small in diameter. PS nanofiber has larger surface area compare to PS films due to its built up from small diameter of fibers. These special properties of nanofibers will enhance and wider its application in industry such as filter, membrane, drug delivery and many more. Figure 8(c) and (d) show the image of PS nanofiber after been coated with copolymer. The surface of the nanofiber becomes rough and thicker indicates the presence of the P(ANI-*co*-*m*-ABA). 10 % PS nanofiber has higher thickness of coating compare to 15 % PS nanofiber due to its small diameter which is 0.15 µm compare to 15 % with diameter 0.21 µm. The smallest

diameter has higher surface to volume ratio thus increasing the amount of copolymer can be deposited onto the nanofiber. The last Figure 9(a) and (b) shows the surface morphology of the PS/GP films before and after coated with copolymer. The image of PS/GP films is quite similar to the image of PS films where the surface of the film is smooth with the presence of some air bubble trapped inside the film. After copolymer is coated on top of PS/GP film, the surface of the film becomes rough and become thicker too.

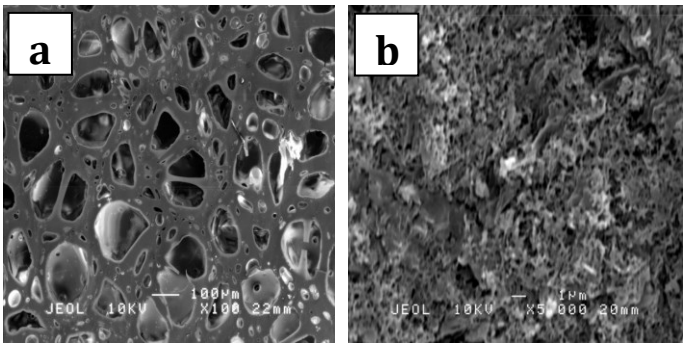


Figure 7. SEM image of (a) PS film and (b) P(ANI-*co*-*m*-ABA)/ PS film

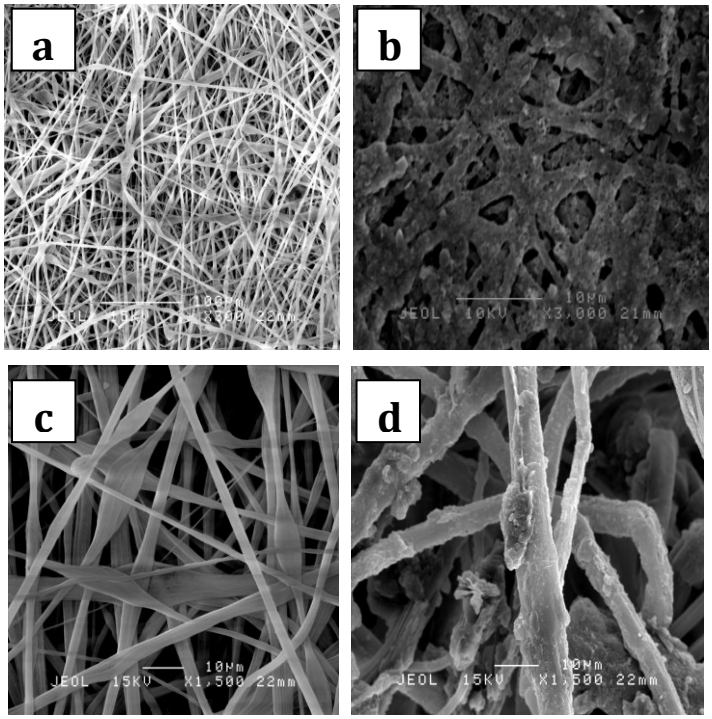


Figure 8. SEM image of (a) 10 % PS nanofiber, (b) P(ANI-*co*-*m*-ABA)/ 10 % PS nanofiber, (c) 15 % PS nanofiber and (d) P(ANI-*co*-*m*-ABA)/ 15 % PS nanofiber

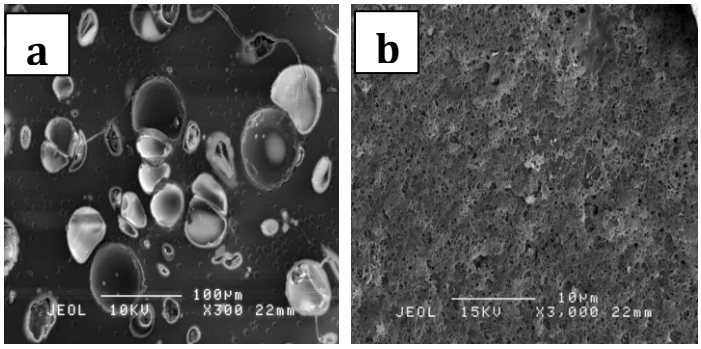


Figure 9. SEM image of (a) PS/graphene film and (b) P(ANI-*co*-*m*-ABA)/ PS/graphene film.

Electrical conductivity of the composite fibers

Electrical conductivity was measured by four-probe method (Stejskal and Gilbert 2002). Table 1 shows the conductivity values for PS nanofiber before and after coated with copolymer. Both of PS nanofiber at 10 % and 15 % before undergoes *in situ* polymerization show no conductivity value which indicates that PS nanofibers have no electrical conductivity. The copolymer coated of P(ANI-*co*-*m*-ABA)/PS nanofibers showed the conductivity of PS/P(ANI-co-m-ABA) nanofibers up to 0.26 S cm^{-1} for 10 % PS and 0.17 S cm^{-1} for 15 % PS. The composite of copolymer with PS nanofiber increase the conductivity values thus indirectly will increase the electrical conducting properties of PS as well.

Table 1. Conductivity measurement of P(ANI-*co*-*m*-ABA)/PS fiber composite

Sample	**Conductivity (S cm^{-1})**
10 % PS fiber	0.00
P(ANI-*co*-*m*-ABA)/10 % PS fiber	0.26
15 % PS fiber	0.00
P(ANI-*co*-*m*-ABA)/15 % PS fiber	0.17

Table 2 demonstrates the value of conductivity of PS film when graphene is added into the polymer film. Graphene is well known material that can conduct electrical with great efficiency. Incorporation of graphene into PS film increases the conductivity value. The conductivity value for PS film after adding graphene increased to 0.74 Scm^{-1}.

Table 2. Conductivity measurement of P(ANI-*co*-*m*-ABA)/PS/GP composite films

Sample	**Conductivity (S cm^{-1})**
PS film	-0.25
P(ANI-*co*-*m*-ABA)/PS/GP films	0.74

Conclusion

In this work, P(ANI-*co*-*m*-ABA) was deposited on PS film and nanofiber using *in situ* polymerization method. The composites were synthesized varying the amount of aniline and *m*-ABA in the composites and also varying the polymerization time. The copolymer was incorporated on PS nanofiber to become composite, hence increasing the

mechanical strength and electrical properties of the whole polymer. The structures were confirmed by FT–IR spectroscopy. The copolymer formation was confirmed by UV–Vis spectroscopy and electrical measurements. The surface morphology showed a nanofibrous structure. The conductivity of the composite increased with the addition of graphene.

Acknowledgement

The authors gratefully acknowledge to Dr Lim Hong Ngee for the supply of rGO. The authors also would like to acknowledge the financial support from the Ministry of Higher Education and Graduate Research Fellowship for the sponsorship.

References

1. Bahgat, A. A., Sayyah, S. M., and Abd-Elsalam, H. M. (2003). Study of ferroelectricity in polyaniline. *International Journal of Polymeric Materials and Polymeric Biomaterial*, 52(6): 499 – 515.
2. Abdul Rahman, N., Gizdavic-Nikolaidis, M., Ray, S., Eastal, A. J., Travas-Sejdic, J. (2010). Functional electrospun nanofibres of poly(lactic acid) blends with polyaniline or poly(aniline-co-benzoic acid), *Synthetic Metals,* 160: 2015 – 2022.
3. Ashran, V., Seydewitz, V. and Michler, G.H. (2011). Micromechanical properties and ductile behavior of electrospun polystyrene nanofibers, *Applied Polymer Science,*135: 1663 – 1673.
4. Tahir, Z., Alocilja, E. C. and Grooms, D. L. (2005). Polyaniline synthesis and its biosensor application. *Biosensors and Bioelectronics*, 20: 1690 – 1695.
5. Stejskal, J. and Gilbert, R. G. (2002). Polyaniline: preparation of a conducting polymer. *Pure Applied Chemistry*, 74(5): 857 – 867.
6. Gerard, M., Chaubey, A. and Malhotra, B. D. (2002). Application of conducting polymers to biosensors. *Biosensors and Bioelectronics*, 17: 345 – 359.
7. Gospodinova, N. and Terlemezyan, L. (1998). Conducting polymers prepared by oxidative polymerization:polyaniline. *Progress Polymer Science*, 23: 1443 – 1484.
8. Huang, Z.-M., Zhang, Y. Z., Kotaki, M. and Ramakrishna, S. (2003). A review on polymer nanofibers by electrospinning and their applications in nanocomposites. *Composite Science and Technology*, 63: 2223 – 2253.
9. Inzelt, G. (2008). Conducting polymers: A new era in electrochemistry. *Berlin: Springer,* 53: 123 – 135.
10. Wang, S., Tan, Z., Li, Y., Sun, L. and Zhang, T. (2006). Synthesis, characterization and thermal analysis of polyaniline/zro2 composites. *Thermochimica Acta*, 44: 191 – 194.
11. Wu, C. G., Liu, Y. C. and Hsu, S. S. (1999). Assembly of conducting polymer/metal oxide multilayer in one step. *Synthetic Material,* 102: 1268 – 1269.

Malaysian Journal of Analytical Sciences, Vol 20 No 5 (2016): 1042 - 1051
DOI: http://dx.doi.org/10.17576/mjas-2016-2005-08

MALAYSIAN JOURNAL OF ANALYTICAL SCIENCES
Published by The Malaysian Analytical Sciences Society
ISSN 1394 - 2506

FREE FATTY ACIDS SEPARATION FROM MALAYSIAN HIGH FREE FATTY ACID CRUDE PALM OIL USING MOLECULAR DISTILLATION

(Pemisahan Asid Lemak Bebas daripada Minyak Sawit Mentah Berasid Lemak Bebas Tinggi Melalui Penyulingan Molekul)

Murad Awadh Bahadi[1, 2], Abd-Wali Japir[2], Nadia Salih[2], Jumat Salimon[2]*

[1]*Faculty of Education and Sciences,*
Hadhramout University, Yemen
[2]*School of Chemical Sciences and Food Technology, Faculty of Science and Technology,*
Universiti Kebangsaan Malaysia, 43600 UKM Bangi, Selangor, Malaysia

**Corresponding author: jumat@ukm.edu.my*

Received: 14 February 2016; Accepted: 23 May 2016

Abstract

Molecular distillation is industrially useful in the purification of highly oxidative oils and fats, and their derivatives. Free Fatty Acids (FFAs) were isolated from high free fatty acid crude palm oil (HFFA-CPO) using molecular distillation. The isolation conditions were set-up with feeder flow rate of 2.3 g/min, wipers speed of 350 rpm, evaporator temperature ranging from 150 °C to 265 °C and pressure at 10 torr respectively. The results showed that the yield of crude palm oil after separation (CPO_{AS}) was 88 % (wt/wt). The physicochemical properties of CPO_{AS} showed a distinct difference in acid value, FFA content, iodine value and hydroxyl value compared to that of HFFA-CPO and it is more favourable for food product usage. The results showed that CPO_{AS} has lower acid value (reduced from 21.3 ± 0.1 to 2.1 ± 0.01 mg NaOH/g), increased iodine value from 50.6 ± 0.2 to 53.5 ± 0.2 mg KOH/g, reduced hydroxyl value from 43.4 ± 0.2 to 25.5 ± 0.1 mg KOH/g and lower FFA content from 9.4 ± 0.1 % to 0.9 ± 0.1 % in CPO_{AS} respectively. The work has proven that molecular distillation is an effective method for the separation of FFA from high free fatty acid crude palm oil.

Keywords: free fatty acid, crude palm oil, molecular distillation

Abstrak

Penyulingan molekul adalah bermanfaat untuk industri bagi penulenan minyak dan lemak yang telah teroksida, serta bahan-bahan terbitannya. Asid lemak bebas (FFA) telah dipisahkan daripada minyak sawit mentah berasid lemak bebas tinggi (HFFA-CPO) menggunakan penyulingan molekul. Keadaan pemisahan telah ditetapkan masing-masing dengan kadar alir suapan pada 2.3 g/min, laju pengelap 350 rpm, suhu penyejat daripada 150 °C hingga 265 °C dan tekanan pada 10 torr. Hasil kajian menunjukkan peratusan hasil minyak sawit mentah selepas proses pemisahan (CPO_{AS}) adalah 88 % (wt/wt). Sifat fiziko-kimia CPO_{AS} menunjukan beberapa perbezaan dalam nilai asid, kandungan FFA, nilai iodin dan nilai hidroksil berbanding dengan HFFA-CPO. Hasil kajian membuktikan CPO_{AS} mempunyai nilai asid yang lebih rendah (menurun daripada 21.3 ± 0.1 kepada 2.1 ± 0.01 mg NaOH/g), nilai iodin meningkat daripada 50.6 ± 0.2 kepada 53.5 ± 0.2 mg KOH/g, nilai hidroksil menurun daripada 43.4 ± 0.2 kepada 25.5 ± 0.1 mg KOH/g dan kandungan FFA menurun daripada 9.4 ± 0.1 % bagi HFFA-CPO kepada 0.9 ± 0.1 % bagi CPO_{AS}. dan menjadikannya lebih sesuai untuk digunakan dalam kegunaan makanan. Kajian ini telah membuktikan bahawa penyulingan molekul adalah suatu kaedah efektif bagi pemisahan FFA daripada minyak sawit mentah berasid lemak tinggi.

Kata kunci: asid lemak bebas, minyak sawit mentah, penyulingan molekul

Introduction

South East Asia and Equatorial Africa are considered the best locations where palm oil is widely grown and produced. In fact, there are mainly two types of oil which can be obtained from palm oil. The first part is known as crude palm oil from the flesh of the fruit (mesocarp), and the second part is palm kernel oil from the seed or kernel. Unripe fruit contains very little oil, but the mesocarp of ripe fruits has an oil content of (70 – 75 %) of its total weight. In Malaysia, production of palm oil is considered as one of the highest among other producing countries, due to the suitable climate and proper management [1, 2]. Crude palm oil (CPO) mainly consists of glycerides and small quantities of non-glyceride components. The non-glyceride components include free fatty acids (FFAs), trace metals, moisture, impurities and minor components [3]. The fatty acid composition of crude palm oil is mainly palmitic (44 %), stearic (4 %), oleic (40.6 %) and linoleic (9.8 %) [4].

According to literatures, Prasanth et al. [5] and Azlan et al. [6] reported, the Malaysian crude palm oil comprises more than (80 %) triacylglyceride, (3 – 8 %) diacylglyceride, less than (3 %) monoacylglyceride and (3 – 4 %) free fatty acids and approximately (1 %) of minor components which include carotenoids, vitamin E (tocopherols and tocotrienols), sterols, phospholipids, glycolipids, and terpenic and aliphatic hydrocarbons. Based on the standards by Malaysian Palm Oil Board (MPOB), the basic quality specifications of CPO are maximum 5 % FFA and 0.25 % of moisture content and impurity respectively [7]. Meanwhile, the Palm Oil Refiners Association of Malaysia (PORAM) specifies lower than 0.1 % FFA content in palm oil [8].

The high level of FFAs in CPO indicates its lower ability due to the enzymeic and microbial lipase reactions of palm fruit, as well as the storage of CPO under bad conditions such as high temperature and high moisture which can affect the quality of oil [9, 10]. The most commonly used methods for FFA separation are molecular distillation, chemical esterification, supercritical extraction, and organic solvent nanofiltration [11, 12]. Chemical esterification with or without catalyst involves separation of FFA from the crude palm oil at high temperature and inert medium with free hydroxyl groups remain in the oil. Supardan and Satriana [12] effectively reduced FFA content from 33.3 % to 1% through esterification with methanol using sulphuric acid as catalyst at 1% (wt/wt). Although high rate of FFA can be removed using chemical esterification, high temperature during distillation would increase the production cost. In another study, Shah and Venkatesan [13] achieved selectively free fatty acids separation from vegetable oil at ambient temperature using 75% aqueous and 80 % isopropyl alcohol as the extraction solvent. The key factor which has contributed to such effective separation is the presence of water in the aqueous isopropyl. As the free fatty acids were transferred into the aqueous isopropyl layer, a progressive decoupling effect was exerted on the alcohol and oil layers and consequently formed immiscible phases.

The molecular distillation process is a useful mechanism to separate and purify high molecular weight materials, as well as compounds that are thermally sensitive such as free fatty acids and vitamins. Furthermore, this technique offers a major advantage that it avoids problems with toxicity among others that use solvents as the separating agent. Molecular distillation processes, enable maximum removal of free fatty acids by manipulating the feed flow rate and temperature of distillation for the extraction of minor components from palm fatty acid distillates. The removal capacity is associated to the yield, purity, and rate of evaporation in terms of concentrations, distribution coefficients, and relative volatilities [14, 15]. In previous study, molecular distillation has been employed to reduce FFAs from soybean oil by varying the operating conditions. High separation was achieved in the distillate with 81.37 % FFA, performed under 140 °C evaporator temperature and 1.87 g/min feed flow rate [15].

The FFA content is an important specification that influences the palm oil quality within the production, storage and marketing stages. The objective of this research work was to extract the FFAs from the HFFA-CPO and to determine the physicochemical properties.

Materials and Methods

Sample collection

Malaysian high free fatty acid crude palm oil (HFFA-CPO) was obtained from a local refinery, Sime Darby, Selangor Malaysia.

Chemicals and reagent
Sodium hydroxide, potassium iodide, Wijs solution, n-hexane, sodium thiosulphate, potassium hydroxide, hydrochloric Acid, acetic anhydride, pyridine and ethyl alcohol were purchased from Sigma-Aldrich.

Free fatty acid separation
Free fatty acid separation from high free fatty acid crude palm oil was carried out using molecular distillation apparatus (Incon ILC-04 SPD, USA). HFFA-CPO of 100 g was added into a feed tank. The conditions of distillation were as follows: 10 torr (pressure), 60 °C (condenser temperature), 150 °C − 270 °C (evaporator temperature), 2.3 g/min feed flow rate and 350 wiper basket speed. After distillation, the distillate and retentate products were collected, weighed and analysed.

Chemical characteristic analysis: *Acid value (AV) & FFA %*
Acid value of oil was determined according to AOCS (1989) standard methods Cd 3a-63[16]. FFA % and acid value in CPO as palmitic acid was calculated using the following equations 1 and 2 below:

$$\%\ \text{FFA as Palmitic acid} = \frac{25.6 \times \text{N} \times V}{W} \quad (1)$$

where the value of 25.6 is the formula for FFA determination is equivalence factors for palmitic acid; the predominant fatty acid in palm oil. N is normality of NaOH, V is volume of NaOH solution used in mL and W is weight of sample.

$$\text{Acid value} = \%\ \text{FFA as palmitic acid} \times 2.19 \quad (2)$$

where the value of 2.19 is the conversion factor for palmitic acid.

Iodine value (IV)
The iodine value was calculated as recommended by the (AOCS 1989) standard methods Cd 1-25 [16] as given in equation 3 below:

$$\text{I.V} = \frac{12.69 \times \text{N}(\text{Vb} - \text{Vs})}{W} \quad (3)$$

where N is the normality of the $Na_2S_2O_3$ solution, Vb is the volume (mL) of $Na_2S_2O_3$ solution used for the blank test, Vs is the volume (mL) of $Na_2S_2O_3$ solution used for the determination of the sample, W is the weight in grams of the sample test portion. The value of 12.69 are used to transfer equivalent thiosulphate to g (iodine). The molecular mass unit or relative molecular unit of iodine is 126.9.

Saponification value and unsaponifiable matter
Saponification value and unsaponifiable matter of oil were determined by adopting the methods by Salimon et al. [17].

Hydroxyl value
Hydroxyl value was determined according to AOCS standard methods Cd 13-60 [16].

Physical characteristic analysis
Colour
The oil colour was determined using a Lovibond tintometer Model F/10508, according to the PORIM test method [18]. The frozen oil samples were melted by placing them in an oven at a temperature of 60 °C. The liquefied samples were placed into an inch cell up to three quarters full, and the colour was determined at 28 °C by achieving the best possible match with the standard colour slides of red and yellow indices.

Viscosity
The viscosity of the HFFA-CPO and CPO_{AS} was determined using a Brook field model RV DV-I+ (U.S.A) Spindle of SO5. The viscosity was read in Pascal second (Pa.s) directly from the viscometer, which was maintained at 1 min and 100 rpm at room temperature.

Moisture Content
The moisture content of HFFA-CPO and CPO_{AS} was determined by using a Moisture Analyzer model AND MX-50. Approximately 5g of CPO was weighed into a moisture dish, and dried in the moisture analyser for 30 minutes at 101 °C.

Refractive Index
The refractive index of HFFA-CPO and CPO_{AS} was determined according to AOCS standard methods Cc 7-25, [16] using a refractometer at 26.5 °C.

Specific gravity
The density of HFFA-CPO and CPO_{AS} was obtained using a delicate balance. An amount 1 mL of oil was placed on a balance, and its weight was recorded at room temperature. Later, the specific gravity was determined according to The Lund relationship [19].

Free fatty acid and fatty acid composition
The fatty acid composition (FAC) of HFFA-CPO and CPO_{AS} were determined using a Gas Chromatography (Shimadzu GC-17A) equipped with a capillary column BPX 70 (30m x 0.25mm x 0.25 µm) and an FID detector. The column temperature was programmed at 120 °C, with an increment of 3 °C per minute up to 245 ^{o}C, whereas the injector and detector temperature were set at 260 °C and 280 °C respectively. High purity helium gas (99.99 %) was used as the carrier gas with a flow rate of 0.3 mL/min. Fatty acid methyl ester (FAME) was prepared with base-catalysed trans esterification according to Salimon et al [17], and using acid-catalysed transesterification proposed by Ichihara et al. [20]. Peaks were identified by comparing with the retention times of the authentic standards.

Analysis of TAG in crude palm oil
Chromatography separation was performed using High performance liquid chromatography (HPLC), model 1525 equipped with refractive index detector and Spherisorb C18 (5 µm; 250 × 4.6 mm) column. HPLC was employed to analyse the triacylglyceride, diacylglyceride, monoacylglyceride and free fatty acid. The parameters of HPLC were carried out according to Cunha et al. [21]. The eluent used was a gradient of acetone (A) and acetonitrile (B). Elution was performed with a solvent flow rate of 0.4 mL/min with a linear gradient as follows: 0 min 30 % B, 20 min 25 % B, 35 min 20 % B and maintained for 20 min before returning to the initial conditions within 3 min. The effluent was monitored with an ELSD detector with the following settings: evaporator temperature of 40 °C, air pressure of 3.5 bar and photomultiplier sensitivity of 6. The samples were prepared by dissolving 0.15 g in 5 mL mixture of acetone: acetonitrile (63.5:36.5) prior to injection into the HPLC.

Fourier transform infrared spectroscopy analysis of crude palm oil
Fourier Transform Infrared Spectroscopy (FTIR) analysis was carried out according to Salimon et al. method [22]. FTIR spectrum was recorded with Perkin Elmer Spectrum GX spectrophotometer in the range of 700−4000 cm^{-1}. FTIR was used to measure functional groups of HFFA-CPO and CPO_{AS}. A very thin film of HFFA-CPO and CPO_{AS} were individually covered on NaCl cells (25 mm i.d × 4 mm thickness) and were used for analysis.

Results and Discussion

Free fatty acid separation
Molecular distillation separates free fatty acids from HFFA-CPO at varying evaporator temperature depending to the boiling points of the fatty acids. It usually operates with a low feeder flow rate of 2.3 g/min and wiper speed of 350 rpm. As the evaporator temperature reached the boiling points of the free fatty acid, the distillate flow rate will increase with the feed flow rate and the highest processing capacity of the unit should be achieved. However, heat transfer limitation between the oils and evaporator will maintain a steady distillate flow rate. At that time when the feed flow rate has been increased, the material volume inside the evaporator is already high. Therefore, the heat

transfer efficiency between the material and the evaporator is reduced due to poor contact with the evaporator walls, thereby, declines the separation ratio [15].

When the HFFA-CPO was subjected to the molecular distillation, it was split in two fractions, the residue and distillate. The residue comprises low PFAD of crude palm oil (CPO_{AS}) and the recovered FFA in the distillate (PFAD). The percentage yield of DFA and CPO_{AS} is shown in Table 1. It shows in the distillate, the DFA yield is 12 % with 97.3 ± 0.1 % acid value which suggest that the distillate contains relatively high percentage of FFA. According to MPOB standards [7], the specified FFA value of a CPO should be lower than 5 % to avoid any defects on the quality of the oil. In this study, the residue has a lower percentage of FFA in CPO_{AS} (0.9 ± 0.1%). Based on these results, the CPO_{AS} in the residue exhibits the property of edible oil, and the FFA recovered in the distillate can be utilized in future industrial applications.

Table1. Yield of DFA and CPO_{AS} after molecular distillation of 100 g HFFA-CPO

	Distillate (PFAD)	**Residue (CPO_{AS})**
Yield (%)	12	88
FFA (%)	97.3±0.1	0.9±0.1

FTIR analysis of HFFA-CPO and CPO_{AS}

Verification of the isolated FFA from HFFA-CPO was carried out using FTIR spectroscopy. The characteristic of main functional groups in HFFA-CPO and CPO_{AS} is given in Table 2.

Table 2. The functional groups of HFFA-CPO and CPO_{AS} in terms of main wavenumber in the FTIR

Functional group	**Wavenumber (cm^{-1})**	
	HFFA-CPO	**CPO_{AS}**
OH stretching (FA)	3473	-
C = C bending vibration (aliphatic)	3006	3005
C-H stretching vibration (aliphatic)	2921,2853	2923, 2853
C = O stretching vibration (ester)	1744	1746
C = O stretching vibration (carboxylic acid)	1714	-
C-H scissoring and bending for methylene	1465	1464
=C–H (cis) Unsaturated	1417	1417
-CH3 sym deformation	1377	1377
-C-O-Stretching vibration(ester)	1238−1165	1237 - 1164
C-H group vibration (aliphatic)	722	722

Notes: HFFA-CPO high free fatty acid crude palm oil, CPO_{AS} crude palm oil after separation

Figure 1 shows the FTIR spectrum of HFFA-CPO where the peaks of C=O for carboxylic acid and ester were clearly seen at 1714 cm^{-1} and 1744 cm^{-1}, respectively. However, the peak of C=O of carboxylic acid disappeared after separation (Figure 1) which proven the effectiveness of the FFA separation process. The C=O (ester) peak in CPO_{AS} appeared at 1746 $cm^{-1}$and the OH stretching also disappeared after molecular distillation as shown in Figure 1.

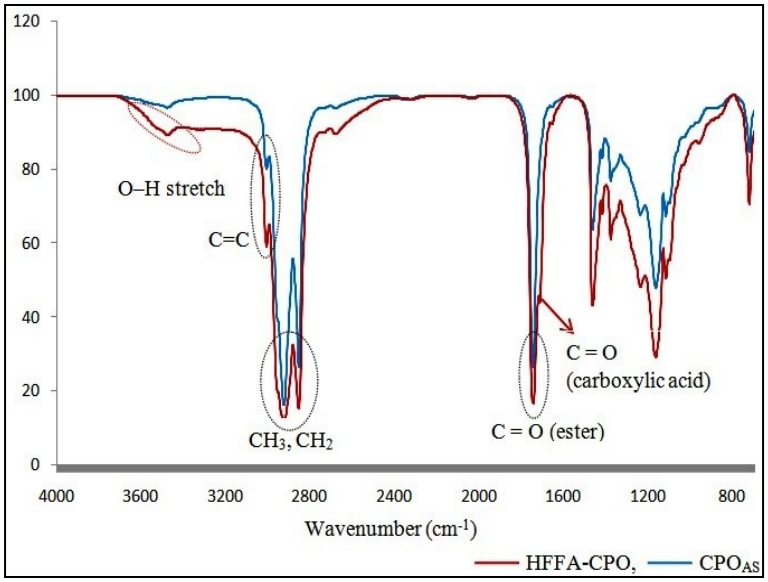


Figure 1. FTIR spectrum of HFFA-CPO and CPO_{AS}

Physicochemical properties of HFFA-CPO and CPO_{AS}

Table 3 presents the physicochemical properties of HFFA-CPO and CPO_{AS}. These properties are different in terms of the acid value, iodine value and hydroxyl value. They have similar physical properties despite the slight differences in their specific parameter values. The result shows that the average value of FFA for HFFA-CPO is high (9.4 ± 0.1%). FFA is one of the most important quality parameters in the palm oil industry as it indicates the level of deterioration of the oil. The FFA limit in Malaysian palm oil mills is 5 % [23], which clearly remarks that the FFA of CPO_{AS} (0.9 ± 0.01 %) is within standard requirement and therefore, is edible. The iodine values of the HFFA-CPO and CPO_{AS} were 50.6 ± 0.2 mg/g and 53.5 ± 0.2 mg/g respectively. This was due to the high content of unsaturated fatty acids in CPO_{AS}. This value is compatible with a typical palm oil [24]. The colour of HFFA-CPO and CPO_{AS} was 50 red and 40 yellow at room-temperature. In addition to that, their refractive value at 28 °C is equal to 1.4669. The CPO_{AS} shows high viscosity at room temperature (0.060 Pa.s) compared to HFFA-CPO (0.052 Pa.s). The results of CPO_{AS}, shown in Table 3, are similar to the physicochemical properties Malaysian crude palm oil standard (CPO_{MS}). Thus, the separation process was optimally conducted and this makes it possible for the product to be used for food industry.

Fatty acid composition

The fatty acid composition and FFA of HFFA-CPO and CPO_{AS} are summarized in Table 4. By comparison, it was proven from this work that the FFA compositions are within the standard permitted by Malaysian palm oil standard (CPO_{MS}) [26]. The results exhibit only a slight difference between the fatty acids composition of HFFA-CPO and CPO_{AS} from the base-catalysed reaction, and the values are within the standard requirements by Malaysian palm oil. Table 2 have shown palmitic acid and stearic acid as the major saturated fatty acids in HFFA-CPO. The values before and after separation are (45.7 %) and (43.9 %) for palmitic acid; (4.3 %) and (4.2 %) for stearic acid respectively. The main unsaturated fatty acids in HFFA-CPO were oleic acid and linoleic acid, with values of (39.5 %) and (9.4 %) respectively, meanwhile in CPO_{AS} the values obtained are (39.8 %) and (10.7 %) respectively.

Table 4 shows that the compositions of fatty acids for CPO_{AS} are within the Malaysian palm oil standard. Furthermore, the composition of FFA in HFFA-CPO and CPO_{AS} from the transesterification with acid catalyst is close to each other, with only minor difference with base-catalysed. FFA of HFFA-CPO and CPO_{AS} Palmitic acid (44 %) and stearic acid (4 %) were the major components of HFFA-CPO and CPO_{AS} obtained from the acid-catalysed transesterification comprises of (44.2 %) palmitic acid and (4 %) stearic acid. Oleic acid and linoleic acid

as the main components of unsaturated fatty acids in HFFA-CPO were recorded as (39.8 %) and (10.7 %) respectively. These values were increased slightly to (39.1 %) and (11.1 %) for CPO_{AS}. In addition, the composition of fatty acids for Distillate of free fatty acid (PFAD) obtained from the acid-catalysed transesterification comprises of lauric acid (0.2 %), myristic acid (0.7 %), palmitic acid (57.4 %), stearic acid (4.8 %), oleic acid (34.6 %) and linoleic acid (2.3 %).

Table 3. Physicochemical properties of HFFA-CPO and CPO_{AS}

Parameter	**HFFA-CPO**	**CPO_{AS}**	**CPO_{MS} [a]**
Iodine value (mg/g)	50.6 ± 0.2	53.5 ± 0.2	50.4 – 53.7
FFA (%)	9.4 ± 0.1	0.9 ± 0.1	< 5 %
Acid value (mg/g)	21.3 ± 0.1	2.1 ± 0.01	< 5 %
Saponification value (mg/g)	203.1 ± 0.1	200.8 ± 0.1	194 – 205
Unsaponifiable matter (%)	0.7 ± 0.1	0.39 ± 0.2	0.19 – 0.44
Average molecular weight (g/mol)	828.7	837.4	-
Hydroxyl value (mg/g)	43.4 ± 0.2	25.5 ± 0.1	-
Specific gravity (g/ml)	0.878	0.841	0.8889 – 0.8896
Refractive index at 28°C	1.4669	1.4669	1.4521 – 1.4541
Moisture content (%)	0.6	0.2	< 0.25 %
Viscosity (28°C) (Pa·s)	0.052	0.060	-
Colour at 28°C	50 R – 40 Y	50 R – 40 Y	-

a: [22], HFFA-CPO: high free fatty acid crude palm oil, CPO_{AS}: Crude palm oil after separation free fatty acid, CPO_{MS}: Malaysian crude palm oil standard.

Table 4. FA composition in HFFA-CPO and CPO_{AS} with base-catalysed transesterification (%) and FFA composition of HFFA-CPO, CPO_{AS} and PFAD with acid-catalysed transesterification

Fatty acid composotion	**Base-catalysed**			**Acid-catalysed**		
	HFFA-CPO %	**CPO_{AS} %**	**CPO_{MS} [a]**	**HFFA-CPO %**	**CPO_{AS} %**	**PFAD %**
C12:0[b]	0.2	0.3	0.2	0.4	0.5	0.2
C14:0	0.9	1.1	1.1	1.1	1.1	0.7
C16:0	45.7	43.9	43.5	44	44.2	57.4
C18:0	4.3	4.2	4.3	4.	4	4.8
C18:1	39.5	39.8	39.8	39.8	39.1	34.6
C18:2	9.4	10.7	10.2	10.7	11.1	2.3
Others	0	0	0.9	0	0	0
Total	100	100	100	100	100	100

a: [26]. b: C12:0 Lauric acid, C 14:0 myristic acid, C 16:0 palmitic acid, C 18:0 stearic acid, C 18:1 oleic acid, C18:2 linoleic acid. HFFA-CPO: high free fatty acid crude palm oil. CPO_{AS}: crude palm oil after separation. CPO_{MS}: Malaysian crude palm oil standard and PFAD: palm fatty acid distillate

Triacylglycerol composition (TAG) profile

The TAG composition in HFFA-CPO and CPO_{AS} with lower free fatty acids was identified according to the equivalent carbon number (ECN). Table 5 shows the TAGs detected for HFFA-CPO and CPO_{AS} from the chromatograph and compared with the Malaysian crude palm oil standard. The HFFA-CPO and CPO_{AS} are composed of at least fourteen important TAGs (Figure 2), whereas (74.2 %) in HFFA-CPO and (84.3 %) in CPO_{AS} depending on the percentage of the MAG and DAG [27]. The dioleoyl-palmitoyl-glycerol (POO) percentage is 25 %, and the percentage of dipalmitoyl-oleoyl-glycerol (POP) is 31% which are higher in CPO_{AS}. The TAGs exist in solid or liquid form depending on the nature of the fatty acids constituent. Most of the triacylglycerols are semi-solid at room temperature due to an equal proportion of saturated and unsaturated fatty acids contain [19]. Table 5 shows that the results of percentage of TAGs for CPO_{AS} are similar to the percentage of TAGs for Malaysian crude palm oil standard (CPO_{MS}). Therefore, this separation was conducted successfully.

Table 5. Triacylglycerol composition of HFFA-CPO and CPO_{AS} (%)

TAGs	**ECNs**	**Composition (%)**		
		HFFA-CPO	**CPO_{AS}**	**CPO_{MS}**[a]
OLL	42.0	0.1	0.2	0.2 – 0.9
PLL	42.6	1.5	1.4	1.3 – 3.4
MLP	43.3	0.2	0.2	0.2 – 1.0
OLO	44.1	0.9	0.9	1.3 – 2.3
PLO	44.7	9.6	10.0	9.0 – 11.2
PPL/PLP	45.3	8.2	8.5	6.5 – 11.0
OOO	46.2	2.5	2.7	3.3 – 6.6
POO/OPO	46.8	20.9	25.0	20.5 – 26.2
PPO/POP	47.4	25.0	31.0	27.1 – 31.0
PPP	48.0	2.3	0.5	0.7 – 7.2
SOO	48.8	0.7	1.0	1.0 – 3.6
POS	49.4	2.2	2.7	4.6 – 5.9
PPS	50.0	0.02	0.1	0.1 – 1.8
SOS	50.0	0.1	0.1	0.1 – 1.4
TAG %		74.2	84.3	≥ 90 %
DAG %		19.9	13.8	< 7.7 %
MAG %		5.9	1.9	≤ 0.5 %

a: [28 – 30], ECNs: equivalent carbon number. HFFA-CPO: high free fatty acid crude palm oil. CPO_{AS}: crude palm oil after separation. CPO_{MS}: Malaysian crude palm oil standard M: myristic, P: palmitic, S: stearic, O: oleic, L: linoleic acid.

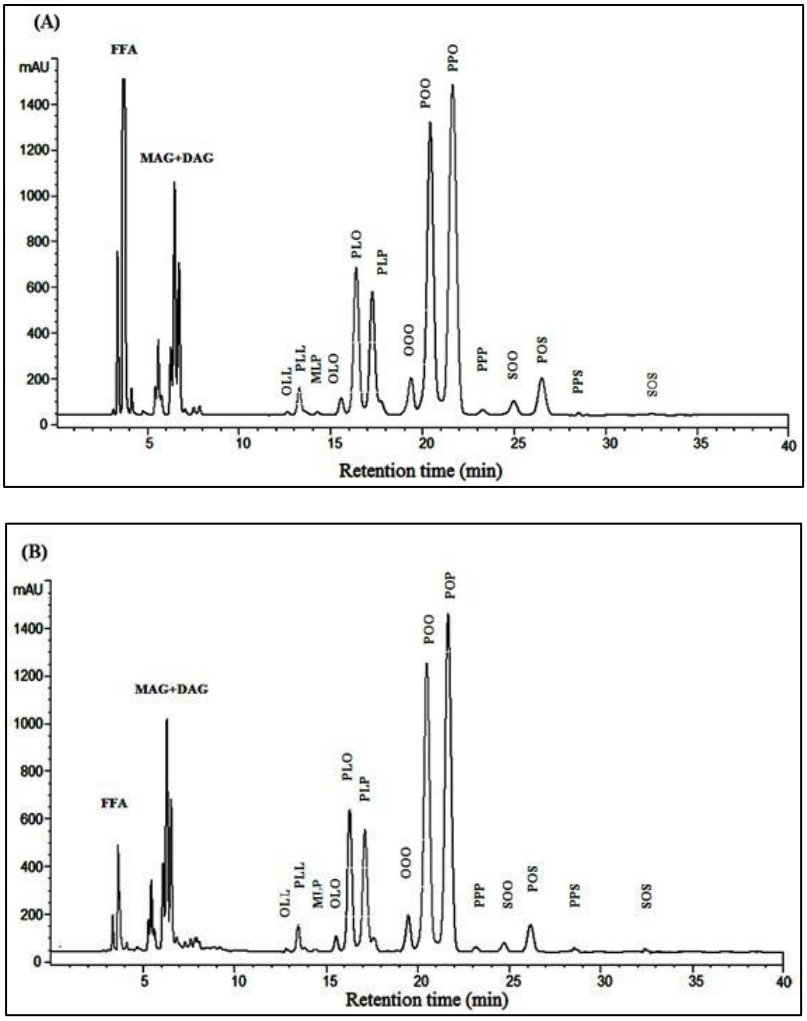


Figure 2. Triacylglycerols (TAGs) profiles chromatograms of (A) HFFA-CPO (B) CPO_{AS}

Conclusion

The high free fatty acids content in crude palm oil is unfavourable condition and need to be reduced for edible oils usage. The separation was accomplished successfully as high percentage of free fatty acids has been isolated from the crude palm oil. The optimum free fatty acid separation process conditions were at 2.3 g/min flow rate, 350 rpm wipers speed, 150 °C to 265°Cevaporator temperature range, and 10 torr pressure. The yield of crude palm oil which is edible favour after the separation (CPO_{AS}) is 88 % (wt/wt). The FFA recovered in the distillate can be utilized in future for industrial applications such as in biolubricant and bioplastic production.

Acknowledgement

We thank UKM for the project funding under university research grant no FRGS/2/2014/ST01/UKM/02/1 and Sime Darby research grant no ST-2014-019.

References

1. Poku, K. (2002). Small-scale palm oil processing in Africa. *FAO Agricultural Services Bulletin*, 148: 1 – 59.
2. Basiron, Y. and Weng, C. K. (2004). The oil palm and its sustainability the oil palm and its sustainability. *Journal of Oil Palm Research*, 16(1): 1 – 10.

3. Nagendran, B., Unnithan, U. R., Choo, Y. M. and Sundram, K. (2000). Characteristics of red palm oil, a carotene- and vitamin E-rich refined oil for food uses. *Food and Nutrition Bulletin*, 21(2): 189 – 194.
4. Tarmizi, A. H. A., Siew, W. L. and Kuntom, A. (2008). Production of palm oil reference materials for the determination of solid fat content. *Journal of Food Quality*, 31(6): 673 – 685.
5. Prasanth Kumar, P. K. and Gopala Krishna, A. G. (2014). Physico-chemical characteristics and nutraceutical distribution of crude palm oil and its fractions. *Grasasy Aceites*, 65(2): 1 -12.
6. Azlan, A., Prasad, K. N., Khoo, H. E., Abdul-Aziz, N., Mohamad, A., Ismail, A. and Amom, Z. (2010). Comparison of fatty acids, vitamin E and physicochemical properties of Canarium odontophyllum Miq. (dabai), olive and palm oils. *Journal of Food Composition and Analysis*, 23(8): 772 – 776.
7. Berger, K.G., (2006). Understanding oils and fats. *Global Oil Fat Business Magazine* 3 (4): 50 – 53.
8. Tan, Y. A. (1994). Analytical techniques in palm oil and palm kernel oil specifications. *Palm Oil Research Institute of Malaysia*, 38(2.49): 45 – 77.
9. Moh, M. H., Tang, T. S., Man, Y. C. and Lai, O. M. (1999). Rapid determination of peroxide value in crude palm oil products using Fourier transforms infrared spectroscopy. *Journal of Food Lipids*, 6(4): 261 – 270.
10. Purseglove, J. W. (1985). Tropical crops–monocotyledons. London: Longman.
11. Cermak, S. C., Kenar, J. A. and Evangelista, R. L. (2012). Distillation of natural fatty acids and their chemical derivatives. *Intech Open Access Publisher*, pp. 109 – 142.
12. Shah, K. J. and Venkatesan, T. K. (1989). Aqueous isopropyl alcohol for extraction of free fatty acids from oils. *Journal of the American Oil Chemists Society*, 66(6): 783 – 787.
13. Supardan, M. D. and Satriana, S. (2009). Esterification of free fatty acid in crude palm oil off grade. *Jurnal Rekayasa Kimia & Lingkungan*, 7(2): 70 – 74.
14. Liu, D., Shi, J., Posada, L. R., Kakuda, Y. and Xue, S. J. (2008). Separating tocotrienols from palm oil by molecular distillation. *Food Reviews International*, 24(4): 376 – 391.
15. Martins, P. F., Ito, V. M., Batistella, C. B. and Maciel, M. R. W. (2006). Free fatty acid separation from vegetable oil deodorizer distillate using molecular distillation process . *Journal from Separation and Purification Technology 48*: 78 – 84.
16. AOCS (1989). Official methods and recommended practices of the American Oil Chemists' Society (4th ed.). Champaign Illinois, USA
17. Salimon. J., Said. M., Ramli. S. and Lazim. M. (2006). Oil and Fat Analysis. UKM Publishing, Bangi, Malaysia.
18. PORIM Test Methods (1995). Kuala Lumpur: Palm Oil Research Institute of Malaysia (PORIM).
19. Gunstone, F. D. (2002). Vegetable oils and food technology: Composition, properties and use, pp 1–352.
20. Ichihara, K. I. and Fukubayashi, Y. (2010). Preparation of fatty acid methyl esters for gas-liquid chromatography. *Journal of Lipid Research*, 51(3): 635 – 640.
21. Cunha, S. C., and Oliveira, M. B. P. P. (2006). Discrimination of vegetable oils by triacylglycerols evaluation of profile using HPLC/ELSD. *Food Chemistry*, 95(3): 518 – 524.
22. Salimon, J., Abdullah, B. M. and Salih, N. (2011). Hydrolysis optimization and characterization study of preparing fatty acids from Jatropha curcas seed oil. *Chemistry Central Journal*, 5(1): 67 – 76.
23. Corley, R. H. V. and Tinker, P. B. (2003). The oil palm. USA: Blackwell, pp. 450 – 471.
24. O'Brien, R. D. (2009). Fat and oils: formulating and processing for applications. 3rd ed. Florida, USA: CRC Press Taylor & Francis Group.
25. Radizian, R., Sue, T. T., and OOI, C., Wong, S. K. (2009). Pocket book of palm oil uses. *Malaysian Palm Oil Board*, Kuala Lumpur, Malaysia.
26. Sambanthamurthi, R., Sundram, K. and Tan, Y. (2000). Chemistry and biochemistry of palm oil. *Progress in lipid research*, 39: 507 – 558.
27. Ku, C. S. and Mun, S. P. (2008). Characterization of seed oils from fresh Bokbunja (Rubus coreanus Miq.) and wine processing waste. *Bioresource technology*, 99(8): 2852 – 2856.
28. Lin, S. W. (2002). 3 palm oil. Vegetable oils in food technology: Composition, properties and uses, 59.
29. Gee, P. T. (2007). Analytical characteristics of crude and refined palm oil and fractions. *European Journal of Lipid Science and Technology*, 109(4): 373 – 379.
30. Gibon, V., De Greyt, W. and Kellens, M. (2007). Palm oil refining. *European Journal of Lipid Science and Technology*, 109(4): 315 – 335.

Malaysian Journal of Analytical Sciences, Vol 20 No 5 (2016): 1052 - 1058
DOI: http://dx.doi.org/10.17576/mjas-2016-2005-09

MALAYSIAN JOURNAL OF ANALYTICAL SCIENCES
Published by The Malaysian Analytical Sciences Society
ISSN 1394 - 2506

PERFORMANCE OF $EGZrO_2$-$EGFe_2O_3$/HY AS PHOTOCATALYST AND ITS EFFICACY IN DECOLORIZATION OF DYE-CONTAMINANTS

(Keupayaan $EGZrO_2$-$EGFe_2O_3$/HY sebagai Fotomangkin dan Keberkesanannya Dalam Penyahwarnaan Bahan Cemar Pewarna)

Muhammad Farhan Hanafi, Norzahir Sapawe*, Mohd Zulkhairi Abdul Rahim, Nurul Nabihah Rahman, Abu Hassan Abd Rahman, Asimi Ana Ahmad

Section of Technical Foundation,
Universiti Kuala Lumpur-Malaysian Institute of Chemical and Bioengineering Technology (UniKL-MICET),
Lot 1988 Vendor City, Taboh Naning, 78000 Alor Gajah, Melaka, Malaysia

**Corresponding author: norzahir@unikl.edu.my*

Received: 17 August 2015; Accepted: 13 June 2016

Abstract

The performance of electrogenerated metals supported on HY zeolite ($EGZrO_2$-$EGFe_2O_3$/HY) was studied under sunlight irradiation for the decolorization of methylene blue (MB) and Congo red (CR) in aqueous solutions. The prepared photocatalysts were examined using X-ray diffraction (XRD), transmission electron microscopy (TEM), and Brunnauer-Emmett-Teller surface area analysis (BET). An amount of 0.375 g L^{-1} $EGZrO_2$-$EGFe_2O_3$/HY was found to be the optimum dosage for 10 mg L^{-1} dyes, which gave almost complete photodecolorization of both MB and CR dye after 2 hours of contact time at pH 9 and pH 7, respectively. In addition, a control experiment was also conducted under similar conditions to confirm the efficacy of the prepared photocatalyst. The simple preparation of the photocatalyst and low amount of metal loading required, with simultaneously existence of synergistic effect from both metal oxides exhibits the great potential of the system that could be applied in textile or other industries wastewater treatment.

Keywords: photocatalyst, dyes, decolorization, sunlight

Abstrak

Keupayaan logam elektrogenerasi disokong pada zeolit HY ($EGZrO_2$-$EGFe_2O_3$/HY) telah dijalankan di bawah sinar matahari untuk penyahwarnaan metilena biru (MB) dan Congo merah (CR) dalam larutan akues. Fotomangkin telah dikaji menggunakan pembelauan sinar X-ray (XRD), mikroskopi elektron transmisi (TEM), dan analisis luas permukaan Brunnauer-Emmett-Teller (BET). Sejumlah 0.375 g L^{-1} $EGZrO_2$-$EGFe_2O_3$/HY telah didapati sebagai dos optimum untuk 10 mg L^{-1} larutan pewarna, yang memberikan penyahwarnaan hampir lengkap bagi kedua-dua pewarna MB dan CR selepas 2 jam tindak balas pada pH 9 dan pH 7. Di samping itu, satu eksperimen kawalan juga telah dijalankan pada keadaan yang sama untuk mengesahkan keberkesanan fotomangkin yang disediakan. Penyediaan yang mudah untuk fotomangkin dan jumlah muatan logam sedikit yang diperlukan, pada masa yang sama dengan kewujudan kesan sinergi dari kedua-dua oksida logam mempamerkan potensi besar untuk sistem ini digunakan dalam industri tekstil atau industri rawatan air sisa yang lain.

Kata kunci: fotomangkin, pewarna, peyahwarnaan, sinar matahari

Introduction

Over the decades, an environmental problems distress on soil and water pollution has become an important issue. In accordance, the major pollutants in wastewater such as organic dyes were produced, wherein about 15% of total

world production of dyes is lost during dyeing processes and is released in textile effluents [1-3]. In Malaysia, about 97% of the dye effluents are mainly come from three industrial classes, which are food, chemical and textiles industry [3]. Among this, about 22% of the total volume of these industrial wastewater is from the textile industry, commonly use basic dyes, such as crystal violet, rhodamine B, methyl violet, methylene blue and etc., to add colour for their final products of wool, silk, cotton, linen and modified acrylic fibres [3-4]. Though, most of the unspent dyes generate undesirable effluents and usually discharged to the environment with or without further treatment [1,5-7]. These effluents run into water bodies and can cause severe problems if not being treated properly as they are toxic, mutagenic and carcinogenic to human life as well as prohibit the photosynthesis of aquatic life even as small quantities as 1 ppm [3, 4]. To overcome this problems, several methods have been reported for the removal of such dyes including chemical and biological oxidation, adsorption, electrochemical oxidation, coagulation and flocculation, ion exchange, and membrane separation [5, 6, 8-10]. However, those methods have their own limitations for example time-consuming, generation of secondary wastes, expensive, and commercially unattractive.

Advanced oxidation processes (AOPs) particularly using semiconductors such as TiO_2, ZnO, WO_3, Fe_2O_3, CuO, ZrO_2, CdS, In_2O_3, SnO_2, etc. as photocatalysts has became attractive and accorded great importance due to its potential to destroy and transform a wide range of harmful dyes at ambient temperature to the simplest form of non-toxic products, CO_2 and water [2-4]. Zeolite is considered to be an important support owing to their high surface area, high thermal stability, eco-friendly nature, and also have reported to provide specific photophysical properties such as control charge transfer and electron transfer processes [3,4]. A review of recent research revealed that some of the succesful examples of metal oxides supported zeolite are TiO_2-HZSM-5, Co-ZSM-5, CuO-X zeolite and Fe-exchange zeolite [3,4,11-13]. Most of the popular one are TiO_2 and ZnO but the report on the ZrO_2 supported zeolite photocatalyst is quite rare. ZrO_2, which have specific optical and electrical properties, possesing both acid-base and redox function, thermal stability, and strong mechanical strength is believed to exhibit a great performance when support on zeolite [3].

Recently, we have reported a new preparation method for an α–Fe_2O_3 and EGZrO_2 supported HY catalyst by a simple and rapid electrochemical process, which possesses high photoactivity in the decolorization of methylene blue [3,14]. The nanosized metal oxides as well as the synergistic interaction between the metal and the support were found to play important roles in the enhancement of the reaction [4]. Further study on the property of that zinc metal oxide showed that it was nanoparticle in size, which showed promising photoactivity in the removal of methyl orange from aqueous solution [15]. Thus, by the corresponding method, we have succeeded to generate a very fine particles metal with higher reactivity.

Herein, as an extension of our study, we attempted to prepared nanoparticles electrogenerated ZrO_2–Fe_2O_3 supported HY zeolite (EGZrO_2–EGFe_2O_3/HY) by using the corresponding novel preparation method which is fast, simple and efficient than other methods with the aim to reduce amount of metal oxide used and tested its photoactivity on the decolorization of methylene blue (MB) and Congo red (CR) towards a green environment. The prepared catalyst was characterized by X-ray diffraction (XRD), transmission electron microscopy (TEM), and Brunnauer-Emmett-Teller of surface area analysis (BET). The performance of photoactivity decolorization was investigated to obtain the optimum conditions.

Materials and Methods

Materials

The HY zeolite had a Si/Al ratio of 80 and was purchased from Zeolyst International. The *N,N*-dimethylformamide (DMF) was purchased from Merck and the naphthalene was obtained from Fluka. The sodium hydroxide (NaOH), hydrochloric acid (HCl), and methylene blue (C.I. 52015 for microscopy) were obtained from QReC™. The platinum (Pt), zirconia (Zr), and iron (Fe) plate cells were obtained from Nilaco Metal, Japan. All of the reagents were analytical grade and were used as received. Deionized water was used for the preparation of the pH solution and adjustments to the pH were performed using a 0.1 M HCl and NaOH solution.

Catalyst preparation

The 1 wt.% EGZrO_2–1 wt.% EGFe_2O_3/HY was prepared following a previously reported protocol [3,4]. A DMF solution (10 mL) containing 0.1 M tetraethylammonium perchlorate was electrolyzed in the presence of a

naphthalene mediator (6 mmol) and HY zeolite (1.5 g) in a normal one-compartment cell fitted with a Pt plate cathode (2 x 2 cm^2) and Zr plate anode (2 x 2 cm^2), then switched to Fe plate anode, at a constant current density of 120 mA/cm^2 under a nitrogen atmosphere at 273 K. Naphthalene was used as a mediator in the system to produce radical anions, which then reduced the metal cations from the anode to give metal nanoparticles. After electrolysis, the mixture was impregnated, oven dried overnight at 378 K and calcined at 823 K for 3 h to yield a white powder ($EGZrO_2$–$EGFe_2O_3$/HY), and finally ready for characterization and photocatalytic testing. Furthermore, the $EGZrO_2$ and $EGFe_2O_3$ photocatalyst was prepared by the same procedure except for the addition of the HY zeolite (1.5 g) prior to electrolysis, and a white powder was obtained as the final product. The required weight percent of the $EGZrO_2$ and $EGFe_2O_3$ supported on HY was calculated based on Faraday's law of electrolysis as expressed in equation 1

$$t = \left(\frac{F}{I}\right)(z \times n) \tag{1}$$

where t = total time for the constant current applied (s); F = 96486 C mol^{-1}, which is the Faraday constant; I = the electric current applied (mA); z = the valency number of ions of substance (electrons transferred per ion); and n = the number of moles of substance (number of moles, liberated n = m/M) [3,4].

Characterization

The crystalline structures of the photocatalyst were studied by X-ray diffraction (XRD) recorded on a D8 Advanced Bruker X-ray diffractometer using Cu K_α radiation at a 2θ angle ranging from 3 to 90°. The phases were identified with the aid of the Joint Committee on Powder Diffraction Standards (JCPDS) files. The morphological properties of the $EGZrO_2$–$EGFe_2O_3$/HY photocatalyst were examined by transmission electron microscopy (TEM) (JEOL JEM-2100F). The textural properties (i.e. specific surface area, pore volume and pore diameter) were determined from nitrogen adsorption-desorption isotherms at liquid nitrogen temperature using a Micromeritics ASAP 2010 instrument. The surface area was calculated with the Brunnauer-Emmett-Teller (BET) method, and the pore distributions were determined by the Barrett-Joyner-Halender (BJH) method. Prior to measurement, all of the samples were degassed at 110 °C to 0.1 Pa.

Reaction testing

The photocatalytic activity of the prepared $EGZrO_2$–$EGFe_2O_3$/HY photocatalyst was tested for the decolorization of MB and CR. A 0.075 mg sample of the photocatalyst was dispersed in 200 mL of 10 mg L^{-1} MB aqueous solution. The adsorption-desorption equilibrium was achieved under dark conditions after 30 min, and the mixture was irradiated for 120 min with constant stirring under sunlight (January to March 2015, between 12 NN until 3 PM with an average intensity 1.315×10^5 Lux unit). However, during the illumination time, no volatility of the solvent was observed. At specific time intervals, 2.5 mL of the sample solution was withdrawn and centrifuged prior measurements of the MB and CR concentration by a UV-vis spectrophotometer (Agilent Technologies Cary 60 UV-vis) using the characteristic adsorption band at 664 nm and 496 nm. The decolorization percentage was calculated as follows (equation 2):

$$Decolorization\ (\%) = \frac{(C_0 - C_t)}{C_0} \times 100 \tag{2}$$

where C_o represents the initial concentration, and C_t denotes a variable concentration.

Results and Discussion

The XRD pattern of 1 wt.% $EGZrO_2$–1 wt.% $EGFe_2O_3$/HY photocatalysts were compared with bare HY, and the results are shown in Fig. 1a. The peak intensity of HY was decreased as the addition of $EGZrO_2$ and $EGFe_2O_3$ due to the presence of foreign substances that could affected the morphology of the HY fingerprint. A series of characteristic peaks were observed for $EGZrO_2$ at 30.2° (101), 35.2° (110), 50.3° (112), and 60.2° (211), which are consistent with the tetragonal (*t*) phase of ZrO_2, and in agreement with JCPDS file PDF No 01-072-2743 (Fig. 1b) [3,14]. Characteristic peaks were observed at 2θ equal to 28.2°, 31.5°, and 34.5° and corresponded to the diffraction patterns of (−111), (111), and (002) of the monoclinic (*m*) phase of ZrO_2 (Fig. 1b) [3,14]. Next, the XRD peaks of $EGFe_2O_3$ (Fig. 1b) were observed at 2θ = 24.1° (012), 33.1° (104), 35.6° (110), 40.7° (113), 49.4° (024), 54.1°

(116), 62.5° (214) and 64.2° (300). These peaks can be indexed to pure rhombohedral symmetry of Fe_2O_3 indicating the crystalline hematite phase (JCPDS file PDF No 00-024-0072) [3,14]. Hence, there is no other diffraction peaks were detected which indicated the purity of the prepared $EGZrO_2$ and $EGFe_2O_3$.

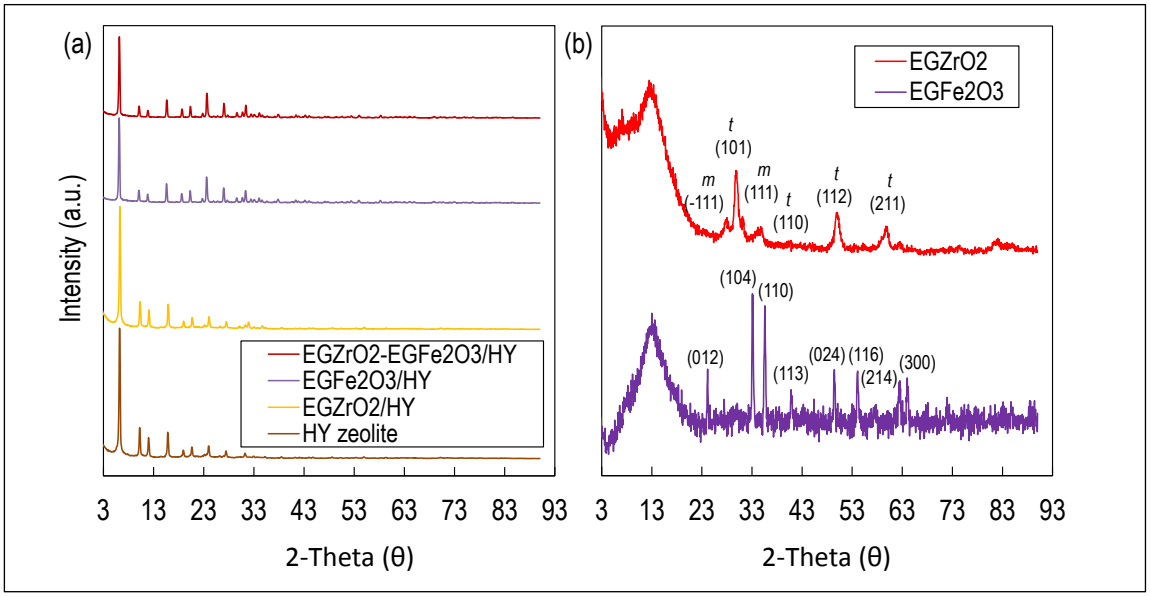


Figure 1. XRD patterns of the photocatalyst

The morphological properties of the 1 wt.% $EGZrO_2$–1 wt.% $EGFe_2O_3$/HY photocatalyst were observed by the transmission electron microscopy (TEM), and the images are presented in Fig. 2, respectively. The value of the interplanar distance (*d*-spacing) of the lattice fringes was estimated from this image was consistent with the value of lattice spacing of $EGZrO_2$ and $EGFe_2O_3$ obtained from the XRD analysis. This agreement confirms that the $EGZrO_2$ and $EGFe_2O_3$ nanoparticles were well dispersed on the HY support.

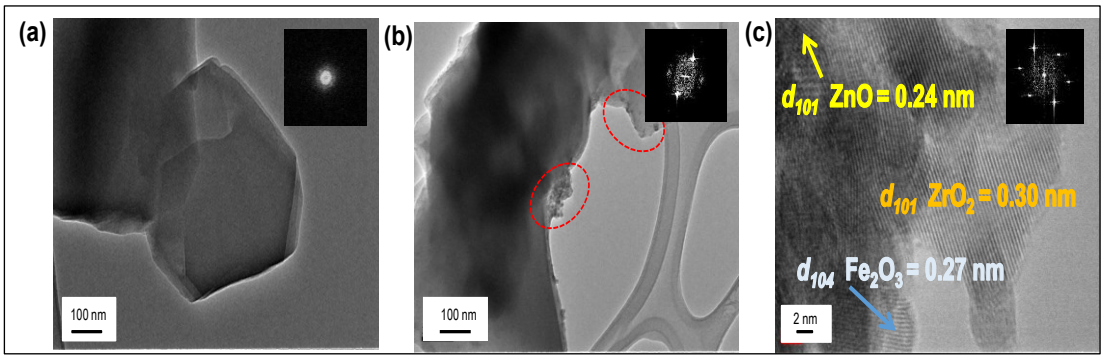


Figure 2. TEM micrographs of 1 wt.% $EGZrO_2$–1 wt.% $EGFe_2O_3$/HY photocatalyst

The surface area analysis data obtained from the BET method as well as the pore volume and pore diameter determined by the Barret-Joyner-Halenda (BJH) desorption isotherms method was tabulated in Table 1. The

addition of $EGZrO_2$ and $EGFe_2O_3$ onto HY decreases the surface area and pore volume, but increases the pore diameter. The decrease in the pore volume may be a reflection of the uneven particle sizes of the catalyst [16-18].

Table 1. The textural properties of the photocatalyst

Catalysts	**Surface area (m^2g^{-1})**	**Pore diameter (nm)**	**Pore volume (cm^3g^{-1})**
HY zeolite	557	2.70	0.376
$EGZrO_2$/HY	505	1.83	0.323
$EGFe_2O_3$/HY	496	1.79	0.222
$EGZrO_2$–$EGFe_2O_3$/HY	536	1.87	0.250

The performance of the prepared 1 wt.% $EGZrO_2$–1 wt.% $EGFe_2O_3$/HY photocatalyst for the decolorization of MB and CR was examined, and the results are shown in Fig. 3. A controlled experiment was conducted for both MB and CR, under six different conditions including photolysis and reaction in the presence of the bare HY, $EGZrO_2$, $EGFe_2O_3$, $EGZrO_2$–$EGFe_2O_3$, and 1 wt.% $EGZrO_2$–1 wt.% $EGFe_2O_3$/HY catalysts. Each experiment was performed under both dark and sunlight conditions. The experiments under dark conditions removed less than 22% of the MB after 2 hours of contact time, which indicated the importance of sunlight in this study. Under photolysis conditions, 2% MB was decolorized because of the degradation of the substance after long exposure to sunlight. No significant effect was observed using bare HY under dark and UV–light conditions where 22% and 27% MB was removed, respectively. The use of $EGZrO_2$, $EGFe_2O_3$, $EGZrO_2$–$EGFe_2O_3$ under sunlight resulted in 32%, 40%, and 67% decolorization of MB, in respectively, which is higher than the same reaction under dark conditions. Indeed, the removal percentage was increased up to 99.8% by using 1 wt.% $EGZrO_2$–1 wt.% $EGFe_2O_3$/HY.

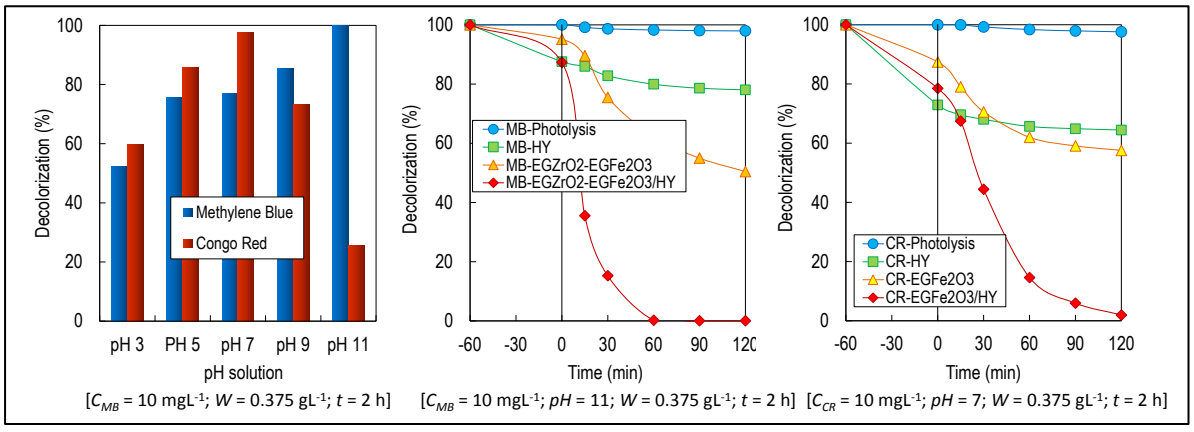


Figure 3. The performance and photoactivity of photocatalyst

Furthermore, for CR dye, less than 17% of the CR was adsorbed under dark conditions after 2 hours of contact time, and no photolysis was occurring after long exposure to sunlight. About 15% and 20% of CR was removed using bare HY under dark and sunlight conditions, in respectively. The $EGZrO_2$, $EGFe_2O_3$, $EGZrO_2$–$EGFe_2O_3$ was resulted in 27%, 34%, and 63% decolorization of CR under sunlight, respectively, indicates the significance the use of sunlight in this study. The 1 wt.% $EGZrO_2$–1 wt.% $EGFe_2O_3$/HY shows the highest removal percentage which accounted 98% decolorization. Based on all above, we can conclude that the porosity of the catalyst surface may play an important role in adsorption, as previously reported in liquid–gas adsorption systems for wastewater

treatment. Good distribution of the $EGZrO_2$ and $EGFe_2O_3$ nanoparticles on the surface of the HY might facilitate their surface contact with sunlight and lead to higher efficiency of the reaction. The synergistic effect from both $EGZrO_2$–$EGFe_2O_3$ and HY were also found to play an important role in enhancing the photodecolorization reaction. This result reveals that $EGZrO_2$–$EGFe_2O_3$/HY is a potential photocatalyst semiconductor.

Conclusion

In this study, the 1 wt.% $EGZrO_2$–1 wt.% $EGFe_2O_3$/HY photocatalyst with enhanced photoactivity was prepared by a simple electrochemical method. The physicochemical properties of the prepared photocatalyst were studied by XRD, TEM, BET surface area analysis. The photocatalyst were evaluated for the decolorization of 10 mg L^{-1} of MB and CR under different pH, at pH 9 and pH 7, using an amount of 0.375 g L^{-1} 1 wt.% $EGZrO_2$–1 wt.% $EGFe_2O_3$/HY after 2 hours of contact time, hence gave removal percentage of 99.8% and 98.0%, in respectively. This system exhibits great potential for improving the quality of the wastewater discharged from textile industry and other industries because of the simple preparation of the photocatalyst and the low amount of metal loading required. It was believed to be extendable to the synthesis of other catalysts with different characteristics and be used in various applications. Furthermore, more technologies and instrument were needed in order to examine and investigate the mechanism pathways of the synthesis of catalyst using this electrolysis system. In addition, it also provides new findings to explore the new structural model of the catalyst.

Acknowledgement

The authors are grateful for the financial support by the Short Term Research Grant (STRG) from Universiti Kuala Lumpur (Grant No. 15047) and Majlis Amanah Rakyat (MARA) Malaysia, and also the Section of Technical Foundation – Malaysian Institute of Chemical and Bioengineering Technology Universiti Kuala Lumpur for their support.

References

1. Mahmoodi, N. M. (2013). Magnetic ferrite nanoparticle–alginate composite: Synthesis, characterization and binary system dye removal. *Journal of Taiwan Institute of Chemical Engineer*, 44: 322 – 330.
2. Jaafar, N. F., Jalil, A. A., Triwahyono, S., Muhid, M. N. M., Sapawe, N., Satar, M. A. H. and Asaari H. (2012). Photodecolorization of methyl orange over α–Fe_2O_3–supported HY catalysts: The effects of catalyst preparation and dealumination. *Chemical Engineering Journal*, 191: 112 – 122.
3. Sapawe, N., Jalil, A. A., Triwahyono, S., Adam, S. H., Jaafar, N. F. and Satar, M. A. H. (2012). Isomorphous substitution of Zr in the framework of aluminosilicate HY by an electrochemical method: Evaluation by methylene blue decolorization. *Applied Catalysis B: Environment*, 125: 311 – 323.
4. Sapawe, N., Jalil, A. A., Triwahyono, S., Sah, R. A. R. N., Jusoh, N. W. C., Hairom, N. H. H. and Efendi. (2013). Electrochemical strategy for grown ZnO nanoparticles deposited onto HY zeolite with enhanced photodecolorization of methylene blue: Effect of the formation of Si–O–Zn bonds. *Applied Catalysis A: General*, 456: 144 – 158.
5. Sapawe, N., Jalil, A. A., Triwahyono, S., Shah, M. I. A., Jusoh, R., Salleh, N. F. M., Hameed, B. H. and Karim, A. H. (2013). Cost–effective microwave rapid synthesis of zeolite NaA for removal of methylene blue. *Chemical Engineering Journal*, 229: 388 – 398.
6. Jalil, A. A., Triwahyono, S., Yaakob, M. R., Azmi, Z. Z. A., Sapawe, N., Kamarudin, N. H. N., Setiabudi, H. D., Jaafar, N. F., Sidik, S. M., Adam, S. H. and Hameed, B. H. (2012). Utilization of bivalve shell–treated *Zea mays* L. (maize) husk leaf as a low–cost biosorbent for enhanced adsorption of malachite green. *Bioresource Technology*, 120: 218 – 224.
7. Jalil, A. A., Triwahyono, S., Sapawe, N., Ahmed, I. H., Aziz, M. A. A. (2014). Low–temperature stabilization of electrolysynthesized tetragonal zirconia, its photoactivity toward methylene blue decolorization. *Desalination and Water Treatment,* 56(9): 1–15.
8. Rodrigues, C. D. S., Madeira, L. M. and Boaventura, R. A. R. (2009). Treatment of textile effluent by chemical (Fenton's Reagent) and biological (Sequencing batch reactor) oxidation. *Journal of Hazardous Material*, 172: 1551 – 1559.
9. Damodar, R. A., You, S. J., Ou, S. H. (2010). Coupling of membrane separation with photocatalytic slurry reactor for advanced dye wastewater treatment. *Separation and Purification Technology*, 76: 64 – 71.

10. Aleksic, M., Kusic, H., Koprivanac, N., Leszczynska, D. and Bozic, A. L. (2010). Heterogenous fenton type processes for the degradation of organic dye pollutant in water – The application of zeolite assisted AOPs. *Desalination*, 257: 22 – 29.
11. Jalil, A. A., Satar, M. A. H., Triwahyono, S., Setiabudi, H. D., Kamarudin, N. H. N., Jaafar, N. F., Sapawe, N. and Ahmad, R. (2013). Tailoring the current density to enhance photocatalytic activity of CuO/HY for decolorization of malachite green. *Journal of Electroanalytical Chemistry*, 701: 50 – 58.
12. Jusoh, N. W. C., Jalil, A. A., Triwahyono, S., Setiabudi, H. D., Sapawe, N., Satar, M. A. H., Karim, A. H., Kamarudin, N. H. N., Jusoh, R., Jaafar, N. F., Salamun, N. and Efendi, J. (2013). Sequential desilication–isomorphous substitution route to prepare mesostructured silica nanoparticles loaded with ZnO and their photocatalytic activity. *Applied Catalysis A: General*, 468: 276 – 287.
13. Jusoh, R., Jalil, A. A., Triwahyono, S., Idris, A., Haron, S., Sapawe, N., Jaafar, N. F., Jusoh, N. W. C. (2014). Synthesis of reverse micelle α–FeOOH nanoparticles in Ionic liquid as an only electrolyte: Inhibition of electron-hole pair recombination for efficient photoactivity. *Applied Catalysis A: General*, 469: 33 – 44.
14. Sapawe, N. (2015). Effective solar-based iron oxide supported HY zeolite catalyst for the decolorization of organic and simulated dyes. *New Journal of Chemistry*, 39: 6377 – 6387.
15. Sapawe, N., Jaafar, N. F., Hairom, N. H. H., Satar, M. A. H., Ariffin, M. N., Triwahyono, S. and Jalil, A. A. (2011). A facile preparation of nanosized ZnO and its use in photocatalytic decorization of methyl orange. *Malaysian Journal of Fundamental and Applied Sciences*, 7: 19 – 23.
16. Sapawe, N., Jalil, A. A. and Triwahyono, S. (2013). One–pot electro–synthesis of ZrO–ZnO/HY nanocomposite for photocatalytic decolorization of various dye–contaminants. *Chemical Engineering Journal*, 225: 254 – 265.
17. Sapawe, N. (2015). Hybridization of zirconia, zinc and iron supported on HY zeolite as a solar-based catalyst for the rapid decolorization of various dyes. *New Journal of Chemistry*, 39: 4526 – 4533.
18. Sapawe, N. and Hanafi, M. F. (2016). Facile one-pot electrolysis of high photoreactive hexacoordinated Si with Zr and Zn catalyst. *RSC Advances*, 5: 75141 – 75144.

Malaysian Journal of Analytical Sciences, Vol 20 No 5 (2016): 1059 - 1065
DOI: http://dx.doi.org/10.17576/mjas-2016-2005-10

MALAYSIAN JOURNAL OF ANALYTICAL SCIENCES
Published by The Malaysian Analytical Sciences Society
ISSN 1394 - 2506

ASSESSMENT OF ANTIOXIDANT ACTIVITY AND TOTAL PHENOLIC CONTENT FROM GREEN COFFEE *Robusta Sp.* BEANS

(Penilaian Aktiviti Antioksidan dan Kandungan Jumlah Fenolik dari Biji Kopi *Robusta Sp*. Hijau)

Raseetha Siva[1]*, Noratikah Rajikin[1], Zaibunnisa Abdul Haiyee[1], Wan Iryani Wan Ismail[2]

[1]*Faculty of Applied Sciences,*
Universiti Teknologi MARA, 40450 Shah Alam, Selangor, Malaysia
[2]*School of Fundamental Sciences,*
Universiti Malaysia Terengganu, 21030 Kuala Terengganu, Terengganu, Malaysia

**Corresponding author: raseetha@salam.uitm.edu.my*

Received: 17 August 2015; Accepted: 23 August 2016

Abstract

Methanol and isopropanol were used as extraction solvent to determine the percentage yield of chlorogenic acid (CGA) in green Robusta (*Coffea canephora)* coffee bean. CGA was extracted by using isolation method with activated carbon to trap the CGA content from the complex compounds in green coffee beans. Results indicated that percentage yield of CGA extracted by using isopropanol was significantly higher (5.21%) compared to methanol (4.55%). Besides, antioxidant activity and total phenolic content were also analyzed. From this study, isopropanol extracted more antioxidant activity and total phenolic content as compared to methanol. For antioxidant activity, isopropanol and methanol extracted 0.48 mg and 0.15 mg of Fe (II) per gram of dry sample, respectively. For total phenolic content, isopropanol and methanol extracted 30.65 mg and 16.26 mg of gallic acid per gram of dry sample, respectively. Isopropanol extraction with ratio 60:40 (isopropanol: water) conserved more CGA content than methanol which was analyzed using high performance liquid chromatography. Chromatogram showed that the retention time of CGA is at 4.68 minutes which is similar to the retention time of standard CGA.

Keywords: green coffee bean, antioxidant, phenolic, methanol, isopropanol

Abstrak

Metanol dan isopropanol telah digunakan sebagai pelarut ekstrak untuk menentukan peratusan hasil asid klorogenik (CGA) di dalam biji kopi hijau Robusta (*Coffea canephora)*. CGA diekstrak dengan menggunakan kaedah pengasingan dengan karbon teraktif berfungsi sebagai perangkap kandungan CGA daripada sebatian kompleks di dalam biji kopi hijau. Keputusan hasil peratusan CGA yang diekstrak oleh isopropanol adalah secara signifikan lebih tinggi (5.21%) berbanding metanol (4.55%). Selain itu, aktiviti antioksidan dan jumlah kandungan fenolik juga telah dianalisis. Daripada kajian ini, pelarut isopropanol mengekstrak lebih banyak aktiviti antioksidan dan jumlah kandungan fenolik berbanding pelarut metanol. Bagi penentuan aktiviti antioksidan isopropanol dan metanol berupaya mengekstrak masing – masing 0.48 mg dan 0.15 mg Fe (II) bagi setiap gram sampel kering. Bagi penentuan jumlah kandungan fenolik, isopropanol dan metanol mengekstrak 30.65 mg dan 16.26 mg asid gallic bagi setiap gram sampel kering. Pengekstrakan isopropanol dengan nisbah 60:40 (isopropanol: air) memelihara lebih kandungan CGA daripada metanol yang dianalisa menggunakan kromatografi cecair prestasi tinggi. Kromatogram menunjukkan bahawa masa tahanan CGA adalah pada 4.68 minit selari dengan masa tahanan larutan piawai CGA.

Kata kunci: biji kopi hijau, antioksidan, fenolik, metanol, isopropanol

Introduction

Overweight or obesity becomes common contributing factors of many unnecessary diseases, such as diabetes mellitus, high blood pressure and cancer. Common causes of the disease are usually due to wrong diet and lack of physical activity [1]. A latest survey in Japan reveals that occurrence of diabetes mellitus is increasing. Furthermore, International Obesity Taskforce (IOTF) reported that up to 1.7 billion people all over the world could eventually be exposed to weight-related health risks [2]. Since these health problems create a big economic impact on health care system in the world, health food supplements are now quite popular among weight observant. Recently, chitosan and citrus (*Citrus aurantium*) fruits are some of the food supplements for weight loss which helps in reduce fat absorption and breaking down fat respectively. Additionally, it has been identified that coffee bean extract releases chlorogenic acid as an inhibitor for the production of glucose in liver and promote insulin secretion [3]. Therefore, further study on chlorogenic acid as weight loss agent can be explored.

Chlorogenic acid (CGA) as shown in Figure 1 belongs to a family of ester consist of caffeic acid and quinic acid [4]. The melting and boiling point of CGA is 205 – 209 ℃ and 665 °C at 760 mmHg, respectively. It is known that CGA solubilizes in ethanol, dimethylsulfoxide and dimethylformamide. Chlorogenic acid is well known as a natural antioxidant that has properties of retarding the oxidation of food products which help keeps the fresh flavor and nutritional value for longer time. This antioxidant also reduces the release of glucose into the bloodstream after a meal [5]. The current commercial source of chlorogenic acid is green coffee beans. It was found that coffee pulp contains natural antioxidants like hydroxycinnamic acids [6].

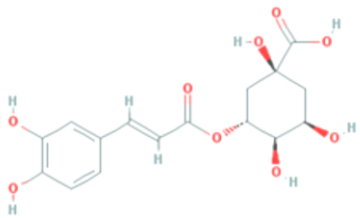


Figure 1. Chemical structure of chlorogenic acid (CGA)

Green coffee beans are basically the seeds from the fruit of coffee trees. The two main green coffee beans that are commonly produced and sold are Arabica coffee (*Coffea arabica*) and Robusta coffee (*Coffea canephora*) [7]. Moreover, coffee is well known as a good source of antioxidant [8]. Coffee also rich with antioxidants and contain of flavonoids. The presence of antioxidant will slow or prevent the oxidation of other chemical. Oxidation can be simplified as gain of oxygen and loss of electron. On the other hand, antioxidants may be either present in two forms which are natural antioxidants and synthetic antioxidants. Natural antioxidants include flavonoids, phenolic, tocopherols (Vitamin E) and also ascorbic acid. About the caffeine and chlorogenic acid content, Arabica generally has less amount of caffeine which is approximately 1.2% and 5.5 to 8.0% of chlorogenic acid while Robusta has 2.2% of caffeine and 7.0 – 10.0% of chlorogenic acid [9]. The post-harvest processing gives effect on the chemical composition of coffee seeds especially in water-soluble components like sugar, caffeine, trigonellie and chlorogenic acid [9].

Nowadays, the worldwide consumption of coffee is increasing in popularity due to their health benefits. These benefits appear to be effected by their antioxidant activity. Antioxidant is a substance that protects living tissues against damage caused by free radicals. Free radicals are species produced during aerobic respiration due to the incomplete reduction of oxygen molecule and directly related to various diseases such as cancer, cardiovascular, inflammatory and neurogenerative pathologies are associated with oxidative stress [10]. Besides fruits and vegetables, plant beverages such as coffee brew have been proposed as an important source of antioxidant in human diet [11, 12]. Additionally, phenolic compounds have an important role in nutritional, organoleptic and commercial

properties of agricultural foodstuffs as they contributed to the sensory properties such as colour, astringency, bitterness and flavour of coffee, because of the interaction between phenolics, mainly procyanidin and glycoprotein in saliva [13].

Solvent extraction technique was used to extract chlorogenic acid from green coffee bean. For this solvent extraction, methanol and isopropanol was used to extract the chlorogenic acid and determine the yield extract. Activated carbon was used to extract the cholorogenic acid content in the filtered extraction [14]. Thus the aim of this study was to compare which solvent (isopropanol or methanol) gives better chlorogenic acid yield antioxidant activity and total phenolic content. Efficient solvent extraction information for antioxidant activity and total phenolic content in green coffee beans was also investigated.

Materials and Methods

Chemicals

Coffee canephora (Robusta coffee) was supplied from Teluk Gong, Klang, Malaysia. All the chemicals were of analytical grade. Folin-Ciocalteu, 3,4,5-trihydroxybenzoic acid (gallic acid), methanol (HPLC grade), acetic acid (HPLC grade) and isopropanol (HPLC grade) were purchased from Merck, Malaysia. The remaining chemicals were purchased from Systerm, Malaysia, listed as follows: Chlorogenic acid, 1,3,5-triazine,2,4,6-tri-2-pyridinyl (TPTZ), 2,2-diphenyl-1-picrylhydrazyl (DPPH), ascorbic acid and $FeCl_3.6H_20$ (ferric chloride hexahydrate).

Equipment's

The water bath (Varian) for extraction of green coffee beans, UV-Vis spectrophotometer (Cary 50 model) and rotary evaporator to dry green coffee bean extract which is located in Universiti Teknologi MARA (UiTM) Shah Alam.

Pre-treatment of samples

Green coffee beans were washed thoroughly with tap water for several times to remove the remaining soil, dirt and contaminants such as tiny stones and other unnecessary particles. The green coffee beans were collected and grinded to form spent ground coffee. The samples were placed in sealed plastic bags and kept at 4 ºC until needed for analysis.

Solvent extraction of chlorogenic acid

Solvent extraction was carried out according to previous method [15]. Approximately 10 g of spent ground coffee was weighed and loaded into glass column. The samples were extracted with selected solvent at samples to solvent ratio 1:10. Solvents mixture of either isopropanol or methanol with water in ratio 60:40 was used for extraction. An amount 100 mL of solvent was added into glass column and allowed it to stand over a period of 5 hours whereas for the methanol water mixture, it was allowed to stand over 24 hours. The activated carbon was used to extract chlorogenic acid content in the filtered extract. The extract was drained and distilled on rotary evaporator at 50 ºC under reduced pressure (40 millibar) and the product was freeze dried and stored at room temperature prior to analysis.

Determination of chlorogenic Acid

The High Performance Liquid Chromatography (HPLC) analysis was performed by using Agilent Technologies 1200 Series (Santa Clara, California, United States) with diode-array detector (DAD) equipped with LiChroCART 250 mm x 4.6 mm i.d. Eclipse Puresper STAR RP-C18 column (5 µm) (Merck, United States), using a binary solvent system: Solvent A, water-acetic acid, 97:3 (v/v); solvent B, methanol and reverse phase. A program of gradient to 100 – 90% A from 0 – 10 minutes, 90 – 30% A for 10 – 32 minutes, 30 – 0% A from 32 – 45 minutes at a flow rate of 1.0 ml/min was used at a wavelength of 320 nm. The sample volume is 20 µL injected into HPLC. An amount 50 ppm of CGA standard was prepared in order to calculate the response factor, R_f for the standard using the following formula adapted from Aishah et al. [16] (equation 1):

$$Response\ Factor, R_f = \frac{amount}{area} \quad (1)$$

The amount of CGA present in the sample was then compared to the standard CGA using the calculated R_f.

Ferric reducing antioxidant power (FRAP)

The FRAP assay was conducted according to method described previously [17]. The FRAP reagent were prepared by mixing acetate buffer (0.3 mol/L), TPTZ (10 mmol/L) and $FeCl_3.6H_20$ (20 mmol/L) in the ratio 10:1:1. FRAP reagent were prepared as required by mixing 25 mL acetate buffer, 2.5 mL TPTZ solution, and 2.5 mL $FeCl_3.6H_2O$ solution. For a volume of 100 µL of the coffee extract, 3.0 mL of the FRAP reagent was added to test tubes with stoppers and the mixture was then left at rest in dark for 30 min at 37 °C. The absorbance of blue colouration was measured against a blank sample at a wavelength of 593 nm, using a UV-Vis spectrophotometer. The calibration curve was prepared using standard solutions of ferrous sulphate at concentration of 0.5 – 2.5 mmol/L. All of the measurements were conducted in triplicate and the results were expressed in mmol Fe^{2+} per litre sample.

Determination of total phenolic content using Folin-Ciocalteu reagent

Total phenolic content in spent ground coffee was determined by using the Folin-Ciocalteu reagent according to the colorimetric method described previously [18]. Approximately 2 mL of filtered extract will be mixed with 30 mL of sodium carbonate solution at 7.5% (w/v) and 7.5 mL of Folin-Ciocalteu reagent. Subsequently, 200 µL of distilled water was added and the solution was mixed. After that, the mixture was heated at 60 ºC for 5 minutes and allowed to cool at room temperature. The absorbance was measured by using spectrophotometer at 700 nm. A calibration curve was made from gallic acid standard solution (100, 150, 200, 250 and 300 mg/L) and the blank was prepared with distilled water. The total phenolic content was expressed as milligram gallic acid equivalent (GAEs) per dry weight material.

Statistical analysis

The results for extraction yield, antioxidant assays and total phenolic determination were expressed as mean ± standard deviation (n= 3). All data were analyzed by one-way analysis of variance (ANOVA) followed by Tukey's multiple comparison test. The level of significance was limited at $p < 0.05$.

Results and Discussion

Assessment of percentage yield and retention times of chlorogenic acid

Solvent extraction method was used to extract chlorogenic acid in green coffee bean which involved two different types of solvent, methanol and isopropanol. Each solvent was mixed with water with ratio of 60:40, respectively. Activated carbon was used to isolate the chlorogenic acid content.

Table 1 shows the percentage yield, concentration and appearance of chlorogenic acid. From the results, the extraction of chlorogenic acid by using methanol was 4.55% (2.28 ppm) while isopropanol was 5.21% (2.61 ppm). The results indicated that the isopropanol solvent extracted significantly higher yield as compared to methanol solvent. This finding is also consistent with previous reports. Chlorogenic acid yield preserved by using isopropanol was about 27% in a ratio of 60:40 as reported previously [15]. The chlorogenic acid yield from green coffee beans using methanol and isopropanol solvent were 4.67% and 5.28% respectively [14]. The mixture of isopropanol and water (60:40) used in this study increased the strength for extracting bioactive compounds such as chlorogenic acid. Attributable to polar nature of isopropanol, the yield of chlorogenic acid generally increases in those solvent, which are isolated using activated carbon [19]. It is widely accepted that higher concentration of phenolic compounds increases antioxidant activity, thus correlating to higher CGA yield [15, 20].

Table 1. Percentage yield, concentration and appearance of chlorogenic acid

Type of Solvent	% Yield of Chlorogenic Acid	Concentration (ppm)	Appearance
Methanol	$4.55^{b} \pm 0.18$	$2.28^{b} \pm 0.18$	Light green
Isopropanol	$5.21^{a} \pm 0.68$	$2.61^{a} \pm 0.68$	Light green

Means with different letters were significantly different at $p < 0.05$

The characterization of chlorogenic acid was conducted to determine retention time of chlorogenic acid standard and sample. Based on the Figure 2a, chromatogram of the standard chlorogenic acid (50 ppm) indicates the retention time at 4.68 minutes. Meanwhile, Figure 2b shows the peak of chlorogenic acid content in green coffee beans. Based on the results, the chromatogram shows the retention time of chlorogenic acid at 4.68 minutes which was similar to the standard of chlorogenic acid. From the results, it is worthy to point that the isolation using activated carbon is suitable to trap the chlorogenic acid from a complex medium such as green coffee beans.

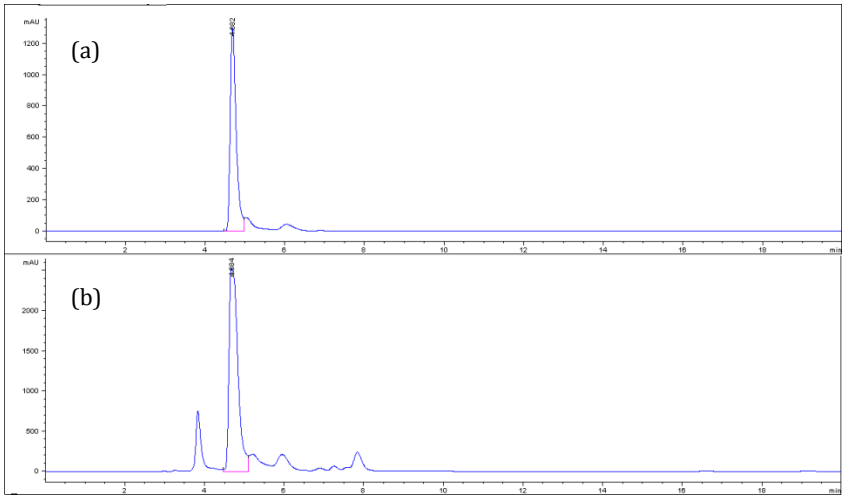


Figure 2. Chromatogram of (a) standard chlorogenic acid (50 ppm) and (b) green coffee beans

Assessment of antioxidant properties and total phenolic content

Table 2 shows the antioxidant activity found in green coffee beans expressed as mg Fe (II) per g dry sample. From the results, the antioxidant activity extracted by methanol solvent was 0.15 ± 0.07. Besides that, the extraction using isopropanol solvent was 0.48 ± 0.19. The antioxidant activity extracted by methanol solvent in spent coffee grounds was 0.109 mg Fe (II)/g dry sample [21].

Table 2. Antioxidant activity of green coffee beans

Type of solvent	**in mg Fe (II)/ g dry sample**
Methanol	0.15^{b} ± 0.07
Isopropanol	0.48^{a} ± 0.19

Means with different letters were significantly different at $p < 0.05$

Meanwhile, Table 3 shows the results on total phenolic content found in green coffee beans. Total phenolic content extracted by isopropanol was significantly higher (30.65 mg GAE/g dry sample) as compared to extraction carried out using methanol (16.26 mg GAE/g dry sample). The total polyphenol conserved by methanol extraction was 16.00 mg GAE/g dry sample [21]. Other than that, the total phenolic content conserved by isopropanol solvent is 31.71 mg GAE/g dry sample [15]. Here again, the isopropanol ratio with water (60:40) extract of green coffee bean showed higher activity as compared to methanol extracts [15].

Table 3. Total phenolic content in green coffee beans

Type of solvent	in mg of GAE/g dry sample
Methanol	$16.26^{b} \pm 0.59$
Isopropanol	$30.65^{a} \pm 0.44$

Means with different letters were significantly different at $p < 0.05$

Extraction solvent plays an important factor that affects the antioxidant capacity and total phenolic content in food materials. Vitamin E and oryzanol that has distinctive antioxidant activities extracted using isopropanol has more yield compared with using hexane as extraction solvent [22]. Isopropanol extract has comparatively higher amount of antioxidant due to the possibility of more polar phenolic compounds and lipids contained in the extract [20]. Antioxidants are extremely crucial in coffee beans to minimize the release of reactive oxygen species (ROS). If production of ROS exceeds the capacity of antioxidant systems, damage to sub-cellular compartments occurs, leading to cell destruction [23]. Hence it is important to maintain the antioxidant and total phenolic pool so that the integrity of green coffee beans is not jeopardized. This would enable the usage of these extracts to be used as ingredients in pharmaceutical industry or as food supplement as CGA implies positive impact on slimming and weight loss.

Conclusion

Higher in percentage yield of chlorogenic acid was found when isopropanol (5.21%) was used as extraction solvent compared to methanol (4.55%) solvent with ratio with water at 60:40. Furthermore, the amount of chlorogenic acid present in green coffee beans has been analyzed by using High Performance Liquid Chromatography (HPLC) with the retention time at 4.68 minutes. Besides that, isopropanol solvent also conserved more antioxidant activity and total phenolic compound. The amount of antioxidant extracted from green coffee bean by using isopropanol was significantly higher 0.48 mg Fe (II)/dry sample compared to methanol 0.15 mg Fe (II)/dry sample. Total phenolic content extracted by isopropanol was also significantly higher (30.65 mg GAE/dry sample) compared to methanol was 16.26 mg GAE/dry sample. The obtained data would be useful for further application of green coffee bean extracts as weight reducing agent in nutraceutical and food supplement industry.

Acknowledgement

The authors would like to thank the Research Acculturation Grant Scheme (RAGS) RAGS/1/2014/STWN03/UITM//2 from the Ministry of Higher Education Malaysia. We would also thank the facilities and assistance obtained from lab staff at Universiti Teknologi MARA during the completion of this research.

References

1. Surh, Y. J. (2003). Cancer chemoprevention with dietary phytochemicals. *Nature Review,* 3: 768 – 780.
2. Kumanyika, S., Jeffery, R. W., Morabia, A., Ritenbaugh, C. and Antipatis V. J. (2002). Report: Obesity prevention: The case for action. *International Journal of Obesity*, 26: 425 – 436.
3. Olthof, M. R., Hollman, P. C., Zock, P. L. and Katan, M. B. (2001). Consumption of high doses of chlorogenic acid, present in coffee or of black tea increseas plasma total homocysteine concentrations in humans. *American Journal of Clinical Nutrition,* 73 (3): 532 – 538.
4. Clifford, M. N., Johnston, K. L., Knigh, S. and Kuhnert, N. (2003). Hierarchical scheme for LC-MSn identification of chlorogenic acids. *Journal of Agricultural and Food Chemistry*, 51 (10): 2900 – 2911.
5. Johnston, K. L., Clifford, M. N. and Morgan, L. M. (2003). Coffee acutely modifies gastrointestinal hormone secretion and glucose tolerance in humans: Glycemic effects of chlorogenic acid and caffeine. *American Journal of Clinical Nutrition*, 78 (4): 728 – 733.
6. Arellano-Gonzalez, M., A., Ramirez-Coronel., A., Torres-Mancera, T., Perez-Morales., G. G. and Saucedo-Castaneda, G. (2011). Antioxidant activity of fermented and non-fermented coffee (*Coffea Arabica*) pulp extracts. *Food Technology,* 49, 374 – 378.

7. Hecimovic I, Belscak-Cvitanovic A., Horzic D. and Komes D (2011). Comparative study of polyphenols and caffeine in different coffee varieties affected by the degree of roasting. *Journal of Food Chemistry,* 129: 991 – 1000.
8. Esquivel, P. and Jimenez, V. M. (2012). Functional properties of coffee and coffee by-products, *Food Research International*, 46 (2): 488 – 495.
9. Garrett, R., Schwab, N. V., Cabral, E. C., Henrique, B. V. M., Ifa, D. R., Eberlin, M. N. and Rezende, C. M. (2014). Ambient mass spectrometry employed for direct analysis of intact Arabica coffee beans. *Journal of the Brazilian Chemical Society*, 25 (7): 1172 – 1177.
10. Dorea, J. and da Costa, T., (2005). Is coffee a functional food? *British Journal of Nutrition*, 93 (6): 773 – 782.
11. Pulido, R., Hernandez G., M. and Saura, C. F. (2003). Contribution of beverages to the intake of lipophilic and hydrophilic antioxidants in the Spanish diet. *European Journal of Clinical Nutrition*, 57 (10): 1275 – 1282.
12. Svilaas, A., Sakhi, A., Andersen, L., Svilaas, T., Strom, E. and Jacobs, D. (2004). Intakes of antioxidants in coffee, wine, and vegetables are correlated with plasma carotenoids in humans. *The Journal of Nutrition*, 134 (3): 562 – 567.
13. Scalbert, A., Johnson, I. T. and Saltmarsh, M. (2005). Polyphenols: Antioxidant and beyond, *American Journal of Clinical Nutrition*, 81: 215S – 217S.
14. Mirna, L., Angelina, A., Gerardo, V., Oscar, G. and Pierre, M. C. (2014). Isolation of green coffee chlorogenic acid using activated carbon. *Journal of Food Composition and Analysis,* 33: 55 – 58.
15. Naidu, M., Sulochanamma, G., Sampathu, S. R. and Srinivas, P. (2008). Studies on extraction and antioxidant potential of green coffee*, Food Chemistry*, 107: 377 – 384.
16. Aishah, B., Cheow, C. S. and Fadhilah, J. (2008). Instrumental analysis of food: practical manual for undergraduates. Universiti Teknologi MARA, pp. 22-24.
17. Benzie, I. F. and Strain, J. J. (1999). Ferric reducing/antioxidant power assay: Direct measure of total antioxidant activity of biological fluids and modified version for simultaneous measurement of total antioxidant power and ascorbic acid concentration. *Methods in Enzymology*, 299: 15 – 27.
18. Singleton, V. L. and Rossi, J. A. (1965). Calorimetry of total phenolic with phosphomoybdic-phosphoungstic acid reagents. *American Journal of Enology and Viticulture*, 16: 144 – 158.
19. Roginsky, V. and Lissi, E. A., (2005). Review of methods to determine chain breaking antioxidant activity in food. *Food Chemistry*, 92: 235 – 254.
20. Zubair, M., Anwar, F. and Shahid, S. A. (2012). Effect of extraction solvents on phenolics and antioxidant activity of selected varieties of Pakistani rice (*Oryza sativa L.*). *International Journal of Agriculture & Biology*, 14: 935 – 940.
21. Mussatto, S. I., Ballesteros, L. F., Martins, S. and Teixeira, J. A. (2011). Extraction of antioxidant phenolic compounds from spent coffee grounds. *Separation and Purification Technology*, 83 (1): 173 –179.
22. Zaidel, D. N. A., Daud, N. S. M., Song, L. K., Muhamad, I. I. and Jusoh, Y. M. M. (2016). Antioxidant properties of rice bran oil from different varieties extracted by solvent extraction methods. *Jurnal Teknologi (Sciences & Engineering)*, 78 (6–12): 107 – 110.
23. Davey, M. W., Van Montagu, M., Inzé, D., Sanmartin, M., Kanellis, A., Smirnoff, N., Benzie, I. J. J., Strain, J. J., Favell, D. and Fletcher, J. (2000). Plant L-ascorbic acid: Chemistry, function, metabolism, bioavailability and effects of processing. *Journal of the Science of Food and Agriculture*, 80(7): 825 –860.
24. Foyer, C. H. and Noctor, G. (2005). Oxidant and antioxidant signalling in plants: A Re-evaluation of the concept of oxidative stress in a physiological context. *Plant, Cell and Environment*, 28(8): 1056 –1071.

Malaysian Journal of Analytical Sciences, Vol 20 No 5 (2016): 1066 - 1072
DOI: http://dx.doi.org/10.17576/mjas-2016-2005-11

MALAYSIAN JOURNAL OF ANALYTICAL SCIENCES
Published by The Malaysian Analytical Sciences Society
ISSN 1394 - 2506

EFFECTS OF RAIN pH, SOIL ORGANIC MATTER, CATION EXCHANGE CAPACITY AND TOTAL LEAD CONTENT IN SHOOTING RANGE SOIL ON THE CONCENTRATION OF LEAD IN LEACHATE

(Kesan pH Hujan, Jirim Organik Tanah, Kapasiti Tukaran Kation dan Kandungan Plumbum di dalam Tanah Lapang Sasar ke atas Kepekatan Plumbum di dalam Air Larut Lesap)

Soon Kong Yong[1]*, Siti Norazieyana Mohd Zin[1], Madinah Jaafar Mad Ariff[2]

[1]*Faculty of Applied Sciences,*
Universiti Teknologi MARA, 40450 Shah Alam, Selangor, Malaysia
[2]*Centre for Foundation Studies,*
Universiti Pertahanan Nasional Malaysia, Kem Sungai Besi, 57000 Kuala Lumpur, Malaysia

**Corresponding author: yongsk@salam.uitm.edu.my*

Received: 17 August 2015; Accepted: 23 May 2016

Abstract

Leaching of lead (Pb) from the shooting range soil may contaminate water resource if rain pH decreases and soil has a low cation exchange capacity (CEC). Over exposure of Pb may cause brain injury and death. In this study, leaching of Pb from shooting range soil was simulated with column leaching test using artificial rain at pH 4 and 7. Soil physico-chemical parameters (i.e. pH, organic matter (OM), and CEC) were determined, and its' correlation with Pb concentrations in soil (Soil Pb) and leachate (Leachate Pb) were studied using Pearson's correlation. Compare to control soil, shooting range soil has higher contents of Pb (12,163 – 17,278 mg/kg, dry weight basis) and sand (64 – 68 %). The CEC value of shooting range soil (193 cmol/kg at pH 7) is lower than those in control soil (85 – 140 cmol/kg at pH 7), possibly due to low contents of clay and OM. There is positive correlation between Soil Pb and Leachate Pb variable pair (r = 0.94; p = 0.06); while Soil OM and Leachate Pb variable pair has a negative correlation (r = -0.94; p = 0.06). In conclusion, the combination of high soil Pb content, low CEC, and low rain pH increases leaching of Pb from shooting range soil.

Keywords: lead shots, heavy metal, groundwater, acid rain, sorption

Abstrak

Larut lesap Pb daripada tanah lapang sasar boleh mencemarkan sumber air jika nilai pH hujan menurun dan tanah mempunyai keupayaan pertukaran kation (CEC) yang rendah. Pendedahan Pb yang keterlaluan boleh menyebabkan kecederaan otak dan kematian. Dalam kajian ini, larut lesap Pb dari tanah lapang sasar telah disimulasikan dengan ujian larut lesap turus menggunakan air hujan tiruan pada pH 4 dan 7. Parameter tanah (iaitu, pH, jirim organik (OM), dan CEC) telah ditentukan, dan dikaji korelasinya dengan kepekatan Pb di dalam tanah dan larut resap dengan menggunakan korelasi Pearson. Berbanding dengan tanah kawalan, kandungan Pb (12163 – 17278 mg/kg, secara berat kering) dan pasir (64 – 68 %) pada tanah lapang sasar adalah lebih tinggi. Nilai CEC tanah lapang sasar (193 cmol/kg pada pH 7) adalah lebih rendah daripada tanah kawalan (85 – 140 cmol/kg pada pH 7), mungkin disebabkan oleh kandungan rendah tanah liat dan jirim organik. Terdapat hubungan yang positif antara pasangan pemboleh ubah Pb tanah dan Pb larut lesap (r = 0.94; p = 0.06); manakala pasangan pemboleh ubah jirim organik tanah dan Pb larut lesap mempunyai korelasi negatif (r = -0,94; p = 0.06). Kesimpulannya, gabungan faktor-faktor seperti kandungan Pb yang tinggi di dalam tanah, nilai CEC tanah yang rendah dan nilai pH hujan yang rendah boleh meningkatkan risiko larut lesap Pb dari tanah lapang sasar.

Kata kunci: peluru plumbum, logam berat, air bawah tanah, hujan berasid, jerapan

Introduction

Soils are reservoirs for many harmful heavy metal pollutants, such as copper, lead, cadmium, aluminium, and etc. These metals are released by anthropogenic activities such as mining, smelting, traffic emission and firearm shooting. Bullet contains lead (90 – 99 %), antimony (1 – 10.5 %), and copper (0.1 %) may be a point source for lead contamination in the shooting range [1]. Total lead concentration in shooting range soils may be as high as 54,000 mg/kg [2]. Lead in bullet is subjected to weathering and may lead to accumulation in soil [3]. Metallic lead will be converted to hydrocerussite ($Pb_3(CO_3)_2(OH)_2$), cerussite ($PbCO_3$), and massicot (PbO) within one week [2].

Lead is toxic to human health especially for children, as it attacks the brain and central nervous system. High level exposure of lead may cause coma, convulsions and even death. Ecological risks of lead at shooting range may also be significant. High level of lead may affect local and migratory, aquatic and terrestrial biota. The risk of lead contamination in groundwater system is higher with high content of lead in shooting range soil [4], and close proximity of groundwater table to the surface of shooting range soil. As groundwater is used as daily drinking water, these contaminations may affect human health.

To the best of our knowledge, there is no study on the risk of lead contamination in groundwater from shooting range soil in Malaysia. Lead contamination in groundwater may depends on the several soil physico-chemical parameters (i.e. soil pH, CEC and OM), and the pH of rain water. The objectives of this study to determine the soil physico-chemical parameters and the soil lead content at the Kem Sungai Besi shooting range, and to simulate the leaching process using artificial rain at various pH values. A correlation study was conducted to determine the risk factors for lead contamination in the groundwater.

Materials and Methods

Soil collection and preparation

Soil samples were collected using the coring technique at a sampling site (3° 3' 0" North, 101° 42' 0" East) located at Kem Sungai Besi, Kuala Lumpur, Malaysia. Baseline soil was taken at the boundary of the shooting range, and is free of the bullets and lead shots. Target 4, 6 and 8 located at the center of the berm were chosen as sampling points. Little vegetation was observed on the target soils (Figure 1a). Three soils replicates were collected at the top, middle and bottom of each targets, and were homogenized to form composite sample (Figure 2).

The soil samples were air dried for 6 days before being sieved to 2 mm. After sieving, the fragment of bullets was hand-picked from the soil sample. The fragments were visibly corroded and have reduced in size, indicating the weathering process of lead shots in the soil (Figure 1b). The soil samples were kept in air-tight plastic container to avoid contact with moisture.



(a) (b)

Figure 1. Shooting range (a) and bullet fragments (b) at Kem Sungai Besi, Kuala Lumpur

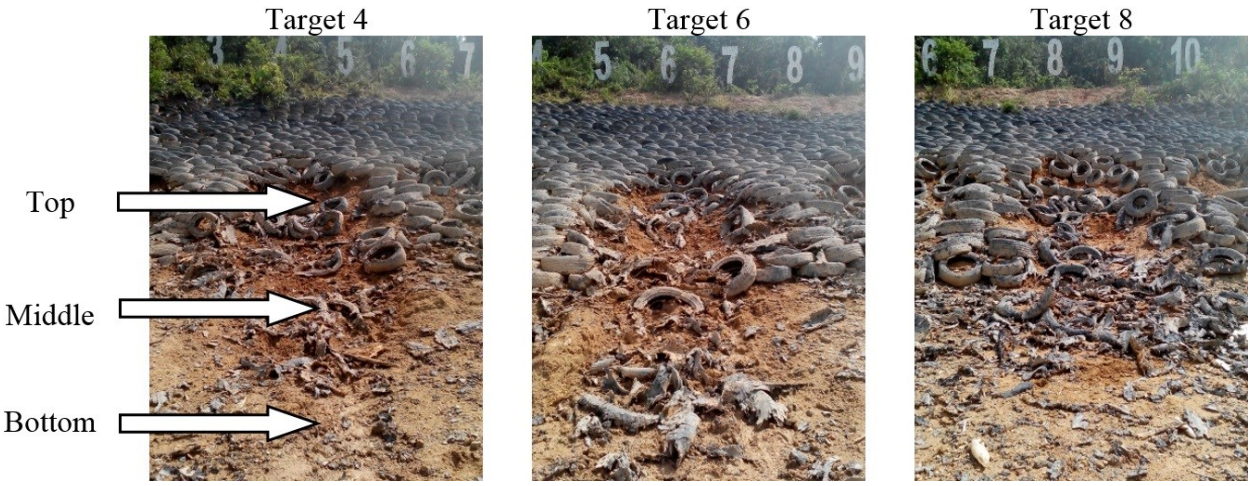


Figure 2. The location of soil sampling points at target 4, 6, and 8

Soil pH

Soil pH was measured on a soil-deionized water suspension (1:1 w/v ratio) using a calibrated pH meter. Twenty grams of soil samples from shooting target were suspended in 20 mL deionized water in a 100 mL beaker. The suspension was mixed using a glass rod and allowed to stand for 30 min with interval stirring at 10 min and again after 1 h to ensure complete homogeneity. The pH reading was taken after immersing the pH meter into the suspension (at about 3 cm depth) for 30 sec at 25 °C.

Soil particle distribution

Soil particles distribution was determined through the hydrometer method. A dispersing solution was prepared by dissolving 40 g sodium hexametaphosphate [$(NaPO_3)_6$] and 10 g of sodium carbonate (Na_2CO_3) in 1 L of volume with deionized water. Sixty millilitres of dispersing solution was poured into a 600 mL beaker containing 40 g of soil sample. The beaker was covered with watch glass and left overnight. The content was stirred for 3 min and then transferred quantitatively into a 1 L calibrated cylinder and was brought to volume with deionized water. To determine the distribution of a mixture of silt and clay, the suspension was mixed in the hydrometer jar. After the paddle is withdrawn, the hydrometer was inserted into the jar and the reading (R_{sc}) was taken after 40 sec. For clay particle distribution determination, the solution was left undisturbed for 4 h before the reading (R_c) was recorded. For the determination of silt in the soil, the suspension was sieved into 50 μm sieve. The sieved soil was washed with water until the sieve is clear. The sand was quantitatively transferred to crucible of known weight. The crucible then was dried in the oven at 105 °C overnight. The crucible was cooled in desiccator and weighed.

Soil organic matter

The organic matter (OM) in the soil was estimated as soil organic carbon (SOC), using the loss-on-ignition method (LOI). Crucibles were dried at 105 °C for at least 1 h and cooled in dessicator for 30 min. About 5.0 g of soil was transferred into the crucible; oven dried overnight at 105 °C, cooled in dessicator and reweighed using an analytical balance. The crucible was placed into a furnace at 450 °C for 4 h, and reweigh after proper cooling. The percentage of LOI and SOC were determined using Eq. 1 and Eq. 2, respectively.

$$\text{LOI} = \frac{(W_3 - W_1) - (W_2 - W_1)}{(W_2 - W_1)} \times 100 \quad (1)$$

$$\text{SOC} = \frac{LOI}{1.72} \quad (2)$$

where W_1 is the weight of empty crucible; W_2 is the weight of crucible and soil samples before ignition; and W_3 is the weight of crucible and soil samples after ignition.

Cation exchange capacity

The CEC values were determined with the sodium acetate method. Four grams of soil sample was mixed with 30 mL of 1.0 N sodium acetate (NaOAc) solution in a 50 mL centrifuge tube for 5 min using a mechanical shaker. Then the content was centrifuged and the supernatant was decanted. The step was repeated thrice using NaOAc solution. Thirty three millilitres of 99 % isopropyl alcohol was added to the centrifuge tube. Then, the tube was shaken in mechanical shaker for 5 min and centrifuged to decant the liquid. This step was repeated for twice. Next, 33 mL of ammonium acetate (NH_4OAc) solution was added into the tube. Then, the tube is shaken for 5 min. The liquid was centrifuged and the supernatant was decanted into a 100 mL volumetric flask. The procedure was repeated twice. The combined washing was diluted to 100 mL with NH_4OAc solution and the solution was analysed using Inductively Couple Plasma- Optical Emission Spectrometry (ICP-OES) for sodium concentration.

Acid digestion of soil sample

About 0.5 g of soil sample was digested in 100 mL beaker using aqua regia solution. The content of the beaker was heated at 100 °C until the volume of acid is decreased to about 5 mL without precipitation. Digested solution was cooled, filtered and diluted to 50 mL in a volumetric flask. The metal composition of the digested solution was analysed using ICP-OES.

Soil column leaching test

A glass column with 13 cm height and 4 cm diameter was used in the column leaching test. This column was packed to about 10 cm height, using composite of soil samples from three targets at the shooting range. The soil composite was transferred to the glass column in small portions to obtain uniform packing. The soil column was pre-wetted with artificial rain (0.01 M $CaCl_2$, pH 7) from the top to bottom in order to displace the air in the soil pores. The soil then was allowed to equilibrate and the excess water was drained off by gravity. Then, 200 mL artificial rainwater was applied to the soil column. To obtain homogenous distribution the solution, the artificial rainwater was applied evenly over the surface of the soil column. The surface of the soil column was covered with a gauze cloth to ensure even distribution of the artificial rain, and to avoid the disturbance of the soil surface by the rain drops. With the aid of peristaltic pump, a total of 600 mL artificial rain was added drop-wise on to the top of the soil column. Soil leaching test was repeated using 0.01 M $CaCl_2$ at pH 4. Leachates were collected in three successive fractions, and were analysed with ICP-OES.

Correlation studies

Correlation of Pb concentrations in leachate fractions (i.e. Leachate Pb) and soil physico-chemical parameters (i.e., Soil Pb, Soil pH, Soil OM, CEC) were analysed with Pearson correlation using SPSS version 13.

Results and Discussion

Physico-chemical properties of shooting range soil

The physico-chemical properties (i.e., pH, OM, CEC), soil composition and lead concentration in shooting range soil are shown in Table 1. The pH of the soil is slightly acidic (i.e. 5.55 to 6.34). The acidity may be due to acid deposition from the atmosphere in Kuala Lumpur [5]. Baseline soil has a similar pH value (5.54) with those at the targets. The percentage of the silt, sand, and clay in the soil are 9%, 66% and 27%, respectively. The soil texture is of sandy clay loam according to United States Department of Agriculture (USDA) soil textural diagram. The OM content for baseline soil is 5.40 %, which is higher than those at the targets (i.e. 1.32 to 1.55 %). Vegetation on top of the baseline soil may have contributed to higher plant biomass and OM contents. Moreover, baseline soil has higher CEC value compared to those at three targets, possibly due to the higher OM contents in baseline soil [6]. However, the CEC value of all soil samples decreased with decreasing pH value. A large CEC value of the soil samples is crucial for holding large amounts of lead cations. However, a combination of low rain pH, low clay

content and OM content in soil may increase the risk for dissolution and mobilization of lead from shooting range soils into groundwater [7].

Table 1. Physico-chemical properties, particle size distribution and concentrations of Pb, Al, Fe, Ca, and K in shooting range soil at target 4, 6 and 8.

Variable	Field soil			
	Baseline	**Target 4**	**Target 6**	**Target 8**
pH	5.54	5.85	6.34	5.55
OM (%LOI)	5.40	1.55	1.37	1.32
% Clay	32	23	26	25
% Silt	13	9	10	8
% Sand	55	68	64	67
CEC- pH 7, (cmol/kg)	193.85	140.21	85.51	85.25
CEC- pH 4, (cmol/kg)	112.15	62.70	54.76	57.00
Pb, (mg/kg, dw)	4.4	17278	14126	12163
Al, (mg/kg, dw)	380	372	347	333
Fe, (mg/kg, dw)	178	152	172	154
Ca, (mg/kg, dw)	132	106	112	16
K, (mg/kg, dw)	27	13	11	13

The concentration of the lead and other metal in shooting range soil is shown in Table 1. The average total lead contents at the targets are 14522 ± 2580 mg/kg, significantly higher than those at the baseline (4.4 mg/kg). The concentration of lead in soil is also the highest compare to other metals, indicating the excessive enrichment of lead in the shooting range soil. The average lead concentration in target soils is 36 times higher than the limits set by United States Environment Protection Agency (USEPA) [8].

Soil column leaching test

Figure 3 shows the average lead concentration in leachate from baseline and target soils, eluted with artificial rain water at pH 7 and 4. Overall, the lead concentration in leachate is higher than the safe limit (0.10 mg/L) set by the Ministry of Natural Resources and Environment [9]. The lead concentration in leachate decreased with successive fractions for all soil samples. The highest lead concentration was recorded in the leachate of target soil at pH 4. Lead concentrations of leachates from target soil are higher than those of baselines soil at pH 4 and 7. High lead content of target soils increases the amount of soluble lead ions in leachate. The concentration of lead is further increased by acidic rain water, possible due to: (1) decrease of CEC of soil, and (2) increased solubility of lead in the soil [10]. This leaching behaviour shows that the risk of leaching of lead is significantly increased in the event of acid rain.

In Table 2, the Pearson's correlation coefficient (r) value for lead concentration in soil (Soil Pb) and leachate (Leachate Pb) variables pair is 0.938, which means the concentration of lead in leachate increases with increasing of lead concentration in soil. The CEC and Soil OM variables pair has positive correlation (r = 0.891). The surface of OM may contain negatively-charged polar functional groups (i.e. carboxylate or phenolic groups) that can attract cations and help increase the CEC value of the soil [11]. The negative r values for Leachate Pb variable with both CEC and Soil OM variables show negative correlations. Decreasing OM and CEC values may depletes the capacity of the soil for retaining Pb ion, thereby, increasing the Pb concentration in leachate. Leachate Pb variable is positively-correlated with Soil Pb variable (r = 0.94; p = 0.06); but is negatively-correlated with the Soil OM variable (r = -0.94; p = 0.06). This indicate that Pb in shooting range soil is the source for Pb ions in the leachate,

and increasing Pb in soil causes higher concentration of Pb in the leachate. High soil OM content may reduce leaching of Pb through sorption with polar functional groups in the OM [12, 13].

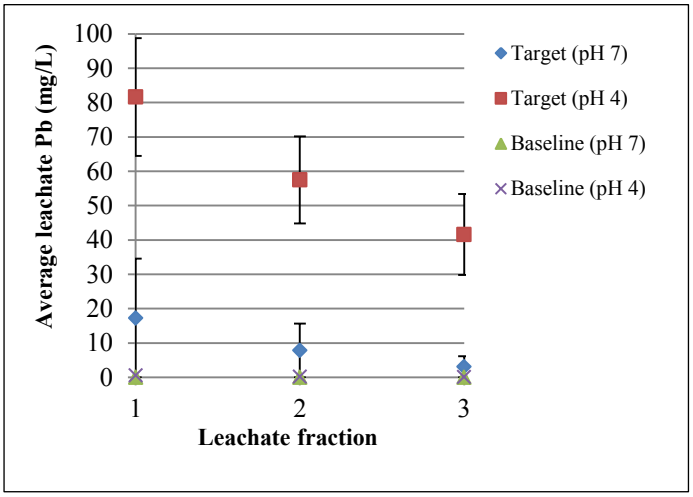


Figure 3. Concentration of lead in leachate (mg/L) from baseline and target soil at pH 4 and 7 as a function of leachate fraction

Table 2. Pearson's correlation coeffeicient (r) and significance level (p) for variables pairs

Variable		Soil Pb	Soil pH	Soil OM	CEC	Leachate Pb
Soil Pb	r	1	0.550	-0.946	-0.705	0.938
	p (2-tailed)		0.450	0.054	0.295	0.062
Soil pH	r	0.550	1	-0.500	-0.485	0.250
	p (2-tailed)	0.450		0.500	0.515	0.750
Soil OM	r	-0.946	-0.500	1	0.891	-0.939
	p (2-tailed)	0.054	0.500		0.109	0.061
CEC	r	-0.705	-0.485	0.891	1	-0.721
	p (2-tailed)	0.295	0.515	0.109		0.279
Leachate Pb	r	0.938	0.250	-0.939	-0.721	1
	p (2-tailed)	0.062	0.750	0.061	0.279	

Conclusion

The risk of leaching of the lead from the shooting range soil at Kem Sungai Besi is a concern due to (1) high concentration of lead in shooting range soil, (2) high percentage of sand in the shooting range soil, (3) lower rain pH value at Kuala Lumpur and Selangor [14], and (4) low CEC value from low soil OM content. On normal radiation practice, soil liming is employed to increase soil pH, and converts lead ions to insoluble hydroxide complexes. However, increasing soil pH may also increase the soluble fraction of the soil OM (i.e. DOM). Lead concentration in leachate may be increased due to an increased formation of soluble lead-DOM complex. In situ remediation method can be used to reduce the possibility of leaching of lead to groundwater. An immediate and economic

solution to this problem is by artificially increasing recalcitrant soil OM (i.e., activated carbon, biochar) to increase immobilization of soil Pb. Further study on the bore waters and air borne particles at the shooting range is warranted to understand the actual migration and impact of soil Pb to water resources.

Acknowledgement

The authors would like to thank the Ministry of Higher Education, Malaysia for financing this project under the Research Acculturation Collaborative Effort (RACE) Grant [600-RMI RACE 16/6/2 (2/2014)], and the Universiti Teknologi MARA for the financial assistance for participation in the SKAM28 conference.

References

1. Clausen, J., Bostick, B. and Korte, N. (2011). Migration of lead in surface water, pore water, and groundwater with a focus on firing ranges. *Critical Reviews in Environmental Science and Technology*, 41(15): 1397 – 1448.
2. Hardison Jr, D. W., Ma, L. Q., Luongo, T. and Harris, W. G. (2004). Lead contamination in shooting range soils from abrasion of lead bullets and subsequent weathering. *Science of the Total Environment*, 328(1–3): 175 – 183.
3. Cao, X., Ma, L. Q., Chen, M., Hardison, D. W. and Harris, W. G. (2003). Lead transformation and distribution in the soils of shooting ranges in Florida, USA. *Science of the Total Environment*, 307(1): 179 – 189.
4. Sorvari, J., Antikainen, R. and Pyy, O. (2006). Environmental contamination at Finnish shooting ranges the scope of the problem and management options. *Science of the Total Environment*, 366(1): 21 – 31.
5. Ayers, G., Peng, L. C., Gillett, R. and Fook, L. S. (2002). Rainwater composition and acidity at five sites in Malaysia, in 1996. *Water, Air, and Soil Pollution*, 133(1-4): 15 – 30.
6. Asadu, C. L. A., Diels, J. and Vanlauwe, B. (1997). A comparison of the contributions of clay, silt, and organic matter to the effective CEC of soils of Subsaharian Africa. *Soil Science*, 162(11): 785 – 794.
7. Darling, C. T. R. and Thomas, V. G. (2003). The distribution of outdoor shooting ranges in Ontario and the potential for lead pollution of soil and water. *Science of the Total Environment*, 313(1–3): 235 – 243.
8. USEPA, (2002). Supplemental guidance for developing soil screening levels for superfund sites. Office of Solid Waste and Emergency Response, USEPA: Washington, D.C.
9. Department of Environment (2009). Environmental quality (control of pollution from solid waste transfer station and landfill) regulations. *PU(A) 433*.
10. Sauvé, S., McBride, M. and Hendershot, W. (1998). Soil solution speciation of lead(II): Effects of organic matter and pH. *Soil Science Society of America Journal*, 62(3): 618 – 621.
11. Liang, B., Lehmann, J., Solomon, D., Kinyangi, J., Grossman, J., O'neill, B., Skjemstad, J., Thies, J., Luizao, F. and Petersen, J. (2006). Black carbon increases cation exchange capacity in soils. *Soil Science Society of America Journal*, 70(5): 1719 – 1730.
12. Yong, S. K., Bolan, N., Lombi, E. and Skinner, W. (2015). Enhanced Zn(II) and Pb(II) removal from wastewater using thiolated chitosan beads (ETB). *Malaysian Journal of Analytical Sciences*, 19(3): 586 – 594.
13. Liew, H. H., Tay, C. C., Yong, S. K., Surif, S. and Abdul Talib, S. (2010). Biosorption characteristics of lead [Pb(II)] by Pleurotus ostreatus biomass. *Proceedings of International Conference on Science and Social Research (CSSR)*. 2010. Kuala Lumpur.
14. Makmom Abdullah, A., Armi Abu Samah, M. and Yee Jun, T. (2012). An overview of the air pollution trend in Klang Valley, Malaysia. *Open Environmental Sciences*, 6(1): 13 – 19.

Malaysian Journal of Analytical Sciences, Vol 20 No 5 (2016): 1073 - 1083
DOI: http://dx.doi.org/10.17576/mjas-2016-2005-12

MALAYSIAN JOURNAL OF ANALYTICAL SCIENCES
Published by The Malaysian Analytical Sciences Society
ISSN 1394 - 2506

EFFECT OF pH ON THE PHYSICOCHEMICAL PROPERTIES AND REDUCIBILITY OF MoVTeNbOx CATALYSTS

(Kesan pH Terhadap Sifat Fizikokimia dan Kebolehturunan Mangkin MoVTeNbOx)

Syazwani Mohd Noor[1], Irmawati Ramli[1,2]*, Taufiq Yap Yun Hin[1,2], Norhazlin Zainuddin[2]

[1]*Centre of Excellence for Catalysis Science and Technology, Faculty of Science*
[2]*Department of Chemistry, Faculty of Science*
Universiti Putra Malaysia, 43400 UPM Serdang, Selangor, Malaysia

**Corresponding author: irmawati@upm.edu.my*

Received: 17 August 2015; Accepted: 25 August 2016

Abstract

A range of MoVTeNbOx catalysts were synthesised by slurry method assisted with a microwave irradiation. The pH of the synthesis solution was varied at pH = 1, 3, 5, and 7 and the obtained solid were calcined in air at 553 K for 1 hour and followed in N_2 at 873 K for 2 hours. The calcined samples were characterised and their reduction properties were evaluated. The pH of the synthesis solution was shown to affect the physicochemical properties where the formation of orthorhombic M1 phase was obtained for catalysts prepared at pH 1 and 3. The reducibility of the catalyst is improved for catalyst prepared at pH 3 as compared to those prepared at pH 1. Although higher synthesised pH (5 and 7) gave much higher reducibility of the metal oxides, however the removable oxygen could be of the unselective ones.

Keywords: MoVTeNbOx catalysts, pH, reducibility, propane, acrylic acid

Abstrak

Satu siri mangkin MoVTeNbOx telah disintesis menggunakan kaedah buburan dibantu oleh radiasi gelombang mikro. Nilai pH bagi larutan sintesis telah dikaji pada pH = 1, 3, 5, dan 7 dan pepejal yang diperolehi telah dikalsin dalam udara pada 553 K selama 1 jam dan diikuti dalam nitrogen pada 873 K selama 2 jam. Sampel terkalsin telah dicirikan dan sifat kebolehturunan telah dikaji. Di dapati, pH bagi larutan sintesis memberi kesan kepada ciri fizikokimia di mana pembentukan fasa ortorombik M1 telah terjadi bagi mangkin yang disediakan pada pH 1 dan 3. Kebolehturunan mangkin ini dipertingkatkan bagi mangkin yang disediakan pada pH 3 berbanding yang disediakan pada pH 1. Walaupun mangkin yang disediakan pada pH yang lebih tinggi (5 dan 7) memberikan kebolehturunan logam oksida lebih tinggi, namun penyingkiran oksigen mungkin menjadi tidak selektif.

Kata kunci: mangkin MoVTeNbOx, pH, kebolehturunan, propana, asid akrilik

Introduction

MoVTeNbOx is a quaternary mixed metal oxide catalyst consists of four different elements which are molybdenum, vanadium, tellurium and niobium. The catalyst is reportedly the most effective catalyst system for the vapour phase catalytic oxidation of propane to form acrylic acid [1-6]. It is because the catalyst contains necessary active sites which is fundamental in propane oxidation [7]. The active MoVTeNbOx system possesses two crystalline phases which are orthorhombic M1 phase, $Te_2M_{20}O_{57}$ (M = Mo, V, Nb), and hexagonal M2 phase, $Te_{0.33}MO_{3.33}$ (M = Mo, V, Nb) [8]. The significant difference exists among these two phases is that the M1 phase contains V^{5+} centres, as an agent for propane activation [4, 7]. Meanwhile, M2 is incapable of activating propane, but it does convert

propylene. Figure 1 suggested the reaction pathway in oxidation of propane to acrylic acid. For the reaction to occur successfully, the catalyst need at least three important active sites. The first site is a V-Mo-O phase for the activation of propane. After hydrogen is successfully abstracted from propane to form propene, a second site which is a Te-Mo-O phase is needed to oxidise propene into aldehyde. Finally, a third site, a V-Mo-O phase is needed for another oxygen insertion to convert aldehyde into acrylic acid. It is recognized that the V^{5+} ion activates alkane by first H abstraction and followed by second H abstraction to produce the allylic radical before the insertion of oxygen [9].

It has been reported that the synthesis parameters affect the properties of the final catalyst. In this context the pH of synthesis solution is of high importance because the chemical composition and phase formation depend closely on it [10-12]. The catalyst precursors suggest the presence of Anderson-type heteropolyanion, $(NH_4)_6TeM_6O_{24}.nH_2O$ in the samples prepared at pH > 3 and favouring the formation of amorphous materials at pH < 3 [12]. The acidity of the catalyst's surface was suggested to affect the binding and reactivity of propene molecules which possess a basic character [13]. Higher synthesis pH promotes the formation of MoO_3 after heat treatment, which is known to be inactive in propane oxidation [10]. The heat-treated (873K in a N_2 stream) samples from precursors prepared at lower pH suggests the presence of $Te_2M_{20}O_{57}$, $Te_{0.33}MO_{3.33}$ (M = Mo, V, Nb) and $Mo_{5-x}(V/Nb)_xO_{14}$ crystalline phases which possibly involved in the active and selective alkane activation to acrylic acid [12].

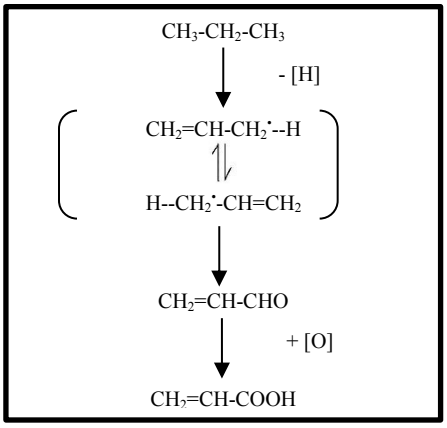


Figure 1. Reaction pathway in oxidation of propane to acrylic acid

In the present work, the MoVTeNbOx catalysts were prepared by using a slurry method assisted with microwave irradiation. During the synthesis, the pH of the solution was varied and its effect on the physicochemical properties and reducibility were studied.

Materials and Methods

Catalyst preparation

$Mo_{1.0}V_{0.3}Te_{0.23}Nb_{0.12}O_x$ catalysts were prepared by a slurry method followed by microwave irradiation according to the patented procedure [14].

Commercial chemicals which were ammonium heptamolybdate tetrahydrate, $(NH_4)_6Mo_7O_{24}.4H_2O$ (Merck), ammonium metavanadate, NH_4VO_3 (Merck), telluric acid, $Te(OH)_6$ (Sigma-Aldrich) and ammonium niobium oxalate, $(NH_4)_2Nb_2(C_2O_4)_5$ (Sigma-Aldrich), were used as the sources for Mo, V, Te and Nb respectively. The microwave used in this study was the conventional Panasonic microwave model no. NN-S554WF (750 W).

The synthesis process begun by dissolving ammonium heptamolybdate tetrahydrate in a 15 ml of irradiated deionised H_2O. The solution was irradiated before ammonium metavanadate was added. The solution was then irradiated, followed by the addition of telluric acid. The irradiated ammonium niobium oxalate solution was added

to the MoVTe suspension that were separately prepared using ammonium niobium oxalate dissolved in 5 ml of deionised H_2O. Finally, the resulting orange slurry formed were irradiated for 3 min. The pH of resultant slurry precursor was recorded with the value of 4.5 (±0. 01) using Thermo-line PHS-3BW digital pH meter.

The pH of the final slurry was adjusted by using 1 M aqueous sulphuric acid for pH range 1 to 3 and 1 M of an aqueous ammonium hydroxide for pH 5 to 7. Then, the solution was left overnight and later dried using a rotary evaporator at 353 K. These samples were denoted as $MVTN_{1p}$, $MVTN_{3p}$, $MVTN_{5p}$, and $MVTN_{7p}$ respectively.

The precursor samples were later calcined for 1 h in air at 553 K to remove the organic substances and followed by 2 h in the N_2 stream at 873 K to control the phase formation of the catalyst. These samples were denoted as $MVTN_{1c}$, $MVTN_{3c}$, $MVTN_{5c}$, and $MVTN_{7c}$ respectively.

Catalyst characterisation

All the catalysts were characterised by the following analytical techniques. Powder X-ray diffraction patterns were collected by using a Shimadzu Model XRD 6000 Diffractometer equipped with CuK_α radiation with wavelength, λ= 1.542 Å which were continuously scanned in the range of $2\theta = 2° - 60°$ at a scanning rate of 2° min^{-1}. Induced coupled plasma-atomic electron spectroscopy (ICP-AES) measurements of bulk MoVTeNbOx compositions were carried out using a model Perkin Elmer Emission Spectrometer Plasma 1000. Fourier Transform Infrared Spectroscopy (FTIR) were analysed using a Perkin Elmer 1725X spectrometer by employing the standard KBr method and the spectra were recorded in the 400 cm^{-1} to 4000 cm^{-1} regions. Field emission-scanning electron microscopy (FESEM) images were collected using Nova 200 NanoLab at an accelerating voltage of 5.0 kV. The aluminium stud was used with the carbon paint was tapped on the sample and coated with gold.

Reducibility study

Temperature programmed reduction in hydrogen (H_2-TPR) analysis was carried out by using ThermoFinnigan TPDRO 1110 Instrument. Before subjecting the catalyst to a reducing environment, it was pre-treated under a N_2 flow by heating sample to 423 K at a heating rate of 10 K min^{-1}. After which, the nitrogen gas was switched to hydrogen (5 % H_2 in Argon) and temperature programming up from 323 K to 1223 K at a heating rate of 10 Kmin^{-1}. The amounts of water, H_2O which was produced was flowed through the thermal conductivity detector.

Results and Discussion

Physicochemical properties of MoVTeNbOx catalysts

The XRD patterns of four precursors prepared at different pH are shown in Figure 2. At pH 1, there are no visible peaks due to metal oxide crystal phase can be observed. The $MVTN_{1p}$ displays two humps at $2\theta = 6°$- 15° and 21° - 35° which reckons that the sample is amorphous due to randomly distributed of atoms in the solid particles [15]. As the pH of synthesis solution increases, the metal oxide peaks become apparent. All of the other three samples ($MVTN_{3p}$, $MVTN_{5p}$, and $MVTN_{7p}$) exhibited sharp peaks at $2\theta = 10.3°$, 12.5°, 13.1°, 16.0°, 18.1°, 23.2°, 25.0° and 27.8° suggesting the orderly arranged of the atoms. The peaks suggested the presence of Anderson-type heteropolyanion $(NH_4)_6TeMo_6O_{24}.7H_2O$ and/or $(NH_4)_7TeMo_5VO_{24}.8H_2O$ [15, 16]. A similar case has been reported, whereby an Anderson-type heteropolyanion, $(NH_4)_6TeMo_6O_{24}.nH_2O$ was formed in samples prepared at pH 3.0– 4.5 whereby at pH < 3 the heteropolyanion partially decomposed with the formation of mostly amorphous materials and at a very low pH 1.0–1.5 indicates the present of polyoxovanadates in the precursors [12]. Therefore, as observed in this work at low pH the crystallinity of heteropolyanion compounds decreases and amorphous materials are observed due to the partial incorporation of heteroatoms or the heteroatoms are highly dispersed on the compounds. The results show that pH influences the incorporation of heteroatoms (V and Nb) on heteropolyanion which determines the formation of active crystalline phases.

The XRD patterns of calcined samples are shown in Figure 3. The peaks evolved for samples synthesised at pH 1 and 3 i.e. $MVTN_{1c}$ and $MVTN_{3c}$, respectively suggests the presence of orthorhombic M1 and hexagonal M2 phases. The presence of both phases can be clearly indicated by $2\theta = 6.6°$, 7.9°, 9.0°, 22.1° and 45° which correspond to orthorhombic M1 (JCPDS: 58-790) meanwhile $2\theta = 22.1°$, 28.3°, 36.2° and 50° correlate to hexagonal M2 phase (JCPDS: 57-1099). On the other hand, the two other samples which are $MVTN_{5c}$ and $MVTN_{7c}$ synthesised at pH 5

and 7 respectively, show the occurrence of hexagonal M2 phase and the additional peaks at 2θ = 7.7°, 8.9°, 22.1°, 24.2° and 31.3° which can be correlated to the existence of tetragonal phase, $(V_{0.07}Mo_{0.93})_5O_{14}$ (JCPDS: 31-1437).

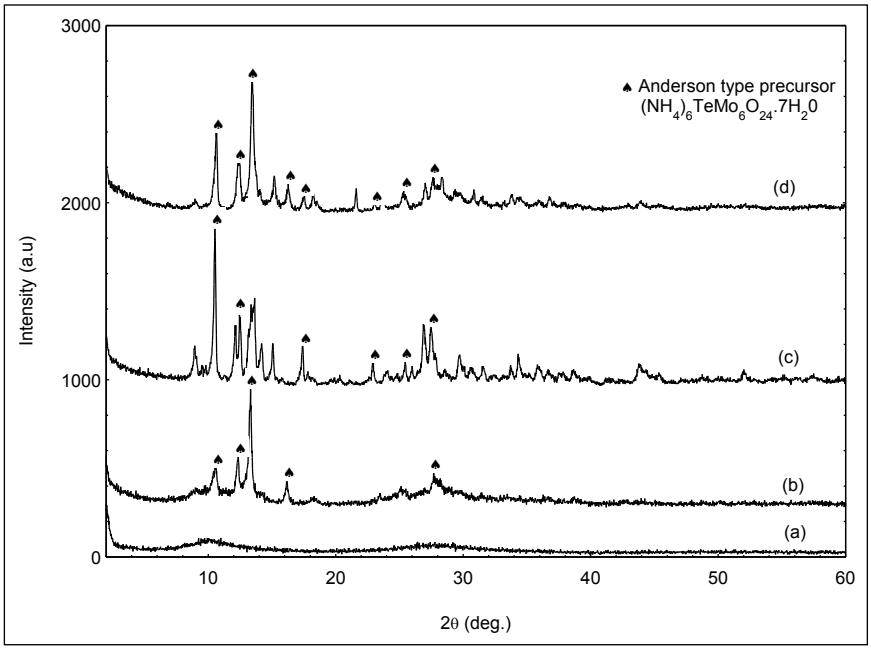


Figure 2. XRD patterns of precursor MoVTeNbOx catalysts (a) $MVTN_{1p}$ (b) $MVTN_{3p}$ (c) $MVTN_{5p}$ (d) $MVTN_{7p}$

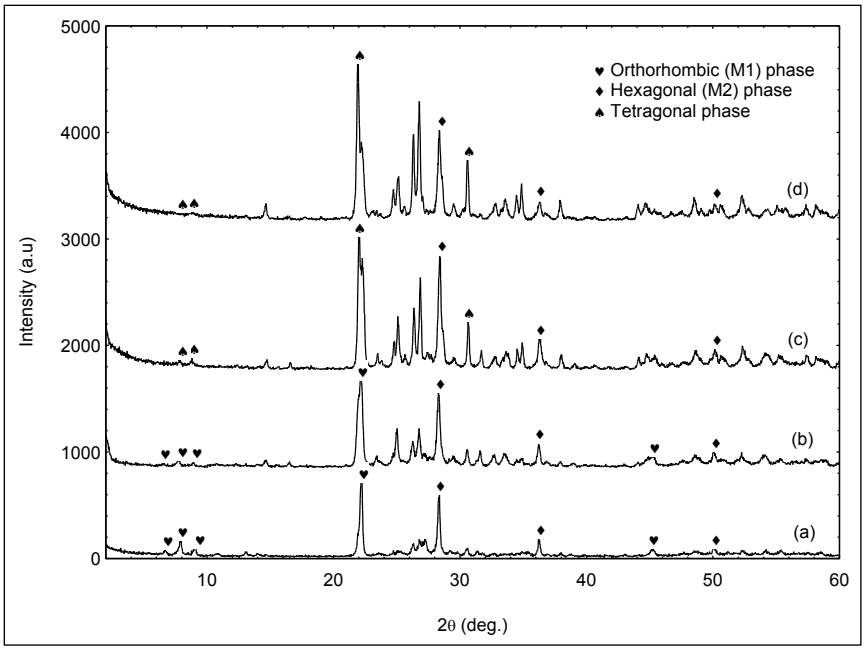


Figure 3. XRD patterns of calcined MoVTeNbOx catalysts (a) $MVTN_{1c}$ (b) $MVTN_{3c}$ (c) $MVTN_{5c}$ (d) $MVTN_{7c}$ [23].

It can be noted that orthorhombic M1, hexagonal M2 and tetragonal phases have the same diffraction peak of 22.1° which suggests that the mixture of phases in the samples [15]. The formation of these phases may be due to the formation of pseudo-amorphous or semi crystalline Anderson-type compound (ammonium containing phase) which has been observed during precursor stage [17].

The crystallite size of the calcined MoVTeNbOx catalysts can be determined by using the full width half maximum (FWHM) for three characteristic peaks of orthorhombic M1 phase at 2θ = 6.6°, 7.9°and 9.0°. The crystallite size was estimated by the using the Debye Scherrer equation as in (1).

$$t = \frac{0.9\lambda}{\beta_{hkl} \cos \theta_{hkl}} \quad (1)$$

where, t = crystallite size, λ = 1.5438 Å, θ = Bragg angle, β_{hkl} = the full width at half maximum (FWHM) of the peak in radian.

The value of crystallite size in Table 1 suggested that the crystallite size of the $MVTN_{1c}$ and $MVTN_{3c}$ samples are 35.12 nm to 36.42 nm respectively. The values are in the nanometer range, which gives a good indication of the pH influence on the catalyst particle size. However, there is no orthorhombic phase were present in $MVTN_{5c}$ and $MVTN_{7c}$, therefore particle size for these samples were not calculated.

Table 1. Crystallite size and bulk composition of $MVTN_{1c}$, $MVTN_{3c}$, $MVTN_{5c}$ and $MVTN_{7c}$

Sample	**2θ (°)**	**FWHM (°)**	**t (nm)**	**Bulk composition[1] (Mo: V: Te: Nb)**
$MVTN_{1c}$	6.5	0.2005	39.8	1.0: 0.29: 0.17: 0.10
	7.7	0.2825	28.2	
	8.6	0.2137	37.4	
			Average: 35.12	
$MVTN_{3c}$	6.6	0.2445	32.6	1.0: 0.29: 0.17: 0.09
	7.7	0.2550	31.3	
	8.9	0.1760	45.4	
			Average: 36.42	
$MVTN_{5c}$	NA[2]			1.0: 0.29: 0.17: 0.09
$MVTN_{7c}$	NA[2]			1.0: 0.29: 0.17: 0.09

Preparative composition of Mo: V: Te: Nb = 1.0: 0.3: 0.23: 0.12, [1]Determined by ICP-AES, [2]NA: Not applicable

The bulk compositions of Mo-V-Te-Nb mixed oxide catalysts determined by ICP-AES are summarised in Table 1. The bulk compositions of all the oxides were not so different from the preparative compositions. The Mo element is justified in all samples as Mo is the main component in the mixture. For all samples, the V element obtained which is 0.29 are closely resemble to the theoretical value of 0.3. The molar ratio of the Mo and V element are important in the catalyst system because these elements are responsible for the structural formation of the MoVTeNbOx catalysts and M1 phase will be formed with Mo:V ratios higher than 0.14 [6,18].

The difference is found in the tellurium contents which were slightly lower in the bulk. A possible explanation for the loss of tellurium could be related to the presence of oxalate anions (reducing agent) from the starting material of

niobium oxalate, which could facilitate the reduction of tellurium cations to metallic Te [19] that were detached away from the structure during calcination. The Nb content is also found lower after calcination in all samples. It has been reported that Nb play the same structural role as vanadium in order to obtain the mono-phasic orthorhombic M1 structure [20]. In the case of the catalyst in this work, the condition of lower amount of Nb gave MoVTeNbOx catalysts containing several phases as has been observed in the XRD analysis. Still, the presence of Nb despite of its amount is important for the stability of the element in the solid structure.

The FTIR spectra of the precursors are shown in Figure 4. The bands around 3178 cm^{-1} and 1441 cm^{-1} are due to the symmetric and asymmetric stretching vibrations of the tetrahedral ammonium cation [16]. The H–O–H bending mode is observed in the range 1668 cm^{-1} and bands at 1301 cm^{-1} could be attributed to stretching and vibration modes of C=O, a stretching combination of C–O and C–C associated with the oxalate anion [15]. Meanwhile, the absorption band at 1101 cm^{-1} is discovered to only exist in sample $MVTN_{1p}$ that can be related to the S=O stretching [21]. This is caused by the presence of sulphate group while incorporating H_2SO_4 during pH adjustment of precursor solution. In this case, only two samples required H_2SO_4 during pH adjustment, which are $MVTN_{1p}$ and $MVTN_{3p}$. However, this peak only intense for $MVTN_{1p}$ and almost unnoticeable for $MVTN_{3p}$. This is due to the reason that the pH of the solution before adjustment was around pH 4.3, so only little amount of H_2SO_4 ions present in the $MVTN_{3p}$ solution, compared to $MVTN_{1p}$. In addition, the sharp peak detected around 884 cm^{-1} corresponds to no vibrations and bands around 623 cm^{-1} can be due to the Mo-O, Te–O and Mo–O–Te vibrations, since the different bands of these vibrations overlapped in this range [16]. The stretching of V=O group and V-O-Me (Me= Mo, Te, Nb) gave the absorption band around 449 cm^{-1}.

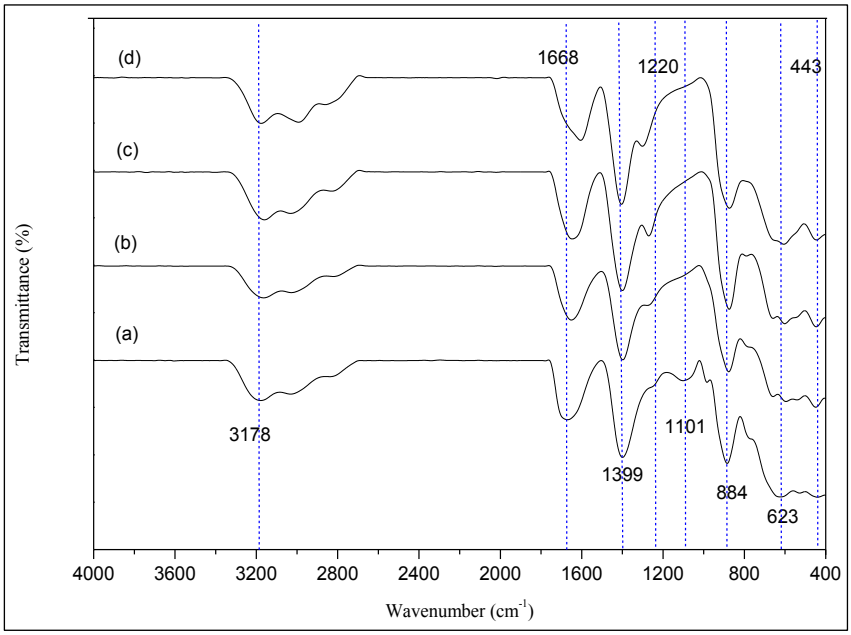


Figure 4. FTIR spectra of precursor MoVTeNbOx catalysts (a) $MVTN_{1p}$ (b) $MVTN_{3p}$ (c) $MVTN_{5p}$ (d) $MVTN_{7p}$

For the calcined samples, there are no bands observed in the region above 1000 cm^{-1} as can be seen in Figure 5, therefore it is sufficient to show spectra of low frequency region [15]. The disappearance of the high frequency region above 1000 cm^{-1} indicates that all of the organic species functional groups such as hydroxyl, sulphate, ammonium and water are completely removed from the samples during calcination. The band at 861 cm^{-1} and 699 cm^{-1} are assigned to asymmetric stretching vibrations of bridging Mo-O-*M* bonds (*M* = Mo, Nb, Te) [12] which lies in the range of 800 – 1000 cm^{-1}. The bands around 530 cm^{-1} and 431 cm^{-1} can be assigned to V = O group and V-O-Me bonds (*M* = Mo, Te, Nb) in the range of 400 – 600 cm^{-1} [16].

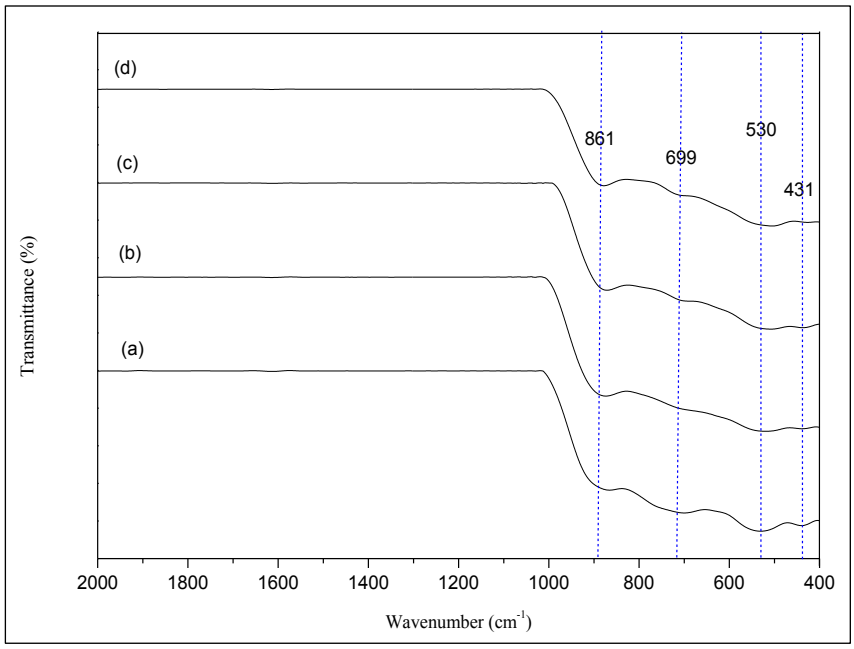


Figure 5. FTIR spectra of calcined MoVTeNbOx catalysts (a) $MVTN_{1c}$ (b) $MVTN_{3c}$ (c) $MVTN_{5c}$ (d) $MVTN_{7c}$

The morphology of calcined catalysts was investigated by FE-SEM analysis. The images are shown in Figure 6. The micrographs display the formation of rod-shaped morphology in all of the samples. This kind of morphology is similar to the reported works [20, 22]. The formation of a rod-shaped morphology could be due to V^{5+} derived from ammonium metavanadate in the synthesis step which contribute to the formation of long and large needles during the slurry synthesis [22]. For catalyst synthesised at pH 1, it gives a more homogeneous and rather disperse particles as compared to catalysts prepared at higher pH. Not to be denied is the presence of other shaped particles, thus stating the mixture of phases in accordance with the XRD patterns which showed mixed phase of the calcined catalyst [12].

Reducibility properties

The study on the catalyst reducibility is important in a mixed metal oxide catalyst used for the oxidation reaction. It will give an indication of the availability of the oxygen for insertion into reactants. During the reduction process, hydrogen gas is in contact with the oxygen species from the surface of the catalyst. The hydrogen is consumed and formed water vapour in the gaseous state as a product, leaving an oxygen vacancy on the catalysts. The interaction of the gas phase hydrogen with catalyst can be represented as in equation (2).

$$H_{2(g)} + O_{(surface)} \longrightarrow H_2O_{(g)} + \square \qquad (2)$$

where (g) = gaseous species, *(*s) = surface or lattice species and □ = oxygen vacancy.

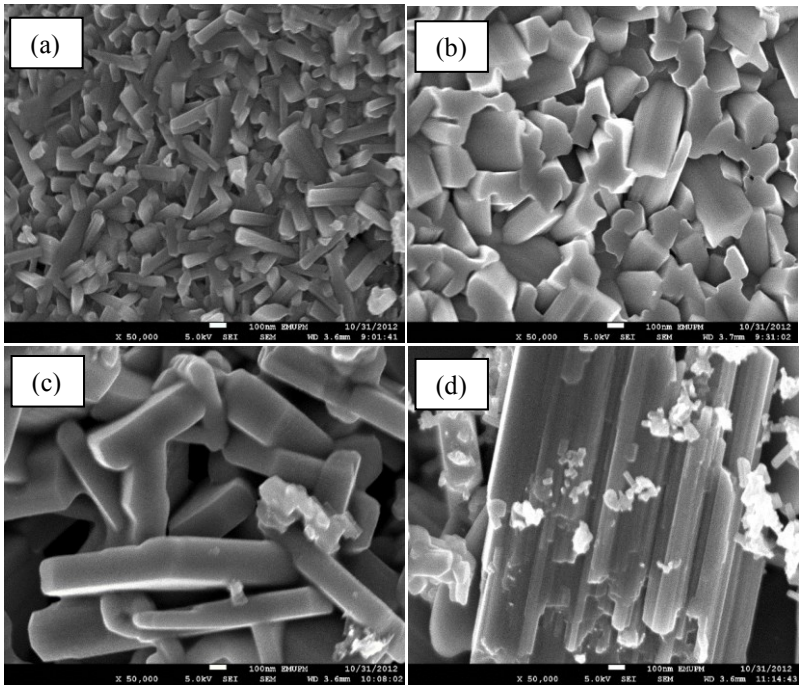


Figure 6. FESEM image of calcined MoVTeNbOx catalysts (a) $MVTN_{1c}$ (b) $MVTN_{3c}$ (c) $MVTN_{5c}$ (d) $MVTN_{7c}$

The reduction profiles of MoVTeNbOx catalysts are shown in Figure 7. There are at least two peak maximum which are overlapped with each other are observed in all of the samples. The occurrence of multiple reduction peaks indicates the presence of a number of reducible metal oxide species present in the catalyst.

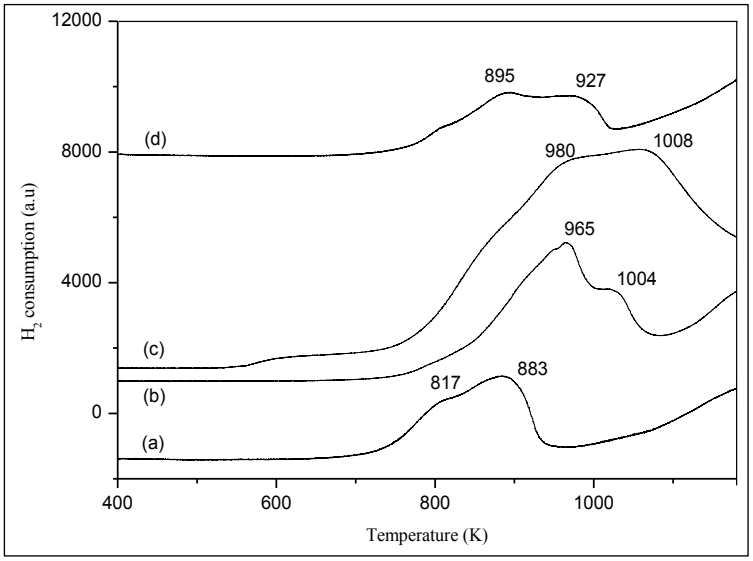


Figure 7. H_2-TPR profiles of calcined MoVTeNbOx catalysts (a) $MVTN_{1c}$ (b) $MVTN_{3c}$ (c) $MVTN_{5c}$ (d) $MVTN_{7c}$

The reduction peak suggests reductive decomposition of metal oxides where MoO_n reduced at 948 K and 995 K for a stepwise reduction of $Mo^{6+} \rightarrow Mo^{4+}$ and $Mo^{4+} \rightarrow Mo^0$ under H_2-TPR, meanwhile VO_n reduced at temperature of 913 K and 943 K from $V_2O_5 \rightarrow VO_2$ [24,25]. Additionally, reduction of Nb^{5+} to Nb^{4+} occur at around 1243 K [26].

The reduction activation energy of the catalysts can be calculated using the modified version of the Redhead equation as stated in equation (3). The results are summarised in Table 2.

$$\frac{E_r}{RT_m^2} = \left(\frac{A_r}{\beta}\right)[H_2]_m \exp\left(\frac{-E_r}{RT_m}\right) \quad (3)$$

where, E_r = reduction activation energy (kcal mol^{-1}), T_m = peak maximum temperature (K) in the rate of production of H_2, A_r = reduction pre-exponential term ($cm^3mol^{-1}s^{-1}$) which is given a standard collision number of 10^{13} cm^3 $mol^{-1}s^{-1}$, β = heating rate (Ks^{-1}) and $[H_2]_m$ is the gas phase concentration of hydrogen (mole cm^{-3}) at the peak maximum.

Table 2. The reduction activation energy, E_r and total O_2 removed determined from H_2-TPR for (a) $MVTN_{1c}$ (b) $MVTN_{3c}$ (c) $MVTN_{5c}$ (d) $MVTN_{7c}$

Sample	**T_{max}, (K)**	**Reduction activation energy, E_r (kJ mol^{-1})**	**O_2 removed (atom g^{-1}) × 10^{21}**
$MVTN_{1c}$	817	136.5	0.72
	883	147.5	1.67
			Total = 2.39
$MVTN_{3c}$	965	161.2	4.67
	1004	167.7	0.94
			Total = 5.61
$MVTN_{5c}$	980	163.7	8.39
	1008	168.4	7.26
			Total = 15.65
$MVTN_{7c}$	895	149.5	1.60
	927	154.9	1.05
			Total = 2.65

The values of reduction activation energy, E_r for all samples is more than 100 kJ mol^{-1} indicates that the oxygen species are strongly bonded. Thus, these strongly bonded oxygen species that has been removed in these samples may be originated from the surface and/ or lattice of the catalyst [27].

Interaction of hydrogen with MoVTeNbOx mixed oxides during H_2-TPR involves the adsorption of hydrogen on all active sites of the molybdenum oxide surface, taken up the oxygen species and caused the reduction of the MoO_n component. The higher amount of oxygen removed indicate the high activity of the catalysts. The amount of oxygen removed of each sample can be estimated by integrating the area under the peak. For catalyst prepared at pH 1, the total amount of removable oxygen is 2.39 x 10^{21} atom g^{-1} whereas the amount is doubled to 5.61 x 10^{21} atom g^{-1} when synthesised at pH 3. This is an indication of the high removable oxygen of the catalyst when prepared at pH 3 which was contributed by the formation of the much desired orthorhombic M1 phase. Although the catalyst prepared at pH 5 gives a much higher of removable oxygen species (15.65 x 10^{21} atom g^{-1}), nevertheless it could be the unselective oxygen species due to the catalyst does not contains the orthorhombic M1 but hexagonal M2 phase instead. The same goes with catalyst prepared at pH 7.

Conclusion

The results revealed that the pH of the slurry strongly influences the formation of crystalline Anderson-type heteropolyanions for catalysts prepared at pH 3, 5 and 7. While the as-synthesised sample at pH 1 showed the presence of pseudo-amorphous materials which allow for the formation of orthorhombic M1 phase upon calcination. The formation of orthorhombic M1 phase is also observed in pH 3 samples (after calcination), but none was found in the other samples. Therefore, high acidity condition is required for the formation of desired catalyst phase. Although, all of the catalysts give similar reduction profiles in the anaerobic hydrogen-TPR, the lattice oxygen that were removed in catalysts which contains orthorhombic M1 could be the selective ones. This is because, the catalysts with M1 phase can undergo charge transfer on the Mo and V sites with the lattice oxygen could be involved in the abstraction of H at the vanadium sites and oxygen insertion at the molybdenum sites. There is a clear relationship between synthesis pH and catalyst properties, suggesting that the reducibility of crystalline phases is a key factor in the propane selective oxidation into acrylic acid.

Acknowledgement

The authors would like to thank the Ministry of Higher Education Malaysia (Fundamental Research Grant Scheme (FRGS), grant number: 5523956) for their financial support.

References

1. Lin, M. M. (2001). Selective oxidation of propane to acrylic acid with molecular oxygen. *Applied Catalysis A: General*, 207 (1-2): 1 – 16.
2. Tu, X., Furuta, N., Sumida, Y., Takahashi, M. and Niiduma, H. (2006). A new approach to the preparation of MoVNbTe mixed oxide catalysts for the oxidation of propane to acrylic acid. *Catalysis Today,* 117 (1-3): 259 – 264.
3. Yu, Z., Zheng, W., Xu, W., Zhang, Y., Fu, H. and Zhang, P. (2009). Effect of preparation conditions on selective oxidation of propane to acrylic acid. *Transactions of Nonferrous Metals Society of China,* 19 (2):476 – 479.
4. Beato, P., Blume, A., Girgsdies, F., Jentoft, R.E., Schlögl, R., Timpe, O., Trunschke, A., Weinberg, G., Basher, Q., Hamid, F.A., Hamid, S.B.A., Omar, E. and Mohd Salim, L. (2006). Analysis of structural transformations during the synthesis of a MoVTeNb mixed oxide catalyst. *Applied Catalysis A: General,* 307 (1): 137 – 147.
5. Ueda, W., Vitry, D., Katou, T., Watanabe, N. and Endo, Y. (2006). Key aspects of crystalline Mo-V-O-based catalysts active in the selective oxidation of propane. *Research on Chemical Intermediates,* 32 (3): 217 – 233.
6. Ushikubo, T., Nakamura, H., Koyasu, Y. and Wajiki, S. (1995). Method for producing an unsaturated carboxylic acid. US Patent 5 380 933.
7. Grasselli, R. K., Buttrey, D. J., DeSanto Jr, P., Burrington, J. D., P., Lugmair, C. G., Volpe Jr, A. F. and Weingand, T. (2004). Active centers in Mo–V–Nb–Te–O_x (Amm)oxidation catalysts. *Catalysis Today,* 91–92: 251 – 258.
8. Ushikubo, T., Oshima, K., Kayou, A. and Hatano, M. (1997). Ammoxidation of propane over Mo-V-Nb-Te mixed oxide catalysts. *Studies in Surface Science and Catalysis,* 112: 473 – 480.
9. Vedrine, J. C. (2016). Heterogeneous partial (Amm) oxidation and degydrogenation catalysis on mixed metal oxides. *Catalysts*, *6*(2):1 – 26.
10. Yu, Z., Zheng, W., Xu, W., Zhang, P., Fu, H. and Zhang, Y. (2011). Crystalline structure of mixed metal oxide catalysts for propane selective oxidation to acrylic acid. *Transactions of Nonferrous Metals Society of China,* 21 (2): 405 – 411.
11. Guan, J., Wang, H., Yang, Y., Liu, B., Yu, X., Ma, Y. and Kan, Q. (2009). Effect of pH on the catalytic properties of Mo–V–Te–P–O catalysts for selective oxidation of isobutane. *Catalysis Letters*, 131 (3-4): 512 – 516.
12. Oliver, J. M., López Nieto, J. M., Botella, P. and Mifsud, A. (2004). The effect of pH on structural and catalytic properties of MoVTeNbO catalysts. *Applied Catalysis A: General,* 257 (1): 67 – 76.
13. Baca, M., Pigamo, A., Dubois, J. L. and Millet, J. M. M. (2005). Fourier transform infrared spectroscopic study of surface acidity by pyridine adsorption on the M1 active phase of the MoVTe(Sb)NbO catalysts used in propane oxidation. *Catalysis Communications,* 6 (3): 215 – 220.
14. Irmawati, R., Muda, A. A., Ismail, A. Z. and Ahangar, H. A. (2016). Malaysian Patent MY 156457.

15. Popova, G.Y., Andrushkevich, T.V., Chesalov, Y. A., Plyasova, L. M., Dovlitova, L. S., Ischenko, E.V., Aleshina, G. I. and Khramov, M. I. (2009). Formation of active phases in MoVTeNb oxide catalysts for ammoxidation of propane. *Catalysis Today,* 144 (3-4): 312 – 317.
16. Botella, P., López Nieto, J. M., Solsona, B., Mifsud, A. and Márquez, F. (2002). The preparation, characterization, and catalytic behavior of MoVTeNbO catalysts prepared by hydrothermal synthesis. *Journal of Catalysis,* 209 (2): 445 – 455.
17. Sanfiz, A. C., Hansen, T. W., Girgsdies, F., Timpe, O., Rodel, E., Ressler, T., Trunschke, A. and Schlogl, R. (2008). Preparation of phase-pure M1 MoVTeNb oxide catalysts by hydrothermal synthesis - influence of reaction parameters on structure and morphology. *Topic in Catalysis*, 50 (1-4): 19 – 32.
18. Naraschewski, F. N., Kumar, C. N., Jentys, A. and Lercher, J. A. (2011). Phase formation and selective oxidation of propane over MoVTeNbOx catalysts with varying compositions. *Applied Catalysis A: General,* 391 (1-2): 63 – 69.
19. Ivars, F., Solsona, B., Hernández, S. and López Nieto, J. M. (2010). Influence of gel composition in the synthesis of MoVTeNb catalysts over their catalytic performance in partial propane and propylene oxidation. *Catalysis Today,* 149 (3-4): 260 – 266.
20. Vitry, D., Morikawa, Y., Dubois, J. L. and Ueda, W. (2003). Mo-V-Te-(Nb)-O mixed metal oxides prepared by hydrothermal synthesis for catalytic selective oxidations of propane and propene to acrylic acid. *Applied Catalysis A: General*, 251 (2): 411 – 424.
21. Pavia, D. L., Lampman, G. M. and Kriz, G. S. (2001). *Introduction to spectroscopy*. United States of America: Thomson Learning, Inc.
22. Lin, M. M. (2003). Complex metal oxide catalysts for selective oxidation of propane and derivatives: II. The relationship among catalyst preparation, structure and catalytic properties. *Applied Catalysis A: General,* 250 (2): 287 – 303.
23. Syazwani M. N, Irmawati R, Taufiq-Yap Y. H, and Zainuddin, N. (2016). Effect of pH on the physicochemical properties of MoVTeNbOx catalysts for oxidation of propane to acrylic acid. *International Journal of Scientific & Technology Research,* 5(1): 40 – 45.
24. Jiang, H. C., Lu, W. M. and Wan, H. L. (2004). The effect of $MoV_{0.3}Te_{0.23}P_xO_n$ catalysts with different phosphorus content for selective oxidation of propane to acrolein. *Journal of Molecular Catalysis A-Chemical*, 208 (1-2): 213 – 217.
25. Wong, M. S., Irmawati, R., Ahangar, H.A., Taufiq-Yap, Y. H, Tan, Y.P. and Muhamad E. N. (2012). Physicochemical studies of Ni-, Co-, Pt- promoted MoVNbOx catalysts synthesised by impregnation method. *Oriental Journal of Chemistry*, 28 (1): 59 – 65.
26. Pereira, E. B., Pereira, M. M., Lam, Y. L., Perez, C. A. C. and Schmal, M., (2000). Synthesis and characterization of niobium oxide layers on silica and the interaction with nickel. *Applied Catalysis A: General*, 197 (1): 99 – 106.
27. Woi, P. M., Irmawati, R. and Taufiq-Yap, Y. H. (2007). Influence of organic species on the characteristics of Mo-V oxides. *Malaysian Journal of Analytical Sciences*, 11(1): 160 – 165.

Malaysian Journal of Analytical Sciences, Vol 20 No 5 (2016): 1084 - 1089
DOI: http://dx.doi.org/10.17576/mjas-2016-2005-13

MALAYSIAN JOURNAL OF ANALYTICAL SCIENCES
Published by The Malaysian Analytical Sciences Society
ISSN 1394 - 2506

EFFECT OF MULTI WALLED CARBON NANOTUBES ON THERMAL CONDUCTIVITY OF POLYLACTIC ACID NANOCOMPOSITE

(Kesan Penambahan Nanotiub Karbon Berbilang Dinding Ke Atas Kekonduksian Terma Polilaktik Asid Nanokomposit)

Adilah Mat Ali[1], Sahrim Hj Ahmad[1]*, Mou'ad A.Tarawneh[2]

[1]*School of Applied Physics, Faculty of Science and Technology, Universiti Kebangsaan Malaysia, 43600 UKM Bangi, Selangor, Malaysia*
[2]*Department of Physics, Collage of Science, Al-Hussein Bin Talal University, P.O. Box 20, Ma'an, Jordan*

**Corresponding author: sahrim@ukm.edu.my*

Received: 10 June 2015; Accepted: 21 July 2016

Abstract

Multi walled carbon nanotubes (MWCNT) hold the increasing interest in many different fields. To employ MWCNT as an effective reinforcement in order to enhance the thermal conductivity of polylactic acid (PLA) modified with liquid natural rubber (LNR), proper dispersion and appropriate interfacial adhesion between MWCNT and PLA/LNR have to be guaranteed. This paper used ultrasonic technique as the method to help to improve the dispersion of MWCNT in PLA/LNR matrix. The result shown that the sample with 3.5 wt.% of MWCNT provided higher thermal conductivity which is believe to be the optimum loading due to better dispersion of MWCNT in PLA/LNR matrix. The 4 wt.% of MWCNT shows decreasing of thermal conductivity due to the presence of agglomeration of MWCNT. The results confirmed by Scanning Electron Microscopy (SEM) micrograph. Fourier Transform Infrared (FTIR) spectra shown that there were no chemical changes happen.

Keywords: polylactic acid, multi-walled carbon nanotubes, thermal conductivity, nanocomposites, ultrasonic

Abstrak

Tiub karbon berbilang dinding (MWCNT) telah menarik minat dalam pelbagai bidang yang berbeza. Bagi memastikan MWCNT dapat digunakan secara berkesan sebagai agen pengukuh dalam peningkatan kekonduksian terma polilaktik asid (PLA)/ cecair getah asli (LNR) nanokomposit, serakan dan lekatan antara muka yang sempurna dan baik di antara MWCNT dan PLA/LNR adalah di antara aspek yang perlu diberi perhatian. Di dalam kertas ini, teknik ultrasonik telah digunakan bagi memastikan membantu penyerakan MWCNT di dalam PLA/LNR matrik. Keputusan menunjukkan sampel yang mengandungi 3.5 wt% MWCNT menghasilkan kekonduksian terma yang tertinggi dengan pencapaian nilai kandungan optima disebabkan oleh serakan yang baik di dalam PLA/LNR matrik. Pada kandungan MWCNT 4 wt%, kekonduksian terma menunjukkan penurunan disebabkan oleh gumpalan MWCNT. Keputusan disahkan oleh Imbasan Elektron Microskopi (SEM) mikrograf. Spektra Fourier Transform Inframerah Spektroskopi (FTIR) pula menunjukkan tiada perubahan kimia yang berlaku.

Kata kunci: polilaktik asid, tiub karbon berbilang dinding, kekonduksian terma, nanokomposit, ultrasonic

Introduction

Recently, carbon nanotube (CNT) has been widely explored and gains much attention to be used as filler in polymer due to their ability to transform an insulating polymer matrix to a conductive composite. CNT developed in 1990s and available as single wall (SWCNT), double wall (DWCNT) and multi wall (MWCNT) [1]. CNT has unique

structure which enables to be filled with polymer and have low percolation threshold concentration [2,3]. CNT not only helps in enhancing in terms of tensile modulus, tensile strength, toughness, glass transition temperature, electrical conductivity but also the thermal conductivity of the polymer composites due to outstanding aspect ratio. CNT incorporated in polymer show thermal conductivity enhancement even at very low loading by forming percolating network. However, it is controlled by many factors such as aspect ratio, dispersion and its interfacial interactions with the polymer matrix.

Even after a decade of research, the potential of employing CNT as reinforcements has become limited because of the difficulties to get good dispersion of CNT during processing and poor interfacial interaction between CNT and polymer matrix. CNT has small diameter in nanometer scale with high aspect ratio (>1000) and extremely large surface area which make the nature of dispersion of CNT differ from other conventional fillers like carbon fibers or spherical particles [1]. Therefore, the basis of CNT dispersion method is introduced here which is ultrasonication which is the most frequently used method for nanoparticle dispersion. This is the method where ultrasound energy is applying in order to agitate particles in the solution by using either an ultrasonic bath or an ultrasonic probe (also known as sonication) [1]. This method is an effective method to disperse CNT in liquids having low viscosity such as water, ethanol and toluene.

In this study, polymer nanocomposites were prepared from biodegradable polymer which is polylactic acid (PLA) with modification using liquid natural rubber (LNR) in order to reduce the brittleness of PLA and filled with MWCNT. The optimal LNR content in the blend was found to be 10 wt.% where it shows it has improve the brittleness and crystallization ability of the PLA [4]. MWCNT was mixed with LNR using ultrasonication method before melt blended with PLA. According to Adilah and Sahrim [5], the tensile strength and Young's modulus of the PLA/LNR/MWCNT nanocomposites which prepared using ultrasonic method shows an improvement compared to the manual method of mixing LNR with MWCNT. The optimum time of ultrasonication was found to be at 1 hour [6]. Thermal conductivity of the polymer nanocomposites produced is discussed in detail.

Materials and Methods

Materials

Polylactic acid of Natureworks IngeoTM Biopolymer 3251D grade supplied by Unic Technology Ltd, China was used as the base polymer matrix. It has a density of 1.24 g/cm^3 and melt flow index of 30-40g/10 minutes (190°C/2.16Kg) with melting temperature between 188 – 210 °C. MWCNT is manufactured by Nanocyl^{TM} having average diameter of 9.5 nm, carbon purity of 90% and surface area of 250 – 300m^2/g. Figure 1 show the MWCNT used in this paper. LNR was produced by using photochemical sensitized degradation technique. NR of SMR L grade which supplied by Malaysian Rubber Board were immersed in toluene and exposing it to ultraviolet radiation for 6 hours.

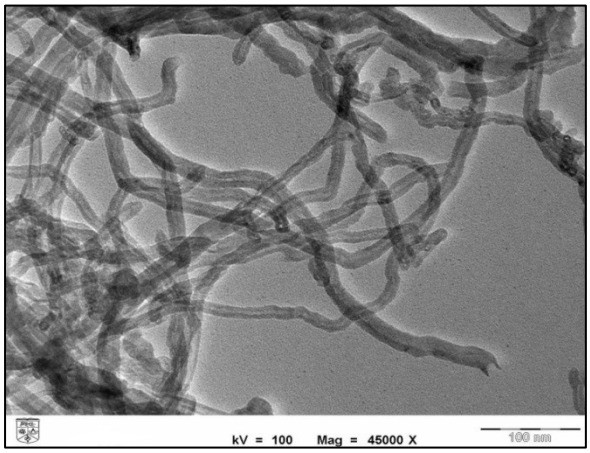


Figure 1. TEM image of pure MWCNT

Preparation of PLA/LNR/MWCNT nanocomposites

PLA/LNR/MWCNT nanocomposites were prepared using melt blending using Haake Rheomix internal mixer. The processing parameter is at 190 °C, rotor speed of 90 rpm with 14 mins of mixing time. The LNR concentration was fixed at 10 wt.%. The MWCNT loading was varied at 0.5, 1.5, 2.5, 3.5 and 4 wt.%. The MWCNT was initially dispersed in the LNR by ultrasonic for 1 hour before melt blended with PLA.

Characterizations of PLA/LNR/MWCNT nanocomposites

To study the effect of MWCNT filler on thermal conductivity of PLA/LNR nanocomposites, the temperature was varied from 30 °C to 180 °C using thermal conductivity analyzer brand NETZSCH and model number LFA 44712-41. The samples used are in disc type having diameter of 12.7 mm and 1 mm in thickness. The Fourier Transform Infrared (FTIR) spectroscopy analysis was carried out on Perkin Elmer spectrum V-2000 spectrometer. The samples were scanned between 700 to 4000 cm^{-1} wave number. The tensile fractured surfaces of the composite were examined by scanning electron microscope (Philips XL 30).

Results and Discussion

Thermal conductivity

The thermal conductivity of a material is dominated by atomic vibration or phonons and electrons. However, for insulating materials, conduction by electrons is generally negligible [1]. Generally, thermal conductivity of polymer/CNT nanocomposites depends on several factors such as the interfacial interactions of the CNT with the polymer matrix, the content and dispersion of the CNT.

From the Figure 2, the PLA/LNR and PLA/LNR with 1.5 wt.% and 3.5 wt.% of MWCNT shows the decreasing trend of thermal conductivity with increasing temperature for all samples. This is due to the presence of defects and large boundaries at the interface of MWCNT/matrix which increase the thermal resistivity as the temperature increase. Phonons mean free path also will be lowered because it was hindered by interfacial boundary of the PLA/LNR matrix. Thus it will reduce the thermal conductivity of the polymer nanocomposites. From this it shows that the interfacial interaction will affect the thermal conductivity of the PLA/LNR nanocomposites. However, at 4 wt% of MWCNT, the graph shows an increment of thermal conductivity with the increasing temperature. At high content of MWCNT in PLA/LNR, MWCNT will provide large surface area and extended shape of MWCNT which will reduce the crystallization of matrix as the temperature increase [7,8]. The large amount of junctions among MWCNT makes the increasing of the thermal conductivity by forming conducting path in the matrix. This shows that the content of MWCNT in matrix will affect the thermal conductivity behavior of the PLA/LNR nanocomposites.

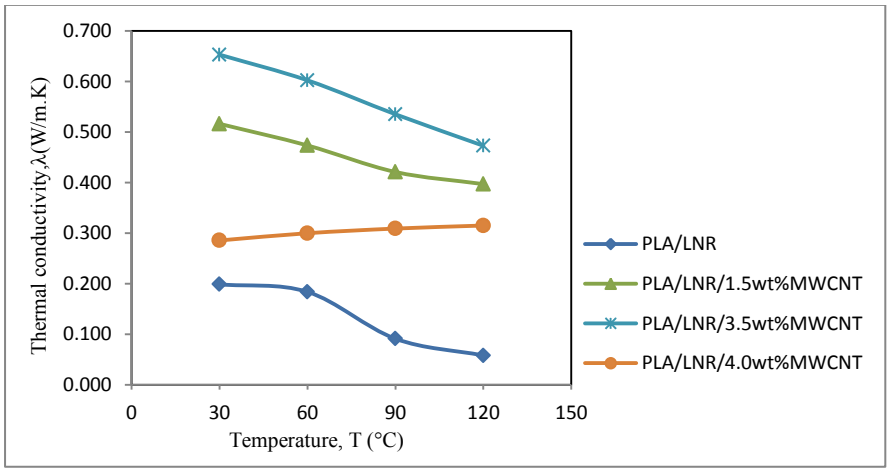


Figure 2. Thermal conductivity dependence of PLA/LNR at different loaded of MWCNT

Figure 3 it shows of thermal conductivities of PLA/LNR nanocomposites containing 1.5 wt.%, 3.5 wt.% and 4 wt.% of MWCNT at 30 °C. It shows remarkable enhancement of thermal conductivity for 1.5 wt.% and 3.5 wt.% of MWCNT compared to 4 wt.% of MWCNT in PLA/LNR. This result obtains due to the presence of highly conductive MWCNT in the PLA/LNR matrix. It provides higher mean free path and higher number of phonons' vibrational modes due to the increasing of crystalline structure. The percolated network of MWCNT inside the PLA/LNR matrix also helps to enhance the thermal conductivity of PLA/LNR nanocomposites. The dispersion of 1.5 wt.% and 3.5 wt.% content of MWCNT in PLA/LNR matrix are better than 4 wt.% of MWCNT as shown in Figure 4. Higher content of MWCNT in the PLA/LNR matrix leads to the reduction of thermal conductivity. This is due to the presence of agglomeration of MWCNT as shown in Fig. 4. The agglomeration of MWCNT will block the phonon travels. This shows that dispersion of MWCNT in matrix plays an important role in enhancing thermal conductivity. From this, the optimum value of thermal conductivity at 30 °C was achieved by 3.5 wt.% of MWCNT content in PLA/LNR. If the MWCNT was added more than this limit, it will give adverse effect to the value of thermal conductivity.

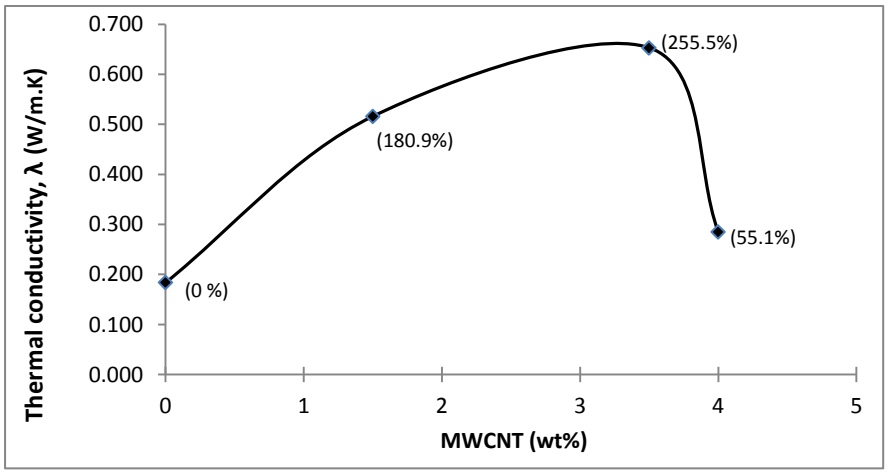
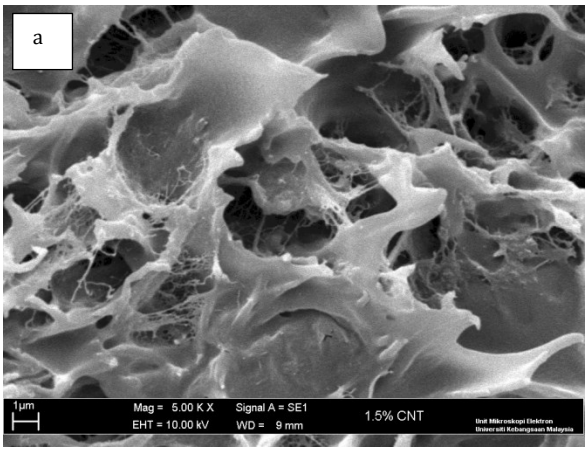
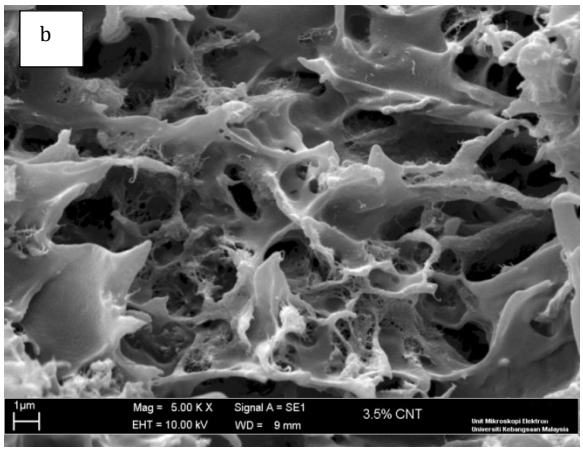


Figure 3. Comparison of thermal conductivities of nanocomposites containing MWCNT with different weight percent at 30 °C (Data in bracket indicate % increase in thermal conductivity against the polymer matrix)





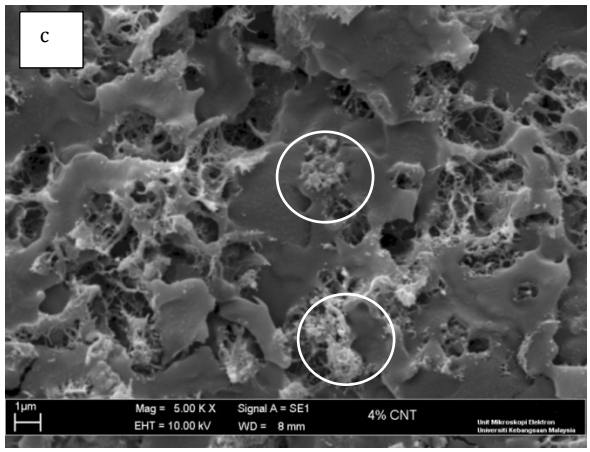


Figure 4. SEM micrograph of a) PLA/LNR at 1.5 wt.% MWCNT b) PLA/LNR at 3.5 wt.% MWCNT and c) PLA/LNR at 4 wt.% MWCNT

FTIR analysis

The FTIR spectra of PLA/LNR and PLA/LNR filled with 3.5 wt.% of MWCNT are given in Figure 5. The IR bands at 2995 and 2849 which is in the single bond stretch region are assigned to the C-H stretch. In the double bond region, the IR band at 1747 is assigned as carbonyl group of C=O bond. The peaks at 868 and 755 are related to the amorphous and crystalline region [4]. The peak at 1080 belongs to C-O-C stretching of the PLA. From that figure, it was found that there were no chemical changes happen.

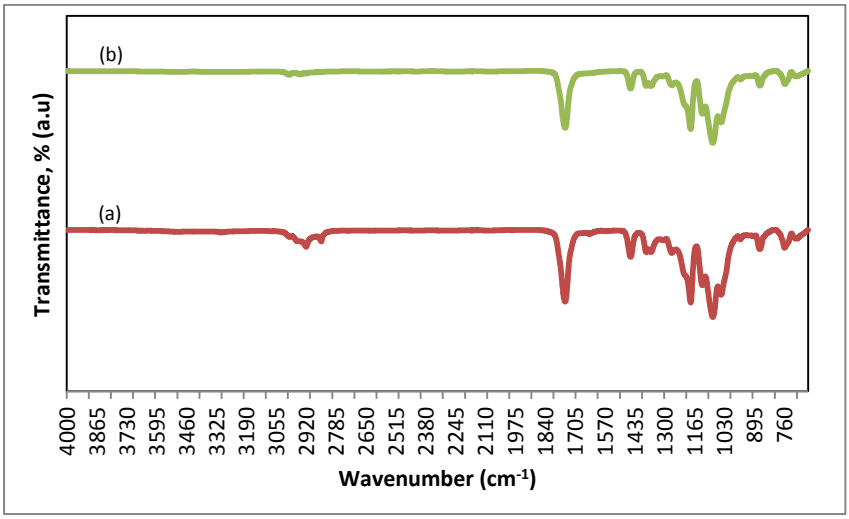


Figure 5. FTIR spectra of a) PLA/LNR and b) PLA/LNR at 3.5 wt.% of MWCNT

Conclusion

Conductive polymer nanocomposites was prepared by impregnating PLA/LNR with MWCNT nanoparticles using melt blending technique. SEM micrographs showed good dispersion for 1.5 wt.% and 3.5 wt.% of MWCNT in PLA/LNR which leads to high thermal conductivity. On the other hand, 3.5 wt.% of MWCNT sample attained the

optimum enhancememt in the thermal conductivity value. FTIR spectra showed that there is no chemical changes occur when PLA/LNR was being added with MWCNT.

Acknowledgement

The authors would like to thank the National University of Malaysia for sponsoring this research work.

References

1. Ma, P. C., Siddiqui, N. A., Marom, G. and Kim, J. K. (2010). Dispersion and functionalization of carbon nanotubes for polymer-based nanocomposites: a review. *Composites: Part A*, 41: 1345 – 1367.
2. Bonnet, P., Sireude, D., Garnier, B. and Chauvet, O. (2007). Thermal properties and percolation in carbon nanotube-polymer composites. *Applied Physics Letter* 91: 201910 – 201913.
3. Lu, C. and Mai, Y. W. (2008). Anomalous electrical conductivity and percolation in carbon nanotube composites. *Material Science* 43(17): 6012 – 6015.
4. Bijarimin, M., Sahrim, A. and Rozaidi, R. (2013). Mechanical, thermal and morphological properties of poly(lactic acid)/natural rubber nanocomposites. *Journal of Reinforced Plastics and Composites*, 32 (21): 1656 – 1667.
5. Adilah, M. A. and Sahrim, A. (2013). Effect of processing parameter and filler content on tensile properties of multi-walled carbon nanotubes reinforced polylactic acid nanocomposites. *AIP Conference Proceeding* 1528: 254 – 259.
6. Mou'ad, A., Hafiz, S. A., SeYong, E. and Kin, T. L. (2013). Sonication effect on the mechanical properties of MWCNTs reinforced natural rubber. *Journal of Composite Materials*, 47(5): 579 – 585.
7. Jin, J., Song, M. and Pan F. T. (2007). A DSC study of effect of carbon nanotubes on crystallization behaviour of poly(ethylene oxide). *Thermochimica Acta,* 45: 25 – 31.
8. Dıez-Pascual A. M., Naffakh M., Gomez M. A., Marco C., Ellis C., Martınez M.T., Anson A., Gonzalez-Domınguez J. M., Martinez-Rubi Y. and Simard B. (2009). Development and characterization of PEEK/carbon nanotube composites. *Carbon.*, 47(13): 3079 – 3090.

Malaysian Journal of Analytical Sciences, Vol 20 No 5 (2016): 1090 - 1094
DOI: http://dx.doi.org/10.17576/mjas-2016-2005-14

MALAYSIAN JOURNAL OF ANALYTICAL SCIENCES
Published by The Malaysian Analytical Sciences Society
ISSN 1394 - 2506

PREPARATION AND CHARACTERIZATION OF EPOXIDISED NATURAL RUBBER (ENR)/POLY (VINYLIDENE FLUORIDE) (PVDF) (ENR/PVDF) COMPOSITE MEMBRANE

(Penyediaan dan Pencirian Membran Komposit Getah Asli Terepoksida (ENR) / Poli (Vinilinida Fluorida) (PVDF) (ENR/PVDF)

Norliyana Mod[1], Farah Hannan Anuar[1,2], Rizafizah Othaman[1,2]*

[1]*School of Chemical Sciences and Food Technology, Faculty of Science and Technology*
[2]*Polymer Research Center, Faculty of Science and Technology*
Universiti Kebangsaan Malaysia, 43600 UKM Bangi, Selangor, Malaysia

**Corresponding author: rizafizah@ukm.edu.my*

Received: 10 June 2015; Accepted: 21 July 2016

Abstract

The focus of this research is to prepare epoxidised natural rubber (ENR)/poly(vinylidene fluoride) (PVDF) (ENR/PVDF) membrane using solution casting method and to characterize the ENR/PVDF membrane using universal tensile machine (UTM) and scanning electron microscope (SEM). Composite membrane of ENR/PVDF was prepared by solution casting technique. The tensile strain increases when ratio of ENR increases in the composite. SEM micrograph shows the compatibility of ENR and PVDF in 40/60 wt% sample but agglomeration of ENR in 60/40 wt% ENR/PVDF sample was observed. The micrograph also shows the existence of pores in the composite membrane which is essential when applying the membrane for separation of gas and waste water treatment.

Keywords: composite membrane, epoxidised natural rubber, poly(vinylidene fluoride)

Abstrak

Fokus kajian ini adalah untuk menyediakan membran getah asli terepoksida (ENR)/ poli (vinilidina fluorida) (PVDF) (ENR/PVDF) menggunakan kaedah penuangan larutan dan untuk mencirikan membran ENR/PVDF menggunakan mesin ujian tensil (UTM) dan mikroskop imbasan elektron (SEM). Membran komposit ENR/PVDF telah disediakan menggunakan teknik penuangan larutan. Rintangan tegangan bertambah apabila ratio ENR bertambah didalam komposit. Mikrograf SEM menunjukkan kesesuaian ENR dan PVDF pada sampel 40/60 wt% tetapi terdapat penggumpalan ENR pada sampel ENR/PVDF 60/40 wt%. Mikrograf juga menunjukkan kehadiran liang pada membran komposit tersebut dimana ianya penting untuk diaplikasikan sebagai membran pemisahan gas dan rawatan air buangan.

Kata kunci: membran komposit, getah asli terepoksida, poli (vinilidina fluorida)

Introduction

Polymer composite is formed when two or more polymers are combined together using various methods such as internal mixture and solution blending. This combination becomes more attentive in polymer industries because it can improve the properties of individual polymer at the end of the process. Combination between thermoplastic polymer and rubber, or known as thermoplastic rubber (TPR) exhibits the properties of elastomeric materials with the possibility of thermoplastic at ambient temperature [1]. Membrane is one of the examples of materials that can

be made from composite polymer. It can be prepared by using solution casting and solvent exchange method. Membrane is a layer that allowed permeation and selectivity of fluid to happen and it usually has a porous support layer to provide mechanical strength to the membrane [2]. Many industries use membrane for the separation of wastewater and gas. The advantages of using membrane are minimum energy of processing, no addition of chemical, environmental friendly and efficient treatment [3].

The combination of epoxidised natural rubber (ENR) with thermoplastic poly (vinylidene fluoride) (PVDF) using internal mixture at high temperature has been reported before [4]. It is found that the tensile strength of PVDF decreased with increasing ENR. PVDF has the properties of high initial modulus, which is brittle and need to be applied as composite. PVDF has many applications as membranes in industries including microfiltration (MF), ultrafiltration (UF), gas separation and pollutant removal from waste water because of the chemical resistivity, thermal stability, and easy to dissolve in variety of solvent. Besides, PVDF is a semi-crystalline polymer, which has different phases of crystallinity named α (form II), β (form I), and γ (form III) [5]. Phases of crystal can be controlled in various ways; such as suitable solvent [6], temperature [7, 8], and addition of additive [9, 10]. ENR is natural rubber which has undergone the addition of epoxide group in the chains by performic epoxidation [11]. ENR is elastic good in tensile strength, oil resistance, and permeable to gas.

Solubility parameter or miscibility between solvent and solute is very important to make composite solution for membrane. The compressibility of solution will be less than that of solvent, so the solute will gain mobility and have some probability of contracting the solvent molecule [12]. Mixing of solvent between tetrahydrofuran (THF) and N,N-Dimethylacetamide (DMAC) has been reported Bagheripour et. al. [13]. THF was used to increase the phase separation time in coagulation bath and preventing macro voids. In current research, PVDF is not soluble in THF. Thus, DMAC was used to make PVDF soluble before combining with ENR. The solubility parameter of each solvent is displayed in Table 1. When the solubility parameter increases, it will be easier for the solvent to dissolve the solute and the non-solvent will be more able to diffuse in membrane casting. So, the exchange of solvent and non-solvent in coagulation bath will be faster and lead to the formation of pores.

The objectives of this paper are to prepare ENR/PVDF membrane in different ratios using solution casting method and to characterize the ENR/PVDF membrane using universal tensile machine (UTM) and scanning electron microscope (SEM). The possibility of using the ENR/PVDF composite as membrane will be discussed.

Table 1. Solubility Parameters

Solvent	**Solubility Parameter (δ)**
THF	11.44
DMAC	11.13
Water	9.4
THF/DMAC (57/43 vol%)	11.30

Materials and Methods

Materials

Epoxidised natural rubber with 50% mol of epoxidation level, ENR-50 (Mw = 640 000 g/mol) was obtained from Rubber Research Institute of Malaysia (RRIM). PVDF (Mw = 543 000 g/mol) in powder form was purchased from Sigma-Aldrich (M) Sdn. Bhd. Tetrahydrofuran (THF) (Mw = 72.11 g/mol) with 99.8% purity was purchased from Systerm Sdn. Bhd. N,N-Dimethylacetamide (DMAC) with 99% purity was purchased from Merck. Distilled water was used in coagulation bath for exchanging between solvent and non-solvent.

Membrane preparation

ENR/PVDF membrane was prepared using different ratios (0/100 wt%, 20/80 wt%, 40/60 wt%, and 60/40 wt%) by solution casting technique. ENR was swelled in THF for 24 hours before vigorously stirred until homogeneous solution was produced. At the same time, PVDF was stirred in DMAC solution in separate container until homogenous. Then, the solution was mixed and continuously stirred for 3 hours. The membrane solution was then degassed for one night to eliminate bubbles. Solution casting was done on a glass plate using a casting knife to get a membrane. After 2 minutes, the membrane was immersed in distilled water for solvent exchange to occur until the white solid membrane formed. Lastly, the sample was dried at ambient temperature and kept in desiccators before testing. The average thickness of the membrane after drying was about 0.02 mm.

Membrane characterization

The membrane had been characterized as follows:

(a) Universal tensile machine (UTM)

The tensile strength of the membrane was measured using Zwick Roell universal tensile machine, Z1.0 model at jogging rate of 50 mm/min. Membranes were tested according to ASTM D412. Prior to that, the samples were cut into the standard dumbbell shape using hollow die punch at ambient temperature. For each membrane, five replications were used and their average values were reported.

(b) Scanning electron microscope (SEM)

The surface morphology of the membrane was obtained by using variable pressure scanning electron microscope (VPSEM) with energy dispersion X-ray (EDX). The model is ZEISS EVO MA 10 (UK) with EDAX Apollo X (USA). The sample was sputter coated with gold before analysis and the magnification used was 5000×.

Results and Discussion

Figure 1 (a) is the appearance of the ENR/PVDF membrane. The colour of the membrane solution becomes dark brown when the colourless solution of PVDF was added into the ENR solution. After the sample was dried at room temperature, it turned into a transparent film as can be seen in Figure 1 (b). The thickness during casting was 0.15 mm and 0.02 mm after it dried. The solvent evaporated from the membrane, resulting to reduce of the overall thickness.

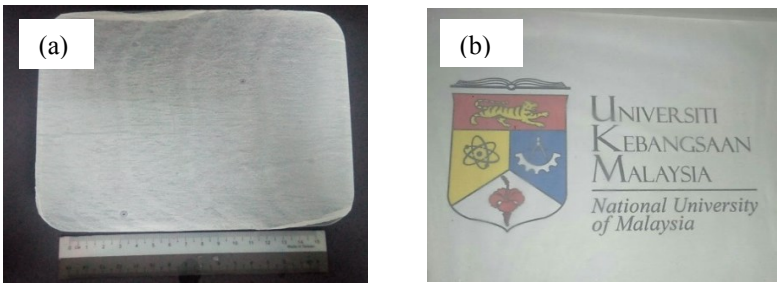


Figure 1. ENR/PVDF membrane for ratio 60/40 wt%

Mechanical properties

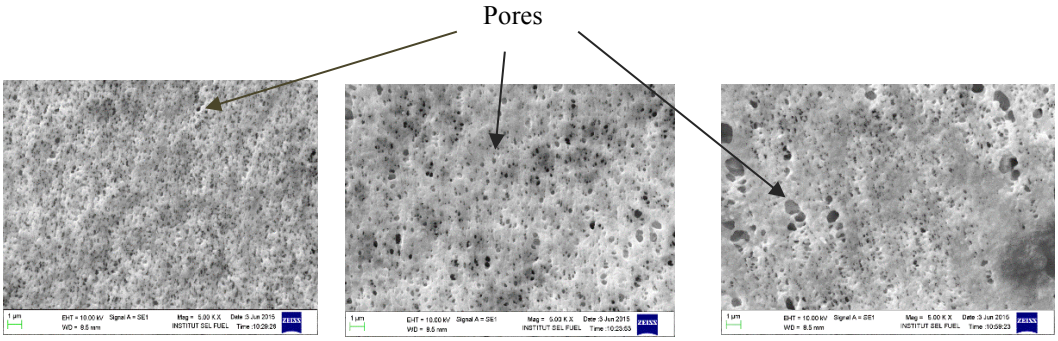
Tensile stress is the resistance of a material towards the force per unit area to the point to tear it apart. While tensile strain is deformation of a solid due to stress that applied. Table 2 shows that the tensile stress decreases with increasing ratio of ENR due to the sample cannot withstand with the force applied. The tensile strain, on the other hand increased. As mentioned before, PVDF is a brittle polymer which is easy to tear apart. Decreasing the ratio of PVDF caused the tensile strain to increase and the addition of ENR introduced a greater chain movement in the membrane. Molecular chain of the sample kept it in metastable state between the amorphous and crystalline states.

Table 2. Tensile stress and tensile strain for ENR/PVDF membrane with different composition

ENR/PVDF Membrane (wt%)	Tensile Stress (MPa)	Tensile Strain (%)
20/80	3.92	8.26
40/60	1.72	14.82
60/40	1.40	15.90

Surface morphology

Figure 3 shows the physical images of ENR/PVDF membrane with different compositions of ENR and PVDF. The micrographs show that pores are present on the surface of all membranes. Random pores were formed due to the property of PVDF and the exchange between solvent and non-solvent during solvent-exchange process. The average pore size for the membranes is shown in Table 3. The pore size increased with the increase ratio of ENR which proven that the addition of ENR caused more chain movement which caused bigger pores on the membrane. This is in a good agreement with previous reported study [14]. For the 60/40 wt% sample (Figure 3c), it can be seen that surface is not even which is due to the agglomeration of ENR in the composite. However, the same problem was not observed on 40/60 wt% (Figure 3b) which make it suitable to be applied as membrane as pores and high tensile strain were observed.



(a) 0/100 wt% (b) 40/60 wt% (c) 60/40 wt%

Figure 3. Scanning electron micrographs of surface for ENR/PVDF at magnification × 5000

Table 3. Average pore sizes of the ENR/PVDF membranes

ENR/PVDF Membrane (wt%)	Average pore size (nm)
0/100	89.32 – 268.9
40/60	157.9 – 625.7
60/40	271.7 – 861.9

Conclusion

As conclusion, ENR/PVDF membrane with different ratios can be prepared by using solution casting method. The thickness of the membrane during casting was 0.15 mm and the average thickness after dried was 0.02 mm. SEM micrographs showed the agglomeration of ENR in the ENR/PVDF solution with the ratio of 60/40 wt% because of

the immiscibility between ENR and PVDF but the 40/60 wt% membrane did not show any incompatability. The increasing ratio of ENR in PVDF had caused the tensile strain to increase and the tensile stress to decrease. Due to the porosity and the tensile property of 40/60 wt% ENR/PVDF composite, it has the potential to be applied to as membrane for gas separation and pollutant removal from wastewater.

Acknowledgement

The authors gratefully acknowledge the financial support from FRGS/2/2013/TK06/UKM/02/1 and 03-01-02-SF1115. We also would like to deliver our grattitude towards Universiti Kebangsaan Malaysia (UKM), Polymer Research Center (PORCE) and SELFUEL, UKM.

References

1. Salaeh, S., Nakason, C., Boiteux, G. and Cassagnau, P. (2013). Co-continuous phase structure and properties of poly(vinylidene fluoride)/epoxidized natural rubber blends. *Advanced Materials Research*, 626: 71 – 74.
2. Bottino, A., Camera-Roda, G., Capannelli, G. and Munari, S. (1991). The formation of microporous polyvinylidene difluoride membranes by phase separation. *Journal of Membrane Science*, 57: 1 –20.
3. Yan, L., Hong, S., Li, M. L. and Li, Y. S. (2009). Application of the Al_2O_3–PVDF nanocomposite tubular ultrafiltration (UF) membrane for oily wastewater treatment and its antifouling research. *Separation and Purification Technology*, 66: 347 – 352.
4. Salaeh, S. (2014). Processing of natural rubber composites and blends: Relation between structure and properties. PhD dissertation, Prince Of Songkla University (Psu) - Pattani (Thailand).
5. Hasegawa, R., Takahashi, Y., Chatani, Y. and Tadokoro, H. (1972). Crystal structures of three crystalline forms of poly(vinylidene fluoride). *Polymer Journal*, 3: 600 – 610.
6. Boccaccio, T., Bottino, A., Capannelli, G. and Piaggio, P. (2002). Characterization of PVDF membranes by vibrational spectroscopy. *Journal of Membrane Science*, 210: 315 – 329.
7. Tao, M.-M., Liu, F., Ma, B.-R. and Xue, L.-X. (2013). Effect of solvent power on PVDF membrane polymorphism during phase inversion. *Desalination*, 316: 137 – 145.
8. Wang, X., Zhang, L., Sun, D., An, Q. and Chen, H. (2009). Formation mechanism and crystallization of poly(vinylidene fluoride) membrane via immersion precipitation method. *Desalination*, 236: 170 – 178.
9. Sulaiman, N. M. N. and Ling, C. K. (2004). Membrane ultrafiltration of treated palm oil mill effluent (POME). *Jurnal Teknologi*, 41(1): 113 – 120.
10. Cao, X., Ma, J., Shi, X. and Ren, Z. (2006). Effect of TiO_2 nanoparticle size on the performance of PVDF membrane. *Applied Surface Science,* 253: 2003 – 2010.
11. Yoksan, R. (2008). Epoxidized natural rubber for adhesive applications. *Kasetsart Jurnal (Natural Science)*, 42: 325 – 332.
12. Sharma, S. K., Singh, G., Kumar, H. and Kataria, R. (2015). Study of solute–solute and solute–solvent interactions of N-acetyl glycine in aqueous D-fructose solutions at different temperatures. *Thermochimica Acta*, 607: 1 – 8.
13. Bagheripour, E., Moghadassi, A. R. and Hosseini, S.M. (2014). Novel nanofiltration membrane with low concentration of polyvinylchloride: Investigation of solvents' mixing ratio effect (dimethyl acetamide/tetrahydrofuran). *Arabian Journal of Chemistry*, 1 – 6.
14. Jon, N., Abdullah, I. and Othaman, R. (2013). Effects of silica on the formation of epoxidised natural rubber/polyvinyl chloride membrane. *Sains Malaysiana*, 42(4): 469 – 473.

Malaysian Journal of Analytical Sciences, Vol 20 No 5 (2016): 1095 - 1103
DOI: http://dx.doi.org/10.17576/mjas-2016-2005-15

MALAYSIAN JOURNAL OF ANALYTICAL SCIENCES
Published by The Malaysian Analytical Sciences Society
ISSN 1394 - 2506

THERMAL BEHAVIORS OF OIL PALM EMPTY FRUIT BUNCH FIBER UPON EXPOSURE TO ACID-BASE AQUEOUS SOLUTIONS

(Perilaku Terma Serabut Tandan Kosong Sawit Selepas Rawatan Larutan Akueus Asid-Alkali)

Nur Syakilla Hassan[1] and Khairiah Haji Badri[1,2]*

[1]*School of Chemical Sciences and Food Technology, Faculty of Science and Technology*
[2]*Polymer Research Center, Faculty of Science and Technology*
Universiti Kebangsaan Malaysia, 43600 UKM Bangi, Selangor, Malaysia

**Corresponding author: kaybadri@ukm.edu.my*

Received: 10 June 2015; Accepted: 21 July 2016

Abstract

The effect of chemical treatment on the chemical composition, functional group, crystallinity and thermal stability of palm oil empty fruit bunch (EFB) fiber were investigated. Chemical treatment was conducted by treating EFB with 10% sodium hydroxide aqueous solution and 2% hydrogen peroxide aqueous solution separately. The results indicated that chemical treatment managed to affect chemical composition of the fiber. FTIR analysis proved the removing of hemicellulose and lignin during the treatment based on the peak disappearance around 1700 cm^{-1} and 1600 cm^{-1}. The XRD diffractogram showed an increase in crystallinity index of the fiber especially for NaOH treatment. Removal the amorphous component of the fiber influences the thermal degradation of the fiber.

Keywords: empty fruit bunch, chemical treatment, thermal properties

Abstrak

Kajian ke atas serabut tandan kosong sawit (EFB) telah dijalankan untuk melihat kesan rawatan kimia terhadap komposisi serabut, kumpulan berfungsi, kehabluran dan kestabilan terma serabut. EFB telah menjalani rawatan kimia menggunakan 10% larutan akues natrium hidroksida dan 2% larutan akues hidrogen peroksida secara berasingan. Hasil kajian menunjukkan rawatan kimia memberi kesan terhadap komposisi kimia serabut. Melalui analisis spektroskopi FTIR, penyingkiran hemiselulosa dan lignin telah berlaku semasa rawatan dijalankan. Keadaan ini dibuktikan melalui kehilangan puncak serapan sekitar 1700 cm^{-1} dan 1600 cm^{-1}. Difraktogram XRD pula menunjukkan peningkatan dalam indek kehabluran bagi serabut yang menjalani rawatan NaOH. Penyingkiran komponen amorfus didapati mempengaruhi degradasi terma serabut EFB.

Kata Kunci: tandan kosong sawit, rawatan kimia, sifat terma

Introduction

Common pretreatment for lignocellulose is to distort the lignocellulosic complex structures of the fiber. The aims of fiber pretreatment are to get rid of lignin and hemicellulose for cellulose extraction and to increase enzyme accessibility; to reduce the crystallinity of cellulose; to increase the porosity of the lignocellulosic materials and for surface modification. Fiber pretreatment can be classified into several categories; that are physical, chemical, biological or a combination of all these methods [1, 2].

Caustic treatment using base aqueous solutions such as sodium hydroxide (NaOH) is one of the most used treatments studied by researchers [1]. NaOH helps the removal of waxes, hemicellulose, pectin and some lignin

monomers [3, 4]. This treatment disturbs the hydrogen bonding in cellulose and hemicellulose, breaking the ester linkages that crosslink lignin and xylan, and deprotonation of phenolic groups [5]. Treatment with high concentration of alkali may rearrange or change the crystalline structure from cellulose type I to cellulose type II [3]. Hydrogen peroxide (H_2O_2) is an oxidizing agent in which it has the ability to decolorize the fiber by removing lignin, hemicellulose and surface impurities. H_2O_2 is always considered as a base even though it is a weak acid (pH ~ 6.2) and often used as bleaching agent in pulp and paper industry. It is often being used on lignocellulose such as oil palm empty fruit bunch fiber (EFB), kenaf, rice husk, bagasse and many others. Different treatments cause various effects to the fiber in term of degree of impurities removed and chemical composition. These also affect the thermal stability of the fiber as reported by previous researchers [6, 7, 8].

EFB as the main feedstock in this research has been intensively studied for decades especially when Malaysia is one of the main producers of palm oil. EFB is the by-product generated after oil refining process. Approximately 400 g of EFB is produced from each bunch of oil palm fresh fruit and it leads to abundancy of EFB biomass [9]. At present, shredded EFB has already been used commercially since it offers several advantages in terms of availability, biodegradability and cost [10]. EFB becomes one of the important lignocelullosic materials and has extensively been used in wood and furniture industry as reinforcement of polymer-based composites. Generally EFB contain 45.0% cellulose, 32.8% hemicellulose and 20.5% lignin [11]. Cellulose is the main component of the cell wall that gives strength to plant. It consists of long carbon chains of polysaccharide. Hemicellulose is a branched polysaccharide containing sugar monomers with shorter chains and various conformations. It exists together with cellulose and lignin in the plant cell wall [12]. On the other hand, lignin is a complex polymer consists of three phenylpropane units which are cross-linked together by alkyl-aryl, alkyl-alkyl, aryl-aryl ether bonds and carbon-carbon bonds [5, 13, 14].

The thermal behavior of the polymer can be explored using thermogravimetric analysis (TGA) and differential scanning calorimetry (DSC). TGA consist of TG curves and DTG curves. TG curve states the decomposition of polymer based on weight loss as a function of temperature while DTG curve reveals the corresponding rate of weight loss. DSC is a thermo analytical technique to determine the thermal transitions of polymer [15, 16]. Our research goal is to investigate the influence of treatment on the thermal characteristic of EFB. Information regarding thermal degradation of natural fiber is considered important for processing temperature in applications related to development of flame retarded products, fiber-reinforced composite and many others [17, 18].

Materials and Methods

Materials

EFB fiber was obtained from Sri Ulu Langat Palm Oil Mill Sdn Bhd, Selangor, Malaysia. It was ground and sieved to obtain a size range of 250 – 315 µm. It was then dried in the oven at 105 °C for 24 hours and was kept in an air-tight container. Sodium hydroxide pellet (NaOH, ~99% purity) and glacial acetic acid (CH_3COOH, 99.8 wt.%) were supplied by Merck (M) Sdn Bhd, Selangor, Malaysia. Hydrogen peroxide (H_2O_2, 30 – 32% purity) was manufactured by Friendemann Schmidt Chemical, Germany.

Fiber treatment

EFB fiber was immersed in 10% NaOH aqueous solution at a ratio of 1:20 at room condition. After 48 hours, the mixture was then filtered through Büchner funnel and rinsed with diluted CH_3COOH until it reached pH 7. The fiber was then dried in an oven at 105 ^{o}C for 24 h following ASTM D2016-65 (Methods of test for moisture content of wood). However, for the H_2O_2 treatment, the EFB fiber was refluxed with 2% H_2O_2 aqueous solution at a ratio of 1:25. The treatment was conducted at 60 – 70 °C with continuous stirring for 3 hours. The mixture was then filtered; rinsed several times until it reached pH 7 and dried in the oven. The treated fibers were labelled as NTF and HTF respectively and were stored in a drying chamber for further analysis.

Characterization

The physicochemical analyses carried out on the samples were determination of moisture content (TAPPI T208 om-84), water solubility (TAPPI T207 om-81), and determination of ethanol-benzene extractives (TAPPI T204 cm-97), holocellulose [19], α-cellulose (TAPPI T203 om-83) and Klason lignin content (TAPPI T222 om-83). Fourier transform infrared spectroscopy (FTIR) analysis was conducted on a spectrophotometer model Perkin Elmer

Spectrum 400. Each spectrum was recorded in a frequency range of 4000 to 650 cm^{-1} using ATR-FTIR technique. The crystallinity of the sample was examined using Bruker X-ray diffractometer model D8-Advance with Cu Kα radiation (λ= 0.15406 nm) and the data were recorded every 0.025° (2θ) within the range of scattering angles from 5° to 60°. Thermogravimetric analysis (TGA) was performed using Perkin Elmer thermal analyzer. The analysis was operated under nitrogen gas atmosphere at a constant heating rate of 10 °C/min heating rate. The glass transition temperatures (T_g) of the samples was carried out using Mettler Toledo differential scanning calorimeter (DSC) in nitrogen gas atmosphere. The samples were first heated to 100 °C to eliminate moisture. Then, the samples were cooled and reheated to 250 °C at a constant heating rate of 10 °C/min.

Results and Discussion

Chemical composition

Lignocellulose is composed of three main components which are cellulose, hemicellulose and lignin. The composition of these three components may differ from one fiber to another. Data of the compositional analysis conducted onto the untreated EFB (UTF), NaOH-treated EFB (NTF) and H_2O_2-treated EFB (HTF) is presented in Table 1.

UTF contained 45.3% cellulose, 35.6% hemicellulose and 17.7% lignin. Generally, treatment with base solution was meant to remove cementing materials exist in the fiber such as lignin, hemicellulose, wax and oil [20]. Upon treatment, NaOH has removed a significant percentage of hemicellulose thus increasing the cellulose content for NTF compared to HTF. The percentages of cellulose, hemicellulose and lignin of HTF were 47.9%, 38.4% and 10.5% respectively. This indicates that hydrogen peroxide was not an efficient delignification agent for the removal of lignin and hemicellulose. On the other hand, NaOH worked effectively as a delignification agent where the lignin content decreased from 17.7 % in the UTF to 9.0% in the NTF.

Table 1. Compositional analysis of the untreated EFB (UTF), NaOH-treated EFB (NTF) and H_2O_2-treated EFB (HTF)

Samples	Composition percentage (%)			
	Cellulose	Hemicellulose	Lignin	Others
UTF	45.3	35.6	17.7	1.4
NTF	62.4	19.9	9.0	8.7
HTF	47.9	38.4	10.5	3.2

Fourier transforms infrared spectroscopy

The structural changes taking place after treatment was determined from the analysis of the FTIR spectra of UTF, NTF and HTF as shown in Figure 1. A peak observed at the region 3600-3200 cm^{-1} indicating hydroxyl (O–H) group in phenolic and aliphatic structures [21]. Peaks at 2850 $cm^{-1}$and 2930 cm^{-1} are attributed to C-H stretching vibration of methyl and methylene group [22]. After the treatment, peak at 2850cm^{-1} diminished due to effect from the reduction of methyl and methylene of cellulose [23]. Differences between these spectra can be observed from the loss of absorption peak at the region 1705-1750 cm^{-1}. These peaks corresponds to the C=O stretching of carbonyl groups in uronic acids or acetyl in hemicellulose [24]. According to Alemdar and Sain (2008), these peaks may also indicate the ester linkage of the carboxylic group in the ferulic and *p*-coumeric acid of lignin and hemicellulose. For NTF spectra, this peak was completely disappeared while the intensity of this peak decreased for HTF spectrum. Both of these related to the removal of lignin and hemicellulose during the treatment [25]. A decrease in the intensity was observed at 1509–1609 cm^{-1} associated to C=C aromatic skeletal vibrations and it was also related to delignification [26]. Differences between NTF and HTF spectra were identified based on peak intensity at specific peaks. At peak around 3300 cm^{-1}, HTF spectrum exhibited low peak adsorption indicating that H_2O_2 treatment may cause more cellulose degradation [23]. FTIR spectra for all samples showed a peak around 898 cm^{-1} which is attributed to the presence of *β*-glycosidic linkage between glucose units in cellulose.

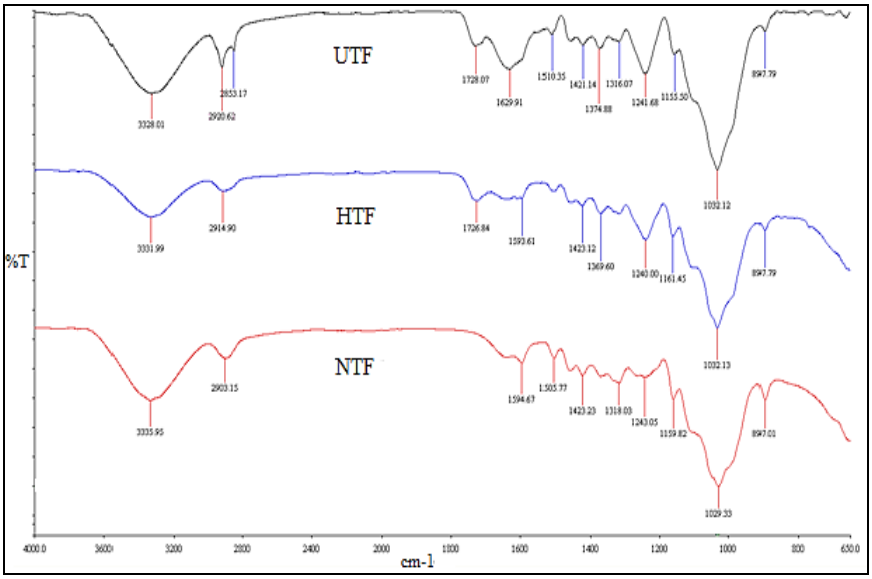


Figure 1. FTIR spectra of UTF, NTF and HTF

X-ray diffraction

X-ray diffraction (XRD) analysis was conducted onto all samples. The diffractogram are as shown in Figure 2 whereas Table 2 tabulated the crystallinity index (CrI) of the samples. Lignocellulose fiber consists of amorphous and crystalline regions that were contributed by the constituents in the fiber [27]. The crystallinity index (CrI) of the sample was calculated using the following equation 1 [28].

$$\text{CrI}, \% = \frac{(I_{002} - I_{AM})}{I_{002}} \quad (1)$$

where I_{002} is the maximum intensity of the lattice diffraction at about $2\theta \cong 22.4°$ and I_{AM} is the intensity attributed to the amorphous portion of sample at $2\theta \cong 18.6°$. From Figure 2, all samples showed similar XRD patterns with two significant peaks at 2θ position around 16.0° and 22.6° contributed by the crystalline regions of cellulose type I [29].

The peak around 22.6° for NTF tends to be more narrow compared to UTF. This is attributed to the increase in crystallinity index of the fiber (46.2 compared to 43.0). It might be due to the removal of amorphous structure of hemicellulose and lignin during the treatment [27]. This situation is parallel to the reduction in the percentages of hemicellulose and lignin (Table 1). Upon treatment, the extracted cellulose is in the form of Cellulose Type I (main peak occurred to be unchanged).There is greater tendency for the transformation of crystalline state from cellulose I to cellulose II to happen when treated with high concentration alkaline solution [20]. However, XRD diffactrograms of HTF and UTF showed similar diffraction pattern with slight reduction in peak intensity of HTF indicating that this treatment has not made any significant changes in the crystal structure of the cellulose [29].

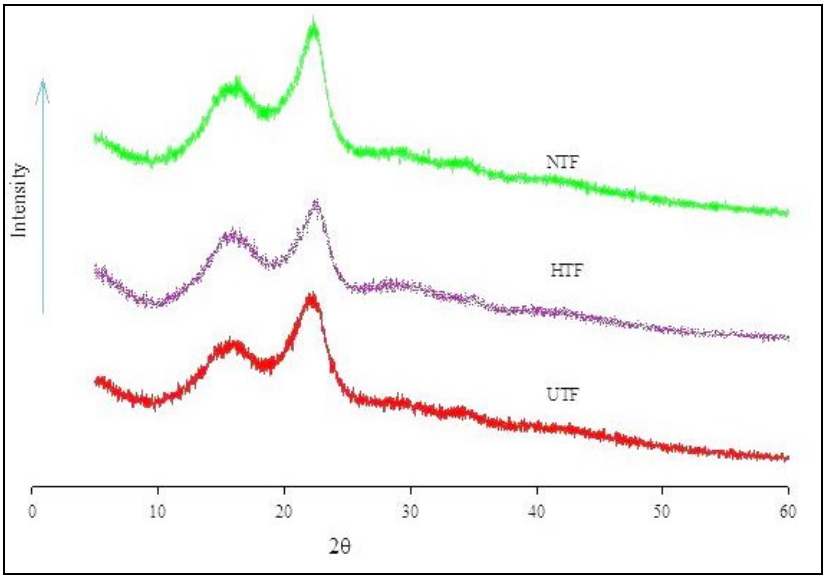


Figure 2. XRD diffactrograms of UTF, NTF and HTF

Table 2. The crystallinity index of the UTF, NTF and HTF

Sample	**UTF**	**NTF**	**HTF**
Crystallinity, %	43.0	46.2	42.6

Thermogravimetric analysis

The TG and DTG curves obtained for UTF, NTF and HTF are presented in Figure 3. The total weight loss was 70.6% for UTF, 81.8% for NTF and 89.3% HTF. The weight loss of the samples is related to the thermal degradation of hemicellulose, cellulose and lignin [7]. The DTG thermogram shows the derivative weight loss as a function of time. The peak observed around 100°C for all sample was connected to moisture loss.

A shoulder observed around 270 °C in the DTG peak of UTF (Figure 3(a)) was mainly related to the decomposition of extractives and hemicelluloses [30]. At this temperature range, the cleavage of glycosidic linkages of cellulose may occur as reported by Deepa et al. (2011) [7]. Major weight loss for UTF occurred around 330°C, contributed by the degradation of cellulose. The weight loss of lignin occurs above 350 °C [7].

The disappearance of a shoulder peak around 270 °C indicated the removal of hemicellulose and extractives upon NaOH treatment. This was confirmed by the FTIR results with the absence of carbonyl group representing the hemicellulose [4]. The decomposition of cellulose for NTF (Figure 3 (b)) was slightly shifted to 345 °C compared to UTF. This may be influenced by the arrangement of the molecular structure of the cellulose. Higher crystallinity means more heat is required to experience thermal degradation [4]. HTF showed two significant peaks in the DTG thermogram. The lower peak (Figure 3 (c)) at 300 °C could be associated to the trace of hemicellulose present after the treatment. A clear sharp peak around 370 °C indicated the degradation of crystalline cellulose. In the study of Brebu and Vasile, lignin thermally decomposed over a broader temperature range of 200 – 500 °C due to different thermal stabilities of various oxygen functional groups from its structure. Thus its scissoring occurred at different temperatures [32].

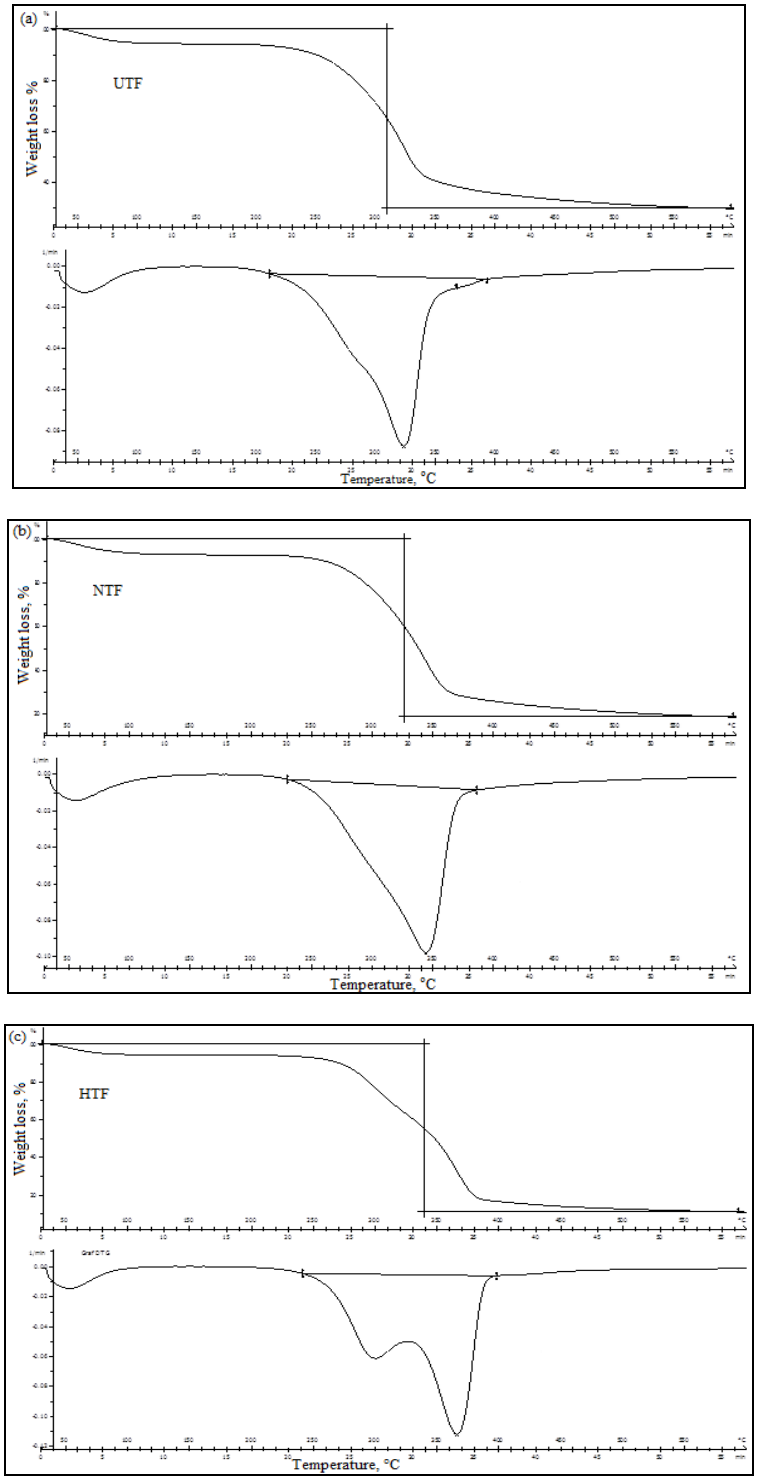


Figure 3. TG and DTG curvesof UT, NTF and HTF

Differential scanning calorimetry

Glass transition temperature or T_g is temperature at which the polymer undergoes a phase change that is from a glassy state a rubbery state. Figure 4 shows DSC thermograms of the samples. T_g of the sample shifted to higher temperature to 186.7°C (NTF) and 185.6°C (HTF) after treatments. These treatments have greater tendency to stabilize the cellulose structure where there was an increase in cellulose crystallinity and hydrogen bonding between the closely packed cellulose chains. More energy is needed to break down the crystalline structure and to cleave the macromolecules for phase transition [31].

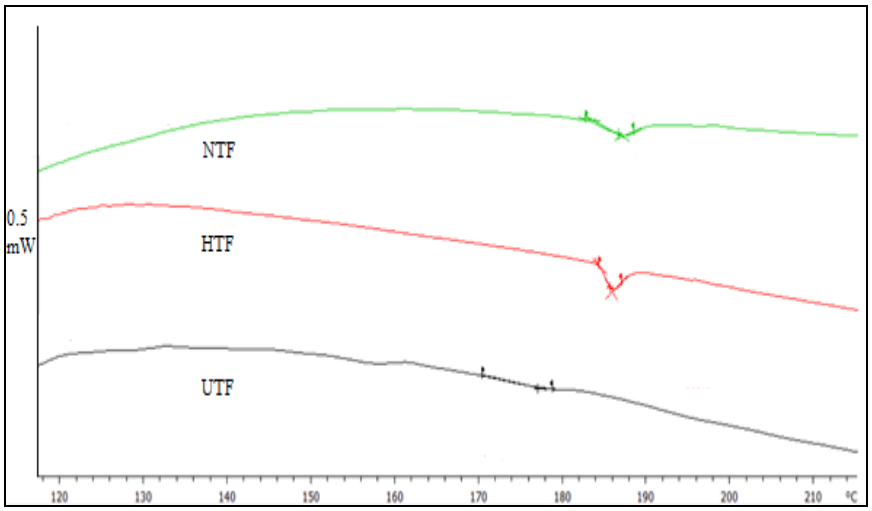


Figure 4. DSC thermograms of UTF, NTF and HTF

Conclusion

The influence of fiber treatments by acid-base approach on the chemical composition, structural and thermal stability has been investigated. Treatments caused the removal of surface impurities, lignin and hemicellulose. Alkaline treatment gave more effect in removing lignin and hemicellulose and exposing more cellulose. Thermal study reveals that thermal stability of fiber increased upon treatment. The thermal stability of the fiber was much related to the composition of the fiber.

Acknowledgement

The authors would like to thank School of Chemical Sciences and Food Technology, Faculty of Science and Technology, Universiti Kebangsaan Malaysia for providing the research facilities. A highly appreciation to the Malaysia Ministry of Higher Education for the funding of the biomass project under grant ERGS/1/2013/STG01/UKM02/2. The authors would also like to thank Malaysia Ministry of Education for the MyMaster to financially support the principal researcher.

References

1. Kumar, P., Barrett, M. D., Delwiche, J. M. and Stroeve P. (2009). Methods for pretreatment of lignocellulosic biomass for efficient hydrolysis and biofuel production. *Industrial and Engineering Chemistry Research*, 48 (8): 3713 – 3729.
2. Harun, N. A. F., Baharuddin, A. S., Mohd Zainudin, M. H., Bahrin, E. K., Nazli Naim, M. and Zakaria, R. (2013). Cellulase production from treated oil palm empty fruit bunch degradation by locally isolated Thermobifida Fusca. *Bioresourse*, 8(1): 676 – 687.
3. Jayabal, S., Sathiyamurthy, S., Loganathan, K. T. and Kalyanasundaram, S. (2012). Effect of soaking time and concentration of NaOH solution on mechanical properties of coir–polyester composites. *Bulletin of Material Science*, 35(4): 567 – 574.

4. Ouajai, S. and Shanks, R. A. (2005). Composition, structure and thermal degradation of hemp cellulose after chemical treatments. *Polymer Degradation and Stability,* 89(2): 327 – 335.
5. Harmsen, P. F. H., Huijgen, W. J. J., Bermúdez López, L. M. and Bakke, R. R. C. (2010). Literature review of physical and chemical pretreatment processes for lignocellulosic biomass. *Food and Biobased Research*. 59: 1 – 49.
6. Brígida, A. I. S., Calado, V. M. A., Gonçalves, L. R. B. and Coelho, M. A. Z. (2010). Effect of chemical treatments on properties of green coconut fiber. *Carbohydrate Polymers*, 79: 832 – 838.
7. Deepa, B., Abraham, E., Cherian, B. M., Bismarck, A., Jonny, J. B., Laly, A. P., Leao, A. L., de Souza, S. F. and Kottaisamy, M. (2011). Structure, morphology and thermal characteristics of banana nano fibers obtained by steam explosion. *Bioresource Technology*, 102 (2): 1988 – 1997.
8. Das, H., Dutta, D., Saikia, P., Kalita, D. and Goswami, T. (2014). Novel Composite Materials from Polymeric Waste and Modified Agro-Fiber. *Applied Science and Advanced Materials International*, 1(1): 3 – 11.
9. Sreekala, M. S., Kumaran, M. G. and Sabu, T. (1997). Oil palm fibers: Morphology, chemical composition, surface modification, and mechanical properties. *Journal of Applied Polymer Science*, 66: 821 – 835.
10. Rayung, M., Ibrahim, N. A., Zainuddin, N., Saad, W. Z., Abdul Razak, N. I. and Chieng, B. W. (2014). The effect of fiber bleaching treatment on the properties of poly(lactic acid)/oil palm empty fruit bunch fiber composites. *International Journal of Molecular Sciences*, 15(8): 14728 – 14742.
11. Ramli, R., Stephen, S. and Jamaludin, M. A. (2002). Properties of medium density fiberboard from oil palm empty fruit bunch fiber. *Journal of Oil Palm Research*, 14(2): 34 – 40.
12. Bulian, F. and Graystone, J. (2009). Wood Coatings: Theory and Practice Theory and Practice. Elsevier, pp 15 – 19.
13. Mankar, S. S., Chaudhari, A. R. and Soni, I. (2012). Lignin in phenol-formaldehyde adhesives. *International Journal of Knowledge Engineering,* 3(1): 116 – 118.
14. Privas, E. and Navard, P. (2013). Preparation, processing and properties of lignosulfonate–flax composite boards. *Carbohydrate Polymers*, 93: 300 – 306.
15. Toledano, A., Serrano, L., Garcia, A., Mondragon, I. and Labidi, J. (2010). Comparative study of lignin fractionation by ultrafiltration and selective precipitation. *Chemical Engineering Journal*, 157 (1): 93 – 99
16. Mohamad Ibrahim, M. N. Zakaria, N. Stephen, C. S. Sulaiman, O. and Hashim, R. (2011). Chemical and thermal properties of lignins from oil palm biomass as a substitute for phenol in a phenol formaldehyde resin production. *Carbohydrate Polymers*, 86: 112 – 119.
17. Yao, F., Wu, Q., Lei, Y., Guo, W. and Xu Y. (2008). Thermal decomposition kinetics of natural fibers: Activation energy with dynamic thermogravimetric analysis. *Polymer Degradation and Stability,* 93: 90 – 98.
18. Ogah, A. O., Afiukwa, J. N. and Englund, K. (2014). Characterization and comparison of thermal stability of agro waste fibers in bio-composites application. *Journal of Chemical Engineering and Chemistry Research*, 1(2): 84 – 93.
19. Browning, B. L. (1967). Holocelluloseas perchlorite method. Methods of wood chemistry. John Wiley and Sons, pp 394 – 396.
20. Abraham, E., Deepaa, B., Pothan, L. A. Jacob, M. and Thomas, S. Cvelbar U. and Anandjiwala R (2011). Extraction of nanocellulose fibrils from lignocellulosic fibers: A novel approach. *Carbohydrate Polymers,* 86:1468 – 1475.
21. Suradi, S. S., Yunus, R. M., Beg, M. D. H. and Yusoz, A. M. F. (2009). Influence pre-treatment on the properties of lignocellulose based biocomposite. National Conference on Postgraduate Research (NCON-PGR). Malaysia.
22. Kumar, R., Mago, G., Balan, V. and Wyman, C. E. (2009). Physical and chemical characterizations of corn stover and poplar solids resulting from leading pretreatment technologies. *Bioresource Technology,* 100: 3948 – 3962.
23. Mohamad Remli, N. A., Md Shah, U. K., Mohamad, R. and Abd-Aziz, S. (2014). Effects of chemical and thermal pretreatments on the enzymatic saccharification of rice straw for sugars production. *Bioresourse,* 9(1): 510 – 522.
24. Sun, X. F., Jing, Z., Fowler, P., Wu Y. and Rajaratnam, M. (2011). Structural characterization and isolation of lignin and hemicelluloses from barley straw. *Industrial Crops and Products*, 33: 588 – 598.
25. Alemdar, A. and Sain, M. (2008). Isolation and characterization of nanofibers from agricultural residues – Wheat straw and soy hulls. *Bioresource Technology*, 99: 1664 – 1671.

26. Mohamad Haafiza, M. K., Eichhorn, S. J., Hassan, A. and Jawaid, M. (2013). Isolation and characterization of microcrystalline cellulose from oil palm biomass residue. *Carbohydrate Polymer*, 93(2): 628 – 634.
27. Joonobi, M., Harun, J., Shakeri, A., Misra, M. and Osman, K. (2009). Chemical composition, crystallinity and thermal degradation of bleached and unbleached Kenaf bast (*Hibicus Cannabinus*) pulp and nanofibers. *BioResource*, 4: 626 – 639.
28. Segal, L., Creely, J. J., Martin, A. E. Jr. and Conrad, C. M. (1959). An empirical method for estimating the degree of crystallinity of native cellulose using the X-ray diffractometer. *Textile Research Journal*, 29: 786 – 794.
29. Poletto, M., Heitor, L., Ornaghi, J., Ademir, J. and Zattera, (2014). Native cellulose: Structure, characterization and thermal properties. *Materials*, 7: 6105 – 6119.
30. Then, Y.Y., Ibrahin, N. A., Zainuddin, N., Chieng, B. W., Ariffin, H. and Wan Yunus, W. M. Z. (2015). Influence of alkaline peroxide treatment of fiber on mechanical properties of oil palm mesocarp fiber/poly(butylene succinate) biocomposite. *Bioresources,* 10(1): 1730 – 1746.
31. Haykiri-Acma, H., Yaman, S. and Kucukbayrak, S. (2010). Comparison of the thermal reactivities of isolated lignin and holocellulose during pyrolysis. *Fuel Processing Technology,* 91: 759 – 764.
32. Brebu, M. and Vasile, C. (2010). Thermal degradation of lignin – A review. *Cellulose Chemistry and Technology,* 44(9): 353 – 363.

Malaysian Journal of Analytical Sciences, Vol 20 No 5 (2016): 1104 - 1111
DOI: http://dx.doi.org/10.17576/mjas-2016-2005-16

MALAYSIAN JOURNAL OF ANALYTICAL SCIENCES
Published by The Malaysian Analytical Sciences Society
ISSN 1394 - 2506

ZETA POTENTIAL AND ENVIRONMENTAL SCANNING ELECTRON MICROSCOPY ANALYSIS IN DEPROTEINISATION OF NATURAL RUBBER LATEX

(Analisis Keupayaan Zeta dan Pengimbas Persekitaran Mikroskopi Elektron di dalam Penyahprotein Lateks Getah Asli)

Nurulhuda Abdullah*, Asrul Mustafa, Mok Kok Lang

Technology and Engineering Division,
Malaysian Rubber Board, 47000 Sungai Buloh, Selangor Darul Ehsan, Malaysia

**Corresponding author: nurulhuda.a@lgm.gov.my*

Received: 10 june 2015; Accepted: 21 July 2016

Abstract

This paper describes the effect of protein denaturants namely, urea and sodium dodecyl sulphate (SDS) in the deproteinisation of high ammonia natural rubber latex (HA-NRL). It had been shown that latex proteins were reduced more in the presence of urea alone (48%) than in the presence of SDS (18%). The synergistic effect when both urea and SDS were used in the latex deproteinisation attributed to the higher protein removal efficacy (55%). Higher zeta potential value was observed when only SDS was used, suggesting higher colloidal stability. Environmental Scanning Electron Microscopy (ESEM) revealed that without SDS, the use of urea single-handedly in the deproteinisation process promoted aggregation of latex particles, possibly due to the dismissal of latex proteins which helped to stabilise latex colloidal. Thus, it is most likely that urea serves as a protein unfolding agent during latex deproteinisation process, while SDS functions as a latex stabiliser with no significant effects on latex proteins discharge.

Keywords: urea, sodium dodecyl sulphate, deproteinisation, zeta potential, environmental scanning electron microscopy

Abstrak

Kertas kerja ini menghuraikan kesan bahan-bahan pengubah sifat protein iaitu urea dan natrium dodekil sulfat (NDS) dalam penyahprotein lateks getah asli tinggi ammonia (HA-NRL). Ia telah menunjukkan bahawa protein lateks lebih banyak dikurangkan dengan kehadiran urea sahaja (48%) berbanding dengan kehadiran NDS sahaja (18%). Keberkesanan penyingkiran protein yang lebih tinggi (55%) mungkin telah disebabkan oleh kesan sinergi apabila kedua-dua urea dan NDS digunakan di dalam penyahprotein lateks. Nilai keupayaan zeta yang tinggi diperhatikan apabila hanya NDS digunakan, menunjukkan kestabilan koloid yang lebih tinggi. Pengimbas Persekitaran Mikroskopi Elektron (ESEM) menunjukkan bahawa tanpa NDS, penggunaan hanya urea dalam proses penyahprotein menyumbang kepada kesan pengagregatan zarah lateks, kemungkinan disebabkan oleh penyingkiran protein lateks yang membantu dalam kestabilan koloid lateks. Oleh yang demikian, besar kemungkinan fungsi utama urea semasa proses penyahprotein lateks adalah sebagai ejen pembuka protein manakala NDS berfungsi sebagai penstabil lateks tanpa kesan ketara pada penyingkiran protein lateks.

Kata kunci: urea, natrium dodekil sulfat, penyahprotein, keupayaan zeta, pengimbas persekitaran mikroskopi elektron

Introduction

Natural rubber (NR) latex in general can be defined as a material that consists stable dispersion of polyisoprene rubber (hydrocarbon) and a large number of non-rubber constituents mainly carbohydrates, lipids, and proteins in an

aqueous serum phase. These non-rubber constituents are dissolved, freely suspended in the aqueous phase or absorbed on the surface of rubber particles [1-3]. During latex concentrate processing through centrifugation for instance, most of the smaller latex particles are removed together with the non-rubbers present in the serum. It is known that not all non-rubbers can be removed completely during the centrifugation process hence commercially supplied NR latex still contains considerable amounts of non-rubbers.

In its native state, NR latex contains about 6% of non-rubbers and the content is reduced to more than half during processing. However, the presence of non-rubbers is regarded imperative not only in conferring stability of rubber latex but also in governing the properties of end products. Any modification in the rubber composition may result in deterioration of properties especially in vulcanisation and cure characteristics [4]. The presence of proteins and other non-rubber linkages are also presumed to provide outstanding mechanical properties of rubber due to strain-induced crystallisation characteristic [5].

On the other hand, the presence of proteins is responsible for certain undesirable properties in NR for instance poor creep, storage hardening, high moisture absorption and poor stress relaxation behaviour [6-7]. Detrimental effects of proteins present in NR were reported in several studies [8-10]. The high moisture uptake in NR is presumably due to interaction of proteins and phospholipids at the terminal chains of rubber with water (moisture). It is generally established that the hardening phenomenon of rubber is attributed to the inter-chain crosslink formation. Proteins and phospholipids at the chain-ends of rubber molecules may interact with water under ambient condition, leads to disruption for branching points due to hydrogen bonding. Thus, when water is removed from the rubber, both functional groups at the terminal chains of rubber will undergo chain-branching and crosslinking which contribute to the gel formation during storage hardening behaviour [10].

The development and production of low protein latexes and products are an important research area ever since the emergence of allergy issues attributed to the latex proteins. Allergic responses are triggered by extractable proteins present in NR latex products especially rubber gloves. Malaysia as one of the largest exporters of latex products is affected by the negative perception of NR latex. Therefore, research in NR latex deproteinisation has continued to balance out the desirable properties which associated with rubber proteins and at the same time to eliminate the adverse proteins.

Generally, proteins can be easily destabilised and its destabilisation is determined by a balance of many competing factors. By nature, a functional native protein is in a folded (F) structure conformation [11-12] and when it loses the conformation (F), it ceases to function. The unfolding (U) process of proteins is called protein denaturation. The stability of protein can be easily affected by slight changes in temperature, pressure or solvent conditions. For instance, the presence of even a small organic molecule in aqueous solution can have profound effect on protein stability, structure, and function. In nature, this occurrence enables the proteins to either retain its stability or promote destabilisation indirectly by controlling the conformational equilibrium between folded (F) to the unfolded (U) structures.

Deproteinisation of NR latex can be achieved using protein denaturants. Urea has a long good reputation as protein denaturant owing to its ability to denature proteins by causing it to unfold. This denaturant has been described elsewhere [13] to produce low protein NR latex. Another common chemical used in latex deproteinsation is sodium dodecyl sulphate (SDS) which is an anionic surfactant [$CH_3(CH_2)_{11}OSO_3Na$]. Owing to the synergistic effect between both chemicals, effective proteins removal was described [14]. It is proposed in urea-SDS protein denaturation mechanism (Figure 1), urea may unfolded the proteins while SDS binds onto the surface of unfolded proteins and imparts negative charges, resulting in the protein to have higher net negative charge compared to its previous state. This phenomenon then creates electrostatic forces which cause the proteins to unfold into rod like shape. The unfolded proteins are then removed during the centrifugation process.

To the best of our knowledge, further elucidation on individual functions of urea and SDS or the combination of both during NRL deproteinisation is obscured hence creating a gap in knowledge. Thus, the aim of this paper is to explicate and address aforesaid gap in scientific knowledge.

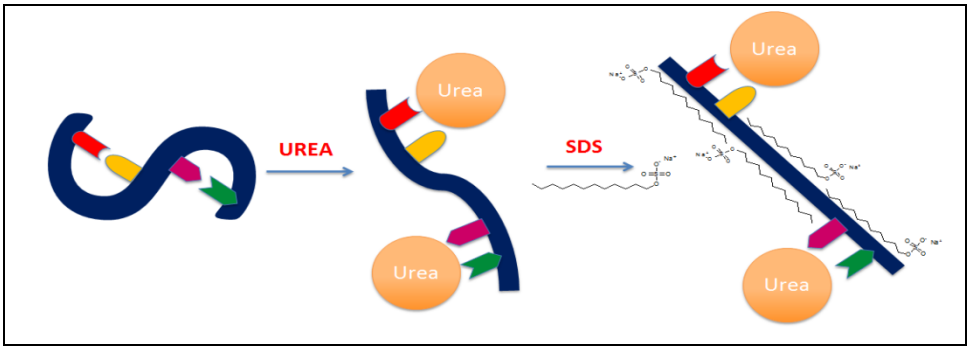


Figure 1. Proposed mechanism on simple protein denaturation via urea – SDS combination treatment

Materials and Methods

Preparation of deproteinised latex

Commercial high ammonia NR latex (HA-NRL) was used for deproteinisation. HA-NRL was incubated with 0.1% urea (w/w) in a mixing vessel under continuous stirring for 1 hour prior to centrifugation. Centrifugation was carried out using the Beckman Coulter Ultracentrifuge Model Optima L-100K at 9,000 rpm and 15 °C. After centrifugation, the cream fraction was collected and redispersed with distilled water followed by addition of SDS 1.0% (w/w). The redispersed cream fraction was stirred for 30 minutes and centrifugation was carried out for the second time. The resulting cream fraction was again collected and redispersed with distilled water to 30% total solid content. The same procedure was repeated for latex treated using 1.0% SDS only and a combination of 0.1% urea with 1.0% SDS respectively.

Characterisation

The protein content in latex samples was determined using the Kjeldahl method which measured the total nitrogen content. About 0.1 g of sample was first weighed and digested in a micro Kjeldahl flask, followed by steam distillation. The distillation result was titrated with concentrated sulphuric acid. The nitrogen content was determined in triplicates and calculated from the titration values.

Particle size and zeta potential of latex were determined using the Brookhaven 90Plus/BI-MAS ZetaPlus. The latex was diluted to 0.01% (w/w) before use. For the Environmental Scanning Electron Microscopy (ESEM), samples were prepared by adding approximately a drop of latex into 1 ml distilled water in Eppendorf tubes. The mixtures were centrifuged and the supernatants discarded. The latex samples were then stained with 1% osmioum tetroxide before viewing under ESEM.

Results and Discussion

Protein contents and zeta potentials

The proteins content and zeta potential characteristic of HA-NRL which were treated with different combinations of either urea, SDS or both denaturants (samples A, B, and C) are tabulated in Table 1. It is evident that the deproteinisation process resulted in a considerable reduction in protein content of the treated latexes.

Evidently, latex treated with urea (sample A) demonstrated approximately 49% protein removal compared to the untreated HA-NRL. In the presence of SDS alone (sample B), only 18% reduction in proteins content was seen. This suggests that SDS might have smaller role and capacity to denature proteins compared to urea.

Urea is found capable to denature proteins by binding onto the protein peptide backbone via hydrogen bonding to the polar moieties of proteins [15-17]. It is also reported elsewhere [18] that urea readily promotes solvation of protein hydrophobic groups whereby partial solubility of hydrocarbon was seen in the presence of aqueous urea. These elements could have contributed to the greater removal of latex proteins, resulted when urea was used, in comparison to SDS in the present study.

Table 1. The effect of protein denaturants on zeta potential and protein content

Treatments	Sample Reference	Proteins Content (%)	Zeta Potential (mV)[1]
High ammonia natural rubber latex (control)	HA-NRL	3.88	-40.78
HA-NRL treated with 0.1% urea	A	1.99	-25.85
HA-NRL treated with 1.0% SDS	B	3.18	-31.32
HA-NRL treated 0.1% urea and 1.0% SDS	C	1.75	-46.32

[1]Zeta potential measured at pH10

From the perspective of SDS, interaction of the anionic surfactant with proteins may also cause denaturation via high affinity binding. SDS is an anionic surfactant which may bind to proteins via sulphate group and positively charged amino side chain, or between the alkyl chain and hydrophobic side chain [19]. An earlier study [19] suggested that the protein unfolding process via SDS might proceed via two different modes which are closely linked to the changes in the micellar structures. That study also established that concentration of surfactants played an important role in the degree of unfolding of the proteins.

This present study shows that the combination of both denaturants resulted in highest protein removal efficacy (55%). However, this is only an increment of about 6% compared to latex treated with urea alone. This slight increment in urea-SDS protein removal indicates a synergistic effect from the two denaturants. Urea may inhibit the effectiveness of SDS to unfold proteins as it is found that in the presence of urea, the SDS hydrocarbon tails readily solvate, aggregation number of SDS micelles reduced and CMC value of SDS increased [18]. Therefore, to further enhance protein removal efficiency, it is suggested that higher than 1% of SDS is required.

With regard to electrostatic stability, the lower protein content resulted from deproteinisation of HA-NRL with urea caused a substantial reduction in zeta potential value from -40.78mV to -25.85mV. Zeta potential analysis gives an indication on surface charge behaviour on rubber particle surface, thus distinct chemical nature of the absorbed layers on the surface of rubber particle is reflected in the difference in the zeta potential value consequently the colloidal stability of natural rubber latex. Adsorbed proteins on the surface of latex particle are reported to contain both acidic and alkaline functional groups that carry positive and negative charge respectively [20]. HA-NRL is composed of phospholipids, carbohydrates, proteins and other non-rubber constituents which contribute charge species that gives high negative zeta potential value [3]. Perturbation of the proteins layer by urea might compensate the surface charge hence compressed the diffuse layer and subsequently reduced the negative zeta potential value [20].

According to the theory of adsorption isotherm [21], charged surfactant like SDS will adsorb onto the surface of latex particles. Reduction in zeta potential value was observed when HA-NRL was treated with 1% SDS. Zeta potential of latex treated with SDS was better than latex treated with urea, suggesting that the former has better colloidal stability than the latter. Interestingly, a higher zeta potential value was observed for sample C which was treated with urea in the presence of SDS whereby its zeta potential surpassed that of HA-NRL alone. This again suggests the synergistic effect of both denaturants when they are used together in deproteinisation of latex.

Factors influencing particle size distribution

Figure 2 depicts particle size distribution of samples HA-NRL, A, B and C. Monomodal size distribution was observed for all samples. Similar size distribution was observed for samples HA-NRL and A, while B and C showed bigger size distributions with sample B recorded the biggest result. Although the proteins content and zeta potential value of sample A were prominently reduced, the particle size distribution was not affected much compared to control (HA-NRL). The narrower and obvious shift to bigger size distribution for sample B (treated with 1.0% SDS) could be due to encapsulation of SDS onto the latex particles which resulted in interference and restricted penetration by photon correlation spectroscopy used in the size measurement method. Moreover due to the

function of SDS as stabiliser, a more distinct and stable domain of rubber particle was formed which restricted inter-particle fusion. This explains the reason why particle size distribution for sample B is narrower and shifted to bigger particle size range.

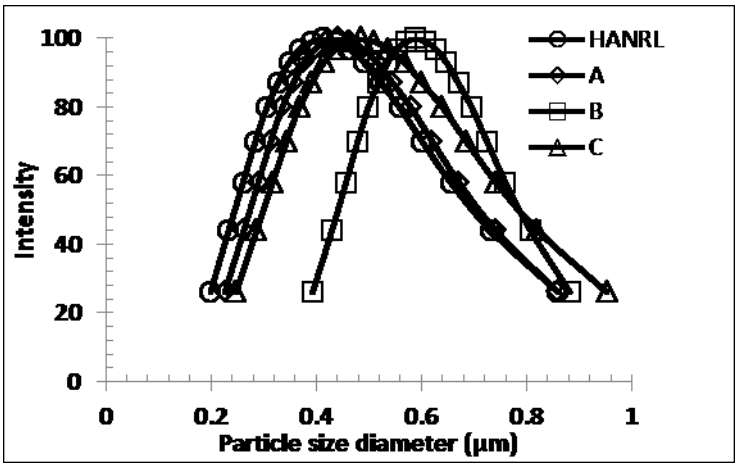


Figure 2. Effect of individual chemical treatment and combination of both chemicals on particle size diameter of deproteinized NRL (A =HANRL treated with 0.1% urea, B = HANRL treated with 1.0% SDS, and C = HANRL treated with 0.1% urea and 1.0% SDS)

Morphological changes in the treated latex samples were studied using ESEM as shown in Figure 3. The micrographs were obtained at 15,000 to 21,000 magnification levels. As observed, rubber particles for all samples exhibited nearly spherical shape. HA-NRL showed strong aggregation of rubber particles with large variation in the size distribution. After the centrifugation process, the smaller rubber particles were removed and the latex particles sizes became more uniformed (Figure 3b and 3d). In the presence of urea alone (Figure 3b), the particles were observed to favour particle inclusion; this may be due to the weakening of the hydrophobic forces when the proteins layers were depleted. In the presence of SDS, the degree of aggregation was less (Figure 3c and 3d). This was due to SDS role which served as a protective layer substituting function of the eliminated proteins. Hence, rubber particles in the presence of SDS were able to preserve their distinctive shape and remained well separated.

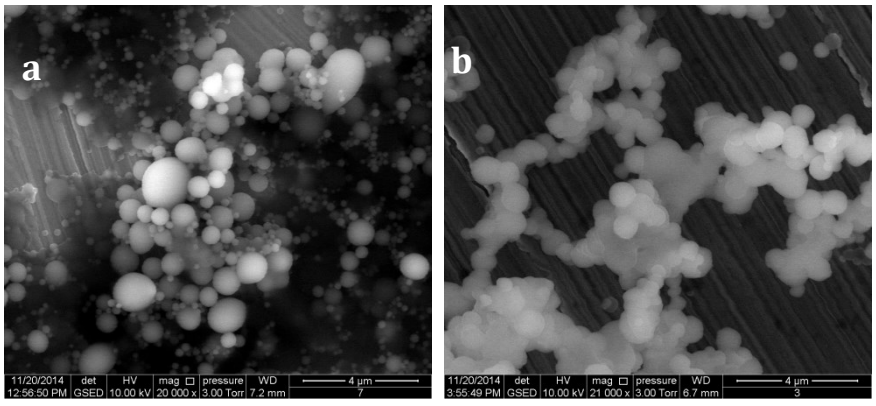


Figure 3. ESEM morphological image of a) HANRL, b) HANRL treated with 0.1% urea, c) HANRL treated with 1.0% SDS and d) HANRL treated with 0.1% urea and 1.0% SDS

It is worth to notify that the primary reason of conducting ESEM analysis is to understand and to have a quick look on the behaviour of rubber particle in a wet condition especially during deproteinisation. This method allows us to gather more information on their shape rather than sizes. The number of particle measured in ESEM is normally small hence it is difficult to collect enough data to give more reliable particle size result. Moreover, it is hard to determine whether or not the particles are merged and aggregated and they will often consider as bigger particle size.

Schematic illustrations on the deproteinisation process using urea, SDS and urea in presence of SDS are shown in Figure 4. It is hoped that this figure will clarify and demonstrate the mechanism of how the rubber particles assemble during deproteinisation process using urea and SDS. The removal of proteins from the surface of rubber particles by urea may create weakens hydrophobic forces of protein layer [15, 22], hence resulting to the merging of rubber particles with adjacent particles (Figure 4a). However, as mentioned earlier, it is uncertain whether the particles are permanently attached together or just in contact with adjacent particle. Treatments with urea will not break the proteins but serves as denaturants which facilitates the removal of proteins from NRL through centrifugation and washing process [23]. When only SDS was used during deproteinisation process, the particle seemed to have an orderly arrangement with a distinct particle shapes and without the particles merging effect (Figure 4b). Interaction of SDS surfactant with NRL surface can be demonstrated as strong interacting systems [24] thus enhance the colloidal stability of rubber particles. This phenomenon will keep the particles away from another therefore particles are well separated. Again, less aggregation was observed when urea and SDS were used mutually (Figure 4c), suggesting the particles protective layer imparted by adsorption of SDS on rubber particle surface.

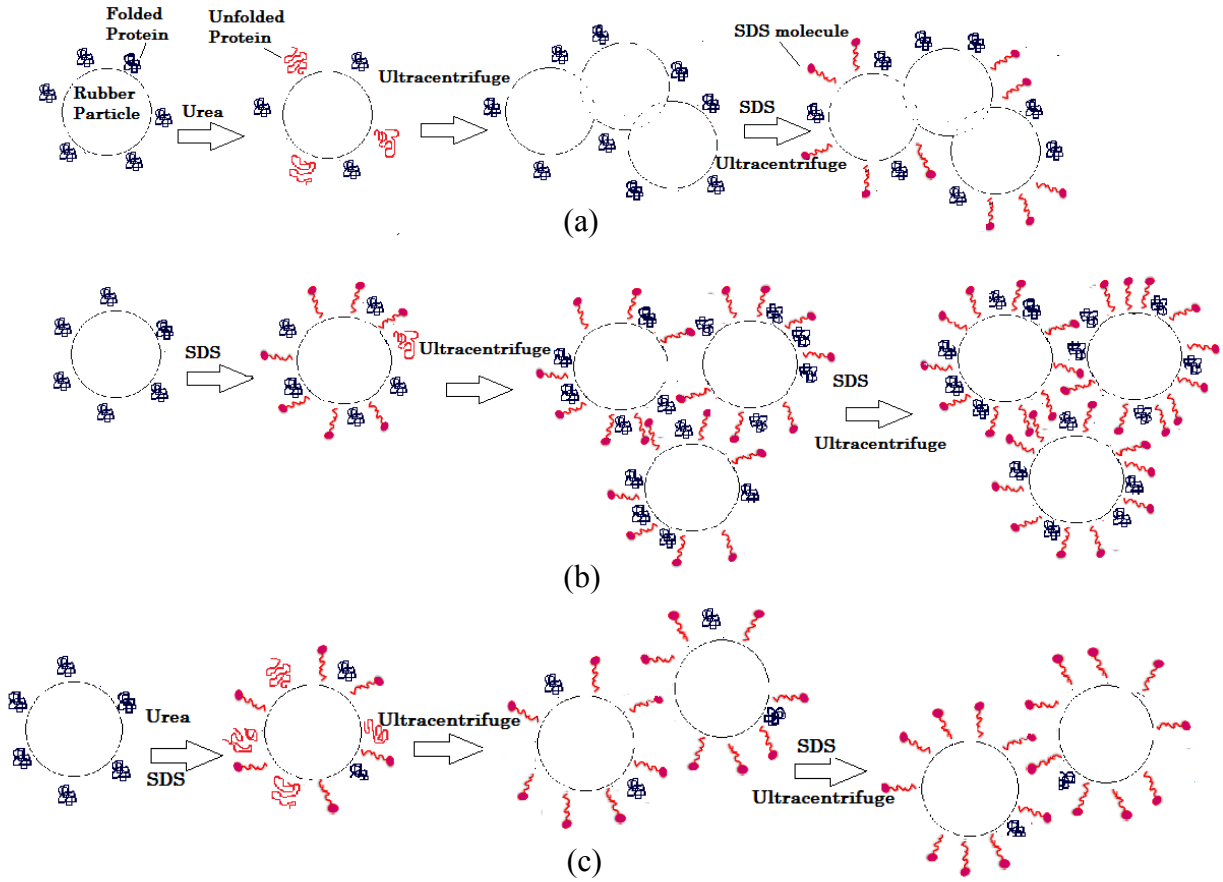


Figure 4. Proposed mechanism and morphological changes during deproteinisation of NRL using a) urea b) SDS and c) urea in the presence of SDS

Conclusion

The function of each denaturant used in the deproteinisation of NRL was examined. This study shows that urea serves as a protein unfolding agent, eliminating the rubber protein protective layer and consequently disrupts the latex colloidal stability, hence promoting particle fusion. The presence of SDS improves the colloidal stability of latex by preserving the colloidal shape of particle and restricting fusion of particle via encapsulation of the rubber particles. This study suggests that in the deproteinisation process, it is most likely that urea functions as a protein unfolding agent whilst SDS serves as a latex stabiliser without distinct effect in the removal of latex proteins.

Acknowledgement

The authors would like to thank the Director General of the Malaysian Rubber Board for permission to publish findings of this study.

References

1. Hasma H. and Subramaniam A. (1986). Composition of lipids in latex of Hevea brasiliensis clone RRIM 501, *Journal Natural Rubber Research,* 1(1):30 – 40.
2. Aprem A. S. and Pal S. N. (2002). Latex allergy and recent developments in deproteinisation of natural rubber latex *Journal of Rubber Research,* 5(2): 94 – 134.
3. Sansatsadeekul, J., Sakdapipanich, J. and Rojruthai, P. (2011). Characterization of associated proteins and phospholipids in natural rubber latex. *Journal of Bioscience and Bioengineering*, 111(6): 628 – 634.
4. Ma'zam Md Said, Ng, K. P., Hasma, H., Mok, K. L., Asrul, M., Lai, P. P. and Saadiah, S. (2004). Low protein natural rubber lattices. *Journal of Rubber Research,* 7(1): 30 – 55.
5. Amnuaypornsri, S., Sakdapipanich, J., Toki, S., Hsiao, B. S., Ichikawa, N. and Tanaka, Y. (2008). Strain-induced crystallization of natural rubber: effect of proteins and phospholipids. *Rubber Chemistry and Technology*, 81(5): 753 – 766.
6. Nor-Hidayaty, K., Shamsul, K., Asrul, M. and Ahmad-Nazir, K. (2011). Comparisons of some properties of deproteinised natural rubber vulcanisates and observations on dynamic load analysis. *Journal of Rubber Research*, 14(3): 129 – 138.
7. Othman, A. and Hasma, H. (1988). Influence of Hevea proteins and amino-acids on properties of natural rubber, *Proceedings International Rubber Technology Conference:* 166 – 177.
8. Burfield, D. R. (1986). Storage hardening of natural rubber: An examination of current mechanistic proposals. *Journal of Natural Rubber Research,* 1(3): 202 – 208.
9. Sakdapipanich, J. T. (2007). Structural characterization of natural rubber based on recent evidence from selective enzymatic treatments. *Journal of Bioscience and Bioengineering*, 103(4): 287 – 292.
10. Sakdapipanich, J. T. and Rojruthai, P. (2012). Molecular structure of natural rubber and its characteristics based on recent evidence. InTech publisher: pp. 159 – 172.
11. Creighton, T. E. (1995). Protein folding: An unfolding story. *Current Biology, 5(4):353-356*
12. Creighton, T. E. (1979). Electrophoretic analysis of the unfolding of proteins by urea. *Journal of Molecular Biology,* 129: 235 – 264.
13. Yamamoto, Y., Kawahara, S., Chaikumpollert, O. and Nghia, P. T. (2013). Protein- free natural rubber, latex thereof, and method for manufacturing said rubber and *US Patent 8476348 B2*
14. Kawahara, S., klinklai, W., Kuroda, H. and Isono, Y. (2004). Removal of proteins from natural rubber with urea. *Polymer Advance Technology,* 15:181 – 184.
15. Rossky, P. J. (2008). Protein denaturation by urea: Slash and bond. *PNAS,* 105(44): 16825 – 16826.
16. Canchi, D. R., Paschek, D. and García, A. E. (2010). Equilibrium study of protein denaturation by urea. *Journal of the American Chemical Society,* 132(7): 2338 – 2344.
17. Bennion, B. J. and Daggett, V. (2003). The molecular basis for the chemical denaturation of proteins by urea. *PNAS,* 100 (9): 5142 – 5147.
18. Ruiz, C. C. (1999). Micelle formation and microenvironmental properties of sodium dodecyl sulphate in aqueous urea solution *Colloids and Surfaces A: Physicochemical and Engineering Aspects,* 147: 349 – 357.
19. Otzen, D. E. (2002). Protein unfolding in detergents: Effect of micelle structure, ionic strength, pH, and temperature. *Biophysical Journal,* 83: 2219 – 2230.

20. *Kemp, A. R. and Straitiff, W. G. (1940). Hevea Latex: Effect of proteins and electrolytes on colloidal behavior. Rubber Chemistry and Technology, 13(4): 705 – 721.*
21. Chen, S. F. (1981). Adsorption of sodium dodecyl sulfate on natural rubber latex particles and determination of specific surface area of the particles. *Rubber Chemistry and Technology,* 54(1): 124 – 133.
22. Jacso, T., Bardiaux, B., Broecker, J., Fiedler, S., Baerwinkel, T., Mainz, A., Fink, U., Vargas, C., Oschkinat, H., Keller, S. and Reif, B. (2013). The mechanism of denaturation and the unfolded state of the α-helical membrane-associated protein Mistic. *Journal of the American Chemical Society,* 135(50): 18884 – 18891.
23. Junoi, S., Chisti, Y. and Hansupalak, N. (2015). Optimal conditions for deproteinizing natural rubber using immobilized alkaline protease *Journal of Chemical Technology and Biotechnology,* 90: 185 – 193.
24. Wei, L. K., Ing, W. K., Badri, K. H. and Ban, W. C. (2013). Formation of protein complex with the aid of polyethylene glycol for deproteinized natural rubber latex *AIP Conference Proceedings* 1571: 871

Malaysian Journal of Analytical Sciences, Vol 20 No 5 (2016): 1112 - 1122
DOI: http://dx.doi.org/10.17576/mjas-2016-2005-17

MALAYSIAN JOURNAL OF ANALYTICAL SCIENCES
Published by The Malaysian Analytical Sciences Society
ISSN 1394 - 2506

THERMAL CHARACTERISTICS OF MICROCRYSTALLINE CELLULOSE FROM OIL PALM BIOMASS

(Sifat Terma Mikrokristal Selulosa Daripada Biojisim Tandan Kosong Sawit)

Fatin Afifah Ahmad Kuthi[1], Nor Rabbi'atul 'Adawiyah Norzali[1], Khairiah Haji Badri[1,2]*

[1]*School of Chemical Sciences and Food Technology, Faculty of Science and Technology*
[2]*Polymer Research Center, Faculty of Science and Technology*
Universiti Kebangsaan Malaysia, 43600 UKM Bangi, Selangor, Malaysia

**Corresponding author: kaybadri@ukm.edu.my*

Received: 10 June 2015; Accepted: 21 July 2016

Abstract

Extracted cellulose from oil palm empty fruit bunch fiber (OPEFB) was subjected to acid hydrolysis in producing microcrystalline cellulose (MCC). The acid hydrolysis was conducted using 1 % (v/v) sulfuric acid (H_2SO_4) at varying temperatures of 120, 130 and 140 °C for an hour. The relationship between the thermal behavior and physical properties was investigated by thermogravimety (TGA/DTG) and differential scanning calorimetry (DSC) as well as x-ray diffractometry (XRD). The hydrolyzed MCC at 120 °C (MCC_A) showed the highest thermal stability temperature and percentage of crystallinity at 250 °C and 65.07% respectively. However, hydrolyzed MCC at 130 °C (MCC_B) and 140 °C (MCC_C) exhibited low thermal stability temperature at 225 °C and 220 °C respectively. The percentage of crystallinity obtained for MCC_B and MCC_C was 61.18% and 60.64% respectively. This study revealed that the degree of crystallinity for cellulose has positive impact on the thermal degradation temperature of the OPEFB-MCC.

Keywords: acid hydrolysis, microcrystalline cellulose, oil palm empty fruit bunch, thermal behavior

Abstrak

Selulosa yang diestrak dari serabut tandan kosong sawit (STKS) dihidrolisis menggunakan asid bagi menghasilkan mikrokristal selulosa (MKS). Hidrolisis berasid dijalankan dengan menggunakan 1 % (v/v) asid sulfurik (H_2SO_4) pada suhu yang divariasikan iaitu 120, 130 dan 140 °C selama sejam. Hubungan antara sifat terma dan sifat fizikal dikaji berdasarkan analisis termogravimetri (TGA/DTG), anlisis kalorimetri imbasan kebezaan (DSC) serta kaedah pembelauan sinar-X (XRD). Peningkatan suhu hidrolisis menunjukkan kesan yang kontra terhadap sifat terma STKS-MKS. MKS yang dihidrolisis pada suhu 120 °C (MKS_A) menunjukkan suhu kestabilan terma dan peratus kehabluran yang paling tinggi iaitu masing-masing pada 250 °C dan 65.07%. MKS yang dihdrolisis pada 130 °C (MKS_B) dan 140 °C (MKS_C) mempamerkan suhu kestabilan terma yang rendah iaitu masing masing pada suhu 225 °C dan 220 °C. Peratus kehabluran yang diperoleh bagi MKS_B dan MKS_C masing-masing adalah 61.18% dan 60.64%. Kajian ini memberi indikasi bahawa darjah kehabluran selulosa memberi kesan positif kepada suhu degradasi terma TKKS-MKS.

Kata kunci: hidrolisis berasid, mikrokristal selulosa, serabut tandan kosng kelapa sawit, sifat terma

Introduction

Oil palm empty fruit bunch (OPEFB) is one of the major agricultural crops generated from palm oil mills in Malaysia. This biomass which is a carbohydrates polymer; comprised of cellulose and hemicellulose and also aromatic polymer called lignin. Despite these three major components, OPEFB also consists of few minor

components such as extractives, inorganic compound and ash [1-3]. Previous study shows that the content of cellulose, hemicellulose and lignin in OPEFB are 44.48%, 27.00% and 17.00% respectively [4]. Figure 1 represents lignocellulosic material structures of the plant cell wall [5].

As a boundless renewable resource, cellulose has a potential on producing environmental friendly and biocompatible products. Cellulose, a glucan polymer that made up from D-glucopyranose units and joined together by β-(1→ 4) - glucosidic bonds [6-8]. Naturally, cellulose resembles in micro fibrils form and composes of crystalline and amorphous region. The 'composite ribbon' micro fibrils bundles are linked by hydrogen bond between the hydroxyl groups and oxygen [9-11]. All native cellulose has been classified as cellulose type I [6]. Studies showed that cellulose type I has intra-molecular hydrogen bond for O(2)H···O(6) and O(3)H···O(5) and the inter-molecular hydrogen bond for O(6)H···O(3') as shown in figure 2 [12-13].

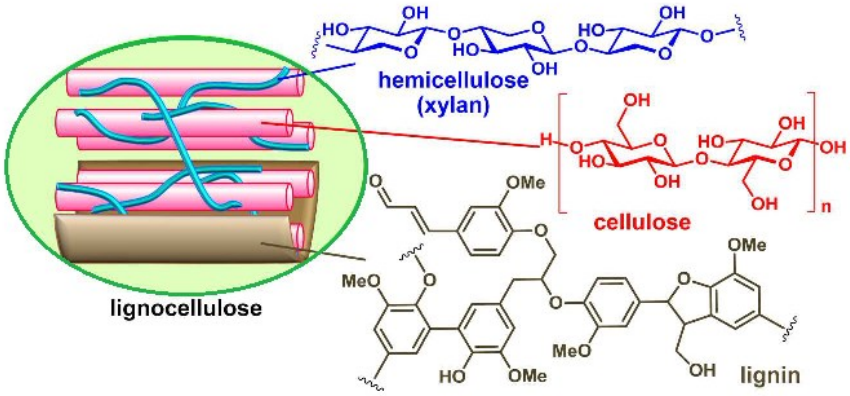


Figure 1. Schematic diagram of lignocellulosic material and their structure

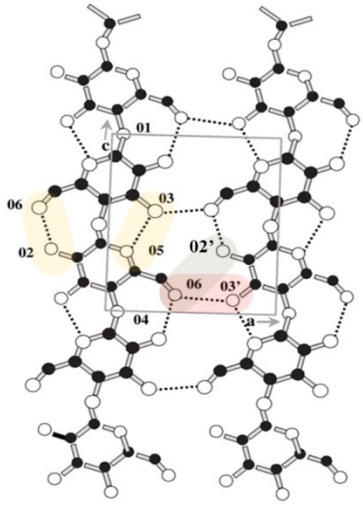


Figure 2. Inter-molecular and intra-molecular hydrogen bonding in cellulose type I

Microcrystalline cellulose (MCC) is defined as a purified, partially depolymerized non-fibrous form of cellulose. MCC is produced by treating cellulose acquired from plant materials using conventional method that is acid hydrolysis. Commercially MCC is produced by woody plants and purified cotton. MCC is white in color, odorless and tasteless crystalline powder. The chemical and physical properties such as crystallinity, moisture content, surface area, molecular weight and porosity are varied depend eloquently on the characteristic of the raw materials and hydrolysis conditions. Commercial MCC produced nowadays have different physicochemical and thermal properties which lead to different functional parameters and applications [7, 14, 15].

MCC is used as a value-added product in food processing, pharmaceutical and cosmetic industries [16]. Today, MCC also being used in producing glucose in order to generate 5-hydroxymethyl furfural (HMF) and levulinic acid as a desirable precursor for catalytic conversion into chemicals and hydrocarbon fuels [17]. Thermal analysis is a technique to prevail the thermal behavior of a material under various conditions. Thermal analysis also determines the changes of a material by noting the temperature at which thermal halt occurred [18, 19]. Azubuike and Okhamafe stated that TGA and DSC analysis also helped to clarify the stability, compatibility and transition of phase of the excipients [7]. In this research, the thermal behavior of MCC from OPEFB was investigated using thermogravimetric analysis (TGA), differential thermal analysis (DTA) and differential scanning calorimetry (DSC). These were employed in order to facilitate the understanding of the possible chemical reactions for the depolymerization of MCC. The MCC was produced by using cellulose extracted from OPEFB through acid hydrolysis at mild concentration and varying hydrolysis temperature of 120, 130 and 140 °C. This work also compared the MCC crystallinity data from X-ray diffraction technique with the thermal stability property.

Materials and Methods

Materials

Oil palm empty fruit bunch fiber (OPEFB) was kindly supplied by Seri Ulu Langat Palm Oil Mills Sdn Bhd, Selangor, Malaysia. The fiber was ground and sieved to obtain fiber size ranging from 315 to 500 μm. Chemicals used for α-cellulose extraction and acid hydrolysis were ethanol (C_2H_5OH; 95% purity, John Kollin Chemicals, UK), sodium chlorite, ($NaClO_2$; 80% purity, Sigma Aldrich, USA) and hydrogen peroxide, (H_2O_2; 30 – 32% purity, Friendemann Schmidt Chemical, Germany). Acetic acid (CH_3COOH; 99.5% purity), sodium hydroxide pellet (NaOH; 99% purity), sulfuric acid (H_2SO_4; 98-99% purity) and toluene (C_7H_8; 99.5%) were purchased from Systerm Sdn Bhd, Selangor, Malaysia. Commercial cellulose microcrystalline powder (Sigma Aldrich, USA) was used as the standard reference.

Method

The prepared OPEFB fibers were dried in a conventional oven at 105 °C for 24 hours and the moisture content was determined. Alcohol-benzene extraction was carried out to remove the extractives such as wax, oil and inorganic substances. This was carried out using ethanol and toluene mixture as the solvent at the ratio of 1:2 by volume for 8 hours following TAPPI T204 cm-97 (Alcohol-benzene solubility of pulp) [20]. The extracted fibre undergone bleaching process to remove lignin by mixing with 25 mL of 10% (v/v) CH_3COOH aqueous solution and 6 g of $NaClO_2$ subsequently under boiling water bath [21]. The mixture was filtered using hardened ash less filter paper (540, Whatman) via Buchner funnel. The whitish yellow filter cake was dried. The filter cake was treated with 75 mL of 17.5% NaOH aqueous solution in a water bath (20 °C). The suspension was filtered and the filter cake was rinsed with 8.3% NaOH aqueous solution followed by 650 mL cold distilled water in order to remove the hemicellulose leaving the α-cellulose in the filter cake. The extracted sample was dried at 105 °C for 24 hours.
Microcrystalline cellulose (MCC) was produced by acid hydrolysis reaction from the dried sample following method proposed by Soom et al. [22]. The reaction was performed by using 1% (v/v) H_2SO_4 diluted solution for an hour at varying temperatures of 120, 130 and 140 °C. The ratio of extracted sample to acid solution was fixed at 1:10. After the reaction was completed, the MCC was rinsed with cold distilled water until it reached pH 7 [7]. The MCC was soaked in 10% (v/v) H_2O_2 diluted solution for 90 min at 60 °C for bleaching purpose [23]. The yield was dried in the oven before further characterization.

Characterizations: X-ray diffraction (XRD)

X-ray diffraction (XRD) analysis was carried out using Bruker X-ray diffractometer (model D8-Advance). The radiation used was Cu-Kα1 at 1.514 Å. All samples were analysed at 2θ of 5° to 60° with the step size of 0.025°/s. The percentage of crystallinity (CrI) was calculated using the following equation (1) [24]:

$$\text{CrI}, \% = \frac{\text{Sc}}{\text{St}} \times 100 \quad (1)$$

where Sc is the area of all crystalline peak and St is the total area including non-crystalline fraction

Thermogravimetric analysis/Differential thermal analysis (TGA/DTA)

Thermogravimetric analysis (TGA) and differential thermal analysis (DTA) were performed using Mettler Toledo model TGA/SDTA 518^e to analyze the thermal behavior of OPEFB, MCC and CMCC samples. The samples were heated from 30 to 600 °C with heating rate of 10 ºC·min^{-1} under nitrogen gas atmosphere [25].

Differential scanning calorimetry

The differential scanning calorimetry (DSC) of the materials was analyzed using Mettler Toledo model DSC 822^e. It was analyzed under nitrogen gas blanket at a flow rate of 20 mL·min^{-1}. The temperature was programmed at 30 to 250 ºC with heating rate of 10 ºC·min^{-1}.

Results and Discussion

X-ray diffraction

The X-ray diffraction (XRD) patterns for all samples are as shown in Figure 3. The main reflection at 2θ=15.0°, 18.0°, 22.6° and 35° were observed for all samples [7,11]. The lattice planes for these reflections were at 101, 10$\bar{1}$, 002 and 040 respectively [7,12]. The free hydroxyl groups present in cellulose are contributed to the rise of various ordered crystal arrangements. This is due to the formation of inter-molecular and intra-molecular hydrogen bonds within the fibrils [26]. Reflections at 15.0°, 18.0°, 22.6° and 35° are typical diffraction signals of polymorph type I which commonly occur in native cellulose [7].

There are two types of natural occurring cellulose called I_α and I_β. Cellulose I_α usually found in bacterial and algae celluloses whereas cellulose I_β is found in higher plant. I_α and I_β exhibited as triclinic and monoclinic unit cells respectively [27]. The changes from polymorph type I to polymorph type II can be seen in the α-cellulose sample. A shoulder around 2θ of 20.4° was observed after alkali treatment was carried out. MCC-OPEFB samples also showed the coexistence of both polymorph types I and II. Two shoulders at 2θ of 20.4° and 12.5° with their respective lattice planes of 110 and 11$\bar{0}$ indicate that acid hydrolysis also contributed in the changes of polymorph type [7, 28].

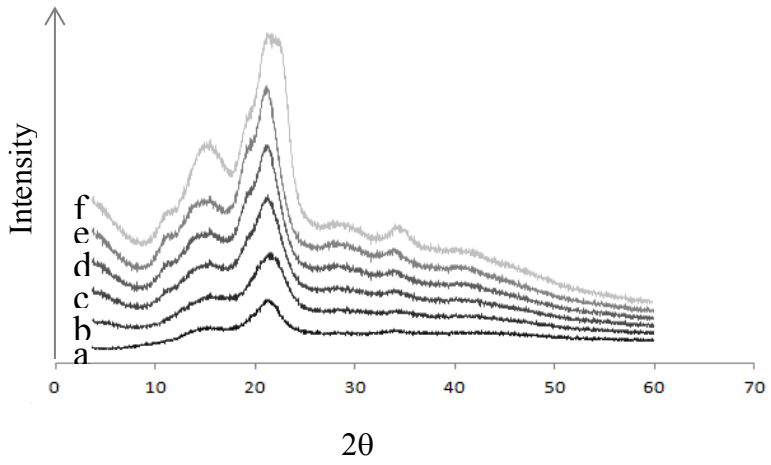


Figure 3. X-ray diffraction patterns of (a) OPEFB; (b) α-cellulose; (c) MCC_A; (d) MCC_B; (e) MCC_C and (f) CMCC

The crystallinity index, CrI (%) of OPEFB, α-cellulose, OPEFB-MCC and CMCC are listed in Table 1. In this study, the crystallinity index was calculated using deconvolution method or curve fitting method. In this method, calculation of CrI is based on the ratio of all crystalline area to the total area [12, 29].

Table 1. Percentage of crystallinity of OPEFB, α-cellullose, OPEFB-MCC and CMCC

Samples	**Crystallinity, CrI(%)**
OPEFB	43.24
α-cellulose	44.78
MCC_A	65.07
MCC_B	61.18
MCC_C	60.64
CMCC	76.19

The crystallinity index increased upon extraction of the α-cellulose. This is possible due to the breakdown of amorphous regions contributed by hemicellulose and lignin [30, 31]. Significant increments of crystallinity index were observed for the acid hydrolyzed samples. This is due to the removal of amorphous part in α-cellulose resulted by the scissoring effect of glycosidic linkages [30]. Higher crystallinity index for CMCC sample was due to the characteristics of the raw material and its hydrolysis condition [14].

Thermal Properties via thermogravimetry analysis (TGA) and differential thermal analysis (DTA)
Figure 3 shows the thermograms of TGA and DTA analyses performed on OPEFB, α-cellulose, OPEFB-MCC and CMCC. Table 2 represents the numerical data from TGA and DTA analyses. The initial weight loss for all samples except CMCC at temperature around 100 °C was attributed to the evaporation of water or moisture [26, 31, 32]. The onset temperature of OPEFB was the lowest compared to other samples. Poletto et al. stated that degradation of hemicellulose which occurs at temperature between 180 to 350 °C [26]. A shoulder in OPEFB DTA curve at 280 °C was suspected belong to hemicellulose since it degrades at a lower temperature compared to lignin and cellulose.

Among the OPEFB-MCC, MCC_A showed the highest onset temperature (250 °C) followed by MCC_B and MCC_C. This is due to the high crystallinity of cellulose in MCC_A. The reorientation of the crystals in cellulose promotes to arise in onset temperature of degradation [33]. According to Poletto et al. (2012), the degradation of cellulose occurs at maximum temperature, (T_{max}) of 350 °C. At this temperature, the scissoring of glycosidic linkage in cellulose happens [26]. The increase in the hydrolytic values lowers both the molecular weight and the T_{max} values. This is attributable to the hydrolytic effect of the crystalline part of the cellulose along with the amorphous hydrolysis [30, 33]. The high onset temperature was observed in CMCC (295 °C) was due to its high percentage of crystallinity [11].

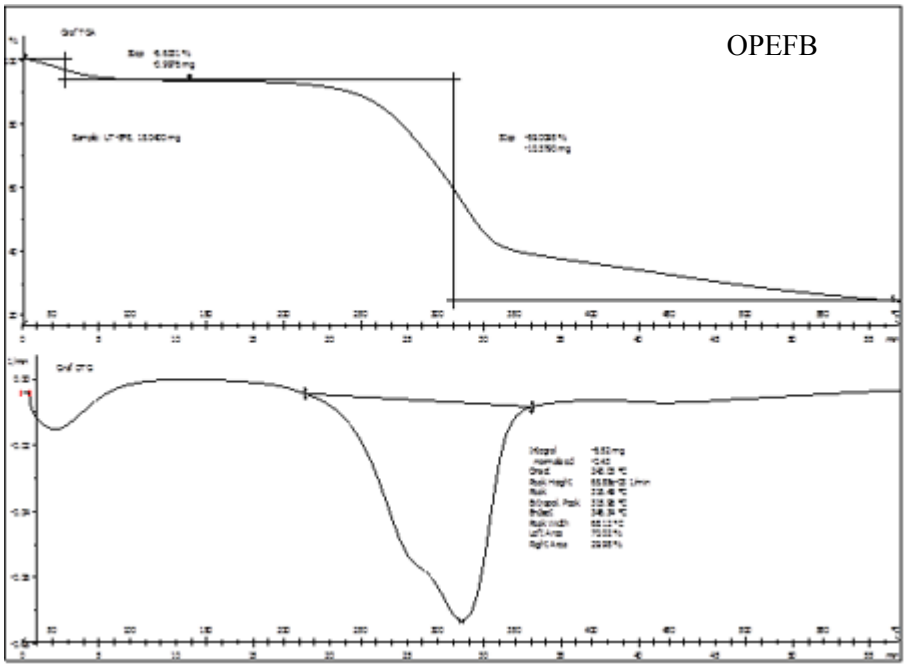


Figure 4 (a). The TGA/DTA curves of OPEFB

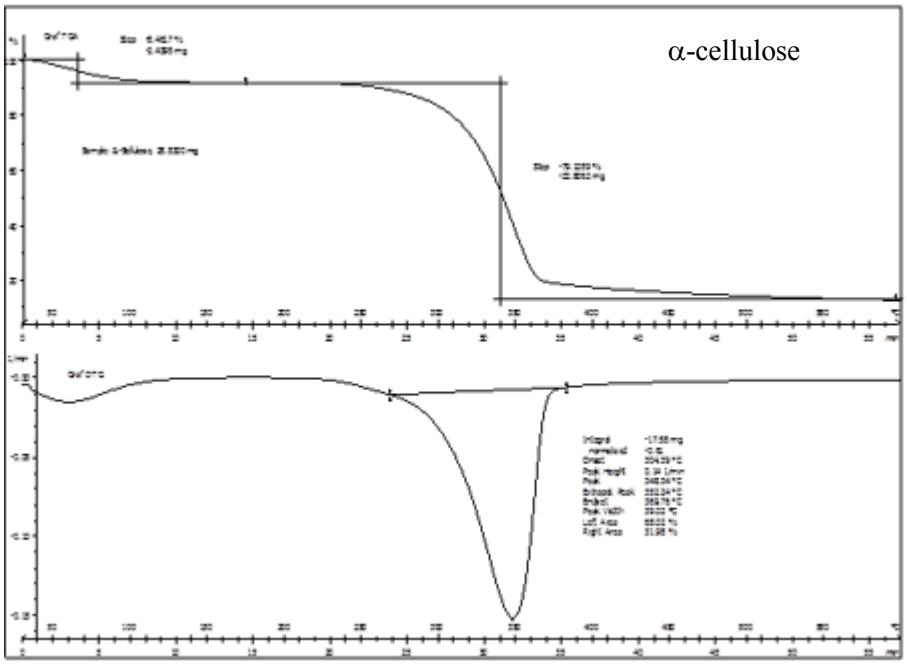


Figure 4 (b). The TGA/DTA curves of α-cellulose

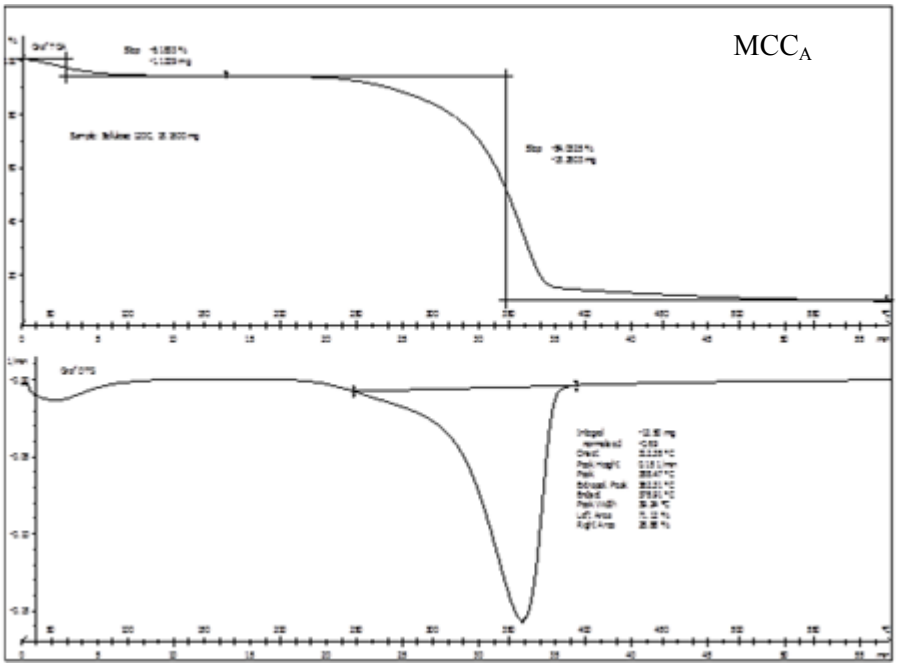


Figure 4 (c). The TGA/DTA curves of MCC_A

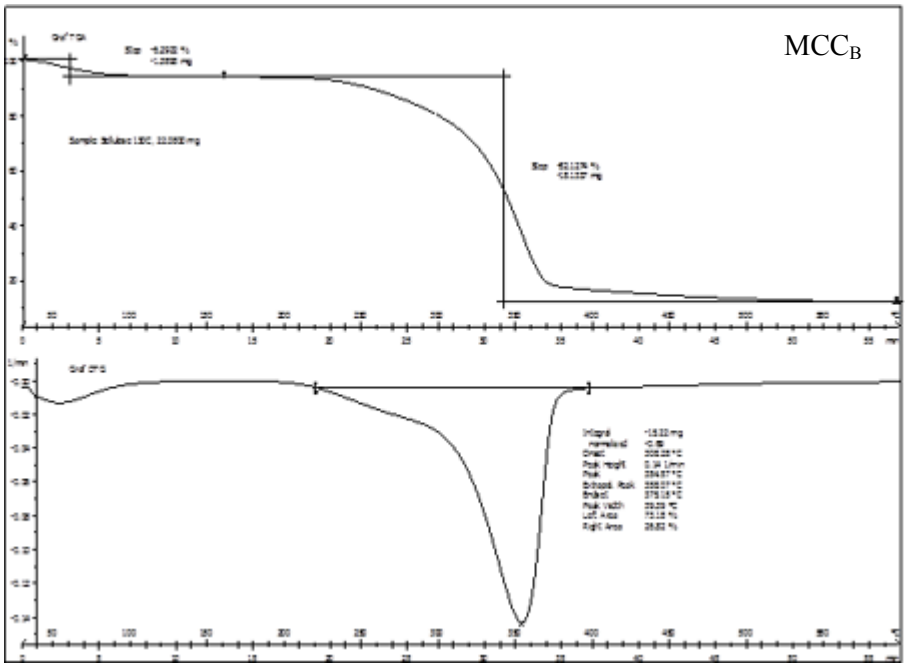


Figure 4 (d). The TGA/DTA curves of MCC_B

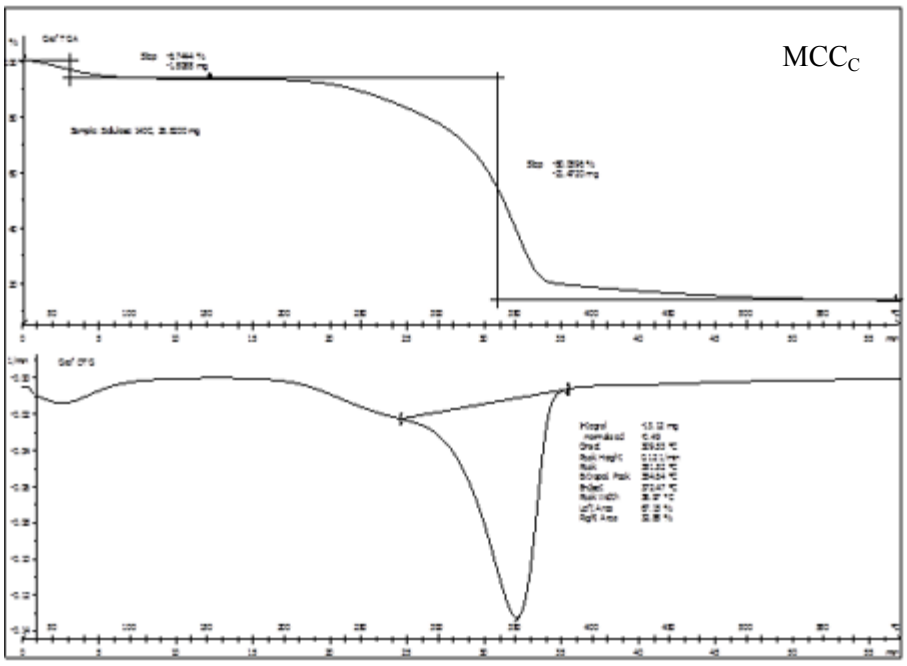


Figure 4 (e). The TGA/DTA curves of MCC_C

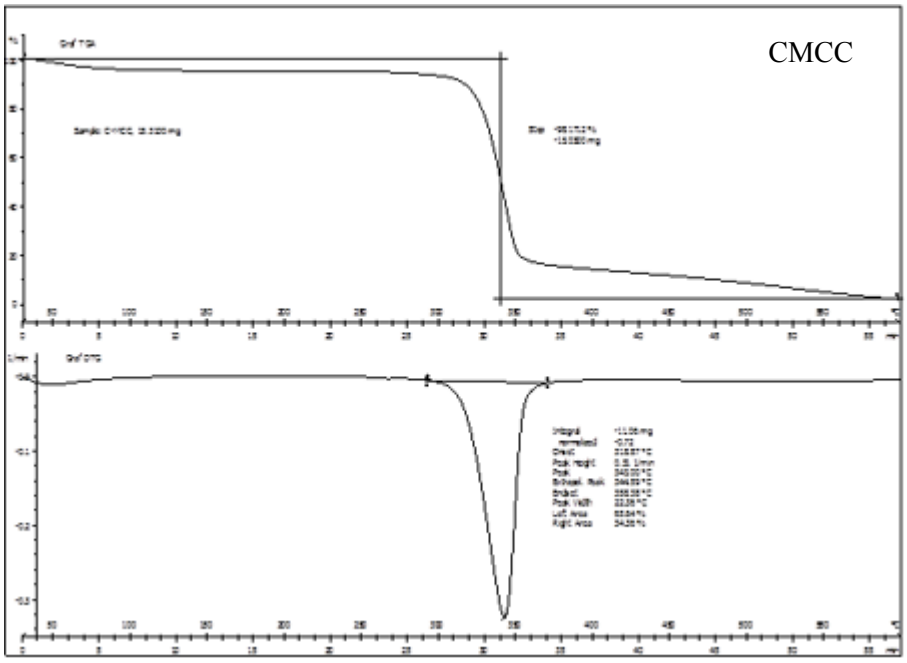


Figure 4 (f). The TGA/DTA curves of CMCC

Differential scanning calorimetry (DSC)

The glass transition temperature, T_g was tabulated in Table 2. The T_g value observed in OPEFB was lower compared to α-cellulose due to the low molecular weight of hemicellulose in OPEFB. Hemicellulose is enriched with many branched structures and also polyose chains [25]. This causes the chain mobility in OPEFB occur at lower temperature. The broad T_g peak on OPEFB was due to the presence of hemicellulose and lignin whereas the broad α-cellulose T_g peak was contributed by the amorphous cellulose. Based on the T_g obtained for the OPEFB-MCC, MCC_A showed high T_g compared to MCC_B and MCC_C. This is due to the acid hydrolysis of the crystalline cellulose at high temperature as discussed earlier. CMMC has the lowest T_g due to its initial physical condition which is powdered form.

Table 2. Thermal properties obtained from TGA and DSC analysis of all samples studied

Samples	T_{onset} (°C)	T_{max} (°C)	T_g (°C)	Weight loss (%)
OPEFB	215	315	182	75.64
α-cellulose	250	349	187	87.57
MCC_A	250	360	178	90.22
MCC_B	225	355	171	88.42
MCC_C	220	350	171	86.80
CMCC	295	345	168	98.17

Conclusion

The thermal behavior of microcrystalline cellulose from oil palm empty fruit bunch (OPEFB) has been investigated. Acid hydrolysis has significantly increased the thermal stability of the OPEFB. However, higher hydrolysis temperature reduced the thermal stability. The MCC_A showed the highest thermal stability and highest percentage of crystallinity.

Acknowledgement

The authors gratefully acknowledge School of Chemical Sciences and Food Technology and Polymer Research Center (PORCE), Faculty of Science and Technology, Universiti Kebangsaan Malaysia for providing the working space and facilities and also to the Ministry of Higher Education (MOHE) for the Exploratory Research Grant Scheme (ERGS) with code no. ERGS/1/2013/STG01/UKM/02/2.

References

1. Sreekala, M. S., Kumaran, M. G. and Thomas, S. (1997). Oil palm fibers: Morphology, chemical composition, surface modification and mechanical properties. *Journal of Applied Polymer Science*, 66: 821 – 835.
2. Law, K. N., Daud, W. R. W. and Ghazali, A. (2007). Morphological and chemical mature of fibers strands of oil empty fruit bunch (OPEFB). *Bioresources*, 2(3): 352 – 362.
3. Abdul Khalil, H. P. S., Alwani, M. S., Ridzuan, R., Kamarudin, H. and Khairul, A. (2008). Chemical composition, morphological characteristic and cell wall structure of Malaysian oil palm fibers. *Polymer-Plastics Technology and Engineering*, 47: 273 – 280.
4. Kuthi, F. A. A. and Badri, K. (2014). Effect of cooking temperature on the crystallinity of acid hydrolysed-oil palm cellulose. *AIP Conference Proceedings*, 1614: 456 – 462.
5. Kobayashi, H. and Fukuoka, A. (2013). Synthesis and utilisation of sugar compounds derived from lignocellulosic biomass. *Green Chemistry*, 5(7): 1740 – 1763.
6. Rowell, R. M., Pettersen, R., Han, J. S., Rowell, J. S. and Tshabalala, M.A. (2005). Cell wall chemistry, Rowell, R. M, Handbook of wood chemistry and wood composites, CRC Press, Florida.

7. Azubuike, C. P. and Okhamafe, A. O. (2012). Physicochemical, spectroscopic and thermal properties of microcrystalline cellulose derived from corn cobs. *International Journal of Recycling of Organic Waste in Agriculture*, 1(9): 1 – 7.
8. Frone, A. N., Panaitescu, D. M. and Donescu, D. (2011). Some aspects concerning the isolation of cellulose micro and nano-fibers. *U.P.B. Scientific Bulletin*, 73(2): 133 – 152.
9. Nishiyama, Y. (2009). Structure and properties of the cellulose microfibril. *Journal of Wood Science*, 55: 241 – 249.
10. Kuthi, F. A. A., Badri, K. dan Azman, M. A. (2014). X-ray diffraction patterns of oil palm empty fruit bunch fibers with varying crystallinity. *Advanced Materials Research*, 1087: 321 – 328.
11. Haafiz, M. K. M., Hassan, A., Zakaria, Z. and Inuwa, I. M. (2014). Isolation and characterization of cellulose. *Carbohydrate Polymers*, 103: 119 – 125.
12. Yuan, L., Wan, J., Ma, Y., Wang, Y., Huang, M. and Chen, Y. (2013). The content of different hydrogen bond models and crystal structure of Eucalyptus fibers during beating, *BioResources*, 8(1): 717 – 734.
13. Kahar, P. (2013). Synergistic effects of pretreatment process on enzymatic digestion of rice straw for efficient ethanol fermentation, Petre, M., Environmental Biotechnology-New Approached Prospective Applications, InTech publisher: pp. 65.
14. Adel, A. M., El-Wahab, Z. H., Ibrahim, A. A and Al-Shemy, M. T. (2011). Characterization of microcrystalline cellulose prepared from lignocellulosic materials. Part II: Physicochemical properties. *Carbohydrate Polymers*, 83: 676 – 687.
15. Trache, D., Donnot, A., Khimeche, K., Benelmir, R. and Brosse, N. (2014). Physico-chemical properties and thermal stability of microcrystalline cellulose isolated from Alfa fibers. *Carbohydrate Polymers*, 104: 223 – 230.
16. Chauhan, R. S., Sapkal, V. S., Sapkal, V. S. and Zamre, G. S. (2009). Microcrystalline cellulose from cotton rags (waste from garment and hosiery industries). *Journal Chemical Sciences*, 7(2): 681 – 688.
17. Wyman, C. E. (2013). Introduction. aqueous pretreatment of plant biomass for biological and chemical conversion to fuels and chemicals, First Edition, Johm Wiley & Sons Ltd.: pp. 1-15.
18. Adel, A. M., El-Wahab, Z. H., Ibrahim, A. A. and Al-Shemy, M. T. (2010). Characterization of microcrystalline cellulose prepared from lignocellulose materials, Part I: Acid hydrolysis. *Bioresources Technology*, 101: 4446 – 4455.
19. Barneto, A. G., Carmona, J. A., Alfonso, J. E. and Serrano, R. S. (2010). Simulation of the thermogravimetry analysis of three non-wood pulps. *Bioresources Technology*, 101: 3220 – 3229.
20. Anon. (1997). Alcohol-benzene solubility of pulp. *TAPPI Testing Procedure* (TAPPI T204 cm-97) USA.
21. Browning, B. L. (1967). Methods of wood chemistry, J. Wiley and Sons, New York: pp. 394 – 396.
22. Soom, R. M., Aziz, A. A., Hassan, W. H. W. and Top, A. G. M. (2009). Solid state characteristics of microcrystalline cellulose from oil palm empty fruit bunch fibre. *Journal of Oil Palm Research*, 21: 613 – 620.
23. Nazir, M. S., Wahjoedi, B. A., Yussof, A.W. and Abdullah, M. A. (2013). Eco-friendly extraction and characterization of cellulose from oil palm empty fruit bunches. *BioResources*, 8: 2161 – 2172.
24. Ciolacu, D., Ciolacu, F. and Popa,V. I. (2011). Amorphous cellulose- structure and characterization. *Cellulose of Chemistry and Technology*, 45: 13 – 21.
25. Harun, N. A. F., Baharuddin, A. S., Zainudin, M. H. M, Bahrin, E. K., Naim, M. N. and Zakaria, R. (2013). Cellulose production from treated oil palm empty fruit bunch degradation by locally isolated Thermobifida fusca. *Bioresources*, 8(1): 676 – 687.
26. Poletto, M., Zattera, A. J., Forte, M. M. C. and Santara, R. M. C. (2012). Thermal decomposition of wood: Influence of wood components and cellulose crystallite size. *Bioresource Technology*, 109: 148 – 153.
27. Poletto, M., Junior, H. L. O. and Zattera, A. J. (2014). Native cellulose: structure, characterization and thermal properties. *Materials*, 7: 6105 – 6119.
28. Rojas, J. (2013). Effect of polymorphism on the particle and compaction properties of microcrystalline cellulose, *InTech Open*: pp. 27 – 46.
29. Terinte, N., Ibbett, R. and Schuster, K. C. (2011). Overview on native cellulose and microcrystalline cellulose I structure studied by x-ray diffraction. *Lenzinger Berichte*, 89: 118 – 131.
30. Haafiz, M. K. M., Eichhorn, S. J., Hassan, A. and Jawaid, M. (2013). Isolation and characterization of microcrystalline cellulose from oil palm biomass residue, *Carbohydrate Polymers*, 93: 628 – 634.

31. Chan, C. H., Chia, C. H., Zakaria, Ahmad, S. I. and Dufresne, A. (2013). Production and characterisation of cellulose and nano-crystalline cellulose from kenaf core wood. *BioResources*, 8: 785 – 794.
32. Peng, Y., Gardner, D. J., Han, Y., Kiziltas, A., Cai, Z. and Tshabalala, M. A. (2013). Influence of drying method on the material properties of nanocellulose I: thermostability and crystallinity. *Cellulose*, 20(5): 2379 – 2392.
33. Mandal, A. and Chakrabarty, D. (2011). Isolation of nanocellulose from waste sugarcane bagasse (SCB) and its characterization. *Carbohydrate Polymers*, 86: 1291 – 1299.

Malaysian Journal of Analytical Sciences, Vol 20 No 5 (2016): 1123 - 1128
DOI: http://dx.doi.org/10.17576/mjas-2016-2005-18

MALAYSIAN JOURNAL OF ANALYTICAL SCIENCES
Published by The Malaysian Analytical Sciences Society
ISSN 1394 - 2506

LATEX PARTICLES MORPHOLOGY OF EPOXIDISED AND HIGH AMMONIA NATURAL RUBBER LATEX FROM ELECTRON MICROSCOPY TECHNIQUES

(Morfologi Partikel Lateks Bagi Lateks Getah Asli Terepoksi dan Lateks Getah Asli Kandungan Tinggi Ammonia daripada Teknik-Teknik Mikroskopi Elektron)

Norhanifah Mohd Yazid*, Fatimah Rubaizah Mohd Rasdi, Asrul Mustafa

Technology and Engineering Division,
Malaysian Rubber Board, 47000 Sungai Buloh, Selangor, Malaysia

**Corresponding author: norhanifah@lgm.gov.my*

Received: 10 June 2015; Accepted: 21 July 2016

Abstract

The rubber latex particle morphology, size and also arrangements of various types of natural rubber latex are investigated in the latex state using Environmental Scanning Microscope (ESEM). Subsequently the changes in the morphology after film formation is observed using Field Emission Scanning Electron Microscopy (FESEM). Prior to film formation, in the latex state, epoxidised natural rubber showed marked differences in latex particle morphology and arrangement compared to high ammonia latex. Subsequently, after the films are formed, the microscopy results exhibited certain dissimilarities between high ammonia and epoxidised natural rubber latex films particularly particle clustering. It is revealed that the high ammonia natural rubber latex film showed distinctly larger spherical shaped latex particles at the surface of the films in contrast to the smaller latex particles as observed in the epoxidised natural rubber latex film. The present study provides insight into the differences in the film formation between high ammonia and epoxidised natural rubber latex, which may also influence the properties of the resulting rubber latex films and latex products.

Keywords: high ammonia natural rubber latex, epoxidised natural rubber latex, film formation, latex particles

Abstrak

Morfologi partikel lateks getah, saiz dan juga susunan pelbagai jenis lateks getah asli dicirikan dalam bentuk lateks menggunakan Mikroskop Imbasan Alam Sekitar (ESEM). Selepas itu perubahan morfologi selepas pembentukan filem diperhatikan menggunakan Mikroskop Elektron Imbasan Medan (FESEM). Sebelum pembentukan filem, dalam bentuk lateks, getah asli terepoksi menunjukkan perbezaan yang ketara dalam morfologi partikel lateks dan susunan berbanding lateks getah asli ammonia kandungan tinggi. Selepas itu, setelah filem terbentuk, analisis mikroskop menunjukkan ketidaksamaan tertentu antara filem lateks getah asli kandungan tinggi ammonia dan lateks getah asli terepoksi terutamanya kelompok partikel. Ia mendedahkan bahawa filem bagi lateks getah asli kandungan tinggi ammonia menunjukkan partikel lateks berbentuk sfera jelas lebih besar di permukaan filem berbeza dengan partikel lateks yang lebih kecil sebagaimana yang berlaku di filem lateks getah asli terepoksi. Kajian ini memberi gambaran tentang perbezaan dalam pembentukan filem di antara lateks getah asli kandungan tinggi ammonia dan lateks getah asli terepoksi, yang juga boleh mempengaruhi sifat – sifat yang terhasil filem lateks getah dan produk getah.

Kata kunci: lateks getah asli kandungan tinggi ammonia, lateks getah asli terepoksi, pembentukan filem, partikel lateks

Introduction

Natural rubber (NR) is an elastomer which has been commercially available for nearly a hundred years and it comes with unique physical and chemical properties which are suitable for tires, gloves, condoms, adhesives and etc. [1]. The application of NR in such products hinges on its ability to undergo strain-induced crystallisation which results in high tensile, tear and fatigue properties [2].

The introduction of chemical modification in NR is carried generally to improve properties, such as oil resistance in order to extend NR latex areas of application and as a new material [2, 3]. One of the chemical modifications is epoxidation which converts NR to epoxidised NR (ENR). Through epoxidation, oxirane (epoxide) is introduced where oxygen atom is added to the unsaturated NR carbon- carbon double [4]. ENR is commercially available in two grades namely ENR-25 (25 mole % epoxide) and ENR-50 (50 mole % epoxide).

Even though epoxidation of NR has been started in 1922 [5], the literatures on ENR latex state is deemed inadequate. This is probably due to the application of ENR was more towards dry rubber application hence more of the research approaches are focused on dry rubber [6-10]. With regards to ENR latex state, information is still lacking especially on latex particle arrangement and film formation.
With regards to the use of microscopy to study rubber, there are research adequate works which described the use of electron microscopy to study rubber latex particle [11-13], however still much of the work utilised dry state latex thin films in their study. The investigation on latex particles morphology using ESEM in the latex or aqueous state and consequently the latex particles packing in films using FESEM has not been yet attempted so far. Hence, in this preliminary work, visualization of chemically modified NR and the subsequent film was carried out by using ESEM and FESEM. The average of latex particles also calculated in this present work.

Materials and Methods

Materials

Concentrated high ammonia natural rubber latex (HA-NRL) was purchased from Lee Rubber, Malaysia Epoxidised natural rubber (ENR 1) and epoxidised natural rubber (ENR 2) latex were obtained from Development of Specialty Rubbers and New Rubber Program, Malaysia Rubber Board with epoxidation level 25% mole. For dilution purposes, distilled water was used throughout the study.

Latex particle morphology using ESEM

HA-NRL and ENR sample and distilled water were mixed in Eppendorf tube prior shaking for a few minutes. Then, the solution was centrifuged for 10 minutes. After that, sample was collected then osmium tetroxide was used to stain the sample. The sample was left to dry for several hours before washing and centrifugation. Then, the sample was ready for ESEM viewing. The morphology of particles was analysed using an ESEM (FEI Quanta). Then, the average of particle size was calculated using ImageJ software (NIH, Freeware).

Film formation and particles packing using FESEM

HA-NRL and ENR samples were stained with osmium tetroxide prior to FESEM analysis. The sample was then air dried in the desiccators on sample stub before coating with thin layer of platinum. Then, surface area of latex film was analysed using FESEM (JOEL JSM-6701F) at 5000 magnification.

Results and Discussion

Latex particle morphology

The ESEM micrographs in Figure 1(a, c, e) present different latexes at latex state. Figure 1a which represents HA-NRL particles packing showed the existence of both spherical and pear shaped latex particles similar with previous studies on NR latex [11-12, 14] where small particles were in spherical or egg shape and large particles were in pear shape. The latex particles were randomly distributed where agglomeration of latex particles could be observed in a close arrangement of latex particles. The large latex particles which in pear shaped were shown to be clustered by smaller latex particles.

After epoxidation (Figure 1c), the arrangement of latex particles changed and agglomeration of particles appeared to be reduced. The latex particles were no longer closer to each other. As result to epoxidation, based on the

micrographs the shape of latex particles could be observed in circular and smaller size only. The pear shaped particle could not be detected in the micrographs (Figure1c and 1e).

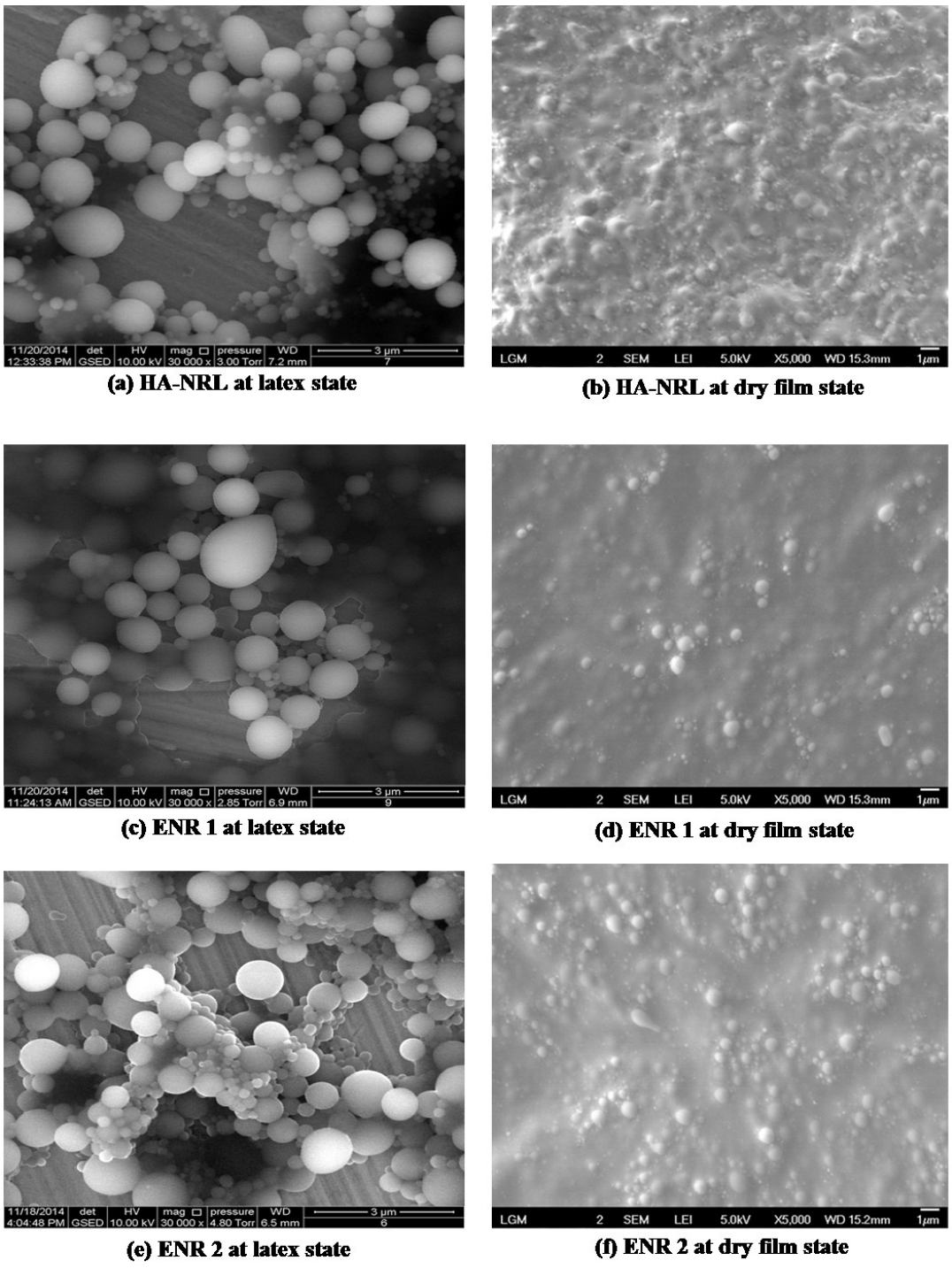


Figure 1. ESEM (a, c, e) and FESEM (b, d, f) micrographs showing of different latexes at various magnification for latex and dry film state.

Meanwhile, for Figure 1e, as could be seen the arrangement of particles was different to Figure 1c where the particles were closer to each other and clustering of smaller particles in between large particles could be seen clearly. The spherical shaped latex particles could be observed whilst the small particles were agglomerated to each other formed larger particles. The similar phenomenon also observed in this micrograph where the pear shaped latex particle could not be observed. This is because ENR 1 and ENR 2 had undergone epoxidation with different propriety processing process. Thus, this could lead to different particle arrangement as seen in the micrographs. So, based on the findings, it is suggested that epoxidation on natural rubber latex has given some effect to latex particles shape and also modified the arrangement of latex particles.

The average of latex particles in the latex state is shown in Figure 2. In the present investigation, average latex size existing in the latex state was measured from the ESEM micrographs. As per stated elsewhere [15], a particle size analysis results merely in 'average' diameter, whether based a number, surface area, volume, is of limited value. The average size of latex particles was in the range of 0.5 to 1.2 μm was taken as the limiting range in this present work because *ImageJ* software has limitation to the smaller size of latex particles. From particle size analysis using laser diffraction the range of particle size for Hevea latex was around 0.01 to 5.0 μm [16] and 0.2 μm to 1.5 μm [17]. Based on Figure 2, the average of particles size between all the latex samples were not much different. This is due to the limitation of measurement by using *ImageJ*. The results were also consistent with result of previous study [15], where the distribution of average particles size based on particles diameter exhibited higher distribution between 700 to 1500 nm. This also explained the average of different latexes exhibited almost similar results to each other.
The average of particles size after drying process for HA-NRL and epoxidation natural rubber latex from FESEM micrographs was measured and the result shown in Figure 2. The trend of latex particles size distribution among HA-NRL, ENR 1 and ENR 2 was similar to result of ESEM micrographs. The size of latex particles after drying showed a reducing trend compared to the ESEM result. This result may have suggested that after drying process, the latex particles size could be reduced in size due to evaporation process at stage I and II which are deformation particles occurred [18].

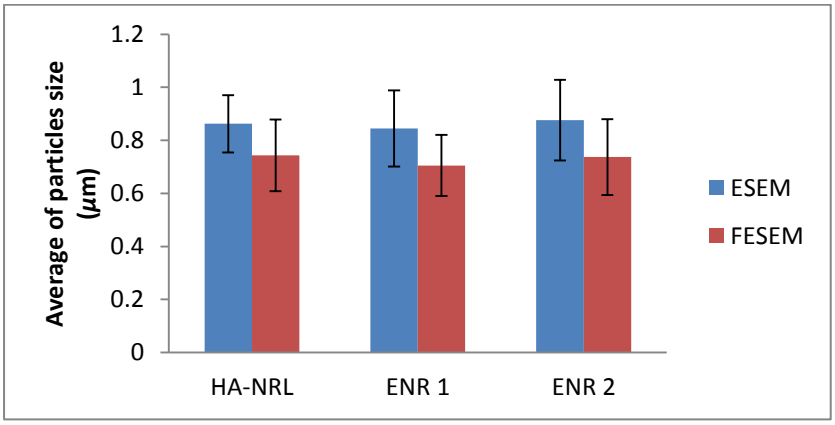


Figure 2. Average latex particles size for different latexes based at latex (ESEM) and dry state (FESEM).

Film formation and particles packing
FESEM micrographs conducted on air dried thin films obtained from HA-NRL, ENR 1 and ENR 2 latex. The features occurred on HA-NRL film were undulation with distinguished latex particles spherical shaped (Figure 1b). Clearly, the polydisperse latex particles distribution could be observed on the surface of formed HA-NRL film even though coalescence of latex particles had already occurred during drying. The core shell structure of HANRL latex particles almost diminished due to occurrences inter-particle diffusion of NR molecules. It is essential in order for

inter-particle mixing of rubber molecules takes place to ensure complete coalescence of the particles as per seen in micrograph. In this case, suggested coalescence and film formation were occurred in same time.

After epoxidation, the surface morphology the film was shown to be in different features compared to HA-NRL latex film. Based on FESEM micrographs (Figure 1d and 1f), the undulation feature on HA-NRL latex film is no longer observable. ENR 1 films exhibited a more coherence films with less distinguishable latex particles. However, in ENR 2 (Figure 1f), clusters of spherical shaped latex particles can be seen on the film surface clearly. The packing of particles could not be observed on the surface morphology in contrast with HA-NRL. This suggested that the changes in latex particles surface morphology are dependent on the type of modification. This is consistent to the ENR 1 and ENR 2 different surface morphology due to the effect processing process. It also could be suggested that inter-particle diffusion process which lead to the coalescence of the particles could be reacted different with HA-NRL.

Conclusion

The interesting findings have been observed using combination of ESEM and FESEM techniques in relation to the elucidation of latex particles arrangement in aqueous latex state and particles packing after the drying of latex to form films. In latex state, it can be suggested that epoxidation contributed to smaller size of latex particles. Subsequently after drying and when films are formed, ENR exhibited a more coherence and less undulating surface in contrast to HA-NRL film.

Acknowledgement

Permission from the Malaysia Rubber Board to present the results is gratefully acknowledged. Thanks are due to Fine Chemicals and Biomaterials staff for technical support. The assistance from Cowen Tan and Ho Oi Kuan from Crest, Malaysia is also gratefully acknowledged

References

1. Yoksan, R. (2008). Epoxidized natural rubber for adhesive applications. *Kasetstart Journal (Natural Science*), 43: 325 – 332.
2. Gelling, I. R. (1988). Chemistry, structure and properties epoxidised natural rubber. *International Rubber Technology Conference*: 415 – 427.
3. Le Bras, J. and Delalande. A. (1950). *Derives Chimiques du Caouchouc Naturel*, Paris, Dunod.
4. Fatimah Rubaizah, M. R, Ngeow, Y. W., Zairossani, M. N. and Md. Aris, A. (2008). ENR-37.5 as a new epoxidised natural rubber (ENR) grade. *International Rubber Conference & Exhibition*: 1 – 11.
5. Pummerer, R. and Burkard, P. A. (1922). On rubber. *Ber*, 55: 3458 – 3472.
6. Baker, C. S. L., Gelling, I. R. and Azemi, S. (1986). Epoxidised natural rubber. *Journal of Natural Rubber Research*, 1(2): 135 – 144.
7. Yong, K. C., Foot, P. J. S., Morgan, H., Cook, S., Tinker, A. J. and Md Aris, A. (2008). Electrically conductive epoxidised natural rubber-polyaniline dodecylbenzenesulfonate blends prepared by solution mixing. *Journal of Rubber Research*, 11(2): 59 – 77.
8. Haidzir, A. R., Gelling, I. R. and Freakley, P. K. (1994). Influence of phase morphology on the properties of natural rubber and epoxidised natural rubber blends. *Journal of Natural Rubber Research,* 9(4): 213 – 225.
9. Suhawati, I., Ismaliza I., Kamarudin A. M. and Shamsul, K. (2013). Sound absorption analysis of foamed rubber composites from kenaf and calcium carbonate. *Journal of Rubber Research*, 16(1): 36 – 44.
10. Dayang Habibah, A. I. H., Shamsul Bahri, A. R. and Nik Intan, N. I. (2013). Morphology, physical and flame retardant properties of epoxidised natural rubber (ENR) organoclay compound. *Journal of Rubber Research,* 16(2): 91 – 100.
11. Van Den Tempel, M. (1952). Electron microscopy of rubber globules in Hevea latex. *Transaction of the Institution of the rubber industry,* 28 (6): 303 – 309.
12. Gomez, J. B. and Hamzah, S. (1989). Particle size distribution in Hevea latex — Some observations on the electron microscopic method. *Journal of Natural Rubber Research,* 4(3): 204 – 211.
13. Southorn, W. A. (1960). Complex particles in Hevea latex. *Nature,* 188: 165 – 166.
14. Hauser, E. A. (1946). The morphology of rubber latex particles. A critical review. *India Rubber World*, 112(4): 461 – 463.

15. Gorton, A. D. T and Pendle, T. D. (1983). Particle size measurement of rubber latices. *Rubber Chemistry and Technology,* 56: 664 – 676.
16. Gazaley, K. F., Gorton, A. D. T. and Pendle, T. D. (1988). In latex concentrate: Properties and composition, Roberts, A.D (ed), Rubber Science and Technology, Chapter 3. Oxford University Press: 63 – 90.
17. Pendle, T. D. and Swinyard, P. E. (1991). The particle size of natural rubber latex concentrates by photon correlation spectroscopy. *Journal of Natural Rubber Research* 6 (1): 1 – 11.
18. Keddie, J. L. and Routh, A. F. (2010). In Fundamental of latex film formation; Process and properties. Parch, H. Chapter 1. Springer: 10 – 18.

Malaysian Journal of Analytical Sciences, Vol 20 No 5 (2016): 1129 - 1137
DOI: http://dx.doi.org/10.17576/mjas-2016-2005-19

MALAYSIAN JOURNAL OF ANALYTICAL SCIENCES
Published by The Malaysian Analytical Sciences Society
ISSN 1394 - 2506

SYNTHESIS OF BIO-BASED HYDROGEL FROM EPOXIDIZED PALM OIL CATALYZED BY FLUOROANTIMONIC ACID HEXAHYDRATE

(Sintesis Hidrogel Berasaskan Bio Daripada Minyak Sawit Terepoksidasi Bermangkinkan Asid Fluoroantimonik Heksahidrat)

Wan Nurhayati Wan Tajulruddin, Abdul Razak Rahmat*, Rohah Abd Majid

Department of Polymer Engineering, Faculty of Chemical Engineering,
Universiti Teknologi Malaysia, 81310 Skudai, Johor, Malaysia

**Corresponding author: k-razak@cheme.utm.my*

Received: 10 June 2015; Accepted: 21 July 2016

Abstract

An epoxidized palm oil-based hydrogel (HPEPO) was synthesized by using ring opening polymerization (ROP) in the presence of fluoroantimonic acid hexahydrate catalyst ($HSbF_6 \cdot 6H_2O$), followed by chemical hydrolysis catalyzed with sodium hydroxide (NaOH). The structural characterization and thermal property of synthesized hydrogel were studied. The successful ring opening of EPO was confirmed by disappearing of epoxy functional group at 833 cm^{-1} in the Fourier transform infrared (FTIR) spectrum. The formation of HPEPO was detected at 2500 cm^{-1} to 3400 cm^{-1} which represents the O-H stretching of carboxylic acid. Based on nuclear magnetic resonance (NMR), the disappearance of epoxy ring group at 2.8 – 3.0 ppm has indicated the completely reacted oxirane ring with the presence of peak at 3.7 ppm corresponded to hydroxyl group. Meanwhile, HPEPO exhibited low thermal stability by having melting temperature around 45 °C to 60 °C in Differential scanning calorimetry (DSC) and as showed by the great percentage of weight loss in thermogravimetric analysis (TGA) curve. However, the formation of char residue was slow, probably due to the formation of hydrogen linkages in hydrogel.

Keywords: hydrogel, epoxidized palm oil, ring opening polymerization, chemical hydrolysis

Abstrak

Hidrogel berasaskan minyak sawit terepoksidasi (HPEPO) telah disintesis menggunakan polimerisasi pembukaan cincin (ROP) dengan kehadiran asid fluoroantimonik heksahidrat ($HSbF_6.6H_2O$) sebagai pemangkin, diikuti dengan hidrolisis kimia yang dimangkinkan oleh natrium hidroksida (NaOH). Pencirian struktur dan sifat termal hidrogel yang disintesis telah dikaji. Kejayaan pembukaan cincin minyak sawit terepoksidasi (EPO) telah disahkan melalui kehilangan kumpulan berfungsi epoksi pada 833 cm^{-1} dalam spektrum Fourier inframerah (FTIR). Pembentukan HPEPO dikesan pada 2500 cm^{-1} hingga 3400 cm^{-1} yang mewakili regangan O-H daripada asid karboksilik. Merujuk kepada resonans magnetik nuklear, kehilangan cincin epoksi pada 2.8 – 3.0 ppm menunjukkan cincin oksiran telah bertindakbalas sepenuhnya dengan kewujudan puncak pada 3.7 ppm sepadan dengan kumpulan hidroksil. Sementara itu, HPEPO telah mempamerkan kestabilan haba yang rendah dengan mempunyai suhu lebur antara 45 °C to 60 °C daripada kalorimetri pengimbasan pembezaan (DSC) dan seperti yang ditunjukkan dalam kehilangan peratusan berat yang besar melalui lengkung analisis Termogravimetri (TGA). Walau bagaimanapun, pembentukan sisa arang didapati perlahan, berkemungkinan disebabkan oleh pembentukan ikatan hidrogen dalam hidrogel.

Kata kunci: hidrogel, minyak sawit terepoksidasi, polimerisasi pembukaan cincin, hidrolisis kimia

Introduction

Natural oil-based materials have been widely used in many industries due to environmental legislation and sustainability. They are used as precursors for many chemical materials such as alcohols (polyols), glycols, olefenic compounds, lubricants, plasticizers and stabilizer for polymers [1,2]. Researchers have successfully synthesized epoxidized natural oils from soybean oil [3], rubber seed oil [4], rapeseed oil [5] and linseed oil.

As one of the major producers of palm oil, Malaysia too has successfully developed epoxidized palm oil as starting materials for various industrial areas [6]. The production of macromonomer polyols through ring opening polymerization of EPO with Lewis acid in tetrahydrofuran [7] and with glycerol [8] has been reported. The benefit of EPO as a starting material is necessary to be explored progressively in order to expand the palm oil commercial value in various industrial areas. A research work completed by Ang et al. [9] have successfully synthesized polyol with high molecular weight and low hydroxyl functionality which is potentially to be used in wood adhesive applications. Clark and Hoong [7] have reported to derive macromonomer polyols from EPO by Lewis acid ring opening reactions in tetrahydrofuran (THF) solvent and reacted with MDI to furnish elastomeric polyurethanes.

This research has utilized EPO due to high reactivity of epoxy ring which can be subsequently converted into many products including polyols. An effort has been made to expand the use of EPO into new area such as hydrogel. Palm oil generally has the average 2.0 – 2.5 functionality as compared to ESO that has higher epoxy functionality. This drawback limits the use of palm oil polyol in the area that need longer molecular chain or higher molecular weight. However, the idea to introduce palm oil polyol with crosslinking network has brought the exploration of polyol into hydrogel.

Hydrogel, can be derived from many synthetic and natural polymers, possess high water absorption capacity and biocompatibility. These attractive properties contribute to wide applications such as in tissue engineering, pharmaceutical, and biomedical fields [10]. Liu et al. [11] have successfully synthesized epoxidized soybean oil (ESO) hydrogel via hydrolysis reaction.This study has adopted ring opening polymerization of EPO to prepare polymeric hydrogel in chemical hydrolysis reaction with the presence of sodium hydroxide (NaOH). The proposed reaction scheme is shown in Fig. 1. To date, no work has been done on the synthesis of hydrogel-based EPO.

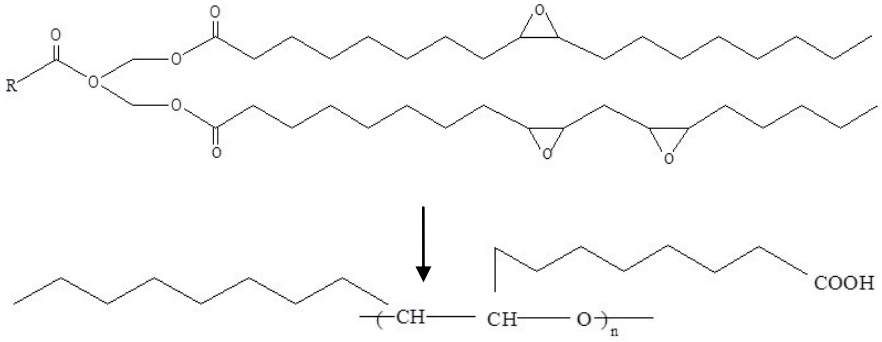


Figure 1. Scheme outlining the synthesis of HPEPO polymers

Materials and Methods

Materials

EPO with 2.7 – 2.9 % oxirane oxygen content (OOC), molecular weight of 1049 g/mol and iodine value of 0.58 eq/100 g value was supplied by Budi Oil (M) Sdn. Bhd. Fluoroantimonic acid hexahydrate catalyst ($HSbF_6 \cdot 6H_2O$) was purchased from Sigma Aldrich while methylene chloride, sodium hydroxide, hydrochloric acid and acetic acid were obtained from Qrec Chemical Co. Ltd.

Sample preparation: *Ring opening polymerization*

EPO was reacted with methylene chloride in the presence of fluoroantimonic acid hexahydrate as catalyst for 3 hours at room temperature to obtain polyol (PEPO) under nitrogen gas environment.

Hydrolysis reaction
PEPO was refluxed in sodium hydroxide for 24 hours before filtered and cooled down to room temperature. The obtained gel was precipitated with hydrochloric acid and washed with water for several times, then washed with acetic acid twice afterwards. The resulting hydrogel (HPEPO) was dried in the oven at 80 °C overnight and further dried in vacuum oven at 70 °C and the weight was measured for every 20 minutes until it reached a constant weight.

Characterization: *FTIR measurements*
Samples of the EPO, PEPO and HPEPO were analyzed using KBr plates. The IR spectra of these samples were recorded on Perkin Elmer IR spectrometer at room temperature with scanning range of 4000 to 400 cm^{-1} for 16 scans.

NMR measurements
The ^{1}H NMR spectrum for the EPO, PEPO and HPEPO samples were recorded quantitatively using a NMR spectrometer model of a Bruker Avance II 400 MHz UltraShield.

DSC measurements
The test was conducted using a DSC-6 Perkin-Elmer on PEPO Aand HPEPO. Samples were placed in the aluminium pan and were scanned from - 60 ^{o}C to 150 ^{o}C and the heating rate of 10 ^{o}C/min.

TGA measurements
A thermogravimetric analysis of the PEPO and HPEPO was carried out on TG (Mettler Toledo, TGA/SDTA851) under nitrogen atmosphere from 30 °C to 600 °C at heating rate of 10°C/min.

Results and Discussion

FTIR analysis
FTIR spectra of EPO, PEPO and HPEPO are presented in Fig. 2. The epoxy group of EPO at 833 cm^{-1} was disappeared in PEPO and HPEPO, indicated the ring opening reaction of epoxy was successfully achieved. Meanwhile, the ester carbonyl band of PEPO (1737 cm^{-1}) has shifted to the lower band in HPEPO (1710 cm^{-1}), implying the formation of strong hydrogen bonding of carboxylic acids dimers in HPEPO. Denisov et al. [12] found that hydrogen bonding and resonance have weaken the C:O bond, resulting in absorption at a lower frequency. Furthermore, a very broad peak observed at around 2500 cm^{-1} to 3400 cm^{-1} which represented the O-H stretching of carboxylic acid, supported the formation of HPEPO hydrogel.

NMR analysis
NMR was done to confirm the formation of polyol. Figures 3, 4 and 5 exhibit the ^{1}HNMR spectrum of EPO, PEPO and HPEPO respectively. From Fig. 3, the highest peak at 1.00 – 1.30 ppm belongs to the CH_2 proton in the fatty acid moiety. The presence of epoxy ring was detected by the peaks at 2.8-3.0 ppm. Meanwhile, the peaks that appeared at 2.7-2.9 ppm were corresponding to the proton adjacent to epoxy cyclic ring groups. Fig. 4 shows the ^{1}HNMR spectrum of PEPO produced. The proton peaks at epoxy cyclic ring group at 2.8-3.0 ppm disappeared and a new small signal at 3.7 ppm has emerged which indicated the presence hydroxyl group of the opened epoxy ring. Similarly, the spectrum of HPEPO in Fig. 5 has shown that there were no peaks from epoxy groups detected, indicating that the epoxy ring has completely reacted.

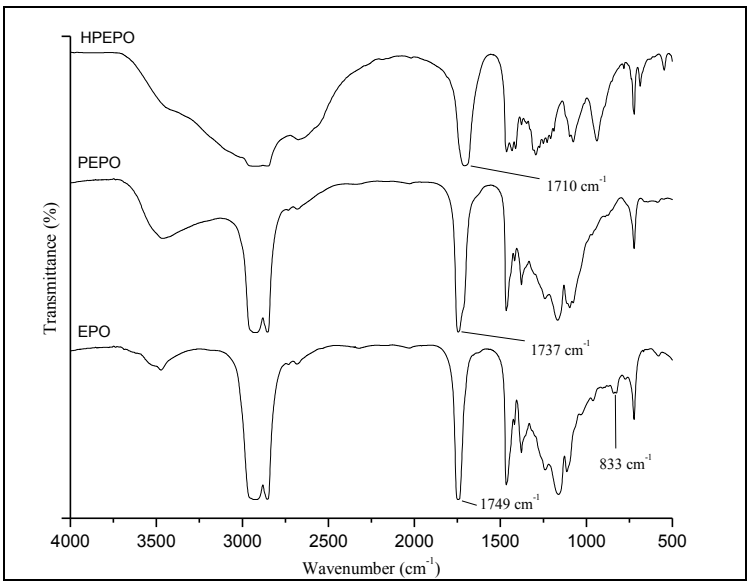


Figure 2. IR spectra for EPO, PEPO and HPEPO

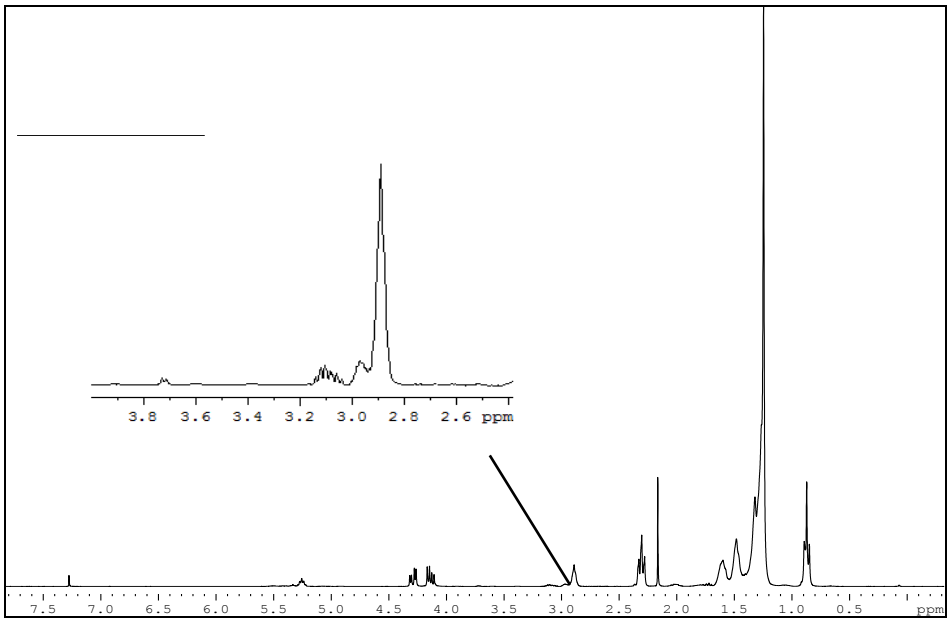


Figure 3. [1]HNMR spectra of EPO

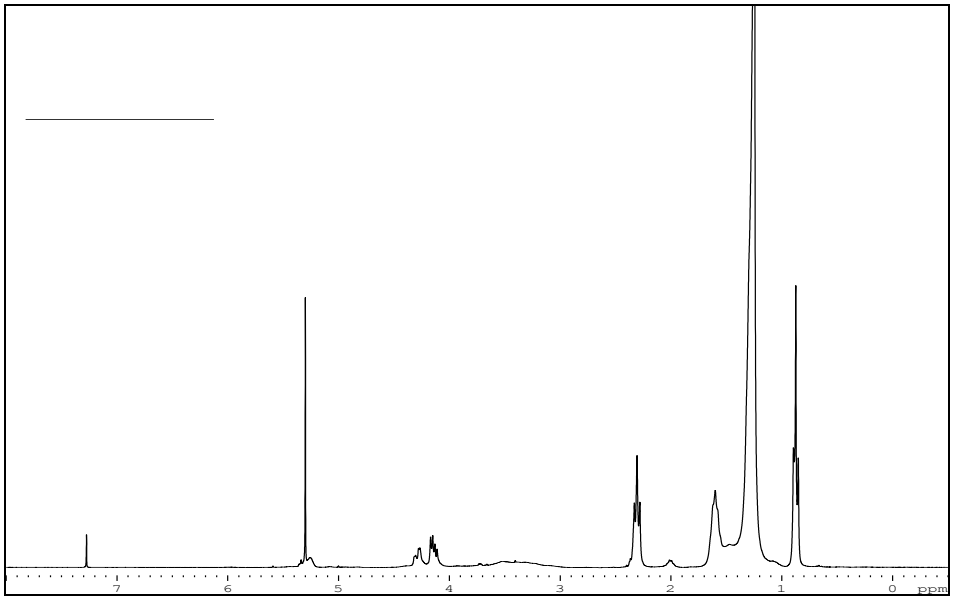


Figure 4. ^{1}HNMR spectra of PEPO

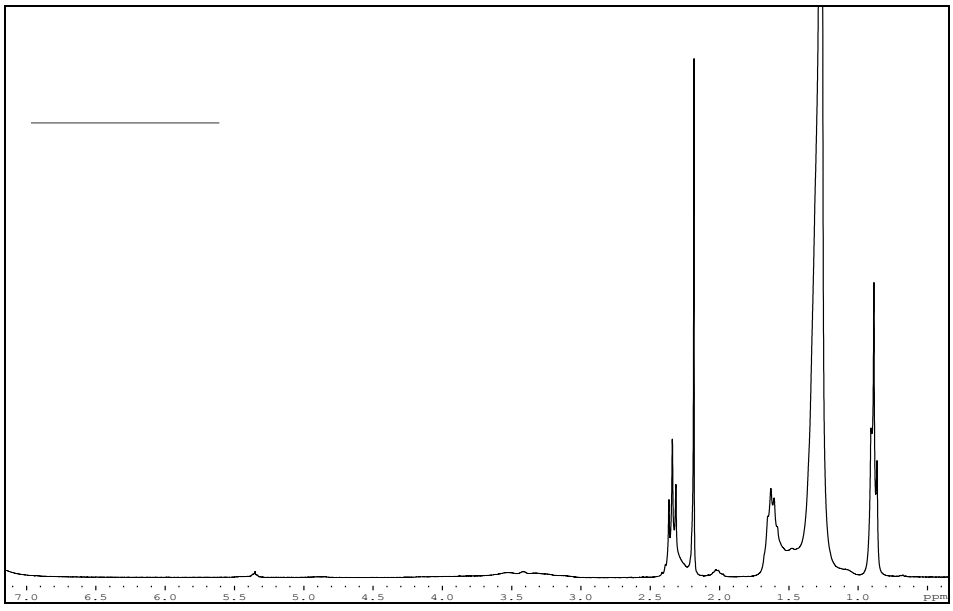


Figure 5. ^{1}HNMR spectra of HPEPO

Differential Scanning Calorimetry

Figure 6 shows the DSC thermograms of PEPO and HPEPO samples. Corresponding to an endothermic process, it can be seen that the DSC heating thermograms of the PEPO and HPEPO samples have shown positive peaks. From the graph, the melting temperature, T_m for PEPO was observed to be at 10 °C while HPEPO has higher in a range between 45 to 60 °C . As related to previous findings reported by Zhang et al.[13] and Rashmi et al. [14], bio-based polyols are typically have low melting temperature due the domain that consists of soft segments that crosslink to

each other. According to Wang and Schuman [15], the composition of the polymer within the cross linked structure plays an important role in thermal behavior, with the inherently flexible structure of fatty acid chain in PEPO reducing the crosslink density to form a less compact crosslinked structure compared to HPEPO. As a result, a polymer with low crosslink network increased its free volume and reduced its viscosity, leading to the decrease in T_m.

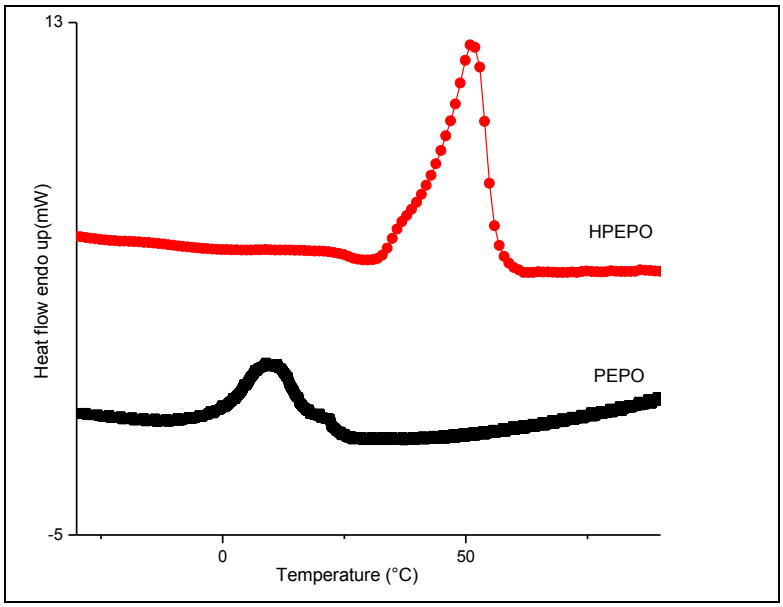


Figure 6. DSC thermograms of PEPO and HPEPO

Thermogravimetric analysis

Fig. 7 shows the TGA curves of PEPO and HPEPO. It can be seen both PEPO and HPEPO exhibited three degradation steps, related to the decomposition of polyunsaturated, monounsaturated and saturated fatty acids as both are palm oil based products, similar to most edible oils [16]. The decomposition in PEPO was not that obvious in the first region with a gradual reduction of weight loss at 5 wt%. On the contrary, HPEPO showed a sharp drop of plateau at about 40 wt%. This is thought due to the synthesis of HPEPO which involves hydrolysis reaction that caused the breakdown of ester linkage [17]. Furthermore, the release of volatile compounds such as hydrocarbon and carboxylic acid also contributes to the great weight loss of the sample [16]. In the second step, PEPO exhibited higher weight loss at 50 wt% compared to 40 wt% weight loss in HPEPO in the temperature ranges from 270 to 390 °C. As illustrated in Fig. 8, the weight loss fell sharply in PEPO as showed by a resolved peak of derivative TG (DTG) curve. In the third step, the char residue formed at above 400 °C, where about ca. 90 wt% and 95 wt% losses occurred in HPEPO and PEPO. However, the rate of degradation of HPEPO was slightly slower than PEPO, probably due to more hydrogen linkages that formed in the hydrogel apart from saturated fatty acids.

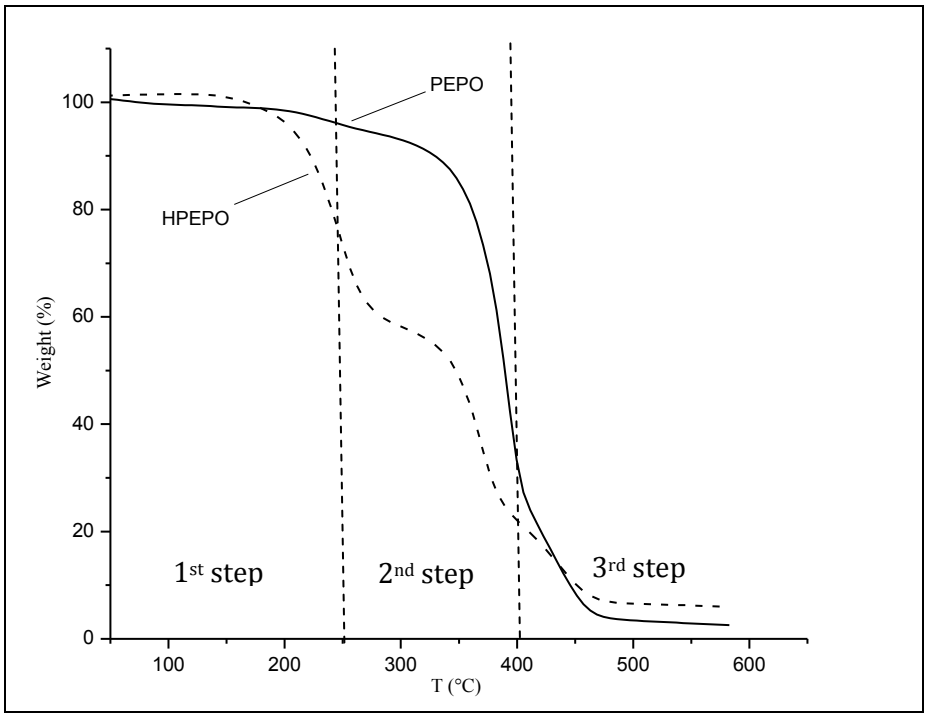


Figure 7. TGA thermogram of PEPO and HPEPO weight loss versus temperature

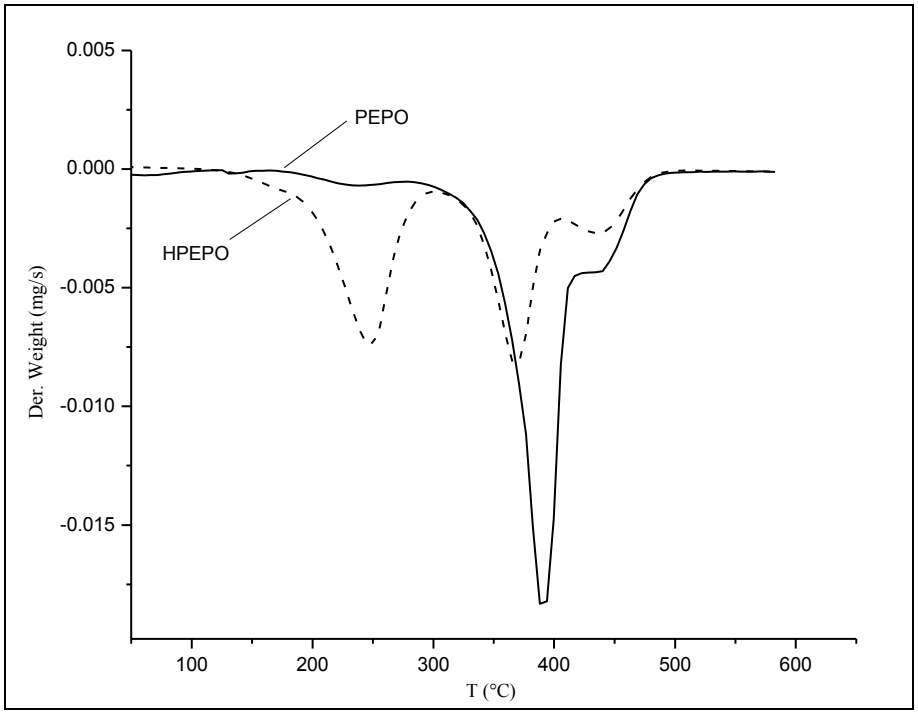


Figure 8. Derivative TG of PEPO and HPEPO versus temperature

Conclusion

The structural and thermal characteristics of epoxidized palm oil based hydrogel were studied. The epoxy ring in EPO had been successfully opened; evidently form the disappearance of 833 cm^{-1} epoxy characteristic band from FTIR spectrum. The formation of hydrogel HPEPO was confirmed with the detection of –OH stretching peaks of carboxylic acid at 2500 cm^{-1} to 3400 cm^{-1}, respectively. This is supported in NMR analysis where the disappearance of epoxy ring group at 2.8 – 3.0 ppm has indicated the completely reacted oxirane ring with the presence of peak at 3.7 ppm corresponded to hydroxyl group. Meanwhile, HPEPO exhibited melting temperature around 45 °C to 60 °C with low thermal stability in the first and the second degradation regions as showed by the great percentage of weight loss against PEPO. However, the formation of char residue was slower in HPEPO, probably due to hydrogen linkages that need higher temperature to be broken.

Acknowledgement

The authors would like to give appreciation for the financial support by the Ministry of Higher Education (MOHE) with FRGS Grant (No:4F215) and Universiti Teknologi Malaysia for providing facilities as this research was conducted.

References

1. Michael, A. R. M., Jurgen, O. M. and Ulrich, S. S. (2007). Plant oil renewable resources as green alternatives in polymer sciences. *Chemical Society Reviews,* 36: 1788 – 1802.
2. Seniha, G. F., Yusuf, Y. A. and Tuncer, E. (2006). Polymer from triglyceride oils. *Progress in Polymer Science,* 31: 633 – 670.
3. Petrovic, Z. S., Zlatanic, A., Lava, C. C. and Sinadinovic-Fiser, S. (2002). Epoxidation of soybean oil in toluene with peroxy acetic and peroxy formic acids-kinetics and side reactions. *European Journal of Lipid Science and Technology,* 104: 293 – 299.
4. Okieimen, F.E., Bakare, O.I., and Okieimen, C.O. (2002). Studies of epoxidation of rubber seed oil. *Industrial Crops and Products,* 15: 139 – 144.
5. Milchert, E. Smagowicz, A. and Lewandowski, G. (2010). Optimization of the reaction parameters of epoxidation of rapeseed oil with peracetic acid. *Journal Chemical Technology and Biotechnology,* 85:1099 – 1107.
6. Vinay, S. and Kundu, P. P. (2006). Addition polymers from natural oils – A review. *Progress in Polymer Science,* 31: 983 – 100.
7. Clark, A. J. and Hoong, S. S. (2013). Copolymers of tetrahydrofuran and epoxidized vegetable oils: Application to elastomeric polyurethanes. *Polymer Chemistry,* 5(9): 3238 – 3244.
8. Yahaya, S. M., Mohd, A. F. and Mohamed, R. (2013). Synthesis and characterization of palm oil based polyol. *Advance Materials Research,* 812: 275 – 280.
9. Ang, K. P., Lee, C. S., Cheng, S. F. and Chuah, C. H. (2013). Synthesis of palm-oil based polyester polyol for polyurethane adhesive production. *Journal of Applied Polymer Science,* 131: 1 – 8.
10. Hoare, T. R. and Kohane, D. S. (2008). Hydrogel in drug delivery: progress and challenges. *Polymer,* 49: 1993 – 2007.
11. Liu, Z. S. and Erhan, S. Z. (2010). Ring-opening polymerization of epoxidized soybean oil. *Journal of Americal Oil Chemical Society,* 87: 437 – 444.
12. Denisov, G. S., Mavri, J. and Sobczyk, L. (2006). Potential energy shape for the proton motion in hydrogen bond reflected in Infrared and NMR spectra. The Netherlands : Springer – Dordrecht.
13. Zhang, L., Huang, M., Yu, R., Huang, J., Dong, X., Zhang, R. and Zhu, J. (2014). Bio-based shape memory polyurethanes (Bio-SMPUs) with short side chains in the soft segment. *Journal of Materials Chemistry A*, 2(29): 11490 – 11498.
14. Rashmi, B. J. Rusu, D. Prashantha, K. Lacrampe, M. F. and Krawczak, P. (2013). Development of bio-based thermoplastic polyurethanes formulations using corn-derived chain extender for reactive rotational molding. *Express Polymer Letters*, 7 (10): 852 – 862.
15. Wang, R. and Schuman, T. P. (2013). Vegetable oil-derived epoxy monomers and polymer blends: A comparative study with review. *Express Polymer Letters,* 7(3) : 272 – 292.

16. Souza, A. G. D., Santos, J. C. O., Conceição, M. M., Silva, M. C. D. and Prasad, S. (2004). A thermoanalytic and kinetic study of sunflower oil. *Brazilian Journal of Chemical Engineering,* 21: 265 – 273.
17. Vashist, A., Shahabuddin, S., Gupta, Y. K. and Ahmad, S. (2013). Polyol induced interpenetrating networks: chitosan-metylmethacrylate based biocompatible and pH responsive hydrogels for drug delivery system. *Journal of Materials Chemistry B.* 1: 168 – 178.

Malaysian Journal of Analytical Sciences, Vol 20 No 5 (2016): 1138 - 1144
DOI: http://dx.doi.org/10.17576/mjas-2016-2005-20

MALAYSIAN JOURNAL OF ANALYTICAL SCIENCES
Published by The Malaysian Analytical Sciences Society
ISSN 1394 - 2506

VIBRATION EXPOSURE ANALYSIS OF POLYDIMETHYLSILOXANE REINFORCED SILICA DERIVED RICE HUSK ASH

(Kajian Pendedahan Getaran Terhadap Polidimetilsiloksana yang Diperkuat Silika Dari Abu Sekam Padi)

Mohd Azham Azmi*, Mohd Syahmi Muin @ Marsayid, Shahruddin Mahzan, Sufizar Ahmad, Hariati Taib

Faculty of Mechanical and Manufacturing Engineering,
Universiti Tun Hussein Onn Malaysia, 86400 Parit Raja, Batu Pahat, Johor, Malaysia

**Corresponding author: azham@uthm.edu.my*

Received: 10 June 2015; Accepted: 21 July 2016

Abstract

The study investigates the vibration and mechanical properties of rice husk silica (RHS) in enhancing the properties of Polydimethylsiloxane (PDMS). The PDMS/RHS composites panel were fabricated by using casting technique and cured at room temperature. PDMS panels were filled with 2 – 12 wt% of RHS. Vibration analysis of PDMS/RHS composites panel were guided by ISO 8662 standard in evaluation of hand arm vibration for hand grinder machine. The vibration exposure analysis showed that application of PDMS/RHS as a vibration absorber successfully decreased the vibration exposure to 46%. Tensile properties analysis conducted using ASTM D412 standard showed that the PDMS/10 wt% RHS properties increased to 9.6% compared to PDMS without RHS. Thus it is concluded that the addition of RHS had improved both properties of PDMS. RHS has successfully acts as a reinforcement when load is applied to the panel and during vibration exposure, RHS has acts as an absorber and distributed the vibration.

Keywords: polydimethylsiloxane, vibration exposure, rice husk silica, tensile properties

Abstrak

Kajian ini dijalankan untuk mengenalpasti sifat – sifat getaran dan tegangan silika sekam padi (RHS) yang digunakan untuk meningkatkan sifat – sifat polidimetilsiloksana (PDMS). Panel komposit PDMS/RHS dihasilkan menggunakan kaedah tuangan dan dirawat pada suhu bilik. Panel PDMS di isi dengan RHS sebanyak 2 – 12 wt%. Analisa getaran panel komposit PDMS/RHS dikendalikan menurut piawaian ISO 8662 bertujuan menilai pendedahan getaran pada tangan bagi penggunaan mesin canai tangan. Keputusan analisa terhadap pendedahan getaran menunjukkan bahawa penggunaan PDMS/RHS sebagai penyerap getaran telah berjaya menurunkan pendedahan getaran sebanyak 46%. Analisa sifat – sifat tegangan yang dijalankan berpandukan piawaian ASTM D412 menunjukkan sifat - sifat PDMS/10 wt% RHS telah meningkat sebanyak 9.6% jika dibandingkan dengan PDMS tanpa RHS. Ini menunjukkan bahawa penambahan RHS telah meningkatkan kedua – dua sifat PDMS. RHS telah berjaya bertindak sebagai penguat apabila beban dikenakan pada panel dan bertindak sebagai penyerap dan penyebar apabila getaran dikenakan.

Kata kunci: polidimetilsiloksana, pendedahan getaran, silika sekam padi, sifat terikan

Introduction

The importance of improving the PDMS vibration properties is to offer a new invention or solution in decreasing the transmitted vibration to human body. Powered tools such as hand powered tools will expose the operators to hand arm vibration syndrome (HAVS) which lead to neurological and/or vascular disorders separately or

simultaneously. Exposure to hand-transmitted vibration can also occur from vibrating work pieces held in the hands of the operator, and from hand-held vibrating controls such as hand grinder [1].

Particulate polymer composites offer interesting mechanical, physical, mixing process and rheological properties resulting from polymer matrix and filler dispersed phase interaction. Polymer matrix and filler requires specific equipment in order to achieve uniform dispersion of fillers in the polymer matrix [2]. The importance of filler addition on polymer is to modify latter properties, either mechanical properties for example stiffness, modulus, etc. or physical properties for conductivity or density or rheological properties such as viscoelasticity or viscosity [3]. This study focuses on improving PDMS properties by usage of silica filler. PDMS or so called as silicone rubber will be filled with naturally derived silica produced *via* rice husk burning. Several previous studies have shown that filling PDMS with reinforced filler will enhance PDMS in terms of its vibration absorption, mechanical and chemical properties [4].

Materials and Methods

RHS derivation

The derivation of the RHS starts by cleaning the rice husk using tap water to remove impurities. Next, wet rice husk was dried in the sun. Dried rice husk converts to RHS by burning process at 700˚C using furnace.

Composites fabrication

PDMS (Dow Jones Xiameter, USA) was applied as matrices and RHS as the reinforcement. Closed mold casting technique had been used to fabricate the composites panel. The PDMS/RHS composites panels were cured at room temperature.

Molecular analysis

Fourier transform infrared spectroscopy (FTIR) was conducted by using Perkin Elmer FTIR Spectrum 100 Spectrometer, USA to analyze the molecular in PDMS/RHS composite panels. Testing specimen preparation and procedures were conducted as per ASTM D2702 - Standard practice for rubber chemicals - determination of infrared absorption characteristics.

Tensile test

Tensile properties as tensile strength, modulus was determined via tensile testing as per ASTM D412 standard test methods for vulcanized rubber and thermoplastic elastomers. Shimadzu AG-1 10kn, Japan was used to conduct the testing. Figure 3.15 shows the Shimadzu AG 10kn universal testing machine attached with tensile jig.

Vibration Test

The vibration properties of PDMS/RHS composite panels were evaluated under BS ISO EN 8622 for testing procedure and BS ISO EN 5349 for Hand Arm Vibration (HAV) measurement. This test method used to determine the average sum frequency weighted acceleration of X, Y, and Z axis and measure the limit of daily vibration exposure of Bosch GWS 8-1 100CE hand grinder to operator. Figure 1. shows the PDMS/RHS composite panels and accelerometer were attached to hand grinder grip. Human vibration meter of Larson Davis's HVM100 were used to measure the hand arm vibration.

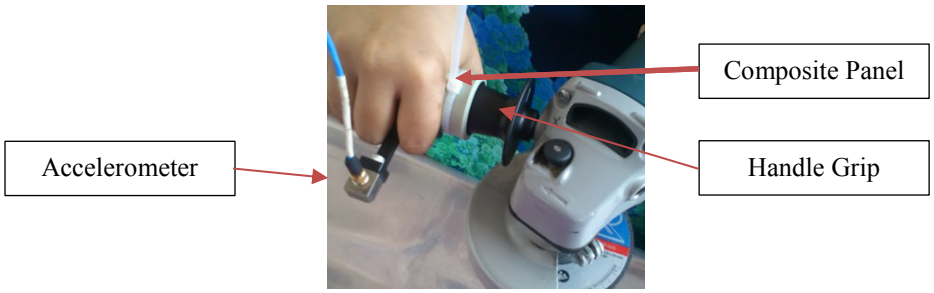


Figure 1. Hand grinder grip attached with composite panels and accelerometer

Results and Discussion

Molecular analysis

Molecular analysis *via* FTIR used to determine and confirm the existence of molecular bonding in the PDMS/RHS composite. The infrared spectra according to the RHS content ranged from 0 to 12% is shown in Figure 2. It was found that the range of wavelength observed referring to presence of PDMS and RHS is from 2963 cm^{-1} to 788 cm^{-1}. The four main peaks have a wavelength of 2968 cm^{-1}, 1260 cm^{-1}, 1012 cm^{-1} and 791 cm^{-1}. The bonds corresponding to the peaks are C-CH_3, Si-CH_3, Si-O-Si and SiO_4 bond respectively similar to observation by Shah et al. and Duo et al. [5, 6]. Those four main peaks have a wavelength of 2968 cm^{-1}, 1258 cm^{-1}, 1008 cm^{-1} and 788cm^{-1} which almost similar to previous studies [5, 6].

The trend of peaks and bonds shows the presence of hydroxyl and silanol group bonding which refer to PDMS and silica bonding respectively. The existence of –CH_3 in first peak (2968 cm^{-1}) and second peak (1260 cm^{-1}) indicated that the reaction between hydroxyl groups on the surface of RHS and PDMS has occurred. The presence of Si in third (1012 cm^{-1}) and fourth peak (791 cm^{-1}) corresponding to silanol groups on the surface of silica decreases after curing [7].

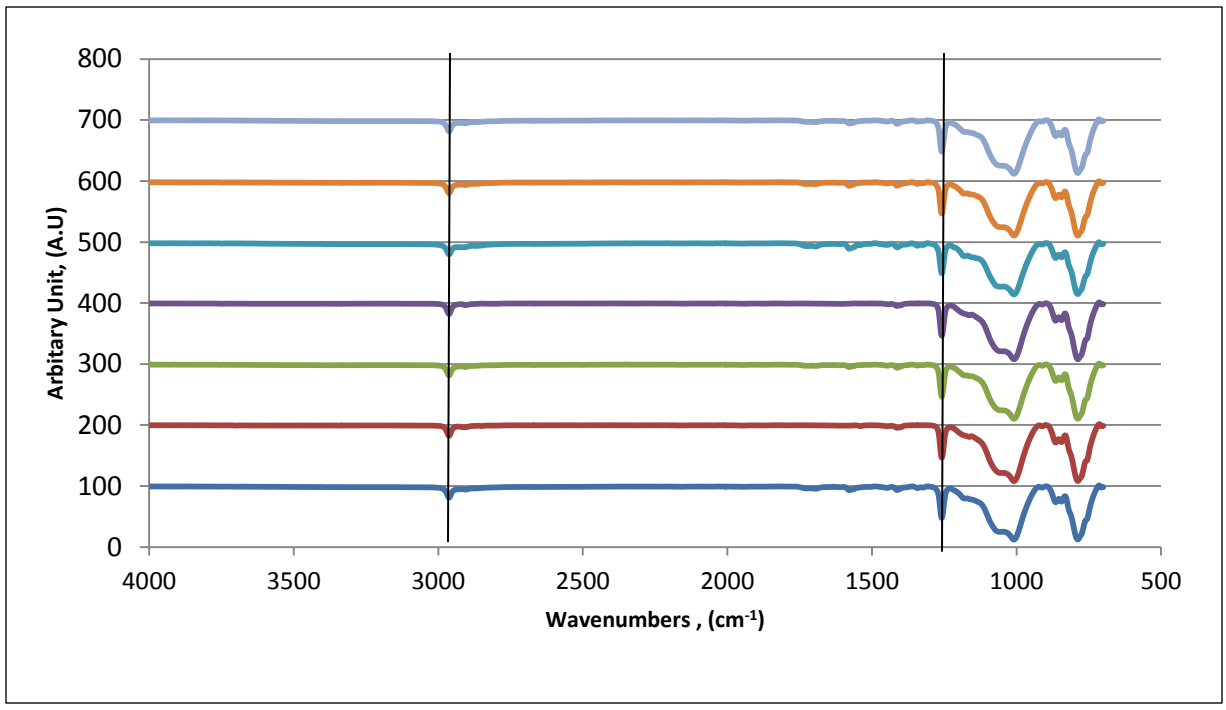


Figure 2. Infrared spectra of PDMS/RHS composite panels

Tensile properties

Tensile properties of PDMS/RHS composites were analyzed in terms of the tensile strength and modulus of elasticity. Figure 3 and Figure 4 shows the results of tensile strength and modulus of PDMS/RHS composites modulus gradually increase with increasing RHS loading. The addition of RHS had increased the tensile strength and modulus properties of PDMS from 5.311 MPa to 5.819 MPa and 1.408 MPa to 2.842 MPa respectively.

Tensile strength and modulus elasticity of composites tend to increase with increment of RHS loading up to 10 wt%. This is ascribed to the greater reinforcing ability by the RHS that may be due to excellent bonding adhesion

between matrix and filler [8]. However, a decline in tensile behavior was observed as the RHS content reaches 12 wt%. This may be due to formation of large SiO_2 aggregates caused by agglomeration of the high SiO_2 content. Subsequently these aggregates contribute to poor an inhomogeneous distribution of SiO_2 in PDMS [9].

The tensile strength and modulus shows a similar trend because of the increment of the RHS loading increased the tensile strength. The elasticity of the composites are indeed proportional to the tensile strength value. Higher tensile strength yields higher modulus of elasticity. However, the strain rate of the composites did not much improve as the addition of RHS caused the composites become stiffer [10].

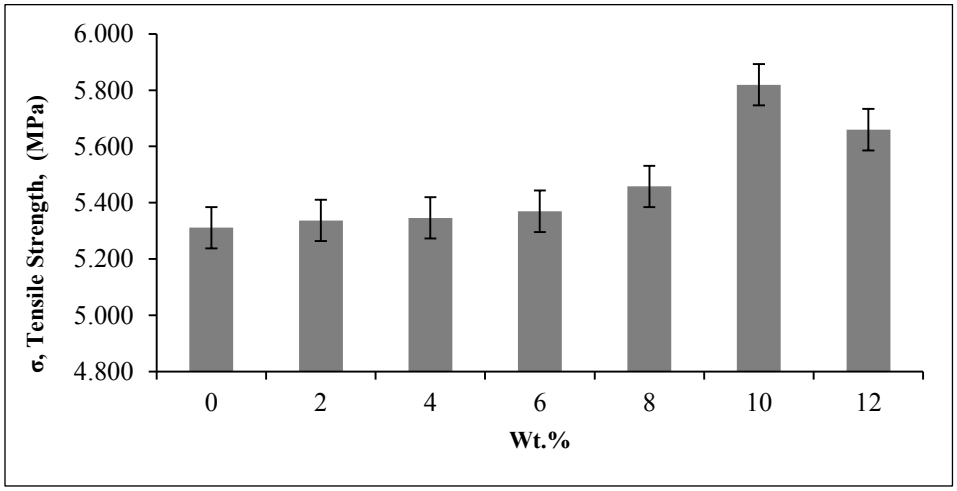


Figure 3. Tensile strength of PDMS/RHS composites

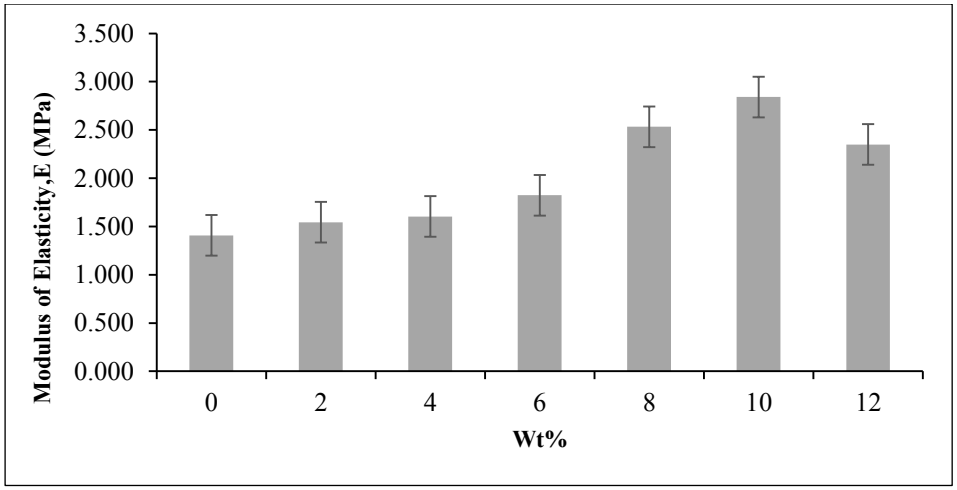


Figure 4. Modulus of PDMS/RHS composites

Vibration properties

Frequency weighted acceleration and vibration exposure time were observed in hand grinder's hand arm vibration measurement. Each measurement used different type of composite panels attachments which ranged from 0 wt% to

12 wt%. The measurement without composite panels attachment also had been studied as a reference. Fig. 5 and Fig. 6 show the results of sum average frequency weighted acceleration and vibration exposure time respectively.

The frequency weighted acceleration values were present the amount of vibration generated during measurement. From the Figure 5 the frequency weighted acceleration were progressively decreased as the filler loading increase. Maximum frequency weighted acceleration decrement occurred at PDMS/4 wt% RHS. However, the frequency weighted acceleration tends to increase at PDMS/6 wt% RHS.

Results showed that the use of PDMS composite panels had significantly decreased the frequency weighted acceleration or vibration of hand arm. The attachment of PDMS without RHS filler hand decreased the frequency weighted acceleration from 11.700 ms^{-2} to 6.360 ms^{-2}. This is due to PDMS properties itself which able to absorb the transmitted vibration [11]. The used of RHS as a filler had improve further the vibration absorption. RHS act as a filler in order to help to distribute the transmitted vibration to every surface in the composite panels body [12]. Compared to unfilled PDMS, the vibration localized at the vibration source, this lead to weak vibration distribution [13]. However, when the used of RHS exceed its limitation and above, 6wt% for this study, its turn out to be insignificant in reducing the vibration due to agglomeration and distribution of filler in the composite panels.

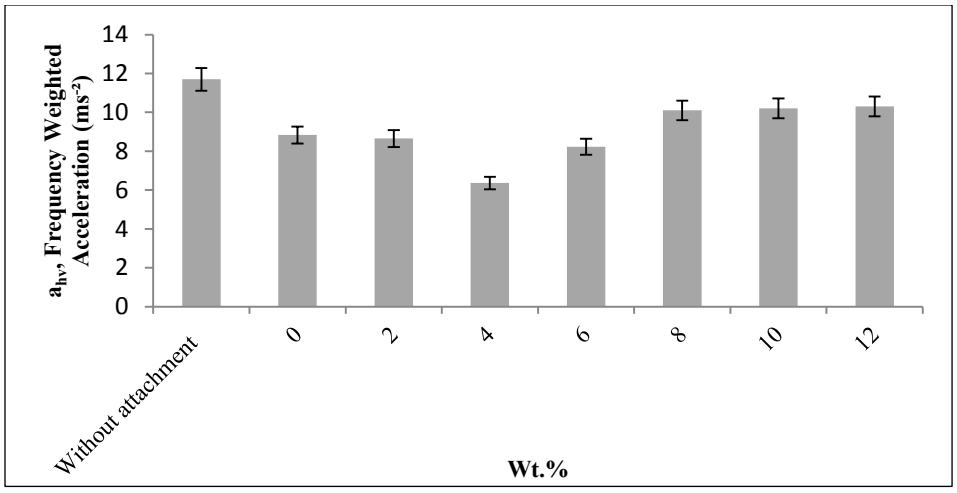


Figure 5. Sum average frequency weighted acceleration

The decrement in frequency weighted acceleration lead to lower hand arm vibration of hand grinder during operation. The lower vibration rate will helps the operator to work at longer time with less hazardous effect. Figure 6 shows the vibration exposure time as per measured during HAV measurement. Without an attachment to hand grinder grip, in 8 hours working duration per day, the operator only allowed to expose with hand grinder vibration for only 0.46 hour. By applying the PDMS/RHS composites panel the vibration exposure time had increased. The maximum vibration exposure time achieved was 1.55 hours with addition 4wt% of RHS. This enhancement will allow the operator to working or expose to the hand grinder vibration in longer duration and improve the productivity.

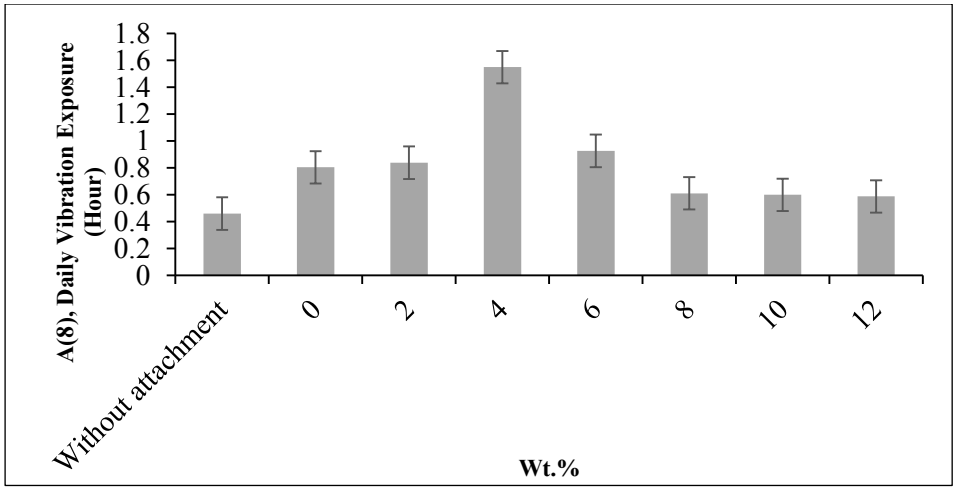


Figure 6. Vibration exposure time

Conclusion

PDMS filled with RHS were successfully fabricated via casting method and cured at 100˚C. Tensile tests revealed that RHS had improve the tensile strength and modulus with the significant enhancement at 10wt% RHS addition. PDMS/4wt%RHS composite panels also improved the productivity of hand grinder operator working hours up to 1.55 hours by reduce the vibration transmitted. This improvement had decreased health effects to the hands-transmitted vibration.

Acknowledgement

Authors are grateful for the KPT's MyBrain15 scholarship to Author 1, RAGS research grant's fund (Ref: R022) and UTHM's short term grant fund (Ref: 1273).

References

1. British Standards Institution (2001). *Mechanical vibration - Measurement and evaluation of human exposure to hand-transmitted vibration - Part 1: General requirements.* London: EN ISO 5349-1.
2. Pal, R. (2010). Rheology of Particulate Dispersions and Composites Surfactant Science. 1st ed. London: Taylor and Francis.
3. Leblanc, J. L. (2010). Filled Polymers: Science and Industrial Applications. 1st ed. Florida: CRC Press.
4. Ahmed, K., Nizami, S. S. and Riza, N.Z. (2014). Reinforcement of natural rubber hybrid composites based on marble sludge/Silica and marble sludge/rice husk derived silica. *Journal of Advanced Research*, 5(2): 165 – 173.
5. Shah, J., Yuan, Q. and Misra, R. D. K. (2009). Synthesis, structure and properties of a novel hybrid bimodal network elastomers with inorganic cross-links: The case of silicone-nanocrystalline titania. *Materials Science and Engineering A*, 523(1-2): 199 – 206.
6. Duo, S., Li, M., Zhu, M. and Zhou, Y. (2008). Polydimethylsiloxane/silica hybrid coatings protecting Kapton from atomic oxygen attack. *Materials Chemistry and Physics*. 112: 1093 – 1098.
7. Yingze, S., Jinhong, Y., Dan, D., Lixian, S. and Nan, J. (2014). Effect of silica particles modified by in-situ and ex-situ methods on the reinforcement of silicone rubber. *Materials and Design*. 64: 687 – 693.
8. Camenzind, A., Schweizer, T., Sztucki, M. and Pratsinis, S. E. (2010). Structure & strength of silica-PDMS nanocomposites. *Polymer*, 51(8): 1796 – 1804.
9. Prasertsri, S. and Rattanasom, N. (2012). Fumed and precipitated silica reinforced natural rubber composites prepared from latex system: Mechanical and dynamic properties. *Polymer Testing*, 31(5): 593 – 605.

10. Yan, Z., Yanwu, Z., Gui, L., Ruoff, R. S., Naiping H., Schaefer, D. W. and Mark, J. E. (2013). What factors control the mechanical properties of poly (dimethylsiloxane) reinforced with nanosheets of 3-aminopropyltriethoxysilane modified graphene oxide? *Polymer*, 54(14): 3605 – 3611.
11. Jones, R. G., Ando, W. and Chojnowski, J. (2001). *Silicon-Containing Polymers: The Science and Technology of Their Synthesis and Applications.* Dordrecht: Kluwer Academic
12. Carponcin, D., Dantras, E., Michon, G., Dandurand, J., Aridon, G., Levallois, F., Cadiergues, L. and Lacabanne, C. (2015). New hybrid polymer nanocomposites for passive vibration damping by incorporation of carbon nanotubes and lead zirconate titanate particles. *Journal of Non-Crystalline Solids*, 409: 20 – 26.
13. Sharma, S. K., Gaur, H., Kulkarni, M., Patil, G., Bhattacharya, B. and Sharma, A. (2013). PZT–PDMS composite for active damping of vibrations. *Composites Science and Technology*, 77: 42 – 51.

Malaysian Journal of Analytical Sciences, Vol 20 No 5 (2016): 1145 - 1152
DOI: http://dx.doi.org/10.17576/mjas-2016-2005-21

MALAYSIAN JOURNAL OF ANALYTICAL SCIENCES
Published by The Malaysian Analytical Sciences Society
ISSN 1394 - 2506

NEW PROCESS DEPROTENISED NATURAL RUBBER (PUREPRENA™): RAW RUBBER, PROCESSABILITY AND BASIC PHYSICAL PROPERTIES

(Proses Baru Getah Asli Nyah Protein (Pureprena™): Getah Mentah, Kebolehprosesan dan Sifat Fizikal)

Rohaidah Abd Rahim*, Teku Zakwan Zaeimoedin, Ahmad Khairul Muhamad and Siti Salina Sarkawi

Engineering & Technology Division,
Malaysian Rubber Board,
RRIM Research Station Sg. Buloh, 47000 Sungai Buloh, Selangor, Malaysia

**Corresponding author: rohaidah@lgm.gov.my*

Received: 10 june 2015; Accepted: 21 July 2016

Abstract

Malaysian Rubber Board has developed a new process deprotenised natural rubber (Pureprena™) by treating fresh natural latex with an industrial enzyme which hydrolyses all naturally-occuring proteins in the latex into water-soluble forms. Further research is carried out to determine the processability performance of Pureprena™ by Mooney viscometer, rubber process analyser and capillary rheometer. The Pureprena™ in bale form has low nitrogen, low ash and volatile matter contents as well as being lighter in color compared to commercial Standard Malaysian Rubber. The rheological results indicate that the Pureprena™ has a comparable rheological behavior with synthetic polyisoprene at low shear rate as determined by RPA and capillary rheometer curves. The measurement by viscometer confirms the rheological behavior at low shear rate. However, Pureprena™ has a faster mill breakdown rate compared to synthetic polyisoprene and SMR at 60 °C. All rubbers were compounded using the soluble efficient vulcanisation system especially for manufacturing engineering rubber products. It was found that Pureprena™ vulcanisate has comparable tensile strength, modulus, resilience and volume swelling in water compared to synthetic polyisoprene vulcanisate.

Keywords: deprotenised natural rubber, soluble efficient vulcanisation cure system, tangent delta, capillary rheometer, rubber process analyser

Abstrak

Lembaga Getah Malaysia telah membangunkan proses baru getah asli nyah protein (Pureprena™) dengan merawat getah asli segar menggunakan enzim perindustrian yang akan menghidrolisis semua protein semulajadi di dalam susu getah kepada bentuk larut-air. Penyelidikan lanjut dijalankan bagi menentukan prestasi kebolehprosesan Pureprena™ menggunakan viskometer Mooney, penganalisa proses getah dan reometer kapilari. Bandela Pureprena™ mempunyai kandungan nitrogen yang rendah, kandungan abu yang rendah dan kandungan jirim meruap serta warna yang lebih cerah berbanding getah komersial Getah Standard Malaysia. Keputusan reologi menunjukkan bahawa Pureprena™ mempunyai kelakuan reologi setanding dengan poliisoprena pada kadar ricih yang rendah dari ujian RPA dan keluk kapilari reometer. Pengukuran dari viskometer mengesahkan kelakuan reologi pada kadar ricih yang rendah ini. Walau bagaimanapun, Pureprena™ mempunyai kadar pecahan yang lebih pantas berbanding sintetik poliisoprena dan SMR pada suhu 60 °C. Penyebatian getah adalah menggunakan sistem pemvulkanan cekap larut khas bagi produk – produk getah kejuruteraan. Ia didapati bahawa Pureprena™ vulkanisat mempunyai kekuatan tensil, modulus, daya tahan dan pembengkakan dalam air yang setanding dengan vulkanisat sintetik poliisoprena.

Kata kunci: getah asli nyah protein, sistem pemvulkanan larut EV, tangen delta, reometer kapilari, penganalisis proses getah

Introduction

Rheological and processability properties of polymer melt are very important in processing of rubbers especially in extrusion and injection molding process due to the high shear rate and pressure involved during the process but are complicated by a number of factors such as flow rate, pressure and temperature. All these factors can affect the rheological properties of polymer and rubber melts [1, 2]. The rheology of polymer melts is considered to be one of the most important factors in determining the processability of a polymer especially for those which required good flow properties such as in calendaring, extrusion and moulding in tyre manufacturing process. Uniformity and consistency in the flow behaviour and processability of rubber are essential in providing the solution to the rubber industries in order to improve productivity, products quality and energy conservation [3]. Thus rubbers with good consistent flow and processability properties for extrusion process can improve productivity and product quality as well as reduce waste and rejects.

The new process deprotenised natural rubber (Pureprena™) has been produced through treating fresh natural latex with an industrial enzyme which hydrolyses all naturally-occuring proteins in the latex into water-soluble forms [4]. The rheological property of Pureprena™ was compared with Standard Malaysian Rubber (SMR), SMR CV which has been produced by Malaysian Rubber Board (LGM) and also synthetic polyisoprene. Both SMR grades of natural rubber were prepared from the same clonal of latex collected from the same field in Kota Tinggi Research Station, Kota Tinggi, Johor and then processed at LGM, Sg Buloh.

Therefore, this research is aim to evaluate the raw properties and processability performance of Pureprena™, SMR CV and synthetic polyisoprene in terms of raw and compound properties. Both rubbers were compounded based on a soluble efficient vulcanisation (EV) typical formulation.

Materials and Methods

Pureprena™ and SMR CV rubbers were produced by LGM. Synthetic polyisoprene, SK1-3 was supplied by Galin Enterprise. Zinc oxide, Permanax TMQ, sulphur, accelerator 1 and 2 were used as the compounding ingredients which act as activator, antioxidant, curing agent and accelerator respectively. Zinc-2-ethylhexanoate (ZEH) and Carbon black N774 were used as activator and filler purchased from Struktol and Cabot (Malaysia) Sdn Bhd., respectively.

Raw rubber properties

The raw rubber test was carried out according to Rubber Research Institute Malaysia (RRIM) internal procedure [5]. The testing were dirt content, ash content, volatile matter and nitrogen content. Ash and dirt content are a measurement of soluble and insoluble impurities in rubber. The presence of large amount of ash and dirt will affect the final rubber properties. Volatile matter determined moisture in raw rubber includes the amount of any material in the rubber which is volatile at 100 °C. A nitrogenous material in the rubber that occurs chiefly as proteins is determined through its nitrogen content. This parameter can provide an estimation of the protein content in the rubber even though it does not give a precise indication.

Processability of raw rubber

The processability study was carried out by using viscometer, Rubber Process Analyser (RPA) and capillary rheometer. The Mooney viscosity was known to be one of the instruments to measure the quality and processability of rubber by using Monsanto automatic Mooney viscometer (MV2000) at 100 °C conducted according to American Standard Testing Method (ASTM D 1646-06) [6, 7]. The viscosity was also measured after mill breakdown for 10 minutes. The effect of viscosity on high shear rate has been carried out by using capillary rheometer Rheograph 75. The capillary rheometer sample was collected after the raw rubber was passed through two roll mill for six times for homogenization and then sheeting out to 6 mm thickness. While for RPA study, the raw rubber in bale form was cut and determined based on frequency sweep mode at 100 °C, 7% strain and ranging of frequency from 0.1 to 20 Hz.

Preparation of compounds

The compounds used in this study are shown in Table 1. The compound with the soluble EV cure system were mixed in two stages in a Banbury internal mixer, BR1600 of capacity 1.6 liters at 70 rpm rotor speed and starting

temperature of 70 °C and additives were added to the master batches by using a two-roll mill at roll temperature of 50 °C. Table 1 shows the formulation used throughout this study. For the evaluation of physical properties, all compounds were cured to their respective optimum cure time, t_{95} at 150 °C by using compression moulding process.

Table 1. Typical formulation for soluble EV formulation

Ingredients	PHR
Rubber	100
N774 black	20
Zinc oxide	4
ZEH[1]	2
Permanax TMQ[2]	2
Accelerator 1	1.44
Accelerator 2	0.7
Sulphur	0.7

[1]Zinc-2-ethylhexanoate,
[2]Polymerised 2,2,4-trimethyl-1,2-dihydroquinoline

Physical properties
All testing is done according to the International Organisation of Standardisation (ISO) procedure by using equipment available in the laboratory. The measurements are hardness (ISO 48), tensile properties (ISO 37), resilience (ISO 4662), compression set (ISO 815) and volume swelling (ISO 1817).

Results and Discussion

Raw rubber properties
The raw rubber properties were analysed and the data obtained are summarised in Table 2. It can be seen in Table 2 that Pureprena™ has a low dirt contents compared to synthetic polyisoprene rubber. Synthetic polyisoprene rubber which based on petroleum has low nitrogen content and volatile matter. A nitrogenous material in the rubber that occurs chiefly as proteins is determined through its nitrogen content. This parameter can provide an estimation of the protein content in the rubber. Result indicates that synthetic polyisoprene rubber has slightly lower protein level. It confirms that deprotenised process brings down the nitrogen content and also produced clean rubber compared to SMR rubber.

Table 2. Raw rubber properties

Property	Pureprena™	Synthetic polyisoprene	SMR
Dirt retained on 44um aperture sieve (% wt, max)	0.003	0.015	0.008
Ash content (%)	0.14	0.26	0.12
Nitrogen content (% wt, max)	0.07	0.04	0.38
Volatile matter (%wt, max)	0.12	0.015	0.23

Mooney viscosity determination
Table 3 shows the Mooney viscosity (V_R) of the rubbers measured by MV2000 at temperature of 100 °C. The results show all rubbers exhibited comparable viscosity at 78.5 ± 1.5 MU. These Mooney viscosity results are in agreement with the viscosity results obtained from RPA discussed above which show that the rubbers did not show a significant difference in viscosity at low shear rate.

Table 3. Mooney viscosity of rubber

Rubber	Mooney viscosity, ML(1+4)@100 °C, MU
Pureprena™	79
Synthetic polyisoprene	77
SMR	80

The effect of viscosity after mastication for 30 minutes showed in Figure 1. It can be seen that Pureprena™ exhibited lower viscosity for all tested time which indicates of easier processing even though, all rubbers have a similar initial viscosity.

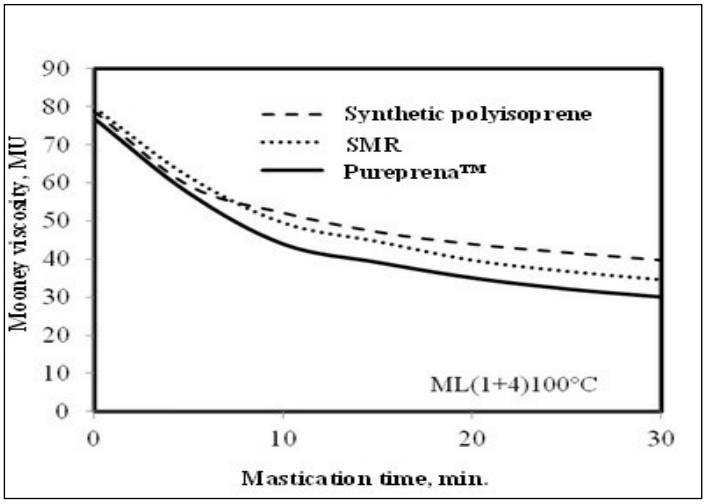


Figure 1. Mill breakdown viscosity of raw rubber determined using viscometer

Viscosity determination by RPA at low shear rate

The effect of shear rate on viscosity determined by RPA is showed in Figure 2. At low shear rate (0.05 – 9sec^{-1}) Pureprena™ , synthetic polyisoprene and SMR exhibited comparable viscosity. This confirms the viscosity behavior as measured by viscometer in Table 3.

Tan delta and elastic modulus determination

The processability characteristics of rubbers can also be assessed by the results of tan delta and elastic torque properties obtained from RPA test. For this test, the values and trend of tan delta and elastic torque with variation in the applied frequency (Hz) was studied. Although the frequency was set from 0.1 to 20 Hz, due to the limitation of the instrument, the actual shear rates applied during the RPA testing was still considered very low that is less than 25 sec^{-1} as compared to those obtained by using capillary rheometer (> 10,000 sec^{-1}). It is known that, the higher the tan delta value the better the processability of the rubber and *vice versa* [8]. It can be seen in Figure 3 that Pureprena™ and synthetic polyisoprene exhibited no significance difference in tan delta at low frequency and become significance as the frequency increased. The higher tan delta value for Pureprena™ indicates better processability than synthetic polyisoprene.

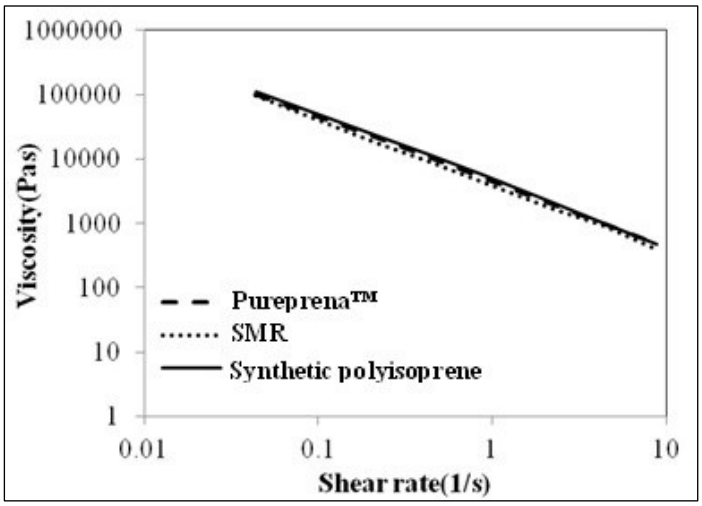


Figure 2. Viscosity responses from frequency sweep of rubbers at 7% strain at temperature of 100 °C

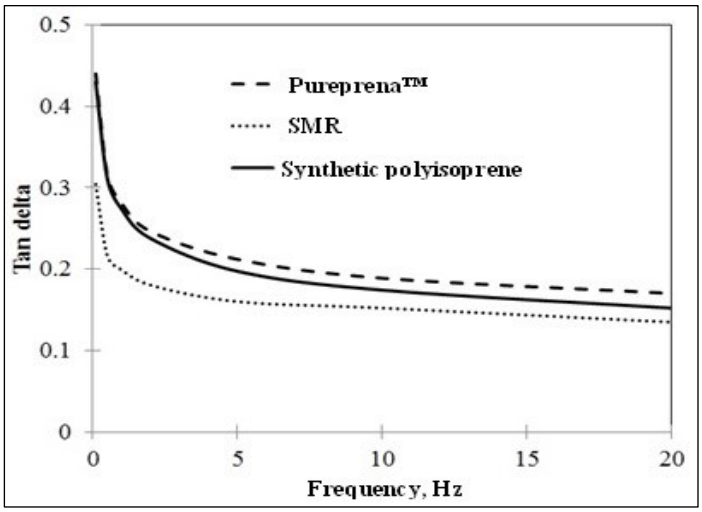


Figure 3. Tan delta response from frequency sweep of rubbers at 7% strain at temperature of 100°C

The elastic torque is the rotational force needed to deform the rubber shape. Normally, high values in elastic torque indicates poor processability of rubber and high energy is needed in its processing due to its high elastic property. As can be observed from the RPA results on raw rubbers as shown in Figure 3 Pureprena™ exhibits lower tangent delta for the range of shear rates tested as compared to synthetic polyisoprene. This is also due to lower elastic modulus of Pureprena™ compared to synthetic polyisoprena as seen in Figure 4.

Viscosity determination by capillary rheometer

The viscosity test was conducted using the capillary rheometer at 100 °C test temperature and employing high shear rates ranging from 100 to 100000 shear rate to study the actual flow behavior of rubbers when shear rate is increased. Viscosity is a measure of the resistance of a fluid (polymer) which is being deformed by shear stress. Low viscosity values indicate good processability and vice versa. For the viscosity results of raw rubber as shown

in Figure 5, it can be observed that all rubbers possess comparable viscosity at low shear rate. However, at high shear rate, synthetic polyisoprene exhibits a lower viscosity curve as compared to Pureprena™ and SMR rubber. Due to its lower viscosity results, it can be deduced that synthetic polyisoprene has lower resistance to flow and hence better flow properties compared to Pureprena™ and SMR rubber.

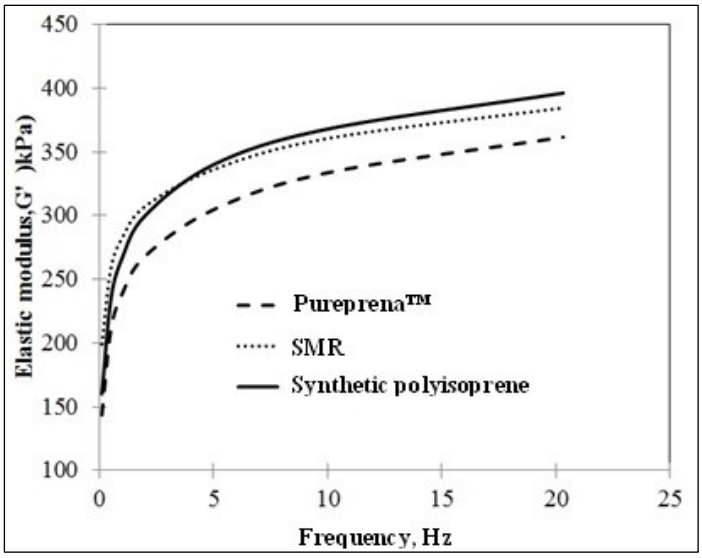


Figure 4. Elastic modulus response from frequency sweep of rubbers at 7% strain at temperature of 100 °C

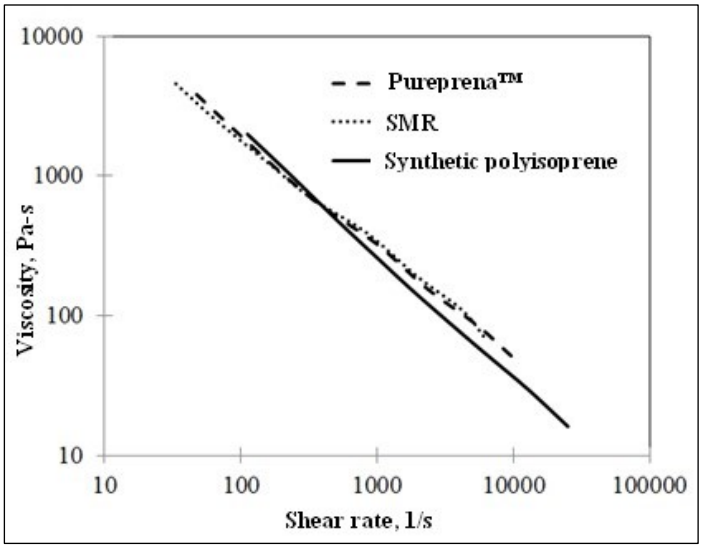


Figure 5. Viscosity of raw rubber determined using capillary rheometer

Basic physical properties of soluble EV vulcanisates

The Pureprena™ and SMR CV compounds were cured at temperature of 150 °C for 12 minutes at cure rate of 2.7 and 2.4 dNm/min, respectively. While, synthetic polyisoprene compound was cured at temperature of 150 °C for 18

minutes at cure rate of 1.6 dNm/min. The basic physical properties of the vulcanisates are shown in Table 4. It was observed that the Pureprena™ and synthetic polyisoprene exhibits almost similar tensile strength, hardness, modulus at 100% elongation, resilience and volume swelling in water. However, Pureprena™ exhibit slightly poor elongation at break and recovery behavior compared to synthetic polyisoprene. The Pureprena™ and SMR exhibited comparable basic physical properties.

Table 4. Basic physical properties of vulcanisates (cured to t_{95} at 150 °C)

Property	**Pureprena™**	**Synthetic polyisoprene**	**SMR**
Hardness, IRHD, 23°C	42	40	41
M100, MPa	0.82	0.83	0.81
M300, MPa	2.60	2.52	2.59
Tensile strength, MPa	24.29	22.64	26.10
Elongation at break, %	700	730	700
Dunlop resilience, % at 23 °C	84	84	85
Compression set, % at 22h/70 °C	12	5	11
Swelling in water, Vol. change, %			
168h/RT	0.1	0.2	0.4
72h/100°C	1.7	1.5	3.8

Conclusion

From the observations and results obtained in this study it showed that deprotenised process brings down the nitrogen content, dirt and volatile matter in the natural rubber. It also found that the new process deprotenised natural rubber produced a low dirt and ash contents compared to synthetic polyisoprene rubber. The RPA study determined that Pureprena™ exhibits better processability compared to synthetic polyisoprene through their higher tangent delta and lower elastic modulus at low shear rate. However, at high shear rate as measured by capillary rheometer, synthetic polyisoprene displayed slightly low viscosity that assumed to be better flow behaviour for the subsequent process. The Pureprena™ and synthetic polyisoprene vulcanisates exhibits comparable basic physical properties such as tensile strength, hardness, modulus at 100% elongation, resilience and water immersion.

Acknowledgement

The authors would like to thank the Management of Malaysian Rubber Board for permission to publish this paper. The assistance from staff of the Silica Dispersion Technology for Green Tyres Programme (GT) for samples preparation, mixing and processability test are gratefully acknowledged.

References

1. Brydson, J. A. (1981). Flow properties of polymer melts. 2nd Ed., George Godwin Ltd, London.
2. Wood, A. K., Read, A. G. G., Lovegrove, J. G. A. (1989). Effect of rheometer design on the measurement of the flow properties of polymer melts. *Plastics and Rubber Processing and Applications*, 12(1): 15 – 20.
3. Rohaidah, A. R. and Teku, Z. Z. (2010). Processability, rheological and physical properties of new process natural rubber. Malaysian Science and Technology Congress, Crystal Crown Hotel, Petaling Jaya, Selangor.
4. Muhamad, A. K., Nur Hidayaty, K. and Zairossani, M. N. (2008). Blue-print for Pureprena Production. Engineering & Technology Division, Malaysian Rubber Board.
5. Tong, N. Y. (1992). RRIM test method for standard Malaysian rubbers in SMR Bulletin No. 7 Revised Edition 1992. Rubber Research Institute of Malaysia.
6. Cantaloube, B. and Cocard, S. (2004). Revisiting the rheological characterisation of NR using Mooney Viscometer. *KGK Kautschuk Gummi Kunststoffe,* 57(4): 168 – 171.

7. ASTM 1646 – 06, Test method for rubber – viscosity, stress relaxation and prevulcanisation characteristics (Mooney Viscometer).
8. Teku, Z. Z., Rohaidah, A. R. and Che Su, M. S. (2011). Rheological and processability properties of new process natural rubber (NPR) for tyre application. *Malaysian Rubber Technology Development* (MRTD), 11: 3 – 16.

Malaysian Journal of Analytical Sciences, Vol 20 No 5 (2016): 1153 - 1158
DOI: http://dx.doi.org/10.17576/mjas-2016-2005-22

MALAYSIAN JOURNAL OF ANALYTICAL SCIENCES
Published by The Malaysian Analytical Sciences Society
ISSN 1394 - 2506

PLASTICIZING POLY(LACTIC ACID) USING EPOXIDIZED PALM OIL FOR ENVIRONMENTAL FRIENDLY PACKAGING MATERIAL

(Peningkatan Fleksibiliti Poli(laktik asid) Menggunakan Minyak Kelapa Sawit Terepoksi untuk Aplikasi Pembungkus Mesra Alam)

Fathilah Binti Ali[1]*, Raina Jama Awale[1], Hanan Fakhruldin[1], Hazleen Anuar[2]

[1]*Department of Biotechnology Engineering, Kulliyyah of Engineering*
[2]*Department of Manufacturing and Materials Engineering, Kulliyyah of Engineering*
International Islamic University of Malaysia, 53100 Kuala Lumpur, Malaysia

**Corresponding author: fathilah@iium.edu.my*

Received: 10 June 2015; Accepted: 21 July 2016

Abstract

Petrochemical based polymers used in packaging materials are causing various environmental problems. Therefore, biopolymers prepared from renewable sources have high potential to substitute the commercially available non-degradable polymer. Poly(lactic acid) (PLA) is one of the biodegradable polymers that can be used to substitute in the application of petrochemical-based polymers. Environmental friendly and biodegradable epoxidized palm oil (EPO) was used as plasticizer in this study and it was incorporated into PLA matrix through solution blending method. The mechanical properties were determined through three-point flexural test and tensile test. Tensile results revealed that the flexibility of PLA can be improved by the addition of epoxidized palm oil (EPO) as plasticizer in the polymer. PLA/EPO blend at ratio 100:10 showed significant flexibility among the other PLA/EPO blends. The thermal properties of neat PLA and PLA/EPO blends were characterized by using Differential Scanning Calorimetry (DSC). The glass transition temperature (Tg) decreased by addition of plasticizer, indicated the chain mobility of PLA increased in the PLA/EPO blends system. The improved flexibility of PLA by using EPO as plasticizer showed that it has high potential to be used as environmental-friendly packaging material.

Keywords: biodegradable polymer, green polymer, poly(lactic acid), environmental friendly packaging material

Abstrak

Barangan dari sumber yang boleh diperbaharui boleh mewujudkan satu platform untuk menggantikan polimer berasaskan petroleum yang diketahui tidak mampu terbiodegradasi. Poli(laktik asid) (PLA) adalah antara polimer yang boleh biodegradasi secara semula jadi dan dipercayai boleh menjadi pengganti bagi penggunaan polimer petrokimia. Pemplastik yang terbiodegradasi boleh digunakan untuk meningkatkan fleksibiliti PLA. PLA/EPO telah dicampurkan dengan nisbah tertentu dan sifat mekanikal dan haba bahan ini telah dikaji. Sifat mekanik polimer/pemplastik ditentukan melalui ujian lenturan mekanik dan ujian tegangan. Hasil kajian tegangan bahan menunjukkan bahawa fleksibiliti PLA boleh dipertingkatkan dengan penambahan minyak kelapa sawat terepoksi (EPO) sebagai pemplastik dalam polimer. Ia telah membuktikan bahawa kandungan 100:10 PLA/EPO adalah nisbah yang paling sesuai untuk campuran PLA/EPO. Ciri – ciri haba diperolehi dengan menggunakan Kalorimeter Pengimbasan Perbezaan (DSC). Pemplastik didapati mengurangkan suhu peralihan kaca PLA. EPO didapati meningkatkan tekanan tegangan dan pemanjangan di dalam PLA/EPO. Peningkatan fleksibiliti PLA menerusi penggunaan EPO membuktikan bahawa PLA/EPO boleh digunakan untuk pengunaan bungkusan mesra alam.

Kata kunci: polimer terbiodegradasikan, polimer hijau, poli(laktik asid), bungkusan mesra alam

Introduction

Flexible materials for packaging industry have been second largest contributor in the industries from way back. Ease of handling and storage, overall cost savings and convenience are among the advantages of flexible packaging. Therefore, these are the keys for its success in packaging industry. There are many polymers that are used in flexible packaging industry but mostly the polymers are non-degradable. The most common polymers utilized in the industry are polypropylene (PP), polyethylene (PE), polyvinyl chloride (PVC), polyethylene terephthalate (PET), and bi-axially oriented polypropylene (BOPP) [1].

At present, most polymeric products are derived from fossil fuels, and these products become non- degradable waste materials and remain in the environment. Consequently, extensive researches are conducted globally to create green polymers from renewable resources which are biodegradable and compostable. Biodegradable polymer is an environmental friendly polymer and has low toxicity. But, it has lower strength, brittle, flammable and high permeability to most of gases and solvents as compared to metals and ceramics, which limits its applications in industry [2, 3]. Reinforcement with additive polymers such as plasticizer and filler can overcome these problems, where the fillers need to be evenly distributed in the polymer matrix to maximize its function [3].

Biodegradable products have been used widely in food, furniture and clothing industries [5]. Therefore, the biopolymers have been researched extensively which can expand potential applications. According to Avérous and Pollet [4], biodegradable polymer is a material that decomposes into other resources such as carbon dioxide, methane, water, inorganic compounds and biomass. There are various types of biodegradable polymer which derived from renewable sources such as natural polymer (agro-polymer), microbial polymer (synthesis from microbial fermentation) and synthetic polymer (renewable bio-derived monomers) [4,5,6].

Poly(lactic acid) (PLA) is a synthetic polymer that derived from renewable sources such as starch derivative. PLA is non-toxic and has high mechanical performance compared to other commercial polymers [7]. PLA can be used for disposable packaging industry as it has good mechanical properties and processability [8,9]. However, the brittleness of PLA causes main drawback in the packaging industry [8]. Thus, many researches have been conducted to improve mechanical properties by addition of plasticizer and fiber in the polymer matrices [9]. For this research, properties of PLA had been improved by the addition of epoxidized palm oil (EPO) as plasticizer through solution blending method. Different types of solvents were utilized to solubilize PLA, in which the solvents have closest solubility parameter with PLA. Therefore, the optimum solvent was chosen to be used for mixing PLA to EPO in various ratios. The optical, thermal and mechanical properties of PLA/EPO blends were reported and discussed.

Materials and Methods

Screening Process

For screening process, the PLA beads were solubilized in different type of solvents such as chloroform, methylene chloride (DCM), dimethylformamide (DMF), tetrahydrofuran (THF) and toluene. The solvents were selected based on the solubility parameter. The PLA/EPO blends were blended at constant speed for overnight.

Samples preparation

Firstly, an amount 0.5 g of PLA was solubilized in five different solvents (chloroform, DCM, DMF, THF, and toluene). Then, 0.05 g of EPO was added into each sample and stirred overnight. The polymer blends were poured slowly into petri dishes and left evaporated at fume hood for 24 hours.

Optimization and sample preparation

Once the optimum solvent was chosen, 30 g of PLA was used to prepare PLA/EPO blends in five different ratios of PLA to EPO (100:5, 100:10, 100:15, 100:20, and 100:30) and neat PLA as reference.

Characterization

XH-406B Tablet Press Machine was used to prepare samples in 0.1 cm thickness of film at 150 °C. Shimadzu Autograph AGS-X Series was used to measure the elongation-at-break of the samples. Differential Scanning Calorimetry (DSC 822) was used to obtain the thermal properties of the samples.

Results and Discussion

Solubility of PLA/EPO blend in different solvents

Samples prepared in five different solutions was shown in Figure 1. This step is to identify the most optimum solvent that can be used for mixing and diffusivity of plasticizer in the PLA solution. Through optical observations, sample prepared from chloroform showed transparency and this indicated homogeneity of PLA and EPO in the solvent. Therefore, chloroform was chosen as the solvent and continued for next step of preparing PLA/EPO blend in different ratios.

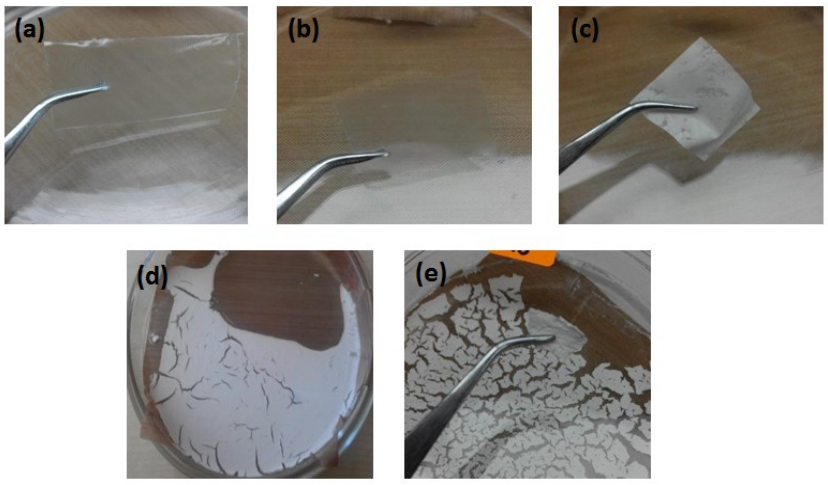


Figure 1. PLA/EPO (100:10) blends in different solutions (a) chloroform, (b) DCM, (c) THF, (d) DMF, and (e) toluene.

Flexural properties of PLA/EPO blends

Flexural strength is the limit of a material to withstand flexural stress without fail. The effects of EPO on the bending stress in the PLA/EPO blends was presented in Figure 2. The bending stress was increased from EPO 5 to EPO 10 and then reduced gradually to EPO content of 15 and 20 wt%. And then, the stress increased again when the EPO content was 30 wt%. This showed that by addition of EPO as plasticizer, it reduced the stress that the blend can endure except for PLA/EPO (100:10). At EPO content of 30 wt%, the increased stress exhibited reduced plasticizing effect at higher loading of EPO. The stress also reflected the ability of PLA/EPO blend (100:10) to resist compression and tension stress simultaneously as shown in Figure 3.

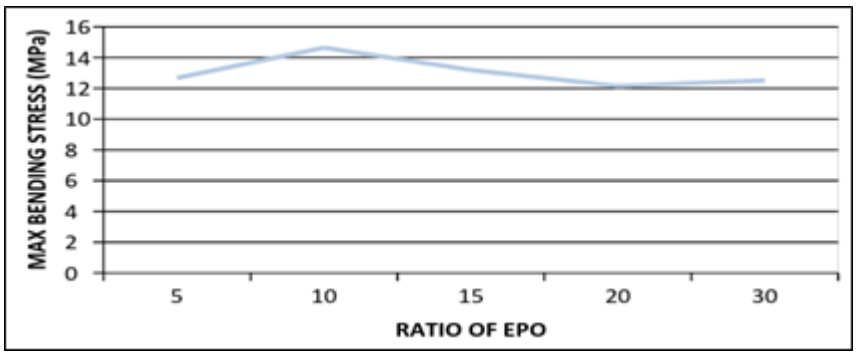


Figure 2. Bending stress of PLA/EPO blends at different ratios

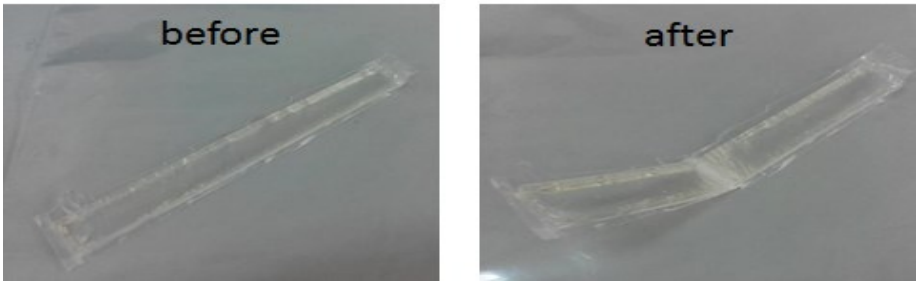


Figure 3. PLA/EPO blend (100:10) sample before and after the bending stress

Tensile properties of PLA/EPO blends

The tensile strength and elongation at break were determined at room temperature (25 °C). The stress-strain curves of neat PLA and PLA/EPO blends was shown in Figure 4. It showed that neat PLA was fractured at low strain whereas the PLA/EPO blends exhibited a ductile behavior with yield indicating plastic deformation behavior. PLA/EPO blends exhibited stress whitening behavior as shown in Figure 5. The similar stress whitening behavior was also observed in other plasticized PLA sample which was due to formation of voids in the samples [10].

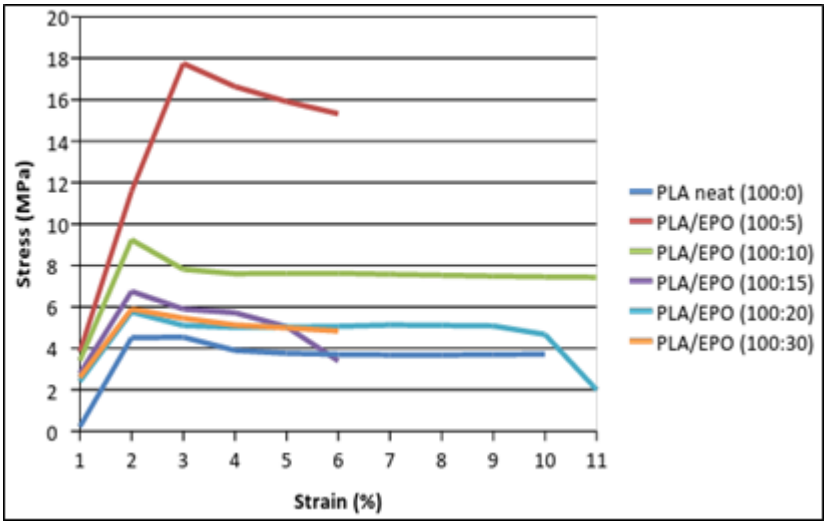


Figure 4. Stress-strain curves of neat PLA and PLA/EPO blends

The elongation-at-break of PLA/EPO blends increased due to plasticization effect of low molecular weight EPO and dispersion of EPO micro droplets in the PLA matrix [10]. The increased flexibility of the PLA/EPO blends was accompanied with decreased in tensile strength, yield stress and modulus. The yield stress of neat PLA decreased from 18.0 MPa to 9.0 MPa for 5 wt% EPO. Addition of 5 wt% EPO significantly improved the tensile strength of PLA/EPO by approximately 50%. Hence, as ratio of EPO increased, the yields stress decreased as reported by Chieng et. al [11]. Meanwhile, at EPO content of 30 wt%, the yield stress decreased to 4.3 MPa and elongation-at-break of 6%. The plasticizing effect reduced at higher loading of EPO, in this case, at 30 wt% the plasticizer has not much effect in the PLA matrix.



Figure 5. Visualization of deformed samples under tensile test

Thermal properties of PLA/EPO blends

The DSC heating thermograms of neat PLA and plasticized PLA blends was illustrated in Figure 6. The DSC curves exhibited three thermal transitions; glass transition (T_g), crystallization (T_c), and melting (T_m) temperatures. The glass transitions of PLA/EPO blends appeared at a lower temperature compared to neat PLA. The glass transition temperatures gradually decreased with increasing EPO content. The T_g of neat PLA decreased from 60.7 °C to 54.9 °C for PLA/EPO (100:15). However, for PLA/EPO (100:30), the glass transition temperature was increased to 60.84 °C. Ali et al. [10] mentioned that there will be no more decrease of T_g at greater amount of epoxidized soybean oil (ESO) in the PLA matrix. In addition, the declination of T_g also exhibited mixing of EPO soft segments into the hard segment phase of PLA. The decrease in T_g showed that there was penetration of EPO segment into the PLA hard segments and increased the chain mobility of PLA.

The crystallization temperature (T_c) of PLA also decreased by addition of EPO which indicated higher chain mobility after the incorporation of EPO. This finding was consistent with plasticized PLA reported by Ali et al. [10], that the cold crystallization temperature of PLA decreased with higher plasticizer content.

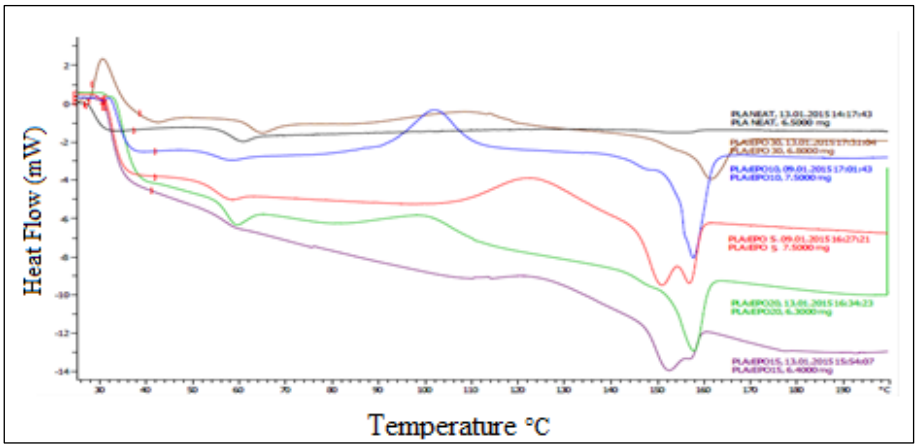


Figure 6. DSC thermograms of neat PLA and PLA/EPO blends

Conclusion

Biodegradable PLA/EPO blend film was successfully prepared through solvent blending method by using chloroform. The flexibility of plasticized PLA increased by addition of EPO and the optimum ratio of EPO was 10 wt%. Thermal properties of PLA/EPO blends showed that the glass transition (T_g), crystallization (T_c), and melting (T_m) temperatures were decreased and the chain mobility of PLA increased. The improved thermal properties of PLA using EPO eased the processability of the blend and this to ensure the blend to be used as environmental friendly packaging material.

Acknowledgement

The author thanked International Islamic University of Malaysia (IIUM) and Kulliyyah of Engineering for the support and fund (EDW B14-131-1016). Mohd Hairi bin Mohd Rasit and Haji Sukiman Sengat are thanked for helping in flexural and thermal characterizations.

References

1. Erin, H. (2009). Flexible packaging: Innovations and developments. Italian Packaging Technology Award, (2): 16 – 17.
2. Silverajah, V. G., Ibrahim, N. A., Wan Yunus, W., Abu Hassan, H. and Woei, C. B. (2012). A comparative study on the mechanical, thermal and morphological characterization of poly(lactic acid)/epoxidized palm oil blend. *International Journal of Molecular Sciences*, 13(5): 5878 – 5898.
3. Shirai, M., Grossmann, M., Mali, S., Yamashita, F., Garcia, P. and Müller, C. (2013). Development of biodegradable flexible films of starch and poly(lactic acid) plasticized with adipate or citrate esters. *Carbohydrate Polymers*, 92(1): 19 – 22.
4. Avérous, L. and Pollet, E. (2012). Biodegradable polymers. *Environmental silicate nano-biocomposites*. London: Springer-Verlag: pp. 14 – 39.
5. Anne, B. (2011). Environmental-friendly biodegradable polymers and composites. *Integrated Waste Management,* 1: pp. 25.
6. Mitrus, M., Wojtowicz, A. and Moscicki, L. (2009). Biodegradable polymers and their practical utility. *Thermoplastic starch.* Weinheim: WILEY-VCH Verlag GmbH & Co. KGaA: pp. 1 – 33.
7. Leja, K. and Lewandowicz, G. (2010). Polymer biodegradation and biodegradable polymers – A Review. *Polish Journal of Environment Studies*, 19(2): 255 – 266.
8. Al-Mullah, E. A. and Ibrahim, N. A. (2012). Poly(lactic Acid) as a biopolymer-based nano-composite. *Products and Applications of Biopolymers,* 28: pp 23.
9. Rasal, R. M., Janorkar, A. V. and Hirt, D. E. (2010). Poly(lactic acid) modifications. *Progress in Polymer Science*, 35(3): 388 – 356.
10. Ali, F., Chang, Y. W., Kang, S. C. and Yoon, J. Y. (2008). Thermal, mechanical and rheological properties of poly (lactic acid)/epoxidized soybean oil blends. *Polymer Bulletin*, 62 (1): 91 – 98.
11. Chieng, B. W., Ibrahim, N. A., Then, Y. Y. and Loo, Y. Y. (2014). Epoxidized vegetable oils plasticized poly(lactic acid) biocomposites: mechanical, thermal and morphology properties. *Molecules,* 19: 16024 – 16038.

Malaysian Journal of Analytical Sciences, Vol 20 No 5 (2016): 1159 - 1170
DOI: http://dx.doi.org/10.17576/mjas-2016-2005-23

MALAYSIAN JOURNAL OF ANALYTICAL SCIENCES
Published by The Malaysian Analytical Sciences Society
ISSN 1394 - 2506

MONTHLY ANALYSIS OF PM_{10} IN AMBIENT AIR OF KLANG VALLEY, MALAYSIA

(Analisis PM_{10} Bulanan di dalam Udara di Lembah Klang, Malaysia)

Mohd Asrul Jamalani[1], Ahmad Makmom Abdullah[1,2]*, Azman Azid[3,4], Mohammad Firuz Ramli[2], Mohd Rafee Baharudin[5], Mahmud Mohammed Bose[1], Rashieda Elawad Elhadi[1], Khaleed Ali Ahmed Ben Youssef[1], Azadeh Gnadimzadeh[1], Danladi Yusuf Gumel[1]

[1]*Air Quality and Ecophysiology Laboratory, Faculty of Environmental Studies*
[2]*Department of Environmental Sciences, Faculty of Environmental Studies*
Universiti Putra Malaysia, 43400 UPM Serdang, Selangor, Malaysia
[3]*UniSZA Science and Medicine Foundation Centre,*
Universiti Sultan Zainal Abidin, Gong Badak Campus, 21300 Kuala Nerus, Terengganu, Malaysia
[4]*Faculty Bioresources and Food Industry,*
Universiti Sultan Zainal Abidin, Tembila Campus, 22200 Besut, Terengganu, Malaysia
[5]*Department of Community Health, Faculty of Medicine and Health Sciences,*
Universiti Putra Malaysia, 43400 UPM Serdang, Selangor, Malaysia

**Corresponding author: amakmom@upm.edu.my*

Received: 14 April 2015; Accepted: 3 August 2016

Abstract

The urbanization in Klang Valley, Peninsular Malaysia over the last decades has induce the atmospheric pollution's risk resulted to negative impact on the environment. The aims of this paper are to identify the spatial-temporal relationship of particulate matter (PM_{10}), to determine the characteristic of each location and to classify hierarchical of the location in relation to their impact on PM_{10} concentration in Klang Valley. The Spearman correlation test indicate that there was strong significant relationship between all the locations (> 0.7; $p < 0.001$) and moderate relationship between Petaling Jaya-Kajang and Kajang-Shah Alam (< 0.7; $p < 0.001$). The principal component analysis (PCA) identifies all four locations have been affected by PM_{10} which were determined as one of the pollutant that deteriorated the air quality. Cluster analysis (CA) has classified the PM_{10} pattern into three (3) different classes; Class 1 (Klang), Class 2 (Petaling Jaya and Kajang) and Class 3 (Shah Alam) based on location. Further analysis of CA would be able to classify the PM_{10} classes into groups depending on their dissimilarities characteristic. Thus, possible period of extreme air quality degradation could be identified. Therefore, statistical and envirometric techniques have proved the impact of the various location on increasing concentration of PM_{10}.

Keywords: particulate matter, Spearman correlation test, principal component analysis, cluster analysis

Abstrak

Proses pembandaran di Lembah Klang, Semenanjung Malaysia sedekad lalu telah mendorong kepada risiko pencemaran atmosfera yang memberi impak negatif kepada alam sekitar. Kajian ini dilakukan bertujuan untuk mengenalpasti hubungkait antara ruang dan tempoh bagi partikel terampai (PM_{10}), menentukan ciri – ciri setiap lokasi dan menentukan pengkelasan hirarki lokasi berhubungan dengan impak kepekatan PM_{10} di Lembah Klang. Ujian korelasi Spearman menunjukkan hubungkait yang kuat antara semua lokasi (> 0.7; $p < 0.001$) dan hubungan

yang sederhana antara Petaling Jaya-Kajang dan Kajang-Shah Alam (< 0.7; $p < 0.001$). Analisis komponen utama (PCA) menentukan semua empat lokasi yang telah terjejas dengan PM_{10} iaitu antara bahan pencemar yang menjejaskan kualiti udara. Analisis kluster (CA) mengelaskan pola PM_{10} kepada tiga (3) kelas berlainan; Kelas 1 (Klang), Kelas 2 (Petaling Jaya dan Kajang) serta Kelas 3 (Shah Alam) berdasarkan lokasi. Analisis lanjutan CA membolehkan pengkelasan kelas PM_{10} kepada kumpulan bergantung kepada ketidaksamaan ciri. Justeru, kemungkinan tempoh kemerosotan kualiti udara yang melampau dapat dikenalpasti. Oleh itu, teknik statistik dan envirometrik telah membuktikan impak pelbagai lokasi terhadap peningkatan kepekatan PM_{10}.

Kata kunci: partikel terampai, ujian korelasi Spearman, analisis komponen utama, analisis kluster

Introduction

Particulate matter is one of the aerosol particles in the atmosphere [1, 2] which has an aerodynamic diameter of less than 10 μm and well known as PM_{10}. PM_{10} has been discovered as major air pollutant in Southeast Asia including Klang Valley, Malaysia [3, 4, 5]. A long term study over 5 decades regarding to air pollution brings up an implication not only to human health but also to the environment [6, 7]. Particulate matter specifically PM_{10} affects human health via inhalation due to its smaller in size and the ability to reach and settle in human respiratory tract which could induce chronic pulmonary disease and asthma [8, 9].

Asia region encounter a major problem due to air particulate matter pollution with the annual average value of total suspended particulate (TSP) which exceeding 300 μgm^{-3} [10]. In Malaysia without the haze issue, the level of PM_{10} is mostly influence by the vehicular and industrial emission [4]. Therefore, this study will define the PM_{10} level in Klang Valley region under normal condition without severe haze issue as the main focus.

Multivariate analysis has been chosen as the final statistical method to analyze, classify and interpret huge number of datasets and has become the most applicable in various field of study recently [11 - 19]. These types of analysis include the application of Principal Component Analysis (PCA) and Hierarchical Agglomerative Cluster Analysis (HACA). The PCA was applying to identify the most significant parameter which relates to spatial and temporal variation [11 - 17, 20, 21, 22]. Meanwhile, HACA was applying to group large data into cluster with differing characteristic between the groups but similar characteristic within the group [23]. Therefore, the aim of this study is to identify the spatial-temporal relationship of PM_{10}, to determine the characteristic of each station and to classify hierarchical of the station that give an impact to PM_{10} concentration in Klang Valley.

Materials and Methods

Background of sampling location

Klang Valley region involves several districts in Selangor and is located in central part of west coast Peninsular Malaysia by the Strait of Malacca to west [24, 25]. Alam Sekitar Malaysia Sdn. Bhd. (ASMA) was appointed by Malaysian Department of Environment (DOE) in establishing, operating and maintaining the continuous air quality monitoring stations. All the stations (S1, S3 and S4) were located within residential area except for Petaling Jaya (S2) which located within industrial area. All the stations within Klang Valley region were affected by heavy traffic which consequently affected by vehicles emissions and the details were shown in the Table 1. The Klang Valley Region which is situated in the central part of Selangor state is illustrated in Figure 1.

The air quality data

The daily-recorded air quality data of PM_{10} at the selected stations within the year of 2000 – 2009 were obtained from Malaysian Department of Environment (DOE). A total of 480 observation data of PM_{10} (12 observations x 4 stations x 10 years) were involved in this study.

Data cleaning

Data treatment technique has been used to treat the missing data in order to obtain a better continuous air quality monitoring data. The missing data in this study has been treated with the method of mean substitution. All the missing data are replacing with the value of mean available neighboring data [27]. Furthermore, other studies stated

that mean substitution method is better and more accurate rather than eliminating the missing value with list wise and pairwise deletion method [28, 29, 30].

Table 1. Continuous air quality monitoring stations within Klang Valley region

Station ID	Air Monitoring Station	Representative Station ID	Representative Name	Coordinates		Background
				Latitude (N)	Longitude (E)	
CA0011	SM(P) Raja Zarina, Klang	S1	Klang	3.0100°	101.4085°	Residential
CA0016	Sek. Keb. Seri Petaling, Petaling Jaya	S2	Petaling Jaya	3.1092°	101.6387°	Industry
CA0023	Country Height, Kajang	S3	Kajang	2.9939°	101.7417°	Residential
CA0025	Sek. Keb. TTDI, ShahAlam	S4	Shah Alam	3.0773°	101.5112°	Residential

Source: Department of Environment [26]

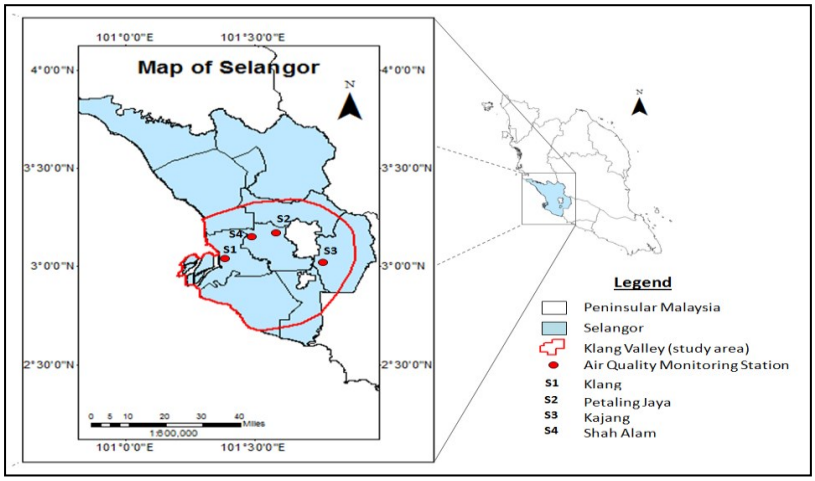


Figure 1. Map of Selangor district which include Klang Valley region

Data analysis

Several types of statistical approach include descriptive analysis, Spearman correlation analysis, principal component analysis (PCA) and cluster analysis (CA) via XLSTAT software has been used in achieving the objective. XLSTAT software has been used as a tool because of its flexibility, multidimensionality and ability to synthesize complex data sets [15]. Any missing value had been treated using mean substitution method.

Spearman correlation test

Spearman correlation test is used for determination of relationship between two variables and also known as Spearman Rho test [31, 32, 33]. This test is one of the non-parametric approaches which is suitable for not normally distributed data and would prefer monotonic graph instead of linear graph. Monotonic relationship shows that the score of variable increases with decreasing the other variables' score either in similar or different rate. The correlation values are in the range between -1 and +1 where the value only shows the strength of correlation between two variables without showing cause and consequence between those two variables [34]. However, the influence and the impact of each other variables can be described. Mathematical formula for calculating Spearman correlation is as follows;

$$r = 1 - \left(\frac{6\,\Sigma\, p^2}{N\,(N^2-1)}\right) \quad (1)$$

where p^2 is define as square root of the variable, and N is a sample size

Principal component analysis (PCA)

Principal component analysis is a procedure for identifying, reducing and arranging items into groups depending on dependent variables and the strength of correlation between those items [12, 15, 16, 35 – 39]. Linear combination of original data set is being generated by the ability of PCA in reducing large amount of data into new sets of variables where the number of principal components is not more than number of original variables [37]. Identification and observation of variation's source taking place after reduction of data set and generally written in the following mathematical equation 2;

$$PC_i = l_{1i}\,X_1 + \, l_{2i}\,X_2 + \, \ldots \, + \, l_{ni}\,X_n \quad (2)$$

where PC_i is define as i^{th} principal component, l_{ji} is define as variable loading and X_j is define as observed variable

Cluster analysis (CA)

CA is an unsupervised pattern recognition identification method, used to split a large group into smaller ones [12] based on homogeneity data. The homogeneous sub-groups will be obtained within the population and gather them into clusters based on similarity of the data [38, 40, 41]. In this study, CA was used for clustering data with the similarities in a group. CA is employed on the normal distribution dataset through the Ward's method by means of Euclidean distances, as a measure of the relationship [11, 12, 16]. The outcome of this method will be demonstrated in a dendrogram form.

Results and Discussion

Statistical analysis of PM_{10}

The monthly values of PM_{10} data in Klang Valley, Selangor have been analyzed and summarized in box plots. The PM_{10} distribution in the air is higher in Klang and Shah Alam compare to Petaling Jaya and Kajang with the range of 154.65μg/m^3 and 104.19μg/m^3 respectively. The mean of PM_{10} is also higher in Klang and Shah Alam compare to the other two stations with the value of 79.97μg/m^3 and 63.32μg/m^3 respectively. Major activities and heavy populated with residential and industrial activities are the main contributors to the higher PM_{10} value in Klang Valley region (Klang and Shah Alam). The details of descriptive statistic of PM_{10} distributions in Klang Valley region for 2000 to 2009 is shown in Table 2 and expressed by box plot in Figure 2.

Determination of air quality relationship

The monthly PM_{10} data in Klang Valley region for 10 years period (2000 to 2009) showed the result is not normally distributed. Parametric test has been used for transformation process via log method. However, the negative result still not normally distributed form. Therefore, the non-parametric test was chosen for the PM_{10} data instead of parametric test. Thus, the Spearman correlation was chosen as the non-parametric approach for determining the relationship between two variables.

Table 2. Descriptive statistic of monthly PM_{10} distributions in Klang Valley region for year 2000-2009

Station	Obs	Min	Max	Range	Q1	Median	Q3	Mean	Var (n)	Std. dev. (n)
Klang	120	39.25	193.90	154.65	55.14	68.39	95.02	79.97	1149.72	33.91
Petaling Jaya	120	26.82	116.97	90.15	45.34	54.06	67.45	58.28	316.60	17.79
Kajang	120	31.01	124.48	93.48	42.30	49.87	61.73	54.03	283.27	16.83
Shah Alam	120	29.67	133.86	104.19	44.71	58.71	80.07	63.32	535.08	23.13

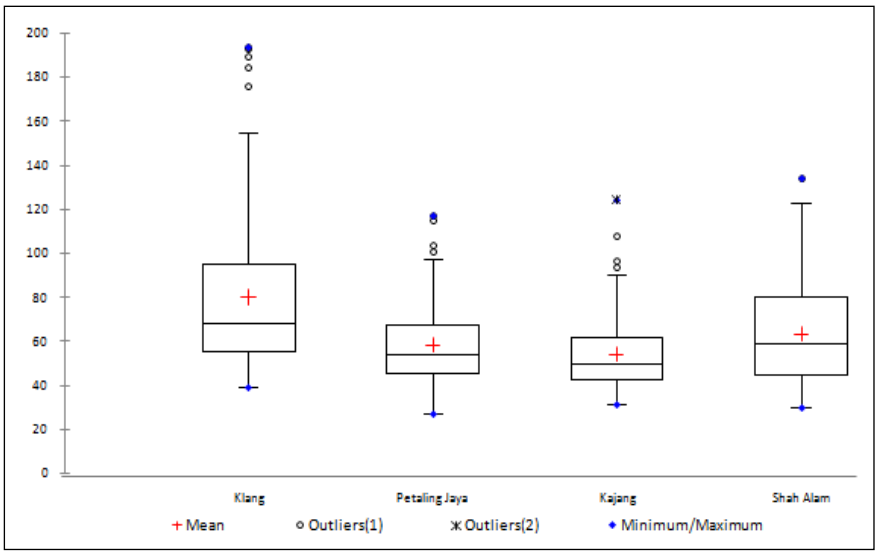


Figure 2. Box Plot of PM_{10} distributions in Klang Valley region for 10 years period (2000 – 2009)

Table 3 showed that all the stations have significant relationship. However, only Klang-Petaling Jaya, Klang-Kajang, Klang-Shah Alam and Petaling Jaya-Shah Alam prove for strong correlation between two stations with the value of 0.732($p < 0.0001$), 0.753($p < 0.0001$), 0.845($p < 0.0001$) and 0.776($p < 0.0001$) respectively. The rest, Petaling Jaya-Kajang and Kajang-Shah Alam showed moderate correlation with the value of 0.678($p < 0.0001$) and 0.602($p < 0.0001$), respectively (Table 4). Klang (S1) was shown to be the main contributor to the PM_{10} level and variation within 10 years period. Based on Malaysian Environmental Quality Report 2004 by Department of Environment, PM_{10} were originating from stationary sources where industries as the highest contributor followed by power plants and the mobile sources from motor vehicles activity [42].

Table 3. Spearman correlation of PM_{10}between Klang Valley regions for 10 years

Year	Variables	Klang	Petaling Jaya	Kajang	Shah Alam
2000-2009	Klang	**1**			
	Petaling Jaya	**0.732**	**1**		
	Kajang	**0.753**	**0.678**	**1**	
	Shah Alam	**0.845**	**0.776**	**0.602**	**1**

Values in bold are different from 0 with a significance level alpha = 0.05

Table 4. Probability value of the spearman correlation of PM_{10} between Klang Valley regions for 10 years

Year	Variables	Klang	Petaling Jaya	Kajang	Shah Alam
2000-2009	Klang	**0**			
	Petaling Jaya	**< 0.0001**	**0**		
	Kajang	**< 0.0001**	**< 0.0001**	**0**	
	Shah Alam	**< 0.0001**	**< 0.0001**	**< 0.0001**	**0**

Values in bold are different from 0 with a significance level alpha = 0.05

Air quality classification using principal component analysis (PCA)

PCA has been applied for identifying the most and less significant location that contributes to air quality in Klang Valley region. Two types of test; Keiser-Meyer-Olkin Measure (KMO) and Barlett's Test of Sphericity have been used in order to assess the sufficiency of the data [13, 37, 38]. KMO test shows the multicolinearity or in simple words, identification of similarity in correlation value exists between two or more items [15]. If there is a similarity in correlation between the items, those items will be measured in similar aspect. The benchmark's value for KMO test is agreed to be more than 0.5 [37, 38]. The KMO value for this study is 0.726 which indicate that there is no serious multicolinearity problem for the Klang Valley's PM_{10} data and suitable to construct PCA. Besides, Barlett's sphericity test also used in identification of the correlation between items and sufficiency of the data to construct the PCA with the benchmark value of less than 0.05 [13, 37, 38]. The result of Barlett'stest showed that the observed PM_{10} data are sufficient to construct PCA with the obtained p-value less than 0.0001. These two sets of test are shown in Table 5.

Table 5. Keiser-Meyer-Olkin Measure (KMO) and Barlett's Test of Sphericity

Types of PCA Test	Test's Variable	Value
Keiser-Meyer-Olkin measure of sampling adequacy		0.726
Barlett's Test of sphericity	Chi-square (observed values)	467.771
	Significant (p-value)	$p < 0.0001$

The Eigenvalue of these data is 3.391 and meet the PCA criterion because of the value larger than one (Eigenvalue > 1). The Eigenvalue shows the proportion of variance in every factor where the variance is significantly increase with increasing number of Eigenvalue [38]. Only 1 Eigenvalue was observed for the PCA analysis as shown in Table 6 because only PM_{10} observation data were used in this study. The scree plot in Figure 3 can prove that only single Eigenvalue involve in this PCA interpretation and the factor that give a large different in variance will be shown clearly by the scree plot [38].

From this study, all of the air quality stations in Klang Valley affected by anthropogenic activity as seen in the F1. From Table 6, it shows that all of the stations gave the positive and strong factor loading [Klang (0.994), Petaling Jaya (0.902), Kajang (0.914) and Shah Alam (0.923)]. Therefore, over past 10 years period (2000 – 2009), particulate matter less than 10 micron (PM_{10}) is one of the most air pollutant that contributed to air quality problem in Klang Valley region. Strong positive factor loading lead to the source of particulate matter from traffic emission in which be the major source of PM_{10} from automobiles' fuel combustion activity [37, 43]. Figure 4 shows the dot matrix position base on factor loading of each air quality stations.

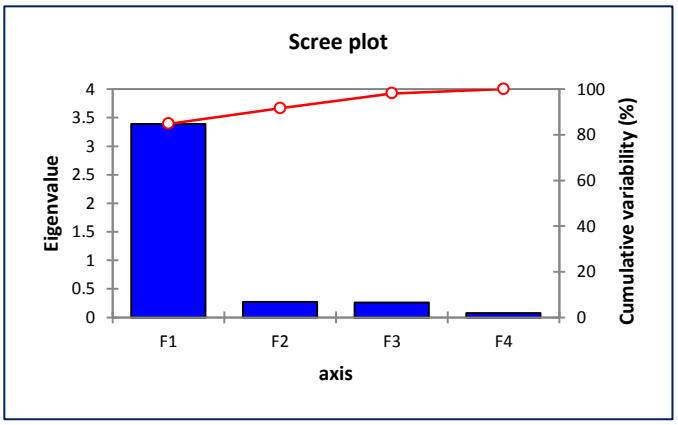


Figure 3. Scree plot of eigenvalue vs cumulative variability (%)

Table 6. Principal component analysis (PCA) interpreted result of PM_{10} data in Klang Valley

Air Quality Station	Factor Loading			
	F1	F2	F3	F4
Klang	0.944	0.141	-0.234	0.185
Petaling Jaya	0.902	-0.246	0.347	0.076
Kajang	0.914	0.356	0.152	-0.123
Shah Alam	0.923	-0.256	-0.250	-0.142
Eigenvalue	**3.391**	0.273	0.261	0.076

The principal components were then being rotated to gain better understanding and interpretation of the data. Varimax rotation was used as a criterion [37] as proposed by other author [44], with only involve the consideration of component with an eigenvalue larger than 1. The variability and cumulative variability for rotated principal component scored both 84.773%. Table 7 shows the percentage of variability and cumulative variability of the PM_{10} data after being rotated with Varimax rotation. On the other hand, Table 8 shows the percentage contribution of PM_{10} in Klang, Petaling Jaya, Kajang and Shah Alam, which are 26.27%, 23.99%, 24.62% and 25.10% respectively. Therefore, it proved that the above statement can be accepted with the average percentage contribution of 25% for each area.

Table 7. Rotated percentage of variability and cumulative variability after Varimax rotation

	F1	F2	F3	F4
Variability (%)	84.773	6.818	6.516	1.893
Cumulative variability (%)	84.773	91.591	98.107	100.000

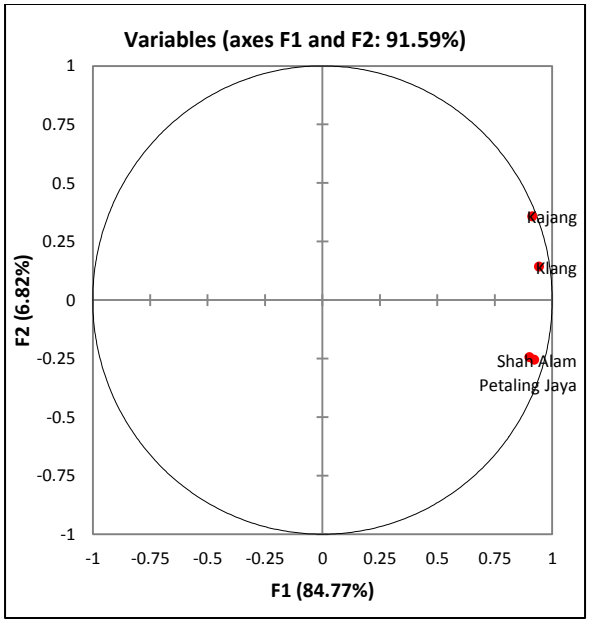


Figure 4. Dot matrix position base on factor loading of each air quality stations in Klang Valley region.

Table 8. Contribution of the variables after Varimax rotation

Contribution (%)	D1
Klang	26.27
Petaling Jaya	23.99
Kajang	24.62
Shah Alam	25.10
Average contribution	25.00
Total contribution	100.00

Air quality pattern using cluster Analysis (CA)

This study focused on four monitoring stations around Klang Valley region, where particulate matter less than 10 microns (PM_{10}) has been chosen for analysis.CA was used as an approach to find and put them into groups depending on their dissimilarity characteristics. PM_{10} pattern which obtained from PCA output have been classified into three (3) different classes; Class 1, Class 2 and Class 3 based on location and can be illustrated in dendrogram such as in Figure 5.

Class 1 refers to air monitoring station in Sekolah Menengah Perempuan Raja Zarina, Klang (CA0011) representative as Klang air monitoring station. This station contributes highest number of dissimilarity to the graph where it is performed alone and giving significant indicator of air quality. In other words, Klang can be represented as a not good air condition. Class 2 covered two different air quality stations which are located in Sekolah Kebangsaan Seri Petaling, Petaling Jaya (CA0016) represent as Petaling Jaya air monitoring station and Country Height, Kajang (CA0023) represent Kajang air monitoring station. Class 3 refers to Sekolah Kebangsaan Taman Tun Dr. Ismail, Shah Alam (CA0025) which represents Shah Alam air monitoring station.

Klang (Class 1) is located near to industrial area and a busy port area originated at Port Klang, while the other two clusters are situated near to both industrial and residential area. The study showed that the sources of pollutant in all stations are affected by motor vehicles, industrial and factories activity. The level of PM_{10} in Klang showed slightly higher concentration due to the port activity which was not found in the other stations [45].

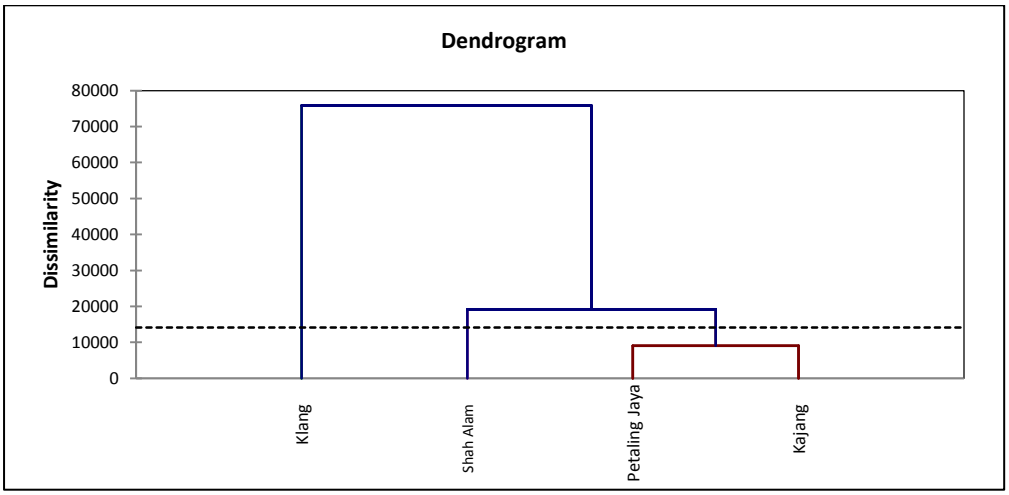


Figure 5. Dendrogram view of cluster analysis for particulate matter (PM_{10}) in Klang Valley

Characteristic of PM_{10} pattern within the Klang Valley region can be identified more using this CA method. This further analysis was discussed based on classes and the groups that might be produced. Figure 6 shows the pattern of $PM_{10}$for three different clusters in Klang Valley based on year.

Throughout the 10 years period from 2000 to 2009, Class 1 (Klang) produces three patterns of group; Group 1 (2008 and 2009) and Group 2 (2002 and 2005). Meanwhile Group 3 (2000, 2001, 2003, 2004, 2006 and 2007) had shown the highest similarity within the year. Based on year 2000 to 2009, Class 2 which refers to Petaling Jaya and Kajang produces four different patterns of group; Group 1 (2008), Group 2 (2009), Group 3 (2003, 2004 and 2005) and lastly Group 4 (2000, 2001, 2002, 2006 and 2007). Class 3 (Shah Alam) produce 3 patterns, Group 1 (2000, 2001, 2006 and 2007), Group 2 (2008 and 2009) and Group 3 (2002, 2003, 2004 and 2005). The above finding shows that the concentration of PM_{10} in the air were the highest at each station; Klang, Petaling Jaya, Kajang and Shah Alam at year 2008 and 2009.

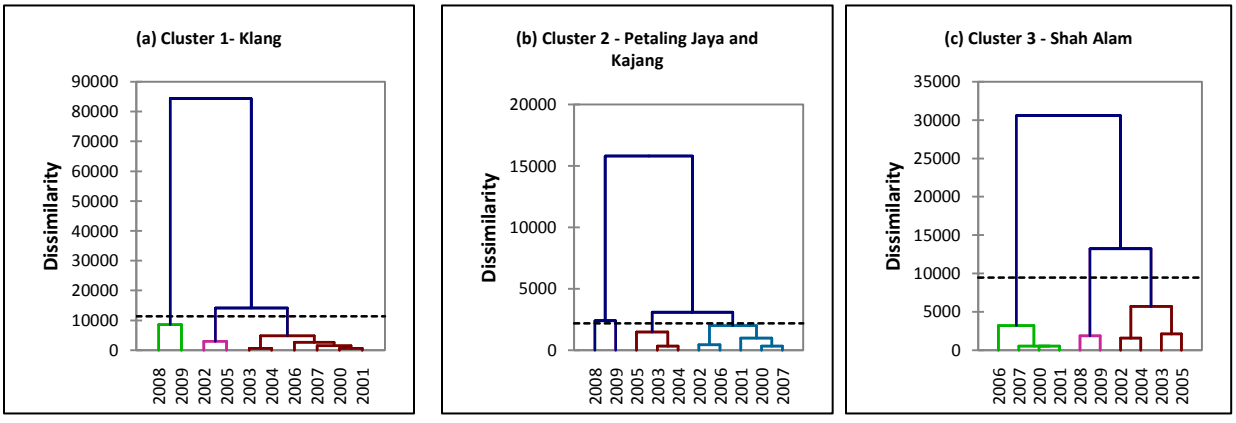


Figure 6. Dendrogram (a – c) view of PM_{10} pattern for three different clusters in Klang Valley based on year

Conclusion

Based on the result, significant relationship of particulate matter (PM_{10}) in Klang Valley, Malaysia and its pattern can be identified using statistical and envirometric technique. The relation between two variables can be determined by using Spearman Correlation Test. Strong correlations (> 0.7 with the p-value < 0.001) were obtained for all stations in determination of significant relationship between 2 stations except for Petaling Jaya-Kajang and Kajang-Shah Alam which recorded moderate correlation value 0.678($p < 0.001$) and 0.602 ($p < 0.001$) respectively. Principal component analysis (PCA) was able to identify the most and less significant location which contributing to the level of PM_{10}. The study found that all four location have been affected by PM_{10} which was determined as one of the air pollutant that contributes to the deterioration of air quality in Klang Valley. On other hand, Cluster analysis (CA) on the other hand was able to classify the PM_{10} into three groups depending on their dissimilarities characteristic. PM_{10} pattern which obtained from PCA output have been classified into three (3) different classes, Class 1 (Klang), Class 2 (Petaling Jaya and Kajang) and Class 3 (Shah Alam) based on location and possible period of extreme air quality degradation could be identified. These statistical and envirometric techniques have proved the impact of the various location on increased concentration of PM_{10}.

Acknowledgement

Gratitude and appreciation to Malaysian Department of Environment (DOE) for their provision of air quality data, and also to supervisor, committee members and colleagues for their efforts in assisting and completing this article.

References

1. Schwartz, J., Dockery, D. W., Neas, L. M., (1996). Is daily mortality associated specifically with fine particles.*Journal of the Air and Waste Management Association 46*(10): 927–939.
2. Shao, Y. P., (2000). Physics and modelling of wind erosion. Atmospheric and oceanographic sciences library, Sydney.
3. Abas, M. R. B., Oros, D. R. and Simoneit, B. R. T. (2004). Biomass burning as the main source of organic aerosol particulate matter in Malaysia during haze episodes. *Chemosphere*, 55: 1089 – 1095.
4. Afroz, R., Hassan, M. N. and Ibrahim, N. A. (2003). Review of air pollution and health impacts in Malaysia. *Environmental Research*. 92: 71 – 77.
5. Azmi, S. Z., Latif, M. T., Ismail, A. S., Juneng, L., Jemain, A. A. (2010). Trend and status of air quality at three different monitoring stations in the Klang Valley, Malaysia. *Air Quality, Atmosphere and Health,* 3: 53 – 64.
6. Gurjar, B. R., Butler, T. M., Lawrence, M. G. and Lelieveld, J. (2008). Evaluation of emissions and air quality in megacities. *Atmospheric Environment,* 42: 1593 – 1606.
7. Ozden, O., Dogeroglu, T. and Kara, S., (2008). Assessment of ambient air quality in Eskisehir, Turkey. *Environment International,* 34: 678 – 687.
8. Nawrot, T. S., Torfs, R., Fierens, F., De Henauw, S., Hoet, P. H. and Van Kersschaever, G. (2007). Stronger associations between daily mortality and fine particulate air pollution in summer than in winter: Evidence from a heavily polluted region in Western Europe. *Epidemiology and Community Health*, 61:146 – 149.
9. Mott, J. A., Mannino, D. M., Alverson, C. J., Kiyu, A., Hashim, J., Lee, Tee., Falter, K., Redd, S. C. (2005). Cardiorespiratory hospitalizations associated with smoke exposure during the 1997 Southeast Asia forest fires, *International journal of Hygiene and Environmental Health,* 2008*:* 75 – 85.
10. Baldasano, J. M., Valera, E., Jiménez, P. (2003). Air quality data from large cities. *The Science of The Total Environment*, 307: 141 – 165.
11. Azid, A., Juahir, H., Amran, M. A., Suhaili, Z., Osman, M. R., Muhamad, A., Abidin, I. Z., Sulaiman, N. H., Saudi, A. S. M. (2015). Spatial air quality modelling using chemometrics techniques: a case study in Peninsular Malaysia. *Malaysian Journal of Analytical Sciences*. 19(6): 1415 – 1430.
12. Azid, A., Juahir, H., Ezani, E., Toriman, M. E., Endut, A., Rahman, M. N. A., Yunus, K., Kamarudin, M. K. A, Hasnam, C. N. C., Saudi, A. S. M. and Umar, R. (2015b). Identification source of variation on regional impact of air quality pattern using chemometric. *Aerosol and Air Quality Research,* 15: 1545 –1558.
13. Azid, A., Juahir, H., Toriman, M. E., Endut, A., Kamarudin, M. K. A., Rahman, M. N. A., Hasnam, C. N. C., Saudi, A. S. M., Yunus, K. (2015). Source apportionment of air pollution: A case study in Malaysia. *Jurnal Teknologi,* 72(1): 83 – 88.

14. Amran, M. A., Azid, A., Juahir, H., Toriman, M. E., Mustafa, A. D., Hasnam, C. N. C., Azaman, F., Kamarudin, M. K. A., Saudi, A. S. M. and Yunus, K. (2015). Spatial analysis of the certain air pollutants using environmetric techniques. *Jurnal Teknologi,* 75(1): 241 – 249.
15. Isiyaka, H. A., Juahir, H., Toriman, M. E., Azid, A., Gasim, B. M. and Kamarudin, M. K. A. (2015). Assessment of the spatial variation and source apportionment of air pollution based on chemometric techniques: A case study in the Peninsular Malaysia. *Jurnal Teknologi,* 77(1): 33 – 44.
16. Isiyaka, H. A. and Azid, A. (2015). Air quality pattern assessment in Malaysia using multivariate techniques. *Malaysian Journal of Analytical Sciences*, 19(5): 966 – 978.
17. Azid, A., Juahir, H., Toriman, M. E., Kamarudin, M. K. A., Saudi, A.S.M., Hasnam, C. N. C., Aziz, N. A. A., Azaman, F., Latif, M. T., Zainuddin, S. F. M., Osman, M. R. and Yamin, M. (2014). Prediction of the level of air pollution using principal component analysis and artificial neural network techniques: A case study in Malaysia. *Water Air Soil Pollution*, 225(8): 1 – 14.
18. Bereton, R. (2003). Chemometrics. Data analysis for the laboratory and chemical plant. Wiley, Chichester.
19. Massart, D. L. and Kaufman, L. (1983). The interpretation of analytical chemical data by the use of cluster analysis, Wiley, New York.
20. Singh, K. P., Malik, A., Mohan, D. and Sintha, S., (2004). Multivariate statistical techniques for the evaluation of spatial and temporal variations in water quality of Chomti River (India) – a case study. *Water Research*, 38(18): 3980 – 3992.
21. Singh, K. P., Malik, A. and Sintha, S., (2005). Water quality assessment and apportionment of pollution sources of Gomti River (India) using multivariate statistical techniques – A case study. *Analytica Chimica Acta*, 538 (1-2): 355 – 374.
22. Kannel, P. R., Lee. S. R., Kanel, S. R. and Khan., S. P. (2007). Chemometrics application in classification and assessment of monitoring locations of an urban river system. *Analytica Chimica Acta*, 582: 390 – 399.
23. McKenna Jr., J. E. (2003). An enhance cluster analysis program with bootstrap significance testing for ecological community analysis. *Environmental Modelling and Software*, 8(2): 205 – 220.
24. Abas, M. R. and Simoneit, B. R. T. (1996). Composition extractable organic matter of air particle from Malaysia: initial study. *Atmospheric Environment,* 30(15): 2779 – 2793.
25. Omar, N. Y. M. J., Abas, M. R. B., Ketuly, K. A. and Tahir, N. M.(2002). Concentration of PAHs in atmospheric particle (PM_{10}) and road side soil particles collected in Kuala Lumpur, Malaysia. *Atmospheric Environment,* 36(2): 247 – 254.
26. Department of Environment (2009), Environmental quality report, Department of Environment Malaysia. Malaysia. Kuala Lumpur.
27. Tsikriktsis, N. (2005). A review of techniques for treating missing data in OM survey research. *Journal of Operations Management*, 24(1): 53 – 62.
28. Chan, L. S. and Dunn, O. J. (1972). The treatment of missing values in discriminant analysis. I. The sampling experiment. *Journal of the American Statistical Association,* 67: 473 – 477.
29. Chan, L. S., Gilman, J. A. and Dunn, O. J. (1976). Alternative approaches to missing values in discriminant analysis. *Journal of the American Statistical Association,* 71: 842 – 844.
30. Raymond, M. R. and Roberts, D. M., (1987). A comparison of methods for treating incomplete data in selection research. *Educational and Psychological Measurement,* 47: 13 – 26.
31. Saudi, A. S. M., Juahir, H., Azid, A., Toriman, M. E., Kamarudin, M. K. A., Saudi, M. M., Mustafa, A. D. and Amran, M. A. (2015). Flood risk pattern recognition by using environmetric technique: A case study in Langat river basin. *Jurnal Teknologi,* 77(1): 145–152.
32. Saudi, A. S. M., Azid, A., Juahir, H., Toriman, M. E., Amran, M. A., Mustafa, A. D., Azaman, F., Kamarudin, M. K. A. and Saudi, M. M. (2015). Flood risk pattern recognition using integrated chemometric method and artificial neural network: A case study in the Johor river basin. *Jurnal Teknologi*, 74(1): 165 – 170.
33. Saudi, A. S. M., Juahir, H., Azid, A., Kamarudin, M. K. A., Kasim, M. F., Toriman, M. E., Aziz, N. A. A., Hasnam, C. N. C. and Samsudin, M. S. (2015). Flood risk pattern recognition using chemometric technique: A case study in Kuantan river basin. *Jurnal Teknologi*, 72(1): 137 – 141.
34. Chua, Y. P. (2013), Spearman correlation test; Book 3, basic research statistic, analysis of likert scale data, Mc Graw-Hill Education (Ed. 2): pp. 242 – 262.

35. Kamaruddin, A. F., Toriman, M. E., Juahir, H., Zain, S. M., Rahman, M. N. A., Kamarudin, M. K. A., and Azid, A. (2015). Spatial characterization and identification sources of pollution using multivariate analysis at Terengganu river basin, Malaysia. *Jurnal Teknologi*, 77(1): 269 – 273.
36. Mutalib, S. N. S. A., Juahir, H., Azid, A., Sharif, S. M., Latif, M. T., Aris, A. Z., Zain, S. M. and Dominick, D. (2013). Spatial and temporal air quality pattern recognition using environmetric techniques: A case study in Malaysia. *Environmental Science: Processes Impacts*, 15: 1717 – 1728.
37. Ul-Saufie, A. Z., Yahya, A. S., Ramli, N. A., Rosaida, N., and Hamid, H. A., (2013). Future daily PM_{10} concentration prediction by combining regression models and feedwork backpropagation models with principal component analysis (PCA). *Atmospheric Environment,* 77: 621 – 637.
38. Chua, Y. P. (2009), Factor analysis and cluster analysis; Book 5, regression test, factor analysis and SEM analysis, Mc Graw-Hill Education: pp. 170 – 299
39. Abdul-Wahab, S. A., Bakheit, C.S. and Al-Alawi, S. M. (2005). Principal component and multiple regression analysis in modelling of ground-level ozone and factors affecting its concentrations. *Environmental Modelling Software*, 20: 1263 – 1271.
40. Markou, M. and Kassomenos, P. (2010). Cluster analysis of five years of back trajectories arriving in Athens, Greece. *Atmospheric Research*, 98: 438 – 457.
41. Masiol, M., Rampazzo, G., Ceccato, D., Squizzato, s., and Pavoni, B. (2010). Characterization of PM_{10} sources in coastal area near Venice (Italy): An application of factor-cluster analysis. *Chemosphere,* 80: 771 – 778.
42. Department of Environment (2011). Environmental Quality Report, Department of Environment Malaysia. Malaysia. Kuala Lumpur.
43. Ghazali, N. A., Ramli, N. A. and Yahya, A. S. (2009). A study to investigate and model the transformation of nitrogen dioxide into ozone using time series plot. *European Journal of Scientific Research* 37(2): 192 – 205.
44. Kaiser, H. F. (1958). The varimax criterion for analytic rotation in factor analysis. *Psycometrika*, 23: 187 – 200.
45. Dominick, D., Juahir, H., Latif, M. T., M. Zain, S. and Aris, A. Z. (2012). Spatial assessment of air quality patterns in Malaysia using multivariate analysis. *Atmospheric Environment,* 60: 172 – 181.

Malaysian Journal of Analytical Sciences, Vol 20 No 5 (2016): 1171 - 1180
DOI: http://dx.doi.org/10.17576/mjas-2016-2005-24

MALAYSIAN JOURNAL OF ANALYTICAL SCIENCES
Published by The Malaysian Analytical Sciences Society
ISSN 1394 - 2506

KLASIFIKASI SEDIMEN MENGGUNAKAN TEKNIK ENVIROMETRIK: SATU KAJIAN KES DI SUNGAI PAHANG, MALAYSIA

(Sediment Classification using Envirometric Technique: A Study Case in Pahang River, Malaysia)

Frankie Marcus Ata[1], Mohd Khairul Amri Kamarudin[1,2]*, Mohd Ekhwan Toriman[1,3], Mohd Saupi Mohd Zin[1], Nur Hishaam Sulaiman[1], Norjima Abd Wahab[1], Sarif Mohd Nasir[3], Jamaluddin Mohamad Saad[3]

[1]*East Coast Environmental Research Institute (ESERI)*
[2]*Faculty of Design Arts and Engineering Technology*
Universiti Sultan Zainal Abidin, Gong Badak Campus, 21300 Kuala Terengganu, Terengganu, Malaysia
[3]*School of Social, Development and Environmental Studies, Faculty of Social Sciences and Humanities,*
Universiti Kebangsaan Malaysia, 43600 UKM Bangi, Selangor, Malaysia

**Corresponding author: mkhairulamri@unisza.edu.my*

Received: 14 April 2015; Accepted: 3 August 2016

Abstract

Masalah sedimentasi merupakan masalah utama sungai di Malaysia. Analisis saiz partikel sedimen di sungai menyediakan maklumat yang berguna dalam menilai kadar dan corak hakisan, pengangkutan dan pemendapan pada sesuatu masa. Bahan-bahan sedimen dikelaskan mengikut saiz seperti pasir, kelodak dan liat. Kajian ini membincangkan hasil kajian mengenai analisis sedimentasi yang dijalankan di Sungai Pahang pada 3 hingga 6 Jun 2015. Sebanyak 13 stesen persampelan telah dipilih. Parameter yang telah diguna bagi tujuan kajian ini berdasarkan kepada jenis taburan saiz partikal sedimen (g). Pengelasan mengikut saiz bahan telah dikira dan ditentukan melalui nilai skala Phi (ø) bagi mengira pelbagai parameter penentuan sedimen seperti min (M), sisihan piawai (D) dan pencongan (S). Di dalam kajian ini, teknik envirometrik digunakan untuk mengelaskan setiap parameter sedimen yang telah dianalisis. Hasil pengelasan mendapati setiap parameter min, pencongan dan sisihan piawai mempunyai tiga kelas utama yang mendominasi iaitu pasir kasar, pasir sederhana dan pasir halus. Analisis saiz partikel sedimen (M) menunjukkan bahawa, di bahagian tebing kanan kiri dan tengah sungai adalah didominasi pasir bersaiz butiran halus dengan nilai phi 2 ke phi 3. Tahap keseragaman sedimen atau sisihan piawai (D) di kawasan kajian mempunyai butiran pasir yang halus dengan skala keseragaman yang buruk direkodkan iaitu phi 1 ke phi 2. Bagi nilai pencongan (S), saiz sedimen yang terdapat di kawasan kajian adalah bersaiz kasar dan sangat kasar iaitu di antara phi -0.1 ke phi -0.3 dan phi -0.3 ke phi -1. Oleh yang demikian, kawasan Sungai Pahang merupakan kawasan yang mudah mengalami perubahan geomorfologi akibat daripada struktur tanihnya yang bersifat mudah dihakis oleh hujan dan perubahan kadar luahan sungai.

Kata kunci: sedimentasi, saiz partikel sedimen, teknik envirometrik, skala phi, Sungai Pahang

Abstract

Sedimentation is a main river problem in Malaysia. Particle size sediments analysis the river provides useful information to evaluate the rate and pattern of erosion, transportation and deposition at a time. The sediments sizes are classified according to sand, silt and clay. This study discusses about the results of sedimentation analysis at the Pahang River from 3 until 6 June 2015. 13 sampling stations were selected. The parameters used in this study are based on grain size distribution (g). Total of different sizes of material classifications were calculated using Phi scale (ø) in older to statistically calculate their mean (M), standard deviation (D) and skewness (S). In this study, envirometrics technique were used to analyzed the classify parameter of this sediments. The classify results for each parameters mean, skewness and standard deviation has dominated by three main class like coarse sand, medium sand and fine sand size. Analysis of particle size sediment (M) shows the middle, right and left bank river is dominated by fine grain size with the phi 2 to phi 3. The uniformity of sediment or standard deviation (D) on the study

areas has a worst with the fine grain sand with the phi 1 to phi 2. For the skewness (S), sediment size in study areas is coarse and very coarse size with phi -0.1 to phi -0.3 and phi -0.3 to phi -1. Therefore, Pahang River areas is an easily to change as a geomorphology landscape that are easily eroded by rain and change of the discharge rate.

Keywords: sedimentation, particle size, envirometrics technique, phi scale, Pahang River

Pengenalan

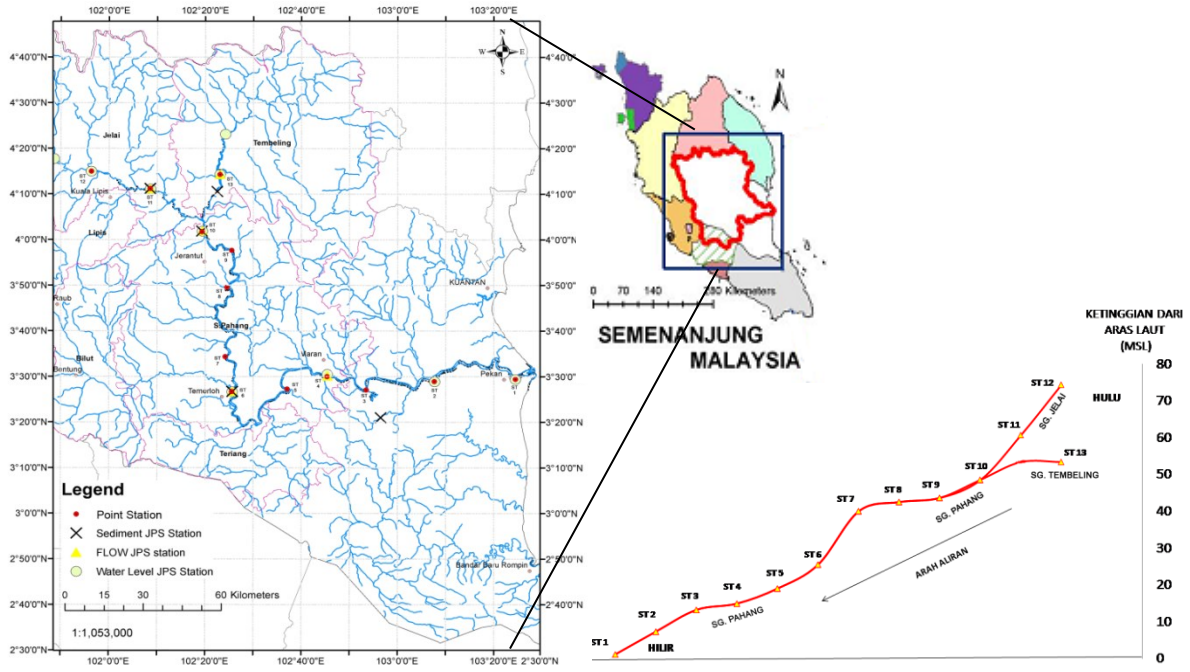
Sedimen atau sedimentasi merupakan sebahagian daripada proses sedimentologi yang berlaku ke atas suatu kawasan lembangan. Sedimen ialah bahan yang terhasil daripada proses luluhawa dan hakisan batuan yang biasanya diangkut oleh agen angin, air dan ais serta diendapkan secara berlapis [1,2]. Sedimen terampai biasanya mempunyai bahan koloid yang bersaiz mikro memerlukan hanya halaju sungai yang rendah untuk mengangkut dari satu titik ke satu titik. Manakala beban dasar sedimen merupakan beban yang bergaris pusat antara 0.2 mm hingga ke 2 mm, bergantung kepada struktur asas batuan dan tanih di sekitar kawasan tersebut [3]. Struktur sedimen pula merupakan struktur yang terbentuk semasa pengenapan atau sejurus selepas bahan sedimen itu dienapkan serta sebelum sedimen termampat [4]. Dengan itu, sedimen memainkan peranan yang penting dalam kitaran yang berkaitan dengan unsur dalam akuatik sekitaran [5]. Sedimen bertanggungjawab bagi mengangkut nutrien dan bahan pencemar yang penting masuk ke dalam sungai. Selain itu, kebanyakan sedimen dalam permukaan air adalah berpunca daripada permukaan hakisan dan mengandungi komponen galian, hakisan batuan dasar dan komponen organik semasa proses pembentukan tanah berlaku [6].

Proses pengangkutan merupakan salah satu dari faktor utama pemendapan sedimen di sepanjang dan muara sungai. Aliran sungai dikatakan mempunyai pengaruh yang besar terhadap pemendapan sedimen terutamanya dalam proses pengangkutan pelbagai jenis beban dari bahagian hulu ke hilir sungai. Terdapat beberapa proses pengangkutan sedimen yang boleh mempengaruhi kadar pemendapan di sesuatu kawasan, antaranya ialah proses golekan, seretan, loncatan, apungan, ampaian dan proses larutan [2,7]. Proses golekan, seretan dan loncatan melibatkan beban sungai yang agak besar dan sederhana besar. Proses ini berlaku disebabkan oleh halaju air yang kuat dan beban ini kebanyakannya dimendap di bahagian hulu sungai yang melibatkan kawasan air terjun dan jeram. Selain dari proses di atas, proses apungan, ampaian dan proses larutan pula boleh mempengaruhi pemendapan sedimen di sepanjang sungai dan muara sungai. Proses ini berlaku disebabkan oleh keadaan dasar sungai yang semakin landai dan menyebabkan aliran air sungai mulai perlahan. Keadaan ini boleh menyebabkan pemendapan sedimen berlaku, biasanya melibatkan sedimen atau bahan mendak yang lebih kecil seperti pasir, lumpur, kelodak dan kerikil yang halus [8]. Masalah sedimentasi yang serius berlaku di Sungai Pahang mendorong kajian ini dijalankan. Bagi mengetahui punca utama berlakunya masalah sedimentasi, kajian analisis sedimentasi ini dilakukan untuk mengetahui struktur tanih yang terdapat di sepanjang Sungai Pahang.

Bahan dan Metodologi

Kajian ini dijalankan pada 3 hingga 6 Jun 2015 dan sebanyak 13 stesen telah dipilih disepanjang Sungai Pahang iaitu bermula dari Sungai Jelai di bahagian Barat Laut Negeri Pahang dengan koordinat 101° 55'49.472" E dan 4° 15'34.355" N. Manakala Sungai Tembeling dibahagian Timur Laut dengan koordinat 102° 28'27.324" E dan 4° 31'14.986" N yang terus mengalir kebawah melalui Bandar Termeloh, Bera, Mentiga dan terus ke pekan dan berakhir di Pahang Tua Muara Sungai Pahang di koordinat 103° 28'16.529" E dan 3° 31'33.478" N (Rajah 1). Bagi memudahkan analisis yang akan dijalan, kawasan kajian akan dipecahkan kepada tiga peringkat iaitu hulu, tengah dan hilir. Peringkat hulu iaitu di Sungai Jelai (Stesen 12 dan Stesen 11), Sungai Tembeling (Stesen 13), Hulu Sg. Pahang (Stesen 10). Peringkat tengah adalah Jerantut, Temerloh dan Bera (Stesen 9, Stesen 8, Stesen 7 dan Stesen 6). Manakala peringkat hilir pula bermula dari Bandar lama Chenor sehingga ke Pekan Pahang (Stesen 5, Stesen 4, Stesen 3, Stesen 2 dan Stesen 1).

Alatan yang digunakan dalam kajian ini adalah seperti pencekup sedimen dan beg plastik bagi tujuan pengambilan sedimen. Tiga replikasi sampel telah di ambil bagi tiap-tiap stesen dan hasil kajian ditunjuk mengikut purata replikasi tersebut. Meter arus, tolok penyukat kedalaman, pita pengukur dan pancang digunakan bagi mengukuran keratan rentas dan had laju air disetiap stesen [9,10]. Kesemua sampel yang diambil kemudiannya dianalisis di dalam makmal.

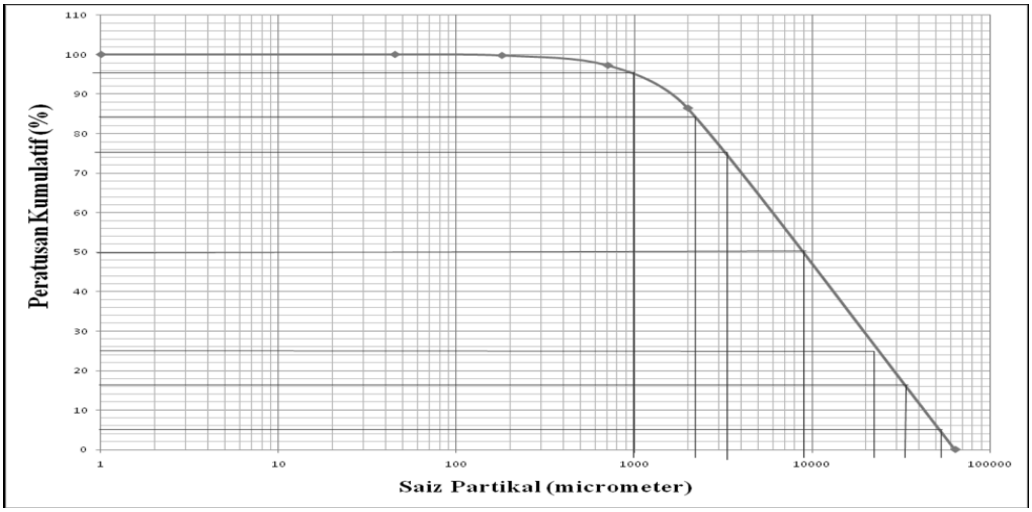


Rajah 1. Peta kawasan kajian melalui pandangan atas dan tepi

Proses pengayakan sedimen akan dijalankan di dalam makmal dengan menyerakkan sedimen di atas plastik bersih dan dibiarkan kering pada suhu bilik. Semasa proses pengeringan yang dijalankan, gumpalan sampel sedimen dipecahkan kepada bahagian-bahagian yang lebih kecil untuk mempercepatkan proses pengeringan. Sampel sedimen dibiarkan kering kemudian dihancurkan dengan menggunakan penumbuk lesung. Sampel tanih tersebut ditimbang sebanyak 100 g dan diayak selama 15 minit dengan menggunakan penggoncang mekanikal. Saiz dulang pengayak yang digunakan di dalam kajian ini adalah 2.0 mm, 0.250 mm, 0.125 mm, 0.063 mm dan pan. Setelah semua sampel tanih dikelaskan serta diasingkan mengikut saiz, sampel tanih tersebut akan dipindahkan ke dalam piring petri dan ditimbang dengan menggunakan neraca eletronik dua titik perpuluhan [11,12]. Berat setiap saiz sampel tanih akan memberikan peratusan saiz tanih. Skala yang akan digunakan di dalam kajian ini adalah mengikut skala Udden-Wentworth.

Menurut kaedah Udden-Wentworth [13,14] untuk memudahkan penganalisisan, pembinaan satu graf arimetik ordinat dengan menggunakan nilai berat yang didapati haruslah dibuat. Skala paksi-x adalah dalam nilai micrometer (µm). Paksi-y adalah nilai skala peratus kumulatif (0 hingga 100%) menggunakan satu skala linear (Rajah 2). Lengkung kumulatif digunakan untuk menentukan nilai micrometer (µm). Saiz phi kemudian ditentukan dengan melihat jadual pengredan saiz partikel sedimen untuk mengetahui setiap nilai phi: (phi pada 5%, phi pada 16% dan sebagainya. Dimana % merujuk untuk peratus kumulatif. Kertas graf yang menggunakan skala log telah digunakan bagi tujuan kajian ini [15].

Bagi kawasan tebing kiri sungai pula, hasil analisis mendapati tiga kelas utama iaitu butiran halus merupakan kelas pertama, diikuti kelas kedua bersaiz butiran kasar dan ketiga bersaiz sederhana. Lokasi yang berada pada kelas pertama iaitu stesen 1, 4, 5, 6, 9, 11 dan 13 dengan saiz butiran antara 125 micrometer hingga 65 micrometer (halus). Stesen 2 dan 3 merupakan kawasan yang mempunyai saiz butiran yang kasar iaitu 1000 micrometer hingga 500 micrometer. Manakala kelas ketiga yang mempunyai saiz butiran antara 500 micrometer hingga 250 micrometer (sederhana) adalah stesen 7, 8, 10 dan 12. Bagi kawasan tengah sungai pula, kelas pertama adalah stesen 1, 9, 10, 11, 12 dan 13 iaitu saiz butiran yang halus, diikuti oleh stesen 2, 6, 7 dan 8 yang bersaiz butiran sederhana dan stesen 3, 4 dan 5 bersaiz kasar.



Rajah 2. Graf Arimetik Ordinat

Beberapa nilai phi akan ditentukan untuk mengira pelbagai nilai statistik bagi Min (M), Sishan Piawai (D), Pencongan (S) dan Kurtosis (K) (Rajah 2) dengan menggunakan persamaan 1 hingga 4 seperti yang ditunjukkan pada Jadual 1 dan 2. Namun begitu, kajian ini lebih membincangkan tentang analisis bagi Min, Sisihan Piawai dan Pencongan pada setiap sampel kajian.

Jadual 1. Nilai phi yang didapati melalui pengiraan daripada analisis pengayakan

Peratus	**ø5**	**ø 16**	**ø 25**	**ø 50**	**ø 75**	**ø 84**	**ø 95**
Nilai Phi	-5.72	-5.14	-4.72	-3.21	-1.84	-1.42	0.0

$$\text{Min (M)} = \frac{\text{ø16} + \text{ø50} + \text{ø84}}{3} \quad (1)$$

$$\text{Sishan Piawai (D)} = \frac{\text{ø84} - \text{ø16}}{4} + \frac{\text{ø95} - \text{ø5}}{6.6} \quad (2)$$

$$\text{Pencongan (S)} = \frac{\text{ø84} + \text{ø16} - 2(\text{ø50})}{2(\text{ø84} - \text{ø16})} + \frac{\text{ø95} + \text{ø5} - 2(\text{ø50})}{2(\text{ø95} - \text{ø5})} \quad (3)$$

Seterusnya, teknik envirometrik yang digunapakai adalah dengan menggunakan perisian tambahan XLStat yang disesuaikan ke dalam perisian Microsoft Excel. Bagi tujuan pengelasan dalam kajian ini, kaedah analisis kluster agglomeratif hierarki (HACA) digunapakai untuk menterjemahkan data mengikut kelas – kelas sedimen yang diperolehi berdasarkan kelas kehomogenan [16]. Aplikasi kaedah ini juga dijangka mampu untuk memperkenalkan dan mengenalpasti ciri sedimen yang sama dan juga masalah yang sama di dalam sub-plot yang akan dibahagikan mengikut kriteria utama dalam pengelasan ini.

Jadual 2. Taksiran bagi saiz taburan, tahap keseragaman dan saiz sedimen untuk skala ukuran Min, Sisihan Piawai dan Pencongan [12]

Skala Ukuran (Min)		**Skala Ukuran (Sisihan Piawai)**		**Skala Ukuran (Pencongan)**	
Saiz Taburan (min)	**Nilai phi**	**Tahap Keseragaman**	**Nilai phi**	**Saiz Sedimen**	**Nilai phi**
Batu besar	-12 ke -8	Sangat baik	< 0.35	Sangat halus	+1.00 ke +0.30
Batu	-8 ke -6	Baik	0.35 ke 0.50	Halus	+0.30 ke +0.10
Batu kecil	-6 ke -2	Sederhana baik	0.50 ke 0.71	Sederhana	+0.10 ke -0.10
Pasir	-2 ke -1	Sederhana	0.71 ke 1.0	Kasar	-0.10 ke -0.30
Butiran sangat kasar	-1 ke 0.0	Buruk	1.0 ke 2.0	Sangat kasar	-0.30 ke -1.00
Butiran kasar	0.0 ke 1.0	Sangat buruk	2.0 ke 4.0		
Butiran sederhana	1.0 ke 2.0	Buruk ekstrem	> 4.0		
Butiran halus	2.0 ke 3.0				
Butiran sangat halus	3.0 ke 4.0				
Kelodak kasar	4.0 ke 5.0				
Kelodak sederhana	5.0 ke 6.0				
Kelodak halus	6.0 ke 7.0				

Hasil dan Perbincangan

Analisis sedimen dalam kajian ini adalah dengan menggunakan ukuran nilai phi (ø) dan micrometer yang diperkenalkan oleh Udden dan Wentworth [13,14]. Parameter yang digunakan bagi menganalisis sampel kawasan tebing kanan, tebing kiri dan tengah sungai adalah min, sisihan piawai dan pencongan.

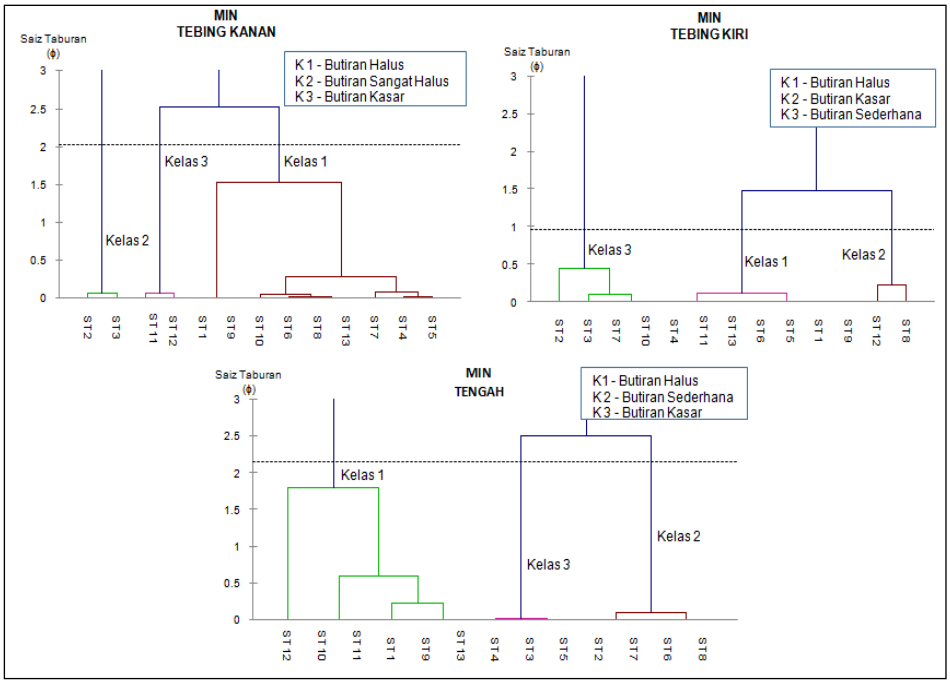
Min (saiz taburan butiran)

Min merupakan saiz taburan butiran sampel tanih yang diperolehi semasa di lapangan. Skala saiz taburan sampel ini terbahagi kepada batu, pasir dan kelodak. Berdasarkan Rajah 3 hasil analisis saiz butiran tanih menggunakan teknik analisis envirometrik mendapati tiga kelas utama saiz butiran yang terdapat di tebing kanan sungai iaitu butiran sangat halus, butiran halus dan butiran kasar. Hasil analisis pengkelasan saiz butiran tanih mendapati bahawa butiran halus iaitu nilai phi 2.0 hingga phi 3.0 merupakan jenis butiran yang paling dominen di semua lokasi persampelan. Antara lokasi yang mempunyai saiz butiran yang halus adalah stesen 1, 4, 5, 6, 7, 8, 9, 10 dan 13, manakala saiz butiran yang sangat halus (phi 3.0 hingga phi 4.0) direkodkan di stesen 11 dan 12. Seterusnya stesen 2 dan 3 pula mencatatkan saiz butiran yang kasar iaitu antara phi 0.0 hingga phi 1.0.

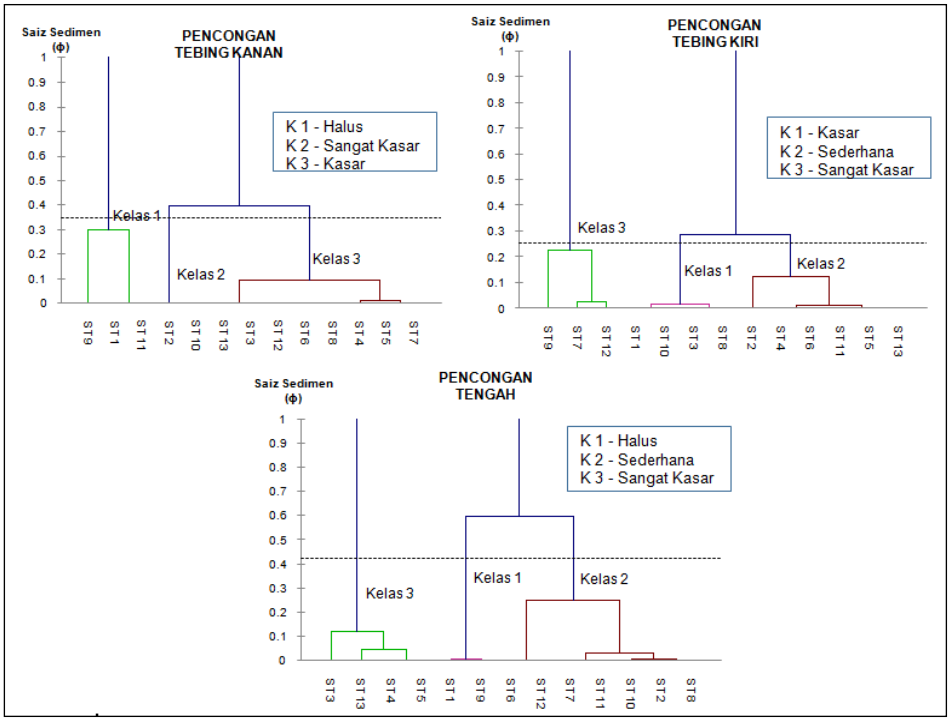
Dapat dirumuskan melalui pengkelasan tersebut bahawa, kawasan di peringkat hulu dan sebahagian kawasan pertengahan Sungai Pahang akan lebih giat berlaku hakisan kerana sifat butirannya yang bersaiz halus, Sungai Pahang di peringkat hulu sehingga sebahagian pertengahan sungai akan mudah mengalami hakisan dan gelongsoran tebing. Saiz butiran yang halus dan sangat halus akan mudah dihakis oleh agen-agen hakisan seperti hujan dan tindakan turbulen arus sungai [17]. Manakala di bahagian hilir pula, jenis butiran yang kasar menunjukkan proses sedimentasi yang giat berlaku kerana arus di kawasan tersebut suda semakin perlahan berbanding di kawasan hulu dan pertengahan Sungai Pahang.

Pencongan (saiz sedimen)

Pencongan merupakan parameter yang digunakan oleh Udden dan Wentworth dalam menentukan saiz sedimen yang terdapat di sesebuah sungai. Berikut merupakan hasli pengkelasan nilai saiz sedimen (pencongan) menggunakan kaedah HACA (Rajah 4). Hasil pengkelasan mendapati empat jenis saiz sedimen yang terdapat pada kawasan tebing kanan, tebing kiri dan kawasan tengah sungai iaitu bersaiz halus, sederhana, kasar dan sangat kasar.



Rajah 3. Hasil pengkelasan saiz butiran (Min) tebing kanan, kiri dan tengah Sungai Pahang menggunakan kaedah HACA



Rajah 4. Hasil pengkelasan saiz sedimen(pencongan) tebing kanan, kiri dan tengah Sungai Pahang menggunakan kaedah HACA

Berpandukan pada Jadual 3, jenis saiz sedimen yang terdapat pada tebing kanan Sungai Pahang adalah didominasi oleh saiz sedimen yang kasar dengan nilai phi antara -0.1 ke -0.30. Stesen-stesen yang mencatatkan saiz sedimen yang kasar adalah stesen 3, 4, 5, 6 7, 8, 10, 12 dan 13. Manakalah stesen 1, 9 dan 11 mencatatkan nilai phi -0.30 ke phi -1.0 iaitu saiz yang sangat kasar. Namun begitu, hanya di stesen 2 sahaja mencatatkan saiz sedimen yang bersaiz halus. Kawasan tebing kiri pula, sedimen yang bersaiz sederhana dengan phi 0 ke phi -0.1 iaitu pada kelas kedua telah direkodkan pada stesen 2, 4, 5, 6, 11 dan 13. Pada kelas pertama pula, dengan saiz sedimen phi -0.1 ke phi -0.3 (kasar) terdapat pada stesen 1, 3, 8 dan 10. Diikuti kelas 3 yang bersaiz sangat kasar, dicatatkan pada stesen 7, 9 dan 12. Seterusnya, di kawasan tengah sungai pula, saiz sedimen bersaiz sederhana iaitu nilai phi 0.1 ke phi -0.1 merupakan saiz yang paling dominen di sepanjang sungai. 8 stesen yang mencatatkan nilai saiz sedimen sederhanan iaitu stesen 2, 6, 7, 8, 10, 11 dan 12. Diikuti kelas 3 dengan nilai phi -0.3 ke phi -1.0 dicatatkan pada stesen 3, 4, 5 dan 13 iaitu bersaiz yang sangat kasar. Saiz sedimen yang halus pula telah didapati di stesen 1 dan 9 dengan nilai phi 0.3 ke phi 0.1.

Jadual 3. Pengkelasan saiz sedimen di lokasi kajian

Pencongan Tebing Kanan	
Kelas 1 (Halus)	ST 1 ST 9 ST 11
Kelas 2 (Sangat Kasar)	ST 2
Kelas 3 (Kasar)	ST 3 ST 4 ST 5 ST 6 ST 7 ST 8 ST 10 ST 12 ST 13
Pencongan Tebing Kiri	
Kelas 1(Kasar)	ST 1 ST 3 ST 8 ST 10
Kelas 2 (Sederhana)	ST 2 ST 4 ST 5 ST 6 ST11 ST 13
Kelas 3 (Sangat Kasar)	ST 7 ST 9 ST 12
Pencongan Tengah	
Kelas 1(Halus)	ST 1 ST 9
Kelas 2 (Sederhana)	ST 2 ST 6 ST 7 ST 8 ST 10 ST 11 ST 12
Kelas 3 (Sangat Kasar)	ST 3 ST 4 ST 5 ST 13

Nilai pencongan bagi suatu sampel berkait rapat dengan bahan mendapan terdapat di dalam sungai. Sebahagian pasir sungai menunjukkan pencongan positif kerana kebanyakan butiran halus yang dimendapkan selepas sungai surut akibat banjir atau hujan, manakala pasir pantai menunjukkan pencongan negatif kerana butiran kasar akan mudah diasingkan oleh pergerakan arus [18]. Bahan enapan bagi kawasan tebing kanan Sungai Pahang adalah berkeadaaan negatif iaitu butiran yang kasar yang mana kawasan tersebut akan mudah mengalami proses hakisan dan pengangkutan serta lebih mudah mengalami perubahan bentuk dan plan sungai.

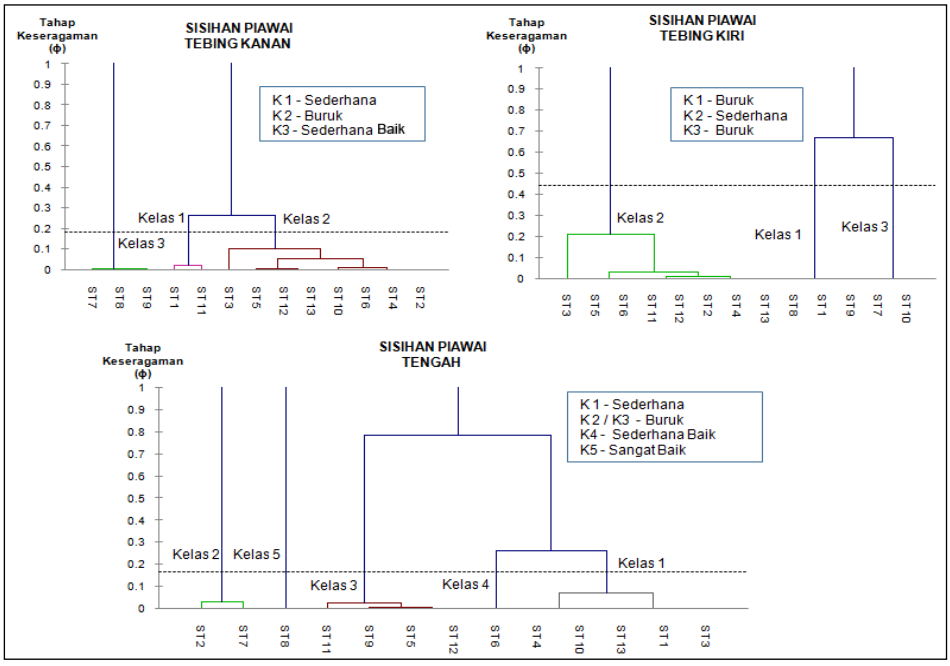
Bagi kawasan tebing kiri pula, saiz kasar yang direkodkan juga mengalami proses yang sama dengan kawasan tebing kanan sungai. Kedua – dua kawasan tebing juga menunjukkan di stesen 1 iaitu bahagian hilir dan stesen 9 pertemuan antara Sungai Jelai, Sungai Tembeling dan Sungai Pahang menunjukkan saiz butiran yang halus, hal ini disebabkan kadar arus yang semakin berkurangan dan proses pemendapan sedimen yang halus tertumpu di kawasan tersebut. Manakala di kawasan tengah sungai pula, saiz sedimen yang bersaiz kasar (negatif) semakin berkurangan iaitu hanya terdapat di stesen 3, 4, 5 dan 13 sahaja berbanding saiz yang halus dan sederhana (positif) yang banyak tertumpu di bahagia tengah sungai. Hal ini menunjukkan, bahagian tengah sungai mempunyai kadar arus yang rendah membolehkan sedimen jenis ini termendap di dasar tengah sungai.

Sisihan piawai (tahap keseragaman)

Parameter ini digunakan untuk menganalisis tahap keseragaman bahan enapan dan tahap keseragaman saiz butiran sampel yang dianalisis. Jadual 4 dan Rajah 5 menunjukkan hasil yang diperolehi selepas analisis pengelasan dijalankan.

Jadual 4. Pengelasan tahap keseragaman sampel di lokasi kajian

Sisihan Piawai Tebing Kanan								
Kelas 1 (Sederhana)	ST 1	ST 2						
Kelas 2 (Buruk)	ST 3	ST 4	ST 5	ST 6	ST 8	ST 10	ST 12	ST 13
Kelas 3 (Sederhana Buruk)	ST 7	ST 9	ST 11					
Sisihan Piawai Tebing Kiri								
Kelas 1 (Buruk)	ST 1	ST 8	ST 9					
Kelas 2 (Sederhana)	ST 2	ST 3	ST 4	ST 5	ST 6	ST 11	ST 12	ST 13
Kelas 3 (Buruk)	ST 7	ST 10						
Sisihan Piawai Tengah								
Kelas 1(Sederhana)	ST 1	ST 3	ST 4	ST 10	ST 13			
Kelas 2 (Buruk)	ST 2	ST 7						
Kelas 3 (Buruk)	ST 5	ST 9	ST 11	ST 12				
Kelas 4 (Sederhana Baik)	ST 6							
Kelas 5 (Sangat Baik)	ST 8							



Rajah 5. Hasil pengkelasan tahap keseragaman (sisihan piawai) tebing kanan, kiri dan tengah Sungai Pahang menggunakan kaedah HACA

Nilai sisihan piawai endapan diukur untuk mengenalpasti proses hakisan yang berlaku bersifat memilih atau sebaliknya. Proses hakisan yang memilih akan menghasilkan butiran sedimen yang halus berbanding hakisan yang tidak seragam akan menghasilkan butiran yang kasar [12,18]. Selepas membuat pengelasan, didapati bahagian tebing kanan sungai didominasi oleh tahap keseragaman yang buruk dengan nilai phi 1.0 ke phi 2.0 iaitu pada stesen 3, 4, 5 ,6, 8, 10, 12 dan 13, sederhana baik dengan nilai phi 0.5 ke phi 0.71 di stesen 7, 9 dan 12 dan tahap sederhana terdapat di stesen 1 dan 2 dengan nilai phi 0.71 ke phi 1.0. Manakala di kawasan tebing kiri pula, hasil pengelasan mendapati terdapat dua jenis keseragaman iaitu jenis buruk dan sederhana.

Hal ini menunjukkan bahawa, bahagian tebing kiri dan tebing kanan sungai mempunyai butiran sedimen bersaiz sederhana kasar dan halus yang boleh menyumbang kepada proses pengangkutan dan pemendapan oleh faktor hakisan. Namun begitu, terdapat beberapa stesen di bahagian kanan tebing yang mengalami hakisan yang tidak memilih iaitu di stesen 7, 9 dan 12 kerana tahap keseragamannya yang sederhana baik dimana saiz butiran sedimennya bersaiz kasar. Seterusnya di bahagian tengah sungai pula, hasli pengelasan mendapati empat kelas tahap keseragaman yang dicatatkan iaitu tahap sangat baik, sederhana baik, sederhana dan buruk. Tahap keseragaman yang buruk didapati di stesen 2, 7, 5, 9, 11 dan 12, tahap keseragaman sederhana terdapat di stesen 1, 3, 4, 10 dan 13. Bagi tahap keseragaman sederhana baik dan sangat baik masing-masing di stesen 6 dan stesen 8. Keseluruhannya, tahap keseragaman yang direkodkan di sepanjang Sungai Pahang adalah berskala buruk iaitu mengalami hakisan yang bersifat memilih kerana saiz butirannya yang diperolehi dalam analisis saiz butiran (Min) menunjukkan butiran halus mendominasi di sepanjang Sungai Pahang.

Kesimpulan

Sungai Pahang mempunyai partikal sedimen yang bersaiz butiran kecil, sederhana dan bersaiz kasar. Butiran kecil ini menunjukkan kawasan tersebut mudah mengalami proses hakisan, pengangkutan dan pemendapan. Selain itu, tahap keseragamannya yang buruk menunjukkan saiz butiran kecil itu lebih mudah dihakis dan diangkut oleh agen-agen hakisan menjadi bahan endapan. Manakala analisis saiz sedimen pula menunjukkan sedimen bersaiz kasar banyak terhasil di sepanjang Sungai Pahang. Hal ini menunjukkan bahawa Sungai Pahang mempunyai struktur tanih yang bersifat pasir dan mudah mengalami perubahan akibat daripada faktor semulajadi dan antropogenik. Sungai Pahang juga akan menjadi semakin dinamik khususnya di bahagian dasar dan tebing sungai yang boleh menyebabkan pelagai masalah yang timbul seperti bencana banjir dan masalah kualiti air yang akhirnya memberi kesan kepada kesihatan persekitaran di dalam Lembangan Sungai Pahang umumnya.

Penghargaan

Kajian ini telah dijalankan melalui dana geran penyelidikan universiti: (UniSZA/2015/GOT/03) dan *Research Acculturation Grant Scheme* (RAGS): (RAGS/1/2015/WABO5/UNISZA/02/1). Penulis merakamkan ucapan jutaan terima kasih kepada Kementerian Pendidikan Malaysia (KPM), Universiti Sultan Zainal Abidin (UniSZA), Universiti Kebangsaan Malaysia dan East Coast Environmental Research Institute (ESERI), UniSZA di atas bantuan yang diberikan.

Rujukan

1. Abdullah N. W and Toriman M. E. (2011). Ciri persekitaran hidrologi dan sedimentasi Sungai Telom, Cameron Higlands. *Jurnal e-Bangi*. 2 (5): 161 – 172.
2. Yang, C. T. (1996). Sediment Transport: Theory and Practice. McGraw-Hill, New York.
3. Toriman M. E., Ata F. M., Kamarudin M. K. A. and Idris M., (2013). Bed-load sediment profile and effect of river bank erosion on river cross-section. *American Journal of Environment Sciences,* 6: 292 –300.
4. Toriman M. E., Kamarudin M. K. A., Abd Aziz N. A., Gasim M. B., Idris M. and Jamil N. R. (2009). Modeling the hydrologic-hydraulic of backwater flow and sediment particle size analysis in Sungai Chini, Pahang. *Jurnal e-Bangi.* 4 (1): 56 – 69.
5. Kamarudin M. K. A., Idris M. and Toriman M. E., (2013). Analysis of *Leptobarbus hoevenii* in control environment at natural lakes. *American Journal of Agriculture Biological Science,* 8: 142 –148.
6. Toriman M. E. (2006). Hakisan muara dan Pantai Kuala Kemaman, Terengganu: Permasalahan dimensi fizikal dan sosial. *Akademika*, 69: 37 – 55.
7. Tongkul F., (2000). *Sedimentologi*. Penerbitan Universiti Kebangsaan Malaysia. Bangi. Selangor. Malaysia.

8. Kamarudin M .K. A., Toriman M. E., Rosli M. H., Juahir H., Azid A., Mohamed Zainuddin S.F., Abdul Aziz N. A. and Sulaiman W. N. A., (2015). Analysis of meander evolution studies on effect from land use and climate change at upstream reach of Pahang River, Malaysia. *Mitigation and Adaptation Strategies for Global Change*, 20 (8):1319 – 1334.
9. Ismail W. R. (1994). *Pengantar Hidrologi*. Dewan Bahasa dan Pustaka. Kementerian Pendidikan Malaysia. Kuala Lumpur. Malaysia.
10. Jaafar O., Toriman M. E., Sharifah Mastura S.A., Gazim M. B., Lan P. I., Abdullah P., Kamarudin M. K. A. and Abdul Aziz N. A. (2010). Modeling the impacts of ringlet reservoir on downstream hydraulic capacity of Bertam River using XPSWMM in Cameron Highlands, Malaysia. *Research Journal of Applied Sciences* 5 (2): 47 – 53.
11. Friedman, G. M and Johnson, K. G. (1982). *Exercises in sedimentology*. New York: Chichester Brisbane Toronto Singapore.
12. Kamarudin M. K. A, Toriman M. E, Sharifah Mastura S. A., Idris M., Jamil N. R and Gasim M. B. (2009). Temporal variability on lowland river sediment properties and yield. *American Journal of Environmental Sciences* 5 (5): 657 – 663.
13. Udden J. A. (1914). Mechanical composition of clastic sediments. *Geological Society of America Bulletin*, 25: 655 – 744.
14. Wentworth C. K. (1922). A scale of grade and class terms for clastic sediments. *Journal of Geology,* 30: 377 – 392.
15. Boltt S. J. and Pey K. (2001). Gradistat: A grain size distribution and statistics package for the analysis of unconsolidated sediments. *Earth Surf. Process. Landforms*, 26: 1237 – 1248.
16. Kamarudin M. K. A, Toriman M. E, Sulaiman N. H, Ata F. M, Gasim M. B, Muhamad A., Yusoff W. A, Mokhtar M., Amran M. A. and Abd Aziz N. A. (2015). Classification of Tropical River using Chemometrics technique: case study in Pahang River, Malaysia. *Malaysian Journal of Analytical Sciences*, 19(5): 1001 – 1018.
17. Toriman M. E., Gasim M. B., Yusop Z., Shahid I., Sharifah Mastura S. A., Abdullah P., Jaafar M., Abd Aziz N. A., Kamarudin M.K.A., Jaafar O., Karim O., Juahir H. & Jamil N. R. (2012). Use of 137Cs activity to investigate sediment movement and transport modeling in river coastal environment. *American Journal of Environmental Science*, 8: 417 – 423.
18. Kairytė, M. and Stevens, R. L. (2015). Composite methodology for interpreting sediment transport pathways from spatial trends in grain size: A case study of the Lithuanian coast. *Sedimentology*. 62(3): 681 – 696.

Malaysian Journal of Analytical Sciences, Vol 20 No 5 (2016): 1181 - 1190
DOI: http://dx.doi.org/10.17576/mjas-2016-2005-25

MALAYSIAN JOURNAL OF ANALYTICAL SCIENCES
Published by The Malaysian Analytical Sciences Society
ISSN 1394 - 2506

PHYTOCHEMICAL SCREENING, TOTAL FLAVONOID AND PHENOLIC CONTENT ASSAYS OF VARIOUS SOLVENT EXTRACTS OF TEPAL OF *Musa paradisiaca*

(Penyaringan Fitokimia, Jumlah Asai Kandungan Flavonoid dan Fenolik Pelbagai Ekstrak Pelarut Tepal *Musa paradisiaca*)

U.S. Mahadeva Rao[1]*, Muhammad Abdurrazak[1], Khamsah Suryati Mohd[2]

[1]*Faculty of Medicine,*
Universiti Sultan Zainal Abidin, Kota Campus, 20400 Kuala Terenganu, Terenganu, Malaysia
[2]*Faculty of Bioresources and Food Industry,*
Universiti Sultan Zainal Abidin, Tembila Campus, 22200 Besut, Terenganu, Malaysia

**Corresponding author: raousm@gmail.com*

Received: 14 April 2015; Accepted: 3 August 2016

Abstract

The objective of this research is to conduct the preliminary phytochemical screening, total flavonoid and phenolic contents assays of various solvent extracts of tepal of *Musa paradisiaca*. Phytochemical screening was carried out according to the method of Trease and Evans, total flavonoid content was measured by the aluminium chloride colorimetric assay and total phenolic content was estimated spectrophotometrically by Folin-Ciocalteau method. - Preliminary phytochemical screening reveals the presence of phenolics, flavonoids, alkaloids, tannins, terpenoids in all the three different extracts (methanolic, ethanolic and aqueous). Tepal methanolic extract has the richest content of both phenolics and flavonoids i.e. (4.27 mg GAE/g and 0.25 mg QE/g) respectively, and aqueous extract was the least i.e. (1.32 mg GAE/g and 0.164 mg QE/g). All the extracts were not significantly different with one another ($p > 0.05$). It can be hypothesised that the high contents of phenolic compounds of tepals of *Musa paradisiaca* indicated that these compounds contribute to the antioxidant activity and can be regarded as promising plant species for natural sources of radical scavenging activity with potential value for treatment of many life threatening diseases.

Keywords: phytochemical, flavonoid, phenolics, *Musa paradisiaca*

Abstrak

Objektif kajian ini adalah untuk menjalankan pemeriksaan awal ke atas ketulenan fitokimia, jumlah kandungan fenolik flavonoid dan pelbagai ekstrak pelarut tepal *Musa paradisiaca***.** Penyaringan fitokimia telah dilaksanakan mengikut kaedah Trease dan Evans, dimana jumlah kandungan flavonoid diukur oleh ujian kalorimetrik aluminium klorida dan jumlah kandungan fenolik dianggarkan secara spektrofotometer dengan kaedah Folin-Ciocalteau. Penyaringan awal fitokimia menunjukkan kehadiran fenolik, flavonoid, alkaloid, tannin dan terpenoid dalam ketiga – tiga ekstrak yang berbeza (metanol, etanol dan akueus). Ekstrak metanol Tepal mempunyai kandungan yang paling tinggi di antara kedua-dua fenolik dan flavonoid iaitu sebanyak 4.27 mg GAE/g dan 0.25 mg QE/g, manakala ekstrak akueus adalah mempunyai kandungan terendah iaitu sebanyak 1.32 mg GAE/g dan 0,164 mg QE/g. Semua ekstrak tidak berbeza secara ketara antara satu sama lain ($p > 0.05$). Oleh itu, hipotesis yang boleh dibuat adalah kandungan yang tinggi sebatian fenolik daripada tepal *Musa paradisiaca* menyumbang kepada aktiviti antioksidan dan boleh dianggap sebagai spesies tumbuhan yang berpotensi untuk merawat pelbagai penyakit yang mengancam nyawa.

Kata kunci: fitokimia, flavonoid, phenolic, *Musa paradisiaca*

Introduction

Consumption of medicinal herbs protects and heals a number of ailments and they have been the principal treatment therapy in prehistoric times until the discovery of synthetic drugs in the nineteenth century [1]. This exploration of biologically active natural products has played an important role in finding new chemical entities (NCEs), for example, approximately 28% of NCEs between 1981and 2002 were natural products or natural product-derived [2]. Health benefits has been derived from bioactive compounds that are commonly found in edible plant parts such as fruits, vegetables, flowers, leaves and have been shown to confer protection against various ailments [3]. Interestingly, many of them are known to contain large amounts of phenolic antioxidants [4]. Phytchemicals have become an intense focus of research interest because of their perceived beneficial effects for health, including anticarcinogenic, antiatherogenic, antiulcer, anti-thrombotic, anti-inflammatory, immunemodulating, antimicrobial, varodialatory, and analgesic effects. Therefore, the search for exploitation of natural antioxidants, especially of plant origin, has greatly increased in recent years [1]. For example, chard extract (*Beta vulgaris* L. var. *cicla)* has been used as a hypoglycaemic agent by diabetic mellitus (DM) patients in Turkey [5] and it has been documented that the number of similarly various phytoconstituent such as epicatechin, rutin, quercetin, nymphayol and flavonoid extracts from *Pterocarpus marsupium* have shown to possess β-cells regeneration capacity [6].

Flavonoids represent the most common and widely distributed group of plant phenolics [7] and are abundant in foods; quercetin and rutin are the flavonoids most abundantly consumed [8]. *Musa paradisiaca* is one of the well-known plants of the *Musaeae* family that have been used in traditional medicine since hundred years to alleviate various diseases and health problems. Active constituent presence in the plants materials might be responsible to the beneficial of human health. The most important of these bioactive compounds of plants are alkaloids, flavonoids, tannins and phenolic compounds [9]. Ethnomedicinal survey around the world revealed that the flowers of *Musa spp.* have been used to treat many illnesses. Its flowers have been traditionally used to alleviate menorrhagia, dysentery, diabetes mellitus [10], heart pain, diarrhea, stomach cramps and infantile malnutrition [11]. It was reported that the extracts of the flowers possess medicinal properties for illness such as diabetes mellitus, anaemia [12] and malaria [13]. Phenolics are the largest group of phytochemicals that account for most of the antioxidant activity in plants or plant products [14].

More than 4000 polyphenols (flavonoids, monophenols and poly phenols) are found in vascular plants. Phenolic compounds such as quercetin, rutin, narigin, catechin, caffeic acid, gallic acid and chlorogenic acid are very important plant constituents [15]. Flavonoids are the largest group of naturally occurring phenolic compounds, which occurs in different plant parts in Free State and as glycosides [16]. They are found to have many biological activities including antimicrobial, mitochondrial adhesion inhibition, antiulcer, antiarthritic, antiangiogenic, anticancer, protein kinase inhibition etc. The flavones and flavonols are the most widely distributed of all the phenolics [17]. Flavonoids are particularly beneficial, acting as antioxidants and giving protection against cardiovascular disease, certain forms of cancer and age related degeneration of cell components. Their polyphenolic nature enables them to scavenge injurious free radicals such as super oxide and hydroxyl radicals [18]. A variety of dietary plant flavonoids inhibits tumor development in experimental animal models [19]. The bi-flavonoids have the pharmacological effects like their ability to inhibit the release of histamines, the adhesion of blood platelets and the action of lens aldose reductase, to block the inflammatory effects of hepatotoxins, and to act as a heart stimulant [20]. Therefore, the objective of this paper is to carry out the phytochemical screening, total contents of both phenolics and flavonoids of various solvent extracts of *Musa paradisiaca.*

Materials and Methods

Preparation of plant extract

The tepals were selectively removed from the bracts, oven dried for one week. It was then crush grinded to fine powder using an electrical grinder. This was then divided into three portion and each portion was soaked in methanol, ethanol and distilled water for 3 days respectively. Each sample was later filtered using Whatmann's No. 1 filter paper. The filtrates were then concentrated at 42 °C to yield a dark brown semi solid using a rotary evaporator (N-1100, Shanghai, Eyela. Co. Ltd, Tokyo, China). This was repeated three times. For each extract, the yield was expressed in percentage by dividing the quantity of dry mass obtained after extraction by the dry weight of the powder used before soaking. Dried extracts were weighed and dissolved in 10% dimethylsulphoxide (DMSO)

to yield a stock solution from which lower concentrations were prepared. The filtrate was then concentrated using an electric incubator. The extract appears as semi-solid greenish brown paste. A stock solution to be used was then prepared by dissolving 100 g of the extract in 50 ml of distilled water.

Preliminary Phytochemical Screening
The phytochemical screening of the extracts was conducted using standard procedures described by Trease and Evans [21]. The following qualitative tests were carried out:

Test for saponins
One mL of the tepal extract was diluted with distilled water to 20 mL and shaken in a graduated cylinder for 15 minutes. The formation of one centimeter layer of foam indicates the presence of saponins.

Test for phenols
A small amount of the ethanolic extract was taken with 1 mL of water in a test tube and 1 to 2 drops of Iron III chloride ($FeCl_3$) was added. A blue, green, red or purple color is a positive test.

Test for glycosides
A small amount of alcoholic extract was taken in 1 mL of water in a test tube and a few drops of aqueous NaOH were added. A yellow coloration indicates the presence glycosides.

Test for flavonoids
One to five drops of concentrated hydrochloric acid (HCl) were added to little amount of ethanolic extract of the plant material. Immediate development of a red colour indicates the presence of flavonoids.

Test for alkaloids
Two mL of extract was taken in a test tube and then 0.2 mL dilute HCl was included, followed by 1 mL of Meyer's reagent. A yellowish coloration indicates alkaloid's presence.

Test for tannins
Five mL of the tepal extract was placed in a test tube and then 2 mL of 5 % of $FeCl_3$ solution was added. A greenish-black precipitate indicates the presence of tannins.

Test for terpenoids
In a test tube containing 2 mL of chloroform, 0.5 mL of extract was added. This is then followed by the addition of 3 mL conc. H_2SO_4 which forms a layer. Reddish brown coloration of the interface indicates terpenoids.

Total phenolic content assay
The total phenolic content (TPC) was carried out by using the method of Folin-Ciocalteu. An aliquot (least amount) (1 mL) of extracts or standard solution of gallic acid (100, 200, 300, 400, and 500 µg/mL) was added to 25 mL of volumetric flask, containing 10 ml of decontaminated water. A blank reagent using distilled water was prepared. One mL of Folin-Ciocalteu phenol reagent was added to the mixture and shaken. After 5 mins 10 mL of 7.5% Na_2CO_3 solution was added to the mixture. The volume was then made up to the mark. Upon completion of incubation for 30-45 minutes at room temperature, the absorbance against the reagent blank was determined at 760 nm with an UV-Visible (Shimadzu Japan). TPC was expressed as mg gallic acid equivalents (GAE) [22].

Total flavonoid content assay
In this method, quercetin was used as the standard to make the calibration curve. 3.2 mg of quercetin was dissolved in 95% ethanol and then diluted to 5, 10, 20, 40, 80, 160, and 320 µg/mL. A calibration curve was made by measuring the absorbance of the dilutions at 415 nm (λ_{max} of quercetin) with a UV-1800 spectrophotometer Shimadzu Japan. Aluminium chloride ($AlCl_3$), 10 % and potassium acetate, 1 M solution was prepared. An amount 50 mg of each extract was accurately weighed and transferred to 10 mL volumetric flask and made up the volume with methanol. 50 µL of each extract stock solution, 2.15 ml ethanol, 0.1 mL $AlCl_3$ 0.1 ml potassium acetate solution and 2.8 mL distilled water were added and mixed well. Sample blank was prepared in a similar way by

replacing $AlCl_3$ with distilled water. Sample and sample blank of all extracts were prepared and their corresponding absorbances were measured at 415 nm. All prepared solutions were filtered through whatmann filter paper before measuring. Total flavonoid content (TFC) was expressed as mg of quercetin equivalent (QE) [23]. TFC was computed by using the following formula:

$$TFC = (R \times D.F \times V \times 100) / W. \quad (1)$$

where, R - result obtained from the standard curve, D.F - dilution factor, V - volume of stock solution, 100 - For 100 g dried plant, W - weight of plants used in the experiment.

Results and Discussion

Percentage yield of extracts

The percentage yield for the various solvent extracts of tepal of *Musa paradisiaca* is shown in Table 1. Ethanolic tepal extract (ETE) has the highest percentage yield when compared to the methanolic and aqueous extract of the flower.

Table 1. Percentage yield of various solvent extracts of tepal of *Musa paradisiaca*

Extract	Initial weight	Final weight	% Yeild
Tepal (methanol)	508.9	7.53	1.50
Tepal (ethanol)	508.9	7.54	1.51
Tepal (aqueous)	508.9	7.13	1.40

Preliminary phytochemical screening

Preliminary phytochemical screening shows the presence of phenols, glycosides, flavonoids, alkaloids, tannins and terpenoids in all three extracts i.e. methanol, ethanol and aqueous. MTE has the highest contents of phenols, followed by the ETE and aqueous tepal extract (ATE) the least. Nonetheless, the aqueous extract possesses flavonoids in abundance. Glycosides, alkaloids, tannins and terpenoids were all found to be present. All extracts were tested negative for saponins.

Total phenolic content (TPC)

The TPC of the extracts was determined by extrapolation from the calibration curve ($Y = 0.18x + 0.1039$; $R^2 = 0.994$) prepared from the gallic acid concentrations (Figure 1) and expressed in mg of gallic acid equivalence (GAE) per gram. The amount of phenolic compounds in the various extracts was obtained from regression equation and the values were expressed in gallic acid equivalence (Figure 2). There was no significant difference ($p > 0.05$) in all the three different extracts.

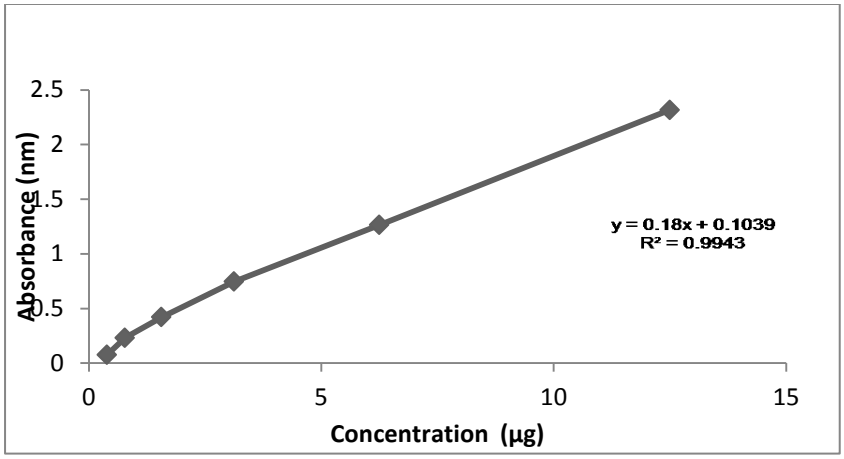


Figure 1. Gallic acid calibration curve

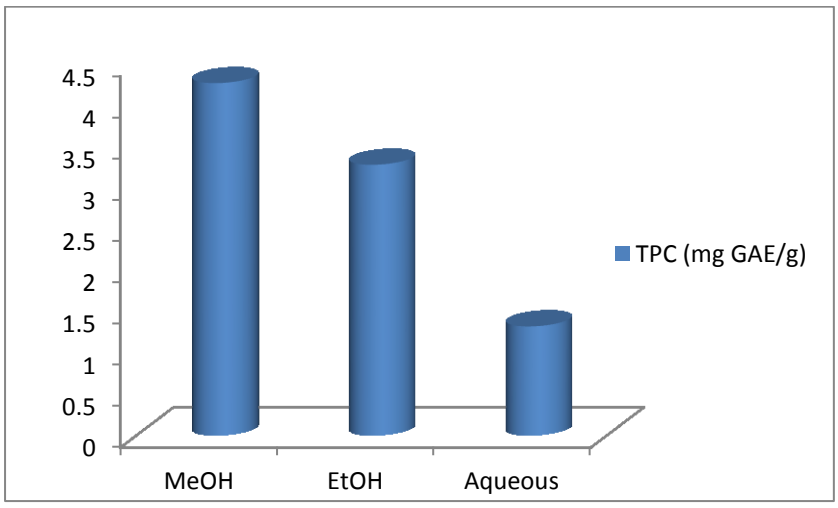


Figure 2. Total phenolic content of various solvent extracts of tepal of *M. paradisiaca*

Total flavonoid content (TFC)

The TFC content of the tepal extracts was also determined by extrapolation from the calibration curve (Y = 0.4638x + 0.0778; R^2 = 0.992) prepared from the quercetin concentrations (Figure 3) and expressed in mg of quercetin equivalence (QE) per gram. The amounts of flavanoid compounds in the various extracts were obtained from regression equation and the values were expressed in quercetin equivalence (figure 4). The values from all the extracts were not significantly different ($p > 0.05$).

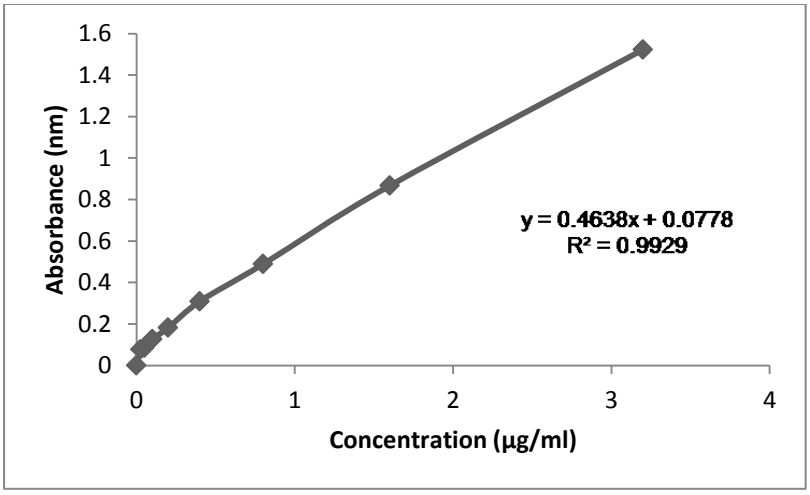


Figure 3. Quercetin calibration curve.

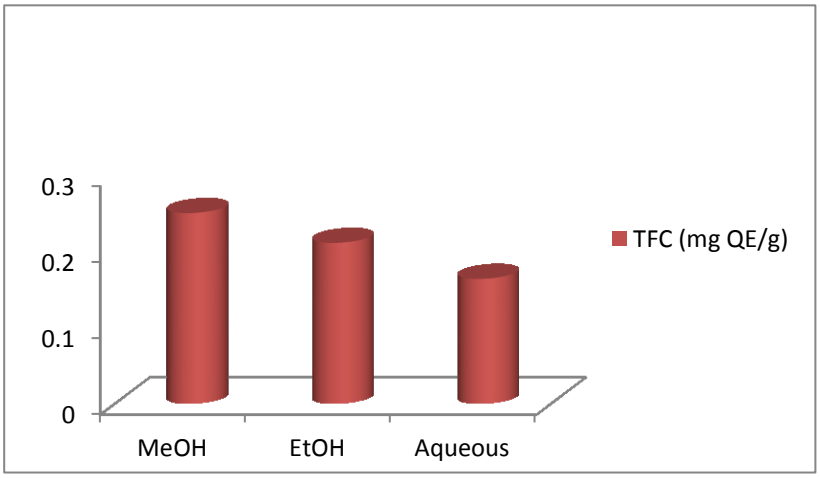


Figure 4. Total flavonoid content of various solvent extracts of tepal of *M. paradisiaca*

Preliminary phytochemical screening reveals the presence of phenols, flavonoids, glycosides, alkaloids, tannins and terpenoids. Saponins were tested negative in all the three different extracts (Table 2). The total phenolic content (TPC) of the tepal (methanolic, ethanolic and aqueous) extracts of *Musa paradisiaca* was determined using the Folin-Ciocalteau method. This method allows the estimation of all the flavonoids, anthocyanins and non-flavonoid phenolic compounds of all the phenolics available in the samples [24]. The results for total phenolic content in the studied plant extracts are presented in the graphs (Figure 2). The results show that MTE has the richest source of phenolics, total phenolic content is 4.272 mg GAE/g while on the contrary, ATE possesses the lowest amount of phenolics i.e. 1.32mg GAE/g. The total phenolic contents did not vary significantly ($p > 0.05$) in different solvent extracts. This is in agreement with the researchers [25,26], who found that yield of total phenolic was dependent on the method and choice of solvent. The recovery of polyphenols from plant materials is influenced by the solubility of the phenolic compounds in the solvent used in the extraction process. Furthermore, solvent polarity will play a key role in increasing phenolic solubility [27]. Thus, it is difficult to produce a standard extraction procedure suitable for phenol extraction of all the plant samples. As the results indicated, it is apparent that the recovery of

phenolic compounds was dependent on the solvents used and their polarity. This may be attributed to the fact that wide range of phenols can dissolve in aqueous methanol mixtures. On the other hand, methanol is a good solvent system for the extraction of polar antioxidants [28]. There is a strong link between phenolic content and free radical scavenging activity [29,30]. Phenolics possess a broad spectrum of biochemical activities such as antioxidant, antimutagenic, anti-carcinogenic and even the ability to modify the gene expression [31]. Polyphenols are the largest group of phytochemicals that account for most of the therapeutic activity in plants or plant products [32]. This plant is generally reported to contain substantial amounts of polyphenols with pharmacological properties which includes flavonoids and tannins [33]. The results obtained in the present study revealed that the level of phenolic compounds in these extracts was considerable and falls within the values of commonly consumed green vegetables. Hence consumption of these plants will enhance the health benefits by absorbing and neutralizing free radicals, quenching singlet oxygen, or decomposing peroxides [3].

Table 2. Preliminary phytochemical screening of various solvent extracts of *Musa paradisiaca*

S.N.	Test	T (MeOH)	T (EtOH)	T (aqueous)
1	Saponin	–	–	–
2	Phenols	+++	++	+
3	Glycosides	++	++	+
4	Flavonoids	+	+	++
5	Alkaloids	+	+	+
6	Tannins	++	+	+
7	Terpenoids	+	+	+

plus (+) indicates the presence and minus (-) signifies absence.

Total flavonoid content (TFC) of different extracts of tepals of *Musa paradisiaca* was determined by $AlCl_3$ method. Determining the total flavonoids by using $AlCl_3$ is based upon the formation of stable complex between $AlCl_3$, keto and hydroxyl groups of flavones and flavonoids. The results for total flavonoid content in the studied plant extracts are presented in the graph (Figure 4). The results show that MTE has the richest source of flavonoids, i.e. total content is 0.25 mg QE/g while on the contrary, ATE possess the lowest amount of flavonoid i.e. 0.164 mg QE/g. this is contrary to the findings of [34] where it was found that ethanolic extract has the highest flavonoid content. Flavonoids display a crucial role in scavenging the free radicals and these are the phyto constituents that should be focused on for investigation of many biological activities. Phytochemicals especially polyphenols constitute a major group of compounds that act as primary antioxidants [15].

More than 4000 polyphenols (flavonoids, monophenols and poly phenols) are found in vascular plants. Phenolic compounds such as quercetin, rutin, narigin, catechin, caffeic acid, gallic acid and chlorogenic acid are very important plant constituents [15]. Medicinal plants are known to produce diverse substances possessing antioxidant properties having ability to protect the human body against cellular oxidation. Anti-oxidation are vital substances which possess the ability to protect the body from damage caused by free radicals inducing oxidative stress [35]. Antioxidant compounds like phenolic acids, polyphenols and flavonoids scavenge free radicals such as peroxide, hydroperoxide of lipid hydroxyl and therefore halt the oxidative mechanism that leads to degenerative diseases [36]. Flavonoids are proactive polyphenolic compounds found in most plants and cannot be synthesized or produced by the humans [37]. It was found to be effective in controlling various biological activities and is anti-inflammatory, anti-angiotic, antimicrobial, antioxidant, reduced hypertension, and has anti-cholesterol properties [38, 39]. In recent times, research interest has been paid to polyphenols and flavonoids as a result of their antioxidant capacity which is principally based on the redox properties of their hydroxyl groups and the structural relationship between different functional groups in their structure which enable them to actively serve as free radical scavengers, reducing agents, singlet oxygen quenchers metal chelators, and hydrogen donors [40].

Conclusion

It can be postulated that the contents of phenolic and flavonoid compounds of tepal of *Musa paradisiaca* contribute to the radical scavenging activity and can be regarded as promising plant species for natural sources of antioxidant with potential value for treatment of many life threatening diseases. The process of extraction and identification of active principles responsible for the free radical scavenging property of tepal extract of *Musa paradisiaca* through bioactivity guided fraction is under progress in order to understand the possible mechanism of action of tepal of *Musa paradisiaca*. Utilization of this tepal will be of advantage to mankind and increased in its consumption will help in prevention of chronic life style diseases.

Acknowledgement

The authors would like to acknowledge the support of Faculty of Medicine, Universiti Sultan Zainal Abidin (UniSZA), for providing the necessary fund on this research work.

References

1. Rao, U. S., Khamsah, S. M., Abdurrazaq, M., Bashir, A. A., Mohaslinda, M. and Rosmawati, M. A. (2014). Taxonomical, Phytochemical and Pharmacological Review of *Musa sapientum var paradisiaca*. *Research Journal of Pharmacy and Technology,* 7(11): 1356 – 1361.
2. Newman, D. J., Cragg, G. M. and Snader, K. M. (2003). Natural products as sources of new drugs over the period 1981–2002. *Journal of Natural Product.* 66 (7): 1022 – 1037.
3. Loganayaki, N., Rajendrakumaran, D. and Manian, S. (2010). Antioxidant capacity and phenolic content of different solvent extracts from banana (*Musa paradisiaca*) and mustai (*Rivea hypocrateriformis*). *Food and Science Biotechnology.* 19(5): 1251 – 1258.
4. Yen, G. C., Duh, P. D. and Tsai, H. L. (2002). Antioxidant and pro-oxidant properties of ascorbic acid and gallic acid. *Food Chemistry.* 79: 307 – 313.
5. Bolkent, S., Yanardag, R., Tabakoglu-Oguz, A. and Ozsoy-Sacan, O. (2000). Effects of chard (*Beta vulgaris* L. var. *cicla*) extract on pancreatic B cells in streptozotocin induced-diabetic rats: A morphological and biochemical study. *Journal of Ethnopharmacol*ogy. 73: 251 – 259.
6. Subash-Babu, P., Ignacimuthu, S., Agastian, P. and Varghese, B. (2009). Partial regeneration of [beta]-cells in the islets of Langerhans by nymphayol a sterol isolated from *Nymphaea stellate* (Willd.) flowers. *Bioorganic and Medicinal Chemistry.* 17: 2864 – 2870.
7. Harborne. J. B. The Flavonoids: (1988). Advances in research since 1980, Chapman and Hall Ltd, New York. 121.
8. Nakamura, Y., Ishimitsu, S. and Tonogai, Y. (2000). Effects of quercetin and rutin on serum and hepatic lipid concentrations, fecal steroid excretion and serum antioxidant properties. *Journal of Health Science,* 46: 229 – 240.
9. Edeoga, H. O., Okwu, D. E. and Mbaebie, B. O. (2005). Phytochemical constituents of some Nigerian medicinal plants. *African Journal of Biotechnology,* 4(7): 685 – 688.
10. Singh, Y. N. (1986). Traditional medicine in Fiji: some herbal folk cures used by Fiji Indians. *Journal of Ethnopharmacology.* 15(1): 57 – 88.
11. Leonard, D. B. (1998). Medicine at your feet: Healing plants of the Hawaiian Kingdom Musa spp.(Mai'a).
12. Mahmood, A., Ngah, N. and Omar, M. N. (2011). Phytochemicals constituent and antioxidant activities in Musa x Paradisiaca flower. *European Journal of Scientific Research*. 66(2): 311 – 318.
13. Bagavan, A., Rahuman, A. A., Kaushik, N. K. and Sahal, D. (2010). In vitro antimalarial activity of medicinal plant extracts against *Plasmodium falciparum*. *Parasitic Research*, 108(2): 15 – 22.
14. Sulaiman, C. and Indira, B. (2012). Total phenolics and total flavonoids in selected Indian medicinal plants. *Indian Journal of Pharmaceutical Science,* 74(3): 258 – 260.
15. Samatha, T., Shyamsundarachary, R., Srinivas, P. and Swamy, R. (2012) Quantification of total phenolic and total flavonoids contents in extracts of *Oroxylum Indicum L*. Kurz. *Asian Journal of Pharmacy and Clinical Research*, 5(4): 177 – 179.
16. John, B. I., Sulaiman, C. T., George, S. A. and Reddy, V. R. (2013). Total phenolics and flavonoids in selected medicinal plants from Kerala. *Intlernational Journal of Pharmacy and Pharmaceutical Science*. 6(1): 406 – 408.

17. Peter, B., Kaufman, J., Warber, C., James, A. and Harry, D. (1999). Natural products from Plants, CRC Press London.
18. Dewick, P. M. (2001). Medicinal natural products. A biosynthetic approach, John Wiley & Sons England.
19. Arnason, J., Mata, R. Romeo, J. (1995). Recent trends in Phytochemistry, (Eds) Plenum Press, New York and London.
20. Harbone, J. B. (1986). Phytochemical methods. Guide to modern techniques of plant analysis (2nd edition. Chapman and Hall) India 1991.
21. Trease, G. E. & Evans, W. C. (1989). *Trease and Evan's Textbook of Pharmacognosy*. 13th Edition. Cambridge University Press, London. 546.
22. Singleton, V. L. and Rossi Jr J. A. (1965). Colorimetry of total phenolics with phosphomolybdic phosphotungstic acid reagents. *American Journal of Enology and Viticulture.* 16: 144 – 158.
23. Kiranmai, M., Kumar, M. and Mohammed, I. (2011). Comparison of total flavanoid content of *Azadirachta indica* root bark extracts prepared by different methods of extraction. *Research Journal of Pharmaceutical Biological and Chemical Science*, 2: 254 – 261.
24. Benvenuti, S., Pellati, F., Melegar, M. and Bertelli, D. (2004). Polyphenols, anthocyanins, ascorbic acid and radical scavenging activity of *Rubus*, *Ribes* and *Aronia*. *Journal of Food Science.* 69: 164 – 169.
25. Goli, A. H., Barzegar, M. and Sahari, M. A. (2005). Antioxidant activity and total phenolic compounds of pistachio (*Pistachia vera*) hull extracts. *Food Chemistry*. 92: 521 – 525.
26. Atmani, D., Chaher, N., Berboucha, M., Ayouni, K., Lounis, H., Boudaoud, H. and Debbache, N. (2009). Antioxidant capacity and phenol content of selected Algerian medicinal plants. *Food Chemistry*, 112: 303 – 309.
27. Naczk, M. and Shahidi F. (2006). Phenolics in cereals, fruits, and vegetables: Occurrence, extraction, and analysis. *Journal of Pharmaceutical and Biomedical Analysis,* 41: 1523 – 1542.
28. Luximon-Ramma, A., Bahorun, T. and Crozier, A. (2003). Antioxidant actions and phenolic and vitamin C contents of common Mauritian exotic fruits. *Journal of the Science of Food and Agriculture*. 83: 496 – 502.
29. Oki, T., Masuda, M., Furuta, S., Nishibia, Y., Terahara, N. and Suda, I. (2002). Involvement of anthocyaninsand other phenolic compounds in radical-scavenging activity of purple-fleshed sweet potato cultivars. *Food and Chemical Toxicology,* 67: 1752 – 1756.
30. Mohammad Reza, S. A., Mahnaz, K., Mannan, H., Maryam J. and Abbas H. (2010). Comparison of antioxidant activity and total phenol contents of some date seed varieties from Iran. *Iranian Journal of Pharmaceutical Research*, 9(2): 141 – 146.
31. Marinova, D., Ribarova F. and Atanassova M. (2005). Total phenolics and total flavonoids in Bulgarian fruits and vegetables. *Journal of Chemical Technology and Biotechnology,* 40(3): 255 – 260.
32. Sulaiman, C. T., Sadashiva, C. T., George, S., Goplakrishnan, V. K. and Balachandran, I. (2013). Chromatographic studies and in vitro screening for acetyl cholinesterase inhibition and antioxidant activity of three Acacia species from South India. *Analytical Chemistry Letters*, 3(2). 111 – 118.
33. Lewis, D. L., Field, W. D. and Shaw, G. P. (1999). A natural flavonoid present in unripe plantain banana pulp (*Musa sapientum* L. var. *paradisiaca*) protects the gastric mucosa from aspirin-induced erosions. *Journal of Ethnopharmacology*. 65: 283 – 288.
34. Joseph, J., Paul, D., Kavitha, M. P., Dineshkumar, B., Menon, J. S., Bhat, A. R. and Krishnakumar, K. (2014). Preliminary phytochemical screening and in vitro antioxidant activity of Banana flower (*Musa paradisiaca* AAB Nendran variety). *Journal of Pharmacy Research.* 8(2): 144 – 151.
35. Ozsoy, N., Can, A., Yanardag, R. and Akev, N. (2008). Antioxidant activity of Smilax excelsa leaf extracts. *Food Chemistry*, 110: 571 – 583.
36. Subramanian, H., Gupta K., Guo, Q., Price, R. and Ali, H. (2011). Mas-related gene X2 (MrgX2) is a novel G protein-coupled receptor for the antimicrobial peptide LL-37 in human mast cells: resistance to receptor phosphorylation, desensitization, and internalization. *Journal of Biological Chemistry.* 286: 44739 – 44749.
37. McCullough, M. L., Peterson, J. J. and Patel, R. (2012). Flavonoid intake and cardiovascular disease mortality in a prospective cohort of US adults 1–4. *American Journal of Clinical Nutrition*. 95(2): 454 – 464.
38. Knekt P., Kumpulainen J., and Jarvinen J. (2002). Flavonoid intake and risk of chronic diseases. *American Journal of Clinical Nutrition*, 76(3): 560 – 568.

39. Liu X, Zhu L, Tan J., Zhou, X., Xiao, L., Yang, X. and Wang, B. (2014). Glucosidase inhibitory activity and antioxidant activity of flavonoid compound and triterpenoid compound from *Agrimonia Pilosa* Ledeb. *BMC Complement Alternative Medicine.* 14(1): 1 – 12.
40. Materska M. and Perucka I. (2005). Antioxidant activity of the main phenolic compounds isolated from hot pepper fruits (*Capsicum annuum* L.). *Journal of Agricultural Food Chemistry.* 53:1730 – 1758.

Malaysian Journal of Analytical Sciences, Vol 20 No 5 (2016): 1191 - 1202
DOI: http://dx.doi.org/10.17576/mjas-2016-2005-26

MALAYSIAN JOURNAL OF ANALYTICAL SCIENCES
Published by The Malaysian Analytical Sciences Society
ISSN 1394 - 2506

IN VITRO NITRIC OXIDE SCAVENGING AND ANTI INFLAMMATORY ACTIVITIES OF DIFFERENT SOLVENT EXTRACTS OF VARIOUS PARTS OF *Musa paradisiaca*

(Aktiviti Pemerangkapan Nitrik Oksida dan Anti-Radang Secara *In Vitro* oleh Ekstrak Pelarut Berbeza dari Pelbagai Bahagian *Musa paradisiaca)*

U.S Mahadeva Rao[1]*, Bashir Ado Ahmad[1], Khamsah Suryati Mohd[2,3]

[1]*Faculty of Medicine,,*
Universiti Sultan Zainal Abidin, Medical Campus, 21400 Kuala Terengganu, Terengganu, Malaysia
[2]*Faculty of Bioresources and Food Industry*
[3]*Agriculture Production and Food Innovation Research Institute*
Universiti Sultan Zainal Abidin, Tembila Campus, 22200 Besut, Terengganu, Malaysia

**Corresponding author: raousm@gmail.com*

Received: 14 April 2015; Accepted: 3 August 2016

Abstract

Inflammatory diseases are an important health concern, and the growing rate is on the rise. Finding a safe drug for these diseases remains an important issue. The study aimed to determine the nitric oxide (NO) scavenging as well as anti-inflammatory activities of *Musa paradisiaca* (banana). *Musa paradisiaca* plant parts used in this study namely tepal, skin (peel) and flesh (pulp) were extracted with methanol (tepal, flesh and skin), ethanol (tepal) and water (tepal) using cold maceration technique. Phytochemicals screening of the extracts was carried out. The ability of the extracts to scavenge NO radical was evaluated using Griess reagent. The anti-inflammatory activity of the extracts was assessed by evaluating the ability of the extract to inhibit RAW 264.7 macrophage cell line from generating harmful NO induced by bacterial lipopolysaccharide (LPS). In order to determine the toxicity of the extracts to the cells while exerting its anti-inflammatory activity,cytotoxicity was measured using MTT [3-(4,5-dimethylthiazol-2-yl)-2,5-diphenyltetrazolium bromide] assay.The extract was found to contain bioactive chemicals like flavonoids, saponins, phenols, etc. Maximum NO radical inhibition of 41.05% was recorded in the tepal aqueous extract, and minimum inhibition of 22.34% was recorded in the flesh extract. All others showed mild inhibition as well. Flesh extract has the highest NO (generated by LP) inhibitory activity, with the maximum inhibition of 52.21% at 250 µg/mL, followed by tepal aqueous extract with maximum inhibition of 48.16% at 62.5 µg/mL. The least inhibition was noted in the tepal methanol extract that has the maximum inhibition of 19.63% at 62.5 µg/mL. The viability of the activated macrophages was not affected by the extracts as confirmed by the MTT assay, thereby indicating that the inhibition of NO synthesis by the extracts was not due to cytotoxic effects. Overall, *Musa paradisiaca* plant parts have the potential as anti-inflammatory and studies in this aspect should be intensified.

Keywords: anti-Inflammation, MTT, *Musa paradisiaca*, RAW 264.7

Abstrak

Penyakit radang merupakan gejala penyakit yang semakin mendapat perhatian dan kadar kedapatan (penyakit) semakin meningkat. Pencarian ubat yang selamat untuk penyakit ini masih menjadi isu penting. Kajian ini bertujuan menentukan aktiviti pemerangkapan nitrik oksida (NO) serta anti radang oleh *Musa paradisiaca* (pisang). Bahagian – bahagian *Musa paradisiaca* yang diguna dalam kajian ini adalah jantung, kulit (kupasan) dan isi (pulpa). Sampel – sampel telah diekstrak dengan metanol (jantung, kulit dan isi), etanol (jantung) dan air (jantung) menggunakan kaedah rendaman sejuk. Penyaringan fitokimia keatas ekstrak telah dijalankan. Keupayaan ekstrak memerangkap radikal NO dinilai menggunakan reagent Griess. Aktiviti anti radang

oleh bahan terekstrak telah ditentukan melalui penilaian terhadap keupayaan menghalang sel makrofaj RAW 264.7 daripada menghasilkan NO yang diaruh oleh lipopolisakarida (LPS) bakteria. Bagi menentukan ketoksikkan ekstrak terhadap sel semasa ianya bertindak sebagai anti radang, tahap sitotiksik telah diukur menggunakan ujian MTT [3-(4,5-dimetiltiazol-2-il)-2,5-difeniltetrazolium bromida]. Kajian mendapati bahawa ekstrak pisang mengandungi bahan kimia bioaktif seperti flavonoids, saponins, fenols, dan lain - lain. Perencatan maksima radikal NO sebanyak 22.34% telah direkodkan bagi ekstrak akueus jantung pisang, dan kadar perencatan minima telah direkodkan pada ekstrak isi pisang. Kesemua ekstrak yang lain menunjukkan perencatan yang rendah. Ekstrak isi pisang mempunyai aktiviti perencatan NO (yang dihasilkan oleh LP) tertinggi dengan perencatan maksima 52.21% pada kepekatan 250 µg/mL, diikuti oleh ekstrak akueus jantung pisang dengan perencatan maksima 48.16% pada kepekatan 62.5µg/mL. Perencatan terendah telah dicatatkan oleh ekstrak metanol jantung pisang, yang mempunyai perencatan maksima 19.63% pada kepekatan 62.5 µg/mL. Kebolehhidupan makrofaj yang diaktifkan tidak terjejas oleh ekstrak sepertimana yang dibuktikan oleh ujian MTT, ia menunjukkan bahawa sintesis NO oleh ektrak bukanlah dari kesan sitotoksik. Secara keseluruhan, bahagian – bahagian *Musa paradisiacal* mempunyai potensi sebagai anti radang dan kajian mengenainya perlu diperluaskan.

Kata kunci: anti radang, MTT, *Musa paradisiaca*, RAW 264.7

Introduction

The body is continuously expose to various noxious agents.This ranges from pathogens (bacteria, viruses, and fungi) to various physical and chemical agents as well as environmental pollutions that result in cell injury or death [1,2]. The body cells resist and eliminate the effect of these agents through an inherent process termed "inflammation".

Recently, the roles of many inflammatory cells and a large number of inflammatory mediators in many pathologies not previously known to be associated to inflammation have been identified. Such pathologies include Alzheimer's disease and cardiovascular disorders including atherosclerosis, as well as cancer [3,4]. For example; acute infection is characterized by elevated myeloperoxidases, ROS and IL-6, which in severe disease serve as an index, in viral and bacterial causes [5], increased nitric oxide (NO) in exhaled air reflected airway inflammation in asthma patients [6,7,8].

Nitric oxide is an important signalling molecule involved in diverse physiological and pathophysiological mechanisms in cardiovascular, nervous and immunological systems. It has contrasting roles in living organisms. It acts as a biological mediator, control blood vessel tone in vascular systems and is an important agent in host defence effector in the immune system. However, it is a free oxygen radical and has cytotoxic effect in pathological processes, particularly in inflammatorydisorders [9-12].Inhibition of iNOS (inducible nitric oxide synthase) may be beneficial for the treatment of inflammatory disease [13,14]. Evidence showed that drugs obtained from natural sources can modulate various inflammatory mediators (arachidonic acid metabolites, peptides, cytokines, excitatory amino acids, *etc*.), the production and/or action of second messengers (cGMP, cAMP, protein kinases, and calcium), the expression of transcription factors such as AP-1, NF-κB, and proto-oncogenes (*c-jun*, *c-fos*, and *c-myc*), and the expression of key pro-inflammatory molecules such as inducible NO synthase (iNOS), cyclooxygenase (COX-2), cytokines (IL-1β, TNF-α), neuropeptides and proteases [15].

Plants have been the basis of many traditional medicine systems throughout the world for thousands of years and remain the primary new source of structurally significant chemical substances that lead to the development of innovative drugs [16,17]. Banana is one of the oldest and well-known fruit worldwide. It has no seeds; it is delicious and available throughout the seasons at an affordable cost. Many traditional uses of banana have been documented. In addition to its nutritional value, a number of biological activities studies have been carried out on banana and these studies prove it to possess bioactivities including anti-hyperglycaemic, anti-ulcerogenic, antioxidant, antihypertensive, cardiac depressant, diuretic, anti-tumoral, bronchodilatory, expectorant, oral contraceptive, antibacterial, antifungal, among others [18].

Hence, the aim of this study is to search for a new safer agent from the medicinal plant that has both NO radical scavenging as well as anti-inflammatory activities is significant to the field of medicine and health sciences.

Materials and Methods

Plant material: Collection and preparation

Musa paradisiaca, fruit and tepal, were obtained from Kuala Terengganu, Malaysia. Samples were identified and authenticated by Dr. Khamsah Suryati Mohd from the Faculty of Bioresources and Food industry, Universiti Sultan Zainal Abidin. The skin (peel) was skinned away and both the skin and the flesh (pulp) were cut and weighed by an electrical balance (1.45kg and 3.28kg) respectively, before dried in a drier at 45 °C, their dry weights were 0.41 kg and 0.21 kg respectively. After drying, samples were blended into powder, using an electrical blender, and the weights were 0.21 kg and 0.10 kg. The tepal was also processed in a similar way and weighed (3kg) and dried at 40 °C and then blended to powder (0.42 kg).

Extraction procedure

The freshly prepared flesh, skin and tepal were extracted twice with methanol (10:2 mL/kg) by cold extraction technique and again with ethanol (for the tepal). The samples were kept in the solvents forthree days at room temperature with regular shaking. Aqueous extraction of the tepal was done by boiling the sample in distilled water at 100 °C on a hot plate. All the extracts were vacuum filtered using Whatman filter paper and made semi-solid by evaporating the solvents using a rotary evaporator.The water extract was concentrated in an oven at 100 °C to obtain the crude extracts. The crude extracts were kept in fresh vials and refrigerated (4 °C) for further use.

Phytochemical screening

The phytochemicals screening of the various solvents extract were carried out using standard procedures as described by Trease and Evans[19]. The following tests were carried out qualitatively.

Test for glycosides

Small amount of the extracts was put in 1 mL of water in a test tube followed by the addition of 1 mL of NaOH. A yellow precipitate indicates the presence of glycosides.

Test for phenols

The extract (5mg) was dissolved in distilled water, and 3 mL of 10% lead acetate solution was added. Bulky white precipitates indicated the presence of phenols.

Test for Flavonoids

A few drops of concentrated hydrochloric acid were added to a small amount of the extract. Immediate development of red color indicates the presence of flavonoids.

Test for Saponins

1 mL of each extract was diluted with distilled water to 20 mL and shaken in a graduated cylinder for 15 min. The formation of foam of about 1cm indicates the presence of saponins.

Pharmacological activities: Nitric oxide (NO) scavenging activity

For the experiment, sodium nitroprusside (10 mM) in phosphate buffered solution (pH = 7.4) was mixed with various concentrations of the extract prepared in 10% DMSO and incubated under light at room temperature for 15 min. The same reaction mixture without the tested extract, but the equal amount of the solvent serves as the control (the last well). After the incubation, 0.05 mL of Griess reagent (1% sulfanilamide, 2% H_3PO_4 and 0.1% N-(1-naphthyl) ethylenediamine dihydrochloride was added. Ascorbic acid was used as positive control. The absorbance was measured at 546 nm and the percentage of NO radical inhibition by the extract was calculated from the formula equation 1 below

$$[(A0–A1) /A0] \times 100. \quad (1)$$

where A0 is the absorbance of the control, and A1 is the absorbance of the extract/standard [20]. IC_{50} value was obtained by drawing the equation of line from the graph of concentration (µg/mL) versus percentage of inhibition.

Anti-inflammatory activity: Materials and reagents

RPMI 1640 media (Gibco), dimethyl sulfoxide (DMSO), lipopolysaccharide (LPS, Escherichia coli) and 3-(4,5-dimethylthiazol-2-yl)-2,5-diphenyltetrazolium bromide (MTT) were purchased from Sigma Chemical Company, fetal bovine serum (FBS)(Gibco) and penicillin/streptomycin (Penstrep)(Gibco).

Cell culture (seeding and treatment)

The macrophage cell line, RAW 264.7 was obtained from the cell culture lab, Faculty of medicine, Universiti Sultan Zainal Abidin. The cells were cultured in Roswell Park Memorial Institute (RPMI, 1640) medium supplemented with 1% pen/strep and 10% heat-inactivated fetal bovine serum. The cell was incubated, in a humidified incubator, in an atmosphere of 5% CO_2 at 37 °C and were subcultured twice before the experiment.

RAW 264.7 cells were seeded onto a 96-well plate (1×10^5 cells/well) and incubated for 24 hours for the experiments. The cells were then treated with the samples at concentrations of 250, 125, 62.5, 31.25, and 15.625 µg/mL and incubated for 1 hour. They were then stimulated with 1µg/mL of LPS for another 24 hours. The supernatant was gently transferred to new 96-well plates and used for NO determination, while the cells remained in the old plate were used for the MTT assay of cell viability. Samples (stock) were dissolved in DMSO, and the working samples were prepared in the media. The effects of the tested extracts were compared with those of L-N^6-(1-iminoethyl) lysine hydrochloride), a known inhibitor of NO production.

MTT [3-(4,5-dimethylthiazol-2-yl)-2,5-diphenyltetrazolium bromide] assay for cell viability

MTT is a pale yellow substrate that is reduced by living cells to yield a dark blue formazan product. This process requires an active mitochondrion, and only freshly dead cells do not reduce significant amounts of MTT. After 24 hours incubation with LPS, MTT was added to the medium for 4 hours. At last, the supernatant was removed, and the formazan crystals were dissolved in DMSO and incubated for more 15 minutes at room temperature. Absorbance was measured at 570nm with reference 630nm. The percentage of dead cells was determined using the formula equation 2.

$$Cell\ viability(\%) = \frac{Test}{Control} \times 100 \quad (2)$$

Nitric oxide assay

Nitric oxide production was assayed by measuring nitrite in the supernatants of cultured RAW 264.7 cells. The assay was carried out as described previously with slight modification [21]. After pre-incubation of RAW 264.7 cells (1×10^5 cells/mL) with LPS (1 µg/mL) for 24 hours, the amount of nitrite, a stable metabolite of NO use as an indicator of NO production, in the culture medium was measured using the Griess reagent (1% sulfanilamide and 0.1% naphthylethylenediamine dihydrochloride in 2.5% phosphoric acid). A volume of 50 µL of the cell culture medium was mixed with 50 µL of the Griess reagent. Subsequently, the mixture was incubated at room temperature for 15 min,and the absorbance was measured at 540 nm in a microplatereader. Fresh culture medium was used as a blank in every experiment. The quantity of nitrite was determined from a sodium nitrite standard curve as expressed in equation 3.

$$Inhibition\ (\%) = \frac{Control-Test}{Control} \times 100 \quad (3)$$

Results and Discussion

Phytochemicals detected in *Musa paradisiaca*

The various solvent extracts of *Musa paradisiaca*, prepared in this work showed the presence of some of the tested phytochemicals like flavonoids, phenols, glycosides among others. Research into natural products often, is aided by ethnopharmacological knowledge and has brought enormous contributions to drug production by providing novel chemical structures and mode of action [22,23]. Methanol and ethanol tepal extracts showed the presence of glycosides and phenols in abundance. Flavonoids and saponins were also detected in these extracts. Tepal aqueous showed the presence of glycosides, phenols, with abundant flavonoids yet saponins are not detected in this extract.

In both skin and flesh methanol extracts, glycosides and phenols were detected with abundant flavonoids in the latter and normal in the former (Table 1).

Table 1. Phytochemicals from the various solvent extracts of *Musa paradisiaca*

Extract	Glycosides	Phenols	Flavonoids	Saponins
Tepal methanol	++	++	+	+
Tepal Ethanol	++	++	+	+
Tepal Aqueous	+	+	++	-
Skin	+	+	++	-
Flesh	+	+	+	-

Note: ++ = present in abundance. + = present. - = Absent

Plant secondary metabolites, are essential sources of many food ingredients and plant chemicals (phytochemicals) [24]. Plants are known to produce many secondary metabolite compounds like alkaloids, cyanogenic glycosides, glucosinolates, flavonoids, saponins, steroids and terpenoids to screen themselves from the attack of naturally occurring pathogens, insect pests and environmental stresses. Recent researches showed that many phytochemicals can protect humans against various diseases [25]. Many phytochemicals are present in herbs, and each has its distinct work. The health benefits attributed to these phytochemicals include; antioxidant, antimicrobial, anti-inflammatory, cancer preventive, antidiabetic and antihypertensive effects [26,27].

Previous studies confirm to the current finding. Research by Jini et al. [28], showed that the flower methanol, ethanol and aqueous extracts of *Musa paradisiaca* containing flavonoids and phenolic compounds. Phytochemical screening of *Musa paradisiaca* flower revealed the presence of glycosides, flavonoids and tannins in ethanolic extract and flavonoids, saponins, glycosides and tannins in ethanol-water extract (1:1) [29]. Preliminary phytochemical screening of dried leaves and fruit peels of *Musa paradisiaca* revealed the presence of some glycosides, anthocyanins, tannins, flavonoids as well as carbohydrates [30,31,32]. These phytochemicals have been reported to play multiple biological and pharmacological roles (antibacterial, antihypertensive, antidiabetic and anti-inflammatory activities) [33].

The obvious roles played by these phytochemicals in both therapeutic and nutritional fields, contribute to the role played by this plant, *Musa paradisiaca* particularly tepal and fruit (skin and flesh) in the field of medicine and health sciences.

Effect of *Musa paradisiaca* on nitric oxide generated by sodium nitroprusside

The extracts showed mild inhibition against the NO produced by the sodium nitroprusside. Maximum inhibition of 41.05% was recorded in the tepal aqueous extract, and minimum inhibition of 22.34% has been registered in the flesh extract; all others showed mild inhibition as well (Table 2).

Table 2. Percentage of NO inhibition by tepal, skin and flesh extracts with the inhibitory concentration

Sample	Maximum inhibition (%)	Concentration (µg/mL)
Tepal methanol	32.36	1000
Tepal ethanol	40.58	250
Tepal aqueous	41.05	1000
Skin	35.94	1000
Flesh	22.34	500
Ascorbic acid	84.43	1000

Nitric oxide is an important chemical mediator produced by endothelial cells, macrophages, neurons, to mention a few and is involved in the regulation of many different physiological processes [34]. An excess amount of NO is associated with several diseases [35], such as its implication in inflammation, cancer and other pathological conditions. It is produced in biological tissues by specific nitric oxide synthases (NOSs), which metabolize arginine to citrulline in which process it is formed via a five electron oxidative reaction [36]. Incubation of solutions of sodium nitroprusside in PBS at 25 $^{\circ}$C resulted in the linear time dependent nitrite production, which is reduced by the tested extracts. Powdered drug of plant parts of Drymariadiandra Blume were separately extracted with methanol-water in ratio 4:1. The extracts from this plant of both hill and plain areas executed very less scavenging power against NO [37].

Effect of *Musa paradisiaca* – tepal, skin and flesh on LPS induced NO (anti-inflammatory activity) and RAW 264.7 cell viability

The Griess reaction, a spectrophotometric determination of nitrite level, was carried out to measure the nitrite levels in the conditioned medium of RAW 264.7 cells treated with LPS. Sodium nitrite ($NaNO_2$) was used as a standard compound for the standard curve (Figure 1). The NO concentrations were obtained using the standard curve equation: $y = 0.005x + 0.0589$, where y is absorbance at 540 nm and x is the NO concentration in µM. The inhibitory activity of the extracts towards NO generated by LPS-activated macrophage was obtained from the calculated value of x.

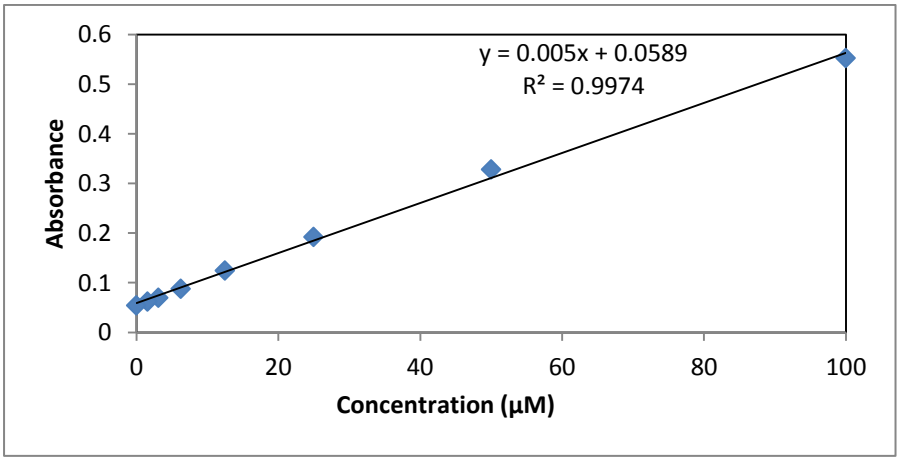


Figure 1. $NaNO_2$ standard curve, use to obtain NO concentration.

The results from this findings showed that flesh extract has the highest NO inhibitory activity, with the maximum inhibition of 52.21% at 250 µg/mL, followed by tepal aqueous extract with maximum inhibition of 48.16% at 62.5 µg/mL. The least inhibition was noted in the tepal methanol extract that has the highest inhibition of 19.63% at 62.5 µg/mL (Table 3). The inhibition of NO, generated by the LPS induced macrophage, by the extracts is similar to that of NO generated by sodium nitroprusside, as discussed in the NO radical scavenging assay. This proves that *Musa paradisiaca* has NO inhibitory activity, which signifies its anti-inflammatory activity.

Table 4 and Figure 2 showed that the number of viable activated macrophages was not altered by the extracts as determined by MTT assay. This indicates that, the inhibition of NO synthesis by the extracts was not due to cytotoxic effects.

The higher NO inhibition by the fruit correspond to the epidemiological data that suggest that lower incidences of certain chronic diseases such as atherosclerosis, arthritis, diabetes, acquired immune deficiency syndrome (AIDS)

are associated with frequent intake of fruits and vegetables [38,39,40]. Flavonoids constituent may also contribute to this activity as many studies prove that consumption of flavonoid-rich foods exhibited regression of inflammatory diseases [41].

Table 3. Maximum NO (generated by LPS) inhibitory concentration of *Musa paradisiaca* tepal, skin and flesh extracts and their concentrations.

Sample	Maximum NO inhibition (%)	Concentration (µg/mL)
Tepal methanol	19.63	62.5
Tepal ethanol	46.08	125
Tepal aqueous	48.16	62.5
Skin	30.6	250
Flesh	52.21	250
Standard	52	250

Table 4. Maximum and minimum percent cell viability of *Musa paradisiaca* tepal, skin and flesh and their various concentrations

	Cell viability (%)			
Sample	Maximum	Concentration (µg/mL)	Minimum	Concentration (µg/mL)
Tepal methanol	102.4	62.5	15	250
Tepal ethanol	119.84	62.5	75	250
Tepal aqueous	83.43	15.625	36	250
Skin	87.14	15.625	43	250
Flesh	100.36	62.5	68	250
Standard	90.97	62.5	80.96	250

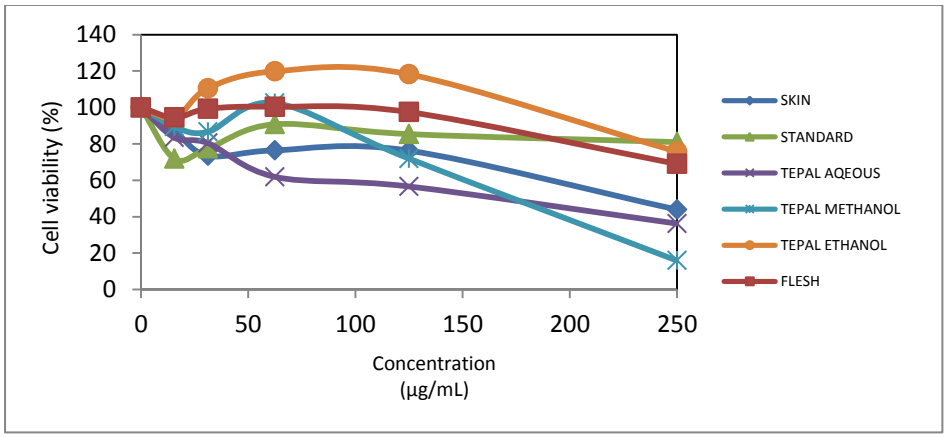


Figure 2. Percent cell viability of the tepal, skin and flesh extracts as determined by MTT

Inflammation is the normal physiological and immune response to tissue injury. More blood supply, enhanced vascular permeability and migration of immune cells occur at the damaged sites. The inflammatory process is a protective reaction that takes place in response to trauma, infection, tissue injury or noxious stimuli [42,43,44]. In this process, activated inflammatory cells (neutrophils, eosinophil, mononuclear phagocytes and macrophages) released abnormal levels of NO, prostaglandin E2 (PGE2) and cytokines, such as interleukin (IL)-1ß, IL-6, and tumour necrosis factor (TNF).These substances not only cause cell and tissue damage but also activate macrophages in diseases like rheumatoid arthritis and chronic hepatitis [45 – 48].

NO is the main product, which formationis regulated by the NOSs. The NOSs include iNOS (inducible nitric oxide synthases), eNOS (endothelial nitric oxide synthases) and nNOS (neuronal nitric oxide synthases). Most significantly, iNOS is highly expressed in macrophages and its activation leads to organ destruction in some inflammatory and autoimmune diseases [49,50]. During inflammation, macrophages play a fundamentalrole in controlling many different immunopathological phenomena, including the overproduction of pro-inflammatory cytokines and inflammatory mediators such as IL-1ß, IL- 6, NO, iNOS, COX-2 and TNF. Indeed, many of inflammatory stimuli, such as LPS and proinflammatory cytokines, activate immune cells to up-regulate such inflammatory states, and these are therefore useful targets in the development of new anti-inflammatory drugs and investigation of the anti-inflammatory molecular mechanisms of a potential drug [51,52]. LPS stimulation alone has been demonstrated to induce iNOS transcription and its protein synthesis, in murine macrophage RAW 264.7 cells, with a corresponding rise in NO production. Moreover, LPS stimulation has also been shown to induce IκB proteolysis and NF-κB nuclear translocation [53,54]. Hence, this cell system is a splendid model for drug screening and the subsequent evaluation of potential inhibitors against iNOS and NO production.

Varieties of phytoconstituents are responsible for anti-inflammatory activity in plants, including phenolics, alkaloids, and terpenoids [55] and phenols are among the phytochemical presents in the extracts. Plants are blessed with many different phytochemical such as, vitamins, phenolics, terpenoids, lignins, tannins, flavonoids, quinones, coumarins, alkaloids, amines, betalains, and other metabolites, which are rich in antioxidant activity [56,57]. Several researches have shown that many of these antioxidant compounds possess anti-inflammatory, anti-atherosclerotic, anti-tumor, anti-mutagenic, anti-carcinogenic, anti-bacterial, and anti-viral activities [58,59]. Saponins present in the tepal ethanol extract may as well, contribute to its anti-inflammatory activity, as soybean saponins were reported to downregulate the expression of PGE2 and NO metabolism at mRNA and protein levels, showing these saponins as chemicals that possess chemopreventive activity through the downregulation of COX-2 or iNOS [60]. Another report also showed that saponins from quinoa possess potent anti-inflammatory activities [61].

Many compounds from medicinal plants origin have been demonstrated as inhibitors of the expression of iNOS in LPS-activated macrophages. Their structures can be categorized as sesquiterpene [62,63], polyacetylenes [64] and lignans [65]. Thus, plants demonstrating inhibitory activity against NO production will be promising candidates for the isolation of active components exhibiting iNOS inhibitory activity, which may have therapeutic potential for the treatment of inflammation accompanying overproduction of NO.

These results indicate that flesh, tepal ethanol and aqueous extracts may suppress NO generation by inhibiting the NOS enzyme activity similar to the NOS inhibitor L-N^6-(1-imino ethyl) lysine hydrochloride (the standard). It is recommended that the extracts, which inhibits NO production through inhibiting iNOS enzyme activity, has beneficial therapeutic effects in the management of inflammatory diseases. These results showed that the tepal ethanol, aqueous and flesh extracts, did not alter the cell viability even at 250 µg/mL. Therefore, inhibition of LPS-induced NO production by these extracts was not due to its cytotoxicity on the cells.

Conclusion

Musa paradisiaca (banana) is a plant that has been used since ancient times both as nutrient and in the treatment of many diseases. The plant is a good candidate for evaluating the nitric oxide scavenging as well as anti-inflammatory potentials due to its proven positive pharmacological activities by many researchers. Both tepal and fruit extracts

demonstrated good nitric oxide scavenging as well as anti-inflammatory activities. Hence, these plant parts need more scientific attention in order to actualize its potentialities in the fields of medicine and health sciences.

Acknowledgement

The researchers acknowledged the effort of chemistry and cell culture labs staff, in the Faculty of Medicine, of Universiti Sultan Zainal Abidin (UniSZA) for their help in this research. The effort of Ainul Syamira, a research assistant at UniSZA, is also appreciated.

References

1. O'Byrne, K. J. and Dalgleish, A. G. (2001). Chronic immune activation and inflammation as the cause of malignancy. *British Journal of Cancer*, 85:473 – 483.
2. O'Byrne, K. J., Dalgleish, A. G., Browning, M. J., Steward, W. P. and Harris, A. L. (2000), The relationship between angiogenesis and the immune response in carcinogenesis and the progression of malignant disease. *European Journal of Cancer*, 36: 151 – 169.
3. Akiyama, H., Barger, S., Barnum, S., Bradt, B., Bauer, J., Cole, G. M., Cooper, N. R., Eikelenboom, P., Emmerling, M. and Fiebich, B. L. (2000). Inflammation and Alzheimer's disease. *Neurobiology of Aging*, 21: 383 – 421.
4. Libby, P., Ridker, P. M. and Maseri, A. (2002). Inflammation and atherosclerosis. *Circulation*, 105: 1135 – 1143.
5. Kulander, L., Pauksens, K. and Venge, P. (2001). Soluble adhesion molecules, cytokines and cellular markers in serum in patients with acute infections. *Scandinavian Journal of Infectious Diseases,* 33: 290 – 300.
6. Bellanti, J. A. (1998). Cytokines and allergic diseases: clinical aspects. *Allergy Asthma Proceeding*, 19: 337 – 341.
7. Romagnani, S. (2000). T-cell subsets (Th1 versus Th2). *Ann. Allergy Asthma. Immunology*, 85: 9 – 21.
8. Silvestri, M., Sabatini, F., Defilippi, A. C., Ghiro, L., Baraldi, E. and Rossi, G. A. (2003). A marker of asthma inflammation: orally exhaled nitric oxide. *Allergy and Clinical Immunology International*, 15: 37 – 43.
9. Alderton, W. K., Cooper, C. E. and Knowles, R. G. (2001). Nitric oxide synthases: structure, function and inhibition. *Biochemical Journal*, 357(P3): 593 – 615.
10. Bogdan, C. (2001). Nitric oxide and the immune response. *Nature Immunology*, 2(10): 907 –916.
11. Dawn, B. and Bolli, R. (2002). Role of nitric oxide in myocardial preconditioning. *Annals of the New York Academy of Sciences*, 962: 18 – 41.
12. Moncada, S. and Higgs, E. A. (1991). Endogenous nitric oxide: physiology, pathology and clinical relevance. *European Journal of Clinical Investigation,* 21(4): 361 – 374.
13. Aktan, F., Henness, S., Roufogalis, B. D. and Ammit, A. J. (2003). Gypenosides derived from *Gynostemma pentaphyllum* suppress NO synthesis in murine macrophages by inhibiting iNOS enzymatic activity and attenuating NF-B-mediated iNOS protein expression. Nitric Oxide: *Biology and Chemistry*, 8(4): 235 – 242.
14. Kroncke, K. D., Fehsel, K. and Kolb-Bachofen, V. (1998). Inducible nitric oxide synthase in human diseases. *Clinical Experimental Immunology*, 113(2): 147 – 156.
15. Kim, Y. S., Young, M. R., Bobe, G., Colburn, N. H. and Milner, J. A., (2009). Bioactive food components, inflammatory targets, and cancer prevention. *Cancer Prevention Research*, 2: 200 – 208.
16. Fabricant, D. S. and Farnsworth, N. R. (2001). The value of plants used in traditional medicine for drug discovery. *Environmental Health Perspective*, 109: 69 – 75.
17. Jachak, S. M. and Saklani, A., (2007). Challenges and opportunities in drug discovery from plants. *Current Science*, 92: 1251 – 1257.
18. Sharma, P. C., Yelne, M. B., Dennis and Kadali J. J. (2002). In: Data base on medical plants used in Ayurveda and Siddha. *New Delhi: Public Printing*, 5: 78 – 93.
19. Trease, G. E. and Evans, W. C. (1989). Trease and Evan's Textbook of Pharmacognosy. 13th Ed. London: *Cambridge University Press*: pp. 546
20. Sreejayan, N. and Rao, M. N. A. (1997). Nitric oxide scavenging by curcuminoids. *Journal of Pharmacy and Pharmacology*, 49(1): 105 – 107.
21. Yoon, W. J., Kim, S. S., Oh, T. H., Lee, N. H. and Hyun, C. G. (2009). *Abies koreana* essential oil inhibits drug-resistant skin pathogen growth and LPS-induced inflammatory effects of murine macrophage. *Lipids*, 44: 471 – 476.

22. Sheeba, M. S. and Asha, V. V. (2006). Effect of *Cardiospermum halicacabum* on ethanol-induced gastric ulcers in rats. *Journal of Ethnopharmacology*, 106(1): 105 – 110.
23. Bohlin, L., Goransson, U., Alsmark, C., Weden, C. and Backlund, A. (2010). Natural products in modern life science. *Phytochemistry Reviews*, 9(2): 279 – 301.
24. Doss, A. and Anand, S. P. (2012). Preliminary phytochemical screening of *Asteracanthalongifolia* and *Pergularia daemia*. *World Applied Science Journal*, 18(2): 233 – 235.
25. Kubmarawa, D., Khan, M. E., Punah, A. M. and Hassan, M. (2008). Phytochemical screening and antibacterial activity of extracts from *Parkia clappertoniana* keay against human pathogenic bacteria. *Journal of Medical Plants Research*; 2(12): 352 – 355.
26. Savithramma, N., Linga Rao, M. and Suhrulatha, D. (2011). Screening of medicinal plants for secondary metabolites. *Middle-East Journal of Science Research*; 8: 579 – 584.
27. Rupasinghe, H. P., Jackson, C. J., Poysa, V., Berado, C. D., Bewley, J. D. and Jenkinson, J. (2003). Soyasapogenol A and B distribution in Soybean (Glycine max (L.) Merr.) in relation to seed physiology, genetic variability and growing location. *Journal of Agricultural and Food Chemistry*, 51: 5888 – 5894.
28. Jini, J., David, P., Kavitha, M. P., Dineshkumar, B., Jalaja S. Menon, Bhat, A. R. and Krishnakumar, K. (2014). Preliminary phytochemical screening and in vitro antioxidant activity of Banana flower (*Musa paradisiaca AAB Nendran variety*). *Journal of Pharmacy Research*, 8(2): 144 – 147.
29. Sunil Jawla, Kumar, Y. and Khan, M. S. Y. (2012). Antimicrobial and antihyperglycemic activities of *Musa paradisiaca* flowers. *Asian Pacific Journal of Tropical Biomedicine*, 2(2): 914 – 918.
30. Anhwange, B. A. (2008). Chemical composition of *Musa sapientum* (Banana) peels. *Journal of Food Technology*, 6(6): 263 – 268.
31. Archibald, J. G. (1949). Nutrient composition of banana skins. *Journal of Dairy Science*; 32: 969 –971.
32. Alisi, C. S., Nwanyanwu, C. E., Akujobi, C. O. and Ibegbulem, C. O. (2008). Inhibition of dehydrogenase activity in pathogenic bacteria isolates by aqueous extracts of *Musa paradisiaca* (var Sapientum). *African Journal of Biotechnology*, 7(12): 1821 – 1825.
33. Middleton, E. J. and Kandaswanmi, C. (1992). Effects of flavonoids on immune and inflammatory cell function. *Biochemical Pharmacology*, 43(6): 1167 –1179.
34. Lata, H. and Ahuja, G. K. (2003). Role of free radicals in health and disease. *Indian Journal of Physiology Allied Science*, 57: 124 – 128.
35. Lalenti, S., Moncada, M. and Di Rosa (1993). Modulation of adjuvant arthritis by endogenous nitric oxide. *British Journal of Pharmacology*, 110: 701 – 705.
36. Ross, R. (1993). The pathogenesis of atherosclerosis: A perspective for the 1990's. *Nature*, 362: 801- 809.
37. Palash, M., Tarun, K. M. and Mitali, G. (2009). Free-radical scavenging activity and phytochemical analysis in the leaf and stem of *Drymaria diandra* Blume. *International Journal Integrative Biology,* 7(2): 81 – 83.
38. Ames, B. N., Shigenaga, M. K. and Hagen, T. M. (1993). Oxidants, antioxidants and the degenerative diseases of aging. *Proceeding National Academy Science*, 90: 7915 – 7922.
39. Chu, Y. F., Sun J., Wu X. and Liu, R. H. (2002). Antioxidant and antiproliferative activities of common vegetables. *Journal Agricultural and Food Chemistry*, 50: 6910 – 6916.
40. Choi, C. W., Kim, S. C., Hwang, S. S., Choi, B. K., Ahn, H. J., Lee, M. Y., Park, S. H. and Kim, S. K. (2002). Antioxidant activity and free radical scavenging capacity between Korean medicinal plants and flavonoids by assay-guided comparison. *Plant Science*, 163: 1161 – 1168.
41. Mennen, L. I., Sapinho, D., de Bree, A., Arnault, N., Ber Trais, S., Galan, P. and Hercberg, S. (2004). Consumption of foods rich in flavonoids is related to a decreased cardiovascular risk in apparently healthy French women. *Journal of Nutrition*, 134(4): 923 – 926.
42. Zedler, S. and Faist, E. (2006). The impact of endogenous triggers on trauma-associated inflammation. *Current Opinion in Critical Care*, 12: 595 – 601.
43. Mariathasan, S. and Monack, D. M., (2007). Inflammasome adaptors and sensors: intracellular regulators of infection and inflammation. *Nature Review of Immunology*, 7: 31 – 40.
44. Choy, C. S., Hu, C. M., Chiu, W. T., Lam, C. S., Ting, Y., Tsai, S. H. and Wang, T. C. (2008). Suppression of lipopolysaccharide-induced of inducible nitric oxide synthase and cyclooxygenase-2 by *Sanguisdraconis*, a dragon's blood resin, in RAW 264.7 cells. *Journal of Ethnopharmacology*, 115: 455 – 462.

45. Vane, J. R., Mitchell, J. A., Appleton, I., Tomlinson, A., Bishop-Bailey, D., Croxtall, J. and Willoughby, D. A. (1994). Inducible isoforms of cyclooxygenase and nitric-oxide synthase in inflammation. *Proceedings of the National Academy of Sciences*, 91: 2046 – 2050.
46. Kasama, T., Miwa, Y., Isozaki, T., Odai, T., Adachi, M. and Kunkel, S. L. (2005). Neutrophil-derived cytokines: potential therapeutic targets in inflammation. *Current Drug Targets - Inflammation and Allergy*, 4: 273 – 279.
47. Wolf, A. M., Wolf, D., Rumpold, H., Ludwiczek, S., Enrich, B., Gastl, G., Weiss, G. and Tilg, H., (2005). The kinase inhibitor imatinib mesylate inhibits TNF-{alpha} production in vitro and prevents TNF-dependent acute hepatic inflammation. *Proceedings of the National Academy of Sciences*, 102: 13622 – 13627.
48. Cheon, H., Rho, Y. H., Choi, S. J., Lee, Y. H., Song, G. G., Sohn, J., Won, N. H. and Ji, J. D. (2006). Prostaglandin E2 augments IL-10 signaling and function. *Journal of Immunology*, 177: 1092 – 2100.
49. Esposito, E. and Cuzzocrea, S., (2007). The role of nitric oxide synthases in lung inflammation. *Current Opinion in Investigational Drugs*, 8: 899 – 909.
50. Murakami, A. and Ohigashi, H. (2007). Targeting NOX, INOS and COX-2 in inflammatory cells: Chemoprevention using food phytochemicals. *International Journal of Cancer*; 121: 2357 – 2363.
51. Zeilhofer, H. U. and Brune, K., (2006). Analgesic strategies beyond the inhibition of cyclooxygenases. *Trends Pharmacology Science*, 27: 467 – 474.
52. Jachak, S. M. (2007). PGE synthase inhibitors as an alternative to COX-2 inhibitors. *Current Opinion in Investigational Drugs*, 8: 411 – 415.
53. Xie, Q. W., Kashiwabara, Y. and Nathan, C. (1994). Role of transcription factor NFkappa B/Rel in induction of nitric oxide synthase. *Journal of Biology Chemistry*, 269: 4705 – 4708.
54. Henkel, T., Machleidt, T., Alkalay, I., Konke, M., Ben-Neriah, Y. and Baeuerle, P. A. (1993). Rapid proteolysis of I kappa B-alpha is necessary for activation of transcription factor NF-kappa B. *Nature*, 365: 182 – 185.
55. Arya, V. and Arya, M. L. (2011). A review on anti-inflammatory plant barks. *International Journal of Pharmtech Research*, 3: 899 – 908.
56. Zheng, W. and Wang, S. Y. (2001). Antioxidant activity and phenolic compounds in selected herbs. *Journal of Agricultural and Food Chemistry*, 49(11): 5165 – 5170.
57. Cai, Y. Z., Sun, M. and Corke, H. (2003). Antioxidant activity of betalains from plants of the *Amaranthaceae*. *Journal of Agricultural Food Chemistry*, 51(8): 2288 – 2294.
58. Sala, A., Recio, M. D., Giner, R. M., Manez, S., Tournier, H., Schinella, G. and Rios, J. L. (2002). Antiinflammatory and antioxidant properties of *Helichrysum italicum*. *Journal Pharmacy and Pharmacology*, 54(3): 365 – 371.
59. Rice-Evans, C. A., Miller, N. J., Bolwell, P. G., Bramley, P. M. and Pridham, J. B. (1995). The relative activities of Plant-derived polyphenolic flavonoid. *Free Radical Research*, 22: 375 – 383.
60. Kang, J. H., Sung, M. K., Kawada, T., Yoo, H., Kim, Y. K., Kim, J. S. and Yu, R. (2005). Soybean saponins suppress the release of proinflammatory mediators by LPS-stimulated peritoneal macrophages. *Cancer Letters*, 230: 219 – 227.
61. Yao, Y., Yang, X., Shi, Z. and Ren., G. (2014). Anti-inflammatory activity of saponins from quinoa (*chenopodium quinoa* willd.) seeds in lipopolysaccharide-stimulated RAW 264.7 macrophages cells. *Journal of Food Science*, 79(5): 1021 – 1022.
62. Reddy, A. M., Lee, J. Y., Seo, J. H., Kim, B. H., Chung, E. Y., Ryu, S. Y., Kim, Y. S., Lee, C. K., Min, K. R. and Kim, Y. (2006). Artemisolide from *Artemisia asiatica*: nuclear factor-kappaB (NF-kappaB) inhibitor suppressing prostaglandin E2 and nitric oxide production in macrophages. *Archives Pharmacal Research*, 29: 591 – 597.
63. Choi, Y., Lee, M. K., Lim, S. Y., Sung, S. H. and Kim, Y. C. (2009). Inhibition of inducible NO synthase, cyclooxygenase-2 and interleukin-1beta by torilin is mediated by mitogen-activated protein kinases in microglial BV2 cells. *British Journal of Pharmacology*, 156: 933 – 940.
64. Kim, J. M., Lee, P., Son, D., Kim, H. and Kim, S. Y. (2003). Falcarindiol inhibits nitric oxidemediated neuronal death in lipopolysaccharide-treated organotypic hippocampal cultures. *Neuroreport*, 14: 1941 –1944.

65. Kim, B. H., Hong, S. S., Kwon, S. W., Lee, H. Y., Sung, H., Lee, I. J., Hwang, B. Y., Song, S., Lee, C. K., Chung, D., Ahn, B., Nam, S. Y., Han, S. B. and Kim, Y. (2008). Diarctigenin, a lignan constituent from *Arctium lappa*, down-regulated zymosan-induced transcription of inflammatory genes through suppression of DNA binding ability of nuclear factor-kappaB in macrophages. *Journal Pharmacology and Experimental Therapeutics*, 327: 93 – 401.

Malaysian Journal of Analytical Sciences, Vol 20 No 5 (2016): 1203 - 1216
DOI: http://dx.doi.org/10.17576/mjas-2016-2005-27

MALAYSIAN JOURNAL OF ANALYTICAL SCIENCES
Published by The Malaysian Analytical Sciences Society
ISSN 1394 - 2506

ANTIULCER ACTIVITY OF *Musa paradisiaca* (BANANA) TEPAL AND SKIN EXTRACTS IN ULCER INDUCED ALBINO MICE

(Aktiviti Antiulser dari Ekstrak Jantung dan Kulit *Musa paradisiaca* (Pisang) pada Tikus Albino Teraruh Ulser)

U.S Mahadeva Rao[1], Bashir Ado Ahmad[1]*, Khamsah Suryati Mohd[2,3], Thant Zin[1]

[1]*Faculty of Medicine,*
Universiti Sultan Zainal Abidin, Medical Campus, 21400 Kuala Terengganu, Terengganu, Malaysia
[2]*Faculty of Bioresources and Food Industry*
[3]*Agriculture Production and Food Innovation Research Institute*
Universiti Sultan Zainal Abidin, Tembila Campus, 22200 Besut, Terengganu, Malaysia

**Corresponding author: dambash011@yahoo.com*

Received: 14 April 2015; Accepted: 3 August 2016

Abstract

The current use of ulcer drugs is limited due to its side effects and potentiality of relapse. This study aimed to ascertain the antiulcer potentials of the tepal and skin extracts of banana *Musa paradisiaca*. The parts were processed and extracted using methanol by maceration. Phytochemicals content of both parts were screened. Twenty-five albino mice were used in *in vivo* analysis. The mice were treated with 100 mg/kg of tepal and skin extract as well as cimetidine for seven days followed by administration of indomethacin. The animals were sacrificed, and the removed stomachs were prepared for the evaluation of ulcer index and gastric wall mucus. pH and volume were measured from the gastric juice. The results revealed that banana's tepal and skin extracts contain phytochemicals like phenols, flavonoids and etc. The tepal and skin extracts prevented the IND+PYL induced ulcer by 68.80 ± 20.53% and 43.22 ± 14.82% respectively. Significant rise ($p < 0.05$) in gastric juice pH (3.79 ± 0.24) was noticed in the banana's tepal treated group. However, the decrease in gastric juice volume and increased gastric wall mucus by both tepal and skin were not statistically significant ($p > 0.05$). Findings from this study shows that banana's tepal and skin were able to prevent IND+PYL induced ulcer by strengthening the gastric mucosa and decreasing the gastric juice acidity.

Keywords: banana's tepal, banana's skin, indomethacin, *Musa paradisiaca,* preventive index.

Abstrak

Penggunaan ubat ulser pada masa kini adalah terhad disebabkan kesan sampingan dan potensi kambuh. Kajian ini bertujuan menentukan potensi antiulser dari ekstrak jantung dan kulit pisang *Musa paradisiaca*. Bahagian – bahagian ini telah diproses dan diekstrak menggunakan metanol melalui kaedah rendaman. Kandungan fitokimia kedua – dua bahagian telah disaring. Dua puluh lima tikus albino telah digunakan dalam analisis *in vivo*. Tikus – tikus ini telah diberi rawatan dengan 100mg/kg ekstrak jantung dan kulit pisang serta simetidin selama tujuh hari di ikuti dengan rawatan dengan indomethacin. Haiwan dikorbankan selepas 8 hari rawatan, dan perut dikeluarkan bagi penilaian indeks ulser dan mukus dinding perut. pH dan jumlah jus gastrik juga diukur. Hasil kajian mendapati bahawa ekstrak jantung dan kulit pisang mengandungi beberapa fitokimia seperti fenol, flavonoid, dan lain – lain. Ekstrak jantung dan kulit ini menghalang ulser yang diaruh dengan IND+PYL masing – masing sebanyak 68.80 ± 20.53% dan 43.22 ± 14.82%. Peningkatan yang signifikan ($p < 0.05$) pada pH jus gastrik (3.79 ± 0.24) telah diperhatikan dalam kumpulan yang dirawat dirawat dengan jantung pisang. Walau bagaimanapun, penurunan dalam jumlah jus gastrik dan meningkatkan mukus dinding perut oleh kedua – dua ekstrak adalah tidak signifikan secara statistik ($p > 0.05$). Dapatan dari kajian ini menunjukkan bahawa jantung dan kulit pisang dapat mencegah ulser yang diaruh dengan IND+PYL melalui penambahan mukosa perut dan pengurangan keasidan jus gastrik.

Kata kunci: jantung pisang, kulit pisang, indomethacin, *Musa paradisiaca,* indeks pencegahan

Introduction

Ulcers are simply lesions penetrating the thickness of the gastrointestinal tract (G.I.T) mucosa [1]. The etiology of gastro-duodenal (peptic) ulcer has therefore developed when aggressive factors such as, increased HCL and pepsin secretion, parietal cell mass, and gastrin production, dominate the defensive factors (PGs, increased mucous cells etc) [2,3].

Indomethacin, a NSAID (methylated indole derivative), was introduced in 1963 for the management of inflammatory diseases such as rheumatoid arthritis, degenerative joint diseases, gout, and acute musculoskeletal disorders [4,5]. However it was later found to be injurious to tissues. These injurious effects have been ascribed to the production of reactive oxygen species (ROS) [6,7], which lead to oxidative stress and initiation of lipid peroxidation [7], infiltration of inflammatory cells [8,9]. Pylorus ligation also induced ulcers by increasing the accumulation of gastric acid and pepsin that lead to auto digestion of the gastric mucosa and the breakdown of gastric mucous [10]. Hence, indomethacin and pylorus ligation were used to induce ulcer in this research.

The major idea behind treating ulcers is to lower the amount of acid that the stomach makes, to neutralize the acid and to protect the injured area so it can have time to heal [1]. However, most of the commonly used antiulcer drugs, namely antacids, H2- blockers and proton pump inhibitors, etc. that mainly act by reducing the aggressive factors are reported to have adverse effects, development of tolerance and increased the incidence of relapses during ulcer therapy [11]. The expensive costs and toxic effect of these agents, necessitate efforts to find a suitable protective agent, for the treatment of peptic ulcer disease from natural products of plants, which afford better protection and decrease the incidence of relapse that is affordable by all classes of people. Interestingly, herbal drugs mostly augment the defensive factors such as mucin secretion, cellular mucus, bicarbonate secretion and mucosal blood flow [12].

Banana is one of the oldest and well-known fruit worldwide. The leaf and stem of banana are use to treat diarrhoea; the stem is good for asthenia and wounds, and the leaf for the treatment of inflammation, headache and rheumatism [13]. Besides to its nutritional value, a number of biological activities studies have been carried out on banana and these studies prove it to possess bioactivities including anti-hyperglycaemic, antiulcerogenic, antioxidant, antihypertensive, cardiac depressant, diuretic, anti-tumoral, bronchodilatory, expectorant, oral contraceptive, abortifacient, antibacterial, antifungal and etc. [14]. Therefore, this study was carried out to evaluate the antiulcer effect of *Musa paradisiaca* tepal (a part mostly considered as a waste) and skin, against indomethacin plus pylorus ligation induced gastric injury in mice.

The economy of developing countries has a lot to do with the health status of its citizen. The rising incidence of ulcer has involved both adults and children. The solution to ulcer will help in controlling health status, societal and physical well-being as well as economic uplift of individuals, families, companies and nation at large.

Materials and Methods

Collection and preparation

Banana fruit and tepal, were purchased from Kuala Terengganu, Malaysia; samples were identified and authenticated by Dr. Khamsah Suryati Mohd from the Faculty of Bioresources and Food industry, Universiti Sultan Zainal Abidin. The skin (peel) was removed from the fruit, sliced, and weighed using electrical balance (1.45kg). It was then dried in a drier at 45°C; the dry weight is 0.41 kg. After drying, it was blended to powder, using an electrical blender, and the weight is 0.21 kg. The tepal was also prepared in a similar way and weighed (3kg) and dried at 40 $^{\circ}$C and then blended to powder (0.42 kg).

Extraction procedure

The prepared skin and tepal were extracted twice with methanol (10:2 mL/kg) by cold extraction technique. The samples were put in the solvents for about 3 days at room temperature with regular shaking. All the extracts were

vacuum filtered using Whatman number one filter paper and concentrated at 40 °C using a rotary evaporator. The crude extracts were kept in a fresh vials and refrigerated at 4°C for further study.

Phytochemical screening of the extracts
The phytochemicals screening of the various solvents extract were carried out using standard procedures [15].

Test for glycosides
Small amount of the extracts was put in 1 mL of water in a test tube followed by the addition of 1 mL of NaOH. A yellow precipitate indicates the presence of glycosides.

Test for phenols
The extract (5mg) was dissolved in distilled water and 3 mL of 10% lead acetate solution was added. A bulky white precipitates indicated the presence of phenols.

Test for Flavonoids
A few drops of concentrated hydrochloric acid were added to a small amount of the extract. Immediate development of red colour indicates the presence of flavonoids.

Test for Saponins
An amount 1 mL of each extract was diluted with distilled water to 20 mL and shaken in a graduated cylinder for 15 min. The formation of foam of about 1cm indicates the presence of saponins.

Evaluation of antiulcer activity
Swiss albino mice of both sexes (30-35g), obtained from UniversitI Sains Malaysia Pinang, were utilized in this experiment. The animals were kept in cages with proper bedding. The bedding was regularly changed to prevent coprophagy. The animals were put up in an ambient temperature of 22 ± 1ºC in a 12 hours light–dark bicycle. They were fed a standard balanced diet and given free access to water *ad libitum*. All animals were fasted for 24 hours [16] to ensure an empty stomach before use in the experiment. The experiments were designed and conducted to meet the ethical norms approved by University Sultan Zainal Abidin, Malaysia, animal ethical committee (UniSZA/AEC/14/006).

Study design
The experimental models were acclimatized for one week. They were then randomly grouped into five groups comprising of five mice each. Group I served as normal control, which received 0.3ml/30g distilled water for 7 days. Group II or IND+PYL group was induced with indomethacin at a single dose of 48 mg/kg [17] body weight (b.wt) on the 7th day of the experiment. Group III or TPM group was also orally administered methanol extract of the tepal at a dose of 100 mg/kg b. wt and then indomethacin at a single dose of 48 mg/kg on the 7th day, one hour after the last treatment. Group IV or SKM and V or CIM were treated in the same manner as group III. All animals were allowed to fast overnight. On the 8th day, pylorus was ligated using silk sutures as per the method [18] under light ether anaesthesia, taking care not to temper with the blood vessels. Then after the abdominal wall was closed by suturing and the animals were allowed to recover from the anaesthesia for 4 hours, ketamine was used to euthanize it. Each stomach was removed and opened along the greater curvature, washed with 0.9% saline and examined for macroscopic mucosal lesions, with the aid of magnifying glass (x10), and then put inside a container containing 10% formasaline and kept for histopathological studies. The gastric content was carefully collected for analysis.

Calculation of macroscopic ulcer index (U.I)
The severity of the ulceration was graded according to the scale that is a modification of the score [19].

(0 - Normal gray colored stomach), (0.5 - Pink to red coloration of the stomach), (1 - Spot ulcer), (1.5 - Haemorrhagic streak), (2 - Number of ulcers less than 5), (3 - Number of ulcers more than or equal to 5), (4 - Ulcer with bleeding) and (5 - Perforation of the gastric/duodenal wall).

Ulcer Index was calculated by summing the entire number of ulcers plus the severity of the ulcer. The preventive index (P.I) of the extract administered was obtained by using the equation 1[20].

$$P.I = \frac{U.I\ of\ indomethacin\ group - U.I\ of\ test\ group}{U.I\ of\ indomethacin\ group} \times 100 \quad (1)$$

Determination of gastric juice volume and pH

After the gastric contents were collected and centrifuged at 1000 rpm for 10 min. The volume of the supernatant was determined in mL. The pH of the supernatant was measured using a pH meter [21,22].

Assessment of gastric wall mucus

Alcian blue binding to gastric wall mucus was determined by a modified method of Corne [23]. The stomach of each mice was weighed and immediately transferred to 10 mL of 1% (w/v) alcian blue solution (in 0.16 M sucrose solution, buffered with 0.05 mL sodium acetate, pH 5) for 2 hours at room temperature. After 2 hours, the stomachs were removed, rinsed with 0.25 M sucrose solution to remove excess dye after 15 and 45 minutes, and the dye complexed with gastric wall mucus was extracted with 10 mL of 0.5M $MgCl_2$ solution by intermittent shaking for 1 minute at 30 minutes' intervals for 2 hours. The stomachs were removed and 5 mL of each aliquot of $MgCl_2$ solution containing the alcian blue eluted from each stomach was shaken with 4 mL of diethyl ether. The aqueous phase was separated out, centrifuged at 4000 x g for 16 min and the absorbance of the supernatant was measured at 580 nm. The amount of alcian blue bound per stomach in micrograms was determined using a standard calibration curve. Alcian blue was the standard compound used.

Histopathological studies: Tissue preparation

After the lesions seen in the stomachs had been noted, each stomach was then placed in 10% formasaline. After 24 hours of fixation followed by embedding, using closed type automated embedding machine, in a paraffin block, it was then trimmed and cut into sections of 5 microns, the ribbon obtained was put in a water bath (56^oC), fished out onto a glass slide and stained with haematoxylin-eosin stain for histological assessment of the gastric mucosa [24].

Results and Discussion

Phytochemicals present in *Musa paradisiaca* tepal and skin

The tepal and skin methanol extracts of *Musa paradisiaca*, prepared in this work showed the presence of the tested phytochemicals like flavonoids, phenols and glycosides.

Investigations into natural products often, is guided by ethno-pharmacological knowledge, and has brought tremendous contributions to drug production by providing novel chemical structures and mechanisms of action [25,26]. Tepal methanol extract showed the presence of glycosides and phenols in abundance. Flavonoids and saponins were also detected in this extract. Skin methanol extract also contains glycosides and phenols yet saponins are absent (Table 1).

Table 1. Phytochemicals from the tepal and skin methanol extracts of *Musa paradisiaca*

Extract	Glycosides	Phenols	Flavonoids	Saponins
Tepal	++	++	+	+
Skin	+	+	++	-

Note: ++ = present in abundance. + = present. - = Absent

Plant secondary metabolites, are important sources of many food ingredients and plant chemicals (phytochemicals) [27]. Recent researches showed that many phytochemicals can protect humans against various diseases [28]. Many phytochemicals are present in herbs, and each has its distinct work. The health benefits attributed to these

phytochemicals include; antioxidant, antimicrobial, anti-inflammatory, cancer preventive, antidiabetic and antihypertensive effects [29,30].

Preliminary phytochemical screening of dried leaves and fruit peels of *Musa paradisiaca* unveil the presence of some glycosides, anthocyanins, tannins, flavonoids as well as carbohydrates [31-33]. These phytochemicals have been reported to play multiple biological and pharmacological roles (antibacterial, antihypertensive, antidiabetic and anti-inflammatory activities [34].

Several phytochemicals in different parts of banana from different solvent extracts have been reported by several researchers. Many flavonoids and related compounds (Leucocyanidin, quercetin, and its 3-O-galactoside, 3-O-glucoside and 3-O-rhamnosyl glucoside) were isolated from the unripe pulp of plantain [35,36]. Serotonin, norepinephrine, tryptophan, indole compounds, tannin, starch, iron, crystallizable and non-crystallizable sugars, vitamin C, B-complex vitamins, fats, mineral salts were detected in the fruit pulp of *M. paradisiaca var. sapientum* [37]. The preliminary phytochemical screening carried out indicated *M. paradisiaca var. sapientum* peels contain some secondary metabolites such as glycosides, alkaloids, saponins, volatile oil, flavonoids and tannins [38]. The phytochemical screening of ethanolic and methanolic extracts of *Musa paradisiaca* confirmed the presence of some secondary metabolites. Ethanolic extract was found to have alkaloids, flavonoids, steroids, tannins, glycosides etc., whereas the methanolic extract revealed the presence of alkaloids, saponins, xanthoproteins and glycosides [39].

The roles of these phytochemicals as both therapeutics and nutrients makes these parts (tepal and skin) of the plant have medicinal and nutritional values. This work confirmed the presence of most of these phytochemicals in the parts above.

Effect of *Musa paradisiaca* tepal and skin on ulcer index

Ligation of pylorus causes erosion due to stimulation of acid and pepsin in the abdomen [18], leading to autodigestion of the gastric mucosa and the breakdown of the gastric mucosal barrier [40]. Prostaglandins (PGs) shows a protective effect on the stomach mucosa and causes an increase in bicarbonate secretion, maintain mucosal blood flow and repair. Hence, the increase in mucosal lesions is caused by suppressing PGs synthesis by NSAIDs. For this reason, indomethacin plus pylorus ligation model was used in our study to induce severe ulceration in mice. The number of lesions seen on the gastric mucosa is an indication of the severity of ulcer disease [41]. Non-parametric Kruskal-Wallis followed by Mann-Whitney tests were used for the statistical analysis.

According to this result (Table 2), administration of indomethacin coupled to ligation of the pylorus in IND+PYL group showed significant increase in ulcer index (16.20 ± 5.70) when compared to the normal control group ($p = 0.005$). Pre-treatment with cimetidine significantly ($p = 0.009$) decreases the ulcer index. Tepal pre-treatment also significantly decreases ($p = 0.027$) the ulcer index when compared to the induced group. However, the decrease in ulcer index in skin pre-treated group is not significant ($p = 0.074$). The cimetidine pre-treated group decreased the ulcer index to 3.6 ± 1.20 giving 72.14% protection. Meanwhile, the tepal and skin extracts reduced the ulcer index to 3.60 ± 1.20 and 6.90 ± 2.10 giving 68.80% and 43.22% protection respectively. This protection (preventive index) observed in both the tepal and skin is not statistically significant from the protection observed in cimetidine ($p = 0.249$).

The gastric mucosal integrity depends on the balance between HCL, pepsin (aggressive factors) and the protective factors as mucus and bicarbonate secretion, prostaglandins, mucosal blood flow, nitric oxide [42]. Hence, the main guidelines for the treatment are aimed not only at blocking the acid secretion, but also on the increased production of factors responsible for protecting the gastric mucosa, thus preventing epithelial damage [43]. The present study proves the preventive effect of *Musa paradisiaca* tepal and skin methanol extracts, as they significantly decreased the induced ulcer.

Table 2. Effect of tepal and skin pre-treatments on ulcer index and preventive index in IND+PYL induced ulcer

Sample (n=5)	Ulcer Index (Mean ± SE)	Preventive index (Mean ± SE)
Control	0.00±0.00[c]	Nil
IND+PYL	16.20±5.70[a,d]	Nil
Tepal pre-treated	3.80±1.60[b]	68.80±20.53[e]
Skin pre-treated	6.90±2.10[a]	43.22±14.82[e]
Cimetidine pre-treated	3.60±1.20[b]	72.14±13.49[e]

[a,b]Man-Whitney U test showed that, tepal methanol and cimetidine showed significant decrease in ulcer index. However, the decrease in skin extract is not statistically significant, when compared to the induced group (IND+PYL) [a]. [c,d]Man-Whitney U test showed a significant formation of ulcer in IND+PYL group when compared to the normal control group. [e]Kruskal-Wallis test showed no significant difference in ulcer prevention (Preventive ulcer index) exerted by the tepal, skin as well as the standard cimetidine drug.

Effect of Musa paradisiaca tepal and skin on gastric juice volume and pH

The current study showed that, the methanolic skin and tepal extracts of *Musa paradisiaca,* as well as cimetidine, lower the volume of the gastric juice compared to the induced group (IND+PYL). The volume of the gastric juice was found to be 0.86 ± 0.13mL in the induced (IND+PYL) group, but tepal brought it down to 0.40 ± 0.04mL. Cimetidine and skin also reduced the volume to 0.46 ± 0.08 mL and 0.64 ± 0.13 mL respectively (Figure 1), although not statistically significant.

Significant increase in pH was observed in the tepal and cimetidine pre-treated groups as presented in Fig. 1. The pH value in the induced group (IND+PYL) was found to be 2.48 ± 0.2. This is significantly (p = 0.012) increased to 3.79 ± 0.24 by the tepal extract in a similar way to the standard drug, cimetidine, 3.98 ± 0.11 (p = 0.009) when compared to the induced group. The increase in pH by the skin extract is not statistically significant (p = 0.203) when compared to the induced group. This may be due to its less chemical components than the tepal or may be higher dosage is needed. However, it also increases the gastric juice pH to 2.99 ± 0.32 (Figure 1).

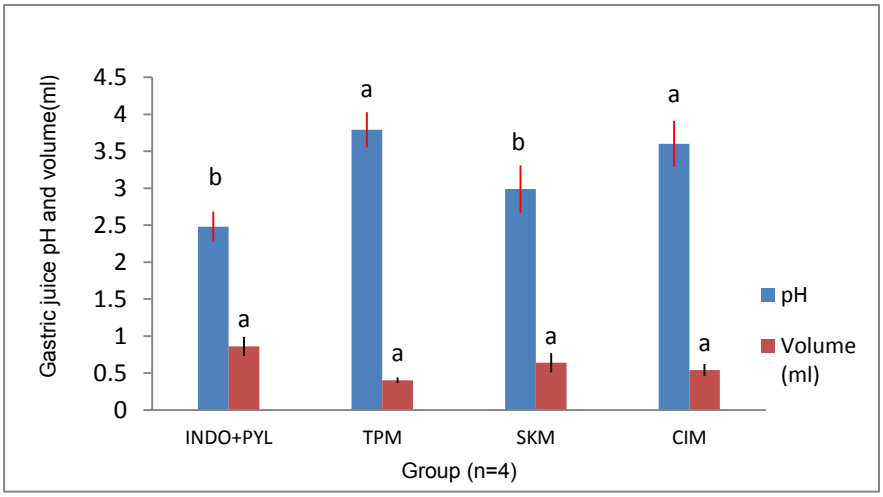


Figure 1. Gastric juice pH and volume

Tepal methanol (TPM), cimetidine (CIM) and skin methanol (SKM) pre-treated groups showed no significant gastric juice volume reduction when compared to the induced group (INDO+PYL).

CIM and TPM showed a significant rise in pH when compared to the induced group (INDO+PYL). SKM showed no statistical significance when compared to the induced group.

Effect of Musa paradisiaca tepal and skin on gastric wall mucus

Figure 2 showed the impact of the tepal and skin extracts on the measured gastric wall mucus. Both the tepal and skin showed increased gastric mucus but not statistically significant ($p = 0.339$) when compared to the induced group (IND+PYL). The group pre-treated with the standard cimetidine drug also decreases the gastric mucus in a similar way to the tepal and skin.

The research shows the effects of tepal and skin against indomethacin plus pylorus ligation induced gastric ulcers. The gastric ulcers in the pylorus ligated animal are mainly due to increased gastric HCL secretion leading to the destruction of mucosal barrier and autodigestion of the gastric mucosal layer. In ulcer induced models there is, normally, a significant increase in the level of acid and pepsin [44]. Indomethacin also increases pepsinogen secretion [45].

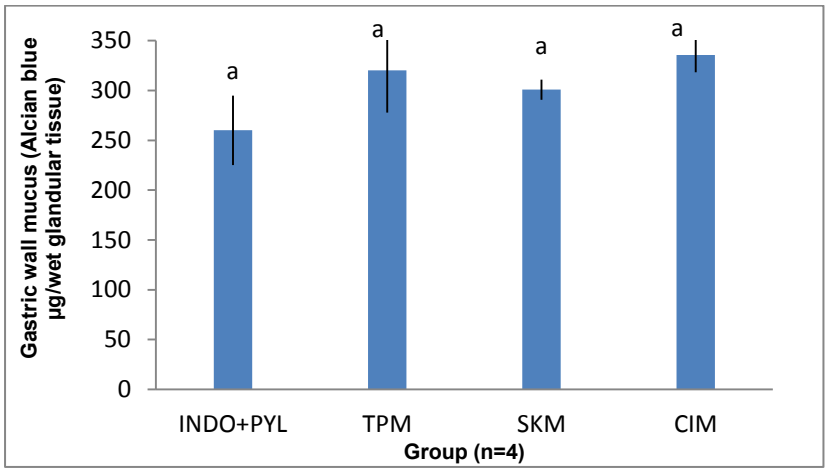


Figure 2. Increase in gastric wall mucus by the extracts.

The rise in the gastric wall mucus (GWM) by both the TPM and SKM is not statistically significant when compared to the induced group (INDO+PYL).

The volume of acid present in gastric secretion which comprises HCL, pepsinogen, mucus, bicarbonate, intrinsic factor and protein reflects acid volume. Exposure of the open lumen of the stomach to accumulating acid could facilitate ulceration [46]. Another aggressive factor responsible for ulcers is the amount of "acid present in the gastric juice. Over secretion of histamine contributes to increased secretion of gastric juice" [47]. When the concentration of hydrogen ions in gastric juice decreases, it indicates high pH. The genesis of ulcer and gastric damage is made easy by hydrogen ions that serve as another aggressive factor [48].

Administration of tepal, skin and cimetidine at a dose of 100 mg/kg decreased gastric juice volume and increased gastric the juice pH when compared to the ulcer induced group. The increase in pH implies a decrease in gastric acidity which can occur through the decline in pepsin activity. Hence, the extracts prevent ulcer possibly by preventing overproduction of gastric acid.

Mucus serves as the first line of defence against ulcerogenic agents. It is secreted by the mucous neck cells and shields the gastric mucosa. Mucus secretion is an essential factor in the protection of the gastric mucosa from the gastric erosions and has been regarded as a significant defensive entity in the gastric mucus barrier [49]. Increased mucus secretion by the gastric mucosal cells can protect gastric ulceration by several mechanisms, like decreasing of stomach wall friction during peristalsis and gastric contractions, increasing the buffering of acid in gastric juice and by acting as an effective barrier to back diffusion of H^+ ions [50]. *Musa paradisiaca* skin and tepal was found to augment the gastric mucus by decreasing the gastric juice acidity and lowering its volume, which are all evident in this work.

Topical and systemic effects of NSAIDs in the gastrointestinal mucosa are associated with mucosal damage in both the upper and lower GIT [51]. The systemic effects of NSAIDs involve the inhibition of prostaglandin production (by affecting COX-1 function), which defect bicarbonate and mucus secretion. Indomethacin induce a direct irritation effect by increasing free radical formation and H^+ ion transport [52]. Indomethacin causes ulcer mainly on the glandular (mucosal) part of the stomach [53]. The extracts (100 mg/kg) may also offer gastroprotection by enhancing the mucus wall thickness and antioxidant activity, since it was found to have an excellent DPPH radical scavenging activity [54] as well as the augmentation of the gastric wall mucus. It is possible that the cytoprotective action *M. paradisiaca* is mediated via the action of endogenous prostaglandin, which stimulate mucus secretion and plays an important role in ensuring mucosal integrity against the actions of various deleterious agents [55].

Several studies on the antiulcer efficacy of different parts of *Musa paradisiaca* var. *sapientum* were carried out, and it conforms to the current finding. A study conducted by Koffuor [56], showed that, the aqueous extract of *Musa paradisiaca* (0.2 – 0.8 mg/kg) treated mice gave a significant ($P < 0.001$) reduction in the gastric ulceration, induced by acetic acid, similar to the esomeprazole treated group. The flower extract of *Musa paradisiaca* has been described to possess antioxidant as well as antiulcer activity [57,58]. Methanolic extract of *M. sapientum var. paradisiaca* showed antiulcer and mucosal defensive factors in normal and non-insulin dependent diabetes mellitus rats [59]. Studies with *M. paradisiaca var. sapientum* have shown its ulcer protective and healing activities through its predominant effect on various mucosal defensive factors and they resolved that its antioxidant activity may be implied in its ulcer protective activity [57]. A previous study reported that dried unripe banana powder contains flavonoid leucocyanidin and a significant protective role against aspirin-induced erosions was seen [55].

The significant increase in the antiulcer activity of *Musa paradisiaca* skin and tepal, could also be attributed to the presence of flavonoids and glycoside, which are shown to be present in the both tepal and skin extracts. In this study, the tepal extract showed better antiulcer activity as well as more abundant glycosides and phenols than the skin extract. The skin extract that showed antiulcer activity and also contains abundant flavonoids (Table 1). Among the phytochemicals present in the extracts, saponins and flavonoids are referred to as antiulcer compounds [60]. These phytochemical constituents of the extracts could explain its antiulcer activity. Furthermore, several plants containing high amounts of saponins have been shown to possess antiulcer activity in several experiments [61,62], probably acting as an activator of mucus membrane protective factors [63]. Moreso, the gastroprotective effect of flavonoids has been previously reported [64].

Phenolic compounds cause the augmentation of mucus production and anti-inflammatory action due to their free radical scavenging activity [65]. The tepal and the skin extracts of *Musa paradisiaca* were found to have a large amount of total phenolic content [54]. The presence of phenolic compounds in the extracts may be a contributing factor towards the significant reduction of ulcer index observed in the pre-treated groups. *Musa paradisiaca* contains a glycoside called “aucubin” which has antihistaminic activity [66]. Thus, the antihistaminic activity may be one of the mechanisms through which plant extracts prevent ulcer progression.

Mucosal defence and repair mechanisms are relevant in protecting the integrity of the mucosal layer, and resultant inhibition of these mechanisms could lead to necrosis. Examples of such defense mechanisms include preepithelial factors (mucus-bicarbonate-phospholipid barrier), surface epithelial cells connected by tight junctions, bicarbonate and mucus production, prostaglandins, heat shock proteins and blood flow through the mucosal vessels [67]. The extracts in effect, may directly protect the mucosal layer from harmful substances such as NSAIDs (indomethacin), acids and alcohol and stimulate mucosal regeneration.

Macroscopic observation

Figure 3 showed the representative stomachs of mice after indomethacin plus pylorus ligation induced gastric ulcer. Oral administration of indomethacin (48 mg/kg) and ligation of pylorus produced superficial or deep erosions, bleeding, and antral ulcers. This is similar to the reports of Zhu and Kaunitz [3] and Lanza [68] in which prostaglandin and protective mucus function were inhibited by NSAIDs.

Nevertheless, pre-treatment with *Musa paradisiaca* skin and tepal significantly reduced the ulcer severity. Tepal and cimetidine were able to cause a significant reduction in ulcer indices compared to the ulcer induced group which caused a significant increase in the ulcer indices. Moreover, tepal and cimetidine have the same protective action against the induced ulceration. The decrease in ulcer indices is in line with those of Goel [69] who reported the reduction in ulcer indices on treatment with vegetable *Musa paradisiaca* in aspirin induced rats [69].

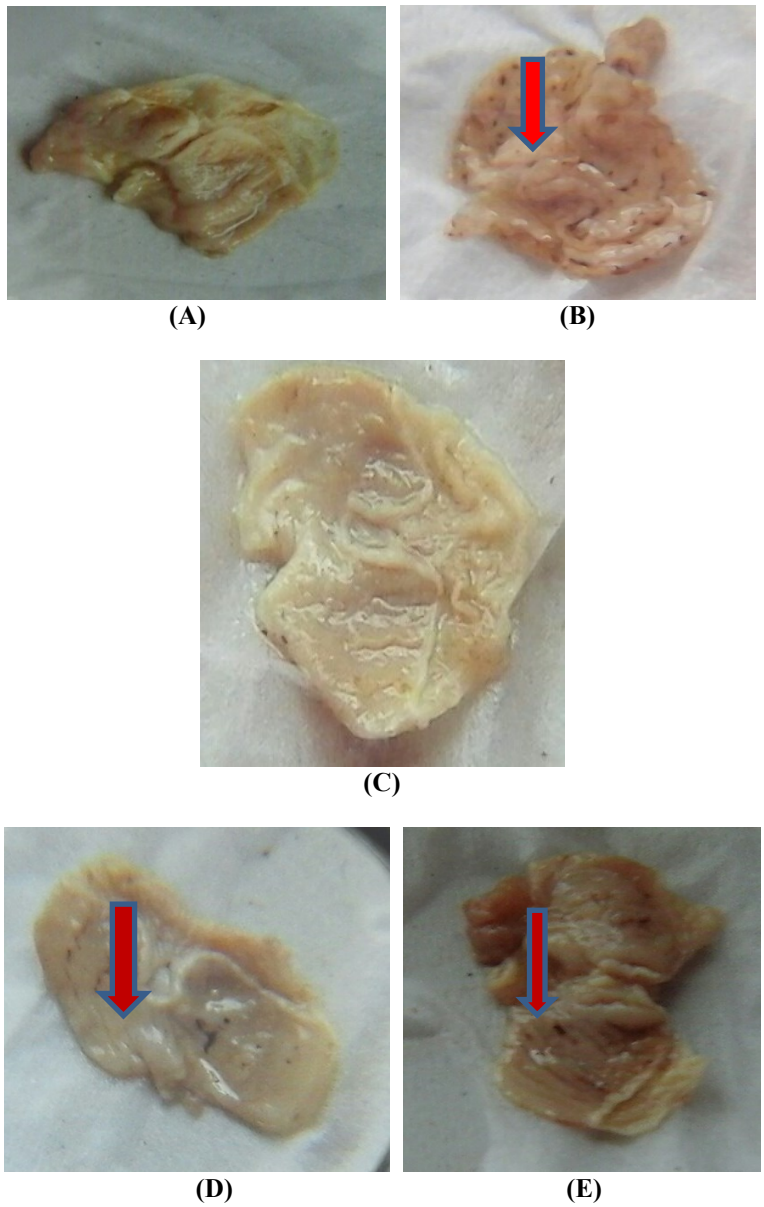


Figure 3. Gross view of mice stomachs after pre-treatment and ulcer induction.

A: control stomach, showing normal gastric mucosa. B: ulcer induced stomach, showing various lesions and some inflammation. C: Tepal pre-treated stomach, showing a highly significant preventive effect against the IND+PYL induced ulceration. D: Skin pre-treated stomach, showing a mild preventive effect against IND+PYL induced ulceration. E: Cimetidine pre-treated stomach, showing prevention against the IND+PYL induced ulcer in the similar way as in C.

Histopathological studies

This study also showed that, the administration of indomethacin at 48 mg/kg body wt. and the ligation of the pylorus, induced histological lesions in mucosal and submucosal regions as revealed by histological examinations compared to control group (Figure 4). This finding conforms to that of several studies in which ulcer was induced using indomethacin [8, 70,71].

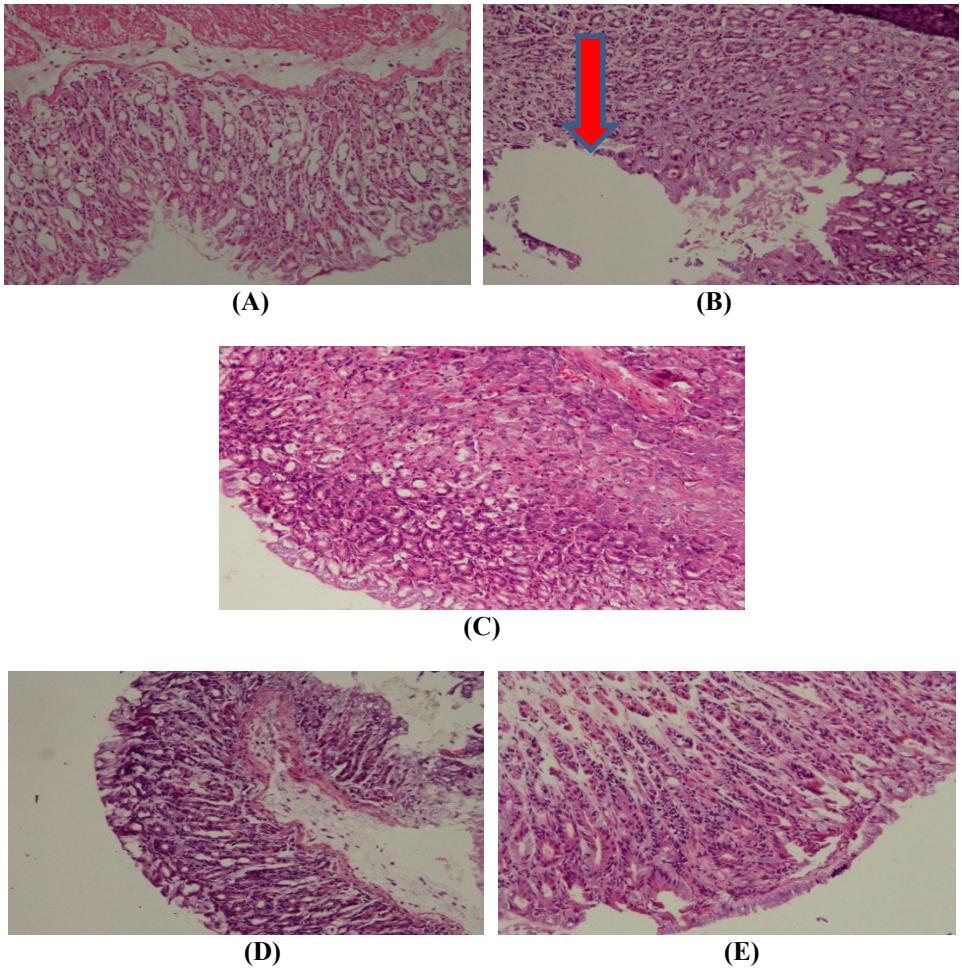


Figure 4. The histological view (x 100) of the stomach of mice

Control group showing intact mucosa (A). IND+PYL (B) induced highlighting the areas of congestion and erosions. Tepal pre-treated (C) showing intact mucosa. Skin pre-treated (D), with intact mucosa and decreased oxyntic cells in superficial half of mucosa and cimetidine (reference drug) pre-treated (E) also showing intact mucosa.

Conclusion

In the present study, it was found that, the tepal extract has the highest preventive ulcer index that is statistically not significant when compared to standard drug (cimetidine), against the indomethacin plus pylorus ligation induced ulceration. Also the same tepal and the skin extract showed a promising reduction of gastric juice volume, increasing pH and strengthening of the gastric wall mucus. Phytochemical screening revealed the presence of flavonoids, saponins, glycosides and phenols in the extracts, which are especially higher in the tepal extract, which could be the reason for its higher antiulcerogenic action recorded in this work. Further investigations are needed to confirm the use of these parts of banana for ulcer treatment.

Acknowledgement

The researchers acknowledged the effort of Chemistry lab and animal house staff, in the Faculty of Medicine and Faculty of Bioresources and Food Industry, of Universiti Sultan Zainal Abidin (UniSZA) for their help in this research. The effort of Mrs. Ummi Akrimmah Binti Yim, a technician in Histopathology lab, Faculty of Medicine, UniSZA, is also appreciated. Regard to Eng. Dr. Rabiu Musa Kwankwaso (Kwankwasiyya) for sponsoring the study.

References

1. Amandeep, K., Robin, S. Ramica, S. and Sunil, K. (2012). Peptic ulcer. *International Research of Journal of Pharmacy*, 3 (6): 34 – 38.
2. Wallace, J L. (2001). Mechanisms of protection and healing: current knowledge and future research. *American Journal of Medicine*, 110: 19 – 23.
3. Zhu, A. and Kaunitz, J. (2008). Gastric mucosal defense. *Current Gastroenterol Reports*, 10: 548 – 554.
4. Robbin, S. L., Kumar, V. and Ramzi, C (2003). Acute and chronic inflammation In: *Basic pathology. 7th Edition. Philadelphia. W.B. Company*: pp. 333.
5. Suleyman, H., Demircan, B. and Karagoz, Y. (2007). Antiinflammatory and side effects of cyclooxygenase inhibitors. *Pharmacology Reports*, 59 (3): 247 – 258.
6. Chattopadhyay, I., Bandyopadhyay, U., Biswas, K., Maity, P. And Banerjee, R. K. (2006). Indomethacin inactivates gastric peroxidase to induce reactive oxygen- mediated gastric mucosal injuty and curcumin protects it by preventing peroxidase inactivation and scavenging reactive oxygen. *Free Radical Biology Medicine*, 40(8):1397 – 1408.
7. Naito, Y. and Yoshikawa, T (2006). Oxidative stress involvement and gene expression in indomethacin induced gastropathy. *Redox Reports*, 11: 243 – 253.
8. Motawi, T. K., Abd Elgawad, H. M. and Shahin, N. N. (2008). Gastroprotective effect of leptin in indomethacin-induced gastric injury. *Journal of Biomedicine Science*, 15: 405 – 412.
9. Abraham, C., Hart, J., Locke, S. M. and Baker, A. L. (2008). A case of indometacin-induced acute hepatitis developing into chronic autoimmune hepatitis. *Nature clinical practice gastroenterol Hepatol*, 5(3): 172 -176.
10. Kannappan, N., Jaikumar, S., Manavalam, R. and Kotti Muthu, A. (2008). Antiulcer activity of methanolic extract of *Jatropa curcas* (Linn.) on aspirin-induced gastric lesions in wistar rats. *Pharmacology Online*, 1: 279 – 293.
11. Narayana, K. R., Reddy, M. S., Chaluvadi, M. R. and Krishna, D. R.(2001). Bioflavonoids classification pharmacology, biochemical effects and therapeutic potential. *Indian Journal of Pharmacology*, 33: 2 – 16.
12. Goel, R. K. and Sairam, K. (2002). Antiulcer drugs from indigenous sources with emphasis on *Musa sapientum, Tamrabhasma, Asparagus racemosus* and *Zingiber officinale. Indian Journal of Pharmacology,* 34: 100 – 110.
13. Marie-Magdeleine, C., Udino, L., Philibert, L., Bocage, B. and Archimede, H. (2014). In vitro effects of *Musa paradisiaca* extracts on four developmental stages of *Haemonchus contortus*. *Research in Veterinary Science*, 96: 127 – 132.
14. Sharma, P. C., Yelne, M. B., Dennis, J. J. Kadali. (2002) In: Data base on medical plants used in Ayurveda and Siddha. *New Delhi: Public Printing*, 5: 78 – 93.
15. Trease, G. E., Evans, W. C. (1989) Trease and Evan's Textbook of Pharmacognosy. *13th Edition London: Cambridge University Press*: pp. 546.

16. Mahmood, A., Mariod, A. A., Al-Bayaty, F. and Abdel-Wahab, SI. (2010). Antiulcerogenic activity of Gynura procumbens leaf extract against experimentally- induced gastric lesions in rats. *Journal of Medical Plants Research* ,4 (8): 685 – 691.
17. Morise, Z., Komatsu, S., Fuseler, J. W., Granger, D. N., Perry, M., Issekutz, A. C. and Grisham, M. B. (1998). ICAM-1 and P-selection expression in a model of NASID – induced gastropathy. *American Journal of Physiology*, 274: 246 – 252.
18. Shay, M., Kamarov, S. A., Fels, D., Meranz, D., Gruenstein, H. and Siplet, H. (1945). A simple method for uniform production of gastric ulceration in the rat. *Gastroenterology,* 5: 43 – 61.
19. Kunchandy, J., Khanna, S. and Kulkarni, S. K. (1985). Effect of α2 - agonists clonidine, guanfacine and B-HT 920 on gastic acid secretion and ulcers in rats. *Archives Internasional de pharmacodynamie et de therapie,* 275: 123 – 138.
20. Hano, J., Bugajski, J. and Danek, L.(1976). Effect of adrenergic blockade on gastric secretion altered by catecholamines in rats. *Archivum immunologiae et therapiae experimentalis (Warsz)*, 24 (4): 507 – 524.
21. Srivastava, V., Viswanathaswamy, A. H. and Mohan, G. (2010). Determination of the antiulcer properties of sodium cromoglycate in pylorus-ligated albino rats. *Indian Journal of Pharmacology*, 42 (3): 185 – 188.
22. Vinothapooshan, G. and Sundar, K. (2010). Anti-ulcer activity of Mimosa pudica leaves against gastric ulcer in rats. *Research Journal of Pharmaceutical, Biological and Chemical Sciences*, 1 (4): 606 – 614.
23. Corne, S. J., Morrisey, S. M. and Woods, K. J. (1974). A method for the quantitative estimation of gastric barrier mucus. *Journal of Physiology*, 2452: 116 – 117.
24. Bancroft, D., Stevens, A. and Turmer, R. (1996). Theory and practice of histological technique*, 4th edition, Churchill Living Stone, Edinburgh, London, Melbourne*: pp. 47 – 67.
25. Sheeba, M. S. and Asha V. V. (2006). Effect of Cardiospermum halicacabum on ethanol-induced gastric ulcers in rats. *Journal of Ethnopharmacology*, 106 (1): 105 – 110.
26. Bohlin, L., Goransson, U., Alsmark, C., Weden, C. and Backlund, A. (2010). Natural products in modern life science. *Phytochemistry Reviews,* 9 (2): 279 – 301.
27. Doss, A. and Anand, SP. (2012). Preliminary Phytochemical Screening of Asteracanthalongifolia and Pergularia daemia. *World Applied Science Journal,* 18(2): 233 – 235.
28. Kubmarawa, D., Khan, M. E., Punah, A. M. and Hassan, M. (2008). Phytochemical screening and antibacterial activity of extracts from *Parkia clappertoniana* keay against human pathogenic bacteria. *Journal of Medical Plants Research*, 2 (12): 352 - 355.
29. Savithramma, N., Linga Rao, M. and Suhrulatha, D. (2011). Screening of medicinal plants for secondary metabolites. *Middle-East Journal of Science Research*, 8: 579 – 584.
30. Rupasinghe, H. P., Jackson, C. J., Poysa, V., Berado, C. D., Bewley, J. D. and Jenkinson, J. (2003). Soyasapogenol A and B distribution in Soybean (Glycine max (L.) Merr.) in relation to seedphysiology, genetic variability and growing location. *Journal of Agricultural and Food Chemistry,* 51: 5888 – 5894.
31. Anhwange, B. A. (2008). Chemical composition of Musa sapientum (Banana) peels. *Journal of Food Technology*, 6 (6): 263 – 268.
32. Archibald, J. G. (1949). Nutrient composition of banana skins. *Journal of Dairy Science,* 32: 969 – 971.
33. Alisi, C S., Nwanyanwu, CE., Akujobi, C O. and Ibegbulem, C O. (2008). Inhibition of dehydrogenase activity in pathogenic bacteria isolates by aqueous extracts of Musa paradisiaca (var Sapientum). *African Journal of Biotechnology*, 7 (12): 1821 – 1825.
34. Middleton, E. J. and Kandaswanmi, C. (1992). Effects of flavonods on immune and inflammatory cell function. *Biochemistry Pharmacology*, 43 (6): 1167 – 1179.
35. Lewis D. A. and Shaw, G. P. (2001). A natural flavonoid and synthetic analogues protect the gastric mucosa from aspirin-induced erosions. *Journal of Nutrition Biochemistry,* 12 (2): 95 – 100.
36. Ragasa, C. Y., Martinez, A., Chua, J. E. Y. and Rideout, J. A. (2007). A triterpene from *Musa errans*. *Philippine Journal of Science*, 136 (2): 167 – 171.
37. Ghani, A. (2003). Medicinal plants of Bangladesh: Chemical constituents and uses. 2nd Ed. *The Asiatic Society of Bangladesh, Dhaka, Bangladesh*: pp. 315.
38. Ehiowemwenguan, G., Emoghene, A. O. and Inetianbor, J. E. (2014) Antibacterial and phytochemical analysis of banana fruit peel. *IOSR Journal of Pharmacy,* 4 (8): 18 – 25.

39. Mallikarjuna, R., Prasad, S. H. K. R. and Jyothirmayi, N. (2012). Efficacy of ripened and unripened fruit extracts of *Musa X Paradisiaca L. (Bontha Cultivar)* against human pathogens. *International Journal of Pharmacy and Pharmaceutical Science*, 4(1): 457 – 458.
40. Sairam, K., Rao, CV., Dorababu, M., Kumar, V., Agrawal, V. K. and Goel, R. K. (2002). Antiulcerogenic activity of methanolic extract of *Emblica officinalis*. *Journal of Ethnopharmacology*, 82: 1 – 9.
41. West, G. B. (1982).Testing for drugs inhibiting the formation of gastric ulcers. *Journal of Pharmacology Methods*, 8: 33 – 37.
42. Lam, E. K. Y., Tai, E. K. K., Koo, M. W. L., Wong, H. P. S., Wu, W. K. K., Yu, L., So, W. H. L. And Cho, W. C. H. (2007). Enhancement of gastric mucosal integrity by *Lactobacillus rhamnosus* GG. *Life Science*, 80: 2128 – 2136.
43. Moraes, T. M., Kushima, H., Moleiro, F. C., Santos, R. C., Rocha, L. R. M., Marques, M. O., Vilegas, W. and Hiruma-Lima, C. A. (2009). Effects of limonene and essential oil from *Citrus aurantium* on gastric mucosa: role of prostaglandins and gastric mucus secretion. *Chemico-Biology International*, 180: 499 – 505.
44. Goel, R. K. and Bhattacharya, S. K. (1991). Gastroduodenal mucosal defense and mucosal protective agents. *Indian Journal of Experimental Biology,* 29: 701 – 714.
45. Mahmoud, M. K., Mohamed, Z. G. and Dalaal, A. (2001). Protective role of nitric oxide in indomethacin induced gastric ulceration by a mechanism independent of gastric acid secretion. *Pharmacological Research*, 43(5): 463 – 467.
46. Olsen, C. E. (1988). Glutathione modulates toxic oxygen metabolite injury of canine chief cell monolayers in primary culture. *Americal Journal of Physiology,* 254: 49 – 56.
47. Grossman, M. I. (1978). Control of gastric secretion in gastrointestinal disease. *Patho physiology- diagnosis and management. Sleisenzer, M.H, Fordtran, J.S., editors. 2nd ed. W B Saunders Co, Philadelphia*: pp. 640 – 659.
48. Lullmann, H., Mohr, K., Ziegler, A. and Bieger, D. (2000). *Color Atlas of Pharmacology. 2nd ed. Thieme Stuttgart, New York*: pp. 166.
49. Goel, R. K., Maitri, R. N. and Mukobandhyay, K. (1994). *Indian Journal of Experimental Biology*, 32: 559 – 561.
50. Sanmugapriya, E. and Venkatraman, S. (2007). Antiulcerogenic potential of Strychnos potatorum Linn seeds on Aspirin plus pyloric ligation-induced ulcers in experimental rats. *Phytomedicine*, 14: 360 – 365.
51. Sostres C. and Lanas A. (2011). Gastrointestinal effects of aspirin. *Nature Reviews Gastroenterology and Hepatology*, 8 (7): 385 – 394.
52. Sharma, A., Chibber, S. S. and Chawala, H. M. (1980). Isocaviunin 7-gentiobioside, a new isoflavone glycoside from Dalbergia sissoo. *Phytochemistry*, 19 (4): 715.
53. Nwafor, P. A., Effraim, K. D. and Jacks, T. W. (1996). Gastroprotective effects of acqeous extracts of *Khaya senegalensis* bark on indomethacin-induced ulceration in rats. *West African Journal Pharmacology and Drug Research*: 46 – 50.
54. Bashir, A. A., Khamsah, M. M., Abdurrazak, M., Mahadeva Rao, U. S. and Thant, Z. (2015). Phytochemical screening, antioxidant activity of pure syringing in comparison to various solvents extracts of *Musa paradisiaca* (banana) (fruit and flower) and total phenolic contents. *International Journal of Pharmacy and Pharmaceutical Science*, 7 (5): 242 – 246.
55. Lewis, D. A., Fields, W. N. and Shaw, G. P. (1999) A natural flavonoid present in unripe plantain banana pulp (Musa sapientum L. var. paradisiaca L) protects the gastric mucosa from aspirin-induced erosion. *Journal of Ethnopharmacology*, 65 (3): 283 – 288.
56. Koffuor, G. A., Ainoonson, G. K., Amponsah, K. I., Addotey, J. N., Asiamah, E. A., Akuffo, S. K., Adutwum, K. and Bandoh, R. F. (2013). Anti-ulcerant activity of an aqueous fruit extract of *Musa x para-disiaca* on acetic acid-induced gastric ulceration in ICR mice. *Journal of Medical and Biomedical Science*, 2 (2): 30 – 39.
57. Goel, R. K., Sairam, K. and Rao, C. V. (2001). Role of gastric antioxidant and anti-Helicobactor pylori activities in antiulcerogenic activity of plantain banana (*Musa sapientum var. paradisiaca*). *Indian Journal of Experimental Biology*, 39 (7): 719 – 722.
58. Vadivelan, R., Elango, K., Suresh, B. and Ramesh, B. R. (2006). Pharmacological validation of *Musa paradisiaca* bhasma for antiulcer activity in albino rats - a preliminary study. *Ancient Science of Life*, 25 (3-4): 67 – 70.

59. Mohan Kumar, M., Joshi, M. C., Prabha, T., Dorababu, M. and Goel R. K. (2006). Effect of plantain banana on gastric ulceration in NIDDM rats: Role of gastric mucosal glycoproteins, cell proliferation, antioxidants and free radicals. *Indian Journal of Experimental Biology,* 44: 292 – 299.
60. Lewis, D. A. and Hanson, P. J. (1991). Anti-ulcer drugs of plant origin. In: Ellis, G. P., West, G. B. (EDS.), *Progress medicinal chemistry, Elsevier Science Publishers, London*, 28: 2001 – 2031.
61. Yesilada, E. and Takaishi, Y. (1999). A saponin with anti-ulcerogenic effect from the flowers of *Spartium junceum*. *Phytochemistry*, 51 (7): 903 – 908.
62. Morikawa, T., Li, N., Nagatomo, A., Matsuda, H., Li, X., Yoshikawa, M. (2006). Triterpene saponins with gastroprotective effects from tea seed (the seeds of *Camellia sinensis*). *Journal of Natural Products,* 69 (2): 185 – 190.
63. Saito, H., Lee, Y. M., Takagi, K., Shoji, S. and Kondo, N. (1977). Pharmacological studies of Panacis Japonici Rhizoma. I. *Chemical and Pharmaceutical Bulletin*, 25 (5): 1017 – 1025.
64. Reyes, M., Martin, C., Alarcon de la Lastra, C., Trujillo, J., Toro, M. V. And Ayuso, M. J. (1996) Antiulcerogenicity of the flavonoid fraction from Erica andevalensis Cabezudo-Rivera. *Z Naturforsch C*, 51 (7-8): 563 – 569.
65. Di, C. G., Mascolo, N., Izzo, A. and Capasso, F. (1999): Old and new aspects of a class of natural therapeutic drugs. *Life Science*, 65: 337 – 353.
66. Ahlborn M. L. (2013). Plantain: the benefits of the use of plantain in herbal preparations. *[www.herballegacy.com]Availableat:http://www.herballegacy.com/Ahlborn_Medicinal.ht ml* [Date Access on: July 12 2015].
67. Laine, L., Takeuchi, K. and Tarnawski, A.(2008). Gastric mucosal defense and cytoprotection: Bench to Bedside. *Gastroenterology*, 135 (1): 41 – 60.
68. Lanza, F. L. Chan, F. K. and Quigley, E. M. (2009). Guildelines for prevention of NSAID complicated ulcer. *American Journal of Gastroenterology*, 104(3): 728 – 738.
69. Goel, R. K., Chakrabarti, A. and Sanyal A. K. (1985). The effect of biological variables on the anti-ulcerogenic effect of vegetable plantain banana. *Planta Medica*, 51: 85 – 88.
70. Ajeigbe, K., Oladejo, E., Emikpe, B., Asuk, A. and Olaleye, S. (2012). The dual modulatory effect of folic acid supplementation on indomethacin-induced gastropathy in the rat. *Turkey Journal of Gastroenterology*, 23(6): 639 – 645.
71. Fleishman, M. Y., Zhivotova, E. Y., Lebedko, O. A. Deigin, V. I. and Timoshin, S. S. (2009). Protective effect of dermorphin analogue sedatin on indomethacininduced injury to the gastric mucosa. *Bulletin Experimental Biology and Medicine*, 148 (1): 60 – 63.

Malaysian Journal of Analytical Sciences, Vol 20 No 5 (2016): 1217 - 1224
DOI: http://dx.doi.org/10.17576/mjas-2016-2005-28

MALAYSIAN JOURNAL OF ANALYTICAL SCIENCES
Published by The Malaysian Analytical Sciences Society
ISSN 1394 - 2506

A STUDY OF MICROBE AIR LEVELS IN SELECTED ROOMS OF A HOSPITAL CULTIVATED ON TWO CULTURE MEDIAS

(Kajian Tahap Mikrob dalam Udara yang Di Kultur Pada Dua Media Kultur di dalam Bilik Hospital Terpilih)

Che Noraini Che Hasnam[1], Hafizan Juahir[1]*, Azman Azid[1], Mohammad Azizi Amran[1], Fazureen Azaman[1], Ahmad Dasuki Mustafa[1], Zarizal Suhaili[1], Sukri Md. Ismail[1], Khairul Affendi Yusof[2], Cik Fatimah Nadia Che Hasnam[1]

[1]*East Coast Environmental Research Institute (ESERI),*
Universiti Sultan Zainal Abidin, Gong Badak Campus, 21300 Kuala Terengganu, Terengganu, Malaysia
[2]*Faculty of Industrial Sciences and Technology,*
Universiti Malaysia Pahang, Lebuhraya Tun Abdul Razak, 26300 Gambang, Kuantan, Pahang, Malaysia

**Corresponding author: hafizanj@unisza.edu.my*

Received: 14 April 2015; Accepted: 3 August 2016

Abstract

The levels of airborne microbe in hospital are unknown previously in Terengganu. Typically, fungi and bacteria are usually presented in indoor environments and cause of human health effects. The aim of this descriptive study was to investigate the level of airborne microbial pollution in the indoor air of the selected hospital rooms. A total of 8 rooms were investigated for this study. Sampling was conducted with an Eco-Mas 100 Single-Stage Microbial Air Impactor and counting plates containing two selective media, Rose Bengal Chloramphenicol Agar (RBCA) and Sabouraud Dextrose Agar (SDA). Air sampling was taken for 5 min at an airflow rate of 28.3 L/min. A medium-low level of bacterial and fungal concentrations (8 to 38 CFU/m^3 for RBCA and 2 to 149 CFU/m^3 for SDA), respectively were found in indoor air quality of the hospital. The highest microbe air levels for RBCA was measured in the washing room, while the highest microbe air levels for SDA was measured in the reprocessing room of hemodialysis unit. The culturable airborne bacterial and fungal concentrations on SDA agar were higher than those on RBCA. The most common culturable airborne microbes were *Penicillium* and *Cladosporium*. In addition, the use of RBCA rather than SDA significantly improved the fungal yield. The study also revealed that no indoor atmosphere in the hospital is completely free from microorganisms.

Keywords: hospital, indoor air quality, airborne microbe, colony counts

Abstrak

Tahap mikrob bawaan udara di hospital tidak di ketahui sebelum ini di Terengganu. Lazimnya, kulat dan bakteria terdapat dalam persekitaran dalaman dan menyebabkan kesan terhadap kesihatan manusia. Tujuan kajian deskriptif ini adalah untuk menyiasat tahap pencemaran mikrob bawaan udara di dalam bangunan bilik – bilik yang terpilih di hospital. Sejumlah 8 buah bilik telah disiasat untuk kajian ini. Pensampelan telah dijalankan dengan menggunakan Eco-Mas 100 Impaktor Udara Mikrob Tahap Tunggal dan plat yang mengandungi dua media terpilih iaitu *Rose Bengal Chloramphenicol Agar* (RBCA) and *Sabouraud Dextrose Agar*. Pensampelan udara dijalankan selama 5 minit pada kadar aliran udara 28.3 L/min. Satu tahap kepekatan sederhana rendah bakteria dan kulat (8 hingga 38 CFU/m^3 untuk media RBCA dan 2 hingga 149 CFU/m^3 untuk media SDA) masing – masing ditemui dalam kualiti udara dalam bangunan hospital tersebut. Tahap udara mikrob yang tertinggi untuk RBCA diukur di bilik cuci, manakala tahap udara mikrob yang tertinggi untuk SDA diukur di bilik pemprosesan semula unit hemodialisis. Kepekatan bakteria dan kulat bawaan udara yang dikultur pada agar SDA adalah lebih tinggi daripada agar RBCA. Mikrob bawaan udara lazimnya yang didapati dari media kultur ialah *Penicillium* and *Cladosporium*. Penggunaan media RBCA adalah ketara lebih baik berbanding media SDA dalam penghasilan kulat. Kajian juga mendedahkan bahawa tiada keadaan persekitaran tertutup di dalam hospital yang bebas sepenuhnya dari mikroorganisma.

Kata kunci: hospital, kualiti udara dalam bangunan, mikrob bawaan udara, pengiraan bilangan koloni

Introduction

Indoor air quality resulting from high levels of fungi (mold) and bacteria become a critical issue in the world and are therefore ubiquitous [1]. This is because of people spend most of their time indoors which is about 90 percent exposure to many types of pathogens [2,3,4]. Recently, an increasing number of people have experienced adverse health effects because of their indoor environments like infections, toxic reactions and hypersensitivity pneumonitis [5,6,7]. This is due to indoor microbial exposure has been related to a range of serious public health hazard and well-being of the population [8].

Hospital is an important facility of public place associated with the environmental exposure of humans. Besides, hospital is referred as a special public place [9]. In addition, the number of people is much higher in hospital every day compared to other public places. The effect of hospital in indoor air quality to humans is more significant, therefore this study has forwarded because there are very little studies that focused on the indoor airborne microbial in hospital in Malaysia especially in Terengganu. Fungi are common in indoor environments and about 10% of people have affected with fungal allergy like allergic bronchitis, chronic obstructive pulmonary disease and asthma [1,10]. Therefore, the airborne in indoor environment of the hospital is essential for the health of patients and medical personnel.

The culturable methods are still widely used generally with impactors and it is a sterile method [11]. The plates have been put in the impactor and grows as a colony, it is then counted as a colony-forming unit, or CFU [12]. This method is easy to implement and low cost thus reproducing the most common culturable conditions regarding total airborne microbial from a particular procedure [13]. According to study by Pasquarella et al. [14], bacterial levels less than 39 CFU/dm^2/h with passive sampling were considered as acceptable values for the air microbial contamination. While the recommended maximum limits set by the American Conference of Governmental Industrial Hygienists with the culturable count for total bacteria is not to exceed 500 CFUs/m^3 [15]. Meanwhile, the hospital was considered as a middle risk in which 50 CFUs/m^3 identified an acceptable microbiological quality in the operative areas [16].

The objective of this study is to calculate the number of colony as CFU/m^3 on two cultivated media, RBCA and SDA and to identify the types of colonies grows on the respective media through their specific colour, and morphology. This study is in line with the study by Yassin and Almouqatea [1], which state that the growth behavior and patterns on different agar need to be evaluated.

Materials and Methods

Study sites

Sampling was performed in eight selected rooms in the Hospital Sultanah Nur Zahirah (HSNZ) namely washing room, endoscopy room, isolation C (haemodialysis unit), isolation B (haemodialysis unit), CAPD room, ward 7A, and negative pressure room.

Media

Media used for sampling included RBCA and SDA (Hi Media Company Limited, India). Sabouraud Dextrose Agar consist of peptone 10 gl^{-1}, glucose 40 gl^{-1}, agar 15 gl^{-1} and Rose Bengal Chloramphenicol Agar consist of agar 15.5 gl^{-1}, chloramphenicol 0.1 gl^{-1}, dextrose 10 gl^{-1}, magnesium sulfate 0.5 $gl^{-1,}$ monopotassium phosphate 1 gl^{-1}, mycological peptone 5 gl^{-1} and rose bengal 0.05 gl^{-1} were prepared.

Sampling procedure

Air was sampled using a MAS-100 Microbial Air Sampler (Merck) for standard 90 mm petri dishes which contain Rose Bengal Chloramphenicol Agar (RBCA, Merck) and Sabouraud Dextrose Agar (SDA) to collect air sample. The microbial air sampler was located at a height of about 1.1 m to 1.5 m from the floor of the sampling sites to simulate location of the breathing zone of a seated person [9,17]. The air sampler was sterilised with 70% ethanol before using. Air sampling was taken for 5 min at an airflow rate of 28.3 L/min. Duplicates of each plate were used

in each stations. After the sampling, the petri dishes contained RBCA and SDA were incubated in an inverted position for a period of 3 to 7 days at room temperature (25 – 27 ^{o}C) as per standard procedures [18,19]. After the desired duration of agar incubation, the colonies formed on each plates were counted and the counts obtained were averaged. According to the standard conversion table for accounting particles at single impaction sites, the transformed colony forming units (CFU) appeared to be similar to the original counted which were expressed in CFU/m^3 [17].

Identification of fungi and bacteria

Isolates with different colony morphologies were selected from RBCA and SDA for identification. A stereoscopic light microscope with a magnification of 40x and 100x was used for identification of the fungi and bacteria. The fungi and bacteria were identified due to their typical colony and morphology characters based on [18, 20-23].

Results and Discussion

The levels of occurrence of the bacteria and fungi identified in the indoor air from eight different rooms in the hospital are represented in Tables 1 and 2. As stated from Table 1 and Table 2, the high CFU/m^3 is found after incubation of 7 days which this is the optimum time different species need to grow. Additionally, the trend of growth of colony counts illustrated that as times increases there is progressively more time for microbial to divide new cells. In this study, it shows that longer incubation times were associated with the highest CFU count obtained in the washing room and reprocessing room which were 38 CFU/m^3 and 149 CFU/m^3 respectively. On the other hand, negative pressure room can be classified as a clean area but there also has a growth of colony on both media; RBCA media and SDA agar which the counts were 25 CFU/m^3 and 11 CFU/m^3 respectively. However, the values obtained for negative pressure room were within the acceptable levels of microbial count.

Table 1. Colony Forming Unit/Plate for RBCA Media

Location/incubation	3 days	5 days	7 days
Washing room	1 small pink colony 27 small white colonies 1 medium yellow colony	4 small pink colonies 12 medium white colonies 6 medium yellow colonies 8 small black colonies	9 small pink colonies 15 medium white colonies 7 medium yellow colonies 7 small black colonies
Endoscopy room	2 small pink colonies 4 small white colonies 2 small yellow colonies	3 small black colonies 7 small white colonies 2 medium yellow colonies	7 medium white colonies 2 medium yellow colonies 7 medium black colonies
Isolation C (haemodialysis unit)	6 small pink colonies 11 small white colonies 2 medium yellow colonies	8 small pink colonies 7 small white colonies 5 medium yellow colonies 11 small black colonies	9 small pink colonies 8 small white colonies 6 medium yellow colonies 11 medium black colonies
Isolation B (haemodialysis unit)	11 small white colonies	4 small black colonies 5 medium white colonies 6 medium yellow colonies	5 medium white colonies 3 medium yellow colonies 8 small black colonies
Reprocessing room (haemodialysis unit)	27 small white colonies 3 medium yellow colonies	9 small black colonies 10 medium white colonies 5 medium yellow colonies 3 small orange colonies	1 small pink colony 9 medium white colonies 12 medium yellow colonies 10 medium black colonies

Table 1 (cont'd). Colony Forming Unit/Plate for RBCA Media

Location/incubation	3 days	5 days	7 days
CAPD room	4 small pink colonies 2 small white colonies 2 medium yellow colonies	5 small black colonies 5 small white colony 3 medium yellow colonies	4 small pink colonies 2 small white colonies 3 medium yellow colonies 6 small black colonies
Ward 7A	2 small pink colonies 8 small white colonies 1 medium yellow colony	3 small pink colonies 10 medium white colonies 1 medium black colony	3 small pink colonies 1 small white colony 9 medium yellow colonies 7 small black colonies
Negative pressure room	2 small pink colonies 9 small white colonies 2 medium yellow colonies	1 small pink colony 14 small white colonies 3 medium black colonies 2 small red colonies	2 small pink colonies 4 small white colonies 14 medium yellow colonies 5 small black colonies

Table 2. Colony Forming Unit/Plate for SDA Media

Location/incubation	3 days	5 days	7 days
Washing room	3 small black colonies 2 small white colonies 2 medium yellow colonies	3 large black colonies 5 large white colonies 2 medium yellow colonies	2 big fungi colonies
Endoscopy room	2 small pink colonies 14 small white colonies 3 medium yellow colonies 2 small pink colonies 16 small orange colonies	6 medium black colonies 12 large white colonies 14 medium yellow colonies 3 medium orange colonies	7 medium grey colonies 1 large white colony
Isolation C (hemodialysis unit)	3 small black colonies 55 small white colonies	11medium black colonies 18 medium white colonies 3 medium yellow colonies	2 fungi colonies 6 medium black colonies
Isolation B (haemodialysis unit)	12 small white colonies 9 medium black colonies	2 large black colonies 3 medium white colonies 3 medium yellow colonies 5 medium grey colonies	5 medium grey colonies 3 medium white colonies 2 medium yellow colonies 1 large black colony
Reprocessing room (haemodialysis unit)	129 small black colonies	135 medium black colonies	149 medium black colony 1large black colony

Table 2 (cont'd). Colony Forming Unit/Plate for SDA Media

Location/incubation	3 days	5 days	7 days
CAPD room	1 small orange colony 21 small white colonies 1 medium yellow colony	7 medium black colonies 14 medium white colonies 3 medium yellow colonies	1 large white colony 4 medium yellow colonies 6 medium black colonies
Ward 7A	2 small black colonies 20 small white colonies 8 medium yellow colonies	3 medium black colonies 20 medium white colonies 7 medium yellow colonies 1 large white colony	1 medium grey colony 21 medium white colonies 8 medium yellow colonies 5 medium black colonies 1 small orange colony
Negative pressure room	1 large black colony 15 small white colonies 2 medium yellow colonies 5 small orange colonies	1 medium black colony 12 medium white colonies 2 medium yellow colonies 4 medium grey colonies	5 medium grey colonies 6 medium yellow colonies 1 large black colony

In the present study the air quality of all of the selected rooms were found to be good, with acceptable values for the air microbial counts, since the microbial levels were lower than 50 CFU/m^3 which in the range from 8 – 38 CFU/m^3 for RBCA media and 2 – 149 CFU/m^3 for SDA media except for the microbial level in reprocessing room of hemodialysis unit Figure 1.

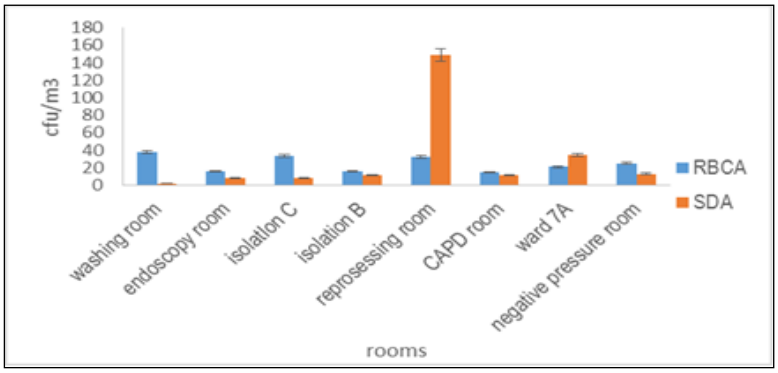


Figure 1. Mean value of microbial counts in each room for RBCA media and SDA media

In this experiment the plates were incubated for a distinct period of time. Figure 2 shows RBCA agar after three, five and seven days of incubation. After incubating the plate, a variety of organism species are grown with increasing times of days of incubation. In this study, it shows that average numbers of fungi on RBCA media was the highest in washing room because it is the place where chemicals most widely used for the purposes of washing medical apparatus before and after operation and preparation for the operation procedures. Figure 3 shows SDA

agar plate after three, five and seven days of the air sampling in reprocessing room. The reprocessing room at hemodialysis unit shows the highest number of colony. The viable cells counted in the reprocessing room and washing room were significantly higher than those found in other rooms because of inadequate ventilation and air filtration system in those rooms.

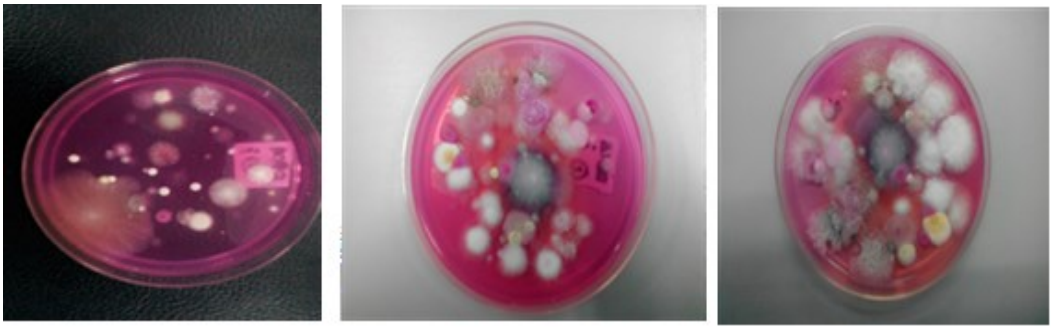


Figure 2. RBCA agar plate after 3, 5 and 7 days of the air sampling in washing room (the highest concentration of fungi on RBCA) of the hospital HSNZ

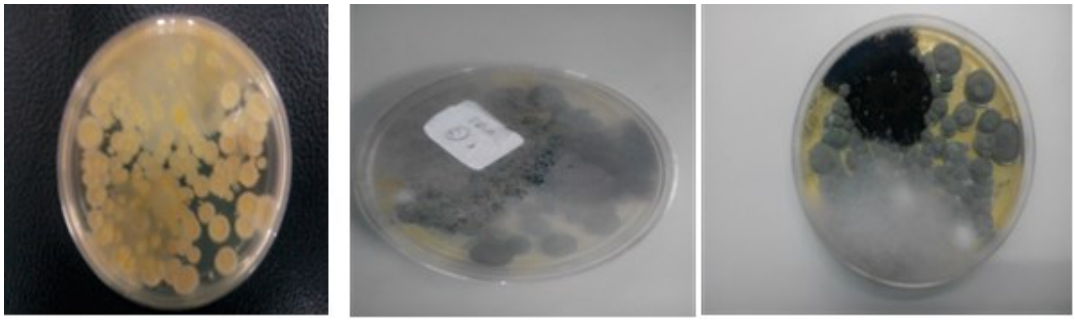


Figure 3. SDA agar plate after 3, 5 and 7 days of the air sampling in reprocessing room (hemodialysis unit) (the highest concentration of fungi on SDA) of the hospital HSNZ

In the present study, totally five different fungi were collected. The most dominant fungi were identified as *Cladosporium* sp. (85%), *Penicillium* sp. (48%), *yeast* sp. (28%), *Mucor* sp. (25%), and *Aspergillus* sp. (12 %). This indicated that indoor environment of each selected location in the hospital provides more favorable conditions for the survival of fungi. In addition, chloramphenicol used in RBCA media was included for the elimination of bacterial colonies in fungal culture while rose Bengal reduced the growth of fungi which eased identification of individual colonies [24]. This result is in line with the finding of earlier researcher by Guiamet et al. [25], who studied in indoor air sampling showed the similar identification of fungi that were *Aspergillus* sp. and *Penicillium* sp. as the most abundant microorganisms because of the microbes can be easily cultivated in the indoor environments.

Conclusion

The current study clearly indicates that there have a growth of airborne fungi and bacteria on two cultivated medias in the hospital even the room environment is clean. Bacteria show higher growth on SDA media while slow growing of fungi on RBCA media. The use of RBCA rather than SDA significantly improved the fungal yield. The lowest detection level of the colony counts was calculated as 2 CFU/m^3 in washing room while the highest detection level of the colony counts was calculated as 149 CFUs/m^3 in reprocessing room of hemodialysis unit respectively.

The evaluation of colony counts in the hospital rooms provides a continuous control for airborne microbial growth and it is important to identify the level of bacterial and fungal in the hospital work environment over the time for the health reassurance of patients and hospital team.

Acknowledgement

The authors are grateful to the Director and staffs of the hospital where fieldwork was undertaken for their cooperation during this study. The first author would like to thank Ministry of Higher Education for the My Brain 15 scholarship that has been given to support this research study. The first author would also like to acknowledge East Coast Environmental Research Institute (ESERI) for providing research facilities.

References

1. Yassin, M. F. and Almouqatea, S. (2010). Assessment of airborne bacteria and fungi in an indoor and outdoor environment. *International Journal of Environmental Science Technology*, 7 (3): 535 – 544.
2. US Environmental Protection Agency (2003). An office building occupant's guide to indoor air quality. Indoor air quality publications.
3. Mentese, S., Arisoy, M., Rad, A. Y. and Gullu, G. (2009). Bacteria and fungi levels in various indoor and outdoor environments in Ankara, Turkey. *Clean*, 37(6): 487 – 493.
4. Wu, M-J., Feng, Y-S, Sung, W-P. and Surampalli, R. Y. (2011). Quantification and analysis of airborne bacterial characteristics in a nursing care institution. *Air & Waste Management*, 61: 732 – 739.
5. Sunesson, A-L., Vaes, W. H. J., Nilsson, C-A., Blomquist, G., Andersson, B. and Carlson, R. (1995). Identification of volatile metabolites from five fungal species cultivated on two media. *Applied Environmental Microbiology*, 61(8): 2911 – 2918.
6. Gorny, R. L., Reponen, T., Willeke, K., Schmechel, D., Robine, E., Boissier, M. and Grinshpun, S. A. (2002). Fungal fragments as indoor air biocontaminants. *Applied Environmental Microbiology,* 68(7): 3522 – 3531.
7. Fracchia, L., Pietronave, S., Rinaldi, M. and Martinotti, M. G. (2006). The assessment of airborne bacterial contamination in three composting plants revealed site-related biological hazard and seasonal variations. *Journal of Applied Microbiology,* 100(5): 973 – 984.
8. Brodie, E. L, De Santis, T. Z., Parker, J. P., Zubietta, I. X., Piceno, Y. M. and Andersen, G. L. (2007). Urban aerosols harbor diverse and dynamic bacterial populations. *Proceedings of the National Academy of Sciences USA,* 104(1): 299 – 304.
9. Wang, X., Bi, X., Sheng, G. and Fu, J. (2006). Hospital indoor $PM_{10}/PM_{2.5}$ and associated trace elements in Guangzhou, China. *Science of the Total Environment*, 366: 124 – 135.
10. Pasanen, A. L., Lappalainen, S. and Pasanen, P. (1996). Volatile organic metabolites associated with some toxic fungi and their mycotoxins. *Analyst*, 121: 1949 – 1953.
11. Pitkaranta, M., Meklin, T., Hyvarinen, A., Nevalainen, A., Paulin, L., Auvinen, P. E. Lignell, U. and Rintala, H. (2011). Molecular profiling of fungal communities in moisture damaged buildings before and after remediation - a comparison of culture-dependent and culture-independent method. *Bio Med Central Microbiology*. 11: 235.
12. Harrel, S. K. and Molinari, J. (2004). Aerosols and splatter in dentistry: A brief review of the literature and infection control implications. *Journal of American Dental Association*, 135: 429 – 437.
13. Manarte-Montiro, P., Carvalho, A., Pina, C., Oliveira, H. and Manso, M. C. (2013). Air quality assessment during dental practice: Aerosols bacteria counts in an universitary clinic. *Revista Portuguesa de Estamatologia Medicina Dentaria Cirurgia Maxilofacial*, 54(1): 2 – 7.
14. Pasquarella, C., Pitzurra, O. and Savino, A. (2000). The index of microbial air contamination. *Journal of Hospital Infection*, 46: 241 – 256.
15. Jense, P. A. and Schafer, M. P. (1998). Sampling and characterization of bioaerosol. *NIOSH Manual of Analytical Methods*, 1(15): 82 – 112.
16. Cellini, L., Di Campli, E., Di Candia, M. and Chiavaroli, G. (2001). Quantitative microbial monitoring in a dental office. *Public Health*, 115: 301 – 305.
17. Rajasekar, A. and Balasubramaniam, R. (2011). Assessment of airborne bacteria and fungi in food courts. *Building and Environment*, 46: 2081 – 2087.
18. Barnett, H. L. and Hunter, B. B. (1999). Illustrated genera of imperfect fungi. 4th Edition, American Phytopathological Society, St. Paul, Minnesota.

19. Suerdem, T. B. and Yildirim, I. (2009). Fungi in the atmospheric air of Canakkale province in Turkey. *African Journal of Biotechnology*, 8(18): 4450 – 4458.
20. Pitt, I. J. and Hocking, D. A. (1985). Fungi and food spoilage. Academic Press, London.
21. Pitt, I. J. (2000). A laboratory guide to common *Penicillium* species. 3rd Edition. North Ryde, N.S.W., Australia.
22. Klich, M. A. (2002). Identification of common *Aspergillus* Species. 1st Edition. Utrecht, The Netherlands.
23. Watanabe, T. (2002). Soil and seed fungi. In morphologies of cultured fungi and key to species. Lewis Publishers, Boca Raton, Boston, London, Washington D.C
24. Goh, I., Obbard, J. P., Viswanathan, S. and Huang, Y. (2000). Airborne bacterial and fungal spores in the indoor environment: a case study in Singapore. *Acta Biotechnologica*, 20: 67 – 73.
25. Guiamet, P. S., Rosato V., Saravia, S. G., Garcia, A. M. and Moreno, D. A. (2012). Biofouling of crypts of historical and architectural interest at La Plata Cemetery (Argentina). *Journal of Cultural Heritage*, 13: 339 – 344.

Malaysian Journal of Analytical Sciences, Vol 20 No 5 (2016): 1225 - 1232
DOI: http://dx.doi.org/10.17576/mjas-2016-2005-29

MALAYSIAN JOURNAL OF ANALYTICAL SCIENCES
Published by The Malaysian Analytical Sciences Society
ISSN 1394 - 2506

SALTWATER INTRUSION ANALYSIS IN EAST COAST OF TERENGGANU USING MULTIVARIATE ANALYSIS

(Analisis Pencerobohan Air Masin di Kawasan Pantai Timur, Terengganu Menggunakan Analisis Multivariat)

Norsyuhada Hairoma[1]*, Muhd Barzani Gasim[1,2], Azman Azid[1,2], Haniff Muhamad[1], Nur Hishaam Sulaiman[1], Zuriati Khairuddin[1], Ahmad Dasuki Mustafa[1], Fazureen Azaman[1], Muhammad Azizi Amran[1]

[1]*East Coast Environmental Research Institute (ESERI),*
Universiti Sultan Zainal Abidin, Gong Badak Campus, 21300 Kuala Terengganu, Terengganu, Malaysia
[2]*Faculty Bioresources and Food Industry,*
Universiti Sultan Zainal Abidin, Tembila Campus, 22200 Besut, Terengganu, Malaysia

**Corresponding author: nsyuhadahairoma@gmail.com*

Received: 14 April 2015; Accepted: 3 August 2016

Abstract

Coastal aquifer groundwater is vulnerable to saltwater contamination as it is located near the coastline. Therefore, a study is conducted to confirm all the major source of pollutants on coastal groundwater based on 13 sampling wells that located close to Terengganu coastline as well as to assess the intensity of saltwater intrusion into the wells. Measurements of selected water quality parameters such as dissolve oxygen (DO), electrical conductivity (EC), total dissolve solid (TDS), salinity, pH, turbidity and total suspended solid (TSS) were obtained from each well by using certified scientific instruments. Data were analysed by using multivariate techniques which involves principle component analysis (PCA) and cluster analysis (CA). CA was performed by using hierarchical agglomerative cluster analysis (HACA) technique. PCA yielded two PCs where PC1 forms composite factor loadings of TDS, salinity and EC that represented the saltwater intrusion meanwhile, PC2 formed composite factors of turbidity, TSS and TDS that represented the anthropogenic pollutions. CA successfully classified sampling wells into seven clusters; Extreme High (EH), Very High (VH), High (H), Moderate (M), Low (L), Very Low (VL) and Extreme Low (EL) where each cluster represented the saltwater intrusion intensity in decreasing order.

Keywords: groundwater, coastal aquifer, saltwater intrusion, multivariate techniques

Abstrak

Air bawah tanah dari akuifer pantai terdedah kepada pencemaran air masin kerana ia terletak berhampiran pantai. Oleh itu, satu kajian dijalankan untuk mengesahkan sumber utama pencemaran kepada air bawah tanah pantai berdasarkan 13 telaga pensampelan yang terletak berhampiran kawasan pantai Terengganu serta untuk menilai keamatan pencerobohan air masin ke dalam telaga.Pengukuran parameter kualiti air seperti oksigen terlarut (DO), kekonduksian elektrik (EC), jumlah pepejal terlarut (TDS), kemasinan, pH, kekeruhan dan jumlah pepejal terampai (TSS) diambil dari setiap telaga dengan menggunakan peralatan saintifik. Data dianalisis menggunakan teknik multivariat iaitu analisis komponen utama (PCA) dan analisis kelompok (CA). CA dilakukan menggunakan teknik analisis kelompok hierarki agglomeratif (HACA). PCA menghasilkan dua PC yang mana, PC1 membentuk faktor komposit TDS, kemasinan dan EC yang mewakili pencerobohan air masin manakala, PC2 membentuk faktor komposit kekeruhan, TSS dan TDS yang mewakili pencemaran antropogenik. CA berjaya mengelaskan telaga pensampelan kepada tujuh kelompok; Tinggi Ekstrem (EH), Sangat Tinggi (VH), Tinggi (H), Sederhana (M), Rendah (L), Sangat Rendah (VL) dan Rendah Ekstrem (EL) yang mana setiap kelompok mewakili keamatan pencerobohan air masin dalam urutan berkurangan.

Kata kunci: air bawah tanah, akuifer pantai, kemasukan air masin, teknik multivariat

Introduction

Water plays a critical role in human life because human need water to stay alive and to carry out daily activities either as in domestic uses or economic uses. As human population keeps growing over times, the demands for water keep increasing as well. For Malaysia, it is a tropical country and thus, receiving an adequate amount of rainfall throughout the year. Supposedly, available water should be enough to cater the needs of its people. However, there are still some states that are experiencing a water shortage crisis [1]. Another alternative for freshwater supply is from groundwater. Groundwater is defined as subsurface water and can be either stored in confined or unconfined aquifer. These aquifers can be distinguished by the water components and type of surface and subsurface water interaction [2]. Water stored as groundwater is originated from surface water that seep slowly into the ground. It takes a long time to fill up the groundwater storage. In contrast, groundwater can be extracted easily by drilling a well into aquifer. Extraction of groundwater without a proper management may lead to imbalance rate of recharge and discharge. As a result, it causes threat to this valuable water resource.

Besides, groundwater aquifer is also vulnerable to saltwater contamination [3]. This kind of threat is generally related to aquifers that located close to coastline. These aquifers are known as coastal aquifers. Theoretically, freshwater and saltwater are of different density and thus, these waters should not mix up. Instead, freshwater and saltwater was separated by a zone known as transition zone containing brackish water. This zone kept freshwater and saltwater in natural equilibrium [4, 5]. The location of the transition zone is not fixed as it is can either move further inland or towards the sea depending on several factors. The movement can be map or visualize by adopting hydrogeochemical and geophysical technique [6]. In a normal condition, freshwater will be flowing into the sea. A reversed situation can occur where the saltwater is flowing into the freshwater under the influences of natural events and anthropogenic activities [7 - 9].

This unfavourable situation caused a great concern to peoples living along the coast since long time ago. This is because of a further movement of saltwater toward the land will lead to saltwater intrusion into coastal aquifer that containing their main freshwater supply [7 - 11]. Contamination of 2 – 3% of saltwater into coastal aquifer will increase the waters salinity and resulting in water quality degradation [8]. This problem is also experienced by residence living along Terengganu coastline which is the area of this study. Most of the residents in this area still use groundwater withdrawn from the drilled wells. Some of them use the water only for basic uses such as for watering crops and livestock drinking water. The rest of them used the well water as their main water supply due to financial issues. In conjunction to this problem, a study is carried out to confirm the major sources of groundwater quality pollutants based on sampling wells that located along Terengganu coastline and to assess the intensity of saltwater intrusion into the wells.

Materials and Methods

Study area

Terengganu is located on the east coast of Peninsular Malaysia [12]. Specifically, it is located between longitudes 102.25 °E to 103.50 °E and latitude 4 N to 5.50 °N. The size of Terengganu is approximately 1,295, 638.3 hectares with coastline bordered by South China Sea and stretching 225 km from Besut to Kemaman [12]. It received an average rainfall of ± 400 mm per annum during the northeast monsoon season from November to March, meanwhile ± 190 mm per annum during the other months [12, 13]. Its average temperature is from 29 °C to 32 °C throughout the year [14]. Sampling areas were located along the Terengganu coastline (Figure 1).

Generally, Terengganu coastline is dominated by Quaternary rock of marine and continental deposits [15]. It is specifically known as Holocene beach ridges derived from Matang Gelugor Member. It is comprises of sand, gravel and sandy clay deposits in littoral and marine environment [16, 17]. In the hydrogeology perspective, Quaternary sediment is characterized by high porosity and excellent permeability that allowed water to be stored in between the grains [18]. Carboniferous rock and minor intrusive rock also present along the centre and south of Terengganu coastline.

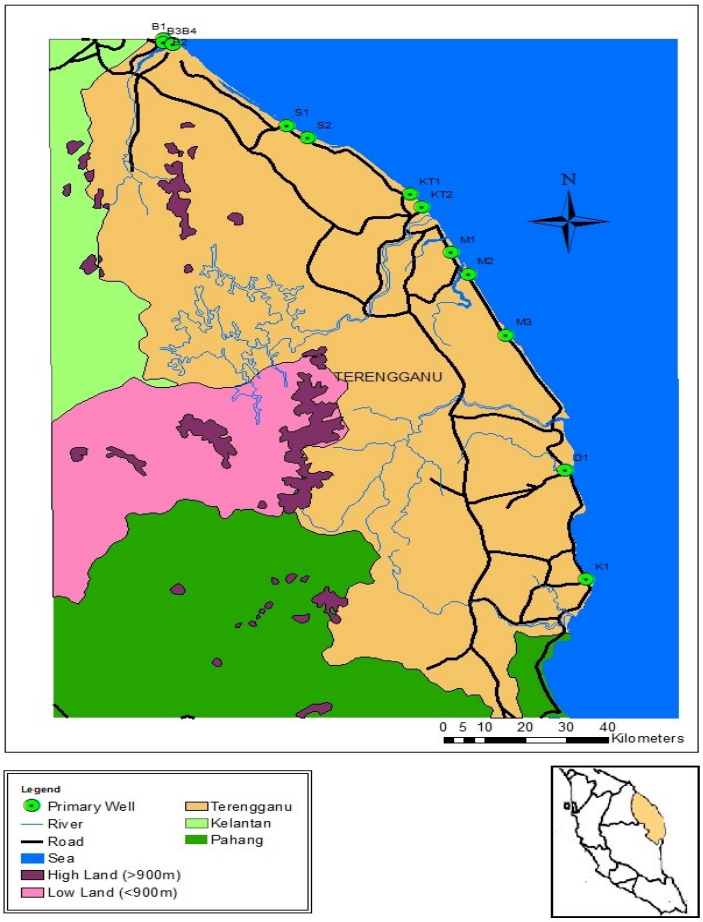


Figure 1. Location of sampling wells (Primary Well) along Terengganu coastline

Data collection

Samplings were carried out at 13 private wells, located closely to Terengganu coastline from July to August 2015 (Table 1). Samplings were conducted monthly by performing in situ measurements of selected water quality parameters such as dissolve oxygen (DO), electrical conductivity (EC), total dissolve solid (TDS), salinity, pH, turbidity and total suspended solid (TSS) . DO, EC, TDS, salinity and pH were measured using YSI 556 Handheld Multiparameter meter. Turbidity was measured using 2100Q Portable Turbidimeter and TSS was measured using HACH DR 900 Multiparameter Handheld meter. Global Positioning System (GPS) was used to locate the exact coordinates of sampling wells.

Multivariate analysis

A numbers of physiochemical parameters can be used to determine the groundwater quality namely total dissolve solid (TDS), dissolve oxygen (DO), total suspended solid (TSS), salinity, electrical conductivity (EC), chloride, biochemical oxygen demand (BOD) and pH value. However, it is difficult to define the main factors that control groundwater quality since there are too many data. Multivariate analysis such as principal component analysis and cluster analysis is suggested to be one of the best solutions to re-define the meaning of a mass of data. Therefore, multivariate analysis is employed to achieve the objective of this study.

Table 1. Coordinate location of sampling wells

Sampling Well	Latitude	Longitude
B1	5.8339°	102.5553°
B2	5.8241°	102.5566°
B3	5.8216°	102.5754°
B4	5.8202°	102.5774°
S1	5.5951°	102.8262°
S2	5.5605°	102.8736°
KT1	5.4039°	103.0992°
KT2	5.3686°	103.1241°
M1	5.2435°	103.1872°
M2	5.1825°	103.2256°
M3	5.0135°	103.3096°
D1	4.6387°	103.4383°
K1	4.3361°	103.4858°

Principal component analysis (PCA)

PCA identify the principle components (PCs) of data sets by transforming the original variables into new variables [19 – 23]. The input data matric (variables x cases) used for this method was [7 x 52]. PCs with eigenvalues more than 1.0 computed from PCA process is considered as significant PCs. These PCs were then rotated and the count of PCs was used as rotation factor in varimax normalization process. Two significant varifactors (VFs) of eigenvalues more than 1.0 explaining 67.44% of the total variance of water quality data set were yielded [24]. Each VF contains a list of factor loadings that explains the major sources of groundwater pollutant.

Cluster analysis (CA)

Cluster analysis is technique for data classification based on their similarities or closeness [22, 23, 25]. It is done by performing hierarchical agglomerative cluster analysis (HACA) on selected parameters spatially or temporally. In this study, spatial cluster analysis is applied onto selected parameters to group the sampling wells into a few clusters. Sampling wells that grouped as a cluster are homogenous to each other meanwhile, sampling wells between clusters were heterogeneous.

Results and Discussion

Identification of source of pollutant

Corresponding VFs, loadings and variance resulted from PCA are presented in Table 2. Bolded values in Table 2 indicated the strong and moderate factor loadings with absolute loading values of >0.75 and 0.75 – 0.50, respectively. These factor loadings were considered as important factors that influence water quality [26]. The un-bolded values represent the weak factor loadings with absolute loading values of 0.50 – 0.30 and have minor contribution for this water quality study.

VF1, explaining 48.66% of total variance, has strong positive loadings on EC, TDS and salinity. This composite factor represents the saltwater intrusion into coastal aquifer. These factors combination proposed that the dissolved solid engaged in PC1 was dissolved salts supplied by high salt contents of seawaters through saltwater intrusion process. Thus, it can be emphasized that groundwater samples from study area are highly susceptible to saltwater intrusion as it is located near to coastline.

Table 2. Factor loadings after Varimax rotation from PCA of sampling wells.

Variables	VF1	VF2
Turbidity (NTU)	-0.281	**0.743**
TSS	0.273	**0.577**
DO (mg/L)	-0.109	**-0.598**
EC (mS cm^{-1})	**0.956**	-0.035
TDS (mg/L)	**0.975**	0.0004
Salinity (ppt)	**0.976**	-0.002
pH	0.649	-0.259
Eigenvalue	3.424	1.297
% Total variance	48.66	18.78
Cumulative % variance	48.66	67.44

Values in bold indicate strong and moderate loadings

VF2, explaining 18.78% of total variance, has positive moderate loading on turbidity, positive moderate loading on TSS and negative moderate loading on DO. This composite factor is proposed to represent the anthropogenic pollution such as waste dumping into wells. The small suspended solid originated from the waste act like a barrier for the direct light entering the wells. It would be able to reach the well base only by scattering through the small spaces in between the particles. The measure of amount of light scattered of these particles is known as turbidity. This explains the association of total suspended solid with turbidity. If the amount of total suspended solid is high, the turbidity would be high as well. In contrast, increasing amount of turbidity and total suspended solid has inverse relationship with dissolved oxygen. The oxygen is suggested to be used up by microorganism for decay process [27].

Spatial clustering

A further analysis on saltwater intrusion which was identified from the VF1 composite factor is done by applying spatial clustering. Parameters included in VF1 composite factor are EC, TDS and salinity. The aim of this application is to cluster the sampling wells according to the range of EC, TDS and salinity readings. Results of this analysis revealed six main clusters. The results of cluster analysis of each parameter are shown in Figures 2, 3 and 4, respectively. Interestingly, all parameters have classified the sampling wells into seven statistically significant clusters. The count and the sampling wells listed under each cluster were also similar. As stated before, EC, TDS and salinity were related to each other. Therefore, it could explain why sampling wells that listed below each cluster is the same for all parameters.

The result of EC, TDS and salinity cluster analysis is suggested to represent the intensity of saltwater intrusion and is shown as a summary in Figure 5. Overall, CA revealed that sampling well B3 is intruded by extremely high (EH) saltwater intrusion compared to other stations followed by very highly (VH) intruded well B4, highly (H) intruded well KT1, moderately (M) intruded well B1, low or less (L) intruded well M3, and very low (VL) intruded well S2, KT2, M1 and D1. EH cluster is characterised by extremely high EC (3965.25 µS/cm), extremely high TDS (2384.5 mg/L) and extremely high salinity (1.89 ppt) compared to other clusters. VH cluster has very high EC (1278.6 µS/cm), very high TDS (1161.88 mg/L) and very high salinity (0.905 ppt).

H cluster has high EC (1094.75 µS/cm), high TDS (608.05 mg/L) and high salinity (0.52 ppt). M cluster is characterised by moderate EC (556.25 µS/cm), moderate TDS (326.14 mg/L) and moderate salinity (0.24 ppt). L cluster has low EC (331.95 µS/cm), low TDS (175.52 mg/L) and low salinity (0.18 ppt). VL clusters has very low EC (246.9 – 321.68 µS/cm), very low TDS (147.89 – 194.01 mg/L) and very low salinity (0.10 – 0.14 ppt). On the other hand, the least or extremely low (EL) intruded sampling wells are B2, S1, M2, K1. This cluster has extremely

low EC (140.15 – 189.15 µS/cm), extremely low TDS (84.34-111.96 mg/L) and extremely low salinity (0.06 – 0.09 ppt).

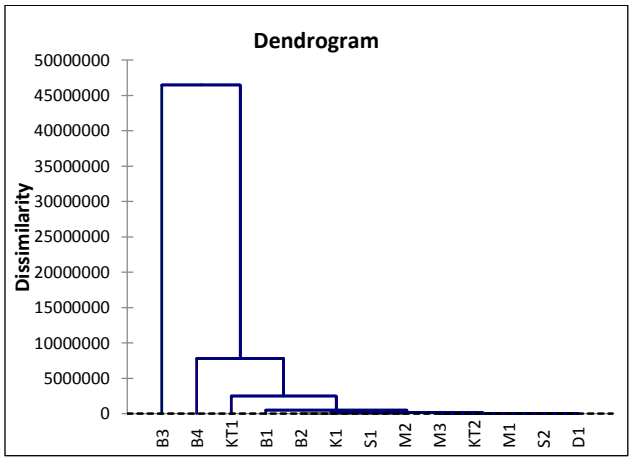


Figure 2. Dendrogram of spatial classification for EC of sampling wells along Terengganu coastline

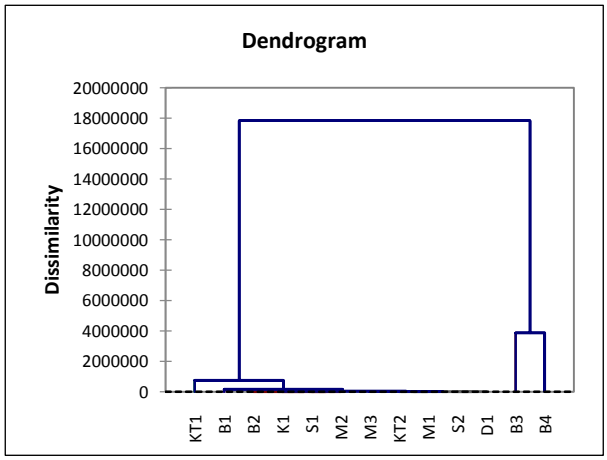


Figure 3. Dendrogram of spatial classification for TDS of sampling wells along Terengganu coastline

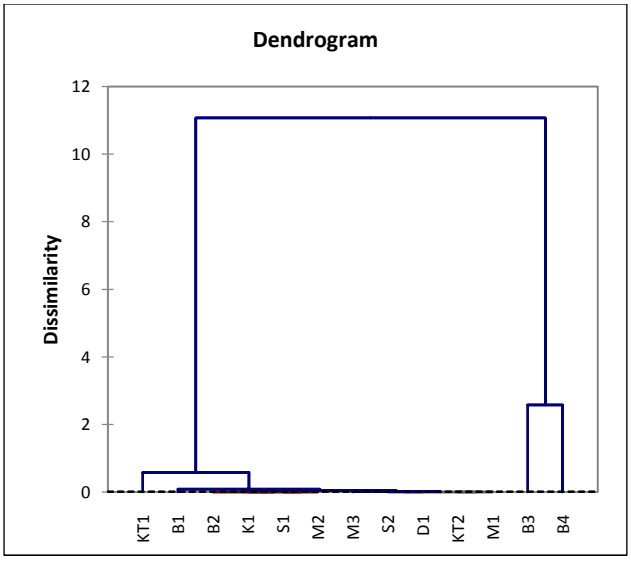


Figure 4. Dendogram of spatial classification for salinity of sampling wells along Terengganu coastline

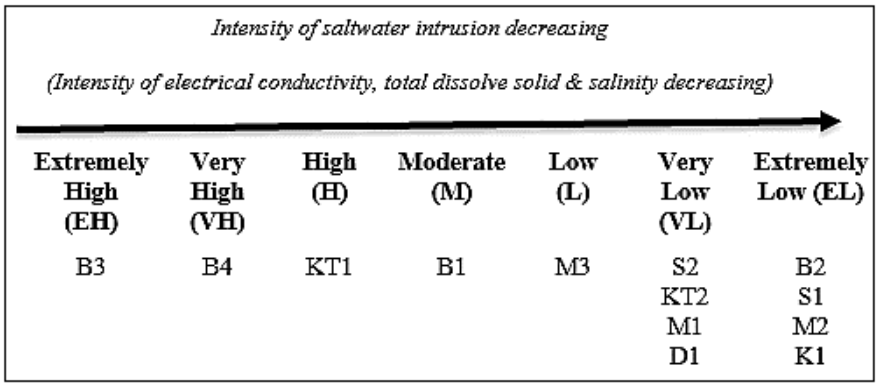


Figure 5. Saltwater intrusion intensity based on EC, TDS and salinity cluster analysis of sampling well along Terengganu coastline

Conclusion

According to principle component analysis (PCA) technique, two pollutants that affect the groundwater quality of sampling wells that located along Terengganu coastline are the saltwater intrusion and the anthropogenic pollutions such as waste dumping into the wells. Next, cluster analysis performed on EC, TDS and salinity has grouped sampling wells into seven clusters; EH, VH, H, M, L, VL, EL. The extremely high (EH) intruded by saltwater is groundwater of sampling well B3 compared to other wells, very highly (VH) intruded well is B4, highly (H) intruded is KT1, moderately (M) intruded is B1, less or low (L) intruded is M3, very low intruded sampling wells are S2, KT2, M1 and D1 meanwhile, extremely low intruded wells are B2, S1, M2 and K1.

Acknowledgement

This research is fully supported by FRGS/2/2014/STWN06/UNISZA/01/1(RR 082) research grant. The authors would like to express an appreciation to the East Coast Environmental Research Institute (ESERI), Universiti Sultan Zainal Abidin (UniSZA) for giving advice, guides, support and for the use of their research facilities.

References

1. Che-Ani, A. I., Shaari, N., Sairi, A., Zain, M. F. M., and Tahir, M. M. (2009). Rainwater harvesting as an alternative water supply in the future. *European Journal of Scientific Research* 34(1): 132 – 140.
2. Green, T. R., Taniguchi, M., Kooi, H., Gurdak, J. J., Allen, D. M., Hiscock, K. M., Treidel, H. and Aureli, A. (2011). Beneath the surface of global change: Impacts of climate change on groundwater. *Journal of Hydrology,* 405: 532 – 560.
3. Choudhury, K., Saha, D. K., and Chakraborty, P. (2001). Geophysical study for saline water intrusion in a coastal alluvial terrain. *Journal of Applied Geophysics,* 46(3): 189 – 200.
4. Abdullah, M. H., Raveena, S. M., and Aris, A. Z. (2010). A numerical modelling of seawater intrusion into an oceanic island aquifer, Sipadan Island, Malaysia. *Sains Malaysiana* 39(4): 525 – 532.
5. Werner, A. D., Bakker, M., Post, V. E. A., Vandenbohede, A., Lu, C., Ataie-ashtiani, B., Simmons, C. T., and Barry, D. A. (2013). Seawater intrusion processes, investigation and management: Recent advances and future challenges. *Advances in Water Resources*, 51: 3 – 26.
6. Samsudin, A. R., Haryono, A., Hamzah, U. and Rafek, A. G. (2008). Salinity mapping of coastal groundwater aquifers using hydrogeochemical and geophysical methods: A case study from north Kelantan, Malaysia. *Environmental Geology*, 55(8): 1737 – 1743.
7. Priyanka, B. N., and Mahesha, A. (2015). Parametric studies on saltwater intrusion into coastal aquifers for anticipate sea level rise. *Aquatic Procedia*, 4: 103 – 108.
8. Abd-Elhamid, H. F. and Javadi, A. A. (2011). A density-dependant finite element model for analysis of saltwater intrusion in coastal aquifers. *Journal of Hydrology*, 401(3): 259 – 271.

9. Yao-Dong, D., Xu-Hua, C., Xian-Wei, W., Hui, A., Hai-Lai, D., Jian, H. and Xiao-Xuan, W. (2013). A review of assessment and adaptation strategy to climate change impacts on the coastal areas in South China. *Advances in Climate Change Research*, 4(4): 201 – 207.
10. Chang, S. W., Clement, T. P., Simpson, M. J. and Lee, K. K. (2011). Does sea-level rise have an impact on saltwater intrusion? *Advances in Water Resources* 34(10): 1283 – 1291.
11. Tomaszkiewicz, M., Abou, N. M. and El-Fadel, M. (2014). Development of a groundwater quality index for seawater intrusion in coastal aquifers. *Environmental Modelling & Software* 57: 13 – 26.
12. Gasim, M. B., Khalid, N. A., and Muhamad, H. (2015). The influence of tidal activities on water quality of Paka River Terengganu, Malaysia. *Malaysian Journal of Analytical Sciences*, 19(5): 979 – 990.
13. Toriman, M. E., Gasim, M. B., Ariffin, N. H., Muhamad, H. and Hairoma, N. (2015). The influence of tidal activities on hydrologic variables of Marang River, Terengganu, Malaysia. *Malaysian Journal of Analytical Sciences*, 19(5): 1099 – 1108.
14. Sharif, S. M., Kusin, F. M., Asha'ari, Z. H. and Aris, A. Z. (2015). Characterization of water quality conditions in the klang river basin, malaysia using self-organizing map and k-means algorithm. *Procedia Environmental Sciences*, 30: 73–78.
15. Raj, J. K., Tan D. N., and Abdullah W. H. (2009). Cenozoic stratigraphy. In *Geology of Peninsular Malaysia.* Kuala Lumpur: University of Malaya: pp. 164 – 168.
16. Hassan, K. B. (1989). Significance of palynology in late quaternary sediments in Peninsular Malaysia. *Geological Society of Malaysia* 24: 57 – 66.
17. Saghravani, S. R., Yusoff, I., Wan Md Tahir, W. Z. and Othman, Z. (2015). Estimating recharge based on long-term groundwater table fluctuation monitoring in a shallow aquifer of Malaysian tropical rainforest catchment. *Environmental Earth Sciences,* 74(6): 4577 – 4587.
18. Feseker, T. (2007). Numerical studies on saltwater intrusion in a coastal aquifer in Northwestern Germany. *Hydrogeology Journal*, 15(2): 267 – 279.
19. Biglari, A. and Sutherland, J. C. (2015). An a-posteriori Evaluation of principal component analysis-based models for turbulent combustion simulations. *Combust and Flame*, 162(10): 4025 – 4035.
20. Tantra, R., Oksel, C., Robinson, K. N., Sikora, A., Wang, X. Z. and Wilkins, T. A. (2015). A method for assessing nanomaterial dispersion quality based on principal component analysis of particle size distribution data. *Particuology,* 22: 30 – 38.
21. Parente, A. and Sutherland, J. C. (2013). Principal component analysis of turbulent combustion data: Data pre-processing and manifold sensitivity. *Combustion and Flame,* 160(2): 340 – 350.
22. Kasim, M. K., Juahir, H., Tawnie, I., Azid, A., Saudi, A.S.M., Samsudin, S., Toriman, M.E., Fazli, B.M., and Hasnam, C.N.C. (2015). Environmetric techniques application in water quality assessment: A case study in Linggi River basin. *Jurnal Teknologi (Sciences & Engineering)* 74(1): 151–157.
23. Aminu Ibrahim, A., Juahir, H., Toriman, M.E., Mustapha, A., Azid, A. and Isiyaka, H.A. (2015). Assessment of surface water quality using multivariate statistical techniques in the Terengganu River basin. *Malaysian Journal of Analytical Sciences,* 19(2): 338 – 348.
24. Maritan, L., Holakooei, P. and Mazzoli, C. (2015). Cluster analysis of XRPD data in ancient ceramics: What for? *Applied Clay Science,* 114: 540 – 549.
25. Shrestha, S. and Kazama, F. (2007). Assessment of surface water quality using multivariate statistical techniques: A case study of the Fuji river basin, Japan. *Environmental Modelling & Software,* 22(4): 464 – 475.
26. Liu, C. W., Lin, K. H. and Kuo, Y. M. (2003). Application of factor analysis in the assessment of groundwater quality in a blackfoot disease area in Taiwan. *Science of the Total Environment*. 313(1): 77 – 89.
27. Mokhtar, M., Bahari, I., and Poon, A. (2001). Kualiti air di sekitar kawasan perindustrian Balakong, Lembangan Langat. *Malaysian Journal of Analytical Sciences* 7(1): 129 – 138.

Malaysian Journal of Analytical Sciences Vol 20 No 6 2016

Articles 17-31 are selected papers from "The 28th Symposium of Malaysian Chemical Engineers (SOMChE 2015), 'Towards Net Carbon Neutrality', 21 - 22 October 2015, Palm Garden Hotel, IOI Resort, Putrajaya; organised by Department of Chemical & Process Engineering, UKM & Fuel Cell Institute, UKM."

Guest Editor: Edy Herianto Majlan

Articles 32-36 are selected papers from the "International Conference on Applied Science and Technology (ICASIT 2015) for Chemistry and Environment Symposium, 24-26 February 2015, Grand Lexis, Port Dickson, Negeri Sembilan, Malaysia; organised by Faculty of Applied Science, Universiti Teknologi MARA, Shah Alam, Selangor, Malaysia."

Guest Editor: Rohaya Ahmad

Page

1. STUDIES OF INTERACTION BETWEEN TETRABUTYLAMMONIUM BROMIDE BASED DEEP EUTECTIC SOLVENT AND DNA USING FLUORESCENCE QUENCHING METHOD AND CIRCULAR DICHROISM SPECTROSCOPY 1233
(Kajian Interaksi antara Pelarut Eutektik Mendalam Berasaskan Tetrabutilamonium Bromida dan DNA Menggunakan Kaedah Pelindapkejutan Pendarfluor dan Spektroskopi Edaran Dikroisme)
Rizana Yusof, Haslina Ahmad, Mohd Basyaruddin Abdul Rahman

2. SYNTHESIS OF ISOXAZOLIDINE VIA 1,3-DIPOLAR CYCLOADDITION OF N-4-TERT-BENZYLIDENE NITRONE AND MALEIMIDE IN IMIDAZOLIUM-BASED IONIC LIQUIDS 1241
(Sintesis Sebatian Isoxazolidina Melalui Tindakbalas 1,3-Dwikutub Pensiklotambahan N-4-Tetra-Benzilidina Nitron dan Maleimida dalam Cecair Ionik Berasaskan Imidazolium)
Nur Liyana Sakinah Johari, Siti Nashwa Mohd Poad, Nur Hasyareeda Hassan, Nurul Izzaty Hassan

3. RADIOLOGICAL RISK ASSESSMENT FROM THE INTAKE OF VEGETABLES AND FRUITS IN MALAYSIA 1247
(Penilaian Risiko Radiologi dari Pengambilan Sayur-Sayuran dan Buah-Buahan di Malaysia)
Wahmisari Priharti and Supian Bin Samat

4. VOLTAMMETRIC DETERMINATION OF REACTIVE BLACK 5 (RB5) IN WASTE WATER SAMPLES FROM THE BATIK INDUSTRY 1254
(Penentuan Voltammetrik Bagi Reaktif Black 5 (RB5) Dalam Sampel Air Sisa Dari Industri Batik)
Nur Syamimi Zainudin, Mohamad Hadzri Yaacob, Noor Zuhartini Md Muslim

5. IN-SILICO IDENTIFICATION OF POTENTIAL PROTEIN ARGININE DEIMINASE IV (PAD4) INHIBITORS 1269
(Pengenalpastian In-Silico yang Berpotensi Sebagai Perencat Protein Arginin Deiminase IV (PAD4))
Zalikha Ibrahim, Bimo Ario Tejo, Muhammad Alif Mohammad Latif, Roghayeh Abedi Karjiban, Abu Bakar Salleh, Mohd Basyaruddin Abdul Rahman

6. SYNTHESIS AND PHYSICOCHEMICAL CHARACTERIZATION OF CATIONIC POLYMERIC 1278

SURFACTANT FROM *Dioscorea pyrifolia* STARCH
(Sintesis dan Pencirian Fizikokimia Surfaktan Polimer Kationik daripada Kanji *Dioscorea pyrifolia*)
Elmi Sharlina Md. Suhaimi, Wan Yaacob Wan Ahmad, Azwan Mat Lazim

7. THE INFLUENCE OF CALCINATION TEMPERATURE ON IRON OXIDE (α-Fe_2O_3) TOWARDS CO_2 ADSORPTION PREPARED BY SIMPLE MIXING METHOD 1286
(Kesan Suhu Pengkalsinan Ferum Oksida (α-Fe_2O_3) Disediakan Melalui Kaedah Campuran Ringkas Terhadap Penjerapan CO_2)
Azizul Hakim, Mohd. Ambar Yarmo, Tengku Sharifah Marliza, Maratun Najiha Abu Tahari, Wan Zurina Samad, Muhammad Rahimi Yusop, Mohamed Wahab Mohamed Hisham, Norliza Dzakaria

8. ENHANCED REDUCIBILITY OF Mg-DOPED MoVTeNbOx MIXED OXIDE CATALYSTS FOR PROPANE OXIDATION REACTION 1299
(Penambahbaikan Kebolehturunan Mangkin Mg-Terdop-MoVTeNbOx Terhadap Proses Pengoksidaan Propana)
Wong Hong Ren, Irmawati Ramli, Taufiq Yap Yun Hin

9. SYNTHESIS, CHARACTERIZATION AND ELECTOCHEMICAL STUDIES OF 4-METHOXYBENZOYLTHIOUREA DERIVATIVES 1311
(Sintesis, Pencirian dan Kajian Elektrokimia Terhadap Terbitan 4-Metoksibenzoiltiourea)
Karimah Kassim, Noor Khadijah Mustafa Kamal, Adibatul Husna Fadzil

10. DETERMINATION OF TOTAL ORGANIC CARBON CONCENTRATION IN SURFICIAL SEDIMENTS OF SUNGAI PINANG, PENANG, MALAYSIA 1318
(Penentuan Jumlah Karbon Organik dalam Sedimen Permukaan di Sungai Pinang, Pulau Pinang, Malaysia)
Ong Meng Chuan, Fok Fei Mei, Yong Jaw Chuen

11. SYNTHESIS AND CHARACTERIZATION OF EPOXIDIZED NEOPENTHYL GLYCOL DIOLETE AS AN INTERMIDIATE OF BIOLUBRICANT 1329
(Sintesis dan Pencirian Epoksida Dioleat Neopentil Glikol Sebagai Bahan Perantara Biopelincir)
Vanitah Rajaendran, Jumat Salimon, Rahimi M.Yusop

12. DEGRADATION OF METHYLENE BLUE DYE BY CuO-BiVO4 PHOTOCATALYSTS UNDER VISIBLE LIGHT IRRADIATION 1338
(Degradasi Pewarna Metilena Biru oleh Fotomangkin CuO-BiVO4 Di Bawah Sinaran Cahaya Nampak)
Abdul Halim Abdullah, Wan Tze Peng, Mohd Zobir Hussein

13. PESTICIDES RESIDUES IN AGRICULTURAL SOILS AND ITS HEALTH ASSESSMENT FOR HUMANS IN CAMERON HIGHLANDS, MALAYSIA 1346
(Residu Racun Serangga dalam Tanah Pertanian dan Penilaian Kesihatan Terhadap Manusia di Cameron Highlands, Malaysia)
Yang Farina, Md Pauzi Abdullah, Nusrat Bibi, Wan Mohd Afiq Wan Mohd Khalik

14. INTERCALATION STUDY OF CURCUMIN INTO ZINC LAYERED HYDROXIDE 1359
(Kajian Mengenai Penyisipan Kurkumin ke dalam Zink Hidroksida Berlapis)
Adila Mohamad Jaafar, Asma Najaj Anuar, Norhayati Hashim, Fatin Hanifah Ayob

15. ENZYMATIC GLYCEROLYSIS OF METHYL LAURATE UTILIZING *Candida antarctica* Lipase b 1365
(Gliserolisis Berenzim oleh Metil Laurat Menggunakan Lipase b *Candida antarctica*)

Norul Naziraa Ahmad Jamlus, Jumat Salimon, Darfizzi Derawi

16. EFFECT OF HEAT TREATMENTS ON THE YIELD, QUALITY AND STORAGE STABILITY OF OIL EXTRACTED FROM PALM FRUITS 1373
(Kesan Rawatan Haba Terhadap Peratus Pengekstrakan Minyak, Kualiti dan Kestabilan Semasa Penyimpanan Minyak yang Diekstrak Daripada Buah Kelapa Sawit)
Hasimah Kasmin, Azwan Mat Lazim, Roila Awang

17. MICROWAVE-ASSISTED SYNTHESIS OF MESOPOROUS SILICA NANOPARTICLES AS A DRUG DELIVERY VEHICLE 1382
(Sintesis Partikel Nano Silika Berliang Meso Dibantu Gelombang Mikro Sebagai Medium Penyebaran Ubat)
Nur Hidayatul Nazirah Kamarudin, Aishah Abdul Jalil, Sugeng Triwahyono, Sharifah Najiha Timmiati

18. METHANE ADSORPTION PERFORMANCE OF THE PALM KERNEL SHELL-DERIVED CARBON MATERIAL ACTIVATED USING CO_2-STEAM SEQUENTIAL COMBINATION 1390
(Prestasi Penjerapan Gas Metana oleh Karbon Teraktif Isirong Kelapa Sawit dengan Menggunakan Gabungan CO_2-Stim Secara Turutan)
Mohd Saufi Md Zaini and Syed Shatir A. Syed Hassan

19. Ba-SAPO-34 ZEOLITE MEMBRANE FOR CO_2 AND N_2 PERMEATION 1397
(Resapan Gas CO_2 dan N_2 Melalui Membran Zeolit Ba-SAPO-34)
Thiam Leng Chew, Jun Wei Lim, Abdul Latif Ahmad

20. INFLUENCE OF HIGHLY CONCENTRATED SODIUM HYDROXIDE (NaOH) TOWARDS FORMATION OF HIGHLY ORDERED TIO_2 NANOTUBES (TNT) STRUCTURE 1405
(Pengaruh Kepekatan Sodium Hidrosida (NaOH) yang Tinggi terhadap Pembentukan Struktur Bertertib Nanotiub TiO_2 (TNT))
Masturah Abdullah and Siti Kartom Kamarudin

21. EFFECT OF pH ON FLUX DECLINE DURING FRACTIONATION OF GLUCOSE FROM CELLULOSE HYDROLYSATE THROUGH A POLYSULFONE MEMBRANE 1413
(Kesan pH pada Penurunan Fluks bagi Pemeringkatan Glukosa daripada Hidrolisis Selulosa Melalui Membran Polisulfon)
Masniroszaime Md Zain and Abdul Wahab Mohammad

22. OPTIMIZATION OF CHLOROPHYLL EXTRACTION FROM *Gynura procumbens* 1421
(Pengoptimuman Proses Pengekstrakan Klorofil daripada *Gynura procumbens*)
Zurina Zainal Abidin, Wan Noraznorin Mohamad, Mahtab Samadi

23. SURFACE CHARACTERIZATION ON ALKALI-HEAT-TREATMENT ON TITANIUM ALLOY 1429
(Pencirian Rawatan Alkali-Haba ke atas Permukaan Aloi Titanium)
Nurul Hazwani Hanib, Fazlena Hamzah, Zarina Omar, Istikamah Subuki

24. OPTIMIZATION OF THERMOPHILIC BIOHYDROGEN PRODUCTION BY MICROFLORA OF PALM OIL MILL EFFLUENT: CELL ATTACHMENT ON GRANULAR ACTIVATED CARBON AS SUPPORT MEDIA 1437
(Pengoptimuman Pengeluaran Biohidrogen Termofilik oleh Mikroflora Efluen Kilang Minyak Sawit: Lampiran Sel Pada Karbon Berbutir Aktif Sebagai Media Sokongan)
Nur Syakina Jamali and Jamaliah Md Jahim

25. PHYSICO-CHEMICAL AND BIOLOGICAL CHANGES DURING CO-COMPOSTING OF MODEL KITCHEN WASTE, RICE BRAN AND DRIED LEAVES WITH DIFFERENT MICROBIAL 1447

INOCULANTS
(Perubahan Fiziko-Kimia dan Biologi dalam Pengkomposan Bersama Sisa Dapur, Dedak Padi dan Daun Kering dengan Mikrob Inokulan Yang Berbeza)
Yee Van Fan, Chew Tin Lee, Chee Woh Leow, Lee Suan Chua, Mohamad Roji Sarmidi

26. PREPARATION OF LANTHANUM STRONTIUM COBALT OXIDE POWDER BY A MODIFIED SOL-GEL METHOD 1458
(Penyediaan Serbuk Lantanum Strontium Kobalt Oksida Melalui Kaedah Sol-Gel Terubahsuai)
Abdullah Abdul Samat, Mahendra Rao Somalu, Andanastuti Muchtar, Nafisah Osman

27. ADSORPTION OF CADMIUM (II) IONS BY POLYACRYLONITRILE-BASED ACTIVATED CARBON NANOFIBERS/MAGNESIUM OXIDE AS ITS ADSORBENTS 1467
(Karbon Nano-Gentian Teraktif Berasaskan Poliakrilonitril/Magnesium Oksida Sebagai Penjerap untuk Penjerapan Ion Kadmium (II))
Faten Ermala Che Othman, Norhaniza Yusof, Juhana Jaafar, Ahmad Fauzi Ismail, Norfadhilatuladha Abdullah, Hasrinah Hasbullah

28. THE EFFECT OF VARIOUS PRETREATMENT METHODS ON EMPTY FRUIT BUNCH FOR GLUCOSE PRODUCTION 1474
(Kesan Kaedah Prarawatan Berbeza Terhadap Tandan Kosong Kelapa Sawit Bagi Penghasilan Glukosa Ringkas)
Nurul Hazirah Che Hamzah, Masturah Markom, Shuhaida Harun, Osman Hassan

29. POLYIMIDE MEMBRANES FOR ORGANIC SALTS RECOVERY FROM MODEL BIOMASS FERMENTATION 1481
(Membran Poliimida untuk Pengumpulan Garam Organik daripada Model Sup Penapaian Biojisim)
Nadiah Khairul Zaman, Rosiah Rohani, Abdul Wahab Mohammad

30. PRODUCTION OF BIOGAS THROUGH ANAEROBIC DIGESTION OF *Cabomba furcata* IN DIGESTER BATCH SYSTEM 1491
(Penghasilan Biogas Melalui Pencernaan Anaerobik daripada *Cabomba furcata* di dalam Sistem Penghadam Kelompok)
Siti Afifah Muda, Omar Syah Jehan Elham, Hassimi Abu Hasan, Siti Rozaimah Sheikh Abdullah

31. POLYANILINE MULTI-COATED ONTO POLYVINYLIDENE FLUORIDE AND SILICON ELASTOMER FOR PRESSURE FILTRATION MEMBRANES 1498
(Polianilin Multi-Lapis Bersalut pada Polivinilidin Fluorida dan Elastomer Silikon untuk Membran Penurasan Bertekanan)
Fatimah Ibrahim, Rosiah Rohani, Abdul Wahab Mohammad

32. REDUCTION BEHAVIOUR OF TUNGSTEN DIOXIDE BY VARIOUS CONCENTRATION OF CARBON MONOXIDE 1510
(Kelakuan Penurunan Tungsten Dioksida oleh Kepekatan Berbeza Karbon Monoksida)
Fairous Salleh, Alinda Samsuri, Tengku Shafazila Tengku Saharuddin, Mohamed Wahab Mohamed Hisham, Rizafizah Othaman, Mohd. Ambar Yarmo

33. SYNTHESIS AND CHARACTERIZATION OF OXADIAZOLE DERIVATIVES FROM BENZIMIDAZOLE 1515
(Sintesis dan Perincian Terbitan Oksadiazol Dari Benzimidazol)
Norizan Ahmat, Nik Khairunissa Nik Abdullah Zawawi, Muhammad Taha, Nor Hadiani Ismail, Noraishah Abdullah

34. THE EFFECT OF POLYMER CONCENTRATION AND SURFACTANT TYPES ON NANOFILTRATION-SURFACTANT MEMBRANE FOR TEXTILE WASTEWATER 1524
(Kesan Kepekatan Polimer dan Jenis Surfaktan pada Membran Surfaktan Penurasan-Nano untuk Air Sisa Tekstil)
Sarah Husnaini Zainal, Abdul Rahman Hassan, Mohd Hafez Mohd Isa

35. THREE FLAVONOL GLYCOSIDES FROM *Calliandra surinamensis* Benth 1530
(Tiga Flavonol Glikosida daripada *Calliandra surinamensis* Benth)
Siti Muhayyah Omar, Norizan Ahmat, Nik Fatini Nik Azmin

36. ISOLATION OF OLIGOSTILBENES FROM *Shorea bracteolate* 1535
(Pemisahan Oligostilbene daripada *Shorea bracteolate*)
Norhazana Norizan, Norizan Ahmat, Yana Maulana, Zurina Shameeri

Malaysian Journal of Analytical Sciences, Vol 20 No 6 (2016): 1233 - 1240
DOI: http://dx.doi.org/10.17576/mjas-2016-2006-01

MALAYSIAN JOURNAL OF ANALYTICAL SCIENCES
Published by The Malaysian Analytical Sciences Society
ISSN 1394 - 2506

STUDIES OF INTERACTION BETWEEN TETRABUTYLAMMONIUM BROMIDE BASED DEEP EUTECTIC SOLVENT AND DNA USING FLUORESCENCE QUENCHING METHOD AND CIRCULAR DICHROISM SPECTROSCOPY

(Kajian Interaksi antara Pelarut Eutektik Mendalam Berasaskan Tetrabutilamonium Bromida dan DNA Menggunakan Kaedah Pelindapkejutan Pendarfluor dan Spektroskopi Edaran Dikroisme)

Rizana Yusof[1], Haslina Ahmad[1,2], Mohd Basyaruddin Abdul Rahman[1,2]*

[1]*Department of Chemistry, Faculty of Science*
[2]*Enzyme and Microbial Technology Research Centre (EMTech)*
Universiti Putra Malaysia, 43400 UPM Serdang, Selangor, Malaysia

**Corresponding author: basya@upm.edu.my*

Received: 17 August 2015; Accepted: 17 August 2016

Abstract

The interaction of tetrabutylammonium bromide (TBABr)-based deep eutectic solvents (DESs) with calf thymus DNA (ct-DNA) was investigated by fluorescence and circular dichroism (CD) spectroscopy. The influences of hydrogen bond donors (HBDs), with respect to chain lengths and the presence of OH group were determined through ethidium bromide (EB) fluorescence quenching. Based on the quenching process, it was concluded that hydrophobic interactions were responsible for the DES ability to quench EB from EB-bound DNA. The strong electrostatic attraction between TBA^+ cation on DES and negative charge phosphate DNA was proved from fluorescence and CD spectroscopy. DNA was able to maintain its double helical structure at 25 °C with a concentration of 25% DES.

Keywords: binding, deep eutectic solvent, tetrabutylammonium bromide, fluorescence quenching, circular dichroism spectroscopy

Abstrak

Ikatan antara pelarut eutektik mendalam berasaskan tetrabutilammonium bromida (TBABr) dengan 'calf thymus' DNA (ct-DNA) telah diuji dengan spektroskopi pendarfluor dan edaran dikroisme (CD). Pengaruh penderma ikatan hidrogen (HBDs) berdasarkan panjang rantai dan kehadiran kumpulan OH telah ditentukan melalui pelindapkejutan pendarfluor etidium bromida (EB). Berdasarkan proses pelindapkejutan, dapat dirumuskan bahawa ikatan hidrofobik berperanan dalam menentukan keupayaan DES untuk menyingkirkan EB daripada EB-terikat DNA. Tarikan elektrostatik yang kuat antara kation TBA^+ pada DES dengan cas negatif fosfat DNA telah dibuktikan daripada kedua-dua spektroskopi pendarfluor dan CD. DNA berupaya mengekalkan struktur heliks berganda pada suhu 25 °C dan kepekatan DES pada 25%.

Katakunci: ikatan, pelarut eutektik mendalam, tetrabutilammonium bromida, pelindapkejutan pendarfluor, spektroskopi edaran dikroisme

Introduction

DNA is a biomacromolecule that plays an important role in the living organism because it stores the genetic information for cell replication and transcription. The potentials of DNA were increasingly recognized especially in the applications of biosensors, catalytic membranes, absorbing membranes and support for catalysts [1,2]. However, DNA is unstable in aqueous solution, resulting in denaturation of nucleic acid structure after 1 month of storage at ambient temperature [3]. Over the past few years, new solvents that can retain the DNA helical structure has been researched. Mamajanov et al. were among the first to propose deep eutectic solvent (DES) as an alternative solvent to maintain DNA helical structure and it was found that choline chloride: urea can maintain the DNA native structure [4]. However, the stability of DNA in the DES depends on the ability of DNA to maintain its helical structure, that could change during the interaction of DNA with other molecules. Recently, Sharma et al. found that hydrogen bonding and electrostatic interactions between bio-ionic liquids and DNA were found to be responsible for the long-term stability of DNA [5]. This finding enhanced the importance of studying the mode of interaction between DNA-DES to provide a stable medium for DNA.

Herein, the study of binding between tetrabutylammonium bromide (TBABr)-based DES and DNA by fluorescence quenching and CD spectroscopy was reported. The capability of DESs to quench EB from EB-bound DNA was explored using different HBDs with varying chain lengths and the number of OH group. In previous literature, it was reported that increasing the alkyl chain length of the cation in ionic liquid (IL) aided the quenching process [6]. In this study, the effect of HBDs chain length in DES on the quenching process was studied. The mode of interactions as well as stability of DESs in DNA were investigated.

Materials and Methods

Materials

Tetrabutylammonium bromide (TBABr), 1,3-propanediol and 1,5-pentanediol were supplied by Fluka Chemical (Reidstr, Steinheim, Germany) with 98% purity. Ethylene glycol was purchased from R&M (Essex, UK) and glycerol was from J.T. Baker (Phillipsburg, NJ, USA). All chemicals were used without further purification. Deoxyribonucleic acid extracted from calf-thymus in the sodium salt form was purchased from CalBioChem. Ethidium bromide (EB) was purchased from Sigma-Aldrich (USA). Deionized water type III was used throughout the experiments.

Synthesis of deep eutectic solvent (DES)

TBABr salt was mixed with four different hydrogen bond donors (HBDs); ethylene glycol, 1,3-propanediol, 1,5-pentanediol and glycerol. The formation of DES mixture between TBABr and HBDs were done at molar ratio of 1:3. The mixtures were heated at 60 °C and stirred at 250 rpm until colourless solution was observed. The mixtures were cooled to room temperature and sealed tightly in vials. DES mixtures were prepared accordingly to the method reported by Yusof et al. [7].

Preparation of reagent solution

Ethidium bromide (EB) stock solution (1.27×10^{-3} mol L^{-1}) was prepared by dissolving 0.01 g of EB in 20 mL volumetric flask and stored in a cool and dark place. The dilution of EB stock solution was done for fresh preparation of 0.5 μM EB.

Preparation of DNA stock solution

A stock solution of DNA was prepared by dissolving an appropriate amount (about 250 mg) of the solid DNA in deionized water type III and stored at 4 °C for about 24 hours. The solution was stirred until homogeneous DNA solution was produced. The solution was sonicated at a 40% amplitude, with setting of 30s on and 50s off for 20 minutes by the Digital Sonifier (Branson).

The final concentration and purity of the DNA stock solution was measured using UV–vis spectrophotometer (AV-650). Diluted DNA stock solution (3 mL) in 1 cm pathlength cuvette was placed in the instrument. The absorbance at 260 nm was measured and corrected with the corresponding deionized water as a blank. The absorbance of the DNA was measured three times to obtain the average absorbance. The sample was scanned from 1000 nm to 290 nm. The concentration of DNA stock solution was calculated from Beer's Law equation 1:

$$A = \varepsilon cl \quad (1)$$

where A is the absorbance value, ε is an extinction coefficient constant (6600 $M^{-1} \cdot cm^{-1}$ at 260 nm expressed in terms of base molarity), c is the concentration of solution (M) and l is a light path length (cm).

The purity of DNA solution was determined by measuring the ratio of the absorbance of the DNA stock solution (at 260 nm) to that of the absorbance of protein (at 280 nm)[6]. The DNA solution was considered pure if the ratio of A_{260}/A_{280} was above 1.8.

Fluorescence measurements

Fluorescence emission of the solution was measured by using Cary Eclipse fluorescence spectrophotometer. In this study, EB was used as an intercalator. About 3 mL of 0.5 μM EB was placed into 1 cm cuvette. The fluorescence spectra of the mixtures were recorded in the wavelength range of 550 to 750 nm with excitation wavelength at 510 nm. Both the excitation and emission slits were set at a diameter of 5 nm. A solution of DNA (0.83 μM) was titrated into the cuvette, and allowed to reach equilibrium for 3 minutes. The emission spectrum was recorded. The DNA was titrated continuously into EB by increasing the DNA concentration from 0.83 μM to 12.5 μM, while the concentration of EB was at 0.5 μM.

The prepared solution of DNA-bound EB was titrated with DES. The titration was done by increasing the concentration of the DES: 0.025, 0.075, 0.175, 0.30, 0.45, 0.63, 0.83, 1.08, 1.38 and 1.73 M into the same cuvette, while maintaining the concentration of DNA-bound EB. The solution was incubated for 3 minutes before the emission spectra were measured. The fluorescence emission spectra were recorded after each addition of the DES solution into the EB-bound DNA. This procedure was repeated for all the newly synthesized DES; TBABr:EG, TBABr:1,3-PD, TBABr:1,5-PD and TBABr:Gly.

Circular dichroism measurements

Circular dichroism spectroscopic measurements were performed by JASCO J-810 spectrophotometer equipped with a Peltier temperature controller (PTC-423s) and a water circulation unit. A fixed amount of DNA (300 μM) was solubilized in 25% hydrated DESs at room temperature, 25 °C. A quartz cuvette with a pathlength of 1.0 cm was used with a bandwidth at 1.0 nm and set at standard sensitivity. The measurements were taken at 320 to 200 nm wavelengths. Three scans were collected for each sample with a scan speed of 50 nm/min and the average value taken. A spectrum of blank solution was recorded and subtracted from the spectra of DES and DNA complexes.

Results and Discussion

The synthesis of DES

TBABr salt was mixed with different HBDs; ethylene glycol (EG), 1,3-propanediol (1,3-PD), 1,5-pentanediol (1,5-PD) and glycerol (Gly) at 60°C with a molar ratio of 1:3. A clear homogenous liquid was observed after 2 to 3 hours of heating. Figure 1 shows the structures of the newly synthesized TBABr-based DES.

The concentration and purity of DNA stock solution

Figure 2 shows a broad absorption spectrum of DNA at 210 to 310 nm in the UV region with a maximum absorption at 260 nm. The final concentration of DNA stock solution was estimated to be 0.0133M with the calculated A_{260}/A_{280} as 1.8. This high ratio ensures a purity of DNA used for the experiments, as it was sufficiently free from protein contamination. The maximum absorption at 260 nm is an indicator of the chromophoric groups present in purine (adenine and guanine) and pyrimidine (cytosine and thymine) moieties that is responsible for the electronic transitions [8].

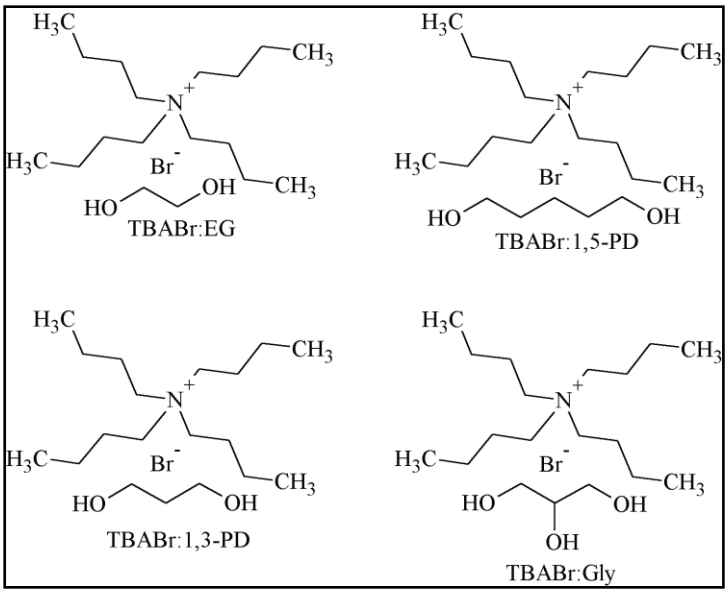


Figure 1. The newly synthesized TBABr-based DES

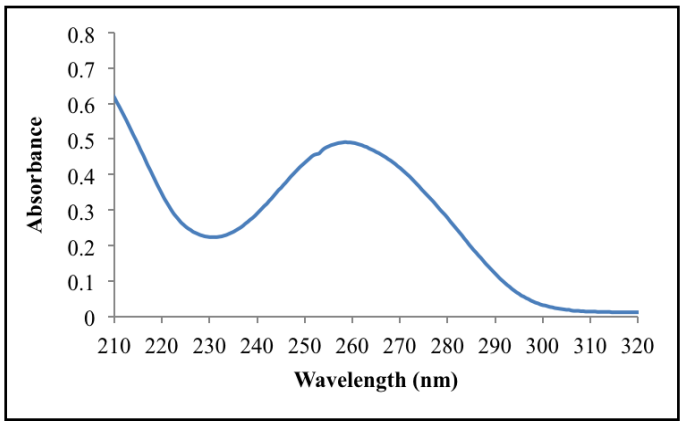


Figure 2. Absorbance spectrum of DNA in the UV region with a maximum absorption at 260 nm

Fluorescence quenching measurements

Fluorescence spectroscopy is one of the most common methods used to study DNA binding. The high sensitivity of fluorescence able to detect the polarity changes causes spectral shifts in both the excitation and emission spectra of molecules [8]. In this work, a known intercalator, ethidium bromide (EB) was used as a fluorescence probe to intercalate the double helix of DNA. EB can be easily intercalated into the adjacent base pairs and stretch the double helix structures of DNA as it is made up of polycyclic, aromatic and planar structure [6, 8, 9]. Through intercalation, the DNA has to unwind in order to let the intercalator fit between the two base pairs. This process causes the DNA helix lengthening by 3.4 Å as the bases are pushed apart hence resulting in conformational changes of the sugar group [10].

Figure 3 shows the emission intensity of free EB at 610 nm when excited at 510 nm. The addition of DNA into free EB has increased the emission intensity with the peak shifted to a shorter wavelength (595 nm). The planar hydrophobic EB was shielded from the aqueous bulk solvent upon intercalation, which resulted in the increase of emission intensity.

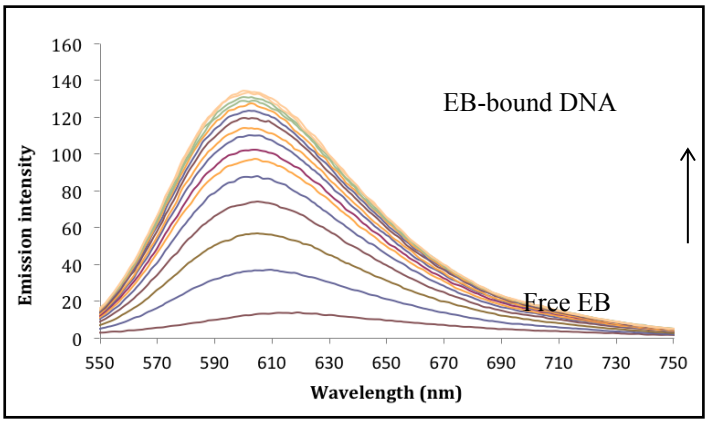


Figure 3. Emission intensity of free EB (610 nm) and EB-bound DNA (595 nm)

The effect of increasing DNA concentration towards the emission intensity was plotted in Figure 4. The emission intensity rapidly increased with the addition of 0.83 µM to 9.17 µM DNA. The intercalation of EB into empty space between the base pairs of DNA happens at this point. The emission intensity increased very slowly during the addition of 11.6 µM up to 12.5 µM DNA, hence suggesting that the base pair on DNA was fully packed with EB at 11.6 µM DNA. The numbers of empty spaces were reduced and the intercalation of EB into DNA base pair was almost saturated.

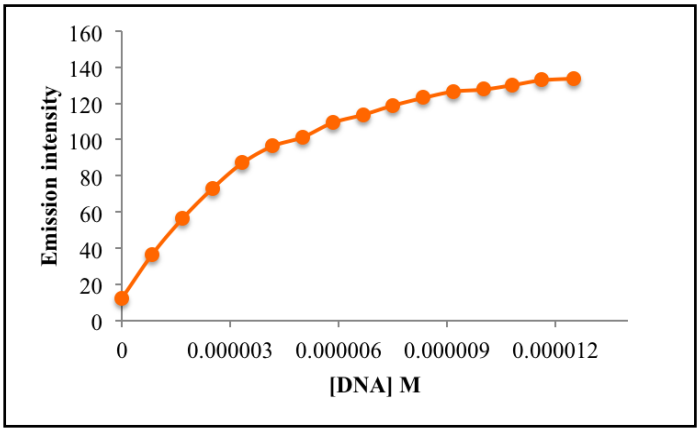


Figure 4. Emission intensity of free EB (0.5 µM EB) with addition of 0.83 µM to 12.5 µM DNA

The strength of newly synthesized DESs to quench EB-bound DNA was determined. DES was titrated into saturated EB-bound DNA in increasing DES concentration; 0.025, 0.075, 0.175, 0.300, 0.450, 0.630, 0.830, 1.080, 1.380 and 1.730 M. Figure 5 shows that the emission intensities steadily decreased with the addition of four different DESs from 0.025M to 0.830 M. During titration, TBA^+ from DES, condensed the DNA and formed

compact molecular structures through electrostatic interaction between TBA^+ and the negative charge of phosphate on DNA [11]. DES acts as a competing molecule that inhibits the intercalation of EB. This process caused the EB to dissociate from DNA and move into the aqueous solvent, resulting in the decrease of emission intensity. Then, the continuous addition of DES from 1.08 to 1.73 M into EB-bound DNA resulted in no observable change of the emission intensity, indicating the complete removal of EB from DNA base pairs.

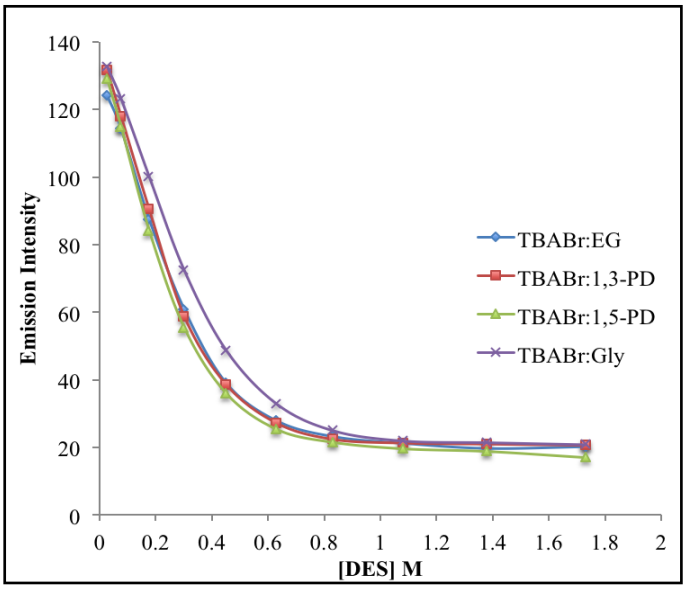


Figure 5. The quenching of EB-bound DNA by addition of different DESs (0.025 to 1.73M)

All synthesized DESs are sufficiently strong to quench the intercalation of EB from EB-bound DNA. From this study, the effect of HBD in quenching was observed, in terms of chain length and presence of OH group. The highest quenching efficiency of DES was shown in order of TBABr:1,5-PD, followed by TBABr:1,3-PD, TBABr:EG to TBABr:Gly. TBABr:1,5-PD has the longest chain length of HBD contributing to the largest hydrophobic effect. The quenching process was caused by the hydrophobic interactions between hydrophobic part of DNA bases and hydrocarbon chain of DES [6]. TBABr:1,5-PD contains five $–CH_2$ groups on 1,5-pentanediol compared to the TBABr:1,3-PD and TBABr:EG which contain of three and two $–CH_2$ groups, respectively. The less number of $–CH_2$ groups reduces the hydrophobic effect, hence decreasing the ability to quench EB. This quenching study suggested that length of HBD has affects the ability of DES to quench EB from EB-bound DNA. This trend is in agreement with the previous reported literature on the binding studies of ILs and DNA, which claimed the quenching efficiency increased with longer alkyl chain lengths of cation in IL[11]. The presence of OH group on DES also plays an important role in the quenching process. Both TBABr:1,3-PD and TBABr:Gly have a similar number of $–CH_2$ groups on HBD. However, TBABr:Gly shows a weaker ability to quench EB from DNA when compared to TBABr:1,3-PD. The presence of three OH groups on glycerol compared to the two OH groups on 1,3-propanediol reduces the hydrophobic effect on DES, in turn decreasing the ability of the TBABr:Gly to remove EB from EB-bound DNA. These results confirmed the importance of hydrophobic effect of DES in destabilizing the DNA-bound EB complex.

Circular dichroism spectroscopy

Circular dichroism (CD) spectroscopy is an optical technique that is usually used to analyze the conformational structures of macromolecules, such as DNA. DNA normally exists as double stranded with two polynucleotide chains in opposite directions to form a double helical structure of Watson-Crick base pairs. DNA can exist in many different conformations; right-handed double helical structure of A- and B-conformation of DNA as well as left-

handed of Z-conformation of DNA. However, the most common and stable DNA structure in solution is the B-conformation of DNA. In order to study the conformation of DNA in DES, the secondary structure on one of the synthesized DES; TBABr:1,5-PD was analyzed by CD. The DES was diluted in aqueous system at fixed concentration of 25%. The effect of DESs concentration to DNA will be studied in the next publication. The study of DNA stability in DES was carried out as DNA is very sensitive towards any changes in its environment such as pH, temperature or concentration [12].

Figure 6 shows the secondary structure of DNA at 25 °C in 25% hydrated TBABr:1,5-PD and its control, DNA in aqueous solution at 25 °C. The positive band at 275 nm and the negative band at 245 nm are due to the π- π base stacking and the helicity of DNA, respectively, indicating the characteristics of B-conformation DNA [3]. When DNA was added into 25% of TBABr:1,5-PD, the magnitude of positive and negative bands increased and decreased respectively. The shift at both the positive and negative bands indicates an electrostatic mode of interaction between the cationic TBA^+ in DES and anionic phosphate charge of DNA [11]. This observation agreed with the flouorescence results and concluded that DNA in 25% of TBABr:1,5-PD maintained its B-conformation as both positive and negative bands were observed at the same wavelength. This hypothesis was supported by the UV-vis absorbance graph as shown in Figure 6(b), where the curves of DNA in DESs are similar to the control.

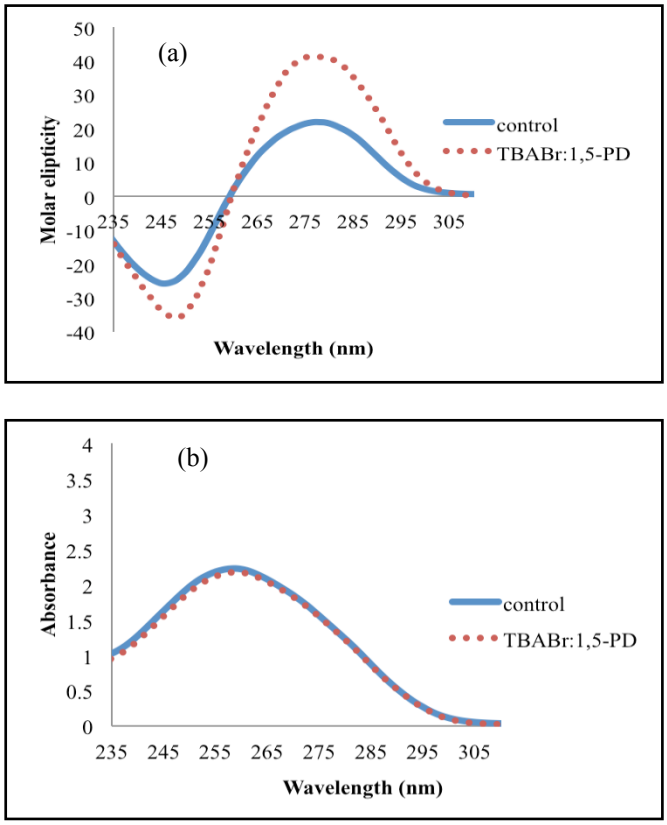


Figure 6. (a) CD spectra (b) absorbance spectra of DNA in 25% hydrated TBABr:1,5-PD as compare to the control at 25 °C. The control was DNA in aqueous solution.

Conclusion

All synthesized DESs; TBABr:EG, TBABr:1,3-PD, TBABr:1,5-PD and TBABr:Gly were strong enough to displace the intercalation of EB from DNA. The strongest DES that quenched EB from DNA was the one that was most

hydrophobic with the longest HBD and the least OH group, TBABr:1,5-PD. Hydrophobic interactions contributes to the ability of DESs to quench DNA from EB. The affinity of DESs toward DNA was due to the electrostatic interactions between the TBA^+ cation of DES and phosphate backbone of DNA. These hypotheses were confirmed by fluorescence and CD spectroscopy. DNA was able to maintain its B-conformation in TBABr:1,5-PD at 25 °C with 25% concentration.

Acknowledgement

This work was supported by Research University Grant Scheme (RUGS), (Grant No. 9341900), Universiti Putra Malaysia, Malaysia. Rizana Yusof thanks Universiti Teknologi MARA (UiTM), Malaysia and the Ministry of Higher Education Malaysia for the financial support throughout her Ph.D.

References

1. Cheng, Q., Benson, D. R., Rivera, M. and Kuczera, K. (2006). Influence of point mutations on the flexibility of cytochrome b5: molecular dynamics simulations of holoproteins. *Biopolymers,* 83, 297 –312.
2. Marrazza, G., Chianella, I. and Mascini, M. (1999). Disposable DNA electrochemical biosensors for environmental monitoring. *Analytica Chimica Acta,* 387: 297 – 307.
3. Vijayaraghavan, R., Izgorodin, A., Ganesh, V., Surianarayanan, M. and MacFarlane, D. R. (2010). Long-term structural and chemical stability of DNA in hydrated ionic liquids. *Angewandte Chemie International Edition,* 122: 1675 – 1677.
4. Mamajanov, I., Engelhart, A. E., Bean, H. D. and Hud, N. V. (2010). DNA and RNA in anhydrous media: duplex, triplex, and G-quadruplex secondary structures in a deep eutectic solvent. *Angewandte Chemie International Edition,* 49: 6310 – 6314.
5. Sharma, M., Mondal, D., Singh, N., Trivedi, N., Bhatt, J. and Prasad, K. (2015). High concentration DNA solubility in bio-ionic liquids with long-lasting chemical and structural stability at room temperature. *RSC Advances* 5: 40546 – 40551.
6. Ding, Y., Zhang, L., Xie, J. and Guo, R. (2010). Binding characteristics and molecular mechanism of interaction between ionic liquid and DNA. *Journal of Physical Chemistry B,* 114: 2033 – 2043.
7. Yusof, R., Abdulmalek, E., Sirat, K., and Rahman, M. B. A. (2014). Tetrabutylammonium bromide (TBABr)-based deep eutectic solvents (DESs) and their physical properties. *Molecules,* 19: 8011 –8026.
8. Sirajuddin, M., Ali, S. and Badshah, A. (2013). Biology drug-DNA interactions and their study by UV-visible, fluorescence spectroscopies and cyclic voltametry. *Journal of Photochemistry and Photobiology B: Biology,* 124: 1–19.
9. Street, N. S. (1995). Criteria for the mode of binding of DNA binding agents. *Bioorganic and Medicinal Chemistry,* 3: 723 – 728.
10. Beckford, S. R. J. (2012). Biophysical characterization of the binding of homologous anthraquinone amides to DNA. Doctoral Dissertation, Georgia State University, United State.
11. Manojkumar, K., Prabhu Charan, K. T., Sivaramakrishna, A., Jha, P. C., Khedkar, V. M., Siva, R., Jayaraman, G. and Vijayakrishna, K. (2015). Biophysical characterization and molecular docking studies of imidazolium based polyelectrolytes–DNA complexes: Role of hydrophobicity. *Biomacromolecules,* 16: 894 – 903.
12. Corrêa, D. H. A. and Ramos, C. H. I. (2009). The use of circular dichroism spectroscopy to study protein folding, form and function. *African Journal of Biochemistry Research,* 3: 164 – 173.

Malaysian Journal of Analytical Sciences, Vol 20 No 6 (2016): 1241 - 1246
DOI: http://dx.doi.org/10.17576/mjas-2016-2006-02

MALAYSIAN JOURNAL OF ANALYTICAL SCIENCES
Published by The Malaysian Analytical Sciences Society
ISSN 1394 - 2506

SYNTHESIS OF ISOXAZOLIDINE VIA 1,3-DIPOLAR CYCLOADDITION OF N-4-TERT-BENZYLIDENE NITRONE AND MALEIMIDE IN IMIDAZOLIUM-BASED IONIC LIQUIDS

(Sintesis Sebatian Isoxazolidina Melalui Tindakbalas 1,3-Dwikutub Pensiklotambahan N-4-Tetra-Benzilidina Nitron dan Maleimida dalam Cecair Ionik Berasaskan Imidazolium)

Nur Liyana Sakinah Johari, Siti Nashwa Mohd Poad, Nur Hasyareeda Hassan, Nurul Izzaty Hassan*

School of Chemical Science and Food Technology, Faculty of Science and Technology, Universiti Kebangsaan Malaysia, 43600 UKM Bangi, Selangor, Malaysia.

**Corresponding author: drizz@ukm.edu.my*

Received: 1 April 2016; Accepted: 11 August 2016

Abstract

The development of environmentally friendly methodologies for pericyclic reactions such as Diels Alder reaction is astonishing. Nevertheless, this is still scarce for the rest of pericyclic reactions. In this work, diastereosiomeric cycloadducts were formed via 1,3-dipolar cycloaddition between *N*-4-Tert-Benzylidene nitrone and maleimide in imidazolium-based ionic liquids (ILs) at 25 °C. Cycloaddition between nitrone **1** and maleimide **2** give diastereoisomeric adducts with 1:1 and 1:2 *trans*/*cis* ratio in two ionic liquids, [Bmim][PF_6] and [Bmim][BF_4], respectively. [Bmim][PF_6] give the desired cycloadducts in 43% yield compared to only 18% yield in [Bmim][BF_4]. In comparison, when the similar reaction was conducted in chloroform, the diasteroeisomeric mixture favoured *trans* isomer in 6:0.2 ratio. We reasoned that the repulsive van der Waals interactions favouring *exo* transition state was assisted by imidazolium ionic liquids. Thus, ILs have shown great potential as second reaction media in dipolar cycloaddition reactions.

Keywords: pericyclic reactions, 1,3-dipolar cycloaddition, imidazolium ionic liquids

Abstrak

Tindak balas Diels Alder merupakan contoh tindak balas perisiklik yang mesra alam serta mendapat perhatian ramai. Namun begitu, contoh lain tindak balas perisiklik masih lagi terhad. Melalui kajian ini, tindak balas 1,3-dwikutub pensiklotambahan di antara *N*-4-Tetra-Benzilidina nitron dan maleimida dalam cecair ionik imidazolium pada suhu 25 °C telah dijalankan. Pensiklotambahan antara nitron **1** dan maleimida **2** telah menghasilkan sikloaduk diastereoisomerik dengan nisbah *tran/cis* 1:1 dan 1:2 bagi kedua-dua cecair ionik, [Bmim][PF_6] dan [Bmim][BF_4]. Hasil sikloaduk dalam cecair ionik [Bmim][PF_6] adalah sebanyak 43% berbanding hanya 18% di dalam [Bmim][BF_4]. Apabila tindak balas yang sama dijalankan dalam pelarut kloroform, ianya memberikan sikloduk diastereosiomerik dalam nisbah 6:0.2 dengan menyebelahi isomer *trans.* Kami beranggapan bahawa interaksi repulsif Van der Waals mendorong keadaan peralihan ekso dengan bantuan cecair ionik imidazolium. Oleh yang demikian, cecair ionik mampu memainkan peranan penting sebagai media kedua di dalam tindak balas dwikutub pensiklotambahan.

Kata kunci: tindak balas perisiklik, 1,3-dwikutub pensiklotambahan, cecair ionik imidazolium

Introduction

Cycloaddition reactions belong to an important group of organic reactions called pericyclic, that are characterized by concerted mechanism proceed *via* cyclic transition states [1]. Woodward-Hoffman rules are used to predict the

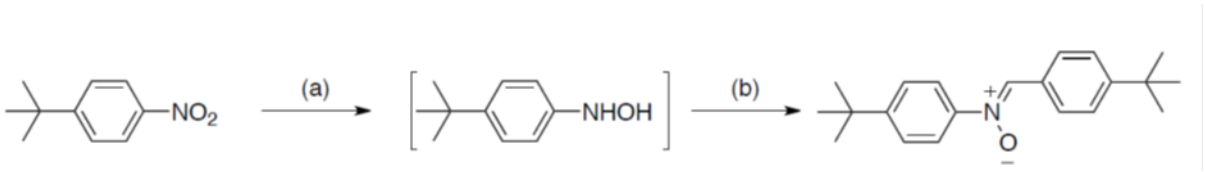
stereochemical features of this pericyclic reaction [2]. In cycloaddition reactions, two or more unsaturated systems react to give a cycle with one less unsaturation. Ionic liquids (ILs) have proved to be alternative solvents and catalysts for the development of the pericyclic reactions [3]. In most cases, an important improvement on the yields and reaction rates has been observed. Hazra et al. observed a good yield in the formation of tetracyclic pyrrolidine/isoxazolidine fused pyrano[3,2-h]quinolines via intramolecular 1,3-dipolar cycloaddition in [Bmim][PF_6] [4].

Thus, the 1,3-dipolar cycloaddition (1,3-DC) reactions has been considered as versatile protocol to generate new C-C bonds, leading to five-membered heterocycles, an essential skeleton in the synthesis of natural products [5]. This reaction furnishes pairs of racemic diastereoisomeric cycloadducts, labelled as *trans* and *cis* with respect to the endo and exo transition states. These two products have markedly different geometries with *trans* diastereoisomer possess an open geometry compared to closed geometry of cisdiastereoisomer. In the case of *cis* isomer, all protons are positioned on the same side with regards to the isoxazolidine ring while in the *trans* isomer, the nitrone-derived hydrogen atom is rendered *trans* to the two hydrogen atoms originally located on the maleimide group.

Not only being regioselective, 1,3-DC also can be highly stereoselective [6]. The mixture of diastereoisomers are obtained depending on the electronic nature of the substituents appended on the two reagents. This outcome originated from the interplay of two generally opposing forces in the transition states, whereby attractive π orbital overlap of unsaturated substituents will favour an endo transition state leading to the formation of isoxazolidine trans. On the other hand, repulsive van der Waals steric interactions favour an exo transition state.

Typically, many cycloaddition reactions conducted in ionic liquids (ILs) was Diels-Alder reaction [7]. Nonetheless, the 1,3-dipolar cycloaddition reaction in ILs has not much received attention. The early attempt was reported by Dubreuil and Bazureau in 2000 [8]. Significant rate accelerations and improved yields of cycloadducts were observed for the reaction of imidate and 2-ethoxybenzaldehyde in [Emim][BF_4], [Emim][PF_6] and [Emim][NfO] respectively. Olga and co-workers have studied extensively the $Er(OTf)_3$ catalyzed 1,3-DC reaction in [Bmim][OTf] which also significantly increase the yield of cycloadducts [9]. Recently, more studies are carried out with the effort to synthesize spiroheterocycles using azomethineylides via catalyzed 1, 3-DC reactions [10, 11, 12].

Herein, we described the 1,3-DC reaction between nitrone **1** and maleimide **2** in room temperature ILs. Initially, the nitrone **1** were prepared in two steps synthesis, starting from 4-Tert-Butylnitrobenzene, which first reduced to hydroxylamine derivatives using Rh/C and hydrazine monohydrate. Subsequently, condensation reaction takes place with 4-Tert-Butylbenzaldehyde (Scheme 1). Maleimide **2** was synthesized by simple condensation reaction of maleic anhydride and *p*-toluidine in acetic acid.



Scheme 1. Synthesis of nitrone **1**. Reagents and yields: (a) Rh/C, NH_2NH_2•H_2O, THF, rt, 4 h; (b) 4-Tert-Butylbenzaldehyde, EtOH, rt, 16 h, 44%.

Materials and Methods

Chemical and reagent

Starting materials and reagents used in the reactions were obtained commercially from Sigma Aldrich, Acros Organic and Friendemann Schmindt, were used without purification, unless otherwise indicated. All other reagents and solvents were purified after receiving from commercial suppliers.

Instrument

^{1}H nuclear magnetic resonance (NMR) spectra were recorded with a JEOL spectrometer (400 MHz) using tetramethylsilane (TMS) as internal standard. ^{13}C NMR spectra were recorded on the same instrument at 100 MHz.

The coupling constant (J) are given in Hz. IR spectra were obtained with a Perkin Elmer Spectrum GX machine as film or as KBR pellets for all the products. Mass spectroscopy (MS) spectra were recorded with a Bruker instrument. The progression and/or completion of the reactions were monitored by thin-layer chromatography (TLC) using 0.25 mm silica gel plates (Merck Kieselgel $60F_{254}$ UV indicator),while column chromatography was performed with silica gel (Merck Kieselgel) 600-200 mesh.

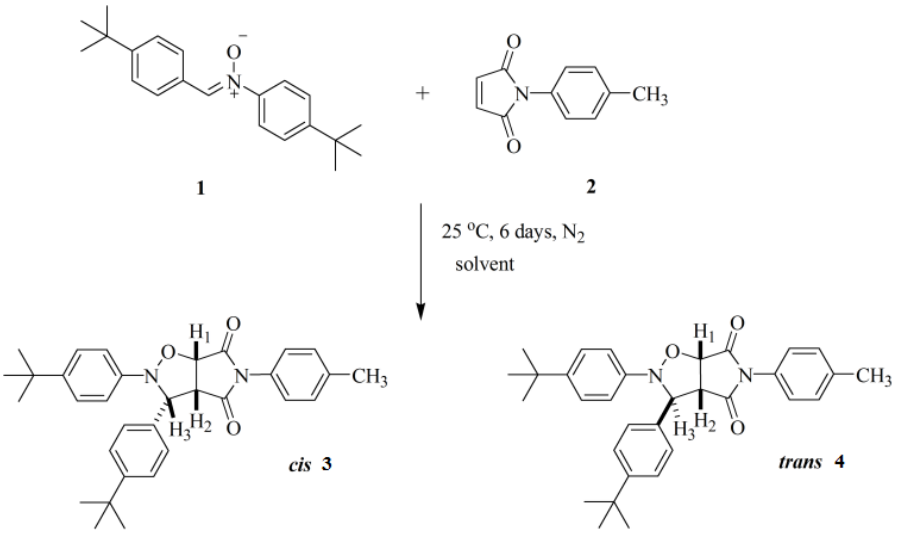
Synthesis of (Z)-4-Tert-Butyl-N-(4-Tert-Butylbenzylidene)aniline oxide 1

4-Tert-Butylnitrobenzene (0.56 g, 3.12 mmol) was dissolved in THF (15 mL). Rhodium (20 mg, 30 wt.% on carbon, wet) and hydrazine monohydrate (0.19 mL, 3.75 mmol) was added and the progress of the reaction was monitored by TLC. After completion, the solution was filtered through Celite pad and concentrated under reduced pressure to obtain the intermediate hydroxylamine which was directly used in the next step without further purification. The hydroxylamine was dissolved in EtOH (15 mL) and 4-Tert-Butylbenzaldehyde (0.51 mL, 3.12 mmol) was added dropwise to the solution. The reaction mixture was left stirred in the absence of light for 16 hours at ambient temperature. The solvent was concentrated *in vacuum* and the residue was purified by column chromatography (SiO_2, gradient Cyclohexane:EtOAc:Et_3N) to give nitrone **1** as yellow solid (44%).

Synthesis of novel diasteromeric isoxazolidine derivatives (3 & 4) in ionic liquid

The 1,3-DC reaction between nitrone **1** and maleimide **2** was carried by stirring out at room temperature under inert atmosphere in the absence of light for six days. The progress of the reaction was monitored using thin layer chromatography. The cycloadducts were carefully isolated using diethyl ether and cyclohexane and concentrated by evaporation under reduced pressure. The residue was purified by column chromatography (SiO_2, gradient hexane: ethyl acetate) affording both diastereoisomers *cis* and *trans* as colourless solid. [Bmim] with anion BF_4 and PF_6 were used as recyclable solvents for 1,3-dipolar cycloaddition reaction of nitrone **1** with maleimide **2** to produce novel isoxazolidine derivatives. The synthesis of the diastereoisomeric adducts were also conducted in chloroform for comparison (Scheme 2).

In a typical procedure, 1 mmol of nitrone **1** was mixed with an equivalent of maleimide **2** in [Bmim][BF_4] (2 ml) under stirring at room temperature and the progress of the reaction was monitored by TLC. After completion of reaction, the reaction mixture was washed with diethyl ethers (3 × 10 ml). The combined organic layers were concentrated *in vacuum* and the resulting product was directly charged on silica gel column and eluted with a mixture of ethyl acetate:hexane to afford pure isoxazolidines.



Scheme 2. Synthesis of diastereoisomeric cycloadducts 3 and 4 via cycloaddition between nitrone **1** and maleimide **2** at 25 °C

Results and Discussion

[Bmim][PF_6] was found to give better yield of 43% as to compare with only 18% in [Bmim][BF_4] (Table 1). This results is in agreement from previous observation from other studies involving cycloaddition reactions in imidazolium based ILs. Chakraborty and Luitel have demonstrated the application of imidazolium ILs as solvents in their cycloaddition reaction of *N*-Benzyl fluoronitrone with maleimide derivatives. In all cases, they found the ratio of the diastereoisomer is 3:1, favouring *cis* cycloadduct [13]. Ganesh et al. also observed similarly the exclusive formation of *cis* fused products in highly stereoselectivity intramolecular 1,3-dipolar cycloaddition of azomethineylides as well as nitrones[14].

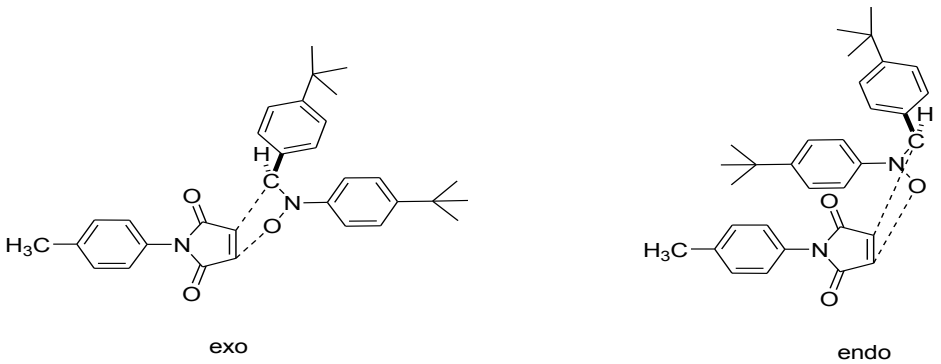
Table 1. 1,3-Dipolar cycloaddition reactions of nitrone **1** with maleimide **2**

Entry	Solvent[a]	*cis* (3)/*trans* ratio(4)[b]	Yield (%)
1	[Bmim][BF_4]	2:1	18
2	[Bmim][PF_6]	1.1:1	43
3	$CHCl_3$	0.2:6	36

[a]Reaction conditions: nitrone **1** (1 mmol), maleimide **2** (1 equivalent), 2 mL of respective ILs or 4 mL of $CHCl_3$, N_2 atmosphere, rt, [b]Cycloadducts were characterized by IR, ^{1}H NMR, ^{13}C NMR and MS spectral data

In the case of *cis* cycloadduct, the prominent signal for proton H_3 and H_1 are both doublet, while triplet for H_2. By contrast, *trans* cycloadducts, signal for proton H_3 is singlet while doublet for H_1 and H_2. It is shown that [Bmim][BF_4] and [Bmim][PF_6] gave cycloadducts in 1:2 and 1:1.1 ratio, respectively, favouring *cis* diastereoisomer. This results is staggering given that a typical uncatalyzed 1, 3-DC of nitrone and maleimide in chloroform leads to the solely formation of *trans* cycloadduct with the ratio of 6:0.2. In addition, mass spectral analysis of the cycloadducts provided evidence for the success of the cycloaddition reactions. The mass spectrum shows the present of molecular ion peak at the base peak m/z = 519.26, 497.27 and 332.20, respectively.

For the formation of major cycloadduct, these results can be rationalized by an exo approach of nitrone which has Z configuration while an endo approach leads to the formation of minor cycloadduct (Scheme 3).



Scheme 3. Exo/ endo approach of nitrone to maleimide in cycloaddition reaction

ILs have shown powerful catalytic properties to accelerate the Diels Alder reaction due to its ionic features. We do believe that ILs contribute to the accessibility of exo transition state, which in return give more *cis* diastereoisomer.

In the meantime, we are trying to investigate further this kind of reactions with elongated 1,3-dipole compounds and dipolarophiles.

Characterization

Representative data for synthesis of (Z)-4-Tert-Butyl-N-(4-Tert-Butylbenzylidene)aniline oxide 1: M.p. = 152.5 – 154.4 °C; ^{1}H NMR (300.1 MHz, $CDCl_3$): δ_H 8.35 - 8.30 (2H, m, ArH), 7.88 (1H, s, CH), 7.72 – 7.67 (2H, m, ArH), 7.52 – 7.46 (4H, m, ArH), 1.35 (18H, s, CH_3); ^{13}C NMR (75.5 MHz, $CDCl_3$): δ_c154.4 (ArC), 153.3 (ArC),146.8 (ArC), 134.2 (CH), 129.1 (ArCH), 128.3 (ArC),126.1 (ArCH), 125.7 (ArCH), 121.4 (ArCH), 35.2 (qC), 35 (qC), 31.4(CH_3), 31.$_3$(CH3); MS (ES^+) m/z 332.0 ([M+Na]$^+$, 95), 641.0 (100); HRMS (ES^+) *m/z* calculated for $C_{21}H_{27}NONa$ 332.1990 [M+Na]$^+$, found 332.1994.

Representative data for cis cycloadduct 3: Mp: 196.6-196.8 °C; ^{1}H NMR (400 MHz; $CDCl_3$) δ_H 7.41 (2H, d, *J*= 8.40 Hz, ArC*H*), 7.37 (2H, d, *J*= 8.40 Hz, ArC*H*), 7.27 (2H, d, *J*= 9.16 Hz, ArC*H*), 7.13 (2H, d, *J*= 8.08 Hz, ArC*H*), 7.05 (2H, d, *J*= 8.80 Hz, ArC*H*), 6.68 (2H, d, *J*= 8.44 Hz, ArC*H*), 5.30 (1H, d, *J*= 8.04 Hz, C*H*), 5.06 (1H, d, *J*= 8.80 Hz, C*H*), 4.03 (1H, t, *J*= 8.44 Hz, C*H*), 2.31 (3H, s, CH_3), 1.30 (9H, s, CH_3), 1.26 (9H, s, CH_3);^{13}C NMR (100 MHz; $CDCl_3$) δ_C173.2 (C=O), 156.3, 151.8, 149.2, 146.3, 145, 141.4, 138.5, 137.2, 132, 131.3, 129.7, 127.4, 117.3 (*C*H), 71.2 (*C*H), 54.6 (*C*H), 34.8 (quat.*C*), 34.5 (quat.*C*), 31.5 (*C*H_3), 31.2 (*C*H_3), 21.2 (*C*H_3); IR ν_{max} (KBr) cm^{-1}: 2956.05 cm^{-1} (sp^3 CH), 1608.84 cm^{-1} and 1461.15 cm^{-1} (aromatic C=C), 1722.79 cm^{-1} (C=O), 1197.36 cm^{-1} (C-N), MS (ESI^+) m/z 519.26 ([M+ Na]$^+$, 100%).

Representative data for trans cycloadduct 4*:* Mp: 196.5-196.7°C; ^{1}H NMR (400 MHz,$CDCl_3$) δ_H7.52 (2H, d, *J*= 8.44 Hz, ArC*H*), 7.44 (2H, d, *J*= 8.44 Hz, ArC*H*), 7.26 (2H, d, *J*= 8.80 Hz, ArC*H*), 7.09 (2H, d, *J*= 9.16 Hz, ArC*H*), 7.06 (2H, d, *J*= 9.88 Hz, ArC*H*), 6.34 (2H, d, *J*= 8.44 Hz, ArC*H*), 5.78 (1H, s, C*H*), 5.07 (1H, d, *J*= 7.32 Hz, C*H*), 4.01 (1H, t, *J*= 7.32 Hz, C*H*), 2.29 (3H, s, CH_3), 1.34 (9H, s, CH_3), 1.28 (9H, s, CH_3); ^{13}C NMR (100 MHz; $CDCl_3$) δ_C173 (C=O), 1561.1, 146.7, 145.8, 143.7, 139.3, 139.1, 136, 135.9, 129.8, 129.6, 128.4, 128.3, 113.9 (*C*H), 69.6 (*C*H), 57.3 (*C*H), 34.5 (quat.*C*), 34.3 (quat. *C*), 31.5 (*C*H_3), 31.3 (*C*H_3), 21.2 (*C*H_3); IR ν_{max} (KBr) cm^{-1}: 2956.05 cm^{-1}, 1608.84 cm^{-1}and 1461.15 cm^{-1} (aromatic C=C), 1722.79 cm^{-1} (C=O), 1197.36 cm^{-1} (C-N); MS (ESI^+) m/z 497.27 ([M+ H]$^+$, 100%).

Conclusion

Considering the environmental pollution by using conventional organic solvents, ILs have become an alternative reaction media for the development of green synthetic strategies in 1,3-DC. Two ionic liquids, [Bmim][BF_4] and [Bmim][PF_6] has facilitated the course of 1,3 DC of nitrone and maleimide with improved results on the yield of the cycloadducts. In the future, we would like to explore the use of microwaves as conventional heating sources. ILs will be heated very quickly, thus, providing shorter reaction times and efficient reaction due to microwave irradiation.

Acknowledgement

The authors express their gratitude to School of Chemical Sciences and Food Technology, Faculty of Science and Technology and Centre for Research and Instrument, Universiti Kebangsaan Malaysia for laboratory and instrumental facilities. This work received financial assistance from Universiti Kebangsaan Malaysia (GUP-2014-015 and DIP-2015-015).

References

1. Fleming, I. (1998). Pericyclic reactions. Oxford: Oxford Chemical Primers: pp. 67
2. Woodward, R. B. and Hoffmann, R. (2004). The conservation of orbital symmetry. *Verlag Chemie Academic Press,* 104 : 2939 – 3002.
3. Visser, A. E., Bridges, N. J. and Rogers, R. D. (2013). Ionic liquids: Science and applications. ACS Symposium Series 1117. *American Chemical Society*: 259 – 270.
4. Hazra, A., Bharitkar, Y. P., Maity, A., Mondal, S. and Mondal, N. B. (2013). Synthesis of tetracyclic pyrrolidine/isoxazolidine fused pyrano[3,2-h]quinolines via intramolecular 1,3-dipolar cycloaddition in ionic liquid. *Tetrahedron Letters*, 54(32): 4339 – 4342.

5. Nishwaki, N. (2014). Methods and applications of cycloaddition reactions in organic syntheses. *John Wiley and Sons*, 9: 223 – 240.
6. Huisgen, R. and Weinberger, R. (1985). The first two step 1,3-dipolar cycloadditions: Non-stereospecificity. *Tetrahedron Letters*, 26: 5119 – 5122.
7. Kumar, A., Deshpande, S. S. and Pawar, S. S. (2003). Diels-Alder reactions in ionic media: rate enhancement with green chemistry. *National Academy Science Letter-India*, 26 (9-10): 232 – 250.
8. Dubreuil, J. F. and Bazureau, J. P. (2000). Rate accelerations of 1,3-dipolar cycloaddition reactions in ionic liquids. *Tetrahedron Letters,* 41(38): 7351 – 7355.
9. Bortolini, O., Nino, A. D., Maiuolo, L., Russo, B., Sindona, G. and Tocci, A. (2007). 1,3-cycloaddition of nitrones in ionic liquids catalyzed by Er(III): an easy access to isoxazolidines. *Tetrahedron Letters,* 48: 7125 – 7128.
10. Domingo, L. R., Aurell, M. J., Arno, M. and Saez, J. A. (2007). Toward an understanding of the 1,3-dipolar cycloaddition between diphenylnitrone and a maleimide: bisamide complex. A DFT analysis of the reactivity of symmetrically substituted dipolarophiles. *Journal of Molecular Structure*, 811: 125 –133.
11. Jain, R., Sharma, K. and Kumar, D. (2012). Ionic liquid mediated 1,3-dipolar cycloaddition of azomethine ylides: A facile and green synthesis of novel dispiro heterocycles. *Tetrahedron Letters*, 53: 1993 – 1997.
12. Rajesh, S. M., Bala, B. D. and Perumal, S. (2012). Multi-component, 1,3-dipolar cycloaddition reactions for the chemo-, regio- and stereoselective synthesis of novel hibrid spiroheterocycles in ionic liquid. *Tetrahedron Letters*, 53: 5367 – 5371.
13. Chakraborty, B. and Luitel, G. P. (2013). Synthesis of some novel fluoro isoxazolidine and isoxazolidine derivatives using N-benzyl fluoronitrone via cycloaddition reaction in ionic liquid. *Journal of Chemical Sciences*, 125: 1071 – 1077.
14. Ganesh, P., Prabal, B. and Smita, R. G. (2006). Construction of enantiopure pyrrolidine ring system via asymmetric [3+2]-cycloaddition of azomethine ylides. *American Chemical Society*, 106(11): 4484 – 4517.

Malaysian Journal of Analytical Sciences, Vol 20 No 6 (2016): 1247 - 1253
DOI: http://dx.doi.org/10.17576/mjas-2016-2006-03

MALAYSIAN JOURNAL OF ANALYTICAL SCIENCES
Published by The Malaysian Analytical Sciences Society
ISSN 1394 - 2506

RADIOLOGICAL RISK ASSESSMENT FROM THE INTAKE OF VEGETABLES AND FRUITS IN MALAYSIA

(Penilaian Risiko Radiologi dari Pengambilan Sayur-Sayuran dan Buah-Buahan di Malaysia)

Wahmisari Priharti and Supian Bin Samat*

School of Applied Physics, Faculty of Science and Technology,
Universiti Kebangsaan Malaysia, 43600 UKM Bangi, Selangor, Malaysia

**Corresponding author: sbsamat@ukm.edu.my*

Received: 3 May 2016; Accepted: 3 August 2016

Abstract

The activity concentration of natural radionuclides ^{226}Ra, ^{232}Th and ^{40}K in vegetables and fruits in central zone of Malaysia were measured using gamma spectrometry. This is for the purpose of assessing the radiological risk in term of ingestion dose and cancer risk. The total ingestion dose from the consumption of vegetables were found to be 0.469 ± 0.003, 0.326 ± 0.005 and 0.232 ± 0.003 mSv/y for infants, children and adults respectively. Whereas the total ingestion dose from the consumption of fruits for infants, children and adults were 0.349 ± 0.005, 0.283 ± 0.007 and 0.195 ± 0.004 mSv/y respectively. The estimated cancer risk from the consumption of vegetables and fruits were 8.13×10^{-4} and 6.83×10^{-4} respectively for adults. The results obtained for activity concentration, dose and risk were found to be below the internationally recommended level. This indicates that the vegetables and fruits consumed in Malaysia would not pose any significant radiological impact to the population.

Keywords: activity concentration, gamma spectrometry, ingestion dose, natural radionuclides, risk assesment

Abstrak

Kepekatan aktiviti radionuklid semulajadi ^{226}Ra, ^{232}Th and ^{40}K dalam sayur-sayuran dan buah-buahan di Malaysia bahagian tengah telah diukur menggunakan spektrometer gama. Ini bertujuan untuk menilai risiko radiologi dalam istilah dos dimakan dan risiko kanser. Didapati jumlah dos dimakan dari pengambilan sayur-sayuran adalah 0.469 ± 0.003, 0.326 ± 0.005 and 0.232 ± 0.003 mSv/tahun masing-masing bagi bayi, kanak-kanak dan dewasa. Manakala jumlah dos dimakan dari pengambilan buah-buahan bagi bayi, kanak-kanak dan dewasa adalah masing-masing 0.349 ± 0.005, 0.283 ± 0.007 and 0.195 ± 0.004mSv/tahun. Risiko kanser dari pengambilan sayur-sayuran dan buah-buahan bagi orang dewasa masing-masing dijangkakan sebanyak 8.13×10^{-4} dan 6.83×10^{-4}. Kesemua hasil yang diperolehi dalam kajian ini bagi kepekatan aktiviti, dos dan risiko didapati berada di bawah aras yang dibenarkan oleh badan antarabangsa. Ini menunjukkan bahawa sayur-sayuran dan buah-buahan yang diambil di Malaysia tidak menimbulkan bahaya radiologi yang ketara terhadap manusia.

Kata kunci: kepekatan aktiviti, spektrometer gama, dos dimakan, radionuklid semula jadi, penilaian risiko

Introduction

The total annual radiation dose received by a member of the population each year is 3.01 mSv. About 79.73% of this number is contributed by natural radiation sources (2.4 mSv/y) and the rest 20.27% by man-made radiation sources (0.61 mSv/y) [1]. It is clear that the natural radiation sources is the main contributor to the total annual radiation dose. One component of this natural radiation sources is the ingestion dose (0.29 mSv/y) that are mainly contributed by ^{238}U and ^{232}Th series (0.12 mSv/y) and ^{40}K (0.17 mSv/y) [2].

Ingestion dose was received by human beings from the consumption of food contaminated with different radionuclides [3]. One of important food that can contributes to better health of human is vegetables and fruits [4]. According to Ministry of Health Malaysia, vegetables and fruits are categorized into the most second important food after rice and grains. Therefore, it is recommended to take these kind of food for at least 5 servings a day (approximately 400 g/d) [5].

Since the amount of recommended intake is quite big, it is important to monitor the radiological effect from the consumption of vegetables and fruits. This matter has become a great concern as has been reported by many researchers in different part of the world. From eleven different countries, 58 types of vegetables have been studied with seven common types namely spinach, carrot, cucumber, tomato, pumpkin, green bean and potato [6-16]. However in Malaysia, only 16 types of vegetables have been studied with spinach and cucumber as the common type [17, 18]. Studies conducted in ten different countries reported that 26 types of fruits have been studied with eight common types namely apple, pear, orange, mango, banana, papaya, grapes and watermelon [6-16]. Whereas in Malaysia, only nine types of fruits have been studied i.e. apple, orange, mango, banana, papaya, star fruit, pineaple, rambutan and durian [17].

The present work is intended to (a) to determine the activities of ^{226}Ra, ^{232}Th and ^{40}K; (b) to assess the ingestion doses (due to these three radionuclides) incurred to the infants (1–2 years), children (7–12 years) and adults (> 17 years), (c) to compare these activities and doses with the previous local and international results, and (d) to estimate the consequent health risk due to the presence of those radionuclides in the vegetables and fruits. This work is also conducted to complete the precedent researches carried out by the authors on some food products such as milk and water [19, 20].

Materials and Methods

Sample collection

Twelve different samples of commonly eaten vegetables and fruits were collected. All the samples were purchased from the local market in central zone of Malaysia. All vegetables and three fruits sample (banana, papaya and mango) were locally produced in Malaysia whereas the remaining three fruits sample i.e. apple, orange and pear were imported from China, Korea and Australia respectively.

Sample preparation

All vegetables and fruits samples were prepared following the IAEA procedure [21]. They were made into powder to follow the geometry of standard silica powder (4 cm height in 10 cm polyethilene beaker). First, they were washed and minced to get a small size. The unused part such as skin and seeds were discarded. Samples were then oven dried at 80 ^{o}C for 48 hours or until they reached constant mass. The dried sample were pulverized and sieved until they become 500 μm homogen powder. The powdered samples were then kept in a sealed tight polyethilene beaker for 30 days to achieve secular equilibrium. For every types of samples, three samples were prepared to obtained the average activity concentration. This means, 36 samples (= 12 × 3 samples) has been prepared for these two categories of samples.

^{226}Ra, ^{232}Th and ^{40}K measurement

The radionuclides ^{226}Ra, ^{232}Th and ^{40}K count, N in the vegetables and fruits sample were measured using gamma ray spectrometry system with high purity germanium detector (HPGe). The detector was connected to MCA card (Accuspec B) and Genie-2000 analysis software. The detector energy resolution was 1.8 keV at 1.33 keV of ^{60}Co gamma ray peak and the relative efficiency was 30% at the same energy peak [22]. Each measurement was carried out for 43,200 second (12 hours). The count of each radionuclides were resulted from the line energy peaks emited directly by the corresponding radionuclide (1460 keV for ^{40}K) or by the radionuclides daughter (352 and 609 keV for ^{226}Ra and 239, 583 and 911 keV for ^{232}) [17]. The equation 1 used to calculate the activity concentration, A and its uncertainty was expressed below [21, 23]:

$$A = \frac{N}{\varepsilon \times t \times P_{\gamma} \times M_s} \quad (1)$$

where ε is the detector efficiency, t is measurement time, P_γ is the γ-ray emission probability (%) and M_s is the mass of the sample (kg). To conceal the minor photopeaks for each sample, the minimum detectable activity (MDA) was calculated using the formula originally defined by Currie [24].

$$\text{MDA} = \frac{2.71 + 4.66\,\sigma}{t \times \varepsilon \times P_\gamma} \quad (2)$$

where σ is the uncertainty of background count. The present measuring system recorded the MDA of 0.30, 0.34 and 2.88 Bq/kg for ^{226}Ra, ^{232}Th and ^{40}K respectively.

Dose and risk calculation

From the ^{226}Ra, ^{232}Th and ^{40}K activities, the ingestion dose D (mSv/y) can be calculated using the following relationship (equation 3) [25]:

$$D = A \times I \times E \quad (3)$$

where I (kg/y) is the annual intake of the vegetables and fruits [26] and E (Sv/Bq) is the ingestion dose conversion factor of the radionuclide [27]. The values of I and E for the three age categories are given in Table 1. The dose contributed from three radionuclides ^{226}Ra, ^{232}Th and ^{40}K were summed to obtain the total dose, D_T. If it is assumed that the life-span of an average individual, L is 70 years [28, 29] and the the cancer risk factor for low doses, RF is 5 × 10^{-5} (1/mSv) [1], the cancer risk R can be estimated from:

$$R = D_T \times L \times RF \quad (4)$$

Table 1. The annual intake, I and the ingestion dose conversion factor, E for infants, children and adults

Age Category	I (kg/y)		E (× 10^{-8} Sv/Bq)		
	Vegetables	Fruits	^{226}Ra	^{232}Th	^{40}K
Infants (1–3 years)	12.96	23.01	96	45	4.20
Children (7–12 years)	25.92	46.02	80	29	1.30
Adults (> 17 years)	38.88	69.03	28	23	0.62

Results and Discussion

The measured activity concentration, A of ^{226}Ra, ^{232}Th and ^{40}K in six samples of vegetables and six samples of fruits, their ranges and their average values were shown in Table 2. It was shown that the activity concentration in some samples of vegetables and fruits were not detectable. For vegetables, the detected activity concentration ranged from 0.60 ± 0.57 to 5.64 ± 0.65 Bq/kg for ^{226}Ra, 0.41 ± 0.32 to 4.40 ± 0.49 Bq/kg for ^{232}Th and 398.85 ± 6.89 to 1072.59 ± 10.25 Bq/kg for ^{40}K. The average activity concentration of ^{226}Ra, ^{232}Th and ^{40}K were found to be 1.38 ± 0.21, 1.06 ± 0.12 and 791.51 ± 3.66 Bq/kg respectively. For fruits, the detected ^{226}Ra activity concentration ranged from 0.90 ± 0.64 to 3.83 ± 0.56 with an average value of 1.22 ± 0.17, ^{232}Th activity concentration ranged from 0.56 ± 0.48 to 2.22 ± 0.38 with an average value of 0.77 ± 0.12 and the ^{40}K activity concentration ranged from 75.39 ± 4.78 to 651.64 ± 9.75 with an average value of 288.63 ± 2.83, all in Bq/kg.

For both types of sample, the highest activity concentration were found to be ^{40}K followed by ^{226}Ra and ^{232}Th. This same pattern has also been reported by many previous work as shown in Table 3. The activity concentration of previous results for vegetables samples ranged from 0.049 to 48.80, 0.001 to 25.36 and 0.79 to 1190.45 Bq/kg for ^{226}Ra, ^{232}Th and ^{40}K respectively. For fruits samples, they ranged from 0.009 to 8.15, 0.001 to 32.30 and 20.94 to 439.53 for ^{226}Ra, ^{232}Th and ^{40}K respectively. In comparison with this range, the present results are in agreement with the previous results. This is because all the averaged value of the present results lie clearly within the range of the previous results.

Table 2. ^{226}Ra, ^{232}Th and ^{40}K measured activity concentration, A from vegetables and fruits

Sample	Name	Activity concentration, $A \pm \Delta A$ (Bq/kg)		
		^{226}Ra	^{232}Th	^{40}K
Vegetables	Spinach	5.64 ± 0.65	4.40 ± 0.49	998.04 ± 9.13
	Carrot	ND[a]	ND	398.85 ± 6.89
	Broccoli	1.29 ± 0.62	ND	664.54 ± 8.75
	Pumpkin	ND	0.41 ± 0.32	682.90 ± 6.92
	Tomato	0.76 ± 0.63	ND	932.11 ± 11.02
	Cucumber	0.60 ± 0.57	1.55 ± 0.44	1072.59 ± 10.25
	Range	0.60 – 5.64	0.41 – 4.40	398.85 – 1072.59
	Average	2.07 ± 0.31[b]	2.12 ± 0.24[b]	791.51 ± 3.66
Fruits	Apple	2.58 ± 0.58	1.84 ± 0.42	151.49 ± 5.69
	Banana	ND	ND	401.59 ± 5.85
	Orange	ND	ND	279.74 ± 7.70
	Pear	3.83 ± 0.56	2.22 ± 0.38	75.39 ± 4.78
	Papaya	0.90 ± 0.64	0.56 ± 0.48	651.64 ± 9.75
	Mango	ND	ND	171.95 ± 6.61
	Range	0.90 – 3.83	0.56 – 2.22	75.39 – 651.64
	Average	2.44 ± 0.34[b]	1.54 ± 0.25[b]	288.63 ± 2.83

[a)]ND = Not detectable (MDA for ^{226}Ra, ^{232}Th and ^{40}K were 0.30, 0.34 and 2.88 Bq/kg respectively). [b)]Due to the ND, respectively two and three out of six ^{226}Ra and ^{232}Th activities of vegetables and respectively three and three out of six ^{226}Ra and ^{232}Th activities of fruits were undetected. Therefore, this average was calculated from detected values only.

Table 3. The measured activity concentration, A in vegetables and fruits in comparison with the previous reported values

Activity concentration (Bq/kg)						Country [References]
Vegetables			Fruits			
^{226}Ra	^{232}Th	^{40}K	^{226}Ra	^{232}Th	^{40}K	
–	–	93.29	–	–	86.93	Spain [6]
–	–	0.79	–	–	34.91	Syria [7]
0.18	0.20	48.15	–	–	–	Iran [8]
1	-	116.04	0.74	-	42.00	Egypt [9]
0.075	0.012	-	0.027	0.001	–	China [10]
–	–	74.30	–	–	52.90	Lebanon [11]
0.049	0.001	68.39	0.009	0.001	20.94	Korea [12]
0.51	1.33	57.64	0.46	1.62	69.88	India [13]
1.90	2.40	80.30	–	–	–	India [14]
2.60	2.92	163.40	1.30	1.56	111.00	Italy [15]
7.67	20.24	75.47	8.15	32.30	75.55	Indonesia [16]
1.22	1.95	1190.45	1.61	1.22	439.53	Malaysia [17]
48.80	25.36	1017.94	–	–	–	Malaysia [18]
0.049–8.80	0.001–25.36	0.79–1190.45	0.009–8.15	0.001–32.30	20.94–439.53	Range of previous study [6-18]
2.07	2.12	791.51	2.44	1.54	288.63	Present study

Table 4. Calculated ingestion dose, *D* from the intake of ^{226}Ra, ^{232}Th and ^{40}K in vegetables and fruits for three age categories

Type	Age Category	Ingestion Dose (mSv/y)			
		$D \pm \Delta D$			$D_T \pm \Delta D_T$ [(a)]
		^{226}Ra	^{232}Th	^{40}K	
Vegetables	Infants	0.026 ± 0.004	0.012 ± 0.001	0.431 ± 0.002	0.469 ± 0.003
	Children	0.043 ± 0.006	0.016 ± 0.002	0.267 ± 0.001	0.326 ± 0.005
	Adults	0.023 ± 0.003	0.019 ± 0.002	0.191 ± 0.001	0.232 ± 0.003
Fruits	Infants	0.054 ± 0.008	0.016 ± 0.003	0.279 ± 0.003	0.349 ± 0.005
	Children	0.090 ± 0.013	0.021 ± 0.003	0.173 ± 0.002	0.283 ± 0.007
	Adults	0.047 ± 0.007	0.024 ± 0.004	0.124 ± 0.001	0.195 ± 0.004

[(a)] $D_T = D_{\text{Ra-226}} + D_{\text{Th-232}} + D_{\text{K-40}}$

Upon comparing these two values, it was found that for vegetables: (a), the *D* due to intake of ^{226}Ra and ^{232}Th for three age categories were below the UNSCEAR annual ingestion dose. Hence, it was automatically below the annual radiation dose from natural sources, (b) only the *D* due to intake of ^{40}K for children and adults were below the UNSCEAR annual ingestion dose, whereas for infants, the *D* value were higher. However, it is still below the value of annual radiation dose from natural sources, (c) the *D* due to total intake of three radionuclides for infants and children are higher than the UNSCEAR annual ingestion dose by a factor of 1.57 and 1.04 respectively, however they are still below the value of annual radiation dose from natural sources.

The comparison results for fruits: (a) the *D* due to intake of ^{226}Ra, ^{232}Th and ^{40}K for three age categories were below the UNSCEAR annual ingestion dose. Hence, it was automatically below the annual radiation dose from natural sources, (b) the *D* due to total intake of three radionuclides were also below the UNSCEAR annual ingestion dose except for infants (higher by a factor of 1.08). However, it is still below the value of annual radiation dose from natural sources. To provide a better understanding of these results, the dose comparison were shown in Figure 1.

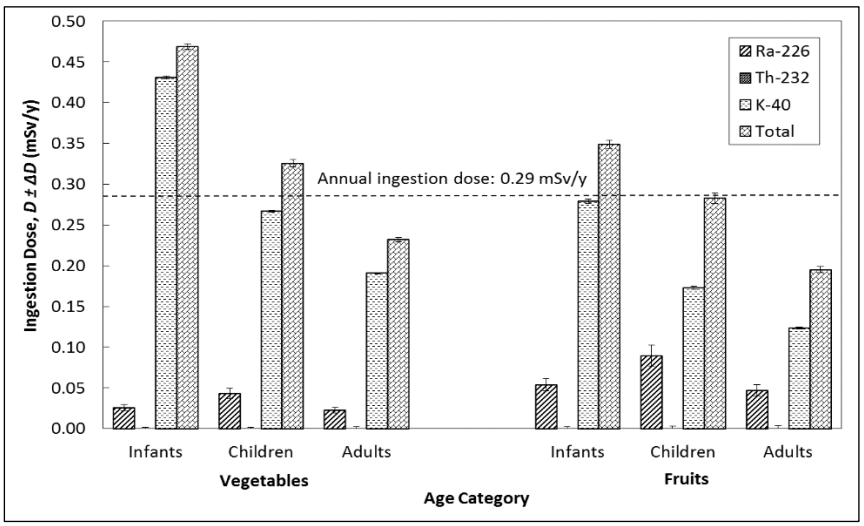


Figure 1. Ingestion dose of infants, children and adults from the intake of radionuclides ^{226}Ra, ^{232}Th and ^{40}K in vegetables and fruits. The dose contributed by ^{232}Th is in the range of 0.012 – 0.019 mSv/y for vegetables and 0.016 – 0.024 mSv/y for fruits, therefore they hardly can be seen.

The *D* for infants and children for both vegetables and fruits were found to be higher than adults despite the lower value of intake *I* (Table 1). This is due to the higher value of *E* (ingestion dose conversion factor) for each radionuclide. The *E* value for infants were found to be higher by adults in the range of 1.96 – 6.77, whereas for children in the range of 1.26 – 2.86. Following the formula of $D = A \times I \times E$, for the same *A*, it makes sense that the *D* is higher when the *E* is higher.

The cancer risk *R* of 8.13×10^{-4} and 6.83×10^{-4} were estimated corresponding to the adult total ingestion dose of 0.232 and 0.195 mSv/y for vegetables and fruits respectively. These risk are significantly lower than the risk estimated by UNSCEAR from total natural radiation dose of 2.4 mSv/y i.e. 8.4×10^{-3}. The reduction by a factor of 10.34 and 12.31 respectively for vegetables and fruits deduces that the vegetables and fruits in Malaysia are safe for human consumption.

Another approach from Cohen and Lee [32] were also used to estimate the health risk posed from the intake of vegetables and fruits. The avoid confusion, these authors estimated the health risk in terms of day loss. It is estimated that an average loss of 9.9 days from continuos exposure of 1 mSv/y throughout life. Based on the total dose of 0.215 and 0.159 mSv/y, the estimated life expectancy for adults is shorten by only 2.13 and 1.57 days due to the consumption of vegetables and fruits respectively. It is therefore concluded that the vegetables and fruits consumed by Malaysian population would not pose any significant radiological impact on health and cancer risk to the population.

Conclusion

The ingestion dose due to the activity concentration of ^{226}Ra, ^{232}Th and ^{40}K in vegetables and fruits in Malaysia were found to be below natural radiation exposure reported by UNSCEAR. It was also comparable to published value reported by other researchers. The estimated risk has no significant health hazard as they were also below the UNSCEAR cancer risk factor. Therefore, it is concluded that the vegetables and fruits available in Malaysia are radiologically safe for human consumption. The data reported here will provide a baseline radiometric values for natural radionuclides in vegetables and fruits and also the radiological risk indices associating with them.

References

1. IAEA (2004). Radiation, people and the environment : A broad view of ionising radiation, its effects and uses as well as the measures in place to it safely. Vienna: International Atomic Energy Agency: pp. 14.
2. UNSCEAR (2000). Sources and effects of ionizing radiation. New York: United Nations: pp. 140.
3. Khan, H., Chaudhry, Z., Ismail, M. and Khan, K. (2010). Assessment of radionuclides, trace metals and radionuclide transfer from soil to food of Jhangar Valley (Pakistan) using gamma-ray spectrometry. *Water, Air, & Soil Pollution*, 213(1-4): 353 - 362.
4. Othman, K. I., Karim, M. S. A., Karim, R., Adzhan, N., Halim, N. A. and Osman, S. (2012). Factors influencing fruits and vegetables consumption behaviour among adults in Malaysia. *Journal of Agribusiness Marketing*, 5: 29 - 46.
5. Ministry of Health (2010). Malaysian dietary guidelines. Putrajaya: Ministry of Health Malaysia. pp. 1 - 4.
6. Hernández, F., Hernández-Armas, J., Catalán, A., Fernández-Aldecoa, J. C. and Landeras, M. I. (2004). Activity concentrations and mean annual effective dose of foodstuffs on the island of Tenerife, Spain. *Radiation Protection Dosimetry,* 111(2): 205 - 210.
7. Al-Masri, M. S., Mukallati, H., Al-Hamwi, A., Khalili, H., Hassan, M., Assaf, H., Amin, Y. and Nashawati, A. (2004). Natural radionuclides in Syrian diet and their daily intake. *Journal of Radioanalytical and Nuclear Chemistry,* 260(2): 405 - 412.
8. Hosseini, T., Fativand, A. A., Barati, H. and Karimi, M. (2006). Assessment of radionuclides in imported foodstuffs in Iran. *International Journal of Radiation Research,* 4(3): 149 - 153.
9. Saleh, I .H., Hafez, A. F., Elanany, N. H., Motaweh, H. A. and Naim, M. A. (2007). Radiological study on soils, foodstuff and fertilizers in the Alexandria region, Egypt. *Turkish Journal of Engineering & Environmental Sciences*, 31(1): 9 - 17.
10. Quan, W., Hongda, Z., Tiqiang, F. and Qingfen, L. (2008). Re-estimation of internal dose from natural radionuclides for Chinese adult men. *Radiation Protection Dosimetry*, 130(4): 434 - 441.

11. Nasreddine, L., El Samad, O., Hwalla, N., Baydoun, R., Hamzé, M. and Parent-Massin, D. (2008). Activity concentrations and mean annual effective dose from gamma-emitting radionuclides in the Lebanese diet. *Radiation Protection Dosimetry,* 131(4): 545 - 550.
12. Choi, M. S., Lin, X. J., Lee, S. A., Kim, W., Kang, H. D., Doh, S. H., Kim, D. S. and Lee, D. M. (2008). Daily intakes of naturally occurring radioisotopes in typical Korean foods. *Journal of Environmental Radioactivity,* 99(8): 1319 - 1323.
13. Shanthi, G., Kumaran, J. T. T., Gnana Raj, G. A. and Maniyan, C. G. (2009). Natural radionuclides in the South Indian foods and their annual dose. *Nuclear Instruments and Methods in Physics Research Section A: Accelerators, Spectrometers, Detectors and Associated Equipment,* 619(1–3): 436 - 440.
14. Khandaker, M. U., Jojo, P. J. and Kassim, H. A. (2012). Determination of primordial radionuclides in natural samples using HPGe gamma-ray spectrometry. *APCBEE Procedia,* 1: 187 - 192.
15. Desideri, D., Meli, M., Roselli, C., Forini, N., Rongoni, A. and Feduzi, L. (2014). Natural radionuclides in Italian diet and their annual intake. *Journal of Radioanalytical and Nuclear Chemistry,* 299(3): 1461 - 1467.
16. Syarbaini, S., Warsona, A. and Iskandar, D. (2014). Natural radioactivity in some food crops from Bangka-Belitung islands, Indonesia. *Atom Indonesia,* 40(1): 27 - 32.
17. Tawalbeh, A. A. (2013). Radiological impact of naturally occurring radionuclides from dietary intakes of adults in central zone of Malaysian Peninsular. School of Applied Physics. Bangi: Universiti Kebangsaan Malaysia.
18. Saeed, M. A., Zainal, N. J., Hossain, I., Javed, M. A. and Mubarak, A. A. (2014). Measurements of natural radionuclides in vegetables by gamma spectrometry. *Journal of Applied Spectroscopy* 81(3): 541 - 545.
19. Priharti, W., Samat, S. B., Yasir, M. S. and Garba, N. N. (2015). Assessment of radiation hazard indices arising from natural radionuclides content of powdered milk in Malaysia. *Journal of Radioanalytical and Nuclear Chemistry,* 307(1): 297 - 303.
20. Priharti, W., Samat, S. B. and Yasir, M. S. (2015). Measurement of natural radionuclides in Malaysian bottled mineral water and consequent health risk estimation. *AIP Conference Proceedings*, 1678: 040012.
21. IAEA (1989). Measurement of radionuclides in food and the environment: A guidebook technical reports No. 295. Vienna: International Atomic Energy Agency: pp. 56 - 69.
22. Samat, S. B. and Priharti, W. (2015). Determination of fano factor and pre-amplifier noise from the measurement of energy resolution of a HPGe detector. *Sains Malaysiana,* 44(5): 761 - 764.
23. Samat, S. B. and Evans, C. J. (1992). Statistics and nuclear counting: Theory, problems and solutions. Selangor: Universiti Pertanian Malaysia.
24. Currie, L. A. (1968). Limits for qualitative detection and quantitative determination. *Analytical Chemistry*, 40(3): 586 - 693.
25. Alamoudi, Z. M. (2013). Assessment of natural radionuclides in powdered milk consumed in Saudi Arabia and estimates of the corresponding annual effective dose. *Journal of American Science,* 9(6): 267 - 273.
26. Ministry of Health (2006). Food consumption statistics for central zone for adult population aged 18-59 years. Putrajaya: Ministry of Health Malaysia: pp. 165 - 174.
27. ICRP (2012). Compendium of Dose Coefficients based on ICRP Publication 60: ICRP Publication 119. Oxford: Pergamon Press: pp. 71 - 86.
28. IAEA (1988). Facts about low-level radiation. Vienna: International Atomic Energy Agency.
29. Lilley, J. S. (2001). Nuclear physics principle and applications. England: John Wiley & Sons Inc.
30. Badran, H. M., Sharshar, T. and Elnimer, T. (2003). Levels of 137Cs and 40K in edible parts of some vegetables consumed in Egypt. *Journal of Environmental Radioactivity,* 67(3): 181 - 190.
31. Chibowski, S. (2000). Studies of radioactive contaminations and heavy metal contents in vegetables and fruit from Lublin, Poland. *Polish Journal of Environmental Studies,* 9(4): 249 - 253.
32. Cohen, B. L. and Lee, I. S. (1991). Catalog of risks extended and updated. *Health Physics*, 61: 317 -335.

Malaysian Journal of Analytical Sciences, Vol 20 No 6 (2016): 1254 - 1268
DOI: http://dx.doi.org/10.17576/mjas-2016-2006-04

MALAYSIAN JOURNAL OF ANALYTICAL SCIENCES
Published by The Malaysian Analytical Sciences Society
ISSN 1394 - 2506

VOLTAMMETRIC DETERMINATION OF REACTIVE BLACK 5 (RB5) IN WASTE WATER SAMPLES FROM THE BATIK INDUSTRY

(Penentuan Voltammetrik Bagi Reaktif Black 5 (RB5) Dalam Sampel Air Sisa Dari Industri Batik)

Nur Syamimi Zainudin[1,2], Mohamad Hadzri Yaacob[1]*, Noor Zuhartini Md Muslim[1]

[1]*School of Health Sciences, Forensic Science Programme*
Universiti Sains Malaysia, 16150 Kubang Kerian, Kelantan, Malaysia
[2]*Faculty of Applied Science,*
Universiti Teknologi MARA Cawangan Pahang, Kampus Jengka, 26400 Bandar Jengka, Pahang, Malaysia

**Corresponding author: hadzri@usm.my*

Received: 19 April 2016; Accepted: 30 September 2016

Abstract

A cyclic voltammetry (CV) and differential pulse cathodic stripping voltammetry (DPCSV) studies of RB5 in Britton-Robinson buffer (BRB) at a hanging mercury dropping electrode (HMDE) are described. CV was carried out by cathodic and anodic potential scan over the range of +200 mV to -800 mV with no accumulation time and three well-defined pH-dependent cathodic peaks were observed. The effects of different scan rates, pH of BRB, repetitive cycle and increasing concentrations on the peak height and peak potential of the analyte were studied. The results showed that RB5 dye was adsorbed and irreversibly reduced at the mercury electrode, mainly under diffusion controlled in the optimum pH 4.0 of BRB. By using DPCSV, pH of BRB and various instrumental parameters such as scan rate, accumulation time, accumulation potential and pulse amplitude that may affect the peak height of RB5 were investigated and optimized for RB5 determination. Under the optimized parameters, the peak height was found to be linear with RB5 concentration in the range from 2.5 x 10^{-7} mol L^{-1} to 2.0 x 10^{-6} mol L^{-1}. A detection limit (3SD/m) of 1.3 x 10^{-8} mol L^{-1} was achieved. The precision of the developed method in terms of RSD was 0.55% for intra-day measurement and 0.55%, 0.24% and 0.40%, for inter-day measurements, respectively. The developed method was successfully applied in the determination of RB5 in batik wastewaters with the mean recovery of 83.97 ± 4.78% to 97.93 ± 5.45% (0.5 x 10^{-6} mol L^{-1}), 95.91 ± 2.68% to 103.49 ± 1.32% (1.0 x 10^{-6} mol L^{-1}) and 99.17 ± 0.75% to 105.12 ± 0.28% (2.0 x 10^{-6} mol L^{-1}). The developed method is considered sensitive, precise, accurate, rugged, robust, fast and low cost for routine analysis of RB5 dye in batik wastewaters over the UV-VIS spectrometry method.

Keywords: Reactive Black 5, differential pulse cathodic stripping, Britton-Robinson buffer, hanging mercury dropping electrode, batik wastewater samples

Abstrak

Kajian voltammetri berkitar (CV) dan voltammetri perlucutan denyut kebezaan (DPCSV) terhadap pewarna RB5 dalam larutan penimbal Britton-Robinson (BRB) menggunakan elektrod jatuhan raksa tergantung (HMDE) dihuraikan. CV dijalankan dengan mengimbas potential kathodik dan anodik dari +200 mV ke -800 mV tanpa masa pengumpulan dan tiga puncak diperhatikan selepas imbasan. Kesan perbezaan kadar imbasan, pH BRB, imbasan berkitar yang berulang dan peningkatan kepekatan RB5 ke atas ketinggian dan nilai keupayaan puncak dikaji. RB5 yang dijerap dan diturunkan secara tidak berbalik pada permukaan elektrod merkuri adalah dibawah kawalan difusi pada pH BRB yang optimum iaitu 4.0. Dengan menggunakan DPCSV, pH BRB dan parameter-parameter peralatan yang memberi kesan kepada ketinggian puncak seperti kadar imbasan, masa pengumpulan, keupayaan pengumpulan dan amplitud denyut telah dioptimumkan untuk analisis RB5. Ketinggian puncak berkadar terus dengan kepekatan RB5 dalam julat dari 2.5 x 10^{-7} mol L^{-1} hingga 2.0 x 10^{-6} mol L^{-1}. Had pengesanan adalah 1.3 x 10^{-8} mol L^{-1}. Ketepatan (RSD) kaedah yang dibangunkan adalah 0.55% untuk hari yang sama, manakala 0.55%, 0.24% dan 0.40% untuk tiga

hari yang berbeza. Kaedah yang dibangunkan berjaya diuji bagi penentuan RB5 dalam air sisa batik dengan purata kebolehdapatan 83.97 ± 4.78% sehingga 97.93 ± 5.45% (0.5 x 10^{-6} mol L^{-1}), 95.91 ± 2.68% sehingga 103.49 ± 1.32% (1.0 x 10^{-6} mol L^{-1}) dan 99.17 ± 0.75% sehingga 105.12 ± 0.28% (2.0 x 10^{-6} mol L^{-1}). Kaedah yang dibangunkan adalah sensitif, tepat, lasak, teguh, cepat dan menjimatkan bagi analisis rutin kandungan RB5 dalam air sisa batik berbanding kaedah spektrofotometri UV-VIS.

Kata kunci: Reaktif Black 5, voltammetri perlucutan denyut kebezaan, penimbal Britton-Robinson, elektrod jatuhan raksa tergantung, sampel air sisa batik

Introduction

The textile industry is considered as one of the major water consumers. It utilizes a large volume of water and chemicals for the wet processing of the textiles and can contribute to the water bodies pollution [1, 2]. Homemade batik industry is a part of the textile industry and preliminary studies have shown that wastewaters discharged from this particular industry contain dyes, heavy metals, grease, wax and also suspended solids with high chemical oxygen demand (COD) [3, 4].

Azo dyes are considered as the oldest and the largest class of synthetic organic dyes. They are also considered as dyes with the largest shade range and are commonly used [5]. They account for 60% to 70% of the total organic dyes, have bright and high colour intensity, extensively used in textile, food, drug, cosmetic, automobile, leather and in the paper making industries [6, 7, 8].

Reactive Black 5 (RB5) or [2,7-naphthalenedisulfonic acid, 4-amino-5-hydroxy-3,6-bis ((4 - ((2 (sulfooxy) ethyl) sulfonyl) phenyl) azo)-tetrasodium salt], which chemical structure is shown in Figure 1, is categorized in the reactive vinyl sulphonate azo dye due to the presence of –N=N- bonds combined with vinylsulphone as the reactive groups [9]. The two azo groups which act as chromophores enable the dyes to absorb light in the visible spectrum and are also responsible for the corresponding colours. These reactive groups are covalently bonded to –OH or –NH_2 groups that are present in the materials to give excellent wash fastness property [10, 11, 12].

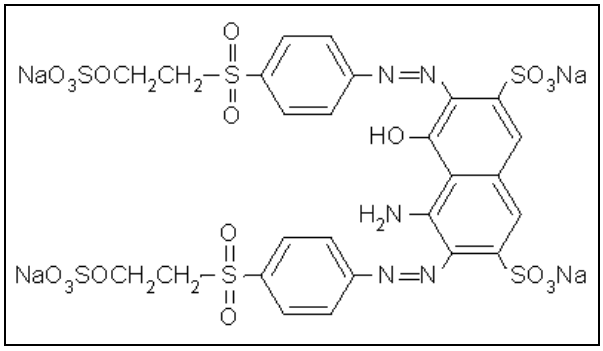


Figure 1. Chemical structure of RB5

Several analytical methods for the analysis of azo dyes and their intermediates in various samples have been developed and most of the methods are based on the electrophoresis, chromatographic and spectroscopic method [13, 14]. The voltammetric method allows for an analysis without or with minimal samples pre-treatment, has comparable selectivity and sensitivity over the chromatographic method, applicability over a wide concentration range, fast analysis, low cost on instrumentation and maintenances and is able to perform both individual and simultaneous analyses [15, 16].

This paper describes the cyclic voltammetric (CV) studies of RB5 dye using a hanging mercury dropping electrode (HMDE) as the working electrode in the Britton-Robinson buffer (BRB) to obtain qualitative information on the

electrochemical reactions such as reversibility, adsorption and diffusion characteristics of a system. Differential pulse cathodic stripping voltammetric (DPCSV) studies of RB5 dye using the same HMDE and in the same BRB had then been carried out for RB5 dye determination in the wastewaters from local batik factories. With regards to the voltammetry method, no DPCSV technique for RB5 dye determination has been reported so far. It is also rarely reported for the analysis of azo dyes containing two azo groups in their chemical structures.

Materials and Methods

Materials

All chemicals used in this study were of analytical grade reagent and all solutions were prepared in deionized water. The RB5 dye standard (MW = 991.82 $gmol^{-1}$) was obtained from Sigma Aldrich, UK. For the preparation of 2.0 x 10^{-4} $molL^{-1}$ RB5 dye stock solution, 20 mg of the RB5 dye standard was dissolved in 100 mL volumetric flask. The standard working solution of 2.0 x 10^{-5} $molL^{-1}$ was prepared by the appropriate dilution of the stock solution. BRB solution as the supporting electrolyte was prepared in 1000 mL deionized water, composed of a mixture of 2.47 g boric acid (R&M Chemicals, Canada), 2.30 mL glacial acetic acid (R&M Chemicals, Canada) and 2.70 mL ortho-phosporic acid (R&M Chemicals, Canada). Sodium hydroxide (Systerm, Italy) with the concentration of 0.1 M was used to adjust the pH of the BRB solution to the desired value. High purity mercury, 99.99% (Merck, Germany) was used for HMDE.

Instrumentations

The voltammetric experiments were carried out using VA 757 Computrace Metrohm Voltammetric Analyzer with 663 VA Stand (Metrohm, Switzerland), consisted of Multi-Mode Electrode (MME) and a 40 mL capacity voltammetric cell. The MME consisted of a HMDE as the working electrode (WE), a platinum wire as the auxiliary electrode (AE) and an Ag/AgCl as the reference electrode (RE). The VA 757 was connected to a computer for data processing and for all pH measurements, the pH meter (Hanna Instruments, UK) was employed.

Voltammetric measurement:

Cyclic voltammetry

BRB solution with the volume of 9 mL was placed into a voltammetric cell and purged by a stream of purified nitrogen for at least 15 minutes. RB5 dye standard solution (2.0 x 10^{-3} $molL^{-1}$) with the volume of 1 mL was then spiked to give a final concentration of 2.0 x 10^{-4} $molL^{-1}$ and the solution was repurged for 2 minutes. The RB5 dye was scanned from +200 mV to -800 mV (cathodic direction) and switched to +200 mV (anodic direction) with a scan rate (v) of 25 mV/s in various pH of the BRB solution (pH 2.0 to 12.0). The effect of various v (25 to 200 mV/s), the effect of repetitive cycle (1 to 5 cycles) and the effect of dye concentrations on the peak height (I_p) and peak potential (E_p) of RB5 dye were investigated.

Differential pulse stripping voltammetry

BRB solution with the volume of 9 mL was placed into the voltammetric cell and purged by a stream of purified nitrogen for at least 15 minutes. RB5 dye standard solution (2.0 x 10^{-5} $molL^{-1}$) with the volume of 1 mL was then spiked to give the final concentration of 2.0 x 10^{-6} $molL^{-1}$ and the solution was repurged for 2 minutes. The initial operational parameters applied for the voltammetric measurements were the initial potential (E_i) = +150 mV, final potential (E_f) = -700 mV, v = 15 mV/s, accumulation time (t_{acc}) = 0 s, accumulation potential (E_{acc}) = 0 mV and pulse amplitude = 50 mV. Parameters such as v, t_{acc}, E_{acc} and pulse amplitude were optimized to increase the response of the developed method.

The developed method was validated for linearity, limit of detection (LOD), limit of quantification (LOQ), precision, repeatability, accuracy, ruggedness and robustness to verify the suitablity for the extended purposes according to the approach proposed by Miranda et al. [17]. The LOD and LOQ were calculated by the equations; LOD = 3 SD/m and LOQ = 10 SD/m, where SD is the standard deviation of the three replicate determinations of the RB5 dye at the lowest concentration on the calibration curve and m is the slope of the regression equation [18]. The RB5 dye standard solution at the concentration of 2.0 x 10^{-6} $molL^{-1}$ was applied for intra-day and inter-day precision, ruggedness and robustness with five replicate (n=5) measurements. The ruggedness of the developed method was investigated using the same voltammetry analyzer (VA 757), but had been conducted by two different analysts [19] and was also analyzed by using two different voltammetry analyzers (VA 757 and VA 797) but only

conducted by one analyst [20] under the same optimum parameters. The robustness was carried out by examining the effect of a small variation of v, t_{acc}, time interval analysis after RB5 dye standard preparation and pH of BRB solution on the response.

Collection, preservation and analysis of wastewaters from the batik industry

Wastewaters from the batik industry were obtained from nine batik factories, located at Kota Bharu and Pantai Cahaya Bulan, Kelantan, Malaysia. The wastewaters were collected from two different dyebaths at each factory. The wastewaters were analyzed using the developed DPCSV technique without the prior samples pre-treatment and extraction by spiking 1 mL of the wastewater samples into the 9 mL BRB solution.

Recovery studies of the RB5 dye in wastewaters from the batik industry

To study the accuracy and reproducibility of the developed DPCSV technique, recovery experiments were carried out using the standard addition method.

UV-VIS Spectrophotometry analysis of the RB5 dye

The results obtained by the developed DPCSV technique were compared with the UV-VIS Spectrophotometry method using Spectrophotometer Cary 100, USA. The double beam mode was employed for the overall analysis from the start wavelength of 700 nm to the stop wavelenghth of 300 nm with the rate of 600 nm/min.

Results and Discussion

Electrochemical behaviour of the RB5 dye

Cyclic voltammetric studies of the RB5 dye were carried out in 0.04 M BRB solution from pH 2.0 to 12.0 with v of 25 mV/s. From the cyclic voltammogram obtained, BRB solution at pH 4.0 was observed to be the optimum condition with I_p of 298 nA for RB5 dye reduction at the HMDE, as shown in Figure 2. Three well-defined reduction peaks at -79.80 mV, -258 mV and -568 mV were obtained for the first, second and third peak, respectively. No oxidation peaks were observed which confirmed that the RB5 dye was irreversibly reduced at the mercury electrode. The second reduction peak was referred to as the analytical signal due to its higher sensitivity compared to the first and third reduction peak of the RB5 dye [21].

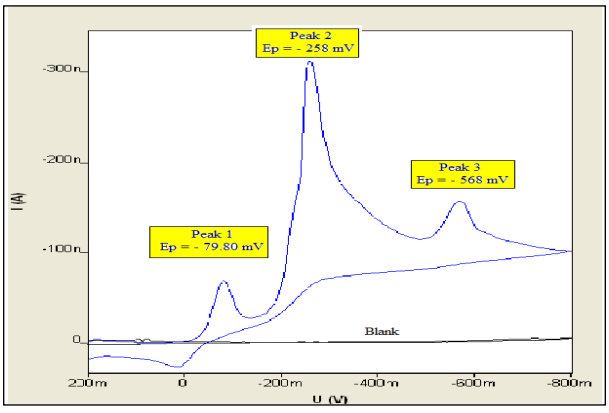


Figure 2. Cyclic voltammogram of 2 x 10^{-4} $molL^{-1}$ RB5 dye in BRB solution at pH 4.0.Experimental condition: E_i = +200 mV, E_{switch} = -800 mV, E_f = +200 mV and v = 25 mV/s

The first two obtained reduction peaks were suggested due to the subsequence reduction process of the two azo groups to amines. Both hydroxyl and amino groups were electron donating substituents in the RB5 dye compound. The first reduction peak was suggested from the reduction process of the azo with the hydroxyl group and followed by the reduction process of the other azo with amino group, which gave the second reduction peak on the

voltammograms. The reduction process of the azo with amino group was more difficult due to the electron distribution in this functional group [22].

The effect of pH of BRB solution on the E_p was studied from pH 2.0 to 12.0. The results showed that the E_p of RB5 dye was shifted to the more negative potentials with the increased pH indicating that the electron transfer was accompanied by proton transfer in the reduction process [23, 24]. The reduction process was easier to take place in a medium rich with H^+ ions and more difficult in a medium with low H^+ ions [25] and the reduction process of RB5 dye was pH dependent [26, 27].

The effects of scan rate (v) from 25 to 200 mV/s on the E_p and I_p of the RB5 dye were observed under the same experimental conditions. The results showed that by increasing the v, the E_p shifted to more negative potentials and accompanied with the increase of the I_p. The increase of I_p indicated an adsorption phenomenon of the RB5 dye at the surface of the mercury electrode [28, 29]. A linear relationship was observed between log I_p against log v with a slope of 0.5282 (R^2 = 0.9982, n = 6), as shown in Figure 3. The slope of 0.5282 was close to the theoretical value of 0.5, which indicated that the reduction process of RB5 dye was mainly controlled by diffusion [30, 31].

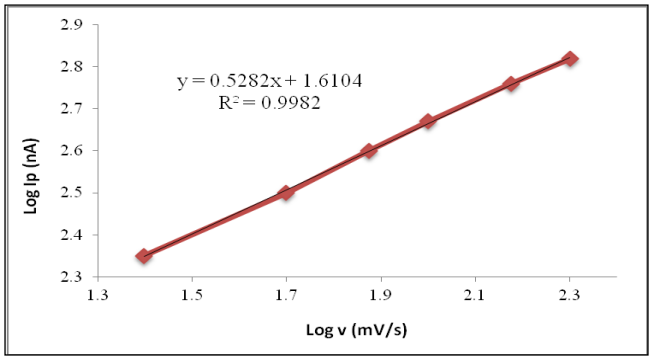


Figure 3. Plot of I_p to the log v for 2 x 10^{-4} molL^{-1} RB5 dye in BRB solution at pH 4.0

The effect of the RB5 dye concentrations was investigated and the results showed that the E_p of RB5 dye at -258 mV showed no significant change in the peak position and the I_p of the RB5 dye increased with the increasing concentration of RB5 dye. This phenomenon confirmed the adsorption of the RB5 dye at the mercury electrode surface [32]. No new peak was observed with the increasing RB5 dye concentration at both the cathodic and anodic directions, which indicated that the obtained reduction peaks were due to respective RB5 dye and not from other electroactive species that may be present in the BRB solution [33].

The effect of repetitive cycles on the I_p of the RB5 dye was studied with five cycles. The I_p decreased in the second cycle and was almost constant for the third, fourth and fifth cycle, as shown in Figure 4. This meant that the variation of I_p was controlled by diffusion in the experimental condition [34] and RB5 dye had the adsorption behaviour at the surface of the mercury electrode [35].

Differential pulse stripping voltammery of the RB5 dye: The effects of pH of BRB solution

Differential pulse cathodic stripping voltammetry of 2 x 10^{-6} molL^{-1} RB5 dye was studied in 0.04 M BRB solution from pH 2.0 to 12.0. BRB solution at pH 2.5 was considered as the optimum pH since the highest I_p and well-defined shape of the first reduction peak were obtained. The voltammogram of RB5 dye in BRB solution at pH 2.5 is shown in Figure 5. The E_p of RB5 dye peak shifted to more negative potentials as the pH of BRB solution increased, indicating the involvement of H^+ in the reduction process of RB5 dye [36].

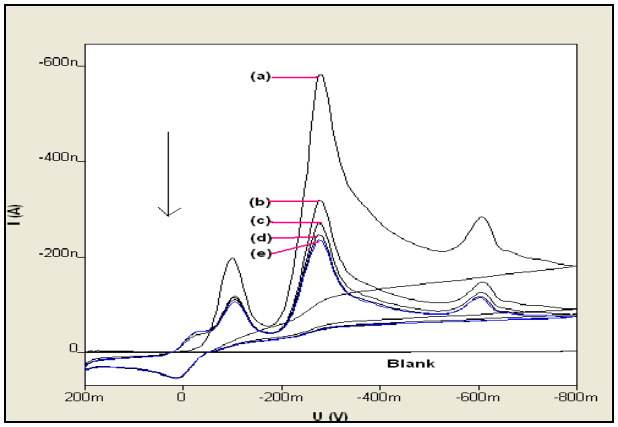


Figure 4. Cyclic voltammograms of repetitive cycles of 2 x 10^{-4} $molL^{-1}$ RB5 dye in BRB solution at pH 4.0. (a) First (b) second (c) third (d) fourth and (e) fifth cycle

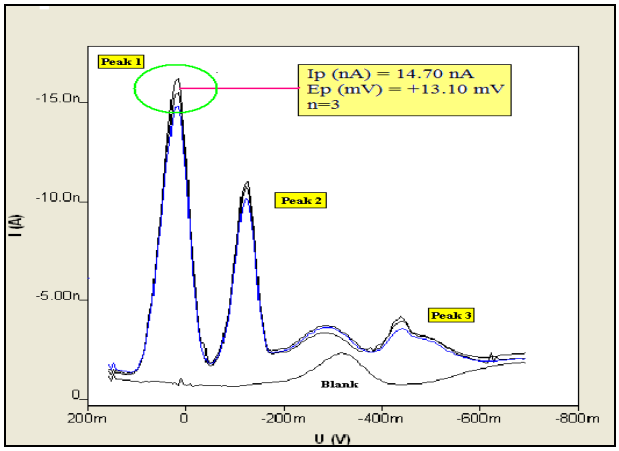


Figure 5. Voltammogram of 2 x 10^{-6} $molL^{-1}$ RB5 dye in BRB solution at pH 2.5. Parameters conditions: E_i = +150 mV, E_f = -700 mV, v = 15 mV/s, t_{acc} = 0 s, E_{acc} = 0 mV and pulse amplitude = 50 mV

Optimization of the operational parameters

It is very important to optimize all the parameters that may influence the measurements in order to obtain the optimum response [37]. The effects of scan rate (v), accumulation time (t_{acc}), accumulation potential (E_{acc}) and pulse amplitude on the I_p of 2 x 10^{-6} $molL^{-1}$ RB5 dye were studied in the BRB solution at pH 2.5.

The effect of scan rate (v)

The relationships of I_p of the RB5 dye to various v such as 5, 10, 15, 30 and 40 mV/s were observed using the unoptimum parameters. The v of 5 mV/s was chosen as the optimum condition since it gave the highest I_p of the first reduction peak of the RB5 dye which was 16.10 nA.

The effect of accumulation time (t_{acc})

Accumulation of electroactive species at the electrode contributed to a high response in the electroanalytical measurements [38]. Accumulation time (t_{acc}) is the period of time given for the RB5 dye to accumulate onto the mercury electrode surface before being analyzed. The dependence of I_p on the t_{acc} was studied at concentration of 2 x 10^{-6} $molL^{-1}$ RB5 dye over the range from 0 to 110 s.

At t_{acc} of 0 s, the first reduction peak of RB5 dye gave a higher I_p compared to the second reduction peak. The I_p of the second reduction peak had become dominant, starting from t_{acc} of 10 s and onwards. The second reduction peak was referred as the analytical signal for further optimization since it showed higher I_p as the t_{acc} increased. From Figure 6, the I_p increased with the increasing t_{acc} from 0 to 80 s, then became constant with the longer times. The t_{acc} of 80 s was chosen as the optimum condition with I_p of 121 nA at E_p of -88 mV.

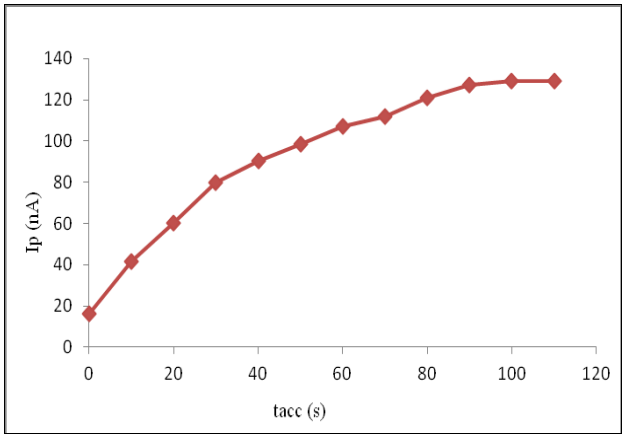


Figure 6. Effect of various t_{acc} on the I_p of second reduction peak of 2 mg/L RB5 dye in BRB solution at pH 2.5. Initial instrumental parameters were E_i = +150 mV, E_f = -650 mV, v = 5 mV/s, E_{acc} = 0 mV and pulse amplitude = 50 mV

As suggested by Tavares et al. [39], the increase of I_p with t_{acc} was due to the accumulation of RB5 dye at the mercury electrode surface in a larger amount, since longer time was given for the accumulation process to occur. The constant I_p that was obtained at longer 90 s had been suggested due to the saturation of the accumulated RB5 dye at the electrode surface [40].

The effect of accumulation potential (E_{acc})

Accumulation potential (E_{acc}) was the potential for the RB5 dye to be accumulated at the surface of mercury electrode, whereas an optimum E_{acc} was the most appropriate potential for the accumulation process to take place. The effect of E_{acc} on the I_p of the second reduction peak was evaluated over the range of 0 to -100 mV for 2 x 10^{-6} $molL^{-1}$ RB5 dye. The maximum response was observed at E_{acc} of 0 mV with I_p of 120 nA at E_p of -82.10 mV. It indicated that the accumulation of RB5 dye at the electrode surface effectively occured at 0 mV.

The effect of pulse amplitude

According to De Lima et al. [41], pulse amplitude is one of the factors that affect the sensitivity of voltammetric measurements. The effect of pulse amplitude on the I_p was studied by measuring 2 x 10^{-6} $molL^{-1}$ RB5 dye within the range of 25 to 125 mV of pulse amplitude, under the previous optimum parameters. Figure 7 shows that the I_p has sharply increased at the range of pulse amplitude from 25 to 75 mV and slowly decreased at higher values. The E_p has shifted towards less negative directions as the values of pulse amplitude increased.

The pulse amplitude of 75 mV was noted as the optimum condition due to the highest I_p observed which was 223 nA with E_p at -65.50 mV. By changing the pulse amplitude, the E_i was changed from +150 mV to +250 mV and the E_f was changed from -650 mV to -600 mV in order to observe the first reduction peak on the voltammograms.

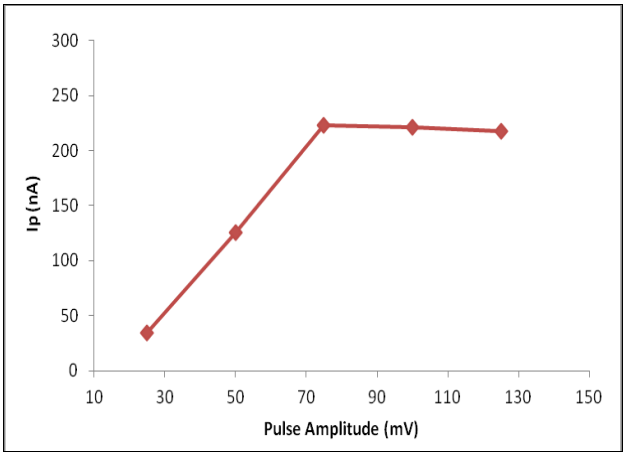


Figure 7. Effects of various pulse amplitudes on the I_p of 2 mg/L RB5 dye in BRB solution at pH 2.5. Initial instrumental parameters were E_i = +150 mV, E_f = -650 mV, v = 5 mV/s, t_{acc} = 80 s and E_{acc} = 0 mV

By applying these optimized parameters, the I_p was enhanced about 24 times, compared to the obtained I_p by using the unoptimized parameters which was 9 nA at E_p of -121 mV. Table 1 shows the optimum supporting electrolyte and instrumental parameters of the developed DPCSV technique of 2 x 10^{-6} $molL^{-1}$ RB5. These optimum parameters were then used to validate the developed method.

Table 1. Optimum supporting electrolyte and instrumental parameters of the developed DPSCV technique

Supporting Electrolyte and Instrumental Parameters	**Optimum Value**
Britton-Robinson Buffer (BRB)	pH 2.5
Initial Potential, E_i (mV)	+250
End Potential, E_f (mV)	-600
Scan Rate, v (mV/s)	5
Accumulation Time, t_{acc} (s)	80
Accumulation Potential, E_{acc} (mV)	0
Pulse Amplitude (mV)	+75

Validation of the developed method: Linearity, limit of detection, limit of quantification

The applicability of the developed DPCSV technique as an analytical method for the determination of RB5 dye standard solution was examined by measuring the obtained I_p as the function of concentration under the optimum operational and instrumental parameters as shown in Table 1.

Two linear regions were observed and the I_p of RB5 dye tended to maintain, starting at the concentration of 1.6 x 10^{-5} $molL^{-1}$. As suggested by Geremedhin et al. [42] and Radi et al. [43], this phenomenon may be due to the limited adsorption of RB5 dye at the mercury electrode, which resulted from the saturation of the electrode surface. As shown in Figure 8, the first linear region demonstrated its linearity from 2.5 x 10^{-7} $molL^{-1}$ to 2.0 x 10^{-6} $molL^{-1}$ at five different concentrations of RB5 dye standard solution. The constructed calibration graph was represented by the linear equation of I_p (nA) = 115.61 x – 10.31 with a correlation coefficient (R^2) of 0.9998. The second region was linear from 3.0 x 10^{-6} $molL^{-1}$ to 1.4 x 10^{-5} $molL^{-1}$ with the regression equation of I_p (nA) = 11.76 x + 211.56 and R^2 of 0.9987. The first linear region demonstrated a bigger slope than the second region, thus it was applied for RB5

dye determination since a higher sensitivity had been offered for analysis [44]. The calculated LOD for the standard solution was 1.3 x 10^{-8} molL^{-1} and the LOQ was found to be 4.3 x 10^{-8} mol L^{-1}.

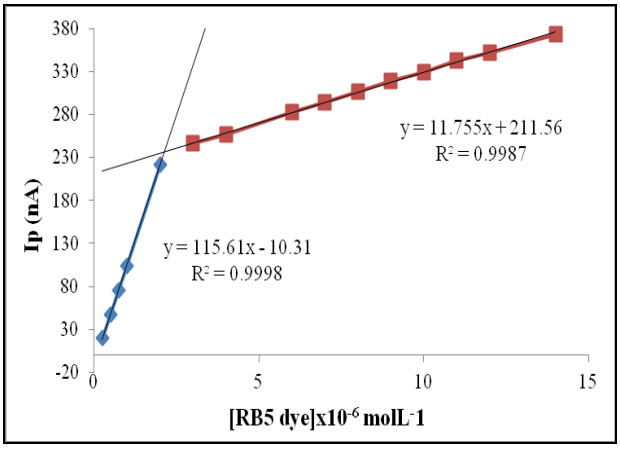


Figure 8. Two linear curves of RB5 dye in BRB solution at pH 2.5. (a) 2.5 x 10^{-7} to 2.0 x 10^{-6} molL^{-1} and (b) 3.0 x 10^{-6} to 1.4 x 10^{-5} molL^{-1}

Precision

The precision of the developed technique for RB5 dye determination was determined in five replicate measurements (n=5) at a concentration of 2.0 x 10^{-6} molL^{-1} [45]. The relative standard deviation (RSD) of 0.55% had been achieved for the measurements which indicated that the developed method was precise and confidence as the value was less than 2% [46]. The intra-day and inter-day repeatability studies were carried out by measuring 2.0 x 10^{-6} molL^{-1} RB5 dye for five replicates in three consecutive days using the developed technique. The RSD values for day 1, 2 and 3 were 0.55%, 0.24% and 0.40%, respectively which also indicated that the developed method was precise and confidence.

Accuracy

The accuracy of the developed technique was tested by spiking three known different concentrations of RB5 dye which were 5 x 10^{-7} molL^{-1}, 1.0 x 10^{-6} molL^{-1} and 2.0 x 10^{-6} molL^{-1} into a voltammetric cell containing BRB solution [47]. These spiked RB5 dye standard solutions were measured in three replicates (n=3) and the discovered amounts of the spiked solutions in the cell were calculated using the equation of I_p (nA) = 115.61 x – 10.31, where x is the found concentrations of RB5 dye in the voltammetric cell. The satisfactory recoveries of 99.94 ± 3.15%, 99.16 ± 1.80% and 100.61 ± 1.09% were respectively achieved for the spiked concentrations of 5 x 10^{-7} molL^{-1}, 1.0 x 10^{-6} molL^{-1} and 2.0 x 10^{-6} molL^{-1}.

Ruggedness

The RSD values were 0.49% and 0.38% for the first and second analyst, respectively for the measurements using the same voltammetry analyzer (VA 757). The RSD values were 0.49% and 0.20% for the analysis using the respective VA 757 and VA 797 (different voltammetry analyzers) by the first analyst. From the two-tailed *F* test, there were no significant differences between the obtained variances for RB5 dye when the measurements were performed by two different analysts with the same voltammetry analyzer and by the same analyst with two different voltammetry analyzers at the 5% significance level. Hence, the results indicated that the developed technique was considered rugged.

Robustness

By the two -tailed *F* test at 95% confidence level, none of small variations of the *v* (3 and 7 mV/s), t_{acc} (78 and 82 s), time interval analysis after the standard preparation (0, 30 and 60 minutes) and pH of BRB solution (pH 2.3 and 2.7)

had significantly influenced the obtained I_p of RB5 dye at the concentration of 2.0 x 10^{-6} molL^{-1} with five replicate (n=5) measurements [48, 49].

Determination of RB5 dye in wastewaters collected from the batik industry

To evaluate the application to a real samples analysis, the developed DPCSV technique was used to analyze RB5 dye in wastewater samples which were collected from the local batik factories. The wastewater samples were analyzed by the developed technique under optimum parameters without any sample pre-treatment. Table 2 shows the content of RB5 in the collected batik wastewater samples.

Table 2. The concentrations of RB5 dye in the batik wastewater samples from the first and second dyebath

Samples (First Dyebath)	Concentration of RB5 (x 10^{-6} mol/L)	Samples (Second Dyebath)	Concentration of RB5 (x 10^{-6} mol/L)
S1-A1	0.493	S1-B1	N.D
S2-A1	N.D	S2-B1	N.D
S3-A1	0.324	S3-B1	N.D
S4-A1	0.236	S4-B1	N.D
S5-A1	N.D	S5-B1	N.D
S6-A1	0.421	S6-B1	0.235
S7-A1	0.183	S7-B1	N.D
S8-A1	N.D	S8-B1	N.D
S9-A1	N.D	S9-B1	N.D

N.D: not detected

To verify these results, recovery experiments were carried out by spiking three different concentrations of RB5 standard solution with the concentrations of 0.5 x 10^{-6}, 1.0 x 10^{-6} and 2.0 x 10^{-6} molL^{-1} into the wastewaters collected from the batik factories that did not contain RB5 dye. The experiments were carried out using four wastewater samples (S1-B1, S2-B1, S5-B1 and S8-B1) with three replicate (n=3) measurements per each spiked concentration. The recoveries achieved for 0.5 x 10^{-6}, 1.0 x 10^{-6} and 2.0 x 10^{-6} molL^{-1} RB5 dye were from 83.97 ± 4.78 to 97.93 ± 5.45%, 95.91 ± 2.68 to 103.49 ± 1.32% and 99.17 ± 0.75 to 105.12 ± 0.28%, respectively. According to the *t*-test (two-tailed), there were no significant differences between the recovery and spiked value at the 95% confidence level with degree of freedom (n-1=2), since all the calculated *t* values in the experiment were lower than the theoretical *t* value, which was 4.303 [50, 51]. These good recovery values indicated that the matrixes did not affect the determination of RB5 dye in batik wastewater samples and it was suggested that the developed method can be applied for RB5 dye determination in the batik wastewater samples without any sample pre-treatment. The recovery results are listed in Table 3.

Comparison of the results by the developed DPCSV technique and spectrophotometry method

The performance of the developed DPCSV technique in determining the RB5 dye was then compared against UV-VIS spectrophotometry [52]. Spectrophotometry measurements of RB5 dye in the range of 300 to 700 nm had shown that the highest absorbance was obtained at 596 nm which was attributed to the diazo groups and responsible for the blue colour of the dye solution [53]. The calibration curve was constructed and a linear range was found from 1.0 x 10^{-6} to 1.5 x 10^{-4} molL^{-1} with the regression equation of $y = 0.0225 x + 0.0287$ ($R^2 = 0.9991$), as shown in Figure 9. The LOD and LOQ were 0.4 x 10^{-7} molL^{-1} and 1.3 x 10^{-7} molL^{-1}, respectively.

Table 3. Analytical results of RB5 dye in batik wastewater samples using the developed technique

Samples	Spiked[a] amount ($x10^{-6}$ $molL^{-1}$)	Found[a] amount ($x10^{-6}$ $molL^{-1}$)	Recovery ± SD (%)	RSD (%)
S1-B1	0.5	0.44	88.30 ± 7.69	8.71
	1.0	0.97	97.37 ± 1.42	1.46
	2.0	1.99	99.75 ± 0.66	0.66
S2-B1	0.5	0.44	88.07 ± 7.99	9.07
	1.0	0.98	98.30 ± 3.60	3.66
	2.0	2.10	105.12 ± 0.28	0.27
S5-B1	0.5	0.42	83.97 ± 4.78	5.69
	1.0	0.96	95.91 ± 2.68	2.79
	2.0	1.99	99.61 ± 0.43	0.43
S8-B1	0.5	0.49	97.93 ± 5.45	5.57
	1.0	1.03	103.49 ± 1.32	1.28
	2.0	1.98	99.17 ± 0.75	0.76

[a]Average of three replicate measurements for each spiked concentration

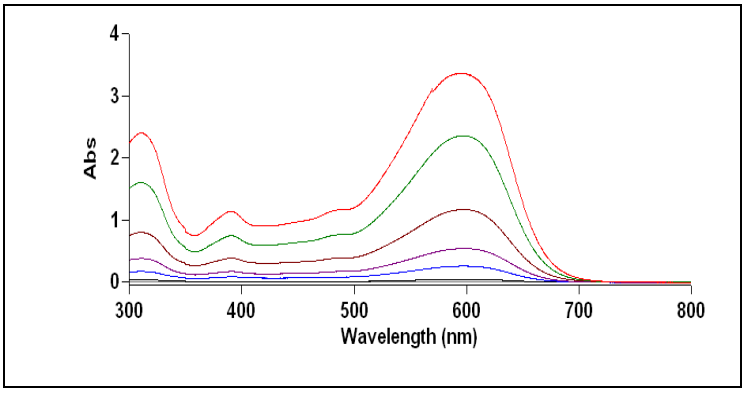


Figure 9. Spectra of RB5 dye with increasing concentration from 1.0 x 10^{-6} to 1.5 x 10^{-4} $molL^{-1}$

The results obtained by both developed DPCSV and spectrophotometry method in analyzing RB5 dye in the several wastewaters samples collected from the batik factories were then compared, as shown in Table 4. The developed DPCSV technique can be considered more sensitive as it had an ability to detect and determine the dye at a lower level compared to the UV-VIS Spectrophotometry method.

Table 4. The concentrations of RB5 dye in the batik wastewater samples using two different methods

Samples	Concentration of RB5 (x 10^{-6} mol/L)	
	DPSV	UV-VIS
S1-A1	0.493	0.471
S2-A1	N.D	N.D
S3-A1	0.324	N.D
S4-A1	0.236	N.D
S5-A1	N.D	N.D
S6-A1	0.421	N.D
S7-A1	0.183	N.D
S8-A1	N.D	N.D
S9-A1	N.D	N.D

N.D: not detected

Conclusion

The developed DPCSV technique had been succesfully applied to determine the RB5 dye in wastewaters from the batik industry. The present method had an advantage that no prior extractions or samples pre-treatment were required. It was also found to be practically rapid, convenient, sensitive, accurate, precise, rugged, robust and low in cost compared to the UV-VIS Spectrophotometry method. Therefore, it could be an excellent alternative method for the routine determination of RB5 dye in batik wastewaters samples.

Acknowledgement

The authors gratefully acknowledge Universiti Sains Malaysia (USM) for awarding the Short Term Grant No: 304/PPSK/61312057. We would also like to thank Metrohm (Malaysia) Sdn Bhd for allowing us to use their instrument and also to all the laboratory staff of the School of Health Sciences, USM, Malaysia for their co-operation and assistance.

References

1. Ellouze, E., Tahri, N. and Amar, R. B. (2012). Enhancement of textile wastewater treatment process using nanofiltration. *Desalination,* 286: 16 – 23.
2. Norasikin, O., Mili, N., Siti, N. Z. and Nurul, A. B. M. (2010). Extraction of remazol brilliant orange 3R from textile wastewater using tetrabutyl ammonium bromide. *Jurnal Teknologi,* 53: 29 – 39.
3. Nora'aini, A. and Suhaimi, N. S. (2009). Performance evaluation of locally fabricated asymmetric nanofiltration membrance for batik industry effluent. *World Applied Sciences Journal,* 5: 46 – 52.
4. Cristóvão, R. O., Tavares, A. P. M., Ferreira, L. A., Loureiro, J. M., Boaventura, R. A. R. and Macedo, E. A. (2009). Modeling the discoloration of a mixture of reactive textile dyes by commercial laccase. *Bioresource Technology,* 100: 1094 – 1099.
5. Xu, G., O'Dea, J. J. and Osteryoung, J. G. (1995). Surface reduction study of monoazo dyes by adsorptive square wave voltammetry. *Dyes and Pigments,* 30: 201 – 223.
6. Muthukumar, M., Karuppiah, M. T. and Raju, G. B. (2007). Electrochemical removal of C.I acid orange 10 from aqueous solution. *Separation and Purification Technology,* 55: 198 – 205.
7. Bogdanowicz, R., Fabiańska, A., Golunski, L., Sobaszek, M., Gnyba, M., Ryl, J., Darowicki, K., Ossowski, T., Janssens, S. D., Haenen, K. and Siedlecka, E. M. (2013). Influence of the boron doping level on the electrochemical oxidation of the azo dyes at Si/BDD thin film electrodes. *Diamonds and Related Materials,* 39: 82 – 88.
8. Solís, M., Solís, A., Pérez, H. I., Manjarrez, N. and Flores, M. (2012). Microbial decolouration of azo dyes: A review. *Process Biochemistry,* 47: 1723 – 1748.

9. Tunc, O., Tanacı, H. and Aksu, Z. (2009). Potential use of cotton plant wastes for the removal of remazol Black B reactive dye. *Journal of Hazardous Materials,* 163: 187 – 198.
10. Yavuz, Y. and Shahbazi, R. (2012). Anodic oxidation of Reactive Black 5 dye using boron doped diamond anodes in a bipolar trickle tower reactor. *Separation and Purification Technology,* 85: 130 –136.
11. Méndez-Martínez, A. J., Dávila-Jiménez, M. M., Ornelas-Dávila, O., Elizalde-González, M. P., Arroyo-Abad, U., Sires, I. and Brillas, E. (2012). Electrochemical reduction and oxidation pathways for Reactive Black 5 dye using nickel electrodes in divided and undivided cells. *Electrochimica Acta,* 59: 140 – 149.
12. Jović, M., Stanković, D., Manojlović, D., Andelković, I., Milić, A., Dojčinović, B. and Roglić, G. (2013). Study of the electrochemical oxidation of reactive textile dyes using platinum electrode. *International Journal of Electrochemical Sciences,* 8: 168 – 183.
13. Bersier, P. M. and Berseir, J. (1986). Polarography and voltammetry of dyes and intermediates. *Trends in Analytical Chemistry,* 5(4): 97 – 102.
14. Pinheiro, H. M., Touraud, E. and Thomas, O. (2004). Aromatic amines from azo dye reduction: Status review with emphasis on direct UV spectrophotometric detection in textile industry wastewaters. *Dyes and Pigments,* 61: 121 – 139.
15. Fogg, A. G., Zanoni, M. V. B., Yusoff, A. R. H. M., Ahmad, R., Barek, J. and Zima, J. (1998). Polarographic and voltammetric determination of triazine-based reactive azo dyes with 4-carboxypyridyl and 1,4-diazabicyclo[2,2,2]octanyl (DABCO) leaving groups. *Analytica Chimica Acta,* 362: 235 – 240.
16. Švorc, L., Sochr, J., Svĭtková, J., Riejav, M. and Bustin, D. (2013). Rapid and sensitive electrochemical determination of codeine in pharmaceutical formulations and human urine using a boron-doped diamond film electrode. *Electrochimica Acta,* 87: 503 – 510.
17. Miranda, M. P., del Rio, R., del Valle, M. A., Faundez, M. and Armijo, F. (2012). Use of fluorine-doped tin oxide electrodes for lipoic acid determination in dietary supplements. *Journal of Electroanalytical Chemistry,* 668: 1 – 6.
18. Yardım, Y. and Şentürk, Z. (2013). Electrochemical evaluation and adsorptive stripping voltammetric determination of capsaicin or dihydrocapsaicin on a disposable pencil graphite electrode. *Talanta,* 112: 11 – 19.
19. Jain, R. and Rather, J. A. (2011). Stripping voltammetry of tinidazole in solubilized system and biological fluids. *Colloids and Surfaces A: Physicochemical and Engineering Aspects,* 378: 27 – 33.
20. Gaber, A. A. A., Ahmed, S. A. and Rahim, A. M. A. (2013). Cathodic adsorptive stripping voltammetric determination of Ribovirin in pharmaceutical dosage form, urine and serum. *Arabian Journal of Chemistry,* Article in Press.
21. Rather, J.A. and Wael, K. D. (2012). C60-funtionalized MWCNT based sensor for sensitive detection of endocrine disruptor vinclozolin in solubilized system and wastewater. *Sensors and Actuators B: Chemical,* 171-172: 907 – 915.
22. Guaratini, C. C. I., Fogg, A. G. and Zanoni, M. V. B. (2001). Assesment of the application of cathodic stripping voltammetry to the analysis of diazo reactive dyes and their hydrolysis products. *Dyes and Pigment,* 50: 211 – 221.
23. Menek, N. and Karaman, Y. (2006). Polarographic and voltammetric investigation of 6'-butoxy-2,6-diamino-3,3'-azodipyridine. *Dyes and Pigments,* 68: 101 – 108.
24. Mo, Z., Zhang, Y. M., Zhao, F., Xiao, F., Guo, G. and Zeng, B. (2010). Sensitive voltammetric determination of Sudan I in food samples by using Gemini surfactant-ionic liquid-multiwalled carbon nanotube composite film modified glassy carbon electrodes. *Food Chemistry,* 121: 233 – 237.
25. Ucar, M., Polat, K., Solak, A.O., Toy, M. and Aksu, M. L. (2010). The electrochemical behavior of 2-halogenated derivatives of 4-methoxyazobenzene at a mercury electrode. *Dyes and Pigments,* 87: 55 –61.
26. Wu, Y. (2010). Electrocatalysis and sensitive determination of Sudan I at the single-walled carbon nanotubes and iron (III)-porphyrin modified glassy carbon electrodes. *Food Chemistry,* 121: 580 – 584.
27. Vilaseca, C., Quintana, M.C., Vicente, J., Hernández, P. and Hernández, L. (2008). Electrochemical analysis of the alanine phenylthiohydantoin derivative by cathodic stripping voltammetry. *Analytical Biochemistry,* 379: 91 – 95.
28. Bagheri, A. and Hosseini, H. (2012). Electrochemistry of raloxifane on glassy carbon electrode and its determination in pharmaceutical formulations and human plasma. *Bioelectrochemistry,* 88: 164 – 170.
29. Aşangil, D., Taşdemir, İ. H. and Kılıc, E. (2012). Adsorptive stripping voltammetric methods for determination of aripiprazole. *Journal of Pharmaceutical Analysis,* 2(3): 193 – 199.

30. Ardila, J. A., Sartori, E. R., Rocha-Filho, R. and Fatibello-Filho, O. (2013). Square-wave voltammetric determination of bezafibrate in pharmaceutical formulations using a cathodically pretreated boron-doped diamond electrode. *Talanta,* 103: 201 – 206.
31. Jain, R. and Vikas. (2011). Voltammetric behavior of antimalarial drug artesunate in solubilized systems. *Colloids and Surfaces B: Biointerfaces,* 88: 729 – 733.
32. Malode, S. J., Shetti, N. P. and Nandibewoor, S. T. (2012). Voltammetric behavior of theophylline and its determination at multi-wall carbon nanotube paste electrode. *Colloids and Surface B: Biointerfaces,* 97: 1 – 6.
33. Hadzri, M.Y. (2006). Stripping voltammetric methods for the determination of aflatoxin compounds. PhD thesis, Universiti Teknologi Malaysia.
34. Guo, Y. J., Pan, J. H. and Jing, W. J. (2004). Determination of Orange II and the supramolecular system of Orange II with cyclodextrins by polarography. *Dyes and Pigments,* 63: 65 – 70.
35. Brahman, P. K., Dar, R. A. and Pitre, K. S. (2013). Adsorptive stripping voltammetric study of Vitamin B1 at multi-walled carbon nanotube paste electrode. *Arabian Journal of Chemistry,* Article in Press.
36. Gupta, V. K., Jain, R., Agarwal, S., Mishra, R. and Dwivedi, A. (2011). Electrochemical determination of antihypertensive drug irbesartan in pharmaceuticals. *Analytical Biochemistry,* 410: 266 – 271.
37. Rievaj, M., Švorc, L. and Bustin, D. (2013). Green electrochemical sensor for environmental monitoring of pesticides: Determination of atrazine in river waters using a boron-doped diamond electrode. *Sensors and Actuators B: Chemical,* 181: 294 – 300.
38. Jain, R. and Sharma, R. (2012). Cathodic adsorptive stripping voltammetry of an anti-emetic agent Granisetron in pharmaceutical formulation and biological matrix. *Journal of Pharmaceutical Analysis,* 2(6): 443 – 449.
39. Tavares., E. M., Carvalho, A. M., Gonçalves, L. M., Valente, I. M., Moreira, M. M., Guido, L. F., Rodrigues, J. A., Doneux, T. and Barros, A. A. (2013). Chemical sensing of chalcones by voltammetry: *trans*-Chalcone, cardamonin and xanthohumol. *Electrochimica Acta,* 90: 440 – 444.
40. Chaiyo, S., Chailapakul, O., Sakai, T., Teshima, N. and Siangproh, W. (2013). Highly sensitive determination of trace copper in food by adsorptive stripping voltammetry in the presence of 1,10-phenanthroline. *Talanta,* 108: 1 – 6.
41. De Lima, F., Gozzi, F., Fiorucci, A. R., Cardoso, C. A. L., Arruda, G. J. and Ferreira, V. S. (2011). Determination of linuron in water and vegetable samples using stripping voltammetry with carbon paste electrode. *Talanta,* 83: 1763 – 1768.
42. Geremedhin, W., Amare, M. and Admassie, S. (2013). Electrochemically pretreated glassy carbon electrode for electrochemical detection of fenitrothion in tap water and human urine. *Electrochimica Acta,* 87: 749 – 755.
43. Radi, A. E., Khafagy, A., El-Shobaky, A. and El-Mezayen, H. (2013). Anodic voltammetric determination of gemifloxacin using screen printed carbon nanotube. *Journal of Pharmaceutical Analysis,* 3(2): 132 – 136.
44. Sadeghi, S., Motaharian, A. and Moghaddam, A. Z. (2012). Electroanalytical determination of sulfasalazine in pharmaceutical and biological samples using molecularly imprinted polymer modified carbon paste electrode. *Sensors and Actuators B: Chemical,* 168: 336 – 344.
45. Yang, G., Chen, Y., Li, L. and Yang, Y. (2011). Direct electrochemical determination of morphine on a novel gold nanotube arrays electrode. *Clinica Chimica Acta,* 412: 1544 – 1549.
46. Salles, M. O., Naozuka, J. and Bertotti, M. (2012). A forensic study: Lead determination in gunshot residues. *Microchemical Journal,* 101: 49 – 53.
47. Skrzypek, S., Mirčeski, V., Ciesielski, W., Sokolowski, A. and Zakrzewski, R. (2007). Direct determination of metformin in urine by adsorptive catalytic square-wave voltammetry. *Journal of Pharmaceutical and Biomedical Analysis,* 45: 275 – 278.
48. Elqudaby, H. M., Mohamed, G. G., Ali, F. A. and Eid, S. M. (2011). Validated voltammetric method for the determination of some antiprotozoa drugs based on the reduction at an activated glassy carbon electrode. *Arabian Journal of Chemistry*, 6: 327 – 333.
49. Mohamed, D. and Tawakkol, S. N. (2013). Fluorimetric determination of diosmin and hesperidine in combined dosage forms and in plasma through complex formation with terbium. *Bulletin of Faculty of Pharmacy Cairo University,* 51: 81 – 88.
50. Baig, J. A., Kazi, T.G., Shah, A. Q., Kandhro, G. A., Afridi, H. I., Arain, M. B., Jamali, M. K. and Jalbani, N. (2010). Speciation and evaluation of Arsenic in surface water and groundwater samples: A multivariate case study. *Ecotoxicology and Environmental Safety,* 73: 914 – 923.

51. Bergamini, M. F., Santos, D. P. and Zanoni, M. V. B. (2010). Determination of isoniazid in human urine using screen printed carbon electrode modified with poly-$_L$-histidine. *Bioelectrochemistry,* 77: 133 – 138.
52. Radi, A. E., Mostafa, M. R., Hegazy, T. A. and Elshafey, R. M. (2012). Electrochemical study of vinylsulphone azo dye Reactive Black 5 and its determination at a glassy carbon electrode. *Journal of Analytical Chemistry,* 67: 890 – 894.
53. Rivera, M., Pazos, M. and Sanromán, M. Á. (2011). Development of an electrochemical cell for the removal of Reactive Black 5. *Desalination,* 274: 39 – 43.

Malaysian Journal of Analytical Sciences, Vol 20 No 6 (2016): 1269 - 1277
DOI: http://dx.doi.org/10.17576/mjas-2016-2006-05

MALAYSIAN JOURNAL OF ANALYTICAL SCIENCES
Published by The Malaysian Analytical Sciences Society
ISSN 1394 - 2506

IN-SILICO IDENTIFICATION OF POTENTIAL PROTEIN ARGININE DEIMINASE IV (PAD4) INHIBITORS

(Pengenalpastian *In-Silico* yang Berpotensi Sebagai Perencat Protin Arginina Deiminase IV (PAD4))

Zalikha Ibrahim[1,4], Bimo Ario Tejo[2], Muhammad Alif Mohammad Latif[1], Roghayeh Abedi Karjiban[1], Abu Bakar Salleh[3], Mohd Basyaruddin Abdul Rahman[1,3]*

[1]*Macromolecular Simulation Laboratory, Department of Chemistry, Faculty of Science, Universiti Putra Malaysia, 43400 UPM Serdang, Selangor, Malaysia*
[2]*Faculty of Applied Science, UCSI University, No. 1, Jalan Menara Gading, UCSI Heights, 56000 Cheras, Kuala Lumpur, Malaysia*
[3]*Enzyme Microbial and Technology (EMTech), Universiti Putra Malaysia, 43400 UPM Serdang, Selangor, Malaysia.*
[4]*Department of Pharmaceutical Chemistry, Kulliyyah of Pharmacy, International Islamic University Malaysia, Bandar Indera Mahkota Campus, 25200 Kuantan, Pahang, Malaysia*

**Corresponding author: basya@upm.edu.my*

Received: 17 August 2015; Accepted: 3 July 2016

Abstract

Protein Arginine Deiminase IV (PAD4) is a promising target for treating rheumatoid arthritis. Here, an *in-silico* screening was performed using PAD4 crystal structure against National Cancer Institute Diversity Set III compounds. Results obtained from the docking studies showed that the compounds have high affinity towards the protein. Visual inspections of the top compounds indicated that they preferred to bind at the front door of the catalytic pocket instead of the back door. The current results from this screening could provide a basis for the development of new PAD4 inhibitors.

Keywords: protein arginine deiminase IV, PAD4, virtual screening, NCI diversity set, structure-based

Abstrak

Protin arginina deiminase IV (PAD4) adalah sasaran yang berharapan untuk merawat artritis reumatoid. Di sini, satu saringan *in-silico* telah dilakukan menggunakan struktur kristal PAD4 terhadap molekul dari Set Beraneka Institut Kanser Nasional III. Keputusan dari pengdokan molekular menunjukkan molekul-molekul tersebut mempunyai daya tarikan yang tinggi terhadap protin. Pemeriksaan secara visual ke atas molekul teratas menunjukkan mereka mempunyai kecenderungan untuk terikat di pintu hadapan poket katalisis daripada di pintu belakang. Keputusan daripada pencarian ini boleh menjadi asas kepada penemuan perencat PAD4 yang baru.

Kata kunci: protin arginina deiminase IV, PAD4, pencarian maya, set beraneka NCI, struktur berasas

Introduction

Protein citrullination is a post-translational modification process, which converts peptidyl-bound arginine into peptidyl-bound citrulline (see Figure 1) [1]. This process is catalyzed by calcium-dependent enzyme called protein arginine deiminase (PAD) [2]. To date, there are five PAD isozymes reported, namely PAD1, PAD2, PAD3, PAD4 and PAD6, where each of them has specific expression place in human body [3]. Among all isozymes, PAD4 has

been linked to an inflammatory disease called rheumatoid arthritis [4]. Overexpression of PAD4 and citrullinated products was found to break the immune system tolerance and produce autoantibody responses against them, which consequently leads to the disease onset. Therefore, modulation of PAD4 activities is considered as an alternative therapeutic strategy against the disease.

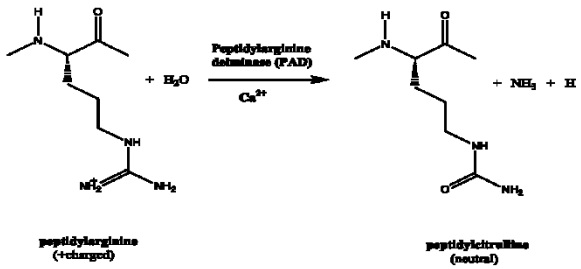


Figure 1. Citrullination process to convert peptidylarginine to peptidylcitrulline

Many researches have been conducted to design and discover PAD4 inhibitors. Based on the crystal structure of PAD4 in complex with small substrate, benzoyl-arginine amide [5], the citrullination process was catalyzed by four key residues, namely D350, H471, D473 and C645. These residues are arranged in a close proximity causing the overall shape of the pocket to be considerably narrow and deep. This significantly influenced PAD4 drug designs and studies were aimed at discovering an improved binding to one or more of the key residues [6-8]. Recent reports on PAD4 inhibitors [9] showed that the GSK199 and GSK147 compounds were binding the protein via another entrance of the catalytic pocket. The anchoring by residue N588 helps the GSK compounds to interact with H471 and distracts the protein activity. The knowledge about the entrance or the 'back door' has expanded the overall view of the pocket (see Figure 2).

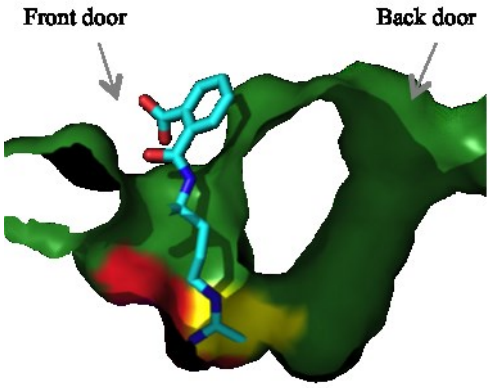


Figure 2. Two accessible doors of PAD4 catalytic pocket. Ligand such as *o*-F-amidine (rendered as blue stick) is bound at the front door. The main catalytic residue C645 is colored in yellow and H471 is colored in red.

Structure-based virtual screening (SBVS) has become an essential tool for drug pre-screening [10]. This approach is dependent on three-dimensional structures of target of interest i.e. protein, in which specific location on the protein can be aimed. The underlying concept in SBVS is the use of molecular docking algorithm to predict ligand poses corresponds to target of interest [11]. The method to evaluate the poses may include binding energies/affinities and reasonable binding interactions. SBVS has been applied in the previous PAD4 inhibitor screening [12]; however, the study was limited to exploring the PAD4 front door. Considering the potential of the PAD4 back door, it is

important that both doors should participate during the screening process. Here, we report SBVS performed using PAD4 crystal structure. The subjects of this study are from the National Cancer Institute Diversity Set 3 (NCIDS3), which is a compilation of pharmacophores with diverse skeleton and functional groups [13]. The poses of the compounds were predicted and evaluated computationally. It is hoped that the findings from this study can provide insight for searching and improvising PAD4 inhibitors.

Materials and Methods

Molecular docking

All molecular docking procedures were performed using AutoDock Vina program [14]. The crystal structure of PAD4 in complex with *o*-F-amidine inhibitors (PDB ID: 3B1U) [8] was used as receptor and control docking. Compounds from the previous PAD4 inhibitor screening report were used as reference compounds [15]. The NCIDS3 containing a total of 1880 ligands were downloaded in mol format from the ZINC database [16]. AutoDockTools version 1.5.6 [17] was used to add polar charges, assign Gasteiger charge [18] and prepare the input files.

Covalent docking protocol was applied exclusively for the control since the inhibitor was bound to PAD4 irreversibly [19-20]. This was achieved by docking a water molecule while setting the covalently bonded co-crystallized ligand, *o*-F-amidine to the thiol group of C645 as flexible residue. The volume of the grid box was 27 Å by 31 Å by 36 Å with a 1.0 Å spacing. The grid box was placed on the coordinate of -26.69, 14.74 and -28.8 centered on H640 to encompass both possible binding sites, namely the front door and the back door. The exhaustiveness was set to 8, while the number of run was set to 9. For the reference compounds and NCIDS3 ligands, conventional rigid protein and flexible ligand docking were performed while maintaining all the docking parameters.

In this work, the NCIDS3 ligands are referred to by their NCI index number (also known as the NSC number). For each ligand, the highest-affinity conformation of the docking result was selected as the docked pose for the ligand. The complexes were sorted by lowest binding affinity values. Complexes with predicted binding affinity equal to or less than -8.0 kcal/mol were filtered based on Lipinski's rule of 5 [21], here describes as: 1) molecular weight less than 500 g/mol, 2) number of hydrogen bond donor less than 5, 3) number of hydrogen bond acceptor less than 10 and 4) log P value less than 5. Only compounds that fulfilled all the criteria were further inspected. Analysis of the docking results was performed using AutoDock Vina shell script. The two-dimensional ligand structures were retrieved from chemicalize.org [22]. Analysis of binding interaction was performed using LigPlot^{+} [23]. Visualization and rendering routines for the docking complexes were done using Pymol version 1.4.1 [24].

Results and Discussion

Validation of docking parameters

The *o*-F-amidine ligand was redocked in consistent manner as seen in the crystal structure as shown in Figure 3. The all-atom RMSD of the predicted pose with respect to its crystallized pose was 1.06 Å. The main difference between the docked pose and the crystallized pose was observed at the benzene carboxylate group. The group was interacting with inconsistent hydrophobic contact. Autodock 4 [25] was also tested as alternative docking tool, however higher RMSD value was found as compared to the one obtained using Vina. The redocking was successful, indicating that dependability of AutoDock Vina in predicting ligand experimental pose.

In conventional virtual screening routine, the accuracy of any computational docking protocol is assessed using inhibitors with known activity against the target. It is a vital step in order to justify the current parameters used. Here in our case, we look forward to ensure that the protocol was suitable and reliable to distinguish and rank PAD4 inhibitors. To achieve the goal, a set of compounds with known PAD4 inhibitions (here labeled as S1 to S12) reported by Bozdag et al. was used [15].

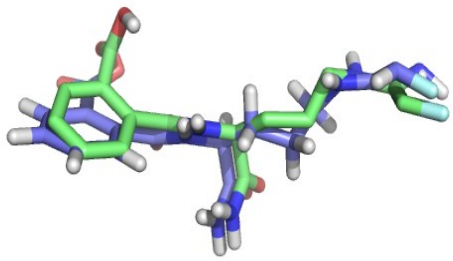


Figure 3. Redocking of *o*-F-amidine. The docked pose was rendered in green, while the crystallized structure was in purple

Table 1 showed the experimental inhibition, experimental rank, predicted binding affinity and predicted rank for compounds S1-S12. As can be seen from the table, it was obvious that Vina fairly predict the ranking of each compound. There was undoubted correlation between the compounds which having the high inhibition and its predicted binding affinity. Visual inspection of the docked poses showed that 11 out of 12 compounds have preference to bind at the front door; only compound S5 was seen to occupy the back door. Although the compounds with low inhibition were not in the exact rank, but it did pick the overall binding trend. Vina was able to distinguish between the high-ranked compounds (i.e. compound S11) and the low-ranked compounds (i.e. compound S4). These results suggested that predicted ranking reflect the experimental ranking with moderate degree of accuracy.

Table 1. Predicted binding affinity and ranks for compounds by Bozdag et al. [15]. The experimental inhibitions were listed for reference purposes.

Compound	% Inhibition at 10 µM	Experimental Rank	Predicted Binding affinity (kcal/mol)	Predicted Rank
S1	6	7	-5.7	7
S2	3	9	-6.0	6
S3	5	8	-6.2	5
S4	1	10	-5.2	8
S5	7	6	-6.0	6
S6	5	8	-4.8	9
S7	3	9	-6.2	5
S8	8	5	-6.8	4
S9	10	3	-6.9	3
S10	34	2	-7.3	2
S11	36	1	-7.4	1
S12	9	4	-5.5	8

Structure-based virtual screening of NCIDS3

It is interesting to observe that ligands from NCIDS3 are in similar predicted binding affinity window as the known PAD4 inhibitors [15]. The plot of number of ligands with respect to their binding affinity range as shown in Figure 4 followed a bell-shaped trend, with majority population lies within the range of -6.0 kcal/mol. In prior to this study, focus was given to compounds that were predicted to have binding affinity equal to or less than -8.0 kcal/mol. This cut-off criterion of -8.0 kcal/mol was imposed as the first filter to yield compounds with predicted binding affinity lower than the predicted binding affinity of the known PAD4 inhibitors (see Table 1) [15]. Even though this NCIDS3 screening have not yet been validated experimentally, the work here is promising, given that half of the shortlisted compounds were predicted to be binding the protein via similar interacting residues with that seen in the crystal structure [8]. All shortlisted compounds were observed to dock at the traditional front door area instead of the back door. The top 11 compounds together with their predicted binding affinity were listed in Table 2.

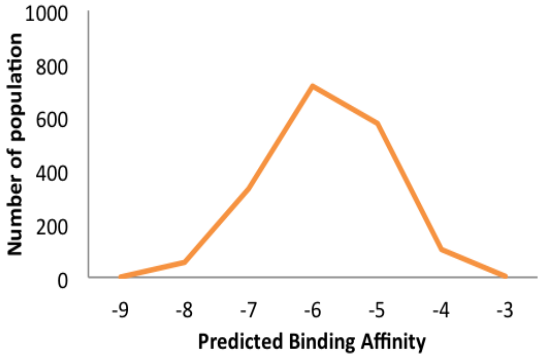


Figure 4. Binding affinities distribution of all NCIDS3 compounds towards PAD4 crystal structure (PDB ID: 3B1U)

Table 2. List of potential PAD4 inhibitors

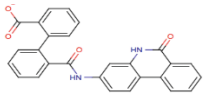
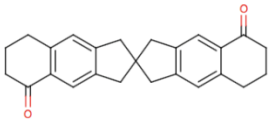
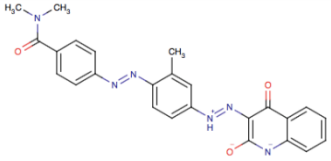
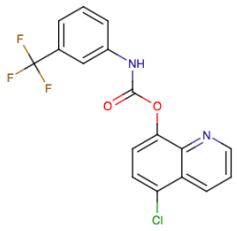
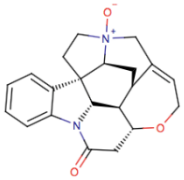
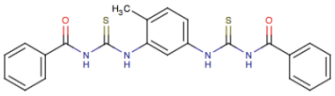
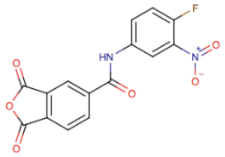
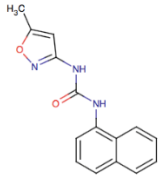
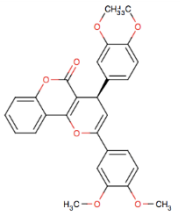
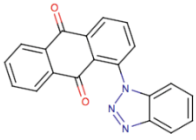
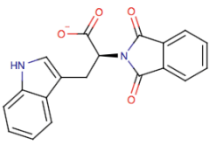
Number	NSC number	Structure	Predicted Binding Affinity (kcal/mol)
1	127133		-8.8
2	670283		-8.6
3	58052		-8.4

Table 2 (cont.). List of potential PAD4 inhibitors

Number	NSC number	Structure	Predicted Binding Affinity (kcal/mol)
4	377852		-8.4
5	24951		-8.3
6	5856		-8.2
7	215629		-8.2
8	203837		-8.1
9	211490		-8.1
10	80313		-8.0
11	401077		-8.0

The ligands were found to linger around the front door region. None of the compounds were able to approach the main catalytic residue C645, possibly because of ring skeleton possesses by each compound. An example of the docked poses was depicted in Figure 5a. There was no specific trend in the type of ligand; but it was observed that each of them contains carbonyl group to assist interactions. For example, Compound 6. As can be seen in Figure 5b, Compound 6 made four hydrogen bonds and six hydrophobic contacts at the front door region. The first two hydrogen bonds were formed between the indole nitrogen of W347 and guanidinium nitrogen of R374 with the carbonyl group of Compound 6. The third hydrogen bond was established between the carbonyl group of R639 backbone and nitrogen atom of Compound 6. Another hydrogen bond was formed between the hydroxyl group of S468 and nitrogen atom of Compound 6. The compound also formed non-hydrogen-bonding interactions with G403, S406, V469, L578 and H640.

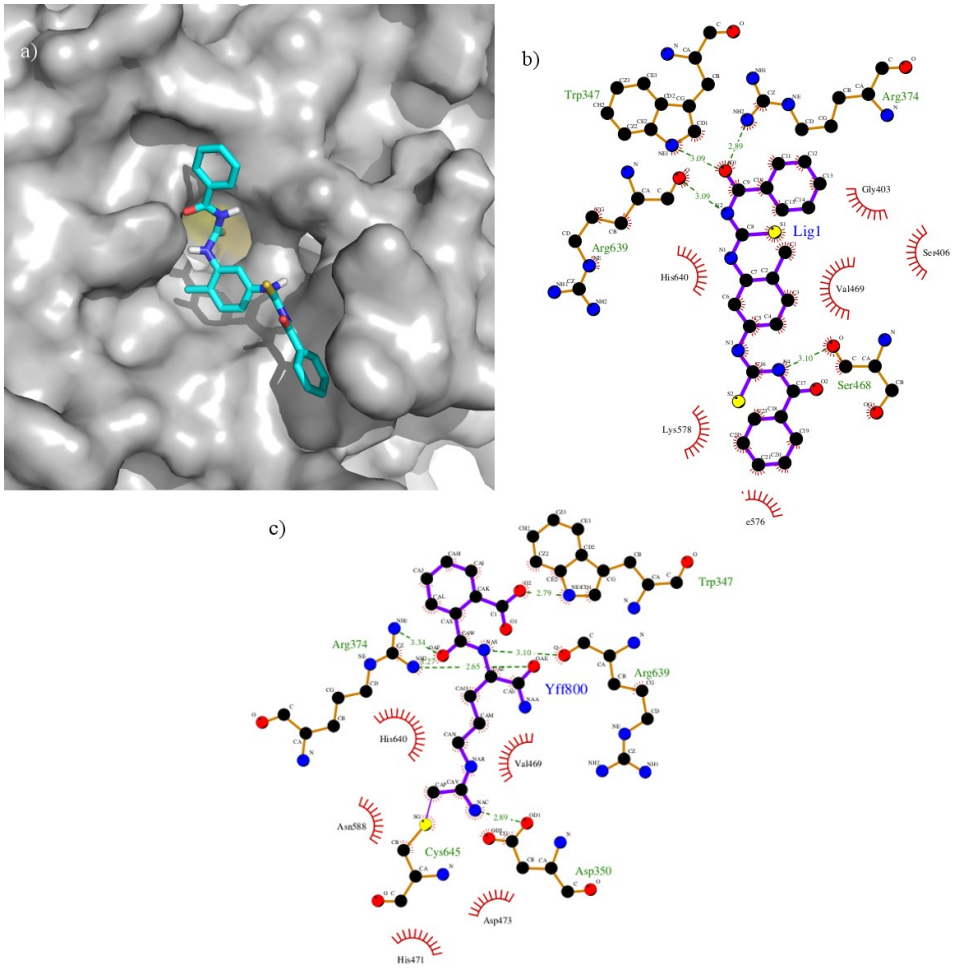


Figure 5. a) Docked pose of Compound 6 (rendered in cyan stick). PAD4 was shown as grey surface. C645 was colored in yellow. Other parts of the protein were discarded for visualization purpose, b) Interaction between PAD4 and Compound 6, c) Interaction of PAD in complex with *o*-F-amidine as reference [8].

Although Compound 6 did not interact with the main catalytic residue, C645, it interacted with important residues at the mouth of the pocket such as R374 and W347. Such interactions were also seen in PAD4-substrate/inhibitor complexes, as illustrated in Figure 5c. Arginine has high tendency to facilitate hydrogen bonds, since it is possible for the guanidinium side chain to donate five hydrogen bonds. Previous mutagenesis study revealed that the residue

R374 was important in PAD4 substrate recognition [26]. The role of W347 was also been studied [8,26]. Located at the line of the active site, the residue was observed to assist interaction via its indole nitrogen. Based on the above information, it is anticipated that the shortlisted compounds in theory would interfere with the binding of substrate to the catalytic residues. Undoubtedly, these compounds will need further optimization because of their current binding interaction. For improved binding, elongation of the compounds towards the active site tunnel may be required.

It is noticeable that the shortlisted compounds preferred to occupy the front door rather than the back door. This may be due to the use of bound front door protein structure. Since the back door did not contain any ligand, the shape of this entrance was not visibly made to occupy a ligand. To exclude the bias, it is suggested to use multiple protein structures to accommodate binding site dynamics in future screening.

Conclusion

SBVS has been successfully performed on PAD4 crystal structure using ligands from NCIDS3. This work indicates that NCIDS3 could serve as a good dataset for searching potential PAD4 inhibitors. All shortlisted compounds have preference to occupy the front door with good binding affinities. The compounds are ready to be tested experimentally. It may not be adequate to use only single protein structure in virtual screening, as binding site dynamics is unattainable. Future works suggested include flexible protein-flexible ligand docking and ensemble-based virtual screening.

Acknowledgement

This work was supported by Exploratory Research Grant Scheme (ERGS/1-2013/5527108) under Ministry of Education (MOE), Malaysia. Zalikha Ibrahim acknowledges International Islamic University Malaysia (IIUM) and Ministry of Higher Education (KPT) for her study leave and fellowship.

References

1. van Venrooij, W. J. and Pruijn, G. J. M. (2000). Citrullination: a small change for a protein with great consequences for rheumatoid arthritis. *Arthritis Research*, 2: 249 – 251.
2. Jones, J., Causey, C., Knuckley, B., Slack-Noyes, J. L. and Thompson, P. R. (2009). Protein arginine deiminase 4 (PAD4): Current understanding and future therapeutic potential. *Current Opinion in Drug Discovery and Development*, 12(5): 616 – 627.
3. Vossenaar, E. R., Zendman, A. J., van Venrooij, W. J. and Pruijn, G. J. (2003). PAD, a growing family of citrullinating enzymes: Genes, features and involvement in disease. *BioEssays*, 25(11): 1106 – 1118.
4. van Boekel, M. A. Vossenaar, E. R., van den Hoogen, F. H. and van Venrooij, W. J. (2002). Autoantibody systems in rheumatoid arthritis: Specificity, sensitivity and diagnostic value. *Arthritis Research*, 4(2): 1 –7.
5. Arita, K., Hashimoto, H., Shimizu, T., Nakashima, K., Yamada, M. and Sato, M. S. (2004). Structural basis for $Ca(^{2+})$-induced activation of human PAD4. *Nature Structure Molecular Biology*, 11(8): 777 – 783.
6. Luo, Y., Knuckley, B., Lee, Y. H., Stallcup, M. R. and Thompson P. R. (2006). A fluoroacetamidine-based inactivator of protein arginine deiminase 4: design, synthesis, and in vitro and in vivo evaluation. *Journal of the American Chemical Society*, 128(4): 1092 – 1093.
7. Luo, Y., Arita, K., Bhatia, M., Knuckley, B., Lee, Y. H., Stallcup, M. R. and Thompson P. R. (2006). Inhibitors and Inactivators of Protein Arginine Deiminase 4: Functional and Structural Characterization. *Biochemistry*, 45(39): 11727 – 11736.
8. Causey, C. P., Jones, J. E., Slack, J. L., Kamei, D., Jones, L. E., Subramanian, V., Knuckley, B., Ebrahimi, P., Chumanevich, A. A., Luo, Y., Hashimoto, H., Sato, M., Hofseth, L. J. and Thompson, P. R. (2011). The development of *N*-*α*-(2-carboxyl)benzoyl-*N*-5-(2-fluoro-1-iminoethyl)-$_L$-ornithine amide (*o*-F-amidine) and *N*-*α*-(2-carboxyl)benzoyl-*N*-5-(2-chloro-1-iminoethyl)-$_L$-ornithine amide (*o*-Cl-amidine) as second generation protein arginine deiminase (PAD) inhibit. *Journal of Medicinal Chemistry*, 54(19): 6919 – 6935.
9. Lewis, H. D., Liddle, J., Coote, J. E., Atkinson, S. J., Barker, M. D., Bax, B. D., Bicker, K. L., Bingham, R. P., Campbell, M., Chen, Y. H., Chung, C. W., Craggs, P. D., Davis, R. P., Eberhard, D., Joberty, G., Lind, K. E., Locke, K., Maller, C., Martinod, K., Patten, C., Polyakova, O., Rise, C. E., Rudiger, M., Sheppard, R. J., Slade, D. J., Thomas, P., Thorpe, J., Yao, G., Drewes, G., Wagner, D. D., Thompson, P. R., Prinjha, R. K. and Wilson,

D. M. (2015). Inhibition of PAD4 activity is sufficient to disrupt mouse and human NET formation. *Nature Chemical Biology*, 11(3): 189 – 191.
10. Kalyaanamoorthy, S. and Chen, Y. P. P. (2011). Structure-based drug design to augment hit discovery. *Drug Discovery Today*, 16(17-18): 831 – 839.
11. Kubinyi, H. (1998). Structure-based design of enzyme inhibitors and receptor ligands. *Current Opinion. Drug Discovery and Development*, 1(1): 4 – 15.
12. Teo, C. Y., Shave, S., Chor, A. L. T., Salleh, A. B., Rahman, M. B. B. A., Walkinshaw, M. D., and Tejo, B. A. (2012). Discovery of a new class of inhibitors for the protein arginine deiminase type 4 (PAD4) by structure-based virtual screening. *BMC bioinformatics*, 13(Supplementary 17): S4.
13. National Cancer Institute Diversity Set III (NCIDS3). Access online from *https://dtp.cancer.gov*
14. Trott, O. and Olson, A. J. (2010). AutoDock Vina: improving the speed and accuracy of docking with a new scoring function, efficient optimization, and multithreading. *Journal of Computational Chemistry*, 31(2): 455 – 461.
15. Bozdag, M., Dreker, T., Henry, C., Tosco, P., Vallaro, M., Fruttero, R., Scozzafava, A., Carta, F. and Supuran, C. T. (2013). Novel small molecule protein arginine deiminase 4 (PAD4) inhibitors. *Bioorganic and Medicinal Chemistry Letters*, 23(3): 715 – 719.
16. Irwin, J. J. and Shoichet, B. K. (2004). ZINC- a free database of commercially available compounds for virtual screening. *Journal of Chemical Information and Modeling*, 45(1): 177 – 182.
17. Sanner, M. F. (1999). Python: a programming language for software integration and development. *Journal of Molecular Graphics & Modelling*, 17(1): 57 – 61.
18. Gasteiger, J. and Marsili, M. (1980). Iterative partial equalization of orbital electronegativity - a rapid access to atomic charges. *Tetrahedron*, 36(22): 3219 – 3228.
19. Morris, G. M., Huey, R., Lindstrom, W., Sanner, M. F., Belew, R. K., Goodsell, D. S., and Olson, A. J. (2009). AutoDock4 and AutoDockTools4: Automated docking with selective receptor flexibility. *Journal of Computational Chemistry*, 30(16): 2785 – 2791.
20. Ortar, G., Morera, E., De Petrocellis, L., Ligresti, A., Moriello, A.S., Morera, L., Nalli, M., Ragno, R., Pirolli, A. and Di Marzo, V. (2013). Biaryl tetrazolyl ureas as inhibitors of endocannabinoid metabolism: modulation at the N-portion and distal phenyl ring. *European Journal of Medicinal Chemistry*, 63: 118 –132.
21. Lipinski, C. A., Lombardo, F., Dominy, B.W. and Feeney, P. J. (2001). Experimental and computational approaches to estimate solubility and permeability in drug discovery and development settings. *Advanced Drug Delivery Reviews*, 46(1): 3 – 26.
22. Instant Cheminformatics Solution (2015). Access online from *www.chemicalize.org* (accessed on June 2015).
23. Laskowski, R. A. and Swindells, M. B. (2011). LigPlot^{+}: Multiple ligand–protein interaction diagrams for drug discovery. *Journal of Chemical Information and Modeling*, 51(10): 2778 – 2786.
24. DeLano, W. L. (2002). The PyMOL Molecular Graphics System.
25. Morris, G. M., Goodsell, D. S., Halliday, R. S., Huey, R., Hart, W. E., Belew, R. K. and Olson, A. J. (1998). Automated docking using a Lamarckian genetic algorithm and an empirical binding free energy function. *Journal of Computational Chemistry*, 19(14): 1639 – 1662.
26. Arita, K., Shimizu, T., Hashimoto, H., Hidaka, Y., Yamada, M. and Sato, M. (2006). Structural basis for histone N-terminal recognition by human peptidylarginine deiminase 4. *Proceedings of the National Academy of Sciences*, 103(14): 5291 – 5296.

Malaysian Journal of Analytical Sciences, Vol 20 No 6 (2016): 1278 - 1285
DOI: http://dx.doi.org/10.17576/mjas-2016-2006-06

MALAYSIAN JOURNAL OF ANALYTICAL SCIENCES
Published by The Malaysian Analytical Sciences Society
ISSN 1394 - 2506

SYNTHESIS AND PHYSICOCHEMICAL CHARACTERIZATION OF CATIONIC POLYMERIC SURFACTANT FROM *Dioscorea pyrifolia* STARCH

(Sintesis dan Pencirian Fizikokimia Surfaktan Polimer Kationik daripada Kanji *Dioscorea pyrifolia*)

Elmi Sharlina Md. Suhaimi, Wan Yaacob Wan Ahmad*, Azwan Mat Lazim

School of Chemical Sciences and Food Technology, Faculty of Science and Technology
Universiti Kebangsaan Malaysia, 43600 UKM Bangi, Selangor, Malaysia

**Corresponding author: wanyaa@ukm.edu.my*

Received: 21 April 2016; Accepted: 3 October 2016

Abstract

Cationic starch-based polymeric surfactant, 2-hydroxy-3-(N,N,N-trimethylammonium)propyloxy starch (S-ETAC) from *Dioscorea pyrifolia* tubers, was synthesized by etherification using 2,3-epoxytrimethylammonium chloride (ETAC) in the mass ratio of ETAC/starch (St) of 0.15:1, 0.25:1, 0.5:1, 1:1, 2:1 g/g and sodium hydroxide as a catalyst in aqueous medium. The degree of substitution (DS) and reaction efficiency (RE) were calculated using the percentage of nitrogen derived from the elemental analysis. The study found that the more the ETAC used, the higher the DS (0:11 to 0.76), but the RE decreased (69% to 35%). This S-ETAC was characterized by using the solubility and swelling power tests as well as attenuated total reflectance - Fourier transform infra-red (ATR - FTIR) spectroscopy, differential scanning calorimetry (DSC) and X-ray diffraction (XRD) to prove the reaction occurs at the starch structure.

Keywords: cationic starch, etherification, *Dioscorea pyrifolia*

Abstrak

Surfaktan polimer berasaskan kanji kationik, kanji 2-hidroksi-3-(N,N,N-trimetilammonium)propiloksi (S-ETAC) dari ubi *Dioscorea pyrifolia*, telah disintesis melalui tindak balas pengeteran menggunakan 2,3-epoksitrimetilammonium klorida (ETAC) dalam nisbah jisim ETAC/kanji (St) 0.15: 1, 0.25: 1, 0.5: 1, 1: 1, 2: 1 g/g dan natrium hidroksida sebagai pemangkin dalam medium akueus. Darjah penukargantian (DS) dan kecekapan tindak balas (RE) telah dikira menggunakan peratusan nitrogen yang diperolehi daripada penganalisis unsur. Kajian ini mendapati bahawa lebih banyak ETAC yang digunakan, semakin tinggi DS (0.11 kepada 0.76), tetapi RE menurun (69% kepada 35%). S-ETAC dicirikan dengan menggunakan ujian keterlarutan dan kuasa pembengkakkan serta spektroskopi transformasi Fourier inframerah - jumlah pantulan teratenuat (FTIR - ATR), kalorimetri pengimbas pembezaan (DSC) dan pembelauan sinar-X (XRD) untuk membuktikan bahawa tindak balas berlaku pada struktur kanji.

Kata kunci: kanji kationik, pengeteran, *Dioscorea pyrifolia*

Introduction

Starch modification is an alternative industry nowadays to meet the growing demand, reduce the cost of raw materials and reduce environmental pollution. The usage of native starch is usually limited due to its physicochemical properties that are not water-soluble and tend to form a non-stable emulsion. Thus, starch modification via physical, chemical or biological is used to increase the functionality that able to expand into to industrial use and has better features in terms of functional group and solubility [1]. Chemically modified starch

typically involves esterification, etherification or oxidation of hydroxyl groups on the α-D-glucopyranosyl of the starch structure. Most of the commercialized starches produced by adding reactants and organic solvents to the starch solution at control pH 7-9 for esterification [2] and pH 11-12 for etherification at temperatures above 60 °C [2, 3].

Cationic starches from sources such as corn, tapioca, wheat and potato have been widely used in the production of paper, textiles, cosmetics and treatment of waste water because they can improve the properties of surface, viscosity, retention performance and change the properties of colloids [2]. Cationic starches commonly used in most products which contained 0.1 – 0.4% nitrogen (< 0.05 DS) [2]. In previous studies, modified corn starch used quaternary ammonium group and dioxane-water-THF as the medium to produce cationic starch with DS 1.37 [3]. Reaction of corn starch with quaternary ammonium in the ionic liquid produced cationic starch with DS of 0.99 [1]. Homogenous reaction conditions using medium DMSO can increase the DS compared to heterogeneous reaction condition in ethanol/water medium [4]. Although there are several ways of obtaining cationic starches with high DS, the use of harmful solvents, difficult in purification process and high cost of solvents limits the production of the cationic starches. Conventional methods which use a lot of organic solvents are not only reduce the DS but also increase pollution to the environment [1].

Dioscorea pyrifolia is a monocot plants possess edible tubers, grown and sold in markets at east coast states of Malaysia [5]. The tubers are called "Ubi Itik" among the people in these states. Although cationic starches from sources as corn, tapioca, wheat and potato is an important product in the industry [2], the preparation and properties of cationic starch from *Dioscorea pyrifolia* tubers are not been reported yet. The information on the modified starch from this plant is still limited to the industry. In this study, a cationic starch-based surfactant from *Dioscorea pyrifolia* tubers is synthesized through etherification of ETAC and aqueous NaOH as a catalyst (Figure 1) using semi-dry method. The effect of the increasing ETAC in the NaOH/water medium was investigated with the calculation of the degree of substitution (DS) and reaction efficiency (RE) using percentage of nitrogen obtained from elemental analyzer. Then, the S-ETAC is characterized to ensure that the reaction occurs in the structure of the starch.

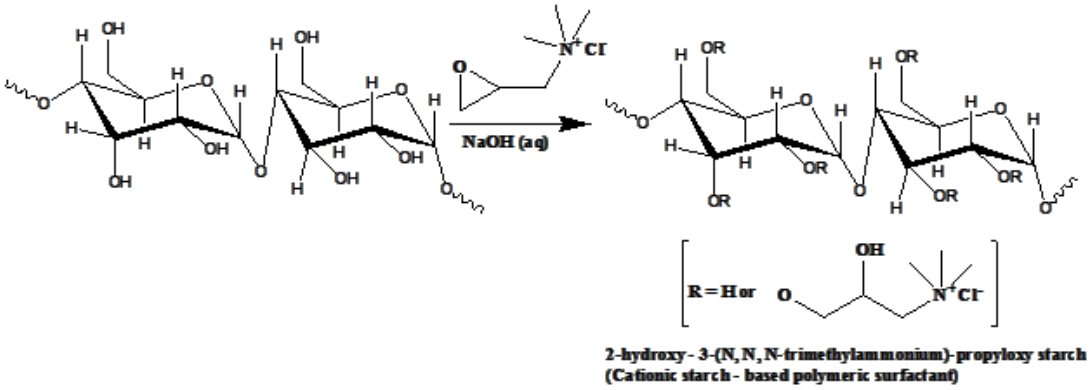


Figure 1. Synthesis of cationic starch-based polymeric surfactant

Materials and Methods

Materials

Starch was extracted from *Dioscorea pyrifolia* tubers taken in Kelantan, Malaysia. Chemicals used in this study are 2,3-epoxytrimethylammonium chloride (Sigma-Aldrich, >90%, technical grade), sodium hydroxide (R & M Chemical, 95%), ethanol (R & M Chemical, 95%, analytical grade) and acetone (EMSURE, 99.5%, analytical grade). Sodium hydroxide solution was prepared using deionized water.

Synthesis of cationic starch-based surfactant

The cationic starch-based polymeric surfactant was prepared by semi-dry process in a series of mass ratio ETAC:St starting with 0.15:1, and varying the masses of ETAC to 0.25, 0.5, 1 and 2 in 4 mL of 0.1 g/mL NaOH solution. The process was initiated by putting 1.5 g ETAC in a beaker containing the NaOH solution and stirred for 5 minutes. Then 10 g of starch incorporated into the solution and stirred, resulting in dough. It was heated in a water bath at 80 °C for 2 hours, and 4 mL water was added into the beaker to stop the reaction. Ethanol (5 mL) was added to the beaker and stirred to wash away the unreacted reagents. Next, acetone (10 mL) was added into the beaker so that the S-ETAC precipitates. The S-ETAC was rinsed three times with ethanol before dried in an oven at 50 ^{o}C. This S-ETAC was pulverized and sieved (600 µm pore size). This method has been reported by Lin et al. [6] with slight modifications.

Degree of substitution and reaction efficiency

The DS value is important to know the average number of ETAC replacement into the anhydrous glucose unit (AGU) of the starch structure. The actual and theoretical DS and RE (%) of the reaction were calculated by the percentage of nitrogen derived from the elemental analysis (Thermo-Finnigan, EA 1112 CHNS Analyzer series, Italy) using equations (1), (2), and (3), respectively:

$$\text{Actual DS} = \frac{(162.15 \text{ x N})}{(1401 - 151.64 \text{ x N})} \quad (1)$$

$$\text{Theoretical DS} = \frac{\text{W1}/151.64}{\text{W2}/162.15} \quad (2)$$

$$\text{RE (\%)} = \frac{\text{Actual DS}}{\text{Theoretical DS}} \text{ x } 100 \quad (3)$$

where N is the percentage of the nitrogen determined by elemental analysis, the 162.15 is the molar mass of anhydrous glucose units (AGU) in the starch, the molar mass of 151.64 is hydroxypropyltrimethylammonium chloride, 1401 is 100 times the mass of the nitrogen atom, W1 and W2 are the masses of ETAC and starch used [6, 7].

Solubility and swelling power

Native starch and S-ETAC incorporated into the different vials contained distilled water (1% w/v) and stirred for 30 minutes at room temperature before being cooled/heated at different temperatures (25, 35, 45, 55, 65, 75, 85 and 95 °C) for 1 hour. The starch slurry was cooled to room temperature, poured in a centrifuge tube and centrifuged at 3000 rpm for 15 minutes. The supernatant was gently put into a vial and dried in an oven at 110 ^{o}C. Wet starch in the centrifuge tube was weighed before dried. Different starch slurry was used for each different temperature and analysis carried out in triplicate [8]. Solubility and swelling power were calculated using equations (4) and (5), respectively.

$$\text{Solubility (\%)} = \frac{\text{mass of dry supernatant}}{\text{mass of dry starch}} \text{ x } 100 \quad (4)$$

$$\text{Swelling power (g/g)} = \frac{\text{mass of wet starch}}{\text{mass of dry starch} - \text{mass of dry supernatant}} \quad (5)$$

Fourier transform infrared analysis

S-ETAC and native starch (30 mg) were determined using a Fourier Transform Infra-Red – Attenuated Total Reflectance (FTIR-ATR Spectra 2000 Perkin Elmer) at 4000 to 650 cm^{-1} at spectral resolution of 4 cm^{-1} [6].

Differential scanning calorimetry

Differential Scanning Calorimetry (DSC 822 Mettler Toledo) was used to measure the gelatinization temperatures and enthalpies of the native starch and S-ETAC. DSC was calibrated with indium and empty aluminum pan was used as blank. Slurry of starch and water in a mass ratio of 1: 3 was placed in aluminum pan, sealed and let for 1

hour. Then the aluminum pan containing the sample was heated from 25 to 100 °C at a heating rate of 10 °C/min [9].

X-ray diffraction

The degree of crystallinity of starch and S-ETAC can be determined using X-ray diffraction (Bruker D8 Advance). The samples were put in special containers and diffraction patterns recorded in a reflection 5 – 80° (2θ) at room temperature, operating at 40 kV and 40 mA with Cu Kα radiation, k = 0.5406 nm [1, 10].

Results and Discussion

Degree of substitution and reaction efficiency

The actual DS (0.11, 0.16, 0.30, 0.48 and 0.76) in this study was increased as the mass ratio of ETAC:St increases (0.15:1, 0.25:1, 0.5:1, 1:1, 2:1), compared with theoretical DS (0.16, 0.27, 0.53, 1.07 and 2.14) (Figure 2 (a)). The percentage of RE decreases with the increasing amounts of ETAC by, 69, 59, 56, 45 and 35 % (Figure 2 (b)). The results show that the more the amounts ETAC added, the lower the RE (%) of the reactions. Kavaliauskaite et al. [11] produced a cationic starch having a DS of 0.2 to 0.85 using different ratios of reactant and different conditions at a temperature of 45°C for 24 to 48 hours. Wang et al. [3] also produced cationic starches with DS 0.27 to 1.37 using dioxane-tetrahydrofuran-water as the reaction medium at 60 °C for 4 – 8 hours. Wang and Xie [1] produced a cationic starch having a DS 0.19 to 0.99 using ionic liquid as the reaction medium at 70 °C for 24-72 hours. Lin et al. [6] also produced cationic starches with DS between 0.13 and 0.26 at 80 °C for 2 hours from waxy maize starch. All of the above studies using different starches, ETAC, NaOH ratios and different solvents. The findings of this study will give information about the reaction to produce a cationic starch using faster and more environmentally friendly method because it does not use organic solvents as well as the yield is easily purified.

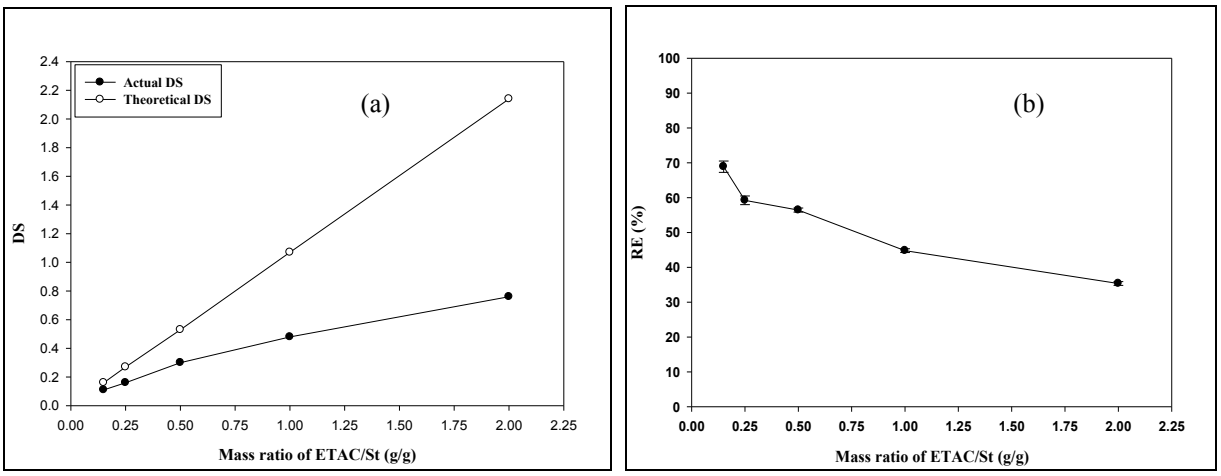


Figure 2. (a) Actual and theoretical DS and (b) RE (%) of S-ETAC at difference mass ratio of ETAC/St (g/g)

Solubility and swelling power

Solubility and swelling power of starch and S-ETAC are shown in Figure 3. Solubility of native starch and S-ETAC increased as temperature increased (Figure 3 (a)) but solubility S-ETAC increased dramatically at temperatures above 75 ^{o}C. This means that the reaction of starch and ETAC molecules produced will increase solubility of S-ETAC in water from 43.5 to 109.7% compared to the native starch. Modification of the structure of starch causes steric hindrance and repulsion between starch molecules, thereby facilitating the absorption of water in the crystalline regions in the starch granules [6]. Swelling power of native starch and S-ETAC also increase as the temperature increases (Figure 3 (b)). Swelling power increases because of the repulsion of the starch molecules cause water to penetrate into the S-ETAC molecules thus increased the swelling power between 124 and 548% compared to the native starch. Lin et al. [6] produces the cationic starch (using dry methods) that have higher

swelling power than the native starch but the solubility index is lower than the native starch. In this study, solubility and swelling power of the cationic starch are higher than the native starch. This may be caused by the gelatinization occurs during the reaction (using a semi-dry method) which causes the cationic starch produced is more soluble than the native starch.

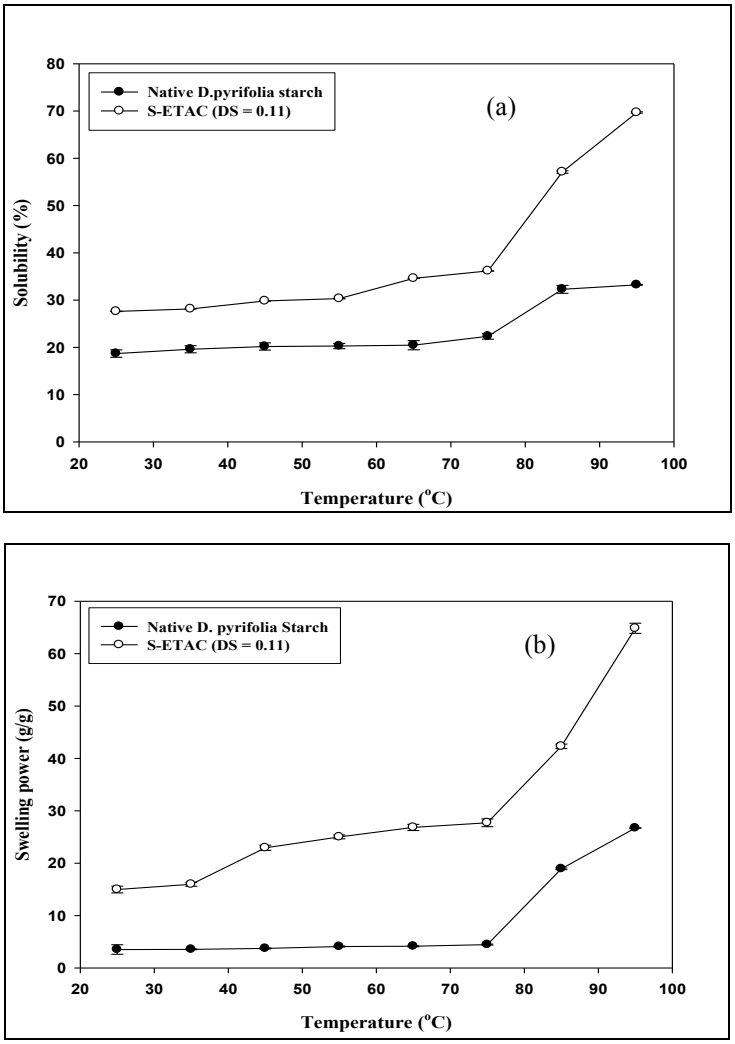


Figure 3. (a) Solubility (%) and (b) swelling power (g/g) of native starch and S-ETAC

Fourier transform infrared analysis (FTIR)

Figure 4 shows FTIR spectra of the native starch and S-ETAC. Infrared profile shows not much difference between the two spectra. Starch backbone shows at 3294 (-OH stretching), 2928 (-CH stretching), 1149, 1078, 996 (C-O stretching), 1363 (C-H deformation) and 1642 cm^{-1} (major peak of starch). The highlight of the S-ETAC at 855 cm^{-1} (-CN deformation) and 1483 cm^{-1} (C-N stretching) proved that the ETAC structure is bonded on the structure of starch. This finding is similar to findings reported by Wang and Xie [1], Wang et al. [3], and Lin et al. [6].

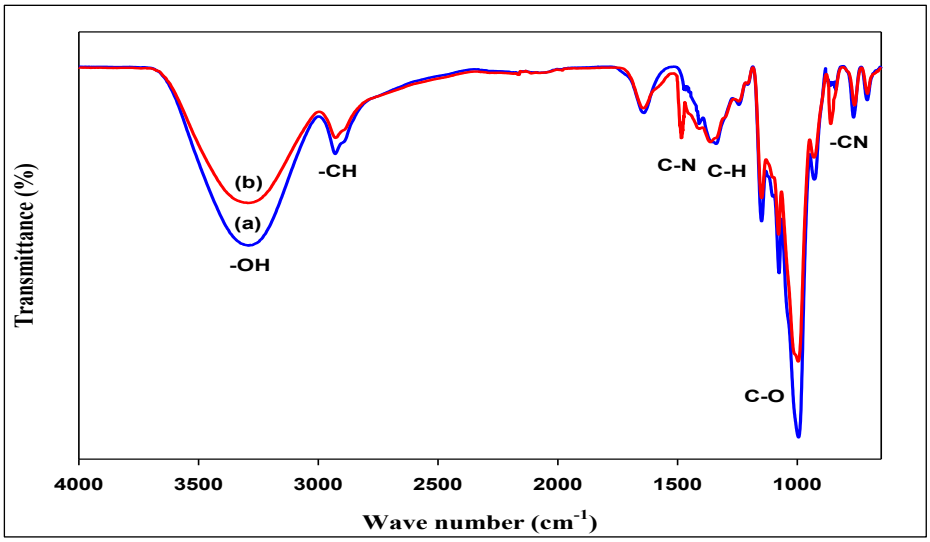


Figure 4. FTIR spectra of (a) native starch and (b) S-ETAC (DS = 0.11)

Differential scanning calorimetry (DSC)

Figure 5 shows the DSC termogram for the native starch and S-ETAC. Gelatinization temperature of native starch was at 71 ^{o}C (onset temperature), 75 ^{o}C (peak temperature) and 78 ^{o}C (conclusion temperature) (Figure 5 (a)), while gelatinization endotherm was not detected in the S-ETAC (Figure 5 (b)). The reaction between the starch and ETAC makes the gelatinization temperature of S-ETAC cannot be determined. This finding is similar to that previous study reported in Zhang et al. [12] using cationic acetylcholine groups as reagent for etherification of potato starch. The interaction between starch and ETAC will loosen starch structure causing starch molecules more easily absorb water during heating. The starch heating at high temperature of 80 °C caused the water to enter the starch granules so hydrogen bonds within and outside of the starch molecules are disrupted and swell. At high temperature, starch crystallites become unstable and disordered due to thermal motion and swelling force. Next, water will fully enter into starch crystallites region and breaks up the order of starch crystallites. The order of starch crystallites will destroy and turned into amorphous form. Thus, gelatinization temperature disappeared. These results confirmed by the X-ray diffraction analysis.

X-ray diffraction (XRD)

X-Ray diffraction patterns of the native starch (a) and S-ETAC (b) shown in Figure 6 are used to determine the changes of crystalline structure. Native starch showed crystallization of type-C pattern, while the diffraction pattern of S-ETAC changed to single broad peak with reduced intensity. This is due to starch crystallites region partly destroyed and converted into amorphous form after etherification of native starch with ETAC molecules. The amorphous properties from XRD pattern have been previously discussed by Wang et al. [3] and Zhang et al. [12]. The loss of crystallites region is caused by alkaline environment and water during etherification of starch. Therefore, these cationic starches have potential as flocculants because the presence of amorphous and solubility properties are important in practical point of view to improve its ability to form a colloidal or solution in cold water especially in waste water treatment plant [3]. It also has potential as additive to increase the viscosity of colloidal emulsion.

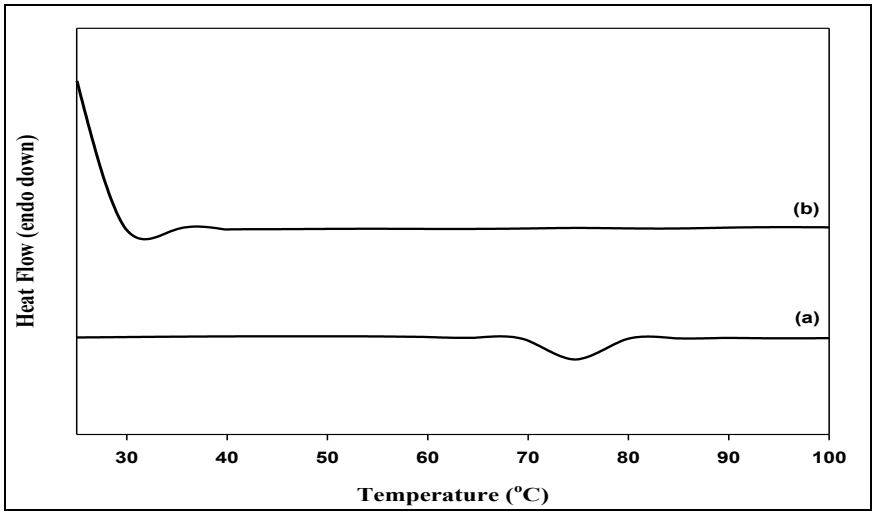


Figure 5. DSC termogram of (a) native starch and (b) S-ETAC (DS = 0.11)

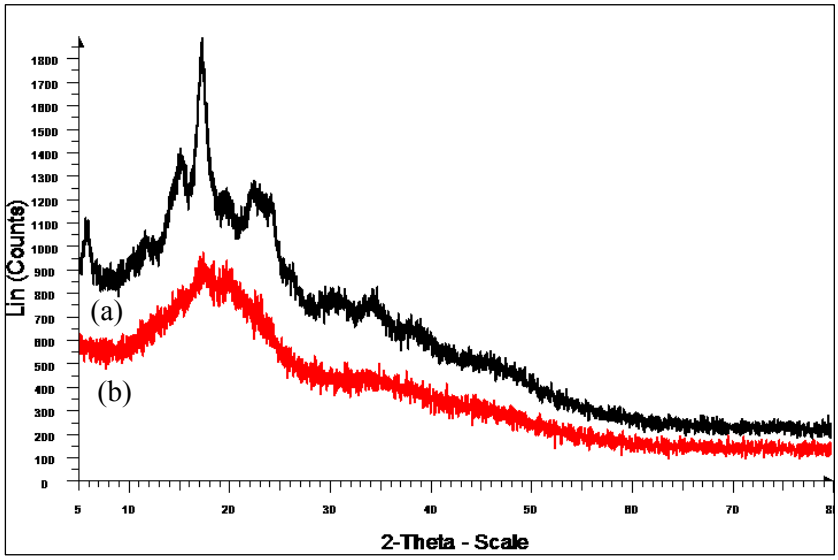


Figure 6. XRD patterns of (a) native starch and (b) S-ETAC (DS = 0.11).

Conclusion

Cationic starch-based polymeric surfactant (S-ETAC) from *Dioscorea pyrifolia* starch tubers has been successfully synthesized in a series of mass ratio ETAC:St at a temperature of 80 °C for 2 hours and the optimum reaction is in ratio of 0.15:1, which has a DS 0.11 and RE 68%. S-ETAC was characterized using the solubility and swelling power tests as well as analyses of ATR-FTIR, DSC and XRD. The results showed that the S-ETAC produced has a solubility and swelling power better than the native starch. The S-ETAC was high in solubility and swelling power in water. Preparation of S-ETAC is also more environmentally friendly, inexpensive and can be produced on a large scale. Further study is to characterize surface properties of S-ETAC to replace petroleum-based surfactant of similar character.

Acknowledgement

The authors wish to thank the Ministry of Higher Education (MOHE) Malaysia, Ministry of Education (MOE) Malaysia, Universiti Kebangsaan Malaysia (UKM) and Centre for Research and Instrumentation Management (CRIM) for providing research grants FRGS/1/2014/ST01/UKM/03/1, DLP-2014-019, GUP-2014-079, GUP-2016-014, KOMUNITI-2014-010 and PRGS/1/2014/TK04/UKM/03/1 to support this study and Hadiah Latihan Persekutuan (HLP) scholarship for Elmi Sharlina Md Suhaimi.

References

1. Wang, Y. and Xie, W. (2010). Synthesis of cationic starch with a high degree of substitution in an ionic liquid. *Carbohydrate Polymers*, 80 (4): 1172 – 1177.
2. Chiu, C. and Solarek, D. (2009). Modification of starches. starch: Chemistry and technology. New York: Academic Press: pp. 629 – 655.
3. Wang, P., Wu, X., Dong-Hua, X., Kun, X., Ying, T., Xi-Bing, D. and Wen-Bo, L. (2009). Preparation and characterization of cationic corn starch with a high degree of substitution in dioxane-THF-water media. *Carbohydrate Research*, 344 (7): 851 – 855.
4. Heinze, T., Haack, V. and Rensing, S. (2004). Starch derivatives of high degree of functionalization preparation of cationic 2-hydroxy-propylthrimethylammonium chloride starches. *Starch/Starke*, 50: 487 – 492.
5. Burkill, I. H. (1966). A dictionary of the economic products of the Malay Peninsula. Kuala Lumpur: Government of Malaysia and Singapore. I (A - H).
6. Lin, Q., Qian, S., Li, C., Pan, H., Wu, Z. and Liu, G. (2012). Synthesis, flocculation and adsorption performance of amphoteric starch. *Carbohydrate Polymers*, 90 (1): 275 – 283.
7. Zhang, M. (2007). Synthesis of cationic hydrolyzed starch with high DS by dry process and use in salt-free dyeing. *Carbohydrate Polymers*, 69: 123 – 129.
8. Jiang, Q., Gao, W., Li, X., Xia, Y., Wang, H., Wu, S., Huang, L., Liu, C. and Xiao, P. (2012). Characterization of starches isolated from five *Dioscorea* L. Species. *Food Hydrocolloids*, 29 (1): 35 – 41.
9. Chen, G., Zhang, B., Zhao, J. and Chen, H. (2013). Improved process for the production of cellulose sulfate using sulfuric acid / ethanol solution. *Carbohydrate Polymers*, 95 (1): 332 – 337.
10. Regina, S. A. S., Yaacob, W. W. A., Shazrul, F., Nurul, I. H. and Azwan, M. L. (2016). Transformation of crystalline starch nanoparticles into high luminescent carbon nanodots: Toxicity studies and their application. *Carbohydrate Polymers*, 137: 488 – 496.
11. Kavaliauskaite, R., Klimaviciute, R. and Zemaitaitis, A. (2008). Factors influencing production of cationic starches. *Carbohydrate Polymers*, 73: 665 – 675.
12. Zhang, B., Ni, B., Lu, S., Cui, D., Liu, M., Gong, H. and Han, F. (2012). Synthesis and characterization of novel potato starch derivative with cationic acetylcholine groups. *International Journal of Biological Macromolecules*, 50: 701 – 706.

Malaysian Journal of Analytical Sciences, Vol 20 No 6 (2016): 1286 - 1298
DOI: http://dx.doi.org/10.17576/mjas-2016-2006-07

MALAYSIAN JOURNAL OF ANALYTICAL SCIENCES
Published by The Malaysian Analytical Sciences Society
ISSN 1394 - 2506

THE INFLUENCE OF CALCINATION TEMPERATURE ON IRON OXIDE (α-Fe_2O_3) TOWARDS CO_2 ADSORPTION PREPARED BY SIMPLE MIXING METHOD

(Kesan Suhu Pengkalsinan Ferum Oksida (α-Fe_2O_3) Disediakan Melalui Kaedah Campuran Ringkas Terhadap Penjerapan CO_2)

Azizul Hakim[1]*, Mohd. Ambar Yarmo[1], Tengku Sharifah Marliza[1,2], Maratun Najiha Abu Tahari[1], Wan Zurina Samad[1], Muhammad Rahimi Yusop[1], Mohamed Wahab Mohamed Hisham[1], Norliza Dzakaria[1,3]

[1]*Catalysis Research Group, School of Chemical Sciences and Food Technology, Faculty of Science and Technology, Universiti Kebangsaan Malaysia, 43600 UKM Bangi, Selangor, Malaysia*
[2]*Catalysis Science and Technology Research Centre, Faculty of Science, Universiti Putra Malaysia, 43400 UPM Serdang, Selangor, Malaysia*
[3]*School of Chemistry and Environmental, Faculty of Applied Science, University Teknologi Mara (UiTM) Negeri Sembilan, Kampus Kuala Pilah, Pekan Parit Tinggi, 72000 Kuala Pilah, Negeri Sembilan, Malaysia*

**Corresponding author: azizulhakim2442@gmail.com*

Received: 7 February 2016; Accepted: 3 July 2016

Abstract

Synthesized iron oxide, α-Fe_2O_3 used for CO_2 capturing was prepared by a simple mixing method and calcined at temperatures in a range of 350 – 850 °C. CO_2 adsorption isotherms at 25 °C and 1 atm found that the sample namely s450 that calcined at 450 °C gave the highest CO_2 adsorption activity with the adsorption capacity of 17.0 $mg_{CO2}/g_{adsorbent}$. Monodentate carbonate, bidentate carbonate and bicarbonates formation were observed on s450 through the IR spectra. The basicity of s450 was identified by chemisorption of CO-TPD which contains weak, medium and strong basic sites with CO total adsorbed amount of 1.99 cm^3/g. It was found that s450 calcined at 450 °C has certain crystallite peaks that abruptly increased through the XRD diffractogram. The texture properties of s450 generated high porosity and more uniform sphere shape particle size with high surface area (50.5 m^2/g). Furthermore, it is composed of trimodal distribution for pore size distribution curve desirable for CO_2 adsorption.

Keywords: CO_2 capture, adsorption, iron oxide, solid adsorbent, porosity

Abstrak

Penjerapan CO_2 terhadap ferum oksida, α-Fe_2O_3 yang disintesis melalui kaedah campuran ringkas dan dikalsin pada suhu 350-850 °C. Penjerapan isoterma CO_2 pada suhu bilik, 25 °C and 1 atm mendapati sampel s450 yang dikalsin pada suhu 450 °C menunjukkan aktiviti penjerapan CO_2 paling tinggi dengan keupayaan penjerapan sebanyak 17.0 $mg_{CO2}/g_{penjerap}$. Spektrum IR telah membuktikan pembentukan spesis monodentat karbonat, bidentat karbonat dan bikarbonat pada s450. Sifat bes s450 yang dikenalpasti menggunakan jerapan kimia CO-TPD dimana jumlah CO yang dijerap oleh tapak bes lemah, sederhana dan kuat adalah 1.99 cm^3/g. Difraktogram XRD pula menunjukkan terdapat beberapa puncak kekisi yang meningkat. Tekstur s450 pula mempunyai keporosan yang tinggi dan bentuk sfera yang lebih sekata serta luas permukaan yang tinggi (50.5 m^2/g). Tambahan lagi, graf taburan saiz liang s450 juga terdiri daripada taburan jenis trimodal yang menjadi salah satu faktor penting dalam penjerapan CO_2.

Kata kunci: penjerapan CO_2, penjerapan, ferum oksida, penjerapan pepejal, keporosan

Introduction

The main concern worldwide over the recent years is renewable energy which could generate for the rest of decades without worrying about the depletion of sources in the earth. Human population and consumption are directly proportional with the addition of technology provided and yet keep growth explosively which completed with extensive research and development in the industry and academic. This progressive situation made human realized with considerable attentions were paid to the green technology by using the anthropocentric environmental ethics which is people centered as an approach to reduce environmental pollutions and save the earth and future generation. It gave rise to anthropocentric individuals to feel the environment should be protected because of its value in maintaining or enhancing the quality of life for human [1].

Rapid growth development resulting in harmful air pollutants released into the atmosphere which became the major contribution in the global warming and several issues on urban smog, acid rain, and health problems contributed from emission of anthropogenic CO_2 [2]. The CO_2 in atmosphere, one of the major greenhouse gases, is now higher than the safety limit for the atmospheric CO_2 level of 350 ppm. According to the National Oceanic and Atmospheric Administration (NOAA) in U.S, the CO_2 level was higher than the safety limit since 80's and to date on September 2015 was approximately 397.63 ppm. Furthermore, the increased CO_2 growth rate about 2.0 ppm/year gives rise to the mitigating measure of capturing CO_2 [3].

According to Freund and Roberts [4], chemisorbed species is connected with the formation of $CO_2^{\delta-}$, the anionic molecule, which involves the charge transfer from the metal to the molecule. Consequently, the α-Fe_2O_3 decorated as the basic oxide where the CO_2 chemisorption involves the basic sites that act as electron donors and are associated with O_2^- ions localized on surface defects [5]. The physisorption is found in almost all cases whereas the chemisorbed species are only observed under very specific conditions: the surfaces have to be either atomically rough, containing a high defect: density in order to stabilize the chemisorbed species, or are alkali metal modified surfaces [4].

Metal oxides of calcium oxide (CaO) were among the earliest studies in the CO_2 capture that has promising properties of high adsorption capacity [6]. However, it consumed high energy during the desorption process up to 900 °C which is economically not favourable. Thus, the capability of the alternative adsorbents from the metal oxides was studied. The desorption process that required heat to dissociate formed carbonate can be explained by the interaction of CO_2 as adsorbate on the adsorbent which depends on its binding energy. In fact, others than alkali metal and alkali earth metal oxides, several metal oxides have been reported for a single crystal oxide that shows its capability in the CO_2 capture. Kwon et al. [7] reported the dissociation carbonate product on lanthanum sesquioxide (La_2O_3) using the IR frequencies at 500°C. Furthermore, the desorption temperature was increased to 700 °C when higher pressure was used during the CO_2 adsorption [8]. Silver oxide (AgO) exhibited desorption temperature at 247°C that was observed under the scanning tunnelling microscopy (STM) [9]. Meanwhile, Yoshikawa [10] discovered the order of dissociation of the different carbonate species (bicarbonate, monodentate, bidentate and polydentate carbonate) on cerium oxide (CeO_2) at the temperature range of 50 – 450 °C. Among the copper oxides (CuO and Cu_2O), it was found that copper (II) oxide (CuO) showed a higher adsorption capacity by physisorbed of 17.7 mg CO_2/g adsorbent and chemisorbed of 9.5 mmol/g with three times regeneration without significant loss of performance [11]. Our works reported that NiO exhibited adsorption capacity of 14.1 and 87.0 mg CO_2/g adsorbent by physio- and chemisorption respectively, with the desorption temperature range of 400 – 460 °C [12].

Previous studies of iron oxides, α-Fe_2O_3 as adsorbent showed evidence on the presence of various carbonate species formations such as monodentate, bidentate, and bicarbonate forms on the metal oxides adsorbent surface [13-17]. These studies described carbonates formation using the Fourier transfer infra red (FTIR) spectroscopy to analyze the configuration of C-O interaction with iron oxide surface. Ismail et al. [18] reported CO_2 adsorption by using the iron material from a steel-pickling waste (97 wt% $FeSO_4.7H_2O$). The original material was roasted at 700 °C for 5 hours in air, oxygen, and nitrogen prior to the adsorption process. However, none of these researches reported the basicity active site that contributes to CO_2.

In this study, α-Fe_2O_3 was synthesized by using a simple mixing method in order to obtain the preferable surfaces. The α-Fe_2O_3 was synthesized by using a low cost method to identify the optimum calcination temperature and quantify the basicity properties. Hence, the amount of CO_2 adsorbed physically at room temperature, 25°C and 1 atm was measured using the volumetric adsorption technique.

Materials and Methods

Sample preparation

The analytical grade iron (III) nitrate nonahydrate ($Fe(NO_3)_3 \cdot 9H_2O$, 98%) and ethanol (C_2H_5OH, 99.7%) were purchased from Sigma-Aldrich, USA and Systerm, Malaysia respectively. The bulk α-Fe_2O_3 obtained from BDH, United Kingdom was treated by calcined under nitrogen flow at 150 °C for 1 hour. The simple mixing method is very useful to produce α-Fe_2O_3 nanoparticles with low cost of starting materials. This method was modified from literature reported by Dong et al. [19]. The $Fe(NO_3)_3 \cdot 9H_2O$ was weighed to 16.16 g and dissolved in 20 ml distilled water to have concentration of 2 M. To this solution, ethanol was added with a volume percentage of 25% from the distilled water used and stirred for 1 hour at room temperature. The concentration of 2 M precursor was found to be the shortest time formation with a connection of large number of $Fe(OH)_3$ fine particles. Ethanol acts as a stabilizer for the colloidal particles avoid aggregation [19]. The solution was sonicated for 20 minutes to obtain better homogeneous condition and dried with vigorous stirring at the temperature of 80 – 100 °C. The dried solid was ground and kept in an oven for 24 hours at 110 °C. Finally, it was calcined under the air flow at the temperature ranging from 350 – 850 °C. The samples were labeled by the calcination temperatures namely: bulk, s350, s450, s550, s650, s750 and s850.

Characterization

These samples were characterized with Bruker AXS D8 Advance type with X-ray radiation source of Cu Kα (40 kV, 40 mA) to obtain the X-ray Diffraction (XRD) pattern. The crystal structures were verified by recording 2θ diffraction angle from 10° to 90° at wavelength (λ = 0.154 nm). The diffraction pattern obtained was matched with a standard diffraction data (JCPDS) file for identification of the crystalline phase composition.

The physical surface analysis of N_2 adsorption-desorption was conducted at 77 K in a Micromeritics ASAP 2020 instrument to determine the textural surface properties of the prepared samples. The catalysts were degassed at 200°C for 6 hours prior to analysis. The volumetric adsorption apparatus was used to determine the surface area and N_2 adsorption-desorption isotherm using the BET equation [20]. Pore volumes and pore size distribution were determined by Barret–Joyner–Halenda (BJH) method and applied based on the adsorption branch. The *t*-plot method was used to calculate the non-microporous (or external) surface area considerable as the mesoporous surface area [21-23]. The total pore volumes were estimated to be the liquid volume of adsorbate (N_2) at a relative pressure. All surface areas were calculated from the N_2 adsorption isotherms by assuming the area of a N_2 molecule to be 0.162 nm^2 [20]. The CO_2 adsorption behaviors of the sorbents were evaluated using the above mentioned instrument and evaluated at 25°C and 1 atm with circulated water bath and using 99.9% of purified CO_2 gas as adsorbate.

The particle sizes and morphology of the catalysts were measured by the transmission electron microscopy (TEM, CM12 Philips) which is equipped with an electron gun 200 kV. The synthesized of α-Fe_2O_3 before and after the exposure with CO_2 (5% and 15% of CO_2) as well as after temperature programmed desorption (TPD) at 650°C were examined using the Fourier transform infrared (FTIR) spectroscopy. The spectra of the samples were recorded between 4000 and 650 cm^{-1} in spectrum 400, FTIR Spectrometer (Perkin Elmer, UK) using the Attenuated Total Reflection (ATR) method for the sample preparation technique.

The basicity properties of catalysts were performed by the TPD from a conventional apparatus of Chemisorption Analyzer, Micrometrics 2920 Chemisorb. This instrument is equipped with a thermal conductivity detector (TCD). Approximately 50 mg of catalyst was preheated to 150°C to remove the moisture for 30 minutes before it was cooled down to 30°C under the pure He gas flow rate of 30 mL/min. The catalyst was exposed with a gas mixture of 5% CO in He in a constant temperature of 40°C under flow rate 30 mL/min for 60 minutes. The pure He gas again was introduced to the catalyst for the purpose of removing excess of the weak physically adsorbed CO at 50°C for 30 minutes. The TPD required ice to trap the moisture which was placed in the container of instrument prior to the

measurements and heated to 900°C with the heating rate of 10°C/min under pure He. The samples after the CO_2-TPD analysis by using 5% and 15% CO_2 were collected using above mentioned conditions and observed through FTIR.

Results and Discussion

XRD pattern

The X-ray diffractograms of bulk and synthesized α-Fe_2O_3 were determined and are represented in Figure 1. The peaks observed at d-values of 3.68, 2.70, 2.52, 2.20, 1.84, 1.69, 1.60, 1.49, 1.45, 1.34, 1.31, 1.26, 1.22, 1.19, 1.16, 1.14, 1.10 Å in all catalysts correspond to the rhombohedral phase of hematite, α-Fe_2O_3 with lattice parameters a=5.0356 and c=13.7489 (matched with JCPDS number 33-0664). The diffractograms show that the crystal formation of hematite phases can be seen at the calcination temperature of 350°C. Nevertheless, the crystallite peaks appear at this temperature had lower intensity compared to the bulk hematite especially on crystallites (018), (208), (10 10), (220), (306), (128), (02 10), (134) and (226). The s450 was found to have a better crystallinity of synthesized α-Fe_2O_3 among others. The crystallite peaks of (024), (116), (214) and (300) were abruptly increased for the calcined α-Fe_2O_3 at 450°C. The XRD pattern for the calcination temperatures ranging at 550 – 850 °C had similar intense of crystallinity.

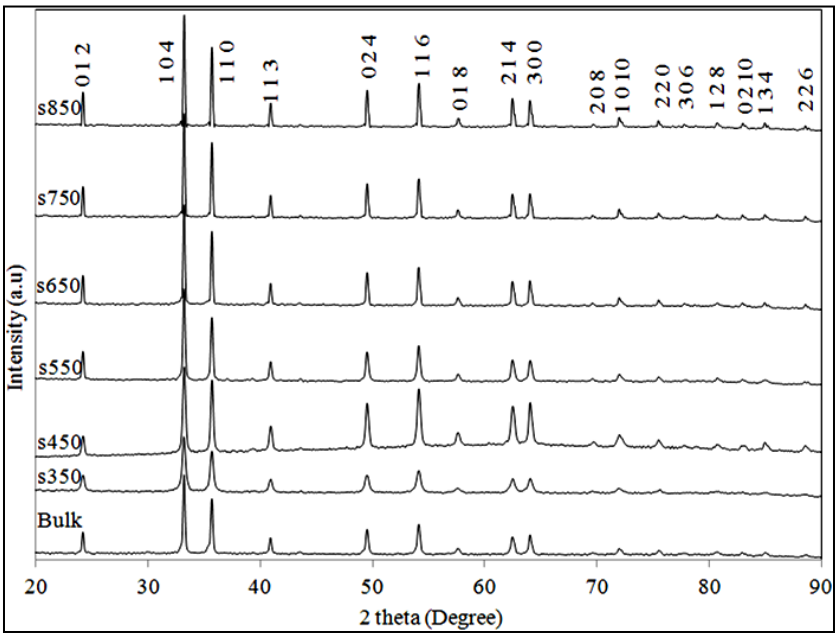


Figure 1. XRD patterns of α-Fe_2O_3 at different calcination temperatures

Textural properties

The N_2 adsorption-desorption isotherms, specific surface areas, and pore volumes for the bulk and synthesized α-Fe_2O_3 are presented in Figure 2 and Table 1, respectively. The isotherms for all samples are type III profile according to the IUPAC isotherms of classification with typical sloping adsorption and desorption branches covering a large range of relative pressure (P/P_o) where the adsorbent-adsorbate interaction is weak, but could be obtained with certain porous adsorbents [24]. It was proven from the H3 type hysteresis based on the isotherms ascribed from plate-like particles giving rise to slit-shaped pores from the adsorbent. The adsorbents showed large ranges of pore diameters which do not exhibit any limiting adsorption at high P/Po [20]. The adsorbents consist of mesoporous and macroporous structure in all samples based on the isotherms. It is interesting to note that s450 has the largest hysteresis area (Figure 2) compared to others which indicate the highest mesoporous and macroporous structure on the surface. The mesopore surface area with pore size ranging between 2 to 50 nm was evaluated by the

t-plot method. The macropore structure of bulk α-Fe_2O_3 was contributed more than mesopore since the mesopore surface area was smaller (3.9 m^2/g) than s650 (4.2 m^2/g) (Table 1). For s350, the temperature of 350 °C was not enough to create better pore structure. However, the sample s450 calcined at 450 °C created better pore structure which leads to a high surface area (50.5 m^2/g). Hence, the total pore volume was increased which is desirable for the adsorption behavior. This ascribed to the calcined α-Fe_2O_3 at a particular temperature provided the capability in generating well pore structure nor produced fine particles. At the temperature higher than 450 °C, it was found to be not efficient to obtain a high porosity α-Fe_2O_3. The constituent crystallites of the hematite grew and sintered resulting from the increased of thermal exposure, eventually generated smaller pores and also reduced the BET surface area. The low specific surface area indicative of less-defined porosity was observed for s550 and above. The bulk α-Fe_2O_3 exhibited better adsorption rather than s650 and above.

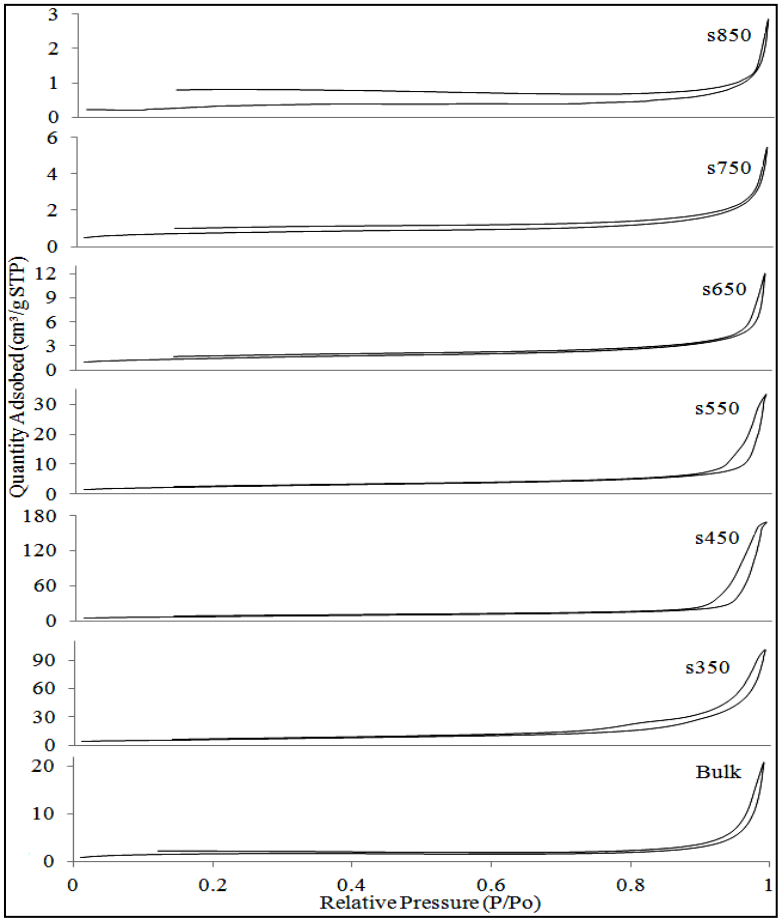


Figure 2. The effect of calcination temperature on α-Fe_2O_3 towards N_2 adsorption-desorption isotherms

Pore size distribution

The highest N_2 adsorption with the widest range of pore size can be seen from the pore size distribution curve illustrated in Figure 3. The distribution shows a wide range of pore sizes categorized under mesoporous and macroporous. A trimodal distribution was observed clearly for α-Fe_2O_3 calcined at 450 °C whereas the rest adsorbents established similar distribution and several multimodal distributions. The trimodal distribution has overcome the monomodal which appears to produce an enhancement in the surface area of the synthesized metal oxides [25]. It is interesting to note that s450 has three maximum pore diameter (652, 907 and 1271 Å) located in a

wide pore structure. These pores exhibited narrow pore size distribution compared to the others which are indicative of good porosity for gas adsorption retained based on the pore size distribution and BET surface area obtained.

Table 1. Textural parameters of the samples obtained from the N_2 adsorption-desorption and CO_2 adsorption isotherms

Calcination Temperature (°C)	BET Surface area (m^2/g)	Mesopore Surface area (m^2/g)	Total Pore volume (cm^3/g)	Pore diameter (Å)	CO_2 Adsorption at 25 °C (cm^3/g)	Adsorption Capacity at 25 °C ($mg_{CO2}/g_{adsorbent}$)
Bulk	5.7	3.9	0.022	154	1.53	3.0
s350	23.1	20.6	0.124	215	2.91	5.7
s450	50.5	27.0	0.227	371	8.66	17.0
s550	9.3	8.9	0.039	168	1.17	2.3
s650	5.0	4.2	0.012	96	1.11	2.2
s750	2.6	1.7	0.006	91	0.94	1.8
s850	1.2	1.9	0.003	98	0.76	1.5

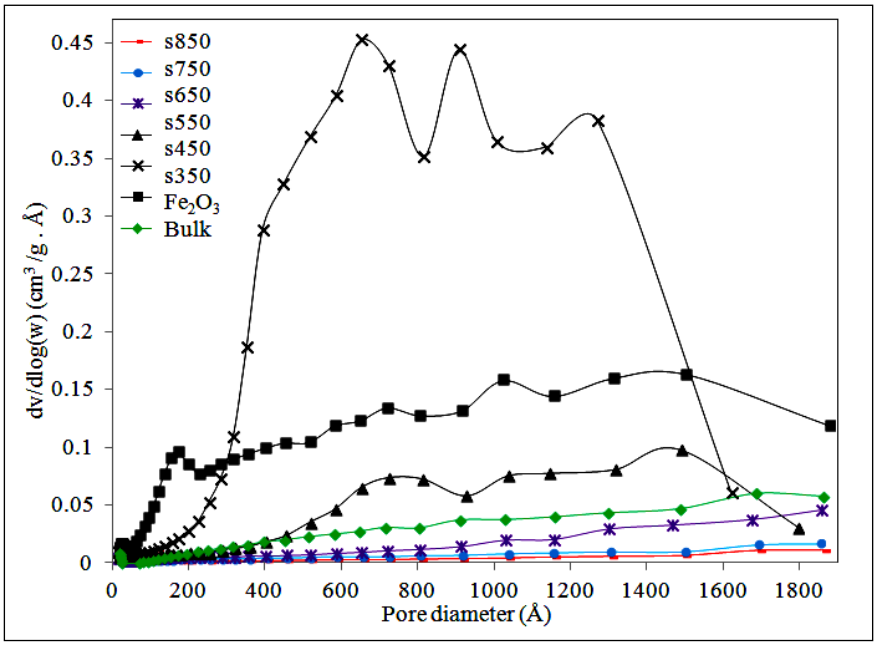


Figure 3. Pore size distribution of synthesized α-Fe_2O_3 by BJH method

Pore structure of the adsorbents

The bright field TEM micrographs of α-Fe_2O_3 prepared with increased calcination temperature are illustrated in Figure 4 to observe its crystallographic and morphological structure. The bulk α-Fe_2O_3 has larger crystallite size particles at 160.5 nm with aggregation and less pore structure which has agreement with the mesopore surface area based on N_2 adsorption-desorption isotherms. For s350, it did not show very good morphology and aggregation of

the particles with particle size range 12.6 to 57.0 nm. Nonetheless, small and uniform particle sizes of α-Fe_2O_3 particles with range of 24.5 to 56.0 nm were generated for s450. The pore structures well distributed on the particles surface are also easily seen from Figure 4. The one-hour calcination temperature of 550 °C was enough to make the particle size of s550 became larger (44.2 to 90.3 nm). At 650 °C, s650 exhibited more particles changing to ellipsoid with larger particle range of 73.0 to 119.2 nm and fine pore structure was observed. According to Dong et al. [19], particles changed at a higher temperature of 700 °C for longer calcination time of three hours. The porous images in Figure 4 for synthesized α-Fe_2O_3 by using simple mixing method could provide improvement in the porosity rather than bulk sample. The high porosity surfaces provide more active sites and space which are responsible in attracting CO_2.

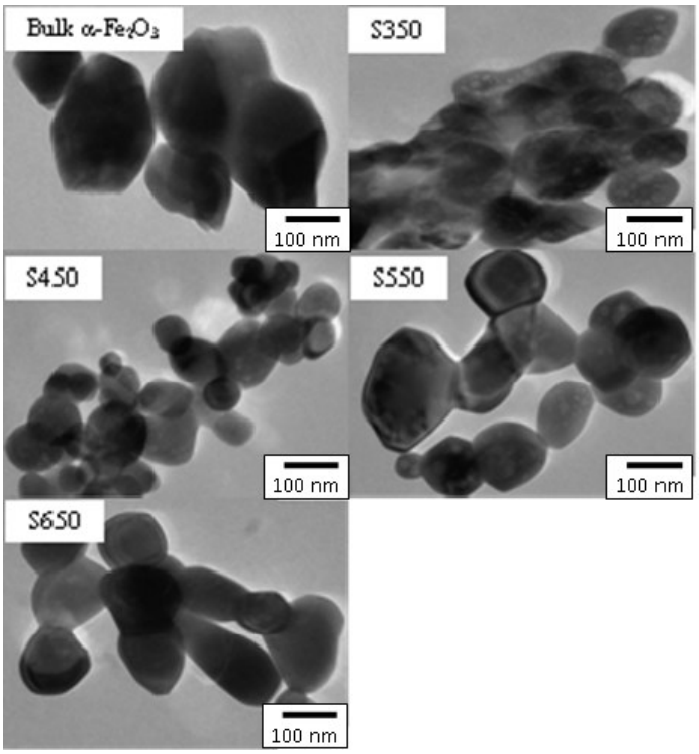


Figure 4. TEM view of synthesized α-Fe_2O_3 particles

Base strength distribution by CO-TPD analysis

The s450 was chosen based on the morphology studies, and used for the basicity measurement by TPD with CO as the probe molecule due to having the desirable properties in the CO_2 adsorption. Although CO_2 has been used worldwide for this purpose, somehow it could appear to be proper probe molecule because of its acidic in nature. The basic of adsorbent would attract the acidic gas easily to form various interaction modes. The CO-TPD profile in the literatures varies depending on the adsorption condition of CO. The broad desorption or high intensity peak indicative of CO has been adsorbed. The CO-TPD peaks represent the base strength distribution of the adsorbent are shown in Figure 5. The range of weak, medium and strong basic sites were estimated from the area under their TPD curve of 40 – 200, 200 – 400, >400 °C respectively. The temperature ranges chosen for the weak, medium and strong basic sites are CO-TPD observed from the most catalyst [26, 27]. The strengths of the basic sites are expressed in the temperature range wherein the CO_2 chemisorbed on the basic sites was desorbed. The CO-TPD curve showed maximum temperature of 170 °C (weak base), 314°C (medium base) and 641 °C (strong base) with the desorption quantity of 0.14, 0.42 and 1.43 cm^3/g respectively. This adsorbent had total amount of 1.99 cm^3/g resulting a potential adsorbent in CO_2 adsorption.

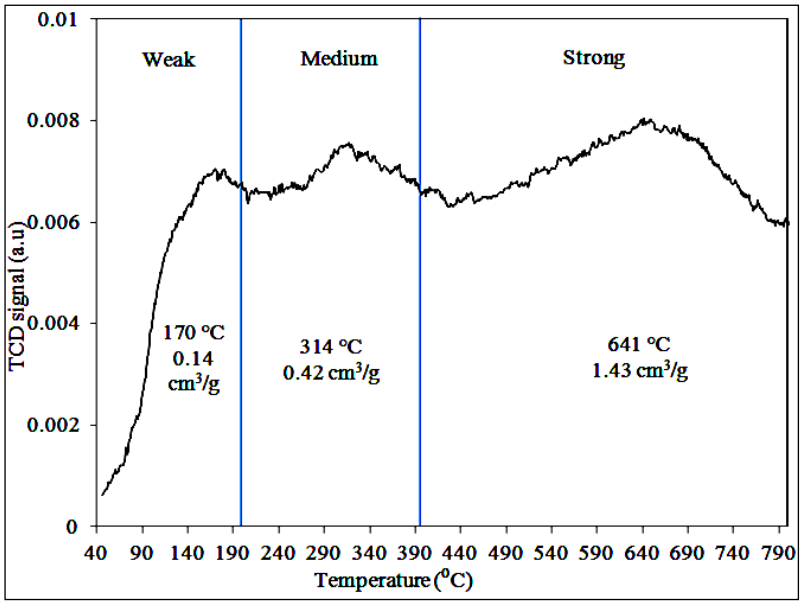


Figure 5. Base strength distribution from TPD profile of CO adsorption (CO-TPD) for s450

Formation of carbonate

The IR spectra for s450 obtained before and after being exposed to CO_2, and after desorption of CO_2 are shown in Figure 6 and vibrational frequencies assignments are tabulated in Table 2. The position of the bands at 1226 and 1630 cm^{-1} are indicative of the bicarbonate species for C-OH bending mode and asymmetry O-C-O vibrational modes of adsorbed bicarbonates respectively [15-17, 28]. The bicarbonate can be easily identified by its OH peak at 3639 cm^{-1} [15-17, 28]. Other peaks observed at 1038 and 1399 cm^{-1} were associated with the monodentate structures of carbonate from IR spectra with C-O stretches and symmetry O-C-O vibrational mode respectively [15-17]. The 1399 cm^{-1} peak only appeared for α-Fe_2O_3 with 5% CO_2 of exposure. The weak contributions around 1245 and 1554 cm^{-1} agreed with the formation of surface bidentate carbonate species with symmetry (O-C-O) and asymmetry (O-C-O) stretching respectively [15-17, 29] as a consequence of the adsorption of CO_2 on a metal oxide surface. In all spectra, the CO band from bridging CO_2 at 2035 cm^{-1} was more intense for α-Fe_2O_3 exposed with 15% CO_2 [30]. The intensity pattern of peak 2162 cm^{-1} was similar where C=O bonded with hydroxyl groups having weak acidic properties [31]. The broad IR absorption band at 3370 cm^{-1} was the characteristic of H-O-H bonding of the H_2O molecules which shows the presence of hydroxyl groups [32]. The intensities of hydroxyl group were found to be reduced and partially removed after CO_2-TPD at 650 °C due to the thermal exposure. Additionally, there was also a broad OH stretching region of 2700 to 3706 cm^{-1} for all spectra but more intense for those exposed with 5% and 15% CO_2 which was caused from moisture in the gas mixture. The adsorption band at 918 cm^{-1} was corresponded to the Fe-O-H deformation due to the source of gas containing traces amount of moisture that led to the hydroxide compound formation on metal oxide surface [33, 34].

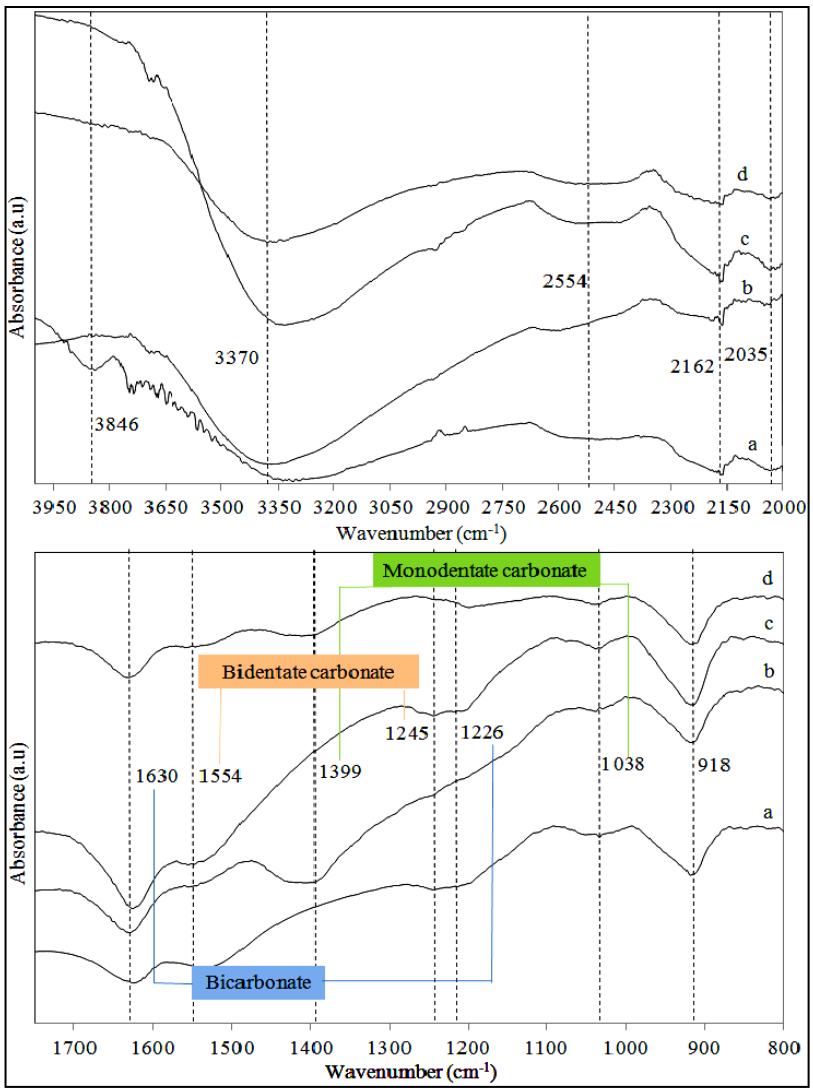


Figure 6. IR spectra of (a) s450 before CO_2 adsorption, (b) α-Fe_2O_3 at 450 °C exposed with 5% CO_2, (c) α-Fe_2O_3 at 450 °C exposed with 15% CO_2 and (d) α-Fe_2O_3 at 450 °C after CO_2-TPD at 650 °C

Table 2. Vibrational modes of IR spectroscopy for s450 adsorbed product after CO_2 adsorption and CO_2-TPD at 650 °C

Vibrational Modes	**Frequency (cm^{-1})**	**References* (cm^{-1})**	**References**
Bicarbonate (HCO_3^-)			
Asymmetry O-C-O	1630	1555-1720	[15-17, 28]
C-OH	1226	1220-1269	[15-17, 28]
O-H	3639	3600-3627	[15-17, 28]

Table 2 (cont'd). Vibrational modes of IR spectroscopy for s450 adsorbed product after CO_2 adsorption and CO_2-TPD at 650 °C

Vibrational Modes	**Frequency (cm^{-1})**	**References* (cm^{-1})**	**References**
Carbonate (CO_3^{2-})			
Monodentate			
C-O	1038	1040	[15-17]
Symmetry O-C-O	1399	1380-1395	[15-17]
Bidentate			
Symmetry O-C-O	1245	1243-1355	[15-17, 29]
Asymmetry O-C-O	1554	1535-1670	[15-17, 29]
Bridging CO_2	2035	2035	[30]
CO_2 bonded to O-H	2162	2160-2162	[31]
H-O-H	3370	3370	[32]
Fe-O-H	918	800-920	[33, 34]

CO_2 adsorption

CO_2 adsorption isotherms of the adsorbents at 25 °C and 1 atm are shown in Figure 7 and the adsorption capacity is tabulated in Table 1. The CO_2 adsorption branch began from the monolayer that was on the adsorbent surface and continued with the multilayer adsorptions that is known as physisorption. The bulk α-Fe_2O_3 shows the adsorption capacity was 1.53 cm^3/g. For the synthesized α-Fe_2O_3, the CO_2 adsorption capacity varies with the different calcination temperature parameters. s450 exhibited the highest BET surface area and total pore volume, showed the highest CO_2 adsorption capacity (17.0 mg_{CO2} / $g_{adsorbent}$) at 25 °C and 1 atm. The amounts of CO_2 adsorbed onto the synthesized α-Fe_2O_3 decreased progressively as the calcination temperature was increased which was influenced by poor surface area as a consequence of the sintering effect of the adsorbent. It also has a higher volume of narrower pores with trimodal distribution of the pore size as shown in Figure 3, that provides more spaces to capture CO_2. The adsorption capacity for s350 was rather higher than the rest of temperatures ascribed to crystallite grew and not exposed to the high thermal treatment that lead to sintering. The adsorption capacity for bulk α-Fe_2O_3 which was treated at 150 °C under N_2 recorded a higher value than s550 and above. In addition, the adsorbed weights (CO_2) of all the adsorbents are in the following order: 450 > 350 > bulk > 550 > 650 > 750 > 850. In fact, a linearly proportional relationship between the adsorptive capacity and surface area is suggested. Higher surface area provides more active sites to attract CO_2 which resulting in high adsorption capacity. Overall, the simple mixing method could save more energy on the calcination temperature compared to Ismail et al. [18] work which required 700°C for the CO_2 adsorption purpose.

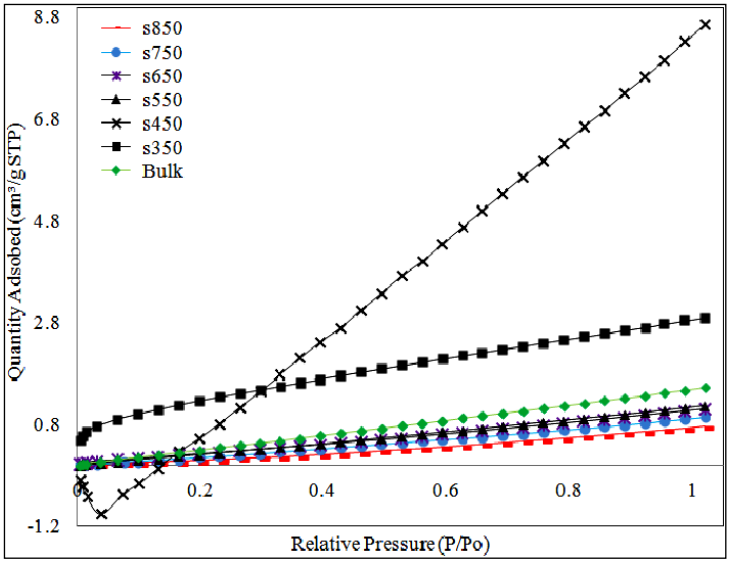


Figure 7. The effect of calcination temperatures on CO_2 adsorption isotherms at 25 °C and 1 atm

Conclusion

The calcination temperature of α-Fe_2O_3 at 450 °C by using a simple mixing method generated sphere particle size of fine particles with high BET surface area, mesopore surface area, and total pore volumes. These features provide an enhancement in CO_2 adsorption at 25 °C and 1 atm with the highest adsorption capacity among all adsorbents was 17.0 $mg_{CO2}/g_{adsorbent}$. Furthermore, the total basic site presence for all three weak, medium and strong basic site was 1.99 cm^3/g. The striking peak was observed at strong base site with amount of 1.43 cm^3/g. The IR spectra described various configurations of CO_2 interacted with α-Fe_2O_3 surface by monodentate, bidentate and bicarbonate forms although exposed with low concentration of 5% of CO_2.

Acknowledgement

The authors wish to thanks Universiti Kebangsaan Malaysia (UKM) for funding this project under research grant number LRGS/BU/2011/USM-UKM/PG/02, BKBP-FST-K003323, ETP-2013-066 and TD-2014-024 from Ministry of Higher Education (MOHE) Malaysia and Centre of Research and Innovation Management (CRIM) UKM for the instruments facilities.

References

1. Gagnon, S. C. and Barton, M. A. (1994). Ecocentric and anthropocentric attitudes toward the environment. *Journal of Environmental Psychology*, 14: 149 – 157.
2. Song, C. S. (2006). Global challenges and strategies for control, conversion and utilization of CO_2 for sustainable development involving energy, catalysis, adsorption and chemical processing. *Catalysis Today*, 115: 2 – 32.
3. Global Monitoring Division, National Oceanic and Atmospheric Administration (NOAA), U.S. Department of Commerce. 2015. Available from http://www.esrl.noaa.gov/gmd/ccgg/trends/#mlo _full. [Access online 24 September 2015].
4. Freund, H. J. and Roberts, M. W. (1996). Surface chemistry of carbon dioxide. *Surface Science Reports*, 25: 225 – 273.
5. Son, W. J., Choi, J. S. and Ahn, W. S. (2008) Adsorptive removal of carbon dioxide using polyethyleneimine-loaded mesoporous silica materials. *Microporous and Mesoporous Materials*, 113: 31 – 40.
6. Abanades, J. C. (2002). The maximum capture efficiency of CO_2 using a carbonation/ calcination cycle of CaO/$CaCO_3$, *Chemical Engineering Journal*, 90: 303 – 306.

7. Kwon, J. H., Dai, M., Halls, M. D., Langereis, E., Chabal, Y. J. and Gordon, R. G. (2009). In situ infrared characterization during atomic layer deposition of lanthanum oxide. *Journal of Physical Chemistry C*., 113: 654 – 660.
8. Rosynek, M. P. and Magnuson, D. T. (1977). Infrared study of CO_2 adsorption on lanthanum sesquioxide and trihydroxide. *Journal of Catalysis*, 48: 417 – 421.
9. Okawa, Y. and Tanaka, K. (1995). STM investigation of the reaction of Ag-O added rows with CO_2 on a Ag (ll0) surface. *Surface Science*, 344: 1207 – 1212.
10. Yoshikawa, K., Sato, H., Kaneeda, M. and Kondo, J. M. (2014). Synthesis and analysis of CO_2 adsorbents based on cerium oxide. *Journal of CO_2 Utilization*, 8: 34 – 38.
11. Wan Isahak, W. N. R., Che Ramli, Z. A., Ismail, M. W., Ismail, K., Yusop, R. M., Mohamed Hisham, M. W. and Yarmo, M. A. (2013). Adsorption–desorption of CO_2 on different type of copper oxides surfaces: Physical and chemical attractions studies. *Journal of CO_2 Utilization*, 2: 8 – 15.
12. Hakim, A., Wan Isahak, W. N. R., Abu Tahari, M. N., Yusop, M. R., Mohamed Hisham, M. W., and Yarmo, M. A. (2014). Temperature programmed desorption of carbon dioxide for activated carbon supported nickel oxide: The adsorption and desorption studies. *Advanced Materials Research*, 1087: 45 – 49.
13. Seyller, T., Borgmann, D. and Wedler. G. (1998). Interaction of CO_2 with Cs-promoted Fe (110) as compared to Fe (110) /K + CO_2. *Surface Science*, 400: 63 – 79.
14. Ramis, G., Busca, G. and Lorenzelli. V. (1991). Low-temperature CO_2 adsorption on metal oxides: Spectroscopic characterization of some weakly adsorbed species. *Materials Chemistry and Physics*, 29: 425 – 435.
15. Ferretto, L. and Glisenti, A. (2002). Study of the surface acidity of an hematite powder. *Journal of Molecular Catalysis A: Chemical*, 187: 119 – 128.
16. Lefevre. G. (2004). In situ Fourier-transform infrared spectroscopy studies of inorganic ions adsorption on metal oxides and hydroxides. *Advance in Colloid and Interface Science*, 107: 109 – 123.
17. Baltrusaitis. J., Schuttlefield, J., Zeitler, E. and Grassian, V. H. (2011). Carbon dioxide adsorption on oxide nanoparticle surfaces. *Chemical Engineering Journal*, 170: 471 – 481.
18. Ismail, H. M., Cadenhead D. A. and Zaki, M. I. (1997). Surface reactivity of iron oxide pigmentary powders toward atmospheric components: XPS, FESEM, and gravimetry of CO and CO_2 adsorption. *Journal of Colloid and Interface Science*, 194: 482 – 488.
19. Dong, W. T., Wu, S. X., Chen, D. P., Jiang, X. W. and Zhu, C. S. (2000). Preparation of α-Fe_2O_3 nanoparticles by sol-gel process with inorganic iron salt. *Chemistry Letters*, 496 – 497.
20. Condon, J. B. (2006). *Surface* area and porosity determinations by physisorption measurements and theory, 1st ed., Elsevier, UK: pp. 1 – 28.
21. Hu, Z. H., Srinivasan, M. P. and Ni, Y. M. (2001). Novel activation process for preparing highly microporous and mesoporous activated carbons. *Carbon*, 39: 877 – 886.
22. Puziy, A. M., Poddubnaya, O. I., Martinez-Alonso, A., Suarez-Garcia, F. and Tascon, J. M. D. (2002). Synthetic carbons activated with phosphoric acid II. Porous structure. *Carbon*, 40: 1507 – 1519.
23. Kennedy, L. J., Mohan das, K. and Sekaran, G. (2004). Integrated biological and catalytic oxidation of organics/ inorganics in tannery wastewater by rice husk based mesoporous activated carbon-Bacillus sp. *Carbon*, 42: 2399 – 2407.
24. Sing, K. S. W., Everett, D. H., Haul, R. A. W., Moscou, L., Pierotti, R. A., Rouquerol, J. and Siemieniewska, T. (1985). Reporting physisorption data for gas/solid systems with special reference to the determination of surface area and porosity. *International Union of Pure and Applied Chemistry*, 57 (4): 603 – 619.
25. Gauden, O. A., Terzyk, A. P., Jaroniec, M. and Kowalczyk, P. (2007). Bimodal pore size distributions for carbons: Experimental results and computational studies. *Journal of Colloid and Interface Science*, 310: 205 – 216.
26. Choudhary, V. R., Mulla, S. A. R. and Uphade, B. S. (1999). Oxidative coupling of methane over alkaline earth oxides deposited on commercial support pre-coated with rare earth oxides. *Fuel*, 78: 427 – 437.
27. Kus, S., Otremba, M., Torz, A. and Taniewski, M. (2002). Further evidence of responsibility of impurities in MgO for variability in its basicity and catalytic performance in oxidative coupling of methane. *Fuel*, 81: 1755 – 1760.
28. Di Cosimo, J. I., Diez, V. K., Xu, M., Iglesia, E. and Apesteguia, C. R. (1998). Structure and surface and catalytic properties of Mg-Al basic oxides. *Journal of Catalysis*, 178: 499 – 510.

29. Su, C. M. and Suarez, D. L. (1997). In situ infrared speciation of adsorbed carbonate on aluminium and iron oxides. *Clays and Clay Mineral*, 45(6): 814 – 825.
30. Rebenstorf, B. (1991). Modified chromium/silica gel catalysts: An FTIR study of the addition of alkali metal ions. *Acta Chemica Scandinavica*, 45: 1012 – 1017.
31. Belskaya, O. B., Danilova, I. G., Kazakov, M. O., Mironenko, R. M., Lavrenov, A. V. and Likholobov, V. A. (2012). FTIR spectroscopy of adsorbed probe molecules for analyzing the surface properties of supported Pt (Pd) Catalysts, In T. Theophile (Ed.). Infrared Spectroscopy - Materials Science, Engineering and Technology, In Tech., Croatia: pp. 149 – 178
32. Chauhan, S. M. and Chakrabarty, B. S. (2014). Lead (Pb) doped fluoride nanocrystals: structural and optical properties. *International Journal of Advanced Research*, 2 (7): 607 – 614.
33. Bishop, J. L., Murad, E., Madejova, J., Komadel, P., Wagner, U. and Scheinost, A. C. (1999). Visible, Mossbauer and infrared spectroscopy of dioctahedral smectites: Structural analyses of the Fe-bearing smectites Sampor, SWy-1 and SWa-1*: 11th International Clay Conference*, Ottawa: pp. 413 – 419.
34. Taylor, R. M. (1980). Formation and properties of Fe (II) Fe (III) hydroxyl-carbonate and its possible significance in soil formation. *Clay Mineral*, 15: 369 – 382.

Malaysian Journal of Analytical Sciences, Vol 20 No 6 (2016): 1299 - 1310
DOI: http://dx.doi.org/10.17576/mjas-2016-2006-08

MALAYSIAN JOURNAL OF ANALYTICAL SCIENCES
Published by The Malaysian Analytical Sciences Society
ISSN 1394 - 2506

ENHANCED REDUCIBILITY OF Mg-DOPED MoVTeNbOx MIXED OXIDE CATALYSTS FOR PROPANE OXIDATION REACTION

(Penambahbaikan Kebolehturunan Mangkin Mg-Terdop-MoVTeNbOx Terhadap Proses Pengoksidaan Propana)

Wong Hong Ren, Irmawati Ramli*, Taufiq Yap Yun Hin

Centre of Excellence for Catalysis Science and Technology,
Department of Chemistry, Faculty of Science,
Universiti Putra Malaysia, 43400 UPM Serdang, Selangor, Malaysia

**Corresponding author: irmawati@upm.edu.my*

Received: 17 August 2015; Accepted: 29 August 2016

Abstract

A series of magnesium-doped MoVTeNbOx (MVTN-Mg) catalysts, as well as undoped sample (MVTN) was prepared by microwave-assisted slurry method followed by calcination in nitrogen at 873 K for 2 hours. The catalysts were further post-treated in aqueous hydrogen peroxide. The physicochemical properties of the catalysts were investigated using X-ray diffraction (XRD), surface area measurement using Brunauer-Emmett-Teller (BET) method, Fourier Transform Infrared (FTIR) and Field Emission Scanning Electron Microscopy (FESEM) which showed the formation of orthorhombic M1 phase, $Te_2M_{20}O_{57}$ (M = Mo, V or Nb) when doped with Mg at a molar ratio of Mg/Mo of 0.06. Temperature Programmed Reduction in hydrogen (H_2-TPR) results indicated the enhanced reducibility of the Mg doped catalysts as opposed to the undoped ones, signifying the apparent high activity of the catalyst.

Keywords: magnesium, dopant, microwave-assisted slurry method, reducibility, propane oxidation

Abstrak

Mangkin MoVTeNbOx (MVTN) dan mangkin MoVTeNbOx yang didopkan magnesium (MVTN-Mg) telah dihasilkan melalui kaedah buburan berbantukan oleh penyinaran gelombang mikro. Prekursor telah dikalsinkan dalam nitrogen pada suhu 873 K and seterusnya dirawat dengan hidrogen peroksida. Sifat fisikokimia mangkin yang dikaji dengan menggunakan pembelauan sinar-X (XRD), pengukuran luas permukaan dengan kaedah Brunauer-Emmett-Teller (BET), spektroskopi inframerah transformasi Fourier (FTIR) dan medan elektron-mikroskopi imbasan elektron (FESEM) menunjukkan pembentukan fasa ortorombik M1, $Te_2M_{20}O_{57}$ (M = Mo, V atau Nb) apabila mangkin didopkan magnesium dengan nisbah molar Mg/Mo adalah 0.06. Keputusan penurunan terprogram suhu dengan hidrogen (H_2-TPR) mendedahkan penambahbaikan kebolehturunan mangkin Mg-MoVTeNbOx berbanding dengan mangkin tanpa dopan dan dengan demikian ini menandakan aktiviti mangkin yang tinggi.

Kata kunci: magnesium, dopan, kaedah buburan dibantu oleh penyinaran gelombang mikro, kebolehturunan, pengoksidaan propana

Introduction

Multicomponents MoVTeNbOx catalysts have been recognized as the most promising catalyst in giving high activity and selectivity in propane partial oxidation to acrylic acid [1]. Typically, MoVTeNbOx catalysts present as main crystalline phases of orthorhombic M1 phase $Te_2M_{20}O_{57}$ (M = Mo, V or Nb) [2-11] and hexagonal M2 phase

$Te_{0.33}MO_{3.33}$ (M = Mo, V or Nb) [4-10]. Each of the individual elements in the mixed oxide catalysts has its own role in converting propane to acrylic acid. It was proposed that propane adsorbed on the V^{5+} site of the catalyst surface through the formation of resonance structure with V^{4+}, hence the catalyst must be in a reduced state. Te^{4+} strategically positioned with the bonding distance of its surface, abstract the α-hydrogen of propane to form propylene [12]. Further process is followed by the insertion of oxygen at Mo^{6+} site, thus forming acrolein and followed by another oxygen insertion at the same site to form acrylic acid [13]. Nb^{5+} site is needed to stabilize the product (acrylic acid) from further oxidation into CO and CO_2 [14]. The ability of MoVTeNbOx to be reduced is a prime condition for a successful catalyst as this will activate it into reacting with the incoming reactant (propane). The reducibility of the catalyst is determined by subjecting it into reducing environment such as CO and hydrogen followed by the quantification of the amount of oxygen removed. The onset of reduction process and the peak maxima for the reduction give an indication of the extent of reduction of the metal oxides.

The catalyst properties may also be further improved by the introduction of metal ions into the lattice [15-21]. Promoter such as cobalt has been reported successful in modifying the properties of $(VO)_2P_2O_7$ through the formation of crystalline form of V^{4+} (vanadyl pyrophosphate, $(VO)_2P_2O_7$), $CoPO_4$ phase and a small amount of V^{5+} (β-$VOPO_4$ phase). It also plays a role in having an effect on the reducibility of the catalyst through oxygen diffusion within the lattice of the $(VO)_2P_2O_7$ catalyst that have dramatically increased the specific rate of butane oxidation into forming maleic anhydride three times as compared to the undoped ones [22]. There is also a study done on incorporating potassium into the MoVSb mixed oxide catalysts to affect the catalytic ability. It was found that the conversion of propane was slightly decreases. However, with an appropriate amount of this alkaline metal, it drastically increases the selectivity of acrylic acid about 2 to 3 times as compared to undoped catalysts. In addition, a decrease in the selectivity of undesired products (acetic acid, carbon monoxide and carbon dioxide) could be seen [23-26].

Pure M1 phase MoVTeNbOx can be obtained directly by hydrothermal synthesis [27,28] in an autoclave heated at 448 K in a nitrogen atmosphere with a synthesis time of 72 h. The synthesis method is mainly characterized by its high solvent effect and equilibrium conditions which lead to the formation of the favoured crystalline phase. Another approach is by using a slurry method [29,30] on the basis of a non-solution precursor. This condition inevitably contributes to the multiphase MoVTeNbOx system in which the species is always present in different valence states due to its non-equilibrium state.

In the present work, a microwave-assisted slurry method has been developed for the synthesis of MoVTeNbOx catalysts, promoted and undoped ones. The method allows intimate mixing of the metal species in a homogeneous state under atmospheric pressure in a very short time. This method is derived from the patented method developed by this research group [31].

Materials and Methods

Catalysts preparation

The undoped (MVTN) and magnesium-promoted MoVTeNbOx (MVTN-Mg) catalysts with a Mo/V/Te/Nb/Mg molar ratio of 1/0.3/0.23/0.12/x (x = 0.02, 0.04, 0.06, 0.08, 0.10) were prepared via microwave assisted slurry method. Ammonium heptamolybdate tetrahydrate, $(NH_4)_6Mo_7O_{24}.4H_2O$ (Merck), ammonium metavanadate, $(NH_4)VO_3$ (Merck), telluric acid, $Te(OH)_6$ (Sigma-Aldrich), ammonium niobium oxalate, $(NH_4)_2Nb_2(C_2O_4)_5$ (Sigma-Aldrich), and magnesium nitrate hexahydrate, $Mg(NO_3)_2.6H_2O$ (Bendosen Laboratory Chemicals) were used as metal sources for each of the elements. Appropriate amount of different metal salts was added in sequence into deionized water beginning ammonium heptamolybdate tetrahydrate and followed by ammonium metavanadate, telluric acid and magnesium nitrate hexahydrate to give solution A. Each time after the metal salt was added, the solution was subjected to microwave irradiation for 1.5 minutes. While solution B was obtained by dissolving ammonium niobium oxalate in deionized water and was also subjected to 1.5 minutes microwave irradiation. After that, the two solutions were mixed and the resulting orange slurry was aged for overnight to homogenise the particle distribution. The slurry was then dried by using a rotary evaporator at 353 K to give a sample precursor. Calcination was then carried out to the precursor where it was heated at 553 K for 1 h in air and at 873 K for 2 h under nitrogen flow. Post treatment process was done by washing the solid with 30% hydrogen peroxide. The peroxide was

removed through centrifugation, and the solid was dried in an oven at 373 K for overnight. The Mg containing catalysts are designated as MVTN-Mg(x), x being the Mg/Mo molar ratio.

Catalysts characterization

The BET surface area of the catalysts was determined by using a Thermo Finnigan Sorptomatic Instrument model 1990 series with adsorption of nitrogen at 77 K.

Powder X-ray diffraction (XRD) patterns were collected by employing a Shimadzu 6000 X-ray diffractometer using Ni filtered CuK_{α} radiation with wavelength λ=1.542Å. The catalysts were ground and put on a horizontal sample holder. The XRD patterns were recorded in the 2° to 60° 2Θ range at a scanning rate of 2.0° min^{-1}.

Fourier-Transform Infrared (FT-IR) analysis was carried out at room temperature in the 280 – 4000 cm^{-1} region with a Perkin Elmer 1725X spectrophotometer. The pellets were prepared with mixing a catalyst sample with 200 mg of dry KBr and pressed into disks.

The morphology of the catalysts was obtained by using a Nova 200 Nanolab Field Electron Scanning Electron Microscope (FE-SEM). The surface catalyst images were recorded at an accelerating voltage of 15 kV and magnification of 100,000.

Reducibility study

Temperature programmed reduction in hydrogen (H_2-TPR) was performed by using a Thermo Finnigan TPDRO 1100 apparatus, utilizing a thermal conductivity detector (TCD). Before subjecting the catalysts to the reducing gas, the samples were first treated by flowing nitrogen at room temperature for half an hour to remove any weak species that might present on the surface. After which the nitrogen gas flow was switched to 5.1% H_2 in argon gas with a flow rate of 25 ml min^{-1} at a heating rate of 10 K min^{-1} from room temperature up to 1223 K. The mass spectrometer records the evolution of water continuously during the course of the reaction.

Results and Discussion

Characterisation of as-synthesised samples

XRD patterns of the as-synthesised samples (before calcination) are displayed in Figure 1. The reflections are found in the 2θ = 5 – 15° and 25 – 30° range. These reflections are typical of Anderson-type structure $(NH_4)_6TeMo_6O_{24}.7H_2O$ as reported by Evans et al. [32] and $(NH_4)_7TeMo_5VO_{24}.8H_2O$ reported by Sun et al. [33] which indicates the presence of heteropoly compounds (HPCs). The narrow diffractions observed in undoped sample becomes broad bands when Mg was added signifying that the HPCs slowly turns into pseudo-crystallines with increasing amount of Mg.

Figure 2 shows the FTIR spectra of as-synthesised samples taken in the range of wavenumber 280 – 4000 cm^{-1}. All samples give FTIR spectra with practically identical bands. The bands at 576 cm^{-1} are assigned to a V=O group and/or V-O-*M* bonds (*M* = V, Nb). Whereas the absorption bands at 483, 630, 678, and 883 cm^{-1} could be assigned to heteropoly-telluromolybdates, $(NH_4)_6TeMo_6O_{24}.7H_2O$ [34,35] in accordance with the XRD results. The bands at 3400 – 3550 cm^{-1} are associated to the symmetric and anti-symmetric O-H bending modes of lattice water, while the bands at 1650 cm^{-1} could be related to H-O-H bending modes [36,37]. Additionally, the asymmetric and symmetric stretching vibration of ammonium cation ($\nu(NH_4^+)$) are determined by the band at 1425 cm^{-1}, and at 3000 and 3200 cm^{-1} respectively [34-36].

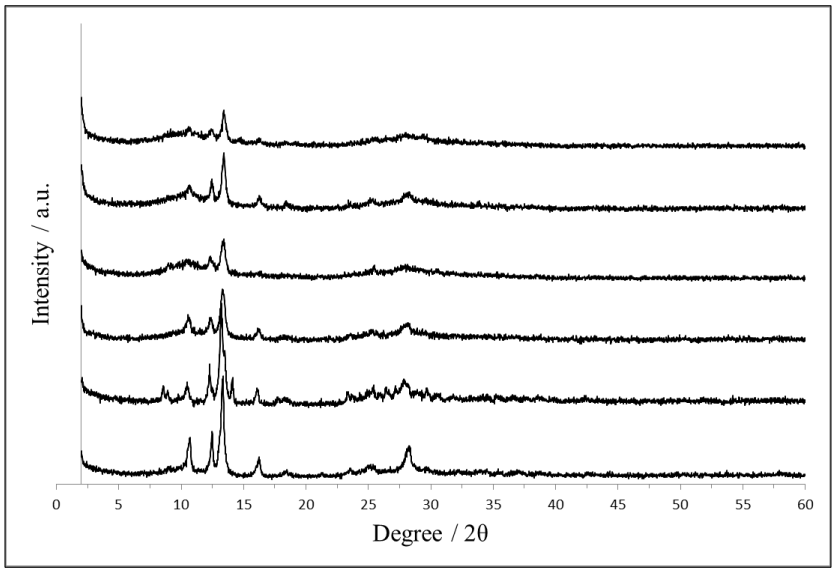


Figure 1. XRD patterns of magnesium free and magnesium containing catalyst precursors: (a) MVTN, (b) MVTN-Mg (0.02), (c) MVTN-Mg (0.04), (d) MVTN-Mg (0.06), (e) MVTN-Mg (0.08) and (f) MVTN-Mg (0.10)

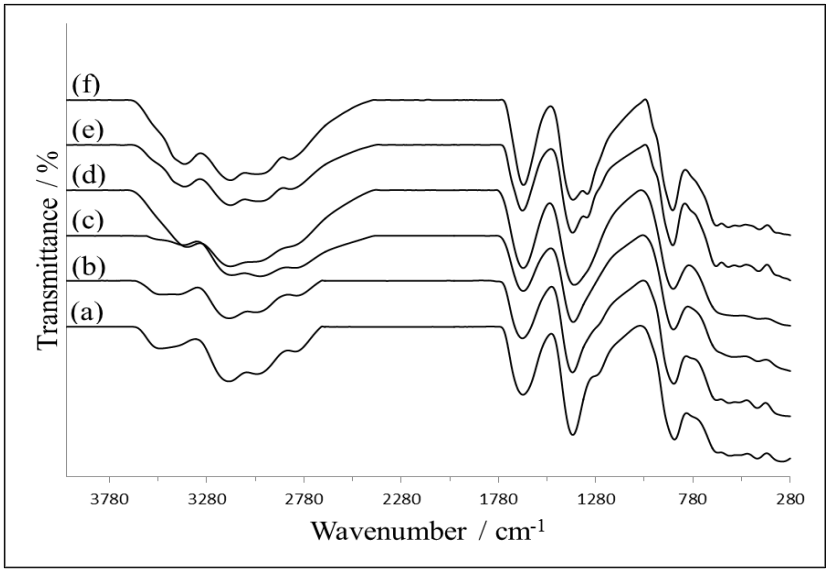


Figure 2. FTIR spectra of magnesium free and magnesium containing catalyst precursors: (a) MVTN, (b) MVTN-Mg (0.02), (c) MVTN-Mg (0.04), (d) MVTN-Mg (0.06), (e) MVTN-Mg (0.08) and (f) MVTN-Mg (0.10).

Characterization of calcined catalysts

The XRD patterns of the calcined catalysts are shown in Figure 3. All of the samples show a similar diffraction peaks with five prominent peaks at 2θ = 22.1°, 28.2°, 36.2°, 45.0° and 50.0°. Termed as the "famous five", however, it was reported that the MoVTeNbOx catalysts containing these peaks did not work effectively [38],

suggesting they are not the key drivers of a successful MoVTeNb mixed oxide catalysts. These five peaks associated with the presence of hexagonal M2, $Te_{0.33}MO_{3.33}$ (*M* = Mo, V and Nb) phase [39-41] which is isomorphous to that of $Sb_4M_{10}O_{31}$ phase [10], and hexagonal tungsten bronze (HTB)-type phase [42]. The formation of M2 phase is common since it is usually started to form at 723 K [43]. It is also noted the development of new peaks in the range of 2θ = 6.7 – 10.0°. These peaks are assigned to orthorhombic M1, $Te_2M_{20}O_{57}$ (*M* = Mo, V and Nb) phase [43,44].

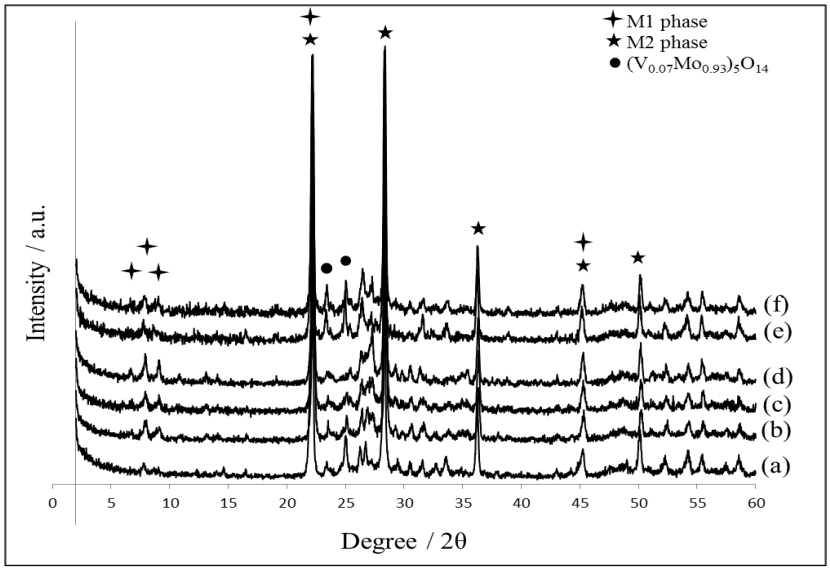


Figure 3. XRD patterns of magnesium free and magnesium containing calcined catalysts: (a) MVTN, (b) MVTN-Mg (0.02), (c) MVTN-Mg (0.04), (d) MVTN-Mg (0.06), (e) MVTN-Mg (0.08) and (f) MVTN-Mg (0.10).

In the case of post-treated catalysts, $Te_2M_{20}O_{57}$ (*M* = Mo, V and Nb) orthorhombic M1 was the crystalline phase mainly observed (Figure 4) which can be identified with the peaks at 2θ = 6.7°, 7.8°, 9.0°, 22.1°, 26.2°, 26.8°, 27.2°, 29.2° and 35.4° [7]. Thus it can be concluded that the post treatment with an aqueous solution of hydrogen peroxide leads to the selective removal of the hexagonal M2 phase from the Mg-doped and undoped MoVTeNbOx catalysts containing M1 and M2 phase mixtures [45]. However, additional phase of tetragonal $(V_{0.07}Mo_{0.93})_5O_{14}$ (JCPDS File No. 31-1473) can be found. Comparison of the XRD patterns of the Mg-promoted with undoped catalysts revealed that the appearance of phase reflections at 2θ = 23.3, 24.6 and 31.5° in undoped catalysts corresponds to the rich tetragonal $(V_{0.07}Mo_{0.93})_5O_{14}$ phase. This phase was slightly diminished when Mg was added until the molar ratio of Mg/Mo was 0.06, suggesting the incorporation of Mg in catalyst lattice is responsible for the suppression of the tetragonal crystallization step. However, beyond that amount (molar ratio = 0.06) the crystallization of tetragonal phase was started to taken over. The XRD patterns of the formed structural material of MVTN-Mg(0.06) catalyst is quite similar to the one observed in the case of monophasic MoVTeNbOx orthorhombic M1 phase which were hydrothermally synthesized [27,28].

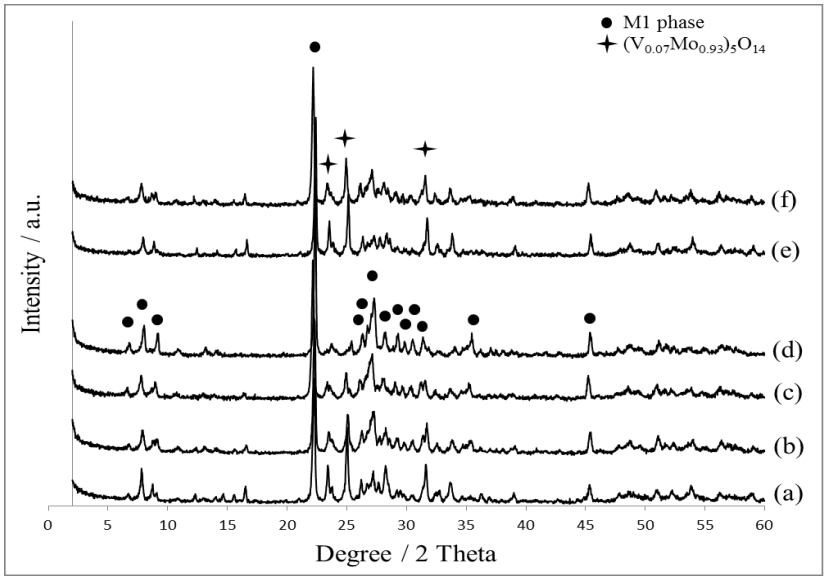


Figure 4. XRD patterns of magnesium free and magnesium containing post-treated catalysts: (a) MVTN, (b) MVTN-Mg (0.02), (c) MVTN-Mg (0.04), (d) MVTN-Mg (0.06), (e) MVTN-Mg (0.08) and (f) MVTN-Mg (0.10)

FTIR spectra of post-treated catalysts are shown in Figure 5. The FTIR spectra of bulk MVTN and MVTN-Mg samples composed of M1 and tetragonal phases show absorption bands at 357 cm^{-1} indicates the existence of Mo-O-Mo bridge with symmetric stretching vibration [34]. Meanwhile, the band that is related to the anti-symmetric vibration of Mo-O-*M* (*M* = V, Nb, Te) bridging bonds which appear around 700 – 900 cm^{-1} is observed at 745 cm^{-1}. The bands at 560 cm^{-1} may probably presents a V=O group and/or V-O-*M* (*M* = Mo, Nb, Te) bonds. The symmetric stretching vibration of Mo=O group that is around 900 – 1000 cm^{-1} is identified by the absorption band at 910 cm^{-1} [46,47]. The most highlighted difference among IR spectra is an intensity of the bands for the catalysts containing tetragonal phase due to the improved crystallization of this phase. The broad bands at higher region (at around 3000 cm^{-1} – 3400 cm^{-1}) could be attributed as symmetric and anti-symmetric O-H bending modes of lattice water. The absorption bands at about 1650 cm^{-1} could be assigned to the presence of H-O-H bending modes [36,37]. This is due to the incomplete drying of post-treated catalysts after washing with hydrogen peroxide. The deviation caused by the containing water was eliminated as pre-treatment was carried out before catalysts were characterised.

The morphology of post-treated catalyst was investigated by FESEM analysis. In general, all of the catalysts were found to have a similar morphology of small rod shaped crystallites as shown in Fig. 6. Such kind of morphology was already been reported by López Nieto and his research team, and are commonly observed for M1 phase crystals [48]. The particle size is rather homogeneous with apparent edges and pointed corners that agreed well with the sharp peaks observed in XRD results. There is no clear effect of the addition of promoter to the catalyst morphology.

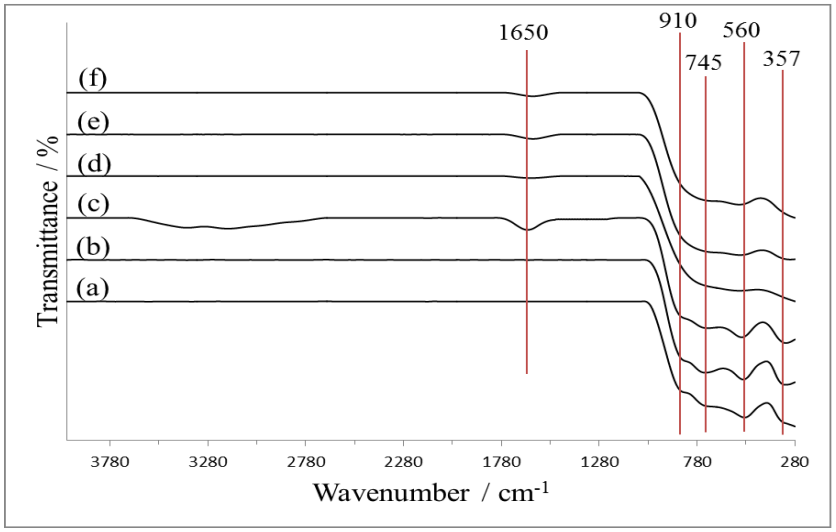


Figure 5. FTIR spectra of magnesium free and magnesium containing post-treated catalysts: (a) MVTN, (b) MVTN-Mg (0.02), (c) MVTN-Mg (0.04), (d) MVTN-Mg (0.06), (e) MVTN-Mg (0.08) and (f) MVTN-Mg (0.10)

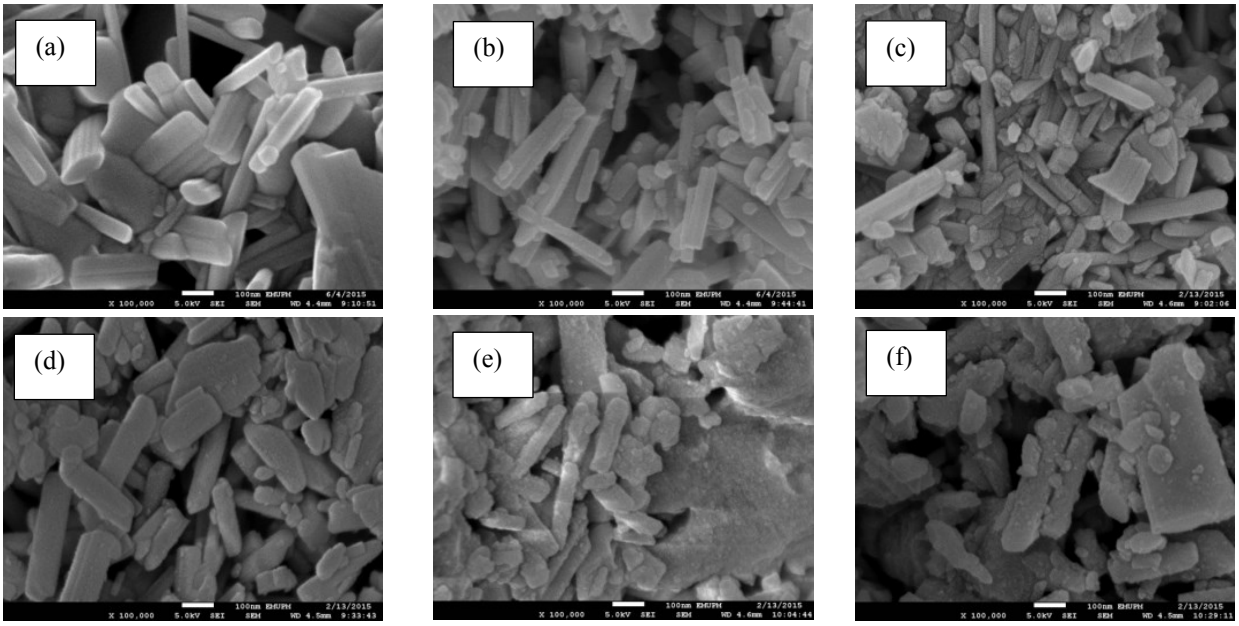


Figure 6. FESEM images of magnesium free and magnesium containing post-treated catalysts: (a) MVTN, (b) MVTN-Mg (0.02), (c) MVTN-Mg (0.04), (d) MVTN-Mg (0.06), (e) MVTN-Mg (0.08) and (f) MVTN-Mg (0.10)

BET surface area of MVTN and MVTN-Mg catalysts are shown in Table 1. Low surface area (3.3 – 4.2 m^2 g^{-1}) is observed in all calcined samples. Therefore, there is no significant effect of magnesium addition to the catalyst crystal structure. However, when the catalysts were post-treated with hydrogen peroxide, the surface area value

significantly improved (13.4 – 20.4 m^2 g^{-1}). This could be related to the selective removal of M2 phase during the post treatment that contributed to the smaller particle size.

Table 1. General characteristics of heat-treated and post-treated catalysts

Catalysts	BET Surface Area (m^2 g^{-1})		TPR Results[a]		
	Heat-treated	Post-treated	T_{max} (K)	E_r (kJ mol^{-1})	O_2 Removed (atom g^{-1})
MVTN	3.3	13.4	930	155.36	2.56×10^{21}
MVTN-Mg (0.02)	3.9	20.1	825	137.82	1.74×10^{21}
			908	151.68	7.72×10^{20}
					2.51×10^{21}
MVTN-Mg (0.04)	3.9	20.4	809	147.00	2.18×10^{21}
			866	158.53	3.87×10^{20}
					2.57×10^{21}
MVTN-Mg (0.06)	4.2	18.8	845	141.16	3.76×10^{21}
			902	150.68	1.64×10^{21}
			928	155.02	1.47×10^{21}
					6.87×10^{21}
MVTN-Mg (0.08)	3.3	15.3	1009	168.55	4.99×10^{21}
MVTN-Mg (0.10)	3.6	21.3	978	163.38	5.61×10^{21}

[a] TPR results of post-treated catalysts

Catalyst reducibility study

The TPR profiles of MVTN and MVTN-Mg catalysts are shown in Figure 7. The analysis was done by flowing hydrogen over the catalyst while temperature was increased at a heating rate of 10 K/min from room temperature to 1223 K. The hydrogen upon interacts with surface oxygen will reacts to form water as the product. The evolution of water was recorded continuously during the course of reaction.

The interaction between the gas phase hydrogen with the surface oxygen can be represented as follows:

$$H_2(g) + O(s) \rightarrow H_2O(g) + \square$$

where (g), (s), and □ denotes gas, surface and vacancy.

Comparison of the peak profiles show that the undoped catalyst (MVTN) has a broad peak with maximum temperature (T_m) occurs at 930 K. The catalyst is less reducible as stipulated by the slow climbing of the reduction peak. On the other hand, all of the promoted catalysts (MVTN-Mg) show a different reduction profile with the peak climbing start immediately after the catalyst started to reduced. The T_m can be found as low as 825 K (for sample MVTN-Mg (0.02)). There is also a presence of other peak maxima in these Mg-promoted catalysts which signify the kinetically different of oxygen species present in the catalysts. The onset of reduction for Mg-promoted catalysts was at 650 K which is coincidence with the reaction temperature for propane oxidation. Meanwhile, the undoped catalyst showed the onset of reduction at about 770 K which indicated the less reducible of this sample.

For the undoped MVTN catalyst, the reduction of pure *M*On (*M* = Mo, V) was at 948 K and 995 K [49]. Both Mo and V species undergo stepwise reduction from $Mo^{6+} \rightarrow Mo^{4+}$ and $Mo^{4+} \rightarrow Mo^0$, and $V^{5+} \rightarrow V^{4+}$ and $V^{4+} \rightarrow V^0$,

respectively. Therefore, the reduction peak observed in this catalyst at 930 K could be attributed to the reduction of both species. Additionally, Nb^{5+} might also be reduced to Nb^{4+} at higher reduction temperature of more than 1000 K as indicated by Pereira et al. [50] in their work on Nb_2O_5.

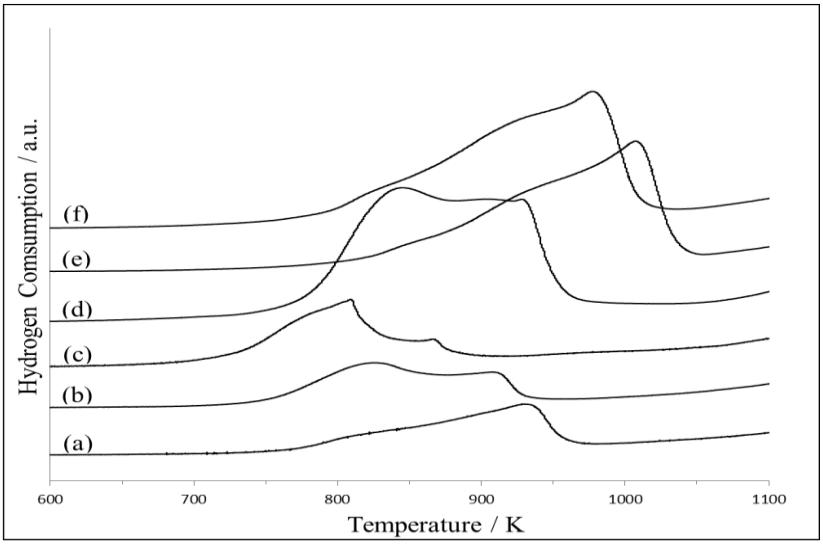


Figure 7. TPR profiles of magnesium free and magnesium containing post-treated catalysts: (a) MVTN, (b) MVTN-Mg (0.02), (c) MVTN-Mg (0.04), (d) MVTN-Mg (0.06), (e) MVTN-Mg (0.08) and (f) MVTN-Mg (0.10)

Meanwhile, the lower peak maximum given by the Mg-promoted MoVTeNbOx catalysts indicated the positive contribution of promoter. The Mg metals might be well dispersed on the catalyst's surface and formed weaker bonds with oxygen species that promote the reducibility of the catalysts. The reduction profiles of MVTN-Mg catalysts are due to the reduction of MoO_n, VO_n, NbO_n and also from $MgO \rightarrow Mg^0$. For MoO_n, the species reduced from $Mo^{6+} \rightarrow Mo^{4+}$ and $Mo^{4+} \rightarrow Mo^0$, for VO_n, the reduction occurs from $V^{5+} \rightarrow V^{4+}$ and $V^{4+} \rightarrow V^0$, and NbO_n reduces from $Nb^{5+} \rightarrow Nb^0$ [49,50].

The amount of removable oxygen can be quantified by calculating the area under the peak and the value of the reduction activation energy, E_r, can be obtained from the modified version of the Redhead equation 1:

$$\frac{E_r}{RT_m^2} = \left(\frac{A_r}{\beta}\right)[H_2]_m exp\left(\frac{E_r}{RT_m}\right) \quad (1)$$

where T_m is the peak maximum temperature (K) in the rate of reaction of H_2, E_r is the reduction activation energy (kJ mol^{-1}), R is the gas constant (J K^{-1} mol^{-1}), β is the heating rate (K s^{-1}), A_r is the reduction pre-exponential term (cm^3 mol^{-1} s^{-1}) which is given the value of a standard collision number of 10^{13} cm^3 mol^{-1} s^{-1} and $[H_2]_m$ is the gas phase concentration of hydrogen (mol cm^{-3}) at the peak maximum.

The values obtained are listed in Table 1. The total number of oxygen atoms released by the undoped and Mg-promoted MoVTeNbOx catalysts are found similar (~2.56 x 10^{21} atom g^{-1}). Close inspection revealed that the Mg-promoted catalysts are more reducible as indicated by the ability of the catalyst to be reduced at lower temperature. Hence, the oxygen species in these promoted catalysts are more labile signifying the higher activity of the promoted catalysts. It is also important to note that the MVTN-Mg (0.06) sample have the highest total amount of oxygen removed. The oxygen species in this catalyst is more reducible at lower temperature as compared to others due to the existence of orthorhombic M1 phase in this sample that facilitates the oxygen removable.

The reduction activation energy, E_r value > 100 kJ mol^{-1} is high for all samples suggesting that the oxygen being removed are surface and lattice oxygen species. The circumstance that the reduction study was done in an anaerobic condition contributed to these findings. There is no weakly bonded oxygen present in these catalysts as shown by no peak evolution at lower temperature (less than 650 K). Therefore, the surface and lattice oxygen removed in this works are the strongly bonded ones that could be playing an important role in the catalytic activity of the catalysts. It has been reported that the oxidation of propane to acrylic acid requires surface and lattice oxygen to be selectively inserted into the intermediate to form final product. The present of weakly bonded oxygen will somehow assist in the C-C bond breakage that might lead to the formation of unwanted products such as acetic acid, CO and CO_2 [51].

Conclusion

Magnesium doped MoVTeNb mixed oxides were successfully synthesized by microwave-assisted slurry method, calcined in nitrogen at 875 K for 2 h and followed by post treatment with hydrogen peroxide. It was found that the incorporation of magnesium into the catalyst lattice were greatly affected the catalyst properties as can be clearly seen in the formation of crystalline phases as observed in the XRD. A highly pure orthorhombic M1 phase that is reported important in the catalyst activity for propane oxidation have successfully derived when the loading of Mg/Mo was in the molar ratio of 0.06. Adding less or more that will give mixture of phases with the present of tetragonal phase became more dominant. The Mg-doped catalysts show a high reducibility property when subjected to reducing agent which is an important property for an oxidation catalyst. The oxygen in the doped catalysts are more labile to be removed at lower temperature with high amount of oxygen removable as the consequence of the weak interaction of the oxygen with the Mg species over the surface of the catalyst.

Acknowledgement

The authors would like to thank the Ministry of Higher Education Malaysia (Fundamental Research Grant Scheme (FRGS), grant number: 5524811) for their financial support.

References

1. Ushikubo, T., Nakamura, H., Koyasu, Y. and Wajiki, S. (1997). US Patent 5,380,933 (1995). *Mitsubishi Kasei Corporation*.
2. Popova, G. Y., Andrushkevich, T., Chesalov, Y. A., Plyasova, L., Dovlitova, L., Ischenko, E. and Khramov, M. (2009). Formation of active phases in MoVTeNb oxide catalysts for ammoxidation of propane. *Catalysis Today,* 144(3): 312 - 317.
3. Amakawa, K., Kolen'ko, Y. V., Villa, A., Schuster, M. E., Csepei, L.-I., Weinberg, G. and Prati, L. (2013). Multifunctionality of crystalline MoV(TeNb) M1 oxide catalysts in selective oxidation of propane and benzyl alcohol. *ACS Catalysis, 3*(6): 1103 - 1113.
4. Ushikubo, T., Oshima, K., Kayou, A. and Hatano, M. (1997). Ammoxidation of propane over Mo-V-Nb-Te mixed oxide catalysts. *Studies in Surface Science and Catalysis,* 112: 473 - 480.
5. Asakura, K., Nakatani, K., Kubota, T. and Iwasawa, Y. (2000). Characterization and kinetic studies on the highly active ammoxidation catalyst MoVNbTeOx. *Journal of Catalysis,* 194(2): 309 - 317.
6. Tsuji, H. and Koyasu, Y. (2002). Synthesis of MoVNbTe(Sb)Ox composite oxide catalysts via reduction of polyoxometalates in an aqueous medium. *Journal of the American Chemical Society,* 124(20): 5608 - 5609.
7. Oliver, J., Nieto, J. L., Botella, P. and Mifsud, A. (2004). The effect of pH on structural and catalytic properties of MoVTeNbO catalysts. *Applied Catalysis A: General,* 257(1): 67 - 76.
8. Grasselli, R. K., Burrington, J. D., Buttrey, D. J., DeSanto Jr, P., Lugmair, C. G., Volpe Jr, A. F. and Weingand, T. (2003). Multifunctionality of active centers in (amm) oxidation catalysts: from Bi–Mo–O x to Mo–V–Nb–(Te, Sb)–Ox. *Topics in Catalysis, 23*(1-4): 5 - 22.
9. García-González, E., López Nieto, J., Botella, P. and González-Calbet, J. (2002). On the nature and structure of a new MoVTeO crystalline phase. *Chemistry of Materials,* 14(10): 4416 - 4421.
10. Tsuji, H., Oshima, K. and Koyasu, Y. (2003). Synthesis of molybdenum and vanadium-based mixed oxide catalysts with metastable structure: Easy access to the MoVNbTe(Sb)Ox catalytically active structure using reductant and oxoacid. *Chemistry of Materials,* 15(11): 2112 - 2114.
11. Ueda, W. and Oshihara, K. (2000). Selective oxidation of light alkanes over hydrothermally synthesized Mo-VMO (M= Al, Ga, Bi, Sb, and Te) oxide catalysts. *Applied Catalysis A: General,* 200(1), 135 - 143.

12. Grasselli, R. K., Buttrey, D. J., DeSanto, P., Burrington, J. D., Lugmair, C. G., Volpe, A. F. and Weingand, T. (2004). Active centers in Mo–V–Nb–Te–O x (amm) oxidation catalysts. *Catalysis Today,* 91: 251 - 258.
13. Grasselli, R. K. (2005). Selectivity issues in (amm) oxidation catalysis. *Catalysis Today,* 99(1): 23 - 31.
14. Ueda, W., Vitry, D., Kato, T., Watanabe, N. and Endo, Y. (2006). Key aspects of crystalline Mo-VO-based catalysts active in the selective oxidation of propane. *Research on Chemical Intermediates,* 32(3): 217 - 233.
15. Schacht, L., Navarrete, J., Schacht, P. and Ramírez, M. A. (2010). Influence of Vanadium oxidation states on the performance of V-Mg-Al mixed-oxide catalysts for the oxidative dehydrogenation of propane. *Journal of the Mexican Chemical Society,* 54(2): 69 - 73.
16. Pless, J. D., Bardin, B. B., Kim, H.-S., Ko, D., Smith, M. T., Hammond, R. R. and Poeppelmeier, K. R. (2004). Catalytic oxidative dehydrogenation of propane over Mg–V/Mo oxides. *Journal of Catalysis,* 223(2): 419 - 431.
17. Lee, K., Yoon, Y.-S., Ueda, W. and Moro-Oka, Y. (1997). An evidence of active surface MoOx over MgMoO4 for the catalytic oxidative dehydrogenation of propane. *Catalysis Letters, 46*(3-4): 267 - 271.
18. Yoon, Y. S., Ueda, W. & Moro-oka, Y. (1995). Oxidative dehydrogenation of propane over magnesium molybdate catalysts. *Catalysis Letters,* 35(1-2): 57 - 64.
19. Cadus, L., Gomez, M. and Abello, M. (1997). Synergy effects in the oxidative dehydrogenation of propane over $MgMoO_4$-MoO_3 catalysts. *Catalysis Letters,* 43(3-4): 229 - 233.
20. Morales, E. and Lunsford, J. H. (1989). Oxidative dehydrogenation of ethane over a lithium-promoted magnesium oxide catalyst. *Journal of Catalysis,* 118(1): 255 - 265.
21. Conway, S. J. and Lunsford, J. H. (1991). The oxidative dehydrogenation of ethane over chlorine-promoted lithium-magnesium oxide catalysts. *Journal of Catalysis,* 131(2): 513 - 522.
22. Mahdavi, V. & Hasheminasab, H. R. (2015). Liquid-phase efficient oxidation of cyclohexane over cobalt promoted VPO catalyst using tert-butylhydroperoxide. *Journal of the Taiwan Institute of Chemical Engineers*, 51: 53 - 62.
23. Ivars, F., Solsona, B., Botella, P., Soriano, M. and Nieto, J. L. (2009). Selective oxidation of propane over alkali-doped Mo–V–Sb–O catalysts. *Catalysis Today,* 141(3): 294 - 299.
24. Botella, P., Concepción, P., Nieto, J. L. and Solsona, B. (2003). Effect of potassium doping on the catalytic behavior of Mo–V–Sb mixed oxide catalysts in the oxidation of propane to acrylic acid. *Catalysis Letters,* 89(3-4): 249 - 253.
25. Ivars, F., Solsona, B., Soriano, M. and Nieto, J. L. (2008). Selective oxidation of propane over AMoVSbO catalysts (A= Li, Na, K, Rb or Cs). *Topics in Catalysis,* 50(1-4): 74 - 81.
26. Ueda, W., Endo, Y. and Watanabe, N. (2006). K-doped Mo–V–Sb–O crystalline catalysts for propane selective oxidation to acrylic acid. *Topics in Catalysis,* 38(4), 261 - 268.
27. Sanfiz, A. C., Hansen, T. W., Girgsdies, F., Timpe, O., Rödel, E., Ressler, T. and Schlögl, R. (2008). Preparation of phase-pure M1 MoVTeNb oxide catalysts by hydrothermal synthesis—influence of reaction parameters on structure and morphology. *Topics in Catalysis,* 50(1-4): 19 - 32.
28. Vitry, D., Morikawa, Y., Dubois, J. and Ueda, W. (2003). Mo-V-Te-(Nb)-O mixed metal oxides prepared by hydrothermal synthesis for catalytic selective oxidations of propane and propene to acrylic acid. *Applied Catalysis A: General,* 251(2): 411 - 424.
29. Lin, M. M. (2003). Complex metal-oxide catalysts for selective oxidation of propane and derivatives: I. Catalysts preparation and application in propane selective oxidation to acrylic acid. *Applied Catalysis A: General,* 250(2): 305 - 318.
30. Tu, X., Furuta, N., Sumida, Y., Takahashi, M. and Niiduma, H. (2006). A new approach to the preparation of MoVNbTe mixed oxide catalysts for the oxidation of propane to acrylic acid. *Catalysis Today,* 117(1): 259 - 264.
31. Irmawati, R., Ahmad Afandi, M., Ahmad Zaidi, I. and Hossein Abbastabar, A. (2011). Patent pending No. PI2011003855.
32. Evans Jr, H. T. (1968). Refined molecular structure of the heptamolybdate and hexamolybdotellurate ions. *Journal of the American Chemical Society,* 90(12): 3275 - 3276.
33. Sun, Y., Liu, J. and Wang, E. (1986). Preparation and properties of some new 6-heteropoly-tellurate compounds of tungsten and molybdenum containing vanadium. *Inorganica Chimica Acta,* 117(1): 23 - 26.

34. Ratheesh, R., Suresh, G. and Nayar, V. (1995). Infrared and polarized raman spectra of M6 $[TeMo_6O_{24}]\cdot 7H_2O$ [M= K, NH_4] and $(NH_4)_6[TeMo_6O_{24}]\cdot Te(OH)_6.7H_2O$ single crystals. *Journal of Solid State Chemistry,* 118(2): 341 - 356.
35. Botto, I., Cabello, C. and Thomas, H. (1997). $(NH_4)_6[TeMo_6O_{24}]\cdot 7H_2O$ Anderson phase as precursor of the $TeMo_5O_{16}$ catalytic phase: thermal and spectroscopic studies. *Materials Chemistry and Physics,* 47(1): 37 - 45.
36. Botella, P., Nieto, J. L. and Solsona, B. (2002). Selective oxidation of propene to acrolein on Mo-Te mixed oxides catalysts prepared from ammonium telluromolybdates. *Journal of Molecular Catalysis A: Chemical,* 184(1): 335 - 347.
37. Nakamoto, K. (1970). Infrared spectra of inorganic and coordination compounds. 2nd Edition. Wiley Science, New York.
38. Lin, M. M. (2003). Complex metal oxide catalysts for selective oxidation of propane and derivatives: II. The relationship among catalyst preparation, structure and catalytic properties. *Applied Catalysis A: General,* 250(2): 287 - 303.
39. Deniau, B., Millet, J., Loridant, S., Christin, N. and Dubois, J. (2008). Effect of several cationic substitutions in the M1 active phase of the MoVTeNbO catalysts used for the oxidation of propane to acrylic acid. *Journal of Catalysis,* 260(1): 30 - 36.
40. Ischenko, E., Andrushkevich, T., Popova, G. Y., Bondareva, V., Chesalov, Y., Kardash, T. Y. and Ischenko, A. (2010). Formation of active component of MoVTeNb oxide catalyst for selective oxidation and ammoxidation of propane and ethane. *Studies in Surface Science and Catalysis,* 175: 479 - 482.
41. Popova, G. Y., Andrushkevich, T., Aleshina, G., Plyasova, L. and Khramov, M. (2007). Effect of oxalic acid content and medium of thermal treatment on physicochemical and catalytic properties of MoVTeNb oxide catalysts in propane ammoxidation. *Applied Catalysis A: General,* 328(2): 195 - 200.
42. Magneli, A. (1953). Studies on the hexagonal tungsten bronzes of-potassium. *Acta Chemica Scandinavica,* 7: 315 - 324.
43. Girgsdies, F., Schlögl, R. and Trunschke, A. (2012). In-situ X-ray diffraction study of phase crystallization from an amorphous MoVTeNb oxide catalyst precursor. *Catalysis Communications,* 18: 60 - 62.
44. Murayama, H., Vitry, D., Ueda, W., Fuchs, G., Anne, M. and Dubois, J. (2007). Structure characterization of orthorhombic phase in MoVTeNbO catalyst by powder X-ray diffraction and XANES. *Applied Catalysis A: General,* 318: 137 - 142.
45. Deniau, B., Bergeret, G., Jouguet, B., Dubois, J. and Millet, J. (2008). Preparation of single M1 phase MoVTe(Sb)NbO catalyst: Study of the effect of M2 phase dissolution on the structure and catalytic properties. *Topics in Catalysis,* 50(1-4): 33 - 42.
46. Bart, J., Cariati, F. and Sgamellotti, A. (1979). Mixed-valence effects in tellurium-molybdenum oxides. *Inorganica Chimica Acta,* 36: 105 - 112.
47. Bart, J., Petrini, G. and Giordano, N. (1975). Solid-state equilibrium relations in the Ternary Systems TeO_2-MoO_3-MoO_2 and TeO_2-MoO_3-Te. *Zeitschrift für anorganische und allgemeine Chemie,* 413(2): 180 - 192.
48. Botella, P., Nieto, J. L., Solsona, B., Mifsud, A. and Márquez, F. (2002). The preparation, characterization, and catalytic behavior of MoVTeNbO catalysts prepared by hydrothermal synthesis. *Journal of Catalysis,* 209(2): 445 - 455.
49. Jiang, H., Lu, W. & Wan, H. (2004). The effect of $MoV_{0.3}Te_{0.23}P_xO_n$ catalysts with different phosphorus content for selective oxidation of propane to acrolein. *Journal of Molecular Catalysis A: Chemical,* 208(1): 213 - 217.
50. Pereira, E. B., Pereira, M. M., Lam, Y., Perez, C. A. and Schmal, M. (2000). Synthesis and characterization of niobium oxide layers on silica and the interaction with nickel. *Applied Catalysis A: General,* 197(1): 99 - 106.
51. Ramli, I., Botella, P., Ivars, F., Meng, W. P., Zawawi, S. M. M., Ahangar, H. A. and Nieto, J. M. L. (2011). Reflux method as a novel route for the synthesis of MoVTeNbOx catalysts for selective oxidation of propane to acrylic acid. *Journal of Molecular Catalysis A: Chemical,* 342: 50 - 57.

Malaysian Journal of Analytical Sciences, Vol 20 No 6 (2016): 1311 - 1317
DOI: http://dx.doi.org/10.17576/mjas-2016-2006-09

MALAYSIAN JOURNAL OF ANALYTICAL SCIENCES
Published by The Malaysian Analytical Sciences Society
ISSN 1394 - 2506

SYNTHESIS, CHARACTERIZATION AND ELECTOCHEMICAL STUDIES OF 4-METHOXYBENZOYLTHIOUREA DERIVATIVES

(Sintesis, Pencirian dan Kajian Elektrokimia Terhadap Terbitan 4-Metoksibenzoiltiourea)

Karimah Kassim[1,2]*, Noor Khadijah Mustafa Kamal[1], Adibatul Husna Fadzil[3].

[1]*Faculty of Applied Sciences*
[2]*Institute of Science*
Universiti Teknologi MARA, 40450 Shah Alam, Selangor, Malaysia
[3]*Faculty of Applied Sciences,*
Universiti Teknologi MARA (Perak), Kampus Tapah, 35400 Tapah Road, Tapah, Perak, Malaysia

**Corresponding author: karimah@salam.uitm.edu.my*

Received: 17 August 2015; Accepted: 11 October 2016

Abstract

Three new 4-methoxybenzoylthiourea derivatives namely *N*-phenyl-*N'*-4-methoxybenzoylthiourea (A), *N*-(2-methoxy-phenyl)-*N'*-4-methoxybenzoylthiourea (B) and *N*-(2-nitrophenyl)-*N'*-4-methoxybenzoylthiourea (C) has successfully synthesized and characterized by elemental analysis, Fourier Transform Infrared (FTIR), proton (^{1}H) and carbon (^{13}C) Nuclear Magnetic Resonance (NMR) spectroscopy. Result obtained for IR showed the presence of important bands of the compounds such as ν(N-H), ν(C=O), ν(C-N) and ν(C=S) which were observed at 3200 cm^{-1}, 1670 cm^{-1}, 1200 cm^{-1} and 700 cm^{-1}, respectively. The ^{1}H chemical shifts for CONH and CSNH had been observed around 9 ppm and 12 ppm, respectively. For the ^{13}C resonance, the signal of C=O and C=S had been observed at 180 ppm and 200 ppm, respectively. The efficiency of the synthesized compounds was investigated as corrosion inhibitor of mild steel in 1.0 M H_2SO_4 by using linear polarization resistance (LPR) technique.

Keywords: 4-methoxybenzoylthiourea, spectroscopy, corrosion inhibitor

Abstrak

Tiga terbitan 4-metoksibenzoiltiourea iaitu *N*-fenil-*N'*-4-metoksibenzoiltiourea (A), *N*-(2-metoksifenil)-*N'*-4-metoksi benzoiltiourea (B) and *N*-(2-nitrofenil)-*N'*-4- metoksibenzoiltiourea (C) telah berjaya disintesis dan dicirikan dengan penganalisis unsur, spektroskopi infra merah (IR), proton (^{1}H) dan karbon (^{13}C) resonans magnet nuklear (RMN). Hasil daripada IR menunjukkan kumpulan penting dalam sebatian seperti ν(N-H), ν(C=O), ν(C-N) and ν(C=S) yang terdapat pada 3200 cm^{-1}, 1670 cm^{-1}, 1200 cm^{-1} and 700 cm^{-1}. Anjakan kimia ^{1}H untuk CONH dan CSNH telah dilihat pada 9 ppm dan 12 ppm. Bagi resonans ^{13}C, C=O dan C=S dapat dilihat pada 180 ppm dan 200 ppm. Keberkesanan sebatian yang disintesis telah dikaji sebagai perencat kakisan keluli lembut dalam 1.0 M H_2SO_4 dengan menggunakan teknik rintangan polarisasi linear.

Kata kunci: 4-metoksibenzoiltiourea, spektroskopi, perencat kakisan

Introduction

Corrosion prevention by using organic inhibitors is one the most practical ways to protect metal in acidic medium [1] The studies on it had attracted many attentions of researchers [2,3]. Corrosion inhibitors are substances that may retard or slow down the corrosion rate when added in small concentration to the system. Organic inhibitors containing nitrogen (N), sulphur (S) and oxygen (O) atoms are considered to be the effective and potential corrosion inhibitors [3-6]. The inhibitors that have these atoms in their structure may induce greater adsorption of the

compounds onto the metal surfaces which leads to the formation of a corrosion protecting film. In addition, the stability of the adsorbed inhibitor film on the metal surface also depends on functional groups [9,11,12].

Thiourea and its derivatives were reported to be the potential corrosion inhibitors as compared with other organic compounds because thiourea molecules contain one S atom and two N atoms [6-8]. These atoms act as centre of adsorption that forms a protective layer on the metal surface from the corrosive attack [9-10]. The corrosion inhibition of thiourea is greater in acidic media because this inhibitor acts simultaneously in both anodic and cathodic areas. Thiourea molecules are very effective inhibitors for steel in acidic conditions because S atom is easily protonated in acidic solution and a stronger electron donor than nitrogen [16].

In this study, a series of 4-methoxybenzoylthiourea derivatives with different substituent groups were synthesized and tested as potential corrosion inhibitor in 1.0 M H_2SO_4 to achieve inhibition efficiency more than 90%. The effect of different substituent group on the inhibition efficiency at different inhibitors' concentrations were also has been studied.

Materials and Methods

Physical measurement

All reactions were performed under an ambient atmosphere and no special precautions were taken to exclude air or moisture. The chemicals (4-methoxybenzoyl chloride, ammonium thiocyanate, aniline, *o*-Anisidine, 2-nitroaniline) and solvents (acetone and acetonitrile) were purchased from Sigma Aldrich and were used without further purification. Melting points were measured using BÜCHI Melting Point B-545. Infrared spectra were recorded using FTIR Perkin Elmer 100 Spectrophotometer in the spectral range of 4000 to 400 cm^{-1} by using KBr pellet. ^{1}H and ^{13}C NMR spectra were obtained from Bruker Advance III 300 Spectrometer at room temperature. The elemental analyses of compound were performed by CHNS Analyzer FLASH 2000 series.

Synthesis of *N*-phenyl-*N'*-4-methoxybenzoylthiourea (A)

Freshly prepared 5mmol (0.85 g) of 4-methoxybenzoyl chloride in 15 ml acetone was added to equal molar of ammonium thiocyanate (0.38 g). The solution was stirred about 20 min. The precipitate formed was discarded and the solution was kept. An amount of 5 mmol (0.46 ml) of aniline was mixed with the previous solution and undergo refluxed for 3 hours. The solution was poured into a beaker containing ice cubes. The resulting precipitate was collected by filtration, washed ethanol and purified by recrystallization with acetonitrile. Figure 1 show the chemical structure of *N*-phenyl-*N'*-4-methoxybenzoyl thiourea (A).

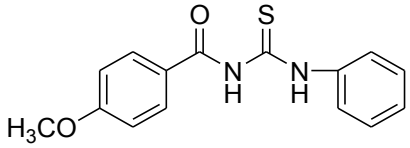


Figure 1. Chemical structure of *N*-phenyl-*N'*-4-methoxybenzoyl thiourea (A)

Synthesis of *N*-(2-methoxyphenyl)-*N'*-4-methoxybenzoylthiourea (B)

Similar procedure as the above, this compound was synthesized by reacting 4-methoxybenzoyl chloride (5 mmol, 0.85 g), ammonium thiocyanate (5 mmol, 0.38 g) and *o*-Anisidine (5 mmol, 0.62 g). Figure 2 show the chemical structure of N-(2-methoxyphenyl)-N'-4-methoxybenzoyl thiourea (B).

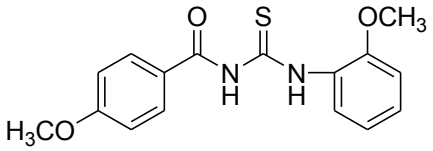


Figure 2. Chemical structure of *N*-(2-methoxyphenyl)-*N'*-4-methoxybenzoyl thiourea (B)

Synthesis of *N*-(2-nitrophenyl)-*N*'-4-methoxybenzoylthiourea (C)
This compound was prepared by similar procedure as above with 4-methoxybenzoyl chloride (5 mmol, 0.85 g), ammonium thiocyanate (5 mmol, 0.38 g) and 2-nitroaniline (5 mmol, 0.69 g). Figure 3 show the chemical structure of N-(2-nitrophenyl)-N'-4-methoxybenzoyl thiourea (C)

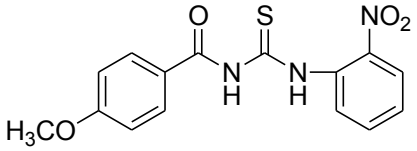


Figure 3. Chemical structure of *N*-(2-nitrophenyl)-*N*'-4-methoxybenzoyl thiourea (C)

Linear polarization resistance (LPR) technique
This method was carried out in a three-electrode cells consist of Silver-silver chloride (Ag/AgCl) as a reference electrode, platinum as a counter electrode and the mild steel sample as working electrode. The working electrode was prepared by embedding a rod with a mild steel sample in epoxy resin. The exposed surface area of the sample was 0.065 cm^2. The measurements by AUTOLAB potentiostat/galvanostat instrument equipped with NOVA software. The polarization curves were recorded at a rate of 0.5 mV s^{-1}. Prior to analysis, the working electrode was polished with emery paper, washed with distilled water, dried and finally immersed in the tested solution for an hour to achieve steady state. The tested solution used was sulphuric acid (H_2SO_4) with or without compound A, B and C.

Results and Discussion

Physical measurement
Table 1 shows the percentage yield, colour, melting point and elemental percentage of compound A, B and C. The composition values of the calculated and experimental for elemental analysis are in good agreement. Meanwhile, Table 2 shows the important FTIR adsorption bands, ^1H and ^{13}C NMR chemical shifts for the three compounds.

Table 1. Percentage yield, colour, melting point and elemental analysis for compound A, B and C

Compound	Percentage yield (%)	Colour	Melting point (°C)	Elemental analysis (Experimental) (%) C	H	N	S
A	52.9	White	140	62.94 (61.00)	4.90 (4.92)	9.79 (9.06)	11.19 (10.42)
B	63.1	White	138	60.76 (60.84)	5.06 (4.95)	8.86 (8.56)	10.12 (9.29)
C	58.7	White	142	54.38 (59.46)	5.06 (4.31)	12.69 (10.87)	9.67 (8.50)

Table 2. FTIR absorption bands, NMR proton (^{1}H) and carbon (^{13}C) shifts for compound A, B and C

Compound	FTIR				NMR ^{1}H		^{13}C	
	ν(NH)	ν(C=O)	ν(CN)	ν(C=S)	CONH	CSNH	C=O	C=S
A	3338.89	1655.58	1179.81	690.91	9.07	12.80	179.20	206.97
B	3222.93	1667.92	1221.54	712.89	9.03	12.90	179.06	207.15
C	3247.56	1670.21	1178.62	708.25	9.10	12.85	177.06	207.17

Linear polarization resistance

The polarization curves of mild steel in 1.0 M H_2SO_4 in the absence and presence of 4-methoxybenzoyl thiourea derivatives are shown in Figures 4 – 6. The corrosion parameters such as corrosion potential (E_{corr}), corrosion current density (i_{corr}), anodic Tafel slope (b_a), cathodic Tafel slope (b_c) and inhibition efficiency (IE%) are listed in Table 3. As compared with the H_2SO_4 without the presence of any inhibitor or also known as blank, it can be observed that i_{corr} decrease in the presence of the inhibitors and decrease as the concentration of the inhibitors increases. The decrease of these values with the presence of inhibitor and increasing inhibitors concentration indicates that there are inhibiting natures of the thiourea derivatives [13,14].

Table 3. LPR parameters of mild steel in 1.0 M H_2SO_4 containing different concentrations of A, B and C

Compound	Concentration (M)	b_a (V/dec)	b_c (V/dec)	E_{corr} (V)	i_{corr} (A/cm^2)	Corrosion rate (mm/year)	IE %
Blank	-	0.1339	0.0380	-0.4287	2.02E-04	2.3425	-
A	1 x 10^{-5}	0.0308	0.0214	-0.4119	5.83E-05	0.6767	71.1
	1 x 10^{-4}	0.1138	0.0256	-0.3941	5.39E-05	0.6258	73.3
	1 x 10^{-3}	0.0618	0.0208	-0.3693	4.13E-05	0.47919	79.6
B	1 x 10^{-5}	0.1042	0.0349	-0.4045	6.53E-05	0.7581	67.7
	1 x 10^{-4}	0.0697	0.0258	-0.3944	3.48E-05	0.4036	82.8
	1 x 10^{-3}	0.0570	0.0199	-0.3744	2.60E-05	0.3017	87.1
C	1 x 10^{-5}	0.1282	0.0406	-0.4226	0.00012	1.3890	40.6
	1 x 10^{-4}	0.0665	0.0340	-0.4110	6.43E-05	0.7460	68.2
	1 x 10^{-3}	0.1225	0.0460	-0.3900	6.36E-05	0.7386	77.6

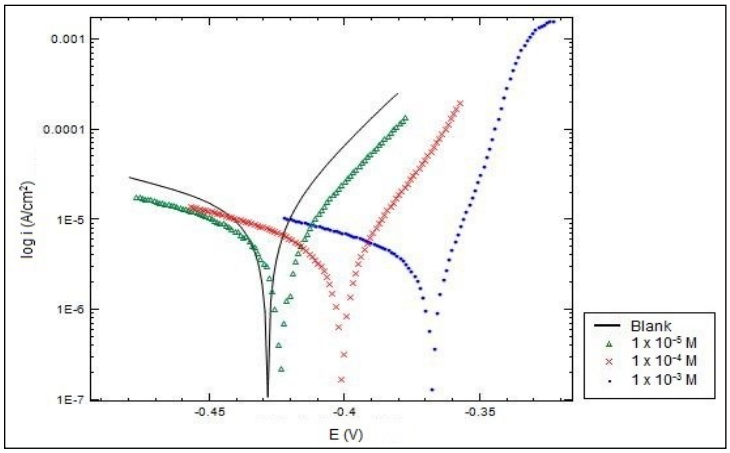


Figure 4. Polarization curves of various concentration of compound A in 1.0 M H_2SO_4

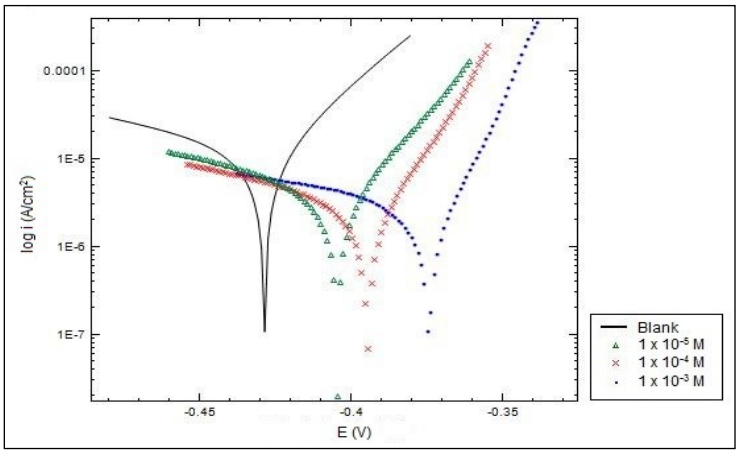


Figure 5. Polarization curves of various concentration of compound B in 1.0 M H_2SO_4

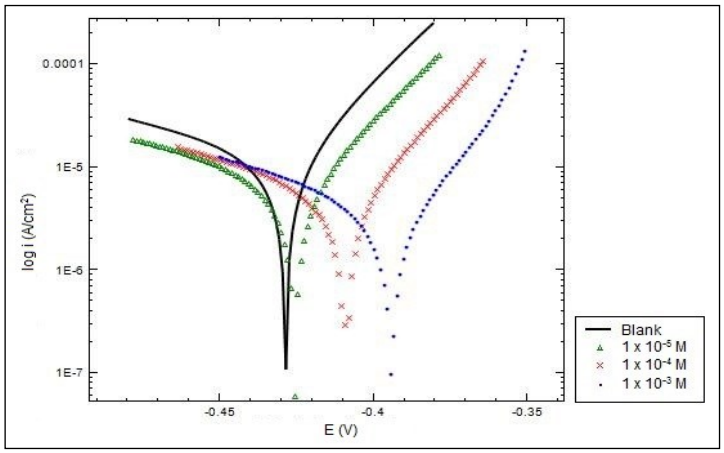


Figure 6. Polarization curves of various concentration of compound C in 1.0 M H_2SO_4

From Table 3, the E_{corr} values shown slight changes in the presence of the inhibitors. This means that the thiourea derivatives are mixed-type inhibitor in 1.0 M H_2SO_4. In addition, the average displacement of E_{corr} is not more than 85 mV, which suggest that these compounds are mixed-type inhibitors [13] even though the polarization curves shift toward the positive side with respect to blank. It also can be observed that the values of b_c did not change drastically with the addition of the compounds showing that thiourea derivatives did not affect the hydrogen evolution reaction [9]. The changes in b_a values with the inhibitors concentration shows that may alter the metal dissolution process. Results from this technique shows that the efficiency of these compounds increased as the concentration of corrosion inhibitor increased. The IE% of the inhibitor was calculated based on the i_{corr} values obtained from the measurement using the following formula equation 1 [15]:

$$\text{IE } \% = \frac{I'_{corr} - I_{corr}}{I'_{corr}} \quad (1)$$

where I'_{corr} and I_{corr} are the corrosion current densities in the absence and presence of an inhibitor, respectively.

Among these three compounds, compound B has the highest IE% which is 87.1%. The presence of different substituent in each compounds affect the IE%. Since compound B has methoxy substituent which is classified as electron donating group, it donates electrons to the system and make it electron rich. This enables the compound to form a protective layer on the metal surface. Unlike compound C which posses electron withdrawing group substituent (NO_2), the substituent will withdraw electrons from the system and make it unstable. Thus, forming a less effective layer. The order of the effectiveness of the compounds as corrosion inhibitors are B > A > C.

Conclusion

N-phenyl-*N'*-4-methoxybenzoylthiourea (A), *N*-(2-methoxyphenyl)-*N'*-4-methoxybenzoylthiourea (B) and *N*-(2-nitrophenyl)-*N'*-4-methoxybenzoylthiourea (C) has been successfully synthesized and characterized. Compound B with methoxy substituent has the highest IE% which is 87.1%. This compound has the potential as an effective corrosion inhibitor that can be used in acid pickling process in chemical or petroleum industries.

Acknowledgement

The authors are grateful to the Ministry of Higher Education of Malaysia for the research grant no. 600-FRGS/2/2013/ST01/UITM/02/6 and the Faculty of Applied Sciences, Institute of Science and Universiti Teknologi MARA for providing research facilities.

References

1. Likhanova N. V., Olivares-Xometl O., Guzmán-Lucero D., Domínguez-Aguilar M. A., Nava N., Corrales-Luna M. and Mendoza M. C. (2011). Corrosion inhibition of carbon steel in acidic environment by imidazolium ionic liquids containing vinyl-hexafluorophosphate as anion. *International Journal of Electrochemical Science*, 6: 4514 – 4536.
2. Kadhum A. A. H., Mohamad A. B., Hammed L.A., Al-Amiery A. A., San N. H and Musa A. Y. (2014). Inhibition of mild steel corrosion in hydrochloric acid solution by new coumarin. *Materials*, 7: 4335 –4348.
3. Selvakumar P., Karthik B.B. and Thangavelu C. (2013). Corrosion inhibition study of stainless steel in acidic medium – An overview. *Research Journal of Chemical Sciences*, 3(4): 87 – 95.
4. Yaro A. S. and Abdulaaima D. A. (2012). Phenyl thiourea as corrosion inhibitor for mild steel in strong hydrochloric acid. *Iraqi Journal of Chemical and Petroleum Engineering*, 13(2): 1 – 9.
5. Karthikeyan S., Harikumar S., Venkatachalam G., Naranayan S. and Venckatesh R. (2012). The inhibitive action of cyclohexyl thiourea on the corrosion and hydrogen permeation through mild steel in acidic solutions. *International Journal of ChemTech Research*, 4(3): 1065 – 1071.
6. Gopiraman M., Selvakumaran N., Kesavan D. and Karvembu R. (2012). Adsorption and corrosion inhibition behaviour of *N*-(phenylcarbamothioyl)benzamide on mild steel in acidic medium. *Progress in Organic Coatings*, 73: 104 – 111.
7. Edrah S. and Hasan. S. K. (2010). Studies on thiourea derivatives as corrosion inhibitor for aluminum in sodium hydroxide solution. *Journal of Applied Science Research*, 6: 1045 – 1049.
8. Khaled K. F. (2010). Experimental and molecular dynamic study on the inhibition performance of some nitrogen containing compounds for iron corrosion. *Material Chemistry and Physics*, 124: 760 –767.

9. Torres V. V., Rayol V. A., Magalhães M., Viana G. M., Aguiar L. C. S, Machado S. P., Orofino H. and D'Elia E. (2014). Study of thiourea derivatives synthesized from a green route as corrosion inhibitors for mild steel in HCl solution. *Corrosion Science*, 79: 108 – 118.
10. Torres V. V., Amado R. S., de Sá C. F., Fernandez T. L., Riehl C. A. S., Torres A. G, and D'Elia E. (2011). Inhibitory action of aqueous coffee ground extracts on the corrosion of carbon steel in HCl solution. *Corrosion Science*, 53: 2385 – 2392.
11. Khaled K. F. (2010). Experimental, density function theory calculations and molecular dynamics simulations to investigate the adsorption of some thiourea derivatives on iron surface in nitric acid solutions. *Applied Surface Science,* 256: 6753 – 6763.
12. Sanyal B. (1981). Organic compounds as corrosion inhibitors in different environments – A review. *Progress in Organic Coating.* 9: 165 – 236.
13. Gopiraman M., Selvakumaran N., Kesavan D., Kim I. S. and Karvembu R. (2012). Chemical and physical interactions of 1-benzoyl-3,3-disubstituted thiourea derivatives on mild steel surfaces: Corrosion inhibition in acidic media. *Industrial & Engineering Chemistry Research*, 51: 7910 – 7922.
14. Li X., Deng S. and Fu H. Allyl thiourea as a corrosion inhibitor for cold rolled steel in H_3PO_4 solution. *Corrosion Science*, 55: 280 – 288.
15. Tang T., Zhang F., Hu S., Cao Z., Wua Z. and Jing W. (2013). Novel benzimidazole derivatives as corrosion inhibitors of mild steel in the acidic media. Part I: Gravimetric, electrochemical, SEM and XPS studies. *Corrosion Science*, 74: 271 – 282
16. Ali, S.A., Saeed, M.T. and Rahman, S.V. (2003). The Isoxazolidines: A new class of corrosion inhibitors of mild steel in acidic medium, *Corrosion Science*, 45 (2): 253 – 266.

Malaysian Journal of Analytical Sciences, Vol 20 No 6 (2016): 1318 - 1328
DOI: http://dx.doi.org/10.17576/mjas-2016-2006-10

MALAYSIAN JOURNAL OF ANALYTICAL SCIENCES
Published by The Malaysian Analytical Sciences Society
ISSN 1394 - 2506

DETERMINATION OF TOTAL ORGANIC CARBON CONCENTRATION IN SURFICIAL SEDIMENTS OF SUNGAI PINANG, PENANG, MALAYSIA

(Penentuan Jumlah Karbon Organik dalam Sedimen Permukaan di Sungai Pinang, Pulau Pinang, Malaysia)

Ong Meng Chuan*, Fok Fei Mei, Yong Jaw Chuen

School of Marine and Environmental Sciences
Universiti Malaysia Terengganu, 21030 Kuala Terengganu, Terengganu, Malaysia

**Corresponding author: ong@umt.edu.my*

Received: 17 August 2015; Accepted: 11 October 2016

Abstract

The concentration of total organic carbon (TOC) and mean size sediment in a total of 24 samples of surficial sediment were determined. From the results of study, the concentration of TOC (5.33%) was found high nearby the housing area at Sungai Pinang. At the downstream of the river tend to have higher concentration of TOC (1.05% - 5.33 %) while at the upstream tend to have low degree of TOC in surficial sediments (0.36% - 0.78%). The major contribution in TOC contamination at the bottom part of the river maybe due to anthropogenic activities such as waste effluent from urban runoff, industrial activities and boat activities. Apart from that, the mean grain size was probably an important factor that influences the TOC content in surficial sediment at Sungai Pinang. This is because the distribution of the mean grain size that had similar trend to TOC. In addition, the high correlation relationship between TOC and mean grain size were observed and it had accounted for $r = 0.67$ owing to fine particles of sediment which had provided a large binding capacity for the sorption of organic carbon. Moreover, fine sediment probably indicates slow hydrodynamic energy at the downstream. It might affect the chemical sorption process and allow the particulate organic carbon to accumulate at the bottom of the water column. Thus, fine sediment maybe playing dominant role in the content of TOC in surficial sediment at Sungai Pinang.

Keywords: total organic carbon, mean size sediment, surficial sediments, Sungai Pinang

Abstrak

Kandungan jumlah karbon organik (TOC) dan purata saiz sedimen di dalam 24 sampel sedimen permukaan telah ditentukan. Dari hasil kajian ini, kepekatan TOC (5.33%) didapati tinggi berhampiran dengan kawasan perumahan di Sungai Pinang. Di kawasan hilir sungai tersebut mempunyai kepekatan TOC yang lebih tinggi (1.05% - 5.33%) manakala di kawasan hulu sungai mempunyai kepekatan yang rendah dalam permukaan sedimen (0.36% - 0.78%). Kemungkinan punca utama untuk pencemaran TOC di bahagian hilir sungai adalah dari aktiviti antropogenik seperti sisa buangan daripada bandar, aktiviti perindustrian dan aktiviti bot. Selain itu, purata saiz partikel kemungkinan adalah faktor penting menpergaruhi kandungan TOC dalam sedimen permukaan di Sungai Pinang. Ini kerana taburan purata saiz partikel mempunyai corak yang sama dengan TOC. Tambahan pula, hubungan korelasi antara TOC dan purata saiz partikel didapati tinggi dalam sedimen permukaan, iaitu $r = 0.67$ disebabkan saiz partikel yang halus memperolehi kapasiti pengikatan yang luas untuk penyerapan karbon organik. Selain itu, sedimen yang halus berkemungkinan menunjukkan tenaga hidrodinamik yang perlahan di bahagian hiliran. Hal ini berkemungkinan mempengaruhi proses penyerapan dan pengumpulan zarah karbon organik di bahagian bawah turus air. Oleh itu, sedimen yang halus berkemungkinan besar memainkan peranan yang paling dominan kepada kandungan TOC yang dalam sedimen permukaan di Sungai Pinang.

Kata kunci: jumlah karbon organik, purata saiz sedimen, sedimen permukaan, Sungai Pinang

Introduction

In general, total organic carbon (TOC) includes all of organic carbon compounds contain in sediment [1,2]. The amount of organic matter that can be stored in river sediment is influenced by several factors, for instances, the types and sources of organic compounds introduced, sediment texture, grain particle size and sedimentation [3,4]. In previous sediment geochemical-related research studies, TOC has been proved to be playing a dominant controlling factor as it manipulates the distribution of other components, including chemical component and biological component in aquatic environment [1,5]. The quantity of organic and inorganic chemical contaminants in sediments such as hydrophobic organic compounds and total mercury respectively were reported to have high correlation with TOC [6,7,8,]. This is because the organic matter is regulating the mobility of those pollutants in sediment [6,7,8]. In addition, some researchers are calculating the fraction of TOC with total sulfur while some other researchers determine the relationship between TOC and total nitrogen for the purpose of evaluation of the type of sedimentary environment and elucidate the dynamic of organic matter in sediment [2,3,9]. Hence, TOC is one of the important chemical sediment quality measurements that has been widely used in environmental evaluation analysis [1,8].

Surficial sediment was used as environment indicator in this present study. Surficial sediment is acting as the sink of TOC and other chemical pollutants as it is able to accumulate all the substances that have settled down on the bottom of water column, including particulate organic carbon and sediment particles which is attached with organic carbon substance [3,5,9]. Thus, surficial sediment is capable of reflecting the latest deposited pollution history [2,10]. On one hand, the strength of preservation of chemical components in surficial sediment is much greater and consistence [10]. However, some contaminants in sediment may return into water system if there is an environmental alteration [10]. Therefore, surficial sediment has been widely used as environmental tool by researchers.

It is important to determine the TOC content at Sungai Pinang because it is one of seven most contaminated river basins in Malaysia according to the Department of Environment (DOE) [11,12]. Based on National Water Quality Standards for Malaysia (NWQS), the water quality of Sungai Pinang basin was classified under IV which is very polluted in year 1999 [13]. In addition, previous study by Saad et al. [13] had concluded that the water quality of Sungai Pinang had degraded and was classified under V showing a very high level of chemical oxygen demand (COD) which was 1219.33 mg/L, very low in dissolved oxygen (DO) which account for < 1.0 mg/L and the temperature ($^{\circ}$C) of water was not categorized in normal range. Apart of that Sungai Pinang is surrounded by heavy industrial and urban areas, the river mouth is an important channel in the distribution of carbon matters [9,14]. Thus, the surficial sediment of Sungai Pinang is exposure to various chemical compound contamination which is contained in the bottom of the water.

In the recent years, Malaysia Environment Quality report (2012) showed that the water quality in Sungai Pinang estuary had improved to class ÏII [15]. However, chemical pollutants that is adsorbed onto the surface sediment, both inorganic and organic pollutants might be released back into water column if there is a sudden change in water quality [2,5]. The increment of toxicity level of pollutants eventually will give adverse impacts on the entire food web in the aquatic ecosystem [3,5]. Therefore, determination of TOC content (%) in the surface sediment is a vital piece of information to Department of Environment (DOE) or policy maker to take further actions in minimizing the anthropogenic discharge.

In the light of these reasons, the aim of the present study is to determine the concentration of TOC (%) in surface sediments at Sungai Pinang. Those results can be established as a baseline assessment of sediment quality. In addition, particle size of sediment is playing an important role in controlling the concentration of chemical components in sediment [5,16]. Therefore, the second objective is to reveal the relationship between TOC (%) and mean size sediments (Ø).

Materials and Methods

Study area

The sampling location is at Sungai Pinang (5° 24' N; l00^{o} 19' E) located in Penang Island, which situated in the northeast of Peninsular Malaysia (Figure 1). This research study was carried out on 20th of July in year 2013. In

order not to miss any hotspot that might contain extreme level of TOC, a total of 24 sampling stations was deployed along Sungai Pinang that is about 100 m apart from each other (Figure 2). The distance between P1 and P21 are about 2.47 km. The total area of Sungai Pinang basin is about 50.97 km^2 [13,17,18]. According to Malaysian Meteorological Department (MMD), Malaysia was having dry weather condition with low rainfall distribution that had accounted for less than 200 mm of precipitation in July of year 2013. Sungai Pinang was surrounded by 70% of wet markets with warehouses, small industrial facilities, residential areas, slaughter houses, and working areas which have a potential to release high amount of waste and toxic chemicals [13,17].

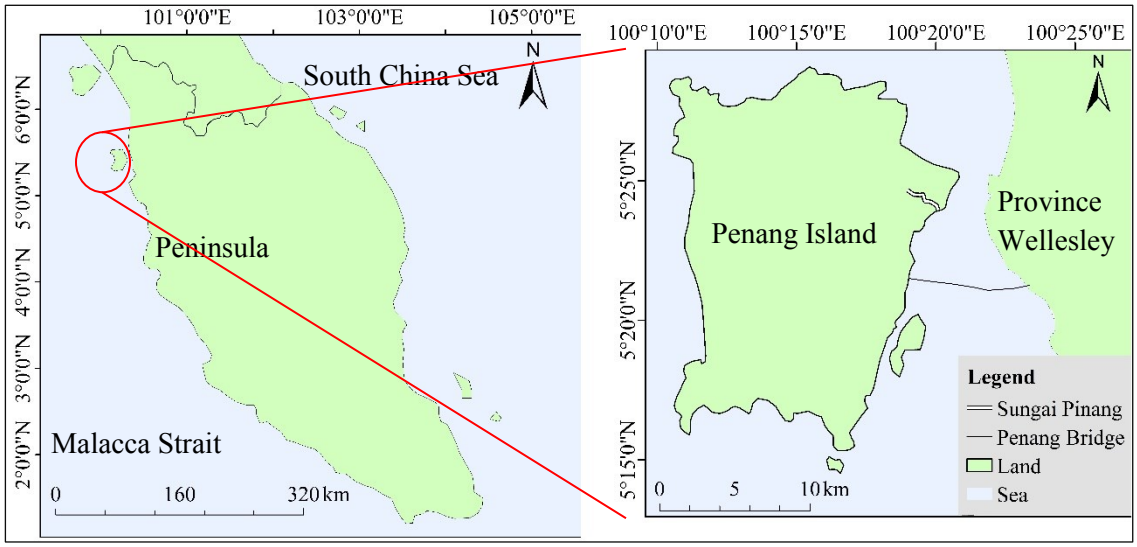


Figure 1. Sampling activity was conducted at Penang Island which is located at Northeast of Peninsular Malaysia

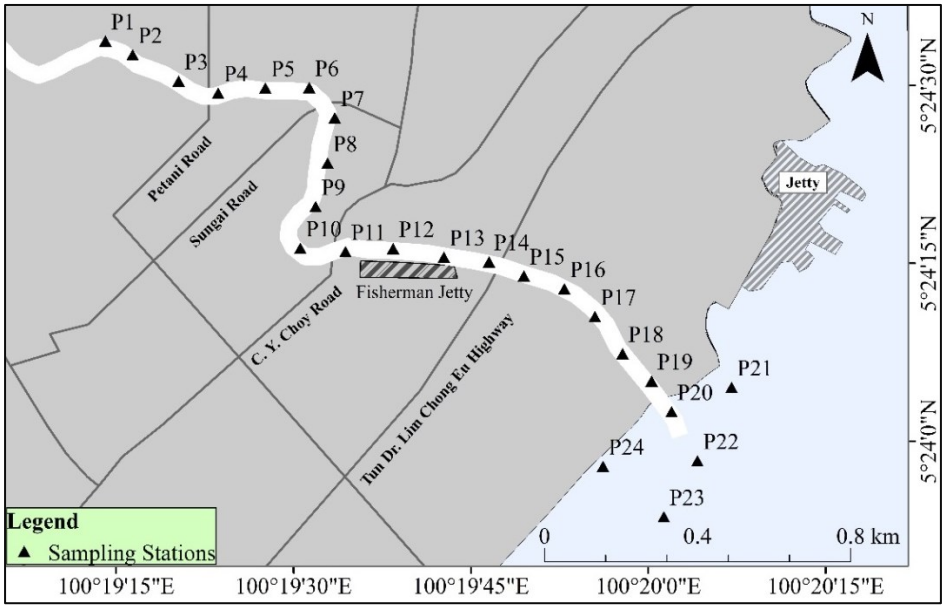


Figure 2. A total of 24 sampling locations was deployed along Sungai Pinang and its river mouth in Penang Island, Penang, Malaysia

For preparation of sampling activity, all apparatus including plastic spoon and polythene bag were cleaned with 10% of nitric acid and rinsed with distilled water. About 5 cm depth of the surface sediment samples were collected by Ponar grab. Precaution was taken to make sure the grab is firmly closed to ensure the maximum preservation of fine sediments samples, so that the reading for the size fractions of sediment is accurate [19]. The actual coordinate of sampling stations is recorded by using Global Positioning System (GPS). In order to minimize the chemical and biological reaction, sediments samples were kept at low temperature (< 4 ^{o}C) in an ice-box during sampling and is stored in a freezer after it is transferred back to the laboratory [19,20]. The sediment samples were dried using oven at 60 ^{o}C and weighed using electronic balance until consistency of samples weight was achieved [20]. The dried sediment samples were proceeded into two separate analyses.

Extraction method for total organic carbon

Wet oxidation method by means of titration was used to determine the TOC content in surficial sediment as it is simple, low in costing, and less equipment is needed for titration [21]. A total of 10 mL of 1 N potassium dichromates ($K_2Cr_2O_7$) was added into 0.5 g of sediments samples, standard solution (0.03 g of glucose) and blank solution (cleaned boiling tube) separately. Next, 20 mL of concentrated sulphuric acid (H_2SO_4) was added into the mixture. If the mixture sediments samples had changed into green color, 5 mL of $K_2Cr_2O_7$ will be added subsequently to ensure the mixture turn brown. The total volume of $K_2Cr_2O_7$ was recorded.

The mixtures were then heated to complete the digestion process for 30 minutes by using boiling bath water on a laboratory hot plate. Once 30 minutes is up, all the boiling tubes were set aside for cooling to allow the exothermic reaction to take place. The mixtures were rinsed with 200.0 mL of distilled water and transferred into Erlenmeyer flask (Standard solution and Blank solution should go through titration first before the titration of sediments sample solution). A volumes of 10.0 mL phosphoric acid (H_3PO_4) and 1 mL of indicator diphenylamine ($C_6H_5.2H_2O$) were added into the Erlenmeyer flask. A dark blue solution was observed.

The initial reading of the volume of Ferrous Sulfate ($Fe_2SO_4.7H_2O$) in the burette was recorded. The mixtures were then titrated with $Fe_2SO_4.7H_2O$ and mixed well with Orbital shaker. End point was reached when the solution turn into a light green in color [6]. The final reading for the volume of $Fe_2SO_4.7H_2O$ in burette was recorded. Percentage of carbon for glucose solution (Standard solution) was approximately 36 ± 5%. The calculation formula was applied to obtain percentage (%) of organic carbon, as shown in equation 1 below:

$$\text{Organic Carbon (\%)} = \frac{(V1-V2)\text{ x } 0.003\text{ x } 100}{\text{Weight of sample (g)}} \quad (1)$$

Where V1 is define as Volume of Potassium dichromate used (mL), V2 is define as Volume of Ferrous sulfate titrated (mL) and 10 mL of dichromate and 3 mg of carbon = 0.003 g carbon

Sediment characteristic analysis method for coarse sediment

Dry sieve method was used to determine the mean size of coarse sediment. A total of 200 g of dried sediment was sieved by using Sieves and Shaker for 10 minutes. A total of 14 different mesh size sieves was arranged consecutively downward from larger mesh size to fine size as follows: 4000 µm, 2800 µm, 2000 µm, 1400 µm, 1000 µm, 710 µm, 500 µm, 355 µm, 250 µm, 18 µm, 125 µm, 90 µm, 63 µm and < 63µm. Sediment samples retained in each layer of sieve were weighted by using an electronic balance. The reading of weight in each sieve was recorded [22]. Mean value can be computed by a moment method, as shown in equation 2 below:

$$\text{Mean } (\emptyset) = \frac{\sum \text{fm}}{n} \quad (2)$$

where f is defined as percentage weight of each grade of particle size (%), m is median of each particle in size in Ø and *n* is defined as total number of sample in 100 when f = %

Sediment characteristic analysis method for fine sediment

Laser diffraction method was used for the determination of the mean size of fine sediment. A total of 1.5 g of sediment samples was transferred into a centrifuge tube and 5 mL of 10% of Calgon solution was added. The

Calgon solution was used to disperse the bonded particle sediments [23]. The mixture was then topped up with distilled water to 50 mL and the grain size sediments were analyzed by using Particle Size Analyzer (PSA) [24].

Results and Discussion

Figure 3 shows the distribution of TOC (%) in surficial sediments of Sungai Pinang. According to the figure, the range was from 0.36% at P4 to 5.33% at P10 with the mean of 2.16%. The trend of TOC (%) remained steady at the upstream zone (from P1 to P9) and followed by a sharp rise at P10. The content of TOC remained constant and followed by a gradual decreased after P20. Housing area was observed at nearby P10 which had the highest TOC concentration at the studied river which is 5.33%. Additionally, there were a high number of fishing boats nearby P12 during sampling activities. In overall, the downstream zone of the river (from P13 to P24) showed that it was having high mean value of TOC concentration which accounted for 3.04% in comparison with upstream zone of the river, 1.28% (from P1 to P12).

TOC concentration is one of the measurements to estimate the amount of organic matters preserved in sediment [1,25]. The contribution of high in TOC concentration at Sungai Pinang might possibly be coming from the continuous deposit of organic matter from terrestrial, dead organisms, urban runoff, untreated waste effluent from industrial factories [1,25,26]. Additionally, variety of chemical wastes, for instance, fuel oil from boat activities which is shown at P12 was probably a major contributor of TOC concentration in surficial sediment [27,28]. This phenomenon can be seen at the Cape Town harbor which had an intense vessel traffic. It had suggested that the wastes discharges from shipping activities might be cause the elevated level of TOC concentration in surficial sediments [28]. In addition, it has been reported that high correlation relationship between total petroleum hydrocarbon and TOC concentration in surficial sediment was observed [27]. According to the research done by Ali et al. [27], it had mentioned that the possible sources of elevation in total petroleum hydrocarbon was closely related to shipping activities and it promotes the deposition of TOC content in surficial sediments.

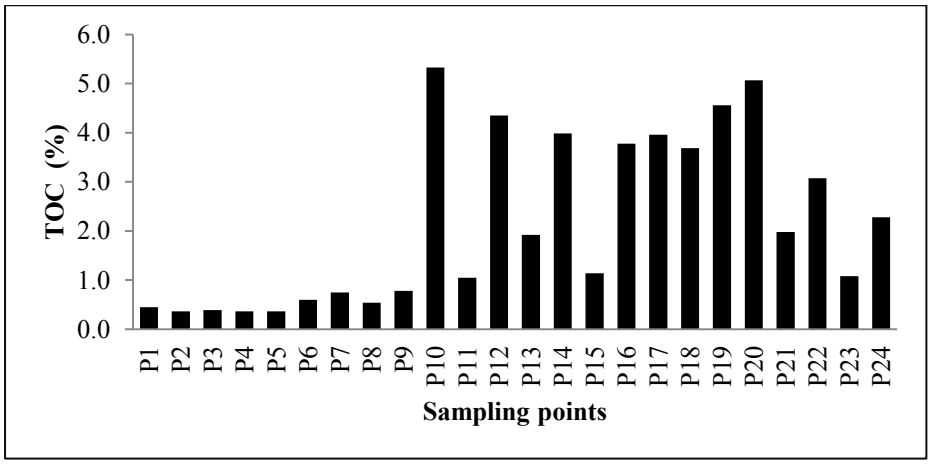


Figure 3. Distribution of TOC (%) in surficial sediments of Sungai Pinang, Penang

Apart from that, grain size sediment would be playing an important role which affects the organic matter bound to surface sediments [25,29]. The fine sediments have been known to be a preference for sorption of chemical compound [4,25,30]. Hence, it is indicated that sediment at lower catchment might possibly have wider surface area to volume ratio of binding site for organic compounds absorption [20,30]. In addition, fine particle sediment may denote slow hydrodynamic energy and particulate OC in water column have enough time to be absorbed on surficial sediment [20,30].

After P20 which is located at the river mouth, it tends to have a lower concentration of TOC and this phenomenon is similar to the estuary of Mahi River, India. Dinakaran and Krishnayya [14] had suggested that the sediment in the estuary might be affected by backwater system. In addition, the other physical components including tidal alteration might influence the level of TOC in sediments at river mouth [2].

The effect of high content of OC in surficial sediment might have contributed to the depletion of DO at the bottom of water column at the downstream of Sungai Pinang [1]. This is because high number of organic matter is promoting the growth of anaerobic bacteria which needs the DO to carry out their microbial activities [1,7].

Although high content of organic matter in aquatic environment may not contribute to a significant threat to human health, it will enhance the synergic effects when it is associated with other chemical compounds and nutrient availability [3,5,7]. It has been reported that TOC concentration is one of the important chemical factors that regulates the behavior of other chemical components in sediments [1,2,5]. Thus, determination of TOC concentration in surficial sediment is taken into the account of environment characteristic analysis [1, 2].

The comparison concentration of TOC (%) in surficial sediment of Sungai Pinang and other regions are shown in Table 1. From the table compassion, Sungai Pinang recorded higher TOC level compared to other rivers such as Sungai Klang basin [31], Sungai Langat [32], Yangtze Estuary [33], Changhua River Estuary [34], Pearl River Estuary [35], Danube River [36] and Beijiang River [37] except Port Klang in Malaysia [20]. Different environmental condition of each study location might probably give different results on TOC content in the surficial sediment. Port Klang, Malaysia has the highest concentration of TOC compared to present study as it reported that the source of TOC concentration probably caused by the discharge of chemical contaminants from shipping area and industrial wastes, weak water current as well as high portion of fine-sized grains sediments [20]. Thus, the fine grain size might be acting as synergic effects in concentration of TOC.

Table 1. Comparison of concentration TOC in surface sediments of Sungai Pinang to published data from similar habitat environments

Area	**TOC (%)**	**References**
Sungai Pinang	2.16 – 5.33 (2.16)	Present study
Malaysia Region		
Sungai Klang	0.19 – 4.5	[31]
Port Klang, Selangor	5.35 – 24.88	[20]
Sungai Langat	0.08 – 3.42	[32]
Others Region		
Yangtze Estuary, China	0.098 – 0.82 (0.436)	[33]
Changhua River Estuary, China	0.01 – 0.88 (0.55)	[34]
Pearl River Estuary	0.48 – 1.14	[35]
Danube River, Serbia	0.2 – 2.82	[36]
Beijing River, China	1.29 ± 0.82	[37]

Figure 4 shows the sediments mean size (Ø) in surficial sediments of Sungai Pinang. The mean grain size was classified according to Wentworth size class [38]. From the grain size sediments analysis, the largest particle size of sediments was recorded at P2 in which is under the coarse grain size category (-0.67Ø), while the finest particle size of sediments was located at P23 (5.46Ø) which was classified as medium silt. The average of mean size of sediments of the 24 sampling stations at Sungai Pinang was 2.63Ø. The trend showed the particle size of sediments decreases gradually from upstream of river towards river mouth.

The upper river catchment had higher composition of coarse sediments compared to downstream. According to [2,20], the environmental changes of river such as transportation and process of sedimentary as well as distribution of material input would affect the grain size of sediments. Additionally, upstream zone tends to have coarser grain size sediments which have a higher possibility of strong hydraulic energy which causes the fine sediment particles to have a shorter residence time which reduces the deposits at the bottom of water column [4, 33,39]. Moreover, silt and clay have more loose fabric with higher degree of porosity and permeability, which is easier to be transported to downstream and leave coarser sediments on the river bed [25,40].

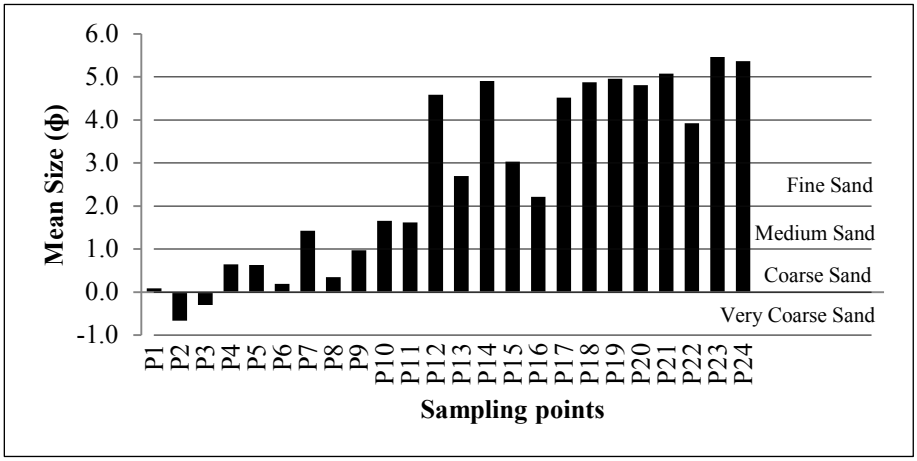


Figure 4. Variation of mean sediment size (Ø) in surficial sediments of Sungai Pinang, Penang

The type of surface sediments at Sungai Pinang varies from coarse sand to medium silt. Figure 5 shows the average sediments texture percentage (%) in surficial sediments of Sungai Pinang. The trend of sand grain size (63 – 2000 µm) decreases towards the river mouth while for the trend of silt and clay grain size is shown to be vice versa. From the result of sediments texture percentage (%), it was shown that the highest proportion for the category of silt grain size (4 – 63 µm) was found at P23 which was accounted for 81.39% whereas for the category of clay grain size (< 4 µm) was found in P21, 4.72% was observed.

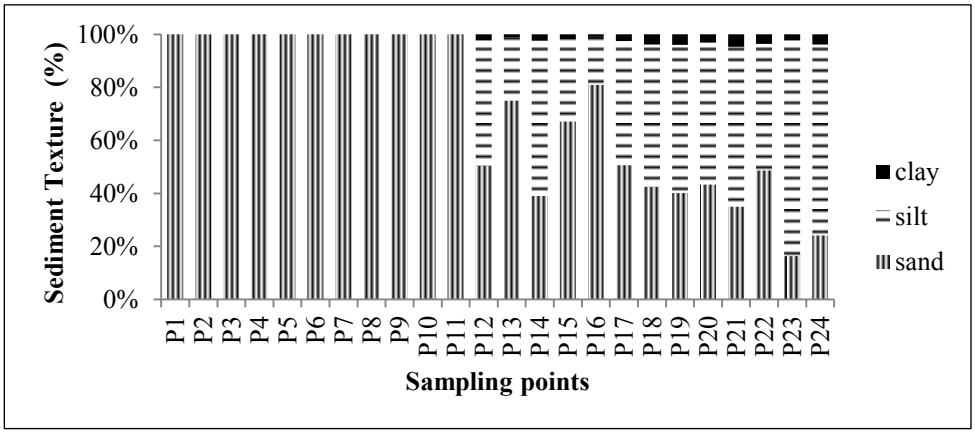


Figure 5. An average percentage sediments texture (%) in surficial sediments of Sungai Pinang, Penang

Downstream tend to have high proportion of slit and clay grain size sediments. It indicates that it might have a low hydrodynamic condition at the estuary [20,30]. The low water flow condition leads to sediments being suspended in water column to have more time to sink and redeposited at the bottom [20]. The consequences of river transportation were found in many rivers such as Klang River [20], Juru River, Malaysia [41] and Keelung River drainage basin, Taiwan [42] Furthermore, estuary has been well known as a settlement for sedimentation during tidal period and tends to have higher sedimentation rate [20, 41].

Generally, fine particle sediments are well known as dominant controlling factors to regulate the TOC concentration in surficial sediment [14,20,33]. Figure 6 shows the correlation relationship of high percentage of TOC concentration is directly proportional to fine sediments size and it is accounted for $r = 0.67$. It was suggesting that the finer grain size sediments might be a significant factor in controlling the TOC content in surficial sediments at Sungai Pinang [14,20,34]. This is because the fine sediments are providing a larger specific surface area and binding sites for organic carbon absorption [4,33,40]. This phenomenon also can be seen at Port Klang, Malaysia as it is reported that the fine grain size sediment had a significant positive correlation with TOC concentration [20].

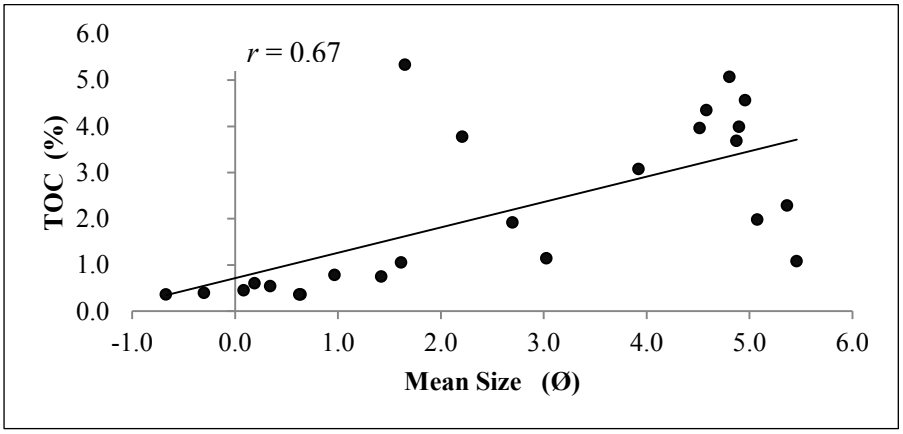


Figure 6. Correlation between TOC (%) and mean sediments size (Ø) in surficial sediments of Sungai Penang

Conclusion

In conclusion, the highest concentration of TOC (5.33%) at Sungai Pinang was found nearby housing area. At the downstream of Sungai Pinang tend to have a high concentration of TOC (1.05% - 5.33%). This is because the fine particle of sediments had provided larger binding sites to organic carbon for absorption. Apart from that, the fine sediments were probably denoted slow hydrodynamic energy at the downstream. It might strengthen the absorption process and lead to accumulation of TOC at the bottom of water column. Thus, the grain size sediment might be playing an important role as controlling factor of concentration of TOC in surficial sediments at Sungai Pinang. The results of present study are a necessity in making assessment of sediment quality and ecological risk. This is because the TOC is one of the controlling factors in regulating the chemical and biological compounds in surficial sediments. The chemical organic and inorganic pollutants such as polycyclic aromatic hydrocarbons (PAHs) and heavy metals respectively in surficial sediments can be the secondary source of water pollution if there is an environmental change. Consequently, it will give a deleterious health effects on living organisms in aquatic environment.

Acknowledgement

This research was conducted with funding from the Ministry of Higher Education Malaysia (MOHE), under the Niche Area Research Grant Scheme (NRGS) project number 53131 and Fundamental Research Grant Scheme (FRGS) 59299. The authors wish to express their gratitude to Oceanography and Biodiversity Laboratory, School of Marine and Environmental Sciences teams for their invaluable assistance and providing the facilities to carry out

the research. We are grateful to our editors and referees for their invaluable comments that helped improve this manuscript.

References

1. Lazăr, L., Gomoiu, M.T., Boicenco, L. and Vasili, D. (2012). Total organic carbon (TOC) of the surface layer sediments covering the seafloor of the Romanian black sea. *Geo-Eco-Marina,* 18: 121 – 132.
2. Hossain, G. M. and Bhuiyan, M. A. H. (2016). Spatial and temporal variations of organic matter contents and potential sediment nutrient index in the sundarbans mangrove forest, Bangladesh. *KSCE Journal of Civil Engineering*, 20 (1): 163 – 174.
3. Anawar, H. M., Yoshioka, T., Konohira, E., Akai, J., Freitas, M. C. and Tareq, S. M. (2010). Sources of organic carbon and depositional environment in the Bengal delta plain sediments during the holocene period. *Limnology*, 11 (2): 133 – 142.
4. Manju, M. N., Resmi, P., Kumar, Ratheesh, C. S., Gireeshkumar, T. R., Chandramohanakumar, N. and Joseph, M. M., (2016). Biochemical and stable carbon isotope records of mangrove derived organic matter in the sediment cores. *Environmental Earth Sciences*, 75: 565 – 580.
5. Naji, A., Ismail, A. and Ismail, A. R. (2010). Chemical speciation and contamination assessment of Zn and Cd by sequential extraction in surface sediment of Klang River, Malaysia. *Microchemical Journal,* 95 (2): 285 – 292.
6. Kwaansa-Ansah, E. E., Voegborlo, R. B., Adimado, A. A., Ephraim, J. H. and Nriagu, J. O. (2012). Effect of pH, sulphate concentration and total organic carbon on mercury accumulation in sediments in the volta lake at yeji, ghana, *Bulletin of Environmental Contamination and Toxicology*, 88 (3): 418 – 421.
7. Shoham-Frider, E., Azran, S. and Kress, N. (2012). Mercury speciation and total organic carbon in marine sediments along the Mediterranean coast of Israel. *Bulletin of Environmental Contamination and Toxicology,* 63 (4): 495 – 502.
8. Hall Jr, L. W. and Anderson, R. D. (2014). Relationship of bifenthrin sediment concentrations to grain size and total organic carbon in California waterbodies: Implications for ecological risk. *Bulletin of Environmental Contamination and Toxicology,* 93 (6): 764 – 768.
9. Zhao, C., Liu, S., Dong, S., Isange, S., Liu, Q., An, N. and Li, X. (2015). Spatial and seasonal dynamics of organic carbon in physically fractioned sediments associated with dam construction in the middle Lancang-Mekong River. *Journal of Soils and Sediments,* 15 (11): 2323 – 2333.
10. Mei, J., Li, Z., Sun, L., Gui, H. and Wang, X. (2011). Assessment of heavy metals in the urban river sediments in Suzhou City, Northern Anhui Province, China. *Procedia Environmental Sciences,* 10: 2547 – 2553.
11. Daud, H. (2008). The water quality monitoring system/ program & pollution control. Retrieved from Water Environment Partnership in Asia Web Site: http://www.wepa-db.net/pdf/0810malaysia/f.pdf
12. Usali, N. and Ismail, M. H. (2010). Use of remote sensing and GIS in monitoring water quality. *Journal of Sustainable Development,* 3 (3): 228 – 238.
13. Saad, F. N., Rahman, N. N., Kadir, M. O. and Omar, F. M. (2008). Identification of pollution sources within the Sungai Pinang River Basin. *Proceeding of the Malaysian Research Group International Conference, Manchester, United Kingdom*: pp. 478 – 485.
14. Dinakaran, J. and Krishnayya, N. S. R. (2011). Variations in total organic carbon and grain size distribution in ephemeral river sediments in Western India. *International Journal of Sediment Research*, 26 (2): 239 – 246.
15. Department of Environment (2012). *Malaysia Environment Quality Report*. Department of Environment Malaysia: pp. 112.
16. Meng, J., Yao, P., Yu, Z., Bianchi, T. S., Zhao, B., Pan, H. and Li, D. (2014). Speciation, bioavailability and preservation of phosphorus in surface sediments of the Changjiang estuary and adjacent East China Sea inner shelf. *Estuarine, Coastal and Shelf Science,* 144: 27 – 38.
17. Maznah, W. O. and Mansor, M. (2002). Aquatic pollution assessment based on attached diatom communities in the Pinang River basin, Malaysia. *Hydrobiologia*, 481(1): 229 – 241.
18. Misnan, N. and Rindam, M. (2012). Morfometri lembangan sungai-sungai utama di Pulau Pinang. *Malaysia Journal of Society and Space,* 8(3): 71 – 81.
19. Ong, M., Menier, D., Shazili, N. and Kamaruzzaman, B. (2013). Geochemical characteristics of heavy metals concentration in sediments of Quiberon Bay waters, South Brittany, France. *Oriental Journal of Chemistry,* 29 (1): 39 – 45.

20. Sany, S. B., Salleh, A., Rezayi, M., Saadati, N., Narimany, L. and Tehrani, G. M. (2013). Distribution and contamination of heavy metal in the coastal sediments of Port Klang, Selangor, Malaysia. *Water, Air, and Soil Pollution,* 224 (4): 1 – 18.
21. Tung J. W. T. and Tanner, P. A. (2003). Instrumental determination of organic carbon in marine sediment. *Marine Chemistry,* 80 (2-3): 161 – 170.
22. Folk, R. L. (1980). Petrology of sedimentary rocks Austin: University of Texas Libraries
23. Ong, M. C., Kamaruzzaman, B. Y., Shazili, N. A. and Rosnan, Y. (2006). Distribution and normalization of lead, copper and zinc in Terengganu , Malaysia. *Journal Sustainability Science and Management,* 1: 74 – 84.
24. Plumb, R. H. (1981). Procedures for handling and chemical analysis of sediment and water samples. Retrieved from United State Environmental Protection Agency: http://yosemite.epa.gov/r10/CLEANUP.NSF/ph/T4+Technical+Documents/$F
25. Özkan, E. Y. (2012). A New assessment of heavy metal contaminations in an eutrophicated bay (Inner Izmir Bay, Turkey). *Turkish Journal of Fisheries and Aquatic Sciences,* 12: 135-147.
26. Swarnalatha, K., Letha, J. and Ayoob, S. (2013). An investigation into the heavy metal burden of Akkulam–Veli Lake in South India. *Environmental Earth Sciences,* 68 (3): 795 – 806.
27. Ali, S. A. M., Payus, C. and Ali, M. M. (2015). Surface sediment analysis on petroleum hydrocarbon and total organic carbon from coastal area of Papar to Tuaran, Sabah. *Malaysian Journal of Analytical Sciences*, 19 (2): 318 – 324.
28. Okoro, H. K., Fatoki, O. S., Adekola, F. A., Ximba, B. J. and Snyman, R. G. (2016). Spatio-temporal variation of organotin compounds in seawater and sediments from Cape Town Harbour, South Africa using gas chromatography with flame photometric detector (GC-FPD). *Arabian Journal of Chemistry*, 9 (1): 95 – 104.
29. Mulligan, C., Fukue, M. and Sato, Y. (2010). Sediment contamination and sustainable remediation. London: CRC Press.
30. Li, G., Cao, Z., Lan, D., Xu, J., Wang, S. and Yin, W. (2007). Spatial variations in grain size distribution and selected metal contents in the Xiamen Bay, China. *Environmetal Geology,* 52 (8): 1559 – 1567.
31. Naji, A. and Ismail, A. (2011). Assessment of metals contamination in Klang River surface sediments by using different indexes. *EnvironmentAsia,* 4(1): 30 – 38.
32. Adnan, N. H., Zakaria, M. P., Juahir, H. and Ali, M. M. (2012). Faecal sterols as sewage markers in the Langat River, Malaysia: Integration of biomarker and multivariate statistical approaches. *Journal of Environmental Sciences,* 24(9): 1600 – 1608.
33. Zhao, S., Feng, C., Wang, D., Liu, Y. and Shen, Z. (2013). Salinity increases the mobility of Cd, Cu, Mn, and Pb in the sediments of Yangtze Estuary: Relative role of sediments' properties and metal speciation. *Chemosphere,* 91 (7): 977 – 984.
34. Hu, B., Cui, R., Li, J., Wei, H., Zhao, J., Bai, F., Song, W. and Ding, X. (2013). Occurrence and distribution of heavy metals in surface sediments of the Changhua River estuary and adjacent shelf (Hainan Island). *Marine Pollution Bulletin,* 76 (1-2): 400 – 405.
35. Wang, F., Wang, W. X. and Huang, X. P. (2012). Spatial distribution of gut juice extractable Cu, Pb and Zn in sediments from the Pearl River Estuary, Southern China. *Marine Environmental Research,* 77: 112 – 119.
36. Relić, D., Đorđević, D. and Popović, A. (2011). Assessment of the pseudo total metal content in alluvial sediments from Danube River, Serbia. *Environmental Earth Science,* 63(6): 1303 – 1317.
37. Chen, L. G., Huang, Y. M., Peng, X. C., Xu, Z., Zhang, S., Ren, M., Ye, Z. and Wang, X. (2009). PBDEs in sediments of the Beijiang River, China: Levels, distribution, and influence of total organic carbon. *Chemosphere,* 76 (2): 226 – 231.
38. Wentworth C. K. (1922). A scale of grade and class terms for clastic sediments. *Journal of Geology*, 30: 377 – 392.
39. Satpathy, K. K., Mohanty, A. K., Prasad, M. V., Natesan, U. and Sarkar, S. K. (2012). Studies on the variations of heavy metals in the marine sediments off Kalpakkam, East Coast of India. *Environmental Earth Science,* 65 (1): 89 –101.
40. Kamaruzzaman, Y. and Ong., M. C., (2009). Geochemical proxy of some chemical elements in sediments of Kemaman River estuary, Terengganu, Malaysia. *Sains Malaysiana,* 38 (5): 631 – 636.
41. Idriss, A. A. and Ahmad, A. K. (2013). Heavy metals nickel and chromiumin sediments in the Juru River, Penang, Malaysia. *Journal of Environmental Protection,* 7: 1245 – 1253.

42. Huang, K. M. and Lin, S. (2003). Consequences and implication of heavy metal spatial variations in sediments of the Keelung River Drainage basin, Taiwan. *Chemosphere,* 53 (9): 1113 – 1121.

Malaysian Journal of Analytical Sciences, Vol 20 No 6 (2016): 1329 - 1337
DOI: http://dx.doi.org/10.17576/mjas-2016-2006-11

MALAYSIAN JOURNAL OF ANALYTICAL SCIENCES
Published by The Malaysian Analytical Sciences Society
ISSN 1394 - 2506

SYNTHESIS AND CHARACTERIZATION OF EPOXIDIZED NEOPENTHYL GLYCOL DIOLETE AS AN INTERMIDIATE OF BIOLUBRICANT

(Sintesis dan Pencirian Epoksida Dioleat Neopentil Glikol Sebagai Bahan Perantara Biopelincir)

Vanitah Rajaendran[1], Jumat Salimon[1], Rahimi M.Yusop[1,2]*

[1]*School of Chemical Sciences and Food Technology, Faculty of Science and Technology, Universiti Kebangsaan Malaysia, 43600 UKM Bangi, Selangor, Malaysia*
[2]*Regenerative Medicine Cluster, Advance Medical and Dental Institute, Universiti Sains Malaysia, 13200 Bertam Kepala Batas, Pulau Pinang, Malaysia*

**Corresponding author: rahimi@ukm.edu.my*

Received: 4 April 2016; Accepted: 5 August 2016

Abstract

Neopenthyl glycol dioleate (NPGDO) is a biolubricant base that was formed via esterification process with oleic acid. The presence of oleic acid leads to poor oxidative stability. In this study, epoxidation reaction between NPGDO, formic acid and hydrogen peroxide has been carried out to produce epoxidized NPG dioleate (ENPGDO) which acts as the intermediate of biolubricant. Epoxidized oil can be further modified for better properties. The temperature for this reaction was 40 °C and the molar ratio of NPGDO:formic acid:hydrogen peroxide was 1:3:4. The reaction had taken place for 3 hours. The presence of the epoxy in the product was confirmed through Fourier Transform Infrared (FTIR). The structure of ENPGDO was confirmed using both proton and carbon Nuclear Magnetic Resonance (^{1}H-NMR and ^{13}C-NMR) analysis. The product was found to have 218 (viscosity indeks), 205 °C (flash point), −18 °C (pour point) and 197 °C (oxidative stability). The relative conversion of oxirane (RCO) for ENPGDO was 97.5%.

Keywords: biolubricant, neopenthyl glycol, oleic acid, epoxidized NPG diolete

Abstrak

Dioleat neopentil glikol (DONPG) merupakan bahan asas biopelincir yang dihasilkan melalui tindak balas pengesteran dengan asid oleik. Kehadiran asid oleik menjadikan kestabilan oksidatifnya rendah. Di dalam penyelidikan ini, pengepoksidaan antara DONPG, asid formik dan hidrogen peroksida dilakukan bagi menghasilkan epoksida dioleat NPG (EDONPG) yang bertindak sebagai bahan perantara biopelincir. Modifikasi kimia dilakukan ke atas EDONPG menghasilkan sifat yang lebih baik. Suhu bagi tindak balas ini adalah 40 °C dan nisbah molar DONPG: asid formik: hidrogen peroksida adalah 1:3:4. Masa tindak balas adalah 3 jam. Kehadiran epoksi di dalam produk ditentukan melalui spektroskopi Fourier transformasi inframerah (FTIR). Struktur EDONPG pula ditentukan melalui proton dan karbon spektroskopi resonan magnetik nuklear (^{1}H-NMR and ^{13}C-NMR). Pencirian fizikal produk dimana indeks kelikatan produk adalah (218), takat kilat (205 °C), takat tuang (−18 °C) dan kestabilan oksidatif (197 °C). Relatif pertukaran oksirana (RCO) produk ialah 97.5%.

Kata kunci: biopelincir, neopentil glikol, asid oleik, epoksida dioleat NPG

Introduction

Biolubricant is a perfect substitute of mineral-based lubricants. The utilization of renewable feedstock to produce biolubricants has overcome the depletion of source problem faced by mineral-based lubricants. The biodegradable feedstock reduces environment pollution issues [1]. Biolubricants also have high viscosity index, high flash points,

good lubricity and less toxic properties. Hence, the subject of biolubricant has become the key interest by researchers and highly favourable by consumers. Although, biolubricants may have poor low temperature properties, as well as low oxidative and thermal stability [2] which require improvements through chemical modifications such as epoxidation and oxirane ring opening.

The highly reactive epoxide is a three-membered cyclic ether that suits the characteristic of an excellent raw material for further chemical modification. This chemical modification such as oxirane ring opening could improvise the properties of a product to make it more practical for industrial uses [3]. Epoxide products have extensively been used as a plasticizer and additive in biolubricant [4]. It is rather crucial for biolubricants to have a good oxidative stability as it reflects the quality and shelf life of the oil. Therefore, epoxidation could be performed to produce oil with better oxidative stability.

Recently, a growing body of literature has established the relavence of vegetable oil or unsaturated fatty acids epoxidation. The epoxidized carbon double bond provides a space for further reactions. Epoxidation on mustard oil was carried out which resulted in better oxidative sability [5]. The improvement on oxidative stability was achieved by converting the double bond in oil into oxirane ring. Epoxidation process can be carried out with and without the presence of catalyst. A catayst is used to produce higher yield and percentage of RCO.

In this study, the main purpose was to develop a biolubricant intermediate from NPGDO via epoxidation. Epoxidation was conducted without catalyst. Optimization of epoxidation was carried out to produce ENPGDO with higher yield and maximum percentage of RCO at mild condition. Epoxidized NPGDO act as an intermediate of biolubricant.

Materials and Methods

Materials

The NPGDO used was synthesized in the laboratory. It was prepared via esterification between NPG and oleic acid in ratio 1:2 at 130 °C for 4 hours with 2% of sulphuric acid as a catalyst. The NPGDO was purified. Hydrogen peroxide, formic acid and sodium chloride used in this experiment were purchased from Systerm. The sodium hydrogen bicarbonate and sodium sulphate were purchased from R&M Chemicals.

Epoxidation procedure

The NPGDO was added into a 250 ml three-necked round bottom flask which was equipped with thermometer, magnetic stirer and a stopper. Formic acid was added according to mole ratio ranging from 1:1 up to 1:5 of NPGDO:formic acid. The round bottom flask was attached to a condenser with heating mantle. Temperature and reaction time were tested at 20 °C to 60 °C and 2 hours up to 6 hours respectively. Peroxide acid was then added drop wise into the flask for 60 minutes. Mole ratio of NPGDO to peroxide acid used in this experiment was 1:1 to 1:5. At the end of the reaction, the mixture was washed with 100 mL of 5% of sodium bicarbonate, 100 mL of 5% sodium chloride and 100 mL of distilled water to remove the acidity. It was then dried overnight with magnesium sulphate. The ethyl acetate solvent used in the mixture to extract oil was removed using a rotary evaporator [6].

Epoxidized NPG dioleate analysis

The oxirane oxygen content (%OOC) were calculated according to AOCS recommended practices. The relative conversion to oxirane was calculated using the following expression (equation 1) as reported by Michelle [3]:
Relative conversion to oxirane content:

$$\mathrm{RCO} = OOc/OOt \tag{1}$$

where, OOc is define as experimental oxygen oxirane and OOt is define as theoretical maximum oxirane oxygen from the expression (equation 2);

$$OO_{\mathrm{t}} = \left(\frac{IV_{\mathrm{O}}/2Ai}{100+(IV_{\mathrm{O}}/2Ai)A_{\mathrm{O}}}\right) Ao \times 100 \tag{2}$$

where, A_i (126.9) and A_0 (16) are atomic weight of iodine and oxygen respectively. Meanwhile, IV_0 is the initial iodine value of sample.

Formation of epoxy was confirmed by using Perkin Elmer GX FTIR in the range of 400 cm^{-1} to 4000 cm^{-1}. Subsequently, the ENPGDO was analysed with ^{1}H NMR and ^{13}C NMR using Bruker ARX-600 for structure conformation. Tetramethyl Silen (TMS) were used as internal standard with deuterochloroform as solvent.

Epoxidized NPG dioleate physicochemical analysis

The improvement in the characteristics of NPGDO and ENPGDO were analysed. For the pour point and oxidative stability, Differential Scanning Calorimetri (DSC) was used. The flash point was determined using ASTM D92 method (ASTM1965). The viscosity of the sample was analysed using Rhemometer Anton Paar at 40 ºC and 100 ºC. For the calculation of viscosity index (VI), ASTM 2270 method (ASTM 1964), the equation 3 or 4 was used as below:

For oils of 0 to 100 VI:

$$VI = [(L- U) / (L-H)] \times 100 \quad (3)$$

where, U is define as kinematic viscocity of oil in centistokes at 40 °C, L and H is value from Table L and H based on kinematic viscocity (cSt) at 100 °C.

For oils of 100 VI and greater:

$$VI = [((\text{antilog } N) - 1) / 0.00715] = 100 \quad (4)$$

where, U is define as kinematic viscocity of oil in centistokes at 40 °C, Y is define as kinematic viscocity of oil in centistokes at 100 °C, and L and H is the value from Table L and H based on kinematic viscocity (cSt) at 100 °C.

Results and Discussion

Neopentyl glycol (NPG) is a polyhydic alcohol. It does not contain hydrogen in β position as glycerol. β hydrogen atom can lead to partial defragmentation into unsaturated compound at high temperature. This compound will later undergo polymerization and form precipitates [7]. In this study, NPG was esterified with oleic acid to form NPGDO. Unsaturation leads to poor oxidative and thermal stability. Meanwhile saturated fatty acid will cause poor low temperature properties. Monounsaturated oleic acid gives moderate oxidative stability and better low temperature properties. It also provides space for chemical modification to improve the properties of NPGDO [7].

Epoxidation of olefin is an important reaction for further chemical modification on NPGDO. The double bond of oleic acid in NPGDO causes the poor oxidative stability. The oxidative and thermal stability have been improved via epoxidation. Epoxidized oil acts as antirust in biolubricant. The biodegradability of oil remains the same [8]. Figure 1 shows the reaction scheme of epoxidized NPG dioleat. Epoxide is a compound with a cyclic ether with three-ring atom which is highly strained. Due to this, it is very reactive and treated as an intermediate for further reaction [3].

The optimization for this reaction was done to obtain ENPGDO in high yield with high oxygen oxirane content (OOC) and high percentage of RCO. OOC value describes the weight percent of oxirane oxygen in a molecule. It shows the conversion of unsaturation to epoxy groups [9]. Figure 2 shows the effect of different mol ratio of NPGDO:formic acid on percentage of RCO. From Figure 2, the highest percentage of RCO is at mol ratio 1:3.

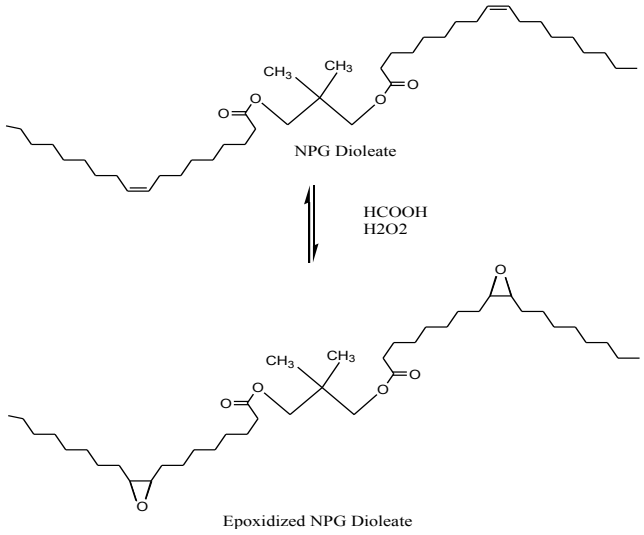


Figure 1. Reaction scheme for the epoxidized NPG dioleate

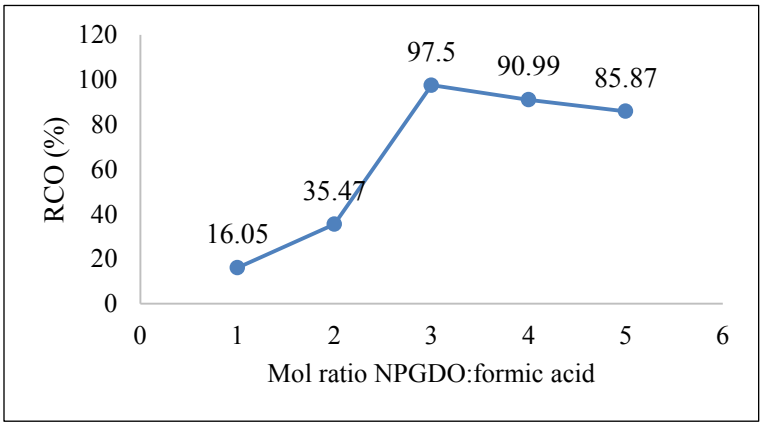


Figure 2. Effect of mol ratio NPGDO:formic acid on percentage of RCO

Figure 3 shows the percentage of RCO in accordance to mol ratio of NPGDO:hydrogen peroxide. The highest percentage of RCO can be seen at mol ratio 1:4. Figure 4 shows the effect of temperature towards the percentage of RCO. At 40 ºC, highest percentage of RCO was obtained. Figure 5 shows the correlation between time of rection on percentage of RCO which remarks 97% as the highest percentage of RCO, obtained after 3 hours of reaction.

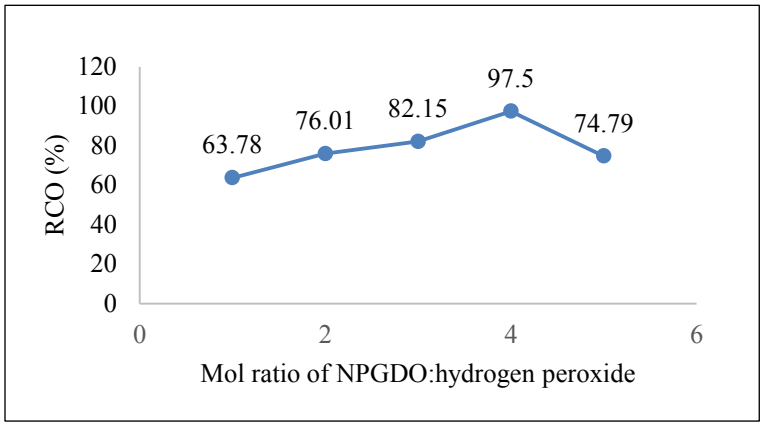


Figure 3. Effect of mol ratio NPGDO: hydrogen peroxide on percentage of RCO

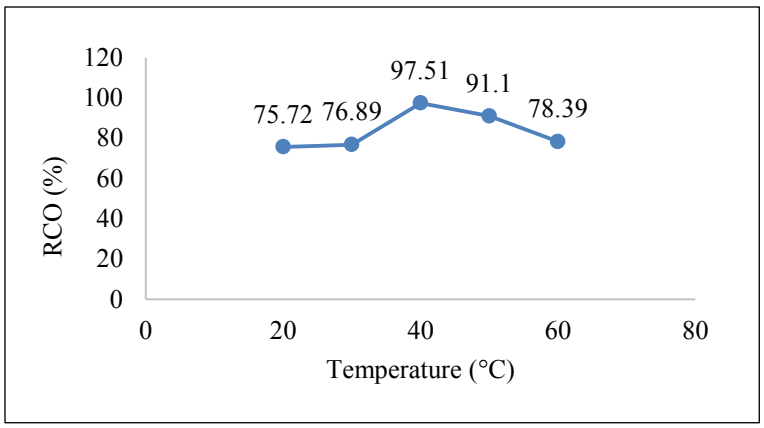


Figure 4. Effect of temperature on percentage of RCO

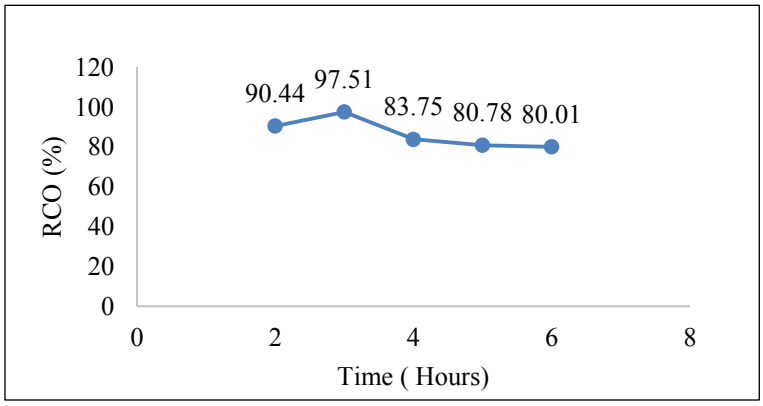


Figure 5. Effect of time of reaction on percentage of RCO

From the optimization graph, it can be concluded that the best condition for the formation of ENPGDO was obtained at 40 ºC for 3 hours. The mol ratio of NPGDO:formic acid:hydrogen peroxide was 1:3:4. The yield obtained was at average 83%. The percentage of OOC was high at 4.3% and the percentage of conversion of double bond in NPG dioelate to epoxy ring was 97%. The formation of ENPGDO was confirmed with Fourier Transform Infrared (FTIR) analysis. Figure 6 shows the comparison of FTIR spectrum before and after epoxidation of NPGDO. Peaks at 821.25 cm^{-1} and 933.33 cm^{-1} represent the C–O–C stretching of epoxide. There is no peak in the range of 3000 cm^{-1} to 3100 cm^{-1} which indicates that all the double bond in NPGDO has been converted into epoxide. The O–H stretching band that should have been appeared between 3200 cm^{-1} to 3400 cm^{-1} is also absent. This proves that ring opening did not occur.

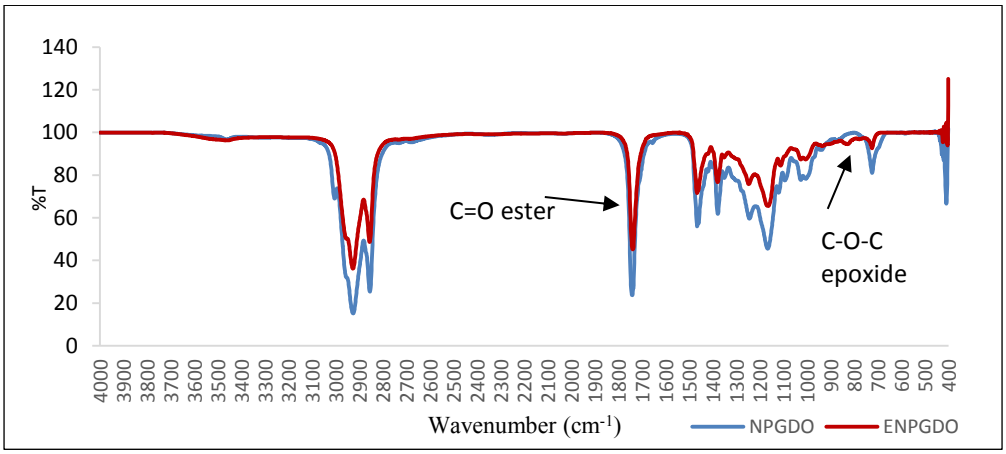


Figure 6. Comparison of FTIR spectrum between NPGDO and ENPGDO

The structural conformation was validated with Nuclear Magnetic Resonance (NMR). Figure 7 shows the ^{1}H NMR spectra.

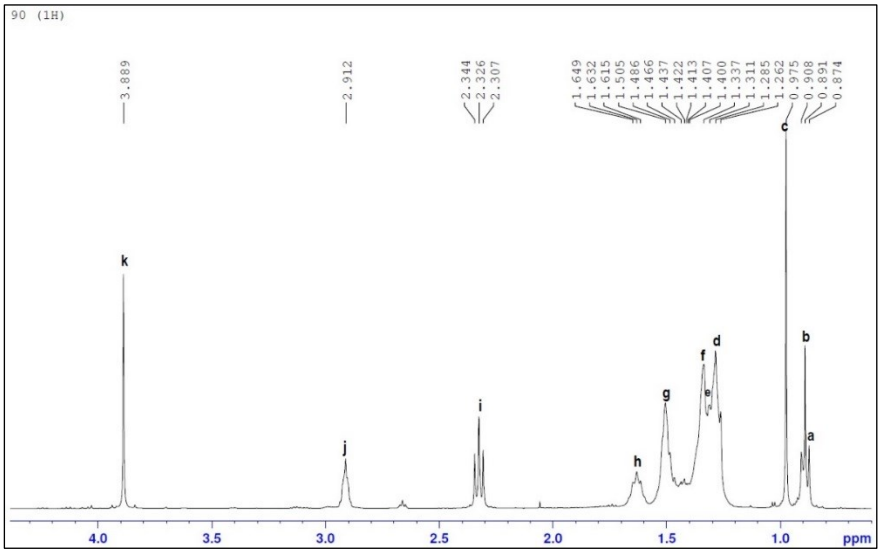


Figure 7. ^{1}H NMR spectra for epoxidized NPG dioleate

Label on Figure 8 represents respective signals on ^{1}H NMR spectra. The peak at 2.9 ppm corresponds the the proton attached to the epoxide group. The absence of peak at 5.381 ppm proves that all double bond has been converted to epoxides. Figure 9 shows the ^{13}C NMR spectra and label on Figure 10 represents respective signals on the ^{13}C NMR spectra. The absence of peak at 120 ppm to 140 ppm prove the absence of double bond in the product. Meanwhile the peak at chemical shift 57 ppm proves the formation of epoxide in the product.

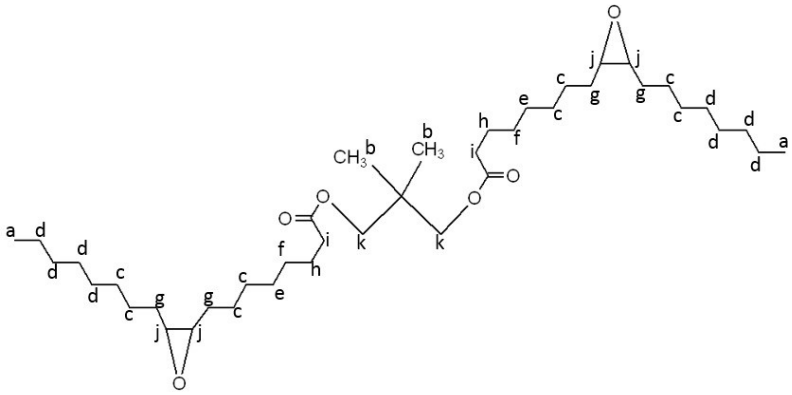


Figure 8. Structure representing signals on ^{1}H NMR spectra

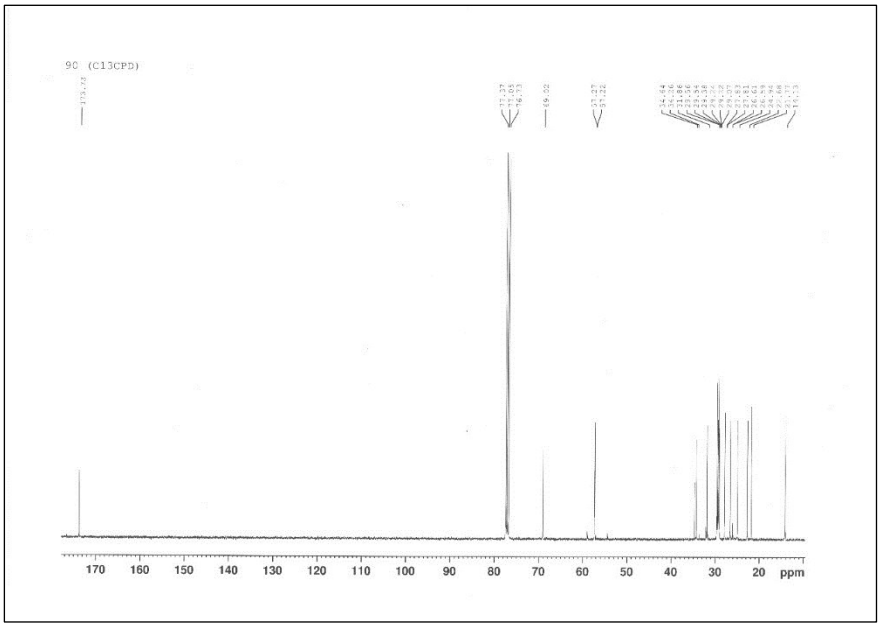


Figure 9. ^{13}C NMR Spectra for epoxidized NPG dioleate

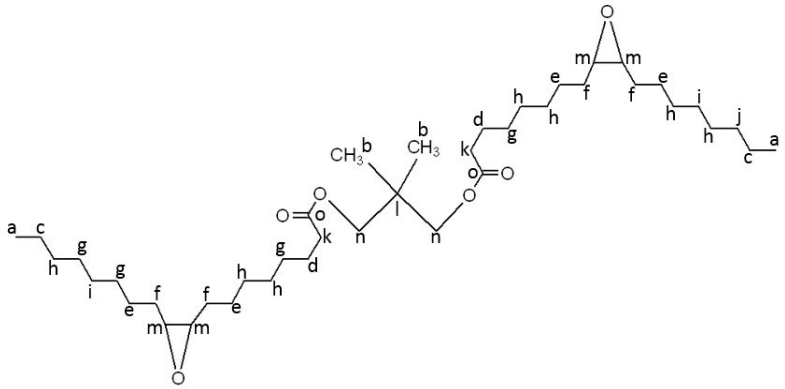


Figure 10. Structure representing signals on ^{1}H NMR spectra

The oxidative stability measures oil resistance towards oxidation. It is important as it reflects the shelf life of the oil [10]. The oxidative stability of ENPGDO has been increased from 177 ºC to 197 ºC. Oxidative stability increased as the number of hydroxyl group decreased by forming free radicals. This have resulted in oxidative degradation [11]. The absence of double bond in the product have led to better oxidative stability. The flash point of epoxide is 205 °C, which is significantly high to ensure safety during use. The ENPGDO possess a pour point of −18 °C, which is higher than NPGDO which is −44 ºC. The pour point is a very important low temperature flow property where it indicates the lowest temperature at which the sample can be poured from a tilted jar [12]. The pour point tends to improve with the attachement of ester. The presence of this large branching group in the middle or end of the chain will have a steric hindrance effect, hence inhibit the formation of crystals [11]. The viscosity index of the epoxidized NPG dioleate is 218. The viscocity index increased as the molecular weight of product increased [13]. Through epoxidation, the oxidative stability and flash point have been improved compared to NPGDO. The viscocity index and pour point properties had decreased compared to NPGDO. These properties can be further improved by chemical modification of ENPGDO which acts as a biolubricant intermediate. The oxirane ring provides the site for further modification to obtain better properties.

Conclusion

The ENPGDO was succesully produced in high yield which was 83% with high percentage of OOC (4.3%). The RCO of epoxide was also high, that was 97%. The optimized condition for epoxidation process was at 40 ºC for 3 hours, and the ratio of NPG dioleate to formic acid to hydrogen peroxide was 1:3:4. The oxidative stability of epoxide increased to 197 ºC. The ENPGDO has −18 ºC of pour point and 205 ºC of flash point. The viscosity index of the epoxide was achieved as 218. The physicochemical properties of epoxide can be further modified through ring opening and other processes for better properties.

Acknowledgement

Authors thanked Universiti Kebangsaan Malaysia for providing the fund IP-2014-070, FRGS/2/2014/ST01/UKM/01/2 and all the staff from the Faculty of Science and Technology, Universiti Kebangsaan Malaysia for giving full support in completing this research.

References

1. Bart, J. C. J., Cavallaro, S. and Gucciardi, E. (2013). Biolubricants: Science and Technology. UK: Woodhead Publiching Limited.
2. Bilal, S., Mohammed-Dabo, I. A., Nuhu, M., Kasim, S. A., Almustapha, I. H. and Yamusa, Y. A. (2013). Production of biolubricant from *Jatropha Curcas* seed oil. *Journal of Chemical Engineering and Materials Science*, 4(6): 72 – 79.
3. Fong, M. N. F. and Salimon, J. (2012). Epoxidation of palm kernel oil fatty acids. *Journal of Science and Technology,* 4(2): 87 – 98.

4. Petrovic, Z., Zhang, W., Javni, I. and Guo, X. A. (2003). Polymer concrete containing vegetable oil- based polyurethanes and method for their preparation. US Patent 090016.
5. Ravindra, D. K., Priya, S. D., Sujay, U. M. and Pramod, P. M. (2013). Epoxidation of mustard oil and ring opening with 2- ethylhexanol for biolubricant with enhanced thermo- oxidative and cold flow characteristics. *Industrial Crops and Products,* 49: 586 – 592.
6. Meyer, P. P., Techaphattana, N., Manundawee, S., Sangkeaw, S., Junlakan, W. and Tongurai, C. (2008). Epoxidation of soybean oil and jatropha oil. *Thammasat Internasional Journal Science Technology,* 13: 1 – 5.
7. Gryglewicz, S., Piechocki, W. and Gryglewicz, G. (2003). Preparation of polyol esters based on vegetable and animal fats. *Bioresource Technology*, 87: 35 – 39.
8. Xuedong, W., Xingang, Z., Shengong, Y., Haigang, C. and Dapu, W. (2000). The study of epoxidized rapseed oil used as a potential biodegradable lubricant. *Journal of the American Oil Chemists Society,* 77(5): 561 – 563.
9. Rafiee- Moghaddam, R., Salimon, J., Jelas Haron, M. D., Jahangirian, H., Shah Ismail, M. H., Hosseini, S. and Rezayi, M. (2014). Lipase epoxidation optimizing of jatropha curcas oil using perlauric acid. *Digest Journal of Nanomaterials and Biostructures,* 9(3): 1159 – 1169.
10. Salimon, J., Bashar, M. A., Rahimi, M. Y. and Nadia, S. (2014). Synthesis, reactivity and application studies for different biolubricants. *Chemistry Central Journal*, 8:16 – 27.
11. Nadia, S., Salimon, J., Emad, Y. and Bashar, M. A. (2013). Biolubricant basestock from chemicaly modified plant oils: Ricinoleic acid based- tetraesters. *Chemistry Central Journal*, 7: 128 – 141.
12. Salimon, J., Nadia, S. and Emad, Y. (2012). Improvement of pour point and stability of synthetic ester basestocks for biolubricant applications. *Arabian Journal of Chemistry,* 5: 193 – 200.
13. Salimon, J., Nadia, S. and Bashar, M. A. (2011). Improvement of physicochemical characteristic of monoepoxide linoleic acid ring opening for biolubricant base oil. *Journal of Biomedicine and Biotechnology,* 2011: 1 – 8.

Malaysian Journal of Analytical Sciences, Vol 20 No 6 (2016): 1338 - 1345
DOI: http://dx.doi.org/10.17576/mjas-2016-2006-12

MALAYSIAN JOURNAL OF ANALYTICAL SCIENCES
Published by The Malaysian Analytical Sciences Society
ISSN 1394 - 2506

DEGRADATION OF METHYLENE BLUE DYE BY CuO-$BiVO_4$ PHOTOCATALYSTS UNDER VISIBLE LIGHT IRRADIATION

(Degradasi Pewarna Metilena Biru oleh Fotomangkin CuO-$BiVO_4$ Di Bawah Sinaran Cahaya Nampak)

Abdul Halim Abdullah[1,2]*, Wan Tze Peng[2], Mohd Zobir Hussein[1,2]

[1]*Institute of Advanced Technology*
[2]*Department of Chemistry, Faculty of Science*
Universiti Putra Malaysia, 43400 UPM Serdang, Selangor, Malaysia

**Corresponding author: halim@upm.edu.my*

Received: 17 August 2015; Accepted: 13 October 2016

Abstract

Bismuth vanadate ($BiVO_4$) and a series of Cu-loaded $BiVO_4$ (CuO-$BiVO_4$) photocatalysts were prepared via precipitation and wet impregnation methods respectively. The samples were characterized by X-ray diffractometry (XRD), transmission electron microscopy (TEM) and the band gap energy was elucidated via UV-visible diffuse reflectance spectroscopy (DRS). Spherically-shaped particles of the photocatalysts were obtained which contained mixtures of monoclinic and tetragonal $BiVO_4$ phases. The particle sizes of the photocatalysts ranged from 20 to 100 nm and band gap energies varied from 2.47 to 2.53 eV. The photodegradation efficiency of the photocatalysts was evaluated by degrading methylene blue (MB) dye under visible-light irradiation. The optimum conditions for the photocatalytic degradation were determined based on wt% Cu loaded, mass loading, initial dye concentration and pH. 1 wt% CuO-$BiVO_4$ exhibited the highest photocatalytic activity where the complete removal of 10 mgL^{-1} of MB was obtained at pH 10 when 0.8 g of the catalyst was used under 4 hours of 18W fluorescent light irradiation.

Keywords: copper oxide-bismuth vanadate, visible light photocatalyst, semiconductor, methylene blue

Abstrak

Bismut vanadat ($BiVO_4$) dan satu siri fotomangkin CuO-$BiVO_4$ masing – masing telah disediakan melalui kaedah pemendakan dan impregnasi basah. Pencirian sampel menggunakan pembelauan Sinar-X (XRD), transmisi elektron mikroskopi (TEM) dan tenaga jurang jalurnya melalui spektroskopi UV-Vis pantulan resap (DRS). Fotomangkin yang berbentuk sfera mengandungi campuran fasa monoklinik dan tetragonal $BiVO_4$ telah dihasilkan. Saiz zarah fotomangkin adalah antara julat 20 – 100 nm dan tenaga jurang jalurnya adalah 2.47 – 2.53 eV. Keberkesanan fotodegradasi pemangkin telah dinilai dengan menyingkirkan pewarna metilena biru (MB) di bawah sinaran cahaya nampak. Keadaan optimum bagi degradasi fotopemangkinan adalah berdasarkan % berat Cu yang dimuatkan, muatan jisim, kepekatan awal pewarna dan pH. 1% berat CuO-$BiVO_4$ menunjukkan aktiviti fotopemangkinan adalah paling tinggi di mana penyingkiran peratusan MB menghampiri 100% 10 mgL^{-1} of MB di bawah keadaan optimum iaitu pH 10 dengan 0.8 g pemangkin digunakan yang didedahkan di bawah sinaran 18W cahaya pendarfluor selama 4 jam.

Kata kunci: kuprum oksida- bismut vanadat, fotomangkin cahaya nampak, semikonduktor, metilena biru

Introduction

Photocatalytic degradation is a promising method for the treatment of wastewater containing organic and inorganic pollutants. The process begins with the activation of the photocatalyst by light irradiation followed by the

degradation of the pollutants to harmless products. The use of titanium dioxide (TiO_2) as a photocatalyst in this process has been extensively studied [1]. However, TiO_2 is only effective under UV light. Thus, with the intention to utilize solar radiation to degrade wastewater pollutants, the search for efficient visible-light driven photocatalysts has attracted many researchers. Two approaches have been employed; doping of TiO_2 and synthesizing non-TiO_2 based photocatalysts. Several reports have shown that although the band gap of TiO_2 reduced after doping, the quantum efficiency of TiO_2 also reduced due to the formation of recombination centers [2, 3]. Hence there has been renewed interest in producing non–TiO_2 based visible-light photocatalysts with better properties.

Several complexes such as Fe_2O_3, WO_3, $BiVO_4$, Bi_2WO_6 and Ag_3PO_4 [4-8] have been tested as visible light photocatalysts. Among these complexes, monoclinic scheelite $BiVO_4$ with a band gap energy of 2.4 eV has been reported to be an effective photocatalyst thus attracting considerable attention [9]. This photocatalyst has been synthesized via several methods including polyol, sol-gel, hydrothermal and polymer assisted co-precipitation methods [10-14]. However, the photocatalytic activity of pure $BiVO_4$ has been reported to be comparatively low. Several researchers have observed enhanced photocatalytic activity of $BiVO_4$ when metals such as iron and thallium [15-16], and metal oxides such as Ag_2O, Bi_2WO_6, CuO, Cu_2O and WO_3 [11, 17-20] were doped on the $BiVO_4$ surface. The enhancement in activity was reported to be due to the suppression of photogenerated electrons and holes recombination at the photocatalyst/co-catalyst interfaces.

In this study, a series of CuO-$BiVO_4$ photocatalysts were prepared via impregnation to evaluate the effect of CuO loading on the photocatalytic efficiency of the photocatalysts in degrading methylene blue dye (MB) under low-wattage visible-light irradiation. The optimal conditions for the photocatalytic degradation of MB were also determined.

Materials and Methods

Preparation of the photocatalysts

An amount of 0.1 M of bismuth (III) nitrate pentahydrate solution was prepared by dissolving 10 mmol of bismuth (III) nitrate pentahydrate (Acros) in 10 mL of concentrated nitric acid (65%, Fischer Scientific)) and 90 mL of deionized water. Separately, 0.1 M of ammonium metavanadate was prepared by dissolving 10 mmol of ammonium metavanadate (Aldrich) in 100 mL of deionized water at 80 °C. Upon cooling to room temperature, the solutions were mixed and continuously stirred for 30 minutes and left overnight for precipitation to occur. The yellow precipitate that formed was washed with deionized water, collected via centrifugation and oven-dried at 70 °C overnight. The dried sample was ground and calcined in air at 550°C for 1 hour.

The CuO-$BiVO_4$ catalysts were prepared by suspending 3.962g of $BiVO_4$ in an ethanolic solution (3:1 ethanol: water) containing copper (II) nitrate trihydrate (Acros) that would yield 0.25 – 1.25 wt % of Cu. The suspension was magnetically stirred until almost all the ethanol evaporated. The slurry obtained was then oven-dried at 70 °C overnight and the resulting powder was calcined at 300 °C for 4 hours.

Characterization of the photocatalysts

X-Ray Diffraction (XRD) analyses of the prepared photocatalysts were performed on a Shimadzu XRD-6000 Diffractometer with Nickel-filtered Cu Kα radiation (λ = 1.5406 Å), over a 2θ range of 10-60º. The diffuse reflectance spectra (DRS) of the photocatalysts were recorded using a UV-Vis spectrophotometer (Lambda 35, Perkin Elmer, USA) equipped with an integration sphere. The microstructure of the photocatalysts was recorded using a transmission electron microscope (Hitachi H-7100). The amount of Cu incorporated into the $BiVO_4$ catalysts was analyzed using the Thermo Scientific S Series Atomic Absorption Spectrometer.

Photocatalytic activity

The photocatalytic activity of the synthesized photocatalysts was evaluated by analyzing the degradation of methylene blue (MB, BDH) under visible-light irradiation (18-watt Cool Day fluorescent light-bulb, Philips) at room temperature. A desired amount of the photocatalyst was suspended in 1 L of 10 mg/L MB solution. Prior to the visible-light illumination, the suspension was magnetically stirred for 30 min ($BiVO_4$) or 45 min (CuO-$BiVO_4$) in the dark, for adsorption-desorption equilibrium. Air was bubbled continuously into the suspension by an aquarium air pump to maintain constant oxygen saturation in the solution throughout the 4 hours reaction period. At

specific time intervals, 5 mL of the suspension was drawn and filtered through cellulose nitrate membrane filters (0.45 µm) to separate the photocatalyst from the solution. The concentration of MB was determined at λ_{max} = 664 nm during the photocatalytic degradation process by a Perkin Elmer Lambda 35 UV-Vis spectrophotometer. The percentage of photodegradation of MB was calculated using equation 1:

$$\text{Photodegradation (\%)} = (C_0\text{-}C)/C_0 \times 100\% \quad (1)$$

where C_0 was the initial concentration of MB and C was the concentration of MB at time t.

Results and Discussion

Characteristics of the photocatalysts

Figure 1 shows the XRD patterns of pure $BiVO_4$ and Cu–$BiVO_4$ with different Cu contents. Characteristic peaks of the monoclinic scheelite $BiVO_4$ phase were observed at 2θ = 28.8º, 30.5º, 39.8º and 53.5º with clear splitting peaks at 2θ = 18.8º, 35º, 47º, 58.4º (JCPDS No. 00-014-0688). Weak peaks corresponding to the tetragonal $BiVO_4$ phase were also observed at 24.4º and 32.7º (JCPDS No. 00-014-0133). This indicated the presence of both $BiVO_4$ phases with monoclinic scheelite as the dominant phase. No diffractive peaks corresponding to CuO were found for any of the CuO-$BiVO_4$ photocatalysts in this work due to the low amount of copper used in the synthesis. To ensure the presence of Cu, the CuO-$BiVO_4$ photocatalysts were digested in aqua regia and analysed by AAS. As listed in Table 1, the Cu content obtained matched well with the calculated values.

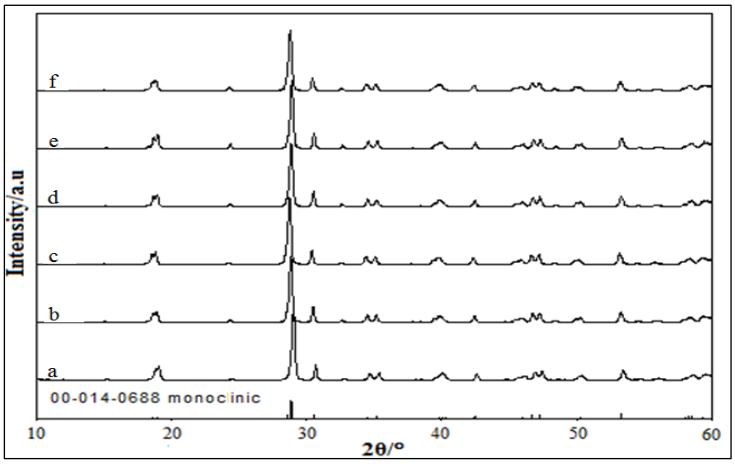


Figure 1. XRD patterns of (a) pure $BiVO_4$ and CuO-$BiVO_4$ at different Cu loading; (b) 0.25, (c) 0.50, (d) 0.75, (e) 1 and (f) 1.25 wt %.

Table 1. Physical properties of the synthesized $BiVO_4$ and CuO-$BiVO_4$ photocatalysts

Samples	Cu content (% wt)	Average Particle Size (nm)	Band Gap Energy (eV)
$BiVO_4$		40.2	2.47
0.25 wt% CuO-$BiVO_4$	0.247	60.6	2.47
0.50 wt% CuO-$BiVO_4$	0.522	40.2	2.52
0.75 w% CuO-$BiVO_4$	0.808	36.3	2.52
1 wt% CuO-$BiVO_4$	1.066	34.1	2.52
1.25 wt% CuO-$BiVO_4$	1.381	37.0	2.53

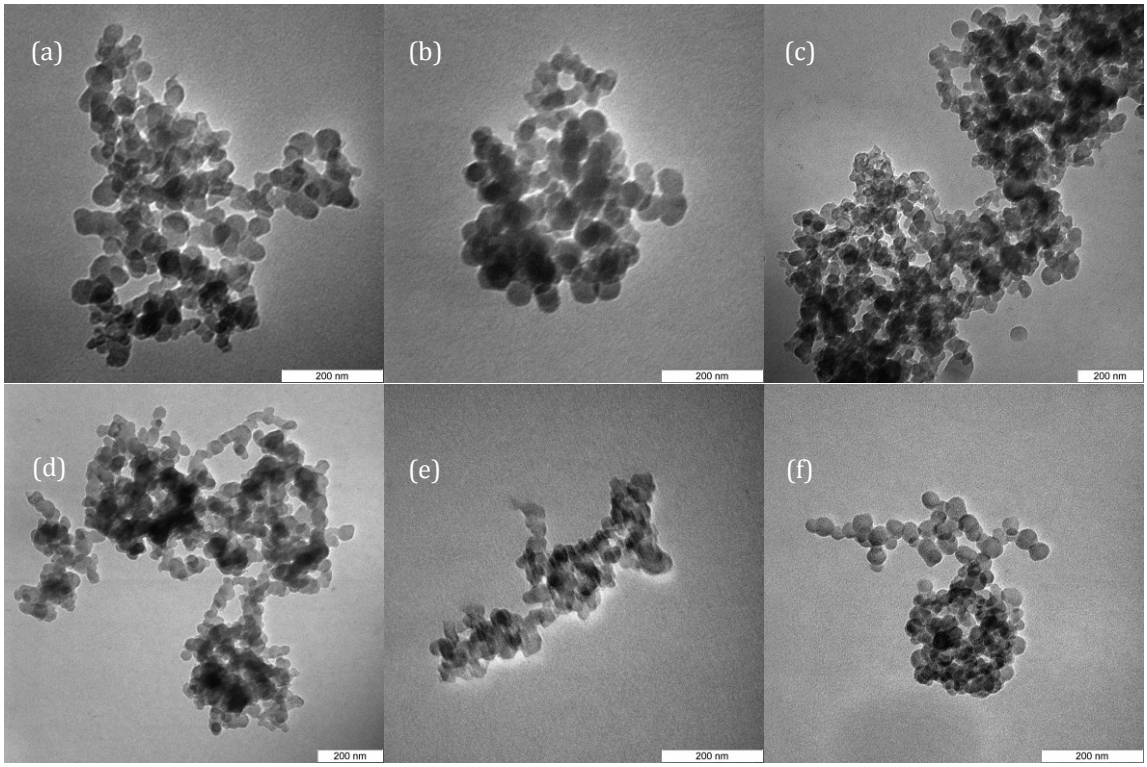


Figure 2. TEM images of (a) pure $BiVO_4$ and CuO-$BiVO_4$ at different Cu loading; (b) 0.25, (c) 0.50, (d) 0.75, (e) 1 and (f) 1.25 wt%.

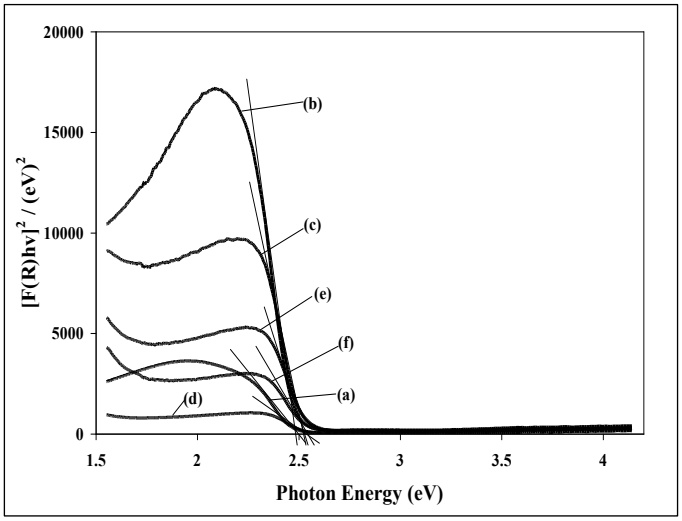


Figure 3. Tauc's plot of $BiVO_4$ and CuO-$BiVO_4$ photocatalysts at different Cu loading; (b) 0.25, (c) 0.50, (d) 0.75, (e) 1 and (f) 1.25 wt% for the determination of optical band gap energy

Photocatalytic degradation of methylene blue

The photocatalytic performance of $BiVO_4$ and CuO-$BiVO_4$ photocatalysts in the degradation of MB and their kinetics study are shown in Figure 4. In the absence of a photocatalyst (Figure 4a), 5% of the MB dye was photolysed under visible-light irradiation while in dark conditions; only approximately 5% of the MB dye was adsorbed on the surface of the photocatalysts. The photocatalytic degradation efficiency of MB steadily increased from 40% to 92% when $BiVO_4$ was doped with increasing amounts of CuO up to 1 wt%. As illustrated in Figure 4b, the photodegradation of MB followed a pseudo first-order reaction. The UV-Vis spectra that displays the progressive degradation of MB by the 1wt% CuO-$BiVO_4$ photocatalyst, as a function of time are shown in Fig 5. The enhancement in the photoactivity of CuO-$BiVO_4$ was attributed to efficient separation of the photogenerated electrons and holes. The band gap energy of CuO and BiVO4 has been reported as 1.70 eV and 2.45 eV, respectively. Since the calculated energy level of the conduction band of CuO (0.46 eV) was higher than that of $BiVO_4$ (0.34 eV), the photoexcited electrons on the conduction band of $BiVO_4$ were not transferred to the conduction band of CuO. Instead the holes were transferred to the valence band of CuO, resulting in a separation of the electron-hole pairs, thereby subsequently increasing the photocatalytic activity [21]. However, at CuO loading higher than 1 wt%, lower photocatalytic activity was observed because CuO acts as a recombination center of photoinduced electron-hole pairs leading to a reduction in photocatalytic activity [21-22]. Thus, 1 wt% CuO-$BiVO_4$ was used as the model photocatalyst for the remainder of this study.

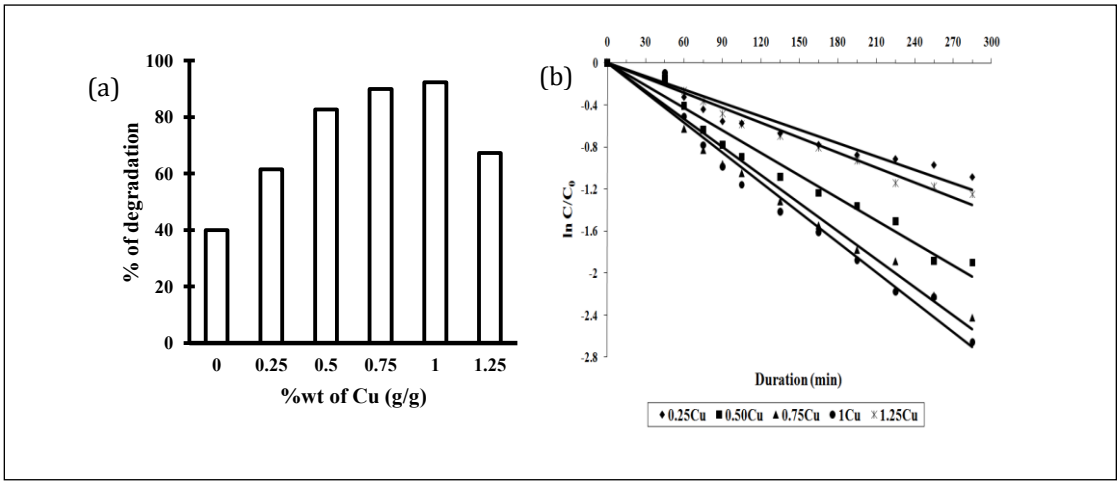


Figure 4. (a) Photocatalytic degradation efficiency and (b) kinetics of pure $BiVO_4$ and Cu-loaded $BiVO_4$ in the degradation of MB (catalyst dosage = 600 mg, initial MB concentration = 10 mg/L and natural pH)

The effect of mass of the 1 wt% CuO-$BiVO_4$ photocatalyst, initial concentration and pH of the MB solution on the degradation efficiency of MB is illustrated in Figure 6. Figure 6a showed that the photodegradation of MB increased proportionally with the amount of photocatalyst loading until 800 mg, after which the photodegradation decreased (1000 mg). The increase in the photocatalytic degradation efficiency of MB was due to the increase in the effective surface area of the photocatalyst, consequently enhancing light absorption and generating more surface active sites for the degradation reaction. The decrease in the efficiency beyond the optimum photocatalyst loading (800 mg) might be attributed to the light scattering effect and agglomeration of the photocatalyst particles in the solution [23].

The photocatalytic degradation of MB at various initial concentrations (10 – 30 mg/L) was studied using 800 mg of 1 wt% CuO-$BiVO_4$. Figure 6b showed that the percentage of degradation decreased with increasing MB concentration. It was also found that the rate of the MB photodegradation was unaffected by change in MB concentration, thus the amount of MB degraded did not change significantly. The maximum amount of MB that could be degraded by 1 wt% CuO-$BiVO_4$ was 10.5 mg/g at any MB concentration.

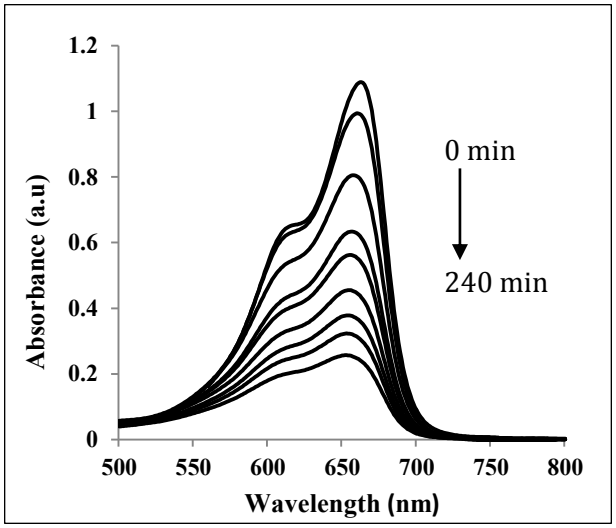


Figure 5. UV-Vis spectra of MB recorded at 30 min intervals during the photodegradation using 1 wt% CuO-$BiVO_4$ photocatalyst. (Catalyst dosage = 600 mg, initial MB concentration = 10 mg/L and natural pH)

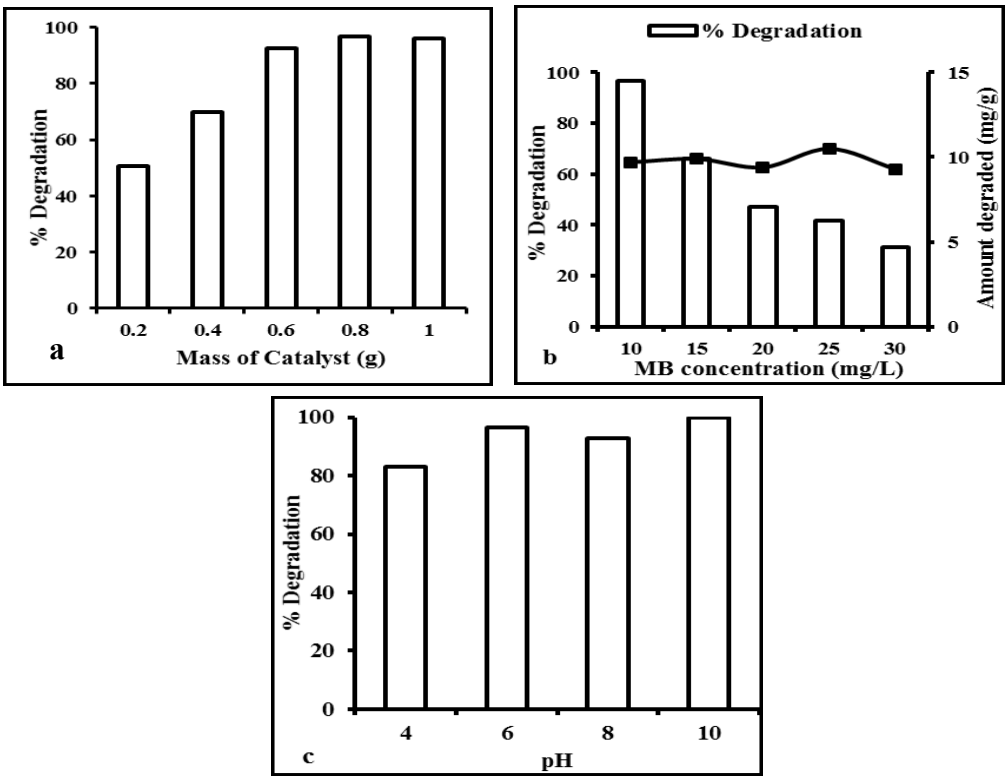


Figure 6. Photocatalytic degradation of methylene blue under different (a) mass of catalyst used, (b) concentrations and (c) pH of the methylene blue solution while keeping the other parameters constant. (Catalyst dosage = 800 mg, initial MB concentration = 10 mg/L and natural pH)

Figure 6c shows the photocatalytic efficiency of the CuO-$BiVO_4$ photocatalyst in the degradation of 10 mg/L MB solution at different initial pH levels. The photocatalytic degradation of MB increased from 83% to 96% when the pH was increased from 4 to 6 but did not show any significant difference after that till a pH of 10. In the photocatalytic mechanism, the holes can react with the added OH^-, in alkaline conditions, to produce hydroxyl radicals (Equation 2) which subsequently can degrade the pollutant. At the same time the holes themselves can also degrade the pollutant (Equation 4).

$$h^+ + HO^- \rightarrow \bullet OH \quad (2)$$

$$\bullet OH + \text{organic pollutant} \rightarrow \text{product of degradation} \quad (3)$$

$$h^+ + \text{organic pollutant} \rightarrow \text{product of degradation} \quad (4)$$

It was hence expected that the rate constant at pH 10 would be higher than that of pH 6 as more hydroxyl radicals were produced to degrade the MB dye. For confirmation, the rate constant of the reaction, k_{app}, at pH 6 – 10 was determined. It was found that although the degradation of MB reached 100% at pH 10, the calculated rate constant, k_{app}, remained almost constant, with value of $0.011 min^{-1}$ at pH 6 and $0.012\ min^{-1}$ at pH 10. This indicated that the photodegradation of the 10 mgL^{-1} MB was mainly due to the reaction between the holes and the MB molecules.

Conclusion

A series of CuO-$BiVO_4$ photocatalysts were successfully prepared via impregnation of nanocrystalline $BiVO_4$. Structural studies indicated that the synthesized photocatalysts were spherical with a particle size range of 20 to 100 nm and were dominated by the monoclinic scheelite crystalline phase. The photocatalytic activity of the pure $BiVO_4$ photocatalyst, prepared by a simple precipitation method, was enhanced with CuO loading and the highest photodegradation efficiency of MB was obtained at 1 wt% CuO content. The optimized conditions for the photodegradation of MB were catalyst dosage = 800 mg, initial concentration and pH of the MB solution = 10 mg/L and 10, respectively.

Acknowledgement

The authors would like to acknowledge the research grant from the Ministry of Higher Education (FRGS-01-01-07-143FR) and Universiti Putra Malaysia's Graduate Research Fellowship (T.P. Wan) for supporting this research.

References

1. Fujishima, A., Hashimoto, K. and Watanabe, T. (1999). TiO_2 photocatalysis: Fundamentals and applications. BKC, Tokyo.
2. Yin, S., Yamaki, H., Komatsu, M., Zhang, Q., Wang, J., Tang, Q., Saito, F. and Sato, T. (2003). Preparation of nitrogen-doped titania with high visible light induced photocatalytic activity by mechanochemical reaction of titania and hexamethylenetetramine. *Journal of Materials Chemistry*, 13 (12): 2996 – 3001.
3. Livraghi, S., Votta, A., Paganini, M. C. and Giamello, E. (2005). The nature of paramagnetic species in nitrogen doped TiO_2 active in visible light photocatalysis. *Chemical Communication*, 41(4): 498 – 500.
4. Cheng, X. L., Jiang, J. S., Jin, C. Y., Lin, C. C., Zeng, Y. and Zhang, Q. H. (2014). Cauliflower like α-Fe_2O_3 microstructures: Toulene-water interface assisted synthesis, characterization and application in wastewater treatment and visible light photocatalysis. *Chemical Engineering Journal*, 236(1): 139 – 148.
5. Sanchez-Martinez, D., Martinez-de la Cruz, A. and Lopez-Cuellar, E. (2011). Photocatalytic properties of WO_3 nanoparticle obtained by precipitation in presence of urea as complexing agent. *Applied Catalysis A-General*, 398(1-2):179 – 186.
6. Sun, J., Chen, G., Wu, J., Dong, H. and Xiong, G. (2013). $BiVO_4$ hollow spheres: Bubble template synthesis and enhanced photocatalytic properties. *Applied Catalysis B-Environmental*, 132: 304 – 314.
7. Zhang, F. J., Xie, F-Z., Liu J., Zhao, W. and Zhang, K. (2013). Rapid sonochemical synthesis of nano laminar like Bi_2WO_6 as efficient visible light active photocatalyst. *Ultrasonics Sonochemistry*, 20: 2009 – 2015.
8. Bi, Y., Ouyang, S., Umezawa N., Cao, J. and Ye, J. (2011). Facet effect of single-crystalline Ag_3PO_4 sub-microcrystals on photocatalytic properties. *Journal of American Chemical Society*, 133: 6490 – 6492.
9. Wang, F., Shao, M., Cheng, L., Hua, J. and Wei, X. (2009). The synthesis of monoclinic bismuth vanadate nanoribbons and studies of photoconductive, photoresponse and photocatalytic properties. *Materials Research*

*Bulleti*n, 44(8): 1687–1691.
10. Abdullah, A. H., Moey, H. J. M. and Yusof, N. A. (2012). Response surface methodology analysis of the photocatalytic removal of methylene blue using bismuth vanadate prepared via polyol route. *Journal of Environmental Sciences*, 24(9): 1694 – 1701.
11. Shan, L., Mi, J., Dong, L., Han, Z. and Liu, B. (2014). Enhanced photocatalytic properties of silver oxide loaded bismuth vanadate, *Chinese Journal of Chemical Engineering*, 22: 909 – 913.
12. Lin, X., Yu, L., Yan, L, Li, H., Yan, Y., Liu, C. and Zhai, H. (2014). Visible light photocatalytic activity of $BiVO_4$ particles with different morphologies. *Solid State Sciences*, 32: 61 – 66.
13. Bian, Z-Y., Zhu, Y-Q., Zhang, J-X., Ding, A-Z. and Wang, H. (2014). Visible light driven degradation of ibuprofen using abundant metal loaded $BiVO_4$ photocatalyst. *Chemosphere*, 117: 527 – 531.
14. Garcia-Perez, U. M., Sepulveda-Guzman, S. and Martinez-de la Cruz, A. (2012). Nanostructures $BiVO_4$ photocatalyst synthesized via polymer assisted co-precipitation method and their photocatalytic properties under visible light irradiation. *Solid State Sciences*, 14: 293 – 298.
15. Chala, S., Wetchakun, K., Panichphant, S., Inceesungvorn, B. and Whetchakun, N. (2014). Enhanced visible-light-response photocatalytic degradation of methylene blue on Fe-loaded $BiVO_4$ photocatalyst. *Journal of Alloys and Compounds*, 597: 129 – 135.
16. Karunakaran, C. and Kalaivani, S. (2014). Enhanced visible-light photocatalysis by hydrothermally synthesized thallium doped bismuth vanadate nanoparticle. *Materials Science in Semiconductor Processing*, 27: 352 – 361.
17. Ju, P., Wang, P., Li, B., Fan, H., Ai, S., Zhang, D. and Wang, Y. (2014). A novel calcined $Bi_2WO_6/BiVO_4$ heterojunction photocatalyst with highly enhanced photocatalytic activity, *Chemical Engineering Journal*, 236: 430 – 437.
18. Min, S., Wang, F., Jin, Z. and Xu, J. (2014). Cu_2O nanoparticles decorated $BiVO_4$ as an effective visible light driven p-n heterojunction photocatalyst for methylene blue degradation, *Superlattices and Microstructures*, 74: 294 – 307.
19. Gao, X. M., Wu, Y. F., Wang, J., Fu, F., Zhang, L. P. and Niu, F. X. (2011). The preparation of CuO-$BiVO_4$ and its enhanced photocatalytic properties for degradation of phenol. *Advanced Materials Research*, 356 – 360: 1253 – 1257.
20. Cho, S. K., Park, H. S., Lee, H. C., Nam, K. M. and Bard, A. J. (2013). Metal doping of $BiVO_4$ by composite electrodeposition with improved photoelectrochemical water oxidation. *Journal of Physical Chemistry C*, 117: 23048 – 23056.
21. Jiang, H. Q., Endo, H., Natori, H., Nagai, M. and Kobayashi, K. (2009). Fabrication and efficient photocatalytic degradation of methylene blue over CuO/$BiVO_4$ composite under visible-light irradiation. *Materials Research Bulletin*, 44(3): 700 – 706.
22. Kohtani, S., Hiro, J., Yamamoto, N., Kudo, A., Tokumura, K. and Nakagaki, R. (2005). Adsorptive and photocatalytic properties of Ag-loaded $BiVO_4$ on the degradation of 4-*n*-alkylphenols under visible light irradiation. *Catalysis Communications*, 6(3): 185 – 189.
23. Das, R., Sarkar, S., Chakraborty, S., Choi, H. and Bhattacharjee, C. (2014). Remediation of antiseptic components in wastewater by photocatalysis using TiO_2 nanoparticle. *Industrial and Engineering Chemical Research*, 53(8): 3012 – 3020.

Malaysian Journal of Analytical Sciences, Vol 20 No 6 (2016): 1346 - 1358
DOI: http://dx.doi.org/10.17576/mjas-2016-2006-13

MALAYSIAN JOURNAL OF ANALYTICAL SCIENCES
Published by The Malaysian Analytical Sciences Society
ISSN 1394 - 2506

PESTICIDES RESIDUES IN AGRICULTURAL SOILS AND ITS HEALTH ASSESSMENT FOR HUMANS IN CAMERON HIGHLANDS, MALAYSIA

(Residu Racun Serangga dalam Tanah Pertanian dan Penilaian Kesihatan Terhadap Manusia di Cameron Highlands, Malaysia)

Yang Farina[1, 2]*, Md Pauzi Abdullah[1, 2], Nusrat Bibi[1,3], Wan Mohd Afiq Wan Mohd Khalik[1]

[1]*School of Chemical Sciences and Food Technology, Faculty of Science and Technology, Universiti Kebangsaan Malaysia, 43600 UKM Bangi, Selangor, Malaysia*
[2]*Centre for Water Research and Analysis, Faculty of Science and Technology, Universiti Kebangsaan Malaysia, 43600 UKM Bangi, Selangor, Malaysia*
[3]*Department of Chemistry, Faculty of Science, Sardar Bahadur Khan Women University, Quetta, Pakistan*

**Corresponding author: farina@ukm.edu.my*

Received: 16 May 2016; Accepted: 21 September 2016

Abstract

Soil contamination is one of the sensitive issue in agricultural region of Cameron Highlands, Malaysia, which is a largest vegetable producer. Organochlorine pesticides (OCPs), organophosphorus pesticides (OPPs) and pyrethroids pesticides (PYRs) concentrations were measured in 35 soil samples of selected crops. Among OCPs, the average concentration in the soil of these crops grown was in the order of cauliflowers > cabbage > broccoli > lettuce > celery > spinach > mustard, while for OPPs; spinach > broccoli > cabbage > cauliflower > celery > lettuce > mustard > and for PYRs it was broccoli > cabbage > cauliflower > spinach > mustard > celery > lettuce. For risk assessment life time average daily dose (LADD) of ΣOCPs, ΣOPPs and ΣPYRs for adults were calculated at 2.1 x 10^{-7} – 1 x 10^{-6} mg kg^{-1} d^{-1}, 1.46 x 10^{-11} – 3.6 x 10^{-10} mg kg^{-1} d^{-1} and 1.28 x 10^{-12} – 3.42 x 10^{-12} mg kg^{-1} d^{-1} meanwhile for children 5.3 x 10^{-8} – 2.7 x 10^{-7} mg kg^{-1} d^{-1}, 3.8 x 10^{-11} – 9.4 x 10^{-10} mg kg^{-1} d^{-1} and 8.8 x 10^{-12} – 1.6 x 10^{-10} mg kg^{-1} d^{-1}. The hazard quotient (HQ) was ≤ 1 indicating less health risks for humans. Principal Component Analysis (PCA) indicates a strong correlation of high pesticides residual concentration of the soil of crops (cauliflower, cabbage and broccoli) with soil properties (pH and organic content) thus influencing its mobility and persistence whereas for other crops soil the decrease residual concentration might be related to crop type, rotation, roots exude, rhizosphere effect, or a rapid disappearance of pesticides after application.

Keywords: organochlorine, organophosphorus, pyrethroids, gas chromatography, multivariate analysis

Abstrak

Pencemaran tanah merupakan salah satu daripada isu yang sensitif dalam kawasan pertanian di Cameron Highlands, Malaysia, di mana ianya merupakan kawasan pengeluar sayur yang terbesar di Malaysia. Kepekatan racun serangga organoklorin (OCPs), organofosforus (OPPs) dan piretroid (PYRs) telah diukur dalam 35 sampel tanah dari tanaman yang terpilih. Berikut merupakan tertib kepekatan OCPs dalam tanah dari tanaman kubis bunga > kubis > brokoli > salad > sederi > bayam > sawi, manakala untuk OPPs adalah bayam > brokoli > kubis > kubis bunga > saderi > salad > sawi dan untuk PYRs adalah brokoli > kubis > kubis bunga > bayam > sawi > saderi > salad. Bagi penilaian risiko purata jangka hayat dos harian (LADD) untuk ΣOCPs, ΣOPPs dan ΣPYRs untuk dewasa adalah 2.1 x 10^{-7} – 1 x 10^{-6} mg kg^{-1} d^{-1}, 1.46 x 10^{-11} – 3.6 x 10^{-10} mg kg^{-1} d^{-1} dan 1.28 x 10^{-12} – 3.42 x 10^{-12} mg kg^{-1} d^{-1}, manakala kanak – kanak 5.3 x 10^{-8} – 2.7 x 10^{-7} mg kg^{-1} d^{-1}, 3.8 x 10^{-11} – 9.4 x 10^{-10} mg kg^{-1} d^{-1} dan 8.8 x 10^{-12} – 1.6 x 10^{-10} mg kg^{-1} d^{-1}. Darjah bahaya (HQ) adalah ≤ 1 iaitu menjelaskan bahawa ianya kurang berisiko terhadap kesihatan manusia.

Analisis komponen utama (PCA) menunjukkan terdapat korelasi yang kuat untuk kepekatan residu racun serangga yang tinggi daripada tanah untuk tanaman (kubis bunga, kubis, dan brokoli) dengan ciri – ciri tanah (pH dan kandungan organik) sekali gus mempengaruhi mobiliti dan pengekalannya manakala untuk tanah tanaman lain kepekatan residu berkurangan mungkin disebabkan oleh faktor yang berkaitan jenis tanaman, kitaran, rembesan akar – akar, kesan rezosfera, atau kehilangan racun yang cepat selepas penggunaannya.

Kata kunci: organoklorin, organofosforus, piretroid, kromatografi gas, analisis multivariat

Introduction

Pesticides pollution is extensively contaminating the environment due to its uncontrolled usage that degrades soil functions by degrading its biological activity and ability to remove pollutants that result in reduction of crop yield. Soil is regarded as a reservoir of xenobiotic that may be adsorbed to organic matter in soil and retained for decades or might be transported or degraded. Literature already proved that decomposition of these pesticides is less from soil to aquatic environment; therefore, it is even more threatening for future generations. Europe has already discussed the persistence behavior of pesticides in the Frame of Directive 91/414/EEC [1]. Soil system is relatively static and beyond human controls [1]. WHO/FAO [2] estimated 3 million cases of acute and severe pesticides poisoning with some 220,000 deaths and also reveals that largest human acute toxicity is caused by OPPs. One of the major soil contaminants are organophosphorus pesticides (OPPs), organochlorine pesticides (OCPs) and pyrethroids (PYRs). It can move in environment by volatilization, infiltration, runoff and transport along food chain [3,4].

Organophosphorus pesticides are highly toxic; it has the ability to penetrate the cells of living organism. They are moderately polar and are mobile to leach and can be retained on vegetation that can affect the environment and food chain [5]. It not only effects the pests but also other microorganisms like fungi and bacteria that brings nutrients to the roots of plants so effecting the healthy interaction and replacing it with chemicals [6]. In contrast to OCPs, OPPs are less persistent but this behavior varies from few days to month and sometimes years depending upon the texture and organic content of soil [7]. Sorption, volatilization, solubility in water, hydrolysis or oxidation, photo-degradation and biodegradation are some of the important factors dealing with the fate of OPPs in the environment [8].

PYRs are basically used for paralyzing insects and are less toxic and persistent than OCPs and OPPs. It is often used in combination with OPPs to enhance their insecticidal activity. It is considered to be the most widely used insecticide for vegetables farming in Malaysia and about 60% of farmers in use permethrin to control pests in the Cameron Highlands Malaysia [9].

Organochlorine pesticides are used worldwide due to its extensive insecticidal property and its use is prohibited due to high persistence (>10 years) and lipophilicity like DDT and β-HCH having higher stability and bio-accumulative property [10]. To understand the fate of OCPs globally it is necessary to know its fate in the tropical regions since they are considered as “net emissions” of OCPs to their “net sinks” Polar Regions. DDTs breakdown very slowly into its metabolites DDD and DDE. Among HCHs, the β-isomer is the most stable and persistent while α-isomer is more volatile and dissipates quickly [11].

However, the use of these pesticides might cause alteration in local environment including death of farm animals, and also risks to human health [12]. Due to their properties of having hydrophobic, strong sorption to soil organic matter, and resistant to degradation such as DDT and HCH they might persist for longer period of time in environment. The human exposure might occur due to occupational exposure or direct consumption of these vegetables and in this case the inhalation, ingestion can be one of the main reason for exposure since agriculture is becoming the occupation and norm of the people in this region and this exposure might cause several toxicological health effects [13,14].

The objective of this study is to identify and quantify the multi-residue of OCPs, OPPs and PYRs pesticides in soils of selected vegetables on the basis of its wide distribution and economic importance in agricultural region of Malaysia, Cameron Highlands and also to evaluate its correlation with physiochemical properties since the

degradation of pesticides depends upon the microbiological, physical and chemical properties while the sorption depends upon the organic content of soil and its pH because of its effect on soil properties such as electric charge and ionic strength [15]. The third objective is to access human health risks associated with soil contamination.

Materials and Methods

Chemicals

Pesticides standards were obtained from Dr. Ehrenstorfer (Augsberg, Germany) with highest purity certificate. Individual pesticides stock solution of 1000 ppm was prepared in acetone and stored in glass bottles at < –16 °C. Working pesticides mixture solution was prepared from stock solution and stored at 4 °C. Acetone, Hexane, ethyl acetate and anhydrous sodium sulphate of analytical grade were from Merck (Darmstadt, Germany and Friendmann Schmidt Chemical). Combo SPE Florisil (500 mg 6 mL^{-1}) packed was obtained from Restek (USA). The rotary evaporator (model A 1000s, Eyela), Soxhlet apparatus (Acott Lab Supplies Sdn. Bhd., Malaysia), Cellulose extraction thimbles with dimension 30 mm x 80 mm (Whatmann, England) and laboratory test sieve (Endecotts Limited, England) were used in the present study.

Sample collection and preparation

Cameron Highlands is the second largest producer of vegetables to Malaysia. Thus, it remarkably very important agricultural and environmentally sensitive area for Malaysia. It is situated in Pahang state having an estimated area of 712 km^2. Its location lies between 04° 20' N – 4° 37' N and 101° 20' – 101° 36' E and its altitude is between 1280 – 1830 m above sea level. Average daily temperature and annual rainfall is between 14 - 21 ˚C and 2800 mm.

In this study, seven different sampling sites were chosen as shown in Figure 1. The distance between station to station is 5 km Kg Raja – Tanah Rata, 13 km (Tanah Rata – Telom), 19.3 km (Telom – Brinchang), 4 km Brinchang – Telom), 8 km (Tanah Rata – Habu) and 3 km (Habu – Ringlet). The spraying pattern varies at each sampling points during both wet and dry seasons. About 64% of farmers spray more frequently every 7 - 9 days. However, during the wet seasons, the spraying pattern is even more frequent of about 4 – 6 days between each spraying. The highest being of 1 – 3 days' interval recorded at upper part of the valley. High humidity and continuous cultivation caused the contamination of river in highland by OCPs and OPPs due to enormous use in plant protection [16,17].

A total of 35 soil samples (0 – 10 cm) soil layer, consisting of three soil samples of approximately 1 – 2 kg for each corresponding vegetable were taken randomly from the cultivated horizon of seven different sites of agricultural region (Figure 1) by a stainless steel scoop wrapped in aluminum foil and placed in polyethylene bags stored in dark and transported to laboratory as soon as possible. These soil samples differed in terms of soil properties and land usage. Each soil sample was divided into two parts, one for pesticide analysis and other for soil geochemical properties. Samples were registered with sample location and site description. Soil samples were placed in amber glass bottles and stored at -18 ˚C until extraction. Soil samples were frozen, oven dried and homogenized by 80-mesh steel sieve.

Soil samples were frozen, oven dried and homogenized by 80-mesh steel sieve. A 15 g of dried weight sample was spiked by 1 mL of mixture of pesticides solution and was placed in thimble along with 6 – 7 g of anhydrous sodium sulphate and extracted with 150 mL of acetone: hexane (1:1) in soxhlet apparatus for 4 hours. The extract was concentrated to 3 mL by rotary evaporator (40 °C). The cleanup was done by Florisil (500 mg 6 mL^{-1}) priory conditioned by 5 mL of methanol and the sorbent were not allowed to dry during conditioning and loading steps. Sample loading was performed at 5 mL min^{-1} column and eluted with ethylacetate: hexane (1:1) and the final extract was concentrated by nitrogen gas up to 1 mL and analyzed by gas chromatography – electron capture detector (GC-ECD).

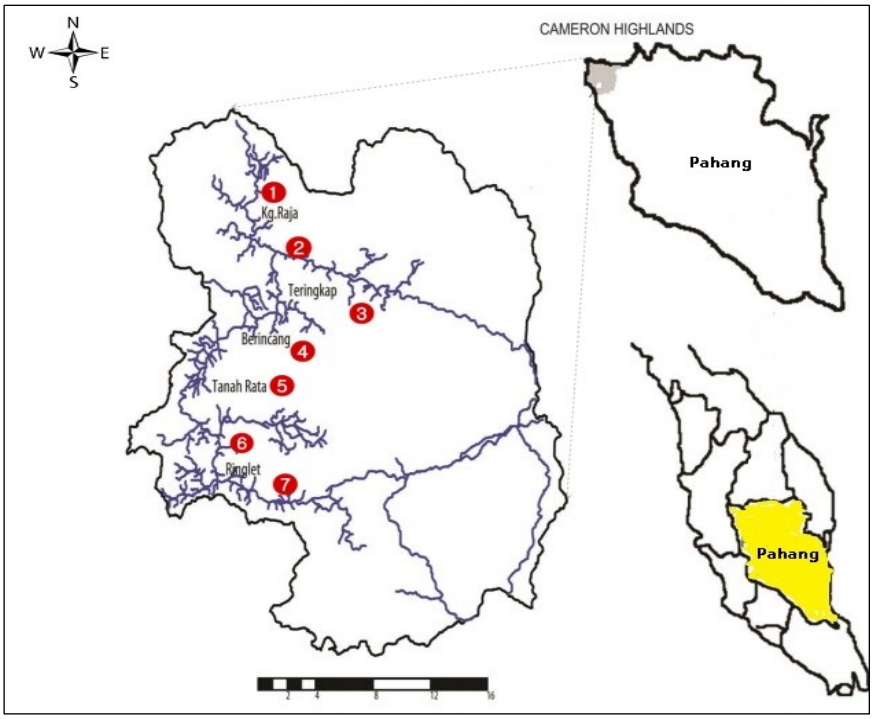


Figure 1. Map showing study area and sampling location (label in red)

Human exposure to pesticides and the consequent health risks associated with it was estimated by the equation given by USEPA. In this study the life time average daily dose (LADD) of pesticides and hazard quotient (HQ) were calculated through soil ingestion according to US Environmental Protection Agency and Agency for Toxic Substances and Disease Registry [13,18,19]. The following equations 1 and 2 were used for estimating the LADD and HQ:

$$\text{LADD (mg kg}^{-1}\text{ day}^{-1}\text{)} = (\text{Cs x IRF X EF x ED})/\text{BW x AT}) \quad (1)$$

$$\text{Hazard Quotient (HQ)} = \text{LADD/RFD} \quad (2)$$

where Cs is the pollutant concentration in soil (mg kg^{-1}), IR is soil ingestion rate (100 mg d^{-1} for adults) [18], F is the conversion factor unit, EF is the exposure frequency (365 days/year), ED is the lifetime exposure duration (adults, 70 years; children, 12 years), BW is a body weight (adults, 70 kg; children, 27 kg) [18] and AT is the averaging time for carcinogens (EF x ED). RFD is the reference dose for particular compound in mg/kg day^{-1} [13].

Soil pH was determined from water: soil (5:1) slurry by using soil pH meter. The organic matter content was determined by loss on ignition in which soil sample were first dried in oven at 104 °C for 24 hours and then the organic matter was combusted to ash and CO_2 at temperature between 500 – 550 °C and the loss on ignition (LOI) was calculated by the following equation 3 [20].

$$LOI_{550} = [(DW_{105} - DW_{550})/DW_{105}] \text{ x } 100 \quad (3)$$

Particle size was used to evaluate the soil texture. USDA classification scheme was used as reference in particle size analysis. The dry method of sieve analysis was performed by weighing 500 g of oven dried sample and separated

through three size of fractions (< 0.05 mm, 0.05 mm -2 mm and 2mm). The empty sieve and pan was weighed to 0.1 g and the mass of soil size of each fraction was weighed and mass fraction was calculated.

Analytical quality control

Pesticides concentrations were determined by external standard method using the peak areas of samples and five levels calibration curves of the standards. The peak was identified by their respective retention times of each standard. Cross contamination of all solvents and chemicals was checked by running a procedural blank. Linearity was estimated by an external calibration curve which was constructed at 5 calibration points by triplicate analysis ranging from 0.5 – 3 mg L^{-1}. These calibration curves were linear with r^2 value ranging from 0.990 – 0.995. The precision was established by triplicate analysis and extraction during accuracy studies. Acceptable precision was a value less than 20 %.

The recovery was calculated at two fortification levels with addition of known quantity of standard. For this purpose, pesticide free samples were collected from the remote areas for spiked samples. Samples were spiked at concentration of 1 mg kg^{-1} and 0.5 mg kg^{-1} with a pesticide mixture. The spiked and non-spiked samples were processed separately as real samples in triplicate. The average recoveries of OCPs were within a range 68% – 98%, (±2.37% - 16.5%), OPPs ranges between 75% – 103%, (±1.1% – 10.7%) and SPY ranges between 68% – 95%, (± 1% – 7%), respectively. The limit of detection and limit of quantification were calculated according to the IUPAC recommendation, three times the standard deviation of seven soil samples spiked at lowest concentration. The limit of detection (LOD) for analytes ranges between 0.04 ng g^{-1} – 0.4 ng g^{-1}, 0.8 ng g^{-1} – 1.8 ng g^{-1} and from 3.8 ng g^{-1} – 5 ng g^{-1} for OCPs, OPPs and PYRs, respectively. Multivariate statistical analysis namely principle component analysis was used for interpretation of data (Minitab Inc., State college, USA).

Instrumentation

Varian chrome pack CP-3800 gas chromatography was used to analyze pesticides residue content. The instrument equipped with ^{63}Ni electron capture detector and a 30 m x 0.32 mm i.d (0.25 µm film thickness), HP-MS 5ms fused silica capillary column. Nitrogen gas (99.99%) was used as a carrier at a flow rate of 1.5 mL min^{-1}. Oven temperature was kept at 90 °C for 1 min than increased to 170 °C at a rate of 3.5 °C min^{-1} and finally to 280 °C at rate of 5 °C/min. The injector and the detector temperature were adjusted to 250 °C and 300 °C. An amount of 2 µL of each sample was injected to GC-ECD for separation and quantitative analysis.

Results and Discussion

Concentration of organochlorine pesticides

The sum of ΣOCPs concentration were 44.1±19.3 µg kg^{-1}, 49.1±19.0 µg kg^{-1}, 25.8±18.3 µg kg^{-1}, 28.4±19.4 µg kg^{-1}, 28.1±18.5 µg kg^{-1}, 37.2±18.4 µg kg^{-1}, 13.7±16.3 µg kg^{-1} in soils of crops cabbage, cauliflower, spinach, celery, lettuce, broccoli and mustard (Table 1). The total concentration of OCPs (sum of α-HCH, β-HCH γ-HCH, DDE, DDD, DDT, endosulfan) in the soil of these crops ranges as ND – 13.3 µg kg^{-1} in cabbage, cauliflower (ND – 13.3 µg kg^{-1}), spinach (ND – 55.3 µg kg^{-1}, celery (ND – 6.6 µg kg^{-1}), lettuce (ND – 8 µg kg^{-1}), broccoli (ND – 4 µg kg^{-1}), and mustard (ND – 3.3 µg kg^{-1}). The observed trend of concentration of studied OCPs in these studies were γ-HCH (23.9%) > endosulfan (21.7%) > DDE (18.1%) > DDD (11.7%) > α-HCH (11.5%) > β-HCH (7.7%) > DDT (4.5%). The OCPs concentration in the soils of these crops decreases in the following order cauliflowers > cabbage > broccoli > celery > lettuce > mustard. Among HCHs the concentration decreases in the following order γ-HCH > α-HCH > β-HCH. This might be due to some new inputs for HCHs or its slow degradation rate. DDTs ranges as DDE > DDD > DDT showing its degradation and historical inputs. This high concentration of DDE shows the aerobic environment in surface soil [21] and this also shows that the degradation of the DDT is related to the physical property like pH in this case found to be higher (8.5) as an average for the soil of brassica leafy vegetables. Thus, its enhancing the degradation factor in soil of these crops. The ΣOCPs concentration observed in these studies were compared with other agriculture sites such as Mexico (36.91 – 389.31 µg kg^{-1}) and (5.2 – 316.4 µg kg^{-1}) [10, 21], China (7.82 – 765 µg kg^{-1}) [11] and India (1231 – 1734 ng g^{-1}) [2].

Table 1. Concentration of OCPs in agricultural soil of Cameron Highlands

Compounds	Concentration in Soil Sample of Vegetables (μg kg^{-1})						
	Cabbage	Cauliflower	Spinach	Celery	Lettuce	Broccoli	Mustard
α-HCH	2.6±0.4	13.3±0.8	4.66±0.4	ND	ND	4.6±0.5	1.3±2.2
β-HCH	3.3±5.2	4.0±7.4	2.6±1.2	ND	ND	4.0±5.8	4.0±1.9
γ-HCH	6.0±1.8	6.6±1.5	6.6±1.9	10.6±7.5	6.6±2.4	12.6±1.8	6±6.42
DDE	10.6±5.5	10.6±1.9	0.6±2.9	8.6±2.4	6.6±1.4	2.0±2.4	1.8±4.5
DDD	9.3±0.7	2.6±1.6	2.0±0.1	0.6±4.1	6.6±1.2	5.13±2.8	0.6±1.2
DDT	2.0±4.9	2.0±5.1.0	2.0±10.9	0.6±3.4	1.3±8.7	2.3±2.4	ND
Endosulfan	10±0.7	10±1.0	7.3±0.8	8.0±2.5	7.0±4.8	6.6±2.7	ND
Σ OCPs	44±19.3	49.1±19	25.76±18.3	28.4±19.9	28.1±18.5	37.23±18.4	13.7±16.3

β-HCH is the most stable, symmetrical structure and does not degrade easily in soil so in degradation process other HCH isomers will convert back to β-isomer and in soil its concentration will keep on increasing during degradation process that is why in many studies the ratio of β/α+γ is used to identify the historical pollution sources. If β/α+γ-HCH is higher than 0.5 would mean that it is due to historical pollution and if less than 0.5 would mean new sources has been introduced [3]. In current studies the majority of soil samples of their respective vegetables showed negative values indicating that the new sources accounted more for HCH pollution. This indicates the importance of pesticides spraying method, wind dispersion, leaching, wash out and volatilization that accounts for 80 – 90% of HCH from other farms to natural farms which is enhanced at high temperature, humidity, and intense solar radiation in tropical regions [11,22,23].

In the case of DDTs, DDE/DDT the ratio was higher than 1. The value for DDT > 1 indicating its historical inputs or its degradation by microbial activity or by enzymes secreted by root exudates or it can be due to high temperature [24]. The spatial distribution analysis of OCPs was investigated. The DDTs values were higher at Kuala Terla station ranging from 11 – 40 μg kg^{-1}. The maximum value at Kuala Terla station arises due to aerobic metabolites DDE of DDT. This results might be because of past usage of DDT in the agricultural area. The spatial distribution of HCHs and DDTs were not same at all sites. At seven sampling sites the sequence pattern for DDTs family were DDE> DDD> DDT. For HCH concentrations, the highest HCHs were found at Brinchang ranging from 1.3 – 26.6 μg kg^{-1}. This maximum value arises due to the presence of β-HCH the most stable isomer of HCHs indicating the past usage of HCH at this site. The highest endosulfan concentration was found at Kuala Terla of about 5 μg kg^{-1}. Among all sites, the Kuala Terla site seems to be most polluted by the OCPs indicating an extensive agricultural activity in this region and the illiteracy of the farmers also contributing to it. The lowest OCPs concentration was found at Habu station.

Human health risk assessment of OCPs

Health assessment was based on the assumption that human beings might be exposed to pesticides contaminated soil through ingestion, dermal contact or inhalation. The study area is an agricultural area so the farmers might be at great risk and since the compounds are persistent and hydrophobic so they would have higher affinity with soil particles. Therefore, the LADD of pesticides and HQ were calculated through soil ingestion [13,18,19] (Table 2). In this study we included adults of 70-year-old and children of 12 years of age exposed for all the days in a year during their life span. The estimated LADD of total OCPs for adults and children through soil ranged between 2.1×10^{-8} – 1×10^{-7} mg kg^{-1} d^{-1} and 5.3×10^{-8} – 2.7×10^{-7} mg kg^{-1} d^{-1} with the mean values as 5.2×10^{-7} mg kg^{-1} d^{-1} and 1.3×10^{-7} mg kg^{-1} d^{-1} (Table 2). HQ for human adults for sum of OCPs are 6.7×10^{-5}, 8×10^{-6}, 1.6×10^{-5} and for children was 3×10^{-5}, 4×10^{-6}, 8.6×10^{-6} (Table 3) which were lower than the acceptable risk levels. Thus, it indicated that the daily dose is below the proposed guidelines of USEPA 2012 [13].

Table 2. Concentration of OCPs and its life time average daily dose for humans through soil ingestion

Compounds	Concentration (μg kg^{-1})		(LADD mg kg^{-1} d^{-1})			
			Adults		Children	
	Range	Mean	Range	Mean	Range	Mean
α-HCH	2.6 – 13.3	3.8	3.7 x 10^{-9} – 1.9 x10^{-8}	5.4 x 10^{-8}	1.9 x 10^{-8} – 9.8 x10^{-8}	2.8 x 10^{-8}
β-HCH	0.6 – 4	2.5	8.5x 10^{-10} – 5.7 x 10^{-9}	3.6 x 10^{-8}	4.4 x 10^{-9} – 2.9 x 10^{-8}	1.9 x 10^{-8}
γ-HCH	3.3 – 12.6	7.8	4.7 x 10^{-9} – 1.8 x 10^{-7}	1 x 10^{-7}	2.4 x 10^{-8} – 9.3 x 10^{-8}	5.7 x 10^{-8}
DDE	2 – 17.3	6.0	2.8 x 10^{-9} – 2.5 x 10^{-8}	8.5 x 10^{-8}	1.4 x 10^{-8} – 4.8 x 10^{-8}	4.4 x 10^{-8}
DDD	0.6 – 9.3	3.8	8.6 x 10^{-10} – 1.3 x 10^{-8}	5.5 x 10^{-8}	4.4 x 10^{-9} – 6.8 x 10^{-8}	2.8 x 10^{-8}
DDT	2 – 6.6	1.5	2.8 x 10^{-9} – 9.4 x 10^{-9}	2 x 10^{-8}	1.5 x 10^{-8} – 1.2 x 10^{-7}	1.0 x 10^{-8}
Endosulfan	3.3 – 10	7.0	4.7x 10^{-9} – 1.4 x 10^{-8}	1 x 10^{-8}	4.4 x 10^{-9} – 1.2 x 10^{-7}	5.0 x 10^{-8}
Total OCPs	14.4 – 73.1	32.4	2.1 x 10^{-8} – 1.0 x 10^{-7}	4.6 x 10^{-7}	5.3 x 10^{-8} – 2.7 x 10^{-7}	2.4 x 10^{-7}

Table 3. Hazard quotients to humans due to OCPs

Pesticide	Reference dose (mg kg^{-1})	LADD (mg kg^{-1} d^{-1})		Hazard Quotient		Health risk
		Adults	Children	Adults	Children	
Σ HCHs	3 x 10^{-3}	2.4 x 10^{-7}	1 x 10^{-7}	6.7 x 10^{-5}	3 x 10^{-5}	No
Σ DDTs	2 x 10^{-2}	1.6 x 10^{-7}	8.3 x 10^{-8}	8 x 10^{-6}	4 x 10^{-6}	No
Endosulfan	6 x 10^{-3}	1.0 x 10^{-8}	5 x 10^{-8}	1.6 x 10^{-5}	8.6 x 10^{-6}	No

Concentration of organophosphorus and pyrethroids

The sum of ΣOPPs concentration were 45.1±7.2 μgkg^{-1}, 34.9±10.3 μgkg^{-1}, 65.8 ±2.3 μgkg^{-1}, 22.7 ±19.8 μg kg^{-1}, 15.5±16.4 μg kg^{-1}, 15.5±57.6 μg kg^{-1}, 14.7±18.9 μg kg^{-1}in the soil of crops cabbage, cauliflower, spinach, celery, lettuce, broccoli and mustard (Table 4). The sum of total concentration of OPPs (dimethoate, diazinon, chlorpyriphos, malathion, parathion methyl, parathion ethyl) in the soil of these crops ranges as ND-20 μg kg^{-1} in cabbage, ND – 26 μg kg^{-1} in brocolli, 0.2 – 8 μg kg^{-1}in celery, ND – 20 μg kg^{-1} in spinach, ND – 8 μg kg^{-1} in lettuce, and ND – 3.3 μg kg^{-1} in mustard. The OPPs concentration in these soil crops decreases in the following order spinach > broccoli > cabbage > cauliflower > celery > lettuce > mustard. This shows the same trend as that of OCPs except the spinach soil indicating that loose structure of soil of these vegetables might decrease the concentration of pesticides due to leaching or via exposure of these plots to the rainfall and since this part has a tropical climate so the decrease in concentration might be due to high temperature, moisture and intense microbial activity [17]. The observation of pesticides residue for spinach soil is highly contaminated by OPPs and mustard soils the least which might be due to the cultivation process of these crops or the type of irrigation system. The observed trend of concentration of studied OPPs in these studies were parathion ethyl (25.3%) > dimethoate (23.8%) > diazinon (21%) > malathion (14.3%) > chlorpyriphos (13.3 %) > parathion methyl (2.2 %). The slight high concentration of OPPs as compared to OCPs in the soil of these crops might be because these vegetables are more susceptible towards the insects or due to easily degradation of OPPs that's is why these are applied frequently and there can be a possibility that insects have developed a low level of resistance towards these pesticides. These OPPs concentration was higher than other studies in Cameron Highland (< 0.01 – 0.06 mg kg^{-1}) [17], 16.68 ng g^{-1} for dimethoate [25]. The spatial distribution of OPPs were not same at all sites. Among stations the highest concentration for OPPs were found at Kuala Terla ranging from 4.6 – 15 μg kg^{-1} where dimethoate accounted the most indicating its extensive use over the vegetables. The lowest concentration of OPPs were found at Telom region ranging from ND – 0.02 μg kg^{-1}.

The sum of ΣPYRs concentration were 7.9±12.7 μg kg^{-1}, 7.9 ±15.1 μg kg^{-1}, 3.6 ±14.2 μg kg^{-1}, 1.3 ±2.7 μg kg^{-1}, 1.3±1.6 μg kg^{-1}, 10.8±1.1 μg kg^{-1} and 2.7±12.4 μg kg^{-1} in the soil of crops cabbage, cauliflower, spinach, celery, lettuce, broccoli and mustard showing that the sum of residual concentration is same in cabbage and cauliflower soil and in celery and lettuce (Table 4). The total concentration of PYRs (sum of permethrin and fenvelerate) for soil ranges between ND – 1.3 μg kg^{-1} in cabbage, ND – 1.3 μg kg^{-1} in celery, ND – 0.6 μg kg^{-1} in lettuce, ND – 6.6 μg kg^{-1} in cauliflower, ND – 5.3 μg kg^{-1} in broccoli, ND – 6.6 μg kg^{-1} in spinach and ND –1.3 μg kg^{-1} in mustard. The observed trend of concentration studied for PYRs were fenvelerate (62.2%) > permethrin (37.7%). This does indicate the usage of pyrethroids pesticides in Cameron Highlands as already been reported [8]. PYRs seemed to be the least detected pesticides among all sites indicating its less use in study area. However, the highest concentration was found at Kuala Terla of which fenvelerate accounted the most (10 μg kg^{-1}).

Table 4. Concentration of OPPs & PYRs pesticide in agricultural soil of Cameron Highlands

Compounds	Concentration in Soil Sample of Vegetables (μg kg^{-1})						
	Cabbage	**Cauliflower**	**Spinach**	**Celery**	**Lettuce**	**Broccoli**	**Mustard**
Dimethoate	6.6±1.8	6.6±3.55	26.6±0.81	0.6±3.2	0.06±3.49	20±1.76	0.6±5.7
Diazinon	20±1.1	13.3±2.2	20±1.8	0.6±5.6	0.06±3.8	ND	0.6±0.9
Parathion methyl	0.6±1.6	0.6±1.78	1.3±3.67	0.2±2.4	0.2±2.4	1.3±3.4	1.46±1.1
Parathion ethyl	9.3±1.27	9.3±1.54	6.6±5.6	8±3.5	3.3±2.75	20±1.4	8.6±3.55
Chlorpyriphos	4.6±0.3	4.6±0.49	5.3±1.51	5.3±4.8	5.3±0.5	5.3±5	3.3±1.24
Malathion	4±1.13	0.4±0.78	6±0.3	8±0.3	6.6±3.6	11±6.2	0.66±6.5
Σ OPPs	45.1±7.2	34.8±10.34	65.8±2.3	22.7±19.8	15.5±16.4	57.6±17.76	14.6±19.0
Permethrin	1.3±5.8	1.3±7.5	0.26±4.9	1.3±2.67	1.3±1.56	6±1.09	2±3.5
Fenvelerate	6.6±6.9	6.6±7.6	3.3±9.3	ND	ND	4.8±1.3	0.66±8.9
Σ PY	7.9±12.7	7.9±15.1	3.5±14.2	1.3±2.67	1.3±1.56	10.8±2.3	2.6±12.4

*ND = not detected

Human health risk assessment for OPPs and PYRs

In this study we included adults of 70 years old and children of 12 years of age exposed for all the days in a year during their life span. The estimated LADD of total OPPs for adults and children through soil ranged between 6.9 x 10^{-9} – 3.6 x 10^{-7} mg kg^{-1} d^{-1} and 3.6 x 10^{-8} – 1.8 x 10^{-6} mg kg^{-1} d^{-1} (Table 5). HQ of OPPs for human adults was 5.7 x 10^{-6}, 1.6 x 10^{-5}, 3.8 x 10^{-7}, 3.3 x 10^{-6}, 2.5 x 10^{-8}, 6.9 x 10^{-7}, while for children was 3 x 10^{-5}, 8 x 10^{-5}, 1.9 x 10^{-6}, 1.7 x 10^{-5}, 1.3 x 10^{-7}, 3.5 x 10^{-6} (Table 5) which were lower than the acceptable risk levels indicating that the daily dose is below the proposed guide lines of USEPA 2012 [12]. For PYRs the LADD adults ranges as 3.7 x 10^{-9} – 3.4 x 10^{-8} mg kg^{-1} d^{-1} and for children as 6 x 10^{-9} – 1.7 x 10^{-8} mg kg^{-1} d^{-1} with the mean values as 7 x 10^{-9} mg kg^{-1} d^{-1} and 1.7 x 10^{-8} mg kg^{-1} d^{-1}. The HQ by fenvelerate and permethrin for adults is 2.2 x 10^{-7}, 5.4 x 10^{-8} and for children is 1 x 10^{-6}, 2.8 x 10^{-7} (Table 6).

Table 5. Concentration of OPPs and PYRs and its life time average daily dose for humans through soil ingestion

Compound	Concentration (μg kg^{-1})		(LADD mg kg^{-1} d^{-1})			
			Adults		Children	
	Range	Mean	Range	Mean	Range	Mean
Dimethoate	0.06 – 200	8.0	$8.6 \times 10^{-11} – 2.9 \times 10^{-7}$	1.1×10^{-8}	$4.4 \times 10^{-10} – 1.5 \times 10^{-6}$	5.9×10^{-8}
Diazinon	0.6 – 23	7.7	$8.5 \times 10^{-10} – 3.3 \times 10^{-8}$	1.1×10^{-8}	$4.4 \times 10^{-9} – 1.7 \times 10^{-7}$	5.7×10^{-8}
ParathionMethyl	0.2 – 12	0.8	$2.8 \times 10^{-13} – 1.7 \times 10^{-8}$	1.1×10^{-9}	$1.5 \times 10^{-9} – 8.9 \times 10^{-8}$	6.0×10^{-9}
Parathion Ethyl	0.2 – 10	9.3	$3.0 \times 10^{-10} – 1.4 \times 10^{-8}$	1.3×10^{-8}	$1.5 \times 10^{-9} – 7.4 \times 10^{-8}$	6.9×10^{-8}
Malathion	2 - 3	5.2	$2.9 \times 10^{-9} – 4.2 \times 10^{-9}$	7.4×10^{-9}	$1.5 \times 10^{-8} – 2.2 \times 10^{-8}$	3.8×10^{-8}
Chlorpyriphos	1.8 – 5.3	4.8	$2.6 \times 10^{-9} – 7.6 \times 10^{-9}$	6.8×10^{-9}	$1.3 \times 10^{-8} – 3.9 \times 10^{-8}$	3.5×10^{-8}
Total OPPs	4.9 – 253.3	35.8	$6.9 \times 10^{-9} – 3.6 \times 10^{-7}$	5.1×10^{-8}	$3.6 \times 10^{-8} – 1.8 \times 10^{-6}$	2.7×10^{-7}
Fenvelerate	0.6 – 2	3.1	$9.0 \times 10^{-10} – 3.0 \times 10^{-8}$	4.3×10^{-9}	$4.4 \times 10^{-9} – 1.5 \times 10^{-8}$	2.3×10^{-8}
Permethrin	0.2 – 0.4	1.9	$3.0 \times 10^{-10} – 6 \times 10^{-10}$	2.7×10^{-9}	$1.5 \times 10^{-9} – 3 \times 10^{-9}$	1.4×10^{-8}
Total PY	0.8 – 0.6	5.0	$3.7 \times 10^{-9} – 3.4 \times 10^{-8}$	7.0×10^{-9}	$6.0 \times 10^{-9} – 1.7 \times 10^{-8}$	3.7×10^{-8}

Table 6. Hazard quotients to humans due to OPPs and PYRs

Pesticide	Reference dose (mg kg^{-1})	LADD (mg kg^{-1} d^{-1})		Hazard Quotient		Health Risk
		Adults	Children	Adults	Children	
Dimethoate	2×10^{-3}	1.1×10^{-8}	5.9×10^{-8}	5.7×10^{-6}	3×10^{-5}	No
Diazinon	7×10^{-4}	1.1×10^{-8}	5.7×10^{-8}	1.6×10^{-5}	8×10^{-5}	No
Parathion Methyl	3×10^{-3}	1.1×10^{-9}	6.0×10^{-9}	3.8×10^{-7}	1.9×10^{-6}	No
Parathion Ethyl	4×10^{-3}	1.3×10^{-8}	6.9×10^{-8}	3.3×10^{-6}	1.7×10^{-5}	No
Malathion	3×10^{-1}	7.4×10^{-9}	3.8×10^{-8}	2.5×10^{-8}	1.3×10^{-7}	No
Chlorpyriphos	1×10^{-2}	6.8×10^{-9}	3.5×10^{-8}	6.9×10^{-7}	3.5×10^{-6}	No
Fenvelerate	2×10^{-2}	4.3×10^{-9}	2.3×10^{-8}	2.2×10^{-7}	1.1×10^{-6}	No
Permethrin	5×10^{-2}	2.7×10^{-9}	1.4×10^{-8}	5.4×10^{-8}	2.8×10^{-7}	No

Relationship of soil properties with pesticides residue

The soil samples were analyzed for three physico-chemical properties including texture, pH, and organic carbon content (Table 7). These parameters are important in order to study the mobility and degradation behavior of pesticides. Soil properties influence the fate of the pesticides in soil e.g. the organic content of soil, clay content and the soil pH. As increase in organic content increases the binding forces by bonding with the hydrophobic compounds in the soil thus reducing their mobility. This correlation among the residue of pesticides and soil properties is shown by a biplot (Figure 2) by using the PCA, which is a powerful tool for pattern recognition, classification and modeling and other aspects of data evaluation. It was performed on data of pesticides in soil under study showing the relationship among 17 variables.

Table 7. Physico-chemical properties of soil

Textures (%)			pH	Organic Carbon (%)
Coarse Sand	Fine sand	Clay and Silt		
68	17	12	7 – 8	17.6

Four principal components with Eigen value >1 accounts for 98% of total variance sets show a high residual concentration of pesticides in soil of brassica vegetables like cabbage, cauliflower, broccoli as compared to other leafy vegetable. Secondly TOC and pH are not separated by larger distance and are more correlated with DDT, DDD, DDE, endosulfan, ∝-HCH, permethrin, diazinon, chloripyrphos and diazinon in the soils of brassica vegetables like cabbage, cauliflower and broccoli and it also shows that the organic content and pH of the soil is more correlated with the soils of these crops as compared to other leafy vegetables (mustard, celery and lettuce) thus reducing pesticides mobility due to strong hydrophobic interactions [26]. This shows that the amount of pesticides usage depends upon crop type; the soil of brassica leafy vegetables is more contaminated and it might be possible that these vegetables has the ability to accumulate more OCPs because of the roots of these vegetables exudes organic compounds consisting of 20-30% of photosynthetic compounds which supports pesticides movement [27] while the decrease in the soil concentration of other leafy vegetables is due to in situ biomass burning during harvesting time of crop cultivation that favors the volatilization of these OCPs [10].

There can be several factors contributing in these observations of these high residual content in brassica vegetables which can be due to a close cultivation of these vegetables in the small field or the procedures used by the farmers for crop protection would be similar for these plants in case of other leafy vegetables the less association of soil with pesticides residues might be because rapid disappearance of pesticides after application or the high rotation frequency of unproductive culture before completely grown [1]. There can also be a possibility that the roots of these vegetables release dehydrohalogenase enzymes that dechlorinate the organohalogenated compounds or there can be enhance degradation due to rhizosphere effect which is the influence of the root system on uptake of contaminants via soil [27]. Biplot also shows a strong correlation between pH 7 – 8, and organic content (14%) with the OCPs like DDT, endosulfan and HCHs showing a hydrophobic interaction between the soil particles and pesticides. This indicates a strong pesticide-soil organic interaction masking the acidity and alkalinity of soil [28].

There is not a significant correlation between most of the OPPs with pH and organic content of soil except diazinon indicating that adsorption of polar OPPs decreases with increase pH (7 – 8). However, endosulfan showed a significant correlation indicating that higher pH is favoured for adsorption of neutral pesticides in soil. These results are similar to the studies reported by Krishna and Philip [29] that pesticides adsorption is maximum between pH 2-8. In this case the persistence of these OPPs in the soil of these crops might be due to its adsorption on the clay fraction of soil because of its polar nature as clay particles has a small size and its combination with the organic content is useful because both of these are associated of their mutual interaction of molecular attraction and surface charges [30]. It might also be possible that inhibition of microbial degradation is responsible for holding these pollutants in soil rather than the organic content. It is also had been proved by other studies that in case if polar pesticides are not correlated with the organic content of soil than it has the ability to relate with other factors of soil such as inorganic matter, calcium concentration cation exchange capacity [30,31]. There is also a possibility that under the influence of roots of the brassica vegetables has the ability to facilitate the movements of these chemicals from soil towards the rhizosphere soil from where they are taken up by the roots [32], that is why these vegetables have high concentration of pesticides.

Biplot also indicates that mixture of pesticides has been used on crops and that might also influence the persistence of these pesticides [25]. Diazinon is an exceptional to other OPPs as it seemed to be more correlated with the organic content and pH of soil showing that at high pH diazinon is more persistent than other OPPs and it has also more association with organic content that's why cannot be broken easily by water thus cannot be removed by leaching [30,33]. This is in agreement reported previously by Chapman and Cole [28] that maximum correlation of diazinon and chlorpyriphos at high pH. This high correlation of diazinon and chlorpyriphos as compared to other OPPs might also be because of increased difficulty to access the adsorption sites of soil by other pesticides due to increased concentration [34], this increased sorption correlates with the sorption studies [35], suggesting the high sorption based on organic content and the k_{ow} of these pesticides. In the case of pyrethroids, permethrin is more correlated with the organic content in these vegetable soils as compared to fenvelerate showing its adsorption with the organic content this correlate with the studies of other researchers [9]. Biplot also indicates that pesticides are originating from different sources as farmers use mixture of pesticides to have more residual effect.

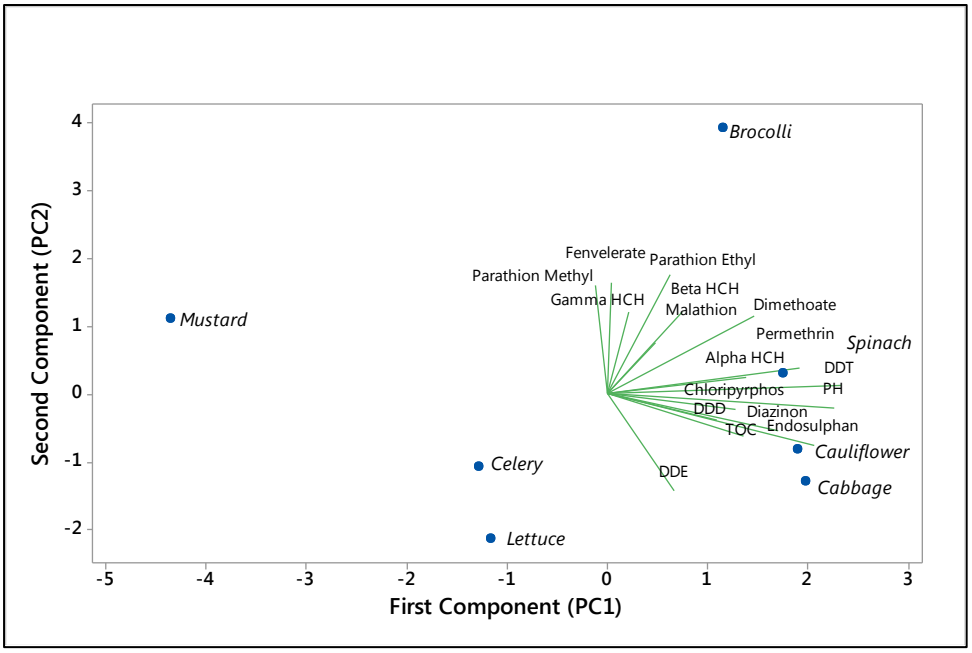


Figure 2. Biplot of two component loading (PC1 x PC2)

Conclusion

Despite restriction on OCPs, the residues of these pesticides were found in the agricultural soil of Cameron Highlands. The average highest concentration of DDT and γ-HCH indicates the presence of both new and historical input sources for HCHs while historical inputs for DDTs contamination or its slow degradation. The highest concentration for OCPs in soil of these crops were seen as cauliflowers > cabbage > broccoli > celery > lettuce > mustard. The OPPs concentration were higher indicating its continuous use in soil of these crops following order as spinach > cabbage > broccoli > cauliflower > celery > lettuce > mustard. Among PYRs, permethrin was used in high concentration and in soil crops its concentration follows as following order broccoli > cabbage > cauliflower > spinach > celery > lettuce > mustard. These results also show that the farmers prefer to use mixture of these pesticides as they believe it is more effective than using a single kind. PCA shows high residual concentration in soil of brassica vegetables and indicated that the presence of these pesticides in the soil is more correlated with type of crop, its cycle or crop protection and it also shows that most of OCPs and permethrin was more correlated with the total organic content and pH of soil. Meanwhile in some cases OPPs and fenvelerate were not as correlated with the pH and organic content indicating its less adsorption on the organic content of soil. The health risk assessment showed that though residues of these contaminants were found in these soil during both less and high frequent spraying by farmers but it poses no health risks to humans working in this agricultural region as the HQs were less than one (≤1).In conclusion it is noteworthy to remark that soil total organic content has reduced the mobility for most of the pesticides in the soil of brassica vegetables (cabbage, cauliflower, broccoli) as it has effect on the leachability, biodegradability, volatility, persistence and bioactivity of these pesticides.

Acknowledgement

Authors wish to thank the Government of Malaysia for grant FRGS/2/2013/STO1/UKM/01/2 and Universiti Kebangsaan Malaysia for DPP-2015-053. Technical help from the Centre of Water Research and Analysis (ALIR) and the School of Chemical Sciences and Food Technology is gratefully acknowledged. We wish to thank the Higher Education Commission, Pakistan for the award of scholarship and Sardar Bahadur Khan Women University (SBKWU), Quetta, Pakistan for study leave.

References

1. Gonçalves, C., Da Silva, J. C. E. and Alpendurada, M. F. (2006). Chemometric interpretation of pesticide occurrence in soil samples from an intensive horticulture area in North Portugal. *Analytica Chimica Acta*, 560: 164 – 171.
2. Mishra, K., Sharma, R. C. and Kumar, S. (2012). Contamination levels and spatial distribution of organochlorine pesticides in soils from India. *Ecotoxicology Environment Safety*, 76: 215 – 225.
3. Shi, R., Lv, J. and Feng, J. (2011). Assessment of pesticide pollution in suburban soil in South Shenyang, China. *Bulletin of Environmental Contamination and Toxicology,* 87: 567 – 573.
4. El-Shahawi, M. S., Hamza, A., Bashammakh, A. S. and Al-Saggaf, W.T. (2010). An overview on the accumulation, distribution, transformations, toxicity and analytical methods for the monitoring of persistent organic pollutants. *Talanta,* 80:1587 – 1597.
5. Ng, W. F., Teo, M. J. K. and Lakso, H. A. (1999). Determination of organophosphorus pesticides in soil by headspace solid-phase microextraction. *Fresenius' Journal of Analytical Chemistry,* 363: 673 – 679.
6. Derbalah, A. S., Ismail, A. and Hamza, A. (2013). Monitoring of organophosphorus pesticides and bioremediation chlorpyrifos in soil. *Egyptian Journal of Plant Production Research,* 1: 115 – 132.
7. Sattar M. A. (1990). Fate of organophosphorus pesticides in soils. *Chemosphere*, 20: 387 – 396.
8. Ragnarsdottir, K. V. (2000). Environmental fate and toxicology of organophosphate pesticides. *Journal of the Geological Society*, 157: 859 – 876.
9. Ismail, B. S. and Kalithasan, K. (2004). Adsorption, desorption, and mobility of permethrin in Malaysian soils. *Journal of Environmental Science and Health Part B,* 39: 419 – 429.
10. Velasco, A., Hernández, S., Ramírez, M. and Ortíz, I. (2014). Detection of residual organochlorine and organophosphorus pesticides in agricultural soil in Rio Verde Region of San Luis Potosi, Mexico. *Journal of Environmental Science and Health, Part B: Pesticides, Food Contaminants, and Agricultural Wastes,* 49: 498 – 504.
11. Gao F., Jia, J. and Wang, X. (2008). Occurrence and ordination of dichlorodiphenyltrichloroethane and hexachlorocyclohexane in agricultural soils from Guangzhou, China. *Archives of Environmental Contamination and Toxicology,* 54:155 – 166.
12. Bempah, C. K., Donkor, A., Yeboah, P. O., Dubey, B. and Osei-Fosu, P. (2011). A preliminary assessment of consumer's exposure to organochlorine pesticides in fruits and vegetables and the potential health risk in Accra Metropolis, Ghana. *Food Chemistry,* 128: 1058 – 1065.
13. Kumar, B., Verma, V.K., Mishra, M., Gaur, R., Kumar, S. and Sharma, C.S. (2014). DDT and HCH (Organochlorine Pesticides) in residential soils and health assessment for human populations in Korba, India. *Human and Ecological Risk Assessment: An International Journal,* 20: 1538 – 1549.
14. Arias-Estévez M., López-Periago, E., Martínez-Carballo, E., Simal-Gándara, J., Mejuto, J. C. and García-Río, L. (2008). The mobility and degradation of pesticides in soils and the pollution of groundwater resources. *Agriculture, Ecosystems & Environment*, 123: 247 – 260.
15. Weng, T. K. and Chee, B. W. (2015). Water quality monitoring using biological indicators in Cameron Highlands Malaysia. *Journal of Sustainable Development,* 8: 28 – 42.
16. Heiri, O., Lotter, A. F. and Lemcke, G. (2001). Loss on ignition as a method for estimating organic and carbonate content in sediments: Reproducibility and comparability of results. *Journal of Paleolimnology*, 25: 101 – 110.
17. Ngan, C. K., Cheah, U. B., Abdullah, W. W., Lim, K. P. and Ismail, B. S. (2005). Fate of chlorothalonil, chlorpyrifos and profenofos in a vegetable farm in Cameron Highlands, Malaysia. *Water, Air, & Soil Pollution*: *Focus,* 5:125 – 136.
18. Agency for Toxic substances and Disease Registry (2005). Toxicological profile for hexachlrocyclohexanes. US Public Health Service, Atlanta, GA, USA.
19. United States Environmental Protection Agency (1989). Risk assessment guide for super fund. Human health evaluation manual, Part A. EPA 540-1-89-002.USEPA, Washington DC.
20. Shukor, N. S. A., Khazaai, S. N. M., Hussain, Z. M. and Jan, S. L. M. (2015). Degradation behavior of chlorpyrifos in spinach (*Spinacia oleracea*) and soil. *Malaysian Journal of Analytical Sciences* 19(4), 722 – 729.

21. Velasco, A., Rodríguez, J., Castillo, R. and Ortíz, I. (2012). Residues of organochlorine and organophosphorus pesticides in sugarcane crop soils and river water. *Journal of Environmental Science and Health, Part B: Pesticides, Food Contaminants, and Agricultural Wastes,* 47: 833 – 841.
22. Miglioranza, K. S. B., de Moreno, J. E., Moreno, V. J., Osterrieth, M. L. and Escalante, A. H. (1999). Fate of organochlorine pesticides in soils and terrestrial biota of "los padres" pond watershed, Argentina. *Environmental Pollution,* 105: 91 – 99.
23. Gonzalez, M., Miglioranza, K. S., Aizpún de Moreno J. E. and Moreno, V. J. (2003). Organochlorine pesticide residues in leek (*Allium porrum*) crops grown on untreated soils from an agricultural environment. *Journal Agricultural and Food Chemistry,* 51: 5024 – 5029.
24. Vig, K., Singh, D. K., Agarwal, H. C., Dhawan, A. C. and Dureja, P. (2001). Insecticide residues in cotton crop soil. *Journal of Environmental Science and Health, Part B: Pesticides, Food Contaminants, and Agricultural Wastes,* 36: 421 – 434.
25. Crisanto, T., Sanchez-Martin, M. J., Sanchez-Camazano, M. and M. Arienzo (1994). Mobility of pesticides in soils. influence of soil properties and pesticide structure. *Toxicological & Environmental Chemistry,* 45: 97 – 104.
26. Gonzalez, M., Miglioranza, K. S., Aizpún, J. E., Isla, F. I. and Peña, A. (2010). Assessing pesticide leaching and desorption in soils with different agricultural activities from Argentina (Pampa and Patagonia). *Chemosphere,* 81: 351 – 358.
27. Pereira, R. C., Camps-Arbestain, M., Garrido, B. R., Macías, F. M. and Monterroso, C. (2006). Behaviour of α-, β-, γ-, and δ-Hexachlorocyclohexane in the soil–plant system of a contaminated site. *Environmental Pollution,* 144: 210 – 217.
28. Chapman, R. A. and Cole, C. M. (1982). Observations on the influence of water and soil pH on the persistence of insecticides. *Journal of Environmental Science & Health Part B*, 17: 487 – 504.
29. Krishna, K. R. and Philip, R. (2008). Adsorption and desorption characteristics of lindane, carbofuran and methyl parathion on various Indian soils. *Journal of Hazardous Materials* 160: 559 – 567.
30. Vagi, M. C, Petsas, A. S., Kostopoulou, M. N. and Lekkas, T. D. (2010). Adsorption and desorption processes of the organophosphorus pesticides, dimethoate and fenthion, onto three Greek agricultural soils. *International Journal of Environmental and Analytical Chemistry,* 90: 369 – 389.
31. Rodriguez-Cruz, M. S., Sanchez-Martin, M. J. Andrades, M. J. and Sánchez-Camazano, M. (2006). Comparison of pesticide sorption by physicochemically modified soils with natural soils as a function of soil properties and pesticide hydrophobicity. *Soil and Sediment Contamination,* 15:401 – 415.
32. Tao, S., Xu, F. L., Wang, X. J., Liu, W. X., Gong, Z. M. and Fang, J.Y. (2005). Organochlorine pesticides in agricultural soil and vegetables from Tianjin, China. *Environmental Science & Technology*, 39(8): 2494 – 2499.
33. Getzin, L. W. (1968). Persistence of diazinon and zinophos in soil: Effects of autoclaving, temperature, moisture, and acidity. *Journal of Economic Entomology,* 61: 1560 – 1565.
34. Nemeth-Konda, L., Füleky, G., Morovjan, G. and Csokan, P. (2002). Sorption behaviour of acetochlor, atrazine, carbendazim, diazinon, imidacloprid and isoproturon on Hungarian agricultural soil. *Chemosphere,* 48: 545 – 552.
35. Kanazawa, J. (1989). Relationship between the soil sorption constants for pesticides and their physicochemical properties. *Environmental Toxicology and Chemistry,* 8: 477 – 484.

Malaysian Journal of Analytical Sciences, Vol 20 No 6 (2016): 1359 - 1364
DOI: http://dx.doi.org/10.17576/mjas-2016-2006-14

MALAYSIAN JOURNAL OF ANALYTICAL SCIENCES
Published by The Malaysian Analytical Sciences Society
ISSN 1394 - 2506

INTERCALATION STUDY OF CURCUMIN INTO ZINC LAYERED HYDROXIDE

(Kajian Mengenai Penyisipan Kurkumin ke dalam Zink Hidroksida Berlapis)

Adila Mohamad Jaafar[1]*, Asma Najaj Anuar[1], Norhayati Hashim[2], Fatin Hanifah Ayob[1]

[1]*Department of Chemistry, Faculty of Science,*
Universiti Putra Malaysia, 43400 UPM Serdang, Selangor, Malaysia
[2]*Department of Chemistry, Faculty of Science and Mathematics*
Universiti Pendidikan Sultan Idris, 35900 Tanjong Malim, Perak, Malaysia

**Corresponding author: adilamj@upm.edu.my*

Received: 17 August 2015; Accepted: 5 October 2016

Abstract

Zinc layered hydroxide (ZLH) intercalated with curcumin was successfully prepared by ion exchange method. The synthesised nanocomposite was characterised by Powder X-ray diffraction (PXRD) and Fourier transform infrared spectroscopy (FTIR). The obtained intercalation compound, ZLH-curcumin nanocomposite (ZiCUR), showed a basal spacing of 10.0 Å when 0.01M of curcumin solution was used in the synthesis. The shifting in the stretching frequency of the curcumin anion provides strong evidence that the anion is bonded to the ZLH through electrostatic force. In FTIR, after intercalation, there is a noticeable shift of the O-H stretching vibrational bands. This is due to the formation of strong hydrogen bonds between curcumin and –OH groups in ZLH. Thus, this indicates that curcumin anions are present in the sample and were intercalated between positively charged ZLH layers, as indicated by the characteristics of PXRD pattern.

Keywords: zinc layered hydroxide, curcumin, ion exchange method

Abstrak

Zink hidroksida berlapis (ZHB) disisip bersama kurkumin telah berjaya disediakan menggunakan kaedah pertukaran ion. Komposit nano yang telah di sintesis dicirikan menggunakan X-ray Serbuk Pembelauan dan Spektroskopi Infra Merah Transformasi Fourier. Sebatian interkalasi yang diperoleh iaitu komposit nano zink hidrosida berlapis-kurkumin, menunjukkan jarak basal sebanyak 10.0 Å apabila kepekatan 0.01M larutan kurkumin digunakan semasa proses sintesis. Perubahan pada frekuensi anion kurkumin menunjukkan bukti yang kukuh di mana anion telah dilekatkan kepada ZHB menggunakan daya elektrostatik. Melalui Spektroskopi Infra Merah Transformasi Fourier, selepas interkalasi, perubahan yang ketara pada O-H regangan jalur getaran dapat di lihat. Hal ini kerana, pembentukan ikatan hidrogen yang kuat antara kurkumin dan kumpulan -OH di dalam ZHB. Maka, ia menunjukkan bahawa anion kurkumin hadir di dalam sampel dan telah disisipkan antara lapisan ZHB yang bercas positif, seperti mana yang ditunjukkan oleh ciri – ciri corak Spektroskopi Infra Merah Transformasi Fourier.

Kata kunci: zink hidroksida berlapis, kurkumin, kaedah pertukaran ion

Introduction

According to the World Health Organization, open injuries have the potential for serious bacterial wound infections, including gas gangrene and tetanus, and these, in turn, may lead to long term disabilities, chronic wound or bone infection, and death [1]. Wound infection is particularly of concern when injured patients are presented late for definitive care. Problems, such as lack of knowledge about how to diagnose and treat wounds and lack of funding to

proper therapies, medical technologies and trained wound-care professionals, will lead to millions of untreated and mistreated patients each year.

Turmeric, (*Curcuma longa* L.), has been used in traditional medical applications since ancient times. The principal curcuminoid in turmeric is curcumin [2], which was extensively studied as antibacterial compound. The wound healing ability of curcumin, involving the mechanisms of reduced inflammation, granulation, and remodelling of the tissue, was intensively examined in rats and guinea pigs. The recent studies have highlighted that punch wounds in curcumin-treated animals healed much faster than curcumin untreated animals [3] [4]. However, the curcumin molecule is unstable and therefore, demonstrates limited biological activity and practical applications. In this study, in order to stabilize the curcumin, attempts were made by intercalating curcumin into layered metal hydroxide.

Layered metal hydroxide can be classified as layered double hydroxide (LDH) and layered hydroxide salt (LHS). Layered double hydroxide (LDH) nanocomposite is a class of inorganic material with a chemical composition represented by the general formula, $[M^{2+}_{1-x}\ M^{3+}_{x}\ (OH)_2]^{x+}\ [A^{n-}_{x/n}.mH_2O]$, where M^{2+} and M^{3+} are divalent and trivalent metal cations, respectively [5]. Previous studies have shown that curcumin intercalated into Mg/Al LDH exhibited excellent wound healing properties [6]. However, to the best of our knowledge, the application of a Zinc layered hydroxide salt (LHS) as a host has yet to be explored.

Zinc layered hydroxide (ZLH) is represented by the general formula of $M^{2+}(OH)_{2-x}(A^{m-})_{x/m}.nH_2O$, where M^{2+} in this case is the metal cation Zn^{2+} and A^{m-} is the counter ion [7]. The ZLH structure consists of positively charged layers that can expand or contract depending on the nature of the interlayer anions. In this current investigation, we study the intercalation of curcumin into interlayer galleries of ZLH via ion exchange method, as well as properties of the resulting ZLH-curcumin intercalation compound. This direct method involved a direct reaction between the curcumin solution and the zinc oxide (ZnO) precursor. Compared with other LHS synthesis methods, like urea hydrolysis [8], structural memory effects [9], co-precipitation [10] and solid state reactions [11], ion exchange method was chosen as the best method because it is simple, environmentally friendly, and economical as it involves fewer chemicals and fewer steps.

Materials and Methods

Materials

Zinc oxide, 99%, curcumin ($C_{21}H_{20}O_6$ molecular weight 368.3799 g/mol), 98%, and sodium hydroxide, 99% purity, were purchased from Acros Organics (Geel, Belgium) and Merck (Darmstadt, Germany), respectively. Chemicals were used without further purification. Deionized water was used throughout the experiment.

Synthesis of zinc layered hydroxide intercalated with curcumin

The curcumin-intercalated ZLH was prepared using the ion-exchange method [12,13,14]. An amount of 100 mL of Curcumin at 0.01 M was added to the aqueous solution containing 1.0 g ZnO. The mixture was stirred vigorously for 2 hours at room temperature. The reaction mixture was aged at 70 °C for 18 hours before the resulting slurry was centrifuged, washed with water, dried in an oven at 70 °C, and kept for further characterisation.

Characterisation

Powder X-ray diffraction (PXRD) patterns were recorded with a XRD-6000 (Shimazdu, Kyoto, Japan) using CuKα radiation (λ = 1.5418 Å) at 30 kV and 30mA. Fourier transform infrared (FTIR) spectra were recorded over the range of 400 – 4000 cm^{-1} on a Perkin-Elmer Spectrum 100 (Perkin-Elmer, Waltham, Massachusetts, USA) equipped with a universal attenuated total reflectance (ATR) accessory.

Results and Discussion

Powder X-ray diffraction analysis

Figure 1 shows the PXRD patterns of ZnO and ZLH-curcumin nanocomposite (ZiCUR). The PXRD pattern of ZnO showed characteristics of high crystallinity peaks. However, in ZiCUR, the peak of ZnO phase still dominated the PXRD pattern, which is due to an incomplete reaction. The intercalation occurred when the ZnO was transformed to ZLH and the curcumin anion was intercalated between the layers. This can be observed by the presence of peaks at a lower 2θ value, as shown in the diffraction patterns of ZiCUR. The expansion of the basal spacing recorded at

10.0 Å was caused by a larger molecular size of curcumin, as well as the spatial arrangement of the anion in the interlayer space. From previous studies, it was proposed that the formation of ZiCUR from ZnO occurred in three steps through a dissociation-deposition mechanism [15,16,17]. The first step described in Eq. 1 involves hydrolysis of ZnO in water. When ZnO particles are immersed in the water, the surface of ZnO hydrolyses to form a layer of $Zn(OH)_2$. The layer of $Zn(OH)_2$ that is formed then becomes more soluble than ZnO in the presence of acid to become Zn^{2+} and OH^- (Eq. 2). Finally, the Zn^{2+} species, hydroxyls, H_2O, and curcumin anions (CA^-) in the solution react to generate the layered intercalation compound (Eq. 3). The process is repeated until all the ZnO phase and the $Zn(OH)_2$ phase has completely converted to the layered compound. ZiCUR is formed from the host-guest interactions, namely electrostatic attraction, hydrogen bonding, and van der Walls forces [18]. The mechanism of dissociation-deposition is described in the equations below:

$$ZnO + H_2O \rightarrow Zn(OH)_2 \quad (1)$$

$$Zn(OH)_2 \rightarrow Zn^{2+} + 2OH^- \quad (2)$$

$$Zn^{2+} + 2OH^- + CA^- + H_2O \rightarrow Zn^{2+}(OH)_{2-x}(CA^-)_x nH_2O \quad (3)$$

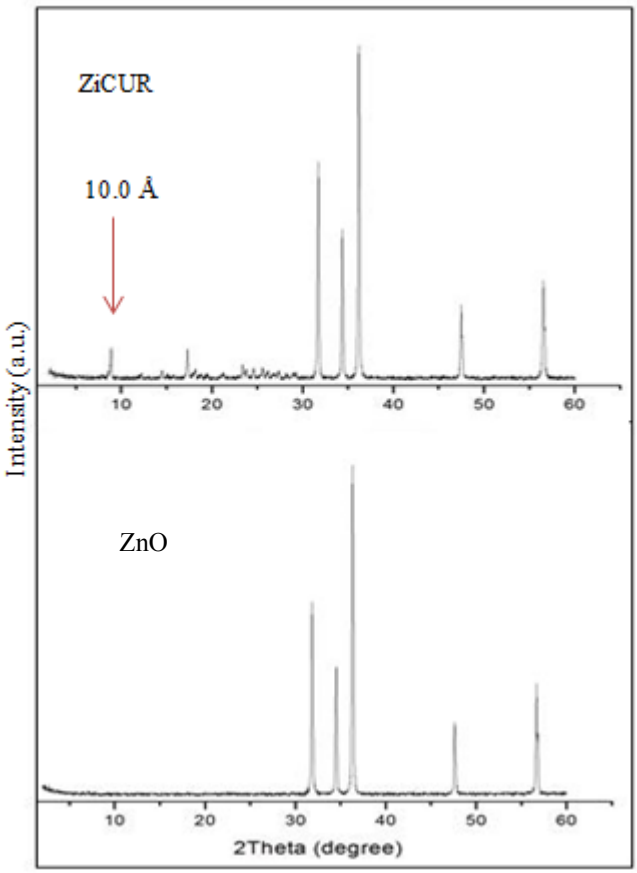


Figure 1. PXRD patterns of ZnO and ZiCUR compounds

Fourier transform infrared analysis

The presence of the curcumin in the ZLH interlayers was also elucidated by FTIR spectroscopy, which supported the PXRD results [19]. Figure 2 exhibited the FTIR spectrum of pure ZnO, curcumin, and ZiCUR. The sharp and

intense peak of ZnO at the lower wavenumber range, 400 cm^{-1} is due to the Zn-O sublattice stretching vibration [20]. Similar absorption bands could also be observed for the ZiCUR, as it possesses the same functional group. The FTIR spectra of curcumin showed strong characteristic vibrations at 1592 cm^{-1} attributed to C=C bending and 1270 cm^{-1} to C-O stretching. Trans-C-H out-of-plane bend for curcumin was detected at 960 cm^{-1}. The C-H monosubstitution band for phenyl group could be detected at 720 cm^{-1}, 809 cm^{-1}, and 856 cm^{-1}.

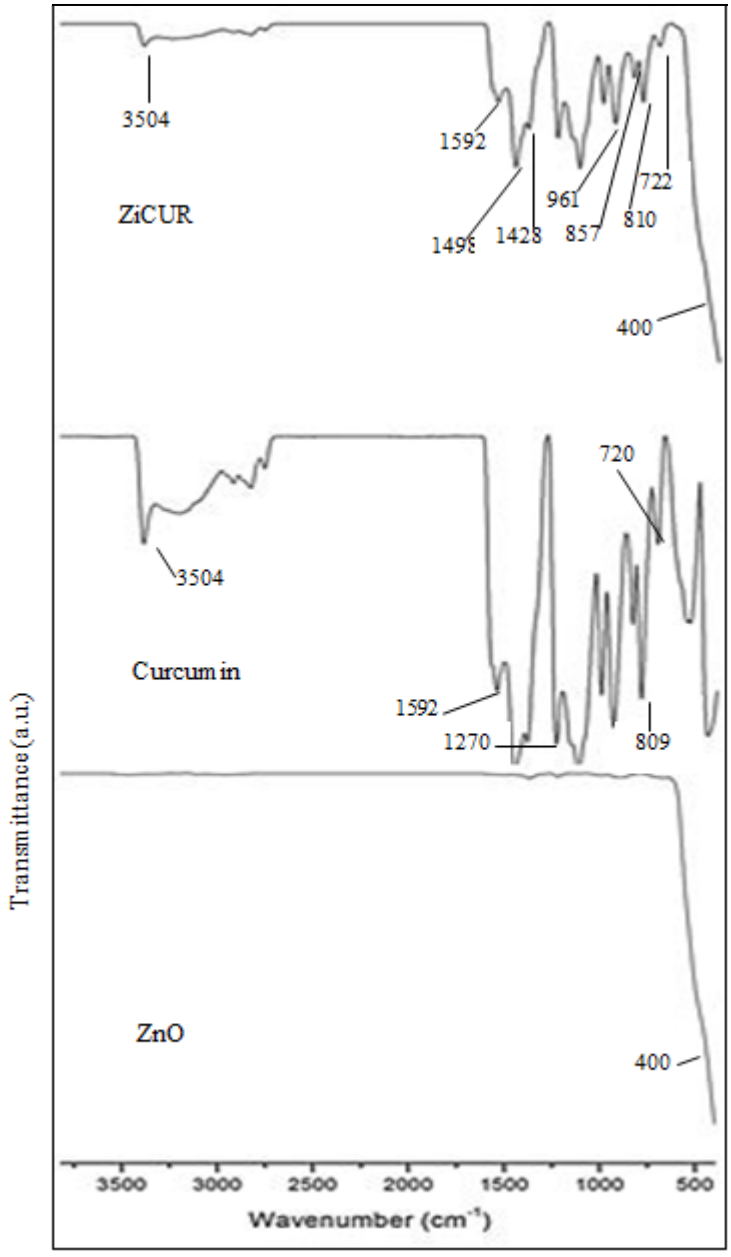


Figure 2. FTIR spectra of ZnO, Curcumin and ZiCUR compounds

On the other hand, the intercalation compound exhibited most of the vibrations assigned of curcumin, although several vibrations shifted due to the interaction between the curcumin anion and the interlayer. In particular, vibrations were due to trans-C-H out of plane bend at 961 cm^{-1} and C-H monosubstitution band at 722 cm^{-1}, 810 cm^{-1} and 857 cm^{-1}. COO^- stretching of intercalated curcumin anion overlapped and appeared at 1498 cm^{-1} and 1428 cm^{-1}. The C=C stretch in intercalated ZLH also overlapped at 1592 cm^{-1}. The broad band at 3504 cm^{-1} was assigned to the O-H stretching of vibration of interlayer water molecules. These results indicate that both curcumin and ZnO functional groups were present in the compound and further confirmed the intercalation of curcumin between positively charged ZLH layers, as indicated by the characteristics of PXRD pattern.

Conclusion

The curcumin anion was successfully intercalated into the Zn layered hydroxide by the ion exchange method. The interlayer spacing of ZiCUR obtained by PXRD characterization suggests the successful intercalation reactions between ZLH nanolayers and curcumin. The FTIR spectra further confirmed the presence of curcumin in the ZLH. The product, therefore, is hoped to demonstrate future potential as wound dressings for human skin.

Acknowledgement

The authors thank the Ministry of Higher Education for funding this project under grant FRGS- 5524557. The author (Asma Najaj Anuar) is grateful to the Department of Chemistry Faculty of Science Universiti Putra Malaysia for providing the essential laboratory facilities and Universiti Putra Malaysia for Graduate Research Fellowship.

References

1. Wound Reach Foundation (2015). Online from http://www.woundreach.org/why-wounds/the-challenge [Accessed date 2015-06-27].
2. Gadekar, R., Saurabh, M. K., Thakur, G. S. and Saurabh, A. (2012). Study of formulation, characterisation and wound healing potential of transdermal patches of curcumin. *Asian Journal of Pharmaceutical and Clinical Research,* 5(4): 225 – 230.
3. Bharat, B., Kumar, A., Aggarwal, M. S. and Shishodia, S. (2005). Curcumin derived from turmeric (*Curcuma Longa*): A spice for all seasons. *Phytopharmaceuticals in Cancer Chemoprevention,* 23: 351 – 387.
4. Kamkanam, M., Samindra, S. and Kottegoda, N. (2014). Encapsulation of curcumin into layered double hydroxides. *Nanotechnology Reviews,* 3(6): 579 – 589.
5. Aminu, U. K., Hussein, M. Z., Fakurazi, S. and Arulselvan, P. (2014). Layered double hydroxide nanocomposite for drug delivery systems; bio-distribution, toxicity and drug activity enhancement. *Chemistry Central Journal,* 8: 47 – 55.
6. Cao, G. T., Xing, F. F., Wang, P. and Ni, Z. M. (2008). Synthesis, characterization and release of curcumin-intercalated Mg-Al-layered double hydroxides. *Chinese Journal of Inorganic Chemistry,* 24(6): 956 – 963.
7. Ramli, M., Hussein, M. Z. and Yusoff, K. (2013). Preparation and characterization of an anti-inflammatory agent based on a zinc-layered hydroxide-salicylate nanohybrid and its effect on viability of Vero-3 cells. *International Journal of Nanomedicine,* 2013 (8): 297 – 306.
8. Kang, H., Leoni, M., He, H., Huang, G. and Yang, X. (2012). Well-crystallized CO_3^{2-} - type LiAl-LDH from urea hydrolysis of an aqueous chloride solution. *European Journal of Inorganic Chemistry,* 2012(24): 3859 – 3865.
9. Hussein, M. Z., Ghotbi, M. Y., Yahaya, A. H. and Rahman, M. Z. A. (2009). Synthesis and characterization of (zinc-layered-gallate) nanohybrid using structural memory effect. *Materials Chemistry and Physics,*113 (1): 491 – 496.
10. Hussein, M. Z., Jaafar, A. M., Yahaya, A. H. and Zulkarnain, Z. (2009). The effect of single, binary and ternary anions of chloride, carbonate and phosphate on the release of 2, 4-dichlorophenoxyacetate intercalated into the Zn-Al-layered double hydroxide nanohybrid. *Nanoscale Research Letters,* 4 (11): 1351 – 1357.
11. Rajamathi, M. and Kamath, P. V. (2001). Urea hydrolysis of cobalt(II) nitrate melts: synthesis of novel hydroxides and hydroxynitrates. *International Journal of Inorganic Materials,* 3 (7): 901 – 906.
12. Hussein, M. Z., Rahman, N. S. S. A., Sajiro, S. H. and Zainal, Z. (2012). Herbicide-intercalated zinc layered double hydroxide nanohybrid for a dual-guest controlled release formulation. *International Journal of Molecular Sciences,* 13: 7328 – 7342.

13. Hashim, N., Muda, Z., Hamid, S. H., Isa, I. M., Kamari, A., Mohamed, A., Hussein, M. Z. and Ghani, S. A. (2014). Characterization and controlled release formulation of agrochemical herbicides based on zinc-layered hydroxide-3-(4-methoxyphenyl) propionate nanocomposite. *Journal of Physical and Chemical Sciences,* 1(4): 1 – 6.
14. Hashim, N., Hussein, M. Z., Isa, I. M., Kamari, A., Mohamed, A., Jaafar, A. M. and Taha, H. (2014). Synthesis and controlled release of cloprop herbicides from cloprop-layered double hydroxide and cloprop-zinc-layered hydroxide nanocomposites. *Open Journal of Inorganic Chemistry,* 4: 1 – 9.
15. Bang, S., Lee, S., Ko, Y., Park, J., Shin, S., Seo, H. and Jeon, H. (2012). Photocurrent detection of chemically tuned hierarchical ZnO nanostructures grown on seed layers formed by atomic layer deposition. *Nanoscale Research Letters,* 7: 290 – 301.
16. Hussein, M. Z., Ali, S. H. A., Zainal, Z. and Hakim, M. N. (2011). Development of antiproliferative nanohybrid compound with control release property using ellagic acid as the active agent. *International Journal of Nanomedicine,* 6: 1373 – 1383.
17. Xingfu, Z., Zhaolin, H., Yiqun, F., Su, C., Weiping, D. and Nanping, X. (2008). Microspheric organization of multilayered ZnO nanosheets with hierarchically porous structures. *Journal Physical Chemistry C,* 112: 11722 – 11728.
18. Mohsin, S. M. N., Hussein, M. Z., Sajiro, S. H., Fakurazi, S., Arulselvan, P. and Hin, T.Y.Y. (2013). Synthesis of (cinnamate-zinc layered hydroxide) intercalation compound for sunscreen application. *Chemistry Central Journal,* 7(1): 26 – 32.
19. Lv, L., Sun, P., Gu, Z., Du, H., Pang, X., Tao, X., Xu, R. and Xu, L. (2009). Removal of chloride ion from aqueous solution by ZnAl-NO_3 layered double hydroxide as anion-exchanger. *Journal of Hazardous Materials,* 161: 1444 – 1449.
20. Hussein, M. Z., Hashim, N., Yahya, A. H. and Zainal, Z. (2010). Synthesis and characterization of [4-(2,4-dichlorophenoxybutyrate)-zinc layered hydroxide] nanohybrid. *Solid State Sciences*, 12: 770 – 775.

Malaysian Journal of Analytical Sciences, Vol 20 No 6 (2016): 1365 - 1372
DOI: http://dx.doi.org/10.17576/mjas-2016-2006-15

MALAYSIAN JOURNAL OF ANALYTICAL SCIENCES
Published by The Malaysian Analytical Sciences Society
ISSN 1394 - 2506

ENZYMATIC GLYCEROLYSIS OF METHYL LAURATE UTILIZING *Candida antarctica* Lipase b

(Gliserolisis Berenzim oleh Metil Laurat Menggunakan Lipase b *Candida antarctica*)

Norul Naziraa Ahmad Jamlus, Jumat Salimon, Darfizzi Derawi*

School of Chemical Sciences and Food Technology, Faculty of Science and Technology, Universiti Kebangsaan Malaysia, 43600 UKM Bangi, Selangor, Malaysia

**Corresponding author: darfizzi@ukm.edu.my*

Received: 1 February 2015; Accepted: 29 August 2016

Abstract

Enzymatic glycerolysis using *Candida antarctica* lipase b (CALB) as catalyst was studied. Production of monolaurin was optimized based on two selected types of CALB, varying enzyme concentrations and reaction time. Novozyme-435 (N-435) and *Aspergillus oryzae* were used in this study. About 47.6% of monolaurin was synthesized using N-435 at a 5% enzyme concentration within 24 hours of reaction time. Characterizations were performed using different techniques namely gas chromatography-flame ionization detector (GC-FID), thin layer chromatography (TLC) and Fourier transform infrared spectroscopy (FTIR) analysis.

Keywords: methyl laurate, enzymatic glycerolysis, monolaurin, Novozyme-435, *Aspergillus oryzae*

Abstrak

Tindak balas gliserolisis berenzim menggunakan lipase b *Candida antarctica* (CALB) telah dikaji. Penghasilan monolaurin dioptimumkan berasaskan dua jenis CALB, kepekatan enzim dan masa tindak balas. Novozym-435 (N-435) dan *Aspergillus oryzae* digunakan dalam kajian ini. Sebanyak 47.6% monolaurin telah berjaya disintesis menggunakan N-435 pada kepekatan enzim 5% dalam tempoh 24 jam masa tindak balas. Pencirian dijalankan menggunakan teknik analisis berbeza seperti kromatografi gas (GC), kromatografi lapisan nipis (TLC) dan spektroskopi inframerah transfomasi Fourier (FTIR).

Kata kunci: metil laurat, gliserolisis berenzim, monolaurin, Novozym-435, *Aspergillus oryzae*

Introduction

Enzymatic glycerolysis reactions were reported to be carried out in a mild reaction condition, low temperature with solvents that are not harmful towards the environment. With the proliferated interest in green and moderate chemical reaction, enzymatic reaction is attractively favored in researches that produce edible products such as monoacylglycerol (MAG) and diacylglycerol (DAG) [1].

MAG which is the glycerol monoester of fatty acids exhibits surfactant and emulsifying properties that advocates mixing of hydrophilic and lipophilic substances. MAG is extensively used in food, detergent, cosmetics, pharmaceutical formulations and plasticizer. Monolaurin (ML) is a medium-chain monoacylglycerol (MAG) with 12 carbons. The industry highly anticipates MAG of various fatty acids due to its unique feature that prevents microbial activity among diverse microorganisms including gram-positive, gram-negative bacteria, spore-forming bacteria, yeasts, filamentous fungi and developed viruses. In particular, ML compounds are able to dissolve and

penetrate into the phospholipid layer of bacterial cell and disintegrate the membrane layer. Thus, ML compounds inhibit bacterial cell reproduction by hindering cell replications [2]. A natural occurring ML exists as an active ingredient in breast milk, which acts as a booster to the infant's immune system [3].

So far, search on literature revealed studies which were focused on the synthesis reaction. MAG could be synthesized by promoting methyl oleate upon a strongly basic MgO via glycerolysis. The catalyst activity decreased with calcination temperature following a trend similar to the site density of the strong base [4]. Furthermore, 2-MAG can be produced from *Echium plantagineum* seed oil and marinol with three purification methods, silica gel column chromatography, liquids-liquids extraction and low temperature crystallization [5]. In addition, it can also be produced from canarium oil by enzymatic reaction using immobilized lipase from *Mucor miehei*, of which has a specific activity towards triacylglycerol (TAG)[6]. Besides that, 2-MAG was produced by enzymatic glycerolysis of omega-3-polyunsaturated fatty acid using short path distillation (SPD) of an acylglycerols mixture [7]. Additionally, the production of 2-MAG done via glycerol esterification of functionalized SBA-15 mesoporous catalyst has been carried out [8].

Lipases are stable enzyme and the general classes of enzymes that break down fat molecules. Lipases are often obtained from animals, plants and recombinant microorganisms. The physiological role of lipases (water-soluble triacylglycerol acylhydrolases) is the catalytic conversion of tri-glycerides into di- or mono-glycerides, fatty acids and glycerol [9]. Extracellular lipases from *Candida sp., Pseudomonas sp., Thermomyces lanuginosus and Rhizomucor miehei* have been investigated by a considerable number of studies to be employed in the biodiesel synthesis [10]. Lipases are hydrolases that catalyze the hydrolysis of fatty acid esters found in living organisms [11].

Candida Antarctica lipase b (CALB) is one of the most effective lipases in the synthesis of ester [12]. The structure as shown in Figure 1. It is an enzyme extracted from yeast. Compared to bacteria, yeasts are easier to handle and grow. This enzyme is commonly used in organic synthesis reactions and as a biocatalyst that is associated to its stereoselectivity and thermal stability. CALB does not show interfacial activation compared to other lipases. This enzyme is optimized at pH 7. CALB generally convert straight-chain acid, which prefers 5 to 12 carbon atoms. This is because bulky acyl groups restrict the size of the binding pocket. CALB is an effective biocatalyst for promoting high FAME production yield [13].

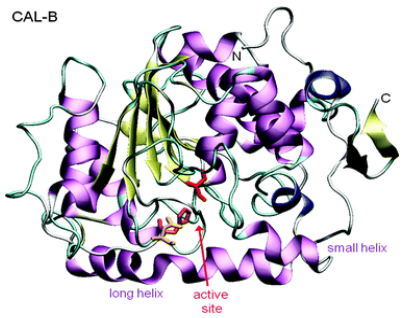


Figure 1. Crystal structure of the lipase CAL-B [17]

Novozyme-435 (N-435) is a heterogeneous biocatalyst system that consists of lipase b from CALB immobilized on a hydrophobic carrier. During esterification and transesterification of sugars, nucleosides and steroids, N-435 has an extraordinary ability to provide high regioselectivity [14]. Previously, a research found that the enzyme showed low activity in the presence of water and proposed a reaction to be done in an anhydrous medium for efficient catalyst activity. N-435 can be used ten times without loss of significant activity [11].

Aspergillus oryzae is a filamentous fungus that has ability to secrete large amounts of hydrolytic enzymes [15]. It is used as a host because it has high protein productivity in the expression of heterogeneous gene using improved

promoters [16]. In this research, we aimed to produce ML with the highest composition through enzymatic glycerolysis of methyl laurate with two selected *Candida antarctica* lipase b *(CALB),* Novozyme-435 (N-435) and *Aspergillus oryzae* with differences concentration of enzyme and reaction time.

Materials and Methods

Raw materials

Glycerol 99%, methyl laurate $C_{13}H_6O_2$, Novozyme-435, CALB *Aspergillus oryzae*, sodium chloride, sodium hydroxide, sodium bicarbonate, chloroform, diethyl ether and ethyl-ethanol were purchased from Sigma Aldrich.

Enzymatic glycerolysis of methyl laurate

Reaction ratio between glycerol and methyl laurate was ratio 1:1 (mol/mol). About 5 g of glycerol reacted with 11.64 g of methyl laurate. Concentrations of enzyme were tested at 3%, 5% and 10% based on the weight of glycerol. Mixtures were heated at 50 °C for 6, 12, 18, 24 and 30 hours in oven shaker with a speed of 250 rpm. Once the reaction ended, the sample was post-treated with 60 mL of sodium bicarbonate solution, 60 mL of sodium chloride solution, 60 mL of sodium hydroxide solution, 60 mL of distilled water, 80 mL of chloroform and 40 mL of ethanol. Unreacted glycerol and water as by-products were dissolved in ethanol, while the desired product was dissolved in chloroform. Products were separated using separating funnel and sample was further purified to isolate monolaurin from by-products (dilaurin and trilaurin) using solid phase extraction (SPE) method. Schematic reaction for enzymatic glycerolysis of methyl laurate was illustrated in Figure 2.

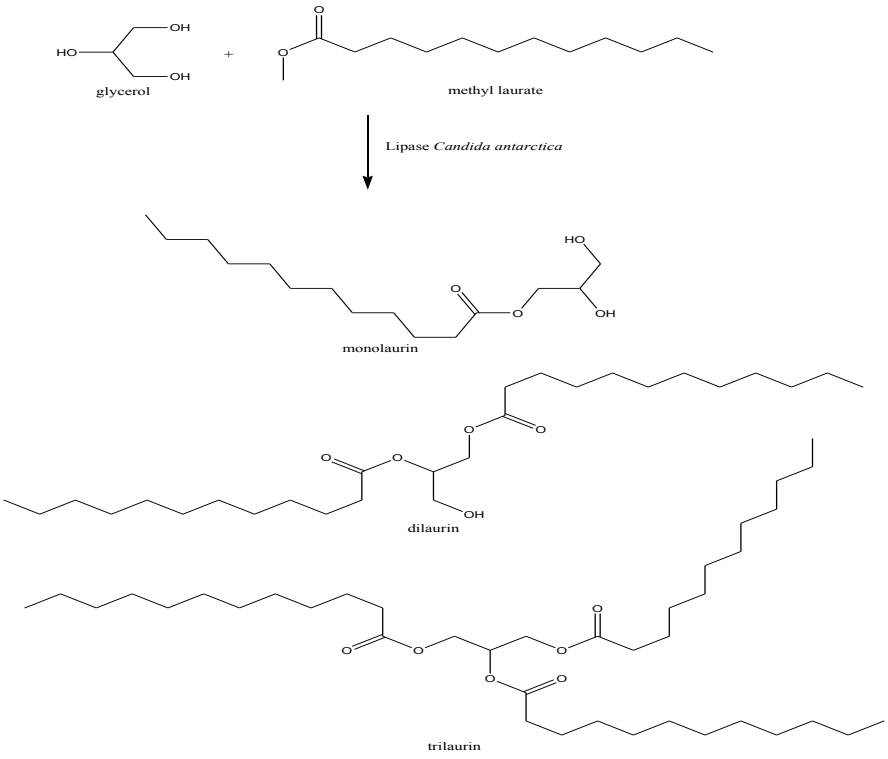


Figure 2. Enzymatic glycerolysis of methyl laurate

Characterization

A series characterization was performed using three different techniques namely thin layer chromatography (TLC), gas chromatography-flame ionization detector (GC-FID) and Fourier transform infrared spectroscopy analysis. A total of 100 mL of TLC mobile phase used toluene: chloroform: acetone with the ratio 70:20:10 (v/v) [18]. GC-FID

analysis is carried out using a capillary column DB-5HT column (30 m × 0.25 mm × 0:10 m). The operator setting GC-FID as follow; the temperature of the injector 250 °C, a temperature of detector 400 °C, initial temperature of 100 °C (1 minute), the final temperature of 380 °C (25 minutes) with a rate of increase of 5 °C/minutes and the carrier gas is nitrogen gas. The sample was prepared by adding 0.03 mL of reaction sample with 1.0 mL ethyl acetate.

Results and Discussion

Figure 3 and 4 represents the production of ML at different enzyme concentration (3%, 5% and 10% by weight) using N-435 and CALB *Aspergillus oryzae*. It is apparent that reaction using N-435 5%wt exhibits higher ML production with 47.6% of conversion in 24 hours of enzymatic glycerolysis. The lowest composition of ML production was 14.4% using CALB from *Aspergillus oryzae*. Hence, it could conceivably be inferred that N-435 is more effective for the synthesis of ML than *Aspergillus oryzae*. It is relevant to hypothesize that N-435 was immobilized on an acrylic resin. In general, acrylic resin is a robust support material for the enzyme which increased thermo stability [14]. Robust material was required to prevent the enzyme from entering the organic media. The lipase hydrolyzed not only produce ML but also dilaurin (DL) and trilaurin (TL). N-435 has higher specificity production toward ML and DL while *Aspergillus oryzae* specificity toward TL.

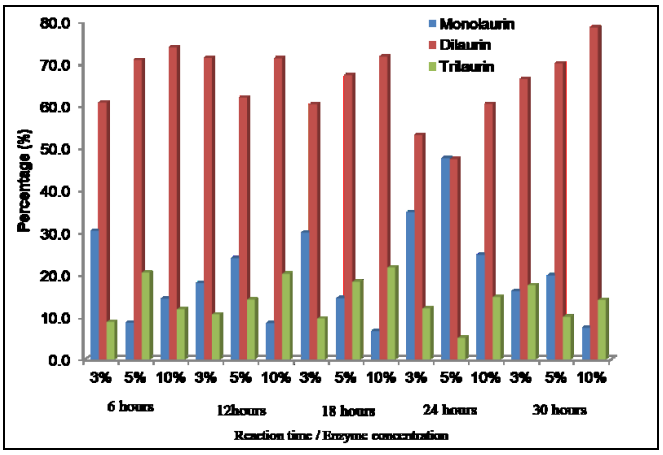


Figure 3. Product composition against concentration of Novozyme-435 and reaction time

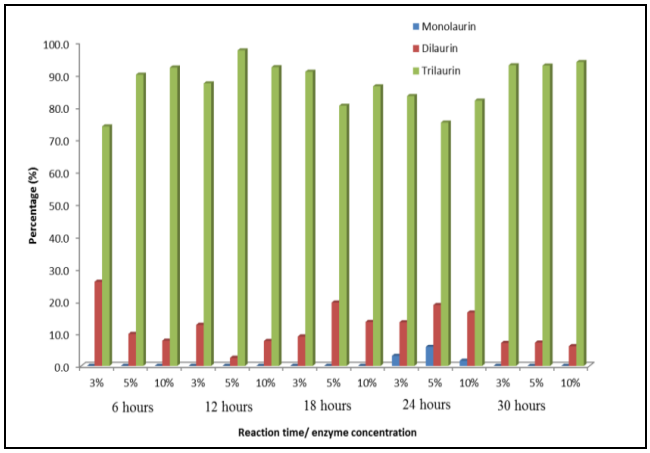


Figure 4. Product composition against concentration of *Candida Antarctica* lipase b from *Aspergillus oryzae* and reaction time

Thin layer chromatography

Separation using TLC was explained by the differences in affinity degree on the plates among the occurring components (Figure 5). Therefore, adsorption depended on the interaction of certain components with the stationary phase [19]. Sample dripped on TLC plates was known as the substrate. Substrates with higher polarity were adsorbed first because the interaction between the substrate and the stationary phase was very strong. This study chemically produced ML, DL and TL from enzymatic glycerolysis. Theoretically, ML has two OH groups and was higher in polarity than DL and TL. Both DL and TL moved slower than ML during elution process due to the hydrogen bonds that formed with the stationary phase. Sample chromatogram was compared with the reference [20].

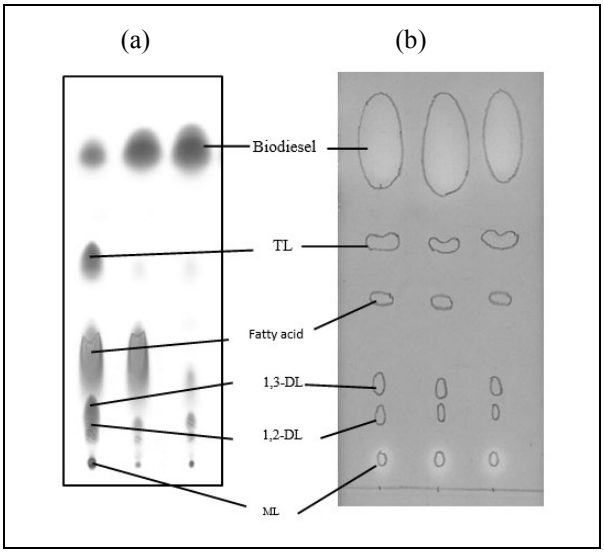


Figure 5. TLC Plate of glycerolysis reaction (a) reference TLC on lipid separation [20] and (b) TLC of sample

Gas chromatography analysis

Synthesized ML was directly compared with the standard mixtures of ML, DL and TL chromatogram (Figure 6). The percentage of ML composition was determined based on the total area of the chromatogram [21]. A relevant idea from a previous study mentioned that fatty acids of methyl esters with similar carbon chain have the same response factor and volatility. Therefore, the sample can be directly compared with the peak area to determine the composition [18]. While, Figure 7 shows a single peak GC chromatogram of purified ML after solid phase extraction (SPE) was performed. Thus, the synthesized ML has been successfully separated and purified from the side products (dilaurin and trilaurin).

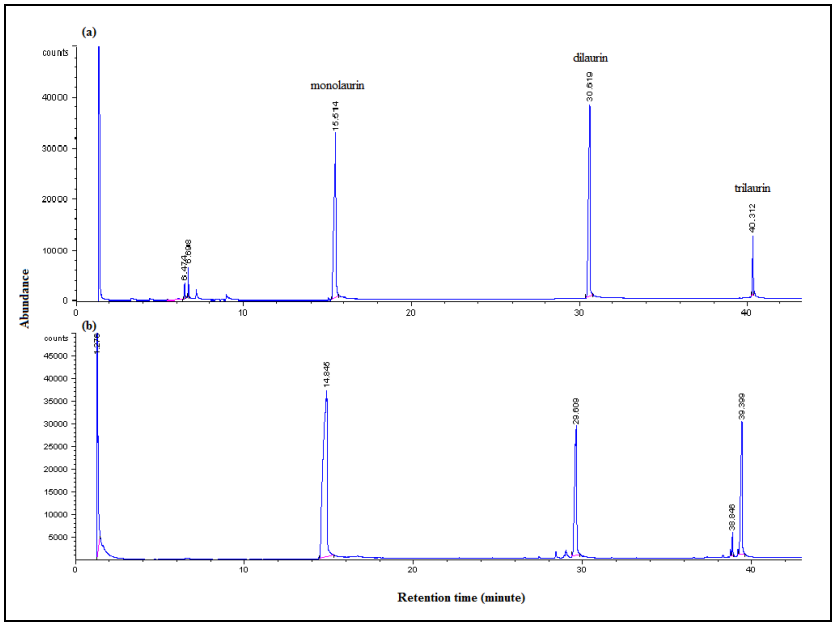


Figure 6. Comparison of GC-FID chromatogram (a) synthesized ML (b) standard mixtures of ML, DL, TL

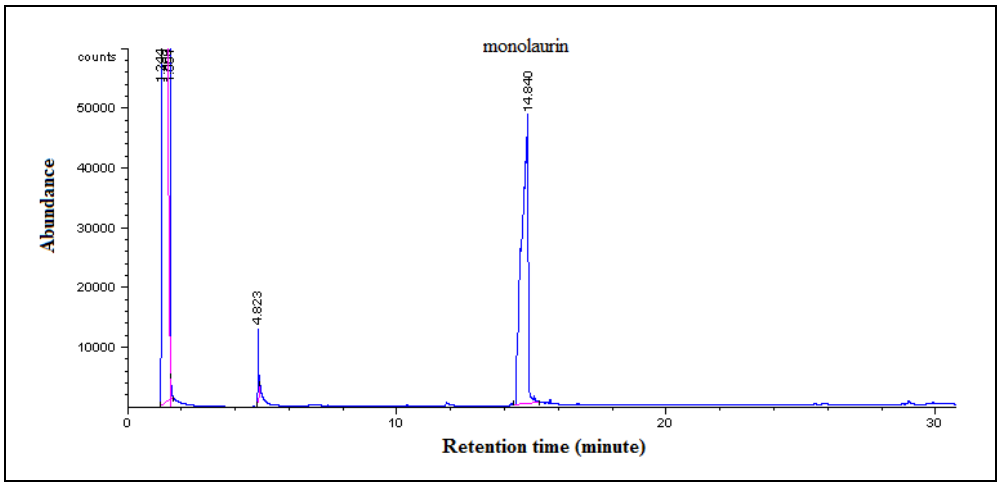


Figure 7. GC chromatogram of purified monolaurin

Infrared spectra

Figure 8 shows comparison of methyl laurate and purified monolaurin infrared spectra. Based on the figure, the present of hydroxyl group can be confirmed by looking at the O-H stretching broad band spectrum at wavenumber 3205 cm^{-1}. It proves the glycerolysis reaction has been successfully performed.

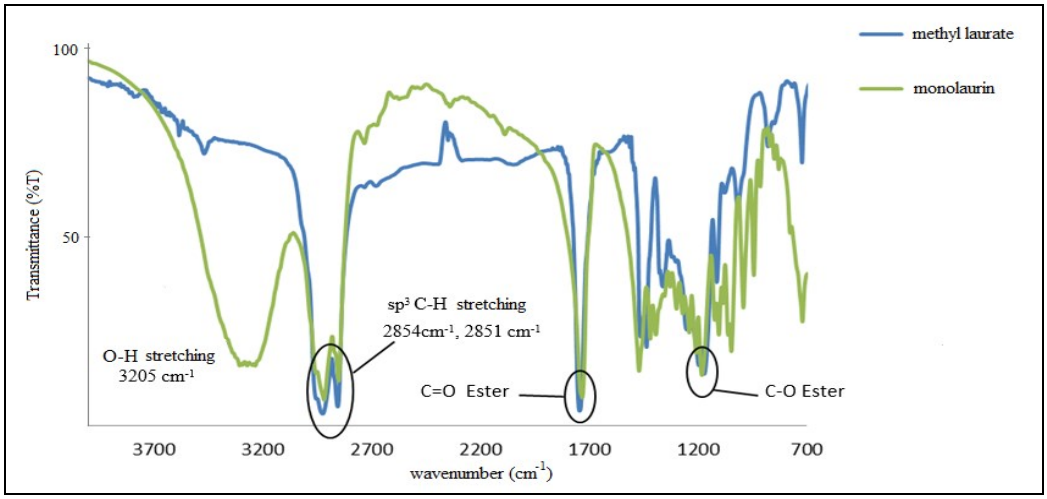


Figure 8. Comparison of infrared spectra between monolaurin and methyl laurate

Conclusion

Monolaurin was successfully synthesized (47.6% yield) and purified by enzymatic glycerolysis of methyl laurate which catalyzed by *Candida antarctica* lipase b. The optimum glycerolysis reaction conditions was using CALB (N-435) 5%wt at 24 hours of reaction time. Monolaurin was successfully characterized using TLC, GC-FID and FTIR analysis techniques. Acrylic resin that bonded onto CALB (N-435) was a robust support material because it restrained the enzyme from getting into the organic media.

Acknowledgement

The authors would like to acknowledge the Universiti Kebangsaan Malaysia for the research facilities and financial support through research grant no. GGPM-2014-033. Also, thanks to the Ministry of Higher Education for the funding through fundamental research grant, FRGS/2/2014/ST01/UKM/02/2 and MyBrain15 scholarship.

References

1. Kathryn, M. K. and Wong, C. H. (2001). Review article enzymes for chemical synthesis. *International Weekly Journal of Science,* 409: 232 – 240.
2. Projan, S. J., Brown-Skrobot, S. and Schlievert, P. M. (1994). Glycerol monolaurate inhibits the production of B-lactamase, toxic shock syndrome toxin-1 and other staphylococcal exoproteins by interfering with signal transduction. *Journal of Bacteriology*, 176: 4204 – 4209.
3. Mansor, T. S. T., Che Man, Y. B., Shuhaimi, M., Abdul Afiq, M. J. and Ku Nurul, F. K. M. (2012). Physicochemical properties of virgin coconut oil extracted from different processing methods. *International Food Research Journal*, 19: 837 – 845.
4. Ferrettia, C. A., Fuenteb, S., Ferullob, R., Castellanib, N., Apesteguíaa, C. R. and Di Cosimoa, J. I. (2012). Monoglyceride synthesis by glycerolysis of methyl oleate on MgO, catalytic and DFT study of the active site. *Applied Catalysis A, General*, 413 – 414: 322 – 331.
5. Cervera, M. A. R., Veneges, E., Bueno, R. R., García, I. R. and José Luis, G. G. (2013). Acyl migration evaluation in monoacylglycerols from Echium plantagineum seed oil and Marinol. *Journal of Bioscience and Bioengineering*, 115: 518 – 522.
6. Rahmana, H., Anggadiredjaa, K. and Sitompulb, J. P. (2015). Synthesis and characterization of 2-monoacylglycerols from Canarium oil. *Procedia Food Science*, 3: 162 – 173.
7. Solaesa, A. G., Sanz, M. T., Falkeborg, M., Beltrán, S. and Zheng, G. (2016). Production and concentration of monoacylglycerols rich in omega-3 polyunsaturated fatty acids by enzymatic glycerolysis and molecular distillation. *Food Chemistry*, 190: 960 – 967.

8. Hermida, L., Abdullah, A. Z. and Mohamed, A. R. (2011). Synthesis of monoglyceride through glycerol esterification with lauric acid over propyl sulfonic acid post-synthesis functionalized SBA-15 mesoporous catalyst. *Chemical Engineering Journal*, 174: 668 – 676.
9. Stergioua, P. Y., Foukisa, A., Filippoub, M., Koukouritakib, M., Parapoulib, M., Theodoroua, L. G., Hatziloukasb, E., Afendrab, A. , Pandeyc, A. and Papamichaela, E. M. (2013). Advances in lipase-catalyzed esterification reactions. *Biotechnology Advances,* 31: 1846 – 1859.
10. Guldhea, A., Singha, P., Kumaria, S., Ismail, Rawata., Permaulb, K. and Buxa, F. (2016). Biodiesel synthesis from microalgae using immobilized *Aspergillus niger* whole cell lipase biocatalyst. *Renewable Energy*, 85: 1002 – 1010.
11. Amanda, A., Miranda, L. S. M. and Rodrigo, O. M. A. (2013) Lipases, valuable catalysts for dynamic kinetic resolutions. *Biotechnology Advances*, 31: 1846 – 1859.
12. Hauerlandováa, I., Lorencováb, E., Buňkab, F., Navrátila, J., Kristýna, Janečkováa. K. and Buňkovác, L. (2014). The influence of fat and monoacylglycerols on growth of spore-forming bacteria in processed cheese. *International Journal of Food Microbiology*, 182 – 183: 37 – 43.
13. Ramirez, M. 2013. *Candida Antarctica* lipase b, Enzyme Report. University of Georgia, Athens, Georgia, United States.
14. Poojari, Y. and Clarson, S. J. (2013). Thermal stability of Candida antarctica lipase b immobilized on macroporous acrylic resin particles in organic media. *Biocatalysis and Agricultural Biotechnology*, 2: 7 – 11.
15. Tamalampudi, S., Talukder, M., Hama, S., Numata, T., Kondo, A. and Fukuda, H. (2007). Development of recombinant Aspergillus oryzae whole-cell biocatalyst expressing lipase-encoding gene from Candida antarctica. *Applied Microbiology and Biotechnology,* 75: 387 – 395.
16. Adachia, D., Hamab, S., Nakashimac, K., Bogakie, T., Oginoa, C. and Kondoa, A. (2013). Production of biodiesel from plant oil hydrolysates using an Aspergillus oryzae whole-cell biocatalyst highly expressing Candida antarctica lipase b. *Bioresource Technology*, 135: 410 – 416.
17. Marco, K., Geraldine, S. L., Abirami, S. and Ping, W. (2011). On the different roles of anions and cations in the solvation of enzymes in ionic liquids. *Physical Chemistry,* 13: 1649 – 1662.
18. Fontana, J. D., Zagonel, G., Vechiatto, W. W., Costa, B. J., Laurindo, J. C., Fontana, R., Pelisson, L., Jorge, B. H. and Lanças, F. M. (2009). Simple TLC-screening of acylglycerol levels in biodiesel as an alternative to GC determination. *Journal of Chromatographic Sciences,* 47: 844 – 846.
19. Fuchsa, B., Süßa, R., Kristin, T. K., Eibischa, M. and Schillera, J. (2011). Lipid analysis by thin-layer chromatography - A review of the current state. *Journal of Chromatography A*, 1218(19): 2754 – 2774
20. Fedosova, S. N., Braskb, J. and Xua, X. (2011). Analysis of biodiesel conversion using thin layer chromatography and nonlinear calibration curves. *Journal of Chromatography A*, 1218: 2785 – 2792.
21. Myller S. C., Márcio A. M., David M. M. P., Inês, S. R. and Paulo, A. Z. S. (2012). Chromatographic analyses of fatty acid methyl esters by HPLC-UV and GC-FID. *Journal of the Brazilian Chemical Society*, 23: 763 – 769.

Malaysian Journal of Analytical Sciences, Vol 20 No 6 (2016): 1373 - 1381
DOI: http://dx.doi.org/10.17576/mjas-2016-2006-16

MALAYSIAN JOURNAL OF ANALYTICAL SCIENCES
Published by The Malaysian Analytical Sciences Society
ISSN 1394 - 2506

EFFECT OF HEAT TREATMENTS ON THE YIELD, QUALITY AND STORAGE STABILITY OF OIL EXTRACTED FROM PALM FRUITS

(Kesan Rawatan Haba Terhadap Peratus Pengekstrakan Minyak, Kualiti dan Kestabilan Semasa Penyimpanan Minyak yang Diekstrak Daripada Buah Kelapa Sawit)

Hasimah Kasmin[1, 2], Azwan Mat Lazim[2], Roila Awang[1]*

[1]*Engineering & Processing Research Division,*
Malaysian Palm Oil Board, No. 6, Persiaran Institusi, Bandar Baru Bangi, 43000 Kajang, Selangor, Malaysia
[2]*School of Chemical Sciences and Food Technology, Faculty of Science and Technology,*
Universiti Kebangsaan Malaysia, 43600 UKM Bangi, Selangor, Malaysia

**Corresponding author: roila@mpob.gov.my*

Received: 17 August 2015; Accepted: 29 August 2016

Abstract

This paper presents the impact of heat treatments on the yield and quality of the palm oil using solvent extraction techniques. Heating temperature range from 70 to 90 °C and heating time range from 30 to 90 min were studied. The quality parameters measured were free fatty acids (FFA), deterioration of bleaching index (DOBI), carotene content, oxidative stability and fatty acid composition of the oil. These parameters were used to determine CPO quality which has been stored for 3 months. It was found that the yield significantly increased with the increasing of heating temperature and time. The optimum parameter was achieved with heating temperature of 90 °C and heating time of 60 min via wet heating. Optimum oil yield obtained was 24% with 0.93% FFA content, 6.10 DOBI, 938.42 ppm carotene content and oxidative stability of 26.87 hours. Fatty acid composition (FAC) of oil extracted showed a reduction in unsaturated fatty acids as the heating duration increased. After 3 months of storage, 60 min of heating time via wet heating process was recorded the lowest increment of FFA (1.32%) and low reduction of DOBI value (0.41). However, carotene content gave the highest loss with 113.54 ppm towards the end of the storage.

Keywords: crude palm oil, heat treatments, oil yield, oil quality, storage stability

Abstrak

Kajian ini bertujuan untuk menganalisis kesan rawatan haba semasa pensterilan ke atas peratus pengekstrakan minyak dan kualiti minyak sawit mentah (MSM) dengan menggunakan pelarut bagi mengekstrak MSM. Suhu dan masa pensterilan yang berlainan telah digunakan bagi mengekstrak MSM iaitu suhu pensterilan dari 70 hingga 90 °C manakala masa pensterilan dari 30 hingga 90 min. Kesan rawatan haba ke atas peratus pengekstrakan minyak telah dijalankan. Kualiti MSM yang diekstrak iaitu asid lemak bebas (ALB), indeks pemerosotan terhadap pelunturan (DOBI), kandungan karotena, kestabilan oksidatif dan komposisi asid lemak telah dicirikan. Parameter ini digunakan untuk menentukan kualiti MSM yang telah disimpan selama 3 bulan. Hasil kajian mendapati peratus pengekstrakan minyak meningkat secara signifikan dengan kenaikkan suhu dan masa. Hasil optimum pada tahap maksimum iaitu sebanyak 24% telah dicapai pada suhu pensterilan 90 °C dan masa pensterilan 60 min dengan menggunakan pemanasan basah. Kualiti minyak pula menunjukkan kandungan ALB sebanyak 0.93%, DOBI sebanyak 6.10, kandungan karotena sebanyak 938.42 ppm dan kestabilan oksidatif selama 26.87 jam. Selepas 3 bulan penyimpanan, masa pemanasan selama 60 min menggunakan pemanasan basah telah menunjukkan peningkatan kandungan ALB dan penurunan bacaan DOBI yang paling rendah iaitu masing-masing 1.32% dan 0.41. Namun, kandungan karotena didapati merosot paling tinggi iaitu sebanyak 113.54 ppm.

Kata kunci: minyak sawit mentah, rawatan haba, peratus pengekstrakan minyak, kualiti minyak, kestabilan minyak

Introduction

Palm oil fruitlets are usually subjected to sterilization as a first step of the milling process. This process is carried out by steam sterilization of the bunches in sterilizers which are steam pressurized to as high as 40 psi at a temperature of 140°C. The objectives of the sterilization process are to prevent free fatty acids (FFA) build up in the oil, soften the palm fruitlets and loosen the fruit on the bunch to facilitate stripping. It also helps to break up the oil bearing cells of the fruit mesocarp to release maximum oil during the digestion process [1]. After sterilization, the bunches are threshed in rotating threshers to detach the individual fruits. The detached fruits are then further soften and mashed in digesters, where the oil is extracted by screw pressing [2]. The crude palm oil is then clarified, purified and go through the oil vacuum dryer to be dried before it is stored in purified oil storage tank [3]. The conventional palm oil milling process as afore described does not involve solvent extraction. Instead, it is a combination of physical and mechanical approaches.

Strict quality control is practiced in the mill to ensure the least amount of deterioration of oil quality during the milling process. Fats and oils are graded by their acid and free fatty acid (FFA) contents, which are as an index to determine their quality. Palm oil contains about 45% of saturated palmitic acid and 39% of mono-unsaturated oleic acid [4]. Fatty acids play a very important role in fats and oils because of their health implications in the human diet and properties in industrial processes. The type of fatty acid determines the nutritional status and storability of the oil. Oil with higher levels of monounsaturated fatty acids such as oleic acid or polyunsaturated fatty acids such as linoleic or linolenic are more desirable for human consumption than saturated fatty acids. However, from the processing perspective, higher levels of polyunsaturated fatty acids contribute to oil oxidative instability, short shelf life, and rancidity.

The conventional sterilization process also involves with high temperature, wet treatment and mechanical screw pressing which creating an environment favorable to the chemical and enzymatic reaction of hydrolysis including oxidation. Thus, researches have been done to look into the possibility of utilization of dry heating coupled with solvent extraction process. The influenced of heating time [2, 5 – 8] also has been investigated on the quality of crude palm oil (CPO). Solvent extraction and lower heating time was able to gives higher oil yield as well as good quality than conventional screw press. However, variations of time entail biochemical modifications of fat, which are explained by the variation of the free fatty acid and the degree of oxidation [6].

The aim of this research are to determine the effect of heating parameters of dry and wet heating process coupled with solvent extraction to increase oil yield as well as minimize the production of FFA and the oxidation of the fat. Stability of palm oil stored at room temperature after three months periods were also analyzed. Quality parameters measured were FFA, DOBI and carotene content to determined degradation by oxidation under these heating time conditions.

Material and Methods

All solvents and chemical used were analytical and chromatographic grades. Palm fruits were obtained from Palm Oil Milling Technology Centre (POMTEC) of Malaysian Palm Oil Board (MPOB) in Negeri Sembilan, Malaysia.

Processing palm fruitlets: Experimental design

Sterilization of oil palm fruits were carried out by studying the effects of heating temperature and time. In this study, oil palm fruits obtained from the mill were cleaned to remove any dirt on the surface followed by heated at required temperature and time under dry and wet condition using electrical oven (Memmert, UM 400, 1400 watt, 50/60 Hz) and heating bath (Buchi B-490, 1400 watt, 50/60 Hz) respectively.

Sterilization of oil palm fruits at different heating temperature and time

Oil palm fruits were heated at 70, 80 and 90°C for fix heating time at 90 min. Meanwhile, oil palm fruit were heated at 90°C at different heating time of 30, 45, 60 and 90 min.

Oil yield
The mesocarp of the fruits was peeled and the nuts were removed. The peel mesocarp were soaked in the hexane for 24 h at a solvent to fruit ratio of 1:1 (v/w) and latter pressed using fruit press expeller. The extraction solution was filtered through a whatman filter paper No. 1. Solvent of the filtrate was then removed from the oil at 60°C via vacuum rotary evaporator. The yield of palm oil extract was determined using equation (1) below.

$$\% \text{ oil yield} = \frac{x}{y} \times 100 \quad (1)$$

where, *x* is define as mass of oil extracted (g) and y is defined as mass of oil palm fruits (g).

Physicochemical analyses of extracted oil: Chemical analysis
Free fatty acid (FFA) content of the extracted oil was determined by using MPOB test method p2.5:2004 [9]. Sodium hydroxide solution (0.1M) was prepared and standardized with potassium hydrogen phthalate. A known mass of the oil sample was dissolved in neutralised iso-propanol and the free acids were neutralised with sodium hydroxide. FFA values were expressed as palmitic acid (%). A mean value of duplicate samples was calculated.

Deterioration of Bleachability Index (DOBI) was also determined according to MPOB test method p2.9:2004 [9]. DOBI is defines as the ratio of the spectrometric absorbance at 446 nm to that 269 nm. A known mass of the oil was dissolved in n-hexane in 25 ml volumetric flask and dilute to the mark. The absorbance reading of the solution at 446 nm and 269 nm was taken using Hitachi U-2000 Spectrophotometer (Japan). A mean value of duplicate samples was calculated.

Carotene contents were carried using MPOB test method p2.6:2004 [9]. A known mass of the oil was dissolved in n-hexane in a 25 ml volumetric flask and dilute to the mark. The absorbance reading of the solution at 446 nm was taken using Hitachi U-2000 Spectrophotometer (Japan). A mean value of duplicate samples was calculated. The carotene content is expressed as ppm β – carotene and is calculated as equation (2) below.

$$\beta\text{-carotene (ppm)} = 25 \times \frac{383}{100\,\mathrm{W}}(\mathrm{a_s} - \mathrm{a_b}) \quad (2)$$

where, a_s is define as absorbance of the sample a_b is define as cuvette error and w is define as weight of the sample in gram.

Oxidative stability
The rancimat method was used to determine oxidative stability by using a Metrohm 743 Rancimat. An amount 3.0 g of oil sample was prepared in a reaction vessel and placed in a heating block. The block temperature and air flow were set at 110 °C and 10 L/h respectively. A mean value of duplicate samples was calculated.

Fatty acid composition
Fatty acid composition (FAC) was measured by conversion of the oil sample to their fatty acid methyl esters (FAME) according to the method described in MPOB test method (2004) with a minor modification. FAME was prepared by adding 50 mg of oil into 6 ml methanolic sodium hydroxide (0.5 M). The mixture was heated on the steam bath for 10 minutes. 7 ml of boron trifluoride methanol (20%) was added and further heated for 2 min followed by 5 ml of hexane and heated for 1 min. The solution was removed from heat and 15 ml of saturated sodium chloride solution was added to the solution. FAME was collected and dried over anhydrous sodium sulphate for 1 to 2 hours.

Storage of palm oil extract
Samples of oil extract from different heating time via wet heating were stored at room temperature with a temperature range of 28 °C to 32 °C for 3 months. Stability of oil was observed by measuring the changes in FFA, DOBI and carotene content. A mean value of duplicate samples was calculated.

Results and Discussion

Oil Yield

Effect of temperature

The dependence of oil yield on temperature was determined at 70, 80, and 90 °C for fix heating time at 90 min. Figure 1 shows the effect of temperature on the oil yield. As expected, the oil yield was low at lower temperature. In this study, heating temperature of 90 °C is found to be adequate for optimum oil yield. Significant result is in agreement as reported by [10]. According to Baryeh [10] higher temperatures led to greater oil yield for both dry and wet heating process. Furthermore, results obtained suggested that the heating temperature should not be above 100°C for optimum yield. This is due to the increasing in yield was very small and also involving extra cost.

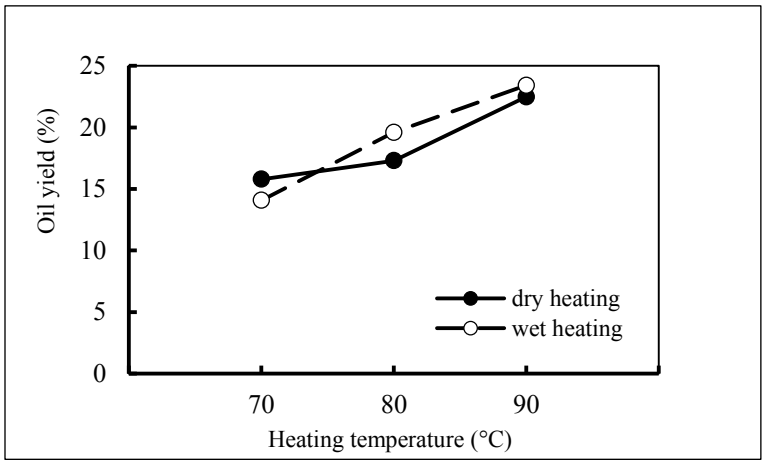


Figure 1. Effect of temperature on oil yield at heating time of 90 min

Effect of time

Heat penetration is the key factor in sterilization of palm fruitlets. Inefficient penetration of heat supply leads to lower oil production. In addition, heating duration also played a crucial part in ensuring the heated fruit remained in good condition for subsequent oil extraction. The oil yield showed the efficiency of solvent extraction process and the effect of different heating duration on the oil content (Fig. 2). The results show that the oil yield increases with increasing duration time for dry (18.86% – 20.99%) and wet (21.64% - 24.55%) heating process. Higher oil yield was obtained when longer heating duration was used as more cell walls of the palm fruits had been ruptured due to heat generated. The results obtained were in good agreement with previous findings [5,6]. According to Malaysian Oil Palm Statistic in 2009, the average oil extraction rate from conventional sterilization and screw pressing in commercial palm oil mill was recorded as 20.21% [11].

Long heating duration caused the palm fruits to be overcooked and increment yield of burnt mesocarp. In contrast, moderate heating period giving a competent time to loosen the nuts from its mesocarp while keeping the yield high to reach the required standard as recommended by MPOB. Maximum oil yield of 24.55% was achieved at 90 min of heating time via the wet heating. However of all trials made, it was found that optimum range period of heating time was between 45 to 60 min via wet heating. Above 45 min heating time, the rise in yield nearly insignificant.

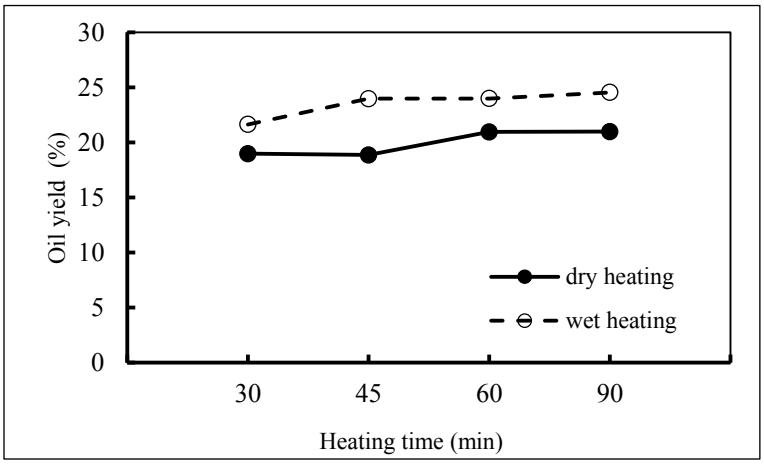


Figure 2. Effect of time on oil yield at heating temperature of 90 °C

Physicochemical analyses of extracted oil

Chemical analysis

Oil extracted from various heating time were selected to be further characterized. The quality of extracted oil using dry and wet heating are shown in Table 1. It is noted that oil extracted using the wet heating approach gave better quality compared to the dry heating. The results obtained from this study proposed the techniques used was able to produce better quality extracted oil set against the commercial CPO for all heating time used.

Table 1. Effect of heating time on oil quality

Heating Time (min)	Quality of Oil					
	FFA (%)		DOBI		Carotene Content (ppm)	
	Dry	Wet	Dry	Wet	Dry	Wet
30	4.97	1.20	4.52	6.25	595.31	806.78
45	2.45	1.15	5.21	5.57	588.98	791.76
60	2.37	0.93	6.06	6.10	846.09	938.42
90	1.42	0.99	6.09	5.42	930.01	763.10
Commercial CPO	< 5.0[a]		> 2.8[b]		500 – 700[c]	

[a] [19]; [b] [20]; [c] [21]

FFA value was gradually decreased as the duration of the heating time was increased for all the heating time. This is due to termination of hydrolysis enzyme in fruits. The lowering of FFA content hence contributed to higher DOBI value. Unfortunately, this situation not helping in increasing the carotene content. Therefore, both FFA and DOBI values gave no effect on the carotene content.

Unsaturated fatty acids contents

The TAG in palm oil partially defines most of the physical characteristics of the palm oil such as melting point and crystallization behavior [12]. Figure 3 shows the unsaturated fatty acid composition for both dry and wet heating process. Unsaturated fatty acid content slightly drops with the time after 60 min exposure, due to long term heating

duration. The composition of fatty acid obtained was within the reported range for all heating duration used. The ranges for unsaturated fatty acid in commercial crude palm oil (CPO) is between 47.5% - 51.8% [4].

Lower unsaturated fatty acid was obtained when longer heating duration was applied as more cell walls of the palm fruits had been ruptured due to heat generated. Similar observation was also observed by Macaire et al. in their study of kernel oil [13]. Owolarafe et al. [14] reported similar results when they studied the micro-structural characterization of palm fruit.

The oil extracted show narrow range in unsaturated fatty composition for dry and wet heating processes (with different only 0.11% – 2.33%). Oil extracted from wet heating show lower unsaturated fatty acid content compared with dry heating process. Wet heating process possesses water to facilitate rupturing of oil cells and destruction of the cell wall [14]. Thus their unsaturated fatty acids fix oxygen and oxidize easily.

The slightly higher content of fatty acid for dry heating compared to wet heating was due to this fatty acid remains trapped in cells. Heat penetration of dry heating was not efficiently penetrated into the fruit but only the outer surface of the fruit. Increases in heating time thus hardened the mesocarp and reduce the chances of the disintegration of the cell content, consequently blocking site from exposing to oxygen and the enzymes to attack double bond.

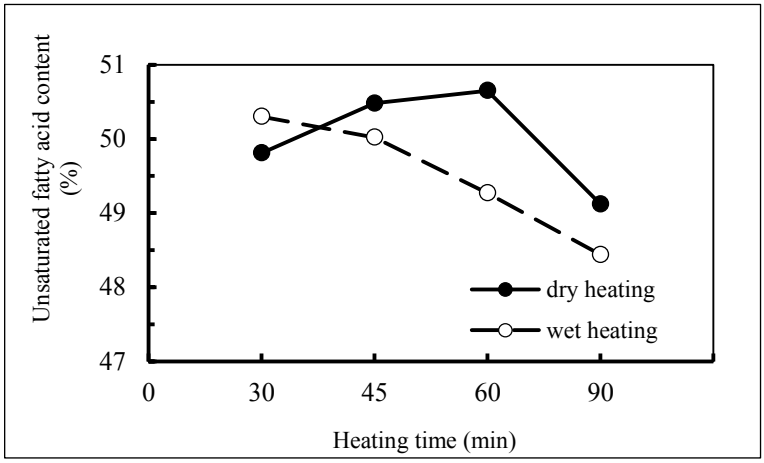


Figure 3. Content of unsaturated fatty acids at various heating time

Oxidative stability

Rancimat test is usually carried out to determine the oxidative stability by considering the Rancimat induction period (RIP). The RIP values represent the stability of the sample. The greater the RIP value, the sample is less susceptible towards oxidation [15]. Figure 4 shows the oxidative stability for both dry and wet heating process varied between 20.56 – 26.87 h. Oxidative stability (RIP) in CPO is >25 hours [15].

In this study, heating duration less than 45 min did not achieve comparable RIP to that of commercial CPO. Higher RIP (25.51 – 26.87 hours) was obtained after 45 and 60 min of heating duration. This result showed that oxidative stability increased with increasing heating duration. At 60 min of heating, the oil extracted from dry and wet heating recorded the highest oxidative stability.

During the heating time, oxidative stability increases due to heating assistance to break the cellular membrane of the fruit mesocarp. In this study, results shows the wet heating has higher oxidative stability compared to dry heating

process. The findings relatively significant to the results obtained from unsaturated fatty acid and FFA content respectively (Figure 3 and Table 1).

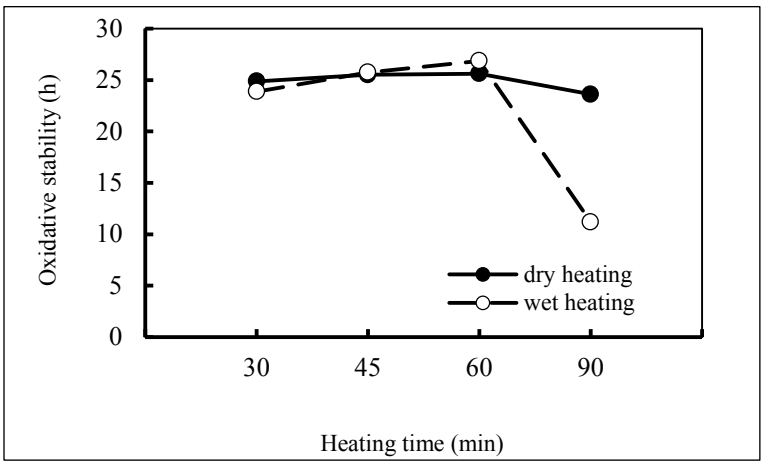


Figure 4. Oxidative stability of oil extracted at various heating time

Storage stability

It is essential to any palm oil mill to extract CPO with excellent quality and stability. The oil stabilities during storage are vital parameter for ensuring that oil appears the good performance at elevated temperature. Table 2 shows the initial value of FFA, DOBI and carotene content for dry and wet heating process before storage at room temperature. For all heating time used, dry heating process gives higher value of FFA compared to wet heating process therefore higher deterioration. Thus, oil sample from wet heating process will produce better quality storage oil in terms of lower FFA content.

Table 2. Initial value of FFA, DOBI and carotene content in palm oil extract at different heating time

Heating Time (min)	Quality of Oil					
	FFA (%)		DOBI		Carotene Content (ppm)	
	Dry	Wet	Dry	Wet	Dry	Wet
30	2.49	2.36	3.17	3.79	754.13	746.09
45	2.64	2.24	2.40	3.64	762.09	779.65
60	2.17	1.95	3.03	3.65	762.80	880.60
90	2.03	1.44	3.23	3.49	717.87	710.20

Figure 5 shows the changes in quality of palm oil extracted at different heating time via wet heating. The quality of extracted oil was determined before and after 3 months storage at room temperature. After 3 months storage, 60 min of heating time recorded the lowest increment of FFA, 1.32 as well as lowest reduction of DOBI value, 0.41. This finding was due to higher initial carotene content that helps to decrease the rate of oxidation or prolong the induction period by interrupting the oxidation reaction. However, it suffers the highest loss of carotene content,

113.54 ppm towards the end of storage. Similar findings of carotene content loss have been reported by Noor Akhmazilla et al. [8].

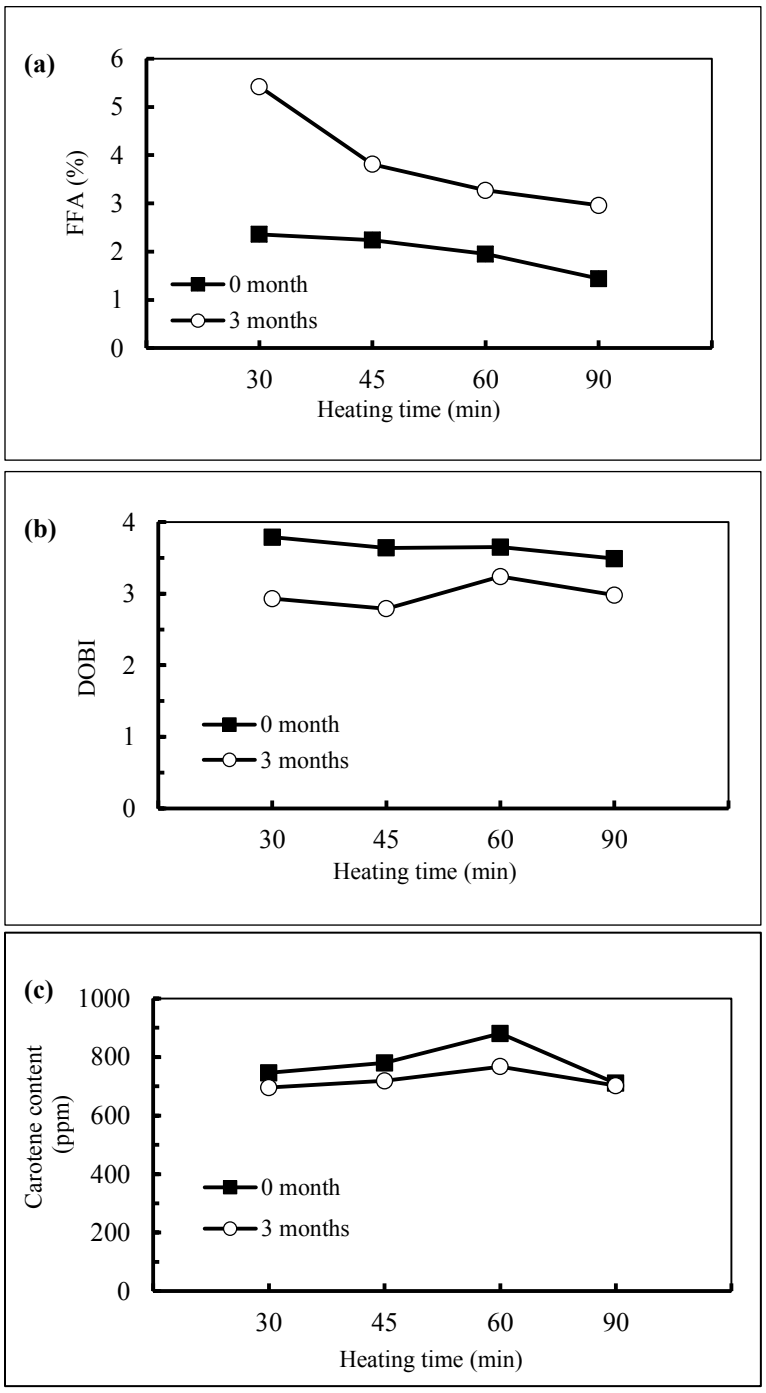


Figure 5. (a) FFA (b) DOBI and (c) Carotene content of extracted oil via wet heating before and after 3 months storage

Conclusion

Heat treatments during sterilization process are an important factor in determining oil yield and quality of extracted oil. This study showed that the temperature and time gave effect on the yield of extracted oil. Wet heating gives higher oil yield than dry heating process. However, dry heating and wet heating process had little effect on quality of extracted oil. This study has revealed that heating temperature at 90 °C and heating time at 60 min via wet heating extract higher oil yield, better CPO quality and good storage stability. The oil extraction yield can be further increased by optimizing other extraction technique. Other quality parameters could also be measured to support the efficiency of the heat treatment used during sterilization.

Acknowledgement

The authors like to thank the Director General of MPOB for financial support and Universiti Kebangsaan Malaysia (UKM) for supporting this work. Thanks also to the Engineering and Processing Division for laboratory facilities as well as from Advanced Oleochemical Technology Center for quality analysis.

References

1. Mahidin, M. R. (1998). Quality improvement in the production of Malaysian palm oil. *Palm Oil Development*, 9: 15 - 21.
2. Chow, M. C. and Ma, A. N. (2007). Processing of fresh palm fruits using microwaves. *Journal of Microwave Power & Electromagnetic Energy*, 40 (3): 165 - 173.
3. Ariffin, A. A. (1991). Chemical changes during sterilization process affecting strippability and oil quality. In Seminar on Developments in Palm Oil Milling Technology and Environmental Management: pp. 2 - 12.
4. PORIM (1991). International Palm Oil Conference Chemistry & Technology. pp. 269.
5. Cheng, S. F., Mohd Nor, L. and Chuah, C. H. (2011). Microwave pretreatment: A clean and dry method for palm oil production. *Journal of Industrial Crops and Products*, 34: 967 - 971.
6. Nu'man, A. H., Ng, M. H., Choo, Y. M. and Ma, A. N. (2012). Dry heating of palm fruits: Effect on selected parameters. *American Journal of Engineering and Applied Sciences*, 5(2): 128 - 131.
7. Mohd Fauzi, N. A., Sarmidi, M. R. and Chua, L. S. (2011). Metabolites profiling of heat treated palm oil extract. *Journal of Applied Sciences,* 11(13): 2376 - 2381.
8. Mohd Fauzi, N. A. and Sarmidi, M. R. (2011). Extraction of heat treated palm oil and their stability on β-carotene during storage. *Journal of Science and Technology*, 2(1): 45 - 54.
9. Malaysian Palm Oil Board (2004). MPOB Test Methods. Malaysian Palm Oil Board, Ministry of Primary Industries, Malaysia.
10. Baryeh, E. A. (2001). Effect of palm oil processing parameters on yield. *Journal of Food Engineering*, 48(1): 1- 6.
11. Malaysian Palm Oil Board (2010). Malaysian Oil Palm Statistic 2009. Kajang. Malaysia.
12. Sambanthamurthi, R., Sundram, K. and Tan, Y. A. (2000). Chemistry and biochemistry of palm oil. *Progress in Lipid Research*, 39: 507 - 558.
13. Macaire, W. H., Bernard, T., Noel, T., Felicite, T. M., Cesar, K., Michel, L. and Jacques, F. (2010). Extraction of palm kernel oil in Cameroon: effects of kernels drying on the oil quality. *Journal of Food Technology*, 8(1): 1 - 7.
14. Owolarafe, O. K. and Faborode, M. O. (2007). Micro-structural characterisation of palm fruit at sterilisation and digestion stages in relation to oil expression. *Journal of Food Engineering,* 85: 598 –605.
15. Yung, C. L., Choo, Y. M., Cheng, S. F., Ma, A. N., Chuah, C. H. and Yusof, B. (2006). The effect of natural and synthetic antioxidants on the oxidative stability of palm diesel. *Fuel*, 85: 867 - 870.
16. Noraini, S. and Siew, W. L. (1990). Quality control measures in palm oil industry. Palm Oil Dev.
17. Vijaya, S., Choo, Y. M., Muhammad, H., Hasyim, Z. and Yew, A. T. (2010). Life cycle assessment of the production of crude palm oil (part 3). *Journal Oil Palm Research,* 22: 895 - 903.
18. Chong, C. L. (1994). Chemical and physical properties of palm oil and palm kernel. Selected readings on palm oil and its uses. Malaysia: Palm Oil Research institute of Malaysia: pp. 60 - 67.

Malaysian Journal of Analytical Sciences, Vol 20 No 6 (2016): 1382 - 1389
DOI: http://dx.doi.org/10.17576/mjas-2016-2006-17

MALAYSIAN JOURNAL OF ANALYTICAL SCIENCES
Published by The Malaysian Analytical Sciences Society
ISSN 1394 - 2506

MICROWAVE-ASSISTED SYNTHESIS OF MESOPOROUS SILICA NANOPARTICLES AS A DRUG DELIVERY VEHICLE

(Sintesis Partikel Nano Silika Berliang Meso Dibantu Gelombang Mikro Sebagai Medium Penyebaran Ubat)

Nur Hidayatul Nazirah Kamarudin [1]*, Aishah Abdul Jalil[2,3], Sugeng Triwahyono[4], Sharifah Najiha Timmiati[5]

[1]*Department of Chemical and Process Engineering, Faculty of Engineering and Built Environment, Universiti Kebangsaan Malaysia, 43600 UKM Bangi, Selangor, Malaysia*
[2]*Department of Chemical Engineering, Faculty of Chemical and Energy Engineering*
[3]*Centre of Hydrogen Energy, Institute of Future Energy*
[4]*Department of Chemistry, Faculty of Science Universiti Teknologi Malaysia, 81310 UTM Johor Bahru, Johor, Malaysia*
[5]*Institute of Fuel Cell, Universiti Kebangsaan Malaysia, 43600 UKM Bangi, Selangor, Malaysia*

**Corresponding author: nhnazirah@ukm.edu.my*

Received: 21 October 2015; Accepted: 14 June 2016

Abstract

Nanotechnology has been utilized in medicine for therapeutic drug delivery and the development of treatments for a variety of diseases and disorders. Mesoporous silica nanoparticles (MSN), which combine both unique properties of nanomaterials and mesostructured substances, have aroused special attention in biomedical research field due to its great advantages in many aspects such as well biocompatible, unique properties of tunable pore size and structure, large surface areas and pore volumes, controllable morphology and modifiable surfaces, high chemical and thermal stabilities. In this study, the microwave was utilized to synthesize MSN under 100 W, 300 W and 450 W heating powers. All MSNs was tested for adsorption and release of an anti-inflammatory and anti-cancer drug, ibuprofen. The characterization revealed that the MSN prepared under 450 W (MSN450) produced the most ordered and prominent mesoporous structure compared to lower power applied. MSN450 exhibited the highest ibuprofen adsorption, followed by MSN300 and MSN100, confirming that more ordered MSN demonstrated higher adsorptivity toward ibuprofen. For the release study, MSN450 showed the slowest release rate of ibuprofen, followed by MSN300 and MSN100. All MSNs was found to exhibit good activity for the ibuprofen adsorption and release.

Keywords: microwave, mesoporous silica, ibuprofen, adsorption, drug delivery

Abstrak

Teknologi nano telah digunakan dalam bidang perubatan untuk penyampaian ubat terapeutik dan pembangunan rawatan untuk pelbagai penyakit dan gangguan. Partikel nano silika mesoliang, yang menggabungkan kedua-dua ciri-ciri yang unik bahan nano dan bahan struktur meso, telah membangkitkan perhatian khusus dalam bidang penyelidikan bioperubatan kerana kelebihan yang besar dalam banyak aspek seperti bioserasi, ciri-ciri unik bolehubah saiz liang dan struktur, kawasan permukaan dan isipadu liang yang besar, morfologi bolehkawal dan permukaan boleh ubahsuai, serta tinggi kestabilan kimia dan haba. Dalam kajian ini, gelombang mikro telah digunakan untuk mensintesis partikel nano silika mesoliang (MSN) dibawah kuasa pemanasan 100 W, 300 W dan 450 W. Semua MSN telah diuji untuk penjerapan dan pembebasan ubat anti-radang dan anti-kanser, ibuprofen. Pencirian mendedahkan bahawa MSN yang disediakan di bawah 450 W (MSN_{450}) menghasilkan struktur paling tersusun dan terbaik dibandingkan dengan kuasa lebih rendah. MSN_{450} telah mencapai penjerapan ibuprofen tertinggi, diikuti dengan MSN_{300} dan MSN_{100}, mengesahkan bahawa MSN yang lebih tersusun menunjukkan penjerapan ibuprofen lebih tinggi. Untuk kajian

pembebasan, MSN_{450} menunjukkan kadar pembebasan ibuprofen paling rendah, diikuti dengan MSN_{300} dan MSN_{100}. Semua MSN ditemui mencapai keaktifan yang baik untuk penjerapan dan pembebasan ibuprofen.

Kata kunci: gelombang mikro, silica berliang meso, ibuprofen, penjerapan, penyampaian ubat

Introduction

In recent years, mesoporous silica nanoparticles (MSNs) have been well developed as effective drug storage vehicles in drug delivery systems due to their large pore volume (~1cm^3/g), high surface area (> 1000 m^2/g), ease of functionalization, low toxicity and biodegradability [1-3]. Exclusively in drug delivery, mesoporous silica is often used with modification to suit treatment needs. The study of the loading and release of drugs into/from mesoporous silica is in high demand for the development of tissue regeneration, transdermal therapy, and cell regulation due to the biocompatibility of this material.

The traditional synthesis method of mesoporous materials is the hydrothermal route, which uses a certain number of surfactants, as well as acid or alkali to compose a mixed aqueous preparation. Next, inorganic sources are added and heated to crystallize, followed by filtration, drying, and calcination or extraction to remove the template. Although finely ordered mesoporous materials are obtained, the process is time and energy consuming [4]. Heating solids in the conventional system leads to an uneven temperature distribution due to poor heat transfer into the bulk of the material. The outer temperature may be substantially higher than the inner one, because the material itself acts as an insulator. In these modern days where scientific findings and technology go hand in hand, any improvement to a synthesis technique that saves time in the synthesis of new materials or improves the properties of materials would be extremely beneficial. It is known that hydrothermal synthesis of inorganic materials using microwave (MW) heating promotes nucleation and can reduce the synthesis time and particle size significantly in comparison with the conventional convection heating method [5-6]. Besides, with faster polymerization under MW irradiation, it was also found that the swelling rate of the material was much higher compared to a material prepared by conventional heating.

In this study, we synthesized the MSN by co-condensation methods, and the physicochemical properties of the MSNs were characterized using X-ray powder diffractometer (XRD), Transmission Electron Microscopy (TEM), and Field Emission Scanning Electron Microscopy (FESEM). The performances of the three MSNs were then examined on the adsorption and release of ibuprofen, a non-steroidal anti-inflammatory drug widely used in the treatment of pain and inflammation in rheumatic disease and other musculoskeletal disorders. Millions of kilograms of ibuprofen are produced and consumed annually by humans; thus, the application of MSN to ibuprofen delivery is crucial and ever continuing research [7]. The influences of structure and morphologies of the MSNs towards the model drug delivery system were discussed in brief.

Materials and Methods

Cetyltrimethylammonium bromide (CTAB), ethylene glycol (EG), and tetraethyl orthosilicate (TEOS) were purchased from Merck Sdn Bhd, Malaysia. Ammonium hydroxide (NH_4OH) was obtained from QRec, Malaysia. The synthesis procedure was as follows. CTAB, EG, and NH_4OH were dissolved in 700 mL of water. After vigorous heating, TEOS were added to the mixture to give a white micelle solution. After stirring for 2 hours, the white solution was moved into a beaker and deposited in the microwave oven under heating power settings of 100, 300, and 450 W in 8, 4 and 1 hour, respectively. The variation of time was decided according to the complete evaporation of the solvent mixture for the purpose of shorten the drying time before preceded to calcination. The mixture was kept under continuous stirring and the sample was collected by centrifugation. The obtained gel was heated at 110 °C for 24 hours followed by calcination at 550 °C.

The crystallinity of catalysts was measured with a Bruker Advance D8 X-ray powder diffractometer with Cu Kα (λ = 1.5418 Á) radiation as the diffracted monochromatic beam at 40 kV and 40 mA. Transmission electron microscopy (TEM) was carried out using a JEOL JEM-2100F micro-scope. The samples were ultrasonically dispersed in acetone and deposited on an amorphous, porous carbon grid. The surface morphology and surface

elemental analysis of the samples were performed using FESEM-EDX (JEOL JSM-6701F) with an accelerating voltage of 15 kV. The samples were coated with platinum by electro-deposition under vacuum prior to analyses.

Powdered mesoporous samples were loaded with ibuprofen by soaking them into an ethanol solution of ibuprofen followed by continuous stirring for 24 hours at 310 K. Ibuprofen loaded samples were recovered by filtration, washed with ethanol and dried for 24 hours at 313 K. During the process, aliquots of 2 mL were withdrawn at pre-determined time intervals and centrifuged in a Hettich Zentrifugen Micro 120 before being analyzed by UV–Vis spectrophotometer (Agilent Technologies) to determine the residual concentration of ibuprofen. Each set of experiments was performed three times. The adsorption band of ibuprofen was taken at a maximum wavelength (λ_{max}) of 264 nm. The ibuprofen release profile was obtained by adding the drug-impregnated powders in a simulated body fluid (SBF) at 37 °C under continuous stirring. The drug concentration in the release fluid for the different release time was determined using UV/VIS spectrophotometer.

Results and Discussion

Figure 1 shows FESEM and TEM images of the MSNs at different microwave power levels, respectively. Comparing the three MSNs in Fig. 1 (a, b, c) FESEM analysis revealed spherical particles with smooth surface for the MSN prepared at microwave power of 450 W; however, irregular particles with a rough surface were formed at a microwave power of 100 W. Moreover, the TEM images in Fig 1 (d, e, f) shows clusters of hexagonally-ordered silica nanoparticles approximately 30–45 nm in size. The average particle sizes and ordering of the hexagonal silica were increased with increasing microwave power, since MSN_{450} exhibited more visible long-range silica arrangement. This may be due to the enhanced assembly of parallel CTAB chains upon increasing the microwave power, which resulted in an increased of silica hydrolysis; thus, a more ordered silica arrangement was formed compared to the MSN prepared at a low microwave power [8].

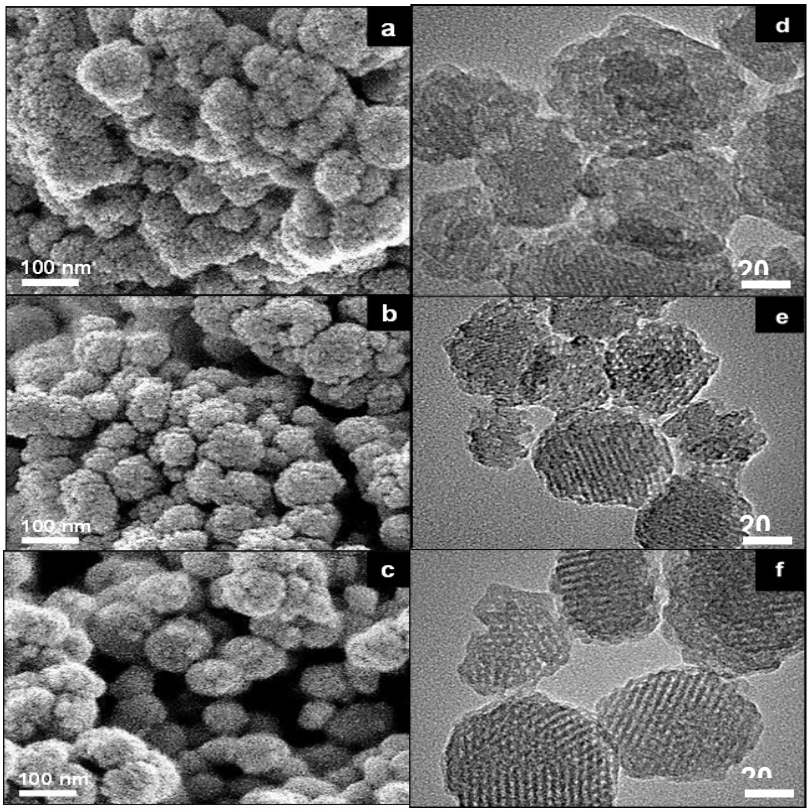


Figure 1. FESEM images of (a)MSN_{100}; (b)MSN_{300}; (c)MSN_{450}; and TEM image of (d)MSN_{100}; (e)MSN_{300}; (f)MSN_{450}

Hence, it can be stated that the crystal growth of MSN was greatly influenced by the microwave power, which resulted in different morphology and particle sizes. It is presumed that these properties will affect MSN behavior regarding ibuprofen adsorption [9]. Indeed, the microwave synthesis of MCM-41 has been reported earlier [10]. In the report, the MCM-41 was synthesized by the composition of synthesis materials of CTAB, TMAOH, TEOS and H_2O, while MSN was synthesized using CTAB, ethylene glycol, NH_4OH, TEOS and H_2O. Different particle size was obtained, which is 100 nm for the former, and 30–45 nm for the latter. This may be due to the difference in the composition led to the different crystal growth for both materials.

Figure 2 demonstrates the difference in the hexagonal density of all MSNs in the low *2θ* region. The pattern illustrates the reflection of a typical MCM-41 type material, which consists of an ordered hexagonal array of parallel silica tubes and can be indexed assuming a hexagonal unit cell as (100), (110), and (200) [11]. Since the materials were not crystalline at the atomic level, no reflections were observed at higher angles.

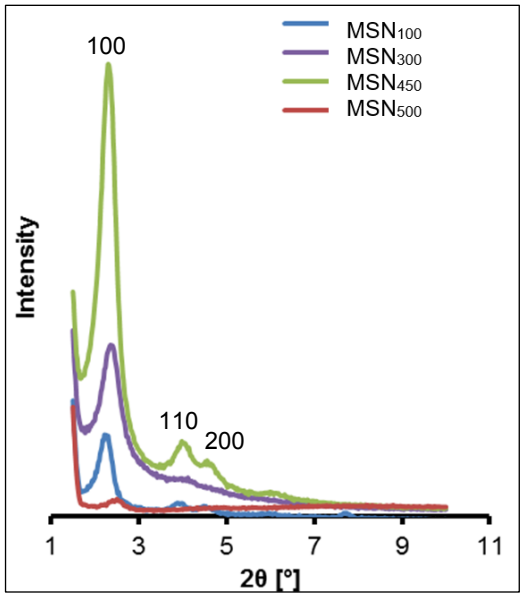


Figure 2. X-ray diffraction patterns of all MSNs

A substantial increment of the diffraction peak intensity corresponding to the (100) reflection was observed upon increasing the microwave power from 100 to 450 W, indicating the alteration of the long-range ordering of the mesoporous structure, while the MSN structure was unchanged. Although the appropriate synthesis time was given to all of the MSN for well crystal growth, the MSN prepared under 450 W exhibited higher crystallinity and silica order as compared to 300 W and 100 W. This may be related to the higher instantaneous microwave power delivery and consequently higher microwave electric field at 450 W during synthesis. While the microwave power was also further increased up to 500 W but disordered structure was obtained, this may be due to the fast drying (30 min) led to the incomplete condensation of TEOS and molecular assembly.

A similar observation was reported for the synthesis of iron-platinum nanoparticles using variable microwave power, in which the XRD data revealed an increase in the peak intensity upon increasing the microwave power from 120 to 420 W [12]. After increasing microwave power, the degree of hydration of the CTAB chains may also increase and their interaction with silica species in the solution becomes stronger, in combination with the increasing rate of hydrolysis and polymerization of the TEOS source that led to the formation of more ordered silica. This may also be related to the effect of synthesis temperature, wherein the temperature rapidly rose when the

microwaves coupled directly with the molecules of the entire reaction mixture, which led to the instantaneous localized superheating of the substance [13]. A less ordered structure of SBA-16 prepared at a lower temperature was reported due to the low degree of Pluronic F127 chain hydration, which resulted in weaker interactions with the silica species [14].

Based on the characterization results, the mechanism for the formation of MSNs using microwaves is proposed. The use of microwave power of 100 W seemed inadequate since it formed poorly crystalline, irregular mesoporous MSN structures with a small surface area. Since to the electromagnetic field generated by microwaves affects the enhancement of crystal growth, a low microwave power with a short irradiation time was probably insufficient to provide the homogeneous heating required for optimal crystal growth [15]. The irregularities in the structure were presumed to be a consequence of the formation of ''hot spots'' at certain locations in the microwave reactor.

A similar result was reported regarding the disruption of the ferrite structure due to ''hot spots'' or areas that induce a localized enhancement in the reaction rate [9]. On the contrary, the use of a microwave power of 450 W generated a more homogeneous and uniform silica order. Although the ''hot spots'' phenomenon also occurred at 450 W, it is presumed that the strong thermal supply directed the micelles to accumulate faster than at 100 W of microwave power. As a result, the MSN formed at 450 W displayed a more highly ordered structure (Figure 3). These differences in MSN characteristics were presumed to affect the adsorption and release pattern of ibuprofen.

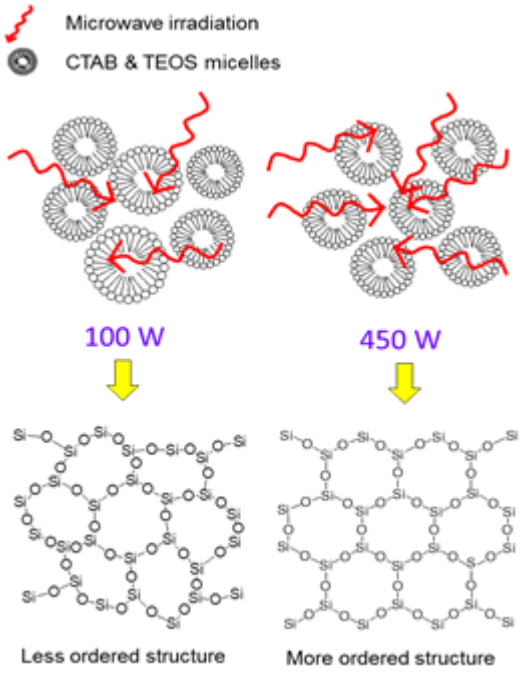


Figure 3. Formation of hexagonal order of MSN_{100} and MSN_{450}

Ibuprofen was used as a model drug to evaluate the adsorptivity and drug storage ability of the synthesized MSNs (Figure 4a). MSN_{450} displayed the highest adsorption rate at the first 6 hours and almost complete adsorption was achieved with 98.3% adsorption after 7 hours. The MSN_{300} and MSN_{100} demonstrated almost similar pattern of adsorption with 81.3% and 74.1%, respectively. Although the MSNs had almost the same chemical structure, ibuprofen adsorption increased with an increase in the microwave power used during MSN synthesis. This result implies that the differences in the material properties resulted in variable ibuprofen adsorption behavior.

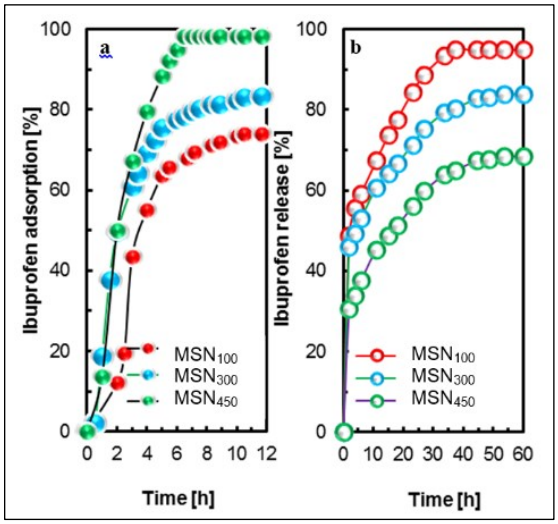


Figure 4. Adsorption (a) and release (b) of ibuprofen by all MSNs

Based on the characterization by TEM and FESEM, the variation in microwave power led to dissimilar patterns in the material's structure. In parallel with the crystallinity, increasing the microwave power also resulted in the enhancement of hexagonal order and the range of the silica. The complete adsorption of ibuprofen by MSN_{450} was probably caused by the higher surface area and fewer irregularities in the morphology that resulted in a more accessible surface as compared to MSN_{300} and MSN_{150}.

It is of great importance to comprehensively understand the drug delivery profiles using in vitro simulated body fluid (SBF) before creating a suitable controlled formulation of mesoporous silica materials for use in vivo. The concentration of ibuprofen released in SBF as a function of time was determined by monitoring changes in the absorbance by UV–Vis spectroscopy at a wavelength of 264 nm. The release rates are shown in Figure 4b. The ibuprofen released fastest from MSN_{100}, followed by MSN_{300} and MSN_{450}. MSN_{450} displayed the slowest release rate of ibuprofen with only 65% of the release percentage of MSN_{300} and MSN_{100} within the same contact time. The ibuprofen release of MSN_{300} and MSN_{100} were 81% and 95% release, respectively. MSN_{100}, with a less ordered silica arrangement, showed the highest release percentage and the fastest drug release rate before equilibrium was reached.

Since the pore surface chemistry of the mesoporous silica was quite similar, it is presumed that the difference in drug delivery behavior may be reasonably attributed to the pore structure of the MSN structure. In fact, a similar pore diameter and drug molecule size allows for sustained release owing to the size confinement effect; thus, the loaded drug can be released at a relatively high rate when the pore size of the MSN is much larger than the size of the drug molecule [16].

On the contrary, MSN-MW_{450}, which is presumed to have the largest and similar average pore distribution due to its most ordered structure did not exhibit the fastest release rate. This observation demonstrated the presence of diffusion process constraints during the release process, probably influenced by the pathway (the channel length of silica) of mesoporous silica, as discussed in the XRD characterization. The long ordered channels of MSN_{450} retained ibuprofen molecules, rendering the rapid release of drug molecules from the surface unfavorable. In a similar report, fast ibuprofen release was observed with MCM-41, which was characterized by a short channel length [17]. Hence, the length of the pathway is one of the most important factors when investigating drug delivery behavior, in addition to other factors such as the pore size, surface chemistry, and pore geometry of mesoporous silica.

The phenomenon of the adsorption and release of ibuprofen molecules is proposed according to the XRD, FESEM, and TEM results. Increasing the microwave power was found to form enhanced hexagonal order and range of silica, which led to a greater surface area, pore width and pore volume. The fewer irregularities in the morphology and a better silica arrangement were found to improve ibuprofen adsorption.

Conclusion

The enhancement of crystal growth was observed in the formation of mesoporous silica nanoparticles synthesized with variable microwave power in the range of 100 – 450 W. The use of low heating power (100 W) resulted in low crystallinity, an irregular mesoporous structure and a low surface area of MSN_{100}, which on the contrary, highest heating power produced more crystallized and better silica arrangement. In relation to the adsorption properties, MSN_{450} demonstrated the highest ibuprofen adsorption (98.3%), followed by MSN_{300} (81.3%) and MSN_{100} (74.1%), confirming that the difference in the material properties was a contributing factor in ibuprofen adsorption. By exhibiting the most crystallized structure, complete adsorption of ibuprofen by MSN_{450} was probably caused by fewer irregularities in its morphology that resulted in a more accessible surface compared to MSN_{300} and MSN_{150}. In accordance, MSN_{450} showed the slowest release rate of adsorption due to its wide pore diameter and long range of silica order.

Acknowledgement

The authors are grateful for the financial support by the Research University Grant from Universiti Teknologi Malaysia (Grant No. 02H76), the awards of MyPhD Scholarship (Nur Hidayatul Nazirah Kamarudin) from Ministry of Higher Education, Malaysia, and to the Hitachi Scholarship Foundation for their support.

References

1. Sayari, A. and Hamoudi, S. (2001). Periodic mesoporous silica-based organic-inorganic nanocomposite materials. *Chemistry of Materials*, 13(10): 3151 – 3168.
2. Liu, X., Li, J., Zhou, L., Huang, D. and Zhou, Y. (2005). Adsorption of CO_2, CH_4 and N_2 on ordered mesoporous silica molecular sieve. *Chemical Physics Lett*ers, 415(4-6): 198 – 201.
3. Karim, A. H., Jalil, A. A., Triwahyono, S., Sidik, S. M., Kamarudin, N. H. N., Jusoh, R., Jusoh, N. W. C. and Hameed, B. H. (2012). Amino modified mesostructured silica nanoparticles for efficient adsorption of methylene blue. *Journal of Colloid and Interface Science,* 386(1): 307 – 314.
4. Yu, Q., Hui, J., Wang, P., Xu, B., Zhuang, J. and Wang, X. (2012). Hydrothermal synthesis of mesoporous silica spheres: Effect of the cooling process. *Nanoscale,* 4: 7114 – 7120.
5. Newalkar, B. L., Olanrewaju, J. and Komarneni, S. (2001). Microwave-hydrothermal synthesis and characterization of zirconium substituted SBA-15 mesoporous silica. *The Journal of Physical Chemistry B*, 105: 8356 – 8360.
6. Hwang, Y. K., Chang, J. S., Kwon, Y. U. and Park, S. E. (2004). Microwave synthesis of cubic mesoporous silica SBA-16. *Microporous and Mesoporous Mat*erials, 68: 21 – 27.
7. Jalil, A. A. Kurono, N. and Tokuda, M. (2002). Synthesis of the precursor of anti-inflammatory agents by cross-coupling using electrogenerated highly reactive zinc, *Synthesis*, 18: 2681 – 2686.
8. Ballem, M. A., Cordoba, J. M. and Oden, M. (2010). Influence of synthesis temperature on morphology of SBA-16 mesoporous materials with a three-dimensional pore system. *Microporous and Mesoporous Materials*, 129: 106 – 111.
9. Chen, B., Wang, Z., Quan, G., Peng, X., Pan, X., Wang, R., Xu, Y., Li, G. and Wu, C. (2012). In vitro and in vivo evaluation of ordered mesoporous silica as a novel adsorbent in liquisolid formulation. *International Journal of Nanomedicine,* 7: 199 – 209.
10. Wu C. G. and Bein, T. (1996). Microwave synthesis of molecular sieve MCM-41. *Chemical Communications*, 925 – 926.
11. Heikkila, T., Santos, H. A., Kumar, N., Murzin, D.Y., Salonen, J., Laaksonen, T., Peltonen, L., Hirvonen, J. and Lehto, V. P. (2010). Cytotoxicity study of ordered mesoporous silica MCM-41 and SBA-15 microparticles on Caco-2 cells. *European Journal of Pharmaceutics and Biopharmaceutics,* 74: 483 –494.
12. Acharya, S. and Singh, K. (2011). Microwave-assisted chemical reduction routes for direct synthesis of (fct) L10 Phase of Fe-Pt. *Journal of Microwave Power Electromagnetic Energy,* 45: 63 – 69.
13. Hayes, B. L. (2002). Microwave synthesis: Chemistry at the speed of light. CEM Publishing: Matthews, NC.

14. Yu, C., Fan, J., Tian, B. and Zhao, D. (2004). Morphology development of mesoporous materials: a colloidal phase separation mechanism. *Chemistry of Materials,* 16: 889 – 898.
15. Cheng, H., Cheng, J., Zhang, Y. and Wang, Q. M. (2007). Large-scale fabrication of ZnO micro-and nano-structures by microwave thermal evaporation deposition. *Journal of Crystal Growth,* 299: 34 – 40.
16. Qu, F., Zhu, G., Lin, H., Sun, J., Zhang, D., Li, S. and Qiu, S. (2006). Drug self-templated synthesis of ibuprofen/mesoporous silica for sustained release. *European Journal of Inorganic Chemistry,* 19: 3943 – 3947.
17. Qu, F., Zhu, G., Lin, H., Zhang, W., Sun, J., Li, S. and Qiu, S. (2006). A controlled release of ibuprofen by systematically tailoring the morphology of mesoporous silica materials. *Journal of Solid State Chemistry.* 179: 2027 – 2035.

Malaysian Journal of Analytical Sciences, Vol 20 No 6 (2016): 1390 - 1397
DOI: http://dx.doi.org/10.17576/mjas-2016-2006-18

MALAYSIAN JOURNAL OF ANALYTICAL SCIENCES
Published by The Malaysian Analytical Sciences Society
ISSN 1394 - 2506

METHANE ADSORPTION PERFORMANCE OF THE PALM KERNEL SHELL-DERIVED CARBON MATERIAL ACTIVATED USING CO_2-STEAM SEQUENTIAL COMBINATION

(Prestasi Penjerapan Gas Metana oleh Karbon Teraktif Isirong Kelapa Sawit dengan Menggunakan Gabungan CO_2-Stim Secara Turutan)

Mohd Saufi Md Zaini and Syed Shatir A. Syed Hassan*

Faculty of Chemical Engineering,
Universiti Teknologi MARA, 40450 Shah Alam, Selangor, Malaysia

**Corresponding author: shatir@salam.uitm.edu.my*

Received: 21 October 2015; Accepted: 14 June 2016

Abstract

A study was conducted to prepare activated carbon from $ZnCl_2$-treated oil palm kernel shell using the sequential combination of carbon dioxide and steam (CO_2 + steam) as activated agent. The development of pores of activated carbon and methane adsorption on the prepared activated carbon were investigated. The results show that the sequential combination of CO_2 and steam was a good combination producing activated carbon with high total pore volume of 1.0 cm^3/g and BET surface area of 1548.0 m^2/g. The resultant activated carbon contained microporous and mesoporous structure with a nearly balance volume percentage. The highest methane uptake in this study was 145.89 V/V at 10 bar and ambient temperature.

Keywords: activated carbon, palm kernel shell, methane adsorption, porosity development

Abstrak

Satu kajian telah dijalankan bagi menyediakan karbon teraktif daripada isirong kelapa sawit yang dirawat bersama $ZnCl_2$ dengan menggunakan agen pengaktifan karbon dioksida dan stim secara berturutan. Dalam kajian ini, pembangunan liang pada karbon teraktif dan penjerapan gas metana telah dikaji. Hasil dari kajian ini menunjukkan bahawa kombinasi secara urutan bagi gas karbon dioksida dan stim merupakan kombinasi agen pengakifan yang baik dan menghasilkan karbon teraktif yang mempunyai jumlah isipadu liang yang tinggi iaitu 1.0 cm^3/g dan luas kawasan BET sebanyak 1548.0 m^2/g. Karbon teraktif yang terhasil juga mempunyai kandungan liang mikro dan liang meso yang hampir seimbang. Hasil kajian ini, penjerapan gas metana yang tertinggi adalah 145.89 V/V pada 10 bar dan suhu ambien.

Kata kunci : karbon teraktif, isirong kelapa sawit, penjerapan gas metana, pembangunan liang

Introduction

A sustainable energy supply and environmental protection are the challenges faced by the world presently. Conserving the sustainable energy is vital in order to ensure the security and the consistency of supply and the diversification of the various energy resources. The search for alternative fuel for vehicles has been actively pursued nowadays due to the issue of sustainability, energy and oil market crisis, and the increased awareness of environmental protection

Methane gas is a promising alternative fuel. It is a clean gas and can be found through various resources such as lake, swamp, landfill and also from fossil fuel. However because of its very low energy density, storing large amounts of methane in a limited volume is very challenging for its application like gas-powered vehicles. A new revolution of natural gas storage technology has been developed through adsorption in porous materials

(activated carbon) which known as adsorbed natural gas (ANG). By using this technique, methane gas can be stored in the same amount as conventional tank but at a lower pressure. The activated carbon provides "extra room" for storing methane gas. The force exerted by the carbon atom inside the pores attract a lot of methane gas molecules into the pores, thus the amount of the bulk of gas will reduce. As a result, the pressure of tank can be kept as low as possible while maintaining high density of methane in the pores.

Extensive studies have been performed to enhance the ability of adsorbing methane gas through activated carbon produced from low cost agriculture waste precursors [1-3]. Production of the most suitable activated carbon for the gas adsorption application usually requires consideration of various factors such as chemical agent, impregnation ratio, activation temperature, and activation time [4]. One of the crucial factor contributing to the pore development of activated carbon is activation agents [5]. Different agents may influence differently in the properties, the activation rate and the yield of carbon material.

There are two main steps in producing activated carbon: i) the carbonisation of raw precursors in the absence of oxidising gas and ii) the activation of carbonisation product (char) using activation agent (physical, chemical or combination of both). Physical activation is widely used and can be applied to all raw materials. Generally, the precursors will undergo carbonisation process in the presence of inert gas at 500 – 800 °C followed by the activation by oxidising gas such as steam, CO_2 or their mixture at 800 – 1100 °C. During carbonisation, the precursors undergo three main stages: i) the elimination of water, ii) the primary pyrolysis (i.e. thermal decomposition of carbonaceous materials to form basic char structure, light gases and tar) and iii) the consolidation of char structure [6]. In the activation step, some carbons are eliminated by the activation agent to form gases via reactions (1) or (2), thus develop the porosity in the carbonised materials

CO_2 activation

$$C + CO_2 = 2CO \quad (1)$$

Steam activation

$$C + H_2O = CO + H_2 \quad (2)$$

Although large amount of researches have been conducted with steam, CO_2 or their simultaneous combination (i.e. mixture) as activating agent for different types of carbonaceous material [5, 7, 8], very few of the previous works has addressed the effect of CO_2-steam activation sequences on the pore development for methane adsorption application. This study is therefore aimed in investigating the methane adsorption performance from palm kernel shell derived activated carbon using the sequential combination (as opposed to the usual simultaneous combination) of CO_2 + steam activation. Our findings provide additional insight into developing an efficient activation procedure for producing high quality activated carbon for methane adsorption.

Materials and Methods

Raw material preparation

Oil palm kernel shells (PKS) were used as activated carbon precursors in this study. PKS were obtained from Sime Darby Research and Development Centre (R&D) in Carey Island, Malaysia. PKS samples were washed with distilled water to remove dust and impurities. The washed PKS were sundried for 48 hours and further dried in an oven at 110 °C overnight to remove moisture and to preserve from biological degradation. The dried PKS were crushed and sieved to obtain particles sizes in the range of 0.5 to 1.0 mm.

Preparation of activated carbon

Dried PKS with the mass of 110 (±0.1) g were mixed into 220 mL solution (98% purity from Acros Organics) of 55% (w/w) zinc chloride. The mixture was stirred by a magnetic stirrer in a beaker at 80 °C for 3 hours. The mixture was then dried in an oven at 110 °C until the PKS achieved complete dryness. Figure 1 shows the experimental setup for carbonisation and activation processes. The setup consists of a double layer stainless steel reactor. The treated-PKS was carbonised under nitrogen flow of 192 cm^3/min until the temperature reached 900 ^oC. N_2 gas was then switched to CO_2 and followed by steam sequentially for 2 hours. The activated carbon obtained was washed under stirring with 0.1M of hydrochloric acid for one hour and further washed with hot distilled water six times (30 minutes each) to remove the remaining chemicals.

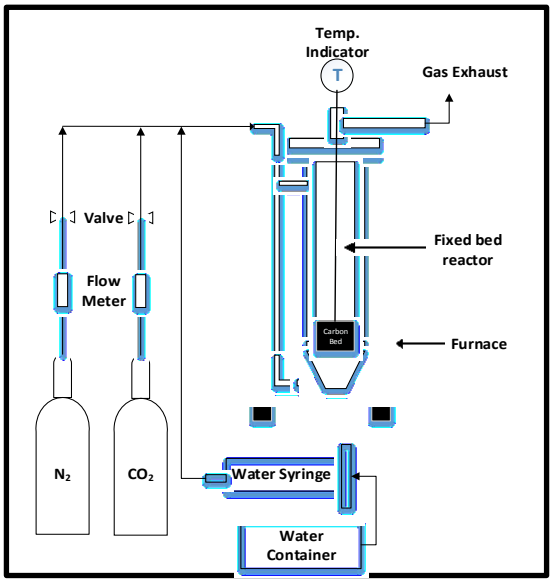


Figure 1. Schematic diagram of the preparation of activated carbon

Methane adsorption by volumetric method

An amount 20 (±0.1) g of activated carbon sample was weighed and placed into high pressure stainless steel adsorbent cell and degassed for several hours to remove any impurity at room temperature. Schematic diagram of experimental set-up is shown in Figure 2. Two pressure transmitters model TPS20-G27F8-00 (range 0 – 20 kg/cm^3 with accuracy ± 0.001) manufactured by Murr Electronic were used to measure the pressure. The temperature condition of the experiment was within the range of 300 (±0.1)K up to 303 (±0.1)K. Methane gas was injected using needle valve up to 10(± 0.001) bar continuously. The number of mol of methane uptake was determined from the mass balance by the application of ideal gas equation of states (3).

$$n_{ads} = \frac{1}{M_w}\left[\left(\frac{P_{r1}}{Z_{r1}} - \frac{P_{r2}}{Z_{r2}}\right)\frac{V_{gl}}{RT} - \left(\frac{P_{ad2}}{Z_{ad2}} - \frac{P_{ad1}}{Z_{ad1}}\right)\frac{V_{ad}}{RT}\right] \quad (3)$$

where M_w is molecular weight of methane gas, V_r is volume of reference cell and V_{ad} is volume of adsorption cell.

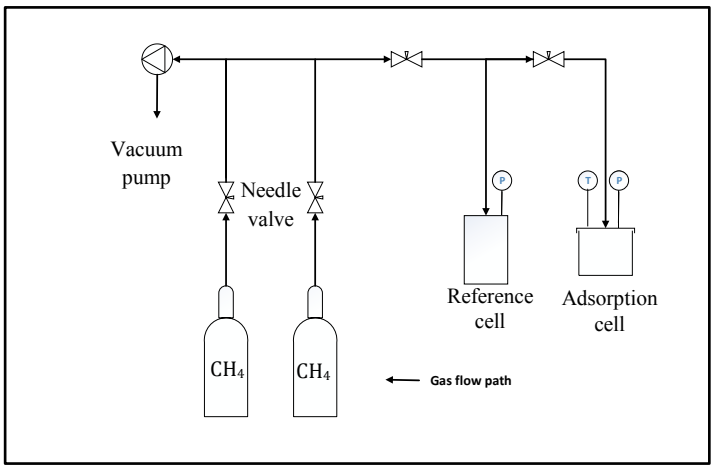


Figure 2. Schematic diagram of methane adsorption unit

Results and Discussion

Proximate and ultimate analysis

Based on the proximate and ultimate analyses the volatile matter of the PKS is 62% and the carbon content of 48%. Sufficient amount of volatile content is important, since the evolution of volatiles during carbonisation and activation processes results in making more porous structures in activated carbon [9]. The high carbon content contributes to structural strength of activated carbon [10]. After activation process (using steam + CO_2 agents), the volatile content of PKS (activated carbon) decreased drastically from 62.15% to 13.8% whilst the fixed carbon increased from 34.85 % to 69.59%. This is because at high degree of activation the volatile were removed through thermal decomposition aided by activation agent (CO_2 + Steam) leaving the residual elementary carbon atom (fixed carbon). Thus, it can be seen in Table 1 that the percentage of carbon (C) was also increased which subsequently caused in decrease to the other elements.

Table 1. Proximate and ultimate analysis of raw PKS and activated carbon PKS

Sample	Proximate Analysis (wt. %)				Ultimate analysis (wt. %)			
	Moisture	Volatile Matter	Fixed carbon	Ash	C	H	N	O
Raw PKS	1.60	62.15	34.85	1.4	47.9	7.2	1.0	43.9
AC PKS	7.01	13.80	69.59	9.6	68.7	3.0	2.1	26.2

Characteristics of prepared activated carbon

The activated carbon was characterised by N_2 adsorption/ desorption, BET surface and pore size distribution analyses. Figure 3 shows the adsorption/desorption isotherm of nitrogen at 77K. It can be ascertained from the graph that the isotherm of activated carbon belongs to the Type IV of IUPAC classification [11] representing adsorption isotherm with hysteresis. The Type IV shape follows the same path as Type II at lower relative pressure. The sharp "knee" suggests that a considerable amount of micropores are present, and the slop of the plateau at high relative pressure is due to multilayer adsorption on non-microporous, i.e. mesoporous [12]. This indicates that the porous structures of the activated carbon are mainly microporous and mesoporous. According to Kundu et al. [13], intensive activation would increase the elimination of low molecular weight volatiles that causes development in pore. The use of CO_2 changes the structure (especially the outer one) of char, leaving more active site to be used for steam to generate microporous structure at a faster rate. In addition, at high temperature (900°C) the microporous structure was collapsed to result in the formation of mesoporous activated carbon.

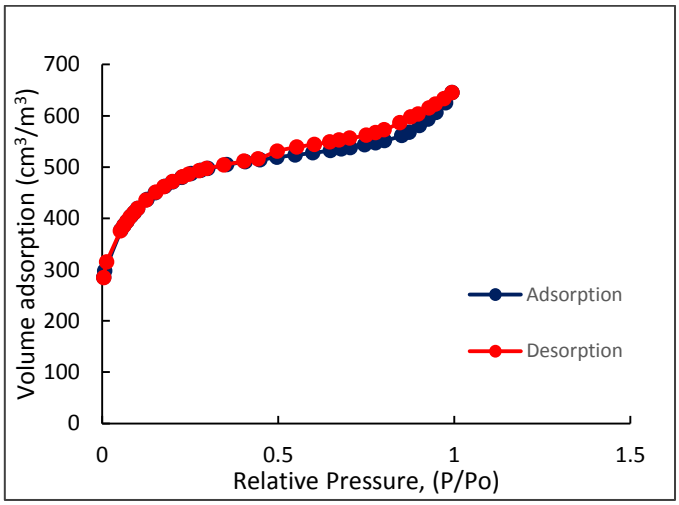


Figure 3. N_2 adsorption on activated carbons produced at the optimum conditions

From the nitrogen adsorption isotherm analysis, the BET surface area and total pore volume of the activated carbon were 1551 m^2/g and 1.00 cm^3/g, respectively. According to Rodriguez-Reinoso et al., steam activation aids enhancement and continuously develops microporosity which would produce more selective attack on the carbon structure, while CO_2 activation tends to enhance the size of micropores to produce more mesoporous and macroporous volume. Therefore, the combination using CO_2 as the first agent and steam as the second agent is a good combination to improve the porosity since CO_2 enlarges the existing pores allowing steam to penetrate deep into or inside porous structure and creates more new pores in the carbon, resulting in a higher surface area and pore volume. Furthermore, with $ZnCl_2$ impregnation, the removal of the volatiles through the pore passage was not hindered since $ZnCl_2$ acts as a dehydrating agent during activation that inhibit tar formation and other liquid clogging, thus increasing number of porosity [14].

Figure 4 illustrates the distribution of pore development by DFT analysis of nitrogen isotherm. Based on the graph, the observed peaks are in the range of 1 to 3 nm, indicating that majority of pores are located within microporous and initial mesoporous range, thus it can be concluded that the result obtained is consistent with the N_2 isotherm trend discussed above. The proportion of micropores (58%) and mesopores (42%) of the activated carbon in this study are nearly balance. It can be inferred that, at low degree of activation, the microporous structure was initially developed and it was progressively widens with increase in degree of activation.

Methane adsorption

The activated carbon prepared using combination of CO_2 + steam underwent further analysis of methane adsorption. The activated carbons prepared from single activation of steam and CO_2 were also prepared at the same conditions for comparative study. Figure 5 shows the methane uptake (mol/kg) of all the three activated carbons. The methane gas were charged continuously until the pressure reached 10 bar and measured at 293.15K. It can be seen clearly, methane uptake increases linearly with the pressure. The results agree well with a previous study by Arami-Niya et al. [15]. High amount of methane adsorption is expected when the adsorption has large surface area and high total pore volume. In this study, it is suggested that the porosity of activated carbon prepared using combination of CO_2 + steam is well developed compared to other set of conditions. It is clearly shown in Table 2, the BET surface area and total pore volume are double the amount of other activated carbons. However higher percentage of microporous structure can be observed when using single activation agent.

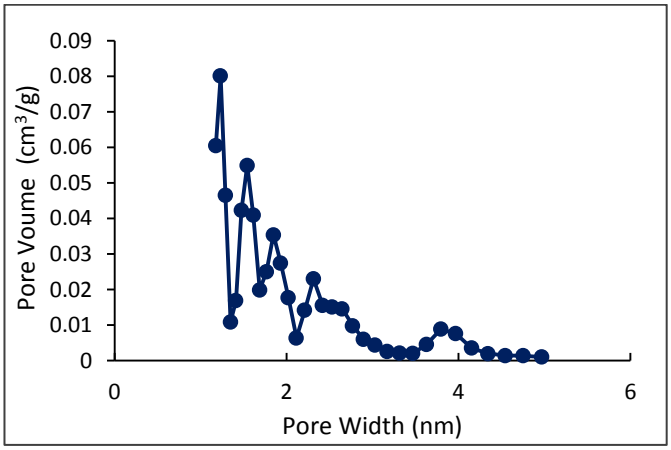


Figure 4. DFT pore size distribution of activated carbon at optimum conditions

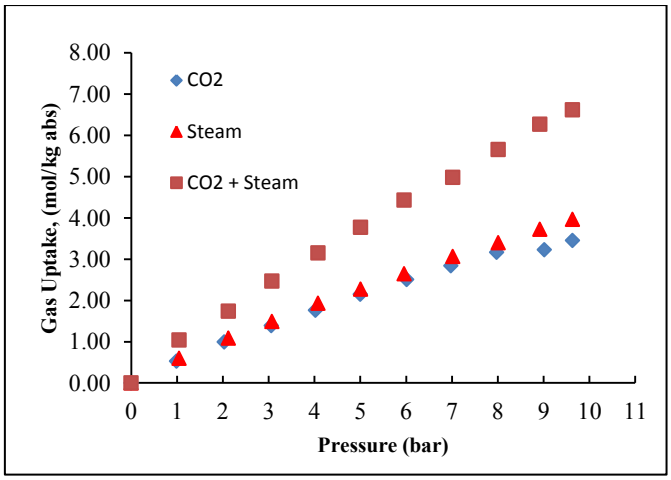


Figure 5. Methane uptake of activated carbons prepared at different conditions.

Table 2. Characteristics of porosity of activated carbons

Sample	SBET (m^2/g)	V_{total} (cm^3/g)	$V_{Microporous}$ (cm^3/g)	Microporous (%)	$V_{Mesoporous}$ (cm^3/g)	Mesoporous (%)
CO_2 + Steam	1548.0	1.000	0.580	58.00	0.420	42.00
Steam	798.2	0.459	0.449	97.99	0.009	2.01
CO_2	787.0	0.435	0.359	82.46	0.076	17.54

It is widely known that steam is more reactive than CO_2. According to thermochemical dissociation of water and carbon dioxide, the hydrogen-oxygen bond of water molecule is relatively easier to break compared to the carbon-oxygen bond, explaining the higher reactivity of steam than CO_2 [11,16]. Nevertheless, with suitable total pore size distribution, the pore wall of the activated carbon provides relatively strong attractive forces to the surrounding gas molecules. The energy of gas molecules slowly lowered as it passes through narrow space. As a result, gas molecules are packed densely within pore networks of the carbon [17]. Since the diameter size of methane gas is about 0.4nm [18], thus to obtain the highest gas adsorption, the pore size of activated carbon must be bigger than the size of two molecules of methane (0.8nm) [19]. Less methane adsorption capacity is expected when activated carbon has low surface area, low volume and has very large pore size diameter.

Thus, in this study, the average pore size diameter, total pore volume and surface area can be regarded as suitable dimension for methane gas adsorption. Therefore, high capacity of methane gas is favourably adsorbed into activated carbon. Similar results were reported by Daud et al. [20], and Azevedo et al. [21], on the porosity development.

Simultaneously, the methane uptake was analysed in term of volume basis. The volume of activated carbon is determined by compressing a known amount of activated carbon at 200 bar. The highest methane uptake of the three activated carbons are shown in Figure 6. The methane storage was measured at 293.15K and 10 bar. As can be seen in the Figure 5, the activated carbon prepared using combination of CO_2 + steam activation agent recorded the highest storage of 145.89 V/V compared to other mode of activation. According US Department of Energy, the practical storage capacity for gas-powered vehicles is 180 V/V at 35 bar [21]. Thus it can be concluded that, the methane uptake of activated carbon prepared under sequential combination of CO_2 + steam activation agent nearly achieved the desired storage capacity for vehicle application.

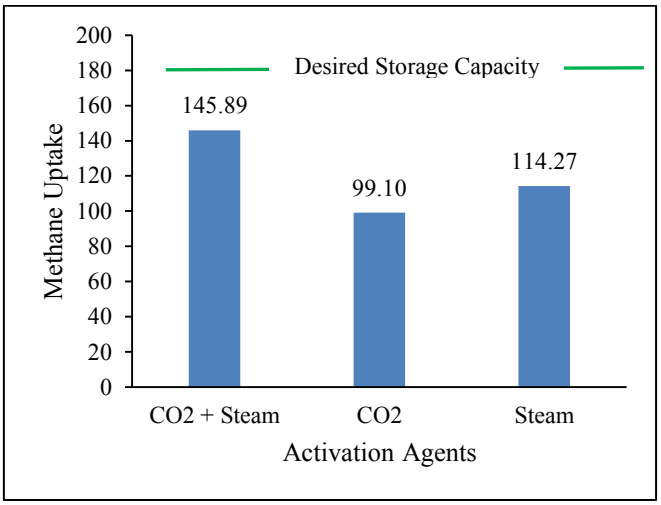


Figure 6. Methane Uptake in volumetric based

Conclusion

Palm kernel shell is regarded as suitable precursors for production of activated carbon. The activation with $ZnCl_2$ under combination in sequence of CO_2 and followed by physical activation proved to be an efficient method in production of activated carbon for methane adsorption. This preparation method leads to high BET surface area (1548.00 m^2/g) and high pore volume (1.00 cm^3/g) with proper dimension of pore size distribution (1 – 3 nm). The sequential combination of CO_2 and steam is a good combination since CO_2 tends to open the outer structure of activated carbon allowing steam with higher rate of reaction strike deep inside activated carbon to develop more pore volume. Methane adsorption capacities of various activated carbons prepared at combination of activation agent and single activation agent were determined at 293.15K and 10 bar on mass basis as well as on the volume basis. Among the three different activated carbons, the higher methane uptake on the mass and volume basis was found in activated carbon prepared under combination of activation agent owing to its high surface area, and large total pore volume.

Acknowledgment

This study was financially supported by the Ministry of Higher Education (MoHE) via the Fundamental Research Grant Scheme (project no: FRGS/1/2013/TK07/UiTM/02/2). Mohd Saufi Md Zaini is thankful to UiTM and MoHE for the scholarship award.

References

1. Solar, C., Blanco, A. G., Vallone, A. and Sapag, K. (2010). Adsorption of methane in porous materials as the basis for the storage of natural gas. *Natural Gas*: pp. 205.
2. Arami-Niya, A., Daud, W. M. A. W. and Mjalli, F. S. (2010). Using granular activated carbon prepared from oil palm shell by $ZnCl_2$ and physical activation for methane adsorption. *Journal of Analytical and Applied Pyrolysis*, 89: 197 – 203.
3. Najibi, H., Chapoy, A. and Tohidi, B. (2008). Methane/natural gas storage and delivered capacity for activated carbons in dry and wet conditions. *Fuel*, 87(1): 7 – 13.
4. Ahmadpour, A., Okhovat, A. and Mahboub, M. D. (2013). Pore size distribution analysis of activated carbons prepared from coconut shell using methane adsorption data. *Journal of Physics and Chemistry of Solids*, 74(6): 886 – 891.
5. Molina-Sabio, M., Gonzalez, M. T., Rodriguez-Reinoso, F. and Sepúlveda-Escribano, A. (1996). Effect of steam and carbon dioxide activation in the micropore size distribution of activated carbon. *Carbon*, 34(4): 505 – 509.
6. Rodriguez-Reinoso, F. and Molina-Sabio, M. (1992). Activated carbons from lignocellulosic materials by chemical and/or physical activation: an overview. *Carbon*, 30(7): 1111 – 1118.

7. Minkova, V., Marinov, S. P., Zanzi, R., Björnbom, E., Budinova, T., Stefanova, M. and Lakov, L. (2000). Thermochemical treatment of biomass in a flow of steam or in a mixture of steam and carbon dioxide. *Fuel Processing Technology*, 62(1): 45 – 52.
8. Carrott, P. J. M., Carrott, M. R., Guerrero, C. I. and Delgado, L. A. (2008). Reactivity and porosity development during pyrolysis and physical activation in CO_2 or steam of kraft and hydrolytic lignins. *Journal of Analytical and Applied Pyrolysis*, 82(2): 264 – 271.
9. Manocha, S. M. (2003). Porous Carbon. Department of Materials Science, Sandar Patel Univeristy, India.
10. Herawan, S. G., Hadi, M. S., Ayob, M. R. and Putra, A. (2013). Characterization of activated carbons from oil-palm shell by CO_2 activation with no holding carbonization temperature. *The Scientific World Journal*, 2013: 1 – 7.
11. Rodriguez-Reinoso, F., Martin-Martinez, J. M., Prado-Burguete, C. and McEnaney, B. (1987). A standard adsorption isotherm for the characterization of activated carbons. *Journal of Physical Chemistry*, 91: 515 – 516.
12. Rouquerol, J., Rouquerol, F., Llewellyn, P., Maurin, G. and Sing, K. S. (2013). Adsorption by powders and porous solids: principles, methodology and applications. 2nd ed. London: Academic Press Inc.(London) Ltd.
13. Kundu, A., Gupta, B. S., Hashim, M. A. and Redzwan, G. (2015). Taguchi optimization approach for production of activated carbon from phosphoric acid impregnated palm kernel shell by microwave heating. *Journal of Cleaner Production*, 105: 420 – 427.
14. Guo, J. and Lua, A. C. (2000). Textural characterization of activated carbons prepared from oil-palm stones pre-treated with various impregnating agents. *Journal of Porous Materials*, 7(4): 491 – 497.
15. Arami-Niya, A., Daud, W. M. A. W. and Mjalli, F. S. (2011). Comparative study of the textural characteristics of oil palm shell activated carbon produced by chemical and physical activation for methane adsorption. *Chemical Engineering Research and Design*, 89(6): 657 – 664.
16. González, J. F., Encinar, J. M., González-García, C. M., Sabio, E., Ramiro, A., Canito, J. L. and Gañán, J. (2006). Preparation of activated carbons from used tyres by gasification with steam and carbon dioxide. *Applied Surface Science*, 252(17): 5999 – 6004.
17. Prasetyo, I., Yunanto, R., & Ariyanto, T. (2011). Methane storage by methane hydrate formation within water-saturatedporous carbon: The effect of mesoporosity. Chemical Engineering Department, Gadjah Mada University, Indonesia.
18. Mosher, K. (2011). The impact of pore size on methane and CO_2 adsorption in carbon. Stanford University, United Kingdom.
19. Almansa, C., Molina-Sabio, M. and Rodríguez-Reinoso, F. (2004). Adsorption of methane into $ZnCl_2$-activated carbon derived discs. *Microporous and Mesoporous Materials*, 76(1): 185 – 191.
20. Daud, W., Ashri, W. M., Ali, W. S. W. and Sulaiman, M. Z. (2003). Effect of activation temperature on pore development in activated carbon produced from palm shell. *Journal of Chemical Technology and Biotechnology*, 78(1): 1 – 5.
21. Azevedo, D. C., Araujo, J. C. S., Bastos-Neto, M., Torres, A. E. B., Jaguaribe, E. F. and Cavalcante, C. L. (2007). Microporous activated carbon prepared from coconut shells using chemical activation with zinc chloride. *Microporous and Mesoporous Materials*, 100(1): 361 – 364.

Malaysian Journal of Analytical Sciences, Vol 20 No 6 (2016): 1397 - 1404
DOI: http://dx.doi.org/10.17576/mjas-2016-2006-19

MALAYSIAN JOURNAL OF ANALYTICAL SCIENCES
Published by The Malaysian Analytical Sciences Society
ISSN 1394 - 2506

Ba-SAPO-34 ZEOLITE MEMBRANE FOR CO_2 AND N_2 PERMEATION

(Resapan Gas CO_2 dan N_2 Melalui Membran Zeolit Ba-SAPO-34)

Thiam Leng Chew[1]*, Jun Wei Lim[2], Abdul Latif Ahmad[3]

[1]*Department of Chemical Engineering, Faculty of Engineering*
[2]*Department of Fundamental and Applied Sciences*
Universiti Teknologi PETRONAS, 32610 Bandar Seri Iskandar, Perak Malaysia
[3]*School of Chemical Engineering, Engineering Campus,*
Universiti Sains Malaysia, 14300 Penang, Malaysia

**Corresponding author: thiamleng.chew@utp.edu.my*

Received: 21 October 2015; Accepted: 14 June 2016

Abstract

Membrane separation technology is gaining importance nowadays in reducing the emission of carbon dioxide (CO_2) as greenhouse gas due to the global climate change. Gas permeation studies play significant role in reflecting the potential of the membranes in separating the gas mixtures. In this study, Ba-SAPO-34 zeolite membrane was formed by membrane synthesis process using microwave (MW) heating and followed by membrane ion-exchange process with Ba^{2+} cation. The Ba-SAPO-34 zeolite membrane was investigated for its performance in the CO_2 and N_2 gases permeation studies. The effects of permeation temperature (30 – 180 ^oC) and pressure difference (100 – 500 kPa) across the membrane on the gas permeation performance of the Ba-SAPO-34 membrane were studied. CO_2 single permeance of ~9.4-19.5 x 10^{-8} mol/m^2.s.Pa and N_2 single permeance of ~0.635-0.694 x 10^{-8} mol/m^2.s.Pa were obtained for gases permeation through Ba-SAPO-34 membrane performed under the range of permeation temperature and pressure difference across the membrane studied. Maximum CO_2/N_2 ideal selectivity of 29.6 was obtained for gases permeation through Ba-SAPO-34 membrane at 30 ^oC and 100 kPa pressure difference.

Keywords: Ba-SAPO-34, membrane, gas permeation

Abstrak

Teknologi membran pemisahan adalah semakin penting pada masa kini dalam mengurangkan pelepasan karbon dioksida (CO_2) sebagai gas rumah hijau disebabkan oleh perubahan iklim sejagat. Kajian resapan gas memainkan peranan yang penting dalam mencerminkan potensi membran dalam pemisahan campuran gas. Dalam kajian ini, membrane zeolit Ba-SAPO-34 telah dibentuk melalui proses sintesis membran dengan menggunakan pemanasan gelombang mikro dan diikuti oleh proses pertukaran ion membran dengan kation Ba^{2+}. Membran zeolit Ba-SAPO-34 tersebut telah dikaji untuk prestasinya dalam kajian resapan gas CO_2 dan N_2. Kesan suhu resapan (30 – 180 ^oC) dan perbezaan tekanan (100 – 500 kPa) merentasi membrane terhadap prestasi resapan gas membrane Ba-SAPO-34 telah dikaji. Ketelapan tunggal CO_2 sebanyak ~9.4-19.5 x 10^{-8} mol/m^2.s.Pa dan ketelapan tunggal N_2 sebanyak ~0.635-0.694 x 10^{-8} mol/m^2.s.Pa telah diperolehi bagi resapan gas melalui membran Ba-SAPO-34 di bawah julat suhu resapan dan perbezaan tekanan merentasi membran yang dikaji. Kememilihan CO_2/N_2 sebanyak 29.6 (maksimum) telah diperolehi bagi resapan gas melalui membran Ba-SAPO-34 pada 30 ^oC dan perbezaaan suhu sebanyak 100 kPa.

Kata kunci: Ba-SAPO-34, membran, resapan gas

Introduction

Reduction in emissions of greenhouse gases is becoming one of the major environmental issues due to the increase in global temperature, which is likely to bring several drawbacks such as disturbance in ecosystems and rise in sea

levels. The increasing concentration of greenhouse gas, in particular carbon dioxide (CO_2), in the atmosphere in recent years has drawn attention of many researchers around the globe. The CO_2 separation from nitrogen (N_2) is among the worldwide concern nowadays in restricting the emission of CO_2 from large emission sources, i.e. flue gas from power plants. In the industrial post-combustion capture for fossil fuel combustion process, CO_2/N_2 separation remains an engineering challenge in removing the CO_2 from the flue gas emitted. In view of this issue, there are increasing number of articles published by the researchers with the aim to explore potential processes for separation and recovery of CO_2 from different sources [1-5]. Conventional technologies used for CO_2 separation from gas mixtures includes absorption using amine based solvents and pressure swing adsorption [6, 7]. However, the drawbacks of these conventional technologies are complexity of the system, high energy consumption for solvent regeneration, equipment corrosion and flow problems caused by viscosity of solvent [8, 9].

Membrane processes appear to be a promising alternative for gas permeation and separation. Polymer membranes, which have been widely investigated for gas permeation and separation, offer advantages such as low cost and ease of preparation. However, the disadvantages of polymer membranes, such as possible occurrence of plasticization due to high CO_2 partial pressure, poor chemical, thermal and mechanical strength, limit their performance in the application [10–12]. Zeolite membranes are gaining increasing interest for gas permeation and separation, in view of their uniform pore structure, high chemical, thermal and mechanical stability [13,14].

There have been extensive studies on different zeolite membranes for gas permeation and separation [12,15 – 19]. Silicoaluminophosphate, SAPO-34 membrane has been studied extensively for gas permeation and separation due to its small pore structure [6,17, 20,21]. Conventionally, the SAPO-34 membranes were prepared by hydrothermal synthesis method. Microwave (MW) heating emerged as a potential technology offering number of advantages against conventional hydrothermal heating such as shorter synthesis time, rapid heating rate and production of small zeolite crystals with narrow size distribution [22–24]. To our best knowledge, our group has been the first to report synthesis of SAPO-34 zeolite membrane using MW heating [25].

In the present study, Ba-SAPO-34 membrane was prepared using MW heating followed by ion-exchange process. In our previous work reported [26], the CO_2/CH_4 gas separation of Ba-SAPO-34 membrane was investigated. In the present study, the Ba-SAPO-34 membrane was tested for single gas permeation of CO_2 and N_2. The effects of permeation temperature and pressure difference across the membrane on the CO_2 and N_2 single gas permeation performance of the Ba-SAPO-34 membrane were studied.

Materials and Methods

Ba-SAPO-34 membrane preparation

α-alumina disc with thickness of 3 mm and diameter of 25 mm was used as the support where the membrane was deposited on. The Ba-SAPO-34 membrane was prepared according to the procedures described in our previous work [26].

Gas permeation studies

Figure 1 show the setup diagram of the gas permeation studies. The disc-shaped Ba-SAPO-34 membrane was placed in a stainless steel module and the module was sealed using silicone gaskets in order to avoid any gas leakage from the module during gas permeation studies. Total feed flow of 60 ml/min was applied for single gas permeation of CO_2 and N_2 through Ba-SAPO-34 membrane. Pure CO_2 or N_2 gas was fed to the membrane using a mass flow controller. By closing the end of the retentate side of the membrane module, the feed pressure was controlled while the permeate pressure was kept at atmospheric pressure in order to vary the pressure difference between 100 and 500 kPa across the membrane. The temperature of the gas permeation was controlled between 30 and 180 ^oC by using an oven where the stainless steel module was placed.

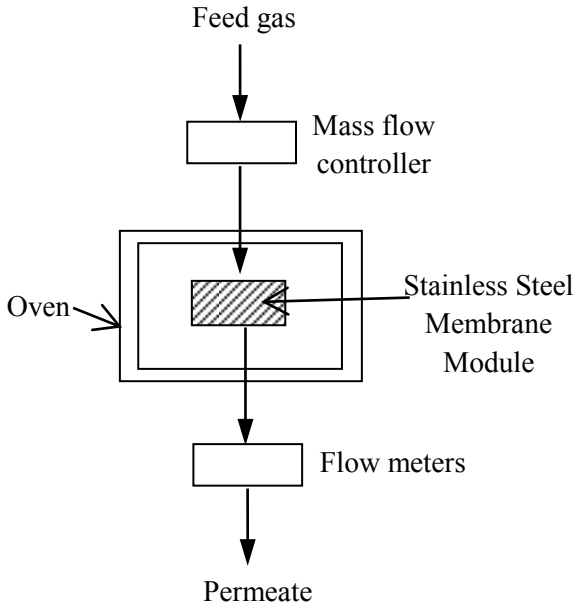


Figure 1. Setup diagram of the gas permeation studies

Flux, J_i (mol/m^2.s) of component gas *i* was calculated as shown in Equation (1).

$$J_i = \frac{n_i}{A \cdot t} \tag{1}$$

where $\frac{n_i}{t}$ is the molar flow rate of component *i* (mol/s), A is the effective permeation area of the membrane (m^2), the component *i* may refer to CO_2 or N_2.

Permeance, P_i (mol/m^2.s.Pa) of component gas *i* was calculated as shown in Equation (2).

$$P_i = \frac{J_i}{\Delta p_i} \tag{2}$$

where Δp_i is the pressure difference of component *i* across the membrane (Pa).

The ideal selectivity of the membranes, $\alpha_{CO_2/N_2}^{ideal}$ was calculated from the ratio of single gas permeance as shown in Equation (3).

$$\alpha_{CO_2/N_2}^{ideal} = \frac{P_{CO_2}}{P_{N_2}} \tag{3}$$

Results and Discussion

Gas permeation studies

Figure 2 presents the effect of pressure difference on the single gas fluxes through Ba-SAPO-34 membrane. The single gas flux of CO_2 and N_2 increased linearly with increase in pressure difference across the membrane. In the range of temperature (30 – 180 ^oC) and pressure difference (100 – 500 kPa) studied in current study, CO_2 displayed higher single gas fluxes even though CO_2 possess higher molecular weight than N_2. The gas flux is the sum of micropore diffusion and surface diffusion [27]. It was relatively easier for CO_2 diffusion through the micropore

framework of Ba-SAPO-34 due to smaller kinetic diameter of CO_2 compared to N_2. In addition, Li et al. [28] reported that the strength of adsorption of CO_2 gas molecules on SAPO-34 framework was higher than those of N_2 gas molecules. Owing to larger quadruple moment of CO_2, CO_2 was more strongly adsorbed on Ba-SAPO-34 pore framework and followed by stronger surface diffusion through the pore framework compared to N_2. The combination effect of micropore diffusion and surface diffusion explains the higher CO_2 single gas flux compared to N_2 in the present study.

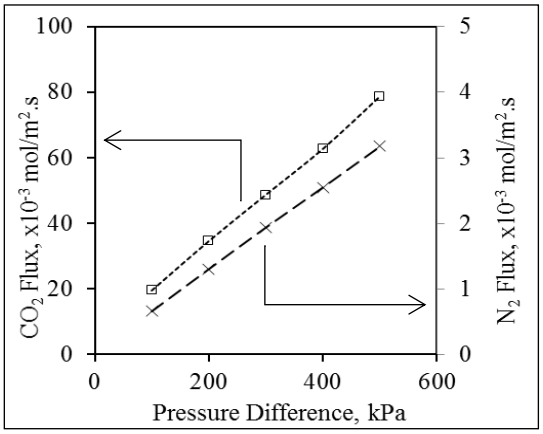


Figure 2. Single gas fluxes of CO_2 and N_2 through Ba-SAPO-34 membrane as a function of pressure difference at 30 ^oC.

Figure 3 shows the effect of pressure difference on the single gas permeances through Ba-SAPO-34 membrane at 30 ^oC. Gas permeance was calculated by dividing the gas flow with pressure difference of that respective gas. The CO_2 single gas permeance decreased from ~19.5 to ~15.7×10^{-8} mol/m^2.s.Pa and the N_2 single gas permeance decreased from ~0.659 to ~0.635×10^{-8} mol/m^2.s.Pa when the pressure difference increased from 100 to 500 kPa at 30 ^oC. The drop in CO_2 gas permeance was a result of adsorption-controlled permeation mechanism reported by Bernal et al. [29]. Owing to high adsorption strength of CO_2 on Ba-SAPO-34 pore framework, feeding pure CO_2 to the membrane at temperature as low as 30 ^oC brought the surface coverage of CO_2 on the retentate side of the membrane close to saturated level. Further increase in the CO_2 pressure difference increased the CO_2 single gas flux, but the increase was not adequate to compensate for the higher increase of pressure difference, which resulted in decrease in CO_2 single gas permeance (flux per pressure difference).

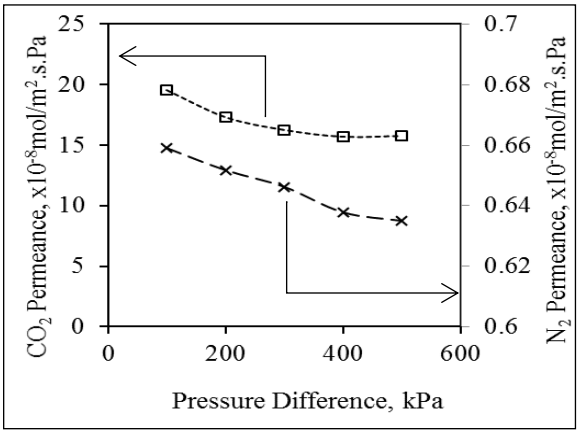


Figure 3. Single gas permeances of CO_2 and N_2 through Ba-SAPO-34 membrane as a function of pressure difference at 30 ^oC

Figures 4 and 5 shows the effect of temperature on the single gas fluxes and single gas permeances, respectively through Ba-SAPO-34 membrane at 100 kPa pressure difference. Generally, surface diffusion decreases but micropore diffusion increases with increase in temperature. In present study, the CO_2 single gas flux and permeance dropped with increase in permeation temperature from 30 to 180 ^oC due to reduction of surface coverage of CO_2 on the Ba-SAPO-34 pore framework with increase in temperature [6]. N_2 exhibited trend of rise in single gas flux and permeance with increase in temperature. This indicated that the micropore diffusion dominated the diffusion of N_2 through Ba-SAPO-34 pore framework instead of surface diffusion.

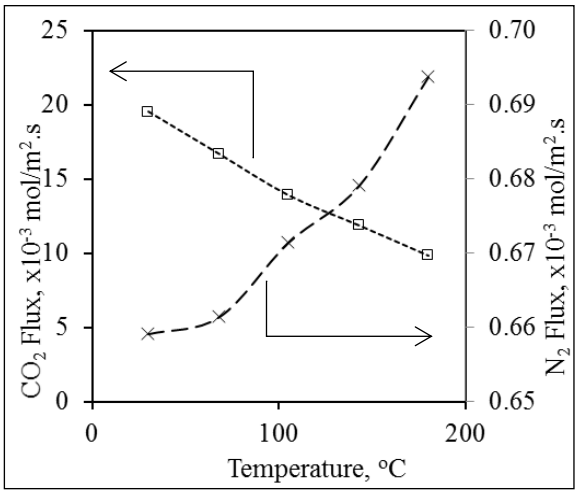


Figure 4. Single gas fluxes of CO_2 and N_2 through Ba-SAPO-34 membrane as a function of temperature at 100 kPa pressure difference across the membrane

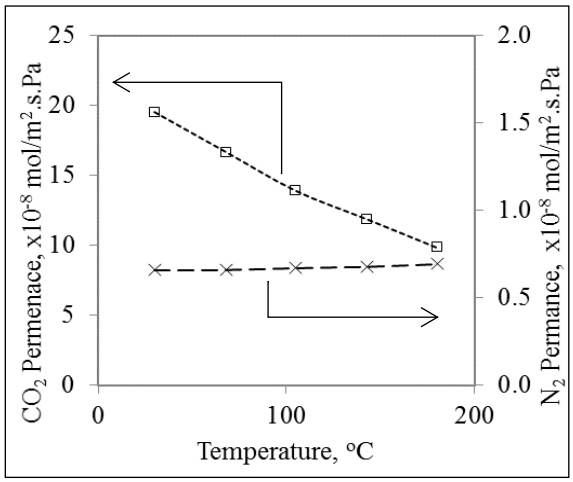


Figure 5. Single gas permeances of CO_2 and N_2 through Ba-SAPO-34 membrane as a function of temperature at 100 kPa pressure difference across the membrane

Figure 6 presents the effect of pressure difference on the CO_2/N_2 ideal selectivities through Ba-SAPO-34 membrane at different temperatures. The CO_2/N_2 ideal selectivity decreased from ~29.6 to ~24.8 with increase in pressure difference from 100 to 500 kPa at 30 ^oC. This phenomenon was due to higher extent of drop in CO_2 single gas

permeance compared to N_2 single gas permeance when the pressure difference was increased from 100 to 500 kPa as shown in Figure 3.

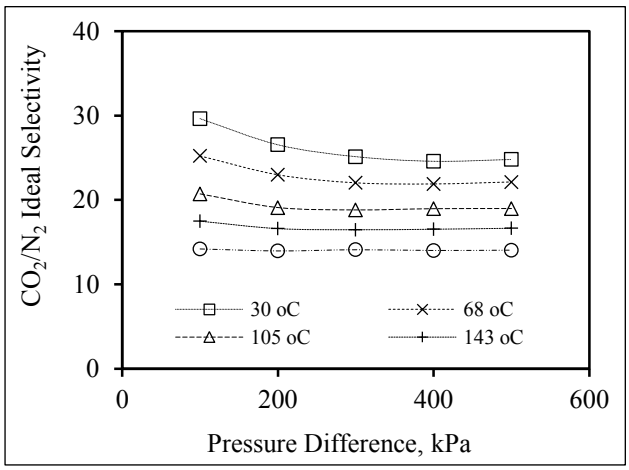


Figure 6. Ideal selectivities of CO_2/N_2 through Ba-SAPO-34 membrane as a function of pressure difference for different temperatures

As shown in Figure 6, it was found that the extent of drop in CO_2/N_2 ideal selectivities at higher temperature of 68 ^oC was lesser than the decline at 30 ^oC. As temperature was further increased to 180 ^oC, there was nearly no change in all the ideal selectivities with increase in pressure difference. This was due to the lower surface coverage of CO_2 on the membrane at higher temperature [28], which led to lower decrease in CO_2 permeances with increase in pressure difference at higher temperature. Therefore, increase in temperature from 30 to 180 ^oC resulted in the gradually dropped CO_2 adsorption strength on the membrane, and hence led to the reduced extent of change in the ideal selectivities with the change of pressure difference from 100 to 500 kPa in present study. Overally, maximum CO_2/N_2 ideal selectivity of 29.6 was obtained for gases permeation through Ba-SAPO-34 membrane at 30 ^oC and 100 kPa pressure difference.

Conclusion

Ba-SAPO-34 zeolite membrane was successfully formed by membrane synthesis process using microwave (MW) heating and followed by membrane ion-exchange process with Ba^{2+} cation. The Ba-SAPO-34 zeolite membrane was investigated for its gas permeations of CO_2 and N_2 under varying permeation temperature (30 – 180 ^oC) and pressure difference (100 – 500 kPa) across the membrane. In all of the range of permeation temperature and pressure difference studied in current study, CO_2 displayed higher single gas fluxes than N_2 due to (1) smaller kinetic diameter of CO_2 compared to N_2 and (2) stronger adsorption of CO_2 on Ba-SAPO-34 pore framework and subsequently followed by surface diffusion through the pore framework compared to N_2. Both CO_2 and N_2 single gas fluxes were found to increase with increase of pressure difference from 100 to 500 kPa. The N_2 single flux increased but the CO_2 single flux decreased with increase in permeation temperature from 30 to 180 ^oC, indicating that micropore diffusion dominated N_2 diffusion but surface diffusion dominated CO_2 diffusion through the Ba-SAPO-34 membrane in present study. CO_2 single permeance of ~9.4-19.5 x 10^{-8} mol/m^2.s.Pa and N_2 single permeance of ~0.635-0.694 x 10^{-8} mol/m^2.s.Pa were obtained for gases permeation through Ba-SAPO-34 membrane performed under the range of permeation temperature and pressure difference across the membrane studied. Maximum CO_2/N_2 ideal selectivity of 29.6 was obtained for gases permeation through Ba-SAPO-34 membrane at 30 ^oC and 100 kPa pressure difference.

Acknowledgement

The authors gratefully acknowledge the financial support received under LRGS grant (grant number: 304/PJKIMIA/6050296/U124). The financial and technical support from Universiti Teknologi PETRONAS, STIRF grant (cost centre: 0153AA-D64) and Carbon Dioxide-Mission Oriented Research (CO_2-MOR) in Universiti Teknologi PETRONAS are also acknowledged. The author thanks the guidance provided by Prof. Subhash Bhatia.

References

1. Bredesen, R., Jordal, K. and Bolland, O. (2004). High-temperature membranes in power generation with CO_2 capture. *Chemical Engineering and Processing*, 43: 1129 – 1158.
2. Favre, E. (2007). Carbon dioxide recovery from post-combustion processes: Can gas permeation membranes compete with absorption? *Journal of Membrane Science*, 294: 50 – 59.
3. Granite, E. J. and O'Brien, T. (2005). Review of novel methods for carbon dioxide separation from flue and fuel gases. *Fuel Processing Technology*, 86: 1423 – 1434.
4. Lin, H. and Freeman, B. D. (2005). Materials selection guidelines for membranes that remove CO_2 from gas mixtures. *Journal of Molecular Structure*, 739: 57 – 74.
5. Yang, H., Xu, Z., Fan, M., Gupta, R., Slimane, R. B., Bland, A. E. and Wright, I. (2008). Progress in carbon dioxide separation and capture: A review. *Journal of Environmental Sciences*, 20: 14 – 27.
6. Li, S. and Fan, C.Q. (2010). High-flux SAPO-34 membrane for CO_2/N_2 separation. *Industrial and Engineering Chemistry Research*, 49: 4399 – 4404.
7. Lu, G.Q., Diniz da Costa, J. C., Duke, M., Giessler, S., Socolow, R., Williams, R. H. and Kreutz, T. (2007). Inorganic membranes for hydrogen production and purification: A critical review and perspective. *Journal of Colloid Interface Science*, 314: 589 – 603.
8. Gray, M. L., Soong, Y., Champagne, K. J., Pennline, H., Baltrus, J. P., Stevens Jr, R.W., Khatri, R., Chuang, S. S. C. and Filburn, T. (2005). Improved immobilized carbon dioxide capture sorbents. *Fuel Processing Technology*, 86: 1449 – 1455.
9. Zheng, F., Tran, D. N., Busche, B. J., Fryxell, G. E., Addleman, R. S., Zemanian, T. S. and Aardahl, C. L. (2005). Ethylenediamine-modified SBA-15 as regenerable CO_2 sorbent. *Industrial and Engineering Chemistry Research*, 44: 3099 – 3105.
10. Fang, M., Wu, C., Yang, Z., Wang, T., Xia, Y. and Li, J. (2015). ZIF-8/PDMS mixed matrix membranes for propane/nitrogen mixture separation: Experimental result and permeation model validation. *Journal of Membrane Science*, 474: 103 – 113.
11. Shirazian, S. and Ashrafizadeh, S. N. (2015). LTA and ion-exchanged LTA zeolite membranes for dehydration of natural gas. *Journal of Industrial and Engineering Chemistry*, 22: 132 – 137.
12. Wu, T., Wang, B., Lu, Z., Zhou, R. and Chen, X. (2014). Alumina-supported AlPO-18 membranes for CO_2/CH_4 separation. *Journal of Membrane Science*, 471: 338 – 346.
13. Lee, I. and Jeong, H.-K. (2011). Synthesis and gas permeation properties of highly b-oriented MFI silicalite-1 thin membranes with controlled microstructure. *Microporous and Mesoporous Material*, 141: 175 – 183.
14. Michalkiewicz, B. and Koren, Z. C. (2015). Zeolite membranes for hydrogen production from natural gas: State of the art. *Journal of Porous Materials*, 22: 635 – 646.
15. Das, N., Kundu, D. and Chatterjee, M. (2010). The effect of intermediate layer on synthesis and gas permeation properties of NaA zeolite membrane. *Journal of Coatings Technology and Research*, 7: 383 – 390.
16. Himeno, S., Tomita, T., Suzuki, K., Nakayama, K., Yajima, K. and Yoshida, S. (2007). Synthesis and permeation properties of a DDR-type zeolite membrane for separation of CO_2/CH_4 gaseous mixtures. *Industrial and Engineering Chemistry Research*, 46: 6989 – 6997.
17. Li, S., Zong, Z., James Zhou, S., Huang, Y., Song, Z., Feng, X., Zhou, R., Meyer, H. S. and Carreon, M.A. (2015). SAPO-34 membranes for N_2/CH_4 separation: Preparation, characterization, separation performance and economic evaluation. *Journal of Membrane Science*, 487: 141 – 151.
18. Sato, K., Sugimoto, K., Sekine, Y., Takada, M., Matsukata, M. and Nakane, T. (2007). Application of FAU-type zeolite membranes to vapor/gas separation under high pressure and high temperature up to 5 MPa and 180 °C. *Microporous and Mesoporous Materials*, 101: 312 – 318.
19. Sebastián, V., Kumakiri, I., Bredesen, R. and Menéndez, M. (2007). Zeolite membrane for CO_2 removal: Operating at high pressure. *Journal of Membrane Science*, 292: 92 – 97.

20. Hong, M., Li, S., Falconer, J. L. and Noble, R. D. (2008). Hydrogen purification using a SAPO-34 membrane. *Journal of Membrane Science*, 307: 277 – 283.
21. Tian, Y., Fan, L., Wang, Z., Qiu, S. and Zhu, G. (2009). Synthesis of a SAPO-34 membrane on macroporous supports for high permeance separation of a CO_2/CH_4 mixture. *Journal of Material Chemistry*, 19: 7698 – 7703.
22. Motuzas, J., Julbe, A., Noble, R. D., van der Lee, A. and Beresnevicius, Z. J. (2006). Rapid synthesis of oriented silicalite-1 membranes by microwave-assisted hydrothermal treatment. *Microporous and Mesoporous Materials*, 92: 259 – 269.
23. Li, Y. and Yang, W. (2008). Microwave synthesis of zeolite membranes: A review. *Journal of Membrane Science*, 316: 3 – 17.
24. Zhu, G., Li, Y., Zhou, H., Liu, J. and Yang, W. (2008). FAU-type zeolite membranes synthesized by microwave assisted in situ crystallization. *Material Letters*, 62: 4357 – 4359.
25. Chew, T., Ahmad, A. L. and Bhatia, S. (2011). Rapid synthesis of thin SAPO-34 membranes using microwave heating. *Journal of Porous Materials*, 18: 355 – 360.
26. Chew, T. L., Ahmad, A. L. and Bhatia, S. (2011). Ba-SAPO-34 membrane synthesized from microwave heating and its performance for CO_2/CH_4 gas separation. *Chemical Engineering Journal*, 71: 1053 – 1059.
27. Poshusta, J. C., Noble, R. D. and Falconer, J. L. (1999). Temperature and pressure effects on CO_2 and CH_4 permeation through MFI zeolite membranes. *Journal of Membrane Science*, 160: 115 – 125.
28. Li, S., Falconer, J. L. and Noble, R. D. (2008). SAPO-34 membranes for CO_2/CH_4 separations: Effect of Si/Al ratio. *Microporous and Mesoporous Materials*, 110: 310 – 317.
29. Bernal, M. P., Coronas, J., Menéndez, M. and Santamaría, J. (2004). Separation of CO_2/N_2 mixtures using MFI-Type zeolite membranes. *AIChE Journal*, 50: 127 – 135.

Malaysian Journal of Analytical Sciences, Vol 20 No 6 (2016): 1405 - 1412
DOI: http://dx.doi.org/10.17576/mjas-2016-2006-20

MALAYSIAN JOURNAL OF ANALYTICAL SCIENCES
Published by The Malaysian Analytical Sciences Society
ISSN 1394 - 2506

INFLUENCE OF HIGHLY CONCENTRATED SODIUM HYDROXIDE (NaOH) TOWARDS FORMATION OF HIGHLY ORDERED TIO_2 NANOTUBES (TNT) STRUCTURE

(Pengaruh Kepekatan Sodium Hidrosida (NaOH) yang Tinggi terhadap Pembentukan Struktur Bertertib Nanotiub TiO_2 (TNT))

Masturah Abdullah[1] and Siti Kartom Kamarudin[1, 2]*

[1]*Fuel Cell Institute*
[2]*Department of Chemical and Process Engineering, Faculty of Engineering and Built Environment*
Universiti Kebangsaan Malaysia, 43600 UKM Bangi, Selangor, Malaysia

**Corresponding author: ctie@vlsi.eng.ukm.my*

Received: 21 October 2015; Accepted: 14 June 2016

Abstract

In this study, titanium dioxide nanotubes (TNT) were synthesis according to different concentration of sodium hydroxide (NaOH). The main purpose of this study was to investigate the effect of the high concentration NaOH towards formation of TiO_2 nanotubes structure. TNT was synthesized via hydrothermal method that was performed in a Teflon line stainless steel autoclave by using different concentration of NaOH (6 M to 12 M). The hydrothermal time and temperature is placed constantly for 24 hours and 110 ^oC respectively. The characterization of TNT was performed by Field Emission Transmission Electron Microscopy (FESEM), X-ray Diffraction (XRD), Fourier Transform Infrared Spectroscopy (FTIR) and Energy Dispersive X-ray (EDX) analysis for better understanding of its nanotubes structure and the chemical bonding present. Based on characterization analysis, the formation of nanotubes was in systematic arrangement and makes it easier for loading of noble catalyst. Furthermore, the replacement of sodium content by hydrogen ion, H^+ also seem to be increasing after the acid washing treatment. The investigation result proven that the best concentration of NaOH for TiO_2 nanotubes formation was 10 M (TNT-10).

Keywords: TiO_2 nanotubes, hydrothermal reaction, concentration of sodium hydroxide

Abstrak

Melalui kajian ini, nanotiub titanium dioksida disintesiskan mengikut kepekatan sodium hidrosida (NaOH) yang berbeza. Tujuan utama kajian ini adalah untuk mengkaji kesan kepekatan NaOH yang tinggi terhadap pembentukan struktur nanotiub. Nanotiub titanium dioksida (TNT) dihasilkan dengan menggunakan kaedah hidrotermal menggunakan turus teflon autoklaf keluli anti karat dengan mempelbagaikan kepekatan NaOH (6 M hingga 12 M). Tempoh dan suhu proses hidrotermal masing-masing dibiarkan sekata selama 24 jam dan 110 ^oC. Pencirian TNT dijalankan dengan menggunakan Mikroskopi Elektron Pengimbasan Pancaran Medan (FESEM), Pembelauan Sinar X (XRD), Spektroskopi Inframerah Transformasi Fourier (FTIR) dan Tenaga Serakan Sinar X (EDX) bagi memahami dengan lebih mendalam mengenai struktur nano dan juga ikatan kimia yang wujud. Berdasarkan analisis yang dijalankan, didapati nanotiub berada dalam keadaan yang sistematik dan memudahkan penempatan pemangkin adi. Tambahan pula, penggantian kandungan sodium oleh H^+ juga meningkat selepas proses pembasuhan menggunakan asid. Keputusan ujikaji menunjukkan kepekatan 10 M (TNT-10) adalah yang terbaik bagi menghasilkan nanotiub TiO_2.

Kata kunci: nanotiub TiO_2, tindak balas hidrotermal, kepekatan sodium hidroksida

Introduction

Since the discovery of carbon nanotubes (CNT) in 1990s, researchers are eager to find and develop more nanotubular structures with different types of materials that can be used for variable purpose. Due to over corrosive of carbon based materials, it seems to be less interesting for catalytic application and alternative materials is needed for overcoming the crucial problem. Titanium dioxide nanotubes (TNT) are one of the exclusive nanomaterial with nanotubular shape that can provide large surface area for deposition of noble catalyst in catalytic system. Moreover, the non-corrosive, environmentally friendly and inexpensive materials are the factors that make it interesting for TNT to be suitable candidate among other nanostructure materials. The strong metal support and high-stability in elevated temperature make it more preferable as potential nanostructure for various applications in science and technology field. TNT is promising nanomaterial due to its high properties that suitable for various applications in fuel cell technology, solar cell, storage energy material [1] and also gas sensing properties [2]. TNT receives numerous attention in fuel cell technology as different roles for each type of fuel cell including as catalyst support for main catalyst [3-6], photocatalyst [7-10], gas sensor [2,11,12] and composite membrane [13,14]. For the synthesized method, TiO_2 nanotubes can be produced via three common methods: (i) electrochemical anodization, (ii) template assisted and (iii) hydrothermal method. Anodization employs the using of power source for obtaining steady current in which longer nanotubes were achieved with larger anodization voltage [15]. However, the higher fabrication cost make it less ideal as the best method for synthesizing TNT.

Template assisted method can be performed by using stabilize template that was already in tube form and nanotubes was grown by using chemical vapor deposition (CVD) system [16] but due to the product that was hard to remove and may damage the structure of nanotubes itself make it less favorable among researchers as it can waste the materials itself. For hydrothermal method, it is more favorable due to lower apparatus cost and high quality products [17] but limit by long operation hours which is take for 24 hours or longer for a complete hydrothermal reaction. Furthermore, in hydrothermal method, a highly concentrated NaOH (10 M ~ 11 M) was used for producing highly nanostructure nanotubes together with TiO_2 (Degussa P25) powder. Nanotubes of titanium dioxide from hydrothermal method was firstly reported in 1998 by Kasuga et al. [18] with large surface area of 400 m^2/g and afterward research was still undergoing after that year for better quality of TiO_2 nanotubes by the same person [19,20]. In this research, hydrothermal method was applied in fabrication process of TiO_2 nanotubes and the brief method was discussed in the next section below.

Materials and Methods

Materials

For hydrothermal process, TiO_2 (P25 Degussa) powder with particle size of 21 nm was obtained from Sigma-Aldrich and NaOH in pellet form was purchased from Macron-USA. Hydrochloric acid with purity of 36.5 – 38% was purchased from J.T. Baker-USA for washing purpose to remove Na^+ ions.

Synthesis of TiO_2 nanotubes

Hydrothermal method was used in the synthesis process of TNT. The synthesis of TiO_2 nanotubes was started by mixing 50 ml of highly concentrated solution of NaOH varied from 6 M to 12 M with TiO_2 powder (3.0 g) and stirred for two hours to allow dispersion. After that, the hydrothermal reaction was performed by using Teflon line stainless steel autoclave at 110 ^oC for 24 hours. Next, the solution was collected and undergone washing process by using 0.1 M HCl and deionized water until pH 7. The crystal sample was then filtered and dried overnight at 80 ^oC in order to obtain pure product of TNT. Lastly, the TiO_2 nanotubes in powder form were obtained by undergoing calcinations process at 400 ^oC for 2 hours. The sample was then labeled as TNT-6, TNT-8, TNT-10 and TNT-12 based on the concentration of NaOH used which are 6 M, 8 M, 10 M and 12 M. The prepared samples were then characterized by FESEM, FTIR, EDX and XRD analysis for knowing the morphology, sodium content, crystal and bonding structure of TiO_2 nanotubes.

Characterization of TiO_2 nanotubes

The morphology structure of TiO_2 nanotubes was viewed by field emission scanning electron microscopy (FESEM) analysis. The structure of TiO_2 nanotubes (TNT) and chemical bonding present in the sample were examined by using X-ray diffraction (XRD) and Fourier Transform Infrared Spectroscopy (FTIR) analysis. The sodium content

was obtained from Energy dispersive x-ray (EDX) analysis. The data was then analyzed for further understanding of its nanostructure.

Results and Discussion

In hydrothermal method, TiO_2 nanotubes was obtained during the reaction of high concentration of NaOH and pure TiO_2 powder in Teflon line stainless steel autoclave. The process of TiO_2 nanotubes generation can be defined by sequence reaction step below:

i) High concentrated alkaline reaction

At the first reaction step, the high concentrated of NaOH (alkaline solution) will reacted with TiO_2 powder at temperature of 110°C for 24 hours. The sodium titanate ($Na_2Ti_2O_5.H_2O$) was the main product.

$$2TiO_2 + 2NaOH \longrightarrow Na_2Ti_2O_5.H_2O \quad (1)$$

ii) Replacement of Na^+ to H^+

The hydrogenotitanate was formed during the ion exchange between Na^+ and H^+ that happened during the acid wash treatment.

$$Na_2Ti_2O_5.H_2O + xH^+ \longrightarrow HxNa_{2-x}Ti_2O_5.H_2O + xNa^+, \quad (0 \leq x \leq 2) \quad (2)$$

iii) Dehydration process

The dehydration process is carried out by undergone drying process at 80 °C and followed by calcination process at high temperature for two hours. The reaction consists of two steps which can be seen below:

$$H_2Ti_2O_5.H_2O \longrightarrow H_2Ti_2O_5 + H_2O \quad (3)$$
$$H_2Ti_2O_5 \longrightarrow 2TiO_2 + H_2O \quad (4)$$

Field emission scanning electron microscopy (FESEM)

The morphology structure of TiO_2 nanotubes was viewed by field emission electron microscopy (FESEM). Figure 1 shown the image of TNT by FESEM as the hydrothermal product with different concentration of sodium hydroxide used (6 M, 8 M, 10 M and 12 M). From the image, it can be seen that only TNT-10 shown the complete structure of nanotubes TiO_2 with random alignment. The nanotubes were likely formed in overlapping with each other. Furthermore, the smooth and well-forming shape of TNT can be seen clearly. The nanotubes structure of TNT-6 was not discovered but instead of aggregated solid granules of TiO_2 nanoparticles was detected. This formation was due to the fact that at low concentration (< 6 M), the rate of Ti ion diffusion was too low with low alkaline solution. As for TNT-8, the early stage formation of TNT can be seen with non-complete tube-structure with agglomerate product formed [21]. As for TNT-12, the tube structure was disappeared and amorphous nanoparticles was discovered. This result can be correlated with Huang et al. [22] that also get the same result in which at too high concentration of NaOH, the amorphous particle is formed. During that condition, the alkaline solution tend to be very viscous and thus limited the diffusion of Ti (IV) ion (equation 1) due to the dissolution of Titania precursor. Besides, the crystallite titanate formed are said to be unstable in extreme condition (high alkaline solution) and decomposition rate of the crystallite titanate was faster. From this analysis, we can say that the concentration of NaOH was strongly influenced the formation of nanotubes TiO_2. As the concentration of alkaline solution was low (< 6 M), the nanotubes structure does not form instead of nanogranules generated while at too high concentration of alkaline solution, the amorphous nanoparticles was discovered with packed agglomerate. The best condition of synthesis TiO_2 nanotubes was 10 M.

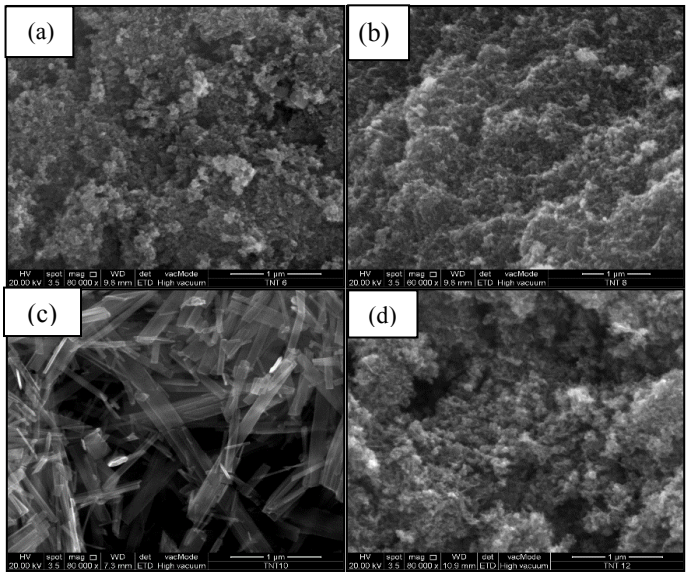


Figure 1. FESEM images of TNT after hydrothermal reaction at scale of 1 μm: (a) 6 M, (b) 8 M, (c) 10 M and (d) 12 M

X-ray diffraction (XRD)

The nanostructure of TiO_2 nanotubes was characterized by using X-ray diffraction (XRD) that were scanned from 10° to 90° at 2θ. Figure 2 illustrated the XRD pattern of titanium dioxide nanotubes that were fabricated by using different concentration of NaOH during hydrothermal treatment. Based on the XRD spectrum, the anatase peak of TiO_2 nanotubes for all concentrations can be detected at $2\theta = 25^o$, 37° and 47° which mark as "A" and rutile phase at $2\theta = 27^o$, 36° and 41° which mark as "R". The result indicated that there is mixture of both anatase and rutile phases in the TiO_2 nanotubes for all types of concentration used. The XRD pattern for TNT-6 and TNT-12 exhibit the same pattern while TNT-8 and TNT-10 show a bit different pattern with almost same properties. Both TNT-8 and TNT-10 gave the highest intense peak around d_{110} (25°) which means that the strong peak of TiO_2 nanotubes. In another word, it can be said that there are larger amount of Ti-O nanotubes bond at the peak compared to another two samples. The intense peak at d_{110} (25°) shown that there is interlayer spacing in tetragonal system with lattice constant value tabulated in Table 1. Moreover, the intense peak at d_{110} (25°) also decrease when approaching d_{600} peak (27.4^o). This proven that there was loss of water molecule during the dehydration process. The crystallite size for TNT-6, TNT-8, TNT-10 and TNT-12 were 140.2 A, 143.7 A, 137 A and 81.4 A respectively. Moreover, the relative ratio of d_{110}/d_{600} peaks can determined the content of Na^+ and was presented in Table 1 [23]. The ratio of d_{110}/d_{600} in Table 1 was seem to be increase as the theta increase which indicated that the Na+ content was decreased because of the replacement of Na^+ by H^+ was happened during the acid washing treatment after the hydrothermal treatment [4]. XRD analysis suggested that the TNT-8 and TNT-10 exhibit almost similar properties to TiO_2 nanotubes by previous studies [3, 4, 23, 24].

Table 1. XRD data for TiO_2 nanotubes

Lattice Constant	d_{110} (25°)	d_{600} (27.4^o)	d_{110}/d_{600}
a	3.872	4.6257	0.84
b	3.872	4.6257	0.84
c	9.616	2.9806	3.23

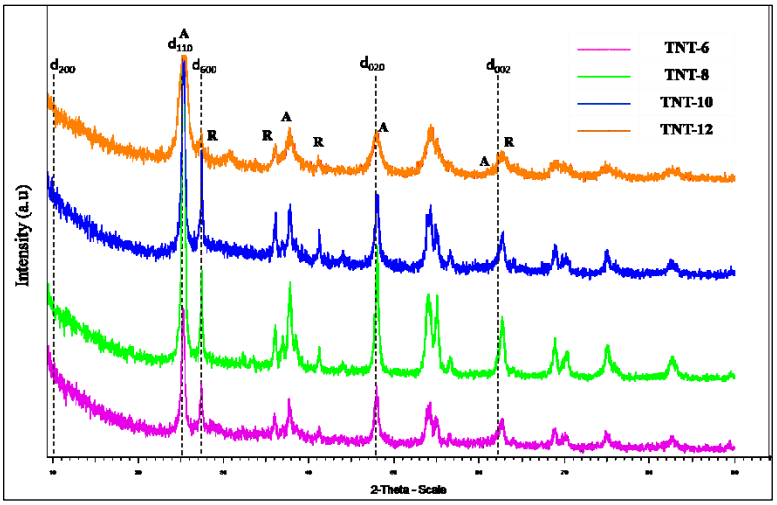


Figure 2. XRD spectrum for TNT-6, TNT-8, TNT-10 and TNT-12

Fourier transform infrared spectroscopy (FTIR)

The chemical bonding structure of prepared sample was checked by using FTIR analysis. Figure 3 present the FTIR spectra for TNT-6, TNT-8, TNT-10 and TNT-12. At 3200 to 3400 cm^{-1} wavenumbers, the strong intensity peak was discovered which ensured that there was O-H bond (hydroxyl group) present for all NaOH concentrations [5]. This result shows that there was large amount of O-H group on the surface of TiO_2 nanotubes due to stretching mode of Ti-OH bond. The sample TNT-10 exhibits the greatest vibrational modes for OH groups. Besides, the strong peaks were also discovered at 1400 to 1600 cm-1 which corresponds to the TiO_2 nanotubes bond that was present [6]. For TNT-12, the peak at this point was not strong enough as it shown the lowest peak among another three samples. This is compatible with the previous analysis (FESEM and XRD) as there were no nanotubes detected instead of amorphous nanoparticles TiO_2 was detected. The discovery of TiO_2 nanotubes bond was also due to the fact that the Ti-O planes was started to scroll to be nanotubes and give rise to site of bronsted acid and at the same time, it tend to modify the Lewis acid site rapidly [25]. In general, pure TiO_2 which in anatase, rutile and brookite phase, Lewis acid site was majorly in it but after NaOH concentration was take into the pure TiO_2, the bronsted acid site was formed directly. As the larger bronsted acid site generated, better nanostructure of TiO_2 nanotubes was achieved and formed. The large amount of O-H group in the TiO_2 nanotubes can be enhance for the purpose of the deposition of metal particles that ease the process of the dispersion and conjunction of the particles in the nanotubes surface. As overall, it can be said that the 10 M (TNT-10) concentration of NaOH was the best result as it has the highest peak intensity for both types of functional group which are hydroxyl group and TiO_2 nanotubes. The result totally suggests that the formation of TiO_2 nanotubes was influenced by the concentration of NaOH used during the hydrothermal reaction.

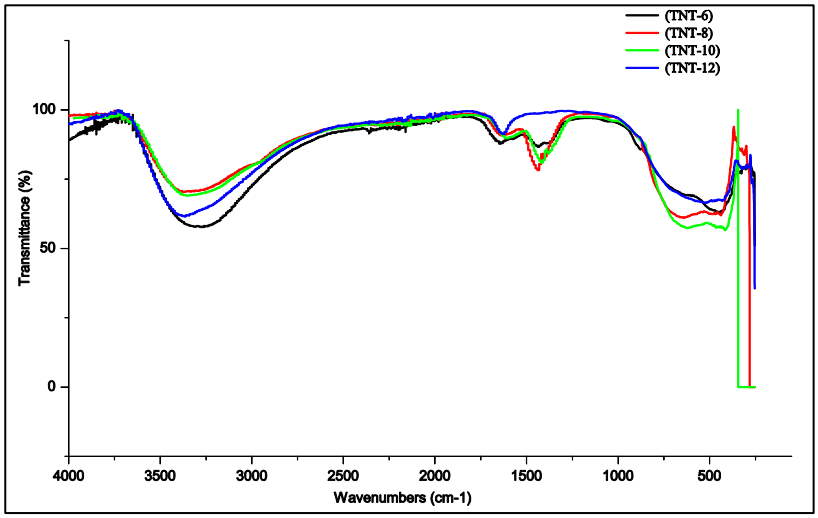


Figure 3. FTIR analysis for TNT-6, TNT-8, TNT-10 and TNT-12

Energy dispersive X-ray (EDX)

The energy dispersive x-ray (EDX) analysis was studied to determine the sodium content in TiO_2 nanotubes. The EDX pattern of various TNTs synthesized can be seen in Figure 4. The amount of Ti, O and Na was obtained in atomic percentage. The atomic ratio of Na to Ti was calculated and shown in Figure 5. Based on the bar chart in Figure 5, TNT-10 presented the lowest value (0.0504) of atomic ratio Na/Ti which directly indicated that many sodium ions was replaced by hydrogen ions during acid washing process with HCl. The loss of Na+ could enhance the rolling process of TiO_2 nanosheet into TiO_2 nanotubes. As for TNT-12, it shown highest value (0.1511) of atomic ratio which means that there is still huge amount of sodium ions even after ther acid washing process which also conjugated that there was least amount of TiO_2 nanotubes formed during hydrothermal reaction. The result can be correlated with FESEM analysis as we can see that as amorphous nanoparticle TiO_2 was generated instead of TiO_2 nanotubes for TNT-12. The lower amount of sodium ions, the higher amount of H+ ions was replaces during ion exchange process. When this condition happened, it will tend to increase the process of TiO_2 nanosheet rolling into TiO_2 nanotubes [23]. The result from EDX was compatible with the previous analysis and ensured that TNT-10 shown the greatest feature of nanotubes.

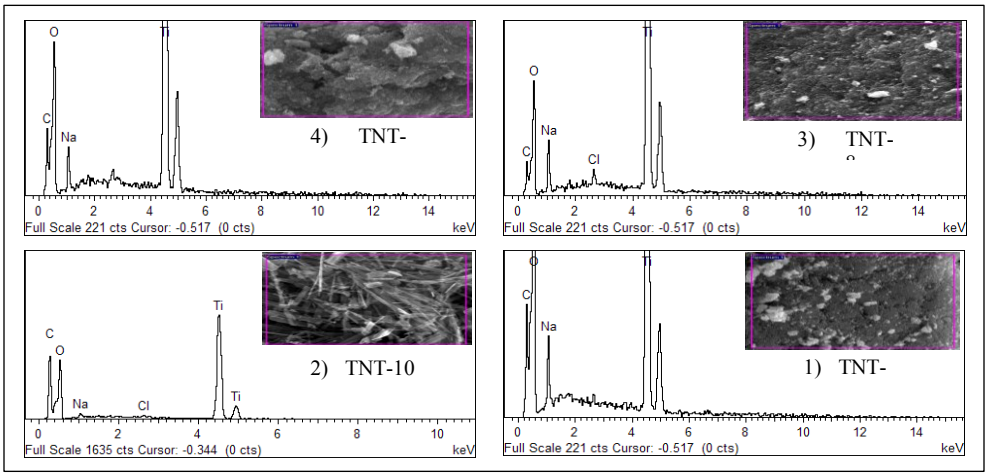


Figure 4. EDX pattern of various TNT synthesized

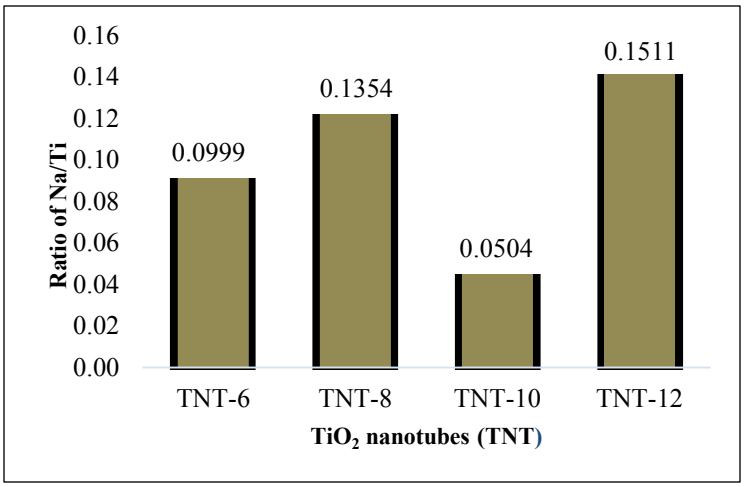


Figure 5. Value of atomic ratio of Na/Ti

Conclusion

The formation of TiO_2 nanotubes was successfully investigated by using different types of NaOH concentration (6 M, 8 M, 10 M and 12 M) during hydrothermal reaction. The effect of NaOH concentration was analyzed by using FESEM, XRD, FTIR and EDX analysis. Based on the four analysis, TNT-10 shown the best performance based on the FTIR, FESEM and EDX analysis while TNT-8 and TNT-10 was the best sample based on XRD analysis as it leads with high properties of TiO_2 nanotubes. In FESEM, only TNT-10 shown the greatest formation of TiO_2 nanotubes with clearly structure while for another samples do not show any clear tube formation. For FTIR analysis, the broad and strong vibrational peak was discovered on TNT-10 while for EDX analysis, the least amount of atomic ratio Na/Ti was obtained in TNT-10 sample which indicated that more Na+ ion was replaced by H+ ion during acid wash process with HCl. The result also suggests that the formation of TiO_2 nanotubes was strictly affected by the concentration of NaOH used in fabrication process during the hydrothermal reaction take places. The suitable concentration of NaOH for synthesized TiO2 nanotubes was 10 M which in moderate concentration. Too low concentration of alkaline solution does not help the TNT formation while too high concentration of alkaline solution lead to rupture structure of TiO_2 nanotubes with amorphous nanoparticle detected.

Acknowledgement

The authors gratefully acknowledge financial support for this work by Universiti Kebangsaan Malaysia under Grant No.: GUP-2014-071 and Malaysian of Education (MOE) for LRGS/2013/UKM-UKM/TP/01.

References

1. Kim, J. H., Kang, H. K., Woo, S. G., Jeong, G., Park, M. S., Kim, K. J., Yu, J. S., Yim, T., Jo, Y. N., Kim, H. and Zhu, K. (2014). Oriented TiO_2 nanotubes as a lithium metal storage medium. *Journal of Electroanalytical Chemistry*, 726: 51 – 54.
2. Perillo, P. M. and Rodriguez, D. F. (2012). The gas sensing properties at room temperature of TiO_2 nanotubes by anodization. *Sensors and Actuators B: Chemical*, 171: 639 – 643.
3. Abida, B., Chirchi, L., Baranton, S., Napporn, T. W., Kochkar, H., Léger, J. M. and Ghorbel, A. (2011). Prepar ation and characterization of Pt/TiO_2 nanotubes catalyst for methanol electro-oxidation. *Applied Catalysis B: Environmental*, 106(3): 609 – 615.
4. Abida, B., Chirchi, L., Baranton, S., Napporn, T. W., Morais, C., Léger, J. M. and Ghorbel, A. (2013). Hydroge notitanates nanotubes supported platinum anode for direct methanol fuel cell. *Journal of Power Sources*, 241: 429 – 439.
5. Dong, B., He, B. L., Chai, Y. M. and Liu, C. G. (2010). Novel Pt nanoclusters/titanium dioxide nanotubes composites for hydrazine oxidation. *Materials Chemistry and Physics*, 120: 404 – 408.

6. Dong, B., He, B. L., Huang, J., Gao, G. Y., Yang, Z. and Li, H. L. (2008). High dispersion and electrocatalytic activity of Pd/titanium dioxide nanotubes catalysts for hydrazine oxidation. *Journal of Power Sources*, 175(1): 266 – 271.
7. Gan, Y. X., Gan, B. J. and Su, L. (2011). Biophoto fuel cell anode containing self-organized titanium dioxide nanotube array. *Materials Science and Engineering: B*, 176(15): 1197 – 1206.
8. Liang, H-C., Li, X-Z. and Nowotny, J. (2010). Photocatalytical properties of TiO_2 nanotubes. *Solid State Phenomena*, 162: 295 – 328.
9. Sun, Y., Wang, G. and Yan, K. (2011). TiO_2 nanotubes for hydrogen generation by photocatalytic water splitting in a two-compartment photoelectrochemical cell. *International Journal of Hydrogen Energy*, 36(24): 1 5502 – 15508.
10. Sun, Y. and Yan, K. P. (2014). Effect of anodization voltage on performance of TiO 2 nanotube arrays for hydrogen generation in a two-compartment photoelectrochemical cell. *International Journal of Hydrogen Energy,* 39: 11368 – 11375.
11. Han, C. H., Hong, D. W., Kim, I. J., Gwak, J., Han, S. D. and Singh, K. C. (2007). Synthesis of Pd or Pt/ titanate nanotube and its application to catalytic type hydrogen gas sensor. *Sensors and Actuators B: Chemical*, 128(1): 320 – 325.
12. Lee, J., Kim, D. H., Hong, S. H. and Jho, J. Y. (2011). A hydrogen gas sensor employing vertically aligned TiO_2 nanotube arrays prepared by template-assisted method. *Sensors and Actuators B: Chemical*, 160(1): 1494 – 1498.
13. Jun, Y., Zarrin, H., Fowler, M. and Chen, Z. (2011). Functionalized titania nanotube composite membranes for high temperature proton exchange membrane fuel cells. *International Journal of Hydrogen Energy*, 36(10): 6073 – 6081.
14. Matos, B. R., Isidoro, R. A., Santiago, E. I., Tavares, A. C., Ferlauto, A. S., Muccillo, R. and Fonseca, F. C. (2015). Nafion–titanate nanotubes composites prepared by in situ crystallization and casting for direct ethanol fuel cells. *International Journal of Hydrogen Energy*, 40(4): 1859 – 1867.
15. Song, H., J. Shang, and C. Suo (2015). Fabrication of TiO_2 nanotube arrays by rectified alternating current anodization. *Journal of Materials Science & Technology*, 31(1): 23 – 29.
16. Karaman, M., Sarıipek, F., Köysüren, Ö. and Yıldız, H. B. (2013). Template assisted synthesis of photocatalytic titanium dioxide nanotubes by hot filament chemical vapor deposition method. *Applied Surface Science*, 283: 993 – 998.
17. Ju, J., Shi, Y. and Wu, D. (2012). TiO_2 nanotube supported Pd-Ni catalyst for methanol electro-oxidation. *Powder Technology*, 230: 252 – 256.
18. Kasuga, T., Hiramatsu, M., Hoson, A., Sekino, T. and Niihara, K. (1998). Formation of titanium oxide nanotube. *Langmuir*, 14(12): 3160 – 3163.
19. Kasuga, T. (2006). Formation of titanium oxide nanotubes using chemical treatments and their characteristic properties. *Thin Solid Films*, 496(1): 141 – 145.
20. Kasuga, T., Hiramatsu, M., Hoson, A., Sekino, T. and Niihara, K. (1999). Titania nanotubes prepared by chemical processing. *Advanced Materials*, 11(15): 1307 – 1311.
21. Liu, W., Sun, W., Han, Y., Ahmad, M. and Ni, J. (2014). Adsorption of Cu (II) and Cd (II) on titanate nanomaterials synthesized via hydrothermal method under different NaOH concentrations: Role of sodium content. *Colloids and Surfaces A: Physicochemical and Engineering Aspects*, 452: 138 – 147.
22. Huang, J., Cao, Y., Deng, Z. and Tong, H. (2011). Formation of titanate nanostructures under different NaOH concentration and their application in wastewater treatment. *Journal of Solid State Chemistry*, 184(3): 712 – 719.
23. Sui, X. L., Wang, Z. B., Li, C. Z., Zhang, J. J., Zhao, L. and Gu, D. M. (2014). Effect of pH value on $H_2Ti_2O_5$/ TiO_2 composite nanotubes as Pt catalyst support for methanol oxidation. *Journal of Power Sources*, 272: 196 – 202.
24. Sui, X. L., Wang, Z. B., Yang, M., Huo, L., Gu, D. M. and Yin, G. P. (2014). Investigation on C–TiO 2 nanotubes composite as Pt catalyst support for methanol electrooxidation. *Journal of Power Sources*, 255: 43 – 51.
25. Camposeco, R., Castillo, S., Mejia-Centeno, I., Navarrete, J. and Gómez, R. (2014). Effect of the Ti/Na molar ratio on the acidity and the structure of TiO_2 nanostructures: Nanotubes, nanofibers and nanowires. *Materials Characterization*, 90: 113 – 120.

Malaysian Journal of Analytical Sciences, Vol 20 No 6 (2016): 1413 - 1420
DOI: http://dx.doi.org/10.17576/mjas-2016-2006-21

MALAYSIAN JOURNAL OF ANALYTICAL SCIENCES
Published by The Malaysian Analytical Sciences Society
ISSN 1394 - 2506

EFFECT OF pH ON FLUX DECLINE DURING FRACTIONATION OF GLUCOSE FROM CELLULOSE HYDROLYSATE THROUGH A POLYSULFONE MEMBRANE

(Kesan pH pada Penurunan Fluks bagi Pemeringkatan Glukosa daripada Hidrolisis Selulosa Melalui Membran Polisulfon)

Masniroszaime Md Zain and Abdul Wahab Mohammad*

Department of Chemical Engineering and Process, Faculty of Engineering and Built Environment, Universiti Kebangsaan Malaysia, 43600 UKM Bangi, Selangor, Malaysia

**Corresponding author: drawm@ukm.edu.my*

Received: 21 October 2015; Accepted: 14 June 2016

Abstract

Concentrating glucose after enzymatic hydrolysis of lignocellulosic biomass is an important step in order to prepare the stream to undergo the fermentation process. However, glucose itself can be inhibitor for the enzymatic hydrolysis, hence in situ glucose removal is recommended. Ultrafiltration represents a promising procedure for isolation of enzymes from hydrolysate and for the removal of glucose. One of the obstacles in successfully utilizing ultrafiltration's membranes has been due to the membrane fouling. The flux behavior of polysulfone (PSF) membrane was studied in concentrating glucose from cellulose hydrolysate during dead end ultrafiltration. Different pH of solutions was used and Kumar's model was applied to analyse the fouling mechanism. The minimum fouling was obtained at pH solution above the IEP due to protein-protein and membrane-protein repulsions alleviating aggregation and fouling. Cake formation blocking was identified as the dominant mechanism for flux decline.

Keywords: enzyme hydrolysis, lignocellulosic biomass, ultrafiltration, polysulfone, fouling

Abstrak

Pemekatan glukosa selepas hidrolisis enzim bagi penghasilan bioetanol daripada biojisim lignoselulosa merupakan langkah yang penting bagi penyediaan untuk proses fermentasi selanjutnya. Penuras ultra menjadi pilihan bagi kaedah yang berpotensi untuk penyekatan enzim dan penyingkiran glukosa daripada larutan hidrolisis. Namun, salah satu rintangan bagi penggunaan maksima bagi penuras ultra adalah kotoran. Kriteria fluks bagi membran polisulfon di kaji dari pemekatan glukosa oleh larutan hidrolisis selulosa di penuras ultra hujung mati. Larutan yang berlainan pH digunakan untuk mengkaji profil fluks dan model Kumar digunakan untuk menganalisis mekanisma kotoran. Kotoran yang minima diperolehi pada larutan yang mempunyai pH yang lebih tinggi daripada nilai titik isoelektrik larutan hidrolisis. Halangan pembentukan kek telah dikenalpasti sebagai mekanisma yang dominan bagi pengurangan fluks.

Kata kunci: hidrolisis enzim, biojisim lignoselulosa, penuras ultra, polisulfon, kotoran

Introduction

Biorenewable products from lignocellulosic biomass has been the focus of attention around the world due to the depletion of petroleum derived product and its advantages of environmental friendly, cheap and widely available [1,2]. The main routes to produce fuels from biomass requires three major steps (1) pretreatment to delignify and

liberates cellulose and hemicelluloses from the matrix, (2) enzymatic hydrolysis to depolymerize carbohydrate polymers to release free sugars, and (3) fermentation [3]. The streams resulted from the pretreatment and enzymatic hydrolysis contains dilute sugars, along with excess components such as enzymes and biomass. The sugars released from hydrolysis may inhibit enzyme significantly, hence retarding the rate of enzymatic degradation [4,5]. In order to increase the conversion of enzymatic hydrolysis, the removal and concentration of the sugars from the hydrolysate can contribute towards not only in improving the hydrolysis but also in recovering the used enzymes. This can help to decrease the cost of enzymatic hydrolysis by reducing the consumption of enzyme [6,7].

Ultrafiltration (UF) membrane process provided an opportunity for retaining the free enzyme from discharge with the effluent after hydrolysis while at the same time separating the glucose for the subsequent fermentation process. The application of ultrafiltration membranes in biorefinery as an integrated process widens the scope of possible operating strategies, such as product removal and enzyme recycling to reduce the enzyme costs and enhance the hydrolysis [8]. The main drawback have been noted with the reduction of permeate flux over time in ultrafiltration, caused by the accumulation of feed component in the membrane porous structure, chemical interaction between solutes and membrane materials on the membrane surface. These macromolecules especially the polysaccharides caused the decrease in the permeate flow through the membrane which can be attributed to the fouling of its surface where the non-permeating solutes tending to form a gel layer [9,10].

A number of studies have shown that ultrafiltration is feasible to recover the enzymes and at the same time remove the fermentable sugars. However, limited study has been conducted on fouling characteristics and mechanism of cellulose hydrolysate and the effects of pH. For this study, a hydrophilic type membrane, polysulfone (PSF) with 20kDa MWCO was employed in a dead-end UF filtration mode. The influence of solution's pH and permeate flux was studied and the mechanism of fouling was modeled using Kumar's model.

Membrane blocking model was adopted by Kumar et al. [11], which was modified from the model by J. Hermia and J. Granger. Table 1 shows the linearized equation of the model. For the cake formation model, cake was formed when the particles larger than the average pore size accumulated on the membrane surface. For standard pore blocking, the particles in the fluids entered the pores and adhered to the innerpore walls, thus the adhesion of particles to the walls decreased the available pore diameter and increased the resistance of the membrane. For complete pore plugging model, the particles plugged individual pores and the flow diverted to other pores that plugged successively.

Table 1. Blocking filtration model

Type of Blockage	**Characteristic Equation**
Cake formation model	$\frac{t}{V} = X_1 V + Y_1$
Standard pore blocking	$\frac{t}{V} = X_2 V + Y_2$
Complete pore plugging model	$\frac{dV}{dt} = Y_3 - X_3 V$

Materials and Methods

Materials

Polysulfone commercial ultrafiltration (UF) membranes were chosen in order to minimize uncertainties with respect to the membrane material. The 20 kDa PSF membrane was purchased from Koch. The high purity cellulose was used to prepare the feed solution and was supplied by Sigma Aldrich. The analytical grade glucose, citric acid, tri-sodium citrate were purchased from Nacalai Japan and used as foulant model in the feed solution.

Characterization of model cellulose hydrolysate

In this study, a model of cellulose hydrolysate was formed by mixing microcrystalline cellulose powder, glucose and cellulase enzymes. The hydrolysate was analyzed for molecular weight and isoelectric point (IEP). 6% (w/w)

microcrystalline cellulose, 33.3 g/l glucose and 8FPU cellulase were added in reverse osmosis water and mixed well for 30 minutes. Gel electrophoresis in denaturing conditions was performed in sodium dodecyl sulfate (SDS-PAGE) according to the method by Laemmli (1970) resolving gel consisted of 15% polyacrylamide in Tris-HCl (1.5M, pH 8.8), while stacking gel consisted of 4.5% polyacrylamide in Tris-HCl (1.0 M, pH 6.8). Sample solutions were mixed at 1:2 (v/v) ratios with the sample buffer and heated at 90 °C for 3 minutes before loading. Aliquots of 40 – 42 µL samples were loaded into individual wells and a constant current was passed through the gel for 2 h to obtain separation of the peptides. Protein markers 10 – 260 kDa was used for molecular-weight determination. The gel sheets were stained with Gelcode Blue Safe Protein stain [12]. As for the determination of isoelectric point (IEP) of cellulose hydrolysate, the zeta potential at a given pH was recorded by a zeta potential titration apparatus using Malvern Zetasizer Nano ZS, UK. The IEP of the hydrolysate was determined where the zeta potential was zero at the pH value.

Ultrafiltration process

The 20 kDa polysulfone membrane purchase from Koch was employed throughout the present study. The active membrane surface area was 14.67 cm2. Fresh membranes were soaked in pure water overnight prior to each run to remove the preservative liquids from the manufacturer before used. Experiments were performed in the dead end stirred cell (Sterlitech HP4750). The stirred cell is equipped with single blade stirrer and rotates at 500 rpm to minimize the layer formation of high solution concentration in the adjacent areas at membrane surface and to prevent the formation of a series vortex in the cell. The operation pressure in the system was maintained by nitrogen gas. The feed solution was conducted under constant pressure at 2 bar. Permeate flux was calculated based on the mass of permeate collected on the balance for about 60 minutes.

Analytical methods

Glucose content was analysed by HPLC (Agilent G1311A) equipped with refractive index (RI) detector and Rezex ROA column (300 x 7.80mm). An amout 0.005 N H2SO4 was used as the mobile phase as a flow rate of 0.6 ml/min and the column temperature was maintained at 60 °C. Protein concentration was measured by the Bradford protein assay using bovine serum albumin (BSA) as standard [13].

Result and Discussion

Characterisation of cellulose hydrolysate

Fractionation is controlled by the membrane pore size and the operating parameters. Determination of molecular size of the retained macromolecules is essential as size can be the criterion for separation. UF membranes retain 90% of molecular mass in daltons of a macrosolute, so a specific small molecule can be fractionated into permeate from the hydrolysate. In concentrating glucose via ultrafiltration process, glucose will be allowed to pass through membrane pores while the enzymes will be retained for recycle. Molecular weight of cellulose hydrolysate was analyzed by SDS polyacrylamide gel electrophoresis (Figure 1). From Figure 1 it was shown that the molecular weight of hydrolysates was 70 kDa. Similar result has also been reported by Andersen et al. [14] as 70 kDa calculated with the average cellulase enzyme in MW.

Amino acids in the protein contain both a basic and an acidic group because of the amphoteric character that can be positive or negative charge depending on the pH of the solution. If the amino acids did not migrate in the electrical field, which is it is not positive nor is negative charge, this conditions called as the IEP of the amino acids [15]. The isoelectric point is one of the characteristics parameter for a protein, as different proteins have different value of isoelectric point. IEP has important effects on the properties of cellulose hydrolysate solution in membrane process. By adjusting the pH, a complete separation of various proteins can be obtained. The isoelectric point of cellulose hydrolysate was 3.9.

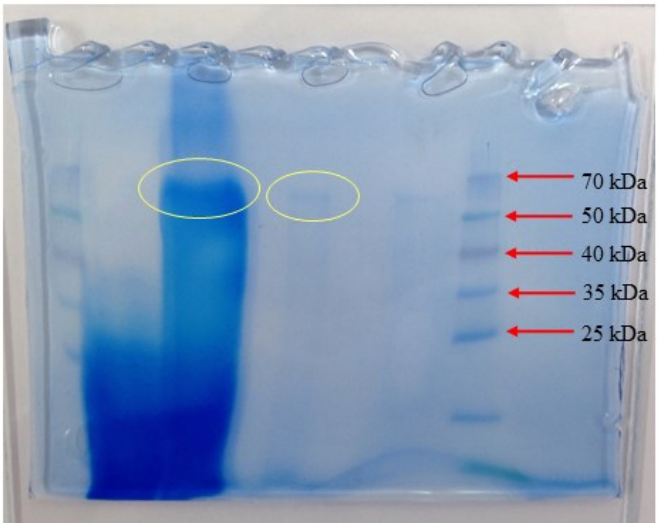


Figure 1. Electrophoresis profile of the cellulose hydrolysis

Effect of pH

The interaction between membrane and solute in different pH was studied in the dead-end stirred ultrafiltration with constant operating pressure at 2 bar. Figure 2 shows the fouling behaviour of cellulose hydrolysate for several pHs illustrated in terms of permeate flux relative to initial water flux (J/Jo). Initially the fouling behaviour for all solution can be seen as rapid flux decline and followed by gradual flux decline. It is noted that the permeate flux was responsive to the solution pH, thus low pH value exhibited severe flux decline as compared to high pH value. Similar experiment trends were reported by other researchers [7,16,17].

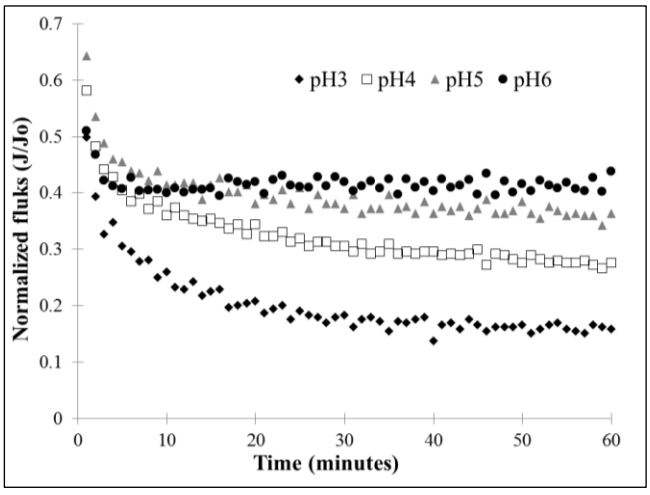


Figure 2. Normalized flux declines of cellulose hydrolysate in different pH of solution

The feasibility of fractionation depends on charge, thus more charged ions are retained better than monovalent ions [18]. In addition, the counterion exchange process between the ion exchanger and the counterions in the external solution has to be considered, specifically proteins of large molecular weight [19]. The net charge of the

macromolecular protein due to pH-based interactions of various constituent groups is positive if the pH is less than the isoelectric point; the net charge is negative if the solution pH is more than the IEP. Thus, as long as the solution pH is different from the IEP, the protein surface has some net positive or net negative charges.

All these could explain why the lowest permeate flux was obtained at pH below the hydrolysate's IEP (~pH3). Figure 3 illustrates the observation for pH3. Below the IEP, both the cellulose hydrolysate (positively charged) and PSF membranes (negatively charged) have opposite charges, thus attraction forces are dominant over repulsion forces and affect the initial flux decline rate at the initial fouling stage. At pH of solution near to IEP (~pH4), the solubility of a protein built out of amino acids is minimum and has tendency to form aggregates with other molecules [10]. As the pH was raised to pH 5 and pH 6 (away from the IEP), observation shows that the protein solubility increases and lead to much lesser accumulation on the membrane surface.

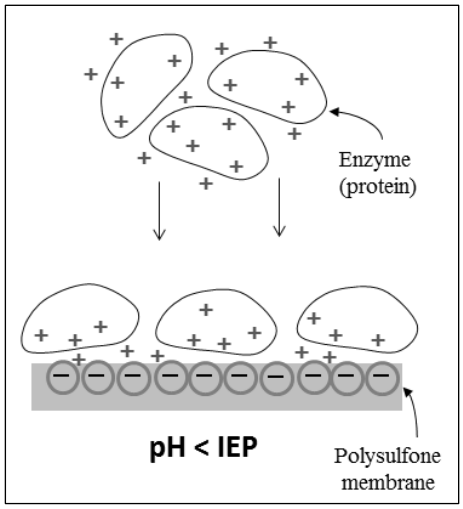


Figure 3. Schematic illustration of possible configurations of cellulose hydrolysate at pH lower than IEP

The membrane blocking resulted from the accumulation on the membrane surface would affected the permeation of glucose in the process. As illustrated in Figure 4, the permeation of glucose at pH 3 is the lowest compared to other pH, indicating that much glucose was unable to pass through the PSF membrane because of the blocking by the protein on the membrane surface, while at pH 5 the permeation of glucose is the highest.

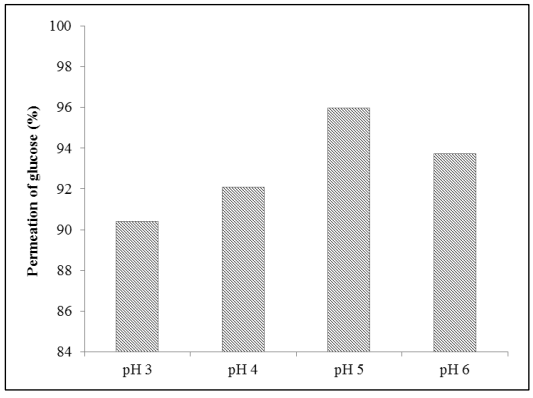


Figure 4. Permeation of glucose in different pH

Fouling mechanism

Kumar's equation was applied to identify the mechanism of fouling during ultrafiltration of cellulose hydrolysate. Y-axis and X-axis according to Table 1 was fitted using Matlab R2012a (Figure 5). The best fit parameter was obtained by minimizing the sum of squared residuals (SSR) that could explain the experimental data rationally (Table 2).

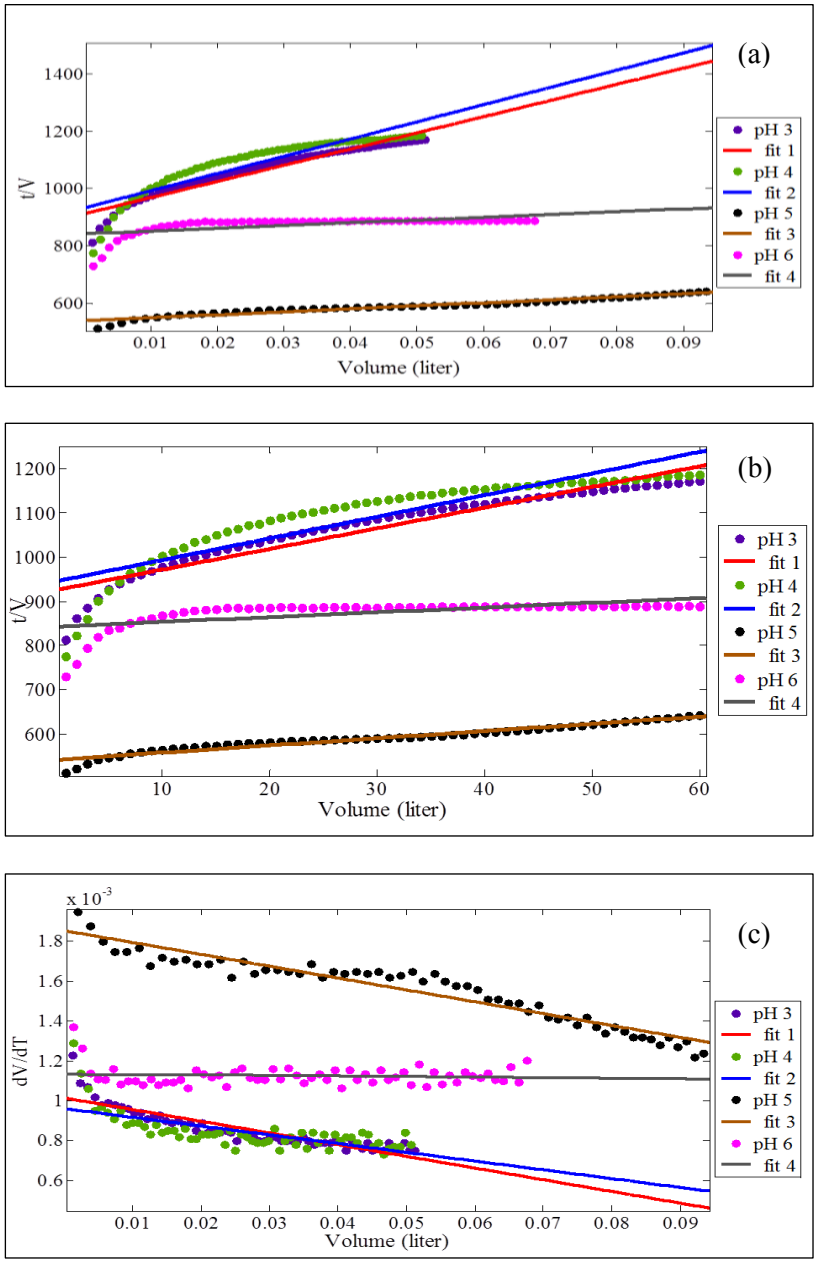


Figure 5. Cake formation model (a), standard pore blocking (b) and complete pore plugging model (c) for cellulose hydrolysate ultrafiltration

It may be observed from the figure that the fitting of experimental data to the all three types of blocking, the best fitting occurred in pH5, as the values of R^2 were higher than others R^2 values, which were mostly above 0.9. Thus

this indicated that at pH5 the possibility that the flux decline could be controlled by the combination of the three blocking model. Solution at pH3 were fouled mainly by cake formation, which could explain the electrostatic attraction between particles of protein and the fresh membrane that lead to the formation of cake layer impeding the entrance of molecules into the membrane pore and keeps them back on the cake layer.

Table 2. The value of R^2 obtained from the experimental data in the study of the effect of pH solution upon membrane fouling

pH	Cake Formation Mode	Standard Pore Blocking	Complete Pore Plugging Model
3	0.9282	0.9084	0.7968
4	0.8117	0.7937	0.8558
5	0.9449	0.9453	0.9133
6	0.3753	0.3769	0.0107

Similar results have also been observed for glucose permeation in hollow fibre membrane whereby formation of thin layer of cake denoted the membrane blocking [6]. Blocking mechanism for filtration at pH6 was found to be unsuitable with the fitted model, may be due to the less accumulation of protein on membrane surface due the stronger electrostatic repulsion between protein and the PSF membrane.

Conclusion

It has been shown that solution pH has significant effect on the extent of cellulose hydrolysate fouling in membrane process. At higher solution pH (pH 5 and 6), the samples showed minimum membrane flux decline due to protein-protein and membrane-protein repulsions alleviate aggregation and fouling. The permeate flux decline profiles of all the solution were compared to the Kumar's model. These results showed that the fouling at pH5 was predominantly contributed by three types of blocking. Under all the solution pH, it was observed that the values of R^2 of cake formation model were always greater than those obtained from other fouling mechanisms. This indicates that the cake formation model dominated in fouling studies, and followed by standard pore blocking and complete pore plugging model.

Acknowledgement

This study was financially supported by the LRGS grant (LRGS/2013/UKM-UKM/PT/03) from Ministry of Higher Education and Universiti Kebangsaan Malaysia.

References

1. Qi, B., Luo, J., Chen, G., Chen, X. and Wan, Y. (2012). Application of ultrafiltration and nanofiltration for recycling cellulase and concentrating glucose from enzymatic hydrolyzate of steam exploded wheat straw. *Bioresource Technology*, 104: 466 - 472.
2. Ishola, M. M., Jahandideh, A., Haidarian, B., Brandberg, T. and Taherzadeh, M. J. (2013). Simultaneous saccharification, filtration and fermentation (SSFF): A novel method for bioethanol production from lignocellulosic biomass. *Bioresource Technology*, 133: 68 - 73.
3. Narayanaswamy. N., D., P., Verma, S. and Kumar, S. (2013) Chapter 1: Biological pretreatment of lignocellulosic biomass for enzymatic saccharification, in Z. Fang (ed.), Pretreament techniques for biofuels and biorefineries. Springer Berlin Heidelberg: pp. 3 - 34).
4. Ma, T., Kosa, M. and Sun, Q. (2014) Chapter 7: Fermentation to bioethanol/biobuthanol in A.J. Ragauskas (ed.) Materials for biofuels. World Scientific, 4: 155 - 185.
5. Gautam, A. and Menkhaus, T. J. (2014) Performance evaluation and fouling analysis for reverse osmosis and nanofiltration membranes during processing of lignocellulosic biomass hydrolysate. *Journal of Membrane Science*, 451: 252 - 265.

6. Hwang, K. J., Tsai, H.-Y. and Chen, S.-T. (2014). Enzymatic hydrolysis suspension cross-flow diafiltration using polysulfone hollow fiber module. *Journal of Membrane Science*, 454: 418 - 425.
7. Maiti, S. K., Lukka Thuyavan, Y., Singh, S., Oberoi, H. S. and Agarwal, G. P. (2012). Modeling of the separation of inhibitory components from pretreated rice straw hydrolysate by nanofiltration membranes. *Bioresource Technology*, 114: 419 - 427.
8. Echavarría, A. P., Ibarz, A., Conde, J. and Pagán, J. (2012). Enzyme recovery and effluents generated in the enzymatic elimination of clogging of pectin cake in filtration process. *Journal of Food Engineering*, 111: 52 - 56.
9. Wang, C., Li, Q., Tang, H., Yan, D., Zhou, W., Xing, J. and Wan, Y. (2012). Membrane fouling mechanism in ultrafiltration of succinic acid fermentation broth. *Bioresource Technology*, 116: 366 - 371.
10. de Barros, S. T. D., Andrade, C. M. G., Mendes, E. S. and Peres, L. (2003). Study of fouling mechanism in pineapple juice clarification by ultrafiltration. *Journal of Membrane Science*, 215: 213 -224.
11. Mahesh Kumar, S., Madhu, G.M. and Roy, S. (2007). Fouling behaviour, regeneration options and on-line control of biomass-based power plant effluents using microporous ceramic membranes. *Separation and Purification Technology*, 57: 25 - 36.
12. Suhimi, N. M., Mohammad, A.W. and Jahim, J. M. (2013). Production and characterization of hydrolyzed collagen derived from enzymatic hydrolysis of type-B gelatin. *Proceeding of the 8th CIGR Section VI International Technical Symposium - Advanced Food Processing and Quality Management:* pp 304.
13. Bradford, M. M. (1976). A rapid and sensitive method for the quantitation of microgram quantities of protein utilizing the principle of protein-dye binding. *Analytical Biochemistry*, 72: 248 - 254.
14. Andersen, N., Johansen, K. S., Michelsen, M., Stenby, E. H., Krogh, K. B. R. M. and Olsson, L. (2008). Hydrolysis of cellulose using mono-component enzymes shows synergy during hydrolysis of phosphoric acid swollen cellulose (PASC), but competition on Avicel. *Enzyme and Microbial Technology*, 42: 362 - 370.
15. Mulder, M. (2000). Basic principles of membrane technology. pp 387.
16. Lim, Y. P. and Mohammad, A.W. (2012). Influence of pH and ionic strength during food protein ultrafiltration: elucidation of permeate flux behavior, fouling resistance, and mechanism. *Separation Science and Technology*, 47: 446 - 454.
17. Lakra, R., Saranya, R., Thuyavan, Y. L., Sugashini, S., Begum, K. M. S. and Arthanareeswaran, G. (2013). Separation of acetic acid and reducing sugars from biomass derived hydrosylate using biopolymer blend polyethersulfone membrane. *Separation and Purification Technology*, 118: 853 - 861.
18. Ribeiro, H. S., Janssen, J. J. M., Kobayashi, I. and Nakajima, M. (2010) Chapter 7: Membrane emulsification for food applications in Peinemann, K.V, Nunes, S. P. and Giorno, L. (eds.) Membrane for food applications: pp. 129 - 131.
19. Sirkar, K.K. (2014) Separation of molecules, macromolecules and particles. *Cambridge University Press*: pp. 295 - 305.

Malaysian Journal of Analytical Sciences, Vol 20 No 6 (2016): 1421 - 1428
DOI: http://dx.doi.org/10.17576/mjas-2016-2006-22

MALAYSIAN JOURNAL OF ANALYTICAL SCIENCES
Published by The Malaysian Analytical Sciences Society
ISSN 1394 - 2506

OPTIMIZATION OF CHLOROPHYLL EXTRACTION FROM *Gynura procumbens*

(Pengoptimuman Proses Pengekstrakan Klorofil daripada *Gynura procumbens*)

Zurina Zainal Abidin*, Wan Noraznorin Mohamad, Mahtab Samadi

Department of Chemical and Environmental Engineering, Faculty of Engineering, Universiti Putra Malaysia, 43400 UPM Serdang, Selangor, Malaysia

**Corresponding author: zurina@upm.edu.my*

Received: 21 October 2015; Accepted: 14 June 2016

Abstract

Gynura procumbens (Sambung nyawa) is a bicolor (green and red) herbal plant, which is widely grown in Asia. This herbs are famously used for medicinal purposes as a safe alternative to chemical-based medicine. Recent studies proved that this plant has anti-herpes simplex virus, anti-flammatory and anti-hyperglycaemic properties. This work investigates the extraction of chlorophyll a and b in *Gynura procumbens* using Solid liquid extraction method. The solid to solvent ratio, temperature, solvent used and extraction time were varied to determine the optimum conditions for extraction. It was found that at 80 °C in 90 minutes with 2:5 solid to solvent ratio was the most favorable condition to extract chlorophyll a and b. Five valuable compounds were found from GC-MS analysis, which are 2-hexanal, phenol, oleic acid, copaene and phytol. This implies that *Gynura procumbens* promises a good source of many useful bioactive compounds.

Keywords: *Gynura procumbens*, sambung nyawa, chlorophyll, extraction, optimization

Abstrak

Sambung Nyawa ialah pokok herba dwi-warna yang tumbuh secara meluas di Asia. Herba ini sangat popular digunakan sebagai bahan alternatif yang selamat bagi tujuan perubatan berbanding ubatan berunsurkan bahan kimia. Penyelidikan terbaru membuktikan bawaha pokok ini anti-virus herpes simplex, anti-keradangan dan anti-sifat hiperglisemia. Eksperimen ini menyiasat tentang pengekstrakan klorofil a dan b dalam *Gynura procumbens.* Menggunakan pengekstrakan cecair pepejal. Nisbah cecair pepejal, suhu, pelarut dan masa mengekstrak telah dimanipulasi untuk menentukan keadaan yang optimum untuk proses pengekstrakan tersebut. Keputusan eksperimen mendapati bahawa pengekstrakan selama 90 minit pada suhu 80°C serta nisbah cecair pepejal 2:5 merupakan kondisi yang paling sesuai untuk mengekstrak klorofil a dan b. Lima kompoun berharga telah ditemui melalui keputusan analisa GC-MS iaitu 2-heksanal, fenol, asid oleik, copaene and fitol. Keputusan ini mencadangkan potensi *Gynura procumbens* sebagai sumber yang baik kepada sebatian bioaktif.

Kata kunci: *Gynura procumbens*, sambung nyawa, klorofil, pengekstrakan, pengoptimuman

Introduction

For centuries, many plants have been used as a traditional medicine. However, the interest for natural products have grown significantly in recent years [1,2,3]. In the market, nowadays, there are tremendous numbers of natural products, which have a phyto origin such as food additives, cosmetics, and medicines [4]. One of the well-known medicinal plants in South-east Asia is *Gynura procumbens (Lour.) Merr.*, which is locally known as Sambung nyawa in Malaysia. *Gynura procumbens* is a fast growing evergreen herb from family of Compositae or Asteraceae and it is mostly found in Thailand, Malaysia, Indonesia, and Philippines [1,5].

The leaves of *Gynura procumbens* have been traditionally used for the treatment of eruptive fevers, rashes, kidney diseases, migraines, constipation, hypertension, cancer and diabetes mellitus, inflammation, rheumatism, viral diseases of skin, migraine, and constipation [5 – 9]. Modern research also has provided evidence for the above-mentioned medicinal properties of *Gynura procumbens*. For instance, Rosidah et al. [10] maintained that the ethanolic extract of *G. procumbens* showed anti-hyperglycaemic and anti-hyperlipidaemic activities in diabetic rats [5,9, 11,12]. Furthermore, *Gynura procumbens* has been reported to possess anti-herpes simplex virus, anti-hyperglycemic, anti-hyperlipidemic [13], anti-hypertensive effects [8], anti-hyperlipidemic [12,13], anti-sterility, anti-oxidative capabilities, and it has been found to be useful for prevention of rheumatism [5 – 7,9,12,13]. In addition, ethanol and methanol extracts from the leaves of *Gynura procumbens* showed anti-diabetic effects in streptozotocin (STZ)-induced diabetic rats [12]. Rosidah et al. [10] also reported that *Gynura procumbens* leaves increase insulin secretion in the insulin-secreting cell line [14]. According to Zurina et al. [15], it was reported that the aqueous extract of *Gynura procumbens* not only decreases the blood glucose levels, but also increase the glucose uptake by muscle tissues in STZ-induced diabetic rats [14].

Strong body of research supported the fact that chemical contents of *Gynura procumbens* leaf are flavonoid, glycoside kuersetin, phenolate acid, triterpenoid, alkaloid, saponin, and tannin [7,14]. Generally, most of the green vegetables and fruits contain chlorophyll, which accounts for their green colour. Chlorophyll a and b are the major pigments that can be found in the extract of green plants [16]. The presence of chlorophylls has also been observed in the solvent extract from leaves of *Gynura procumbens* [17,18,19]. Chlorophylls have been used as a traditional medicine for therapeutic and as antioxidant [17, 20]. Kaewseejan, et al. [17] reported that the usage of chlorophylls in human diet has increased significantly in recent years. According to Guil-Guerrero et al. [20], chlorophylls have antioxidant, anticarcinogenic, and cytotoxic activity, so, they may ameliorate drugs' side effects [17]. Chlorophyll has been used for many purposes. In chemical industry, chlorophylls have been used as natural dyes. Chlorophyll is registered as a food additive (colorant), and its E number is E140. Chefs use chlorophyll to colour a variety of foods and beverages such as pasta and absinthe. Other than that, in medical field chlorophyll has been introduced as bioactive compound which can help in blood production.

Hence, given the importance of chlorophylls and its beneficial compounds, the aim of this study is to extract the chlorophyll a and b in *Gynura procumbens* at optimum condition.

Materials and Methods

Sample preparation

The leaves of *Gynura procumbens* were bought from Pusat Herba, Taman Pertanian Universiti (TPU). The leaves were washed by distilled water to avoid contaminants on the surface of the leaves. After drying, the leaves were freshly stored at 4 °C for subsequent experiments.

Solvent extraction

The fresh leaves of *Gynura procumbens* were cut into small pieces before the extraction. Then, an amount 0.5 g of sample was used for each experiment and soaked in 5 ml of solvent in a test tube. In order to find the best solvent for this extraction, three different solvents (water, methanol, and ethanol) were used in each extraction. The conical flask was then covered with aluminum foil to avoid contamination and to protect from sunlight that may causes unwanted reaction. Water bath machine was used to heat the samples for extraction at different temperature and time. After each experiment, the extracts were filtered through a Whatman No.1 filter paper and the absorbance value measured by using Shimadzu UV-Vis spectrophotometer.

Ultraviolet visible spectrophotometer

In this study, Shimadzu ultraviolet visible (UV-Vis) spectrophotometer was used in determining chlorophyll content. The extract collected after filtration of samples through Whatman No.1 filter paper were filled in the cuvette. Chlorophyll-a showed maximum absorbance at 665 nm while chlorophyll-b at 652 nm. Then, the chlorophyll-a and chlorophyll-b content (μg/ mL) were calculated using equations 1 and 2 for ethanol-based extraction as reported by Kaewseejan et al. [17]:

$$\text{Chlorophyll-a} = 16.72\ (A665) - 9.15\ (A652) \quad (1)$$

$$\text{Chlorophyll-b} = 34.09\ (A652) - 15.28\ (A665) \quad (2)$$

The wavelengths used were at 666 nm for chlorophyll-a absorbance and 653nm for chlorophyll-b absorbance. The equations 3 and 4 were used for methanol-based extraction to determined chlorophyll-a and –b content:

$$\text{Chlorophyll-a} = 15.65\ (A666) - 7.340\ (A653) \quad (3)$$

$$\text{Chlorophyll-b} = 27.05\ (A653) - 11.21\ (A666) \quad (4)$$

Gas chromatography mass spectrometry

Extracted samples were analysed using Shimadzu gas chromatography mass spectrometry (GC/MS). A 30 m × 250 µm × 0.25 µm capillary column was used. The temperature used for this analysis was from 50 to 325 ˚C while the pressure was up to 10.5 psi. The injection volume was 3.0 µL. Split less mode was used and helium gas with the flow of 1mL/min and pressure of 10.5 psi was used as carrier gas. Response Surface Methodology software was used to obtain a mathematical model for extraction of chlorophylls.

Results and Discussion

The fresh leaves of *Gynura procumbens* were extracted by solvent extraction method, which is a traditional method to obtain chlorophylls.

Optimization of extraction method

The conventional extraction process can vary in different temperatures, solid/ liquid ratio, solvent, and time. So, the effect of these parameters was studied in order to find the optimum conditions, in which highest yield of chlorophylls was extracted.

Effect of solvents

As mentioned earlier, three different types of solvents of methanol, ethanol, and water were employed. The extractions were done at different times, from 5 to 30 minutes. The results from each solvent varied in the extracted amount of chlorophyll-a and chlorophyll-b. As Figure 1 depicts, one of the highest yield of chlorophyll-a was extracted using methanol as a solvent and followed by ethanol and water respectively. 30 minutes of extraction was found to be the best extraction time to obtain the highest amount of chlorophyll-a (34.63 µg/ml) by methanol. While the concentration of chlorophyll-a extracted by ethanol and water were 32.03µg/ml and 0.281µg/ml respectively.

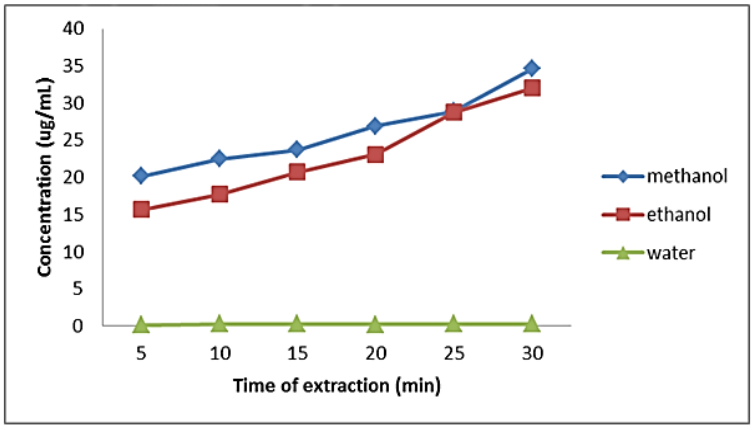


Figure 1. Concentration of chlorophyll-a against time of extraction at different solvents

Meanwhile, the highest yield of chlorophyll-b was extracted by using methanol as a solvent and followed by ethanol and water. After 30 minutes of extraction, the concentration of chlorophyll-b extracted by methanol was 6.82 µg/ml. While the concentration of chlorophyll-b extracted by ethanol and water was 6.08 µg/ml and 0.12 µg/ml respectively (Figure 2). Therefore, it clearly shows that methanol extracted the highest yield of chlorophylls compared to ethanol and water. The reason of these phenomena is because chlorophylls are readily soluble in alcohol, mostly insoluble in non-polar alkanes like butane and hexane, and has unique relationships with polar water, due to its polarity and the presence of ionic groups. Chlorophylls are basically composed of hydrocarbons, which are mostly insoluble in water.

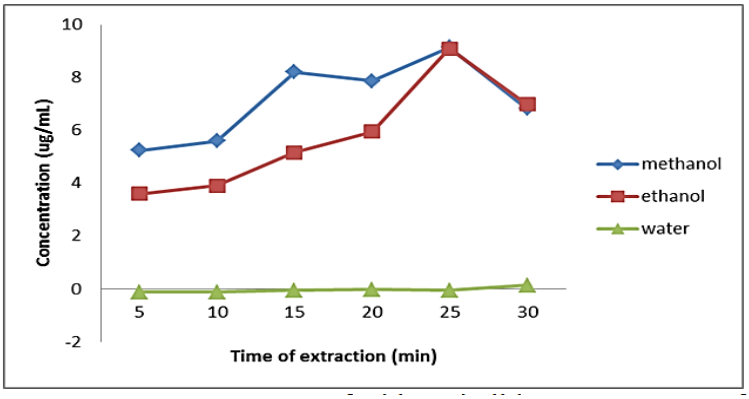


Figure 2. Concentration of chlorophyll-b against time of extraction of different solvent

Since the yield of chlorophylls were almost the same for ethanol and methanol extract, hence ethanol was chosen as solvent for the rest of experiments. This is because ethanol poses less threat to human consumption and health risks [21].

Effect of solid to solvent ratio

In this experiment, solid to solvent ratio was varied from 1:5 to 5:5 g/ml. The time of extraction was set to be at 30 minutes and 120 minutes. Figures 3 and 4 below shown the results obtained. As it is depicted in Figures 3 and 4, the optimum ratio for highest yield of chlorophylls was at 2:5 g/ml in 120 minutes of extraction. The concentration of chlorophyll-a and b was 72.32 µg/ml and 32.62 µg/ml respectively, while half of these amounts were extracted in 30 minutes. So, the result showed that the yield of chlorophylls doubled by increasing the time of extraction. The highest yield of chlorophylls at solid to liquid ratio of 2:5 mg/ml may be explained by the fact that at this ratio better mass transfer between sample and solvent occurs in comparison to other ratios.

Effect of extraction temperature

In this part, temperatures of extraction were varied from 40 to 80 ˚C at the constant solid to solvent ratio (2:5) and 30 minutes extraction time to find the optimum temperature. As it shows in Figure 5, the concentration of chlorophyll-a and b increase with respect to temperature from 41.47 µg/ml and 16.57 µg/ml to 84.78 and 77.63 µg/ml. At higher temperatures, plant cell wall, which is hydrocarbon chain and consists of phospholipid layer, breaks easier and the compounds in the leaf can leave the cell wall [22]. Higher temperatures also increase the solubility of sample in solvent and hence help to shorten the extraction time by increasing the mass transfer of solute into solvent. Based on the results, highest amount of chlorophylls was extracted at the 80 ˚C. The finding regarding the optimum temperature was consistent with the findings of other research such as Bucić-Kojić, et al. [23].

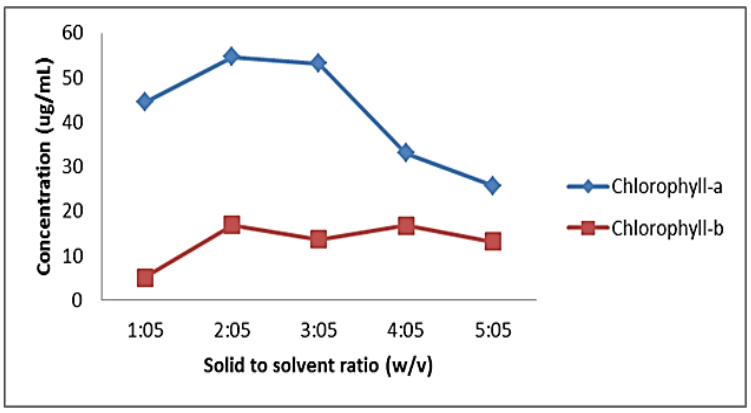


Figure 3. Concentration of chlorophyll against solid to solvent ratio for 30 minutes

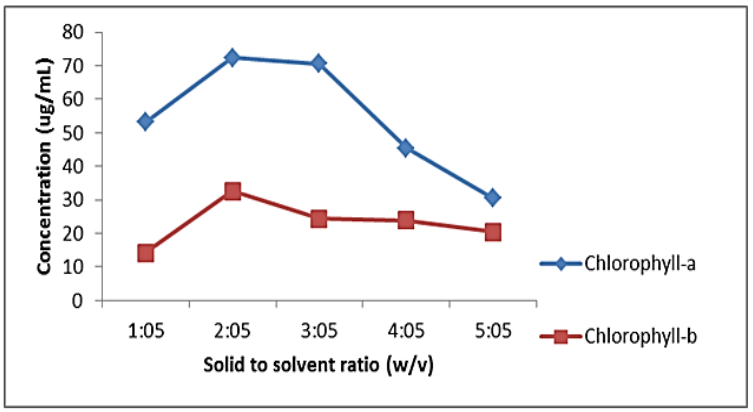


Figure 4. Concentration of chlorophyll at different solid to solvent ratio for 120 minutes

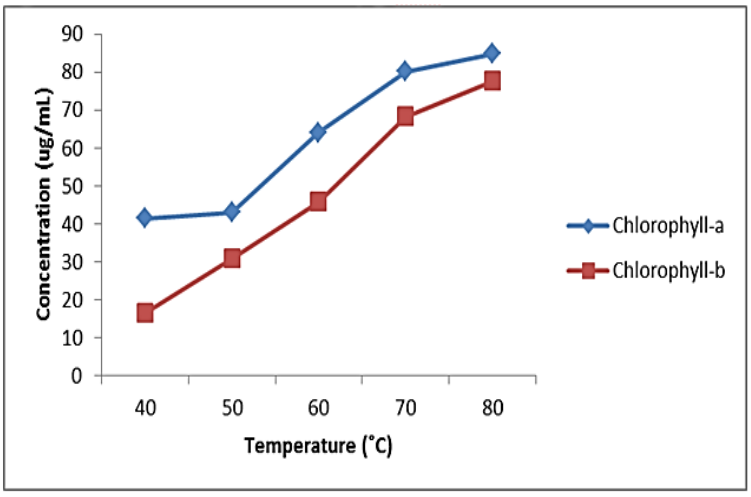


Figure 5. Concentration of chlorophyll against temperature

.

Effect of extraction time

In order to find the optimum time of extraction, constant amount of solid to solvent ratio and temperature was set at different times of extraction ranging from 5 to 120 minutes. Figure 6 shows results of concentration chlorophyll at constant temperature of 80 ˚C while the time of extraction was varied throughout the experiment. From the graph we can see that the concentration of chlorophyll increased as time of extraction increased. However, at 120 minutes of extraction the concentration decreased because the ethanol had vaporized totally and the mixture become dry in the conical flask. In 5 minutes of extraction concentration of chlorophyll obtained was 58.20 µg/ml for chlorophyll-a and 33.41 µg/ml for chlorophyll-b, while maximum amount of chlorophyll-a and chlorophyll-b obtained at 90 minutes of extraction with 173.25 µg/ml and 165.54 µg/ml respectively.

Thus as mentioned earlier, high temperature helps to reduce time of extraction with higher yield of extraction. In this case, the optimum time was 90 minutes at 80 ˚C for extraction highest amount of chlorophylls. Therefore, based on the results, the optimum parameters for conventional extraction of chlorophylls from *G. procumbens* leaves were at 80 ˚C for 90 minutes of extraction and solid to solvent ratio 2:5 g/ml.

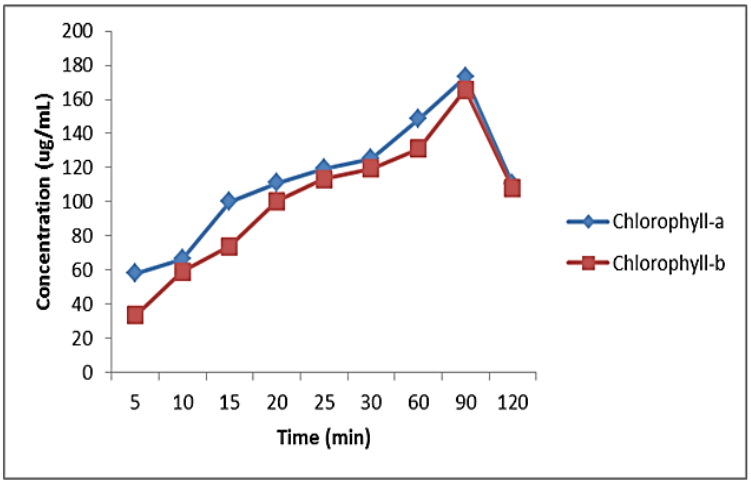


Figure 6. Concentration of chlorophyll against time of extraction at constant temperature (80˚C)

Response surface methodology

In order to find the mathematical model for the extractions, Response surface methodology software was used based on the obtained results for extraction of Chlorophylls at different solid to solvent ratio, temperature, and extraction time (three parameters). Central composite design and Box-Behnken design for historical data was used for each extraction method. Analysis of variance (ANOVA) was employed to evaluate the significance of each variable on the resulted model. Linear model was suggested for extraction of chlorophyll-a and chlorophyll-b by conventional method (equation 5 and 6).

$$\text{Chlorophyll-a concentration} = + 90.30 - 6.67A + 22.71B + 38.38C \quad (5)$$

$$\text{Chlorophyll-b concentration} = + 19.21 + 6.05A + 31.83B + 42.45C \quad (6)$$

where; A = Ratio (g/ml), B = Temperature (˚C) and C = Time (minutes)

As it shows in the Figure 7, the desirable concentration of chlorophylls obtained at 80 ˚C and 90 minutes of extraction by conventional method.

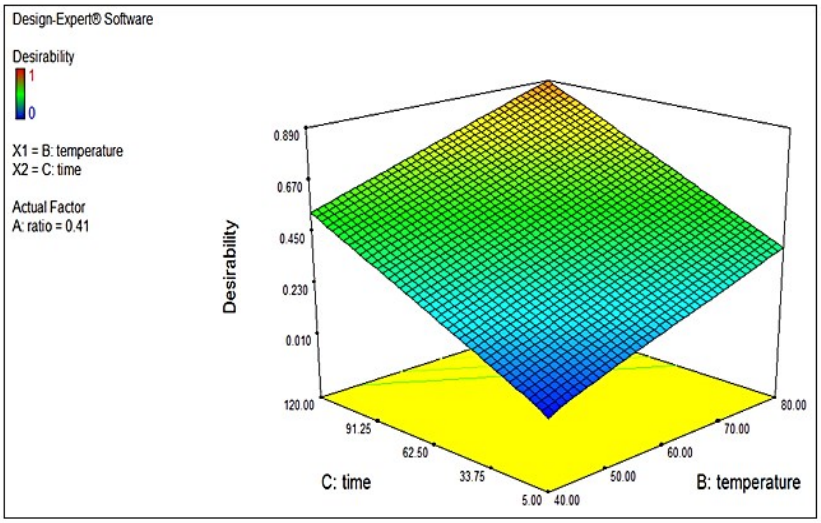


Figure 7. Desirability of concentration of chlorophyll for conventional extraction by optimization analysis

Gas chromatography-mass spectrometry analysis

The chemical compounds of ethanolic extracts obtained by solvent extraction from the leaves of *Gynura procumbens* were identified by GC-MS. The results showed five identified compounds. The identified compounds from solvent extraction sample were 2-hexenal, phenol, oleic acid, copaene and phytol. All the identified compounds are valuable and useful in medicine and they can be the reason of *Gynura procumbens* traditional medicinal usage, but further investigation is needed.

Conclusion

Based on the results, the highest yield of chlorophylls was extracted by conventional method at 80 ˚C with solid to solvent ratio of 2:5 mg/ml for 90 minutes. Also the samples extracted by conventional extraction method contained valuable compounds, which are useful in medicine. In short, the extract from leaves of *Gynura procumbens* has a promising medicinal potential and it can be used as a natural source of chlorophylls.

Acknowledgement

We would like to thank En Termizi Zakaria from Biochemical Engineering Laboratory for all his help.

References

1. Abrika, O., Yam, M., Asmawi, M., Sadikun, A., Dieng, H. and Hussain, E. (2013). Effects of extracts and fractions of gynura procumbens on rat atrial contraction. *Journal of Acupuncture and Meridian Studies*, 6: 199 – 207
2. Yesilada, E. (2005). Past and future contributions of traditional medicine in the health care system of the Middle-East. *Journal of Ethnopharmacology*, 100: 135 – 137.
3. Stepp, J. R. and Moerman, D. E. (2001). The importance of weeds in ethnopharmacology. *Journal of Ethno-pharmacol*, 75: 19 – 23.
4. Jiao, J., Gai, Q.-Y., Fu, Y.-J., Zu, Y.-G., Luo, M., Zhao, C.-J. and Li. C. Y. (2013). Microwave-assisted ionic liquids treatment followed by hydro- distillation for the e fficient isolation of essential oil from Fructus forsythiae seed. *Separation & Purification Technology*, 107: 228 – 237.
5. Ng, H., Poh, T.-F., Lam, S.-K. and Hoe, S.-Z. (2013). Potassium channel openers and prostacyclin play a crucial role in mediating the vasorelaxant activity of *Gynura procumbens*. *BMC Complementary Alternative Medicine*, 13: 188 – 199 .
6. Perry, L. (1980). Medicinal Plants of East and Southeast Asia. Cambridge: MIT Press.

7. Lee, H.-W., Hakim, P., Rabu, A. and Abdullah Sani, H. (2011). Antidiabetic effect of *Gynura procumbens* leaves extracts involve modulation of hepatic carbohydrate metabolism in streptozotocin-induced diabetic rats. *Journal of Medicinal Plants Research*, 6(5): 796 – 812.
8. Hoe, S. Z., Lee, C. N., Mok, S. L., Kamaruddin, M. Y. and Lam, S. K. (2011). *Gynura procumbens Merr.* Decreases blood pressure in rats by vasodilatation via inhibition of calcium channels. *Clinics (Sao Paulo)*, 66(1): 143 – 150.
9. Mahmood, A., Abdalbasit A., M., Fouad, A.-B. and Siddig Ibrahim, A.-W. (2010). Antiulcerogenic activity of *Gynura procumbens* leaf extract against experimentally-induced gastric lesions in rats. *Journal of Medicinal Plants Research*, 4(6): 685 – 691.
10. Rosidah, Y., Sadikun, A., Ahmad, M., Akowuah, G. and Asmawi, M. (2009). Toxicology evaluation of standardized methanol extract of *G. procumens*. *Journal of Ethnopharmacology*, 123: 244 – 249.
11. Chan, L., Lim, S. and Pan, L. (2009). Micropropagation of *Gynura procumbens (Lour.) Merr.* an important medicinal plant. *Journal of Medicinal Plants Research*, 3:105 – 111.
12. Zhang, X. and Tan, B. (2000). Anti-diabetic property of ethanolic extract of *Andrographis paniculata* in streptozotocin-diabetic rats. *Acta Pharmacology Sin*inca, 21(12):1157 – 1164.
13. Zhang, X. and Tan, B. (2000). Effects of an ethanolic extract of *Gynura procumbens* on serum glucose, cholesterol and triglyceride levels in normal and steptozotocin-induced diabetic rats. *Singapore Medical Journal*, 41: 9 – 13.
14. Ahmed Issa, I. and Bule, M. H. (2015). Hypoglycemic effect of aqueous and methanolic extract of *Artemisia afra* on alloxan induced diabetic swiss albino mice. *Evidence-Based Complementary and Alternative Medicine*, 2015: 1 – 5.
15. Zurina, H., Mun, F. Y. and Mariam, A. (2010). Antidiabetic properties and mechanism of action of *Gynura procumbens* water extract in streptozotocin-induced diabetic rats, *Molecules*, 15: 9008 – 9023.
16. Hojnik, M., Škerget, M. and Knez, Ž. (2007). Isolation of chlorophylls from stinging nettle (*Urticadioica* L.). *Separation and Purification Technology*, 57(1): 37 – 46.
17. Kaewseejan, N., Puangpronpitag, D. and Nakornriab, M. (2012). Evaluation of phytochemical composition and antibacterial property of *Gynura procumbens* extract. *Asian Journal of Plant Sciences*, 11(2):77 – 82.
18. Hew, C. and Gam, L. (2010). The identification of high abundant proteins in the leaves of *Gynura procumbens*. *Biotechnology & Biotechnological Equipment*, 24(4): 2132 – 2136.
19. Bhore, S. J., Ravichantar, N. and Loh, C. Y. (2010). Screening of endophytic bacteria isolated from leaves of Sambung Nyawa (*Gynura procumbens (Lour.) Merr.)* for cytokinin-like compounds. *Bioinformation*, 5(5): 191–197.
20. Guil-Guerrero, J. L., Rebolloso-Fuentes, M. M. and Isasa, M. T. (2003). Fatty acids and carotenoids from Stinging Nettle (*Urticadioica L.*). *Journal of Food Composition and Analysis*, 16(2): 111 – 119.
21. Shi, L., Macinko, J., Starfield, B., Politzer, R., Wulu, J. and Xu, J. (2005a). Primary care, social inequalities, and all-cause, heart disease, and cancer mortality in U.S. Counties. *American Journal of Public Health*, 95: 674 – 680.
22. Simon, E. (1974). Phospholipids and plantmembranepermeability. *New Photologist*, 73: 377 – 420.
23. Bucić-Kojić, A., Planinić, M., Tomas, S., Jokić, S., Mujić, I., Bilić, M. and Velić, D. (2011). Effect of extraction conditions on the extractability of phenolic compounds from lyophilised fig fruits (*Ficus carica L.*). *Polish Journal of Food and Nutrition Sciences*, 61(3): 195 – 199.

Malaysian Journal of Analytical Sciences, Vol 20 No 6 (2016): 1429 - 1436
DOI: http://dx.doi.org/10.17576/mjas-2016-2006-23

MALAYSIAN JOURNAL OF ANALYTICAL SCIENCES
Published by The Malaysian Analytical Sciences Society
ISSN 1394 - 2506

SURFACE CHARACTERIZATION ON ALKALI-HEAT-TREATMENT ON TITANIUM ALLOY

(Pencirian Rawatan Alkali-Haba ke atas Permukaan Aloi Titanium)

Nurul Hazwani Hanib[1], Fazlena Hamzah[1]*, Zarina Omar[2], Istikamah Subuki[1]

[1]*Biocatalysis & Biobased Material Research Group, Green Technology & Sustainable Development Research Community, Chemical Engineering Faculty, Universiti Teknologi MARA, 40450 Shah Alam, Selangor, Malaysia*
[2]*Chemical Engineering Faculty, Universiti Teknologi MARA, 23200 Bukit Besi, Dungun, Terengganu, Malaysia*

**Corresponding author: fazlena@salam.uitm.edu.my*

Received: 21 October 2015; Accepted: 14 June 2016

Abstract

Coating of apatite in a biomimetic fluid is an alternative technique for metallic coating. Key element for effective biomimetic apatite coating depends on the surface material that can be enhanced by physical and chemical pre-treatment process. Two different preparations of Titanium alloy (Ti6Al4V) have been studied namely *as* received (*as*-Ti) and abraded (*ab*-Ti) with SiC paper. Both samples were then immersed in 5M NaOH and 5M KOH at temperature of 60 °C for 24 hours. A passive oxide layer covered on the surface of Ti6Al4V generally changed to form alkali (Na/K) titanate layer which is mechanically unstable. Therefore, alkali-treated Ti6Al4V were heat-treated at 700 °C for 1 hour to consolidate a mechanically stable structure of amorphous alkali titanate layer. Both samples before and after heat treatment were characterized using field emission scanning electron microscope, 3D surface metrology, contact angle goniometry and X-ray diffraction. The result indicates that *as*-Ti treated in 5 M KOH showed an existence of porous network structure.

Keywords: titanium, active surface, alkali treatment, heat treatment

Abstrak

Penyalutan apatit dalam cecair biomimetik adalah teknik alternatif untuk salutan logam. Faktor utama dalam penyalutan logam dengan apatit secara biomimetik yang berkesan adalah bergantung kepada sifat permukaan bahan/logam. Sifat permukaan logam boleh ditambah baik melalui proses pra-rawatan secara fizikal dan kimia. Dua persediaan yang berbeza ke atas aloi Titanium (Ti6Al4V) telah dikaji iaitu seperti yang diterima (*as-Ti*) dan telah dilelas (*ab-Ti*) dengan kertas pasir silikon karbida (SiC). Kedua-dua sampel kemudiannya direndam ke dalam 5M NaOH dan 5M KOH pada suhu 60 °C selama 24 jam. Satu lapisan oksida pasif yang meliputi atas permukaan Ti6Al4V umumnya berubah untuk membentuk lapisan alkali (Na/K) titanat yang secara mekanikal adalah tidak stabil. Oleh itu, Ti6Al4V yang telah mengalami pra-rawatan alkali telah melalui proses pemanasan haba pada suhu 700 °C selama 1 jam untuk mengukuhkan kestabilan struktur mekanikal lapisan amorfus alkali titanat. Kedua-dua sampel sebelum dan selepas rawatan haba telah dianalisa menggunakan mikroskop elektron imbasan pancaran medan, metrologi permukaan 3D, sudut sentuhan goniometri dan pembelauan sinar-X. Hasil daripada kajian ini menunjukkan bahawa as-Ti yang dirawat dengan 5M KOH menunjukkan jelas kewujudan struktur jaringan berliang.

Kata kunci: titanium, permukaan aktif, rawatan alkali, rawatan haba

Introduction

Titanium and its alloy are widely used as dental, orthopaedic and maxillofacial implant materials due to their mechanical properties. It has a good biocompatibility, high corrosion resistance and better strength to the weight ratio as compared to 316L stainless steel. However, bone tissue does not bond directly to these materials due to the micromotion which leads to the formation of fibrous tissue encapsulated after implantation and drove to the loosening effects [1].

Enhancement of cell attachment and bone ingrowth promotion between cell-implant can be improved by coating with a bioactive surface such as calcium phosphate based material (i.e. hydroxyapatite) [2]. Various methods were introduced in producing calcium phosphate/ hydroxyapatite coating on titanium such as electrochemical deposition [3], sol-gel precipitate [4] and plasma spray coating [5]. High processing temperature in plasma spray easily induced decomposition of hydroxyapatite[6]. Indeed, the biomimetic process is one of the promising techniques for bioactive coating which conducted at the ambient temperature by immersion in simulated body fluid (SBF). This technique has ability in promoting uniform coatings on the porous and complex metal surface.

For optimizing rate of hydroxyapatite coating on the implant surface, pre-treatment of the metal is required to initiate an active surface. Many methods of pre-treatment on titanium surface before immersion into SBF solution has been widely studied, including sandblasting [7], alkali or acid treatment [8,9], heat treatment [10] or in a combination of these three approaches [11]. Nucleation of apatite is observed on alkali-heat treated metal after 4 weeks immersion in SBF which improved surface bioactivity with the formation of alkali titanate layer [12,13]. Chemical surface treatment changed Ti implant surface to form hydrogel layer (alkali titanate layer).

Thus, the present study aimed to explore different Ti metal surface preparations with and without SiC paper abrasion towards the formation of alkali titanate layer.

Materials and Methods

Material and chemical selection

Titanium alloy Ti6Al4V ELI (Ti), ASTM F136, Grade 23 long cylinder rods was cut into a small disc samples with diameter 5.5 mm and thickness of 5mm. Samples received in a mirror-liked polished and were categorized into two (2) groups of as received (*as*-Ti) and treated surface (*ab*-Ti). *ab*-Ti surface were abraded with silicon-carbide (SiC) paper up to #1000 grit. Then, *as*-Ti and *ab*-Ti disc were cleaned in acetone, ethanol and distilled water for 10 minutes each, consecutively in the ultrasonic bath (NEYTech, 208H, USA).

Alkali and heat treatment

Surface modification of alkali-heat treatment was conducted using established method from Krupa et al. [11], Kim et al. [14] and Qu & Wei [15] with some modification. The alkali treatment is a process of surface etching and was performed by soaking both *as*-Ti and *ab*-Ti disc in 50 ml of 200g/L NaOH and 50 ml of 280.53g/L KOH aqueous solution for 24 hours at 60 °C for each group. After 24 hours soaking in a water bath of 60 °C, *as*-Ti and *ab*-Ti discs were then rinsed thoroughly with distilled water and dried overnight at room temperature. Then, *as*-Ti and *ab*-Ti discs were heat-treated at 700 °C for 1 hour dwelling time with the heating rate of 3 °C/min in a CARBOLITE furnace (CARBOLITE, ELF 11/14B, UK) and allowed to cool down in the furnace after the heating process. Surface morphology, crystallinity, topography and wettability of Ti6Al4V were examined and studied using field emission scanning electron microscope (FESEM), X-ray diffraction (XRD), 3D surface metrology and contact angle goniometry, respectively.

Surface characterization

Surface roughness

Roughness of *as*-Ti and *ab*-Ti was analysed using optical 3D surface metrology (Alicona, InfiniteFocus, Austria). 3D surface metrology system operated based on combination of small depth of focus of an optical microscope setting at 5X optical zoom with vertical scanning. The analysis was conducted on the total surface area of Ø5.5mm by setting at 3x3 scan frame. Roughness profile calculated automatically using its software based on a line drew across the 2D image of scan surface. Average roughness measurement was taken from 3 different drew lines.

Surface wettability

The wettability of *as*-Ti and *ab*-Ti was determined using contact angle goniometry (AST Products, Inc, VCA-3000S, Massachusetts USA). The contact angle was measured using distilled water drops at room temperature. The angle was calculated manually from the baseline of surface-water contact. Image of water droplet was captured for measurement at about 15 seconds after delivery by using static sessile drop method. Average of three readings of contact angle was taken from each sample.

Surface morphology

Morphology for all samples of Ti treated was observed by using field emission electron microscope, FESEM **(**Carl Zeiss, *SUPRA* 40VP, Germany). The images were captured at magnification of 1k, 5k and 20k at accelerating voltage of 10kV.

Surface structure

Surface structural changes on Ti6Al4V treated specimen were examined by using X-ray diffraction, XRD (Rigaku, D/Max 2200-PC, Japan). All specimens were analyzed at 2θ angles from 10° to 90° with scan speed of 1° per minute.

Results and Discussion

Surface roughness

The surface roughness of *as*-Ti and *ab*-Ti when treated with NaOH and KOH at ambient and high temperature is illustrated in Figure 1.

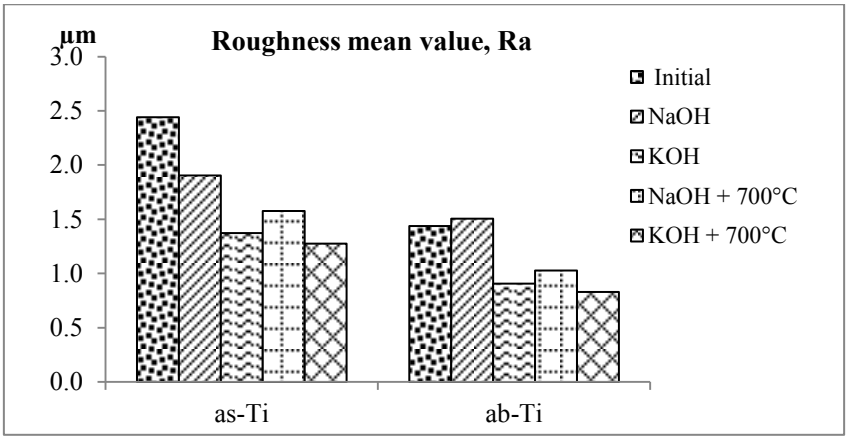


Figure 1. Mean surface roughness of alkali and alkali-heat treated on *as*-Ti and *ab*-Ti

The aim of the analysis is to determine the effect of alkali-heat treated *as*-Ti and *ab*-Ti render the resultant surfaces roughness. The results indicate that the mean value of surface roughness (Ra) on *as*-Ti and *ab*-Ti were 2.44±0.80µm and 1.44±0.40µm, respectively. Abrasion of SiC paper diminished uneven surface on *as*-Ti and lower the surface roughness of *ab-Ti* up to 41%. Initial soaking of *as*-Ti and *ab*-Ti in NaOH gave the Ra value ~0.3-0.5µm greater than Ra in KOH treatment. Alkali treatment leads to the development of submicron- or nano roughness on Ti surface[16] Theoretically, potassium was slightly reactive than sodium. This might cause the outer layer of oxide Ti surface to completely dissolved and activated to form a more homogeneous oxide film. The profile value of the surface roughness changed given a lower value as well. From the Figure 1, the surface roughness of *as*-Ti is decreased after treated with NaOH while it is increased slightly for the case of treating the *ab*-Ti with NaOH. Alkali etching is a process of corroding the surface of Ti. The even surface of *ab*-Ti after abraded with SiC paper was destroyed by NaOH etching process. Hence, Ra value after NaOH treatment is slightly increased. Meanwhile, for the case of *as*-Ti, the rough surface was attacked by NaOH etching reaction that attenuates surface roughness.

ab-Ti that start with lower Ra (1.44±0.40µm) apparently showed value is decreased to 0.83±0.01µm after alkali-heat treated. Heating changed the surface roughness concurrently with the change of surface morphology structure as per in FESEM image (Figure 3 and Figure 4). From the previous studies, a mean surface roughness of 1.38µm and 0.20µm did not differ significantly in the percentage of cell attachment [17]. On the other hand, the effect of SiC paper abrasion on the surface Ti did not show a significant impact in increasing the value of Ra as expected. Therefore, surface roughness value (Ra) range from 1.5µm to 2.0µm is a good start in promoting alkali titanate layer.

Surface wettability

Figure 2 shows the surface wettability study of *as*-Ti and *ab*-Ti. The contact angles of *as*-Ti and *ab*-Ti were 85.05±1.53° and 81.62±2.66°, respectively. A contact angle value indicates the affinity of the Ti surface work towards water molecules. As the contact angle value goes higher, the surface properties become more hydrophobic.

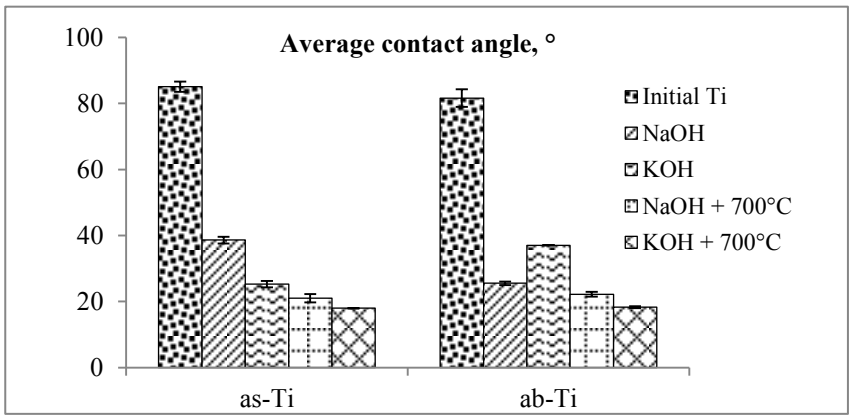


Figure 2. The contact angles measurement of alkali and alkali-heat treated on *as*-Ti and *ab*-Ti

Along the process treatment, *as*-Ti contact angles consistently decreased after alkali-heat treatment. Meanwhile, *ab*-Ti indicates otherwise, which *ab*-Ti after KOH etching is slightly hydrophobic than *as*-Ti with a difference of ~10°. On the other hand, NaOH etching *as*-Ti and *ab*-Ti, the water contact angles drastically reduced to 38.64±1.03° and 25.54±0.53° respectively. A similar result was reported by Zhou et al. [18]. In the case of NaOH etching, higher contact angle of *as*-Ti than *ab*-Ti is due to the presence of inhomogeneous porous network structure in the as-Ti surface (Figure 3b). A large clump cloud-like structure act as a multiscaled roughness of pillars forced the droplet of water to remain in Cassie state which increases the hydrophobicity of *as*-Ti [16]. Meanwhile in a KOH etching case, a porous network structure observed on the surface of *as*-Ti (Figure 3d) which contributed to geometrical air trapping effect due to wetting of hydrophilic pores [19]. Thus, lower the contact angle measurement. Analysis within *as*-Ti group found that KOH etching increased the wettability of the surface with contact angle value of 25.27±0.95° lower than NaOH etching of 38.64±1.03°. Similar results also reported by Kim et al. [16]. Potassium ion has a better reactivity compared to sodium ion. Hence, during the etching process, potassium ion etched and incorporated into the microstructure of passive oxide layer TiO_2 which slightly greater than sodium ion. Moreover, an attraction of hydroxyl group changed the wettability of treated Ti surfaces.

According to the result, chemical and heat treatment result in more hydrophilic surface of *as*-Ti and *ab*-Ti by lowering the contact angle. This can occur due to the reaction on the surface of Ti after chemical-heat treatment that creates the pores which contribute to the hydrophilic structure of Ti. This experiment had not shown obvious differences with the abrasion SiC paper on *as*-Ti surface. According to Rosales-Leal et al., the surface abraded with silicon carbide leaves an excess carbon which potentially modified surface energy[20].

Surface morphology

The surface morphology of *as*-Ti and *ab*-Ti before and after alkali-heat treatment is shown in Figure 3 and Figure 4 respectively. The visible abrasive mark on *ab*-Ti (Figure 4a) was affected the resultant surface structure after NaOH and KOH etching. The formation of porous network structure on *ab*-Ti surface was twice smaller than *as*-Ti. Clearly seen a porous structure on KOH treated at 60 °C with the presence of cloudy dense image (Figure 3d) compared with NaOH etching. However, *ab*-Ti alkali treated had not shown obvious different in morphology structure as shown in Figure 4b and Figure 4d.

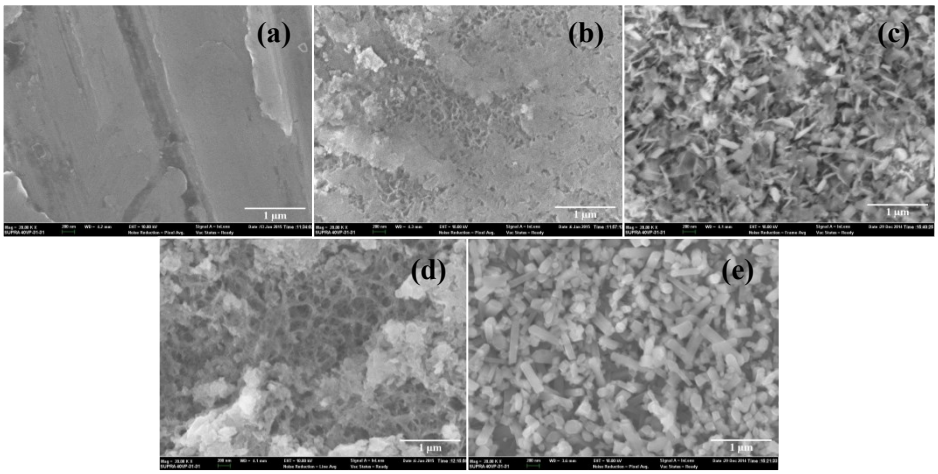


Figure 3. FESEM images at 20k magnification on the surface of *as*-Ti (a), after 5M NaOH-treated (b), after 5M NaOH-heat treated (c), after 5M KOH treated (d) and after 5M KOH-heat treated (e)

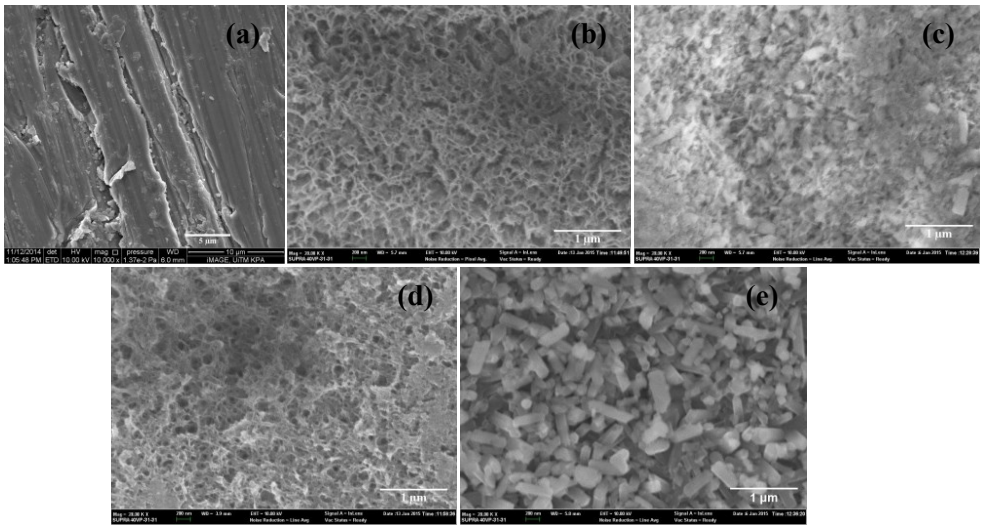


Figure 4. FESEM images at 10k magnification on the surface of *ab*-Ti (a); 20k magnification after 5M NaOH-treated (b), after 5M NaOH-heat treated (c), after 5M KOH treated (d) and after 5M KOH-heat treated (e)

Examination on *as*-Ti and *ab*-Ti surface revealed porous network structure was fully densified to form a homogenous flake-like shape structure (Figure 3c and Figure 4c) on its surface. According to Wei et al., no apatite

formation on the flake-like structure of NaOH-heat treated at 700°C due to heat treatment had changed the surface structure [21]. On the other hand, Ciobanu et al. [22] and Qu & Wei [15] shared similar findings of uniform petal rose-like morphology on Ti surface. Both claimed that petal rose-like structure was HA layer that exhibited on the treated after soaking in modified supersaturated calcification solution (M-SCS) and SBF at medium pH, respectively. Petal rose-like structure of HA coating layer on Ti surface is believe could enhance the osteoinductive and biochemical properties of coating by modification of physical structure [22].

A homogenous rod-like shape structure was observed on heat treated surface after soaking in KOH for 24 hours at 60 °C (Figure 3e and Figure 4e). The porous structure of KOH-treated was fully densified after heat treatment at 700 °C. A potassium hexatitanate ($K_2Ti_6O_{13}$) rod-like structure was observed by Wang et al. [23] and Li et al. [24], which produced from a mixing of potassium carbonate/nitrate and titanium dioxide powder as initial.

Surface structure

Figure 5 and Figure 6 show the XRD patterns of the surfaces of *as*-Ti and *ab*-Ti subjected to heating process at 700°C after soaking in NaOH and KOH, respectively.

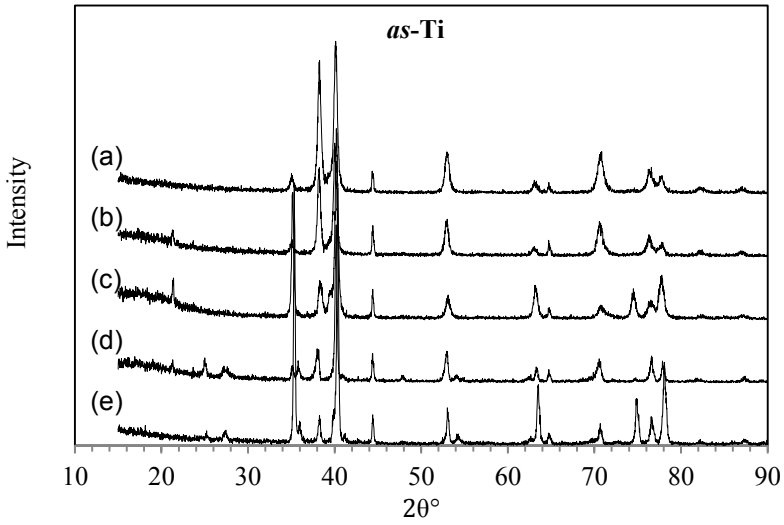


Figure 5. XRD pattern of as-Ti (a); after KOH treated at 60 °C (b); after NaOH treated at 60 °C (c); heat treated after soaking in KOH (d) and heat treated after soaking in NaOH (e)

The aim of XRD analysis is to determine surface structural changes or phase composition present on the treated Ti surface. A small bump was detected around 2θ = 21-22° in Figure 5 (b, c and d) on *as*-Ti. Results indicate a thin layer of either monoclinic phase of potassium titanate ($K_2Ti_6O_{13}$) [24] or sodium titanate ($Na_2Ti_6O_{13}$) depending on alkali solution that *as*-Ti was soaked in. Minor decrease of $K_2Ti_6O_{13}$ or $Na_2Ti_6O_{13}$ peak was hardly observable due to relatively high heating temperature (700 °C). However, neither potassium titanate nor sodium titanate major peak was detectable on *ab*-Ti surface as pattern on in Figure 6.

Meanwhile, at 2θ = 25-28° small amount of rutile (TiO_2) peak were detected for all specimens after heat treated except for *ab*-Ti after soaking in NaOH. These additional peaks indicate that titanium was further oxidized and formed oxide layers with a rutile structure. Other peaks most the same as initial Ti pattern for both *as*-Ti and *ab*-Ti which presenting the peaks of titanium. Intensity different from each treatment due to phase amount and sharp peak indicates phase crystallinity.

During the alkali (KOH/NaOH) etching at 60 °C for 24 hours, the passive oxide layer, TiO_2 partially dissolves into the alkaline solution because of hydroxyl group easily attacked hydrated TiO_2 which will produce negatively charged hydrates on the Ti specimen surface. Negatively charged species easily combined with alkali ions and result

in the formation of alkali titanate hydrogel layer which then densified and dehydrated to form amorphous or crystalline alkali titanate layer after heat treatment [25].

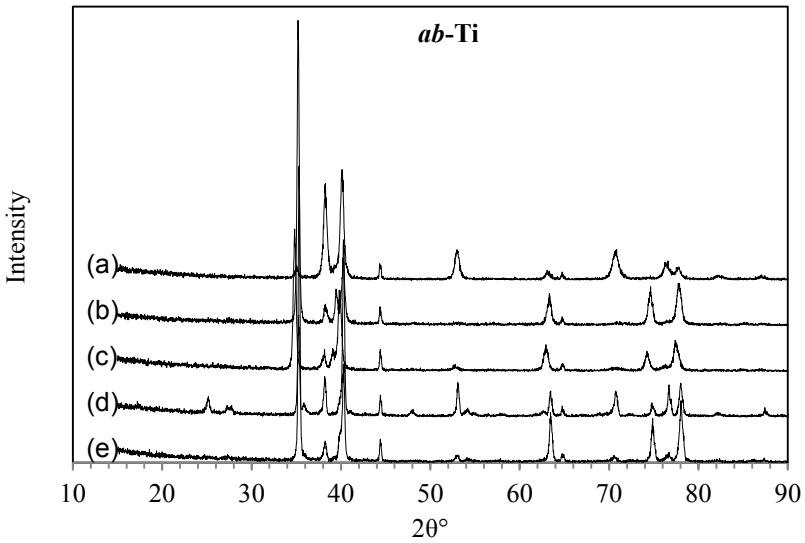


Figure 6. XRD pattern of abraded Ti with SiC paper, as received Ti (a); after KOH treated at 60 °C (b); after NaOH treated at 60 °C (c); heat treated after soaking in KOH (d) and heat treated after soaking in NaOH (e)

Theoretically, Wei et al. [21] claimed that more sodium ions can be released from thicker sodium titanate layer. This leads to easily apatite formation in SBF by increase amount OH^- concentration that release from titanate layer. Hence, further study is suggested to investigate the effect of temperature after alkali treatment on as-Ti.

Conclusion

In this study, roughness, wettability, morphology structure and crystallinity of as-Ti and ab-Ti alkali treated at ambient and 700 °C does not show an obvious different measurement. In fact, as-Ti treated with KOH showed a better porous network structure which is required for good bonding of apatite formation. For the future study, the apatite formation ability on the treated Ti surface in SBF is suggested to be tested.

Acknowledgement

The present study was made possible through a Research Acculturation Grant Scheme by University Technology MARA (600-RMI/RAGS5/3(71/2013)) and also facilities and constant encouragement from Faculty of Chemical Engineering, University Technology MARA is gratefully acknowledged.

References

1. Viceconti, M., Muccini, R., Bernakiewicz, M., Baleani, M. and Cristofolini, L. (2000). Large-sliding contact elements accurately predict levels of bone–implant micromotion relevant to osseointegration. *Journal of Biomechanics*, 33 (12): 1611 – 1618.
2. Narayanan, R., Seshadri, S. K., Kwon, T. Y. and Kim, K. H. (2008). Calcium phosphate-based coatings on titanium and its alloys. *Journal of Biomedical Material Research Part B: Applied Biomaterials*, 85 (1): 279 – 299.
3. Zhang, Q. & Leng, Y. (2005). Electrochemical activation of titanium for biomimetic coating of calcium phosphate. *Biomaterials*, 26 (18): 3853–3859.
4. Liu, D., Yang, Q. and Troczynski, T. (2002). Sol–gel hydroxyapatite coatings on stainless steel substrates. *Biomaterials*, 23: 691 – 698.

5. Wang, H., Eliaz, N., Xiang, Z., Hsu, H. P., Spector, M. and Hobbs, L. W. (2006). Early bone apposition in vivo on plasma-sprayed and electrochemically deposited hydroxyapatite coatings on titanium alloy. *Biomaterials*, 27 (23): 4192 – 4203.
6. Jaworski, R., Pawlowski, L. and Petit, F. (2009). Suspension plasma sprayed titanium oxide and hydroxyapatite coatings in thermal spray 2009. *Proceedings of the International Thermal Spray Conference,*10: 156 – 162.
7. Li, P. (2002). Biomimetic nano-apatite coating capable of promoting bone ingrowth. *Journal of Biomedical Materials Research*, 66A (1): 79–85.
8. Bocardo, J. C. E., Heredia, M. A. L., Cortés, D. A., Ramírez, A. M. and Robles, J. M. A. (2005). Apatite formation on cobalt and titanium alloys by a biomimetic process. *AZo Journal Materials Online*, 1–15.
9. Müller, F. A., Bottino, M. C., Müller, L., Henriques, V. A. R., Lohbauer, U., Bressiani, A. H. and Bressiani, J. C. (2008). In vitro apatite formation on chemically treated (P/M) Ti-13Nb-13Zr. *Dental Materials*, 24 (1): 50 – 56
10. Rohanizadeh, R., Al-Sadeq, M. and Legeros, R. Z. (2004). Preparation of different forms of titanium oxide on titanium surface: Effects on apatite deposition. *Journal of Biomedical Materials Research Part A*, 71(2): 343 – 352.
11. Krupa, D., Baszkiewicz, J., Mizera, J., Borowski, T., Barcz, A., Sobczak, J. W., Biliński, A., Lewandowska-Szumieł, M. and Wojewódzka, M. (2009). Effect of the heating temperature on the corrosion resistance of alkali-treated titanium. *Journal of Biomedical Materials Reserach Part A*, 88(3): 589 – 598.
12. Kokubo, T. (1996). Formation of biologically active bone-like apatite on metals and polymers by a biomimetic process. *Thermochimica Acta*, 280/281: 479 – 490.
13. Kokubo, T., Kim, H.-M., Miyaji, F., Takadama, H. and Miyazaki, T. (1999). Ceramic–metal and ceramic–polymer composites prepared by a biomimetic process. *Composite Part A: Applied Science and Manufacturing*, 30 (4): 405 – 409.
14. Kim, H. M., Miyaji, F., Kokubo, T. and Nakamura, T. (1997). Bonding strength of bonelike apatite layer to Ti metal substrate. *Journal of Biomedical Materials Reserach*, 38 (2): 121 – 127.
15. Qu, H. and Wei, M. (2008). The effect of temperature and initial pH on biomimetic apatite coating. *Journal of Biomedical Materials Research Part B: Applied Biomaterials*, 87(1): 204 – 212.
16. Kim, C., Kendall, M. R., Miller, M. A., Long, C. L., Preston, R., Humphrey, M. B., Madden, A. S. and Tas, A. C. (2013). Comparison of titanium soaked in 5M NaOH or 5M KOH solutions. *Materials Science and Engineering C*, 33: 327 – 339.
17. Mustafa, K., Wennerberg, A., Wroblewski, J., Hultenby, K., Lopez, B. S. and Arvidson, K. (2001). Determining optimal surface roughness of TiO_2 blasted titanium implant material for attachment, proliferation and differentiation of cells derived from human mandibular alveolar bone. *Clinical Oral Implants Research*, 12 (5): 515 – 525.
18. Zhou, H., Nabiyouni, M. and Bhaduri, S. B. (2013). Microwave assisted apatite coating deposition on Ti6Al4V implants. *Materials Science and Engineering C,* 33(7): 4435 – 4443.
19. Whyman, G and Bormashenko, E. (2011). How to make the cassie wetting state stable? *Langmuir*, 27(13): 8171 – 8176.
20. Rosales-Leal, J. I., Rodríguez-Valverde. M. Mazzaglia, A., G., Ramón-Torregrosa, P. J., Díaz-Rodríguez, L., García-Martínez, O., Vallecillo-Capilla, M., Ruiz, C. and M. A. Cabrerizo-Vílchez, (2010). Effect of roughness, wettability and morphology of engineered titanium surfaces on osteoblast-like cell adhesion. *Colloids Surfaces A Physicochemical and Engineering Aspects*, 365 (1–3): 222 – 229.
21. Wei, M., Kim, H.-M., Kokubo, T. and Evans, J. H. (2002). Optimising the bioactivity of alkaline-treated titanium alloy. *Materials Science and Engineering C*, 20 (1–2): 125 – 134.
22. Ciobanu, G., Carja, G., Ciobanu, O., Sandu, I. and Sandu, A. (2009). SEM and EDX studies of bioactive hydroxyapatite coatings on titanium implants. *Micron*, 40 (1): 143 – 146.
23. Wang, X., Liu, S. J., Qi, Y. M., Zhao, L. C. and Cui, C. X. (2014). Behavior of potassium titanate whisker in simulated body fluid. *Materials Letters*, 135: 139 – 142.
24. Li, J., Zhang, Y. C. and Zhang, M. (2012). Low temperature preparation and optical properties of K2Ti6O13. *Materials Letters*, 79: 136–138.
25. Kim, H.-M. and Miyaji, F. (1996). Preparation of bioactive Ti and its alloys via simple chemical surface treatment. *Journal of Biomedical and Materials Research*, 32: 409 – 417.

Malaysian Journal of Analytical Sciences, Vol 20 No 6 (2016): 1437 - 1446
DOI: http://dx.doi.org/10.17576/mjas-2016-2006-24

MALAYSIAN JOURNAL OF ANALYTICAL SCIENCES
Published by The Malaysian Analytical Sciences Society
ISSN 1394 - 2506

OPTIMIZATION OF THERMOPHILIC BIOHYDROGEN PRODUCTION BY MICROFLORA OF PALM OIL MILL EFFLUENT: CELL ATTACHMENT ON GRANULAR ACTIVATED CARBON AS SUPPORT MEDIA

(Pengoptimuman Pengeluaran Biohidrogen Termofilik oleh Mikroflora Efluen Kilang Minyak Sawit: Lampiran Sel Pada Karbon Berbutir Aktif Sebagai Media Sokongan)

Nur Syakina Jamali[1,2] and Jamaliah Md Jahim[1]*

[1]*Department of Chemical and Process Engineering, Faculty of Engineering and Built Environment, Universiti Kebangsaan Malaysia, 43600 UKM Bangi, Selangor, Malaysia*
[2]*Department of Chemical and Environmental Engineering, Faculty of Engineering, Universiti Putra Malaysia, 43400 UPM Serdang, Selangor, Malaysia*

**Corresponding author: jamal@ukm.edu.my*

Received: 21 October 2015; Accepted: 14 June 2016

Abstract

In this study, the biohydrogen production by microflora of palm oil mill effluent (POME) from glucose and xylose fermentation were investigated. Synthetic medium was prepared based on sugar composition present in POME at 7 g/L of glucose and 3 g/L of xylose was used as substrate carbon source. Prior to optimization, 10% of microflora POME was acclimatized in the synthetic medium with the help of granular activated carbon as their support media until consistent hydrogen percentage at 44 ± 1.7% was obtained. Optimization that was conducted using response surface methodology (RSM) by quadratic model of central composite design was found to give optimum parameters of thermophilic microbial growth at pH 6, temperature 60 °C and 10% (v/v) of sludge percentage. Results obtained for hydrogen productivity (1.32 ± 0.01 mmol H_2/L.h, 32.36 ± 0.75 ml H_2/L.h) and hydrogen yield (1.22 ± 0.10 mol H_2/mol sugar consumed) from an average of experimental data reached small error of different (0.8%, 1.0% and 8.3%) to predicted RSM data at optimum condition respectively. The model provided a useful approach for biohydrogen production by POME microflora sludge by using granular activated carbon as their support media.

Keywords: biohydrogen, thermophilic, palm oil mill effluent, synthetic medium, optimization

Abstrak

Melalui kajian ini, penghasilan biohidrogen oleh mikroflora sisa kilang minyak sawit (POME) dari glukosa dan xilosa penapaian telah dikaji. Media sintetik telah disediakan berdasarkan komposisi gula yang terkandung dalam POME sebanyak 7 g/L glukosa dan 3 g/L xilosa telah digunakan sebagai sumber substrat karbon. Sebelum pengoptimuman dijalankan, 10% daripada mikroflora POME telah disesuaikan dalam media sintetik dengan bantuan karbon berbutir aktif sebagai media sokongan mereka sehingga peratusan hidrogen secara konsisten pada 44 ± 1.7% telah diperolehi. Pengoptimuman yang dijalankan dengan menggunakan kaedah gerak balas permukaan (RSM) oleh model kuadratik reka bentuk komposit berpusat telah mendapati bahawa parameter optimum bagi pertumbuhan mikrob termofilik adalah pada pH 6, suhu 60 °C dan 10% (v/v) peratusan enapcemar. Keputusan yang diperolehi untuk pengeluaran hidrogen (1.32 ± 0.01 mmol H_2/L.h, 32.36 ± 0.75 ml H_2/L.H) dan hasil hidrogen (1.22 ± 0.11 mol H_2/mol gula yang digunakan) oleh nilai purata daripada kajian hanya memperolehi sedikit perbezaan (0.8%, 1.0% dan 8.3%) data perolehan saranan RSM pada keadaan optimum. Model ini telah menyediakan pendekatan yang berguna untuk penghasilan biohidrogen oleh enapcemar mikroflora POME dengan menggunakan karbon aktif berbutir sebagai media sokongan mereka.

Kata kunci: biohidrogen, termofilik, sisa kilang minyak sawit, media sintetik, pengoptimuman

Introduction

Fossil fuels have been broadly used to fulfil the needs of developed and undeveloped nations. Burning of fossil fuel in power generation contributes to major environmental destruction, climate changes, greenhouse gasses, and health problems. Hydrogen has been recommended as a new sustainable energy substitutes to fossil fuels because it is non-polluting to the environment and renewable. It only produces water as by-product when burns. Among the conventional hydrogen production technologies, biological hydrogen production through dark fermentation has received great attention due to its potential as an inexhaustible, economical, and carbon-neutral fuel [1, 2].

In Malaysia, wastewater known as palm oil mill effluent (POME) from oil palm industry is considered as an important renewable biomass energy source because it comprises of a mixture of carbohydrates. The high nutrient content in the biomass makes it as an ideal source of sugar feedstock and potentially to be used as fermentation medium in anaerobic treatment processes [2]. Former reports have utilized POME as a substrate for hydrogen production, however these studies only focused on suspended cell cultures, which are usually ineffective or difficult to be monitored in continuous process. Low cell density and washout of bacteria with effluents may happen from the reactor at shorter hydraulic retention time (HRT) in the suspended process [2, 3].

Considering the low biomass in the suspended systems, employing biofilms would appear to be a better approach since biofilms promote higher biomass density and more resistant to changes in environmental conditions. Support carriers like granular activated carbon (GAC) have been well recognised as a support medium in thermophilic fermentation because it can perform effectively at high working temperatures, has a high surface area and highly porous structure that enable to sustain cell feasibility and colonization density [4].

In the view of above, the current research work aimed to evaluate the viability of thermophilic hydrogen production using GAC in an immobilised attached-biofilm system culture. Hence, in a process of developing the biofilm, environmental parameters such as cultivation temperature, initial pH of the culture medium and microbial inoculums play an important role in determining the optimum conditions for ideal microbial growth. Synthetic media comprised of mimicking sugar composition in POME was developed and used as a fermentation media. The optimization of the operating microbial growth condition is essential to attain the maximum hydrogen productivity and hydrogen yield. Response surface methodology (RSM) is recognise as a numerical method which is used in the formation of an empirical model to evaluate the effects of operating process parameters on the desired responses studied. In this regard, RSM was used to determine the relationship between the responses studied, the necessary controllable input factors and represents a sequence of mathematical practises by giving a model equation in evaluating the thermophilic hydrogen production.

Materials and Methods

Microorganism and medium

Microorganism used in this research study was obtained from mixed culture POME-sludge from the sludge pit at Sime Darby Plantation, West Oill Mill, Pulau Carey, Selangor, Malaysia. The synthetic medium used was slightly modified from [4] and contained (per litre of deionized water): NH_4Cl 1.0 g, NaCl 2.0 g, $MgCl_2.6H_2O$ 0.5 g, $CaCl_2.2H_2O$ 0.05 g, $K_2HPO_4.3H_2O$ 1.5 g, KH_2PO_4 0.75 g, $NaHCO_3$ 2.6 g, yeast extract 2.0 g. The mixed cultures sludge was cultivated in the synthetic medium contained glucose and xylose as the sole carbon and energy source.

Sludge growth conditions

The inoculums were grown in 200 ml working volume provided 10% (v/v) of sludge with 90% (v/v) of synthetic medium in batch cultivation in 250 ml modified Scott Duran. The opening mouth of 250 ml Scott Duran was fabricated by allowing the free flow of gas produced from fermentation medium to gas collection in inverted measuring cylinder which contained HCl solvent (pH 2). The HCl solvent was used to prevent biogas dissolved in the liquid and disappear to environment.

The microbial support carrier used in the cultivation process were granular activated carbon (GAC) with particle size of 2 – 3 mm. The cell attachment were studied by adding 1 to 1 GAC weight (g) to heat treated POME sludge volume (ml) ratio as a support media for the inoculum sludge in the serum bottle. The pH of the cultures initially

was adjusted to pH 6 and they were cultivated in a water bath shaker at a temperature of 60 °C and 200 rpm for 48 hours cultivation at 43±2% H_2 gas percentage (OD 0.7 – 0.8 at 600 nm).

Optimization in serum bottles

The optimization of growth parameters at thermophilic condition was designed based on response surface methodology by using Design Expert version 6.0.6. Central composite design was used to optimize the manipulating factors. A total of 20 experiments need to be carried out based on the 3 selected growth parameters namely pH, temperature (°C), and sludge composition (v/v) and resulting to hydrogen productivity rate, HPR (mmol H_2/L.h and ml H_2/L.h) and the hydrogen yield (mol H_2/mol substrate consumed) as the outcomes responses. pH and temperature are one of the most important factors to be regulated in anaerobic digestion processes [5,6].

The optimum conditions were predicted using quadratic equation. Experiments were conducted in triplicates after the optimize parameters were obtained. Analyses of variances (ANOVA) was used as the chosen model to analysis the results obtained and generating the 3D plots. The center line of pH 6, temperature 60 °C and sludge percentage 10(%) was chosen based on thermophilic hydrogen production from sucrose fermentation [4].

The optimization experiments were conducted using 50 ml working volume in 100 ml anaerobic crimped-seal bottles with subsequent flushing of the headspace with nitrogen gas for 1 L/h to create an anaerobic condition. The fermentation was carried out in a water bath shaker by adjusting the temperature according to desire experimental temperature. Samples were analyzed at every 5 hours interval until stationary phase of growth profile was obtained and the cumulative hydrogen productivity was calculated.

Analysis of hydrogen production

Biogas productions were analyzed for CO_2 and H_2 by gas chromatography, using (GC, model SRI 8600C, USA) consist with two detectors, helium ionization detector (HID) and the thermal conductivity detector (TCD). Highly purity helium gas (MOX 99.99%) was used as carrier gas at 25 ml/min. The samples gases were injected to the GC using a gas-tight syringe (0.5 ml injection volume) at 43 °C temperature and pressure 2.7 psi initially and followed by a ramping of 30 °C per minute and been hold for 10 min once the temperature reached 220 °C.

A modified Gompertz equation was performed to quantify the cumulative hydrogen production in the batch experiment by using Matlab 7.9.0 (R2009b). Theoretically, the modified Gompertz equation used in this research was expressed as equation 1 below [5]:

$$Ht = Hm.\exp\{-\exp[(Rm.e/Hm)(\lambda-t)+1]\} \quad (1)$$

where Ht is the cumulative hydrogen production (ml), Hm is the maximum hydrogen production (ml), Rm is the maximum hydrogen production rate (ml/h), e is euler number, λ is the lag phase time (h), and t is the incubation time (h). In this study, the data presented also considered the cumulative of total biogas to compare with the cumulative hydrogen production. Therefore the modified Gompertz was also applied to quantify the total biogas production.

Determination of sugar concentration

Samples were prepared by filtration through a 0.22 µm syringe filter in vials tube and sugar concentration and the soluble volatile fatty acids (VFAs) were quantified by HPLC analysis using an Agilent 1200 HPLC system (California, USA) with a REZEX ROA column (Phenomenex, USA) equipped with a refractive index detector (RID). The mobile phase used was 5 mM H_2SO_4 at a constant 0.6 mL min^{-1} at room temperature. Standard curves of every peak detection were generated at different concentration until straight line R squared was obtained.

Yield and productivity

The amount of sugars consumed and the hydrogen productions obtained were used to calculate the hydrogen yields and the productivity. Yields were expressed as moles of hydrogen per moles of sugar consumed. The VTAs production were used to quantify the capability of the microorganism to reach highest theoretical yields. The maximal volumetric hydrogen productivity was calculated based on the highest percentage of hydrogen gas obtained during the exponential phase of the growth profile in the batch fermentation.

FESEM microbial morphology

The view image of the cell that attached on the surface of GAC after conducting the experimental model validation was further observed with Field Emission Scanning Electron Microscopy (FESEM). The GAC samples were prepared using a Critical Point Dryer (Model Leica EM CPD 300, Leica Microsystems, Germany) for 1 hour and 30 minute prior to be viewed with the FESEM. An amount of 4% glutaraldehyde was used to fix the samples of GAC-attached biofilm for 12 − 24 hours at 4 °C. The samples were then washed with 0.1 M phosphate buffer solution three times per ten minutes each. A series of alcohol dilutions at 30, 50, 70, 80, 90, and 100% (w/w) alcohol were used to dehydrate the samples. The dehydrated samples were then transferred to the CPD and were sputter-coated with platinum before being analyzed with FESEM.

Results and Discussion

Optimization of biohydrogen production

Results of manipulating the selected key factors used during fermentation process towards the hydrogen productivity and yield for each experimental condition produced was shown in Table 1. Based from the experimental conditions shown in Table 1, the hydrogen productivity range from 0.01 to 1.70 mmol H_2/L.h, 0.14 to 41.69 ml H_2/L.h and the hydrogen yield range from 0.06 to 1.61 mol H_2/mol substrate consumed. Results obtained shown the variation of hydrogen production under similar fermentation conditions but with different variable parameters (pH, temperature and sludge percentage) were indicated the importance of each selected parameter on the thermophilic fermentative hydrogen production.

Table 1. Numeric factors of experimental designs with three independent variables and hydrogen productivity and hydrogen yield

Run	pH	Temp	Sludge	Hydrogen		
				Productivity		Yield
		(°C)	(%)	(mmol H_2/L.h)	(ml H_2/L.h)	(mol H_2/mol substrate)
1	6.00	60.00	10.00	1.21	29.50	1.18
2	6.00	60.00	10.00	1.13	27.69	1.20
3	6.84	60.00	10.00	0.42	10.22	0.73
4	5.50	65.00	15.00	0.03	0.66	0.45
5	6.50	65.00	15.00	0.94	22.89	0.98
6	5.16	60.00	10.00	0.01	0.25	0.15
7	6.00	68.41	10.00	0.15	3.61	0.45
8	6.00	60.00	18.41	0.23	5.66	1.01
9	6.00	60.00	10.00	1.36	33.39	1.35
10	6.00	60.00	10.00	1.09	26.68	1.33
11	6.00	60.00	10.00	1.43	34.97	1.31
12	6.50	55.00	15.00	0.29	7.02	0.62
13	6.00	60.00	1.59	0.17	4.22	0.57
14	6.00	60.00	10.00	1.70	41.69	1.61
15	5.50	55.00	5.00	0.70	17.21	0.82
16	5.50	65.00	5.00	0.01	0.14	0.04
17	6.00	51.59	10.00	0.03	0.85	0.06
18	6.50	55.00	5.00	0.86	20.98	0.82
19	6.50	65.00	5.00	0.18	4.38	0.48
20	5.50	55.00	15.00	0.55	13.50	0.77

The predicted responses at centre point at pH 6, temperature 60 °C and sludge percentage 10(v/v) were 1.32 ± 0.23 mmol H_2/L.h, 32.32 ± 5.61 ml H_2/L.h and 1.33±0.15 mol H_2/mol substrate consumed (total of glucose and xylose consumed). The responses as a function of three independent factors are shown in the regression equation after performing the analysis of variances. The quadratic polynomial relating the factors and the responses are shown as equation 2, 3, 4, respectively.
HPR (mmol H_2/L.h):

$$1.31 + 0.12A – 0.08B + 0.01C – 0.32A2 – 0.36B2 – 0.32C2 + 0.15AB +0.04AC + 0.19BC \quad (2)$$

HPR (ml H_2/L.h):

$$32.05 + 2.97A – 1.90B + 0.28C – 7.80A2 – 8.86B2 – 7.90C2 + 3.65AB + 0.97AC + 4.59BC. \quad (3)$$

Hydrogen yield (mol H_2/mol substrate consumed):

$$1.33 + 0.13A – 0.03B + 0.10C – 0.28A2 – 0.34B2 – 0.15C2 + 0.14AB - 0.01AC + 0.14BC \quad (4)$$

where A is the pH, B is the temperature (°C) and C is the sludge percentage (v/v).

Statistical analysis (ANOVA)
An analysis of variance (ANOVA) was conducted to investigate the significance of fit for the quadratic model based on experimental data Table 2 and 3, respectively. The p-value was used to investigate the significance of each coefficient and the degree of interaction between each of the independent factors studied. The independent variables of selected factors are more significant with greater F-value and small p-value [7]. From analysis of ANOVA for response data of hydrogen productivity (mmol H_2/L.h) as summarize in Table 2, the model F-value of 5.76 implies the model was significant. There was only a 0.57% chance that a model F-value this large could occur due to noise. Values of Prob > F of 0.0057 less than 0.05 indicated model terms were significant. The lack of fit F-value of 2.53 implies the lack of fit is not significant relative to the pure error. There is a 16.55% chance that a lack of fit F-value this large could occur due to noise.

Table 2. ANOVA for the response H_2 productivity (mmol H_2/l.h)

	Statistics					
Source	**Sum of Squares**	**DF**	**Mean Square**	**F-Value**	**Prob > F**	**Remark**
Model	4.81	9	0.53	5.76	0.0057	Significant
A	0.20	1	0.20	2.16	0.1720	
B	0.08	1	0.08	0.89	0.3677	
C	0.00	1	0.00	0.02	0.8931	
A^2	1.46	1	1.46	15.78	0.0026	
B^2	1.89	1	1.89	20.37	0.0011	
C^2	1.50	1	1.50	16.21	0.0024	
AB	0.18	1	0.18	1.91	0.1966	
AC	0.01	1	0.01	0.13	0.7218	
BC	0.28	1	0.28	3.03	0.1122	
Residual	0.93	10	0.09			
Lack of Fit	0.66	5	0.13	2.53	0.1655	Not Significant
Pure Error	0.26	5	0.05			
Cor Total	5.74	19				
Coefficient of determination, R^2 = 0.838; adjusted R^2 = 0.693						

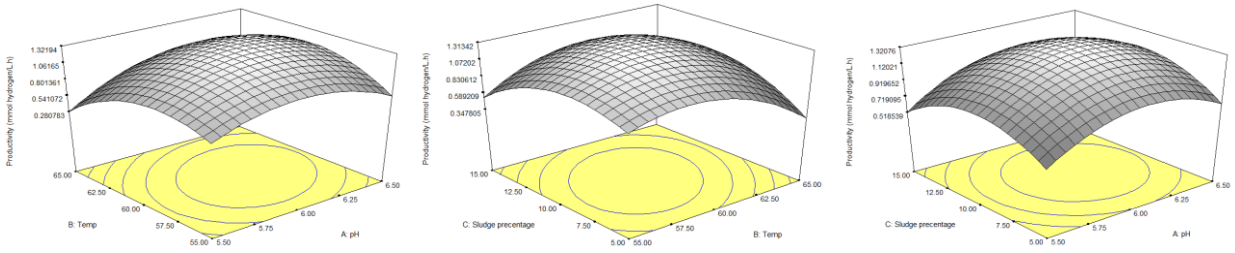
For hydrogen yield response, statistical ANOVA was shown that the model F-value of 8.19 implies the model was significant (Table 3). There was only a 0.14% chance that a model F-value this large could occur due to noise. Values of Prob > F of 0.0014 was shown less than 0.0500 indicated model terms were significant. The lack of fit F-value of 2.87 implies the lack of fit is not significant relative to the pure error. There is a 9.56% chance that a lack of fit F-value this large could occur due to noise. The model terms with p-value greater than 0.10 indicate they are insignificant. The large F-value clearly suggest that the variance in the response can be explained by the regression equation [8].

Table 3. ANOVA for the response H_2 yield (mol H_2/mol substrate consumed)

Statistics						
Source	**Sum of squares**	**DF**	**Mean Square**	**F-Value**	**Prob > F**	**Remark**
Model	3.41	9	0.38	8.19	0.0014	Significant
A	0.23	1	0.23	4.99	0.0495	
B	0.01	1	0.01	0.27	0.6136	
C	0.14	1	0.14	3.08	0.1100	
A^2	1.12	1	1.12	24.10	0.0006	
B^2	1.70	1	1.70	36.62	0.0001	
C^2	0.34	1	0.34	7.41	0.0215	
AB	0.16	1	0.16	3.39	0.0952	
AC	0.00	1	0.00	0.01	0.9155	
BC	0.16	1	0.16	3.54	0.0893	
Residual	0.46	10	0.05			
Lack of Fit	0.34	5	0.07	2.87	0.1360	Not Significant
Pure Error	0.12	5	0.02			
Cor Total	3.88	19				
Coefficient of determination, $R^2 = 0.871$; adjusted $R^2 = 0.756$						

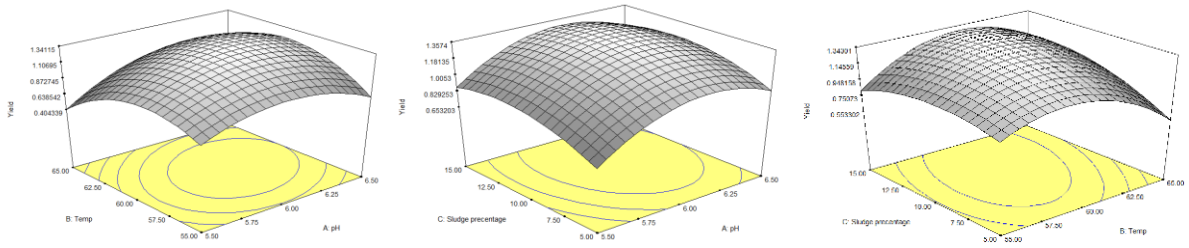
Effect of selected factors on response variables

3D plots are a useful approach in interpreting the response surface. Each 3D plot represent the effect of two independent variables at an optimum level at which the third variable was maintained as constant value. The 3D plot shape indicates whether the mutual interaction between the variables are significant or insignificant. Figure 1 shows the effect between two variables at which the third variable was constant. 3D plots are estimates and if data from repeated experiments were used in the same design, the response of the exchange will change to some extent [9,10].



(a) (b) (c)

Figure 1. 3D plots for different experimental conditions. H_2 productivity (mmol H_2/l.h) as a function of (a) pH and temperature, (b) sludge percentage and temperature, and (c) sludge percentage and pH.



(a) (b) (c)

Figure 2. 3D plots for different experimental conditions. H_2 yield (mol H_2/mol substrate consumed) as a function of (a) pH and temperature, (b) pH and sludge percentage, and (c) temperature and sludge percentage

Validation of the models

Three experimental replications from suggested optimum condition by RSM (pH 6, temperature 60 °C and sludge percentage 10% (v/v)) were conducted to confirm the model validity. From the RSM, the estimated responses of the hydrogen productivity and yield were 1.31 mmol H_2/L.h, 32.04 ml H_2/L.h and 1.33 mol H_2/mol sugar consumed in batch fermentation experiments respectively.

The actual experimental data obtained was tabulated in Table 4. From experimental data, the hydrogen productivity of 1.32 ± 0.01 mmol H_2/L.h obtained in this study was comparable to the predicted data by RSM with only up to 0.76% error of differences. Change in unit of productivity to ml H_2/L.h would not give much different of error compare in unit of mmol H_2/L.h. For yield of hydrogen, 4.4% error of different between the experimental of 1.27 ± 0.11 to predicted data by RSM of 1.33 (mol H_2/mol sugar consumed). Experimental data obtained was also analyzed by modified Gompertz equation as tabulated in Table 4.

Table 4. Confirmation of model validity based from optimum condition predicted by RSM

Model experiment	**Hydrogen**			**Modified Gomertz equation parameter values for H_2 production (per working volume)**		
	Productivity		**Yield**	**Hm**	**Rm**	**λ**
	mmol H_2/L.h	**ml H_2/L.h**	**mol H_2/ mol sugar**	**ml**	**ml/h**	**h**
Predicted Value	1.31	32.04	1.33	-	-	-
Experimental Value	1.32 ± 0.01	32.36 ± 0.75	1.22 ± 0.10	44.17 ± 10.31	3.31 ± 0.39	4.90 ± 0.31
Error (%)	0.8	1.0	8.3	-	-	-

From the statistical quality of modified Gompertz equation, biohydrogen production from experimental data (R^2 = 0.982), it could be inferred that the predicted result are in good agreement with the experimental data. The maximum hydrogen production of 44.17 ± 10.31 ml H_2 and the hydrogen production rate based on the Gompertz equation was 3.31 ± 0.39 ml H_2/h with lag phase of 4.90 ± 0.31h has explained that at optimum condition of thermophilic fermentative hydrogen production, the hydrogen production rate obtained was capable to reach high hydrogen production rate.

Graph of cumulative biohydrogen and biogas production (ml) over fermentation time (hour) were plotted in Figure 3 by using Matlab 7.9.0 (R2009b). 42.0 ± 1.6% of hydrogen gas obtained (44.17 ± 10.31 ml) from total biogas produced (105.0 ± 20.81 ml).

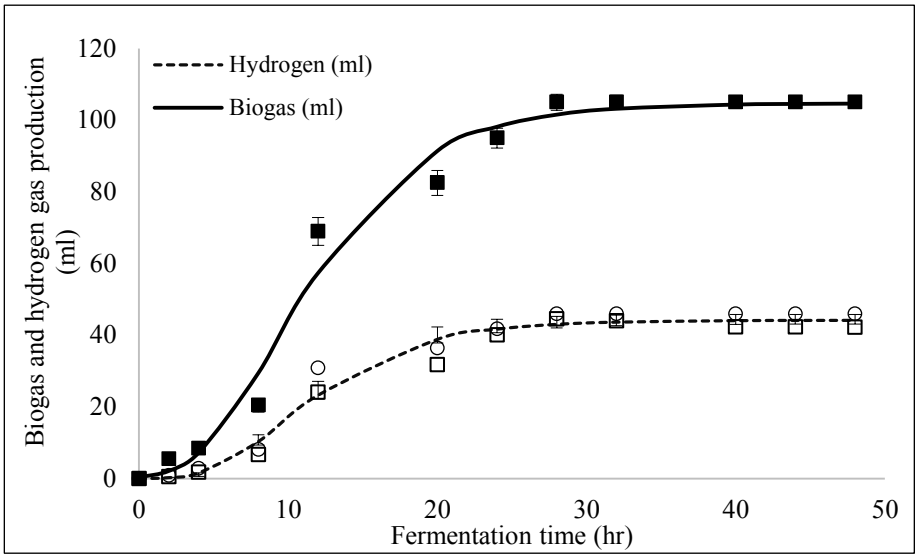


Figure 3. Hydrogen and biogas production (ml) examined by using modified Gompertz equation

FESEM images

The images of microbial cell culture were further observed under Field Emission Scanning Electron Microscope (FESEM). Figure 4(a) represents clean GAC meanwhile 4(b) shows the image of attached cell on GAC after cultural at optimum conditions obtained from the RSM. Figure 4(a) shows that the porosity of clean GAC were acted as suitable place for sludge to self-attach in the pore provided thus forming high density of microbial population, while the images of 4(b) shows that the cells have been successfully adhered on the GAC surface, forming a biofilm attached cell. Immobilisation by adhesion through self-attachment of microorganism and activated carbon is noticeably enhanced cultural cell density at thermophilic operating condition. The GAC provide a structural template directing cell growth and prominent to increase hydrogen production performance compared to suspended culture [11, 12].

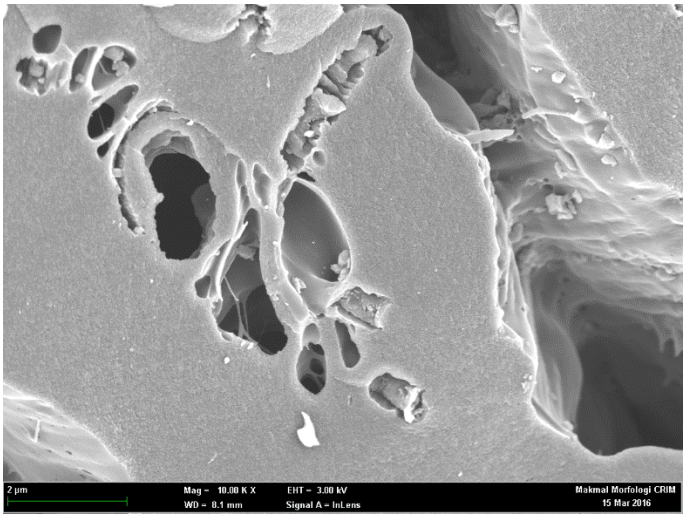


Figure 4(a). FESEM image of clean GAC in the cultural medium at 10.00k x magnification

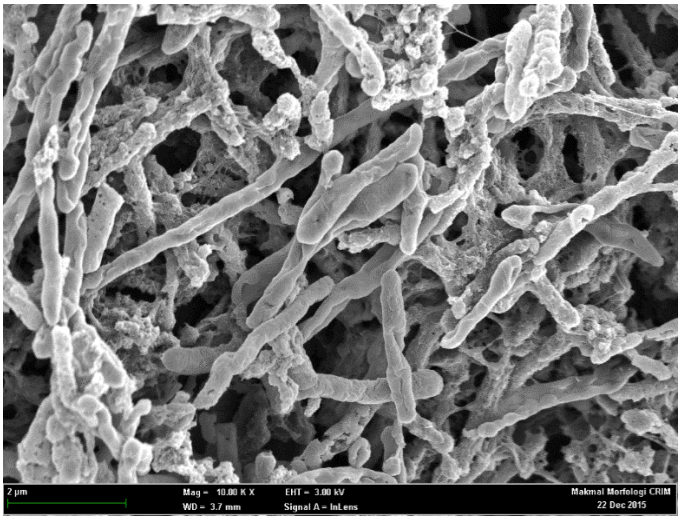


Figure 4(b). FESEM image of attached cell on micro-pores GAC in the cultural medium at 10.00k x magnification

Conclusion

The present study emphasize the mutual effects of the selected parameters in thermophilic biohydrogen production. In this study, the optimum condition obtained from the selected growth parameters were identified to reach optimum through experimental data. The experimental data obtained for hydrogen productivity was 1.48 ± 0.27 in mmol H2/L.h, 36.14 ± 6.65 in ml H2/L.h, and hydrogen yield 1.27 ± 0.11 mol H2/mol sugar consumed at pH 6, temperature 60°C and sludge percentage 10% with error of different 11.3, 11.3 and 4.4% from estimated data by RSM respectively. Under high temperature at thermophilic condition, the hydrogen community producer become energetically favorable and hydrogen consuming reactions become less favorable. The quadratic design model from initial central composite design based on RSM for selected parameters and responses factors were significant to each other. The model provided a useful approach for biohydrogen production by POME microflora sludge by using granular activated carbon as their support media.

Acknowledgement

The authors wish to acknowledge the profound financial support from Sime Darby Plantation, Sdn Bhd under project Zero Waste Technology, Trust Area Biohydrogen (KK-2015-002).

References

1. Levin, D. B., Pitt, L. and Love M. (2004). Biohydrogen production: prospects and limitations to practical applications. *International Journal of Hydrogen Energy*, 29: 173 – 185.
2. Mohammed, M., Salmiaton. A., Azlina W. W., Amran M. M., Fakhru'l-Razi A. and Taufiq-Yap Y. (2011). Hydrogen rich gas from oil palm biomass as a potential source of renewable energy in Malaysia. *Renewable and Sustainable Energy Reviews,* 15: 1258 – 1270.
3. Ismail, I., Hassan, M. A., Abdul Rahman, N. A. and Soon, C. S. (2010). Thermophilic biohydrogen production from palm oil mill effluent (POME) using suspended mixed culture. *Biomass and Bioenergy,* 34: 42 – 47.
4. Lutpi, N. A. and Jahim, J. M. (2014). Thermophilic fermentative hydrogen production using granular activated carbon immobilized mixed microflora. *Australian Journal of Basic and Applied Sciences,* 8: 134 – 137.
5. Chen, W. H., Chen, S.Y., Khanal S. and Sung S. (2006). Kinetic study of biological hydrogen production by anaerobic fermentation. *International Journal of Hydrogen Energy*, 31: 2170 – 2178.

6. Espinoza-Escalante F. M., Pelayo-Ortiz C., Navarro-Corona J., Gonzalez-Garcia Y., Bories A. and Gutierrez-Pulido H. (2009). Anaerobic digestion of the vinasses from the fermentation of *Agave tequilana* Weber to tequila: The effect of pH, temperature and hydraulic retention time on the production of hydrogen and methane. *Biomass and Bioenergy*, 33(1): 14 – 20.
7. Atkinson, A. C. (2011). Optimum experimental design. *International Encyclopedia of Statistical Science. Springer Berlin Heidelberg,* pp. 1037 – 1039.
8. Kim, H. M., Kim, J, G., Cho, J. D. and Hong, J. W. (2003). Optimization and characterization of UV-curable adhesives for optical communication by response surface methodology. *Polymer Testing*, 22: 889 – 906.
9. Myers, R. H., Douglas C., Montgomery, and Anderson-Cook, C. M. (2001). Response surface methodology: Process and product optimization using designed experiments. *John Wiley & Sons.*
10. Montgomery D. C. (2001). Design and analysis of experiments. *5th ed. New York: John Wiley and Sons*.
11. Jamali N. S. J., Jahim J. M., Isahak W. N. R. W., and Abdul P. M. (2016). Particle size variations of activated carbon on biofilm formation in thermophilic biohydrogen production from palm oil mill effluent. *Energy Conversion and Management*. Article in press.
12. Jamali N. S. J., Jahim J. M., and Isahak W. N. R. W. (2016). Biofilm formation on granular activated carbon in xylose and glucose mixture for thermophilic biohydrogen production. *International Journal of Hydrogen Energy*, 41(6): 21617 - 21627.

Malaysian Journal of Analytical Sciences, Vol 20 No 6 (2016): 1447 - 1457
DOI: http://dx.doi.org/10.17576/mjas-2016-2006-25

MALAYSIAN JOURNAL OF ANALYTICAL SCIENCES
Published by The Malaysian Analytical Sciences Society
ISSN 1394 - 2506

PHYSICO-CHEMICAL AND BIOLOGICAL CHANGES DURING CO-COMPOSTING OF MODEL KITCHEN WASTE, RICE BRAN AND DRIED LEAVES WITH DIFFERENT MICROBIAL INOCULANTS

(Perubahan Fiziko-Kimia dan Biologi dalam Pengkomposan Bersama Sisa Dapur, Dedak Padi dan Daun Kering dengan Mikrob Inokulan Yang Berbeza)

Yee Van Fan[1], Chew Tin Lee[1]*, Chee Woh Leow[1], Lee Suan Chua[2], Mohamad Roji Sarmidi[2]

[1]*Faculty of Chemical and Energy Engineering*
[2]*Institute of Bioproduct Development*
Universiti Teknologi Malaysia, 81310 Johor Bahru, Johor. Malaysia

**Corresponding author: ctlee@utm.my*

Received: 21 October 2015; Accepted: 14 June 2016

Abstract

Disposal of food waste either by land-filling or incineration will cause environmental pollution and engaged in high treatment cost. Composting can be a viable food waste management, however, less research works have focused on the degradation of small scale kitchen waste. In this study, co-composting of model kitchen waste, dried leaves and rice bran were inoculated with four different sources of microbial inoculants (MI) namely commercial Effective Microorganism (EM), *Tempeh*, *Tapai*, a mixture of *Tempeh* and *Tapai* and water as a control. It was found that the temperature of all four composting materials with MI can be heated up to a higher temperature (>50 ^{o}C) than the control and produced less offensive smells. All composts ended with a neutral or weakly alkaline pH value (pH 7 – 8) and a C:N ratio of around 10 which indicating the maturation of composts. For enzymatic activities, the highest activity of amylase (73 – 129 U/g) and cellulase (75 – 148 U/g) occurred at the beginning of the composting process. The maximum activities of lipase (5 – 10 U/g) and protease (46 – 72 U/g) were at the middle stage of the composting process. The germination indexes of the five composts were larger than 100% indicating non-phytotoxic. Although the temperature profile and odour performance were outstanding in the presence of MI, most other parameters did not show significant differences when co-compositing of small scale model kitchen waste was carried out with an adequate initial C:N ratio and moisture content. Further study is needed to distinguish the potential beneficiary effects of MI for the composting of kitchen waste. Nevertheless, the comparable performance of *Tempeh* and *Tapai* with EM in composting suggested that *Tempeh* and *Tapai* can be used to substitute the function of EM as a cheaper and more available microbial source for the household.

Keywords: composting, kitchen waste, effective microorganisms, *tempeh*, *tapai*

Abstrak

Pelupusan sisa makanan sama ada di tapak pelupusan atau pembakaran akan menyebabkan pencemaran alam sekitar dan menglibatkan kos rawatan yang tinggi. Pengkomposan merupakan cara pengurusan sisa makanan yang berpotensi tetapi kerja penyelidikan terkini kurang memberi tumpuan kepada degradasi sisa dapur yang berskala kecil. Melalui kajian ini, sisa model dapur, daun kering dan dedak padi telah dirawat dengan empat sumber mikrob yang berbeza iaitu komersial Mikroorganisma Efektif (EM), Tempeh, Tapai, campuran Tempeh dan Tapai dan air sebagai kawalan. Didapati bahawa suhu keempat – empat bahan kompos yang dirawat dengan inokulan mikrob boleh mencapai suhu yang lebih tinggi (>50 ^{o}C) berbanding kawalan dan menghasilkan bau yang kurang busuk. Semua kompos telah berakhir dengan nilai pH yang neutral atau beralkali lemah (pH 7-8) dengan nisbah C:N lebih kurang 10 yang menunjukkan kematangan kompos. Untuk aktiviti enzim, aktiviti tertinggi amilase (73 – 129 U/g) dan selulase (75 – 148 U/g) berlaku pada awal proses pengkomposan. Manakala, aktiviti maksimum lipase (5 – 10 U/g) dan protease (46 – 72 U/g) berada di peringkat pertengahan proses pengkomposan. Indeks percambahan kelima-

lima kompos adalah lebih besar daripada 100% menunjukkan ketiadaan fitotoksik. Walaupun profil suhu dan prestasi bau adalah cemerlang, inokulan mikrob tidak menunjukkan keperluannya dari segi aspek – aspek lain. Keperluan inokulan mikrob dalam proses pengkomposan sisa dapur perlu ditentusahkan secara lebih mendalam dengan analisis yang lain. Walau bagaimanapun, prestasi inokulasi yang disediakan daripada tempeh dan tapai adalah setanding dengan EM. Ini mencadangkan bahawa ia boleh menggantikan EM sebagai sumber yang lebih murah dan lebih tersedia kepada rumah tangga.

Kata kunci: pengkomposan, sisa makanan, mikroorganisma efektif, tempeh, tapai

Introduction

Malaysia has implemented mandatory separation of waste at source starting from September 2015 [1]. Households are required to separate their solid waste before disposal. This action was critical to support effective waste management in order to minimize the management cost, environment pollution and to converse energy. Landfilling and incineration are not suitable for the disposal of kitchen waste as kitchen waste contains high moisture and organic matter contents. Pay-as-you-throw food waste policy as implemented in other countries such as in the Northern Europe, Japan and Korea is a best practice to encourage food waste reducing and recycling. Composting provides an alternative way to convert organic waste into useable and saleable compost. Composting can be a lengthy process and with the possibility of producing immature or low-quality compost when the composting techniques are sub-optimal.

There are two extreme opinions on the uses of microbial inoculants (MI) during composting. Some of them stated that MI is able to increase enzymatic activities [2,3], promote biodegradation of organic matter [4,5] and accelerate the process [4,6]. In contrast, part of them suggests that microbial community naturally present in the waste is able to carry out the degradation satisfactorily when optimum environmental conditions were given [7, 8,9]. In this study, co-composting of model kitchen waste, rice bran and dried leaves in the total size of 4 kg under five different treatments were used to study the necessity and effect of MI for composting. Four MI were tested, namely, the commercial Effective Microorganism^{TM} and three formulations of MI prepared accordingly to the concept of Takakura method [10] using locally available fermented food namely *Tempeh*, *Tapai*, and a mixture of *Tempeh* and *Tapai* where water was used as the control. Various parameters including temperature, moisture content, pH value, C: N ratio, odour performance as well as four enzymatic assays were monitored along the composting process and the resultant compost was evaluated by germination test.

Materials and Methods

Preparation of microbial inoculants (MI)

The microbial inoculants (MI) from *Tempeh* and *Tapai* were prepared as followed: An amount 200 g of brown sugar was dissolved in 3 L of distilled water and autoclaved at 121 ^{o}C for 15 min. Next, 100 g of *Tempeh* and 100 g of *Tapai* was separately added into two 5 L containers each of which contained 3 L of brown sugar solution to produce the respective MI for *Tempeh* and *Tapai*. The containers were placed in room temperature at a static condition for 2 – 3 days until the optical density reading was 0.7 at 545 nm with the appearance of sweet and sour smells and a layer of mold which is an indicator of success fermentation as stated by Takakura [10, 11]. The commercial MI Effective Microorganism^{TM} (EMRO Malaysia Sdn Bhd, Johor, Malaysia) was activated according to the user manual where one part of EM stock was mixed with one part of molasses and twenty part of water for 5 – 7 days until the pH was below 3.5.

Composting of kitchen waste

Composting was carried out in plastic bins under static condition. Aeration of these passively aerated composting was improved with the use of shredded dried leaves as bulking agents, the breathable fabric was used to cover the plastic bin and controlled turning was conducted manually once in a week instead of using an air pump or blower. Each composting bin consists of a total of 4 kg composting materials (2 kg kitchen waste, 1 kg dried leaves,1 kg rice brain) with the initial C:N of around 25:1. Each bin was mixed with different compositions of microbial inoculants (MI) to prepare five composts (Te, Ta, Te+Ta, EM and water as a control) as summarized in Table 1. The model kitchen waste was prepared according to Hafid et al. [12]. The dried leave collected from the landscape within the campus of Universiti Teknologi Malaysia (UTM) was autoclaved before being mixed with the model kitchen waste and the rice bran as purchased from Syarikat Faiza Sdn. Bhd, Batu Pahat, Malaysia.

Each composting material (4 kg) as stated above was mixed with 1.2 L of MI or water (for control) to achieve the acceptable level of initial moisture content between 40 – 60% using the squeeze test [13]. The moisture content of the compost was also monitored weekly based on the dry oven method at 105 ^{o}C for 24 hours [14]. The initial C:N ratio and the moisture content along the composting process were fixed within the suggested range for efficient composting [15].

Table 1. Composition of composting materials

Compost	Composition
Te	Composting material + MI (1.2 L *Tempeh* solution)
Ta	Composting material + MI (1.2 L *Tapai* solution)
Te+Ta	Composting material + MI (0.6 L *Tempeh* solution and 0.6 L *Tapai* solution)
EM	Composting material + MI (1.2 L commercial EM)
Wa (Control)	Composting material + 1.2 L distilled water

Physico-chemical analysis

The temperature of compost was determined daily using thermometer where three-points were measured at 50% depth [9]. Odour performance was examined by smelling [16]. Simple random sampling method [17] was used to obtained representative samples for laboratory analysis where five sub-samples [18] with a total weight of 50 – 70 g was selected. pH values were indicated using SI Analytics Handylab 680FK with the extraction ratio of 1 g of composts in 5 ml of distilled water [19]. For C:N ratio, it was firstly dried at 60 ^{o}C, ground and analyzed using CHNS/O elemental analyzer [6].

Phytotoxicity was evaluated by the effects on seed germination and root growth of aqueous compost extracts prepared from 1.5 g of solid (dry basis) with 15 ml of distilled water (1:10), shaked for one hour at room temperature before centrifuged for 20 min at 5000 rpm. The supernatant was filtered and 5 ml of extract was placed in a Petri dish with 10 radish seeds. Two replicates per sample were incubated at room temperature in dark condition for 72 h. A control test was prepared with distilled water. The number of germinated seeds and their root length was measured. The relative seed germination (RSG), relative root elongation (RRE) and germination index (GI) were calculated using the formulation (equation 1 – 3) as follow [6]:

$$\text{RSG}\ (\%) = \frac{\text{number of seeds germinated in the aqueous extract}}{\text{number of seeds germinated in control}} \times 100\% \quad (1)$$

$$\text{RRE}\ (\%) = \frac{\text{mean root length in the aqueous extract}}{\text{mean root length in control}} \times 100\% \quad (2)$$

$$\text{GI}\ (\%) = \frac{\text{RSG} \times \text{RRE}}{100} \quad (3)$$

Biological analysis

Enzymatic activities were evaluated weekly during the composting process. Amylase, cellulose, protease and lipase activity of all the five samples was determined using aqueous compost extracts extracted using different buffer solution. Amylase activity was evaluated using 1.1% w/v soluble starch as substrate [20]. The colorimetric determination of reducing sugar released from 2% w/v carboxymethyl cellulose was used to estimate the cellulase activity [21]. Glucose was used as a standard substrate for both assays. Protease activity was quantified using 0.65% casein as substrate and tyrosine as standard [22]. Lipase activity was analyzed using 10 µL of *p*-nitrophenyl butyrate as substrate and nitrophenol as standard [23]**.** All measurements were performed in duplicates and calculated in the unit of micrograms per minute per grams (U/g).

Results and Discussion

Temperature

The change of temperature during the composting process indicated the change of microbes in the composts. The high temperature is the results of the accumulation of microbial metabolic warmth and indicating the occurrence of degradation where organic matter was being transformed. Composting is required to go through a thermophilic phase to ensure the safety of compost from pathogens [24]. According to Sundberg et al., thermophilic temperatures are approximately from 45 to 70 ^{o}C [25]. It was found that the temperature of all four composting materials with microbial inoculants (MI) can be heated up higher (>50 ^{o}C) than the control as shown in Figure 1.

The control (composting materials without MI) was not heated up to 45 ^{o}C for at least three days continuously. The maximum temperature was 46 ^{o}C and appeared for only two days. This was probably that the compost contained less diverse communities of microorganisms compared to the inoculated composting materials [9,26]. The composting materials with MI produced from fermented food performed better than those inoculated with EM as their temperature rose higher and continued for a longer period. Among all, Te+Ta shows the best temperature profile. It has a longer thermophilic phase which has continued for 8 days and was heated up to 52 ^{o}C.

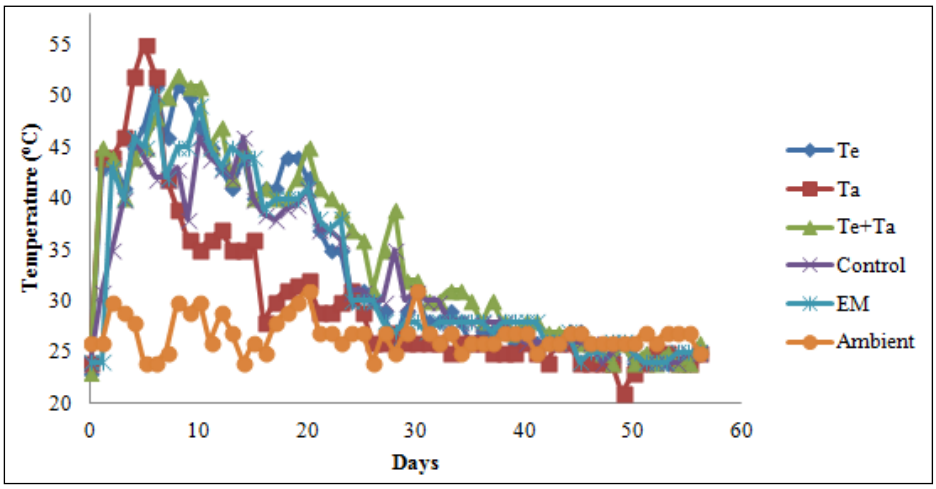


Figure 1. Temperature profile of the composting materials

In this study, the temperatures of the five composting materials started to enter cooling phase after 3 weeks of composting. This suggests that the maturation and stabilization of organic matter have been reached. However, the drop in temperature can be due to the lost of composts volume and lead to insufficient self-insulation as the composting scale in this study was initially undersized [26]. Consequently, it makes the use of temperature for predicting maturation less effective. Therefore, the temperature profile is employed together with other additional parameters to further determine the maturity and stability of composts. The ambient temperatures were ranged between 24 to 31°C during the composting process.

pH value and odour

After 8 weeks, the pH values of all composts were approximately at neutral (7 – 8) as shown in Figure 2 which indicating the stability of organic matter [27]. There were no significant different ($p > 0.05$) between the compost with and without microbial inoculants (MI) in term of pH. According to the pH profile, all of the five composting materials were no longer acidic in week 3.

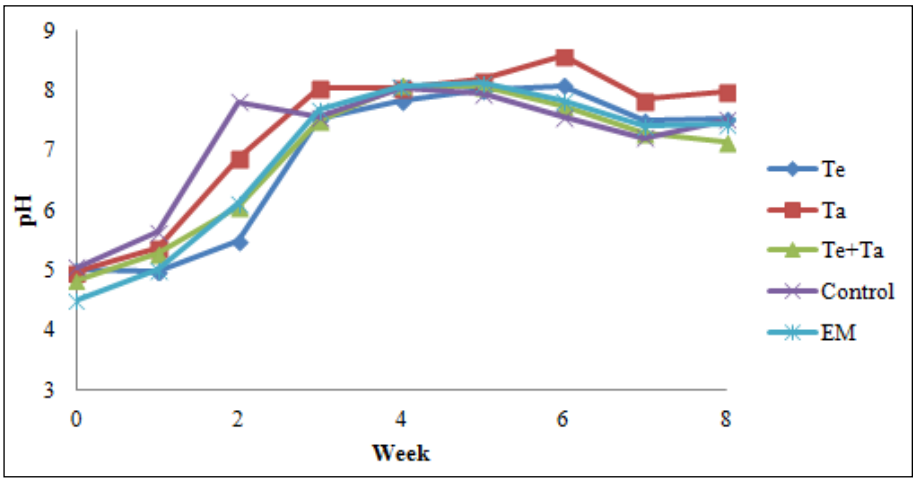


Figure 2. pH profile of the composting materials

In contrast, there are notable differences in term of the odour of the composts. Table 2 shows the summary of odour produced during the composting. The unpleasant smell of the composting materials decreased with time [16]. MI successfully suppressed the growth of bad microbes that contributed to foul smell by week 3. By comparison, control set produced very unpleasant smells which were pungent on week 1 and 2. These results correlate with the pH profiles where the pH values were higher than the others in the control samples. According to Miller et al., high pH leads to the loss of N through ammonia volatilization that was associated with the odour problem [28]. Besides, composts with MI produced earthy smells faster than the control. Among the compost treated with MI, Te+Ta produced earthy smell in the shortest time which was on week 4.

Table 2. Odour performance of composting materials

Week/ Sample	Te	Ta	Te + Ta	Control	EM
0	+++	+++	+++	+++	+++
1	++	++	++	++	++
2	++	++	++	+	++
3	+++	+++	+++	+	+++
4	++++	++++	+++	++	+++
5	++++	++++	+++	+++	++++
6	++++	++++	++++	+++	++++
7	++++	++++	++++	++++	++++
8	++++	++++	++++	++++	++++

+ very unpleasant, ++ moderate unpleasant, +++ odourless, ++++ earthy

C:N ratio

Figure 3 shows the changes of C:N ratio. For all samples including for the control, the C:N ratio decreased significantly with time and stabilized on week 2 which means that significant degree of degradation took place in

the first 3 weeks. C:N ratio decreased as the carbon content in the compost valorised as carbon dioxide along the composting process. Although nitrogen might lose due to volatilization, it does not contribute to the increase of C:N ratio as the decrease of carbon is more markedly during the composting process. The values of C:N for all of the composts in week 8 was less than 10, indicating the approaching of the mature stage [29]. The C:N ratio of about 10 is the ideal ratio for well-matured compost [30] but as C:N ratio was highly depending on the initial and type of feedstock used, two or more parameters are needed to verify the maturity of compost. There was no significant different ($p > 0.05$) between the compost with and without microbial inoculants (MI) in term of C: N ratio. These phenomena might have suggested that the degradation rate was similar in all cases.

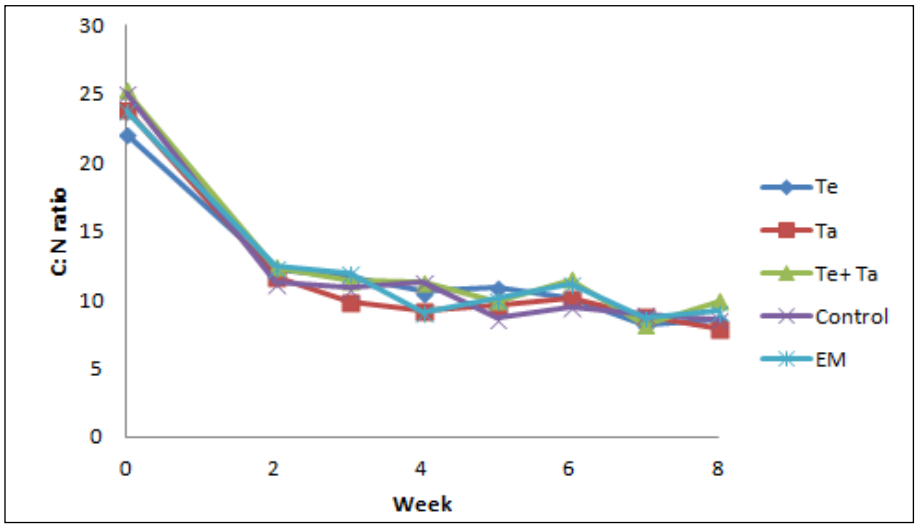


Figure 3. Changes of C: N ratio during the composting process

Enzymatic assays

Enzymes are the main mediators of degradation process and they control the degradation rates of different substrate [16]. Measurement of enzymatic activities illustrates the enzymes which participate in the bioconversion of the composting materials. In this study amylase, cellulase, lipase and protease were measured during composting due to the possible available inducers in the composting materials. The enzymatic assays (amylase, cellulose, lipase and protease) for all composts, namely Te, Ta, Te+Ta, EM and Wa (control), showed a similar ending trend as shown in Figure 4 to 7. The lower activity during the end phase indicated the completion of decomposition process [11]. The cellulase and protease activity decreased and stabilized on week 3 while amylase, lipase was on week 4 and 5, respectively. Figure 4 to 7 are plotted using the average values from the duplicated test.

Referring to Figure 4, the highest activity of amylase occurred at the beginning of the composting process and decreased gradually until a stabilized level. This trend was similar to the finding by Ismail et al., the high activity at the beginning could be due to the starchy materials available in the kitchen waste which was easier to be degraded [16].

Cellulose activity also has an analogous trend with amylase, the maximum activity occurred at the beginning as shown in Figure 5. These findings agree with the result that has been stated by Gómez-Brandón et al. in the composting of cattle manure where the cellulase activity was low during the active and maturation stage [31]. However, the decline shown in the cellulase activity was sharper than that for the amylase activity. This was most probably due to the limited substrate (cellulose) in the composting materials.

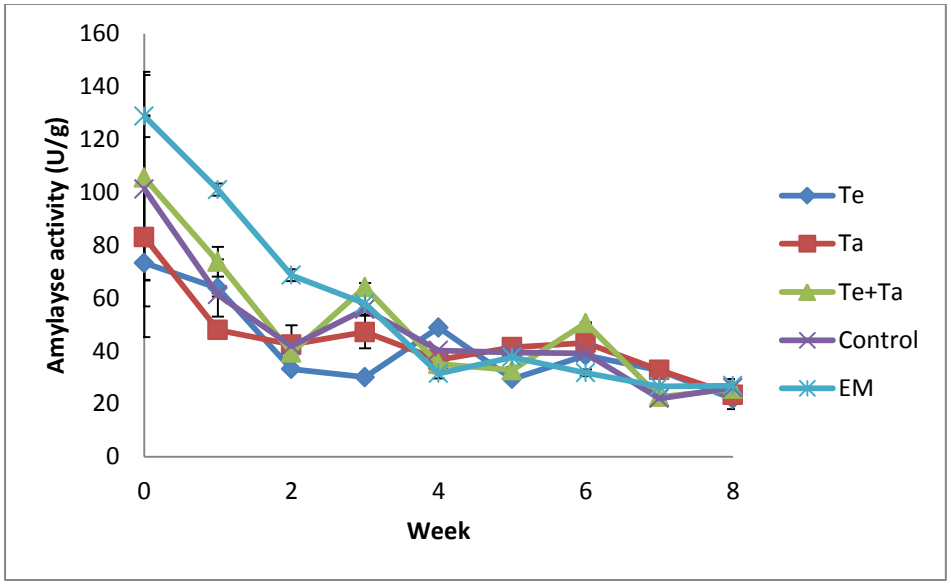


Figure 4. Amylase activity of composting materials

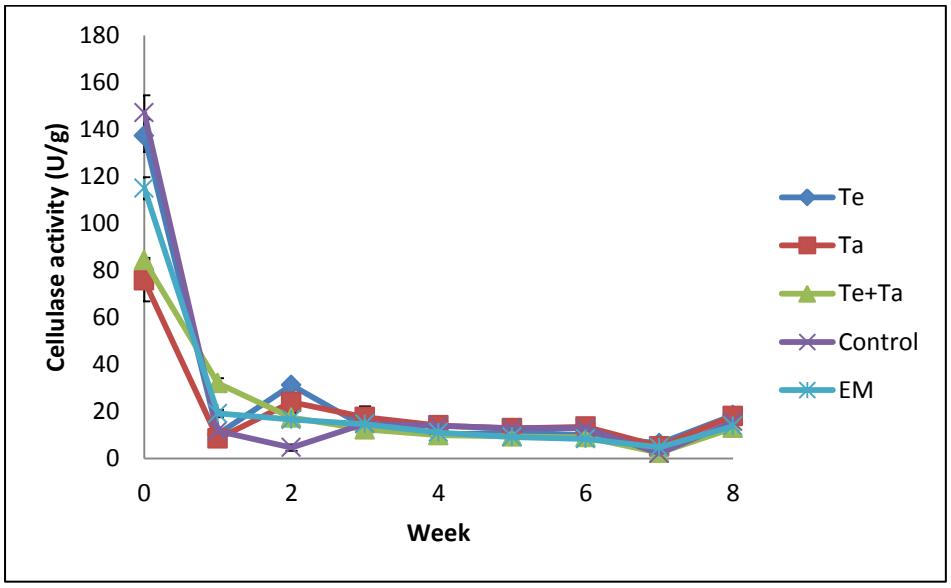


Figure 5. Cellulase activity of composting materials

The composting material used in this study was made up of kitchen waste, rice bran and dried leaves. These materials contained recalcitrant carbon due to the present of lignin. Lignin minimizes the accessibility of cellulose to microbial enzymes. Rice bran contains 27% cellulose, 37% hemicellulose, 5% lignin [32], the available and easier degradable cellulose was mainly from rice bran and kitchen waste. Therefore, the dramatic decrease in the cellulase activity was likely due to the fast degradation in the beginning contributed by the easier degrading cellulose materials and the low remaining cellulose content after one week. Moreover, the type of cellulase determined in this study is endoglucanase. The enzymatic hydrolysis of cellulose requires endoglucanase,

exoglucanase and cellobiases to work together [33], the later composting process might be taken over by exoglucanase or cellobiases.

On the other hand, the lipase and protease activity shows a pattern that is normally obtained in the previous studies where the enzymatic activities increased with time as the composting proceeded until a maximum activity at the middle stage followed by a declining trend [11,34]. These results indicated the capability of microorganisms in synthesizing enzymes essential for hydrolysis of various complexes organic compounds. Figure 6 and 7 shows the lipase and protease activities respectively.

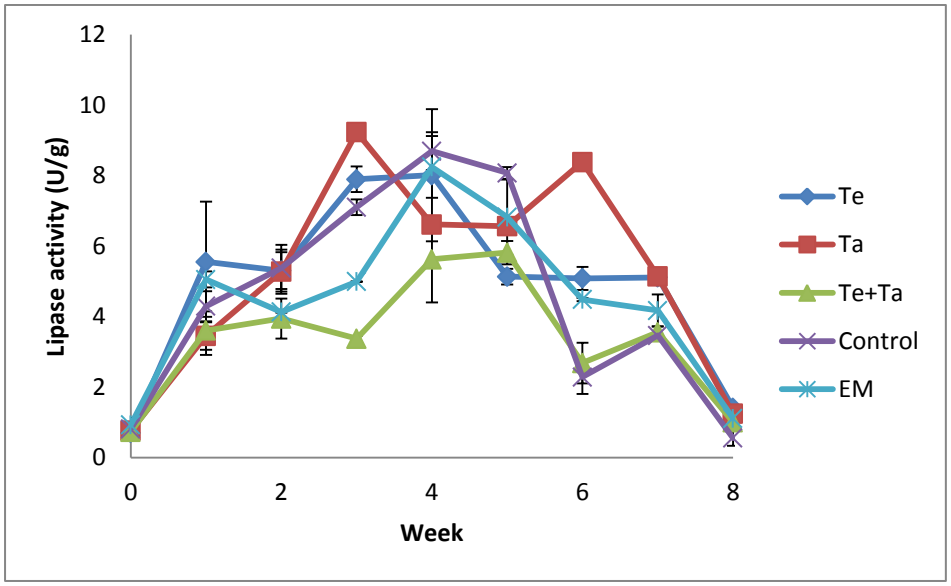


Figure 6. Lipase activity of composting materials

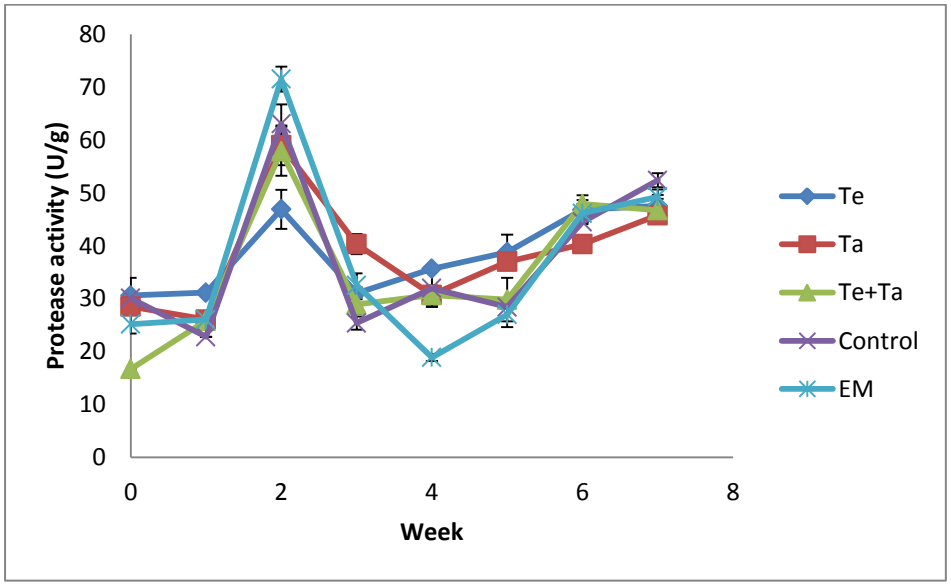


Figure 7. Protease activity of composting materials

No significant different was found among the composting materials inoculated with or without microbial inoculants (MI). The enzymatic activities of the composting materials treated with MI developed from the fermented food were almost the same as the composting materials treated with EM and also with bare water. In term of the total accumulated enzymatic activity along the whole composting process for a 8 weeks duration, EM has the highest amylase activity (510.47 U/g), Te has the highest cellulase (247.63 U/g) as well as protease activity (347.13 U/g) and Ta has the highest lipase activity (46.64 U/g). Table 3 shows the maximum enzymatic activity occurred during the composting process. The maximum amylase and cellulase activity occurred on the initial stage of composting process (week 0). While the maximum lipase and protease activities were observed on week 4 and week 2, respectively.

Table 3. Maximum enzymatic activity during the composting process

Maximum activity (U/g)	**Composts**				
	Te	**Ta**	**Te+Ta**	**Water (Control)**	**EM**
Amylase	73.23	83.03	105.48	101.2	128.82
Cellulase	137.3	75.64	84.25	147.03	114.94
Protease	46.87	58.98	57.86	63.06	71.5
Lipase	8.01	9.23	5.62	8.69	8.24

Germination Index

All composts showed non-phytotoxic (> 80%) on germination test using radish seeds [29]. Table 4 shows the germination index of composts on week 8. Measurement of phytotoxic present in the compost is an accurate and efficient method to check the maturation of organic matter. The results obtained indicated that all composts have matured within two months time. By comparison, it was far faster than the normal duration of traditional composting (6 months to 1 year), vermicomposting (3 – 6 month) and Takakura home composting method (3 months).

Table 4. Germination index on week 8

Composts	**Germination Index (%)**
Te	317.93 ± 23.06
Ta	321.32 ± 7.47
Te+Ta	323.37 ± 97.31
Control	401.57 ± 86.92
EM	306.05 ± 97.01

Conclusion

Based on the results, it shows the potential of using *Tempeh* and *Tapai* as microbial inoculants (MI) to degrade small scale kitchen waste. The technique is user-friendly and the sources of MI are readily accessible by households. The temperature profile and odour performance of Te, Ta, Te +Ta were outstanding. Besides, the enzymatic assays are comparable with the composting performance of EM even though no difference can be indicated when compared with the control (water). In addition, the pH values, C: N ratio and germination index of the five composts under different treatments also showed satisfactory values. According to the examined parameter, all of the composts were in matured stage within two-month duration of composting or even earlier. The continuous

study can be carried out on the humic acid content, nutrient content and pathogen analysis to further comparing the effectiveness of *Tempeh* and *Tapai* as MI against EM and water.

Acknowledgement

The authors are grateful to Universiti Teknologi Malaysia (UTM) and Ministry of Science, Technology and Innovation, Malaysia (MOSTI) for the financial grants of Vot 10H28 and Vot 4S058 respectively. This work was also partially funded by UTM Sustainability Flagship Project Vot No. 01G67 and UTM Research University Grant Vot No. 04H09.

References

1. The Star (2014). Govt to gradually introduce mandatory waste separation from Sept 2015. *The Star*. www.thestar.com.my/News/Nation/2014/11/15/waste-sorting-mandatory-sept-2015/ [Assessed 28 April 2016].
2. Hubbe, M. A., Nazhad, M. and Sánchez, C. (2010). Composting as a way to convert cellulosic biomass and organic waste into high-value soil amendments: A review. *Bioresources,* 5(4): 2808 – 2854.
3. Payel, S., Mukesh, M. and Rajni, S. (2011). Microbial consortium: A new approach in effective degradation of organic kitchen wastes. *International Journal of Environmental Science and Development*, 2 (3): 170 – 174.
4. Xi, B., Zhang, G. And Liu, H. (2005). Process kinetics of inoculation composting of municipal solid waste. *Journal of Hazardous Materials*, 124(1): 165 – 172.
5. Patidar, A., Gupta, R. and Tiwari, A. (2012). Enhancement of bio-degradation of bio-solids via microbial inoculation in integrated composting and vermicomposting technology. *Scientific Report*, 1(5): 1 – 4.
6. Saad, N. F. M., Ma'min, N. N., Zain, S. M., Basri, N. E. A. and Zaini, N. S. M. (2013). Composting of mixed yard and food wastes with effective microbes. *Jurnal Teknologi*, 65(2): 89 – 95.
7. Stabnikova, O., Ding, H. B., Tay, J. H. and Wang, J. Y. (2005). Biotechnology for aerobic conversion of food waste into organic fertilizer. *Waste Management and Research*, 23(1): 39 – 47.
8. Nair, J. and Okamitsu, K. (2010). Microbial inoculants for small scale composting of putrescible kitchen wastes. *Waste Management*, 30(6): 977 – 982.
9. Abdullah, N., Chin, N. L., Mokhtar, M. N. And Taip, F. S. (2013). Effects of bulking agents, load size or starter cultures in kitchen-waste composting. *International Journal of Recycling of Organic Waste in Agriculture*, 2(1): 1 – 10.
10. Norlidah, R. (2010). Home composting: Step-by-step guide to Takakura composting, *The Star*. [Assessed 28 April 2016].
11. Ying, G. H. and Ibrahim, M. H. (2013). Local knowledge in waste management: A study of Takakura home method. *Journal of Environmental Science*, 2: 528 – 533.
12. Hafid, H. S., Nor'Aini, A., Omar, F. N., Phang, L., Suraini, A. and Hassan, M. A. (2010). A comparative study of organic acids production from kitchen wastes and simulated kitchen waste. *Australian Journal of Basic and Applied Sciences*, 4(4): 639 – 645.
13. The United States Department of Agriculture (1998). Estimating soil moisture by feel and appearance. Washington, D.C.
14. Kutsanedzie, F., Rockson, G. N., Aklaku, E. D. and Achio, S. (2012). Comparisons of compost maturity indicators for two field scale composting systems. *International Research Journal of Applied and Basic Science*, 3(4): 713 – 720.
15. Hubbe, M. A., Nazhad, M. and Sanchez, C. (2010). Composting as a way to convert cellulosic biomass and organic waste into high-value soil amendments: A review. *Bioresources,* 5(4): 2808 – 2854.
16. Ismail, K. A., El-Din, H. M. S., Mohamed, S. M., Latif, A. B. M. A. and Ali, M. A. M. (2013). Monitoring of physical, chemical, microbial and enzymatic parameters during composting of municipal solid wastes: A Comparative Study. *Journal of Pure Applied Microbiolology*, 8(1): 211 – 224.
17. Food and Agriculture Organization of the United Nations. (2000). Simple soil, water and plant testing techniques for soil resource management. Rome, Italy.
18. Woods End Research Laboratory. (2000). Compost quality standard and guidelines. Compost quality in America.
19. Shyamala, D. and Belagali, S. (2012). Studies on variations in physico-chemical and biological characteristics at different maturity stages of municipal solid waste compost. *International Journal of Environmental Sciences*, 2(4): 1984 – 1997.

20. Mishra, S. and Behera, N. (2008). Amylase activity of a starch degrading bacteria isolated from soil receiving kitchen wastes. *African journal of biotechnology*, 7(18): 3326 – 3331.
21. Ghose, T. (1987). Measurement of cellulase activities. *Pure and Applied Chemistry*, 59(2): 257 – 268.
22. Cupp-Enyard, C. (2008). Sigma's non-specific protease activity assay-casein as a substrate. *Journal of Visualized Experiments*, 19: 1 – 2.
23. Margesin, R., Feller, G., Hämmerle, M., Stegner, U. and Schinner, F. (2002). A colorimetric method for the determination of lipase activity in soil. *Biotechnology Letters*, 24(1): 27 – 33.
24. Bernal, M. P., Alburquerque, J. A. and Moral, R. (2009). Composting of animal manures and chemical criteria for compost maturity assessment: A review. *Bioresource Technology*, 100(22): 5444 – 5453.
25. Sundberg, C., Smårs, S. and Jönsson, H. (2004). Low pH as an inhibiting factor in the transition from mesophilic to thermophilic phase in composting. *Bioresource Technology*, 95(2): 145 – 150.
26. Dickson, N., Richard, T., Kozlowski, R. and Sobel, P. L. (1991). Composting to reduce the waste stream: a guide to small scale food and yard waste composting. *Northeast Regional Agricultural Engineering Service*: pp 1 – 53.
27. Pan, I. and Sen, S. (2013). Microbial and physico-chemical analysis of composting process of wheat straw. *Indian Journal of Biotechnology*, 12(1): 120 – 128.
28. Miller, F. C., Macauley, B. J. and Harper, E. R. (1991). Investigation of various gases, pH and redox potential in mushroom composting Phase I stacks. *Animal Production Science*, 31(3): 415 – 423.
29. Cheng, K. H., Huang, M. C., Lu, M. F., Chou, Y. J. and Lin, J. J. M. (2013). Assessment of degree of maturity of compost produced by different kitchen waste composting methods. *Advanced Materials Research*, 652: 1642 – 1651.
30. Pathak, A. K., Singh, M. M. and Kumar, V. (2011). Composting of municipal solid waste: a sustainable waste management technique in Indian cities – A review. *International Journal of Current Research*, 3(12): 339 – 246.
31. Gómez-Brandón, M., Lazcano, C. and Domínguez, J. (2008). The evaluation of stability and maturity during the composting of cattle manure. *Chemosphere*, 70(3): 436 – 444.
32. Baig, M., Zetzl, C. and Brunner, G. (2005). Conversion of extracted rice bran and isolation of pure bio-ethanol by means of supercritical fluid technology. *10th European Meeting on Supercritical Fluids,* N(3): 1 – 6.
33. Zhang, Y. P., Hong, J. and Ye, X. (2009). Cellulase assays. Protocol biofuels. *Springer*, 581: 213 – 231.
34. Raut, M., William, S. P., Bhattacharyya, J., Chakrabarti, T. and Devotta, S. (2008). Microbial dynamics and enzyme activities during rapid composting of municipal solid waste – a compost maturity analysis perspective. *Bioresource Technology*, 99(14): 6512 – 6519.

Malaysian Journal of Analytical Sciences, Vol 20 No 6 (2016): 1458 - 1466
DOI: http://dx.doi.org/10.17576/mjas-2016-2006-26

MALAYSIAN JOURNAL OF ANALYTICAL SCIENCES
Published by The Malaysian Analytical Sciences Society
ISSN 1394 - 2506

PREPARATION OF LANTHANUM STRONTIUM COBALT OXIDE POWDER BY A MODIFIED SOL-GEL METHOD

(Penyediaan Serbuk Lantanum Strontium Kobalt Oksida Melalui Kaedah Sol-Gel Terubahsuai)

Abdullah Abdul Samat[1], Mahendra Rao Somalu[1]*, Andanastuti Muchtar[1,2], Nafisah Osman[3]

[1]*Fuel Cell Institute*
[2]*Department of Mechanical and Materials Engineering, Faculty of Engineering and Built Environment*
Universiti Kebangsaan Malaysia, 43600 UKM Bangi, Selangor, Malaysia
[3]*Faculty of Applied Sciences,*
Universiti Teknologi MARA, 02600 Arau, Perlis, Malaysia

**Corresponding author: mahen@ukm.edu.my*

Received: 21 October 2015; Accepted: 14 June 2016

Abstract

A simple low temperature synthesis route has been presented for the preparation of single perovskite phase of $La_{0.6}Sr_{0.4}CoO_{3-\delta}$ (LSCO) for cathode application in intermediate temperature proton conducting solid oxide fuel cell (SOFC). A wet chemical method namely a modified sol-gel method has been applied in this work. In this method, a combined citric acid and ethylenediaminetetraacetic acid (EDTA) has been used as a chelating agent. Ethylene glycol (EG) and activated carbon (AC) have been used as surfactants in this process. The synthesized powders were characterized by X-ray diffractometer (XRD), scanning electron microscope (FESEM) equipped with energy dispersive X-ray (EDX) spectrometer and particle size analyzer (PSA) for phase formation, morphology and particle size analysis, respectively. XRD result revealed that a single LSCO perovskite phase for both surfactants formed at calcination temperature of 900 °C. The produced single phase powders consist of homogeneous and almost identical shape of particles as shown in SEM images. However, the powder prepared using EG has a smaller average particle size diameter as compared with the powder prepared using AC which is 149 nm and 190 nm, respectively.

Keywords: modified sol-gel, surfactant, cathode, solid oxide fuel cell, single perovskite phase of $La_{0.6}Sr_{0.4}CoO_{3-\delta}$

Abstrak

Satu kaedah sintesis ringkas pada suhu rendah telah dibentangkan untuk menyediakan fasa tunggal perovskit $La_{0.6}Sr_{0.4}CoO_{3-\delta}$ (LSCO) bagi aplikasi katod di dalam konduktor proton sel bahan api oksida pepejal (SFOP) suhu sederhana. Satu kaedah kimia basah, iaitu, kaedah sol-gel terubahsuai telah digunakan dalam penyelidikan ini. Melalui kaedah ini, gabungan asid sitrik dan asid atelindiamintetrasetik (EDTA) telah digunakan sebagai agen pengikat. Etilena glikol (EG) dan karbon teraktif (AC) telah digunakan sebagai surfaktan dalam proses ini. Serbuk yang disintesis telah dicirikan dengan menggunakan pembelauan sinar-X (XRD), mikroskop elektron pengimbas (SEM) dilengkapi dengan spektroskopi sinar-X sebaran tenaga (EDX) dan penganalisis saiz zarah (PSA) bagi analisis pembentukan fasa, morfologi dan saiz zarah, masing-masing. Keputusan XRD menunjukkan fasa tunggal perovskit LSCO bagi kedua-dua surfaktan telah terbentuk pada suhu pengkalsinan 900 °C. Serbuk berfasa tunggal yang terhasil terdiri daripada zarah yang homogen dan mempunyai bentuk yang hampir sama seperti ditunjukkan dalam imej SEM. Walau bagaimanapun, serbuk yang dihasilkan menggunakan EG mempunyai purata diameter saiz zarah yang lebih kecil iaitu 149 nm berbanding serbuk yang dihasilkan menggunakan AC iaitu 190 nm.

Kata kunci: sol-gel terubahsuai, surfaktan, katod, proton sel bahan api oksida pepejal, fasa tunggal perovskit $La_{0.6}Sr_{0.4}CoO_{3-\delta}$

Introduction

Nowadays, solid oxide fuel cells (SOFCs) have received considerable attention worldwide. It has been deemed as one of the most promising future power generation as if offers few remarkable advantages including high energy conversion efficiency, low/zero pollutant emission and fuel flexibility compared to the conventional energy power generator. The challenge in the SOFC development is to lower the operating temperature from high (800 - 1000 °C) to intermediate (500 - 700 °C) temperatures. The fabrication cost is then expected to be reduced which would boost the commercialization of such energy conversion devices [1,2].

One the most promising SOFC technologies operating at intermediate temperature is proton conducting SOFC (H^+-SOFC). However, only few reports have dealt with H^+-SOFC technology especially in cathode materials for the H^+-SOFC in the literature [3-6]. In this context, our main goal is to synthesis suitable cathode materials for the H^+-SOFC.

In the last two decades, cobaltite oxides have been widely studied due to the fact that many of these compounds have shown good electrical conductivity and remarkable thermoelectric properties that could be used in practical applications. Among these oxides, lanthanum cobaltite, $LaCoO_3$-based materials are frequently employed as cathode material for H^+-SOFC. The material does not form oxygen vacancies at temperatures below 600 °C and it is therefore a pure electronic conductor in the expected operating temperature range of the H^+-SOFC. Additionally, the material has shown to be stable with no phase changes were observed after 350 hours stability test at 600 °C in air as well as in humidified air (ρH_2O = 0.2 atm) [4]. Furthermore, the $LaCoO_3$ does not react with solutions of barium cerate-zirconate at temperatures below 1100 °C due to its stability in air and wet atmosphere [7].

To this date, $LaCoO_3$-based cathode material such as strontium-doped $LaCoO_3$, $LaSrCoO_3$ is still lack in the literature particularly for H^+-SOFC application which uses barium cerate-zirconate as its electrolyte. Therefore, in this present work, a ceramic based on $LaCoO_3$ material which is $La_{0.6}Sr_{0.4}CoO_{3-\delta}$ (LSCO) has been prepared to be used as cathode material for H^+-SOFC application later. The LSCO material was synthesized by a modified sol-gel method. This method allows the preparation of a single crystalline materials at relatively low processing temperature with good stoichiometry control and preserves the homogeneity of the composition along with relatively large surface area after heat treatment [8,9]. Two different surfactants namely, ethylene glycol (EG) and activated carbon (AC) have been used in producing the LSCO materials and their effects on phase formation, morphology and particle size of the produced powders have been presented in this work.

Materials and Methods

$La_{0.6}Sr_{0.4}CoO_{3-\delta}$ (LSCO) powder was prepared via a modified sol-gel method. Citric acid and ethylenediaminetetraacetic acid (EDTA) was used as a combined chelating agent; ethylene glycol (EG) and activated carbon (AC) were used as surfactants. Analytical grade of metal nitrate salts of lanthanum, $La(NO_3)_3.6H_2O$, strontium, $Sr(NO_3)_2$ and cobalt, $Co(NO_3)_3.6H_2O$ were used as precursor materials. A mixture of these precursor materials was firstly dissolved in 100 mL deionized water. Then, calculated amount of citric acid was added into the solution mixture with stirring. Next, calculated amount of EDTA was slowly added into the solution mixture. After that, pH of the solution was adjusted to be 0.5. Finally, the respective surfactant (EG and AC) was added and the solution was continuously stirred and heated for several hours to obtain a viscous gel. The resulting viscous gel was dried at 150 ºC (12 hours) and 250 ºC (5 hours) accordingly. The as-synthesized powder was calcined at temperatures of 500, 600, 700, 800 and 900 ºC with heating/cooling rate of 5 ºC min^{-1} for 5 hours. The LSCO prepared with the EG and AC as surfactant and caclcined at different calcination temperatures are labelled as EG500, EG600, EG700, EG800, EG900, AC500, AC600, AC700, AC800 and AC900, respectively.

X-ray diffractometer (XRD Bruker D8 Advance) using a monochromatic Cu-K_α radiation source (λ = 0.1540 nm) with Ni-filtered was used to confirm the phase formation of LSCO perovskite powder. The XRD was operated at 40 kV and 30 mA using a step scan procedure of 0.02º s^{-1} for 2 theta (θ) ranging from 20º to 80º. The percentage of perovskite phase present in the calcined powders was calculated using equation (1) as proposed by Swarts and Shrout [10].

$$\text{Perovskite phase} = \frac{I_p}{I_p + I_m} \times 100\% \quad (1)$$

The *Ip* refers to the maximum intensity of the perovskite phase and *Im* is the maximum intensity of the impurity phases. Morphology of the powder was examined by a Merlin Compact Zeiss field emission scanning electron microscope (FESEM) equipped with energy dispersive X-ray (EDX) spectrometer. The imaging was performed in Secondary Electron (SEI) mode using an accelerating voltage of 15 kV at magnification of 15000 times. Particle size distribution analysis of the powders was done using Nano-ZS Particle Size Analyzer (PSA) manufactured by Malvern using deionized water as a dispersant.

Results and Discussion

Phase formation analysis

Figures 1 and 2 show the XRD profiles of LSCO powders prepared with different surfactants and calcined at different calcination temperatures, respectively. Both of the XRD profiles have almost similar patterns. The strongest peaks of all the XRD patterns were matched with Joint Committee of Powder Diffraction Standards (JCPDS) file no. 48-0121 with cubic (Pm-3m) structure. The pronounce peaks can be indexed to their Miller indices (hkl) of (100), (110), (111), (200), (210), (211), (220), (300) and (310), accordingly. Besides that, some additional peaks corresponded to the trace of impurity phases such as cobalt oxide (CoO), strontium oxide (SrO) and strontium cobalt oxide ($SrCoO_x$) were also presence in the XRD patterns of the calcined powders.

As the calcination temperature increases, the peaks intensity in both XRD profiles was further enhanced and become the dominant phase. The calcined powders at 500, 600, 700 and 800 °C have shown weak crystallinity of the LSCO perovskite phase since the trace of the impurity phases appeared in their XRD patterns. The full crystallization of a single perovskite phase of LSCO was formed at calcination temperature of 900 °C for the powders prepared using both surfactants. The works done by Tao et al. [8], Heel et al. [11] and Acuña et al. [12] also obtained a single phase of the LSCO at calcination temperature of 900 °C but using different synthesis methods namely citrate-EDTA, flame spray and free-drying, accordingly. Furthermore, as the calcination temperature increases, the calculated amount of perovskite phase percentage also increased. A summary of phase formation analysis was presented in Table 1.

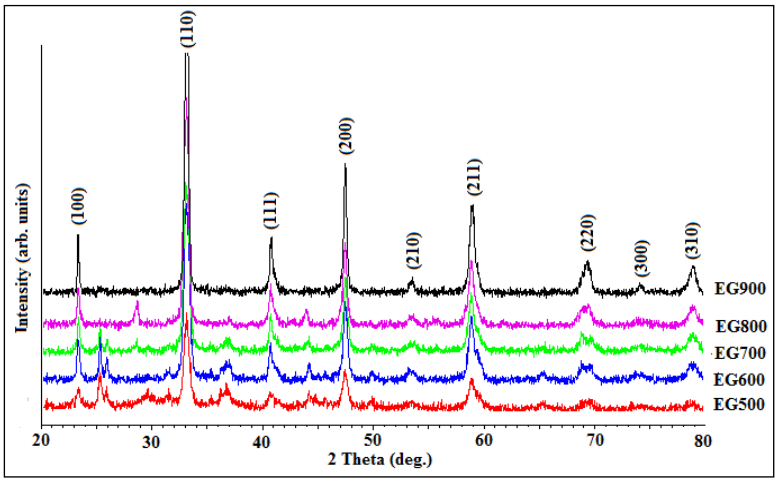


Figure 1. XRD patterns of the powders after calcined at various temperatures prepared using ethylene glycol (EG) as a surfactant

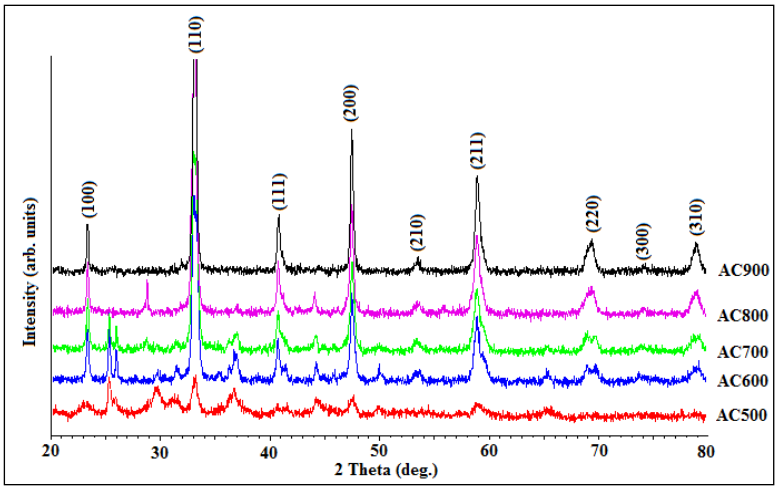


Figure 2. XRD patterns of the powders after calcined at various temperatures prepared using activated carbon (AC) as a surfactant

Table 1. A summary of phase formation analysis

Sample	Crystalline Phase	Percentage of Perovskite Phase (%)
EG500	LSCO, CoO, SrO, $SrCoO_x$	73.06
EG600	LSCO, CoO, SrO, $SrCoO_x$	79.47
EG700	LSCO, CoO, SrO, $SrCoO_x$	86.55
EG800	LSCO, CoO, $SrCoO_x$	90.25
EG900	LSCO	100.00
AC500	LSCO, CoO, SrO, $SrCoO_x$	50.57
AC600	LSCO, CoO, SrO, $SrCoO_x$	72.39
AC700	LSCO, CoO, SrO, $SrCoO_x$	84.34
AC800	LSCO, CoO, $SrCoO_x$	89.59
AC900	LSC0	100.00

Powder morphology and particle size distribution analysis

SEM micrographs of the single LSCO perovskite phase powders of the EG900 and AC900 are shown in Figure 3. The powders consist of homogeneous and almost identical particles. They are basically spherical in shape. The particles are well connected with each other and formed well-bonded porous network. Figures 4 and 5 show the EDX patterns of LSCO in EG900 and AC900 powders, respectively. The figures reveal the presence of lanthanum (La), strontium (Sr), cobalt (Co), oxygen (O) and carbon (C) peaks in the powders.

The analysis of elemental composition of each of the element in the EG900 and AC900 powders is presented in Table 2 and Table 3, accordingly. The weight percent (wt %) of each element is obtained from the EDX analysis and has been used to calculate the mole fraction. The site fractions were calculated assuming pure ABO_3 perovskite phase of LSCO with La and Sr on A-sites and Co only on B-sites. From the table, it can be seen that the elemental fraction of La/Sr in the EG900 was close to the nominal fraction of LSCO. However, the elemental fraction of La/Sr in the AC900 is slightly deviated from the nominal fraction. Additionally, residual carbon element is higher in the

AC900 compared to the EG900 as the activated carbon contains many C element. The high residual carbon content might block the La/Sr from being detected in the EDX spectrum which then contributes to the deviation.

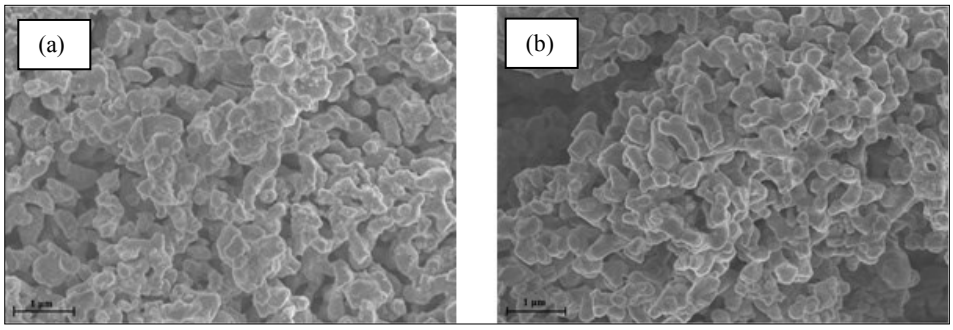


Figure 3. SEM micrographs of (a) EG900 powder and (b) AC900 powder

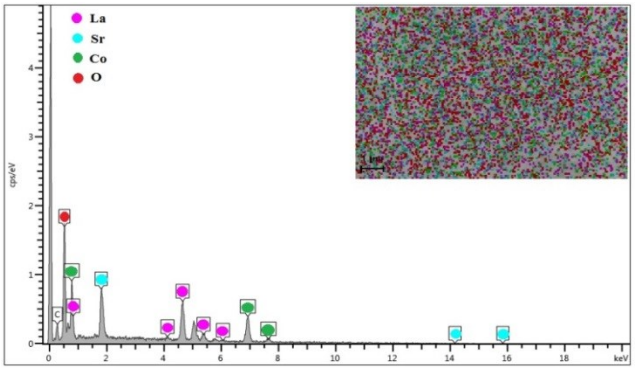


Figure 4. EDX spectrum of EG900 powder

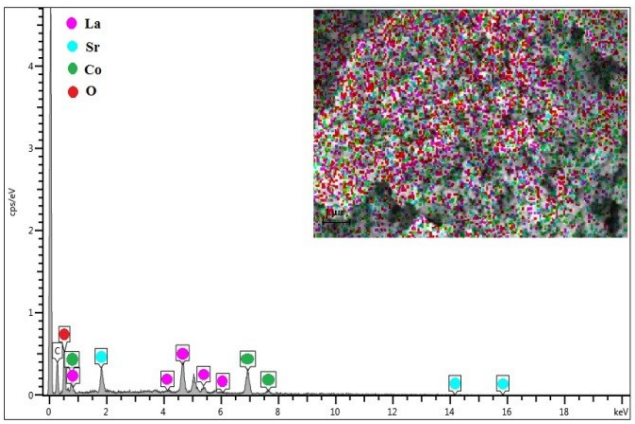


Figure 5. EDX spectrum of AC900 powder

Table 2. EDX data of weight percentage (wt %) and Mole fraction for EG900 powder

Element	Wt. %	Formula Wt.	Mole	Calculated Mole Fraction	Nominal Mole Fraction
La	37.15	138.905	0.267	0.61	0.60
Sr	12.65	87.620	0.144	0.33	0.40
Co	25.65	58.933	0.435	1.00	1.00
				1.94	**2.00**
O	17.75	15.999	1.109		
C	6.80	12.011	0.566		

Table 3. EDX data of weight percentage (wt %) and mole fraction for AC900 powder

Element	Wt. %	Formula Wt	Mole	Calculated Mole Fraction	Nominal Mole Fraction
La	36.20	138.905	0.261	0.56	0.60
Sr	11.00	87.620	0.126	0.27	0.40
Co	27.45	58.933	0.466	1.00	1.00
				1.83	**2.00**
O	13.65	15.999	0.853		
C	11.60	12.011	0.966		

Table 4 shows the average particle size of secondary particles for EG900 and AC900 powders measured using PSA. It can be seen that the average particle size of the EG900 is smaller than the average particle size of the AC900. The bimodal particle size distribution of the EG900 and AC900 powders are shown in Figure 6 and Figure 7, respectively. Two groups of particle size were observed in the particle size distribution for both samples. For EG900, the powder sample showed about ~ 87% of its particles lying between ~ 450 and 1300 nm and only ~ 13% in the ~ 160 - 340 nm range. For AC900, the powder sample showed about 85% of its particles lying between ~ 530 and 1300 nm and only 15% in the ~ 190 - 400 nm range. The difference in the particle size diameter and particle size distribution between both powders might be resulted from the properties of the surfactants used as they have different molecular structure and different relative bond strength towards compound (metal cations) during synthesizing process. Besides that, surfactant complexes concentration might also contribute to the results as it affects particle growth pathways which then leading to various morphologies.

Table 4. Average particle size diameter of EG900 and AC900 powders measured using PSA

Sample	Average Particle Size Diameter (nm)
EG900	751.2
AC900	1046.3

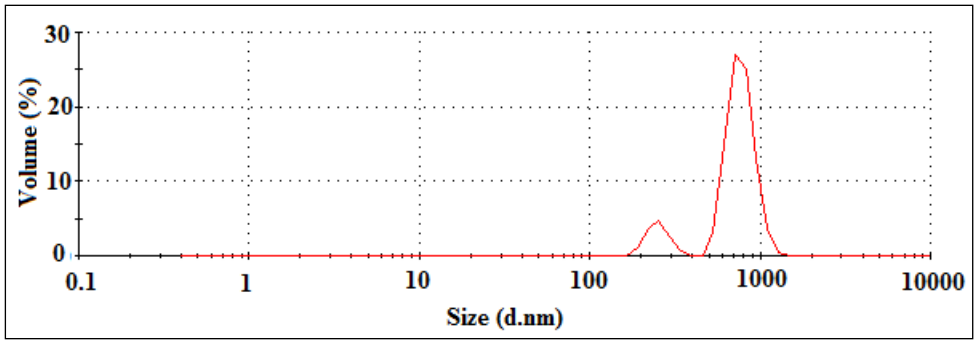


Figure 6. The bimodal particle size distribution of the EG900 powders

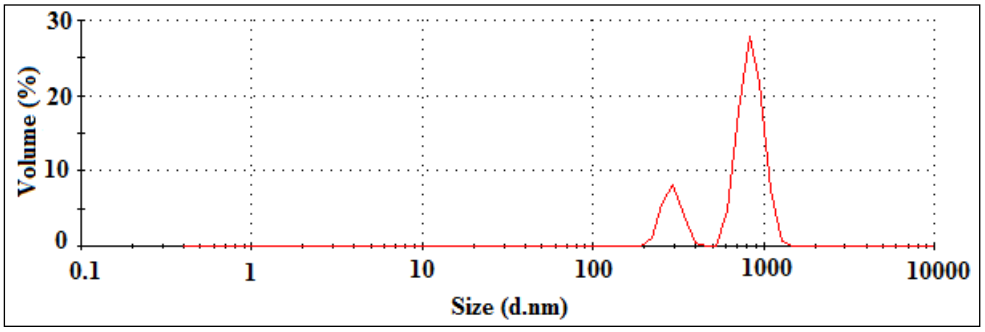


Figure 7. The bimodal particle size distribution of the AC900 powders

Table 5 shows the comparison of particle size diameter of primary particles obtained from this work with another reported works. It can be seen that the particle size obtained from this work is bigger than those reported works. The discrepancy between the results is due to the different synthesis methods and chemical agents used such as chelating agent, fuel or surfactant for the production of LSCO-based powders. The different synthesis methods with different chemical agents will produce materials with different microstructures and properties. Additionally, all the reported works have optimized or controlled their synthesizing parameters such as the amount of surfactant, pH and others in order to produce the nano-size powder but not for this work. Therefore, to obtain the nano size particles (< 100 nm) of LSCO, the relative bond strength and concentration of surfactant will be studied and controlled in our future work and the progress will be reported elsewhere.

Table 5. Average particle size diameter of LSCO powders produced by various methods

Synthesis method	**Chemical agent**	**Calcination temperature (°C)**	**Average particle size diameter (nm)**	**Reference**
Modified sol-gel	EG as surfactant	900	~ 149[a]	[This work]
	AC as surfactant	900	~ 190[b]	
Solution-combustion	Glycine as fuel	1100	50	[13]

Table 5 (cont'd). Average particle size diameter of LSCO powders produced by various methods

Synthesis method	Chemical agent	Calcination temperature (°C)	Average particle size diameter (nm)	Reference
Citrate-EDTA	Poly-EG as surfactant	900	60	[8]
Flame spray	Acetic acid as fuel	900	50	[11]
Citrate complexing	Citric acid as complexing agent	1100	150 - 250	[12]
Metal organic deposition	Propionic acid as chelating agent	700	17 - 90	[14]

[a,b]measured using image processing software from SEM analysis

Conclusion

LSCO powders was successfully prepared using a modified sol-gel method with different surfactants namely ethylene glycol (EG) and activated carbon (AC). A single perovskite phase of LSCO was obtained at calcination temperature of 900 °C for both surfactants as confirmed by XRD measurement. The pure phase powders of EG900 and AC900 obtained consists of uniform particle size with almost identical spherical shape as revealed by the SEM analysis. EDX measurement confirmed the presence of La, Sr, Co, O and C elements in both powders. Elemental fraction of La/Sr in the AC900 powder is slightly deviated from its nominal fraction. Both of the powders have different particle size diameter and particle size distribution as confirmed by particle size analyzer. The EG900 and AC900 powders have average particle size diameter of 751.2 nm and 1046.3 nm for secondary particles, and 149 nm and 190 nm for primary particle, respectively. Proton conducting SOFC cathode fabricated using EG900 powder is expected to perform better than AC900 powder due to the fact that the former has finer particle size with reduced residual carbon.

Acknowledgement

The authors would like to thank the Ministry of Higher Education (MOHE) for the Fundamental Research Grant Scheme (FRGS/2/2013/TK06/UKM/02/9) and Universiti Kebangssan Malaysia (UKM) via research sponsorship of DLP-2014-004. Abdullah Abdul Samat is thankful to MOHE and Universiti Malaysia Perlis (UniMAP) for the SLAB/SLAI scholarship. Facility support from Center for Research and Instrumentation Management (CRIM) of UKM and Universiti Teknologi MARA (UiTM) is gratefully acknowledged.

References

1. Tao, Z., Bi, L., Yan, L., Sun, W., Zhu, Z., Peng, R. and Liu, W. (2009). A novel single phase cathode material for a proton-conducting SOFC. *Electrochemical Communication,* 11(3): 688 – 690.
2. Handal, H. T. and Thangadurai, V. (2013). Evaluation of chemical stability, thermal expansion coefficient, and electrical properties of solid state and wet-chemical synthesized Y and Mn-codoped CeO_2 for solid oxide fuel cells. *Journal of Power Sources*, 243: 458 – 471.
3. Bi, L., Fabbri, E. and Traversa, E. (2012). Novel $Ba_{0.5}Sr_{0.5}(Co_{0.8}Fe_{0.2})_{1-x}Ti_xO_{3-\delta}$ (x = 0, 0.05, and 0.1) cathode materials for proton-conducting solid oxide fuel cells. *Solid State Ionics,* 214: 1 – 5.
4. Goupil, G., Delahaye, T., Gauthier, G., Sala, B. and Joud, F. L. (2012). Stability study of possible air electrode materials for proton conducting electrochemical cells. *Solid State Ionics*, 209 – 210: 36 – 42.
5. Ling, Y., Wang, F., Zhao, L., Liu, X. and Lin, B. (2014). Comparative study of electrochemical properties of different composite cathode materials associated to stable proton conducting $BaZr_{0.7}Pr_{0.1}Y_{0.2}O_{3-\delta}$ electrolyte. *Electrochimica Acta*, 146: 1 – 7.
6. Yu, T., Mao, X. and Ma, G. (2014). Performance of cobalt-free perovskite $La_{0.6}Sr_{0.4}Fe_{1-x}Nb_xO_{3-\delta}$ cathode materials for proton-conducting IT-SOFC. *Journal Alloys Compounds*, 608: 30 – 34.

7. Tolchard, J. R. and Grande, T. (2007). Chemical compatibility of candidate oxide cathodes for $BaZrO_3$ electrolytes. *Solid State Ionics,* 178(7–10): 593 – 599.
8. Tao, Y., Shao, J., Wang, J. and Wang, W.G. (2008). Synthesis and properties of $La_{0.6}Sr_{0.4}CoO_{3-\delta}$ nanopowder, *Journal of Power Sources*, 185(2): 609 – 614.
9. Shao, Z., Zhou, W. and Zhu, Z. (2012). Advanced synthesis of materials for intermediate-temperature solid oxide fuel cells. *Progress in Materials Science*, 57(4): 804 – 874.
10. Wongmaneerung, R., Yimnirun, R. and Ananta, S. (2009). Effect of two-stage sintering on phase formation, microstructure and dielectric properties of perovskite PMN ceramics derived from a corundum $Mg_4Nb_2O_9$ precursor. *Materials Chemistry and Physics*, 114(2–3): 569 – 575.
11. Heel, A., Holtappels, P. and Graule, T. (2010). On the synthesis and performance of flame-made nanoscale $La_{0.6}Sr_{0.4}CoO_{3-\delta}$ and its influence on the application as an intermediate temperature solid oxide fuel cell cathode. *Journal of Power Sources*, 195(19): 6709 – 6718.
12. Acuña, L. M., Peña-Martínez, J., Marrero-López, D., Fuentes, R. O., Nuñez, P. and Lamas, D.G. (2011). Electrochemical performance of nanostructured $La_{0.6}Sr_{0.4}CoO_{3-\delta}$ and $Sm_{0.5}Sr_{0.5}CoO_{3-\delta}$ cathodes for IT-SOFCs. *Journal of Power Sources*, 196(22): 9276 – 9283.
13. Bansal, N. P. and Zhong, Z. (2006). Combustion synthesis of $Sm_{0.5}Sr_{0.5}CoO_{3-x}$ and $La_{0.6}Sr_{0.4}CoO_{3-x}$ nanopowders for solid oxide fuel cell cathodes. *Journal of Power Sources*, 158(1): 148 – 153.
14. Hayd, J., Dieterle, L., Guntow, U., Gerthsen, D. and Ivers-Tiffée, E. (2011). Nanoscaled $La_{0.6}Sr_{0.4}CoO_{3-\delta}$ as intermediate temperature solid oxide fuel cell cathode: Microstructure and electrochemical performance. *Journal of Power Sources,* 196(17): 7263 – 7270.

Malaysian Journal of Analytical Sciences, Vol 20 No 6 (2016): 1467 - 1473
DOI: http://dx.doi.org/10.17576/mjas-2016-2006-27

MALAYSIAN JOURNAL OF ANALYTICAL SCIENCES
Published by The Malaysian Analytical Sciences Society
ISSN 1394 - 2506

ADSORPTION OF CADMIUM (II) IONS BY POLYACRYLONITRILE-BASED ACTIVATED CARBON NANOFIBERS/MAGNESIUM OXIDE AS ITS ADSORBENTS

(Karbon Nano-Gentian Teraktif Berasaskan Poliakrilonitril/Magnesium Oksida Sebagai Penjerap untuk Penjerapan Ion Kadmium (II))

Faten Ermala Che Othman, Norhaniza Yusof*, Juhana Jaafar, Ahmad Fauzi Ismail, Norfadhilatuladha Abdullah, Hasrinah Hasbullah

Advanced Membrane Technology Research Center,
Faculty of Chemical and Energy Engineering,
Universiti Teknologi Malaysia, 81310 Johor Bahru, Johor, Malaysia

**Corresponding author: norhaniza@petroleum.utm.my*

Received: 21 October 2015; Accepted: 14 June 2016

Abstract

In this work, activated carbon nanofibers (ACNFs) from precursor polyacrylonitrile (PAN) and magnesium oxide (MgO) were prepared via electrospinning process. The morphological properties of the PAN/MgO-based ACNFs were characterized by using Scanning Electron Microscopy (SEM) and the specific surface area (SSA) were investigated using nitrogen adsorption, Brunauer-Emmett-Teller (BET) methods. Moreover, the functional groups were analyzed by using Fourier Transform Infrared (FTIR). Besides that, the sorption study has been conducted in order to determine the adsorption capacity between electrospun ACNFs/MgO, pristine ACNFs and granular activated carbon (GAC) towards cadmium (II) ions. The results showed that the SSA of modified ACNFs (198.80 m^2/g) is significantly higher compared to the precursor ACNFs (15.43 m^2/g), however the SSA obtained is quite lower compared to the average theoretical value. SEM micrograph of pristine ACNFs depicted more compact nanofibers compared to aligned nanofibers with average diameter of 200-700 nm. Under batch adsorption study, it was found out that Cd(II) removal of both ACNFs and ACNFs/MgO is higher compared to the commercial GAC. It has been demonstrated that the adsorption capacity of both electrospun ACNFs (ACNFs/MgO and pristine ACNFs) is higher when compared to the adsorption capacity of commercial GAC towards Cd (II) ions.

Keywords: polyacrylonitrile, activated carbon nanofiber, magnesium oxide, cadmium (II) ion adsorption

Abstrak

Kajian ini membincangkan tentang proses penyediaan karbon nano-gentian teraktif (ACNFs) berasaskan poliakrilonitril (PAN) dan magnesium oksida (MgO) melalui teknik putaran elektro. Ciri-ciri morfologi bagi ACNFs telah dicirikan menggunakan Mikroskopi Elektron Pengimbasan (SEM) dan luas permukaan kawasan tertentu (SSA) telah disiasat menggunakan kaedah penjerapan nitrogen, Brunauer-Emmett-Teller (BET). Selain itu, kumpulan berfungsi dianalisis dengan menggunakan Inframerah Transformasi Fourier (FTIR). Melalui kajian ini juga, kapasiti penjerapan diantara ACNFs, ACNFs/MgO dan karbon berbutir teraktif (GAC) terhadap ion (II) kadmium telah dijalankan. Hasil kajian menunjukkan bahawa SSA daripada ACNFs yang telah diubah suai (198.80 m^2/g) adalah lebih tinggi berbanding dengan pelopor ACNFs (15.43 m^2/g), walau bagaimanapun SSA yang diperoleh agak rendah berbanding dengan nilai purata teori. SEM mikrograf bagi pelopor ACNFs menunjukkan nano-gentian yang lebih padat berbanding nano-gentian berstruktur sejajar dengan diameter purata 200-700 nm. Di bawah kajian penjerapan berkumpulan, pembuangan ion (II) kadmium bagi kedua-dua ACNFs dan ACNFs/MgO adalah lebih tinggi berbanding dengan GAC komersial. Hal ini telah membuktikan bahawa kapasiti penjerapan kedua-dua ACNFs yang diperbuat daripada kaedah

putaran elektro (ACNFs/MgO dan ACNFs) terhadap ion (II) kadmium adalah lebih tinggi jika dibandingkan dengan kapasiti penjerapan GAC.

Kata kunci: poliakrilonitril, karbon nano-gentian teraktif, magnesium oksida, penjerapan ion kadmium (II)

Introduction

Nowadays, water contamination by heavy metals remains a major environmental concern as heavy metals persistently present in water subjected by their non-degradable properties [1]. Besides, their tendency to being over-accumulated in biosystem will negatively affect public health and environment despite they play roles in biochemical processes at trace level [2,3,4]. Among the common heavy metals that present in water, cadmium (Cd) has attracted great attention for the studies of its removal as this metal are proved to pose adverse effects on human health even at minimum level [5]. Moreover, the emission of Cd may occur naturally or anthropogenically.

Various methods have been implied upon removal of cadmium laden in water streams such as ion exchange, precipitation, coagulation-flocculation and flotation where each of this method possesses their own limitations more likely to be incomplete removal, generation of secondary waste and inefficient removal efficacies [6,7]. Adsorption is another technique that is frequently applied for removal of heavy metals laden in water. There is wide range of adsorbents available; one good example is activated carbon nanofibers (ACNFs) as it has small inter-fibrous pore size with high porosity and also high specific surface area per unit mass that will lead to high adsorption capacity [8]. One of the challenges to activate the nanofibers is to increase the SSA and capacitance without damaging the graphitic fiber structure, which controls their mechanical properties [9].

Many polymers can be used for preparation of carbon nanofibers such as polyacrylonitrile (PAN), pitch and cellulose. Out of the aforementioned polymers, PAN is an excellent polymer selection because of its outstanding properties which contains a proper functional group(s), adsorbent for metal ion removal, inexpensive, common commercial product and can easily prepared into nanofibers by electrospinning. Preparation of ACNFs with incorporation of nano-scaled metal oxides such as magnesium oxide (MgO) has received great attention as it can solve the major concern of large pores of ACNFs upon removal of heavy metals. Moreover, many previous studies have been conducted on sole MgO due to its large SSA and were proven to be good adsorbent [10]. Thus, in this study the adsorption capacity of prepared ACNFs/MgO were determined and compared with neat PAN-based ACNFs and commercial granular activated carbon (GAC).

Materials and Methods

Materials

Polyacrylonitrile (PAN) with MW of 150, 000 was purchased from Sigma-Aldrich. Dimethylformamide (DMF; ~99.98% purity), magnesium oxides (MgO, ≥99% trace metal basis) and activated carbon (GAC, untreated, granular, 8-20 mesh) were also purchased from Sigma-Aldrich (USA). Stock solution of 1000 mg/L cadmium ions was prepared by using analytical grade cadmium (II) chloride, which was further diluted to the required concentrations before used.

Preparation of PAN nanofibers with dimethylformamide and metal oxides

The dope solution was prepared by adding 1 wt% of MgO into 89 wt% of DMF. The mixture was stirred for at least 5 hours to ensure the MgO dispersed well in the solution before adding up the PAN 10 wt%. The dope was left to stir for 24 hours. The electrospinning process was carried out at fixed electric field of 12kV, the infusion rate is 1 ml/hour and the distance of the tip of needle to the collector is 20 cm, where aluminium foils were used as the collectors.

Activation of PAN-based carbon nanofibers

In stabilization process, the nanofibers were heated up until 275 °C in the furnace (Carbolite) from room temperature with pure air gas flow rate of 0.2 L/min at heating rate of 2 °C/min with resting time of 30 minutes at 275 °C. The treated nanofibers were further heated up until 600 °C with nitrogen gas flow rate of 0.2 L/min at heating rate of 5 °C /min with 30 minutes of dwelling time and were left for cooling down until room temperature.

For activation process, the carbonized nanofibers were burnt in the tube furnace until 800 °C at rate of 5 °C/min with carbon dioxide gas flow rate of 0.2 L/min and 30 minutes of dwelling time.

Characterization

The surface properties, such as morphology and composition of various adsorbents were determined using scanning electron microscopy (SEM) and the specific surface area were investigated using nitrogen adsorption Brunauer-Emmett-Teller (BET). Fourier Transform Infrared (FTIR) analysis was used to analyze the functional groups appeared in the ACNFs.

Batch adsorption study

Adsorption study of Cd ions was analyzed by investigating the effect of initial concentration upon adsorption rate of Cd. 0.05 g of the prepared samples were placed into conical flask containing 50 mL of Cd solution with initial concentration of 3 ppm respectively. The samples were agitated on rotary shaker with the speed of 180 rpm at 30 °C for 48 hours to reach equilibrium [11,12]. The sample solutions were later filtered and examined by using Atomic Absorption Spectrometer (AAS).

The adsorption capacity of the GAC, ACNFs and ACNFs/MgO and the percentage of removal of metallic ions by adsorbent were calculated by following Equation (1) [13].

$$q_t = \frac{(C_0 - C_t)V}{W} \quad (1)$$

and the removal efficiency was calculated using Equation (2).

$$R(\%) = \frac{(C_0 - C_t)}{C_0} \times 100 \quad (2)$$

where C_o and C_t are the initial and final concentration of the metallic solution (mg/L), V is the volume of the solution (L), and M is the weight of the adsorbent used (g) [11].

For batch adsorption study, the ACNFs were rinsed with distilled water in order to eliminate any residual solutions. Then, the ACNFs were further dried in oven at room temperature. Desorption of ACNFs have been used to identify the recovery rate and reusability PAN-based ACNFs/MgO. Desorption of metal ions were carried out by immersing the ACNFs in 1M HCl and agitated at 30 ^{o}C with speed of 100 rpm for 5 h. The concentration of Cd ions in the solution was analyzed using atomic absorption spectrometer (AAS) and the desorption ratio (D) was calculated as Equation 3 follows:

$$D(\%) = \frac{mg\ of metal\ desorbed}{mg\ of\ metal\ ion\ adsorbed\ into\ ACNFs} \times 100 \quad (3)$$

Results and Discussion

SEM for morphology characterization

Figure 1 (a and b) showed that both neat PAN-based ACNFs and modified ACNFs (ACNFs/MgO) possessed straight line fibers, bent fibers, rougher and wrinkled fibers due to the shrinkage effect during pyrolysis process. Moreover, in Figure 1(b), the presence of MgO in the ACNFs can be observed by the presence of white spots while the appearance of few beads was believed due to capillary instability [14] during electrospinning.

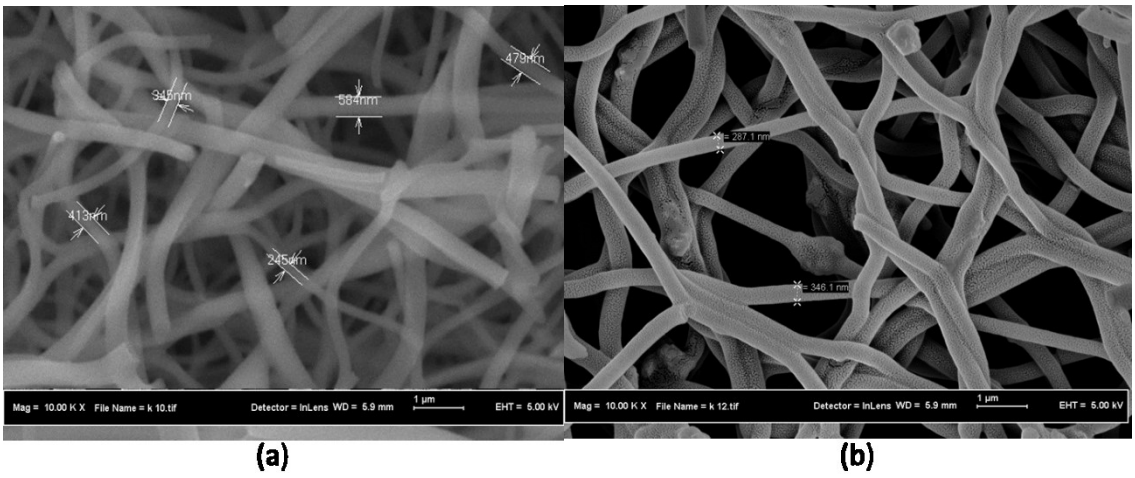


Figure 1. SEM images of (a) ACNFs; and (b) ACNFs/MgO with 10000x magnification

Meanwhile, in comparison of physical observation of SEM micrographs between neat ACNFs and ACNFs/MgO, it can be found that the average diameter of ACNFs without metal oxide is 413.2 ± 128.8 nm (Figure 1a) while for ACNF with MgO is 316.6 ± 41.72 nm as shown in Figure 1(b). As expected, the diameter of ACNFs/MgO is smaller compared to the neat ACNF, as smaller diameter will lead to larger SSA [15,16]. However, even the diameter of the ACNFs obtained not in nano-meter range (below 100 nm), still this study was a success as this result is comparable to other studies on ACNFs.

BET analysis for specific surface area

In this study, the single point BET method was employed to analyze nitrogen adsorption isotherms in order to determine the specific surface area (SSA) of ACNFs and ACNFs/MgO compared to commercial GAC.

Table 1. BET specific surface area of GAC, ACNF, ACNF/MgO

Samples	BET surface area (m^2/g)
GAC	729.82
ACNF	15.43
ACNF/MgO	198.80

From Table 1, the pristine ACNFs show the lowest SSA of 15.43 m^2/g while GAC has the highest SSA of 752.60 m^2/g. Theoretically, the SSA of both ACNFs and ACNFs/MgO were expected to be much higher compared to the results obtained as tabulated in Table 1. For instance, in a study conducted by Dadvar et al. [17], they have obtained SSA of ACNFs/MgO of 600 m^2/g and it was expected in future study, the results for ACNFs/MgO at least comparable or exceeded this value. The low SSA obtained in this study might be due to the incomplete pyrolysis process where the temperature used not high enough to create new micropores instead creating macro- and mesopores that led to low SSA. In our future study, the higher activation temperature with slower heating rate will be used in order to make sure the nanofibers undergo complete pyrolysis stage [18,19].

FTIR for functional group studies

Typically, PAN-based nanofibers will show the existence of CH_2, C≡N, C=O, C−O and C−H bonds but after activation all of these transition compounds were expected to evolve as volatilities and only carbon and hydrogen

atoms remain [20]. As shown in Figure 2, there are six major peaks observed located at 2330.98, 2115.36, 1997.37, 1791.34, 1095.37 and 476.12 cm^{-1}. The peak 2330.98 cm^{-1} is assigned as O-H stretch from strongly hydrogen-bonded- COOH. Peaks 2115.36 and 1997.37 cm^{-1} basically attributed to the strong stretching of C=C groups while peaks 1791.34 cm^{-1} and 1095.37 cm^{-1} indicated as stretching vibrations of C-O groups and C-C stretching, respectively. Last of all, peak 476.12 cm^{-1} were the proofs of the existence of MgO in the ACNFs as the MgO bonds are expected to be presence in the range of 600-450 cm-1 [21]. These detected functional groups may play vital role for adsorption of Cd(II).

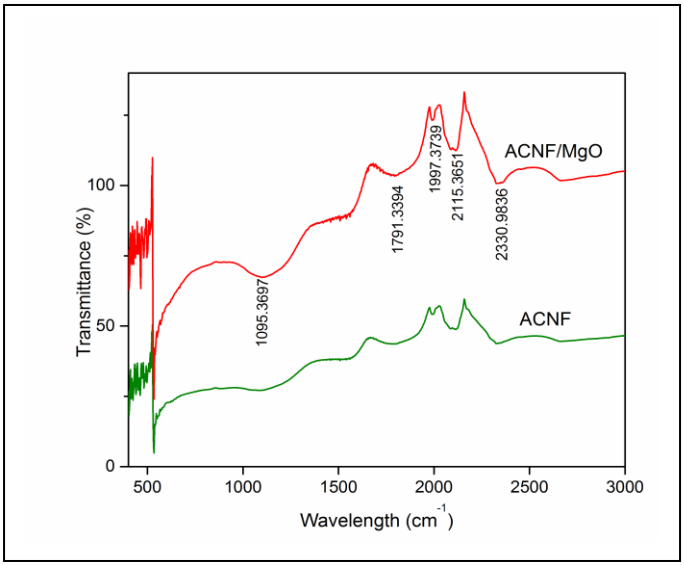


Figure 2. FTIR spectrum of both ACNF and ACNF/MgO

Batch adsorption studies

In this research, the adsorption of heavy metals onto activated carbon nanofibers has been studied using batch-adsorption technique. This study was carried out to examine the adsorption performance of GAC, ACNFs and ACNFs/MgO for the removal of Cd from aqueous solution.

Table 2 shows the percentage removal of cadmium for GAC, ACNFs and ACNFs/MgO it show promising results of 97%, 100% and 100%, respectively. The obtained results revealed that both ACNFs and ACNFs/MgO has good adsorption capacity and effective for the removal of heavy metals from wastewater. Moreover, previous studies have shown that MgO was one of the good adsorbent with high SSA and the incorporation between ACNFs and MgO has proven to be good adsorbent [22] for Cd removal. Based on the results obtained, it can be said that both ACNFs and ACNFs/MgO can be good adsorbent for Cd removal.

Table 2. Removal of cd on GAC, ACNF AND ACNF/MgO

Samples	Removal of Cd (%)
GAC	97
ACNF	100
ACNF/MgO	100

Conclusion

This study investigated the adsorption capabilities of different types of activated carbon on cadmium as a function of adsorbent. Although GAC showed highest SSA compared to both ACNFs, however it was found that pristine and modified ACNFs provided better performance compared to commercial GAC in removal of cadmium from aqueous solution.

Acknowledgement

The authors would like to acknowledge the financial support from the Malaysian Ministry of Education and Universiti Teknologi Malaysia under GUP grants (Q.J130000.2542.05H46 and Q.J130000.2546.12H54) and HICOE grant (R.J090301.7846.4J179). The author would also like to acknowledge the technical and management support from Research Management Centre (RMC), Universiti Teknologi Malaysia.

References

1. Li Y., Wang Y.B., Gou X., Su Y.B. and Wang G. (2006). Risk assessment of heavy metals in soils and vegetables around non-ferrous metals mining and smelting sites, Baiyin, China. *Journal of Environmental Sciences*, 18(6): 1124 – 1134.
2. Kumar R., Isloor A. M., Ismail A. F. and Matsuura T. (2013). Synthesis and characterization of novel water soluble derivative of chitosan as an additive for polysulfone ultrafiltration membrane. *Journal of Membrane Science*, 40: 140 – 147.
3. Meybeck M., Kuusisto A., Makela A. and Malkki R. (1996). Water quality monitoring: a practical guide to the design and implications of freshwater quality studies and monitoring programmes, Water quality. Eds. London, UK: Chapman and Hall.
4. Saeed K., Park S.Y. and Oh T. J. (2012). Preparation of hydrazine-modified polyacrylonitrile nanofibers for the extraction of metal ions from aqueous media. *Journal of Applied Polymer Science,* 121(2): 869 – 873.
5. Vila G., Luger A. and Clodi M. (2012). B-type natriuretic peptide modulates ghrelin, hunger, and satiety in healthy men. *Diabetes*, 61: 2592 – 2596.
6. Barakat M. A. (2011). New trends in removing heavy metal from industrial wastewater. *Arabic Journal of Chemical*, 4: 38 – 41.
7. Fu F. and Wang Q. (2011). Removal of heavy metal ions from wastewater: A review. *Journal of Environment Management*, 92: 20 – 25.
8. Liang Y., Wu D. and Fu R. (2013). Carbon microfibers with hierarchical porous structure from electrospun fiber-like natural biopolymer. *Scientic Reports*, 3: 1119 – 1124.
9. Mao X., Hatton T. and Rutledge G. (2013). A review of electrospun carbon fibers as electrode materials for energy storage. *Current Organic Chemistry*, 17(13): 1390 – 1401.
10. Zahida R., Rabia N., Durr-e-Shahwar, Muhammad Raza S. and Shujat A. (2014). Utilization of magnesium and zinc oxide nano-adsorbents as potential materials for treatment of copper electroplating industry wastewater. *Journal of Environmental Chemical Engineering*, 2(1): 642 – 651.
11. Desta M. B. (2013). Batch sorption experiments: Langmuir and Freundlich isotherm studies for the adsorption of textile metal ions onto teff straw agricultural waste. *Journal of Thermodynamics*, 2013: 1 – 6.
12. Vijayakumar G., Tamilarasan R. and Dharmendirakumar M. (2012). Adsorption, kinetic, equilibrium and thermodynamic studies on the removal of basic dye rhodamine-B from aqueous solution by the use of natural adsorbent perlite. *Journal of Materials and Environmental Science*, 3(1): 157 – 170.
13. Kampalanonwat P. and Supaphol P. (2014). The study of competitive adsorption of heavy metal ions from aqueous solution by aminated polyacrylonitrile nanofibers mat. *Energy Procedia*, 56: 142 – 151.
14. Zussman E., Chen X., Ding W., Calabri L., Dikin D. A., Quintana J. P. and Ruoff R. S. (2005). Mechanical and structural characterization of electrospun PAN-derived carbon nanofibers. *Carbon*, 43: 2175 – 2185.
15. Huang Z. M., Zhang Y. Z., Kotaki M. and Ramakrishna S. (2003). A review on polymer nanofibers by electrospinning and their applications in nanocomposites. *Composites Science and Technology*, 63(15): 2223 – 2253.
16. Drew C., Liu X., Ziegler D., Wang X.Y., Bruno F. F., Whitten J., Samuelson L. A. and Kumar J. (2003). Metal oxide-coated polymer nanofibers. *American Chemical Society*, 3(2): 143 – 147.
17. Dadvar S., Tavanai H. and Morshed M. (2012). Effect of embedding MgO and Al_2O_3 nanoparticles in the precursor on the pore characteristics of PAN based activated carbon nanofibers. *Journal of Analytical and Applied Pyrolysis*, 98: 98 – 105.

18. Abdullah A. H., Kassim A., Zainal Z., Hussein M. Z., Kuang D., Ahmad F. and Wooi O.S. (2001). Preparation and characterization of activated carbon from gelam wood bark. *Malaysian Journal of Analytical Sciences*, 7(1): 65 – 68.
19. Bonso J. S., Kalaw G. D. and Ferraris J. P. (2014). High surface area carbon nanofibers derived from electro-spun PIM-1 for energy storage applications. *Journal of Materials Chemistry A*, 2: 418 – 424.
20. Arshad S. N., Naraghi M. and Chasiotis I. (2011). Strong carbon nanofibers from electrospun polyacrylonitrile, *Carbon*, 49: 1710 – 1719.
21. Hofmeister M., Keppel E. and Speck K. (2003). Adsorption and reflection infrared spectra of MgO and other diatomic compounds. *Monthly Notices of the Royal Astronomical Society*, 345(1): 16 – 38.
22. Rajagopalan S., Koper O., Decker S. and Klabunde K. J. (2002). Nanocrystalline metal oxides as destructive adsorbents for organophosphorus compounds at ambient temperatures. *Chemistry-A European Journal*, 8(11): 2602 – 2607.

Malaysian Journal of Analytical Sciences, Vol 20 No 6 (2016): 1474 - 1480
DOI: http://dx.doi.org/10.17576/mjas-2016-2006-28

MALAYSIAN JOURNAL OF ANALYTICAL SCIENCES
Published by The Malaysian Analytical Sciences Society
ISSN 1394 - 2506

THE EFFECT OF VARIOUS PRETREATMENT METHODS ON EMPTY FRUIT BUNCH FOR GLUCOSE PRODUCTION

(Kesan Kaedah Prarawatan Berbeza Terhadap Tandan Kosong Kelapa Sawit Bagi Penghasilan Glukosa Ringkas)

Nurul Hazirah Che Hamzah[1], Masturah Markom[1]*, Shuhaida Harun[1], Osman Hassan[2]

[1]*Department of Chemical and Process Engineering, Faculty of Engineering and Built Environment*
[2]*School of Chemical Sciences and Food Technology, Faculty of Science and Technology*
Universiti Kebangsaan Malaysia, 43600 UKM Bangi, Selangor, Malaysia

**Corresponding author: masturahmarkom@ukm.edu.my*

Received: 21 October 2015; Accepted: 14 June 2016

Abstract

In this study, a pretreatment of empty fruit bunch (EFB) using supercritical carbon dioxide (SC-CO_2), acid and alkaline were investigated for glucose yield from enzymatic hydrolysis. The chemical composition, X-ray diffraction (XRD) and Scanning Electron Microscopy (SEM) analysis of EFB before and after pretreatment were determined. From this study, the chemical composition of EFB (% g/g dry biomass) before pretreatment for cellulose, hemicellulose and Klason lignin were recorded as 36.7%, 22.8%, and 24.2%, respectively. After pretreatment, the highest cellulose composition was obtained from EFB treated with alkaline followed by acid and SC-CO_2 which gave the results of 48.5%, 47.7% and 38% respectively. The glucose yield after enzymatic hydrolysis for untreated EFB was 17% (w/w). After pretreatment, the glucose yield increased to 84.4%, 34% and 24% for alkaline, acid and SC-CO_2 of the treated EFB, respectively. Other than that, XRD analysis showed increase in the crystallinity index after each pretreatment. Morphology analysis showed the surface of the treated EFB looked swollen and ruptured as compared with the surface of the untreated EFB. Between the three pretreatments, alkaline pretreatment gives the highest cellulose composition and glucose yield. Thus, it shows that alkaline pretreatment was the best pretreatment method on EFB compared to acid and SC-CO_2 pretreatments.

Keywords: empty fruit bunches, enzymatic hydrolysis, pretreatment, glucose

Abstrak

Melalui kajian ini prarawatan tandan buah kosong (TKKS) menggunakan kaedah supergenting karbon dioksida (SC-CO_2), asid dan alkali telah dilakukan untuk mendapatkan hasil glukosa daripada hidrolisis berenzim. Analisis komposisi kimia, pembelauan sinar-X (XRD) dan mikroskopi pemgimbasan elektron (SEM) terhadap TKKS sebelum dan selepas prarawatan telah ditentukan. Dari kajian ini komposisi kimia TKKS (% g/g biomas kering) sebelum prarawatan bagi selulosa, hemiselulosa dan lignin ialah 36.7%, 22.8%, and 24.2%. Selepas prarawatan, komposisi selulosa yang paling tinggi diperolehi daripada TKKS terawat dengan prarawatan alkali diikuti dengan prarawatan asid dan SC-CO_2 iaitu 48.5%, 47.7% dan 38%. Hasil glukosa selepas hidrolisis berenzim bagi TKKS yang tidak terawat ialah 17% (w/w). Selepas prarawatan, hasil glukosa telah meningkat kepada 84.4%, 34% dan 24% bagi prarawatan alkali, asid dan SC-CO_2. Selain daripada itu, analisis XRD menunjukkan peningkatan indeks penghabluran terhadap TKKS terawat. Analisis morfologi menunjukkan perubahan pada permukaan TKKS terawat dimana ia kelihatan bengkak dan pecah berbanding dengan permukaan TKKS yang tidak terawat. Antara ketiga-tiga kaedah prarawatan, prarawatan alkali memberikan komposisi selulosa dan hasil glukosa yang paling tinggi. Oleh itu, kajian ini menunjukkan bahawa prarawatan alkali adalah kaedah prarawatan terbaik terhadap TKKS berbanding prarawatan asid dan SC-CO_2.

Kata kunci: tandan kosong kelapa sawit, hidrolisis berenzim, prarawatan, glukosa

Introduction

Malaysia produces approximately 43% of the world's palm oil supply and is the second largest exporters in the world after Indonesia, which produces 44% of palm oil [1]. Crude palm oil production has increased every year due to high demand in the market which also leading to massive production of biomass in the form of trunks, fronds, fibers, shells and empty fruit bunch (EFB) [2]. The potentials of this biomass are yet to be fully exploited that currently leads to waste disposal problems [3].

EFB is a lignocellulosic material consists of carbohydrate sugars, lignin, extractives and ash with inorganic minerals. Carbohydrate sugars such as cellulose and hemicellulose, which can be used as a source of biomass energy when hydrogen is produced via bioconversion process. However it is difficult to yield high amount of reducing sugars from bioconversion of lignocellulosic materials as its end product due to their complex structure and component [4]. Thus, EFB has to undergo pretreatment in order to break the complex structure of lignocellulosic and thus improves enzymatic hydrolysis process for the production of high sugar yields [5].

Many studies have been done on pretreatment of lignocellulosic biomass material either physical, chemical or biological [6]. Chemical pretreatments using acid and alkaline have been claimed as a potential technique for lignocellulose degradation [7]. Acid pretreatment is one of the most extensively studied pretreatment methods that results in hydrolyzes hemicellulose from lignocellulose [8]. Alkaline pretreatment disrupts the cell wall by breaking down the α-ether linkages between lignin and/or hemicelluloses and solubilized thus increasing the enzymatic digestibility of cellulose [9].

Besides the most widely used of chemical methods, physico-chemical pretreatment such as supercritical carbon dioxide (SC-CO_2) has also been of interest in recent years because it uses a low-cost of CO_2, non-toxic and environmentally friendly [10]. During pretreatment, CO_2 molecules penetrate into the micropores of lignocellulose and destroy the structure of the biomass by rapidly release CO_2 [11].

The objectives of this research are to characterize the chemical composition of EFB and to study the effects of alkaline, acid and supercritical carbon dioxide (SC-CO_2) pretreatments on EFB for sugar production during enzymatic hydrolysis.

Materials and Methods

Materials

Empty fruit bunch fibers (EFB) were collected from Sime Darby Sdn. Bhd. palm oil milling, Pulau Carey, Selangor, Malaysia. The EFB was dried using oven (less than 10 wt. % moisture content) and then was milled into particles (0.25 – 0.42 mm). The samples were stored at room temperature until they were used for the pretreatment process. The CO_2 gas was purchased from Gas Pantai Timur, Malaysia and had the purity of 99.9%. The commercial enzymes used in this study were cellulase enzyme and β-glucosidase purchased from Sigma Aldrich.

Pretreatment procedure

Three pretreatment methods were employed in this study. The SC-CO_2 pretreatment was carried out in static type at 75% moisture content, 250 bars and 130 °C. An amount 5g of samples was introduced into a high pressure stainless steel reactor vessel. The supercritical CO_2 was fed into the reactor until desired pressure after the system reached the set temperature. Then, the system was maintained at constant pressure and temperature for 60 min. After the reaction process finished, the supercritical CO_2 was immediately released to atmospheric pressure [12]. NaOH and H_2SO_4 solution at concentration level 4% were used to pretreat EFB. The samples were treated in a 250 mL Erlenmeyer flask at temperature of 121 °C for 1 hour and with ratio of biomass to liquid was 1:10. Later, the treated fibers were washed until all chemicals used were removed [13]. Then, the treated fibers were dried in an oven at 50 ºC overnight.

Enzymatic saccharification

Enzymatic hydrolysis of untreated and treated EFB were carried out in 250 mL Erlenmeyer flasks containing 1% (w/v) glucan loading in 0.05 M citrate buffer, pH 4.8 and together with desired cellulase and cellobiase enzymes.

Cellulose and cellobiase enzymes were added at 60 FPU per g glucan loading and 64 ρNPGU per g glucan loading, respectively. An amount of 10% sodium azide was added at concentration of 20 mg/mL act as an antibiotic. The saccharification was done in a shaker incubator at 200 rpm at 37 ºC for 48 hours. Samples were taken periodically, filtered and stored at -8 °C for sugar determination using High Performance Liquid Chromatography (HPLC) [14].

Analytical method

The chemical composition of EFB was determined according to NREL standard method [15]. In this method, the structural carbohydrates and insoluble lignin (Klason lignin) in biomass were analyzed. The sugar monomers in untreated and treated EFB fiber samples after enzymatic hydrolysis were determined by high performance liquid chromatography. HPLC system (Model G1311A, Agilent Technologies) equipped with reflective index detector and Rezex ROA column was used for the analysis. The mobile phase used was 0.005 N sulfuric acid with a flow rate of 0.6 mL/min at 60 °C. The samples were centrifuged for 5 minutes and filtered with 0.2 µm syringe filter for HPLC analysis. The glucose yield from EFB was measured based on the glucose released after both pretreatment and enzymatic hydrolysis as proposed by Srinivasan and Ju [16].

Scanning electron microscope

SEM analysis was conducted using SEM model Philips XL30 to determine the surface changes before and after pretreatment. For sample preparation, the samples were coated with a thin layer of gold using sputter coater system Model Q150 RS.

X-ray diffraction

The crystallinities of untreated and pretreated Tamarix solids were measured using a Bruker D8 Advance instrument. The data analysis was calculated from XRD data and determined based on the formula by Segal follows [17]**.**

$$CrI = 100 \times [(I002\text{-}Iam)/I002] \quad (1)$$

where I002 is the maximum intensity of 002 reflections from the crystalline and amorphous portions at about $2\theta = 22.5^{\circ}$, and Iam is the minimum intensity of diffraction from the amorphous portion at a $2\theta \approx 18.7^{\circ}$ of the EFB fibers in most literatures [18]. During the calculation, the height of (002) peaks were used at a $2\theta \approx 22^{\circ}$, while the intensity of Iam was taken at a $2\theta \approx 16^{\circ}$.

Results and Discussion

Effect of various pretreatments on chemical composition of EFB

The chemical compositions of untreated and treated EFB fibers were shown in Figure 1. Chemical composition of untreated EFB fiber for cellulose, hemicellulose and Klason lignin were 36.7%, 22.8%, and 24.2%, respectively. The cellulose, hemicellulose and lignin content in untreated EFB fiber were similar to that reported by Chong et al. who studied the chemical composition of EFB [8]. These results proved that more than 30% -50% of EFB component is cellulose, followed by hemicellulose 20% - 30% and lignin 15% - 20% of the overall components in biomass [4,19]. After pretreatment, it was observed that the composition of cellulose increased in the treated EFB as the results after SC-CO_2, acid and alkaline pretreatment were 38%, 47.7% and 48.5%, respectively. While the composition of hemicellulose was increased after SC-CO_2 and alkaline pretreatment but decreased after acid pretreatment as the results obtained were 25.5%, 29.1% and 0.012% respectively.

The composition of Klason lignin showed that the percentages reduced after SC-CO_2 and alkaline pretreatment but increased after acid pretreatment which were calculated at 23.8%, 20.4% and 31.2%, respectively. The result showed differences in the composition of EFB after pretreatments because of different effects of pretreatment on EFB fiber. SC-CO_2 is a physicochemical pretreatment in which at supercritical conditions and high temperatures, carbonic acid possibly formed by the interaction of SC-CO_2 with water and may have hydrolyzed hemicellulose [20]. Whereas acid and alkaline are chemical pretreatment which chemically changing the structure of lignocellulose EFB and destroying its crystalline structure [6]. The acid pretreatment enhances the hydrolysis of hemicelluloses and portion of amorphous cellulose while alkaline pretreatment disrupts the cell wall by dissolving hemicelluloses and lignin from lignocellulose [21,22].

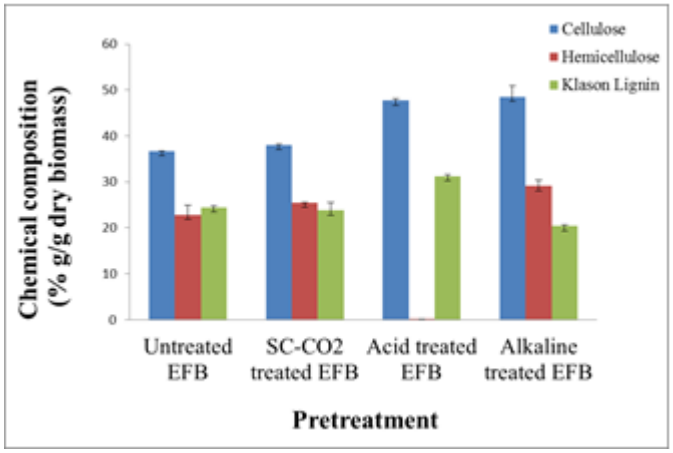


Figure 1. Chemical compositions of untreated, supercritical carbon dioxide, acid and alkaline treated EFB.

Effect of various pretreatments on glucose yield

The trends of glucose yield after 48 hours' enzymatic hydrolysis over different pretreatments were shown in Figure 2. After enzymatic hydrolysis, the glucose yield for untreated compared with supercritical carbon dioxide, acid and alkaline treated EFB were calculated at 17%, 24%, 34% and 84.4%, respectively. The results showed that all the three pretreatments caused an increase of the glucose yield after enzymatic hydrolysis compared to untreated EFB. The highest glucose yield was obtained in EFB treated with 4% NaOH showing that alkaline pretreatment gave significant effect on glucose yield. Alkaline pretreatment enhancing enzymatic hydrolysis by removing lignin that linked to both hemicellulose and cellulose from lignocellulose [2]. Acid and SC-CO_2 pretreatment also help in enzymatic hydrolysis however the glucose yield is lower than alkaline pretreatment. During acid and SC-CO_2 pretreatment, most of the hemicellulose was hydrolyzed leaving lignin as a barrier that preventing penetration of enzymes and difficult for the enzyme to access the cellulose [4].

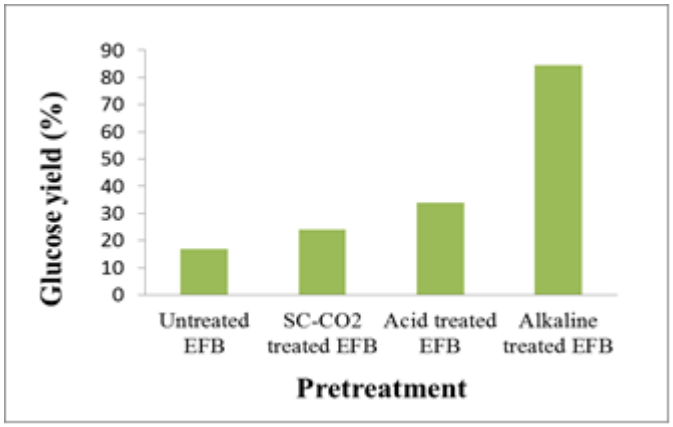


Figure 2. Glucose yield of the enzymatic hydrolysis for untreated, supercritical carbon dioxide, acid and alkaline treated EFB after 48 hours enzymatic hydrolysis.

X-ray diffraction analysis

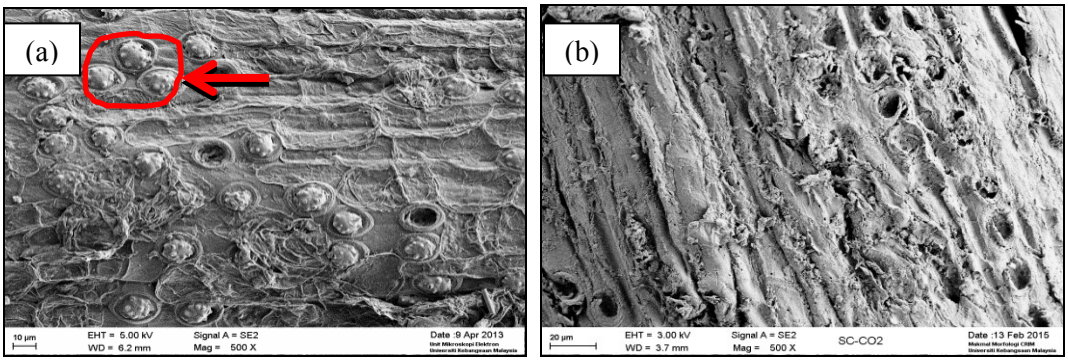
Table 1 showed the crystallinity index of untreated EFB, SC-CO_2 treated EFB, acid treated EFB and alkaline treated EFB. Crystallinity index for each sample was calculated using the formula by Segal et al. [17]. It was determined that crystallinity index of cellulose in untreated EFB was 44%. The crystallinity increased after each pretreatment as for SC-CO_2 treated EFB (45.3%), acid treated EFB (47%) and alkaline treated EFB (50%), respectively. Crystallinity index had been used in various studies to interpret the changes in the structure of cellulose after pretreatment [23]. Cellulose crystallinity index was the main factor affecting the hydrolysis since degradation of cellulose crystallinity will increase the rate of enzymatic hydrolysis [24]. This concept was used because cellulose structure can be divided into two parts which amorphous part that was easy to hydrolyze and crystalline part that was more difficult to hydrolyze [23]. However, in this study, it showed that the crystallinity index was increased for each pretreatment similarly in previous studies conducted by Singh et al. [21] on rice straw using alkaline pretreatment which increased the crystallization index of 2.35%. Therefore, it can be concluded that the crystallization is not the only factor affecting the enzymatic hydrolysis of biomass but other parameters such as hemicellulose and lignin also involve in enhancing the enzymatic hydrolysis.

Table 1. Chemical compositions of untreated, supercritical carbon dioxide, acid and alkaline treated EFB

Samples	**Crystallinity Index (%)**
Untreated EFB	44
SC-CO_2 treated EFB	45.3
Acid treated EFB	47
Alkaline treated EFB	50

Scanning electron microscopy

Scanning electron microscopy (SEM) analysis was used to observe the structure changes in EFB before and after pretreatment. Figure 3 shows SEM images of EFB samples for (a) untreated EFB (b) SC-CO_2 treated EFB (c) acid treated EFB and (d) alkaline treated EFB. From the SEM images, it showed that untreated EFB had a rough surface with the silica bodies on the surface strand. The structure looked very rigid and solid because the surface of the fiber was covered by a layer of matrix material like lignin or waxes. On the other hand, after pretreatment the SEM showed the structural damage EFB. After SC-CO_2 pretreatment process, the structure of EFB became porous and visible cracks formed were seen due to quick release of CO_2 [25]. A significant effect can be observed after alkaline and acid pretreatment where these pretreatments caused greater disruptions on the fiber structure by destroying the cell wall, hydrolyzing lignin or hemicellulose of lignocellulose and creating number of large pores [14]. Thus after pretreatment more cellulose was exposed to the enzymes, resulting in increment of glucose yield.



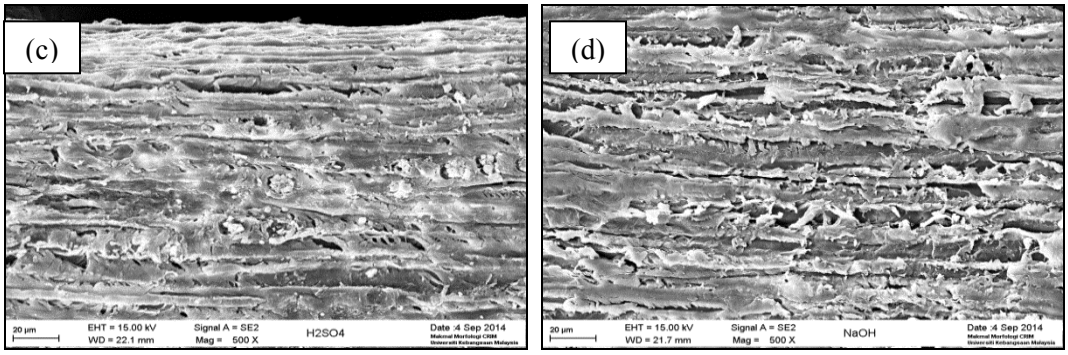


Figure 3. SEM images of EFB samples (a) untreated EFB, (b)SC-CO_2 treated EFB, (c) acid treated EFB and (d) alkaline treated EFB; Arrow indicates silica bodies on the EFB strand

Conclusion

In summary, SC-CO_2, acid and alkaline pretreatment on EFB enhances the glucose yields of enzymatic hydrolysis. The highest glucan composition and glucose yield were obtained from EFB treated with alkaline followed by acid and SC-CO_2. After pretreatment, SEM images demonstrated that the structure of treated EFB was swollen and ruptured as compared with the untreated EFB. A significant effect can be observed after alkaline and acid pretreatment which were the chemical pretreatment. XRD analysis showed increase in the crystallinity index for EFB treated using SC-CO_2, acid and alkaline pretreatment by 1.3%, 3% and 6% compared to untreated EFB. Therefore based on these findings, it could be concluded that alkaline pretreatment using NaOH was the best pretreatment method on EFB which gives the highest glucose yield through enzymatic hydrolysis.

Acknowledgement

The authors would like to thank Universiti Kebangsaan Malaysia and KURSI UKM-Yayasan Sime Darby (UKM-YSD) for sponsoring this work.

References

1. Shuit, S. H., Tan, K. T., Lee, K. T. and Kamaruddin, A. H. (2009). Oil palm biomass as a sustainable energy source: A Malaysian case study. *Energy,* 34(9): 1225 – 1235.
2. Shamsudin, S., Md Shah, U. K., Zainudin, H., Abd-Aziz, S., Mustapa Kamal, S. M., Shirai, Y. and Hassan, M. A. (2012). Effect of steam pretreatment on oil palm empty fruit bunch for the production of sugars. *Biomass and Bioenergy,* 36: 280 – 288.
3. Yaakob, M. Y., Hasoloan, H. I. P., Yahaya, S. H. and Said, M. R. (2012). Solid fuel from empty fruit bunch fiber and waste papers part 3: ash content from combustion test. *Global Engineers & Technologists Review*, 2(3): 26 – 32.
4. Ariffin, H., Hassan, M. A., Kalsom, M. S. U., Abdullah, N. and Shirai, Y. (2008). Effect of physical, chemical and thermal pretreatments on the enzymatic hydrolysis of oil palm empty fruit bunch (OPEFB). *Journal of Tropical Agriculture and Food Sciences,* 36(2): 259 – 268.
5. Zheng, Y., Pan, Z. and Zhang, R. (2009). Overview of biomass pretreatment for cellulosic ethanol production. *International Journal of Agricultural and Biological Engineering,* 2: 51 – 69.
6. Taherzadeh, M. J. and Karimi, K. (2008). Pretreatment of lignocellulosic wastes to improve ethanol and biogas production: A review. *International Journal of Molecular Sciences,* 9: 1621 – 1651.
7. Misson, M., Haron, R., Ahmad, M. F., Aishah, N. O. R. and Amin, S. (2009). Pretreatment of empty palm fruit bunch for lignin degradation. *Jurnal Teknologi,* 50: 89 – 98.
8. Chong, P. S., Jahim, J. M., Harun, S., Lim, S. S., Mutalib, S. A., Hassan, O. and Nor, M. T. M. (2013). Enhancement of batch biohydrogen production from prehydrolysate of acid treated oil palm empty fruit bunch. *International Journal of Hydrogen Energy,* 38: 9592 – 9599.
9. Varga, E., Schmidt, A. S., Réczey, K. and Thomsen, A. B. (2003). Pretreatment of corn stover using wet oxidation to enhance enzymatic digestibility. *Applied Biochemistry and Biotechnology,* 104: 37 – 50.

10. Lü, H., Ren, M., Zhang, M. and Chen, Y. (2013). Pretreatment of corn stover using supercritical CO_2 with water-ethanol as co-solvent. *Chinese Journal of Chemical Engineering,* 21(5): 551 – 557.
11. Yin, J., Hao, L., Yu, W., Wang, E., Zhao, M., Xu, Q. and Liu, Y. (2014). Enzymatic hydrolysis enhancement of corn lignocellulose by supercritical CO_2 combined with ultrasound pretreatment. *Chinese Journal of Catalysis,* 35(5): 108 – 119.
12. Narayanaswamy, N., Faik, A., Goetz, D. J. and Gu, T. (2011). Supercritical carbon dioxide pretreatment of corn stover and switchgrass for lignocellulosic ethanol production. *Bioresource Technology,* 102(13): 6995 – 7000.
13. Ying, T. Y., Teong, L. K., Abdullah, W. N. W. and Peng, L. C. (2014). The effect of various pretreatment methods on oil palm empty fruit bunch (EFB) and kenaf core fibers for sugar production. *Procedia Environmental Sciences,* 20: 328 – 335.
14. Iberahim, N. I., Jahim, J. M., Harun, S., Nor, M. T. M. and Hassan, O. (2013). Sodium hydroxide pretreatment and enzymatic hydrolysis of oil palm mesocarp fiber. *International Journal of Chemical Engineering and Applications*, 4(3): 101 – 105.
15. Sluiter, A., Hames, B., Ruiz, R., Scarlata, C., Sluiter, J., Templeton, D. and Crocker, D. (2008). Determination of structural carbohydrates and lignin in biomass. Biomass analysis technology team laboratory analytical procedure.
16. Srinivasan, N. and Ju, L.-K. (2012). Statistical optimization of operating conditions for supercritical carbon dioxide-based pretreatment of Guayule Bagasse. *Biomass and Bioenergy,* 47: 451 – 458.
17. Segal, L. G. J. M. A., Creely, J. J., Martin, A. E. and Conrad, C. M. (1959). An empirical method for estimating the degree of crystallinity of native cellulose using the X-ray diffractometer. *Textile Research Journal*, 29(10): 786 – 794.
18. Xiao, L., Sun, Z., Shi, Z. and Xu, F. (2011). Impact of hot compressed water pretreatment on the structural changes of woody biomass for bioethanol production. *Bioresources,* 6: 1576 – 1598.
19. Kelly-Yong, T. L., Lee, K. T., Mohamed, A. R. and Bhatia, S. (2007). Potential of hydrogen from oil palm biomass as a source of renewable energy worldwide. *Energy Policy,* 35: 5692 – 5701.
20. Kim, K. H. and Hong, J. (2001). Supercritical CO_2 pretreatment of lignocellulose enhances enzymatic cellulose hydrolysis. *Bioresource Technology,* 77(2): 139 – 144.
21. Singh, R., Shukla, A., Tiwari, S. and Srivastava, M. (2014). A review on delignification of lignocellulosic biomass for enhancement of ethanol production potential. *Renewable and Sustainable Energy Reviews,* 32: 713 – 728.
22. Xiao, B., Sun, X. and Sun, R. (2001). Chemical, structural, and thermal characterizations of alkali-soluble lignins and hemicelluloses, and cellulose from maize stems, rye straw, and rice straw. *Polymer Degradation and Stability,* 74(2): 307 – 319.
23. Park, S., Baker, J. O., Himmel, M. E., Parilla, P. A. and Johnson, D. K. (2010). Cellulose crystallinity index: Measurement techniques and their impact on interpreting cellulase performance. *Biotechnology for Biofuels,* 3: 1 – 10.
24. Hassan, O., Ling, T. P., Maskat, M. Y., Illias, R. M., Badri, K., Jahim, J. and Mahadi, N. M. (2013). Optimization of pretreatments for the hydrolysis of oil palm empty fruit bunch fiber (EFBF) using enzyme mixtures. *Biomass and Bioenergy,* 56: 137 – 146.
25. Gao, M., Xu, F., Li, S., Ji, X., Chen, S. and Zhang, D. (2010). Effect of SC-CO_2 pretreatment in increasing rice straw biomass conversion. *Biosystems Engineering,* 106(4): 470 – 475.

Malaysian Journal of Analytical Sciences, Vol 20 No 6 (2016): 1481 - 1490
DOI: http://dx.doi.org/10.17576/mjas-2016-2006-29

MALAYSIAN JOURNAL OF ANALYTICAL SCIENCES
Published by The Malaysian Analytical Sciences Society
ISSN 1394 - 2506

POLYIMIDE MEMBRANES FOR ORGANIC SALTS RECOVERY FROM MODEL BIOMASS FERMENTATION

(Membran Poliimida untuk Pengumpulan Garam Organik daripada Model Sup Penapaian Biojisim)

Nadiah Khairul Zaman, Rosiah Rohani*, Abdul Wahab Mohammad

Department of Chemical and Process Engineering,
Faculty of Engineering and Built Environment,
Universiti Kebangsaan Malaysia, 43600 UKM Bangi, Selangor, Malaysia

**Corresponding author: rosiah@ukm.edu.my*

Received: 21 October 2015; Accepted: 14 June 2016

Abstract

Succinic acid displays promising properties as a precursor for synthesizing valuable chemicals. However, its recovery experiences difficulty due to the formation of by-products with similar physicochemical properties, namely acetate and formate. The succinate separation process via pressure filtration membrane technology demonstrates polyimide (PI) membrane as a potential candidate due to its high resistance and selectivity to many organic solvents from its imide groups, an important feature in separation of biomass fermentation broth. This study aims to investigate the performance of newly synthesized PI (P84) membrane prepared by phase inversion for succinate recovery from fermentation broth (simulated model solution is used). PI polymer composition 14 – 17 wt% were cast to investigate the effect of varying polymer compositions on the performance of NF membrane determined from the recovery of succinate, and removal of formate and acetate from ternary organic salt solutions at concentration range between 10 – 50 g/L. PI membrane (15 wt%) shows the highest selective succinate retention of 73%. Succinate selective retention was observed to increase whereas rejection of by-products decreased at increasing mixed salt solution concentration from 20 – 50 g/L. Field Emission Scanning Electron Microscope (FESEM) results showed a PI membrane with dense and thick top layer, with porous middle substructure to support membrane performance.

Keywords: polyimide, nanofiltration membrane, succinate, biomass fermentation, mixed salt solution

Abstrak

Asid suksinik mempunyai kepentingan sebagai pelopor dalam mensintesis bahan kimia yang bernilai. Namun, pengumpulannya menghadapi kesukaran kerana pembentukan satu lagi produk sampingan yang mempunyai sifat fizikokimia yang sama seperti asetat dan format. Dalam proses pemisahan/pengumpulan suksinat menerusi tekanan teknologi membran penapisan, membran poliimida (PI) didapati berpotensi sebagai calon membran kerana ia bersifat perintang yang tinggi kepada banyak pelarut organik dan juga mempunyai pemilihan yang tinggi ke atas air melalui kumpulan imida yang penting dalam pengasingan sup penapaian biojisim. Oleh itu, kajian ini bertujuan untuk menyiasat prestasi membran PI (P84) yang baru disintesis dan disediakan dengan teknik fasa songsangan dalam bidang pengumpulan suksinat dari sup penapaian (model simulasi digunakan). Kepekatan PI polimer sebanyak 14 – 17 wt% telah disediakan dan kesan kepekatan polimer dalam penyediaan membran PI telah disiasat untuk mencapai membran PI berprestasi tinggi yang ditentukan dari pengumpulan suksinat dan penyingkiran asetat dan format pada julat kepekatan antara 10 – 50 g/L. Melalui kajian ini, membran PI (15 wt%) menunjukkan pengumpulan suksinat tertinggi sebanyak 73%. Pengumpulan suksinat diperhatikan meningkat manakala penyingkiran produk sampingan berkurangan dengan peningkatan kepekatan garam campuran dari 20 – 50 g/L. FESEM yang menunjukkan lapisan atas membran PI yang padat dan tebal serta lapisan substruktur tengah yang berliang untuk menyokong prestasi membran PI.

Kata kunci: poliimida, nanopenurasan, suksinat, penapaian biojisim, garam campuran

Introduction

Succinic acid is a dicarboxylic acid (consists of two carboxyl) and is of high interest as a precursor for synthesizing a variety of valuable chemicals in the production of food [1], pharmaceutical products [2], and in the chemicals industry [3,4]. The versatility of succinic acid has attracted many attentions to find an alternative production route over the traditional process of using petroleum feedstock due to long-term environmental concern. This thus gives rise to the production of succinic acid from fermentation process using abundant biomass for a cleaner technology approach. Presently, studies have reported high production of succinate at various amounts via fermentation process when using different producing bacteria; 50 g/L by *Mannheimia succiniciproducens* [5], 83 g/L by *Anaerobio-spirillum succiniciproducens* [6], 99.2 g/L by *E. coli* [7] and 100 g/L by *Actinobacillus succinogenes* [8]. However, along with the succinic acid production, other by-products such as acetic acid, formic acid, lactic, and pyruvic acids (depending on the producing bacteria) with similar physicochemical properties were also produced [9]. In addition to that, the requirement of pre-treating the fermentation broth prior to succinic acid separation has made the downstream processing of succinic acid difficult and costly which could mount up to about 50 – 70% of the production cost [10].

Many separation processes have been intensively studied for the separation/recovery of succinic acid including precipitation and crystallization [11], reactive extraction [12] and chromatography [13]. However these processes are subjected to limitations of either low recovery rate or purity, contamination of process by impurities, high energy consumptions or the need of frequent regeneration [14]. Among the separation technologies, intensive study using membrane filtration including microfiltration, ultrafiltration and nanofiltration (NF) have been carried out using commercial membranes [15-19]. Initial study was carried out by Glassner in 1992 on succinic acid purification process using integrated desalination electrodialysis and bipolar membrane electrodialysis. The former stage is applied to separate the ionic species such as acids from the fermentation broth containing the uncharged compounds such as sugars, saccharides or proteins. The charged molecules then passed through a membrane, and sodium succinate was collected. Meanwhile at the latter stage, bipolar membrane electrodialysis is used to convert sodium succinate into succinic acid while recycling back the NaOH to maintain the pH of the fermentation broth. However, this type of membrane filtration was found to be prone to low product yield due to loss of succinic acid and membrane pollution [20]. Later, succinic acid separation from fermentation broth was investigated using ultrafiltration. Wang et al. carried out a study on succinic acid separation which focused more on the membrane fouling mechanism in treating succinate acid from fermentation broth using dead-end ultrafiltration. Their study investigated the type of fouling experienced by different membranes including RC 10 kDa, PES 30 kDa, PES 100 kDa, and PES 10 kDa during succinate separation using Hermia's model. It was found that most of the membranes tended to foul by cake layer or concentration polarization [21].

Among membrane filtration separation technologies, NF membranes for acid mixtures separation was highly reported due to the NF membrane characteristic that has high selectivity towards divalent anions compared to monovalent anions especially for separation of divalent anion from multivalent anions solution [15, 19]. Choi et al. [16] reported the retention of succinic acid using NF membrane, NF270 of Filmtec. The retention of organic salts was found to be dependent on the molecular weight cut off (MWCO) of membrane. Furthermore, the retention of succinic acid was over 90% irrespective of operating pressure and concentration due to close molecular weight (MW) of succinic acid to the MWCO of the NF270 membrane used. However for organic acid with lower MW (i.e. formic acid, acetic acid and propionic acid) than the MWCO of membrane, the retention is found to be dependent on the operating pressure and concentration. They also reported that the retention of succinic acid increases with increasing pH, depending on the degree of dissociation [16].

Therefore, the successful recovery of succinate/succinic acid using the commercial polymeric NF membrane has become the main motivation of this study. In this work an investigation on the succinate recovery from biomass fermentation broth was carried out using newly synthesized PI NF membrane fabricated via phase inversion, which to our knowledge has not yet been investigated in this field of succinate recovery from fermentation broth. The introduction of PI in the field of recovering succinate from fermentation broth is due to its excellent chemical resistance, good thermal and mechanical properties, easy processing, and good solubility in a variety of common solvents. It also possesses high negative surface charge that could effectively impede bio-fouling unlike the

commercial membranes [22]. This material is also chosen due to its recent introduction in organic solvent separation [23,24], which is found to be also suitable for the targeted application in purifying the biomass fermentation broth that is composed of a complex mixture of alcohol, organic acid/salts, sugars, and biomass. A robust membrane such as PI polymer is required to withstand the extreme environment during separation and recovery of the desired product.

In this study, succinate retention was investigated based on the manipulation of polymer compositions during the doped solution preparation. This varying composition is expected to give different morphologies of the membrane thus influencing the retention of desired product. Phase inversion was used as it created an asymmetric membrane suitable for the application targeted. In the phase inversion, the cast polymer is immersed in a coagulation-bath containing poor solvent (non-solvent) such as water to create polymer rich and polymer lean phases from the diffusion of non-solvent into the cast film and of solvent out of it, inducing liquid-liquid demixing due to thermodynamic instability [22]. The former and latter polymer phases are then subsequently transformed into membrane matrix and membrane pores respectively [25]. The fabricated membranes were characterized using FESEM and salt retention to determine the membrane morphologies and retention properties. The performance of the fabricated membranes was also tested with a modelled ternary solution consisting succinate, formate, and acetate at different concentrations to investigate the selective recovery of succinate from the ternary solution.

Materials and Methods

Materials

For membrane preparation, polyimide (P84) fibers was purchased from Good Fellow and dried overnight at 120 °C prior to use. N–methyl–2–pyrrolidinone (NMP, Merck) was used as solvent. De-ionized H_2O was used as coagulation media while 2–propanol (2–PrOH, Merck) was used for membrane post-treatment. For model solution preparation, succinic acid (with molecular weight [MW] 118.09 g/mol, R&M Chemicals), formic acid (MW 46.03 g/mol, R&M Chemicals) and acetic acid (MW 90.09 g/mol, R&M Chemicals) were used to prepare the model fermentation broth solution at different concentration for retention analysis. Sodium hydroxide (NaOH, R&M Chemicals) was used to adjust pH to 7.0. All chemicals were used without further purification.

Membrane preparation

Homogeneous PI solutions were prepared by adding NMP solvent to the PI chopped fibers, which was subsequently heated at 60 °C for 4 hours until completely dissolved. The solution was stirred overnight until homogeneous for casting at room temperature using an automated film applicator (Elcometer 4340, UK). The cast speed, membrane thickness and evaporation time were set at 10 cm/s, 250 μm and 30 s, respectively. After casting, membrane films were exposed to ambient air to allow evaporation of the solvents and subsequently immersed in a coagulation bath of de-ionized water at room temperature for 10 min, after which the de-ionized water was replaced to remove all solvents. For post treatment by a solvent exchange procedure to avoid pore collapse upon drying, all cast membranes were immersed in 2–PrOH for 3 hours [26] and finally air dried naturally [27].

Salt rejection

To determine the level of membrane separation towards divalent and monovalent anions, salt rejections were carried out using dead end filtration cell (HP4750 Stirred Cell, Sterlitech) with a filtration area of 0.00146 m^2. A fixed pressure of 20 bar was used with feed consisting of NaCl and Na_2SO_4 at 20 mM concentration each. The salt rejection of membrane was determined by analysing the salt permeate using conductivity meter (METTLER TOLEDO). The flux was calculated based on the following Equation (1) while retention was calculated based on the following Equation (2):

$$J = \frac{\Delta V}{A.t} \tag{1}$$

where J is the flux ($L/m^2.h$), V is the volume of permeate (L), A is the effective area of membrane (m^2) and t is time (h).

$$R\ (\%) = \left[1 - \left(\frac{C_P}{C_R}\right)\right] \quad (2)$$

where R is the percentage retention, C_P is the concentration of permeate and C_R is the concentration of retentate.

Membrane morphology

For membrane morphology, membrane cross-sections were observed with field emission scanning electron microscopy (FESEM) (SUPRA 55VP, ZEISS). Dried membrane samples were fractured in liquid nitrogen and mounted on aluminum stubs for platinum sputter-coated using sputter-coater (QUORUM Q150RS, UK) to make samples appear to have electrical conductivity. The samples were observed in standard high-vacuum conditions of 5 kV.

Succinate recovery

The recovery of succinate from multi-salt solutions using PI membranes were carried out using dead end filtration cells similar as in salt retention analysis. After every run, membranes used were rinsed with ultra-pure water until the initial water flux was recovered. Please note that the flux and rejection calculation are based on the salt rejection also. The flux and rejection were measured at various mixed-salt solution concentrations between 10 – 50 g/L at 15 bar. All mixed-salt solution concentrations were carried out at 1:1:1 ratio of succinate, formate, and acetate respectively (for simplification, 33.33:33.33:33.33 ratio in percentage).

The organic acid salts were measured using a high performance liquid chromatography (HPLC) (G1313A series, Agilent) with a separating column (REZEX ROA ORGANIC ACID H+ [8%], 300 x 7.8 mm, PHENOMENEX). The analysis was run with a refractive index (RI) detector at column temperature of 60 °C. An amount 0.005 M H_2SO_4 was used as the mobile phase at 0.6 ml/min of flow rate [19].

Results and Discussion

Salt retention

A desired NF membrane is a membrane that possesses high rejection of divalent anions while low rejection of monovalent anions. This means the succinate is to be retained in the retentate while other organic salts (formate and acetate) are to be removed in the permeate in this study. In order to investigate the retention of monovalent and divalent anions of the synthesized membranes, four different compositions of PI in the range of 14 – 17 wt% were prepared and tested using 20 mM of NaCl (monovalent anion) and Na_2SO_4 (divalent anion).

Table 1. NaCl and Na_2SO_4 retention and solution flux of PI membrane at different composition

PI membranes composition (wt%)	Flux for NaCl ($L/m^2.h$)	Rej. for NaCl (%)	Flux for Na_2SO_4 ($L/m^2.h$)	Rej. for Na_2SO_4 (%)
14	35.34	9.94	34.52	18.90
15	15.41	6.57	15.31	39.10
16	6.26	60.16	5.94	52.19
17	1.51	66.89	1.92	53.84

Table 1 shows the retention of each salt and the solution flux. From the results, it was observed that the fabricated PI membrane started to show NF characteristics at composition above 14 wt% based on the retention of NaCl and/or Na_2SO_4 of above 20%. Based on The DOW Chemical Company membrane specification, a typical NF membrane shows retention of dissolved salts between 20–80% [28]. Figure 1 shows the comparison between the retention of monovalent and divalent anions at different membrane compositions. Among the tested membranes, PI at 15 wt% composition shows the largest retention difference between monovalent anion, Cl^- and divalent anion, SO_4^{2-} with approximately 83% retention difference. It was also observed that below 15 wt% PI, the divalent anions shows

higher retention compared to monovalent anions but above 15 wt% PI, monovalent anion has slightly higher retention than the divalent anion. It seemed that below 15 wt% PI composition, Donnan exclusion and sieve effect play important roles in ion separation while above 15 wt%, only Donnan exclusion acted as the major factor in the ion separation [19,29]. From the salt retention test, 15 wt% PI shows the highest potential for selective retention of succinate from mixture solution containing both mono- and divalent anions (Cl^- and SO_4^{2-} respectively) as it shows the highest retention difference between these two anions.

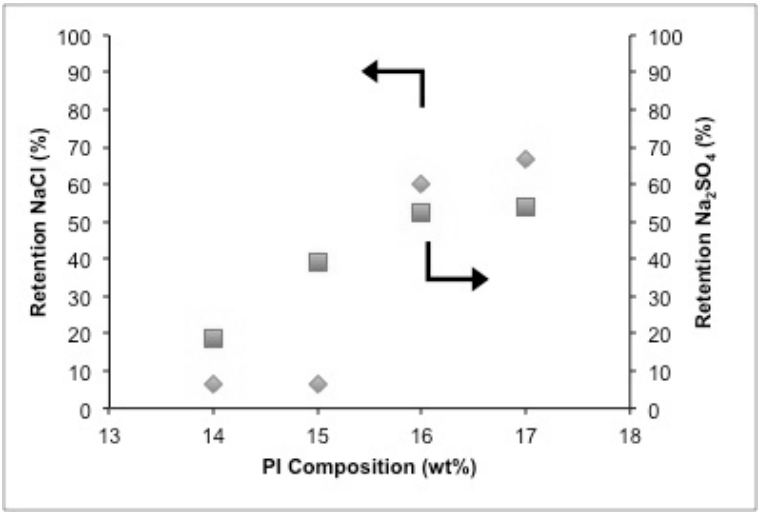


Figure 1. Comparison between retention of NaCl and Na_2SO_4 using PI membrane at different doped solution compositions (14, 15, 16 and 17 wt%). (Membrane synthesis conditions: membrane thickness of 250 µm, evaporation time of 30s. Filtration conditions: 20 bar, room temperature)

Membrane morphology

In order to further investigate the influence of polymer composition on the retention performance, the morphology of the membranes were examined using FESEM. Figure 2 shows the magnified cross-sections of PI membranes at different composition between 14 – 17 wt% of PI. Overall cross-section of the PI membrane images shows three layers of i) thin top skin layer, ii) intermediate nodular structure and iii) finger like porous sub-structure with macro voids. This top skin layer and nodular structure indicated an NF membrane properties as reported by [22,24]. The images observed as in Figure 2(c), within 10 µm of the top skin layer of the membranes exhibit dense sponge like morphologies leaving small channels reaching the surface of the membrane. At increasing PI composition, the membrane skin layer was observed to become denser while the middle sub-structure became less porous especially above 15 wt% PI composition. This observation explained the overall increase in retention of the tested solutes and the reduction in fluxes at composition higher than 15 wt%. The phenomenon is due to the slow down and delay on the non-solvent in diffusion and demixing of the polymer/non-solvent interface upon immersion when a higher composition of PI is used and thus resulting in a denser skin layer [22]. A dense skin layer may strongly affect the transport process of solute during rejection process thus making the rejection of the ions to be more effective. This result will be further discussed in the succinate recovery in the following section.

Meanwhile for the surface morphology of the fabricated membrane at different PI compositions, the FESEM images as in Figure 2(d) show an overall rough surface area at magnification of 100000x. It is also observed that as the composition of PI increases, the surface morphology becomes more wrinkled, which increases the surface roughness of the membrane. Lin et al. reported that the increase in surface roughness indicates that the membrane would have higher retention [30], which is in agreement with the results of salt retention test presented in Table 1. The results show that the retention of monovalent and divalent salt increases from 6.64 to 66.89% and from 18.9 to 53.84% respectively with increasing PI composition from 14 to 17 wt%.

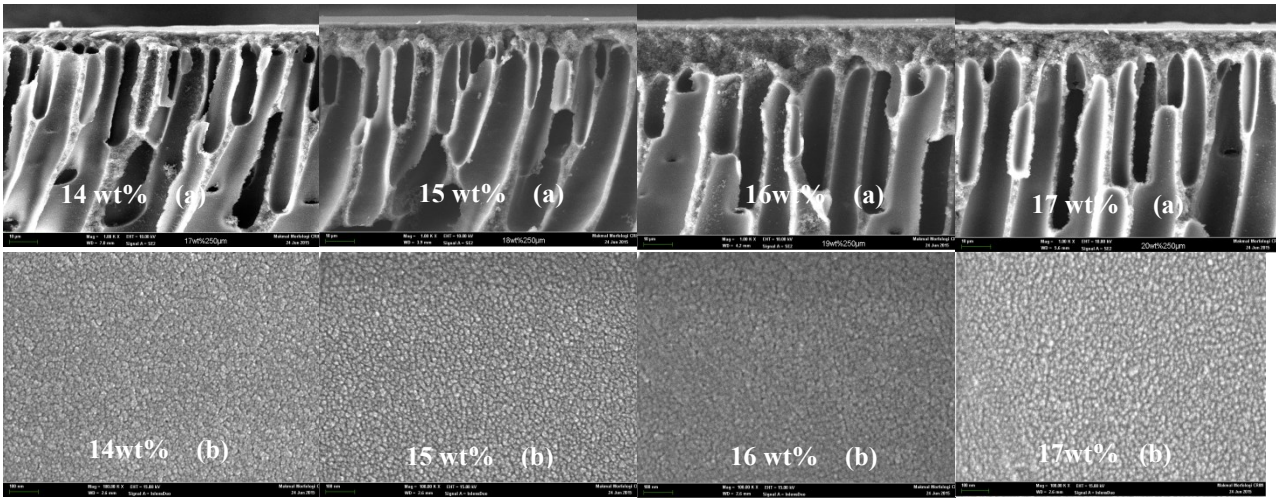


Figure 2. Effect of PI compositions (14, 15, 16 and 17 wt%) on morphology of membranes: (a) cross-section 500x and B) surface 100,000x (Membrane synthesis conditions: membrane thickness: 250 μm, evaporation time of 30s).

Succinate recovery

The performance of the membrane was also tested for the retention of succinate from ternary solution containing succinate, formate, and acetate at different concentration between 10 – 50 g/L. Figure 3 represents the flux of the ternary solutions and Figure 4 shows the succinate retention at different polymer compositions. From Figure 3, overall it was observed that the fluxes of ternary solution decreases with increasing concentrations, and polymer composition with 14 wt% PI membrane showed the highest fluxes. Meanwhile Figure 4 shows that the retention of succinate overall increased as the polymer composition increased irrespective of the ternary solution concentration. This observation is in agreement with the morphology of the membrane obtained in Figure 2(b) where the membrane skin layer becomes denser as the polymer composition increases thus resulting in the reduction of fluxes and increase of succinate retention. Similar results were also reported in previous studies using PI for rejection of isopropanol [22] and toluene [24].

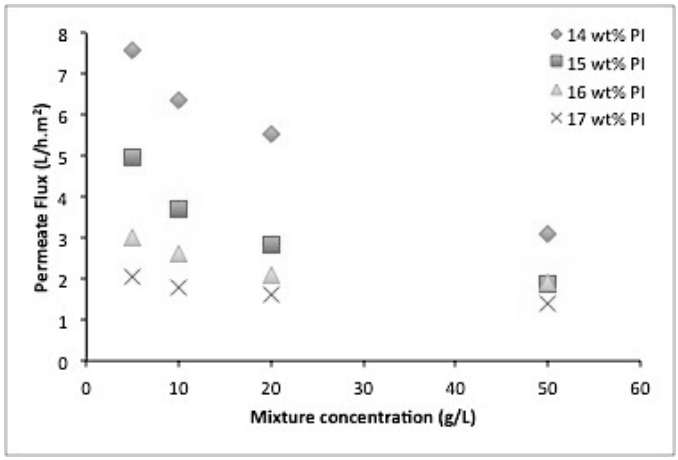


Figure 3. Permeate flux of mixed salt solution as a function of mixture concentrations for 4 different PI compositions (14, 15, 16 and 17 wt% PI). (Membrane synthesis conditions: membrane thickness of 250 μm, evaporation time of 30s. Filtration conditions: 15 bar, room temperature).

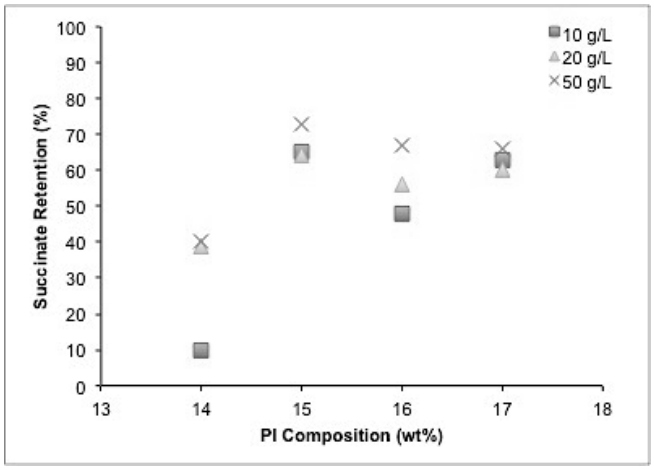


Figure 4. Succinate retention from 10, 20 and 50 g/L mixed salt solution concentrations as a function of PI composition (14 – 17 wt%) PI. (Membrane synthesis conditions: membrane thickness of 250 µm, evaporation time of 30s. Filtration conditions: 15 bar, room temperature).

However, for the selective separation of succinate in the mixed salt solution, in which succinate is recovered (retained in the retentate) while acetate and formate are removed in the permeate, 14 wt% PI membrane shows poor performance compared to the 15 wt% PI. Figure 5(a) shows that the retention of succinate by PI membrane at 14 wt% is approximately 40% for all concentration tested except at 10 g/L mixed salt solution concentration, in which a lower retention of 10% was obtained. The retention of formate and acetate were also found to be equivalent or higher than succinate retention indicating that 14 wt% PI membrane is not suitable for the selective separation of succinate. Such phenomenon can be explained by the large MWCO of membrane determined from the low retention of NaCl (MW = 58.44 g/mol) and Na_2SO_4 (MW = 142.04 g/mol) obtained in Table 1.

As the polymer composition increases to 15 wt% as shown in Figure 5(b), it was observed that succinate was able to be selectively retained while removing acetate and formate at high concentration of above 10 g/L. The succinate retention increased from 64 to 73%, while the retention of formate reduced from 42 to 39%, and acetate retention did not change much with the increasing of ternary solution concentration from 20 – 50 g/L. This increase in difference between succinate, formate, and acetate retentions indicates that the selectivity of succinate increases at high mixture concentration. It is expected that, if multiple filtrate tests are carried out, higher succinate retention and selectivity could be achieved. In a normal practice, multi-run/multi-celled, and integrated system of membrane coupled with other separation technologies are usually applied to get higher selectivity.

The increase in selectivity observed at increasing concentration could be explained by the pumping effect of monovalent anion (formate and acetate) by the divalent anion (succinate) [19]. Having a higher valency, divalent anions tend to stay further away from the membrane surface due to strong repulsion while pushing monovalent anions towards the membrane surface to meet electroneutrality in the membrane phase. Consequently this increases the concentration of monovalent anions in the membrane phase, thus the monovalent ions permeate preferentially at higher fraction compared to the divalent ions resulting in the observed lower retention of acetate and formate, compared to succinate [19]. This phenomenon was also found to be more significant at higher mixed salt solution concentration of above 10 g/L as observed in Figure 5(b) because at higher concentration, succinate, a divalent anion could effectively balance the charge of counter ion, Na^+ thus acetate/formate is no longer required for electroneutrality, causing its retention to decrease [31]. Moreover it was also observed that the retention of formate decreases more compared to acetate at increasing mixed salt solution concentration from 20 to 50 g/L. This can be explained by the smaller degree of dissociation of formic acid (pK_a 3.8) compared to acetic acid (pK_a 4.7), thus formic acid was more completely dissociated than acetic acid at the pH tested [15,32].

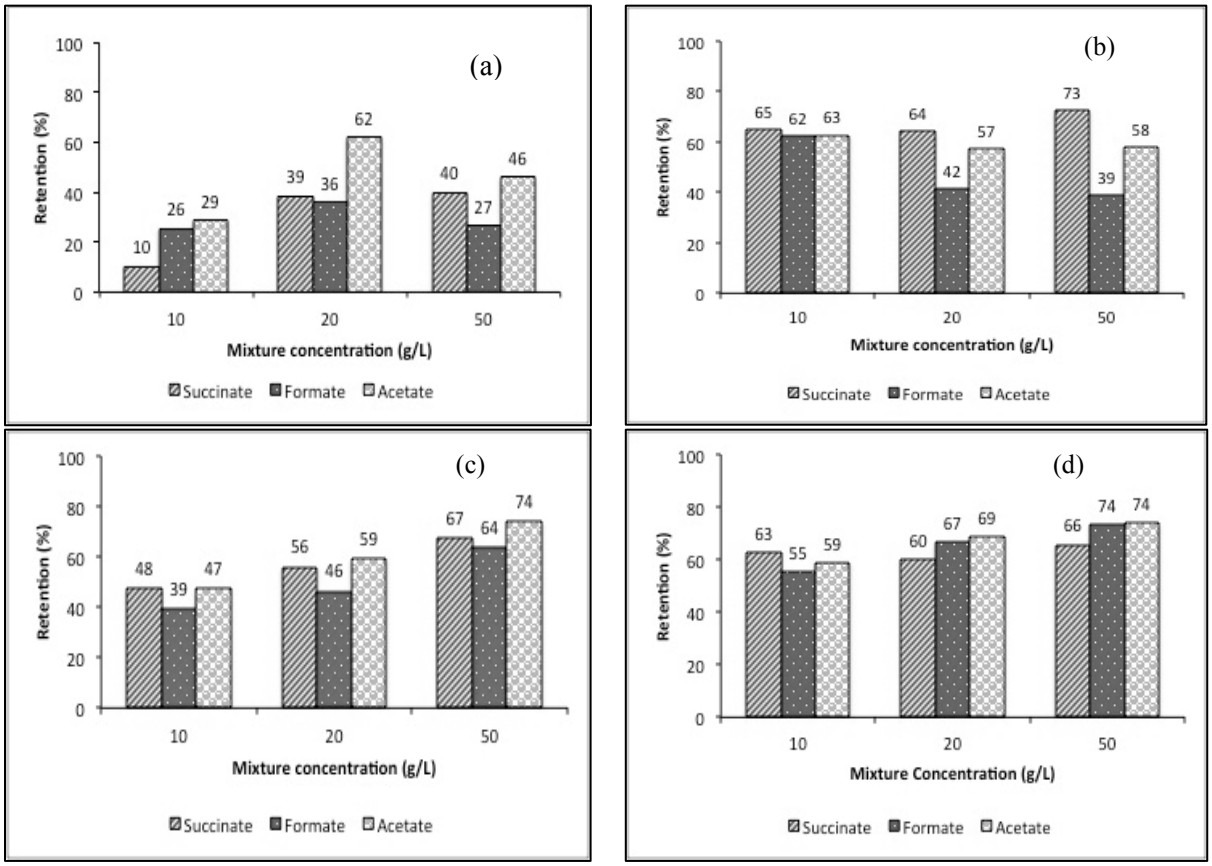


Figure 5. Retention of succinate, formate and acetate from mixed salt solution at 10, 20 and 50 g/L concentrations for (a) 14, (b) 15 (c) 16 and (d) 17 wt% PI membranes. (Membrane synthesis conditions: membrane thickness of 250 μm, evaporation time of 30s. Filtration conditions: 15 bar, room temperature).

However, when the polymer composition increased above 15 wt%, it was observed that succinate was not able to be selectively separated from the mixed salt solutions irrespective of the concentration of salt solutions tested, as shown in Figures 5 (c) and (d). All compounds (succinate, formate, and acetate) show similar retention percentage and only slight increase in succinate selectivity was observed as the mixture concentration increases from 10 to 50 g/L. This result is found to be consistent with the salt retention test that was carried out as discussed in section 3.1. Membranes with higher PI composition of above 15 wt% show a reduction in the retention difference between monovalent and divalent anions. Thus it is not suitable for selective separation of divalent anions from solution containing both monovalent and divalent anions.

Conclusion

Overall, PI shows high potential to be fabricated into NF membrane via phase inversion by manipulating the polymer composition. The NF characteristic was observed when PI composition is above 14 wt% based on the salt retention obtained. Based on the salt retention of NaCl and Na_2SO_4, 15 wt% PI membrane was found to have relatively low retention to monovalent ions and high retention to divalent ions. It also shows the best performance in selectively separated and retained succinate while rejecting formate and acetate from the model fermentation broth solution. The highest succinate retention of 73% was obtained at 50 g/L mixture solutions. Succinate selectivity was also observed with increasing mixture solution concentration from 20 to 50 g/L which was determined from the reduction in formate retention from 42 to 39%. As the test was only carried out in a single test with single cell

filtration, it is expected that a higher purity can be achieved with a multi-run/multi-celled or/and integrated system of membrane coupled with other separation technologies processes, which are usually used in a normal practice. FESEM images showing dense and thick skin layer with porous substructure resembling common NF membrane morphology also supported the result of the succinate retention.

Acknowledgement

The authors gratefully acknowledge the Ministry of Higher Education (MOHE) of Malaysia for providing financial support under the Long Term Research Grant Scheme (LRGS/2013/UKM-UKM/ PT/03 & LRGS/2013/UKM-UKM/PT/01), the Department of Chemical and Process Engineering, Universiti Kebangsaan Malaysia and MyBrain by MOSTI for the PhD scholarship.

References

1. Chimirri, F., Bosco, F., Ceccarelli, R., Venturello, A. and Geobaldo, F. (2010). Succinic acid and its derivatives: fermentative production using sustainable industrial agro food by-products and its applications in the food industry. *Italian Journal of Food Science,* 22: 119 - 125.
2. Sener, A., Kadiata, M. M., Ladrie`re, L. and Malaisse, W. J. (1997). Synergistic insulinotropic action of succinate, acetate, and glucose esters in islets from normal and diabetic rats. *Endocrine*, 7: 151 - 155.
3. Kurzrock, T. and Weuster-Botz, D. (2010). Recovery of succinic acid from fermentation broth. *Biotechnolology Letter,* 32: 331 - 339.
4. Delhomme, C., Weuster-Botz, D. and Khun, F. E. (2009). Succinic acid from renewable resources as a C4 buildig-block chemical-a review of the catalytic possibilities in aqueous media. *Green Chemistry,* 11: 13 - 26.
5. Song, H., Lee, J. W., Choi, S., You, J. K., Hong, W. H. and Lee, S. Y. (2007). Effects of dissolved CO_2 levels on the growth of Mannheimia succiniciproducens and succinic acid production. *Biotechnology and Bioengineering,* 98: 1296 - 1304.
6. Meynial-Salles, I., Dorotyn, S. and Soucaille, P. (2008). A new process for the continous production of succinic acid from glucose at high yield, titer, and productivity. *Biotechnology and Bioengineering,* 99: 129 - 135.
7. Vemuri, G. N., Eiteman, M. A. and Altman, E. (2002). Succinate production in dual-phase *Escherichia coli* fermentations depends on the time of transition from aerobic to anaerobic conditions. *Journal of Industrial Microbiology and Biotechnology,* 28: 325 - 332.
8. Guettler, M. V., Rumler, D. and Jain, M. K. (1999). Actinobacillus succinogenes sp.nov., a novel succinic-acid-producing strain from the bovine rumen. *International Journal of Systematic Bacteriology,* 49: 207 - 216.
9. Li, Q., Wang, D., Wu, Y., Li, W. L., Zhang, Y. J., Xing, J. M. and Su, Z. G. (2010). One step recovery of succinic acid from fermentation broths by crystallization. *Separation and Purification Technololgy,* 72: 294 - 300.
10. Arora, M. B., Hestekin, J. A., Snyder, S. W., Martin, E. J. S., Lin, Y. J., Donnelly, M. I. and Sanville M. C. (2007). The separation biorector: a continuous separation process for the simultaneous production and direct capture of organic acids. *Journal of Separation Science and Technology,* 42: 2519 - 2538.
11. Bechthold, I., Brezt, K., Kabasci, S., Kopitzky, R. and Springer, A. (2008) Succinic acid: A new platform chemical for biobased polymers from renewable resources. *Chemical Engineering and Technology,* 31: 647 - 654.
12. McKinlay, J. B., Vieille, C. and Zeikus, J. G. (2007). Prospects for a biobased succinate industry. *Applied Microbiology & Biotechnology*. 76: 727 - 740.
13. Huh, Y. S., Jun, Y.-S., Hong, Y. K., Song, H., Lee, S. Y. and Hong, W. H. (2006). Effective purification of succinic acid from fermentation broth produced by *Mannheimia succinicproducens. Process Biochemistry,* 41: 1461 - 1465.
14. Nam, H.-G., Park, K.-M., Lim, S. S. and Mun, S. (2011). Adsorption equilibria of succinic acid and lactic acid on amberchrom CG300C resin. *Journal of Chemical and Engineering Data*, 56: 464 - 471.
15. Cao, Y., Zhang, R., Sun, C., Cheng, T., Liu, Y. and Xian, M. (2013). Fermentative succinate production: an emerging technology to replace the traditional petrochemical processes. *BioMed Research International,* 2013: 1 - 12.
16. Choi, J.-H., Fukushi, K. and Yamamoto, K. (2008). A study on the removal of organic acids from wastewaters using nanofiltration membranes. *Separation and Purification Technology,* 59: 17 - 25.

17. Staszak, K., Wozniak, M. J., Karas, Z., Staniewski, J. and Prochaska, K. (2013). Application of nanofiltration in the process of the separation of model fermentation broth components. *Polish Journal Chemical Technology,* 15(4): 1 - 4.
18. Yao, Z., Wu, H., Liu, H., Li, S. and Jiang, M. (2008). Method for separation succinic acid from anaerobic fermentation broth. Chinese Patent CN 200610086003.7
19. Wu, H., Jiang, M., Wie, P., Lei, D., Yao, Z. and Zuo, P. (2011). Nanofiltration method for separation of succinic acid from its fermented broth. Chinese Patent CN 200910025531.5.
20. Kang, S. H. and Chang, Y. K. (2005). Removal of organic acid salts from simulated fermentation broth containing succinate by nanofiltration. *Journal of Membrane Science,* 246: 49 - 57.
21. Datta, R., Glassner, D. A., Jain, M. K. and Vick Roy, J. R. (1992). Fermentation and purification process for succinic acid. U.S. Patent 5,168,055.
22. Wang, C., Li, Q., Tang, H., Yan, D., Zhou, W., Xing, J. and Wan, Y. (2012). Membrane fouling mechanism in ultrafiltration of succinic acid fermentation broth. *Bioresource Technology,* 116: 366 -371.
23. Vandezande, P., Li, X., Gevers, L. E. M. and Vankelecom, I. F. J. (2009). High throughput study of phase inversion parameters for polyimide-based SRNF membranes. *Journal of Membrane Science,* 330: 307 - 318.
24. Valadez-Blanco, R. and Livingston, A. G. (2009). Solute molecular transport through polyimide asymmetric organic solvent nanofiltration (OSN) membranes and the effect of membrane-formation parameters on mass transfer. *Journal of Membrane Scienc,* 326: 332 - 342.
25. See-Toh, Y. H., Ferreira, F. C. and Livingston, A. G. (2007). The influence of membrane formation parameters on the functional performance of organic solvent nanofiltration membranes. *Journal of Membrane Science* 299: 236 - 250.
26. Vankelecom, I. F. J., De Smet, K., Gevers, L. E. M., and Jacobs, P. A., (2005). Nanofiltration. principles and applications. Ed. de A.I. Schäfer, A.G. Fane, T.D. Waite ; pról. de Robert J. Petersen, Elsevier.
27. Lee, J., Chae, H.-R., Won, Y. J., Lee, K., Lee, C.-H., Lee, H. H., Kim, I.-C. and Lee, J.-M. (2013). Graphene oxide nanoplatelets composite membrane with hydrophilic and antifouling properties for wastewater treatment. *Journal of Membrane Science,* 448: 223 - 230.
28. Qiao, X., Chung, T.-S. and Pramoda, K. P. (2005). Fabrication and characterization of BTDA-TDI/MDI (P84) co-polyimide membranes for the pervaporation dehydration of isopropanol. *Journal of Membrane Science,* 264: 176 - 189.
29. DOW. *Dow Water and Process Solutions - Levels of Separation of IX, RO, NF, UF and CFT* (2015). DOW answer center. The DOW company.
30. Peeters, J. M. M., Boom, J. P., Mulder, M. H. V. and Strathmann, H. (1998). Retention measurements of nanofiltration membranes with electrolyte solutions. *Journal of Membrane Science,* 145: 199 - 209.
31. Lin, S. W., Sicairos, S. P. and Navarro, R. M. F. (2007). Preparation, characterization and salt rejection of negatively charged polyamide nanofiltration membranes. *Journal of Mexican Chemical Society,* 51: 129 - 135.
32. Krieg, H. M., Modise, S. J., Keizer, K., and Neomagus, H. W. J. P. (2004) Salt rejection in nanofiltration for single and binary salt mixtures in view of sulphate removal. *Desalination*, 171: 205 -215.
33. Van der Burggen, B., Schaep, J., Wilms, D. and Vandecasteele, C. (1999). Influence of molecular size, polarity and change on the retention of organis molecules by nanofiltration. *Journal of Membrane Science,* 156: 29 - 41.

Malaysian Journal of Analytical Sciences, Vol 20 No 6 (2016): 1491 - 1497
DOI: http://dx.doi.org/10.17576/mjas-2016-2006-30

MALAYSIAN JOURNAL OF ANALYTICAL SCIENCES
Published by The Malaysian Analytical Sciences Society
ISSN 1394 - 2506

PRODUCTION OF BIOGAS THROUGH ANAEROBIC DIGESTION OF *Cabomba furcata* IN DIGESTER BATCH SYSTEM

(Penghasilan Biogas Melalui Pencernaan Anaerobik daripada *Cabomba furcata* di dalam Sistem Penghadam Kelompok)

Siti Afifah Muda[1,3]*, Omar Syah Jehan Elham[2,3], Hassimi Abu Hasan[3], Siti Rozaimah Sheikh Abdullah[3]

[1]*Section of Process, Chemical Engineering Technology,*
Universiti Kuala Lumpur-Malaysian Institute of Chemical & Bioengineering Technology (UniKL-MICET),
Lot 1988 Bandar Vendor Taboh Naning, 78000 Alor Gajah, Melaka, Malaysia
[2]*Faculty of Chemical Engineering,*
Universiti Teknologi MARA, Cawangan Johor, Kampus Pasir Gudang, 81750 Masai, Johor, Malaysia
[3]*Department of Chemical and Process Engineering, Faculty of Engineering and Built Environment,*
Universiti Kebangsaan Malaysia, 43600 UKM Bangi, Selangor, Malaysia

**Corresponding author: sitiafifahm@unikl.edu.my*

Received: 21 October 2015; Accepted: 14 June 2016

Abstract

Biogas is produced from decomposition of organic waste such as sewage sludge, animal manure, and municipality solid wastes by microorganisms in anaerobic conditions. Biogas, which consist mainly of methane is a renewable energy source. It can be used for heating, power generation or upgrading to natural gas quality. In this study, the anaerobic treatability and biogas generation potential of *Cabomba furcata* (*C. furcata*) were examined in batch digesters. *C. furcata* collected from Chini Lake, Pahang was utilized as a substrate in biogas production. Slurry samples of *C. furcata* were prepared in 2 different mixture i.e., *C. furcata*/water ratio (1:1, 1:2 and 1:3) and *C. furcata*/inoculums ratio (1:1, 1:2 and 1:3). Throughout the experiment, the pH range was 5.5 to 7.0 while temperature range was 25 to 30 °C to enable anaerobic digestion in mesophilic condition for a retention time of 28 days. The results showed that the maximum methane production achieved at ratio of 1:3 for both mixture *C. furcata*/water and *C. furcata*/inoculums with production percentages up to 1.1 and 11.9%, respectively. Moreover, the result indicated that the production of methane increased as the retention time increased. Therefore, native plant of *C. furcata* is a great potential as a substrate in the production of biogas for future renewable energy.

Keywords: *Cabomba furcata*, methane production, anaerobic digestion, renewable energy

Abstrak

Biogas terhasil daripada penguraian sisa organik seperti kumbuhan enapcemar, baja haiwan dan sisa pepejal perbandaran oleh mikroorganisma dalam keadaan anaerobik. Biogas terdiri daripada metana sebagai sumber tenaga yang boleh diperbaharui. Ia boleh digunakan untuk pemanasan, penjanaan kuasa atau peningkatan kepada kualiti gas asli. Melalui kajian ini, kebolehrawatan anaerobik dan kebolehan penjanaan biogas oleh *Cabomba furcata* (C. *furcata*) telah diperiksa di dalam penghadam kelompok. C. *furcata* telah dikumpul dari Tasik Chini, Pahang dan digunakan sebagai substrat dalam penghasilan biogas. Sampel cair *C. furcata* disediakan dengan 2 campuran yang berlainan i.e., nisbah *C. furcata*/air (1:1, 1:2 dan 1:3) dan nisbah *C. furcata*/inokulum (1:1, 1:2 dan 1:3). Sepanjang kajian dijalankan, nilai pH adalah 5.5 hingga 7.0 manakala julat suhu ialah 25 – 30 °C menjadikan keadaan operasi penghadaman anaerobik sebagai mesofilik dan masa tahanan selama 28 hari. Keputusan kajian menunjukkan penghasilan biogas yang maksimum berlaku pada nisbah 1:3 untuk kedua-dua campuran *C. furcata*/air dan *C. furcata*/inokulum dengan peratusan penghasilan masing - masing meningkat kepada 1.1 dan 11.9%. Selain itu, keputusan juga menunjukkan penghasilan semakin meningkat apabila masa tahanan meningkat. Oleh itu, *C. furcata* mempunyai potensi yang bagus sebagai substrat dalam penghasilan biogas untuk tenaga yang boleh diperbaharui pada masa depan.

Kata kunci: *Cabomba furcata*, penghasilan metana, penghadaman anaerobik, tenaga yang boleh diperbaharui

Introduction

Biogas is one of the clean renewable energy where the source is easily controlled such as organic waste. Biogas is produced from decomposition of organic material by microorganisms in absence of oxygen. Besides that, biogas also can be produced by anaerobic digestion or fermentation of biodegradable materials such as biomass, fertilizer, municipal waste, crop, crop residue and other plants. Biogas consist of methane, carbon dioxide, nitrogen, hydrogen, hydrogen sulfide and oxygen. In Malaysia, the source for biogas generation such as agriculture waste, animal manure, domestic waste, crops, household waste and others are widely available. Using these materials as biogas sources can provides a number of advantages such as reduce the utilization of fossil fuel, increase farmers income and provide employment opportunities. In addition, biogas production has a great potential to produce neutral carbon dioxide that can prevent the occurrences of emission of greenhouse gases into the atmosphere and simultaneously reduce air pollution as well.

Anaerobic digestion is one of widely used process and attractive method for converting organic waste into for biogas as alternative energy sources [1]. Anaerobic digestion is a natural process in which bacteria decompose the carbon in organic matter. The digestion occurs in three process steps which are hydrolysis, acidogenesis and methanogenesis. In hydrolysis stage, complex organic compounds are broken down by hydrolytic bacteria. Subsequently, in the acidogenesis stage, compounds are further broken into simple molecules by acid-forming bacteria. Then, in methanogenesis stage, methanogenic bacteria will convert the acids into methane gas and carbon dioxide. These processes occur without the presence of oxygen [2]. A few studies have been conducted on biogas production using aquatic plants by applying anaerobic digestion process such as water hyacinth [3], *Eichhornia azurea, Pistia stratiotes* and *Salvini* [4], and water hyacinth and water chest nut [5].

Cabomba furcata is a fully submerged aquatic plant that grows readily in Chini Lake, Pahang. Unfortunately, *C. furcata* gives negative impact towards ecosystem in Chini Lake. Recent research indicates *C. furcata* adversely affects water quality by imparting colour and taint. Cabomba thickets interfere with swimming, boating and fishing, increased the habitat of disease carriers like mosquitoes and reduce habitat available other native plants, fish and others species [6]. Recommendations to utilize an aquatic plant as a renewable feedstock is a good solution for controlling overgrowth of *C. furcata*, save the ecosystem and cost effective. Therefore, this study was conducted to evaluate the potential of *C. furcata* as a substrate for biogas production in a batch digester. The effect of substrate/water ratio and substrate/inoculums ratio were also investigated extensively.

Materials and Methods

Substrate and inoculums

C. furcata plant was used as a substrate for biogas production. The plant was collected from Chini Lake, Pahang while inoculums of activated sludge was obtained from sewage treatment plant located in Putrajaya.

C. furcata preparation

The raw sample of *C. furcata* was weighted and transferred into six different 2000 mL conical flasks, as batch digesters for carrying out the anaerobic digestion process. Each conical flask contained 500 g of *C. furcata* substrate at different ratio of sample mixture. Conical flask 1, 2 and 3 were filled with 500, 1000 and 1500 g of water for 1:1, 1:2 and 1:3 of *C. furcata*/water ratio respectively. Meanwhile, conical flask labelled with 4, 5 and 6 contained 500, 1000 and 1500 g of inoculums for 1:1, 1:2, 1:3 of *C. furcata*/inoculums ratio respectively as shown in Table 1.

Setup of anaerobic digester

Anaerobic digester system was setup using 2000 mL conical flask and 1000 mL cylinder that filled with water was upturned to trap gas produced during experiment. Both unit was connected using silicon tube as depicted in Figure 1. Each reactor consists of different sample mixture as stated in Table 1. Laboratory anaerobic digester system was developed as shown in Figure 1.

Table 1. Sample preparation method

Digester	Sample Mixture	Mixture Ratio
1	500 g *C. furcata* + 500 g water	1:1
2	500 g *C. furcata* + 1000 g water	1:2
3	500 g *C. furcata* + 1500 g water	1:3
4	500 g *C. furcata* + 500 g inoculums	1:1
5	500 g *C. furcata* + 1000 g inoculums	1:2
6	500 g *C. furcata* + 1500 g inoculums	1:3

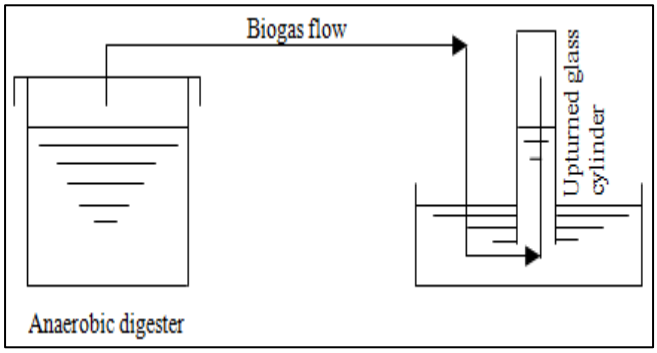


Figure 1. Schematic diagram for anaerobic digester system

Results and Discussion

Effect of *C. furcata*/water ratios

As can be seen in Figure 2, a graph of percentage of biogas production versus time was plotted for the sample mixture of *C. furcata* and water for once in week until 28 days. Cumulative biogas production for sample mixture of 1:1 and 1:2 *C. furcata*/water ratio increased according to time but for ratio of 1:3 *C.furcata*/water the biogas production increased after day 22 onwards. For sample mixture of 1:1 and 1:2 *C. furcata*/water there were no CH_4 detected during 28 days. Meanwhile for sample mixture of 1:3 *C. furcata*/water ratio produced 1.1% of CH_4 started on day 22. At ratio of 1:1 of *C. furcata*/water only 3.6%, 4.4%, 2.1% and 1.4% CO_2 were produced on day 7, 14, 21 and 28, respectively and only 61.3% hydrogen was detected on day 28. The sample mixture of 1:2 *C. furcata*/water ratio produced 0.95% of CO_2 and 50.9% of H_2 on day 7. Biogas composition majorly consists of methane and carbon dioxide. Meanwhile, nitrogen, hydrogen, hydrogen sulphide and oxygen are minority gases produced during digestion process [7]. Others gases produced during this study might consist of nitrogen, oxygen and hydrogen sulphide. Based on the results, only sample mixture of 1:3 *C. furcata*/water produced 1.1% CH_4. The methane produced from the digestion process could be initiated from native microbes that naturally attached to the *C. furcata*. On top of that, sample mixture of 1:3 *C. furcata*/water has higher fluid properties compared to others. According to Sara and Veronica [7], fluid properties is an important parameter for feedstock to facilitate the methane bacteria to contact with feedstock and makes the digestion faster.

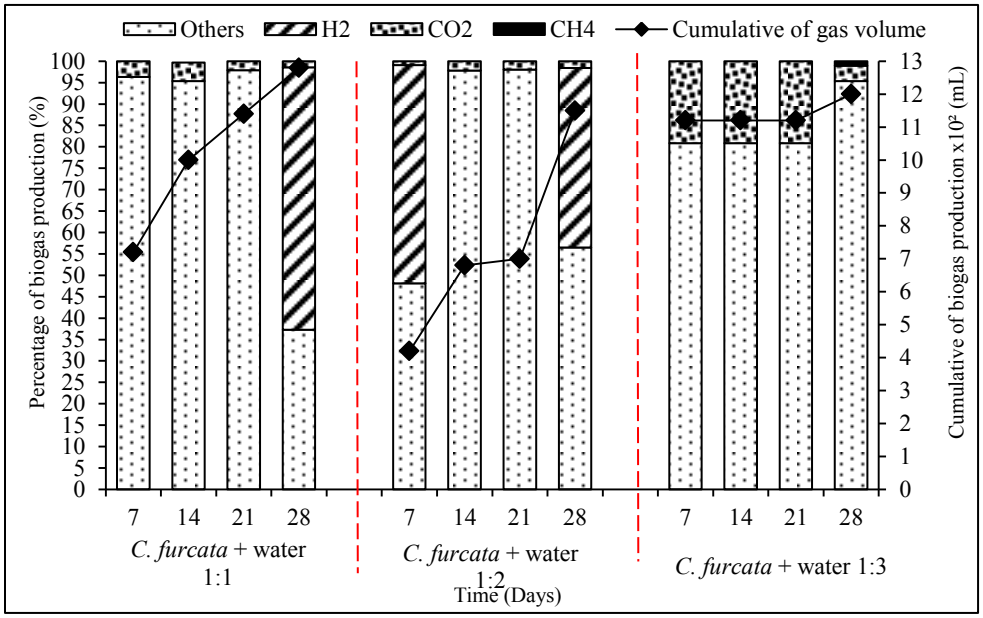


Figure 2. Biogas production from *C. furcata*/water slurry at different ratio

Effect of *C. furcata*/inoculums ratios

In Figure 3, the cumulative biogas production for sample mixture of *C. furcata*/inoculums ratio (1:1, 1:2, and 1:3) increased according to time. For sample mixture of 1:1 *C. furcata*/inoculums ratio, no CH_4 detected. Otherwise, CO_2 detected on days 7, 14, 21 and 28 as 1.3%, 2.7%, 2.6% and 2.7% respectively while 49.3% of hydrogen produced on day 7. However, for sample mixture of 1:2 *C. furcata*/inoculums ratio, about 2.1% of methane detected within days 22 to 28 followed by CO_2 produced on days 7, 14, 21 and 28 as 1.2%, 8.2%, 3.5% and 7.3% respectively. But H_2 only produced on day 7 about 85.1%. The percentage of CH_4 yield increase can be seen for sample mixture of 1:3 *C. furcata*/inoculums ratio up to 11.9% during 28 days. While, CO_2 production increase day by day as 2.2%, 5.5%, 3.1% and 8.5% on day 7, 14, 21, and 28 respectively. H_2 only detected on 7, 14 and 28 as much as 58.7%, 37.0 and 49.4% respectively. Based on the previous research, Neo et al. [8] reported that wheat straw produced highest percentage of biogas production up to 59% when inoculated with cattle manure. Other than that, Sunorso et al. [9] proved that substrates (manure) and inoculums (rumen fluid) exhibit higher cumulative biogas production. Besides, Abu Darieh et al. [10] reported that, methane yield produced from grass mixed with inoculums up to 80%. As a result, inoculums is one of the most important factor affecting the biogas production. In order to produce high CH_4 content, inoculums that contain high microbial loading needs to be added in the mixture of biomass to initiate the biochemical processes from anaerobic digester [11]. During this digestion, CO_2 produced is less than 10% for the sample mixture of 1:1 *C. furcata*/inoculums ratio and 1:2 *C. furcata*/inoculums ratio compared to H_2 produced up to 85% for 1:3 *C. furcata*/inoculums ratio. H_2 and CO_2 are the two other products converted by acidifying bacteria during acidogenesis stage. Khanal et al. [12] reported that optimum pH for hydrogen produced is at pH 5. Content of liquid in the digester is the main factor in producing of CO_2. Reducing in CO_2 level in gas phase resulted from higher liquid content in digester and elevated the concentration CO_2 dissolved in water [13].

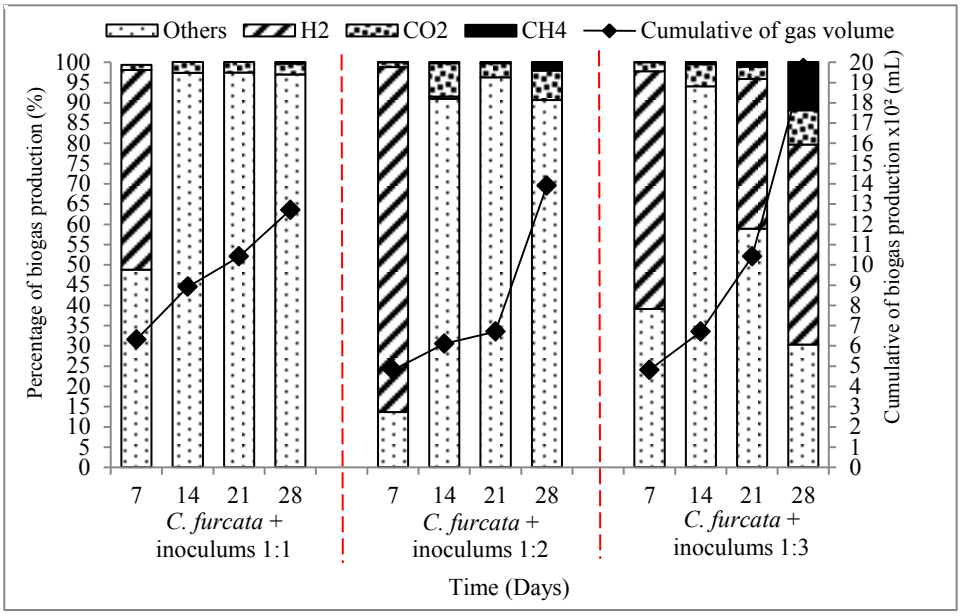


Figure 3. Biogas production from *C. furcata*/inoculums slurry at different ratios

Variation of pH and temperature during CH_4 production

During digestion occurred, the variation pH value was monitored and plotted in Figure 4. pH value and temperature were monitored regularly at every 3 days and continued until 35 days. The profile of the pH and temperature for both types of sample mixture were similar. The pH value dropped from an initial reading of around pH 5.5 - 6.9 for all samples. The decline of pH reading from 4.5 to 5 for each sample causes acidic conditions that lead to the failure of methanogenic activity because it inhibits of microbial growth. This occurs when the pH value drops below 6.5 [14]. Based on these factors, the sample mixture of 1:3 *C. furcata*/water ratio managed to produce little CH_4 on the 28th day since the final of pH value in the range of 5 - 6.2 because the pH is less acidic. Similarly, sample mixture of 1:3 *C. furcata*/inoculums, which resulted in the highest percentage of CH_4 as final pH value of the sample was approaching pH 6.5 that suitable for bacteria involved in anaerobic digestion. During the digestion process, protein degradation might occur and result in increasing ammonia presence that contributed to the elevated pH during day 17 for all sample mixtures and had inhibited the process [15]. The pH value decreased on day 20 due to the utilization of ammonia by microbes as nitrogen source for growth. As a result, pH decreased below than 6.5, and the conversion of mainly H_2 or CO_2 to methane and, acetate acid to methane and carbon dioxide by methanogenic bacteria could be reduced during methanogenesis process [16].

As shown in to Figure 5, the temperature for all the samples in the range of 25 - 30°C during the digestion. Ozmen and Aslanzadeh [17] reported that the possible temperature for anaerobic digestion from 3 to 70 °C and for mesophilic conditions in the range of 20 – 40 °C. It means that the process of digestion occurred within the mesophilic range. The temperature control of the process is important to ensure the optimum temperature range for the bacteria during methanogenic activity. Based on Figure 2 and Figure 3, the highest percentage of CH_4 produced in mesophilic condition up to 11.9 %. However, according to Tchobanogous et al. [18], this digestion temperature in this study considered as optimal temperature for the support of biological-reaction rate.

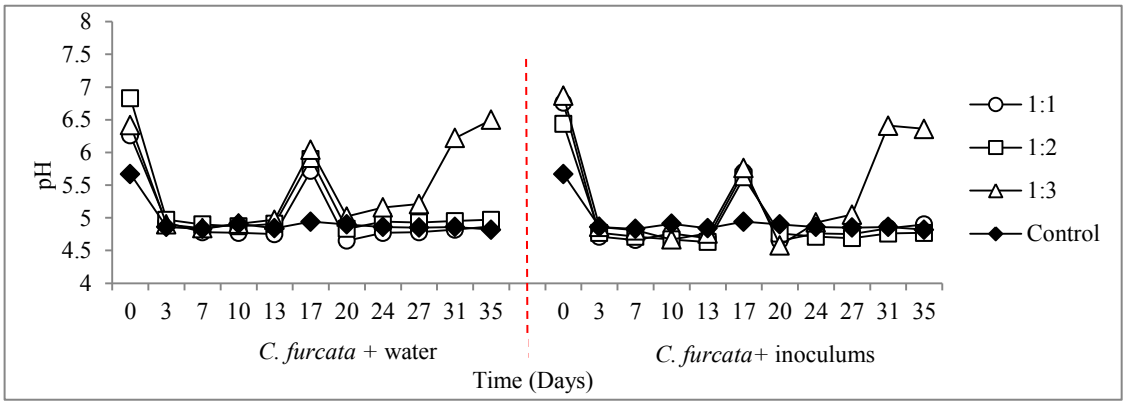


Figure 4. Comparative of pH value in anaerobic digestion process

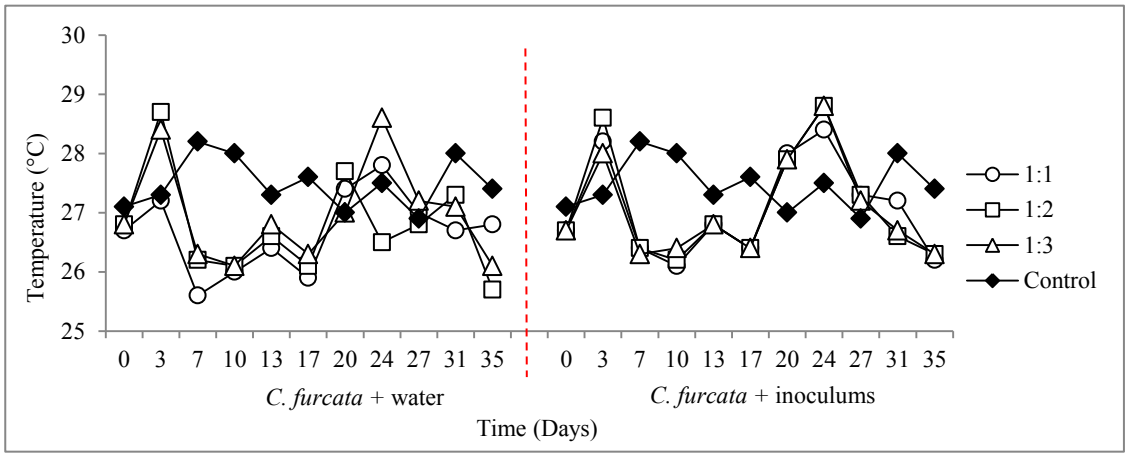


Figure 5. Comparative of temperature in anaerobic digestion process

A sample mixture of *C. furcata*/inoculums shows the percentage increase in CH_4 quite significantly up to 11.9% for sample mixture of 1:3 *C. furcata*/inoculums ratio as shown in Figure 3. This is because this sample contained of highest soluble/degradable organic load for methanogens. Verma et al. [5] reported that the role of the inoculums, supplying microbial culture and a slurry substrate to begin the process methanogenisis assume equals importance in biogas production. Besides that, the retention time which the period spent by the feed or substrate inside the digester has a significant effect on methane production. The appropriate retention time for mesophilic bacteria is around 20 days. If the retention time is in the short period, the concentration of methane in the formed biogas is less than 50% and it is not longer combustible [7]. This was proven by the highest amount of biogas produced which started from days 22 for sample mixture of 1:3 *C. furcata*/water ratio and 1:3 *C. furcata*/inoculums ratio.

Conclusion

The result revealed that *C. furcata* has a great potential for utilization as substrate in biogas production. In mesophilic phase, the cumulated biogas volume increased with respect to substrate/water ratio and substrate/inoculums ratio. The most important finding in this research is that the sample mixture ratio of the substrate significantly affect the biogas production. The sample mixture of *C. furcata*/inoculums produced up to 11.9% of CH_4 during 28 days of anaerobic digestion process compared to sample mixture of *C. furcata*/water ratio only produced about 1.1% of CH_4. Besides that, activated sewage sludge can be used as inoculums for anaerobic digestion since it has important roles for start-up of the biochemical processes from anaerobic digesters.

Acknowledgement

This research was financially supported by the Ministry of Education (MOE) through Grant No. ERGS/1/2013/TK05/UKM/02/2 and Universiti Kebangsaan Malaysia with Grant No. GGPM-2013-075.

References

1. Gelegenis, J., Georgakakis, D., Angelidaki, I., Christopouolou, N. and Goumenaki, M. (2007). Optimization of biogas production from olive–oil mill wastewater, by co-digesting with diluted poultry manure. *Applied Energy*, 84: 646 – 663.
2. Teodorita, A. S., Rutz, D., Prassl, H., Kottner, M., Finsterwalder, T., Volk, S. and Janssen, R. (2008). Biogass Handbook.University of Southern Denmark, Denmark.
3. Kunatsa, T. and Mufundirwa, A. (2013). Biogas production from water hyacinth case of Lake Chivero - Zimbabwe. *International Journal of Recent Technology and Engineering,* 2 (2): 138 – 142.
4. Pereira, R. G., Pereira, M. C. D. E., Silva, J. G., Abreu, F. L. B. and Lameira, V. J. (2011). Production and characterization of biogas obtained from biomass of aquatic plants. *International Conference on Renewable Energies and Power Quality* (ICREPQ'11). Canary Island Convention Centre Spain.
5. Verma, V. K., Singh, Y. P. and Rai, J. P. N. (2007). Biogas production from plant biomass used for phytoremediation of industrial wastes. *Bioresource Technology,* 98: 1664 – 1669.
6. Department of Agriculture, Fisheries and Forestry (2012). Cabomba. *The State of Queensland Fact Sheet*. Access from https://www.daf.qld.gov.au/__data/assets/pdf_file/0005/72896/IPA-Cabomba-PP30.pdf [10 February 2013].
7. Sara, S. R. and Veronica, M. S. (2009). Biogas production from waste of the shrimp manufacture in Sisimiut. *Arctic Technology*: pp. 1 – 48.
8. Neo, S., Vintila, T. and Bura, M. (2012). Conversion of agriculture wastes to biogas using as inoculums cattle manure and activated sludge. *Scientific papers: Animals Sciences and Biotechnologies,* 45(1): 328 – 334.
9. Sunarso, Johari, S., Widiasa, I. N. and Budiyono. (2012). The effect of feed to inoculums ratio on biogas production rate from cattle manure using ramen fluids as inoculums. *International Journal of Waste Resources*, 2(1): 1 – 4.
10. Abu-Dahrieh, J. K., Orozco, A., Ahmad, M. and Rooney, D. (2011). The potential for biogas production from grass. *Jordan International Energy Conference*: pp. 1 – 8.
11. Mateescu, C. and Constantinescu, I. (2011). Comparative analysis of inoculums biomass for biogas potential in the anaerobic digestion. *U.P.B. Scientific Bulletin: Series B, 73(3)*: 99 – 104.
12. Khanal, S. K., Chen, W. H., Li, L. and Sung, S. (2004). Biological hydrogen production: Effects of pH and intermediate product. *International Journal Hydrogen Energy,* 29: 1123 – 1131.
13. Deublein D. and Steinhauser, A. (2011). Biogas from waste and renewable resources. An introduction. 2nd Edition, Revised and Expended edited, Wiley-VCH, Weinheim, Germany.
14. Franco, A., Mosquera-Corral, A., Campos, J. L. and Roca, E. (2007). Learning to operate anaerobic bioreactors. *Communicating Current Research and Educational Topics and Trends in Applied Microbiology:* pp. 618 – 627.
15. Neves, L., Oliveira, R. and Alves, M. (2003). Influence of inoculum activity on the bio-methanization of a kitchen waste under different waste/inoculum ratios. *Process Biochemistry*, 39(12): 2019 – 2024.
16. Zimeminski, K. and Frac, M. (2012). Methane fermentation process as anaeorbic aigestion of biomass: transfromations, stages and microorganism. *African Journal of Biotechnology*, 11(18): 4127 – 4139.
17. Ozmen, P. and Aslanzadeh, S. (2009). Biogas production from municipal waste mixed with different portions of orange peel. Synopsis of Master thesis. University of Boras, Sweden.
18. Tchobanoglous, G., Burton, F. L. and Stensel, H. D. (2003). Waste-water engineering: Treatment and reuse. Fourth edition. Tata McGraw-Hill Publishing Company Limited, New Delhi: pp.1819.

Malaysian Journal of Analytical Sciences, Vol 20 No 6 (2016): 1498 - 1509
DOI: http://dx.doi.org/10.17576/mjas-2016-2006-31

MALAYSIAN JOURNAL OF ANALYTICAL SCIENCES
Published by The Malaysian Analytical Sciences Society
ISSN 1394 - 2506

POLYANILINE MULTI-COATED ONTO POLYVINYLIDENE FLUORIDE AND SILICON ELASTOMER FOR PRESSURE FILTRATION MEMBRANES

(Polianilin Multi-Lapis Bersalut pada Polivinilidin Fluorida dan Elastomer Silikon untuk Membran Penurasan Bertekanan)

Fatimah Ibrahim, Rosiah Rohani*, Abdul Wahab Mohammad

Department of Chemical and Process Engineering,
Faculty of Engineering & Built Environment,
Universiti Kebangsaan Malaysia, 43600 UKM Bangi, Selangor, Malaysia

**Corresponding author: rosiah@ukm.edu.my*

Received: 21 October 2015; Accepted: 14 June 2016

Abstract

In this study, silicone rubbers were used to achieve the desire absorbing properties of PANI onto polyvinylidene fluoride (PVDF) microporous support. Poly (methyl-vinyl ether-alt-maleic acid) (PMVEA) polymeric acid was used as acid dopant to enhance the membrane filtration performance. Initially PVDF micro-porous support was dip-coated with silicone rubber elastomer solution followed by deposition with PANI by *in-situ* chemical oxidative polymerisation techniques using two-compartment cell in presence of PMVEA and ammonium persulfate as the oxidizing agent. The PANI multilayer composite membranes were characterized by gravimetric for PANI content measurement namely Scanning Electron Microscope (SEM), Fourier-Transform Infrared (FTIR), Differential Scanning Calorimetry (DSC) and contact angle. The PANI content was found to be more than 30 %. SEM, FTIR and DSC analysis have confirmed the presence of PANI onto the multilayers membrane while the contact angle of the membrane in presence of high loading PANI was 0 ^{o} indicating the super hydrophilicity than without the PANI presence of 78.8 ^{o}. The pressure filtration of PANI multilayer composite filtration membrane with a range of polyethylene glycols at different molecular weights was obtained based on the high flux up to 904.11 L/m^2.h and reasonable molecular weight cut off of below 20,000 g/mol were obtained for the synthesized membrane.

Keywords: polyaniline, silicone elastomer, polyvinylidene fluoride, chemical oxidative polymerisation, polymeric acid

Abstrak

Melaui kajian ini, getah silikon telah digunakan untuk mencapai keinginan menyerap sifat-sifat PANI ke polivinilidin fluorida (PVDF) sokongan mikrobeliang. Poli (vinil metil-eter-alt-asid malik) (PMVEA) asid polimer digunakan sebagai asid pendopan untuk meningkatkan prestasi penapisan membran. Pada mulanya mikro-berliang sokongan PVDF telah disalut dengan larutan elastomer getah silikon diikuti dengan pemendapan PANI oleh teknik pempolimeran kimia oksidatif sel *in-situ* menggunakan dua bahagian sel dengan kehadiran PMVEA dan ammonium persulfat sebagai agen pengoksidaan. Membran komposit PANI multilapis telah dicirikan secara gravimetrik untuk mengukur kandungan PANI, seperti Mikroskop Imbasan Elektron (SEM), Inframerah Transformasi Fourier (FTIR), kalorimeter pengimbasan pembezaan (DSC) dan sudut sentuhan. Kandungan PANI didapati melebihi 30%. Analsis SEM, FTIR dan DSC telah mengesahkan kehadiran PANI pada membran PANI multilapisan manakala sudut sentuhan membran dengan kehadrian PANI yang tinggi adalah 0 ° menunjukkan keadaan super hidrofilik berbanding tanpa kehadiran PANI adalah 78.8 °. Tekanan penapisan membran komposit PANI multilapis dengan pelbagai julat polietilena glikol pada berat molekul yang berbeza telah diperolehi berdasarkan fluks yang tinggi sehingga 904.11 L/m^2.h dan berat molekul yang munasabah iaitu di bawah 20.000 g/mol bagi membran yang telah di sintesis.

Kata kunci: polianilin, elastomer silikon, polivinilidin fluorida, pempolimeran oksidatif kimia, asid polimer

Introduction

Interest in conducting polymer from polyaniline (PANI) has grown due to its conducting properties: electronically conductive and electrochemically active polymer [1], good redox properties and high environmental stability, relatively simple synthesis, and also low cost [2-7]. These advantages have led PANI to be used in numerous applications including filtration membranes [8], battery electrodes [9, 10], electromagnetic shielding devices [11], and anticorrosion coatings [12-14]. To cope with the rising energy costs, emerging contaminants, stricter environmental regulations, and industrial demand, the next generation of filtration membranes must be more selective, robust, and require low chemical and energy inputs. New membrane materials must be explored to meet these goals in applications such as water and wastewater treatment, in addition to other well-established industrial, biomedical and analytical separations [8]. High permeation flux and high selectivity are the essential requirement for successful separation membrane. One way of achieving this is by self-synthesizing filtration membranes that meet the criteria. Additionally this membrane can be tailored utilizing intrinsic polymer such as PANI to meet specific requirement for the targeted application. The fabrication of high-performance multilayer composite membrane specifically from PANI base from microporous support substrate is essential to obtain the most suitable surface structure, roughness and surface porosity for the separation.

Multilayer composite membrane has been reported for various applications especially for water filtration [15-18]. The multilayer composite membrane usually has three layers and can be divided into two types based on the membrane configuration: (selective layer)/(gutter layer)/(support substrate) and (sealing or protective layer)/ (selective layer)/(support substrate) [19-21]. In the former, the selective layer might be as thin as a few tens nanometers and slightly defective; the gutter layer is a permeable material which serves as a channelling and adhesive medium between the selective layer and the support substrate. In the latter, the selective layer is thicker (about 0.04 ± 1 mm) and essentially defect-free. The sealing or protective layer not only functions as a protective layer but also improves the membrane performance [21]. Therefore this motivates the synthesis of the multilayer composite membrane to be used in the field of pressure filtration namely nano- (NF) and ultra-filtration (UF). The used of PANI in forming multilayer composite membranes have been reported in the application of fuel cell [22], desalination of saline water that consists of charged solutes [17, 23], separation of carbon dioxide from methane [24] and also as electrochemical energy storage [25]. However the application in pressure filtration membrane under neutral solutes has yet to be reported.

The main aim of this work is to fabricate multilayer composite membrane from PANI coated with silicone elastomer onto PVDF and further characterize it. Multilayer composite membrane is prepared in the form of (sealing or protective layer)/(selective layer)/(support substrate) in series. PANI works as the sealing layer, silicone rubber as the selective layer acts as barrier to attach more PANI onto PVDF (support substrate). Silicone rubber is used for selective support as it has low density, easy to form, good chemical resistance and weather resistant [26]. The functionalization of silicone rubber has been reported can improve the membrane performance either in pervaporation, gas separation or extraction to serve for better separations [27-29]. Chemical oxidative polymerization of aniline is conducted in the presence of 1M HCl to dilute the aniline and ammonium persulphate (APS) to form PANI. These aniline and APS solutions further reacted in a specially fabricated two compartment cell, each solution is filled at each side of the cell and the PVDF membrane is sandwiched between the cell. Meanwhile polymeric acid of poly (methyl- vinyl ether-alt-maleic acid) (PMVEA) is used as the dopant for functionalizing the PANI together with HCl. PANI doped with PMVEA was reportedly used for covalent attachment of oligonucleotides through the carboxylic acid functionality [30, 31]. The chemical structure of PANI, PVDF, silicone rubber and PMVEA used for producing the multilayer composite membrane is presented in Figure 1.

The characterization of the synthesized membranes was performed using Fourier Transform Infrared (FTIR) spectroscopy. Thermal properties of the membrane were investigated by Differential Scanning Calorimetry (DSC) while surface morphology is investigated by Scanning Electron Microscope (SEM). Drop shape analysis was used to examine surface wettability changes contact angles (θ) for liquid water droplets on the multilayer membrane surfaces. The performance of the multilayer membrane is tested via rejection of different molecular weights (MW) of neutral and non-charged solutes from Polyethylene glycols (PEG) in a dead-end filtration. Solutions with

different molecular weight (MW) were used for the identification of the nominal pore sizes of the membrane fabricated [32,33].

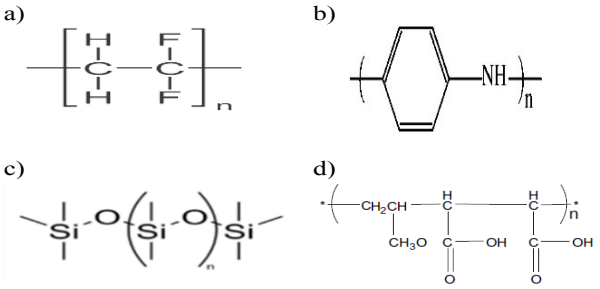


Figure 1. Chemical structure of a) PVDF, b) PANI, c) Silicone rubber and, d) PMVEA

Materials and Methods

Materials

Aniline monomer, poly (methyl vinyl ether-alt-maleic acid) (PMVEA), of MW 216,000 g/mol and ammonium persulfate (APS) were obtained from Aldrich Chem. Co. The microporous polyvinylidene fluoride (PVDF) membrane (0.1 µm) was purchased from Hangzhou ANOW Microfiltration Co. Ltd., China. Liquid silicone elastomer was purchased from Portal Trading, Penang, Malaysia. N-hexane and hydrochloric acid (HCl) were supplied by Merck and used as received.

Preparation of PVDF/silicone membranes

The commercial microporous PVDF membranes were kept in a desiccator for overnight and weighed. Next, the membranes were dipped in 50% ethanol solution for 1 min and washed with ultrapure water to loosen the shrunken membrane pores due to the long-term storage [34]. The dipped membranes were then coated with a mixture of 3 wt.% of silicone (with curing agent) and 97% n-hexane for 30 minutes. This was to ensure that membrane surface has been completely covered by the mixture of silicone and curing agent [19]. The ratio of silicone to curing agent was fixed at 10:1.The silicone coated layer membranes were then cross-linked with each other by keeping the silicone coated membranes in an oven at 60 ^{o}C for 1 hour [21].

Multilayer membrane composites

The microporous PVDF coated with silicone rubber were further coated with PANI in presence of polymeric acid from PMVEA to enhance the performance of the multilayer coated membranes for application in pressure filtration especially in UF and NF range. The polymerization of PANI onto the silicone coated PVDF support was performed by sandwiching aniline/PMVEA and APS aqueous solutions in a specially fabricated two-compartment cell via diffusion technique. The schematic diagram of the cell is presented in Figure 2. Silicone elastomer, which was initially coated on PVDF microporous support, was clamped in between the two cell loaded with aniline and APS aqueous solutions, respectively, in a way to enhance the absorption of PANI/PMVEA onto the microporus PVDF/silicone support. Initially, 0.8 mol.L^{-1} aniline and 4 wt.% PMVEA were dissolved in 1 M HCl while the molar ratio of APS to aniline in the final solution was set at 1: 1.25 mol.mol^{-1}. The stirring speed was maintained at 400 rpm and a stainless steel ring clamp was used to tighten the two compartment cells where the membrane was placed in the middle of the cells. During the polymerization period, aniline/PMVEA and APS oxidant solutions were allowed to counter-diffuse, simultaneously, through the silicone/PVDF coated membrane. After the polymerization reaction for 6 h completed, the multilayer composite membrane was removed from the cell, cleaned with ultrapure water several times and further soaked in 1M HCl for 24 hours to achieve a complete protonation and doping of PANI in the membranes [6].

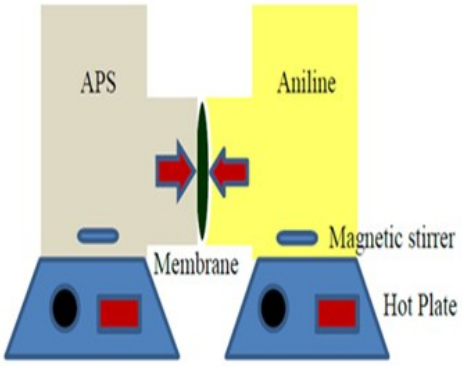


Figure 2. Schematic diagram of the two-compartment cell

PANI deposition levels in the base membranes were measured by using the gravimetric technique. The PANI deposition was calculated by measuring the weight difference between the modified and silicone/PVDF membranes. The PANI/PMVEA deposition % PANI was calculated using Equation (1):

$$\text{PANI/PMVEA (\%)} = \frac{Wf - Wi}{Wf} \text{ X } 100 \quad (1)$$

where, W_i is the initial weight of PVDF/silicone membrane before PANI/PMVEA coating and W_f is the final weight of the multilayer membrane after polymerization.

Membranes characterization

Fourier transform infrared spectroscopy (FTIR) spectra of the multilayer membranes were recorded using Thermo Scientific, Nicolet 6700 FT-IR (ATR) at a resolution of 4 cm^{-1} using pressed potassium bromide (KBr) pellets in a transmittance mode. A wavenumber between 4000 to 600 cm^{-1} was scanned for 16 times with the scan time of 1 min.

The surface and cross-sectional morphology of the multilayer membranes were examined with Scanning Electron Microscopy (SEM) (Leo 1550 VP) using activation voltage ranging from 2 kV to 5 kV. For cross-sectional morphology, the membranes were initially dipped in liquid nitrogen to crack the membrane. All membranes were coated with gold with thickness of 6 nm by using Polaron SC 500 prior to analyses. Samples were mounted on a Aluminium stub and further analyzed in SEM.

Meanwhile, the thermal investigation of the membranes was measured using DSC under an inert static flowing of nitrogen gas. The temperature was increased at a rate of 10 $^{o}C\ min^{-1}$ with temperature range between 25 ^{o}C to 500 ^{o}C.

Easy Drop Goniometer (Kruss GmbH, Germany) was used to determine the membranes' contact angle (^{o}) via dropping a water droplet with a volume of 2 mL onto the film surface and a high speed camera was used to record the droplet permeation images. The measurements were carried out in air at room temperature. At each activation potential, an average contact angle was determined from measurements of 3 separate droplets within a region of 2 mm^2.

Sterlitech HP4750 Stirred Cell was used to obtain the water flux and the rejection of the synthesized membrane having an active surface area of 14.6 cm^2 using Equation (2) [33,35,36]. Membrane water filtration properties were determined by using pure water flux measurement at pressure ranged from 1 to 5 bar at 27 ^{o}C.

$$\text{Flux, J} = \frac{V}{A \times t} \quad (2)$$

where, J is the permeate flux ($L.m^{-2}.h^{-1}$), V is volume of permeate (L), A is effective membrane area (m^2) and t is operating time (h).

Molecular weight cut-off (MWCO) value was obtained from the PEG rejection profile of the multilayer membranes from 90% molecular rejection which were calculated using Equation (3). Solute rejection (SR) of the multilayer membranes were evaluated with various MW of PEG solutions from 6000 to 20 000 $g.mol^{-1}$ with concentration of 100 $mg.L^{-1}$ at 5 bar.

$$SR\ (\%) = \left[1 - \frac{C_p}{C_f}\right] x\ 100 \quad (3)$$

C_f and C_p are the polyethylene glycol concentrations in the feed solution and permeate solution, respectively [37]. The concentration of PEG was determined based on their absorbency in a UV-spectrophotometer at a wavelength of 535 nm.

Results and Discussion

Gravimetric PANI/PMVEA content

PANI/PMVEA deposition amount in the based membrane supports were measured by using the gravimetric technique. The PANI/PMVEA coated onto the composite membrane support was calculated by measuring the weight difference between modified and coated PVDF membranes with silicone elastomer (Table 1). The results showed that longer reaction time resulted in higher PANI deposition onto the membrane to form the PANI/PMVEA multilayer membrane. The highest PANI/PMVEA coating of 61.8% was obtained at 10 hours while the lowest of 32.4% was obtained at 6 hours. In this work, PANI/PMVEA was assumed to be deposited inside the pores and on the surface of the silicone/PVDF membrane during the polymerization period in the two-compartment cell (refer Figure 2). PANI has formed in bulk membrane by the counter-diffusion of aniline and oxidant (APS) through the membrane [6]. The amount of PANI/PMVEA deposited onto the membrane was calculated via gravimetry technique. During the polymerization process, PANI deposition was initiated on the aniline-facing side of the membrane and maintained its asymmetric growth in the bulk membrane throughout the polymerization.

Table 1. The amount of PANI/PMVEA deposited (%) onto silicone/PVDF

Polymerisation Time (h)	PANI/PMVEA Deposition (%)
6	32.4
8	40.0
10	61.8

Donnan exclusion may be used to explain the deposition mechanism of PANI onto microporous support in the diffusion cell [38]. In the polymerization period using the two-compartment cell, APS solution was used in the compartment with ANI. The negatively charged $S_2O_8^{2-}$ species would then be generated from the decomposition of APS on the support polymer. This resulted in the polymerisation of PANI from positively charged anilinium ions ($C_6H_5NH^3+$) onto the ANI-facing side of the diffusion cell. This occurred right after the mixing of the monomer and oxidant attached to the microporous support sites. Subsequently, the PANI polymerisation would be enriched on the surface of the ANI-facing side of the membrane, through a continuous polymerisation process with a counter diffusion of ANI and APS with time. The surface coverage and in-bulk PANI deposition increased with the polymerisation time.

Similar phenomenon was observed upon coating of PANI onto other supports. The difference in coating amount between the supports over the time can be explained by the difference in the support layer's interaction with PANI (the in-situ chemical oxidative polymerisation of PANI onto PVDF has been reported to be inhibited by the nature

of the PVDF matrix compared to polyethylene terpthalate (PET)) [39]. High amounts of PANI coating have also been reported for PET [39] and Nylon 6 [40] supports. This indicates that it is the physicochemical interaction of ANI with the hydrogen bonding of the NH_2-group of the ANI molecule with the silicone/PVDF that plays the role, as this is similar to the interaction with the carboxyl group in PET [39] and Nylon 6 [40]. Thus, in presence of silicone layer, it is assumed that the coating would be much better on the membrane support rather than directly coated onto the pure PVDF surface.

FTIR analysis

Figure 3 shows the FTIR spectra of the PANI/PMVEA multilayer membranes in comparison to the PVDF and silicone/PVDF coated membranes. The main peaks at 1588 and 1584 cm^{-1} correspond to the C=C stretching deformation of quinoid and benzenoid rings, respectively. The 1259.7 cm^{-1} band is assigned to the C-N stretching of the secondary aromatic amine. The peak at 796.1 cm^{-1} is assigned to an out-of-plane deformation of C-H in the 1,4-disubstituted benzene ring. A peak at 1291.9 cm^{-1}, ascribed to the $C\text{-}N^+$ stretching vibration in the polaron structure, is also observed, indicating that the PANI is in a doped state [31]. In addition to the common peaks representing PANI, a peak at 1716.5 cm^{-1} that belongs to the C=O stretching vibration of a carboxylic acid group is seen in the spectra of PANI–PMVEA indicating the presence of the polymeric acid (PMVEA) that was incorporated into the PANI structure.

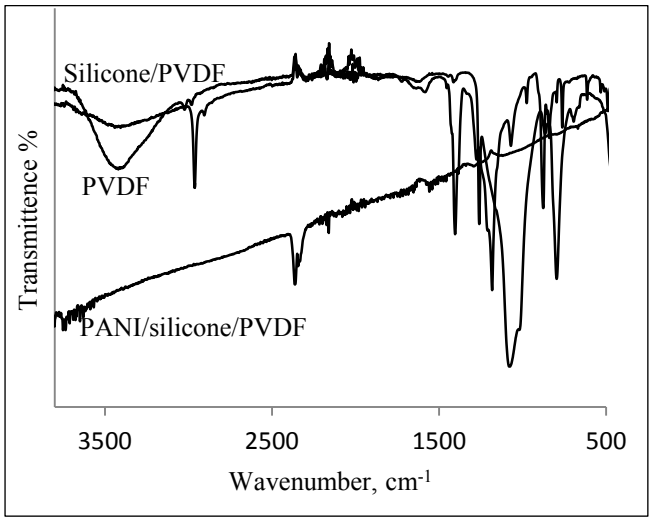


Figure 3. vFTIR spectra for the PANI/PMVEA, silicone/PVDF, PVDF multilayer composite membranes

Morphology of multilayer membranes

SEM images of the PANI/PMVEA composite membrane obtained from the chemical oxidation of aniline are shown in Figure 4. The images reveal that the molecular structure of the PVDF without coating is totally different with the PVDF/silicone. Figure 4(b) shows the silicone structural image on the surface of the PVDF membrane. The images of the coated PANI/PMVEA at different (%) in Figure 4(c), 4(d) and 4(e) are found to possess lumpy and granular morphological structures and the PANI/PMVEA growth seems to be bigger at a higher polymerisation time. From these three images, a better deposition of PANI/PMVEA can be seen in Figure 4(c) and 4(d) compared to 4(e) although higher PANI/PMVEA content was obtained at 10 hours polymerization time (refer Table 1). The more reaction times are taken for polymerization, the more PANI/PMVEA is coated on the silicone/PVDF surface.

From the SEM images, the morphology of PVDF membranes have changed after silicone elastomer is coated onto them. The polymerisations of PANI/PMVEA onto the micro-supports have altered the morphology of silicone elastomer onto PVDF. The molecular structure of the multilayer membrane is also affected by polymeric acid

involved and the properties of oxidant (APS) which is hydrophilic [31]. The formation of molecular structure happens through hydrogen bonding and hydrophilic/hydrophobic interaction that act as a template. The scanning electron micrograph in Figure 4(a) shows the surface morphology of the PVDF support. The surface was smoother compare the pristine PVDF (Figure 4(a)). The PVDF/silicone (Figure 4(b)) is rougher but the roughness of PVDF/silicone/PANI is lesser than the PVDF/silicone after coated with PANI. The deposition of PANI/PMVEA layer on the membrane support increases with the polymerisation time [6].

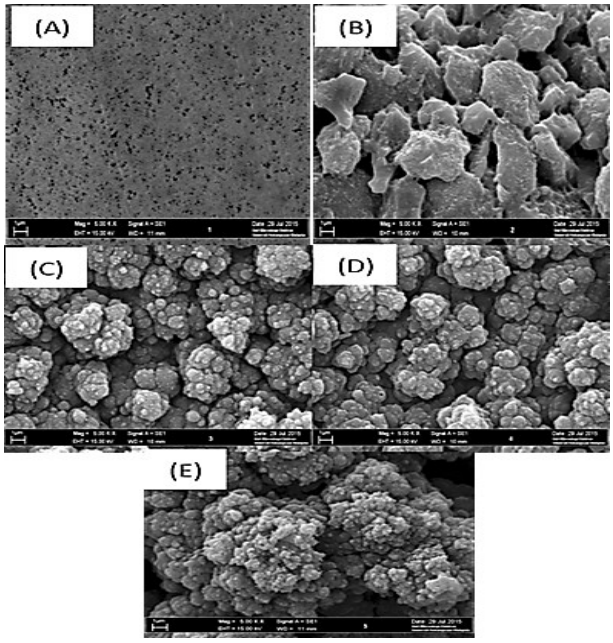


Figure 4. SEM surface images obtained; (a) PVDF support, (b) silicone/PVDF support, (c) PANI/silicone/PVDF 6 h (50%), (d) PANI/silicone/PVDF 8 h (63.3%) and (e) PANI/silicone/PVDF 10 h (83.3%) with the PMVEA, Magnification 5000 x.

Contact angle (CA) analysis

The contact angle (CA), θ, of a liquid drop on a solid surface is a useful measurement of the interactions at the solid-vapor, solid liquid, and liquid-vapor interface. The surface tension of a material determines its wettability. Typically, high CA values are an indication of low wettability, whereas low CA values correspond to high wettability [24,41]. Table 2 shows the equilibrium values of contact angle onto the membrane. The different contact angle shows the wettability of the membrane either possesses hydrophilic or hydrophobic characteristic. Based on the table, the coated membrane with PANI at all different polymerisation time has completely changed their characteristic of the PVDF/silicone support used from hydrophobic to hydrophilic properties. The contact angles recorded at 0° for the newly synthesized membrane shows that it possesses super-hydrophilic properties based on the lowest contact angles recorded. This is probably because the membranes were doped with 1 M HCl that protonate the PANI, and give the highest contact angle value. This result indicates a preliminary data for the pressure filtration of the membrane, which would be highly permeable in water. Therefore the flux is expected to be high thus a good membrane is produced. The membrane flux value is presented in the following section.

Table 2. Contact angle values of the different form membranes

Sample	Contact Angle (^{o})
PVDF	78.8
Silicone/PVDF	143
PANI-PMVEA/silicone/PVDF	
6 hours	0
8 hours	0
10 hours	0

Thermal properties of multilayer membrane

Figure 5 shows the melting temperatures of PVDF and PANI/silicone/PVDF composites membranes at different PANI content. The DSC curve peaks indicates the endothermic processes, where energy is required to break the bonds in the successive elimination of H_2O, CO and CO_2. The first peak is the evaporation of moisture and residual organic solvent in the membrane. The second peak is the endothermic process of the loss of the doping acid instead of a glass transition [42]. The sharp melting peak of PVDF is observed at 250 ^{o}C. The peaks representing PANI and silicon rubber is observed at 280 and 170 ^{o}C, respectively. The elimination of water molecules can be clearly seen at 100 ^{o}C especially for the PANI coated membranes. This is because PANI membrane in the form of emeraldine (doped with acids) carries high hydroxyl molecules, which will be evaporated at their boiling temperature. Meanwhile no shift in the peaks were observed for the major components of PVDF, PANI and silicone indicating the stability of the components used to produce the membrane.

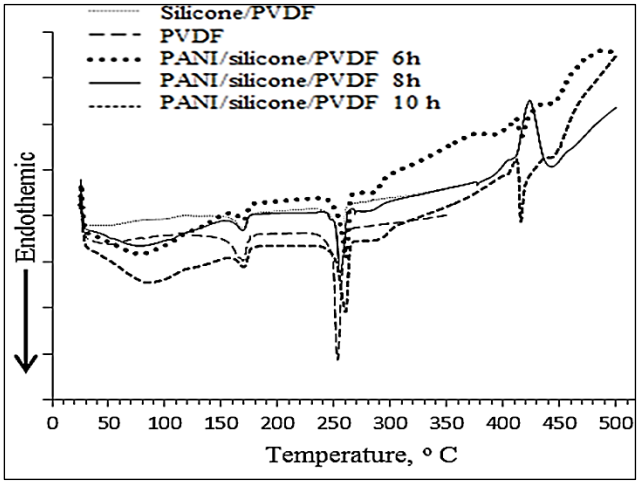


Figure 5. DSC for the different polymerization times of multilayer membranes

Based on the physical, chemical, morphological and thermal properties of the membranes analyzed in this work, the synthesized membranes are found to possess reasonable properties suitable for the application in pressure filtration. For example, the contact angles of the membranes have shown super-hydrophilic properties upon addition of the PANI/PMVEA indicating high water permeation and flux. The presence of PANI/PMVEA is supported by the FTIR, SEM and DSC analysis. Though the intrinsic properties of the membranes are confirmed from these analyses, the best membrane that could be used for pressure filtration at different polymerization time is yet to be identified. Further characterization for the membrane performances in pressure filtration is presented in the next section.

Multilayer pressure filtration membrane test

The permeation performances of the synthesized membranes were investigated by the water flux and the PEG rejection. Figure 6 and Table 3 show the respective variation of flux and rejection profile for membrane with different polymerization times performed at different pressure. Figure 6 shows the PANI membrane produced at 6 hours polymerisation has high water flux followed by the membranes produced at 8 and 10 hours, respectively. The highest water flux was recorded at the lowest polymerisation time of 6 hours. This result is supported by the membrane morphological properties with higher PANI % that have a tighter structure resulting in a lower flux value.

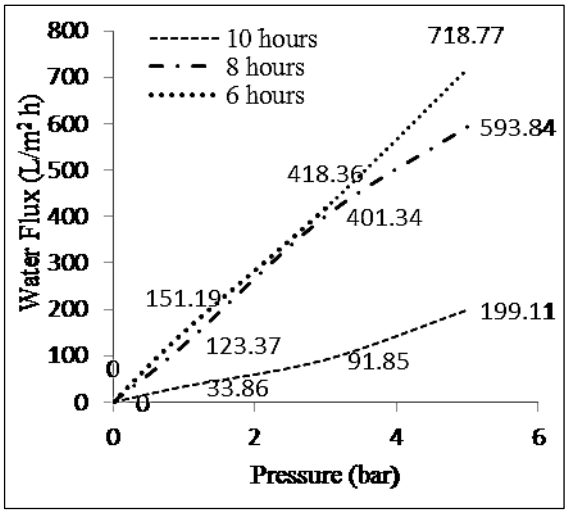


Figure 6. Water flux of multilayer filtration membrane

Table 3. Rejection of PEG below 20,000 g/mol

PANI Content %	Polymerisation Times (h)	Permeate Flux ($L/m^2.h$) (3 bar)		Rejection PEG (g/mol)	
		6000	10 000	6000	10 000
32.4	6	904.1	799.3	39.3	18.7
40.0	8	233.8	208.8	10.7	3.04
61.8	10	297.3	257.5	39.1	5.81

Membrane rejection at different MWs of PEG (presented in Table 3) shows that the lowest polymerisation times resulting the lowest PANI % have a comparable rejection value with the 10 hours polymerisation time, though the PANI content % is almost doubled for 10 hours. These results can be supported by the SEM images where the PANI deposition at higher polymerisation time than 6 hours does not help in sealing the membrane pores but has elongated the polymer on the membranes surface. It is expected that longer polymerization time supposed to form a better surface coverage. However, bigger micelles are formed and elongated (refer Figure 4 (e)). This has caused un-even coating as well as inconsistent porosity at different membrane area. The same results were reported by [31,43] under extended polymerisation time causing the PANI/PMVEA to form a micelle structure and elongate on the polymer surface. Therefore the rejection is found to be not improving by prolonging the reaction time. Lower rejection is obtained possibly due to the pores leakage on the membranes at higher pressure (5 bar) during the compaction prior to the PEG filtration. This is supported by the presence of filtration traces of PANI observed in the permeate stream

after the compaction process. Based on this result also, it can be concluded that the membrane prepared at 6 hours possesses the highest rejection and the highest flux to be further tested for a higher MW PEG.

Conclusion

PANI/PMVEA multilayer composite membranes were fabricated by chemical polymerization in a specially fabricated two-compartment cell. The amount of PANI/PMVEA % coated onto the silicone/PVDF support has increased with the increase in polymerisation time. The physical, chemical, thermal and morphological characteristic of the PVDF/silicone elastomer microporous support has changed in the presence of PANI/PMVEA. FTIR spectra have confirmed the incorporation of polymeric acid (PMVEA) into the PANI. DSC analysis has confirmed that the multilayer coating does not change much on the thermal stability of the membranes based on the melting peaks position. Contact angle shows that the water permeability of the membrane has twisted from hydrophobic to super-hydrophilic in presence of HCl doped PANI/PMVEA. The water flux of multilayer membrane decreased with the increased in PANI/PMVEA content. The higher PANI % gave the lowest water and permeate flux. The rejection result shows that the membrane has reasonable rejection at 6 hours than 8 or 10 hours while maintaining the highest flux than the others. It is suggested by optimizing the polymerization time will enhance the rejection properties of the membrane.

Acknowledgement

The authors are thankful to the Ministry of Higher Education (MOHE) of Malaysia for their financial support under the Fundamental Research Grant Scheme (FRGS/2/2013/TK05/UKM/02/4) and the Long Term Research Grant Scheme (LRGS/2013/UKM-UKM/PT/03), Department of Chemical and Process Engineering, Universiti Kebangsaan Malaysia and MyMaster by MOSTI for the MSc scholarship.

References

1. Montazami, R., Jain, V. and Heflin, J. R. (2010). High contrast asymmetric solid state electrochromic devices based on layer-by-layer deposition of polyaniline and poly (aniline sulfonic acid). *Electrochimica Acta*, 56(2): 990 – 994.
2. Abdolahi, A., Hamzah, E., Ibrahim, Z. and Hashim, S. (2012). Synthesis of uniform polyaniline nanofibers through interfacial polymerization. *Materials*, 5(8): 1487 – 1494.
3. Tokarský, J., Maixner, M., Peikertová, P., Kulhánková, L. and Burda, J. V. (2014). The IR and Raman spectra of polyaniline adsorbed on the glass surface; comparison of experimental, empirical force field, and quantum chemical results. *European Polymer Journal*, 57: 47 – 57.
4. Detsri, E. and Dubas, S. T. (2009). Interfacial polymerization of water-soluble polyaniline and its assembly using the layer-by-layer technique. *Journal of Metals, Materials and Minerals*, 19(1): 39 – 44.
5. Vivekanandan, J., Ponnusamy, V., Mahudeswaran, A. and Vijayanand, P. S. (2011). Synthesis, characterization and conductivity study of polyaniline prepared by chemical oxidative and electrochemical methods. *Archives of Applied Science Research*, 3(6): 147 – 153.
6. Qaiser, A. A. (2010). Electrochemical composite membranes based on intrinsically conducting polymers synthesis and characterization. University of Aucklannd: Auckland. pp. 1 – 192.
7. Supri, A. G., Ammar, Z., Yeon, A., Shakaff, M., Hassan, A., Noor, M. and Ahmad, P. (2012). Enhancing conductive polymer performance using eggshell for ammonia sensor. *Journal of Physical Science*, 23(2): 73 – 83.
8. Guillen, G. R. and Hoek, E. M. (2010). Development and testing of "smart" nanofiltration membranes. University of California: Los Angeles: pp 1 – 46.
9. Ali, Y., Kumar, V., Sonkawade, R. G. and Dhaliwal, A. S. (2012). Fabrication of polyaniline nanofibers by chronopotentiometry. *Advance Materials Letters*, 3: 388 – 392.
10. Gomes, E. C. and Oliveira, M. A. S. (2012). Chemical polymerization of aniline in hydrochloric acid (HCl) and formic acid (HCOOH) media. Differences between the two synthesized polyanilines. *American Journal of Polymer Science*, 2(2): 5 – 13.
11. Saikia, P. J. and Sarmah, P. C. (2011). Investigation of polyaniline thin film and Schottky junction with aluminium for electrical and optical characterization. *Materials Sciences and Applications*, 2(8): 1022 –1026.

12. Sapurina, I. Y. and Shishov, M. A. (2012). Oxidative polymerization of aniline: Molecular synthesis of polyaniline and the formation of supramolecular structures. Chapter in Book, Dr. Ailton De Souza Gomes (Ed.), InTech Publisher.
13. Tiwari, A. and Singh, V. (2007). Synthesis and characterization of electrical conducting chitosan-graft-polyaniline. *Express Polymer Letters*, 1(5): 308 – 317.
14. Jelmy, E. J., Ramakrishnan, S., Devanathan, S., Rangarajan, M. and Kothurkar, N. K. (2013). Optimization of the conductivity and yield of chemically synthesized polyaniline using a design of experiments. *Journal of Applied Polymer Science*, 130(2): 1047 – 1057.
15. Devi, M. G., Al Omairi, K. A. S., Feroz, S. and Ali, S. M. (2013). Treatment of textile industry effluent using multilayer thin films. *International Journal of Engineering Research and Technology*, 2 (7): 701 – 706.
16. Sagidullin, A., Meier-Haack, J. and Scheler, U. (2005). Water diffusion through asymmetric polymer membranes and polyelectrolyte multilayers. *Diffusion Fundamentals*, 2: 131 – 132.
17. Ashraf, M. A., Maah, M. J., Qureshi, A. K., Gharibreza, M. and Yusoff, I. (2013). Synthetic polymer composite membrane for the desalination of saline water. *Desalination and Water Treatment*, 51(16-18): 3650 – 3661.
18. Hassanien, A. M., El-Hashash, M. A., Mekewi, M. A., Guirguis, D. B.and Ramadan, A. M. (2013). Fabrication of polyvinyl alcohol/cellulose acetate (PVA/CA/PEG) antibacterial membrane for potential water purification application. *Hydrology: Current Research*, 4: 146 – 152.
19. Ye, Z., Chen, Y., Li, H., He, G. and Deng, M. (2005). Preparation of a novel polysulfone/polyethylene oxide/silicone rubber multilayer composite membrane for hydrogen–nitrogen separation. *Materials Chemistry and Physics*, 94: 288 – 291.
20. Shieh, J. J. and Chung, T. S. (2000). Cellulose nitrate-based multilayer composite membranes for gas separation. *Journal of Membrane Science*, 166: 259 – 269.
21. Chung, T-S., Shieh, J-J., Lau, W. W-Y., Srinivasan, M. P. and Paul, D. R. (1999). Fabrication of multi-layer hollow fiber membranes for gas separation. *Journal of Membrane Science*, 152: 211 – 225.
22. Abu, S., Kim, Y. H., Kim, C., Park, Y., Gopalan, A. I., Lee, K. P. and Choi, S. J. (2013). Preparation and characterization of MWCNT-g-poly (aniline-co-DABSA)/Nafion® nanocomposite membranes for direct methanol fuel cells. *Bulletin of the Korean Chemical Society*, 34(9): 2657 – 2662.
23. Amado, F. D. R., Gondran, E., Ferreira J. Z. Rodrigues M. A. S. and Ferreira C. A. (2004). Synthesis and characterisation of high impact polystyrene/polyaniline composite membranes for electrodialysis. *Journal of Membrane Science*, 234(1-2): 139 – 145.
24. Blinova, N.V. and Svec, F. (2012). Functionalized polyaniline-based composite membranes with vastly improved performance for separation of carbon dioxide from methane. *Journal of Membrane Science*, 423 – 424: 514 – 521.
25. Zhu, J., Chen, M., Qu, H., Zhang, X., Wei, H., Luo, Z. and Guo, Z. (2012). Interfacial polymerized polyaniline/graphite oxide nanocomposites toward electrochemical energy storage. *Polymer*, 53(25): 5953 – 5964.
26. Morari, C., Balan, I., Pintea, J., Chitanu, E. and Iordache, I. (2011). Electrical conductivity and electromagnetic shielding effectiveness of silicone rubber filled with ferrite and graphite powders. *Progress in Electromagnetics Research M*, 21: 93 – 104.
27. Achalpurkar, M. P., Kharul, U. K., Lohokare, H. R. and Karadkar, P. B. (2007). Gas permeation in amine functionalized silicon rubber membranes. *Separation and Purification Technology*, 57(2): 304 –313.
28. Mohamed, F., Hasbullah, H., Jamian, W. N. R., Rani, A. R. A., Saman, M. F. K., Salleh, W. N. H. W. and Ismail, A. F. (2015). Morphological investiggation of poly(lactic acid) asymmetric membrane. *Journal of Engineering Science and Technology*: 1 – 8.
29. Saritha Chandran A. (2008). Polaniline coated short nylon fiber/elastromer composites: electrical and microwave characteristic, Thesis in Faculty of Technology, Cochin University of Science and Technology: Kerala, India.
30. Matsuura, T. (1993). Synthetic membranes and membrane separation processes. CRC press.
31. Zhang, L., Peng, H., Sui, J., Kilmartin, P. A. and Travas-Sejdic, J. (2008). Polyaniline nanotubes doped with polymeric acids. *Current Applied Physics*, 8(3): 312 – 315.
32. Strathmann, H. (2011). Introduction to membrane science and technology. Wiley-VCH verlag & Co, Germany.

33. Rohani, R., Hyland, M. and Patterson, D. (2011). A refined one-filtration method for aqueous based nanofiltration and ultrafiltration membrane molecular weight cut-off determination using polyethylene glycols. *Journal of Membrane Science*, 382(1): 278 – 290.
34. Kang, S. H. and Chang, Y. K. (2005). Removal of organic acid salts from simulated fermentation broth containing succinate by nanofiltration. *Journal of Membrane Science*, 246(1): 49 – 57.
35. Yilmaz, F. (2007). Polyaniline: synthesis, charaterization, solution properties and composites, Thesis Polymer Science and Technology, School of Natural and Applied Sciences.
36. Jaleh, B., Gavary, N., Fakhri, P., Muensit, N. and Taheri, S. M. (2015). Characteristics of PVDF membranes irradiated by electron beam. *Membranes*, 5(1): 1 – 10.
37. Alam, J., Dass, L. A., Alhoshan, M. S., Ghasemi, M. and Mohammad, A. W. (2012). Development of polyaniline-modified polysulfone nanocomposite membrane. *Applied Water Science*, 2(1): 37 – 46.
38. Iyoda, T., Ohtani, A., Honda, K., & Shimidzu, T. (1990). Diaphragmatic chemical polymerization of pyrrole in the Nafion film. *Macromolecules*, 23(7): 1971 – 1976.
39. Pud, A., Ogurtsov, N., Korzhenko, A. and Shapoval, G. (2003). Some aspects of preparation methods and properties of polyaniline blends and composites with organic polymers. *Progress in Polymer Science*, 28(12): 1701 – 1753.
40. Sung, W. B. and Im Seung, S. (1998). Physical properties and doping characteristics of polyaniline-nylon 6 composite films. *Polymer*, 39(2): 485 – 489.
41. Sironi, A., Marinotto, D., Riccardi, C., Zanini, S., Guerrini, E., Della Pina, C. and Falletta, E. (2015). Effect of salicylic acid and 5-sulfosalicylic acid on UV-Vis spectroscopic characteristics, morphology, and contact angles of spin coated polyaniline and poly (4-aminodiphenylaniline) thin films. *Journal of Spectroscopy*, 2015: 1 – 8.
42. Zhang, X., Zhu, J., Haldolaarachchige, N., Ryu, J., Young, D. P., Wei, S. and Guo, Z. (2012). Synthetic process engineered polyaniline nanostructures with tunable morphology and physical properties. *Polymer*, 53: 2109 – 2120.
43. Zhang, X., Chan-Yu-King, R., Jose, A. and Manohar, S. K. (2004). Nanofibers of polyaniline synthesized by interfacial polymerization. *Synthetic Metals*, 145(1): 23 – 29.

Malaysian Journal of Analytical Sciences, Vol 20 No 6 (2016): 1510 - 1514
DOI: http://dx.doi.org/10.17576/mjas-2016-2006-32

MALAYSIAN JOURNAL OF ANALYTICAL SCIENCES
Published by The Malaysian Analytical Sciences Society
ISSN 1394 - 2506

REDUCTION BEHAVIOUR OF TUNGSTEN DIOXIDE BY VARIOUS CONCENTRATION OF CARBON MONOXIDE

(Kelakuan Penurunan Tungsten Dioksida oleh Kepekatan Karbon Monoksida yang Berbeza)

Fairous Salleh[1]*, Alinda Samsuri[1,2], Tengku Shafazila Tengku Saharuddin[1], Mohamed Wahab Mohamed Hisham[1], Rizafizah Othaman[1], Mohd. Ambar Yarmo[1]

[1]*Catalyst Research Group, School of Chemical Sciences and Food Technology, Faculty of Science and Technology, Universiti Kebangsaan Malaysia, 43600 UKM Bangi, Selangor, Malaysia*
[2]*Centre for Defense Foundation Studies, Universiti Pertahanan Nasional Malaysia, Kem Sungai Besi, 57000 Kuala Lumpur, Malaysia*

**Corresponding author: fairoussalleh@gmail.com*

Received: 24 February 2015; Accepted: 27 October 2015

Abstract

The reduction behaviour of tungsten dioxide (WO_2) under both non-isothermal and isothermal conditions in various concentrations of carbon monoxide (CO) were investigated by using temperature-programmed reduction (TPR) and X-ray diffractometry (XRD) techniques. The influences of carbon monoxide concentration (20 and 40% v/v CO in N_2) on the reducibility of WO_2 to tungsten metal W have been investigated in the temperature range 40 – 900 ºC. The TPR profile shows that reduction using 40% CO produce higher thermal conductivity detector (TCD) signal in comparison by using 20 % CO. XRD results show that, by increasing the concentration of CO, the intensity of WO_2 decreases and tungsten carbide (WC) peak appeared. Moreover, holding the reduction time for 30 min in 20 and 40% of CO resulted in the formation of new peak of tungsten hemi carbide (W_2C) and WC, respectively. It can be concluded that by using CO, reduction steps comprise of $WO_2 \rightarrow W \rightarrow W_2C \rightarrow WC$. The reduction behaviour of WO_2 is strongly dependent on the concentration of CO and hold time of reaction. Furthermore, excess of CO by isothermal reduction results in the formation of WC.

Keywords: tungsten dioxide, tungsten, tungsten carbide, carbon monoxide

Abstrak

Kelakuan penurunan tungsten dioksida (WO_2) melalui penurunan bukan isotermal dan isotermal menggunakan kepekatan karbon monoksida (CO) berbeza telah dikaji dengan menggunakan suhu penurunan berprogram (TPR) dan pembelauan sinar-X (XRD). Kesan kepekatan karbon monoksida (20 dan 40% v/v CO dalam N_2) terhadap kadar penurunan WO_2 kepada W telah dikaji dalam suhu 40 – 900 °C. Profil TPR menunjukkan bahawa penurunan dengan menggunakan 40% CO menghasilkan isyarat TCD lebih tinggi berbanding dengan menggunakan 20% CO. Keputusan XRD menunjukkan bahawa, dengan meningkatkan kepekatan CO, keamatan WO_2 menurun dan puncak tungsten karbida (WC) muncul. Selain itu, dengan penambahan masa tindak balas selama 30 minit menggunakan 20 dan 40% CO menghasilkan puncak baru masing-masing tungsten hemi karbida (W_2C) dan WC. Dapat disimpulkan bahawa dengan menggunakan CO, langkah penurunan terdiri daripada $WO_2 \rightarrow W \rightarrow W_2C \rightarrow WC$. Tingkahlaku penurunan WO_2 amat bergantung kepada kepekatan CO dan penambahan masa tindak balas. Tambahan pula, pendedahan kepada CO berlebihan daripada penurunan isotermal menyebabkan pembentukan WC.

Kata kunci: tungsten dioksida, tungsten, tungsten karbida, karbon monoksida

Introduction

Tungsten is used in four main different applications that are WC, as an alloy additive, pure tungsten, and tungsten chemicals [1]. Due to superior properties, such as high melting point (3422 °C), high conductivity, thermal and chemical stability, high hardness and strength, etc. Tungsten is widely used in the contemporary industry and especially for high-temperature structural applications [2]. Tungsten is often used because of its superior thermal properties and low vapour pressure. The best known its application is as lamp filament and as electron emitters because it can be used at very high temperature. Furthermore, tungsten also used as organic tungsten dyes and pigments that can be used in variety materials. While, tungsten carbide is the most common hard materials in use today for cutting tools and other high strength application due to its high hardness at high temperatures [1].Tungsten oxides are frequently used as raw materials for recovering metal tungsten powder by reduction process for hardmetal industry and doping process for decades [1].

To further lower the temperature of oxide reduction, a reducing agent can be used [3]. The reducing agent can be hydrogen, carbon, methane, magnesium and carbon monoxide [2,4]. Tungsten oxide having several compositions like $WO_{2.9}$, $WO_{2.72}$, WO_2, WO and W_3O [5]. Venables et al. [6] studied the reduction of WO_3 with carbon monoxide using TGA. The intermediate phases $W_{20}O_{58}$, $W_{18}O_{49}$ and WO_2 were observed in the reduction, and the final product is WC. Generally reduction of tungsten oxide divided into two stages: (i) a low-temperature stage (< 777 ºC) which reduce $WO_3 \rightarrow WO_2$ involving formation and reduction of three intermediate sub oxide of ($WO_{2.96}$, $WO_{2.9}$ and $WO_{2.72}$, and (ii) high temperature stage which reduce WO_2 to W at > 777 ºC [5]. Studies on reduction of WO_3 using hydrogen and carbon monoxide as reducing agent have been published. However, there are limited studies were reported on the reduction of WO_2. This work focuses on the reduction of tungsten WO_2 in the presence of different concentration of CO as reducing agent. The effects of isothermal reduction on the formation of the product were also investigated.

Materials and Methods

Chemicals and raw materials

$WO_2 \geq 99\%$ and $W \geq 99\%$ powder Sigma Aldrich was used. The gas mixture CO in N_2 (20, and 40 vol % of CO) from MOX was used as reducing agents.

Reduction of WO_2

Reduction of WO_2 was performed using TPR instrument Micromritics Autochem 2920 Chemisorption Analyzer apparatus. An amount 5 – 8 mg of the samples were introduced in nonisothermal mode up to 900 °C under two different concentration of gas mixture of 20% and 40% of (CO in N_2) with a heating rate of 10 ºC/min with flow rates 20 ml/min. In another experiment, the measurement was carried out using the same method, and continued with isothermal mode at 900 °C for 30 min, under the similar reducing gas.

Characterization method

XRD analysis of samples were performed using XRD's Bruker AXS D8 Advance type with X-ray radiation source of Cu Kα (40kV, 40 mA) to record the 2θ diffraction angle from 10° to 80° at wavelength (λ = 0.154 nm) of 1 g sample. For identification purposes of crystalline phase composition, diffraction pattern obtained were matched with standard diffraction data (JCPDS) files.

Results and Discussion

Thermodynamic consideration data

Thermodynamic analysis of WO_2 was performed for the reduction as in Equation 1 and CO as a reducing agent. The Gibbs free energy change due to reaction and the equilibrium composition of the oxides were calculated. From the calculation, clearly indicates that the reduction by CO reaction is spontaneous (ΔG_r = +6 up to +15 kcal/mol) temperature 400 to 1000 ºC. Enthalpy (ΔH_r) reduction is endothermic, where the value of ΔH_r is +24 kcal/mol.

$$WO_2 + 2CO \rightarrow W + 2CO_2 \quad (1)$$

TPR analysis

The TPR profile obtained for non-isothermal and isothermal reduction of WO_2 under 20% and 40% CO in N_2 as reducing gas shown in Figure 1. Profile (a) indicates that reduction by 20% CO in N_2 of WO_2 up to 900ºC while (b) is reduction by 40% CO in N_2 of WO_2. The shoulder and peaks monitor in the both profile look quite similar. However, for reduction using 40% CO produce higher signal in comparison by using 20% CO. It is due to the low rate of reaction which resulted to low reducibility in 20% CO in N_2. A similar TPR experiment was performed on a sample of WO_2 and continued with isothermal condition at 900 ºC for 30 minutes. According to the profile, no obvious peak was observed upon holding the reaction time for 30 minutes for all the reactions. The residual obtained after reduction were then subjected to XRD analysis for recording XRD pattern.

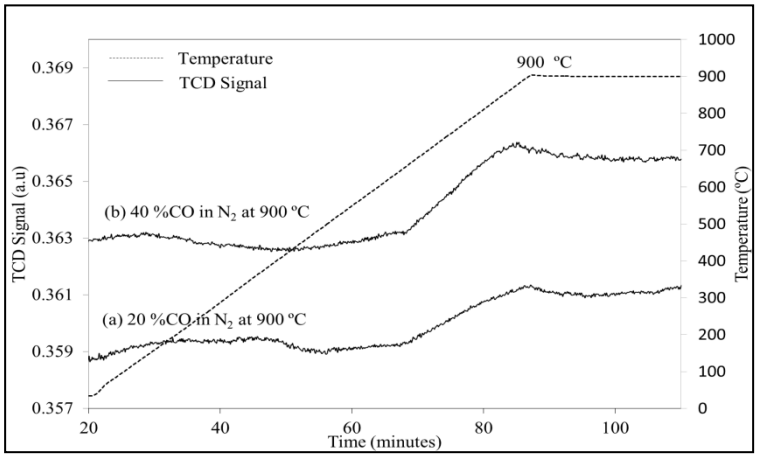


Figure 1. TPR profile obtained for non-isothermal and isothermal reduction of WO_2 by 20% and 40% (CO in N_2) up to 900 ºC and hold for 30 minutes respectively

XRD analysis

The X-ray diffraction patterns of the reduction product were analyzing to study the behavior of WO_2 reduction. The comparison of sample XRD pattern of the non-isothermal reduction under various concentration of CO in N_2 (20% and 40%) was in Figure 2. From the results, the non-isothermal reduction product of WO_2 under 20% and 40% CO in N_2 were rather similar with small reduction which 3 peaks of W metal assigned (JCPDS 04-0806) and major peak of remaining unreduced WO_2 (JCPDS 32-1393) was observed. However, reduction product by 40% CO shown low intensity of crystalline phase of W metal in comparison of reduction product by 20% CO which shown higher intensity of W. Nevertheless, by increasing the concentration of CO lead to the appearance of a new peak of WC (JCPDS 51-0939). From the results, it was obvious shown that by increasing the concentration of CO, the intensity of WO_2 decreases and WC peak appeared due to transformation of W phase to WC [6].

The reduction was continued for isothermal reduction at same temperature for 30 min. The XRD pattern were compared to the various concentration of CO in N_2 (20 and 40%) in Figure 3. From the results, isothermal reduction with 20% CO showed in identifying of higher intensity of W metal in comparison to reduction with 40% CO. The limited formation of W phases may attribute to the excessing CO introduced to the system which results to the formation of carbide. It was in agreement with previous study [6], where the formation of WC was transform from W metal phase. The XRD pattern shows the new peak observed correspond to the W_2C and WC appeared under gas of 20% CO and 40% CO respectively.

It can be concluded that, higher the concentration of CO introduced to the system, lead to the formation of WC. The WC observed in XRD pattern is in agreement to previous study working on VI transition metal carbide catalysts. It is obvious that suitable concentration of CO and reaction time need to consider in order reducing WO_2 to W metal. It is probably since, among phase transitions in the reduction of WO_3 to W, from $WO_3 \rightarrow WO_{2.9}$, $WO_{2.9} \rightarrow W_{18}O_{49}$,

and $W_{18}O_{49} \rightarrow WO_2$ and $WO_2 \rightarrow W$, transition WO_2 to W proceed very limited [7]. It was matched with the thermodynamic calculation in Eq. (1) where the enthalpy value for reduction WO_2 to W and WO_3 to W are endothermic and exothermic respectively in carbon monoxide atmosphere. The traces of WO_3 were observed in the pattern of reduction WO_2 sample; this is probably due to the slight oxidation on the WO_2 commercial sample prior undergoing the reduction process.

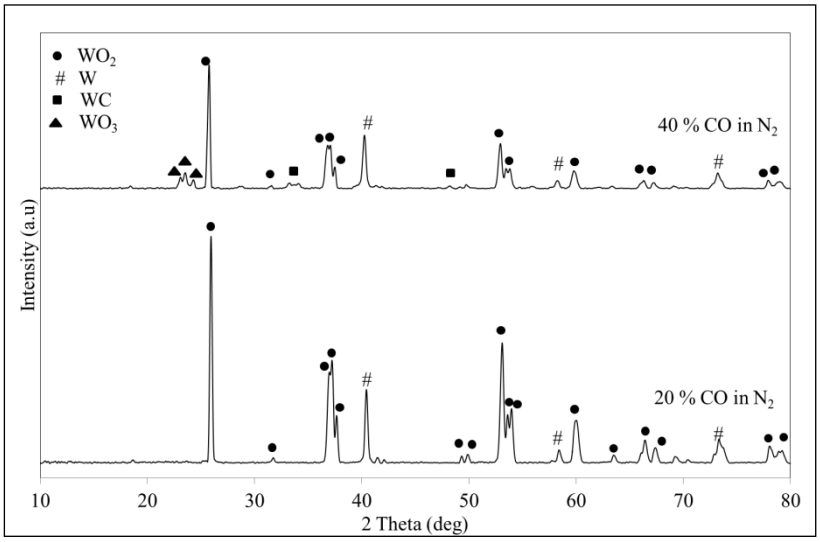


Figure 2. XRD profile obtained for non-isothermal reduction of WO_2 by 20% and 40% (CO in N_2) up to 900 ºC

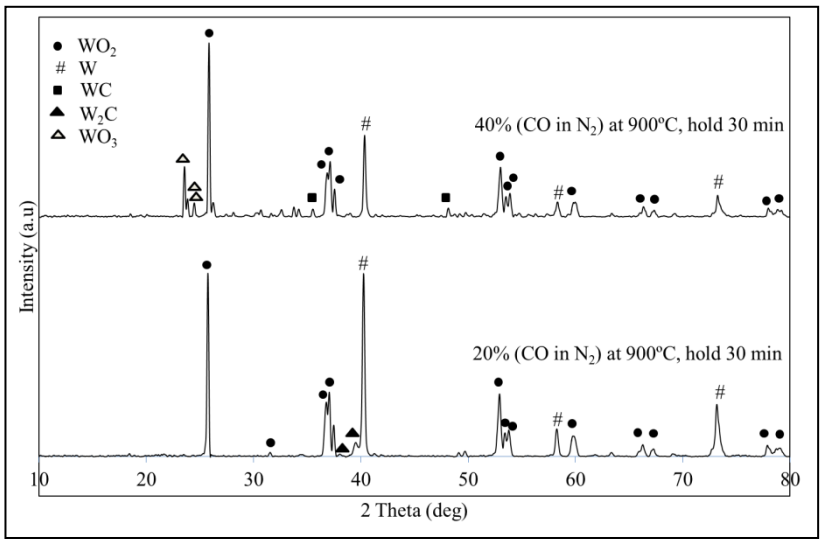


Figure 3. XRD profile for isothermal reduction of WO_2 by 20 and 40 % (CO in N_2) up to 900 ºC and hold for 30 min

Conclusion

Tungsten (IV) oxide (WO_2) samples were characterized using the TPR and XRD methods to investigate the reduction behavior. The WO_2 was reduced to W and some remaining unreduced WO_2 in both concentrations. However, by increasing the concentration of CO to 40%, the remaining WO_2 peaks were decreases and low crystalline phase of W peaks were observed. Furthermore, reduction of WO_2 is improved by hold the reaction at 900 ºC for 30 min. It can be proved by formation of higher peak of W phase for both concentrations compared to nonisothermal reduction. However, excess of CO introduced lead to the formation of tungsten semi carbide (W_2C) and tungsten carbide (WC) under 20% and 40% CO in N_2 respectively.

Acknowledgement

The author s wish to thank Ministry of Higher Education (MOHE) and Universiti Kebangsaan Malaysia (UKM) for funding this project under research grant number LRGS/BU/2011/USM-UKM/PG/02, BKBP-FST-K003323-2014, FRGS/2/2013/TK06/UKM/02/3, ETP-2013-066 and Centre of Research and Innovation Management (CRIM) for the instruments facilities.

References

1. Ricceri, R. and Matteazzi, P. (2003). A study of formation of nanometric W by room temperature mechanosynthesis. *Journal of Alloys and Compounds,* 358: 71 – 75.
2. Baghdasaryan, A. M., Niazyan, O. M., Khachatryan, H. L. and Kharatyan, S. L. (2014). DTA/TG study of tungsten oxide and ammonium tungstate reduction by (Mg + C) combined reducers at non-isothermal conditions. *International Journal Refractory Metals & Hard Materials.* 43: 216 – 221.
3. Jiqiao, L., Baiyun, H. and Zhiqiang, Z. (2001). Determination of physical characterization of tungsten oxides. *International Journal Refractory Metals & Hard Materials,* 19 (2): 79 – 84.
4. Kwak, J. H., Han, G. Y. and Yoon, K. J. (2013). Zirconia supported tungsten oxides for cyclic production of syngas and hydrogen by methane reforming and water splitting. *International Journal of Hydrogen Energy*, 38: 8293 – 8305.
5. Zaki, M. I., Fouad, N. E., Mansour, S. A. A. and Muftah, A. I. (2011). Temperature-programmed and X-ray diffractometry studies of hydrogen reduction course and products of WO_3 powder: Influence of reduction parameters. *Thermochimica Acta*, 523 (1–2): 90 – 96.
6. Venables, D. S. and Brown, M. E. (1997). Reduction of Tungsten Oxides with Carbon Monoxide. *Thermochimica Acta*, 291: 131 – 140.
7. Xiang-wei, W. U., Jing-song, L. U. O. and Bi-zhi, L. U. (2009). crystal growth of tungsten during hydrogen reduction of tungsten oxide at high temperature. *Transactions of Nonferrous Metals Society of China*, 19: 785 - 789.

Malaysian Journal of Analytical Sciences, Vol 20 No 6 (2016): 1515 - 1523
DOI: http://dx.doi.org/10.17576/mjas-2016-2006-33

MALAYSIAN JOURNAL OF ANALYTICAL SCIENCES
Published by The Malaysian Analytical Sciences Society
ISSN 1394 - 2506

SYNTHESIS AND CHARACTERIZATION OF OXADIAZOLE DERIVATIVES FROM BENZIMIDAZOLE

(Sintesis dan Perincian Terbitan Oksadiazol Dari Benzimidazol)

Norizan Ahmat[1, 2]*, Nik Khairunissa Nik Abdullah Zawawi[1,2], Muhammad Taha[1,2], Nor Hadiani Ismail[1,2], Noraishah Abdullah[1]

[1]*Faculty of Applied Sciences,*
Universiti Teknologi MARA, 40450 Shah Alam, Selangor, Malaysia
[2]*Atta-ur-Rahman Institute for Natural Product Discovery,*
Universiti Teknologi MARA, Puncak Alam Campus, 42300 Bandar Puncak Alam, Selangor, Malaysia

**Corresponding author: noriz118@salam.uitm.edu.my*

Received: 24 February 2015; Accepted: 27 October 2015

Abstract

Heterocyclic compounds of benzimidazole and oxadiazole are considered as important class of compounds in medicinal chemistry because of their interesting diversified biological activities. A series of new benzimidazole bearing oxadiazole derivatives have been conveniently synthesized by intermolecular oxidative cyclization of benzimidazole benzoyl hydrazide promoted by iodobenzene diacetate as an oxidant. The structures of the synthesized compounds were characterized by spectroscopic methods namely ^{1}H Nuclear Magnetic Resonance (NMR), Infrared (IR), Mass Spectrometry (MS) and melting point.

Keywords: synthesis, benzimidazole, oxadiazole, hydrazide, nuclear magnetic resonance

Abstrak

Sebatian heterosiklik daripada benzimidazol dan oksadiazol dianggap sebagai satu kelas sebatian penting dalam kimia perubatan kerana aktiviti biologinya yang pelbagai. Satu siri baru terbitan oksadiazol dari benzimidazol telah disintesis dengan mudah oleh siklisasi oksidatif antara molekul daripada benzoil hidrazida benzimidazol dimangkin oleh diasetat iodobenzena sebagai oksidan. Struktur sebatian disintesis telah dicirikan oleh kaedah spektroskopik seperti ^{1}H Resonans Magnet Nukleus (NMR), Inframerah (IR), Spektrometri Jisim (MS) dan takat lebur.

Kata kunci: sintesis, benzimidazol, oxadiazol, hidrazida, resonan megnetik nukleus

Introduction

Benzimidazole and oxadiazole have received attention in recent years due to widespread applications notably in the field of medicinal chemistry due to their privileged biological activity. Recently, benzimidazole derivatives have been reported as antidiabetic [1], antimicrobial [2-3], antiviral [4-6] antispasmodic [7] and antiasthmatic [8] agents. Similarly, oxadiazole derivatives are also recognized for their pharmacological importance and are reported to possess wide spectrum of activities such as antibacterial [9-11], antifungal [12] anti-inflammatory [13-14] analgesic [15], anticonvulsant [16-17], hypoglycemic [18] and anticancer [19] properties. The synthesis of both compounds has emerged as an essential need for development of new pharmaceutical entities.

In the present study, a series of novel oxadiazoles were synthesized from benzimidazole and their physical characterization are reported. The structures of the synthesized compounds were characterized using different spectroscopic methods namely ^{1}H Nuclear Magnetic Resonance (NMR), Infrared (IR), Mass Spectrometry (MS) and melting point.

Materials and Methods

Melting point was taken on Buchi M-560 melting point instrument and was uncorrected. IR spectra were recorded on a Spectrum One FT-IR spectrometer (Perkin Elmer), using KBr discs and values were signified in cm^{-1}. The ^{1}H NMR and ^{13}C NMR spectra were measured on Bruker 500 Ultrashield Plus NMR (500 MHz) in DMSO-*d*6 as solvent, using tetramethylsilane (TMS) as an internal standard, and chemical shifts are expressed as ppm. ESI MS were determined on Agilent 6330 Ion Trap, using positive/negative mode. HR-ESI-MS were determined on Agilent 6224 TOF-LC/MS using positive mode.

Synthesis of methyl 4-(5,6-dimethyl-1H-benzo[d]imidazol-2-yl)benzoate (a)

Sodium metasulfite adduct was synthesized according to literature protocol [20]. Equimolar solution of sulphite adduct and 4,5-dimethyl-*O*-phenylenediamine in DMF was refluxed for 6 hours. After the completion of reaction, it was poured into ice water and the solid product (a) was filtered, dried and crystallized.

Synthesis of 4-(5,6-dimethyl-1H-benzo[d]imidazol-2-yl)benzohydrazide (b)

A solution of compound (a) (40 mmol) in methanol (50 ml) was refluxed for 12 hours in the presence of hydrazine hydrate (95%) mixture (10 ml). The reaction mixture was evaporated and the residue was washed with water, filtered, dried, and crystallized.

General procedure for the synthesis of 4-(5,6-dimethyl-1H-benzo[d]imidazol-2-yl) benzohydrazide Schiff bases (1-14)

Equimolar mixture of 4-(5,6-dimethyl-1H-benzo[d]imidazol-2-yl) benzohydrazide (0.280 g, 0.01 mol) selected aldehyde (0.01 mol), in *n*-butanol (25 mL) containing acetic acid (1 mL) was heated under reflux for 3 hours. The reaction mixture was filtered, dried and crystallized.

General procedure for the synthesis of 2,5-disubstituted-1,3,4-oxadiazoles (15-28)

Compounds **1-14** (100 mg, ±0.25 mmol) were dissolved in DMF (5 ml) and iodobenzenediacetate (IBD) (±0.27 mmol) were added [21]. The content was stirred overnight and the progress of reaction was monitored by thin layer chromatography. Cold water was added and the precipitate obtained was filtered, washed with diethyl ether and dried to afford **15-28**.

Results and Discussion

Characterization: methyl 4-(5,6-dimethyl-1H-benzo[d]imidazol-2-yl)benzoate (a)

Light brown solid; yield (96%); m.p. 208.9 °C; IR(KBr) (ν_{max}, cm^{-1}): 2954, 1720, 1273, 1107. ^{1}H NMR (500 MHz, DMSO) δ: 2.33 (s, 6H, CH_3-5,6-benzimidazole), 3.88 (s, 3H, OCH_3-benzoate), 7.39 (s, 2H, H-4,7-benzimidazole), 8.09 (d, J = 8.4 Hz, 2H, Ar), 8.27 (d, J = 8.4 Hz, 2H, Ar). ESI MS (m/z): 280.1 (M^+).

4-(5,6-dimethyl-1H-benzo[d]imidazol-2-yl)benzohydrazide (b)

Light brown solid; yield (93%); m.p. 316.5 °C; IR(KBr) (ν_{max}, cm^{-1}): 3020, 1625, 1560, 1350. ^{1}H NMR (500 MHz, DMSO) δ: 2.33 (s, 6H, CH_3-5,6-benzimidazole), 4.56 (s, 2H, NH_2), 7.32 (s, 1H, H-7-benzimidazole), 7.46 (s, 1H, H-4-benzimidazole), 7.98 (d, J = 7.5 Hz, 2H, Ar), 8.21 (d, J = 7.5 Hz, 2H, Ar), 9.88 (s, 1H, NH-hydrazide), 12.74 (s, 1H, NH-benzimidazole). ESI MS (m/z): 280.1 (M^+).

(E)-4-(5,6-dimethyl-1H-benzo[d]imidazol-2-yl)-N'-(3-fluorobenzylidene) benzohydrazide (1)

Light brown solid; yield 89%; m.p. 324.3 °C; IR(KBr) (ν_{max}, cm^{-1}): 3465, 1657, 1557, 1276, 1237. ^{1}H NMR (500 MHz, DMSO) δ: 2.34, 2.35 (s, 6H, CH_3-5,6-benzimidazole), 7.31 (m, 2H, Ar), 7.55 (m, 4H, Ar), 8.09 (d, J = 7.7 Hz, 2H, Ar), 8.29 (d, J = 8.0 Hz, 2H, Ar), 8.51 (s, 1H, CH=N), 12.05 (s, 1H, NH-hydrazide), 12.80 (s, 1H, NH-benzimidazole). ESI MS (m/z): 386.2 (M^+).

(E)-4-(5,6-dimethyl-1H-benzo[d]imidazol-2-yl)-N'-(2-hydroxybenzylidene) benzohydrazide (2)
Light brown solid; yield (90%); m.p. 352.7 °C; IR(KBr) (ν_{max}, cm^{-1}): 3427, 1623, 1291. ^{1}H NMR (500 MHz, DMSO) δ: 2.35 (s, 6H, CH_3-5,6-benzimidazole), 6.99 – 6.92 (m, 2H, Ar), 7.33 (t, *J* = 7.7 Hz, 1H, Ar), 7.41 (s, 2H, H-4,7-benzimidazole), 7.58 (d, *J* = 7.4 Hz, 1H, Ar), 8.11 (d, *J* = 8.2 Hz, 2H, Ar), 8.30 (d, *J* = 8.2 Hz, 2H, Ar), 8.69 (s, 1H, CH=N), 11.28 (s, 1H, NH-hydrazide), 12.19 (s, 1H, NH-benzimidazole). ESI MS (m/z): 384.3 (M^-).

(E)-4-(5,6-dimethyl-1H-benzo[d]imidazol-2-yl)-N'-(3-hydroxybenzylidene) benzohydrazide (3)
Light yellow solid; yield (90%); m.p. 316.1 °C; IR(KBr) (ν_{max}, cm^{-1}): 3200, 1642, 1560, 1271. ^{1}H NMR (500 MHz, DMSO) δ: 2.34 (s, 6H, CH_3-5,6-benzimidazole), 7.13 (d, *J* = 7.2 Hz, 1H, Ar), 7.24 (s, 1H, Ar), 7.28 (t, *J* = 7.7 Hz, 1H, Ar), 7.41 (s, 2H, H-4,7-benzimidazole), 8.08 (d, *J* = 7.9 Hz, 2H, Ar), 8.28 (d, *J* = 8.0 Hz, 2H, Ar), 8.41 (s, 1H, CH=N), 9.66 (s, 1H, OH), 11.88 (s, 1H, NH-hydrazide), 12.80 (d, *J* = 1.0 Hz, 1H, NH-benzimidazole). ESI MS (m/z): 384.3 (M^-).

(E)-N'-(3,4-dimethoxybenzylidene)-4-(5,6-dimethyl-1H-benzo[d]imidazol-2-yl) benzohydrazide (4)
Light yellow solid; yield (92%); m.p. 316.4 °C; IR(KBr) (ν_{max}, cm^{-1}): 3434, 1658, 1564, 1272. ^{1}H NMR (500 MHz, DMSO) δ: 2.35, 2.34 (s, 6H, CH_3-5,6-benzimidazole), 3.84 (s, 6H, OCH_3-3,4-Ar), 7.05 (d, *J* = 8.2 Hz, 1H, Ar), 7.23 (d, *J* = 7.8 Hz, 1H, Ar), 7.33 (s, 1H, Ar), 7.38 (s, 1H, Ar), 7.47 (s, 1H, Ar), 8.07 (d, *J* = 8.1 Hz, 2H, Ar), 8.28 (d, *J* = 8.1 Hz, 2H, Ar), 8.42 (s, 1H, CH=N), 11.83 (s, 1H, NH-hydrazide), 12.81 (s, 1H, NH-benzimidazole). ESI MS (m/z): 428.3 (M^+).

(E)-4-(5,6-dimethyl-1H-benzo[d]imidazol-2-yl)-N'-(4-nitrobenzylidene) benzohydrazide (5)
Light yellow solid; yield (92%); m.p. 323.6 °C; IR(KBr) (ν_{max}, cm^{-1}): 3269, 1637, 1560, 1519, 1343, 1282. ^{1}H NMR (500 MHz, DMSO) δ: 2.33, 2.35 (s, 6H, CH_3-5,6-benzimidazole), 7.32 (s, 1H, H-7), 7.46 (s, 1H, H-4), 8.00 (d, *J* = 8.1 Hz, 2H, Ar), 8.09 (d, *J* = 7.7 Hz, 2H, Ar), 8.32 – 8.27 (m, 4H, Ar), 8.57 (s, 1H, CH=N), 12.23 (s, 1H, NH-hydrazide), 12.83 (s, 1H, NH-benzimidazole). ESI MS (m/z): 413.3 (M^+).

(E)-4-(5,6-dimethyl-1H-benzo[d]imidazol-2-yl)-N'-(4-fluorobenzylidene) benzohydrazide (6)
Light brown solid; yield (94%); m.p. 330.7 °C; IR(KBr) (ν_{max}, cm^{-1}): 3256, 1630, 1287, 1236. ^{1}H NMR (500 MHz, DMSO) δ: 2.34 (s, 6H, CH_3-5,6-benzimidazole), 7.32 (t, *J* = 8.6 Hz, 2H, Ar), 7.40 (s, 2H, Ar), 7.87 – 7.78 (m, 2H, Ar), 8.08 (d, *J* = 8.0 Hz, 2H, Ar), 8.28 (d, *J* = 8.1 Hz, 2H, Ar), 8.49 (s, 1H, CH=N), 11.96 (s, 1H, NH-benzimidazole). ESI MS (m/z): 386.9 (M^-).

(E)-4-(5,6-dimethyl-1H-benzo[d]imidazol-2-yl)-N'-(4-methoxybenzylidene) benzohydrazide (7)
Light brown solid; yield (91%); m.p. 276.0 °C; IR(KBr) (ν_{max}, cm^{-1}): 3234, 1611, 1512, 1258. ^{1}H NMR (500 MHz, DMSO) δ: 2.34 (s, 6H, CH_3-5,6-benzimidazole), 3.82 (s, 3H, OCH_3), 7.04 (d, *J* = 8.6 Hz, 2H, Ar), 7.51 – 7.29 (m, 2H, Ar), 7.71 (d, *J* = 8.5 Hz, 2H, Ar), 8.08 (d, *J* = 8.2 Hz, 2H, Ar), 8.28 (d, *J* = 8.2 Hz, 2H, Ar), 8.44 (s, 1H, CH=N), 11.83 (s, 1H, NH-benzimidazole). ESI MS (m/z): 398.9 (M^-).

(Z)-N'-(4-chlorobenzylidene)-4-(5,6-dimethyl-1H-benzo[d]imidazol-2-yl)benzohydrazide (8)
Light brown solid; yield (90%); m.p. 338.7 °C; IR(KBr) (ν_{max}, cm^{-1}): 3253, 1634, 1565, 1286, 669. ^{1}H NMR (500 MHz, DMSO) δ: 2.34, 2.36 (s, 6H, CH_3-5,6-benzimidazole), 7.33 (s, 1H, Ar), 7.47 (s, 1H, Ar), 7.55 (d, *J* = 8.0 Hz, 2H, Ar), 7.79 (d, *J* = 8.1 Hz, 2H, Ar), 8.08 (d, *J* = 7.9 Hz, 2H, Ar), 8.28 (d, *J* = 8.0 Hz, 2H, Ar), 8.49 (s, 1H, CH=N), 12.01 (s, 1H, NH-hydrazide), 12.80 (s, 1H, NH-benzimidazole). ESI MS (m/z): 402.3 (M^+).

(E)-4-(5,6-dimethyl-1H-benzo[d]imidazol-2-yl)-N'-(pyridin-4-ylmethylene) benzohydrazide (9)
Light brown solid; yield (90%); m.p. 306.7 °C; IR(KBr) (ν_{max}, cm^{-1}): 3277, 1634, 1560, 1288. ^{1}H NMR (500 MHz, DMSO) δ: 2.33 (s, 6H, CH_3-5,6-benzimidazole), 7.40 (s, 2H, Ar), 7.69 (s, 2H, Ar), 8.10 (d, *J* = 7.2 Hz, 2H, Ar), 8.30 (d, *J* = 7.9 Hz, 2H, Ar), 8.48 (s, 1H, CH=N), 8.67 (s, 2H, Ar), 12.22 (s, 1H, NH-benzimidazole). ESI MS (m/z): 369.3 (M^+).

(E)-N'-(3-chlorobenzylidene)-4-(5,6-dimethyl-1H-benzo[d]imidazol-2-yl) benzohydrazide (10)
Light brown solid; yield (91%); m.p. 358.5 °C; IR(KBr) (ν_{max}, cm^{-1}): 3422 (NH), 1651, 1564, 1282, 704. ^{1}H NMR (500 MHz, DMSO) δ: 2.33 (s, 6H, CH_3-5,6-benzimidazole), 7.40 (s, 2H, Ar), 7.49 (s, 2H, Ar), 7.71 (s, 1H, Ar), 7.81

(s, 1H, Ar), 8.09 (d, *J* = 7.6 Hz, 2H, Ar), 8.29 (d, *J* = 7.8 Hz, 2H, Ar), 8.47 (s, 1H, CH=N), 12.09 (s, 1H, NH-benzimidazole). ESI MS (m/z): 402.3 (M^+).

(E)-4-(5,6-dimethyl-1H-benzo[d]imidazol-2-yl)-N'-(2-methylbenzylidene) benzohydrazide (11)
Light brown solid; yield (93%); m.p. 323.8 °C; IR(KBr) (ν_{max}, cm^{-1}): 3057 (NH), 1637, 1275. ^{1}H NMR (500 MHz, DMSO) δ: 2.34 (s, 6H, CH_3-5,6-benzimidazole), 2.47 (s, 3H, CH_3), 7.35 – 7.26 (m, 3H, Ar), 7.40 (s, 2H, H-4,7-benzimidazole), 7.89 (d, *J* = 7.3 Hz, 1H, Ar), 8.10 (d, *J* = 8.0 Hz, 2H, Ar), 8.29 (d, *J* = 8.0 Hz, 2H, Ar), 8.80 (s, 1H, CH=N), 11.92 (s, 1H, NH-benzimidazole). ESI MS (m/z): 382.3 (M^+).

(E)-4-(5,6-dimethyl-1H-benzo[d]imidazol-2-yl)-N'-(4 hydroxybenzylidene) benzohydrazide (12)
Light yellow solid; yield (91%); m.p. 313.4 °C; IR(KBr) (ν_{max}, cm^{-1}): 3198 (NH), 1610, 1272. ^{1}H NMR (500 MHz, DMSO) δ: 2.35 (s, 6H, CH_3-5,6), 6.86 (d, *J* = 8.2 Hz, 2H, Ar), 7.40 (s, 2H, H-4,7-benzimidazole), 7.59 (d, *J* = 8.2 Hz, 2H, Ar), 8.07 (d, *J* = 8.1 Hz, 2H, Ar), 8.27 (d, *J* = 8.1 Hz, 2H, Ar), 8.39 (s, 1H, CH=N), 9.95 (s, 1H, NH-hydrazide), 11.74 (s, 1H, NH-benzimidazole). ESI MS (m/z): 384.3 (M^+).

(E)-4-(5,6-dimethyl-1H-benzo[d]imidazol-2-yl)-N'-(pyridin-3-ylmethylene) benzohydrazide (13)
Light yellow solid; yield (92%); m.p. 348.3 °C; IR(KBr) (ν_{max}, cm^{-1}): 3194, 1647, 1552, 1281. ^{1}H NMR (500 MHz, DMSO) δ: 2.33 (s, 6H, CH_3-5,6-benzimidazole), 7.40 (s, 2H, Ar), 7.50 (s, 1H, Ar), 8.10 (d, *J* = 7.5 Hz, 2H, Ar), 8.17 (d, *J* = 6.9 Hz, 1H, Ar), 8.30 (d, *J* = 7.7 Hz, 2H, Ar), 8.55 (s, 1H, Ar), 8.63 (s, 1H, Ar), 8.89 (s, 1H, CH=N), 12.12 (s, 1H, NH-hydrazide), 12.81 (s, 1H, NH-benzimidazole). ESI MS (m/z): 369.3 (M^+).

(E)-4-(5,6-dimethyl-1H-benzo[d]imidazol-2-yl)-N'-(3 methylbenzylidene) benzohydrazide (14)
White solid; yield (93%); m.p. 321.2 °C; IR(KBr) (ν_{max}, cm^{-1}): 3422, 1656, 1564, 1283. ^{1}H NMR (500 MHz, DMSO) δ: 2.33, 2.35, 2.38 (s, 9H, $3CH_3$-5,6-benzimidazole, 3''-Ar), 7.27 (d, *J* = 6.9 Hz, 1H, Ar), 7.33 (s, 1H, H-7), 7.37 (t, *J* = 7.3 Hz, 1H, Ar), 7.47 (s, 1H, H-4), 7.54 (d, *J* = 7.1 Hz, 1H, Ar), 7.59 (s, 1H, H-2''), 8.08 (d, *J* = 7.6 Hz, 2H, Ar), 8.28 (d, *J* = 7.8 Hz, 2H, Ar), 8.46 (s, 1H, CH=N), 11.93 (s, 1H, NH-hydrazide), 12.82 (s, 1H, NH-benzimidazole). ESI MS (m/z): 382.3 (M^-).

2-(4-(5,6-dimethyl-1H-benzo[d]imidazol-2-yl)phenyl)-5-(3-fluorophenyl)-1,3,4-oxadiazole (15)
Pale yellow powder, yield: 0.075 g (75%), m.p.: 346.5 °C. IR (KBr) (ν_{max}, cm^{-1}): 3308, 1611, 1317, 1262, 1070, 999, 848. ^{1}H NMR (500 MHz, DMSO) δ: 2.34, 2.36 (s, 6H, CH_3-5,6-benzimidazole), 7.34 (s,1H, Ar), 7.48 (s, 1H, Ar), 7.54 (td, 1H, *J* = 8.6, 1.9, Ar), 7.55 (t, 1H, *J* = 7.6 Hz, Ar), 7.72 (dd, 1H, *J* = 13.8, 8.0 Hz, Ar), 8.03 (dd, 2H, *J* = 15.7, 8.6 Hz, Ar), 8.33 (d, 2H, *J* = 8.5 Hz, Ar), 8.38 (d, 2H, *J* = 8.4 Hz, Ar), 12.9 (s, 1H, NH). HR-ESI-MS: m/z 384.2288 (M^+).

2-(5-(4-(5,6-dimethyl-1H-benzo[d]imidazol-2-yl)phenyl)-1,3,4-oxadiazol-2-yl)phenol (16)
Pale yellow powder, yield: 0.081 g (81%), m.p.: 375.7 °C; IR (KBr) (ν_{max}, cm^{-1}): 3235, 1612, 1317, 1256, 1155, 1062.^{1}H NMR (500 MHz, DMSO) δ: 2.33, 2.36 (s, 6H, CH_3-5,6-benzimidazole), 7.18 – 7.05 (m, 2H, Ar), 7.34 (s, 1H, Ar), 7.56 – 7.42 (m, 2H, Ar), 7.97 (dt, 1H, *J* = 10.1, 5.1 Hz, Ar), 8.26 (d, 2H, *J* = 8.5 Hz, Ar), 8.38 (d, 2H, *J* = 8.5 Hz, Ar), 10.36 (s, 1H, OH), 12.89 (s, 1H, NH). HR-ESI-MS: m/z 382.2325 (M^+).

3-(5-(4-(5,6-dimethyl-1H-benzo[d]imidazol-2-yl)phenyl)-1,3,4-oxadiazol-2-yl)phenol (17)
Pale yellow powder, yield: 0.082 g (82%); m.p.: 369.9 °C; IR (KBr) (ν_{max}, cm^{-1}): 3236, 1610, 1315, 1262, 1069, 1008.^{1}H NMR (500 MHz, DMSO) δ: 2.33 (s, 6H, CH_3-5,6-benzimidazole), 7.06 (d, 1H, *J* = 6.6 Hz, Ar), 7.40 (s, 2H, Ar), 7.45 (t, 1H, *J* = 7.8 Hz, Ar), 7.54 (s, 1H, Ar), 7.59 (d, 1H, *J* = 7.5 Hz, Ar), 8.25 (d, 2H, *J* = 8.3 Hz, Ar), 8.35 (d, 2H, *J* = 8.3 Hz, Ar), 10.04 (s, 1H, OH). HR-ESI-MS: m/z 382.1843 (M^+).

2-(3,4-dimethoxyphenyl)-5-(4-(5,6-dimethyl-1H-benzo[d]imidazol-2-yl)phenyl)-1,3,4-oxadiazole (18)
Pale yellow powder, yield: 0.076 g (76%); m.p.: 293.4 °C; IR (KBr) (ν_{max}, cm^{-1}): 3255, 1611, 1315, 1275, 1106, 1025. ^{1}H NMR (500 MHz, DMSO) δ: 2.33, 2.35 (s, 6H, CH_3-5,6-benzimidazole), 3.88, 3.92 (s, 6H, OCH_3-3'',4''-Ar), 7.20 (d, 1H, *J* = 8.5 Hz, Ar), 7.39 (s, 2H, Ar), 7.65 (d, 1H, *J* = 1.9 Hz, Ar), 7.76 (dd, 1H, *J* = 8.4, 2.0 Hz, Ar), 8.28 (d, 2H, *J* = 8.5 Hz, Ar), 8.36 (d, 2H, *J* = 8.5 Hz, Ar), 12.87 (s, 1H, NH). HR-ESI-MS: m/z 426.2690 (M^+).

2-(4-(5,6-dimethyl-1H-benzo[d]imidazol-2-yl)phenyl)-5-(4-nitrophenyl)-1,3,4-oxadiazole (19)
Pale yellow powder, yield: 0.076 g (76%); m.p.: 361.2 °C; IR (KBr) (ν_{max}, cm^{-1}): 3302, 1612, 1523, 1340, 1264, 1108, 1082. ^{1}H NMR (500 MHz, DMSO) δ: 2.34, 2.36 (s, 6H, CH_3-5,6-benzimidazole), 7.35 (s, 1H, Ar), 7.49 (s, 1H, Ar), 8.33 (d, 2H, *J* = 8.4 Hz, Ar), 8.40 (d, 2H, *J* = 8.4 Hz, Ar), 8.45, 8.48 (d, 4H, *J* = 8.9 Hz, Ar), 12.90 (s, 1H, NH). HR-ESI-MS: m/z 411.2255 (M^+).

2-(4-(5,6-dimethyl-1H-benzo[d]imidazol-2-yl)phenyl)-5-(4-fluorophenyl)-1,3,4-oxadiazole (20)
Pale yellow powder, yield: 0.083 g (83%); m.p.: 372.7 °C; IR (KBr) (ν_{max}, cm^{-1}): 3292, 1610, 1318, 1264, 1164, 1002, 845. ^{1}H NMR (500 MHz, DMSO) δ: 2.34, 2.36 (s, 6H, CH_3-5,6-benzimidazole), 7.34 (s, 1H, Ar), 7.49 (d, 2H, *J* = 9.0 Hz, Ar), 7.54 (d, 2H, *J* = 9.0 Hz, Ar), 8.26 (dd, 2H, *J* = 8.8, 5.4 Hz, Ar), 8.30 (d, 2H, *J* = 8.5 Hz, Ar), 8.38 (d, 2H, *J* = 8.5 Hz, Ar), 12.90 (s, 1H, NH). HR-ESI-MS: m/z 384.2288 (M^+).

2-(4-(5,6-dimethyl-1H-benzo[d]imidazol-2-yl)phenyl)-5-(4-methoxyphenyl)-1,3,4-oxadiazole (21)
Pale yellow powder, yield: 0.077 g (77%); m.p.: 342 °C; IR (KBr) (ν_{max}, cm^{-1}): 3244, 1614, 1311, 1263, 1174, 1033. ^{1}H NMR (500 MHz, DMSO) δ: 2.34, 2.36 (s, 6H, CH_3-5,6-benzimidazole), 3.89 (s, 3H, OCH_3-4''-Ar), 7.20 (d, 2H, *J* = 8.8 Hz, Ar), 7.34 (s, 1H, Ar), 7.48 (s, 1H, Ar), 8.12 (d, 2H, *J* = 8.8 Hz, Ar), 8.28 (d, 2H, *J* = 8.4 Hz, Ar), 8.37 (d, 2H, *J* = 8.5 Hz, Ar), 12.89 (s, 1H, NH). HR-ESI- MS: m/z 396.2500 (M^+).

2-(4-chlorophenyl)-5-(4-(5,6-dimethyl-1H-benzo[d]imidazol-2-yl)phenyl)-1,3,4-oxadiazole (22)
Pale yellow powder, yield: 0.075 g (75%); m.p.: 369.7 °C; IR (KBr) (ν_{max}, cm^{-1}): 3280, 1611, 1317, 1264, 1093, 1016, 844. ^{1}H NMR (500 MHz, DMSO) δ: 2.34, 2.36 (s, 6H, CH_3-5,6-benzimidazole), 7.35 (s, 1H, Ar), 7.48 (s, 1H, Ar), 7.74 (d, 2H, *J* = 8.5 Hz, Ar), 8.20 (d, 2H, *J* = 8.5 Hz, Ar), 8.30 (d, 2H, *J* = 8.4 Hz, Ar), 8.37 (d, 2H, *J* = 8.4 Hz, Ar), 12.92 (s, 1H, NH). HR-ESI-MS: m/z 400.2004 (M^+).

2-(4-(5,6-dimethyl-1H-benzo[d]imidazol-2-yl)phenyl)-5-(pyridin-4-yl)-1,3,4-oxadiazole (23)
Pale yellow powder, yield: 0.068 g (68%); m.p.: 373.0 °C; IR (KBr) (ν_{max}, cm^{-1}): 3051, 1612, 1571, 1321, 1272, 1061, 1002. ^{1}H NMR (500 MHz, DMSO δ: 2.35 (s, 6H, CH_3-5,6-benzimidazole), 7.41 (s, 2H, Ar), 8.10 (d, 2H, *J* = 5.5 Hz, Ar), 8.33 (d, 2H, *J* = 8.4 Hz, Ar), 8.39 (d, 2H, *J* = 8.4 Hz, Ar), 8.89 (d, 2H, *J* = 4 Hz, Ar). HR-ESI-MS: m/z 367.1948 (M^+).

2-(3-chlorophenyl)-5-(4-(5,6-dimethyl-1H-benzo[d]imidazol-2-yl)phenyl)-1,3,4-oxadiazole (24)
Pale yellow powder, yield: 0.071 g (71%); m.p.: 356.2 °C; IR (KBr) (ν_{max}, cm^{-1}): 3053, 1614, 1316, 1266, 1032, 1003, 847. ^{1}H NMR (500 MHz, DMSO) δ: 2.33, 2.35 (s, 6H, CH_3-5,6-benzimidazole), 7.34 (s, 1H, Ar), 7.48 (s, 1H, Ar), 7.69 (t, 1H, *J* = 8, 7.5 Hz, Ar), 7.75 (d, 1H, *J* = 8 Hz, Ar), 8.14 (d, 1H, *J* = 7.5 Hz, Ar), 8.22 (s, 1H, Ar), 8.32 (d, 2H, *J* = 8 Hz, Ar), 8.37 (d, 2H, *J* = 8 Hz, Ar), 12.89 (s, 1H, NH). HR-ESI-MS: m/z 400.2009 (M^+).

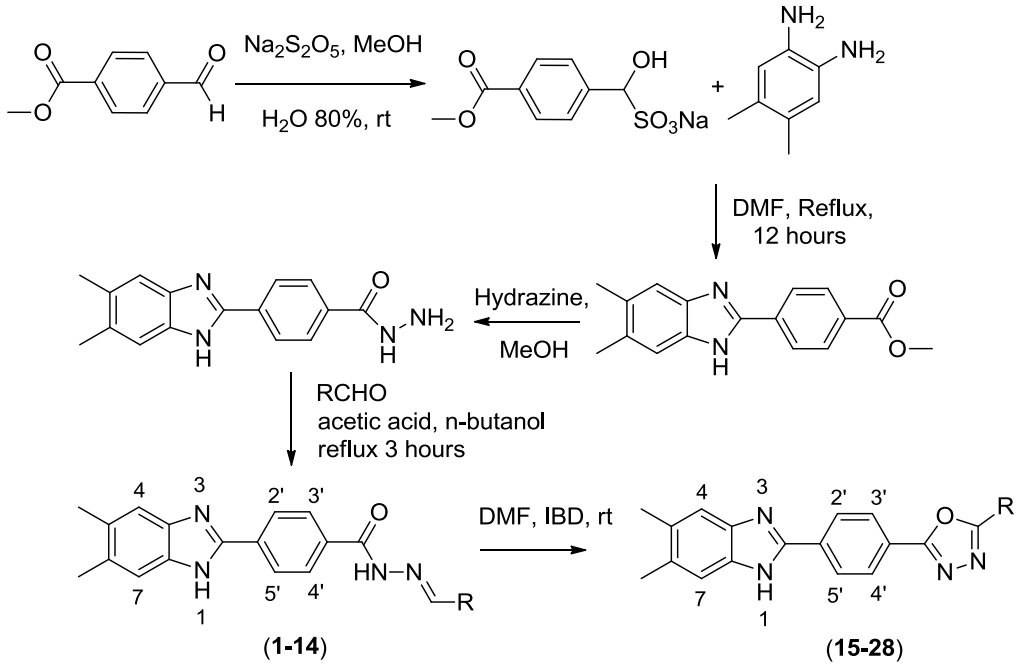
2-(4-(5,6-dimethyl-1H-benzo[d]imidazol-2-yl)phenyl)-5-(o-tolyl)-1,3,4-oxadiazole (25)
Pale yellow powder, yield: 0.083 g (83%); m.p.: 348.1 °C; IR (KBr) (ν_{max}, cm^{-1}): 3179, 1614, 1317, 1287, 1055, 1000. ^{1}H NMR (500 MHz, DMSO) δ: 2.34, 2.36 (s, 6H, CH_3-5,6-benzimidazole), 2.73 (s, 3H, CH_3-2''-Ar), 7.34 (s, 1H, Ar), 7.52 – 7.44 (m, 3H, Ar), 7.56 (td, 1H, *J* = 7.5, 1.1 Hz, Ar), 8.13 (d, 1H, *J* = 7.6 Hz, Ar), 8.28 (d, 2H, *J* = 8.5 Hz, Ar), 8.38 (d, 2H, *J* = 8.4 Hz, Ar), 12.88 (s, 1H, NH). HR-ESI-MS: m/z 380.2535 (M^+).

4-(5-(4-(5,6-dimethyl-1H-benzo[d]imidazol-2-yl)phenyl)-1,3,4-oxadiazol-2-yl)phenol (26)
Pale yellow powder, yield: 0.079 g (79%); m.p.: 335 °C; IR (KBr) (ν_{max}, cm^{-1}): 3200, 1609, 1315, 1263, 1079, 1016. ^{1}H NMR (500 MHz, DMSO) δ: 2.34 (s, 6H, CH_3-5,6-benzimidazole), 7.00 (d, 2H, *J* = 8.5 Hz, Ar), 7.41 (s, 2H, Ar), 8.01 (d, 2H, *J* = 8.5 Hz, Ar), 8.25 (d, 2H, *J* = 8.3 Hz, Ar), 8.36 (d, 2H, *J* = 8.3 Hz, Ar), 10.40 (s, 1H, Ar). HR-ESI-MS: m/z 382.2328 (M^+).

2-(4-(5,6-dimethyl-1H-benzo[d]imidazol-2-yl)phenyl)-5-(pyridin-3-yl)-1,3,4-oxadiazole (27)
Pale yellow powder, yield: 0.073g (73%); m.p.: 327.9 °C; IR (KBr) (ν_{max}, cm^{-1}): 3326, 1611, 1565, 1317, 1257, 1054, 999. ^{1}H NMR (500 MHz, DMSO) δ: 2.34, 2.35 (s, 6H, CH_3-5,6-benzimidazole), 7.36 (m, 2H, Ar), 7.48 (s, 1H, Ar), 8.00 (t, 1H, *J* = 4.6 Hz, Ar), 8.25 (d, 2H, *J* = 8.4 Hz, Ar), 8.37 (d, 2H, *J* = 8.4 Hz, Ar), 12.91 (s, 1H, NH). HR-ESI-MS: m/z 367.1932 (M^+).

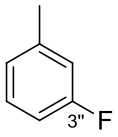
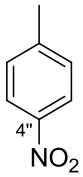
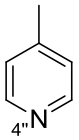
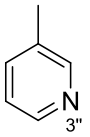
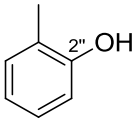
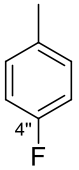
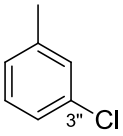
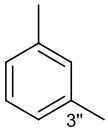
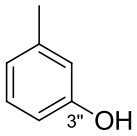
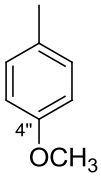
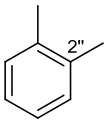
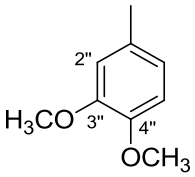
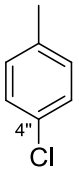
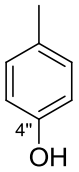
2-(4-(5,6-dimethyl-1H-benzo[d]imidazol-2-yl)phenyl)-5-(m-tolyl)-1,3,4-oxadiazole (28)
Pale yellow powder, yield: 0.079 g (79%); m.p.: 315.4 °C; IR (KBr) (ν_{max}, cm^{-1}): 3198, 1612, 1314, 1274, 1080, 999.^{1}H NMR (500 MHz, DMSO) δ: 2.33, 2.35 (s, 6H, CH_3-5,6-benzimidazole), 2.45 (s, 3H, CH_3-3''-Ar), 7.33 (s, 1H, Ar), 7.48 (d, 2H, *J* = 9.3 Hz, Ar), 7.54 (t, 1H, *J* = 7.6 Hz, Ar), 7.97 (d, 1H, *J* = 7.6 Hz, Ar), 8.00 (s, 1H, Ar), 8.28 (d, 2H, *J* = 8.4 Hz, Ar), 8.37 (d, 2H, *J* = 8.4 Hz, Ar), 12.88 (s, 1H, NH). HR-ESI-MS: m/z 380.2536 (M^+).

The synthesis of the target compounds began with the synthesis of sodium metasulfite adduct according to the literature protocol [5]. The resulting sulfite adduct was refluxed with 4,5-dimethyl-*O*-phenylenediamine in DMF for 6 h to give the arylester substituted benzimidazole. The benzohydrazide of benzimidazole was formed by refluxing arylester of benzimidazole with methanolic hydrazine hydrate (Scheme 1). The synthesis of benzimidazole benzohydrazide Schiff bases (**1-14**) was accomplished by reacting different aldehydes with benzimidazole benzohydrazide in *n*-butanol in the presence of a catalytic amount of acetic acid as shown in Scheme-1. A series of new 2, 5-disubstituted-1,3,4-oxadiazoles (Table 1) have been accomplished in excellent yields by the oxidation of of various aryl aldehydes with one equivalent of iodobenzenediacetate (IBD) in DMF. Compounds **15-28** were synthesized based on the reported procedure.



Scheme 1. Synthesis of oxadiazole derivatives from benzimidazole benzoyl hydrazide

Table 1. Benzimidazole benzohydrazide bearing oxadiazole derivatives

Comp. No.	R	Comp. No.	R	Comp. No.	R	Comp. No.	R
1, 15		5, 19		9, 23		13, 27	
2, 16		6, 20		10, 24		14, 28	
3, 17		7, 21		11, 25			
4, 18		8, 22		12, 26			

The IR spectra of the synthesized compounds exhibited characteristic absorption bands at 1600 – 1700 cm^{-1} and 3100 – 3300 cm^{-1} due to carbonyl or C=N; and NH group, respectively. The ^{1}H NMR spectra of compounds **1-14** showed two singlets due at N=CH and NH, respectively. The structure of all compounds was confirmed by their spectral data (IR, ^{1}H NMR, LCMS) and melting point. The characterization of products **15-28** was based upon a careful comparison of their IR and ^{1}H NMR spectra with those of **1-14**. IR spectra of **15-28** were found to be transparent in the region of NH stretch and CO stretch. In ^{1}H NMR spectra of **15-28** the disappearance of their singlet due to N=CH and NH proton confirms the oxidation of **1-14** into **15-28**.

Conclusion

A series of new 2,5-disubstituted-1,3,4-oxadiazoles derivatives of benzimidazole (**15-28**) were synthesized in good yield and characterized by ^{1}H NMR, IR, MS spectroscopic methods and melting point. A further study to acquire information concerning the pharmacological activity is in progress.

Acknowledgement

The authors would like to acknowledge Faculty of Pharmacy, Universiti Teknologi MARA Puncak Alam, Ministry of Education Malaysia and Universiti Teknologi MARA for the financial support under RAGS grant 600-RMI/RAGS/5/3/ (2/2012).

References

1. Subudhi, B. B., Panda, P. K., Kundu, T., Sahoo, S. and Pradhan, D. J. (2007). Synthesis and biological evaluation of benzimidazole and thiazolidinone derivatives. *Pharmaceutical Research,* 6 (2): 114 – 118.

2. Afaf, H. E., Fanmy, H. H. and Abdelwad, S. H. (2000). Synthesis and antimicrobial activity of some new benzimidazole derivatives. *Molecules,* 5(12): 1429 – 1438.
3. Ozden, S., Karatas, H., Yildiz, S. and Goker, H. (2004). Synthesis and potent antimicrobial activity of some novel 4- (5,6-Dichloro-1H-benzimidazol-2-yl)-N-substituted benzamides. *Archiv der Pharmazie* 337: 556 – 562.
4. Tebbe, M. J., Spitzer, W. A., Victor, F., Miller, S. C., Lee, C. C., Sattelberg, T. R., McKinney, E. and Tang, J. C. (1997). Antirhino/enteroviral vinylacetylene benzimidazoles: a study of their activity and oral plasma levels in mice. *Journal of Medicinal Chemistry*, 40 (24): 3937 – 3946.
5. Migawa, M. T., Girardet, J. L., Walker, J. A., Koszalka, G. W., Chamberlain, S. D., Drach, J. C. and Townsend, L. B. (1998). Design, synthesis, and antiviral activity of alpha-nucleosides: D- and L-isomers of lyxofuranosyl- and (5-deoxylyxofuranosyl) benzimidazoles. *Journal of Medicinal Chemistry*, 41 (8): 1242 – 1251.
6. Sidwell, R. W. and Huffman, J. H. (1971). Use of disposable micro tissue culture plates for antiviral and interferon induction studies. *Applied Microbiology*, 22 (5): 797 – 801.
7. Aydin, S., Beis, K. and Can, D. D. (2003). Analgesic and antispasmodic activities of 2-(2-nitro-phenyl)-1H-benzimidazole 5-carboxylic acid: evidence for the importance of the 2-(O-substituted phenyl) group. *Pharmazie*, 58: 405 – 408.
8. Kumar, V. R., Vaidya, S. D., Kumar, B. V. S., Bhise, U. N., Bhirud, S. B. and Mashelkar, U. C. (2008). Synthesis, anti-bacterial, anti-asthmatic and anti-diabetic activities of novel *N*-substituted-2-(4-phenylethynyl-phenyl)-1*H*-benzimidazoles and *N*-substituted 2[4-(4,4-dimethyl-thiochroman-6-yl-ethynyl)-phenyl)-1*H*-benzimidazoles. *European Journal Medicinal Chemistry,* 43 (5): 986 – 995.
9. Padmavathi, V., Reddy, G. S., Padmaja, A., Kondaiah, P. and Shazia, A. (2009). Synthesis, antimicrobial and cytotoxic activities of 1,3,4-oxadiazoles, 1,3,4-thiadiazoles and 1,2,4-triazoles. *European Journal of Medicinal Chemistry*, 44 (5): 2106 – 2112.
10. El-Emam, A. A., Al-Deeb, O. A., Al-Omar, M. A. and Lehmann, J. (2004). Synthesis, antimicrobial, and anti-HIV-1 activity of certain 5-(1-adamantyl)-2-substituted thio-1,3,4-oxadiazoles and 5-(1-adamantyl)-3-substituted aminomethyl-1,3,4-oxadiazoline-2-thiones. *Bioorganic and Medicinal Chemistry*, 12 (19): 5107 – 5113.
11. Kadi, A. A., El-Brollosy, N. R., Al-Deeb, O. A., Habib, E. E., Ibrahim, T. M. and El-Emam, A. A. (2007). Synthesis, antimicrobial, and anti-inflammatory activities of novel 2-(1-adamantyl)-5-substituted-1,3,4-oxadiazoles and 2-(1-adamantylamino)-5-substituted-1,3,4-thiadiazoles. *European Journal of Medicinal Chemistry,* 42 (2): 235 – 242.
12. Sahin, G., Palaska, E., Ekizoglu, M. and Ozalp, M. (2002). Synthesis and antimicrobial activity of some 1,3,4-oxadiazole derivatives. *Farmaco II*, 57 (7): 539 – 542.
13. Amir, M., Javed, S. A. and Kumar, H. (2007). Synthesis of some 1,3,4-oxadizole derivatives as possible anti-inflammatory agents. *Indian Journal of Chemistry Section B,* 46: 1014 – 1019.
14. Wagle, S., Adhikari, A. V., Kumari, N. S. (2008). Synthesis of some new 2-(3-methyl-7-substituted-2-oxoquinoxalinyl)-5-(aryl)-1,3,4-oxadiazoles as potential non-steroidal anti-inflammatory and analgesic agents. *Indian Journal of Chemistry,* 47: 439 – 448.
15. Najer, H., Giudicelli, R., Moral, C. and Menin, M. (1996). Synthesis of some 5- aryl- 2- dimethylamino-1,3,4-oxadiazoles with anti -inflammatory action. *Bulletin de la Societe chimique de France,* 1: 153 – 159.
16. Almasirad, A., Tabatabai, S. A., Faizi, M., Kebriaceezadeh, A., Mehrabi, N., Dalvandi, A and Shafiee, A. (2004). Synthesis and anticonvulsant activity of new 2-substituted-5- [2-(2-fluorophenoxy)phenyl]-1,3,4-oxadiazoles and 1,2,4-triazoles**.** *Bioorganic and Medicinal Chemistry Letters*, 14 (20): 6057 –6059.
17. Zarghi, A., Tabatabai, S. A., Faizi, M., Ahadian, A., Navabi, P. and Zanganeh, V. A. (2005). Synthesis and anticonvulsant activity of new 2-substituted-5-(2-benzyloxyphenyl)-1,3,4-oxadiazoles. *Bioorganic and Medicinal Chemistry Letters*, 15 (7): 1863 – 1865.
18. Burbuliene, M. M., Jakubkiene, V., Mekuskeine, G., Vdrenaite, E., Smicius, R. and Vainilavicius, P. (2004). Synthesis and anti-inflammatory activity of derivatives of 5-[(2-disubstitutedamino-6-methyl-pyrimidin-4-yl)-sulfanylmethyl]-3H-1,3,4-oxadiazole-2-thiones. *Farmaco II*, 59 (10): 767 – 774.
19. Sengupta, P., Dash, D. K., Yeligar, C. V., Murugesh, K., Rajalingam, D., Singh, J. and Maity, T. K. (2008). Evaluation of anticancer activity of some 1,3,4-oxadiazole derivatives. *Indian Journal of Chemistry Section B*, 147: 460 – 462.

20. Taha, M., Ismail, N. H., Jamil, W., Rashwan, H., Kashif, S. M., Sain, A. A., Adenan, M. I., Anouar, E. H., Ali, M., Rahim, F. and Khan, K. M. (2014). Synthesis of novel derivatives of 4-methylbenzimidazole and evaluation of their biological activities. *European Journal of Medicinal Chemistry,* 84: 731 – 738.
21. Prasanna Kumar, B. N., Mohana, K. N., Mallesha, L. (2013). Synthesis of N-[{5-Aryl-1,3,4-oxadiazole-2-yl}methyl]-4-methoxyaniline derivatives and their anticonvulsant activity. *Journal of Chemistry,* 2013: 1 – 8.

Malaysian Journal of Analytical Sciences, Vol 20 No 6 (2016): 1524 - 1529
DOI: http://dx.doi.org/10.17576/mjas-2016-2006-34

MALAYSIAN JOURNAL OF ANALYTICAL SCIENCES
Published by The Malaysian Analytical Sciences Society
ISSN 1394 - 2506

THE EFFECT OF POLYMER CONCENTRATION AND SURFACTANT TYPES ON NANOFILTRATION-SURFACTANT MEMBRANE FOR TEXTILE WASTEWATER

(Kesan Kepekatan Polimer dan Jenis Surfaktan pada Membran Surfaktan Penurasan-Nano untuk Air Sisa Tekstil)

Sarah Husnaini Zainal, Abdul Rahman Hassan*, Mohd Hafez Mohd Isa

Industrial Membrane Technology Laboratory, Department of Industrial Chemical Technology,
Faculty of Science and Technology,
Universiti Sains Islam Malaysia, 71800 Nilai, Negeri Sembilan, Malaysia

**Corresponding author: abdrahman@usim.edu.my*

Received: 24 February 2015; Accepted: 27 October 2015

Abstract

In this study, an asymmetric nanofiltration-surfactant (NFS) membrane was prepared via simple dry/wet phase inversion technique. A newly dope formulation consisting of different surfactants (SDS, CTAB) and polymer concentration (17 wt% - 21 wt%) were developed. The effect of these parameters on dyes performance in terms of dyes flux, rejection and morphological structure were examined. Experimental data showed that, at different ranges of polymer concentration, NFS membranes shows low permeation flux of dyes ranging from 9.256 L/m^{2}h to 14.315 L/m^{2}h at 4 bar operating pressure. Significantly, the addition of SDS and CTAB surfactants were found to promote the increasing of dyes flux and rejection up to 79.698 L/m^{2}h and 99.5% respectively. Addition of surfactant shows the membrane surface morphology with upper layer and support layer consists of finger-like structure, finger-like channel, macrovoids and spongy structure.

Keywords: nanofiltration, surfactant, flux, rejection, morphological structure

Abstrak

Dalam kajian ini, membran surfaktan penurasan-nano telah disediakan melalui teknik fasa berbalik kering/basah mudah. Satu formulasi baru polimer yang terdiri daripada surfaktan yang berbeza (SDS,CTAB) dan kepekatan polimer (17 wt% - 21 wt%) telah disediakan. Kesan parameter ini terhadap prestasi pewarna dari segi fluks warna, penolakan dan struktur morfologi telah diperiksa. Data ujikaji menunjukkan bahawa, pada jarak yang berbeza kepekatan polimer, keputusan fluks membran NFS menyerap rendah pewarna antara 9.256 L/m^{2}h kepada 14.315 L/m^{2}h pada 4 bar tekanan operasi. Lebih penting lagi, penambahan SDS dan CTAB sebagai surfaktan didapati menggalakkan peningkatan fluks pewarna dan penolakan sehingga masing – masing adalah 79.698 L/m^{2}h dan 99.5%. Penambahan surfaktan menunjukkan morfologi permukaan membran dengan lapisan atas dan lapisan sokongan yang terdiri daripada struktur jejari, saluran jejari, makrovoid dan struktur lembut.

Kata kunci: penurasan-nano, surfaktan, fluks, penolakan, struktur morfologi

Introduction

Nanofiltration (NF) membrane one of the promising technologies which has been largely developed and commercialized for the separation of neutral and charged solutes in the aqueous solutions. NF membranes has two remarkable features which are has molecular weight cut-off (MWCO) between reverse osmosis (RO) membranes

and ultrafiltration (UF) membranes ranges from 200 to 2000 Da. The other advantage of NF where it can separate electrolytes due to the materials containing charged groups [1]. According to these features, the separation mechanisms involve both steric and electrostatic partitioning effects between the membrane and external solutions. The combination between steric and electrostatic allows NF membranes more effective for the separations of mixtures of organic molecules and salts. An NF membranes main feature is that most of them are charged either positively or negatively depends on their materials [2].

In this study, asymmetric nanofiltration membranes were prepared via dry/wet phase inversion techniques. This technique has been introduced by Loeb and Sourirajan which is the most extensively used technique for the preparation of asymmetric membranes. In this technique, the solution was cast on a substrate/glass was immersed and precipitated in a water bath. In dry/wet phase inversion technique, solvent in the casting solution was exchanged with non-solvent and phase separation will occurs in the film. This will be resulted to the morphology of asymmetric membranes showing a dense top layer and porous sub-layer membranes [3]. Addition of surfactant as additive in the polymer solution was the new materials used in formulating new NF membranes. Surfactant has been used in soaps, laundry detergents, dishwashing liquids and shampoos are organic chemicals that reduce surface tension in water and other liquids. Surfactant also can be considered as amphiphilic due to the two parts which are hydrophilic and hydrophobic parts [4].

Addition of surfactant has been studied by several researchers which gives high membrane performance. According to Tsai et al. [5], addition of surfactants in the casting solution can influence the formation process of macrovoids. Moreover, the size of macrovoids decreases when the surfactant content increase [5]. Furthermore, Amirilargani et al. [6] discovered that addition of non-ionic surfactant in the casting solutions shows that the macrovoids and finger-like pores in the sub-layer can be induced or suppressed depending on their miscibility. It was also found that the addition of small amount of surfactant will increase the water content, porosity and thickness of the prepared membranes [6].

Materials and Methods

Chemicals and raw materials

Polyethersulfone (PES) was purchased from SOLVAY Advanced Polymers Company (RADEL A-300). 1-Methyl-2-Pyrrolidone (NMP) with analytical purity of 99.5% (Merck), ethanol and n-hexane (Merck) was used as pre-treatment solutions in membrane fabrication. Polyethylene glycol (PEG) with average molecular weight of 600g/mol (Merck) used as additive. Cetyltrimethylammonium bromide (CTAB) with molecular weight of 364.5g/mol from EMD Chemicals and Sodium dodecyl sulfate (SDS) with molecular weight of 288.37g/mol (Merck) were used as surfactant addition in the polymer solution. Methyl violet from Blulux Laboratory Reagents and Methyl blue (Merck) were used as synthetic dyes.

Membrane preparation and fabrication

NMP was used to dissolve polymer in polymer solution method. NMP was heated at about 50 °C and PES was dissolved. PEG 600 was added when polymer has been dissolved. The solution was stirred for 8 hours to get homogenous solution. Then, surfactant was added 3 hours before the polymer solution was completed. After formation of polymer solution has been completed, casting process will take place in fabricated thin film of membrane. The casting process was conducted at room temperature (30±2 °C). Small amount of polymer solution was poured onto glass plate as support layer with casting knife setting at 150 μm. After the membrane has been casted, the glass plate support together with membrane was immersed into the coagulation bath. When the coagulation process was completed, the membrane was immersed in water bath for 24 hours before it was immersed in ethanol for another 24 hours. Finally, the resulted membrane was soaked in n-hexane for 2-3 hours before dried at room temperature at least for 24 hours. The prepared polymer solution concentration was varied from 17 wt% to 21 wt%.

Membrane performance evaluation

The permeation test was conducted by using a simple dead-end permeation cell. Prior to the testing, each membrane was subjected for the passages of the first 10 ml permeate was collected. The pure water permeation was calculated using equation 1 below:

$$\text{Pure Water Permeation} = \frac{\text{Volume of Permeate Solution Collected}}{\text{Effective Membrane Area x Time}} \quad (1)$$

To study the effect of dyes rejection, operating pressure at 4 bar was used to obtain respective flux. Permeation flux test of dyes was carried out using three types of dyes (methyl violet, methyl blue, acid orange) at 3 different concentrations (10ppm, 15ppm, 20ppm). The volume flux and rejection was calculated using formula equation 2 below:

$$\text{Percentage of Rejection} = 1 - \frac{\text{Concentration Permeate}}{\text{Concentration Feed}} \times 100\% \quad (2)$$

Results and Discussion

Dyes permeation flux and rejection

Three different dyes were used in this study (Methyl Violet, Methyl Blue, and Acid Orange) in order to determine the membrane performance in terms of permeation flux and dye rejection. Three different concentrations (10 ppm, 15 ppm, 20 ppm) of Methyl Violet has been used in order to find the significance difference of each prepared membrane and each concentration will give difference permeation flux and rejection results. Figure 1(a) shows the permeation flux of Methyl Violet at three different dyes concentration of membrane with SDS surfactant. Since 10 ppm is the lowest dye concentration, it shows highest flux among other concentration of about, 38.836 L/m^{2}h. However, the permeate flux keep increasing as polymer concentration increase up to 79.697 L/m^{2}h. The rejection of 10 ppm concentration of Methyl Violet shows that as polymer concentration increase, the rejection will decrease from 79% to 66.2%. Unlike the lower dye concentration, at 13.776 L/m^{2}h, the membrane can reject dye only 33.3% at 15ppm dye concentration. Since polymer concentration also plays an important role in this study, the color rejection of Methyl Violet increase sharply up to 79% at higher polymer concentration (21 wt%). As dye concentration increase to 20 ppm, the permeate flux decreased to 11.0843 L/m^{2}h. However, for 20 ppm of dye concentration, the three different polymer concentrations resulted to the same rejection. Research revealed that addition of surfactants in casting solution will influence the formation of macrovoids [7].

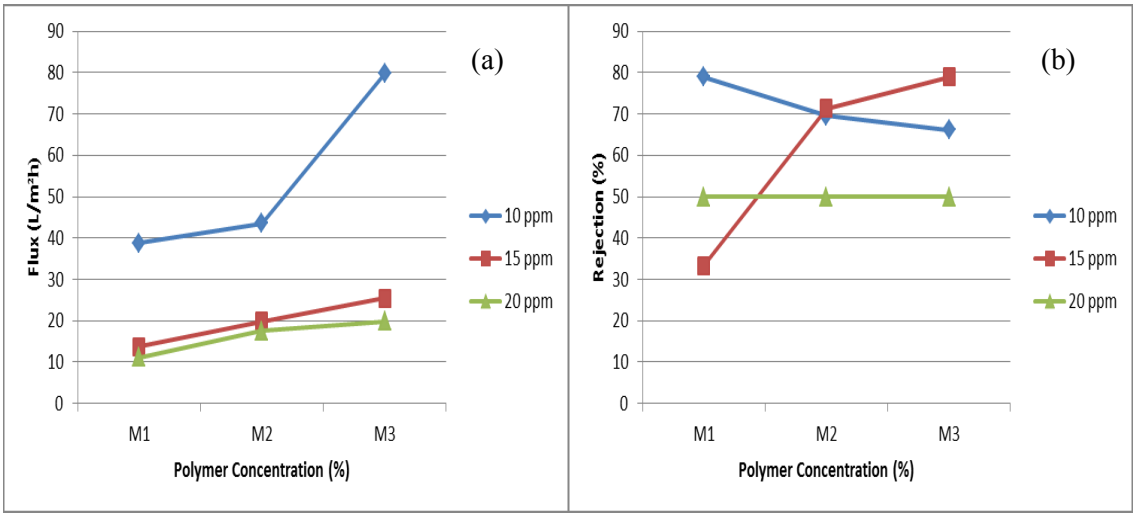


Figure 1. (a) Permeate flux and (b) % rejection of Methyl Violet

Experimental data shows that addition of SDS in polymer solution is not good for dyes rejection. Figure 2(a) and 2(b) shows permeation flux and percentage rejection of Methyl Blue when CTAB was used as surfactant. The highest permeate flux were obtained from the lowest polymer concentration at the lowest dye concentration. At 44.565 L/m^{2}h, M1 can remove dye of about 99.2% at 10ppm dye concentration. The results also show that, as polymer concentration increased, the permeate flux decreased up to 13.682 L/m^{2}h and increase the rejection to 99.5% for M3. According to Rahimpour et al. [7], addition of CTAB surfactant in polymer solution will gives membrane with large pores that formed in the sub-layer of the membrane. Moreover, addition of CTAB was known to be capable to increase the porosity of membrane support layer and result in high rejection of Methyl Blue [8]. At 15 ppm of dye concentration, the permeate flux shows the same results where the flux decrease when polymer concentration increase from 27.758 L/m^{2}h to 9.272 L/m^{2}h. Moreover, the rejection of Methyl Blue at 15ppm dye concentration increasing up to 99.1% for M3. An amount of 21wt% PES shows 8.972 L/m^{2}h of permeation flux and can reject dye up to 99.9% at 20 ppm of dye concentration.

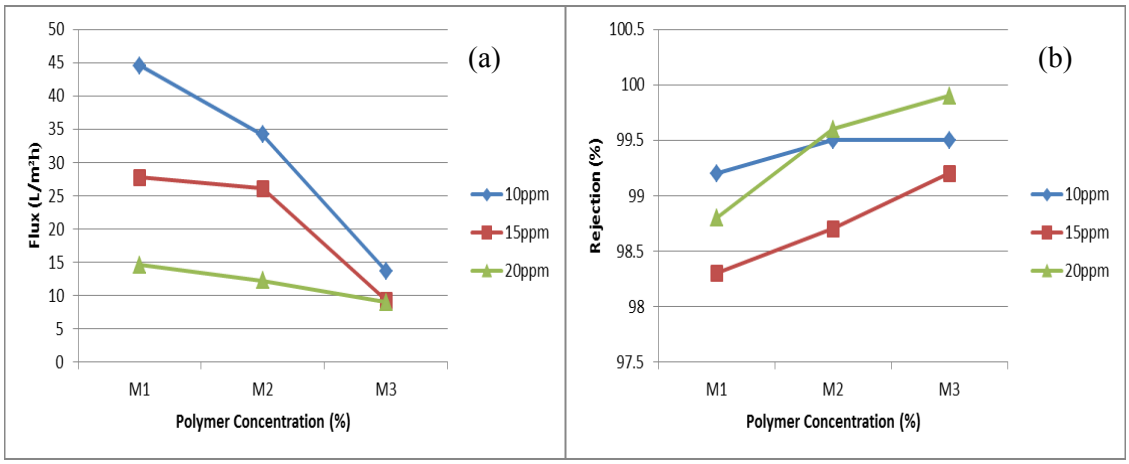


Figure 2. (a) Permeate flux and (b) % rejection of Methyl Blue

In order to complete the study, acid orange also was used to test the membrane performance (Figure 3). The same trend shown between Methyl Blue and Acid Orange in which the permeation flux decreased as polymer concentration increased with increasing of dye concentration. On the other hand, the rejection of acid orange was increased as polymer concentration increase also with increasing of dye concentration. At 51.044 L/m^{2}h, M1 gives dye rejection of 90.7% for 10 ppm dye concentration. Research proved that concentration of feed solutions is one of parameters that affects the membrane performance [9]. Permeate flux of Acid Orange decreased and rejection also increased when dye concentration increased. For 15 ppm dye concentration, M1 gives 46.898 L/m^{2}h of permeation flux and decreased to 15.871 L/m^{2}h indicate as the polymer concentration increased to M3 (21 wt%). Permeation flux of Acid Orange decreased and has increased the rejection up to 94.9%. Furthermore, morphological structures of prepared membrane also was the most important parameters that gives high or low rejection towards dye solutions. At 12.175 L/m^{2}h, 20 ppm of Acid Orange dye concentration gives 94.1% of dye rejection. This can be conclude that, for Acid Orange with lower molecular weight will decreased the permeation flux and increased the rejection as polymer concentration increased as well as dye concentration increased.

Morphological study

Figure 4a shows the image of nanofiltration membrane without surfactants. It can be seen that the resultant asymmetric membranes consist of dense top-layer and finger-like substructure. The cross-sectional image revealed that increasing of polymer concentration will increase the number of pores on the top-layer of the membranes. The long finger-like substructure is the key towards the performance of membranes. The support layer is thick that make the solutions harder to pass through the membranes. Addition of small amount SDS surfactant was shown by Figure

4b where different morphological structure produced. SDS makes the membrane structure more porous in terms of formation of larger macrovoids. Moreover, the support layer of membranes also containing microvoids that leads to the lower mechanical strength of the membrane. In order to study the effect of different type of surfactant on membrane performance, Figure 4c shows SEM image of membrane with CTAB. Addition of CTAB on polymer solution shows the formation of long finger-like structure across the substructure of the membrane. From the previous study, the SEM images shows the formation of large pores in the sub-layer of membrane with addition of CTAB. This phenomenon is due to the miscibility of the surfactant and coagulant. Other than that, addition of CTAB revealed that it will induces and extends the formation of macrovoids as well as finger-like pores in the support layer of membranes [10]. From the experimental data, membrane with CTAB shows lower flux and high rejection of dyes.

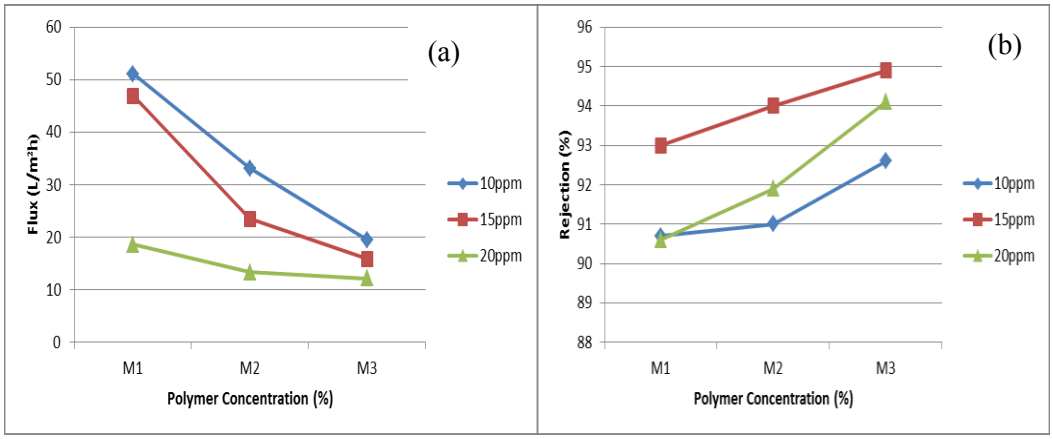


Figure 3. (a) Permeate flux and (b) % rejection of Acid Orange

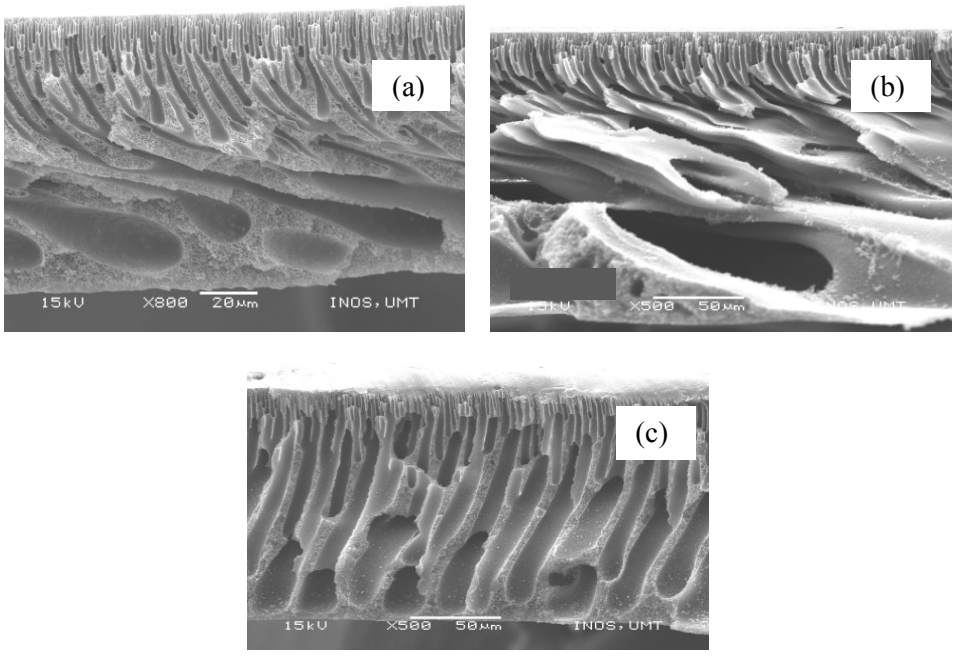


Figure 4. SEM images on (a) NF membrane (b) NF membrane with SDS and (c) NF membrane with CTAB at 800x of magnification

Conclusion

Experimental data shows the highest rejection of dyes was obtained by membrane contains CTAB as surfactant. Increased the rejection p to 99.9% it could be comparable to commercial membrane in the industry. With fine morphological structure consists of dense top-layer, long finger-like structure and stable support layer, membrane with CTAB is the best membranes to be used in textile industries in Malaysia. Besides, CTAB is readily available and very economical to use in making membrane.

Acknowledgement

The authors would like to thank the Research Management Centre (RMC), Universiti Sains Islam Malaysia (USIM) and KPT for financing the project under the Exploratory Research Grant Scheme (USIM/ERGS-FST-33-50113).

References

1. Wang, X. L., Shang, W. J., Wang, D. X., Lu, L. and Tu, C. H. (2009). Characterization and applications of nanofiltration membranes: State of the art, *Desalination*, 236: 316 – 326.
2. Ismail, A. F. and Hassan, A. R. (2004). The deduction of fine structural details of asymmetric nanofiltration membranes using theoretical models. *Journal of Membranes Science*, 231: 25 – 36.
3. Ismail, A. F. and Hassan, A. R. (2006). Formation and characterization of asymmetric nanofiltration membrane: Effect of shear rate and polymer concentration. *Journal of Membrane Science*, 270: 57 – 72.
4. Kowalska, I., Korbutowicz, M. K., Nowak, K. M. and Winnicki, T. (2004). Separation of anionic surfactants on ultrafiltration membranes. *Desalination*, 162: 33 – 40.
5. Tsai, H.A., Li, L. D., Lee, K. R., Wang, Y. C., Li, C. L., Huang, J. and Lai, J. Y. (2000). Effect of surfactant addition on the morphology and pervaporation performance of asymmetric polysulfone membranes. *Journal of Membrane Science*, 176: 97 – 103.
6. Amirilargani, M., Saljoughi, E. and Mohammadi, T. (2009). Effects of Tween-80 concentration as a surfactant additive on morphology and permeability of flat sheet polyethersulfone (PES) membrane. *Desalination*, 249: 837 – 842.
7. Rahimpour, A., Madaeni, S. S. and Mansourpanah, Y. (2007). The effect of anionic, non-ionic and cationic surfactants on morphology and performance of polyethersulfone ultrafiltration membranes for milk concentration. *Journal of Membrane Science*, 296: 110 – 121.
8. Akbari, A., Remigy, J. C. and Aptel, P. (2002). Treatment of textile effluent using a polyamide-based nanofiltration membrane. *Chemical Engineering and Processing*, 41: 601 – 609.
9. Huang, J., Liu, L., Zeng, G., Li, X., Peng, L., Li, F., Jiang, Y., Zhao, Y. and Huang, X. (2014). Influence of feed concentration and transmembrane pressure on membrane fouling and effect of hydraulic on the performance of ultrafiltration. *Desalination*, 335: 1 – 8.
10. Saedi, S., Madaeni, S. S., Shamsabadi, A. A. and Mottaghi, F. (2012). The effect of surfactants on the structure and performance of pes membrane for separation of carbon dioxide from methane. *Separation and Purification Technology*, 99: 104 – 119.

Malaysian Journal of Analytical Sciences, Vol 20 No 6 (2016): 1530 - 1534
DOI: http://dx.doi.org/10.17576/mjas-2016-2006-35

MALAYSIAN JOURNAL OF ANALYTICAL SCIENCES
Published by The Malaysian Analytical Sciences Society
ISSN 1394 - 2506

THREE FLAVONOL GLYCOSIDES FROM *Calliandra surinamensis* Benth

(Tiga Flavonol Glikosida daripada *Calliandra surinamensis* Benth)

Siti Muhayyah Omar, Norizan Ahmat*, Nik Fatini Nik Azmin

Department of Chemistry, Faculty of Applied Sciences,
Universiti Teknologi MARA, 40450 Shah Alam, Selangor, Malaysia

**Corresponding author: noriz118@salam.uitm.edu.my*

Received: 24 February 2015; Accepted: 27 October 2015

Abstract

Calliandra surinamensis or Pinkpowder puff is a tropical shrub, named after Suriname. In Borneo, such as Sarawak and East Kalimantan area, it was known as "daun assam jawa". This species belonging to the family of Leguminosae and subfamily of Mimosoideae originated from tropical America. *Calliandra surinamensis* has been used in folk medicine to treat various diseases and infections such as cough, wound healing and inflammation. In this study, the flowers of *Calliandra surinamensis* was extracted by successive extraction. The phytochemical procedures adopted were vacuum liquid chromatography (VLC), and radial chromatography (RC). Phytochemical investigation of *Calliandra surinamensis* flower afforded three flavonol glycosides identified namely (1) 3-*O*-rhamnosylkaempferol (2) 3-*O*-rhamnosylmyricetin and (3) Myricetin-3-*O*-heptoseptanoside. The molecular structures of the isolated compounds were established based on spectroscopic methods such as 1D-NMR (^{1}H, ^{13}C, DEPT) and 2D-NMR (COSY, HMQC, HMBC) and comparison with literature.

Keywords: leguminosae, *Calliandra surinamensis*, 3-*o*-ramnosilkaempferol, 3-*o*-ramnosilmyricetin, myricitrin-3-*o*-heptoseptanoside

Abstrak

Calliandra surinamensis atau Pinkpowder puff adalah pokok renek tropika, dinamakan sempena nama Negara Surinam di Utara Amerika Selatan. Di Borneo seperti kawasan Sarawak dan Kalimantan Timur, ia dikenali sebagai "daun asam jawa". Spesies daripada keluarga Leguminosae dan subkeluarga Mimosoideae ini berasal dari Amerika bahagian tropika [4]. *Calliandra surinamensis* telah digunakan dalam perubatan tradisional untuk merawat pelbagai penyakit dan jangkitan seperti batuk, penyembuhan luka dan keradangan. Melalui kajian ini, bunga – bunga *Calliandra surinamensis* telah diekstrak melalui pengekstrakkan berturut-turut. Prosedur fitokimia yang digunakan adalah kromatografi cecair vakum (VLC) dan kromatografi jejarian. Kajian fitokimia daripada bunga *Calliandra surinamensis* telah menghasilkan tiga flavonol glikosida yang dikenalpasti sebagai (1) 3-*O*-ramnosilkaempferol (2) 3-*O*-ramnosilmyricetin dan (3) myricetin-3-*O*-heptoseptanosida. Struktur molekul sebatian terpencil telah dikenalpasti berdasarkan kaedah spektroskopi seperti 1D-NMR (^{1}H, ^{13}C, DEPT) dan 2D-NMR (COSY, HMQC, HMBC) serta perbandingan dengan data literatur.

Kata kunci: leguminosae, *Calliandra surinamensis*, 3-*o*-rhamnosilkaempferol, 3-*o*-rhamnosilmyricetin, myricitrin-3-*o*-heptosepta-nosida

Introduction

The genus *Calliandra* is one of the largest genera of the Leguminosae (Fabaceae), with approximately 200 species. It grows mostly in the tropical and sub-tropical regions of America with a few native also found in Madagascar and India. Various species in the genus have been reported for the treatment of eye diseases, diarrhea, indigestion [1],

diabetes and obesity [2]. Previous studies on the phytochemistry of several *Calliandra* species revealed different classes of compounds such as flavonoids, diterpenes, triterpenes, amino acids and polyphenols.

In the search of biologically active and interesting compounds from plants, the investigation on *Calliandra surinamensis* was carried out. *Calliandra surinamensis* locally known in Malaysia as "Kaliandra bunga merah" is a flowering plant endemic to southern Asia, Africa, Australia and America. Previous investigation reported the stem bark was used as traditional medicine by the folklore to treat various diseases and infections, antioxidants and antimicrobial activity [3,4]. The knowledge on isolation of the chemical constituents from this species is still limited. A preliminary study by Falodun and Qiu [5] on the rootbark of the plant reported some secondary metabolites such as flavonoid, β-sitosterol 3-*O*-β-D-glucopyranoside and recursterol. This paper reports on the isolation and structure elucidation of flavonoid compounds from the flower of *Calliandra surinamensis* which has not been reported before.

Materials and Methods

Experimental procedures

The ^{1}H-NMR and ^{13}C-NMR spectra were recorded on a Bruker 300 Ultrashield NMR spectrometer (Switzerland) measured at 300 and 75 MHz, respectively, using chloroform-D and methanol-D (Merck) as solvent. Chemical shifts are reported in δ ppm (part per million) with coupling constants given in Hertz (Hz). The infrared (IR) spectra were recorded using Perkin-Elmer 1600 series FTIR spectrometer (USA) using KBr pellets. The ultraviolet (UV) spectra were recorded on Shimadzu UV-Vis 160i spectrometer. The mass spectra were measured on Perkin Elmer Clarus 600T spectrometer 70 eV. Vacuum liquid chromatography (VLC) used Silica gel 60, 70-230 mesh ASTM (Merck 1.07747), Radial chromatography used Si-gel 60 PF254 (Merck 1.07749). For TLC analysis, pre-coated silica gel plates (Merck Kieselgel 60 GF254 0.25 mm) were used and visualized under UV light [6].

Plant material

The fresh flowers of *Calliandra surinamensis* was collected from the Universiti Teknologi MARA Shah Alam, Malaysia in September 2011. Botanical identification was done by a taxonomist Prof. Dr Mohd Nazip Suratman from Faculty of Applied Sciences, Universiti Teknologi MARA, Malaysia.

Extraction and isolation procedure

The dried powdered of flower (70 grams) of *Calliandra surinamensis* was defatted in methanol (40 $^{\circ}$C – 60 $^{\circ}$C) for 48 hours repeated for three times and was evaporated under reduced pressure to give brown residues. The methanol extract (40 g) was subjected to vacuum liquid chromatography (VLC) using gradient elution system of Hexane: EtOAc. Thirty-nine fractions from two separate fractionations were obtained and spotted on TLC and similar profile was pooled to yield four major fractions. Further purification of fraction 4 by radial chromatography (silica gel, $CHCl_3$: MeOH) yielded compound 1 (1.21 mg). Compound 2 and 3 also were obtained from radial chromatography.

Results and Discussion

Three flavonol glycosides isolated from the flower of *Calliandra surinamensis* were identified as 3-*O*-rhamnosylkaempferol, 3-*O*-rhamnosylmyricetin and myricetin-3-*O*-heptoseptanoside (Figure 1).

3-*O*-rhamnosylkaempferol (1)

Yellow solid. MS m/z: 432, $C_{21}H_{20}O_{10}$. UV λ_{max} nm (MeOH) 265 and 342. IR ν_{max} (KBr):1675 and 3197 cm$^{-1.}$ For ^{1}H NMR and ^{13}C NMR data, see Table 1.

Compound 1 was obtained as yellow solid and the mass spectral of the data gave a molecular weight of $C_{21}H_{20}O_{10}$ corresponding to 21 carbon in ^{13}C NMR spectral data. ^{1}H NMR spectra of compound 1 showed signals for aromatic hydrogen at δ_H 6.39 (d, J=2.1) and 6.21 (d, J=2.1) indicated H-6 and H-8, respectively at ring A of the flavonol skeleton. The ortho-coupled hydrogen at signal δ_H 7.79 (d,J=9.0) and 6.96 (d, J=9.0) were assigned for H-2'/6' and H-3'/5', respectively at ring B. A signal at δ_H 5.39 (d, J=1.2) was assigned to the anomeric proton of H-1''. One sugar moiety detected at C-3 of ring C assigned as rhamnose unit gave signals at δ 5.39 (d, J=12), 4.24 (dd, J=3.3, 1.5), 3.73 (dd, J=9.3,3.6), 3.35 (d, J=1.8), 3.31-3.33 (m) and 0.94 (d, J=5.7).

The APT NMR spectrum displayed 18 signals corresponding to 21 resonances. A signal at δc 178.20 was appointed to carbonyl carbon (C=O) attached to oxygen at C-4 whereas other signals at δc 98.42, 93.34, 115.11 and 130.50 were corresponded to quaternary carbon attached to OH at C-6, C-8, C-3'/5' and C-2'/6', respectively. Additional of one rhamnose unit at C-3 of ring C was proved by signals at δc 102.09, 70.51, 70.63, 71.76, 70.70 and 16.24. This compound was previously isolated from the leaves of *Schima wallichii* and was reported to have potential for anti-cancer therapeutics [7].

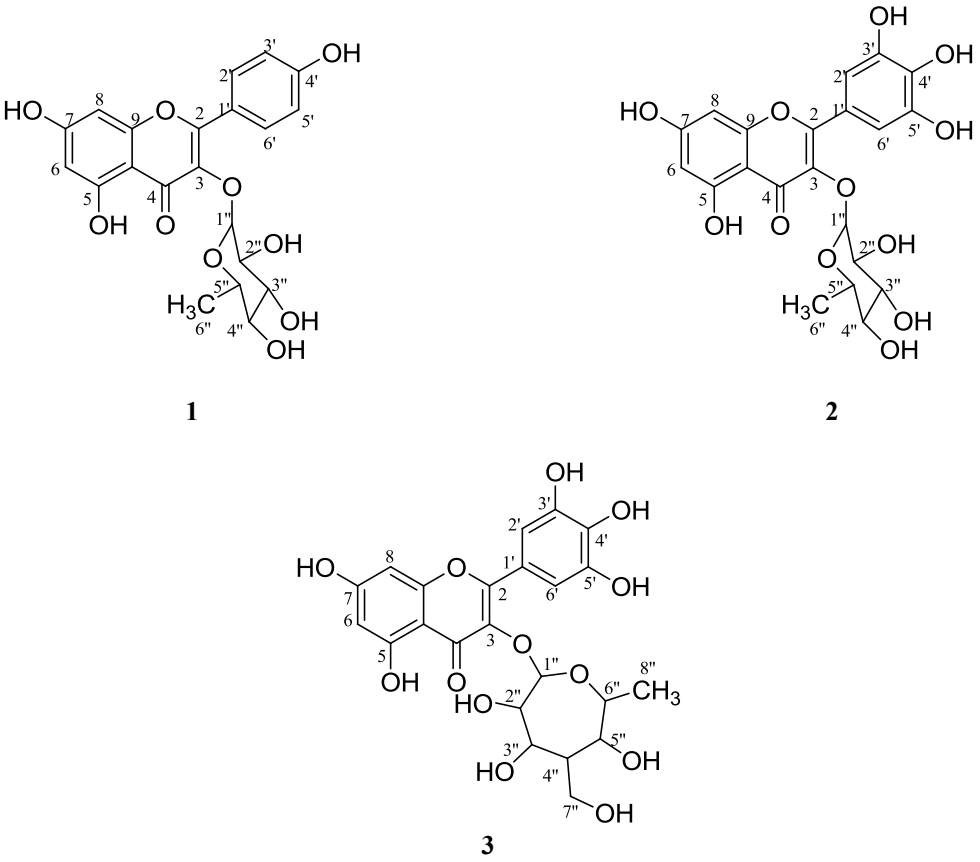


Figure 1. Structures of compound 1-3

3-*O*-rhamnosylmyricetin (2)
Mass Spectrum m/z: 464, $C_{21}H_{20}O_{12}$. UV λ_{max} nm (MeOH) 258, 302 and 352. IR ν_{max} (KBr): 1678 and 3186 cm^{-1}. For ^{1}H NMR and ^{13}C NMR data, see Table 1.

Compound 2 was obtained as yellow solid. The mass spectral of the data exhibit an M+ at m/z 464, corresponding to molecular weight $C_{21}H_{20}O_{12}$. Its ^{1}H NMR and ^{13}C NMR spectral data for 2 were closely related to compound **1** except that the AA'BB'-type coupling system in the B-ring of 1, was replaced by an AB-type coupling system in B-ring for 2. The ^{13}C NMR spectrum exhibited 16 signals corresponding to 17 carbon resonances. Signals at δ_C 178.24 was appointed to carbonyl carbon attached to oxygen (C-4) whereas other signals at δ_C 145.01 and δ_C 148.40 were corresponded to a quarternary carbon attached to OH at C-3' and C-5' respectively. Rhamnose was presence at C-3, [δ_C 102.1, 70.4, 70.6, 71.8, 70.6, 16.25 ppm] as similar to compound **1**. This compound was isolated from the leaves of *Myrica rubra* and showed good anti-inflammatory activity [8].

Myricetin-3-*O*-heptoseptanoside (3)
Mass Spectrum m/z: 508, $C_{23}H_{24}O_{13}$. UV λ_{max} nm (MeOH) 245 and 252. IR ν_{max} (KBr): 1679 and 3174 $cm^{-1.}$ For ^{1}H NMR and ^{13}C NMR data, see Table 1.

Compound 3 was obtained as pale yellow solid. The mass spectral of the data exhibit an M+ at m/z, corresponding to molecular weight $C_{23}H_{24}O_{13}$. Compound 3 gave the ^{1}H NMR and ^{13}C NMR spectra shown in Table 1, show the aglycone moiety at signal δ 6.79 (d, J=1.8), 6.92 (d, J=2.1), 7.92 (dd, J=2.1,16.8) and 7.48 (d, J=8.4). The APT NMR spectrum exhibited 18 signals corresponding to 21 resonances. Signals at δ_C 179.2 was appointed to carbonyl carbon attached to oxygen (C-4) whereas other signals at δ_C 146.0 and δ_C 149.3 were corresponded to a quarternary carbon attached to OH at C-3' and C-5' respectively. Additional of one sugar moiety at C-3 was confirmed with extra signals detected at δ_C 103.1, 71.5, 72.9, 73.4, 64.0, 71.6, 71.7 and 17.2. Thus, compound 3 was determined to be myricitrin-3-*O*-heptoseptanoside and this is the first report on the isolation of this constituent.

Table 1. Spectroscopic data (^{1}H NMR and ^{13}C NMR) for compounds 1-3

Position	1		2		3	
	δ_H (Hz)	δ_C (ppm)	δ_H (Hz)	δ_C (ppm)	δ_H (Hz)	δ_C (ppm)
2	-	161.82	-	161.81	-	161.66
3	-	134.80	-	134.82	-	135.86
4	-	178.20	-	178.24	-	179.26
5	-	164.50	-	164.47	-	165.43
6	6.21 (d,J = 2.1)	98.42	6.15 (d,J=2.1)	98.39	6.22 (d,J=1.8)	99.45
7	-	164.50	-	164.47	-	162.79
8	6.39 (d,J = 2.1)	93.34	6.32 (d,J=2.1)	93.29	6.39 (d,J=2.1)	94.35
9	-	157.14	-	157.12	-	158.13
10	-	104.51	-	104.48	-	105.54
1′	-	121.21	-	121.54	-	122.62
2′	7.79 (d,J = 9.0)	130.50	7.28 (dd, J=1.8,12.9)	115.50	7.92 (d, J=7.8)	116.24
3′	6.96 (d,J = 9.0)	115.11	-	145.01	-	146.00
4′	-	160.18	-	157.91	-	158.92
5′	6.96 (d,J = 9.0)	115.11	-	148.40	-	149.38
6′	7.79 (d,J = 9.0)	130.50	6.86 (d,J=8.1)	114.95	6.94 (d, J=8.4)	115.39
	rhamnose		rhamnose		heptoseptanoside	
1″	5.39 (d,J = 1.2)	102.09	5.29 (d,J=1.2)	102.13	5.37 (s)	103.15
2″	4.24 (dd,J = 3.3, 1.5)	70.51	4.16 (m)	70.49	4.25 (s)	71.52
3″	3.73 (dd,J = 9.3, 3.6)	70.63	3.71(dd,J=3.3,9.3)	70.63	3.33 (s)	72.90
4″	3.35 (d,J = 1.8)	71.76	3.24 (2H, complex)	71.83	3.61 (dd,J=6.9)	73.47
5″	3.31 – 3.33 (m)	70.70	3.24 (2H, complex)	70.68	3.61 (dd,J=6.9)	64.05
6″	0.94 (d,J=5.7)	16.24	0.89 (d,J=6.0)	16.25	4.25 (s)	71.63
7″					3.78 (d,J=3.0)	71.77
8″					0.97 (d,J=6.0)	17.26

Conclusion

Three flavonol glycoside compounds identified as 3-*O*-rhamnosylkaempferol (1), 3-*O*-rhamnosylmyricetin (2) and myricetin-3-*O*-heptoseptanoside (3) were successfully isolated from the flower of *Calliandra surinamensis.*

Acknowledgement

The authors would like to thank Institute of Graduate Studies (IGS) of UiTM under the Graduate Service Scheme and Conference Support Fund (IGS/JTA/FUND/2012(1)) and Faculty of Applied Sciences, Universiti Teknologi MARA for financing this research project.

References

1. Allen, O.N and Allen, E.K. (1981). Book: The leguminosae, a source book of characteristics, uses and nodulation, pp. 125 – 126.
2. Koji, Y., Kazuyoshi, Y., Atsushi, H. and Tomio, N. (2006). A blood glucose increase inhibitor prepared from *Calliandra haematocephala* (*Calliandra*, Leguminosae) leaf extract. Japan. Kokai Tokyo Koho, JP 2006232750 A 20060907.
3. Irabor, E. E. I, Falodun, A., Obasuyi, O., Ofoegbu, C. O., Abiodun, S. O. and Umujeyan, K. (2007). Antimicrobial evaluation of methanolic extract of *calliandra surinamensis* on some pathogenic organism. *Acta Poloniae Pharmaceutica-Drug Research,* 63(5): 449 – 451.
4. Camazine, S. and Robert, A. (1980). A study of ethnobotany of the Zuni Indians of New Mexico. *Journal of Ethnopharmacology,* 2: 365 – 388.
5. Falodun, A. and Qiu, S. (2010). Isolation and characterization of chemical principles from rootbark of *Calliandra surinamensis*. *Nigerian Journal of Biochemistry and Molecular Biology,* 25(2): 17 – 22.
6. Sofowora, A. (1984). A screening plants for bioactive agents: In medicinal plants and traditional medicine in Africa. Spectrum Books Limited. 1st edition. John Wiley and Sons, London.
7. Diantini, A., Subarnas, A., Lestari, K., Halimah, E., Susilawati, Y., Supriyatna., Julaeha, E., Achmad, T. H., Suradji, E. W., Yamazaki, C., Kobayashi, K., Koyama, H. and Abdulah, R. (2012). Kaempferol-3-o-rhamnoside isolated from the leaves of *Schima wallichii* Korth. Inhibits MCF-7 breast cancer cell proliferation through activation of the caspase cascade pathway. *Oncology Letters,* 3: 1069 – 1072.
8. Kim, H. H., Kim, D. H., Kim, M. H., Oh, M. H., Kim, S. R., Park, K. J. and Lee, M. W. (2013). Flavonoid constituents in the leaves of *Myrica rubra* Sieb. et zucc. with anti-inflammatory activity. *Achieves of Pharmacological Research*, 36(12): 1533 – 1540.

Malaysian Journal of Analytical Sciences, Vol 20 No 6 (2016): 1535 - 1538
DOI: http://dx.doi.org/10.17576/mjas-2016-2006-36

MALAYSIAN JOURNAL OF ANALYTICAL SCIENCES
Published by The Malaysian Analytical Sciences Society
ISSN 1394 - 2506

ISOLATION OF OLIGOSTILBENES FROM *Shorea bracteolate*

(Pemisahan Oligostilbene daripada *Shorea bracteolate*)

Norhazana Norizan[1], Norizan Ahmat[1,2]*, Yana Maulana[3] , Zurina Shameeri[1]

[1]*Faculty of Applied Sciences,*
Universiti Teknologi MARA, 40450 Shah Alam, Selangor, Malaysia
[2]*Atta ur Rahman Institute for Natural Product Discovery*
Universiti Teknologi MARA, Puncak Alam Campus, 42300 Bandar Puncak Alam, Selangor, Malaysia
[3]*Department of Chemistry,*
Institut Teknologi Bandung, Jalan Ganesha 10, Bandung 40132, Indonesia

**Corresponding author: noriz118@salam.uitm.edu.my*

Received: 24 February 2015; Accepted: 27 October 2015

Abstract

Phytochemical investigation has been carried out on the stem bark of *Shorea bracteolate* . Three known oligomeric stilbene compounds, namely vaticanol A (1), stepnophyllol C (2) and hopeaphenol A (3) were isolated from the acetone extract of the plant. The structure of the isolated compounds were determined based on the analysis of spectroscopic data, including Nucleus Magnetic Resonance (NMR), Ultra Violet (UV), Infrared (IR) and comparison with literature.

Keywords: ε-viniferin, hopeaphenol, Vaticanol A, Stepnophyllol C, *Shorea bracteolate*, dipterocarpaceae

Abstrak

Kajian fitokimia telah dilakukan ke atas bahagian kulit batang *Shorea bracteolate.* Tiga sebatian oligomerik stilbene iaitu vatikanol A (1), stepnofilol C (2) dan hopeafenol A (3) telah diasingkan daripada ekstrak aseton *S. bracteolate*. Struktur sebatian-sebatian ini telah ditentukan menggunakan analisis data spektroskopi termasuk Resonans Magnet Nukleus (NMR), Ultra Violet (UV), Infra merah (IR), dan perbandingan dengan literatur.

Kata kunci: ε-viniferin, hopeaphenol, Vaticanol A, Stepnofilol C, *Shorea bracteolate*, dipterocarpacea

Introduction

Shorea is a subfamily of Dipterocarpaceae family. A large number of stilbene derivatives have been isolated from plants belonging to the families of the Vitaceae, Leguminosae and Dipterocarpacea [1]. Plants of the largest subfamily, Dipterocarpoideae, are the sources of resveratrol oligomers (oligostilbenoids), sesquiterpenes, and triterpenes [2]. Until now, the chemistry of Dipterocarpaceae is relatively less known. This is because the early research on Dipterocarpaceae was mainly focused on the chemical compounds of their resins such as terpenoid, sesquiterpenoid and triterpenoid. In the last two decades, the phytochemical research on Dipterocarpaceae has shifted rapidly. This is due to the fact that oligomeric resveratrol compounds have been found to be the main polyphenols. They include stilbene dimers, trimers, tetramers, hexamers, heptamers and octamers with various molecular framework resulting from different oxidative condensations of revesratrol monomers. These compound also show a variety of important bioactivities such as anti inflammatory, antibacterial, antifungal, cytotoxicity, chemopreventive and hepatoprotective. They also inibit topoisomerase II, gastic ATPase and 5α-reductase reaction [3].

Shorea bracteolate called white meranti is widely distributed in Sumatera, Peninsular Malaysia, Indonesia and Singapura. The tree grows up to 50 m in height and the timber is light hardwood. This paper reports the isolation and structure determination of a stilbene dimer, a stilbene trimer and a stilbene tetramer form the plant.

Materials and Methods

General experimental procedure

^{1}H and ^{13}C spectra were recorded in acetone-D on Bruker 300 Ultrashield NMR spectrometer measured at 300 and 125 MHz. IR spectrums and UV spectra were recorded on the Perkin Elmer spectrum on FT-IR spectrometer and Shimadzu UV-vis 160i instruments, respectively. Melting point was measured by Fisher Johns. Optical rotations were determined using a Perkin-Elmer 341 polarimeter in MeOH. Vacuum liquid chromatography (VLC) was carried out using Si-gel Merck 60 GF254 (230 – 400 mesh), while column chromatography (CC) was used Si-gel Merck 60 (200 – 400mesh) and TLC analysis on precoated Si-gel Merck Kieselgel 60 F254 0.25mm, 20 x 20 cm plates.

Plant material

The stem bark of *Shorea bracteolate* was collected in 2009 and a voucher specimen had been deposited at the UPM.

Extraction and isolation procedure

The stem bark of *S. bracteolate* was dried and cut into small pieces and ground to powder about 1mm mesh size using a grinder. The sample was extracted with acetone and the extract was evaporated in vacuo at 40 ^{0}C to yield a crude extract. The crude extract was fractionated using (VLC) to give 6 fractions. Fraction 3 (F3**)** was subjected to multiple radial chromatography (RC) to afford Compound 1**.** Fraction 4 (F4**)** was subjected to VLC using a series of increasing polarity solvent from 40% hexane/60% ethyl acetate to 90% ethyl acetate/10% methanol to give 5 fractions. Subfraction F43 was resubjected again to VLC to give 12 fractions. Similar TLC profile were pooled together to give 4 fractions. Subfraction F432 was then subjected to radial chromatography (RC) and CC to give Compound 2 [C: A: M (9:0.5:0.5)]. F44 was subjected to RC and PTLC to give Compound 3 [C: M (9:1)].

Results and Discussion

Investigation on the tree bark of *Shorea bracteolate* have resulted in the isolation of three oligostilbenoid compounds which successfully characterized as vaticanol A **(**1**)**, stepnophyllol C **(**2**)** and hopeaphenol A **(**3**).** Compound 1 was obtained as a yellow powder. The ^{1}H-NMR spectrum showed three sets of *ortho*- coupled aromatic protons. They were assignable to three 4-hydroxyphenyl groups at 7.28(2H, d, J=8.4, $H_{2a,6a}$), 6.83(2H ,dd, J=8.4, $H_{3a,5a}$), 7.07(2H, d, J=8.4, $H_{2b,6b}$), 6.60(2H, dd, J=8.7, $H_{3b,5b}$), 6.55(2H, dd, J=8.7, $H_{2c,6c}$) and 6.37(2H, dd, 8.4, $H_{3c,5c}$). It also showed a 3,5-dihydroxyphenyl group at 6.27 (1H, d, J=2.1, $H_{10c,14c}$), 6.21 (1H, 2.1, H_{12c}), a set of *meta*- coupled aromatic protons at 6.09(1H ,d, 2.4, H_{12a}), 6.48(1H, d, 2.4, H_{14a}), aromatic proton of a penta-substituted benzene ring at 6.22(br, s, H_{12b}), four unit of aliphatic methine protons coupled at 5.17(br, s, H_{7b}), 4.52 (br ,s ,H_{8b}), 3.64(1H, d, 7.8, H_{7c}), 4.19(br, s, H_{8c}), a set of aliphatic protons at 6.18(br, s, H7a) and 4.52 (br, s, H_{8a}). From these characteristics, it was suggested that the compound 1 is vaticanol A [4]. Figure 1 show the structure of vaticanol A.

Compound 2 was obtained as brownish powder. The ^{1}H NMR spectrum showed the presence of two sets of *ortho*-coupled aromatic proton at δ7.12 (2H, d, J=15Hz, $H_{2(6)a}$), 6.76(2H, d, J=15Hz, $H_{3(5)a}$), 6.76 (2H, d, J=15Hz, $H_{2(6)b}$), 6.58 (2H, d, J=15Hz, $H_{3(5)b}$), a 3,5-dihydroxyphenyl group δ6.29 (1H, br s, H_{10a}), 6.32 (1H, s, H_{12a}), a singlet aromatic proton 6.21 (1H, s, H_{12b}), two broad aliphatic protons δ4.30 (1H, br s ,H_{7b}), 3.98 (1H, br s, H_{8b}), two mutually coupled aromatic aliphatic hydrogens 5.32(1H,d,J=5Hz, H_{7a}) and 4.32 (1H,s,H_{8a}). From these characteristics, it was suggested that the compound 2 is stepnophyllols C [5]. Figure 2 shown the structure of stepnophyllols C.

Malaysian Journal of Analytical Sciences, Vol 20 No 6 (2016): 1535 - 1538
DOI: http://dx.doi.org/10.17576/mjas-2016-2006-36

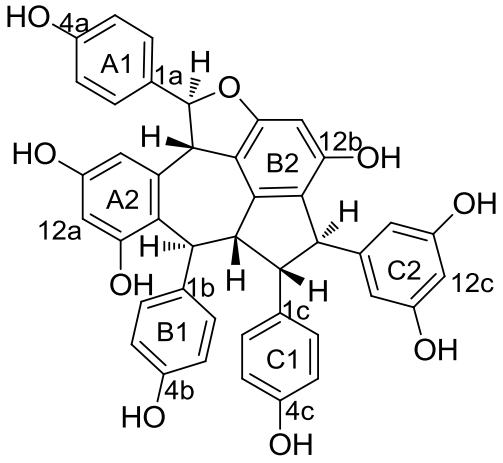


Figure 1. Structure of Vaticanol A

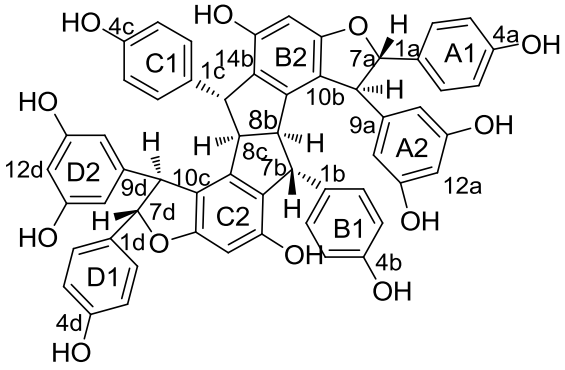


Figure 2. Structure of Stepnophyllols C

Compound 3 was obtained as a yellowish amorphous powder. The ^{1}H NMR spectrum showed the presence of eight *ortho*- coupled aromatic proton. They were assignable to four 1,4- disubstituted aromatic ring δ7.25 (2H, d, J=8.5Hz, $H_{2(6)a)}$), 6.84 (2H, d, J=8.5Hz, $H_{3(5)a}$), 7.52 (2H,d,J=8.5Hz, $H_{2(6)a'}$), 6.93 (2H, dd, J=8.5Hz, $H_{2(6)b}$, $_{3(5)a'}$), 6.56 (2H,d,J=8.5Hz, $H_{3(5)b}$), 6.32 (2H,m, $H_{2(6)b', 3(5)b'}$). Futher analysis of the ^{1}H NMR spectrum revealed a four set of 1,2,3,5 tetrasubstituted aromatic ring, 6.33 (1H,m, H_{12a}), 6.22 (1H,s, H_{14a}), 6.38 (1H,m,$H_{12a'}$), 6.40 (1H,s, $H_{14a'}$), 6.05 (1H, d, J=2.1Hz, H_{12b}), 5.90 (1H,m, $H_{14b,12b'}$), 5.01 (1H, d, J=2.1), a sequence of two vicinal methine doublets 5.83 (1H,d, J=13Hz, H7a), 4.41 (1H,d, J=13Hz,H8a), 5.73 (1H,d, J=8.5Hz, H7a'), 5.43 (1H,d,J=8.5Hz,H8a') and four contiguous methine multiplets 5.06 (1H,d, J=5.0Hz, H7b), 4.30 (1H,dd, J=5.0Hz, H8b), 4.73 (1H,d,J=4.5Hz, H7b'), 2.65 (1H,dd,J=5, H8b'). From these characteristics, it was suggested that the compound 3 is hopeaphenol A [6]. Figure 3 shown the structure of hopeaphenol A.

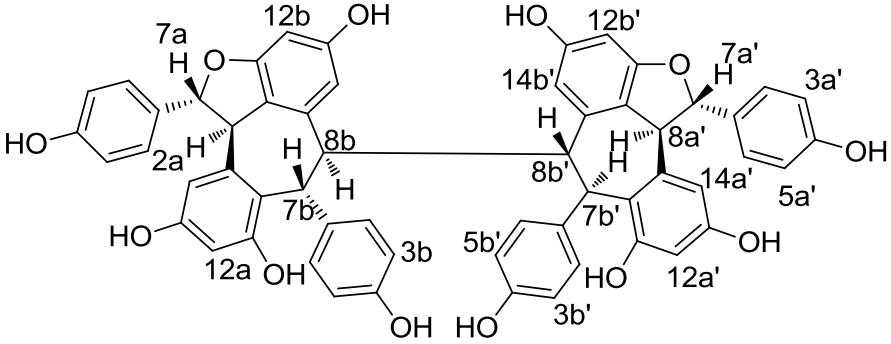


Figure 3. Structure of Hopeaphenol A

Conclusion

Three oligostilbenes, Vaticanol A **(**1**)**, Stepnophyllol C **(2)** and hopeaphenol A **(**3**),** were successfully isolated from the acetone extract of the stem bark of *Shorea bracelate.*

References

1. Sotheeswaran, S and Pasupathy, V. (1993). Distribution of resveratrol oligomers in plants. *Phytochemistry,* 32: 1083-1092
2. Seo, E. K. and Douglas, K. A. (2000). Bioactive constituents of the family Dipterocarpaceae. In: Atta-ur-Rahman (ed) studies in natural products chemistry. *Elsevier*, 23: 531 – 561.
3. Hakim, E. H. (2002). Oligostilbenoid dari tumbuh – tumbuhan Dipterocarpaceae. *Bulletin of the Indonesia Society of Natural Products Chemistry,* 2(1): 1 – 19.
4. Tanaka, T., Ito, T., Nakaya, K., Iunuma, M. and Riswan, S. (2000). Oligostilbenoids in stem of *Vatica rassak*. *Phytochemistry*, 54: 63 – 69.
5. Masayoshi, O. Toshiyuki, T., Munekazu, I., Charles, L. and Burandt, Jr. (1998). Phenolic compounds isolated from the roots of *Sophora stenophylia*. *Chemical and Pharmaceutical Bulletin*, 46(4): 663 –668.
6. Joanna, R., Zgoda-Pols., A., Freyer, J. L., Killmer, B. J. and Porter, R. (2002). Antimicrobial resveratrol tetramers from the stem bark of *Vatica oblongifolia ssp.oblongifolia*. *Journal of Natural Product*, 65: 1554 – 1559.